REPORT DOCUMENTATION PAGE

Form Approved OMB No. 0704-0188

Public reporting burden for this collection of information is estimated to average 1 hour per response, including the time for reviewing instructions, searching existing data sources, gathering and maintaining the data needed, and completing and reviewing the collection of information. Send comments regarding this burden estimate or any other aspect of this collection of information, including suggestions for reducing this burden to Washington Headquarters Services, Directorate for Information Operations and Reports, 1215 Jefferson Davis Highway, Suite 1204, Arlington, VA 22202-4302, and to the Office of Management and Budget, Paperwork Reduction Project (0704-0188), Washington, DC 20503.

1. AGENCY USE ONLY (Leave blank)	2. REPORT DATE	3. REPORT TYPE AND DATES COVERED
	8 May 1998	Conference Proceedings

4. TITLE AND SUBTITLE

XVI International Conference on Thermoelectrics, 26 August 1997 - 29 August 1997

5. FUNDING NUMBERS

F6170897W0097

6. AUTHOR(S)

Conference Committee

7. PERFORMING ORGANIZATION NAME(S) AND ADDRESS(ES)

DLR Institute of Materials Research
Linder Hohe
D-51140 Koln
Germany

8. PERFORMING ORGANIZATION REPORT NUMBER

N/A

9. SPONSORING/MONITORING AGENCY NAME(S) AND ADDRESS(ES)

EOARD
PSC 802 BOX 14
FPO 09499-0200

10. SPONSORING/MONITORING AGENCY REPORT NUMBER

CSP 97-1042

11. SUPPLEMENTARY NOTES

12a. DISTRIBUTION/AVAILABILITY STATEMENT

Approved for public release; distribution is unlimited.

12b. DISTRIBUTION CODE

A

13. ABSTRACT (Maximum 200 words)

The Final Proceedings for XVI International Conference on Thermoelectrics, 26 August 1997 - 29 August 1997

Thermoelectric Materials: bulk materials, thin films, heterostructures; preparation & processing techniques; characteristics of structure and transport properties; modeling.

DTIC QUALITY INSPECTED 2

14. SUBJECT TERMS

Electronic Devices, Avionics, Materials, Sensor Technology

15. NUMBER OF PAGES

800

16. PRICE CODE

N/A

17. SECURITY CLASSIFICATION OF REPORT	18. SECURITY CLASSIFICATION OF THIS PAGE	19. SECURITY CLASSIFICATION OF ABSTRACT	20. LIMITATION OF ABSTRACT
UNCLASSIFIED	UNCLASSIFIED	UNCLASSIFIED	UL

SIXTEENTH

INTERNATIONAL CONFERENCE ON THERMOELECTRICS

PROCEEDINGS, ICT '97

AUGUST 26-29, 1997 **DRESDEN, GERMANY**

14 SESSIONS — 175 PAPERS

- **Chalcogenides-Based Materials**
- **Bismuth Antimony Alloys**
- **High Temperature Materials**
- **Composite Materials: Theory & Experiment**
- **Low Dimensional Materials; Quantum Wells**
- **Functionally Graded Material**
- **Silicide Alloys**
- **Skutterudites**
- **Power Generation**
- **Peltier Cooling: Devices, Reliability**
- **Measurements and Sensors**
- **Thermal Devices, Systems and Applications**

SPONSORED BY:

Sächsisches Staatsministerium für Wissenschaft und Kunst

Deutsche Forschungsgemeinschaft

European Commission, Directorate General XII

United States Air Force European Office of Aerospace Research and Development

Institute of Solid State and Materials Research Dresden

The International Thermoelectric Society

The Institute of Electrical and Electronics Engineers, Inc.

The Components, Packaging, and Manufacturing Technology Society, IEEE

DISTRIBUTION STATEMENT A
Approved for public release;
Distribution Unlimited

IEEE CATALOG NUMBER 97TH8291
ISSN 1094-2734



Proceedings ICT'97

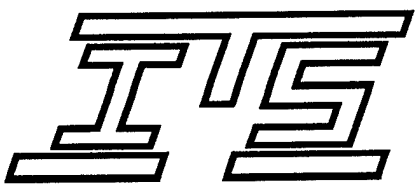
XVI International Conference on Thermoelectrics

August 26 - 29, 1997

Hotel Art'otel Dresden
Germany

19980519 044

Organized by
Institute of Solid State and Materials Research Dresden
Thermoelectric Group



International
Thermoelectric Society



Institute of Electrical and
Electronics Engineers, Inc.



Institut für Festkörper-
und Werkstofforschung
Dresden

1997 PROCEEDINGS, Sixteenth International Conference on Thermoelectrics (ICT)

PERMISSION TO REPRINT OR COPY:

Abstracting is permitted with credit to the source. Libraries are permitted to photocopy beyond the limits of U.S. copyright law for private use of patrons those articles in this volume that carry a code at the bottom of the first page, provided the per-copy fee indicated in the code is paid through the Copyright Clearance Center, 222 Rosewood Drive, Danvers, MA 01923 U.S.A. Instructors are permitted to photocopy isolated articles for non-commercial classroom use without fee. For other copying, reprint, or re-publication permission, write to IEEE Copyrights Manager; 445 Hoes Lane, PO Box 1331; Piscataway, NJ 08855 U.S.A. All rights reserved.

Copyright ©1997 by the Institute of Electrical and Electronics Engineers, Inc.

PRINTED IN THE UNITED STATES OF AMERICA

Additional copies of this PROCEEDINGS may be purchased from:

IEEE Service Center
445 Hoes Lane
Piscataway, NJ 08855-1331 USA
Phone: +1-732-981-0060
or 1-800-678-IEEE

Refer to the IEEE Catalog Number, printed below.

IEEE Catalog Number	97TH8291
ISBN	0-7803-4057-4 Softbound Edition 0-7803-4058-2 Microfiche Edition
ISSN	1094-2734

Layout, composition, and compilation by Chappell Enterprises

Word of Greeting



The conversion of heat into electric power and vice versa using the thermoelectric effect is of major importance for very different areas of technological application - for example, the cooling of highly integrated electronic components or the recycling of waste heat in power plants.

The most recent advances in the field of materials development give cause to expect that this conversion can be even more efficiently applied in the future than has been the case so far. Against this background, international research efforts in which physical knowledge is combined with application-oriented development are to be welcomed.

Special credit goes to the International Thermoelectric Society for offering those researchers, developers, producers, and users interested in thermoelectricity a global forum for the discussion and further development of this technology. The International Thermoelectric Society has played a major part in the current boom of thermoelectricity. The fact that the annual meetings have been held for some years now on an alternating basis in the USA, Japan and Europe takes due account of the increasing globalization of science and research.

I am particularly pleased that this year's meeting of the International Thermoelectric Society is taking place in Germany for the first time at the Institute of Solid State and Materials Research in Dresden. This can be interpreted as due recognition of the high standard of materials research in Dresden. I wish the XVIth Annual Meeting every success and hope it will be rewarding for all participants.

Dr. Jürgen Rüttgers
Federal Minister of Education, Science, Research and Technology

Preface

The International Conference on Thermoelectrics 1997 was the XVI[th] annual meeting of the International Thermoelectric Society and the first held in Germany. The conference was hosted by the Institute of Solid State and Materials Research Dresden (IFW Dresden) and organized by ist the Thermoelectric Team. The conference was held under the auspicies of the Saxon State Minister of Science and Arts. It was supported by the International Thermoelectric Society (IST), European Thermoelectric Society (ETS), and Bundesministerium für Bildung, Wissenschaft, Forschung und Technologie (BMBF) and sponsored by several German and International Organizations.

The XVI ICT followed the traditional concept of the ICT series and covered a broad range of topics in thermoelectric research, development and application. A total of 248 scientists, engineers and manufacturers of 23 countries attended the conference. Large groups came from Japan (61), Germany (54), USA (40), Russia (24), Ukraine (13), Korea (10), France (8) and Israel (7).

A total of 181 papers were actually presented including 6 plenary and 16 invited papers. 74 of the contributed papers were given in oral and 85 in poster presentation. This was the largest number of presented papers and the second largest attendance within the ICT series. This indicates the increasing interest in thermoelectrics worldwide.

The scientific programme was organized in three main subjects covering the following topics: (i) State-of-the-art thermoelectric materials, (ii) Novel thermoelectric materials, (iii) Thermoelectric devices, systems and applications.

Many highlights were set by the invited and contributed papers. In this preface only some of the high-quality reports can be mentioned: Rare-earth filled skutterudites, heterostructure integrated thermoionic refrigeration, epitaxial heterostructures based on layered thermoelectrics, papers on transition metal compounds and on thermoelectric microcoolers. Due to the high qualitiy of the reports we could find the best paper and poster awards only by consistent restricting to presentations by young scientists. The best paper award was confered to R. Martin-Lopez (Ecole des Mines, Nancy) for her paper on thermoelectric properties of mechanically alloyed Bi-Sb, the best poster award to K.Fess (University Konstanz) for his paper on the thermoelectric properties of the skutterudite $CoSb_3$.

According to the ICT tradition a technical exhibition was held concurrently to the technical sessions featuring the latest devices and products from TE companies as well as products and equipments related to thermoelectricity. 13 companies and research institutes of 6 countries presented their products. For the ICT'97 exhibition TE thin films sensors and generators have been presented for the first time. Many attendees have used the opportunity to contact the developers and manufacturers of TE devices and products and to continue in the mutual exchange of ideas and projects.

According to the feedback from many attendees it appears that the ICT'97 was a success. As chairmen of this conference we would like to thank all who have contributed to this success. First of all thanks are due to the members of the Organizing Committee for their engaged efforts during many months and the authorities of the Host Institute IFW Dresden for their continuous support. Thanks also to the members of the International Advisory Committee for many helpful advices and recommendations.

Last but not least we want to thank the following institutions for their sponsoring: the Saxon State Ministry of Science and Arts, Deutsche Forschungsgemeinschaft, European Commission - Secretariat General XII, European Office of Aerospace Research and Development of the US Air Force and Components, Packaging and Manufacturing Technology Society (CPMT) of IEEE. Only by the generous sponsoring of these institutions the Organizing Committee was in the position to support many attendees and to organize vital parts of both the scientific and social programme.

Armin Heinrich, Joachim Schumann

CONTENTS

PART A

Plenary Lectures

Novel Thermoelectric Materials

Skutterudites: An Update (invited paper) 1
J.-P. Fleurial, T. Caillat, and A. Borshchevsky, *Jet Propulsion Laboratory, Pasadena CA 91109 , USA*

Low Dimensional Thermoelectrics (invited paper) 12
M. S. Dresselhaus[1], X. Sun[1], S. B. Cronin[1], T. Koga[2], K. L. Wang[3], and G. Chen[3]
[1] *Massachusetts Institut of Technology, Cambridge MA 02139, USA*
[2] *Harvard University, Cambridge, MA 02138, USA*
[3] *University of California, Los Angeles, CA 90405, USA*

Rare Earth Thermoelectrics (invited paper) 21
G. D. Mahan, *University of Tennessee, Knoxville TN 37996-1200, USA*

Thermoelectric Devices, Systems and Applications

Status and Future Prospects on the Development of Thermoelectric Power Generation 28
Systems Utilizing Combustion Heat from Municipal Solid Waste (invited paper)
Takenobu Kajikawa, *Shonan Institute of Technology, Fujisawa, Kanagawa 251, Japan*

Current State of Peltier Cooling (invited paper) 37
John Stockholm, *Marvel Thermoelectrics, Vernouillet, F-78540 Marsinval, France*

Sensor Applications of Thermoelectric Thin-Films (invited paper) 47
Sander van Herwaarden, *Xensor Integration, 2601 DE Delft, Netherlands*

PART B

State-of-the-Art Thermoelectric Materials

Session: Chalcogenides - $(Bi,Sb)_2(Te,Se)_3$ Based Materials

Optimization of $(Bi,Sb)_2(Te,Se)_3$ - Based Thermoelectrics 56
Applications for Low - Temperature (invited paper)
M. V. Vedernikov, V. A. Kutasov, L. N. Luk`yanova, and P.P. Konstantinov
A.F. Ioffe Physical-Technical Institute, St. Petersburg 194021, Russia

Doping Effects on the Electronic Structures of Bi_2Te_3 and Thermoelectric Properties 63
Sunao Sugihara[1], Seiji Kawashima[1], Isaku Yonekura[1], Hiroaki Suzuki[1], and Rika Sekine[2]
[1] *Shonan Institute of Technology,Fujisawa, Kanagawa 251, Japan*
[2] *Shizuoka University, Shizuoka 422, Japan*

Defect Structure of Undoped and Pb-Doped Bi_2Se_3 Single Crystals 68
J. Horak[1] , P. Lostak[2], J. Navratil[1,2], and S. Karamazov[2]
[1] *Institute of Inorganic Chemistry, Prague, Czech Republic*
[2] *University of Pardubice, Czech Republic*
[3] *Joint Laboratory of Solid State Chemistry, Academy of Sciences of the Czech Republic and Unversity of Pardubice, Pardubice, Czech Republic*

Peculiarities of Electrophysical Properties of Bi_2Te_3 Doped with Sn 72
M. K. Zhitinskaya[1], S. A. Nemov[1], and T. E. Svechnikova[2]
[1] *State Technical University, St. Petersburg 195251, Russia*
[2] *Baikov Institute of Metallurgy, Moscow 117334, Russia*

Fabrication and Characterization of Bi_2Te_3- Sb_2Te_3 Based Thermoelectric Materials by Powder-Extrusion-Sintering Technique 76
Byoung-Gue Min[2], Kyung-Wook Jang[1], Dow-Bin Hyun[3] and Dong-Hi Lee[2]
[1] *Hanseo University, Chungnam 352-820, Korea*
[2] *Yonsei University, Korea*
[3] *Korea Institute of Science and Technologie*

Effect of Extrusion Process on the Thermoelectric Properties of Hot-Extruded *n*-type $Bi_2Te_{2.85}Se_{0.15}$ Compounds 81
J. H. Seo[1], D. M. Lee[3], K. Park[2], C. H. Lee[1]
[1] *Inha University, Inchon 402-751, Korea*
[2] *Chung-ju National University, Chungju 380-702, Korea*
[3] *Pusan Business Office, Pusan 616-110, Korea*

Thermoelectric Properties of *p*-Type Bi-Sb-Te Based Material Prepared by PIES Method with Conventional Ball Milling Process 85
Shuzo Kagawa[1], Hideki Satake[1], Masanori Sakamoto[1], Atsushi Yamamoto[2], and Toshitaka Ohta[2]
[1] *KUBOTA Corporation, Amagasaki 661, Japan*
[2] *Electrotechnical Laboratory, AIST, Tsukuba 305, Japan*

Layer by Layer Growth of Bi_2Te_3 Epitaxial Thermoelectric Heterostructures 89
Yu. A. Boikov[1,2], V. A. Danilov[2], T. Claeson[1] , D. Erts[1,3]
[1] *Chalmers University of Technologie and Goteborg University, Goteborg S-41296, Sweden*
[2] *A.F. Ioffe Physico-Technical Institute, St. Petersburg 194021, Russia*
[3] *Institute of Chemical Physics, Latvia University, Riga, Latvia*

Crystalline Structure and Thermoelectric Properties Versus Growing Conditions of Sputtering-Deposited $(Bi_{1-x}Sb_x)_2Te_3$ Films with $0 \leq x \leq 0.85$ 93
M. Stölzer, V. Bechstein, and J. Meusel
Martin Luther Universität, Halle 06099, Germany

Structural and Electrical Characterization of Thin Bi_2Te_3 Films Grown with MBE 97
S. Kikuchi[1], Y. Iwata[2], E. Hatta[3], J. Nagao[4], and K. Mukasa[3]
[1] *Hokkaido Tokai University, Sapporo 005, Japan*
[2] *Aisin Cosmos R&D Co., Aichi 448, Japan*
[3] *Hokkaido University, Sapporo 060, Japan*
[4] *Hokkaido National Industrial Research Institute, Sapporo 062, Japan*

Transport Properties of $Bi_2Te_{2.4}Se_{0.6}$ Thin Films 101
V. Damodara Das, and S. Selvaraj
Indian Institute of Technology, Chennai 600036, Madras, India

Peculiarities of the Figure of Merit Temperature Dependence in *n*-$Bi_2(Te,Se)_3$ Solid Solution at Low Charge Carrier Concentration 105
L. N. Luk'yanova, G. T. Alekseeva, P.P Konstantinov, V. A. Kutasov
A.F.Ioffe Physical-Technical Institute, St.Petersburg 194021, Russia

Electrophysical Properties of $Bi_2Te_{2.85}Se_{0.15}$ Single Crystals Doped with Copper 109
T. E. Svechnikova[1], N. M. Maksimova[1], and P. P. Konstantinov[2]
[1] *Baikov Institute of Metallurgy, Moscow 117334, Russia*
[2] *A.F. Ioffe Institute, St. Petersburg 194021, Russia*

Electrophysical Properties of Sb_2Te_3 Single Crystals Doped with Tin, Selenium, Bismuth 111
L. D. Ivanova, Yu. V. Granatkina, and Yu. A. Sidorov
A. A. Baikov Institute of Metallurgy, Moscow 117334, Russia

Optimization of Hot-Pressed *n*-type SbI_3-Doped $Bi_2Te_{2.85}Se_{0.15}$ Compounds 114
J. Seo[1], M. Ju[1], K. Park[2], J. Kim[3], C. Lee[1]
[1] *Inha University, Inchon 402-751, Korea*
[2] *Chung-ju National University, Chungbuk 380-702, Korea*
[3] *Korea Academy of Industrial Technology, Siheung, Kyunggi-do 429-450, Korea*

Influence of Growth Conditions on Structure, Composition Homogeneity and Mechanical Properties of Thermoelectric Crystals for Coolers 118
V. T. Bublik, V.V. Karataev, V. B. Osvenski, T. B. Sagalova, V. B. Ufimtsev, and A. M. Frolov
Institute of Chemical Problems for Microelectronics, Moscow 109017, Russia

Peculiarities of Production *n*-$Bi_2(Te, Se)_3$ and *p*-$(Bi, Sb)_2Te_3$ in Conditions of Structural Superplasticity 122
O. B. Sokolov, S. Ya. Skipidarov, N. I. Duvankov, and E. V. Zaitsev,
Nord Co, Moscow109383, Russia

Effects of a Reduction Treatment and Te Doping on Thermoelectric Properties of $(Bi_{1-x}Sb_x)_2Te_3$ Fabricated by Mechanical Alloying 127
H. C. Kim[1], J. S. Choi[1], H. J. Kim[1], D.-B. Hyun[2], and T. S. Oh[1]
[1] *Hong Ik University, Seoul 121-791, Korea*
[2] *Korea Institute of Science and Technology, Seoul 136-791, Korea*

Structural-Chemical Characterization of Semiconductors Using the Seebeck and Thermal Conductivity Quality Factors 131
Donald Tuomi, *Tuomi Associates, Arlington Hts., IL 60005-2320, USA*

Peltier Cooling of Superconducting Electronics 138
J. W. Straehle[1], S. Rath[2], K. -J. Klingesberger[1] , T. Nissel[1], S. G. Doettinger[1,3], Chr. A. Doettinger[4], R. P. Huebener[1], S. Kemmler-Sack[2]
[1] *Physikalisches Institut, Universität Tübingen, Tübingen 72076, Germany*
[2] *Institut für Anorganische Chemie, Universität Tübingen, Tübingen 72076, Germany*
[3] *Department of Applied Physics, Stanford University, Stanford, CA 94305-4090, USA*
[4] *Institut für Kunststoffprüfung und Kunststoffkunde, University of Stuttgart, Stuttgart 70569, Germany*

Transport Coefficients of InSb in a Strong Magnetic Field 142
Hiroaki Nakamura[1], Kazuaki Ikeda[2], and Satarou Yamaguchi[1]
[1] *National Institute for Fusion Science, Toki-City 509-52, Japan*
[2] *The Graduate University for Advanced Studies, Toki-City 509-52, Japan*

Structural and Electrical Properties of Flash Evaporated $(Bi_{0.4}Sb_{0.6})_2Te_3$ Alloy Thin Films 147
V. Damodara Das, P. Gopal Ganesan, *Indian Institute of Technology, Chennai 600036, Madras, India*

Bismuth-Telluride Films Prepared by Vacuum-Arc Plasma Method for Thermoelectrical Transducers 151
I. Gasenkova
Institute of Electronics, Belarus Academy of Sciences, Minsk 220090, Belarus

Geometric Contribution to the Measurement of Thermoelectric Power and Nernst Coefficient in a Strong Magnetic Field 155
K. Ikeda[1], Hiroaki Nakamura[2], Satarou Yamaguchi[2]
[1] *The Graduate University for Advanced Studies, Toki-city 509-52, Japan*
[2] *National Institute for Fusion Science, Toki-City 509-52, Japan*

Thermal Conductivity of Solid Solutions $(Bi_ySb_{1-y})_2Te_3$ for y=0.7-0.8 Grown by Method of Zone Melting 159
A. I. Anukhin
Scientific-Production Firm MODUL, Kiev 252022, Ukraine

Flash Evaporated Layer of $(Bi_2Te_3$-$Bi_2Se_3)$(N) and $(Bi_2Te_3$-$Sb_2Te_3)$(P) Used as Micro-Module-Peltier 163
A. Foucaran , A. Sackda , A. Giani , F. Pascal- Delannoy , and A. Boyer
Centre d' Electronique et de Micro-optoelectronique de Montpellier, Montpellier 34095, France

Bi_2Te_3 Thin Films Grown by MOCVD Process 167
A. Boulouz , A. Giani , F. Pascal- Delannoy , A. Foucaran and A. Boyer
Centre d' Electronique et de Micro-optoelectronique de Montpellier, Montpellier 34095, France

Session: Bismuth Antimony Alloys

Galvanomagnetic and Thermoelectric Measurements on Polycrystalline $Bi_{88}Sb_{12}$ 171
H. J. Goldsmid, E. H. Volckmann, *Marlow Industries, Dallas, TX 75238, USA*

Magneto-Thermoelectric Properties of Undoped and Doped Bi-Sb Single Crystals 176
V. M. Grabov[1], O. N. Uryupin[2]
[1] *Herzen Russian State Pedagogical University, St. Petersburg 194021, Russia*
[2] *A. F. Ioffe Physical - Technical Institute, St. Petersburg 194021, Russia*

Energy Conversion by Galvanomagnetic and Thermomagnetic Effects with the Use of $Bi_{88}Sb_{12}$ Alloys 180
M. Sakurai[1], N. Satoh[1], S. Tanuma[2], and I. Yoshida[1]
[1] *Department of Solid State Physics, Iwaki Meisei University, Fukushima 970, Japan*
[2] *Hayama, Kanagawa 240-01, Japan*

Influence of the Consolidation Technique on the Thermoelectric Properties of Mechanically Alloyed Bi-Sb 184
R. Martin-Lopez[1], A. Dauscher[1], X. Devaux[1], B. Lenoir[1], H. Scherrer[1], M. Zandona[2]
[1] *Laboratoire de Physique des Matériaux, Nancy F-54042, France*
[2] *Laboratoire de Science et Génie des Matériaux Métalliques, Nancy F-54042, France*

Observation of a Power Factor Enhancement in MBE-Grown $Bi_{1-x}Sb_x$ Alloy Thin Films 188
S. Cho[1], A. DiVenere[1], G. K. Wong[1], J. B. Ketterson[1] , J. R. Meyer[2] , and C. A. Hoffman[2]
[1] *Northwestern University, Evanston IL 60208, USA*
[2] *Naval Research Laboratory, Washington DC 20375, USA*

Determination of Carrier Mobilities and Densities from 192
Galvanomagnetic Coefficients in Undoped $Bi_{0.96}Sb_{0.04}$ Alloy
B. Lenoir[1], M. O. Selme[1], A. Demouge[1], H. Scherrer[1], Yu. I. Ravich[2], Yu. V. Ivanov[2]
[1] *Laboratoire de Physique des Matériaux, Ecole des Mines, Nancy F-54042, France*
[2] *A.F. Ioffe Physico-Technical Institute, St. Petersburg 194021, Russia*

Determination of the Longitudinal Thermo-Galvanomagnetic Coefficients 196
E. H. Volckmann, H. J. Goldsmid
Marlow Industries, Dallas TX 75238, USA

Observation of the Grain Size Influence on the Thermoelectric Properties 199
of Polycrystalline Bismuth - Antimony Alloys
X. Devaux, F. Brochin, A. Dauscher, B. Lenoir, R. Martin-Lopez, H. Scherrer, and S. Scherrer
Laboratoire de Physique des Matériaux, Ecole des Mines, Nancy 54042, France,

Thermoelectric Properties of Sintered Bi Using Plasma-Treated Powder 203
Y. H. Lee, R. Isobe, M. Yomura, I. Nakamoto, and T. Koyanagi
Department of Electrical and Electronic Engineering, Yamaguchi University, Tokiwadai, Ube 755, Japan

Session: High Temperature Materials - Si-Ge Alloys, Tellurides, Borides, Oxides

Powder Processing of Thermoelectric Materials - 207
Focusing on SiGe with New Sintering Technique (invited paper)
Teruo Noguchi, *Vacuum Metallurgical Co., Chiba-ken 289-12, Japan*

Microstructure and Thermoelectric Properties 215
of Arc-Melted Silicon Borides
Lidong Chen, Takashi Goto, Jianhui Li, Eiji Aoyagi, Toshio Hirai
Institute for Materials Research, Tohoku University, Sendai 980-77, Japan

Electronic Transport in *p*-type and *n*-type β-Rhombohedral Boron 219
R. Schmechel[1], H. Werheit[1], V. Kueffel[1], T. Lundström[2]
[1] *Solid State Physics Laboratory, Gerhard Mercator University, Duisburg 47048, Germany*
[2] *Institute of Chemistry, Uppsala University, Uppsala 75121, Sweden*

Hopping Carrier Mobilities and Thermoelectric Properties 224
of Oxide Materials with Perovskite-Related Structure
Michitaka Ohtaki, Tsutomu Tokunaga, Koichi Eguchi and Hiromichi Arai
Department of Materials Science and Technology, Kyushu University, Kasuga-shi, Fukuoka 816, Japan

Thermoelectric Properties of *n*-type $(Pb_{1-x}Ge_x)Te$ Fabricated 228
by Hot Pressing Method
J. S. Choi[1], H. J. Kim[1], H. C. Kim[1], T. S. Oh[1], D.-B. Hyun[2], H. W. Lee[3]
[1] *Department of Metallurgy and Materials Science, Hong Ik University, Seoul 121-791, Korea*
[2] *Korea Institute of Science and Technology, Seoul 136-791, Korea*
[3] *Korea Electro Technology Research Institute, Kyungnam 641-120, Korea*

Structure and Transport Properties of Microcrystalline SiGe Films 232
F. Edelman[1], M. Stölzer[2], T. Raz[1], Y. Komem[1], C. B. Vining[3], H. Zeindl[4], and P. Zaumseil[4]
[1] *Technion-Israel Institute of Technology, Haifa 32000, Israel*
[2] *FG Angewandte Physik, Martin-Luther-Universität, Halle.06120, Germany*
[3] *ZT Services Inc., Auburn, AL 36830-7113, USA*
[4] *Institut für Halbleiterphysik, Frankfurt/(Oder) 15230, Germany*

A Study for Thermoelectric Properties of Ni Doped SiC Sintered Thermoelectric Semiconductor 236
Yoichi Okamoto[1], Kazuhiko Kato[1], Jun Morimoto[1], Toru Miyakawa[2]
[1] *Department of Materials Science and Engineering, Natl. Defense Academy, Hashirimizu 110-20, Japan*
[2] *Chiba Institute of Technology, Chiba 275, Japan*

Thermoelectric Properties of ZnO Doped with the Group 13 Elements 240
Toshiki Tsubota, Michitaka Ohtaki, Koichi Eguchi, and Hiromichi Arai,
Department of Materials Science and Technology, Kyushu University, Kasuga-shi, Fukuoka 816, Japan

Dependence of the Phonon Drag on Zn Concentration in Cd_{1-x} Zn_xTe in the Range $0 < x < 0.1$ 244
S. Vackova[1], K. Zdánský[2], L. Scherbak[3], P. Fejchouk[3], M. Ilaschouk[4]
[1] *Faculty of Mathematics and Physics, Charles University, Praha 12116, Czech Republic*
[2] *Institute of Radio Engineering and Electronics, Academy of Sciences, Praha 18251, Czech Republic*
[3] *Faculty of Chemistry, State University of Chernovtsi, Chernivtsi 274000, Ukraine*
[4] *Faculty of Physics, State University of Chernovtsi, Chernivtsi 274000, Ukraine*

Crystal Grain Size Dependence of Thermoelectric Properties for Sintered PbTe by Spark Plasma Sintering Technique 247
S. Yoneda[1], E. Ohta[1], H. T. Kaibe[2], I. Shiota[3], K. Takahashi[4], Y. Shinohara[5], Y. Imai[5], and I. A. Nishida[5]
[1] *Department Materials Science, Keio University, Yokahama, Kanagawa 223, Japan*
[2] *Department Electronics and Information Eng., Tokyo Metropolitan University, Tokyo 192-0,*
[3] *Department Environmental Chem. Eng., Kogakuin University, Tokyo 192*
[4] *Vacuum Metallurgical Co., Chiba 289-12, Japan*
[5] *National Research Institute for Metals, Ibaraki 305, Japan*

High-Temperature Oxidation Behavior of PbTe and Oxidation-Resistive Glass Coating 251
Lidong Chen, Takashi Goto, Rong Tu, and Toshio Hirai,
Institute for Materials Research, Tohoku University, Sendai 980-77, Japan

Influence of Potential Barriers on the Thermoelectric Properties of PbTe Thin Films 255
Z. Dashevsky
Department of Materials Engineering, Ben-Gurion University of the Negev, Beer-Sheva 84105, Israel

Thermoelectric Power and Figure Merit of Pb-Sn-Te Alloy Thin Films 259
V. Damodara Das
Department of Physics, Indian Institute of Technology, Chennai 600036, Madras, India

Comparisons of the Thermoelectric Properties of *n*-type PbTe Fabricated with Different Powder Processing Methods 263
J. S. Choi[1], H. J. Kim[1], H. C. Kim[1], D.-B. Hyun[2], and T. S. Oh[1]
[1] *Department of Metallurgy and Materials Science, Hong Ik University, Seoul 121-791, Korea*
[2] *Korea Institute of Science and Technology, Seoul 136-791, Korea*

Session: Silicides - β-$FeSi_2$, Mg_2Si, Me-Si alloys

Semiconducting Transition Metal Silicides: Electronic Structure, Electrical and Thermoelectrical Properties (invited paper) 267
H. Lange[1], S. Brehme[1], W. Henrion[1], A. Heinrich[2], G. Behr[2], H. Griessmann[2], A. B. Filonov[3], and V. E. Borisenko[3]
[1] *Hahn-Meitner-Institut, Berlin 12489, Germany*
[2] *Institut für Festkörper- und Werkstofforschung, Dresden 01069, Germany*
[3] *Belarusian State University of Informatics and Radioelectronics, Minsk 220027, Belarus*

Thermoelectric Properties of Magnesium Silicide Processed 275
by Powdered Elements Plasma Activated Sintering Method
Takenobu Kajikawa[1], Keisuke Shida[1], Sunao Sugihara[1], Mamoru Ohmori[2], and Toshio Hirai[2]
[1] *Shonan Institute of Technology, Fujisawa 251, Japan*
[2] *Institute for Materials Research, Tohoku University, Sendai 980, Japan*

Temperature Dependence of Thermal Conductivity 279
for $Mg_2Si_{1-x}Ge_x$ Solid Solution
Hiromasa T. Kaibe[1], Yasutoshi Noda[2], Yukihiro Isoda[3], Isao A. Nishida[3]
[1] *Department Electronics and Information Eng., Tokyo Metropolitan University, Tokyo 192-03, Japan*
[2] *Department Materials Science, Tohoku University, Sendai 980, Japan*
[3] *National Research Institute for Metals, Ibaraki 305, Japan*

Influence of Production Parameters on 283
the Thermoelectric Properties of Mg_2Si
M. Riffel[1], and J. Schilz[2]
[1] *Laboratoire de Physique des Matériaux, Ecole des Mines, Nancy F-54042, France*
[2] *German Aerospace Research Establishment, Köln 51147, Germany*

Thermoelectric Properties of β-$FeSi_2$ Single Crystals Prepared 287
with 5N Source Material
A Heinrich, G. Behr, and H. Griessmann
Institut für Festkörper- und Werkstofforschung, Dresden 01701, Germany

Drag Effects in β-Iron Disilicide 291
M. I. Fedorov, V. K. Zaitsev, Yu. V. Ivanov, V. V. Popov, and M. A. Khazan
A. F. Ioffe Physical-Technical Institute, St. Petersburg 194021, Russia

Fabrication of Ternary Iron Disilicides as Thermoelectric Semiconductors 295
by Sintering Using Elemental Powders
Yoriko Ohta[1], Seiji Miura[2], and Yoshinao Mishima[2]
[1] *Dept. of Materials Science and Engineering, Tokyo Institute of Technology, Yokohama 226, Japan*
[2] *Precision and Intelligence Laboratory, Tokyo Institute of Technology, Yokohama 226, Japan*

Rhenium Silicide Thin Films: Structural Analysis of the $ReSi_{2-\delta}$ Phase 299
W. Pitschke, A. Heinrich, J. Schumann
Institut für Festkörper- und Werkstofforschung, Dresden 01171, Germany

Preparation of Iridium Silicide Thin Films 303
by Means of Electron Beam Evaporation
R. Kurt, W. Pitschke, A. Heinrich, J. Schumann, and K. Wetzig
Institut für Festkörper- und Werkstofforschung, Dresden 01069, Germany

Aging Properties of Thermally Sprayed Iron Disilicide 307
K. Schackenberg[1], E. Müller[1], J. Schilz[1], W. A. Kaysser[2], G. Langer[2], and E. Lugscheider[2]
[1] *Deutsche Forschungsanstalt für Luft- und Raumfahrt, Köln 51140, Germany*
[2] *Rhein.- Westf. Technische Hochschule, Aachen 52056, Germany*

Effect of Powder Treatment by Mechanofusion Process 311
on Thermoelectric Properties of $FeSi_2$ System
Takuji Kita, Kiyoshi Nogi, Hiroshi Nagai, and Mizuki Kohno
Osaka University, Suita, Japan

Effect of Dispersed Si-Phase on the Thermoelectric Properties 315
of $FeSi_2$ Prepared by Mechanical Alloying and Sintering
Byoung-Gue Min, and Dong-Hi Lee
School of Materials Science and Engineering, Yonsei University, Seoul 120-749 , Korea

PART C

Novel Thermoelectric Materials

Session: Skutterudites

Expanding the Investigation of the Thermoelectric Properties of Rare-Earth-Filled-Skutterudites 321
George S. Nolas[1], Hylan B. Lyon[1], J. L. Cohn[2], T. M. Tritt[3], and G. A. Slack[4]
[1] *Research and Development Division, Marlow Industries, Dallas TX 75238, USA*
[2] *Department of Physics, University of Miami, Coral Gables, FL, USA*
[3] *Department of Physics and Astronomy, Clemson University, SC 29634, USA*
[4] *Department of Physics, Rensselaer Polytechnic Institute, Troy, New York, USA*

Effects of Doping Pd/Pt in $CoSb_3$ Crystals on Electrical and Thermoelectric Properties 326
H. Tashiro[1], Y. Notohara[2], T. Sakakibara[3], H. Anno[4], and K. Matsubara[4]
[1] *Toyo Kohan Co., Kudamatsu 744, Japan*
[2] *Kyushu Matsushita Electric Co., Fukuoka 812, Japan*
[3] *Aisin Cosmos R & D Co., Kariya 448, Japan*
[4] *Science University of Tokyo in Yamaguchi, Onoda 756, Japan*

Thermoelectric Properties of the Skutterudite-Related Phase $CoSn_{1.5}Te_{1.5}$ 330
Y. Nagamoto, K.Tanaka, and T. Koyanagi,
Department of Electrical and Electronic Engineering, Yamaguchi University, Tokiwadai, Ube 755, Japan

Effects of Defects and Impurities on Electronic Properties in $CoSb_3$ 334
K. Akai, H. Kurisu, T. Shimura, and M. Matsuura,
Faculty of Engineering, University of Yamaguchi, Ube 755, Japan

Preparation and Thermoelectric Properties of $CoSb_3$ Thin Films on GaAs (100) Substrate 338
H. Anno[1], T. Sakakibara[2], Y. Notohara[3], H. Tashiro[4], T. Koyanagi[5], H. Kaneko[1], and K. Matsubara[1]
[1] *Science University of Tokyo in Yamaguchi, Onoda 756, Japan*
[2] *Aisin Cosmos R&D Co., Kariya 448, Japan*
[3] *Kyushu Matsushita Electric Co., Hakata-ku, Fukuoka 812, Japan*
[4] *Toyo Kohan Co., Kudamatsu 744, Japan*
[5] *Yamaguchi University, Tokiwadai, Ube 755, Japan,*

Electronic Transport Properties of *p*-type $CoSb_3$ 343
H. Anno[1], H.Tashiro[2], Y. Notohara[3], T. Sakakibara[4], K. Hatada[1], K. Motoya[5], H. Shimizu[1], and K. Matsubara[1]
[1] *Science University of Tokyo in Yamaguchi, Onoda 756, Japan*
[2] *Toyo Kohan Co., Kudamatsu 744, Japan*
[3] *Kyushu Matsushita Electric Co., Fukuoka 812, Japan*
[4] *Aisin Cosmos R&D Co., Kariya 448, Japan*
[5] *Science University of Tokyo in Yamaguchi, Noda 278, Japan*

Transport Properties of the Skutterudite $CoSb_3$ 347
K. Fess, E. Arushanov, W. Käfer, Ch. Kloc, K. Friemelt, and E. Bucher,
Universität Konstanz, Konstanz D-78457, Germany

Grain Size Effects on Thermoelectric Properties of Hot-Pressed $CoSb_3$ 351
H. Nakagawa[1], H. Tanaka[1], A. Kasama[1], H. Anno[2], and K. Matsubara[2]
[1] *Japan Ultra-high Temperature Materials Research Institute, Yamaguchi 755, Japan*
[2] *Faculty of Science and Engineering, Science University of Tokyo in Yamaguchi, Yamaguchi 756, Japan*

Microstructures and Thermoelectric Properties of Spin-Cast $Co_{0.97}Cr_{0.03}Sb_3$ Ribbons 356
T. Morimura, H. Kitagawa, M. Hasaka, and S. Kondo,
Department of Materials Science and Engineering, Nagasaki University, Nagasaki 852 Japan

Thermoelectric Properties of $Fe_{1-x}Ni_x Sb_3$ Ribbons 360
M. Hasaka, H. Kitagawa, K. Matano, T. Morimura, and S. Kondo,
Department of Materials Science and Engineering , Nagasaki University, Nagasaki 852, Japan

Session: Functionally Graded Material

Development of FGM Thermoelectric Materials in Japan - The State of the Art (invited paper) 364
Ichiro Shiota[1], and Isao A. Nishida[2]
[1] *Department of Environmental Chemical Eng., Kogakuin University, Tokyo 192, Japan*
[2] *National Research Institute for Metals, Ibaraki 305, Japan*

Preparation and Characterization of Segmented-Type Thermoelectric Branches of Bi_2Te_3/PbTe 371
Y.Noda[1], Y.-S.Kang[2], and M.Niino[2]
[1] *Department of Materials Science, Tohoku University, Sendai 980-77, Japan*
[2] *National Aerospace Laboratory, Kakuda Research Center, Kakuda, Miyagi 981-15, Japan*

Bismuth-Telluride / Iron-Disilicide Segmented Thermoelectric Elements: Patterning, Preparation and Properties 375
J. Schilz[1], L. Helmers[1], Y. S. Kang[2], Y. Noda[2], and M. Niino[2]
[1] *German Aerospace Research Establishment, Köln 51147, Germany*
[2] *National Aerospace Laboratory, Kakuda Research Center, Kakuda, Miyagi 981-15, Japan*

Preparation and Evaluation of PbTe-FGM by Joining Melt-Grown Materials 379
M. Orihashi[1], Y. Noda[2], L. Chen[1], Y.-S. Kang[3], A. Moro[3], and T. Hirai[1]
[1] *Institute for Materials Research, Tohoku University, Sendai, Miyagi 980-77, Japan*
[2] *Graduate School of Engineering, Tohoku University, Sendai, Miyagi 980-77, Japan*
[3] *National Aerospace Laboratory, Kakuda Research Center, Kakuda, Miyagi 981-15, Japan*

Improved Materials for Thermoelectric Conversion (Generation) 382
Z. Dashevsky[1], I. Drabkin[2], V. Korotaev[2], and D. Rabinovich[1]
[1] *Department of Materials Engineering, Ben-Gurion University, Beer-Sheva, Israel*
[2] *Institute of Rare Metals, Moscow 109017, Russia*

Thermoelectric Properties of Segmented Pb-Te Systems with Graded Carrier Concentrations 386
Y. Shinohara[1], Y. Imai[1], Y. Isoda[1], I. A. Nishida[1], H. T. Kaibe[2], and I. Shiota[3]
[1] *National Research Institute for Metals, Ibaraki 305, Japan*
[2] *Tokyo Metropolitan University, Tokyo 192-03, Japan*
[3] *Kogakuin University, Tokyo 192, Japan*

Evaluation of Monolithic and Segmented Thermoelectric Materials by Using a Large-Temperature-Span Apparatus 390
Y. S. Kang[1], S. Moriya[1], K. Kisara[1], M. Niino[1], Y. Noda[2], L. Chen[3], T. Sudo[4]
[1] *National Aerospace Laboratory, Kakuda Research Center, Kakuda, Miyagi 981-15, Japan*
[2] *Department of Materials Science, Tohoku University, Sendai, Miyagi 980-77, Japan*
[3] *Institute for Materials Research, Sendai, Miyagi 980-77, Japan*
[4] *National Space Development Agency, Kakuda, Miyagi 981-15 Japan*

Catalytic Furnaces with Thermogenerators 394
L. I. Anatychuk, and V. Ya. Mikhailovsky, *Institute of Thermoelectricity, Chernovtsy 274000,, Ukraine*

Low-Temperature Thermoelectric Cooling under Optimal Legs Inhomogeneity 397
in the Optimal Nonuniform Magnetic Field
L. I. Anatychuk, and L. N. Vikhor, *Institute of Thermoelectricity, Chernovtsy 274000, Ukraine*

Session: Composite Materials - Theory & Experiment

Thermoelectric Tensor and Figure of Merit for a Composite Medium: 401
Some Exact Bounds (invited paper)
David J. Bergman, *School of Physics and Astronomy, Tel Aviv University, Tel Aviv 69978, Israel*

Thermoelectric Properties of Bi and Bi_2Te_3 Composites (invited paper) 404
T.E. Huber, and R. Calcao, *Polytechnic University, Brooklyn, NY 11201, USA*

Thermoelectric Properties of Heterogenous, ... 409
Manyphase and Composite Materials
Yu. Goryachev, M. Siman, and L. Fiyalka, O. Shvartsman
Institute of Material Problems, Kiev 252142, Ukraine

On the Theory of Thermopower 413
in Random Two-Component Semiconductor Systems
I. I. Fishchuk, *Institute for Nuclear Research, Kiev 252022, Ukraine*

Session: Low-Dimensional Materials - Quantum Well Structures

Characterization of *p*-Type PbEuTe/PbTe MQW Structures 416
with High Thermoelectric Figures of Merit in the PbTe Quantum Wells (invited paper)
T. C. Harman, D. L. Spears, D. R. Calawa, S. H. Groves, and M. P. Walsh,
Lincoln Laboratory, Massachusetts Institute of Technology, Lexington MA 02173, USA

Thermoelectric Transport in Low Dimensional Superlattice Systems 424
(invited paper)
Thomas L. Reinecke[1], and D. A. Broido[2]
[1] *Naval Research Laboratory , Washington DC, 20375, USA*
[2] *Department of Physics, Boston College, Chestnut Hill, MA 02167, USA*

On the Use of Bismuth in Quantum Wells 429
A. Dauscher, B. Lenoir, O. Boffoué, X. Devaux, R. Martin-Lopez, and H. Scherrer
Laboratoire de Physique des Matériaux, Ecole des Mines, Nancy F-54042, France

Thermoelectric Properties of Multilayered p-type Si-Ge Thin Films 434
A. Yamamoto[1], H. Kato[2], S. Kuwashiro[2], M. Takimoto[3],
T. Ohta[1], K. Miki[1], K .Sakamoto[1], T. Matsui[2], and K. Kamisako[3]
[1] *Electrotechnical Laboratory, MITI, Japan*
[2] *Nagoya University, Japan*
[3] *Tokyo University of Agriculture and Technology, Tokyo 192, Japan*

Thermoelectric Properties of Superlattices 438
S. V. Melnichuk, S. V. Kosyachenko, and V. M. Vozny
Institute of Thermoelectricity, Chernovtsy 274000, Ukraine

Effects of One-Dimensional Quantum Structures 442
on the Thermoelectric Figure of Merit
A. Casian[1], I. Sur[1], A. Sandu[1], H. Scherrer[2], and S. Scherrer[2]
[1] *Technical University of Moldova, Kishinau, MD 2004, Moldova*
[2] *Laboratoire de Physique des Materiaux, Ecole des Mines, Nancy F- 54042, France*

Session: New Materials - Low κ, Intermetallics, Complex Structures

New Low Thermal Conductivity Materials 446
for Thermoelectric Applications (invited paper)
T. Caillat and J.-P. Fleurial,
Jet Propulsion Laboratory, California Institute of Technology, Pasadena, CA 91109, USA

Potential of Quasicrystals and Quasicrystal Approximants 454
for New and Improved Thermoelectric Materials (invited paper)
Terry M. Tritt[1,2], M. L. Wilson[1], A. L. Johnson[1], S.LeGault[3], and R. Stroud[4]
[1] *Department of Physics and Astronomy, Clemson University, Clemson, SC 29634, USA*
[2] *Materials Science and Engineering Department, Clemson University,*
[3] *Department of Physics and Astronomy, McGill University, Montreal, Canada,*
[4] *Naval Research Laboratory, Washington DC 20375, USA*

Complex Bismuth Chalcogenides as Thermoelectrics (invited paper) 459
D.-Y. Chung[1], T. Hogan[2], J. Schindler[2], L. Iordanidis[1], P. Brazis[2],
C. Kannewurf[2], B. Chen[3], C. Uher[3], and M. G. Kanatzidis[1],
[1] *Dept. of Chemistry, Michigan State University, East Lansing , MI 48824, USA*
[2] *Dept.of Electrical and Computer Engineering, Northwestern University, Evanston IL 60208, USA*
[3] *Dept. of Physics, University of Michigan, Ann Arbor. MI 48109, USA*

Thermoelectric Properties of β-Zn_4Sb_3 Doped with Sn 463
T. Koyanagi, K. Hino, Y. Nagamoto, H. Yoshitake, and K. Kishimoto
Faculty of Engineering, Yamaguchi University, Tokiwadai, Ube 755, Japan

Huge Thermoelectromotive Force Generated by Porous Ceramics of Y_2O_3 467
K. Koumoto, W. S. Seo, and S. Ozawa,
Graduate School of Engineering, Nagoya University, Chikusa-ku, Nagoya 464-01, Japan

Enhanced Thermoelectric Efficiency Near a Conductivity Threshold 471
G. D. Guttman, E. Ben-Jacob, and D. J. Bergman
School of Physics and Astronomy, Tel Aviv University, Tel Aviv 69978, Israel

Thermopower and Thermal Transport 476
in Metal - *p*-type Semiconductor - Metal Structure
Yu. G. Gurevich[1], G. N. Logvinov[2], O. I. Lyubimov[3], O. Yu. Titov[1]
[1] *Department of Physics, CINVESTAV , Mexico D. F. 07000, Mexico*
[2] *Teacher Training University, Ternopil 282009, Ukraine*
[3] *Physics Department, Kharkov State University, Kharkov 310077, Ukraine*

Crystal Structure and Thermoelectric Properties 481
of the Mixed Layered Compounds of the $(GeTe)_N(Bi_2Te_3)_M$ Homologous Series
L. E. Shelimova[1], O. G. Karpinsky[1], M. A. Kretova[1], E. S. Avilov[1], and J.-P. Fleurial[2]
[1] *A. A. Baikov Institute of Metallurgy, Moscow 117911, Russia*
[2] *Jet Propulsion Laboratory, Pasadena, CA 91109, USA*

Transport Properties of ZrNiSn-Based Intermetallics 485
Ctirad Uher[1], Siqing Hu[1], Jihui Yang[1], Gregory P. Meisner[2], and Donald T. Morelli[2]
[1] *Dept. of Physics, University of Michigan, Ann Arbor, MI 48109, USA*
[2] *Physics and Physical Chemistry Dept., GM Research and Development Ctr., Warren, MI 48090, USA*

Thermoelectric Properties of MNiSn (M=Ti, Zr,Hf) Single Crystals and Related Alloys 489
W. Käfer, K. Fess, Ch. Kloc, K. Friemelt, and E. Bucher
Universität Konstanz, Konstanz D-78457, Germany

Effect of Isoelectronic Substitution of Thermopower and Resistivity of $Hf_{1-x}Zr_xTe_5$ 493
R. T. Littleton IV[1], M. L. Wilson[1], C. R. Feger[2], M. J. Marone[1], J. Kolis[2,3], T. M. Tritt[1,3], and F. Levy[4]
[1] *Department of Physics and Astronomy, Clemson University,*
[2] *Department of Chemistry, Clemson University,*
[3] *Materials Science and Engineering Department, Clemson University, Clemson, SC 29634, USA*
[4] *Institut de Physique Applique , Lausanne, Switzerland*

IR-Reflection Study of Sintered SiC/Al Thermoelectric Semiconductors 496
Toru Miyakawa[1], Y. Okamoto[2], T. Kawahara[2], S. V. Ordin[3], M. I. Fedorov[3], and Y. Miida[1]
[1] *Dept. of Computer Science, Chiba Institute of Technology, Chiba 275, Japan*
[2] *Dept. of Materials Science & Engineering, Nat'l.Defense Academy, Yokosuka 239, Japan*
[3] *A.F. Ioffe Physico-Technical Institute, St. Petersburg 194021, Russia*

Synthesis of Zn_4Sb_3 Compound by PIES Method 500
A. Yamamoto[1], T. Ichizuka[2], H. Takazawa[1], T. Ohta[1], T. Kajikawa[2]
[1] *Electrotechnical Laboratory, MITI, Energy Fundamentals Division, Tsukuba, Ibaraki 305, Japan*
[2] *Shonan Institute of Technology, Japan*

Low Temperature Thermoelectric Power of Amorphous Alloys Al-Y-Ni 504
K. Pekala, *Institute of Physics, Warsaw University of Technology, Warsaw PL-02524, Poland*

Transport Study of Hg - Based High Temperature Superconductors 507
M. Pekala[1], H. Bougrine[2,3], I. Sargankova[4], and M. Ausloos[2]
[1] *Chemistry Dept., Warsaw University, Warsaw PL-02089, Poland*
[2] *SUPRAS, Inst. de Physique, Universite de Liege,*
[3] *SUPRAS, Inst. d'Electricite Montefiore, Universite de Liege, Liege B-4000, Belgium*
[4] *Institute of Experimental Physics, Slovak Academy of Sciences, Kosice 04353, Slovakia*

Magneto -Thermoelectric Studies of High Temperature Superconductors 511
M. Pekala[1], and M. Ausloos[2]
[1] *Chemistry Dept., University of Warsaw, Warsaw PL-02089, Poland*
[2] *SUPRAS, Inst. de Physique, Universite de Liege, Liege B-4000, Belgium*

MgAgAs Structure Type Solid Solutions as a New Thermoelectric Material 516
L. P. Romaka, Yu. V. Stadnyk, A. M. Goryn, Yu. K. Gorelenko, and R. V. Skolozdra
Inorganic Chemistry Dept., Lviv State University, Lviv 290005, Ukraine

Electronic Transport in Amorphous Ni-P Alloys 520
F. Skoropad, and B. Stadnyk, *State University "Lviv Polytechnic", Lviv 290646, Ukraine*

Thermoelectric Properties of Transition-Metal Oxide $NaCo_2O_4$ System 523
H. Yakabe[1], K. Kikuchi[1], I. Terasaki[2], Y. Sasago[3], and K. Uchinokura[3]
[1] *Frontier Technology Research Institute, Tokyo Gas Co, Yokohama 230, Japan*
[2] *Dept. of Applied Physics, Waseda University, Tokyo 169, Japan*
[3] *Dept. of Applied Physics , University of Tokyo, Tokyo 113, Japan*

Thermoelectric Properties of Hot-Pressed $YbAl_3$ Compound Over Temperature Range 150-800K 528
D. M. Rowe, Gao Min, and V. L. Kuznetsov,
School of Engineering, University of Wales, Cardiff CF2 3TF, South Wales, UK

PART D

Thermoelectric Devices, Systems and Applications

Session: Power Generation - Terrestrial and Space Applications

Development of Improved Modules for the Economic Recovery of Low Temperature Waste Heat (invited paper) 532
D. M. Rowe
Centre for Thermoelectric Engineering, Cardiff CF2 3TF, South Wales, UK

Research Project on the Effective Use of Untapped Thermal Energy from Garbage Incineration etc. (invited paper) 539
M. Niino[1], T. Ohshima[1], and K. Matsubara[2]
[1] *National Aerospace Laboratory, Kakuda, Miyagi 981-15, Japan,*
[2] *Dept. of Electronics, Science University of Tokyo in Yamaguchi; Japan*

Examples of Power from Waste Heat for Gas Fields 547
John C. Bass[1], and Robert.L. Farley[2]
[1] *Hi-Z Technology, Inc., San Diego CA 92126, USA*
[2] *Power Sources, Inc., Farmington, NM, USA*

Thermoelectric Power Generator Design and Selection from TE Cooling Module Specifications 551
Richard J. Buist, and Paul G. Lau,
TE Technology, Inc., Traverse City, MI 49686, USA

A Study of Commercial Thermoelectric Generation in a Processing Plant of Combustible Solid Waste 555
Akira Tsuyoshi[1], Shuzo Kagawa[2], Masanori Sakamoto[2], and Kenji Matsuura[3]
[1] *Kobe City College of Technology, Kobe 651-21, Japan*
[2] *KUBOTA Corporation, Japan*
[3] *Osaka University, Japan*

Nuclear Thermoelectric Power Units in Russian, USA and European Space Agency Research Programs 559
A. A. Pustovalov,
BIAPOS Company, Moscow 117334, Russia

Calculation of Thermoelectric Power Generation Performance Using Finite Element Analysis 563
Paul G. Lau, and Richard J. Buist,
TE Technology, Traverse City, MI 49686, USA

Effect of Electrons and Phonons Temperature Mismatch on Thermoelectric Properties of Semiconductors 567
Lev P. Bulat,
Dept. of Electrical Engineering, State Academy of Refrigeration, St. Petersburg 191002, Russia

Thermoelectric Self-Powered Hydronic Heating Demonstration 571
Daniel T. Allen[1], and Jerzy Wonsowski[2],
[1] *Hi-Z Technology Inc., San Diego, CA 92126, USA*
[2] *Gas Research Centre, Loughborough, UK*

Low Power Thermoelectric Generator - 575
Self-Sufficient Energy Supply for Microsystems
M. Stordeur, and I. Stark,
Gesellschaft zur Fertigung von Dünnschicht-Thermogenerator-Systemen.mbH, Halle 06118, Germany

Thermoelectric and Heat Transfer Properties in a New-Type Module 578
Composed of Hamburger-Type Elements
Y. Tanji[1], Y. Nakagawa[2], S. Moriya[1], M. Niino[1], M. Yasuoka[2], R. Sato[3], and Y. Tada[4]
[1] *NAL Kakuda Research Center, Kakuda, Japan, 981-15*
[2] *Tohoku Institute of Technology, Sendai, Japan, 982*
[3] *Tohoku Gakuin University, Tagajo, Japan, 985*
[4] *JAST, Sendai, Japan, 981-31*

Grid-Independent Power Supply for Repeaters in Mobile Radio Networks 582
Using Photovoltaic/Thermoelectric Hybrid Systems
W. Roth, R. Kügele, A Steinhüser, W. Schulz, and G. Hille
Fraunhofer Institute for Solar Energy Systems, Freiburg D-79100, Germany

Thermal Generators for Waste Heat Utilization` 586
L. I. Anatychuk, Yu. Yu. Rozver, K. Misawa, N. Suzuki
Institute of Thermoelectricity, Chernovtsy 274000, Ukraine

Functionally Graded Materials and New Prospects for Thermoelectricity Use 588
L. I. Anatychuk, and L. N. Vykhor,
Institute of Thermoelectricity, Chernovtsy 274000, Ukraine

Thermoelectric Generator Modules and Blocks 592
L. I. Anatychuk, V. V. Razinkov, Yu. Yu. Rozver, and V. Ya. Mikhailovsky
Institute of Thermoelectricity, Chernovtsy 274000, Ukraine

Thermoelectric Eddy Currents. Calculation and Control Methods 595
L. I. Anatychuk, and O. J. Luste,
Institute of Thermoelectricity, Chernovtsy 274000, Ukraine

Thermoelectric Semiconductor and Electrode - 599
Fabrication and Evaluation of SiGe / Electrode
K. Hasezaki[1], H. Tsukuda[1], A. Yamada[1], S. Nakajima[2], Y. Kang[3] , and M. Niino[3]
[1] *Mitsubishi Heavy Industries, Nagasaki 582, Japan*
[2] *Nagasaki Shipyard & Machinery Works, Nagasaki 582, Japan*
[3] *National Aerospace Laboratory, Kakuda Research Center, Japan*

Thermoelectric Generator for Underwater Wellhead 603
Philippe Dubourdieu[1], Gery Tribou[1], and Steve Byrne[2]
[1] *Department of Technology and Development DCN, Cherbourg, 50115, France*
[2] *TOTAL OIL MARINE, Aberdeen, Scotland, UK*

The Use of Thermoelectric Converters for the Production 607
of Electricity from Biomass
Markus Doloszeski , and Alfred Schmidt, *Technical University Wien A-1060, Austria*

Session: Peltier Cooling - Devices, Reliability, Microcoolers, New Principles

Comprehensive Research of the Institute of Thermoelectricity, Ukraine 611
on the Theory, Material Science and Applications of Thermoelectricity (invited paper)
L. I. Anatychuk, *Institute of Thermoelectricity, Chernovtsy 274000, Ukraine*

A Critical Evaluation of Today's Thermoelectric Modules 619
Todd M. Ritzer, Paul Lau, and Andy Bogard, *TE Technology Inc, Traverse City, MI 49686, USA*

Influence of Difference in Dice Properties on Figure 624
of Merit of Thermoelectric Cooler
I. A. Drabkin, *Institute of Chemical Problems for Microelectronics, Moscow 109017, Russia*

Thermal Properties of Commercial Thermoelectric Modules 628
Rafael Palacios, and Miguel Angel Sanz-Bobi,
Instituto de Investigacion, Universidad Pontificia Comillas, Madrid 28015, Spain

Problems of Thermoelectric Devices Reliability 632
L. I. Anatychuk, and O. J. Luste, *Institute of Thermoelectricity, Chernovtsy 274000, Ukraine*

Heterostructure Integrated Thermionic Refrigeration 636
Ali Shakouri, and John E. Bowers,
Dept. of Electrical and Computer Engineering, Univ. of California, Santa Barbara, CA 93106, USA

Thermoelectric Microcoolers for Thermal Management Applications 641
J.-P. Fleurial, A. Borshchevsky, M. A. Ryan, W. Phillips, E. Kolawa, T. Kacisch, and R. Ewell,
Jet Propulsion Laboratory, Pasadena, CA 91109, USA

Micro Thermoelectric Coolers for Integrated Applications 646
Lance Rushing, Ali Shakouri, Patrick Abraham, and John E. Bowers
Dept. of Electrical and Computer Engineering, Univ. of California, Santa Barbara, CA 93106, USA

Fast Thermoelectric Microcoolers 650
Vadim Galperin, *MGNPP "OSTERM", St. Petersburg 190031, Russia*

Fabrication of a Miniature Thermoelectric Module with Elements 653
Composed of Sintered Bi-Te Compounds
M. Kishi, Y. Yoshida, H. Okano, H. Nemoto, Y. Funanami, M. Yamamoto, and H. Kanazawa
Seiko Instruments Inc, Chiba 271, Japan

Peltier Current Lead Experiments with a Thermoelectric Semiconductor near 77K 657
S. Yamaguchi[1], H. Nakamura[1], K. Ikeda[1], S. Tobise[2], K. Koumoto[2], T. Sakurai[3],
I. Yoshida[3], and S. Tanuma[3]
[1] *National Institute for Fusion Science, Nagoya, Toki 509-52, Japan*
[2] *Nagoya University, Nagoya 464-01, Japan*
[3] *Iwaki Meisei University, Iwaki 970, Japan*

New Physical Point of View on the Peltier Effect 661
O. Yu. Titov[1], G. Gonzalez de la Cruz[1], G. N. Logvinov[2], and Yu. G. Gurevich[1]
[1] *Dept of Physics, CINVESTAV, Mexico D.F 07000, Mexico*
[2] *Ternopil Pedagogical State University, Ternopil, Ukraine*

A New Concept of Porous Thermoelectric Module Using a Reciprocating Flow 664
for Cooling/Heating System (Numerical Analysis for Heating System)
Shigeru Tada, Ryozo Echigo, and Hideo Yoshida, *Tokyo Institute of Technology, Tokyo 152, Japan*

Quality Testing of Two-Stage Thermoelectric Cascades 668
Solomon M. Gorodetskiy[1], Richard J. Buist[2], and Paul G. Lau[2]
[1] *Cryotherm Company, St. Petersburg 197348 Russia*
[2] *TE Technology, Inc., Traverse City, MI 49686, USA*

Precise Methods and Equipment for Thermoelectric 672
Cooling Modules Parameters Measurement
L. I. Anatychuk, N. I. Varich, and A. A. Shchedrin,
Institute of Thermoelectricity, Chernovtsy 274000, Ukraine

Rapid Method of Defining the Quality of Multistage Thermoelectric Cooler 676
Based on Measurements of Voltage from Every Stage
I. A. Drabkin, and O. Jouranlev,
Institute of Chemical Problems for Microelectronics, Moscow 109017, Russia

Generalized Formulas to Express Maximum Temperature Difference 679
for Two-Stage Thermoelectric Cooling Modules
Dow-Bin Hyun[1], N. V. Kolomoets[1], Tae-Sung Oh[2], Jong-Seung Hwang[1], and Jae-Dong Shim[1]
[1] *Korea Institute of Science and Technology, Seoul 130-650, Korea*
[2] *Dept. of Metallurgy and Materials Science, Hong Ik University, Seoul 121-791, Korea*

Novel High Performance Thermoelectric Microcoolers 683
with Diamond Substrates
V. Semeniouk[1] , and Jean-Pierre Fleurial[2]
[1] *Odessa State Academy of Refrigeration, Thermion Company, Odessa 270009, Ukraine*
[2] *Jet Propulsion Laboratory, Pasadena, CA 91109, USA*

The Effectiveness of Water Vapor Sealing Agents When Used 687
in Application with Thermoelectric Cooling Modules
Michael J. Nagy, *TE Technology, Inc., Traverse City MI 49686, USA*

A Method of Diode Parallel to Improve the Reliability 690
of the Thermoelectric Coolers
Zhang Jianzhong, Zhang Hua, Wang Tiemin, Chen Song, and Ji Zhaonan
Tianjin Institute of Power Sources, Tianjin 300381, P.R. China

Thermoelectric Coolers with Vortex Apparatus 693
G. A. Smolyar, *Institute of Thermoelectricity, Chernovtsy 274000, Ukraine*

Thermoelectric Cooling Devices Based on Bismuth Telluride Alloys: 697
Data of the Patent Documentation of the USSR and Russia
B. Sh. Malkovitch, *"Cryotherm" Company, St. Petersburg 197348, Russia*

Modeling and Minimization of Intercascade Thermal Resistance 701
in Multi-Stage Thermoelectric Coolers
V. A. Semeniouk, and D. B. Bezverkhov, *State Academy of Refrigeration, Odessa 270009, Ukraine*

Thermoelectric Cascade for Cryosurgical Destroyer 705
T. Wartanowicz[1], A. Czarnecki[2]
[1] *Institute of Heat Engineering, University of Technology, Warsaw PL 02089, Poland*
[2] *Foundation of Applied Physics, Warsaw PL 02089, Poland*

Reliability Investigation of Semiconductor Coolers 708
Liu Zhenmao[1], Wang Xilian[1], Liu Xiaowei[1], Quan Wuyun[1], Sun Shufang[1], Ye Shuichi[1],
Lui Jingwei[1], and Chen Lunqiang[2]
[1] *Harbin Institute of Technology, Harbin, China*
[2] *Pengxian Refrigeration and Air Conditioning Equipment Company, China*

Session: Measurements and Sensors

Thermal Conductivity in Thin Films - Experimental Methods and Theoretical Interpretation (invited paper) 711
F. Völklein, and T. Stärz
Faculty of Physical Technology, Fachhochschule Wiesbaden, Rüsselsheim D-65428, Germany

Thermal and Electrical Imaging of Surface Properties with High Lateral Resolution (invited paper) 719
E. Oesterschulze, and R. Kassing
Institute of Technical Physics, Universität GH Kassel, Kassel D-34109, Germany

Thermal Conductivity Measurement and Microscopy of Thin Film Structures 726
G. T. Borca-Tasciuc[1], G. Chen[1], D. Wang[2], and K. L. Wang[2]
[1] *Mechanical and Aerospace Engineering Department, UCLA, Los Angeles, CA 90095, USA*
[2] *Electrical Engineering Department, UCLA, Los Angeles, CA 90095, USA*

Damped Thermoelectric Waves 730
C. B. Vining, *ZT Service Inc., Auburn , AL 36830, USA*

A 256 Pixel Linear Thermopile Array Using Materials with High Thermoelectric Efficiency 734
E. Kessler, U. Dillner, V. Baier, and J. Müller
Institute of Physical High Technology, Jena D-07702, Germany

Thermoelectric Detection of Photothermal Signals in Semiconductors 738
G. N. Logvinov[1], M. N. Kasyanchuk[1], Yu. G. Gurevich[2], and G. Gonzales de la Cruz[2]
[1] *Ternopil Pedagogical State University, Ternopil 282009, Ukraine*
[2] *Dept. de Fisica, Centro de Investigacion y de Estudios Avanzados del IPN, Mexico 07000, Mexico*

Eddy Thermoelectric Currents. Measuring Devices on their Basis 741
L. I. Anatychuk, and O. J. Luste, *Institute of Thermoelectricity, Chernovtsy 274000, Ukraine*

Film Manometric Thermocouple Transducer 745
R. Bychkovskyi, *State University "Lviv Polytechnic", Lviv 290646, Ukraine*

The Thermocouple Temperature Instability 748
B. M. Goltsman[1], and Yu. I. Ravich[2]
[1] *A.F. Ioffe Physical-Technical Institute, St. Petersburg 194021, Russia*
[2] *Technical University, St. Petersburg, Russia*

Unsteady-State Thermoelectric Response for a Thermal Pulse in Semiconductors 749
G. N. Logvinov[1], Yu. V. Drogobychsky[1] ,Yu. G. Gurevich[2], A. F. Carbalo Canchez[2], and O. Yu. Titov[2]
[1] *Institute of Thermoelectricity, Chernovtsy 274000, Ukraine*
[2] *Dept. de Fisica, Centro de Investigasion y de Estudios Avanzados del I.P.N., Mexico 07000, Mexico*

Features of Thermoelectromotive Force in Au/*p*-Ge Junctions 753
S. Ashmontas, J. Gradauskas, A. Suziedėlis, and G. Valusis
Semiconductor Physics Institute, Vilnius 2600, Lithuania

Nature of Thermoelectric Anisotropy in Semiconductors at the Lower Temperatures 757
Eduard V. Osipov, and Algirdas Aulas,
Semiconductor Physics Institute, Vilnius 2600, Lithuania

Determination of Structural Changes and Temperature Distributions within Crystals 761
V. P. Shafranyuk, *Institute of Thermoelectricity, Chernovtsy 274000, Ukraine*

About the Possibilities of Transverse Thermoelectromotion Force in the Case of Optical Media 764

A. A. Ascheulov[1], I. V. Gutsul[2], A. I. Rarenko[2],

[1] *Institute of Thermoelectricity, Chernovtsy 274000, Ukraine*

[2] *Chernovtsy State University, Chernovtsy 274000, Ukraine*

Devices for Temperature Measurement and Laser Profile Analysis Using $YBa_2Cu_3O_{7-\delta}$ Atomic Layer Thermopiles 768

W. Brozio, F. Wolf, C. Ferstl, O. Kus, F. Lankes, T. Honke, J. Betz, and K. F. Renk

Institut für Angewandte Physik, University Regensburg, Regensburg D-93040, Germany

Skutterudites: An Update

J.-P. Fleurial*, T. Caillat and A. Borshchevsky
Jet Propulsion Laboratory/California Institute of Technology,
4800, Oak Grove Drive, MS 277-207, Pasadena, CA 91109
*jean-pierre.fleurial@jpl.nasa.gov

Abstract

Materials with the skutterudite crystal structure possess attractive transport properties and have a good potential for achieving ZT values substantially larger than for state-of-the-art thermoelectric materials. Studies conducted at JPL on $CoAs_3$, $RhAs_3$, $CoSb_3$, $RhSb_3$ and $IrSb_3$ have shown that p-type conductivity samples are characterized by carriers with low effective masses and very high mobilities, low electrical resistivities and moderate Seebeck coefficients. The carrier mobilities of n-type samples are about an order of magnitude lower, but low electrical resistivities and relatively large Seebeck coefficients can still be obtained at high doping levels. The room temperature lattice thermal conductivities of these binary skutterudites was found to be 7 to 10 times larger than that of Bi_2Te_3. This results in low ZT values at 300K, though very heavily doped n-type $CoSb_3$ samples can achieve ZT~1 at 600°C. Several research groups, mostly in the U.S., are now working on understanding and optimizing the transport properties of skutterudites. Most of the efforts are focusing on reducing the lattice thermal conductivity by filling the empty octant cages in the skutterudite structure with rare earth atoms. Additional approaches have also been pursued at JPL, in particular the formation of solid solutions and alloys, and the study of novel ternary skutterudite compounds. Recent experiments have demonstrated that ternary compounds such as $Ru_{0.5}Pd_{0.5}Sb_3$ and filled skutterudites such as $CeFe_4Sb_{12}$ had much lower lattice thermal conductivity. High ZT values have been obtained for several filled skutterudites in the 500-700°C temperature range, but figures of merit at 300K are still low. This paper reviews recent experimental and theoretical results on skutterudites with a particular emphasis on the transport properties of ternary compounds and filled compositions. The latest results obtained at JPL are presented and the possibility of obtaining high ZT values near room temperature is discussed.

Introduction

The need for more efficient thermoelectric devices has driven the study of novel semiconducting and semimetallic materials. While even modest improvements in the maximum dimensionless figure of merit ZT - currently achieved by state-of-the-art Bi_2Te_3 alloys - would be meaningful for near room temperature applications [1], thermoelectric power generators which could operate in the 200 to 1000°C temperature range are facing very stiff competition from other energy conversion technologies. This is true in particular for high power (over 200 W) automobile waste heat recovery and space applications [2,3]. For thermoelectrics to be attractive, to successfully challenge competing conversion systems and to develop new wide ranging applications, ZT must attain an average value of 1.5 to 3.0, depending on the type and temperature range of the targeted application. This rationale has led to a systematic search for advanced thermoelectric materials with a good potential for maximum ZT values of 2.0 to 3.0. Studies at the Jet Propulsion Laboratory (JPL) resulted in the identification of several promising classes of materials, and in particular semiconductors with the skutterudite crystal structure [4]. Following JPL's efforts, there are now several laboratories in the United States and other countries investigating skutterudites for their thermoelectric properties. This increasing interest in skutterudites is linked to their unusual electrical and thermal transport properties which offer attractive possibilities for high ZT values. This paper will briefly review the large body of experimental data obtained to date on binary and ternary skutterudites, emphasizing common characteristics, and will attempt to provide some guidelines for optimizing thermoelectric properties near room temperature.

Crystal Structure, Existence and Composition

The prototype of the cubic skutterudite crystal structure (space group Im3) is the $CoAs_3$ compound [5]. The unit cell contains square radicals of the pnicogen atoms, $[As_4]^{4-}$. This anion, located in the center of the smaller cube, is surrounded by 8 trivalent transition metal Co^{3+} cations. The unit cell consists of 8 smaller cubes, or octants, described above but two of them do not have the $[As_4]^{4-}$ anions in the center. This is necessary to keep the ratio $Co^{3+}:[As_4]^{4-} = 4:3$. Thus, a typical coordination structure results with $Co_8[As_4]_6 = 2Co_4[As_4]_3$ composition and 32 atoms per cell, as depicted in Figure 1. Taking into account one-half of the unit cell and its empty octant, one can represent the skutterudite formula as $\square T_4Pn_{12}$, where $\square$ is the empty octant, T is the transition metal and Pn is the pnicogen atom. If considering a simple bonding scheme [6], each transition metal contributes 9 electrons and each pnicogen contributes 3 electrons to the covalent bonding, for a valence electron count (VEC) total of 72 for each $\square T_4Pn_{12}$ unit. The VEC is a useful number in determining semiconducting skutterudite compositions. A filled skutterudite structure is simply derived from the skutterudite structure by inserting one atom in the empty octants, as illustrated in Figure 1.

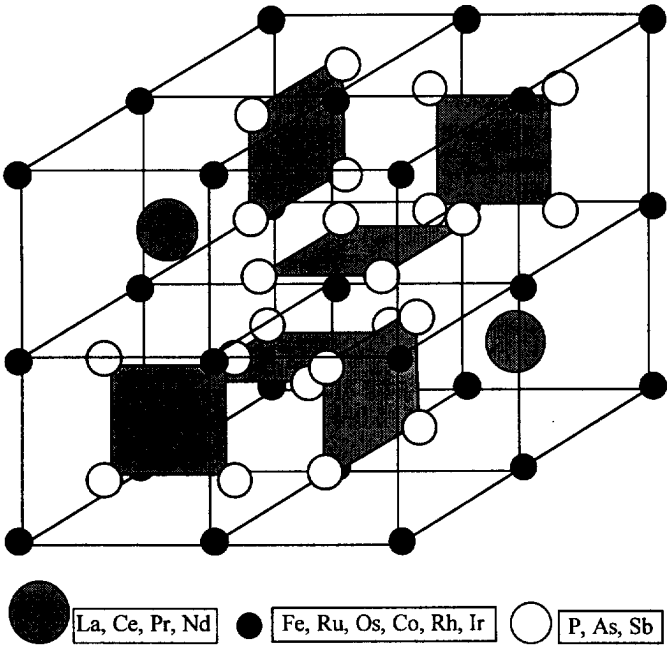


Figure 1: Skutterudite crystal structure: 32 atoms, a cubic frame with 8 transition metals, 24 pnicogens distributed in six square radicals and located in only six of the eight octants. Two rare earth elements located in the two remaining octants form a completely filled structure.

Binary compounds

Table 1. Lattice parameter a, decomposition temperature T_m, band gap Eg, of binary skutterudite compounds

Compound	a (Å)	T_m (°C)	E_g (eV)	reference
CoP_3	7.7073	>1000	0.43*	7
$CoAs_3$	8.2043	960	0.69*	8
$CoSb_3$	9.0385	850	0.63*	9
RhP_3	7.9951	>1200	-	10
$RhAs_3$	8.4427	>1000	>0.85*	8
$RhSb_3$	9.2322	900	0.80*	9
IrP_3	8.0151	>1200	-	6
$IrAs_3$	8.4673	>1200	-	11
$IrSb_3$	9.2533	1141*	1.18*	4
NiP_3	7.8190	>850	metallic	12
PdP_3	7.705	>650	metallic	13

* JPL findings

There are eleven $\square T_4Pn_{12}$ binary skutterudites reported in the literature (see Table 1). The nine semiconducting compositions are formed with all nine possible combinations of T = Co, Rh, Ir and Pn = P, As, Sb. The existence of two more skutterudite phosphides was determined: NiP_3 and PdP_3. However, in these two compounds, the total VEC is 73, resulting in metallic behavior [15].

Known values for the lattice parameter, peritectic decomposition temperature and band gap of these nine binary compounds are reported in Table 1. Decomposition temperatures for CoP_3, RhP_3, $RhAs_3$, IrP_3 and $IrAs_3$ are only lower limit estimates. We have calculated the band gap values of $IrSb_3$, $RhSb_3$, $CoSb_3$, $RhAs_3$, $CoAs_3$, and CoP_3 from high temperature Hall effect measurements [14]. The p-type $RhAs_3$ sample was still not fully intrinsic at the highest temperature of measurement, thus the value of 0.85 should only be considered a lower limit. Less heavily doped samples must be obtained to accurately determine the band gap of $RhAs_3$. The value obtained for CoP_3 is only preliminary because the sample used for measurement contained CoP_2 inclusions. For the arsenides and antimonides, the band gap increases in sequence from the Co- to the Ir-based compounds as well as from the antimonides to the arsenides.

Ternary compounds

Table 2: Lattice parameter a, decomposition temperature T_m, band gap Eg, electronegativity difference ΔX of ternary skutterudite compounds

Compound	a (Å)	T_m (°C)	E_g (eV)	ΔX	Ref.
$CoGe_{1.5}S_{1.5}$	8.0170	~1000	-	0.49	[16]
$CoGe_{1.5}Se_{1.5}$	8.3076*	~800	1.50*	0.47	[16]
$CoGe_{1.5}Te_{1.5}$*	8.7270*	~800	-	0.37	
$CoSn_{1.5}Se_{1.5}$*	8.7259*	~800	-	0.50	
$CoSn_{1.5}Te_{1.5}$*	9.1284*	~800	>2.0*	0.40	
$RhGe_{1.5}S_{1.5}$	8.2746	> 800	-	0.49	[17]
$IrGe_{1.5}S_{1.5}$	8.297	> 800	-	0.49	[17]
$IrGe_{1.5}Se_{1.5}$	8.5778*	> 800	1.38*	0.47	[17]
$IrSn_{1.5}S_{1.5}$	8.7059	> 800	-	0.52	[17]
$IrSn_{1.5}Se_{1.5}$*	8.9674*	> 800	1.24*	0.50	
$IrSn_{1.5}Te_{1.5}$*	9.3320*	>800	2.56*	0.40	
$Fe_{0.5}Ni_{0.5}Sb_3$	9.0904	729 *	~0.16*	0.12	[18]
$Fe_{0.5}Pd_{0.5}Sb_3$*	9.2060*	-	-	0.12	
$Fe_{0.5}Pt_{0.5}Sb_3$*	9.1950*	-	-	0.12	
$Ru_{0.5}Ni_{0.5}Sb_3$*	9.1780*	-	-	0.11	
$Ru_{0.5}Pd_{0.5}Sb_3$*	9.2960*	647 *	~0.60*	0.12	[19]
$Ru_{0.5}Pt_{0.5}Sb_3$*	-	-	-	0.12	
$Fe_{0.5}Ni_{0.5}As_3$	8.2560	-	-	0.21	[20]
$FeSb_2Se$*	-	-	-	0.29	
$FeSb_2Te$*	9.1120*	556*	~0.27*	0.24	
$RuSb_2Se$*	9.2570*	-	-	0.21	
$RuSb_2Te$*	9.2680*	810*	1.20*	0.16	
$OsSb_2Te$*	9.2980*	>800	-	0.15	
$PtSn_{1.2}Sb_{1.8}$	9.3900	-	-	0.18	[21]
$NiGeP_2$*	7.9040*	-	-	0.18	
$NiGeBi_2$*	9.4400	-	-	-	

*JPL findings

The existence of many ternary skutterudites has been determined. Nine ternary compounds have been reported in the literature and seventeen more have been discovered at JPL (see Table 2). Ternary skutterudite composition are derived from binary compounds by keeping a total VEC of 72. Using $\square Co_4Sb_{12}$ ($CoSb_3$) as an example, substituting trivalent Co (Co^{3+}) by divalent Fe (Fe^{2+}) and tetravalent Pd (Pd^{4+}), results in $\square Fe_2Ni_2Sb_{12}$ ($Fe_{0.5}Ni_{0.5}Sb_3$). If instead Sb is replaced by Sn and Te, then $\square Co_4Sn_6Te_6$ ($CoSn_{1.5}Te_{1.5}$) is obtained. If substitutions occur on both transition metal and pnicogen site, then $\square Fe_4Sb_8Te_4$ ($FeSb_2Te$) is obtained. It appears likely that more ternary skutterudites will be found, in particular among phosphides and arsenides. Using Pauli's scale, the electronegativity difference was calculated for the ternary compounds reported here. $Fe_{0.5}Ni_{0.5}Sb_3$ and $FeSb_2Te$ are two ternary phases derived from $CoSb_3$, and the calculated band gap values, 0.16 and 0.27 eV respectively, are much smaller than the 0.63 eV value for $CoSb_3$. Similar results are obtained for $Ru_{0.5}Pd_{0.5}Sb_3$ (0.6 eV), which is derived from $RhSb_3$ (0.8 eV). The lower band gap values are consistent with the lower decomposition temperatures. This is not the case of $RuSb_2Te$ however, which has a band gap of 1.20 eV. As seen in Table2, it is interesting to note that the larger band gap values are indeed found in the most ionic compositions, corresponding to substitution on the pnicogen site. In addition, the lattice parameter of the ternary compounds is consistently larger than the one obtained for their binary analog. On average, the lattice parameter increases by 0.7%, 1.1% and 0.6% when substitutions respectively occur on the transition metal site, the pnicogen site , or both sites simultaneously.

Filled compounds

A large number of these compounds have been known for some time (see for example [15, 22-25]), where the filling atom is typically a rare earth lanthanoid, though other compositions with actinoids Th and U, [22, 26] as well as alkaline earths Ca, Sr and Ba [25,27] have also been reported. For a typical filled skutterudite composition such as $LaFe_4P_{12}$, the rare earth element contributes 3 electrons, but due to the divalent Fe (Fe^{2+}), the total VEC is only 71. This deficit results in metallic behavior for most simple filled ternary compounds. Only $CeFe_4P_{12}$, UFe_4P_{12} and $CeFe_4As_{12}$ have been reported as semiconductors, a result attributed to the higher electronegativity of phosphorus in particular which is favorable to tetravalent Ce (Ce^{4+}) instead of trivalent Ce (Ce^{3+}). However, it must be noted that Ce was found to be of intermediate valence in $CeFe_4P_{12}$. Compounds based on Th ($ThFe_4P_{12}$ has been reported) should also been semiconducting since Th is exclusively tetravalent. More recent results on filled skutterudite antimonides [28-30] based on $LaFe_4Sb_{12}$ and $CeFe_4Sb_{12}$ have shown that Fe can be replaced by Co, leading to a more semiconducting behavior in these materials. However, it was found that as Co substitution increases, the number of filling La or Ce atoms simultaneously decreases. It thus appears that the VEC of filled skutterudites can vary from 71 to 72, depending on the valency of the filling atom.

Solid solutions.

The only solid solutions between binary skutterudite compounds previously reported in the literature show that CoP_3 and $CoAs_3$ form a complete range of solid solutions which obey the Vegard's rule and that the system $CoAs_{3-x}Sb_x$ has a miscibility gap in the region of x = 0.4 to 2.8 [31]. More recent experimental work at JPL has shown that there is a large number of skutterudite binary and ternary compounds, including filled skutterudites, which form solid solutions, at least in some limited range of composition [32,33].

Table 3. Existence of skutterudite solid solutions

Compound	Partial Range	Full Range
CoP_3		$CoAs_3$*
$CoAs_3$	$CoSb_3$* , $IrAs_3$	
$CoSb_3$	$CoAs_3$* , $Fe_{0.5}Ni_{0.5}Sb_3$, $FeSb_2Te$	$IrSb_3$, $CeFe_4Sb_{12}$
$RhSb_3$	$CoSb_3$	$IrSb_3$
$IrAs_3$	$CoAs_3$, $IrSb_3$	
$IrSb_3$	$CoSb_3$, $IrAs_3$	$RhSb_3$, $RuSb_2Te$
$Fe_{0.5}Ni_{0.5}Sb_3$	$CoSb_3$, $IrSb_3$, $Ru_{0.5}Pd_{0.5}Sb_3$	$Ru_{0.5}Pd_{0.5}Sb_3$
$Ru_{0.5}Pd_{0.5}Sb_3$	$CoSb_3$, $IrSb_3$	$Fe_{0.5}Ni_{0.5}Sb_3$
$FeSb_2Te$	$CoSb_3$, $RuSb_2Te$	
$RuSb_2Te$	$FeSb_2Te$	$IrSb_3$
$CeFe_4Sb_{12}$	$CeRu_4Sb_{12}$	$CoSb_3$

*literature results

Thermoelectric Properties of Binary Compounds

Electrical properties

The antimonides $CoSb_3$, $RhSb_3$, $IrSb_3$, and arsenides $CoAs_3$, $RhAs_3$ all exhibit semiconducting behavior, with band gap values ranging from 0.63 to 1.18 eV. These band gap values were calculated from the high temperature variations of the electrical resistivity and Hall coefficient [14]. Almost no data are available for the binary phosphides. Due to the exceptionally high hole mobilities, p-type skutterudites exhibit high electrical conductivity values, ranging from 2 to $5x10^5$ $\Omega^{-1}m^{-1}$ for a hole concentration of $1x10^{19}$ cm^{-3}. The room temperature mobility values of p-type skutterudites are 1 to 100 times higher than those for p-type Si and GaAs at similar carrier concentrations, as seen in Figure 2. $RhSb_3$ exhibits the greatest hole mobility, 8000 $cm^2V^{-1}s^{-1}$ for a carrier concentration of $2.5x10^{18}$ cm^{-3}, which is about 70 times higher than p-type GaAs and still 5 times higher than n-type GaAs [9]. This is due to small hole effective mass values (as low as 0.07 m_o for $RhSb_3$). Due to the preparation techniques used,

skutterudite samples with carrier concentrations lower than $7.0x10^{16}$ cm^{-3} could not been obtained so far [9]. The temperature dependence of the carrier mobilities of the skutterudites also compare favorably with those of state-of-the-art semiconductors. Even at a temperature of 550°C, the hole mobility of $IrSb_3$ was observed to be 600 $cm^2V^{-1}s^{-1}$ for a carrier concentration of $6.5x10^{18}$ cm^{-3} -about 4 times the value obtained for n-type Si, in spite of the polycrystalline, small grain structure of the $IrSb_3$ samples [34]. Acoustic phonon scattering of the charge carriers was found to be the dominant mechanism at 300K for undoped skutterudites [35].

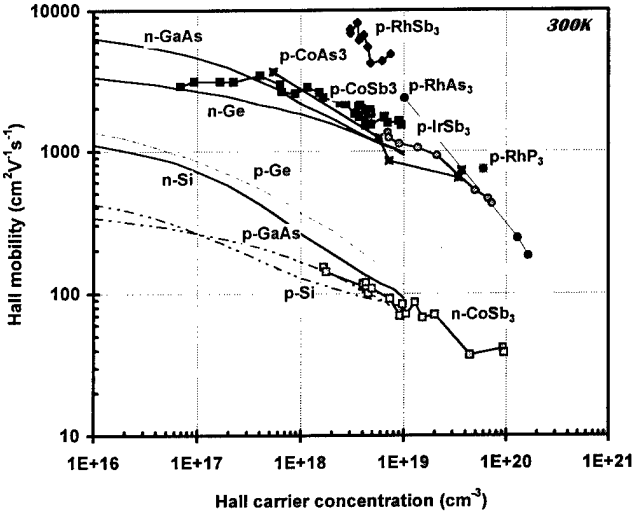


Figure 2: Room temperature Hall mobility values as a function of carrier concentration for several skutterudite compounds. Results are compared to those obtained for state of the art electronic p-type (solid lines) and n-type (dotted lines) semiconductors: Si, Ge and GaAs.

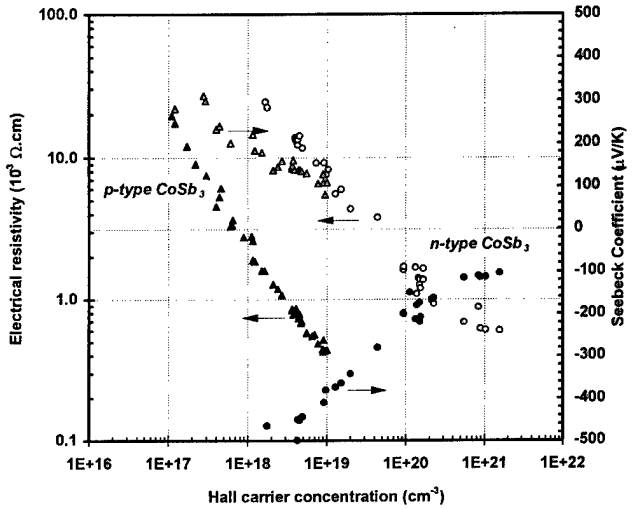


Figure 3: Room temperature electrical resistivity and Seebeck values as a function of carrier concentration for $CoSb_3$.

Skutterudites with n-type conductivity have been obtained by doping with selected elements such as Ni, Pd, Pt and Te [34, 35]. The electron mobilities of n-type $CoSb_3$, also plotted in Figure 2, are comparable to the values obtained for p-type Si and GaAs. The calculated electron effective mass, 3.1 m_o, is much larger than the hole effective mass, 0.28 m_o, in $CoSb_3$. Experimental results obtained on $CoAs_3$ and $IrSb_3$ suggest a similar behavior. It is interesting to note that these characteristics of skutterudites are the opposite of those found for Si, Ge and most III-V compounds, where the electron effective mass is significantly smaller than the hole effective mass.

These very different characteristics lead to interesting variations of the electrical resistivity and Seebeck coefficient with carrier concentration and temperature. The room temperature variations of both transport properties are reported in Figure 3 for $CoSb_3$ as a function of the carrier concentration obtained from measurement of the Hall coefficient. It can be seen that to achieve the same electrical resistivity values n-type $CoSb_3$ samples must have carrier concentrations about fifty times higher than n-type samples. However, because of the large electron effective masses, the n-type Seebeck coefficient values are also much larger than p-type Seebeck coefficient values for the same carrier concentration.

In addition to detailed optical measurements [36], lattice dynamics studies [37,38], the electronic band structure of $CoSb_3$ has also been calculated from first principles [39]. Calculations indicated the presence of unusual features for several binary skutterudites [39,40], including the presence of a single valence band crossing the high temperature "pseudogap", resulting in an actual 50 meV gap in $CoSb_3$ and no gap in $CoAs_3$ and $IrSb_3$. In addition the gap-crossing valence band follows a linear dispersion and peculiar carrier mobility and Seebeck coefficient carrier concentration dependences were predicted. These theoretical predictions have since been completely validated by detailed experimental data [35,41].

Thermal conductivity

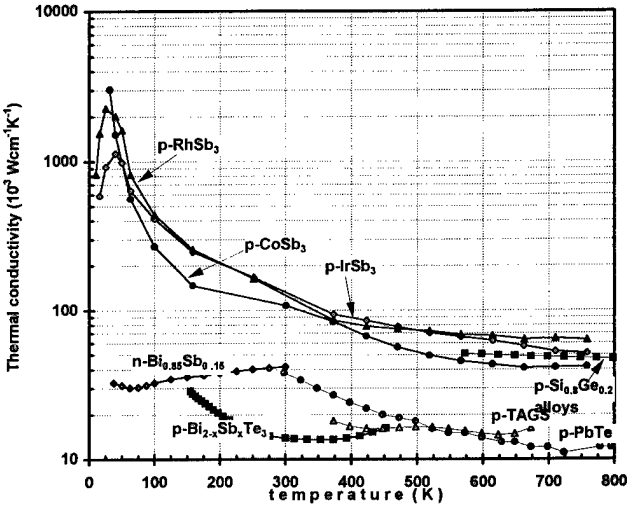


Figure 4: Thermal conductivity as a function of carrier concentration for binary skutterudite antimonides. Results are compared to those obtained for state of the art thermoelectric materials.

The thermal conductivity of lightly-doped p-type $CoSb_3$, $RhSb_3$ and $IrSb_3$ samples is plotted as a function of temperature in Figure 4. These results are similar to those obtained for $CoAs_3$ and $RhAs_3$ [8]. A simple calculation using the Wiedemann-Franz law shows that 90 to 95% of the total thermal conductivity is due to the lattice contribution near room temperature. At high temperatures, acoustic phonon scattering is mostly responsible for the decrease in thermal conductivity with a T^{-1} dependence [35]. Below room temperature, the very sharp rise in thermal conductivity with decreasing temperature was attributed to the dominance of the phonon-phonon Umklapp scattering, and was indicative of the purity of the measured samples [41].

When compared to state-of-the-art thermoelectric materials (10-40 $mWcm^{-1}K^{-1}$), the thermal conductivity of binary skutterudites (100-150 $mWcm^{-1}K^{-1}$) is too high to result in high figures of merit.

Heavily Doped n-type $CoSb_3$

As discussed in the preceding sections, both p-type and n-type $CoSb_3$ can achieve similarly attractive electrical properties, with power factor values in the 25-30 $\mu W/cmK^2$ range. However, because the optimum carrier concentration must be 50 times higher in n-type samples (~ $5x10^{20}$ cm^3), there are important differences in thermal conductivity and figure of merit values between p-type and n-type samples. The thermal conductivity of heavily doped n-type $CoSb_3$ samples was recently measured [35] and experimental data are shown in Figure 5. For lightly doped samples, the lattice thermal conductivity at 100°C is about 80 $mWcm^{-1}K^{-1}$ but for more heavily doped samples, the value decreases to about 44 $mWcm^{-1}K^{-1}$ ($1x10^{20}$ cm^{-3}) and can be as low as 32 $mWcm^{-1}K^{-1}$ ($1x10^{21}$ cm^{-3}). The total thermal conductivity of the most heavily doped sample is actually higher than the one doped at $1x10^{20}$ cm^{-3} because of the large electronic contribution (proportional to the electrical conductivity).

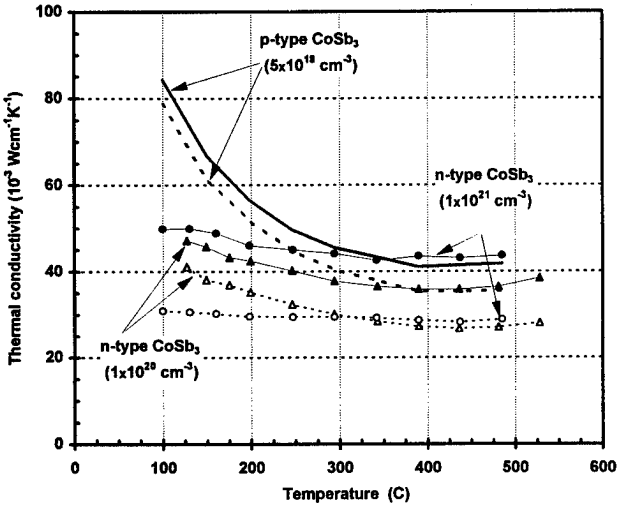


Figure 5: Lattice (dotted lines) and total (plain lines) thermal conductivity as a function of temperature for $CoSb_3$ samples with various doping levels.

The temperature dependence of the lattice thermal conductivity becomes weaker for more heavily doped samples, indicating that electron-phonon scattering is responsible for the large decrease in lattice thermal conductivity. This is an interesting finding because charge carrier phonon scattering would scatter the phonons with low frequency and if coupled with point defect scattering (by forming solid solutions) could result in very low lattice thermal conductivity values. The combination of point defects and charge carrier scattering was utilized in Si-Ge alloys [42]. Because of lower carrier concentrations, this scattering mechanism has not been identified yet in p-type samples. For optimum carrier concentrations, maximum ZT values in very heavily doped n-type $CoSb_3$ samples can reach 0.9 to 1.0 in the 550-600°C temperature range.

Ternary Compounds

Only limited information is available in the literature about the electrical and thermal properties of ternary skutterudite compounds. Some results obtained at JPL on six ternary skutterudites, $FeSb_2Te$, $RuSb_2Te$, $OsSb_2Te$, $Fe_{0.5}Ni_{0.5}Sb_3$, $Ru_{0.5}Pd_{0.5}Sb_3$, $IrSn_{1.5}Se_{1.5}$ and $IrSn_{1.5}Te_{1.5}$ are reported in Figures 6, 7 and 8. $FeSb_2Te$, $Fe_{0.5}Ni_{0.5}Sb_3$ and $Ru_{0.5}Pd_{0.5}Sb_3$ appear to be heavily doped semiconductors with carrier concentrations values ranging from $1x10^{20}$ to $1x10^{21}$ cm^{-3}. However, $Ru_{0.5}Pd_{0.5}Sb_3$ samples showed good carrier mobility values (about 40 cm^2/Vs near room temperature), and the a hole effective mass of $0.28m_o$ was calculated [19]. $Fe_{0.5}Ni_{0.5}Sb_3$ and $Ru_{0.5}Pd_{0.5}Sb_3$ also have low Seebeck coefficient values and mixed conduction effects are apparent in $Fe_{0.5}Ni_{0.5}Sb_3$ (n-type Seebeck, p-type mobility). Relatively high Seebeck coefficients are obtained for semimetallic p-type $FeSb_2Te$ at elevated temperature, which is surprising considering the very high carrier concentration and small bandgap.

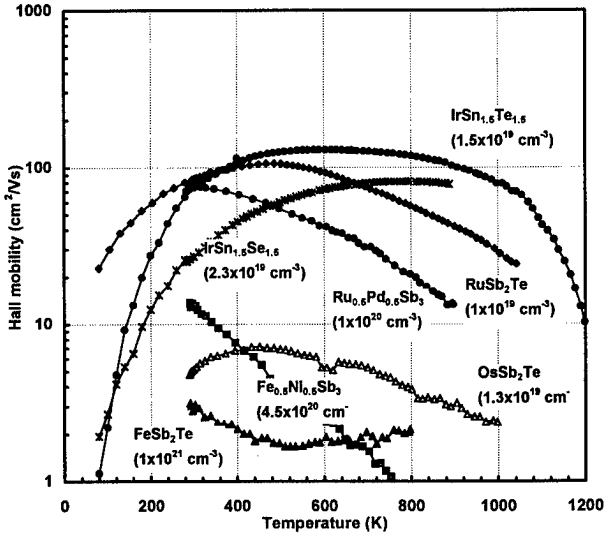


Figure 6: Hall carrier mobility as a function of temperature for several ternary skutterudite compounds. Carrier concentration levels are also reported.

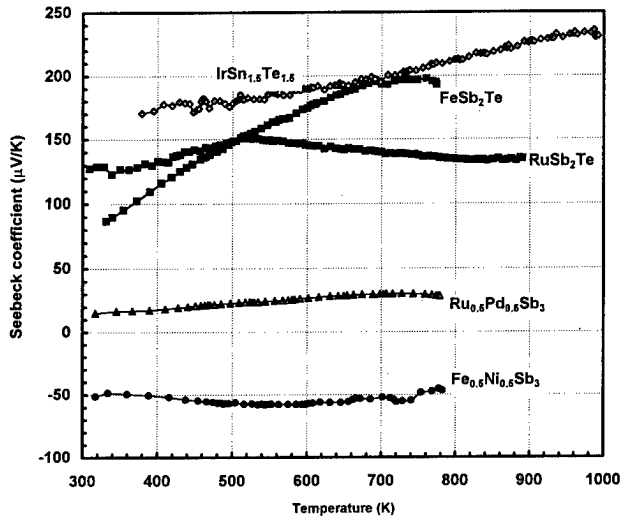


Figure 7: Seebeck coefficient as a function of temperature for several ternary skutterudite compounds.

$RuSb_2Te$, $IrSn_{1.5}Se_{1.5}$ and $IrSn_{1.5}Te_{1.5}$, have semiconducting behavior with typical carrier concentrations of $1x10^{19}$ cm^{-3}, carrier mobility ranging from 50 to 100 $cm^2V^{-1}s^{-1}$ and Seebeck coefficient ranging from 120 up to 250 μVK^{-1}. All three compounds were also found to have relatively large bandgap values (over 1.2 eV). It is interesting to note that these latter materials only have one type of transition metal. Dopants, such as Ni and Te, were found to be quite ineffective in changing the carrier concentration of $FeSb_2Te$, $RuSb_2Te$ and $Ru_{0.5}Pd_{0.5}Sb_3$. From these initial experimental data, it is clear however that significant departures from the band structure and doping behavior of binary skutterudites exist in ternary skutterudites. This is confirmed in the next section when we analyze results of thermal conductivity measurements.

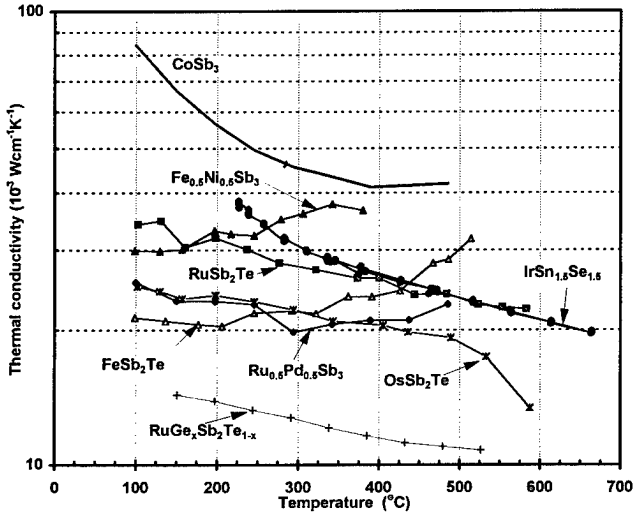


Figure 8: Thermal conductivity as a function of temperature for several ternary skutterudite compounds. Results are compared to those obtained for lightly doped $CoSb_3$.

The experimental data on the high temperature thermal conductivity of six ternary compounds, $FeSb_2Te$, $RuSb_2Te$, $OsSb_2Te$, $Fe_{0.5}Ni_{0.5}Sb_3$, $Ru_{0.5}Pd_{0.5}Sb_3$ and $IrSn_{1.5}Se_{1.5}$ and one quaternary phase, $RuGe_{0.2}Sb_2Te_{0.8}$ are plotted in Figure 8 [19, 43]. The results are compared to the data on lightly doped p-type $CoSb_3$. The lattice contribution to the thermal conductivity is greatly reduced in these materials, with room temperature values ranging from 15 to 30 $mW.cm^{-1}K^{-1}$. The low thermal conductivity values of these compounds, while very encouraging, are nevertheless a bit surprising considering that the atomic mass and volume differences introduced by the substituting anion/cation are fairly small. This indicates that additional mechanisms must be involved.

A possible explanation for the unusually high phonon scattering rate could be that transition metal elements have mixed valence states and electrons are transferred between the different ions, thus scattering the phonons in this process [43, 44]. When substituting trivalent Co (Co^{3+}) in $CoSb_3$ by Ru and Pd to form the stoichiometric $Ru_{0.5}Pd_{0.5}Sb_3$ composition, it is assumed that the valence state of Ru, and Pd, are Ru^{2+} and Pd^{4+} respectively. Systematic shifts from the stoichiometric $Ru_{0.5}Pd_{0.5}Sb_3$ were revealed by microprobe analysis [19]. Results indicate that the Ru:Pd atomic ratio can vary substantially from the expected 1:1 value and that there is a significant number of vacancies on the transition metal sublattice. To compensate for the Pd deficit and excess Sb in the samples, the Ru must adopt a mixed valence state, *i.e.*, Ru^{2+} and Ru^{4+}. Such valence fluctuations were recently confirmed by x-ray absorption near-edge structure analysis [44].

Such stoichiometric shifts are also found for the other ternary skutterudites and experimental data for samples prepared at JPL are presented in Table 4. Based on electron microprobe analysis, each composition can be recalculated to conform to the $T^{3+}X_3^{-1}$ stoichiometry, adding vacancies to the metal sublattice when needed. The valence ratio v of the mixed valence transition metal (for example $[Ru^{2+}]/[Ru^{4+}]$) was then determined from the ionic formula. The lattice thermal conductivity calculated from the measured thermal conductivity at room temperature using the Wiedemann-Franz law is also reported in this table.

Table 4: Valence Fluctuations in Low Thermal Conductivity Ternary Skutterudites, where v is the valence ratio (e.g. $[Ru^{2+}]/[Ru^{4+}]$) and λ_L is the lattice thermal conductivity in 10^{-3} W/cmK.

Composition (at%)	Ionic Formula	v	λ_L
$Fe_{12.8}Ni_{11.9}Sb_{75.2}$	$Fe^{2+}_{0.51}Ni^{4+}_{0.49}Sb^{-1}_3$	--	29
$Ru_{12.3}Pd_{10.6}Sb_{77.1}$	$[]_{0.11}Ru^{2+}_{0.28}Ru^{4+}_{0.20}Pd^{4+}_{0.41}Sb^{-1}_3$	1.4	15
$Fe_{25.1}Sb_{52.0}Te_{22.9}$	$Fe^{2+}_{0.91}Fe^{3+}_{0.09}Sb^{-1}_{2.1}Te^{0}_{0.9}$	10.4	23
$Ru_{22.4}Sb_{49.7}Te_{25.3}$	$[]_{0.10}Ru^{2+}_{0.79}Ru^{4+}_{0.11}Sb^{-1}_{1.98}Te^{0}_{1.02}$	7.2	28
$Os_{24.6}Sb_{50.5}Te_{24.9}$	$[]_{0.02}Os^{2+}_{0.98}Os^{4+}_{0.02}Sb^{-1}_{2.03}Te^{0}_{0.97}$	32.3	25
$Ru_{24.0}Ge_{4.7}Sb_{50.6}Te_{20.7}$	$[]_{0.05}Ru^{2+}_{0.75}Ru^{4+}_{0.2}Ge^{-2}_{0.18}Sb^{-1}_{2.0}Te^{0}_{0.82}$	3.7	14
$Ir_{23.3}Sn_{38.3}Te_{38.4}$	$[]_{0.07}Ir^{3+}_{0.65}Ir^{4+}_{0.28}Sn^{-2}_{1.5}Te^{0}_{1.5}$	2.3	42

Although ternary compounds have rather low thermal conductivity values, it is difficult to control their electrical properties. When doping ternary skutterudites, and supposing that the electron exchange mechanism is indeed present, changes in carrier concentration are not easy to achieve because dopants can be compensated by small fluctuations in the overall valence of the transition metals.

Fe-based Filled Skutterudites

Recent studies have focused on Fe-based filled skutterudites, investigating the electronic band structure of $CeFe_4P_{12}$ and $CeFe_4Sb_{12}$ [45] and the transport properties of $LaFe_{4-x}Co_xSb_{12}$ and $CeFe_{4-x}Co_xSb_{12}$ compositions [28-30]. These materials are particularly attractive because of the possibility of dramatic reductions in the lattice thermal conductivity due to the "rattling" of the filling atom in the two empty octants present in the skutterudite structure [46]. As briefly discussed in a preceding section, the VEC in filled skutterudites such as $LaFe_4Sb_{12}$ is only 71, resulting in metallic behavior. This is because La brings only three electrons (La is exclusively trivalent) to compensate for the four electron deficit due to the presence of Fe (instead of say, Co). It also has been demonstrated that Ce is nearly trivalent at temperatures higher than 100K [30]. The study of the $CeFe_{4-x}Co_xSb_{12}$ compositions was thus driven by the expectation of returning to a semiconducting $CoSb_3$-like behavior. The high temperature electrical and thermal transport properties of the $CeFe_{4-x}Co_xSb_{12}$ filled skutterudite samples have been measured from 25 up to 650°C. The temperature dependence of the electrical resistivity, Seebeck coefficient and thermal conductivity are reported in Figures 9, 10 and 11, respectively.

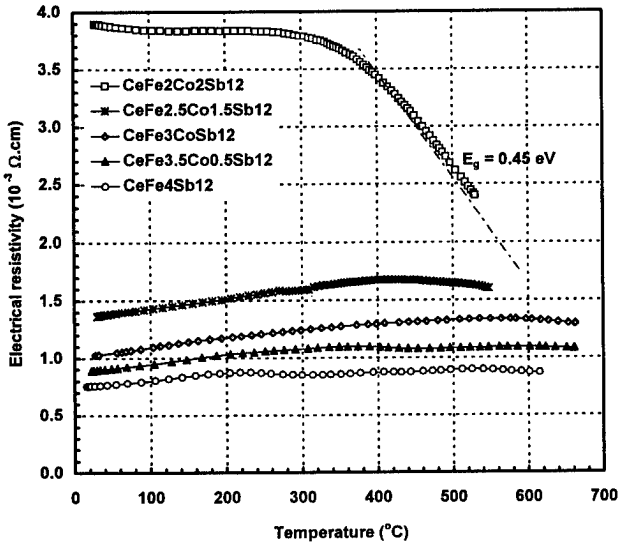


Figure 9: High temperature variations of the electrical resistivity of p-type $CeFe_{4-x}Co_xSb_{12}$ filled skutterudites.

The results show that the Fe-rich compositions have a semimetallic behavior (very high carrier concentration of about $5x10^{21}$ cm^{-3} and low carrier mobilities of 2-5 $cm^2V^{-1}s^{-1}$) with a low electrical resistivity, which increases slightly with temperature. However, the $CeFe_2Co_2Sb_{12}$ sample demonstrated a more semiconducting behavior, with a bandgap value of 0.45 eV determined from high temperature electrical resistivity measurements

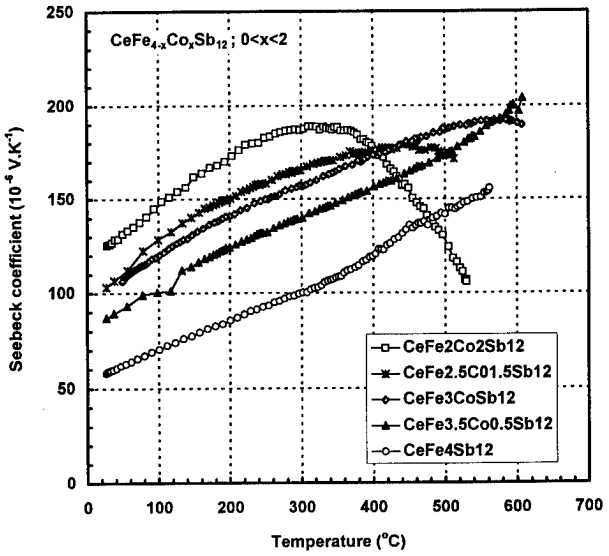


Figure 10: High temperature variations of the Seebeck coefficient of p-type $CeFe_{4-x}Co_xSb_{12}$ filled skutterudites.

What is most surprising is the magnitude of the Seebeck coefficients, ranging from 55 to 125 μVK^{-1} at 25°C and increasing steadily with temperature. Again, the intrinsic regime is obtained in $CeFe_2Co_2Sb_{12}$ for temperatures over 350°C. These values are comparable to those obtained for other p-type binary skutterudites except that here the carrier concentration is two to three orders of magnitude higher. This is attributed to the fact that these materials behave similarly to heavy fermions systems: the hybridization between Ce and the transition metal (Fe or Co here) creates a small bandgap and carriers possess large effective masses resulting in a low mobility but unusually high Seebeck coefficient [45,47].

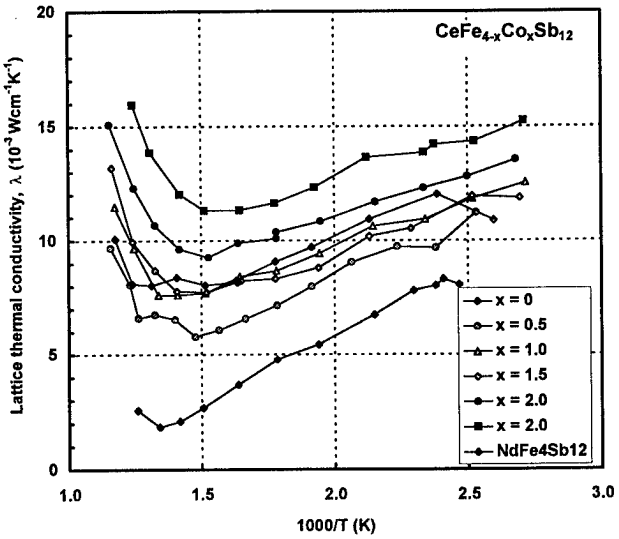


Figure 11: Lattice thermal conductivity as a function of inverse temperature for $CeFe_{4-x}Co_xSb_{12}$ filled skutterudites.

As shown in Figure 11, the lattice thermal conductivity of filled skutterudites is much lower than the values obtained for $CoSb_3$. The $CeFe_4Sb_{12}$ sample has a room temperature thermal conductivity of about 24 $x10^{-3}Wcm^{-1}K^{-1}$ at room temperature and increasing up to 27 $x10^{-3}Wcm^{-1}K^{-1}$ at 575°C. Based on the low electrical resistivity value ($0.5x10^{-3}\Omega cm$), the lattice contribution to the thermal conductivity was estimated at 12 $x10^{-3}Wcm^{-1}K^{-1}$. This demonstrates that the combination of the "rattling" atom and very high carrier concentration ($5x10^{21}$ cm^{-3}) very effectively scatter the phonons, and results in an extremely low lattice thermal conductivity. Similar low thermal conductivity values have also been obtained on $IrSb_3$-based filled skutterudite compositions [48,49].

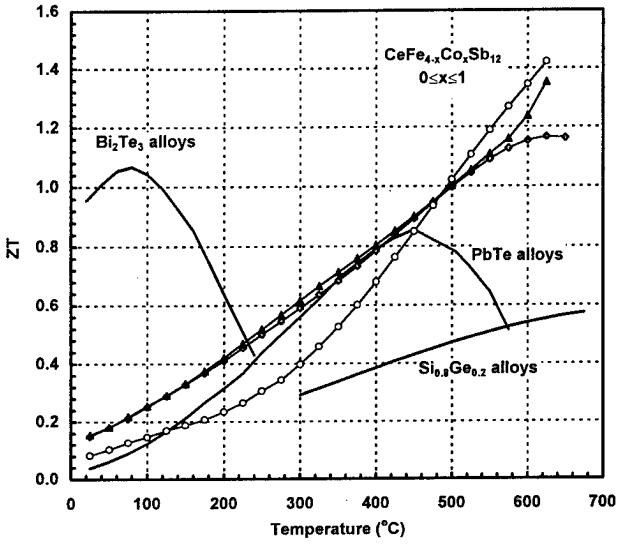


Figure 12: ZT as a function of temperature for $CeFe_{4-x}Co_xSb_{12}$ samples, with $0<x<1.0$.

The combination of the low electrical resistivity, moderate Seebeck coefficient and low thermal conductivity resulted in high ZT values at temperatures above 400°C for the Fe-rich compositions (Figure 12). A maximum ZT value of 1.4 has been achieved to date at a temperature of 600°C [28]. High ZT values have also been reported on similar compositions filled with La instead of Ce [29]. However, because of the semimetallic behavior of the $CeFe_{4-x}Co_xSb_{12}$ compositions it is difficult to control carrier concentration, obtain n-type conductivity samples and optimize the thermoelectric properties at various temperatures. To do so requires the preparation of semiconducting filled skutterudites with good carrier mobility values.

Skutterudites for Low Temperatures

Electron microprobe analysis of a series of $CeFe_{4-x}Co_xSb_{12}$ has demonstrated that the amount of Ce filling decreases with increasing substitution of Fe by Co. One can rewrite those compositions with the following formula, $Ce_fFe_{4-x}Co_xSb_{12}$, where f represent the fraction of Ce filling (f =1 represents complete filling). In addition to Co, substitution of Fe by Ni and Ru has also been investigated recently. The variations of the filling fraction f as a function of x have been plotted in Figure 13 for the three different ranges of compositions. The two solid lines represent the expected transition for Ni and Co from p-type to n-type (when the VEC reaches 72), taking into account both f and x variations. When Fe is totally replaced by Co, only a very small amount of Ce remains in the sample (f = 0.07) while completely filled $CeRu_4Sb_{12}$ can be prepared (f=1). This is attributed to the fact that Ru and Fe are isoelectronic. The dotted line was calculated based on a $CeFe_4Sb_{12}$-$Ce_{0.065}Co_4Sb_{12}$ range of "solid solution" compositions. $Ce_fFe_{4-x}Ni_xSb_{12}$ compositions with $x > 1.5$ have not yet been synthesized, but it is clear that at equivalent concentrations, Ni substitution results in less Ce filling than Co substitution. However, because Ni donates two electrons instead of only one for Co when replacing Fe, the decrease in carrier concentration and corresponding change in properties with increasing x is much stronger for $Ce_fFe_{4-x}Ni_xSb_{12}$.

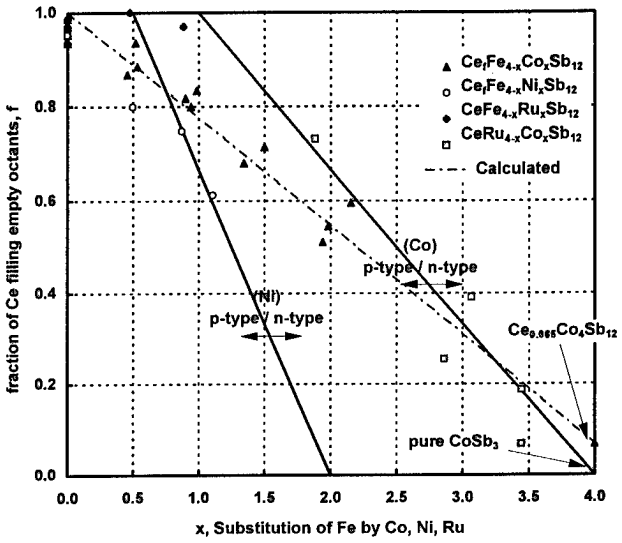


Figure 13: Ce filling fraction (f) for $Ce_fFe_{4-x}M_xSb_{12}$ samples as a function of Fe substitution by M (x) with M = Co, Ni and Ru. No decrease in Ce filling is observed for $Ce_fFe_{4-x}Ru_xSb_{12}$ samples.

While it is clear that filling the skutterudite structure contributes to the low lattice thermal conductivity, high carrier concentrations and valence fluctuations could also strongly scatter phonons in the compositions studied so far. Indeed, a typical carrier concentration value of $5x10^{21}$ cm^{-3} is obtained for $CeFe_4Sb_{12}$ at 300K, while a carrier concentration of $4x10^{20}$ cm^{-3} was measured for both $Ce_{0.51}Fe_{2.1}Co_{1.9}Sb_{12}$ and $Ce_{0.75}Fe_{3.1}Ni_{0.9}Sb_{12}$ compositions. The Co-based sample has 51% of its voids filled with Ce while the Ni-based sample has 75% of filled voids, but their lattice thermal conductivity is nearly identical, 16 to $17x10^{-3}Wcm^{-1}K^{-1}$, to be compared with a value of $12x10^{-3}Wcm^{-1}K^{-1}$ for $CeFe_4Sb_{12}$.

Another interesting result is the fact that no decrease in lattice thermal conductivity was observed when Ru was substituted for Fe. It seems that the point defects generated by a Ru atom on the Fe site do not contribute any further to the overall scattering rate, possibly because void fillers already scatter phonons in a wide frequency domain. Very recent experimental data obtained at JPL on $Ce_fRu_{4-x}Co_xSb_{12}$

samples suggests another possibility. Figures 14, 15 and 16 respectively present Hall mobility, Seebeck coefficient and thermal conductivity variations with temperatures for selected Fe-based, Ru-based and Co-based filled skutterudites. The actual filling fraction as determined from electron microprobe analysis is also reported.

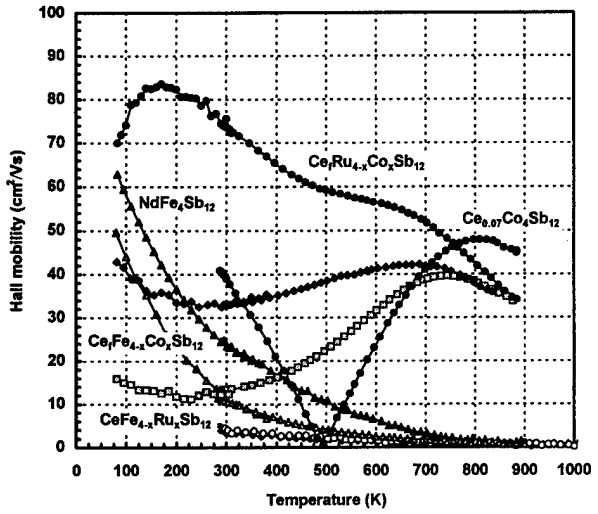


Figure 14: Hall carrier mobility as a function of temperature for various Fe-, Ru-, and Co-based filled skutterudites.

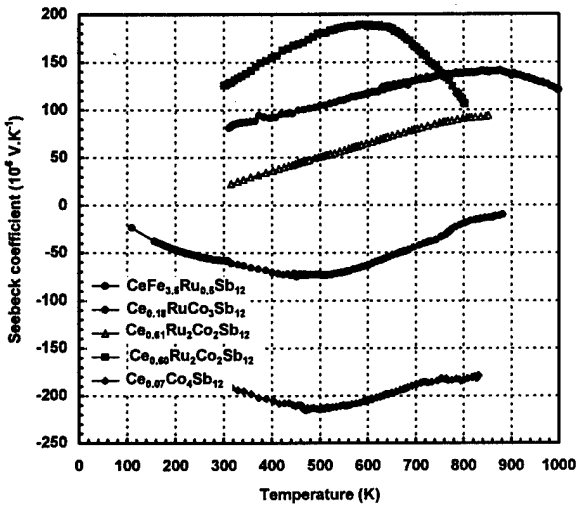


Figure 15: Seebeck coefficient as a function of temperature for various Fe-, Ru-, and Co-based filled skutterudites.

The data show that there are very significant differences between filled skutterudite compositions containing some amount of Fe and those which only have Ru and Co. Much higher p-type carrier mobility (up to 75 $cm^2V^{-1}s$-1 at room temperature) are obtained for an 18% filled $Ce_fRuCo_3Sb_{12}$ sample. Comparable compositions with Fe have been reported to have very poor mobilities [50]. In addition n-type $Ce_fRuCo_3Sb_{12}$ and $Ce_fCo_4Sb_{12}$ samples were successfully prepared. These n-type samples show mixed conduction effects very similar to those observed in n-type $CoSb_3$ and $IrSb_3$. The filling of just 7% of the empty octants of a semiconducting $CoSb_3$ sample resulted in a large drop in the room temperature lattice thermal conductivity, from 95 to about 35 $10^{-3}Wcm^{-1}K^{-1}$. Substitution of Co by Ru and a subsequent increase in Ce filling succeeded in further reduction in the lattice thermal conductivity, likely due to a combination of point defect and increased void filling phonon scattering.

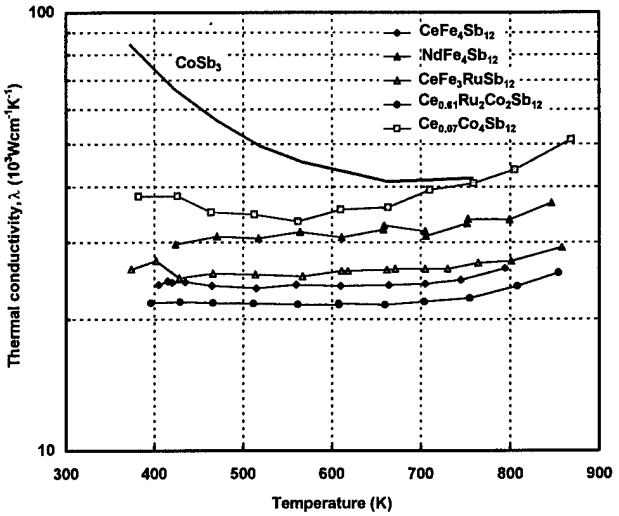


Figure 15: Thermal conductivity as a function of temperature for various Fe-, Ru-, and Co-based filled skutterudites. Results are compared to p-type $CoSb_3$ data.

However, Fe-based filled skutterudites, despite much higher carrier concentrations, consistently possess larger p-type Seebeck coefficient and lower lattice thermal conductivity. It is interesting to note that qualitatively similar remarks can be made for the $FeSb_2Te$ and $Fe_{0.5}Ni_{0.5}Sb_3$ ternary compounds compared to their Ru-based analogs, $RuSb_2Te$ and $Ru_{0.5}Pd_{0.5}Sb_3$. First principle electronic band structure calculations of Ru-based filled skutterudites would be of great interest [51]. Even though these new results are not fully understood, the preparation of p-type and n-type semiconducting filled skutterudites with filling fractions of up to 60% offers new possibilities for optimizing their thermoelectric properties near room temperature.

Conclusion

The properties of binary skutterudite compounds are very attractive for thermoelectric applications. However, their lattice thermal conductivity values are too high, in particular at low temperatures. Several approaches to significantly reduce the thermal conductivity of skutterudites have been identified: heavy doping, solid solution formation, valence fluctuations, and void filling. Ultimately, a combination of these approaches should be employed to reach a lattice thermal conductivity close to the theoretical minimum. Recent results have shown that high ZT values substantially larger than 1.0 can be obtained for some skutterudite solid solutions and filled compositions at temperature near 600°C. New experimental data on Ru-based semiconducting filled skutterudite compositions offer a promising approach for achieving high ZT in skutterudites at lower temperatures.

Acknowledgments

The work described in this paper was carried out at the Jet Propulsion Laboratory/California Institute of Technology, under contract with the National Aeronautics and Space Administration. The authors would like to thank Dr. D.T. Morelli, Dr. D.J. Singh and Prof. Glen A. Slack for many helpful discussions. This work is supported by the U.S. Office of Naval Research, Grant No. N00014-95-F-0068.

References

1. H. Lyon, Proceedings, Materials Research Society Spring Meeting, Symposium Q, ed. T. Tritt, (1997).

2. A. Schock, *Proceedings, 14th International Conference on Thermoelectrics*, ed. M. Vedernikov, Ioffe Physico-Technical Institute, p. 231 (1995).

3. D.T. Morelli, *Proceedings, 15th International Conference on Thermoelectrics,* ed. T. Caillat (IEEE Catalog 96TH8169), p. 112 (1996).

4. T. Caillat, A. Borshchevsky, and J.-P. Fleurial, Proceedings, 7th International Conference on Thermoelectrics, ed. K. Rao, University of Texas at Arlington, p. 98 (1993).

5. Oftedal, I., Z. Kristallogr., 66, 517 (1928).

6. S. Rundqvist and N.-O. Ersson, Arkiv for Kemi, 30 (10), 103 (1968).

7. W. Biltz and M. Heimbrecht, Z. Anorg. Allgem. Chem. 241, 349 (1939).

8. T. Caillat, J.-P. Fleurial, and A. Borshchevsky, *Proc. 30th Intersoc. Ener. Conv. Engin. Conf.*, Orlando, Florida, August 3-7, (1995).

9. T. Caillat, J.-P. Fleurial, and A. Borshchevsky, J. Crystal Growth, 166, 722-726 (1996).

10. J. P. Odile, S. Soled, C. A. Castro, A. Wold, Inorganic Chemistry, 17, 2, 283 (1978).

11. A. Kjekshus and G. Pedersen, "The Crystal Structure of $IrAs_3$ and $IrSb_3$", Acta Cryst., 14, 1065-1070 (1961).

12. S. Rundqvist and E Larsson, Acta Chem. Scand. 13, 551 (1959).

13. S. Rundqvist, Nature, 185, 31 (1960).

14. J.-P. Fleurial, T. Caillat, A. Borshchevsky, *Proc. 13th Intl. Conf. on Thermoelectrics*, AIP Press No. 316, 40-44, Kansas City, MO (1994).

15. W. Jeitschko and D. Braun, Acta. Cryst., B33, 3401-3406 (1977).

16. R. Korenstein, S. Soled, A. Wold, G. Collin, Inorganic Chemistry, 16, 9, 2344 (1977).

17. A. Lyons, R. P. Gruska, C. Case, S. N. Subbarao, A. Wold, Mat. Res. Bul., 125 (1978).

18. A. Kjekshus, T. Rakke, Acta Chemica Scandinavica, A28, 99 (1974).

19. T. Caillat, J. Kulleck, A. Borshchevsky, and J.-P. Fleurial, J. Appl. Phys. vol. 79, 11, 1141 (1996).

20. H. D. Lutz, G. Kliche, J. Solid State Chemistry, 40, 64 (1981).

21. S. Bahn, T. Gödecke, , K. Schubert, J. of Less-Common Metals, 19, 121 (1969).

22. G. P. Meisner, M. S. Torikachvili, K. N. Yang, M. B. Maple, R. P. Guertin, J. Appl. Phys., 57, 1, 3073 (1985).

23. D. Jung, M. H. Whangbo, S. Alvarez, Inorganic Chemistry, 29, 2252 (1990).

24. F. Grandjean, A. Gérard, D. J. Braun, W. Jeitschko, J. Phys. Chem. Solids, 45, 8/9, 877 (1984).

25. N. T. Stetson, S. M. Kauzlarich, H. Hope, Journal of Solid State Chemistry, 91, 140 (1991).

26. D. J. Braun and W. Jeitschko, J/ Less Common Metals, 76, 33 (1980).

27. M. E. Danebrock, C. B. H. Evers and W. Jeitschko, J. Phys. Chem. Solids, 57 (4) 381 (1996).

28. J.-P. Fleurial, A. Borshchevsky, and T. Caillat, D. T. Morelli, and G. P. Meisner, *Proceedings, 15th International Conference on Thermoelectrics,* ed. T. Caillat (IEEE Catalog 96TH8169), p. 91 (1996).

29. B.C. Sales, D. Mandrus and R.K. Williams, Science, Vol. 22, 1325-1328 (1996).

30. B. Chen, J.H Xu, C. Uher, D.T. Morelli, G.P. Meisner, J.-P. Fleurial, T. Caillat and A. Borshchevsky, Phys. Rev. B. 55 (3) 1476-1480 (1997).

31. N. Mandel, J. Donohue, Acta Cryst., B27, 2288 (1971).

32. A. Borshchevsky, J.-P. Fleurial, C.E. Allevato, and T. Caillat, , *Proc. 13th Intl. Conf. on Thermoelectrics*, AIP Press No. 316, 3-6, Kansas City, MO (1994).

33. A. Borshchevsky, J.-P. Fleurial, and T. Caillat, *Proceedings, 15th International Conference on Thermoelectrics,* ed. T. Caillat (IEEE Catalog 96TH8169), p. 112 (1996).

34. T. Caillat, A. Borshchevsky, and J.-P. Fleurial, J.-P., *Proc. 13th Intl. Conf. on Thermoelectrics*, AIP Press No. 316, 31-34, Kansas City, MO (1994).

35. T. Caillat, A. Borshchevsky, and J.-P. Fleurial, J. Appl. Phys. 80 (8) 4442-4449 (1996).

36. J. Ackermann and A. Wold, J. Phys. Chem. Solids, 38, 1013 (1977).

37. G.S. Nolas, G.A. Slack, T. Caillat and G.P. Meisner, J. Appl. Phys. 79 (5) 2622-2626 (1996).

38. J.L. Feldman and D.J. Singh, Phys. Rev. B, 53 (10), 6273-6282 (1996).

39. D.J. Singh and W.E. Pickett, Phys. Rev. B, 50 (11), 235 (1994).

40. M. Llunell. P. Alemany, S. Alvarez and V. P. Zhukov, Phys. Rev. B, 53 (16), 10605-10609 (1996).

41. D.T. Morelli, T. Caillat, J.-P. Fleurial, A. Borshchevsky, J. Vandersande, B. Chen and C. Uher, Phys. Rev. B, 51 (15), 9622-9628 (1995).

42. J. P. Dismukes, L. Ekström, E. F. Steigmeier, I., Kudman, and D. S. Beers, J. Appl. Phys., vol. 35, p. 2899 (1964).

43. G. A. Slack, J.-P. Fleurial, and T. Caillat, Naval Research Reviews, Vol. XLVIII, 23-30 (1996).

44. G.S. Nolas, V.G. Harris, T.M. Tritt and G.A. Slack, J. Appl. Phys. 80 (11) 6304-6308 (1996).

45. L. Nordstrom and D.J. Singh, Phys. Rev. B, 53 (3), 9622-9628 (1996).

46. G. A. Slack, Thermoelectric Handbook, ed. by M. Rowe (Chemical Rubber, Boca Raton, FL), p. 407 (1995).

47. D.T. Morelli and G.P. Meisner, J. Applied Physics 77, 3777 (1995)

48. G. S. Nolas, G. A. Slack, T. M. Tritt, and D. T. Morelli, J. Applied Physics 79 (8) 4002-4008 (1996).

49. T. M. Tritt, G. S. Nolas, G. A. Slack, A.C. Ehrlich, D.J. Gillespie and J.L. Cohn ,J. Applied Physics 79 (11) 8412-8418 (1996).

50. D.T. Morelli, private communication.

51. D.J. Singh, private communication.

Low Dimensional Thermoelectrics

M. S. Dresselhaus
Department of Electrical Engineering and Computer Science, Massachusetts Institute of Technology, Cambridge MA 02139-4307

T. Koga
Division of Engineering and Applied Sciences, Harvard University, Cambridge, MA 02138

X. Sun, S. B. Cronin
Department of Physics, Massachusetts Institute of Technology, Cambridge MA 02139-4307

K.L. Wang and G. Chen
School of Engineering, University of California, Los Angeles, CA 90024

ABSTRACT

Enhanced ZT has been predicted theoretically for low dimensional electronic systems under appropriate experimental conditions. Enhanced ZT has been observed experimentally within 2D quantum wells of PbTe, and good agreement between theory and experiment has been obtained. The advantages of low dimensional systems for thermoelectric applications are described, and prospects for further enhancement of ZT are discussed.

INTRODUCTION

The usefulness of thermoelectric materials for refrigeration or power generation applications is typically expressed by the dimensionless quantity ZT where T is the temperature (in degrees Kelvin) and Z is the thermoelectric figure of merit

$$Z = \frac{S^2\sigma}{\kappa}. \qquad (1)$$

Here S is the thermoelectric power or Seebeck coefficient, σ is the electrical conductivity and κ is the thermal conductivity. Clearly high ZT requires high S, high σ, and low κ. Since an increase in S normally implies a decrease in σ because of carrier density considerations, and since an increase in σ implies an increase in the electronic contribution to κ as given by the Wiedemann–Franz law, it is very difficult to increase Z in typical thermoelectric materials. The best commercial 3D thermoelectric material is in the $Bi_{2(1-x)}Sb_{2x}Te_{3(1-y)}Se_{3y}$ family with room temperature $ZT \approx 1$ for $Bi_{0.5}Sb_{1.5}Te_3$.[1] It is generally considered that only incremental improvements in the ZT of this system are possible. For this reason, efforts are being expended in the identification of new families of materials with a high density of states at the Fermi level[2–4] and with cage-like structures partially occupied by constituent rattling atoms to reduce the lattice thermal conductivity.[5,6] This approach appears to be promising, and values of $ZT \simeq 1.4$ have been achieved in $CeFe_4Sb_{12}$ at $T = 900\,K$.[7]

Reduced dimensionality [as occurs in quantum wells (2D) or quantum wires (1D)] offers another strategy for enhancing ZT,[8,9] because of (1) enhancement of the density of states near E_F leading to an enhancement of the Seebeck coefficient, (2) increased carrier mobilities at a given carrier concentration due to quantum confinement, modulation doping and δ-doping phenomena, (3) opportunities to take advantage of the anisotropic Fermi surfaces in multi-valley semiconductors, (4) increased boundary scattering of phonons at the barrier-well interfaces, while effectively preserving carrier mobilities by exploiting the different length scales for phonon and electron scattering, and (5) the different temperature dependences of the transport properties and intrinsic carrier excitations in low dimensional systems relative to 3D systems. The dependence of the S, σ, κ, on quantum well thickness is, of course, the principal method for enhancing ZT, both through quantum confinement effects and reduced thermal conductivity due to interface scattering.[8,10–13]

Calculations based on the simplest possible model for a quantum confined two-dimensional (2D) electron gas,[8] and described in the next section, indicate that it should be possible to obtain significant enhancement in ZT for a good thermoelectric material when prepared as a 2D quantum well. Specific calculated results for ZT vs quantum well width d_W are shown in Fig. 1 for a Bi_2Te_3 quantum well. Even greater enhancement in ZT is predicted for Bi_2Te_3 when prepared as a 1D quantum wire.[10,14]

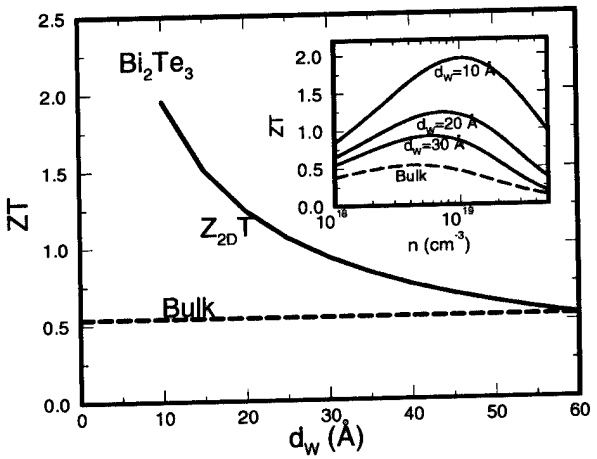


FIG. 1. Dependence of ZT on the width of the quantum well for a Bi_2Te_3-like material at the optimum doping level for transport in the highest mobility direction. The inset shows the dependence of ZT on carrier concentration n, and demonstrates that the optimum carrier density depends on the given quantum well width.

0-7803-4057-4/97 $10.00 ©1997 IEEE

The results of Fig. 1 suggest that a good thermoelectric material in 3D might be expected to exhibit even higher ZT values in reduced dimensions. It is shown in Fig. 1 that for any quantum well width d_W, it is important to optimize the electro-chemical potential ζ in order to maximize ZT. The calculations for Bi_2Te_3 indicate that this optimization of ζ leads to an optimization of the carrier doping level, and the inset to Fig. 1 shows that the optimum carrier density for n-type (111) PbTe quantum wells increases with decreasing d_W.

Furthermore, as discussed below, some materials which are not favorable for high ZT in 3D may exhibit high ZT in 2D.[15] However, the confinement lengths required for enhanced ZT are quite small for a Bi_2Te_3-like material (see Fig. 1) especially in comparison to the lattice constant which is $\approx$10 Å in the c-direction. Thus, it may not be possible to realize such an enhancement in ZT for Bi_2Te_3 quantum wells experimentally for both materials science issues (pertaining to interface integrity) and physics-related issues (pertaining to quantum confinement and the applicability of band theory models) in the limit of very small d_W. Since the solutions of the Schrödinger equation for a particle in a box $E_n = \hbar^2\pi^2 n/(2m^* d_W^2)$ scale with quantum well width d_W, similar enhancements of ZT would be expected to occur at larger quantum well widths for materials with light effective mass components in the direction of quantum confinement. We show below that this concept is correct.

In this paper we discuss very simple theoretical models that show enhancement of ZT in 2D quantum wells, experimental proof-of-principle of the enhanced ZT in n-type PbTe quantum wells, advantages of quantum well structures for achieving enhanced ZT more generally, approaches for modeling the thermal conductivity in calculations for ZT, strategies for using temperature dependent phenomena to increase ZT in quantum wells, and finally the advantages of bismuth as a low dimensional thermoelectric material.

THEORETICAL MODELING

In the simplest model for thermoelectricity in 2D quantum well structures, it is assumed that the electrons in the valence and conduction bands are in simple parabolic energy bands and that the electrons occupy only the lowest (n=1) sub-band of the quantum well. The electronic dispersion relations are then given by

$$\mathcal{E}(k_x, k_y) = \frac{\hbar^2 k_x^2}{2m_x} + \frac{\hbar^2 k_y^2}{2m_y} + \frac{\hbar^2 \pi^2}{2m_z d_W^2}, \qquad (2)$$

where d_W is the width of the quantum well, and m_x, m_y, and m_z are the effective mass tensor components of the constant energy surfaces. It is further assumed that the current flows in the x direction and that quantum confinement is in the z direction. Solution of Boltzmann's equation for S, σ, and κ_e (the electronic contribution to the thermal conductivity) then yields[8] the following expression for the dimensionless figure of merit in 2D

$$Z_{2D}T = \frac{\left(\frac{2F_1}{F_0} - \zeta^*\right)^2 F_0}{\frac{1}{B_{2D}} + 3F_2 - \frac{4F_1^2}{F_0}}, \qquad (3)$$

where the Fermi–Dirac related function F_i is given by

$$F_i = F_i(\zeta^*) = \int_0^\infty \frac{\xi^i \, d\xi}{e^{(\xi - \zeta^*)} + 1}, \qquad (4)$$

and $\zeta^* = \zeta/k_BT$ is the reduced chemical potential relative to the edge of the first sub-band. The expression for B_{2D} in Eq. (3) is sensitive to the materials properties of the quantum well, and B_{2D} is given by

$$B_{2D} = \frac{1}{2\pi d_W}\left(\frac{2k_BT}{\hbar^2}\right)\frac{k_B^2 T (m_x m_y)^{1/2}\mu_x}{e\kappa_{ph}}, \qquad (5)$$

where μ_x is the carrier mobility for current flow in the x direction and κ_{ph} is the phonon contribution to the thermal conductivity. Equation 5 shows that B_{2D} (and therefore $Z_{2D}T$) is increased by increasing the effective mass components m_x and m_y, by increasing the carrier mobility in the direction of current flow, and by decreasing the quantum well width d_W as much as possible, as discussed below.

The results for Z_{2D} in a quantum well are to be contrasted to the corresponding 3D results:[8,14]

$$Z_{3D}T = \frac{\frac{3}{2}\left(\frac{5F_{3/2}}{3F_{1/2}} - \zeta^*\right)^2 F_{1/2}}{\frac{1}{B_{3D}} + \frac{7}{2}F_{5/2} - \frac{25F_{3/2}^2}{6F_{1/2}}}, \qquad (6)$$

where B_{3D} in Eq. (6) is given by

$$B_{3D} = \frac{1}{3\pi^2}\left(\frac{2k_BT}{\hbar^2}\right)^{3/2}\frac{k_B^2 T (m_x m_y m_z)^{1/2}\mu_x}{e\kappa_{ph}}, \qquad (7)$$

so that for bulk thermoelectrics, it is desirable to have all the mass components and the carrier mobility as large as possible.

To obtain explicit results for $Z_{2D}T$, a model for the phonon contribution to the thermal conductivity κ_{ph} is needed. Three approaches are discussed in this paper: (1) κ_{ph} is conservatively approximated using 3D experimental data; (2) κ_{ph} is taken from 3D experimental data for the phonon mean free path $\ell < d_W$, while $\ell = d_W$ is used in the expression $\kappa_{ph} = C_v v\ell/3$ for $\ell > d_W$, where C_v and v are respectively the heat capacity and the velocity of sound; (3) κ_{ph} is obtained from a more detailed treatment of the scattering of phonons by the interface between the quantum wells and the barriers.

The expressions for Z_{3D} and Z_{2D} both depend on the electrochemical potential ζ, and therefore on the carrier concentration, which can be controlled experimentally to achieve the maximum ZT for each thermoelectric material at the desired temperature of operation, and at the desired quantum well thickness (see inset to Fig. 1). The quantities B_{3D} and B_{2D} are particularly sensitive to the electronic structure and to the sample quality of each thermoelectric material. In the next section, we review the observation of enhanced Z_{2D} in n-type PbTe quantum wells.

EXPERIMENTAL PROOF-OF-PRINCIPLE

PbTe was chosen as the quantum well for demonstrating proof-of-principle of enhanced ZT in a 2D system because of its desirable thermoelectric and materials science properties. Regarding its thermoelectric properties, PbTe has a reasonably high room temperature ZT in bulk form ($ZT \simeq 0.4$), reflecting the high carrier mobility, multiple anisotropic carrier pockets, and low thermal conductivity that can be achieved under isoelectronic alloying. In addition, calculations indicated that carrier confinement and enhanced ZT could be achieved for quantum well widths < 100 Å.[16] It was also known that high mobility quantum well superlattices could be prepared with PbTe as the quantum well material and $Pb_{1-x}Eu_xTe$ as the barrier material,[17,18] with well controlled and stable interfaces, using epitaxial growth techniques, such as molecular beam epitaxy. Good lattice matching and similar thermal expansion coefficients[19] across the interfaces permitted the preparation of PbTe/PbEuTe superlattices with ~100 superlattice periods.[20] Experiments by Harman[20] indicated that Bi could be introduced into the $Pb_{0.927}Eu_{0.073}Te$ barrier region, yielding quantum wells with carrier concentrations $> 10^{19}$ electrons/cm^3 within the quantum well. These experiments further indicated that the Hall mobility in the quantum wells would be comparable to and in some cases better than that in the best 3D films prepared with a comparable doping level in the same apparatus.[20] Measurements by Hicks *et al.*[14] corroborated that quantum confinement could be achieved for $x = 0.073$, where the band offsets for the conduction and valence bands were calculated to be 171 meV and 140 meV, respectively, for a band gap of 630 meV in the barrier regions and 319 meV in the quantum wells at 300 K.[17] The band gap in the barrier region is found from infrared measurements to be 630 meV, while the band offset of 171 meV was found from analysis of optical data[17] and the bandgap in the quantum well region is from the literature.

Experimental results for the quantity S^2n on a number of n-type PbTe quantum wells for a variety of quantum well widths from 17 Å to 55 Å are given as points in Fig. 2(a) as a function of quantum well width (or equivalently the thickness d_W), and in Fig. 2(b) as a function of doping level (as determined from Hall effect measurements). Using the value for the Hall mobility $\mu_{\rm Hall} = 1400$ cm^2/Vs for n-type carriers in PbTe, a value of the power factor $S^2\sigma$ was obtained as a function of quantum well width d_W at the optimum doping level. The solid curves in Figs. 2(a) and (b) were obtained with no adjustable parameters using the envelope function approximation to calculate the bound states and using literature values for the electronic band parameters and other physical properties of PbTe.[17] Enhancement of the power factor in the 2D PbTe quantum wells by a factor of 3–4 over 3D bulk values was thus demonstrated in n-type PbTe. The experimental data in Fig. 2 clearly shows that a greater enhancement in S^2n is achieved with decreasing quantum well widths, at least for quantum wells down to ~20 Å. The bound states in the quantum wells that were used to calculate the curves in Fig. 2 were all obtained by applying the general theoretical model described in this paper to the specific material PbTe, using literature values for the parameters for the 2D electronic band structure for PbTe quantum wells.[16] Proof-of-principle for enhanced ZT in 2D quantum wells is provided by the good fit of the experimental points to the calculated curves in Fig. 2. Further corroboration is provided by the good agreement between the infrared transmission measurements and the calculated bound state energies as shown in Fig. 3.[16] From the solid curves in Fig. 2(b), the optimum carrier concentration as a function of quantum well thickness can be inferred. The results show that the optimum doping concentrations increase with decreasing quantum well widths d_W for n-type PbTe, consistent with the results in Fig. 1 for Bi_2Te_3. The best room temperature values that were obtained for the n-type PbTe quantum wells are a power factor of 130 μW/cmK^2 and a thermoelectric figure of merit of $Z_{2D}T = 1.2$.

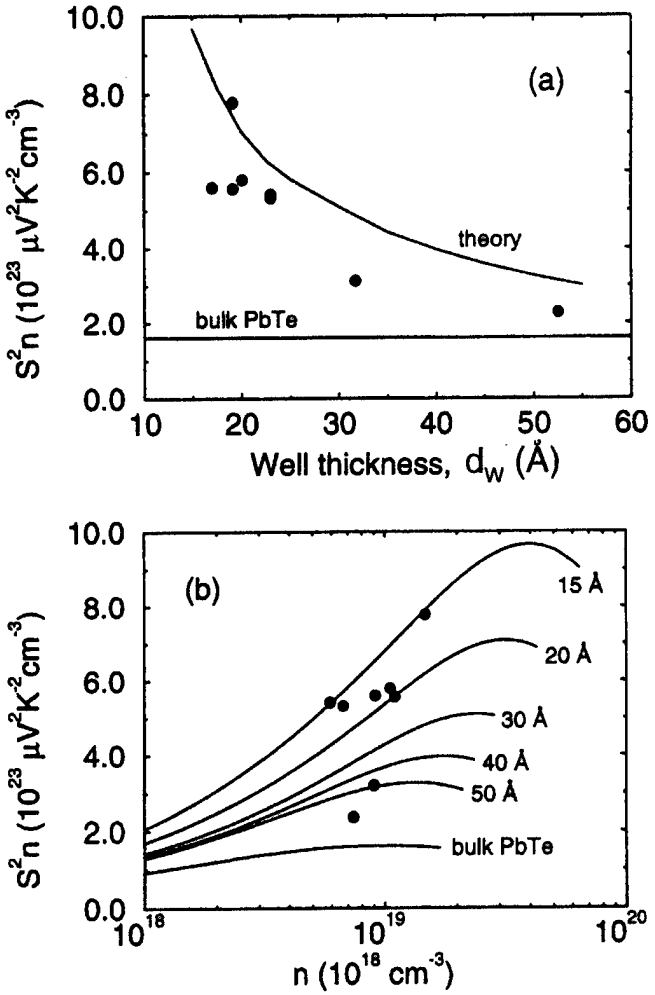


FIG. 2. (a) S^2n results for n-type (Bi-doped) PbTe/$Pb_{0.927}Eu_{0.073}Te$ MQWs (full circles) as a function of quantum well thickness d_W at 300 K. For comparison, the best experimental bulk PbTe value for S^2n is also shown. Calculated results for optimum doping are shown as a solid line. (b) S^2n results for the same PbTe/$Pb_{0.927}Eu_{0.073}Te$ MQW sample (full circles) as a function of carrier density n at 300 K. Calculated results for different indicated well thicknesses are shown as solid curves.[16]

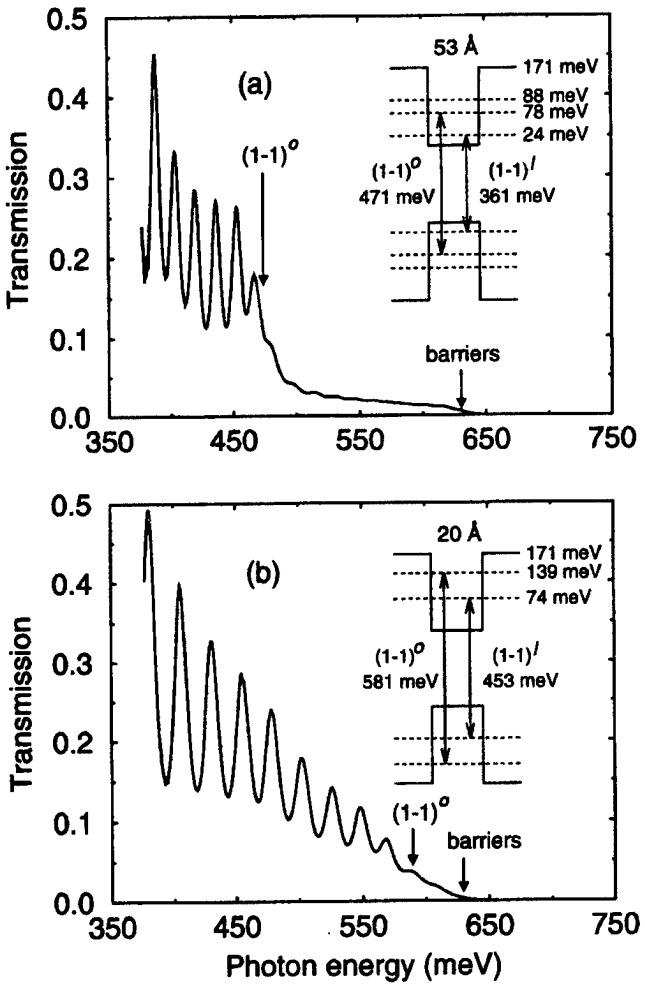


FIG. 3. Optical transmission vs photon energy at 300 K for (a) a PbTe/$Pb_{1-x}Eu_xTe$ ($x = 0.073$) MQW sample with a 53-Å well and a 560-Å barrier and (b) a MQW sample with a 20-Å well and a 430-Å barrier. Insets show the results of EFA calculations of the quantum well energy levels and the interband transition energies.[16] The superscripts o and l refer to the oblique and longitudinal subbands associated with the two carrier types shown in the inset to Fig. 4.

ADVANTAGES OF QUANTUM WELLS FOR ACHIEVING HIGH ZT

Having demonstrated enhancement of ZT in quantum wells of a specific material, we would now like to review the advantages of 2D quantum wells over bulk materials from a more general vantage point, in the hope of identifying other materials systems that might be even more favorable than PbTe for low dimensional thermoelectric applications. Calculations carried out on other materials suggest that $Si/Si_{1-x}Ge_x$, $Bi_{1-x}Sb_x$, $Bi_{2(1-x)}Sb_{2x}Te_{3(1-y)}Se_{3y}$, and p-type PbTe are all favorable quantum well materials for enhanced 2D thermoelectric performance. Our theoretical model suggests that if a material is a good thermoelectric in 3D, it should be even better in 2D, and still better in 1D, although greater enhancement through reduced dimensionality is possible for some materials systems than for others.

Quantum confinement associated with a quantum well system is expected to give rise to an increase in the magnitude of the Seebeck coefficient $|S|$ for the same carrier density, with the increased $|S|$ arising from an increase in the density of electron states at the Fermi level for the 2D electron gas. Experimental evidence for the enhancement of $|S|$ for n-type PbTe quantum wells is found in Fig. 4, which shows a significant enhancement in $|S|$ for quantum wells of about 20 Å well widths, while the larger 40 Å n-type PbTe quantum wells show about the same $|S|$ as bulk samples of the same carrier concentrations (see also Fig. 2). It should be noted that the entire contribution to the Seebeck coefficient for the whole sample comes from the quantum wells, since the barrier regions make no contribution to $|S|$.

Also shown in Fig. 4 is the projection of the electron carrier pockets for (111) n-type PbTe. The high Seebeck coefficient for the PbTe quantum wells is attributed to the relatively high density of states for carriers in the oblique carrier pockets shown in the inset to the figure.

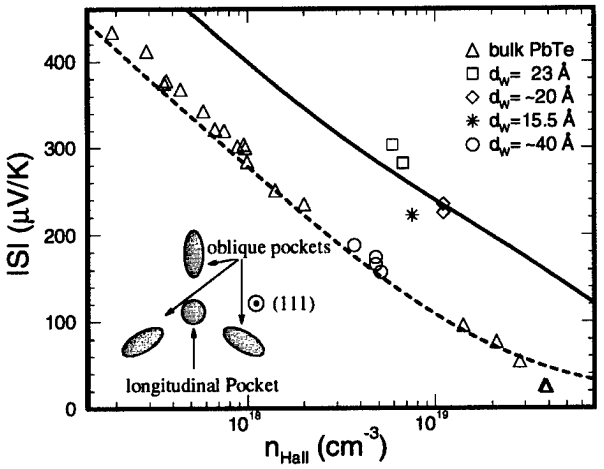


FIG. 4. Dependence of the absolute value of the room temperature Seebeck coefficient S on carrier concentration in n-type PbTe for bulk samples (open triangles) and quantum wells with various widths d_W as indicated. For n-type semiconductors, S is negative so that S decreases in magnitude for increasing carrier concentration n. The inset shows the projection of the electron carrier pockets on a plane normal to the (111) growth direction.

The theoretical analysis given above shows that increased carrier mobility leads to higher ZT values in all cases (3D, 2D and 1D). Experimentally, enhancement in the carrier mobility relative to bulk values can be achieved using the attributes of low dimensional systems, including quantum confinement, modulation doping and δ-doping techniques. In this way the dopants can be introduced into the barrier regions, far from the quantum wells where the carriers are located, thereby greatly reducing the carrier scattering by the impurity dopant ions that are responsible for the carrier generation. This advantage of 2D quantum well systems should be of particular importance at low temperature where electron-phonon scattering is less important and impurity scattering tends to be the dominant scattering mechanism. Figure 5 shows that the additional carrier scattering at the interfaces between the quantum wells and barriers is

more than compensated by the beneficial effects of carrier confinement and modulation doping,[20] so that the carrier mobility in the quantum well tends to increase as the quantum well width decreases to 19 Å, for which the highest mobilities were observed experimentally.[20] A number of experimental and theoretical studies have been carried out to show that the quantum well/barrier interfaces can significantly increase the phonon-phonon scattering.[21] It is generally believed that the interface is more effective in scattering phonons than in electron scattering because of the different length scales that are involved in these scattering processes. However, systematic studies to simultaneously measure the thermal conductivity and carrier mobility are needed to study this phenomenon in detail.

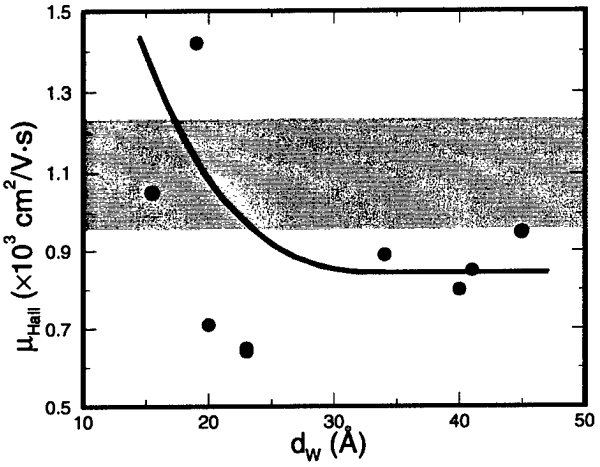


FIG. 5. Hall carrier mobility μ_{Hall} as a function of the quantum well width d_W for PbTe/$Pb_{1-x}Eu_xTe$ MQWs (closed circles). The data are taken from Ref. [20]. The shaded region indicates the range of carrier mobilities for similarly grown bulk PbTe for comparison. The solid line is a guide to the eye.

A third advantage of the 2D aspects of quantum wells is the exploitation of the anisotropy of the constant energy surfaces of typical multi-valleyed semiconductors. For 3D systems, the k-space anisotropic effects of the various ellipsoidal carrier pockets tend to cancel when summing over the contributions from all the ellipsoids to the transport properties of a multi-valleyed cubic semiconductor, such as PbTe or Si. However, the symmetry-lowering introduced by the quantum well superlattice periodicity allows the possibility of better exploiting the anisotropy of the individual ellipsoidal carrier pockets.[22] This anisotropy is illustrated in the inset to Fig. 4. The contributions to the power factor from the four carrier pockets for n-type PbTe are equivalent in 3D but not in 2D where the 2D Fermi surface is projected in the (111) direction to give one longitudinal (circular) pocket and three oblique (elliptical) constant energy surfaces, as shown in the inset to Fig. 4. The thermoelectric properties of (111) PbTe multiple quantum wells are dominated by the three elliptical carrier pockets which have higher density of states masses ($m^* = 0.308m_0$) than the longitudinal carrier pocket, $m^* = 0.0334m_0$ [see Eq. (5)]. Semiconductors with favorable low dimensional thermoelectric properties should have (1) a large number of equivalent carrier pockets, (2) highly anisotropic constant energy surfaces, and (3) high carrier mobilities. In selecting the superlattice growth direction, attention should be given to maximizing the effect of the anisotropic Fermi surface toward enhancing ZT. For example, theoretical predictions[23] indicate that n-type PbTe superlattices grown along the (001) direction should have an even higher Seebeck coefficient and ZT than for the case of (111) n-type PbTe quantum wells.

Isoelectronic alloying, which is commonly used in 3D thermoelectric systems to reduce the phonon contribution to the thermal conductivity, can also be used effectively in quantum well superlattices, both in the quantum well regions and in the barrier regions. In addition, it may be possible to use δ-doping with appropriate species both as a source for carriers and as a method to effectively increase the band gap of the barrier region. For example δ-doping with carbon or with SiC ($E_g = 2.9$ eV) within the $Si_{1-x}Ge_x$ barrier region of a $Si/Si_{1-x}Ge_x$ superlattice could be used to effectively increase the band gap within the barrier region, so that smaller barrier widths would be needed for quantum confinement.[24] The δ-doping approach thus could lead to reduced κ for the superlattice thermoelectric material due to both a reduction in the barrier widths and increased phonon scattering at the SiC interfaces within the barrier region.

In addition to the advantages of 2D quantum well thermoelectrics mentioned in this section, there are a variety of temperature-dependent effects where quantum wells offer additional advantages, as discussed below.

THERMAL CONDUCTIVITY MODELS

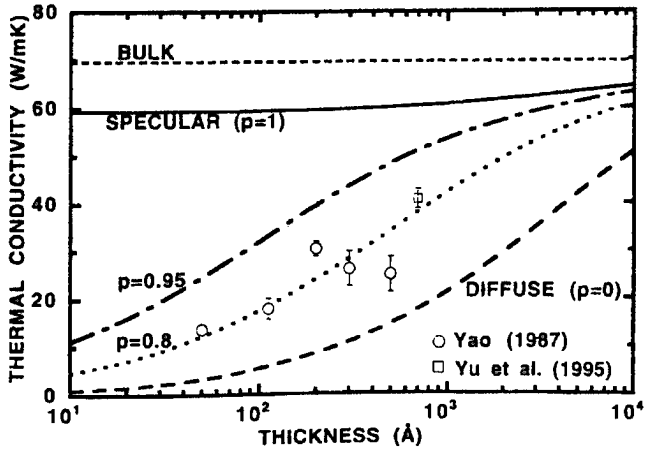


FIG. 6. Room temperature thermal conductivity as a function of the layer thickness for GaAs/AlAs MQWs superlattices, assuming equal layer thicknesses for the quantum well (GaAs) and the barrier (AlAs).[21]

Thus far, many of the models for the thermoelectric figure of merit of multi-quantum well superlattices have focussed on either the power factor $S^2\sigma$ with simplistic treatments given for the lattice contribution κ_{ph} to the thermal conductivity.[10,15,16] The electronic contribution κ_e to the thermal conductivity is conventionally modeled in terms of the Wiedemann–Franz law

$$\kappa_e = L_0 \sigma T \tag{8}$$

where the electrical conductivity σ for MQWs is generally available from experimental data, and the Lorenz number $L_{0\,(2D)}$ for 2D systems is found from the Boltzmann equation to be

$$\kappa_e = L_{0\,(2D)} = \left(\frac{k_B}{e}\right)^2 \left(\frac{3F_2(\zeta^*)}{F_0(\zeta^*)} - \frac{4F_1(\zeta^*)^2}{F_0(\zeta^*)^2}\right), \tag{9}$$

in which the Fermi–Dirac integral function $F_i(\zeta^*)$ is given by Eq. (4) and $L_{0\,(2D)}$ is dependent on the reduced electrochemical potential ζ^*. For many thermoelectric materials $L_{0\,(2D)}$ may be significantly lower than the value of 2.45×10^{-8} WΩ/K^2 conventionally used for metals and degenerate semiconductors, and for some semiconducting thermoelectric materials $L_{0\,(2D)}$ could be reduced from this value by as much as 50% or even more, due to nonparabolicity of the energy bands and to the details of the carrier scattering mechanism.

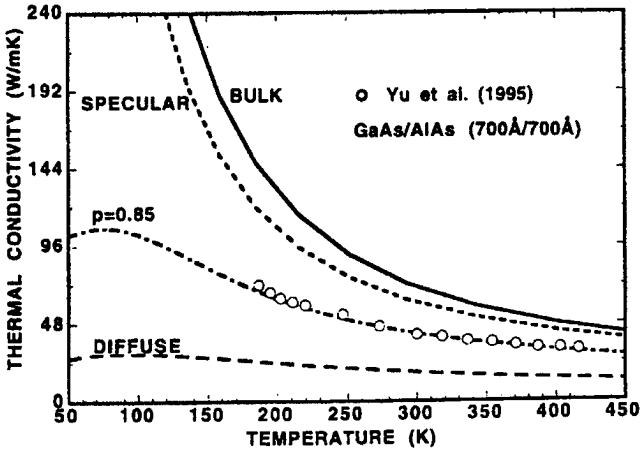


FIG. 7. Thermal conductivity as a function of temperature for a GaAs/AlAs MQWs structure.[21]

Regarding the lattice contribution to the thermal conductivity, two simplistic models have been employed for the case of n-type PbTe MQWs. In the first approach, $\kappa_{\rm ph}$ is approximated by the 3D bulk value, $\kappa_{\rm ph} = \kappa_B$, which overestimates $\kappa_{\rm ph}$ because of the neglect of the interface scattering between the quantum wells and the barriers. In the second approach, $\kappa_{\rm ph}$ is assumed to be equal to κ_B when the phonon mean free path ℓ is smaller than the quantum well width d_W, but $\kappa_{\rm ph}$ is approximated by $\kappa_{\rm ph} = C_v v d_W/3$ when $\ell > d_W$ and where C_v and v are, respectively, the heat capacity at constant volume and the velocity of sound. The second approach was used for example to construct Fig. 1. A third more quantitative approach would incorporate the actual phonon distribution present in PbTe and would consider the detailed scattering mechanisms for each of the phonon branches. Such a detailed treatment for $\kappa_{\rm ph}$ is not yet available for PbTe or any other quantum well system for which thermoelectric data are available, though progress has been made in this direction.[11,25] The availability of such a more detailed model for $\kappa_{\rm ph}$ would allow the procedures, used to optimize the thermoelectric performance of 2D quantum well superlattices, to focus on the optimization of $(ZT)_{SL}$, the figure of merit of the whole superlattice directly rather than the optimization of the power factor $S^2\sigma$.

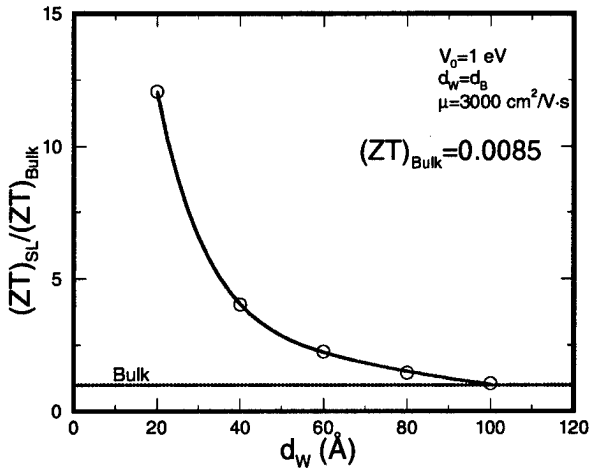


FIG. 8. Plot of the ratio of ZT for the GaAs/AlAs Γ-point multi-quantum well superlattice normalized to that of bulk GaAs, using values of $V_0 = 1$eV and $\mu = 3000$ cm^2/Vsec for the band offset and electron mobility in the MQW system, respectively, and equal values of the quantum well (d_W) and barrier (d_B) widths.

On the other hand, detailed thermal conductivity modeling has been carried out in the case of GaAs/AlAs MQWs where the quantum well thickness (GaAs) was assumed to be equal to that for the barrier material (AlAs).[21] Calculations of the thermal conductivity as a function of d_W are shown in Fig. 6, where it is seen that interface scattering is important, especially for interfaces with a significant amount of diffuse phonon scattering which is characterized by the parameter p. The experimental data for the thermal conductivity of GaAs/AlAs MQWs are fit[21] with $p = 0.85$, where $p = 1$ refers to specular scattering, while $p = 0$ denotes totally diffuse scattering. For $p = 0.85$, the calculations show that, for $d_W < 30$Å, $\kappa_{\rm ph}$ drops below the thermal conductivity of 9 W/mK for an $(GaAs)_{1-x}(AlAs)_x$ alloy with $x = 0.5$. Figure 7 shows that the effect of phonon interface scattering is more important as the temperature is lowered below room temperature and interface scattering becomes less important with increasing temperature above room temperature. It is of interest to note that fits to the experimental quantum well thickness dependence data of Fig. 6 and to the temperature dependence data of Fig. 7 yield the same value of p.

With the availability of the data for $\kappa_{\rm ph}$ as a function of d_W in Fig. 6 for GaAs/AlAs MQW structures, the simplest possible model was constructed for the power factor $S^2\sigma$ for GaAs/AlAs Γ-point quantum wells, using the formulae given in Eqs. (2) – (5) and the assumption $d_W = d_B$, consistent with the assumption used for the thermal conductivity plot of Fig. 6. Values of $V_0 = 1$eV and $\mu = 3000$ cm^2/Vsec were taken for the band offset and the room temperature carrier mobility, respectively, for the MQW GaAs/AlAs system and the results for the whole superlattice $(ZT)_{SL} = S^2\sigma T/\kappa$ normalized to the

bulk value $(ZT)_{\text{bulk}}$ are shown in Fig. 8 as a function of d_W. The calculated results for $(ZT)_{SL}/(ZT)_{\text{bulk}}$ in Fig. 8 are qualitatively similar to the model calculations shown in Fig. 1 and to published curves for other quantum well systems, such as Bi[15] and Si.[22,24] The curve for the MQW superlattice in Fig. 8, however, characteristically shows a smoother and more gradual increase in the magnitude of ZT below ~50Å than was obtained by the crude models previously used for κ_{ph} in MQW systems. Extending these more realistic models for κ_{ph} to PbTe and to other materials where thermoelectric data are now becoming available will be a high priority project for the near future.

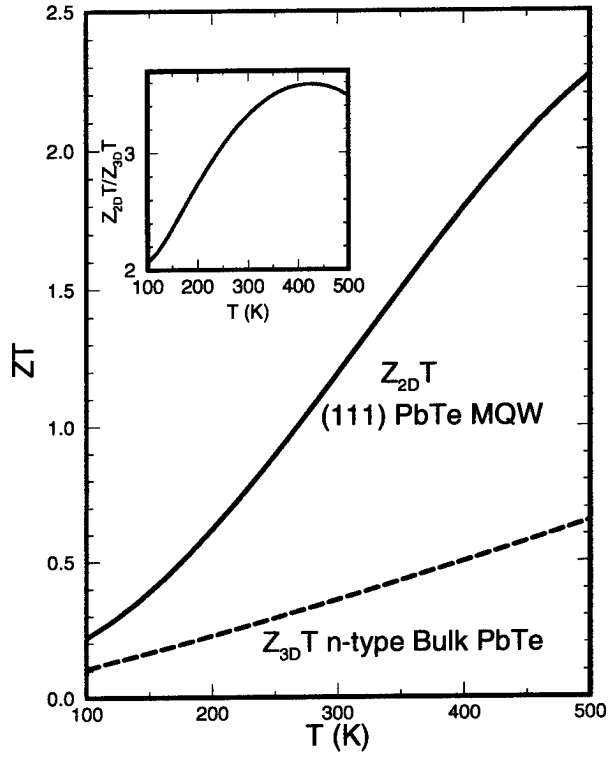


FIG. 9. Theoretical estimation of $Z_{2D}T$ as a function of T (using temperature-dependent band parameters) for the best n-type PbTe quantum well sample in Ref.[20]. The calculation is based on a two-band model which includes temperature dependent bound state levels for longitudinal and oblique subbands and temperature-dependent band parameters (see inset to Fig. 3).[16] For comparison, we show a calculation for the temperature dependence of ZT for a bulk sample. The inset shows a plot of the ratio Z_{2D}/Z_{3D} as a function of temperature.

TEMPERATURE DEPENDENCE

Since all of the transport properties (e.g., S, σ, κ) have different temperature dependences in 2D and 3D, differences in the temperature dependence of ZT are expected for low dimensional systems. For typical thermoelectric materials, ZT tends to increase with increasing temperature in the extrinsic carrier density range. The lower value of ν in the temperature dependence of the carrier mobility $\mu \sim T^{-\nu}$ the greater the increase in ZT with T. Because of differences in the scattering mechanisms in quantum wells, ν tends to be lower in quantum wells than in bulk materials. These effects need to be studied systematically in low dimensional systems at high doping levels characteristic of thermoelectric materials.

Once temperatures are reached where thermal carrier generation becomes significant, the approximate cancellation between the thermally excited electron and hole carrier contributions to the Seebeck coefficient S leads to a reduction in ZT as a function of temperature. Thus $(ZT)_{\text{max}}$ occurs at higher temperatures for wider gap (E_g) semiconductors, since intrinsic carrier excitation begins to occur at higher T as E_g increases. Bulk materials exhibiting an increase in E_g with increasing T (such as PbTe) will tend to push $(ZT)_{\text{max}}$ to higher temperatures, thereby increasing the maximum value of ZT that can be reached. On the other hand, materials (such as Si and GaAs), where E_g decreases with increasing T, the opposite effect is expected. Thermal diffusion across the quantum well-barrier interfaces will become important with increasing T, and this effect will limit the temperature range where quantum wells can be used for practical thermoelectric applications.

Quantum well thermoelectrics are also of particular interest for low temperature applications, where there are presently no thermoelectrics with high ZT values, though there could be a real need for such materials for the cooling of high T_c superconducting devices. The reduction in carrier-impurity scattering associated with modulation doping and δ-doping could be of particular importance at low temperature for 2D thermoelectrics, for which the carrier concentrations necessary to achieve the optimum doping condition tend to be very high. Since the interface scattering cross-section for phonons would be expected to be less sensitive to temperature than phonon-phonon scattering, this scattering mechanism for the lattice thermal conductivity could be especially important at low temperature where the phonon density is not so high.

Figure 9 shows a model calculation for the temperature dependence of $Z_{2D}T$ for n-type PbTe quantum wells using temperature-dependent band parameters found in the literature.[26] The parameters used in the calculation of $Z_{3D}T$ were for the best available crystalline samples, which correspond to lower carrier concentrations, lower doping levels, and therefore higher mobilities than those used for the quantum well thermoelectric samples. The band parameters used for calculating $Z_{2D}T$ also correspond to the best n-type sample that has been studied at room temperature.[16,20] A temperature dependence of $T^{-2.5}$ was used for the carrier mobility for the 3D case while a somewhat weaker $T^{-2.1}$ was used for the 2D case. The electronic thermal conductivity κ_e was estimated from σ using the Wiedemann–Franz law for both the 2D and 3D samples. A temperature dependence of $\kappa_{\text{ph}} \sim T^{-1}$ was assumed, and the same $\kappa_{\text{ph}}(T)$ data were used for the 3D and 2D cases.

Figure 9 also shows that the calculated $Z_{2D}T$ for n-type (111) PbTe exceeds $Z_{3D}T$ over the entire temperature range from 100 to 500 K and that the ratio

$Z_{2D}T/Z_{3D}T$ shown in the inset also tends to increase with increasing T until about 400 K, where saturation occurs and this is followed by a small decrease in the ratio Z_{2D}/Z_{3D} at yet higher temperatures.

The calculated results indicate that $Z_{2D}T \sim 2$ above 400 K, with further increases in $Z_{2D}T$ expected at higher temperatures. We feel that the approximations used to make the theoretical estimation for $Z_{2D}T$ in Fig. 9 are conservative. Non-parabolic effects, which are not taken into account in our present model, are expected to give further enhancement of $Z_{2D}T$ for elevated temperatures and therefore should yield a further increase in $Z_{2D}T$. Also the effect of electron-electron scattering should be more important in the MQW samples because of the higher carrier concentrations that are generally employed for MQW thermoelectrics relative to bulk thermoelectrics. Such carrier-carrier effects were not taken into account in these calculations, but are expected to have a large effect on reducing $L_{0\,(2D)}$. Such effects will be studied further in future work.

BISMUTH AS A LOW DIMENSIONAL THERMOELECTRIC

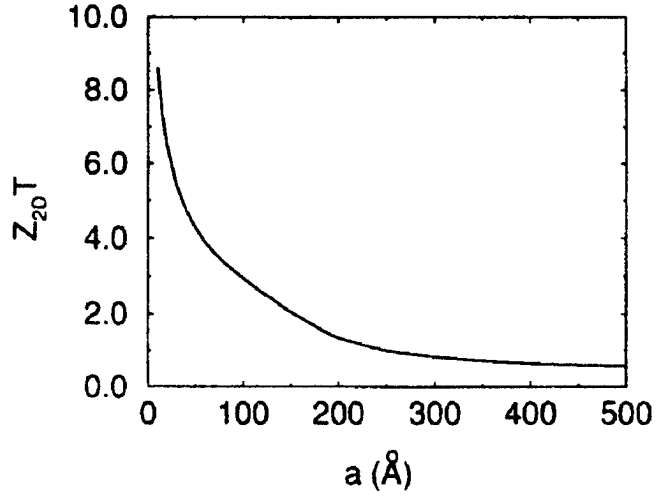


FIG. 10. Dependence of $Z_{2D}T$ on quantum well width a for a Bi well in the highest mobility (binary) direction.[15]

Bismuth is a very attractive material for low dimensional thermoelectricity because of the large anisotropy of the three ellipsoidal constant energy surfaces for electrons at the L point in the rhombohedral Brillouin zone ($m_x^* = 0.00651m_0$, $m_y^* = 1.362m_0$, $m_z^* = 0.00993m_0$), and the high mobility of the carriers ($\mu = 3.5 \times 10^4$ cm^2/Vs for light mass electrons in the binary direction with a carrier density 2×10^{18}/cm^3 at 300 K).[27–29] As the quantum well width decreases, the lowest bound state in the conduction band rises above the highest bound state in the valence band, inducing a semimetal-semiconductor transition. If the 2D bismuth system is then doped to the optimum doping level, a large enhancement in $Z_{2D}T$ is predicted (see Fig. 10) with decreasing quantum well width.[15]. Of particular interest is the observation that the $Z_{2D}T$ enhancement is large for quite large quantum well widths. For example, Fig. 10 predicts a $Z_{2D}T \sim 4$ at room temperature for a 50 Å Bi quantum well. Such quantum well widths should be achievable experimentally, if one could only identify a suitable barrier material.

Bismuth can be alloyed isoelectronically with antimony to yield a high mobility and highly desirable thermoelectric properties. From what is known about the bismuth-antimony phase diagram (Fig. 11), it should be possible to prepare both n-type and p-type $Bi_{1-x}Sb_x$ quantum wells for x in the range $0.09 < x < 0.17$. In this narrow composition range, the lowest conduction band and the highest valence band are both at the L point in the Brillouin zone, and both bands have very similar highly anisotropic constant energy surfaces giving rise to high mobility carriers as well as high density of states effective masses.

Bismuth and $Bi_{1-x}Sb_x$ are highly desirable low dimensional thermoelectric materials because of their large Fermi surface anisotropy, high mobility carriers, very long electron mean free paths, heavy mass ions to effectively scatter phonons to yield low phonon mean free paths, and opportunities to achieve $Z_{2D}T$ enhancement for both n-type and p-type doping. Bi and $Bi_{1-x}Sb_x$, however, have a serious deficiency for 2D quantum well applications because of the unavailability until the present time of a suitable barrier material. Several research groups are now working to identify a suitable barrier material.

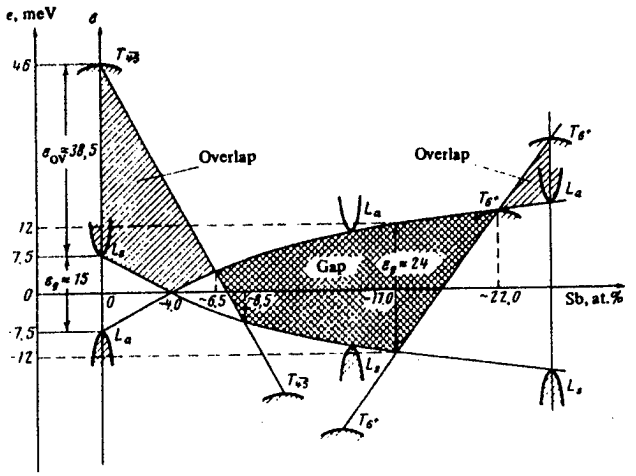


FIG. 11. Bi – Sb phase diagram and the implied electronic structure. The region of the semiconducting alloys is cross hatched.[30,31]

CONCLUSIONS

At present, $Z_{2D}T \sim 1.2$ has been achieved experimentally in n-type PbTe quantum wells at room temperature. On the basis of model calculations, values of $Z_{2D}T > 2$ are expected at higher temperatures. It is likely that high $Z_{2D}T$ values will soon be demonstrated in other quantum well systems. Quantum well systems offer advantages both for low temperature and high temperature thermoelectric performance. However, the utilization of quantum wells in a real thermoelectric material will require much effort to reduce the barrier widths and the

thermal conductivity, and to develop suitable barrier materials for the most promising 2D thermoelectrics. Because of the many trade-off constraints that govern thermoelectric performance, model calculations are especially valuable for optimizing the superlattice and materials parameters to maximize $Z_{2D}T$. The inclusion of more realistic models for the lattice thermal conductivity is expected to increase the reliability of these models significantly in the near future.

ACKNOWLEDGMENTS

The authors would like to thank G. Dresselhaus, T. C. Harman and P. C. Eklund for valuable discussions. The authors gratefully acknowledge support by the US Navy under Contract No. N00167-92-K-0052 (MIT), and ONR under URI (UCLA). Support from the Honda Corporation for temperature dependent studies is gratefully acknowledged.

---

[1] H. J. Goldsmid, *Electronic Refrigeration* (Pion, London, 1986).

[2] G. D. Mahan, Physics Today **March** (1997).

[3] G. D. Mahan. In *Solid State Physics*, edited by H. Ehrenreich and F. Spaepen. Academic Press, 1996.

[4] G. D. Mahan, Proc. Natl. Acad. Sci. USA **93**, 7436–7439 (1996).

[5] G. A. Slack and V. G. Tsoukala, J. Appl. Phys. **76**, 1665 (1994).

[6] G. A. Slack. In *CRC Handbook of Thermoelectrics*, edited by D. M. Rowe, page 407, CRC Press, New York, 1995.

[7] J.-P. Fleurial. In *Proceedings of the 15th IEEE International Conference on Thermoelectrics*, edited by J.-P. Fleurial, Pasadena, CA, 1996. IEEE Catalogue Number 96TH8169.

[8] L. D. Hicks and M. S. Dresselhaus, Phys. Rev. B **47**, 12727–12731 (1993).

[9] L. D. Hicks and M. S. Dresselhaus. In *Semiconductor Heterostructures for Photonic and Electronic Applications: MRS Symposia Proceedings, Boston, volume* **281**, edited by C. W. Tu, D. C. Houghton, and R. T. Tung, page 821, Materials Research Society Press, Pittsburgh, PA, 1993.

[10] L. D. Hicks and M. S. Dresselhaus, Phys. Rev. B **47**, 16631 (1993).

[11] J. O. Sofo and G. D. Mahan, Appl. Phys. Lett. **65**, 2690 (1994).

[12] D. L. Broido and T. L. Reinecke, Phys. Rev. B **51**, 13797 (1995).

[13] D. A. Broido and T. L. Reinecke, Appl. Phys. Lett. **67**, 1170 (1995).

[14] Lyndon D. Hicks. *The effect of quantum-well superlattices on the thermo-electric figure of merit.* PhD thesis, Massachusetts Institute of Technology, June 1996. Department of Physics.

[15] L. D. Hicks, T. C. Harman, and M. S. Dresselhaus, Appl. Phys. Lett. **63**, 3230 (1993).

[16] L. D. Hicks, T. C. Harman, X. Sun, and M. S. Dresselhaus, Phys. Rev. B **53**, R10493–R10496 (1996).

[17] Shu Yuan, H. Krenn, G. Springholz, and G. Bauer, Phys. Rev. B **47**, 7213 (1993).

[18] G. Springholz, G. Ihninger, G. Bauer, M. M. Oliver, J. Z. Pastalan, S. Romaine, and B. B. Goldberg, Appl. Phys. Lett. **63**, 2908 (1993).

[19] G. Springholz and G. Bauer, Appl. Phys. Lett. **62**, 2399 (1993).

[20] T. C. Harman, D. L. Spears, and M. J. Manfra, J. Electron. Mater. **25**, 1121 (1996).

[21] Gang Chen, J. Heat Transf.: Trans. ASME **119**, 220 (1997).

[22] M. S. Dresselhaus, X. Sun, S. B. Cronin, T. Koga, G. Dresselhaus, and K. L. Wang. In *Thermoelectric Materials - New Directions and Approaches: MRS Symposia Proceedings, San Francisco, volume* **478**, edited by T. M. Tritt, M. G. Kanatzidis, H. B. Lyon, Jr., and G. Mahan, page 55, Materials Research Society Press, Pittsburgh, PA, 1997.

[23] T. Koga, S. B. Cronin, T. C. Harman, X. Sun, and M. S. Dresselhaus, (unpublished).

[24] X. Sun, M. S. Dresselhaus, K. L. Wang, and M. O. Tanner. In *Thermoelectric Materials - New Directions and Approaches: MRS Symposia Proceedings, San Francisco, volume* **478**, edited by T. M. Tritt, M. G. Kanatzidis, H. B. Lyon, Jr., and G. Mahan, page 169, Materials Research Society Press, Pittsburgh, PA, 1997.

[25] D. A. Broido and T. L. Reinecke, Appl. Phys. Lett. **70**, 2834 (1997).

[26] R. Dornhaus, G. Nimtz, and B. Schlicht, *Narrow-Gap Semiconductors* (Springer-Verlag, Berlin, 1985). Springer Tracts in Modern Physics, Volume 98.

[27] R. T. Isaacson and G. A. Williams, Phys. Rev. **185**, 682 (1969).

[28] M. S. Dresselhaus. In *Proceedings of the Conference on the Physics of Semimetals and Narrow Gap Semiconductors*, edited by D. L. Carter and R. T. Bate, page 3, Pergamon Press, New York, NY, 1970.

[29] W. M. Yim and A. Amith, Solid State Electronics **15**, 1141–1165 (1972).

[30] N. B. Brandt, S. M. Chudinov, and V. G. Karavaev, Sov. Phys. JETP **34**, 368 (1972).

[31] J. S. Lannin, Phys. Rev. B **19**, 2390 (1979).

Rare Earth Thermoelectrics

G.D. Mahan
Department of Physics and Astronomy
University of Tennessee, Knoxville, TN 37996-1200, and
Solid State Division, Oak Ridge National Laboratory
Oak Ridge, TN 37831-6030

Abstract

We review the thermoelectric properties of metallic compounds which contain rare-earth atoms. They are the group of metals with the largest value ever reported of the Seebeck coefficient. An increase by 50% of the Seebeck would make these compounds useful for thermoelectric devices. The largest Seebeck coefficient is found for compounds of cerium (e.g., $CePd_3$) and ytterbium (e.g., $YbAl_3$). Theoretical predictions are in agreement with the maximum observed Seebeck. We discuss the theoretical model which has been used to calculate the Seebeck coefficient. We are solving this model for other configurations $(4f)^n$ of rare-earth ground states.

Introduction

There is a need to find new materials suitable for thermoelectric applications[1–5]. Present materials are good at room temperature and above. New materials at high temperature are always useful for power generation devices. There is also a need for new materials at low temperatures for refrigeration. They would be used in cooling for superconducting magnets and electronics. Generally, a good thermoelectric material must have high values of the electrical conductivity and Seebeck coefficient, while having a small value of the thermal conductivity.

Most metals are unsuitable for thermoelectric applications because they have a small Seebeck coefficient[6]. Metallic compounds containing rare-earth compounds are an exception to this rule-of-thumb[7]. The highest values of the Seebeck coefficient are obtained in rare-earth compounds of cerium or ytterbium[5, 8] such as $YbAl_3$ or $CePd_3$ where $|S| \sim 100\mu V/K$. Some of the materials with high value of the Seebeck and power factor are shown in table 1. We also include bismuth telluride for comparison.

Compound	T (K)	S	ref.	ρ	ref.	P_f
Bi_2Te_3	300	240		1700		35
$CeSn_3$	150	50	[9–11]	25	[9, 12]	100
$CePd_3$	140	125	[13, 14]	170	[13, 14]	92
YbPd	250	-104	[15]	145	[15]	75
$YbAl_3$	300	-90	[16]	45	[16]	180

TABLE I. Seebeck coefficient S in units of $\mu V/K$, resistivity ρ in units of $\mu\Omega$cm, and Power factor ($P_f = S^2/\rho$) in units of $\mu W/(K^2\ cm)$.

These are the highest values of the Seebeck coefficient ever reported for metals. Also note the large power factors compared to bismuth telluride. Unfortunately the large value of the thermal conductivity prevents these materials from having large values of the figure of merit Z. $CePd_3$ has a value of $ZT \approx 0.4$. Many other compounds containing Ce or Yb have been found to have values of the Seebeck coefficient which are lower[5, 8] than those in table 1.

The large value of the thermal conductivity in these materials is due to thermal conduction by electrons. This contribution is given accurately by the Wiedemann-Franz law[17, 18] which relates the electronic part of the thermal conductivity K_e to the electrical conductivity σ

$$K_e = \frac{\pi^2}{3}\sigma T\left(\frac{k_B}{e}\right)^2 \tag{1}$$

The W-F law can be used to prove an inportant inequality for the figure of merit. Since everything in the denominator of the formula for ZT is positive

$$ZT = \frac{\sigma T S^2}{K_e + K_\ell} < \frac{\sigma T S^2}{K_e} \tag{2}$$

$$ZT < \left(\frac{S}{S_0}\right)^2 \tag{3}$$

$$S_0 = \frac{\pi}{\sqrt{3}}\left(\frac{k_B}{e}\right) = 156\mu V/K \tag{4}$$

where we used the W-F law in arriving at eqn. (3). Both theory [19] and experiment [20] suggest that the W-F law is valid in rare-earth compounds. However, experimental data[21, 22] shows that the phonon part of the thermal conductivity is relatively large at low temperature. Thus (2) is really an inequality, and the Seebeck needs to be larger than S_0 at low temperatures in order that $ZT \geq 1$.

The large value of the Seebeck coefficient in Ce and Yb compounds is caused by the *Kondo resonance*[23]. This resonance is a sharp feature in the density of states of the conduction electrons at energies very near to the chemical potential. This feature appears to be a delta function when plotted on a large energy scale. However, when plotted on a fine energy scale, one finds that the Kondo resonance has an energy width $\Delta E = k_B T_K$, where k_B is Boltzmanns constant and T_K is the *Kondo temperature.* The actual method of calculating the Kondo resonance, and temperature, are described in the next section. When

calculating the Seebeck coefficient, the Kondo resosnance causes a broad peak in the Seebeck coefficient $S(T)$ as a function of temperature T. This broad peak has its maximum at, or at least very close to, the Kondo temperature.

The Kondo resonance is due to spin fluctuations. Most rare-earth ions in metals have a magnetic moment due to the partially occupied f-shell. A conduction electron, when scattering from the rare-earth ion, can flip its spin while also flipping the moment of the f-electrons. This process causes the resistivity $\rho(T)$ to rise at low temperature, which is called the *Kondo effect*. Later theoretical work showed that this spin-flip scattering caused the energy resonance near to the chemical potential, which we now call the Kondo resonance. The Kondo resonance, and the high value of the Seebeck coefficient, are caused by the conduction electrons interacting with the spin fluctuations. Most theoretical calculations of this phenomena start from a theoretical model proposed by Anderson[39].

Numerous theoretical calculations have solved the Anderson model to obtain the Seebeck coefficient for Ce or Yb. They generally predict the value of 100 μV/K, in agreement with the observed maximum[24- 38]. These values are obtained by four different methods: Gunnarsson and Schönhammer[24, 25], the non-crossing approximation[26, 28–30] slave-boson techniques[27], and renormalization group techniques[33–36]. The non-crossing approximation is described below.

An interesting question is whether other rare-earth compounds, besides Ce or Yb, can have a Seebeck coefficient which is higher than 100 μV/K. In talking with experimentalists in this field, most admit that they have not tried very hard to find mixed valent materials composed of other rare-earths, once the Ce and Yb compounds became fashionable. However, compounds have been made with other rare-earths, and none show a Seebeck as large as 100μV/K. This raises the interesting question of whether any of them are capable of having a larger Seebeck coefficient than this apparent maximum. Theoretical calculations of energy levels indicate that mixed valent materials are possible with other rare earths. So we have started a series of calculations to calculate the Seebeck coefficient for the general configuration $(4f)^n$ where the occupancy integer spans the range $1 \leq n < 14$.

We have used the non-crossing approximation to extend these calculations to all values n of the f-orbital occupancy. We solve the single site Anderson model[23] for the case of a level with degeneracy N_f. We find the Kondo resonance for the case that the ground state has L electrons in the f-orbital, where $0 < L < N_f$. The Seebeck coefficient is calculated as a function of temperature for every value of L. We find that the Seebeck coefficient is largest for $L = 1$ and declines in value as L increases. This suggests that large Seebeck coefficients are not possible in mixed valent systems besides those of cerium or ytterbium. Generally we find that the Kondo resonance becomes smaller when L is increased.

A realistic calculation of the Seebeck for the configuration $(4f)^n$ requires that one include the various splittings of the f-levels due to spin-orbit and other interactions.This has only been done for Ce [25, 26, 38] which has $L = 1$. We are in the process of doing this calculation for $L = 2$ which corresponds to Pr. It is difficult to guess the results which will be found when we split the levels. The Seebeck coefficient is sensitive to a number of features of the Kondo resonance, such as the width and aymmetry. Any change in parameters changes both these features, which compete against each other for determining the size of the Seebeck coefficient.

Single-Site Anderson Model

The most popular theoretical model for describing the rare earth compounds was introduced by P.W. Anderson[39, 23]

$$H = H_0 + V \tag{5}$$

$$H_0 = \sum_{k\nu} \varepsilon_k C^\dagger_{k\nu} C_{k\nu} + \varepsilon_f \sum_\mu n_\mu + U \sum_{\mu>\nu} n_\mu n_\nu \tag{6}$$

$$n_\mu = f^\dagger_\mu f_\mu \tag{7}$$

$$V = \frac{1}{\sqrt{N}} \sum_{k\nu} V_{k\nu} [f^\dagger_\nu C_{k\nu} + C^\dagger_{k\nu} f_\nu] \tag{8}$$

where V is the hybridization interaction between the band electrons (k) and the localized electrons f_μ. It describes processes whereby the conduction electrons hop on and off the localized f-shell of the rare-earth. The on-site Coulomb repulsion is U and ε_f is the eigenvalue for a single f-electron. The eigenvalue and degeneracy factor Z_n for the f-electrons are, in the absence of hybridization

$$E_n = n\varepsilon_f + \frac{n(n-1)}{2} U \tag{9}$$

$$Z_n = \begin{pmatrix} N_f \\ n \end{pmatrix} \tag{10}$$

3+	nf	S	L	J	2J+1	Δ_-	Δ_+
Ce	1	1/2	3	5/2	6	1.8	3.2
Pr	2	1	5	4	9	3.8	1.9
Nd	3	3/2	6	9/2	10	5.2	1.5
Pm	4	2	6	4	9	5.5	1.6
Sm	5	5/2	5	5/2	6	5.4	0.3
Eu	6	3	3	0	1	7.9	
Eu	7	7/2	0	7/2	8	1.9	8.6
Gd	7	7/2	0	7/2	8	8.5	3.7
Tb	8	3	3	6	13	3.2	2.2
Dy	9	5/2	5	15/2	16	4.9	1.5
Ho	10	2	6	8	17	5.8	1.4
Er	11	3/2	6	15/2	16	5.9	1.8
Tm	12	1	5	6	13	5.5	1.1
Yb	13	1/2	3	7/2	8	7.4	0.9

TABLE II. Ground state degeneracy (2J+1) for mostly 3+ rare earths ions according to Hund's Rules. Values for Δ_+ and Δ_- from Herbst and Wilkins[40].

The ground state degeneracy of a rare-earth ion are given according to Hund's rules. These are shown in table 2. The Anderson model ignores the splittings of the f-orbital due to spin-orbit and other factors. It gives the wrong degeneracy Z_n instead of $(2J+1)$. In a future paper we will include these realistic splittings of the f-levels. The present calculation is intended to be a solution of the Anderson model as given in eqns (5)-(8).

The eigenvalue expression (9) is parabolic in the level occupancy n. Since $\varepsilon_f < 0$ then the minimum energy is found near to $n \sim 1/2 - \varepsilon_f/U$. Define L as the value of n which has the lowest value of E_n. We can increase L by decreasing the value of ε_f towards larger negative values, while keeping U fixed.

Mixed valence occurs when the number of f-electrons can fluctuate between n and $n \pm 1$. This fluctuation is the origin of the spin fluctuations. The hybridization interaction causes mixing whenever $|E_L - E_{L\pm1}|$ is a small energy. The standard nomenclature[40] is to define the two excitation energies out of the ground state as

$$\Delta_- = E_{L-1} - E_L = -[\varepsilon_f + (L-1)U] \tag{11}$$

$$\Delta_+ = E_{L+1} - E_L = \varepsilon_f + LU \tag{12}$$

$$U = \Delta_+ + \Delta_- \tag{13}$$

Values of $\Delta_\pm$ have been calculated for the rare-earth metals in ref. [40] and are shown in table 2. Generally they find one value which is small ($\Delta \sim 1.0$eV) while the other is larger so that $U \sim 6 - 8$ eV. We assume that similar values apply to the rare-earths when they are in metallic compounds.

We are doing a series of numerical calculations where we keep fixed the important values of $\Delta_\pm = E_{L\pm1} - E_L$, while varying $\varepsilon_f = -0.5 - U(L-1)$ to change L. We choose $\Delta_- = 0.5$eV.

First we discuss the properties of the Hamiltonian H_0 without the hybridization V. This interaction is included in the following section. The Green's function for the f-states in the absense of the hybridization term is

$$\mathcal{G}_f(i\omega_m) = -\sum_\mu \int_0^\beta d\tau e^{i\omega_m \tau} < T_\tau f_\mu(\tau) f_\mu^\dagger > \tag{14}$$

This can be written exactly for the nonintracting states. We employ the notation $N_f = 14$ to denote the number of states for a single f-electron. The degeneracy of the having n-electrons in the f-state is Z_n as defined above.

$$\mathcal{G}_f(i\omega_m) = \frac{1}{Z}\sum_{n=0}^{N_f} Z_n e^{-\beta E_n}\{\frac{N_f - n}{i\omega_m + E_n - E_{n+1}} + \frac{n}{i\omega_m + E_{n-1} - E_n}\} \tag{15}$$

$$A_f(\omega) = -2\Im[G_f(\omega)] \tag{16}$$

$$A_f(\omega) = \frac{2\pi}{Z}\sum_{n=0}^{N_f} Z_n e^{-\beta E_n}\{(N_f - n)\delta(\omega + E_n - E_{n+1}) + n\delta(\omega + E_{n-1} - E_n)\} \tag{17}$$

$$Z = \sum_0^{N_f} Z_n e^{-\beta E_n} \tag{18}$$

The spectral function $A_f(\omega)$ is obtained by the analytic continuation $i\omega_m \rightarrow \omega + i\eta$ and then taking twice the imaginary part.

Let E_L be the lowest eigenvalue ($n = L$) and assume that L is neither 0 nor N_f. The most important terms in the summation is when $n = L-1, L, L+1$ which gives the approximation

$$Z = Z_L \mathcal{Z} e^{-\beta E_L} \tag{19}$$

$$\mathcal{Z} = 1 + \frac{L}{N_f + 1 - L}e^{-\beta\Delta_-} + \frac{N_f - L}{L+1}e^{-\beta\Delta_+} \tag{20}$$

$$A_f(\omega) = \frac{2\pi}{\mathcal{Z}}[L\delta(\omega + \Delta_-)(1 + e^{-\beta\Delta_-}) + (N_f - L)\delta(\omega - \Delta_+)(1 + e^{-\beta\Delta_+}) + e^{-\beta\Delta_-}\frac{L(L-1)}{N_f + 1 - L}\delta(\omega + E_{L-2} - E_{L-1}) + e^{-\beta\Delta_+}\frac{(N_f - L)(N_f - L - 1)}{L+1}\delta(\omega + E_{L+1} - E_{L+2})] \tag{21}$$

The spectra has four peaks. Two are below the chemical potential and two above. We follow custom and ignore the last two terms in $A_f(\omega)$ and include only the peaks at $\omega = -\Delta_-, \Delta_+$. For the case that $L = 1$ then the third term is missing since there is no state $L-2$. For the case that $L = N_f - 1$ the $L+2$ term is missing.

Self-Energy of Electrons

The hybridization interaction V in eqn(8) describes the processes whereby a conduction electron can hop on or off the f-shell of the local atom. This process leads to several important new effects. The first is a new energy parameter defined as

$$\Gamma(E) = \frac{\pi}{N}\sum_k V_k^2 \delta(E - \varepsilon_k) \tag{22}$$

This function is assumed to be a constant, independent of energy. Its value for the rare-earths is about 0.1 eV. The second effect is that the resonance lines at $\omega = -\Delta_-, \Delta_+$ become broadened by an amount proportional to Γ. The third new effect is that a new resonance peak appears in $A_f(\omega)$ near to zero energy. This is the Kondo resonance, and it is the important feature for the calculation of the Seebeck coefficient.

In the prior section we showed that there were energy levels associated with having n-electrons in the f-state. Introduce a Green's function for this state

$$G_n(\omega) = \frac{1}{\omega - E_n - \Sigma_n(\omega)} \tag{23}$$

The hybridization interaction causes the self-energy $\Sigma_n(\omega)$. We calculate this function using the method of

ref.[26]. First consider the result for the self-energy in the second-order of perturbation theory

$$\Sigma_n(\omega) = nS^{'(0)}_{n-1}(\omega) + (N_f - n)S^{(0)}_{n+1}(\omega) \quad (24)$$

$$S^{(0)}_{n+1}(\omega) = \frac{1}{N}\sum_k \frac{V_k^2 n_k}{\omega - (E_{n+1} - \varepsilon_k) + i\eta} \quad (25)$$

$$S^{'(0)}_{n-1}(\omega) = \frac{1}{N}\sum_k \frac{V_k^2 (1-n_k)}{\omega - (E_{n-1} + \varepsilon_k) + i\eta} \quad (26)$$

There are two terms. The first term ($f^\dagger C_k$) in V adds an electron to the f-level, which changes n to $n+1$, while destroying a band electron in the state k. This process is proportional to the occupation number n_k of the band electrons. The second term ($C_k^\dagger f$) in V takes an electron out of the f level, which changes n to $n-1$, while adding an electron to the band. This process is proportional to the probability $(1-n_k)$ that the band state is unoccupied.

Arguments of $S^{(0)}$ are Green's functions G_n without the self-energies. The "Non-Crossing Approximation "(NCA)[26, 38] is to evaluate these Green's functions while including these self-energies. Put the self-energies in the denominators

$$\Sigma_n(\omega) = nS^{'}_{n-1}(\omega) + (N_f - n)S_{n+1}(\omega) \quad (27)$$

$$S_{n+1}(\omega) = \frac{1}{N}\sum_k V_k^2 n_k G_{n+1}(\omega + \varepsilon_k) \quad (28)$$

$$S^{'}_{n-1}(\omega) = \frac{1}{N}\sum_k V_k^2 (1-n_k) G_{n-1}(\omega - \varepsilon_k) \quad (29)$$

The above equations are a self-consistent definition for the self-energies. They are solved by iteration on the computer. We find that self-consistency is obtained only after many iterations.

We assume a Lorentzian density of states

$$g(\varepsilon) = \frac{2D}{\varepsilon^2 + D^2} \quad (30)$$

and place the chemical potential at $\varepsilon = 0$. The parameter D is an effective band width and the hybridization width is $\Gamma = \pi g(0) V(0)^2 = 2\pi V(0)^2/D$. In $S^{'}_n(\omega)$ we can change variables $\varepsilon \to -\varepsilon$ which now makes $S^{'}_n = S_n$. Thus we actually only evaluate the integrals of the form

$$S_n(\omega) = \frac{\Gamma}{\pi}\int \frac{d\varepsilon}{1 + (\varepsilon/D)^2} n_F(\varepsilon) G_n(\omega + \varepsilon) \quad (31)$$

f-electron Green's Function

The final step is to calculate the spectral function of the f-electron in the NCA. We must also include in the thermal averages the feature that the interactions give a spread in energy. Our result is

$$A_f(\omega) = \frac{1}{Z}\sum_{n=0}^{N_f} Z_n \int \frac{dE}{2\pi} e^{-\beta E} A_n(E)\{nA_{n-1}(E-\omega) + (N_f - n)A_{n+1}(E+\omega)\} \quad (32)$$

$$Z = \sum_{n=0}^{N_f} Z_n \int \frac{dE}{2\pi} e^{-\beta E} A_n(E) \quad (33)$$

A detailed derivation of these equations is given in refs. [26, 41]. These equations are similar in spirit to those of ref.[26]. They took the limit that $U \to \infty$ which eliminated all states with $n > 1$. They only had the two states of $n = 0, 1$ in their system and $L = 1$. Here we include all of the states with different values of n. We fix the value U=6 eV. We choose $\varepsilon_f = -0.5 - U(L-1)$ (in units of electron Volts) to have a variety of values so that we have different occupancies L in the f-state, while keeping fixed the values of $\Delta_- = -0.5$ eV, $\Delta_+ = 5.5$ eV. We make an approximation in our numerical solution of retaining only the states with $n = L-1, L, L+1$ in our self-consistent solution. We also choose $N_f = 6$ in order to compare with previous calculations.

Results and Discussion

Fig. 1 shows a graph of the spectral function $A_f(E)$ as a function of E (in eV) for the case that: $L = 1, N_f = 6, \varepsilon = -0.5$eV, $U = 6.0$eV at a temperature T=50 K.The narrow peak near to zero energy is the Kondo resonance. The two broad peaks, one above and one below zero, are at the energies of $\Delta_\pm$. The Kondo resonance is quite visible.

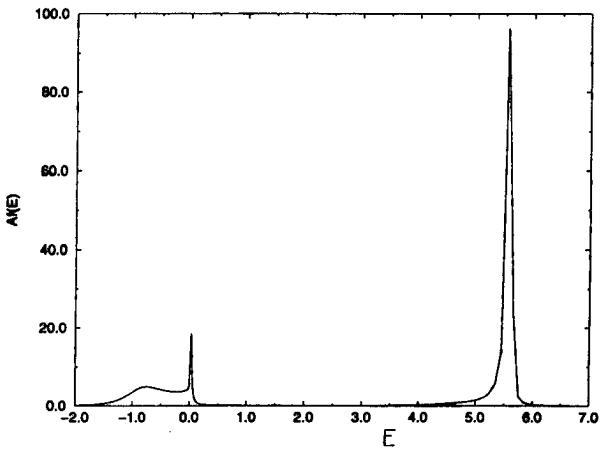


FIG. 1. The spectra function $A_f(E)$ of the f-electron as a function of energy E in eV. The Kondo resonance appears at zero energy.

The Kondo resonance is a real feature of the density of states of rare-earth compounds. It can be observed directly in photoemission and related spectroscopies, although the results are often controversial[42- 47].

We calculated the Kondo resonance in more detail as a function of temperature and L. We fixed $N_f = 6, U, \Delta_-$, and Δ_+, as described above, and varied the value of L by using $\varepsilon_f = -0.5 - U(L-1)$. The size of the Kondo resonance decreases in value as L increases. The largest Kondo resonance is the case $L = 1$ and the smallest is

the case with $L = 5$. The factors which are changing in these calculations are $(n, N_f - n)$ or $(L, N_f - L)$ in eqns (27,32). These factors relate to the degeneracy of the various levels as given by the factor of Z_n. If we do a more realistic calculation for f-electrons, with the factors which split the levels into sublevels, then we will reduce these factors[38].

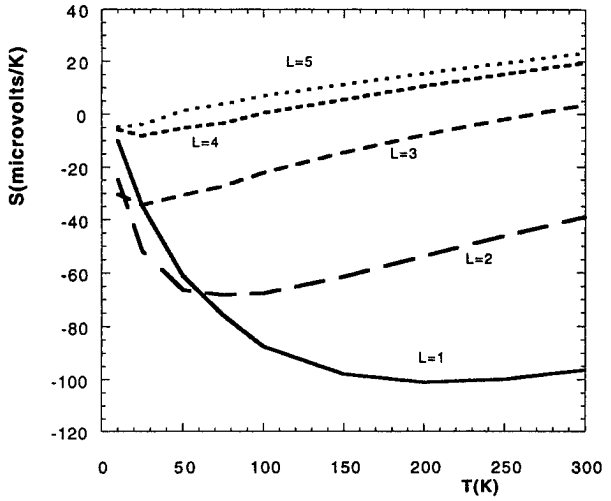


FIG. 2. Seebeck coefficient as a function of temperature between 25K and 300 K. The maximum value of the Seebeck coefficient occurs near to the Kondo temperature T_K. The maximum value of the Seebeck coefficient, and T_K, both decline with increasing values of L. Other parameters the same as in fig.2.

Figure 2 shows the Seebeck coefficient for $N_f = 6$ as a function of temperature for different values of L. The Seebeck coefficient is calculated in the usual fashion[5, 26]. Start from the usual formulas

$$\sigma = e^2 \int_{-\infty}^{\infty} dE \left(-\frac{\partial n_F(E)}{\partial E} \right) \Sigma(E) \tag{34}$$

$$T\sigma S = e \int_{-\infty}^{\infty} dE \left(-\frac{\partial n_F(E)}{\partial E} \right) \Sigma(E)(E - \mu) \tag{35}$$

$$\Sigma(E) = C\tau(E) \tag{36}$$

$$\frac{1}{\tau(E)} = \frac{1}{\tau_0} + cA_f(E) \tag{37}$$

The factor $\Sigma(E)$ contains the density of states of the band electrons as well as their average velocity and mean free path. We assume that the lifetime $\tau(E)$ has the only significant energy dependence in $\Sigma(E)$, which arises because the band electrons hybridize with the local electrons on the f-shells of the rare-earth atoms. The constant lifetime τ_0 is from impurity scattering and perhaps phonons. The factors of c and C are constants. Note that it is the inverse of $\Sigma(E)$ which is proportional to $A_f(E)$. The Kondo resonance makes a dip in the energy dependence of $\Sigma(E)$. The above formulas are derived in [5]. The Seebeck coefficient for these cases is shown in fig.(2) as a function of temperature. The largest Seebeck value is for $L = 1$, and the values decrease in size when L increases. This agrees with the observation that the Kondo resonance is getting smaller. The Kondo resonance causes the large values of the Seebeck [5, 26]. The Seebeck coefficient peaks at a temperature near to the Kondo temperature. The peak in our calculated Seebeck coefficients declines with increasing values of L. For $L \geq 3$ it is below 50 K and the peak is off the figure to the left. However, one can see that even at the peak value the Seebeck will be small for these cases. Besides this peak, due to the Kondo resonance, the Seebeck coeficients tends to rise linearly with temperaure, as is typical of metals.

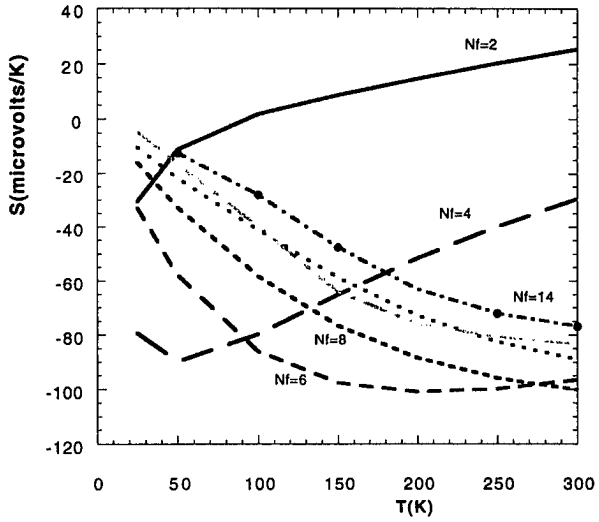


FIG. 3. Calculated Seebeck cofficient as a function of temperature for $L = 1$, U=6.0 eV, $\Delta_- = 0.5$ eV, $\Delta_+ = 5.5$ eV for different values of N_f.

The Seebeck coefficient has a large value when the Kondo resonance is large and asymmetric. The largest asymmetry is when $L, N_f - L$ differ by as much as possible. This happens when $L = 1$, or when $L = 5$ in the case of $N_f = 6$. However, because of our choice that Δ_- is smaller than Δ_+, the large Kondo resonance happens for $L = 1$. If we reverse the magnitudes of Δ_- and Δ_+ then the largest result is for $L = 5$. The mapping of $\Delta_- \rightarrow \Delta_+, \Delta_+ \rightarrow \Delta_-, L \rightarrow N_f - L$ leaves the results unchanged. The case for Yb corresponds to $N_f = 8, \Delta_+$ small and Δ_- large. It will have values similar to those for $N_f = 6, L = 1$ shown in the figures.

Since the largest Seebeck coefficient is for the case of one f-electron in the ground state, we were curious how it varied with N_f. One can choose different values of N_f, in steps of two, depending upon the crystal field, spin-orbit, or other factors which split the original degeneracy of 14. These results are shown in figure 3. Again we used $U = 6$ and $\Delta_- = 0.5$ and $\Delta_+ = 5.5$, all in electron volts. The

maximum Seebeck is for N_f in the range of 6-8, which are the cases of Ce and Yb, respectively.

So far our calculations show that the Seebeck and Kondo temperature decline in value as one considers values L of f-level occupancy larger than one. The same conclusion applies to f-holes. Of course, in mixed valence systems, the ground state configuration $(4f)^L$ will change as the occupancy fluctuates. Here we denote L as the principle valence. These results suggest that Ce and Yb will have the largest values of the Seebeck coefficient among all of the rare-earth compounds. This theoretical conclusion is in accord with the experimental observations.[8].

I wish to acknowledge many helpful conversations with Drs. Brian Sales, Frank DiSalvo, and Mirek Bartkowiak. All have contributed to my education in this field. I also acknowledge research support from a Grant from the Defense Advanced Research Projects Agency, from the University of Tennessee, and from Oak Ridge National Laboratory, managed by Lockheed Martin Energy Research Corp. for the U.S. Department of Energy under contract number DE-AC05-96OR22464.

---

[1] D.M. Rowe and C.M. Bhandari, *Modern Thermoelectrics* (Reston, 1983)

[2] H. J. Goldsmid, *Electronic Refrigeration* (Pion, London, 1986)

[3] C. Wood, "Materials for Thermoelectric Energy Conversion", Rep. Prog. Phys. **51**, 459 (1988)

[4] G.A. Slack, in *CRC Handbook of Thermoelectrics*, ed. D.M. Rowe (CRC Press, 1995) pg 407-440

[5] G.D. Mahan, "Good Thermoelectrics", In *Solid State Physics* **51**, ed. H. Ehrenreich and F. Spaepen (Academic Press, 1998, in press)

[6] F.J. Blatt, P.A. Schroeder, C.L. Foiles, and D. Greig, *Thermoelectric Power of Metals* (Plenum, 1976)

[7] R.J. Gambino, W.D. Grobman and A.M. Toxen, "Anomalously large thermoelectric cooling figure of merit in the Kondo systems $CePd_3$ and $CeIn_3$", Appl. Phys. Lett. **22**, 506 (1973)

[8] D. Jaccard and J. Sierro, "Thermoelectric Power of Some Intermediate Valence Compounds", *Valence Instabilities* ed. P. Wachter and H. Boppart (North-Holland, 1982) pg 409

[9] J. Sakurai, T. Ohyama and Y. Komura, "Thermoelectric Power and Electrical Resistivity of $Ce(In_{1-x}Sn_x)_3$, and $(Ce_{1-x}La_xIn_3$", JMMM **52**, 320 (1985)

[10] J.R. Cooper, C. Rizzuto, and G. Olcese, "Magnetic Susceptibility, Electronic Specific Heat and Transport Properties of some Intermediate Compounds of Cerium", J. de Phy. **C1-32**, 1136 (1971)

[11] J. Sakurai, H. Kamimura, and Y. Komura, "Thermoelectric Power of $Ce(Pb_{1-x}Sn_x)_3$",JMMM **76** & **77**, 287 (1988)

[12] B. Stalinski, Z. Kletowski and Z Henkie, "Electrical Resistivity of $RESn_3$ Single Crystals (RE = La, Ce, Pr, Nd)", phys. stat. sol.(a) K165 (1973)

[13] H. Sthiol, D. Jaccard, and J. Sierro, "Thermoelectric Power of $CePd_{3+\epsilon}$", in *Valence Instabilities*, ed. P. Wachter and H. Boppart (North-Holland, 1982) pg 443

[14] Y. Ijiri and F.J. DiSalvo, "Thermoelectric properties of $R_xCe_{1-x}Pd_3$ (R=Y, $La_{0.5}Y_{0.5}$, Nd)", Phys. Rev. B **55**, 1283 (1997)

[15] R. Potts, W. Boksch, G. Leson, B. Politt, H. Schmidt, A. Freimuth, K. Keulerz, J. Langen, G. Neumann, F. Oster, J. Röhler, U. Walter, P. Weidner, and D. Wohlleben, "Magnetic Order and Other Phase Transitions in Mixed-Valent YbPd", Phys. Rev. Lett. **55**, 481 (1985)

[16] H.J. van Daal, P.B. van Aken and K.H.J. Buschow, "The Seebeck Coefficient of $YbAl_2$ and $YbAl_3$", Phys. Lett. **49A**, 246 (1974)

[17] G. Wiedemann and R. Franz, Ann. Phys. **89**, 497 (1853)

[18] J.M. Ziman, *Electrons and Phonons* (Clarendon, Oxford, 1960) pg 260

[19] A.K. Bhattacharjee and B. Coqblin, "Thermal Conductivity of cerium compounds", Phys. Rev. B **38**, 338 (1988)

[20] E. Bauer, "Thermal Conductivity of Ce and Yb Based Kondo Systems", in *Transport and Thermal Properties of f-Electron Systems* ed. G. Oomi (Plenum, 1993) pg 133

[21] B.C. Sales (private communication)

[22] C. Jones and F. DiSalvo (private communication)

[23] G.D. Mahan, *Many-Particle Physics* (Plenum, Second Ed., 1990) Chapter 11

[24] O. Gunnarsson and K. Schönhammer, "Double occupancy of the f orbital in the Anderson model for Ce Compounds", Phys. Rev. B **31**, 4815 (1995)

[25] O. Gunnarsson and K. Schönhammer, "Many-Body Formulation of Spectra of Mixed Valence Systems", in *Handbook on the Physics and Chemistry of Rare Earths*, ed K.A. Gschneider, L. Eyring and S. Hüfner (North-Holland, 1987) Vol. 10, pg 103

[26] N.E. Bickers, D.L. Cox and J.W. Wilkins, "Self-Consistent Large-N expansion of Dilute Magnetic Alloys", Phys. Rev. B **36**, 2036 (1987)

[27] N.E. Bickers, "Reviews of Techniques in the large-N Expansion for dilute magnetic alloys", Rev. Mod. Phys. **59**, 845 (1987)

[28] A. Houghton, N. Read and H. Won, "1/N Expansion for the Transport Coefficients of the Single-Impurity Anderson Model", Phys. Rev. B **35**, 5123 (1987)

[29] D.L. Cox and N. Grewe, "Transport Properties of the Anderson Lattice", Z. hys. B **71**, 321 (1988)

[30] T.S. Kim and D.L. Cox, "Theory of One-Channel versus Multichannel Kondo Effect for Ce^{+3} Impurities", Phys. Rev. Lett. **75**, 1622 (1995)

[31] H. Schweitzer and G. Czycholl, "Resistivity and Thermopower of Heavy Fermion Systems", Phys. Rev. Lett. **67**, 3724 (1991)

[32] H.L. Neal and D.J. Collins, "Transport Coefficients for the Anderson Model", Phys. Rev. B **48**, 4299 (1993)

[33] H.O. Frota and L.N. Oliveira, "Photoemission spectroscopy for the spin-degenerate Anderson Model", Phys. Rev. B **33**, 7871 (1986)

[34] A. Schiller and V. Zevin, "Degenerate Anderson-impurity Model with Finite On-site Coulomb Interaction", Phys.

Rev. B **47**, 9297 (1993)
[35] T.A. Costi and A.C. Hewson, "Transport Coefficients of the Anderson Model", J. Phys. CM**5**, L361 (1993)
[36] A.C. Hewson, *The Kondo Problem to Heavy Fermions* (Cambridge, 1993)
[37] S. Suzuki, O. Sakai and Y. Shimizu, "Magnetic Excitations and Transport Coefficients of the Impurity Anderson Model", J. Phys. Soc. Jpn **65**, 4034 (1996)
[38] T.S. Kim and D.L. Cox, "Scaling analysis of a model Hamiltonian for Ce^{+3} impurities in a cubic metal", Phys. Rev. B **54**, 6494 (1996)
[39] P.W. Anderson, "Localized Magnetic States in Metals", Phys. Rev. **124**, 41 (1961)
[40] J.F. Herbst and J.W. Wilkins, "Calculation of 4f Excitation Energies in Metal", in *Handbook on the Physics and Chemistry of Rare Earths* ed. K.A. Gschneider, L. Eyring and S. Hüfer (North-Holland, 1987) Vol. 10, pg. 321
[41] G.D. Mahan, "Seebeck Coefficient for the Anderson Model", Phys. Rev. B (in press)
[42] F. Patthey et al, "Characterization of the hybridized $4f$ states in $YbAl_3$ by high energy spectroscopies", Phys. Rev. B **36**, 7697 (1987)
[43] S.-J. Oh et al, "Observation of Kondo resonance in $YbAl_3$", Phys. Rev. B **37**, 2861 (1988)
[44] J.-M. Imer et al, "Comment on 'Observation of Kondo resdonance in $YbAl_3$'", Phys. Rev. B **46**, 1864 (1992)
[45] S.J. Oh et al, "Reply to 'Comment on Observation of Kondo Resonance in $YbAl_3$'", Phys. Rev. B **46**, 1866 (1992)
[46] L.H. Tjeng et al, "Temperature Dependence of the Kondo Resonance in $YbAl_3$", Phys. Rev. Lett. **71**, 1419 (1993)
[47] R.I.R. Blyth et al, "Temperature-invariant valence band $4f$ photoemission features in the heavy-fermion compound $YbAl_3$", Phys. Rev. B **48** 9497 (1993)

Status and Future Prospects on the Development of Thermoelectric Power Generation Systems Utilizing Combustion Heat From Municipal Solid Waste

Takenobu Kajikawa
Shonan Institute of Technology, Fujisawa, Kanagawa, Japan 251
Tel:+81 466 34 4111, Fax:+81 466 35 8897, E-mail: kajikawa@elec.shonan-it.ac.jp

Abstract

The characteristics of combustion heat from the municipal solid waste are fitted for a large-scale application of thermoelectric power generation potentially. In the paper the status and the future prospects on the development of thermoelectric power generation systems to recover electricity from this heat source in Japan are reviewed and discussed. The experimental results on three different types, small-scale (500 W class) thermoelectric power generation systems installed in the real municipal solid waste processing systems to demonstrate the technological feasibility and to extract the technological problems are briefly introduced. The conceptual designs of small scale system for the next phase of the R&D program are presented. From the view point of large-scale realization the thermoelectric material and modules configurations to adapt for this application are also discussed. The case study on the marginal cost estimation shows the cost reduction to less than 0.4-0.5 Million Yen/kW to make a profit on this system.

Introduction

Among a lot of applications of thermoelectric power generation, the system utilizing combustion heat of municipal solid waste has received particular attention in recent years because it is highly possible to respond to the social needs to solve the problems on processing solid waste.

In Japan municipal solid waste per capita is discharged about 1.1 kg/day recently. Because of limited space more than 75% of the solid waste is burned. It is socially acceptable that the solid waste processing system should be located near the resident area to process the solid waste discharged by the residents' own, not the strangers. Hence, small incinerator systems are constructed at each town and each small local government. There is one incinerator system per 60,000 residents on an average. It means that a lot of small and medium scale heat sources are dispersed.

On the other hand, 1 kg solid waste contains about 10,000 kJ/kg in enthalpy, while the additional energy is required to burn it. It is the most acceptable that the solid waste should be processed with the energy contained in itself at least from the viewpoint of global environmental protection issue and the conservation of fossil fuel resources.

In consideration of these situations, it can be said that a thermoelectric power generation system, which has no scale effect and high reliability, is the most suitable system to utilize the combustion heat efficiently[1]. As the system scale would be several tens kW to several thousands kW in power output, for the thermoelectric manufacturing process the mass-production effect can be expected to reduce the cost substantially. Moreover, the spin-off effects are also anticipated greatly.

The Japanese national project entitled "Research on Efficient Utilization of Unused Energy Sources Such As Heat of Combustible Solid Waste" started with the special coordination funds for promoting science and technology by Science and Technology Agency in FY1995.The objective is to establish the technology on the thermoelectric power generation system recovering unused heat source to improve the energy conversion efficiency for regional energy systems. The major research items concerned with this application consist of the followings:

1) Development of the manufacturing for the thermoelectric power generation module.
2) Development of system technology for the thermoelectric application to small , medium and large incinerators
3) Development of optimum design and evaluation technique for various types of thermoelectric power generation systems adapted to incinerator system conditions.

The R&D term will be five or six years divided with two phases. Twelve research organizations of industrial, governmental and academic have joined in it.

Another R&D activity on thermoelectric power generation system for the utilization of combustion heat of municipal solid waste has been promoted by Japan Waste Research Foundation supported by the Ministry of Health and Welfare since 1991. The objective of this project is to verify the improvement of the energy conversion efficiency for the power generation system combined with a small or medium scale solid waste processing

0-7803-4057-4/97 $10.00 ©1997 IEEE

system due to thermoelectric energy conversion based on the existing technology. The present phase is from FY1996 to FY1998. The major research items are as follows:

1) Experimental study on the establishment of the suitable thermoelectric power generation system in the incinerator system
2) Conceptual design and cost evaluation of the thermoelectric power generation system for a small or medium scale incinerator.

The committee (Chair: Prof. N.Hirayama) on the development of utilization of combustion heat of solid waste using novel method such as thermoelectrics has been established to promote this project in parallel with the working group consisted of 16 private companies.

In this paper the status and future prospects on the development of the thermoelectric power generation systems utilizing heat of municipal solid waste as one of the promising applications are reviewed from various aspects.

The first is to introduce the quantitative and qualitative characteristics on municipal solid waste as the energy resource. The second is to present the system classification and examples of conceptual design. The third is to review three experimental studies for real incinerator systems to verify the technological feasibility and extract the technological problems on this application. The fourth is to discuss about the technological problems and future prospects including cost aspect and the approaches to solve them ,and the last is to summarize this review as conclusions.

Resource Evaluation

In order to efficiently use the combustion heat of municipal solid waste for a thermoelectric power generation system, it is necessary to clarify quantitative and qualitative characteristics on the concerned energy resource in detail.

The total amount of municipal solid waste in Japan is annually produced about 50 Million ton/year. The increment rate is gradually increasing even though the campaign for reducing the amount of solid waste by local government is achieved. More than 75% of total amount is burned, while the other is reclaimed to low ground , where tends to be limited from the environmental issue. About 2000 incinerator systems of more than 50 ton/day have been in operation in Japan. The number of large scale systems processing more than 150 ton/day is only about 22%. The numbers of small scale systems of several tens kg/day are more than 100,000. The numbers of the incinerators increase year by year gradually.

The expense for processing solid waste is about 24,450 Million dollars annually in Japan. It means that the expense for 1 ton solid waste is 420$/ton and the expense per capita is 164$/year.

The Rankine cycle power generation systems installed with large scale units for 146 sites have been in operation to generate 550MW, which means 30 Billion kWh in electricity annually.

In addition to the municipal solid waste, the amount of solid waste rejected from industrial sector is estimated 397 Million tons per year, about 8 times of municipal solid waste. Now most of it is reclaimed to low ground. The location for reclaiming are restricted year and year. About 50 systems have been in operation to generate 247MW in electricity by the Rankine cycle system at present It will be important to apply the thermoelectric power generation system to this field in the future.

Concerning the quality of the energy resource, mean heat of combustion for high grade solid waste is 12,500kJ/kg, while that for low grade one is 7,100kJ/kg. The quality is not constant regionally and daily. The temperature variation of combustion gas is shown in Fig.1, where the variation range is from 873K to 1433 K and temperature change from 1433K to 1233K for one hour as an example. Moreover,it is careful that the combustion gas is very chemically reactive for peculiar temperature range and contains some contents of ash.

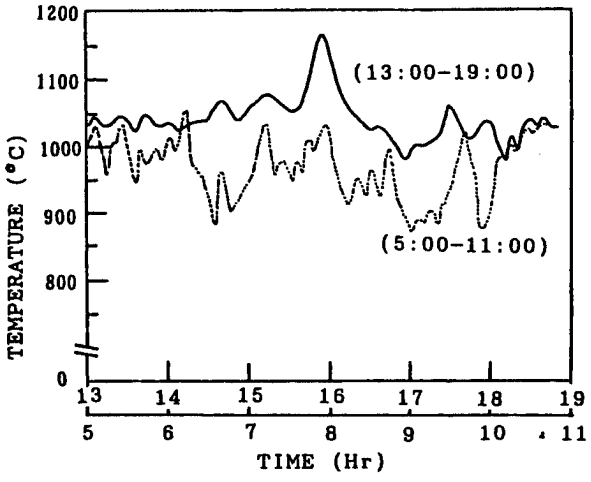


Fig.1 Temperature variation of combustion gas for a real incinerator

System Classification and Conceptual Designs

System

Solid waste processing systems are classified from the point of thermoelectric energy conversion system as capacity (large;>200ton/day,medium,small;<50ton/day,Mini;~100kg/day), quality of solid waste (High;~12,500 kJ/kg, Medium;~10,000 kJ/kg, Low;~7100kJ/kg), operating mode (Continuous, Intermittent), location (Near city, Remote) , and utilization (Heat, Electricity, Both). Operating mode depends on the system capacity so far. However, in order to suppress the reaction of toxic products such as Dioxins all of incinerators will be operated in non-stop run even for a small scale system by the regulation in future.

The types of thermoelectric power generation systems installed into the incinerator system are classified with 1) system constitution (Independent system from other heat utilization, Combination system with other heat utilization), 2) power utility (Stand alone, Grid connection), and 3) installation place (Furnace wall-embedded type, Inserted-in-gas duct type, Separated type from the incinerator but connected with heat transmitter(Hot air type, Heat pipe type), Coexist-with -boiler type).

A proper type of thermoelectric power generation system can be selected in due consideration of given conditions for existing solid waste processing systems. Concerning the type of installation place in the incinerator system, various heat exchanging systems from combustion gas to thermoelectric elements and from thermoelectric elements to heat sink system are considered as shown in Fig.2.

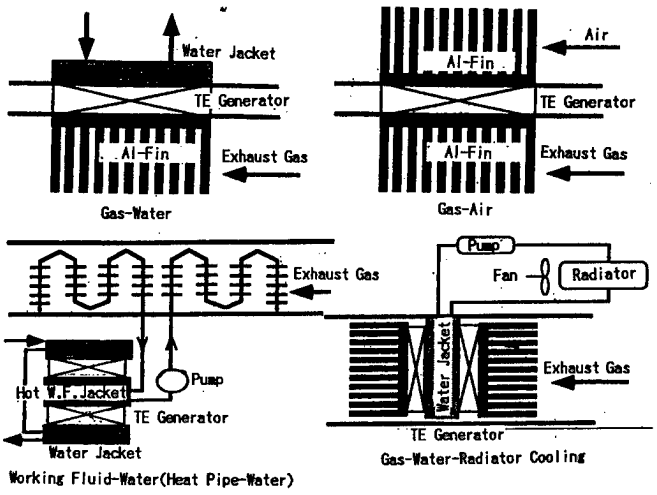


Fig.2 Classification of heat exchanging system for TE generator applying to the incinerator

Conceptual Designs

The conceptual design of thermoelectric power generation system embedded in the furnace wall for a 1000 kg/day (i.e.,200 kg/h and 5 h in operation per day) incinerator was carried out. The system configuration is shown in Fig.3. The size of a furnace for a mini scale incinerator can be calculated from the equation as V=HG/Q, where V,H,G,and Q are volume of a furnace, heat of combustion, processing rate and heat duty of a furnace respectively. Heat duty of a furnace is about 290kW/m^3 for such a scale. In the case of 200kg/h system, the volume is 4m^3. The available surface area embedding thermoelectric power generation modules was estimated 3.6m^2. The specifications on the module are shown in Table 1. As the combustion temperature reaches more than 1173K, Si-Ge elements were used. The percentage of available heat to overall input thermal energy was assumed 25%, the system energy conversion efficiency would be 2.5% based on 10.1% in thermoelectric energy conversion efficiency. The power output was 29kW in DC at the thermoelectric modules. The gross power output was estimated 23.2 kW in AC through inverter of which efficiency was 80%., while the auxiliary power was about 15kW. The power density was 6.4kW/m^2 at 800K in temperature difference between the hot side and cold side of the thermoelectric element [2].

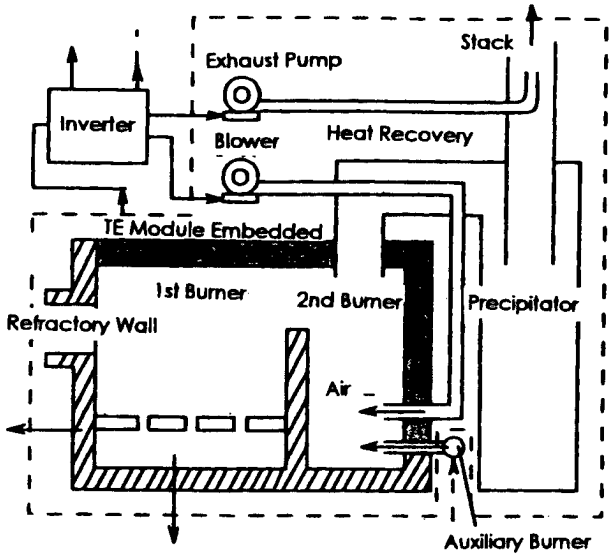


Fig.3 Configuration of a mini-scale incinerator

Table 1 Specifications of thermoelectric module

TE Material	Si-Ge
Fig. of Merit	0.75×10^{-3} K^{-1}
TE Leg Hight	32 mm
Hot Junction Temp.	1123 K
Cold Junction Temp.	323 K
Temp. Difference	800 K
Efficiency	10.1 %
Heat Flux	80.4 kW/m^2

Another conceptual design of thermoelectric power generation system was carried out on the basis of the existing incinerator of 40 ton/day. This incinerator has a gas cooling system through the outlet of the burner. At this part water is sprayed to reduce the gas temperature adapting for next stage, which is a hot air heat exchanger of 523 K. For example, about 80 ton/day in water flow rate is sprayed in it. This enthalpy drop can be used to generate electricity with thermoelectric power generation system.

Hot air type system to install it into the incinerator was considered. For this system the high temperture air heat exchanger is replaced instead of the gas cooling system to make hot air, which transfers heat to the hot junction for thermoelectric power generation system. The outlet of hot air through thermoelectric module is connected with the inlet of the stack as shown in Fig.4. The conceptual design specifications for each grade of the solid waste are summarized in Table 2. Hot air temperature is designed 853K provided with an advanced heat exchanger, while hot air temperature is 523K by the present technology. When the energy conversion efficiency is assumed 5%, the power output for high graded solid waste is obtained 171 kW. The heat sink system is used with a cooling tower system.

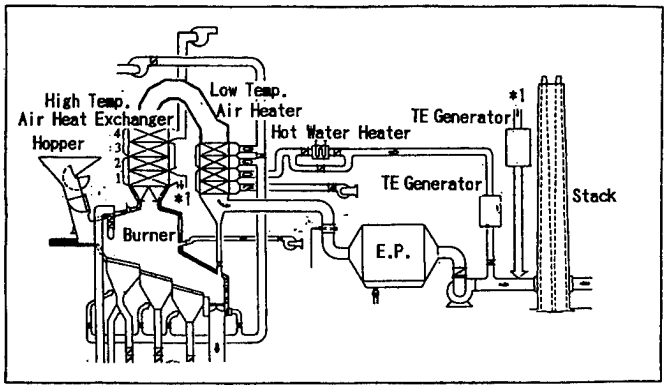


Fig.4 Conceptual configuration of High Temperature Air Heat Exchanger type

Table 2 Temperature allocation for High Temp. Air Type system

Item/Quality of Solid Waste	High	Standard	Low
Heat Duty (kW)	3428	2445	880
Inlet Gas Temp. (K)	1223	1223	1223
Outlet Gas Temp. (K)	727	775	857
Inlet Air Temp. (K)	373	373	373
Outlet Air Temp. (K)	853	853	853
Gas Flow Rate (Nm^3/h)	17,650	14,090	10,280
Air Flow Rate (Nm^3/h)	18,900	13,480	4,850
Tube Wall Temp. at 1st Stage (K)	1003	1062	1029
at 2nd Stage (K)	848	924	967
at 3rd Stage (K)	718	803	899
at 4th Stage (K)	607	694	829
Energy Conversion Eff.(%)	5.0	5.0	5.0
Power Output (kW)	171	122	44

On-site Experiments

Experiments on three types of 500 W class thermoelectric power generation system installed in a real incinerator have been carried out to verify the technological feasibility and to extract the technological problems. It is an ordinary manner to proceed the national R&D project in Japan. These types are 1) Hot air type, 2)Heat pipe type, and 3) Furnace wall-embedded type.

Hot Air Type[3]

The field test of thermoelectric power generation system was carried out for the real incinerator ,in which the processing amount was 40 ton/day and the operating time was 16h/day. The thermoelectric unit was inserted in the hot air duct connected with hot air heat exchanger as shown in Fig.5. In the nominal conditions hot air temperature is 523 K and outlet temperature is 503 K. The coolant at the heat sink is used water, of which inlet temperature and outlet one are 296 K and 305 K respectively.

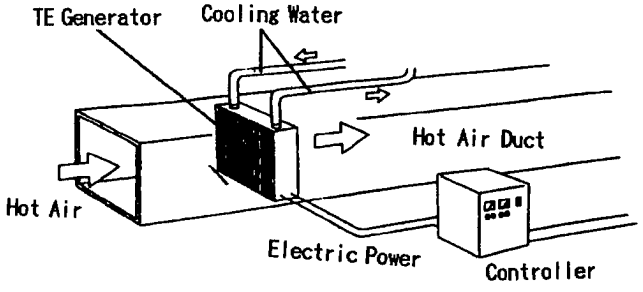


Fig.5 Schematic diagram of the field test for Hot Air type

For the wind tunnel test before the field test, at $T_{hot\ air}$ =505 K and T_{water} =296 K, power output was obtained 429W ,when load

voltage =23.8 V and load current =18 A in the case of 12 modules times 7 stages (total 84 modules). As the initial trouble on cooling was happened, the 35 modules alive were installed to the real incinerator. The experimental result for the field test is shown in Fig.6. The internal resistance was found 0.5 Ω. The power output per module was 6.57 W/module. The enegy conversion efficiency was about 4% to 3.5%.

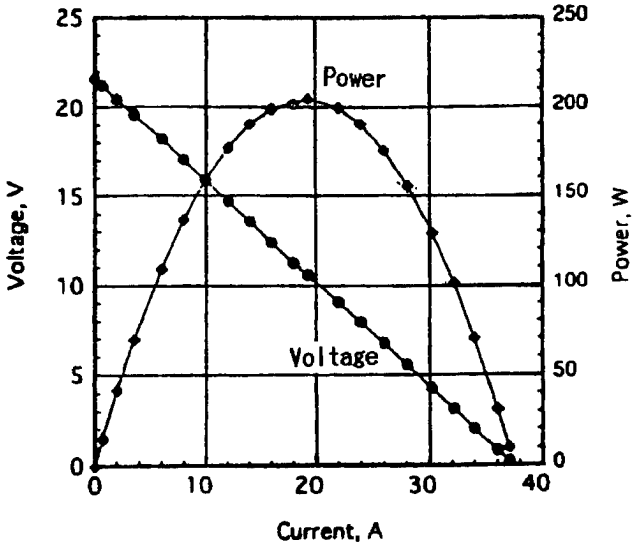


Fig.6 Performance of power output for Hot Air type field test

The power variation with time is shown in Fig.7. The inlet temperature was changed from 544 K to 518 K, so that power output varied with input condition from 214W to 175W. The variation of power was proportional to square of temperature variation. These are good agreement with the theoretical estimation. The experiment was stopped for short duration, because the performance degradation was large due to the deterioration of the adhesion between electrode and thermoelectric elements caused by many ON/OFF operations. As expected, it is recognized that the durability of junction between electrode and element is very much important. As the heat source is clean, hot air, there are no problems on corrosion and fouling . Concerning hot air temperature, its temperature is limited less than 573 K from the economical heat exchanger tube material at present.

Heat Pipe Type [4]

A 500W class thermoelectric power generation system has been tested in the real incinerator of 40 ton/day . The heat pipe type experimental facility has been located at the inlet of the stack. The heat pipes were inserted in the gas duct before the stack to extract thermal energy, which was used as a hot side source in a thermoelectric power generation system. Figure 8 shows the

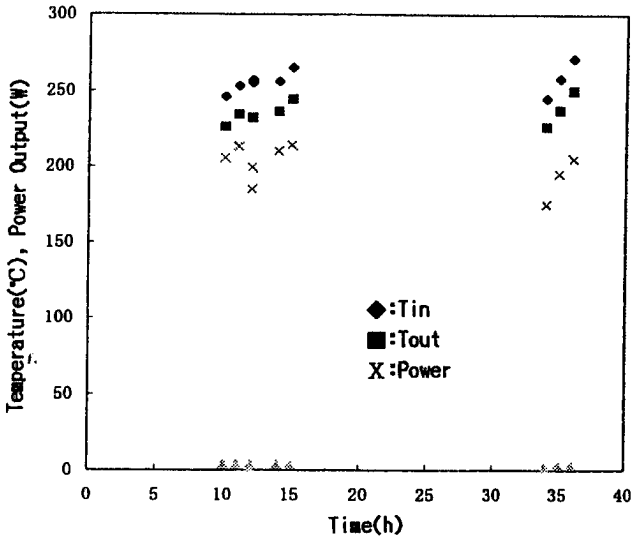


Fig.7 Power output and temeprature variation with time

cross-sectional view of the heat pipe type experimental facility. One unit was consisted of 3 modules, in which 49 couples of Bi-Te elements were used. Totally 24 units could generate 500 W in electricity. The heat collecting part was fin tube made of copper, of which fin thickness was 0.6mm and fin pitch was 5mm. The working fluid was Fluoride Carbon (vapor pressure is 0.8 MPa at 298 K). As the heat pipe is tilted at 7 degree, working fluid can circulate by gravity.

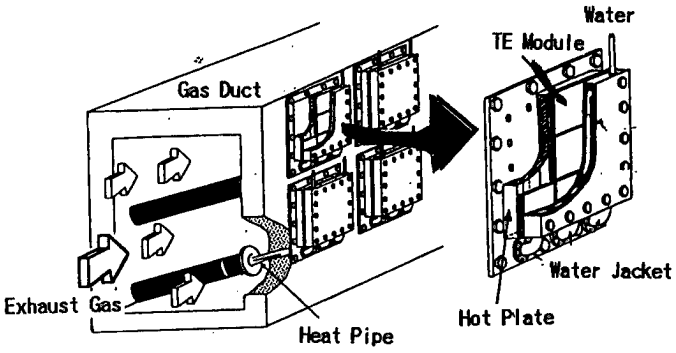


Fig.8 Configuration of Heat Pipe type test facility

DC power output at Tgas=513 K and gas velocity =18 m/s was 570 W. Operating hour is 16 hours per day. Start-up and shut-down tests were carried out more than 100 times. The steady state reaches about half an hour. The characteristics of power output (DC and AC) are shown in Fig.9. The power output were gradually decreasing with time. At the initial one month the degradation rate was 0.55%/day. The reason is considered to be caused by the ash deposition on the fin surface mainly.

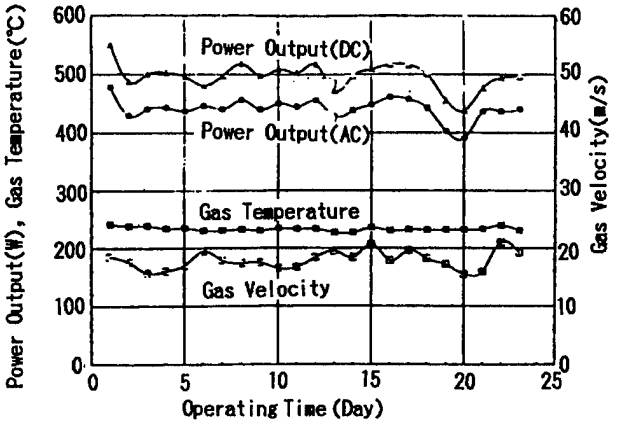


Fig.9 Characteristics of power output,gas temperature and gas velocity

Wall embedded type

Two sets of a 500 W wall-embedded type test facility were installed at the upper portion of the furnace and at the exhaust gas duct near the stack in the Fluidized bed type incinerator. It can process 36.5 ton/day for 16 hours operation. The test unit is consisted of 4 modules, which can generate 125 W for each using Pb-Te thermoelectric elements made by Global Thermoelectric Inc.,. The surface of the test unit was set up on the same level as other refractory wall. The specification of the experimental facility is summarized in Table 3.

Table 3 Specifications of Wall-embedded type test facility

Size	480 ϕ mm x 204mm
Module	192 ϕ mm x 84 mmx 4 modules
Thermoelectric Element	Pb-Te-Sn 80 couples x 4
Power Output	500 W (at 8W/m² in Heat Flux)
Load Voltage	28 V
Load Current	18 A
Heat Duty	10kW
Coolant	Water

The combustion gas temperature changed from 1073 K to 1223 K. The gas flow rate changed from 6570 to 15,120 Nm^3/h at the same time. The temperature at the surface of the test unit changed from 993 K in maximum to 843 K for one operation. At the upper portion of the furnace the maximum power output was only 135 W at 4.8 W/cm^2 in heat flux.The experimental data were substantially lower than the designed values because of insufficient heat flux. It suggests that the module design should be adapted to the properties of the heat source. The test has been continued to detect the long run effect in the real incinerator system.

Technological Problems and Future Prospects

Economic Aspect

According to the experimental results of several thermoelectric power generation systems in the real incinerator the technological feasibility has been verified, although some technological problems were extracted. It is very important to consider the system from the point of economic aspect in order to be smoothly accepted with the present incinerator systems and society. At the present phase there is no detailed investigation on economic aspect of this application but the preliminary one.

The case study on the cost estimation was achieved on the basis of the existing thermoelectric module technology.

The evaluation was achieved the account of the difference of the construction cost for each component as compared with the conventional system in order to estimate the marginal cost.

The thermoelectric power generation system is replaced instead of the gas cooling system for a stoker type incinerator of 50 ton/day and for a fluidized bed type one of 40 ton/day. The amount of electricity bought from the electric power company for 15 years is saved with the introduction of the thermoelectric power generation system. The enthalpy of solid waste and the power density are assumed to be 8360 kJ/kg and 5.7 kW/m^2 respectively.The total power output is about 300kW. The baseline cost of the thermoelectric element per 1kW and power generation unit are estimated to be 1.2 Million Yen/kW and 2.4 Million Yen/kW(2 times of thermoelectric element cost). The cost account is shown in Table 4 [6]. The results mean that the additional investment should be needed 431 Million Yen for a stoker type and 500 Million Yen for a fluidized bed type.

Table 4 Cost account based on 1.2Million ¥/kW of TE element

Component/System	Stoker Type	Fluidized Bed Type	
Building	±0	±0	Million Yen
Gas Cooling System	-105	-84	
Thermoelectric Element	+725	+766	
Auxiliary Components	+260	+250	
Buying Electricity	-449	-432	
Balance	+431	+500	

Based on this investigation the marginal cost of thermoelectric element can be estimated to be 0.487 Million Yen/kW (~4.35 $/W) for the former, and 0.416 Million Yen/kW (~3.8 $/W) for

the latter respectively. These values are about 1/3 of the existing element cost. The cost less than these costs is competitive with the conventional system and becomes the goal for the development of this application.

Technological Problems

According to the above-mentioned characteristics and experimental and theoretical works on this application, the peculiar points of the thermoelectric power generation system recovering heat of solid waste are summarized as follows:

1) Temperature range is wide; that is , from 1300 K to room temperature.
2) The temperature of the heat source is variable and unstable hourly, daily, monthly and annually.
3) The combustion gas contains ash and is chemically reactive for peculiar temperature range.
4) The power capacity is large, and total numbers of thermoelectric elements are huge as compared with other applications.
5) The main mission of the overall system is to process the solid waste and not to generate electricity.

The technical problems to be solved are picked up from these peculiar points and several experiences. The high priority in the technological problems can be discussed from the points of software and hardware as follows:

Concerning the former, these are:

1) To achieve the most useful design of the thermoelectric power generation system in consideration of power generating cost and the environmental conditions such as site and heat sink.

   Multi-dimensional design method including the transient behavior [5] and total design method in consideration of heat transfer mechanism and heat transfer method such as radiator type or hot working fluid type and so on for both hot and cold sides should be established.
2) To properly select the power conditions(Power capacity, Voltage, Current) of an unit or module in consideration of reliability, controllability, responsibility and redundancy of the system.

At present they are considered to be next phase problems.

Concerning the latter, these are;

1) To develop the high performance , inexpensive and safe thermoelectric element over the wide temperature range.

   The goal of the thermoelectric element to be developed is conceptually shown in Fig. 10. In the figure solid circles represent the existing technology. The dotted circles represent advanced elements. At present it seems that Bi-Te element is located close to the marginal goal line.

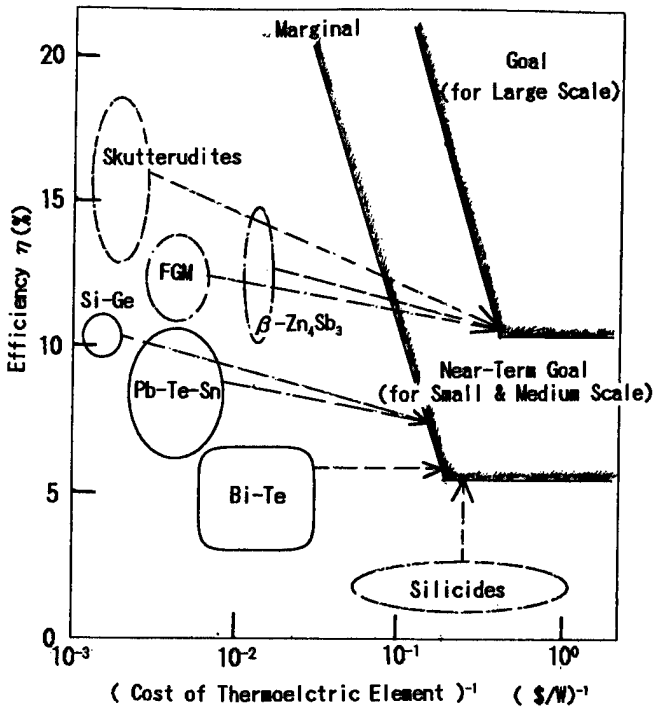


Fig.10 Goal of TE elements for this application

2) To develop the thermal stress relaxation module or stress -free thermoelectric module in order to have the durability for more than 15 years and for many times start-up and shut -down operations.

   The experimental results of durability test is shown in Fig.11[7]. The test modules is ceramic plate sandwich type Bi-Te modules, of which electrode and element is soldered by Sn-Pb type solder. The added heat is changed from 300K to 453 K for three hours. One cycle time is 6 hours. According to the experiment, the modules were broken up to 200-240 cycles. It is very severe results. It suggested that the module configuration should be changed to the stress-free module such as shown in Fig. 12 [8] for example.
3) To develop the countermeasure to the chemically reactive environment and the deposition of fly ash such as air blowing system.

   In order to avoid the performance degradation due to the ash deposition, an improved experiment was carried out by NKK group [2]. In the experiment air blowing for ten minutes per day was operated to the module surface embedded to the furnace wall. The stable characteristics could be obtained as shown in Fig.13 . It can be said that air blowing is effective to keep the electrical performance stable. It is necessary to

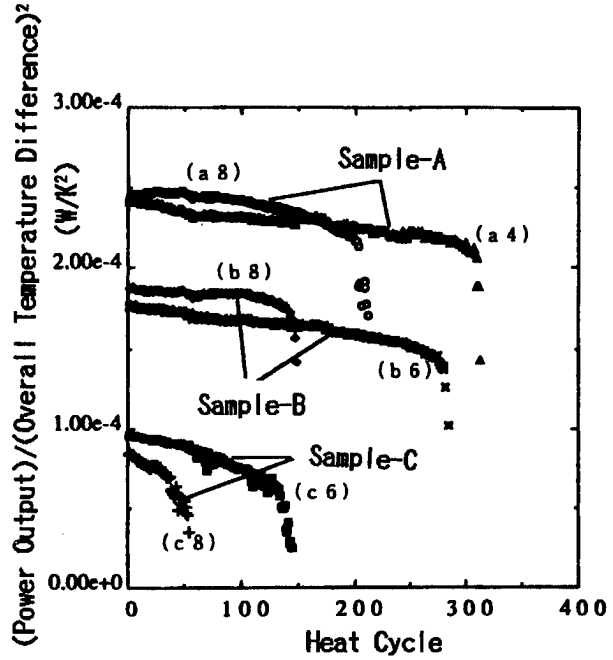


Fig.11 Heat cycle test of TE modules[7]

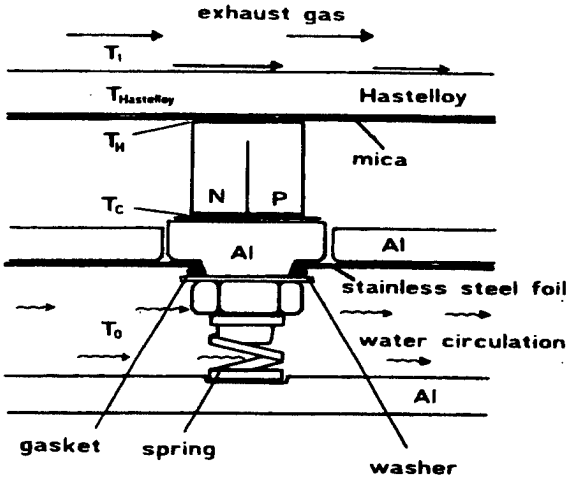


Fig.12 Strain relief configration of TE module[8]

estimate optimum air blowing conditions such as flow rate, interval and duration in consideration of temperature reduction effect and additional auxiliary power for a practical large scale system.

4) To develop the reliable mass-productive fabrication processing of thermoelectric module and unit by applying industrial robotics.

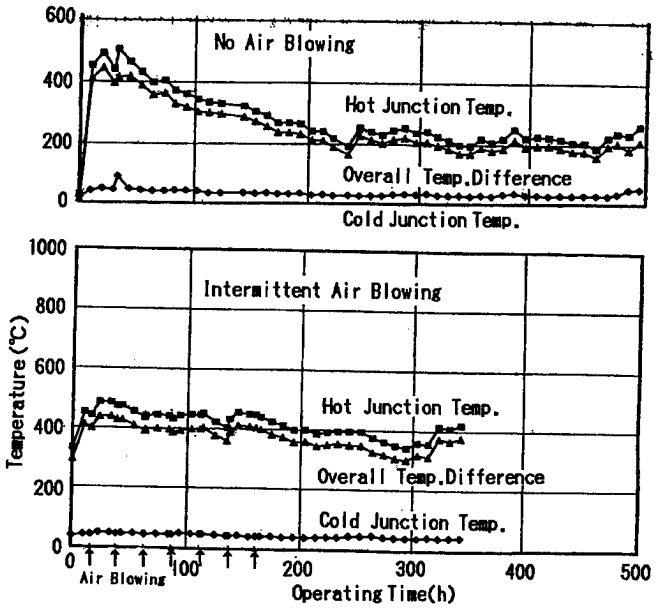


Fig.13 Air blowing effect on wall-embedded type TE module

Future Prospects

At present the R&D stage of this application is situated in the preliminary phase which includes several small scale experiments for real incinerators and some conceptual designs under the national projects in Japan. Moreover, many technological problems to be solved and their approaches were discussed. It can be said at least that the potential market size of this applications very large in the thermoelectric industry and the thermoelectric system is advantageous in principle to this application as compared with other power generation system such as the Rankine cycle system from the view point of the adaptability to the energy source.

The market penetration scenarios of the thermoelectric power generation system are considered as shown in Table 5. As the first generation a small scale less than 100kW thermoelectric power generation system will be used for a self-sustaining incinerator system. Figure 14 shows the approving condition of thermoelectric performance for a self-sustaining incinerator. As mentioned in Fig.10. it is necessary to reach 5% of energy conversion efficiency for thermoelectric power generation system.

The key is the development of durable thermoelectric modules and low-cost ,high -reliability mass-production processing for the first generation. And for the next generation the development of advanced thermoelectric materials of high performance is

essential in parallel with the first phase.

This application surely has large spin-off effect to other waste heat sources from automobile, industrial process and many dispersed heat sources.

Table 5 Market penetration scenarios for TE system utilizing heat of combustible solid waste

Generation	Capacity	TE Material	Heat Exchanging Type
I	<100kW	Bi-Te	Hot Air(523-573K)
II	<100kW	Bi-Te/Pb-Te	Wall-embedded
III	~300kW	Bi-Te/Pb-Te	High Temp. Hot Air /Wall-embedded
IV	~300kW	Advanced TE	Advanced Tech.
V	Large Scale	Advanced TE	Advanced Tech.

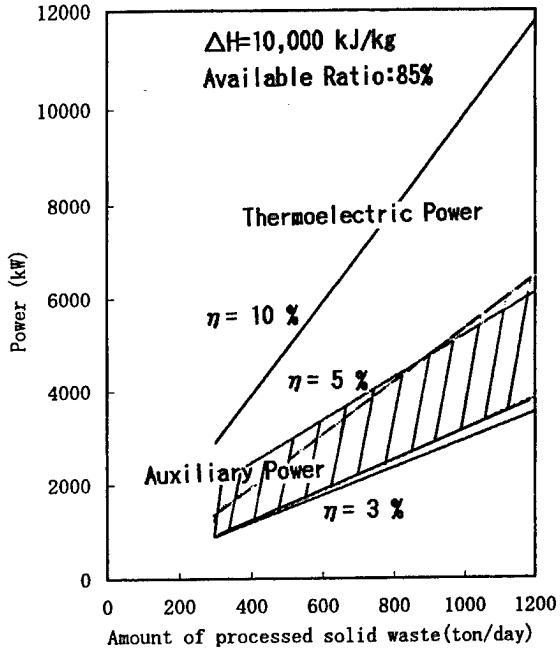


Fig.14 Approving conditions of TE system efficiency for self-sustaining incinerator system

Conclusions

The survey on the feasibility of thermoelectric power generation system utilizing combustion heat of solid waste has been done from various aspects such as resource evaluation, system characterization, on-site experiments , cost estimation and so on.

In consideration of the characteristics of solid waste as energy source, it can be said in principle that a thermoelectric power generation system , which has no scale effect and is high reliable, is the most suitable power generation system to utilize the combustion heat from a mini-scale to large scale efficiently. It is necessary to select a proper heat exchanging system fitting the incinerator system condition. Due to several on-site experiments the technological problems have been extracted and some approaches have been discussed. In particular, it was clarified that the problems on durability and heat transmission were very important.

In conclusion, although there are technological and economic problems to be solved, the thermoelectric system is advantageous to the utilization of heat of solid waste as compared with other systems. The further research and development with this aim should be highly encouraged.

Acknowledgments

The author would like to express his gratitude to Dr. M.Niino,NAL,Dr.Y.Tada,JAST,Dr.I.Higashi,Fuji Elec.Inc.,and Mr.H.Tsuboi,NKK to fruitful collaboration for this survey.

References

[1] T.Kajikawa et al, advancement of Thermoelectric Energy Conversion Systems in Japan,Proc. of XI ICT, 175-180(1992)

[2] T.Kajikawa,Thermeoelctric Power Generation Systems Recovering Heat From Combustible Solid Waste in Japan, Proc. of XV ICT,343-351(1996)

[3] Y.Tada,N.Endou,T.Oshima,Y.Tanji,An Experimental Study on Thermoelectric System by Hot Air in an Incinerator, Proc. of 7th Symposium on Environment Technology (1997)

[4] I.Hikashi, A.Simizu, M.Toraguchi, Thermoelectric Generator, Technical Rept. of IEICE (1997)

[5] T.Kajikawa, Development of Thermoelectric Power Generation System Utilizing Heat of Solid Waste, J. of Advanced Science,7,3&4,133-137(1995)

[6]Japan Waste Research Foundation, Report on Utilization Combustion Heat of Solid Waste(1996)

[7] Y.Hori et al, Analysis on Thermo-mechanical Stress of Thermoelectric Module, Proc. of 1997 IEE Power&Energy Symposium 262-263(1997)

[8] U.Birkholz,D.O.Gruden, Conversion of Waste Exhaust Heat in Automobiles Using FeSi2-Thermoelements, Proc. of 7th ICTEC, 124-128(1988)

Current state of Peltier cooling

John G. Stockholm
Marvel Thermoelectrics. 11 rue Joachim du Bellay, Marsinval, 78540 Vernouillet, France.
Tel: (33)1 3971 6914, Fax: (33)1 39716823, e mail: marveljs@imaginet.fr

Abstract.

The performances of Peltier cooling depend first of all, on the thermoelectric properties of the thermoelectric (TE) materials and secondly on the thermal design. A survey will be given of present and future TE materials, bulk and thin film. The technologies of manufacturing the materials and of manufacturing TE modules (a rigid assembly of TE couples) will be presented with future trends. Cooling systems from milliwatts to kilowatts with temperature differentials from a few K to more than 100 K will be examined. Present day and pending applications will be reviewed.
The figure of merit Z is the best overall parameter to characterize TE material.
We will examine, for a standard air-air modular cooling unit, the influence of higher values of Z, on the cooling power and the coefficient of performance COP (= cooling power/electrical power). Also the influence on the cost of the system will be estimated. The COP of TE is compared to the COP of a small HFC type compressor.
The aspect of development cost will be addressed as it is a major drawback to the increase of new developments.

1) Introduction

We shall use the abbreviation TE for the word thermoelectric. This paper attempts to satisfy the layman and the specialist. For the past few years there is a renewed interest in Thermoelectricity, also all the work done over the past 30 years in all the countries of the former Soviet Union is slowly emerging. We hope that some of the ideas proposed below will encourage discussion and development.

2) Thermoelectric materials.

2.1 Characterization

The best way to characterize a thermoelectric material is the coefficient of merit $Z = s^2/(\rho*\kappa)$
where s = Seebeck coefficient V/K
ρ = electrical resistivity Ω*m
κ = thermal conductivity W/(m*K)

There has to be an n type material which has a negative Seebeck coefficient and a p type material with a positive Seebeck coefficient. The basic cooling sub-assembly is the thermoelectric couple shown as a sketch in Fig. 1, then comes the thermoelectric module see photograph in Fig. 1 which consists of TE couples in series electrically and in parallel thermally. These are manufactured industrially all over the World.

Thermoelectric semiconductor materials were discovered and developed in the 1950's. For cooling around 300 K bismuth tellluride based compounds are still the best. The improvement since 1960 has essentially been in quality control.

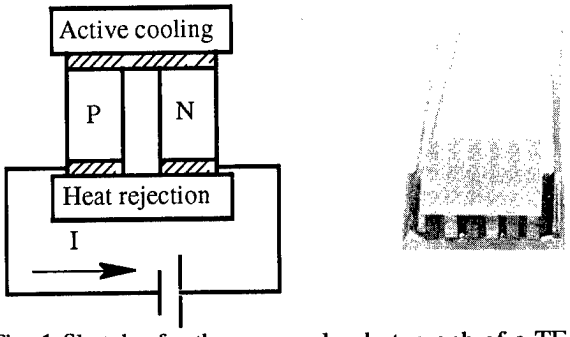


Fig. 1 Sketch of a thermocouple-photograph of a TE module (Thermion) base 8*6 mm

Typical easy to remember values for bismuth telluride at ambient temperature are:

s = ± 200	μV/K
ρ = 10	$\mu\Omega$*m
κ = 1.5	W/(m*K)
Z = 2.67*10^-3	K^{-1}.

These materials are anisotropic, the performances are obviously better when they are oriented in the most favorable way.

2.2 Experimental characterization

The characterization with high accuracy is very difficult. A paper by Uher [1] gives an excellent survey of all the methods used. The most difficult parameter to measure is the thermal conductivity. Harman [2] developed a method to measure directly the coefficient of merit Z. This measurement is relatively easy to do, it has the tremendous advantage of being a cross check of Z calculated from the 3 parameters s, ρ and κ measured independently. The difference between the calculated Z and the Z measured directly gives one an idea of the inaccuracies involved. Therefore all values announced by a laboratory or a company must be considered with a degree of precaution.

2.3 Manufacturing processes

There are quite a few ways these materials can be manufactured, we will give the most commonly ones used.
The following pertains to bismuth telluride.

1) Crystal grown

There are many ways to grow such crystals. The best crystals are mono-crystals meaning that the manufacturing process produces an ingot consisting of one crystal.

- The Traveling heater method known as THM is considered to produce the best mono-crystals. This method is presently mainly used for research because the method is a very slow one.
- Bridgman, Zone refining and Czchrowlsy are used in industry.

2) Sintered materials

There are 3 methods:

- cold sintering which produces a non oriented material with lower performances
- hot sintering which produces an oriented material

for bismuth telluride compounds this method produces an excellent p type material (Z up to 3.0 *10^-3 K^-1, but the n type material has so far always had a Z that does not exceed 2.4*10^-3 K^-1.

- extruded material

This process is used to manufacture rods of TE material like spaghetti with diameter greater than 1 mm. Interestingly this process produces an oriented material, that can be used directly by slicing perpendicularly to the rod (the current must flow parallel to the axis of the rod).

3) Thin film deposition

There are two categories: the first is by electrodeposition, the second by vacuum deposition. The latter has numerous processes such as sputtering, molecular beam epitaxy etc.

2.4 Temperature ranges of present day TE materials

2.4.1 Bismuth telluride

This material generally includes Selenium for the n type material. Normally the maximum of Z is around 300 K. It can be shifted as a function of temperature by changing the composition and the doping of the material.

This material can be optimized to have a maximum Z of 2.5*10^-3 K^-1 at 200 K Anukhin [3].

The maximum of Z as temperature increases is around 350 K, this material is generally used for electricity generation but can be used also for cooling. The maximum temperature at which bismuth telluride can be used is a function of its internal degradation as a function of temperature. It is generally accepted that this TE material should not be continuously used above 250 °C, though certain compositions can withstand short periods up to 275 and even 300 °C. This temperature range is interesting for cyclic cooling and heating to check reliability of electronic components.

2.4.2 Bismuth antimony.

This compound unfortunately only exists as an n type, Lenoir [4] Goldsmid [5] proposed that one can use a superconductor for the other leg, then the overall Z is close to the Z of the n leg.

2.5 Materials of the near future.

After over 30 years of stagnation in the development of TE materials, there is a renewal of interest in this area. There are two families: bulk type material and thin film materials. The following is a brief survey for non material specialists so that they have some idea of the research work that is being done.

2.5.1 Bulk type materials.

An extensive materials search has been done at the Jet Propulsion Laboratory (Pasadena ,California, USA): JPL [6]. The most promising materials are skutterdurites which are a class of compounds based on the mineral skutterdurite : CoAs3. There are nine binary semiconducting compounds in this group, the first one to be studied was IrSb3. Slack [7] has examined the thermoelectric properties of skutterdurites.

These materials of cubic structure have two vacant sites Slack has proposed to place in those sites a "rattling atom" which would considerable reduce the thermal conductivity and lead to materials with a ZT of the order of 1. This value of ZT = 1 is no marked improvement but many specialists feel that one should be able to considerably increase it for skutterdurites.

Numerous other materials are also being studied, in particular intermetallics such as TiNiSn, Kohl [8] and organic compounds. These have been studied for many years but the major obstacle to be solved was their stability in time, it seems that this problem has been solved.

2.5.2 Thin films.

The term thin film is a very simplistic term to cover new families of materials that consist of very thin films that are superlattices one of which is quantum wells. The TE properties are those parallel to the plane. This must not be forgotten so the electrical current and the heat flow are parallel to the plane.

The quantum well was first studied by Hicks and Dresselhaus [9]. At the 1997 Spring Materials Research Society Meeting in San Francisco the theoretical work by Dresselhaus [10] associated with the experimental work on PbTe by Harman [11] constituted a proof of principle of the quantum wells. Dresselhaus considers that the time frame, for this to reach industry, is 10 years away. PbTe was studied because a barrier was available which was not the case for bismuth telluride.

The quantum well consists of a very thin layer of material (between 1 and 100 nm) sandwiched between two barriers. So a system would consist of a stack of alternatively active films and of barrier films.

It is necessary to indicate that the Z values given for 2D materials does not include the barrier. The barrier decreases the Z as heat flows through it and therefore increases the overall thermal conductivity of the films. Until now only the quantum wells have been studied, and the barriers have not yet been optimized.

From the above we see that nothing is on the short term horizon, but there is at last very reasonable hope that we shall see within 7 to 15 years new materials which will considerably increase the performances of cooling systems and will open up new markets.

A cooling system consists of an active TE material and a technology to mechanically and thermally link the material to the heat sources. For the bulk material of the future all present day technology development will contribute to the system design.

For thin films it is another subject, especially as we saw that the plane of the thin films will be perpendicular to the heat sources. This will require the development of a whole new technology.

2.6 Unexplored thermoelectric physical processes.

We must not forget the potential physical processes that have not been studied, Anatychuk [12] presented a table showing all the thermoelectric physical processes. Very few have been studied in fact, essentially those, with an electric field continuous in time. For low temperatures the magnetic enhancements has been studied they are the Nernst, Ettinghausen Riggi etc. effects.

The influence of pressure and of magnetic fields has not been systematically studied. There are areas that should be explored. An area of potential interest is the one with variable electric and magnetic fields. Work has been done in some of these areas Strachan [13] combined an electric field with a variable pressure (piezo-electric) but to date Strachan's results have not been confirmed .

The author believes that these areas are worth studying.

There are two technologies to connect the TE material to the heat sources.[14]. The most common one uses thermoelectric modules as shown in Fig. 1, the other integrates the TE material to the heat exchangers which are used to conduct the electrical current from one piece of TE material (n type) to the next piece of TE material (p type) [15].

3) Thermoelectric modules: single stage

3.1. TE modules with a ceramic

The great majority of thermoelectric modules consist of the assembly of thermoelectric couples between two ceramic plates see Fig. 1. The ceramic must be a good dielectric insulator, have mechanical strength, have a thermal expansion compatible with the copper connectors between the pieces of TE material and have a good thermal conductivity. The compactness of the TE material is generally such that the area of TE material is about 40 % of the area of the ceramic plate

Generally alumina (Al_2O_3) with a thermal conductivity below 25 W/(m*K) is the ceramic. Beryllium oxide which has a much higher thermal conductivity of 250 W/(m*K) is also used but it is expensive and its manufacturing and machining creates a toxic dust. Aluminum nitride is an excellent material with excellent properties and a very high thermal conductivity of 180W/(m*K). The cost of this material which five years ago was very high is now coming down and is a very valid material.

3.2 TE modules without a ceramic

Modules that are manufactured without a ceramic support are more compact as the thermoelectric elements are only separated by a thin electrical insulator with a thickness of about 0.1 mm, so the compactness can exceed 90 %.

These modules nevertheless require an electrical insulation between the copper connectors and the heat exchangers. Generally one uses a thin organic insulator such as Mylar or Kapton.

The performances of a thermoelectric module depend primarily on the quality of the thermoelectric material and to a minor extend on the thermal conductivity of the electrical insulator whether it be a ceramic or an organic electrical insulator. We will address the subject of the interfacing of the module with the heat exchangers further on.

3.3 Interfacing of TE modules.

The interface with the lowest thermal resistance is a soldered interface. Present day applications generally interface modules with a ceramic, with a thermal grease such as a zinc oxide powder in a silicone oil. There are also thermal pads. These interfaces have the advantage of allowing the ceramic to freely expand thermally. This is at the detriment of a certain thermal surface resistance between the ceramic and the metallic heat exchanger which is of the order of $0.35*10^{-4}$ K*m^2/W (0.35 K*cm^2/W).

An alumina ceramic with a thickness of 0.6 mm and a thermal conductivity of 25 W/(m*K) has thermal area resistance of 0.24 cm2*K/W, this is similar to the value of the interface resistance. A Kapton sheet 50 micrometers thick has a thermal bulk surface resistance of 0.5 K*cm2/W, but it has two interfaces of around 0.35 K*cm2/W each.

When both sides are extriorly mehanically independent both sides can be soldered. For certain applications it is possible to solder one of the ceramics to the heat exchanger. In this case the ceramic has a metallization on its outside surface. The soldered interface has a thermal resistance which is decreased by a factor of ten, which make it very interesting. Generally one solders the cold side ceramic, because the thermal expansion is much less than on the hot side. Soldering large surfaces requires considerable care and its application is essentially a matter of cost.

3.4 Integrated heat exchangers.

By this term we mean associating the "ceramic" with the heat exchanger. Until now the market for TE modules was for "universal modules" that can be installed in many different ways to many different heat exchangers.

The trend to day with an increasing market for TE modules estimated at about a 15 % annual increase, is such that soon it may be economically valid to manufacture TE modules for a specific application with the heat exchangers being an integral part of the TE module.

Two technologies are emerging.

3.4.1 Anodized aluminum heat exchangers

With an electrically insulating anodization.

The concept is to manufacture the TE modules onto the heat exchanger [16]. TE modules are commercially sold with an integrated heat exchanger consisting of finned aluminum plates

Thermally this concept is very interesting, the main disadvantage is the difference in thermal expansion between the aluminum and the copper connectors, it may be advantageous to replace the copper connectors with aluminum connectors?. This technology probably very economic has yet to be confirmed from the reliability point of view.

3.4.2 Aluminum nitride heat exchangers.

The advantage of aluminum nitride is that it is an excellent thermal conductor and an excellent electrical insulator combined with a high mechanical strength. It's cost is decreasing every year.

So a TE module can be made with this ceramicmaterial with an appropriate outside surface for the heat exchange.

The cost for prototype parts made with aluminum nitride are still very expensive but for large annual requirements the cost will come down.

This concept leads to a completely new technology for the assembly of several or many modules together. The main difficulties will be

- to have a structure to hold the modules together
- to obtain reliable sealed circuits
- to absorb the thermal expansion.

Such systems are presently being studied and will probably be commercially available in the next few years. The performances will be better than present day assemblies.

4) Multistage TE modules

These TE modules produce a high ΔT and give a low cooling power. The applications are numerous for spot cooling in particular of detectors.
Some TE companies just sell the multistage modules, other companies manufacture and sell detectors with their in house made multistage modules.
The lowest temperature one can reach from ambient is around 160 K [17].

Another application is to drop the temperature a few K but at very low temperatures. At temperatures below 200 K bismuth telluride has a very low Z. The best material today is n type bismuth antimony with a superconducting second leg. to our knowledge such modules are not available commercially. The manufactures use them for their own detectors. So not much information is available about them.

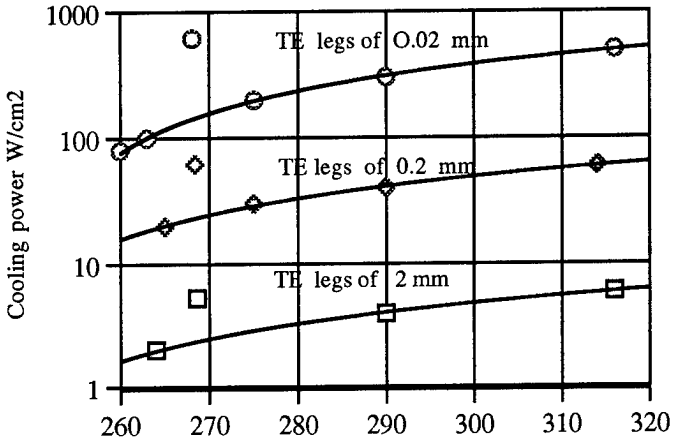
5) Applications.

Below we have reviewed most present day applications and have divided into categories more or less by cooling power and temperature range.

5.1 Electronic chip spot cooling.
This application is a growing market as more and more components require cooling. The main trend is towards higher and higher heat flux densities which is requiring development work.

5.1.1 Present day technology.
Today certain CPU's are cooled thermoelectrically. The TE module cools the CPU and on the heated side there is a heat exchangers and generally a small fan. The small unit is either designed for assembly to the CPU during manufacturing or as a commercially sold add on component that clips onto the CPU. The modules used have TE legs with a length generally between 1 and 1.5 mm

5.1.2 Micro devices with thick and thin films.
This is a new area of development [18]. The substrates are diamond or aluminum nitride: AlN. The advantage of having shorter TE legs is that the cooling power density increases as the legs get shorter. See Fig. 2



T hot = 330 K diamond substrates Cold side temperature K
Fig. 2 Cooling power density for different leg lengths from[18]

We note that with a ΔT of 50 K the cooling power density in W/m2 increases 10 fold each time the leg length decreases by a factor of 10 from 2 mm to 0.2 mm to 20 μm. and has a value of 3 MW/m^2 (300 W/cm^2), these are very high heat flux densities. The applications are for the cooling of electronic chips. For example an 8 watt chip today dissipates 30 W/cm2 and future power amplifiers will dissipate 100 W/cm2. with these micro coolers one shall be able to maintain the temperature of the active layers of the electronic device from a few degrees to tens of degrees below the temperature of the substrate on which the device is mounted. This reduction in temperature increases reliability, lifetime and clock speed.

5.2 Biological applications
More and more biological samples require cooling for them to be conserved and examined often under a microscope.

5.3 Temperature stabilization.
Thermoelectrics is the ideal solution when one needs to stabilize a temperature and when small cooling and heating powers are required. the field is enormous in particular in the biological sciences where often it is critical that the temperature be maintained constant to within a tenth of a degree C.

Certain electronic components have important properties that vary with temperature, the most common one is the laser diode that is very sensitive to temperature. This market has not developed as fast as people thought. Komatsu of Japan developed a sophisticated robot to manufacture automatically small TE modules of a few mm by a few mm for this application. The robot is presently operated well below full capacity. The interesting fact is that a robot has been successfully built to manufacture small modules, so expertise has been accumulated leading the way for the future when larger modules could be manufactured automatically.

5.4 High ΔT multistage modules.
These modules are generally for detectors of all sorts: infra-red, X ray, gamma ray etc. because lowering the temperature reduces the noise and increases the sensitivity. The objective has been 170 K. This is obtainable, but still requires considerable electrical power. Better TE materials will reduce the electrical power. Development in this area is due to the military applications.

5.5 Standard range up to 50 W
There is a big World market for TE modules with a ceramic sizes of 30*30 and 40*40mm. The applications are "infinite" from industrial applications to consumer products such as picnic coolers. This market is the one that has made thermoelectrics known to many people. A new potential market, especially in the US is the water cooler market.
There is presently no special breakthrough, cost is the most important factor. The manufacturers of the applications sacrifice performance for cost. They install generally only one TE module and operate it close to its maximum cooling power hence at a very low Coefficient of performance COP

COP = cooling power W / electrical power W
which often gives thermoelectricity a reputation for a very bad efficiency when it is not quite that bad.

5.6 Range up to 50 W with a higher ΔT.

For quite a few years now two stage modules manufactured generally with three ceramics of the same size have been commercialized. These TE modules allow one to obtain slightly greater ΔT's between the cold ceramic and the hot ceramic. The increase is of the order of 10 to 15 K. A typical application is a refrigerator that makes ice.

5.7 Range 50 to 200 W.

The small home refrigerator has a cooling power of 75 W this increases as the size of the refrigerator. A few months ago the Japanese company Matsushita announced the manufacturing and commercialization of small thermoelectric refrigerators for hotel rooms. The main advantage of TE being the absence of the noise of a compressor. These refrigerators that contain food and drink are quite sophisticated in that they are computer controlled. Matsushita announced a yearly production of 50 000 units. Their publicity was misleading in that they compare their performances with that of "cheap" picnic coolers so announce a considerable improvement in performance which already exists in systems properly designed.

This application is nevertheless very important because it creates an awareness and more and more refrigerators will be thermoelectric though thermoelectricity is not ready to replace the compression cycle from an efficiency point of view.

This example is very interesting because it is a reality and we can use it to make comparisons between compression cycle and thermoelectricity. This is the object of paragraph 7.

This range corresponds to space cooling for electronic cabinets, the World leader in this field is TECA (Chicago Illinois USA) who make off the shelf TE air-air coolers in this range. Their standard product Americool® 4000 See Fig. 3. It is an air to air unit, designed so that they can be stacked, Fig. 3 shows 4 units stacked together

5.8 Cooling powers greater than 200 W

The TECA unit referenced above is designed so that up to 10 units can be installed in parallel on both air circuits. This gives cooling powers in the range of 1 kW.

Marvel has developed a standard TE building block with a nominal cooling power of 150 W with a $\Delta T = 0$ between the inlet air flows and a COP = 1. See Fig. 4 Marvel TEBB AA6 These temperature conditions are standard for electronic cooling when the user wants to keep the inside temperature of the enclosure equal to the outside temperature without any air going from the outside to the inside and vice versa. This TE air-air building block is designed so that it can be assembled in series and in parallel on both air circuits. In this way one can obtain much greater temperature drops than with units that can only be assembled in parallel.

Applications for these building blocks are numerous: first of all they are an economic way to build feasibility prototypes and to obtain small productions series. The design is for all uses including where there is condensation of moisture in the air, so performances are not optimized for a given application, but they are sufficiently good for most applications. Numerous feasibility studies have been done for the air conditioning of drivers cabs of trains. This appears to be an excellent application because the cooling powers do not exceed 10 kW and are generally around 6 kW.

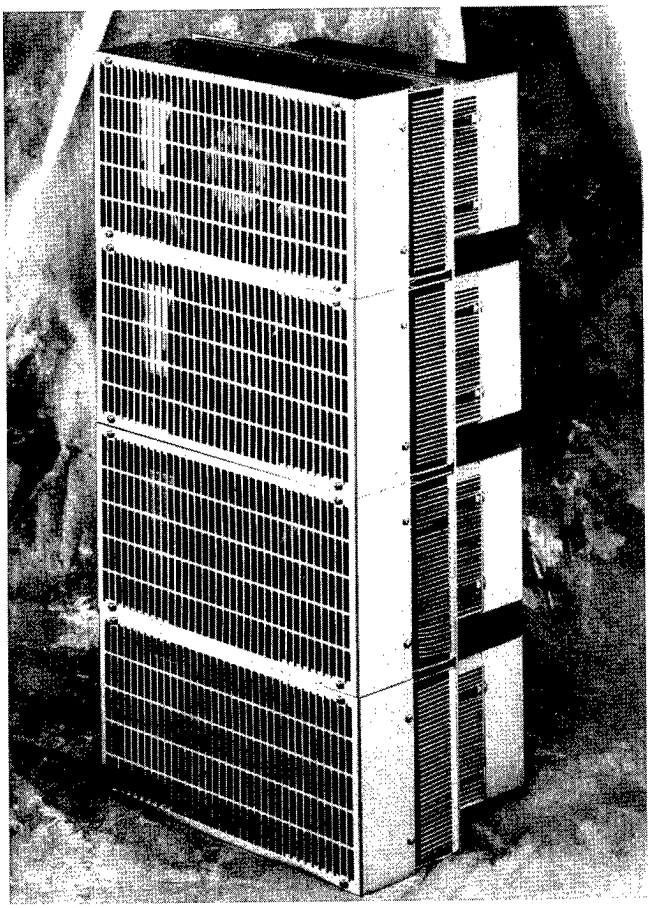


Fig. 3 Americool® 4000

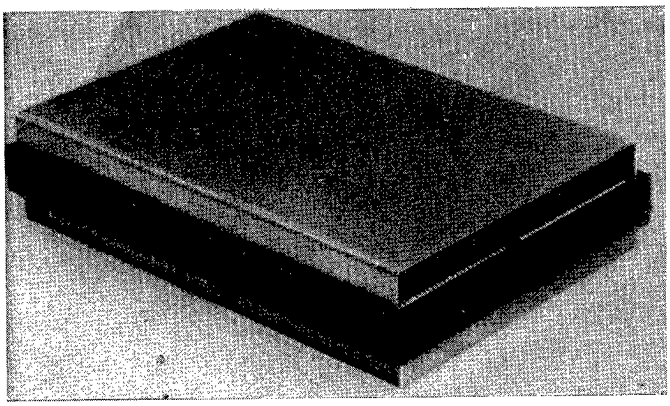


Fig. 4 Photograph of Marvel Thermoelectric building block air-air TEBB6 Dimensions: 275*185*70 mm

We must not forget that large TE systems were initially developed in the 1960's. The administrative building of S. C. Johnson by Frank Lloyd Wright in Racine Wisconsin USA was equipped in 1965 with 30 units of TE air conditioning with heat rejection to water, manufactured by Carrier Corporation. A photograph was taken by the author in 1973 of a unit placed on the floor. After 8 years they were mainly having power supply problems. A few years later the units were taken out for lack of spares.

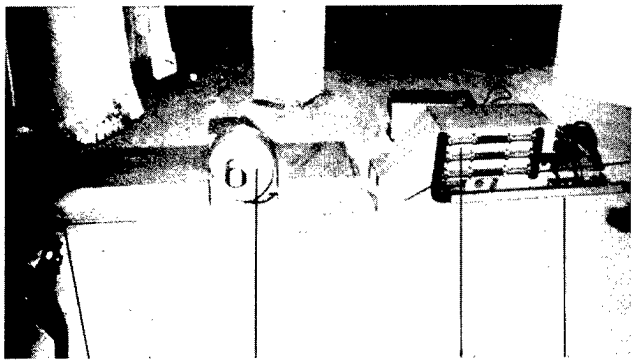


Fig. 5 TE air conditioning at S. C. Johnson by Carrier Corp. Cooling power 1,5 kW heating power 1.8 kW

Then a railway coach was TE air conditioned with 20 kW of cooling and 32 kW of heating, designed and manufactured in the late seventies by Air Industrie [19] see photograph in Fig. 6 below. It was in commercial operation for over 10 years on the French Railways without a thermoelectric failure, there were only maintenance problems with the power supply and the controls.

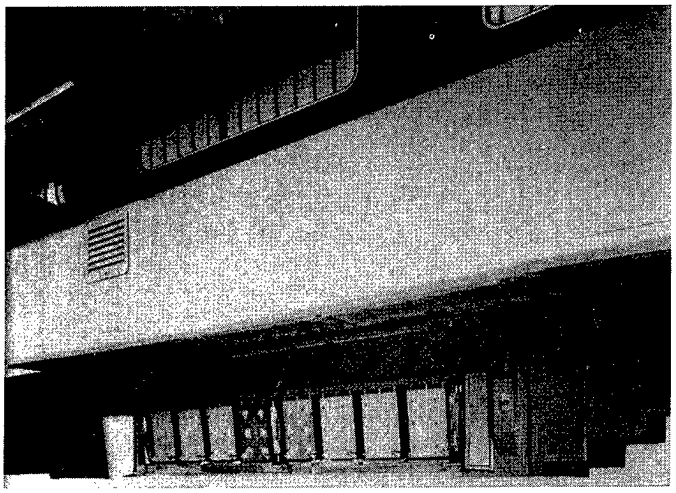


Fig. 6 TE air conditioning unit of a passenger railway coach

For large water cooling units, there are no commercially available units all equipment's are designed for a specific application such as for submarine use. A cabinet is shown in Fig. 7 that produces 15 kW of chilled water with heat rejection to a water circuit [20]. It was developed by the same team that developed the TE railway air conditioning Many of these cabinets are now installed and are in operation on a submarine.

All these applications has proved the technical reliability of such systems, but not the economic. We do not see today any more applications for cooling powers in the tens of kW range. These applications will only emerge economically for specific applications when a new generation of TE materials with Z's at least double of present day materials become industrial.

6) Influence of Z on the performances of a standard TE building block (TEBB)

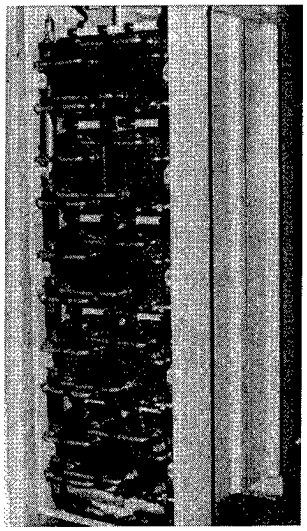


Fig. 7 TE water cooling cabinet for a submarine application. Dimensions 1800*600*900 mm

The influence of the Z of TE material on the performances of a system vary on the type of system. For a multistage cooler the overall performances depend on the module performances and on the heat exchanger on the hot side. We will not address this example as the module manufacturer can calculate the performances.

We will examine an air to air TE building block designed for 6 large thermoelectric modules. These building blocks are designed so that they can be placed in parallel and in series to make up a big system. We will examine a single building block

6.1 Description of the TE Building Block. (TEBB)
The TEBB is designed to contain 6 TE modules with ceramics ranging in size between 40*40 and 62*62 mm. See Fig. 4 Photograph Marvel TEBB AA6

The air to air TEBB is cross flow so that the TEBBs can be placed in parallel and in series on each of the air circuits. See Fig. 8 Schematic of 8 TEBB AA6 which shows 8 TEBBs.

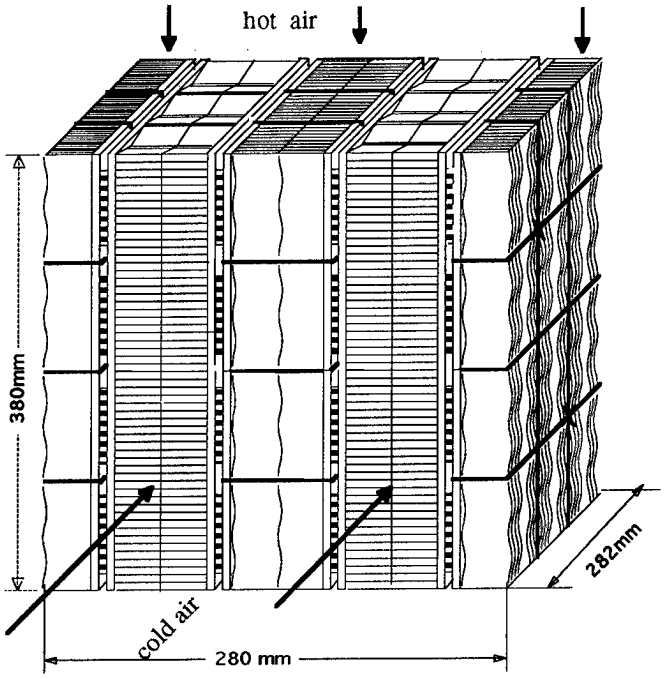


Fig. 8 Schematic of 8 TEBB AA6

6.2 Performances of TE building block.
The performances for the TEBB with a commercial TE module

Melcor CP5-31-06 L are given in Fig. 9 The nominal conditions are those used for electronics:

- both inlet air temperatures are equal to 25 °C.

With a COP =1 the cooling power is of 135 W

- the air flow rates are such that the cooled air velocity is 2 m/s and the heated air flow velocity is 4 m/s.

6.3 Influence of Z on the performances.

We have examined the influence of Z between 2.44 and $8.5*10^{-3}$ K^{-1} of a hypothetical TE material to see how it influences the performances of the Marvel air-air TEBB6. We used the simple thermal-thermoelectric mathematical model [21]. the air flow velocities through the heat exchangers are of 3 m/s on the cooled side and 6 m/s on the heated side. The thermal resistance's between he ceramics of each Melcor CP5-31-06 TE modules and the air flows are for the cooled side 0.24 K/W and for the heated side 0.17 K/W.

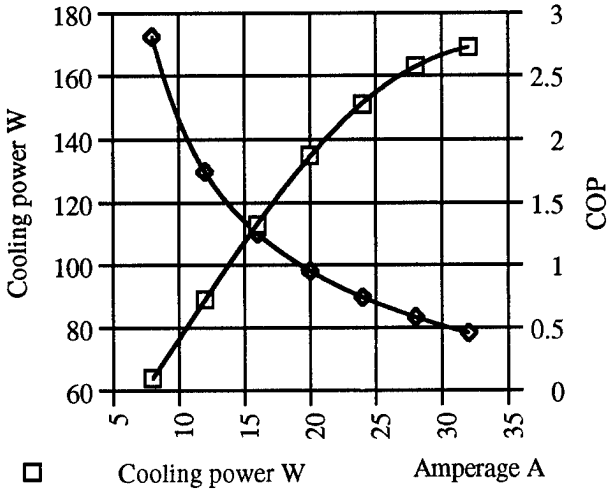
We used the following formulae from Melcor expanded around 23 °C (not from O K as the Melcor formulae are given)

ρ = (10.85+0.0535*(tm_Te-23)
+ 0.0000628*(tm_Te-23)^2)/1000000 Ω*m

s = (210.9+0.344*(tm_Te-23)
- 0.0009904*(tm_Te)^2)/1000000 V/K

κ = (1.659-0.00332*(tm_Te-23)+0.0000413*(tm_Te-23)^2) W/(m*K)

The values of Melcor material at 23 °C correspond to the first number in the expansion.



Air inlet temperatures
hot side 25 °C 50 %RH air 2 m/s: 9.1 g/s ΔP = 24 Pa
cold side 25 °C 50 %RH air 4 m/s 27.3 g/s ΔP = 46 Pa

Fig. 9 Marvel air-air TEBB6 Cooling power and COP.

The hypothetical material has properties ρ, s and κ. We chose the values by taking the initial values of the Melcor material then we multiplied them by the factors given below.

	Values of 1000*Z						
	2.44	3.02	3.72	4.61	5.7	6.3	8.5
k factor of ρ	1	0,9	0.9^2	0.9^3	0.9^4	0.9^4	0.9^5
k factor of κ	1	0.9	0.9^2	0.9^3	0.9^4	0.9^5	0.9^5
k factor of s	1	1	1	1	1	1	1.1

For each case with the set of values of ρ, s and κ with a corresponding Z, we calculated the Cooling power and COP as a function of ΔT between the two air flows and the electical current through the TE modules.

To obtain 2D graphs from 3D data, we chose to present the results for a given ΔT between the two air flows. We chose 30 K as being an industrially valid temperature difference.

$$\Delta T = \frac{(T \text{ heated in} + T \text{ heated out})}{2} - \frac{(T \text{ cold} + T \text{ cold out})}{2}$$

= 30 K

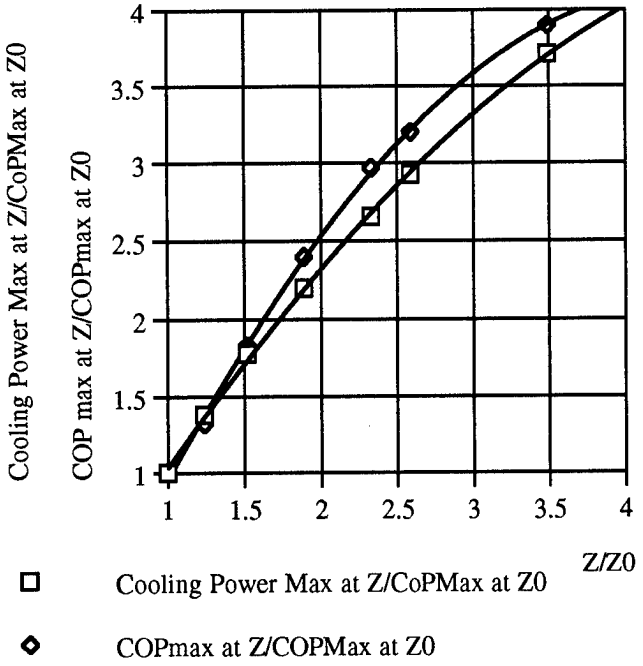
With ΔT= 30 K, we calculated for each case the maximum cooling power and the maximum of COP and the corresponding electrical currents through the TE modules.

The nominal values for $Z = 2.44*10^{-3}$ K^{-1}.

Are: Maximum cooling power 152 W

COP Max. = 0.39

Fig. 10 gives the relative values



Marvel air-air TEBB with DT = 30 K between the air flows.

Fig. 10 Relative Maximum Cooling power and COP max. for average ΔT between the air flows = 30 K

We must not forget that these two values correspond to two different values of the electrical current. So we examined an "industrial" case, we took the average of these two electrical currents which corresponds to a current that would be used industrially.

We chose severe conditions. A constant ΔT between the average temperature between the two air circuits of 30 K

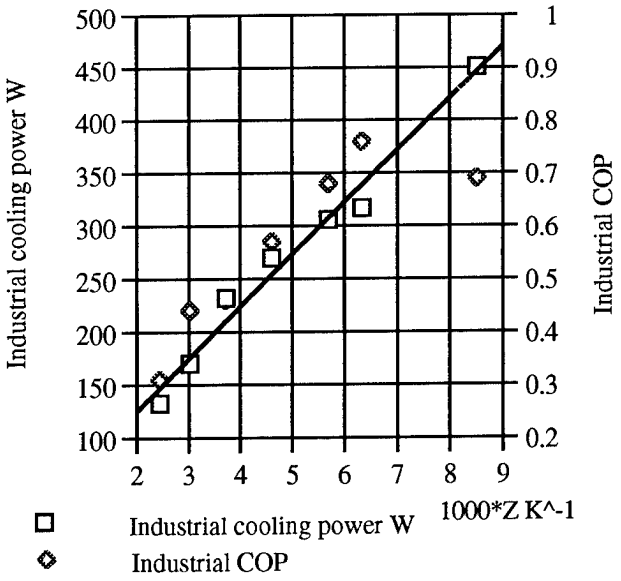
We defined an industrial operating point such that

I ind = [I(Pmax) +I (COPmax)]/2

$$\Delta T = \frac{(T \text{ heated in} + T \text{ heated out})}{2} - \frac{(T \text{ cold} + T \text{ cold out})}{2}$$

= 30 K

Examining the results of the calculations shown in Fig. 11, we realized that the criteria chosen for the "industrial current" was not ideal, we got a dispersion of points, that can only be explained by the arbitrary choices of ρ, σ and κ. The curves are relatively regular up till Z = 6.3*10-3. Then the COP drops off. The only explanation we can find is that up to a Z of $6.3*10^{-3}$ the s remained unchanged then for Z =$8.3*10^{-3}$ we increased s.



Electrical current= (current of Pmax + current of COP max)/2

Average temperature between the two air flows = 30 K

Fig. 11 Industrial cooling power and Industrial COP with average ΔT between the two air flows of 30 K

This graph shows that from a 1000*Z of 2.4 to 8.5 the cooling power increases by a factor of 3, but the COP then leveled off at 0.7. We examined the results of the calculations and saw that for 1000Z =8.3 we could increase the COP to =1 but the cooling dropped to 338 W.
The ΔT max. which corresponds to zero cooling power was not systematically examined but with a Z of 6.3 $*10^{-3}$ K^{-1}. It exceeds 120 K.

6.4 Estimated influence of Z on the cost of the TE building block.
The cost of a TE unit is proportional to the number of TEBBs and to the yearly production. Examining the above graphs, we consider that assuming a conservative value today of Z = $2.4*10^{-3}$ when Z reaches $6*10^{-3}$ the cost will be divided by more than two and at the same time the COP will have more than doubled.

7) Comparison between a TE module and a small compressor

We are giving this because a lot of general statements are made on the subject but few numbers. So we have examined the COP of small HFC R134a compressors of 60 W and 75 W of electrical power at 60 Hz and 50 Hz (courtesy of Japan air conditioning, heating and refrigeration news). Fig. 12 shows the COP as a function of the temperature difference between condensor at 45 °C and evapoerator, ambient being 32.2 °C.

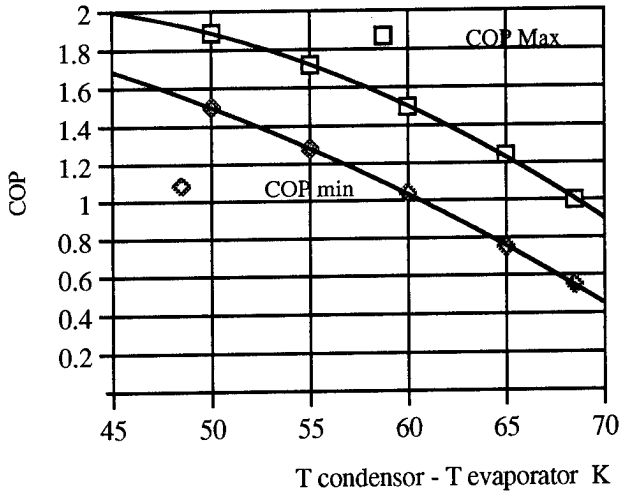


Fig. 12 COP of a compressor with HFC R134a.

It is dangerous to use the same temperature differences for an equivalent TE system, nevertheless it is interesting to compare the above performances with those of a TE module with today's Z = 2.44*10-3. A compressor operates essentially at constant electrical power, but a TE system can be operated with different electrical powers (electrical current) so we must choose a value for the electrical current. See Fig. 13 and 14

We want to compare the compressor operating with a ΔT = 50 K to the above module. We see that with this ΔT and an electrical current of 50 A we obtain 30 W with a COP = 0.18. This is to be compared with a COP between 1.5 and 1.9 for a compressor. The conclusion is that today we are very far from the COP of a compressor for the range of a few hundred watts of cooling.

Nevertheless we must not forget the advantages of a TE system which are reliability, no potentially hazardous fluid, flexibility etc.

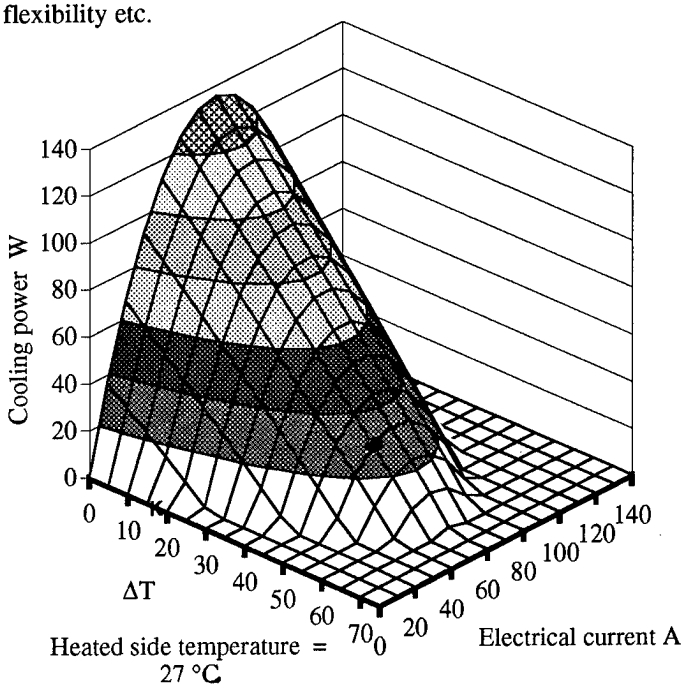


Fig. 13 Cooling power of a Melcor CP5-31- 06

The COP is given in Fig. 14

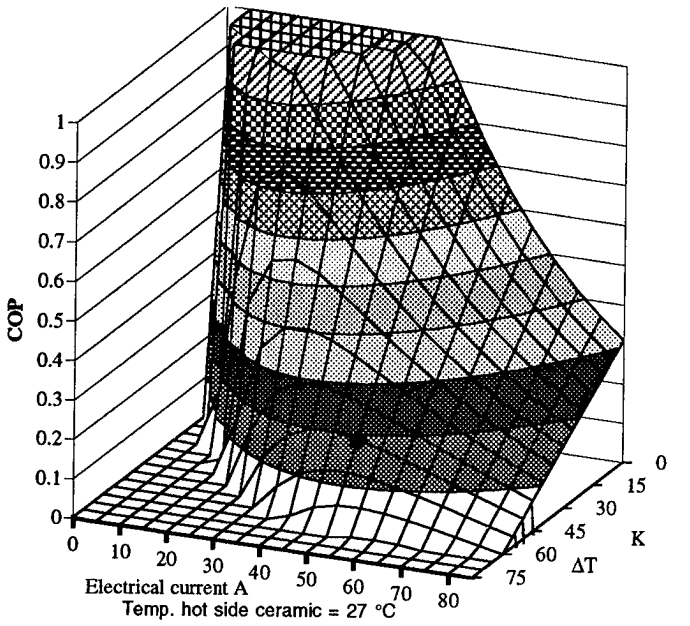


Fig. 14 Melcor module CP5-31-06 COP

8) Economics of TE cooling and development costs.

A predominant parameter is the annual requirements. As annual
quantities increase the costs go down. For very large annual quantities such as those encountered in the automotive industry the cost is essentially material cost, the manufacturing and assembly costs become the minor component.

8.1 Raw TE material costs
For cooling today bismuth telluride is the only valid material. Material costs vary as a function of purity and of annual quantity, the following values are approximate and correspond to annual quantities per ton and purities between 4 and five nines.

Bi: $10/kg
Te: $70/kg
Sb: $80/kg
Se: $45/kg

New materials may use:

Zn: $1.20/kg
Cd: $1.50/kg
Co: $43/kg

with these values the raw materials cost for a bismuth telluride that contains Sb and Se will be around $70/kg.

8.2 TE material costs.
Bismuth telluride is available on the World market, the price per kg for one ton a year is around $250. This is very variable as it depends on the Z of the material, this value if for a $Z = 2.5*10^{-3} K^{-1}$.

8.3 TE module costs.
One can in a very simplistic way calculate the module cost based on the amount of TE material and come up with a $/kg of TE material in a module. Comparisons are only valid for very similar modules as the cost increases considerably as the size of the TE elements decrease.
A major parameter is once again the annual requirements. TE module manufacturers generally give cost for orders up to 1000 modules, for larger quantities there is always negotiation. An estimation of the relative cost as a function of quantity is given in [22].
For medium and large cooling power TE modules the cost per kg of TE material assembled into a module is around $1500, for annual orders corresponding to a ton of TE material in the TE modules.

8.4 TE system costs.
The predominant parameter is the influence of the annual production, but the technology of the system will depend on the annual production. Obviously the level of production at which the technology changes depends on many parameters to simplify when dealing with large cooling systems with cooling powers in excess of hundreds of watts the "magic number is 1000 kg year of TE material.

Today the TE module manufacturers produce TE modules that are relatively universal, this means that they can produce large annual quantities. The user who only requires much smaller quantities profits by the series effect of the TE module manufacturer.
The difference is that the annual quantities so far for TE systems is small except for some devices that require only one TE modules such as specific spot electronic cooling, or the picnic cooler.

8.5 Development costs.
This aspect is generally considerably under estimated. Big systems require extensive R and D. That is why developing a multi-use building blocks is economical, because the thermoelectric R and D has been done and then there is only left to do the mechanical assembly.
Systems require that a test bench be built to measure the overall performances and also endurance testing is a necessity to ensure the reliability of the system.
It is very difficult to estimate on a general basis development costs. When experience in designing and building TE systems is already available then the development cost decreases considerably. Unfortunately there is no book on the Design and Technology of TE cooling systems,

8.6 New TE materials
The new materials which are on the horizon may contain Zn and Cd which are very cheap and Co is about half the price of Te so from the raw material aspect we may see a considerable decrease in cost.

Today we do not know the manufacturing processes that will be required to make from these raw materials a good TE material, but we can hope that the processes will be analogous to those used today so the manufacturing costs should be similar. As the raw materials are cheaper and the performances are considerably better, we should see a big increase in annual quantities and this should also contribute to bring down the cost of the TE material.
Many applications will only develop if the cost of the TE material is considerably lower than today.

9) Conclusions

Peltier cooling has progressed very slowly over the past 35 years. In fact many large applications of the past have proven the advantages of thermoelectrics but the economics are very rarely valid for large systems. For the past 4 years money has been invested into the study of new materials, They are 7 to 15 years away. New areas of thermoelectrics deserve research such as those where there are magnetic fields, variable currents and perhaps mechanical stresses.
Thermoelectrics has not taken off yet. It will come but in probably only 10 to 15 years. Then it may increase like the area of microelectronics today.

References

[1] C. Uher: Thermoelectric property measurements, Naval Research Reviews, four/1996 vol. XLVIII Office of Naval Research, Dept. of the Navy US p 44 - 55
[2] T. C. Harman, J. appl. Phy. 29, 1373 (1958)
[3] A.I. Anukhin, S. Y. Skipidarov, O. B. Sokolov Thermoelectric and semiconducting properties iof $(Bi_{1-y}Sb_y)2Te_3$ solid solutions grown by zone melting. Teh 12 th International conference on Thermoelectrics Nov 9-11 Yokohama, Japan. Editor K. Matsuura. Institute of electrical engineers Japan.
[4] B. Lenoir, A. Dauscher, X Devaux, R Martin-Lopez, Y. I. Ravich, H. Scherrer, S. Scherrer Bi-Sb alloys: an Update; The 15 Interantional conference on Thermoelectrics March 26-29 1996 Pasadena U. S. A. IEEE Catalog N° 96TH8169 pp 1-13
[5] K.K. Gopinathan, H.J.Goldsmid,D.N. Mathews, K.R.N. Taylor Passive Thermoelements, Procceding of 7th International conference on thermoelectrics Arlington Texas. U.S.A. pp 58-61 (1988)
[6] J. P. Fleurial, A. Borshchevsky, T.Caillat and Richard Ewell"New materials and devices for thermoelectric applications" Proceedings of the 32nd Intersociety Energy Conversion Engineering Conference, July 27- August 1, Honolulu, Hawai, (2), 1080-1086, (1997)
[7]G.A. Slack The themroelectricproperties of skutterdurites, Naval Research Reviews,four/1996 vol XLVIII Office of Naval Research, Dept. of the Navy USA
p 23 - 30
[8] H. Kohl, A. P. Ramirez, W Kaefer, K. Fess, Ch Thurner, Ch Kloc and E. Bucher "New class of materials MNiSn" Thermoelectric materials-New Directions and Approaches; Matreaials Research Society Symposium Proceedings vol 478 March 31 - April 3 1997. San Francisco CA USA.
[9] L. D. Hicks, M. S. Dresselhaus "The effect of quantum well structures on thermoelectric figure of merit" Presented at 1 st National thermogenic cooler Workshop Sept. 17 1992 Fort Belvoir. VA. USA
[10]M. S. Dresselhaus, X. sun, S. B. Cronin, T. KOga, G. Dresselhaus, and K.L. Wang, "Prospects for high Z in 2 D systems", Thermoelectric materials - New Directions and Approaches; Materials Research Society Symposium Proceedings vol. 478 March 31 - April 3 1997. pp 55 - 66 San Francisco CA USA.
[11] T. D. Harman, D. L. Spears, M. P. Walsh, X. sun, S. B. Cronin, and M. S. Dreselhaus "High thermoelectricFigures of merit in PbTe Quantum Wells"
to be published in the Proceedings of ICT'97 Dresden
[12] L. I. Anatychuk , " Rational areas of investigation and application of thermoelectricity", Journal of Thermoelectricity Vol. 1 N° 1 Oct. 1993.pp 5-19 Institute of Thermoelectricity, Chernivtsi, Ukraine.
[13] H. Aspden, J. S. Strachan "Solid-state thermoelectric refrigeration" Intersociey energy convrsion engineering conference, 1993 pp 1891-1896 American Chemical Society.
[14] J. G. Stockholm CRC Handbook of Thermoelectricity D. M. Rowe Ed. CRC press Boca Raton Fl. USA chapter 54
[15] J. G. Stockholm CRC Handbook of Thermoelectricity D. M. Rowe Ed. CRC press Boca Raton Fl. USA chapter 53
[16] T.I. Lushkina, A. M . Blagorodov, V. I. Dubov, "Thermoelectric metal base module"14 th International conference on Thermoelectrics June 27-30 1995.
St.Petersburg, Russia. pp 428-429
[17] G. Mahan B. Sales, J Sharp, "Thermoelectric material: new approach to an old problem" Physics Today March 1997 p 42- 47.
[18] J. P. Fleurial, A. Borshchevsky, T Caillat, R Ewell, New materials and devices for thermoelectric applications IECEC 1997 American chemical society paper N° 97419 p1080 - 1085
[19] J. G. Stockholm, L. Pujol-Soulet. "Prototype thermoelectric air conditioning of a passenger railway coach " 4 th International Conference on Thermoelectric Energy Conversion. Arlington Texas, March 1982 .
[20] Thermoelectric Cooling for Naval applications . J. G. Stockholm , P. M. Schlicklin. 7th International Conference on thermoelectric Energy Conversion. Arlington TX., March 1988
[21] J. G. Stockholm, D.W. Stockholm. "Thermoelectric modeling of a cooling module with heat exchangers" XI th International Conference on Thermoelectrics, Arlington, Texas, USA October 1992.
[22] J. G. Stockholm Future prospects in thermoelectric cooling systems Proceedings 12 th ICT November 1993 K. Matsuura Editor

Sensor applications of thermoelectric thin films

Sander van Herwaarden

Xensor Integration, POBox 3233, 2601 DE Delft, the Netherlands
Tel +31-15-2578040 Fax +31-15-2578050

0 ABSTRACT

This paper describes state of the art in thermal micro-sensors, as fabricated using thin-film and silicon technology. After defining thermal sensor types, the major thermal sensors are described. It also considers the physical and thermal effects on which the sensor action is based, and gives an introduction in the technology and design methodology of present day thermal micro-sensors.

I INTRODUCTION

Thermoelectric Thin Films: Ideal for Thermal Sensors
After the industrial revolution of the 19th century and the electronics revolution of the last decades, we are now on the brink of the information technology revolution of the 21st century. An important side effect of the information-technology revolution is its ever increasing need of data on the environment. For this, we need sensors which can measure every aspect of life, and transduce the related physical signals into electrical signals. The computer then does the rest.

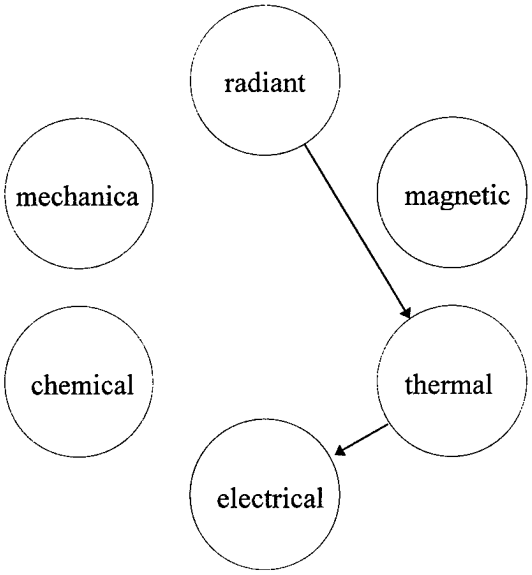


Figure 1: The six signal domains, with indicated the transduction of a thermal infrared sensor.

An often-used classification of sensors distinguishes six domains into which physical signal can be classified [1]: mechanical, chemical, magnetic, radiant, thermal and electric, see Fig.1.

Thermoelectric thin films are of importance to a class of sensors called thermal sensors. Thermal sensors transduce non-thermal signals into thermal signals, and then into electrical signals (indicated in Fig.1). For this second transduction, the thermoelectric effect is often used. It has the advantage over other methods to transduce from thermal to electric, that it is a self-generating effect, which means that the power needed for the electrical signal originates from the thermal signal. The advantage lies in the fact, that there cannot be any offset, since there cannot be a non-zero output signal without input signal (and power). Moreover, biasing is not required either.

II ANALYSIS OF THERMAL SENSING

Thermal power sensors and thermal conductance sensors
In thermal sensors, the transduction of the input signal to the output signal is carried out in two transduction steps, first the input signal is transduced into a thermal signal, and then, the thermal signal is transduced into the electrical output signal. An important distinction among thermal sensors is that between thermal power sensors and thermal conductance sensors [2].

Thermal power sensors
In the thermal power sensors the input signal which is measured by the sensor is a (thermal) power, which is used to generate the (electrical) power of the sensor's output signal. Therefore, there can be no output signal if the input signal is zero. These (so-called self-generating) sensors have no offset, and need no biasing. Especially for this class of sensors, the thermoelectric thin films are ideal. The operation of the thermal power sensors takes place in three steps.

1) The nonthermal signal C is transduced into the thermal signal heat P, by means of sensor-specific transduction action Q.

$$P = Q\,C \tag{1}$$

2) The heat P is converted into the thermal signal temperature difference ΔT, by means of a thermal structure with thermal resistance R.

$$\Delta T = R\,P \tag{2}$$

0-7803-4057-4/97 $10.00 ©1997 IEEE

3) The temperature difference ΔT is transduced into an electrical voltage U, by means of a temperature difference sensor S.

$$U = S\,\Delta T \tag{3}$$

In total, the transfer U/C of a thermal power sensor is described by:

$$U/C = Q\,R\,S. \tag{4}$$

Here, Q is governed by the physical transduction processes underlying the sensor physics, R is the thermal resistance of the sensor's active area to the ambient, often enhanced by using micro-machining techniques, while S may be the sensitivity $N\alpha_s$ of a thermopile with Seebeck coefficient α_s, consisting of N couples.

Thermal conductance sensors

In the case of thermal conductance sensors, the input signal C influences the thermal conductance G between sensitive area and ambient. To measure the thermal conductance, the sensor is biased with a heating power P. In this class of (so-called modulating) sensors the importance of a self-generating second transduction such as the thermopile is less important, but it can be convenient in some circumstances. The transfer in the thermal conductance sensors is as follows.

1) The nonthermal signal C is transduced into the thermal signal conductance G, by means of sensor-specific transduction action Q (with G_o as the offset of the sensor).

$$G = Q\,C + G_o \tag{5}$$

2) The conductance G is converted into the thermal signal temperature difference ΔT, by means of the (internally generated) thermal heat P.

$$\Delta T = P / G \tag{6}$$

3) The temperature difference ΔT is transduced into an electrical voltage U, by means of a temperature difference sensor S.

$$U = S\,\Delta T \tag{7}$$

For thermal conductance sensors, the total transfer can no longer be written in a multiplicative form, instead we find:

$$U = P\,S\,/\,(\,Q\,C + G_o). \tag{8}$$

This exposes the offset-containing character of modulating sensors. As for step 3), in some thermal conductance sensors, the electrical signal takes on another form, for instance a current or resistance value, depending upon the type of temperature difference sensor used (thermopile, Pt100, transistor).

III MAJOR THERMAL SENSORS

Overview of thermal sensors

At present at least ten different types of thermal sensor can be distinguished. Five of them belong to the thermal power class (self-generating), five to the thermal conductance class (modulating). They are listed in Table 1, and will be briefly discussed below. For a more extensive description, please consult [2]. With the exception of the psychrometer, all these sensors have been realized in in both silicon and thin-film technology.

Table 1: Overview of thermal sensors, signals they measure, and operation principles.

Sensor	Measures
thermal power sensors:	
microcalorimeter	concentration
psychrometer	humidity
infrared sensor	infrared radiation
RMS converter	AC-electrical power
EM-field sensor	EM fields
thermal conductance sensors:	
flow sensor	fluid flow
vacuum sensor	vacuum pressure
thermal conductivity sensor	fluid type
accelerometer	acceleration
thermal properties sensor	material properties

Microcalorimeter

The microcalorimeter measures the heat that is developed during chemical reactions. Bataillard describes various applications [3]. You can create a chemical reaction between two solutions in the reaction volume of the sensor (near the active area of the thermal sensor) by supplying them to this volume via two tubes. Alternatively, you can immobilize a catalyst or enzyme on the active area of the microcalorimeter, which will initiate the chemical reaction once the (single) solution comes into contact with it, see Fig. 2. This setup ensures that the transfer of reaction heat to the sensor is optimized. It is even possible to measure the heat of micro-organisms such as bacteria immobilized near the active area of the microcalorimeter. In this way, the heat produced by the bacteria (of the order of 1 pW per bacteria) can be a measure for the concentration of nutrients in the solution, such as glucose, or of the growth rate of bacteria or the influence of farmaceuticals when sufficient glucose is present.

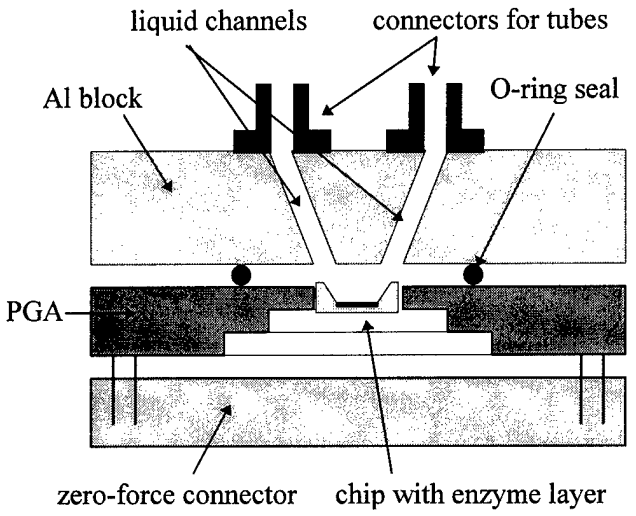


Figure 2: Cross section of a liquid micro-calorimeter chip with enzyme coating in PGA ceramic housing, clamped between an aluminum heat-sink block with liquid channels, and a connector [4].

Psychrometer

In this sensor the relative humidity of air is detected by measuring the psychrometric temperature depression ΔT_{psych} of a wetted thermometer as a result of evaporation. This sensor is therefore based on a physical phase transition (see, for instance, [5] for more details).

Infrared Sensor

From the transduction point of view this is a fairly simple sensor. The transduction from radiation to heat is carried out by a black absorber, which can have an efficiency up to 99%. The first transduction step from incident radiation density P''_{inc} (in W/m^2) to thermal power P is

$$P = Q\, P''_{inc}$$

$$Q = \alpha\, A_D\, \tau_{filter}.$$

The absorptivity α is between 0 and 1, and denotes the fraction of infrared radiation power which is absorbed by the black coating. Various types of black coatings are used for silicon infrared sensors. A simple and efficient method is to use the silicon oxide and silicon nitride layers present in all semiconductor production processes, for which Lenggenhager [6] found an absorption on the order of 50% for radiation wavelengths of 7-14 μm. Porous metal coatings such as gold black are used to fabricate very black layers, absorbing more than 99% of radiation over the entire infrared spectrum. The method used at Xensor Integration is to spin-coated the sensor-wafers by a black polymer. This layer is patterned just like any other thin film on silicon, and will withstand further processing of the wafer. This is in contrast to coatings such as gold black, which are very vulnerable and cannot be handled once they are applied.

A_D is the sensitive area of the sensor (usually the area that is coated black), while τ_{filter} is the transmission of the filter that is usually incorporated in the encapsulation of the sensitive element of the sensor. This filter can be broadband, transmitting infrared radiation with wavelengths between 2-14 μm. This can be used for an application such as non-contact temperature measurement, which is a big market for thermoelectric infrared sensors. It can be high-pass, 7-14 μm, for detection of objects at room temperature emitting radiation at wavelengths at typically 10 μm (intrusion alarm). An interesting application is in the game saver (of Xensor Integration and Terra Care), a fast IR sensor with amplifier used to detect bird's nests in the mowing field. When mowing, on-line detection allows temporary lifting of the mowing apparatus, thus saving the nest (see Fig. 3).

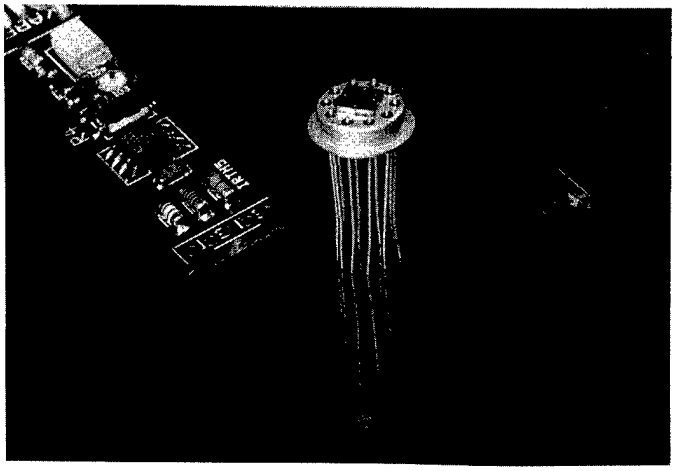


Figure 3: Infrared-sensor based game saver (Terra Care & Xensor Integration), which detects the heat of game or bird's nests in the mowing field during the mowing.

The filter can also be band-pass, transmitting, for instance, radiation at a wavelength which is in the absorption band of a gas. In this way, a gas sensor can be constructed in which the radiation intensity is measured in a reference path and a path where the gas mixture under investigation is present. The difference in intensity is due to the presence of radiation-absorbing gas. This method is used, especially, for CO_2 and CO, since few other good methods exist to detect CO_2.

RMS converter and EM-field sensor

These devices are used to perform a calorimetric measurement of the power of AC-electric signals [7] and EM-fields [8] by dissipating the electrical and electro-magnetic signals in a resistor or a wave-guide termination. RMS-convertors are important in precision AC-measurements, and a very nice example is the AC-DC RMS converter developed by Fluke, based on micro-structures made in standard IC-technology, in which bipolar transistors act as temperature sensors, suspended in mid-air by their aluminum connection wires (see Fig. 4). Here, the reasonable sensitivity of a transistor (2 mV/K) combined with only a few connection wires to the ambient make a good thermal design [9].

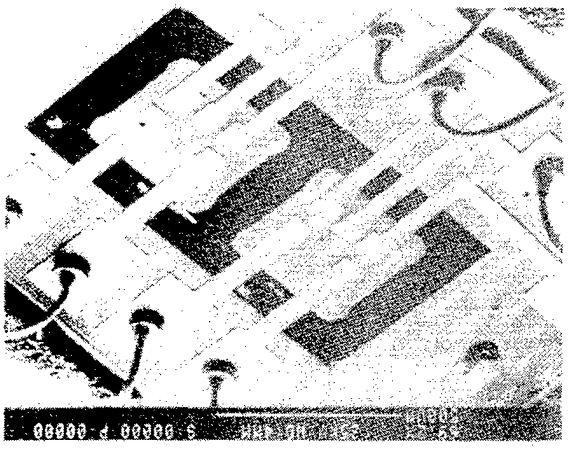


Figure 4: Scanning electron micrograph of the transistor-sensed thermal converter, showing the two islands [9] (photo courtesy of John Fluke Mfg.Co.Inc., Everett, WA 38206, USA).

Flow sensor

Flow sensors are based on the transfer of heat to moving fluids. This effectively increases the overall thermal conductance between sensor and ambient. For flow sensors the physics of the second and third step in the transduction process are just as simple as for all thermal sensors, but the similarity ends here. The physics of the first transduction step, from flow to thermal, and also the encapsulation of the sensor, are both much more complicated than for most other sensors.

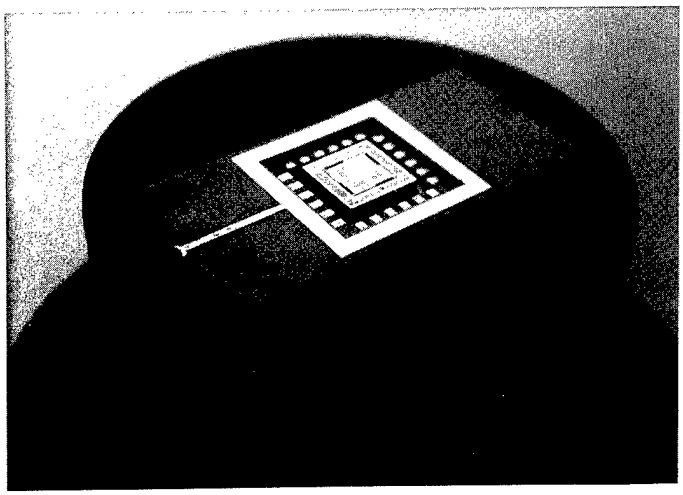


Figure 5: Integrated thermal wind flow sensor made of a silicon membrane suspended by four narrow silicon beams [10].

What is more, the encapsulation has a great influence on the first transduction step, because it influences the type of flow. There is laminar flow when the fluid flows along straight flow lines, and turbulent flow when fluid flows in irregular patterns and the local flow direction has no direct link with the average flow direction. In microstructures laminar flow is often encountered, although for thermal windmeters, microturbulent flow is also encountered (see [5], Par. 7.4). The dependence of the heat transfer on flow velocity is different for laminar and turbulent flow. Fig. 5 shows an experimental wind flow sensor of Delft University [10]. Flow sensors are the most difficult thermal sensors that exist. At the same time, they are commercially, together with infrared sensors, the most requested sensors. The fields of applications for flow sensors are too numerous to mention. However, because there has to be a thermal interaction between sensor and flow, thin-film versions of flow sensors are applicable only in well-controlled and favorable conditions. Honeywell [11] has succeeded in making such a thin film flow sensor, shown in Fig. 6. However, many industrial applications require more robust technologies.

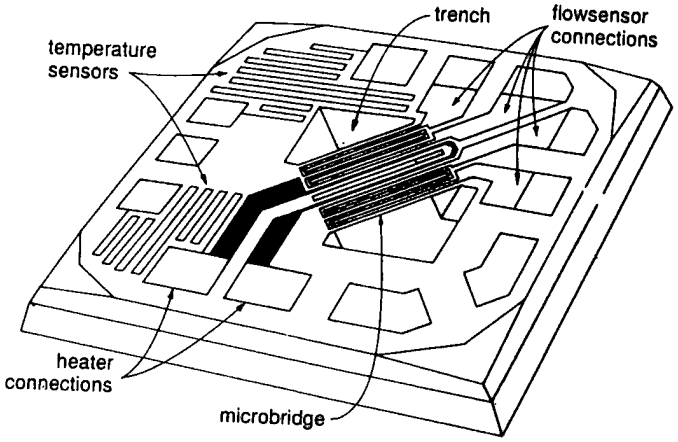


Figure 6: The double-bridge thermal mass flow sensor made by Honeywell [11].

Vacuum sensor and Conductivity sensor

This sensor measures gas pressures below atmospheric pressure by measuring the pressure-dependent thermal conductivity of gases [12], [13]. At very low pressures, when the mean distance between collisions of molecules is much larger than the distance between two surfaces, heat transfer between the surfaces is by individual molecules; and the rate of heat transfer is therefore proportional to the rate with which molecules hit the surface, which is the absolute pressure. At higher pressures (atmospheric for surfaces 500 μm apart, but very high pressures for surface micromachined devices [14]), molecules transfer their heat not from surface to surface, but by collisions among themselves. Doubling the pressure will double the number of molecules transferring heat, but the distance over which they transport the heat (the mean free path between collisions) is halved, and the thermal conductivity of the gas is now independent of pressure. This can be seen in Fig. 7.

The conductivity sensor is similar to the vacuum sensor, since it measures the thermal conductance of the gas enveloping the sensor. However, in this case the conductance does not depend upon the pressure, but, at atmospheric pressure, upon the gas type (or liquid type) instead, since all gases have different thermal conductivities. For instance, for air the thermal conductivity is κ=26 mW/Km at room temperature; hydrogen

has the highest conductivity at more than 180 mW/Km; for helium it is about 150 mW/Km; while gases such as argon (18 mW/Km) and xenon (6 mW/Km) are even less conductive than air. The pressure dependence for low pressures, and the gas type dependence at atmospheric pressure is nicely illustrated by the thermal conductance experienced by a thermal sensor at various ambients and pressures, see Fig. 7.

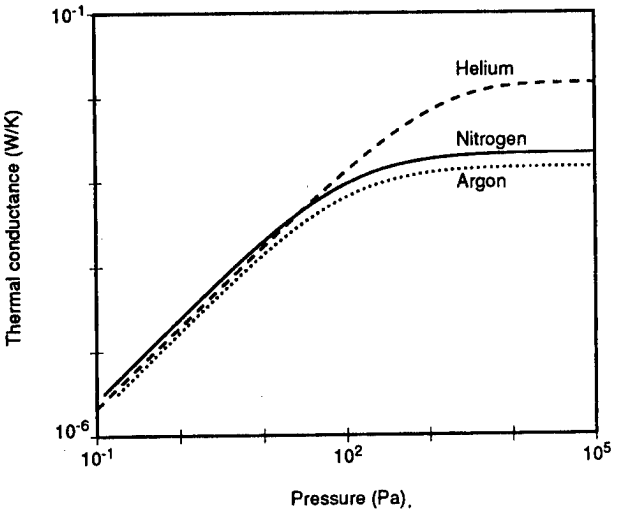


Figure 7: Output of a floating-membrane thermal conductivity sensor versus pressure for three different gases.

Mechanical Sensors

In mechanical thermal sensors such as the accelerometer, the mechanical signal (acceleration) is converted into force F by means of a seismic mass m and a closed membrane. Subsequently the force is converted into a gap size (change) D by means of mechanical springs with spring constant K (using damping characteristics of the enveloping gas to obtain the proper frequency behavior). Finally, the gap size is transduced into a temperature difference by the thermal conductance of the gas in the gap, see Fig. 8.

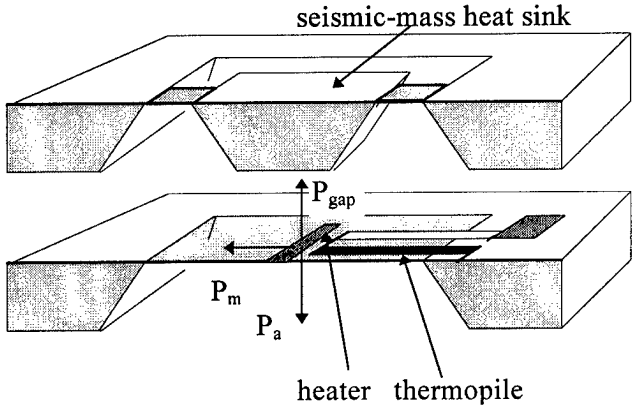


Figure 8: Exploded view of a thermal accelerometer, with indicated the heat flows in the membrane, down to the housing, and the signal-heat flow P_{gap} in the acceleration-dependent gap to the seismic mass.

The physical principle of the thermal accelerometer does not differ much from that of the capacitive accelerometer. The gap distance is now measured thermally, instead of capacitively [15]. However, the thermal accelerometer is much younger, and therefore its commercial potential is still unknown.

Thermal properties sensor

Thermal sensor structures can also be used to measure the thermal properties of thin films and of the sensor materials themselves. In general, an absolute measurement is made of the thermal resistance and the thermal time constants of a certain structure. With the modern micromachined structures such as the floating membrane or cantilever beam, measurements have become relatively simple. Figure 9 shows a structure where a silicon island containing bipolar transistors is suspended in a closed silicon-nitride membrane, a variation on the floating-membrane structure [16]. A similar technology arrives at several isolated p-type mono-silicon thermopile strips suspended underneath a dielectric membrane, isolated from each other by ECE-etch removal of any silicon between the strips [17].

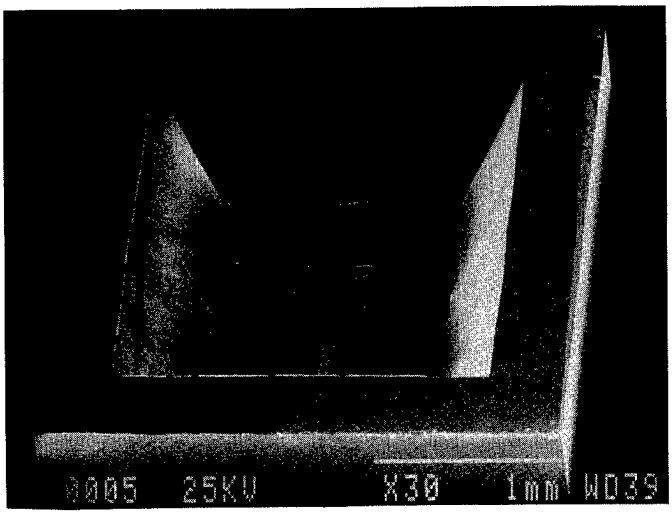


Figure 9: SEM photograph of a thermal properties sensor consisting of a silicon island suspended in a silicon nitride closed membrane (Photo courtesy of DIMES, Delft University).

The measurements are performed in vacuum, so that only conduction in the solid material adds to the measured conductances (radiation effects are usually not significant in size). In this way, the thermal conductance κ and capacitance c_p of various materials has been determined, see Table 3 ([5], p. 288; [16], [18]).

Table3: Typical thermal properties of freqeuntly encountered materials in thermal sensors.

Material	conductivity (W/Km)	capacitance (J/kgK)
silicon (mono)	150	700
silicon dioxide (thermal)	1½	730
Si-nitride (low-stres LPCVD)	3	700
polysilicon	≈30	770
aluminum(/1%Si)	≈200	

IV THERMAL STRUCTURES

Heat Transfer Mechanisms

In most thermal power sensors, the heat is generated in or on the active area of the sensor itself, and the transduction takes place in or on the sensor itself. In some, the transport of the non-thermal power to the sensor involves heat transfer mechanisms. In thermal conductance sensors, on the other hand, the non-thermal signal influences the thermal conductance of the sensor to the ambient directly around the sensor, instead of acting on the sensor itself. Here, heat transfer mechanisms are always essential to the operation of the sensor. There are four heat transfer mechanisms [19], listed in Table 2, together with an indication of their magnitude. Usually, conduction and convection are more significant than radiation (and phase transition).

Table 2 Overview of heat transfer mechanisms and their magnitude for a 500 μm dimension typical of microsensors.

Effect	W/Km^2	Remarks
Radiation		
between black surfaces	6	at room temperature
	500	at 1000°C
Conduction		
between surfaces 500 μm apart:		
- air at vacuum	1	1 Pa pressure
- air	50	atmospheric pressure
- water	1 200	
- silicon	300 000	
Convection		
for sensors 500 μm long:		
- free convection	-	often negligible in microstructures
- forced convection air	150	1 m/s flow
- forced convection water	15 000	1 m/s flow
Phase transition		
temperature difference not required for the phase transition heat transfer to occur, so no heat transfer coefficient can be given.		

Conduction is always present, but in thermal conductance sensors the first transduction step can be based on it, through the thermal conduction G_{cond} between the active area of the sensor and the ambient. The thermal conductance between two parallel surfaces of area A at distance D can be described by

$$G_{cond} = \kappa A/D$$

where κ is the thermal conductivity of the medium present between the surfaces. The sensor action may be based on the dependence of the physical signal

- on κ (pressure dependence: vacuum sensor/Pirani gauge; fluid-type dependence: thermal conductivity and overflow sensor),
- on D (plate-spacing dependence: accelerometer), or
- on all three parameters κ, D and A (thermal properties sensor).

Convection, the second mechanism for thermal conductance sensors, is heat transfer to moving fluids, as in flow sensors. Usually convection is not relevant in other sensors than flow sensors. The sensor action can be based on the flow velocity dependence of the Reynolds number (as in flow sensors), and in rare cases on the pressure dependence of the viscosity and the conductivity, also constituents of the Reynolds number (as in some Pirani gauges for vacuum measurement near atmospheric pressure).

Radiation is transfer of heat by means of electromagnetic waves, either as infrared radiation (thermal radiation), or in other forms, such as microwaves or magnetic fields which generate heat in a dissipative layer (hysteresis in a magnetic layer, for instance). It is a self-generating effect, and therefore the basis of a thermal power sensor. The heat transfer between parallel plates, which, for both plates around room temperature, is equal to

$$G_{ir} = \varepsilon \times 6 \text{ W/m}^2\text{K}$$

where ε is the emissivity or absorptivity of the plate (one plate is assumed to be black with emissivity $\varepsilon = 1$). All materials emit infrared radiation, but usually that does not contribute significantly to the heat exchange of a thermal sensor with the ambient.

Phase transition is the last mechanism of heat transfer. Here we can think, for instance, of the heat generated by evaporation. Phase transitions are often encouraged by forced convection though, which influences the thermal conductance. Still, this is also a self-generating effect. Just like radiation, phase transitions generate their own thermal power (be it negative or positive). A peculiarity of heat transfer by phase transition is that in some situations heat can be transferred from a cold to a hot object, where normally heat flows from a hot to a cold object.

Design and technology of thermal structures

An important step in the thermal sensor transduction sequence is the conversion in the thermal domain. Optimisation of this step requires optimisation of the thermal structure of the sensor. Thin-film sensor technology is often based on silicon technology, combining standard IC processing technology and additions of thin film technology to obtain advanced sensor technology. Sensors based on other technology are also reported, such as micro-calorimeters using thin films on mica. Silicon technology is based on silicon substrates with amazingly good thermal conduction, which usually leads to

thermal sensors with insignificant sensitivity and significant interference from thermal conduction paths to the ambient, if no measures are taken. So, designing thermal sensors almost always involves micro-machining of silicon. For thermal power sensors, the idea is to create an active area where the heat of the non-thermal process is induced (such as the area with the black absorber of an infrared radiation sensor), give it the optimum size while maximising the thermal isolation with respect to the ambient. For thermal conductance sensors the same idea applies, since the change in the external thermal conductance can best be measured by a sensor with negligible internal thermal conductance. Because of this, there are really only a few thermal structures relevant, and designing thermal sensors can be brought back to the design of a few relevant structures. For instance, infrared sensors and micro-calorimeters both require very good thermal isolation and a large active area. On the other hand, RMS converters and properties sensors do not require a large active area (a simple heating resistor will do) not a good thermal isolation, since they are modulating sensors, where optimum transfer in terms of Volts per Watt is less important. Flow sensors are in between, they require a large active area to sense the flow, but thermal isolation is again less important if sufficient heating power is present. Vacuum sensors are more sensitive to good thermal isolation. Finally, devices such as flow sensors and micro-calorimeters working with liquids do not require very good thermal isoltaion.

Concluding, thermal sensor design requires making an active area of the required size, with the required thermal isolation. When using silicon technology for micromachining, we have three major choices to design the thermal isolation [20]:

- back-side bulk micro-machining (BMM)
- front-side bulk micro-machining (FMM)
- surface micro-machining (SMM)

These alternatives are presented schematically in Fig. 10.

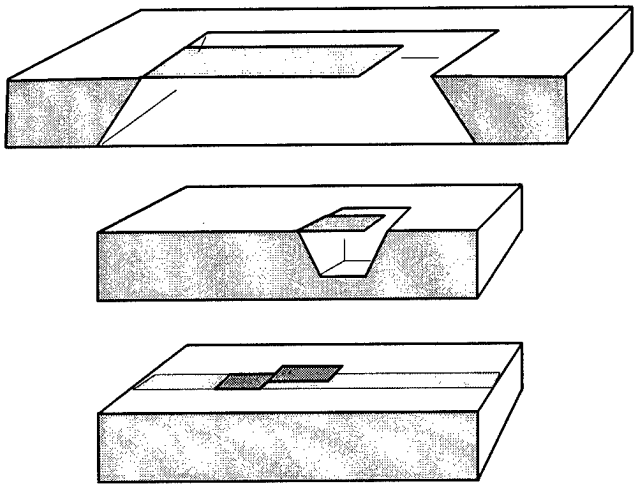


Figure 10: Three micro-machining techniques in silicon sensor technology: from top to bottom: a cantilever beam fabricated by back-side bulk, front-side bulk and surface micromaching.

As can be seen, the size of devices in back-side micromachining is nearly unlimited. The micro-calorimeters shown in Fig. 11 have a (0.5 μm thick silicon-nitride) membrane of 8.5×8.5 mm. To obtain this, the device is 10×10 mm large. Using front-side micromachining reduces the device size, since the etch cavity slopes inwards instead of outwards. This is especially attractive for small devices. Moreover, large devices are more difficult to fabricate because the anisotropic nature of the etching (indicated by the 55° edge of the etch cavities) makes underetching of cantilever beams more difficult.

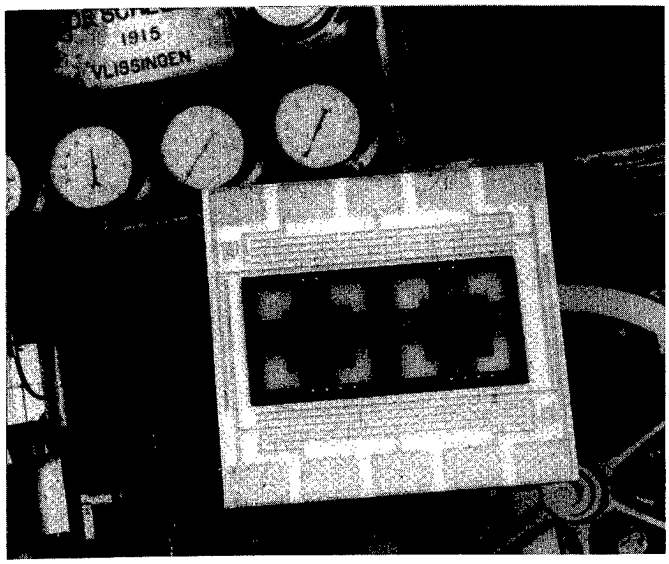


Figure 11: Photograph of a dual micro-calorimeter for nuclear experiments, containing a silicon island suspended in a silicon nitride membrane, with polysilicon thermopiles from four sides. The sensors are mounted on a ceramic carrier with venting holes (Xensor Integration & IRI, Delft University).

Front side micromachined devices are usually smaller than back side machined devices. This can be seen in the SEM of such a structure shown in Fig. 12. Alignment of such devices is easier since all layers are on the same side.

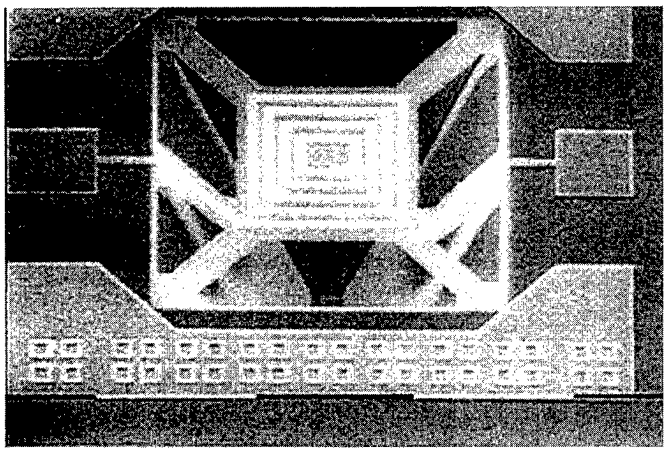


Figure 12: Front-side bulk micro-machined structure with a free hanging membrane suspended by four beams, featuring double metallisation on LPCVD low-stress SiN. The bars on the bottom indicate 100 μm (photo courtesy of DIMES, Delft University, [21]).

Surface micro-machined structures also have all layers at the front side. The size of these kind of structures is limited only by the design, and the control over tensile and compressive stresses of the structures. However, the vertical dimension of the separation between beams and substrate is limited to only one or two micrometers. For thermal sensors this technology is mainly interesting to devices being operated in a very good vacuum (below 1 mPa) such as the surface micromachined bolometer array developed at the National Optics Institute in Quebec, Canada [22], or to vacuum sensors, where the small gap results in a very good range (well up to atmospheric pressure [14]).

V TEMPERATURE SENSORS

Apart from the technology to achieve a thermal isolation, the choice for the sensing elements is also important, and influences both thermal structure and technology. In particular, devices can be based upon mono-silicon devices such as bipolar or CMOS transistors, resistors, thermopiles or even more complicated circuits. Or you can use thin film structures using silicon as substrate. In those cases, the micro-structures are often based on oxide or nitride membranes carrying the thin-film sensing devices. Here, poly-silicon resistors and thermopiles are very common for thermal sensors, since they can be made using standard (CMOS or bipolar) processing. But also more efficient thermoelectric materials such as Bismuth-Telluride compounds are being used [23], be it that they are not standard, and are less easily combined with electronics. In general, the choice for thermoelectric devices to measure the temperature differences in a thermal sensor is not at all trivial. Many sensors use resistors, with their convenient bridges of Wheatstone. In the case of modulating sensors, there is offset anyway, and thermopiles do not offer that many advantages as in the case of self-generating sensors. For self-generating sensors such as infrared sensors and micro-calorimeters, efficient thermopiles can be quite attractive to maximise performance. Here, new technologies to obtain very high figure of merit materials are promising.

VI DISCUSSION

Many thermal sensors have been devised so far. Some of them are already very commercialized (such as infrared sensors for intrusion alarms), others are stil very novel (accelerometer), or not even fabricated in silicon technology (psychrometer). Interesting also is the great difference that exists in the applicability of various thermal sensors. Infrared sensors are very simple devices because they can be hermetically sealed during encapsulation. The same applies to RMS converters, which are also becoming more and more popular in semiconductor versions. For flow sensors, the story is different. Research on semiconductor flow sensors has by now become very impressive, but the difficulties encountered by encapsulation and its influence on the sensor make the commercial success of a semiconductor version of this sensor still insignificant.

Another impediment to commercial success for thermal sensors is the scarcety of foundries capable and willing to fabricate such devices on a commercial basis, even if the numbers are not so large. Especially in Europe, where foundries for single steps are less common than in silicon valley, having your devices made can be difficult. But here, the work of the group of Prof. Baltes of Zurich, using standard CMOS foundries to make thermal sensors [24], [25], is quite interesting and opens up the way to new applications.

VII REFERENCES

[1] S. Middelhoek and S.A. Audet: Silicon Sensors (Academic Press, London, 1989) 6.

[2] A.W. van Herwaarden, Physical Principles of Thermal Sensors, Sensors and Materials, 8 (1996) 373-387

[3] P. Bataillard: Calorimetric Sensing in Bioanalytical Chemisty: Principles, Applications and Trends, Trends in Analytical Chemistry, vol.12, no. 10 (1993) 387

[4] A.W. van Herwaarden, P.M. Sarro, J.W. Gardner and P. Bataillard: Micro-Calorimeters for (Bio)Chemical Measurements in Gases and Liquids, Sensors and Actuators A43 (1994) 24.

[5] G.C.M. Meijer and A.W. van Herwaarden: Thermal Sensors (IOP Publishing, Bristol 1994).

[6] R. Lenggenhager: CMOS Thermoelectric Infrared Sensors, PhD dissertation (ETH No. 10744, Zurich 1994) 37

[7] M. Klonz and T. Weimann: Increasing the Time-Constant of a Thin-Film Multi-Junction Thermal Converter for Low Frequency Application, IEEE Trans Instrum. Meas IM-40 (1991) 350.

[8] S. Kodato, T. Wakabayashi, New Structure for DC-65 GHz Thermal Power Sensor, Proc. Transducers '97, 16-19 June 1997, Chigaco, USA, 1279-1282

[9] R. Goyal and B.T. Brodie, Recent Advances in Precision AC Measurements, IEEE Trans. Instr. Meas, IM-33 (1984) 164-167

[10] B.W. van Oudheusden and A.W. van Herwaarden, High-Sensitivity 2-D Flow Sensor with an Etched Thermal Isolation Structure, Sens. & Act., A21-A23 (1990) 423-430

[11 R.G. Johnson and R.E. Higashi, A Highly Sensitive Silicon Chip Microtransducer for Air Flow and Differential Pressure Sensing Applications, Sens & Act, 11 (1987) 63-72

[12] A.W. van Herwaarden and P.M. Sarro: Performance of Integrated Thermopile Vacuum Sensors, J. Phys. E: Sci. Instrum. 21 (1988) 1162.

[13] G.H. Chapman, N. Sawadsky, P.P.S. Juneja, Phase Sensitive Techniques Applied to a Micromachined Vacuum Sensor, SPIE, vol. 2882 (1996) 266-277

[14] B.C.S. Chou, J.-S. Shie, An Innovative Pirani Pressure Sensor, Proc. Transducers '97, 16-19 June 1997, Chigaco, USA, 1465-1468

[15] U.A. Dauderstädt, P.M. Sarro, S. Middelhoek, Temperature Drift of a Thermal Accelerometer, Proc.

Transducers '97, 16-19 June 1997, Chigaco, USA, 1209-1212

[16] P.M. Sarro, A.W. van Herwaarden and W. van der Vlist: A Silicon - Silicon Nitride Membrane Fabrication Process for Smart Thermal Sensors, Sensors and Actuators A, 41-42 (1994) 666.

[17] Z. Olgun, O. Akar, H. Kulah, T. Akin, An Integrated thermopile Structure with High Responsivity using any Stnadrd CMOS Process, 1263-1266

[18] O. Paul and H. Baltes: Thermal Conductivity of CMOS Materials for the Optimization of Microsensors, J. Micromech. Microeng 3 (1993) 110.

[19] A.J. Chapman: Heat Transfer, 4th ed. (MacMillan, New York, 1984).

[20] P.M. Sarro, P.J. French, P.J.T. Gennissen, New Developments in the Integration of Micromachined Sensors, 26-36

[21] Y. Sun, H. van Zeijl, J.L. Tauritz, R.G.F. Baets, Suspended Membrane Inductors and Capacitors for Applications in Silicon MMIC'S, International Microwave Symposium, 17-21 June 1996, San Francisco, CA, USA

[22] H. Jerominek, M. Renaud, N.R. Swart, F. Picard, T.D. Pope,M. Levesque, M. Lehoux, G. Bilodeau, M. Pelletier, D. Audet, P. Lambert, Micromachined VO_2-based Uncooled IR Bolometric Detector Arrays with Integrated CMOS Readout Electronics, SPIE, vol. 2882 (1996) 111-121

[23] M. Zieren, J.M. Köhler, A Micro-Fluid Channel Calorimeter using BiSb/SB thin Film Thermopiles, Proc. Transducers '97, 16-19 June 1997, Chigaco, USA, 539-542

[24] N. Schneeberger, O. Paul, H. Baltes, Optimization of CMOS Infrared Detector Microsystems, SPIE, vol. 2882 (1996) 122-131;

[25] U. Münich, D, Jaeggi, K. Schneeberger, A. Schaufelbühl, O. Paul, H. Baltes, J. Jasper, Industrial Fabrication Technology for CMOS Infrared Sensor Arrays, Proc. Transducers '97, 16-19 June 1997, Chigaco, USA, 205-208

Optimization of $(Bi,Sb)_2(Te,Se)_3$ - based thermoelectrics for low-temperature applications.

M.V. Vedernikov, V.A. Kutasov, L.N. Luk'yanova, and P.P. Konstantinov

A.F. Ioffe Physical-Technical Institute, 194021 St. Petersburg, Russia
Tel.: +7/812/515-9180, Fax: +7/812/515-6747, E-mail: M.Vedernikov@shuvpop.ioffe.rssi.ru.

Abstract

General situation with thermoelectric cooling at temperatures below 200 K is discussed. The problem of optimization of $(Bi,Sb)_2(Te,Se)_3$ - based thermoelectrics for operation in this temperature range is distinguished as the actual one especially in connection with a possible practical application of high-temperature superconductors. Then detailed results of the first systematic study of n-type $Bi_2Te_{3-x-y}Se_xS_y$ and p-type $Bi_{2-x}Sb_xTe_{3-y}Se_y$ are presented. The composition of solid solutions and the current carrier concentration were optimized. Thermopower, electrical and thermal conductivity were measured at 80-350 K, and thermoelectric figure of merit was calculated. Figure of merit for both type materials was increased significantly for the temperatures near 100-150 K. These optimized materials were used for the fabrication of the special low-temperature thermoelectric modules. These modules were tested, and temperature 130 K and 124 K on the cold junction of 2 types of 6-stages coolers was achieved.

Introduction: On cooling at T<200 K.

This report is based on a cycle of investigations carried out by the Laboratory for Physics of Thermoelements of Ioffe Institute during last decade. It contains more detailed data than that published earlier.

First of all we would like to explain why we consider a temperature range below 200 K as a special subject at a study of thermoelectric cooling.

Absolute majority of thermoelectric coolers operate today near the room temperature in range $T_{room}\pm$ few tens degrees centigrade. This is why thermoelectric properties and figure of merit of thermoelectrics used are studied in detail in this temperature interval. The best modern $(Bi,Sb)_2(Te,Se)_3$ - based materials are characterized by figure of merit value $Z = (3 - 3.2)\cdot10^{-3}$ K^{-1} at T_{room}. The value of ΔT_{max} is (68-70) K for a thermoelement fabricated from these materials. Deeper cooling is produced by multistage cascade modules. ΔT_{max} up to approximately 140 K is proclaimed for them. We have no information on conditions at which they are used really.

We can suggest however:

1. Their hot junctions are at temperature not lower than T_{room};
2. Many of them have not-zero heat load, and, respectively, their real ΔT is significantly less than ΔT_{max}.

These mean that thermoelectrics of multistage modules operate really at T>200 K. One can suppose that such a situation is a reason why the thermoelectric properties of $(Bi,Sb)_2(Te,Se)_3$ - based materials are studied much less at T<200 K than at higher temperatures. We don't know any detailed, systematic study of these materials at T<200 K which could allow to optimize their properties for usage at these temperatures.

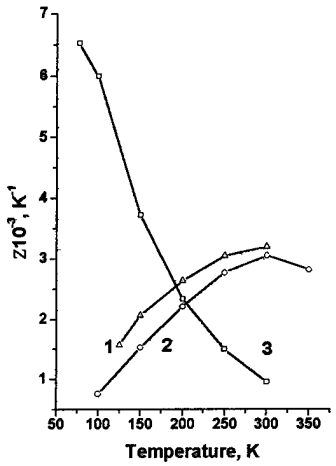


Fig.1. Temperature dependence of thermoelectric figure of merit Z for standard $(Bi,Sb)_2(Te,Se)_3$-based thermoelectrics (1: p-type, 2: n-type) and n-type $Bi_{0.85}Sb_{0.15}$ alloy (3)

A real impulse for initiating of investigations at T<200 K was given by the discovery of superconductors with high critical temperature T_c (HTCS). After the discovery of yttrium- and bismuth-type HTCS with T_c near 100 K there existed during several years a great hope to achieve soon higher T_c. This would open a possibility to cool a HTCS-object to $T<T_c$ without the usage of liquid nitrogen. It is natural to consider thermoelectric cooling among other alternative methods of cooling. But as to thermoelectric method it has a special feature which can be important at control of HTCS-devices: thermoelement is a heat pump, electrically controled. It allows to change temperature in the range $T_c\pm\Delta T$ by means of simple change of current direction through a cooler. Of

course, in order to realize an effective cooler one should have thermoelectrics effective enough in operating temperature range.

What did one know on efficiency of thermoelectrics 10 years ago? On Fig.1 a general information of that time is presented. Curves 1 and 2 show the figure of merit for the real standard $(Bi,Sb)_2(Te,Se)_3$ - based materials which are optimized for usage near T_{room}. One can see that Z falls rapidly with lowering of temperature and has low values near 100 K. On the contrary, Z of Bi-Sb alloy rises with temperature fall and achieves very good value at T=100 K. But there exists only n-type material, and it could be used practically with a bad p-type leg from $(Bi,Sb)_2(Te,Se)_3$ - standard material only. Therefore one could formulate on that moment the next directions of investigation for improvement of situation with low-temperature cooling:

1. Search for new thermoelectrics which would be more effective than the mentioned above.
2. Usage of the known thermoelectrics which are better than $(Bi,Sb)_2(Te,Se)_3$ - based materials.
3. Optimization of $(Bi,Sb)_2(Te,Se)_3$ - based materials for low-temperature application.
4. Usage of Bi-Sb alloys as a n-type leg in combination with a thermoelectrically passive leg of HTCS material.

According to our information there were no fruitful ideas 10 years ago in the direction 1, this is why we didn't attempt to work in this direction. As for the direction 2, it was indicated above that only n-Bi-Sb alloys are known as the more effective material. For their practical usage one needs to have an effective enough p-leg. Two ways would be possible for work in this direction: to develop effective p-type Bi-Sb leg, and to improve significantly p-$(Bi,Sb)_2(Te,Se)_3$ - based materials for the low temperatures. As to p-Bi-Sb, an opinion predominates now that, if not principally, but practically it is impossible to create p-type conductivity in these alloys. A goal of improvement of p-$(Bi,Sb)_2(Te,Se)_3$ - based materials coincides with the goal of the direction 3 of our list to optimize $(Bi,Sb)_2(Te,Se)_3$ - based thermoelectrics for low-temperature application. This topic was the subject of the Laboratory activity in the last decade and it is a base for this report. At last, the direction 4: thermoelement of n-Bi-Sb and thermoelectrically passive superconducting leg was realized successfully at the Laboratory. This subject was reported at the preceding international conferences on thermoelectrics and in «CRC Handbook on Thermoelectrics» [1, 2, 3].

Methods and results of optimization

For preparation of crystals a method of the directional crystallization (zone levelling) was used under the conditions which prevent concentration supercooling. The growth installation was of a laboratory scale, the diameter of crystal rod is 10 mm, and the length is about 150 mm. The rates of crystallization were at the most 0.5 mm/min and the temperature gradient at the crystallization front was at the most 200 K/cm. The cleavage planes in the rods were oriented along the crystallization axis and block-crystalline structure of the rods allowed to cutout (by electric spark cutting) single crystal samples for studying the anisotropy of thermoelectric properties. Samples for measurement of thermopower, electrical and thermal conductivity were cylinders of 10 mm in diameter and 10-12 mm length.

A possibility of optimization of thermoelectric properties of $(Bi,Sb)_2(Te,Se)_3$- based materials for effective operation in the different temperature intervals is a consequence of two fundamental results of the theory of thermoelectric energy conversion by semiconductors [4]. The first establishes a proportionality between figure of merit Z and so called «material's parameter» β which includes microscopic parameters of a thermoelectrics:

$$ZT \propto \beta;\ \beta=\text{constant}\cdot(m^*/m_0)^{3/2}\mu\cdot\kappa_L^{-1}T^{5/2} \qquad (1)$$

Here m^* and μ are effective mass and mobility of current carriers, m_0 is free electron mass, and κ_L is lattice thermal conductivity. At introduction of any dopants in $(Bi,Sb)_2(Te,Se)_3$ or alteration of ratio of components of these complicated compounds β can alter due to alteration of microscopic parameters and κ_L. The second result is that ZT depends on current carriers density n. Therefore n should be optimized for each temperature range.

Special feature of these thermoelectrics is a strong temperature dependence of Z with a maximum near the room temperature - see Fig.1. At alteration of components ratio and dopation this typical curve shifts up-down and to the right-left. This process was studied in detail near the room temperature for different impurities, different composition of solid solution, and resulted in values of Z which were indicated here in Introduction and shown on Fig.1. It is known for a long time that the curve Z(T) can shifted to the left so that its left slope will be above than the left slope of the standard curves on Fig.1. A new example of such a low-temperature material one can find in [5]. But we indicated in Introduction that there is no systematic study of this problem. This is why, if one may assert $Z=3.2\cdot10^{-3}$ K^{-1} as the best value for T_{room}, he cannot call a maximum possible value of Z for temperature 100 K. So, we believe our study is the first systematic experiment on low-temperature optimization of $(Bi,Sb)_2(Te,Se)_3$ - based thermoelectrics.

As to optimal current carrier concentration, we didn't use an introduction of chalcogenide impurities ($CdCl_2$, $BiBr_3$, and so on) in n-type materials that could results in decrease of low-temperature carrier mobility. Extra stoichiometric Te changes current carrier concentration too, and this method of optimization was used.

As to alteration of a composition of solid solution, one should operate in different manner for n-and p-type bismuth-antimony chalcogenides. Let us consider at first n-type materials. $Bi_2Te_{3-x}Se_x$ solid solutions are the most widely used materials for n-leg of cooling modules. Besides these materials, there is information on more complex solid solution formed by substitution of atoms in both anion and

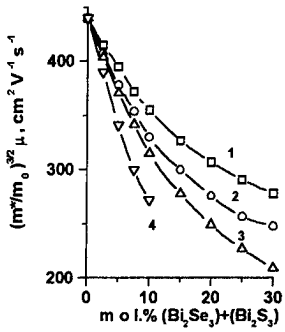


Fig.2. Dependence of $(m^*/m_0)^{3/2}\mu$ parameter on composition of n-$Bi_2Te_{3-x-y}Se_{x-y}S_y$ solid solutions. T=300 K.
1 - $(Bi_2Te_3)_{1-x}$ - $(Bi_2Se_3)_x$;
2 - $(Bi_2Te_3)_{1-x-y}$ - $(Bi_2Se_3)_x$ - $(Bi_2S_3)_y$ for x = 2y;
3 - $(Bi_2Te_3)_{1-x-y}$ - $(Bi_2Se_3)_x$ - $(Bi_2S_3)_y$ for x = y;
4 - $(Bi_2Te_3)_{1-y}$ - $(Bi_2S_3)_y$.

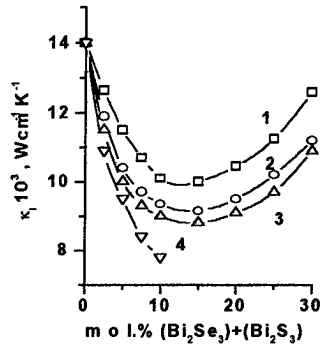


Fig.3. Dependence of lattice thermal conductivity κ_l on composition of n-$(Bi_2Te_{3-x-y}Se_xS_y)$ solid solutions at T=300 K.
1 - $(Bi_2Te_3)_{1-x}$ - $(Bi_2Se_3)_x$;
2 - $(Bi_2Te_3)_{1-x-y}$ - $(Bi_2Se_3)_x$ - $(Bi_2S_3)_y$ for x = 2y;
3 - $(Bi_2Te_3)_{1-x-y}$ - $(Bi_2Se_3)_x$ - $(Bi_2S_3)_y$ for x = y;
4 - $(Bi_2Te_3)_{1-y}$ - $(Bi_2S_3)_y$.

cation sublattice of bismuth telluride. These compounds have high thermoelectric efficiency at 300 K (b) as well as at lower temperatures [5,6]. We investigated such a complex systems too but here only thermoelectric properties of the next solid solution system will be considered in detail:

$Bi_2Te_{3-x-y}Se_xS_y$ at conditions x=y and x=2y, $0 \le x+y \le 0.9$

A value $(m^*/m_0)^{3/2}\cdot\mu$ is calculated from experimental data on thermoelectric power α and electrical conductivity σ assuming acoustic scattering is predominant. So-called scattering parameter r for acoustic scattering mechanism is equal to -0.5 (r is an index of a power in the dependence of relaxation time τ on energy: $\tau=\tau_0\cdot E^r$). Fig.2 shows that the

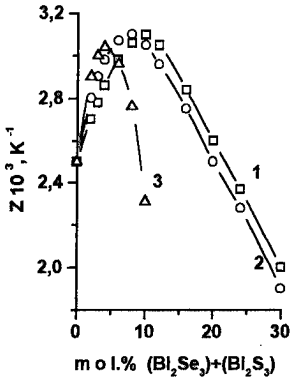


Fig.4. Dependence of figure of merit Z on composition of n-$Bi_2Te_{3-x-y}Se_xS_y$ solid solutions.
1 - $Bi_2Te_{3-x}Se_x$; 2 - $Bi_2Te_{3-x-y}Se_xS_y$, 3 - $Bi_2Te_{3-y}S_y$.

strongest changes of $(m^*/m_0)^{3/2}\cdot\mu$ are observed in the range of a small concentration of second component. The $(m^*/m_0)^{3/2}\cdot\mu$ parameter decreases continuously with increase of x,y for all considered n-type compositions.

Thermal conductivity κ was measured on samples of the same compositions and concentrations as samples for electrical conductivity and thermopower measurement. An electron part of thermal conductivity κ_e was calculated in accordance with Wiedemann-Franz law for scattering parameter r=-0.5. Lattice thermal conductivity κ_L in the temperature range of impurity conductivity was calculated as a difference between a measured thermal conductivity κ and its electron part κ_e. The dependences of κ_L on composition of solid solution are shown on Fig.3. One can see there κ_L has a minimum. This minimum is associated with the ordering owing to complete substitution of $Te^{(2)}$ atoms in the five-layer packet $Te^{(1)}$-Bi-$Te^{(2)}$-Bi-$Te^{(1)}$ by Se atoms in $Bi_2Te_{3-x}Se_x$ solid solution. A similar picture is observed in $Bi_2Te_{3-x-y}Se_xS_y$ too where $Te^{(2)}$ sites are replaced by Se and S atoms.

It follows from the above discussion that $(m^*/m_0)^{3/2}\cdot\mu$ and κ_L decrease when molar concentration of the second and third components increases in pseudo-binary or pseudo-ternary solid solutions of Bi_2Te_3 with Bi_2Se_3 and Bi_2S_3. However $(m^*/m_0)^{3/2}\cdot\mu$ decreases less rapidly than κ_L. This is the primary reason for the growth of Z at 300 K: Fig.4 shows that Z has a maximum in $Bi_2Te_{3-x}Se_x$ for x=0.3. When x is increased further, the thermoelectric efficiency falls. The behavior of Z in other n-type solid solutions based on Bi_2Te_3 is, on the whole, similar to that $Bi_2Te_{3-x}Se_x$. However there is still some difference. According to Fig.4 values of $Z=(3\text{-}3.1)\cdot10^{-3}$ K^{-1} are attained at 300 K with various concentrations of the second component: with y=0.06÷0.1 in $Bi_2Te_{3-y}S_y$ and with x+y=0.24 in $Bi_2Te_{3-x-y}Se_xS_y$. A similar

pattern is observed in other solid solutions, including

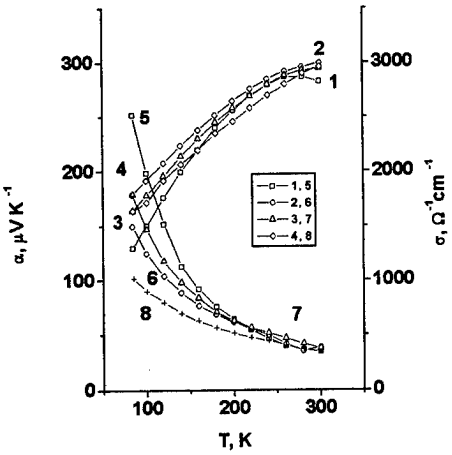


Fig.5. Temperature dependence of thermoelectric power α (curves 1-4) and electrical conductivity σ (curves 5-8) in n- $Bi_2Te_{3-y}Se_y$ solid solutions y= 0.12, 0.3, 0.36 for curves 1 and 5; 2 and 6; 3 and 7, respectively. n- $Bi_{1.88}Sb_{0.12}Te_{2.64}Se_{0.36}$ solid solution (curves 4,8).

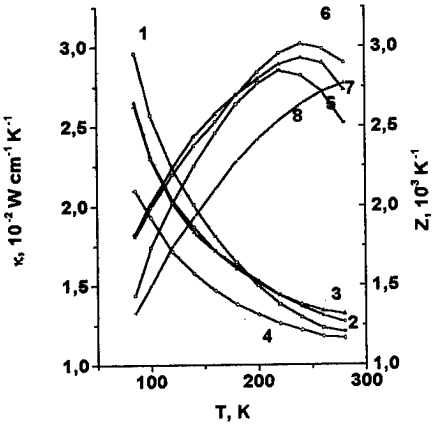


Fig.6. Temperature dependence of thermal conductivity κ (curves 1 - 4) and figure of merit Z (curves 5 - 8) in n- $Bi_2Te_{3-y}Se_y$; y= 0.12, 0.3, 0.36 for curves 1 and 5; 2 and 6; 3 and 7, respectively. n-$Bi_{1.88}Sb_{0.12}Te_{2.64}Se_{0.36}$ solid solution (curves 4, 8).

$Bi_{2-z}Sb_zTe_{3-x-y}Se_xS_y$. However the results of our investigations of these compositions are not discussed in this paper.

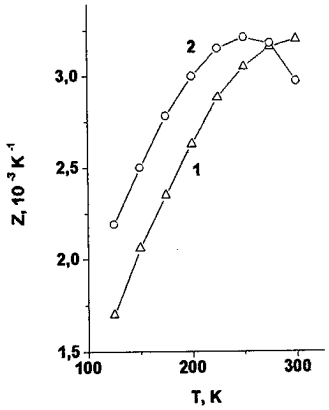


Fig.7. Temperature dependence of figure of merit Z in standard (1) and optimized (2) n-$Bi_2Te_{2.7}Se_{0.3}$ solid solution.

Different isovalent atom substitutions in the bismuth telluride sublattices can change the properties of these materials substantially and this would make it possible to extend the temperature range of application of thermoelectric cooling. We included in this discussion some data on thermoelectric properties of n-type $Bi_{2-x}Sb_xTe_{3-y}Se_y$ solid solution too. Here a part of Bi atoms are substituted by Sb: x=0.12, y=0.36. This material attracted our attention because it has very good figure of merit at 300 K: $Z=3.1\cdot10^{-3}$ K^{-1} when $n=1\cdot10^{19}$ cm^{-3}. But the same composition with low current carrier concentration (optimized for lower temperatures) didn't demonstrate good thermoelectric quality at low temperatures. It may be seen on Figs. 5 and 6, where temperature dependences of thermopouwer, electrical and thermal conductivity, and figure of merit are presented for this alloy and for some compositions of the system $Bi_2Te_{3-x}Se_x$ discussed above.

Thus the best material of n-type for low-temperature application among considered here is $Bi_2Te_{2.7}Se_{0.3}$ with carrier concentration $n=2\cdot10^{18}$ cm^{-3} and thermopower α=300-310 μVK^{-1} at the room temperature. Its figure of merit is shown on Fig.7 in comparison with data for standard material (which is the best near T_{room}).

Naturally p-type alloys near the room temperature are studied very detailed too. It is ascertained the Sb is an acceptor impurity and the composition p-$Bi_{0.5}Sb_{1.5}Te_3$ is the most effective material at this temperature. Lead impurity increases a current carrier concentration and efficiency at higher temperature. For usage at lower temperature one should decrease concentration. It is possible to achieve this effect by introduction of extra stoichoimetric tellurium as it was made with n-type material. But a solubility of extra Te in $Bi_{0.5}Sb_{1.5}Te_3$ is limited. This is why one cannot diminish a hole concentration enough and obtain the most effective low-temperature material by this method.

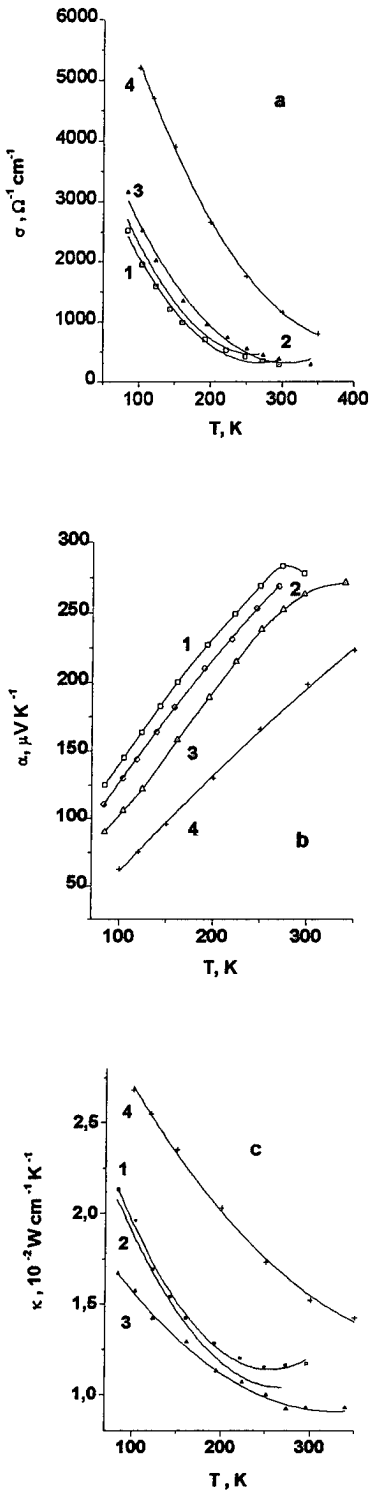


Fig.8. Temperature dependence of electrical conductivity σ (a),thermopower α (b), and thermal conductivity κ (c) in p-$Bi_{2-x}Sb_xTe_{3-y}Se_y$ solid solutions.
1: x = 1.0, y = 0.06; 2: x = 1.2, y = 0.09;
3: x = 1.3, y = 0.09; 4: x = 1.5, y = 0.

In order to feel about a possible method to solve this problem, we analysed data of Stary et al [8] and Stordeur et al [9] for alloys with reduced contents of Sb in p- $Bi_{2-x}Sb_xTe_3$ ($0.8<x<1.5$). In [8] calculations were fulfiled that showed a slower decrease of concentration of antisite defects of Bi on Te site than Sb on the same sites when x is decreased. This is why a decrease of Sb contents (decrease of x) results in decrease of current carrier concentration too. This conclusion was confirmed experimentally in [9] where thermoelectric properties of $Bi_{2-x}Sb_xTe_3$ at 300 K were measured on single crystals. It is possible to conclude from these data that at diminishing of x from 1.5 to 0.8 effective mass of density of states diminishes but mobility rises. As a result product $(m^*/m_0)^{3/2}\cdot\mu$ remains constant approximately in the whole interval of composition. As to lattice thermal conductivity, many researchers indicated on existence of a wide minimum in $\kappa_L(x)$ dependence for $Bi_{2-x}Sb_xTe_3$ at $0.8<x<1.6$ (300 K). Thus p-type $Bi_{2-x}Sb_xTe_3$ materials with lowered antimony contents seem to be of interest for a solution of our problem. But this conclusion bases on data for the room temperature. For creation of low-temperature materials one should lower their current carrier concentration optimally: by one order of magnitude approximately.

Compositions with x=1.3, 1.2, 1.0 were studied in this investigation. For diminishing of hole concentration extra stoichoimetric Te was introduced but for further diminishing a part of Te was substituted by Se. According to ideas of paper [8] this substitution increases a polarity of bonds and decreases, due to this, a density of antisite defects. Thus the combination $Bi_{2-x}Sb_xTe_{3-y}Se_y$ was studied with $y\leq 0.09$.

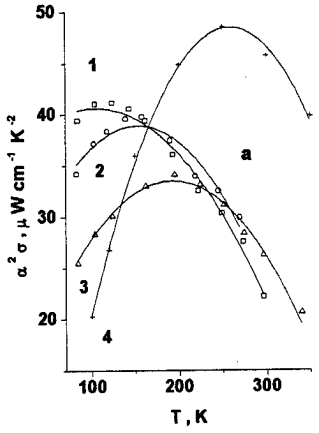
Fig. 8 shows results of measurement of electrical conductivity, thermopower, and thermal conductivity at 80-350 K. One can see from Fig. 8b that all samples at the room temperature are in mixed conduction temperature range: a thermopower maximum is observed. Hall effect was measured for all these samples too, and evaluation of current carrier density at 220-240 K (in range of impurity conduction) from Hall coefficient showed its minimum value $(2\text{-}3)\cdot 10^{18}$ cm^{-3}. An analysis of $\alpha(T)$ and $\sigma(T)$ dependences for r=-0.5 shows the calculated angular coefficients t for these materials are close to that for standard material with x=1.5, y=0:

$$t = \frac{d\ln[(m^*/m_0)^{3/2}\mu]}{d\ln T}$$

t=-1.5 for sample with x=1.2, y=0.09

t=-1.3 for sample with x=1.0, y=0.06.

Absolute magnitudes of parameter $(m^*/m_0)^{3/2}\cdot\mu$ at T=240 K for the same alloys with $x<1.5$ differ from standard material not more than 10%. This means the introduction of a small amount of Se in solid solution at lowered values of x doesn't influence significantly charge carrier scattering (doesn't rise it). But owing to lowered charge carrier density, these materials are characterized by high thermopower values. This results in high values of power factor $\alpha\cdot\sigma^2$ at low temperatures, much more than for standard composition: Fig. 9a.



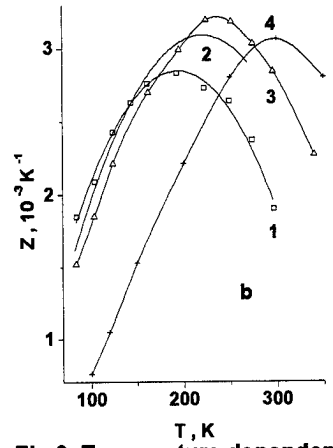


Fig.9. Temperature dependence of power coefficient $\alpha^2\sigma$ (a) and figure of merit Z (b) in p-$Bi_{2-x}Sb_xTe_{3-y}Se_y$ solid solutions. 1: x = 1.0, y = 0.06; 2: x = 1.2, y = 0. 09; 3: x = 1 3, y = 0.09; 4: x = 1.5, y = 0.

Now one can see also that partial substitution of Te by Se results in significant decrease of thermal conductivity in the whole temperature range: Fig. 8c. Together these two processes considered above ($\alpha\cdot\sigma^2$ up, κ_L down) lead to increase of figure of merit at low temperatures in comparison with the standard material: curves 1,2,3 - and 4, respectively, on Fig. 9b. Optimized materials have significantly higher ZT - parameter: at 80, 150 and 210 K values 0.1, 0.4, and 0.64 are achieved instead of 0.03, 0.28, and 0.57, respectively, for standard $Bi_{0.5}Sb_{1.5}Te_3$ composition.

Testing of optimized materials in low-temperature cascade modules.

Testing of low-temperature optimized materials at real temperatures, for wich they were developed, was the important part of the project. Its results were presented at one

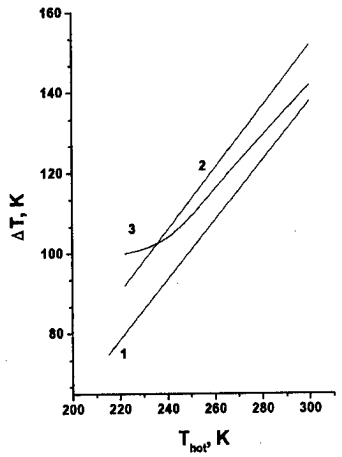


Fig.10. Temperature difference on modules tested vs. hot side temperature: 1 - 4-stage module; 2 - 6-stage module based on $(Bi,Sb)_2(Te,Se)_3$ - thermoelectrics; 3 - 6-stage module with the coldest stage including n-$Bi_{0.85}Sb_{0.15}$ leg.

of the recent ICT [10], although in short enough form. Here we are reporting only principal points of this work.

We used a special temperature regime of the testing: a hot junction of the module tested was at T=223 K which is a temperature of «dry ice» (solid CO_2 - it means that temperature of hot junction was maintained during a testing by means of «dry ice»). It was made for economy of the time and money because the module stages for interval 223 - 300 K would be highly cumbersome and expensive but it is possible today to design these stages theoretically, without any additional experiment. First 2 stages, counting from the hot junction, were made from standard materials, and what is more, from standard modules of the Russian thermoelectric company Osterm. Other, colder stages were made from the optimized materials, prepared at our laboratory and described above. Modules as a whole were assembled by Osterm by means of its standard technology. Then all testings of modules were performed at the laboratory.

Achieved results are presented on Fig.10. It is necessary to note that the 4-stage module was the first in this series, then better materials were developed and these improved materials were used in 6-stages modules. The first 6-stage module (curve 2) was made from $(Bi,Sb)_2(Te,Se)_3$ alloys. Then the second 6-stage module was created where the coldest, 6th stage had n-leg from very effective $Bi_{0.85}Sb_{0.15}$ alloy and p-leg from optimized $Bi_{2-x}Sb_xTe_{3-y}Se_y$ alloy. Bi-Sb leg was surrounded by a miniature permanent magnet system because optimal magnetic field increases thermoelectric figure of merit of this material very significantly. In all modules thermoelements and stages were connected in series and supplied by the same electrical current. Temperature T_{cold} on the cold junction of 4-stage module was 142 K (curve 1). 6-stage module (curve 2) produced ΔT=93 K and had

T_{cold}=130 K. Modernized 6-stage module with Bi-Sb (curve 3) produced ΔT=99 K and had T_{cold}=124 K. At all these testings there was a heat load on the coldest stage about 10 mW (by a heat flow through measuring thermocouple).

It was important not only to know what the lowest temperature is accessible experimentally. It was very important also to be convinced of good enough coincidence of calculated and experimental values of ΔT_{max} of the coolers. This confirmed a reliability of our measurements of thermoelectric properties as well as high quality of the assembling technology.

Conclusion

The study performed allows for the first time to consider in realistic manner a possibility of thermoelectric cooling at 80-150 K with $(Bi,Sb)_2(Te,Se)_3$ - based thermoelectrics. It can be a base for investigation of another compositions, with including of another components in solid solution.

Acknowledgements

One of the authors (M.V.V.) is happy to thank the Organizing Committee of ICT'97 and specially its Chairman Prof. A.Heinrich for the very important support of his participation in the Conference.

References

[1] M.V. Vedernikov, V.L. Kuznetsov, A.V. Ditman, B.T. Melekh, and A.T. Burkov «Efficient thermoelectric cooler with a thermoelectrically passive high T_c superconducting leg» Proc. of the X Int. Conf. on thermoelectrics (ICT'91), Cardiff, UK (1991) 96.

[2] V.L. Kuznetsov, M.V. Vedernikov, P. Jandl, U. Birkholz «Investigation of maximal possibility of thermoelectric cooling at liquid nitrogen temperature». Proc. of the XII Int. Conf. on thermoelectrics (ICT'93), Yokohama, Japan (1994) 424.

[3] M.V. Vedernikov and V.L. Kuznetsov «Cooling thermoelements with superconducting leg», CRC Handbook of thermoelectrics, Ed. by D.M. Rowe, N.Y.-L. (1995) 642.

[4] A.F. Ioffe «Semiconductor Thermoelements and Thermoelectric Cooling» (1957) Infosearch, London.

[5] V.A. Semenyuk, L.D. Ivanova, and T.E. Svechnikova «Peculiarities of applications of single crystal of bismuth and antimony chalcogenides solid solution in miniaturized coolers» Izv. RAN, ser. Neorg. Mater., 31 (1995) 32 (in Russian).

[6] W.M. Yim and F.D. Rosi «Compound tellurides and their alloys for Peltier cooling». Sol. St. Electr. 15 (1972) 1121.

[7] H.J. Goldsmid «Electronic Refrigeration», Pion, London (1985) 227.

[8] Z. Stary, J. Horak, M. Stordeur, and M. Stolzer «Antisite defects in $Sb_{2-x}Bi_xTe_3$ mixed crystals» J. Phys. and Chem. Solids, 49 (1988) 29.

[9] M. Stordeur, M. Stolzer, H. Sobotta, and V.Riede «Investigation of the valence band structure of thermorlectric $(Bi_{1-x}Sb_x)_2Te_3$ single crystals». Phys. Stat. Sol. (b). 150 (1988) 165.

[10] M.V. Vedernikov, V.A. Kutasov, V.L. Kuznetsov, L.N. Luk'yanova, P.P. Konstantinov, Yu.I. Ageev, G.T. Alexeeva, Yu.I. Ravich, M.I. Fedorov, E.A. Izupak, L.N. Gladkikh, I.M. Bash «Thermoelectric cooling to 130 K and lower temperature» Proc. of the XIII Int. Conf. on thermoelectrics (ICT'94), Kansas City, USA (1994) 185.

Doping Effects on the Electronic Structures of Bi_2Te_3 and Thermoelectric Property

Sunao Sugihara, Seiji Kawashima, Isaku Yonekura and
Hiroaki Suzuki
Shonan Institute of Technology, Tsujido Nishi kaigan, Fujisawa, Japan,251
Tel: +81/466/34-4111, Fax:+81/466/36-1594, E-mail:sugihara@mate.shonan-it.ac.jp
Rika Sekine
Shizuoka Universtiy, Ohya836 Shizuoka, 422
Tel: +81-54-238-4754, Fax: +81-54-237-3384,E-mail:scrsekine@sci.shizuoka.ac.jp

Abstract

The electronic structures of n- and p- Bi_2Te_3 were clarified using the molecular orbital method of Discrete Variational X α setting two kinds of cluster such as Bi_7Te_6 and Bi_6Te_7. The present computational study was focused on the changes of electronic structures by doping another atom to the original bismuth telluride. The computational results revealed bonding strength between atoms and contour map of electron density. The atoms of Bi and Sb possessing 6p or 5p electrons are polarized to be more positive than their formal charges when doping (original Bi_2Te_3 in the case of Bi), meanwhile Ag and Cu turned to be negative. The gaps between the occupied and unoccupied levels became smaller by doping the atoms such as Ag and Cu leading to a lower electrical resistivity. Furthermore, bond strength between the center-Bi and Te in the cluster 1 (C-1) enhanced due to doping Ag or Cu as well as that of the center-Te and Bi in the cluster 2 (C-2) did. We elucidated the experimental data including electrical resistivity and Seebeck coefficient associating with the calculated electronic structures.

Introduction

Bi_2Te_3 has become popular as a cooling device and electric power generation at relatively low temperatures as well. However, the efficiency has still been low although it is higher than the other thermoelectric materials so far. In order to improve the situation, there are a lot of studies for developing the materials with better efficiency, such as fabrication process of pressing and sintering of the powders, control of powder particle size, measuring methods of material properties, etc. To understand the basic electronic structure of Bi_2Te_3, Drabble et al. [1] explained the crystal consisting of Van der Waals force, covalent bonding and ionic bonding from the view point of the formal charge and the bond length, and also the theoretical approach by the tight binding method was studied by Pecheur et al. [2]. However, there have been no discussions of electronic structures of Bi_2Te_3 with the thermoelectric properties. Recently, Mishra et al. reported the electronic structure of Bi_2Te_3 and Bi_2Se_3 using the linear muffin- tin potential method in the atomic sphere approximation [3]. It may be, however, difficult to elucidate thermoelectric properties from their effective charges.

The basic characteristics of thermoelectric materials are much related to microstructures of the polycrystals and the electronic structures. We have experimentally developed the relationship between morphology and thermoelectricity in the former subject. For the latter subject, the present study includes the computer simulation to design the n- and p- Bi_2Te_3 and to associate the electronic structure with the actual thermoelectric properties based on our experiments.

0-7803-4057-4/97 $10.00 ©1997 IEEE

We use the one of molecular orbital methods such as a Discrete Variational X α [4] which consists of construction of the cluster, defining the basis functions, the symmetry of the cluster, etc. By means of this calculation, the bonding natures, density of states, effective charges of each atom and contour map of electron density are discussed with characteristics of thermoelectricity. The calculations are performed on n- and p- Bi_2Te_3 and to show the effectiveness of doping Ag or Cu to the Bi_2Te_3.

Calculation

The cluster models of Bi_2Te_3 were set every layer [5]; cluster 1 (Bi_7Te_6) and cluster 2 (Bi_6Te_7) along C axis in the unit cell. In the cluster 1 (C-1), Bi atom is surrounded by six atoms of Bi in the same plane (ring), and each 3 Te atom upper and lower the ring. Meanwhile, the cluster 2 (C-2) contains a centered- Te atom and the six Te atoms in the same plane (ring), including each 3 Bi atom upper and lower the ring. The doping was performed by replacing Ag or Cu for Bi in the cluster C-1 and for Te in the cluster C-2 as well.

The DV-X α method involves the local density approximation applied to the exchange correlation potential introduced by Slater. The calculation were carried out in the symmetry of each cluster with C3V, non-spin and non-relativistic method. The potential well depth is 0.5 (atomic unit) and the width is-5 (Hartree). The basis functions of Bi were 5d, 6s and 6p, and 4d, 5s and 5p orbitals for Sb and Te. Moreover, 3d, 4s, 4p (vacant level) for Cu and 4d, 5s, 5p (vacant level) for Ag.

Specimen preparation

The specimens for thermoelectric measurement were prepared by milling the Bi_2Te_3 ingots and the powders less than 150 μ m in diameter were pressed at 190 MPa, then followed by sintering for 2 hrs at 723 K in Ar gas. The sintered pellets were cut in a rectangular shape with an approx. size 5×5×12mm. Seebeck coefficient and electrical resistivity were measured by a 4 probe-method with the temperature difference of about 10 K between both ends longitudially.

Results and Discussion

Table 1 shows effective charges for every cluster (C-1 and C-2) indicating the substitution of Ag or Cu for Bi(C-1) and the substitution of Ag or Cu for Te (C-2). Both Ag and Cu atom tends to be negative charge that means the electrons surrounded Ag or Cu, meanwhile ring -Bi becomes positive in the C-1, and upper and lower Bi becomes positive as well. The bond orders corresponding to bonding strength are indicated in Table 2 to show bigger figures when Ag or Cu is doped into the Bi_2Te_3 in the both C-1 and C-2 clusters. The meaning of "center/above ring" is center atom like Ag in C-1(Ag) and the upper Te. These results may suggest that the Bi_2Te_3 layer in longitudinally becomes stronger. The densities of states for the Ag- doped cluster, Ag(C-1)are shown in Fig. 1. As well known in the electronic configuration of Ag, the 4d orbital has full electrons in default presenting higher density of states in Fig.1(a). Meanwhile,

Table 1. Effective charges for each cluster.

	center	ring-Bi	upper-Te	lower-Te
C-1(Bi)	0.308(Bi)	0.036	-0.101	-0.071
C-1(Ag)	-0.189(Ag)	0.114	-0.085	-0.08
C-1(Cu)	-0.353(Cu)	0.161	-0.114	-0.906
	center	ring-Te	upper-Bi	lower-Bi
C-2(Te)	0.044(Te)	-0.144	0.167	0.107
C-2(Ag)	-0.391(Ag)	-0.137	0.204	0.2
C-2(Cu)	-0.497(Cu)	0.086	0.202	0.136

Table 2 . Bond orders between atoms in each cluster.

	center / above ring	center / below ring
C-1(Bi)	0.142	0.031
C-1(Ag)	0.194	0.242
C-1(Cu)	0.319	0.226
C-2(Te)	0.198	0.03
C-2(Ag)	0.348	0.303
C-2(Cu)	0.205	0.355

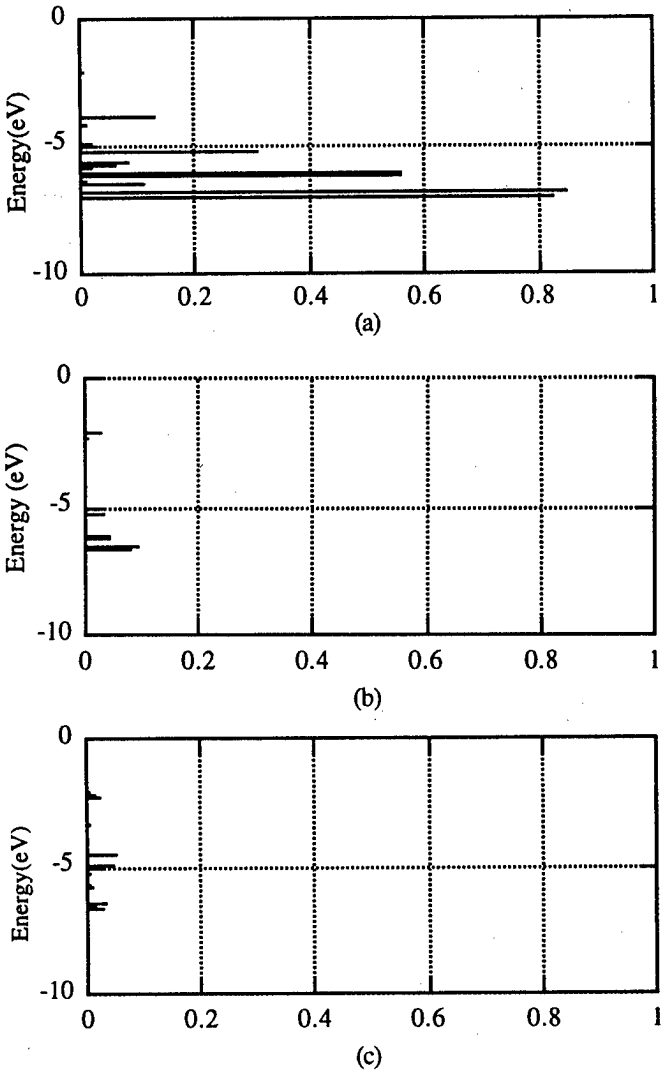


Fig1. Density of states for each energy for Ag-doped cluster Ag(C-1), (a)Ag4d, (b)Ag5s and (c)Ag5p.

5p orbital in Fig1(c) is characterized as a vacant level for electron presumably.

Figure 2 shows the energy level structures for both clusters of Bi_2Te_3; Ag-doped cluster with C-1 in upper and with C-2 in lower diagrams. Generally, n- and p- Bi_2Te_3 are said to be a degenerated semiconductors. The doping of Ag or Cu attributed to decrease the gap between the levels of HOMO (Highest Occupied Molecular Orbital) and LUMO (Lowest Unoccupied Molecular Orbital). The narrowed gap seems to cause the lowering of electrical resistivity for both C-1(Ag) and C-2(Cu). The degenerated conduction band suggested to play an important role for enhancing Seebeck coefficient which can be described by the difference of electron energy between the degenerated conduction band level and the Fermi level .The degenerated conduction band in the Ag

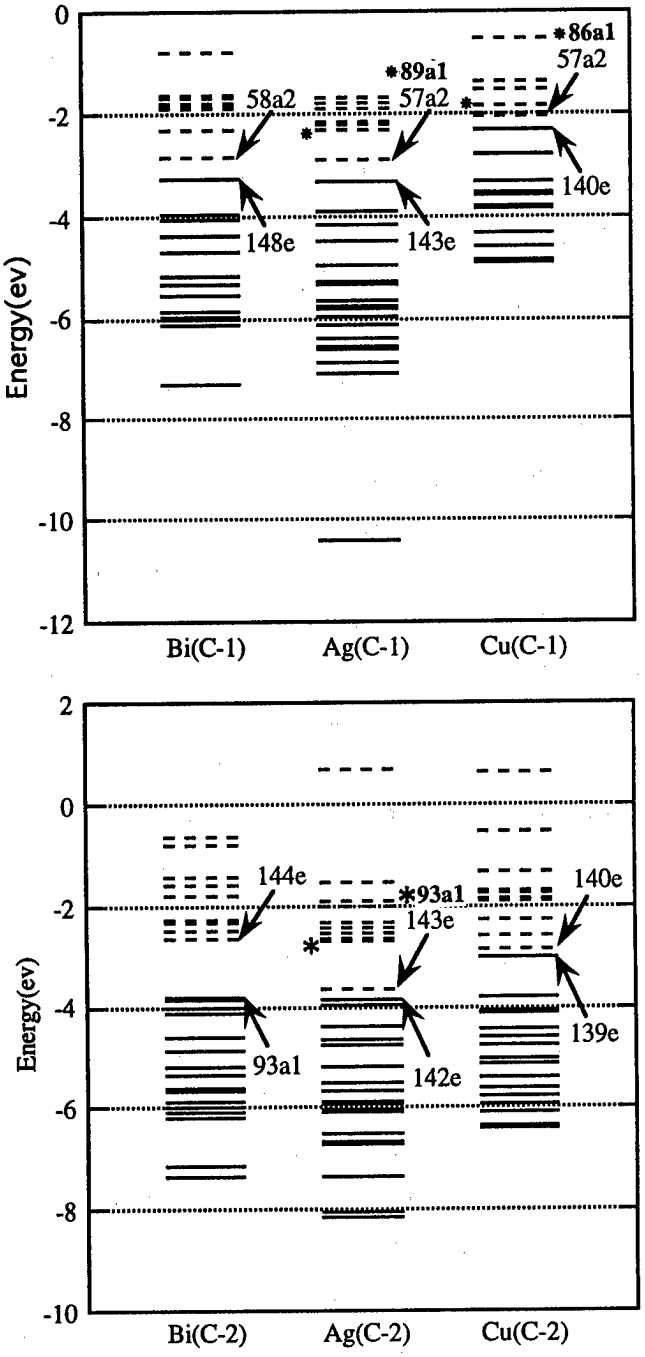


Fig.2 Energy level structures of Bi2Te3 and Ag-, Cu- doped cluster (C-1 and C-2).

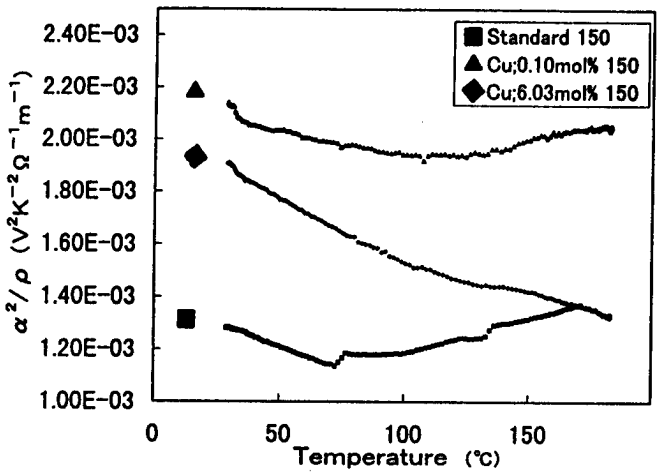


Fig. 3 α^2/ρ for Bi_2Te_3(particle size 150μm), and Cu−dopedBi_2Te_3(n) of 0. 10 and 6. 03mol% with 150μm.

doping was presumed with existing of the 5p (89a1) and 4d (143e) for the C-1 and the C-2, respectively, and in the Cu doping the band appears with 3d, 4s and 4p levels (86a1) for the C-1, and 3d and 4p(140e) for the C-2. In the case of Ag(C-2), there was the vacant level of 93a1 above the LUMO level of 143e, where the Ag 4d level has a population of 0.05. The Ag(C-1) presented the vacant level of 89a1 just above 57a2 (LUMO). The vacant level of a dopant above the LUMO is considered to be important for enhancing Seebeck coefficient to result in the larger difference of $E-E_f$ (E: conduction electron energy, E_f: Fermi energy). Meanwhile, the electrical resistivity is estimated to depend upon the difference of just HOMO and LUMO regardless of a dopant energy level. Therefore, the vacant level relating to a dopant energy level should have a possibility to accept electrons and also a smaller energy gap between HOMO and LUMO should be required for lower electrical resistivity and higher Seebeck coefficient.

We can compare the experimental data to show Seebeck coefficient and electrical resistivity (α^2/ρ) when Cu (0.1 and 6.03 mol%) is doped in n-Bi_2Te_3 as shown in Fig. 3. The 0.1mol% Cu- doping showed the largest Seebeck coefficient for the smallest resistivity. At room temperature, the resistivity was $1\times10^{-5}\Omega$m and $2\times10^{-5}\Omega$m for Cu-doping and Ag-doping, respectively. Figure 4 shows the electrical resistivity for the Ag- doped Bi_2Te_3.

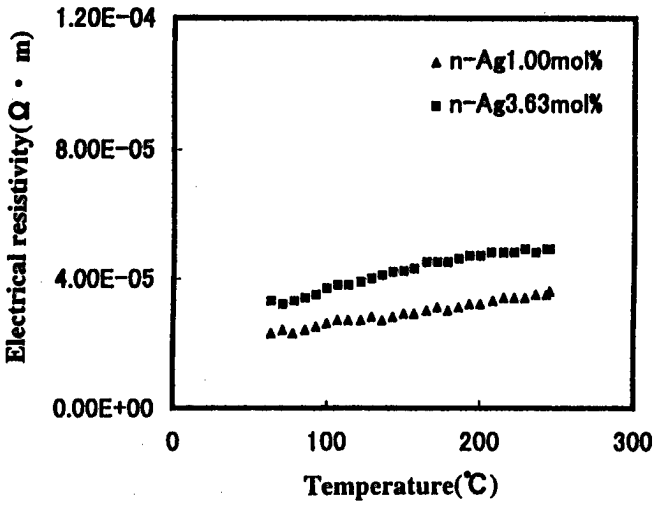


Fig. 4 Electrical resistivity for Ag-doped Bi_2Te_3 (n)

Conclusion

The electronic structures of the metal doped-Bi_2Te_3 were discussed concerning with the experimental data of electrical resistivity and Seebeck coefficient. The conclusions come out as following;

1)We found that the metals of Ag and Cu have possibility to enhance the bonding strength of Bi_2Te_3 layer according to the bond order by the computational calculations.

2) The higher Seebeck coefficient and lower electrical resistivity can be possibly obtained through controlling the electronic structures by doping of proper amount of the metals. The calculational results can bring the thermoelectrical new concept.

References

[1]J.R.Drabble and C.H.L.Goodman, J. Phys. Chem. Solids, 5(1958)142.

[2]P.Pecheur and G.Tounssaint,"Tight-Binding Studies of Crystal Stability and Defects in Bi_2Te_3" J.Phys. Chm. Solids,55

(1994)327.

[3] S.K.Mishra, S.Satpathy and O.J.Jepsen, "Electronic structure and thermoelectric properties of bismuth telluride and bismuth selenide", J.Phys: Condens,Matter 9(1997)461.

[4] H.Adachi, "Quantum Chemistry for Materials", Sankyo Shuppan Pub.Co.Inc. 1993 [in Japanese].

[5]S.Sugihara, S.Kawashima and I.Yonekura, " Electronic Structure of Bi_2Te_3 and thermoelectric Property", Submitted to Relativistic Symposium for DV-X α at Shizuoka University, June 7, 1997.

Defect Structure of Undoped and Pb-Doped Bi_2Se_3 Single Crystals

J. Horák(a), P. Lošťák (b), J. Navrátil (c), S. Karamazov (b)
(a) Institute of Inorganic Chemistry, Academy of Sciences of the Czech Republic, Prague, Czech Republic, (b) Faculty of Chemical Technology, University of Pardubice, Czech Republic, (c) Joint Laboratory of Solid State Chemistry, Academy of Sciences of the Czech Republic and University of Pardubice, Pardubice, Czech Republic
Tel.:(+42 40) 582 111, Fax: (+42 40) 514 530, E-mail: lostak @ hlb. upce. cz

Introduction

The Bi_2Se_3 crystals rank among the group of layered semiconductors of tetradymite structure (space group $R\bar{3}m - D_{3d}^5$). The crystal lattice of Bi_2Se_3 is formed by a periodic arrangement of layers aligned perpendicular to the trigonal axis c. Each layer is composed of five atomic planes arrangement according to the following pattern:

... Se^1 Bi Se^2 Bi Se^1 ... Se^1 Bi Se^2 Bi Se^1 ...

Between Se^1 atomic planes of neighbouring atoms there is a van der Waals gap. This compound is a component of material applied in thermoelectric devices as solid state coolers or generators [1]. Therefore, studies of the effect of native and crystal defects caused by impurity atoms in the crystal structure of Bi_2Se_3 are interesting both for basic and applied research.

In spite of a considerable attention devoted to the investigation of Bi_2Se_3 crystals, there is not an unambiguous model of defects in these crystals. It is known that their structural and point defects are associated with the deviation of their composition from the stoichiometric one. These defects influence considerably .the concentration of free current carriers in these crystals. Therefore the investigation of some physical properties which are governed by the concentration of free current carriers gives information on the nature of these defects and their concentration in crystal structures.

In this paper we present the results of the study of some transport coefficients and optical properties in the IR region at both undoped and Pb-doped Bi_2Se_3 single crystals with the aim to explain some anomalies in the dependence of the concentration of free current carriers on the content of incorporated Pb atoms.

Experimental

The starting Bi_2Se_3 and Bi_2Se_3(Pb) polycrystalline material was synthesized from the elements Bi, Pb and Se of 5N purity in evacuated conical silica ampoules at 1073 K for 48 hours. The growth of the crystals was carried out in the same ampoule by means of a modified Bridgman method using a suitable temperature gradient and a pulling rate of 1.3 mm/h.

The obtained single crystals, 50 to 60 mm in length and 8 mm in diameter, could be easily cleaved. Their trigonal axis *c* was always perpendicular to the pulling direction so that the (0001) plane was parallel to the ampoule axis. The orientation of the cleavage faces was carried out using the Laue back-diffraction technique, which confirmed that these faces were always (0001).

The Pb content, c_{Pb}, in the samples was determined using atomic absorption spectrometry.

On the prepared samples of the dimensions 15x3x(0.1-0.2)mm^3 the value of the Hall constant $R_H(\mathbf{B} \parallel \mathbf{c})$ has been determined (**B** is the magnetic induction). A stationary magnetic field having an induction of 1.1 T was used: the samples were fed from a current source the frequency of which was 170 Hz. Contacts to the samples for the measurement of the Hall voltage were made so that a thin platinum wire 0.05 mm in diameter coated with an indium layer was connected to the crystal by a capacitor discharge, the current contacts were made by an indium solder.

The Seebeck coefficient α has been measured for the direction $\Delta T \perp \mathbf{c}$, that is $\alpha(\Delta T \perp \mathbf{c})$, in the temperature range of 100 to 400 K: the temperature difference between the cold and hot junctions did not exceed 10 K.

The results of performed measurements are presented both in Table 1 and Fig. 1.

Sample No.	C_{Pb} ($10^{24}.m^{-3}$)	$R_H(B \parallel c)$ ($10^{-6}m^3C^{-1}$)	$\alpha(\Delta T \perp c)$ ($\mu V.K^{-1}$)
1	0	-0.235	-63
2	4.22	-0.203	-58
3	4.51	-0.214	-55
4	8.49	-0.248	-53
5	13.08	-0.270	-58
6	26.12	-0.384	-69
7	36.11	-0.507	-87

Table 1. Values of the Hall constant $R_H(\mathbf{B} \parallel \mathbf{c})$ and the Seebeck coefficient $\alpha(\Delta T \perp \mathbf{c})$.

Spectral dependences of the reflectance R in the plasma resonance frequency range were measured at room temperature in unpolarized light on natural (0001) cleavage faces using a FT-IR spectrometer Biorad FTS 45. The geometry of the experiment was such that the electric field vector **E** of the electromagnetic radiation was always perpendicular to the trigonal c-axis, i.e.$\mathbf{E} \perp \mathbf{c}$.

The transmittance spectra on thin samples with thickness of the order of 1 μm were measured at room temperature using the same spectrometer. The radiation was unpolarized but the orientation of the samples towards the incident radiation always fulfilled the condition of $\mathbf{E} \perp \mathbf{c}$.

In order to get information on the changes in the concentration dependences of free current carriers, the experimental obtained curves R = f(ν) were fitted using the equations for the real and imaginary parts of the dielectric constant obtained from the Drude-Zener theory [2]. The obtained values of the plasma-resonance

frequency ω_p were used for the calculation of the ratio $N/m_\perp^*$ from the expresion

$$\omega_p=(Ne^2/\varepsilon_o\varepsilon_\infty m_\perp^*)^{1/2}, \quad (1)$$

where N is the concentration of free current carriers (i.e.

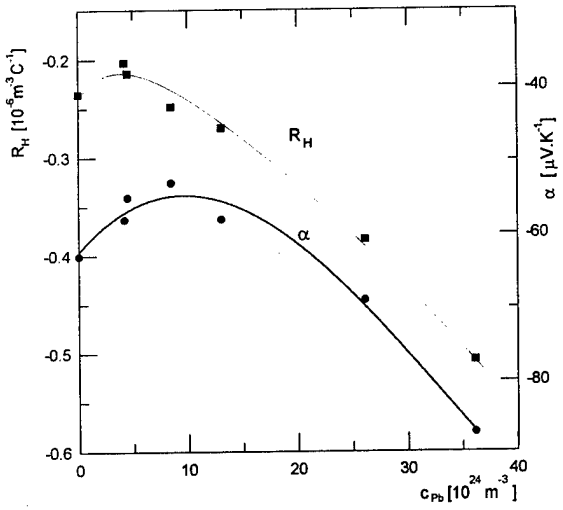


Fig. 1 Dependences of the Hall constant R_H and the Seebeck coefficient α on the Pb content for Pb-doped Bi_2Se_3.

electrons in Bi_2Se_3), e the electron charge, ε_o the dielectric constant of vacuum, ε_∞ the high-frequency dielectric constant, and $m_\perp^*$ the effective mass of the current carriers in the direction perpendicular to the trigonal c-axis. The obtained results are presented in Fig. 1.

The results of the transmission measurements were used for the determination of the spectral dependence of the absorption coefficient K; from the spectral course of the short-wavelength absorption edge K^2 vs. ($h\nu$ - $E_{g,opt}$). The values of the optical gap width $E_{g,opt}$. were determined supposing the direct allowed transitions. The obtained results are presented in Fig. 2.

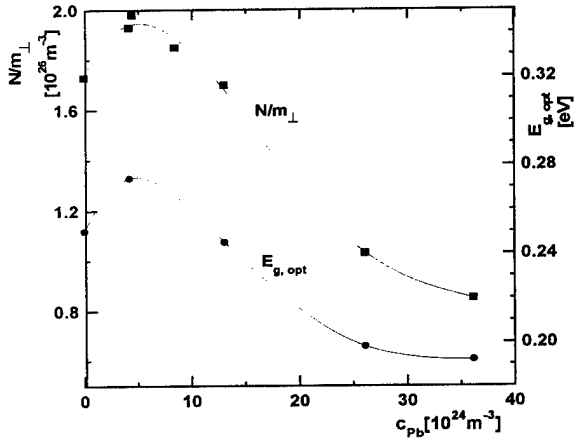


Fig. 2 Dependences of the ratio $N/m_\perp^*$ and the value of $E_{g,opt}$ on the Pb content in Pb-doped Bi_2Se_3.

Discussion

The obtained dependences of transport parameters and optical parameters in the IR region on the Pb content reveal extremes at the low concentration of Pb atoms. In order to explain the origin of this effect we consider not only the formation of substitutional defects formed by Pb atoms incorporated into the Bi-sublattice, i.e. Pb'_{Bi}, but also the interaction of these defects with native defects of the Bi_2Se_3 crystal..

Bi_2Se_3 crystals prepared from the stoichiometric melt reveal an overstoichiometric content of Bi [3]. The surplus of Bi in the Bi_2Se_3 lattice can result in the formation of following native defects:

a) vacancies in the Se-sublattice carrying two positive charges $V_{Se}^{\bullet\bullet}$,

b) antisite defects formed by Bi atoms incorporated in Se-sublattice carrying one negative charge Bi'_{Se},

c) Bi - Bi double layers situated in the van der Waals of the layered crystal [4],

d) seven-layer-lamellae $Bi_3Se''_{4_4}$, nine-layer-lamellae $Bi_4Se''_5$.

We note that the relations between the content Bi - Bi double layers and the concentration of free current carriers has not been studied yet.

As the concentration of overstoichiometric Bi atoms in the Bi_2Se_3 crystals prepared from the melt of stoichiometric composition is of the order of 10^{19} atoms cm^{-3}, we can make a simplification supposing that the concentration of unoccupied vacancies in the Bi sublattice $[V_{Bi}^{z'}]$ is much lower than the concentration of Se vacancies $[V_{Se}^{\bullet\bullet}]$ and also much lower than the concentration of antisite defects or the content of the seven.layer-lamellae, i.e.

$$[V_{Bi}^{z'}] << [V_{Se}^{\bullet\bullet}]; \qquad [V_{Bi}^{z'}] << [Bi'_{Se}];$$

and

$$[V_{Bi}^{z'}] << [Bi_3Se'_4].$$

The above given discussion on possible native defects in the Bi_2Se_3 crystal structure can results in the proposal of the following model :

a) native defects are formed at the temperature of the solidification the melt T_m,
b) concentration of native defects does not change under the temperature of T_m (our approximation),
c) the formation of native defects is a nearly equilibrium process which can be described by the equation

$$Bi_{Bi} + V_{Se}^{\bullet\bullet} + (3+z)e' \Leftrightarrow Bi'_{Se} + V_{Bi}^{z'}. \quad (2)$$

The above given model of point defects make it possible to explain the observed extremes in the dependences of physical parameters on the Pb-content in the studied crystals as a result of interaction of incorporated Pb atoms with native defects of the Bi_2Se_3 lattice. This conclusion results from the following ideas. The incorporation of Pb atoms into the Bi sublattice results in an increase of the polarity of bonds between the substitution defect Pb'_{Bi} and the neighbour Se atoms results in an increase of the ionicity of the crystal. As a

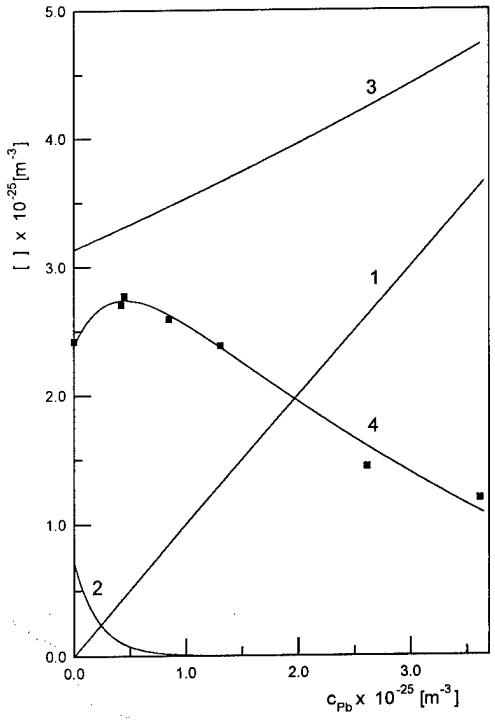


Fig. 3: Fit of the dependence of the free carrier concentration on Pb content, $n = f(c_{Pb})$, in the Pb-doped Bi_2Se_3 samples: 1-concentration of defects Pb'_{Bi}, 2-concentration of antisite defects Bi'_{Se}, 3-concentration of free electrons compensating the charges of doubly charged $V^{\bullet\bullet}_{Se}$, 4-theoretical $n = f(c_{Pb})$ dependence. The points represent experimental data on the concentration of free electrons.

consequencethe energy necessary for the transition of Bi atoms into the Se sublattice in the Se^{II} position also increases. It means that the energy of the formation of antisite defects increases and in agreement with the equation (2) the concentration of free current carriers increases. In this way can explain an increase in the concentration of free electrons in the region of a low Pb content. When overstoichiometric Bi atoms form seven-layer-lamellae, then an increase in the electron concentration can be described by the following equation

$$2Bi_3Se'_4+Pb+Se_2(g)\Leftrightarrow PbBi_2Se_4+2Bi_2Se_3+2e' \quad (3)$$

When the concentration of antisite defects, or eventually seven-layer -lamellae is sufficiently suppressed, only substitution defects Pb'_{Bi} are formed, which results in a decrease in the concentration of free electrons. This behavior can be described by the following equation

$$(2V_{bi}+3V_{se})+2Pb+3/2Se_2(g)+2e' = 2Pb'_{Bi}+3Se_{Se}. \quad (4)$$

The process described above generates free carriers in the first step and suppresses the concentration of free carriers in the second step and in this way describes qualitatively the observed dependence of free carrier concentration on the Pb content in Bi_2Se_3 crystals. With regard to the proposed model we have tried to calculate the change in the concentration of native defects including the changes in the energy of formation of these defects.

The concentration of free electrons N can be obtained from the crystal electroneutrality condition

$$N = 2[V^{\bullet\bullet}_{Se}] - [Bi'_{Se}] - [Pb'_{Bi}]. \quad (5)$$

The concentration of antisite defects can be described by the relation given in our previous paper [5] as

$$[Bi'_{Se}] = k_1 \frac{N_{Bi}}{2} \exp\left(-\frac{E_{AS}}{k_B T_m}\right), \quad (6)$$

where k_1 is a term describing the probability of forming an antisite defect in the Bi_2Se_3 unit regardless of any energy considerations, N_{Bi} is the concentration of Bi atoms in trhe unit volume of Bi_2Se_3 crystal, E_{AS} is the energy of formation of antisite defects, k_B is the Boltzmann constant and T_m is the melting point of the crystal.

In the crystal with a high dopant content (in our case of Pb) the bonding conditions are changed to a certain measure and thus also the formation energy of AS defects E_{AS} depending on the impurity content in a given crystal. A change in the formation energy is denoted as ΔE_{AS}; in the calculation we consider its magnitude to be proportional to the content of incorporated Pb atoms.

When we describe in a similar way also the concentration of vacancies $[V^{\bullet\bullet}_{Se}]$, then the equation (5) takes the form

$$N = 2N_{Se}\exp\left(-\frac{E_V + \Delta E_V(c_{Pb})}{k_B T_m}\right) - k_1 \frac{N_{Bi}}{2}\exp\left(-\frac{E_{AS} + \Delta E_{AS}(c_{Pb})}{k_B T_m}\right) - c_{Pb}, \quad (7)$$

where N_{Se} is the concentration of Se atoms in a unit crystal volume, E_V is the formation energy of vacancies $V^{\bullet\bullet}_{Se}$, ΔE_V is the change in the energy of formation of Se-vacancies caused by the incorporation of Pb-atoms into the crystal structure..

The equation (7) was used for fitting the $N = f(c_{Pb})$ dependence. The values of N were determined from the values of the ratio $N/m_\perp$, obtained by the interpretation of reflection spectra in the plasma-resonance frequency region using in a first approximation the constant value of $m_\perp = 0.14\ m_0$. For the calculation of the formation energy of the antisite defect in the undoped Bi_2Se_3 crystal was used as E_{AS}=0.59 eV. The result of fitting is shown in Fig.3.

From this figure it is evident, that with an increasing Pb-content in the Bi_2Se_3 crystals a steep decrease in the concentration of antisite defects takes place, whereas the

concentration of Se-vacancies increases. The value of formation energy E_{AS}=0.59 eV for the undoped crystal increased to 2.04 eV for the crystal with $c_{Pb} = 3.6.10^{19}$ cm^{-3}; simultaneously the formation energy E_V decreased from 0.61 to 0.58 eV.

Conclusions

The dependence of free electrons concentration on the content of doping Pb atoms in Bi_2Se_3 crystals reveals a pronounced maximum in the region of a low Pb content. The existence of such a maximum can be explained by an interaction of incorporated Pb atoms with negatively charged native defects of Bi_2Se_3. Such defects can be presented by antisite defects or defects of the type of seven-layer-lamellae.

References

[1] U. Birkholz, „Thermoelektrische Bauelemente", Amorphe und polykristalline Halbleiter, Ed. W. Heywang, Springer, Berlin 1984, p. 77.

[2] O. Madelung, Handbuch der Physik, Vol. XX, Ed. S. Flügge, Springer, Berlin 1957,p. 210.

[3] G. Offergeld, J. van Cakenberghe, „Determination de la composition a fusion congruente de semiconducteurs binaires par analyse thermique differentielle", J. Phys. Chem. Solids**1** (1959) 310.

[4] E. Gaudin, S. Jobic, M. Evain, R. Brec, J. Rouxel, „Charge balance in some Bi_xSe_y phases through atomic structure determination and band structure calculations", Mater. Res. Bull. **30** (1995) 549.

[5] J. Horák, Z. Starý, P. Lošťák, J. Pancíř, „Anti-site defects in n-Bi_2Se_3 crystals", J. Phys. Chem. Solids **51** (1990) 1353.

Acknowledgment

This work has been supported by the grant No. 202/95/0042 of the Grant Agency of Czech Republic.

Peculiarities of electrophysical properties of Bi_2Te_3 doped with Sn.

M.K. Zhitinskaya[1], S.A. Nemov[1], T.E. Svechnikova[2].

[1]State Technical University, 29 Polytechnicheskaya, 195251 St-Petersburg, Russia
Tel.: (812)5133256, Fax: (812) 2342877, E-mail: marina@nym.spb.ru

[2]A.A.Baikov Institute of Metallurgy, Russia Acad.Sci., Moscow, Russia

Abstract

The influence of doping with Sn atoms is investigated in details. The method of additional doping with electroactive impurities is used. The peculiarities of kinetic coefficients of Bi_2Te_3 doped with Sn and J simultaneously are discussed. There is good reason to believe that these peculiarities are due to Sn-resonant states.

Introduction

Bismuth telluride is the main component of alloies used for thermoelectric devices for middletemperature region. Therefore the search for different methods of thermoelectrical efficiency increase of Bi_2Te_3 and its alloies is important for production. One of the methods is the use of resonant scattering of the charge carriers. The resonant scattering can take place when the impurity levels appear on the background of allowed spectrum. The presence of impurity resonance states in semiconductors can give the new possibilities in control of their physical properties.

According to published and our data [1-4] the Sn impurity in Bi_2Te_3 create the impurity states with the most probability. Theoretical calculations made by methods of strong bond [1] lead to conclusion that impurities of IV group substituted to Te^I in Bi_2Te_3 create resonant states. Doping of Bi_2Te_3 by Sn atoms was investigated experimentally by the authors [2-4]. In the bismuth telluride doped with Sn atoms the peculiarities in temperature- and press- dependences of electroconductivity (σ_{ij}) and Hall coefficients (R_{ijk}) were observed, that can be interpreted as presence of impurity states. But these peculiarities are not as strong as the peculiarities induced by Tl in lead telluride. The point is that there are usually many intrinsic defects in Bi_2Te_3, in particular, the antistructure defects (AS), that leads to high hole concentration. The complex structure of valence band consisting of two subbands with a small energy gap ($\Delta \cong$ 0,02eV) makes the situation even more complicated.

Investigations of resonant levels associated with group III elements in IV-VI semiconductors [5] testified that the method of additional doping with an electroactive impurity, which does not create level itself, is very efficient for detection of impurity levels. Electroactive impurity changes the degree of occupancy of the allowed and impurity bands. The existance of an impurity band is indicated by stabilization (pinning) of the chemical potential, when the concentration of the additional impurity is varied. In the case of tin-doped bismuth telluride the iodine which exhibits a strong donor behavior can be used as an additional impurity.

Experiment and results

The investigations of the transport coefficients are made on single crystals of bismuth telluride doped with tin and double-doped with tin and iodine. The composition of the samples doped with tin is described by the chemical formula $Bi_{2-X}Sn_XTe_3$, where X=0; 0.002; 0.005; 0.007; 0.01 (X=0.01 corresponds to $6*10^{19}cm^{-3}$). The samples double-doped with tin and jodine are the samples $Bi_{2-X}Sn_XTe_3$ + $YSbJ_3$ with X=0.005 and with additional impurity SbJ_3: Y= 0.05; 0.1; 0.15 weight %. All crystals were grown by Chochralskij method. The perfection of crystals was verified by STM-images with scanning tunneling microscope and by concentration dependence of Nernst-Ettingshausen effect [6]. The Sn and J impurities content was controlled with chemical test. The homogeneity of impurity distribution along the samples was estimated by measuring of Seebeck coefficient with the aid of a thermoprobe at 300 K.

We determined the following independent components of the transport tensors: the Hall coefficients R_{123} and R_{321}, the thermoelectric powers S_{11} and S_{33}, the electrical conductivity σ_{11} and the Nernst-Ettingshausen coefficients Q_{123} and Q_{132}. In this notation the number 3 indicates the trigonal axis of a crystal. The subscripts of the coefficients represent the following, in the order they appeared: the first is used for the direction of the measured electric field, the second for the direction of the electric current or the temperature gradient, and the third for the direction of the magnetic field.

The measurements were carried out mainly in the temperature range 77 - 420 K. The carrier density was determined from the expression $n, p = I\, q^* R_{321}(77\,K)\, I^{-1}$.

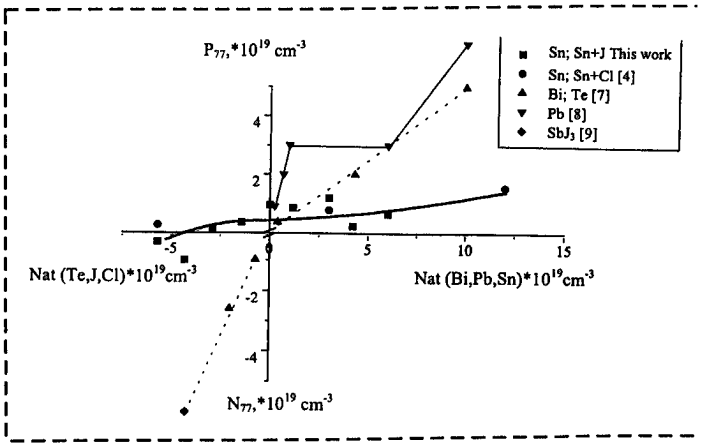


Fig. 1 The dependence of hole concentration (p) against of doped Sn impurity.

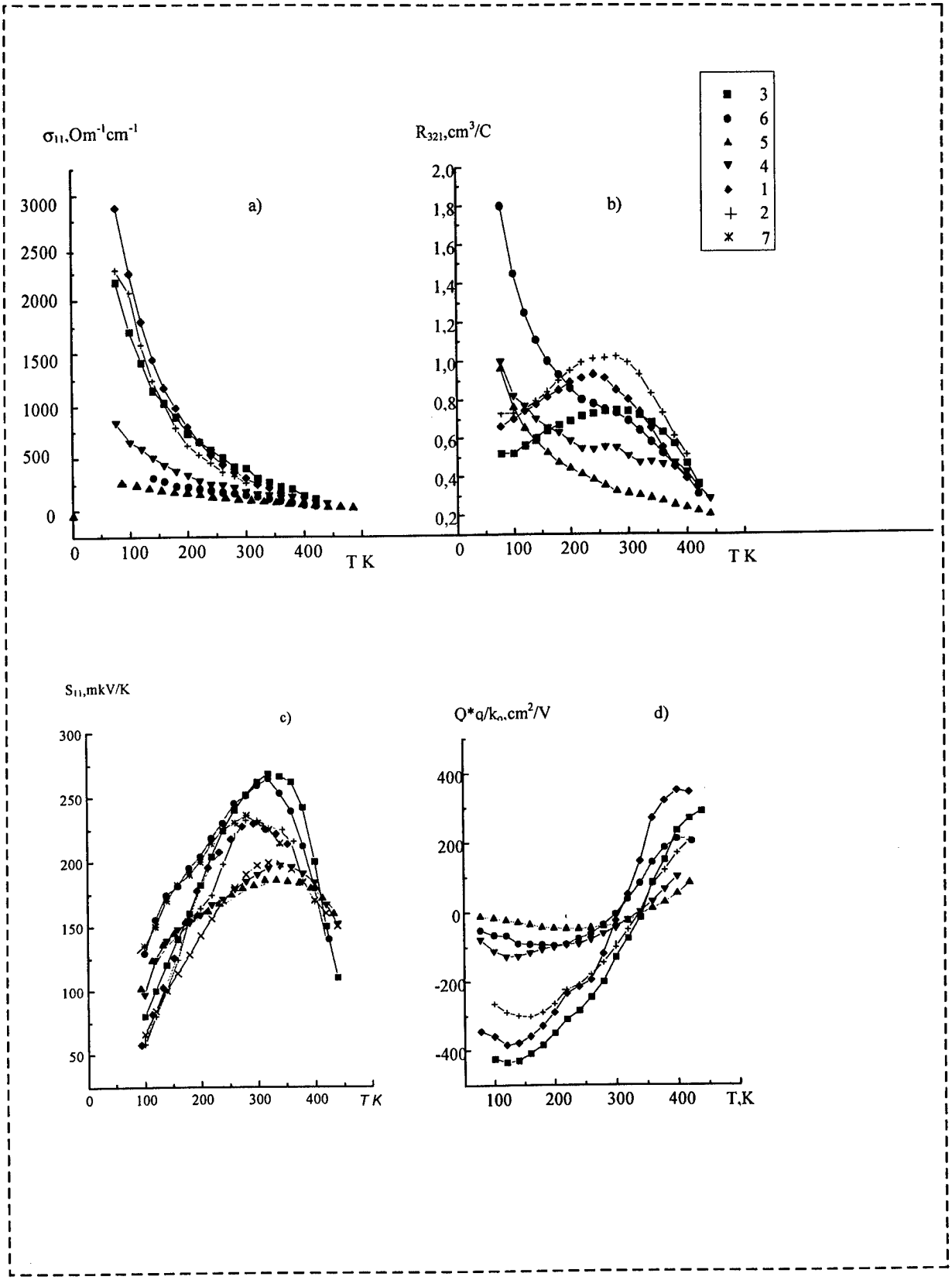


Fig. 2 The temperature dependences: a) - of the Hall mobility $R_{123}\sigma_{11}$; the kinetic coefficients: b) - Hall R_{123}; c) - Seebeck S_{11} ; d) - TNEE Q_{123}. X_{Sn}: 1 - 0; 2 - 0.002; 3 - 0.005; 4 - 0.007; 5 - 0.01; 6 - 0.005 and 0.05weight% SbJ_3; 7 - [4].

The dependences of hole concentration (p) on of doped Sn impurity amount are shown in Fig.1 There are presented our data, the data of [4] on Bi_2Te_3 doped with Sn and $CdCl_2$ and data of [7-9] on Bi_2Te_3 doped with donor and acceptor impurities (Te,Bi,Pb,SbJ_3). Usually the hole concentration in Bi_2Te_3 grows proportionally to amount of doping impurity atoms. Lead activity depends on its site in a lattice and could range from 1,4 - 1,7 h/atom [9], jodine electrical activity is 1,3 - 1,4 h/atom. In contrary to these facts, we observe the low changes of hole concentration in tin-doped Bi_2Te_3. At the doping with Sn atoms in amount N_{Sn} = (1,2 - 6)*10^{19}cm^{-3} the carriers concentration is changed in the small interval (6 - 8,5)*10^{18}cm^{-3} .We observe the stabilization of hole concentration.

The data on Bi_2Te_3 double-doped with tin and electroactive impurities (this work - with SbJ_3, [4] - $CdCl_2$) are shown on Fig 1 also. We can see different action of J and Cl atoms on Bi_2Te_3 and on $Bi_{2-X}Sn_XTe_3$. In the latter case the concentration changes are considerably smaller.

The temperature dependences of the kinetic coefficients are shown on Fig.2. For small tin-doped $Bi_{2-X}Sn_XTe_3$ (X=0.002 ; 0.005) they are similar to those obtained earlier for the undoped samples Bi_2Te_3. For big tin-doped $Bi_{2-X}Sn_XTe_3$ (X=0.007 ; 0.01) and for the samples double-doped with tin and jodine there are peculiarities in temperature dependences of kinetic coefficients: the decrease of Hall coefficients in all temperature range; the decrease of hole mobilities, determined from electroconductivity and from Nernst-Ettingshausen effects.

Fig.3 shows isoterms of the Seebeck and Nernst-coefficients and Hall-mobility on the hole concentration. These dependences have a clearly defined minimum at low temperature in the case of big tin or tin-jodine doped samples, when hole density is of the order of (3 - 5)*10^{18}cm^{-3}. Earlier we obtained the similar peculiarities on Bi_2Te_3 doped with In atoms. In the case of In doped Bi_2Te_3 we observed the decrease of Seebeck coefficient, but in the case of Sn-doped Bi_2Te_3 the Seebeck coefficient increases at this hole concentration.

Discussion

The strong temperature dependence R(T) and sharp decreases of charge carriers mobilities are common features for $A^{IV}B^{VI}$ semiconductors with impurity resonant states [5]. The stabilization of carrier concentration was explained by the existence of impurity states underground of allowed states. Therefore it is quite natural to link the observed dependences of R(T), sharp decrease of hole mobility and stabilization of hole concentration in Bi_2Te_3:Sn with existence of resonant states. However, in order to prove that it is really the impurity states we should give additional arguments. Really, when this compound is doped, especially with metals (for example, Pb, Sn, In or Tl), the number of defects and the degree of the inhomogeneities of compound increase. Note, that in inhomogeneous semiconductors a situation, in which the temperature dependences of the transport coefficients (specifically, the Hall coefficient) can simulate the behavior of homogeneous semiconductor with impurity levels is possible. However, in our work [6] we confirmed the high quality of the Sn-doped samples by the data on transverse Nernst-Ettingshausen effect (TNEE). Therefore, the peculiarities of the transport coefficients experimentally observed on these crystals can be explained by

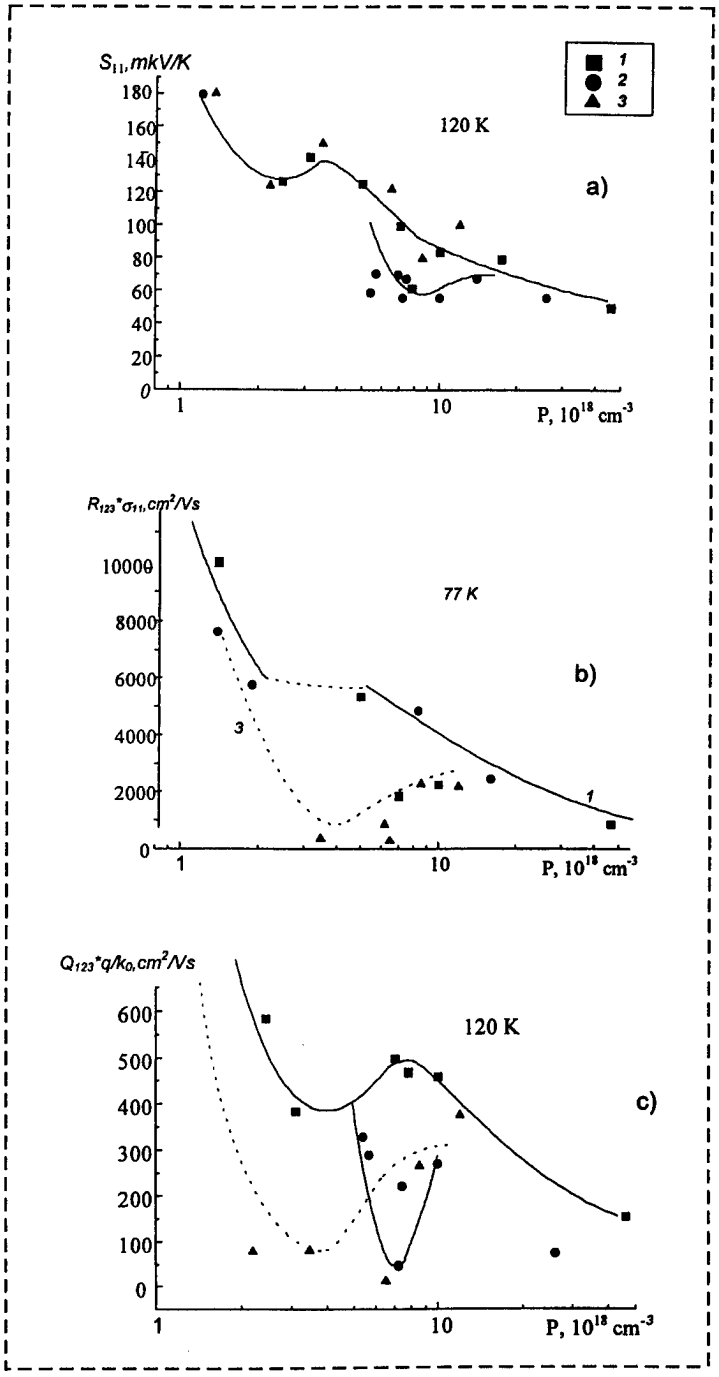


Fig. 3 Isoterms of the concentration dependences: a) -S_{11}; b) - R_{123} * σ_{11}; c) - Q_{123}. The curve 1 - Bi_2Te_3 without doping atoms; 2 - with In; 3 - with Sn.

the differences in the energy spectrum of samples with and without tin in other words by the presence of impurity resonant levels.

Our experimental results enabled us to determine the parameters of the energy band structure of $Bi_{2-X}Sn_XTe_3$ solid solutions such as effective density mass m* and energy gap ε_g. In our recent work [3] we reported about the calculations of these parameters. Note that they are the same as for the case of undoped Bi_2Te_3 and we observe some increase of m* and ε_g for the samples doped with Sn.

The estimation of the value hemical potential was made by the methods of [5]. The extrapolation of temperature dependence of chemical potential to T=0 gives the energy of impurity states equal to ε = 0,02 - 0,03 eV. It was shown that level connected with Sn atoms is situated among subbands of valence band. The estimation of density state function we carry out using the expression $\alpha_{\infty} = S^*q/k_0 + Q_{123}*q/R_{123}\sigma_{11}k_0$. It is an isotropic value and it depends only on chemical potential μ^*. The method was described in details in [3]. For the energies of 0,02 - 0,03 eV the encrease of density state function was obtained. This increase can be explained by the appearance of Sn-impurity states near the edge of the second valence band. And observed minimum in hole concentration dependences of Hall and Nernst mobilities - by resonant scattering of holes on Sn levels.

The influence of resonant scattering of charge carriers on kinetic coefficients is considered in review [10]. In this review there was shown that the resonant scattering is highly selective in respect of the carrier energy: only the carriers with energy, close to energy of impurity states, are strongly scattering. When the Fermi level position is of the order of k_0T higher than the resonant level, the carriers with relatively low energies ($\varepsilon-\mu < 0$) are scattered much more strongly than those with high energies ($\varepsilon-\mu > 0$). The average energy of carriers in flow increases and hence the thermoelectric power increases too. If the mobility of carriers does not decrease too much due to resonant scattering, the thermoelectric figure of merit $Z = S^2\sigma/\kappa$ (κ is the thermal conductivity) can increase. Note that our data show the increase of S in the some samples Bi_2Te_3 doped with Sn. But only two of them (NN 89,90) with X_{Sn} = 0.002 and 0.005 have the encrease of thermoelectric efficiency ($S^2\sigma$). These samples have some increase of S and small decrease of hole mobility. It can be assumed that the Sn-states are filled by holes of intrinsic defects (AS) and correlation of Fermi level position and the resonant energy takes place at this Sn concentration .

Conclusion

Thus the data obtained in this work (i.e. the fact of presence of impurity Sn-level) permit to hope on the improvement of figure of merit in A^VB^{VI} compounds traditionally used for middletemperature thermoelectric performances by the use of resonant impurity states.

Acknowledgments

We would like to express grateful appreciation to prof.V.I. Kaidanov who attracted of our attention to the investigation of resonant states in compounds A^5B^6. We also would like to thank to N.Yu. Ispolov for help in creation of the computer's maket of this article.

References

[1] P. Pecheur, G. Toussaint, "Tight binding studies of crystal stability and defects in Bi_2Te_3", Proc. VIIIth Int. Conf. on Thermoelectric Energy Conversion, Nancy (1989) 176.

[2] V.A. Kulbachinskii, M. Inoue, M. Sasaki, H. Negishi, W.X. Gao, K. Takase, Y. Giman, J. Horak, P. Lostak, "Valence-band energy spectrum of solid solutions of narrow-gap-semiconductor $Bi_{2-X}Sn_XTe_3$ single crystals", Phys. Rev. B, **50** (1994) 16921.

[3] M.K. Zhitinskaya, S.A. Nemov, T.G. Abaidulina, T.E. Svechnikova, "Thermoelectrical properties and energy band spectrum p-Bi_2Te_3, doped with element of III or IV grop", Proc. of the XIVth Int. Conf. on Thermoelectrics (ICT95) St. Petersburg, Russia, 1995, 56.

[4] G.T. Alekseeva, P.P. Konstantinov, V.A. Kutasov, L.N. Luk'yanova, Yu.I. Ravich, "Nonisovalent substitution of atoms in the cation sublattice of bismuth telluride", Fiz. Tverd Tela (St. Petersburg), **38** (1996) 2998-3004.

[5] V.I. Kaidanov and Yu.I. Ravich, "Deep and resonant states in $A^{IV}B^{VI}$ semiconductors", Usp. Fiz. Nauk Sov. Phys. Usp. **28** (1985) 31.

[6] M.K. Zhitinskaya, S.A. Nemov, T.E. Svechnikova, "Effect of inhomogeneities of Bi_2Te_3 crystals on the transverse Nernst-Ettingshausen effect", Fiz. Tekh. Poluprov. **34** (1997) 441-443.

[7] J.-P. Fleurial, L. Gailliard, R. Triboulet, H. Scherrer, S. Scherrer, "Thermal properties of high quality single crystals of bismuth telluride - part I: Experimental characterization", J. Phys. Chem. Sol., **49** (1988) 1237.

[8] H. Sьssmann, A. Priemuth, U. Pruhl, "Doping properties of Pb and Ge in Bi_2Te_3 and Sb2Te_3", Phys. Stat. Sol. (a) **82** (1984) 561.

[9] W.M.Yum, F.D.Rosi, "Compound tellurides and their alloys for Peltier cooling - a Review", Solid-State Electronics **10** (1972) 1121.

[10] V.I. Kaidanov, S.A. Nemov, Yu.I. Ravich, "Resonant scattering of carriers in IV-VI semiconductors", Fiz. Tekh. Poluprovodn. **26** (1992) 201-222.

Fabrication and Characterization of Bi_2Te_3-Sb_2Te_3 based Thermoelectric Materials by Powder-Extrusion-Sintering Technique

Byoung-Gue Min, Kyung-Wook Jang*, Dow-Bin Hyun** and Dong-Hi Lee

School of Materials Science and Engineering, Yonsei University
**Department of Materials Science and Engineering, Hanseo University*
*** Korea Institute of Science and Technology*
Tel. : 82-2-361-2834, Fax : 82-2-312-5375, E-mail : metphys@bubble.yonsei.ac.kr

ABSTRACT

Despite high thermoelectric performance, the commercial applications of Bi_2Te_3-Sb_2Te_3 based thermoelectrics are limited mainly because of production cost due to complicated processing steps. In this study, a new approach to the powder-extrusion-sintering method, which is intended to fabricate a sound sintered material by the simultaneous application of pressure and heat, was investigated. This method is expected to be suitable for low cost production of Bi_2Te_3-Sb_2Te_3 materials because of the possibility of semi-continuous fabrication processing. It was possible to achieve high density ($\geq$95% of theoretical density) products by adjusting variables, such as; die angle, die hole length, powder size, extrusion pressure and temperature. Thermoelectric properties of sintered specimens were measured, and discussed to achieve optimum fabrication conditions.

I. INTRODUCTION

It is a common practice to fabricate Bi_2Te_3-Sb_2Te_3 based thermoelectric material by methods of a single crystal growing[1, 2] or sintering[3, 4, 5, 6]. These methods, however, have some drawbacks such as high production cost, low efficiency, and difficult control of compositions. Naturally, new methods, which could overcome such drawbacks, have been sought[7, 8, 9]. Powder extrusion-and-sintering could be one of the candidates for economical mass production of thermoelectric materials.

In this study, a novel Powder-Extrusion-Sintering (PES) process, which allows sintering and extrusion simultaneously, is examined for the production of Bi_2Te_3-Sb_2Te_3 based materials. The core of this technique is the application of high electric current (resistance heating) and pressure to the powder mass in an extrusion die in order to complete shaping and sintering within a short period of time (typically 5 to 20 : minutes). It is found that this approach can produce thermoelectric materials having the desired cross-sectional shape and size under a semi-continuous fabrication process. Furthermore, the short reaction time might provide a limited variation in compositions and microstructures of this material[10, 11]. It is also possible to obtain anisotropic thermoelectric properties due to the aligned texture microstructures along the extrusion direction[12, 13].

P-type $Bi_{0.5}Sb_{1.5}Te_3$ and n-type $Bi_2Te_{2.25}Se_{0.75}$ were used to demonstrate the feasibility of this new approach. The PES process was examined at various conditions of temperature, pressure, die dimension and extrusion time along with the composition and particle size of powders. From trial and errors, it was possible to find the process and material condition which can produce sound specimens of high densities ($\geq$95% of theoretical density). Thermoelectric properties of the specimens were investigated and analyzed in conjunction with sinterability, microstructure and appearance.

II. EXPERIMENTALS

Preparation procedures of p- and n-type powders are the same as described elsewhere[3]. That is, ① pure (4-nine grade) elements of Bi, Te, Sb, Se, etc. were vacuum sealed into a silica tube after weighing, ② melted and vibrated for 2 hours, and ③ cooled and crushed (pulverized) into powders inside the glove box under an Ar atmosphere. For p-type $Bi_{0.5}Sb_{1.5}Te_3$, relatively large amounts of Te (2 ~ 5wt%) were added, only 0.05 ~ 0.2 wt% of SbI_3 was added for n-type $Bi_2Te_{2.25}Se_{0.75}$ as a dopant. Powders of four different particle sizes (60, 100, 150 and 210 μm) were employed in this experiment.

PES apparatus, as shown in Photo 1 and Fig 1, consists of a vacuum chamber, a hydraulic ram, a direct current supply, a die assembly and auxiliary control units. Pressuring and resistance heating were applied to the powder mass in the die to complete sintering and extrusion simultaneously through the process cycle. In addition to the pressure gauges and thermocouples which monitors the whole extrusion and sintering cycle, a LVDT was attached to the ram in order to record the amount of extrusion.

0-7803-4057-4/97 $10.00 ©1997 IEEE

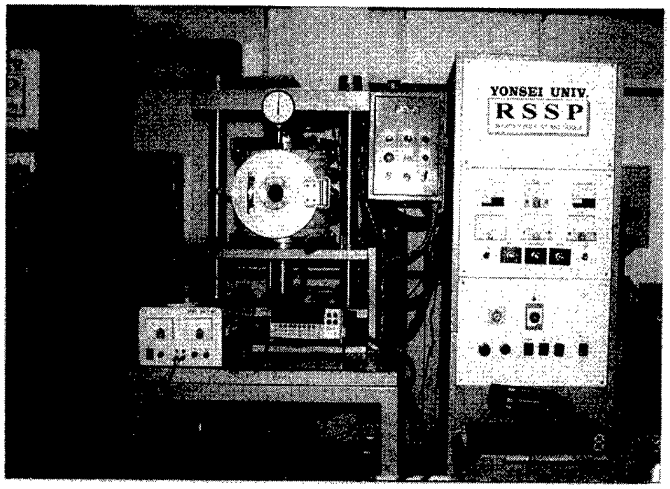
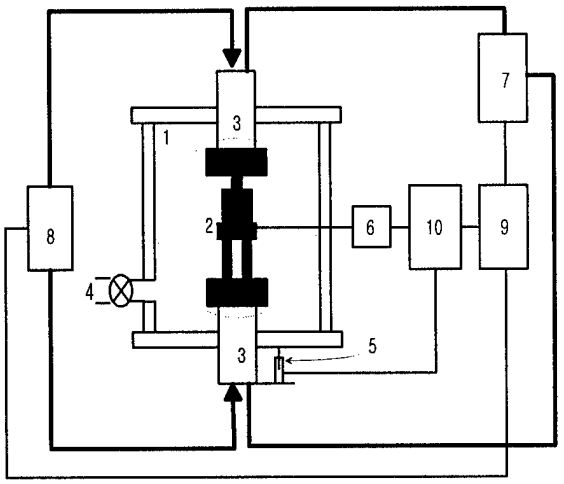


Photo 1. Power Extrusion Sintering apparatus



1. vacuum chamber
2. die assembly with compact
3. water cooled electrode
4. vacuum system
5. LVDT
6. pyrometer
7. DC and AC power supply
8. servo controlled hydraulic system
9. process control unit
10. digital multichannel recorder

Figure 1. Schematic illustration of PES arrangement

The shape and dimension of die assembly is shown in Fig 2. It resembles a conventional extrusion die assembly, but for this experiment, several dies having different values of extrusion angles (θ : 30° , 45° and 60°), die hole lengths (ℓ : 2, 5 and 10㎜) and extrusion ratios (R = D/d : 3 and 10) were used to examine effects on the final product. For this apparatus, rod shaped specimens (diameters : 1.5 ~ 5㎜) of as long as 120㎜ in length were fabricated. Powders were pre-compacted into a cylindrical mass (diameter : 15㎜, length : 22㎜, density ≈ 93%) at a cold compaction pressure of 300kgf/cm^2. Each green compact was loaded into the extrusion die cavity and held for about 3 minutes of heating-up period at low extrusion pressures.

The die assembly was heated up to predetermined temperatures of 300 ~ 400℃ by the application of a high density direct current (250 ~ 350A) through die assembly. As soon as the sintering temperature was reached, it was extruded by applying high extrusion pressures ranging from 100 to 200MPa, depending on other variables.

Ⅲ. RESULTS AND DISCUSSION

1. Effects of variables on PES

Fig 3 shows a typical behaviour of the present PES cycle; the variation of temperature and amount of extrusion is plotted with time as a function of particle size of powders, extrusion pressure and die angle.

In order to obtain a high density (≥95%) material, higher temperatures and longer times were required for larger size powders irrespective of p- or n-type material. In general, n-type materials needed higher temperatures than p-type materials for densities of equivalent.

Variations in die dimensions (θ , ℓ and R) revealed the effect on the process as predicted, i.e. for larger θ , ℓ and R, higher temperatures and pressures were required. In cases of $\theta > 60°$ and $\ell < 5$mm, surface cracks on the specimens which were so severe that it was not possible to cut-out a sound thermoelement from such a product. This tendency was pronounced as the particle size and extrusion rate (slope of extrusion curve in Fig 3) were increased.

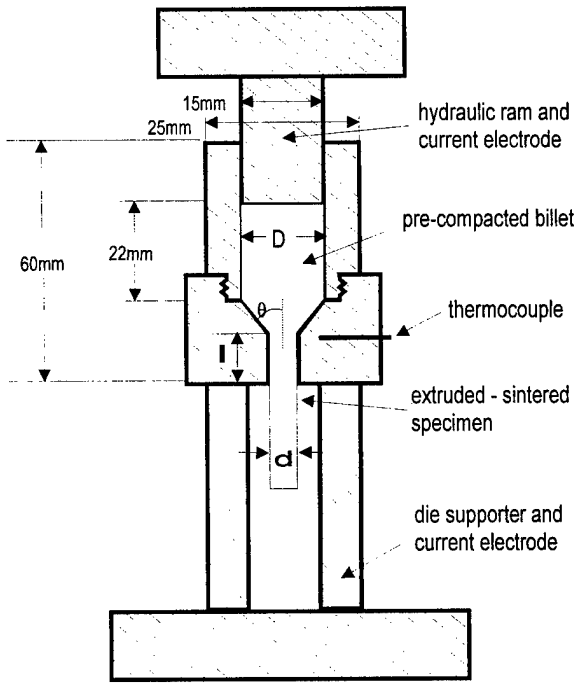


Figure 2. Detail of die assembly

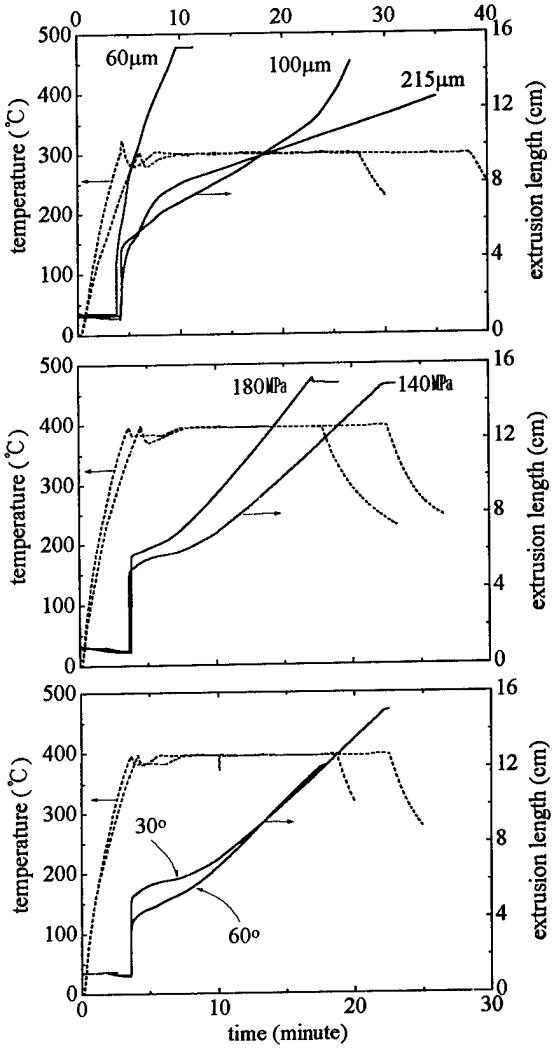


Figure 3. Effects of variables on PES cycle

From the above mentioned data, the following conditions (Tab. 1) were obtained for optimum fabrication of sound materials, of which thermoeletric properties were reproducible. As in Photo 2, the PES specimens showed a sound appearance and dense microstructure at relatively low extrusion pressures of this experiment [11]. When PES conditions, such as temperature, extrusion rate (pressure), particle size and die dimensions of θ and ℓ, were not properly selected undesirable surface cracks appeared with internal pore in addition to lower sintered density.

Samples ($\approx 10 \times 1.5 \times 1.5$ and $\approx 7 \times 7 \times 1$ mm^3) taken from positions marked "x" of PES specimens (Photo 2), which were extruded-and-sintered relatively later than other parts of the PES specimen, showed a very high density($\approx$97% of theoretical density). The measurements of thermoelectric properties (σ , α and Z) were carried out for these samples unless otherwise mentioned.

Table 1. Selected PES conditions employed in this experiment and final state of specimen.

Average particle size	45 mm
extrusion / sintering temp.	300 ℃ (p-type) 395 ℃ (n-type)
current density	250 A (p-type) 350 A (n-type)
extrusion / sintering time	20 min
die angle, θ	30°
die hole length, l	10 mm
extrusion ratio, R	3
sintered density	97.1% (p-type) 96.9% (n-type)
surface appearance	good

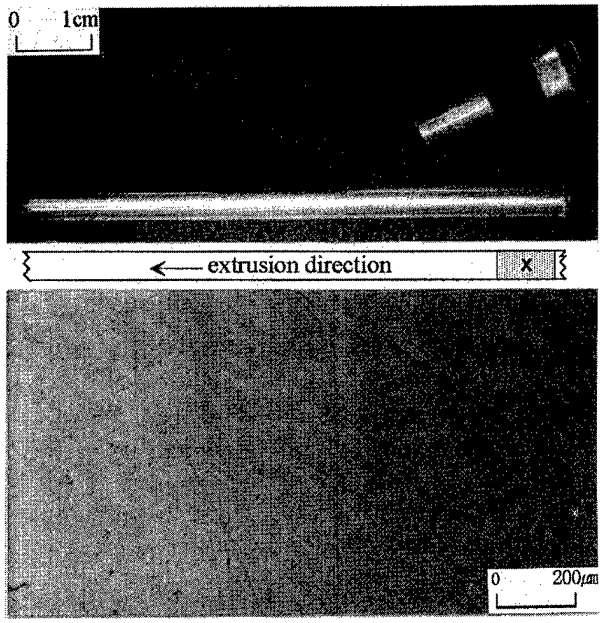


Photo 2. Appearance and micrograph(at "x" position) of PES specimen

2. Thermoelectric Properties

Together with results of Hall measurements (carrier concentration and mobility), values of σ , α and Z measured at room temperature for p- and n-type specimens are shown in Tab. 2.

Table 2. Thermoelectric properties measured at room temperature.

N-type / P-type	σ ($\Omega^{-1}cm^{-1}$)	α (μV/K)	Z ($x10^{-3}$/K)	κ ($x10^{-2}$W/cmK)	C ($x10^{19}/cm^3$)	μ (cm^2/Vs)	ref.
single crystal	1735 / 613	-204 / 252	2.01 / 2.6	3.59 / 1.5	-	-	[14]
sintered	1080 / 830	-166 / 210	1.66 / 2.2	1.8 / 1.68	- / 305	- / 305	[14]
PES	1271 / 451	-103 / 222	0.79 / 1.38	1.71 / 1.61	0.31 / 2.61	2563 / 108	present work

(C: carrier concentration, μ: Hall mobility)

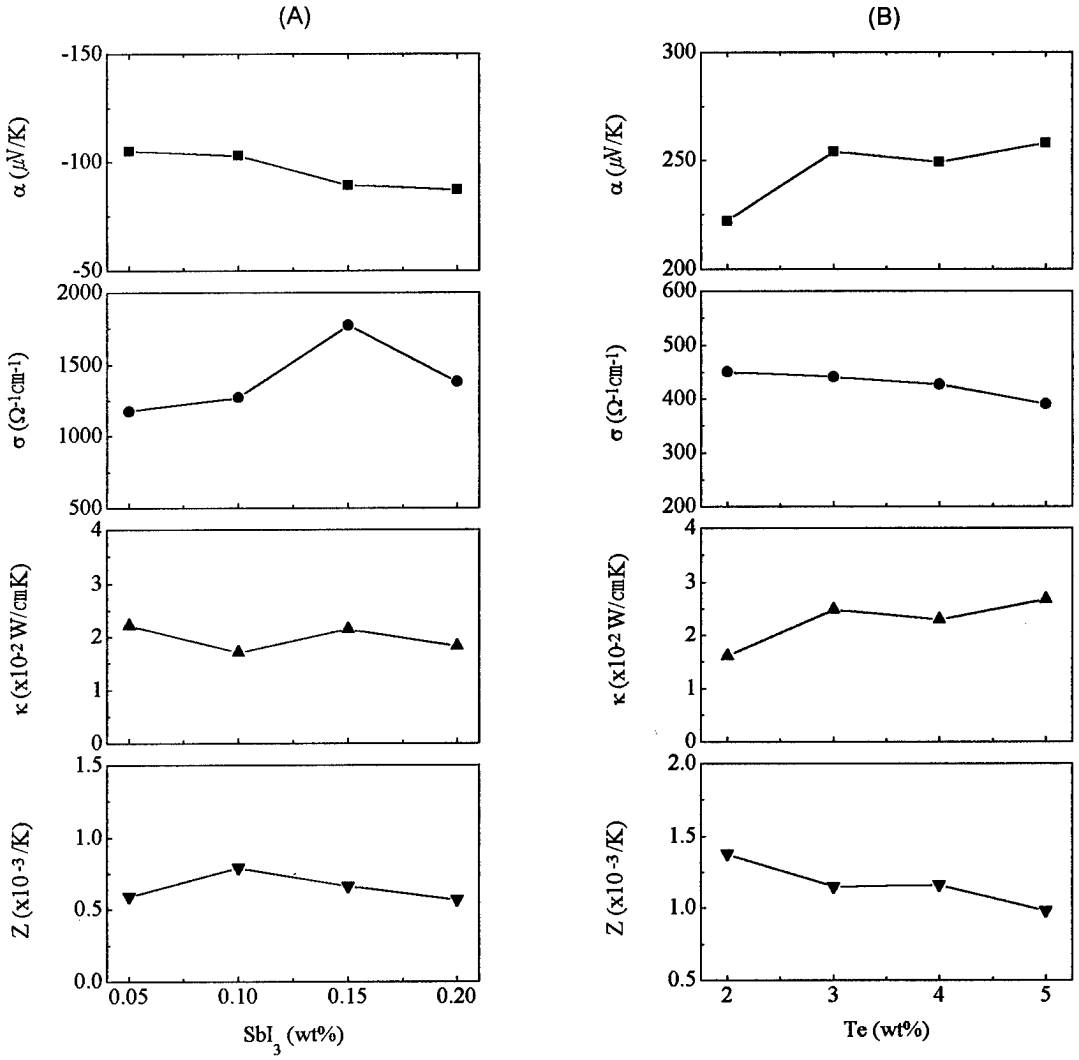


Figure 4. Variation of thermoelectric properties with compositional change.
(A) N-type material (B) P-type material

Values available from other methods are also shown for comparison. It is indicated from Tab. 2 that the values of thermoelectric properties for the PES specimens were relatively lower than those of the other methods, such as single crystals, sintered or hot-pressed materials[8, 14].

However, considering the fact that the properties and appearance of PES specimens were changed significantly with material and processing variables, it is expected that the improvement of properties, microstructures and appearance will be possible if variables are more carefully adjusted. Particularly, controlling material variables, such as composition and particle size of different types of powders, is believed to be one relatively easy way for improvement, compared to control process variables, such as θ, ℓ, R, temperature,

pressure and time. With this in mind, the variation of thermoelectric properties with compositional changes were investigated using the PES specimens (See Fig 4). From these results, it is recognized that, with specific process variables, different values of thermoelectric properties can be achieved through slight changes in composition. Particle or grain size effects can be also utilized to improve thermoelectric properties by blending powders for proper size and size distribution[10, 15]

IV. CONCLUSION

With this new approach of a PES method for the fabrication of Bi_2Te_3-Sb_2Te_3 based materials, the following results were obtained;

1. As given in Tab. 1, it was possible to obtain high density ($\geq$95%) materials having reasonably good surface and microstructure by adjusting several variables in this method.

2. The thermoelectric properties, α, σ and Z measured at room temperature for the specimens showed relatively lower values compared to the other process, even though the density of specimen was nearly equivalent to that of other methods.

3. It is expected, however, that the thermoelectric properties may be improved if the material variables, such as composition and powder size are carefully selected. Some data collected from the compositional variations demonstrated certain possibility of this expectation.

ACKNOWLEDGEMENTS

The authors would like to show their appreciation to Korea Institute of Science and Technology for the financial support. (Contract No. 96HN-063)

REFERENCES

[1] W.M.Yim and F.D.Rosi, "Compound telluride and their alloys for Peltier cooling-A review", Solid state Electronics, **15** (1972) 1121-1140

[2] A.C.Yang and F.D.Shepherd, "N- and P-type single crystal Bithmuth Telluride", J.Electrochem.Soc., **108** (1961) 197

[3] Kyung-Wook Jang and Dong-Hi Lee, "Thermoelectric properties of hot-pressed p-type $(Sb_2Te_3)_{0.70}(Bi_2Te_3)_{0.25}(Sb_2Se_3)_{0.05}$ pseudo-ternary materials", J. Korean Inst. of Met. and Mater., **32**(5) (1994) 609-615

[4] M.M. Ibrahim, N. Afity, M.M. Hafiz and M. A. Mahmoud, "Electrical conductivity and thermoelectric power of powder compacts of the system $Bi_{1-x}Te_x$", Powder Metall. Int., **20** (1988) 21

[5] F.A.A. Amin, A.S.S. Al-Ghaffari, M.A.A. Issa, A.M. Hassib, "Thermoelectric properties of fine grained (75%Sb_2Te_3-25%Bi_2Te_3) p-type and (90%Bi_2Te_3-5%Sb_2Te_3-5%Sb_2Se_3) n-type alloys", J. Mater. Sci. **27** (1992) 1250-1254

[6] A.F. Semizorov, "A study of pressed thermoelectric materials based on Bi_2Te_3-Sb_2Te_3-Sb_2Se_3 solid solutions", Inorg. Mater. **31** (6) (1995) 675-677

[7] Seok-Ho Son, Kyung-Wook Jang and Dong-Hi Lee, "Thermoelectric properties of n-type $Bi_2Te_{2.4}Se_{0.6}$ prepared by novel sintering process", Korean J. Mater. Res. **7** (5) (1997) 374-380

[8] Hyun-Soo Shin, Heon-Phil Ha, Dow-Bin Hyun, Jae-Dong Shim and Dong-Hi Lee, "Thermoelectric properties of 25%Bi_2Te_3-75%Sb_2Te_3 solid solution prepared by hot-pressing method", J. Phys. Chem. Solids **58** (4) (1997) 671-678

[9] T. Ohta, A. Yamamoto and T. Tanaka, "Thermoelectric properties of undoped polycrystal $(Bi_2Te_3)_{0.2}(Sb_2Te_3)_{0.8}$ by PIES method", Proc. 13th Int. Conf. On thermoelectrics (Kansas city, MO, 1994), 267

[10] a) J.Jaklovszky, R. Ionescu, N. Nistor and A.Chiculita, "Grain size effect on the figure of merit of sintered solid solutions based on Bi2Te3", Phys. Stat. Sol., (a) **27** (1975) 329

b) R. Ionescu, J.Jaklovszky, N. Nistor and A.Chiculita, "Grain size effects on thermoelectrical properties of sintered solid solutions based on Bi_2Te_3", Phys. Stat. Sol., (a) **27** (1975) 27

[11] Nikolay A. Sidorenko, "Brittle thermoelectric semconductors extrusion under high hydrostatic pressure", Proc. 13th Int. Conf. on thermoelectrics(Kansas city, MO, 1994), 260-266

[12] F.D. Rosi, B. Abeles, and V. Jensen, "Materials for thermoelectric refrigeration", J. Phys. Chem. Solids, **10** (1959) 191

[13] C.H.Champness, P.T.Chang and P.Parekh, Thermoelectric properties of Bi_2Te_3-Sb_2Te_3 alloys", Canadian J. Phys., **43** (1965) 653

[14] Kyung-Wook Jang, "Study on the improvements of thermoelectric properties of Bi_2Te_3-based thermoelectric semiconductors", Ph.D. thesis, Yonsei university (1994)

[15] A.A. Joraide, "Thermoelectric properties of fine-grained sintered $(Bi_2Te_3)_{25}$-$(Sb_2Te_3)_{75}$ p-type solid solution", J. Mater. Sci. **30** (1995) 744-748

Effect of extrusion process on the thermoelectric properties of hot-extruded n-type $Bi_2Te_{2.85}Se_{0.15}$ compounds

J. H. Seo,* D. M. Lee,** K. Park,*** C. H. Lee*
*Dept. of Metallurgical Engineering, Inha University, Inchon 402-751, Korea
**Pusan Regional small & Medium Business Office, Pusan, 616-110, Korea
***Dept. of Materials Eng., Chung-ju National University, Chungbuk 380-702, Korea

Abstract

The n-type $Bi_2Te_{2.85}Se_{0.15}$ compounds were fabricated by the hot extrusion under in the temperature range of 300 to 440 ℃ under an extrusion ratio of 20:1. The microstructure and thermoelectric properties of the compounds were studied. It was found that the compounds was highly dense. The density was increased with increasing the temperature. Also, equiaxed fine grains (~1.0 ㎛) were formed because the dynamic recrystallization occurred during the extrusion. The hot extrusion gave rise to a slightly preferred orientation of grains. The small grain size and preferred orientation of grains and the high density contributed to an improvement in the thermoelectric properties. The highest figure of merit (2.62×10^{-3}/K) was obtained at 440 ℃. In addition, the SbI_3 dopants significantly increased the figure of merit. The values of the figure of merit for 0.05 wt% SbI_3-doped $Bi_2Te_{2.85}Se_{0.15}$ compounds hot extruded at 440 ℃ was 3.05×10^{-3}/K.

Introduction

The Bi_2Te_3 and related alloy are most often used in thermoelectric devices and extensively studied on fabrication methods. The electrical and thermal properties of single crystals are highly anisotropic. Therefore, controlling the microstructure is important to increase the thermoelectric properties in sintered materials, because sintered material is composed of random mixed fined grain crystals. It has been previously reported that the theraml conductivity was reduced by grain boundary scattering of long wavelength phonon in Ge-Si alloys [1][2]. Therefore, fine grained Bi-Te alloy are expected to reduce thermal conductivity by phonon scattering at grain boundary. The grain refinement can be achieved by hot extrusion. In this work, we fabricated the n-type SbI_3-doped $(Bi_2Te_3)_{0.95}(Bi_2Se_3)_{0.05}$ compounds by hot extrusion, and then investigated effects of extrusion temperature and dopant on the thermoelectric properties.

Experimental Procedure

The n-type $(Bi_2Te_3)_{0.95}(Bi_2Se_3)_{0.05}$ compounds undoped and doped with 0.05 wt% and 0.1 wt% SbI_3 were selected for this study. The starting materials were the powders of Bi, Te, Se, and SbI_3 with >99.99 % purity. The powder mixtures in SiO_2 tube was heated at 700 ℃ using rocking furnace. The solidified ingot was crushed using Al_2O_3 bowl and then seived to prepare powders with 45-74 ㎛ size. To remove the oxygen developed, the resulting powders were reduced in hydrogen atmosphere at 360 ℃ for 4 hours. The powders were compacted and pressed at 420 ℃ under 200 MPa in Ar. Subsequently, billets were hot extruded in the temperature range 300-440 ℃ at steps of 70 ℃ under an extrusion ratio of 20:1 and a ram speed of 50 mm/min. The density of the and hot-extruded compounds was measured by pycnometer (Micrometric Co.). The prefered orientation of grains was investigated by X-ray diffraction (XRD). Transmission electron microscopy(TEM) was used to examine the microstructure. To measure the Seebeck coefficient α, heat was applied to the specimen, which was placed between the two Cu discs. The thermal conductivity κ was measured

0-7803-4057-4/97 $10.00 ©1997 IEEE

by the static comparative method using a transparent SiO_2 (κ =1.36 W/Km at room temperature) as a standard sample in 5×10^{-5} torr. The electrical resistivity ρ was measured by the four-probe technique.

Results and discussion

Effect of extrusion temperature

The n-type SbI_3-doped $Bi_2Te_{2.85}Se_{0.15}$ compounds were relatively dense. The relative density increased with increasing the extrusion temperature. The density was achieved up to 99.5 % of theoretical density, which was obtained at 440 ℃. Also, high-quality extruded bars without any defects such as tearing, orange peel, and blister were obtained in the hot extrusion temperature of 300-440 ℃.

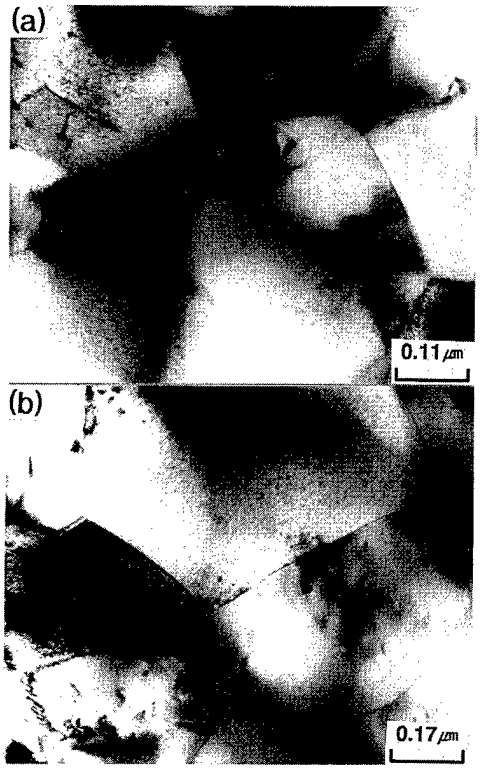


Fig. 1. TEM bright field images from the (a) perpendicular and (b) parallel sections to the hot extrusion direction for the compounds hot extruded at 440 ℃.

Fig. 1(a) and (b) show the TEM bright field images from the perpendicular and parallel sections to the extrusion direction, respectively, for the compounds extruded at 440 ℃. It is evident that the grains are small equiaxed (~1.0 ㎛) and contain many dislocations because of the dynamic recrystallization (DRX) during the extrusion. The grain size of is much smaller than that of hot pressed compounds [3].

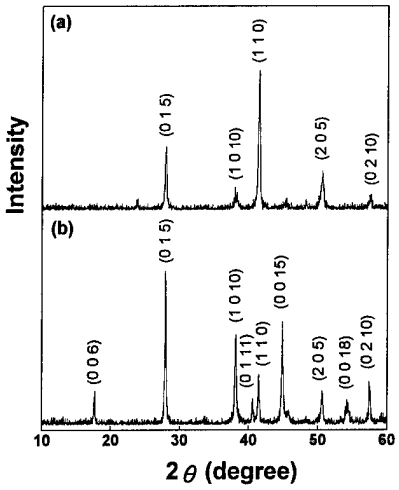


Fig. 2. XRD patterns obtained from the (a) perpendicular and (b) parallel sections to the hot extrusion direction for the compounds hot extruded at 440 ℃.

Fig. 2 (a) and (b) show the XRD patterns obtained from the perpendicular and parallel sections to the extrusion direction, respectively, for the compounds extruded at 440 ℃. The intensity of (0 0 6), (0 0 15), and (0 0 18) planes is only observed at the parallel section, strongly indicating that the hot extrusion gave rise to a preferred orientation of grains. As shown in Fig. 3 with increasing the extrusion temperature, the carrier concentration n_c is decreased and the mobility μ is slightly increased. Fig. 4 shows the variation of Seebeck coefficient α and electrical resistivity ρ with the extrusion temperature. The relationship between the $|\alpha|$ and n_c can be expressed as follows: $|\alpha| \approx r - \ln n_c$ where, r is the scattering factor [4]. This figure represents that the absolute value of Seebeck coefficient $|\alpha|$ increased with the extrusion temperature probably because of the decrease in carrier concentration. The electrical resistivity can be expressed as the following relationship: $\rho = 1/n_c e\mu$. The electrical resistivity increased with

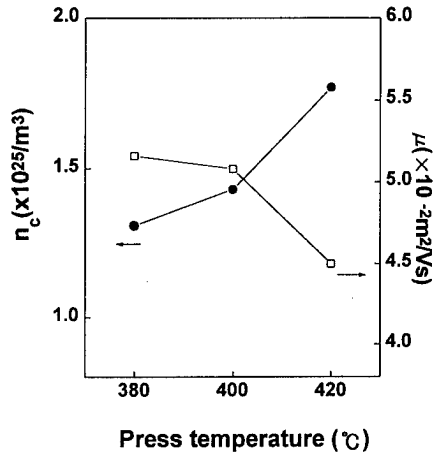


Fig. 3. Carrier concentration n_c and mobility μ as a function of the hot pressing temperature.

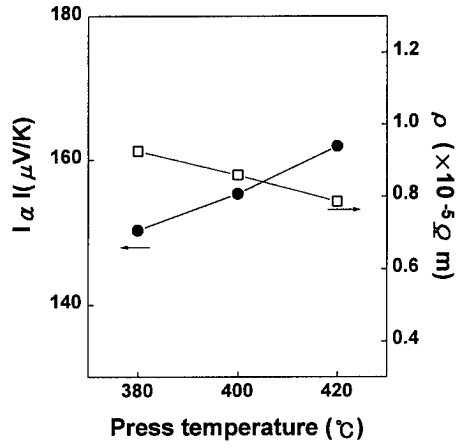


Fig. 4. Variation of Seebeck coefficient α and electriccal resistivity ρ with hot pressing temperature.

The increase in carrier mobility results from the porosity decrease. The variation of Seebeck coefficient α and relative resistivity ρ with the pressing temperature is shown in Fig. 4. The relationship between the α and n_c can be expressed as follows: $\alpha \approx r - \ln n_c$, where r is the scattering factor [6]. As the pressing temperature is increased, the Seebeck coefficient is slightly increased because of the decrease in carrier concentration. Also, the relative resistivity is slightly decreased with increasing the pressing temperature. The relative resistivity can be expressed as the following relationship: $\rho = 1/n_c e \mu$. Therefore, it seems that with increasing the pressing temperature, the slight decrease in relative resistivity would result from an increase in mobility and a slight decrease in carrier concentration. Fig. 5 shows the thermal conductivity κ of the compounds hot pressed at various temperatures. It is increased with the pressing temperature probably because of the density increase. The figure of merit Z was calculated using the following equation: $Z = \alpha^2/\rho\kappa$. Fig. 6 shows the figure of merit Z of the compounds hot pressed at various temperatures. The figure of merit was increased with the pressing temperature because of a slight decrease in resistivity, an increase in Seebeck coefficient, and a slight increase in thermal conductivity. The compounds hot pressed at 420 ℃ shows the highest figure of merit (Z=2.35×10^{-3}/K).

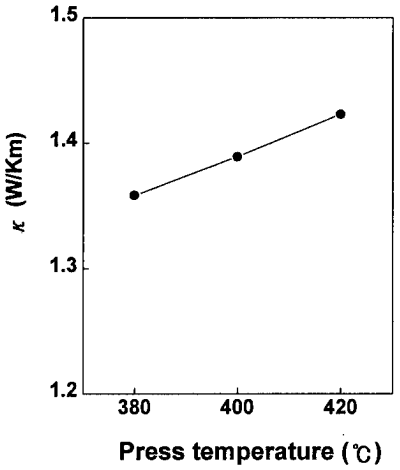


Fig. 5. Thermal conductivity as a function of the hot pressing temperature.

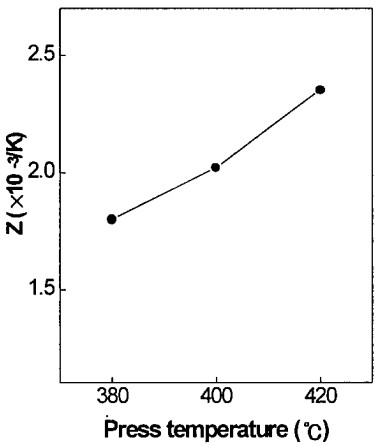


Fig. 6 Figure of merit Z of the compounds hot pressed at various temperatures.

electrical resistivity ρ decreased with the dopant contents because the carrier concentration n_c increased with the dopant contents. In addition, the thermal conductivity κ decreased with the dopant contents due to phonon scattering by ionized impurities. This table represents that the SbI_3 dopant significantly increases the figure of merit.

Table 1. Variation of thermoelectric properties with SbI_3 dopant contents for the n-type compounds hot extruded at 440 ℃

	Contents of SbI_3 dopant (wt %)		
	0.01	0.05	0.1
n_c ($\times 10^{25}/m^3$)	2.44	2.77	3.53
μ ($\times 10^{-2} m^2/Vs$)	1.64	2.68	2.22
α ($\mu V/K$)	-208.3	-183.8	-161.5
ρ ($\times 10^{-5} \Omega m$)	1.557	0.839	0.798
κ (W/Km)	1.369	1.319	1.249
Z ($\times 10^{-3}/K$)	2.04	3.05	2.62

Conclusions

1. The grains of the n-type 0.1 wt% SbI_3-doped $(Bi_2Te_3)_{0.95}(Bi_2Se_3)_{0.05}$ compounds fabricated by hot extrusion were fine equiaxed (~1.0 ㎛) owing to the dynamic recrystallization during the extrusion.
2. The hot extrusion gave rise to a slight orientation of grains.
3. The highest figure of merit (2.62×10^{-3}/K) was obtained at 440 ℃due to the scattering of phonon by fine grain.
4. SbI_3 dopants significantly increased the figure of merit. The values of the figure of merit for n-type 0.05 wt% SbI_3-doped $Bi_2Te_{2.85}Se_{0.15}$ hot extruded at 440 ℃ was 3.05×10^{-3}/K.

Acknowledgement

We would like to thank the support from the University Basic Research Support Fund (1998) of Korea Ministry of Information and Communication.

References

1. D. M. ROWE, *Applied Energy* **24**, (1986) 139
2. H. J. GOLDSMID and A. PENN, *Phys. Lett.* **27A**, (1986) 523.
3. J. Seo, K. Park, C. Lee, and J. Kim, edited by M. G. Kanatzidis, H. B. Lyon, Jr., G. Mahan, and T. M. Tritt, *Thermoelectric Materials-New Directions and Approaches*, Materials Research Society Symp. Proc. Vol. 478, San Francisco, CA, 1997 (in press).
4. K. UEMURA and I. NISHIDA, in *"Thermoelectric Semiconductors and Their Application"*, (Nikkan-Kogyo Shinbun Press, Tokyo, Japan, 1988).
5. J. E. PARROTT, *J. Phys.* C **2**, (1969) 147.
6. W. M. YIM, E. V. FITZKE, and F. D. ROSI, *J. Mater. Sci.* **1**, (1966) 52.
7. K. W. Jang, D. H. Lee, *J. of the Korean Inst. of Met. & Mater.* **32**, (1994) 609

Thermoelectric properties of p-type Bi-Sb-Te based material prepared by PIES method with conventional ball milling process

Shuzo Kagawa[1], Hideki Satake[1], Masanori Sakamoto[1],
Atsushi Yamamoto[2] and Toshitaka Ohta[2]

1 Technology Development Laboratory, KUBOTA Corporation, Japan
2 Electrotechnical Laboratory, AIST, MITI, Japan
(Tel. +81-6-494-7569 Fax. +81-6-494-7696 E-mail: s-kagawa@gkn.kubota.co.jp)

Abstract

For the development of energy saving processes for producing thermoelectric materials, the PIES (Pulverized and Intermixed Elements Sintering) method is known as a suitable one.

In this study, a high figure of merit p-type Bi-Sb-Te based thermoelectric material was obtained by the oxygen free PIES method. The electrical resistivity of p-type $(Bi_2Te_3)_{0.175}(Sb_2Te_3)_{0.825}$ material was reduced to 0.8×10^{-5} ohm•m and Seebeck coefficient was obtained 2.4×10^{-4} V/K by fabrication in the oxygen free atmosphere process. The maximum ZT value was almost 1.0.

Moreover, it was demonstrated that the improvement in figure of merit value was obtained even if the intermixed powder of elements was prepared by a conventional ball milling process in stead of the high energy ball milling process. The PIES methods using a low energy ball milling process is suitable for mass-production because of its cost efficiency.

Introduction

Thermoelectric materials are eagerly being developed for power generation by utilizing the low-temperature waste heat from garbage furnaces or factory waste. For such power generation purposes, the cost reduction for thermoelectric modules is one of the important factors. Therefore we are aiming at 1$ for 1W electric power generation.

Bi-Sb-Te thermoelectric modules are generally fabricated by conventional single crystal growth, but such fabrication processes provide materials with low mechanical strength and they are difficult to upscale for mass-production.

Therefore we developed an improved fabrication process based on PIES (Pulverized and Intermixed Elements Sintering) method in which powder metal was used and crystallized by hot pressing without melting.[1, 2, 3, 4] P type thermoelectric elements fabricated by the PIES method in an oxygen free atmosphere indicated a high figure of merit and high mechanical strength. This process is suitable for mass-production and larger size module fabrication by using conventional low energy ball milling.

Experimental procedure

The raw materials used were the single powder metals of Bi, Sb, Te (purity: over 99.999%) with the mean particle size smaller than 100um. The specified amounts of raw materials were weighed out, placed in a ball milling bottle with YSZ (Yttrium Stabilized Zirconium, ZrO_2 95%) balls, and sealed. These processes were executed inside a high purity nitrogen atmosphere (purity: over 99.999%). More specifically, we used a glove box which could be evacuated and we substituted nitrogen for air. The composition of p-type materials used was $(Bi_2Te_3)_{0.175}(Sb_2Te_3)_{0.825}$ and with no dopant material. This composition rate has been found to be most suitable in obtaining a high figure of merit.[5] They were mixed and pulverized for 20 hours using a conventional ball milling process.

The ball milled powder was placed into the press mold which was made of alloy tool steel, again applying the high purity nitrogen atmosphere. They were then heated to 500℃ for almost 1 hour in the preheating furnace. At the temperature of 500℃, hot pressing took place for 1 minute. Five pressure conditions were applied such as 25, 50, 100, 200, 300 MPa. After pressing, the hot pressed sample was immediately taken out from the mold and quenched. The sample size was 45mm in diameter and almost 10mm thick.

Result

Resistivity was measured by 4-terminal method with the applied voltage of alternately turned DC 100mA in order to compensate the effects on the sample by temperature difference due to Peltier effect. Figure 1 presents the electric resistivity to the press direction. At the temperature of 300K, the values are almost the same and sufficiently low at $0.80\sim0.87\times10^{-5}$ Ω•m regardless of the pressure.

Seebeck coefficient was calculated by thermoelectromotive force measured. A sample was inserted into a Nb electrode 20mm in diameter. The temperature difference of 10 Kelvin was provided to the press direction. Figure 2 presents the Seebeck coefficients. Their values are higher than 2×10^{-4} V/K at the higher temperature region.

0-7803-4057-4/97 $10.00 ©1997 IEEE

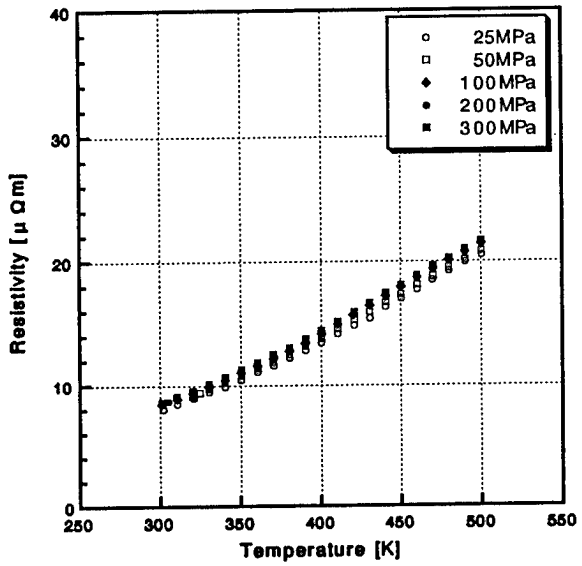


Fig. 1 Electric resistivity

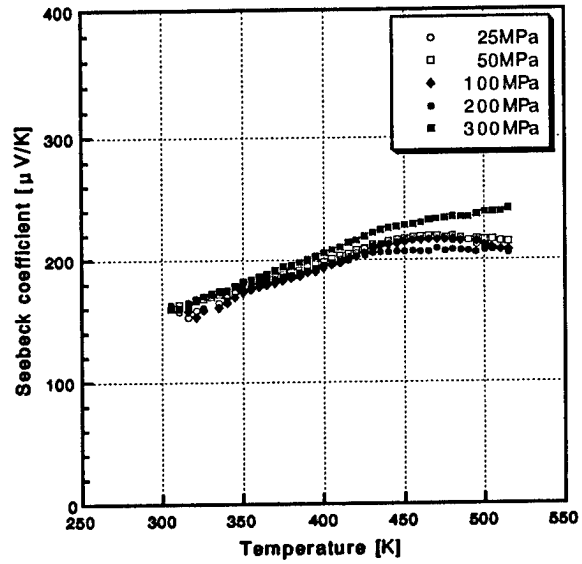


Fig. 2 Seebeck coefficient

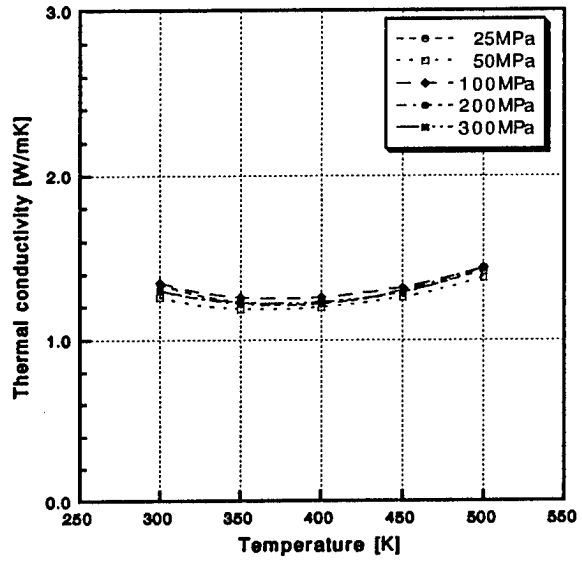


Fig. 3 Thermal conductivity

Thermal conductivity was calculated with thermal diffusivity measured by the laser flash method and specific heat measured by adiabatic scanning calorimetry. Figure 3 shows the thermal conductivity. They are between 1.2～1.5 W/m•K.

According to such data, the figure of merit was calculated and exhibited in Figure 4. They were almost equal regardless of pressure, but it was slightly larger at the high pressure condition of 300MPa. The maximum ZT value of 1.01 was obtained at the temperature of 450K with 300MPa pressure.

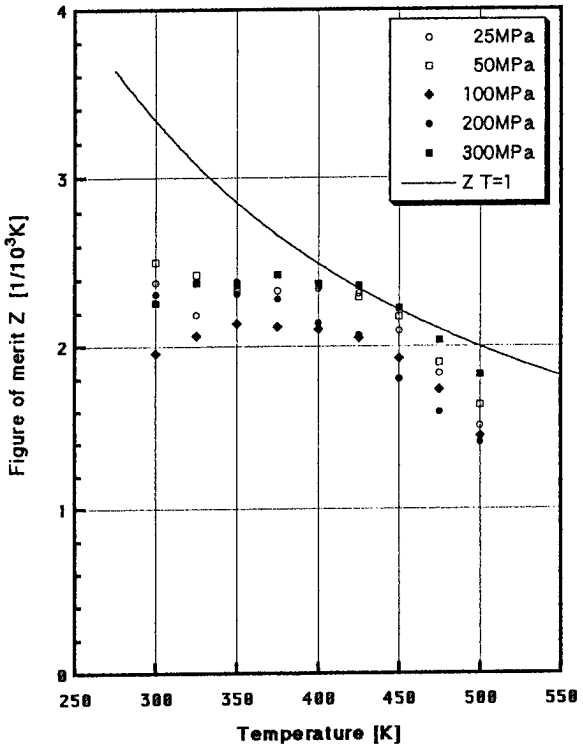


Fig. 4 Figure of Merit

The above thermoelectric properties were almost the same regardless of the direction, vertical or horizontal. The obtained hot pressed bodies were sufficiently dense and the relative densities were almost 97～98% in all cases as exhibited in Table 1.

Table. 1 Relative density

Pressure	Specific gravity	Relative density
25 MPa	6.508 g/cm^3	96.9 %
50 MPa	6.537 g/cm^3	97.4 %
100 MPa	6.538 g/cm^3	97.4 %
200 MPa	6.591 g/cm^3	98.2 %
300 MPa	6.558 g/cm^3	97.7 %

Discussion

Figure 5 shows X-ray diffraction patterns of powder after ball milling process and hot pressed samples. Diffraction peaks of single metals of Bi, Sb and Te were observed in a ball milled powder. But, diffraction peaks of oxides were not observed. On the other hand in hot pressed samples, there were diffraction peaks of solid solutions in stead of single metals. These patterns of hot pressed results were almost the same regardless of the pressure.

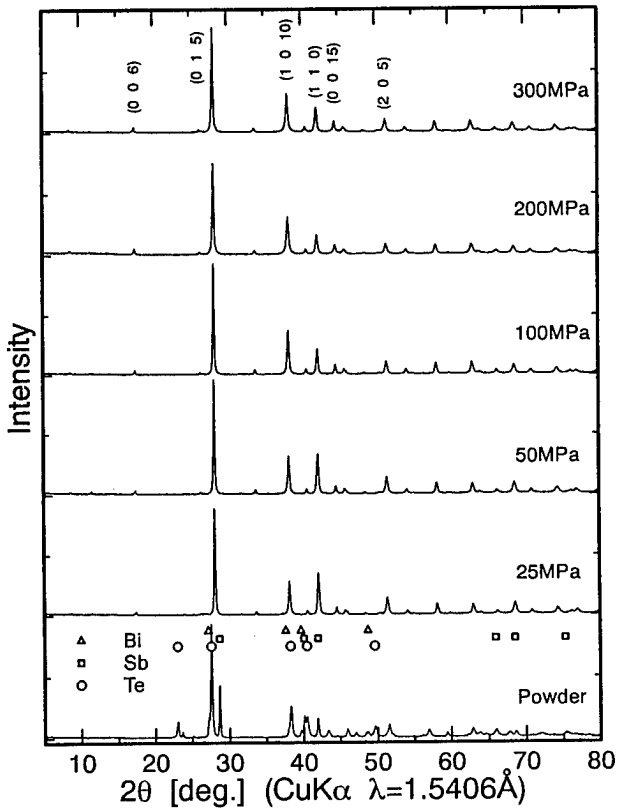


Fig. 5 X-ray diffraction patterns of podwer after ball milling and hot preessed samples

Up to now, mechanical alloying (MA) was normally performed in order to accelerate the crystallization. In this experiment, press time is as short as 1 minute, but if the following conditions were satisfied, crystallization is sufficient. That is to say, (1) oxygen free process, (2) uniformity mixed fine particles, (3) exact stoichiometric composition. In other words, MA is not an essential condition in PIES process.

Figure 6 shows carrier concentration and electric resistivity graph. All of the carrier concentrations were within $3\sim4x10^{19}cm^{-3}$ which is the most suitable region. Also, hole mobility is as high as 200 $cm^2/V\cdot sec$ at all samples. Electric resistivities obtained are $0.8\sim0.9x10^{-5}$ $\Omega\cdot m$ which is as low as single crystal's value $0.91x10^{-5}$ $\Omega\cdot m$[6], $0.89x10^{-5}\Omega\cdot m$[7] reported. The resistivity is related to oxygen contents, and higher oxygen density makes higher resistivity.

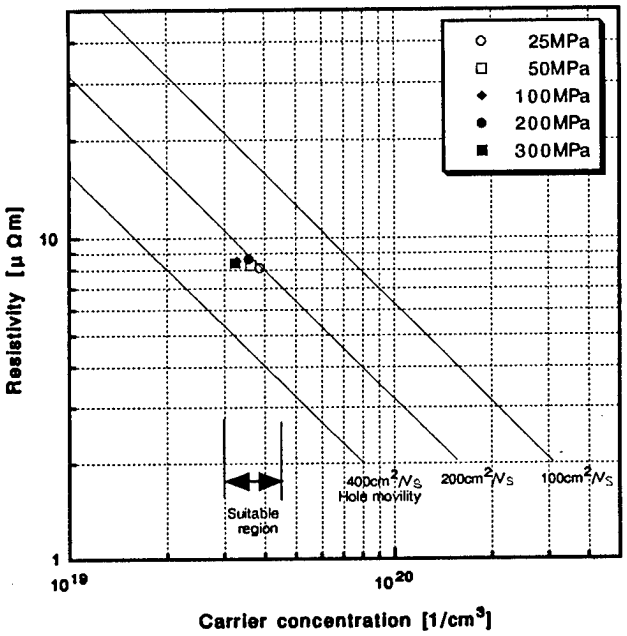


Fig. 6 Carrier concentration and electric resistivity

The quantitative analysis of oxygen of hot pressed sample was done by inert gas carrier melting infrared absorptionmetric method. The value obtained was 820ppm. As our measured data, it is not as low as 100ppm of single crystal result, but it is low enough as compared with 3,900ppm of the conventional process result without using glove-box. The wet ball milling method using such as ethanol as a solvent contained a rather higher oxygen density of 26,500ppm.[8]

Dr.Tokiai reported the oxygen was concentrated at the grain boundary[3]. So, it is shown that the fully controlled oxygen free PIES method makes crystallization proceed easily because of the no precipitate at the grain boundary. Therefore, if the oxygen concentration is low enough, this leads to low electric resistivity and a high figure of merit in these press conditions.

Figure 7 shows the SEM image of powder after ball milling. They were mostly ground to fine particles with irregular shape. The milling process for 20hours made the average sizes below 10um. Figure 8 and 9 show the SEM images of hot pressed samples cut parallel and vertical to the press direction, respectively. The grains grew considerably to several micrometers up to 20um after only 1 minute hot pressing. There is no difference independent of any direction unlike that of a single crystal.

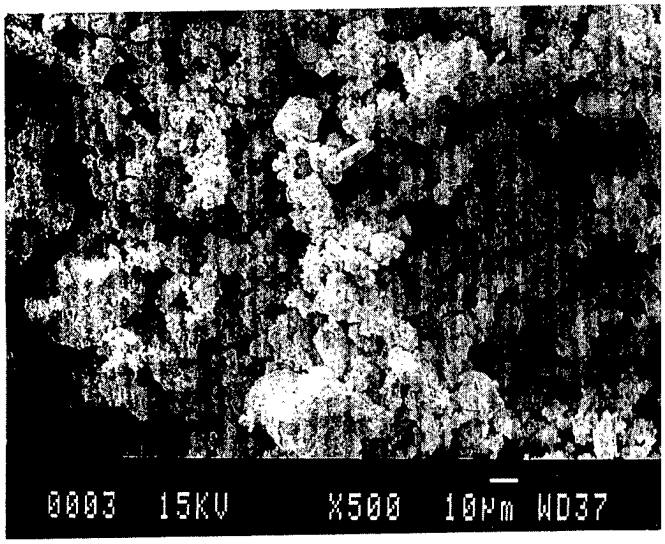


Fig. 7 SEM image of powder after ball milling

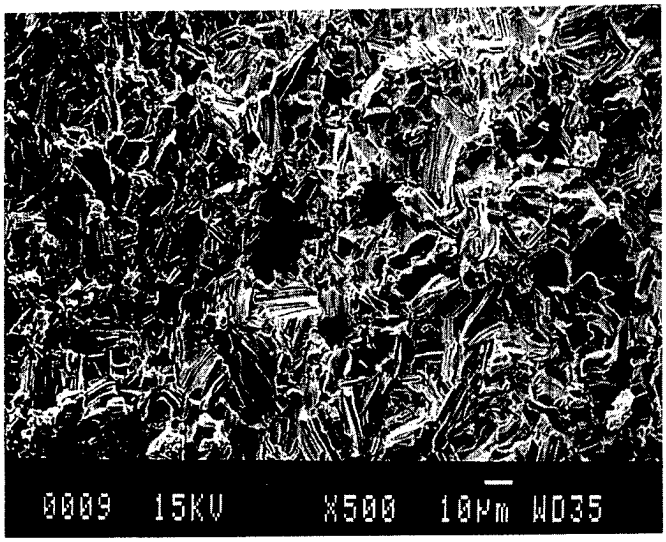


Fig. 8 SEM image of hot pressed sample cut parallel to the press direction

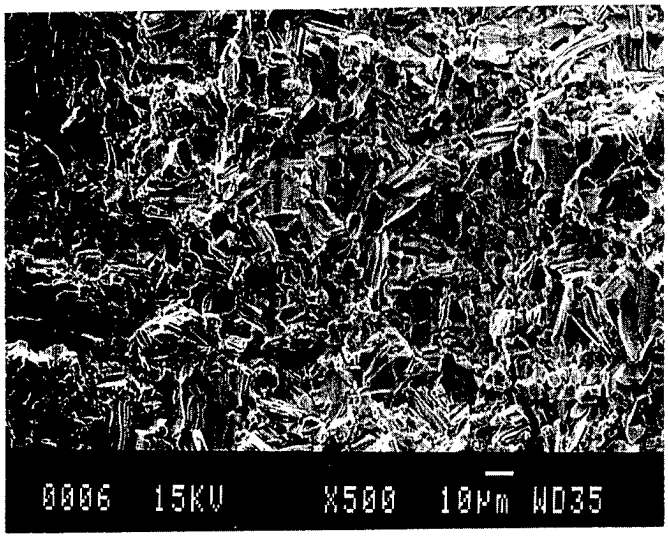


Fig. 9 SEM image of hot pressed sample cut vertical to the press direction

Generally, there was strong orientation dependence in electrical characteristics in the case of using pulverized Ingot. However, the PIES method using single powder metals has no orientation dependence as expected in SEM image and electrical characteristics. Therefore, there is big advantage in that it is not necessary to arrange direction properly in assembling the module.

Conclusions

A high figure of merit non-oriented p-type Bi-Sb-Te thermoelectric element was realized by the PIES method applying conventional ball milling process. The maximum ZT value is almost 1.0 at the temperature of 450K.

The mechanical alloying (MA) process is not always necessary for crystallization in the PIES methods. However, there is a more important factor, that is the oxygen free process. An oxygen concentration lower than 1,000 ppm is desirable.

The conventional ball milling process is simple and easy. This improved process needs only lower energy ball milling, extremely short time (almost 1min) and low pressure (below 25MPa) hot pressing. Therefore, it is suitable for the industrial fabrication process of thermoelectric module for power generation.

References

[1] T.Ohta, T.Uesugi, T.Tokiai. M.Nosaka and T.Kazikawa, Proc. the 8th Int. Conf. on Thermoelectric Energy Conversion, Ins. Nat. Polytech. Lorraine (1989) 7-11.

[2] T.Ohta, T.Tokiai. M.Nosaka and T.Kazikawa, "Proceedings of the 9th International Conference on Thermoelectrics", Jet Propulsion Laboratory California Institute of Technology (1990) pp. 16-26

[3] T.Tokiai, T.Uesugi and K.Koumoto, J. Ceram. Soc, Japan, 103, 904-910 (1995)

[4] I.Yashima, T.Sato and Y.Tochio, T.Tokiai, J. Ceram. Soc, Japan, (Japanese version), 105, 152-155 (1997)

[5] A.Yamamoto,T.Ohta, "Proceedings of the Materials Reserch Society", Vol.478, to be published. (1997)

[6] W.M.Yim, E.V.Fitzke and F.D.Rosi, J.Mater. Sci., 1, 52-65 (1966)

[7] T.Caillat, L.Gailliard, H.Scherrer and S.Scherrer, J.Phys.Chem. Solids, 54, 575-581 (1993)

[8] T.Tokiai, T.Uesugi and K.Koumoto, J. Ceram. Soc, Japan, 103, 784-790 (1995)

Layer by layer growth of Bi_2Te_3 epitaxial thermoelectric heterostructures

Yu.A. Boikov[1,2], V.A. Danilov[2], T. Claeson[1], D.Erts[1,3]

[1]Chalmers University of Technology and Goteborg University, S-41296 Goteborg, Sweden

[2]Ioffe Physico-Technical Institute RAS, 194021 St.Petersburg, Russia

[3]Institute of Chemical Physics, Latvia University, Riga, Latvia

Abstract

Epitaxial films of n- and p-type (0001)Bi_2Te_3 with carrier concentrations between $1x10^{18}$ and $8x10^{19}$ cm^{-3} have been grown by hot wall epitaxy at the surface of mica. Granular textured films have been grown on barium fluorine substrates. A regular system of growth steps of 1 nm height was observed at the surface of the Bi_2Te_3 films grown on mica at 600K. The spirals ($m \approx 10^6$ cm^{-2}) were detected by AFM at the surface of the thermoelectric films when substrate temperature was increased to 640K. Steps at the surface of freshly cleaved BaF_2 substrate promote the formation of a grains in the Bi_2Te_3 film and rough surface. The $\alpha^2\sigma$ for the Bi_2Te_3 films with electron and hole conductance at 300K was in the range 40-60 $\mu Wcm^{-1}K^{-2}$.

Introduction

Thermoelectric materials based on bithmuth telluride possess the highest values of figure of merit $Z = \alpha^2\sigma/\chi$ [1] (T=300K), α - Seebeck coefficient, σ - electrical conductivity, and χ - thermal conductivity. Polycrystalline thin films of bithmuth chalcogenides have been successfully used to fabricate thermoelectric micro generators and micro coolers [1]. Scattering of phonons and electrons at grain boundaries and interfaces might dramatically influence the heat and charge carrier transports in ceramic samples and thin films [2].

Single crystalline $(Bi,Sb)_2(Te,Se)_3$ films, combined with thin dielectric layers in epitaxial multilayer heterostructure, look attractive for development of a new thermoelectric materials with improved Z [3]. To enhance the product of $\alpha^2\sigma$ for the multilayer, thin dielectric layers have to be inserted equidistantly into the thermoelectric film with a separation of a few Bi_2Te_3 unit cells.

Processing conditions (substrate temperature T_s, composition of the vapor phase) as well as the state of the substrate influence dramatically the $(Bi,Sb)_2(Te,Se)_3$ film structure. To grow the $(Bi,Sb)_2(Te,Se)_3$ epitaxial film in-situ, the substrate temperature T_s has to be fixed in the range 300 - 450C [4]. Because of intensive re evaporation of chalcogen from the surface of the growing layer, magnetron sputtering as well as flash and e-gun evaporation are ineffective for formation of high quality $(Bi,Sb)_2(Te,Se)_3$ films at T_s > 250C. Hot wall epitaxi [5] was successfully used to eliminate uncontrollable loss of Te during the growth of Bi_2Te_3 and $Bi_{0.5}Sb_{1.5}Te_3$ films at high T_s [4].

To combine Bi_2Te_3 films with dielectric layers in multilayer heterostructure, there has to be a small mismatch in lattice parameters and thermal expansion coefficients of the thermoelectric and insulating material. The insulating layers have to be grown at about the same processing conditions as the thermoelectric ones. Chemical interactions between Bi_2Te_3 and intermediate dielectric layers have to be negligible.

Features of growth and doping of epitaxial Bi_2Te_3 films are topics of this study.

Experimental procedure

Bi_2Te_3 films with a thickness of 0.05 - 20 μm were grown by hot wall epitaxy [4]. A p-type (hole concentration - $3x10^{19}$ cm^{-3}) Bi_2Te_3 single crystal was used as source material. The vapor phase formed during the Bi_2Te_3 powder (~ 500x500x30 μm) sublimation in carbon crucible was directed by "hot wall" towards the substrate. Thin, freshly cleaved plates of (0001)mica and (111) BaF_2 were used as substrates. The surface of the mica was atomically flat, but a high density of a steps was detected by AFM at the surface of the barium fluorine. The substrate temperature T_s during film growth was fixed in the range 570 - 670K.

The structure and the phase composition of the films were investigated by x-ray diffraction Philips PW 1710 ($\theta/2\theta$). The in-plain orientation of the films on the substrate was investigated by electron micro diffraction.

The surface morphology was investigated by Atomic Force Microscopy (AFM).

To optimize the charge carrier density in the thermoelectric film, a separate source of tellurium was inserted in the growth chamber.

The σ, α and Hall coefficient R_x of the Bi_2Te_3 films were measured in the temperature range 77 - 500K.

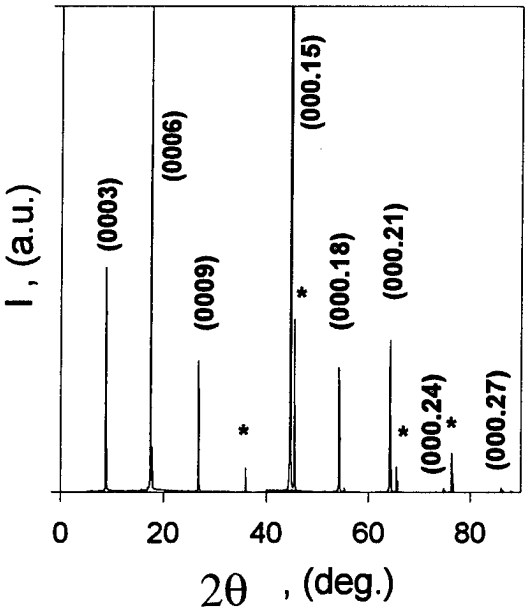
Experimental results

c-axis ([0001]Bi_2Te_3 normal to substrate surface) films of Bi_2Te_3 were grown epitaxially at the surface of (0001)mica, Fig.1a. The films grown on (111)BaF_2 were well c-axis oriented and possess preferential orientation of the grains in axb plain. The grain sise was in the range 0.5 -3 μm.

0-7803-4057-4/97 $10.00 ©1997 IEEE

The CuK_α doublet for (000.21) diffraction peak was well resolved for Bi_2Te_3 films (T_s = 600 - 640K), Fig.1b.

a)



b)

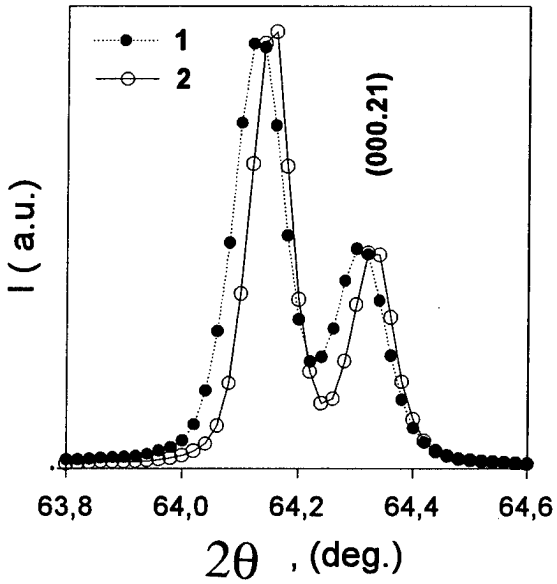
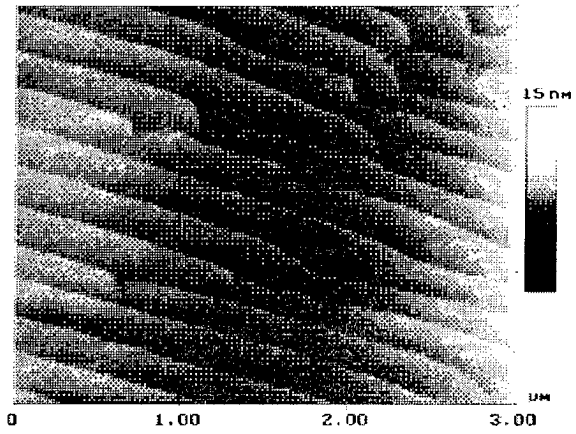
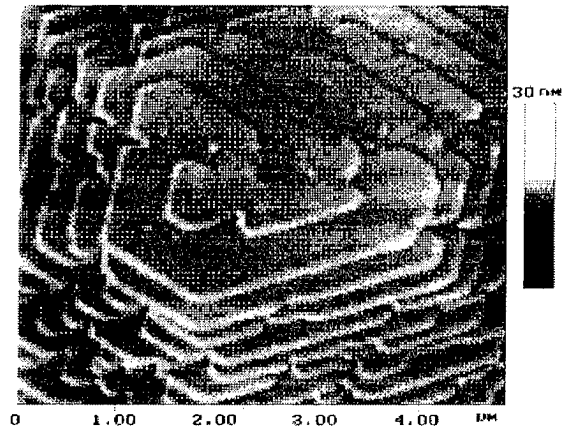


Fig.1. X-ray CuK_α, θ/2θ scan for p -Bi_2Te_3 film (d = 500 nm) grown on mica substrate at 600K (a), (000.21)Bi_2Te_3 peaks for Bi_2Te_3 films grown on mica substrate (b) at 640K (1) and 600K (2)

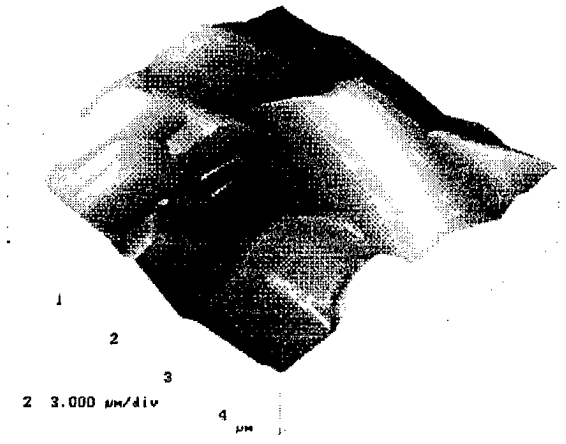
The Full Width at Half Maximum (FWHM) for the (000.21) x-ray peak was about 0.07° for the film grown on mica at 600K. The c-axis lattice parameter for p-Bi_2Te_3 film grown at T_s = 600K (c= 30.453Å) was decreased as compared with the data for the bulk single crystals [1].



a).



b).



c).

Fig.2 Regular system of steps was observed by AFM at the surface of the (0001)Bi_2Te_3 grown on mica at (a) $T_s \approx$ 600K , spirals were detected at the surface of the films grown on mica at 640K (b). Because of granular structure, surface of the films grown on (111)BaF_2 at 600K was rough (c) .

The FWHM of the x-ray peaks as well as c-axis parameter (30.463Å) of the Bi_2Te_3 films increased essentially when T_s was increased up to 640K, see Fig.1b. The increase in the c-axis parameter might be attributed to a higher concentration of the anti site deffects (Bi replaced by Te) in the films grown at higher Ts. Bi atom possess larger covalent radius as compared with Te one. An increase of c-axis parameter for the Bi_2Te_3 films with increase of the T_s is well correlated with higher hole concentration, see Fig.3a, and increase of FWHM of x-ray peaks, Fig.!b. Traces of (10$\underline{1}$5) x-ray peaks were detected in the x-ray scans for Bi_2Te_3 films grown on BaF_2.

A regular system of steps with a height 1 nm was observed by AFM at the surface of the thermoelectric films grown on mica at $T_s \approx 600K$, Fig.2a. The separation between an adjacent steps L, dependent from T_s, at T_s=600K L≈200 nm. Due to a growth of spirals, the (0001)Bi_2Te_3 film surface became rough when the T_s was increased up to 640K, Fig.2b. The density of screw dislocations **m** was about 10^6 cm^2.

The (000l)Bi_2Te_3 films grown on (111)BaF_2 were well in-plain oriented, but there was small (few degrees) mis orientation of the grains relative the substrate normal..

As follow from the Hall data, the Bi_2Te_3 films grown at T_s=300 - 400C possessed hole (p-type) conductivity with hole concentration between $1x10^{18}$ cm^{-3} and $8x10^{19}$ cm^{-3}. An excess of tellurium was induced into the vapor phase from a separate source to grow Bi_2Te_3 films with electron (n-type) conductivity.

Discussion

$A_2^{V}B_3^{VI}$ thermoelectric materials have layered structures . The layers consist of the atoms of the same sort. In the case of Bi_2Te_3, the layers along the c-axis alternate in the following sequence: - Bi - Te^1 - $\underline{Te^1 - Bi - Te^2 - Bi - Te^1}$ - Te^1 - Bi - [1]. Five layers Te^1 - Bi - Te^2 - Bi - Te^1 are called quintet. An interaction of Te^1 atoms at the boundary of an adjacent quintets is weak - Van der Waals type[1].

Evaporation and sublimation of the bismuth telluride (δ - phase) at temperatures around the melting point are accompanied by dissociation of the Bi_2Te_3 molecules [1]

$$Bi_2Te_3 \Rightarrow 2BiTe|sol + 1/2Te_2|vap \quad (1)$$

There is an essential difference in partial pressures of tellurium and BiTe at temperatures in the range 400 - 500C. The BiTe (γ - phase) are sublimated congruently.

The anisotropy of the surface free energy and growth rate influence essentially the orientation of stable Bi_2Te_3 nuclei and determine, to a large extend, the orientation of the film on the substrate.

The variation of the Gibbs free energy ΔG of the system - vapor phase - substrate - nuclease during nucleation may be presented as

$$\Delta G = dG_vV + \gamma_1S_1 + (\gamma_2 - \gamma_3 + E)S_2 + \mu_i dN_i \quad (2)$$

dGv - variation of the volume free energy during the formationof of nucleus, V - nucleus volume, γ_1, γ_2 and γ_3 - surface free energies of the nucleus surface, substrate/nucleus interface and substrate surface, S_1 and S_2 - nucleus surface and nucleus/substrate interface area, E - elastic strain energy of the nucleus/substrate system, $\mu_i = d\Delta G/dNi|_{v,Si}$, N_i - number of the Bi_2Te_3 molecules in the nucleus.

Due to a low value of the γ_1S_1 for heavily packed (0001) planes of Bi_2Te_3, c-axis oriented nuclei became stable at first and, thus, determine Bi_2Te_3 film orientation under condition of high mobility of the condensed particles. The in-plain orientation of the nuclei is determined by minimization of the elastic strain energy of the system nucleus/substrate. Because of weak interaction of the atoms at the boundary of quintet, Bi_2Te_3 films might be grown epitaxially on a substrate having a large mismatch ($\Delta a \approx 10\%$ in the case of Bi_2Te_3 film on (0001)mica).

The hexagonal plane lattice of atoms at the surfaces of (0001)mica and (111)BaF_2 promotes in-plane alignment of the (0001)Bi_2Te_3 nuclei.

Due to a small mismatch for (000l)Bi_2Te_3 and (111)BaF_2 ($\Delta a \approx 1$), Bi_2Te_3 nuclei are well in-plain oriented. Steps at a substrate surface might promote formation of a grains with an inclination of c-axis relative to the normal to the substrate plane and a formation of a net of two - dimensional defects in the thermoelectric film volume.

The layer by layer growth mode is realized during Bi_2Te_3 film growth on mica substrates at temperatures about 600K as follow from x-ray and AFM data, see Fig.1 and 2a. The step height is equal to the quintet thickness (~ 1 nm). It is a Bi_2Te_3 surface terminated by Te^1 atoms (quintet boundary) which possess the lowest values of the surface free energy. A high mobility of condensed particles and close to stoichiometric composition of a adsorbed phase are necessary to accomplish a layer by layer growth of the Bi_2Te_3. Due to an intensive tellurium re evaporation from the surface of the growing film, the adsorbed phase is deficient in chalcogen at $T_s \geq 640K$. Micro inclusions of secondary phases at the film surface are responsible for nucleation of the screw dislocation and film growth with a spirals.

The c-axis for Bi_2Te_3 nuclei formed near the steps at the surface of a freshly cut BaF_2 substrate might be essentially inclined relative to the substrate normal. Because of low growth rate for a Bi_2Te_3 along the c-axis, there is essential difference in the sizes for c-axis oriented grains and those with inclined c-axis. Steps at BaF_2 substrate surface combined with anisotropy of Bi_2Te_3 growth rates promote formation of a films with rough surface, see Fig.2c.

Layer by layer growth of Bi_2Te_3 films might be followed by a tree dimensional one in the case of a low mobility of adsorbed particles. A (10$\underline{1}$5) oriented grains were detected by x-ray in the Bi_2Te_3 films grown at T_s<570K.

The charge carrier concentration in the p- and n-type Bi_2Te_3 films was essentially dependent of T_s and the

tellurium super saturation in the growth chamber. By varying T_s and the temperature of separate tellurium source, it was possible to optimize charge carrier concentration in the films, see.Fig.3a.

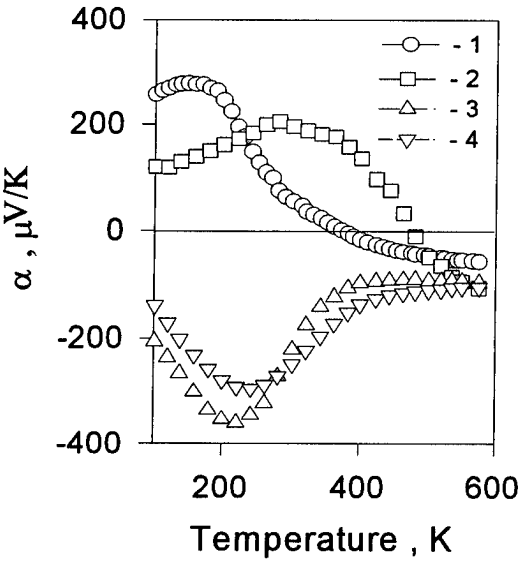
As result of tellurium selective re evaporation. from the regions near the grain boundaries, net of "channels" deficient with chalcogen might be formed in the poly crystalline thermoelectric film grown at high T_s (T_s > 550K). Tellurium deficient grain boundaries do not interfere essentially a hole mobility in the Bi_2Te_3 films but the "channels" are a potential barriers for an electrons.

In the absence of degeneracy it have been found that hall mobility of charge carriers in the p- and n- type Bi_2Te_3 films grown on mica at T_s = 600K was proportional to $T^{-1.8}$ and $T^{-2.3}$ respectively (T = 100 -300K). Due to higer mobility of electrons as compared with that for holes, Seebeck coefficient for an epitaxial Bi_2Te_3 films is negative in the case of intrinsic conditions, see Fig.3a. Because of potential barriers at a grain boundaries , electron mobility in n-type Bi_2Te_3 films grown on (111)BaF_2 was suppressed and $d\sigma/dT$ was positive. The power parameter for the best n- and p-type Bi_2Te_3 films was in the range 40-60 $\mu Wcm^{-1}K^{-2}$, see Fig.2 and 3.

Conclusion

A layer by layer growth mode may be realized for the Bi_2Te_3 film on mica substrate under condition of a high mobility of condensed particles and a closed to stoichiometric composition of the adsorbed phase. High quality (0001)Bi_2T_3 epitaxial films with smooth surface

a)



b)

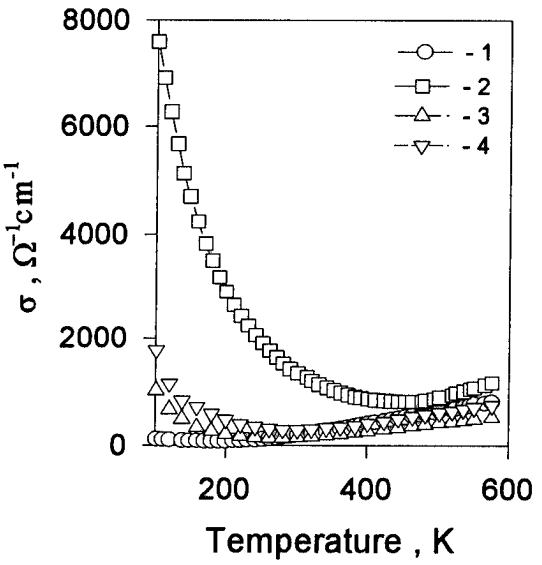


Fig.3. Temperature dependencies of Seebeck coefficient α (a) and electrical conductivity σ (b) for the - Bi_2Te_3 films grown by hot wall epitaxy on (0001)mica substrate. 1,2 - p-type films grown at T_s = 600K and 640K respectively, 3,4 - n-type films grown at T_s = 600K To grow films with electron conductivity, vapor phase was enriched by Te . Tellurium source temperature during the film formation was fixed at 720K for (3) and 740K for(4) .

might be grown by hat wall epitaxy on a mica substrates at temperatures around 600K.The concentration of electrons and holes in the films can be optimized by varying T_s and the tellurium super saturation in the growth chamber.

References

[1]. B.M.Goltsman, V.A. Kudinov, I.A. Smirnov, Semiconductor thermoelectric materials based on Bi_2Te_3, Nauka, Moscow , (1972), 14, 235

[2]. Yu.A.Boikov , B.M.Goltsman, V.A.Kutasov, Bi_2Te_3 film structure influence on the thermal conductivity, Phys.Solid State, **20** (1978) .1316-1318 .

[3] L.D. Hicks and M.S. Dresselhause, Effect of quantum well structures on the thermoelectric figure of merit, Phys.Rev. **B 47** , (1993) , 12727 .

[4] Yu.A.Boikov, O.S.Gribanova, V.A.Danilov, and V.A. Kutasov, Mobility of holes in compositionally nonuniform polycrystalline p-type Bi_2Te_3 films, Sov.Phys.Solid state , **32** (1990) , 2056 .

[5] A.Lopez-Otero, Hot wall epitaxy, Thin Solid Films, **49** (1978) . 3 .

Crystalline structure and thermoelectric properties versus growing conditions of sputtering-deposited $(Bi_{1-x}Sb_x)_2Te_3$ films with $0 \le x \le 0.85$

M. Stölzer, V. Bechstein, J. Meusel
Martin Luther University, Dept. of Physics, 06099 Halle, Germany
E-mail: stoelzer@physik.uni-halle.de

Abstract

$(Bi_{1-x}Sb_x)_2Te_3$ films of about 1 µm thickness were deposited on Kapton substrates by means of DC magnetron sputtering. Four different targets were used with compositions according to $(Bi_{1-x}Sb_x)_2Te_3$ + 20 at% Te and x=0, 0.5, 0.75 and 0.85.

The temperatures of substrates T_S and of a hot-wall environment T_e were altered in the range of 220...320 °C and 150...390 °C, respectively. A previous paper [1] pointed out that any oversupply between 5 and 50 at% Te is sufficient for achieving nearly stoichiometric films in the range of substrate temperature of interest.

Composition and crystalline structure were studied using WDX, SEM and XRD. Films grown at $T_S < 290°C$ had rough surfaces and week texture. Above $T_S = 290°C$ the films were strongly (0 0 n) textured and had smooth surfaces. Annealing at 300 or 350°C increased the size of the crystallites but their orientation was unchanged. This behaviour was independent on the composition x.

The transport properties depend significantly on Sb-Bi ratio x, substrate and environment temperatures and annealing. High carrier mobilities could only be achieved together with low carrier concentrations and at $T_S \approx 250°C$ after annealing. Films best suited for thermoelectric applications (highest power factor at room temperature) had the composition $(Bi_{0.15}Sb_{0.85})_2Te_3$, the conductivity σ=1140 $\Omega^{-1}cm^{-1}$, the carrier mobility μ=360cm²/Vs and the Seebeck coefficient S=182µV/K.

Introduction

The development of high quality Bi_2Te_3 type films for miniaturized thermoelectric applications is a technological challenge. Apart from a high figure of merit Z, there are some additional requirements to fulfill. Mechanically stable and highly adhesive films are needed for photolithographic patterning. If possible, the film deposition process should be cheap and easy.

Using flash evaporation technique [2, 3] or hot wall epitaxy [4], it is possible to achieve $Z \approx 3 \cdot 10^{-3} K^{-1}$ for p-type material, wich is the same as in state-of-the-art bulk material. However, these deposition methods are not good suited for an industrial production process, because they are difficult to control or use very high substrate temperatures.

In this paper, we report new promising results of sputtered $(Bi_{1-x}Sb_x)_2Te_3$ films. Magnetron sputtering is an established high deposition rate technique, which can produce films of high adhesivity.

It is well known, that the thermoelectric properties of $(Bi,Sb)_2Te_3$ are mainly determined by the deviation from the stoichiometric composition. Earlier investigations on sputtered V_2VI_3 semiconductor films [6,7] showed a lack of Tellurium of several at%, probably caused by different sticking coefficients of the elements and preferential resputtering during the film growth. A. Wagner et al. [8] used sputtering targets of the composition $(Bi,Sb)_2Te_4$ to avoid this problem.

Figure 1 shows results of high precision wave-length dispersive X-ray analysis (WDX) from our preliminary experiments on $(Bi_{0.25}Sb_{0.75})_2Te_3$ films (see [1] for details). The curves have a plateau between 220 and 300°C. Within this region, Te concentration does almost not depend on the oversupply in the vapour phase and only very slightly depend on the substrate temperature. However, the Te content is about 0.5 at% too small which results in rather high carrier concentrations and low Seebeck coefficients.

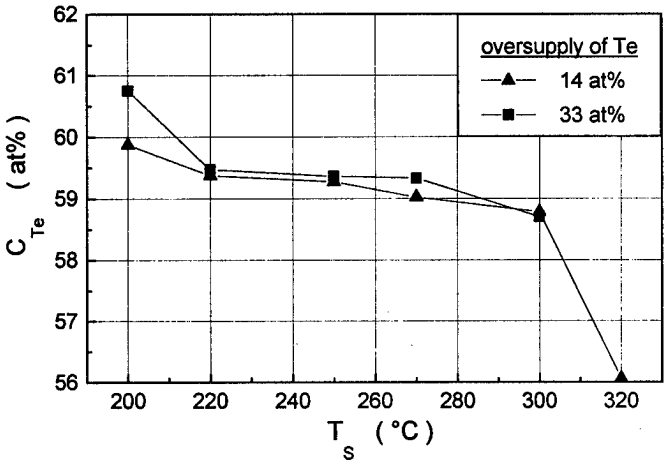


Fig. 1: Te concentration vs. substrate temperature and Te oversupply in the vapour phase in sputtered $(Bi_{0.25}Sb_{0.75})Te_3$ films (without heated shield)

The aim of our following work was, to overcome this problem and to use the concentration plateau for developing a stable deposition process of high quality thermoelectric $(Bi_{1-x}Sb_x)_2Te_3$ films.

Film preparation

Films of 1...2 µm thickness were deposited on 130µm Kapton substrates using a 90 mm magnetron source at low argon pressure ($3 \cdot 10^{-3}$mbar) and a deposition rate of about 1 nm/s. The background pressure in the vacuum chamber was 10^{-5} mbar. Sputtering source and substrate were surrounded by a cylinder of the "environmental" temperature T_e (see figure 2).

Extensive work was done for measuring and controlling the temperature T_S of the substrate foils, because this is the most important parameter which influences the film properties. A constant temperature over a large area was achieved with the

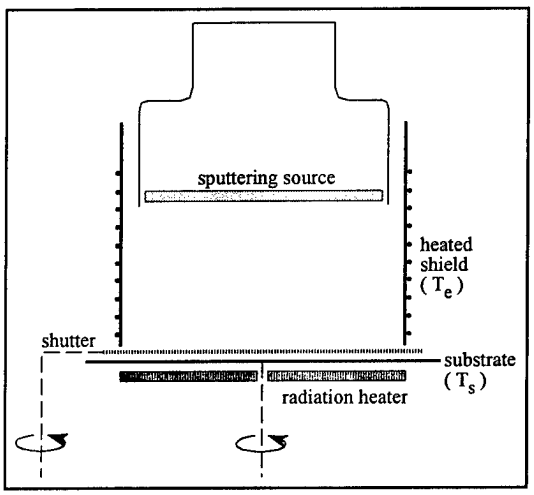


Fig. 2: schematic view of the sputtering arrangement

help of a "black" radiation heater close to the substrate. During film growth, T_S was held constant with an error of ±10K, at the beginning it was about 20K lower.

Sputtering targets of the composition $(Bi_{1-x}Sb_x)_2Te_3$ + 20 at% Te (x=0, 0.5, 0.75 and 0.85) have been produced by a melting process from 99.999% pure material. Sample structures for transport measurements were made by photolithographic patterning and wet etching. Annealing procedures were carried out in evacuated ampoules after patterning and cutting the samples.

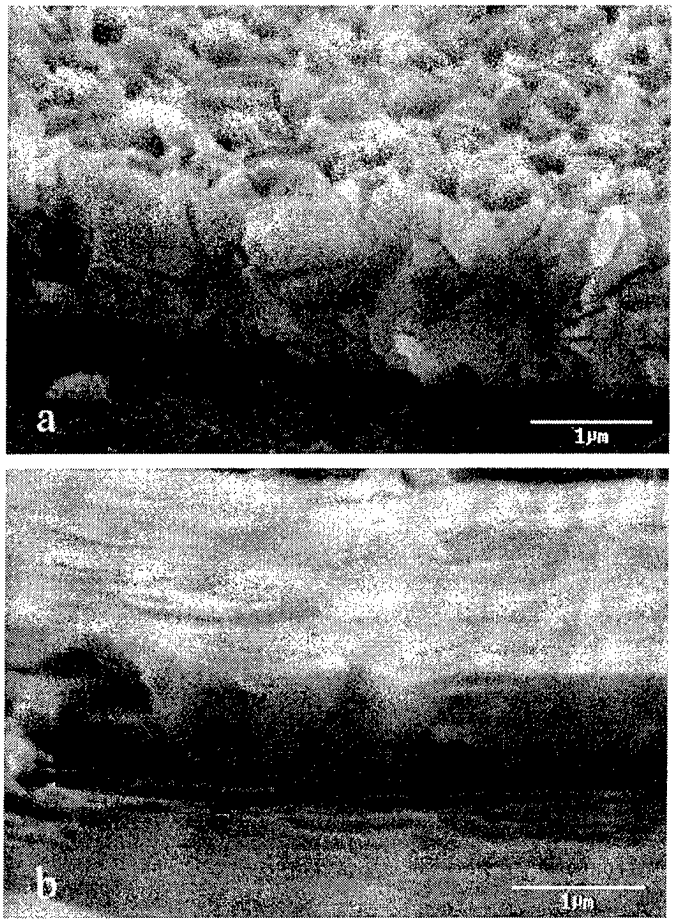


Fig. 3: SEM micrographs of sputtered $(Bi_{1-x}Sb_x)_2Te_3$ films on Kapton. a) T_S=260°C , b) T_S=300°C

Results and discussion

Texture and morphology of the films are essentially determined by the substrate temperature T_S and are largely independent of the Sb-Bi relation x. Typical samples can be seen in figure 3 and the corresponding X-ray diffraction pattern in figure 4. Films grown below 290°C are rough and more or less disordered but grown at T_S=300°C they are very smooth and strong (0 0 n) textured. Even higher growing temperatures are not suited to produce films of high thermoelectric quality because the Te concentration becomes to small (see fig. 2). Annealing up to 10 hours at 300°C or 350°C does not change the XRD pattern significantly, while the average grain size of disordered films is increased by a factor of about two.

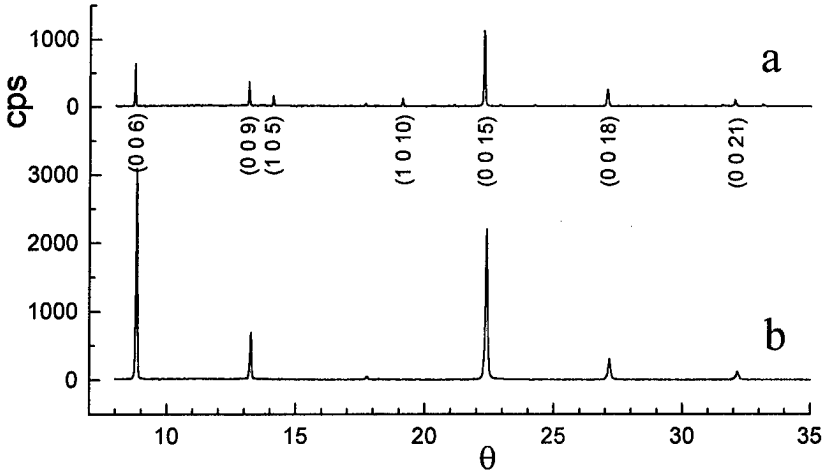


Fig. 4: XRD pattern corresponding to fig.3. a) T_S=260°C - week (0 0 n) texture, additional peaks occur, b) T_S=300°C - strong (0 0 n) texture

The deviation from stoichiometry at a certain T_S can be influenced by the shield temperature T_e. Within a heated environment, the reevaporated Te atoms are not immediately pumped away by the cold chamber but remain close to the substrate. That results in a somewhat higher Te content in the film.

This effect can be measured as an increase of the Seebeck coefficient. Fig. 5 shows the thermopower depending on the substrate temperature T_S and the temperature of the environment T_e. All samples have been annealed after deposition in the same manner (1h 350°C or 3h 300°C). In conformity with the slight decrease of the Te concentration measured by WDX (Fig. 1), the thermopower becomes smaller with increasing T_S. Raising the shield temperature T_e above T_S results in a strong increase of the thermopower to a maximum of 225 µV/K. At $T_S \geq 300$°C it is not possible to build enough Tellurium into the film anymore for getting that high thermopower. (The last point at T_e=390°C is probably due to a somewhat to high T_S.) The maximum obtainable Seebeck coefficient can be shifted to 250 µV/K (see figure 6) through longer annealing, this value marks the solubility boundary of Te in $(Bi_{0.25}Sb_{0.75})_2Te_3$.

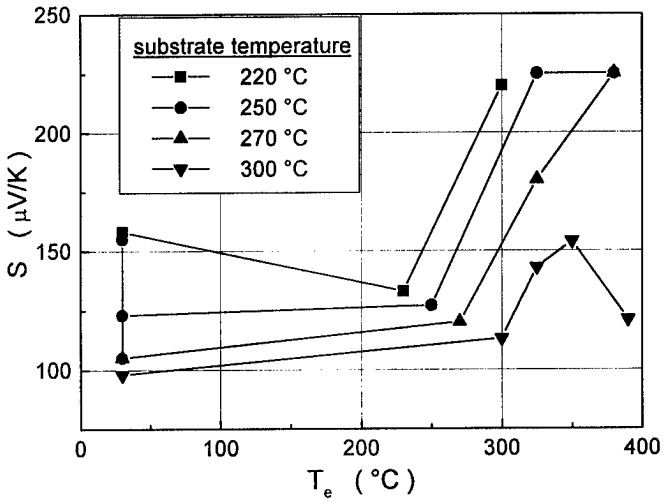


Fig. 5: Thermopower of annealed $(Bi_{0.25}Sb_{0.75})_2Te_3$ films depending on substrate and environmental temperatures T_S and T_e

Carrier mobility

Unfortunately the Seebeck coefficient, depending on the Te concentration via carrier concentration, can not be optimized without affecting the carrier mobility. This shall be discussed with the aid of fig. 6. In this figure, the thermopower S, the conductivity σ, the thermoelectric power factor $S^2\sigma$ and the Hall mobility μ_H of a large amount of samples (all data available) with different growing conditions (220°C ≤ T_S ≤ 300°C, 30°C ≤ T_e ≤ 390°C, annealed 1...10h at 350°C) are plotted versus $1/e\rho_H$. This term represents approximately the carrier concentration p which is related to the Hall coefficient ρ_H according

$$\rho_H = \frac{1}{e\,p}\; R_H\; B_{eff}.$$

(R_H is the scattering factor and B_{eff} an effective structure factor calculated from the tensor components B_{ijk} according to the film texture.) For a comparison with the well known properties of single crystals, theoretical curves have been calculated based on experimental data of a Bridgman grown $(Bi_{0.25}Sb_{0.75})_2Te_3$ sample from [10], using the Drabble-Wolfe model [9] (6 valley valence band, parabolic energy dispersion, pure carrier scattering on acoustic phonons) and the model parameters (effective masses and density-of-states mass, structure and scattering factor of Hall coefficient, relaxation time) published in [10]. The model parameters for nontextured polycristals were calculated as an average over the three directions in space.

From fig. 6 some remarkable facts can be seen:

(i) All data points (except ✳: x=0.85) including references are well arranged along curves, despite the large differences in their growth conditions, morphology and texture.

(ii) The thermopower is very close to the theoretical curves, while the conductivity and hence the power factor are lower.

(iii) Usually the Hall mobility is about two times lower compared to the single crystals model. At low carrier concentrations, however, there is a strong increase and the mobility matches its theoretical limit.

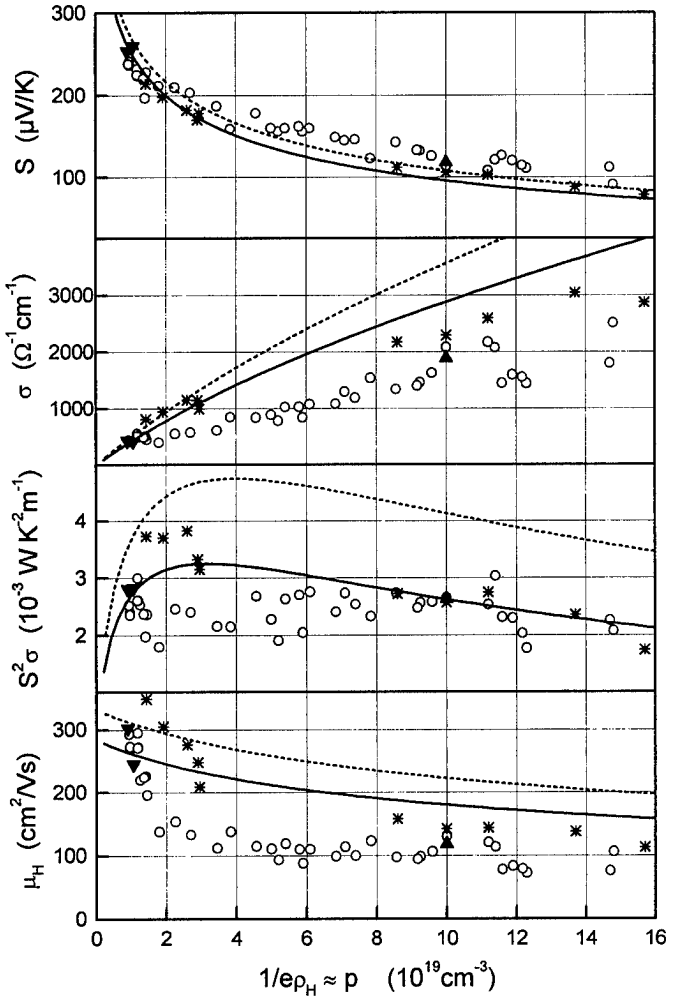


Fig. 6: Thermoelectric properties of sputtered $(Bi_{1-x}Sb_x)_2Te_3$ films vs. carrier concentration. ○ x=0.75, ✳ x=0.85, ▲ x=0.75 (Ref. [8]), ▼ x=0.75 (flash evaporated, Ref. [3], Theory (x=0.75, based on Refs. [9, 10]): —— non-textured, ---- (0 0 n) textured

This effect is not related to the films texture as one would expect. Well oriented samples (i. e. fig. 3b and [8]) have rather high carrier concentration and low mobility, and less textured rough samples (i. e. fig. 3a) show low carrier concentrations and high mobility. We suppose that it is related to the solubility of Tellurium in $(Bi_{1-x}Sb_x)_2Te_3$. The mobility increases, when the Te concentration is close to its upper solubility limit. Probably, the growth kinetics is responsible for this effect, but details are not yet known.

Material optimisation

This assumption is now to be used for improving the thermoelectric properties of $(Bi_{1-x}Sb_x)_2Te_3$ films. The theoretical maximum of the power factor is near $p=4\cdot10^{19}cm^{-3}$ (fig. 6) were the carrier mobility attainable is just low. The solubility limit of Te can be shifted to lower values by changing to a higher Sb-Bi ratio x [11]. We expect then the increase of the mobility to appear already at higher carrier concentrations.

Included in fig. 6 are data points (✳) of $(Bi_{0.85}Sb_{0.15})_2Te_3$ samples. They show indeed the expected increase of the mobility near $p\approx3\cdot10^{19}cm^{-3}$. This results in significantly higher

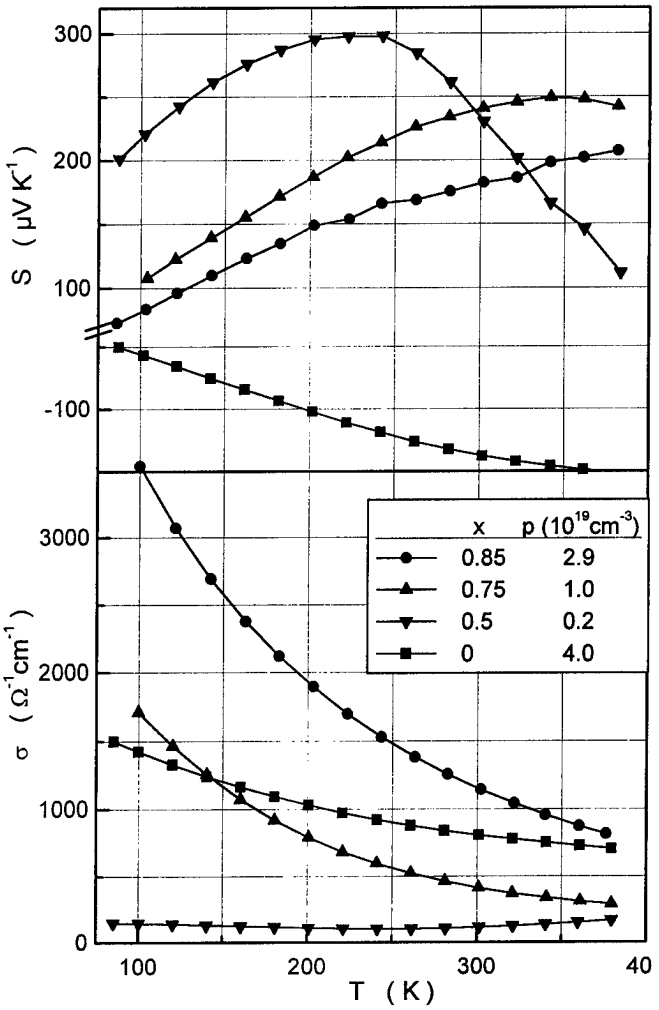


Fig. 7: Thermopower and electrical conductivity vs. temperature and values of carrier concentration (textbox, at 200K) of sputtered $(Bi_{1-x}Sb_x)_2Te_3$ films with maximum mobility (T_S=260°C and T_e=380°C)

values of the thermoelectric power factor.

The optimal growth conditions for achieving the highest mobility and lowest carrier concentration (after annealing at 350°C) were found to be T_S=260°C and T_e=380°C. In fig. 7, thermopower and electrical conductivity of $(Bi_{1-x}Sb_x)_2Te_3$ films with various Sb-Bi ratios x are plotted, which are grown by magnetron sputtering under these conditions. The carrier concentrations calculated from Hall coefficient at 200K are given in the legend.

With decreasing x, more tellurium is incorporated into the films and the hole concentration decreases. At x=0.5 the film is nearly intrinsic at room temperature, and low conductivity and a very high thermopower at low temperatures is observed. For x<0.5 the films should become n-type, which is verified for Bi_2Te_3 (x=0).

Conclusion

The well established sputtering technique was used to produce $(Bi_{1-x}Sb_x)_2Te_3$ films. The substrate temperature T_S was found to be the most important deposition parameter which influences both texture and Te concentration of the films. In addition, the incorporation of Te could be influenced by a heated environment.

Films of high crystalline perfection but moderate thermoelectric properties have been grown at T_S=300°C, and films of high thermoelectric quality but rough morphology at $T_S \approx 260$°C.

As a result of the investigation of a large amount of samples including references of sputtered and flash evaporated $(Bi_{0.25}Sb_{0.75})_2Te_3$ films, a rule can be formulated:

A high carrier mobility within the films can be achieved only when the concentration of tellurium is maximum. i. e. at its upper solubility limit.

Because the solubility limit of Te depends on the Sb-Bi ratio x, the carrier concentration can be easily tuned by changing x without affecting the mobility. Following this idea, a maximum power factor of $3.9 \cdot 10^{-3} WK^{-2}m^{-1}$ was realized with the composition $(Bi_{0.15}Sb_{0.85})_2Te_3$.

References

[1] M. Stölzer, V. Bechstein, J. Meusel: Deposition of $(BiSb)_2Te_3$ films by magnetron cosputtering from two targets - first results. Proc. of the XV Int. Conf. on Thermoel. p. 422, Pasadena 1996

[2] F. Völklein et al.: Transport properties of flash-evaporated $(Bi_{1-x}Sb_x)_2Te_3$ films I: Optimization of film properties. Thin Solid Films **187**, 253-262 (1990)

[3] M. Stölzer, M. Stordeur and I. Stark: Preparation of highly effective p-$Bi_{0.5}Sb_{1.5}Te_3$ and n-$Bi_2Te_{2.7}Se_{0.3}$ films. Proc. of the XV Int. Conf. on Thermoel. p. 445, Pasadena 1996

[4] Yu.A. Boikov et al.: Electrophysical parameters of epitaxial n-type Bi_2Te_3 films. Fizika Tverdogo Tela **33**, 3414-19 (1991).

[5] A. Mzerd et al.: Effect of substrate temperature on crystal growth of Bi_2Te_3 on single crystal Sb_2Te_3. J. Mat. Sci. Lett. **13**, 301-304 (1994).

[6] Y. H. Shing et al.: Sputtered Bi2Te3 and PbTe films. J. Vac. Sci. Technol. A 1 (2), 503-506 (1983).

[7] H. Noro, K. Sato and H. Kagechika: The thermoelectric properties and crystallography of Bi-Sb-Te-Se thin films grown by ion beam sputtering. J. Appl. Phys. 73 (3), 1252-1260 (1993).

[8] A. V. Wagner et al.: Synthesis and evaluation of thermoelectric multilayer films. ICT XV, Pasadena 1996

[9] J. R. Drabble, R. D. Groves, R. Wolfe; Proc. Phys. Soc. **71**, 430 (1958)

[10] M. Stordeur, M. Stölzer, H. Sobotta and V. Riede, Investigation of the Valence Band Structure of Thermoelectric $(Bi_{1-x}Sb_x)_2Te_3$ Single Crystals. phys. stat. sol. (b) **150**, 165 (1988)

[11] H. Scherrer and S. Scherrer: Bismuth Telluride, Antimony Telluride and their solid solutions. in: Handbook of Thermoelectrics, ed. by M. Rowe, p. 225, CRC Press 1995

Structural and electrical characterization of thin Bi_2Te_3 films grown with MBE

Satoru Kikuchi, Yuji Iwata*, Eiji Hatta**, Jiro Nagao*** and Koichi Mukasa**

Faculty of Engineering, Hokkaido Tokai University, Hokkaido, Sapporo 005, JAPAN
*Aisin Cosmos R&D Co., Ltd, Kariya, Aichi 448, JAPAN
**Nanoelectronics Laboratory, Hokkaido University, Hokkaido, Sapporo 060, JAPAN
***Hokkaido National Industrial Research Institute, MITI, Hokkaido, Sapporo 062, JAPAN
Tel.: +81-11-706-6539, Fax: +81-11-706-7803, E-mail: kikuchi@nano.hokudai.ac.jp

Abstract

Thin Bi_2Te_3 films were grown on $Al_2O_3(0001)$ substrates with molecular beam epitaxy (MBE). X-ray diffraction (XRD) was used to confirm the orientation and crystalline quality of the films, the c-axis was oriented normal to the film surface. It was found that the full width at half-maximum intensity (FWHM) of diffraction peaks in XRD pattern depends on the deposition conditions such as substrate temperature and the flux ratio. The reflection high-energy electron diffraction (RHEED) pattern of the deposited films shows a streak pattern at the initial stage of growth. Electrical resistivity, carrier concentrations and Hall mobility were measured in the temperature range from 77K to 300K. The film with narrower FWHM exhibited a lower carrier concentration (5.1×10^{19} cm^{-3}) and electrically intrinsic characteristics around room temperatures. For the first time a clear separation of slopes of the Hall mobility in thin Bi_2Te_3 film is observed. On the other hand, the films with wider FWHM, which have higher carrier concentrations, exhibited a metallic behavior. The electrical properties are closely related to the variation of FWHM of diffraction peaks in the XRD pattern.

Introduction

A high thermoelectric figure of merit ($Z=\alpha^2\sigma/\kappa$) leads to a high performance of thermoelectric devices [1], where α is a Seebeck coefficient, σ is an electrical conductivity, and κ is a thermal conductivity. Recently, new approaches using superlattices and quantum-well structures of semiconductors have been reported to improve the thermoelectric figure of merit [2], [3]. The systems of Bi_2Te_3 compounds have attracted considerable attention because of their high thermoelectric figure of merit around room temperatures [4], so that superlattices and quantum-well structures composed of Bi_2Te_3 films can be expected to have an improved thermoelectric figure of merit. It is well known that the thermoelectric figure of merit is strongly related to the carrier concentration [5]. So it is required that the thin films in their structures are epitaxially grown, which are expected to have a low carrier concentration. This leads us to investigate optimization of carrier concentration in these systems.

Many workers have reported growth of thin Bi_2Te_3 films by several methods and characterization of their electrical properties. For example thin Bi_2Te_3 films were prepared by co-evaporation [6], sputtering [7], hot wall epitaxy method (HWE) [8] and flush evaporation [9]. However, the films are polycrystalline or nonstoichiometric resulting in high carrier concentrations at room temperature. On the other hand Mzerd and Charles et al. reported deposition experiments of stoichiometric thin Bi_2Te_3 films on glass [10], single crystal Sb_2Te_3 [11]-[13] and Si(111) [14] substrates by using MBE, however they did not report on electrical properties.

In this paper, we present the crystal structure and electrical properties of thin Bi_2Te_3 films grown with MBE using a $Al_2O_3(0001)$ substrate which has a small lattice mismatch (8%) in the a-axis plane of Bi_2Te_3.We have studied the behavior of the electrical properties as a function of full width of half maximum intensity (FWHM) in diffraction peaks of x-ray diffraction (XRD) pattern in order to investigate the correlation between film structures and electrical properties.

Experimental

We have grown thin Bi_2Te_3 films by using molecular beam epitaxy (MBE). Base pressure of our growth chamber is kept below 5×10^{-10} Torr. High purity (99.9999%) bismuth and tellurium are used as source materials that are treated by hydrogen deoxidization method. $Al_2O_3(0001)$ substrates (12 mm $\times$12 mm$\times$0.5 mm t) are used to grow the films. The substrate surface is prepared by chemical etching in a hot solution of 85 % phosphoric acid for 5 minutes, thermal treatment at 700 ℃ for 1hr and 950 ℃ for 15 minutes in the growth chamber before growth [15]. The Bi_2Te_3 thin films were evaluated by reflection high-energy electron diffraction (RHEED) during the growth and θ-2θ XRD after the growth. The film thickness was then measured using a Salone surface profilometer. The deposition rate of thin Bi_2Te_3 films was controlled to be 0.5 Å/sec. The typical substrate temperatures are 170 ℃ and 200 ℃. The source temperature is held constant at 540 ℃ for bismuth and varied between 250 ℃ and 280 ℃ for tellurium. Table I shows the deposition conditions of thin Bi_2Te_3 films in this work. A beam flux monitor (BFM) monitored the molecular beam flux of source materials. Energy dispersive x-ray spectroscopy (EDX) con-

0-7803-4057-4/97 $10.00 ©1997 IEEE

firmed the composition of the Bi_2Te_3 films. Electrical resistivity and Hall coefficient were measured by van der Pauw method in the temperature range from 77K to 300K under high vacuum (10^{-5}torr). A magnetic field of 3000 gauss was applied in the measurement of the Hall coefficient. The electrical contacts to the leads were made through Au films (500 Å), which were deposited by conventional vacuum evaporation using a suitable metal mask on to the Bi_2Te_3 films.

TABLE I Deposition conditions

Sample	Substrate Temperature (°C)	Flux ratio F(Te)/F(Bi)	Thickness (Å)	Composition (at.%)
A	200	3.1	780	$Bi_{40}Te_{60}$
B	170	2.6	1000	$Bi_{40}Te_{60}$
C	200	2.4	860	$Bi_{42}Te_{58}$

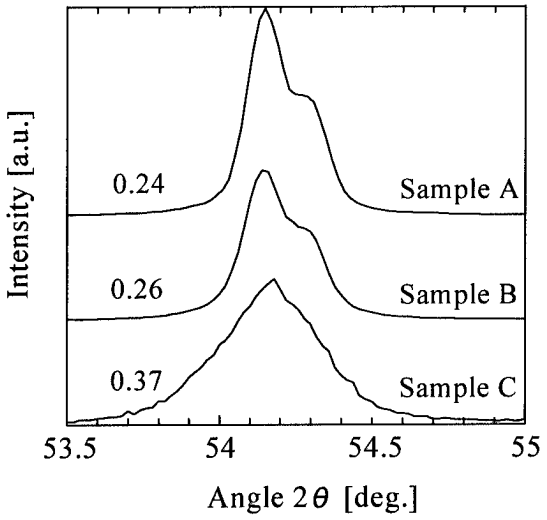


Fig. 2. Variation of FWHM of (00018) diffraction peaks for three films with different growth conditions.

Results and Discussion

Epitaxal growth of films is affected by the surface condition of the substrate. In our experiments, the substrates were thermally treated after chemical etching. Applying this treatment, we obtained a clean surface of the Al_2O_3(0001) substrate which was confirmed by the RHEED pattern. During growth of Bi_2Te_3 films initially a streak pattern is observed, which suggests that the film surface is very smooth and that epitaxal growth of thin Bi_2Te_3 film is achieved.

We measured the electrical resistivity, carrier concentration and Hall mobility of three samples which were prepared under different growth conditions and investigated the correlation

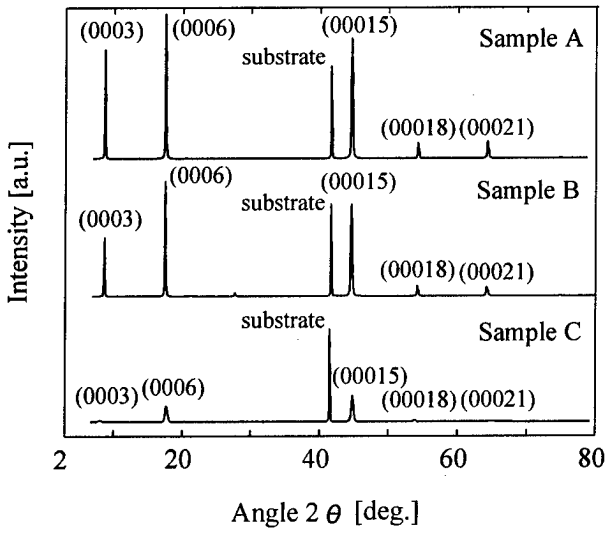


Fig. 1. XRD patterns of thin Bi_2Te_3 films grown on Al_2O_3(0001) substrate.

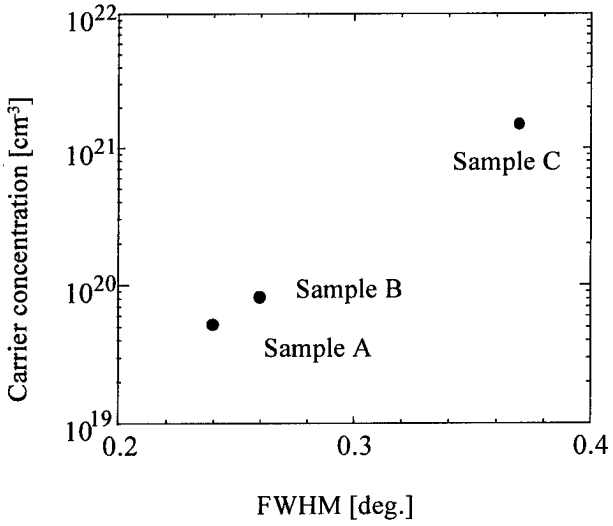


Fig. 3. Carrier concentrations (at 300 K) of thin Bi_2Te_3 films as a function of FWHM of (00018) peaks

between the crystalline quality and electrical properties. Figure 1 shows XRD patterns of the Bi_2Te_3 films for which the electrical measurements were made. Predominant c-axis orientation was found for all samples. The full width at half-maximum intensity (FWHM) of diffraction peaks is closely related to crystalline quality, because the width of XRD peaks is related to a variety of factors such as crystallite size, non-uniform strain, and stacking faults. In addition, a narrower FWHM is associated with a larger crystallite size by the Scherrer equation [16]. Therefore we estimated the FWHM of (00018) peaks in the XRD pattern to evaluate the crystalline

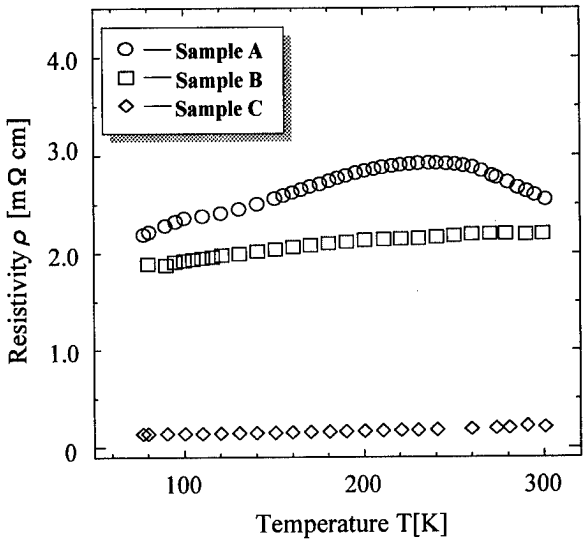


Fig. 4. Temperature dependence of resistivity of thin Bi_2Te_3 films

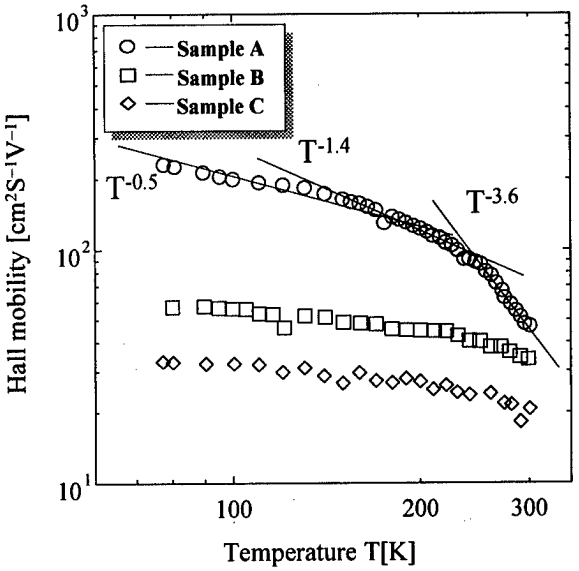


Fig. 6. Temperature dependence of Hall mobility of thin Bi_2Te_3 films

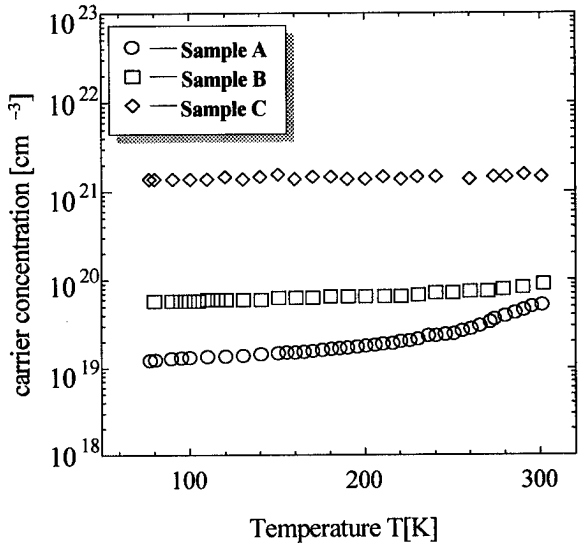


Fig. 5. Temperature dependence of carrier concentrations of thin Bi_2Te_3 films

quality of three sample.

Figure 2 shows the variation of FWHM of (00018) peaks for the three samples with the different growth conditions. In comparison to the other films (samples B and C), the pattern of sample A has a narrower FWHM, which corresponds to higher crystalline quality. This result suggests that the crystalline quality is strongly affected by the growth conditions such as substrate temperature and the flux ratio.

Figure 3 shows the relationship between the FWHM of (00018) peaks and the carrier concentrations at 300 K. In the case of the film with narrower FWHM (sample A), the carrier concentration is lower than the other films with wider FWHM (samples B and C), in which the carrier concentrations are over 10^{20} cm^{-3}. The increase of carrier concentration is likely to be caused by a larger number of defects in samples B and C [17].

Figures 4 and 5 shows the temperature dependence of carrier concentration and electrical resistivity, respectively. In sample A, the carrier concentration decreases monotonously with decreasing temperature, which indicates a semiconducting behavior in this temperature region. The resistivity has a maximum value at 230 K. Since the resistivity decreases above 230 K, the film is found to be in the intrinsic region. We can estimate the energy gap E_g to be about 100 meV, which is close the value of bulk single crystals [18]. On the other hand, in samples B and C, the carrier concentrations were almost independent of temperature and the resistivity decreases slightly with decreasing temperature, which suggests metallic behavior in this temperature region.

Figure 6 shows the temperature dependence of Hall mobility. The sample A has the highest value and some different slopes are observed in the curve. The appearance of these slopes can be explained by the dominance of different scattering mechanisms in different temperature regions. The temperature dependence of the Hall mobility in the intermediate temperature region is found to be $T^{-1.4}$, which shows that acoustic phonon scattering is dominant. On the other hand, the higher slope at higher temperatures suggests that polar optical phonon scattering is dominant. The clear separation of slopes and the appearance of a higher slope at higher temperatures were observed for the first time in the thin Bi_2Te_3 films of this work. It emphasizes the fact that a good crystalline quality could be achieved using the MBE method for the growth of thin Bi_2Te_3 films. The samples B and C have lower mobilities than sample A and the separation of slopes is not clear for these films. The relation between the FWHM as a measure of crystalline quality and the mobility is the following: in films with wider FWHM, the density of crystallite boundaries is

relatively higher, so that the Hall mobility is smaller due to stronger scattering at crystallite boundaries. Growth conditions that lead to a larger crystallite size could reduce the grain boundary scattering of carriers. From the above results, we believe that there is a strong correlation between the film structures and electrical properties.

Conclusions

We studied the crystal structures and electrical properties of thin Bi_2Te_3 films grown on $Al_2O_3(0001)$ substrates by MBE. XRD patterns show that the films are c-axis oriented and Streak RHEED patterns are observed at the early stage of growth. The crystalline quality was estimated by FWHM of (00018) diffraction peaks in XRD pattern. It is found that the crystalline quality is very sensitive to the deposition conditions. The carrier concentration, electrical resistivity and Hall mobility in the temperature range from 77K to 300K were measured for films with three different crystalline qualities. The FWHM of XRD peaks versus carrier concentration shows correlation between the crystalline quality and electrical properties. The film with narrower FWHM had a lower carrier concentration and higher value of Hall mobility, and an electrically intrinsic region of the resistivity was found around room temperatures. For the first time a clear separation of slopes of the Hall mobility in thin Bi_2Te_3 film is observed. The other films, which had wider FWHM, exhibited a metallic behavior, and carrier concentrations were over 10^{20} cm^{-3} and Hall mobility was lower values. The above results suggest that Bi_2Te_3 film with high crystalline quality and good electrical properties can be grown by MBE.

Acknowledgments

We would like to thank to Dr. T. Yoshimoto of Hokkaido Tokai University and Dr. K. Sueoka and Mr. N. Sasa of Nanoelectronics Laboratory of Hokkaido University, Dr. M. Kimura of JEOL Co., Ltd for their valuable discussion on this work.

References

[1] H. J. Goldsmid, "Electronic Refrigeration", Pion Limited, London (1986) pp. 7.

[2] L. D Hicks, T. C Harman and M. S. Dresselhaus, "Use of quantum-well superlattices to obtain a high thermoelectric figure of merit from nonconventional thermoelectric materials", Appl. Phys. Lett. **63** (1993) 3230.

[3] R. Venkatasubramanian, M. L. Timmons and J. A. Hutchby, "Monollthlicaly interconnected, superlattice-structured thermoelements (MISST) in Bi_2Te_3, Sb_2Te_3 and Bi_2Se_3 materials for thermoelectric cooling devices", Proc. 12th int. conf. on thermoelectrics (1993) 332.

[4] H. J. Goldsmid, "Electronic Refrigeration", Pion Limited, London (1986) pp. 89.

[5] D. M. Rowe, "CRC Handbook of thermoelectrics", CRC Press, Florida (1995) pp. 44.

[6] J. George and B. Pradeep, "Preparation and properties of co-evaporated bismuth telluride [Bi_2Te_3] thin films", Solid State Commun. **56** (1984) 117.

[7] Y. H. Shing, Y. Chang, A. Mirshafii, L. Hayashi, S. S. Roberts, J. Y. Josefowicz, and N. Tran, "Sputterd Bi_2Te_3 and PbTe thin films", J. Vac. Sci. Technol. **2** (1983) 503.

[8] M. Ferhat, B. Liautard, G. Brun, J. C. Tedenac, M. Nouaoura, L. Lassabatere, "Comparative studies between the growth characteristics of thin films deposited on SiO_2, Si(100), Si(111)", J. Cyrst. Growth **167** (1996) 122.

[9] V. Damodara Das and N. Soundararajan, "Size and temperature effects on the thermoelectric power and electrical resistivity of bismuth telluride thin films", Phys. Rev. B **37** (1988) 4522.

[10] E. Charles, E. Groubert and A. Boyer, "Structural and electrical properties of bismuth telluride films grown by the molecular beam technique", J. Mater. Sci. Lett. **7** (1988) 575.

[11] A. Mzerd, D. Sayah, J. C. Tedenac and A. Boyer, "Crystal growth of Bi_2Te_3 on single-crystal substrate Sb_2Te_3 by molecular beam epitaxy", Int. J. Electronics **77** (1994) 291.

[12] A. Mzerd, D. Sayah, J. C. Tedenac and A. Boyer, "Effect of substrate temperature on crystal growth of Bi_2Te_3 on single crystal Sb_2Te_3", J. Mater. Sci. Lett. **13** (1994) 301.

[13] A. Mzerd, D. Sayah, J. C. Tedenac and A. Boyer, "Optimal crystal growth condition of thin films of Bi_2Te_3 semiconductor", J. Cyrst. Growth **140** (1994) 365.

[14] A. Mzerd, D. Sayah, G. Brun, J. C. Tedenac and A. Boyer, "Crystal growth and sticking coefficient of Bi_2Te_3 thin films on Si(111) substrate", J. Mater. Sci. Lett. **14** (1995) 194.

[15] M. Imamura, K. Ogawa, M. Tokubuchi and M. Nakahara, "Magneto-optical properties of CdMnTe films on quartz glass and sapphire substrates in the transparent, visible region", IEEE Trans. Magn. **30** (1994) 4936.

[16] B. E. Warren, "X-ray diffraction", Addison-Wesley, Massachusetts (1969) pp. 251.

[17] S. N. Chizhevskaya, L. E. Shelimova, "Electroactive and electroinactive dopants in Bi_2Te_3 and their interaction with antisite defects", Inorganic Mater. **31** (1995) 1083.

[18] S. Shigetomi and S. Mori, "Electrical properties of Bi_2Te_3", J. Phys. Soc. Japan **11** (1956) 915.

Transport Properties of $Bi_2Te_{2.4}Se_{0.6}$ Thin Films

V. Damodara Das and S. Selvaraj
Thin Film Laboratory, Department of Physics
Indian Institute of Technology, Madras, Chennai 600 036, INDIA
Tel.: +91-44-2351365 Extn.3221, FAX: +91-44-2350509, E-mail: vddas@acer.iitm.ernet.in

Abstract

High efficiency thermoelectric thin film converters find applications as miniature energy sources which can deliver low power at high output voltage and also as IR detectors and sensors in new developments like microelectronics, space applications, medicine, etc.. $Bi_2Te_{3-x}Se_x$ chalcogenide is an important thermoelectric material which needs to be investigated for its thermoelectric properties in the thin film state. In this paper we present our results on thermoelectric properties of $Bi_2Te_{2.4}Se_{0.6}$ thin films. Annealed thin films of $Bi_2Te_{2.4}Se_{0.6}$ material, grown on glass plates held at room temperature by the flash evaporation technique in a vacuum of 2×10^{-5} torr, were investigated for their thermoelectric and electrical properties in the temperature range 300 K-480 K. The non-stoichiometry problem as encountered in the thermal evaporation method is avoided in this simple flash evaporation technique as evidenced from the $EDAX$ compositional analysis. Structural analysis indicated the polycrystalline nature of the films with hexagonal structure. Grain size was calculated from the electron micrograph. Thermoelectric studies indicated n-type conductivity. As temperature increases, thermoelectric power of the films increases in the low temperature range and then decreases after reaching a maximum. This is explained to be due to the evaporation of volatile components. The important physical parameters like Fermi energy, power index of the energy dependent mean free path expression and carrier concentration were evaluated from these measurements using the size effect theory.

Introduction

Bi_2Te_3 based thermoelectric materials find applications as IR detectors, sensors and power generators etc.. Thin film thermoelectric converters with high efficiency can be used as miniaturized energy sources which can deliver low power at high output voltage [1,2]. Recently Il-Ho-Kim et al showed that thermoelectric power generators based on Bi-Sb-Te-Se thin film modules can produce microwatt level power at high voltage (of the order of a volt) [3]. Bulk materials of $Bi_2(Te_{1-x}Se_x)_3$ compounds have been almost thoroughly studied by various researchers. But it is still needed to investigate the peculiar properties of $Bi_2(Te_{1-x})Se_x$ materials in the thin film state especially the size effect on the electrical and thermoelectric properties. It is well established that Bi_2Te_3 forms continuous solid solution with Bi_2Se_3 and thermoelectric figure of merit can be improved in these solid solutions. Bi_2Te_3 crystallizes in hexagonal structure with space group $R\bar{3}m$. In this paper we present our results on thermoelectric studies of $Bi_2Te_{2.4}Se_{0.6}$ thin films prepared by the flash evaporation technique.

Experimental

Bulk alloy $Bi_2Te_{2.4}Se_{0.6}$ compound was prepared by melting the elements in a quartz ampoule. The procedure of preparation of the bulk alloy is described elsewhere [5]. The homogeneity of the alloy and alloy formation were checked by using the X-Ray Diffraction (XRD) technique. Then the alloy was grinded into small granular particles. Thin films of different thicknesses were prepared on clean glass plates using the thermal flash evaporation technique in a vacuum of 2×10^{-5} torr. The lateral dimension of the films were 6.5 cm $\times$ 1 cm. The powdered particles of the alloy were taken in a basket to which a long hollow tube is attached so that the powdered particles fall through the tube and then fall on to a pre-heated basket type tantalum boat. The basket which contains the powdered particles was vibrated using a relay arrangement so that the particles fall on to the preheated tantalum boat. The falling rate of the particles into the boat was controlled by controlling the voltage applied to the relay using a variac so that the deposition rate was maintained at an average of 10-15 Å/sec. The rate of deposition and thickness of the films were indicated by a quartz crystal monitor (model QCT-101). The substrate (glass plates) cleaning procedure is as follows. The glass plates were kept in chromic acid for two days. After that they were shaken using an ultrasonic vibrator in soap solution for half an hour. Then they were washed with deionised water and then dried. The substrates were kept at room temperature at a distance of about 25 cm from the source. It is known that as-grown films of Bi_2Te_3 based materials show poor thermoelectric properties due to the presence of frozen-in defects, residual stress and inhomogeneity in composition. Thus, it is required that the films should be given heat treatment. Hence, all the films were annealed in vacuum at a temperature of 460 K and were used for the investigations. The crystal structure and microstructural analysis of the films was done using XRD, Selected Area Diffraction (SAD), Transmission Electron Microscopy (TEM) techniques. The composition of the films was analyzed using (Energy Dispersive Analysis of X-rays) EDAX facility attached to the transmission electron microscope.

0-7803-4057-4/97 $10.00 ©1997 IEEE

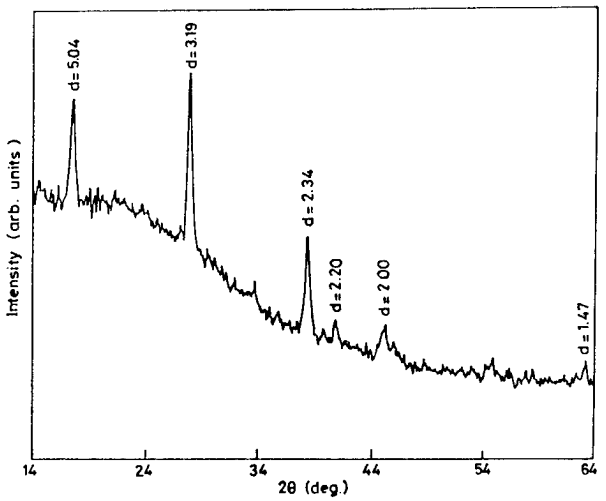


Figure 1: Typical XRD pattern of a thin film (1650 Å)

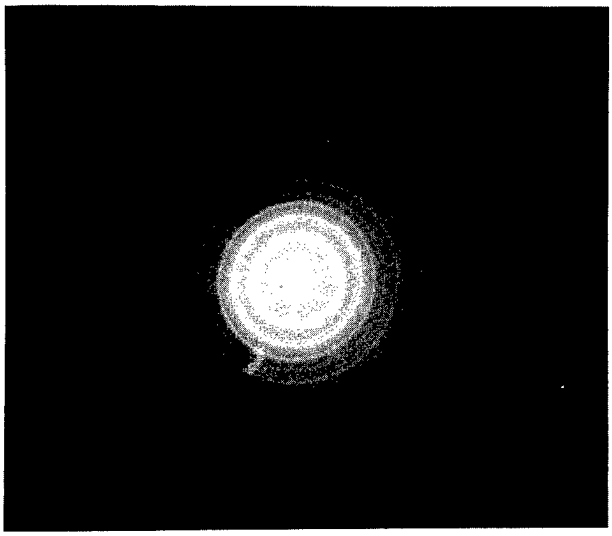


Figure 2: SAD photograph of a thin film (1650 Å)

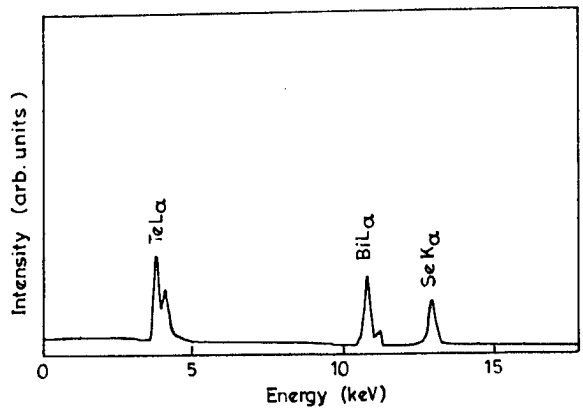


Figure 3: EDAX spectrum of a thin film (450 Å)

Results and Discussion

Strucural Analysis

X-ray diffractogram of a typical film (fig.1) shows the polycrystalline nature of the film. Comparison of d-values with the ASTM d-values confirms the hexagonal nature of the film (Table I). Fig.3 shows the EDAX spectrum of thin film of thickness 450 Å. The grain size of the film was calculated from the electron micrograph (fig.4) using the formula: G.S = 1.5l/mn, where l is length of n grains and m the magnification. The d-values were also obtained from the (SAD) (Selected Area Diffraction) (fig.2) pattern and are compared in Table I. It is found that the d-values and matching with the XRD d-values. Also it can be observed that the d-values are in between the Bi_2Te_3 and Bi_2Se_3 d-values which is in agreement with the fact that as Se, which has smaller atomic size, content increases the lattice parameters decreases [4].

TABLE I

Comparison of *d*-values of the films obtained from XRD and electron diffraction data with ASTM standard d values of Bi_2Te_3 (set 15-863) and Bi_2Se_3 (set 12-732) materials.

ASTM d values Å		h k l	d values observed Å	
Bi_2Te_3	Bi_2Se_3		XRD	SAD
5.08	4.80	006	5.04	
3.22	3.03	015	3.19	3.12
2.38	2.23	$10\underline{1}0$	2.34	
2.24	2.10	$01\underline{1}1$	2.20	2.20
2.031		$00\underline{1}5$	2.00	
1.81	1.78	205		1.77
1.40	1.32	125	1.47	1.39
1.27	1.23	$2\underline{1}10$		1.24

Thermoelectric Studies

Thermal emf of the films was measured in the temperature range 300 K- 480 K using the integral technique in which one end of the film was kept at constant temperature (room temperature) and the other end was heated at a controlled rate using a heater. The heating rate was controlled by a computer using a relay switch. Copper pads were used for electrical contacts with the films at both the ends. As temperature of one end is heated, thermal emf is developed across the film which was measured using a Keithley multi meter. Copper-constantan thermocouples were used for measuring the temperature of the hot and cold ends. Thermoelectric power of the films was calculated from the measured thermal emf as a function of temperature by taking derivatives at different temperatures using spline functions.

Fig.5 shows the thermoelectric power versus temperature plot. It was observed that the hot end of the films was positive which indicates that electrons are the majority carriers and the films are n-type. It is seen from fig.5 that thermoelectric power of the films increases with temperature and then decreases after reaching a maximum. This is explained to be due to the loss of Te from the films as evidenced from

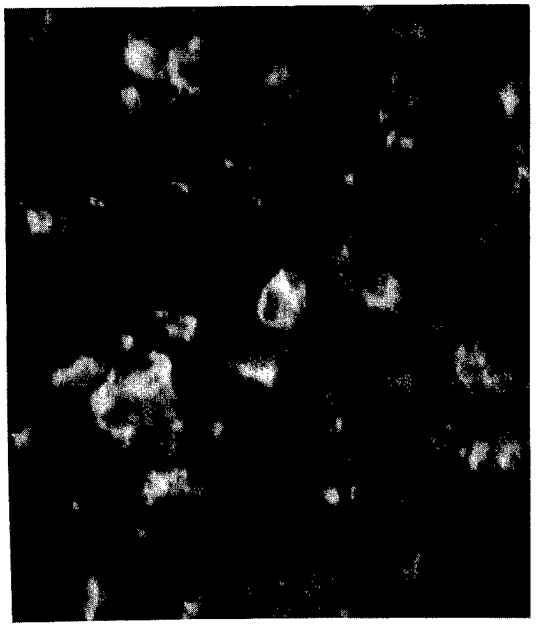


Figure 4: TEM photograph of a typical film (mag. 37,000) G.S = 220 Å

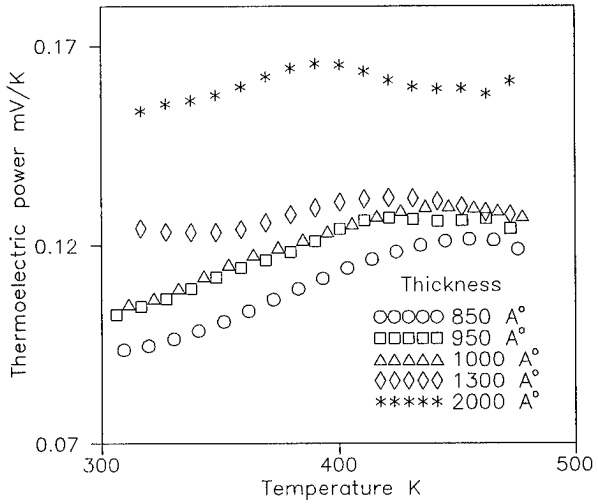


Figure 5: Plot of thermoelectric power versus Temperature

the EDAX spectrum (Fig.3). The expected atomic percentage of the alloy is Bi - 40 %, Te - 48 % and Se 12 %. The EDAX spectrum indicates that the observed composition of the annealed films is: Bi - 45.89%, Te - 38.41% and Se - 13.70%, whereas the as-grown film indicated the composition as: Bi - 41.14%, Te - 48.58% and Se - 10.28%. This indicates that the heat treatment during annealing results in loss of Te. The tellurium vacancy created thus can contribute to hole conduction in the films. This is observed by us in $Bi_2Te_2Se_1$ thin films [5]. Also it is observed that as thickness of the films increases, thermoelectric power increases. This is explained by the size effect theories as follows:

We have explained the size effects on electrical resistivity of polycrystalline thin films using the simpler effective mean free path model developed by Tellier [6]. This model has been successfully extended to calculate the thermoelectric

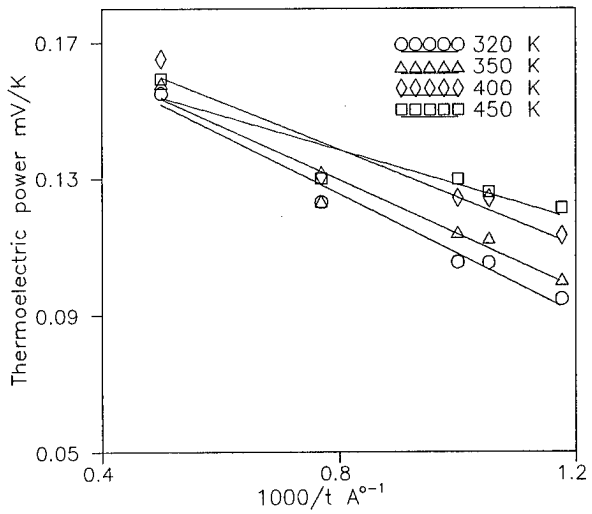


Figure 6: Plot of thermoelectric power and reciprocal thickness

power of polycrystalline films by Pichard et al [7]. According to this model, thermoelectric power of polycrystalline thin films can be expressed as,

$$S_F = S_g[1 - \frac{3(1-p)l_g}{8t}(\frac{U_g}{1+U_g}] \quad (1)$$

where, S_g is the thermoelectric power of infinite thick film, i.e. bulk material (hypothetical) having the same microstructure of the films and is given by,

$$S_g = \frac{\pi^2 k^2 T}{3eE_F}(1+U_g) \quad (2)$$

where

$$U_g = (\frac{\partial ln l_g}{\partial ln E}) \quad (3)$$

l_g is the effective mean free path which can be calculated from the slope of resistivity versus reciprocal thickness plot. This parameter U_g determines the energy dependence of the mean free path of the charge carriers in the infinitely thick film. From the expression (1) it is found that a plot of thermoelectric power of polycrystalline thin films versus reciprocal thickness is linear and the parameters U_g and S_g can be determined from the slope and intercept of the plot respectively if we know the mean free path (l_g). Once we get these parameters we can calculate the Fermi energy using the expression (2) and the electron concentration using the expression,

$$n = \frac{4\pi}{\pi^{1/2}}(2\pi m^* kT/h^2)^{3/2} F_{1/2} \quad (4)$$

where, m^* is the effective mass of electrons and $F_{1/2}$ is the Fermi integral.

Fig.6 shows the plot between thermoelectric power and reciprocal thickness and it is seen that the experimental points are fairly fitting to a straight line. The value of l_g was taken similarly for these films from the resistivity

versus reciprocal thickness plots at different temperatures. Using these values the parameters mentioned above were calculated and are shown in the Table II. It is seen that thermoelectric power (S_g) of the infinitely thick film increases with temperature and starts decreasing at around 450 K. The U_g parameter values are positive which indicates that the mean free path of the carriers increases with temperature. Also it is seen that Fermi energy increases with temperature and hence the carrier concentration.

Conclusions

Thickness dependence of thermoelectric power of the $Bi_2Te_{2.4}Se_{0.6}$ films is explained by the effective mean free path model. Various parameters are evaluated from the size effect analysis. Decrease of the thermoelectric power of the films at high temperature is attributed to the partial evaporation of Te from the films. Size effect analysis indicates that Fermi level increases with temperature which reveals that large number of charge carriers are generated from the donor states in the films and hence the carrier concentration increases. Structure of the film was confirmed by XRD and SAD.

TABLE II
Variation of various physical parameters with temperature

Temperature K	S_g μV/K	U_g	E_f meV	n $\times 10^{20}$ cm^{-3}
320	195.7	0.19	47.5	2.89
350	193.3	0.20	53.2	3.38
400	195.2	0.22	61.5	4.15
450	179.6	0.23	75.7	5.44

References

[1] U.A.Arifov, A.I.Kulagin, N.I.Erzin, N.V.Makov, B.Tursunov and H.Saidvalieva, "Variation of the thermoelectric properties of the solid solution $Bi_2Te_{2.4}Se_{0.6}$ in the course of deposition", Appl.Solar Energy vol.**10**, pp.63-65 (1974)

[2] Y.A.Arifov, N.I.Erzin, A.I.Kulagin et al, "Structure and Properties of Films Based on Bismuth Telluride and Selenide", Appl.Solar Energy vol.**11** pp.3-5 (1975)

[3] Il-Ho Kim and Dong-Hi Lee, "Thin Film Thermoelectric Generator Cell of Bi-Sb-Te-Se System", 15th International Conference on Thermoelectrics p.425-429, (1996)

[4] V.F.Bankina and N.Kh.Abrikosov, "The Bi_2Te_3 System", Russ.J.Inorg.Chem., vol.**9**, pp.509-512 (1964)

[5] V.Damodara Das and S.Selvaraj, "Size and Temperature Dependence of Electrical Resistance and Thermoelectric Power of $Bi_2Te_2Se_1$ Thin Films", J.Appl.Phys. (communicated)

[6] C.R.Tellier, "A Theoretical Description of Grain Boundary Scattering by an Effective Mean Free Path Model", Thin Solid Films, **51**, 311-317, (1978)

[7] C.R.Pichard, C.R.Tellier and A.J.Tosser, J.Phys.F., "Thermoelectric Power of Thin Polycrystalline Metal Films in an Effective Mean Free Path Model" **10**, p.2009 (1980)

PECULIARITIES OF THE FIGURE OF MERIT TEMPERATURE DEPENDENCE IN n-Bi_2 (Te, Se)$_3$ SOLID SOLUTION AT LOW CHARGE CARRIER CONCENTRATION

Luk`yanova L.N., Alekseeva G.T., Konstantinov P.P., Kutasov V.A.

A.F. Ioffe Physical- Technical Institute, RAS, St. Petersburg, Russia
Tel.: 7/812/515-9247, Fax: 7/5156747, Email: luk@exd.ioffe.rssi.ru

Abstract

A study has been made temperature dependence of the thermoelectric properties of n-Bi_2 (Te, Se)$_3$ solid solutions (x=0.3 and 0.36). An optimal charge carrier concentration in the low temperature range (80-120) K was provided with addition of excess Te. Minimum of Z = f(T) relation was observed near by 120 K, than the value of Z is increased when the temperature falls to 80 K. It is may be explained with an absence of interband scattering of carriers at the studied carrier concentrations ($(0.8 - 1)\cdot 10^{18}$ cm^{-3}).

In recent years there have been some problems which required more deep cooling than one-stage thermoelectric module can be provided. The interest to develop of low temperatures (80-120) K by means of many stage thermoelectric cooling is explained by successes in the high-T_c-superconductivity studies and in the range of the sensor devices. The results of these studies are shown that it is required to diminish the charge carrier concentration in n-$Bi_2(Te,Se)_3$ solid solutions for increasing the figure of merit Z and using of these materials at more lower temperatures. The optimal low carrier concentration was provided with the addition of the excess Te, this made it possible to eliminate at low temperatures the additional scattering due to dopiness based on chalcogenides ($CdCl_2$, $BiBr_3$ and so on).

One of the main parameter, determining the figure of merit Z is the value of β [1]:

$$\beta = \frac{2(2\pi)^{3/2}}{h^3 e} k_o^{7/2} (m^*/m_o)^{3/2} \mu_o T^{5/2} \kappa_l^{-1} \quad (1)$$

m^* and μ_o are the effective mass of the density of states and the mobility of the carrier concentration including degeneracy; κ_l is the thermal conductivity of the crystal lattice.

The product of $(m^*/m_0)^{3/2}\mu_0$ can be obtained from the measured values of the thermoelectric power α and electrical conductivity σ for some scattering mechanism. The main scattering mechanism is usually that by acoustic vibrations of the crystal lattice, for which the scattering parameter is r = -0.5 (r is the power exponent in the energy dependence of the relaxation time $\tau = \tau_0 E^r$). Other scattering mechanisms (by atoms of the second components of a solid solution, the scattering by the cores of ionized impurities) and interband scattering mechanism, including due to complicated band structure of the solid solutions are not taken into account. Therefore, the effective scattering mechanism assuming these scattering processes is used [2, 3] with the effective scattering parameter r_{eef}, which takes into account peculiarities of the band structure and scattering mechanisms. In the samples of n-$Bi_2(Te,Se)_3$ solid solutions r_{eff} values at T=80 K are equal to (-0.38) - (-0.4) and varied to -0.6 at the room temperature [2, 3]. The r_{eff}-values close to them which were determined in ref [4] for n-$Bi_2Te_{2.85}Se_{0.85}$ solid solution. .

The samples of n-$Bi_2Te_{3-x}Se_x$ solid solutions were grown by directed crystallization method in conditions excluding a concentration overcooling. The studied range of the carrier concentrations was $n \le 4\cdot 10^{18}$ cm^{-3}. The charge carrier concentration was determined trom measuring of Hall cefficients in a weak magnetic field [5].

Temperature dependence of the parameter $(m^*/m_0)^{3/2}\mu_0$ in n-$Bi_2Te_{3-x}Se_x$ (x=0.3; 0.36) solid solutions is shown in Fig. 1. The angle coefficients $s = d\ln[(m^*/m_0)^{3/2}\mu_0]/d\ln T$ were calculated from the product of $(m^*/m_0)^{3/2}\mu_0$. The $d\ln[(m^*/m_0)^{3/2}\mu_0] / d\ln T$ dependence is

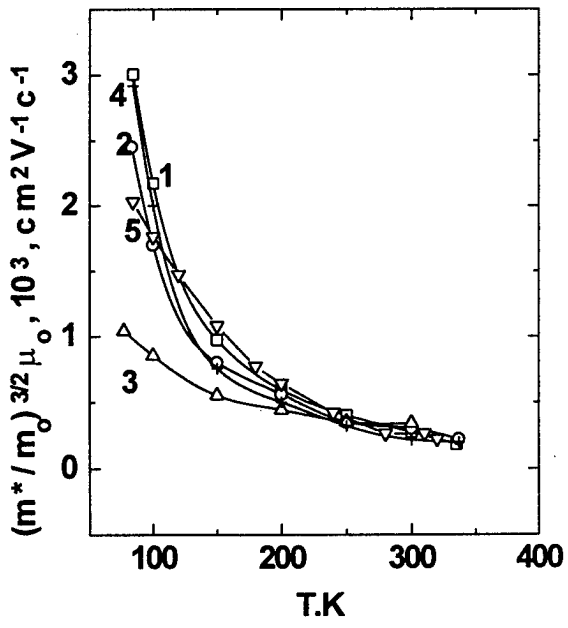


Fig. 1. Temperature dependence of the $(m^*/m_0)^{3/2}\mu_0$ parameter in n-$Bi_2Te_{3-x}Se_x$ solid solutions.
x: 1, 2, 3 - 0.3; 4, 5 - 0.36.

shown to be nonlinear functions throughout the temperature interval studied. The values of |s| are very high and equal to 2.0 - 2.3 at low carrier concentrations (0.8 - 1)·10^{18} cm^{-3} (Fig. 1, curves 1, 2, 4). With growth of the temperature |s|-values is decreased to 1.5-1.6. The parameter $(m^*/m_0)^{3/2}\mu_0$ is decreased with growth of the carrier concentrations to ($n=4\cdot10^{18}$ cm^{-3}) (Fig. 1, curves 3) and the angle coefficients |s| falls to 1.1-0.9 due to increasing of the number of scattering centers.

To calculate of β parameter, which determines the figure of merit Z, the thermal conductivity of the crystal lattice κ_l is evaluated with account of r_{eff}. A whole thermal conductivity in the range of the impurity conductivity of semiconductor:

$$\kappa=\kappa_e+\kappa_l \qquad (2)$$

κ_e- the electron thermal conductivity was calculated using the Wiedemann-Franz law in the form:

$$\kappa_e=L\sigma T \qquad (3)$$

L = L(r, η) - Lorentz number was determined for the effective scattering parameter ($r=r_{eff}$):

$$L=\left(\frac{k}{e}\right)^2\left[\frac{(r+7/2)F_{r+5/2}(\eta)}{(r+3/2)F_{r+1/2}(\eta)}-\frac{(r+5/2)^2F^2_{r+3/2}(\eta)}{(r+3/2)^2F^2_{r+1/2}(\eta)}\right] \qquad (4)$$

where the Fermi integral is

$$F_r(\eta)=\int_0^\infty [x^r/e^{x-\eta}]dx \qquad (5)$$

and η is the reduced Fermi level.

The relations $\ln(\kappa_l)$ = Fln(T) were calculated in accordance with (2) - (5) and they were close to linear over the interval 80-300 K in the samples with low carrier concentrations. The angle coefficients m = $d\ln\kappa_l/d\ln T$ are equal to m ≈ -0.4 at the studied concentrations. In the samples with more high carrier concentration up to ($n=4\cdot10^{18}cm^{-3}$) weak variation of m -value is observed in low- and high temperature ranges and m is equal to -0.4 -0.5, respectively. Variation of the angle coefficients m comparing with Bi_2Te_3 (for a purely acoustic scattering mechanism (r = -0.5) m ≈ -1 [1]) is connected with increasing in the contribution of the additional thermal resistance on introduction of neutral atoms participating in the formation of the substitution solid solutions.

The calculation of β (Fig. 2) is shown that the angle coefficients t = $d\ln\beta$ / $d\ln T$ are different in the low and high temperature regions and change from 0.6 - 0.8 to 1.6 - 1.8 at low n (Fig. 2, curves 1,2), and from 1.4 - 1.5 to 1.6 - 1.8 with growth carrier concentration (Fig. 2, curves 3). A weak reduce β- value at low temperatures in the samples with low carrier concentration comparing with high n indicates to possible increasing of the figure of merit Z at low temperatures.

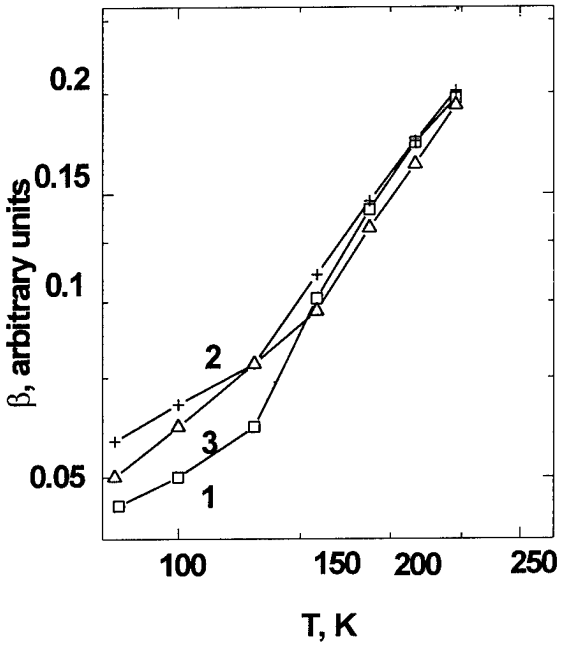


Fig. 2. Temperature dependence of β parameter in n-$Bi_2Te_{3-x}Se_x$ solid solution.
x: 1, 3 - 0.3; 2 - 0.36.

The temperature dependence of Z is shown in Fig. 3. It is noted that a slowing-down of the value of Z in low temperature range is observed in the samples of n-$Bi_2Te_{3-x}Se_x$ (x=0.3; 0.36) solid solutions at the carrier concentration close to n = (2.5 - 3)·$10^{18}cm^{-3}$ when the thermoelectric power is α = (315 - 320) μV K^{-1} at the room temperature (Fig. 3, curves 3, 6). Over the temperature interval (80 - 120) K at α ≥ (320 - 330) μV K^{-1} (T = 300 K) a growth of Z up to (2.2 - 2.3) $10^{18}cm^{-3}$ was observed instead of usual decreasing of Z with temperature in the optimal for these temperatures low carrier concentration (0.8 -1)·10^{18} cm^{-3} (Fig.3, curves 1,2,5). So behavior of Z = F(T) relation can be traced to the absence of interband scattering, because additional band in the conduction band of the solid solution does not fill at the studied carrier concentrations.

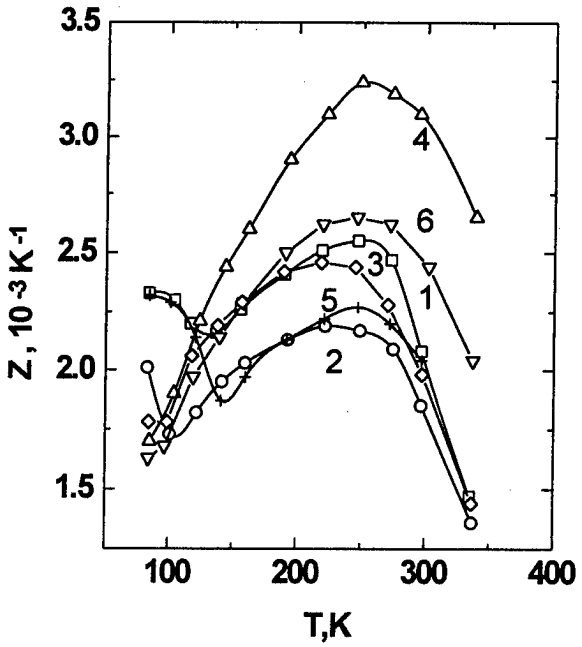


Fig.3. Temperature dependence of the figure of merit in n-$Bi_2Te_{3-x}Se_x$ solid solution.
x: 1, 2, 4, 6 - 0.3; 3,5 - 0.36.

The low absolute maximum of Z (not above to $2.6 \cdot 10^{-3} K^{-1}$) may be explained by deviation of the considered carrier concentration from the optimal one at T > 120 K. In the sample with carrier concentration $n=4 \cdot 10^{18} cm^{-3}$ the value of Z is equal to $\sim 1.7 \cdot 10^{-3} K^{-1}$ in the low temperature range and Z_{max} is observed at T = 240 K (Fig.3, curves 4). Note that for materials customarily used at the room temperatures Z = (0.6 - 1.1)$\cdot 10^{-3} K^{-1}$ at low temperatures. Thus, n-$Bi_2Te_{3-x}Se_x$ samples at low carrier concentration without interband scattering will give substantially higher values Z and product ZT, which determines the efficiency of thermoelectric power conversion.

Variation of Z in n-$Bi_2Te_{3-x}Se_x$ solid solution in the low temperature range can be analyzed in common with studies of galvanomagnetic effects in weak magnetic fields. In ref. [6] temperature dependence of the ratios of the components of tensor of the density of states effective mass m_i/m_j and the angle of rotation of the principal axes of the constant-energy ellipsoids relative to the crystallographic axes θ was determined in the samples of n-$Bi_2Te_{3-x}Se_x$ with the different carrier concentrations. The analyze of the ratios of m_i/m_j give rise to determine the relationship of the principal axes of the constant-energy ellipsoids and their orientation relative to the crystallographic axes. The Cartesian coordinate system in which the X(1) axis (binary direction) is along the twofold axis the Y(2) axis (bisectrix) is in the reflection plane, and the Z(3) (trigonal) direction is parallel to the threefold rotation axis is used [7, 8].

In n-$Bi_2Te_{3-x}Se_x$ solid solution the relationship of the principal axes of the ellipsoids is: $m_2 > m_3 > m_1$ with account of the turn on the angle θ relative to bisectrix axis [9], that is the ellipsoids is compressed to the binary axis X. At low carrier concentration ($n \leq 3 \cdot 10^{18} cm^{-3}$) $m_3 \approx m_2$ and the ellipsoids close to ellipsoid of rotation relative to the binary axes (Fig. 4)

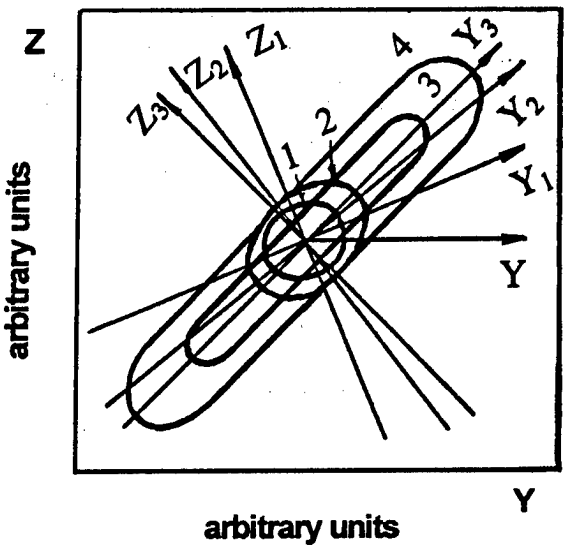


Fig. 4. Orientation and form of the constant-energy ellipsoids at the different temperatures and carrier concentrations in n-$Bi_2Te_{3-x}Se_x$ solid solution.
T, K: 1, 3 - 80; 2, 4 - 200.
$n.10^{-18} cm^{-3}$: 1, 2 - 1.5; 3,4 - 4.

In some of ref. [10-12] the ratios m_i/mj are determined for a purely isotropic scattering mechanism. However, solid solutions based on Bi_2Te_3 exhibit a strong anisotropy of the transport properties due to anisotropy of the effective mass and the scattering anisotropy which is from the anisotropy of elastic vibrations of a crystal. Because it is necessary to introduce the relaxation time tensor in an analysis of the experimental results. [8.12]. From analysis of the galvanomagnetic effects in weak magnetic fields in n-$Bi_2Te_{3-x}Se_x$ solid solution in accordance with many-valley model of the energy spectrum with anisotropic carrier scattering we calculated ratios of the components of the relaxation time tensor τ_{ij} / τ_{11} on temperature [6]. It is found that the anisotropy of carrier scattering increases on increase in the carrier concentrations and anisotropy of carrier scattering in the (0001) cleavage plane is much less than at right-angles along the direction <111> coinciding with Z axis. It therefore follows that the increase of the figure of merit Z in the investigated solid solution and the anisotropy of carrier scattering are correlated, so that the figure of merit Z is higher in the low temperature range when the constant energy surfaces are the ellipsoids of rotation along the binary axis X. In this case the anisotropy of the carrier scattering is less, especially in the cleavage plane (0001).

References

[1] B.M.Goltsman, V.A. Kudinov, and I.A. Smirnov, Semiconductor Thermoelectric Materials Based on Bi_2Te_3 [in Russian], Nauka, Moskow. (1972) 320.

[2] V.A. Kutasov, L.N. Luk`yanova, "Carrier Density Dependence of the Effective Scattering Parameter of the Solid Solutions Based on Bithmuth Telluride", Fiz. Tverd. Tela **26** (1984) 2501 (Soviet Physics Solid State. **26** (1984) 1515).

[3] V.A. Kutasov, L.N. Luk`yanova, "Carrier- density dependence of the anisotropy parameter of n-type Bi_2Te_3 and solid solutions derived from it", Fiz. Tverd. Tela. **28** (1986) 899), (Soviet Physics Solid State. **28** (1986) 502).

[4] H. Kaibe Y. Tanaka, M. Sakata, and Nishida, "Anisotropic galvanomagnetic and thermoelectric properties of n-type Bi_2Te_3 single crystal with the composition of a useful thermoelectric cooling material" J. Phys. Chem. Solids. **50** (1989) 945.

[5] G.T. Alekseeva, P.P. Konstantinov, V.A. Kutasov, L.N. Luk,yanova, Yu. I. Ravich, "Nonisovalent substitution of atoms in the cation sublattice of bismuth telluride", Fiz. Tverd. Tela. **38** (1996) 2998), (Soviet Physics Solid State. **38** (1996) 1639.

[6] V.A. Kutasov, L.N. Luk`yanova, "Anisotropy of carrier scattering in $Bi_2Te_{3-x}Se_x$ and $Bi_{2-y}In_yTe_3$ solid solutions", Fiz. Tverd. Tela **32** (1990) 488), (Soviet Physics Solid State. **32** (1990) 282).

[7] L.P. Caywood and G.R. Miller, "Anisotropy of the constant-energy surfaces in n-type Bi_2Te_3 and Bi_2Se_3 from galvanomagnetic coefficients", Phys. Rev. B, **2** (1970) 3210.

[8] H.A.Ashworth J.A. Rayne, and R.W. Ure, Transport properties of Bi_2Te_3", Phys. Rev. **3**, (1971) 2646.

[9] V.A. Kutasov, L.N. Luk`yanova, "The conduction band parameters and scattering mechanisms in solid solutions based on Bi_2Te_3", Phys. Stat. Sol. B. **154** (1989) 699.

[10] J.R. Drabble R.D. Groves and R. Wolfe, "Galvanomagnetic effects in n-type bithmuth telluride", Proc. Phys. Soc. **71** (1958) 430.

[11] O. Beckman, P. Bergvall, and K. Tripathi, Doping Studies of $Bi_2(TeSe)_3$ Alloys, Ark. fur Fys. **B28**, (1965) 215.

[12] B.A. Efimova, V.L. Novikov, and A.,G. Ostroumov, Anisotropy of the galvanomagnetic properties in n-Bi_2Te_3", Fiz. Tverd. Tela **4** (1962) 302.

Electrophysical properties of $Bi_2Te_{2.85}Se_{0.15}$ single crystals doped with copper

T.E. Svechnikova, N.M. Maksimova
Baikov Institute of Metallurgy, Russian Academy of Sciences, Moscow, Russia
Tel.: 095/135-9611, Fax: 095/135-8680, E-mail: svechn@lesr.imet.ac.ru
P.P. Konstantinov
Ioffe Physical-Technical Institute, Russian Academy of Sciences, St. Petersburg, Russia

Abstract

The influence of copper addition on thermoelectric and electrophysical properties of $Bi_2Te_{2.85}Se_{0.15}$ solid solutions grown by the Czochralski technique is studied. The effective segregation coefficient of copper K_{eff} = 0.2 is determined. Doping with small quantities of copper (up to 0.05 at.% in charge) leads to enhancement of carrier mobility and thermoelectric figure of merit, Z = (3.1 – 3.4) 10^{-3} K^{-1} in the temperature range of 220 – 350K. The single crystals with copper content up to 0.1 at.% in charge are found to retain stability of properties. Annealing at 280℃ for 150 hours did not cause significant change in thermoelectric properties of the samples.

Introduction

Single crystals of $Bi_2Te_{2.85}Se_{0.15}$ solid solution are efficient n-type materials and are recommended for application in thermoelectric coolers operating in the temperature range of 200 – 350 K [1].

The results of studies on doping of this solid solution with the elements from Groups IIB – VB, replacing the positions of bismuth and tellurium atoms in crystal lattice, showed an increase in thermoelectric figure of merit due to reduction of thermal conductivity of crystal lattice and a slight enhancement of mechanical strength of the material [2 – 4]. The element from Group IB, copper, unlike the above-mentioned elements, is an efficient donor addition to $Bi_2Te_{2.85}Se_{0.15}$ [5]. The copper atoms, according to [6], are located in interstitial sites, mainly between the cleavage planes with van der Waals bonds, that leads to strengthening of chemical bonds between quintets and to enhancement of mechanical strength. Therefore, it is of interest to investigate the influence of copper doping on thermoelectric and electrophysical properties, as well as on the stability of the properties, of $Bi_2Te_{2.85}Se_{0.15}$ single crystals.

Experimental

Single crystals of solid solutions with copper content of 0.02 to 0.3 at.% in charge were grown by the Czochralski technique with replenishment of the melt from a liquid phase [3]. The charge was prepared from preliminary synthesized compounds Bi_2Te_3, Bi_2Se_3 and copper by melting them in the proper proportion. We used the materials: bismuth Bi-0000, tellurium Te-0000, Se and Cu of very high purity. The single crystals were grown in the [$10\bar{1}0$] direction normal to the main crystallographic axis C. The crystals had the form of plates of the length ~ 100 mm, width ~27 mm, and thickness 16 – 20 mm. The growth conditions were identical in all cases. The copper content was determined by plasma absorption spectroscopy. From these data the effective segregation coefficient K_{eff} = 0.2 was obtained.

We also measured electrophysical properties of samples cut out of the ends of the crystals at the distance of 80 – 90 mm from the seed (see table).

The dependence of electrical conductivity on thermoelectric power is shown in Fig. 1. The $Bi_2Te_{2.85}Se_{0.15}$ <Cu> single crystal samples with 0.05 at.% Cu have higher values of σ compared to the initial solid solution over the whole investigated range of concentrations. This effect is explained by the increase in carrier mobility (see table) which was calculated on the assumption of an acoustic scattering mechanism. The maximum value of carrier mobility corresponds

Electrophysical properties of $Bi_2Te_{2.85}Se_{0.15}$ <Cu> at room temperature

№	C_{cu}, at% (in the charge)	-α, μV/K	σ, S/cm	κ_p x 10^3, W/(cmK)	Z x 10^3, K^{-1}	n x 10^{19}, cm^{-3}	μ_0 x 10^4, $m^2/(Vs)$
1	-	208	1200	10,6	3,1	3,0	275
2	0,02	214	1130	11,1	3,1	2,5	240
3	0,05	214	1250	11,0	3,4	2,4	380
4	0,10	208	1269	11,3	3,1	2,9	285
5	0,20	215	1130	11,6	3,1	2,5	318
6	0,30	210	1110	11,4	2,9	2,8	280

0-7803-4057-4/97 $10.00 ©1997 IEEE

to the composition with 0.05 at.% Cu in charge. The change of μ has a nonmonotone character and calls for further investigation. Lattice thermal conductivity increases slightly with copper content (table) that can be connected with the reduction of scattering by phonons on the thermal vibrations of crystal lattice upon introduction of copper [5].

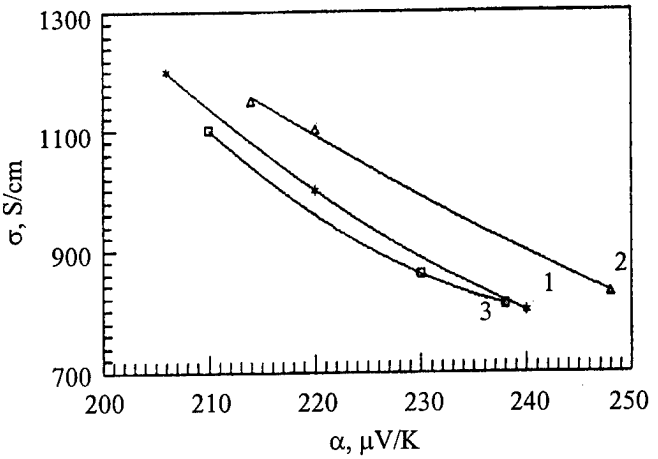


Fig. 1. Dependence of σ on α for single crystals $Bi_2Te_{2.85}Se_{0.15}$ (1) and $Bi_2Te_{2.85}Se_{0.15}$<Cu> with copper content of 0.05 (2) and 0.3 at.% (3).

From measurements of α, σ, and κ in the 100 – 350 K temperature range we found that the maximum values of σ and Z corresponded to the composition with 0.05 at.% Cu (Fig. 2). The maximum value of $Z = 3.4\ 10^{-3}\ K^{-1}$ was obtained in the temperature range of 280 – 320 K. From the analysis of temperature dependencies it follows that the increase in copper content in the solid solution practically does not affect the dependencies α(T) and $\sigma = T^{-m}$. The weakening of temperature dependence of lattice thermal conductivity was observed. For copper content of 0.3 at.% σ and Z decreased compared to the initial composition (Fig. 2).

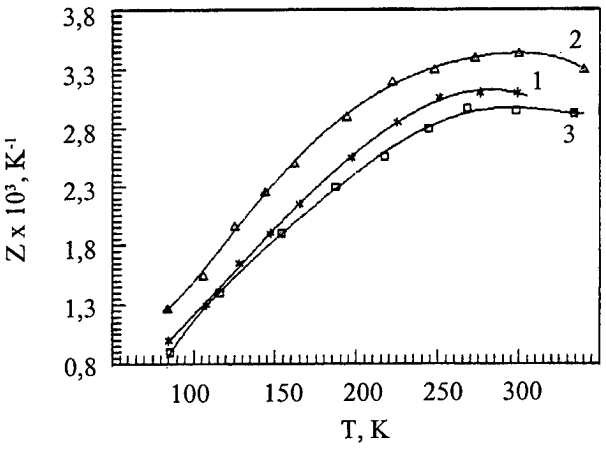


Fig. 2. Temperature dependence of Z for single crystals $Bi_2Te_{2.85}Se_{0.15}$ (1) and $Bi_2Te_{2.85}Se_{0.15}$<Cu> with copper content of 0.05 (2) and 0.3 at.% (3).

To investigate the stability of properties of the $Bi_2Te_{2.85}Se_{0.15}$<Cu> solid solutions we annealed the single crystal samples in air at the temperature 280 C for 150 hours with periodical monitoring of their properties. No release of copper on the sample surfaces was observed.

Thermoelectric power of the samples with copper content up to 0.1 at.% in charge changed for the first 60 hours by 3 – 4%, and electrical conductivity accordingly slightly decreased. On further annealing these properties did not change. For the samples with copper content 0.3 at.% thermoelectric power changed by ~10% and electrical conductivity changed by ~18%.

Conclusion

Single crystals of $Bi_2Te_{2.85}Se_{0.15}$ solid solutions with copper content in charge up to 0.3 at.% were grown by the Czochralski technique in the direction [10$\bar{1}$0]. The effective segregation coefficient of copper $K_{eff} = 0.2$ was determined. The single crystals with 0.05 at.% Cu in charge have high value of thermoelectric figure of merit $Z = 3.4\ 10^{-3}\ K^{-1}$ in the temperature range of 280 – 320 K. The solid solutions doped with copper in amount of up to 0.1 at.% retain stability of properties.

References

[1] V.A. Semenyuk, T.E. Svechnikova, L.D. Ivanova, "Single crystals of solid solutions of chalcogenides of bismuth and antimony and miniature coolers based on them", Advanced Materials 5 (1994) 428.

[2] T.E. Svechnikova, S.N. Chizhevskaya, N.V. Polikarpova, et al., "Influence of CdTe on thermoelectric and mechanical properties of $Bi_2Te_{2.85}Se_{0.15}$ single crystals", J. Inorganic Mater. 28 (1992) 316.

[3] T.E. Svechnikova, S.N. Chizhevskaya, N.V. Polikarpova, "Doping of $Bi_2Te_{2.85}Se_{0.15}$ single crystals with In", Izv. Academ. Nauk SSSR Neorgan. Mater. 23 (1987) 1128.

[4] T.E. Svechnikova, S.N. Chizhevskaya, N.M. Maksimova, et al., "Doping of $Bi_2Te_{2.85}Se_{0.15}$ solid solution with germanium", J. Inorganic Mater. 30 (1994) 161.

[5] T.E. Svechnikova, N.M. Maksimova, P.P. Konstantinov, et al., "Thermoelectric efficiency of $Bi_2Te_{2.85}Se_{0.15}$ single crystals doped with copper", J. Inorganic Mater. 29 (1993) 1442.

[6] M.A. Korzhuev, S.N. Chizhevskaya, T.E. Svechnikova, et al., "Mechanical properties of single crystals of Bi_2Te_3 and $Bi_2Te_{2.85}Se_{0.15}$ doped with copper", J. Inorganic Mater. 28 (1992) 1383.

ELECTROPHYSICAL PROPERTIES OF SB_2TE_3 SINGLE CRYSTALS DOPED WITH TIN, SELENIUM, BISMUTH

Lidia D.Ivanova, Yulia V.Granatkina, Yurii A.Sidorov

A.A.Baikov Institute of Metallurgy of Russian Academy of Science, 117334 Moscow, Russia,
Tel.:+7/095/135-9611, Fax:+7/095/135-8680, E-mail:ivanova@lesr.imet.ac.ru

Abstract

Electrophysical properties (Seebeck coefficient, electro- and thermoconductivities, Hall coefficient and Hall mobility) of Sb_2Te_3 single crystals, doped with tin up to 1 mass.%, selenium up to and bismuth up to 7 mass.% in various crystallographic directions were studied. The single crystals were grown using Czochralski technique with the melt supply through a floating crucible. Using atomic absorption analysis were determined the effective distribution coefficients of the tin and of the selenium in Sb_2Te_3.

The concentration dependencies of elecrophysical properties of doped crystals were studied. It was established that tin atoms act as acceptors and one atom of Sn gave 1.3 holes. Doping of selenium and bismuth decrease deviation from stoichiometric composition of Sb_2Te_3. The possible mechanisms of the incorporation of Sn, Se and Bi atoms into the crystal lattice of Sb_2Te_3 were discussed. At room temperature for the whole crystals the anisotropy of electro- and termoconductivities was highest between the directions parallel and perpendicular of basal planes (2-4). Anisotropy factors of Seebeck coefficient were 0.8-0.9. The temperature dependencies of electroconductivity and Seebeck coefficient in directions parallel and perpendicular of basal planes of the crystals doped with tin in range 100-300 K were studied.

Introduction

The compound Sb_2Te_3 has a rhombohedral crystal structure, spatial group D^5_{3d} (R3m), described by a hexagonal elementary cell which can be represented in the form of a set of layers-quintets, perpendicular to the main crystallographic axis "c". The distance between the quintets is relatively large and the link between them is carried out by forces of the van der Waals type. The link inside the quintets is of the covalent nature with a small fraction of the ion bond. This determines the considerable anisotropy of the thermoelectric and mechanical properties of single crystals of these materials in the directions parallel and perpendicular to the main crystallographic axis. Single crystals of antimony telluride doped tin up to 1 mass.%, selenium and bismuth up to 7 mass.% were grown using Czochralski method of pulling from a melt with liquid-phase make up from floating crucible [1].

The single crystals were grown in the direction perpendicular to the trigonal axis. The crystals have a layered structure with very distinct cleavage planes, perpendicular to the principal crystallographic axis .

Results and discussion.

The tin and selenium content in the crystals was determined by using atomic flame analysis which was performed on a Perkin-Elmer analyzer [2]. The effective distribution coefficients of tin $k_{eff\ Sn}$= 0.8, and selenium $k_{eff\ Se}$ = 1.2 (doping Sb_2Se_3) and $k_{eff\ Se}$ = 0.64 (doping Bi_2Se_3) in Sb_2Te_3 were determined.

Electrophysical properties (Seebeck coefficient, electro- and thermoconductivities, Hall coefficient and Hall mobility), of single crystals of various compositions at room temperature in two crystallographic directions parallel and perpendicular to the cleavage planes were studied. The results of the investigation are summarized in Figs. 1,2 and Tab.1,2.

With increasing Sn content in Sb_2Te_3 Seebeck coefficient is essential lowered, electrical and thermal conductivities are change small (Fig.1, Tab. 1). The concentration dependencies of Seebeck coefficient and Hall mobility for doped with tin crystals were considerable smaller than theoretical values calculated when the parabolic band structure and acoustic scattering mechanism is assumed. We established that tin atoms act as accepters and one atom Sn gave 1.3 holes.

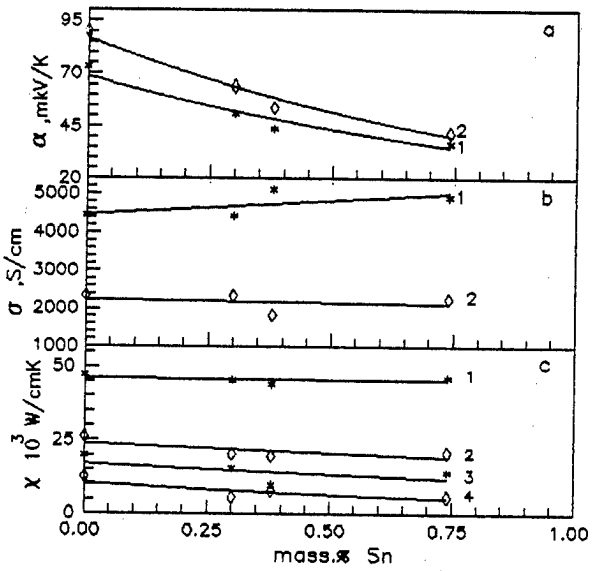


Fig.1. Seebeck coefficient (a), electroconductivity (b), total (1,3) and lattice (2,4) thermocoductivity (c) for Sb_2Te_3 single crystals doped with Sn in direction parallel (1,3) and perpendicular (2,4) of basal planes.

Doped with Se and Bi lead to decrease of electrical and thermal conductivities and carrier concentrations (Fig.2, table 2), Seebeck coefficient decrease for crystal doping 11.6 mol.% Sb_2Te_3 and increase for the crystals Sb_2Te_3 doping Bi_2Se_3 (from 7.4 mol.%) and Bi_2 Te_3 (from 10 mol.%). Doping of Sb_2Te_3 selenium and bismuth decrease deviation from stoichiometric composition of Sb_2Te_3. Selenium replaced tellurium atoms replaced and a part of antimony atoms, which were situated in the tellurium places, therefore, the carrier concentrations decrease.

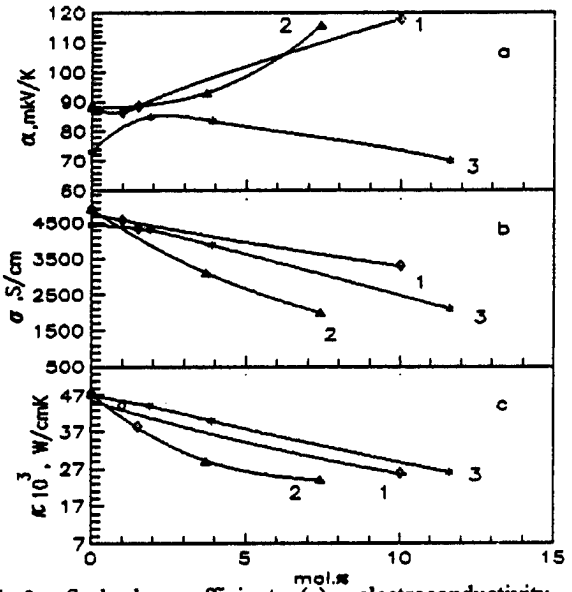


Fig.2. Seebeck coefficient (a), electroconductivity (b), thermocoductivity (c) for Sb_2Te_3 single crystals doped with Bi_2Te_3 (1), Bi_2Se_3 (2), Sb_2Se_3 (3).

At room temperature for the whole crystals the anisotropy of electroand termoconductivities was highest between the directions parallel and perpendicular of basal planes $\sigma_{\parallel}/\sigma_{\perp}$ =1.9-2.8 and $\kappa_{\parallel}/\kappa_{\perp}$=1.8-2.8 for doped with Sn (Tab.1) and $\sigma_{\parallel}/\sigma_{\perp}$=2.5-4.2 and $\kappa_{\parallel}/\kappa_{\perp}$=1.8-3 for doped with Se and Bi (Tab. 2). Anisotropy of Seebeck coefficient in these directions is smaller, the anisotropy factors were $\alpha_{\parallel}/\alpha_{\perp}$=0.8-0.9 (Tab.1,2). The temperature dependencies of electroconductivity and Seebeck coefficient in directions parallel and perpendicular of basal planes of the single crystals of Sb_2Te_3 doped with tin (Fig.3) in range 100-300 K were studied.

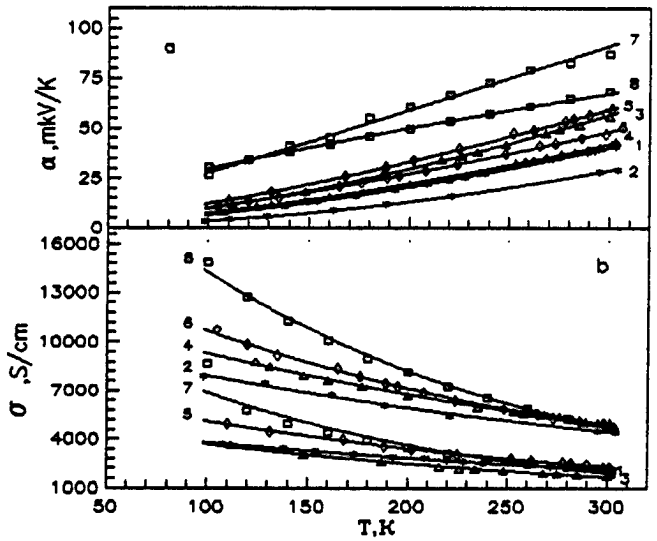


Fig.3. Temperature dependences of Seebeck coefficient (a) and electroconductivity (b) Sb_2Te_3 single crystals (7,8), doped with 0.3 (5,6); 0.38 (3,4); 0.74 (1,2) wt % Sn in direction parallel(2,4,6,8) and perpendicular(1,3,5,7) of basal planes

Calculations of the temperature dependencies of the electroconductivity of the single crystals in direction parallel to basal planes showed that $\sigma \sim T^{-1.5}$ for Sb_2Te_3. In this case one may assume the acoustic scattering mechanism and parabolic band structure, but for Sb_2Te_3 single crystals doped with Sn $\sigma \sim T^{-(1-0.7)}$ that is electroconductivity more feebly depend on temperature (Fig.3). This may be attributed to complex band structure which consist of two under bands with heavy and light holes [3].

Conclusion

The single crystals of Sb_2Te_3 doped with Sn up to 1 mass.%, Se and Bi up to 7 mass.% were grown by Czochralski technique with melt supply. The effective distribution coefficients (k) of Sn k=0.8 and Se k=1.2 (doping Sb_2Te_3) and k=0.64 (doping Bi_2Se_3) were determined in Sb_2Te_3. With increasing Sn content the Seebeck coefficient is lowered. The Sn atoms act as accepters and one atom of Sn gave 1.3 holes. Doped with Se and Bi lead to decrease of electrical and thermal conductivities and carrier concentrations, because decrease deviation from stoichiometric composition of Sb_2Te_3.

For the investigated crystals the factors of the anisotropy of electro- and thermoconductivities were about 2-4, and of the Seebeck coefficient were 0.8-0.9 in the directions parallel and perpendicular to the cleavage planes.

References

[1] L.D.Ivanova, Yu.V.Granatkina, "Transport properties of Sb_2Te_3-Bi_2Te_3 single crystals", Transport in verbindungshalbleitern, MLU, Halle (1990) 91.

[2] N.Ch.Abrikosov, L.D.Ivanova, N.V.Polikarpova, "Thermoelectric properties of the $Sb_{1.5}Bi_{0.5}Te_3$-Bi_2Se_3 solid solutions single crystals doped with Pb", Zh. Neorgan. Materialy, 9 (1987) 1453.

[3] B.Ronnlund, O.Beckman, H.Levy,"Doping properties of Sb_2Te_3 indicating a two valence band model", Phis.Chem.Sol. 8 (1965) 1281.

Composition	Dir.	α (mkV/K)	σ (S/cm)	κ 10^3 (W/cmK)	κ_l 10^3 (W/cmK)	μ (cm^2/Vs)	R10^{-7} (m^3/c)	$p_H 10^{-20}$ (at/cm^3)	$\alpha_\parallel/\alpha_\perp$	$\sigma_\parallel/\sigma_\perp$	$\kappa_\parallel/\kappa_\perp$
Sb_2Te_3,	∥	88	4885	47.6	19.0	418	0.925	0.7	0.8	2.7	2.8
dop.Te	⊥	110	1823	17.0	6.9	156	1.05				
Sb_2Te_3	∥	73	4450	47.0	19.8	347	0.77	0.8	0.8	1.9	1.8
	⊥	90	2340	26.2	12.5	183	0.75				
$Sb_{1.984}Sn_{0.016}Te_3$	∥	51	4926	46.2	14.1	147	0.301	2.1	0.8	2.1	2.3
	⊥	64	2342	20.2	5.5	70	0.306				
$Sb_{1.98}Sn_{0.02}Te_3$	∥	44	5120	44.0	9.9	133	0.269	2.4	0.8	2.8	2.3
	⊥	54	1830	19.5	7.6	48	0.262				
$Sb_{1.981}Sn_{0..019}Te_3$	∥	37	4425	45.5	15.2	72	0.162	3.9	0.9	2.0	2.2
	⊥	42	2260	20.8	5.6	36	0.167				

Table 1: Thermoelectric properties of Sb2Te3 single crystals, doped with Sn, in directions parallel and perpendicular of basal planes at room temperature

Composition\ N cr. / Properties \	1	2	3	4	5	6	7	8	9	10	11
Bi_2Te_3, mol.%	-	-	0.5	1.0	1.5	10.0	-	-	-	-	-
Sb_2Se_3, mol.%	-	-	-	-	-	-	1.9	3.9	11.6	-	-
Bi_2Se_3, mol.%	-	-	-	-	-	-	-	-	-	3.7	7.4
Bi, mass.%	-	-	0.3	0.66	1.0	6.5	-	-	-	2.7	6.6
Se, mass.%	-	-	-	-	-	-	0.74	1,5	4.5	1.4	2.8
Excess Te, mas.%	1.5	-	0.5	1.5	1.5	1.5	0.5	0.5	0.5	1.5	1.5
α, mkV/K	88	73	82	86.5	88.5	118	85	83.5	70	93	116
σ, S/cm	4885	4450	4900	4570	4350	3303	4300	3870	2100	3100	2000
κ 10^3, W/cmK	47.6	47.0	44.5	44.3	38.6	25.8	44.1	40	26	29.2	24
κ_l 10^3, W/cmK	19.0	19.8	15.3	17.3	13.1	7.7	18.6	17	13	11.2	13
p 10^{20}, 1/cm^3	0.7	0.8	0.9	0.6	0.7	0.5	0.5	0.7	0.4	0.6	0.3
m_p 10^4, cm^2/Vs	418	347	362	468	394	402	498	327	375	340	403
m */m_o	0.75	0.67	0.82	0.67	0.75	0.83	0.58	0.71	0.40	0.72	0.58
$\alpha_\parallel$, mkV/K	88	7	82	86.5	118	88.5	85	83.5	70	93	116
$\alpha_\perp$N, mkV/K	110	90	97	105	135	108	102	95	84	116	137
$\alpha_\parallel/\alpha_\perp$	0.8	0.81	0.85	0.82	0.87	0.82	0.83	0.88	0.83	0.80	0.85
σ, S/cm	4885	4450	4900	4570	3303	4350	4300	3870	2100	3100	2000
σ, S/cm	1823	2340	1170	1645	-	-	1740	1155	-	-	700
$\sigma_\parallel/\sigma_\perp$ s /s	2.7	1.9	4.21	2.8	-	-	2.5	13.4	-	-	2.9
κ 10 , W/cmK	47.6	47.0	44.5	44.3	38.6	25.8	44.1	40.0	26.0	29.2	24.0
κ 10 , W/cmK	17.0	26.2	18.3	15.8	14.2	-	15.4	-	-	13.5	8.0
$\kappa_\parallel/\kappa_\perp$	2.8	1.8	2.4	2.8	2.7	-	2.9	-	-	2.2	3.0

Table 2: Electrophysical properties and anisotropy of Seebeck coefficient, electro- and thermoconductivities in directions parallel and perpendicular of basal planes of Sb_2Te_3 single crystals doped with Bi_2Te_3, Sb_2Se_3, Bi_2Se_3 at room temperature

Optimization of hot-pressed n-type SbI_3-doped $Bi_2Te_{2.85}Se_{0.15}$ compounds

J. H. Seo,* M. C. Ju,* K. Park,** J. H. Kim***, C. H. Lee*
*Dept. of Metallurgical Engineering, Inha University, Inchon 402-751, Korea
**Dept. of Materials Eng., Chung-ju National University, Chungbuk 380-702, Korea
***Advanced Manufacturing Processing Division, Korea Academy of Industrial Technology, Siheung, Kyunggi-do 429-450, Korea

Abstract

The n-type SbI_3-doped $Bi_2Te_{2.85}Se_{0.15}$ thermoelectric compounds were fabricated by the hot pressing in the temperature range of 380 to 420 ℃ under 100, 150 and 200 MPa in Ar. The transmission electron microscopy, and X-ray diffraction were used to investigate the detailed microstructure. We fabricated relatively dense compounds. The relative density of the compounds fabricated at 420 ℃ was 99.6 %. The grains of the compounds were preferentially oriented along the perpendicular to the pressing direction through the hot pressing and also the degree of preferred orientation increased with the hot pressing temperature and pressure. In addition, with increasing the hot pressing temperature, the figure of merit was increased due to the increase in density and preferred orientation. The highest figure of merit (2.35×10^{-3}/K)was obtained at 420 ℃ under 200MPa.

Introduction

Bismuth telluride and alloys of Bi_2Te_3 with Bi_2Se_3 are the materials most often used in thermoelectric devices[1][2]. These materials can be made not only single crystals but also cold or hot pressing powder compacts. In general, sintering technique is not effective because the figure of merit of sintered compounds is lower than that of single crystals. However, this thecnique able to reduce the thermal conductivity due to the scattering of phonons caused by grain refinement and improve the figure of merit[3][4]. . In this work, we optimized fabrication condition of hot-pressed n-type SbI_3-doped $Bi_2Te_{2.85}Se_{0.15}$ compounds and then investigated the microstructure and thermoelectric properties of the compounds.

Experimental procedure

To fabricate the n-type $Bi_2Te_{2.85}Se_{0.15}$ compounds doped with 0.1 wt% SbI_3, the starting powders with >99.99 % purity were mixed. The powders mixture was placed into SiO_2 and then, the tube was evacuated below 10^{-4} torr and sealed. The melt in the tube was stirred at 700 ℃ for 6 hours using a rocking furnace to make a homogeneous melt without segregation. The solidified ingot was crushed and sieved to prepare powders with 45-74 ㎛ size. The resulting powders were reduced in hydrogen atmosphere at 360 ℃ for 4 hours. The powders were compacted by the hot pressing in the temperature range 380 to 420 ℃ at steps of 20 ℃ under 100, 150, and 200 MPa in Ar to produce the billets with 30 mm diameter and 6 mm length. The density of the hot-pressed compounds was measured by pycnometer (Micrometric Co.). The preferred orientation of grains was investigated by X-ray diffraction (XRD). Transmission electron microscopy (TEM) was used to examine the microstructure of the compounds. The thermoelectric properties were measured at room temperature along the direction perpendicular to the pressing direction. The specimens with dimensions of 2×2×15 mm and of 4×4×4 mm were cut out of the compounds for the measurements of Seebeck coefficient α and thermal conductivity κ and of the relative

0-7803-4057-4/97 $10.00 ©1997 IEEE

resistivity ρ, respectively. To measure the Seebeck coefficient α, heat was applied to the specimen which was placed between the two Cu discs. The relative resistivity ρ was measured by the four-probe technique. The repeat measurement was made rapidly with a duration smaller than one second to prevent errors due to the Peltier effect. The thermal conductivity κ was measured by the static comparative method using a transparent SiO_2 (κ =1.36 W/Km at room temperature) as a standard sample in 5×10^{-5} torr.

Results and discussion

Microstructure

It was found that the n-type 0.1 wt% SbI_3-doped $Bi_2Te_{2.85}Se_{0.15}$ compounds were relatively dense. The bonding between the powders became strong with increasing the pressing temperature and pressure, resulting in an increase in the relative density. Table 1 shows the relative densities as a function of pressing temperature and pressure.

Table 1. Variation of relative density the n-type $Bi_2Te_{2.85}Se_{0.15}$ compounds hot pressed at various pressing temperature and pressure.

Pressing Temperaure(℃) under 200 MPa	*Relative Density(%)*
380	98.1
400	98.5
420	99.2

Pressing Pressure(MPa) at 420℃	*RelativeDensity(%)*
100	97.9
150	98.5
200	99.2

Fig. 1 shows a TEM bright field image from the perpendicular section to the hot pressing direction for the compounds hot pressed at 420 ℃ under 200 MPa. Fig. 2(a) and (b) show the XRD patterns obtained from the perpendicular and parallel sections, respectively, for the compounds hot pressed at 420 ℃. The intensity of (0 0 6), (0 0 15), and (0 0 18) planes, which are perpendicular to the c-axis, is only observed at the perpendicular section. This indicates that the grains are preferentially oriented along the perpendicular to the pressing direction through the hot pressing. It has previously been reported that the preferred orientation of grains is observed in unidirectionally solidified materials, in which the growing direction is perpendicular to the c-axis [5].

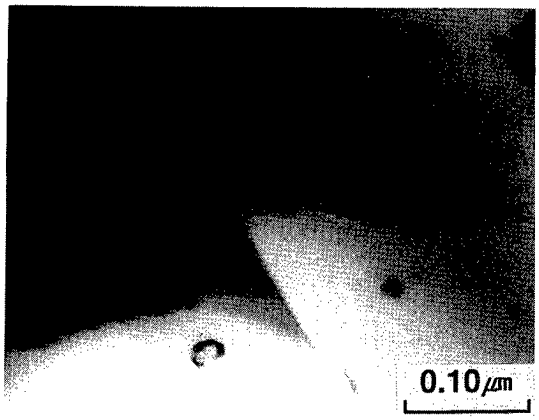


Fig. 1. TEM bright field image from the perpendicular section to the hot pressing direction for the compounds hot pressed at 420 ℃.

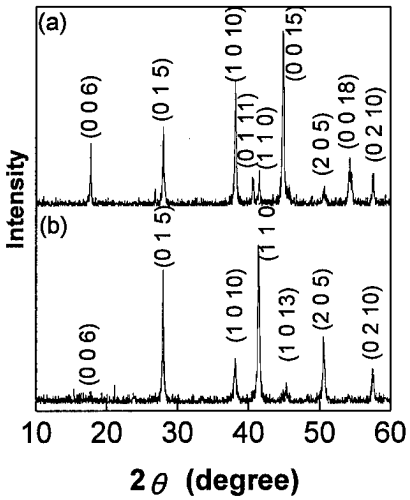


Fig. 2. XRD patterns obtained from the (a) perpendicular and (b) parallel sections to the hot pressing direction for the compounds hot pressed at 420 ℃.

Thermoelectric properties

Fig. 3 shows the carrier concentration n_c and carrier mobility μ as a function of pressing temperature. With increasing the pressing temperature, the carrier concentration is slightly decreased, whereas the mobility is increased.

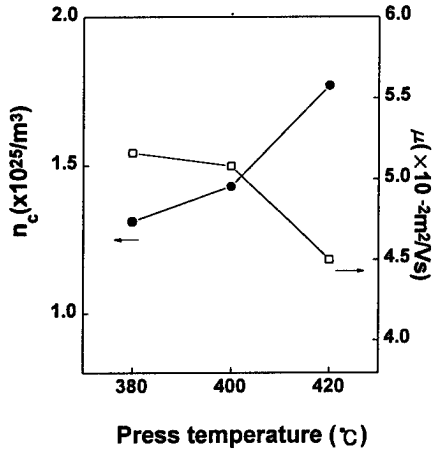


Fig. 3. Carrier concentration n_c and mobility μ as a function of the hot pressing temperature.

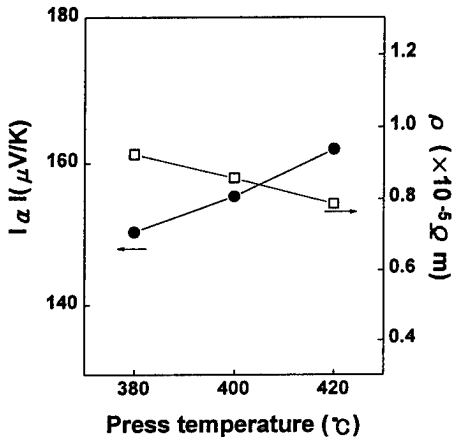


Fig. 4. Variation of Seebeck coefficient α and electriccal resistivity ρ with hot pressing temperature.

The increase in carrier mobility results from the porosity decrease. The variation of Seebeck coefficient α and relative resistivity ρ with the pressing temperature is shown in Fig. 4. The relationship between the α and n_c can be expressed as follows: $\alpha \approx r - \ln n_c$, where r is the scattering factor [6]. As the pressing temperature is increased, the Seebeck coefficient is slightly increased because of the decrease in carrier concentration. Also, the relative resistivity is slightly decreased with increasing the pressing temperature. The relative resistivity can be expressed as the following relationship: $\rho = 1/n_c e \mu$. Therefore, it seems that with increasing the pressing temperature, the slight decrease in relative resistivity would result from an increase in mobility and a slight decrease in carrier concentration. Fig. 5 shows the thermal conductivity κ of the compounds hot pressed at various temperatures. It is increased with the pressing temperature probably because of the density increase. The figure of merit Z was calculated using the following equation: $Z = \alpha^2 / \rho \kappa$. Fig. 6 shows the figure of merit Z of the compounds hot pressed at various temperatures. The figure of merit was increased with the pressing temperature because of a slight decrease in resistivity, an increase in Seebeck coefficient, and a slight increase in thermal conductivity. The compounds hot pressed at 420 ℃ shows the highest figure of merit ($Z = 2.35 \times 10^{-3}$/K).

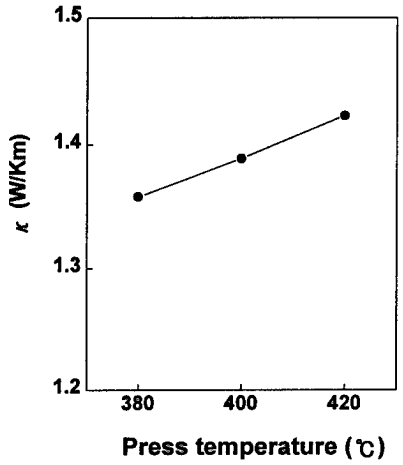


Fig. 5. Thermal conductivity as a function of the hot pressing temperature.

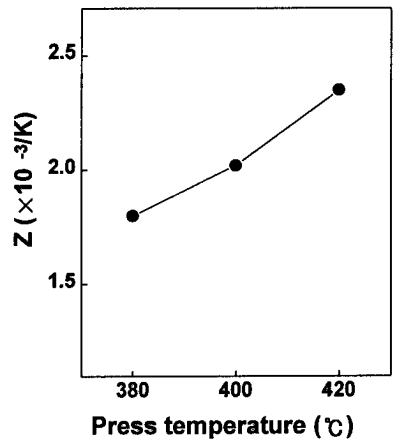


Fig. 6 Figure of merit Z of the compounds hot pressed at various temperatures.

Table 2. Thermoelectric properties of then-type $Bi_2Te_{2.85}Se_{0.15}$ compounds hot pressed at various pressing pressures.

	Hot pressing pressures(MPa) at 420 ℃		
	100	150	200
α ($\mu V/K$)	-131.6	-139.5	-161.9
ρ ($\times 10^{-5}\Omega m$)	0.741	0.753	0.785
κ (W/Km)	1.201	1.212	1.423
Z ($\times 10^{-3}/K$)	1.95	2.13	2.35

Table 2 shows thermoelectric properties as a function of pressing pressures under 420 ℃. With increasing the pressing pressures, the figure of merit is increased. It seems that with increasing the pressing pressures, the increase in figure of merit would result from an increase in the relative densities

Conclusion

1. The density of hot-pressed n-type 0.1 wt% SbI_3-doped $Bi_2Te_{2.85}Se_{0.15}$ compounds was increased with increasing the pressing temperature and pressures.
2. The grains of the compounds were preferentially oriented through the hot pressing and also the degree of preferred orientation increased with the hot pressing temperature.
3. It was found that the figure of merit increased with increasing the pressing temperature and pressures. The figure of merit of the compounds hot pressed at 420 ℃ under 200 MPa was 2.35×10^{-3}/K

Acknowledgement

We would like to thank the support from the University Basic Research Support Fund (1998) of Korea Ministry of Information and Communication.

References

[1] C. H. L. Goodman, *Mater. Res. Bull., 20* (1985) 231.

[2] A. Sher, M. Shiloh, D. Ilzycer and D. Eger, *J. Electronic Mater., 12* (1983) 247.

[3] D. M. ROWE, *Applied Energy* **24**, (1986) 139

[4] H. J. GOLDSMID and A. PENN, *Phys. Lett.* **27A**, (1986) 523.

[5] J. P. Fleurial, L. Gailliard, R. Triboulet, H. Scherrer and S. Scherrer, *J. Phys. Chem. Solids, 49* (1988) 1237.

[6] K. Uemura and I. Nishida, *Thermoelectric Semiconductors and Their Application,* Nikkan-Kogyo Shinbun Press, Tokyo, Japan, 1988.

Influence of growth conditions on structure, composition homogeneity and mechanical properties of thermoelectric crystals for coolers

V.T.Bublik, V.V.Karataev, V.B. Osvenski, T.B.Sagalova, V.B.Ufimtsev and A.M.Frolov

Institute of Chemical Problems for Microelectronics, Moscow Institute of Steel and Alloys
Moscow, Russia

The object of this work is to produce by economical method (vertical zone melting) the polycrystalline textured ingots of p- and n-type thermoelectric materials (TEM) based on antimony and bismuth tellurides and selenides solid solutions with high performance parameters (thermoelectric figure-of-merit Z) and diameter not less than 20 mm.

Following problems were to be solved:

a) the formation of favorable crystallographic orientation with minimum scatter which allows to make use of properties anisotropy to achieve maximum value of Z;

b) preparation of solid solutions with reasonably homogeneous composition (along and across the ingot) and reproducible alloying level;

c) elucidation of causes of mechanical stresses, that are responsible for cracking, to produce material with adequate mechanical properties.

The texture, phase composition, macro- and microscale composition inhomogeneity of solid solution have been studied with X-ray diffraction methods by evaluation of lattice parameter and smearing (broadening) of diffraction maxima. In addition, microheterogeneity was assessed by microhardness measurements coupled with local elemental microanalysis (local X-ray microprobe).

The cracking pattern was correlated with microstructure features (using optical metallography and X-ray topography).

The slip lines formed by indenter prints during microhardness measurements were used for evaluation of cross-sectional disorder of adjacent grains, whose cleavage planes are parallel to ingot axis.

The growth parameters suppressing dendrite crystallization have been determined. As a rule, it is impossible to control the orientation of individual dendrites during dendrite growth and, hence, the structure with randomly oriented grains is formed. Moreover, such structure quite often exhibit substantial degree of chemical inhomogeneity that ultimately can go so far as segregation of solid solution. This phenomenon reveals itself in smearing (Fig. 1a) or even in occurrence of two diffraction maxima (Fig. 1b)

The high axial thermal gradient (≥ 100-120 °C/cm) and flat crystallization front have led to suppression of dendrite crystallization and formation of macrocrystalline structure with beneficial well-defined texture (110) + (100), with C-axis (that is normal to (0001) cleavage plane) be perpendicular to the ingot axis. Just at 10-20 mm distance

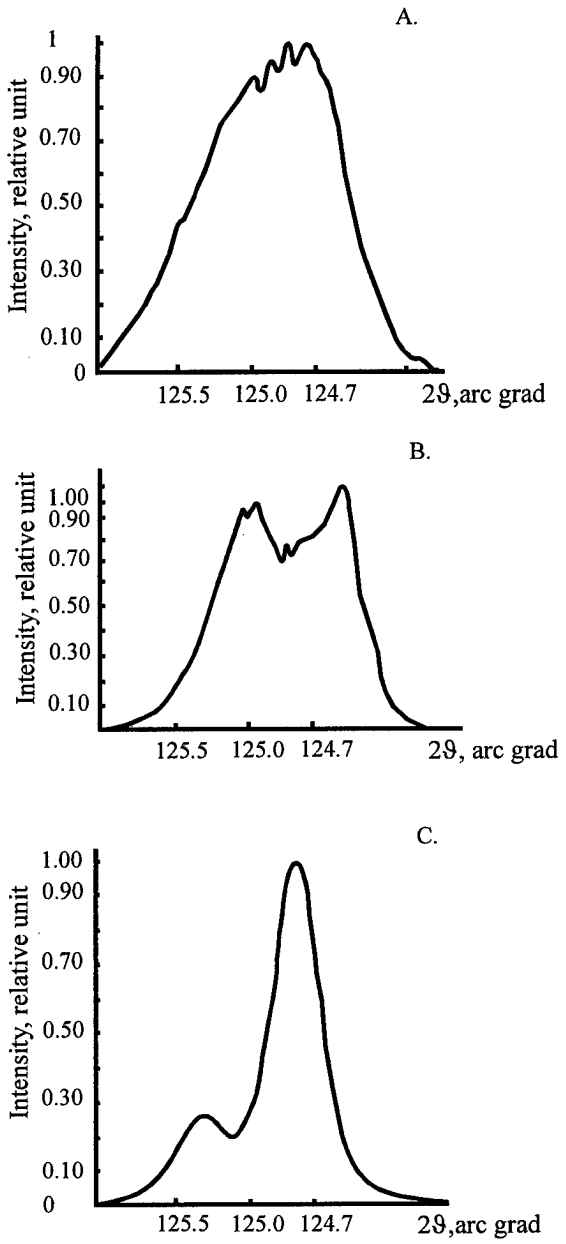


Fig.1 The fragments of diffraction patterns ((220) reflection, n-type ingot) that are specific for crystallization of dendrite type – the absence of resolved doublet (a) and two maxima due to stratification into two solid solutions (b); perfect coarse-grained structure with minimal inhomoheneity – the doublet is resolved, diffraction lines are narrow (c).

from ingot front face the disordered orientation of nucleation zone changes to well-defined structure. The figure 2 illustrates

from ingot front face the disordered orientation of nucleation zone changes to well-defined structure. The figure 2 illustrates the variation of beneficial structure fraction along the ingot length. It is apparent that texture changes little across the ingot.

Fig.1 The fragments of diffraction patterns ((220) reflection, n-type ingot) that are specific for crystallization of dendrite type – the absence of resolved doublet (a) and two maxima due to stratification into two solid solutions (b); perfect coarse-grained structure with minimal inhomoheneity – the doublet is resolved, diffraction lines are narrow (c).

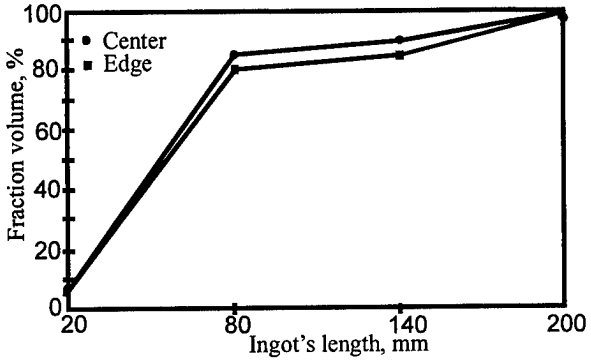


Fig.2: The variation of volume fraction of grains with beneficial texture along n-type ingot.

The evaluation of texture scatter indicated that scatter up to 5 ang deg has negligible effect on Z value [1].

Fig.3 shows the variation of mean composition along ingot length.

This value characterizes the macroscale inhomogeneity and was evaluated using the change of ***a*** lattice dimension along the axis and across the ingot . With exception of rather narrow zones at the beginning and at the end of ingot length the concentration of solid solution remains practically constant and corresponds to n-type $Bi_2Te_{2,7}Se_{0,3}$ and p-type - $Sb_{1,5}Bi_{0,5}Te_3$ compositions.

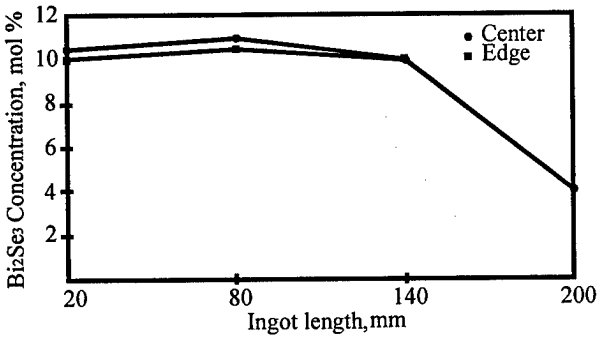


Fig.3:The variation of average composition along and across ingot.

Microheterogeneity that was assessed from diffraction reflections broadening values also substantially decreased (Fig.2c): doublet Kα1-Kα2 was well resolved, the diffraction reflections became narrow.

The important factor for achievement of high thermoelectric properties in n-type ingots is uniform and reproducible doping by introduction of chlorine in the form of nonhygroscopic Bi-Se-Cl compound.

One of important technical problems in preparation of ingots with diameter larger than 20 mm is thermal stress which is responsible for cracking and breakdown of thermoelectric material not only at subsequent machining step during thermoelement fabrication, but not rarely even in the process of ingot cooling . The distinctive property of hexagonal crystal lattice of Bi_2Te_3 type compounds is that the weak Van der Waals forces act between cleavage planes of (0001) type. This results in easy spalling and destruction of crystals in this axial direction. The ingots with very high thermoelectric properties, which were formed under large thermal gradients, are especially susceptible to this cracking tendency. This is explained by the fact that in such crystals the cleavage planes, where material destruction occurs, are oriented along the ingot axis.

The crack formation takes place under the action of tangential thermal stretching stresses which in this case are directed perpendicularly to cleavage planes and reach maximum values at the ingot lateral face. This results in predominance of radial cracks, which run parallel to growth axis and are located mostly at peripheral portions. It must be emphasized that even in the case of crystal growth with flat crystallization front the orthographic pattern is characterized by the presence of radial thermal stresses reaching maximum values in central portion of ingot due to curved axial temperature profile that exists in actual growth conditions. Therefore at some distance from lateral face the formation of circumferential cracks under the action of stretching radial stresses is possible.

The cracks observed in the ingots can be classified as follows:

- intercrystalline type (at grain boundaries);
- transcrystalline type that go inside grain body along cleavage planes;

There is quite definite correlation between the ingot texture features and crack type:

- in original fine-grained and nontextured zone the intercrystalline cracks were mostly observed, very likely at the boundaries of poorly oriented grains. As a rule, these cracks are initiated at ingot periphery;
- in the zone with well-defined double [(11.0) + (30.0)] axial texture, with basal plane (00.1) being parallel to growth axis, the transcrystalline cracks are observed, which at cross-sectional cuts have the form of smooth lines and are related to breakdown at cleavage planes. The cracks are formed both at depth and periphery .

The causes of material destruction (cracks formation) can be as follows:

1. Thermal stresses that were caused by non-linear axial temperature gradient even in the case of flat crystallization front.
2. Compositional microheterogeneity.
3. Anisotropy of thermal expansion ratio in grains with different orientation.

Let us analyze the role of each factor.

The predominance of transcrystalline cracks in the depth of grown ingots that are associated with the breakdown at cleavage planes leads one to conclude that one of principal

causes for cracking the crystal with larger diameter is the formation of thermal stresses related to heat conditions of growth. This conclusion is supported by the fact that in ingots with 20-25 cm diameter which were grown at high thermal gradients (120-150°C/cm) the cracks at cross-sections are often observed in quite substantial amount (3-5 per cross-section). In crystals that were grown with lower axial gradients (not more than 80-100 °C/cm) as in the case of crystals with small diameter the cracking is practically absent. At the same time we must be aware that not only the magnitude of axial gradient but also the curvature of temperature profile is important [2].

According to tentative estimates [3] the spontaneous cracking of crystal in the process of growth or during subsequent machining step, including cutting, takes place at $\sigma/E \approx 10^{-3}$ (where σ is the value of thermoelastic stress, E - elasticity module). Taking into account the elastic constants of bismuth tellurides, reported in [4], the rough estimate of thermoelastic stresses in ingots grown at high temperature gradients is about several kg/mm^2. It must be noted that destruction of TEM crystals takes place at lower values of effective temperature gradients in comparison, for example, with semi-conducting compounds.

Consequently, the special control of thermal conditions of ingot growth to decrease thermoelastic stress magnitude is one of main factors in prevention of cracks formation when producing TEM ingots with larger diameters.

Another important factor is the microheterogeneity of solid solution composition. As was noted above, the microscale inhomogeneity gives rise to broadening of diffraction reflections maxima. We also established that chemical non-uniformity of such kind has quite clearly revealed itself in microhardness measurements and is confirmed by elemental quantitative analysis of main components in solid solution. Fig. 4 shows the variation of microhardness over central zone diameter of n-type ingot while corresponding variations of bismuth, tellurium and selenium content at the same points are shown in Fig.5 a,b,c.

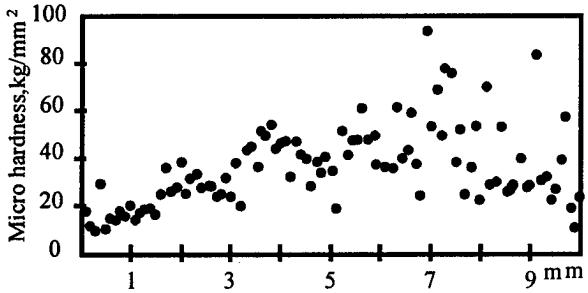


Fig.4:The variation of microhardness in central zone of n-type ingot.

Thus, the presented data demonstrate that even relatively small deviations in content of main solid solutions components (within ± 1 atomic percent) result in significant changes of microhardness (as much as several times).

The cause of microheterogeneity can be the occurence of concentration-dependent supercooling and as a result the distortion of flat crystallization front. In this case the projections at stepwise crystallization front, extending parallel with cleavage plane, are the cause for development of longitudinal stratified inhomogeneity [4]. The pre-condition for concentration-dependent supercooled state is the growth of ingot with lower thermal gradients and sufficiently high growth rates. If the Bi_2Se_3 segregation ratio K > 1, the projections have increased amount of Bi_2Se_3 [4].

According to [4] the critical value of $(G/V)_{cryt}$ ratio for solid solution is equal to $(2\text{-}2.5)\cdot 10^5$ °C/cm (G is axial

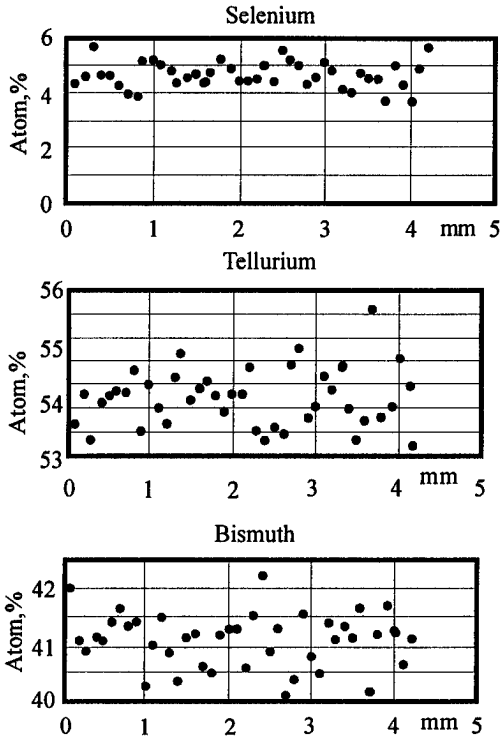


Fig.5:The variation of elemental composition in central zone of the same ingot.

temperature gradient at crystallization front, V is growth rate). The crystals in this work were grown at $G/V \approx (2\text{-}4)\cdot 10^6$ °C/cm. Thus it is impossible to be sure that observed microhererogeneity is associated with distortion of flat crystallization front.

Nevertheless, the assessment of relative microdeformation value ,$\Delta a/a$ (i.e. the change of lattice order in neighbouring microspaces), using (110) and (220) diffraction maxima broadening values gives the value of 10^{-3} order for some n-type crystals and that is quite enough to be the cause of local breakdown (cracking) of material. Fig.6 shows the variation

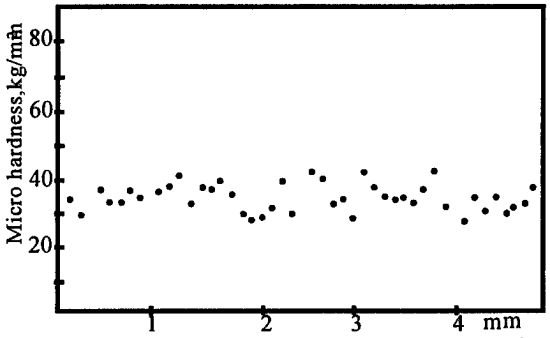


Fig.6:The variation of microhardness in central zone of p-type ingots.

of microhardness in central zone of p-type ingot where any significant deviations from average microhardness value are

practically absent. In this case the development of compositional microheterogeneity is unlikely since the segragation ratio in Sb_2Te_3-Bi_2Se_3 system is near to unity. Probably, this can be one among other causes of crystal lesser susceptibility to cracking.

The assessment of anisotropy role in thermal expansion ratios of adjacent grains in stress development at grain boundaries as a function of adjacent grains orientation and boundary position, demonstrated that due to well defined structure and coarse grain size of ingots the proportion of unfavorably oriented boundaries is small and transcrystalline destruction from thermal expansion anisotropy does not contribute to ingot cracking in great extent.

The optimization of growth conditions results in preparation of sufficiently homogenous ingots with quite acceptable mechanical properties.

Thus, using more efficient process we have solved , for the most part, the technical problems in preparation of TEM ingots with diameter larger than 20 mm:

- with high thermoelectric parameters ($Z \geq 3 \cdot 10^{-3}$ k^{-1});
- with sufficiently uniform solid solution composition;
- with uniform alloying level;
- with beneficial texture to make use of properties anisotropy and provide maximum quality which is peculiar to single crystal;
- with adequate mechanical properties.

References

[1] Bublik V.T. et al , Structure and properties of large diameter zone-melt grown thermoelectric crystals,: Proceedings of the XIY International Conference on thermoelectrics, 1995, pp.33-37

[2] Milvidsky M.G., Osvenski I.B., Structure defects in semiconducting single crystals, Moscow, Metallurgy, 1984

[3] Indenbom V.L., Osvenski I.B., In: Crystal growth, Moscow, Nauka, 1980, vol.13, pp. 240-251

[4] Holtzman B.M., Kudinov V.A., Smirnov I.A., Bi_2Te_3-based semiconducting thermoelectric materials , Moscow, Nauka, 1972, 320 p

PECULIARITIES OF PRODUCTION N-$Bi_2(Te,Se)_3$ AND P-$(Bi,Sb)_2Te_3$ IN CONDITIONS OF STRUCTURAL SUPERPLASTICITY

O.B.Sokolov, S.Ya.Skipidarov, N.I.Duvankov, E.V.Zaitsev

Nord Co., Moscow, RUSSIA

INTRODUCTION

Superplasticity is important, primarily, due to the fact that intensive plastic deformations can be created under low loads, with the formation of material with a homogeneous structure in cross-section. The establishment of conditions providing for the apparent superplasticity acquires special importance for the realization of plastic deformation of thermoelectric materials [1]. For this purpose the authors have investigated the process of hot extrusion of N-$Bi_2(Te,Se)_3$ and P-$(Bi,Sb)_2Te_3$ metal-ceramic billets through conical matrix both in isobaric and isothermic conditions.

ISOBARIC CONDITIONS

In isobaric conditions the temperature dependences of strain rate have been investigated. Strain rate $\dot{\varepsilon}$ (its mean value) was calculated from the values of the degree strain ε and the time of the material residence in the strain concentration zone. In $\lg\dot{\varepsilon}$-1/T (Fig.1) coordinates, where T is the temperature of extrusion, experimental points lie on straight lines correlating with the Arrhenius's equation $\dot{\varepsilon} \sim \exp(-Q/RT)$, where Q is an apparent energy of activation of the plastic flow, R is the Rydberg constant.

Calculations show that in the zone of minimal rates the apparent energy of activation is maximal and amounts to 1.45 eV. With the medium rates the Q value dramatically decreases to 0.79 eV that indicates the changing of the strain mechanizm.

ISOTHERMIC CONDITIONS

In isothermic conditions the pressure dependences of the strain rate have been investigated. To the authors' opinion over 90% of pressure can be attributed to the

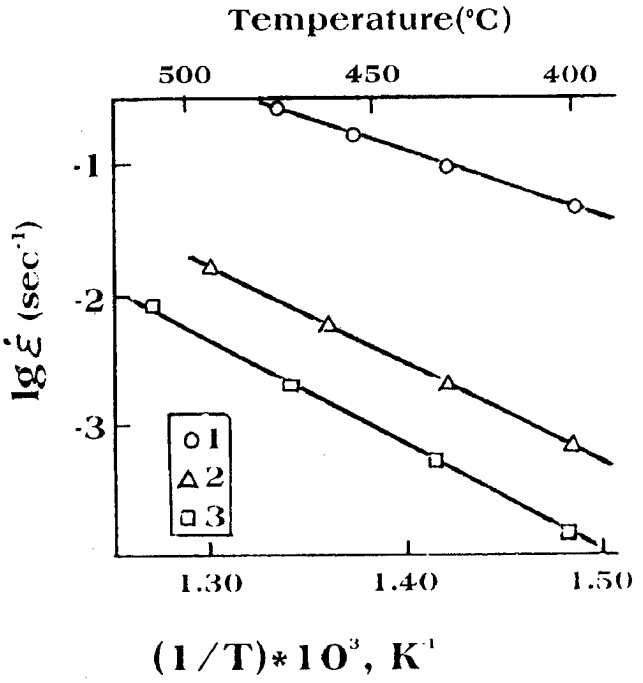


Fig.1. Temperature dependence of N-$Bi_2(Te,Se)_3$ plastic deformation rate under constant pressure of extrusion (kg/mm^2): 1- 50; 2- 80; 3- 100; stretching coefficient k=280.

resistance to the strain of material (S). Some straight-line zones of the obtained curves in logarithmic coordinates (Fig.2) are described by the equation $S = N\cdot\dot{\varepsilon}^m$, where N is a constant, *m* is a strain-rate sensitivity index. The changing incline of straight lines indicates that with the growth of the $\dot{\varepsilon}$ value the *m* value gradually decreases from $\approx$ 0.8 (for the N-type material) at rates $\leq 10^{-2}$ sec^{-1} to lower than 0.2 at maximal rates. It qaulitatively corresponds to the II and III stages of typical curves of superplasticity [2].

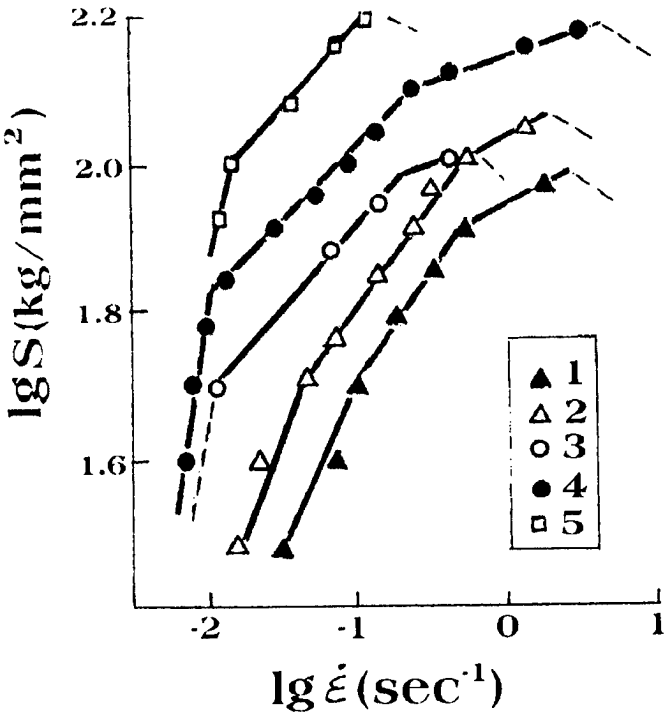


Fig.2. Pressure dependences of N-$Bi_2(Te,Se)_3$ (3, 4) and P-$(Bi,Sb)_2Te_3$ (1,2,5) plastic deformation rate at a constant temperature of extrusion: 480(1). 450(2); 440(3, 4). 400(5); k = 289 (1, 2, 4, 5); k=64 (3).

STRUCTURE

The results of the undertaken research into the structure by method of electronic microscopy (on splits) show that the particles of the original billet are characterized by a clearly demonstrated layer structure (Fig. 3a, 3d). At the initial stage of the process of plastic deformation the phenomenon of mechanical twinning is observed (Fig.3e). At the final stage of plastic deformation the structure is completely recrystallized in the P-$(Bi,Sb)_2Te_3$ material (Fig. 3b, 3c) and to a great extent in the N-$Bi_2(Te,Se)_3$ material (Fig.3f). The mean grain size amounts to approximately 2 - 3 mμ. It indicates, that superplasticity is realized through grain boundary sliding. Although grain boundary sliding (structural superplasticity) is predominant, a certain contribution of the diffusion creep and dislocation creep cannot be excluded. With high strain rates there is not enough time for the processes of recrystallization in the strain concentration zone, and the strain (extrusion) changes from superplasticity to conventional plasticity. In this case the samples demonstrate such a strain structure in which grains and intercrystallite impurities are stretched in the direction of extrusion.

DIFFUSION AND CHARACTERISTICS

To identify the nature of diffusion processes going in conditions of structural superplasticity the original cylinder-shaped billet has a thin interphase boundary. It was a plane stretching along the billet axis and dividing two tellurides which differed in metal composition (Fig.4). Research into diffusion by method of micro-X-ray spectrometry was effected on lateral and axial microsections which were perpendicular to the phase boundary.

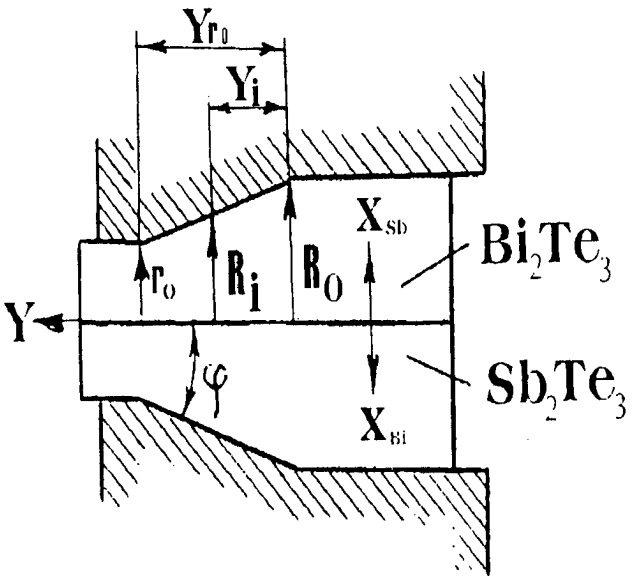


Fig.4. Design of a composite billet for the research into diffusion.

Concentration curves characterizing the distribution of Bi and Sb in pressing residue and extruded samples were taken by the MS-46 ("Cameca") X-ray installation. X-ray characteristical radiation of elements was registered for Sb on the $L_{\alpha 1}$ line and for Bi on the $M_{\alpha 1}$ line. The diameter of the electronic probe amounted to 1 mμ. By the above mentioned curves the depth of Sb penetration into Bi_2Te_3 and that of Bi penetration into Sb_2Te_3 was identified.

Calculations were made with the use of Lyubov-Fastov's equation [3] for the diffusion in plastic deformation media

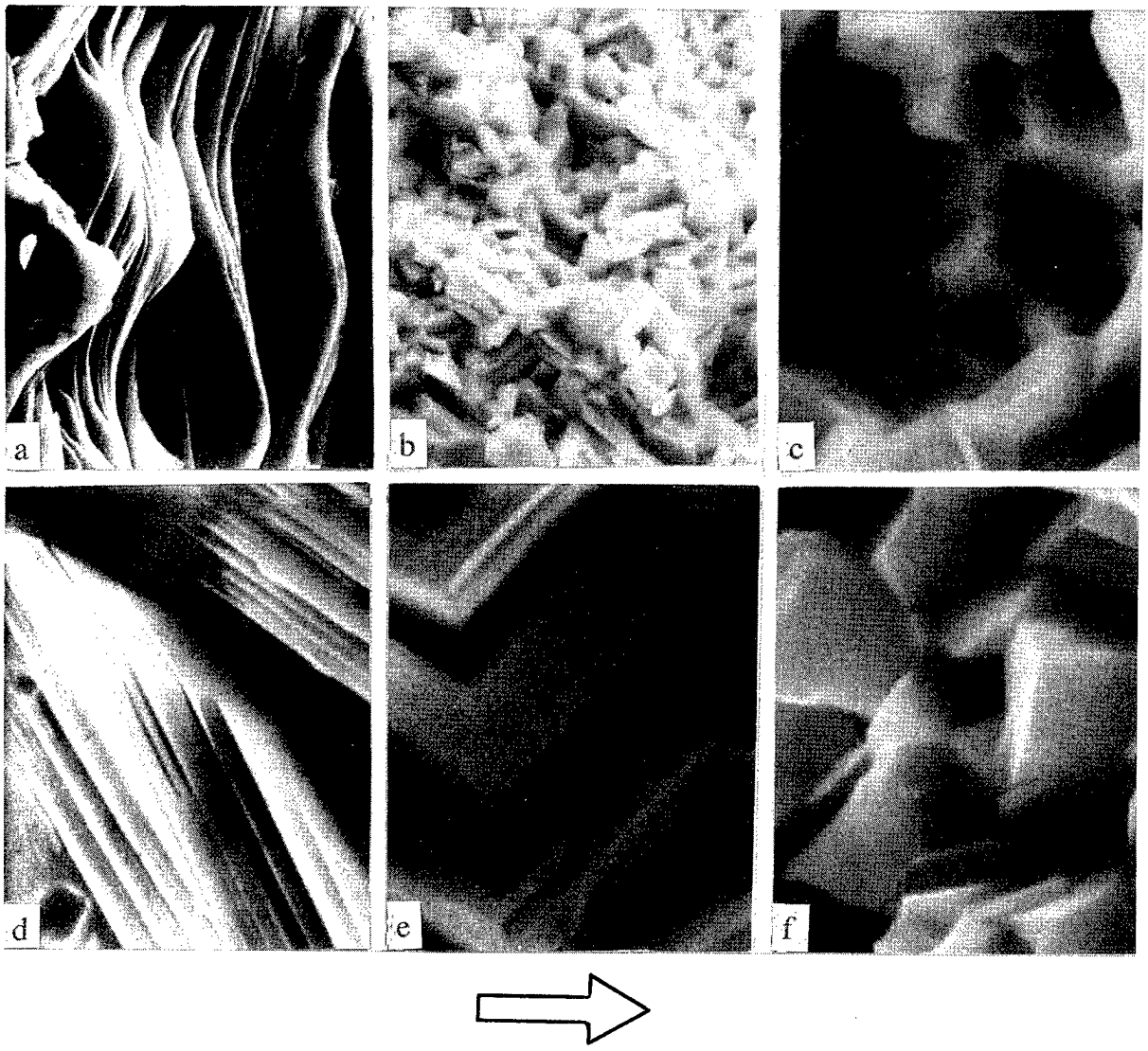


Fig.3. Changing of the microstructure with hot extrusion in conditions of structural superplasticity. P-$(Bi,Sb)_2Te_3$ structure: a - the original billet (10,000x); b - extruded rod (2 300x); c - extruded rod (10,000x). N-$Bi_2(Te,Se)_3$ structure: d- the original billet (10,000x); e - a mechanical twin on the boundary of the strain concentration zone (10,000x); f - extruded rod (10,000x). The arrow indicates the direction of extrusion.

with due account for the initial and boundary conditions which were determined by the geometry of extrusion tool (Fig.4). This equation is of the following form:

$$\frac{\partial C}{\partial \tau} = \frac{\partial^2 C}{\partial \xi^2},$$

where

$$\xi = x \cdot \frac{R_0}{R(t)}, \quad \tau = \int_0^t R_0^2 / R(t)^2 \cdot D(t) \cdot dt.$$

Here, x is an experimentally observed depth of diffusion, ξ is the depth of diffusion with due account for the plastic deformation, τ is the time of diffusion in the period of plastic deformation; C is the concentration of the diffusant; D is the diffusion coefficient.

The equation was solved by the following way. Assuming that the square average value of the displacement of the diffusant is

$$\xi^2 = 2 C_1 \tau,$$

the differentiation result is: $\xi d\xi = C_1 R_o^2 / R^2(t) \cdot D(t) \cdot dt$. The time of passing the y_i layer to the depth of $\Delta y_i = y_i - y_{i-1}$ amount to $\Delta t_i = t_i - t_{i-1}$ Having the time of passing through the Δy_i layer and y_{i-1} layer to the onset of the strain concentration zone one can identify on the basis of experimental data the time of the material residence in the Δy_i layer. The time of the process of deformation is the volume of pressing portion to flown-out material volume per second ratio:

$$t_i = \frac{R_i^3}{3 \cdot V \cdot tg\varphi \cdot r^2},$$

where V is the rate of material flow-out from the conical matrix;

$$\Delta t = \frac{(R_i - R_{i-1}) \cdot (R_i^2 + R_i \cdot R_{i-1} + R_{i-1}^2)}{3 \cdot tg\varphi \cdot r^2 \cdot V}.$$

Assuming that $R_i \approx R_{i-1}$ one can write the expression as follows:

$$\Delta t = \frac{\Delta R_i}{tg\varphi} \cdot \frac{R_i^2}{r^2 \cdot V}.$$

Assuming that $R_i / tg\varphi = y_i$, accordingly

$$\Delta R_i / tg\varphi = \Delta y_i,$$

this expression acquires the following form:

$$\Delta t = \Delta y_i \cdot \frac{R_i^2}{r^2 \cdot V} \approx dt.$$

Then

$$\xi \cdot d\xi = C_1 \cdot D_i \cdot 1/V_0 \cdot dy,$$

where V_0 is the rate of material feeding into the conical matrix. Whence the solution of the Lyubov-Fastov's equation derived with due account for the boundary and original conditions has the following form:

$$D_i = C_1 \cdot V_0 \cdot \xi_i \cdot \frac{\Delta \xi_i}{\Delta y_i},$$

where D_i is a diffusion coefficient of the chemical element in the Δy_i thickness layer of the system under consideration which is located in the conical strain concentration zone at the y_i distance from its onset; C_1 is a constant; $\xi_i = x_i R_o / R_i$ (x_i is the experimentally identified displacement of the diffusant; $2R_i$ is the diameter of the strained billet; $\Delta \xi_i = \xi_i - \xi_{i-1}$; V_o is the rate of the material feeding into the strain zone.

In experiment, on a microsection of the pressing residue in a matrix with a $\varphi = 30^\circ$ entry angle it was discovered that for the investigated elements (Bi and Sb) the $\xi_i(y_i)$ dependence is approximated by a straight line (Fig.5) with an accuracy of ±10%, i.e. $\xi_i = C_2 y_i$ and, accordingly, $\Delta \xi_i = C_2 \Delta y_i$. Then $D_i = C V_o y_i$, where $C = C_1 C_2$.

In the outset of the strain concentration zone ($y_i \geq y_{ro}$), i.e. in the extruded rod, $D_{ro} = C V_o y_{ro}$. It follows, that in the extruded rod the ε strain rate dependence of ξ_{ro} cannot occur that may be attributed to the proportional growth of the diffusion coefficient. The established proportional growth of the diffusion coefficient with the increase of the strain rate in the process of extrusion accounts for the stability of thermoelectric characteristics of extruded rods of N-$Bi_2(Te,Se)_3$ and P-$(Bi,Sb)_2Te_3$ solid solutions within a wide range of $\dot{\varepsilon}$ in conditions of structural superplasticity (Fig.6).

The practical aspect of the undertaken research is the opportunity to spur the processes of diffusion alignment of statistical microinhomogeneities [4] in the process of hot extrusion in conditions of structural superplasticity

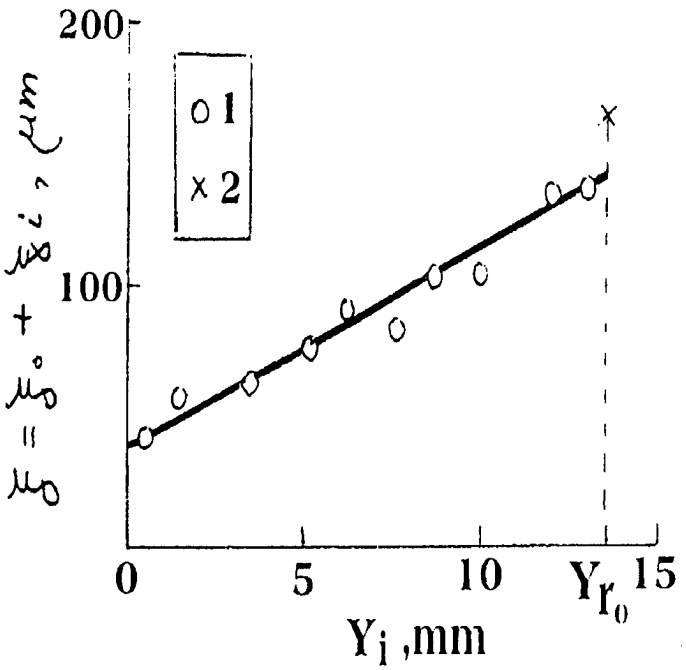


Fig.5. y_i dependence of Bi penetration into Sb_2Te_3: 1 - by the results of the analysis of the pressing residue (k = 44.5; φ = 30°) after extrusion with T = 480° C and V = 0.5 mm/sec.; 2 - data from extruded samples.

through the reduction of the angle (φ) of entry into matrix (see Fig.4). It allows to produce the rods of over 20 mm diameter from N-$Bi_2(Te,Se)_3$ and P-$(Bi,Sb)_2Te_3$ metal-ceramic billets by method of extrusion.

CONCLUSIONS

In isobaric conditions, in the zone of minimal rates of plastic deformation the apparent energy of activation of plastic deformation of the N-$Bi_2(Te,Se)_3$ material is maximal and amounts to 1.45 eV. With medium rates the value of the energy of activation dramatically decreases to 0.79 eV that proves the changing of the strain mechanizm.

For isothermic conditions it was discovered, that with the increase of the strain rate the strain-rate sensitivity index for the N-$Bi_2(Te,Se)_3$ material decreases from the value of ~ 0.8 to that of lower than 0.2 which is attained at maximal rates. It qualitatively corresponds to the II and III stages of typical curves of superplasticity.

The results of the research into the structure by method of electronic microscopy show that the grain boundary sliding is the main micromechanizm of superplasticity of low-temperature thermoelectric materials.

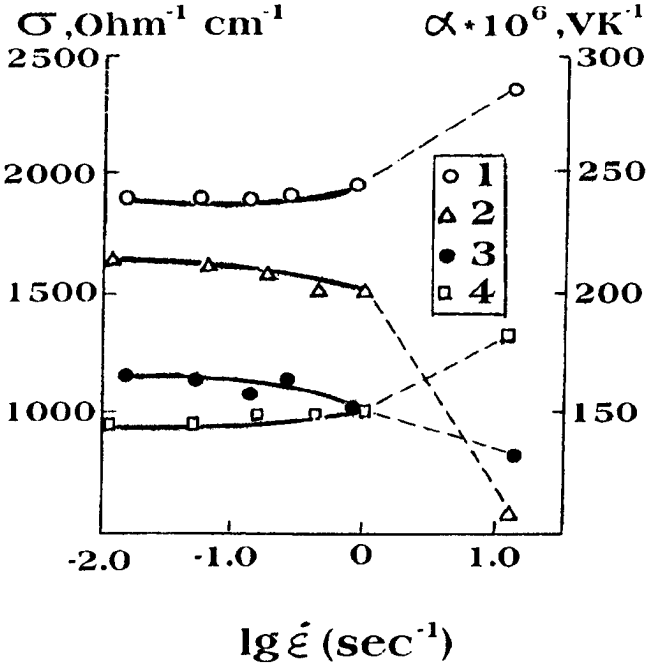


Fig.6. Strain rate dependence of electrical conductivity (1,2) and Seebeck coefficient (3,4) of P-$(Bi,Sb)_2Te_3$ (1,3) and N-$Bi_2(Te,Se)_3$ (2,4) samples extruded at k = 64.

The proportional growth of the diffusion coefficient with the increase of strain rate has been established. It accounts for the absence of strain rate dependence of thermoelectric characteristics of N-$Bi_2(Te,Se)_3$ and P-$(Bi,Sb)_2Te_3$ TE legs if the latter are produced in conditions of structural superplasticity.

REFERENCES

1. O.B. Sokolov, B.A. Efimova. On Resistance to Cracks of Semiconductive Materials, P-PbTe Case Study. Izvestiya AN SSSR. Neorganicheskiye Materialy (Non-organic Materials.). 1992. V.28, No 1. p.61 (in Russian).

2. O.A. Kaibyshev. Plasticity and Superplasticity of Metals, M., Mettalurgiya (Metallurgy), 1975. (In Russian).

3. B.Ya. Lyubov, N.S. Fastov. Physics of Metals and Physical Metallurgy, v.10, 2, 310 (1960), (in Russian).

4. A.I. Anukhin, S.Ya. Skipidarov, O.B. Sokolov. Statistical Micro-Inhomoheneities in $(Bi,Sb)_2Te_3$ Solid Solutions Grown from Melt with Excess Content of Tellurium, Proceedings of the 14th International Conference on Thermoelectric Energy Conversion, St.Petersburg, Russia, 1995, p.65.

Effects of a Reduction Treatment and Te Doping on Thermoelectric Properties of $(Bi_{1-x}Sb_x)_2Te_3$ Fabricated by Mechanical Alloying

Hang-Chong Kim[1], Jae-Shik Choi[1], Hee-Jeong Kim[1], Dow-Bin Hyun[2], and Tae-Sung Oh[1]
[1]Department of Metallurgy and Materials Science, Hong Ik University, Seoul 121-791, Korea,
Phone : 82-2-320-1655, FAX : 82-2-337-8460, e-mail : ohts@wow.hongik.ac.kr
[2]Division of Metals, Korea Institute of Science and Technology (KIST), Seoul 136-791, Korea,
Phone : 82-2-958-5464, FAX : 82-2-958-5379, e-mail : dbhyun@kistmail.kist.re.kr

Abstract
$(Bi_{1-x}Sb_x)_2Te_3$ ($0.75 \leq x \leq 0.85$) thermoelectric materials were fabricated by mechanical alloying and hot pressing at 550℃ for 30 minutes with and without a reduction treatment of the mechanically alloyed powders. When the mechanically alloyed $(Bi_{1-x}Sb_x)_2Te_3$ powders were hot-pressed without a reduction treatment, a maximum figure-of-merit of 2.92×10^{-3}/K at 300K was obtained for x = 0.8 composition. Although the electrical resistivity of the mechanically alloyed $(Bi_{1-x}Sb_x)_2Te_3$ decreased with a reduction treatment of the powders, the figure-of-merit was lowered due to the substantial decrease of the Seebeck coefficient. With addition of 1 wt% excess Te, the figure-of-merit of the reduction-treated $(Bi_{0.2}Sb_{0.8})_2Te_3$ could be improved to be 3.33×10^{-3}/K.

Introduction
As a new processing technique, mechanical alloying process has been investigated to fabricate polycrystalline thermoelectric materials such as Si-Ge alloys and Bi_2Te_3-based alloys [1-3]. Mechanical alloying is a technique in which alloy powders are fabricated from the elemental powders through a sequence of collision events inside a high energy ball mill [4]. Since mechanical alloying occurs near room temperature, this technique can be a cost-saving process for the production of polycrystalline thermoelectric materials compared with the conventional "vacuum melting/grinding" process [1]. Also the vaporization of the chalcogenide elements such as Te and segregation of dopants may be prevented in the powders produced by mechanical alloying, as melting process is not involved during powder fabrication.

In this paper, the effects of a hydrogen-reduction treatment and excess-Te doping on the thermoelectric properties of the mechanically alloyed and hot-pressed $(Bi_{1-x}Sb_x)_2Te_3$ ($0.75 \leq x \leq 0.85$) alloys have been investigated.

Experimental procedure
High purity (> 99.99%) Bi, Sb, and Te granules were weighed for $(Bi_{1-x}Sb_x)_2Te_3$ ($0.75 \leq x \leq 0.85$) compositions and charged in a hardened tool-steel vial with steel balls as milling media under Ar atmosphere. Ball-to-material weight ratio was held at 5 : 1. Mechanical alloying was conducted by shaking the vial at about 1200 rpm using a Spex mill. $(Bi_{0.25}Sb_{0.75})_2Te_3$ and $(Bi_{0.2}Sb_{0.8})_2Te_3$ powders were fabricated by mechanical alloying for 5 hours, and $(Bi_{0.15}Sb_{0.85})_2Te_3$ powders were mechanically alloyed for 6.5 hours. A reduction treatment of the mechanically alloyed powders was performed at 400℃ for 24 hours in (50% H_2 + 50% Ar) atmosphere.

The $(Bi_{1-x}Sb_x)_2Te_3$ powders, with and without a reduction treatment, were cold-pressed at 320 MPa to form 5 mm×5 mm×10 mm compacts, and hot pressed in vacuum at 550℃ for 30 minutes. Fracture surface of the hot-pressed specimens, parallel to the hot-pressing direction, was observed using scanning electron microscopy (SEM). The Seebeck coefficient (α) was measured at 300K by applying a temperature difference of 10℃ at both ends of a specimen using a sub-heater. The electrical resistivity (ρ) and thermal conductivity (κ) were measured at 300K using Harman method in a vacuum of 10^{-5} torr to minimize the thermal conduction through convection, and the figure-of-merit was calculated from $Z = \alpha^2/\rho\cdot\kappa$. Carrier concentration and mobility of the hot-pressed $(Bi_{1-x}Sb_x)_2Te_3$ were obtained using Hall measurements with AC magnetic fields.

Results and Discussion
The Seebeck coefficient and electrical resistivity of $(Bi_{1-x}Sb_x)_2Te_3$ are shown in Fig. 1 with variation of Sb_2Te_3 content x. The thermoelectric properties of $(Bi_{1-x}Sb_x)_2Te_3$ with the reduction treatment are also illustrated in Fig. 1. For $(Bi_{1-x}Sb_x)_2Te_3$ without the reduction treatment, the Seebeck coefficient and electrical resistivity were lowered with increasing Sb_2Te_3 content x. However, the electrical resistivities of $(Bi_{1-x}Sb_x)_2Te_3$ fabricated by mechanical alloying and hot pressing are higher, even without any addition of donor dopant, than ~1 mΩ-cm of the donor-doped single crystals [5-7]. As mechanical alloying occurs by repeated fracture and cold welding of the powders

0-7803-4057-4/97 $10.00 ©1997 IEEE

during vibro-milling process [4], the mechanically alloyed powders are heavily deformed and the surface of powders is easily oxidized even in an atmosphere of low oxygen pressure. It has been reported that heavily-deformed Bi_2Te_3 ingots changes the conduction mechanism from p-type to n-type due to the generation of Te vacancies ($V_{Te}^{\cdot}$) which act as donors [7]. Also the oxygens dissolved in the $(Bi,Sb)_2Te_3$ lattice have an effect to add donor levels [8]. Incorporation of the oxygen into the lattice would be enhanced in the mechanically alloyed powders due to the increase of the vacancy concentration and dislocation density by heavy deformation. Thus, high electrical resistivity of the mechanically alloyed $(Bi_{1-x}Sb_x)_2Te_3$ could be attributed to the reduction of the hole concentration by compensation with electrons generated by $V_{Te}^{\cdot}$ and the powder-surface oxidation. As shown in Fig. 2, the hole concentrations of the mechanically alloyed $(Bi_{1-x}Sb_x)_2Te_3$ were lower than the values reported for the single crystals [5]. The carrier mobilities of the mechanically alloyed $(Bi_{1-x}Sb_x)_2Te_3$ were also lower than ones of the single crystals [5].

As shown in Fig. 3, the mechanically alloyed $(Bi_{1-x}Sb_x)_2Te_3$ exhibited relatively low thermal conductivity (κ_{tot}) of 0.86 ~ 1.35 W/K-m, compared to single crystals [5-7]. Assuming the mechanically alloyed $(Bi_{1-x}Sb_x)_2Te_3$ as a degenerate semiconductor, the Lorenz number was taken as $(\pi^2/3)(k/e)^2$ and the electrical thermal conductivity was calculated from $\kappa_{el} = L_o\sigma T$. ($\kappa_{tot} - \kappa_{ph}$) of the mechanically alloyed $(Bi_{1-x}Sb_x)_2Te_3$ was 0.67 ~ 0.71 W/K-m. Although the mechanically alloyed $(Bi_{1-x}Sb_x)_2Te_3$ exhibited lower $\alpha^2\sigma$ than single crystals [5], a figure-of-merit of 2.96×10^{-3}/K comparable to the values of single crystals was obtained for the mechanically alloyed $(Bi_{0.2}Sb_{0.8})_2Te_3$ due to the low thermal conductivity.

The mechanically alloyed $(Bi_{1-x}Sb_x)_2Te_3$ powders were reduction-treated in (50% H_2 + 50% Ar) atmosphere and hot pressed in vacuum. The Seebeck coefficient and electrical resistivity of $(Bi_{1-x}Sb_x)_2Te_3$ decreased with the reduction treatment. The increase of the hole concentration with the reduction treatment, shown in Fig. 2, may be due to the removal of $V_{Te}^{\cdot}$ and the oxide layer of the powder surface. During the reduction treatment, Bi/Sb vacancies acting as acceptors also could be annealed out. However, more Te vacancies than Bi vacancies would be removed by dislocation climb to the low energy Te-Te planes [8], and hence the hole concentration increased. The figure-of-merit of $(Bi_{1-x}Sb_x)_2Te_3$ was lowered with the reduction treatment (Fig. 3).

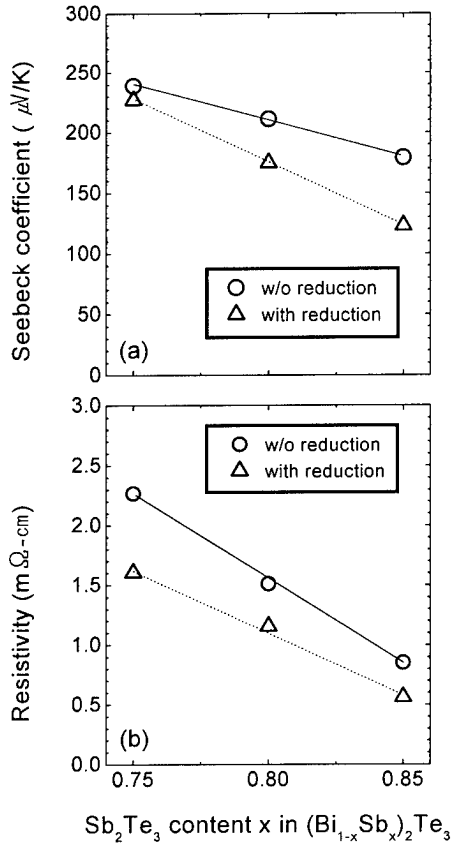


Fig. 1 (a) Seebeck coefficient and (b) electrical resistivity of $(Bi_{1-x}Sb_x)_2Te_3$.

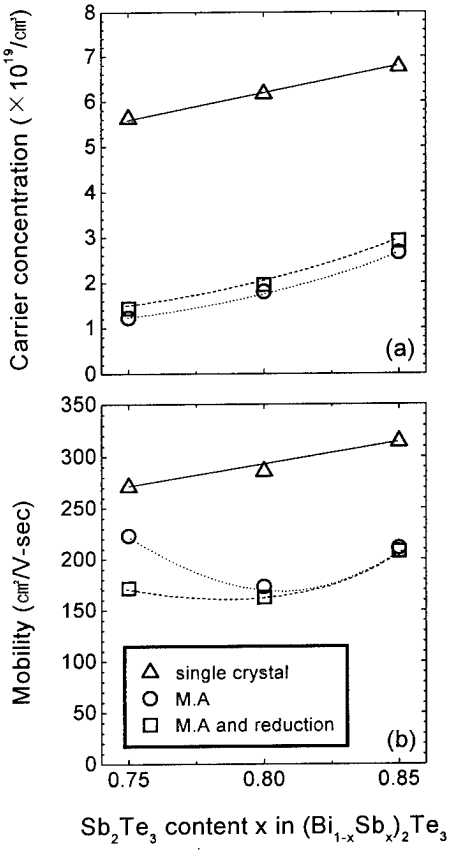


Fig. 2 (a) Hole concentration and (b) mobility of $(Bi_{1-x}Sb_x)_2Te_3$.

As shown in Fig. 4, the grain size of the mechanically alloyed $(Bi_{1-x}Sb_x)_2Te_3$ became remarkably smaller with the reduction treatment. The vacancy concentration and the dislocation density of the mechanically alloyed powders were lowered with the reduction treatment. Then, the diffusion rates of Bi, Sb and Te in the lattice would be decrease and the grain growth of the reduction-treated $(Bi_{1-x}Sb_x)_2Te_3$ seemed to be prohibited during hot pressing. Grain refinement with the reduction treatment might be considered to be due to the removal of the oxide layer on the powder surface, if liquid phase sintering was promoted with the oxide layer. However, the melting point of Bi_2O_3, produced as the oxide layer during oxidation of Bi_2Te_3 [8], is higher than that of $(Bi,Sb)_2Te_3$ alloys, which eliminates the possibility of the liquid phase sintering.

$(Bi_{0.2}Sb_{0.8})_2Te_3$ powders doped with excess Te were fabricated by mechanical alloying, reduction-treated, and hot pressed at 550℃. The thermoelectric properties of excess Te-doped $(Bi_{0.2}Sb_{0.8})_2Te_3$ with and without the reduction treatment, are shown in Fig. 5. Contrary to the fact that the electrical resistivity of the single crystal $(Bi,Sb)_2Te_3$ increased with excess Te doping due to the decrease of the anti-structure defect concentration [6], the electrical resistivity of the mechanically alloyed $(Bi_{0.2}Sb_{0.8})_2Te_3$ decreased with addition of excess Te up to 2 wt%.

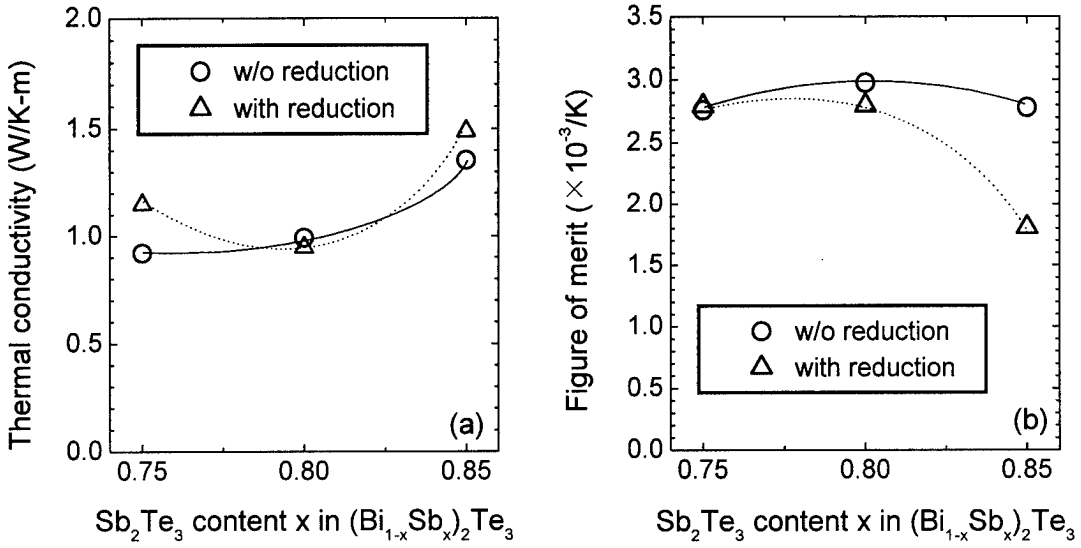


Fig. 3 (a) Thermal conductivity and (b) figure-of-merit of $(Bi_{1-x}Sb_x)_2Te_3$.

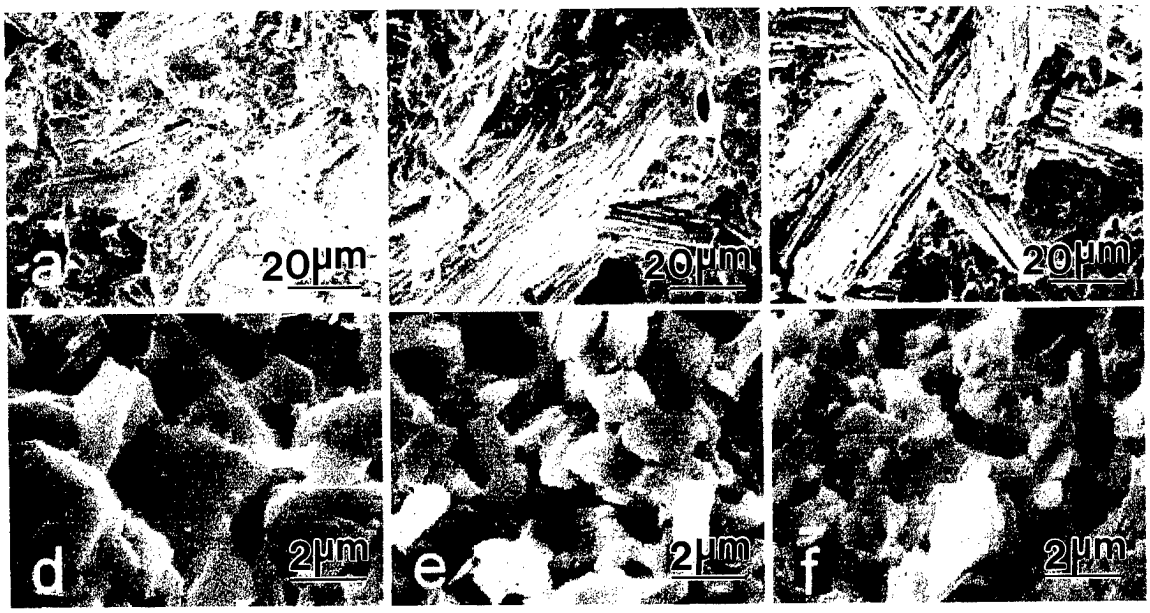


Fig. 4 SEM micrographs of (a) $(Bi_{0.25}Sb_{0.75})_2Te_3$, (b) $(Bi_{0.2}Sb_{0.8})_2Te_3$ and (c) $(Bi_{0.15}Sb_{0.85})_2Te_3$ without a reduction treatment, (d) $(Bi_{0.25}Sb_{0.75})_2Te_3$, (e) $(Bi_{0.2}Sb_{0.8})_2Te_3$ and (f) $(Bi_{0.15}Sb_{0.85})_2Te_3$ with a reduction treatment.

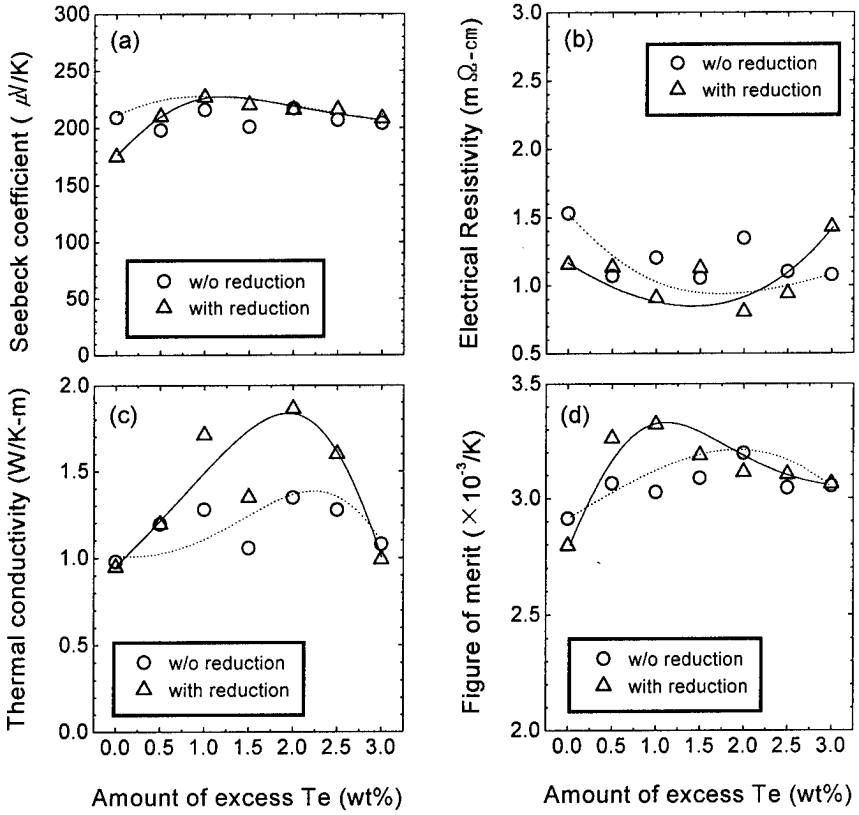


Fig. 5 (a) Seebeck coefficient, (b) electrical resistivity, (c) thermal conductivity, and (d) figure-of-merit of $(Bi_{0.2}Sb_{0.8})_2Te_3$ as a function of the amount of excess Te addition.

This might be due to less generation of Te vacancies during mechanical alloying of the Te-doped powders. It is also plausible that Te vacancies were removed more easily during hot pressing of the excess-Te doped powders due to the incorporation of excess Te into its own site in the lattice. As shown in Fig. 5(a), the Seebeck coefficient increased with addition of excess Te up to about 1 wt%. To fully explain the thermoelectric properties of the mechanically alloyed $(Bi_{0.2}Sb_{0.8})_2Te_3$ with excess Te, further experiments are required. Nevertheless, the figure-of-merit of the mechanically alloyed $(Bi_{0.2}Sb_{0.8})_2Te_3$ was markedly improved with addition of 1 ~ 2 wt% excess Te.

Summary

When the mechanically alloyed $(Bi_{1-x}Sb_x)_2Te_3$ powders were hot-pressed without a reduction treatment, a maximum figure-of-merit of 2.96×10^{-3}/K was obtained for x = 0.8 composition. With the reduction treatment, the electrical resistivity decreased, but the figure-of-merit of $(Bi_{0.15}Sb_{0.85})_2Te_3$ was lowered due to the substantial decrease of the Seebeck coefficient. The figure-of-merit of $(Bi_{0.2}Sb_{0.8})_2Te_3$ could be improved remarkably with the addition of excess Te. A maximum figure-of-merit of 3.33×10^{-3}/K was obtained for the reduction-treated $(Bi_{0.2}Sb_{0.8})_2Te_3$ with 1 wt% excess Te. Without the reduction treatment, 2 wt% Te-doped specimen exhibited a figure-of-merit of 3.2×10^{-3}/K.

Acknowledgment

This work was supported by the Institute of Information Technology Assessment of Korea.

References

[1] B. A. Cook, B. J. Beaudry, J. L. Harringa, and W. J. Barnett, Proc. of the IXth ICT, p.234, 1990.

[2] O. Sh. Gogishvili, I. P. Lavrinenko, S. P. Lalykin, T. M. Melashivili, and L. D. Rogovoy, *ibid*, p.271, 1990.

[3] B. Y. Jung, T. S. Oh, D. B. Hyun, and J. D. Shim, J. Korean Phys. Soc., **31** (1997) 219.

[4] R. Sundaresan and F. H. Froes, J. of Metals, **8** (1987) 22.

[5] J. D. Shim and D. B. Hyun, Proc. of the IXth ICT, p.27, 1990.

[6] W. M. Yim and F. D. Rosi, Solid-State Electronics, **15** (1972) 1121

[7] H. P. Ha, Y. W. Cho, J. Y. Byun, and J. D. Shim, Proc. of the XIIth ICT, p.105, 1993.

[8] J. M. Schultz, J. P. McHugh, and W. A. Tiller, J. Appl. Phys., **33** (1962) 2443.

Structural- Chemical Characterization of Semiconductors Using The Seebeck And Thermal Conductivity Quality Factors

Donald Tuomi
Tuomi Associates, 626 South Kaspar Ave., Arlington Hts. IL 60005
Tel.: 00/847/392-3003; E-mail: dtuomi@juno.com

Abstract

The evaluation of alloy quality utilizing the electron mobility – effective mass product. $\mu_0(m^*/m_0)^{3/2}$, for acoustic mode alloy scattering of electrons, the Seebeck quality factor, Qs, and an empirically defined thermal conductivity quality factor, Qk, provides insight into options for producing improved superior thermoelectric alloys.

Introduction.

In 1961, Tuomi introduced the Seebeck Quality Factor, Qs, (1), to relate the alloy Seebeck coefficient to the electrical conductivity and the thermal conductivity quality factor, Qk, (2), to relate the thermal conductivity to the electrical conductivity of thermoelectric energy conversion alloys. The material parameters supplemented the engineering parameters: the power coefficient and the figure of merit. The Seebeck quality, Qs, is the electron mobility – effective electron mass product, $\mu_o(m^*/m_o)^{3/2}$, for acoustic mode alloy scattering of electrons in units of cm^2/volt sec. The thermal conductivity quality, Qk, is empirically derived as a lattice component of thermal conductivity for a degenerate semiconductor corrected for the reduction in thermal conductivity associated with the alloy doping (3) in units of mw/cmK. The designation of Qs and Qk recognizes the dependence of the variables on material composition and processing. Constant values of Qs and Qk for a series of samples reflect the operation of a pure extrinsic dopant variable as illustrated in Fig. 1 . Alloy samples became characterized by the variables S, ó, k, S^2 ó, Z, Qs, Qk, and M. . The Qs curves in Fig. 2 were used in optimizing cooling alloys. Fig. 3 shows the logarithmic scale form Qs curves used to evaluate literature data. The Qs relationship tp the power coefficient Qs/Qk = M =32.5 is shown in Fig. 4 . The material parameter, M, is related to Z as shown in Fig. 5 .

In 1961, Donald Tuomi and John Horwath began accumulating literature on thermoelectric alloys which, where possible, was evaluated by Qs, Qk, and M.

The private Borg-Warner research program sought alloy options opening thermoelectric energy conversion to larger scale commercial exploitation. At this time, many materials R & D programs were being closed because little progress was evident toward achieving the large scale applications.

Though very high figure of merit alloys were not encountered, significant progress was made in describing the general challenge. The following discussion focuses upon new options revealed through the applications of quality factor analyses.

The Bismuth Tellurides, $(Bi,Sb)_2(Se,Te)_3$

The optimization technology of the bismuth telluride class alloys has been described (4). Examining the general preparative literature for the Qs dependence on the alloy composition and the preparative technology reveals the general challenges of bismuth telluride class optimization (5) .

For the P type bismuth antimonyl telluride alloys the Qs varies with preparative composition and technology as shown in Fig. 6 . Near the 75/25 antimony to bismuth composition a 500 Qs is encountered in a Bridgman sample while the 300 to 400 Qs range is accessible by both grown Bridgman rod and powder metallurgical compact techniques with the latter measured perpendicular to the pressing direction and the former measured parallel to the rod axis (i.e. the crystallographic cleavage plane oriented parallel to growth direction). During annealing the P type powder metallurgical samples recrystallize to form equiaxed grains. A critical variable is equilibrating the solid phase with excess tellurium while minimizing second phase tellurium eutectic degradation of the Qs. In tellurium deficit matrix phase lattice vacancies precipitate as dislocation loops which degrade Qs.

Limited data for a few Bridgman rods grown in the greater than 50% bismuth region show P in the 300-350 Qs range and N type in the 400 Qs range suggesting superior alloys may also be accessible in this region of composition for both types. Neither option has been subject to careful scrutiny.

The Qs for N type bismuth telluroselenide alloys are summarized in Fig. 7 . A clearly defined outlier Qs limit for grown rods is evident between a 525 Qs at the bismuth telluride and slightly greater than 300 Qs at the Bi_2Te_2Se composition with selenium substituting for centrosymmetric tellurium, Te^{II}, with the crystal cleavage plane oriented parallel to the growth axis. The variable Qs for the grown rod class alloys arises from variations in the detailed chemical stoichiometry, the crystal orientations, variations in the cross-sectional compositional homogeneity, inappropriate dopant distributions, improper site occupation by the selenium, as well as second phase peritectic or eutectic phase enhancement or degradation of Qs.

A distinctly lower outlier Qs range, Fig. 8, exists for the powder metallurgical N type alloys with the higher Qs again appearing in the perpendicular to pressing direction; a 270 Qs at the Bi_2Te_3 composition increasing to 300 Qs at the $Bi_2Te_{2.4}Se_{0.6}$ composition. These N type samples are characterized by a deformation twin recrystallization substructure which complicates the interpretation of the anisotropic properties origins.

Superior oriented grown N type rods should be producible near the 500 Qs range as compared to the 300 to 400 Qs of common alloys. Imperfection structure controls are needed in the

crystals to minimize the cleavage degradation of the die for modules.

The P type rods grown in the N type composition field, Fig. 8, have a Qs as high as 500 at the Bi_2Te_3 composition and an outlier near 400 Qs at 0.5 Se substitution for Te[11]. A possibility exists for high quality P type preparation in the normally N type composition field.

The old paradigm regarding the selection of the optimum chemical compositions for good N type as a bismuth telluroselenide and P type as an antimony bismuthyl telluride class alloy may need to be revised.

Unfortunately sufficient literature Qk data for the bismuth telluride class alloys are not available to make a detailed analysis. Variations of Qk may occur in the space averaged properties of test samples so the Qs/Qk = M ratio is improved or degraded depending on the contributing imperfection structures.

The optimization of the bismuth telluride, 2-3, class alloys has not yet been performed in an exhaustive manner to produce the superior alloys for the P and N type legs of modules. The necessary commercial technologies have not been developed.

The Bi-Sb-Te-Se Chemical System

The Bi-Sb - Te-Se, A-B, quaternary system (6) contains several semiconductor alloy systems as shown in Fig. 9 , and conveniently described as the following material classes:

- N type A , Bi-Sb alloys .....~1,500 Qs,
- P type B, Te-Se alloys ..... ~250 Qs,
- N type A_2B_3 alloys B rich ..... ~400-500 Qs,
- P type A_2B_3 alloys A rich ..... ~ 400-500 Qs,
- N type $A_{1+x}B$ peritectic, $Bi_{1+x}Te$ with SbTe and/or BiSe ..... ~300 Qs, when oriented with cleavage plane parallel to growth direction,
- P type $A_{1+x}B$ peritectic, $Sb_{1+x}Te$ with BiTe and/or SbSe ..... ? >50 Qs *,
- N type $A_{2+x}B$ peritectic $Bi_{2+x}Te$ with Sb_2Te and/or Bi_2Se ..... ? <100 Qs*,
- P type $A_{2+x}B$ peritectic Sb_2Te_{1+x} with Bi_2Te and/or Sb_2Se ..... ? < 100 Qs*,
- N type $A_{3+x}B$ peritectic $Bi_{3+x}Te$ ..... ?< 100 Qs*,
- Between A_2B_3 and B at high pressure, perhaps an AB_2 semiconductor, exists with useful characteristics ..... ? <100 Qs*,

*when quench cast and annealed.

In 1962 , Stanley Cook and John Horwath studied the quaternary phase diagram in considerable detail using quench cast and annealed alloy samples. Metallurgical examinations provided information on the approach to phase equilibrium. A useful conceptual perspective emerged on the solidification of the four component alloys during various processing procedures. Later work showed that the quench cast – anneal technique did not necessarily improve the alloy Qs, or alter the overall alloy homogeneity. The quench cast alloy needed to be pulverized and the powder vapor phase composition equilibrated, then reground and annealed.

The general quaternary phase diagram needs to be explored for P type materials which complement the 1,500 Qs of the N type Bi-Sb alloys used in low temperature cooling applications.

The Lead Telluride Alloys

Many studies have explored the thermoelectric properties of lead telluride alloys with and without alloying by homo- and hetero-polar element additions and with variations in dopant additions. The results of an extensive literature survey (7) are conveniently summarized by tabulating the Qs values as a function of the sample electrical conductivity as shown for P and N type in Fig. 10.

Lower electrical conductivity P type includes samples at 330 to 400 Qs which are to be compared to commercial samples in the 200 cm^2/volt sec Qs range. This high Qs suggests that useful P type alloys may be accessible for use in cooling applications since the lead tellurides are octahedral coordination, low thermal conductivity materials.

By contrast, the N type alloys are all below the 300 Qs range from 100 to 6,000 mho/cm. Since the outliers are superior to the commercial class alloys as noted in the bismuth telluride class, further improvements are possible.

The variations in the properties of the lead telluride samples draw attention to the need to delineate the variables controlling the alloy quality and then to practice the best composition control and preparative technology so practical applications become possible. The art needs to be replaced by science.

The recently reported $3.6x10^{-3}$ /K figure of merit for P type lead telluride (8) prepared using a particular art illustrates the need for more detailed studies. Segmenting options exist to improve the Z as a function of temperature performance.

The Si/Ge Alloys.

The Si/Ge system including the dopant is the simplest thermoelectric alloy (9)(10) . The alloys are characterized by a constant Qs as the doping level is changed at constant temperature. With increasing temperature, the Qs of both N and P type increases as shown in Fig. 11 thus providing access to 400 to 500 Qs at high hot side temperatures. As shown, alloying with GaP may improve the Qs values beyond that of the common alloys. The GaP acts as a Si/Ge mineralizer in the processing.

The III/V alloys as well as TAGS material show the Si/Ge temperature dependence of Qs so at higher temperatures appropriately doped alloys possess an improved power coefficient. This contrasts to the other extrinsic alloy classes for which the Qs is temperature independent but may vary with dopant element, alloying agent, composition, and preparative process.

Periodic Table Screening for New Alloys

Ioffee by 1955 (11) had revealed to the world the new opportunities for thermal energy conversion through the use of heavily doped semiconductors. The large market potential and the lack of defined limits to progress resulted in a worldwide program seeking high performance options in cooling and power. Few guiding paradigms for material preparation existed to use in directing the work. The simple Ioffee device theory led to requiring a large power coefficient and figure of merit in alloys processable into modules without developing electrical or thermal contact resistance and having the expected solid state reliability and the needed high performance.

Data appeared from 1955 to 1975 in a large variety of publications worldwide exploring many compounds and alloys seeking the magic potion. Hundreds of laboratories were engaged in the search, each using a particular approach with special combinations of elements from the periodic table. At Borg-

Warner Research Horwath and Tuomi continually surveyed this literature to evaluate the thermoelectric results through the Qs/Qk/M route. From the 770 alloy compilation (12), excluding the familiar useful alloys, emerged 383 P and 278 N type better samples with the Qs values distributed as shown in Fig. 12 . Most are below 100 Qs with few above 200.

The English language literature included Office of Naval Research reports and related others from private laboratories. Extreme pressure was exerted in the laboratories to produce the desired spectacular results based upon a particular limited sampling of element combinations from the periodic table using proprietary laboratory procedures. The difficulties encountered in producing high quality, compound semiconductor alloys did not become well known until commercial electronic devices began to be produced from III/V materials in the middle 70's and later.

The N or P type optimized thermoelectric alloys require using, as base, a compound semiconductor in which an alloying agent minimizes the lattice thermal conductivity and controlled dopant addition optimizes the electrical conductivity for the operational temperature range. This four component alloy system forms from a quaternary phase diagram in which a small composition region contains the desired superior material. An intuitive view of the actual phase diagram compositional tie lines interaction with the metallurgical processes is not easily formulated. Many routes exist to inferior quality alloys but few exist to the desired superior composition.

Some of the guiding paradigms for the exploratory research included the following:

1. The first part of an alloy to freeze represented a unique phase diagram tie line. Only true if super-cooling is absent and the growth rate is sufficiently slow and the initial nucleation readily occurs.
2. Single phase samples are desired before serious thermoelectric measurements are undertaken. Only true under very limited circumstances.
3. The power coefficient data on a few samples are adequate to predict the promise of a composition. Response surface data involving both chemical composition and process technology are important.
4. The thermal conductivity could be estimated for the alloy rather than undertaking the difficult measurement except on very select samples. The alloy thermal conductivity may involve as many complicating variables as the power factor.
5. Three different samples from the same specimen may be used to determine the thermoelectric parameters. All data need to be obtained on the same sample.
6. Quench casting is an adequate technique for rapidly preparing alloy for screening studies. This procedure rather consistently results in low Qs alloys but may provide low thermal conductivity because of the inherently large lattice imperfection density.
7. Simplified pseudo- phase diagrams are adequate for screening studies. Imperfections associated with narrow non-stoichiometry solid solution fields may readily degrade the electron mobility-effective mass product into the poor class.
8. Only semiconductor compounds in the lower right hand of the periodic table have the desired low lattice thermal conductivity. The lattice thermal conductivity depends more strongly upon the coordination chemistry of the compound than upon the simple mass heterogeneity and bond force constant relationships.
9. Long term annealing of alloy samples will bring the material to a desirable equilibrium compositional state with properties approaching optimum states. Samples frequently contain associated defect structures which are not dissociated and dispersed during annealing and degrade the thermoelectric properties.
10. Chemical purity is not an important variable because of the inherent dirtiness of alloys with multiple components. Impurities in the alloy components may function to degrade Qs as well as to place the alloy into minimally optimal electrical conductivity range.
11. The optimization process may be performed by selective adjustment of the basic thermoelectric parameters. The parameters are explicitly related to fundamental space averaged material structural – chemical variables and optimization involves determining the response surfaces of the variables.

It is unfortunate that few laboratories engaged in writing critical reviews of the experiences during the hectic exploratory research period from 1955 to 1965. Such writing would have brought attention to the extensive work remaining to be done to bring the thermoelectric energy conversion heavily doped semiconductors from art to material science.

The data on TiS_2 in Fig. 13 illustrate how the Qs analysis suggested that this material may have promise in thermoelectric applications (13) . Such data illustrate the need for further experimental studies on the compound.

Thermal Conductivity Quality Factors

Attention has focused on the Seebeck quality factors of compounds because only limited thermal conductivity data were obtained on the exploratory materials; the power coefficient was the initial measure of alloy utility. Thermal conductivity data were only obtained on the best samples. This strategy changed when the Harman Z meter became available (14).

The thermal conductivity screening studies of heavily doped semiconductors at American Cyanamid by Spitzer (15) led to clarifying the structural chemical conditions for low thermal conductivities. The local site symmetry of the lattice components proved to be important. The critical variable is having the local site symmetry in the octahedral class as in lead telluride or a more complex octahedral class as in bismuth telluride with the asymmetric $Te^{I}Te^{I}Bi$, $Te^{I}BiTe^{II}$ and symmetric $BiTe^{II}Bi$ sites or as in the bismuth-antimony alloys. The structure should provide access to a large Qs. Alloying may further reduce the lattice thermal conductivities into the amorphous quartz class or less.

The studies brought attention to the need to qualify the simple mass and bond disorder models for low thermal conductivity alloys. Unfortunately the samples were largely quench cast materials so that the Seebeck quality factors were small. A new study is needed in which more optimum alloy preparative procedures are used so that insights could be obtained into the promise present in the low Qk alloys explored.

The Qk survey studies on the common alloys demonstrated its quantitative applicability to a broad range of degenerate, heavily doped, semiconducting materials. The combination of Qs, Qk, and M adequately fit the results at ambient temperatures.

Compositional and processing variables could be related in response surface forms to the thermoelectric materials parameters Qs, Qk and M. The applicability of the ambient temperature data to temperature dependent results on individual samples gave yet another useful perspective on ways materials could be optimized.

Conclusions

The Qs, Qk, and M characterization of heavily doped semiconductors has brought attention to the large number of compositional and processing variable interactions which are important to the optimization of the thermoelectric performance. They provide a route through which much data on a variety of semiconductors may be organized into a coherent whole. The electronic mobility – effective electron mass product, $\mu_o(m^*/m_o)^{3/2}$, is a system variable rather than being a fundamental parameter in solid state theory. It was this reason that the quality factor notation was introduced. The broad applicability range to varied alloys is unexpected and implies the presence of a rather fundamental semiconductor electronic property description based upon acoustic mode – alloy scattering of electrons. The Qs does not depend upon carrier density in the sense that the electron mobility does, it is a constant over a broad range of changing carrier density.

Only on select samples of the best quality is the Qs really the familiar fundamental parameter of solid state theory.. This is really true only in the alloy produced with an 'ideally perfect lattice' as defined by x-ray crystallographers, most materials are better classed as 'ideally imperfect' crystalline alloys. In the better quality powder metallurgical bismuth antimony tellurides the Qs becomes related to the x-ray powder diffraction line half breadth at half height variations, the higher Qs having narrower half breadths, as noted by Dr. Peter Yu at the Borg-Warner Research Center. The difficulty in attaining the best quality class alloys is undoubtedly associated with the challenge of attaining ideal crystal lattice perfection.

Acknowledgements

The kind support of Mike Mikalauskis, President, Thermoelectric Cooling of America, Chicago, Illinois has made possible the preparation of this manuscript and my attending the ITC '97 in Dresden, Germany. Through the encouragement and cooperation of my wife, Ruth, came the spirit to review my files and to try mastering a new computer effectively. All shortcomings and errors fall upon my shoulders. A deep appreciation exists for Yves Palmieri , Bismuth Institute, Antwerp, Belgium for his willingness to accept custody of my unpublished manuscripts. I regret circumstance limited my ability to contribute fully much information to the community. I deeply honor the fellows who strongly supported the research efforts over a number of years. These included Dr. Jack Madigan, deceased, Senior Scientist Physicist; Dr. Allen Reich, physicist; Richard Buist, physicist; Marland Stanley, physicist ; Dave Epley, physics technician, deceased; Stanley Cook, materials scientist; Bharat Kalra, metallurgist; John Horwath, metallurgist; Richard Duenn, measurements technician; Bill Eckhardt, materials technician and other Roy C. Ingersoll Research Center, Borg-Warner Corp. Des Plaines, Illinois, staff members. Special thanks are due to Dr. Donald W. Collier , Director of Research, and Dr. Leonard Sloma, manager of Physics and Electronics, for their steadfast support and commitment through the decades of effort. Each year we all grew more appreciative of the challenging materials science problem presented by thermoelectric energy conversion alloys.

References

1. D. Tuomi, "Thermoelectricity: VII The Seebeck Quality Factor, Qs, 'Semiconductor Characterization Tool," J. Electrochemical Soc. 131 (9) 2101, (1983).
2. D. Tuomi, "Thermoelectricity: VIII The Thermal Conductivity Quality Factor, Qk, A Semiconductor Characterization Tool," J. Electrochemical Soc. 131 (10) 2319 (1983).
3. D. Tuomi, "Thermoelectricity: XII Thermal Conductivity and Bismuth Telluride Alloys," 3/13/87, Unpublished.
4. D, Tuomi, "Thermoelectricity: XVIII From Garbage to Perfection: A Structural - Chemical View of Thermoelectric Materials," The Materials Research Society, Fall Meeting, Anaheim, CA, 1991, Conference Proceedings.
5. Donald Tuomi, "Thermoelectricity: IX The Seebeck Quality of Bismuth Telluride Alloys," Presented 165th Meeting The Electrochemical Society, May 7, 1984, Cincinnati, Ohio .
6. John Horwath and Donald Tuomi, "Thermoelectricity: XIII The Bi-Sb-Te-Se Phases," 11/1/1962, Unpublished.
7. Donald Tuomi, "Thermoelectricity: XIV The Lead Telluride Alloys," 3/13/87 Unpublished.
8. Harry W. Rauch, Sr., Lewis H. Goen, June k. Goen, "Thermoelectric Elements" U.S. Patent 4,717,789, Jan. 5, 1985.
9. Donald Tuomi, "Thermoelectricity: II Phase Diagrams and Imperfection Structures" The Proceedings of The 15th Intersociety Energy Conversion Conf., Seattle, Washington, Aug., 18-22, 1980.
10. Donald Tuomi, "Thermoelectricity: XVI The Seebeck Quality of Silicon/Germanium Alloys," The Proceedings of the First International Thermoelectric Energy Conversion Conference, Sept. 15-17, 1987, Cardiff, Wales, U.K.
11. A. F. Ioffe, "Semiconductor Thermoelements and Thermoelectric Cooling," Infosearch, Ltd. (1957).
12. D. Tuomi, " Thermoelectric Materials Qs Files" .
13. D. Tuomi, "The TiS_2 Files," from Carl A. Kukkonen, et. al., "Transport and Optical Properties of $Ti_{(1\pm x)}S_2$ " Phys. Rev. B, 24 (1981) 1691
14. T. C. Harman, Semiconductor Products, Sept. 1963, 18-20; T.C. Harman,, J. Appl. Phys., 29 (1958) 1373; 30 (1959) 1351.
15. D. P. Spitzer, "Lattice Thermal Conductivity of Semiconductors: A Chemical Bond Approach" J. Phys. Chem. Solids, Pergamon Press, 31 (1970) 19-40, Gr. Br.

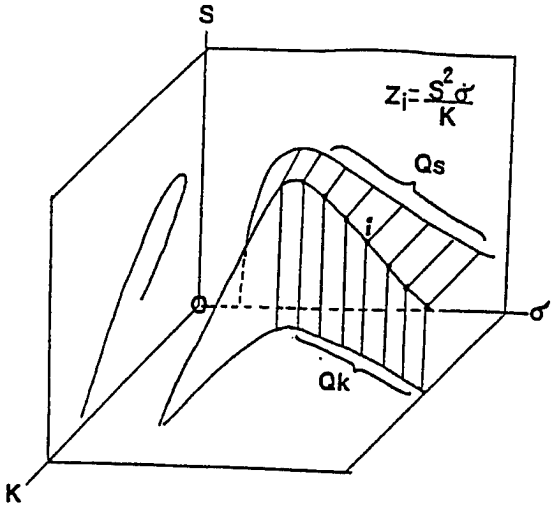


Fig. 1 The three dimensional Seebeck Coefficient, electrical conductivity, and thermal conductivity variables used to derive the figure of merit response surface for a sample doped to change the Fermi level along constant Qs and Qk curves.

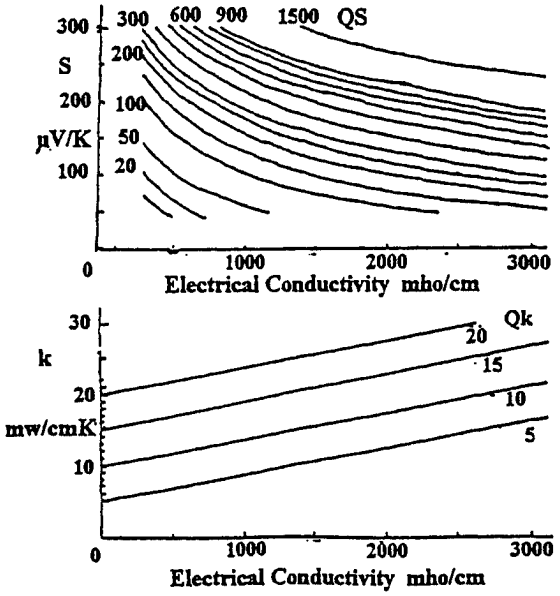


Fig. 2 The Qs and Qk curves used in characterizing experimental samples of bismuth telluride class alloys.

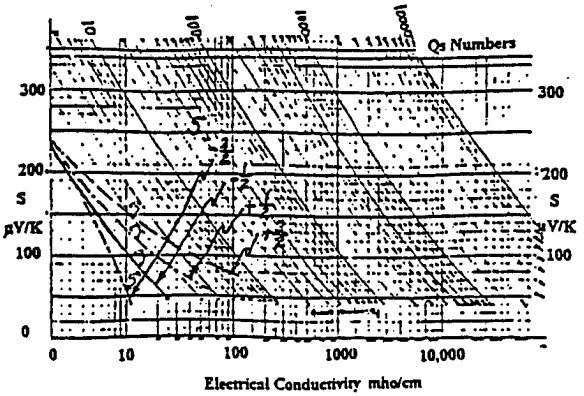


Fig. 3. The semilogarithmic scale Qs curves for extrinsic semiconductor alloys dominated by acoustic mode – alloy electron scattering. Reference curves for the scattering parameter: -3/2, -1/2 (acoustic mode alloy), +1/2 (low temperature, $<T_D$), and +3/2 (Ionized impurity).

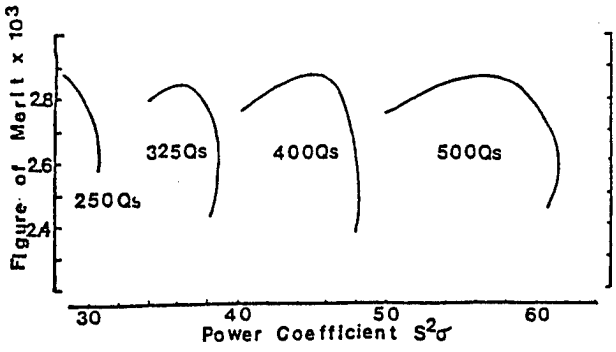


Fig. 4 The interrelationship of the figure of merit and the power coefficient for alloys at variable Qs at constant M= Qs/Qk = 32.5.

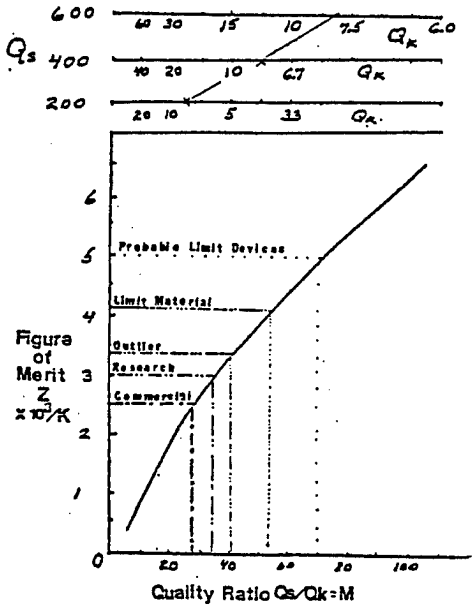


Fig. 5 The relationship of the figure of merit to the quality factor ratio, M = Qs/Qk, illustrating the limitations imposed upon figure of merit through changes in the Qs and Qk. The relative status of bismuth telluride class alloys shown. Device limit includes distributed Peltier effect.

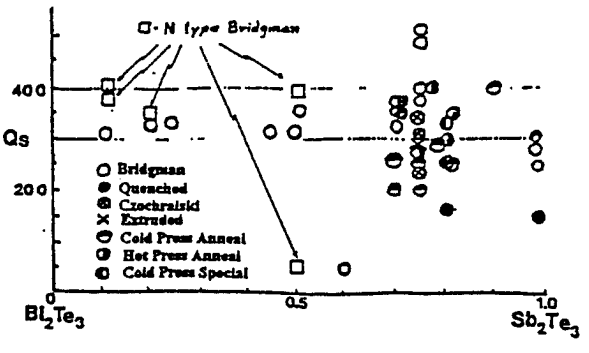


Fig. 6. The P and N type Qs changes with processing and composition for bismuth telluride and antimony telluride alloys, $(Bi_{1-x}Sb_x)_2Te_3$ in samples described in the literature.

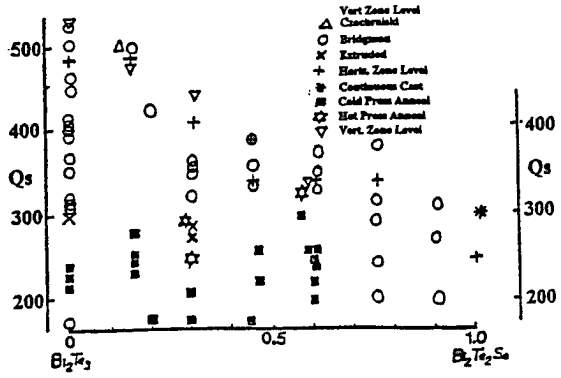


Fig. 7. The N type Qs changes with processing and composition for bismuth telluride and bismuth telluroselenide alloys, Bi_2Te_3 to Bi_2Te_2Se in samples described in the literature.

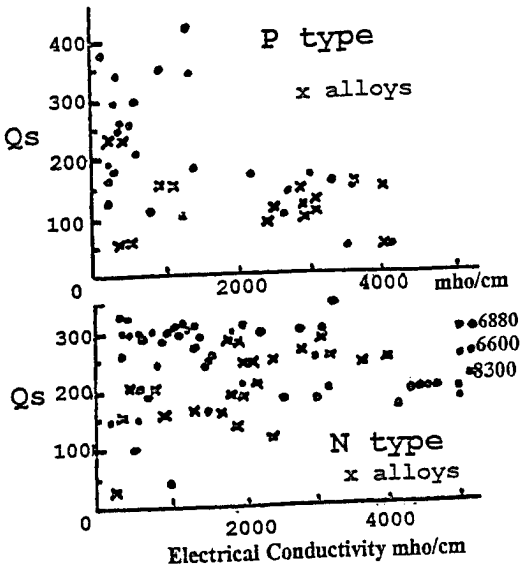


Fig. 10. The Qs versus electrical conductivity for P and N type lead telluride samples from the literature as unalloyed (·) and alloyed (x).

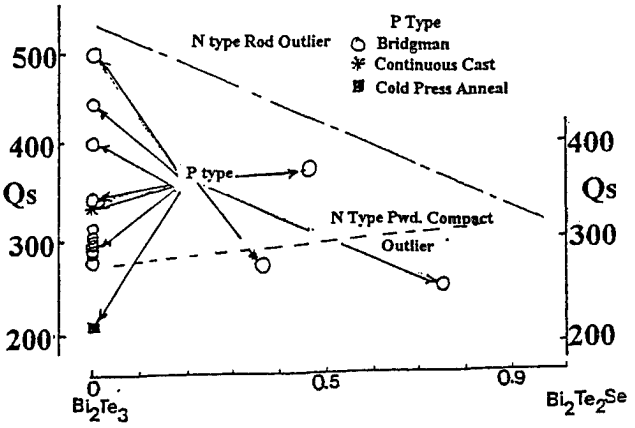


Fig. 8 The Qs of P type samples in the nominally N type composition region.

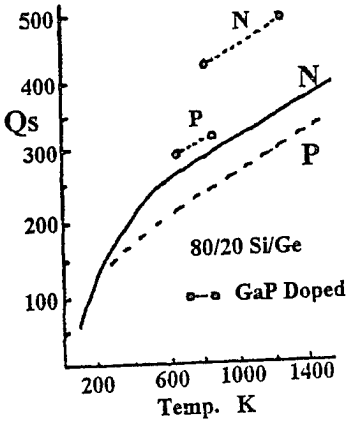


Fig. 11 The Qs versus temperature for P and N type Si/Ge standard sintered alloys and outlier extrinsic GaP doped material.

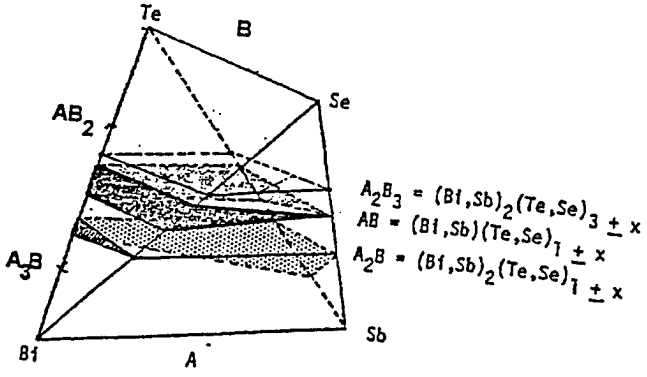


Fig. 9. The Bi-Sb -- Te-Se, A-B, composition tetrahedron.

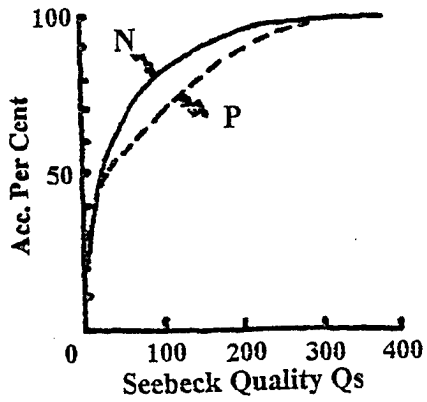


Fig. 12. The number distribution of Qs values for best samples in series of 383 P type and 278 N type exploratory thermoelectric alloys excluding the recognized commercially useful types.

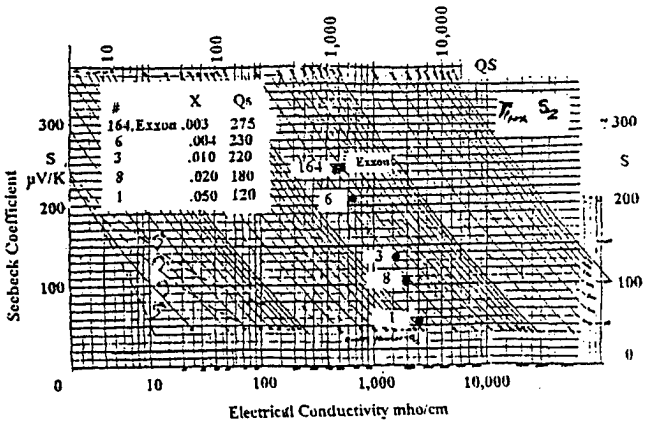


Fig. 13 The Qs data for titanium disulfide, $Ti_{1+x}S_2$, obtained in screening the literature for new thermoelectric alloy options.

Peltier Cooling of Superconducting Electronics

J. W. Straehle[1], S. Rath[2], K.-J. Klingesberger[1], T. Nissel[1], S. G. Doettinger[1,3], Chr. A. Doettinger[4], R. P. Huebener[1], and S. Kemmler-Sack[2]

[1]Physikalisches Institut, Lehrstuhl Experimentalphysik II, University of Tuebingen, Morgenstelle 14, D - 72076 Tuebingen, Germany
[2]Institut fuer Anorganische Chemie, University of Tuebingen, Morgenstelle 18, D - 72076 Tuebingen, Germany
[3]Present address: Department of Applied Physics, Stanford University, CA 94305-4090, USA
[4]Institut fuer Kunststoffpruefung und Kunststoffkunde (IKP), University of Stuttgart, Pfaffenwaldring 32, D - 70569 Stuttgart, Germany

Abstract

The increase of the superconducting transition temperature in some of the cuprate superconductors to values higher than 130 K is generating strong interest in the exploration of Peltier cooling for the operation of superconducting electronics. In this case, we need materials with a sufficiently large figure of merit z down to temperatures near 100 K. We have performed measurements of the Seebeck coefficient, the thermal conductivity and the electric resistivity in the temperature range 80 - 300 K of Bi_2Te_3-based materials with admixtures of Sb and Se, and studied the influence of pulverization and sintering. The resulting z-values are reported. The influence of sintering on the microstructure of the samples has been studied by SEM.

Introduction

The increase of the superconducting transition temperature in some of the cuprate superconductors to values above 130 K is generating strong interest in the exploration of Peltier cooling for the operation of superconducting electronics. In this case cooling of a highly miniaturized superconducting electronic circuit may be already sufficient ("on-chip Peltier cooling"). We need Peltier materials with a sufficiently large figure of merit $z = \frac{S^2}{\kappa \cdot \rho}$ down to temperatures around 100 K. Here, S, κ, and ρ are the Seebeck coefficient, the heat conductivity, and the electric resistivity, respectively. Assuming the value $z = 3 \cdot 10^{-3}\ K^{-1}$ over the whole temperature range and the ambient temperature $T_0 = 283$ K as an example, for a four-stage Peltier cascade we find $T_1 = 228$ K, $T_2 = 189$ K, $T_3 = 161$ K, and $T_4 = 134$ K, where T_i is the temperature on the cold side of stage i. In this calculation we have assumed that the electric power dissipation in each stage has been reduced by a factor of ten compared to the previous stage. Hence, for the first three stages only 80 % of the maximum temperature drop $(T_i\text{-}T_{i+1})_{max} = \frac{1}{2z}\left[\left(2zT_i+1\right)^{1/2}-1\right]^2$ has been used in calculating the values of T_i given above.

For the semiconductors favorable for Peltier cooling because of their relatively small concentration of charge carriers (in contrast to metals), the heat conductivity is dominated by phonons. Hence, it appears favorable to increase the phonon scattering in order to obtain a small value of κ and a large value of z. Motivated by this idea, pulverizing and sintering the Peltier materials has been discussed already many years ago [1]. More recently values of z as high as $(8 - 10) \cdot 10^{-3}$ K^{-1} in the temperature range 100 - 300 K have been reported [2]. Because of these results we have investigated the relevant transport properties S, κ, and ρ in the temperature range 80 - 300 K and studied the influence of pulverization and sintering. So far we have concentrated on Bi_2Te_3-based materials with admixtures of Sb and Se. In this paper we report the first results of our studies.

Experimental Procedures

Our n- or p-doped Peltier materials were prepared from the elements (purity 99.99 % or higher) by melting in a quartz tube at a temperature around 800° C. The polycrystalline alloys were the starting materials for the subsequent powder-metallurgical treatment. The polycrystals were mechanically ground in air to small pieces and then pulverized in a planetary mill using a small admixture of petrol-ether. The powder was placed in oscillating sieves allowing the separation into four fractions with the following grain sizes: smaller than 20 µm, 20 - 32 µm, 32 - 40 µm, larger than 40 µm. Up to now most experiments have been carried out using only a single fraction 0 - 40 µm. The powder was compressed within a steel cylinder using a force in the range 20 - 100 kN. In this way the powder was turned into tablets of 8 mm or 13 mm diameter and 2.0 - 3.5 mm thickness. The sintering of the tablets was performed under Argon atmosphere (containing 8 % H_2) at 400° C for generally a period of 2 - 24 h.

After sintering, the round tablets were used directly to measure the Seebeck coefficient and the heat conductivity. The applied temperature gradient was oriented in axial direction. In order to cover the temperature range 80 - 300 K, the samples were mounted on a sample holder surrounded by a metal can which could be evacuated. During the measurements this metal can was inserted into a liquid nitrogen bath. For establishing the temperature gradient a standard configuration of heater and thermocouples (30 µm wire diameter) was used. For the electric resistivity measurements we have used a standard four-probe method by placing four spring-loaded gold contact pins on the tablet surface.

0-7803-4057-4/97 $10.00 ©1997 IEEE

In addition to the electrical and thermal measurements we have performed x-ray analyses of the samples and studied their microstructure using scanning electron microscopy. Using a spatially resolved eddy current damping method for detecting the local resistivity values, the tablets were found to be homogeneous.

Experimental Results and Discussion

In Fig. 1 we show the quantities κ, ρ, S, and the figure of merit z for p-doped $Bi_{0.52}Sb_{1.48}Te_3$ plotted versus temperature. The triangles refer to the 0.25 wt.-% Se admixture, whereas the circles were obtained for the 0.5 wt.-% Se admixture. The open triangles and circles refer to the samples without sintering whereas the solid triangles and circles indicate the samples sintered for 5 h at 400° C. The compression force was 20 kN and the tablet diameter 8 mm. The samples of Fig. 1 were fabricated using the single 0-40 μm fraction of the powder.

We have also studied the n-doped material $Bi_2Te_{2.4}Se_{0.6}$. In some cases, a curve of the figure of merit versus temperature similar to that shown by the solid circles in Fig. 1 has been obtained. It appears that the alloying of Sb to this material is difficult. However, our studies of this material are not yet completed.

Up to now we have performed only few experiments regarding the influence of the grain size of the powder. However, the sieved fraction where the grains with diameter less than 20 μm have been eliminated, appears favorable, resulting in an appreciable enhancement of the figure of merit, compared to the unsieved material.

We have investigated the influence of sintering on the microstructure of the samples by scanning electron microscopy. Figure 2 shows the surface topography of a p-doped $Bi_{0.52}Sb_{1.48}Te_3$ tablet (13 mm diameter, 80 kN force) before and after sintering (0.5 h, 400° C), respectively. The sintering is seen to result in the formation of small crystals. As indicated by EDX analysis, these crystals consist of Sb. For this SEM analysis the tablet has been fractured and the images shown in Fig. 2 were taken for the same location on the fractured surface. The Sb microcrystals seen in Fig. 2b apparently had been fully developed after the 0.5 h sintering period, and practically remained unchanged during additional sintering periods. During the sintering process the evaporation of Te has clearly been indicated by subsequent x-ray diffraction. It seems likely that the evaporation of Te during the sintering is responsible for the appearance of the Sb microcrystals.

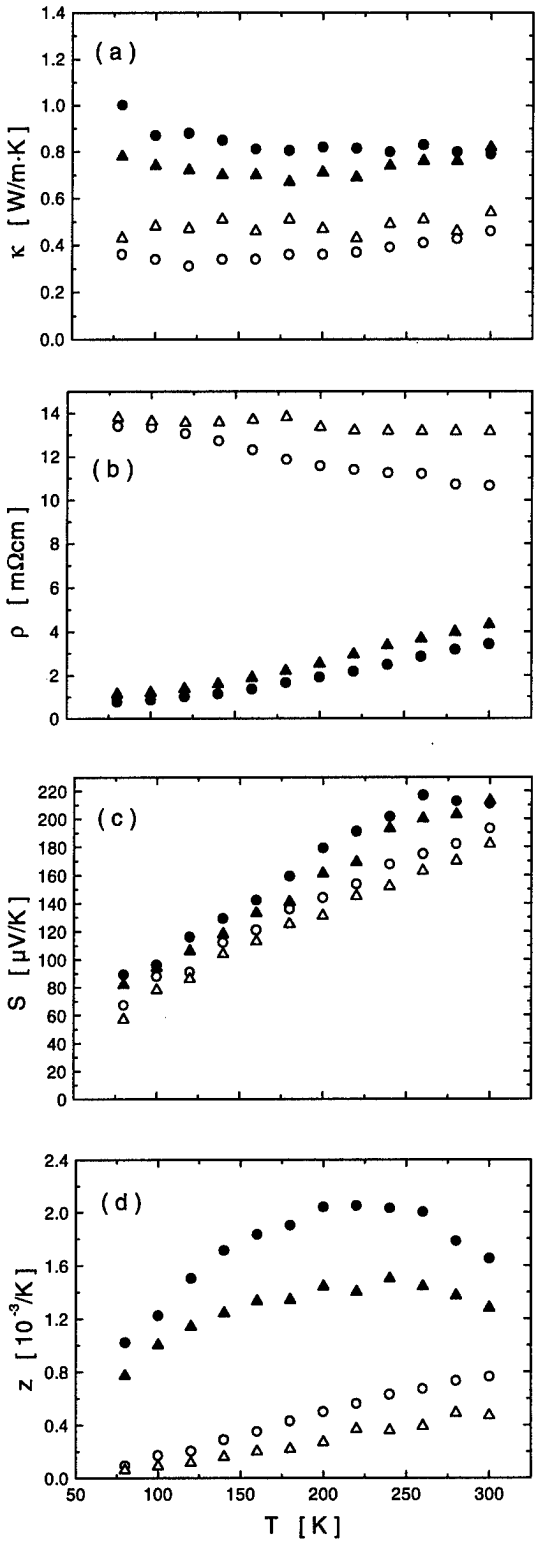
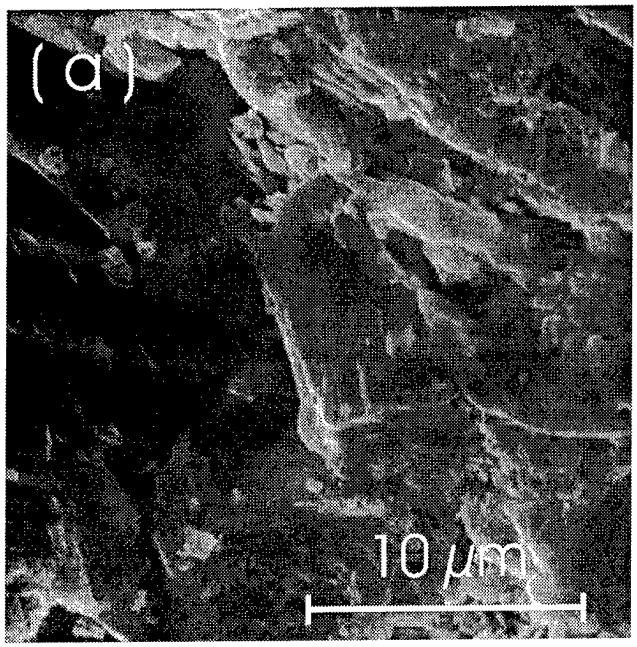


Fig. 1: Heat conductivity κ, electric resistivity ρ, Seebeck coefficient S, and figure of merit z of p-doped $Bi_{0.52}Sb_{1.48}Te_3$ with 0.25 wt.-% (triangles) and 0.5 wt.-% (circles) Se admixture. Open symbols: without sintering; solid symbols: after sintering for 5 h at 400° C.



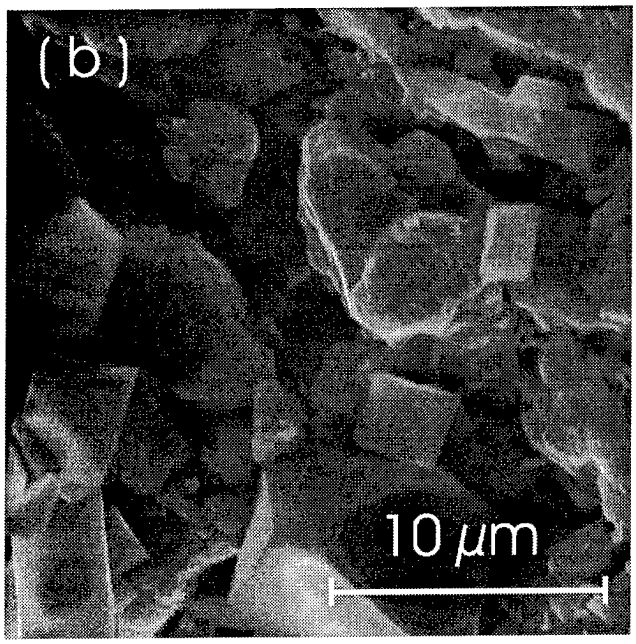
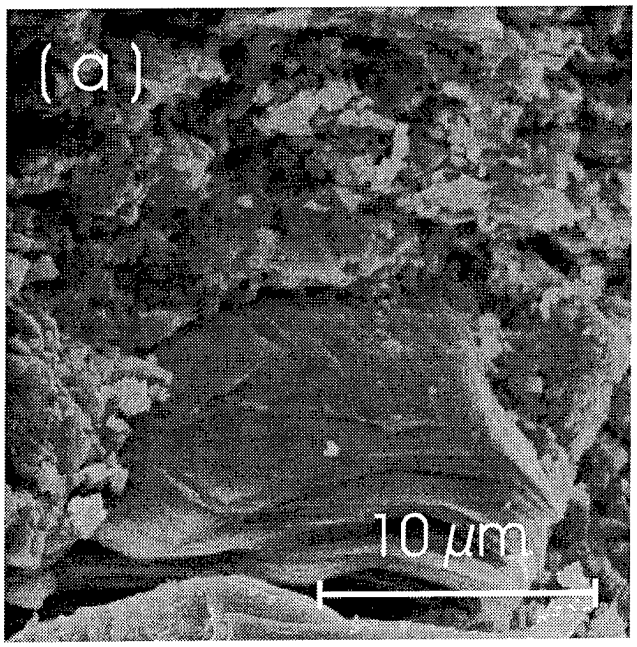


Fig. 2: SEM images of p-doped $Bi_{0.52}Sb_{1.48}Te_3$ before (a) and after (b) sintering. Further details are given in the text.



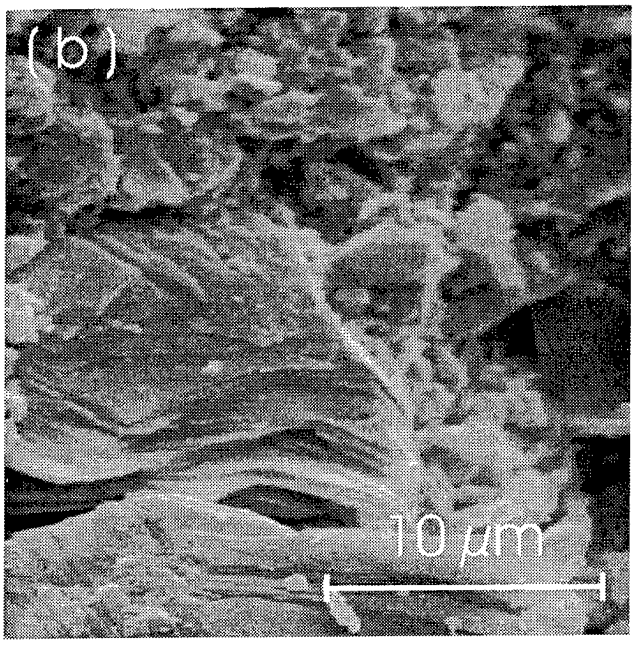


Fig. 3: SEM images of n-doped $Bi_2Te_{2.4}Se_{0.6}$ before (a) and after (b) sintering. Further details are given in the text.

Typical SEM images of the n-doped material $Bi_2Te_{2.4}Se_{0.6}$ (13 mm diameter tablet, 80 kN force) before and after sintering (1 h, 400° C) are presented in Fig. 3. Here we do not see the generation of any microcrystals during the sintering process, similar to the Sb microcrystals of Fig. 2b. Again, the SEM images were taken for the same location on the fractured surface. Generally, for this material during sintering we have observed a distinct intergranular growth leading to a larger microcrystalline structure.

As the main result of our measurements displayed in Fig. 1 we note that the values of the figure of merit of the sintered p-doped material with 0.5 wt.-% Se admixture are appreciably higher than the values without the Se admixture [3, 4]. Further, in the lower temperature regime below about 200 K the z-values of the sintered samples are generally larger than those of the corresponding polycrystals. An additional increase in the values of z can be expected by optimization of the range of grain sizes used for the tablet fabrication. As we see from Fig. 1, the Seebeck coefficient shows an interesting increase due to sintering. Whereas the electric resistivity of the samples without sintering attains relatively high values, ρ is reduced by

a factor up to more than 10 because of sintering. This can be understood in terms of an improvement of the intergranular contacts. The corresponding increase in thermal conductivity due to sintering remains relatively small.

Acknowledgment

This work was supported by the Bundesminister fuer Bildung, Wissenschaft, Forschung und Technologie (Project No. 13N6937/7).

References

[1] U. Birkholz, Halbleiterprobleme, Vol. **VI**, Vieweg, Braunschweig, 1964.

[2] A. A. Joraide, J. Materials Science **30**, 744 (1995).

[3] J. W. Straehle, Thesis, University of Tuebingen, 1996.

[4] K.-J. Klingesberger, Thesis, University of Tuebingen, 1997.

Transport Coefficients of InSb in a Strong Magnetic Field

Hiroaki Nakamura, Kazuaki Ikeda* and Satarou Yamaguchi

National Institute for Fusion Science (NIFS), 322-6, Oroshi-Cho, Toki-City, 509-52 , Japan,
Tel.&FAX +81-52-789-4538, E-mail:hiroaki@rouge.nifs.ac.jp, http://rouge.nifs.ac.jp/~hiroaki/index.html
*Department of Fusion Science, The Graduate University for Advanced Studies(GUAS),
322-6, Oroshi-Cho, Toki-City, 509-52 , Japan.

Abstract

Improvement of a superconducting magnet makes induction of a strong magnetic field easier. This fact gives us a possibility of energy conversion by the Nernst effect. As the first step to study the Nernst element, we measured the conductivity, the Hall coefficient, the thermoelectric power and the Nernst coefficient of the InSb, which is one of candidates of the Nernst elements. From this experiment, it is concluded that the Nernst coefficient is smaller than the theoretical values. On the other hand, the conductivity, the Hall coefficient ant the thermoelectric power has the values expected by the theory.

Introduction

One of the authors, S. Y., proposed[1,2] the direct electric energy conversion of the heat from plasma by the Nernst effect in a fusion reactor, where a strong magnetic field is used to confine a high temperature fusion plasma. He called[1,2] the element which induces the electric field in the presence of temperature gradient and magnetic field, as Nernst element. In his paper[1,2], he also estimated the figure of merit of the Nernst element in a semiconductor model. In his result[1,2], the Nernst element has high performance in low temperature region, that is, 300 - 500 K.

Before his works, the Nernst element was studied in the 1960's[3]. In those days, induction of the magnetic field had a lot of loss of energy. This is the reason why the Nernst element cannot be used. Nowadays an improvement on superconducting magnet gives us higher efficiency of the induction of the strong magnetic field. We started a measuring system of transport coefficients in the strong magnetic field to estimate efficiency of the Nernst element on a few years ago[4].

As the first candidate of the Nernst element, we choose InSb, which is expected to have the high figure of merit according to the single-band model[5]. The experimental results show that the Nernst coefficient is smaller than the theoretical values. On the other hand, the conductivity, the Hall coefficient and the thermoelectric power has the values expected by the theory.

In this paper, we introduce the experimental results and compare the theoretical calculations.

Experiment

Choice of material

We discuss the principle of transport phenomena in a magnetic field and a temperature gradient. This behavior is written by two phenomenological equations[6] as follows:

$$\boldsymbol{E} = \frac{\boldsymbol{J}}{\sigma} + \alpha \nabla T + R_{\mathrm{H}} \boldsymbol{B} \times \boldsymbol{J} + N \boldsymbol{B} \times \nabla T, \qquad (1)$$

$$\boldsymbol{q} = \alpha T \boldsymbol{J} - \kappa \nabla T + N T \boldsymbol{B} \times \boldsymbol{J} + L \boldsymbol{B} \times \nabla T \qquad (2)$$

where $\boldsymbol{E}$ is electrical field, $\boldsymbol{J}$ current density, $\boldsymbol{B}$ magnetic field, T temperature, σ electrical conductivity, α thermoelectric power, R_H Hall coefficient, N Nernst coefficient, κ thermal conductivity and L Righi-Leduc coefficient.

To simplify the discussion of the efficiency, we replace all transport coefficients by averaged quantities, which do not depend on position within a device. In order to estimate efficiency of the Nernst element, it is useful to define the figure of merit Z_N as follows[3]:

$$Z_N \equiv \frac{\sigma (B N)^2}{\kappa} \ . \qquad (3)$$

Using eq.(1), the optimal efficiency of thermomagnetic generators ε_N is given by[3]

$$\varepsilon_N = \varepsilon_C \left(\frac{1 - \delta_N^*}{1 + \frac{T_{low}}{T_{high}} \delta_N^*} \right) , \qquad (4)$$

where T_{high} (T_{low}) is the temperatures of the heating (cooling) block, ε_C the carnot efficiency, $(T_{high} - T_{low}) / T_{high}$, and

$$\delta_N^* = \sqrt{1 - Z_N \left(\frac{T_{low} + T_{high}}{2} \right)} \ . \qquad (5)$$

The value of δ_N^* must be a real number. This fact impose the following restriction as[3]:

$$Z_N \left(\frac{T_{low} + T_{high}}{2} \right) \le 1 \ . \qquad (6)$$

We plot the normalized efficiency, $\varepsilon_N / \varepsilon_C$ in Fig. 1 as a function of the figure of merit. This figure shows that ε_N increases monotonously as Z_N becomes larger. We, therefore, must choose the high-Z_N materials. We consider the transport coefficients to choose them. It is known from the Boltzmann equation that both conductivity and Nernst coefficient are proportional to Hall mobility[7,8]. This fact derives the form[1,4]:

$$Z_N \propto \mu^3. \qquad (7)$$

The equation (7) is a criterion for searching the Nernst element. Under this criterion, we first propose indium antimonide, InSb as a candidate of the Nernst element. To compare the mobility of InSb with the other materials, we summarize the values of the mobilities in Table 1.

Measurement of transport coefficients and results

1) Conductivity and Hall coefficient

The carrier concentration of the InSb crystals investigated is 6.6×10^{20} [m^{-3}] and its mobility 21 [m^2/V/s] at 77K. This sample exhibited intrinsic behavior near room temperature. Copper wires with 50μm-diameter are spark-bonded onto a crystal by using a capacitor discharge. Chromel-Alumel thermocouples, 0.5 mm in diameter, are contact to heating and cooling units with silver epoxy. The temperature of the sample is controlled within 270-370K by the heat bath, the water temperature of which is kept a constant. We induced a strong magnetic field up to 4 Tesla by the superconducting coil to measure magnetoresistance of the sample. Analog signals of the thermocouples and voltage source are amplified and converted to digital data. The personal computer acquires these data and draws figures in real time.

We use the van der Pauw method[9] to measure the conductivity and Hall coefficients. A geometry for the van der Pauw method is shown in Fig. 2. Figure 3(a) shows the temperature dependence of the resistivity at B=0 Tesla. The temperature dependence of the Hall coefficient is represented in Fig. 3(b).

InSb	7.7 [m^2 / V/ s]
HgSe	2.0
HgTe	2.5
InAs	3.3

Table 1: Mobilities of electron near room temperature.

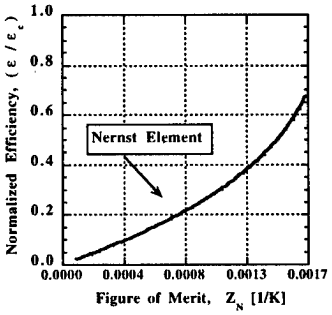


Fig. 1: The maximum efficiency of the Nernst element as a function of Z_N.

2) Thermoelectric power and Nernst coefficient

The sample of measurement of the thermoelectric power and the Nernst element is the same material as the van der Pauw method. However, the shape of the sample is changed from the square to the "bridged shape" (Fig. 4). In order to make temperature gradient in the sample, we used thermofoil heater for a heating copper block side, the water temperature of which is controlled by a low temperature incubator, for a cooling one. Using the heating and cooling units, the temperature difference across the sample was within 10-100K. The thermoelectric voltage, V_α and the Nernst one, V_N have the following relations between the thermoelectric power and the temperature gradient as

$$V_\alpha = L\,\alpha\,\nabla T \approx \alpha\,\Delta T, \qquad (8)$$

$$V_N = w\,N\,B\,\nabla T \approx \frac{w\,N\,B\,\Delta T}{L}, \qquad (9)$$

where ΔT is (T_{high} - T_{low}), w the width of the sample and L the length defined by Fig. 4. Here we define the following physical quantity, β to compare the thermoelectric power and the Nernst effect:

$$\beta \equiv N\,B, \qquad (10)$$

which has the same dimension, [V/K] as α. The results of the measurement of α and β in Figs. (5)-(6). The thermoelectric power doesn't change very much as the magnetic field is induced. On the other hand, the β depends on the magnetic field very much.

In Fig.6(a), we plot the results as the crosses and the theoretical values as the filled circles. The theoretical values are explained in the later. The difference between the experimental results and the theoretical ones is the order of 10. For the strong magnetic field, the results are shown in Fig.6(b).

Analysis and physical quantities

Carrier concentration

In the weak field limit, the Hall coefficient and the carrier con-

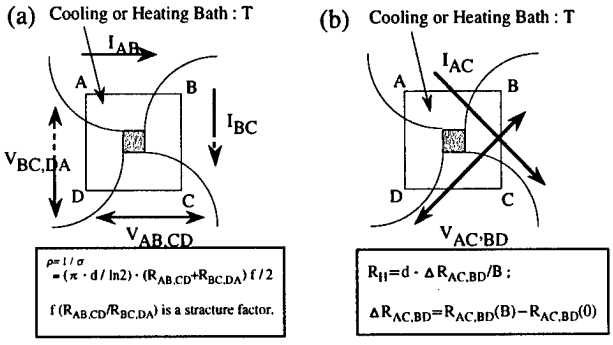


Fig. 2: Sample geometries for performing (a) resistivity and (b) Hall measurements by the van der Pauw method. Size of sample is 4mm×4mm×1mm.

centration has the form[8]

$$R_H = \frac{3\pi}{8|e|}\frac{p - n b^2}{(p + n b)^2} \approx -\frac{3\pi}{8|e|n}, \qquad (11)$$

where we define $b = \mu_n / \mu_p$ and the hole parts are neglected because $b \approx 100$ for InSb[10,11]. Equation (11) and Fig. 3 (b) gives the carrier concentration of the electron in Fig. 7. We can fit the following function of the temperature by the least square method as

$$n(T) = 3.3 \times 10^{20} T^{1.5} \exp\left(-\frac{2600}{kT}\right). \qquad (12)$$

We assume that the sample is in the intrinsic region near room temperature. The carrier concentration of the intrinsic semiconductor is written by[8]

$$n_i(T) = 2\left(\frac{\sqrt{m_n m_p}\, kT}{2\pi\hbar^2}\right)^{\frac{3}{2}} \exp\left(-\frac{E_G}{2kT}\right), \qquad (13)$$

where E_G is the energy gap, m_n the effective mass of the electron, and m_p the effective mass of the hole. Comparing eq. (12) with eq. (13), we obtain

$$E_G \approx 2600 \times \frac{k}{e} = 0.22 \text{ [eV]}, \qquad (14)$$

$$m_n m_p = \left\{\left(\frac{3.3 \times 10^{20}}{2}\right)^{2/3} \frac{2\pi\hbar^2}{k}\right\}^2 \approx 1.7 \times 10^{-2} m_0^2. \qquad (15)$$

Mobility of electron

In the weak field limit, the Boltzmann equation for the single parabolic non-degenerated band model gives the conductivity as follows[8]:

$$\sigma = 1/\rho = |e| n \mu_n \left(1 + \frac{p}{n}\frac{1}{b}\right) \approx |e| n \mu_n, \qquad (16)$$

where we use $b >> 1$ for InSb. Equations (11) and (16) give the mobility of the electron in Fig. 8. The temperature dependence of the mobility of the electron is obtained as

$$\mu_n \approx 7.5 \times \left(\frac{T}{300}\right)^{-1.50} \text{ [m}^2\text{/V/s]}. \qquad (17)$$

The exponent -1.5 denotes that the dominant scattering process is acoustic phonon scattering.

Mobility of hole

In the strong magnetic field limit, the Nernst coefficient of the intrinsic semiconductor becomes[10]

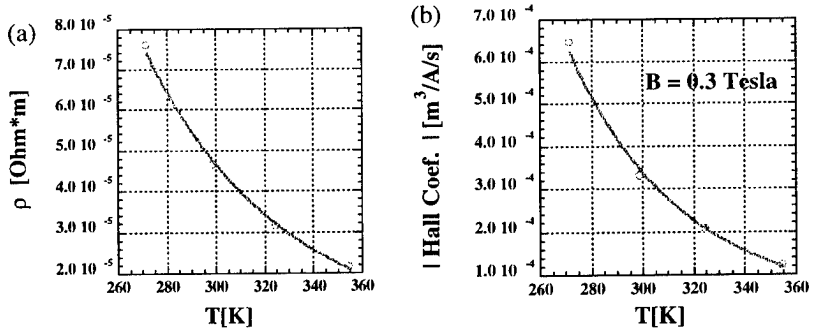


Fig. 3 Resistivity (a) and Hall coefficient (b) of InSb sample as a function of temperature. The closed circles indicate the experimental results. The solid curve is a guide of eyes.

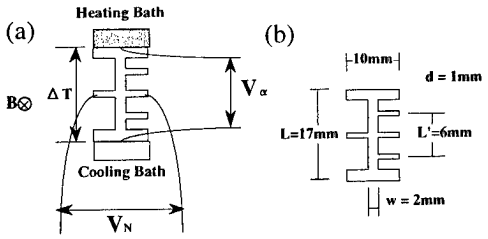


Fig. 4 Shape of the sample for measuring the thermoelectric power and the Nernst effect. This shape is called the "bridged shape".

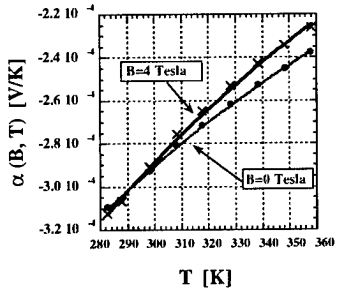


Fig. 5 Thermoelectric power of InSb sample as a function of temperature. The crosses represent experimental results at B=0Tesla. The filled circles indicate the experimental results at B=4 Tesla. The solid curves are guides of eyes.

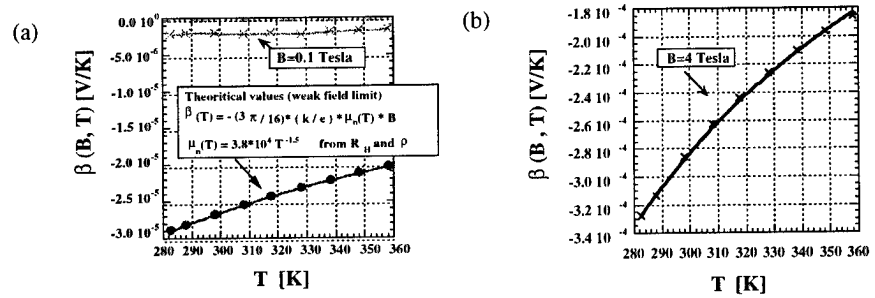


Fig.6 Plot of Nernst effects, $\beta = N \times B$ in the case of B = 0.1 Tesla (a) and 4 Tesla (b). The crosses indicate the experimental results. The filled circles in Fig. (a) were calculated by the single band model with the mobilities which were given from the Hall coefficients and resistivities. In Fig. (b), the solid curve is given by the least square method.

$$N \approx \frac{k}{e}\mu_p\left(4+\frac{E_G}{kT}\right). \qquad (18)$$

Substituting the values of the Nernst coefficient given by the experiment at B =4 Tesla in the eq. (18), we obtain the mobility of the hole in Fig. 9. By the least square method, we also have the temperature dependence of the hole mobility as

$$\mu_p(B=4\text{Tesla}) \approx 0.065 \times \left(\frac{T}{300}\right)^{-1.7} \quad [\text{m}^2/\text{V/s}]. \qquad (19)$$

Fermi level

The thermoelectric power gives the Fermi level as follows[8]:

$$\alpha = \alpha_n \frac{\sigma_n}{\sigma_n+\sigma_p} + \alpha_p \frac{\sigma_p}{\sigma_n+\sigma_p}$$

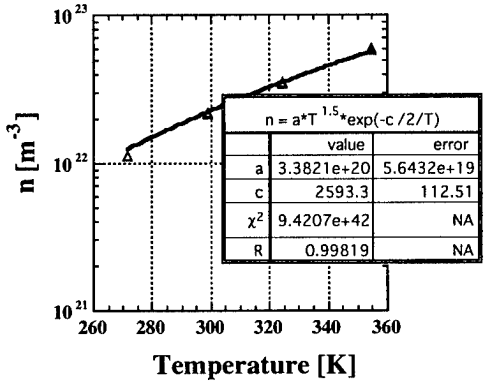


Fig. 7 Temperature dependence of the carrier concentration of the electron. Fitting function is $n(T) = 3.3\times10^{20}T^{1.5}\exp\left(-\frac{2600}{kT}\right)$. Comparing the intrinsic concentration $n_i(T) = 2\left(\frac{\sqrt{m_n m_p}\,kT}{2\pi\hbar^2}\right)^{\frac{3}{2}}\exp\left(-\frac{E_G}{2kT}\right)$, we have

$E_G \approx 2600\times\frac{k}{e} = 0.22$ [eV] and $m_n m_p = 2.9\times10^{-4} m_e$

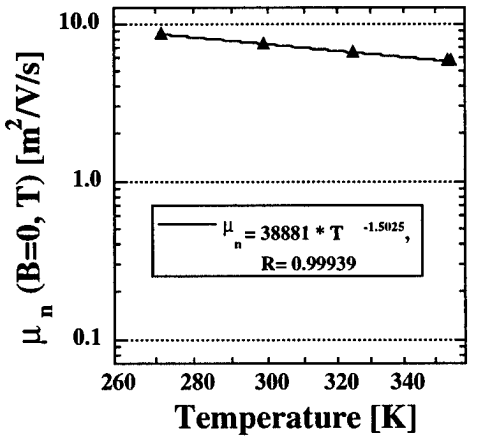


Fig. 8 Temperature dependence of the electron mobility. The experimental results are fitted by $\mu_n \approx 7.5\times\left(\frac{T}{300}\right)^{-1.50}$ [m²/V/s].

$$= \alpha_n\left(\frac{1}{1+\frac{p}{n}\frac{1}{b}}\right) + \alpha_p\left(\frac{\frac{p}{n}\frac{1}{b}}{1+\frac{p}{n}\frac{1}{b}}\right)$$

$$\approx \alpha_n = -\frac{k}{e}\left(2-\frac{\zeta_n}{kT}\right), \qquad (20)$$

where ζ_n is the Fermi level from the edge of the conduction band and negative. Equation (20) and the experimental results of the thermoelectric power give the Fermi level in Fig. 10. In the intrinsic region, the Fermi level becomes[8]

$$\zeta_n = -\frac{E_G}{2} + \frac{3}{4}\ln\left(\frac{m_p}{m_n}\right)\frac{kT}{e} \text{ [eV]}. \qquad (21)$$

Analysis in Fig. 10 gives the temperature dependence of the Fermi level as follows

$$\zeta_n = -0.117 + 3.2\frac{kT}{e} \text{ [eV]}. \qquad (22)$$

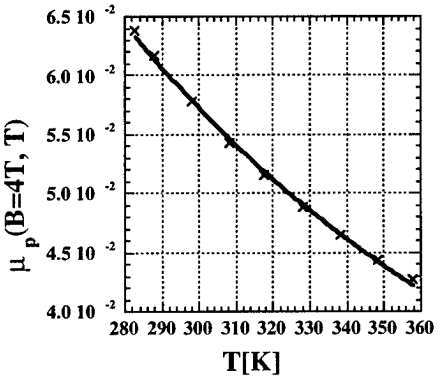


Fig. 9 Temperature dependence of the hole mobility from the Nernst coefficients. The experimental results are fitted by

$$\mu_p(B=4\text{Tesla}) \approx 0.065\times\left(\frac{T}{300}\right)^{-1.7} \quad [\text{m}^2/\text{V/s}].$$

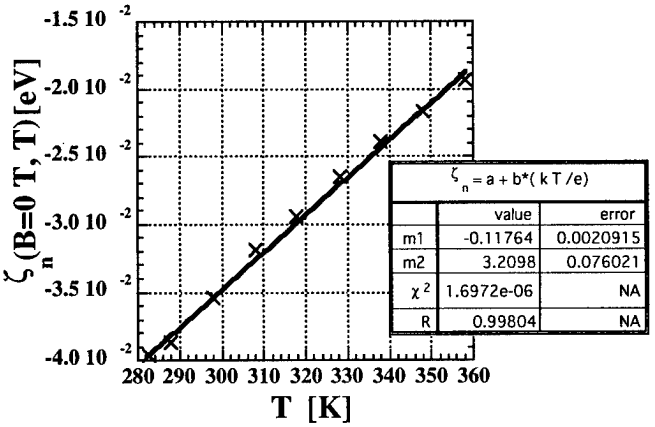


Fig. 10 Temperature dependence of the fermi level. The experimental results are fitted by $\zeta_n = -0.117 + 3.2\frac{kT}{e}$ [eV]. This equation denotes that $E_G \approx 0.23$ [eV] and $\frac{m_p}{m_n} \approx 73$.

From eqs. (21) and (22), the energy gap and the ratio of the effective masses of the electron and the hole is given as

$$E_G \approx 0.23\ [\mathrm{eV}]\ ,\ \frac{m_p}{m_n} \approx 73\ . \qquad (24)$$

Discussion and conclusions

We summarize basic physical quantities obtained by the experiment in Table 2, where the reference values are also written. This table shows that the experimental results are almost coincident with the previous works. It is concluded that the Hall coefficient, the conductivity and the thermoelectric power of InSb near room temperature in the weak field are given by the Boltzmann equation for the non-degenerate parabolic two-band with the acoustic phonon scattering. However, the Nernst coefficient is very smaller than the theoretical value in the weak field. The behavior of the Nernst coefficient in the strong magnetic field is consistent with the two-band model. We try to explain the difference between the experimental and the theoretical values of the Nernst coefficient in the weak field. Moreover we will measure the thermal conductivity in the magnetic field to estimate the figure of merit.

Acknowledgments

The authors are grateful to Dr. Tatsumi in Sumitomo Electric Industries and Prof. Kuroda in Nagoya university for providing semiconductors. We appreciate Prof. Iiyoshi in the National Institute for Fusion Science for his helpful comments.

physical quantity	experimental result	reference value
carrier concentration	$3.3\times10^{20}T^{1.5}\exp\left(\frac{0.22[\mathrm{eV}]}{kT}\right)$	$6\times10^{20}T^{3/2}\exp\left(-\frac{0.26\ [\mathrm{eV}]}{2kT}\right)$
[m^{-3}]	eqs. (12) and (15)	ref. [10,13]
effective mass	$m_n m_p = 1.7\times10^{-2} m_e^2$	$m_n = 0.01359\, m_e$
	eq. (15)	ref.[14]
	$\frac{m_p}{m_n} \approx 73$	$m_p \approx 0.45\, m_e$
	eq.(24)	ref.[15]
mobility * [m^2/V/s]		
electron	$7.5\times\left(\frac{T}{300}\right)^{-1.50}$	$7.7\left(\frac{T}{300}\right)^{-1.66}$
	eq.(17)	ref.[10,11]
hole	$0.065\times\left(\frac{T}{300}\right)^{-1.7}$	$0.085\left(\frac{T}{300}\right)^{-2}$
	at B = 4 Tesla	at B = 0 Tesla
	eq.(19)	ref.[10,11]
Fermi level	$\zeta_n = -0.117 + 3.2\frac{kT}{e}$ [eV]	----------
	eq.(22)	

Table 2 Comparison of the experimental results and the theoretical values.

References

[1] S. Yamaguchi, A. Iiyoshi, O. Motojima, M. Okamoto, S. Sudo, M. Ohnishi, M. Onozuka and C. Uesono, "Direct Energy Conversion of Radiation Energy in Fusion Energy", Proc. of 7th Int. Conf. Merging Nucl. Energy Systems (ICENES), (1994) 502.

[2] S. Yamaguchi, K. Ikeda, H. Nakamura and K. Kuroda, "A Nuclear Fusion Study of Thermoelectric Conversion in Magnetic field", 4th Int. Sympo. on Fusion Nuclear Tech., ND-P25, Tokyo, Japan, April (1997).

[3] T. C. Harman and J. M. Honig, "Thermoelectric and Thermomagnetic Effects and Applications", McGraw-Hill Book Company, (1967), Chap. 7, p. 311.

[4] K. Ikeda, H. Nakamura, S. Yamaguchi and K. Kuroda, "Measurement of Transport properties of Thermoelectric Materials in the Magnetic Field", J. Adv. Sci., **8** (1996) 147, (in Japanese).

[5] H. Nakamura, K. Ikeda, S. Yamaguchi and K. Kuroda, "Transport Coefficients of Thermoelectric Semiconductor InSb", J. Adv. Sci., **8** (1996) 153, (in Japanese).

[6] L. D. Landau, E. M. Lifshitz and L. P. Petaevskii, "Electrodynamics of Continuous Media", 2nd Edition, Pergamon Press, (1984)101.

[7] E. H. Putly, "The Hall Effect and Related Phenomena", London, Butterworth &Co. Ltd., (1960), Chap. 3, p. 66.

[8] K. Seeger, "Semiconductor Physics", Springer-Verlag, (1989).

[9] L. J. van der Pauw, "A Method of Measuring Specific Resistivity and Hall Effect of Discs of arbitrary Shape", Philips Res. Rep., **13** (1958) 1.

[10] O. Madelung, "Physics of III-V Compounds", J. Wiley & Sons, (1964) 115.

[11] J. D. Wiley, "Semiconductors and Semimetals", Vol. **10**, ed. by R. K. Willardson and A.C. Beer, Academic Press, (1975) 169.

[12] L. Sosnowski, "Therm-Electric and Therm-Magnetic Effects", Proc. Int'l School of Physics "Enrico Fermi" XXII , Semiconductors (Academic Press, New York and London 1963) 436.

[13] H. J. Hrostowski, F. J. Morin, T. H. Geballe, and G. H. Wheatley, Phys. Rev., **100** (1955) 1672.

[14] D. M. Zengin, J. Phys., D16, (1983) 635.

[15] D. M. S. Bagguley, M. L. A. Pobinson and R. A. Strandling, Phys. Lett., **6** (1963) 143.

Structural and Electrical Properties of Flash Evaporated $(Bi_{0.4}Sb_{0.6})_2Te_3$ Alloy Thin Films

V. Damodara Das and P. Gopal Ganesan

Thin Film Laboratory, Department of Physics
Indian Institute of Technology, Madras, Chennai - 600 036, INDIA
TEl.: +91-44-2351365 Ext. 3221, Fax: +91-44-2350509, E-mail: vddas@acer.iitm.ernet.in

Abstract

The alloys of $(Bi_{1-x}Sb_x)_2Te_3$ are the best materials currently available for thermoelectric application near room temperature. Thin films of $(Bi_{0.4}Sb_{0.6})_2Te_3$ alloy were prepared by flash evaporation technique onto clean glass substrates held at room temperature in a vacuum of 1×10^{-5} torr. Thickness of the films was monitored by a quartz crystal thickness monitor. Structural characterisation was carried out by X-Ray Diffraction (XRD) and Transmission Electron Microscopy (TEM). It was found that the structure of the alloy films is hexagonal and the films are polycrystalline. Electrical resistivity and thermoelectric measurements were carried out on these films in the temperature range 300 K to 450 K. From the electrical resistivity measurements, the plot of Ln(σ) vs 1000/T was drawn. From the plot of thermoelectric power against temperature, the nature of films has been identified. These parameters are found to influence the figure merit of the alloy films.

Introduction

$V_2(VI)_3$ compounds Bi_2Te_3 and Sb_2Te_3 have been used because of their good thermoelectric properties for the fabrication of thermoelectric devices[1]. Mixed crystals of Bi_2Te_3 and Sb_2Te_3 of appropriate proportions give a p-type material with a thermoelectric figure of merit higher than either of the compounds alone. This is due to a reduction in the mean free path of phonons without a similar reduction in the mean free path of the holes[2]. These crystals crystallize in the series of anisotropic narrow band gap semiconductors with trigonal layer structure (point group $\bar{3}$m, D_{3d}). Many workers have studied the structure and electrical properties of bismuth antimony telluride in the bulk state[3]. However, there are very few works on these materials in the thin films state[4]. In this paper, the structural and electrical properties of $(Bi_{0.4}Sb_{0.6})_2Te_3$ alloy films have been presented.

Experimental

The bulk alloy of $(Bi_{0.4}Sb_{0.6})_2Te_3$ was prepared from 5N pure Bismuth, Antimony and Tellurium which was taken in stoichiometric proportion in a vacuum sealed quartz ampoule. This ampoule was kept in a furnace and the ampoule temperature was increased upto 800°C with a slow rate and the ampoule was maintained at that temperature for 2 days in order to provide thorough mixing of the liquid by shaking the ampoule frequently. The ampoule was then cooled slowly down to room temperature. The ampoule was then broken and the alloy was powered for use as a source material for thin film preparation.

Thin films of $(Bi_{0.4}Sb_{0.6})_2Te_3$ were deposited on clean glass plates held at room temperature by flash evaporation technique in a vacuum of 1×10^{-5} torr. A quartz crystal thickness monitor (model QCT 101) which was attached to the vacuum coating unit, was used to monitor the rate of deposition of the film and also the thickness of the deposited film. The thickness of the deposited film was 1000 Å. These films were annealed by a radiation heater in a vacuum of 1×10^{-5} torr at a temperature of 450 K for one hour.

To investigate the crystal structure of these films, an X-ray diffractometer (Philips PW1373) operated at 35 kV and 20 mA was used with CuKα radiation ($\lambda = 1.542$ Å). X-ray diffraction patterns were recorded automatically with a scanning rate of 2 deg. min^{-1} in the scanning angle 5-90 deg. The microstructure of the films was studied using a philips CM12 Scanning Transmission Electron Microscope (STEM). Compositional analysis was also carried out in the transmission electron microscope using the Energy Dispersive Analysis of X-rays (EDAX) analyser connected to it.

Thermoelectric power measurements were carried out by the integral method in the temperature range 300 - 450 K. Thermal emf generated due to thermal gradient across the film was measured using a Keithley (USA) multimeter (model 196) with respect to copper. The temperature of the hot end of the film-copper junction was monitored by another Keithley multimeter using a copper constantan thermocouple. These two multimeters were interfaced with a 286 AT computer through a IEEE interface bus. The rate of heating and cooling were controlled by the computer using some switching circuits and this was maintained at 90° C/hour. The temperature and thermal emf data were collected by the computer and stored in the hard disk which were used later for further analysis.

Electrical conductivity of the films was measured by the two probe method using large area (1 cm^2) copper pad pressure

0-7803-4057-4/97 $10.00 ©1997 IEEE

contacts. It was verified before hand by current - voltage measurements in both directions (whose plots were linear) that the contacts were ohmic in the required voltage range. The temperature of the film was controlled by a radiation heater in a vacuum of 1×10^{-5} torr and it was measured by a Keithley multimeter using a copper constantan thermocouple. The resistance of the films was measured using a Keithley multimeter (model 196). Hall effect measurements were carried out by means of the four-point direct current Van der Pauw method at room temperature.

Results and Discussion

Structural and Morphological Analysis

From the positions of the peaks of the X-ray diffraction pattern of bulk alloy, the interplaner spacings (d_{hkl}) were determined. The observed d-values are tabulated and compared with the standard d-values of Bi_2Te_3 and Sb_2Te_3 in Table 1. The Miller indices of each of the peaks were identified with the help of ASTM cards (card 836 and card 874 in set 15)[5]. It was found on comparison that the structure of $(Bi_{0.4}Sb_{0.6})_2Te_3$ alloy is also hexagonal and from the observed d-values of the diffraction peaks, the lattice constants of the bulk alloy were evaluated to be a= 4.23 Å and c =30.07 Å.

Figure 1 shows the typical X-ray diffraction pattern of a typical film of $(Bi_{0.4}Sb_{0.6})_2Te_3$. It indicates the polycrystalline nature of the film. X-ray diffractograms of thin films of the sample confirmed that the structure of $(Bi_{0.4}Sb_{0.6})_2Te_3$ films is the same as that of the bulk. The grain size of the films was calculated from the x-ray diffractogram peaks using the Scherrer formula, $L = 0.9\lambda/B cos\theta_B$ where L is the grain size, λ the wavelength of the radiation used, B the full width at half maximum and θ_B the diffraction angle. The grain size of the as-grown film is 140 Å and annealed film is 200 Å . Thus, grain size was found to be high for annealed films compared to as-grown films.

Figure 2 shows the transmission electron micrograph and selected area electron diffraction pattern of a film of thickness 1000 Å. From the electron micrograph, the size of the grains was calculated to be 200 Å. In addition to the XRD pattern, the selected area electron diffraction pattern also indicates the polycrystalline nature of the films. From the diameter of each ring in the selected area electron diffraction pattern, the interplaner distances (d_{hkl}) were calculated. These d-values are also given in the Table 1 and they are comparable with the bulk alloy d-values and the d-values calculated from the XRD pattern of thin films.

The results from the EDAX spectrum are given in Table 2. It is observed that the atomic percentage of Sb and Te are deviated from the expected values by a large and small extent respectively. This can be attributed to the fact that Lα peaks for Sb and Te are very close (3.60 and 3.77 KeV). Due to the resolution limit of the instrument, the apparent deviation of atomic percentage observed is expected for these two elements. Also due to some fractionation and re-evaporation of volatile components, a change in compo-

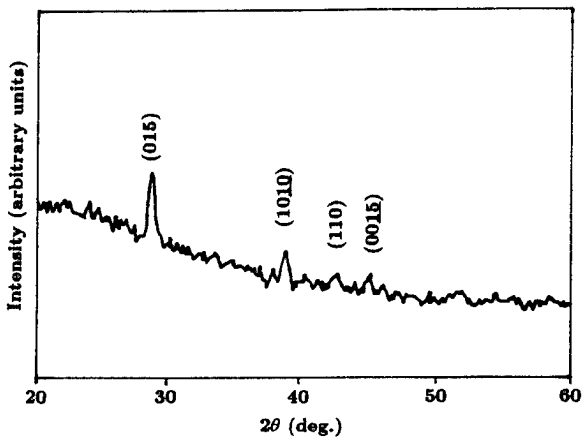
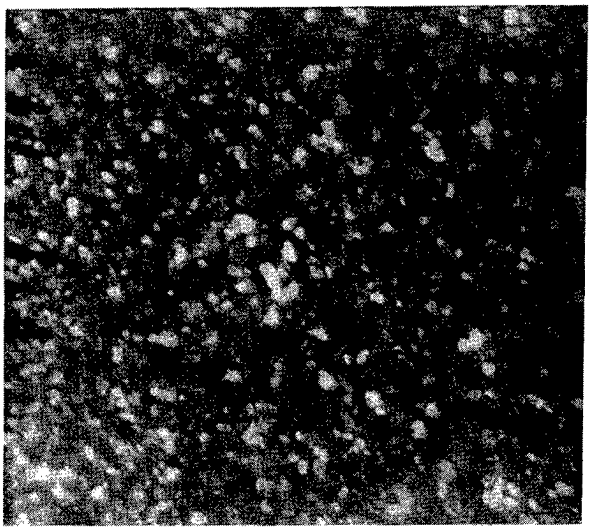
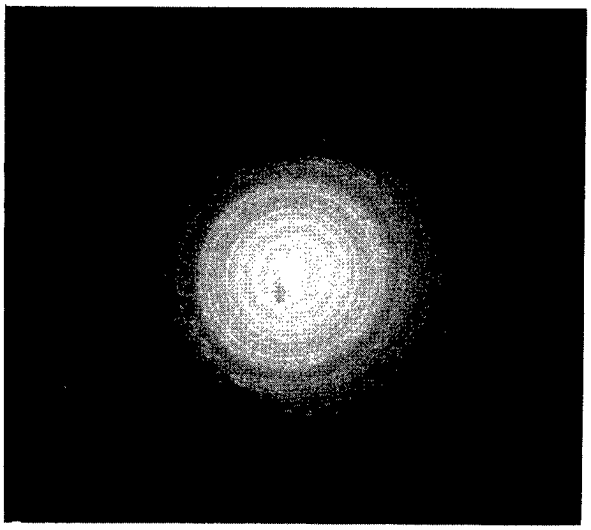


Figure 1: X-ray diffraction pattern of a thin film



(a)



(b)

Figure 2: Electron micrograph (a) and diffraction pattern (b) of a film of thickness 1000 Å

Table 1: Comparison of d - values of $(Bi_{0.4}Sb_{0.6})_2$ Te_3 bulk and thin films from XRD and electron diffraction data with standard d - values.

ASTM d-values (Å)		hkl	Observed d-values (Å)		
			XRD	Film t=1000Å	
Bi_2Te_3	Sb_2Te_3		Bulk	XRD	e-diff.
5.078	5.08	006	5.0463		
3.767		101			3.7333
3.398		104	3.3844		
3.222	3.157	015	3.1742	3.1430	3.2332
2.689		018	2.6615		2.6612
2.376	2.349	10$\underline{1}$0	2.3601	2.3444	2.3534
2.238	2.215	01$\underline{1}$1	2.2200		
2.192	2.130	110	2.1583	2.1417	2.1667
2.031	2.030	00$\underline{1}$5	2.0308	2.0232	
1.995	1.977	10$\underline{1}$3	2.0144		1.9921
1.812	1.766	205	1.7846		1.7894
1.693	1.692	00$\underline{1}$8	1.6933		1.6903
1.611	1.578	02$\underline{1}$0	1.5898		1.5918
1.4901		11$\underline{1}$5	1.4792		1.4827
1.4513	1.450	00$\underline{2}$1	1.4512		
1.414	1.408	01$\underline{2}$0	1.4107		
1.397	1.3597	125	1.3741		1.3747
1.3404	1.3249	11$\underline{1}$8	1.3307		
1.2986		21$\underline{1}$0	1.2818		1.2782

Table 2: Results of EDAX analysis

Elements	Atomic %	
	Observed	Expected
Bi	16.0	16±0.8
Sb	14.5	24±1.2
Te	69.5	60±3.0

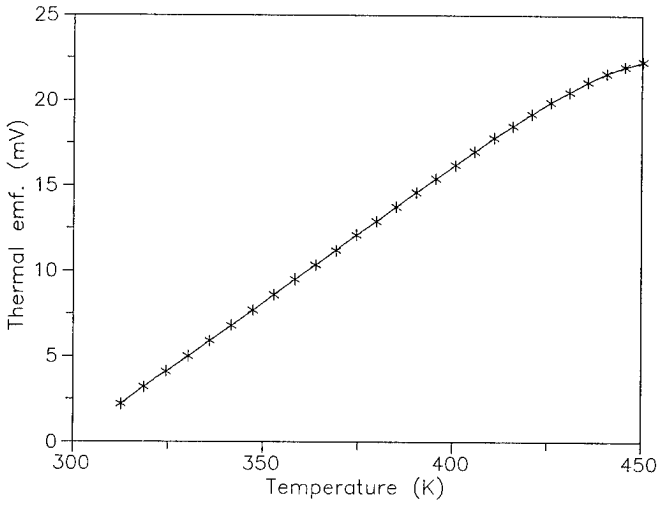


Figure 3: Plot of thermal emf versus temperature

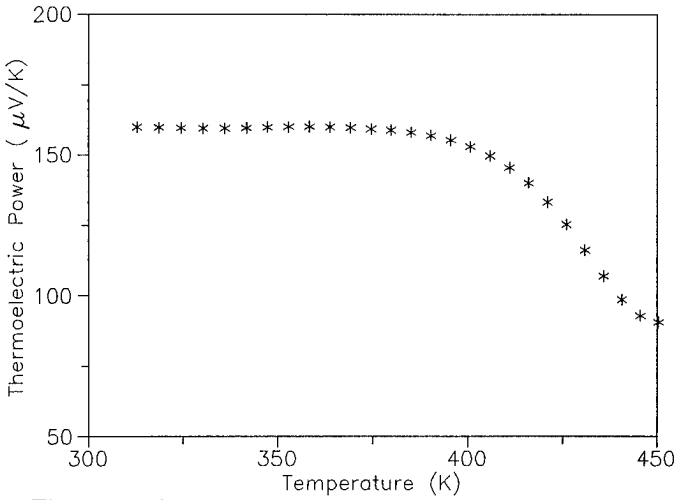


Figure 4: plot of thermoelectric power vs temperature

sition takes place in the films formed.

Thermoelectric power

Figure 3 shows the measured thermal emf for the annealed film in the temperature range 300 - 450 K. It is observed that at low temperatures the thermal emf is nearly linear and at high temperatures, it deviates much from linearity. From the slope of the plot, the thermoelectric power of the film was calculated.

Figure 4 shows the variation of the Seebeck coefficient as a function of temperature. The Seebeck coefficient is temperature dependent and at low temperatures it increases with increasing temperature and at high temperatures it decreases with increasing temperature. This indicates the degenerate nature of the films. From the voltage terminal connected to the cold-end it was found that that end was positive, and hence, the semiconductor was p-type.

Electrical resistivity

Electrical resistivity measurements were carried out for two cycles of heating and cooling. Figure 5 shows the resistivity variation with temperature during heating-cooling cycles for as-grown and annealed films. During the first heating cycle, the resistivity variation is different from all other cycles. But the resistivity variation in the second (and subsequent) heating and cooling cycles retraced the variation in the first cooling cycle. Resistivity during the first heating cycle was considerably higher than that in the first cooling cycle. Irreversible changes occur during the first heating cycle leading to a steep fall in resistance which can be explained by the following:

A large number of non-equilibrium defects which are thermodynamically unstable, are frozen-in during the deposition of a film. During the first heating these defects are annealed out.[6] The substrate, i.e., glass plate is inert towards the film atoms and this causes the re-evaporation of the film material. Another significant effect due to annealing is re-orientation and growth of microcrystallites which leads to the increase in size of the grains. The increase in

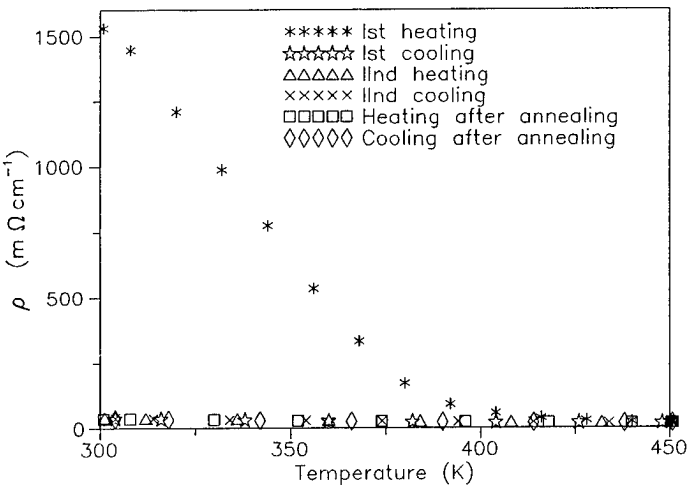


Figure 5: Plot of electrical resistivity vs temperature

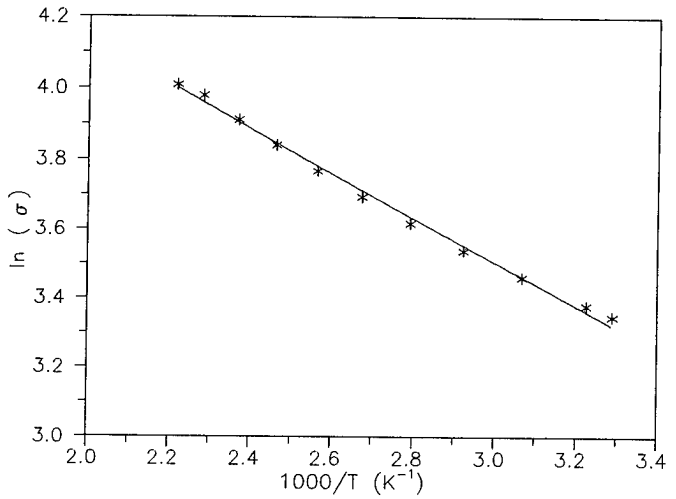


Figure 6: Plot of ln (σ) vs reciprocal temperature

the grain size leads to a reduction in the ratio between grain boundary area and grain volume and consequently in grain boundary scattering. These processes lead to irreversible changes in resistivity.

Figure 6 shows the plot of ln(σ) vs 1/T for annealed films. It is clear from Fig. 6 that the plots are nearly linear. Thus, $(Bi_{0.4}Sb_{0.6})_2Te_3$ thin films studied in the present work exhibit normal semiconducting behaviour of exponential increase of conductivity with temperature in the temperature range studied, after annealing. From the plot of ln(σ) vs 1/T the values of the activation energy have been calculated using the relation [7]:

$$\sigma = \sigma_o \exp\left(\frac{-E_a}{kT}\right)$$

where E_a is the conductivity activation energy and k is the Boltzmann constant. The slight deviation from linearity is due to effects of impurities/defects present in the films. During the deposition of the films, gas molecules, including oxygen will also bombard the substrate simultaneously and these will be trapped in the growing film. This leads to the formation of defects. The oxygen (electronegative) atoms bind electrons and generate holes and cause hole conduction. During annealing, most of these defects are annealed out eventhough the defects which have decay energies higher than the annealing temperature will be still present in the film. Due to the different vapour pressures of the elements, there will be a slight deviation from stoichiometry, i.e., excess or deficiency of a component. These defects produce extra quantum levels distinct from those of the main lattice.

The calculated activation energy value is 55 meV. From the Hall effect study in the magnetic filed of 2.5 K.Gauss, hole concentration was determined at room temperature for annealed films and was found to be $1.2 \times 10^{19} cm^{-3}$.

Conclusions

Thin films of $(Bi_{0.4}Sb_{0.6})_2Te_3$, prepared by flash evaporation were characterized by XRD and Electron Microscopy and Electron Diffraction. These films are polycrystalline with hexagonal structure and the d-values are comparable with the bulk. From the thermoelectric power measurement, it is found that the films are p-type semiconducting. The activation energy for conduction in these films is calculated from the resistivity measurement. The carrier concentration of the films was calculated from the Hall effect measurement. The thermoelectric power depends on the carrier concentration of the film. The thermoelectric figure of merit depends on the thermoelectric power and electrical resistivity of the films.

References

[1] Rowe D.M. and Bhandari C.M., "Modern Thermoelectrics", Holt, Rinehart and Winston, London,(1983) p.103.

[2] C. H. Champness, P. T. Chiang, and P. Parekh, "Thermoelectric properties of $Bi_2Te_3 - Sb_2Te_3$ alloys", Canadian J. Phys., 43 (1965) 653.

[3] M. Stordeur, "The thermoelectric figure of merit in the mixed crystal system p - $(Bi_{1-x}Sb_x)_2Te_3$", Phys. Stat. Sol. (b), 161 (1990) 831.

[4] F. Volklein, V. Baier, U. Dillner and E. Kessler, "Transport properties of flash evaporated $(Bi_{1-x}Sb_x)_2Te_3$ films I: optimization of film properties", Thin Solid Films, 187 (1990) 253.

[5] Joint Committee on Powder Diffraction Standards (JCPDS) diffraction data card 863 for Bi_2Te_3 and 874 for Sb_2Te_3 in set 15 published by American Society for Testing and Materials (ASTM).

[6] V. Damodara Das, "Modified equations for the evaluation of energy distribution of defects in as-grown thin film by Vand's theory", J. Appl. Phys., 55 (1984) 1023.

[7] V. Damodara Das and P. Gopal Ganesan, "Electrical conduction studies on $(Bi_{0.6}Sb_{0.4})_2Te_3$ thin films", Semicond. Sci. Technol. 12 (1997) 195.

BISMUTH-TELLURIDE FILMS PREPARED BY VACUUM-ARC PLASMA METHOD FOR THERMOELECTRICAL TRANSDUCERS

Irina V. Gasenkova

Institute of Electronics, National Academy of Sciences of Belarus, 22 Lagoiski Trakt,
220090 Minsk, Republic of Belarus,
Tel. (37517) 265 64 33, Fax: (37517) 265 25 41, E-mail: inel @ inel.bas-net. by

Abstract

The results of using $(BiSb)_2Te_3$ and $Bi_2(TeSe)_3$ films prepared by pulsed vacuum plasma method in contactless thin-film TET's are presented. The devices are compatible in technology and miniaturization degree with microelectronic structures and, hence, can be used as components of special-purpose integrated devices for converting, processing and measuring of electrical signals. Comparison is made between the parameters of two types of differential transducers of identical design with thermobattery branches made of PbTe/GeTe films (reference device) and $(BiSb)_2 Te_3$ /$Bi_2(TeSe)_3$ films, respectively. The films were deposited by flash evaporation and pulsed plasma methods onto anodic Al_2O_3 wafers used as a base for the device. It is found that the bismuth-telluride TET shows a much higher conversion coefficient as compared to the reference device. Thus, the conversion coefficient increases from 6 to 12 V/W in case of plasma method and from 6 to 8V/W in case of flash evaporation. The conversion coefficient can be further increased by annealing $(BiSb)_2 Te_3$/ $Bi_2(TeSe)_3$ branches in argon. The transducer works at $5\text{-}10^5$ μW input power and 0-100MHz input frequency, with the conversion error <1,5%. Another advantage of the $(BiSb)_2 Te_3$/$Bi_2(TeSe)_3$ TET's is that there is no need for protective film on the branch surface against degradation of device parameters normally found with PbTe/GeTe-based devices due to branch material oxidation. It should also be noted that lower surface resistance of branches subjected to annealing allows formation of thermosensitive elements with lower output resistance on the same wafer area. Besides, for the same rating values of thermosensitive elements, smaller area of dielectric wafer is required and the overall sensor size is smaller.

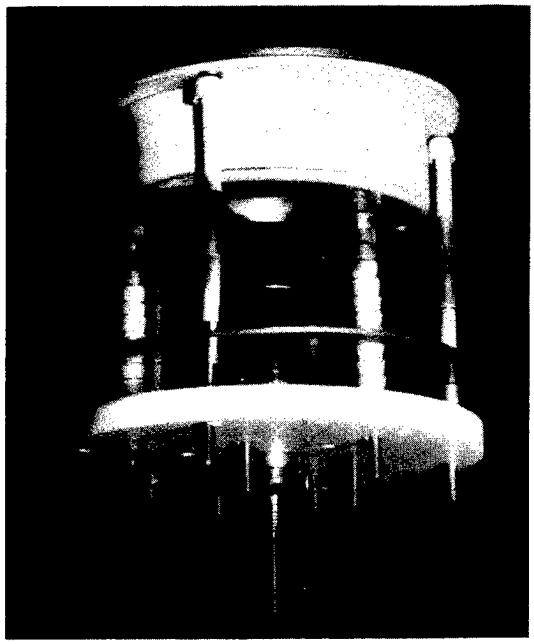
Introduction

The thin-film thermoelectrical measuring transducer (TET) carries out conversion of electrical signals to constant voltage and is employed in such devices as broadband digital voltmeters. The device has been made by using an original technology based on anodic alumina. The method used to form the heating element of the TET makes it possible to fabricate a group of amorphous alumina substrates with nichrome heating elements in a single production cycle by employing photolithography. Because of peculiar properties of the chosen structural elements, the problem of making thermocouple branches is fairly complex owing to low adhesion of film thermoelectric materials to anodic oxide. Thermocouple branches were formed by pulsed vacuum arc-plasma plasma method. Solid solutions based on bismuth telluride such as $(BiSb)_2Te_3$ and $Bi_2(TeSe)_3$ were used as sputtered materials [1]. This paper gives a detailed description of a pulsed vacuum-arc plasma unit employed and contains a discussion of the parameters of thermo-electrical transducers made with branches of different materials.

Pulsed Vacuum Arc Plasma Unit

The $(BiSb)_2Te_3$ and $Bi_2(TeSe)_3$ films were prepared by the pulsed vacuum-arc plasma method in oil-free vacuum of 10^{-5} Pa using the unit demonstrated in Fig. 1. The unit represents a coaxial electrode system with a central electrode of sputtered material and an outer cylindrical electrode between which a high-current vacuum-arc discharge is initiated in vapors of cathode material. The cathode is made in the form of a rod (10 mm in diameter) by pressing powder of sputtered material and is kept in close contact to the conical surface of the insulator by means of a spring, which is necessary for automatic feeding of the cathode consumed during the process. Initiation of the main discharge in the unit is achieved by means of an auxiliary low-power discharge created between the central cathode and coaxially located igniting electrode. The cathode and the igniting electrode are separated by the insulator. The conductive film of cathode material is preliminarily deposited on the insulator surface with its composition corresponding to the required film composition and undergoes vaporization under the action of the current pulse. The plasma fills the gap between the cathode and anode, and the main arc is initiated. During the life of the arc the conductive film on the insulator is recovered. The conductive film resistance is chosen in the range of 2 Ohm to 200 kOhm. The anode and igniting electrode are made of copper, and the insulator is made of high-density alumina. During the discharge, erosion of the anode, igniting electrode and insulator is negligible. Plasma is generated on the butt-end surface of the central cathode. The plasma flux is further accelerated by means of the special magnetic system. Power supply sources for the main discharge and discharge initiation system are characterized by the following respective parameters: capacitance of the capacitor battery varies within 50 to 450 μF and within 0.1 to 3.9 μF; the voltage between the cathode and anode varies up to 1000 V, and between the cathode and igniting electrode up to 900 V; pulse

0-7803-4057-4/97 $10.00 ©1997 IEEE



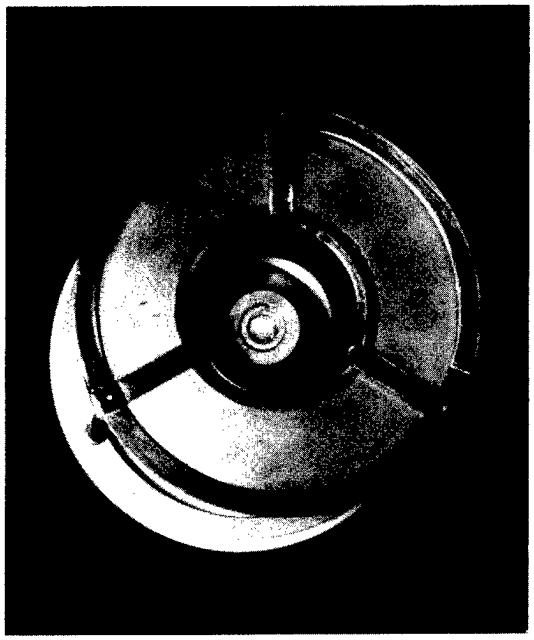


Fig. 1: Appearance of the vacuum-arc plasma unit.

repetition frequency used for plasma generation ranges from 1 to 1000 Hz.

Description of the TET

The TET consists of two identical thin-film multielement contactless conversion units which operate in differential connection scheme. Fig.2 shows a schematic illustration of one of the conversion units. The input part of the transducer represents a heater, and the output part is a thermobattery [2,3]. With an input signal on the heater, the thermo-e.m.f. taken at the output is proportional to the r.m.s. value of the input signal. The value of the thermo-e.m.f. is fed at the input of a voltmeter. In the contactless TET's the heaters and thermobatteries are made as thin

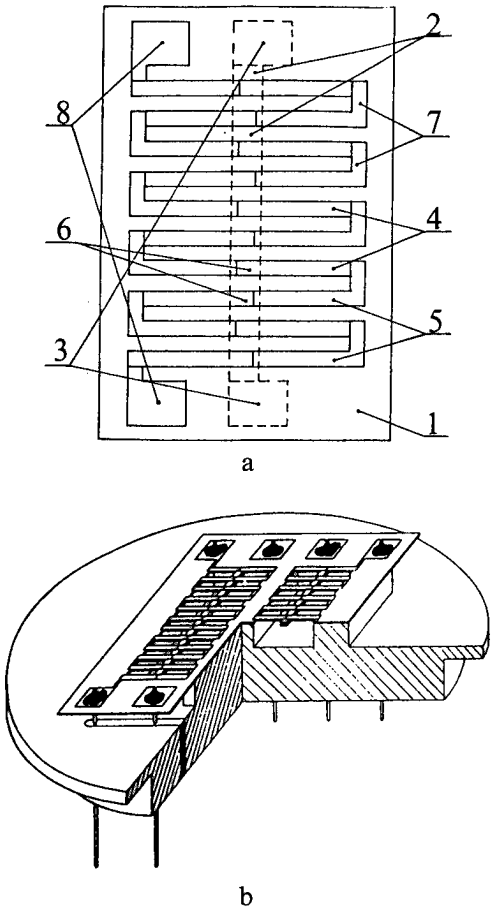


Fig. 2: (a) A schematic image of one of the conversion units: 1 - dielectric substrate, 2 - heater, 3 - contact pads, 4,5 - thermocouple branches, 6 - contact pads for thermobattery, 7 - cold-soldered connection, 8 - hot-soldered connection.
(b) An illustration of the TET.

films placed on the opposite surfaces of a dielectric substrate. The thermobatteries consist of series-connected thermocouples. For convenience, measuring circuits are made of two identical transducers (differentially connected). Such connection reduces a negative influence of the ambient atmosphere (temperature, humidity, pressure, electric interference, etc.). The TET is made on a perforated dielectric substrate of anodic alumina with the dimensions 8.0x4.5x0.03 mm. The substrate was formed by anodizing an aluminium plate 0.07 mm thick in a 3% solution of oxalic acid for 35 + 2 min at 30 mA/cm^2 current density. Then, the heaters were formed by a group technology using photolithography (see Fig. 3).

The nichrome heater was made from a resistive material 0.8 μm thick by ion plasma sputtering. The process was conducted in vacuum not less than 6.6×10^{-4} Pa. Prior to deposition the substrates were heated to (620+10)K and the chamber was filled with argon whose pressure was maintained at 1.2-1.6 Pa during the deposition process. To obtain the required resistance value (ρ = 2.8 Ohm/□) deposition was performed for 20 min at the current of 230-

250 mA on the target. Thin nichrome films were also used as underlayers for formation of nickel metallization. Contact pads 0.6 - 1.0 μm thick were formed on the heater by thermal vacuum evaporation of a material having high electric conductivity (nickel, copper, silver). The thermobattery was formed on the surface opposite to that of the heater. The heater sized 4.6 x 0.2 mm is in thermal contact with 30 thermocouples, each having two branches

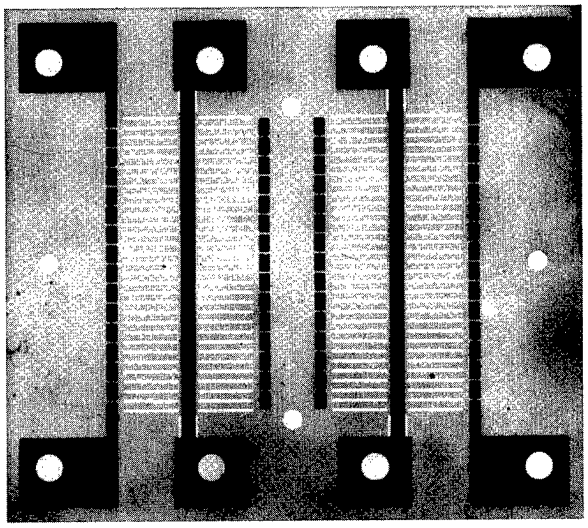


Fig. 3: A finished heating unit of the TET.

sized 1.1 x 0.1 mm. The gap between branches of the two adjacent thermocouples is 0.05 mm. D.C. resistance of the heater was 75 Ohm. The total resistance of the thermobattery consisting of series-connected thermocouples does not exceed 10 kOhm, while the resistance of one branch is 166 Ohm. The TET is sealed in a metalloglass package, and its parameters are measured by special method. The device is tested in the environmental temperature of 240-345 K and humidity of 98% at 295 K. The TET's feature the following characteristics: operation frequency range is 0-100 MHz; deviation from quadratic conversion in the input signal range of 0.05 - 1.0 V does not exceed 0.4%; the conversion error at 100 MHz is not more than 1.5%. As input voltages in the range of 0.03-0.06 V change their polarity, deviation in the conversion coefficient is 0.4%. At voltages higher than 0.06 V, it is not more than 0.1%.

Experimental Results and Discussion

To study the efficiency of $(BiSb)_2Te_3$ and $Bi_2(TeSe)_3$ films prepared by the pulsed vacuum-arc plasma method as thermobattery branch materials, we have made transducer matrices with practically similar parameters and prototypes of a multielement differential thermoelectrical transducer. The following deposition parameters were used: residual gas pressure in the vacuum chamber was not higher than 4 x 10^{-4}Pa; plasma pulse repetition frequency was 20 Hz; capacitance of the discharge battery of the power supply source was 100 μF; the discharge voltage was 160 V; plasma pulse duration was 1.5 ms; the substrate temperature was 470 and 450 K for $(BiSb)_2Te_3$ and $Bi_2(TeSe)_3$, respectively. Surface resistance was controlled in the course of deposition. For p-type films formed by pulsed vacuum-arc plasma method, it was less than 22 Ohm/□, and for n-type branch it was 17 Ohm/□, with the thermo-e.m.f. coefficicents being 106.7 and -90.7 μV/K, respectively. The experimental devices were compared with the reference commercial devices which contained GeTe and PbTe thermobattery branches. P- and n-type branches of GeTe and PbTe were 0.5-0.9 μm thick and had surface resistance of 6 and 8 Ohm/□, respectively. They were deposited by flash evaporation or from Knudsen cell at the rates of 0.0050 and 0.0055 μm/s and substrate temperatures of 435 and 400 K, respectively. Comparison was also made with TET's with $(BiSb)_2Te_3$ and $Bi_2(TeSe)_3$ thermobattery branches produced by the above methods with the deposition rates 0.006 and 0.0035 μm/s, respectively. The basic parameters of the TET's made of different branch materials are given in Table 1.

Table 1. Basic parameters of TET's made by using various methods and materials

Parameter	TET1*		TET2**		Ref. device
	unit A	unit B	unit A	unit B	
Heater resistance (Ohm)	72,5	72,1	74,6	73,7	75
Thermobattery resistance (kOhm)	17,9	18,4	24,2	25,8	25
Conversion coefficient (V/W)	13,5	11,8	8,0	8,0	6

*$(BiSb)_2Te_3$ and $Bi_2(TeSe)_3$ branches deposited by pulsed vacuum-arc plasma method,

**$(BiSb)_2Te_3$ and $Bi_2(TeSe)_3$ branches deposited by vacuum evaporation.

As can be seen, the use of $(BiSb)_2Te_3$ and $Bi_2(TeSe)_3$ results in an increased conversion coefficient with the internal thermobattery resistance being unchanged. For the devices with vacuum evaporated branches, the conversion coefficient is 8 V/W. For the devices with branches made by pulsed vacuum-arc plasma method, the conversion coefficient ranges from 6 to 12 V/W. The pulsed vacuum-arc plasma method made it possible to solve the problem of increasing adhesion of chalcogenide films to alumina, which also allowed us to conduct annealing in inert atmosphere. Thermal annealing of the devices was conducted in Ar at 0.9 atm. pressure for 30 min with temperature being 575, 625 and 675 K. Table 2 illustrates changes in the basic parameters of the experimental TET with chalcogenide branches in the course of annealing in argon atmosphere at 575 K for 30 min. It can be seen from Table 2 that annealing leads to a substantially higher conversion coefficient (up to 17.9 V/W). The higher conversion coefficient is not the only advantage offered by materials based on bismuth telluride and the deposition method employed. Our studies have shown that the films do not practically degrade when stored in air (humidity of

Table 2. The effect of annealing on TET efficiency

Parameter	Before annealing unit A	Before annealing unit B	After annealing unit A	After annealing unit B	Ref. device
Heater resistance (Ohm)	65	65	64.8	64.7	75.0
Thermobattery resistance (kOhm)	18.0	18.14	15.7	15.3	25
Conversion coefficient(V/W)	11.7	11.7	17.9	18,9	6

70-80%) for a year without special packaging. Another advantage is a higher degree of integration achievable in the devices. These peculiarities have been described in detail in our previous paper [4].

Conclusions

The fundamental possibility has been demonstrated of using the pulsed vacuum-arc plasma method for making thermocouple branches from $(BiSb)_2Te_3$ and $Bi_2(TeSe)_3$ in an anodic alumina-based thin-film thermoelectrical transducer. The thermoelectric parameters of bismuth telluride films thus obtained are rather high although our efforts have not been aimed at achieving the best possible results. To gain further improvement of thermoelectric parameters it is desirable that sputtering of the films be conducted using a bulk target material with better characteristics. Our investigations of the composition and microstructure of bismuth telluride films on monocrystalline (NaCl) and amorphous (polyimide) substrates depending on the operation regime of the vacuum-arc plasma unit demonstrate that there is a wide space for further improvements.

Acknowledgments

The author is thankful to Dr. I.L. Grigirishin for fruitful discussions and a substantial support.

References

[1] I.V. Gasenkova, E.I. Tochitsky, "$(BiSb)_2Te_3$ and $Bi_2(TeSe)_3$ films prepared by vacuum arc plasma method: characterization and applications", Proc. of XIV Int. Conf. on Thermoelectrics (ICT'95), St. Petersburg, Russia, 1995.

[2] A.A. Archakov, D.R. Velder, Yu. I. Gorbachyov et al., "Differential thin-film thermoelectric measuring transducer", Teknika Sredstv Svyasi, seriya RIT. **5**(51)(1983)30 (in Russian).

[3] I.V. Gasenkova, "The AVBVI film application as functional elements of thermoelectric transducer", Pribory i Sistemy Upravleniya. **10** (1993) 43 (in Russian).

[4] I.V.Gasenkova, "The use of $(BiSb)_2Te_3$ and $Bi_2(TeSe)_3$ films in thermoelectrical transducers", Journal of Thermoelectricity, **1** (1995) 73.

Geometric contribution to the measurement of thermoelectric power and Nernst coefficient in a strong magnetic field

Kazuaki IKEDA
Department of Fusion Science, The Graduate University for Advanced Studies,
322-6, Orosi-Cho, Toki-City, Gifu-Prefecture, 509-52, Japan
Phone&Fax : +80-52-789-4538, e-mail : ikeda@rouge.nifs.ac.jp

Hiroaki NAKAMURA and Satarou YAMAGUCHI
National Insutitute for Fusion Science (NIFS)

Abstract

On the measurement of thermoelectric power and Nernst coefficient, we used two kinds of shapes for a sample. One is "Bridge shape" and the other is, we call, "Fat-Bridge shape". The latter has 5 times wider main body than the former. We used pure n-InSb in this experiment, whose carrier condensation measured at 77K was 6.6 x 10^{-14} cm^{-3}. The length of sample is 17mm and temperature difference induced between the edges in that direction were about 10°C or 100°C near a room temperature range of 0 to 100°C. Magnetic induction added in the perpendicular direction to temperature gradient was in the range of 0 up to 4 Tesla. In the case of "Fat-Bridge shape", we detected about 10% smaller Nernst coefficient and 1 to 10% smaller thermoelectric power comparing to the "Bridge shape". We suppose this phenomena is due to the geometric contribution on the different shape of samples.

Introduction

We call some semiconductors Nernst element [1,2], which will be able to use for the generation of electric power by applying the Nernst effect. As the fundamental study for the power generation by the Nernst elements, we are studying for the transport properties of its candidates in a magnetic field [3,4]. By measuring their transport coefficients, we will be able to estimate the efficiency of energy conversion.

Experiment

The thermoelectric effect and the Nernst effect can be written respectively in the form,

$$\boldsymbol{E} = \alpha \bullet grad\,\mathrm{T}, \qquad (1)$$

$$\boldsymbol{E} = \mathrm{N} \bullet \boldsymbol{B} \times grad\,\mathrm{T}, \qquad (2)$$

where $\boldsymbol{E}$ is electric field, α thermoelectric power, T temperature, N Nernst coefficient and $\boldsymbol{B}$ magnetic induction.

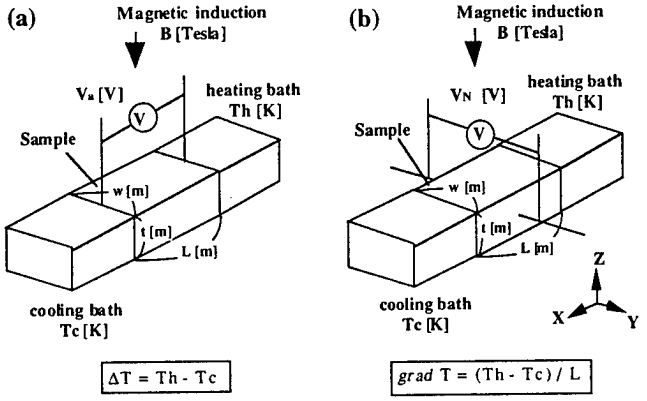


Fig.1 : The scheme of measurement. (a) is for thermoelectric power and (b) is for Nernst coefficient.

Suppose a sample is rectangular parallelepiped and its scale is of length L, width w, thickness t, then a temperature gradient is given in the direction of L. That scheme is indicated to Fig.1.

We can obtain the thermoelectric power α by detecting the potential difference V_α and temperature difference ΔT between edges in the direction of L, and the Nernst coefficient N by temperature gradient $\Delta T/L$ and the magnetic induction B added in the perpendicular direction to temperature gradient and potential difference V_N in the perpendicular direction to both temperature gradient and magnetic induction. They were calculated from eq. (1) and (2) as follows:

$$V_\alpha = \alpha \bullet \left(\frac{\Delta T}{L}\right), \quad hence \quad \alpha = \left(\frac{V_\alpha \bullet L}{\Delta T}\right), \qquad (3)$$

$$V_N = N \bullet B \bullet \left(\frac{\Delta T}{L}\right) \bullet w, \quad hence \quad N = \left(\frac{V_N}{B}\right) \bullet \left(\frac{L}{w}\right). \qquad (4)$$

On this measurement, it is very important that we used two kinds of the shapes for a sample. They are indicated to Fig.2.

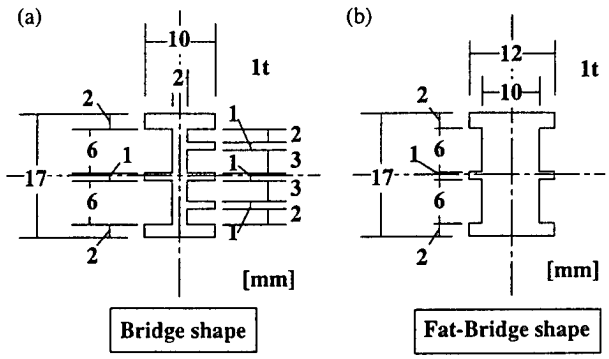


Fig. 2 : The shape of samples. (a) is Bridge shape and (b) is Fat-Bridge shape.

One is called "Bridge shape", that has narrow main body, several legs for measuring leads and wide heads on the edges for having good attachments to heating or cooling bath. We call the other "Fat-Bridge shape", that has 5 times wider body than Bridge one. The samples were cut out from thin wafers at accuracy of about 0.1mm by wire cutter. We measured their scale at precision of within 0.005mm by micrometer.

These samples were located on the sample holder as is indicated to the Fig.3.

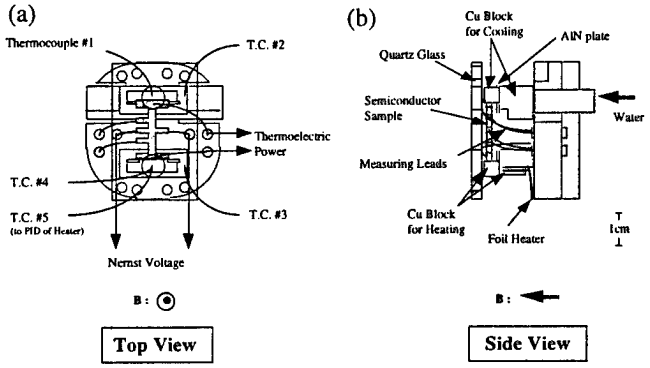


Fig. 3 : Sample holder which is mounted on sample mounter and inserted in the central part of vacuum chamber. (a) and (b) are its top view and side view respectively.

When we make the temperature gradient in the samples, temperatures are controlled by two Cu blocks attached to the edges of sample. One is heated up to about 100°C by foil heater and the other is cooled down to about 0°C by the unfrozen liquid mixed water and ethylene glycol. Temperatures were measured by Chromel-Almuel thermocouples. Measuring leads for voltage signals are 0.5mm diameter wires of the Cu which were welded to sample.

We had the experiment around room temperatures and on the two kinds of temperature conditions. On one condition, the temperature difference of between sample edges is 10 °C, and temperature of cold side is increased 0 up to 80 °C by 10 °C. On the other condition, the cold side is fixed to 0 °C and hot side is 100 °C.

Experimental equipments are indicated to Fig. 4. By using the superconducting magnet coil which is included into the cryostat, magnetic field of 0 to 4 Tesla is generated in the central region of vacuum chamber. The region of 10mm square in the central part of the chamber is stable within 0.1% to the magnetic field strength of central point. We had measurements of physical properties in that region. Inner pressure of chamber was less than 10^{-3} Pa.

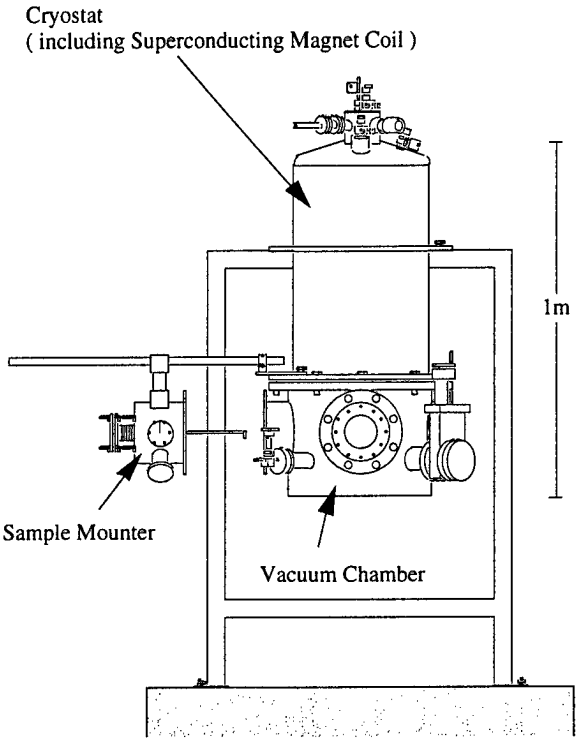


Fig. 4 : The experimental equipments. Superconducting magnet coil, vacuum chamber and sample mounter.

Physical phenomena of temperature and electric field are transduced to voltage signals by thermocouples and leads. As is indicated to Fig. 5, transduced voltage signals are inputted to isolation amplifiers. Then, amplified signals are sent to 16bit A/D converter plugged into a personal computer and are digitized.

The maximum gain of the Amplifier is 2000. We can detect voltage signals in the resolution of 0.15μV at maximum. On

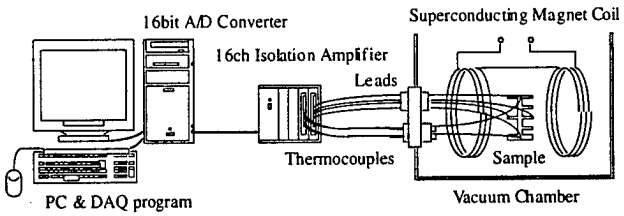


Fig. 5 : Data acquisition system.

this measurement, the precision of the temperature measurement were less than 0.1K and the relative error of the voltage measurement were not exceed 0.5%.

Data analysis and discussion

Figures 6 and 7 shows the dependence of thermoelectric power and Nernst coefficient on magnetic induction respectively. They include data on the conditions that the temperature pairs of heating block and cooling one are set on 0 and 100°C, 10 and 20°C and 80 and 90°C. In Fig. 6, we used

$$\beta = N \bullet B, \qquad (5)$$

as substitute for Nernst coefficient.

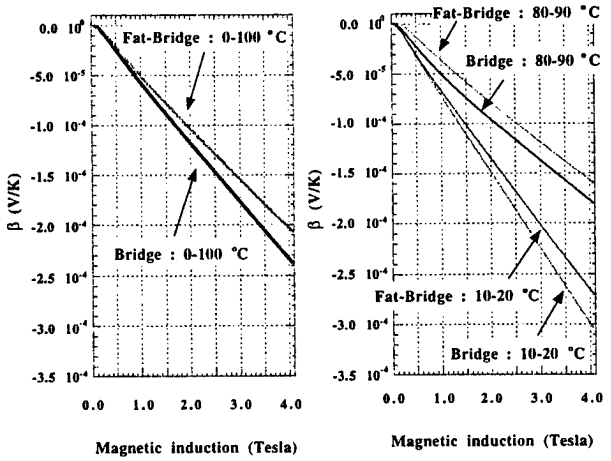


Fig. 6 : The B dependence of β, which is defined as product of Nernst coefficient and magnetic induction.

In very weak and strong magnetic fields, β was linearly decreasing or decreasing with the increase of field strength. It means that Nernst coefficient is nearly constant in their regions. In intermediate fields, there is a transition of N from one constant value to another. Especially in the case of 80-90°C, the sign of coefficient changed. Except in weak field of the case of 80-90°C, the sign of Nernst coefficients was negative on this experiment. These results have qualitative agreements with the investigation of up to 2 Tesla reported in [5]. But we detected the qualitative difference when the shapes of samples were different. At 4 Tesla, Nernst coefficients measured on the Fat-Bridge shape were about 12% smaller than those on the Bridge shape in all cases and that tendencies are similar in strong fields.

In the measurement of thermoelectric powers, the any value on the Fat-Bridge shape was smaller than that on the Bridge shape. But the rate of its reduction were about 8%, 5% and less than 1% in the case of 0-100°C, 10-20°C, 80-90°C respectively.

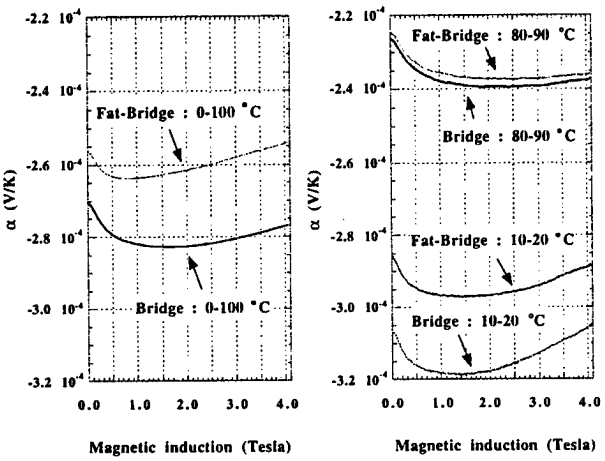


Fig. 7 : The B dependence of the thermoelectric power.

We suppose that the detected differences are apparently and due to the difference of samples' shape. We call it geometrical contribution. To interpret this contribution and the inner state of the samples, more detailed analysis and the theoretical investigation will be proceeded in near future.

Fig.8 shows the dependence of thermoelectric power on magnetic induction, which include the measured and the analytically derived data. The sign of magnetic induction appears the direction to be add. Measured one was not symmetric to the direction of magnetic induction. We suppose this is due to the reason that the positions of measuring leads had the difference in the transverse direction to heat flux and Nernst effect was detected slightly. That component is indicated as the excluded β in Fig.8. Because of the similar mechanism, thermoelectric effect was detected on the measurement of Nernst effect. That appeared as offset voltages apparently, when magnetic induction was equal to zero.

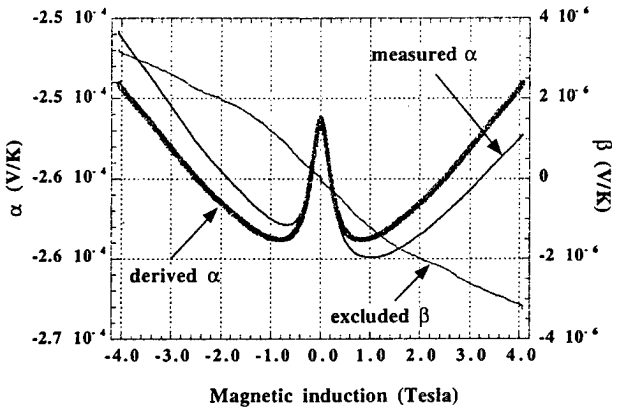


Fig. 8 : Measured α, analytically derived α and excluded β.

To excluded the contaminations on the measured data, we calculate α and β as follows :

$$\alpha = \frac{1}{2}\left\{\left(\frac{V_\alpha(B)}{\Delta T}\right) + \left(\frac{V_\alpha(-B)}{\Delta T}\right)\right\}, \qquad (6)$$

$$\beta = \frac{1}{2}\left(\frac{L}{w}\right)\left\{\left(\frac{V_N(B)}{\Delta T}\right) - \left(\frac{V_N(-B)}{\Delta T}\right)\right\}, \qquad (7)$$

The propriety of these processes are due to the properties that thermoelectric effect is even to the direction of magnetic induction and Nernst effect is odd.

Conclusion

When the magnetic field is added to the semiconductor in which heat flux exist, two components of electric fields are generated inside of it. One is in the origin of thermoelectric effect and the other is Nernst effect. The mixture of these two effects generate the geometric contributions on the measurement of physical properties as we detected on this measurement using "Bridge shape" and "Fat-Bridge shape". This condition is similar to the measurement of the Hall effect [6,7]. When we confirm the physical properties by the measurement, the geometric contributions must be thought of. We shall need to develop the calculation code to interpret the transport properties including the heat and current fluxes in more details and self-consistently.

Acknowledgements

The authors are grateful to Mr. Nishimura in Nishimura factory corporation for the process of samples and Dr. Tatsumi in Sumitomo Electric Industries for providing semiconductors and Prof. Kuroda in Nagoya university for many useful supports. We appreciate Prof. Iiyoshi and Prof. Motojima in the National Institute for Fusion Science for their helpful comments.

References

[1] S. Yamaguchi, A. Iiyoshi, O. Motojima, M. Okamoto, S. Sudo, M. Ohnishi, M. Onozuka and C. Uesono, "Direct Energy Conversion of Radiation Energy in Fusion Energy", Proc. of 7th Int. Conf. Merging Nucl. Energy Systems (ICENES), (1994) 502.

[2] S. Yamaguchi, K.Ikeda, H. Nakamura and K. Kuroda, "A Nuclear Fusion Study of Thermoelectric Conversion in Magnetic field", 4th Int. Sympo. on Fusion Nuclear Tech., ND-P25, Tokyo, Japan, April (1997)

[3] K.Ikeda, H.Nakamura, S.Yamaguchi and K.Kuroda, J. Adv. Sci., **8**, 3&4, 147 (1996), (in Japanese)

[4] H.Nakamura, K.Ikeda, S.Yamaguchi and K.Kuroda, J. Adv. Sci., **8**, 3&4, 153 (1996), (in Japanese)

[5] Ya. Agaev, O. Mosanov, and O. Ismailov, Sov. Phys. Semicond., **1**, 6, 711 (1967)

[6] H. Welker, H. Weiss, Z. Phys. **138**, 322 (1954)

[7] H. Weiss, "Semiconductors and Semimetals 1", Academic, New York (1966)

Thermal Conductivity of Solid Solutions $(Bi_ySb_{1-y})_2Te_3$ for y=0.7—0.8 Grown by Method of Zone Melting

A.I.Anukhin
Scientific- Production Firm "MODUL", Kyiv, Ukraine,
Tel/fax: +38/044/419-9030, Email: hel@osvita.kiev.ua

Abstract

Linear deviation of concentration of excessive tellurium in the melt during zone melting $C=C_0(1+X/l)$, where C_0-start concentration of tellurium in the load, X-zone co-ordinate on the ingot, l-the length of the melting zone, is used for investigating the dependency of thermoelectric qualities of solid solutions $(Bi,Sb)_2Te_3$ on chemical composition distributed along the ingot.

According to the distributed thermoelectric parameters obtained in the temperature rang 150-360K, the general projection of solidus line was made, depicting tellurium for solid solutions $(Bi_ySb_{1-y})_2Te_3$ around chemical composition with the melting temperature close to maximum. There is existing a dependency of distribution of thermoelectric parameters of solid solutions along the ingot on the surface shape of their solidus.

Distribution of remaining thermal conductivity, obtained as a result of subtraction of electron component, calculated on the base Videman Frans law, from the general one, calculated from the Seebeck coefficient, figure of merit and electrical conductivity, depends on ratio of atom parts of bismuth and antimony as well as on excessive concentration of tellurium in the melt. For y>0,5 around room temperature, remaining thermal conductivity is abrupt maximum corresponding to the area of intrinsic conductivity of the ingot.

The maximum of remaining thermal conductivity under y=0,7-0,8 and T=300K reaches the figure of $6,0x10^{-2}$ W/K/cm when at the same time the contribution of ambipole component of conductivity, according to the calculations, under this temperature is not above $6,0x10^{-3}$ W/K/cm.

The most suitable mechanism, which can explain anomaly increase of thermal conductivity in solid solutions with chemical composition corresponding to the area where solidus overlaps with stoichiometric cut, is transition of heat by exitons, too.

Introduction

While using solid state cooling in the low temperature range, it is a problem to get the material with the optimal thermoelectric parameters. To get low temperature thermoelectric material one has to reduce the concentration of charge carriers in the material. The necessary concentration in the most widely used solid solutions $(Bi,Sb)_2Te_3$ is achieved by changing the concentration of tellurium in the melt used for melting of solid solution.

While for solid solutions $(Bi,Sb)_2Te_3$, which are rich with antimony telluride and have p-type conductivity this problem has been successfully fixed, the search for low temperature materials similar to solid solutions with electrical conductivity is still a task to work on.

Unlike the solid solutions enriched with antimony telluride, it is equally easy to get solid solutions $(Bi,Sb)_2Te_3$ enriched with bismuth telluride with hole conduction as well as with electron conduction. At the same time there has not been done enough research to investigate if they can be used as low temperature ones. Meanwhile these solid solutions $(Bi,Sb)_2Te_3$ with the chemical composition close to stoichiometric composition and thus having low specific electric conductivity, may be of interest from the point of view of their use as low temperature material.

Specific thermal conductivity of thermoelectric material together with its electric conductivity and Seebeck coefficient directly determines figure of merit of material.

That is why the purpose of this experiment is to investigate the dependency of these parameters on the concentration of charge carriers in a wide temperature range in the above mentioned solid solutions close in their composition to stoichiometric one.

Method of the Experiment

Growing solid solutions (single phased material) by zone melting technique of Bi_2Te_3-Sb_2Te_3+Te excessive tellurium is moved into the melt by the melting front because the distribution coefficient of tellurium is close to zero. Excessive tellurium concentration in the melt of the zone depends on coordinate X of the zone ingot [1]

$$C=C_0(1+X/l), \qquad (1)$$

Where C_0 - starting concentration of the excessive tellurium in the load, l - length of the melted zone.

According to (1) by the moment of solid solution melting co-ordinate X of the zone corresponds to excessive tellurium concentration in the melt.

Dependency of the tellurium concentration in the melted zone on its coordinate on the ingot allows us to say that there is dependency between the distribution of the thermoelectric qualities along the ingot and concentration of the tellurium in the melt. As a result we can investigate concentration dependency of thermoelectric and thermal properties of the solid solutions $(Bi,Sb)_2Te_3$ using zone melted ingots.

During our investigation by method of vertical zone melting we received the ingots of solid solutions $(Bi_{0.8}Sb_{0.2})_2Te_3$ and $(Bi_{0.7}Sb_{0.3})_2Te_3$ with the length of 12 mm from the load with 2.5% of excessive tellurium. The length of the zone of the melt was 2.0 cm. The low speed of growing which was 1.0 cm/hour provided the growth of single phased solid solutions without any traces of concentration supercooling. The ingots were cut into samples 3x3x5 mm in such way that the 5 mm side was oriented along the growth direction. Discreteness of the coordinate change along the ingot δX=5mm corresponded to the discreteness of the

concentration change of the excessive tellurium in the melt which was equal to

$$\delta C = C_0 \cdot \delta X / l = 0.62\% \qquad (2)$$

Excessive tellurium concentration in the melt was changing in a very wide range from 2.5% to 17.5% (with l=0 and l=12 cm at the beginning and the end of the ingot accordingly).

It is known [1] that in solid solutions $(Bi,Sb)_2Te_3$, enriched by bismuth tellurium, concentration dependency of the physical properties is to some degree alike the same dependency which is a characteristic of bismuth telluride.

According to data [2], chemical composition of the melt, from which bismuth telluride of stoichiometric composition is melted, is rich in tellurium and corresponds to 62.5at%Te+37.5at%Bi (with excessive tellurium concentration in the melt 6.7%). This way, zone coordinate with chemical composition of the melt from which solid solution $(Bi,Sb)_2Te_3$ of stoichiometric composition melting should be expected, is located inside the area of the tellurium concentration change in the zone melt.

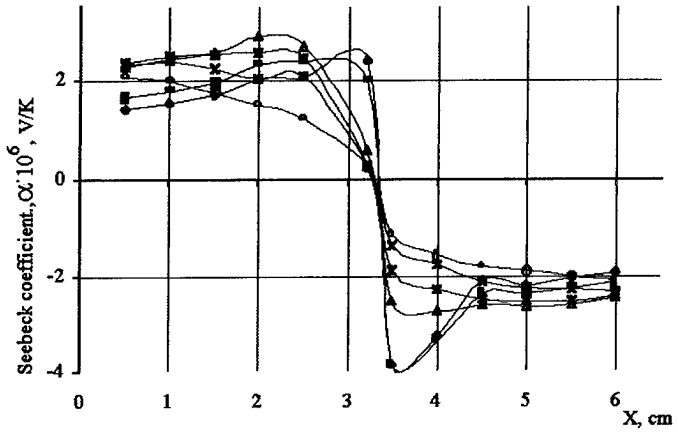


Fig.1. Seebeck coefficient as a function of co- ordinate on the ingot at different temperatures

150 K 180 K 260 K 300 K 330 K 360 K

In other words, coordinate on the ingot, at which charge carrier sign inversion is observed, will be located in the middle part of the ingot. According to formula (1) its meaning equals 3.5 cm.

On the samples the following parameters were measured: figure of merit Z (by Harman method), specific electric conductivity σ, and Seebeck coefficient α in the temperature range 150-360 K. Specific thermal conductivity was calculated on the basis of the obtained data according to the formula

$$K = \alpha^2 \sigma / Z \qquad (3)$$

Metal graphic investigation was done according to the usual procedure on cross and linear sections.

Investigation results

According to metal graphic examination all ingots of solid solutions $(Bi_{0.8}Sb_{0.2})_2Te_3$ and $(Bi_{0.7}Sb_{0.3})_2Te_3$ were single phased excluding the end part of the ingot with the length of 15mm, where laminated non-uniform double phased structure is observed. The second phase insertion appears at the same time along the melting front, which is a sign of the beginning of melting supercooling.

The results of the investigation are shown on example of a solid solution $(Bi_{0.7}Sb_{0.3})_2Te_3$ because there is no principal difference between the properties of solid solutions $(Bi_{0.8}Sb_{0.2})_2Te_3$ and $(Bi_{0.7}Sb_{0.3})_2Te_3$.

In the beginning part of the zone melted ingots with hole conduction and positive Seebeck coefficient are observed. Seebeck coefficient insignificantly increases in the beginning of the ingot under the temperature 200K and less, reaches its maximum, then abruptly lowers at the zero point and then

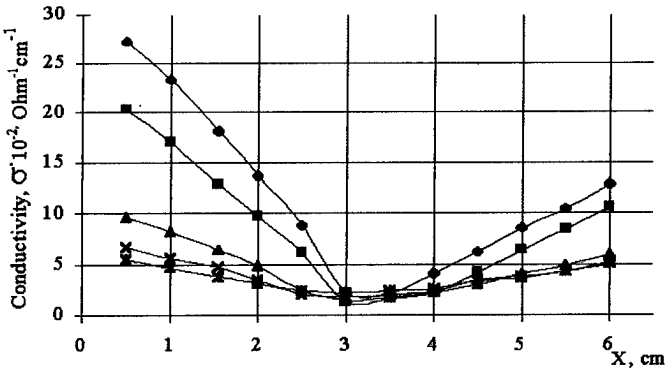


Fig.2. Specific conductivity as a function of co- ordinate on the ingot at different temperatures

150 K 180 K 260 K 300 K 330 K

changes its sign. The change of the sign occurs within the 5 mm length at the point distanced for 3.0 cm from the beginning of the ingot (Fig.1).

Fig.2 shows the distribution on the ingot of electrical conductivity, measured in the process of measuring the figure of merit, on the same samples where Seebeck coefficient was measured at different temperatures. The graphs of electrical conductivity look like broken lines with the break coordinate corresponding to electrical conductivity of the sample - the coordinate of the inversion of hole-type conduction into electron one. The incline angle of the broken lines to the abscissa axis in hole conduction area on the ingot is much bigger than in electron area under low temperature. With the

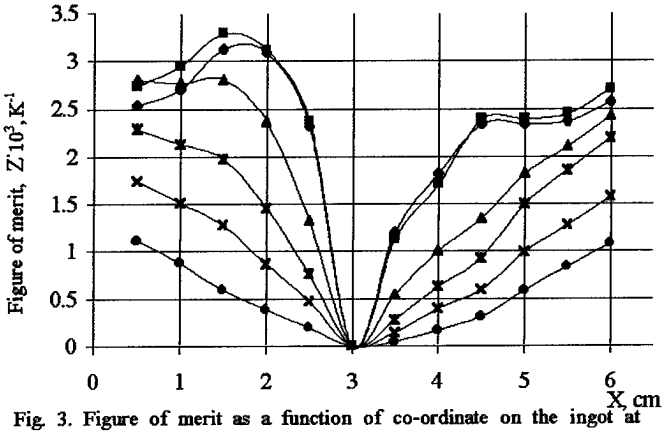


Fig. 3. Figure of merit as a function of co-ordinate on the ingot at different temperatures

150 K 180 K 260 K 300 K 330 K 360 K

temperature increase the incline angle decreases.

Figure of merit along the ingot (Fig.3) decreases in the hole area of the ingot, turns into zero at the point of Seebeck coefficient sign inversion and then increases again in the ingot area with electron conductivity. Figure of merit of solid solution with electron conductivity is lower than one with hole conductivity. In the ingot part close to intrinsic conductivity, figure of merit of the sample increases with the temperature decrease.

Fig.4 shows specific thermal conductivity distribution along the zone melted solid solution $(Bi_{0.7}Sb_{0.3})_2Te_3$, drawn according to the points calculated by formula (1) by subtraction from there an electron component on the basis of Videmann-Frans law under the supposition that degeneration is not present. The same picture shows for comparison remaining thermal conductivity distribution under the temperature 300 K along the ingot of solid solution $(Bi_{0.8}Sb_{0.2})_2Te_3$. Under X=3.0 cm it is impossible to calculate thermal conductivity precisely enough because of the very low figure of merit and Seebeck coefficient even though specific conductivity is relatively high. Nevertheless an obvious maximum is observed on the broken lines of thermal conductivity distribution. It reaches 0.06 W/K/cm under the temperature 300K.

Fig. 5 shows temperature dependency of Seebeck coefficient, presented in a semi logarithmic scale for the samples cut out

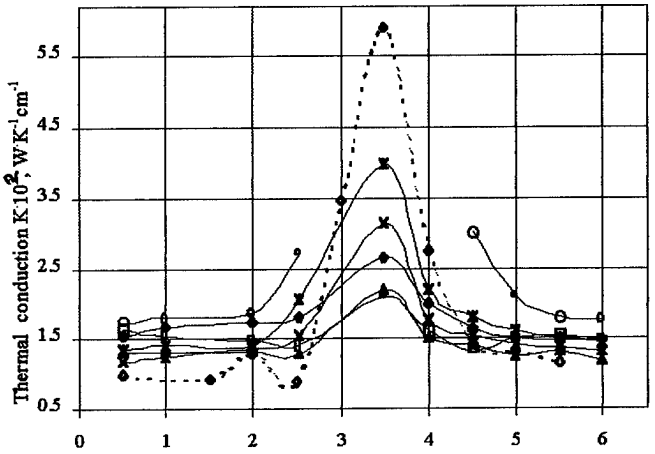


Fig.4. Remaining thermal conduction as a function of co-ordinate on the ingot at different temperatures

of the ingot with hole, intrinsic and electron conductivity. Under low temperatures there is linear part on the curves of the temperature dependency.

The incline angle of linear parts to temperature axis varies for different samples. In hole area of the ingot samples are more distanced from the inversion point, their incline angle is smaller that other areas. Incline angle of linear part of the curve to abscissa axis increases from 150 to 190 μV/K with the increase of sample coordinate. In the ingot part with electron type of conductivity incline angle of Seebeck coefficient curve practically does not depend on sample

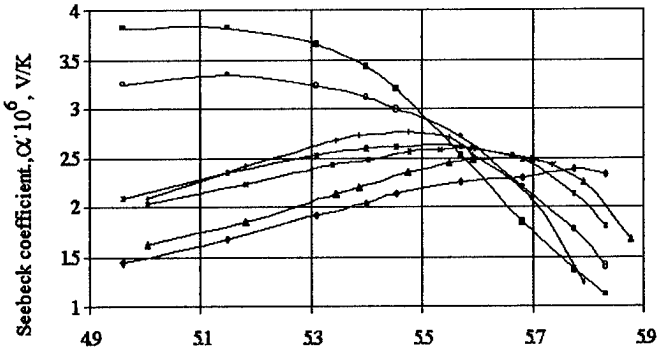


Fig. 5. Seebeck coefficient as a function of temperature for specimens cut out from different parts of the ingot

coordinate on the ingot and remains equal to 146 μV/K. At the same time in samples with electron conductivity cut out of the part of the ingot close to inversion point, maximum of Seebeck coefficient is observed under the temperature closed to 150 K. That is why in the temperature range, which was investigated there is no Seebeck coefficient increase on the temperature dependency curves.

Dependency indices of specific conductivity on the temperature as well as incline angle of the curves to the abscissa axis, depend on the coordinate of the sample on the ingot. It's also important that distribution character for the exponent meaning along the ingot is the same as for the distribution of the Seebeck coefficient incline angle to the abscissa axis (Fig. 6).

Discussion of the Results of the Experiment

The most interesting fact is the presence of the abrupt maximum on the remaining thermal conductivity distribution curve along the zone-melted ingots. With X=3.2 cm in the melt of the zone excessive tellurium concentration compared to stoichiometric composite equals 6.62% or 62.54 at%Te

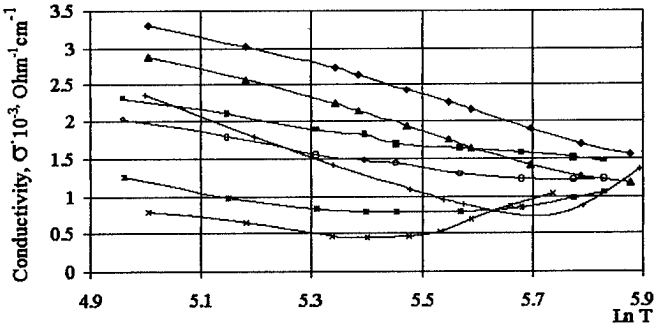


Fig. 6. Conductivity a function of temperature for specimens cut out from different parts of the ingot

using absolute proportions. Bismuth telluride with intrinsic conduction [2] was obtained from the melt containing 62.5at%Te which almost precisely coincides with the meanings received during this investigation for solid solutions of bismuth telluride and antimony telluride, enriched with bismuth telluride. This means that tellurium concentration of 62.5at%Te in the melt may be considered as invariant to the

change of the antimony telluride concentration in solid solutions $(Bi_ySb_{1-y})_2Te_3$ at least for y=0-0.3 under which materials with intrinsic conduction are grown from the melt. It is necessary to mention that the melt with the same tellurium concentration is used for solid solutions $(Bi_ySb_{1-y})_2Te_3$ melting for y=0.2-0.5 with the hole conduction where transition to retrograde dissolution from regular one is observed on solidus line[3].

The difference in line angle slope of hole and electron conduction of solid solutions due to different of doping atom sort: anti-structure tellurium is donor and it gives 2/5 electrons. Anti-structure bismuth is acceptor and it gives 3/5 holes (Fig. 2) as it is known well]. Therefore, the distributions of conductivity along the ingot confirm the chosen method of investigation is correct one. The dependencies of Seebeck coefficient against temperature and also conductivity (Fig. 5 and 6) show preferably intrinsic conduction of searched solid solutions in whole temperature region, if co-ordinate of specimen on the ingot is in the region from 3.0 to 4.0 cm.

The value of remaining thermal conductivity of solid solutions $(Bi_{0.7}Sb_{0.3})_2Te_3$ as well as $(Bi_{0.8}Sb_{0.2})_2Te_3$ which also includes lattice component, in the area of chemical composites with impurity conduction corresponds to the values known for these solid solutions. Ambipole diffusion contribution into thermal conductivity, calculated by [4] and with the energy gap 0.13 eV, is not more than 0,006 W/K/cm.

Independent of ambipole diffusion, non-uniform distribution of the components that occurs as a result of dendrite growth also contributes to thermal conductivity and creates eddy currents. Eddy currents are directly involved in heat transmission and increases thermal conductivity of the thermoelectric material.

In the area where impurity conductivity prevails, concentrated non-uniformity does not influence thermal conductivity too much because the difference between Seebeck coefficients of non-uniform neighboring parts of the ingot is not big. In the part of the ingot near to the area with intrinsic conduction, sub areas with hole and electron conduction can be close to each other. Seebeck coefficient values in this case can be comparable and the contribution to the thermal conductivity of eddy currents occurring in such non-uniform media can be significant. Under the temperature 300K for example specific electrical conductivity of the part of the ingot of solid solution $(Bi_{0.7}Sb_{0.3})_2Te_3$ equals approximately 80 $Ohm^{-1}cm^{-1}$ Fig. 3 and Seebeck coefficient 140 μV/K. Then electron conductivity component contribution will be equal approximately to 0.006 W/K/cm, due to non-uniform distribution of components around intrinsic conduction. Because the mechanisms of heat transmission by ambipole diffusion and eddy currents are independent, their joint contribution to thermal conductivity is not more than 0.012Wt/K/cm. Thermal conductivity of the samples in the maximum of distribution curve in the ingot is higher than the calculated one. This brings us to a conclusion that there could possibly be additional ways of heat transmission in the solid solutions under the investigation, exiton way could be one.

It is necessary to mention that the change of thermal conductivity depending on molar part of bismuth telluride in Bi_2Te_3-Sb_2Te_3 alloys, which were received by zone melting, was also observed in [5]. It was pointed out that with molar parts of bismuth telluride and antimony telluride 1:1, thermal conductivity had the maximum value. The sign inversion of the conduction type took place. At the same time in our investigation the maximum value of thermal conductivity is significantly higher which may be a result of less discreteness of chemical composite from sample to sample which was achieved during our investigation.

In hole conduction solid solutions around the ingot part with intrinsic conduction, maximum figure of merit reaches the point of $3.2 \cdot 10^{-3}$ K^{-1} under low temperatures and is comparable to the figure of merit of traditional thermoelectric material at room temperature. The figure of merit of solid solutions with electron conduction is approximately $2.5 \cdot 10^{-3}$ K^{-1} at temperature 150-170K. Taking into consideration that specific conductivity maximum is in the ingot part where electron conduction prevails, it is possible that electron-hole interaction occurs which leads to the increase of thermal conductivity and that it reaches the maximum when the electron concentration is the lowest. Such interaction does not allow us to receive material of electron conduction with high figure of merit under low temperatures. Nevertheless, even the figure of merit of solid solutions $(Bi_{0.7}Sb_{0.3})_2Te_3$ of electron conduction under the temperature 150-170 K is higher than the figure of merit of the material with electron conduction of traditional composite $Bi_2(Te_{0.9}Se_{0.1})_3$.

Summery

1. In solid solutions $(Bi_{0.7}Sb_{0.3})_2Te_3$ and $(Bi_{0.8}Sb_{0.2})_2Te_3$ obtained as a result of zone melting, sign inversion of the charge carriers is observed when tellurium concentration in the melt equals 62.5at%
2. Solid solutions $(Bi_ySb_{1-y})_2Te_3$ with y=0.7-0.8 of stoichiometric composition with intrinsic conductivity have maximum thermal conductivity due to ambipole diffusion, non-uniform components distribution and exiton excitation.
3. Solid solutions $(Bi_{0.7}Sb_{0.3})_2Te_3$ and $(Bi_{0.8}Sb_{0.2})_2Te_3$ with hole conduction have maximum figure of merit under the temperature T=150-180 K and it reaches $3.2 \cdot 10^{-3}K^{-1}$.
4. Maximum figure of merit of solid solutions $(Bi_ySb_{1-y})_2Te_3$ with y=0.7-0.8 with electron conduction under the investigation reaches the value of $2,510^{-3}K^{-1}$ under the temperature 150-180K.

Reference

[1] A.I.Anukhin, A.A.Aivazov, I.S.Gavrilenko, "Features of zone meltingof complex semiconductors", In Russian .Izv.. An SSSR. Inorganical materials, N5, (1991), 938.

[2] C.B.Satterwaite and R.W.Ure, "Electrical and thermal properties of Bi_2Te_3", Phys. Rev., 108, (1957), 1164.

[3] A.A.Aivazov, A.I.Annukhin. "Thermoelectric properties of Bi_2Te_3— Sb_2Te_3 low temperature materials with hole conductivity",.Proceed. of XII ICT'93, (Nov., 1993), Yokohama, 161.

[4] J.R.Drabble, H,J,Goldsmid, "Thermal conduction in semiconductors", in Russian, M., (1963), 266p.

[5] C.H.Chamness, P.T.Chiang, and P.Parekh, "Thermoelectric properties of Bi_2Te_3-Sb_2Te_3 „alloys", Can. Journ. Of Phys., 43, (1965), 653.

Flash evaporated layers of (Bi_2Te_3-Bi_2Se_3)(N) and (Bi_2Te_3-Sb_2Te_3)(P) used as Micro-Module-Peltier

A. Foucaran, A. Sackda, A. Giani, F. Pascal-Delannoy and A. Boyer.

Centre d'Electronique et de Micro-optoelectronique de Montpellier, UMR 5507 CNRS, Université Montpellier II, Place E. Bataillon, 34095 Montpellier cedex 05 - France

Abstract :

$(Bi_2Te_3)_{0.9}(Bi_2Se_3)_{0.1}$ for N type material powder and $(Bi_2Te_3)_{0.25}(Sb_2Te_3)_{0.75}$ for P type material powder were evaporated by flash evaporation technique. We obtained a value of Z equal to $0.21x10^{-4}$ K^{-1} for α = 40 μV/K and ρ = 50 $\mu\Omega$.m for P type material and Z about $0.17x10^{-3}K^{-1}$ for α = 90 μV/K and ρ = 30 $\mu\Omega$.m for N type material (at 300K), for 1 μm layers thickness deposited over polyimide substrate, before annealing. We show that after annealing at 250°C under He atmosphere, the figure of merit of the layers increases to $Z = 3.2x10^{-3}$ K^{-1} for α = 240 μV/K and ρ = 12 $\mu\Omega$.m for P type material and $Z = 1.6x10^{-3}K^{-1}$ for α = 200 μV/K and ρ = 15 $\mu\Omega$.m for N type material (at 300K). With these fabrication parameters we realised three different structures of Micro-Module Peltier (MMP) junction and we obtained a maximum value for temperature drop between hot and cold sides of about 3.4 K. This result is very promising in order to develop Micro-Module Peltier (MMP).

Introduction :

At present, V_2-VI_3 compounds provide the best materials for thermoelectric cooling between 400K to 200K : particularly (Bi_2Te_3-Bi_2Se_3) alloys for N type material and (Bi_2Te_3-Sb_2Te_3) alloys for P type material because of their high values of the thermoelectric figure of merit Z reaching a maximum value of $3.3x10^{-3}$ K^{-1} [1-2].

Therefore, with increasing interest in thin film thermoelectric devices (sensors area), attempts were made in regard to deposition and investigation of (Bi_2Te_3-Sb_2Te_3) and (Bi_2Te_3-Bi_2Se_3) alloys. Using several deposition techniques [2-3-4-5-6], layers were grown on various substrates as SiO_2 [2], mica [8] or polyimide [7-11].

However, except Kim and al. [3] every deposited layers were (Bi_2Te_3-Sb_2Te_3) alloys (P type material). So the study of (Bi_2Te_3-Bi_2Se_3) (N type material) thin layers deposition is very interesting in the aim of P-N junction realisation for high performance thermoelectric modules.

In this work, we study flash evaporated thin films of (Bi_2Te_3-Bi_2Se_3) and (Bi_2Te_3-Sb_2Te_3) alloys before and after annealing. In fact it is well known that the thermoelectric properties of these materials layers strongly depend on annealing processes [2-9]. In order to investigate performance of ours flash evaporated layers, we elaborated three different structures of MMP, the realisation of a little size Peltier module being a very important challenge in elaboration of news sensors concepts [3-11-12].

Experimental details:

Prior to the beginning of this study, it was determined that alloy compositions of $(Bi_2Te_3)_{0.9}(Bi_2Se_3)_{0.1}$ for N type and $(Bi_2Te_3)_{0.25}(Sb_2Te_3)_{0.75}$ for P type provided deposited layers having high figures of merit.

The evaporated materials $(Bi_2Te_3)_{0.9}(Bi_2Se_3)_{0.1}$ for N type or $(Bi_2Te_3)_{0.25}(Sb_2Te_3)_{0.75}$ for P type, were prepared by mixing pure elements of 5N Bi, Sb, Te, Se in stoichiometric proportions in sealed quartz tube, which was maintained in a H_2 atmosphere at pressure of 1 Pa. To adjust the carrier concentration of the N type material we used SbI_3 and an excess of tellurium for P type material. The quartz tube was placed in a furnace and held at 800°C for 24 hours to make complete alloying. Then it was quenched to room temperature. Electron-probe micro-analysis was used to investigate the formation of homogenous and stoichiometric material. The ingots were crushed to powders. The flash evaporation technique was chosen for growing layers because this method allows the deposition of several elements which exhibit different vapour pressures.

To optimise the deposition parameters, experiments were carried out. We investigated the influence of the powder grains size, crucible temperature and substrate temperature on stoichiometric films composition, crystallisation, kinetic growth, electron-probe micro-analysis, X-ray diffraction. Thermoelectric properties, Seebeck coefficient and electrical resistivity of layers, were measured respectively by a constant temperature gradient method and 4 probes method.

To improve the thermoelectric properties of these layers we operated annealing under He atmosphere, time and temperature of annealing depend on type material.

By using suitable masks, the polyimide substrate (MMP support) are successively coated with the N-material, followed by annealing at 250°C for 100 mn, then P-material and an other annealing at 250°C for 100 mn, then the contacts were deposited by electron-beam evaporation of 500 nm of Ni followed by 1 μm of Cu, and finally the last annealing of the structure at 250°C for 15 mn.

Results :

P type layers ($(Bi_2Te_3)_{0.25}(Sb_2Te_3)_{0.75}$) :

Unannealed flash-evaporated of $(Bi_2Te_3)_{0.25}(Sb_2Te_3)_{0.75}$ layers showed unsatisfactively low values of thermoelectric properties : α = 40 μV/K and ρ = 50 $\mu\Omega$.m and so $Z = 0.21.10^{-4}$ K^{-1} at 300 K. Therefore the annealing procedure was used to improve these properties. In figure 1 we show the evolution of the Seebeck coefficient versus the annealing time

at 250°C and under He atmosphere for two different thickness of layers. After 100 mn, whatever the thickness of the films there is no significant increasing of α.

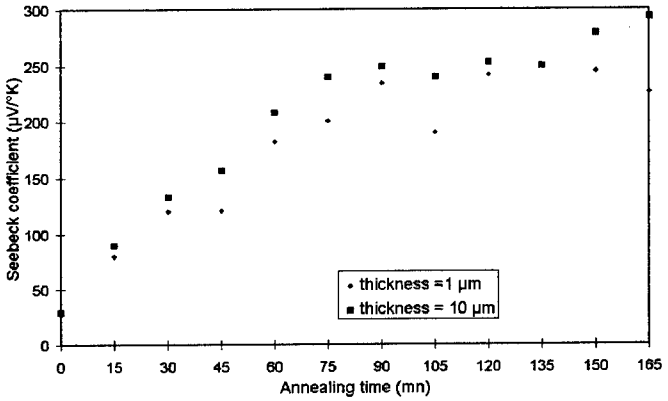


Figure 1 : Variation of the Seebeck coefficient, α, for $(Bi_2Te_3)_{0.25}(Sb_2Te_3)_{0.75}$ layers versus annealing time, at 250°C and under He atmosphere.

For the electrical resistivity, ρ, (figure 2) we observed an important decreasing of ρ versus the annealing time, and after 100 mn there is a stabilisation of ρ. However, the thinner layer (1 µm) presents a better ρ than the more thick (10 µm). It is very difficult to compare these results with these of others authors because our annealing atmosphere (He) and temperature annealing were different from these used in literature. However, the Seebeck parameter and resistivity variations versus annealing time present the same aspect as these found by Volklein and al. [2].

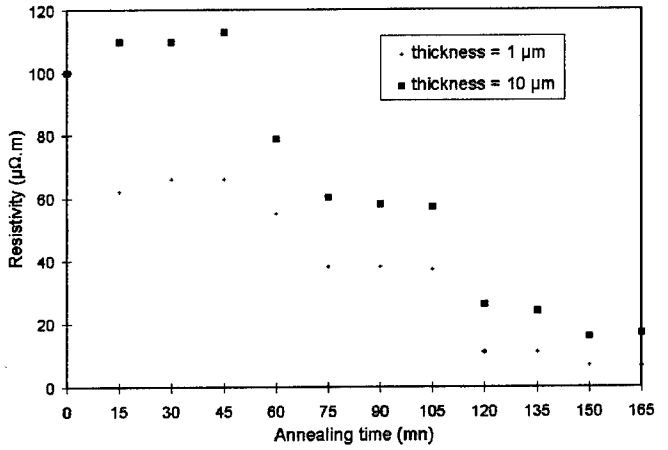


Figure 2 : Variation of electrical resistivity, ρ, for $(Bi_2Te_3)_{0.25}(Sb_2Te_3)_{0.75}$ layers versus annealing time, at 250°C and under He atmosphere.

N type layers ($(Bi_2Te_3)_{0.9}(Bi_2Se_3)_{0.1}$) :

Unannealed flash-evaporated $(Bi_2Te_3)_{0.9}(Bi_2Se_3)_{0.1}$ layers showed thermoelectric properties better than as grown P type films, α = 90 µV/K and ρ = 30 µΩ.m and so $Z = 0.17 \times 10^{-3}$ $.K^{-1}$ at 300 K. However, an annealing at 250°C improves these thermoelectric properties as shown in figure 3 and figure 4 for α and ρ respectively. Moreover, the variation of α versus the annealing time showed the same profile that for the P type material, but we observed a stabilisation of the Seebeck coefficient at a smaller temperature of about 60 mn. For the variation of the electrical resistivity versus the annealing time we had the same evolution for P type but the stabilisation of ρ is reached for annealing time longer than 60 mn. Only one author [3] reports on the annealing of $((Bi_2Te_3)_{0.9}(Bi_2Se_3)_{0.1})$ flash-evaporated N type layers, but anyone have made such studies on the variation of Seebeck coefficient and resistivity versus annealing time or temperature.

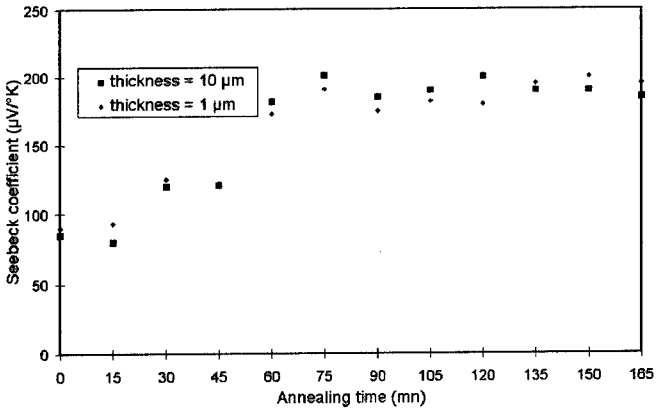


Figure 3 : Variation of the Seebeck coefficient, α, for $(Bi_2Te_3)_{0.9}(Bi_2Se_3)_{0.1}$ layers versus annealing time, at 250°C and under He atmosphere.

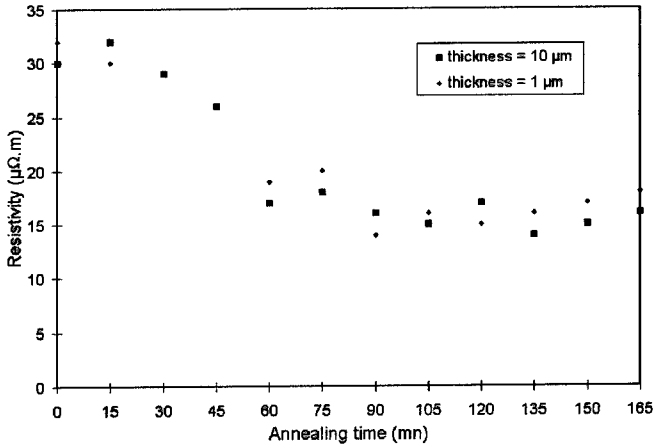


Figure 4 : Variation of electrical resistivity, ρ, for $(Bi_2Te_3)_{0.9}(Bi_2Se_3)_{0.1}$ layers versus annealing time, at 250°C and under He atmosphere.

Micro-Module Peltier (MMP) characterisation :

Three different structure of MMP were investigated. These MMP had the same thickness and physical properties because they were made in the same run for each step of the process fabrication (table 1). The detail of the MMP geometric structure is given in figure-5.

The electrical and geometrical characteristics of each MMP are listed in table 3. MMP1 and MMP3 present almost the same value of contact resistance about 5.10^{-3} $\Omega.cm^2$ which is

MMP FABRICATION		Steps fabrication process of the MMP						
		1 N type layer	2 Annealing of N type layer	3 P type layer	4 Annealing of P type layer	5 contact layer	6 contactlayer	7 Annealing of contacts
Flash deposition parameters for MMP fabrication	g (μm) powder grains size	160<g<250		160<g<250				
	k ($nm.^{s-1}$) growth kinetic	2		3				
	T_C (K) crucible temperature	1123		1073				
	T_S (K) substrate temperature	473		373				
Annealing under He atmosphere	time (mn)		100		130			15
	temperature (K)		250		250			250
Electron beam evaporation	thickness of Ni (μm)					0.5		
	thickness of Cu (μm)						1	

Table 1: Fabrication parameters for the MMP realised by flash evaporation.

in good agreement with the literature for this kind of metal/semiconductor contact [10]. The detail of the MMP geometric structure is given in figure-5.

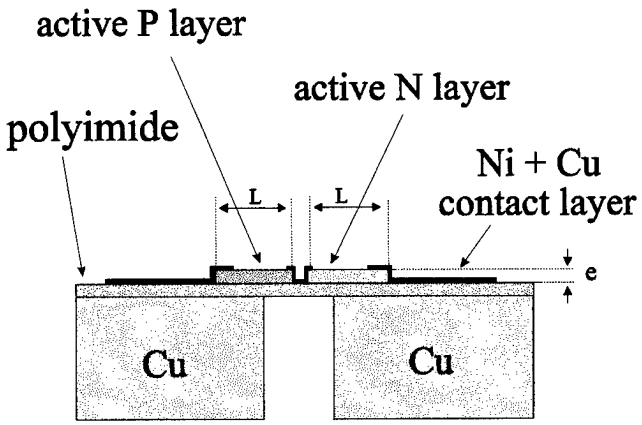


Figure 5 : Schematic drawing of a MMP structure

The electrical and geometrical characteristics of each MMP are listed in table 2. MMP1 and MMP3 present almost the same value of contact resistance about 5.10^{-3} $\Omega.cm^2$ which is in good agreement with the literature for this kind of metal/semiconductor contact [10].
However for the MMP4, which has the longer legs (1000 μm) for P and N type material, we think that the calculated resistance, R_{CAL}, is not a significant result. As a matter of fact, more the legs are long more they are sensitive to the kapton substrate deformation which can involve micro-fissures and then resistivity deterioration of the actives legs (P and N).
Figure 6 shows the variation of temperature difference between hot and cold sides produced by Peltier effect as function of input current for each MMP sample. The maximum temperature difference obtained was 3.4 K for the MMP4 structure for an input current of 14.2 mA.

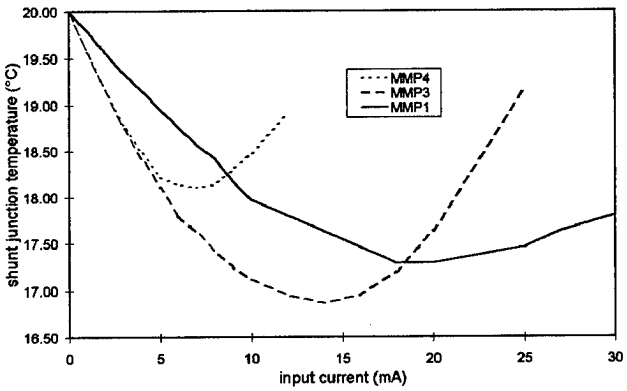


Figure 6 : Temperature difference between hot and cold sides produced by Peltier effect versus the input current.

Conclusion :

In this work we have shown that after annealing (respectively 130 mn and 100 mn for P and N type, at 250°C under He atmosphere) the figure of merit of the layers increases to $Z = 3.2x10^{-3}$ K^{-1} for $\alpha = 240$ μV/K and $\rho = 12$ μΩ.m for P type material and $Z = 1.6x10^{-3}$ K^{-1} for

N° of MMP structure	e(μm) thickness of active layers	L (μm) length of active N or P layer	ρ (μΩ.m) experimental resistivity of P type layer	ρ (μΩ.m) experimental resistivity of N type layer	R_{EXP} (Ω) experimental resistance of MMP	R_C (Ω) contact resistance (Ω)	α ($\mu V.K^{-1}$) experimental Seebeck coefficient of N type layer	α ($\mu V.K^{-1}$) experimental Seebeck coefficient of P type layer
MMP1	20	100	12	15	3.36	2.75	200	240
MMP3	20	500	12	15	6.3	3.57	200	240
MMP4	20	1000	12	15	15.32	9.92	200	240

Table 2 : Thermoelectric and geometrical characteristics of each MMP structure.

α = 200 μV/K and ρ = 15 μΩ.m for N type material (at 300 K). With these fabrication parameters we realised three different structures of MMP and we obtained a maximum value for temperature drop between hot and cold sides of about 3.4K.

This kind of MMP structure offers a very wide domain of possible applications, like humidity sensor or thermopile. These first results are very promising because large possibility of improvements of the MMP structures. Actually we study the optimisation of the legs geometric to increase the Peltier effect and to decrease the Joule effect. The improvement of contact resistance is also analysed.

References :

[1] D.M. ROWE and M. STORDEUR, Thermoelectrics, CRC Press. Inc. (1995), 239.

[2] F. VOLKLEIN, V. BAIER, U. DILLNER and E. KESSLER, Thin Solid Films, 187 (1990), 253.

[3] I.H. KIM and D.H. LEE, Proc. MRS Korca-Mexico Joint Symp. On Adv. Mat. And Tech. (1992), 53.

[4] TOSHITAKA OHTA, TAKENOBU KAJIKAWA and YUKINOBU KUMASHIRO, Electrical Engineering in Japan, Vol. 110, N°4 (1990), 14.

[5] SH. B. ATAKULOV, U. A. GAFUROV and S. A. KAZMIN, Sov. Phys. Semicond. 21, 3, march 1997, 342.

[6] A. MZERD, F. TCHELIEBOU, A. SACKDAF and A. BOYER, Sensors and Actuators A, 46-47, (1995), 387.

[7] YU. BOIKOV, B. M. GOLTSMAN and V. A. KUSATOV, Sov. Phys. Solid State 20, 5, may 1978, 757.

[8] E. CHARLES, E. GROUBERT and A. BOYER, J. Mater. Sci. Lett., 7 (1988), 205.

[9] V. DAMORADA DAS and P. GOPAL GANESAN, Semicond. Sci. Technol. 12 (1997), 195.

[10] U. BIRKHOLZ, R. FETTIG and J. ROSENZWEIG, Sensors and Actuators, 12 (1987), 179.

[11] B. CHINAGLIA, F. VALLANA andG. BOSIO, Energy Conversion, Pergamond Press, Vol. 16, (1976), 55.

[12] P. ANCEY, M. GSCHWIND and O. VANCAUWENBERGHE, Sensors and Actuators, B 26-27 (1995), 303.

Bi_2Te_3 thin films grown by MOCVD process

A. Boulouz, A. Giani, F. Pascal-Delannoy, A. Foucaran and A. Boyer.
Centre d'Electronique et de Micro-optoélectronique de Montpellier, UMII, UMR CNRS n° 5507,
place E. Bataillon, 34095 Montpellier cedex 05 France.
E-mail : giani@cem2.univ-montp2.fr

Abstract

The growth of Bi_2Te_3 thin films by metal organic chemical vapor deposition (MOCVD) using diethytellurium and trimethylbismuth as tellurium and bismuth sources respectively is investigated on pyrex substrate. The results of growth rate, morphology, electrical and thermoelectrical properties as a function of growth parameters are given. The prepared films were always n-type.
Film properties, such as electrical resistivity, mobility, carrier concentration, thermoelectric power and X-ray diffraction were studied at 300 K. Increasing VI/V ratio was found to reduce the electrical resistivity to 12 $\mu\Omega$.m. Hall mobility varies from 28 and 150cm^2/V.s. The figure-of-merit obtained was $Z = 2.48 \times 10^{-3} K^{-1}$. These initial results suggest a significant potential of MOCVD growth for large scale production of thermoelectric material.

Introduction

Until now the best material for thermoelectric applications at room temperature were Bi_2Te_3 and its alloys with Sb_2Te_3 and Bi_2Se_3. They are narrow bandgap semiconductors with layered structure. The interest of thin films is their potential to be used in the micro-fabrication of integrated thermoelectric devices such as sensors.
Thin films of Bi_2Te_3 have already been elaborated by several methods : sputtering deposition [1-2], co-evaporation of the elements [3], flash evaporation [4-6], molecular beam epitaxy [7-8] and metal organic chemical vapor deposition system using Dimethyltelluride (DMTe) [9] and Diisopropyltelluride (DiPTe) [10] as tellurium source. But not work has been reported on Bi_2Te_3 thin films prepared by MOCVD process using DETe as tellurium sources.
The properties of thin films of Bi_2Te_3 have been investigated by many authors. George and Bradeep [11] have reported the electrical properties of Bi_2Te_3 thin films. The effect of the film thickness and deposition temperature on thermoelectric power and resistivity of Bi_2Te_3 thin films, prepared by vacuum evaporation on glass substrates is reported by Damadora et *al.* [12]. Francombe's work [13] on films obtained by dc sputtering from a Bi_2Te_3 cathode on glass substrates indicates a metastable single phase characterized by a composition that ranges from Bi_2Te_3 to approximately BiTe, depending on the substrate temperature during growth.
In the present paper, morphology, growth rate, electrical and thermoelectrical properties of n-type Bi_2Te_3 are described in relationship with the growth parameters.

Experimental

Epitaxial films of Bi_2Te_3 were growth by MOCVD on pyrex substrate, the precursors for Bi and Te were Trimethylbismuth and Diethyltelluride respectively. The experiments were performed in a horizontal reactor [14] at atmospheric pressure. The carrier gas was H_2 with a flow rate equal to 6 slm. The growth temperature are kept at 450 °C for all the runs. The VI/V ratio ($R_{VI/V}$ = P DETe / P TMBi) varied between 4 to 15. In our case, when the VI/V ratio varies, the pressure and flow of V elements were kept constant and equal to 0.5×10^{-4} atm and 18.4 cm^3/mn respectively.
The V and VI group gases are kept separate until the reactor head. To avoid the possibility of any pre-reaction, the TMBi and DETe source were maintained at 5 °C and 20 °C respectively.
The film thickness was measured by stylus profiling at several points (α-step, 1% accurancy).
X-ray diffraction studies were carried out with copper Kα radiation (λ = 1.54051 Å). Seebeck coefficients were calculated from measurement of electromotive force with temperature difference. The electrical resistivity and Hall effect measurements were performed by Van Der- Pauw method at 300 K.

Results and discussion

Table1 gives the standard values of the X-ray powder data given by Francombe [13] along with the data obtained in the present work. From this table, it is clear that the present film contains only Bi_2Te. We observed that the crystalline orientation of the films is independent on VI/V ratio at fixed substrate temperature T = 450 °C.
Figure 1 shows the X-ray diffractogram of typical bismuth telluride film.

The intense and thin lines are observed for the (0001) planes (l = 6,15,18). The additional lines indicate many different orientations.

	Standard pattern [13]		Deposited layer	
hkil*	d (Å)	I/I_0	d (Å)	I/I_0
006	5.078	8	5.012	98
105	3.220	100	3.192	17
0015	2.032	40	2.017	100
0018	1.694	5	1.685	21
2010	1.610	16	1.605	11

Table 1 : X-ray diffraction data for Bi_2Te_3 thin film grown by MOCVD and standard pattern (* the hkil indices are refereed to hexagonal structure cell).

The lattice parameters deduced from the diffraction angle are :

a = 4.34 Å and c = 30.25 Å

these values are closed to those reported for bulk Bi_2Te_3 films (a = 4.38 Å and c = 30.48 Å).

The experimental data of EDS analysis indicate that the stoichiometry of Bi_2Te_3 epiaxial films is essentially constant for all thicknesses and whatever the growth parameters

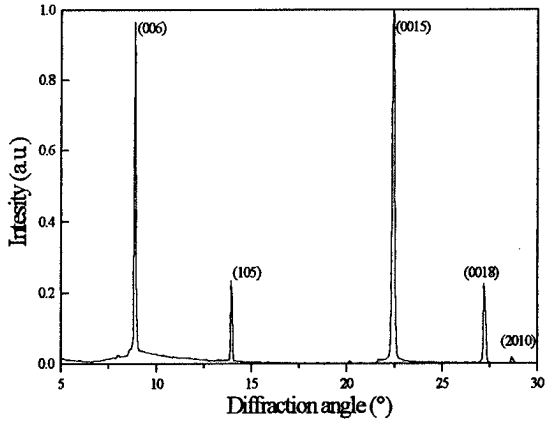


Figure 1 : X-ray diffractogram of a Bi_2Te_3 layer.

For our experimental conditions, the same morphology were observed for different VI/V ratio at substrate temperature equal to 450°C. The SEM micrograph (figure 2) show typical morphology of Bi_2Te_3 layers which correspond to the several crystallites with hexagonal oriented such as their c-axis are perpendicular to substrate plane.

Then the influence of VI/V ratio on the growth rate of n-type Bi_2Te_3 thin films deposited on pyrex substrate was studied. First of all, we found that the growth rate is quite constant in the study range of the VI/V ratio and it is equal to 1.2 µm per hour. The growth rate versus $R_{VI/V}$ is shown in figure 3.

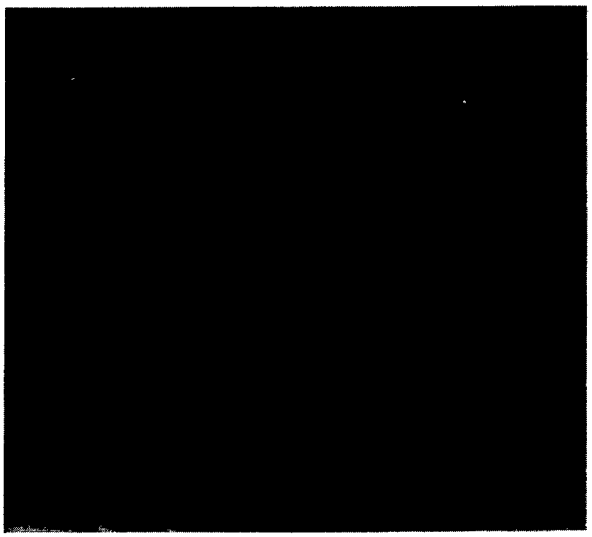


Figure 2 : Surface morphology of Bi_2Te_3 films (1 cm = 20µm).

These mobilities and seebeck coefficient are two to three times higher than those reported in our previous work [9] with DMTe precursor. The high values of µ, N and α are clearly due to a better crystallinity because of a high cracking efficiency for DETe source.

The Hall effect was measured at room temperature. The produced films always have n-type conduction, dependent on the growth parameters and principally of the VI /V ratio. We can explain easily the role of the VI /V ratio : the excess of tellurium present in the vapour phase compensated the losses of this one in the material during the growth.

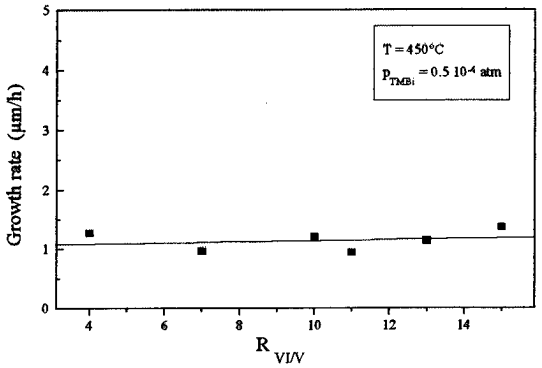


Figure 3 : Growth rate versus VI/V ratio.

Table 2 presents the electrical and thermoelectrical properties of the layers grown under optimal conditions using DMTe [9] and DETe as tellurium sources.

	DETe	DMTe [9]
μ (cm^2 /V.S)	117	50
N (cm^{-3})	4.50×10^{19}	1.6×10^{19}
α (μV/K)	-210	-94
Z (K^{-1})	2.48×10^{-3}	5×10^{-4}

Table 2 : Influence of organometallics sources on electrical and thermoelectrical properties of Bi_2Te_3 thin films at T = 450 °C and R = 7.

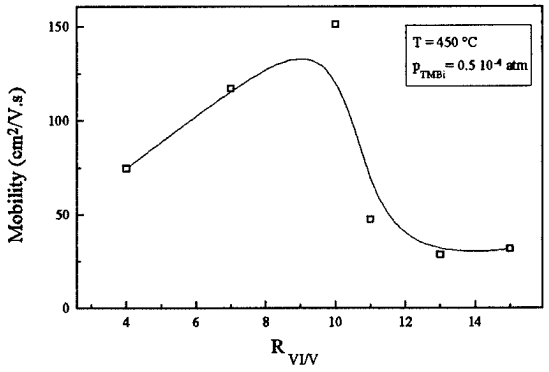


Figure 4 : VI/V ratio dependence on mobility.

The behaviour of Hall mobility as a function of the ratio is indicated in figure 4. Here, we notice that the mobility is higher in R ratio varied between 7 and 12. The best value of mobility was found equal to 151 cm^2 /V.s.

Figure 5 shows the variation of the carrier concentration as function of ratio. We remark a noticeable increase of the carrier concentration from 1.61×10^{19} cm^{-3} to 1.84×10^{20} cm^{-3}. In parallel, the electrical resistivity varies from 52 to 12 $\mu\Omega$.m, we noted that the electrical resistivity have a opposite behaviour when the R ratio increase (figure 6). All the electrical properties are simalar to the values published by Y. Azzouz [15] using the MBE epitaxy.

As know, the performance of the thermoelectric device is essentially related to a figure-of-merit Z of the material which is described by the relation $Z = \alpha^2/k.\rho$ where α is the seebeck coefficient, ρ is the electrical resistivity and k is the thermal conductivity (k is taken equal to 15 mW / cm.K which is the value for the bulk material).

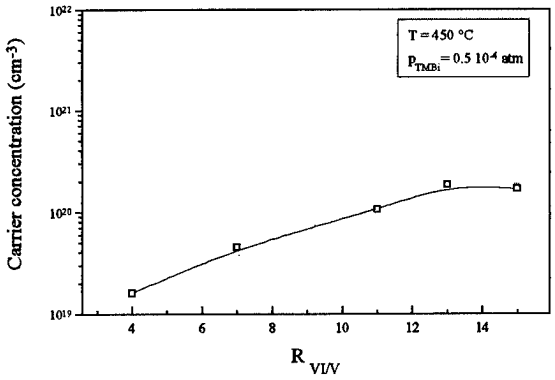


Figure 5 : VI/V ratio dependence on carrier concentration.

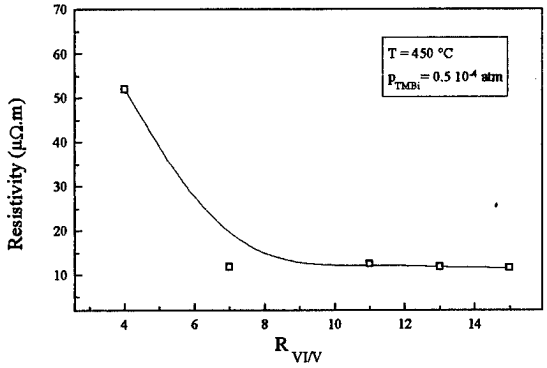


Figure 6 : VI/V ratio dependence on electrical resistivity.

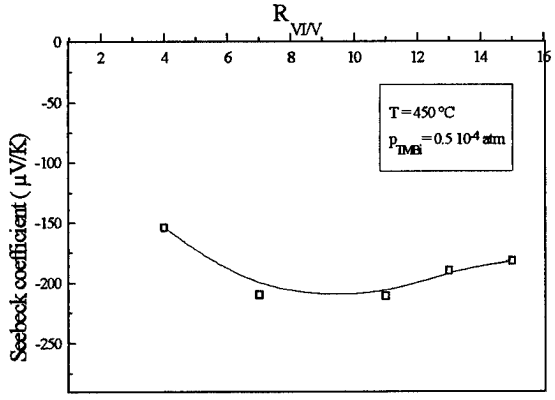


Figure 7 : VI/V ratio dependence on seebeck coefficient.

Figure 7 shows the R ratio dependence of seebeck coefficient. It can seen that as R ratio increase the seebeck coefficient is raised up a maximum of -210 μV/K for the R value equal to 7.

Further increase in R results in a decrease of the seebeck coefficient. In parallel, the same behaviour of figure-of-merit is indicated in figure 8. The best value of Z was found to be equal to 2.48 $x10^{-3}$ K^{-1}.

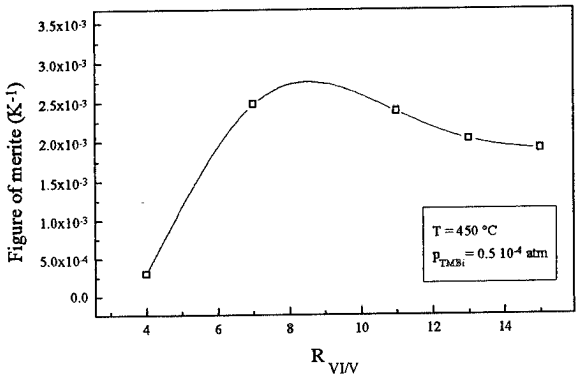


Figure 8 : VI/V ratio dependence on figure of merit.

Conclusion

MOCVD growth of n-type on pyrex substrate has been examined. The growth parameters have been studied to obtain both morphology and crystallinity. The growth to be depend on VI/V ratio. The best results were found for VI/V ratio varied between 6 and 10. In the variation range of these parameter the our results are comparable to the best results obtained by MBE for the same material.

These initial results suggest a significant potential of MOCVD method which is an industrial method and should allow the growth of good quality thick layers for thermoelectric devices.

References

[1] Y.H. Shing, Y. Chang, A. Mirchafti, L.Hayash,. S. S. Robert, J. Y Josefowicz and N. Tran, J. Vac . Sci. Technol. , A, 1 (1983) 503.

[2] H. Noro, k. Sato and H. Kagechika, J. Appl. Phys. 73 (1993) 1252.

[3] J. George and B. Pradeep, Solid State commun. 56 (1985) 117.

[4] F. Völklein, V. Baier, U. Dillner and E. Kessler, Thin solid films, 187 (1990) 253.

[5] N. G. Patel and P. G. Patel, Solid State Electron., 35 (1992) 1269.

[6] T. Tanaka, M. Saki, F. Kiya, Y. Ogawa, K. Mukasa, N Sasa and J. Nago in K. Mastuura(ed), Proc. XII Int. Conf. On thermoelectrics Institute of Electrical Engineers of Japan, Tokyo, (1994), p. 355.

[7] A. Boyer and E.Cissé, Mater. Sci. Eng. B,13 (1992) 103.

[8] E. Charles, E. Groubert and A. Boyer, J. Mater. Sci. Lett., 7 (1988) 575

[9] A.Giani, F. Pascal-Delannoy, A. Boyer, A . Foucaran, M. Gschwind, P. Ancey, Thin soild films, (1997) 9694.

[10] R. Venkatasubramanian, T. Colpitts, E. Watko, M. Lamvik, N. El-Masry, J. of Crystal Growth, 170 (1997) 817-821.

[11] J. George and B. Bradeep, Solide State Commun. 65 (1985) 117.

[12] N. Damadora and N. Soundararajan, Phys. Rev. B 37 (1988) 450.

[13] M. Francombe, Philos. Mag. 10 (1964) 989.

[14] N. J. Mason and P.J. Walker, J. of Crystal Growth, 107 (1991) 181-187.

[15] Y. Azzouz, doctorat thesis (1990), Université Montpellier II, France.

Galvanomagnetic and Thermoelectric Measurements on Polycrystalline $Bi_{88}Sb_{12}$

H. J. Goldsmid and E. H. Volckmann
Marlow Industries, Inc., Dallas, Texas, USA

Abstract

Measurements of the electrical conductivity, Seebeck coefficient, Hall coefficient and magnetoresistance of Se-doped, Sn-doped and undoped $Bi_{88}Sb_{12}$ have been made over the temperature range 100 K to 300 K using transverse magnetic fields of up to 1 tesla. The material was polycrystalline and prepared by powder metallurgy. A simplified two-carrier theory is applied to the analysis of the experimental data and is shown to give a good qualitative description of the results. It is shown that the electrons and light holes have effective masses of the order of one-tenth of the free electron mass. On the other hand, the heavy holes have an effective mass in excess of the free electron mass.

1. Introduction

Although there is no doubt that single crystal Bi-Sb alloys, when properly oriented, have superior thermoelectric and thermomagnetic figures of merit to those displayed by polycrystalline material, there are practical advantages in using samples produced by powder metallurgy. Such advantages include speed of preparation, consistency of composition and mechanical strength. The preferred Bi-Sb ratio is undoubtedly different for thermoelectric and thermomagnetic applications and is probably temperature dependent too. There may also be advantages in adding either a donor or acceptor impurity, e.g., selenium or tin.[1]

The present study is aimed not so much at the optimization of the material but rather at the establishment of a simple model that adequately describes the transport properties of the polycrystalline alloys. Our measurements have been made over the temperature range 100 K to 300 K on samples having the basic composition $Bi_{88}Sb_{12}$, with additions of Se or Sn in the range 0 to 1000 ppm. The electrical and thermal conductivities, the Seebeck coefficient and the Hall coefficient have been measured in a transverse magnetic field of up to 1 tesla. Our present analysis is confined to the electrical conductivity and Seebeck coefficient in zero magnetic field and the Hall coefficient and magnetoresistance at the low magnetic field limit. The magneto-Seebeck effect and the thermal conductivity will be discussed at a later date.

2. Experimental Details

The $Bi_{88}Sb_{12}$ samples were prepared by melting the desired quantities of high purity Bi, Sb and dopants in sealed, quartz ampoules. The tubes were agitated to promote complete mixing of the melt followed by a water quench to minimized segregation during solidification. 99.9999 % Bi and Sb were used after it was found that the impurities in 99.999 % raw materials produced significant variability in undoped samples. Powders were prepared by crushing the ingots via mortar and pestle so that the particles would pass through a 60 mesh screen. The powder was initially consolidated by cold pressing followed by a warm loading step to promote good interparticle contact.

The measurements were made in a cryostat that allowed the stabilization of the temperature at any point between liquid nitrogen temperature and 300 K. Each sample was soldered to copper end plates through which electrical and thermal currents could be introduced. The electric potentials and temperatures at these end plates were measured, allowing the electrical and thermal conductivity and the Seebeck coefficient to be determined as in a typical Harman-type measurement.[2] The Hall coefficient was found using wire probes at the center of the sample.

We generally attempted to make the samples at least four times as long as their width, as measured perpendicular to the direction of the magnetic field. By this means we hoped to avoid any influence on the Hall effect from transverse currents. However, the magnetoresistance clearly involved a contribution from transverse currents near the end plates.[3] As we shall show elsewhere, the magnetoresistance under the condition of zero transverse current can be calculated from the results using our configuration if samples of more than one length-to-width ratio are employed. We actually found very little influence from transverse flows when the magnetoresistance was measured on samples with a 4:1 length-to-width ratio.

3. Theory

A theoretical description of the transport properties of BiSb alloys is complicated by the presence of two types of hole. The energy band structure has been described by Lenoir *et al.*[4] and, using their data for the composition $Bi_{88}Sb_{12}$, the edge of the conduction band lies 20 meV above the edge of the light hole band and 35.7 meV above the edge of the heavy hole band. Strictly then, we should make use of a three-carrier model. However, we are not attempting to give a detailed interpretation of the transport properties at this stage. For example, we shall be ignoring the effect of the scattering law on the partial Hall coefficients of the electrons and holes and we shall ignore the effect of internal currents associated with the anisotropic properties of the grains. Thus, although we take account of the effect of the heavy holes on the concentration of light holes for any given electron concentration, we assume that the mobility of the heavy holes is so small that they make a negligible contribution to the transport coefficients. We hope, then, for example, to describe the undoped alloy by a two-carrier model in which the electron concentration is substantially greater than the light hole concentration.

The four measured parameters, namely the electrical conductivity, σ, the Seebeck coefficient, α, the Hall coefficient, R_H, and the magnetoresistance coefficient, $\Delta\rho/\rho B^2$, are given by[5]

$$\sigma = ne\mu_n + pe\mu_p, \qquad (1)$$

$$\alpha=\frac{n\mu_n\alpha_n+p\mu_p\alpha_p}{n\mu_n+p\mu_p}, \qquad (2)$$

$$R_H=\frac{-n\mu_n^2+p\mu_p^2}{e(n\mu_n+p\mu_p)^2}, \qquad (3)$$

$$\frac{\Delta\rho}{\rho B^2}=\frac{np\mu_n\mu_p(\mu_n+\mu_p)^2}{(n\mu_n+p\mu_p)^2}. \qquad (4)$$

where n and p are the electron and the hole concentrations, μ_n and μ_p are the electron and hole mobilities and α_n and α_p are the partial Seebeck coefficients. It should be noted that the magnetoresistance coefficient, as given by equation (4), goes to zero when there is only one type of carrier, whereas we know that this quantity is finite for extrinsic Bi-Sb. In other words, equation (4) is likely to be a good approximation only when the contributions from the electrons and holes are comparable.

It is convenient to rearrange equations (3) and (4) to obtain

$$\mu_n=-R_He(n\mu_n+p\mu_p)+\left(\frac{Mp\mu_p}{n\mu_n}\right)^{\frac{1}{2}} \qquad (5)$$

and

$$\mu_p=R_He(n\mu_n+p\mu_p)+\left(\frac{Mn\mu_n}{p\mu_p}\right)^{\frac{1}{2}}. \qquad (6)$$

Here the magnetoresistance coefficient is denoted by M.

It is noted that the two partial Seebeck coefficients are related to one another through our knowledge of the energy gap, provided that an assumption is made about the scattering law. For want of any other indication, we shall suppose that the scattering law exponent r is equal to -½. Even so, there are five unknowns to be determined from four measured parameters. This dilemma can be resolved if we can make measurements on a sample in which there is only one type of carrier. We can then find the relationship between partial Seebeck coefficient and concentration for that carrier.

4. Experimental Data

In figures 1 to 4 we show how each of the measured parameters vary with temperatures for each sample. The figures give, respectively, the electrical conductivity, the Seebeck coefficient, the Hall coefficient and the magnetoresistance coefficient. The latter two quantities were found to vary with magnetic field strength so, to obtain consistent results, we selected the values for that field at which the change of resistance was 10%. It was expected that the magnetoresistance at this field strength would correspond to the region for which $\Delta\rho/\rho$ is proportional to B^2.

We see that only the most heavily Sn-doped sample displays positive values for the Seebeck and Hall coefficients and then only at the lowest temperatures.

Most of the samples display variations of the parameters with temperature that are typical of mixed conduction but the two most heavily Se-doped samples behave in a different manner. They have electrical conductivities that fall continuously as the temperature rises while their Seebeck coefficients rise with temperature. Their Hall coefficients are almost temperature independent. All these characteristics are typical of extrinsic conduction.

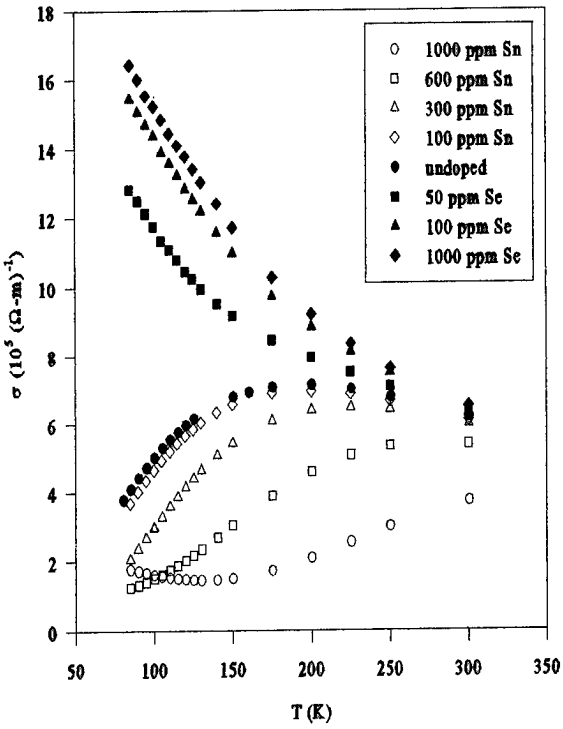


Figure 1. Plots of electrical conductivity against temperature.

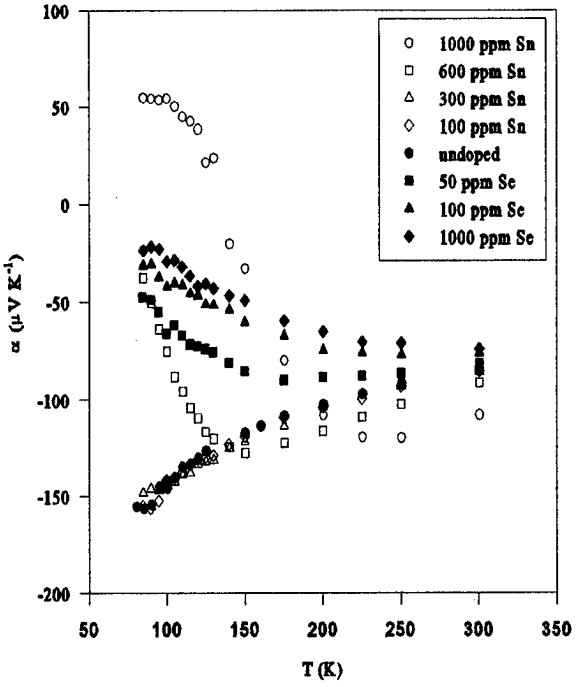


Figure 2. Plots of Seebeck coefficient against temperature.

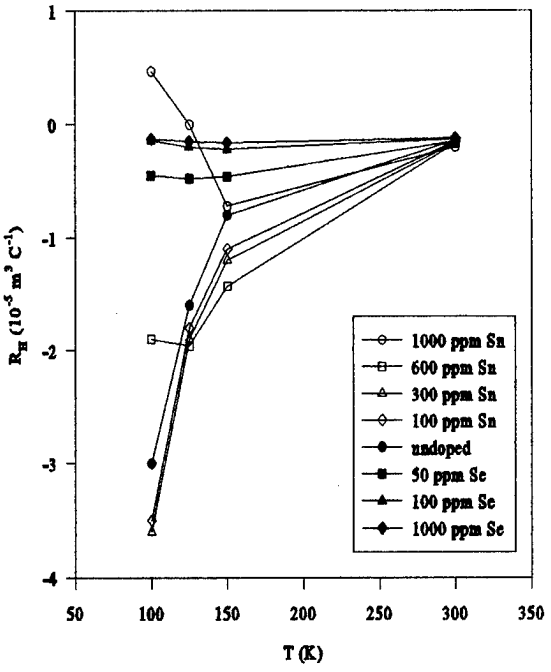


Figure 3. Plots of Hall coefficient against temperature.

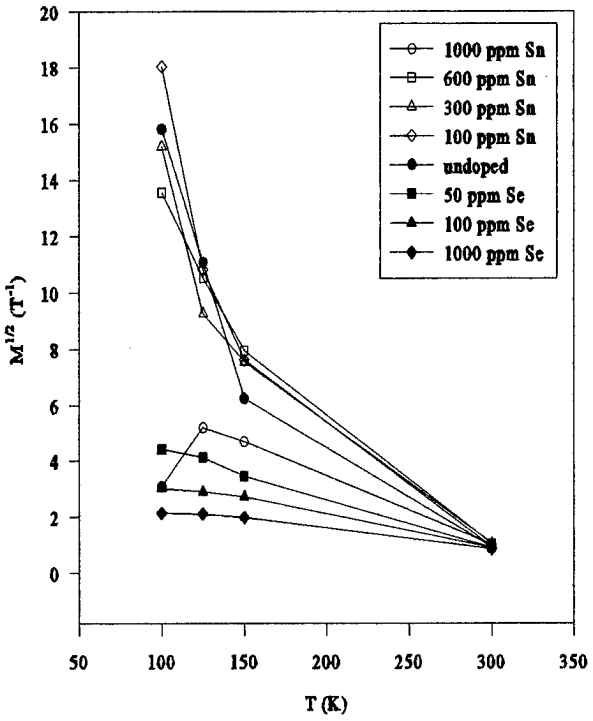


Figure 4. Plots of the square root of the magnetoresistance coefficient against temperature.

5. Analysis of Results

The extrinsic behavior of the samples with nominally 100 ppm and 1000 ppm of Se allows us to analyze their properties in terms solely of the properties of the electrons. The Hall coefficient gives us the electron concentration while the Seebeck coefficient determines the Fermi energy. Consequently we can find the effective mass of the electrons. Interestingly, the quantity, m_n^*, did not appear to vary significantly with either temperature or concentration of dopant. This seems to indicate that the electron band is nearly parabolic, at least for the Fermi energies encountered in our samples. This implies that we can use the same mean value of $m_n^* = 0.122m$ for all our samples.

We have applied the theory of Section 3 to our experimental data using a spreadsheet technique to determine the basic parameters that best fit the results. For each sample at each temperature we have adjusted the electron concentration until, after inserting the measured values of the coefficients, σ, R_H, and M, together with the known value of m_n^*, we have found the value of α to agree with experiment. The final form of the spreadsheet appears as Appendix 1.

In figures 5 and 6 we have plotted the electron and light hole mobilities, respectively, against temperatures. The highest mobilities are found for the undoped and lightly Sn-doped samples. The electron and hole mobilities are comparable with one another though, perhaps unexpectedly, the hole mobility seems significantly higher than that of electrons at 300 K. There

is some apparent anomaly for the sample with 1000 ppm Sn at the lower temperatures but otherwise the results are unremarkable with the mobilities falling rapidly as the temperature rises, except for the Se-doped samples which obviously display strong point defect scattering.

Although we have been able to fit the experimental data without any glaring anomalies, we do not have any spare parameters with which to check the validity of our approach. However, there is a further step that we can take. We can make use of our values for the concentration and Fermi energy of the light holes to determine their effective mass. We have done this for the six samples that display mixed conduction.

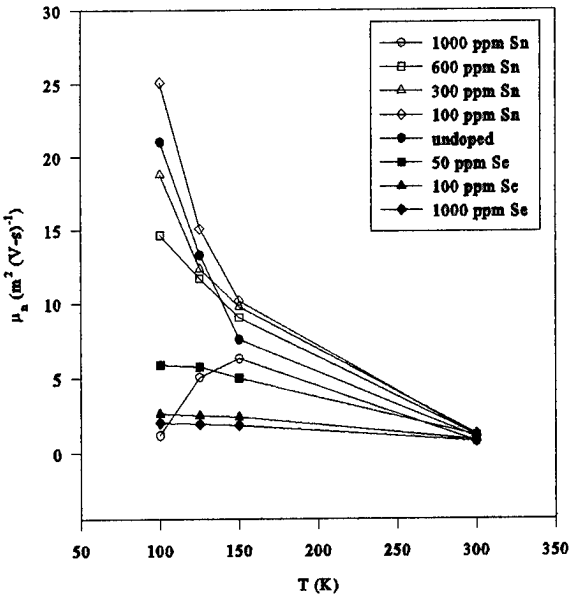


Figure 5. Plots of electron mobility against temperature.

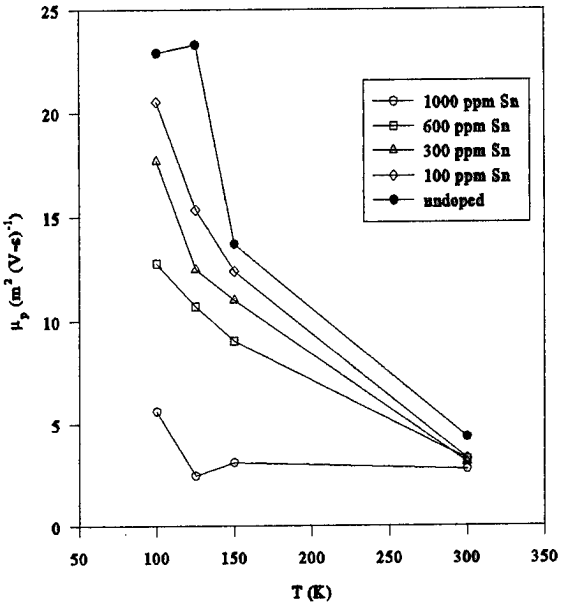


Figure 6. Plots of light hole mobility against temperature.

If we use all the data we obtain a rather wide spread for m_p^* but some of the values are obviously unreliable. For example, the results at 300 K are of doubtful value since the magnetoresistance is invariably very small at this temperature and there is also the likelihood that the neglect of the contribution to the transport processes of the heavy holes is less valid at this temperature. Furthermore, for the 50 ppm Se case it is difficult to attribute properties to the holes since they make very little contribution compared with electrons. The remaining results are given in table 1.

6. Conclusions

It is concluded that a good qualitative description of the galvanomagnetic and thermoelectric properties of polycrystalline $Bi_{88}Sb_{12}$ is given by a two-carrier theory in which bipolar transport is predominant. However, the model clearly needs to be improved if really close agreement with experimental data is to be achieved.

The value for m_p^* at 100 K for the sample with 1000 ppm Sn is clearly anomalous. This sample was unusual in that it displayed a greater magnetoresistance at 125 K and 150 K than it did at 100 K. Otherwise, the values are all of the same order even though they cover a rather wide range from about 0.6m to 0.16m. This suggests that the model is basically sound but needs refinement. The mean value for the effective mass of the light holes is 0.088m. We can probably conclude quite safely that the light holes and the electrons have rather similar effective masses.

We can also deduce a value for the effective mass, m_{p2}^*, of the heavy holes, if we suppose that the total concentration of the holes in the undoped sample is the same as the electron concentration. We calculate the concentration of the heavy holes by subtracting that of the light holes from the electron concentration. Also, by assuming that the gap between the edge of the heavy hole band and the electron band is 35.7 meV, we can determine the Fermi energy of the heavy holes. The mean value for m_{p2}^* turns out to be about 2.4m. This rather large value suggests that the mobility of the heavy holes must be very small but, in view of the fact that they can greatly outnumber the light holes, their neglect in the transport theory can be no more than an approximation.

References

[1] Jandl, P., Birkholz, U., *J. Appl. Phys.*, **76**, 7351 (1994).

[2] Harman, T.C., *J. Appl. Phys.*, **29**, 1373 (1958).

[3] Beer, A. C., "Galvanomagnetic Effects in Semiconductors," 58, Academic Press, New York (1963).

[4] Lenoir, B., Cassart, M., Dauscher, A., Ravich, Yu. I., and Scherrer, H., Proceedings of the Fourteenth International Conference on Thermoelectrics, St. Petersburg (1995).

[5] Putley, E. H., "The Hall Effect and Related Phenomena," 88, Butterworths, Sevenoaks (1960).

Appendix 1. Analysis of Polycrystalline $Bi_{88}Sb_{12}$

doping	T	$ne\mu_n$	$pe\mu_p$	μ_n	μ_p	ne	pe	$F_{1/2}(\eta_n)$	η_n	η_p	α_n	α_p	α
ppm	K	10^5 /Ωm	10^5 /Ωm	m^2 /Vs	m^2 /Vs	10^3 C/m³	10^3 C/m³				μV/K	μV/K	μV/K
0	100	4.05	0.73	21.05	22.90	19.2	3.2	0.517	-0.39	-1.93	-229.6	344.3	-142.0
0	120	5.34	0.61	13.27	23.29	40.2	2.6	0.822	0.29	-2.22	-187.2	267.0	-130.4
0	160	6.28	0.66	7.58	13.71	82.9	4.8	1.100	0.72	-2.17	-164.2	363.2	-114.0
0	300	6.03	0.18	1.03	4.37	587.8	4.1	3.038	2.36	-3.81	-101.5	462.5	-85.1
1000 Sn	100	1.15	0.46	1.19	5.63	96.4	8.2	2.589	2.01	-4.33	-112.0	470.4	54.4
1000 Sn	125	0.75	0.71	5.06	2.48	14.8	28.6	0.285	-1.12	-0.74	-281.7	253.8	-21.3
1000 Sn	150	0.67	0.83	6.30	3.13	10.6	26.5	0.155	-1.63	0.08	-321.0	199.6	-32.9
1000 Sn	300	1.90	0.19	0.74	2.79	257.1	6.8	1.329	0.99	-1.76	-151.3	331.1	-107.5
600 Sn	100	0.86	0.65	14.63	12.77	5.8	5.1	0.157	-1.62	-0.70	-320.5	250.7	-74.9
600 Sn	125	1.45	0.72	11.68	10.70	12.4	6.7	0.239	-1.29	-0.57	-294.9	241.6	-116.9
600 Sn	150	2.25	0.79	9.05	9.05	24.9	8.7	0.363	-0.85	-0.70	-261.6	251.0	-128.4
600 Sn	300	5.07	0.31	1.17	3.29	432.8	9.4	2.237	1.74	-2.51	-121.1	388.5	-91.7
300 Sn	100	2.31	0.66	18.80	17.68	12.3	3.7	0.330	-0.96	-1.36	-269.8	299.9	-143.2
300 Sn	125	3.57	0.72	12.32	12.50	29.0	5.8	0.557	-0.29	-1.57	-222.6	316.7	-132.1
300 Sn	150	4.58	0.85	9.77	11.01	46.9	7.7	0.685	0.02	-1.57	-203.3	316.2	-122.0
300 Sn	300	5.62	0.37	1.23	3.13	457.8	11.8	2.366	1.84	-2.61	-117.7	395.6	-86.0
100 Sn	100	3.75	0.90	25.11	20.52	14.9	4.4	0.401	-0.73	-1.59	-252.9	318.0	-142.4
100 Sn	125	4.98	0.87	15.05	15.35	33.1	5.7	0.636	-0.09	-1.77	-210.2	331.7	-129.6
100 Sn	150	5.72	0.86	10.19	12.40	56.1	6.9	0.820	0.29	-1.84	-187.4	337.3	-118.8
100 Sn	300	5.82	0.28	1.12	3.31	520.4	8.5	2.689	2.09	-2.86	-109.6	413.1	-85.6
50 Se	100	11.54	0.21	5.88	27.45	196.2	0.8	5.268	3.67	-5.99	-73.1	320.0	-66.0
50 Se	125	9.85	0.40	5.75	15.54	171.3	2.6	3.291	2.57	-4.43	-96.1	469.8	-74.0
50 Se	150	8.71	0.46	5.01	10.86	173.7	4.2	2.539	1.97	-3.52	-113.3	451.1	-85.0
50 Se	300	5.97	0.36	1.17	2.72	510.0	13.3	2.636	2.04	-2.81	-110.9	410.2	-81.2

Table 1. Effective mass of the light holes

sample	temperature K	pe 10^3 m^{-1}	η_p	$F_{1/2}(\eta_p)$	m_p^*/m
undoped	100	3.2	-1.93	0.123	0.096
	120	2.6	-2.22	0.096	0.079
	160	4.8	-2.17	0.101	0.090
1000 ppm Sn	100	8.2	-4.33	0.018	0.864
	125	28.6	-0.74	0.367	0.160
	150	26.5	0.08	0.724	0.080
600 ppm Sn	100	5.1	-0.70	0.380	0.062
	125	6.7	-0.57	0.424	0.055
	150	8.7	-0.70	0.380	0.059
300 ppm Sn	100	3.7	-1.36	0.210	0.074
	125	5.8	-1.57	0.173	0.091
	150	7.7	-1.57	0.173	0.092
100 ppm Sn	100	4.4	-1.59	0.169	0.096
	125	5.7	-1.77	0.143	0.102
	150	6.9	-1.84	0.134	0.101

Magneto-thermoelectric properties of undoped and doped Bi-Sb single crystals.

V.M. Grabov[1], O.N. Uryupin[2]
[1]Herzen Russian State Pedagogical University, St. Petersburg, Russia
[2]A.F.Ioffe Physical-Technical Institute, St.Petersburg, Russia
Tel.: +7/812/515-9153, Fax: +7/812/515-6747, E-mail: O.Uryupin@shuvpop.ioffe.rssi.ru

Abstract

Electrical resistivity ρ, Seebeck coefficient α and thermal conductivity κ of $Bi_{1-x}Sb_x$ crystals were measured depending on alloy composition, doping, and crystallographic orientation, temperature in an interval 77-300 K, magnetic field up to 2 T.

To prepare alloys Bi and Sb refined up to 99.9999 at. % were used. The single crystals $Bi_{1-x}Sb_x$ ($0<x<0.15$) were grown up by a horizontal zone recrystallization method at growth rate V=0.05 cm/hours and temperature gradient G=20 K/cm.

It is shown, that the n - type $(Bi_{0.93}Sb_{0.07})<Sn_{0.001\ at.\%}>$ crystals at the temperature of practical interest T=180 K have the following magneto-thermoelectric figure of merit ($Z_{33}(B_2)$): $2.79\cdot10^{-3}$ 1/K at B=0, $4.79\cdot10^{-3}$ 1/K at B=0.25 T, and $4.95\cdot10^{-3}$ 1/K at B=0.50 T.

Caused by magnetic field the changes of transport coefficients and Z are the result of reduction of energy dependence of effective relaxation time, reduction of partial mobility and their distinctions for light and heavy charge carriers, electrons and holes in a magnetic field. The initial conditions for obtaining the highest magneto-thermoelectric figure of merit are formed by doping by donor or acceptor impurity.

Introduction

Progress in the research of thermoelectric and magneto-thermoelectric figure of merit of $Bi_{1-x}Sb_x$ crystals [1-6] are connected essentially with the increase of Bi and Sb purity degree and the perfection of crystal growth methods [5].

Our researches [5, 6] allowed to establish the detailed picture of influence of alloy inhomogenity and also content of doping impurity on thermoelectric characteristics of $Bi_{1-x}Sb_x$ crystals. It was shown, that the highest value of thermoelectric figure of merit Z_{33} is achieved in undoped homogeneous n - type $Bi_{1-x}Sb_x$ crystals at x = 0.07 in the whole temperature region 77 - 300 K [5]. For all (x) $Z_{33}(T)$ passes through a maximum at $T=T_m(x)$. The doping n - type $Bi_{1-x}Sb_x$ crystals by donor impurity (tellurium) leads to some increase of thermoelectric figure of merit at $T<T_m(x)$, and doping by acceptor impurity (tin) leads to such an increase at $T>T_m(x)$ [6]. In work [2, 4] it was established, that the magneto-thermoelectric figure of merit $Z_{33}(B_1)$ of $Bi_{1-x}Sb_x$ single crystals doped by tellurium exceeds much its value for undoped crystals, however for the achievement of maximum value $Z_{33}(B_1)$ high enough values of magnetic fields are required.

The goal of this work was to receive the most complete picture of magnetic field influence on thermoelectric parameters, and also to fulfill the detailed research of physical mechanism of increasing the thermoelectric figure of merit of $Bi_{1-x}Sb_x$ crystals in a magnetic field. For this purpose we studied magnetic field influence on bismuth-antimony crystal thermoelectric figure of merit in the area of temperatures and alloy compositions where tin doped crystals have the highest efficiency without magnetic field.

Experiment

Initial materials of high purity were used to prepare alloys: antimony of 99.9999 % purity and bismuth of 99.999 % . Bismuth was additionally refined up to 99.9999 % [5]. The single crystals were grown up by a horizontal zone recrystallization method applying regimes that ensure obtaining single crystals with homogeneous distribution of components and doping impurities [5, 6]. Samples for the research were cut out by electric erosion method as parallelepipeds with edges, parallel to crystallographic axes C_1, C_2, C_3. Three sample types being differ in crystallographic axis parallel to the longest side of a parallelepiped were used. Used system of coordinates: the axis (x) or (1) is parallel to C_2, the axis (y) or (2) is parallel to C_1, the axis (z) or (3) is parallel to C_3. The transverse magnetic field $B=B_2$ was directed parallel to C_1, for which average cyclotron mobility of electrons is the highest one.

The measurements of transport coefficients $\rho=1/\sigma$, α, κ were performed by stationary methods in the temperature range 77-300 K. [5, 6]. The stationary magnetic field was formed by an electromagnet with an area of uniformity, exceeding sample sizes. The measurements of magnetic field induction were performed by Hall gauge with the error 5%. The errors of measurement of transport coefficient ρ, α, κ were accordingly: 3%, 5% and 7%.

Experimental results

Measurements of electric resistivity, Seebeck coefficient and thermal conductivity dependence on temperature and magnetic field for $Bi_{0.93}Sb_{0.07}$ crystals, having the highest value Z_{33} among homogeneous undoped $Bi_{1-x}Sb_x$ crystals in the interval 80-300 K [5] were carried out. The same transport coefficients were measured for $Bi_{0.93}Sb_{0.07}$ crystals, doped by tellurium and tin. Fig. 1-4 show the dependencies of transport coefficients ρ_{33}, α_{33}, κ_{33} and Z_{33} on magnetic

0-7803-4057-4/97 $10.00 ©1997 IEEE

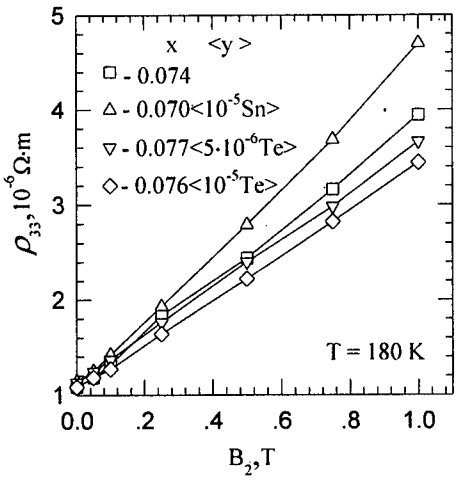


Fig. 1: Dependence of electric resistivity ρ_{33} on magnetic field $B_2 \| C_1$ for $Bi_{1-x}Sb_x$<y> crystals at temperature T=180 K.

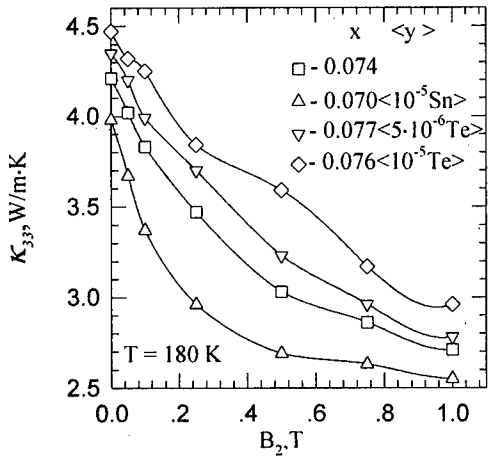


Fig. 3: Dependence of thermal conductivity κ_{33} on magnetic field $B_2 \| C_1$ for $Bi_{1-x}Sb_x$<y> crystals at temperature T=180 K.

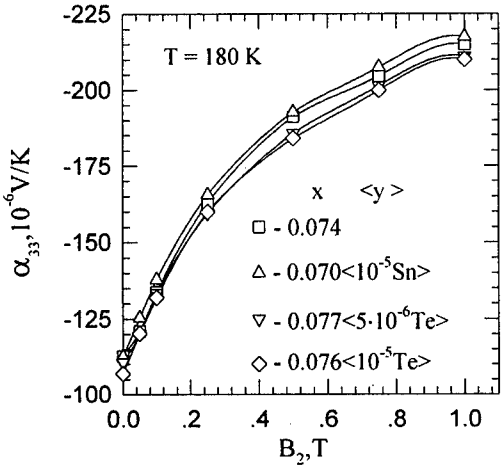


Fig. 2: Dependence of Seebeck coefficient α_{33} on magnetic field $B_2 \| C_1$ for $Bi_{1-x}Sb_x$<y> crystals at temperature T=180 K.

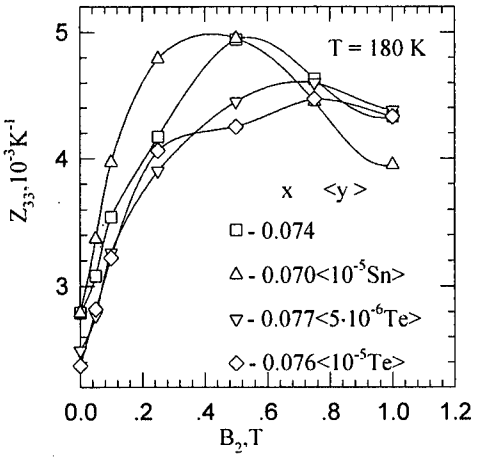


Fig. 4: Dependence of thermoelectric figure of merit Z_{33} on magnetic field $B_2 \| C_1$ for $Bi_{1-x}Sb_x$<y> crystals at temperature T=180 K.

field B_2 for pure and doped $Bi_{0.93}Sb_{0.07}$ crystals at temperature T=180K. That temperature is of interest for application of $Bi_{1-x}Sb_x$ crystals in low temperature stages of thermoelectric coolers.

The dependencies presented on Fig. 1-4, show that in the conditions, when tin doped $Bi_{1-x}Sb_x$ crystals have the highest values of Z_{33}, they have the highest value of $Z_{33}(B_2)$ in a transverse magnetic field. Thus the magnetic field B_m corresponding to the maximum of $Z_{33}(B_2)$ is less than that for undoped and tellurium doped crystals. The highest values of $Z_{33}(B_2)$ for $Bi_{0.93}Sb_{0.07}$<$Sn_{0.001at.\%}$> crystals are reached, mainly, due to lower thermal conductivity and its sharper decrease in a magnetic field.

About the mechanism of magnetic field influence on thermoelectric figure of merit of $Bi_{1-x}Sb_x$ crystal

As it is known [1, 2], the increase of Z(B) of bismuth-antimony crystals at $0<B<B_m$ is caused by the increase of Seebeck coefficient and reduction of thermal conductivity at rather small increase of electric resistance. At $B>B_m$ Seebeck coefficient and thermal conductivity reach saturation, and electric resistance continues to grow so Z(B) reaches a maximum at $B=B_m$ and further decreases. In general it is so, however the complex structure of energy bands of bismuth-type crystal complicates the real dependence Z (B).

Let us consider magnetic field dependence of Seebeck coefficient in $Bi_{1-x}Sb_x$ crystals. In an elementary case it will be bismuth single crystals, tellurium doped up to the level when only electrons of L-extrema of a conduction band participate in the transport phenomena and Seebeck coefficient in absence of magnetic field is isotropic one and corresponds to the partial Seebeck coefficient of electrons.

Fig. 5 shows the dependence of Seebeck coefficient $\alpha_{22}(B_1)$ at T=80 K for Bi<$Te_{0.05at.\%}$> single crystal satisfying specified

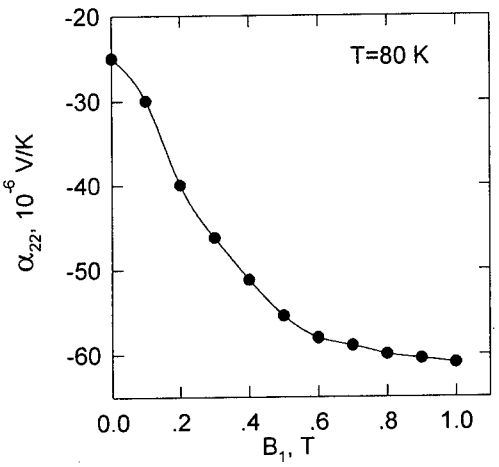


Fig. 5: Dependence of Seebeck coefficient $\alpha_{22}(B_1)$ on magnetic field $B_1 \| C_2$ for Bi<$Te_{0.05\ at.\%}$> single crystal at temperature T=80 K.

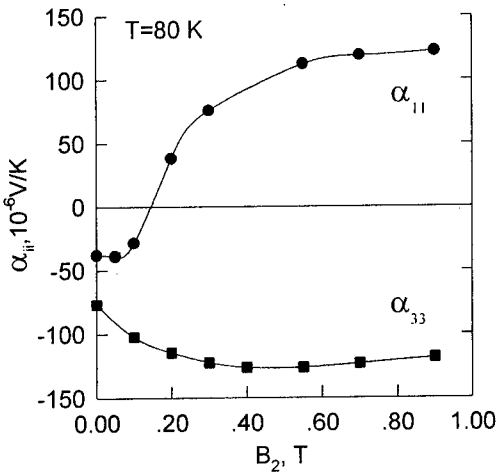


Fig. 6: Dependence of Seebeck coefficient $\alpha_{33}(B_2)$ and $\alpha_{11}(B_2)$ on magnetic field $B_2 \| C_1$ of bismuth single crystals at temperature T=80 K.

conditions. The direction of magnetic field $B_1 \| C_2$, appropriate to the least electron cyclotron mobility, was chosen to show experimentally the opportunity of achievement of Seebeck coefficient saturation. The essential increase of Seebeck coefficient, more than twice, in a magnetic field was observed. It is possible to understand such behavior qualitatively on the basis of elementary theory for the parabolic electron dispersion law :

$$\alpha = \frac{\pi^2}{3}\frac{\mathbf{k}}{\mathbf{e}}\left(\mathbf{r}+\frac{3}{2}\right)\left(\frac{\mathbf{kT}}{\mathbf{E_F}}\right) \qquad (1)$$

where **r** - relaxation parameter, determining the dependence of charge carriers relaxation time τ on energy $\varepsilon=(E/kT)$: $\tau=\tau_0\varepsilon^r$. For the scattering on acoustic phonons **r**=-1/2. The effective relaxation parameter in a strong magnetic field **r***=0, because classically strong magnetic field equalizes the effective mobility of all charge carriers. This change of **r***(B) results in the increase of partial electron Seebeck coefficient in a magnetic field about 1.5 times. The observable more than twice change of Seebeck coefficient is caused by the additional contribution of nonparabolic conductivity band [7]. The transition from the change of Seebeck coefficient in a magnetic field to the saturation is determined by the condition uB=1, differentiating the areas of classically weak and strong magnetic field.

In undoped bismuth crystals Seebeck coefficient is determined by the contribution of electrons and holes:

$$\alpha_{ii} = \frac{\alpha^+\sigma_{ii}^+ + \alpha^-\sigma_{ii}^-}{\sigma_{ii}^+ + \sigma_{ii}^-} \qquad (2)$$

and is negative because at n=p, $u^+ < u^-$ and $\sigma^+ < \sigma^-$.

Fig. 6 shows the dependence of Seebeck coefficient components $\alpha_{33}(B_2)$ and $\alpha_{11}(B_2)$ of bismuth single crystals at T=80 K. The direction $B_2 \| C_1$ was chosen appropriate to the highest value of cyclotron electron mobility. The magnetic field dependence $\alpha_{11}(B_2)$ shows two features: negative Seebeck coefficient achieves the maximum of absolute value and further changes its sign and growth up to the saturation. The dependence $\alpha_{33}(B_2)$ is a similar one, but the value of maximum is significantly higher as in the given direction hole mobility is much less $u_3^+ << u_1^+$. Therefore the maximum and saturation occurs in higher magnetic fields.

The maxima of Seebeck coefficient and thermoelectric figure of merit of n-type crystals are reached in a magnetic fields, appropriate to a condition 0<B<1/u for the electron mobility.

In crystals $Bi_{1-x}Sb_x$ (0<x<0.17) electron mobility is more than that in bismuth owing to the transition from overlapping bands to an energy gap and the reduction of charge carriers concentration. This results in the reduction of the region of magnetic field 0<B<1/u and reduction of magnetic field B_m appropriate to maximum Seebeck coefficient and thermoelectric figure of merit.

Doping by acceptor impurity leads to the increase of thermoelectric figure of merit of n-type crystals at higher temperatures in comparison with undoped crystals, and the increase of electron mobility provides obtaining the maximum of thermoelectric figure of merit at smaller value of magnetic field in comparison with undoped or tellurium doped crystals, as it is seen from the Fig.4.

There is another situation at bismuth crystals and $Bi_{1-x}Sb_x$ (0<x<0.20) alloys doping by donor impurity. In this case, in the region of existence of charge carriers of two signs n>p Seebeck coefficient at saturation remains negative too, so both mechanisms work in one direction, resulting in the increase of Seebeck coefficient and thermoelectric figure of merit.

The separate manifestation of these factors can be seen on Fig. 7 for the $Bi_{0.88}Sb_{0.12}$<$Te_{0.001\ ат.\%}$> crystal at T=80 K and $B_1 \| C_2$. At $B_2 \| C_1$ the action of both factors results in the maximum increase of thermoelectric figure of merit in a magnetic field attaining the value $Z_{33}(B_2) = 1.1 \cdot 10^{-2}\ K^{-1}$ for some $Bi_{1-x}Sb_x$ <Te_y> crystals in the low temperature region [2, 4].

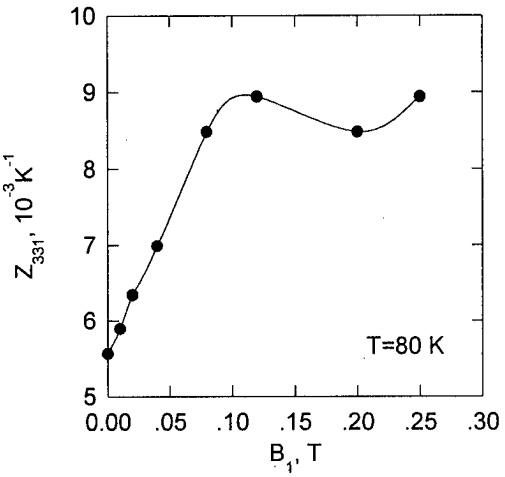


Fig. 7: Dependence of magneto-thermoelectric figure of merit on magnetic field $B_1 \|\ C_2$ for the $Bi_{0.88}Sb_{0.12}$<$Te_{0.001\ ат.\%}$> single crystal at temperature T=80 K.

Conclusions

In conditions when thermoelectric figure of merit Z_{33} of n-type $Bi_{1-x}Sb_x$ <Sn> crystals is the highest, magneto-thermoelectric figure of merit $Z_{33}(B_2)$ of these crystals is the highest too.

Magneto-thermoelectric figure of merit $Z_{33}(B_2)$ of $Bi_{1-x}Sb_x$<Sn> crystals reaches the maximum value at lower magnetic fields in comparison with undoped or tellurium doped crystals.

Caused by magnetic field the change of transport coefficients and Z is the result of reduction of energy dependence of effective relaxation time, reduction of partial mobilities and their distinctions for light and heavy charge carriers, electrons and holes in a magnetic field.

The specified factors work in one direction to increase Z(B) in tellurium doped $B_{1-x}Sb_x$ crystals, that results in the achievement of record value $Z_{33}(B_2)$.

The essential contribution to the increase of Z(B) in tin doped $Bi_{1-x}Sb_x$ crystals caused by the reduction of thermal conductivity in a magnetic field.

References

[1] R. Wolfe and G.E. Smith. «Effects of a Magnetic Field on the thermoelectric properties of Bismuth-Antimony Alloys», Rept. Internat. Conf. Phys. Semicond. Exeter. 1962, London, Institute Phys. And Phys. Soc. (1962) 771-776.

[2] Ivanov G.A., Kulikov V.A., Naletov V.L., Panarin A.F., Regel A.R. «Thermoelectric figure of merit of pure and doped bismuth-antimony alloys in a magnetic field», Phys. Techn. Poluprovodn. **6** (1972) 1296-1299. (in Russian)

[3] Yim W.M., Amith A. «Bi-Sb alloys for magneto-thermoelectric and thermomagnnetic cooling», Solid State Electronics. **15** (1972) 1141-1165.

[4] Belaya A.D., Zayakin S.A., Zemskov V.S., and Ponomarev Y.G. «Service properties of doped Bi-Sb single crystals», Proc. of the Fourteenth International Conference on Thermoelectrics, St.Petersburg, A.F. Ioffe Physical-Technical Institute, 1995, 37-41.

[5] Grabov V.M., Ivanov G.A., Naletov V.L., Bondarenko M.G., Uryupin O.N. «Thermoelectric figure of merit of horizontal zone-leveling prepared bismuth-antimony single crystals», Proc. of the Fourteenth International Conference on Thermoelectrics, St.Petersburg, A.F. Ioffe Physical-Technical Institute, 1995, 115-118.

[6] Grabov V.M., Uryupin O.N., Bondarenko M.G. «Thermoelectric Properties of Doped Bismuth-Antimony Single Crystals», Proc. of the Fifteenth International Conference on Thermoelectrics. Ed. By the Institute of Electrical and Electronics Engineers, USA, 1996, 27-31.

[7] C.B. Thomas and H.J. Goldsmid. «Large magneto-Seebeck effect in an extrinsic Bi-Sb alloy», Phys. Lett. **27A** (1968) 369-370.

Energy conversion by galvanomagnetic and thermomagnetic effects with the use of $Bi_{88}Sb_{12}$ alloys

M.Sakurai*, N.Satoh*, S.Tanuma** and I.Yoshida*

* Department of Solid State Physics, Iwaki Meisei University, Chuodai Iwaki 970 Japan

** 2100-174 Horiuchi, Hayama, Kanagawa 240-01 Japan

Abstract

Galvanomagnetic and thermomagnetic effects were studied in order to serve the solid state energy conversion. A possible merit of the use of magnetic field in these effect is obious because the Seebeck emf (longitudinal Nernst-Ettingshausen effect) or Peltier cooling (Nernst effect) could be enhanced under the magnetic field. Moreover, the Ettingshausen effect generates a temperature gradient under the magnetic field. Such three effects were studied experimentally. On a Bi/Sb sample, the temperature difference due to the Ettingshausen effect for the sample width of 10 mm, and the current density of 1 A/mm² was 23K at the ambient temperature of 100 K and in the magnetic field of 1.0 tesla.

The Nernst temperature difference under the relevant condition was 15.4K for 10 mm length.

Introduction

The solid state means for the energy conversion between electricity and heat is the use of Seebeck effect which is the longitudinal generation of voltage by the temperature gradient and the use of Peltier effect which is the longitudinal temperature difference generation by the electric current.

The application of a magnetic field on both of these effects are called the longitudinal Ettingshausen-Nernst effect and the Nernst effect respectively in which the magnetic field is applied perpendicular to the primary temperature gradient and the primary electric current. Furthermore, there are conjugate two other effects, namely, the transverse Ettingshausen-Nernst effect and the Ettingshausen effect which are only appearing under the magnetic field. The names of these effects are not unique, so we show in Fig.1 the effects and the corresponding names being used in this work. We adopted $Bi_{88}Sb_{12}$ alloy as the sample. Bi and Sb have the similar crystal structure and are both semi-metals. Bi and Sb make all proportion solid solution; among this, the alloys of composition range of 4 to about 60 atomic % Sb is found to be semi-conductor [1]. The maximum band gap 13 meV appears at the composition $Bi_{88}Sb_{12}$ which alloy is also known as the best n-type Seebeck or Peltier material at low temperature [2].

Ettingshausen effect

(pure Bi)

Fig.2 shows one of the measured results on the Ettingshausen effect of a polycrystalline pure Bi of which purity is better than 6 nines. As shown in Fig.1(a), a temperature gradient $\partial T/\partial y$ appears when an electric current I_x and a magnetic field B_z are applied. The relation between I_x, B_z and $\partial T/\partial y$ is

$$\frac{\partial T}{\partial y} = E_t B_z I_x \qquad (1)$$

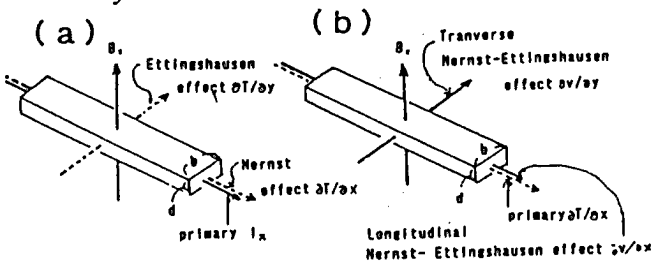


Fig.1 The definition of galvanomagnetic and thermomagnetic effects

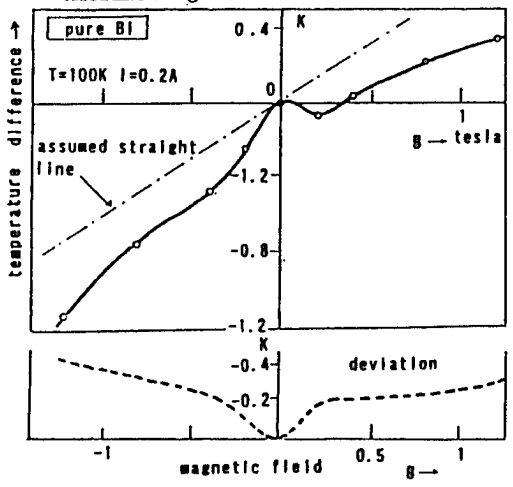


Fig.2 Ettingshausen effect of a pure Bi sample

expressed in Eq.(1).

The Ettingshausen coefficient E_t is normally constant. So the Ettingshausen temperature difference is proportional to both of B_z and I_x which means that a straight line through the origin is expected in Fig.2. Actually, Fig.2 shows a thick curved line as the measurement. In the figure, a straight line is drawn in such a manner that the differences between the straight line and the curved thick line in the both sides of ± magnetic field have the equal magnitudes at the the points of ± 0.5 tesla.

The difference throughout the range of magnetic field is shown by the dashed curve in the lower part of the figure. The cause of this deviation from the straight line is that the positions of the two thermo-junctions which are set to measure the Ettingshausen temperature difference are not along the exact y-direction but shift with each other along the x-direction, therefore the measured voltage includes Nernst effect as an error.. The Nernst effect is principally proportional to B^2 so the deviation curve shoud be symmetric to the ± B as seen by the dashed curve. In fact, the shape of the curve is parabolic only within the magnetic field of ± 0.2 tesla and is more flat in the higher field. The shape of this curve fairly resembles to the measured curve of the Nernst effect which is shown in Fig.5.

By such a consideration, the straight line in the figure has to express the net Ettingshausen effect. The line indicates the converted value of 6.5 Kfor 10 mm length, 1 /mm² and at 100 K and 1 tesla.

($Bi_{88}Sb_{12}$ alloy)

The Ettingshausen temperature difference is shown in Fig.3. The overall appearance is similar to that of the former figure on a pure bismuth. The straight line is drawn in the same manner as the case of Fig.2. The deviation curve is shown in in the lower part of the figure by the dotted line. Different from the former case, the experimental curve is surpassing the deviation curve. This difference means that the setting of two thermojunctions for measuring the effect have a misfit along the x-direction in an opposit way to the former case. The deviation curve in Fig.3 has a little hump around -0.2 tesla. The origin of this hump is not known.

The temperature difference of the deviation curvea at 0.5 tesla is 0.2 K for the current of 2 A, while the Nernst temperature difference in Fig.5 (a) in 100 K and at 0.5 tesla for the current of 2 A is about 2.5 K along 10 mm distance. So the misfit of thermo-junctions along x is estimated as 0.8 mm. This amount of misfit may be rather possible. After such a consideration, the Ettingshausen effect is thought to be expressed by the straight line; the line indicates a converted value of 22 K for 1 A/mm² at 100 K and 1 tesla.

($Bi_{88}Sb_{12}$ doped by 0.002 atm % Te)

The Ettingshausen temperature difference is shown in Fig.4. The overall appearance is similar to the former two cases. The straight line is

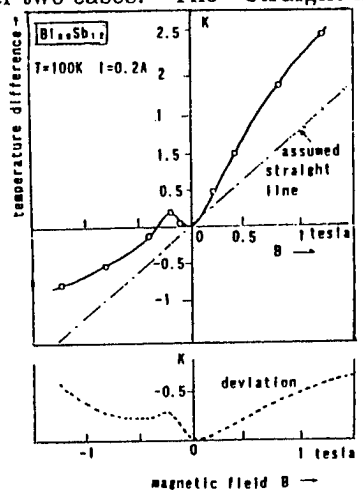


Fig.3 Ettingshausen temperature difference versus the magnetic field.for $Bi_{88}Sb_{12}$

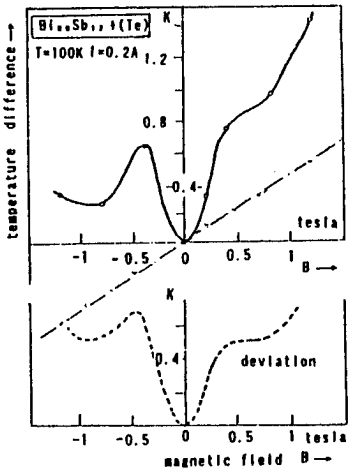


Fig.4 Ettingshausen temperature difference versus the magnetic field for $Bi_{88}Sb_{12}$ + 0.002 atm % Te

shown in Fig.4. The overall appearance is similar to the former two cases. The deviation is drawn in the same manner as the former figure by the dotted line. The deviation is positive, namely the experimental curve is surpassing the straight line as the case of Fig.3.

The dotted curve of the deviation has a hump around -0.5 tesla which is similar to the former one. The origin of this hump is also unknown.

The temperature difference of the deviation curve at 0.5 tesla is estimated as 0.5 K with the width of 16.3 mm except the height of hump for the sample current of 2A and the temperature of 100 K, while the Nernst temperature difference in Fig.5 (b) in 100 K is about 3.3K for the sample current of 2 A along the distance of 16.3 mm. So the misfit of thermo-junctions along x is estimated as 2.5 mm; this value of misfit seems fairly big. Assuming the above misfits as real ones, the net Ettingshausen effect is expressed by the straight lines in Figs.2, 3 and 4. The Nernst temperature difference shown in Fig.5 should obey the quadratic relation to the magnetic field; but the experimental curves obey the B^2 relation only within about ± 0.2 tesla.

It may be unnatural that the Effingshausen effect obeys the B-linear nature to the highest measured field of 1.5 tesla, because the Nernst effect obeys the B-quadratic nature within only 0.2 tesla. Therefore, the idea of regarding the straight line in Fig.2,3 and 4 as the real values for the Ettingshausen effect may be a too much crude approximation. A part of the deviation curves could be attributed to the real effect, although it is not known that how the real effect is separated among the deviation curve.

Nernst effect

The Nernst effect is the longitudinal temperature gradient under the primary current and the perpendicular magnetic field. The experimental results are shown in Fig.5 (a) and (b), where (a) is the result on the $Bi_{88}Sb_{12}$ alloy sample and (b) is the result on the sample of $Bi_{88}Sb_{12}$ + 0.002 atm % Te. The relation of the Nernst temperature difference, the current density and the magnetic field is as follows:

$$\frac{\partial T}{\partial x} = N_e \cdot B_z I_x \qquad (2)$$

The Nernst coefficient N_e is a constant at least in a weak magnetic field. The Nernst effect has a symmetric nature to $\pm B$, and the temperature gradient is quadratic of B. Fig.5 indicates that the symmetry holds but the parabolic change is seen only within $\pm$ 0.2 tesla or less. In the larger field, the effect less changes or even decreases. The mechanism of such a complicated field dependence is not known.

The magnitude of the Nernst temperature differencs for 10 mm length, for instance, at 100 K and in 0.5 tesla are about 2.5 K for Bi/Sb alloy and about 3.3 K for Bi/Sb (0.002Te) alloy. The former value is converted to 15.4 K for 10 mm length, 1 A/mm², 100 K and 1 tesla.

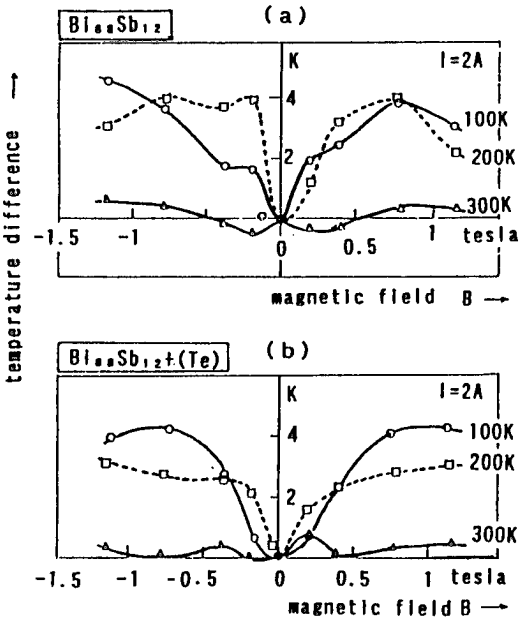


Fig.5 Nernst temperature difference (a) $Bi_{88}Sb_{12}$ sample, (b) $Bi_{88}Sb_{12}$+0.002 atm%Te

Transverse and longitudinal Nernst Ettingshausen effects

The transverse effect is the appearnce of a temperature gradient along y direction, $\partial T/\partial y$, when B_z and $\partial T/\partial x$ are applied. The longitudinal effect is the appearance of an additive temperature gradient along x, $\partial T/\partial x$, when B_z and $\partial T/\partial x$, are applied. These effects were studied on the same Bi/Sb alloy samples and the work was reported elsewhere [3].

Conclusion

(1) Ettingshausen effect and Nernst effect have been measured on $Bi_{88}Sb_{12}$ semiconducting alloys.

(2) The estimated Ettingshausen temperature difference for 10 mm width is 23.0 K with the conditions of the current density of 1A/mm², the ambient temperature 100 K and the magnetic field 1 tesla.

(3) The estimated Nernst temperature difference for 10 mm length is 15.4 K with the same conditions as above.

(4) Doping of 0.002 atomic % Te showed little improvement. A higher level of doping should be investigated.

Reference

[1] S.Tanuma: J. Phys. Soc. Jpn **14** (1959) 1246, **16** (1961) 2349, **16** (1961) 2354, **16** (1961) 2354.

[2] R.Wolfe and G.E.Smith: Appltd Phys. Lett.**1** (1962) 5.

[3] S.Tanuma and M.Sakurai: J. Adv. Sci. **7** (1975) 163.

Influence of the Consolidation Technique on the Thermoelectric Properties of Mechanically Alloyed Bi-Sb

Martin-Lopez R., Dauscher A., Devaux X., Lenoir B., Scherrer H., Zandona M.*

Laboratoire de Physique des Matériaux
* Laboratoire de Science et Génie des Matériaux Métalliques
Ecole des Mines, Parc de Saurupt, 54042 Nancy (France)
Tel.:+33/3/83584170, Fax:+33/3/83579794, E-mail:martinl@mines.u-nancy.fr

Abstract

The aim of this work is multiple : first the synthesis by mechanical alloying of homogeneous $Bi_{85}Sb_{15}$ polycrystalline powder alloys, that have been achieved with an adequate ball to powder weight ratio (10:1), second the consolidation of the powders either by sintering or by hot extrusion in order to try to introduce a texture in the material and finally to measure the thermoelectric properties of the consolidated samples in the 77-300 K temperature range.

Introduction

Bi-Sb semiconducting single crystals are the best conventional materials for low temperature (80 K) thermoelectric cooling. The highest figure of merit has been found for single crystals of an antimony composition close to 15 atomic % [1]. However, it is well known that the poor mechanical properties of these single crystals limit their use in thermoelectric devices.

Powder metallurgy offers the opportunity to increase the mechanical strength of these alloys. Mechanical alloying is a method allowing to obtain solid solutions [2] in a microcrystalline form. This technique was chosen to synthesize Bi-Sb alloys because it offers the possibility to process a homogeneous alloy in a reasonable time. Nevertheless, the thermoelectric performances of polycrystalline samples are generally altered with respect to single crystals due to the anisotropic nature of the Bi-Sb material.

The aim of this work is multiple : first the synthesis of an homogeneous $Bi_{85}Sb_{15}$ polycrystalline powder alloy by mechanical alloying and second the study of the influence of the consolidation technique on the thermoelectric properties of the obtained samples.

Experimental Procedure

Mechanical alloying was carried out in a planetary ball mill (Fritsch, Pulverisette 5) with balls (Ø = 30 mm) and jars (250 cc) in hardened stainless steel.

Base bismuth and antimony of high purity (99.999%) with initial particle sizes of 10 mm were introduced in the vessels in a stoichiometric ratio ($Bi_{85}Sb_{15}$) under an argon atmosphere in a glove box. The vessels were then hermetically sealed in order to preserve the material of a possible oxidation during the ball milling.

Three balls to powder weight ratios (BPR) were used 92:1, 40:1, 10:1. The rotation speed was fixed at 236 r. p. m..

X-ray diffraction (XRD) analyses of the powder samples were performed in a Siemens D-500 diffractometer with the Co-$K_{\alpha 1}$ radiation, in the standard θ–2θ geometry. For the microprobe analyses (CAMEBAX SX 50), the powder samples were first compacted under an uniaxial pressure of 500 MPa during 2 minutes and then polished at 1 µm with alumina powders.

The forming of the material was performed following two different ways : sintering and extrusion. The sintered samples were prepared as follows : the powder is first compacted in the form of cylindrical greens of 10 mm in diameter under an uniaxial pressure of 160 MPa and then the green is submitted to a thermal treatment at 250°C during 60 minutes under an He-H_2 atmosphere. The extrusion of the material was realised at 265°C with an 2.5 extrusion ratio, from cylindrical greens of 25 mm in diameter which present a density of 75% of the theoretical density.

The microstructure of sintered and extruded samples was studied by scanning electron microscopy (SEM) in a JEOL JMS 820 in the secondary electron image mode. The samples were prepared by electrochemical polishing.

In order to determine their transport properties, the sintered and extruded samples were cut with a wire saw into parallelepipeds of typical dimensions 2.5 x 2.5 x 10 mm. All the mesurements of the transport coefficients were performed on the same sample in a experimental set-up described in details elsewhere [3]. Briefly, the thermal conductivity and the thermopower mesurements are measured by means of a four probe steady heater and sink method. A four probe method is used to measure the electrical resistivity. The values are obtained by using small intensities and by recording almost instantaneously the voltage as soon as the electrical circuit is closed.

0-7803-4057-4/97 $10.00 ©1997 IEEE

Results and Discussion

XRD analyses showed that the seeked $Bi_{85}Sb_{15}$ alloy is reached after 15, 3 and 2 hours of milling time for the 10:1, 40:1 and 92:1 ratios, respectively [4].

The microprobe analyses show that the powder obtained with the 10:1 BPR is the most homogeneous as compared to the powders synthesized with the others BPR that present larger dispersions in the antimony content (figure 1). We only used the powders produced with the 10:1 BPR to continue our characterization work on the sinterd and extruded samples.

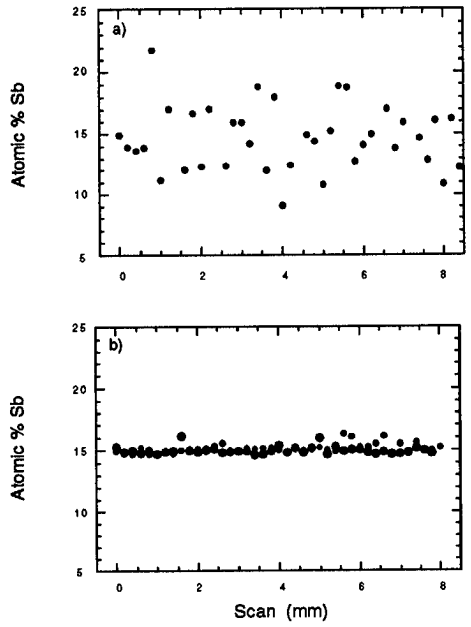


Figure 1 : Microprobe scanning along compacted samples : a) BPR 92:1, milling time 3 h, b) BPR 10:1, milling time 15h.

The sintered samples present a microstructure with grains randomly oriented. The grains have sizes ranging from 2 to 10 µm. In some grains, can be observed parallel broad lines corresponding to the $(0\ 0\ 1)_H$ cleavage planes of each single grain (figure 2).

The original shape of the extruded material is a cylindrical bar which presents a smooth external surface without any damage. This bar was cut to observe the microstructure of the extruded material in both parallel and perpendicular directions to the extrusion direction. The microstructure observed in the two directions are identical (figure 3). The grains have sizes ranging from 2 to 30 µm. A priori, there is no evidence of preferential orientation of the grains. We can again note the presence of lines corresponding to the cleavage planes. Texture analyses [3] show that there are two main orientations in the samples : the $[0\ 1\ 2]_H$ and the $[1\ 1\ 0]_H$ directions, both parallel to the extrusion direction.

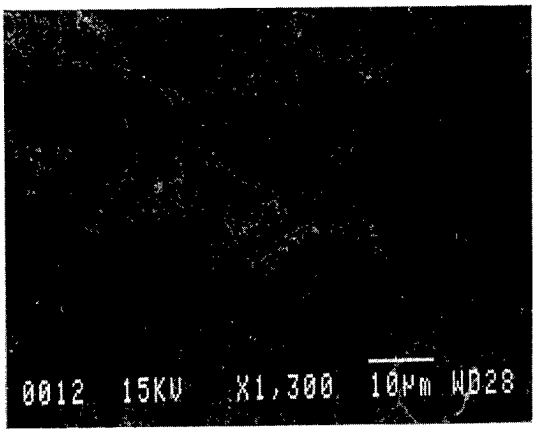
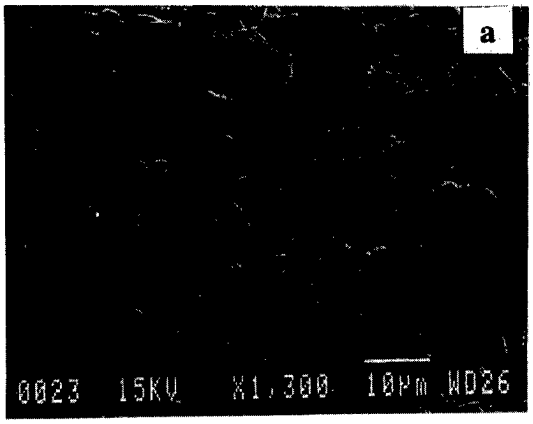


Figure 2 : Microstructure of the sintered samples. The microghaph is token from a sample cut parallel to the pressing direction.



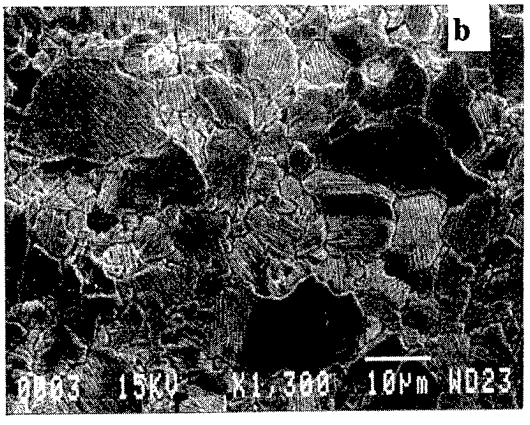


Figure 3 : Microstructure of the extruded samples : a) along the extrusion direction, b) perpendicular to the extrusion direction.

The dependence of the electrical resistivity, thermopower and thermal conductivity were measured as a function of the temperature between 80 and 300 K on the sintered and extruded samples.

The electrical resistivity of both samples increases with decreasing temperature, characteristic feature of a semiconducting behaviour. The electrical resistivity of the sintered sample reaches a maximum value of about 7 μΩm at a temperature of 100 K whereas it still increases at lower temperature for the extruded sample in the considered temperature range (figure 4). The values of the electrical resistivity in both samples are higher than those measured along the trigonal axis (ρ_{33}) of a single crystal of rather close content (14.4%), in all the studied temperature range. It seems that the curves of the two polycrystalline samples are shifted towards higher temperatures compared to that of the single crystal. The higher values of the electrical resistivity result from the polycrystalline nature of the material and from the presence of potential barriers [5] in the sintered and extruded materials. Estimation of the band gap E_g can be calculated assuming the relation :

$$\rho = \rho_0 \exp\left(\frac{-E_g}{2KT}\right) \qquad (1)$$

where K is the Boltzman constant and T the absolute temperature. The estimated band gap is about 19 meV for the sintered material and about 28 meV for the extruded material.

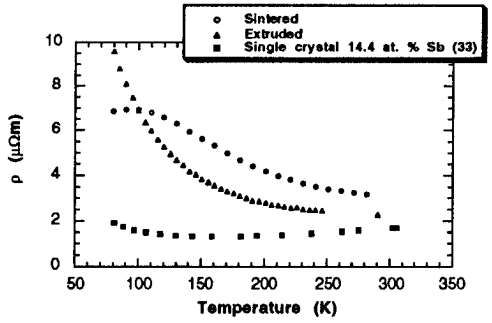


Figure 4 : Electrical resistivity of sintered and extruded samples. Comparaison with the behaviour of a single crystal (14.4 at. % Sb) measured along the trigonal axis.

In figure 5 are reported the results of the thermopower measured on the formed samples in function of the temperature and compared them to those obtained with a single crystal (14.4 at.% Sb) measured along the trigonal axis. Note that the thermopower anisotropy in single crystals is less than 5% in the temperature range 80-300 K [6]. The extruded sample presents, between 80 K and 300 K, absolute thermopower values higher than those of the single crystal with a maximum in absolute value of about 150 μV/K at 90 K. On the other hand, the sintered sample presents larger absolute values than the single crystal for temperatures higher than 110 K, with a maximum in absolute value of about 130 μV/K at 150 K. The large increase of the thermopower for both polycristalline samples could be linked to the presence of potential barriers. This scattering mechanism was reported as being a way to improve the thermoelectric properties [7 - 9].

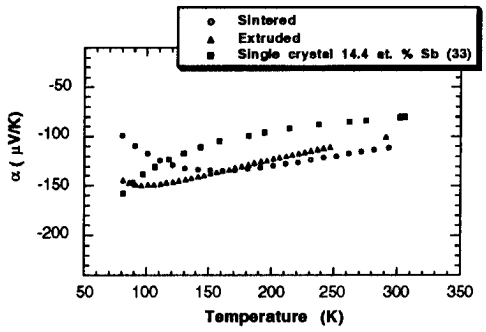


Figure 5 : Thermopower of sintered and extruded samples. Comparaison with the behaviour of a single crystal (14.4 at. % Sb) measured a long the trigonal axis.

In figure 6 are represented the temperature dependences of the thermal conductivity of both extruded and sintered samples. We can observe that between 80 K and approximately 250 K the thermal conductivity of both samples are very slightly lower than those obtained for a single crystal (14.4 at.% Sb) measured along the trigonal axis (λ_{33}). If we take into account the polycrystalline nature of the formed powder samples and the anisotropy of the thermal conductivity in the single crystal the thermal conductivity values of the material presenting non oriented grains would be the weighted average [6] of the two single crystal values, λ_{33} and λ_{11} (mesured along the basal planes). We can obseve that in our samples the thermal conductivity has been considerably reduced with regard to the expected values. This lowering is due to the scattering of the low frequency phonons at the grain boundaries. This phenomenon can be greater for smaller grain sizes of about 1 μm as has been pointed out by Goldsmid [10]. In our case the grain sizes are larger (2-30 μm), and as a consequence the lattice thermal conductivity value is more important, the scattering mechanisms being however still effectives.

From the measurements of the three transport coefficients α, ρ, λ, we deduced the values of the figure of merit Z. In figure 7 are reported the temperature dependences of the figure of merit of both extruded and sintered samples. We have also represented the results of the measurements along the trigonal axis of a single crystal (14.4 at. % Sb) as reported by Lenoir [6] and Yim and Amith [11]. The results show that there is a maximum in the figure of merit of 2.0 10^{-3} K^{-1} at 150 K for the extruded sample. This maximum is lower than the single

crystal value at the same temperature (3.5 10^{-3} K^{-1}). The maximun of the figure of merit is shifted toward higher temperatures as compared with single crystals. Nevertheless between 150 K and room temperature the use of our extruded material will be of interest because of the better mechanical strength of the polycrystalline alloys [12].

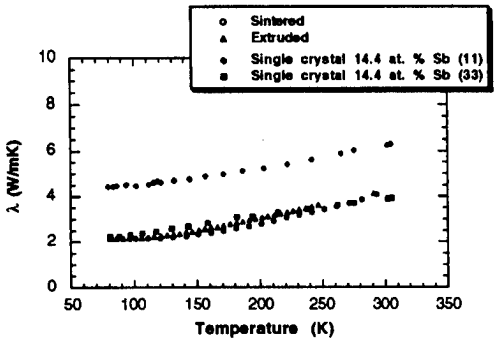


Figure 6 : Thermal conductivity of sintered and extruded samples compared to the thermal conductivity behaviour of a 14.4 % at. Sb content single crystal.

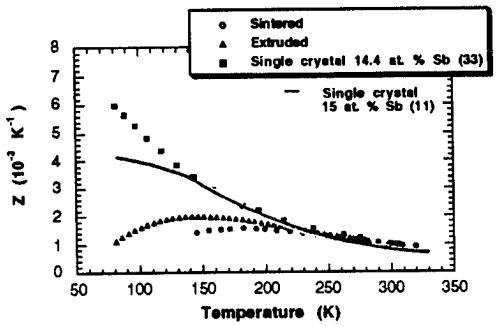


Figure 7 : Figure of merit of sintered and extruded samples compared with the performances of a single crystal of 14.4 at. % Sb content.

Conclusion

1. Mechanical alloying technique carried out with a 10:1 BPR allows to synthesize homogeneous polycrystalline $Bi_{85}Sb_{15}$ powders.
2. Between the two considered consolidation techniques the extrusion is the more powerful. The potential barriers of the extruded material seem to be more effective than those of the sintered materials.

Higher power factor ($\alpha^2\sigma$) values are obtained in the extruded samples with a maximum of figure of merit of 2.0 10^{-3} K^{-1} at 150 K.

References

[1] B. Lenoir, A. Dauscher, M. Cassart, Yu. I. Ravich and H. Scherrer, "Effect of antimony content on the thermoelectric figure of merit of $Bi_{1-x}Sb_x$ alloys", J. Chem. Phys. of Solids, in press (1997).

[2] C. Koch, R. W. Cahn, P. Haasen and E. J. Kramer, "Mechanical milling and alloying", Mater. Sci. and Technology, **7**, (1991) 97.

[3] R. Martin-Lopez, Ph. D. Thesis, INPL, Nancy (France) (1997).

[4] R. Martin-Lopez, B. Lenoir, A. Dauscher, X. Devaux, H. Scherrer, S. Scherrer and M. Zandona, " Bi-Sb semiconductor alloy synthesized by mechanical alloying", Proc. of the II European Workshop on Thermoelectrics (ETS 95), Nancy, France, (1995) 34.

[5] C. H. Seager and T. G. Castner , "Zero-bias resistance of grain boundaries in neutron- transmutation- doped polycristalline silicon", J. Appl. Phys., **49**, (1978) 3879.

[6] B. Lenoir, Ph. D. Thesis, INPL, Nancy (France) (1992).

[7] D. M. Rowe and Gao Min, "Multiple potential barriers as a possible mechanism to increase the Seebeck coefficient and electrical power factor", Proc. of the XIII Int. Conf. on Thermoelectrics (ICT94), Kansas City MO, USA, 1994, AIP Conf. Proc. **316** (1994) 339.

[8] Y. I. Ravich, "Selective carrier scattering in thermoelectric materials", CRC Handbook of Thermoelectrics, Ed. D. M. Rowe, CRC Press, (1995) 67.

[9] Y. Nishio and T. Hirano, " Improvement of the efficiency of thermoelectric energy conversion utilizing potential barriers", Jpn. J. Appl. Phys., **36** (1997) 170.

[10] H. J. Goldsmid, H. B. Lyon Jr. and E. H. Volckmann, "A simplified theory of phonon boundary scattering in solid solutions", Proc. of the XIV Int. Conf. on Thermoelectrics (ICT95), St Petersburg, Russia (1995) 71.

[11] W. M. Yim and A. Amith, "Bi-Sb alloys for magneto-thermoelectric and thermomagnetic cooling" Solid State Electronics. , **15** (1972) 1141.

[12] R. Martin-Lopez, A. Dauscher, B. Lenoir, H. Scherrer, S. Zayakin and L. Ivanova, to be published (1997).

Observation of a power factor enhancement in MBE-grown $Bi_{1-x}Sb_x$ alloy thin films

Sunglae Cho, Antonio DiVenere, George K. Wong, and John B. Ketterson
Department of Physics and Astronomy and Materials Research Center, Northwestern University, Evanston, Illinois 60208, USA

Jerry R. Meyer and Craig A. Hoffman
Naval Research Laboratory, Code 5610, Washington, D.C. 20375-5338, USA

Abstract

Bulk $Bi_{1-x}Sb_x$ is a direct (indirect) gap semiconductor for $0.07 < x < 0.15 (0.15 < x < 0.22)$ with a maximum bandgap of 14-20 meV at $x \approx 0.12$-0.15. Small bandgap $Bi_{1-x}Sb_x$ alloys have been used as the n-type thermoelement for coolers operating around 80K. The optimum operating temperature strongly depends on the magnitude of the bandgap of the material. We have grown BiSb alloy thin films on CdTe(111)B over a wide range of Sb concentrations using molecular beam epitaxy and have observed a maximum bandgap of 40 meV at $x = 0.09$, which is larger than that observed in bulk alloys. Thermoelectric power (TEP) measurements showed that a maximum TEP value occurred in a thin film with $x = 0.09$. This thin-film TEP value was 16% larger than bulk at room temperature. The power factor ($S^2\sigma$) results show that the BiSb alloy thin films peak at a significantly higher temperature (250K) than previously reported for the bulk alloy (80K), which is possibly due to the enhanced bandgap. This bandgap enhancement may be associated with strain effects. The results show significant promise for the use of band-engineered materials in thermoelectric devices.

Introduction

Bi and Sb are semimetals with a rhombohedral structure which have a small energy overlap between the conduction and valence bands, high carrier mobilities, and small effective masses. Because of these properties, Bi and Sb were studied in connection with quantum transport and quantum size effect phenomena. $Bi_{1-x}Sb_x$ can be a semiconductor or semimetal depending on the Sb concentration.[1-9] The band structure is shown in Fig. 1. The addition of Sb to Bi causes the L_s and T bands to move down with respect to the L_a band. At $x=0.04$ the L bands invert[2,3] and at $x=0.07$ the overlap between the hole T and L_a bands disappears[4], resulting in an indirect semiconductor for $x<0.09$. For $0.09<x<0.15$, $Bi_{1-x}Sb_x$ is a direct gap semiconductor. The maximum bandgap of these alloys is in the range 14-20 meV for 12~15 % Sb concentration.[1,6,7] For $x>0.15$, the hole H band lies above the L_a band and we have an indirect semiconductor. Above $x=0.22$, the alloys are semimetallic.

With properties such as a small bandgap, high mobility and a reduced lattice thermal conductivity, semiconducting $Bi_{1-x}Sb_x$ alloys may potentially be used as an n-type thermoelement operating around 80 K. The thermoelectric figure of merit defined by $ZT=(S^2\sigma/\kappa)T$ (where S is the thermoelectric power(TEP) or Seebeck coefficient, σ is the electrical conductivity, and κ is the thermal conductivity) is 0.88 at 80 K in a magnetic field of 0.13 T.[6] It should be noted that the optimum operating temperature and the magnitude of the figure of merit strongly depend on the size of the bandgap of the material. If one could "engineer" the bandgap, the thermoelectric properties could be adjusted. For example, some of us recently showed that quantum confinement induces an energy gap in Bi thin films of thickness <200 Å.[10] In this paper we will discuss the electrical transport properties and TEP of somewhat thicker $Bi_{1-x}Sb_x$ alloy thin films (for which a gap occurs naturally without any quantum confinement) grown on a CdTe(111)B substrate over a wide range of Sb concentrations. Future work will consider quantum confinement with the alloy effects.

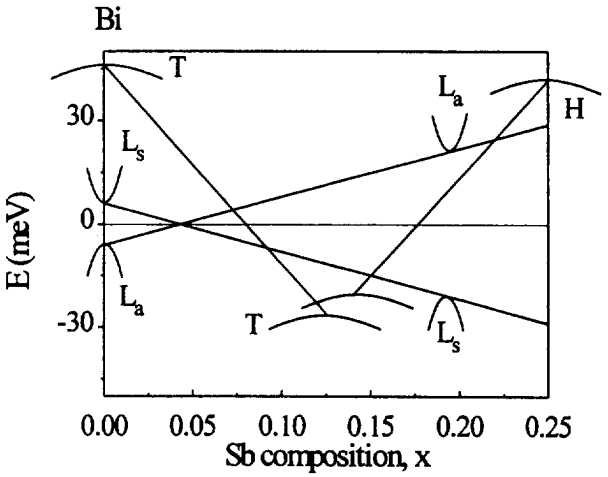


FIG. 1. Energy band structure of $Bi_{1-x}Sb_x$ alloys.

Experiment

$Bi_{1-x}Sb_x$ alloy thin films were grown on semi-insulating CdTe(111)B substrates by molecular beam epitaxy (MBE) with $x=0$, 0.035, 0.05, 0.09, 0.11, 0.14, and 0.16. The base pressure of the growth chamber was in the 10^{-10} Torr range. The growth direction of the $Bi_{1-x}Sb_x$ alloy film on CdTe(111)B is parallel to the trigonal axis. We first deposited a 3000 Å CdTe buffer layer on the CdTe substrate at 250 °C, followed by deposition of the $Bi_{1-x}Sb_x$ layer at a rate of 0.4 Å/s and at a growth temperature of 83 °C. Reflection high-energy electron diffraction (RHEED) was used to examine the specific surface reconstruction of the deposited layers. The composition of Sb was controlled by a quartz thickness monitor. The accuracy of this technique has

been examined and confirmed by inductively coupled plasma (ICP) spectroscopy analysis. The $Bi_{1-x}Sb_x$ epilayers had nominal thicknesses of 1 μm. The lattice constants of Bi and Sb are 4.546 and 4.308 Å, respectively. Consequently the lattice mismatch with CdTe(111)B (4.58 Å) increases from 0.7 % to 6 % between these limits. We measured the TEP and electrical resistivity as a function of temperature. Samples were processed into bar-shape patterns using photolithography and lift-off techniques for electrical measurements. The TEP measurement techniques are discussed elsewhere.[11]

Results and Discussion

The temperature-dependent resistivities of the Bi and BiSb alloy thin films with various Sb compositions are shown in Fig.'s 2(a) and (b). At room temperature, the resistivity differences between the various compositions are small. However, as the temperature decreases, the resistivity behavior varies significantly with Sb concentration. As the Sb concentration increases, the resistivity increases rapidly up to 9 % Sb concentration as shown in Fig. 2(a). Unlike a pure Bi film, the resistivities of the alloys increase with decreasing temperature below room temperature, implying that the dominant bandgap in the alloy is larger than the thermal energy (at 300 K, k_BT~25 meV). It should be noted that the 9 % Sb alloy has the highest resistivity at low temperature. With the further addition of Sb, the resistivity decreases as shown in Fig. 2(b).

In order to analyze the temperature dependent resistivity for a given Sb concentration, Jain[1] used the following exponential law to describe the semiconducting alloys:

$$\rho = \rho_0 \exp(E_g/2k_BT)$$

where ρ_0 is a constant and E_g is an effective bandgap. This relation is based on the assumptions that the contributing bands are parabolic with the same density of states, and that the carriers are scattered primarily by acoustic phonons. [7,12] Despite these approximations, the results obtained may be used to describe, qualitatively, the evolution of the band structure as a function of Sb concentration at low temperature. We have calculated the thermal energy gaps using the above equation, and the results are shown in Fig. 3. The calculated results are compared with similarly calculated literature values for bulk and epitaxial thin films grown on BaF_2(111). [1,6-8] It is seen that the effective bandgaps (defined in the above manner) of thin films grown on CdTe(111) are larger than the bulk values, and that the Sb concentration for the maximum bandgap has shifted to a lower x, from 14-20 meV at $x \approx 0.12$-0.15 in bulk to 40 meV at $x \approx 0.09$ in the thin films grown on CdTe(111). The same analysis yielded a slight enhancement of the bandgaps of BiSb thin films grown on BaF_2 (111) studied by Morelli *et al.*. [9] It must be pointed out that the effective bandgap for thin film and bulk materials may differ. Since there are multiple hole bands (at L, H and T), the band which makes the dominant contribution to the temperature dependence of the resistivity depends on a complex interplay between the bandgap, density of states, mobility and temperature. Surface scattering and strain are present in thin films which are absent in bulk and both are, in general, substrate dependent. Alternatively, the differences between the thin film bandgaps and the earlier bulk results may be due in part to a breakdown of the assumption that acoustic scattering dominates the mobility for the relevant temperature range in the thin films.

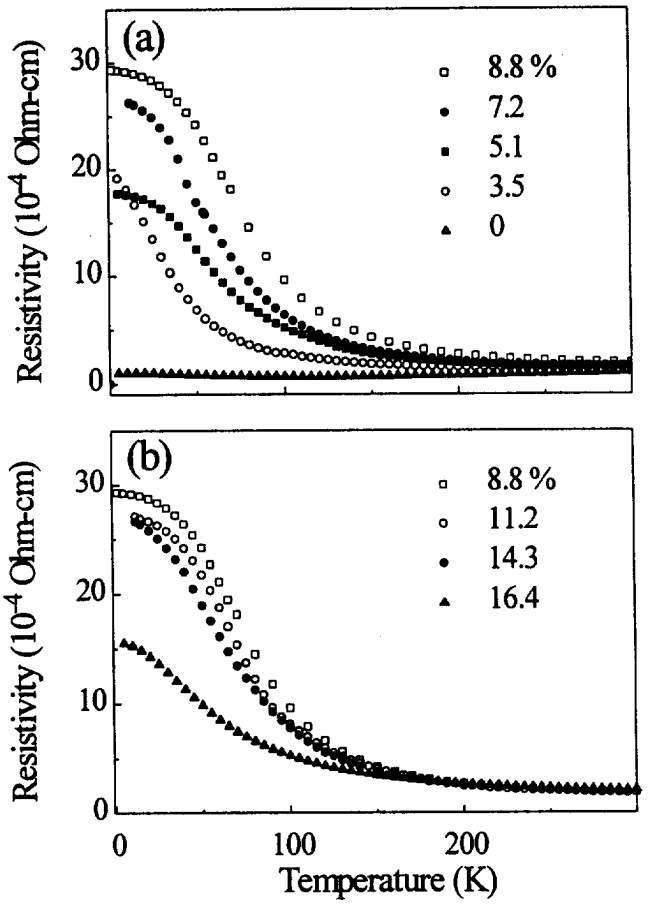


FIG. 2. The temperature dependence of the electrical resistivities of Bi and BiSb alloy thin films with various Sb composition.

In Fig.'s 4(a) and (b), the TEP values for the Bi and BiSb alloy thin films are plotted as a function of temperature between 20 and 300 K. The TEP of a pure Bi film is seen to be in good agreement with the previous single crystal values for conduction perpendicular to the trigonal axis as reported by Gallo *et al.*[13] and Korenblit *et al.*.[14] The TEP values for the alloy thin films are seen to be larger than that for the pure Bi film. The alloy TEPs increase with increasing Sb concentration up to 9 %, as shown in Fig. 4(a), and decrease thereafter with further increase in x, as shown in Fig. 4(b). For a thermoelectric material containing both electrons and holes, the total TEP may be modeled by the relation: $S = (\sigma_e S_e + \sigma_p S_p)/(\sigma_e + \sigma_p)$, where σ_e

and σ_p are the electrical conductivities and S_e and S_p are the TEPs for electrons and holes, respectively. The observed negative TEP implies a higher mobility for electrons than for holes (assuming n = p). The magnitude of the TEP increases with decreasing temperature above a certain temperature. This increase is due to the freeze-out of electrons and holes at low temperature. Thereafter, the magnitude of the TEP decreases linearly with decreasing temperature as in bulk, which is due to the greater degeneracy of the carrier populations.

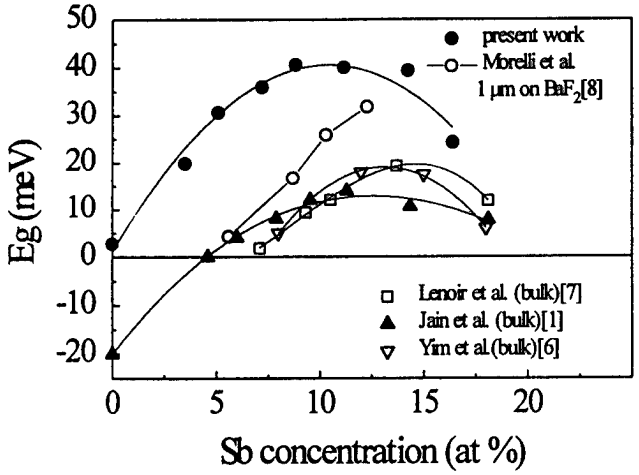


FIG. 3. Bandgap E_g vs Sb concentration.

In Fig. 5, a comparison is made between the thin film and bulk TEPs as a function of Sb concentration at several temperatures. At a given temperature, the maximum TEP occurs at lower Sb concentration in the thin films than in bulk. Two important points are evident in this result: i) the TEPs of the alloy thin films are larger than for bulk alloys (which may be further evidence of an enhanced bandgap in the thin films grown on CdTe(111)B substrates), and ii) the downward movement of the maximum TEP for Sb concentrations between 14 % to 9 % is consistent with the resistivity results (which also show a maximum at 9 %).

In Fig. 6, the temperature-dependent power factor ($S^2\sigma$) for a 7.2 % BiSb alloy thin film is compared with those for bulk Bi and 12 % BiSb alloy crystals. Only samples with the largest experimental power factors from the literature are graphed for ease of viewing. These results show that power factors for the BiSb thin film peak at a significantly higher temperatures (250K) than in previous results for the bulk alloy (80K). This higher temperature maximum for the power factor can be taken as further evidence for an increase in the bandgap for alloy thin films grown on CdTe(111). It is clear that if the conductivity of the films could be improved (e.g. by forming more perfect interfaces and eliminating misfit dislocations through better lattice matching), higher power factors would also be obtained at all temperatures. This, in turn, would require a reduction in substrate interface scattering and doping effects.

The above mentioned explanation for the enhanced effective bandgap involving strain assumes a shift in the relative position of the electron and hole bands. Morelli *et al.* [9] attributed their (slightly) enhanced bandgap in films grown on

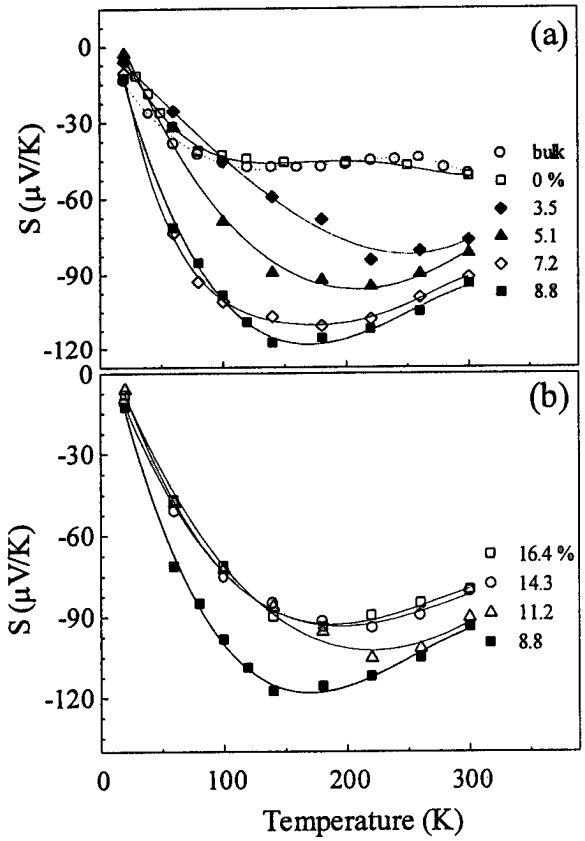


FIG. 4. TEP of Bi and BiSb alloy thin film as a function of temperature.

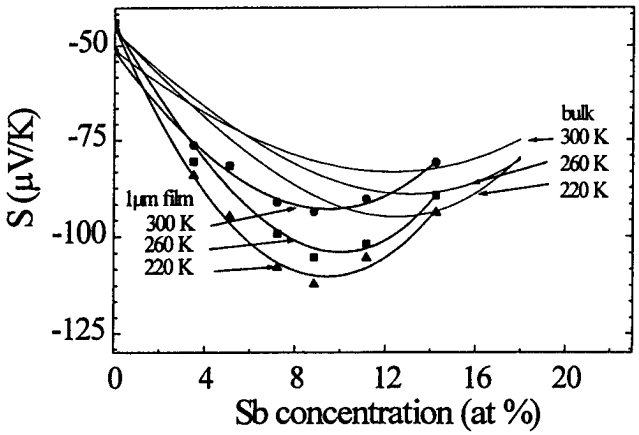


FIG. 5. TEPs of BiSb thin film and bulk crystal as a function of Sb concentration with different temperatures.

$BaF_2(111)$ to a compressive strain caused by the smaller lattice constant of the substrate (4.38 Å). However in our films a tensile strain is expected. Fig. 7 shows the results of a θ-2θ X-ray diffraction study which was used to determine the c-axis lattice constant using a hexagonal unit cell of BiSb films as a function of Sb concentration. For a given Sb concentration, the lattice constant for our films is consistently smaller than that of the bulk, while for thin alloy films on BaF_2 it is larger. Both behaviors are consistent with the expected strain induced by the substrate and the positive Poisson ratio of BiSb. For our films, this strain becomes larger, since the lattice mismatch between BiSb and CdTe increases with increasing x. Theoretical band structure calculations, which may shed some light on this problem, are underway and will be reported elsewhere.[15]

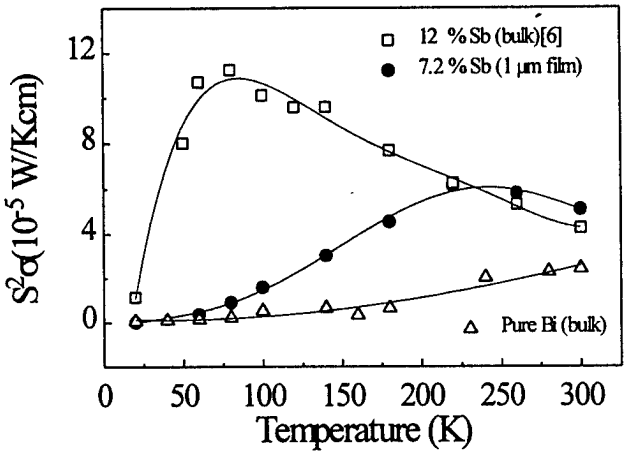


FIG. 6 Power factor vs temperature.

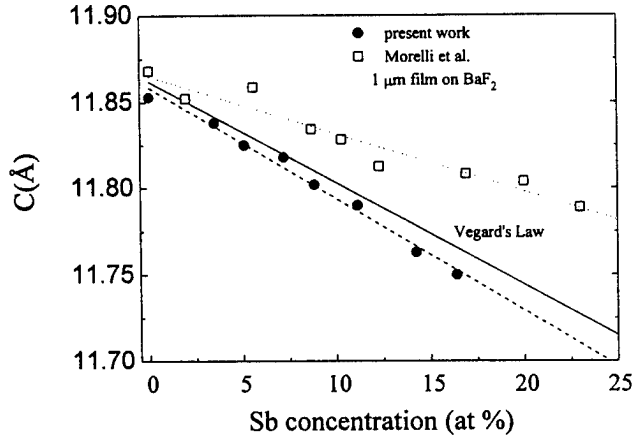


FIG. 7. C-axis lattice constant of Bi and BiSb alloy thin films as a function of antimony concentration. The full line gives results for bulk alloys.

Conclusion

We have grown $Bi_{1-x}Sb_x$ alloy thin films on CdTe(111)B over a wide range of Sb concentrations using MBE, and have observed a maximum effective bandgap of 40 meV at x = 0.09, which is larger than that observed in bulk alloys. It is proposed that this bandgap enhancement may be due to strain effects. TEP measurements show that a maximum value occurs in an alloy thin film with x = 0.09. At room temperature, the thin-film TEP value is 16 % larger than in the bulk alloy. Power factor results show that BiSb alloy thin films peak at a significantly higher temperature (250 K) than previously reported for the bulk alloy (80 K). These results show significant promise for the use of band-engineered Bi-based materials in thermoelectric devices, which will become even more attractive when quantum confinement is introduced.

Acknowledgments

This work was supported by ARPA under Grant No. MDA972-95-1-0020, ONR under Document N0001496WX20241 and DARPA under Grant No. DAAG55-97-1-0130. Use was made of MRL Central Facilities supported by the National Science Foundation, at the Materials Research Center of Northwestern University, under Grant DMR-9120521.

References

1. A. L. Jain, Phys. Rev. **114**, 1518 (1959).
2. S. Golin, Phys. Rev. **176**, 830 (1968).
3. E. J. Tichovolski and J. G. Mavroides, Solid State Commun. 7, 927 (1969).
4. G. A. Mironova, M. V. Sudakaova, and Ta. G. Ponomarev, Sov. Phys. Solid State **22**, 2124 (1980).
5. G. Oelgart, G. Schneider, W. Kraak and R. Herrmann, Phys. Stat. Sol. (b) **74**, K75 (1976).
6. W. M. Yim and A. Amith, Solid-State Electron. **15**, 1141 (1972).
7. B. Lenoir, M. Cassart, J.-P. Michenaud, H. Scherrer and S. Scherrer, J. Phys. Chem. Solids **57**, 89 (1996).
8. D. T. Morelli, D. L. Partin and J. Heremans, Semicon. Sci. Technol. **5**, S257 (1990).
9. J. Heremans, D. L. Partin, C. M. Thrush, G. Karczewski, M. S. Richardson, and J. K. Furdyna, Phys. Rev. B **48**, 11 329 (1993).
10. C. A. Hoffman, J. R. Meyer, F. J. Bartoli, A. DiVenere, X. J. Yi, C. L. Hou, H. C. Wang, J. B. Ketterson, and G. K. Wong, Phys. Rev. B **48**, 1993, 11 43; Phys. Rev. B **51**, 1995, 5535.
11. S. Cho, A. DiVenere, G. K. Wong, J. B. Ketterson, J. R. Meyer and C. A. Hoffman, Solid State Comm. **102**, 673 (1997).
12. D. M. Brown and S. J. Silverman, Phys. Rev. **136**, A290(1964).
13. C. F. Gallo, B. S. Chandrasekhar, and P. H. Sutter, J. Appl. Phys. **34**, 144 (1963).
14. I. Ya. Korenblit, M. E. Kusnetsov, and S. S. Shalyt, Soviet Phys. JETP, **29**, 4 (1969).
15. A. B. Shick, S. J. Youn, and A. J. Freeman (unpublished).

Determination of Carrier Mobilities and Densities from Galvanomagnetic Coefficients in Undoped $Bi_{0.96}Sb_{0.04}$ Alloy

B. Lenoir, M.O. Selme, A. Demouge, H. Scherrer

Laboratoire de Physique des Matériaux
Ecole des Mines, Parc de Saurupt, 54042 Nancy (France)
Tel.:+33/3/83584163, Fax:+33/3/83584163, E-mail:lenoir@mines.u-nancy.fr

Yu. I. Ravich, Yu. V. Ivanov

A.F. Ioffe Physical-Technical Institute, 194021, St. Petersburg (Russia)

Abstract

Carrier mobilities and densities were calculated in $Bi_{0.96}Sb_{0.04}$ alloy in the temperature range 78-300 K. The theoretical model takes into account the particular band structure, the non parabolicity of the conduction band and the complex carrier scattering mechanisms. The adjustable parameters are found by the least-squares method from the experimental values of the twelve galvanomagnetic coefficients in weak magnetic field and of the two components of the thermopower. Calculated values of the Hall and magnetoresistance factors of electrons show a substantial deviation from unity.

Introduction

Detailed study of classical galvanomagnetic effects in Bi-rich $Bi_{1-x}Sb_x$ alloys are lacking in the literature. These alloys are well known materials for their attractive thermoelectric or thermomagnetic properties at low temperatures [1-2].

Galvanomagnetic investigations consist in the determination of the resistivity tensor $\bar{\bar{\rho}}(\bar{B})$ in presence of a magnetic induction B. In the limit of weak fields ($\mu B \ll 1$, where μ is the mobility), only terms in B and B^2 need to be retained in the expansion of this tensor as a power series, leading to a relatively small number of low field measurements. The number of independent coefficients appearing in the expansion is twelve for the Bi-Sb alloys belonging to the point group $R\bar{3}m$. A schematic representation (Fig.1) shows how the band parameters may be phenomenologically deduced from these coefficients.

The galvanomagnetic study of Bi-rich Bi-Sb alloys remains a tedious task from a theoretical point of view. Ravich and co-workers [3-4] have shown that the Hall and magnetoresistance factors of electrons, which are governed by the energy dependence of the relaxation time, differ greatly from unity in bismuth at temperatures higher than 100 K because of the strong non-parabolicity of the dispersion relations for conduction electrons and light holes. The same results seem also to be true in alloys, as shown by Demouge et al. [5] in an analysis of five galvanomagnetic coefficients in the $Bi_{0.96}Sb_{0.04}$ semimetallic alloy. Since the Hall and the magnetoresistance factors of electrons can't be fitted directly with sufficient accuracy, it is necessary to calculate them assuming a scattering model for charge carriers.

In this communication, we report on the temperature dependence of the components of the mobility of electrons and holes in $Bi_{0.96}Sb_{0.04}$ alloy between 78-300 K calculated from a least-squares procedure using the complete set of the twelve independent galvanomagnetic coefficients and the two components of the thermopower. The theoretical model first proposed for Bi [6] is extended here in the alloy. The calculated values of Hall and magnetoresistance factors of electrons in alloy are compared with those of Bi.

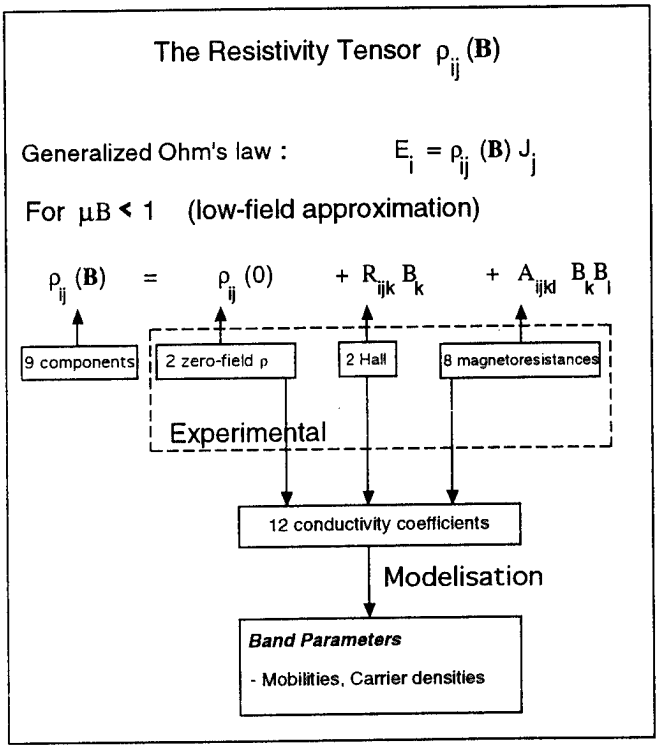


Figure 1: Schematic representation of band parameter calculation from low-field galvanomagnetic measurements for a rhomboedral structure.

Theory

By alloying bismuth with a small amount of antimony, the band structure of bismuth at T = 0 K is qualitatively maintained with a change in the relative position of the different energy bands, and, correspondingly, in the different

band parameters. The addition of Sb to Bi results in a decrease of the overlap between the L-conduction and T-valence bands and to a decrease of the L-point energy gap E_g (Fig. 2). For 4 at.% Sb the direct gap is zero [7-8].

We described the L bands by a two band non parabolic model and the T band by a parabolic model. To calculate the temperature dependences of the transport coefficients, we have to know those of the band structure parameters. However, complete information about them is not available. According to magnetooptic results [9], the energy gap E_g which is zero in $Bi_{0.96}Sb_{0.04}$ at T = 0 K increases noticeably above 80 K, reaching 23 meV at 300 K. We took the temperature dependence of the two small effective masses of the electrons into account by working [10] from the results of magnetooptic measurements [9]. We assumed that both the large effective mass and the components of the effective mass for the T holes were temperature independent. The temperature dependence of the overlap energy of the conduction band with the T-valence band, E_{LT}, is not known and was considered as an adjustable parameter in our model.

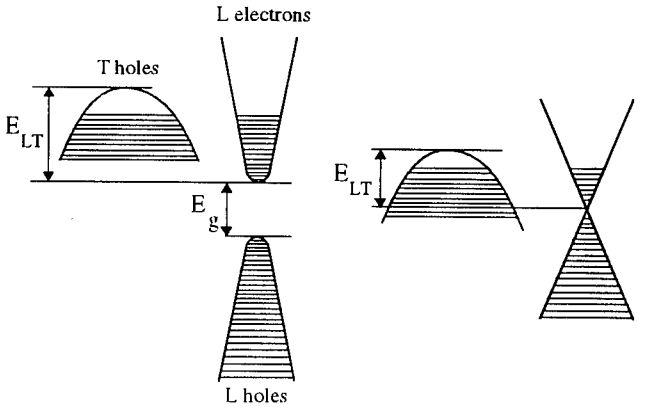


Figure 2: Band structure of Bi (a) and $Bi_{0.96}Sb_{0.04}$ alloy (b) at T = 0 K. E_g and E_{LT} are the direct band gap and the energy overlap, respectively.

We considered the scattering model developed for pure bismuth [6], where both acoustical phonon and interband recombination scattering mechanisms were taken into account. Considering that the energy dependence of the relaxation time for the impurity scattering with a short range potential of isovalent atom of antimony is the same as for the scattering with acoustical phonons, the expansion of this model to alloys is possible. Then the theoretical model involves three scattering parameters : C_N, C_P, xC_N [3,6]. C_N and C_P represent the intensity of L-electrons or T-holes scattering by acoustic phonons and xC_N characterizes the rate of recombination scattering; these parameters will be fitted to obtain the Hall and the magnetoresistance factors, A and M, respectively. Theoretical formulas for the kinetic coefficients, the relaxation times, the Hall and magnetoresitance factors are given in [3,6].

Similarly to the work of Ravich et al. with bismuth [4], we used the twelve independent galvanomagnetic coefficients and the two components of the thermopower in the absence of a magnetic field to determine the parameters of the model by the least-squares method.

For each temperature we selected constants E_{LT}, C_N, C_P, and xC_N. We also selected the angle between the major axis of the ellipsoids of electrons and the plane perpendicular to the trigonal axis of the crystal. However, this angle turned out to be relatively insensitive to the temperature and to have a value close to 7° [10] as in pure Bi [4].

All adjustable parameters values used in the calculation of the carrier mobilities and densities, Hall and magnetoresistance factors are listed elsewhere [10].

Experiments

A $Bi_{0.96}Sb_{0.04}$ single crystalline ingot was grown by the traveling heater method (THM) described in a previous paper [11]. The ingot was 15 mm ID and 150 mm length, and the growth rate was 8 mm/day. In these conditions, the required relation [12] :

$$R.\Delta T < D.G \qquad (1)$$

to avoid constitutional supercooling is satisfied, where R is the growth rate, ΔT the temperature difference between liquidus and solidus ($\Delta T \cong 10°C$ for $Bi_{0.96}Sb_{0.04}$ [13]), G the temperature gradient (estimated at 35°C/cm), and D the binary alloy liquid diffusion constant (about 10^{-5} cm^2/s, as evaluated by Brown and Heumann [13]). After about two centimeters, the grown ingot was composed almost entirely of one single grain. Detailed investigations of the grown alloys, using an electron beam microprobe, show that a high degree of homogeneity is obtained on a microscopic scale [5].
However, some composition variations along the ingot have been found which are believed to be due to changes in the size of the molten zone caused by asymmetric thermal losses during the growth. These fluctuations are especially appreciable at the two ends of the ingot while the inhomogeneity of the central part is rather small, as shown in figure 3.

To obtain values for the twelve phenomenologically independent constants, it is necessary to perform experiments using a number of crystals with various orientations of the magnetic field $\vec{B}$ and the current density $\vec{J}$. We used four samples. The correct crystallographic orientation of the samples was determined by Laue photographs on basal planes obtained by cleaving the crystals in liquid nitrogen. The orientation and probe arrangements are reported in [5]. The measurements were performed with a well adapted set-up allowing strict isothermal conditions for the samples. A

detailed description of the set-up and the measurement techniques are given elsewhere [5,14].

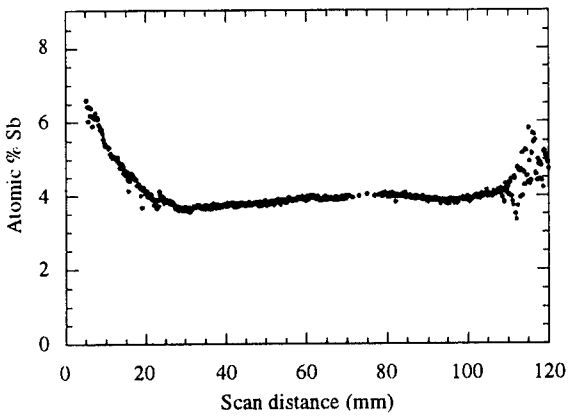


Figure 3: Longitudinal variation in Sb content as determined by electron microprobe analysis in the $Bi_{0.96}Sb_{0.04}$ ingot.

Results

The temperature dependence of the twelve galvanomagnetic coefficients and the two components of the thermopower is reported in [10]. The variations of the large calculated mobilities of electrons μ_1 and μ_3 and holes ν_1 versus temperature are represented in Fig. 4. We also include in the graph those obtained with pure bismuth [4] for comparison.

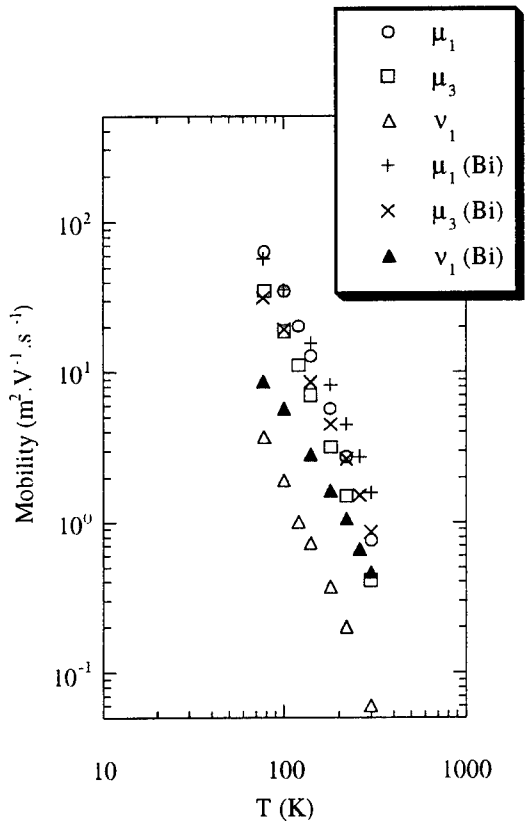


Figure 4: Temperature dependence of carrier mobilities in $Bi_{0.96}Sb_{0.04}$ and in Bi [4].

The electron mobilities follow a $T^{-7.6}$ law whereas ν_1 follows a $T^{-6.7}$ law. It can be seen that the difference between electron and hole mobilities is more important in the alloy than in Bi.

Figure 5 shows the variation of the carrier density with temperature from 78 to 300 K in the alloy. The carrier density varies from 3.10^{23} to 10^{25} m^{-3}. The carrier density in alloy thus changes by roughly two orders of magnitude from 78 to 300 K which is more than in pure bismuth (see Fig. 5).

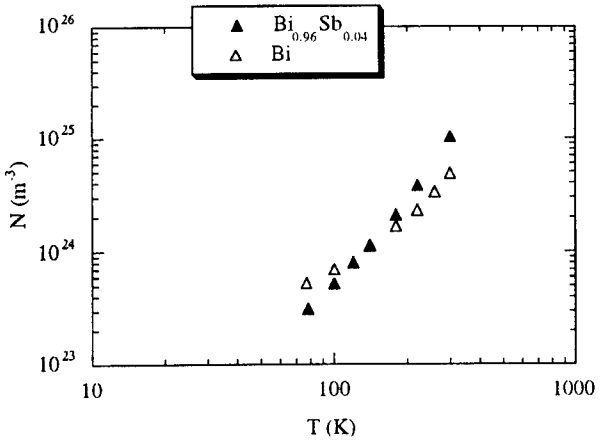


Figure 5: Variation of carrier concentration with temperature in $Bi_{0.96}Sb_{0.04}$ alloy and in Bi [4].

The adjustable parameters found by the least-squares method were used to calculate the Hall and magnetoresistance factors of electrons in alloy. Their variation with temperature is reported in Fig. 6. It can be seen that the Hall and magnetoresistance factors, A and M, differ from unity, especially for temperatures higher than 150 K. Moreover, the values are higher in the alloy than in Bi [4]. The deviation from unity arises from the energy dependence of the relaxation time in the case of a highly non parabolic conduction band. A direct experimental proof of this deviation from unity, is reported in [10], in an analysis of several galvanomagnetic coefficients.

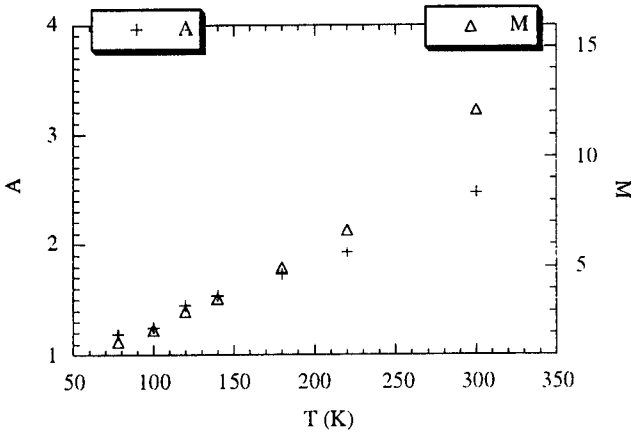


Figure 6: Temperature dependence of A and M in $Bi_{0.96}Sb_{0.04}$ alloy.

Conclusion

Carrier mobilities and densities were calculated in $Bi_{0.96}Sb_{0.04}$ alloy in the temperature range 78-300 K from a theoretical model. The adjustable parameters are found by the least-squares method from the experimental values of the twelve galvanomagnetic coefficients in weak magnetic field and of the two components of the thermopower. Effect of alloying affects more hole than electron mobilities.

The deviation from unity of the Hall and magnetoresistance factors of electrons is more pronounced in alloy than in Bi.

The extension of this study to other antimony contents, especially in the semi-conducting range, is the next step for modelisation of transport properties. Such investigations should undoubtedly contribute to a best comprehension of scattering mechanisms in these alloys .

References

[1] G.E. Smith and R. Wolfe, "Thermoelectric properties of bismuth-antimony alloys", J. Appl. Phys., **33** (1962) 841.

[2] W.M. Yim and A. Amith, "Bi-Sb alloys for magneto-thermoelectric and thermomagnetic cooling", Solid-State Electronics, **15** (1972) 1141.

[3] Yu. I. Ravich and A.V. Rapoport, "Temperature dependences of the carrier mobilities and densities in bismuth", Sov. Phys. Solid State, **34** (1992) 960.

[4] Yu. I. Ravich, Yu. I. Ivanov and A.V. Rapoport, "Thermogalvanomagnetic effects in bismuth", Semiconductors, **29** (1995) 458.

[5] A. Demouge, B. Lenoir, Yu. Ravich, H. Scherrer and S. Scherrer, "Estimation of carrier mobilities and densities in $Bi_{0.96}Sb_{0.04}$ alloys from galvanomagnetic coefficients", J. Phys. Chem. Solids, **56** (1995) 1155.

[6] V.A Nemchinskii and Yu. I. Ravich, "Transport effects in bismuth at 77 K", Sov. Phys. Solid state, **33** (1991) 1165.

[7] E.J. Tichovolsky and J.G. Mavroides, "Magnetoreflection studies on the band structure of bismuth-antimony alloys", Solid State Comm., **7** (1969) 927.

[8] G. Oelgart and R. Herrmann, "Cyclotron masses in semiconducting $Bi_{1-x}Sb_x$ alloys", Phys. Stat. Sol. (b), **75** (1976) 189.

[9] E.E Mendez, Ph. D. Thesis, MIT, (1979).

[10] B. Lenoir, M.O selme, A. Demouge, H. Scherrer, Yu.I. Ravich and Yu.I. Ivanov, to be published.

[11] B. Lenoir, A. Demouge, D. Perrin, H. Scherrer, S. Scherrer, M. Cassart and J.-P. Michenaud, "Growth of $Bi_{1-x}Sb_x$ alloy single crystals", J. Phys. Chem. Solids, **56** (1995) 99.

[12] W.A. Tiller, K.A. Jackson, J.W. Rutter and B. Chalmers, "The redistribution of solute atoms during the solidification of metals", Acta Met., **1** (1953) 428.

[13] D.M. Brown and F.K. Heumann, "Growth of bismuth antimony single-crystal alloys", J. Appl. Phys., **35** (1964) 1947.

[14] J.-P. Issi, J.-P. Michenaud, A. Moureau and P. Coopmans, "The measurements of isothermal galvanomagnetic properties of thermelectric materials", J. Phys. E: Sci. Instrum., **4** (1971) 512.

Determination of the Longitudinal Thermo-galvanomagnetic Coefficients

by E.H. Volckmann and H. J. Goldsmid
Marlow Industries Inc., Dallas, Texas, USA

Abstract

The problems associated with the non-ideal boundary conditions that usually hold in practical galvanomagnetic and thermomagnetic measurements are described. It is then proposed that a novel technique should be used to overcome these problems. This technique involves the use of samples of different length-to-width ratio. Any particular longitudinal thermo-galvanomagnetic coefficient varies with this ratio and it is shown how the value of the coefficient for zero transverse flow can be obtained. All the potential measurements are made at the end contacts and there is no need to apply probes to the side faces. This method is especially easy to use for polycrystalline material since a single sample, in which the width and breadth are different, is then sufficient. Examples of the applications of the technique to a Bi-Sb alloy are given.

Introduction

It is well known[1] that the boundary conditions can have a profound effect on the values of the thermo-galvanomagnetic coefficients of a semiconductor.

There are two ideal conditions. In one of these there is no transverse electric field or temperature gradient, while in the other there is no transverse flow of electric current or heat. The first condition is approached when the length of the sample is very small compared with its width in the direction perpendicular to the transverse magnetic field and can sometimes be realized by use of the so-called Corbino disc configuration.[2] The other condition is approached when the sample is exceedingly long compared with its width. In practice, it is convenient to use samples that are rectangular parallelepipeds with a length that is not many times greater than their width. The galvanomagnetic coefficients for zero transverse electric current can, in principle, be determined to a high degree of accuracy if the Hall probes are at least two sample widths from either of the end contacts and the magnetoresistance probes are at least one sample width from the ends.[3] However, it is difficult to determine the thermomagnetic coefficients for zero transverse current or heat flow since thermometric measurements other than at the ends of the sample are rather unreliable. Furthermore, the act of applying potential probes or thermometers to the side faces of a sample invariably has some effect on the flow pattern.

What is really desirable is the development of some method by which the longitudinal coefficients for one or other of the ideal configurations can be calculated from measurements using a non-ideal arrangement without the need for probes on the side faces. It is our present purpose to outline such a method.

Principle of the Method

The new method makes use of samples of rectangular parallelepipedal shape with as great a length x as possible and with a range of values of the width y perpendicular to the direction of the transverse magnetic field B_z. Preferably all the values of y should be very much less than x. Clearly, the condition of zero transverse electric current and heat flow is more closely approached as y/x becomes smaller. We show that the variation of a particular coefficient with the ratio y/x can be used to predict its value for an ideal sample of infinite length.

Let us suppose that any sample be divided into two regions. One region is the central section that is, say, at least one sample width y from the ends. The other region consists of the end sections that are within y from the ends. In the central region, any longitudinal coefficient will take up the value C for the ideal long sample. Within the other region, the coefficient will vary but may be assumed to have some effective value C^* intermediate between that for very long and very short samples. Suppose, then, that the observed coefficient is C_r for a sample of length-to-width ratio $r = x/y$. The value of C_r will be a weighted average of C and C^* and will be given by $[(x-2y)C + 2yC^*]/x$. Thus,

$$C_r=(1-\frac{2}{r})C+(\frac{2}{r})C^*. \qquad (1)$$

Clearly, C^* can be eliminated by plotting C_r against $1/r$. The required ideal coefficient C is equal to the intercept of the linear plot with the C_r axis.

We would expect the plot to become non-linear for values of r less than about 2, since there would then be no region of the sample for which transverse flow would be negligible. However, it should, in principle, be possible to determine C from only two samples with different values of r provided that both values were greater than about 2. The larger the length-to-width ratios for the two samples, the greater would be the accuracy.

Polycrystalline Material

The application of our technique for the determination of the coefficients for zero transverse flow is particularly simple if the material is polycrystalline and randomly oriented (or if the coefficients do not depend on the direction of the magnetic field). In this case, one can use a single sample provided that its width differs significantly from its breadth and that both these dimensions are substantially smaller than its length.

Consider the two specimens shown in figure 1(a) and (b). Both specimens have the same length-to-width ratio although the actual lengths and widths are different. Suppose that an electric current is passed from one end to the other in each case and that a transverse magnetic field is applied. The equipotential surfaces will take the shapes shown schematically in the two diagrams. Now, suppose that the breadth of the larger sample (a) is equal to the width of the smaller sample (b) and that the larger sample is rotated so that the magnetic field is then perpendicular to its breadth. The new equipotentials are shown schematically in figure 1(c). The disturbed equipotentials in the region of the end contacts are clearly the same in (c) and (b). The effect of rotating

the sample (a) is to provide us with two samples of different length-to-width ratio. We can, therefore, apply equation (1) to the two orientations and eliminate C* to obtain the coefficient C.

We have described the determination of the magnetoresistance coefficient but the same arguments would apply for any of the other longitudinal coefficients e.g. the magneto-Seebeck coefficient and the magneto-thermal conductivity.

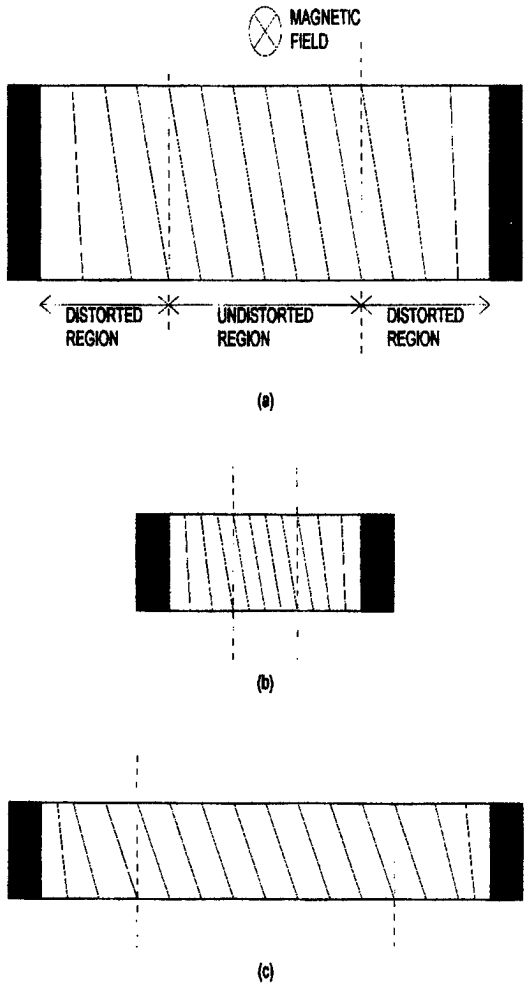


Figure 1. Equipotentials for a current-carrying sample in a transverse magnetic field. (a) Large sample. (b) Small sample with the same length-to-width ratio. (c) Large sample rotated through 90°. The new width is the same as that of the small sample.

Experimental Data

We illustrate the technique for the determination of the magnetoresistance coefficient of undoped polycrystalline $Bi_{88}Sb_{12}$ at 100 K.

We selected samples of about 5 mm length with length-to-width ratios r between 2 and 5. We measured the electrical resistance between the ends of each sample in transverse magnetic fields from zero to 1 T. The electrical resistivity is plotted against $1/r$ in figure 2. As predicted, the plots are linear and allow the resistivity for zero transverse current to be determined accurately from the intercept with the vertical axis.

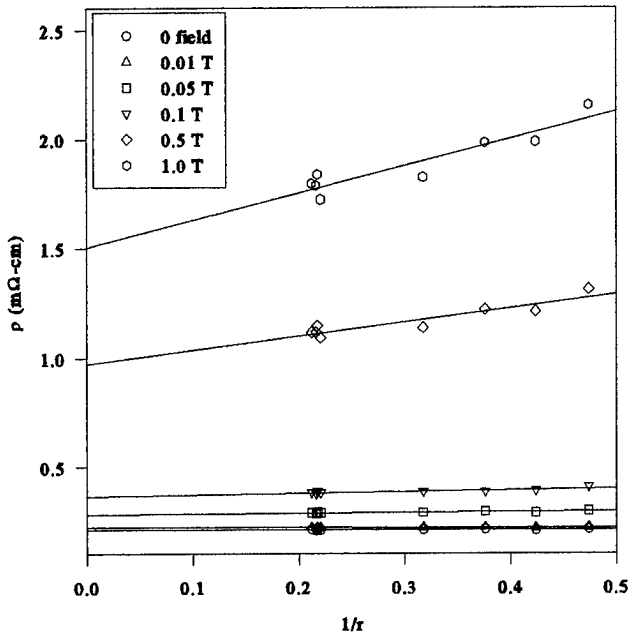


Figure 2. Plots of electrical resistivity between the ends of samples of $Bi_{88}Sb_{12}$ as a function of the width-to-length ratio, $1/r$, in different magnetic fields.

We have also attempted to apply the method to the magneto-Seebeck coefficient and the magneto-thermal resistance but have not yet achieved the same success. This is because there is significantly greater error in the measurements of these two parameters. Thus, as shown in figure 3, the Seebeck coefficient definitely tends to become more negative as $1/r$ falls to zero, but the intercept cannot be determined very accurately. The results are shown for fields of 0.5 T and 1 T.

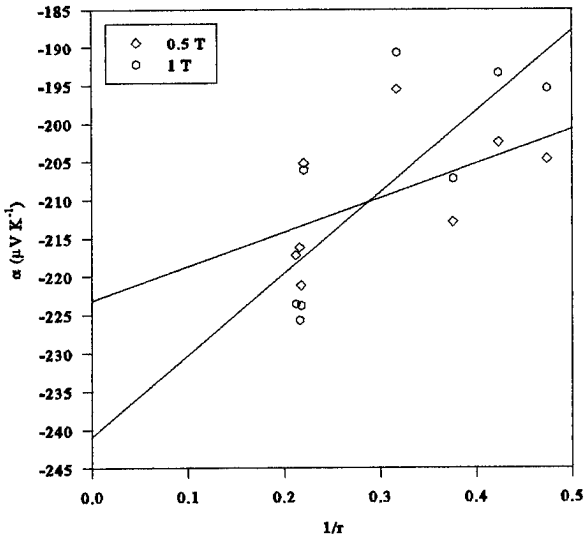


Figure 3. Plot of Seebeck coefficient against $1/r$ for $Bi_{88}Sb_{12}$ in a field of (a) 0.5 T and (b) 1.0 T.

T

There is even more scatter for the thermal conductivity data than for the Seebeck coefficient data and one cannot even determine the trend of the former quantity as $1/r$ changes. It may be, in fact, that the magneto-thermal resistance coefficient is only slightly dependent on the length-to-width ratio because the lattice conductivity acts to reduce any transverse temperature gradients that would otherwise exist.

Conclusions

It is concluded that the technique that has been described allows the longitudinal thermo-galvanomagnetic coefficients to be determined, for the condition of zero transverse flow, without the requirement of probes attached to the side faces of the samples. For polycrystalline material, only a single sample is needed but at least two samples of different length-to-width ratio would be needed for single crystal material.

References

[1] E. H. Putley, "The Hall Effect and related phenoma," Butterworths, London, (1960).

[2] O. M. Cordino, *Nuovo Cim.*, **1**, 393, (1911).

[3] J. R. Drabble and R. Wolfe, *J. Electronics and Control,* **3**, 259, (1957).

Observation of the grain size influence on the thermoelectric properties of polycrystalline bismuth - antimony alloys

X. Devaux, F. Brochin, A. Dauscher, B. Lenoir, R. Martin-Lopez, H. Scherrer, S. Scherrer

Laboratoire de Physique des Matériaux URA CNRS 155, Ecole des Mines, Parc de Saurupt, F-54042 Nancy Cedex, France
Tel.: +33 383 58 41 62, Fax: +33 383 57 97 94, E-mail: devaux@mines-nancy.fr

Abstract

This paper is devoted to the study of the transport properties of polycrystalline $Bi_{86.5}Sb_{13.5}$ alloys. Pellets of polycrystalline alloys were prepared by cold pressing and sintering of ultrafine powders. The average grain size of the bulk materials was adjusted from 0.1 µm to 200 µm. The influence of the microstructure and the grain size on both electrical and thermal conductivity, thermoelectric power and thermoelectric figure of merit is presented.

Introduction

Bi-rich bismuth-antimony alloys are semiconducting materials known for their thermoelectric properties for temperature below 210 K [1]. The properties of Bi-Sb single crystals are strongly anisotropic. Their best thermoelectric performances are observed along their trigonal axis. However the lamellar structure confers to the single crystals a high aptitude to cleavage along the trigonal planes which has largely prevented the use of Bi-Sb alloys in thermoelectric devices. The use of polycrystalline Bi-Sb alloys with a fine grain size could eliminate the cleavage problems. Nevertheless the microstructure will affect the transport properties of the alloys because of electron and phonon scattering at the grain boundaries. A recent theory predicts that for grain size lower than 5 µm, phonon scattering at the grain boundaries should become noticeable [2]. In a previous work, Suse et al. reported that sintered polycrystalline $Bi_{88}Sb_{12}$ alloys with a mean grain size of about 5 µm present a thermoelectric figure of merit twice larger than that of single crystal at 155 K [3]. More recently Volckmann et al. studied the effect of grain size (between 1 µm and 19 µm) on both thermal conductivity and electrical resistivity [4]. They observed that the thermal conductivity decreases as the grain size, but they didn't notice any enhancement of the figure of merit because of a dominating concurrent decrease in the electrical conductivity.
The purpose of the present work is to study the influence of grain size on thermoelectric properties of submicrometric and micrometric polycrystalline $Bi_{86.5}Sb_{13.5}$ alloys.

Experimental procedure

Polycrystalline samples were prepared by sintering $Bi_{86.5}Sb_{13.5}$ powders. The fine powders of Bi-Sb alloy were produced by pulverising a prealloyed ingot in an arc-plasma furnace in an argon-hydrogen atmosphere. Three powders with an average grain size of 0.06, 0.3 and 0.8 µm were prepared. The scatter of the antimony content between the grains of the powder was evaluated lower than 3 at.% of the average content by electron microprobe on population of about hundred grains. A complete description of the powder elaboration was previously published [5]. The powders were collected, stored and cold pressed in a glove box under a high purity argon atmosphere (O_2<0.5 ppm) to avoid any oxygen pollution. Pellets (13 mm of diameter and 3 mm of high) were obtained by cold pressing of freshly synthesised powders in an evacuated stainless steel die. To increase the sintering and to further the grain growth some cold pressed samples were annealed in vacuum during one to ten hours at 250°C, 275°C and 290°C. The density of the pellets was determined by the Archimedes method. The average grain size of consolidated samples was determined from scanning electron micrographs of cross sections of pellets.
Parallelepiped-shaped samples cut from the pellets were used for the investigation of the transport properties. Typical dimensions of a sample were 1.5x1.8x12 mm^3. The electrical resistivity was measured by the four probe method and the thermoelectric figure of merit was evaluated by the Harman method. The thermoelectric power was measured by means of a heat and sink method, i.e. by establishing a stationary temperature gradient by supplying heat at one end of the sample, while the other end is remained at constant temperature. The thermal conductivity was deduced from the three previous factors. Transport measurements were performed from 75 K to 330 K.

Results and discussion

The surface state of the powders and their average diameter have strong influence on the cold consolidation. As it is shown in figure 1, the density of the pellets made with fresh and uncontaminated powders is always higher than that made with powders shortly exposed to air just before pressing. For such air contaminated powders the grains diameter seems to have any influence on the density of the pellets. The uncontaminated powders of diameter 0.3 µm sintered better than the other uncontaminated powders does for pressure lower than 500 MPa. For higher pressure a relative density higher than 97 % was reached whatever the average grain size of the powder.
Figure 2 present a SEM micrograph of a cross section of a 600 MPa cold pressed powder. Most of the grains appear equiaxed. They have a faceted morphology whereas the grains of the powder had a spherical shape before pressing. Cold pressing clean powders leads to a sintering of the powders. At the same time a small grain growth occurs. However we have observed the grain growth remained limited to twice the initial average diameter of the powder. For example, a polycrystalline alloy with a relative density of 97 % and with a grain size of 0.11 µm was prepared by cold pressing at 600 MPa a powder of an average diameter of 0.06 µm.

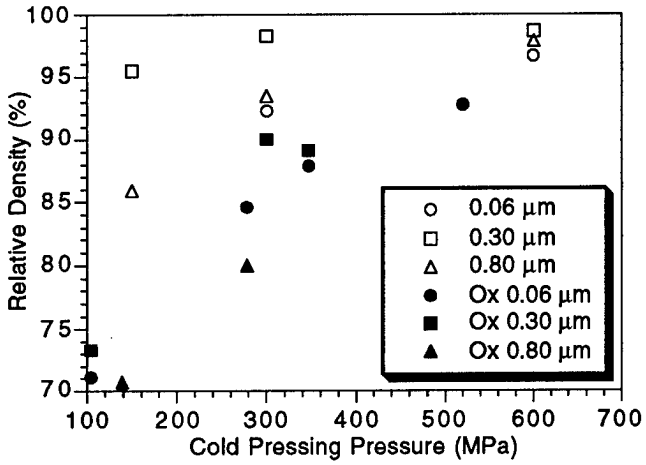


Figure 1: Influence of the pressure and the grain size on the relative density of pellets; Open markers fresh powders; Solid markers air-contaminated powders.

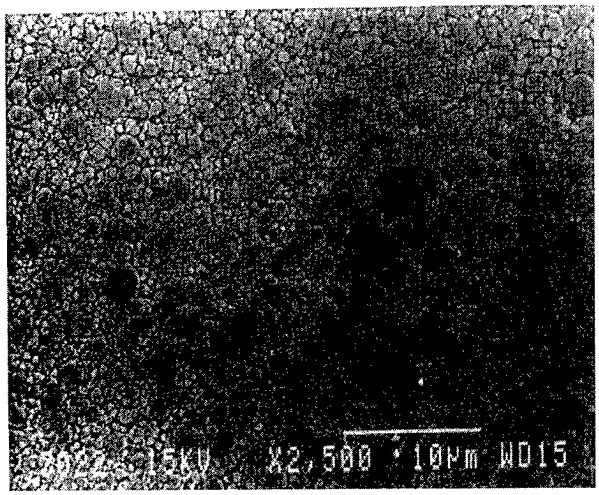


Figure 2: SEM micrograph of a cross section of a 600 MPa cold pressed 0.8 µm powder. Horizontal axe = pressing axe. Mean diameter of grains = 1.6 µm.

To allow the grain growth, some pellets were annealed. Micrographs on figure 3 displays the microstructures which can be obtained by heating a 0.3 µm cold compacted powder. The mean diameter of the grains was initially 0.45 µm in the bulk samples before the heat treatments. The microstructure presented in figure 3-c was obtained by heating specimen at temperature near the solidus line in order to promote the growth in presence of a small quantity of a liquid phase. For this treatment, some small solidified droplets have been observed after the annealing on the surface of the pellets. A part of the molten phase which allowed the grain growth moved up to the surface of the sample and let a few large voids inside the pellets. Starting with a cold compacted sample having grains of mean size of 0.1 µm, it was possible to control the grain size of the sintered sample from 0.1 µm up to 200 µm by a suitable annealing. Polycrystalline compacted powders with relative density larger than 97 % and with mean grain sizes respectively of 0.11 µm, 0.80 µm, 2.5 µm and 100 µm were prepared to measure the effect of the microstructure on the thermoelectric properties.

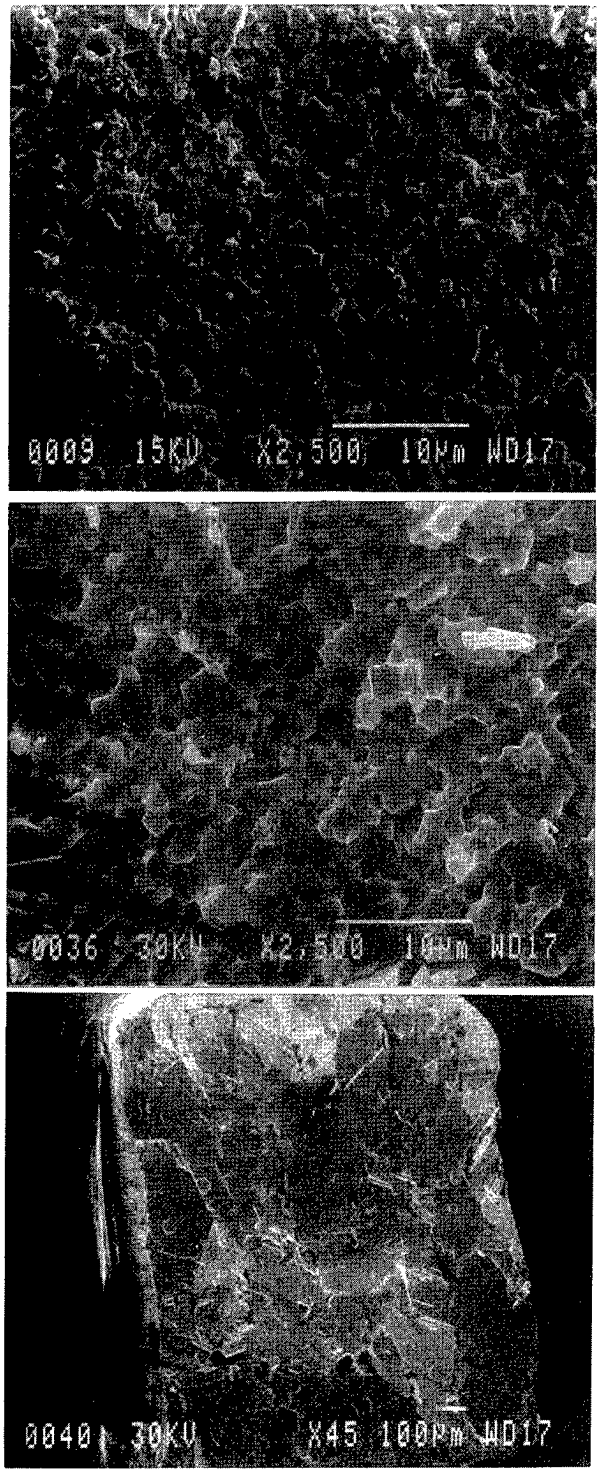


Figure 3: SEM micrographs samples obtained from a 600 MPa cold pressed and vacuum annealed 0.3 µm powder. a) heated 1h at 250°C; average diameter of grains = 0.8 µm. b) annealed 10h at 275°C; mean diameter of grains = 2.5 µm. c) annealed 10h at 290°C; mean diameter of grains = 200 µm.

Because of the strong anisotropy of Bi-Sb single crystals, we compare the transport properties of the polycrystalline samples with those of a single crystal of an intermediate orientation. The transport property of a single crystal of an intermediate orientation was deduced from the arithmetic mean of data measured along the trigonal axis and along the binary axis [6].

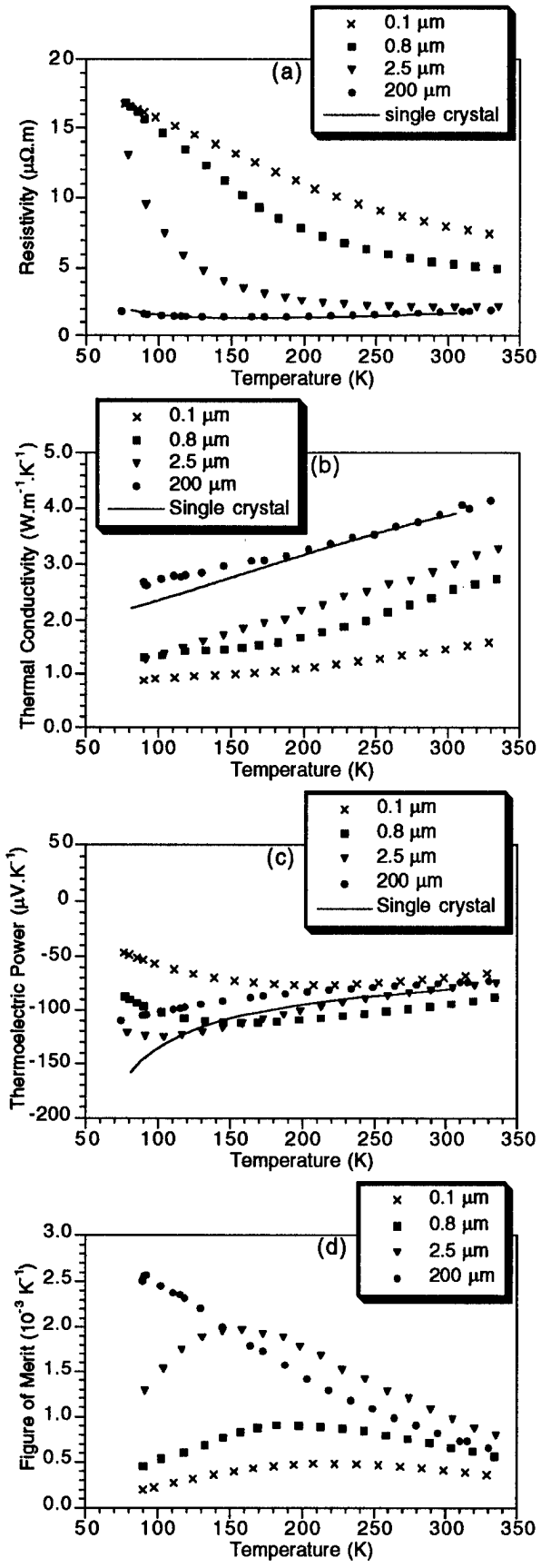


Figure 4: Influence of the grain size on the transport properties of polycrystalline $Bi_{86.5}Sb_{13.5}$ alloy. (a) Electrical resistivity (b) Thermal conductivity (c) Seebeck coefficient (d) Thermoelectric figure of merit.

The polycrystalline sample with the largest grain size (200 µm) present the same behaviour than the single crystal from 80 K to room temperature (figure 4).

The resistivity of micrometric and submicrometric polycrystalline samples decreases when the temperature increases. For grain size lower than 1 µm the resistivity is always higher than that of single crystal and is eight time larger at 80 K. Micrometric specimen present an intermediate behaviour. The level of its electrical resistivity is near those of fine grained materials and reaches that of single crystal at room temperature (figure 4a).

The thermal conductivity of all the studied samples increases with the temperature. Nevertheless the level of the thermal conductivity is all the lower than the mean grain size is small. The thermal conductivity of a 0.11 µm alloy is more than twice lower than that of the single crystal at 80 K and more than three times lower at 300 K. These experimental data confirm that phonon scattering at grain boundaries produce significant reduction in thermal conductivity.

At low temperature the thermoelectric power of polycrystalline alloys is always lower than that of the single crystal. Small grained samples exhibit a very low Seebeck coefficient at 80 K. The values increase slowly with the temperature to reach a maximum an then slowly decreases. For temperatures higher than 200 K the Seebeck coefficient values of polycrystalline samples become comparable to that of single crystal.

The thermoelectric figure of merit of the single crystal and large grained polycrystalline specimen decreases monotonously when the temperature increases. For fine grained alloys the thermoelectric figure of merit increases with the temperature to reach a maximum and decrease monotonously for higher temperatures. The maximum is all the more shifted towards higher temperatures than the grain size diminishes. The decrease of the thermal conductivity obtained for the small grain sizes is not sufficient to compensate the decrease of the electrical conductivity. The decrease of the grain size leads to a decrease of the thermoelectric figure of merit.

The effects observed on the transport properties are probably due to carrier scattering at the grain boundaries. Nevertheless a part of the measured effects may be a manifestation of an additional scattering mechanism induced by other defects such as porosity. The effect of porosity was then considered. In order to study the influence of porosity, two samples were prepared by cold pressing a 0.8 µm sized powder. The first one has 14 % of porosity and the second one only 3 %. The mean grain size of these two samples is about 1 µm. The results reported figure 5 allow to appreciate the effects induced by the porosity on the transport properties.

Significant effects of porosity ware observed on both thermal conductivity and electrical resistivity. The decrease of the thermal conductivity is more significant at low temperature probably because of the dominating of the electronic component of the thermal conductivity at high temperature. It can be noticed that porosity largely increases the resistivity of polycrystalline alloy.

The porosity have a very low infuence on the thermoelectric power as it is shown on figure 5 (c).

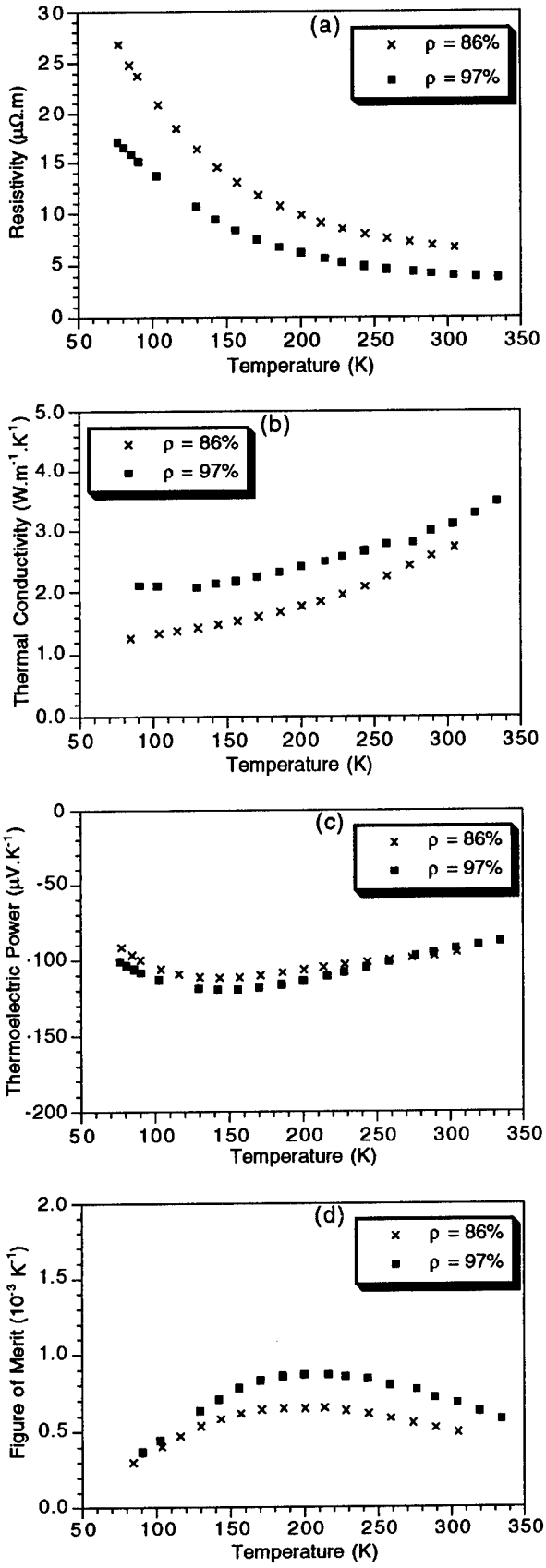


Figure 5: Influence of the porosity of 1.5 μm polycrystalline cold pressed samples on: a) Electrical resistivity b) Thermal conductivity c) Seebeck coefficient d) Thermoelectric figure of merit.

The decrease of the electrical conductivity being greater than that of the thermal conductivity, the thermoelectric figure of merit is lower for the porous specimen.

Conclusion

The use of BiSb ultrafine powders is powerful to elaborate polycrystalline alloys with controlled microstructure. The transport properties of polycrystalline BiSb alloy are strongly affected by their microstructure. The polycrystalline BiSb sample that were prepared exhibit thermal conductivities that decrease with grain size. Nevertheless a dominating concurrent decrease in electrical conductivity results in a decrease of the thermoelectric figure of merit. The apparent dependence of the thermal conductivity on grain size suggests that scattering of phonons is occurring at the grain boundaries.

References

[1] G.E. Smith, R. Wolfe, J. Appl. Phys., **33** (1961) 841.

[2] H.G. Goldsmid, H.B. Lyon, E.V. Volckmann, Proc. of 15th Intern. Conf. on Thermoelectrics, M.V. Vedernikov ed., Ioffe Institute, Saint Petersburg, Russia, 1995, p 16.

[3] Y. Suse, Y.H. Lee, H. Morimoto, T. Koyanagi, K. Matsubara, A. Kawamoto, Proc. of 12th Intern. Conf. on Thermoelectrics, K. Matsuura ed., Yokohama, Japan, 1993, p 248.

[4] E.H. Volckmann, H.J. Goldsmid, J. Sharp, Proc. of 16th Intern. Conf. on Thermoelectrics, Pasadena 1996, p 22.

[5] X. Devaux, F. Brochin, A. Dauscher, B. Lenoir, R. Martin-Lopez, H. Scherrer, S. Scherrer, Nanostructured Materials, **8** (1997) 137

[6] B. Lenoir, M. Cassart, J.P. Micheneaud, H. Scherrer, S. Scherrer, J. Phys. Chem. Solids, **57** (1996) 89

Thermoelectric Properties of Sintered Bi Using Plasma-Treated Powder

Y. H. Lee*, R. Isobe, M. Yomura, I. Nakamoto and T. Koyanagi
Department of Electrical and Electronic Engineering, Yamaguchi University,
2557, Tokiwadai, Ube 755, Japan,
* E-mail : lee@aem.eee.yamaguchi-u.ac.jp

Abstract

Sintered Bi was prepared by using the plasma-treated powder in order to improve their thermoelectric figure of merit. Surfaces of Bi raw powder were modified in the Ar, H_2, O_2 and $SbCl_3$ rf-plasmas prior to sintering, and Bi was sintered using the powder obtained by the spark plasma sintering. For Bi samples sintered using O_2 plasma-treared powder, the electrical conductivity σ was increased in spite of growth of Bi oxcides, as compared with that of the untreated one. The increase in σ is attributed to the increase in the carrier concentration. As a result, the thermoelectric figure of merit at room temperature was improved 1.5 times as high as that of the untreated one. The improvement of thermoelectric properties of sintered Bi was observed also in the case of other gas plasma treatment.

Introduction

The alloying of Bi with Sb constitutes a continuous solid solution with a rhombohedral structure (R3m) [1]. In Bi-Sb alloys, $Bi_{88}Sb_{12}$ is well known as a n-type thermoelement with the significantly high thermoelectric figure of merit at low temperatures [2]. Therefore, this material has been expected to be applied to the thermoelectric cooling, and has been desired to further improve their thermoelectric performance. We has tried to improve the thermoelectric properties of Bi-Sb sintered alloys by controlling their structures using Bi-Sb fine particles [3].

As one of techniques for improvement of properties of thermoelectric materials, the plasma treatement of powder of thermoelectric materials, which is a non equilibrium technique, has been attempted [4]. Using this technique, there is possibility that the carrier conduction and phonon scattering can be controlled by changing the micro-structure of thermoelectric sintered materials. This control can not be realized by the conventional melt process.

We has been investigated the thermoelectric properties of Bi sintered using the plasma treated powder as a preliminary experiment in order to improve the thermoelectric performance of Bi-Sb alloys. In this paper, we report some results on the thermoelectric properties of Bi sintered using O_2, Ar, H_2 and $SbCl_3$-plasma-treated powder. We adopted further two new techniqes, the hydrogen plasma-metal reaction method[5] and the spark plasma sintering method[6]. The hydrogen plasma-metal reaction method was used for obtaining Bi fine particles of several μm in diameter. The spark plasma sintering method was used for sintering Bi. In this paper, the results of O_2-plasma treatment are mainely discribed. Finally, the results of thermoelectric figure of merit of sintered Bi treated using other gases are summarized.

Experimental Procedure

rf-plasma treatment

Bi powder of ~2μm in diameter was generated by the hydrogen plasma-metal reaction method [5]. The treatment of Bi powder obtained was performed by using the plasma reactor as shown in Fig. 1. Powder is set in the container with a rotating fin, and was jumped up to the plasma region by rotating the fin. Reactive gases was introduced from the powder container. The plasma was generated by the induction coil to which a voltage with radio frequency (rf: 13.56MHz) was applied. By exposing the powder to the plasma, surfaces of the powder is modified, for example oxidation, coating, etching etc. In this study, the plasma treatment of Bi powder was carried out at a rf-power of 500W and at a pressure 0.2 Torr for 0.5~2 hours in an O_2, Ar, H_2 and $SbCl_3$ atmosphere. The $SbCl_3$, which is solid at room temperature, was evaporated at 240°C, and was introduced into the plasma reactor with H_2 carrier gas. For O_2 and H_2 gas, we expected that surfaces of Bi powder was oxidized and reduced, respectively. For Ar gas, the atomic state of surfaces was expected to be disorderd by bombardment of Ar^+ ions, leading

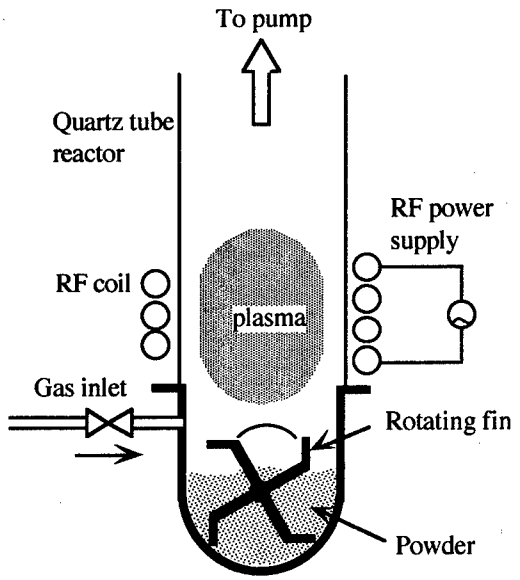


Fig. 1 Schematic diagram of rf-plasma processing system for treating Bi powder.

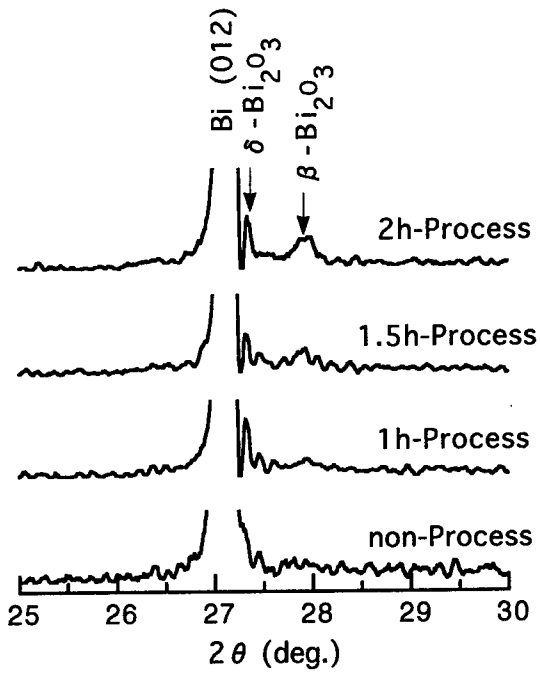


Fig.2 XRD patterns of O_2-plasma-treated powder.

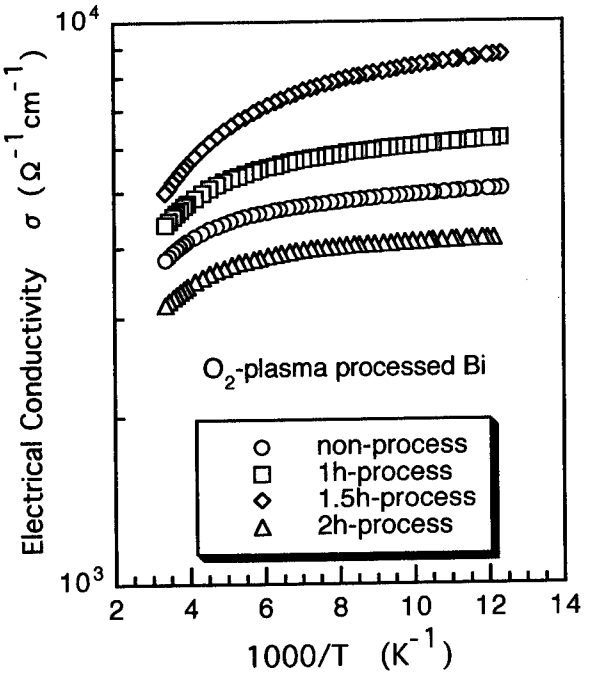


Fig.3 Temperature dependence of electrical conductivity σ of sintered Bi.

to improvement of the density of sintered Bi. The coating of Sb was expected by using $SbCl_3$ gas which was decomposed into Sb and HCl gases by reacting the $SbCl_3$ gas to the H_2 carrier gas.

Sintering of Bi samples

Using Bi powder which was treated with O_2, Ar, H_2 and $SbCl_3$ gases, Bi samples was sintered by the spark plasma sintering at 240°C and 30MPa for 10min in an Ar atmosphere. For comparison, Bi samples was sintered using non-treated Bi powder at the same conditions. In this sintering, joule heat and plasma energy are supplyed to powder particles by passing a pulsed current under an high pressure. As a result, surfaces of powder are activated and is effectively heated [6], which make it possible to sinter thermoelectric materials with a high density at low temperatures and for short sintering times.

Measurements

The obtained powder was identified by the x-ray diffractometry (XRD) analysis. The density of samples was measured by immersion technique using distilled water as the liquid. The Hall measurements, from which the carrier concentration n and Hall mobility μ_H were calculated, were measured in the temperature range from 90 to 300K. Measurements of the Seebeck coefficient S were performed by the standard technique in the temperature range from 90 to 300K. The temperature difference between high and low temperature electrodes was set at 5K. The electrical conductivity σ was measured by the standard four probe method at temperatures ranging from 90 to 300K. The thermal conductivity κ values were determined by using the laser flush method at room temperature.

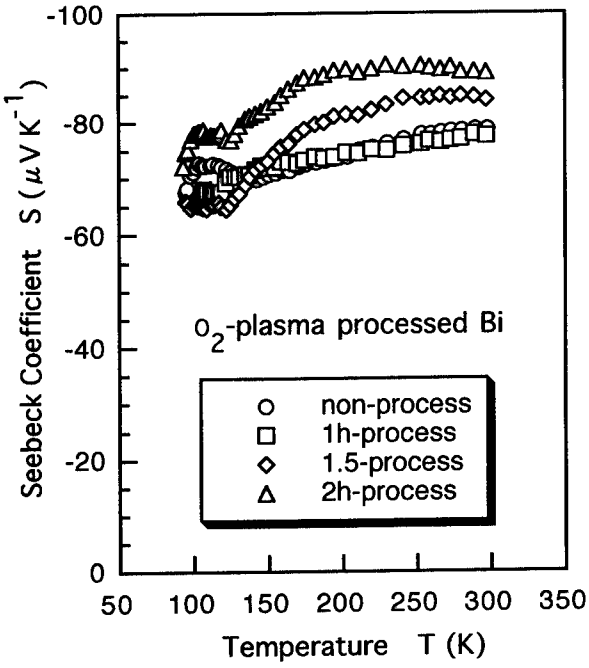


Fig.4 Temperature dependence of Seebeck coefficient S of sintered Bi.

Results and Discussion

Figure 2 shows the x-ray diffraction patterns of O_2-plasma-treated powder at various plasma treatment times, as compared with that of non-treated powder. In these patterns of the O_2-plasma-treated powder, diffraction peaks of β-Bi_2O_3, δ-Bi_2O_3 were identified in addition to a peak of Bi. Their peaks

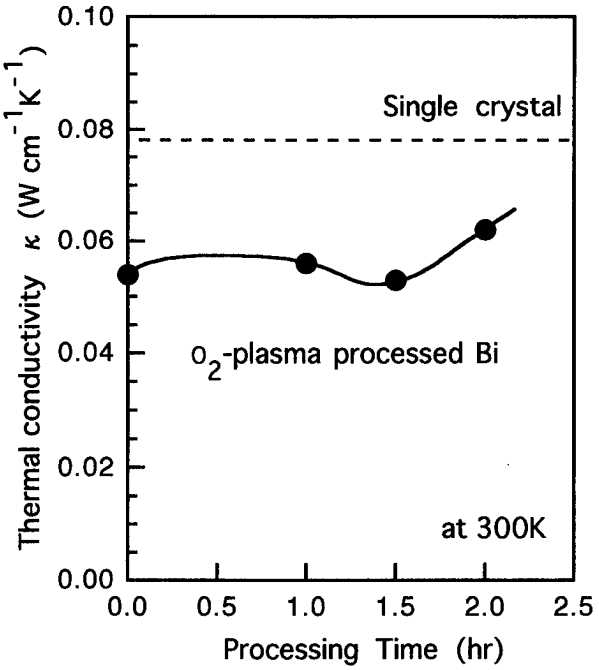


Fig.5 Thermal conductivity κ at room temperature.

intensity increases with an increase in the plasma treatment time. From the result, it was found that the surfaces of Bi powders were oxidized by O_2-plasma treatment.

Figure 3 shows the temperature dependence of electrical conductivity σ for the sintered Bi. Since Bi is a semimetal, σ decreases with increasing temperature. As the plasma treatment time was increased up to 1.5 hours, the values of σ increase in the whole temperature range in spite of oxidation of the powders as shown Fig.2. Above the treatment time of 2 hours, the values of σ decrease, as contrasted with the former case. In order to investigate the reason for the increase in σ, Hall measurements were performed. The carrier concentration n increased up to 1.5 hours and decreased above this time as the plasma treatment time was increased. The Hall mobility μ_H was hardly changed except for the sample treated at 1.5 hours. The values of μ_H for the sample treated at 1.5 hours were slightly larger than those for other samples. From these results, it was found that the increase in σ is attributed to the increase in n. Oxygen is a VI element and is expected to acted for Bi of a V element as a donar. Accordingly, the carrier concentration n increased by doping of Bi with oxygen which was achieved by the O_2-plasma treatment. On the other hand, in the case of O_2-plasma treatment for 2 hours, the Bi_2O_3 layers surrounding Bi powder was grown, resulting in the decrease in values of σ owing to Bi_2O_3 insulating layers at grain boundaries.

Figure 4 shows the temperature dependence of Seebeck coefficient S for the sintered Bi. The values of S monotonously increase with an increase in the plasma treatment time in the temperature range above ~140K. The increase in values of S could not be explained by the dependence of the carrier concentration n on the plasma

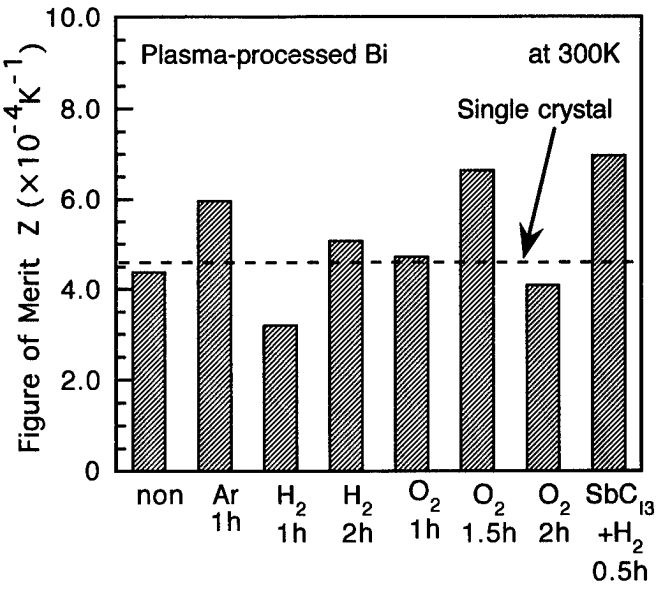


Fig.6 Figure of merit Z at room temperature of sintered Bi.

treatment time. Therefore, the increase values of S is probably related to the structure of grain boundary in sintered samples affected by the O_2-plasma treatment.

Figure 5 shows the thermal conductivity κ at room temperature for the sintered Bi as a finction of the plasma treatment time. The value of κ for a Bi single crystal is indicated by the dotted line in this figure for comparison. Since Bi has an anisotropy, the thermal conductivity is represented by κ_{11} in the perpendicular direction of c-axis and κ_{33} in the parallel direction of c-axis. The value shown in Fig.5 was calculated by κ_{11} and κ_{33} of a Bi single crystal [7], assuming that grains of Bi was randomly oriented [8]. The values of κ for every samples were lower than that of the single crystal. This is closely related to the fact that the grain size of the Bi powder used was as small as ~2μm. The reduction of κ by using fine powders was also reported elsewhere [9]. In this case, no influence of the O_2-plasma treatment on the value of κ could be observed.

In the same way as the above O_2-plasma treatment, the plasma treatment of Bi powder was carried out by using Ar, H_2 and $SbCl_3$ gases. The sintered samples were prepared by using the plasma-treated powder. Figure 6 shows the thermoelectric figure of merit Z of these samples at room temperature. In this figure, the dotted line indicates the value of Z of a Bi single crystal, which was calculated from the values of electrical conductivity (σ_{11}, σ_{33}), Seebeck coefficient (S_{11}, S_{33}) and thermal conductivity (κ_{11}, κ_{33}) in the perpendicular and prallel direction of c-axis [7], assuming grains of Bi was randomly oriented [8]. The values of Z for the every plasma-treated samples were improved, as compared with that of the non-treated one. Further, for some plasma-treated samples the values of Z were larger than those for a Bi single crystal. In the case of the O_2-plasma treatment, the value of Z for sample treated for 1.5 hours is 1.5 times as high as that for non-treated one. From these results, it was found that the

plasma treatment make possible the improvement of figure of merit of Bi.

Conclusion

The sintered Bi was prepared using the plasma-treated powder. The plasma treatment was carried out by using O_2, Ar, H_2 and $SbCl_3$ gases. For the O_2-plasma-treated sintered Bi, although oxidation of Bi powder was identified by the x-ray diffractometry analysis, the electrical conductivity σ increased up to 1.5 hours of the plasma treatment time. The increase in σ is attributed to the increase in the carrier concentration n, suggesting that oxygen acts as a donor. As a result, the thermoelectric figure of merit at room temperature was improved 1.5 times as high as that of the non-treated one. For the Ar, H_2 and $SbCl_3$ plasma-treated samples, the values of Z was higher not only than that for non-treated one, but also, for a part of the samples, than that of a Bi single crystal. From these results, the plasma treatment of thermoelectric material powders found to be reasonably effective for improvement of their thermoelectric figure of merit. Based on these results, the improvement of thermoelectrical properties for Bi-Sb alloys can be expected.

References

[1] M. Hansen and K. Anderko, "Constitution of Binary Alloys", 2nd Ed. (McGraw-Hill Book Company, New York, 1986), p.332.

[2] R.Walfe and G.E.Smith, "Effects of a magnetic field on the thermoelectric properties of a bismuth-antimony alloys", Appl. Phys. Lett. **1** (1962) 5.

[3] Y. H. Lee, R. Isobe, T. Koyanagi and K. Matsubara, "Thermoelectric properties of Bi-Sb sintered alloys prepared under unidirectional high pressure", T. IEE Japan **116-A** (1996) 273 [*in Japanese*].

[4] K. Matsubara, K. Nagao, O. Ueda, T. Miki, T. Koyanagi and I. Fijii, "Iron disilicides: The possibility of improving thermoelectric figure of merit values by rf-plasma processing", Proc. of 12th Int. Conf. on Thermoelectrics, (1993) 233.

[5] S. Ohno and M. Uda, "Generation rate of ultrafine metal particles in hydrogen plasma-metal reaction", J. Japan Inst. Metals **48** (1984) 640 [*in Japanese*].

[6] M. Tokita, "Trends in advanced SPS spark plasma sintering systems and technology", J. Soc. Powder Technology Japan **30** (1993) 790 [*in Japanese*].

[7] W. M. Yim and A. Amith, "Bi-Sb Alloys for Magneto-Thermoelectric and Thermomagnetic Coolong", Solod-State Electron., **15** (1972) 1141.

[8] H. J. Goldsimd and F. A Underwood, "Study of orientation in polycrystalline bismuth telluride allys", Advanced Energy Conversion, **7** (1968) 297.

[9] E. H. Volckmann, H. J. Goldsmid, J. Sharp, "Observation of the effect of grain size on the lattice thermal conductivity of polycrystalline bismuth antimony", Proc. of 15th Int. Conf. on Thermoelectrics, (1996) 22.

Powder Processing of Thermoelectric Materials---focusing on SiGe with New Sintering Technique

Teruo Noguchi

Vacuum Metallurgical Co., Ltd. 516 Yikota, Sambu-machi, Sambu-gun, Chiba-ken, 289-12 JAPAN

Abstract

Big efforts have long been done to develop SiGe alloys known as a promising thermoelectric material for high temperature applications. Because of difficulty in manufacturing, which has resulted in less economical competitiveness, the practical application of the material has been almost limited to the power source for the space satellites. Reduction of manufacturing costs will be inevitable to conduct further industrial applications of the SiGe having high thermoelectric potentiality.

Conventional hot-pressing, including a combination of hot-pressing with mechanical alloying, have contributed to enhancement of the thermoelectric performances[1].

In these several years, Spark-Plasma-Sintering (SPS) or Plasma-Activated-Sintering(PAS) technique have been utilized for processing thermoelectric materials[2,3], in particular, SiGe alloys[4,5]. One of the successful results will be co-sintering of p- and n-type material which can necessarily form a p-n junction to be used as a hot temperature end[4].

This paper will report on the SPS technique we have applied to sinter SiGe alloys together with their properties.

Introduction

A silicon-germanium alloy (SiGe, hereafter) has been known as a suitable thermoelectric material for usage at temperatures as high as 500-1000C. To develop the SiGe material having higher thermoelectric properties, many efforts have been done by many people during the past half century. A fruitful result was obviously seen in the fact that it had successfully applied to the power source for the artificial satellites.

On the other hand, however, applications of the SiGe to many other fields such as industries and /or consumer's lives are still small; almost none. This would be due to expensive costs of manufacture resulting in low cost performances. It is inevitable for the SiGe to reduce manufacturing costs as well as to improve its thermoelectric properties.

Up to now, SiGe has typically processed by powder metallurgical techniques represented by hot pressing[6]. This technique should be regarded to have succeeded to a great extent, in considering that one can control the chemical compositions, metallographic structures, electronic structures, and/or acoustic ones.[7,8]

For these several years, we have been developing SiGe by using a new sintering technique, Spark-Plasma-Sintering (SPS). Our efforts, unfortunately however, have not brought us fully successful results so far from either economical or high performance point of view. Though much more efforts are required for us to be able to supply satisfactory SiGe materials to commercial markets, we would like to report on the results we have obtained so far.

Processing

The process we have been developing to manufacture SiGe thermoelectric materials and elements is shown schematically in Fig.1. Each step of the process will be described in the following sections in detail.

1. Powder Preparation

As starting materials of SiGe to be sintered, powders of the alloy consisting of Si, Ge, and doping elements are prepared by usual processes. The alloys of 80 at.% Si, 20 at.% Ge, and 0.2-1.5 at.% B or P were melt in a vacuum induction melting furnace. To avoid contamination of p- and n-type materials with each other, the furnace has two independent melting chambers for p- and n-type, respectively.

0-7803-4057-4/97 $10.00 ©1997 IEEE

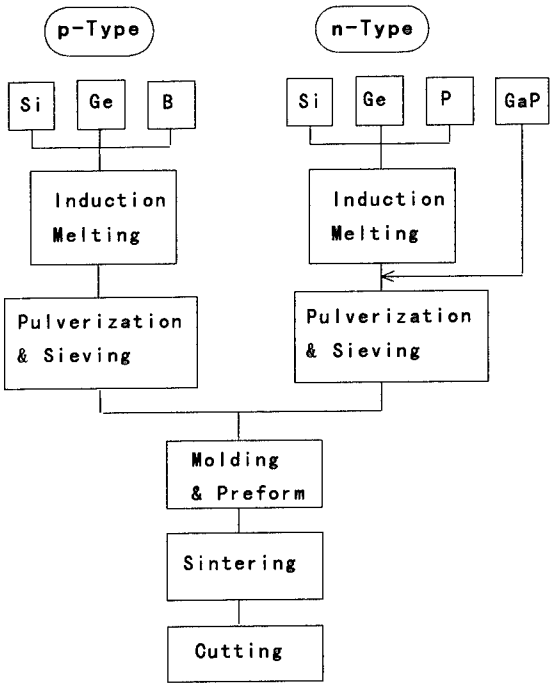


Fig. 1 Process block diagram

The n-type Si-Ge-P alloy was melt in the inert Ar atmosphere of about 1 atmospheric pressure to minimize volatilization of P, while the p-type alloy Si-Ge-B was melt under a vacuum pressure of $1x10^{-5}$ Torrs. The melt was poured onto a water cooled Cu plate to solidify as lumps of the SiGe alloys. These lumps, after coarse cracking by a hammer, were pulverized by a cracking machine into powders of 0.1-0.2mm in diameter. Then the powders were milled down to fine sizes of 5 microns or smaller by a planetary ball mill in Ar atmosphere. The average size of the powder was typically 2-3 microns.

2. Sintering

2.1 Spark Plasma Sintering

Among many sintering techniques available, a hot pressing will be most popular for manufacture of thermoelectric materials, in particular SiGe.

A HIP (Hot Iso-static Pressing)[9] can be included as one of its variant, excluding directions of pressing force. Sintering processes by the hot pressing will be done under a nearly thermal equilibrium given by the ambient heating source. In contrast to them, the SPS technique would not always need equilibrium conditions, and as a most remarkable feature, makes at least partly use of own-heating due to currents flowing in the work. Pressing forces are applied prior to the current flow. Figure 2 shows a schematic drawing of the SPS. A cylindrical graphite die covers the work to be sintered, and the applied current can be shared between the work and the die

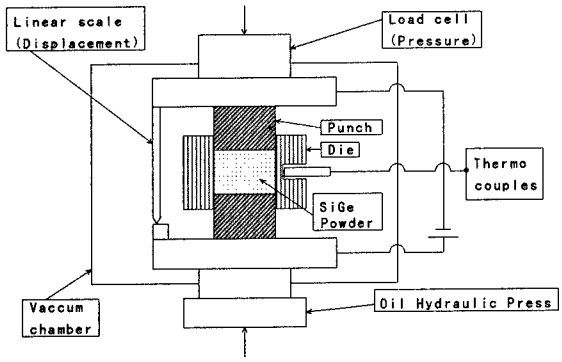


Fig. 2 Schematic drawing of SPS

which functions both as a mechanical restraint from radial displacement and as an ambient heater. It is not known however how much currents is shared in the work, and so the precise distribution of temperatures within the work is also not known. It should be noted here that the applied currents are not simple DC currents, but some impulsive ones with frequency at several hundred Hz. In some analysis[10], such impulsive currents, or impulsive electric fields could play an important role; electric arcing could be caused at many points of contact between particles of the work material, and thus causes triggers of sintering reaction, particularly in its initial stage. This would be the reason why the SPS process can be conducted in a very short time.

The process by using the SPS technique will have certainly a merit of short time sintering, and consequently have a possibility to restrain grain growth during sintering. The process will probably be made under non-equilibrium state of the thermodynamics. This, in turn, makes it difficult to find out optimum operating conditions.

In a similar technique, PAS, the difference with SPS is

very small, and will lie in their current supplying modes; impulsive currents alone for SPS, and initial impulsive currents followed by subsequent direct ones for PAS.

Although the detailed mechanism of sintering processes through the SPS will have to be investigated further from now, the SPS technique is surely advantageous either to synthesize or to join various kind of ceramics relatively easily in a short time.

2.2 Sintering of SiGe by SPS

Prior to sintering, the starting powders were compacted to take a shape of disk like pre-forms having 30-50 mm in diameter and 10-40 mm in thickness. This is required for both easy handling and increasing the electric conductivity of the powders in the initial stage of sintering.

Provided either p-type or n-type SiGe alone is to be sintered, either one kind of the powder is used. If a monolith consisting of p- and n-type SiGe is to be sintered, both kinds of powder are compacted in a pre-form disk so as to be neighbored or to be piled up by turns each other. In this case, however, it must be careful not to mix together p- and n-type powders by interleaving an appropriate barrier. Selection of the layout, horizontal neighboring or vertical piling will be determined in consideration of number of layers, number of kinds of material, their melting points, and so forth.

The first sequence of the operation is vacuum evacuation of the sintering chamber up to $1x10^{-3}$ Torrs, and the applying force by oil hydraulic pressures at about 30 MPa is the next. The applied current is increasing with time, till the work temperatures measured by a R-type thermocouple inserted into the die reaches 1200-1250 ℃. During the sintering process, operating conditions of the SPS apparatus were recorded in a multi-pen recorder. A typical recorder chart is shown in Fig.3 where the temperature of the work, the applied currents, longitudinal displacement in the work, and the derivative of the displacement with regard to time are recorded. It can be observed the time derivative of the displacement changes drastically during sintering. This drastic change in the time derivative of the displacement means that the volume of the work was reducing rapidly with progressing sintering. It is to be noted that the period of sintering was around 1 minute.

Short time sintering like this, unfortunately on the contrary to our expectation, could not always restrain crystalline grain growth. Figure 4 shows a typical metallographic structure of the SiGe sintered by SPS, where average grain sizes are around 10 microns, about 3 times larger than the starting powders. The densities of almost all the specimens are higher than 99%.

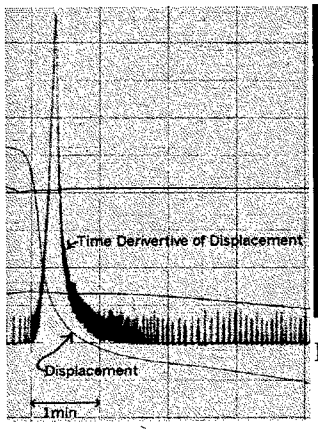


Fig. 3 Recorder chart of SPS operation

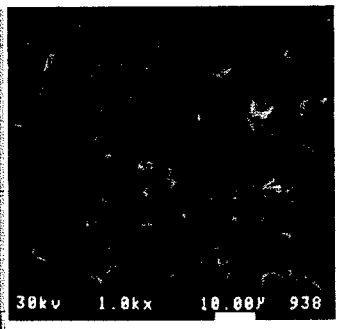


Fig.4 Typical grain structure

2.3 Addition of GaP

Our study to improve the thermoelectric properties by addition of GaP has been in the beginning stage. Tips of GaP were crashed, pulverized, milled by a planetary ball mill, and sieved into three grades, 1 , 3 and 6 microns in averaged size. The powders of GaP were mixed with that of n-type 80Si-20Ge-0.3P before molding. Sintering was followed by SPS, but subsequent heat treatments have not tried yet. Monolithic p/n elements having the GaP added material have not also fabricated. The thermoelectric of the GaP added specimens will be described later.

2.4 Shaping into p/n Joined Elements

In the case with monolithically sintered p/n SiGe

material, the as-sintered disk must be cut into a U-shaped element. Before cutting it, the boundary between p- and n-type materials should be distinguished.

Such a boundary can usually be localized by steep changes in the electrical resistivities or in the polarity of thermoelectric motive forces. For simplicity, however, it is visualized as follows. When the as-sintered material was firstly cut in a plane crossing the p/n boundary by a discharging cutting machine, the boundary is visualized as a subtle line, because of some difference in the discharging conditions. Examples of the resistivity measurement will be shown in the following section.

Photographs of Fig.5a and Fig.5b show respectively examples of a pair and two pairs of monolithic SiGe thermoelectric elements cut in the above mentioned manner.

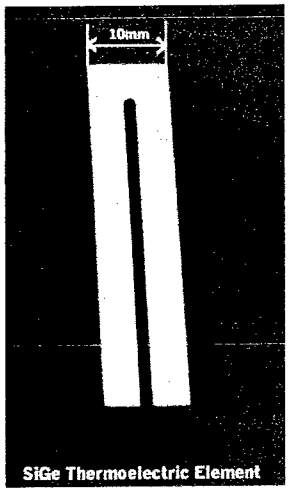


Fig. 5a Monolithic p/n element of SiGe

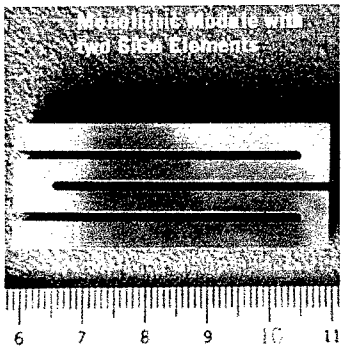


Fig. 5b Monolithic SiGe with two elements

Results

1. Boundaries between p- and n-type SiGe

To distinguish exactly the boundaries p- and n-type material of the monolithically sintered SiGe, the resistivity measurement was employed at the room temperatures. The four-terminal and/or four-probe method, in which the probe was scanned precisely with a computer control, was used for the above purpose. A typical example of the measurement for a specimen of the two p/n-paired SiGe is shown in Fig.6.

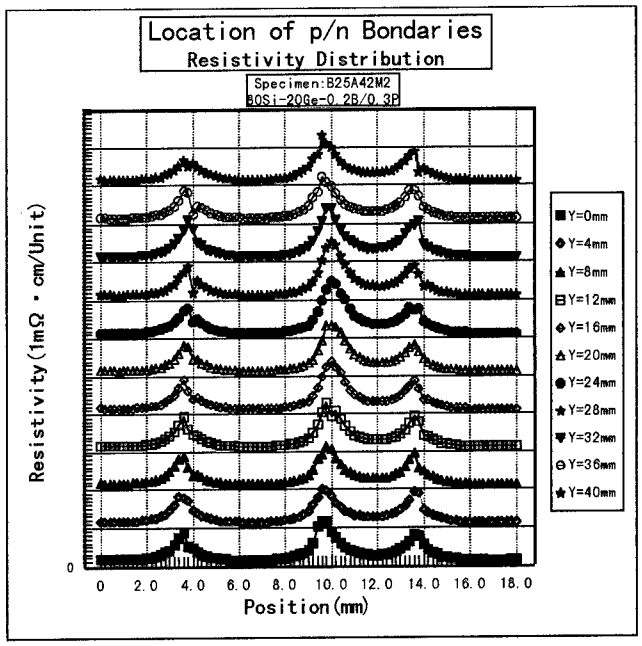


Fig. 6 Distribution of p/n boundary location

From this, two problems become apparent. The first is that resistivities at the p/n boundaries are remarkably high compared with each p- and n-type material zones, and the second is that widths of each zone of p- or n-type material are not always equal, but is likely that n-type regions were spread more.

Both problems will be strongly related to diffusion of doping elements during sintering, The doping element, B and P diffused into the opposite direction each other crossing the initial p/n boundary during sintering. This caused canceling of p- and n-type carriers, and resulted in not only increase in the resistivities but also difference in their distribution. Since this problem will be treated independently later, the second problem is touched here. In the specimen used, the doping level was 0.2at.% and 0.3at.% for p-type B, and n-type P, respectively. The electrical resitivity of both type SiGe of these doping levels lies just before saturation with increasing dopant concentration., and is still variable with small change in dopant concentrations. Specimens consisting of the combination of a little more dopant concentrations, 0.5at.%P and 0.58at.%B were sintered, and as can be seen in Fig.7, the problem of different zone widths was almost solved.

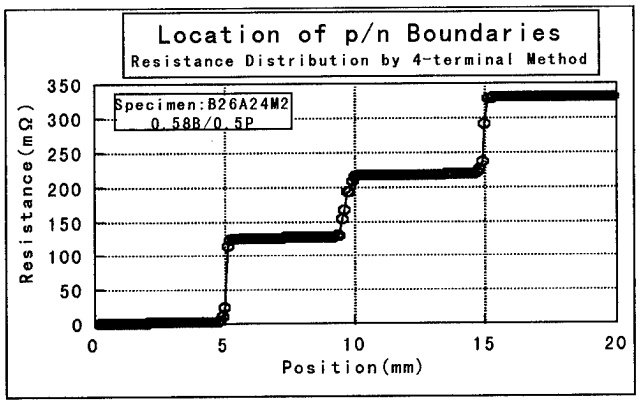


Fig. 7 Improvement of the unequal p/n zone width

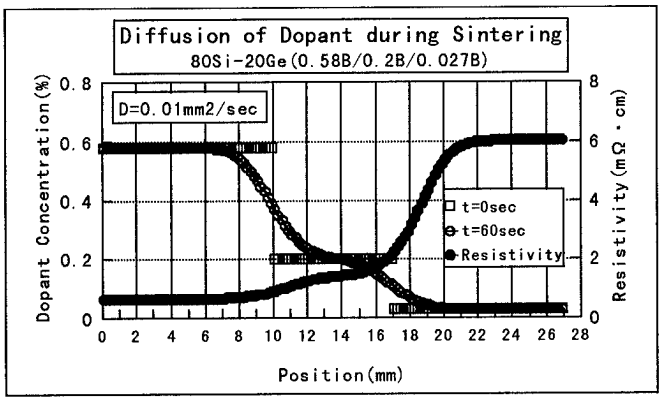


Fig. 9 Calculated distribution of dopant concentration and resistivity

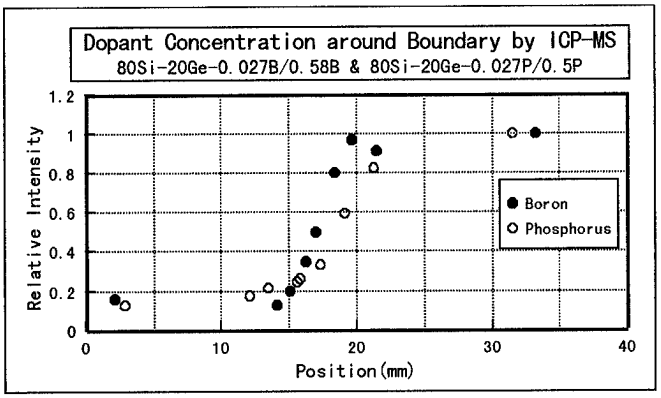


Fig. 10 ICP-MS analysis of dopant concentration

2. Diffusion of Dopants during Sintering

We have been studying FGM (functionally graded material) SiGe where two or three kinds f SiGe with different doping levels are joined stepwise. In order to distinguish the boundary at different doping, precise measurements of resistivity distributions around the joined boundary have been made. As was already reported on some results elsewhere[11], remarkable broadening of the boundary was observed as shown in Fig.8 for the case of p-type FGM and it was speculated that this might have been caused by the diffusion of the doping elements during the sintering.

To clarify the cause, the solution of a simple one dimensional diffusion equation is compared with the results of ICP-MS analysis. Figure 9 shows distributions of the dopant concentration together with the resulting resistivity, both of which were calculated. Comparing Fig.9 with Fig.10, the result of ICP-MS analysis, it would be concluded that the dopants could easily self diffuse in SiGe during sintering, even by SPS which was kept for a short period of about 1 minute. Also the same investigation on n-type FGM revealed that P might diffuse faster than B did.

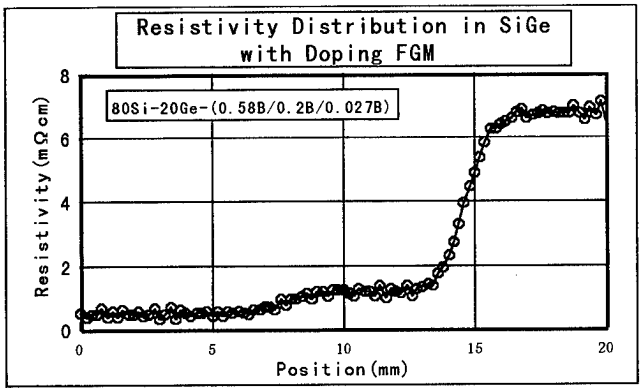


Fig. 8 Boundary around different doping zones

3. Thermoelectric Properties

3.1 Thermal Conductivity

Thermal conductivity was measured by using a Laser Flash Method equipment. Figure 11 shows the typical results obtained for specimens of 80Si-20Ge alloy having B or P doping with 0.2-1.6 at.% concentration and GaP added n-type materials. For n-type materials thermal conductivity does not depend remarkably on P concentrations, while it increases with increase in B concentration for p-type materials. Those values, except 1.6B doped case whose curve looks like somewhat strange, would be within reported ones in preceding works[12]. For the case with GaP doped n-type materials, where the size

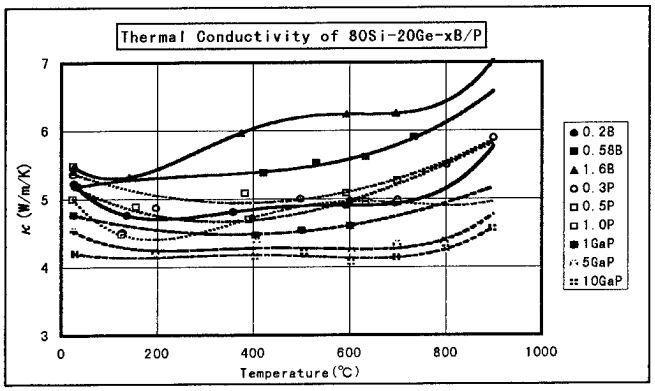


Fig. 11 Typical thermal conductivity of 80Si-20Ge with various doping

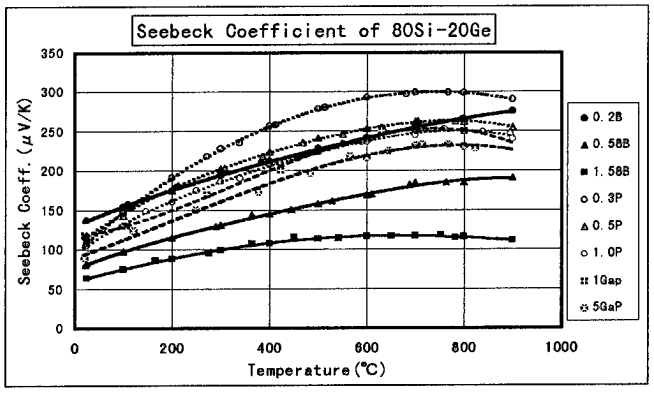


Fig. 12 Typical Seebeck coefficient of 80Si-20Ge with various doping

of GaP powder were 6.5 microns, the thermal conductivity decreases with increasing GaP concentration, probably due to some enhancement in carriers or alloy disorder[13]. The lowest value, 4.1W/m/K, however, is still large compared to those reported in preceding works[14].

As mentioned in the section 2.2, the grain size of our specimens are around 10microns that is not satisfactorily small, and this would be most responsible for still large thermal conductivity in both cases of B or P doping and GaP addition.

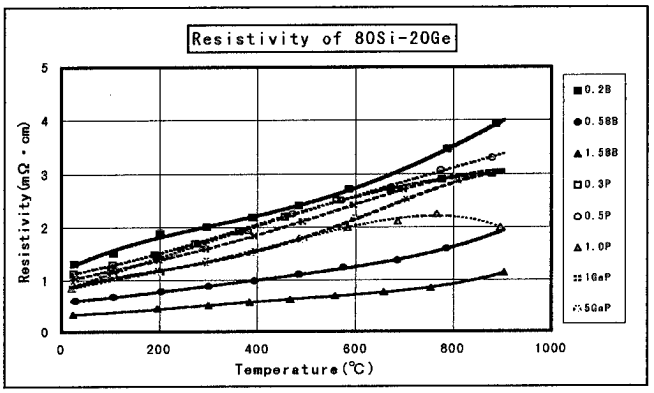


Fig. 13 Typical resistivity of 80Si-20Ge with various

3.2 Electrical Properties

Seebeck coefficients are shown in Fig.12 for materials doped with B or P, and GaP. As can be seen, for the B doped p-type materials their Seebeck coefficients depend strongly on B concentrations, and decrease with increasing B concentrations. The curve for doping with 1.58at.%B will suggests to be over doped. For P doped n-type materials, however, the dependency on P concentrations is small.

All B atoms added could have functioned as p-type charged carriers, whereas P atoms might have some limitation in their solubility in SiGe alloy matrices. Volatilization losses of P also will be responsible. It could be due to solubility enhancement of P that Seebeck coefficients of the GaP doped materials become slightly smaller with increasing GaP content [15].

Electrical resistivity measured by using a usual four-terminal method is shown in Fig.13, for the specimens doped with B or P alone, or additionally doped GaP,respectively. Here also a small difference is observed between 0.3at.%P and 0.5at.%P doped cases. A reason will be in an experimental fact that dependency of the resistivity on P concentrations almost saturates over 0.3at.%. For the specimen doped with 1at.%P, the resistivity, having small difference from those of 0.3 or 0.5at.%P doped cases at room temperatures, is spreading the difference with increasing temperatures, and takes a maximum before 800℃, and then decreases at higher temperatures. This could be explained by enhancement in carrier densities at elevated temperatures [16].

Unfortunately however, because of our very limited knowledge about either carrier concentrations or carrier mobilities, this issue has not been fully understood so far. Only such data at room temperatures are $n=1.5\times10^{26}/m^3$, $\mu=3.6\times10^{-3}m^2/V/s$ for 80Si-20Ge-0.2B, and $n=7.7\times10^{25}/m^3$, $\mu=6.5\times10^{-3}m^2/V/s$ for 80Si-20Ge-0.3P, respectively.

Referring to the report by J.P.Dismukes[17], the above mobility values for both materials may be rather small compared with carrier numbers.

Concerning the GaP added n-type specimens, it is likely to be sure that the resitivity decreases with increasing GaP concentrations as shown in Fig.13. The resistivity reduction reaches 70% in the intermediate temperatures, but becomes small over 600℃, and reaches no difference at last 800℃.

To understand electrical properties of our SiGe specimens better, especially of GaP added materials, it should be absolutely required for us to conduct high temperature annealing and subsequent measurement of carrier numbers as well as mobilities.

3.3 Figure of Merit

The figure of merit for some selected specimens are shown in Fig.14. For both p- and n-type materials, these properties so far are not competitive to those obtained by many preceding works[18-20]. More efforts will be required for us to improve our materials through optimization of electrical and grain structures. Finer control of the manufacturing conditions including heat treatments particularly for n-type GaP added materials will be also inevitable.

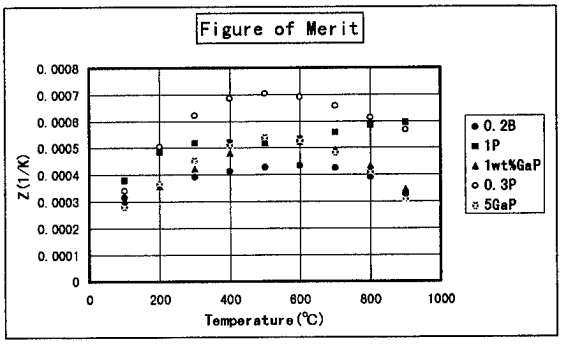


Fig. 14 Figure of merit for 80Si-20Ge alloys

4. Reduction of Resistivity at p/n Junctions

To reduce resitivities around p/n junctions of our monolithically sintered SiGe elements, addition of metal has powders into the boundary region of p- and n-type materials been tried. In molding p- and n-type materials, mixed powders of SiGe with a metal powder such as Ni, Mo, and etc. was interleaved between both materials. A result obtained for specimens using Ni powder is shown in Fig.15. Small addition of metal powder makes the boundary resistivities reduce drastically.

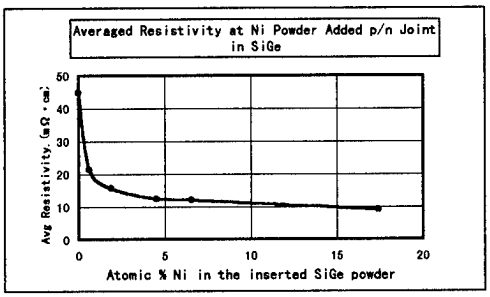


Fig. 15 Reduction of resistivity at p/n boundary by Ni powder addition

5. Power Generation Test by using Monolithic SiGe Element

A preliminary test of the power generation was made for our SiGe monolithic elements. Three kind of power generation modules as shown in Fig.16 were prepared. Each module were connected to variable load resisters, and their hot ends were heated by an infra-red lamp. The output voltages across the load resister and the output currents were measured.

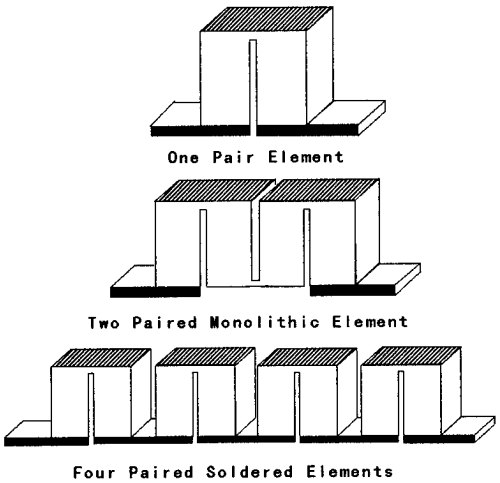


Fig. 16 Module for power generation test

The maximum out put power for each module is plotted in Fig.17, in which the power was normalized as per one pair element. There is no difference between the one pair element and the soldered four pair one, while the two pair monolithic one seems to generate less power. This is simply because the two pair monolith had no electrical shunt at the low temperature end. Consequently three test modules performed identically.

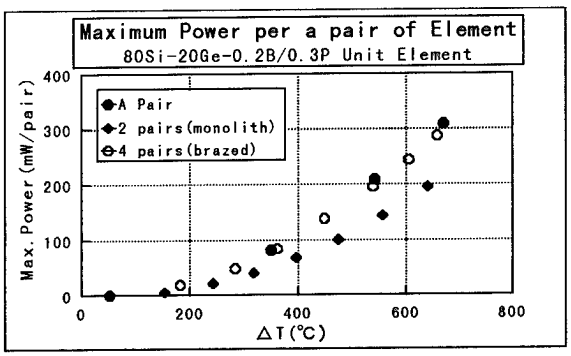


Fig. 17 Result of power generation test

Conclusion

Spark-Plasma-Sintering as one of new sintering technique was described together with its application to development of SiGe thermoelectric alloys. The technique has advantages to make it possible to synthesize materials with difficulty to sinter by other techniques in a short time. However, it may have disadvantage not to adopt easily scaling laws of manufacturing because the sintering process must be conducted under non thermal equilibrium.

In our experiences using SPS, sintering of SiGe alloys with various doping were successfully synthesized in a very short time sintering of about 1minutes. The monolithic elements having p/n SiGe junctions were also manufactured. Even in such a short time sintering, grain growth could not be avoided due to very fast diffusion in the process. As a result, thermoelectric properties of the SiGe alloy with various doping have not been so far fully competitive with preceding works conducted by using hot-press technology. More efforts to avoid the grain growth, and to understand performances of carriers better are required for us to enhance thermoelectric properties. Scaling up with finer control of manufacturing conditions is also needed to establish the reliable and inexpensive process.

Acknowledgment

The author is much indebted to Messrs. T. Mochimaru, T. Takahashi, T. Masuda, and J. Nitta for their cooperation in this work. Sincere thanks are expressed for Dr. I .A. Nishida and Dr. K. Shinohara for their help in Hall measurements.

A part of this work was performed through Special Coordination Funds for promoting Science and Technology Agency of the Japanese Government.

References

[1]B.A. Cook et al: Proc. Int. Soc. Energy Conv. Eng. Conf., 2, 24,1987

[2]Y.S. Kang et al: Preprint at Int. Symp. Functionally Graded Materials, Tsukuba, 1996 (FGM96)

[3]K. Tshuno et al: Proc. 12th Int. Conf. Thermoelectrics, Yokohama,1993 (ICT93)

[4]T. Mochimaru et al: Proc. ICT93

[5]T. Noguchi et al: Preprint at FGM96

[6]R.W. Bunce et al: J. Phys. D:Appl.Phys.,10,1977

[7]C. Vining et al: Proc.10th ICT91,1991

[8]D.M. Rowe: Proc. 4th Int. Conf. Thermoelectrics,1982

[9]S. Sugihara et al: Proc. ICT93

[10]M. Tokita: J. Soc. Powder Tech., Japan, 11, 30, 1993

[11]T.Noguchi et al: Preprint at Proc. FGM96

[12]J.P. Dismukes et al: J. Appl. Phys. 35, 1964

[13]C.M. Bhandari et al : Proc. 2nd ICTEC, 1978

[14]S.L. Draper: NASA Tech. Memo. 100164, Oct.,1987

[15]C. Vining et al: Proc.10th ICT.1991

[16]J.P. Dismukes et al: J. Appl.Phys. 35, 1964

[17]J.P. Dismukes et al: Ditto

[18]C. Vining et al: Ditto

[19]S.L. Draper et al: Int. Soc. Energy. Conv. Eng. Conf., 2, 24, 1989

[20]J.P. Fleurial et al: ICT93

Microstructure and thermoelectric properties of arc-melted silicon borides

Lidong Chen, Takashi Goto, Jianhui Li, Eiji Aoyagi and Toshio Hirai
Institute for Materials Research, Tohoku University, 2-1-1 Katahira, Aoba-ku, Sendai 980-77, Japan
Tel.: +81-22-215-2106, Fax: +81-22-215-2107, E-mail: cld@imr.tohoku.ac.jp

Abstract

Silicon borides in a boron content range of 80 to 94mol% were prepared by arc-melting. As-melted specimens consisted of SiB_n (hexagonal, n=14–49) and free silicon. The free silicon content decreased with increasing boron content in raw materials. The arc-melted specimens were annealed in an argon atmosphere at 1663K. By annealing for 1.8ks, SiB_4 phase formed at the Si-SiB_n boundary. By annealing for more than 5.4ks, SiB_6 phase formed and SiB_4 phase disappeared. SiB_n content increased with increasing annealing time. The annealing for 5.4ks caused a great increase of the Seebeck coefficient.

Introduction

The efficiency of thermoelectric power generation is in proportion to hot junction temperature and the temperature difference between hot- and cold-junctions [1]. Boron-rich silicon borides are one of the candidate materials for thermoelectric conversion because of their moderate Seebeck coefficient (α) and small thermal conductivity (κ) at high temperatures more than 1000K [1, 2-4]. In the Si-B binary system, there are many types of compounds such as SiB_4 (rhombohedral), SiB_6 (orthorhombic) and SiB_n (hexagonal, n=14-49) [5-7]. Among them, SiB_4 has a low thermal conductivity (κ) and high electrical conductivity (σ) but a low Seebeck coefficient (α) [8]. On the other hand, SiB_6 and SiB_n have a large Seebeck coefficient and a low thermal conductivity but a moderately low electrical conductivity.

The authors have reported the thermoelectric properties of arc-melted silicon borides [9]. As-melted silicon borides in the boron content range from 80 to 94mol% consisted of SiB_n and free silicon, in which the free silicon dispersed in a network structure when boron content is less than 90mol%. The free silicon caused the increase of both electrical conductivity and thermal conductivity, but did not increase the thermoelectric figure of merits ($Z=\alpha^2\sigma/\kappa$). By our previous work, proper annealing at 1663K for 1.8ks caused the formation of SiB_4 at the Si-SiB_n boundary and the increase of electrical conductivity and decrease of thermal conductivity without changing the Seebeck coefficient. At the present work, in order to increase Seebeck coefficient, we have carried out annealing for longer time. In this paper, we report the microstructure changes after annealing and their effects on the thermoelectric properties.

Experimental

The mixtures of silicon and boron powders in a boron content range from 80 to 94mol% were pressed into disk-shaped pellets (10 mm thickness and 20 mm diameter) and then arc-melted in an argon atmosphere. The arc-melted samples were then annealed in an argon atmosphere at temperature of 1663K. The phase composition of the resulted specimens was identified by X-ray diffraction (XRD). Rod-like pieces (3x3x15mm) and disk-shaped pieces (2mm thickness and 10mm diameter) were cut out for the electrical conductivity measurement and the thermal conductivity measurement, respectively. Microstructure was observed by transmission electron microscopy (TEM) (JEOL: JEM-1250ARM). Electrical conductivity was measured by using a dc four-probe method. Thermal conductivity was measured by using a laser-flash technique. All the measurements were performed in the temperature range between 300 to 1200 K.

Results and discussion

Specimens containing 80 to 94mol% boron were prepared by arc-melting. By the X-ray diffraction result, all the as-melted specimens consisted of SiB_n and free silicon. The content of free silicon decreased from about 30 to 3vol% as the boron content in raw materials increased from 80 to 94mol%. We reported that the free silicon phase inter-connected to form a network structure when B=80 to 90mol%, while it dispersed isolatedly when B>90mol% [9].

Figure 1 shows the changes of X-ray diffraction pattern of the sample containing 94mol% boron before and after annealing at 1663K for various time. After annealing at 1663K for 5.4ks, the free silicon content decreased and the SiB_n content increased accompanied with SiB_6 phase appearing. The X-ray diffraction pattern of the specimen annealed for 19.8ks was not so different from that for 5.4ks, suggesting that the phase composition has come to not change when the annealing time is over 5.4ks.

0-7803-4057-4/97 $10.00 ©1997 IEEE

Figure 2 (a) and (b) show the TEM microstructures of the SiB_n phase in the specimens annealed for 5.4ks and 19.8ks, respectively. The observed area was SiB_n phase and the electron beam direction is parallel to the crystal orientation of [001]. In the sample annealed for 5.4ks (Fig.2(a)), highly dense stacking faults of about 50nm in width and strong strain contrast were observed. However, in the sample annealed for 19.8ks (Fig.2(b)), the numbers of stacking faults decreased significantly. The size of stacking faults have grown into about 200 to 300nm in width, and the strain contrasts disappeared.

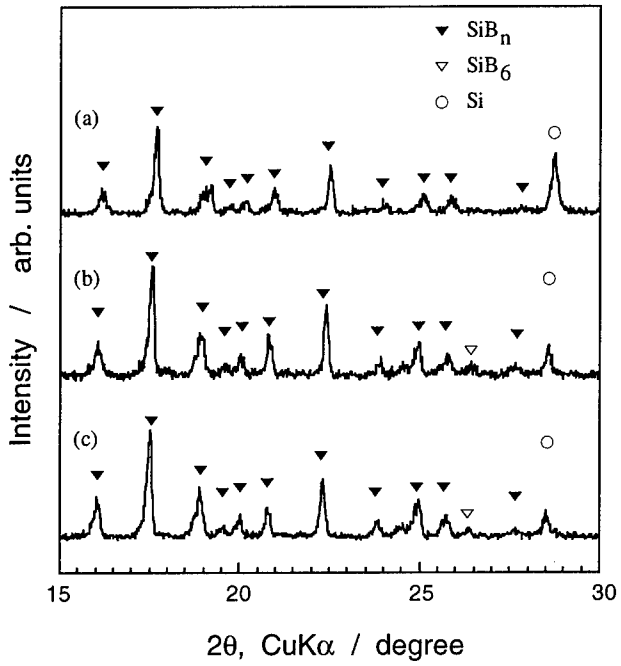


Figure 1. X-ray diffraction patterns of arc-melted silicon boride containing 94mol%B. (a) As-melted; (b) annealed at 1663K for 5.4ks; (c) annealed at 1663K for 19.8ks.

Figure 3 shows the temperature dependence of Seebeck coefficients (α) of arc-melted silicon borides. The α values increased with increasing temperature. The larger the boron contents, the greater the α values. Figure 4 shows the Seebeck coefficient changes of the specimen containing 94mol% boron after annealing. The α values increased when the annealing time was 5.4ks, but decreased when the annealing time was 19.8ks. The changes of Seebeck coefficients of other samples containing various boron contents showed the same tendency; the samples annealed for 5.4ks have the greatest Seebeck coefficients.

Although the samples annealed for 5.4ks and 19.8ks have almost the same phase composition, highly dense stacking faults with strong strain contrasts were observed only in the samples annealed for 5.4ks. The large Seebeck coefficient of these samples may be associated with those stacking faults [10-11].

The electrical conductivity (σ) increased with increasing temperature. The larger the free silicon content, the greater the σ values. Figure 5 shows the changes of electrical conductivity of arc-melted silicon boride containing 94mol% boron before and after annealing. The annealed sample showed smaller σ values than the as-melted sample, but the samples annealed for 5.4ks and 19.8ks have almost the same σ values. This is because the free silicon content decreased after annealing and the phase composition was almost the same for the different annealing time.

The thermal conductivity (κ) decreased with increasing

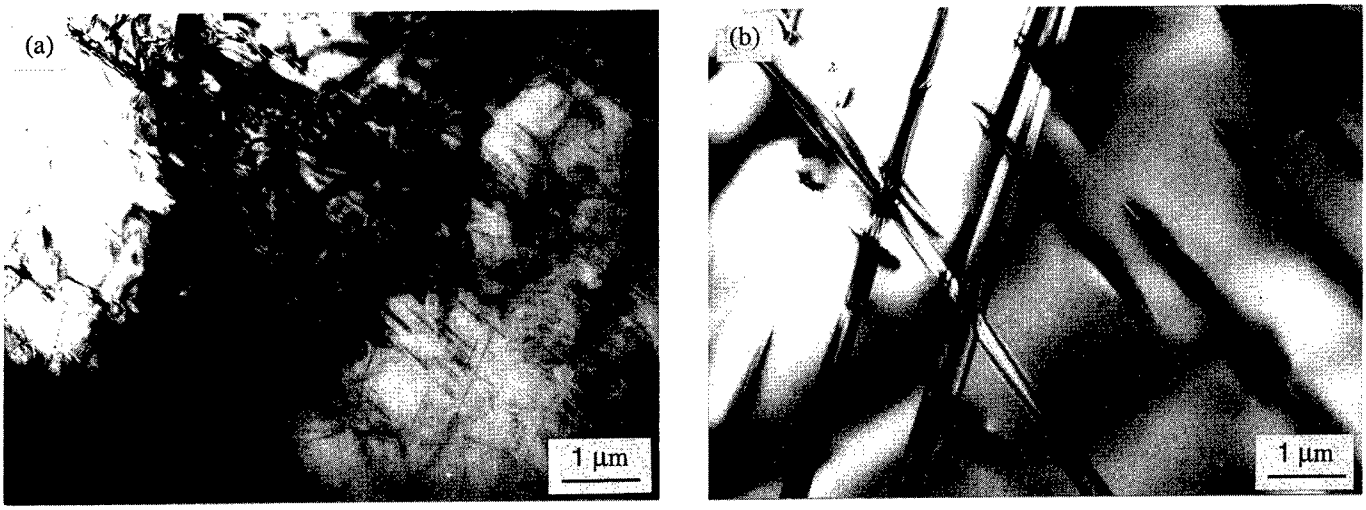


Figure 2. TEM photos of arc-melted silicon boride containing 94mol%B. (a) Annealed at 1663K for 5.4ks; (b) annealed at 1663K for 19.8ks.

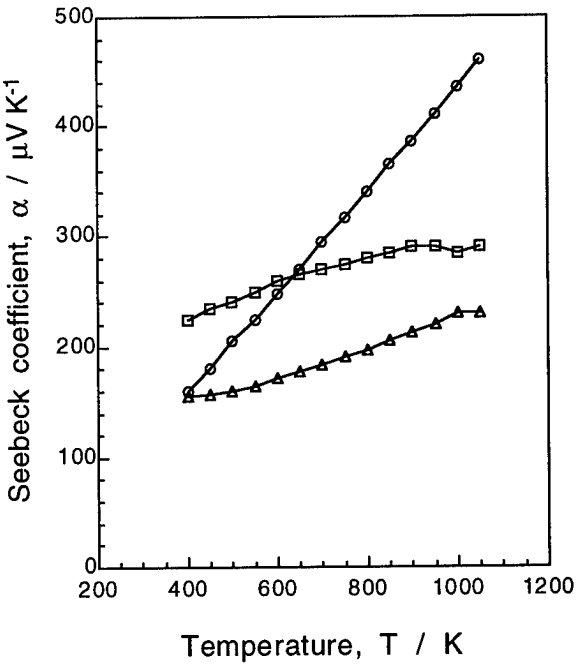


Figure 3. Temperature dependence of Seebeck coefficients of arc-melted silicon borides. (△) 80mol%B; (□) 86mol%B; (○)94mol%B.

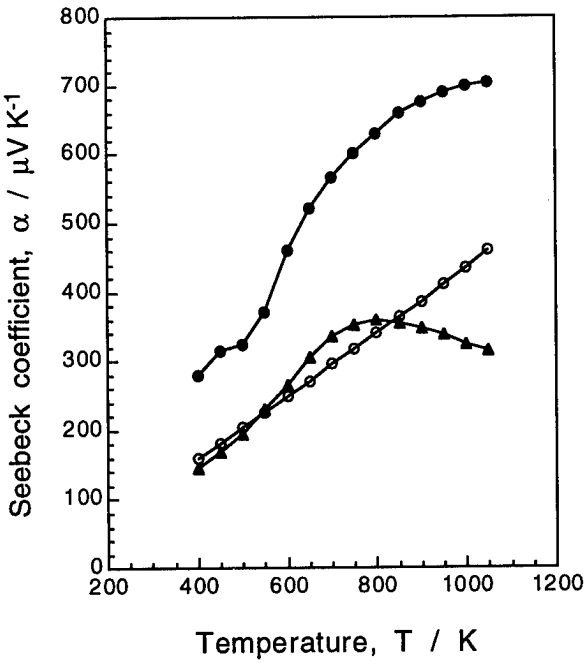


Figure 4. Seebeck coefficient changes of the arc-melted silicon boride containing 94mol%B after annealing. (○) As-melted; (●) annealed at 1663K for 5.4ks; (▲) annealed at 1663K for 19.8ks.

temperature. The larger the free silicon content, the greater the κ values. Figure 6 shows the changes of thermal conductivity of arc-melted silicon boride containing 94mol% boron before and after annealing. The annealed sample showed smaller κ values than the as-melted sample. This is caused by the decrease of free silicon content after annealing.

Figure 7 summarizes the dimensionless figure of merit ($ZT=\sigma\alpha^2T/\kappa$) values of the samples containing 86 and 94mol% boron. The ZT values increased with increasing temperature. The samples annealed for 5.4ks showed greater ZT values than the as-melted samples, but the samples annealed for 19.8ks showed smaller ZT values than the as-melted samples. The sample containing 86mol% boron annealed for 5.4ks showed the highest ZT value of about 0.2 at 1100K.

Conclusion

Silicon borides were prepared by arc melting in argon atmosphere using silicon and boron powders in a boron content range from 80 to 94mol%. As-melted specimens consisted of SiB_n and free silicon. The contents of free silicon decreased from 30 to 3vol% as the boron content in raw materials increased from 80 to 94mol%.

As-melted specimens were annealed in an argon atmosphere at temperatures of 1663K. By annealing for

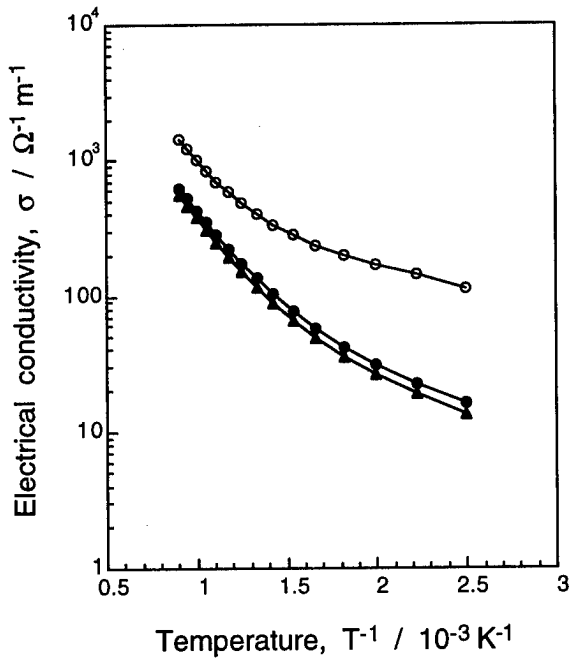


Figure 5. Electrical conductivity changes of the arc-melted silicon boride containing 94mol%B after annealing. (○) As-melted; (●) annealed at 1663K for 5.4ks; (▲) annealed at 1663K for 19.8ks.

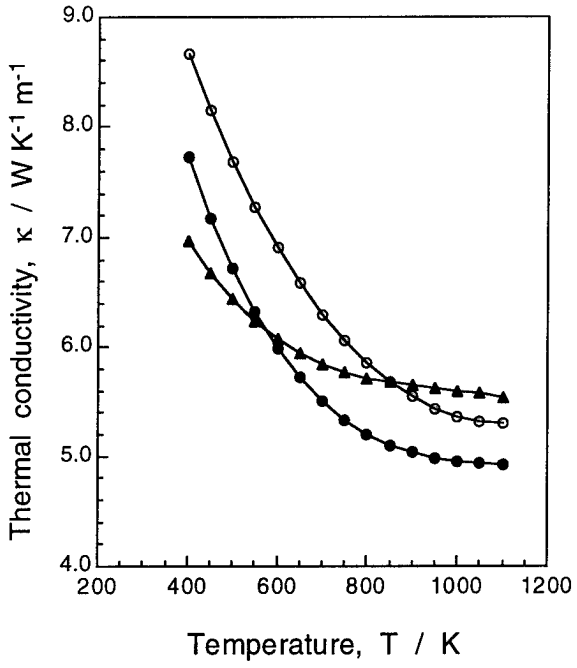


Figure 6. Thermal conductivity changes of the arc-melted silicon boride containing 94mol%B after annealing. (○) As-melted; (●) annealed at 1663K for 5.4ks; (▲) annealed at 1663K for 19.8ks.

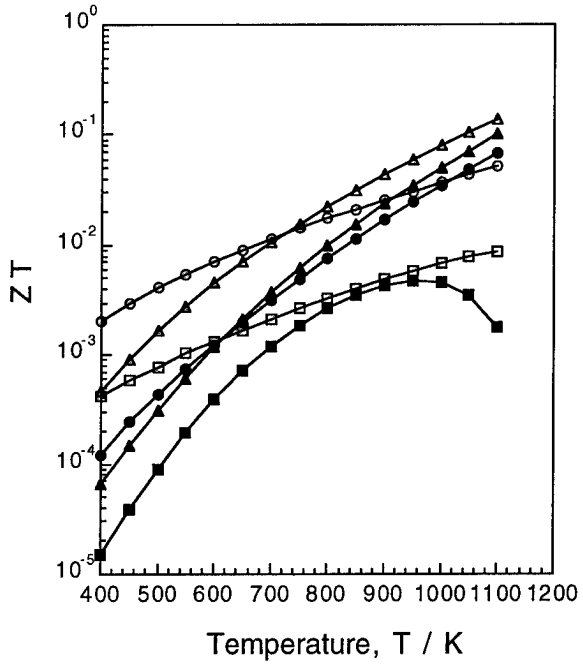


Figure 7. ZT values of the arc-melted silicon boride. (○, ●) As-melted; (△, ▲) annealed at 1663K for 5.4ks; (□, ■) annealed at 1663K for 19.8ks. White marks: 86mol%B; black marks: 94mol%B.

more than 5.4ks, a trace amount of SiB_6 phase formed and SiB_n content increased. In the samples annealed for 5.4ks, highly dense stacking faults and strain contrast were observed. The annealing for 5.4ks caused a great increase of Seebeck coefficient. This may be resulted from the highly dense stacking faults in the SiB_n phase. The dimensionless figure of merit (ZT) was increased significantly by an appropriate annealing.

Acknowledgements

We thank Mr. Y. Hayasaka of IMR, Tohoku University for helping TEM observation. This research was supported in part by the Grant-in-Aid for Scientific Research from the Ministry of Education, Science and Culture, under contact nos. NP0701 and 06453081, also supported by the Special Coordination Funds for Promoting Science and Technology from the Science and Technology Agency of Japan.

Reference

[1] C. Wood, Materials Research Society Symposia Proceedings, Vol 97, Ed. by D. Emin, T. L. Aselage and C. Wood (Materials Research Society, Pittsburgh, 1987), p.335.

[2] C. Wood, D. Emin, R. S. Frigelson and I. D. R. Mackinnon, Materials Research Society Symposia Proceedings, Vol 97, Ed. by D. Emin, T. L. Aselage and C. Wood (Materials Research Society, Pittsburgh, 1987), p.33.

[3] B. Armas and C. Combescure, J. Less-Common Met., 47 (1976) 135.

[4] J. M. Darolles, T. Lepetre and J. M. Dusseau, Phys. Stat. Sol. (a), 58 (1980) K71.

[5] R. W. Olesinski and G. J. Abbaschian, Bull. Alloy Phase Diagrams, 5 (1984) 478.

[6] B. Armas, G. Male and D. Salanoubat, J. Less-Common Met., 82 (1981) 245.

[7] H. F. Rizzo, B. C. Weber and M. A. Schwarz, J. Amer. Ceram. Soc., 43 (1960) 497.

[8] M. Mukaida, T. Goto and T. Hirai, Mater. & Manufacturing Processes, 7 (1992) 625.

[9] L. Chen, T. Goto, J. Li, M. Niino and T. Hirai, Trans. IEE Jpn, 116-A (1996) 248.

[10] L. W. Whitlow and T. Hirano, Proc. 12th Inter. Conf. Thermoelectrics, Ed. by K. Matsuura (IEEJ, Tokyo, 1994), p.39.

[11] T. L. Aselage, D. Emin, C. Wood, I. D. R. Mackinnon and I. Howard, Materials Research Society Symposia Proceedings, Vol 97, Ed. by D. Emin, T. L. Aselage and C. Wood (Materials Research Society, Pittsburgh, 1987), p.27.

Electronic transport in p-type and n-type β-rhombohedral boron

R. Schmechel [a]), H. Werheit [a]), V. Kueffel [a]) and T. Lundström [b])

[a]) Solid State Physics Laboratory, Gerhard Mercator University Duisburg, D 47048 Duisburg, Germany
[b]) Institute of Chemistry, Uppsala University, S 75121 Uppsala, Sweden

Abstract

Controlled doping is required for the promising thermoelectric application of boron-rich solids. β-rhombohedral boron, which is p-type in pure form, can be made n-type by interstitial doping with V, Cr, Fe and Ni, while it remains p-type in the case of Cu and Co doping. Seebeck coefficient, dc electrical conductivity, dynamical conductivity and optical absorption of B:V, B:Fe and B:Co are presented. Irrespective of the carrier type, in all these cases the electronic transport can be described by a superposition of Drude-type and hopping type conduction. Doping to n-type requires the overcompensation of the unoccupied valence and gap states in pure boron by a doping level positioned between conduction band and uppermost intrinsic electron trap. While Fe atoms occupy the suitable interstitial sites statistically, V atoms prefer the A site at lower and preferably occupy D sites at higher metal contents. Irrespective of the lower ionisation energy of the V atoms compared with Fe, the doping efficiency of V is much higher and differs qualitatively from that of Fe.

Introduction

Boron-rich solids are interesting materials for thermoelectric applications, due to a high thermoelectrical force even at high temperatures [1]. The high Seebeck coefficient is typical for semiconductors, whereas a high density of localized states in the band gap prevent the decrease of the Seebeck coefficient at high temperatures. Doping of boron carbide by Si [2] or Al [3] increases the Seebeck coefficient, which demonstrate the important role of doping for a controlled change of the thermoelectrical properties. But a transition from the normally p-type boron carbide to n-type by doping has not yet been realized. Pure p-type β-rhombohedral boron becomes n-type by interstitial doping with the transition metals Fe, V, Cr, Ni [4, 5, 6], whereas it remains p-type for other transition metals like Cu [4] or Co (this work). Doping with the group IV element carbon acting as donor increases the conductivity [7], but does not change the p-type behaviour.

The electronic properties of boron rich solids are mainly related to B_{12} icosahedra, which are essential structural elements in the most boron rich solids. The semiconductor character of icosahedral boron-rich solids is explained by the Jahn-Teller effect distorting the icosahedra and splitting the valence band. The upper split-off band consisting of localized states acts as intrinsic acceptor level [8, 9]. This explains the p-type character of all pure icosahedral boron rich solids. Unfortunately, the complex structure of β-rhombohedral boron (structure formula $(B_{12})_4(B_{28})_2B$) has prevented reliable band structure calculations. The actual energy band scheme of pure β-rhombohedral boron is based on numerous optical, electrical and thermal experiments [10], which are consistent with the split-off valence band model. The split-off energy is about 180 meV; the band gaps of 1.29 and 1.46 eV respectively are indirect allowed. Off the conduction band a series of intrinsic trap states was found. While the energy band structure remains largely unchanged by doping, a transition from p- to n-type occurs, if all the gap states are filled up by electrons. In the case of B:Fe was shown that six electrons per unit cell are required [11]. However, doping with vanadium for example seems to change the electronic structure [12], since the transition to n-type conduction cannot be explained within that energy band scheme.

The charge transport in pure and doped β-rhombohedral boron is not yet understood in detail, but a superposition of hopping conduction between localized states in the band gap and band conduction of free carriers more or less influenced by retrapping processes is evident. In this work, Seebeck coefficient measurements on B:V, B:Co and B:C, dc conductivity of B:V and infrared spectra of B:V, B:Co and B:Fe are presented and discussed with respect to possible transport mechanisms.

Sample material

The metal-doped β- rhombohedral boron samples were obtained by arc-melting lumps of zone-melted boron (Wacker-Chemie, Munich, purity better than 99.99%), with vanadium (Material Research Co., USA, purity better than 99.95%) and Co (Johnson and Mattey Co., England, purity better than 99.99%) respectively. Afterwards the samples were heat treated typically for 48 hours at 1200 °C to guarantee homogeneity. The iron-doped sample is the same as that in [6, 11] and the carbon doped samples are the same as those in [7].

The samples are single-phase, only VB_{32} and VB_{43} contain traces of VB_2, and CoB_{49} and CoB_{66} contain traces of CoB. Crystallographic investigations suggest the solubility limit for B:V to be 1.6 at.% V and for B:Co to be 1.4 at.% Co, but the optical and electrical properties presented below don't show saturation even at high metal concentration.

Experimental details

The Seebeck-coefficient of B:V was measured from 150K to 700K in a vacuum cryostat. The temperature gradient in the sample was produced by a small electrical heater and controlled by thermocouples simultaneously acting as probes for the voltage measurements. Temperature differences of about 1 K were used. The very small size of the available samples (few mm) caused a quantitative error of the measured Seebeck coefficient, while the temperature dependence was hardly impaired. Quantitatively reliable Seebeck coefficients were obtained close to 300 K with a hot-spot method yielding

the average Seebeck coefficient for the used temperature diffenrence of 100K. The correction in Fig. 3 (right ordinate) is performed according to these results.

The conductivity of B:V was measured by the four-probe method according to van der Pau [13]between 100 to 700K. Platinum wire probes were attached by an electrical capacitor discharge.

The reflectivity spectra of B:V, B:Co and B:Fe were measured with a FTIR spectrometer IFS113v (Bruker, Karlsruhe) in the spectral range between 10 and 5000 cm^{-1} at temperatures between 77 and 450K. For low noise levels a lHe-cooled Si-Bolometer was used in the FIR-range, and a lN_2-cooled MCT detector for the MIR range.

From the measured reflectivity spectra the absorption coefficient and the complex dielectric function were numerically calculated by Kramers Kronig transformation using the Hagen-Rubens relation for extrapolation to zero frequency.

Results

DC conductivity of B:V

The dc conductivity results of B:V are presented in Figure 1. While for pure boron the measured conductivity agrees with the results known from literature (see [14]), the results for B:V are about ten times smaller compared with those reported by Slack et al. [4] and Matsuda et al. [15]. Probably sample inhomogeneities or VB_2 precipitation are the reason. The temperature dependence of the conductivity is typical for metal-doped β-rhombohedral boron [4, 15, 16] and meets Mott's law of variable range hopping [17]:

$$\sigma \propto 1/\sqrt{T} \cdot \exp\left(\left(T_0/T\right)^{1/4}\right)$$

in a large temperature range, as demonstrated for VB_{32} in the insert of Figure 1. The deviation above 500K are attributed to thermally excited free carriers in the conduction band. The fit parameters T_0 and the activation energies ε of the high temperature range are listed in Table 1.

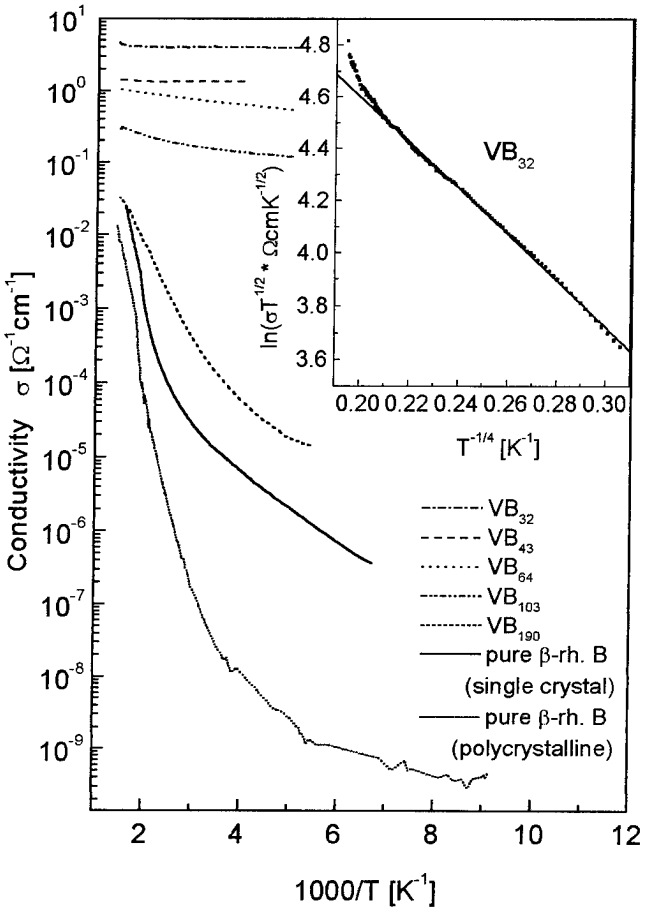


Figure 1: dc conductivity of B:V and pure boron vs. reciprocal temperature. The insert shows the conductivity of VB_{32} plotted according to Mott's law of variable range hopping (straight line).

Seebeck effect measurements

Figure 2 presents the measured Seebeck coefficient at room temperature compared with values taken from literature. For B:Fe the transition from p-type to n-type occurs at 2.5 at. % Fe corresponding to six additional electrons per unit cell [11]. They originate from Fe^{2+} and Fe^{3+} ions and agree with the number of unoccupied valence and gap states in pure boron. In contrast, for B:V only 0.25 at % V is required for the p to n transition. Related to the number of Fe atoms, this would correspond to an unrealistic ionization to V^{24+} and proves therefore that in contrast to Fe the insertion of V atoms causes a considerable change of the electronic band structure of β-rhombohedral boron.

As a typical example for B:V, VB_{190} excepted, Figure 3 shows the temperature dependence of the Seebeck coefficient of VB_{32}. Below 450 K the Seebeck coefficient can be well fitted by Mott's formula for variable range hopping [17]:

$$S \propto \sqrt{T},$$

whereas above 450K a linear behavior occurs which is typical for metals according to:

Table 1: Model parameter T_0 of Mott's variable range hopping model and activation energy ε describing the thermal activated conductivity above 500K of B:V and pure boron

Sample	T_0 [K]	ε [meV]
β-rh. B (polycrystalline)	$5.1(4)\cdot10^9$	625 (3)
β-rh. B (single crystal)	$8.7(6)\cdot10^7$	630 (3)
VB_{190}	$2.9(2)\cdot10^8$	260 (3)
VB_{103}	$1.6(1)\cdot10^5$	56 (4)
VB_{64}	$1.0(1)\cdot10^5$	20 (3)
VB_{43}	$6.1(4)\cdot10^3$	17 (3)
VB_{32}	$6.0(4)\cdot10^3$	22 (3)

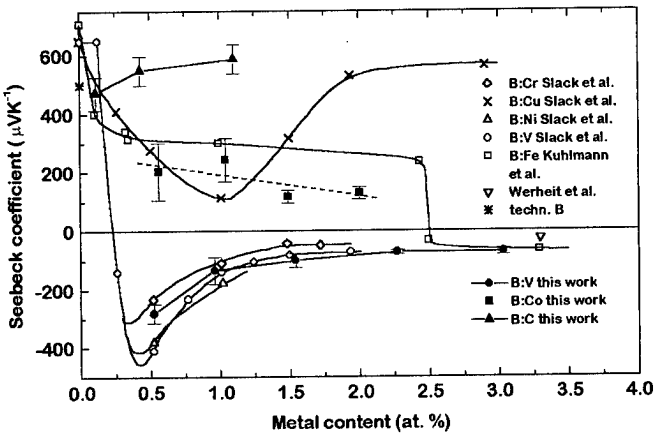


Figure 2: Seebeck coefficient of β-rhombohedral boron with different dopants at room temperature (Werheit et al. [4]; Slack et al. [5]; Kuhlmann et al. [11]; technical B [14].

$$S = \frac{\pi^2}{2}\frac{k_B}{e}\frac{k_B T}{E_F} .$$

At lower temperatures a satisfactory fit of the experimental data is also possible with the theory on the thermoelectric power of a semiconductor near the Anderson transition [17]:

$$S = \frac{k_B}{e}\left\{\frac{\varepsilon}{k_B T} + \left(1+\exp\frac{\varepsilon}{k_B T}\right)\ln\left(1+\exp\frac{-\varepsilon}{k_B T}\right)\right\}$$

when the only fit parameter of the equation ε, describing the distance between Fermi energy and the conduction band edge is taken from Table 1. Up to 300K the Seebeck coefficient of VB_{190} has qualitative the same behavior like that of the other B:V compounds. But above 300K the Seebeck coefficient of VB_{190} decreases with increasing temperature according to the typical semiconductor behavior.

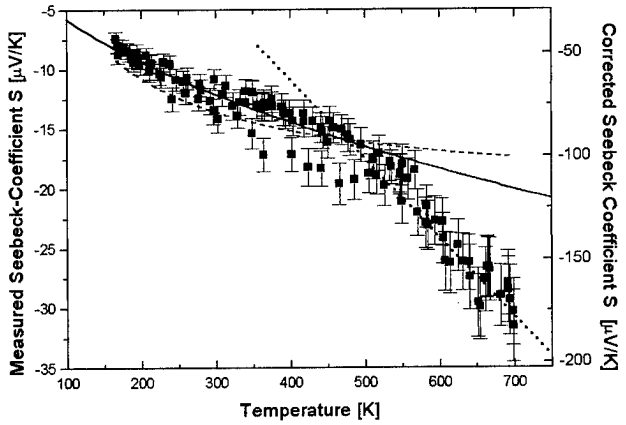


Figure 3: Seebeck coefficient of VB_{32} vs. temperature. Solid line, Mott's formula for variable range hopping; dashed line, theoretical behavior near Anderson transition; dotted line: metallic behavior. Left ordinate, measured values; right ordinate, correction according to room temperature data (see text).

B:Co remains p-type within the range of investigated Co content. Because of the usually much lower ionisation of Co compared with Fe atoms in crystals, a transition to n-type may require Co contents that exceed the solubility limit.

FIR spectra and complex dielectric function

The FIR reflectivity ($\nu \leq 150\ cm^{-1}$) of metal-doped β-rhombohedral boron rapidly increases towards lower frequencies. This behavior is due to the dynamical conductivity and obviously correlated to the quantity of the dc conductivity of the particular samples. To obtain information on the charge transport mechanisms from the spectra, the complex dielectric function was calculated by a Kramers-Kronig analysis and fitted by using different transport models. Reliable results require simultaneous fits to both ε_r and ε_i. For details and numerous examples see [18]. For boron-rich solids in general, satisfactory fits were only possible, when a superposition of Drude-like and hopping-type transport was assumed. As an example, an improved fit to the spectrum of VB_{32} is shown in Fig. 4.

The classical Drude theory was used for the contribution of band-type carriers. For the hopping part the model of Butcher and Morys [19] was used. It is the ac analogon to dc variable-range range hopping, and is based on tunneling of electrons between localized states. According to Dyre [20] this theory is largely independent of the specific relaxation process and therefore at least approximately applicable for boron as well (for detailed discussion see [18]). Of course, this general model does not allow conclusions on specific details of the kind of hopping. Resonant absorption due to carriers between localized states are excluded, since the thermal energy is greater than the photon energy.

From fits like in Figure 4 the density of free carriers was derived as the square root of the plasma frequency of the Drude part, and the density of pairs, between which hopping takes place, results from the hopping part. The obtained results are shown in Figure 5.

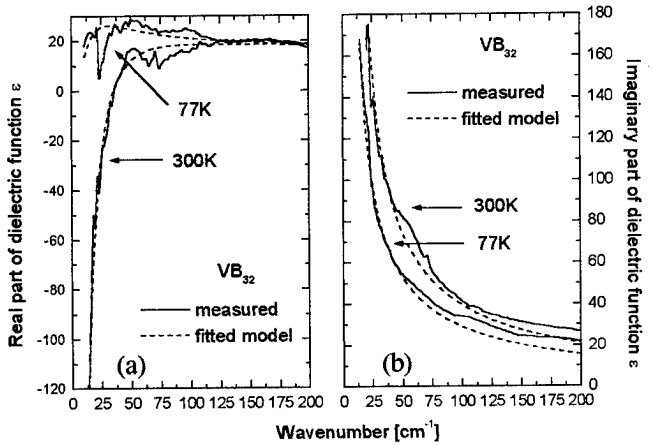


Figure 4: ε_r (a) and ε_i (b) of VB_{32} at different temperatures. Solid lines, experimental; dotted lines, fit by superposition of free carrier-type and hopping-type transport (see text).

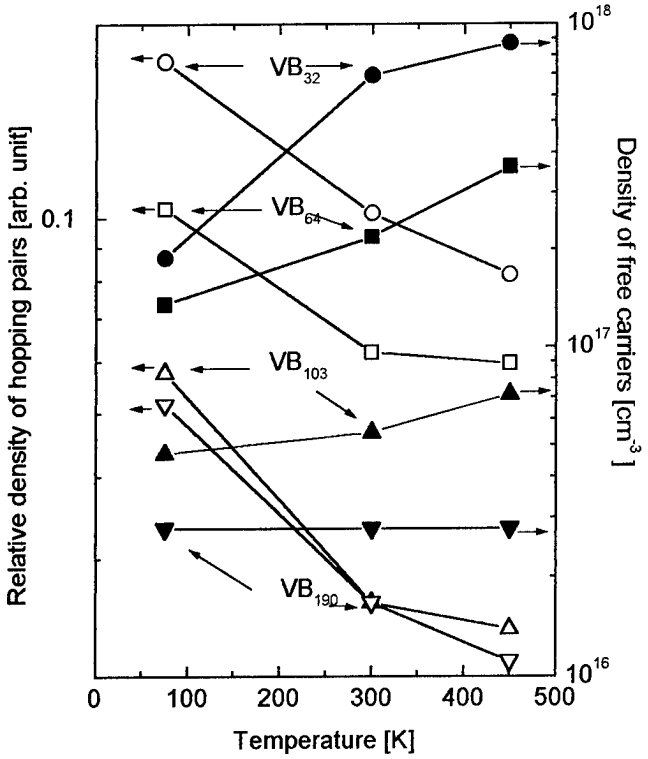


Figure 5: Density of hopping pairs (left ordinate) and density of Drude-type free carriers (right ordinate) of VB_x vs. temperature.

Both densities increase with increasing metal concentration. But, while the density of free carriers increases with temperature, the density of hopping pairs decreases. This is consistent with the observed dc transport, where the hopping processes decrease towards higher temperature, while free carriers becomes prevailing.

The model of hopping-like transport by Pistoulet et al. [21] is based on potential fluctuation in the conduction or valence band. Unfortunately it cannot be applied to boron, because it does not hold for thermal energies comparable or greater than the potential fluctuation like in the case of all measurements presented in this paper.

MIR absorption spectra

Examples of the MIR absorption spectra of B:V, B:Co and B:Fe, which were calculated from the measured reflectivity by Kramers Kronig transformation, are shown in Figure 6. The structures in the range < 0.1 eV are due to phonons, while the broad absorption processes are due to electronic transitions from deep localized gap states into extended band states. The absorption of n-type $FeB_{29.5}$ is not much higher than that of p-type CoB_{49}. Obviously, the slightly higher occupation of localized gap states in $FeB_{29.5}$ is sufficient for the n-type character. Besides of the considerably higher absorption, the spectrum of VB_{32} is qualitatively different, because the absorption starts at much lower energies. A quantitative analysis of the spectrum yields about 50 meV as distance between Fermi level and conduction band edge. This value

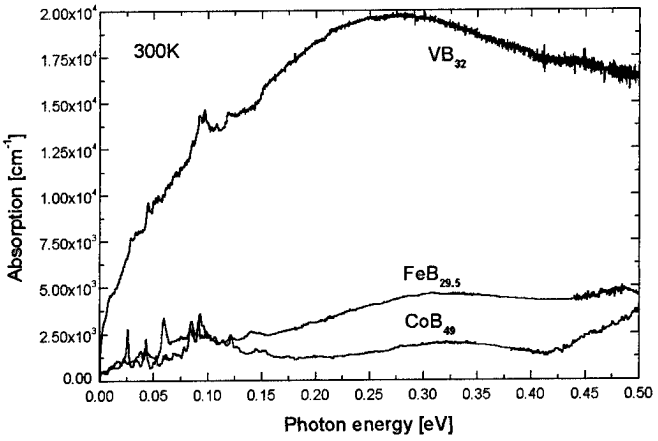


Figure 6: MIR absorption spectra of VB_{32}, $FeB_{29.5}$ and CoB_{49} at 300K

roughly agrees with the thermal activation energy of the electrical conductivity (Table 1). Obviously the uppermost electronic level of interstitially accommodated vanadium in β-rhombohedral boron is well above the electron trap with the lowest ionization energy of 0.188 eV.

Conclusion

The interpretation of dc conductivity, dynamical conductivity and Seebeck effect of B:V requires the assumption of a superposition of free-carrier and of hopping-type transport. Doping of p-type β-rhombohedral boron to n-type is possible by the interstitial accommodation of specific metal atoms, whose doping level must be above the electron trapping levels.

In contrast to Fe, interstitial V atoms considerably modify the band structure of β-rhombohedral boron. Therefore, the efficiency of its electron transfer to the boron structure is much higher.

Up to 700K, the limit of the present investigations, the Seebeck coefficient of higher-doped B:V increases monotonously with temperature.

References

[1] H. Werheit, „Boron-rich solids: a chance for high-efficiency high-temperature thermoelectric conversion!", Mat. Sci. Eng. B29 (1995) 228.

[2] H. Werheit, U. Kuhlmann, M. Laux, R. Telle, „Solid Solutions of Silicon in Boron-Carbide-Type Crystals", J. Alloys Comp. 209 (1994) 181 and Jap. J. Appl. Phys. Series 10 (1994) 86.

[3] R. Schmechel, H. Werheit, K. Robberding, „IR active phonon spectra of B-C-AL compounds with boron carbide structure", J. Solid State Chem. 133 (1997) (in press)

[4] H. Werheit, K. de Groot, W. Malkemper, T. Lundström, „On n-type β-rhombohedral boron", J. less-common Met. 82 (1981) 163.

[5] G.A. Slack, J.H. Rosolowski, C. Hejna, M. Garbauskas, J.S. Kasper, „Semiconductor Properties of Boron", in Proc. 9th Int. Symp. Boron, Borides and Related

Compounds, University of Duisburg, Germany, Sept. 21 - 25, 1987., ed. H. Werheit, University of Duisburg: Duisburg, 1987 p. 132.

[6] U. Kuhlmann, H. Werheit, T. Dose, T. Lundström, „Influence of Interstitially Soluted Iron on Structural, Optical, and Electrical Properties of β-Rhombohedral Boron", J. Alloys Comp. 186 (1992) 187.

[7] H. Werheit, U. Kuhlmann, M. Laux, T. Lundström, „Structural and Electronic Properties of Carbon-Doped β-Rhombohedral Boron", Phys. stat. sol. (b) 179 (1993) 489.

[8] R. Franz, H. Werheit, „Jahn-Teller Effect of the B_{12} Icosahedron and Its General Influence on the Valence Band Structures of Boron-Rich Solids", Europhys. Lett. 9 (1989) 145.

[9] H. Werheit, „On the Electronic Transport Properties of Boron Carbide", in: The Physics and Chemistry of Carbides, Nitrides and Borides; NATO ASI Series E: Applied Sciences Vol. 185, ed. R. Freer, Kluwer Academic Publishers: Dordrecht, 1990 p. 677.

[10] H. Werheit, M. Laux, U. Kuhlmann, „Interband and Gap State Related Transitions in β-Rhombohedral Boron", phys. stat. sol. (b) 176 (1993) 415.

[11] U. Kuhlmann, H. Werheit, J. Pelloth, W. Keune, T. Lundström, „Ionisation of Interstital Iron Atoms in β-Rhombohedral Boron", Phys. Stat. Sol. b 187 (1995) 43.

[12] H. Werheit, R. Schmechel, V. Kueffel, T. Lundström, „On the Electronic Properties of β-Rhombohedral Boron Interstitially Doped with 3d Transition Metals", J. Alloys and Comp. (1997) (in press)

[13] L. J. van der Pau, Philips Research Reports **13** (1958) 1

[14] H. Werheit, „Boron", in Landolt-Börnstein, New Series, Vol. 17e, (1983), p. 9.

[15] H. Matsuda, N. Tanaka, T. Nakayama, K. Kimura, „Structural- and Electronic-Property Investigations on Metal-Doped β-Rhombohedral Boron, J. Phys. Chem. Solids 57 (1996) 1167.

[16] H. Matsuda, T. Nakayama, K. Kimura, Y. Murakami, H. Suematsu, M. Kobayashi, H. Suematsu, „Structural and Electronic Properties of Li- and Cu-Doped β-Rhombohedral Boron Constructed from Icosahedral and Truncated Icosahedral Clusters, Phys. Rev. B 32 (1995) 6102.

[17] N. F. Mott, E. A. Davis, „Electronic Processes in Non-Crystalline Materials", 2nd Edition, Clarendon Press, Oxford 1979.

[18] R. Schmechel, H. Werheit, „On the Dynamical Conductivity in Icosahedral Boron-Rich Solids", J. Phys.: Condens. Matter 8 (1996) 7263.

[19] P. N. Butcher, P. L. Morys, „Exact Solution of the ac Hopping Conductivity Problem at Low Site Density", J. Phys. C: Solid State Phys. 6 (1973) 2147.

[20] J. C. Dyre, „The Random Free-Energy Barrier Model for ac Conduction in Disordered Solids", J. Appl. Phys. 64 (1988) 2456.

[21] B. Pistoulet, F. M. Roche, S. Abdalla, „AC Band Conductivity in Compensated Semiconductors with Potential Fluctuation", Phys. Rev. B 30 (1984) 5987.

Hopping Carrier Mobilities and Thermoelectric Properties of Oxide Materials with Perovskite-related Structure

Michitaka OHTAKI, Tsutomu TOKUNAGA, Koichi EGUCHI, and Hiromichi ARAI

Department of Materials Science and Technology, Graduate School of Engineering Sciences, Kyushu University
6-1 Kasugakoen, Kasuga-shi, Fukuoka 816 JAPAN
Phone: +81-92-583-7527 Fax: +81-92-573-0342 E-mail: ohtakigz@mbox.nc.kyushu-u.ac.jp

Abstract

Thermoelectric properties of perovskite-type oxides are investigated with particular interests in their hopping carrier mobility. A series of partial substitution for metal cations in $CaMnO_3$, a perovskite-type oxide showing small polaron hopping conduction, reveals that larger substituents for both Ca and Mn sites result in higher carrier mobilities. Consequently, Bi and In attain the largest ZT values for the Ca and Mn site substitutions, respectively. Increase in the hopping intersite distance is suggested as a reason of the enhanced mobilities. As a consequence, the largest substituent for the Mn site, In, gives the highest mobility, and thereby brings about the largest power factor for $Ca(Mn_{0.9}In_{0.1})O_3$. Also benefiting from the fairly low thermal conductivity, the In-substituted sample attains $ZT = 0.16$ at 900 °C.

Introduction

Commercialization of high-temperature thermoelectric power generation in practical use are nowadays more and more required with respect to improvement in the energy conversion efficiency for sustainable energy futures. A new family of high-temperature thermoelectric materials recently developed, skutterudites and filled skutterudites, has proven that the empirical limitation of the conventional materials at $ZT \approx 1$ could really be overcome [1-6]. Whereas the band theories can provide essentially good explanations also for the skutterudite-related compounds, some 'exotic' materials for which the conventional band approximation no longer holds have been pointed out to be also interesting (and maybe prospective) in terms of high temperature thermoelectrics [7,8].

In some solids, hopping movement of the localized electrons (or holes) to the adjacent sites would be a good approximation for the electronic charge transport mechanism, rather than a conventional picture of itinerant electrons. Small polaron hopping is frequently observed for ionic solids such as oxides and halides, and is characterized by thermally activated hopping of a localized electronic carrier accompanied by a spatial displacement of the surrounding lattice atoms induced by the Coulomb interactions between the carrier and the polarized crystal lattice [9]. Because hopping conduction should inherently result in low carrier mobilities (generally ≤ 0.1 - $1.0\ cm^2\ V^{-1}\ s^{-1}$), materials with such conduction mechanisms appear to be hopeless judging from the conventional thermoelectric theories [10]. Nevertheless, some compounds having the hopping conduction mechanisms have been revealed to show prospective thermoelectric performance; they include boron carbide and boron-rich borides, and some transition metal silicides [7,8]. These findings imply that materials showing hopping conduction may deserve to examine, even if their mobilities are much lower than the conventional criteria. Furthermore, studies on the thermoelectric properties of materials with hopping conduction mechanisms have so far been very limited. Experimental investigations on the hopping conduction mechanisms with concerns about the thermoelectric properties would be expected to provide a valuable information to researches for novel thermoelectric materials.

We have already reported that the following oxide materials have some potential for high-temperature thermoelectric applications, also being outstandingly advantageous in high stability against heat: In_2O_3-SnO_2 [11], $(Ca_{1-x}A_x)MnO_3$ [12,13], $(Zn_{1-x}Al_x)O$ [14-16], and $(Zn_{1-x}M_x)O$ (M = Ga, In) [17]. Very recently, some other oxide materials such as $(ZnO)_mIn_2O_3$ [18], $CdIn_2O_4$ [19], and $Nd_{2-x}CeCuO_4$ [20] also appeared in the literature in terms of thermoelectric conversion. It seems to be noteworthy that almost all of these oxides can be classified into oxides with 'high' mobility (or having been developed aiming at them). However, $CaMnO_3$-based perovskite-type oxides appear to be an exception, because they are known to exhibit thermally activated hopping conduction. In the present paper, we have focused on these oxides with particular interests in enhancement of the hopping carrier mobility in order to improve the high-temperature thermoelectric properties of the oxides.

Experimental

Sintered samples of $CaMnO_3$-based oxides were prepared by conventional solid-state reaction from powders of $CaCO_3$, $MnCO_3$, and corresponding single oxides of metal substituents. Properly weighed powders were mixed in a nylon-lined ball mill for 24 h, and calcined at 850 °C for 10 h in air. The resulting mixture was pulverized and pressed into a pellet, and then sintered at 1300 °C for 10 h in air. The relative density of all the sintered pellets were confirmed to be more than 95% by the Archimedes' method. The 4-wire measurement of the electrical conductivity, σ, and the steady-state measurement of the Seebeck coefficient, S, were simultaneously carried out on the same sample bar of *ca.* 5 mm × 3 mm × 15 mm in size. The measurement procedures and an experimental setup have been described in detail elsewhere [11,13]. The Hall measurements were carried out by the van der Pauw method at room temperature applying a magnetic field of 0.8 T. The thermal conductivity, κ, was determined from the specific heat capacity and the thermal diffusivity measured by the laser flash technique.

Results and Discussion

1. System $(Ca_{1-x}A_x)MnO_3$

The Ca sites of $CaMnO_3$, being in 12-fold coordination

and often referred as the A sites of the ABO_3 perovskite structure, were first subjected to partial substitution by various tri- or tetravalent metal cations. The oxide $CaMnO_3$ with no substitution was an n-type semiconductor with rather low σ of *ca.* 10^{-1} S cm^{-1} at room temperature. The substitution of the higher valence cations for the Ca sites resulted in a significant increase in σ. Moreover, the temperature coefficient, $d\sigma/dT$, of the samples changed from positive to nearly zero or negative by the substitution. Although negative values of $d\sigma/dT$ usually imply metallic conduction, hopping conduction with a small activation energy would also show negative $d\sigma/dT$. For hopping conduction in which hopping of the charge carriers is thermally activated with the activation energy E_a, the electrical conductivity is given by a general formula as

$$\sigma = (C/T) \exp(-E_a/kT), \quad (1)$$

where k is the Boltzmann constant [21]. The equation predicts a linear relation between log σT and T^{-1}, instead of the usual Arrhenius plots for log σ. The T^{-1} dependence of σT is summarized in Fig. 1 for $(Ca_{0.9}A_{0.1})MnO_3$. In the temperature region below 300 °C, the plots for all the samples lie on the straight lines, confirming the validity of Eq. (1). The reduction of the activation energy of the hopping conduction is also noticeable for the substituted samples. The undoped $CaMnO_3$ showed an activation energy E_a of 0.16 eV, being in good agreement with 0.192 eV reported for $LaCrO_3$ [9] and 0.19 ± 0.01 eV for $LaMnO_3$ [22]. The plots for all the substituted samples except the Sb-substituted one gave small and virtually the same E_a values of 0.02-0.04 eV. For the Sb substitution, the plots below 150 °C appear to yield E_a of *ca.* 0.16 eV, very similar to that of the undoped sample.

The linear relation seen in Fig. 1 strongly suggests that hopping conduction occurs in the $CaMnO_3$-based perovskites. The electrical conductivity of small polaron hopping with the intersite distance a can be written in an adiabatic case as

$$\sigma = ne\mu = nea^2(A_0/T) \exp(-E_h/kT), \quad (2)$$

where n is the carrier concentration, e the electrical charge of the carrier, μ the carrier mobility, E_h the activation energy for hopping motion, and A_0 is the pre-exponential term related to the carrier scattering mechanism [21]. If differences in n, A_0, and E_h between the samples are sufficiently small, Eq. (2) at a certain temperature can give rise to a linear relation between log σ and log a.

Figure 2 clearly depicts the excellent linearity between the logarithm of ionic radii, r_A, of the cation substituents and the logarithm of the electrical conductivity at room temperature, σ_{RT}, for $(Ca_{0.9}A_{0.1})MnO_3$. The carrier concentrations n are assumed to be predominantly governed by the concentrations of the dopant cations. In Fig. 2, the σ_{RT} values for tetravalent cations Pb^{4+} and Sn^{4+} substituting on the divalent Ca sites were therefore adjusted by a factor of 0.5. It should be noted that the ionic radii presented here are the values for 6-fold coordination according to Shannon [23], since we cannot find a complete list of values for 12-coordination, which is actually the case for the A site cations in the perovskite-type oxides. Moreover, as mentioned above, the assumption of almost the same value of E_h may no longer hold, which is certainly so for the Sb-substituted sample. Nevertheless, in spite of the extreme simpleness of the estimation, Fig. 2 suggests that the hopping intersite distance, which presumably varies with the ionic radii of the cation substituents, mainly governs the conductivity at low and intermediate temperatures.

2. System $Ca(Mn_{1-x}B_x)O_3$

Since the formal valence formula of $CaMnO_3$ requires Mn^{4+} with the d^3 electron configuration, the Fermi surface of $CaMnO_3$ should dominantly consist of the 3d electrons of Mn^{4+} in an octahedral symmetry. This means that the localized carrier electrons are mostly located at the Mn sites. It is therefore of much interest to further investigate effects of the Mn site substitution on the hopping behavior and the thermoelectric properties of $CaMnO_3$.

Figure 3 represents the Arrhenius plots of σT for $Ca(Mn_{0.9}B_{0.1})O_3$, where B denotes several typical or transition metal elements. The linear relation observed in Fig. 1 is also obvious for all the samples in the temperature region at least up to 400 °C, confirming that the thermally activated hopping conduction is operative. The substituent cations with the high formal valence numbers such as Sb, Nb, and Bi resulted in the larg-

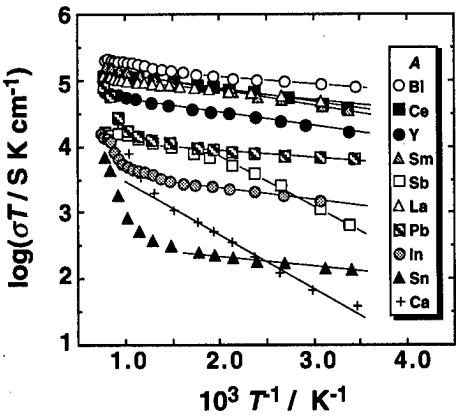


Fig. 1 The Arrhenius plots of σT for $(Ca_{0.9}A_{0.1})MnO_3$.

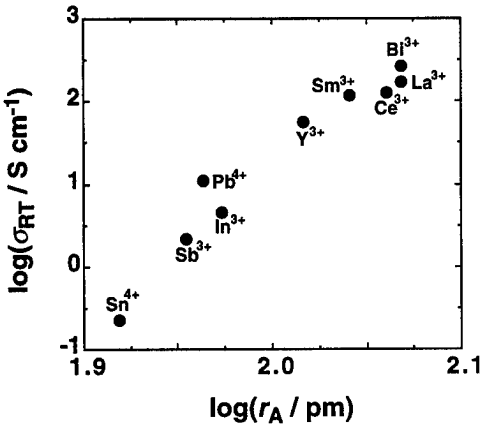


Fig. 2 The electrical conductivity of $(Ca_{0.9}A_{0.1})MnO_3$ at room temperature as a function of the ionic radius of the cation substituent A.

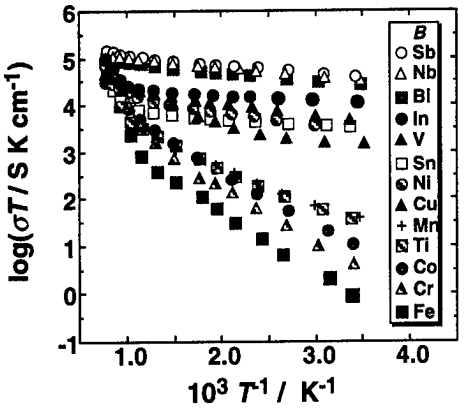


Fig. 3 The Arrhenius plots of σT for $Ca(Mn_{0.9}B_{0.1})O_3$.

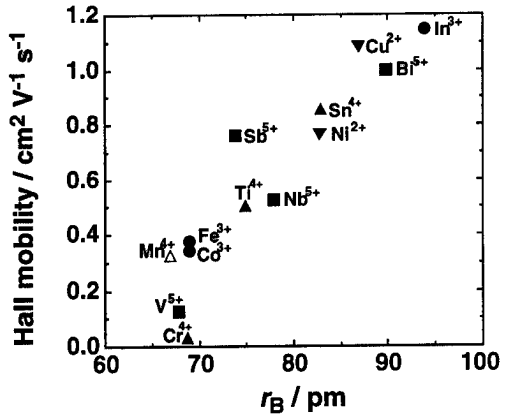


Fig. 4 The Hall carrier mobility of $Ca(Mn_{0.9}B_{0.1})O_3$ at room temperature as a function of the ionic radius of the cation substituent B.

est increase in σ, presumably because of carrier electron doping. It would be also noteworthy that the activation energies of the samples appear to be divided into two groups; those with a much larger σ values compared to the undoped sample are considerably small as 0.02 - 0.05 eV as similar to those seen for the substituted samples in Fig. 1, while those showing no improvement in σ are very similar to that of the undoped $CaMnO_3$. The activation energy of hopping conduction is generally a sum of that for ionization of donor (or acceptor) centers to generate the charge carriers, E_i, and that for hopping motion of the carriers from one site to another, E_h; *i. e.*, $E_a = E_i + E_h$. It is therefore probable that E_i may become negligible for the heavily doped samples for which the carrier concentrations are extrinsically fixed. Since E_h can be derived from the temperature dependence of the Hall mobility, this question should be subjected to further investigations.

The assumption underlying the explanation of the good correlation observed in Fig. 2 was that σ directly reflects the variation in the carrier mobility. We have hence measured the Hall coefficients of $Ca(Mn_{0.9}B_{0.1})O_3$ in order to investigate the real influence of the substitutions on the hopping carrier mobility. Due to our experimental limitations, the Hall measurements in the present study were carried out only at room temperature. Undoped $CaMnO_3$ showed a carrier concentration, n, of 4.2×10^{17} cm^{-3} and a mobility of 0.37 cm^2 V^{-1} s^{-1}. It should be notified that increase in n was obvious for most of the substituted samples, particularly for those by pentavalent cations (Nb, V, Sb, Bi). However, no clear correlation was found between the n values and the valence numbers of the substituents. The Hall carrier mobilities, μ_H, of $Ca(Mn_{0.9}B_{0.1})O_3$ determined at room temperature are summarized in Fig. 4 as a function of ionic radius, r_B, of the substituting cations in 6-fold coordination. Obviously, the larger substituents leads to the higher mobilities, almost regardless of the formal valence numbers of the cation substituents. These results strongly support the hypothesis that the substitution of the lattice points by the larger cations results in the increase in the hopping intersite distance. The highest μ_H value of 1.1 cm^2 V^{-1} s^{-1} was observed for the sample with the largest substituent for the Mn site, In. This value is also consistent with the predicted higher limit of 1.0 - 0.1 cm^2 V^{-1} s^{-1} for the small polaron hopping.

The temperature dependence of the Seebeck coefficient, S, of $Ca(Mn_{0.9}B_{0.1})O_3$ is shown in Fig. 5 for several representative samples. All these samples have negative S, with the absolute values being reduced by the substitutions. This tendency would be ascribed to the increased n, particularly for the samples with Nb, V, Sb, and Bi whose n values were as large as $1 \times 10^{20} - 5 \times 10^{21}$ cm^{-3}. However, the absolute S values appear to be still fairly large even for these heavily doped samples. Even more, the In-substituted sample showed S of -250 μV/K at room temperature, and the absolute value increased almost linearly with increasing temperature at least up to about 800 °C where the intrinsic conduction began to influence, reaching more than -300 μV/K. Such absolute S values are definitely too large for metallic conduction. It is also noteworthy that n of the In-substituted sample was 2.2×10^{20} cm^{-3}, being almost twice higher than that of the Bi-substituted sample. The enhanced μ_H may be responsible for such a large S even at high n. Whereas the general theories of the small polaron hopping conduction predict an almost temperature-independent S [21], linear increase in S with increasing temperature has also been experimentally reported for polaron hopping conduction in $LaCrO_3$ [9] and the hopping between inequivalent sites in boron-rich carbides [24-26].

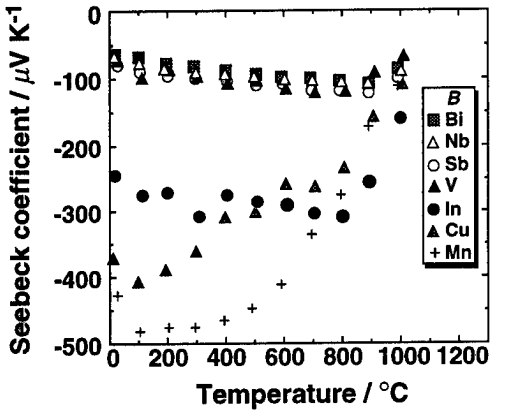


Fig. 5 Temperature dependence of the Seebeck coefficient for $Ca(Mn_{0.9}B_{0.1})O_3$.

The temperature dependence of the power factors, $S^2\sigma$, of $Ca(Mn_{0.9}B_{0.1})O_3$ is plotted in Fig. 6. Clearly, the In-substituted sample shows the largest power factor of all the samples

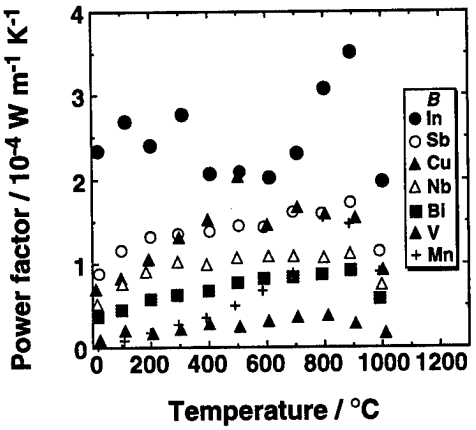


Fig. 6 Temperature dependence of the power factor for $Ca(Mn_{0.9}B_{0.1})O_3$.

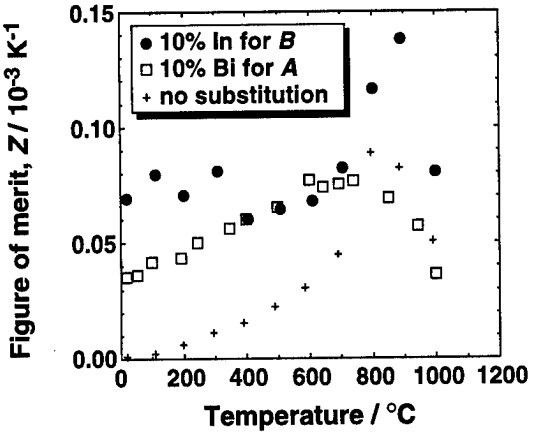


Fig. 7 Temperature dependence of the figure of merit for $Ca(Mn_{0.9}In_{0.1})O_3$, $(Ca_{0.9}Bi_{0.1})MnO_3$, and $CaMnO_3$.

over the whole temperature range. The power factor of the oxide increases up to 900 °C, and then rapidly decreases, attaining a maximum value of 3.5×10^{-4} W m^{-1} K^{-2}. The thermal conductivity, κ, of $Ca(Mn_{0.9}In_{0.1})O_3$ at room temperature was almost the same as that of undoped $CaMnO_3$ as 3.4 W m^{-1} K^{-1}, and decreased with increasing temperature down to 2.6 W m^{-1} K^{-1} at 800 °C.

The figure of merit, $Z = S^2\sigma/\kappa$, of $Ca(Mn_{0.9}In_{0.1})O_3$ is depicted in Fig. 7 in comparison with those of $(Ca_{0.9}Bi_{0.1})MnO_3$ and $CaMnO_3$. The values at 900 and 1000 °C were obtained from κ extrapolated by assuming the T^{-1} proportionality. Improvement in Z is significant for $Ca(Mn_{0.9}In_{0.1})O_3$ in both low and high temperature regions compared with $(Ca_{0.9}Bi_{0.1})MnO_3$, which oxide marked the best Z for the Ca site substitution. The largest Z was 0.14×10^{-3} K^{-1} at 900 °C, yielding a maximum ZT value of 0.16. Although ZT at present is still insufficient for commercialized practical applications, this value appears to be one of the best performance of oxide materials so far investigated. As the largest value of oxide materials, $Z = 0.24 \times 10^{-3}$ K^{-1} has been observed on $Zn_{0.98}Al_{0.02}O$ with $n = 2.2 \times 10^{19}$ cm^{-3} and $\mu_H = 80$ cm^2 V^{-1} s^{-1} [16]. On the other hand, the $CaMnO_3$-based perovskites were here revealed to attain $Z = 0.14 \times 10^{-3}$ K^{-1} on the sample with $n = 2.2 \times 10^{20}$ cm^{-3} and $\mu_H = 1.1$ cm^2 V^{-1} s^{-1}; a comparable Z value was observed even with the 10-fold higher carrier concentration and more than 70 times lower mobility. These facts imply that the hopping conduction mechanism would be advantageous to proceed beyond a theoretical limit predicted for the conventional broadband materials. Enhancement in the hopping carrier mobility of unconventional candidate materials is therefore expected to be of great interest for development of novel thermoelectric materials.

References

[1] T. Caillat, A. Borshchevsky, J.-P. Fleurial, in *Proc. XIth Int. Conf. Thermoelectrics*, Arlington, Texas, 1992 (University of Texas at Arlington Press, Arlington, 1993) p. 98.

[2] G. Slack, V. G. Tsoukala, *J. Appl. Phys.*, **76**(3) (1994) 1665.

[3] D. T. Morelli, G. P. Meisner, *J. Appl. Phys.*, **77**(8) (1995) 3777.

[4] G. S. Nolas, G. A. Slack, D. T. Morelli, T. M. Tritt, A. C. Ehrlich, *J. Appl. Phys.*, **79**(8) (1996) 4002.

[5] B. C. Sales, D. Mandrus, R. K. Williams, *Science*, **272** (1996) 1325.

[6] J.-P. Fleurial, A. Borshchevsky, T. Caillat, D. T. Morelli, G. P. Meisner, in *Proc. XVth Int. Conf. Thermoelectrics*, Pasadena, CA, 1996 (Inst. Electrical Electronics Engineers, Piscataway, NJ, 1996) p. 91.

[7] C. Wood, *Rep. Prog. Phys.*, **51** (1988) 459

[8] C. B. Vining, in *Proc. XIIth Int. Conf. Thermoelectrics*, Yokohama, Japan, 1993 (Inst. Electrical Engineers Jpn., Tokyo, 1994) p. 126.

[9] D. P. Karim, A. T. Aldred, *Phys. Rev. B*, **20** (1979) 2255.

[10] A. F. Ioffe, "Semiconductor Thermoelements and Thermoelectric Cooling", Infosearch, London, 1957.

[11] M. Ohtaki, D. Ogura, K. Eguchi, H. Arai, *J. Mater. Chem.*, **4**(5) (1994) 653.

[12] M. Ohtaki, H. Koga, K. Eguchi, H. Arai, in *Proc. XIIIth Int. Conf. Thermoelectrics*, Kansas City, MO, 1994 (AIP Press, Now York, 1994) p. 115

[13] M. Ohtaki, H. Koga, T. Tokunaga, K. Eguchi, H. Arai, *J. Solid State Chem.*, **120** (1995) 105.

[14] M. Ohtaki, T. Tsubota, K. Eguchi H. Arai, in *Proc. XIVth Int. Conf. Thermoelectrics*, St Petersburg, Russia, 1995 (A. F. Ioffe Physical-Technical Institute, St. Petersburg, 1995) p. 245

[15] M. Ohtaki, T. Tsubota, K. Eguchi, H. Arai, *J. Appl. Phys.*, **79**(3) (1996) 1816.

[16] T. Tsubota, M. Ohtaki, K. Eguchi, H. Arai, *J. Mater. Chem.*, **7**(1) (1997) 85.

[17] T. Tsubota, M. Ohtaki, K. Eguchi, H. Arai, "Thermoelectric Properties of ZnO Doped with the Group 13 Elements", this conference.

[18] H. Ohta, W. S. Seo, K. Koumoto, *J. Am. Ceram. Soc.*, **79**(8) (1996) 2193.

[19] W. S. Seo, H. Sinmachi, K. Koumoto, in *Proc. Annual Meeting Ceram. Soc. Jpn.*, (Ceramic Society of Japan, Nagoya, 1994) p. 206 (in Japanese).

[20] M. Yasukawa, N. Murakami, *J. Soc. Powder Powder Metallur.*, **44**(1) (1997) 50.

[21] H. L. Tuller and A. S. Nowick, *J. Phys. Chem. Solids*, **38** (1977) 859.

[22] J. H. Kuo, H. U. Anderson, and D. M. Sparlin, *J. Solid State Chem.*, **87** (1990) 55.

[23] R. D. Shannon, *Acta Crystallogr.*, **A32** (1976) 751.

[24] C. Wood, D. Emin, *Phys. Rev. B*, **29** (1984) 4582.

[25] D. Emin, *Phys. Rev. Lett.*, **35** (1975) 882.

[26] G. A. Samara, D. Emin, C. Wood, *Phys. Rev. B*, **32** (1985) 2315.

Thermoelectric Properties of n-Type $(Pb_{1-x}Ge_x)Te$ Fabricated by Hot Pressing Method

Jae-Shik Choi[1], Hee-Jeong Kim[1], Hang-Chong Kim[1], Tae-Sung Oh[1],
Dow-Bin Hyun[2], and Hee-Woong Lee[3]
[1]Department of Metallurgy and Materials Science, Hong Ik University, Seoul 121-791, Korea,
Phone : 82-2-320-1655, FAX : 82-2-337-8460, e-mail : ohts@wow.hongik.ac.kr
[2]Division of Metals, Korea Institute of Science and Technology (KIST), Seoul 136-791, Korea,
Phone : 82-2-958-5464, FAX : 82-2-958-5379, e-mail : dbhyun@kistmail.kist.re.kr
[3]Korea Electro Technology Research Institute, Kyungnam 641-120, Korea
Phone : 82-0551-80-1630, FAX : 82-0551-80-1606, e-mail : hwlee@keri.re.kr

Abstract

To investigate the effects of solid solution alloying on the thermoelectric properties of PbTe-based thermoelectric materials, 0.3 wt% Bi-doped $(Pb_{1-x}Ge_x)Te$ alloy powders ($0 \leq x \leq 0.15$) were fabricated by "melting/grinding" process, and hot-pressed at 650℃ and 750℃ for 1 hour in vacuum. At the temperatures ranging from 25℃ to 450℃, the $(Pb_{1-x}Ge_x)Te$ alloys exhibited more negative Seebeck coefficient, higher electrical resistivity and lower thermal conductivity with increasing the GeTe content. The temperature, where the figure-of-merit of $(Pb_{1-x}Ge_x)Te$ reached a maximum, was lowered with increasing the GeTe content x. When hot-pressed at 650℃, 0.3 wt% Bi-doped PbTe and $(Pb_{0.9}Ge_{0.1})Te$ exhibited a maximum figure-of-merit of 1.07×10^{-3}/K at 400℃ and 1.25×10^{-3}/K at 300℃, respectively.

Introduction

PbTe has been widely applied for the thermoelectric generators using various heat sources. It has been proposed that solid solution alloying of thermoelectric materials can improve the figure-of-merit by decreasing the lattice thermal conductivity [1,2]. The concept of solid solution alloying has been in great success for improving the figure-of-merit of $(Bi,Sb)_2(Te,Se)_3$ alloys [2]. The figure-of-merit of PbTe may also be expected to be increased by solid solution alloying with SnTe and GeTe, because substantial phonon scattering can occur due to the lattice distortion introduced by the large differences in atomic masses and sizes of the constituent atoms [3]. However, few work has been reported on the thermoelectric properties of the polycrystalline (Pb,Ge)Te alloys.

In this paper, $(Pb_{1-x}Ge_x)Te$ ($0 \leq x \leq 0.15$) alloys doped with 0.3 wt% Bi as donor dopants were fabricated by "melting/ grinding" process and hot pressing. Microstructure and the thermoelectric properties of the hot-pressed $(Pb_{1-x}Ge)Te$ alloys were characterized with the GeTe content.

Experimental procedure

High purity (> 99.99%) Pb, Ge, and Te granules (~ 5 mm size) were washed with 10% nitric solution, acetone, and distilled water to remove the surface oxide layer. The appropriate amounts of Pb, Ge and Te were weighed to make 40g of $(Pb_{1-x}Ge_x)Te$ ($0 \leq x \leq 0.15$) and charged with 0.3 wt% Bi as donor dopants into a quartz tube. The inside wall of the quartz tube was carbon-coated by acetone cracking. The quartz tube was evacuated to 10^{-5} torr and sealed. Pb, Ge and Te in the quartz tube were melted at 1000℃ for 2 hours using a rocking furnace to ensure the composition homogeneity, and then quenched to room temperature. The $(Pb_{1-x}Ge_x)Te$ ingots were then grown in a zone melting furnace at 1000℃ with a growth rate of 1 mm/min. The $(Pb_{1-x}Ge_x)Te$ powders were obtained by crushing the ingots to 90 ~ 250 μm size. Observation with scanning electron microscopy (SEM) revealed many cracks in each powder, which were formed during crushing. A reduction treatment of the $(Pb_{1-x}Ge_x)Te$ powders was conducted at 400℃ for 24 hours in (50% H_2 + 50% Ar) atmosphere. The $(Pb_{1-x}Ge_x)Te$ powders were cold-pressed at 475 MPa to form 5 mm×5 mm×10 mm compacts, and hot pressed in vacuum for 1 hour at 650℃ and 750℃.

Polished surfaces of the hot-pressed specimens were observed using optical microscopy. Lattice parameters of the $(Pb_{1-x}Ge_x)Te$ alloys were characterized by X-ray Diffraction (XRD). The Seebeck coefficient (α) of the hot-pressed specimens was measured at temperatures ranging from 25℃ to 450℃ by applying a temperature difference of 20℃ at both ends of a specimen using a sub-heater. The electrical resistivity (ρ) and thermal conductivity (κ) were measured using Harman method [4]. All thermoelectric measurements were performed in a vacuum of 10^{-5} torr to minimize the oxidation of the specimens and the thermal conduction through convection. The figure-of-merit was calculated from $Z = \alpha^2/\rho\cdot\kappa$.

0-7803-4057-4/97 $10.00 ©1997 IEEE

Results and Discussion

The $(Pb_{1-x}Ge_x)Te$ ($0 \leq x \leq 0.15$) alloys were fully densified close to the theoretical density by hot pressing at 650℃ and 750℃. XRD patterns of $(Pb_{1-x}Ge_x)Te$ alloys revealed the single phase of the NaCl-type PbTe structure. As shown in Fig. 1, the lattice parameter of the $(Pb_{1-x}Ge_x)Te$ alloys decreased almost linearly with increasing the GeTe content up to x = 0.15, which may indicate the complete solid solution of PbTe and GeTe. In PbTe-GeTe pseudo-binary system, the solubility of GeTe in PbTe is more than 20% at temperatures below 750℃ [5]. Fig. 2 illustrates optical micrographs of the $(Pb_{1-x}Ge_x)Te$ alloys hot-pressed at 650℃. High-density grains of polygonal-shape were developed and the grain sizes were almost the same for all compositions.

The thermoelectric properties of $(Pb_{1-x}Ge_x)Te$ hot-pressed at 650℃ and 750℃ are shown in Fig. 3 and Fig. 4, respectively. The increase of the Seebeck coefficient and the electrical resistivity with increasing the temperature came from the temperature dependence of the carrier mobility. Since the hot-pressed $(Pb_{1-x}Ge_x)Te$ alloys were in extrinsic region up to 450 ℃, as shown in Figs. 3(b) and 4(b), the carrier concentration was saturated in this temperature range. Thus, the increase of the electrical resistivity and the Seebeck coefficient was mainly due to the decrease of μ_e with increasing the temperature. The Seebeck coefficient and the electrical resistivity increased with the GeTe content x, which might be caused by the decrease of the electron concentration due to p-type characteristics of GeTe [6]. For the same composition, $(Pb_{1-x}Ge_x)Te$ hot-pressed at 750℃ exhibited a slightly higher Seebeck coefficient and electrical resistivity than the specimens hot-pressed at 650℃. Powdering process for sintered PbTe has been reported to introduce donor levels by generating electrically-active point defects [7,8]. When the $(Pb_{1-x}Ge_x)Te$ alloys were hot pressed at higher temperature, the point defects introduced by powdering action could be removed more easily, resulting the increase of the electrical resistivity and hence the Seebeck coefficient.

It is worth to emphasize that the thermal conductivity of $(Pb_{1-x}Ge_x)Te$ was lowered with increasing the GeTe content, as shown in Figs. 3(c) and 4(c). It has been proposed that solid solution alloying of VI-IV thermoelectric materials reduces the lattice thermal conductivity by introducing short-range distortions in the lattice [1,3]. Contrary to this, however, the lattice thermal conductivities of PbTe-SnTe alloys were reported to be higher than the value of PbTe [9]. For the $(Pb_{1-x}Ge_x)Te$ alloys, the electrical component of the thermal conductivity was calculated from $\kappa_{el} = L\sigma T$ with taking L as 1.48×10^{-8}. Fig. 5 clearly

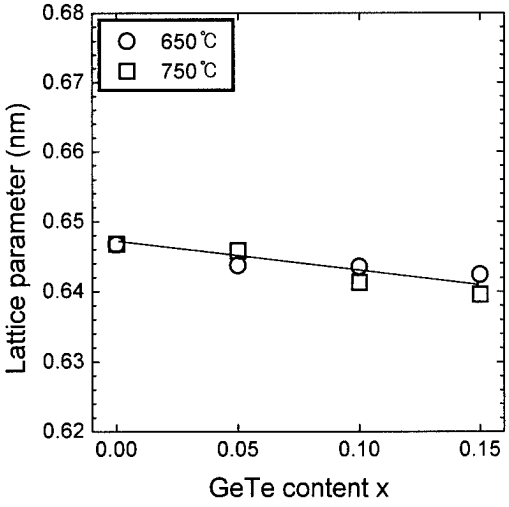


Fig. 1 Lattice parameter of the $(Pb_{1-x}Ge_x)Te$ alloys hot-pressed at 650℃ and 750℃.

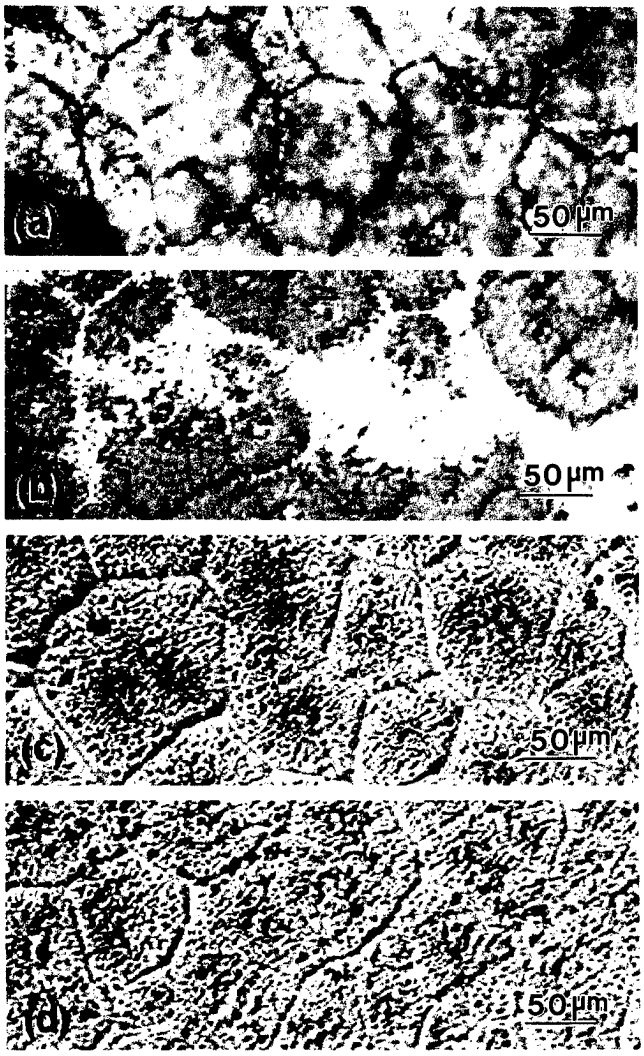


Fig. 2 Optical micrographs of $(Pb_{1-x}Ge_x)Te$: (a) x = 0, (b) x = 0.05, (c) x = 0.1, (d) x = 0.15 (hot-pressing temperature : 650℃)

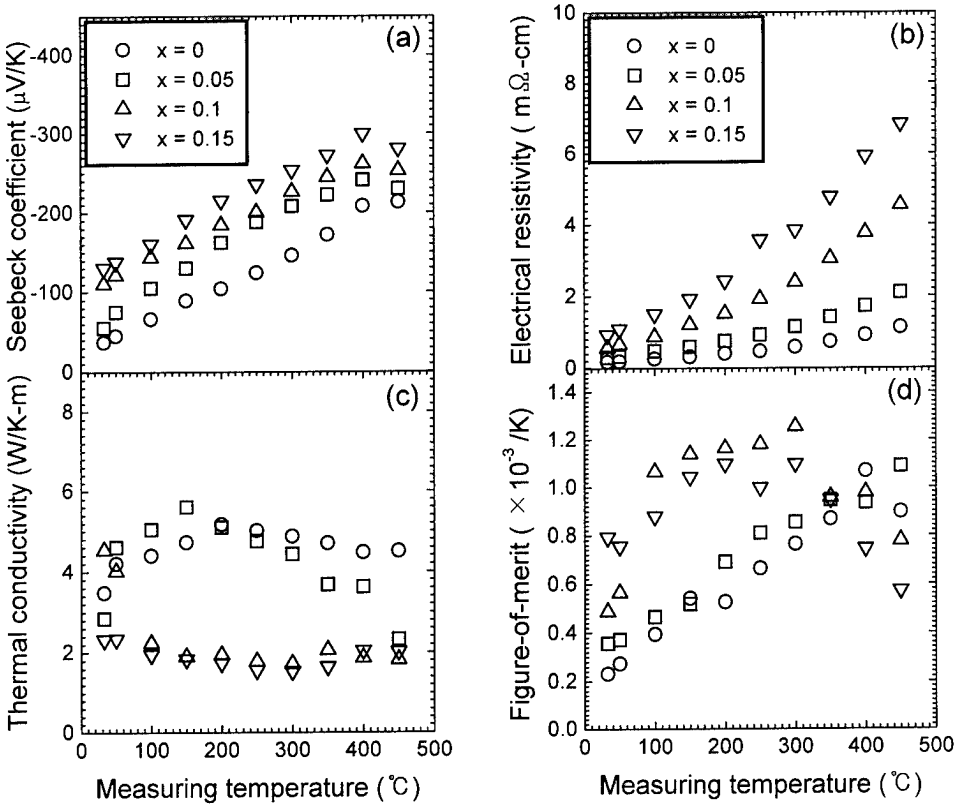


Fig. 3 (a) Seebeck coefficient, (b) electrical resistivity, (c) thermal conductivity, and (d) figure-of-merit of the $(Pb_{1-x}Ge_x)Te$ alloys hot-pressed at 650℃.

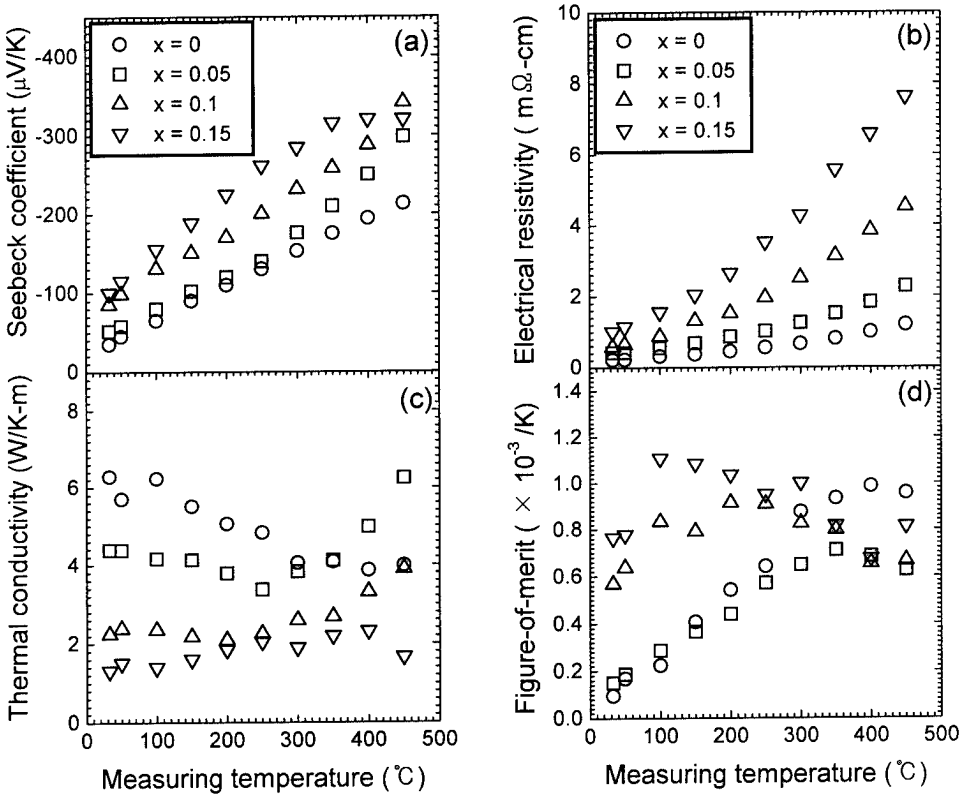


Fig. 4 (a) Seebeck coefficient, (b) electrical resistivity, (c) thermal conductivity, and (d) figure-of-merit of the $(Pb_{1-x}Ge_x)Te$ alloys hot-pressed at 750℃.

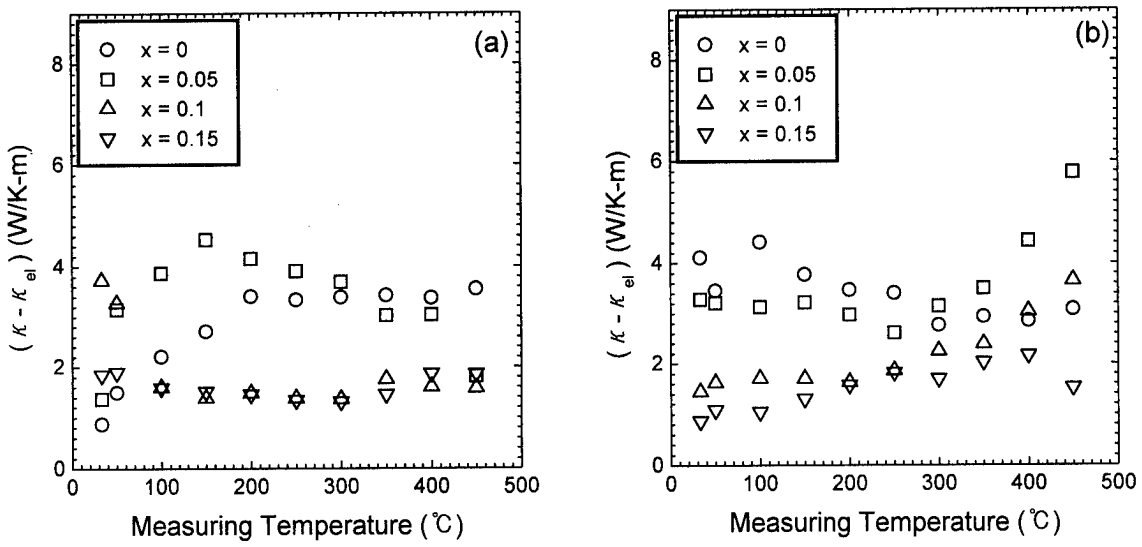


Fig. 5 The variation of ($\kappa - \kappa_{el}$) of the $(Pb_{1-x}Ge_x)Te$ alloys hot-pressed at (a) 650℃ and (b) 750℃.

illustrates the decrease of the ($\kappa - \kappa_{el}$) values with increasing the GeTe content x, especially in the composition range of $0.05 \leq x \leq 0.1$. κ_{el} also decreased with increasing the GeTe content. However, the contribution of κ_{el} to the total thermal conductivity was relatively small, compared with ($\kappa - \kappa_{el}$).

Figs. 3(d) and (4)d illustrate that the temperature, where the figure-of-merit of $(Pb_{1-x}Ge_x)$ Te reached a maximum, was lowered with increasing the GeTe content x and the hot-pressing temperature. When hot-pressed at 650℃, PbTe and $(Pb_{0.9}Ge_{0.1})Te$ exhibited a maximum figure-of-merit of 1.07×10^{-3}/K at 400℃ and 1.25×10^{-3}/K at 300℃, respectively. For $(Pb_{1-x}Ge_x)Te$ hot-pressed at 750℃, a maximum figure-of-merit of 0.99×10^{-3}/K at 400℃ and 1.11×10^{-3}/K at 100℃ was obtained for PbTe and for $(Pb_{0.85}Ge_{0.15})Te$.

Summary

The $(Pb_{1-x}Ge_x)Te$ ($0 \leq x \leq 0.15$) alloys doped with 0.3 wt% Bi were fully densified by hot pressing at 650℃ and 750℃, and the lattice parameter of the alloys decreased almost linearly with increasing the GeTe content. The $(Pb_{1-x}Ge_x)Te$ alloys exhibited more negative Seebeck coefficient, higher electrical resistivity and lower thermal conductivity with increasing the GeTe content. The ($\kappa - \kappa_{el}$) values of the $(Pb_{1-x}Ge_x)Te$ alloys decreased with increasing the GeTe content x, especially in the range of $0.05 \leq x \leq 0.1$. The temperature, where the figure-of-merit of $(Pb_{1-x}Ge_x)Te$ reached a maximum, was lowered with increasing the GeTe content and the hot-pressing temperature. For the $(Pb_{1-x}Ge_x)Te$ alloys hot-pressed at 650℃, $(Pb_{0.9}Ge_{0.1})Te$ exhibited a maximum figure-of-merit of 1.25×10^{-3}/K at 300℃. With hot pressing at 750℃, a maximum figure-of-merit of 1.11×10^{-3}/K was obtained at 100℃ for the $(Pb_{0.85}Ge_{0.15})$ alloy.

Acknowledgment

This work was supported by Korea Electro Technology Research Institute.

References

[1] A. F. Ioffe, S. V. Airapetiants, A. V. Ioffe, N. V. Kolomoets, and L. S. Stil'bans, Dokl. Akasd. Naruk. SSSR, **106** (1956) 981.

[2] W. M. Yim and F. D. Rosi, Solid-State Electronics, **15** (1972) 1121.

[3] D. R. Rowe and C. M. Bhandari, Appl. Phys. Lett., **47** (1985) 255

[4] T. C. Harman, J. H. Cahn and M. J. Logan, J. Appl. Phys., **30** (1959) 9.

[5] N. Kh. Abrikosov, V. F. Bankina, L. V. Poretskaya, L. E. Shelimova, and E. V. Skudnova, Semiconducting II-VI, IV-VI, and V-VI Compounds" p.132, Plenum Press, New York (1969).

[6] N. V. Kolomoets, E. Ya. Lev, and L. M. Sysoeva, Soviet Phys.-Solid State, **5** (1964) 2101.

[7] "CRC Handbook of Thermoelectrics", D. M. Rowe (ed.), p.262, CRC Press, New York (1995).

[8] R. Breschi, A. Olivi, A. Camanzi, and V. Fano, J. Mater. Sci., **15** (1980) 918.

[9] A. A. Machonis and I. B. Cadoff, Trans. Metall. Soc. AIME, **230** (1964) 333.

Structure and Transport Properties of Microcrystalline SiGe Films

F. Edelman[1], M. Stölzer[2], T. Raz[1], Y. Komem[1], C.B. Vining[3], H. Zeindl[4] and P. Zaumseil[4]

1-Materials Engineering Faculty, Technion-Israel Institute of Technology, 32000 Haifa, Israel (e-mail: edelmann@tx.technion.ac.il); 2-Martin-Luther-Universität Halle-Wittenberg, Fachbereich Physik, FG Angewandte Physik, Halle (Saale), Germany; 3-ZT Services, Inc., Auburn, AL 36830-7113, USA; 4-Institut für Halbleiterphysik, Frankfurt (Oder), Germany

Abstract

Amorphous $Si_{1-x}Ge_x$ films (x=0, 0.25, 0.5, 0.75 and 1, having Boron concentrations of $5\cdot10^{18}$, $5\cdot10^{19}$ and $5\cdot10^{20}cm^{-3}$), were deposited at low temperature by a molecular beam processing on SiO_2/Si(001) substrates. Samples were studied by *in-situ* TEM and *in-situ* XRD to follow the crystallization process. In addition, transport properties were studied in samples which were annealed in vacuum by a hot-wall furnace at temperatures between 500 to 900°C for 1 hour. The microstructure of B-doped SiGe films is characterized by a relatively large grain size (about 1μm). The $Si_{0.5}Ge_{0.5}$ films have a rather high and temperature independent Hall mobility (25 to 60 cm^2/Vsec), Seebeck coefficient (~150 to 250 μV/K at room temperature) and conductivity ((200 to 2000 $(Ohm\cdot cm)^{-1}$ at room temperature). Therefore, the highly-doped μc-SiGe films that we produce in the present research project show transport characteristics comparable to the sintered SiGe materials for thermoelectric applications.

I. Introduction

Bulk $Si_{1-x}Ge_x$ is used for thermoelectric applications in the form of sintered powder having a composition varying between x=0.2 and x=0.7 and a grain size ranging from 1 to 100μm. The advantages of $Si_{1-x}Ge_x$ as a thermoelectric material are: 1) low thermoconductivity (λ) having a minimum value at x≈0.5; and 2) high charge carriers mobility. Increase of the figure of merit $Z=S^2\sigma/\lambda$ of SiGe by decreasing the grain size from 100 to 1μm was predicted, but was found to be not effective since while the thermal conductivity is decreased with grain size, the electrical conductivity is also slightly decreased, so that no sufficient change in the figure of merit is observed [1]. Some thermoelectric properties of Ga-doped nanocrystalline SiGe films were recently reported by us [2].

SiGe Peltier elements can be incorporated in a Si chip because SiGe material is compatible with VLSI processing. However, up to now, only one article was published concerning SiGe film application as a thermoelectric integrated element [3].

The main advantages of microcrystalline $Si_{1-x}Ge_x$ films on insulating SiO_2 substrate are: a) clean molecular beam deposition processing, b) wide range of Ge content (x) and doping type/concentrations. Here we present the first results of structure and thermoelectric properties studies of p-type microcrystalline $Si_{1-x}Ge_x$ films.

II. Experimental

B-doped $Si_{1-x}Ge_x$ films, 0.2μm thick, having the composition x=0, 0.25, 0.5, 0.75 and 1, and dopant (B) concentration of $5\cdot10^{18}$, $5\cdot10^{19}$ and $5\cdot10^{20}$ cm^{-3}, were deposited by molecular beam processing on SiO_2/Si(001) substrates at a temperature of 200°C.

In-situ X-Ray Diffraction (XRD) experiments were carried out at ESRF, Grenoble-France. A special high-temperature chamber with vacuum of 10^{-6}Torr was used to detect (220) SiGe reflection during the crystallization process in the temperature range of 300 to 1000°C and exposures from 15 min to 12 h.

The crystallization of the $Si_{1-x}Ge_x$ films was studied also by means of *in-situ* TEM, equipped with a hot stage, at the temperature range between 500 to 800°C, in Max-Planck-Institute of Microstructure Physics, Halle/Saale.

Annealing of the films for measurement of transport properties was done in a hot-wall furnace, having a vacuum near 10^{-7}Torr at temperatures between 600 and 900°C and times between 15 min and 16 hours.

The electrical conductivity σ, the Hall coefficient R_H and the Seebeck coefficient S were measured in the temperature range between 85 and 375K. All measurements were carried out at the Laboratory of Thin Films at Physical Faculty of the Martin-Luther University Halle-Wittenberg.

III. Results and Discussion

III.1. Structure of B-doped $Si_{1-x}Ge_x$ films

After thermal annealing during 1h at T≥450°C (Ge), T≥750°C (Si) and at the intermediate temperatures (SiGe), amorphous films crystallized to the microcrystalline state. Fig.1a shows crystallization kinetics of a-$Si_{0.5}Ge_{0.5}$ films, undoped and B-doped, at 550 and 600°C.

The TEM plan-view in Fig.2 demonstrates a typical microcrystalline morphology of the B-doped ([B]=$5\cdot10^{20}cm^{-3}$) $Si_{0.5}Ge_{0.5}$ film. An average grain size was about 1μm and the film was totally crystallized at 600°C for 1h. Precipitation of SiB_6 in highly B-doped films was observed in course of the *in-situ* TEM experiments at 650-800°C for 15 to 30 min. Selected area diffraction (SAD) in Fig.2 shows SiB_6 (precipitates) reflections (arrows). The morphology of the plate-like precipitates produced striations along <110> directions of SiGe in the large grains, when {001} face oriented perpendicular to the electron beam. Solubility limit of Boron in SiGe is not known, however, upper limit of Boron solubility in Si at T=700°C is only $2\cdot10^{19}cm^{-3}$ and B-phase precipitation in SiGe with [B]=$5\cdot10^{20}cm^{-3}$ [4] is expected.

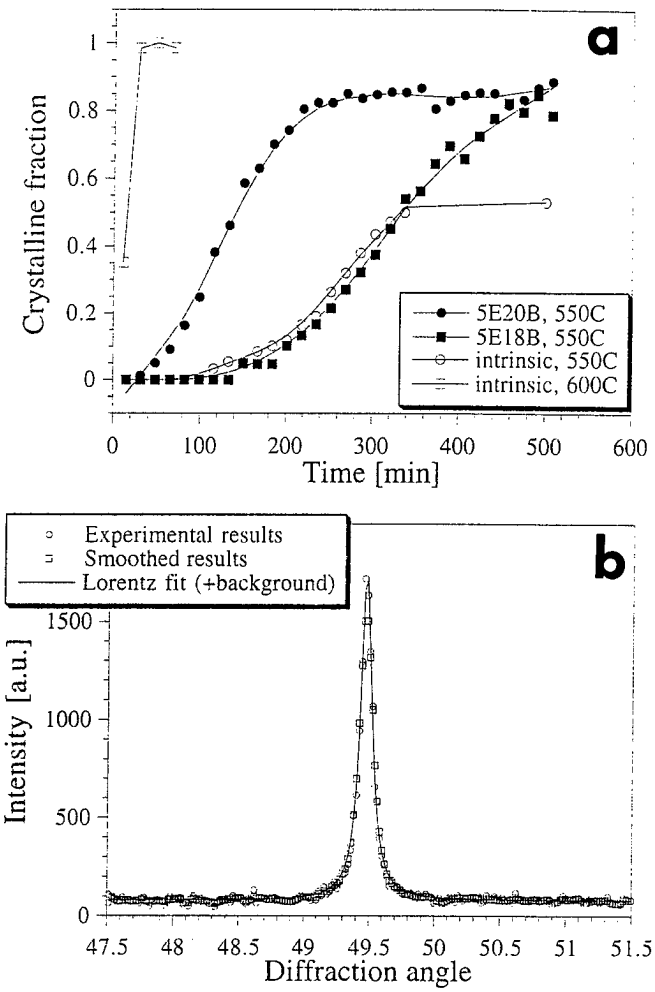


Figure 1. Structure of microcrystalline SiGe films.
(a) Crystallization kinetics of a-$Si_{0.5}Ge_{0.5}$ intrinsic and doped films at 550°C and 600°C via *in-situ* XRD and (b) (220) crystalline $Si_{0.5}Ge_{0.5}$ peak.

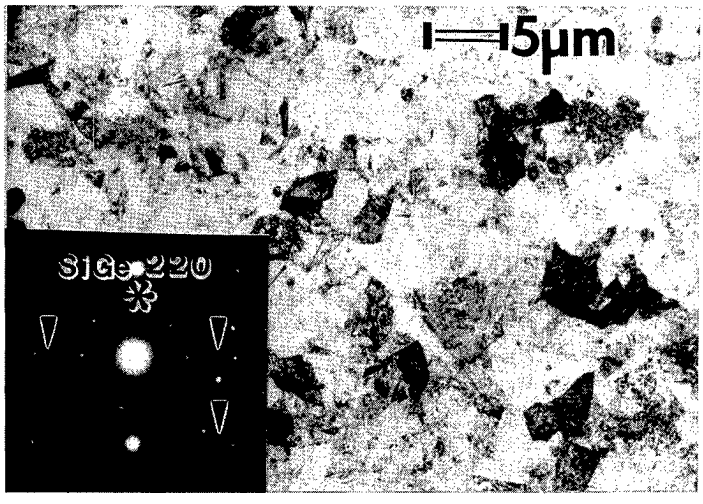


Figure 2. Plan-view TEM micrograph and SAD of $Si_{0.5}Ge_{0.5}$ Boron-doped film ([B]=$5\cdot10^{22}cm^{-3}$) annealed at 600°C for 1h.

III.2. Transport properties of B-doped microcrystalline $Si_{1-x}Ge_x$ Films

Data of Hall mobility, Seebeck coefficient, and power efficiency factor which were measured by us in the temperature range of -188 to 107°C for $Si_{1-x}Ge_x$:B film crystallized at 600°C for 1h are presented as a function of the doping level, Ge content (x) and crystallization temperature in Figs.3-5.

A weak temperature dependence of the carrier concentration (not shown in Figs) , the mobility and, consequently, of the conductivity was found, as expected from degenerated crystalline SiGe material [5,6]. The increase of S (Fig.4) with temperature results in the gain of the power efficiency parameter, $S^2\sigma$.

It is important to notice that after 600 to 800°C annealings for 1 hour, all the $Si_{1-x}Ge_x$ films have a rather high and temperature independent Hall mobility values (Fig.3) in the range of 25 to 60 cm^2/Vsec. All the typical transport characteristics observed for microcrystalline $Si_{0.5}Ge_{0.5}$:B films were also typical for $Si_{0.25}Ge_{0.75}$:B films with [B]=$5\cdot10^{20}cm^{-3}$. The power factor $S^2\sigma$ was found to be practically indifferent to the Ge concentration (x) and the film annealing temperature .

The carrier transport, like in MOS devices, developes via drift process, with a drift mobility (μ_D or μ) typical to this transport. Detailed analysis of the Hall factor $r_H=\mu_H/\mu_D<1$ of epitaxial p-$Si_{1-x}Ge_x$ films with $0<x<0.36$ is given for doping level of [B]=10^{14} to $10^{20}cm^{-3}$ in Ref.7. The main result obtained in Ref.8 is that the value of μ is about 5 to 7 times greater than μ_H, with r_H=0.15 to 0.2 for x=0.36 to 0.17, respectively. Therefore, a hole drift mobility of 200 to 350 cm^2/Vsec is expected in SiGe thermoelectrical transport devices.

Presently, thermoelectric Peltier elements are produced by using SiGe powder sintered or zone-levelled in a bulk form. The first $Si_{1-x}Ge_x$ alloys were studied by RCA group [8] , which reported S value of about 80 to 240 μV/K (depending on x) and a room temperature the Hall hole mobility of the order of 35 to 90 cm^2/Vsec, decreasing with the doping level and Si-content. Later an improved thermoelectric conversion efficiency at T=1000K was reported [9] for a small-grained (3 to 5μm) compacts, compared to a large-grained (>10μm) SiGe samples. A detailed analysis of the mobility and the carrier concentration in sintered p-$Si_{0.7}Ge_{0.3}$ bulk samples [10] showed that the composition and temperature dependence of the mobility, μ, in $Si_{1-x}Ge_x$ alloy can be given by a semi-empiric formula:

$$\mu=[\mu_a/4x(1-x)]\cdot(300/T)^{0.5}, \quad (1)$$

where the parameter μ_a=160cm^2/Vsec. Using this relationship and the data of B solubility in Si, the calculated hole Hall mobility in $Si_{0.7}Ge_{0.3}$ for large grain-size sintered samples, or for single crystal, was found to be in the range from 65 cm^2/Vsec for [B]=$10^{19}cm^{-3}$ to 55 cm^2/Vsec for [B]=$5\cdot10^{21}cm^{-3}$. These values fit with our data, as measured for microcrystalline $Si_{1-x}Ge_x$ films with x=0.25 to 0.75 (Fig.3).

As it was shown in Ref.1, the thermal conductivity of sintered $Si_{0.8}Ge_{0.2}$ samples decreased with decreasing of the particle size (from 134 to 3μm). However, the figure of merit was not significantly increased due to a reduction in the electrical conductivity with grain size decrease. Experimental values measured for hole Hall mobilities varied within the range of 25 to 35 cm^2/Vsec at room temperature. Thermal conductivity data on our microcrystalline films would allow a calculation of Z values for comparison purposes.

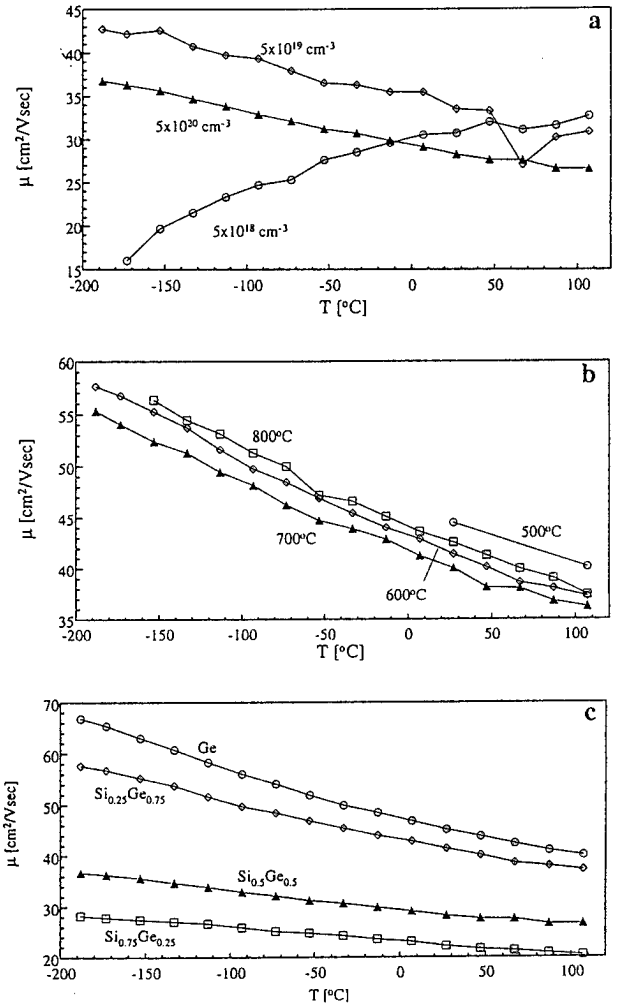


Figure 3. The hole Hall mobility of $Si_{1-x}Ge_x$ films having different Boron concentration, after 600°C/1h annealing (a), films with [B]=$5\cdot10^{20}cm^{-3}$ crystallized at different temperatures (b) and having different Ge content, after annealing at 600°C/1h and containing [B]=$5\cdot10^{20}cm^{-3}$ (c).

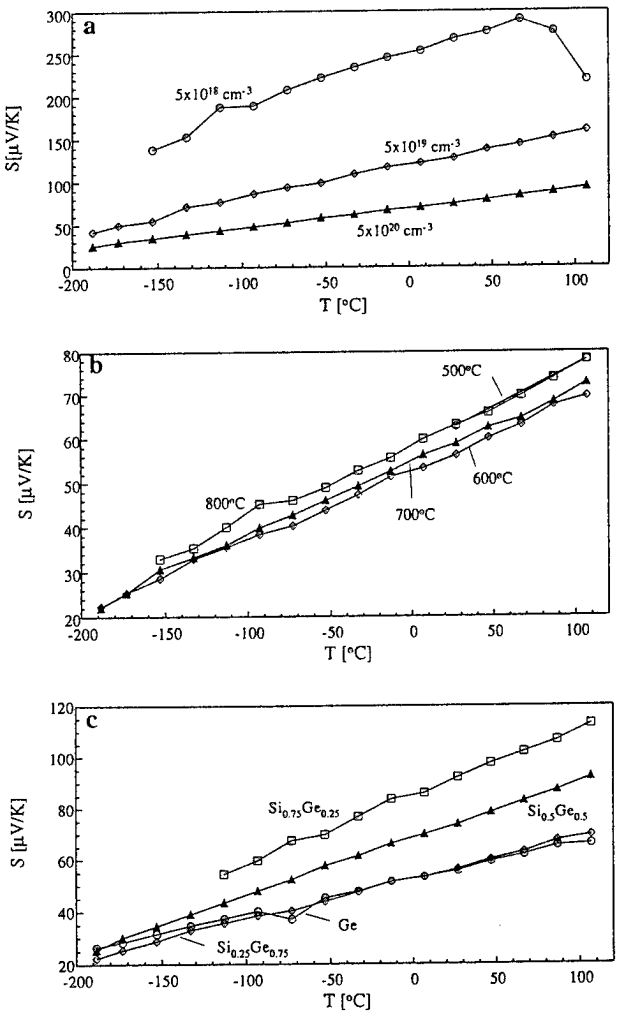


Figure 4. The Seebeck coefficient of $Si_{1-x}Ge_x$ films having different Boron concentration, after 600°C/1h annealing (a), films with [B]=$5\cdot10^{20}cm^{-3}$ crystallized at different temperatures (b) and having different Ge content, annealed at 600°C/1h and containing [B]=$5\cdot10^{20}cm^{-3}$ (c).

IV. Conclusions

(i) Amorphous $Si_{1-x}Ge_x$ films (x=0, 0.25, 0.5, 0.75 and 1, having Boron concentrations of $5\cdot10^{18}$, $5\cdot10^{19}$ and $5\cdot10^{20}cm^{-3}$, were deposited at low temperature by a molecular beam processing on SiO_2/Si(001) substrates and then the films were annealed in vacuum at temperatures between 500 to 900°C for 1 hour. Annealed SiGe films were polycrystalline having an average grain size of ~ 1μm.

(ii) The SiGe films demonstrated Hall mobility of 25 to 60 cm^2/Vsec, Seebeck coefficient of 150 to 250 μV/K) and conductivity 200 to 2000 $(Ohm\cdot cm)^{-1}$ at room temperature.

(iii) Therefore, the μc-SiGe films that we produce in the present research show transport characteristics comparable to the sintered SiGe materials for thermoelectric application.

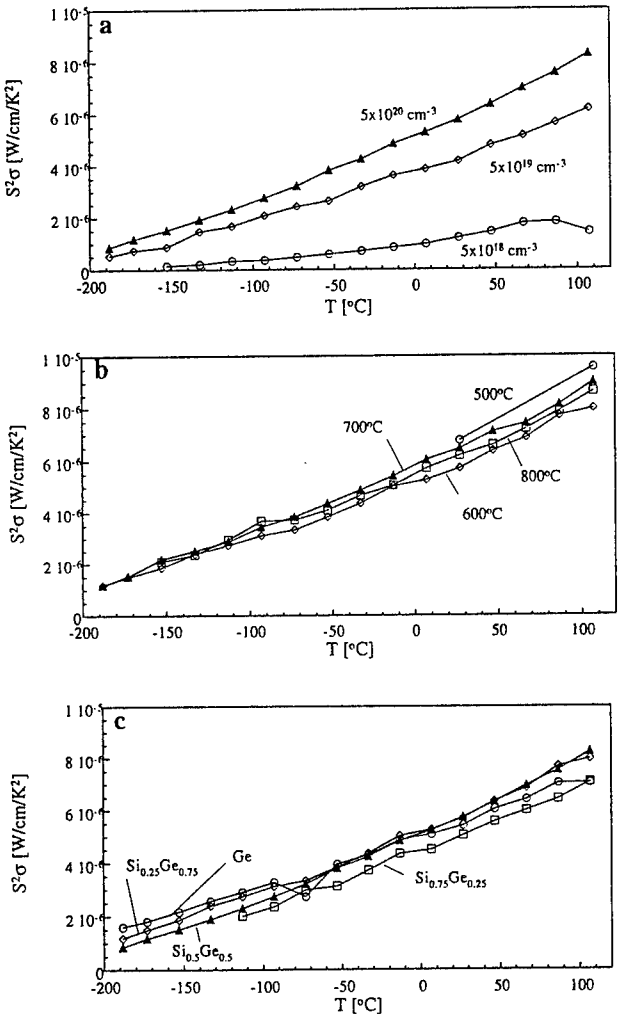


Figure 5. Power efficiency factor of $Si_{1-x}Ge_x$ films having different Boron concentration, after 600°C/1h annealing (a), films with [B]=$5\cdot10^{20}$cm^{-3} crystallized at different temperatures (b) and having different Ge content, annealed at 600°C/1h and containing [B]=$5\cdot10^{20}$cm^{-3} (c).

Acknowledgements

We would like to acknowledge to Dr. Peter Werner and Prof. Ulrich Gösele, Max-Planck-Institute of Microstructural Physics for assisting in *in-situ* TEM studies. This work was financed by Volkswagen Stiftung (grant #040-549). One of us (T.R.) acknowledges for support the Israel Ministry of Science.

References

[1] C.B.Vining, W.Laskow, J.O.Hanson, R.R.Van der Beck, and P.D.Gorsuch, "Thermoelectric properties of pressure-sintered Si0.8Ge0.2 thermoelectric alloys", . Appl. Phys. , **69** (1991) 4333 .

[2] F.Edelman, Y.Komem, M.Stoelzer, P.Werner, and R.Butz, "Nanocrystalline SiGe Films: Structure and Properties", IEEE SIMC-9, Semiconducting and Insulating Materials Conference, Toulouse, (France) - April 29/ May 3, 1996, "Semiconducting and Insulating Materials 1996", Proceeds. of the 9th Conf. on Semicond. a. Insulating Mater. IEEE Operations Center, Piscataway, NJ, USA, 1996, Ed.C.Fontaine, p.205.

[3] P.Van Gerwen, T.Slater, J.B.Chevrier, K.Baert, and R.Mertens, "Thin-film Boron-doped polycrystalline silicon70%-germanium30% for thermopiles", Sensors and Actuators, **A53** (1996) 325.

[4] ***Binary Alloy Phase Diagrams***, Editior-in-Chief T.B.Massalski , ASM (The Materials Information Society), 1992.

[5] K.Seeger, ***Semiconductor Physics***, Springer, Berlin, 1991.

[6] V.I.Fistul', ***Heavily Doped Semiconductors***, Plenum, NY, 1969.

[7] K.B.Joelsson, Y.Fu, W.-X.Ni, and G.V.Hansson, "Hall factor and drift mobility for hole transport in strained Si1-xGex alloys", J. Appl. Phys. **81** (1997) 1264.

[8] J.P.Dismukes, L.Ekstrom, E.F.Steigmeier, I.Kudman, and D.S.Beers, "Thermal and Electrical Properties of Heavily Doped Ge-Si Alloys up to 1300K", J. Appl. Phys. **35** (1964) 2899 .

[9] D.M.Rowe and V.S.Shukla, "The effect of phonon-grain boundary scattering on the lattice thermal conductivity and thermoelectric conversion efficiency of heavily doped fine-grained, hot-pressed silicon germanium alloy", J/ Appl. Phys. **52** (1981) 7421 .

[10] G.A.Slack and M.A.Hussain, "The maximum possible conversion efficiency of silicon-germanium thermoelectric generators", J. Appl. Phys. **70** (1991) 2694 ..

A Study for Thermoelectric Properties of Ni Doped SiC Sintered Thermoelectric Semiconductor

Yoichi Okamoto, Kazuhiko Kato, Jun Morimoto and Toru Miyakawa*

Dept.of Materials Sci.& Eng. Natl.Defense Academy, 1-10-20 Hashirimizu, Yokosuka, Kanagawa 239 Japan
Phone: +81-468-41-3811 ext.3664, Fax: + 81-468-44-5910, E-mail: rshow@cc.nda.ac.jp
*Dept. of Computer Science, Chiba Inst.of Technology, 2-17-1 Tsudanuma, Narashino, Chiba 275, Japan

Abstract

The thermoelectric properties of the p-type SiC/Ni sintered thermoelectric semiconductor have been studied as functions of Ni concentration (from 0.5 wt.% to 5.0 wt.%) and temperature (from RT to 700 ℃). The electrical resistivity decreases drastically for all Ni concentration range compared with other dopants such as Cu, Al and B at room temperature. The electrical resistivity and thermoelectric power decrease with increase temperature. The value of figure of merit Z approaches to 1.4×10^{-4} at around 700 ℃. The condition of the doped impurity atom Ni has been also studied by magnetically. It is confirmed that Ni does not segregate in the SiC sintered sample. We conclude that Ni well diffused into SiC and it is one of the most effective dopant for SiC based thermoelectric materials.

1 Introduction

Recently, strong effort has been directed towards the development of sintered thermoelectric materials [1～5] with improved characteristics at comparatively higher temperatures. We reported the thermoelectric properties of SiC based p-type thermoelectric semiconductor doped with B_4C [5～9], Al [10] and Cu [11,12] over the temperature range from room temperature to 700 ℃. The SiC based system is expected to be useful at higher temperature region because of pyrolytic property and wide gap semiconductor characteristics of SiC. It is revealed that the figure of merit Z of this system reaches up to 10^{-4} K^{-1} at around 700℃ from the measurements of electrical resistivity, thermoelectric power and thermal conductivity on SiC based systems as functions of dopant concentration, temperature and sample porosity. The relatively higher electrical resistivity is responsible to this low Z value which is not enough for practical use. From the results of previous reports[6-12], it is considered that $\mathrm{II_b}$ atom is more appreciable than $\mathrm{III_b}$ atom and far the more $\mathrm{I_b}$ atom is more appreciable than $\mathrm{II_b}$ as a dopant atom. Therefore, Ni, which belongs to VIII, is selected as a dopant atom with ambition to decrease electrical resistivity.

Also from the previous reports [6～12], carrier concentration is still low compared with the dopant concentration. There is accordingly probability that only minor part of the dopant atoms act as the effective electron acceptor and major part of the dopant atoms have no effect on carrier concentration.

Since the same kind of doped atoms act different roles, there must be some differences among the effective atom and non effective atom, such as circumstances of the doped atom. Therefore we must study the diffusion condition of dopant atoms in the sample.

A magnetic approach is available when the atoms of ferromagnetic material diffuse into non-ferromagnetic material. In this case, reduction of the ferromagnetic moment is a good indication of diffusion [13]. It is well known that the ferromagnetic moment of Ni metal linearly decreases when it is diluted by the many kinds of non-ferromagnetic materials such as Cu, Si, *etc.* In the present study, we have chosen ferromagnetic Ni as a dopant, because of following two purposes. One is to study the thermoelectric properties of the SiC doped with ferromagnetic atom Ni and the other is to clarify the diffusion condition into the SiC by using the magnetic measurements.

In this paper we report on the results of the magnetic measurements and the thermoelectric property measurements of SiC/Ni system at room temperature.

2 Experiment

2.1 Sample preparation

Sample preparation procedure is almost the same as described in previous papers[6～12]. β-SiC (Mitsui Toatsu Co., Ltd. MSC-20, 99.7 % up, average particle size 0.15 μm and BET (Brunauer-Emmett-Teller) surface area 19.5 m^2/g) and Ni (Rare Metallic Co.,Ltd., 99.9 % up, 100 mesh pass,) were used as starting materials.

Slurries were made from mixed SiC and 0.5 ～ 5.0 wt. % Ni powders in polyethylene jars with nylon coated iron balls as the grinding media and xylene solution as the mixing agent. After mixing for 20 hours and passing through 75 μm mesh sieve, the slurries were dried. The dried mixture were granulated using 500 μm mesh sieve and pressed into 20 mm $\phi\times$ 6 mm pellet at 10 MPa. Then the pellets sealed into an evacuated rubber tube and then pressed isostatically at 200 MPa.

Each pellet covered with the same compositional powder was placed into a carbon crucible. Sintering procedure was carried out by RF induction. First, the furnace was heated up

0-7803-4057-4/97 $10.00 ©1997 IEEE

to 1100 ℃ at a rate of 20 ℃/min. in vacuum, and Ar gas was introduced up to normal pressure. Then the temperature was raised to the sintering temperature (2100 ℃) at a rate of 10 ℃/min., the sample was kept at this temperature for 2 hours and cooled naturally down to room temperature. Sintered materials were cut into rectangular shaped specimens of 3 × 4 × 8 ~ 10 mm^3 in dimensions.

2.2 Measurement

The crystal properties and constituent of prepared samples were studied by using powder X-ray diffractometer and EPMA (Electron Probe Micro Analyzer). Magnetic hysteresis curve was measured at room temperature by using VSM (Vibrating Sample Magnetometer) and temperature dependence of the magnetization was measured by using SQUID (Superconducting Quantum Interference Device) from liquid He temperature to room temperature. Measurements of thermoelectric power and DC electrical resistivity were made from room temperature to around 700 ℃ and measurements of thermal conductivity was made from room temperature to around 300 ℃. Conventional four proves method was employed in DC electrical resistivity measurement. Thermoelectric power was measured by the standard DC method.

Thermal conductivity measurement was made by a differential phase analysis of PPE(Photo Pyro Electric) signal (ΔL-$\Delta\theta$ analysis)[14,15].

In the PPE method one can measure thermal diffusivity α. Thermal conductivity is given by

$$\kappa = \alpha_{td} \cdot d \cdot C \quad \cdots\cdots (1)$$

here, κ, α_{td}, d and C are thermal conductivity, thermal diffusivity, density and specific heat, respectively. We calculate specific heat of SiC/Ni system from that of SiC and Ni. The values of d and α were measured.

3 Results and Discussion

3.1 Structural property

The crystal properties and composition of prepared samples are studied by using powder X-ray diffractometer. In the diffraction profiles of the 0.5, 1.0, 2.0 and 5.0 wt.% Ni doped sample, there are only diffraction peaks assigned to α -SiC (3C-SiC). There are no additional small peaks invented from unknown impurities.

The cut surfaces of the samples were analyzed by using EPMA to know the spacial distribution of dopant. From the results of EPMA line analysis of the 5.0 wt.% Ni doped sample, the intensity of Ni K_α is almost constant within the noise level. It is concluded that there is no large Ni segregated area. On the other hands, the intensity of Si K_α shows the large fluctuation. Since the packing density of this sample is about 62%, the porous structure of this sample may be responsible for the large fluctuation of the intensity of Si K_α.

3.2 Magnetic measurements

Figure 1-(a) and 1-(b) show the M-H curves of the Ni 5.0 wt.% doped two samples measured at room temperature by using VSM. From these figures, the both samples mainly consists of paramagnetic component and slight ferromagnetic component. The magnetic susceptibility of paramagnetic component is estimated around 2.7×10^{-6} emu/g Oe and saturation magnetization of ferromagnetic component is estimated about 7×10^{-4} emu from the small hysteresis loop. The Ni content is 15.4 mg and 16.0mg since the mass of the samples are 308.1 mg in fig.1-(a) and 319.0 mg in fig.1-(b), respectively. If all dopant Ni segregates, the saturation magnetization of this sample would be 0.838 emu in fig.1-(a) and 0.870 emu in fig.1-(b) at room temperature, respectively. This is corroboration of uniform diffusion of dopant Ni into SiC grain and/or grain boundary.

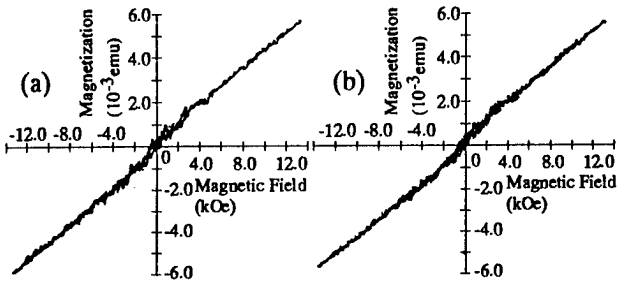


Fig.1 M-H curve of the sample SiC/Ni:5.0 wt.% measured by using VSM at room temperature.

Figure 2 shows temperature dependence of magnetic susceptibility measured from room temperature to liquid He temperature by using SQUID with about 10 Oe magnetic field. Above 100 K, magnetic susceptibility keeps almost constant. On the other hands, below 100 K, it shows some fluctuation. It seems that there are some kind of magnetic ordering. However, in all temperature range, apparent spontaneous magnetization is not observed. We conclude that dopant Ni well diffuses into SiC grain and/or grain boundary. Because, if pure Ni particles and/or Ni high concentration regions are formed, we can detect apparent ferromagnetic component.

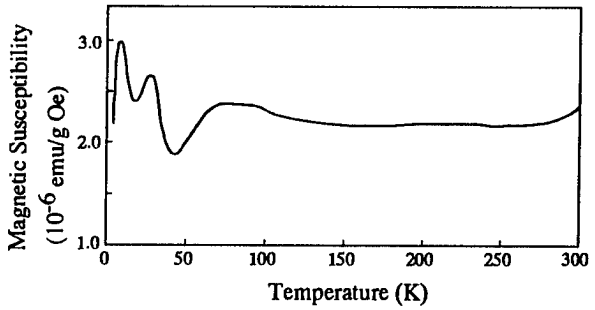


Fig.2 Temperature dependence of the magnetic susceptibility measured by using SQUID with temperature ranging from RT to liquid He temperature.

3.3 Thermal and electrical properties

Figure 3 shows the temperature dependence of electrical

resistivity with Ni concentration as a parameter. As shown in the figure, electrical resisitivity shows semiconductor like temperature dependence but degradation with temperature is rather small compared with the other dopants such as Al, Cu, Ag and B.

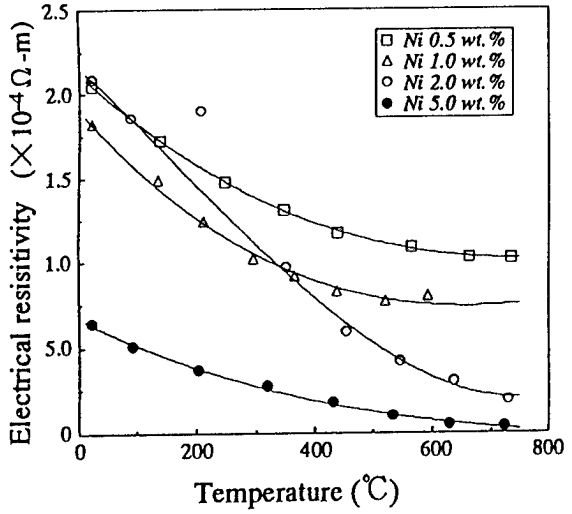


Fig. 3 Temperature dependence of the electrical resistivity with varying the Ni concentration.

No appreciable nonlinearity in the current-voltage characteristics could be observed. We found the minimum in resistivity at 5.0 % Ni concentration. For samples of 0.5 ~ 5.0 % Ni concentration, resistivity at 700 ℃ drops to 1/2 ~ 1/10 of its value at room temperature. And this tendency seem to saturate at higher temperatures. We tried to fit the experimental data by polynomials to interpolate between the measured points for calculation of figure of merit. In the figure, solid curves represent the calculated results of these polynomials.

The values of electrical resistivity have been reduced drastically and these absolute values are almost comparable with the values of with SiC/Cu or SiC/Ag reported in previous papers[5-8] at 700 ℃.

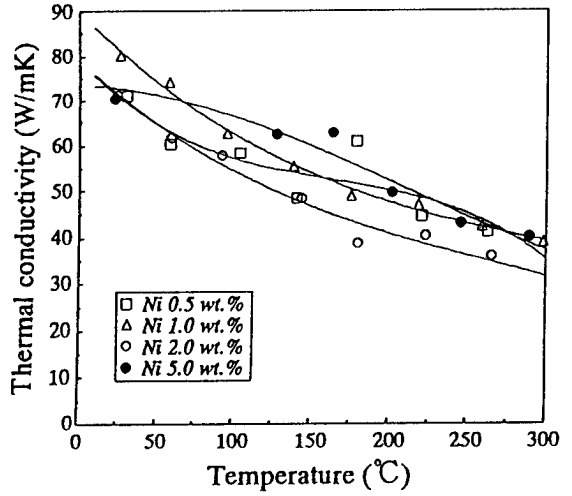


Fig. 4 Temperature dependence of the thermal conductivity measured by PPE method.

Figure 4 shows the temperature dependence of thermal conductivity measured by the PPE method as a function of Ni concentration. All samples show the same monotonous decrease tendency with temperature increase. Therefore, we can say that doping of Ni has no effects on the temperature dependence of the thermal conductivity. Unfortunately, the unstable thermal contact at higher temperatures of the sample to thermal sensor in our experimental system limits the range of thermal conductivity measurements below 300 ℃.

Also, we have fitted the experimental data by polynomials to interpolate the experimental data. In the calculation of the figure of merit, we have used these fitting polynomials under 300 ℃, and we have assumed that thermal conductivity stays constant above 300 ℃.

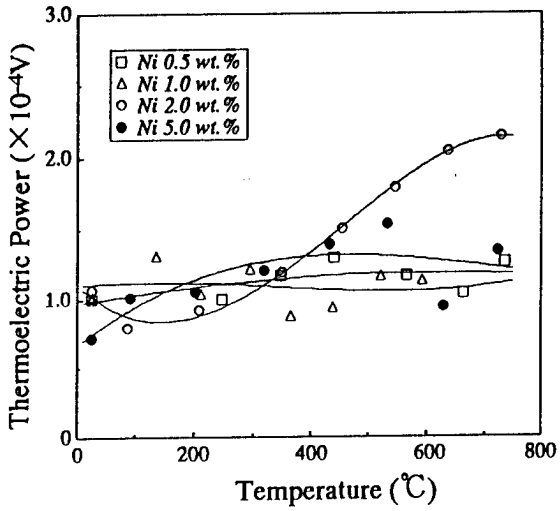


Fig. 5 Temperature dependence of the thermoelectric power measured by the conventional DC method.

Figure 5 shows the temperature dependence of thermoelectric power as a function of Ni concentration. The sample with 2.0 % Ni shows anomalous temperature dependence. The thermoelectric power in other samples show weak increase with temperature and the values are around 100 μV/K.

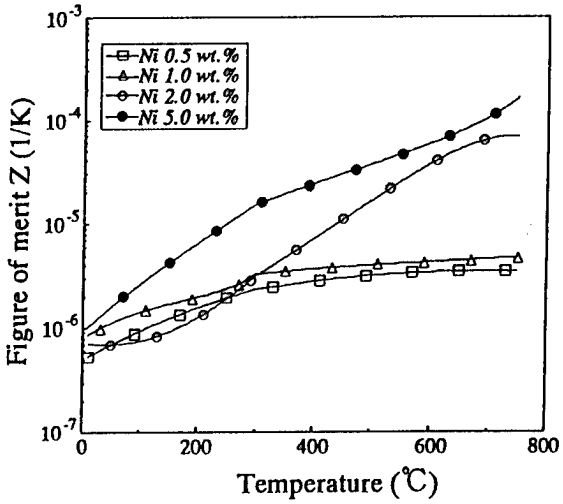


Fig. 6 Temperature dependence of the figure of merit.

The temperature dependence of figure of merit Z in Figure 6 is estimated using fitting polynomials for electrical resistivity, thermal conductivity and thermoelectric power.

At the Ni concentration of 5.0 wt.%, where the figure of merit Z takes its maximum value (1.4×10^{-4} K^{-1}), while thermal conductivity shows the value around 40 W/m-K. The value of thermoelectric power is comparable to one of the practical material such as Bi_2Te_3 system at room temperature. Compared with practical materials, Z value of our present SiC/Ni system is lower by almost a factor of 10. Further reduction of electrical resistivity and thermal conductivity will be a prospective way to achieve a higher value of Z especially at still higher temperature range (>700℃). In this respect, sample preparation of this SiC based system would be an interesting future work.

4. Conclusion

From the magnetic measurements, it is confirmed that dopant Ni well diffused into SiC grain and/or grain boundary and it acts as effective electron acceptor. We found that the sample with Ni concentration 5.0 wt.% can be expected to take the maximum value of figure of merit Z (1.4×10^{-4} K^{-1}) at around 700 ℃. Compared with the one of the criterion for practical use ($Z \geqq 10^{-3}$ K^{-1}), Z value of our present SiC/Ni system is almost within the reach of the criterion. At 700 ℃, the electrical resistivity also takes a minimum value of 3.0×10^{-5} Ω m. The reduction of the electrical resisitivity by doping of impurity atoms is the most effective way to increase the figure of merit Z. Since this SiC/Ni system shows the largest Z value and lowest electrical resistivity in the SiC based systems at room temperature, Ni is found to be a more effective dopant as an acceptor in SiC compared to another dopants such as Al, Cu, Ag and B.

Measurements of thermoelectric characteristics at still higher temperature will also be a challenging task.

Acknowledgments

The authors express their thanks to Associate Professor Hiroshi Yasuoka of Department of Mathematics and Physics and Mr. Makoto Itonaga of Japan Victor Co., Ltd. for their experimental assistance.

References

1) T. Ohta, A. Yamamoto, T. Tanaka, T. Fujimaki, K. Kamisako, "Composition dependence on thermoelectric properties of undoped polycristal $(Bi_2Te_3)_{1-y}(Sb_2Te_3)_y$ prepared by PIES metod": Proc. 14th Int. Conf. on Thermoelectrics (ICT'95), St. Petersburg, Russia, 1995.
2) H. Wada, Y. Okamoto, T. Miyakawa, T. Irie, "Oriented mosaic model analysis of anisotropic thermoelectric properties of heterogeneous materials": J. Mater. Sci. **27** (1992) 881.
3) K. Fukuda, H. Imaizumi, T. Ishii, F. Toyoda, M. Yamanashi, Y. Kibayashi, "Orientational distribution in hot pressed n-type Bi_2Te_3": Proc. 14th Int. Conf. on Thermoelectrics (ICT'95), St. Petersburg, Russia, 1995.
4) H. Wada, M. Watanabe, J. Morimoto, T. Miyakawa, "Photopyroelectric (PPE) determination of thermal deffusivity of $Bi_2Te_{2.85}Se_{0.15}$ sintered thermoelectric semiconductor": J. Mater. Res. **6** (1991) 1711.
5) Y. Okamoto, T. Miyakawa, J. Morimoto, A. Aruga, S. Fujimoto, "Effective medium analysis and equi-Z-contour map for porosity controlled SiC:B_4C system": Proc. 14th Int. Conf. on Thermoelectrics (ICT'95), St.Petersburg, Russia, 1995.
6) Y. Okamoto, A. Aruga, K. Shioi, J. Morimoto, T. Miyakawa, S. Fujimoto, "Thermoelectric properties of B_4C doped SiC" : Proc. 12th Int. Conf. on Thermoelectrics, Yokohama, Japan, 1993.
7) Y. Okamoto, K. Tanaka, A. Aruga, M. Furuta, J. Morimoto, T. Miyakawa, S. Fujimoto, "Thermoelectric properties of porosity controlled SiC/B_4C": Proc. 13th Int. Conf. on Thermoelectrics, KANSAS CITY MO, USA, 1994, AIP Conf. Proc. 316 (1995) 62.
8) Y. Okamoto, A. Aruga, H. Kasai, J. Morimoto, T. Miyakawa, S. Fujimoto, "Temperature dependence of thermoelectric properties of SiC/B_4C": Proc. 13th Int. Conf. on Thermoelectrics, KANSAS CITY MO, USA, 1994, AIP Conf. Proc. 316 (1995) 92.
9) K. Kato, A. Aruga, Y. Okamoto, J. Morimoto, T. Miyakawa, "Temperature Dependence of the Porosity Controlled SiC/B_4C+PSS Thermoelectric Properties": Proc. 4th Int. Symp. Functional Graded Materials <FGM'96>, Tsukuba, 1996 (in press).
10) Y. Okamoto, A. Aruga, H. Tashiro, J. Morimoto, T. Miyakawa, S. Fujimoto, "Temperature dependence of thermoelectric properties of SiC/Al": Proc. 14th Int. Conf. on Thermoelectrics (ICT'95), St. Petersburg, Russia, 1995.
11) Y. Okamoto, K. Kato, K. Asai, J. Morimoto, T. Miyakawa, "The characteristics of high temperature thermoelectric material: sintered SiC/Cu": J. Mater. Sci. (submitted).
12) K. Kato, Y. Okamoto, J. Morimoto, T. Miyakawa: "Thermoelectric properties of density controlled SiC/Cu systems by the addition of polysilastyene": J. Adv. Sci. **9** (1997) 26.
13) Y. Okamoto, T. Koyano, A. Tasaki, "A magnetic study of sintering of ultrafine particles": Jpn. J. Appl. Phys. **26** (1987) 1943.
14) J. Morimoto, Y. Okamoto, T, Miyakawa, "Thermal diffusivity of semiconductors evaluated by differential PPE method": Proc. 12th Symp. Ultrasonic Electronics, Tokyo, 1991, Jpn. J. Appl. Phys. **31**, Supplement **31-1** (1992) 38.
15) A. G. Rosencwaig, A. Gersho, "Photoacoustic and Photoacoustic Spectroscopy" (Academic Press, New York, 1980).

Thermoelectric Properties of ZnO Doped with The Group 13 Elements

Toshiki Tsubota, Michitaka Ohtaki, Koichi Eguchi, and Hiromichi Arai
Department of Materials Science and Technology, Graduate School of Engineering Sciences, Kyushu University
6-1 Kasugakoen, Kasuga, Fukuoka 816 JAPAN
Tel.: +81/92/583-7527, Fax: +81/92/573-0342, E-mail: tsubota@zaikai.kyushu-u.ac.jp

Abstract

Investigation on thermoelectric properties of ZnO doped with the group 13 elements revealed that addition of M_2O_3 (M = Al, Ga, In) to ZnO all increased the electrical conductivity significantly, whereas the absolute values of the Seebeck coefficient moderately decreased. The increase in the electrical conductivity was smaller for the dopant with the heavier element, being in good agreement with a decrease in the carrier mobility. However, the thermal conductivity was also suppressed by Ga and In doping, particularly at the lower temperature region. Even with the smaller power factor values, the figure of merit of $(Zn_{0.98}M_{0.02})O$ (M = Ga or In) was equal to that of the Al-doped one up to ca. 600°C, owing to the suppression of the thermal conductivity.

Introduction

The performance of thermoelectric materials is represented by the figure of merit defined as $Z = S^2\sigma/\kappa$, where σ is the electrical conductivity, S is the Seebeck coefficient, and κ is the thermal conductivity of the material. Because the Carnot efficiency also improves with increasing temperature difference over which the thermoelectric device operates, materials with larger ZT values have been under extensive research. To date, several materials have been developed as high temperature thermoelectric materials; for example, Si-Ge alloys, several metal chalcogenides, transition-metal disilicides, and some boron compounds. Recently, skutterudites and filled skutterudites have been discovered as promising materials with superior transport properties and high thermoelectric performance at moderately high temperatures[1-3].

Many metal oxides are known to be stable at high temperature in air. However, poor electrical conduction appears to be a common belief about metal oxides. Highly ionic characters of oxide materials are generally considered to result in very low carrier mobility. Presumably from this reason, oxides had hardly been studied as thermoelectric materials. Actually, however, rather many oxide materials have been reported to have high electrical conductivities. We have recently pointed out that the oxides such as In_2O_3-based mixed oxides[4], $CaMnO_3$[5, 6], and $(Zn_{1-x}Al_x)O$[7-9] would be promising as new thermoelectric materials at high temperatures. Since then, several researchers have started to study on oxide thermoelectric materials such as $(ZnO)_mIn_2O_3$[10], $CdIn_2O_4$[11], and so on.

We have already reported that $(Zn_{1-x}Al_x)O$ have exceedingly high thermoelectric performance compared to other oxides[7-9]. The addition of Al_2O_3 to ZnO significantly enhances the electrical conductivity, retaining the moderate Seebeck coefficients. The power factors, which evaluates the electrical component of the thermoelectric performance, of $(Zn_{1-x}Al_x)O$ are consequently very large. We have also revealed that polycrystalline samples of $(Zn_{1-x}Al_x)O$ ($0.02<x<0.05$) show the fairly high mobility, which would account for the very large power factors of these oxides. Unfortunately, however, these samples showed the unfavorably high thermal conductivities which limit Z to moderate values. The simple crystal structure and the light constituent elements of $(Zn_{1-x}Al_x)O$ must be the reason for the high thermal conductivities. We confirmed that the lattice thermal conductivity is the principal component of κ of the oxides. If phonon scattering centers can be effectively introduced without scattering the charge carriers, the Z values of these materials will be greatly improved. Since the point defects induced by heavier atoms should be more effective for phonon scattering, in this work we have attempted to reduce κ by using Ga and In as the heavier group 13 elements for dopants.

Experimental

The mixed oxides $(Zn_{0.98}M_{0.02})O$ (M = Al, Ga, In) were prepared from powders of ZnO, Al_2O_3, Ga_2O_3 and In_2O_3 of guaranteed grade. These powders were mixed and pulverized in a nylon-lined ball mill for 24 h. The powder mixture was pressed into a pellet and sintered at 1400°C for 10 h in air. The heating and cooling rate was 200°C h^{-1}. The crystal phases in the samples thus obtained were determined from a powder X-ray diffraction (XRD) study using Cu Kα radiation (Rigaku RINT-1400). The relative densities of all the samples were measured by the Archimedes' method. We simultaneously measured both the electrical conductivities and Seebeck coefficients in air, from room temperature up to 1000°C. The measurement procedures have been described elsewhere in detail[4]. The thermal conductivity was determined from the thermal diffusivity and the specific heat capacity measured by the laser flash technique (ULVAC TC-7000). The Hall

0-7803-4057-4/97 $10.00 ©1997 IEEE

measurements were performed by van der Pauw method at room temperature.

Results and Discussion

Arrhenius plots of the electrical conductivity, σ, are shown in Fig. 1 for $(Zn_{0.98}M_{0.02})O$ (M=Al, Ga, In). The relative densities of all the samples were more than 99%. Since all the samples have dense microstructure, difference in the microstructure of the sintered samples cannot be the main reason for the variation in the σ values. We have reported that Al-doping to ZnO increases σ and changes its behavior from semiconducting to metallic[7-9]. The σ values of the doped samples are in the following order: Al > Ga > In >> undoped ZnO. In other words, σ decreases in order of the atomic weight of the dopant atoms.

The Seebeck coefficients of $(Zn_{0.98}M_{0.02})O$ (M = Al, Ga, In)

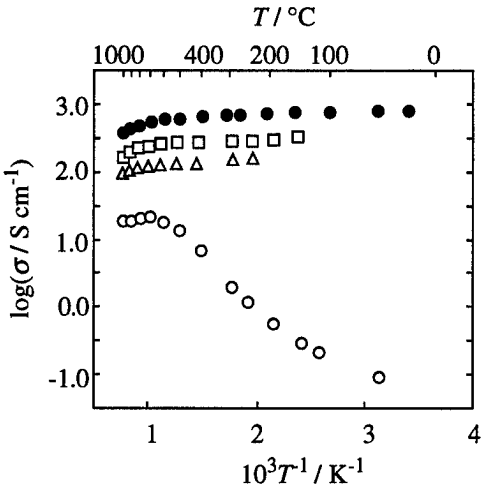


Fig. 1 Arrhenius plots of the electrical conductivities of $(Zn_{0.98}M_{0.02})O$.
M: ○, Zn; ●, Al; □, Ga; △, In

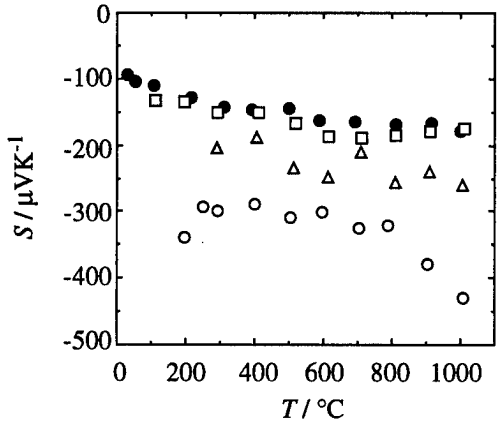


Fig. 2 The Seebeck coefficients of $(Zn_{0.98}M_{0.02})O$ as a function of temperature.
M: ○, Zn; ●, Al; □, Ga; △, In

as a function of temperature are indicated in Fig. 2. The |S| values of the doped samples were all smaller than that of undoped ZnO, and showed a general trend in which the values gradually increase with temperature up to 1000°C. The order of the |S| values was undoped ZnO >> In > Ga ≈ Al. It should be noted that the dependence of |S| and σ on the dopant is in a reciprocal manner.

According to the idea of valence control, it is expected that addition of trivalent elements to ZnO would provide excess electrons and hence result in an increase in the electrical conductivity. We have further measured the Hall coefficients of $(Zn_{0.98}M_{0.02})O$ (M=Al, Ga, In) to estimate the carrier concentration n and the Hall mobility μ_H of these samples. The n and μ_H values measured at room temperature are summarized in Table 1. Even the n value of undoped ZnO was of the order of $10^{23}m^{-3}$. It is well known that ZnO is a nonstoichiometric compound having interstitial Zn atoms, which provide the carrier electrons. All the doped samples had much higher carrier concentrations of the order of $10^{25}m^{-3}$.

It is noteworthy that undoped ZnO has a fairly large μ_H value of $67cm^2V^{-1}s^{-1}$. We have already reported in the previous paper that $(Zn_{1-x}Al_x)O$ $(0.02<x<0.05)$ have high mobilities as similar to the undoped one[9], and suggested that a fairly covalent character of the Zn-O bond is probably responsible for the favorable electrical transport properties. However, it should be noted that the μ_H values of the Ga- and In-doped samples are less than half of that for the Al-doped sample. The smaller μ_H values of the Ga-doped sample compared with the Al-doped one can account for the insufficient improvement in σ for the Ga doping, and even lower σ of the In-doped sample would be ascribed to both the small n and μ_H values.

The $S^2\sigma$ values of $(Zn_{0.98}M_{0.02})O$ (M=Al, Ga, In) are presented in Fig. 3 as a function of temperature. The power factor of ZnO was improved by any of the group 13 doping. The improvement is attributed to the marked enhancement of σ with only moderately suppressing S. The power factor values of $(Zn_{0.98}M_{0.02})O$ (M = Ga or In), however, are about half of that of $(Zn_{0.98}Al_{0.02})O$.

Table 1 The carrier concentration n and the Hall mobility μ_H of $(Zn_{0.98}M_{0.02})O$

M	n / $10^{25}m^3$	μ_H / $cm^2V^{-1}s^{-1}$
Zn	0.052	67
Al	7.2	81
Ga	7.2	33
In	3.2	36

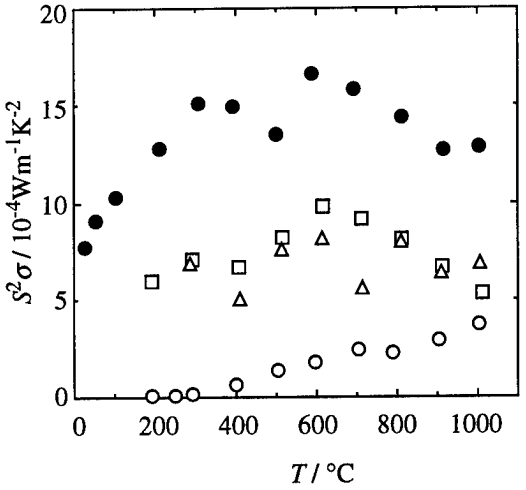


Fig. 3 The power factors of $(Zn_{0.98}M_{0.02})O$ as a function of temperature.
M: ○, Zn; ●, Al; □, Ga; △, In

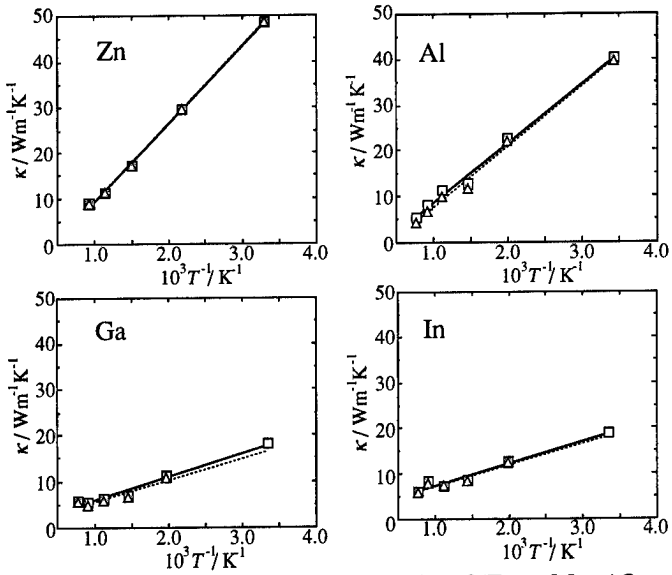


Fig. 5 The thermal conductivity of $(Zn_{0.98}M_{0.02})O$ as a function of inverse temperature.
□, κ; △, $\kappa_{ph} = \kappa - \kappa_{el}$

Fig. 4 depicts the thermal conductivities of $(Zn_{0.98}M_{0.02})O$ (M=Al, Ga, In) as a function of temperature. The κ values of all the samples decrease with increasing temperature and converge in ca. 5 $Wm^{-1}K^{-1}$ at 1000°C. This figure indicates that the κ values of the doped samples are apparently lower than that of undoped ZnO in the low temperature region; particularly the κ values of $(Zn_{0.98}M_{0.02})O$ (M = Ga or In) are less than half of that for undoped ZnO. The thermal conductivity, κ, of solid materials consists of the carrier thermal conductivity (κ_{el}) and the lattice thermal conductivity (κ_{ph}), i.e., $\kappa = \kappa_{el} + \kappa_{ph}$. It is well known that κ_{ph} is proportional to T^{-1} above the Debye temperature (it is usually below room temperature)[12]. The dependence of κ versus T^{-1} shown in Fig. 5 for $(Zn_{0.98}M_{0.02})O$ (M=Al, Ga, In) exhibits a good linearity, which suggests that κ is predominantly consists of κ_{ph}. This is further confirmed in Fig. 5 by a negligible contribution of κ_{el} estimated from the Wiedemann-Franz relation, $\kappa_{el} = L\sigma T$ (L is the Lorentz number.), for which validity for several electronic-conducting oxides has also been confirmed[13]. We can also conclude that the suppressions of κ for $(Zn_{0.98}M_{0.02})O$ (M = Ga or In) are due to the decreases in κ_{ph}. As we have expected, the addition of the heavier group 13 elements, which have similar electron configurations but larger atomic weights compared to Al, was successful to enhance the phonon scattering as confirmed by the suppression of κ_{ph} by the Ga- and In-doping. Nevertheless, the electrical transport properties were also affected mainly with

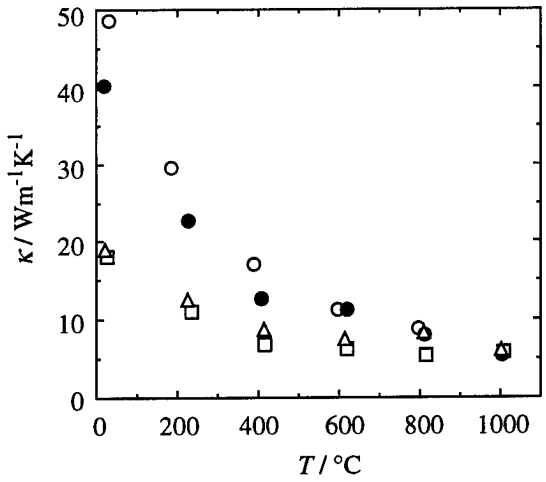


Fig. 4 The thermal conductivities of $(Zn_{0.98}M_{0.02})O$ as a function of temperature.
M: ○, Zn; ●, Al; □, Ga; △, In

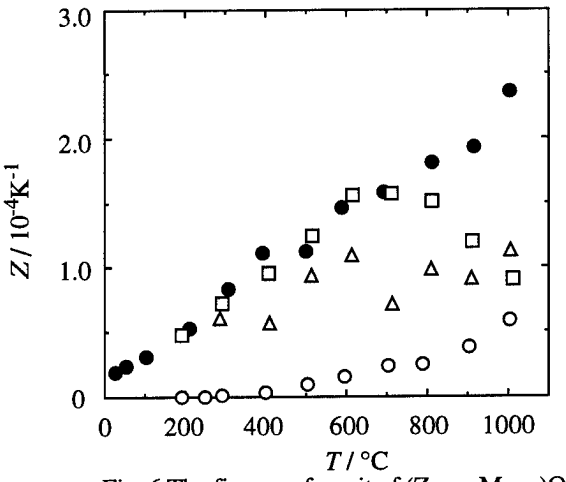


Fig. 6 The figures of merit of $(Zn_{0.98}M_{0.02})O$ as a function of temperature.
M: ○, Zn; ●, Al; □, Ga; △, In

the decreased μ_H values against our expectation.

The figure of merit, Z, of $(Zn_{0.98}M_{0.02})O$ (M = Al, Ga, In) obtained from the σ, S and κ data is displayed in Fig. 6 as a function of temperature. The Al-doped sample surpasses all other samples including undoped ZnO all over the temperature region examined. In spite of the decrease in $S^2\sigma$, the Z values of $(Zn_{0.98}M_{0.02})O$ (M = Ga, In) are virtually equal to that of the Al-doped one up to *ca.* 600°C, benefiting from the suppression of κ. However, because the κ values of these samples converge with increasing temperature, $(Zn_{0.98}Al_{0.02})O$ has larger Z values than Ga- and In-doped samples above 600°C.

Conclusions

Thermoelectric properties of $(Zn_{0.98}M_{0.02})O$ (M = Al, Ga, In) were investigated. Addition of these group 13 elements to ZnO significantly enhanced σ and moderately depressed $|S|$, resulting in the improvement in $S^2\sigma$. The σ values of the samples were in order of Al > Ga > In >> undoped ZnO, being in good agreement with the measurd n and μ_H. The Ga- and In-doping were sucsessful to suppress κ via decreases in κ_{ph}. Consequently, the Z values for the Ga- and In- doped samples reached the values of the Al-doped one up to 600°C in spite of the decrease in $S^2\sigma$. The compatibility between the effective carrier doping and suppression of κ is required for improvement in Z of the ZnO-based thermoelectric materials.

Acknowledgments

The authors thank Mr.Yasuhiro Yamada of the Government Industrial Research Institute, Kyushu, for his kind cooperation on the laser flash measurement of κ. This work was financially supported in part by Research Fellowships of the Japan Society for the Promotion of Science for Young Scientists.

References

[1] T. Caillat, A. Borshchevsky, J.-P. Fleurial, "Preparation and Thermoelectric Properties of p- and n-type $CoSb_3$", in Proc. 13th Int. Conf. Thermoelectrics, ed. B. Mathiprakasam, AIP Press, Now York, 1994, p. 58

[2] G. S. Nolas, G. A. Slack, D. T. Morelli, T. M. Tritt, A. C. Ehrlich, "The effect of rare-earth filling on the lattice thermal conductivity of skutterudites", J. Appl. Phys., **79**(8) (1996) 4002.

[3] A. Borshchevsky, T. Caillat, J.-P. Fleurial, "Solid Solution Formation: Improving the Thermoelectric Properties of Skutterudites", in Proc. 15th Int. Conf. Thermoelectrics, 1996, p. 112

[4] M. Ohtaki, D. Ogura, K. Eguchi, H. Arai, "High-temperature Thermoelectric Properties of In_2O_3-based Mixed Oxides and their Applicability to Thermoelectric Power Generation" J. Mater. Chem., **4**(5) (1994) 653.

[5] M. Ohtaki, H. Koga, T. Tokunaga, K. Eguchi, H. Arai, "Electrical Transport Properties and High-Temperature Thermoelectric Performance of $(Ca_{0.9}M_{0.1})MnO_3$ (M = Y, La, Ce, Sm, In, Sn, Sb, Pb, Bi)", J. Solid State Chem., **120** (1995) 105.

[6] M. Ohtaki, H. Koga, K. Eguchi, H. Arai, "Thermoelectric Properties of $(Ca_{1-x}Bi_x)MnO_3$ Perovskite-type Oxides as a New Material for High Temperature Thermoelectric Conversion", in Proc. 13th Int. Conf. Thermoelectrics, ed. B. Mathiprakasam, AIP Press, Now York, 1994, p. 115

[7] M. Ohtaki, T. Tsubota, K. Eguchi, H. Arai, "High-temperature thermoelectric properties of $(Zn_{1-x}Al_x)O$", J. Appl. Phys., **79**(3) (1996) 1816.

[8] M. Ohtaki, T. Tsubota, K. Eguchi H. Arai, "Thermoelectric performance of ZnO-based mixed oxides as a promising high-temperature material", in Proc. 14th Int. Conf. Thermoelectrics, ed. M. V. Vedernikov, A. F. Ioffe Physical-Technical Institute, St. Petersburg, 1995, p. 245

[9] T. Tsubota, M. Ohtaki, K. Eguchi, H. Arai, "Thermoelectric properties of Al-doped ZnO as a promising oxide material for high-temperature thermoelectric conversion", J. Mater. Chem., **7**(1) (1997) 85.

[10] H. Ohta, W. S. Seo, K. Koumoto, "Thermoelectric Properties of Homologous Compounds in the ZnO-In_2O_3 System", J. Am. Ceram. Soc., **79**(8) (1996) 2193.

[11] W. S. Seo, H. Sinmachi, K. Koumoto, "Synthesis of Spinel-Type Oxides and Their Thermoelectric Properties" (in Jpn.), in Proc. of the Annual Meeting of the Ceramic Society of Japan, Ceramic Society of Japan, Nagoya, Japan, 1994, p. 206

[12] C. Kittel, in Introduction to Solid State Physics, 5th edition, John Wiley & Sons, Inc., New York, 1976.

[13] M. E. Fine, N. Hsieh, "Wiedemann-Franz-Lorenz relation in highly electronic-conducting oxides", J. Am. Ceram. Soc., **57** (1974) 502.

Dependence of the phonon drag on Zn concentration in $Cd_{1-x}Zn_xTe$ in the range $0<x<0.1$

Svìtla Vacková
Charles University, Faculty of Mathematics and Physics, Ke Karlovu 5, 12116 Prague 2, Czech Republic, Tel.:+420/2/2191-1484, Fax: +420/2/2491-1061, E-mail: vackova@karlov.mff.cuni.cz
and Czech Technical University, Prague, Czech Republic

Karel Zdánský
Institute of Radio Engineering and Electronics, Academy of Sciences of the Czech Republic, Chaberská 57, 18251 Prague 8, Czech Republic, Tel.:+420/2/688-1804, Fax: +420/2/688-0222, E-mail: zdansky@ure.cas.cz

Larisa Scherbak and Petro Fejchouk
Faculty of Chemistry, State University of Chernivtsi, Ukraine

Maria Ilaschouk
Faculty of Physics, State University of Chernivtsi, Ukraine

Abstract

Our last results have shown a non-linear dependence of the phonon drag effect on the Zn concentration single crystals of $Cd_{1-x}Zn_xTe$ in the range $0<x<0,1$ with the minimum at $x=0,04$. As the phonon drag (PD) gives information about the interaction between carriers and phonons in the lattice, the reason for the non-linear dependence can be probably found in anomalous structural changes of the crystal lattice. The PD has been studied by the measurement of the Seebeck effect in Cd_{1-x} Zn_xTe. Simultaneously a new method for the measurement of the activation energy of shallow acceptors using the temperature gradient has been described.

Introduction

The II-VI mixed crystals, one of which is $Cd_{1-x}Zn_xTe$, have been the subject of many mainly experimental studies. These crystals are very important because of their multiple applications, which range from radiation detectors to substrates for lattice matched growth of HgCdTe and HgZnTe epitaxial thin films. In paper [1] the abnormal vibrations Cd atoms in $Cd_{1-x}Zn_xTe$ are reported, in [2,3] the influence of ferroelectricity on the electrical properties of $Cd_{1-x}Zn_xTe$ solid solutions and in [4] the optical investigations of defects in $Cd_{1-x}Zn_xTe$ were studied. In spite of these studies a lot of problems is not yet solved. Especially little is known about the dynamics of atoms in these ternary compounds. The introduction of Zn in the CdTe matrix represents in our opinion a factor of crystalline disorder. This assumption is strongly supported by the fact that heat transport properties [5] as well as the carrier transport are strongly influenced by the crystal quality.

Results and Discussion

After 25 years study of phonon drag effect in p and n-CdTe [6] (our results were also quoted in [7]) our attention is now concentrated on solid solutions of $Cd_{1-x}Zn_xTe$ with small concentration of Zn.

As we have shown in [6], the scattering on optical phonons is dominant in electrical transport effects. In the Seebeck effect the phonon drag by optical phonons diminishes (in absolute value) the Seebeck coefficient.

Our samples were grown by modified Bridgman technique elaborated in Laboratories of Chernivtsi State University, Ukraine. For n-CdTe the In contacts were used, for p-type Au was deposited from a $AuCl_3$ solution on split surface of the crystal. While In on n-CdTe forms a perfect ohmic contact, on p-CdTe and on its solid solution with Zn it is not in principal possible to prepare ohmic contacts. This property is used in our new method described below.

The following transport coefficients were measured on all samples: temperature dependence of dc electrical conductivity, Hall and Seebeck coefficients. The samples about $(15\times4\times1.5)$ mm^3 were pressed between two cooper blocks with an electrical heater inside of each block. Similarly as in [6] the experimental value of Seebeck coefficient α_{exp} was compared with the calculated one determined from the carrier concentration α_{th}, the difference $\alpha_{th} - \alpha_{exp} = \alpha_f$ and the

sample No.	Zn content x	carrier conc. (cm^{-3})	α_{th} ($\mu V/K$)	α_{exp} ($\mu V/K$)	α_f ($\mu V/K$)	type
1	0	1×10^{12}	1750	1320	430	p
2	0	2.4×10^{14}	1280	620	660	p
3	0	7.2×10^{15}	980	700	280	p
4	0.03	8×10^{15}	1100	750	350	p
5	0.04	2.1×10^{16}	880	860	20	p
6	0.04	1.4×10^{14}	980	950	30	p
7	0.04	2.7×10^{16}	860	860	0	p
8	0.04	3.2×10^{15}	1060	1000	60	p
9	0.04	2.6×10^{14}	700	650	50	n
10	0.09	1.4×10^{16}	920	760	160	p
11	0.1	8.9×10^{15}	930	430	500	p

Tab.1 Room temperature data of the measured samples

0-7803-4057-4/97 $10.00 ©1997 IEEE

contribution of the phonon drag effect to the Seebeck coefficient was calculated (see Tab. 1.)

The PD effect was found for all concentrations of zinc in the range from 0 to 10 % with the exception of 4 %, where the α_f is very small and its value fluctuates according to an experimental error. The experimental error in the determination of Zn concentration is about 0.5 %. It seems to us that our results are in a good agreement with [5], where the thermal and structural properties of $Cd_{1-x}Zn_xTe$ in the dependence on Zn concentration were compared.

Recently we have described [8] a new method for the study of phonon drag effect provided that the conditions about redistribution of carriers (as was theoretically predicted by Gurevich [9]) are fulfilled. The main idea of the method is following.

When the temperature gradient ∇T is applied on the metal-semiconductor-metal (MSM) system, the electrical conductivity is changing along the sample with the temperature gradient ∇T in dependence on its activation energy ΔE. The change of the electrical current ΔI through the system MSM at a constant voltage U can be described under these conditions as

$$\frac{\Delta I}{I_0} = 1 + \frac{\Delta E \cdot \Delta T}{2kT_0^2} \qquad (1)$$

for $\Delta T << T_0$, k is the Boltzmann constant, I_0 - the electrical current and T_0 - the temperature. The equation (1) gives a straight line for both signs of the temperature gradient ∇T. In the case that the temperature gradient produces the conductivity change only and no other effects, like a large PD effect, are involved, it is easy to determine the activation energy ΔE from the slope of the straight line.

The character of this dependence will be changed in the case, when the temperature gradient produces also other effects, e.g. the PD effect. The PD effect is connected with the redistribution of charge along the temperature gradient as it was shown by Gurevich [9]. Evidently for the redistribution of charge some special conditions must be fulfilled, for instance the presence of two types of carriers (heavy and light holes). From the character of experimental dependence we can decide whether acoustical or optical phonons drag the carriers in a similar way as in Seebeck effect [6].

The fact that there is no possibility to prepare an ohmic contact on a p-type CdZnTe crystal, as mentioned above, is used in our measurements. Reverse biased barrier Au/p-CdZnTe (0<Zn<10 %) in MSM system monitors the changes in the sample and under the temperature gradient brings about additional changes in ΔI for constant voltage U.

We measured at a constant voltage U instead with full I-U characteristic of the system MSM, because the application of temperature gradient mean the shift of I-U characteristic, as we verified many times. The results of our measurements of the sample No.3 are seen on the plot in Fig.1. Linear regressions of the experimental points for $\Delta T>0$ and $\Delta T<0$ are indicated by two straight lines. For the samples numbers 5, 6, 7, 8 and 9 the both straight lines coincide. In our paper [10] we described the experiment keeping the middle temperature T* at a constant value as is suggested in the theory [9], but the theory does not assume the rectifying properties of the contacts. The influence of

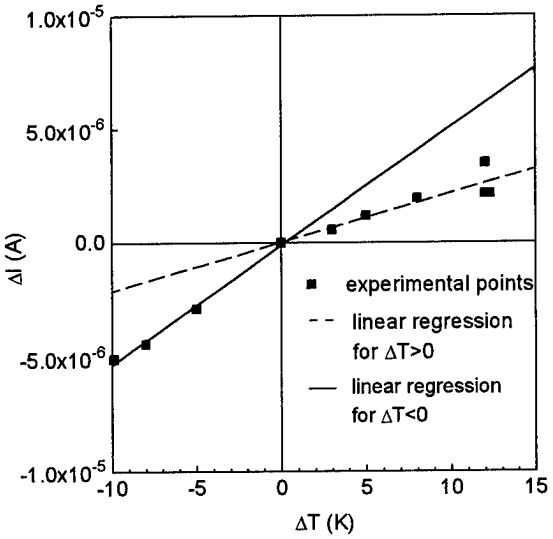


Fig.1. Asymetrical change of the current ΔI in the sample No.3 (Au/p-CdTe/Au) as a function of the temperature difference ΔT for U=2V and T=308K.

rectifying contacts was discussed in [11]. For this reason we decided to keep the temperature of one contact constant and to increase or decrease the temperature of the other one. The temperature gradient ∇T on the system MSM significantly controls the electrical current through the sample, it can enlarge or diminish it in agreement with (1).

Existence of a minimum in the PD dependence on the zinc concentration is unexpected at the first sight. It is well known that CdTe and ZnTe form a continuous series of solid solutions and their lattice parameter is regulated by a linear dependence on x at $x = 0.03 \div 0.05$ [4,5].

A non-linear character of some thermodynamic properties is published in [12] where a minimum in the dependence of the Gibbs factor on the Zn concentration at $x = 0.06 \pm 0.03$ is referred. Because this parameter is governed by the arrangement of the lattice nearest neighbor atoms and their interatomic interactions it can be assumed that near x = 0.04 a change of lattice interactions and lattice parameters falls out. It is known that the energy of an impurity in various lattice sites may depend on its environment. Apparently the increase of impurity content provokes a deviation of thermodynamic functions of the solid solution from the ideal ones. If we take into account the presence of extremes in concentration dependencies of some physical parameters we can assume that the transition from an ideal (in the thermodynamic sense) to non-ideal solid state takes place near x=0.04 in the case of $Cd_{1-x}Zn_xTe$.

This conclusion corresponds to the note in [12] about the fundamentals of solid states $Cd_{1-x}Zn_xTe$ at middle

concentrations. In accordance with the calculation in [12] the structure of $Cd_{1-x}Zn_xTe$ is so arranged that the sublattice of cations is nearly undisturbed (cations are held in their sites in the face-centered cubic lattice) but the anion sublattice is strongly disturbed. The increase of the Zn concentration in CdTe is followed by a shift of Te to form a bond with Zn so that the Zn-Te bond-length is shorter than that of Cd-Te.

References

[1] D. Comedi, R.Kalish, V. Richter, "Abnormal Vibrations of Cd Atoms in $Cd_{1-x}Zn_xTe$", Phys. Rev. Lett., **61,** No. 18, (1988) 2125.

[2] R. Weil, R. Nkum, E. Muranevich, L. Benquiqui, "Ferroelectricity in CdZnTe", Phys. Rev. Lett., **62**, No. 23, (1988) 2744.

[3] L. Benquiqui, R. Weil, E. Muranevich, A. Chack, E. Fredj, "Ferroelectric properties of $Cd_{1-x}Zn_xTe$ solid solutions", J. Appl. Phys. **74** (1) (1993) 513.

[4] W. Standler, D. M. Hofmann, H. C. Alt, T. Muschik, B. K. Meyer, "Optical investigatons of defects in $Cd_{1-x}Zn_xTe$", Phys. Rev. B, **51**, No. 16, (1995) 10619.

[5] M.E.Rodriguez, J. J. Alvarado-Gil, I. Delgadillo, O. Zelaya, H. Vargas, F. Sanchez-Sinencio, M. Tufino-Velazquez, L. Banos, "On the thermal and structural Properties of $Cd_{1-x}Zn_xTe$ in range $0<x<0,3$", Phys. Stat. Sol. (a) **158** (1996) 67.

[6] S. Kubalkova (Vackova), "The influence of optical phonons on Seebeck and Nernst-Ettingshausen Effects in CdTe", phys. stat. sol. (b) **50** (1972) 111.

[7] J. Rosenzweig, U. Birkholz, "Influece of Bipolar Photoconduction on the Thermoelectric Power of CdTe", phys .stat. sol. **71**, (1982) K41.

[8] Yu. G. Gurevich, S. Vackova, K. □dánský, "The phonon drag effect on thermopower in p-CdTe", Proceedings of ICT'96, Pasadena, USA.

[9] Yu. G. Gurevich, O. Yu. Titov, G. N. Logvinov and O. I. Lyubimov, "Nature of the thermopower in bipolar semiconductors", Phys. Rev. B **51** (1995) 6999.

[10] S. Vackova, J. Racko, D. Donoval, Yu. G. Gurevich, "The thermoelectrical and electrical properties of the system Au/p-CdTe/Au", Proceedings of ICT'95, St. Petersburg, Russia

[11] S. Vackova, J. Racko, D. Donoval, Yu. G. Gurevich, P.Fochuk, P. Feichuk, "Analysis of I-U measurements on Au/p-CdTe/Au and Au/p-$Cd_{0.96}Zn_{0.04}Te$/Au systems; the in-fluence of parallel temperature gradient", Proceedings of ECT'95, Nancy, France.

[12] N. Motta, A. Balzarotti, P. Letardi, A. Kisiel, M. T. Czyzyk, M. Zimnal-Starnawska, "Random Distribution Miscibility of $Cd_{1-x}Zn_xTe$ Alloy from EXAFS , J. Cryst. Growth, **72** (1985) 205.

Crystal grain size dependence of thermoelectric properties for sintered PbTe by spark plasma sintering technique

S. Yoneda[1], E. Ohta[1], H. T. Kaibe[2], I. Shiota[3], K. Takahashi[4], Y. Shinohara[5], Y. Imai[5] and I. A. Nishida[5]

[1]Dept. Materials Science, Keio University, Yokohama,Kanagawa 223, Japan
Tel.: +81/45/563/1141-3501, Fax:+81/45/563/0322, E-mail:yoneda@nrim.go.jp
[2]Dept. Electronics and Information Eng., Tokyo Metropolitan University, Hachioji, Tokyo 192-03, Japan
Tel.: +81/426/77/1111-4463, Fax:+81/426/77/2756
[3]Dept. Environmental Chemical Eng., Kogakuin University, Hachioji, Tokyo 192, Japan
Tel.: +81/426/28/4568, Fax:+81/426/28/5647
[4]Vacuum Metallurgical Co., Ltd., Yamatake, Chiba 289-12, Japan
Tel.: +81/475/89/0151, Fax:+81/475/89/1469
[5]National Research Institute for Metals,STA
Tel.: +81/298/59/2637, Fax:+81/298/59/2601

Abstract

Thermal and electrical conduction parameters of the sintered PbTe with different crystal grain sizes Ds were measured over the temperature range from 77 to 350 K, to examine the objective of this study is to examine the possibility of improvement in thermoelectric performance for sintered PbTe by reducing D. The starting powders with particle sizes of 6, 39, 180 and 380 μm were obtained by pulverizing undoped PbTe boule prepared by Bridgman method. Sintering was carried out by spark plasma sintering technique (SPS) under the conditions of sintering temperature of 732-803 K, sintering duration of 60-90 min and sintering pressure of 45 MPa. All the sintered compacts, whose conduction type were p-type, had apparent relative density of more than 99 %. Thermal conductivity κ decreased with reducing D below 200 K, while showed no dependence on D above 200 K . Long-wave phonons are scattered efficiently at grain boundaries only below 200 K. Hall mobility μ_H of the sintered compacts with different Ds were almost same above 200 K. It is concluded that thermoelectric performance for sintered PbTe is not directly affected by controlling D.

Introduction

Sintered material has even more crystal grain boundary in an unit volume the solidified material. The phonon component of thermal conductivity κ_{ph} is reduced by scattering of long-wave length phonon at the grain boundary. Bhandari and Rowe[1] have reported that reducing D has an effect on reducing κ_{ph} of PbTe alloys, resulting that the thermoelectric performance is improved.

The objective of the present study is to examine the possibility of improvement in thermoelectric performance for sintered PbTe by reducing D.

Experimental Procedure

Pb and Te with purity of 99.9999 % were individually weighed out in the atomic ratio1:1. They were loaded into an evacuated quartz tube whose size was 10 mm in diameter and 120 mm in length. The tube was flushed several times with Ar and sealed off under a pressure of about 1×10^{-1} Pa. The crystal growth was carried out by Bridgman technique. The growing conditions were maximum temperature 1223 K in the furnace, thermal gradient of 1.2 K/mm and crystal growth rate of 1.1×10^{-3} mm/s. The conduction type of the whole region of obtained boule was p-type. The boule material was ground into fine powders with a mean particle size of 6, 39, 180 and 380 μm, respectively. The sintered compacts ware prepared by SPS[2] at 732 - 803 K for 3.6×10^{2}-5.4×10^{2} s under 4.5×10^{7} Pa in an atmosphere of Ar+5%H_2. The size of sintered compacts were 15 mm in dia. and 6 mm in thickness. The apparent densities were 8.17-8.23 g/cm^3 which are higher than 99 % of theoretical one. The sintered compacts were all p-type semiconductors. Resistivity ρ, Hall coefficient R_H, thermoelectric power α and κ were measured in the temperature range from 77 to 350 K. Measuring κ was carried out by the static comparative method using transparent quartz as a standard specimen in the vacuum less than 1×10^{-4} Pa.

Results and discussion

Figure 1 shows microstructures of the sintered compacts with starting powder sizes of 6 (a), 39 (b), 180 (c) and 380 μm (d). The D corresponded to the starting particle size. It is confirmed that there is no evidence for the secondary grain growth during the sintering process.

Figure 2 is temperature dependence of R_H for the original boule and the sintered compacts shown in Figure 1. In the temperature range from 77 to 350 K, R_H decreases with

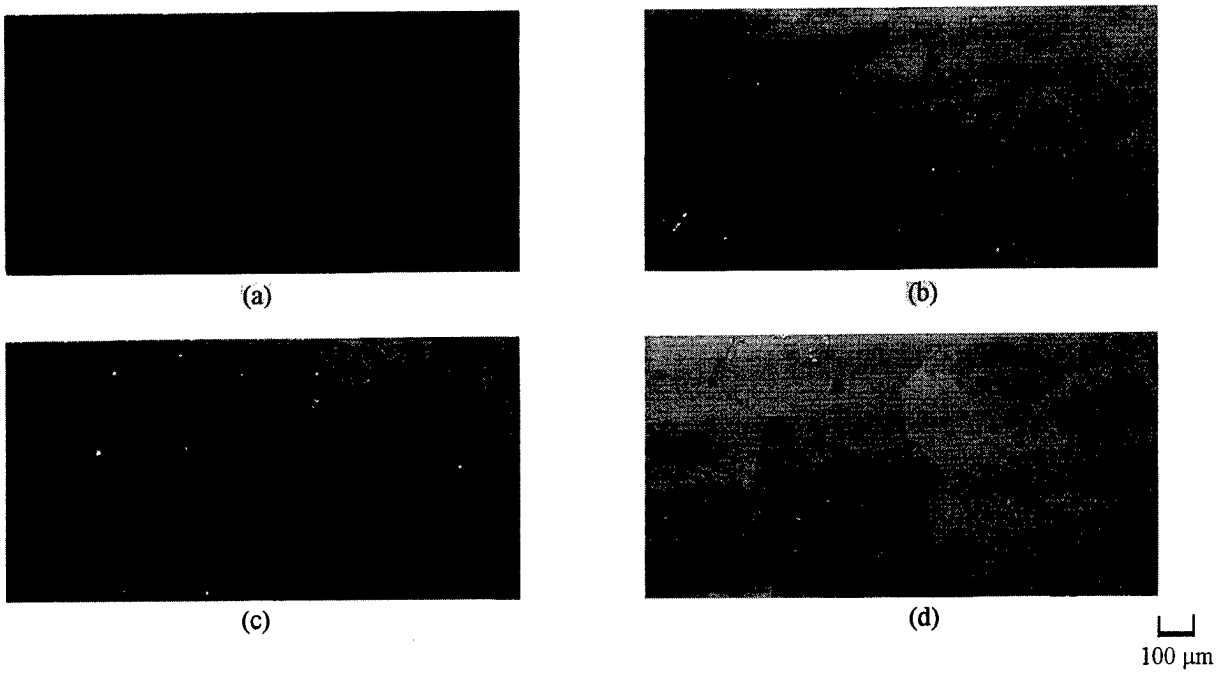


Figure 1: Microstructures of sintered PbTe compacts. (a), (b), (c) and (d) correspond to starting powders with particle sizes of 6, 39, 180 and 380μm, respectively.

decreasing D. The sintered compact with smaller D has higher hole concentration n_p. It is seemed that oxidation in the grain boundary regions and/or crystal grains is caused in the fabrication process of sintered compacts[3].

Figure 3 is temperature dependence of resistivity ρ for the original boule and the sintered compacts shown in Figure 1. In the temperature range from 77 to 250 K, ρ increased with decreasing D and the variations of ρ for the sintered compacts are remarkably different from that of the original boule.

Figure 4 shows temperature dependence of Hall mobility

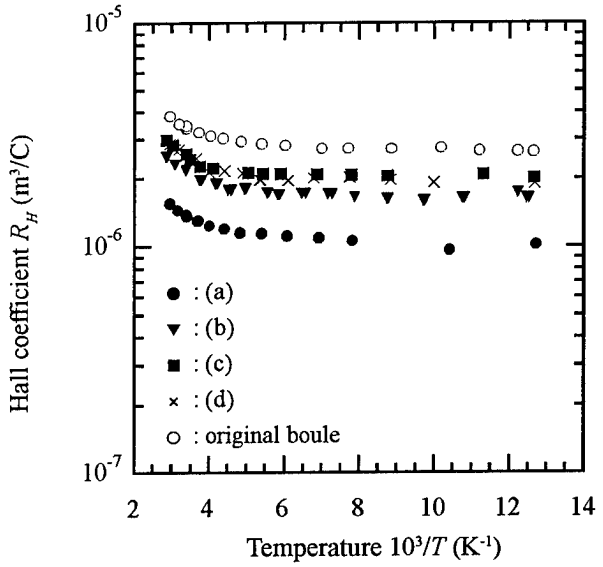


Figure 2: Temperature dependence of Hall coefficient R_H for original boule and sintered compacts shown in Figure 1.

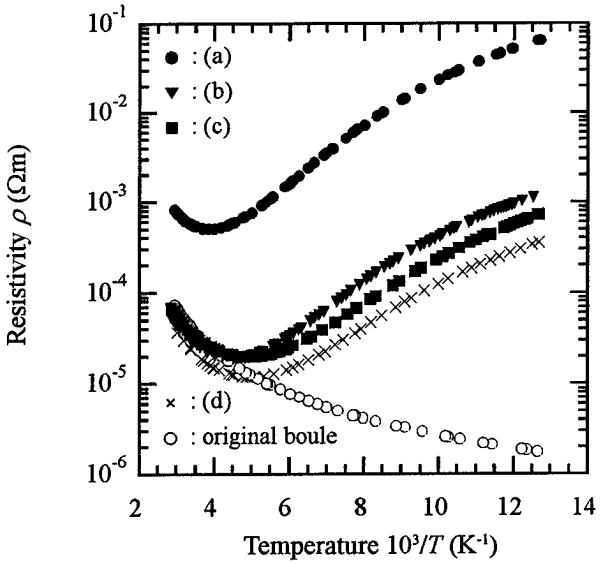


Figure 3: Temperature dependence of resistivity ρ for original boule and sintered compacts shown in Figure 1.

μ_H for the original boule and the sintered compacts shown in Figure 1. All the sintered compacts had the variations of μ_H different from the original boule in the temperature range from 77 to 250 K. This is mainly due to the difference of carrier scattering mechanism. The carrier scattering mechanism is strongly affected by the formation conditions of grain boundaries during SPS. However, the carrier scattering mechanism is not clear and further investigation is required. μ_H of the sintered compacts approaches toward that of the original boule with increasing D above 200 K. This is due to the decrease of mean free path of carrier with increasing temperature and also to the

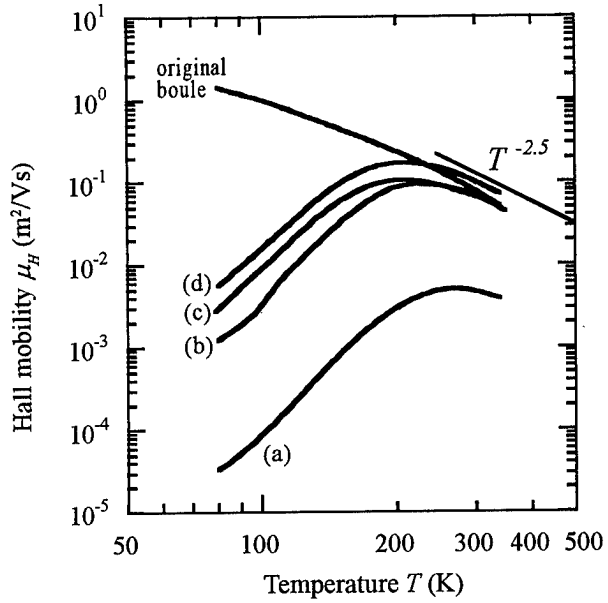


Figure 4: Temperature dependence of Hall mobility μ_H for original boule and sintered compacts shown in Figure 1.

decrease of probability of scattering at crystal grain boundary with the increasing D. The temperature μ_H of all the specimens is proportional to $T^{-2.5}$ above 200 K. This behavior is caused by lattice scattering in a combination of optical- and acoustic-modes[4].

Figure 5 is temperature dependence of thermoelectric power α for the original boule and the sintered compacts shown in Figure 1. α is independent of D in the temperature range from 77 to 350 K. This result agrees with the theoretical analysis obtained by J. Yoshino[5,6].

Figure 6 is temperature dependence of thermal conductivity

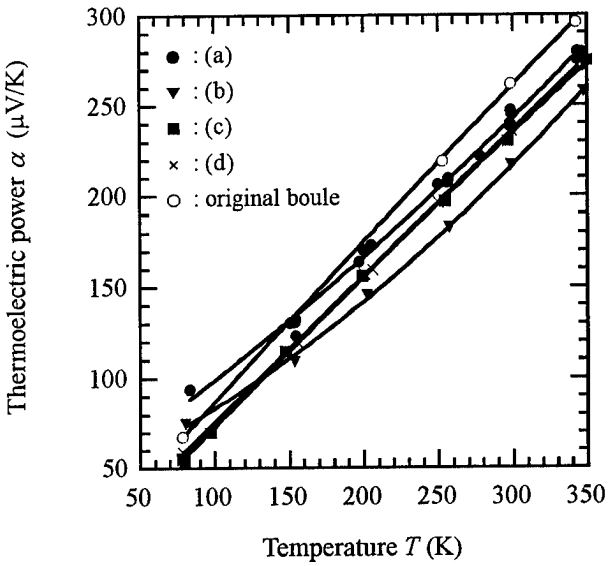


Figure 5: Temperature dependence of thermoelectric power α for original boule and sintered compacts shown in Figure 1.

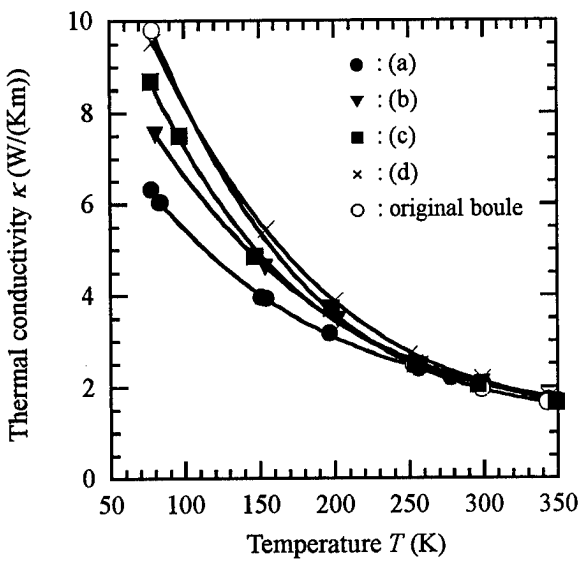


Figure 6: Temperature dependence of thermal conductivity κ for original boule and sintered compacts shown in Figure 1.

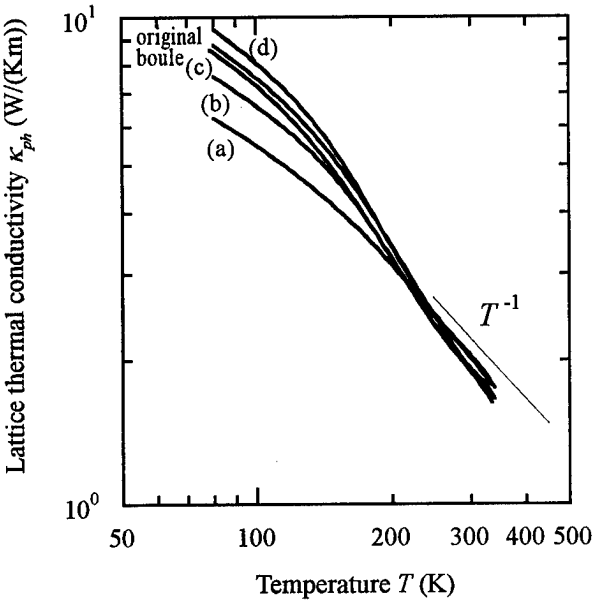


Figure 7: Temperature dependence of lattice thermal conductivity κ_{ph} for original boule and sintered compacts shown in Figure 1.

κ for the original boule and the sintered compacts shown in Figure 1. κ has tendency of decreasing with reduction in D below 250 K. κ is expressed as

$$\kappa = \kappa_{el} + \kappa_{ph}, \tag{1}$$

where κ_{el} and κ_{ph} are electronic and phonon components of κ, respectivity[7] .

κ_{el} is given by

$$\kappa_{el} = LT/\rho, \tag{2}$$

where L is lorentz number. κ_{ph} was separated from κ by using L as 2.45×10^{-8} V^2/K^2 which is valid for metal.

Figure 7 is temperature dependence of κ_{ph} for the original boule and the sintered compacts shown in Figure 1. κ_{ph} of all the specimens was proportional to T^{-1} in the temperature range from 200 to 350 K. Since the Debye temperature θ_D of PbTe is 136 K [8], the condition of $T > \theta_D/2$ is satisfied in this study. It is thought that the Umklapp process is dominant in κ_{ph} and κ_{ph} is proportional to T^{-1}[9]. κ_{ph} decreased with reducing D below 200 K. This tendency is by the effect of long-wave phonon scattering at grain boundaries. κ_{ph} was independent of D above 250 K. J. Yoshino[5,6] reported that improvement of the dimensionless thermoelectric figure of merit for PbTe by controlling with the D is not expected theoretically. Our results experimentally clarify that is not changed by controlling D and that thermoelectric performance is not directly affected by D.

Conclusions

Thermal and electrical conduction parameters of the sintered PbTe with different crystal grain sizes Ds were measured over the temperature range from 77 to 350 K, to examine the objective of this study is to examine the possibility of improvement in thermoelectric performance for sintered PbTe by reducing D. Thermal conductivity decreased with reducing D below 200 K, while showed no dependence on D above 200 K and κ_{ph} was proportional to T^{-1}. Long-wave phonons are scattered efficiently at grain boundaries only below 200 K. Hall mobility of the sintered compacts with different Ds were almost same above 200 K. Thermoelectric power was independent of the grain size in the temperature range from 77 to 350 K. It is concluded that thermoelectric performance for sintered PbTe is not directly affected by controlling D.

References

[1] D.M. Rowe and C.M. Bhandari ,"A Review of Lead Telluride Technology at Uwist" , Proc. of 6th Int. Conf. on Thermoelectrics,Arlington, America, (1986) 43.

[2] T. Noguchi, "Powder processing of thermoelectric materials-Focusing on GeSi with new sintering", Proc. of 16th Int. Conf. Thermoelectrics, Dresden, (1997).

[3] W. D. Lawson,"Oxygen-Free Single Crystals of Lead Telluride, Selenide, and Salfide", J. Appl. Phys. **22**(1952) 495.

[4] R. S. Allgaier and W. W. Scanlon, "Mobility of Electrons and Hole in PbS, PbSe, and PbTe between Room Temperature and 4.2°K", Phys. Rev. **111**(1958) 1029.

[5] J. Yoshino, "Theoretical estimation of thermoelectric figure of merit in sintered materials and proposal of grain size graded structures", Abstracts 4th. Int. Symp. FGM'96, (1996) 106.

[6] J. Yoshino, Report of FGM Project, (1997).

[7] K. Uemura and I. A. Nishida, "Thermoelectric semiconductors and their applications", Nikkan-Kogyo Shinbun-sya, (1988).

[8] K. H. Hellwege and O. Madelung ed., "Landolt-Börnstein", Springer-Verlag Berlin-Heidelberg., **3, 17, f**(1983) 178.

[9] C. Kittel, "Introduction to Solid State Physics, 6th edn.", John Wiley & Sons, Inc., New York, (1986).

High-temperature oxidation behavior of PbTe and oxidation-resistive glass coating

Lidong Chen, Takashi Goto, Rong Tu and Toshio Hirai
Institute for Materials Research, Tohoku University, 2-1-1 Katahira, Aoba-ku, Sendai 980-77, Japan
Tel.: +81-22-215-2106, Fax: +81-22-215-2107, E-mail: cld@imr.tohoku.ac.jp

Abstract

Oxidation of lead telluride (PbTe) is a serious issue for the thermoelectric application. In the present study, the oxidation behavior of PbTe was studied at oxygen partial pressures of 10Pa to 0.1MPa in the temperature range between 700 and 900 K. At moderately low oxygen partial pressures and high temperatures, mass loss was observed and the oxide layers (Pb_3TeO_5 or Pb_5TeO_7) formed on the PbTe surface. At high oxygen partial pressures and low temperatures, mass gain was observed and $PbTeO_3$ or Pb_2TeO_4/$PbTeO_3$ oxide layers formed on the PbTe surface. When the temperature was higher than 819 K, $PbTeO_3$ melted and dropped down from the specimen. Oxidation-resistive glasses were coated on the PbTe surface. The glass-coated PbTe showed excellent oxidation resistance showing no mass change at 773K.

Introduction

Recently, thermoelectric (TE) power generation has been applied to the use of heat energy of combustible solid waste, because the TE power generation system has a good flexibility to the heat source capacity and to the change of either temperature range or heat energy input [1-2]. In general, the temperature of the combustion gas in the solid waste incinerator changes from about 1000K to 500K when the combustion gas flows from the burner to the bottom of chimney. Because the conversion efficiency is in proportion to the hot junction temperature, it is better to equip the TE power generator at a high temperature region.

There are many commercial thermoelectric elements, such as Bi_2Te_3, Sb_2Te_3, PbTe, SiGe and $FeSi_2$. Bi_2Te_3 and Sb_2Te_3 are not valid above 500K, and the conversion efficiency of $FeSi_2$ or SiGe is too low at the temperature range of 500 to 900K. On the other hand, PbTe has a high conversion efficiency at this temperature range. However, the combustion gas from incinerators generally contains corrosive gases, such as HCl and H_2SO_4. Therefore, it is important to understand the oxidation/corrosion behavior of PbTe and to develop an advanced PbTe element having high oxidation/corrosion resistance. In the present study, we investigated the high temperature oxidation behavior of PbTe at the O_2-Ar atmosphere, and developed a glass coating to the PbTe surface to improve the oxidation resistance.

Experimental

Commercial PbTe sintered materials were used in the oxidation experiments. The oxidation experiment was carried out at oxygen partial pressures of 10Pa to 0.1MPa in the temperature range between 700 to 900K for 90ks. The mass changes during oxidation were measured. Figure 1 shows the schematic of the oxidation equipment. The oxidized specimens were investigated by X-ray diffraction (XRD), SEM and EPMA. The oxidation-resistive glasses were coated as follows. Glass paste was prepared by mixing glass powders with polymer agent (α–Terpineol + Cellulose)

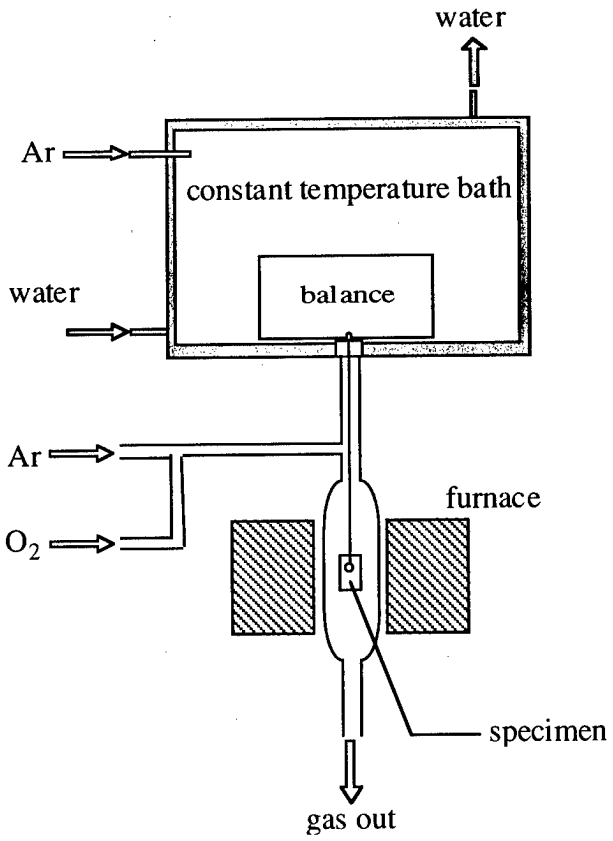


Figure 1. Schematic of oxidation equipment.

and then coated on the PbTe surface. The coated glass pastes were dried at about 400K for 1.8ks and then sintered at 700 to 1000K for 1.8ks. Four types of glass powders, SiO_2-PbO-BaO (glass A), SiO_2-PbO-B_2O_3 (glass B), ZnO-Na_2O-B_2O_3 (glass C) and SiO_2-Na_2O-B_2O_3-PbO-TeO_2 (glass D), were used. The morphology of the glass coatings was observed by SEM. The oxidation experiments of the glass-coated PbTe specimens were also carried out.

Results and discussion

Figure 2 shows the relationship between the mass changes and time at 773K. When oxygen partial pressure (P_{O2}) was 10Pa, mass loss was observed. However, when P_{O2} was more than 100Pa, mass gains were observed and the mass gains obeyed a parabolic law. This suggests that the oxidation reaction could be controlled by a diffusion process through the oxide layer. The amount of mass gain increased with oxygen partial pressure. At every oxidation temperature, the same tendency was observed; at a low P_{O2} region mass loss occurred and at a high P_{O2} region mass gain occurred. The transition P_{O2} from mass loss to mass gain increased with increasing temperature.

Figure 3 shows the typical X-ray diffraction patterns of the oxidized PbTe surface. At every oxidation condition, lead tellurium oxides formed on the PbTe surface, though the oxide composition and/or the oxide polymorphic forms varies with the oxidation temperature and oxygen partial pressure.

Figure 4 summarizes the oxidation behavior at various oxidation conditions. At the area (A) of moderately lower

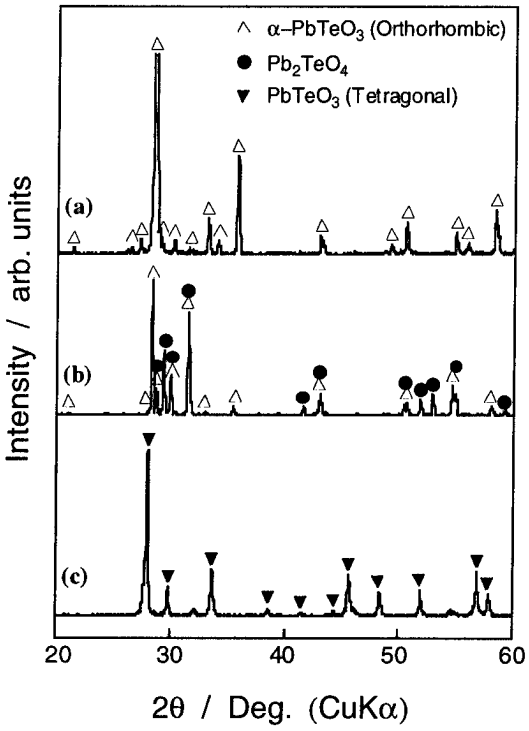


Figure 3. X–ray diffraction patterns of the oxides formed on PbTe surface (a: P_{O2}=5kPa, 773K; b: P_{O2}=20kPa, 773K) and the solidified drops (c: P_{O2}=20kPa, 873K).

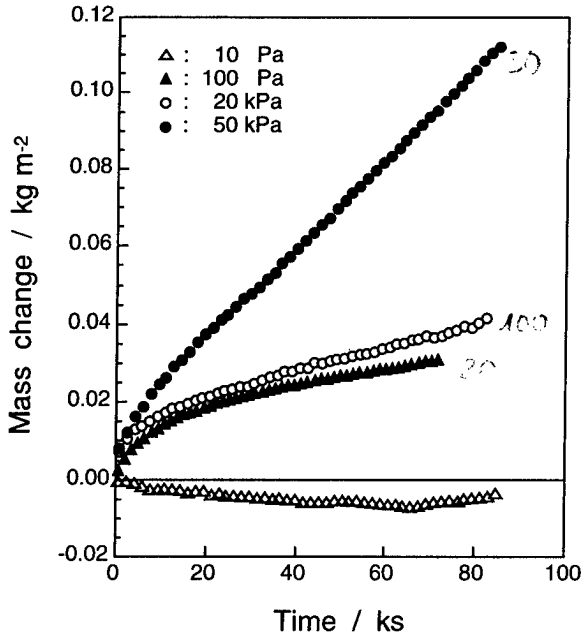


Figure 2. Relationship between mass change and oxidation time at 773K.

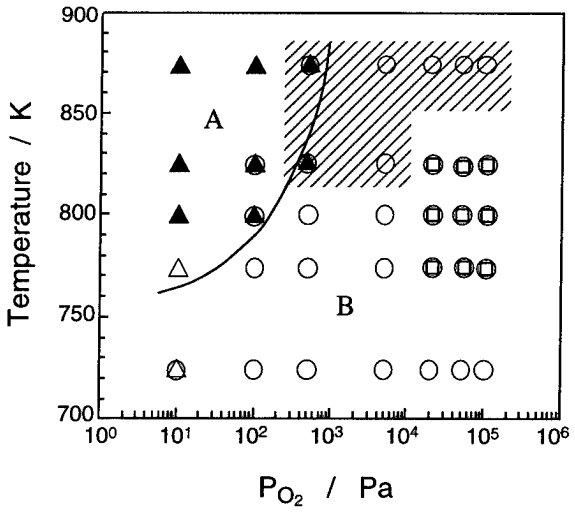


Figure 4. Effect of temperature and oxygen partial pressure on the formation of oxides. Area A: mass loss; area B: mass gain; shadow area: liquid drop formation. (▲) Pb_3TeO_5; (△)Pb_5TeO_7; (○) $PbTeO_3$; (□) Pb_2TeO_4.

oxygen partial pressure and higher temperature, mass losses were observed and mainly Pb_3TeO_5 or Pb_5TeO_7 (lead rich-lead lellurium oxides) formed. At the area (B) of higher oxygen partial pressure and lower temperatures, mass gains were observed and mainly $PbTeO_3$ single phase or $PbTeO_3$/Pb_2TeO_4 two phases formed. SEM observation and EPMA analysis gave the same results with x-ray diffraction. Especially, in the $PbTeO_3$ /Pb_2TeO_4 two phase region, the multi layers of $PbTeO_3$(inner)/Pb_2TeO_4(outer) were observed.

In the $PbTeO_3$ single layer formation region, a liquid phase appeared when the temperature is higher than the melting point of $PbTeO_3$ (819K). The melted $PbTeO_3$ dropped down at a specific time interval. The mass changes with the liquid-drop formation are summarized in figure 5. At first, a slight mass gain occurred and then an abrupt mass loss proceeded. The abrupt mass loss corresponds to the dropping of the liquid phase. The slight mass gain and abrupt mass loss repeated till the sample was consumed out. The higher the oxidation temperature and the oxygen partial pressure, the shorter the mass gain-mass loss period.

In table 1 the melting points of several lead oxides, tellurium oxides and lead tellurium oxides are summarized. The melting points of tellurium oxides and tellurium rich-lead tellurium oxides ($PbTe_5O_{11}$, $PbTe_4O_9$) are lower than those of lead oxides and/or lead rich-lead tellurium oxides (Pb_3TeO_5, Pb_5TeO_7). When the mixture of PbO and TeO_2 was heat-treated, a mass loss due to the evaporation of tellurium oxides was reported [7]. In the present work, the mass loss at the higher oxidation temperature and lower oxygen partial pressure may be caused by the evaporation of tellurium oxides and/or tellurium rich-lead tellurium oxides.

Two types of glasses, glass A and glass D, were coated on to the PbTe surface. The other two type glasses, glass B and glass C, were not well adhered to the PbTe because of the reaction between the glass and PbTe. The SEM observation showed that the glass coatings (A, D) have a thickness of about 30 to 50μm with a dense morphology. The oxidation experiments showed that the oxidation resistance of PbTe was significantly improved by the glass-coating. At temperature of 773K and oxygen partial pressure of 20kPa, no mass change was observed for the glass-coated PbTe specimens (glass D).

Conclusion

The oxidation behavior of PbTe was studied at oxygen partial pressures of 10Pa to 0.1MPa in the temperature range between 700 and 900 K. At moderately low oxygen partial pressures and at high temperatures, mass loss was observed and the oxide layers (Pb_3TeO_5 or Pb_5TeO_7) formed on the PbTe surface due to the evaporation of tellurium oxides or tellurium rich-lead tellurium oxides. At high oxygen partial pressures and low temperatures, mass gain was observed and $PbTeO_3$ layer or Pb_2TeO_4/$PbTeO_3$ multi-layers formed on the PbTe surface. When the temperature was higher than 819 K, $PbTeO_3$ melted and dropped down from the specimen. Oxidation-resistive glasses were coated on the PbTe surface. The glass-coated PbTe showed excellent oxidation resistance showing no mass change at 773K.

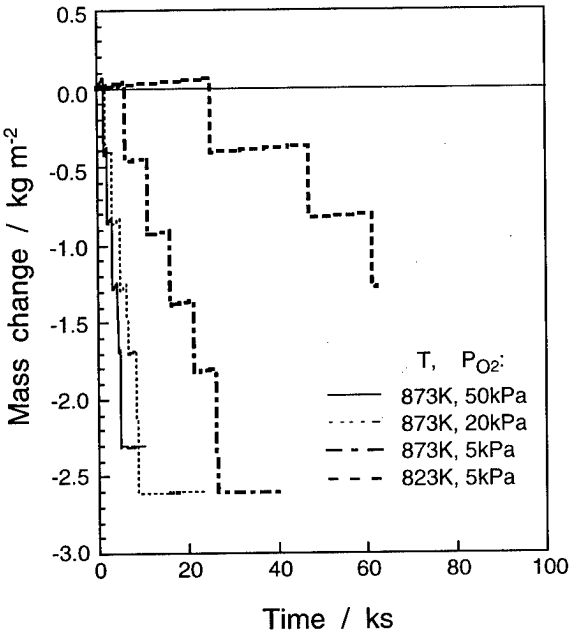


Figure 5. Relationship between mass change and time for the case of liquid-drop formation.

Table 1 Melting points of Pb-Te-O system oxides.

Compound	Melting point (K)	Ref.	Remark
TeO_2	1008	3	
TeO_3	703	4	
$PbTe_5O_{11}$	791	3, 4	peritectic
$PbTe_4O_9$	753	3	peritectic
$Pb_2Te_3O_8$	868	5	
$PbTeO_3$	819	6	
Pb_2TeO_4	1053	3	peritectic
Pb_3TeO_5	1138	6	
Pb_5TeO_7	1137	3	peritectic
PbO	1163	6	

Acknowledgements

This research was supported in part by the Special Coordination Funds for Promoting Science and Technology from the Science and Technology Agency of Japan.

References

[1] T. Kajikawa, M. Ito, I. Katsube and E. Shibuya: AIP Conf. Proceedings 316, 13th Inter. Conf. on Thermoelectrics, Ed. by B. Mathiprakasam and P. Heenan (Amer. Institute of Physics, New York, 1995), p.314.

[2] M. Niino, T. Ohshima and K. Matsubara: in this proceedings.

[3] D. Stavrakieva, Y. Ivanova and J. Pyrov: J. Mater. Sci., **23** (1988) 1871.

[4] D. Dumora and P. Haganmuller: Compt. Rend., Series C, **266** (1968) 276.

[5] D. S. Robertson, N. Shaw and I. M. Young: J. Phys. D: Appl. Phys., **9** (1976) 1257.

[6] O. I. Tananayeva and A. V. Novoselova: Inorg. Mater. USSR, **3** (1967) 163.

[7] I. M. Young: J. Mater. Sci., **14** (1979) 1579.

Influence of potential barriers on the thermoelectric properties of PbTe thin films

Z. Dashevsky

Department of Materials Engineering Ben-Gurion University of the Negev,
P.O.B. 653, Beer-Sheva 84105, Israel

Abstract

The PbTe film, 0.4 - 3 μm thick, were formed on different substrates by the method of flash evaporation. The samples had a single crystal structure with blocks and the angle of misorientation was ≤ 1°. The dimensions of the blocks were ~1 μm for the films on mica. Block boundaries were system of edge dislocations. On one side of each dislocation there was a region of compression and on the other a region of dilatation. Regardless of the sign of the deformation potential, potential energy relief is formed near a block boundary. Estimates obtained using parameters of bulk PbTe have shown that the energy barrier can reach 0.1 eV. The electrical conductivity σ, Seebeck coefficient S, Hall coefficient R, and Nernst-Ettingshausen coefficient Q were measured in 80 - 500 K range. A comparison with bulk PbTe single crystals with the same charge concentration indicates that the films were characterized by a higher parameter $S^2\sigma$. This difference were attributed to energy-selective carrier scattering by potential barriers. The potential relief in PbTe thin films was obtained using an electron-beam induced current. Doping of PbTe films with certain impurities can be used to control their barrier properties.

Introduction

The Group IV telluride compound, among which PbTe is the best known, are a good thermoelectric material [1]. PbTe is its relatively high figure of merit Z, for the n-and p-legs of a thermoelement. The main advantage PbTe is its isotropy (NaCl lattice) in a comparison with the strong anisotropy thermoelectric materials on the base Bi_2Te_3 (hexagonal lattice). In this case it is not possible to grow the thin films with maximal thermoelectric efficiency direction parallel to the substrate (along heat flux).

Secondly, the PbTe fabrication technology is well developed, making it possible to grow samples with high mobility transport to have precise control over the carrier density.

The block (grain) size in wide limits (from 0.01 to some μm) can be varied by the growth rate and substrate temperature. A comparison with bulk single crystals with the same value of carrier density indicated that the films were characterized by a higher thermoelectric power S [3]. These differences were attributed to energy-selective carrier scattering by potential barriers associated with block boundaries. The scattering model on two-dimensional potential barriers is such actual with view point of thermoelectric efficiency optimization. The presence of such barriers with strong selective scattering causes the increase of carrier energy in electron flux from hot to cold end. Electrons with energy E below Fermi energy E_F practically don't take part in charge flux, electrons with $E > E_F$ don't change the mean free path l, which equal l in perfect crystal. In this case we can wait to the obvious increase of specific power $S^2\sigma$ in such samples.

Samples

The PbTe films, 0.4 - 3 μm thick, were prepared by the flash evaporation (FE). FE technique is abundantly described in the literature. We used different substrates: mica, NaCl, BaF_2. X-ray diffraction methods were used to determine the quality of crystals. The high resolution transmission electron microscope (HRTEM) and scanning electron microscope (SEM) also were used for structure investigation. Laue methods for crystal orientation determination and optical methods for crystal perfection assessment. PbTe films had a micro-block structure (substrate temperature Ts ≥ 300 °C) with block orientation (111) plane parallel substrate (mica or BaF_2) and (001) plane parallel NaCl substrate. The dimensions of the blocks achieved 1 - 2 μm for the films on mica and 5 - 6 μm for films on BaF_2 and angle of misorientation of the blocks was ≈ 1°. The surface reflected also the internal structure, which was probably due to some disorientation of the micro-blocks. The block height was equal to the film thickness. The same results were discovered in [2]. Block boundaries were systems of edge dislocations. It was discovered, using an electron-beam (whose current was 10^{-8} A at an applied voltage of 20 kV) the shallow potential relief on block boundaries (Fig. 1). Doping in PbTe can be achieved by the constituent elements that generate structural defects, when in excess of the stoichiometric composition [4].

0-7803-4057-4/97 $10.00 ©1997 IEEE

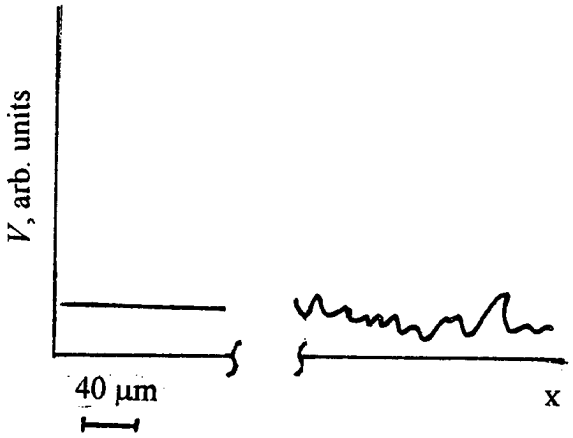


Fig 1: Secondary-electron image of PbTe crystal. Left part - bulk single crystal, right part - thin film (2 μm thick) on mica substrate. An oscillogram shows the induced current signal (T = 300 K).

Thus, for PbTe, carrier concentration is given by

$$n\,(p) = -2[V_{Te}] + 2[V_{Pb}] + 0[I_{Te}] - 1[I_{Pb}], \qquad (1)$$

when the total charge q is negative, electron conductivity predominates and when q is positive, hole conductivity dominates. Here [V] and [I] denote the vacancy and interstitial concentrations of lead and tellurium, respectively. The width of one-phase PbTe compound region for this material is relatively large and extends on both sides of the stoichiometric composition. The crystal composition was changed within the solubility limits by varying the crystal growth conditions and/or subsequent heat treatment parameters. The carrier concentration can, therefore, attain a $5\cdot10^{19}$ cm^{-3} value, for n- and p-type materials, without any doping by foreign impurities.
Also we used impurity doping for the film preparation. In this case evaporation source had composition PbTe<In>. The high solubility of this impurity allows to observe and study the impurity state characteristic manifestations in spite of high intrinsic defect concentration.

Experimental results and discussion

Measurements of the kinetic effects (electrical conductivity σ, Seebeck coefficient S, Hall coefficient R, Nernst-Ettingshausen coefficient Q, and thermal conductivity k) in the temperature interval 80 - 500 K yield the data necessary to determine the figure of merit of the material and also provide information about the fundamental parameters (carrier density, mobility, impurity level, mechanism of scattering) necessary to gain an understanding of the relevant properties.

The transport effects in PbTe films

For PbTe films on BaF_2 substrate, temperature dependence of mobility (temperature interval from 80 to 300 K) obeys a T^{-2} law, which is typical for bulk single crystals. A number of significant features are observed in PbTe films on mica. A comparison of the results obtained for films with results for bulk single crystals [1] showed, that mobility in films was about a half, that in bulk crystals at carrier concentration $n \geq 5\cdot10^{18}$ cm^{-3}(T = 300 K). On the other hand, the absolute value of Seebeck coefficient and ratio $Q/R\sigma$ was more higher in thin films. The calculations of density states effective mass from S, R, σ, and Q gave results which practically didn't differ from the values obtained for bulk PbTe crystals. These results and measurement of optical band gap in the same films expected, that considerable changes S and Q were mainly connected with the appearance of an additional scattering mechanism. The mobility decreasing in thin films by a factor of 2 and more indicated that the relative contribution of this scattering mechanism was approximately the same as that of the phonon scattering, known to dominate the transport effects in bulk PbTe in this temperature range. Effective scattering parameter r in thin films was calculated from experimental values S, R, σ, and Q. The technique of calculations is described in details in [5]. In the case of degenerate state (typical for optimal charge concentration in the thermoelectric applications) effective mobility μ and effective parameter r (in this case r characterizes mixed scattering can be calculated in terms of the parameters specific to each mechanism:

$$\mu = \mu_1\mu_2/(\mu_1 + \mu_2), \qquad (2)$$

$$r = (\mu_2 r_1 + \mu_1 r_2)/(\mu_1 + \mu_2). \qquad (3)$$

Here μ_1, r_1 - mobility and scattering parameter for bulk crystal (phonon mechanism); μ_2, r_2 -parameters for additional scattering mechanism. Using the data of μ_1 and r_1 for the bulk samples [1], we estimated the values of μ_2 and r_2. It was shown, that parameter r_2 is large and positive (more 2) at temperature T = 100 K. In the same time mobility μ_2 is less than μ_1 at T = 100 K and its temperature variation (100 - 300 K) is weak. The value of r_2 and the behaviour of mobility μ_2 are typical for scattering on defects. The same effect was also discovered in p-type PbTe films. Several types of defects, in principle, can influence on transport in thin films. However, as shown in [6], additional

scattering is connected with block boundaries. These block boundaries may act as concentration of electron states whose filling produces a potential barriers (scattering centres). The rise of the Fermi energy E_F increases the population of the boundary states and the barrier height E_b. If $E_b \approx E_F$ such barrier scatters efficiently carriers with energy below E_F and weakly carriers of higher energy. The potential barriers, whose height followed automatically the chemical potential level. A weak two-dimensional potential may result from elastic deformation of a crystal around dislocation. Near an edge dislocation there are always compressed and stretched regions, which give rise to potential wells and humps and this happens for either sign of carrier charge (i.e., it occurs in *n*- and *p*-type materials). Bound states appear in such a potential well. The change of conduction band in plane of block boundary was shown schematically on Fig. 2 for homogeneous distribution of doping impurity [6].

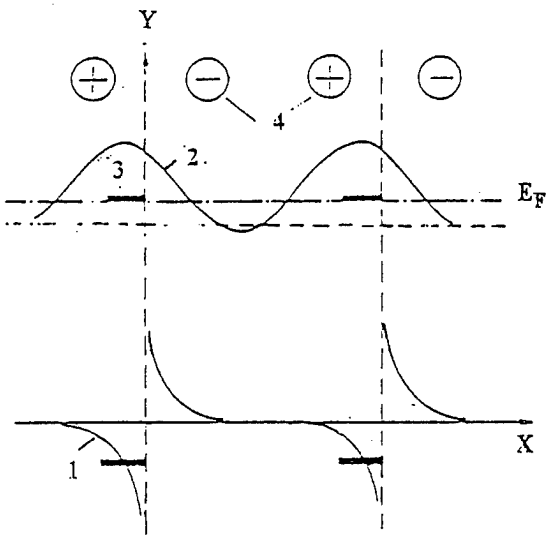


Fig 2: Potential of electron at a block boundary.
1 - deformation potential, 2 - smoother electrostatic potential forming barrier, 3 - localised level, 4 - stress sign ("+ " - dilatation area, "- " - compression area).

These conclusions permit to explain the results of influence of doping impurity on scattering properties of block boundary. Difference between films and bulk samples practically disappears in PbTe films doping In. In this case value of mobility and scattering parameter close to bulk values. Consequently, doping In PbTe films decreases the role of addition scattering of carriers on block boundaries. Atom of In replacing Pb, giving up an electron to conduction band and makes the relevant lattice site positive. It follows, that ionic radius R_{In}^{+++} less than R_{Pb}^{++}, In ions accumulate in the compression regions. Estimates indicate, that the concentrations impurities near dislocations may be one or two orders higher than in block volume. The enrichment of the saddle points of the potential barriers with In ions effectively lowers the percolation level.

Thermal conductivity in PbTe films with block boundaries

Thermal conductivity in PbTe films was measured by the method described in [5]. The carrier contribution was estimated from Wiedemann-Franz relation. The influence of film thickness on the value of the lattice thermal conductivity k_p is not observed. For PbTe films on BaF_2 substrate, temperature dependence of k_p (temperature interval from 80 to 300 K) obeys a T^{-1} law, which is typical for bulk single crystals. The effect of phonon scattering on block boundary is very weak. It is connected with small value of mean free path of phonons in compound PbTe. The influence of boundary scattering of phonons on the thermal conductivity can be increased in solid solutions on the base PbTe. This change is connected with different role of long-wavelength phonons in the thermal conductivity. Such effect was observed in solid solutions on the base Bi_2Te_3 [7]. The lowering of the lattice thermal conductivity in the films of the solid solutions leads to a considerable increase in the *Z*.

Influence of potential relief on minority carriers

Potential relief in these structures can influence complexly on thermoelectric characteristics at high temperature. It is connected with more influence of minority carriers in transport effects. We tried to estimate this process, measuring diffusion length of minority carriers *L* in thin films [8]. With this goal we produced vertical *p-n* junctions in *p*-type films by the method of implantation of zinc in doses of 10^{16} cm^{-2} (the ion energy was 150 keV). Figure 3 shows the induced current signals produced in SEM at temperatures of 300 ad 80 K. We determined *L* of minority carriers in original part (*p*-type PbTe). The values of L_e, determined from the slope of the curve $\ln(V/Vo) = f(x)$, are 5 and 50 μm at temperatures of 300 and 80 K. These diffusion length of carriers in films are longer than the published values for bulk single crystals. The increase in the diffusion length of carriers in films is due to an increase in their lifetime because of the presence of the potential

relief linked with block boundaries. carriers generated by an electron beam in our case (or heat generation) become spatially separated: electrons become localized at the maximum of potential well and holes are localized at the minimum, which retards their recombination.

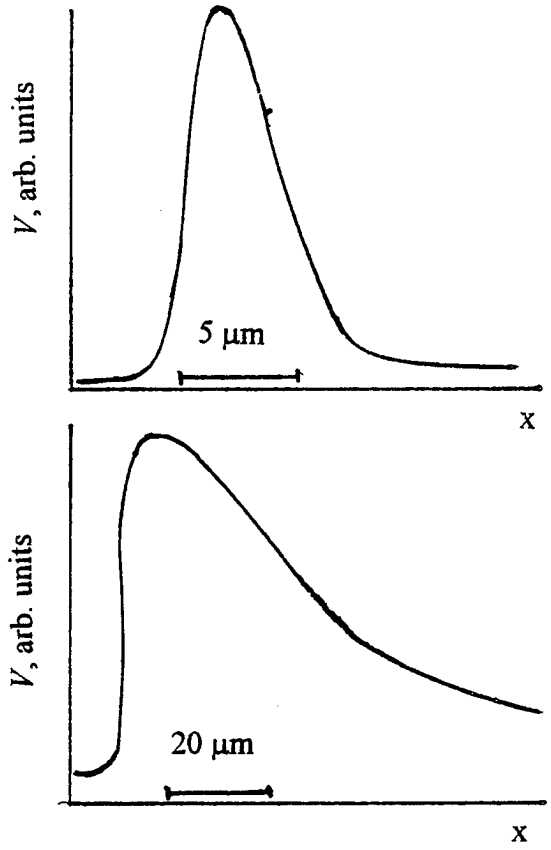


Fig 3: Induced-current signal for vertical *p-n* junction (ion implantation method) in PbTe film, prepared on BaF_2 substrate (the original *p*- type region on the right). Temperature *T*, K: a) 300; b) 80.

An additional check of the reliability of our results was made by applying the another method to determine the diffusion length of carriers. Since the sensitive area of a vertical *p-n* junction in a film is equal to the product of the diffusion length of carriers and the film width, we were abler to determine the diffusion length of carriers from the strength of the photosignal in response to a given flux of the incident infrared radiation. This was done by using the photoelectric parameters of a p-n junction (zero-bias differential resistance, quantum efficiency, *p-n* junction figure of merit). The diffusion length found in this way at T = 80 K are similar to the values quoted above.

Acknowledgments

Author would like to thank Prof. V.I.Kaidanov and coworkers, B.M. Gol'tsman for collaboration, advises and discussions.

References

[1] Yu.I. Ravich, B.A. Efimova, I.A. Smirnov: *Semiconducting lead chalcogenides* (Plenum press New York-London, 1970).

[2] L.I. Bytenskii, T.S. Gudkin, E.K. Iordanishvili, S.A. Kazmin, V.I. Kaidanov, S.A. Nemov, and Yu.I. Ravich, "Influence of potential barriers on thermoelectric properties of lead chalcogenide films", Sov. Phys. Semicond., 11, 894 (1977).

[3] T.S. Gudkin, I.A. Drabkin, V.I. Kaidanov, and O.G. Sterlyadkina, "Characteristics of electron scattering in thin PbTe films", Sov. Phys. Semicond., 8, 1453 (1975).

[4] L. Palmetshofer, "Ion Implantation in IV-VI Semiconductors", Appl. Phys., A34, 139 (1984).

[5] B.M. Goltsman, Z.M.Dashevsky and V.I. Kaydanov: *Film thermoelements: Physics and Application* (Nauka, Moscow, 1985).

[6] L.I. Bytenskii, S.A. Kazmin, V.I. Kaidanov, "Influence of the chemical nature of the dopant on the electrical properties of lead selenide films", Sov. Phys. Semicond., 16, 712 (1982).

[7] Yu. A. Boikov, B.M. Gol'tsman, and V.A. Kutasov, "Effect of structure on the thermal conductivity of Bi_2Te_3 and $Bi_{0.5}Sb_{1.5}Te_3$ films", Sov. Phys. Solid State, 20, 757 (1978).

[8] Z.M. Dashevsky and M.P. Rulenko, "Increase in the diffusion length of carriers in polycrystalline PbTe", Semiconductors, 27, 366 (1993).

Thermoelectric Power and Figure of Merit of Pb-Sn-Te Alloy Thin Films

V. Damodara Das
Thin Film Laboratory, Department of Physics,
Indian Institute of Technology, Madras
Chennai 600 036, INDIA
Tel.: +91-44-2351365 Extn.3221, FAX: +91-44-2350509, E-mail: vddas@acer.iitm.ernet.in

ABSTRACT

This paper describes the results of thermoelectric measurements carried out by our group on Pb-Sn-Te alloy thin films of different compositions, prepared by vacuum thermal flash evaporation. The compositions studied were $Pb_{0.8}Sn_{0.2}Te$, $Pb_{0.6}Sn_{0.4}Te$, $Pb_{0.5}Sn_{0.5}Te$ and $Pb_{0.4}Sn_{0.6}Te$. Thin films of the ternary alloy $Pb_{0.8}Sn_{0.2}Te$ with excess 1% Te doping was also studied to see the effect of excess Te on the thermoelectric properties. Simultaneously electrical resistivity of the films was also measured, and both the thermoelectric power and electrical resistivity data were analyzed by the Effective Mean Free Path model. Out of the compositions studied, it was found that 1% Te excess doped $Pb_{0.8}Sn_{0.2}Te$ alloy thin films showed the best thermoelectric power and figure of merit values. However, these values were lower than the bulk values as is to be expected due to the high electrical resistivity of thin films compared to the bulk. Whereas thermoelectric power of $Pb_{0.8}Sn_{0.2}Te$ thin films was of the order of 240 μV/K, the thermoelectric power of thin films of other compositions was around 150 - 180 μV/K only. It was found that thicker films showed higher figure of merit whereas thinner films showed lower figure of merit. This is due to the fact that thinner film resistivity is higher than the thicker ones due to the classical size effect, i.e., larger additional surface scattering contribution. The details of the results obtained on different composition thin films are discussed.

Introduction

The pseudobinary $Pb_{(1-x)}Sn_xTe$ semiconductors are widely used as IR detectors, optoelectronics devices [1-4] and as thermoelectric devices [5]. These have a wide range of operating temperatures between 300 K and 800 K and, thus, this material is useful above room temperatures. This alloy forms continuous solid solutions and crystallises in rock salt structure throughout the range $0 \leq x \leq 1$. Lattice constant changes from a = 6.327 Å to 6.461 Å on going from $x = 0$ to 1. As x increases, energy gap value decreases linearly and changes over to negative values crossing the zero energy gap at $x = 0.62$. The negative band gap of this material is explained by the band inversion model [6]. Even though there have been many reports on electrical and structural properties of $Pb_{(1-x)}Sn_xTe$ thin films [7-11] there are only few works on thermoelectric properties of thin films of these materials [12-13]. In this paper we give a review of the results on thermoelectric figure of merit of thin films of Pb-Sn-Te alloys of composition $Pb_{0.8}Sn_{0.2}Te$, $Pb_{0.6}Sn_{0.4}Te$, $Pb_{0.5}Sn_{0.5}Te$, $Pb_{0.4}Sn_{0.6}Te$ and 1% excess Te doped films obtained in our laboratory.

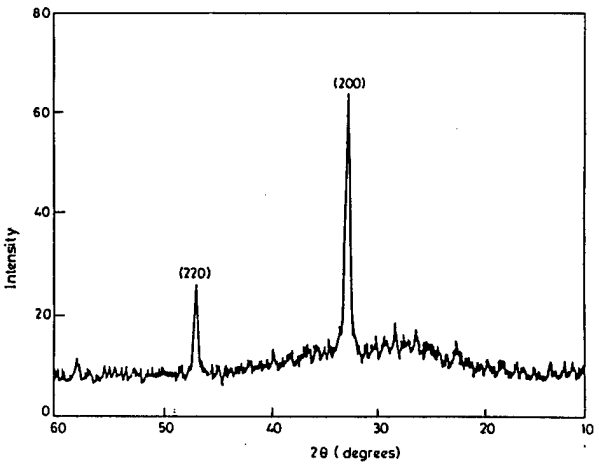
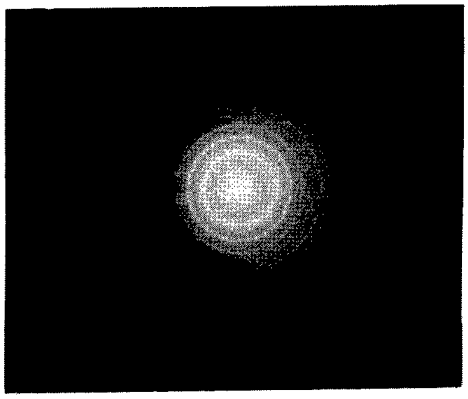


Figure 1: Typical X-Ray Diffraction pattern of a thin film of $Pb_{0.8}Sn_{0.2}Te$ alloy

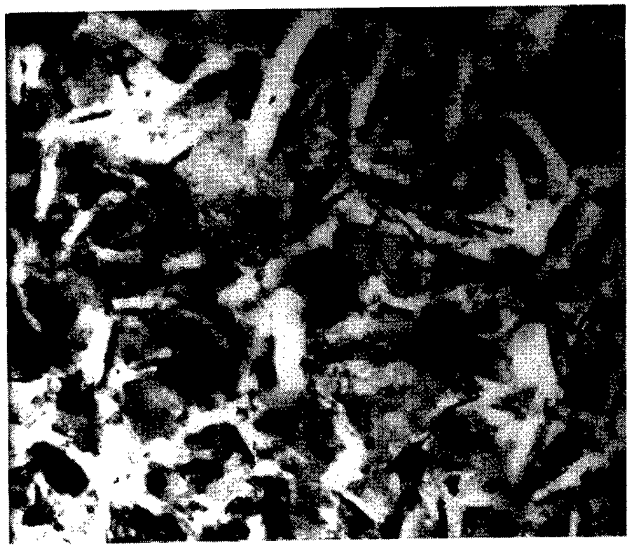
Results and Discussion

Structural Analysis

The structural analysis was done by X-Ray Diffraction (XRD) and Transmission Electron Microscopy (TEM) techniques. The d-values obtained for both bulk and thin films from XRD and SAD (Selected Area Diffraction) patterns were compared with the $ASTM$ d-values of PbTe and SnTe alloys and it was observed that the lattice parameters of the alloys were lying in between those of PbTe and SnTe alloys and increase with the increase of Sn content in the films. Typical XRD pattern of a thin film is shown in Figure 1. All the films were polycrystalline in nature with rock salt structure. Figure 2 shows the TEM and SAD patterns of a film. It was generally observed that the grain size of the films increases with thickness of the films [14]. Also it was observed that there was some noticeable change



a)



b)

Figure 2: a) Typical SAD pattern b) TEM micrograph

in grain size and orientation of the films during the heat treatment while the resistivity of the films was measured.

Thermoelectric Power

Thermoelectric power of all the films was measured in the temperature range 300 K - 500 K using the integral technique. The experimental set up is described elsewhere [15]. In all the cases thermoelectric power of the films increased with the temperature and the sign of thermoelectric power indicated p-type conductivity for all compositions of the alloy studied. It is reported by us in [16] that thermoelectric power of the films of $Pb_{0.8}Sn_{0.2}Te$ alloy is well below the state of the art in this field. But it was suggested that by excess doping of Te in these alloys we can improve the thermoelectric figure of merit. Hence alloy of $Pb_{0.8}Sn_{0.2}Te$ semiconductor with 1% excess doping was prepared and thermoelectric power of thin films of this doped material was measured. Figure 3. shows thermoelectric power of thin films of $Pb_{0.8}Sn_{0.2}Te$ material doped with 1% excess tellurium with reciprocal temperature. Thermoelectric power of a p type semiconductor is given by [17],

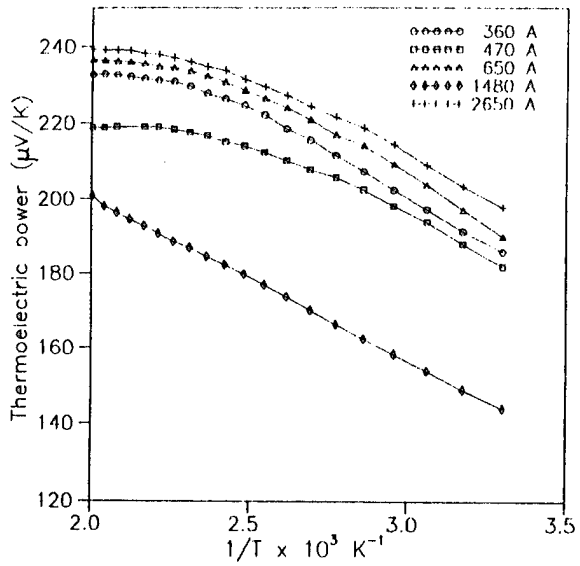


Figure 3: Plot of S versus 1000/T of thin films of 1% excess doped $Pb_{0.8}Sn_{0.2}Te$ alloy.

$$S = (\frac{k}{e}) \quad [\frac{E_F - E_V}{kT} + A] \tag{1}$$

The above equation suggests that a plot of thermoelectric power of the films with reciprocal temperature will be linear if we assume that E_F-E_V=E_0-γ holds good over a wide range of temperatures. Here γ is the temperature coefficient of activation energy. The intercept of the plot gives E_0 and the slope of the plot will give γ. It is seen from the figure that thermoelectric power of the films varies linearly in the low temperature range whereas it saturates in the high temperature range. This suggests that at high temperatures E_F-E_V=E_0-γ becomes constant, i.e., the Fermi level gets pinned at high temperatures. This can be expected because of the fact that the activation energy values are too low ($0.05eV$) and hence at high temperatures there is abundance of excess charge carriers. The details are given in [18]. It is observed that thermoelectric power values vary from 150 μ Volt/K at low temperatures to 240 μ Volt/K at high temperatures in the case of the high thickness films. Thus, in the excess doped material the pinning of the Fermi level at high temperatures limits thermoelectric power to around 240 μ Volt/K. Even though thermoelectric power saturates at high temperature, doping of Te enhances thermoelectric power of the material. Also this has the highest thermoelectric power compared to the other compositions studied and they are described below.

Thermoelectric power variation of $Pb_{0.6}Sn_{0.4}Te$ thin film with temperature was analyzed. It was seen that the initial increase of thermoelectric power with temperature indicates the partial degenerate nature of the thin films. Also it was observed that the maximum value of thermoelectric power of thin film at high temperature is around 170 μ V/K [19].

Figure 4 compares the thermoelectric power of thin film

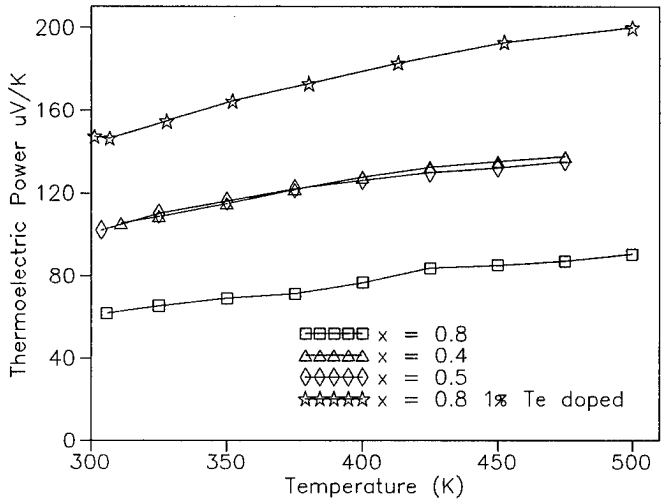


Figure 4: Plot of thermoelectric power versus Temperature of thin films of alloys x = 0.2 (1% Te excess doped), 0.4, 0.5 and 0.8

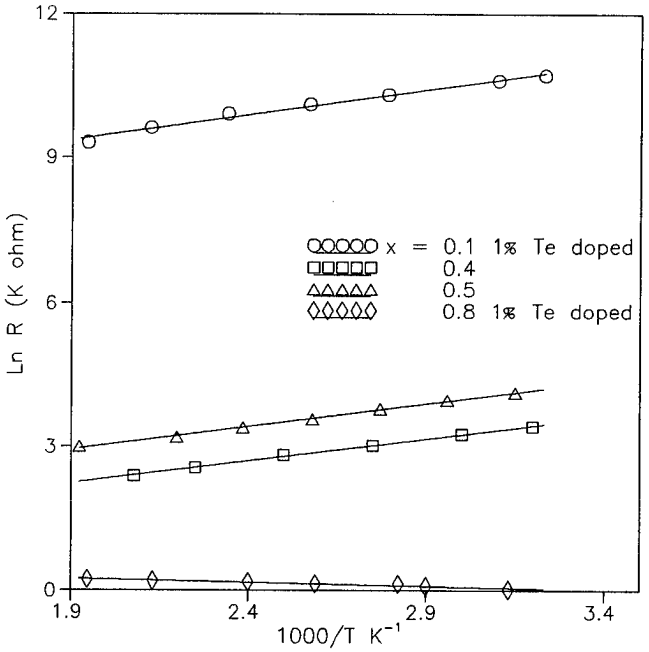


Figure 5: Plot between Ln R versus 1000/T for various alloy thin film.

of thickness around 1000 Å of various alloys studied. It is seen from the figure that $Pb_{0.8}Sn_{0.2}Te$ with 1% excess doped alloy exhibits high thermoelectric power among the alloys studied. Thin films of the alloys with x = 0.4 and 0.5 have more or less the same thermoelectric power. The other alloy with x = 0.8 gives very low thermoelectric power.

Similarly electrical conductivity of the films of all the alloys studied was measured in the temperature range of 300 *K*- 500 *K*. Figure 5. shows the plot between Ln R and 1000/T of thin films of about 1200 Å thickness of various alloys. It is seen that all the films are showing semiconducting nature. Thermoelectric figure of merit was calculated for these films using the reported thermal conductivity values which vary with temperature in the temperature range 300 K - 500 K between $K = 0.023$ W/cm K and 0.04 W/cm K [20]. Figure 6 shows variation of thermoelectric figure of merit with temperature for two different alloy compositions. Figure of merit values of alloys around room temperature with x = 0.4, 0.5, 0.8 and 1% Te doped in x = 0.2 are 5.13 $\times 10^{-6}$, 4.07 $\times 10^{-6}$, 87 $\times 10^{-6}$ and 96 $\times 10^{-6}$ K^{-1} respectively. Even though there is no systematic variation of figure of merit, it is observed that thin films of $Pb_{0.8}Sn_{0.2}Te$ doped with 1% Te doped have very high thermoelectric figure of merit than the other compositions. But these values are low compared to the bulk materials because of the fact that materials in the thin film state show high resistance.

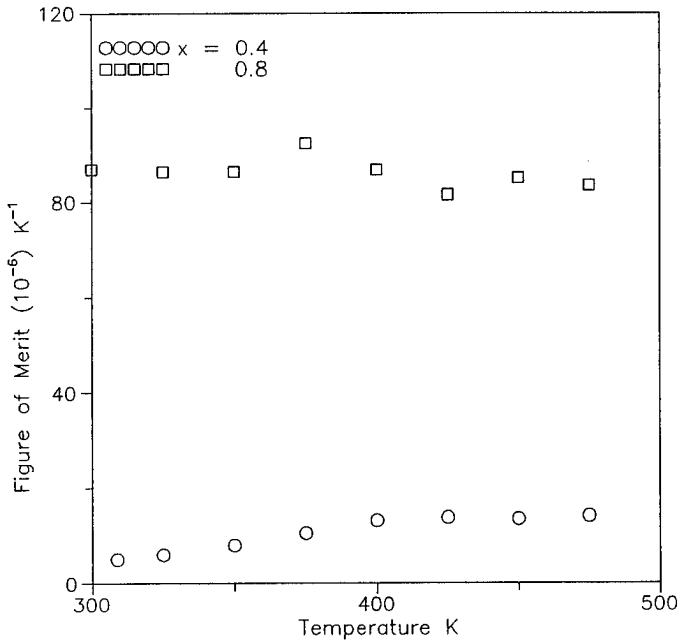


Figure 6: Figure of merit versus Temperature of thin films of x =0.4 and x = 0.8 alloys

Conclusions

A systematic analysis of thermoelectric properties, i.e., thermoelectric power and thermoelectric figure of merit of thin films of $Pb_{1-x}Sn_xTe$ alloys of various compositions indicated that excess doping of Te in the alloy $Pb_{0.8}Sn_{0.2}Te$ enhances thermoelectric figure of merit noticeably. But at high temperatures (500 K) thermoelectric power saturates for this excess doped material and it is attributed to the pin-

ning of the Fermi level. Studies on other compositions (x = 0.8,0.5, 0.6 and 0.4) indicate that thermoelectric power of these alloy thin films varies between 150 μ Volt/K and 180 μ Volt/K (for the high thickness films studied, of about 3000 Å) which is well below that of the doped material. Thus,the composition with x = 0.2 doped with 1% excess Te gives high thermoelectric power and thermoelectric figure of merit. Hence for any device fabrication purpose, this doped material can be preferred.

References

[1] A.M.Andrews, J.A.Higgins, J.F.Longo, E.R.Gertner and J.F.Posko: Appl.Phys.Lett. **21**, (1972) p.285

[2] R.B.Schooler , J.D.Jenson and G.M.Black: Appl.Phys.Lett. **31** (1970) p. 620

[3] C.C.Wang and S.R.Hampton: Solid State Electron. **18**, (1975) p.699

[4] A.R.Calawa: J.Lumin. **7**, (1973) p.477

[5] Yu.I.Ravich, B.A.Efimova, and I.A.Smirov: Semiconducting Lead Chalcogenides (Plenum press, New York, 1970)

[6] J.O.Dimmock, I.Melngails and J.Strauss: Phys.Rev.Lett., **16**, (1966) p.1193

[7] I.Mellingailis and T.C.Harman, Semiconductors and Semimetals edited by R.K.Williardson and A.C.Beer (Academic press, New York, 1970)

[8] S.Takoka, Y.Itoga and K.Murase, Jpn.J.Appl.Phys. **23** (1984) p. 216

[9] Yu.A.Abramyan, K.Z.Papazyan and V.I.Stafeev, Sov.Phys.Semicond. **26**, (1992) p.144

[10] S.C.Das, S.Battacharjee and A.K.Chaudhuri, India Bull.Mater.Sci., **16**, 159 (1993)

[11] V.Damodara Das and C.Bahuleyan, Thin Solid Films, **l274**, (1996), p.55-62

[12] N.N.Putukhova, D.B.Chesmokova and D.A.Yaskov, Sov.Phys.Semicond., **20**, (1986), p.1048

[13] L.V.Bochareva and S.P.Zimin, Sov.Phys.Semicond., **22**, (1988) p.421

[14] V.Damodara Das and C.Bahuleyan, Solid State Commun. **93** 949, (1995)

[15] V.Damodara Das and J.Chandra Mohanty, J.Appl.Phys. **54** (1983) p.977

[16] V.Damodara Das and C.Bahuleyan, National Conference on Thin Film Processing and Applications, Sri Venkateswara University, Tirupati, p.P88, Jan 23-24, 1995

[17] N.F.Mott and E.A.Davis: Electronic process and non-crystalline materials (Clarendon, Oxford 1971), p.235

[18] V.Damodara Das and C.Bahuleyan, Jpn.J.Appl.Phys., **34**, p.534, (1995)

[19] V.Damodara Das and C.Bahuleyan, J.Appl.Phys., **80**, p.1633 (1996)

[20] A.A.Machonis and I.B.Cadoff, Trans.Metall.Soc.AMIE, **230** p.333, (1964)

Comparisons of the Thermoelectric Properties of n-Type PbTe Fabricated with Different Powder Processing Methods

Jae-Shik Choi[1], Hee-Jeong Kim[1], Hang-Chong Kim[1], Dow-Bin Hyun, and Tae-Sung Oh[1]
[1]Department of Metallurgy and Materials Science, Hong Ik University, Seoul 121-791, Korea,
Phone : 82-2-320-1655, FAX : 82-2-337-8460, e-mail : ohts@wow.hongik.ac.kr
[2]Division of Metals, Korea Institute of Science and Technology (KIST), Seoul 136-791, Korea,
Phone : 82-2-958-5464, FAX : 82-2-958-5379, e-mail : dbhyun@kistmail.kist.re.kr

Abstract

Bi-doped n-type PbTe powders were fabricated by mechanical alloying and melting/grinding to compare the thermoelectric properties of the alloys with powder processing methods. Hot pressing of the PbTe powders was conducted at 650℃ and 750℃ for 1 hour in vacuum. When measured at temperatures ranging from 25℃ to 450℃, PbTe fabricated by mechanical alloying exhibited more negative Seebeck coefficient, higher electrical resistivity and lower thermal conductivity, compared to ones prepared by melting/grinding. The temperature for the maximum figure-of-merit shifted to lower temperature for the specimens fabricated by mechanical alloying. When hot pressed at 650℃, 0.3 wt% Bi-doped PbTe fabricated by mechanical alloying and melting/grinding exhibited a maximum figure-of-merit of 1.33×10^{-3}/K at 200℃ and 1.07×10^{-3}/K at 350℃, respectively.

Introduction

As a thermoelectric material having the highest figure-of-merit at around 400℃, PbTe has been widely applied to fabricate the thermoelectric generators using various heat sources.

Conventionally, the powders for sintered PbTe alloys have been fabricated by melting/grinding process [1,2]. In recent years, mechanical alloying has been applied to fabricate polycrystalline thermoelectric materials such as Si-Ge alloys and Bi_2Te_3-based alloys [3,4]. Since mechanical alloying occurs near room temperature, this technique can be a cost-saving process for the production of polycrystalline thermoelectric materials compared with the "vacuum melting/grinding" where a long processing time with high-temperature/large-scale facilities is required.

In this paper, the thermoelectric properties of Bi-doped PbTe fabricated by mechanical alloying and hot pressing were compared with the values of the alloys prepared by melting/grinding.

Experimental procedure

To process the PbTe powders using mechanical alloying, high purity (>99.99%) Pb and Te granules (~5 mm size) were weighed for PbTe composition and charged with Bi up to 0.5 wt% as donor dopants into a hardened tool-steel vial under Ar atmosphere. Ball-to-material weight ratio was held at 5 : 1. Mechanical alloying was conducted by shaking the vial at about 1200 rpm for 210 minutes using a Spex mill.

To prepare the PbTe powders by melting/grinding, Pb and Te granules were weighed to make a ingot of 40g and charged with 0.1 and 0.3 wt% Bi into a carbon-coated quartz tube. The quartz tube was vacuum-sealed at 10^{-5} torr. Pb and Te in the quartz tube were melted at 1000℃ for 2 hours using a rocking furnace and then quenched. The PbTe ingots were grown in a zone melting furnace at 1000℃ with a growth rate of 1 mm/min. The ingots were crushed in an alumina mortar to obtain the powders of 90~250 μm size.

The PbTe powders, fabricated both by mechanical alloying and by melting/grinding, were reduction-treated at 400℃ for 24 hours in (50% H_2 + 50% Ar) atmosphere. The powders were cold-pressed at 475 MPa to form 5 mm×5 mm×10 mm compacts, and hot pressed in vacuum for 1 hour at 650℃ and 750 ℃. Density of the hot-pressed specimens was measured with Archimedes method, and fracture surface parallel to the hot-pressing direction was observed using scanning electron microscopy (SEM). The Seebeck coefficient (α) of the hot-pressed specimens was measured at temperatures ranging from 25℃ to 450℃ by applying a temperature difference of 20℃ at both ends of a specimen using a sub-heater. The electrical resistivity (ρ) and thermal conductivity (κ) were measured using Harman method [5]. All thermoelectric measurements were performed in a vacuum of 10^{-5} torr to minimize the oxidation of the specimens and the thermal conduction through convection. The figure-of-merit was calculated from of $Z = \alpha^2/\rho\cdot\kappa$.

Results and Discussion

Fig. 1 illustrates SEM and optical micrographs of the PbTe prepared by mechanical alloying and melting/

grinding. When hot pressed at 650℃, the undoped PbTe was not fully sintered. However, densification was progressed almost completely and the grain size increased substantially with the addition of 0.1 wt% Bi. Microstructural variation with the Bi content up to 0.5 wt% was not noticeable. When hot-pressed at 650 ℃, the sintering density of the mechanically alloyed PbTe was improved from 93% to the almost full density with addition of Bi more than 0.1 wt%. From this result with Fig. 1, it might be expected that Bi dopant acted as a sintering aid during hot pressing of PbTe. Fig. 1(d) illustrates that densification and the grain growth occurred for the undoped specimen by hot-pressing at 750℃. As shown in Fig. 1(e) and (f), the grain sizes of the PbTe prepared by melting/grinding were much larger than ones of the mechanically alloyed PbTe, which might be due to the difference of the powder sizes before hot-pressing.

Figs. 2 and 3 show the thermoelectric properties of the PbTe mechanically alloyed and hot pressed at 650 ℃ and 750℃, respectively. The undoped PbTe exhibited the negative Seebeck coefficients, and thus n-type conduction. Although PbTe may be either p-type or n-type according to the Pb/Te stoichiometric ratio [1], powdering process for sintered PbTe has been reported to introduce donor levels [2,6].

The Seebeck coefficient and electrical resistivity decreased remarkably with addition of 0.1 wt% Bi. However, variations of these properties, especially at lower temperatures, were not so appreciable with further addition of Bi. From these results with the microstructural behavior in Fig. 1, it may be suggested that the solubility of Bi in PbTe is around 1 wt%. The Seebeck coefficient and electrical resistivity of the undoped PbTe decreased substantially by hot pressing at 750℃, which could be attributed to the microstructural change shown in Figs. 1(a) and (d). For the undoped PbTe, a substantial grain growth occurred by hot pressing at 750℃, resulting in the decrease of the electrical resistivity and hence the Seebeck coefficient. Then, the decrease of the electrical resistivity and the Seebeck coefficient with the addition of Bi, shown in Fig. 2, were not only due to the increase of the electron concentration, but also due to the increase of the carrier mobility with densification and grain growth.

For the specimens hot-pressed at 650℃, 0.3 wt% Bi-doped PbTe exhibited a maximum figure-of-merit of 1.33×10^{-3}/K at 200℃. When hot pressed at 750℃, a maximum figure-of-merit of 1.27×10^{-3}/K at 250℃ was obtained for the 0.1 wt% Bi-doped PbTe

Fig. 4 illustrates the thermoelectric properties of the 0.1 wt% Bi and 0.3 wt% Bi-doped PbTe, which were prepared by melting/grinding. The Seebeck coefficients and electrical resistivities of the specimens prepared by melting/grinding were lower than the values of the mechanically alloyed PbTe, which might be due to the different degree of surface oxidation of the powders

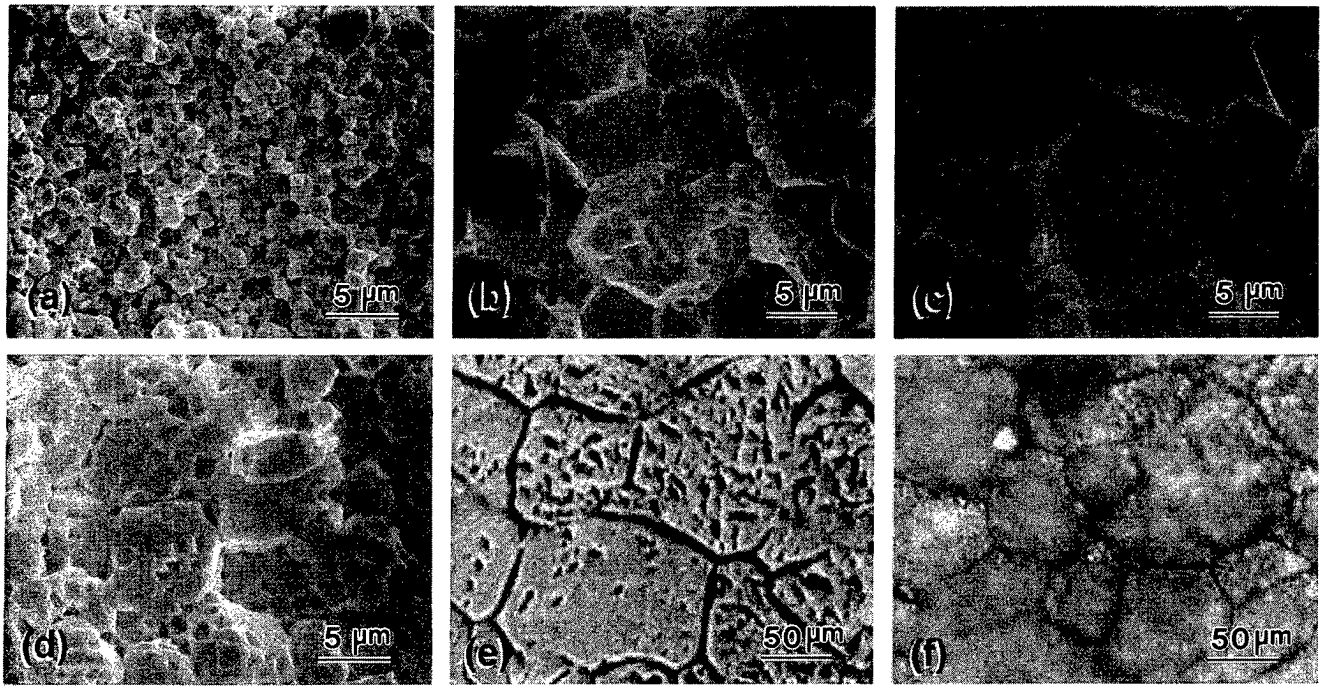


Fig. 1 SEM micrographs of the mechanically alloyed PbTe with Bi addition of (a) 0 wt%, (b) 0.1 wt%, (c) 0.3 wt% (hot-pressed at 650℃) and (d) 0 wt% (hot-pressed at 750℃), and optical micrographs of PbTe prepared by melting/grinding with (e) 0.1 wt% Bi and (f) 0.3 wt% Bi (hot-pressed at 650℃).

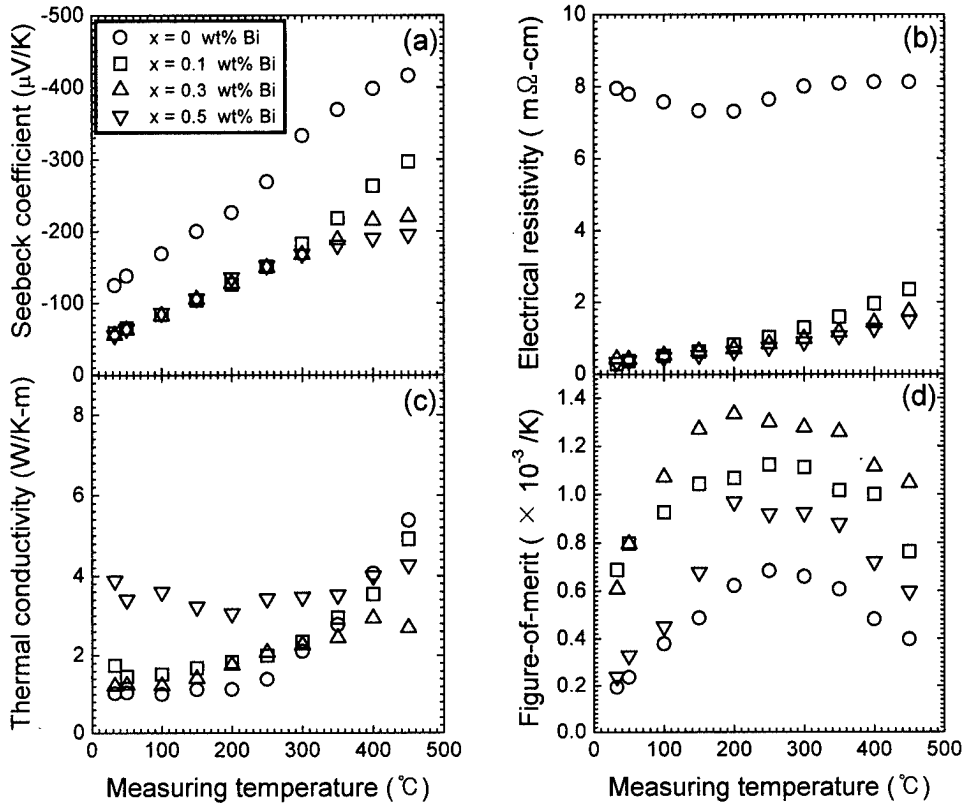


Fig. 2 (a) Seebeck coefficient, (b) electrical resistivity, (c) thermal conductivity, and (d) figure-of-merit of PbTe fabricated by mechanical alloying (hot-pressing temperature : 650℃).

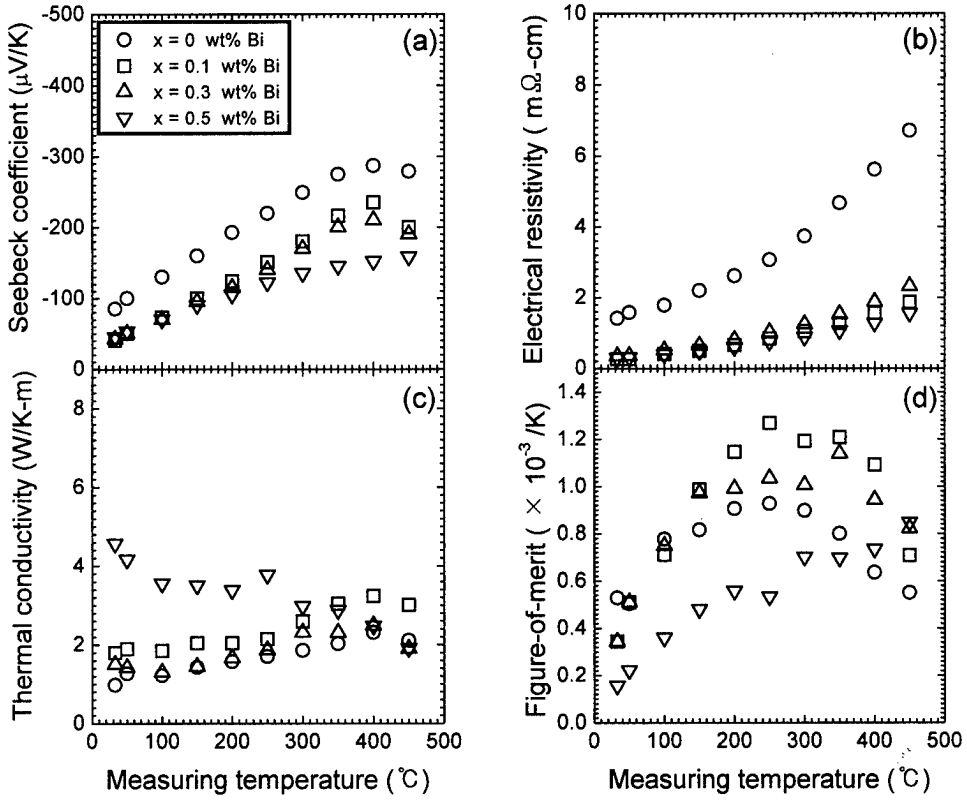


Fig. 3 (a) Seebeck coefficient, (b) electrical resistivity, (c) thermal conductivity, and (d) figure-of-merit of PbTe fabricated by mechanical alloying (hot-pressing temperature : 750℃).

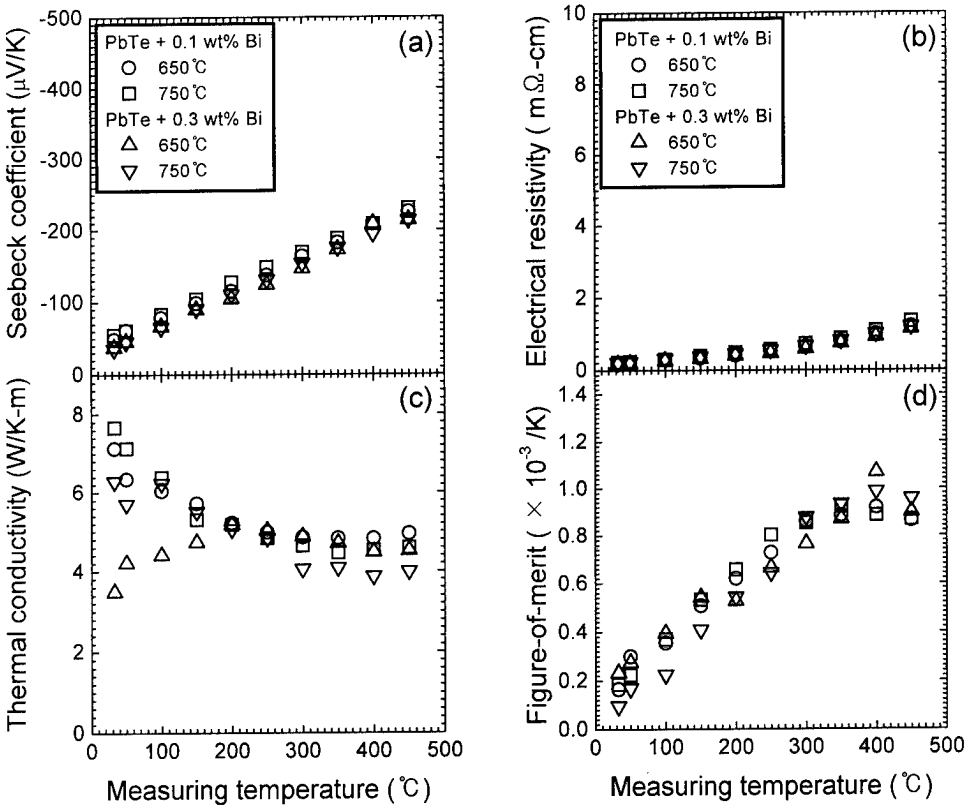


Fig. 4 (a) Seebeck coefficient, (b) electrical resistivity, (c) thermal conductivity, and (d) figure-of-merit of PbTe fabricated by melting/grinding (hot-pressing temperature : 650℃ and 750℃).

before hot pressing. As mechanical alloying occurs by repeated fracture and cold welding of the powders [7], the surface of the mechanically alloyed powders is more easily oxidized than the powders prepared by melting/grinding. Contrary to the case of Bi_2Te_3 alloys where the oxygen acts as a donor dopant [8,9], the oxygen is a p-type dopant for PbTe [6,10], As shown in Fig. 4(d), the maximum figure-of-merit shifted to higher temperature, compared to ones for the mechanically alloyed PbTe. A maximum figure-of-merit of 1.07×10^{-3}/K at 400℃ was obtained for the 0.3 wt% Bi-doped PbTe, which was hot-pressed at 650℃.

Summary

The Seebeck coefficients and electrical resistivities of the PbTe prepared by melting/grinding were lower than the values of the mechanically alloyed specimens, which might be due to the different degree of surface oxidation of the powders before hot pressing. The temperature for the maximum figure-of-merit shifted to lower temperature for the specimens fabricated by mechanical alloying. When hot pressed at 650℃, the 0.3 wt% Bi-doped PbTe fabricated by mechanical alloying and melting/grinding process exhibited a maximum figure-of-merit of 1.33×10^{-3}/K at 200℃ and 1.07×10^{-3}/K at 350℃, respectively.

Acknowledgment

This work was supported by the Korea Electric Power Corporation through an EESRI research project.

References

[1] "CRC Handbook of Thermoelectrics," D. M. Rowe (ed.), p.257, CRC Press, New York (1995).

[2] R. Breschi and V. Fano, J. Mater. Sci., **20** (1985) 990.

[3] B. A. Cook, B. J. Beaudry, J. L. Harringa, and W. J. Barnett, Proc. of the IXth Int. Conf. on Thermoelectric, p.234, 1990.

[4] B. Y. Jung, T. S. Oh, D. B. Hyun, and J. D. Shim, J. Korean Phys. Soc., **31** (1997) 219.

[5] T. C. Harman, J. H. Cahn and M. J. Logan, J. Appl. Phys., **30** (1959) 9.

[6] R. Breschi, A. Olivi, A. Camanzi, and V. Fano, J. Mater. Sci., **15** (1980) 918.

[7] R. Sundaresan and F. H. Froes, J. of Metals, **8** (1987) 22.

[8] J. M. Schultz, J. P. McHugh, and W. A. Tiller, J. Appl. Phys., **33** (1962) 2443.

[9] D. M. Gel'fgat and Z. M. Dashevskii, Inorg. Mat., **19** (1984) 1172.

[10] W. D. Lawson, J. Appl. Phys., **23** (1952) 495.

Semiconducting Transition Metal Silicides: Electronic Structure, Electrical and Thermoelectrical Properties

H. Lange, St. Brehme, W. Henrion

Hahn-Meitner-Institut, Abteilung Photovoltaik, Rudower Chausssee 5, D-12489 Berlin, Germany, Tel.: +49-30-67053-354, Fax: +49-30-67053-333, E-mail: lange@hmi.de

A. Heinrich, G. Behr, H. Griessmann

Institut für Festkörper- und Werkstofforschung Dresden, Helmholtzstr. 20, D-01069 Dresden, Germany, Tel.: +49-351-4659-533, Fax: +49-351-4659-537, E-mail: aheinrich@ifw-dresden.de

A.B. Filonov, V.E. Borisenko

Belarusian State University of Informatics and Radioelectronics, P. Browka 6, 220027 Minsk, Belarus, Tel.: +375172-398869, Fax: +375172-310914, E-mail: victor@nano.rei.minsk.by

Abstract

The actual knowledge existing on electronic structure determinations for semiconducting transition metal silicides obtained from band structure calculations and investigations of optical interband spectra is reviewed. The emphasis is put on the information available for the semiconducting 3d transition metal silicides which is combined with recently gained experimental and theoretical data for the semiconducting 4d and 5d transiton metal silicides. From band structure studies and optical investigations it is concluded that most semiconducting transition metal silicides are indirect-gap materials. An electrical data analysis indicates that all non-intentionally doped semiconducting silicides exhibit hole conduction with relatively high carrier concentrations even in epitaxial films and single crystals. The experimental electron to hole mobility ratios are less than unity, i.e. mobilities of electrons are usually much lower than those of holes. Effective masses seem to be ≥ 1 free electron mass for most semiconducting silicides. The extensive work done on the electrical and thermoelectrical properties of semiconducting iron disilicide thin films and single crystals will be considered in more detail.

Introduction

Semiconducting transition metal silicides are a class of semiconductors which are considered to be promising for thermoelectric applications. In recent years considerable progress has been achieved in the growth of epitaxial layers and also of single crystals for a series of semiconducting transition metal silicides. This allows a deeper understanding of their fundamental electronic and electrical properties. Only few silicides are reported to be semiconducting. As a rule these include Si-rich phases with transition metals from the VI. to the VIII. Group of the Periodic Table. Now nine semiconducting transition metal silicides are known: $CrSi_2$, $MnSi_x$, ß-$FeSi_2$, Ru_2Si_3, $ReSi_{1.75}$, OsSi, Os_2Si_3, $OsSi_2$, and Ir_3Si_5. Theoretical estimates also predict metastable hexagonal $MoSi_2$ and WSi_2 to be small-gap semiconductors. Most efforts are concentrated on the ß-phase of $FeSi_2$. On the one hand, this is due to the availablitiy of the components Fe and Si and the non-toxicity of the compound and the preparation process. On the other hand, ß-$FeSi_2$ exhibits interesting physical properties being attractive for optoelectronics, photovoltaics, thermoelectrics.

Crystallographic structure

The semiconducting silicides crystallize in a variety of crystallographic structures. A compilation of structural data is contained in [1]. Most of the semiconducting silicides crystallize in the orthorhombic structure. Some of them are isostructural, i.e. the disilicides of Os and Fe as well as Ru_2Si_3 and Os_2Si_3. Thus, the formation of solid solutions on their basis over the whole composition range can be expected. The crystallographic structure of ß-$FeSi_2$ has been studied most thoroughly [2]. The orthorhombic unit cell contains 16 molecules. There are two crystallographically inequivalent lattice sites for both Fe and Si with slightly differing distances to nearest neighbours. Ru_2Si_3 and Os_2Si_3 are so-called defect-type $TiSi_2$ chimney-ladder compounds. In previous investigations semiconducting Re silicide was reported to have the composition $ReSi_2$ and to crystallize in the orthorhombic structure. In recent work [3] the structural properties of semiconducting Re silicide were reinvestigated, it was found that the stable composition is $ReSi_{1.75}$ and space group is P1. Higher manganese silicide $MnSi_x$ has the most complicated structure of all semiconducting silicides. For x in the range between 1.71 and 1.75 several tetragonal phases exist [4],, all of them have similar tetragonal cells. They are composed of manganese-silicon subcells which are stacked along the c-axis yielding elementary cells of different size and chemical composition.

Electronic structure

Trends in electronic structure

The principal picture of the electronic structure of metallic silicides derived in numerous previous theoretical and experimental investigations [5,6,7] is generally also valid for their

semiconducting counterparts. Main attention has been paid to the 3d transition metal silicides. The electronic structure of the transition metal silicides is dominated by transition metal d states. The common characteristics of the valence band density of states of the silicides are non-bonding d states near the Fermi energy E_F, the bonding p-d hybridized states which determine the stability of the silicide extending to about 6 eV below E_F and the Si s states situated about 10 to 14 eV below E_F. Compared to the elemental transition metals the non-bonding d band is narrowed, as the atomic d bands are driven farther apart and the hopping integrals decrease due to the insertion of the Si atoms in the crystal lattice. With increasing atomic number Z in the series of 3d transition metals the d-derived states vary substantially appearing first as broad band of mostly empty states at the beginning of the transition metal row to a narrow band of fully occupied states. Whereas the occupied d-derived states move to greater binding energy within the transition metal row, the antibonding p-d combinations appear mostly above E_F and their energetic position remains nearly invariant in the series of 3d silicides. The Si s-derived states overlap relatively little with the Si p and the metal d states and are weakly involved in chemical bonding. The calculations have shown that there is only small charge transfer in silicides, usually less than 1 % of the valence charge/atom. This means that ionicity does not contribute to bond formation.

Band structure studies of semiconducting transition metal silicides

Electronic structure calculations have been recently carried out for the disilicides of Cr, Fe, Os, as well as for the semiconducting phase of Ru silicide. First estimates have been also carried out for $ReSi_{1.75}$. In all cases the semiconducting nature of these compounds could be theoretically verified.

Most of these studies were concentrated on ß-$FeSi_2$. Already in the first calculations, e.g. [8], the nature of the gap was one of the most important questions. It has been pointed out in [8] that the gap formation in ß-$FeSi_2$ is related to a Jahn-Teller-like crystal-structure deformation of the fluorite-type γ-phase of $FeSi_2$. A particularly strong coupling of the band edge states to the lattice has been found to be a characteristic feature of ß-$FeSi_2$. The conduction band exhibits two energetically close valleys at Y and around the Λ points of the Brillouin Zone with strongly differing electron effective masses. The highest valence band maximum is at the Λ point, a second maximum energetically shifted to higher binding energies is situated at the Y point. Calculations of the electronic structure of this compound performed in the augmented plane wave (APW) [9], the linear muffin-tin orbital (LMTO) in the local density approximation (LDA) [8,10], the empirical tight-binding scheme [11], as well as by an ab-initio full-potential linearized APW method [12] agree that the nature of the lowest gap at 0.78 eV is rather structure sensitive. A slight decrease in the nearest-neighbour distance induces a change in the gap nature from indirect into direct. A second direct gap appears at the Y point at about 0.82 eV.

Recently the electronic structure of $OsSi_2$, which is isostructural to ß-$FeSi_2$, has been calculated with the LMTO method in the LDA scheme [13]. The conduction band minimum has shifted from the Λ to the Γ point and is energetically higher than that at the Y point. The valence band has extrema at the Λ and Y points. Thus, this material is an indirect-gap semiconductor, its lowest gap value is 0.95 eV. A second direct gap occurs at at the Y point which amounts to 1.14 eV. For $OsSi_2$ the regions of bonding Si-p and Os-d states and non-bonding metal d states are shifted to higher energies with respect to ß-$FeSi_2$. This is probably due to the stronger overlap of Os d and Si p functions causing a greater bonding/antibonding splitting.

Band structure calculations for hexagonal $CrSi_2$ carried out by LMTO, LAPW, and ASW methods (for references see [1]) agree that this material is an indirect gap semiconductor, the theoretical gap values range between 0.21 and 0.38 eV. The gap occurs between the valence band maximum at the L point and the conduction band minimum at the M point. The lowest direct gap values range between 0.37 and 0.48 eV, this gap occurs at the M point.

All previous calculations of the electronic structure of $ReSi_2$ have predicted this material to be a metal with very high conductivity [14]. This theoretical conclusion is possibly due to the wrong (tetragonal) crystal structure used in the calculation and the assumption that the chemical composition is $ReSi_2$. When considering the structural refinement results for this semiconductor, i.e. chemical composition $ReSi_{1.75}$ and space group P1, the theoretical studies [15] indeed revealed semiconducting indirect-gap character, with gap values in correspondence with the experimental ones.

First band structure calculations for Ru_2Si_3 have been carried out recently by several groups using the full-potential linearized APW method [16] and the LMTO method [17,18] in the LDA approximation. All calculations predict a direct band-gap character for this compound, the theoretical gap values obtained range between 0.40 and 0.46 eV.

A compilation of theoretical gaps together with gap energies from optical and elecrical measurements is given in Table 1.

Optical interband spectra

One of the most powerful methods of probing the electronic structure of semiconductors are optical interband investigations. We have performed intensive studies of the optical interband properties of semiconducting silicides over a broad energy range from the infrared up to 24 eV. Fig. 1 shows an overview of the spectral distribution of the real and imaginary parts of the dielectric function of ß-$FeSi_2$ films. The spectra are characterized by three features of decreasing intensity with increasing photon energy: the first most intensive one occurring between 1 and 2 eV, the second one at about 4.5 eV, and the third one of lowest intensity around 14.5 eV. In terms of our density of states calculations for ß-$FeSi_2$ [10] we interpret these structures as follows: These are due to transitions from the valence band into the antibonding conduction band states, the first one starting from the non-bonding group of d states, the second one has its origin in optical transitions from the group of bonding states distribution, and finally the weak structure at 14.5 eV arises from the broad distribution of Si s states not involved in chemical bonding.

Table 1
Theoretical and experimental energy gaps of semiconducting silicides as well as gap nature. Unless indicated, the experimental gap values are determined from optical measurements.

phase	experimental energy gap (eV)	type of gap, experimental	theoretical energy gap (eV)	type of gap, theoretical
$CrSi_2$	0.35 [19] 0.5 [19] 0.67 [20] 0.9 [20] 0.27-0.35 [1]) 0.42 [1]) [21]	indirect direct indirect direct	0.21-0.38 (references see [1]) 0.37-0.47 (references see [1])	indirect direct
$MnSi_x$	0.45-0.47 [22,23] 0.66 [24] 0.78-0.83 [25] 0.4-0.45 [2])	indirect direct direct		
β-$FeSi_2$	0.765 [10] 0.78 [2]) [26] 0.79 [2]) [27] 0.83-0.89, most probable RT direct gap value 0.87 eV, for references see [1]	indirect indirect indirect direct	0.44 [28] 0.742 [10] 0.78 [12] 0.46 [28] 0.8 [8] 0.825 [10] 0.82 [12]	indirect quasi-direct quasi-direct direct direct direct direct
Ru_2Si_3	0.7 [3]) [29] 1.09 [3]) [30] 0.44 [4]) [29]		0.45 [5]) [15] 0.46 [5]) [16] 0.40 [5]) [17]	direct direct direct
$ReSi_2$ ($ReSi_{1.75}$)	0.12-0.15 [31] 0.36 [31] 0.16-0.2 [1]) second gap at 0.3 eV [1]) [32]	indirect direct	0.16 [14] 0.36 [14]	indirect direct
OsSi	0.34 [1]) [33]			
Os_2Si_3	2.3 [1]) [33]			
$OsSi_2$	1.4 [1]) [34] 1.8 [1]) [32]		0.95 [13] 1.14 [13]	indirect direct
Ir_3Si_5	1.2 [35] 1.57 [23]	direct direct		

[1]) Lowest gap values obtained from electrical measurements.
[2]) $E_g^{ind} + h\nu_p$, the energy of the participating phonon is $h\nu_p = 35$ meV according to [10].
[3]) Low-temperature modification, obtained from electrical measurements.
[4]) High-temperature modification, obtained from electrical measurements.
[5]) Low-temperature modification.

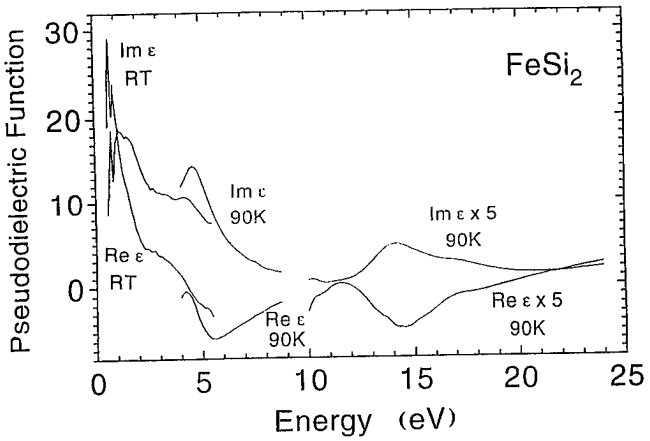


Fig. 1. Overview of spectral distribution of real and imaginary parts of the dielectric function up to 24 eV for ß-$FeSi_2$

Fig. 2 shows the degree of agreement presently achieved for the low-energy range up to 5 eV of the spectral distribution of optical constants. The optical spectra have been calculated with and without account of f electrons within LDA approximation by using the semirelativistic LMTO method. The experimental spectra were determined ellipsometrically on epitaxial ß-$FeSi_2$ films. The influence of the f electrons becomes more prominent in the high-energy region. As seen from the figure, the theoretical spectra reproduce all main features of the experimental spectra and even finer spectral details. A similarly good agreement between theoretical and experimental optical spectra in has been obtained for semiconducting Ru_2Si_3 [17].

In Fig. 3 the imaginary parts of the dielectric function are compared for the semiconducting transition metal silicides $MnSi_x$, $CrSi_2$, and ß-$FeSi_2$ as well as for the semiconducting 5d transition metal silicide Ir_3Si_5. A close resemblance in the spectra for the silicides in the 3d series is clearly seen. This resemblance even holds for Ir_3Si_5. For this material the low-energy features are shifted to higher energies compared to the 3d transition metal silicides. This is in correspondence with the stronger bonding/antibonding splitting compared to 3d silicides. However, the position of the s-like states not involved in chemical bonding is approximately the same in the silicides. The optical interband spectra for the 5d semiconducting Re silicide fit into this general trend.

The band structure calculations have revealed a dominant d character of states on both sides of the gap. Therefore across-gap oscillator strengths of semiconducting silicides might be orders of magnitude smaller than e.g. for typical zincblende-type materials. Therefore optical gap and gap nature determinations by extrapolating the relevant information from power-law plots of optical data might become problematic for semiconducting silicides considering that usually pronounced absorption tails exist for all semiconducting silicides, even for epitaxial layers, which extend far into the interband gap. These could mask interband features having a low oscillator strength. This has been shown for $CrSi_2$ (see [1]) and is also observed for Ru_2Si_3. Care has also to be taken in case of Mn and Ir silicides in assigning the gap values obtained to lowest interband gaps in these materials.

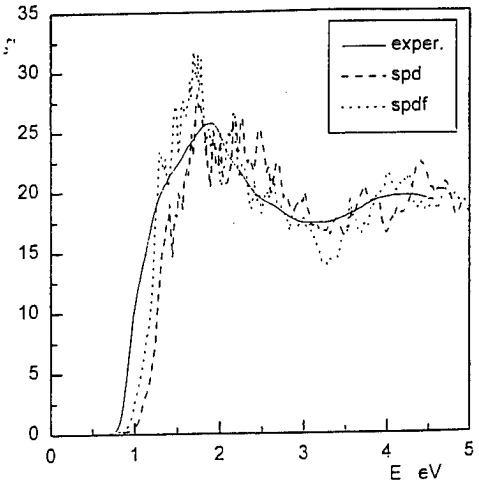


Fig. 2. Experimental ε_2 spectra of ß-$FeSi_2$ upto 5 eV compared with theory calculated with and without f electrons

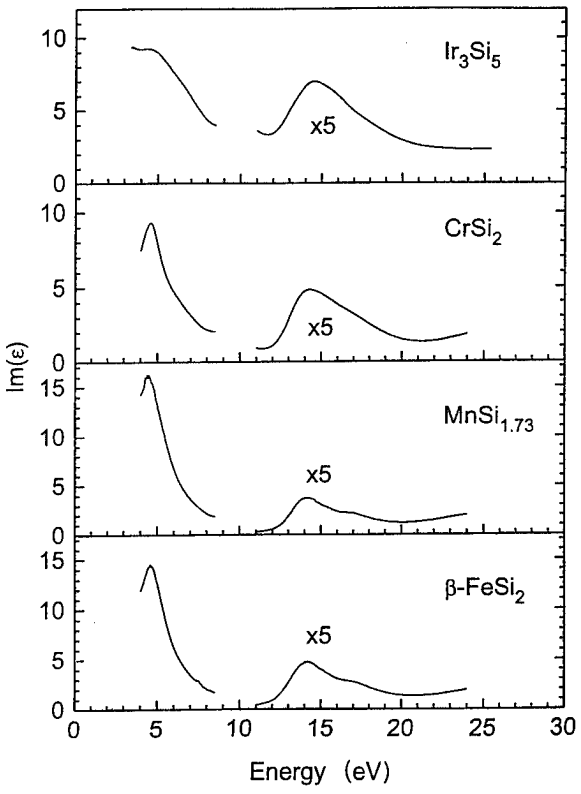


Fig. 3. Imaginary parts of the dielectric function at high photon energies for ß-$FeSi_2$, $CrSi_2$, $MnSi_x$, and Ir_3Si_5

Electrical properties

The study of the electrical properties of semiconducting silicides was a main research activity for many years because of the possible use of these materials in thermoelectric applications. Special attention has been paid to the 3d transition metal silicides. Most extensive investigations have been carried out on ß-$FeSi_2$. Although less information is available for the other semiconducting silicides, some general conclusions can be drawn for the whole class of these compounds.

Not intentionally doped semiconducting silicides are usually p-type materials. The nature of the defects responsible for the p-type character is not known. A conversion to n-type is possible by the addition of transition metals with a larger number of d electrons than the metal they replace. This has been shown for ß-$FeSi_2$ and Ru_2Si_3 by adding Co, Ni, Pt, or Pt, or also Rh, Ir, Ga, P in the latter compound. Mn, Cr, V, and Ti give p-type in ß-$FeSi_2$ and Ru_2Si_3 [36,37] (see also [1]). The activation energies of most n- and p-type dopands range between 0.05 and 0.14 eV. In some cases solubilities of dopands of the order of several at% were found. Occasionally n-type conduction is observed in ß-$FeSi_2$ epitaxial films with Si excess. Around room temperature acoustic phonon scattering seems to be a dominant carrier scattering mechsnism in many semiconducting silicides. Low-temperature scattering mechanisms are less well known.

In Table 2 a summary of room temperature electrical parameters is given for films and single crystals of semiconducting silicides. The data for polycrystalline films often exhibit a large scatter which is related to their structural quality.

The carrier concentrations are relatively high even in epitaxial films and crystals. They usually range between 10^{18} and 10^{20} cm^{-3}. Lowest carrier concentrations of 10^{16} cm^{-3} have been obtained on high-purity single crystals of ß-$FeSi_2$. Maximum room temeparture mobilities are between 10 and 40 cm^2/Vs for ß-$FeSi_2$ epitaxial films and crystals. In polycrystalline films they can drop to < 1 cm^2/Vs. The electron to hole mobility ratio is much less than unity, i.e. the mobilities of electrons are much lower than those of holes. Effective masses seem to be ≥ 1 m_o for most semiconducting silicides.

We have performed electron paramagnetic resonance (EPR) measurements on ß-$FeSi_2$ single crystals doped with Co, Ni, Mn, or Cr in order to get insight into the incorporation of dopands into the lattice [38]. The main features of the EPR spectra could be explained using a spin Hamiltonian with electronic spin 1/2. From the good agreement achieved between measured and simulated hyperfine structures which reflect the interaction of dopands with the lattice, it is concluded that all transition metal dopands replace Fe in different amounts on its two non-equivalent lattice sites. The electron spin 1/2 indicates that the impurity states are occupied by an electron for Ni and Co, and by a hole for Mn and Cr.

Recently, quite interesting new results were obtained on the electrical and thermoelectrical properties of undoped ß-$FeSi_2$ single crystals grown under high-purity conditions wih 5N Fe and Si, both electrical resistivity and thermopower were found to depend on the composition within the homogeneity range of ß-$FeSi_2$ [51]. In both doped and undoped ß-$FeSi_2$ the electrical resistivity shown in Fig. 4 reveals a thermally activated behaviour being typical for extrinsic semiconductors. We obtained an activation energy of 40-60 meV for Co dopand, about 80 meV for Cr, ca. 50 meV for Mn, and between about 60 and 95 meV for Ni dopand. At temperatures below 100 K impurity-related hopping processes play the dominant role in electrical transport of ß-$FeSi_2$, characterized by $\ln(\rho) \sim T^{-1/n}$ power laws with n = 2 or 4. A further indication of hopping transport at low temperatures is the occurrence of a negative magnetoresistance which is related to quantum interferences between multiple carrier paths being possible for a carrier which will hop from one site to another one.

In n-type ß-$FeSi_2$ only very low Hall voltages can be measured. A typical temperature dependence of the Hall coefficient R_H of an undoped p-type thin layer on high-resistivity n-type Si substrate is shown in Fig. 5. With decreasing temperature the Hall coefficient strongly decreases and changes sign between 200 and 300 K. Since a change of sign is not expected in a homogeneous semiconductor, this is suggested to be due to the strongly temperature-dependent influence of the substrate caused by the nonideal p-n junction between p-type layer and n-type substrate at higher temperatures, as demonstrated by the reverse I-U characteristics in the insert of Fig. 5. Hole concentrations (p) and hole mobilities (μ) derived from the R_H data for layers on Si substrates correspond to true p and μ values only between the transition from impurity to valence band conduction (about 100 K) and the range without disturbing influence of the substrate (i.e. about 250 K). In Fig. 6 the temperature dependences of Hall mobilities are shown for thin film and crystal. Between RT and 100 K the temperature dependence can be approximated by a power law, T^{-n}. Typical n values for films range between 1.5 and 1.8; a higher vaue of n = 2.15 was obtained for the hydrogen-treated film. The n values for crystals are found to be strongly dependent on the purity of the starting material and the optimization of the growth process [52]. In a first theoretical attempt to simulate the temperature dependence of mobility scattering by acoustic and non-polar optical phonon modes as well as scattering by neutral impurities were found to be main scattering mechanisms, whereas polar optical phonon scattering was considered to be negligible [53]. Extrapolated RT values for layers range between 0.5 and 2 cm^2/Vs. Literature also reports room temperature mobilities of 100 cm^2/Vs or higher for polycrystalline layers on Si, e.g. [27], which are much higher than those of well grown crystals ranging between 20 and 40 cm^2/Vs. Considering the data presented in Fig. 5, this is probably due to the leakiness of the silicide/Si p-n heterojunction and indicates the substrate influence.

A Hall voltage in p-type samples was observed down to the lowest temperatures in all thin films and single crystals investigated. In [54] on the basis of an analysis of characteristic hopping temperatures a metallic character of impurity bands in most doped crystals was deduced. The Hall voltage often reveals a nonlinear dependence on the strength of the magnetic induction at low temperatures which is most pronounced near B = 0 (see Fig. 7). This prevents reliable Hall data analysis below a threshold temperature which amounts to 50-150 K depending on the individual sample. In [56] even a hysteresis effect has been found at low temperatures in doped crystals.

Table 2

Room temperature electrical parameters for non-intentionally doped semiconducting silicides (thin films and bulk material).

phase	resistivity (Ωcm)	hole mobility (cm^2/Vs)	electron to hole mobility ratio b	hole concentration (cm^{-3})	effective hole mass (m_o)
$CrSi_2$	‖c: 0.14 [1] ⊥c: 0.073 [1] [39] 0.01-0.07 [2] [40] 0.02 [3] [21]	‖c: 9.2 [1] ⊥c: 18 [1] [39] 7-18 [2] [40] 2980 [3] [21]	0.01 [1] [39]	6-8x10^{20} [1] [39] 6x10^{19} -2x10^{18}, see [21] 1.1x10^{17} [3] [21]	‖c: 5 [1] ⊥c: 3 [1] [39]
$MnSi_x$	0.004 [41] 0.013 [42] ‖c: 0.0055 ⊥c: 0.001 [44]	1.5 [41] 0.7 [42] ‖c: 0.45 ⊥c: 2.9 [44]	0.02 [41] 0.36 [42]	7.1x10^{20} [42] 1.8-2.3x10^{21} [41] 2.1x10^{21} [44]	12 [43] ‖c: 15 ⊥c: 11 [44]
β-$FeSi_2$	0.1-1 [1] [45] 0.01-1 [2] [26,27]	10-40 [1] [45] 1-10 [2] [26] 90-120 [2] [26,27]	0.1 [1] [45]	10^{17} [1] [45] 10^{18}-10^{19} [2] [26] 10^{17} [27]	1 [1] [45]
Ru_2Si_3	ca. 0.01 [46]	7.3 [46]	0.07 [46]	1x10^{18} [46]	7.5 [46]
$ReSi_{1.75}$ ($ReSi_2$)	0.004-0.008 [1] [32] 0.003-0.01 [2] [48]	370 [1] [3] 9 [2] [32] 50 [2] [47] 150 [4] [47]		4x10^{18} [1] [3] 3.9x10^{19} [2] [32] 3x10^{18} [2] [47] 4x10^{17} [4] [47]	
Ir_3Si_5	0.1-0.01 [2] [49] 6x10^{-4} [1] [50]	2.4 [2] [35]		>10^{20} [2] [49] 3.9x10^{17} [2] [35]	

[1]) Data for single crystals.
[2]) Data for polycrystalline layers.
[3]) Data for epitaxial A-type layers on Si(111).
[4]) After annealing in hydrogen atmosphere at 850 °C.

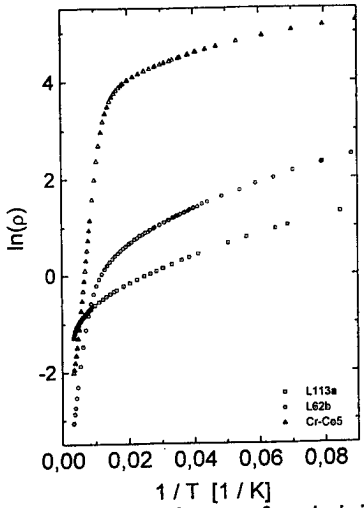


Fig. 4. Temperature dependence of resistivity of non-intentionally doped (L113a) and Co-doped ß-$FeSi_2$ layers (L112b) and Co-doped ß-$FeSi_2$ single crystals (Cr-Co5)

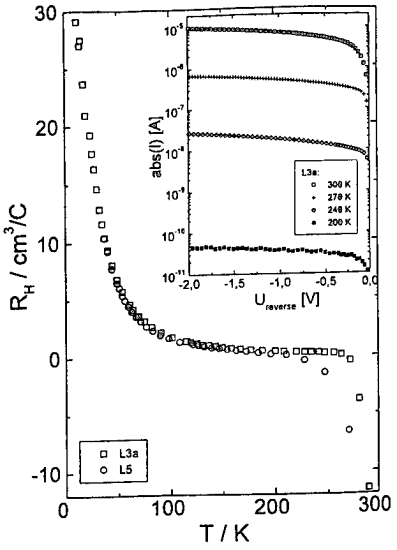


Fig. 5. Temperature dependence of Hall coefficient for a nonintentionally doped layer on 5 kΩcm Si substrate. The insert presents the temperature dependence of the reverse current-voltage characteristcs of the silicide/Si p-n heterojunction

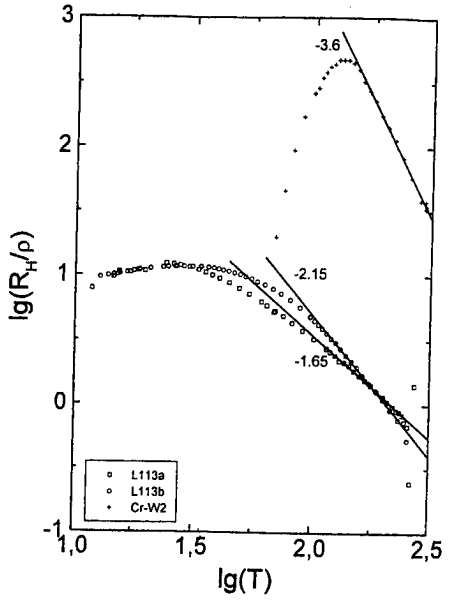


Fig. 6. Logarithmic representation of the apparent Hall mobility of untreated (L113a) and hydrogen-treated (L113b) layers and a Cr-doped crystal (Cr-W2). The slopes of temperature dependences are indicated.

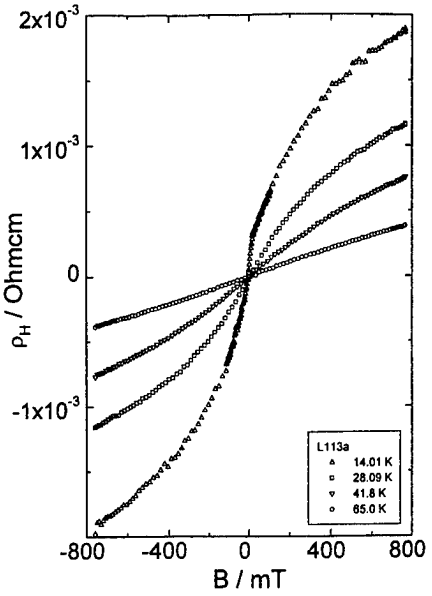


Fig. 7. Dependence of Hall resistivity on strength of magnetic induction for a ß-$FeSi_2$ layer at different temperatures. With decreasing temperature a contribution from the anomalous Hall effect arises.

The cause of the anomalous Hall effect is not quite clear. There are no hints on a magnetic phase transition from EPR [38] or magnetization measurements [45]. Our recent investigations suggest that this phenomenon has an extrinsic origin and is due to deviations from the ideal crystal structure of ß-$FeSi_2$.

The temperature dependence of thermopower of doped ß-$FeSi_2$ single crystals is shown in Fig. 8. Independent of the doping element and of the conductivity type there is a strong increase of thermopower from 70 to 150 K which can be described by a T^n power law with $n \approx 6$. Also the temperature dependence of thermopower below 300 K is similar in most samples and is given by an exponent -0.9 which is also found in undoped crystals. The low temperature maximum therefore seems to be a common characteristic of ß-$FeSi_2$ crystals. Maximum thermopowers of 2000 µV/K are attained. These large values of thermopower cannot be explained by a usual diffusion thermopower. Phonon drag effects play an important role. As seen from Fig. 8, the most pronounced maximum was found in Co-doped crystals with 0.5 at% Co grown with high-purity (5N) Fe. At temperatures above 300 K the thermopower remains approximately constant until the onset of intrinsic conduction at 400 K in undoped and about 600 K in doped single crystals (see Fig. 8).

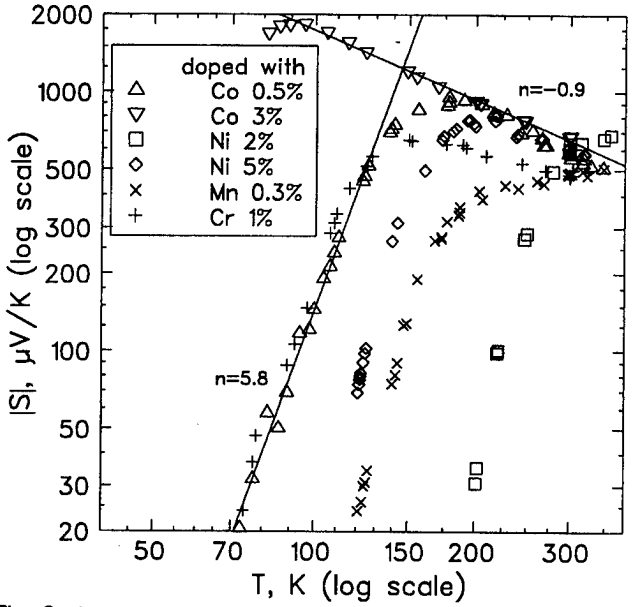


Fig. 8. Absolute value of the thermopower of doped ß-$FeSi_2$ crystals between 4 and 1000 K.

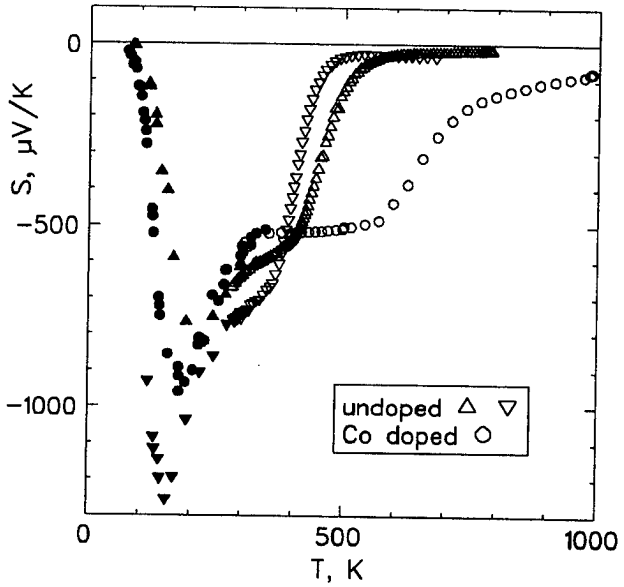


Fig. 9. Thermopower of undoped and cobalt-doped ß-$FeSi_2$ single single crystals versus temperature.

Conclusion

From recent investigations much information has been obtained on the electronic structure and electrical properties of semiconducting silicides. For ß-$FeSi_2$ it could be shown that crystal growth under high-purity and controlled-doping conditions provides deeper insight into the electrical and thermoelectrical properties of this material.

Acknowledgement

This work has been supported by projects granted from Deutsche Forschungsgemeinschaft, Volkswagen-Stiftung and Ministerium für Forschung, Technologie, Bildung und Erziehung.

References

[1] H. Lange, phys. stat. sol. (b) **201**, 3 (1997).

[2] Y. Dusausoy, J. Protas, R. Wandji, B. Roques, Acta Cryst. **B27**, 1209 (1967).

[3] U. Gottlieb, B. Lambert-Andron, F. Nava, et al., J. Appl. Phys. **78**, 3902 (1995).

[4] V.K. Zaitsev, S.V. Ordin, K.A. Rakhimov, A.E. Englyachev, Soviet Phys. - Solid State **23**, 353 (1981).

[5] J.H. Weaver, A. Franciosi, V.L. Moruzzi, Phys. Rev. B **29**, 3293 (1984).

[6] W. Speier, E. van Leuken, J.C. Fuggle, et al., Phys. Rev. B **39**, 6008 (1989).

[7] P.J.W. Weijs, G. Wiech, W. Zahorowski, et al., Physica Scripta **41**, 629 (1990).

[8] N.E. Christensen, Phys. Rev. B **42**, 7148 (1990).

[9] R. Eppenga, J. Appl. Phys. **68**, 3027 (1990).

[10] A.B. Filonov, D.B. Migas, V.L. Shaposhnikov, et al., J. Appl. Phys. **79**, 7708 (1996).

[11] L. Miglio, G. Malegori, Phys. Rev. B **52**, 1448 (1995).

[12] S. Eisebitt, J.-E. Rubensson, M. Nicodemus, et al., Phys. Rev. B **50**, 18330 (1994).

[13] A.B. Filonov, D.B. Migas, V.L. Shaposhnikov, et al., Appl. Phys. Letters **70**, 976 (1997).

[14] B.K. Bhattacharrayya, D.M. Bylander, L. Kleinman, Phys. Rev. B **33**, 3947 (1986).

[15] A.B. Filonov et al., to be published.

[16] W. Wolf, G. Bihlmayer, S. Blügel, Phys. Rev. B **55**, 6918 (1997).

[17] W. Henrion, M. Rebien, H. Lange, V. Antonov, O. Jepson, Thin Solid Films, in the press.

[18] A.B. Filonov et al., to be published.

[19] M.C. Bost, J.E. Mahan, J. Appl. Phys. **63**, 839 (1988).

[20] H. Lange, M. Giehler, W. Henrion, F. Fenske, I. Sieber, G. Oertel, phys. stat. sol. (b) **171**, 63 (1992).

[21] N.G. Galkin, T.V. Veltchko, S.V. Skripka, A.B., Khrustalev, Thin Solid Films **280**, 211 (1996).

[22] M.C. Bost, J.E. Mahan, J. Electronic Mater. **16**, 389 (1987).

[23] H. Lange et al.,phys. stat. sol. (b) **194**, 231 (1996).

[24] V.K. Zaitsev, S.V. Ordin, V.I. Tarassov, M.I. Fedorov, Soviet Phys. - Solid State **21**, 1454 (1979).

[25] Lin Zhang, D.G. Ivey, J. Mater. Sci., Mater. in Electronics **2**, 116 (1991).

[26] K. Radermacher, R. Carius, S. Mantl, Nuclear Instrum. and Methods B **84**, 163 (1994).

[27] D.H. Tassis et al.,J. Appl. Phys. **80**, 962 (1996).

[28] R. Eppenga, J. Appl. Phys. **68**, 3027 (1990).

[29] C.P. Suzs, J. Muller, K. Yvon, E. Parthe, J. less-common Metals **71**, P1 (1980).

[30] C.B. Vining, C.E. Allevato, Proc. 12th Intersoc. Energy Conv. Engng. Conf., Warendale (PA) 1992 (p. 3.489).

[31] R.G. Long, M.C. Bost, J.E. Mahan, Thin Solid Films **162**, 29 (1988).

[32] U. Gottlieb, M. Affronte, F. Nava, O. Laborde, A. Salpice, R. Madar, Appl. Surface Sci. **91**, 82 (1995).

[33] L. Schellenberg, H.F. Braun, J. Muller, J. less-common Metals **144**, 341 (1988).

[34] K. Mason, G. Müller-Vogt, J. Crystal Growth **63**, 34 (1983).

[35] S. Petersson, J.A. Reimer, M.H. Brodsky, et al., J. Appl. Phys. **53**, 3342 (1982).

[36] M. Komabayashi, K. Hijikata, S. Ino, Japan. J. Appl. Phys. **30**, 331 (1991).

[37] C.B. Vining, Proc. 9th Internat. Conf. Thermoelectrics, Pasadena 1991 (p. 249).

[38] K. Irmscher, W. Gehlhoff, Y. Tomm, H. Lange, V. Alex, Phys. Rev. B **55**, 4417 (1997).

[39] P.V. Geld, F.A. Sidorenko, Transition Metal Silicides of Fourth Period, Metallurgiya, Moscow 1971.

[40] F. Nava, T. Tien, K.N. Tu, J. Appl. Phys. **57**, 2018 (1985).

[41] I. Nishida, J. Mater. Sci. **7**, 435 (1972).

[42] Ch. Krontiras, K. Pomoni, M. Roilos, J. Phys. D **21**, 509 (1988).

[43] D. Shinoda, S. Asanabe, Y. Sasaki, J. Phys. Soc. Japan **19**, 269 (1964).

[44] I. Kawasumi, M. Sakata, I. Nishida, K. Masumoto, J. Mater. Sci. **16**, 355 (1981).

[45] E. Arushanov, Ch. Kloc, E. Bucher, Phys. Rev. B **50**, 2653 (1994).

[46] C.B. Vining, C.E. Allevato, Proc. 10th Internat. Conf. Thermoelectrics, Babrow, Cardiff 1991 (p. 167).

[47] I. Ali, P. Muret, T.A. Nguyen Tan, Appl. Surface Sci. **102**, 147 (1996).

[48] T. Sigrist, F. Hullinger, G. Travaglini, J. less-common Metals **92**, 119 (1983).

[49] J. Schumann, D. Elefant, C. Gladun, et al., phys. stat. sol. (a) **145**, 429 (1994).

[50] C.E. Allevato, C.B. Vining, J. Alloys and Compounds **200**, 99 (1993).

[51] A. Heinrich et al., this volume.

[52] St. Brehme, L. Ivanenko, Y. Tomm, et al., Mater. Res. Soc. Symp. Proc. **402**, 355 (1996).

[53] A.B. Filonov, D.B. Migas, V.L. Shaposhnikov, et al., phys. stat. sol. (b) **203**, 183 (1997).

[55] G. Behr et al.., phys. stat. sol. (a) **160**, 549 (1997)

[56] S. Teichert, G. Beddies, Y. Tomm, et al., phys. stat. sol. (a) **152**, K15 (1995).

Thermoelectric Properties of Magnesium Silicide Processed By Powdered Elements Plasma Activated Sintering Method

Takenobu Kajikawa, Keisuke Shida, Sunao Sugihara
Shonan Institute of Technology, Fujisawa, Kanagawa, Japan 251
Mamoru Ohmori, Toshio Hirai
Institute for Materials Research, Tohoku University, Sendai, Miyagi, Japan 980
Tel:+81 466 34 4111, Fax:+81 466 35 8897,E-mail: kajikawa@elec.shonan-it.ac.jp

Abstract

Efficient, inexpensive and non-toxic thermoelectric elements such as silicides should be developed aiming large scale application such as recovering the combustion heat of municipal solid waste, of which the characteristics are greatly fitted for thermoelectric power generation. This paper introduces the characterization and thermoelectric properties of undoped and doped n-type Magnesium Silicide processed by powdered elements spark plasma sintering method. The patterns by powder X-ray diffractometry showed that it had typical polycrystalline phase successfully. Temperature dependence of thermoelectric properties such as the Seebeck coefficient and electrical conductivity were measured for the temperature range from 300 K to 773 K. As a result, power factor value 6.0×10^{-4} (W/mK^2) was obtained at 773 K for a doped sample.

Introduction

Efficient, inexpensive and non-toxic thermoelectric elements such as silicides should be developed aiming large scale application of thermoelectric power generation systems to recover various kinds of rejected heat such as combustion heat of municipal solid waste.

Intermetalic magnesium compounds and their solid solutions have been known as the potentially promising thermoelectric elements [1,2].

Recently a spark plasma sintering method has been attracted as the new and interesting method because it can be said that the diffusion velocity becomes extremely large even at the low temperature due to pulsed electric field superposed on D.C.. It suggests that this peculiar property of the spark plasma sintering method can allow the alloying and sintering formation of thermoelectric element started from the mixture of powdered elements at the same time for the elements of high vapor pressure around the melting point such as magnesium.

This paper presents the thermoelectric properties of undoped and doped n-type Magnesium Silicide elements processed by the powdered elements spark plasma sintering method combined with hot-pressed sintering method in order to establish the improved thermoelectric elements for the medium temperature range from 400K to 800K.

Experiment

Sample preparation

Mg(4N,3-5mm chunk) and Si (5N,300mesh powder) were mixed for the mole fraction of two to one as the starting mixture. In the case of doped alloy the required amount of Antimony(Sb,4N 100mesh powder) as the n-type dopant was mixed with the starting mixture. The starting mixture was processed in the graphite die (50 mm I.D or 20 mm I.D x 20 mm in effective length) by the spark plasma sintering process, which had been developed to sinter the metal powder for short time initially [3]. For this process it can be said that the diffusion constant affected by the pulsed electric field was several tens to hundreds times of the standard value [3]. The conceptual configuration of the spark plasma sintering apparatus is shown in Fig.1. The thermoelectric elements were made under the processing

0-7803-4057-4/97 $10.00 ©1997 IEEE

flow chart as shown in Fig.2. In the case of Sb-doped thermoelectric elements there were many micro-cracks.

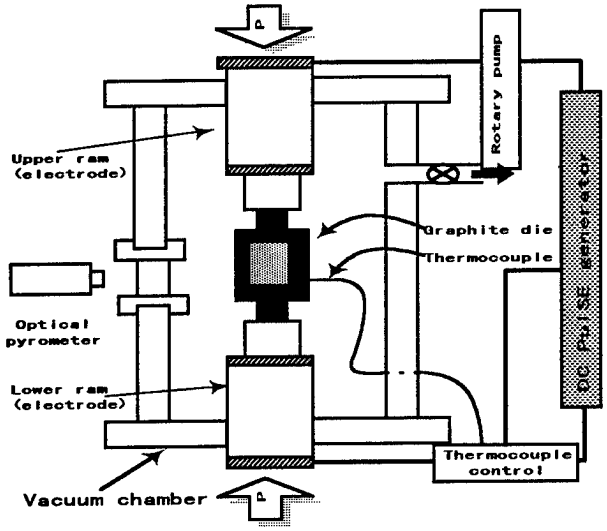


Fig.1. Spark Plasma Sintering System

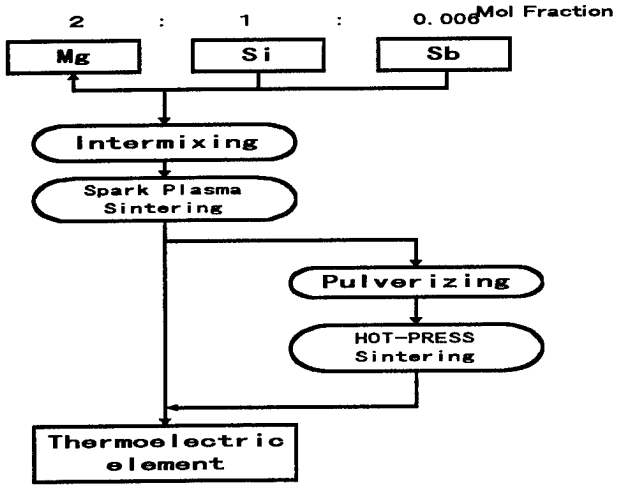


Fig.2. Processing flow chart

Table 1. Sintering conditions

Pressure	Sintering Temp.	Key
20 MPa	973 K	MgSi1
	1073 K	MgSi2
	1098 K	MgSi3
	1103 K	MgSi4
24 MPa	1173 K*	MgSi+Sb0.6mol%

* Hot-press sintering after spark plasma sintering at1103K

Hence, it was hot-pressed again to form the thermoelectric element. The sintering conditions are shown in Table 1. The atmosphere for a spark plasma sintering was in vacuum, and for a hot-pressed was in Argon at 0.103MPa. The amount of dopant were 0.3mol% and 0.6mol% of Antimony.

Characterization

The characterizations of the samples were analyzed with SEM, powder X-ray diffractometry (XRD) and Electron probe microanalysis (EPMA). The density of the samples measured by Aruchimedes' principle and the calculation of the volume and measure weight was almost 100% of theoretical value (d=2.002 g/cm^3) for the sample of more than 1073K in sintering temperature. SEM images showed that the sintered sample of 973 K in sintering temperature had a lot of small pores , but for the samples of more than 1073K polycrystalline phase was established and the micro superstructures due to lattice defects were also grown. The results of XRD for every sintering temperature showed the structure had typical polycrystalline and mono-Mg_2Si phase simply. The XRD patterns for several points verified the samples were homogeneous.

Although the undoped Mg_2Si samples didn't have any micro-cracks, all of the doped samples had many micro-cracks in spite of the same processing. Hence, in these cases the samples were re-sintered by the hot-pressed sintering after pulverized.

The EPMA clarified that mean weight fractions of the samples were Mg:Si:Sb=0.631:0.363:0.006 as compared with the theoretical fractions =0.628:0.363:0.009. In consideration of the accuracy of EPMA the fraction of antimony was estimated to be included well in Mg_2Si alloy partially replacing to silicon site.

Results and Discussion

The temperature dependence of the Seebeck coefficient is shown in Fig.3 for various sintering temperature as a processing parameter at the constant pressure (20MPa). All samples show n-type semiconductor. The characteristics are peculiar for semiconductor, for which the Seebeck coefficient has a peak and decreases for high temperature region because the electrical conductivity increases with

temperature. The behavior of 0.6mol% Sb doped element seems to be different from others, because for low temperature the behavior is similar to others as the semiconductor and for high temperature range the scattering effect is dominant to affect the behavior as shown in the characteristics of electrical conductivity.

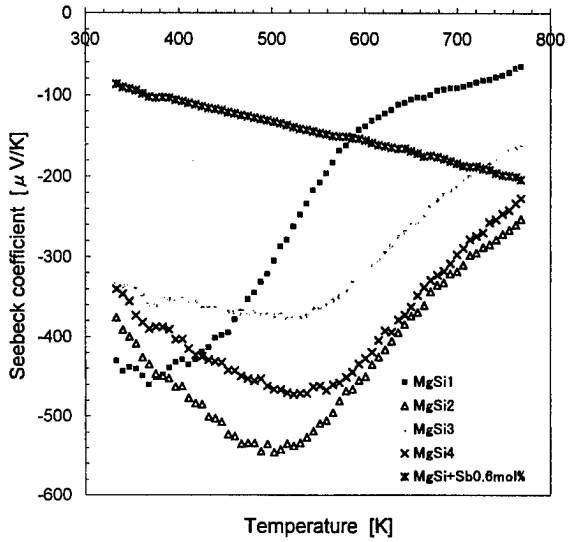


Fig.3. Temperature dependence of Seebeck coefficient

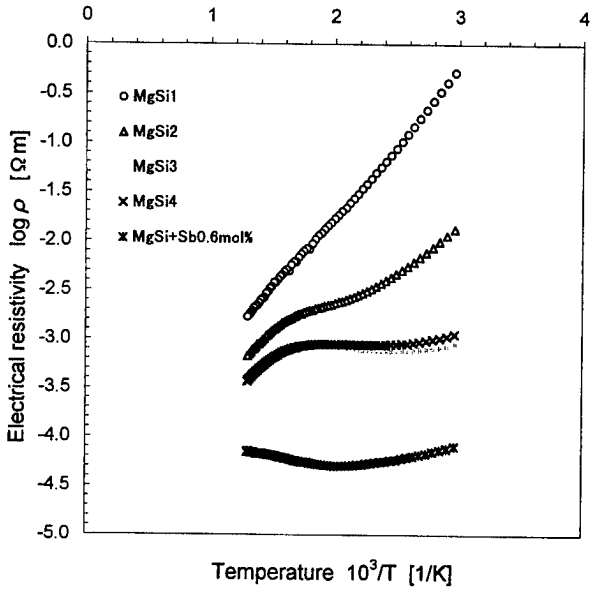


Fig.4. Temperature dependence of electrical resistivity

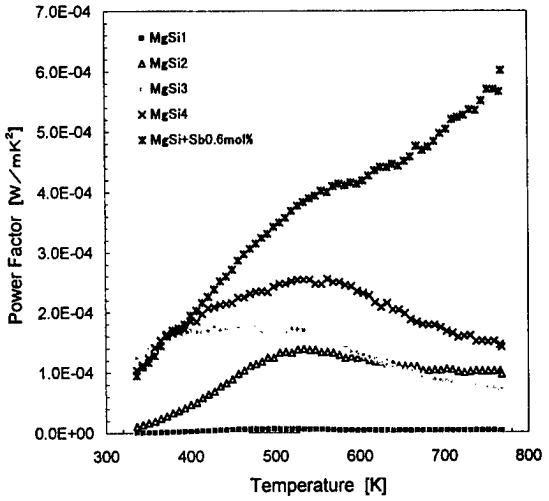


Fig.5. Temperature dependence of power factor

The relationship between ($\log \rho$) and (10^3/T) is shown in Fig.4, where ρ is electrical resistivity. The doping effect is clear. The value for doped sample is higher than these of undoped samples by two orders. Assuming one antimony element supplies one carrier to the thermoelectric element, theoretical carrier concentration for 0.6mol% of Sb is 1.62×10^{26} m^{-3} and the measured value is 1.6×10^{26} m^{-3}. It can be said that Sb behaves as dopant well in the samples.

For 0.6mol% of Sb doped sample the band gap is estimated about 0.7eV in terms of the relationship ρ and 1/T for intrinsic region as compared with 0.65eV for the single crystal [4].

The temperature dependence of the power factor ($\alpha^2\sigma$) is shown in Fig.5 as the results form the Seebeck coefficient α and electrical conductivity σ. For 0.6mol% Sb doped samples the value is increasing with temperature. At 773 K the power factor is obtained 6.0×10^{-4} W/mK^2 in maximum.

The results from measured Hall coefficient at room temperature are summarized in Table 2. Hall mobility for undoped and 0.6mol%Sb doped Mg_2Si is 41.5 cm^2/Vs and 34.1cm^2/Vs respectively. The carrier concentration for each case $1.4\times10^{24}m^{-3}$ and $1.6\times10^{26}m^{-3}$ respectively. The temperature dependence of Hall mobility is shown in Fig.6. The behavior was obtained to be almost flat and slightly decreased with temperature. Generally, mobility μ is represented as $\mu \propto T^{r-3/2}$ where r is scattering factor. As

shown in Fig.6 the approximated equation of the Hall mobility is represented $\mu = 0.1106T^{-0.5438}$,so that scattering factor is about 1.0.The charged impurity scattering and the neutral impurity scattering represent r=3/2 and r=0 respectively [5] . Hence, the behavior suggests that the scattering mechanism is due to the combined mechanism with the charged impurity scattering and neutral impurity scattering.

Table 2. Summary of Thermoelectric Properties

Mg_2Si	Sintering Temp.(K)	Density (g/cm^3)	Hall Coef. (m^3/C)	Carrier Con.(m^{-3})	Mobility (m^2/Vs)
Undoped	1103	2.0	-4.4×10^{-6}	1.4×10^{24}	4.1×10^{-3}
0.3mol%Sb	1173	1.85	-3.5×10^{-7}	1.8×10^{25}	0.7×10^{-3}
0.6mol%Sb	1173	1.88	-3.9×10^{-8}	1.6×10^{26}	3.4×10^{-3}

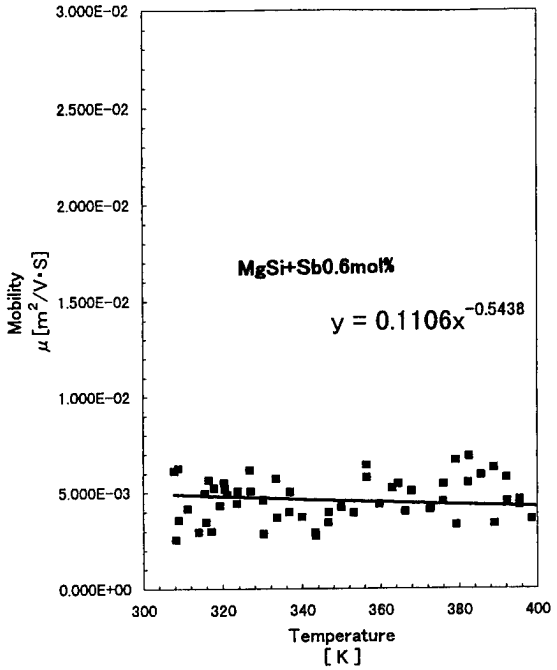


Fig.6 Temperature dependence of Hall mobility

Conclusions

In conclusion, the powdered elements spark plasma sintering method was successfully introduced to make undoped and doped magnesium silicide. The temperature dependence of the Seebeck coefficient, electrical resistivity, power factor and Hall coefficient was investigated. The power factor was obtained 6.0×10^{-4} W/mK^2 at 773K for 0.6mol% Sb doped Mg_2Si element, while the value for undoped element was 2.5×10^{-4} W/mK^2 at 540 K. According to the Hall coefficient measurement, the carrier concentration should be optimized to give the maximum power factor based on Ioffe's theory as the further research.

Acknowledgments

We express our gratitude to Dr. I.A.Nishida, National Research Institute for Metals, Prof.Y.Noda ,Tohoku University and Dr. M.Sakata,Emeritus Prof. of Keio Univ. for continuous support and encouragement. We appreciate Mr. K.Shiraishi's effort, SIT for assistance of our research.

This research is carried out in the research project "Physics and Chemistry of Functionally Graded Materials" under the leadership of Prof. T.Hirai supported by Ministry of Education and Culture.

References

1.C.B.Vining,Thermoelectric Properties of Silicides, CRC Handbook of Thermeoelctrics,277-283(1995)

2.Hiroyuki Kon ,Y.Noda et al, Temperature Dependence of Thermoelectric Properties of $Mg_2Si_{0.6}Ge_{0.4}$, J.of Japan Inst. Metals 55,9,1018-1022(1991)

3.M.Ishiyama,Plasma Activated Sintering System, Proc. of 1993 powder Metallurgy World Congress,931-934(1991)

4. R.J.LaBotz, D.R.Mason, D.F.O'Kane,The Thermoelectric Properties of Mixed Crystals of $Mg_2Ge_xSi_{1-x}$, J. of The Electrochem.Soc. 127-134(1963)

5.Y.Suge,Thermoelectric Semiconductor,Makishoten(1966)

Temperature dependence of thermal conductivity for $Mg_2Si_{1-x}Ge_x$ solid solution

Hiromasa T. Kaibe*, Yasutoshi Noda**, Yukihiro Isoda*** and Isao A. Nishida***

*Dept. Electronics and Information Eng., Tokyo Metropolitan University, Hachioji, Tokyo 192-03, Japan
Tel.: +81/426/77/1111(ext.4463), Fax:+81/426/77/2756, E-mail: kaibe@eei.metro-u.ac.jp

**Dept. Materials Science, Fac. of Engineering, Tohoku University, Sendai 980, Japan
Tel.: +81/22/217/7328, Fax:+81/22/217/7328, E-mail: nodayasu@material.tohoku.ac.jp

***National Research Institute for Metals,STA, Ibaraki 305, Japan
Tel.: +81/298/59/2637, Fax:+81/298/59/2601, E-mail: isoda@nrim.go.jp, albert@nrim.go.jp

Abstract

Thermal conductivity of *n*-type $Mg_2Si_{0.6}Ge_{0.4}$ doped with 8000ppm of Sb were measured over the temperature range from 80 to 350 K. The measurement was carried out by a comparative static method using transparent quartz as a reference specimen.

The carrier concentration at 300 K was 6.25×10^{25} m^{-3} determined from Hall measurement. The Hall coefficient was almost constant over the whole temperature range, which indicates the degenerate state of electrons. Then, κ was separated into two components of phonon κ_{ph} and electron κ_{el} on the basis of Wiedemann-Franz law. Assuming that Lorenz number is 2.44×10^{-8} V^2/K^2 which is a value for a metal and using values of the electrical conductivity σ, it was found that κ_{ph} has a temperature dependence proportional to $T^{-1/2}$ and that point defects related to the mass difference between Si and Ge is predominant for the phonon conduction.

Introduction

The II_2-IV solid solution semiconductor, such as Mg_2SiGe and Mg_2SiSn have been expected as a candidate material for thermoelectric energy conversion in a middle temperature range between 500 and 800 K [1-5]. In order to evaluate the thermoelectric figure of merit *Z*, the thermoelectric properties and thermal conductivities up to 573 K were measured for the undoped samples [6]. The phonon component of κ_{ph} for $Mg_2Si_xGe_{1-x}$ has a minimum value at around x=0.6 [6]. It is widely recognized that optimum carrier concentration must be about 10^{25} m^{-3}. However, no heavily doped II_2-IV compounds were used for middle-temperature energy conversion. In the author's previous study, the thermoelectric properties were investigated for the impurity doped *n*- and *p*-type $Mg_2Si_{0.6}Ge_{0.4}$ at 300 K [3][4]. Their Z values were smaller than those of PbTe, which is the most efficient material as the current thermoelectric generator. $Mg_2Si_{0.6}Si_{0.4}$ has, however, favorable semiconductive properties such as large effective mass m^*, small κ_{ph} and larger energy gap than that of PbTe. Furthermore, the temperature dependence of thermoelectric properties was also investigated for Sb-doped *n*-type and the Ag-doped *p*-type ones [3,5]. Those *Z* have their maximum value around 650 K for both specimens. Especially for *p*-type one, a maximum *ZT*-value amounts to 1.68 at 629 K. However, those estimation used the κ-value at room temperature and temperature dependence of κ was calculated on the basis of Wiedemann-Franz law with σ and κ_{ph} proportional to $T^{-1/2}$

The purpose of this study is to verify the temperature dependence of κ_{ph} for *n*-type $Mg_2Si_{0.6}Ge_{0.4}$ heavily doped with Sb. Then, κ as well as other thermoelectric parameters for the unidirectional solidified *n*-type $Mg_2Si_{0.6}Ge_{0.4}$ dope with Sb of 8000 ppm were investigated as a function of temperature below room temperature.

Experimental procedure

Preparation of *n*-type $Mg_2Si_{0.6}Ge_{0.4}$ doped with Sb of 8000 ppm

The *n*-type $Mg_2Si_{0.6}Ge_{0.4}$ doped with Sb of 8000 ppm was prepared by direct melting of constituent elements of Mg(nominal purity, 99.9%), Si(99.9999%) ,Ge(99.9999%) and Sb(99.999%). The crucible was made of graphite(0.1% ash, Tokai Carbon Ltd.,No. G150). The dimensions of the crucible were 10mm in dia. and 50 mm in length with a cone shaped bottom. The pressure inside the reaction furnace was 0.2 MPa of Ar (99.999%).

Prior to use, the crucible was heated at 1400 K in the stream of 0.1 MPa Ar in order to remove volatile impurities. The $Mg_2Si_{0.6}Ge_{0.4}$ solid solutions was synthesized at 1380 K which was about 20 K higher than the melting point of 1360 K. The temperature gradient was about 10K/cm from top to bottom of the crucible for the purpose of the unidirectional solidification. On cooling, the samples were kept at 1300 K for 3.3 h to homogenize the components and impurity elements and to proceed the grain growth.

The boiling point of Mg under 0.2 MPa Ar was estimated to be 1452 K using Clausius-Clapeyron's equation. The synthesis temperature was kept below the boiling point, which would be effective to surpress the evaporation of Mg. In order

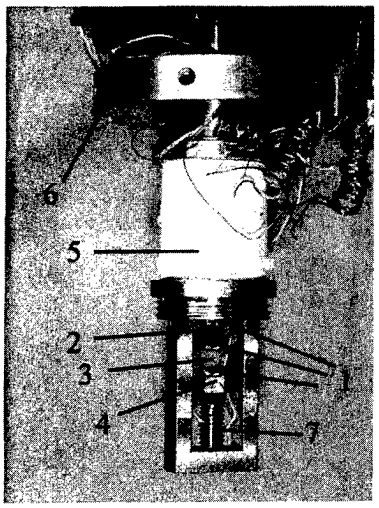


Figure1 Magnified photograph of a sample holder in the cryostat : 1 cupper spacer ; 2 specimen ; 3 reference (SiO_2) ; 4 sub-heater ; 5 main heater ; 6 heat sink ; 7 screw.

to avoid the reaction between the graphite crucible and constituent elements, the synthesis was carried out under the presence of NaCl. The boules obtained were analyzed by EPMA and identified by X-ray diffraction as a single phase of the anti-fluorite type structure.

Measurements of thermoelectric parameters

The measurement of κ was carried out by the comparative static method using transparent quartz (SiO_2) as a reference in a low temperature cryostat. Figure 1 is a magnified photograph of the sample holdre of the cryostat. In case of Fig.1, the metal cap of the sample holder is taken off. For the measurement of κ and thermoelectric power α for *n*-type $Mg_2Si_{0.6}Ge_{0.4}$ doped with Sb of 8000 ppm, the cubic shaped specimen was cut out of the as-grown boule. The SiO_2 with a cubic shape of 4×4×4 mm^3 was also prepared. The comparative method determines κ of a material with respect to that of a suitable reference material. κ of the reference is required to be comparatively close to that of a material to be measured. This is the reason why SiO_2 was selected as a reference material in this case. A sub-heater, reference and the specimen were arranged vertically as shown in Fig. 1. They are rigidly fixed using a screw with a tip made of bakelite. In this apparatus the specimen is separated by copper spacers from a standard specimen and the sub-heater. Each of three copper spacers has 5×5 mm^2 in area and 1 mm in thickness and has a hole with 0.5mm in dia. and 2.5 mm in length at the side. A junction of T-type thermocouple with 76μm in dia. was attached both thermally and electrically at the bottom of the hole by soldering . The temperature differences were given by passing electric current through the sub heater. The heater consists of a cupper bobbin with dimennsions of 5×5 mm^2 in cross section and 10 mm in length, and a constantan wire with 0.1 mm in dia wounded around the bobbin. They are electrically isolated by the teflon film. The resistance of the constantan wire as heater element is 10 Ω. Good thermal contact is obtained by polishing flatly the components of the stack and using silicon grease to reduce contact resistance. Radiation losses are reduced by polishing the surface of the copper spacers in ordrd to reduce their emissivities .

The heat flow is determined by measuring the difference in temperature across the standard specimen. If the ratio of the length to cross sections l/S are given for both reference and specimen as $(l/S)_{ref}$ and $(l/S)_{sp}$, then the thermal conductivity κ is calculated from equation (1).

$$\kappa = \kappa_{ref} \frac{(\Delta P/\Delta T)_{sp}(l/S)_{sp}}{(\Delta P/\Delta T)_{ref}(l/S)_{ref}} \quad (1)$$

where κ_{ref} is the thermal conductivity of the reference and $(\Delta P/\Delta T)_{ref}$ and $(\Delta P/\Delta T)_{sp}$ are power required to give 1K of temperature difference for the reference and the specimen, respectively. They were determined from the linear relationship between the heater power and the temperature difference within 2-3 K. The measurements were carried out for both arranging positions, i.e. one is in a case of the specimen locating at the side of the sub-heater and another is in a case of a reference at the side of the sub-heater as shown in Figure 1 . Then, the heat flux through them were more precisely evaluated comparing to the case of just one arrangement. A heat sink can be set at any required temperature by adjusting the main heater wound round sample holder.

The α was measured simultaneously with κ. α is determined by the relationship between thermoelectromotive force and temperature difference within 2-3 K. Those measurements were carried out over the temperature range from 80 to 350 K in a vacuum below 1.33×10^{-3} Pa.

The σ and the Hall coefficient R_H were measured by the van der Pauw's method using plate like specimen with dimension of 4×4×1 mm^3 which is identical with that used for κ and α measurements.

Table 1 Thermoelectric properties for n-type $Mg_2Si_{0.6}Si_{0.4}$ doped with Sb of 8000 ppm at room temperature.

Type	Carrier conc. ($1/m^3$)	σ ($1/(\Omega m)$)	α ($\mu V/K$)	κ ($W/(mK)$)	Z ($1/K$)
n	6.25×10^{25}	7.81×10^{4}	-97.0	3.35	0.22×10^{-3}

Results and discussion

Table 1 tabulates the thermoelectric properties of n-type $MgSi_{0.6}Ge_{0.4}$ doped with Sb of 8000ppm at room temperature. This specimen corresponds to the sample C in reference [5]. The sample was so brittle that it was very difficult to cut out of the specimen with dimensions of $4\times4\times4$ mm^3. In reference [5], κ for specimen C is 2.45 W/(mK). However, it was measured again and then κ of this specimen was determined to be 3.35 W/(mK) at room temperature. This is mainly due to the more precise estimation of the amount of heat flux through the specimen and SiO_2 reference . The Z is $0.22\times10^{-3}K^{-1}$ which is about one third of the value described in reference [5].

Figure 2 shows the temperature dependence of σ. The Hall coefficient R_H is almost constant in the temperature range from 80 to 300 K, which indicates the degenerate state of conduction electron. The electron density derived from R_H is 6.25×10^{25} m^{-3}. Therefore, σ-T curve can be regarded as a temperature dependence of the drift mobility. Above 100 K, the σ has a temperature dependence proportional to $T^{-1/2}$ which indicates that the mixed alloy scattering is predominant [7]. This is mainly due to the solid solidification between Mg_2Si and Mg_2Ge. In reference [5], it was also reported that above 300 K, the Hall mobility μ_H has rather steep temperature dependence and that carrier-carrier scattering contributes to the electron transport.

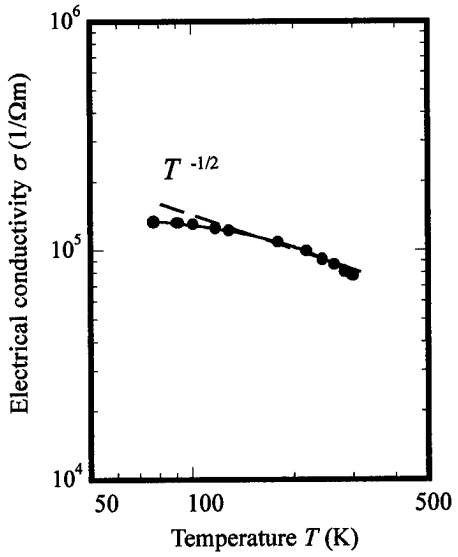


Figure 2 Temperature dependence of the electrical conductivity σ for n-type $MgSi_{0.6}Ge_{0.4}$ doped with Sb of 8000ppm.

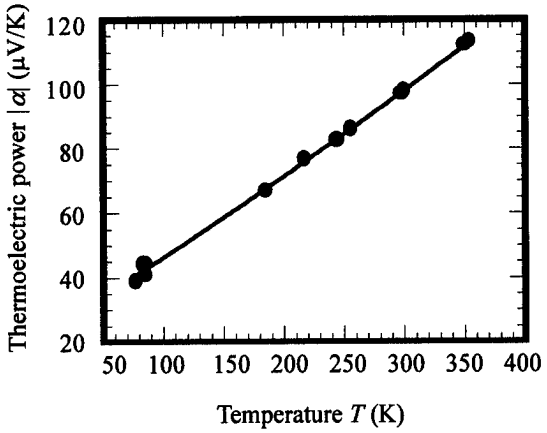


Figure 3 Temperature dependence of the thermoelectric power α for n-type $Mg_2Si_{0.6}Ge_{0.4}$ doped with Sb of 8000ppm.

Figure 3 shows the temperature dependence of the thermoelectric power α for n-type $Mg_2Si_{0.6}Ge_{0.4}$. The α increases linerly with temperature in this temperature region. According to reference[5], α still increses with temperature up to 600 K and then began to decrease because of the onset of the intrinsic conduction.

Figure 4 shows the temperature dependence of κ for n-type $Mg_2Si_{0.6}Ge_{0.4}$. In the figure, the marks of ▲ and ▼ express the arangement of the reference and specimen in measuring κ described in the previous chapter, i.e ▲ and ▼ are in cases of the specimen and reference on the sub-heater side, respectively. The κ decreases monotonously with temperature. In the thermoelectric semiconductors, the κ is given by

$$\kappa = \kappa_{el} + \kappa_{ph}, \tag{2}$$

where κ_{el} is the carrier component of the thermal conductivity [8]. κ_{el} is estimated on the basis of the Wiedeman-Franz law using the Lorentz number L and electrical conductivity σ. Then, κ_{el} is expressed by

$$\kappa_{el} = L\,\sigma T, \tag{3}$$

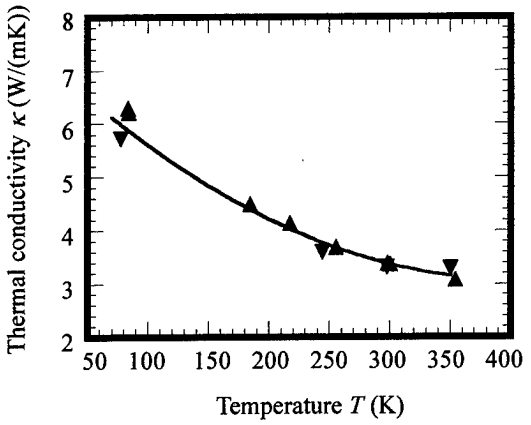


Figure4 Temperature dependence of the thermal conductivity κ for n-type $Mg_2Si_{0.6}Ge_{0.4}$ doped Sb of 8000ppm.

In this case, it is valid to use 2.45×10^{-8} V^2/K^2 for L, which is avilable for metal becaues of the heavy doping with carrier concentration of 6.25×10^{25} m^{-3} and temperature dependence of the R_H.

Figure 5 shows the temperature dependence of κ_{ph} for n-type $Mg_2Si_{0.6}Ge_{0.4}$. The dashed line is $\kappa_{ph}= 51.2T^{-1/2}$ W/(mK) for $Mg_2Si_{0.6}Ge_{0.4}$ reported by R.J.LaBotz et.al. [6]. While their measurements were carried out above room temperature, the κ_{ph}- T curve is in fairly good agreement with their estimation. Then, it is quite valid to apply $T^{-1/2}$ dependence for heavily doped $Mg_2Si_{0.6}Ge_{0.4}$. $T^{-1/2}$ dependence indicates the phonon scattering by point defect due to the large mass difference between Si and Ge[6]. However, temperature dependence of κ_{ph} is slightly different between above and below 170K. Especially, above 170 K, it has temperature dependence of $118.2T^{-0.655}$ W/(mK), which is a combination of point defect and normal Umklapp scattering [6]. And also, below 170 K it has a temperature dependence of $26.6T^{-0.352}$ W/(mK), which is considered to be due to the contribution of the electron-phonon scattering [9] .

Conclusion

For the purpose of verifying the temperature dependence of lattice thermal conductuvity κ_{ph} for n-type $Mg_2Si_{0.6}Ge_{0.4}$ heavily doped with Sb, the thermal conductivity κ as well as other thermoelectric parameters were investigated as a function of temperature. It is found that $T^{-1/2}$ dependence of κ_{ph} is quite valid for the heavily dopen n-type $Mg_2Si_{0.6}Ge_{0.4}$. However, it is also pointed out that the various phonon scattering mechanism such as point defect , normal Umklapp amd electron-phonon scattering contribute toward κ_{ph}.

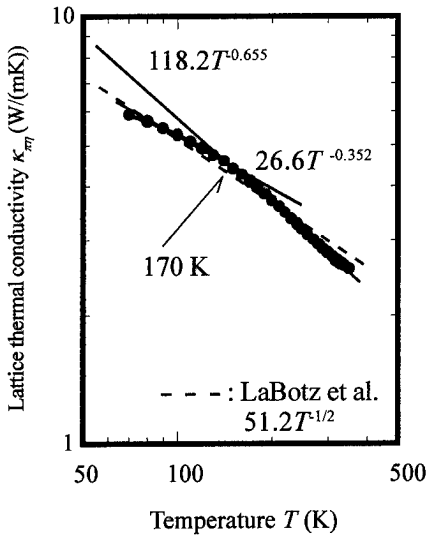


Figure 5 Temperature dependence of the lattice thermal conductivity κ_{ph} for n-type $MgSi_{0.6}Ge_{0.4}$ doped with Sb of 8000ppm.

References

[1] M.Riffel and J.Schilz, "Mechanically alloyed $Mg_2Si_{1-x}Sn_x$ solid solutions as thermoelectric materials", Proc. of the 15th International Conference on Thermoelectrics (ICT'96), Pasadena, USA, p.133,1996.

[2] T.Kajikawa, I.Katsube, S.Sugihara and K.Soejima, "Thermoelectric properties of sintered magnesium compounds", Proc. of the 15th International Conference on Thermoelectrics (ICT'96), Pasadena, USA, p.128,1996.

[3] Y.Noda, H.Kon, Y.Furukawa, I.A.Nishida and K.Masumoto, "Preparation and thermoelectric properties of $Mg_2Si_{1-x}Ge_x$", Proc. of the 12th International Conference on Thermoelectrics (ICT'93), Yokohama, Japan, p.206,1993.

[4] Y.Noda, H.Kon, Y.Furukawa, N.Otsuka, I.A.Nishida and K.Masumot, "Preparation and thermoelectric properties of $Mg_2Si_{1-x}Ge_x$ (x=0.0-0.4) solid solution semiconductors", Mater. , Trans. JIM, 33(1992)845.

[5] Y.Noda, H.Kon, Y.Furukawa, I.A.Nishida and K.Masumot, "Temperature dependence of thermoelectric properties of $Mg_2Si_{0.6}Ge_{0.4}$", Mater. , Trans. JIM, 33(1992),851.

[6] R.J.LaBotz, D.R.Mason and D.F.O'Kanne, "The thermoelectric properties of mixed crystals of $Mg_2Ge_xSi_{1-x}$", J.Electrochem. Soc., 110(1963)127.

[7] B.R.Nag,"Electron transport in compound semicouductor", Springer-Verlag, Berlin Heidelberg New York, (1980), p.174.

[8] K.Uemura and I.A.Nishida, "Thermoelectric Semiconductors and their Applications", Nikkan-Kogyo, Tokyo, (1988),p.145.

[9] J.M.Ziman, "The effect of free electrons on lattice conduction", Phil. Mag. 1(1956)191.

Influence of Production Parameters on the Thermoelectric Properties of Mg_2Si

M. Riffel* and J. Schilz

German Aerospace Research Establishment (DLR), Institute of Materials Research, Linder Höhe, D-51147 Köln, Germany

*present address for all correspondence: Laboratoire de Physique des Matériaux, Ecole des Mines, Parc de Saurupt, F-54042 Nancy

Tel.:+33/3/83584163, Fax:+33/3/83584163, E-mail:riffel@mines.u-nancy.fr

Abstract

According to the literature, Mg_2Si possesses good thermoelectric properties. However, no easy fabrication process for this material is known to date. In this paper we present a new production route based on modified mechanical alloying and hot uniaxial pressing that leads to samples free from oxides. Comparison is made with samples produced by a conventional powdermetallurgical process leading to the contamination with MgO. The samples were examined by differential scanning calorimetry, laser flash-, Hall-, and Seebeck- measurements. The results show that the samples free from oxides have an improved thermal stability, a higher thermal conductivity and a much higher Hall mobility. Thus, the thermoelectric figure of merit z could be improved by a factor of 3.5. Additionally, the electronic transport behaviour of the oxide-free samples was examined. It can be explained by the contribution of an additional conduction band.

Introduction

The three intermetallic compounds Mg_2Si, Mg_2Ge, and Mg_2Sn and their solid solutions are known as promising thermoelectric materials [1,2,3]. Due to the high vapour pressure and the reactivity of Mg, synthesis of these compounds via melt metallurgy is difficult. It has been shown, previously, that mechanical alloying as a new production method to receive powders of these materials has advantages as it avoids the mentioned difficulties [4,5,6]. The current paper focuses on the consolidation of such prepared powders and on the influence of the oxygen content on the thermal and thermoelectric behaviour of the compacts.

Experimental

The mechanical alloying process is described elsewhere [5,7].

The consolidation was performed under high vacuum ($p<10^{-4}$ mbar) through hot uniaxial pressing (HUP) at a pressure of 50 MPa. The sintering temperature was varied from 580 to 900 °C and the sintering time from 10 to 90 minutes.

The amount of oxide content of the samples was calculated from X-ray diffraction (XRD) spectra using a MgO calibration. The differential thermal analysis (DTA) and the differential scanning calorimetry (DSC) characterization was performed in air using a Netzsch DSC404 at a heating rate of 10 K/min. For the measurement of the thermal diffusivity, a Netzsch LFA427 laser flash apparatus was employed, and for the Seebeck measurements a MMR SB100 programmable Seebeck controller. The Hall apparatus using a standard 6 point method is described elsewhere [8].

Preparation of the samples

Although the mechanically alloyed powders itself showed no MgO signal in the XRD measurements and the hot uniaxial pressing occurs in high vacuum, all samples prepared by conventional powdermetallurgy show a MgO signal after consolidation. The amount did not drop below 20 Mol% MgO (e.g. see table 1, samples 1 and 2). The difference in oxide content between sample 1 and 2 was due to a reduction of the hot pressing temperature and by filling the graphite die in argon atmosphere instead of air. Nevertheless, this result is not satisfactory.

sample	powder	T_S (°C)	t_S (min)	MgO (Mol-%)
1	dry	900	15	41
2	dry	700	60	24
3	wet	700	20	~0

Table 1: Oxide content of hot pressed samples

For the third sample, the preparation route has been modified. Prior to the application of pressure onto the pressing punches, the graphite die was degassed for 12 hours in vacuum. Immediately after the degassing the die was filled with the powder. It is important that the powder is still wet from the milling fluid when it is filled into the graphite die. Thus, any oxidation of the Mg that may occur even in the glove box in argon atmosphere can be avoided.

The milling fluid was then removed in the HUP apparatus at an applied pressure of 3.2 MPa in vacuum ($p<10^{-4}$ mbar) at room temperature. Subsequently, the temperature has been raised to 700 °C, and the sample hot pressed for 20 minutes at a pressure of 50 MPa. In this way bulk-Mg_2Si indeed free from MgO could be produced as proved by X-ray diffraction.

Thermal analysis

DTA measurements performed on samples 2 and 3 (table1) are plotted in figures 1 and 2, respectively. The first run of sample 2 shows an endothermic reaction beginning at 60 °C that converts directly into an exothermic one at about 150 °C. The endothermic peak is caused by the evaporation of water and is also visible in the runs 3 and 5. It can be concluded that the sample has absorbed water during the storage in air before these runs. This is confirmed by an weight increase of about 2.5 %. The peak does not occur in the runs 2, 4, and 6 because these runs were performed directly after the previous ones

giving no time for water absorption. The exothermic peak in run 1 is due to the annealing of stresses that has been induced during the hot pressing. It does not occur in any the subsequent run.

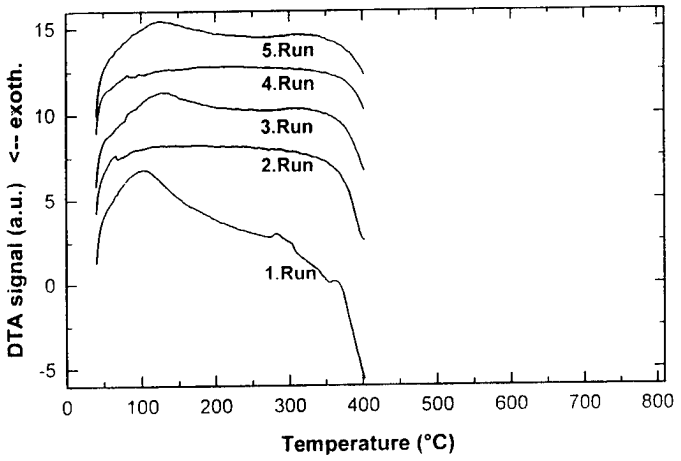


Figure 1: Differential thermal analysis of sample 2

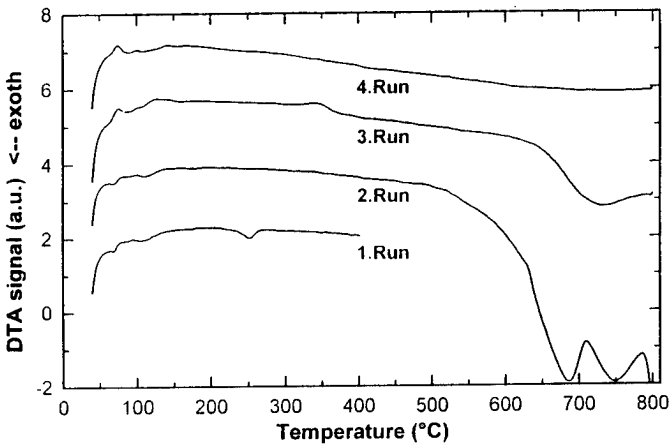


Figure 2: Differential thermal analysis of sample 3

All runs show a strong exothermic peak that begins at between 300 and 350 °C indicating the beginning oxidation of Mg_2Si. With increasing run number this peak becomes more and more flat but even after a heat treatment of 48 hours at 400 °C in air, it still occurs. Though the grown oxide layer slows down further oxidation, it cannot completely stop it, leading eventually to the destruction of the whole sample.

Sample 3 that is free from MgO shows a completely different behaviour. In the first run neither the endothermic peak is visible nor a change in weight could be observed. Only a small exothermic peak at 270°C that belongs to the healing of stress is visible. Because it is much smaller than the one of sample 2 we conclude that the occurrence of MgO is accompanied by an introduction of mechanical stress into the sample during the hot pressing.

The second run was performed up to a temperature of 800 °C. A strong exothermic reaction is visible that begins at about 500 °C and which corresponds to the oxidation of the Mg_2Si. After this run the weight of the sample has increased about 3 %, and its surface was covered with a thin layer of MgO. Due to this surface oxidation the sample can absorb water which is indicated by the small endothermic peaks of run 3. After the third run the sample shows a concomitant increase in the weight of another 3 %.

Much stronger than in sample 2 is the flattening of the exothermic oxidation peak. In the fourth run the signal even disappeared, and no increase in weight could be observed. Thus, the oxidation of sample 3 is a true surface effect forming a protective oxide layer on the surface.

To confirm the dependence of the weight from temperature, a sample free from oxides was heat-treated in the following way: Holding at 100 °C for 1 hour in air, then cooled down and weighted. This procedure was repeated at 200 °C, then at 300 °C, and so on. The result is shown in figure 3.

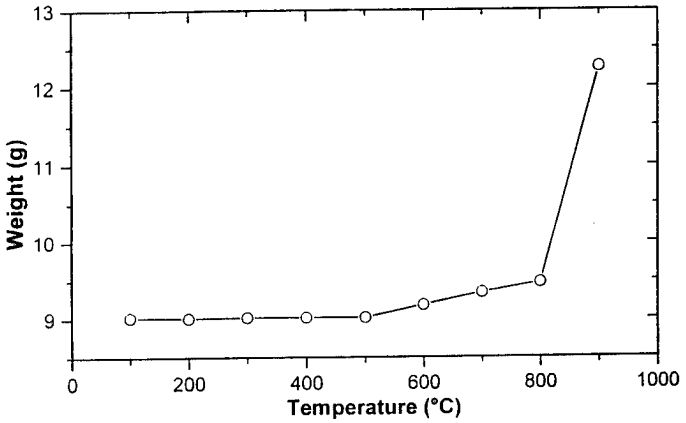


Figure 3: Weight evolution during annealing of sample 3

According to the DTA measurements and in agreement with the literature [6] in terms of oxidation, the sample is stable up to 500 °C. When annealing at temperatures between 600 and 800 °C, a MgO layer on the sample surface forms and a small increase in weight occurs. At these temperatures the oxidation proceeds only slowly and merely as a surface effect. Only when annealing at 900 °C a strong increase in weight can be observed, which indicates an oxidation through the whole sample. This means the destruction through oxidation of Mg_2Si takes place at 900 °C.

Specific heat measurements

As only one publication is available in which the specific heat of Mg_2Si has been measured [9] we carried out calorimetric measurements on the sample free from oxide. Figure 4 shows the measurements by Mannchen/Jacobi together with our results and the theoretical Dulong-Petit saturation value. It can be seen that the literature values as well as our ones monotonously increase with temperature, but that only our measurement asymptotically approximates the Dulong-Petit value. (The slight bend in the curve at about 250-300 °C corresponds to the exothermic peak at 270 °C measured in the first DTA run of sample 3.) The previously measured literature values exceed the Dulong-Petit limit, which is probably due to a non-negligible MgO content in those samples.

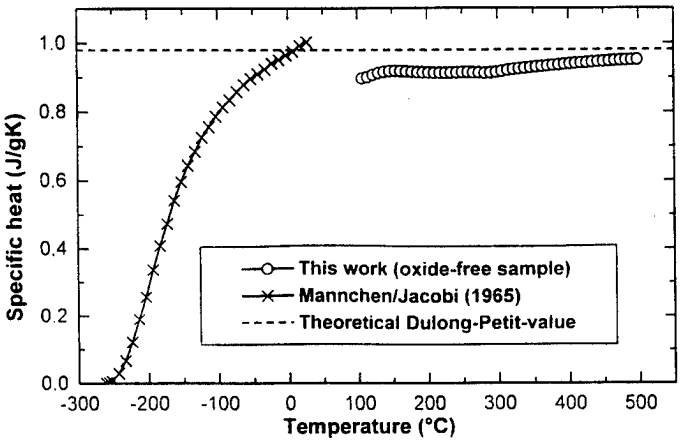


Figure 4: Specific heat of Mg_2Si

Thermoelectric properties

The thermoelectric characterization has been performed in terms of measuring the lattice thermal conductivity and the carrier mobility, i.e. on quantities for which no defined doping is necessary.

The thermal conductivity has been calculated from the measured specific heat, the thermal diffusivity, and the density, which has been geometrically determined. Because the carrier densities are not larger than $3*10^{18}/cm^3$ the electronic contribution to the thermal diffusivity can be neglected. Therefore, in the extrinsic range (T<400 °C), the calculated thermal conductivity values can be directly identified with the lattice thermal conductivities.

In figure 5 the lattice thermal conductivities k_l of sample 3 and a sample with high MgO content are plotted. Over the whole temperature range k_l of sample 3 is about a factor 1.5 higher than the one of the sample with high MgO content. The reason are the disturbances introduced by the MgO.

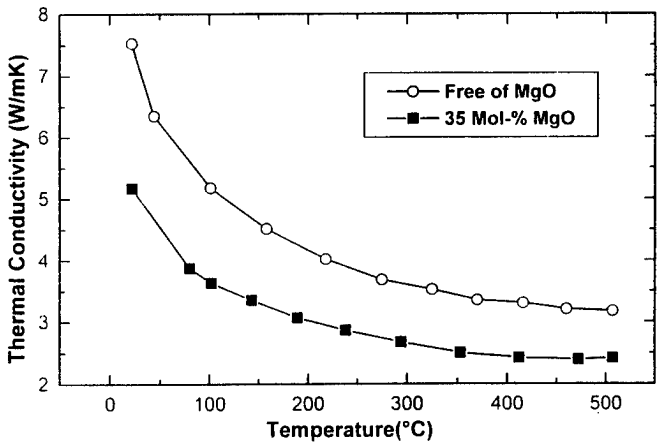


Figure 5: Lattice thermal conductivities of samples with different MgO content.

Figure 6 shows the electron mobilities of the same samples. Sample 3, i.e. the one free from MgO, exhibits a 5 fold higher mobility than compared to the sample with high MgO content and reaches nearly the published values for polycrystalline material [2].

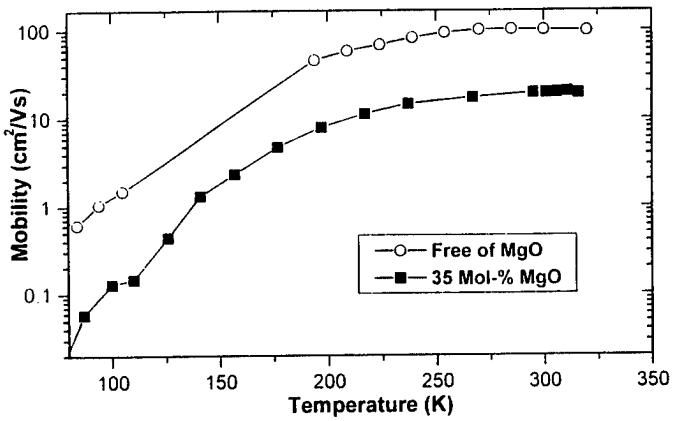


Figure 6: Electron mobility of samples with different MgO contents.

On the other hand, all the samples with a MgO content from 20-41 Mol-% have nearly the same mobilities independent from the production parameters and their carrier densities. We therefore conclude that the MgO content is the reason for their low mobilities. It is a sound to assume that the grains are covered with a layer of MgO which acts as an isolating barrier, thus reducing the carrier mobility.

The thermoelectric characterization shows that the influence of the MgO content is much higher on the mobility than on the thermal conductivity. Consequently, the presented preparation route that leads to samples free from oxides makes it possible to increase the ratio of electron mobility to lattice thermal conductivity, which concomitantly leads to an increase of the thermoelectric figure of merit z by the same factor of 3.5.

Transport mechanisms

The transport behaviour of the sample free from MgO is analysed using temperature dependent measurements of the Hall coefficient R_H and the Seebeck coefficient S (see figures 7 and 8). At temperatures higher than 250 K the transport behaviour can be explained using a simple one band model with a single donor state. In the range 250—320 K, the donor states are thermally activated leading to the normal decrease in R_H. From the slope of $R_H(T)$ the donor activation energy to the conduction band edge is calculated to be 96 meV. Due to the rising of the Fermi niveau, the Seebeck coefficient rises up to a temperature of 320 K. Above this point it decreases, denoting that all donor states are activated.

The temperature dependences of R_H and S in the range 70—250 K cannot be explained in this simple model. An additional energy level must be introduced that can either be a second impurity state or a second conduction band.

Using the model of a second impurity state, it must be located between conduction band and given donor level. In this case electrons are activated with increasing temperature into this level and contribute to conductivity by a hopping mechanism. With increasing number of electrons in this state the density of free states decreases. Thus, the density of mobile electrons in this state decreases and leads to an increase of R_H with T [10].

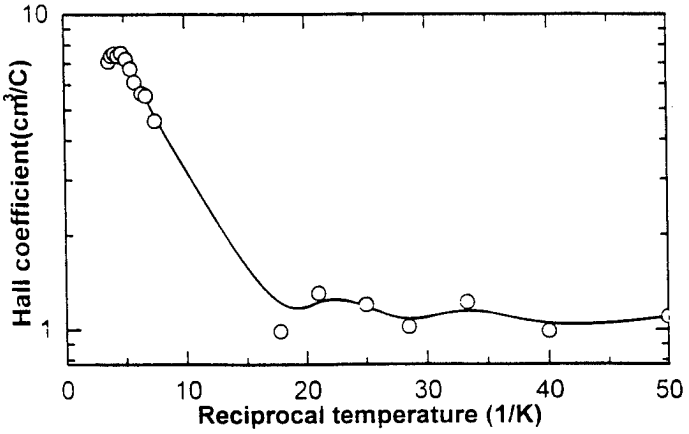


Figure 7: Hall coefficient of Mg_2Si.

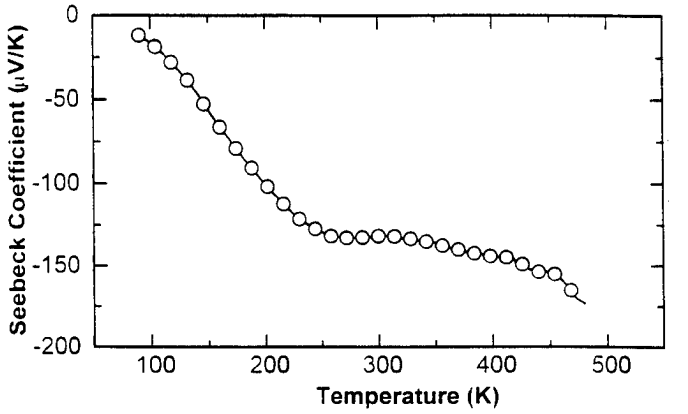


Figure 8: Seebeck coefficient of Mg_2Si

If we consider two conduction bands CB1 and CB2 with $E_{CB2}>E_{CB1}$ there are only electrons in CB1 at low temperatures. At a certain temperature electrons are activated into CB2 (70 K for Mg_2Si, see figure 7). Because the carrier mobility in CB2 is much smaller than in CB1, R_H increases with temperature. Using the theory of Allgaier [11] the ratio of mobilities in the two bands can be calculated to $\mu_1 = 28\mu_2$, and the energy difference between E_{CB2}-E_{CB1} to 18 meV. The ratio of density of states is calculated to be 20.

Assuming that the sum of carriers in the two bands is constant, the strong increase of S with temperature below 250 K can also be explained by the activation of electrons from CB1 into CB2. Because the density of states of CB2 is much higher, the Fermi level decreases and consequently, the Seebeck coefficient increases with temperature.

Conclusions

A powdermetallurgical preparation route that leads to Mg_2Si samples free from oxides has been developed. The samples are thermally stable up to 500 °C in air. Compared to samples which contain oxides, the hall mobility of the carriers is improved by a factor of 5, and the thermoelectric figure of merit by a factor of 3.5. The transport behaviour can be explained by the contribution of an additional band.

Acknowledgment: This work has been supported by the Deutsche Forschungsgemeinschaft, Schwerpunktprogramm Gradientenwerkstoffe. We gratefully acknowledge fruitful discussions with E. Müller and the continuous support by W.A. Kaysser.

References

[1] R.J. LaBotz, D.R. Mason, D.F. O'Kane, "The thermoelectric properties of mixed crystals of $Mg_2Si_{1-x}Ge_x$", J. Electrochem. Soc. **110** (1963) 127.

[2] Y. Noda, H. Kon, Y. Furukawa, I.A. Nishida, K. Masumoto, "Preparation and thermoelectric properties of $Mg_2Si_{1-x}Ge_x$", Proc. of the XIIth Int. Conf. on Thermoelectrics, Yokohama, Japan (1993) 206.

[3] T. Kajikawa, I. Katsube, S. Sugihara, K. Soejima, "Thermoelectric properties of sintered magnesium compounds", Proc. of the XVth Int. Conf. on Thermoelectrics, Pasadena, USA (1996) 128.

[4] M. Riffel, J. Schilz, "Mechanical alloying of Mg_2Si", Scr. Met. **32** (1995) 1951.

[5] M. Riffel, J. Schilz, "Mechanically alloyed $Mg_2Si_{1-x}Sn_x$ solid solutions as thermoelectric materials", Proc. of the XVth Int. Conf. on Thermoelectrics, Pasadena, USA (1996) 133.

[6] J.M. Munoz-Palos, M.C. Christina del Paso, P. Adeva, "Synthesis of Mg_2Si powder by mechanical alloying and its consolidation", Mater. Trans. JIM **37** (1996) 1602.

[7] M. Riffel, J. Schilz, "Mill setting and microstructural evolution during mechanical alloying of Mg_2Si", submitted to J. Mat. Sci.

[8] K. Pixius, "Mechanisches Legieren harter und spröder Materialien", Ph.D. thesis, RWTH Aachen (1996)

[9] W. Mannchen, G. Jacobi, "Die Molwärme des Mg_2Si von 12 bis 300 K", Z. Naturforschung B **20** (1965) 178.

[10] N.F. Mott, E.A. Davis, Electronic Processes in Non-crystalline materials, Clarendon Press, Oxford (1971).

[11] R.S. Allgaier, "Extension of the Aukerman-Willardson two-band Hall coefficient analysis", J. Appl. Phys. **36** (1964) 2429.

Thermoelectric Properties of β-$FeSi_2$ Single Crystals Prepared with 5N Source Material

A. Heinrich, G. Behr, and H. Griessmann

Institut für Festkörper- und Werkstofforschung Dresden
P.O.Box 270016, D-01701 Dresden, Germany
e-mail: aheinrich@ifw-dresden.de

Abstract

Thermopower and electrical conductivity of undoped β-$FeSi_2$ single crystals have been investigated between 4K and 350K in dependence on the deviation from strict stoichiometry within the homogeinity range. The crystals have been prepared by chemical transport reaction in a closed system with iodine as transport agent using high purity source material. Both electrical conductivity and thermopower depend on the composition within the homogeinity range which is explained by different intrinsic defect concentrations at the Si-rich and Fe-rich phase boundaries. Low ohmic material was only obtained by additional doping. At the Si-rich phase boundary the thermopower shows at low temperatures a significant phonon drag contribution with /S/>1000μV/K.

Introduction

The compound β-$FeSi_2$ belongs to the group of semiconducting silicides formed by the transition metals Cr, Mn, Fe, Ru, Re, Os and Ir in the Si rich part of the corresponding phase diagrams [1]. Within this group the disilicide β-$FeSi_2$ is believed to be the most promising thermoelectric material for medium and high temperature applications [2,3]. Many efforts have been made to find suitable doping elements and doping levels for high efficient n-type and p-type material. Both bulk material [2-13] and thin films [14-20] have been considered.

Despite the great interest in thermoelectric and recently also in optoelectronic applications [1] many of the transport properties of β-$FeSi_2$ are still not well understood: The main scattering mechanisms are not known which limit the mobility, unclear is the role of polaron formation in n-type material, uncomplete the knowledge of defect formation and impurity levels. In Fig.1 an example is shown of the influence of unknown doping on the thermopower of β-$FeSi_{2+x}$ thin films. The different results in both the undoped and Co-doped films show that unintentional doping has to be carefully considered in all electrical transport measurements.

As a consequence of the above mentioned problems the question remained open whether β-$FeSi_2$ can be further modified to give improved thermoelectric properties in comparison with the state-of-the-art material. To answer this question also β-$FeSi_2$ single crystals have been investigated in recent years [19, 21-25]. According to their high structural order and defined stoichiometry the β-$FeSi_2$ single crystals can be considered as basis for applied research.

In this paper the electrical conductivity and thermopower undoped of β-$FeSi_2$ single crystals will be discussed which have been prepared with high puritiy source material to control unintentional doping. It will be shown that one needs a purity of at least 5N to obtain information about intrinsic defects. Both the electrical conductivity and thermopower have been found to depend on the deviation from strict stoichiometry.

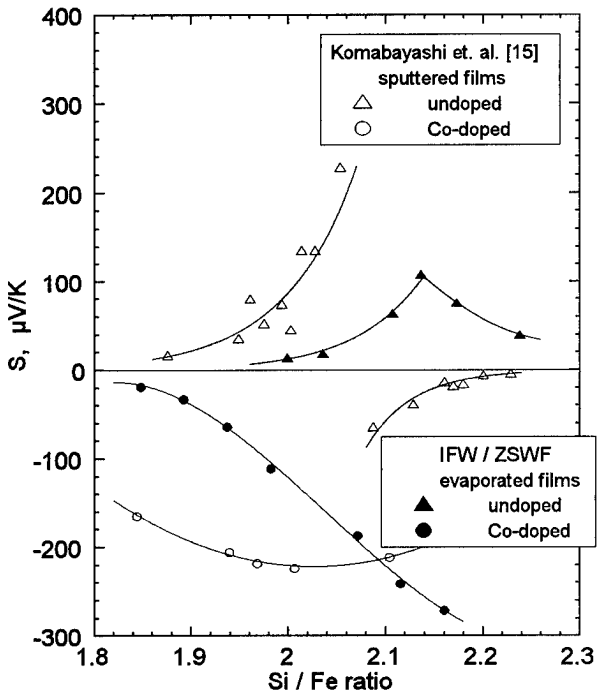


Fig.1 Thermopower S(300K) of undoped and Co-doped β-$FeSi_{2+x}$ thin films (full symbols - own results)

Crystal Growth

To achieve high-purity semiconductor grade β-$FeSi_2$ single crystals it is necessary to use high-purity starting materials and to optimize the whole preparation process to maintain the purity. Ultra-high-purity silicon (5N) was used as available on the market but high-purity iron of 5N was prepared by a special multistep process starting from technological iron powder [26,27]. The remaining impurity concentrations are shown in Table 1.

According to the phase diagram of the Fe-Si system the orthorhombic β-$FeSi_2$ phase does not coexist with the melt and decomposes at 1255K into FeSi and α-$FeSi_2$, which is stable above 1210K. Therefore, the growth of β-$FeSi_2$ single crystals must be carried out below 1210K, and chemical transport reactions or flux growth may be used. To avoid impurity incorporation the transport reaction was performed in closed silica ampoules with a mixed powder of iron (5 N) and silicon (5 N) as source materials and high purity I_2 as the transport medium. A special heat treatment of the silica ampoules was carried out to exclude oxygen and water.

Table 1: Impurity concentrations of Fe and β-$FeSi_2$ detected by mass spectroscopy

Element	Fe-Wire (mass ppm)	β-$FeSi_2$ (mass ppm)
B	< 1	< 1
S	< 1	< 0.1
P	< 1	< 1
Na	< 1	2
Ba	< 1	< 0.1
Cl	2	< 1
Br	< 1	< 0.1
K	< 1	< 1
Ca	< 0.1	2
Ti	< 1	< 1
Cr	< 1	7
Mn	< 1	<0.1
Co	1	1
Pb	< 1	< 0.1
W	< 1	< 0.1
Ni	2	11
Cu	5	2
Zn	< 1	< 1
Ga	1	1
Zr	1	1
Nb	< 0.1	< 1
Sb	< 1	< 0.1
Sn	< 1	< 0.1
As	< 1	< 0.1
Mo	< 2	< 0.1
Ag	< 0.1	1
I	< 0.1	19
Ta[1)]	13	19
C[2)]	10	3)
O[2)]	9	3)
N[2)]	6	3)
H	< 6	3)

1) MS-sample holder consists of Ta
2) 70% of the contents of C, O, N are bound on the surface [19]
3) not determined

The composition of the starting material was chosen to be equal to the atomic ratios Fe/Si = 2, 2.5 and 1.5. With the ratios 2.5 and 1.5 crystals were obtained with the upper and the lower boundaries of the homogeneity range of β-$FeSi_2$, resp. The chemical vapour transport proceeded from the source at T_2 =1323 K to the crystallization zone kept at a temperature T_1 of 100 to 300 K below T_2. In some cases the single crystals have been annealed after the crystal growth at a constant temperature for 100h to achieve a composition in equilibrium with the vapour phase. The single crystals obtained have a needle-like shape with dimensions (after about 10 days growth) of (5 - 10) x 2 x 0.5 mm^3. The crystal structure was checked by X-ray diffraction. The habit of the crystals does not change if different source compositions and different temperatures in the crystallization zone are used. In contrast to the crystals reported in literature before [21], selected crystals have a flat surface indicating that the usual twinning can be avoided in the material of higher purity.

The analyses of impurities in the single crystals (Table I) displays no significant increase in comparison with the starting materials but a decrease in the elements which will not be transported by iodine. Only the concentration of the transport agent iodine is increased to 19 wt. ppm.

Transport Properties of Undoped β-$FeSi_2$ Single Crystals

Thermopower

Fig. 2 shows the influence of the purity of the source material on the thermopower of undoped β-$FeSi_2$. Single crystals prepared with 4N Fe show a positive thermopower (p-type behaviour) but those prepared with 5N Fe negative thermopower (n-type behaviour). The samples of Fig. 2 have been prepared with source material of the atomic ratio 2.0, i.e. their possible deviation from stoichiometry is undefined.

p-type conductivity is usually reported for undoped polycrystalline β-$FeSi_2$ thin films and bulk material made by commercially available Fe of 4N or less purity. The p-type conductivity of undoped β-$FeSi_2$ is obviously caused by unintentional doping and not by intrinsic defects. According to Fig. 2 intrinsic defects are expected to be donors.

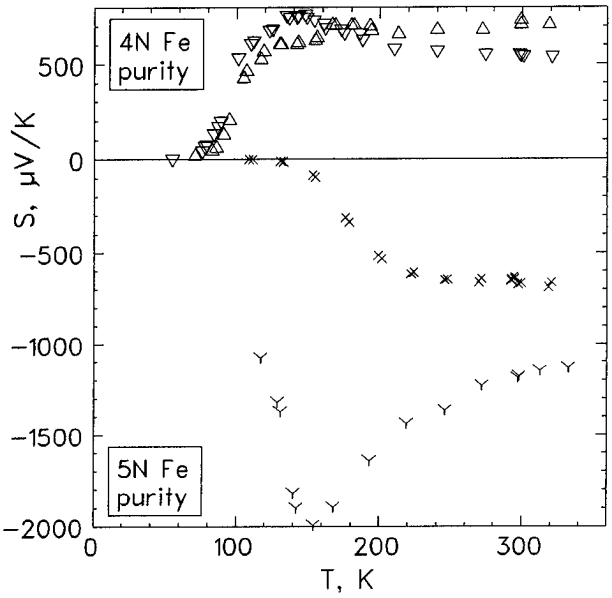


Fig. 2 Thermopower of undoped β-$FeSi_2$ single crystals prepared with 4N and 5N Fe

The general temperature dependence of the thermopower S(T) is obviously independent of the conductivity type. At low temperatures S(T) remains very small near zero up to about 70K, increases sharply up to values of /S/ = 500...800μV/K at 150K and shows a weak temperature dependence until room temperature. Crystals grown with 5N source material show sometimes a much larger low temperature thermopower up to 2000μV/K, see Fig.2 and below. Room temperature values are usually within 450μV/K and 900μV/K and with that much larger than in polycrystalline material.

In Fig. 3 the thermopower S(T) is compared of undoped single crystals prepared with excess of Si and Fe, respectively. The two groups of crystals exhibit different magnitudes and temperature dependences of S(T). Samples of the Si-rich phase boundary show a larger absolute value of the thermopower at room temperature than those of the Fe rich phase boundary. Also the increase of /S(T)/ with decreasing temperature is larger in Si rich samples. The thermopower of Fe rich crystals goes through a maximum between 150K and 200K but in Si rich crystals /S/ increases

down to 100K and reaches values >2000μV/K. Such large values of the low temperature thermpower can not be explained by an usual diffusion thermopower. Phonon drag effects should play an important role [28]. The slope of the increase of /S(T)/∝ T^n below 300K is given by n = 0.8...1.2 (Fig. 4) and with that in the range of usual acustic phonon drag effects.

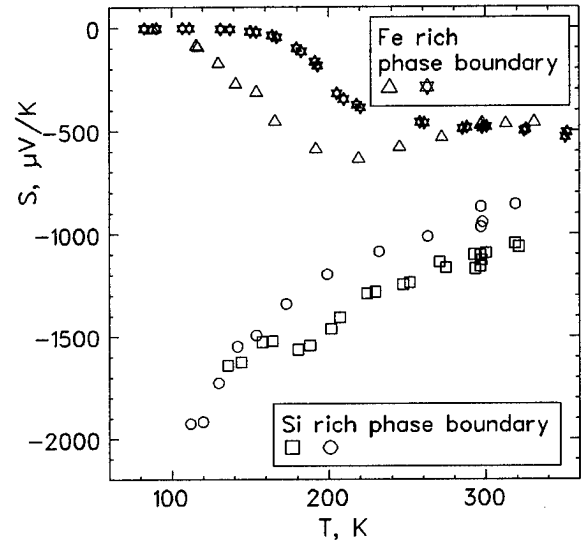


Fig. 3 Thermopower of undoped β-$FeSi_2$ single crystals prepared with 5N source material

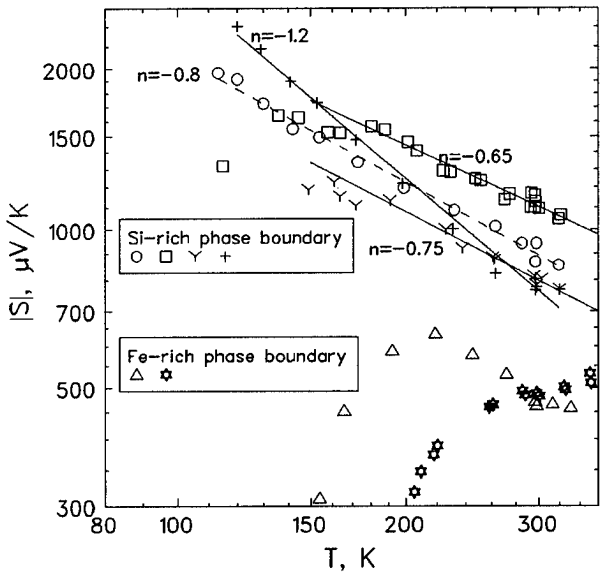


Fig. 4 Thermopower of undoped β-$FeSi_2$ single crystals in the semi-logarithmic plot

Electrical Resistivity

The different behaviour of S(T) of the both groups of crystals is expected to correspond to different behaviour of the electrical resistivity ρ(T). It is of special interest whether low ohmic material can be achieved by changing only the deviation from the strict stoichiometry. Fig. 5 shows ρ(T) normalized to ρ(300K) between 70K and 400K of single crystals grown with 5N source material at the Si rich and Fe rich phase boundaries and with the atomic ratio Si/Fe=2. There is a clear dependence of the slope of ρ(T) above 150K on the composition. The slope of ρ(T) and with that the activation energy at 300K increase with increasing Si/Fe ratio of the source material. On the contrary single crystals grown with 4N source material show irregular behaviour.

The different slopes of ρ(T) remain below 100K In Fig. 6 the resistivity is shown down to 10K. Straight lines are observed in the lg ρ vs. T^{-1} plot with small activation energies indicating impurity band conduction. In plots lgρ vs. $T^{-1/2}$ or $T^{-1/4}$ corresponding to variable range hopping (vrh) no straight lines were found.

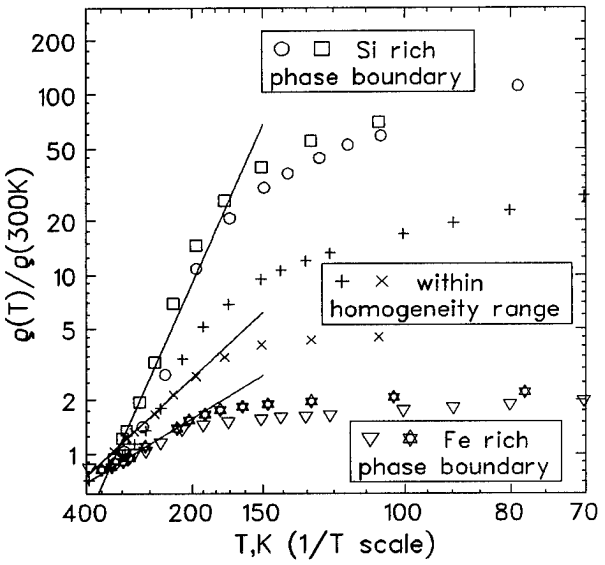


Fig. 5 Resistivity of undoped β-$FeSi_2$ single crystals prepared with 5N source material

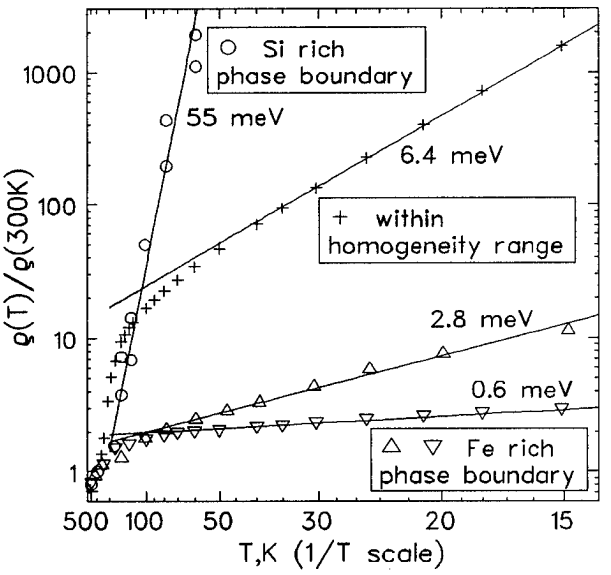


Fig. 5 Resistivity of undoped β-$FeSi_2$ single crystals at low temperatures (see Fig.5)

There is a correspondence between the temperature dependence of the resistivity ρ(T) and the thermpower S(T). The low temperature range of small values of /S(T)/

corresponds to the impurity band conduction and the increase of the thermopower with increasing temperature is in parallel with the decrease of the resistivity according to the activation of carriers from the shallow donor into the conduction band.

Some of the single crystals grown with the ratio Si/Fe = 2.5 show a similar temperature dependence of the resistivity as crystals grown with stoichiometric composition Si/Fe = 2 or with Si/Fe = 1.5. It is still an open question whether this behaviour is caused by unintentional doping which is still present despite the 5N purity of the source material or by different concentrations of intrinsic defects.

The room temperature values of resistivity and thermopower are given in Table 2. There is obviously no dependence of ρ(300K) on the deviation from stoichiometry despite the different temperature dependencies (Fig.5 and 6). All crystals have resistivities at room temperature in the same order of magnitude of 10 to 100Ωcm. It was still not possible to obtain low resistivity crystals only by changing the deviation from stoichiometry and with that the concentration of intrinsic defects. Only by additional doping low resistivity crystals have been obtained, see Table 3. The doping was carried out with stoichiometric source material. Whether the doping effects are different at the Si rich and Fe rich phase boundaries will be published in a forthcoming paper.

Table 2: Electrical parameter at 300K of undoped β-$FeSi_2$ single crystals (see Fig. 5 and 6)

Symbol	Source composition	ρ / Ωcm (300 K)	S / μV/K (300 K)	E_A / meV (T ≈ 300 K)
△	$FeSi_{1.5}$	25	-500	25
✡	$FeSi_{1.5}$	37	-500	28
Y	$FeSi_2$	130	-750	50
×	$FeSi_2$	21	-650	44
○	$FeSi_{2.5}$	35	-800	60
□	$FeSi_{2.5}$	70	-1100	105

Table 3: Electrical parameter at 300K of doped β-$FeSi_2$ single crystals (dopant concentr.: at% in source material)

dopant / at%	ρ / Ωcm	S / μV/K	E_A / meV
Cr 1	0.22	490	80
Co 3	1.1	-650	50
Ni 5	0.45	-620	60

Conclusions:

β-$FeSi_2$ single crystals have been prepared with the Si rich and Fe rich phase boundaries of the homogeneity range using source material of 5N purity. It was shown that this purity of the source material is necessary to avoid unintentional doping. The n-type conduction of the obtained crystals indicates that the dominant intrinsic defect is a donor.

There is a clear dependence of both the thermopower and electrical resistivity on the deviation from strict stoichiometry. In the temperature range between 4K and 350K Fe rich crystals both transport parameters show a much weaker temperature dependence of the resistivity than Si rich crystals. Only in Si rich crystals a strong phonon drag effect was found in the low temperature thermopower. Maximum values up to /S/ = 2000μV/K were found at 100K.

It was still not possible to obtain low ohmic single crystals only by changing the deviation from stoichiometry. Low ohmic crystals have been obtained until now only by additional doping.

References

1. H. Lange, in *Silicide Thin Films-Fabrication, Properties and Applications*, Mater. Res. Soc. Proc. 402, Pittsburgh, PA, 1996, p. 307.
2. I. Nishida, J. Mater. Sci. Soc. Jap. 15, 72 1978).
3. C. B. Vining, in *CRC Handbook of Thermoelectrics*, ed. M. Rowe, CRC Press, 1995, p. 277
4. R.M.Ware and D.J.McNeill, Proc. IEE 111, 178 (1964).
5. U. Birkholz, J. Schelm, phys.stat.sol. (a) 27, 413 (1968).
6. I.D. Ivanova, N.Kh. Abrikosova, E.I.Elagina and V.D. Khostikova, Neorg. Mater. 5, 1933 (1969).
7. I. Nishida, Phys. Rev. B 7, 2710 (1972).
8. G. Waldecker, H. Meinhold and U. Birkholz, phys. stat. sol. (a) 15, 143 (1973).
9. Y. Isoda, T. Ohkoshi, I. Nishida and H. Kaibe, J. Mater. Sci. Soc. Jap. 25, 311 (1989).
10. T. Kojima, phys. stat. sol. (a) 111, 233 (1989).
11. U. Stöhrer, R. Voggesberger, G. Wagner and U. Birkholz, En. Conv. Mgmt. 20, 143 (1990).
12. T. Tokiai and T. Uesugi, J. Am. Ceram. Soc. 78, 1089; J. Ceram. Soc. Jap. 103, 661 (1995).
13. E. Groß, M. Riffel, U. Stöhrer, J. Mat. Res. 10, 34 (1995).
14. M. Komabayashi, K. Hijikata, S. Ido, Jap. J. Appl. Phys. 29, 1118 (1990); 30, 331 (1991).
15. M. Komabayashi and S. Ido, Jap. J. Appl. Phys. 30, 2883 (1991); J. Ceram. Soc. Jap. 100, 21 (1992)
16. K. Matsubara, H. Kuno, Y. Okuno, H. Takaoka and T. Takagi, Proc. ISIAT'83 & IPAT'83, (Kyoto 1983) 1221.
17. M. Powalla, K. Herz, Appl. Surf. Sci. 70/71, 593 (1993)
18. K. Matsubara, K. Kishimoto, K. Nagao, O. Ueda, T.Miki, T. Koyanagi and I. Fujii, in *Proc. XII. Int. Conf. Thermo electrics*, Yokohama, 1993, p.223.
19. A. Heinrich, C. Gladun, A. Burkov, Y. Tomm, S. Brehme and H. Lange, in *Proc. XIV. Int. Conf. Thermoelectrics*, St. Petersburg, 1995, p. 259.
20. S. Teichert, R. Kilper, T. Franke, J. Erben, P. Häussler, W. Henrion, H. Lange and D. Paknin, Appl. Surf. Science 91, 56 (1995).
21. Ch. Kloc, E. Arushanov, M. Wendl, H. Hohl, U. Malang and E. Busher, J. Alloys Comp., 219, 93 (1995).
22. E. Arushanov, Ch. Kloc, H. Hohl and E. Bucher, J. Appl. Phys. 75, 5106 (1994).
23. E. Arushanov, Ch. Kloc and E. Bucher, Phys. Rev. B 50, 2653 (1995); E. Arushanov, E. Bucher, Ch. Kloc, O. Kulikowa, L.Kulyuk and A. Siminel, ibid., 52, 20 (1995).
24. S. Brehme, L. Ivanenko, Y. Tomm, G.-U. Reinsperger, P. Strauß and H. Lange, in Mater. Res. Soc. Proc. 402, Pittsburgh, PA, 1996), p. 355.
25. A. Heinrich, A. Burkov, C. Gladun, G. Behr, K. Herz, J. Schumann and H. Powalla, in *Proc. XV. Int. Conf. Thermoelectrics*, Pasadena, CA, 1996, p. 57.
26. G. Weise, G. Oswian, Kristall & Technik 11, 729 1976).
27. G. Behr, J. Werner, G. Weise, A. Heinrich, A, Burkov and C. Gladun, phys. stat. sol. (a) 160 (1997)
28. C. Herring, Phys. Rev. 96, 163 (1954).

Drag Effects in β-Iron Disilicide

Fedorov M.I, Zaitsev V.K., Ivanov Yu.V., Popov V.V., Khazan M.A.

A.F.Ioffe Physical-Technical Institute, St.Petersburg, Russia

Abstract

The results of experimental study of Seebeck coefficient, electrical and thermal conductivity of pure and doped $\beta-FeSi_2$ polycrystals in the temperature region 4.2-1000K are presented in this paper. The contributions of possible mechanisms of current carrier transport into Seebeck coefficient are discussed. Optical phonon drag effect contribution into Seebeck coefficient is calculated for band conduction mechanism. The reasons of gigantic Seebeck coefficient at low temperature are discussed either.

Introduction

The problem of good thermoelectrics existence among the materials with low mobility was discussed in [1]. $\beta - FeSi_2$ is a representative of such thermoelectrics. Undoped $\beta - FeSi_2$ has high thermal conductivity of crystal lattice ($\sim 9\ W \cdot m^{-1}K^{-1}$) and very low mobility of current carriers ($\sim 1\ cm^2V^{-1}s^{-1}$). Nevertheless doped iron disilicide has a high enough figure of merit $Z = 0.4 \cdot 10^{-3}K^{-1}$ [2]. This fact shows that in $\beta - FeSi_2$ unusual intercommunication between the mobility and thermal conductivity of crystal lattice takes place. The interconnection on our opinion is shown most noticeable in temperature dependencies of Seebeck coefficient. Earlier in [3, 4, 5] it was shown, that Seebeck coefficient of a number of materials on the basis of iron disilicide has features, which can be explained within the framework of neither the usual band theory nor polaron theory. In this paper we shall discuss the contributions of optical phonon drag effect and some other effects into Seebeck coefficient.

Samples and measurement

In this work we used polycrystalline samples prepared by vacuum casting method as described in [6]. Measurements of kinetic coefficients were fulfilled with 4 different installations. The installations have overlapping temperature ranges. The results obtained with different installations in a common temperature range are practically coincide. The error of measurement of electrical conductivity and Seebeck coefficient was less than 5% and that for thermal conductivity less than 10%.

Seebeck coefficient

Fig.1 shows the temperature dependencies of Seebeck coefficient for pure and weakly doped $\beta - FeSi_2$. Some results obtained by Birkholz and Schelm [3] on polycrystalline samples and by Heinrich et al. [5] on single crystals are shown either. The most characteristic feature obtained on the majority of samples is the sharp growth of Seebeck coefficient with temperature practically from zero up to 500 - 800 $\mu V/K$ in the region of 150 - 400 K. At these temperatures practically in all cases the activational growth of electrical conductivity is observed (Fig.2). Earlier we stated the assumption [7], that such behaviour of a Seebeck coefficient can be stipulated by the essential contribution of current carriers drag by optical phonons.

In the paper [4] we estimated the contribution of optical phonon drag effect into Seebeck coefficient for a polaron conduction mechanism. Now we shall discuss such a contribution for a band conduction mechanism.

Optical phonon drag effect for band conduction mechanism

To calculate the contribution of optical phonon drag effect we suggested that the elementary spectra of quasiparticles: $\varepsilon_k = \frac{\hbar^2k^2}{2m}$, $\omega_q = \omega_0 + aq^2$ can be used . Here ω_0 - limiting frequency of longitudinal optical phonons, a - parameter, determining their dispersion. It was assumed, that scattering of carriers on optical phonons is a small perturbation in an electronic subsystem and can be neglected. Thus the electronic Boltsmann equation is easily solved in relaxation time (τ) approximation. Case of small concentration of current carriers was considered. Therefore from all possible relaxation processes in a phonon subsystem the disintegration of an optical phonon on two acoustic ones was taken into account only. The relaxation time of such a process does not depend practically on a wave vector of initial phonon [8].

It simplifies the problem and allows to calculate phonon components of Peltier and Seebeck coefficients for any temperature. In this case the expression for phonon component of Seebeck coefficient S_p can be written as:

$$S_p = \frac{k_B\alpha\Delta\omega}{8e\nu_0} D_r(\eta) \qquad (1)$$

Where α - the dimensionless constant of electron-phonon interaction,

$\Delta\omega = a\kappa^2$,

$\kappa^2 = 2m\omega_0/\hbar$,

ν_0 - Frequency of processes of optical phonon disintegration at $T \to 0$,

r standard parameter, determining power dependence of the relaxation time of current carriers,

$\eta = \hbar\omega_0/k_BT$.

Functions $D_r(\eta)$ for a number of carriers scattering mechanisms are submitted on fig.3.

Temperature dependence of Seebeck coefficient (1) is determined by the function $D_r(\eta)$. Other factors are responsible for the value of effect. At low temperature ($\eta \gg 2$) $D_r(\eta) \propto \eta^{r+2}e^{-\eta}$, at high - $D_r(\eta) \propto \eta^{3/2}$. It is easy to see, that in semiconductors with reasonably large m, a, α and

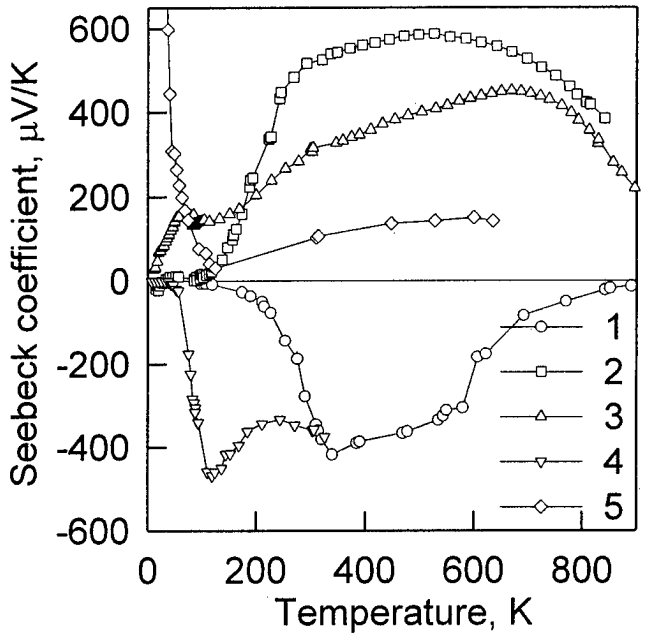


Figure 1: Seebeck coefficient of some materials based on $\beta - FeSi_2$
1 - $FeSi_2$, pure [3], 2 - $FeSi_2$<1%Mn>,
3 - $FeSi_2$<0.01%Co>, 4 - $FeSi_2$<0.7%Co> [5], 5 - $FeSi_{2.01}$

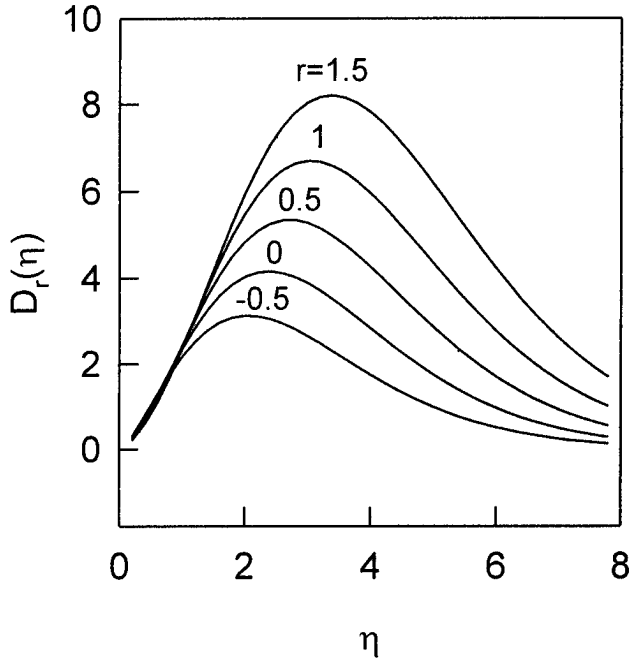


Figure 3: Function $D_r(\eta)$ at various r

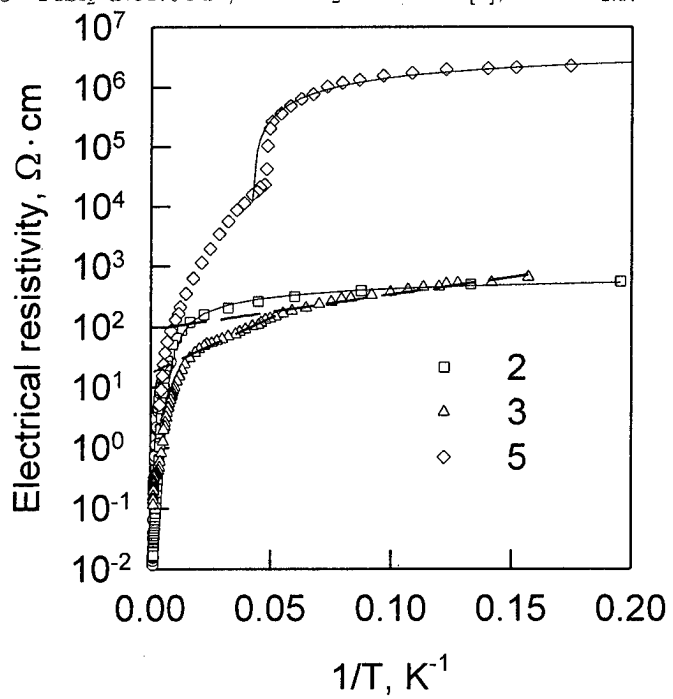


Figure 2: The electrical resistivity of some materials based on $\beta - FeSi_2$.
Symbols - experiment, designations are the same as on Fig.1. Lines - theory: Solid - Kondo-type dependence. Dashed - activational dependence.

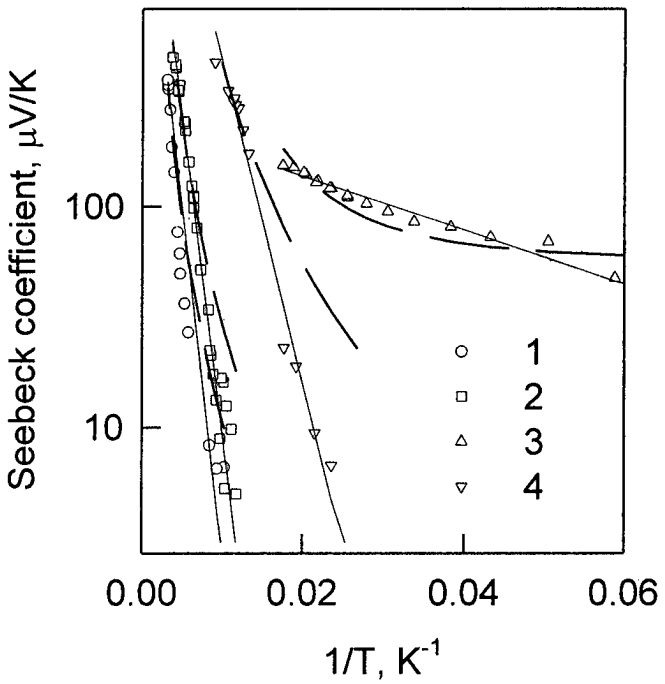


Figure 4: Absolute value of Seebeck coefficient of a number $\beta - FeSi_2$ based materials (symbols, designations are the same as on Fig.1) and fitted contribution of optical phonon drag effect (solid line) and acoustic phonon drag effect (dashed line)

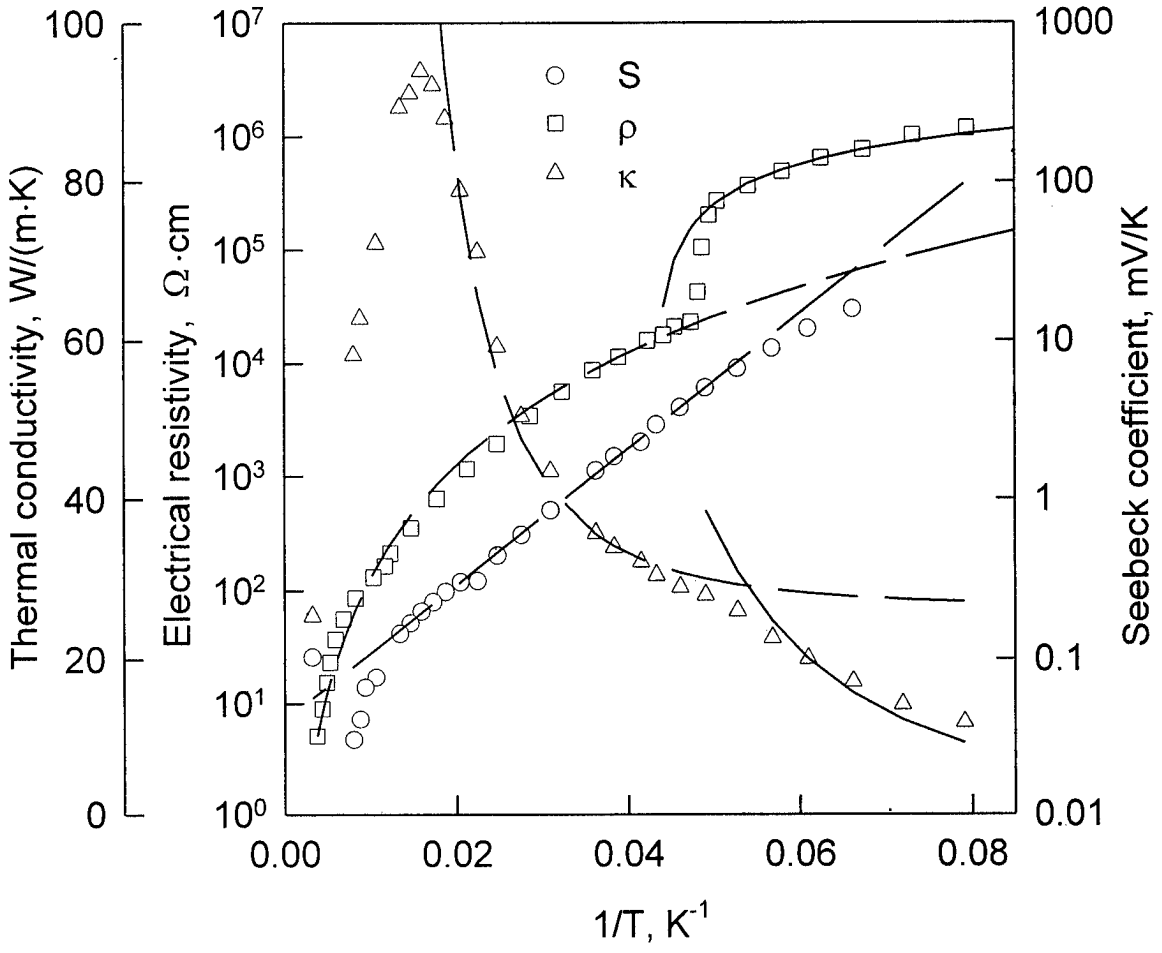


Figure 5: Seebeck coefficient (S), resistivity (ρ) and thermal conductivity (κ) of $\beta - FeSi_{2.01}$. Solid lines describe theoretical dependence at low temperature, dashed lines - those at higher temperature.
Low temperature dependences: $\kappa = \kappa_0 T^3$; $\rho = \rho_0 + k \cdot \ln(T)$.
Higher temperature dependences: $\kappa = \kappa_1 T^3 + d\kappa$; $\rho = \rho_1 T^{-3.3}$; $S = S_0 e^{\frac{\Theta}{T}}$.

small ν_0 the contribution of optical phonons in Seebeck coefficient can appear $\sim k_B/e$ and more. The sign of S_p (for electrons $e < 0$, for holes $e > 0$) at $a > 0$ coincides with the sign of diffusional thermopower.

Discussion

Discussed above theory and the results of Seebeck coefficient estimation for polaron conduction mechanism [4] show that in both case an exponential growth of Seebeck coefficient with temperature should take place. This is the principal distinction from an acoustic phonon drag effect where T^3 dependence takes place. Fig.4 shows Seebeck coefficient of a number $\beta - FeSi_2$ based materials (symbols) and fitted contribution of optical phonon drag effect (solid line) and acoustic phonon drag effect (dashed line). One can see that the exponential dependence of Seebeck coefficient much better describes the experiment than the cubic one.

The theory of optical phonon drag effect stated above cannot describe whole Seebeck coefficient temperature dependence firstly because of existence other contributions into the coefficient and, secondly, because the theory was stated for one optical phonon branch. $\beta - FeSi_2$ unit cell contains 49 atoms and therefore the phonon spectrum must contain 48 branches of longitudinal optical phonons. The study of IR-reflection in reststralen region fulfilled on polycrystals [9] and on single crystals [10] shows about 9 oscillators. The temperature corresponding the oscillator of lowest energy is $\sim$ 300K. The fitting gives the temperatures of phonon activation in the range 90 - 500 K. Now it is impossible to make definite conclusion about the possibility of applying the theory because of lack of knowledge about phonon spectrum. We have data on phonon frequences only for pure $\beta - FeSi_2$ and we know nothing about phonon dispersion. Nevertheless it is possible to say that the optical phonon drag makes an essential contribution in Seebeck coefficient in some cases.

Gigantic Seebeck coefficient in some $\beta - FeSi_2$ based samples

As we reported earlier [11] there are gigantic values of Seebeck coefficient up to 15 mV/K in $FeSi_{2.01}$. As Fig.5 shows there is an exponential growth of Seebeck coefficient when temperature decreasing in the region 70 – 15 K. Simultaneously with the growth of Seebeck coefficient electrical resistivity increases. The growth of resistivity can be described as $T^{-3.3}$ in the region 300 – 20 K and in the region 20 – 4.3 K it can be described by Kondo-type dependence $\rho = \rho_0 + k \cdot \ln(T)$. Such a dependence shows that this growth cannot be explained only by some phonon drag effect because the drag effects do not result in so drastic change of resistivity.

It should be mentioned that the problem of existence of a phase transition in $\beta - FeSi_2$ near $T = 20K$ must be studied. The existence of the phase transition is indicated by the change of temperature dependence type for all measured parameters in this region. The most essential change takes place in the temperature dependence of resistivity.

Kondo-type dependence of resistivity takes place not only in $FeSi_{2.01}$. The similar dependence is observed in the Mn-doped sample although in the Co-doped sample in this temperature range takes place only activational dependence (Fig.2). So, the study of influence of magnetic impurities on thermoelectric parameters of $\beta - FeSi_2$ should be continued.

Conclusion

Study of materials based on $\beta - FeSi_2$ shows that this material has many problems. Solving these problems can show the new ways of search of very effective thermoelectrics.

Acknowledgments

Authors are very thankful to the ICT97 Organizing Committee for financial support that allowed to present this work. The work was supported either by Russian Foundation for Basic Researches, grant N 95-02-04103-a.

References

[1] Zaitsev V.K., Ktitorov S.A., Fedorov M.I. Low Carrier Mobility Materials for Thermoelectric Application. CRC Handbook of Thermoelectrics. ed. by D.M.Rowe., N.Y., CRC Press, (1995) 311.

[2] Ware R.M., McNeil D.J. Iron disilicide as a thermoelectric generator material. Proc. IEE 111 (1964) 178.

[3] Birkholz U., Schelm J. Phys. Stat.sol., 27 (1968) 413.

[4] Zaitsev V.K., Ktitorov S.A., Kaliazin A.E., Fedorov M.I. Proc. of the XIV Int. Conf. On Thermoelectrics, St. Petersburg, (1995) 210.

[5] Heinrich A., Gladun C., Burkov A., Tomm Y., Brehme S., Lange H. Proc. of the XIV Int. Conf. On Thermoelectrics, St. Petersburg, (1995) 259.

[6] Fedorov M.I., Khazan M.A., Kaliazin A.E., Zaitsev V.K., Kartenko N.F., Engalychev A.E. Properties of iron disilicide doped with Ru, Rh, Pd. Proc. of the XV Int. Conf. on Thermoelectrics, Pasadena, CA, USA, (1996) 75.

[7] Zaitsev V.K., Ktitorov S.A., Petrov Yu. V. Materials for thermoelectric converters, Leningrad, (1987) 36.

[8] Bhatt A.R., Kim K.W., Stroscio M.A. J.Appl. Phys. 76 (1994) 3905.

[9] Birkholz U., Finkenrath H., Naegele J., Uhle N. Infrared reflectivity of semiconducting $FeSi_2$. Phys. Stat. sol. 30 (1968) K81.

[10] Arushanov E.K., Carles R., Kloc Ch., Bucher E., Leotin J., Smirnov D.V. Optical studies of monocrystalline $\beta - FeSi_2$. Inst.Phys.Conf.Ser. 155 (1997) 1013.

[11] Fedorov M.I., Zaitsev V.K., Ivanov Yu.V., Popov V.V., Kaliazin A.E., Khazan M.A. Thermoelectric properties of some materials based on $\beta - FeSi_2$ in the low temperature region. Thermoelectrics and their applications, St.Petersburg, (1997) 92.

Fabrication of Ternary Iron Disilisicides as Thermoelectric Semicomductors by Sintering using Elemental Powders

Yoriko Ohta[i], Seiji Miura[ii] and Yoshinao Mishima[iii]

[i] Graduate Student, Mishima Group, Department of Materials Science and Engineering, Tokyo Institute of Technology, 4259 Nagatsuta, Midori-ku Yokohama 226, Japan
Tel&Fax : +81-45-924-5495, e-mail : ohta@materia.titech.ac.jp

[ii] Precision and Intelligence Laboratory, Tokyo Institute of Technology (Now with Division of Materials Science and Engineering, Hokkaido University, N13W8, Kita-ku Sapporo 060, Japan)

[iii] Precision and Intelligence Laboratory (Now with Department of Materials Science and Engineering), Tokyo Institute of Technology, 4259 Nagatsuta, Midori-ku Yokohama 226, Japan

Abstract

Sintering process to fabricate iron disilicides with a fine grain structure is pursued using elemental powders as starting materials. Additions of Al to the binary Fe-Si system are attempted. This is because Al has a considerably lower melting point than Fe and Si and hence liquid Al phase would be involved upon sintering to help accelerating the reaction kinetics to form iron disilicides. Sintering of ternary iron disilicides is attempted also with additions of Co and Cu, the former being an n-type dopant while the latter might promote metal-to-semiconductor transition upon annealing after sintering. Effects of such additions are examined on the sintering kinetics, constituent phases in the products, and their thermoelectric properties. It is shown that fabrication of sintered iron disilicides using elemental powders becomes possible with Al additions, for which a mechanism of sintering in the Fe-Si-Al ternary system is proposed. Also a series of demonstration is given for the changes in thermoelectric properties with difference in doping element.

Introduction

The iron disilicides have been known by their high potential as thermoelectric semiconductors, besides they consist of abundant and economical raw materials and yet have high oxidation resistance as well as chemical stability at high temperatures[1-4].

The partial Fe-Si binary phase diagram is shown in Fig. 1[5]. At the stoichiometric composition, a low-temperature phase of the iron disilicide exists below 1259K as β-$FeSi_2$ having semiconducting properties, while at above 1259K it exists as an eutectic alloy composed of α-$FeSi_2$ and ε-FeSi having metallic properties.

The single phase β-$FeSi_2$ is an intrinsic semiconductor, and it is necessary for use as thermoelectric materials to dope with Al[1,2] or Mn[3,4] as acceptors and with Co[1,2,6] as a donor, since a thermoelement consists of a combination of p- and n-type semiconductors. These dopants have been usually used independently, but it has been reported that thermoelectric properties are improved by complex dopings with Mn-Al or Co-Al[7].

Thermoelectric materials have been usually sintered for better thermoelectric properties and mechanical strength. As-sintered iron disilicide is basically the metallic α phase, being a stable phase at high temperatures, and therefore it is necessary to conduct a heat treatment at a lower temperature to convert the alloy into β phase with semiconducting properties. The kinetics for this conversion has been known to be sluggish[8], but a small amount of Cu doping has been shown to accelerate the kinetics of α to β conversion upon heat treatment[9,10].

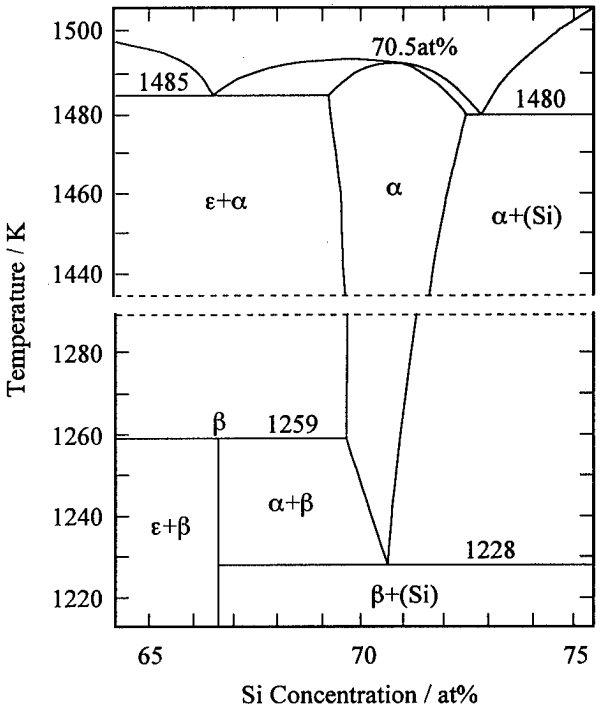


Fig. 1 The partial Fe-Si binary phase diagram.

Sintered iron disilicides have been conventionally fabricated through such a complicated process as sintering the crashed and milled alloys which had once been made through such ingot metallurgy as induction or arc melting[11]. Such a fabrication process has been required since sintering elemental powders of a desired composition with a uniformity has been unsuccessful.

Al have a considerably lower melting point than Fe and Si. Therefore Al doping should affect ternary liquidus temperatures of the compound in the Fe-Si-Al ternary system as compared to the case in the binary Fe-Si system. This is obvious from Fig. 2[12], where isothermal contour for the liquidus surface is shown together with troughs for ternary invariant reactions. Then, in case of sintering using elemental powders, it is expected that Al-rich-liquid-phase containing much of Fe and Si in solution forms at early stages in the sintering time and facilitates the reaction between Fe and Si elemental powders. Since the reaction in this sintering process occurs on a scale of raw powder sizes, if the raw powder are fine enough to react overall, it is also expected that the sintered specimen would not be accompanied by macro segregation.

0-7803-4057-4/97 $10.00 ©1997 IEEE

In this paper, it is presented that fabrication of the sintered iron disilicides using elemental powders becomes possible with addition of elemental Al powder. Also observed and discussed is the change in thermoelectric power with varying kind and amount of additional elements. The elements other than Al are Co as an n-type dopant and Cu as an accelerator for the kinetics of α to β conversion.

Experimental procedure

Nominal compositions of the mixtures, and purities and average particle sizes of elemental powders are shown in Table 1 and 2, respectively. The mixtures are blended in ball milling process for 3days. Green compacts of Fe-Si mixtures with Al, Co and Cu, about 10mm in diameter and about 5 to 30mm in length, are prepared by cold isostatic pressing (CIP) at 370MPa and sintered for 5, 30min or 25hr at 1423 or 1453K in a vacuum (about 10^{-1}Pa). Sintered specimens are then annealed for conversion to β-$FeSi_2$ in evacuated quartz tube at 1073K for 200hr. The constituent phases of specimens are observed by a JEOL JSM-5300 scanning electron microscope (SEM) and identified by energy dispersive X-ray spectroscopy (EDS) JEM JED-2001 operated at 20kV. Thermoelectric power is measured in a vacuum (about 10^{-1}Pa) at temperatures ranging from R.T. to 673K with spot welded Pt-legs during heating and cooling. Heating or cooling rate was about 10K/min and the measurement is recorded by digital multi meter at every 1min.

Results and Discussion

* Mechanism of sintering in the Fe-Si-Al ternary system

SEM micrographs of as-sintered Fe-61.7Si-5Al are shown in Fig. 3. Sintering was conducted at 1453K for (a) 5min, (b) 30min and (c) 25hr. In the specimen sintered for 5min, Fig. 3 (a), white phase which is identified to be ε-FeSi by EDS is surrounded by α-$FeSi_2$ with a darker contrast. It is noted that the boundaries between the two phases are irregular in shape. EDS revealed that Al is mainly contained in α-$FeSi_2$, but not in ε-FeSi. Also in some darker regions in the matrix of α phase, shown by an arrow, are enriched with Al. It is therefore evident that the reaction is incomplete in this sintering condition. Since the ε-FeSi is found as large as the size of raw Fe-powder as has been

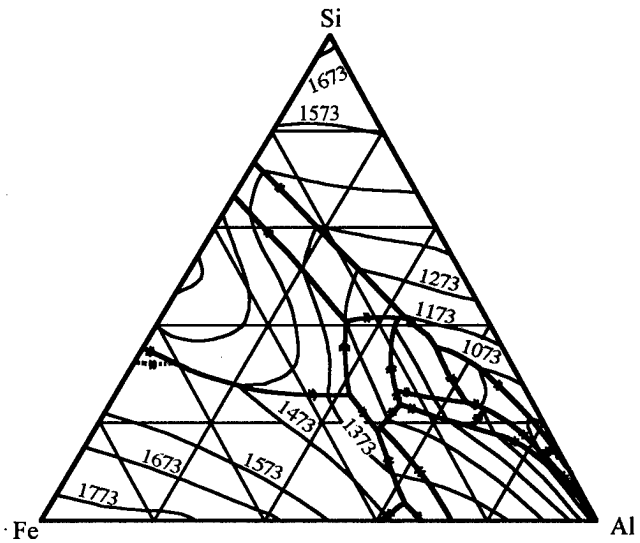


Fig. 2 Liquidus surface in the Fe-Si-Al ternary system.

Table 1 Nominal compositions of green compacts using elemental powders.

Fe	Si	Al	Co	Cu
33.3	61.7	5	-	-
32.97 (33.3)	63.06 (63.7)	2.97 (3)	-	1
32.97 (33.3)	64.05 (64.7)	1.98 (2)	-	1
32.47 (32.8)	63.06 (63.7)	2.97 (3)	0.50 (0.5)	1
31.98 (32.3)	63.06 (63.7)	2.97 (3)	0.99 (1)	1
30.00 (30.3)	63.06 (63.7)	2.97 (3)	2.97 (3)	1
29.01 (29.3)	63.06 (63.7)	2.97 (3)	3.96 (4)	1
28.02 (28.3)	63.06 (63.7)	2.97 (3)	4.95 (5)	1
31.98 (32.3)	64.05 (64.7)	1.98 (2)	0.99 (1)	1

( ) compositions without Cu. [at%]

Table 2 Purity and average particle size of the elemental powders.

	Purity / %	Average particle size / μm
Fe	99	45
Si	99.999	45
Al	99.9	10
Co	99.8	5.22
Cu	99.5	5.98

shown in Table 2, the ε phase is thought to be formed by the diffusion of Si into Fe-particles. It is then considered that progress of reaction in the sintering process depend on the slower diffusion of Fe and the size of raw Fe-particles. The specimen sintered for 30min, Fig. 3 (b), is similar to (a) in appearance though compositions of the each constituent phase seem to reach their equilibrium according to the EDS results. The boundaries between the constituent phases are smooth implying that the reaction has been completed at this stage. In Fig. 3 (c), after being sintered for 25hr, the ε phase becomes remarkably coarse.

On the basis of these results, a mechanism of sintering in the Fe-Si-Al ternary system is proposed. It is shown schematically in Fig. 4 (a) through (c). When the green compact consisting of Fe, Si, and Al powder mixtures as shown in (a) is heated and held at the sintering temperature, Al-liquid-phase should first form and a considerable amount of Fe and Si would dissolve into it. This is the situation shown in (b). Being judged from the liquidus surface which was shown in Fig. 2, the amount of liquid phase at for example 1373 K is as much as five times the volume of aluminum powders added initially, since the alu-

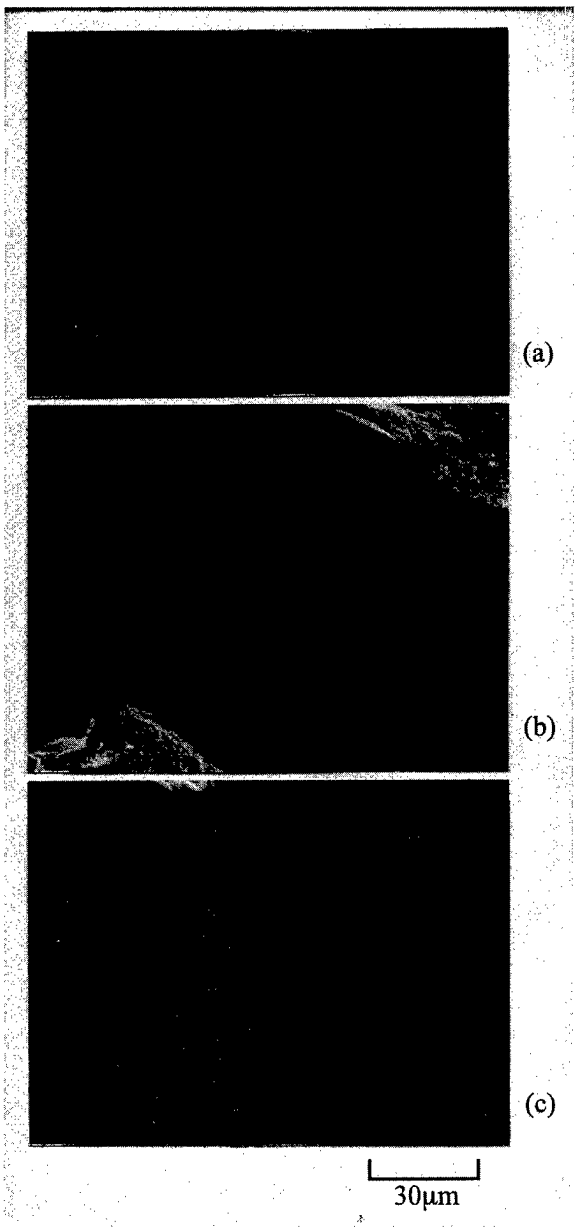


Fig. 3 SEM micrographs of as-sintered $FeSi_2$ with 5at%Al. Sintering was conducted at 1453K for (a) 5min, (b) 30min and (c) 25h.

minum concentration in the liquid coexisting with solid Fe and Si would be as high as 20at%. Under such a condition, α-$FeSi_2$ would form at such sites where the concentration requirement is reached as boundaries between liquid and solid phases. The diffusion of Fe in each solid phase must be slower than that of Si[13]. Furthermore, the solubility of Fe in Si-solid-phase is small[14], while that of Si is large. Therefore, as a result of the preferential diffusion of Si into Fe-particle through the medium of liquid phase, ε-FeSi forms. The sintering process results in forming an alloy composed of ε-FeSi and α-$FeSi_2$ as shown in (c).

* The change in thermoelectric power

Thermoelectric power as a function of temperature for $Fe(Si,2Al)_2$ and $Fe(Si,3Al)_2$ doped with and without 1at%Cu is compared in Fig. 5. These specimens are sintered at 1423K for 30min and then annealed at 1073K for 200hr for a to b conversion. It is the condition for sintering and annealing for all the other specimens described hereafter. It is first found that the thermoelectric power of the specimen with 3at%Al is higher at entire temperature range over that with 2at%Al. Then it is seen that the thermoelectric power of Cu-doped specimens is substantially higher for both cases with the same tendency for the difference in Al level. This should be due to the acceleration of the kinetics of conversion from α to β by Cu as has been reported before[9,10]. In fact SEM observation revealed that the microstructure changes drastically after annealing for α to β conversion in a way that the amount of ε-FeSi becomes very small in volume for Cu-doped specimens.

Thermoelectric power as a function of temperature for $(Fe,Co)(Si,3Al)_2$-1Cu with various Co concentrations after β-annealing is shown in Fig. 6. Note that this composition was found to be the highest in thermoelectric power among the specimens examined in the present work as shown in Fig. 5. The thermoelectric power undergoes a change from positive to negative values for a wide range as Co concentration increases. For the purpose of clarifying the influence of Co concentration, thermoelectric power at 573K as a function of Co-concentration in $(Fe,Co)(Si,3Al)_2$-1Cu is summarized in Fig. 7. As the Co concentration increases, thermoelectric power decreases in the range of p-type at first, however with more than 3at%Co dopings it change into negative in value, becoming n-type, and its absolute value decreases with Co concentration.

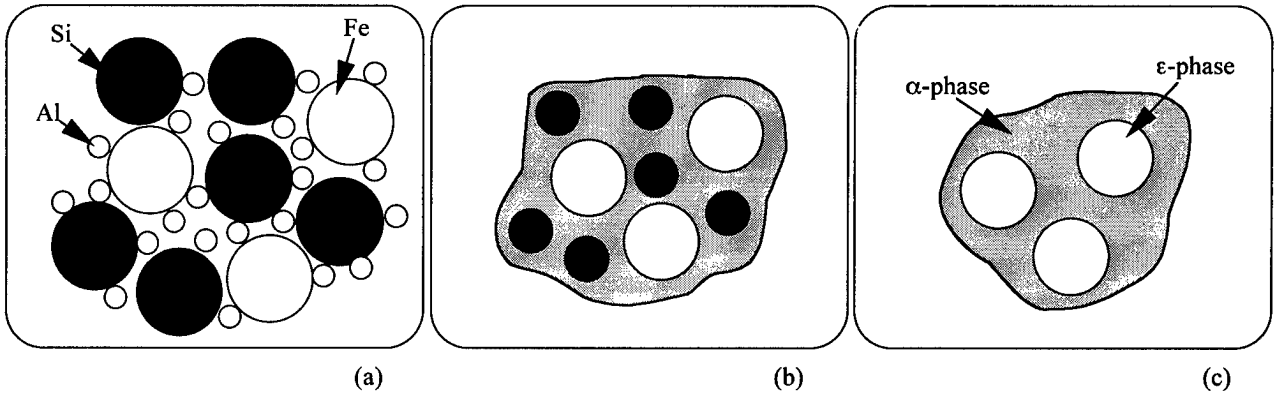


Fig. 4 A proposed mechanism of sintering in the Fe-Si-Al ternary system.
(a) Green Compact. (b) Formation of Al-liquid-phase containing much of Fe and Si in solution, through which Si diffuses into Fe-particle. (c) Final product composed of ε-FeSi and α-$FeSi_2$.

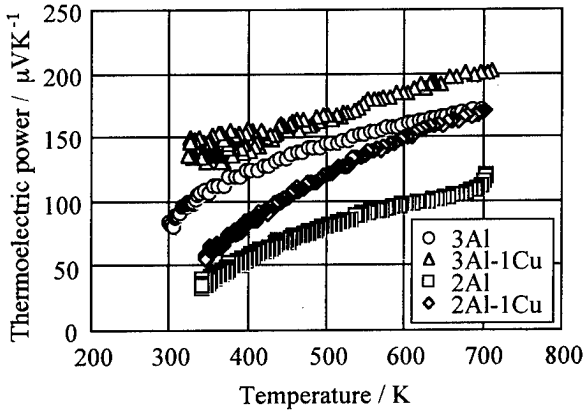


Fig. 5 Thermoelectric power as a function of temperature for $Fe(Si,2Al)_2$ and $Fe(Si,3Al)_2$ doped with and without 1at%Cu after annealing for α to β conversion at 1073K for 200h.

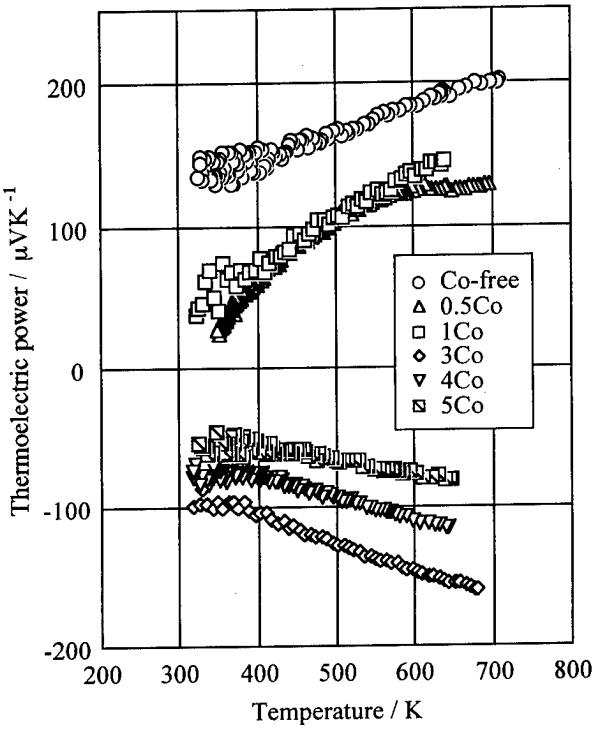


Fig. 6 Thermoelectric power as a function of temperature for $(Fe,Co)(Si,3Al)_2$-1Cu with various Co-concentrations after the annealing for α to β conversion at 1073K for 200h.

It is concluded from Fig. 7 that the maximum thermoelectric power of p-type specimen is resulted by doping with 3at%Al and 1at%Cu, and that of n-type is for doping with 3at%Al, 3at%Co and 1at%Cu within the specimens examined in the present work. Therefore it is shown that the sintering iron disilicides using elemental powders are possible and that the proper composition can be chosen for better thermoelectric power. However, the electrical and the thermal conductivity for these iron disilicides should be investigated in order to evaluate overall thermoelectric properties.

Conclusions

Sintering of iron disilicides with various compositions

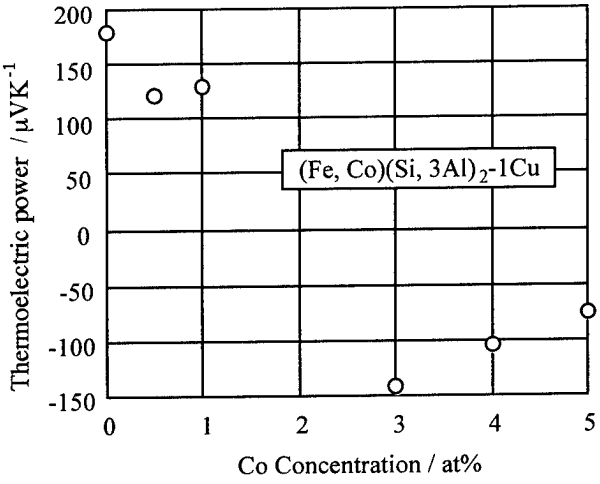


Fig. 7 Thermoelectric power at 573K as a function of Co concentration in $(Fe,Co)(Si,3Al)_2$-1Cu.

are attempted using elemental powders basically in the Fe-Si-Al ternary system with some quaternary additions. The process of sintering has been observed and discussed, and then thermoelectric power has been measured as a function of temperatures to see the effect of composition of the iron disilicides. The followings are the conclusions drawn;

1. Fabrication of iron disilicide using elemental powders becomes possible with Al additions.
2. A mechanism of sintering in the Fe-Si-Al ternary system was proposed in which the liquid phase plays an important role to accelerate the reaction to form iron disilicides.
3. Effect of ternary and quaternary elements on the thermoelectric power is demonstrated systematically. It is found that the maximum thermoelectric power of p-type specimen is resulted with 3at%Al and 1at%Cu additions, and that of n-type is 3at%Al, 3at%Co and 1at%Cu additions.

Reference

1. R.M.Ware and D.J.McNeill : Proc.Inst.Electr.Eng., 111(1964)178
2. U.Birkholz and J.Schelm : Phys.Stat.Sol., 27(1968)413.
3. I.Nishida : Phys.Rev.B7(1973)2710.
4. T.Kojima : Phys.Stat.Sol. (a), 111(1989)233.
5. J.P.Piton and M.F.Fay : C.R.Acad.Sci., C266(1968)514.
6. J.Hesse and R.Bucksch : J.Mater.Sci., 5(1970)272.
7. U.Stohrer : Meas.Sci.Technol., 5(1994)440.
8. T.Sakata, Y.Sakai, H.Yoshida, H.Fujii and I.Nishida : J.Less-Comm.Met., 61(1978)301.
9. I.Yamauchi, A.Suganuma and H.Oonaka : Abstracts of the Japan Institute of Metals, (1994.10)428. (in Japanese)
10. I.Yamauchi, A.Suganuma and H.Oonaka : Abstracts of the Japan Institute of Metals, (1995.4)52. (in Japanese)
11. I.A.Nishida : TETSU-TO-HAGANE, 81(1995)N454. (in Japanese)
12. G.Petzow and G.Effenberg : Ternary Alloys, VCH Verlagsgesellschaft mbH, Weinhelm, vol.5,(1992)421.
13. For example, E.A.Brandes : Smithells metals reference book, Sixth Edition, Butterworth & Co (Publishers) Ltd, (1983).
14. For example, T.B.Massalski : Binary Alloy Phase Diagrams, Second Edition, ASM Internatioal, Materials Park, Ohio, (1990).

Rhenium Silicide Thin Films: Structural Analysis of the $ReSi_{2-\delta}$ - Phase

Wolfram Pitschke, Armin Heinrich, Joachim Schumann

Institut für Festkörper- und Werkstofforschung Dresden, PF270016, D-01171 Dresden, Germany
Tel.:+49 351 4659 354, Fax: +49 351 4659 452, e-mail: pitschke@ifw-dresden.de

Abstract

The structure of the semiconducting $ReSi_{2-\delta}$ phase formed in binary Rhenium Silicide thin films has been studied using X-ray powder diffraction. The films were deposited by magnetron cosputtering onto unheated, oxidized Si-wafers. Subsequent annealing results in crystallization of the amorphous films. By means of Rietveld analysis the unit cell dimensions and the atomic occupation factors of the crystalline phases have been determined. After annaeling the film at T=973K a $ReSi_{2-\delta}$-phase phase was formed the chemical composition of which has been determined to be $ReSi_{1,55}$. Temperature enhancement gave rise to increase the occupation factors of Si resulting in an chemical composition of $ReSi_{1,78}$ at T=1073K. This phase crystallizes with primitive space group P1 and a=0.3138nm, b=0.3118nm, c=0.7688nm and α=89,83°.

Introduction

Among a large variety of transition metal silicides, most of which reveal a metallic behaviour, those silicides which possess semiconducting properties occupy a special place. They have been considered as promising materials for Si-based optoelectronic devices [1] and interesting thermo-electric materials [2].
Within the Re-Si system $ReSi_{2-\delta}$ is a narrow-gap semiconductor, the forbidden gap of which was found to be 0.12 eV [3]. The exact stoichiometry and the crystal structure of $ReSi_{2-\delta}$ has been discussed contradictory in the literature with $0 \leq \delta \leq 0.25$ and tetragonal, orthorhombic and primitive unit cell respectively. In 1941 Wallbaum [4] reported that the structure of this phase was of the $MoSi_2$ type, i.e. space group I4/mmm (tetragonal) with lattice parameters a = 0.3131 nm and c = 0.7676 nm and the atomic positions given in table 1 and illustrated in fig. 1.

	x	y	z	occ.
Re	0	0	0	1
Si	0	0	0.333	1 / 0.8 (Jorda)

Table 1: Atomic positions and occupation numbers of $ReSi_2$ given by Wallbaum [4] and Jorda at al. [5].

Jorda et al. [5] indicated a tetragonal unit cell with a = 0.3132 nm and c = 0.7681 nm but an occupation number of Si of 0.8, i.e. the stoichiometry of the rhenium disilicide is $ReSi_{1,8}$.
Sigrist et al. [6] found an orthorhombic space group (Immm) with a=0.3128nm, b=0.3144nm, c=0.7677nm and the same atom positions and occupation number as given by Wallbaum.
Gottlieb et al. [7] investigated the structure of the $ReSi_{2-\delta}$ phase by means of single crystal X-ray diffractometry and found an breakdown of the orthorhombic symmetry and transition to the primitive space group P1 as a result of uncomplete occupation of Si positions and hence caused marginal deviations of the atomic coordinates, which are given in table 2 (see fig. 2 for the illustration). They determined lattice parameters of a = 0.3138 nm, b = 0.3120 nm , c = 0.7670 nm, and α=89,90°.

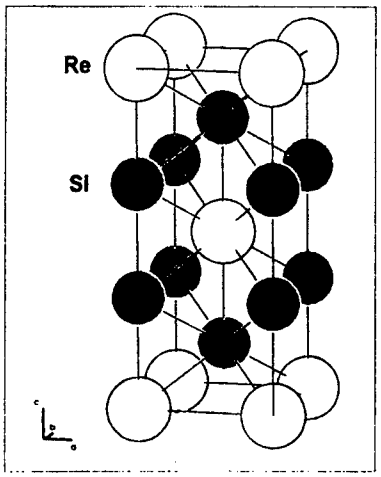


Fig.1: Crystal structure of tetragonal $ReSi_2$

	x	y	z	occ.
Re1	0	0	0	1
Re2	0.5082(9)	0.501(1)	0.5181(3)	1
Si1	0.511(4)	0.529(4)	0.870(2)	1
Si2	-0.034(4)	0.031(4)	0.669(2)	1
Si3	-0.044(6)	-0.027(7)	0.342(2)	0.75
Si4	0.512(6)	0.459(6)	0.190(2)	0.75

Table 2: Atomic positions and occupation numbers of $ReSi_{1,75}$ (space group P1) given by Gottlieb et al. [7].

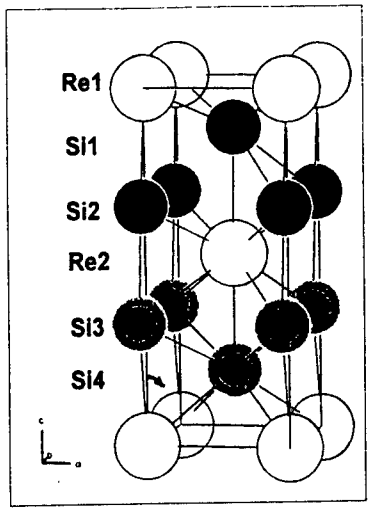


Fig.2:
Crystal structure of monoclinic $ReSi_{1,75}$

Knowledge of the exact crystal structure of $ReSi_{2-\delta}$ is necessary in order to understand its semiconducting transport properties. Assuming an $ReSi_2$ stoichiometry the compound has an odd electron number apparent contradictory with the semiconducting behaviour as follows from band structutre calculations by several autors [8,9]. Henceforward the assumption of lattice defects such as grain boundaries was necessary [10]. Gottlieb et al. could solve this inconsistencies providing a stoichiometry of $ReSi_{1,75}$ with even number of electrons in the formula unit of single crystals.
It's the aim of this paper to determine the crystal structure of the polycrystalline $ReSi_{2-\delta}$ - phase formed in binary $ReSi_x$ thin films.

Method

The structure of the Rhenium Silicide thin films was analysed by means of X-ray diffraction and following Rietveld refinement. The Rietveld method [11] refines a crystal structure by comparing the measured diffraction pattern with that calculated from a known crystal structure.
The scattered intensity of a polycrystalline sample is given by

$$(1) \qquad y_{ci} = sL_K|F_K|^2\phi(2\Theta_i - 2\Theta_K)P_K + y_{bi},$$

where s is the scale factor, K represents the Miller indices, hkl, for a Bragg reflection, L_k contains the Lorentz, polarization, and multiplicity factors, 2Θ is the Bragg angle, P_K is the preferred orientation function, F_K is the structure factor for the Kth Bragg reflection, and y_{bi} is the background intensity at the ith step (see [12] and for the application of the method to thin films [13]). The structure factor F_K is given by

$$(2) \qquad F_K = \sum_j N_j f_j \exp\left[2\pi i\left(hx_j + ky_j + lz_j\right)\right]\exp\left[-M_j\right]$$

where h, k, and l are the Miller indices, x_j, y_j, and z_j are the position parameters, f_j are the atomic scattering factors of the jth atom in the unit cell, M_j is the isotropic temperature factor, and N_j is the site occupancy multiplier for the jth atom site.
A least-squares refinement is used to optimize the structure parameters. The weighted R pattern value

$$(3) \qquad R_{wp}^2 = \frac{\sum_i w_i\left(y_{oi} - y_{ci}\right)^2}{\left(\sum_i w_i y_{oi}^2\right)}$$

is used as an indicator for the estimation of the quality of the refinement, whose limit, for purely statistical fluctuations, is for N observations and P parameters

$$(4) \qquad R_{exp}^2 = \frac{\left(N - P\right)}{\left(\sum_i w_i y_{oi}^2\right)},$$

where $w_i = 1/y_o$ is the weighting factor).
The method allows a quantitative phase analysis without the use of standards, on the assumption that the phases being refined account 100% of the specimen, via the following relation [14]

$$(5) \qquad W_p = \frac{s_p\left(ZMV\right)_p}{\sum_{i=1}^{N} s_i\left(ZMV\right)_i},$$

where W is th weight fraction, p is the value of i for a particular phase among the N phases present, s is the refined scale factor, ZM is the weight of the unit cell in atomic weight units, and V is the volume of the unit cell.

Experimental

Sample Preparation

The films were deposited by magnetron co-sputtering from pure component targets onto unheated Si-wafers with intermediate 1μm thick SiO_2 layer in order to prevent a reaction of the film with the substrate. The film thickness measured by means of a Dectac stylus profilometer was 140 nm.
The composition analysis of the film was carried out by Rutherford backscattering spectroscopy (RBS) and energy dispersive X-ray analysis (EDXS) to be $ReSi_{1.75}$ within an accuracy of ±1at%.
In the as-deposited state the structure of the film was amorphous. Phase formation was achieved by subsequent heat treatment at T = 973 K, 1023 K, and 1073 K respectively under reducing atmosphere.
X-ray photoelectron spectroscopy (XPS) has been applied to investigate contaminations of the surface with Oxygen, Carbon, and Nitrogen. A Si-O(N) layer with a thickness of 3 nm was identified at the surface of the annealed layers.

XRD Measurements

X-ray diffraction patterns were recorded by means of a Philips X'Pert PW3050 (Θ-Θ) diffractometer with programable divergence slit and double detector arm for the selective use of Bragg-Brentano or parallel beam secondary

optics using CoKα radiation (40kV, 40mA). Grazing incidence geometry with an angle of incident X-radiation with the sample surface of Ω=1°=constant was applied to record the patterns of all the annealed samples. Additionally Bragg-Brentano patterns were recorded of the annealed at T=1073K layer in order to verify the results of Rietveld analysis. The patterns were recorded in the range of diffraction angle 2Θ between 20° and 140° with a step size of 0.03° and a counting time of 20 s per step.

Results

Figure 1 shows the resulting diffraction patterns recorded in grazing incidence geometry. In table 3 the identified phases are summerized. The annealed at T=973K layer produces the reflections of $ReSi_{2-\delta}$ major phase embedded in residual amorphous phase. The existence of the latter follows from the characteristic broad peak at about 51,0°(2Θ). Annealing at T=1023K and 1073K has caused additional formation of Re the amount of which increases with increasing annealing temperature. In the same manner the amount of amorphous phase decreases. However, as follows from the Rietveld analysis the residual amorphous phase is not disappeared yet after annealing the layer at T=1073K. A crystalline Si phase could not be detected at all the investigated samples.

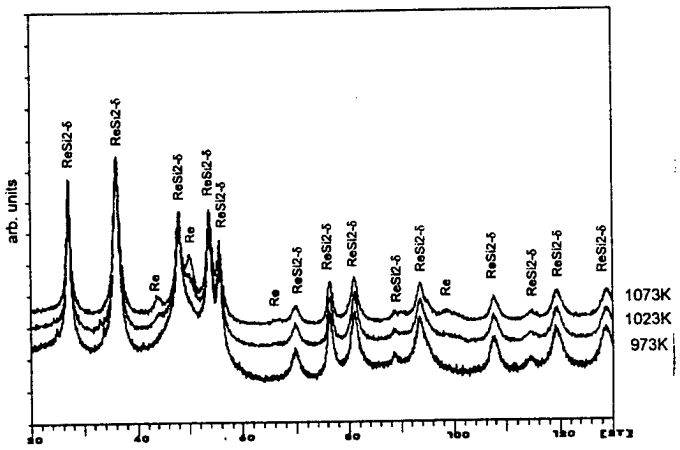


Fig. 3: X-ray diffraction patterns of a $ReSi_{1.75}$ thin film deposited on an oxidized Si-Wafer and subsequent annealed at T=973K, 1023K and 1073K. The patterns were recorded with grazing incidence geometry using CoKα radiation.

temperature	973 K	1023 K	1073 K
amorphous phase	X	X	X
$ReSi_{2-\delta}$	X	X	X
Re		X	X
Si	not detectable	not detectable	not detectable

Table 3: Results of qualitative phase analysis by means of XRD.

In order to clear up the unit cell dimensions of the $ReSi_{2-\delta}$ phase the Rietveld method was applied to the annealed at T=1073K layer using the orthorhombic [6] and the monoclinic unit cell [7] with fixed atomic positions as structure model. In the Rietveld procedure lattice parameters, background parameters, scaling factor, sample displacement and reflection profile parameters were refined.

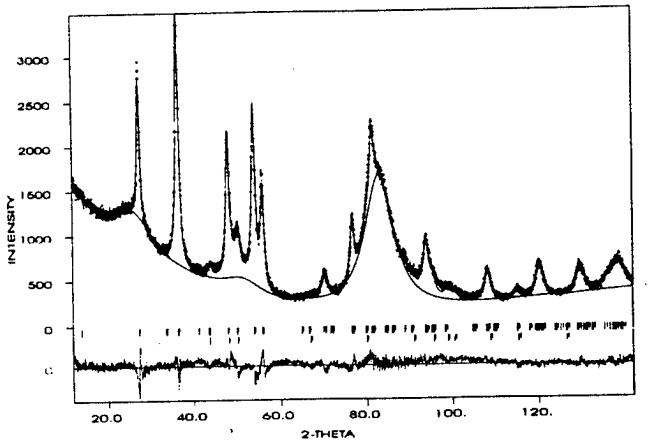


Fig. 4: Final Rietveld plot of the annealed at T=1073K $ReSi_{1.75}$ thin film. The upper trace illustrates the oserved data as crosses, while the calculated pattern is shown by a solid line. Additionally the background function is given describing contributions from the Si-wafer, the SiO_2 intermediate layer and the residual amorphous phase also. The lower trace is a plot of the difference, observed minus calculated intensities. The vertical markers show positions calculated for Bragg reflections.

In Fig. 4 the final Rietveld plot of the diffraction pattern recorded in Bragg Brentano geometry calculated on the basis of Gottliebs model is given. The background was refined using a 4th order polynomial in 2Θ . In addition three broad peaks were refined in the background function caused by the SiO_2 intermediate layer (2Θ=25,5°), by the residual amorphous phase (2Θ=51,0°), and by the Si-wafer (2Θ=82,64°). In table 4 the resulting R-values are given in dependence on the used unit cell and the stoichiometry of $ReSi_{2-\delta}$.

space group	stoichiometry	R_{wp}	R_{exp}	S
Immm (orthorhombic)	$ReSi_2$	7,60	3,60	2,11
P1 (monoclinic)	$ReSi_2$	6,29	3,60	1,75
P1 (monoclinic)	$ReSi_{1.78}$	6,19	3,60	1,72

Table 4: Final R-values of the Rietveld refinement of the $ReSi_{1.75}$ pattern after annealing at T=1073K.

The best agreement between observed and calculated intensities was observed with monoclinic unit cell and a refined stoichiometrie of the $ReSi_{2-\delta}$ - phase of $ReSi_{1.78}$ in accordance with Gottliebs results of single crystal structure. On the basis of this unit cell the diffraction patterns recorded

with grazing incidence geometry were refined yielding the lattice parameters and occupation numbers of Si_3 and Si_4 atoms given in table 5.

temperature / K	973	1023	1073
a / nm	0,3142(1)	0,3138(1)	0,3138(1)
b / nm	0,3120(1)	0,3121(1)	0,3118(1)
c / nm	0,7689(1)	0,7684(1)	0,7688(1)
α / °	89,89(4)	89,97(3)	89,83(3)
$N_{Si3/4}$	0,55(4)	0,78(3)	0,78(3)
stoichiometry of $ReSi_{2-\delta}$	$ReSi_{1,55}$	$ReSi_{1,78}$	$ReSi_{1,78}$

Table 5: Lattice parameters and occupation numbers of Si3/Si4 position as derived from Rietveld refinement on the basis on a monoclinic unit cell of $ReSi_{2-\delta}$ - phase.

The stoichiometry of $ReSi_{2-\delta}$ in the annealed at T=973K layer was determined to be $ReSi_{1,55}$, that means the phase formation process was not finished yet. However, lattice parameters do not differ and agree with the given one by Gottlieb et al. with the exception of the c-axis which was determined to be 0.002nm greater.
The phase content of the annealed at T=1073 K layer was analysed quantitatively. With the constraint that the sum of detectable crystalline phases amounts to 100at% the Rieveld analysis gives 82at% $ReSi_{1,78}$ and 18at% Re. The additional content of an amorphous phase could not be quantified by this method. Using the known stoichiometry of the layer and assuming constant stoichiometry of residual amorphous phase it follows a phase composition of crystalline phases of 62at%$ReSi_{1,78}$ + 13at%Re + 24at%Si , that is 82wt%$ReSi_{1,78}$ +14wt%Re + 4wt%Si. Calculating the diffraction pattern on the basis of this weight fractions it was shown that a weight fraction of 4wt% of Si lies below the detection limit of the X-ray diffraction method as a result of the low atomic scattering factor of Si in comparison with Re and $ReSi_{1,78}$.

Discussion

Rietveld analysis of both the X-ray diffraction patterns of the annaeled at T = 1073K layer recorded with Bragg-Brentano and with grazing incidence geometry provides evidence the $ReSi_{2-\delta}$ - phase to crystallize with $\delta = 0.22$ and primitive unit cell given by Gottlieb et al. [4]. Additionally to the $ReSi_{1,78}$ major phase Re and residual amorphous phase were identified by the X-ray diffraction method. The Si phase could not be proofed to be formed because of its weight fraction below the detection limit.
After annealing the film at a temperature of T=973K the phase formation process of the $ReSi_{2-\delta}$ was not finished yet resulting in additional vacancies of the Si_3 and of the Si_4 atom positions. The stoichiometry of $ReSi_{2-\delta}$ was determined to be $ReSi_{1,55}$. Lattice parameters of the primitive unit cell did not differ and agree with the given one by Gottlieb et al. with the exception of the c axis which was determined to be 0.002nm greater.

The crystallographic results resolve the contradiction between the odd number of electrons in $ReSi_2$ and the experimentally observed semiconducting behaviour. Further investigations of the crystallographic structure of doped $ReSi_x$ thin films are in progress in order to clarify the position of doping atoms possibly arranged at the vacant Si - positions.

Acknowledgement

The authors thank M. Mäder (Forschungszentrum Rossendorf) for the RBS measurements, I. Bächer (IFW Dresden) for the EDXS measurements, and R. Reiche (IFW Dresden) for the XPS measurements. This work was supported by the Deutsche Forschungsgemeinschaft (DFG) under contract no Pi 282/1-1.

References

[1] S.P. Murarka, Silicides for VLSI Applications (Academic Presss, Orlando, FL, 1983).

[2] C.B. Vining, Proc. of the IXth Int. Conf. on Thermo-electr. (1990) 249.

[3] R.G. Long, M.C. Bost, and J.E. Mahan, Thin Solid Films **162** (1988)29.

[4] H.J.Wallbaum, Z. Metallkd. **33** (1941)378.

[5] J.L.Jorda, M.Ishikawa, and J.Muller, J. Less-Common Met. **85** (1982)27.

[6] T. Siegrist, F. Hulliger, and G. Travaglini, J. Less-Common Met. 92 (1983)119.

[7] U. Gottlieb, B. Lambert-Andron, F. Nava, M. Affronte, O. Laborde, A. Rouault, and R. Madar, J.Appl. Phys. **78** (1995) 3902.

[8] B.K. Bhattacharyya, D.M. Bylander, L. Kleinman, Phys. Rev. B**33** (1986)3947.

[9] S. Itho, Mater. Sci. Eng. B**6** (1990)37.

[10] L.M. Chapnik, phys. stat. sol.A**58** (1080) K193.

[11] H.M. Rietveld, J. Appl. Cryst., **2** (1969) 65.

[12] R.A.Young,Ed., The Rietveld Method (New York: Oxford University Press Inc., 1993).

[13] W. Pitschke, Materials Science Forum **228-231** (1996) 171.

[14] R.J. Hill and C.J. Howard, J. Appl. Cryst. **20** (1987) 467.

Preparation of Iridium Silicide Thin Films by Means of Electron Beam Evaporation

R. Kurt, W. Pitschke, A. Heinrich, J. Schumann, and K. Wetzig

Institut für Festkörper- und Werkstofforschung Dresden, PF 270016, D-01171 Dresden, Germany
Tel.:+49 351 4659 354, Fax: +49 351 4659 452, E-mail: r.kurt@ifw-dresden.de

Abstract

Iridium Silicide thin films were prepared by means of electron beam evaporation. The deposition process was monitored by measuring the deposition rates using quartz-crystal oscillators and the temperature at the rear of the substrate. The film composition was determined by means of energy dispersive X-ray analysis (EDX). It changes systematically as a result of the geometric arrangement of the evaporators and of the substrate permitting the preparation of layers with continually varied range of stoichiometry during one deposition experiment. The structure of the layers becomes amorphous when the substrates temperature becomes lower than 373 K during deposition process. The impurity concentration of the layers was determined by means of mass spectrometry to be less than 600 at.-ppm which is about 2 orders of magnitude less than that of layers deposited by means of magnetron sputtering.

Introduction

In the field of thermoelectric materials, the semiconducting transition metal silicides are a group with promising potential of applications in Si-based devices because of the compatibility of preparation technology [1]. Within the Ir-Si system Ir_3Si_5 is a wide-gap semiconductor. The optical gap of it was determined to be 1,56 eV [2], that means doped with a further transition metal iridium silicides may be suitable for the use at high temperatures [3]. In [4] and [5] results of the structure and thermoelectric properties of Ir_xSi_{1-x} thin films prepared by means of magnetron-cosputtering have been reported. The structure of the as-deposited films has been amorphous. Subsequent annealing causes start of crystallization at a temperature of T=960 K and formation of Ir_3Si_5 and Ir_3Si_4 at Ir-enriched, respectively, Ir_3Si_5 and $IrSi_3$ at Si-enriched samples in agreement with the phase diagram [6]. Additionally, a metastable phase was found to exist in a small range of temperature from 960 K up to 1100 K and at film compositions of $0.3 < x < 0.4$. Measurements of the electrical resistivity in low temperature range [7] gave activation energies of about 0.08 eV for layers with Si-concentrations of 64 at.%, which is a typical value for a transition metal impurity state in a semiconductor.

The investigation of intrinsic transport properties and of the influence of dopants requires the dramatic reduction of the impurity concentration which is limited in the magnetron sputtering process by the use of a sputtering gas (argon) partially incorporated into the film. In order to overcome this problem a deposition chamber for the preparation of doped Ir_xSi_{1-x} thin films by means of electron beam evaporation was realized and tested. In this paper we report for first time about properties of undoped binary Iridium Silicide thin films prepared by means of electron beam evaporation in dependence on the deposition parameters.

Experimental results

The deposition system consists of a chamber of 50 cm in diameter equipped with sample manipulator, load lock station, two electron beam evaporators for the major components Ir and Si and a Knudsen cell for thermal effusion of a dopant element. Above the sources in vertical direction there are placed quartz-crystal oscillators (QCO) for the measurement of deposition rates. In Figure 1 the geometric arrangement of the substrate with respect to the evaporator cells is given. Polished corning glass plates with dimensions of 200 mm × 400 mm were used as substrates. The chamber can be evacuated to ultra high vacuum conditions using an ion-getter pump. The control units permit an automatic as well as a manual processing of the layer deposition controlling the power of the cells.

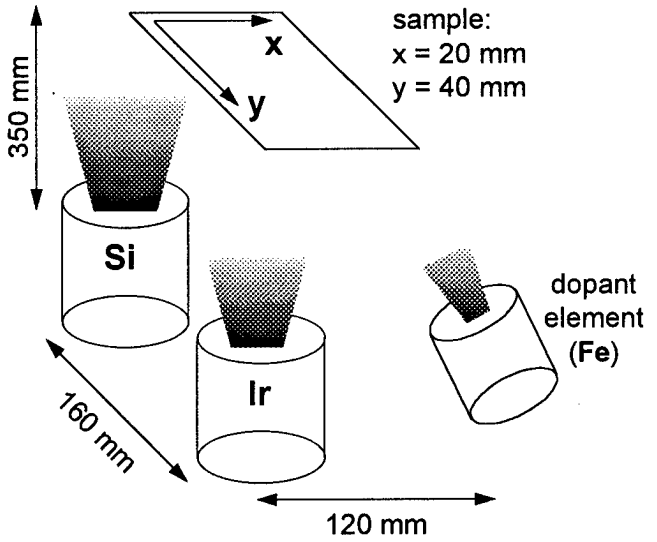


Fig. 1: Schematic view over the set-up for film preparation.

For the test of the preparation unit binary Iridium Silicide thin films were prepared by codeposition from high purity component targets (99,99%) onto inert corning glass. In Table 1 power of sources, processing time, quantities observed by QCO, resulting layer thicknesses determined by a tracing stylus profilometer, and Si-concentrations of three typical films are given.

Tab. 1: Deposition and film parameters. The chemical composition varies systematically over the sample.

				quartz-crystal oscillator (QCO)					tracing stylus	Si-concen tration
sample	Ir-power / kW	Si-power / kW	time / min	Ir-thickn. / nm	Si-thickn. / nm	Ir-rate / nm/min	Si-rate / nm/min	thick. ratio Si/Ir	average thickness / nm	observed by EDX / at.%
1	2.72	1.36	15	1.1	50.5	0.07	3.37	46	65	93.5-96
2	1.95	1.31	22	12.0	73.6	0.55	3.35	6.1	75	64-72
3	2.14	1.24	25	21.2	53.5	0.84	2.15	2.5	66	39-48

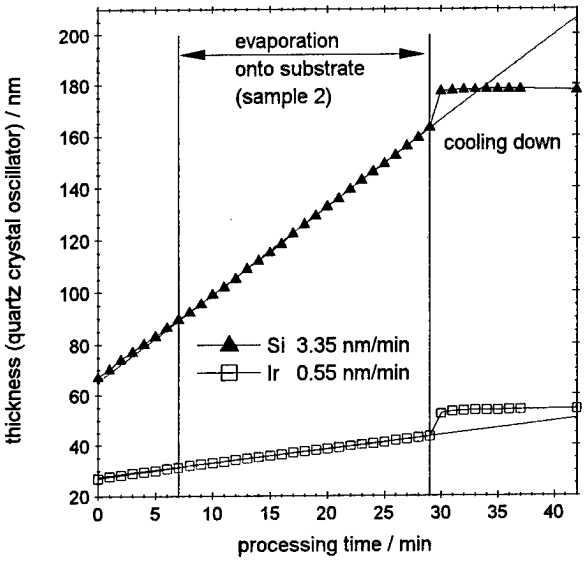


Fig. 2: Recorded thickness deposited on the QCO as a function of time. The ratio of Ir-/ Si-rates can be used as a sensitive parameter to adjust the chemical composition of the films.

In Figure 2 the film thicknesses monitored by QCO during the deposition process of sample 2 are given as a function of processing time. The operational principle of crystal-oscillators first explored by Sauerbrey [8] is given in [9]. A thin crystal wafer is contacted on its two surfaces and makes part of an oscillator circuit. The ac-field induces thickness-shear oscillations in the crystal whose resonance frequency is inversely proportional to the wafer thickness. Mass loading effects in addition of an increment to the thickness and results in change of resonance frequency. The temperature coefficient of frequency (TCF) of the quartz is related to the elastic constants and has positive and negative terms with respect to the natural crystal axes. Usually the crystals are cut into a direction, where the TCF terms compensate each other. However measurements of Phelps [10] have shown that TCF increases at a temperature of T>380 K resulting in an error during thickness determination in dependence on the temperature. Hence the step rise in thickness at t=29 min (see Fig. 2) can be explained by the temperature decrease caused by shut down the evaporator cells.
Recording the thickness measurements was started after optimization of preparation parameters. In order to obtain stable conditions the shutter between substrate holder and evaporation sources was opened after a waiting time of t=7min. Fig. 2 clearly reveals the constant deposition rates of the two evaporators due to the linearity in the given plot. Hence these parameters are suitable for a sensitive deposition monitoring.
After calibration the ratio of Ir/Si-rates can be used for adjustment of chemical composition of the deposited layers.

Generally the resulting film thickness condensed onto the substrate is not given by numerical addition of the silicon and iridium thicknesses. Since the measured quantity of a QCO is the accumulated mass of deposit, conversion into film thickness requires knowledge of the material's density. The latter is usually lower for films than for bulk materials but is not known exactly. Furthermore, the locations of the sensor devices and of the substrate with respect to the source are different, therefore a comparison of the readings observed by quartz crystal oscillators with independently measured film thicknesses on the substrates are necessary.
Hence, the film bordering line originated from substrate holding device shielding from vapour was analysed ex-situ by tracing stylus instrument measuring perpendicular to this line. The evaluation of the height profile along the tracing length of 750 µm using constant force mode (30 mN) only succeeds by background levelling. The latter is necessary due to substrate curvature which is non-linear as a general rule. Measurements were done five times in order to reduce the statistical error. In that way the thickness distribution given in Fig. 3 was investigated as a function of location on the sample relatively to the evaporation sources.

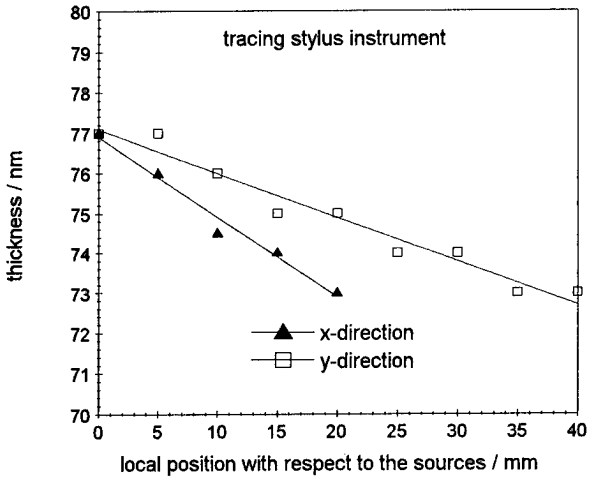


Fig. 3: Thickness distribution in dependence on the deposition arrangement.

The maximum of layer thickness was observed near the source with the highest evaporation rate which was the silicon evaporator in this case. In the x-direction between the two sources a continuous thickness gradient of about 1.1% per 1 cm was observed whereas perpendicular to that in y-direction a higher slope of 2.0% per cm was found. For sample 2 the average film thickness was observed to be 13% less than the value determined by QCO (see also Tab. 1). These deviations are caused by the arrangement factor and materials density, which could not be determined exactly. The films surface roughness was observed to be less than 5 nm, which is acceptable to use in devices.

Microprobe analysis (EDX) was carried out in order to determine the chemical composition. For this purpose several films were simultaneously deposited on glassy carbon substrates arranged on the edge of the sample holder. The Si-concentration profiles of various samples were measured and the ranges of values in the direction between the two evaporation sources are given in Tab. 1. Linear dependence on the local position with respect to the evaporators were observed showing maximal Si-concentrations on that side where the Si-evaporator was situated. For further investigations of the thermoelectric behaviour the range between 60 and 70 at.% Si is of interest. In this range a concentration gradient of about 8 at.% Si was detected. Cutting the sample into stripes perpendicular to the gradient we are able to prepare layers of 3-5 mm width with continually varied range of stoichiometry during one deposition experiment. Deviations of the Si/Ir-ratio in x-direction were not observed within the margin of error.

The temperature in the chamber during the evaporation process was measured using a thermocouple fixed at the rear of the sample holder. The temperature increases proportional with the evaporation time. For sample 2 a slope of temperature versus time of about 2.5 K/min was observed. This was caused by the heat radiation originated from the evaporation sources.
All as-deposited films were analysed by means of the X-ray diffraction method using gracing incidence geometry [11]. Sputtered films have been amorphous in the as-deposited state, because the temperature of the films during the sputtering process is lower than 350 K in general. Using electron beam deposition a few samples have shown small amounts of crystalline phases. The upper diffraction pattern in Fig. 4 shows additionally to the diffuse peaks some sharp reflections caused by the IrSi monosilicide structure. Samples characterised by lower maximum temperature of T<373 K have shown completely amorphous structure (lower curve in Fig. 4). In order to make the results of sputtered films and electron beam evaporated films comparable and to exclude an influence of crystallized non-stoichiometric phases on the phase formation process as well as on the thermoelectric behaviour the temperature controlling was used to prevent a crystallization during the preparation treatment.

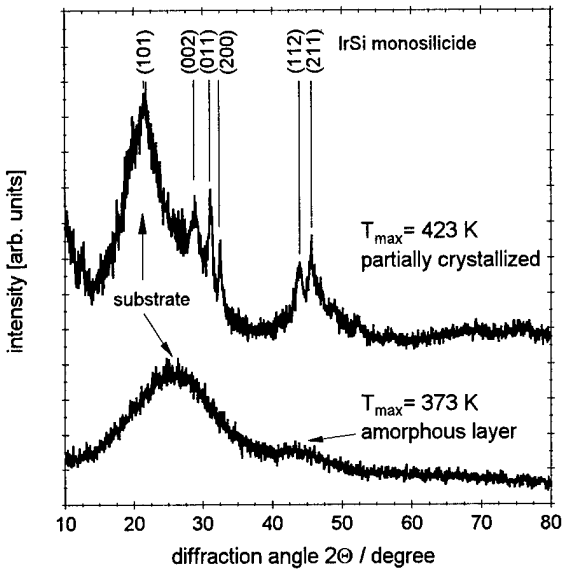


Fig. 4: X-ray diffraction patterns of samples deposited during various temperatures. (CuKα-radiation, angle of incident X-rays with sample surface Ω = 4° = const.)

A spark source mass spectrometer MS 7 was used to carry out ex-situ chemical survey analysis for impurity elements in order to check the effectivity of the UHV-preparation process in comparison with the sputtering process. In Ref. [12] an universal highly sensitive method was described available for examination of thin films simultaneously for all elements of the periodic table. For the spark source mass spectrometry (SSMS) analysis within RF single spark source, a fine probe Ta-electrode is positioned opposite the plane shaped sample electrode which contains the microvolume that is to be vaporized and ionized by discharge. Limits of detection of about 30 at.-ppm are due to the dimension of the area that can be scanned by discharge, which is about 1 cm^2, for the exposure of one mass spectrum [13]. Table 2 shows the observed impurity concentrations for typical species. Ir and Si as well as Ta are not given due to the error in determination of main components concentration and additionally contributions of Si from the substrate and of Ta from the electrode. Corresponding values of investigated sputtered films and films deposited by electron beam evaporation clearly differ from each other. The accuracy of single values is within a range of factor 3. The large amount of Ar incorporated in the sputtered film is unequivocal. The corresponding value for the UHV-deposited film can also be explained by the existence of Ca-atoms due to interference phenomena with the Ar isotope in mass spectrometry. Generally a suppression of the impurity level was achieved.

Tab. 2: SSMS-data of impurity elements

		concentration / at.%	
element	isotope	sputtered film	UHV deposited
Al	27	3.8	0.05
K	39	0.05	< 0.002
Ar / (Ca)	40	3.7	0.06
Ti	48	0.006	0.01
Cr	52	0.07	0.005
Fe	56, 57	0.5	< 0.01
Co	59	0.01	0.007
Ni	60	2.6	0.01
Cu	63	0.01	0.01
Mo	98	0.01	0.006
Ag	107, 109	0.3	0.004

Conclusions and preview

A deposition chamber was realized which permits the preparation of doped clean Ir-Si thin films. The composition can be varied in the range of interest by controlling the evaporation process with in-situ thickness and temperature monitoring. The geometric arrangement causes gradients of thickness and concentration over the sample size. Hence thermoelectric transport properties can be studied systematically in dependence on chemical composition of the films. Using UHV-preparation conditions the impurity level was reduced to an order, which meets the requirements for further studies of the intrinsic properties.

Acknowledgements

The investigation was supported by the Deutsche Forschungsgemeinschaft (DFG) under contract No. Pi 282/1-1. We thank I. Bächer for microprobe analysis, V. Hoffmann for mass spectrometric measurements, and U. Hartmann for technical assistance.

References

[1] C.B. Vining, Proc. IX Conf. Thermoel.,Pasadena, Calif. Inst. Techn. (1990) 249.

[2] J. Schumann, D. Elefant, C. Gladun, A. Heinrich, W. Pitschke, H. Lange, W. Henrion, and R. Grötzschel, phys. stat. sol (a) **145** (1994) 429.

[3] C.E. Allevato and C.B. Vining, Proc. 28th Int. Energy Conv. Eng. Conf., Washington, DC, Aqm. Chem. Soc. (1993) 239.

[4] R. Kurt, W. Pitschke, A. Heinrich, J. Schumann, J. Thomas, K. Wetzig, and A. Burkov, Thin Solid Films (1997) in the press.

[5] R. Kurt, W. Pitschke, A. Heinrich, and K. Wetzig, Materials Science Forum (1997) in the press.

[6] C.E. Allevato and C.B. Vining, J. of Alloys and Compounds **200** (1993) 90.

[7] W. Pitschke, R. Kurt, A. Heinrich, J. Schumann, J. Thomas, and M. Mäder, Proc. XV Int. Conf. Thermoel., Pasadena, Calif. Inst. Techn. (1996) 499.

[8] G. Sauerbrey, Phys. Verhandl., **8** (1957) 113.

[9] Maissel, Glang „Handbook of Thin Film Technology" McGRAW-HILL bock com., New York (1970) I-107

[10] F.P. Phelps, Proc. 11th Ann. Symp. Frequency Control, Fost Moumouth (1957) 256.

[11] T.C. Huang, Advances in X-Ray Analysis **33** (1990) 91.

[12] V. Liebich and H. Mai, Advances in Mass Spectrometry, **6** (1974) 655.

[13] V.I. Derzhiev, G.I. Ramendik, V. Liebich, H. Mai, Int. Journal of Mass Spectrometry and Ion Physics, **32** (1980) 345.

Ageing Properties of Thermally Sprayed Iron Disilicide

K. Schackenberg, E. Müller, J. Schilz, W. A. Kaysser
Deutsche Forschungsanstalt für Luft- und Raumfahrt (DLR), Institut für Werkstoff-Forschung, D-51140 Köln, Germany
E-mail: karsten.schackenberg@dlr.de, Fax: (+49) 2203 696480
G. Langer, E. Lugscheider
Rhein.-Westf. Techn. Hochschule Aachen, Lehr- und Forschungsbereich Werkstoffwissenschaften, D-52056 Aachen, Germany

Abstract
The relation between the microstructure and the thermal and thermoelectric behaviour of thermally sprayed p- and n-type $FeSi_2$ has been investigated in order to identify process variations and operation conditions to obtain good thermoelectric properties. For comparison of materials from different spraying techniques hot pressed standard material is considered. The investigation of the correlation between the thermal and electrical properties on the one hand and microstructural features on the other hand is based on the measurements of transport properties (Seebeck coefficient, thermal diffusivity, electrical conductivity) combined with imaging and analytical methods (REM, EDX, XRD). These are recorded during a step-wise annealing throughout an overall period of 500 h.

Introduction
Thermoelectric energy converters made of iron disilicide offer economically attractive solutions for supplying electronic control and display elements in systems independent of mains connection [1][2]. They become favourable especially when an essential heat flux occurs over a large temperature difference. For an expansion of economically advantageous applications, automation-compatible methods for low-cost production of thermoelectric generators with a high output rate are required. Here thermal spray forming may be promising.

Thermal spraying as consolidation process
Thermal spraying is a well established processing method in surface technology for producing thermal barriers and corrosion- or wear-resistant coatings. From the variety of thermal spray processes we have chosen plasma spraying (PS) for the consolidation of $FeSi_2$ [3][4].
The starting material consists of gas atomised $FeSi_2$-powders doped with Al (2.5 at% of Si is replaced by Al) for p-type or with Co (5 at% of Fe is replaced by Co) for n-type, respectively. The powders have particle sizes of about 70 µm in diameter. An elementary analysis of the powder gave an oxygen content of about 0.09 wt% [5]. These powders are blown into a plasma jet which is produced by an electric discharge in a gas flow. Due to the thermal expansion (temperatures up to 20000 K) the plasma gains a velocity up to 1000 m/s. Therefore the powder particles are heated and partially molten by the hot plasma, accelerated onto a substrate reaching velocities up to 400 m/s, and finally form a bulk material with a flake-like structure.

In order to aggravate oxidation, the processing was carried out under low pressure (vacuum, VPS) or with a gas shielding around the plasma jet (shrouded, SPS). Nevertheless an oxygen content of 0.20 wt% in SPS- and 0.59 wt% in VPS-material was found. Hot pressing as a standard consolidation process delivers only an oxygen content of about 0.17 wt% [5].



Figure 1: REM-micrograph of SPS-$FeSi_2$:Al, as sprayed: The light globulitic areas consist of ε-FeSi.

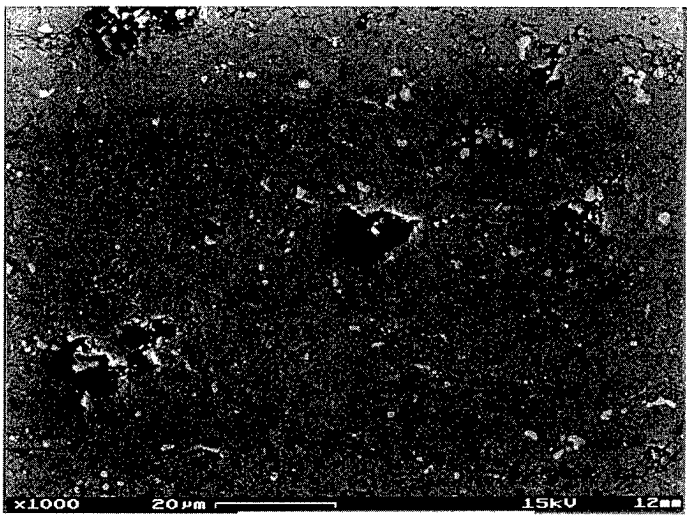


Figure 2: REM-micrograph of VPS-$FeSi_2$:Co, as sprayed: Large dark areas correspond to pores, dark lines to oxides.

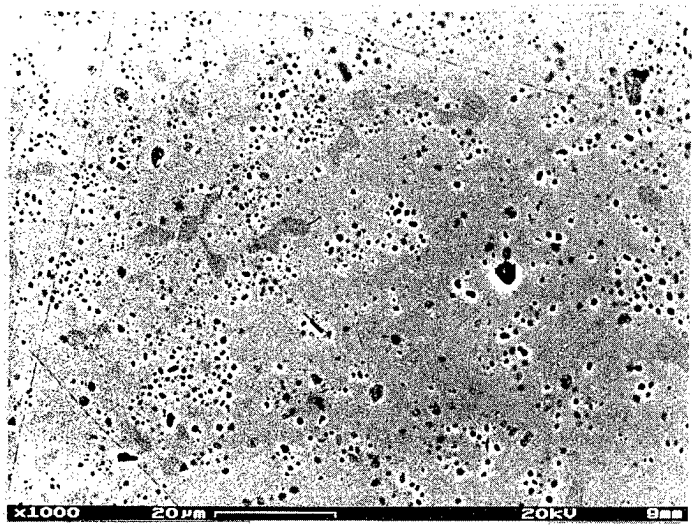


Figure 3: REM-micrograph of HUP-$FeSi_2$:Al, tempered for 100 h at 800 °C. The microstructure shows a lower porosity and a higher homogeneity than thermally sprayed material.

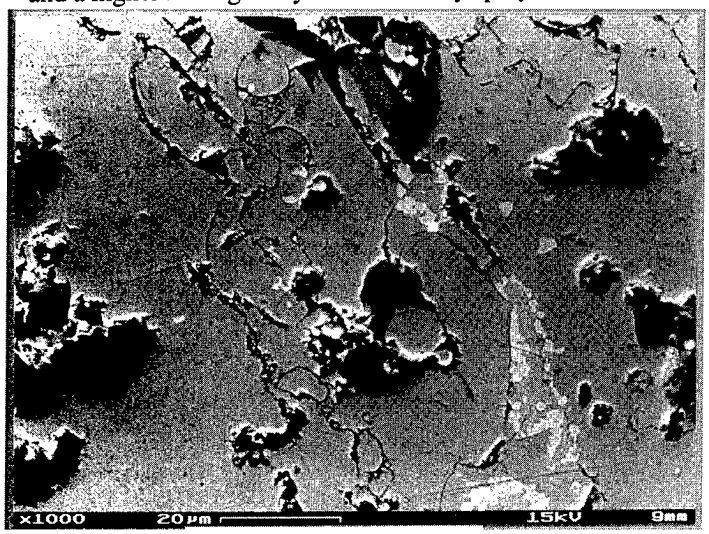


Figure 4: REM-micrograph of SPS-$FeSi_2$:Al, tempered for 100 h at 800 °C. The microstructural curing typical for a sintering process influences the thermoelectric properties as well.

Microstructure of thermally sprayed $FeSi_2$

Hot pressed $FeSi_2$ is very homogenous (figure 3) and has only a low porosity of about 2% [5]. In contrast to that, on a REM-micrograph of the thermally sprayed samples separate particles - so called splats - can be distinguished. The figures 1, 2 and 4 show cross sections perpendicular to the spraying direction of as-sprayed material: SPS provides a distinctly coarser structure than VPS. An interactive image analysis gives a porosity of 5% for SPS and 3% for VPS [5].

The different phases seen in the REM-micrographs have been identified by an EDX analysis: grey areas consist of $FeSi_2$, the smaller, lighter and globulitic phases consist of ε-FeSi. Dark grey areas are pores, separations or oxides. The ε-FeSi and oxide phases reduce the suitability for thermoelectric applications either because of the formation of electrical short circuits (decreasing the Seebeck coefficient S) or by the deterioration of the electrical conductivity σ.

Thermoelectric characterisation of β-$FeSi_2$

Immediately after spraying, $FeSi_2$ exists partially in the metallic high-temperature α-phase (stable above 950 °C) [6] which possesses only very poor thermoelectric properties. In order to convert most of the material into the desired semiconducting β-phase, a short term annealing of about 2 h at 800 °C is required. The thermoelectric properties of plasma sprayed samples treated this way are compared with those of uniaxially hot pressed (HUP) samples as a standard in table 1.

Processing	SPS		VPS	
Doping	Al (p)	Co (n)	Al (p)	Co (n)
Seebeck coeff. S ($\%_{HUP}$)	100	97	122	103
Electr. cond. σ ($\%_{HUP}$)	59	39	47	69
Therm. diff. D_{th} ($\%_{HUP}$)	42	28	78	85
Mass density ρ ($\%_{HUP}$)	93	97	96	99

Table 1: Comparison of the transport properties and mass density of thermally sprayed and uniaxially hot pressed $FeSi_2$ after 2 h annealing at 800 °C, normalised by taking the corresponding values of the HUP-samples as 100%.

The heat capacity of the samples is not given in table 1, as it didn't vary in a significant way with the consolidation processing. In accordance with the higher porosity of the thermally sprayed samples (visible from the REM-micrographs) we found their mass density also decreased by about 5%.

Except for the Al-doped VPS-material the Seebeck coefficient is almost unaffected by the consolidation process. The increase of S for the p-type VPS-sample indicates a loss of electronically effective doping. However, by means of Hall measurements we didn't find any significant difference in the charge carrier density of Al-doped VPS-samples (as sprayed) and HUP-samples (2 h annealed at 800 °C) made of identical powders. From further investigations we expect to see, whether dopant diffusion shows an effect on the Hall coefficient during short and long term annealing at 800 °C.

The electrical conductivity σ and the thermal diffusivity D_{th} of plasma sprayed samples are much smaller than the corresponding values for hot pressed material. This is due to the different microstructure which shows a higher porosity and numerous separations between the splats in plasma sprayed samples. Nevertheless it is remarkable that for VPS the thermal diffusivity of both p- and n-type samples reduces to about 80% of the HUP values, whereas the electrical conductivity lowers to about $50\%_{HUP}$ for p-type and $70\%_{HUP}$ for n-type. On the other hand, for SPS the thermal diffusivity D_{th} is more decreased than the electrical conductivity σ. Therefore in the case of SPS the figure of merit $Z = S^2 \sigma / \kappa$ (with thermal conductivity $\kappa = \rho\ c_p\ D_{th}$) is increased to $156\%_{HUP}$ for p-type and to $133\%_{HUP}$ for n-type, respectively. In contrast to that, for the VPS-samples the figure of merit is slightly decreased to $97\%_{HUP}$ for p-type and to $86\%_{HUP}$ for n-type. The stronger deterioration of the electrical conductivity indicates a dopant loss during the VPS-consolidation process, which mainly impairs the electrical conductivity and leaves the thermal conductivity nearly unaffected.

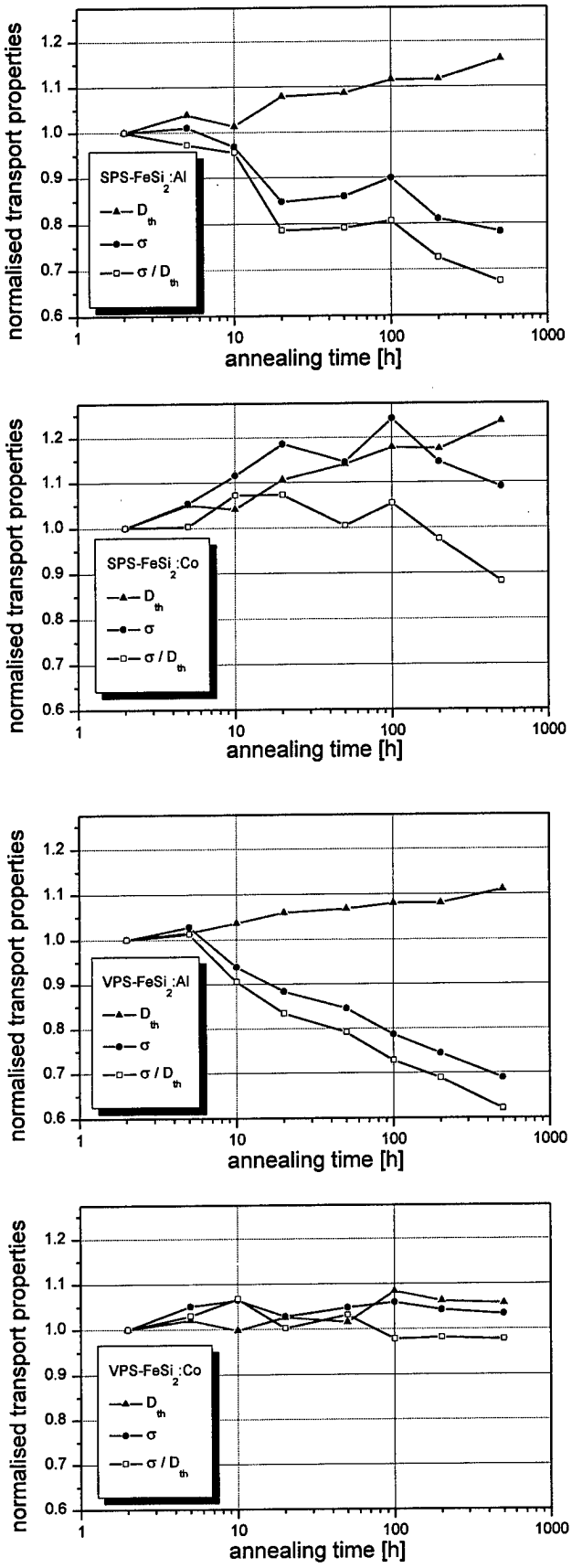


Figure 5: Ageing behaviour of SPS- and VPS-material: Relative change of thermal diffusivity D_{th} and electrical conductivity σ during annealing at 800 °C.

Furthermore the high oxygen content in VPS-samples promotes the formation of oxides as electrically isolating particle boundaries.

Long term annealing

The differences in the thermoelectric performance of materials from the various consolidation processes lead to the question whether a stabilisation of the thermoelectric properties may be achieved by a thermal treatment. The ageing behaviour of the samples tempered at 800 °C for 500 h differs strongly in correspondence with the manufacturing method.

The heat capacity, density and Seebeck coefficient of all samples didn't change in a significant way. Therefore the change of the thermoelectric figure of merit is predominantly determined by the ratio of the electrical conductivity to the thermal diffusivity. For clearness we choose a presentation of the results where the transport properties at 2 h annealing time are taken as 100% and the following annealing steps are normalised according to this value. From the data sets thus resulting from measurements at 100 °C, 200 °C and 300 °C for σ and further up to 800 °C for D_{th}, we finally took the mean curve. The overall annealing behaviour didn't vary significantly for measurements taken at different temperatures.

The ageing behaviour of SPS- and VPS-samples is given in figure 5. The results can be summarised as follows:

1. Hot pressed samples with either Al or Co doping do not change their electrical and thermal conductivities within a limit of about 5%.
2. All samples show an increase in the thermal diffusivity which is typical for a sintering process. The enlargement is only very small in the case of HUP (about 1%) and is most significant in the case of SPS (16% for Al- and 25% for Co-doping); for VPS the change of D_{th} is in between these two limits (about 10%). This behaviour corresponds very well to the different microstructure of the samples: SPS gives the coarsest structure and thus possesses the largest capability for microstructural curing. The curing of microstructural separations can also be observed in the REM-micrographs - compare figures 1 and 4.
3. The change of the electrical conductivity is different for Al and Co doped samples. For Al doping σ generally decreases with progressive annealing. This decrease is smallest for HUP (only less than 5%) and largest for VPS (more than 30%); for Al-SPS the decrease is about 20%. We suggest that the large decrease of σ for VPS can be explained by the high oxygen content in VPS samples which leads to the formation of Al_2O_3 during the annealing process and thus effects a reduction of the charge carrier density. A corresponding increase of the Seebeck coefficient during annealing could not yet be proved.

It is remarkable that for Co-doped SPS the electrical conductivity increases to about 125% at an annealing time of 100 h and afterwards decreases to a 110% level at 500 h. This initial increase of σ corresponds pretty good to the increase of D_{th} which could be well understood as a result of microstructural curing. For an annealing time longer than

100 h the geometrical effect of material curing is apparently overlapped by some process which causes a reduction of the charge carrier density.

4. The thermoelectric properties of the Co-doped VPS-samples are almost as stable as those of the corresponding HUP-samples.

5. Although the figure of merit decreases with progressive annealing according to the ratio σ/D_{th}, its absolute value for SPS after 500 h annealing is still higher than for HUP after a 2 h heat treatment: For p-type SPS-material Z was in the order of $105\%_{HUP,2h}$, for the corresponding n-type material Z even reached $117\%_{HUP,2h}$. There will be further investigations in order to find the asymptotic behaviour of Z.

Correlation between microstructure and activation energy for the α–>β-phase transition

The transition between α- and β-phase is accompanied by an exponential decrease of the thermal diffusivity D_{th} that can be observed in-situ by a laser flash technique. In our investigations we found a delay of up to ½ h preceding the actual phase transition; this delay possibly results from microstructural relaxation and diffusion due to the stoichiometric deviation between α- and β-phase. The slope of the exponential decrease of D_{th} determines the reaction rate. From the temperature dependence of the reaction rate we receive an estimate of the total activation energy for the phase transition by means of an Arrhenius plot. For a Co-doped VPS-sample we find an energy of about 70 kJ/mol, which is only about one third of the corresponding value for SPS-material [7]. This difference indicates that the measured activation energies cannot be explained only by thermodynamical arguments but also by microstructural effects depending on the material's processing.

Short term annealing at high temperature

From a technological point of view it is interesting to know whether a fast microstructural curing without an impairment of the thermoelectric properties can be achieved by an annealing process at a high temperature above 1000 °C. In this sense we studied the behaviour of a Co-doped VPS-sample.

We started with a 20 h annealing at about 800 °C and received an increase in the thermal and the electrical conductivity in the order of about 10%. After that we kept the sample for 2 h at 1000 °C and subsequently for 2 h at 800 °C. The entailed transition to the α-phase and back to the β-phase caused a further small increase of the thermal diffusivity and even a doubling of the electrical conductivity. The latter could be explained by a reduction of β-$FeSi_2$ in favour of iron monosilicide (ε-FeSi), which we observed in an XRD measurement.

This change of the phase constitution could not be reversed even by a long term annealing of more than 400 h at 800 °C. The large share of metallic ε-FeSi leads to a massive deterioration of the Seebeck coefficient and thus strongly reduces the suitability of the material for thermoelectric applications.

Conclusions

Thermally sprayed iron disilicide possesses clearly different thermoelectric properties than the uniaxially hot pressed standard material. Both the thermal diffusivity and the electrical conductivity are essentially reduced for thermally sprayed samples because of the disturbed microstructure on the one hand and an oxygen incorporation during the consolidation process on the other hand.

A fast curing of the microstructure by a high temperature treatment above 1000 °C leads to an irreversible decrease of $FeSi_2$ in favour of FeSi and thus provides material unsuitable for thermoelectric applications.

The long term annealing at 800 °C causes a microstructural curing and thus an increase of the thermal diffusivity. Furthermore we observe a decrease of the electrical conductivity for all Al-doped samples - HUP included. To obtain p-type material with a better stability other dopants will be tested - presumably Mn [8]. The Co-doped thermally sprayed samples are almost as stable as the hot pressed standard material.

References

[1] E. Müller, J. Schilz: Entwicklungsarbeiten in der DLR zur Anwendung thermoelektrischer Energiewandler, 3. FAT-Seminar, Wiesbaden 1996

[2] W. Roth, J. Schilz, A. Steinhüser: Thermoelektrische Wandler als Zusatzstromerzeuger, Forschungsverbund Sonnenenergie „Themen 96/97"

[3] Ch. Schmidt, R. W. Smith, M. Barsoum: Feasibility Study about the Applicability of Plasma Spray to produce $FeSi_2$ Thermoelectric Devices, Drexel University, Philadelphia, 1995

[4] J. Schilz, M. Riffel, R. Mathesius, G. Schiller, R. Henne, R. W. Smith: Plasma spray forming as a novel production method for thermoelectric materials, Proc. XV ICT '96, Pasadena, CA USA, 1996

[5] E. Lugscheider, H. Jungklaus, R. Mathesius, G. Langer, J. Schilz: Processing of thermoelectric material by thermal spraying, Euromat '97

[6] J.-P. Piton, M.-F. Fay: Sur les changements de phases des alliages de compositions voisines de $FeSi_2$, C. R. Acad. Sc. Paris, Serie C, 1968

[7] M. Riffel, J. Schilz, E. Paulussen, S. Sous, F. Dourado, W. Kaysser, R. Mathesius: Preliminary results on plasma sprayed $FeSi_2$, Proc. of the 2nd European Workshop on Thermoelectrics (ETS2), Nancy, 1995

[8] I. A. Nishida: Fabrications and Thermoelectric Properties of Semiconducting Iron Disilicides, Iron and Alloy Vol. 81 (1995), No. 10

Effect of Powder Treatment by Mechanofusion Process on Thermoelectric Properties of $FeSi_2$ System

Takuji KITA, Kiyoshi NOGI, Hiroshi NAGAI, Mizuki KOHNO

Osaka University, Japan

Abstract

The thermoelectric properties of hot-pressed $Fe_{0.91}Mn_{0.09}Si_2$ (mean diameter:D_m=5-10μm) were measured with changing the powder treatment. In order to improve the thermal conductivity and the electrical conductivity, carbon (0, 1 and 2wt%, D_m=0.02-0.3μm) was added and the mechanofusion process was used. The mechanofusion process can produce composite powders with high shear stress and compressive force, allowing a more homogenious compact to be fabricated. As a result, the thermal conductivity was remarkably improved in this system. EPMA analyses showed that extremely fine particles of carbon were dispersed along grain boundaries without aggregation. However, the electrical conductivity decreased in this case. This is probably because the electrical resistivity of carbon black is very high. However, when graphite are added, the MF process would be very effective to improve the figure of merit, because the process can increase the grain boundary with additives and improves the electrical conductivity.

1. Introduction

Thermoelectric materials have been recently investigated in various systems. In particular, the iron-disilicide system is an attractive system, because the system can be used in the air at a high temperature owing to the superior oxidation resistance and the harmless and cheap raw materials [1-5].

In the iron-disilicide system, β-$FeSi_2$ phase has thermoelectric properties, but α-$FeSi_2$ and ε-FeSi phases are metallic and they don't have thermoelectric properties [6,7].

β-$FeSi_2$ is generally produced by a powder metallurgy method because it is very brittle and the method can decrease the thermal conductivity of the material [8-10]. In the sintered material , the state of grain boundaries is an important factor because it affects the electrical and thermal conduction. When adding fine particles, it is necessary to avoid their aggregations and disperse them homogeneously.

The mechanofusion(MF) process is known as a dry powder-coating-process [11-13]. Fig.1 shows a schematic diagram of the MF system used in this study. The system consists of a motionless shaft and a circular chamber rotating at a high speed.

While the chamber is rotating, the powder is compressed into the clearance of the inner piece and receives complicated forces in various states, such as compression, attrition, shearing, and rolling [14]. After the compression, the processed powder is dispersed by the scraper. These actions are repeated during the chamber rotations. Consequently, the surface state of particles is modified [15-19].

In this study, using this mechanism, composite powders were produced so that the grain boundary state of the sintered compacts can be changed. The effect of the powder treatment by the MF treatment on thermoelectric properties is investigated.

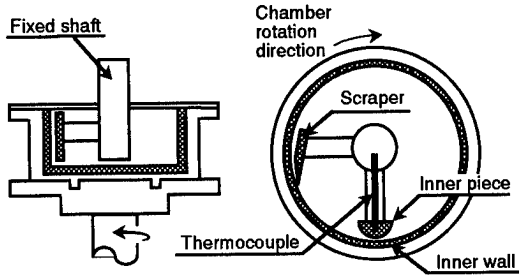


Fig.1 Schematic diagram of mechanofusion system (The gray part is made of SiC, and the other part is made of stainless steal.)

2. Experimental procedure

Fe, Si and Mn were weighed in the ratio of $Fe_{0.91}Mn_{0.09}Si_2$ composition, and melted in a high-frequency induction furnace. The produced alloy were crushed in an alumina mortar, and then, they were ground to powders(mean diameter=5-8μm) with a planetary ball mill.

Carbon fine particles(mean diameter=0.02-0.3μm) were added in the ratio of $x$wt%(x=0, 1, 2) and mixed in an alumina mortar for about 30min. This procedure prevents the fine particles from being blown up by the centrifugal force and from being accumulated on the arms of the shaft at the early stage of the MF process.

These powders were treated by the MF process for 1hr at 900rpm. The inner wall, the inner piece and the scraper were made of SiC. The clearance between the inner piece and the inner wall was about 2mm, and the clearance between the scraper and the inner wall was about 1mm. The temperature was measured by a thermocouple placed inside the end of the inner piece [20]. Some powders were prepared by just being mixed in an alumina mortar for about 30min, without the MF process.

Each obtained powder was hot-pressed(HP) by 1g with a carbon die under a pressure of 25MPa for one hour at 1173K in a vacuum of 1×10^{-2}Pa. The phases existing in the obtained sintered compacts were determined by XRD and the microstructures of the compacts were observed by SEM.

The thermoelectric power and the resistivity were simultaneously measured with the temperature deference of less than 5K between both ends in the temperature range be-

0-7803-4057-4/97 $10.00 ©1997 IEEE

tween 400 and 1173K in an Ar atmosphere. The thermal conductivity was measured by a laser-pulse method between 300 and 1173K.

3. Results and discussions

Fig.2 shows secondary electron micrographs and C-Kα images of the hot pressed $Fe_{0.91}Mn_{0.09}Si_2$-1wt%C samples. It is found that with the MF treatment:(a)(b), C particles are almost homogeneously dispersed along the grain boundaries and the size of aggregation is smaller than three micrometers. Without the MF treatment:(c)(d), on the other hand, the size of aggregation is much larger.

Fig.3 shows the temperature dependence of the thermal conductivity. As shown in this figure, the addition of carbon only does not decrease the thermal conductivity very much. However, the addition of carbon with the MF process decreases the thermal conductivity significantly.

These results indicates that the phonon scattering mainly occurs at the grain boundaries. The MF treatment restrains the grain growth, increasing the amount of grain boundaries.

The MF process decreased the thermal conductivity extremely even in the 1wt%C sample. However, carbon more than 1wt% didn't reduce the thermal conductivities further. This result indicates that 1wt% carbon is enough to prevent the grain growth when it is well dispersed.

Fig.4 shows the temperature dependence of the electrical resistivity.

Contrary to our expectation, the MF process increased the electrical resistivity though there was no change in the non-carbon sample. A possible reason for these phenomena is that the electrical resistivity of the carbon was higher than that of $FeSi_2$.

Carbon black was used as an additive in this study. Its electrical resistivity is dependent on the production process.

Without the MF treatment, the electrical resistivity did not increase very much in the 1wt%C sample. With the MF treatment, it significantly increased even in 1wt%C sample, and increased further in the 2wt%C sample.

It seems that the dispersion of carbon by the MF process had a bad effect on the electrical resistivity. These results do not contradict the hypothesis that electrical resistivity of the carbon used was too high.

The electrical resistivity of graphite is about one thousand times smaller than the carbon black. Therfore, when graphite is used as an additive, the electrical resistivity might be reduced [21].

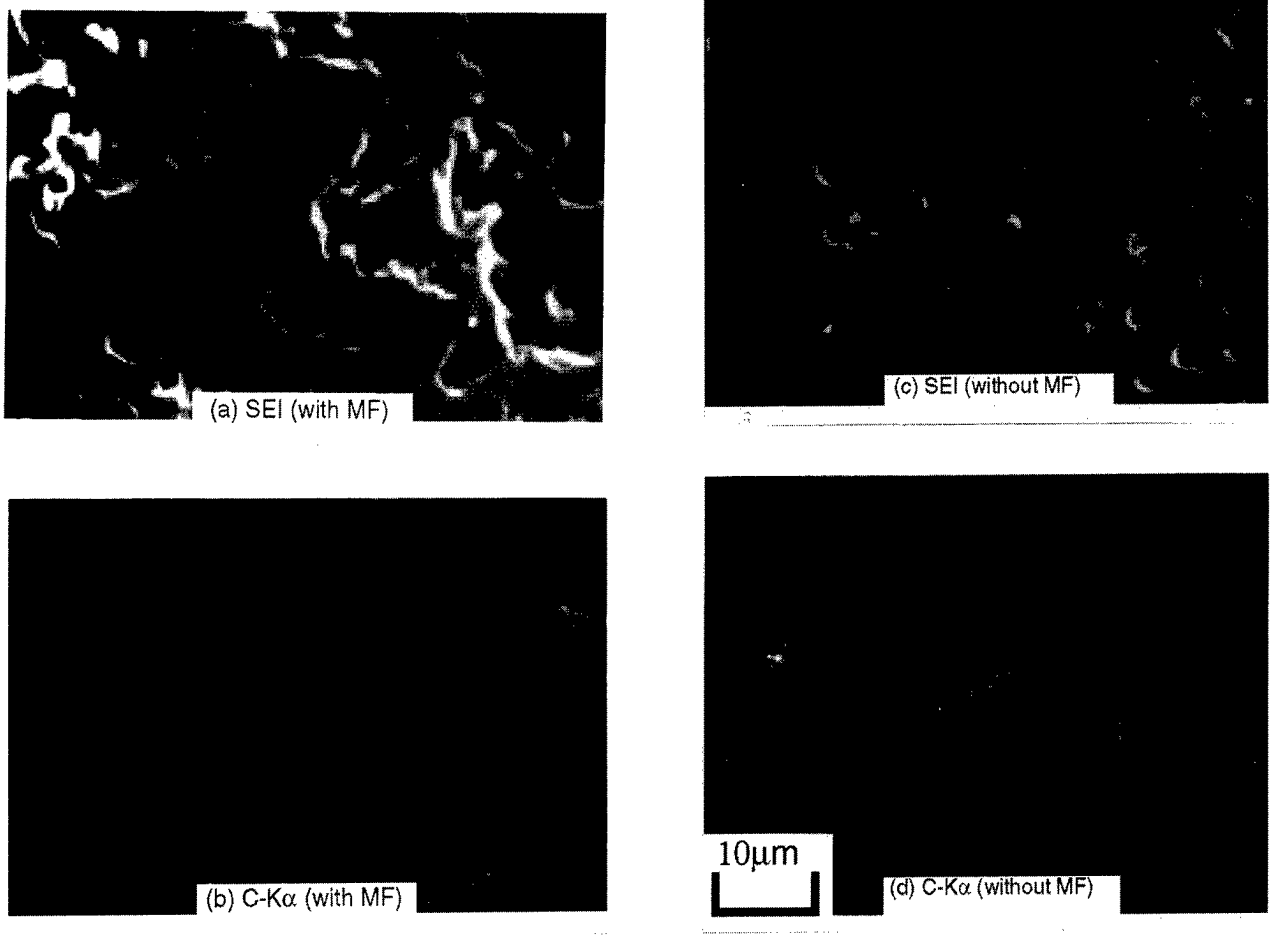


Fig.2 Secondary electron image and X-ray image of C-Kα of sintered $Fe_{0.91}Mn_{0.09}Si_2$-1wt%C.

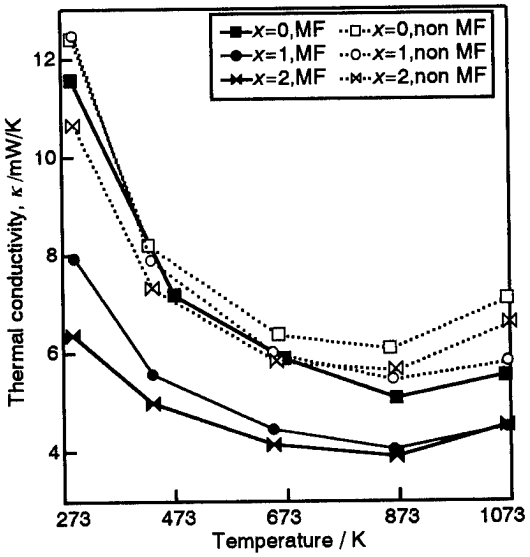


Fig.3 Temperature dependence of thermal conductivity of $Fe_{0.91}Mn_{0.09}Si_2$+$x$wt%C

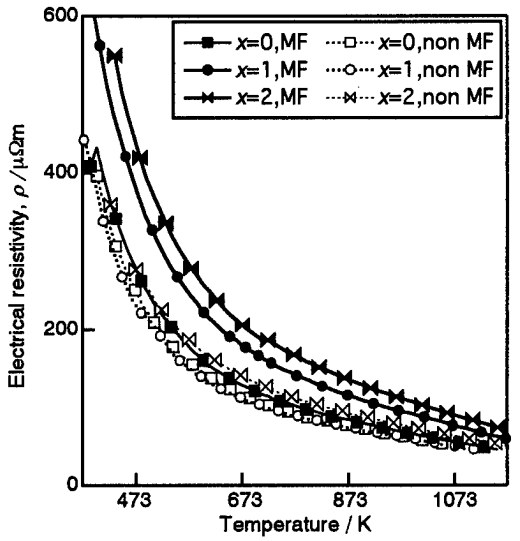


Fig.4 Temperature dependence of electrical resistivity of $Fe_{0.91}Mn_{0.09}Si_2$+$x$wt%C

Fig.5 shows the temperature dependence of the thermoelectric power. The MF process didn't affect the thermoelectric power very much for the carbon added samples, because the amount of added carbon was small.

As shown in Fig.5, the MF process decreased the thermoelectric power of the non-carbon sample. However, the reason of the decrease is still unclear.

Fig.6 shows the temperature dependence of the figure of merit calculated by the following equations.

$$Z=\alpha^2/\rho/\kappa.$$

The figure of merit was not improved by the MF process because the electrical resistivity was increased due to the high resistivity of carbon black.

As a consequence, it was only thermal conductivity that the MF process was able to improve.

However, when graphite are added, the MF process would be very effective to improve the figure of merit, because the process increases the grain boundary with additives and can improve the electrical conductivity.

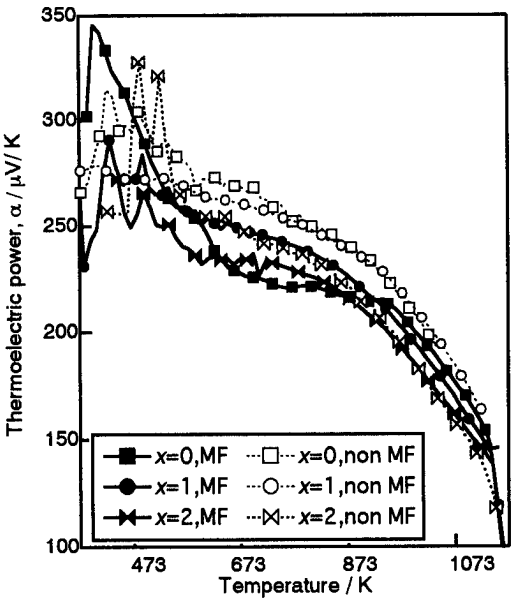


Fig.5 Temperature dependence of thermoelectric power of $Fe_{0.91}Mn_{0.09}Si_2$+$x$wt%C

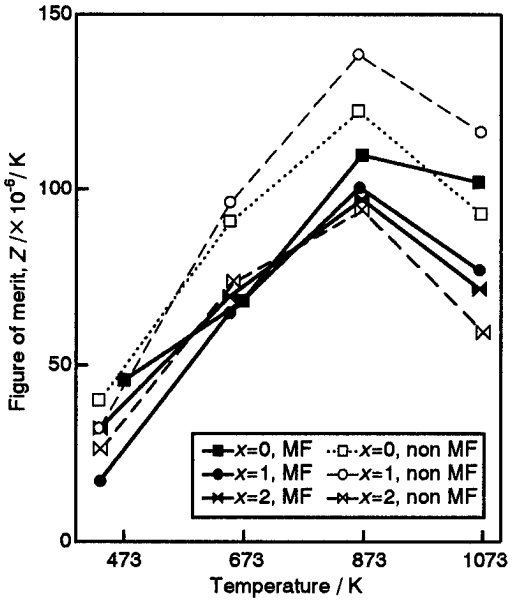


Fig.6 Temperature dependence of firgure of merit of $Fe_{0.91}Mn_{0.09}Si_2$+x wt%C

4. Summary

(1) The mechanofusion process allows carbon particles to be dispersed homogeneously along the grain boundaries of sintered compacts.

(2) The dispersion of an additive by the mechanofusion process restrains the grain growth and decreases the thermal conductivity.

(3) The mechanofusion process was not sble to improve the thermoelectric power and the electrical resistivity because of the high resistivity of carbon black. However, when graphite are added, the MF process would be very effective to improve the figure of merit, because the process increase the grain boundary with additives and improve the electrical conductivity.

5. References

[1] I. Nishida: "Study of Semiconductor-to-Metal Transition in Mn-Doped $FeSi_2$", Phys.Rev., **B7**(1970),2710.

[2] U. Birkholtz and J. Schelm: "Mechanism of electrical conduction in β-$FeSi_2$", Phys. Status Solidi, **27**(1968), 413.

[3] T. Kojima, M. Okamoto and I.Nishida: Proc. 5th Int. Conf. Thermoelectric Energy Conv., March(1984), 56.

[4] H. Nagai: "Effects of mechanical alloying and grinding on the preparation and thermoelectric properties of β-$FeSi_2$", Mat. Trans., JIM, **36**(1995), 365.

[5] M. Komabayashi, K. Hijikata and S. Ido: "Effects of some additives on thermoelectric properties of $FeSi_2$ thin films", Jpn. J. Appl. Phys. **30**(1991),331.

[6] C. R. Acad. Sc. Paris, t.266, **C**(1968), 514.

[7] T. Sakata and I. Nishida: "Thermoelectric properties of semiconducting 3d-transition metal disilicides", Bulletin J. Inst. Met., **15**(1976), 11.

[8] D. M. Rowe and C. M. Bhandari: "Modern Thermoelectrics, Holt", Rinehart & Winston Ltd.,(1983)

[9] S. Shiga, K. Fujimoto, K. Rowiprased, M. Umemoto and I. Okane: "Thermoelectric properties of β-$FeSi_2$ prepared by mechanical alloying", J. Jpn. Powder and Powder Metallurgy, **41**(1994),1308.

[10] J. Yoshino: "Theoretical calculation of thermoelectric figure of merit for sinterd materials", *Keisya Kinou Zairyou Ronbunsyu*(Quarterly of FGM), Jpn,(1994), 223.

[11] Micromeritics Lab., Hosokawa Micron Co.: "Mechanofusion", Nikkan Kogyo Simbun LTD.,(1989)

[12] K. Tanno, T. Yokoyama and K. Urayama: "The production of metal/ceramics composite particles by a mechanofusion process", J. Soc. Powd. Tech., Jpn., **27**(1990),17.

[13] H. Kaga, Y. Taya, I. Shimono and H. Katayama: "Preparation of Al_2O_3/Cu composite particles by vacuum mechanofusion process", J. Jpn. Powder and Powder Metallurgy, **39**(1992), 546.

[14] Tohei Yokoyama, K. Urayama, M.Naito, M. Kato and Toyokazu Yokoyama: "The Angmill mechanofusion system and its applications", KONA, **5**(1987), 59.

[15] M. Naito, A. Kondo, T. Yokoyama: "Applications of comminution techniques for the surface modification of powder materials", ISIJ Int., Vol.33, No.9(1983), 916.

[16] M. Naito: "Powder processing technology to fabricate composite particles by a mechanical method", *Funtai to Kogyo*(Powder Sci. and Eng.), **26**(1994), 31.

[17] K. Tanno, T. Yokoyama, K. Urayama and M. Naito: Prep. Autumn Meeting Soc. Pow. Tech., Jpn., Tokyo,(1988), 97

[18] K. Tanno, K. Urayama and T. Yokoyama: Prep. Autumn Meeting Soc. Pow. Tech., Jpn., Tokyo,(1990), 96

[19] P. R. Mort and R. E. Riman: "Reactive multicomponent powder mixtures prepared by microencapsulation: $Pb(Mg_{1/3}Nb_{2/3})O_3$ synthesis", J. Am. Ceram. Soc., **75**[6](1992),1581.

[20] K.Nogi, M. Naitoh, A. Kondoh, A. Nakahira, K. Niihara, T. Yokoyama: "New method for elucidation of temperature at the interface between particles under mechanical stirring", J. Jpn. Powder and Powder Metallurgy, **43**[3](1996), 396.

[21] K. Saito: "*Mukikagaku Zensyo*(Encyclopedia of Inorganic chemistry) X-2, Boron, Carbon and Germanium", Maruzen, (1965), 253.

Effect of Dispersed Si-phase on Thermoelectric Properties of $FeSi_2$ Prepared by Mechanical Alloying and Sintering

Byoung-Gue Min and Dong-Hi Lee

School of Materials Science and Engineering, Yonsei University, 134 Shinchon-dong Seodaemun-gu Seoul 120-749, Korea,
Tel.: 82-2-361-2834, Fax: 82-2-312-5375, E-mail: metphys@bubble.yonsei.ac.kr

Abstract

While melt-cast $FeSi_2$ requires careful heat-treatment of homogenization and phase transformation to achieve thermoelectric β-phase, the mechanical alloying(M/A) and sintering method is expected to simplify the process. By using the M/A method with elementary Fe and Si coarse powders, very fine powders consisting of FeSi- and Si-phases were obtained. Especially when excess Si was deliberately introduced in the starting materials, the desired microstructure containing finely distributed Si-phase in the matrix of β-$FeSi_2$ was produced by subsequent sintering. The volume fraction of dispersed Si-phase could be controlled within a range of 0.26~0.38 by varying the excess Si content. The shape of the dispersed the Si phase was something like the coral colony of fine finger-shaped protrusions (diameter ≤ 0.5㎛ and length ≤ 3㎛). The size and volume fraction of the Si-phase in the β-$FeSi_2$ matrix was analysed being effective in controlling the thermal conductivity of the sintered mass due to the phonon scattering.

Introduction

Various research efforts have been made to improve the figure of merit by reducing thermal conductivity without any significant losses in the electrical conductivity and thermoelectric power which are directly related to a carrier concentration. Research has shown that the effects of solid solution[1] and second phase dispersion[2] for Bi_2Te_3-based materials, grain refinement[3] and fine particle dispersion[4] for SiGe compounds are all regarded as desirable approaches.

β-$FeSi_2$ was reported to have relatively high thermoelectric properties over a wide range of temperatures from 200 ℃ to 600 ℃ together with good thermal and chemical stability in that temperature range.[5] It also has the merit of low cost of fabrication compared to other high temperature thermoelectrics. According to the phase diagram of a Fe-Si system, several phases are present with changes of composition and temperature, which makes it difficult to obtain pure β-$FeSi_2$ phase material. In reality, a fine eutectoid (mixed) structure consisting of β-$FeSi_2$ and Si phases are formed during the preparation of this compound.[6] The finely dispersed composite of β-$FeSi_2$ and Si phases can hopefully be exploited to improve thermoelectric properties by inducing an effective phonon scattering in the material.[7,8]

β-$FeSi_2$ phase, conventionally produced through several stages, such as melting, casting, powder production, sintering, and subsequently prolonged heat treatments. The recently reported mechanical alloying method (M/A) was found to be suitable for the production of Fe-silicide powders by applying mechanical energy to the mixture of elemental Fe and Si powders.[9,10] Alloyed powders obtained by this technique contained, various phases besides the β-$FeSi_2$ phase. Therefore, it is significant to find optimum sintering conditions which convert effectively non-thermoelectric phases into β-$FeSi_2$ phase, or maintain the β-$FeSi_2$ phase as much as possible. And it is also expected that the variation in initial compositions as well as sintering conditions may be effective in controlling the dispersibility of the fine Si phase in the final microstructures.

By sintering below the stable temperature (937 ℃) of the β-$FeSi_2$ phase in the phase diagram, a sound body of p-type $FeSi_2$ having a high sintered density (≥ 95% of theoretical value) was obtained. In this case, sintering was carried out by the Pressurized-Resistance-Sintering technique; a simultaneous application of high pressure and high density direct current through the die assembly in a vacuum chamber. The detailed procedures are described elsewhere.[11] The sintering temperatures were controlled to find the changes in size of dispersed Si phases in the matrix. Measured thermoelectric properties at high temperatures as well as at room temperature were investigated in conjunction with the microstructural development, such as the size and volume fraction of the dispersoids.

Experimental

M/A was carried out using an alumina attrition mill (volume capacity: 500㎖, impeller rotating speed: 1000rpm) with powder mixtures of elemental Fe(99.9%, 75~150㎛) and Si(>99.99%, <150㎛). The analysis of the powders by this method revealed a final compositions of $(Fe_{0.98}Mn_{0.02})_xSi_2$, in which x is a controlled variable(x= 0.7, 0.8, 0.9 and 1.0). Elemental Mn was doped during the M/A to obtain p-type material. Chemical compositions of the powders (Table 1) were examined by a wet chemical analysis. X-R-D showed

0-7803-4057-4/97 $10.00 ©1997 IEEE

that the powders were a mixture of ε-FeSi and Si phases.

Sintering was performed at temperatures between 760℃ and 850℃ for about 7 minutes under a vacuum atmosphere. It took about two minutes from room temperature to reach the pre-determined sintering temperature, and the isothermal sintering period of time was approximately five minutes. Heat was applied by a high density direct current (≈280Amp) through the graphite die assembly (Ringsdorff, V1364). During the sintering cycle, a relatively low pressure of 20 MPa applied in the heating-up period was switched to a high pressure of 50 MPa as soon as sintering temperature was reached, this was held until cooling-down to room temperature.

Table 1. Chemical compositions and particle size of M/A powders.

composition designation		$(Fe_{0.98}Mn_{0.02})_xSi_2$			
		x = 1.0	x = 0.9	x = 0.8	x = 0.7
chemical composition (at%)	Fe	32.78	30.97	28.41	25.56
	Mn	0.68	0.71	0.74	0.67
	Si	66.54	68.32	70.85	73.77
particle distribution	mean partlcle size(㎛)	1.36	1.60	1.40	1.21
	half-width (㎛)	0.69	0.61	0.78	0.60

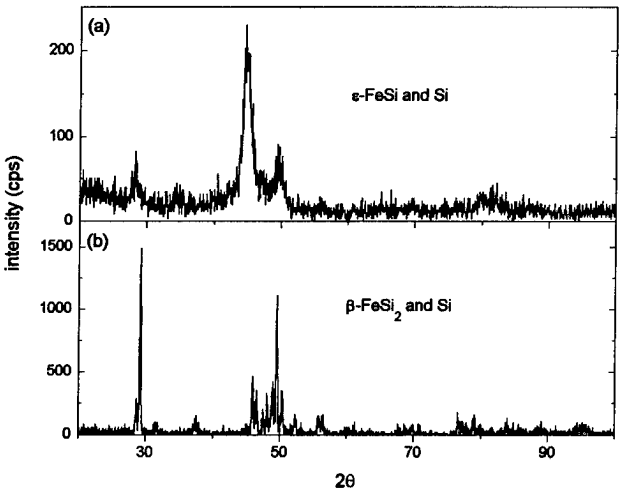


Figure 1. XRD patterns of (a) M/A powders and (b) sintered specimen. [composition : $(Fe_{0.98}Mn_{0.02})_{0.7}Si_2$]

The microstructures of the sintered specimen were examined by SEM, optical microscope and image analyser to evaluate the degree of dispersion (size and average interspacing of dispersed Si phases). Thermoelectric power and electrical conductivity were measured at 500℃ as well as at room temperature, and the values of thermal conductivity were indirectly calculated from the figure of merit obtained by Harman's method. It was confirmed that there were no microstructural changes during the measurement at 500℃ in the sintered specimens. Carrier concentration and Hall mobility were measured at room temperature for the estimation of their effects on thermoelectric properties.

Results and Discussion

Table 1 shows data collected from the analysis of the chemical compositions, the average particle size and the size distribution (half-width of the distribution peak) of powders produced by M/A for 50hrs. No significant deviation in the chemical compositions was observed between the M/A powders and the mixture of starting elemental powders; i. e. the contents of Fe and Si varied by 1% well within experimental-error. Contents of aluminum and carbon, introduced from the alumina ball and the vial during the prolonged period of M/A time, were analysed to be 0.17wt% and 0.01% respectively, which are almost the same levels as the starting materials. The average particle size of a 50hr M/A powder was very small(1.2~1.6㎛) with respect to that of starting powder(≤150㎛). Particle size distribution was fitted with a normal distribution having a half-width of about 0.7㎛. Powders of M/A time shorter than 20hrs consisted of elemental Fe and Si. But X-R-D peaks of the powders became broader with M/A time, which means the powder refinement as well as the lattice distortion of each elements due to the alloying effect. As in Fig. 1(a), it was found that powders M/A-ed for 50hrs or longer consisted of ε-FeSi and Si phase, regardless of composition.

Sintered specimens were very dense (95% of theoretical density) when powders M/A-ed for 50hrs (average particle size ≈1.4㎛) were sintered at 760~850℃ by the aforementioned PRS apparatus. The high density is regarded to be the result of ① M/A induced internal strain in powders and ② heat of formation (ΔH_f = -0.24 kJ/mole) of β-$FeSi_2$ phase from ε-FeSi and Si phases.

Formation of β-$FeSi_2$ phase as well as dispersion of excess Si phase was confirmed by X-R-D (Fig 1 (b)) and TEM selected area diffraction patterns of M/A powders (Photo. 1). Ring patterns of Si phase were overlapped with spot patterns of matrix β-$FeSi_2$ in TEM S.A.D. patterns, which indicate that there were no crystallographic directionality between Si phase and β-$FeSi_2$ matrix.

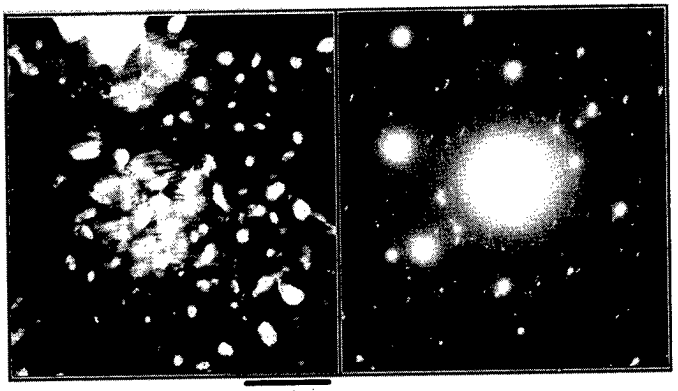


Photo. 1. TEM micrographs and S.A.D. pattern of the specimen sintered at 820℃. [composition : $(Fe_{0.98}Mn_{0.02})_{0.8}Si_2$]

Microstructures of the PRS specimens of various compositions were shown in Photo. 2. The spotty bright regions in the dark matrix of β-$FeSi_2$ phase correspond to Si phases. Selective etching of β-$FeSi_2$ phase showed the remaining Si phase, which consisted of a coral-like-colony of finger-shaped protrusions having aspect ratios of ≥6 (Photo. 3). Diameter and length of the protrusions, which appeared as dispersed phases in 2-d micrographs, varied with sintering temperatures; i.e. the aspect ratios of the protrusions reduced with higher sintering temperature.

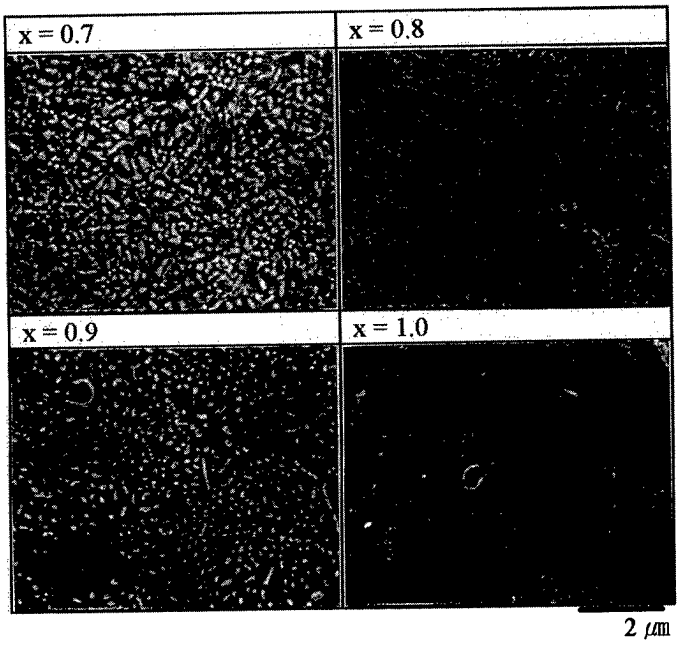


Photo. 2. SEM micrographs of $(Fe_{0.98}Mn_{0.02})_xSi_2$ specimens sintered at 760℃ with varying x (=0.7, 0.8, 0.9 and 1.0).

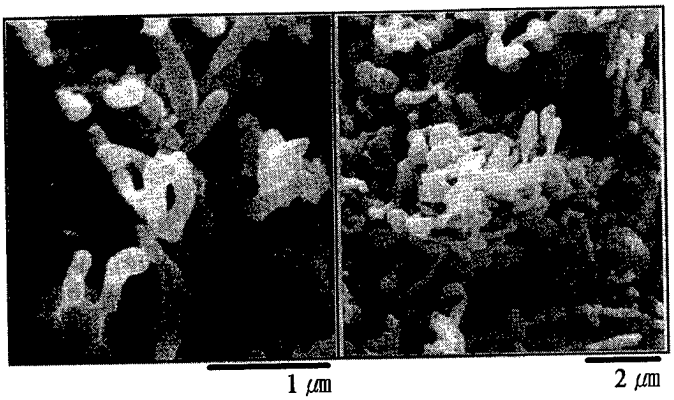


Photo. 3. SEM micrographs showing Si-phases after selective etching of β-$FeSi_2$ phase of the sintered specimen.

Volume fractions of Si phases, analysed by an image analyser, decreased with increment of x in $[(Fe_{0.98}Mn_{0.02})_xSi_2]$, and showed a decreasing tendency with sintering temperature.(Fig. 2)

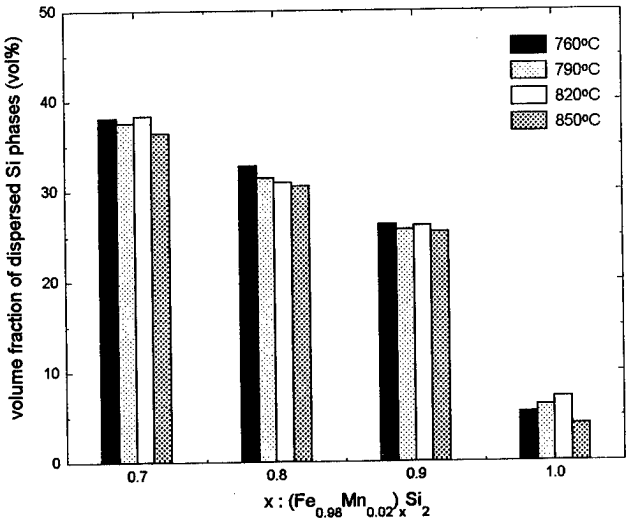


Figure 2. Volume fraction of Si phase in β-$FeSi_2$ matrix v.s. sintering temperatures and compositions.

Fig. 3 shows data on the average size and the interspacing of Si phases in a matrix of β-$FeSi_2$, which were measured by the line intercept method[12] from the micrographs of the specimens sintered at several temperatures. The size of Si phase grew gradually with the increase of sintering temperature, but it was not affected by compositional variation.(Fig. 3(a)) The diameter of Si phases increased from 0.2 to 0.5μm when sintering temperature changed from 760℃ to 850℃, and high sintering temperature and low Si content caused the increment of interspacings between dispersed Si phases.(Fig.

3(b)) Therefore, The volume fraction, size and interspacing of Si phases are controllable by changing conditions of sintering and composition.

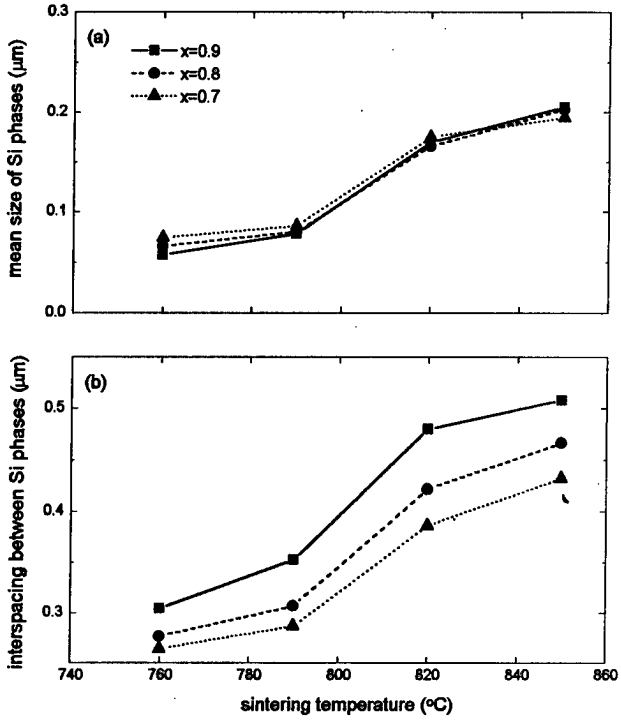


Figure 3. Variations of (a) mean size and (b) interspacing of dispersed Si-phases with sintering temperature.

It is not difficult to imagine that thermoelectric properties of the specimens consisting of β-$FeSi_2$ and fine Si phases would be different from those of ordinary macroscopic composite materials (a mixture of β- $FeSi_2$ and Si phases). If the fine Si phases in a matrix of β-$FeSi_2$ phase have interspacings equivalent to the order of mean free path of carriers or phonons, they could become effective scattering centers.

Variations of Hall measurements (carrier concentration and mobility) with respect to composition and interspacings of Si phases are shown in Fig. 4. Although carrier(holes) concentration did not vary significantly with composition (volume fraction) or interspacings (sintering temperature), the carrier mobility significantly changed with the interspacings. Considering the fact that the mean free path of carriers in β-$FeSi_2$ is the order of 10^2~10^3 Å, the rapid increase of electrical conductivity with interspacings is understandable.

The temperature dependence of electrical conductivity showed an extrinsic behavior in the temperature range from room temperature up to 500 ℃, but changed to intrinsic above 500 ℃, irrespective of compositions and sintering conditions.(Fig. 5)

Fig. 6 shows the data on thermoelectric properties measured at 500 ℃ for specimens of various compositions (volume fraction of dispersed Si phases) and sintered at several temperatures (different interspacings of Si phases).

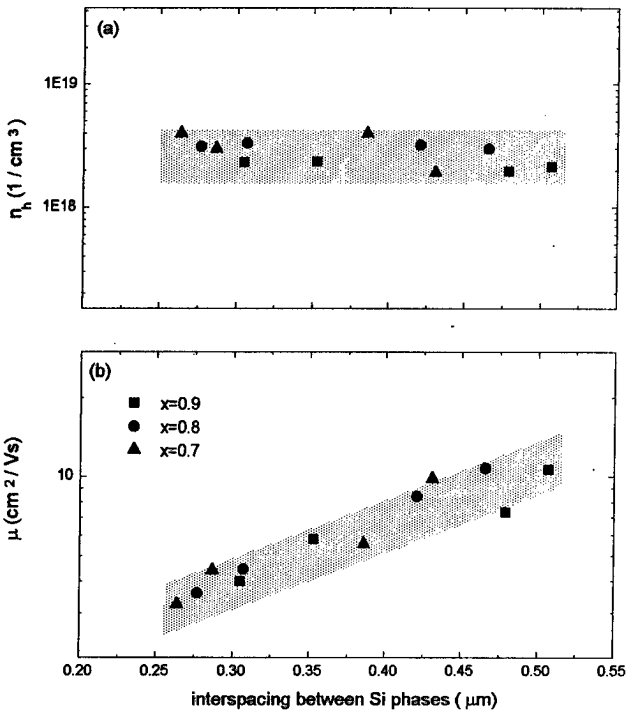


Figure 4. Variations of (a) carrier concentration and (b) mobility as a function of the interspacing between Si phases and the composition.
[x : $(Fe_{0.98}Mn_{0.02})_xSi_2$]

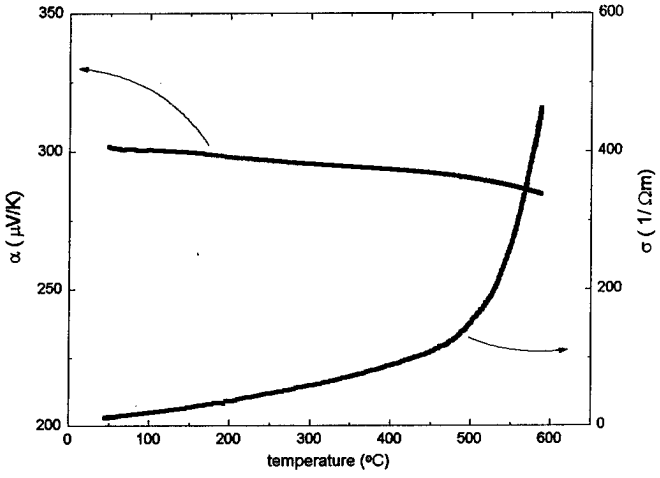


Figure 5. Variations of Seebeck coefficient and electrical conductivity with temperature of the specimen sintered at 820 ℃.
[composition : $(Fe_{0.98}Mn_{0.02})_{0.8}Si_2$]

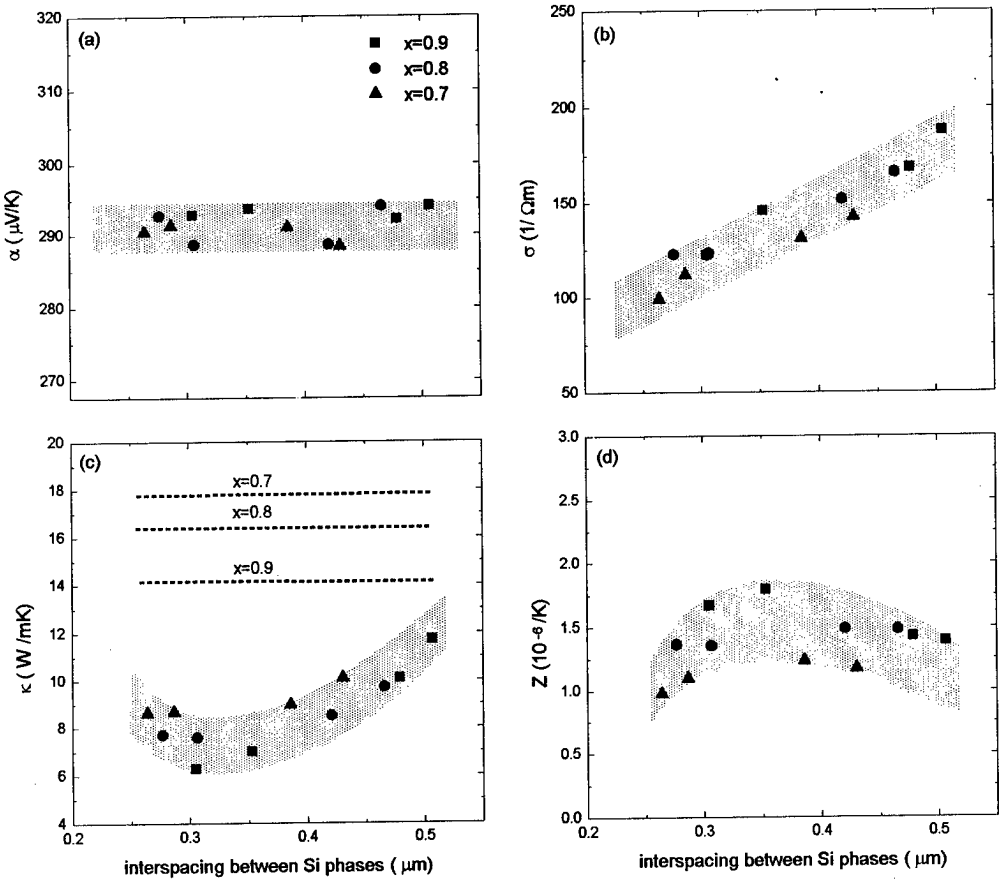


Figure 6. Variations of thermoelectric properties with interspacings of Si phases for the specimens consisting of dispersed fine Si phases in the β-$FeSi_2$ matrix.
(a) Seebeck coefficient (b) Electrical conductivity
(c) Thermal conductivity (d) Figure of merit

Seebeck coefficients measured at 500 ℃ were 285~295 μV /K, and nearly independent of interspacings and compositions. The gradual increment in electrical conductivity with interspacings (sintering temperature) is contrasted with the nearly constant values of Seebeck coefficients for a given composition.

Electrical conductivity varied with composition (volume fraction of Si-phases) and also showed a linear increase with interspacings of Si phases. Recalling Hall measurement data at room temperature,(Fig. 4) this tendency is attributed to increasing carrier mobility.

On the other hand, thermal conductivity increased with interspacings as well as volume fraction of Si-phases.(Fig 6(c)). The variation of thermal conductivity was different from electrical conductivity; i.e. whereas electrical conductivity was linear with interspacings, thermal conductivity showed a higher order relation with the interspacings. If the ordinary composite rule is applicable to the specimen, the conductivities (σ and κ) will be dependent on the composition (volume fraction of Si-phase) only. That implies, the size and interspacings should have no effects on both conductivities as long as the volume fraction of Si-phases is constant. However, as can be seen in Fig. 6, the conductivities (σ and κ) varied with composition as well as the degree of dispersion of Si phases (size and interspacings). The discrepancy between the expectation of the composite rule and the measured values indicates the scattering effect of dispersed Si-phases on the conductivities. The higher order relationship of thermal conductivity with the interspacings especially demonstrates the relative higher scattering of phonons than carriers. This fact can be understood by considering the mean free pathes of carrier (10^2~10^3 Å)and phonons (order of a few μm) as well as the interspacings (0.2~0.5 μm) of Si phases in the specimens.[13]

As expected, the figure of merit has a maximum when plotted with the variation of interspacings. The highest value (1.8×10^{-6}/K) obtained for the specimen having an Si-phase interspacing ≈0.35 μm was stemmed from the different dependency of electrical and thermal conductivities on the Si-phase interspacings. (Remember the Seebeck coefficient is

almost independent of interspacings.) In short, the effectiveness of the scattering of fine Si phases both on electrical and thermal conductivities can be changed if the degree of dispersion(size and interspacing of Si phase in the matrix of the β-$FeSi_2$ phase.) is carefully controlled by conditions of sintering and composition.

Conclusions

In this experiments, Fe-silicide powders of various compositions were prepared by M/A process, and the sintered specimens consisting of dispersed Si phases in a matrix of β-$FeSi_2$ phase were fabricated by PRS technique. The results obtained are as follows;

1. Dense (>95% theoretical density) and sound specimens, consisting of β-$FeSi_2$ and dispersed Si-phases, were obtained when M/A powders of 50 hrs were sintered at temperatures of 760~850 ℃ by the PRS apparatus.
2. The size(0.05~0.2 ㎛) and interspacings(0.2~0.5 ㎛) of the dispersed Si phases in the matrix of β-$FeSi_2$ varied with conditions employed. By adjusting the sintering variables, the degree of dispersion of Si phases(size and interspacings)was controlled.
3. Hall measurements showed that carrier concentration did not vary with composition but the mobility decreased with an increasing amount of Si content(volume fraction of Si phases). Electrical conductivity increased linearly with the interspacings of Si phases, irrespective of the Si-content.
4. Thermal conductivity, however, showed a higher order relationship with the interspacings. Especially it increased rapidly when the interspacings were larger than 0.3 ㎛. Considering the behavior of conductivities(σ and κ), it was concluded that the interspacings were responsible for the relatively high reduction of thermal conductivity due to the phonon scattering effect.

References

[1] A.F. Ioffe, *Semiconductor thermoelements and thermoelectric cooling*, Insforsearch Ltd., London, (1957).

[2] K-W. Jang and D-H. Lee, "Properties of Bi_2Te_3-based thermoelectrics fabricated with porous matrix", Proc. 12th ICT, pp115-120 (1993).

[3] D.W. Rowe and V.S. Shukla, "The effect of grain boundary scattering on the lattice thermal conductivity and thermoelectric conversion efficiency of heavily doped fine grained Si-Ge alloys", J. of Appl. Phys., vol. 52, No. 12, pp7421-7426 (1981).

[4] N.S. Scoville, C.B. Bajgar, J. Rolfe, J-P. Fleurial and J. Vandersande, "Status of p-type SiGe alloys with nano-phase inclusions", Proc. 13th ICT, pp110-114 (1994).

[5] U. Birkholz and J. Schelm, "Mechanism of electrical conduction of β-$FeSi_2$", Phys. Stat. Sol., vol. 27, pp413-425 (1968).

[6] Y-H. Eun, B-G. Min and D-H. Lee, "Transformation behavior of high temperature thermoelectric $FeSi_2$", Korean J. Electron Microscopy, vol. 25, No. 3, pp90-98 (1995).

[7] B-G. Min, Y-H. Eun and D-H. Lee, "Effect of additives on the phase transformation and thermoelectric properties of $FeSi_2$", Proc. 3rd IUMRS-ICA, pp185-191 (1995).

[8] B-G. Min, K-W. Jang and D-H. Lee, "Preparation and characterization of thermoelectric β-$FeSi_2$ phase dispersed with Si", Proc. 15th ICT, pp67-70 (1996).

[9] H. Nagai, "Effects of mechanical alloying and grinding on the preparation and thermoelectric properties of β-$FeSi_2$ (overview)", Materials Transactions, JIM, vol. 36, No. 2, pp363-372 (1995).

[10] M. Umemoto, "Prepartaion of thermoelectric b-$FeSi_2$ doped with Al and Mn by mechanical alloying (overview)", Materials Transactions, JIM, vol. 36, No. 2, pp373-383 (1995).

[11] G-S. Choi, J-Y. Kim and D-H. Lee, "Resistance/spark sintering under pressure of intermetallic TiAl powders", J. of the Korean Inst. of Met. & Mater., vol. 30, No. 7, pp840-847 (1992).

[12] E.E. Underwood, *Quantitative stereology*, Addison-Wesley, p22 (1970).

[13] G. Waldecker, H. Meinhold and U. Birkholz, "thermal conductivity of semiconducting and metallic $FeSi_2$", Phys. Stat. Sol. (a), vol. 15, p143-149 (1973).

Expanding the Investigation of the Thermoelectric Properties of Rare-Earth-Filled Skutterudites

G.S. Nolas and H.B. Lyon
Research and Development Division, Marlow Industries Inc., Dallas, Texas, USA

J.L. Cohn
Department of Physics, University of Miami, Coral Gables, Florida, USA

T.M. Tritt
Department of Physics and Astronomy, Clemson University, Clemson, South Carolina, USA

G.A. Slack
Department of Physics, Rensselaer Polytechnic Institute, Troy , New York, USA

Abstract
There is increasing interest in the skutterudite family of compounds as potential thermoelectric materials mainly due to the marked reduction in the thermal conductivity that occurs when voids in the structure are filled with "guest" atoms. The "rattlling" of these void-fillers atoms damps the phonon propagation through the lattice. The phonon scattering mechanism(s) are not yet compoletely understood. Ongoing research focuses on compensating for the charge of the void-filling ions and finding the optimum void filler that yields maximal reduction in the thermal conductivity while maintaining favorable electronic properties. Thus far published data on Ge and Fe as charge compensators resulting in P-type samples has been reported. In this paper we present data on skutterudites incorporating Sn for charge compensation.

Introduction
The binary skutterudites have the cubic *Im*3 (T_h^5) structure and are of the form AB_3 where A represents a metal atom and B represents a pnicogen atom. There are nine binary semiconducting compounds in this group (A=Co, Rh, and Ir, and B=P, As, and Sb). There are eight formula units per cubic unit cell. The basic conditions for high figure of merit, Z, are a large unit cell, heavy constituent atom masses, low electronegativity differences between the constituent atoms, and large carrier mobilities, as described in Slack,[1] all of which are met in these materials. In addition there are two voids per unit cell in the structure. Skutterudites form covalent structures with low coordination numbers for the constituent atoms and so can incorporate atoms in the voids. The void radii of these nine binary semiconducting compounds have been estimated from x-ray crystallographic data[2] and range from 1.763 Å for CoP_3 to 2.040 Å for $IrSb_3$.

Large x-ray thermal parameters have been observed in filled skutterudites.[3] In both rare earth and alkaline earth-filled skutterudites, the thermal parameter of the filler increases as the ratio of the filler radius to void radius decreases. This seems to indicate that these "guest" atoms "rattle" in the voids more easily when they have more room to do so. The effect of the void-fillers on the optical modes of this structure has also been observed, using Raman Spectroscopy.[4]

The definition of a good thermoelectric material lies in the magnitude of the materials' Z value[5]

$$Z=\frac{S^2\sigma}{\kappa} \qquad (1)$$

where S is the Seebeck coefficient, σ the electrical conductivity, and κ the total thermal conductivity ($\kappa=\kappa_g+\kappa_e$; κ_g and κ_e being the lattice and electronic contributions, respectively.) Since the dimensions of Z are inverse temperature, a more convenient quantity is the dimensionless figure of merit, ZT, where T is the absolute temperature.

From Eq. (1) we see that a good thermoelectric material will have a high electronic conductivity and a low thermal conductivity. The Weidemann-Franz law[6] states that for a good metal $\kappa_e=L_o\sigma T$ where L_o is the Lorenz number. Also in a good metal $\kappa_e >> \kappa_g$. In this special case therefore $ZT=S^2/L_o$ and ZT is limited only by the value of S. We need $S \geq 156\mu V/K$ in order to obtain $ZT \geq 1$ since $L_o=2.443\times10^{-8}\ V^2/K^2$. Most metals have S values of the order of 10 μV/K or less. Semiconductors, which can have much larger S values, are needed for thermoelectric devices. In semiconductors, therefore, estimating κ_e from the Weidemann-Franz law, $ZT= S^2/[L_o+(\kappa_g/\sigma T)]$. This shows the influence of κ_g on ZT.

As explained by Slack[1] the ideal semiconducting material for thermoelectric applications is one which is a "phonon glass and an electron crystal" or PGEC. A phonon glass has the very smallest possible value of κ_g ($=\kappa_{min}$) because the atomic disorder reduces the phonon propagation distances to their absolute minimum value.[7] The electron crystal should appear to the electrons (or holes) as a very perfectly ordered, covalent solid so that the electrons are not scattered very much as they propagate through the crystal. This dual nature of disorder for phonons and order for electrons is the critical characteristic being sought in new and improved thermoelectric materials. The skutterudites have a very special nature that may make this possible.

Recent results indicate ZT~1 at high temperatures.[8,9] This indicates the promise of this materials system, however, care must be taken in suggesting applications at high temperature unless and until the thermoelectric properties, and indeed the stoichiometry, of these compounds are proven stable over time at the proposed operating temperatures. Previous erroneous conclusions[10] due to high temperature material dissociation should serve as a reminder.

In order to increase ZT in the room temperature range a larger reduction in κ_g towards κ_{min} is needed. In addition, more effort is needed in understanding the best dopant for charge compensation. It is evident that the carrier concentration of the filled skutterudite compounds presently under focus cannot be varied substantially, if at all, with the charge compensation techniques attempted thus far. Currently, new avenues are being investigated at Marlow Industries toward this end.

Reducing κ_g

Due to the importance of κ_g on ZT an understanding of the mechanisms that may be employed for reducing κ_g in skutterudites is imperative. These may be listed as known methods for scattering the phonons:

- charge carriers from dopants
- inner-shell excitations (*d*-shell or *f*-shell)
- mixed-valence
- other (grain boundary scattering, precipitates, and dislocations)
- point defect scattering
- void fillers

We will not review all these mechanisms here. In general, however, each one of the phonon scattering mechanisms will scatter phonons in some particular energy range while interacting weakly with all other frequency phonons. For example point defect scattering[11] employing mass fluctuation and strain field scattering results in a Raleigh-type scattering dependence of the mean free path, l, such that $l \propto \omega^{-4}$, where ω is the phonon frequency. This type of phonon scattering mechanism therefore effects the high frequency part of the phonon spectrum. It should be noted that this scattering mechanism has been the main technique in reducing κ_g in an attempt to improve the thermoelectric properties of potential thermoelectric materials. A more effective way in reducing κ_g would be to combine different scattering mechanisms such that different parts of the phonon spectrum can be attacked. This technique was employed in Si-Ge thermoelectrics where lower frequency phonons were scattered by interactions with the free carriers in degenerately doped materials.[12] Mass fluctuation scattering was produced by the Si-Ge alloys. The combination of these two mechanisms produces low κ_g values but these materials still do not possess κ_{min}, as shown by Slack and Hussain.[13] There is still a large part of the phonon spectrum that needs to be attacked in order to obtain κ_{min}.

Phonon Scattering by Void Fillers

Many different atoms have been introduced into the voids in skutterudites.[2,3,8,14] These include alkali earth, lanthanide and actanide ions. The chemical formula for $CoSb_3$, for example, can be written as $\square_2Co_8Sb_{24}$ illustrating the two voids per unit cell. One must also take into account the void radius of the particular compound under investigation. Table I illustrates the array of possible void fillers as well as an estimate of their ionic radii, from Ref. 2. Note that this list is in no way complete. If we place smaller sized atoms in the voids, such as Nd^{3+} for example, these "rattle" about in the larger diameter voids. More loosely bound "rattlers" produce local vibrational modes of lower frequency and are thus more effective in scattering the lower-frequency, heat-carrying phonons. Nolas *et al.*[2] has initiated a study on the effects of the "guest" radius to void radius ratio on κ_g and the results. The smaller the ion in the $IrSb_3$ voids, the larger the disorder that is produced and therefore the larger the reduction in κ_g. An order-of-magnitude decrease in κ_g is observed at room temperature and an even larger reduction below room temperature.

Table I. The average ionic radii, in Å, for ions in 6 and 12 CN sites taken from oxide and fluoride structural data. These ions may not be in a similar symmetry site in the voids of the skutterudites and the actual inter-ion distances may therefore differ. However, the important trend in the sizes of these ions is illustrated.

ion	Na	K	Rb	Cs
charge	+1	+1	+1	+1
12 CN	1.44	1.74	1.87	2.02
6CN	1.13	1.52	1.63	1.84
ion	Sm	Nd	Ce	La
charge	+3	+3	+3	+3
12 CN	1.37	1.40	1.44	1.46
6CN	1.10	1.14	1.17	1.20

The RFe_3CoSb_{12} system, where R=La or Ce, has also proven to possess very low κ_g.[8,15] However, Fe in this system also has a dramatic affect on κ, as shown in Dudkin et al.[16] where 10% Fe substitution for Co in $CoSb_3$ (10%Fe:$CoSb_3$) resulted in a room temperature value of κ that was reduced to one half the value measured for pure $CoSb_3$. We have synthesized a polycrystalline pressed powder sample of 10%Fe:$CoSb_3$ and our measurements are in agreement with these results. At 35 K the reduction in κ is almost an-order-of-magnitude less for 10%Fe:$CoSb_3$ as compared to pure $CoSb_3$. This reduction in κ cannot be explained by the point-defect scattering produced by Fe in the metal sites of $CoSb_3$, using an estimate with Fe in this structure,[4] or experimental data[17] on $FeSb_3$ to estimate the bond distances. This work will be reported elsewhere; the main goal of the present study is to isolate the phonon scattering mechanism(s) introduced by the void-filler atoms in studying their effect on κ_g.

Results and Discussion

In this study we present preliminary results on the transport properties of partially filled skutterudite compounds with the aim of investigating the influence of partial void filling on κ_g. X-ray diffraction, metallographic, and electron-beam microprobe analysis have been employed in the characterization of these compounds. La^{3+} was used as the rare earth filler ion due to the fact that this trivalent rare earth ion has an empty $4f$ shell. In this study we therefore isolate the "rattling" nature of the filled skutterudites from other possible scattering mechanisms caused by $4f$ electrons. Table II shows the samples prepared along with their measured density, and room temperature carrier concentration and mobility. Also shown in Table II is a nominally 100% filled sample, $Co_4LaSn_3Sb_9$. Sn is similar in size and mass to Sb and is therefore not expected to produce much phonon scattering. The amount of La in the voids of uncompensated skutterudite samples reaches saturation at 23%.

Table II. The sample compositions, their fraction of theoretical densities, D%, and the carrier concentration and mobilities measured for the skutterudite samples used in this study. The Hall data were taken using a four probe technique. The $CoSb_3$ and the Sn-compensated samples are P-type, the uncompensated samples are N-type. The cubic unit cell is defined by twice the formula units shown.

Sample	D %	carrier conc. (10^{19} cm^{-3})	mobility (cm^2/V-sec)
Co_4Sb_{12}	97	0.19	270
$La_{0.05}Co_4Sb_{12}$	94	15	20.5
$La_{0.23}Co_4Sb_{12}$	93	63	6.83
$Co_4La_{0.3}Sn_{1.5}Sb_{11}$	94	3.0	121
$Co_4LaSn_3Sb_9$	94	31	16.7

The series of skutterudite compounds used in this work were prepared similarly as described in Nolas *et al.*[2] Densification was accomplished using a graphite die in a hot press. The samples were cut with a wire saw in the shape of parallelpipeds for transport properties measurements, performed as described previously.[18,19]

Figures 1 and 2 show ρ and absolute α, respectively, in the temperature range from 300K down to 6K for the skutterudite samples prepared for this study. The data for $Co_4LaSn_3Sb_9$ is typical in magnitude and temperature dependence to that of P-type heavily doped pnicogen-compensated filled-skutterudite samples. The two N- type samples clearly show a higher $|\alpha|$. From Figure 2 we see that for $La_{0.05}Co_4Sb_{12}$ $|\alpha|$ is similar to that of $CoSb_3$ even though the former sample has a carrier concentration 80 times larger.

The N-type sample behavior is obvious from the fact that the La^{3+} ions donate their electrons without charge compensation towards the goal of 72.0 electron count per cubic unit cell, as described in Tritt *et al.*[20] It should also be noted that the

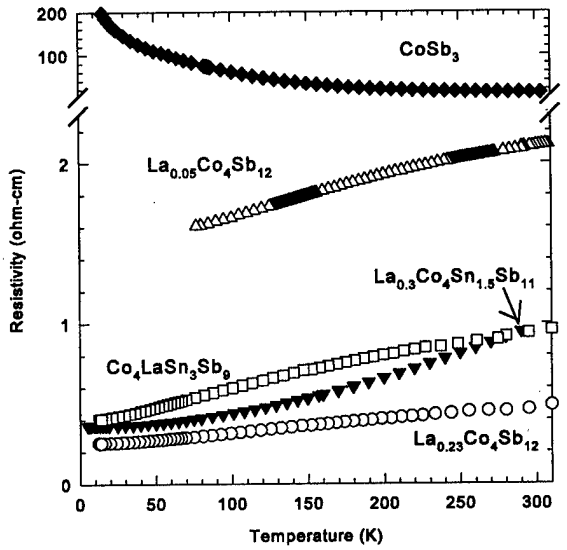


Figure 1. The ρ as a function of temperature from 300K down to 6 K for $Co_4LaSn_3Sb_9$, $Co_4La_{0.3}Sn_{1.5}Sb_{11}$ (solid triangles), $La_{0.23}Co_4Sb_{12}$, $La_{0.05}Co_4Sb_{12}$ and $CoSb_3$.

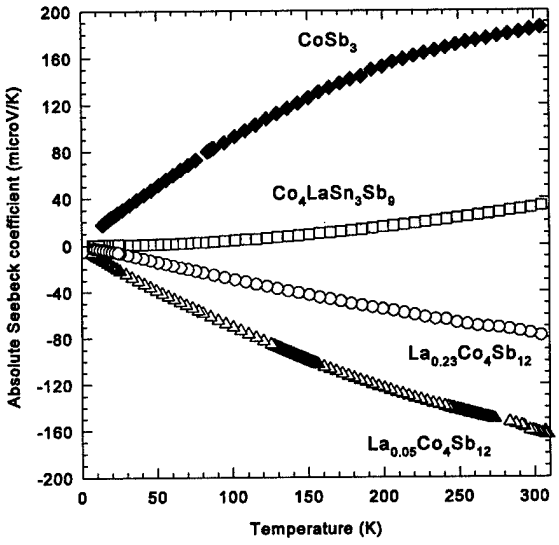


Figure 2. Absolute α as a function of temperature from 300K down to 6 K for $Co_4LaSn_3Sb_9$, $Co_4La_{0.3}Sn_{1.5}Sb_{11}$, $La_{0.23}Co_4Sb_{12}$, $La_{0.05}Co_4Sb_{12}$ and $CoSb_3$.

x=0.05 uncompensated La-filled skutterudite as well as the Sn-compensated samples have a larger carrier mobility than Fe-compensated[8] samples with similar carrier concentration. This suggests a greater carrier scattering due to Fe in this system.

The absolute α values are somewhat dependant on the carrier concentration, as observed from Table II and Figure 2, and the relatively large absolute α for the N-type samples are presumably due to their large effective mass. Band structure calculations predict a heavy conduction band mass in N-type skutterudites.[21] It may be that the La^{3+} ions in these samples do not affect the band structure of $CoSb_3$ a great deal while doping the samples N-type.

Figure 3 shows κ_g in the temperature range from 300 K down to 6 K for the skutterudite samples synthsized in this study. Also in the figure is calculated κ_g due to boundary scattering for 4 and 7 μm grain sizes.[3] The κ_g is isotropic since the skutterudite structure is cubic. From the measured values of ρ, shown in Figure 1, and the Wiedemann-Franz law, with the Lorenz number taken to be $2.44X10^{-8}$ V^2/deg^2,[22] we have estimated and subtracted the κ_e values in Figure 3. The curve for κ_{min} of $CoSb_3$ was calculated following Slack[7] taking the minimum mean free path of the acoustic phonons as $\lambda/2$ instead of λ, as suggested by Cahill *et al.*,[23] where λ is one phonon wavelength. Single crystal results[24]are also shown in Figure 3.

The temperature dependence of κ_g for pure $CoSb_3$ is typical of crystalline compounds. The peak value for our pure $CoSb_3$ (7 μm grain size) is much lower than that of the single crystal due to the effect of boundary scatteing. In the case of the partially filled skutterudites the grain sizes where all ≥4 μm, therefore the magnitude and temperature dependence for all the samples for temperatures greater than 45 K are not due to grain boundary scattering.

From Figure 3 we see that κ_g decreases with increasing La concentration. However, the 100% La-filled sample has κ_g greater than the 30% sample. It appears that partial filling of the skutterudites produces more phonon scattering than in the case of fully-filled skutterudites. This may indicate a point-defect-type scattering effect as well as the dynamic, or "rattling", type scattering mechanism at work in the partially-filled skutterudites resulting in the further reduction of κ_g.

Conclusions

The skutterudite family of compounds continues to be of interest for thermoelectric applications. Their good mechanical properties, low thermal expansion coefficients and cubic crystal structure make them excellent candidates for thermoelectric applications. The key, however, is to substantially reduce κ in this structure with a minimum degradation in the electronic properties. Clearly potential only excists if κ_g can be reduced further towards κ_{min}. Initial results on partially-filled skutterudites are very encouraging both in terms of further κ_g reduction and minimization of carrier scattering. The greatest benefit in the investigation of this system, however, may lie in this new and novel approach, i.e. the PGEC approach, for thermoelectric properties improvements. This may well be the most promising strategy for developing improved thermoelectric materials.

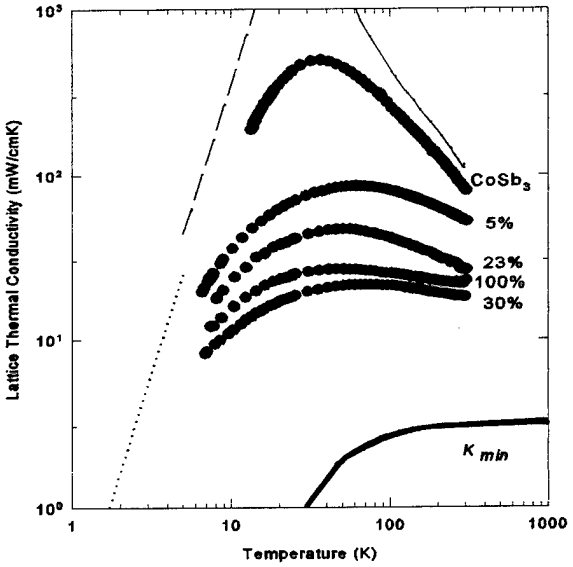


Figure 3. The κ_g vs. temperature for $Co_4LaSn_3Sb_9$ (100% La-filled), $Co_4La_{0.3}Sn_{1.5}Sb_{11}$ (30%), $La_{0.23}Co_4Sb_{12}$ (23%), $La_{0.05}Co_4Sb_{12}$ (5%) and $CoSb_3$. The dotted and dashed lines are calculations for κ_g due to boundary scattering from 4 and 7 μm grain sizes. The κ for a $CoSb_3$ single crystal (solid line) as well as κ_{min} for $CoSb_3$ is also included.

Acknowledgment

This work was supported, in part, by NASA. Grant number NAS9-19358.

References

[1] G.A. Slack, in "CRC Handbook of Thermoelectrics", edited by D.M. Rowe, CRC Press, Boca Raton, FL, 1995, p. 407.

[2] G.S. Nolas, G.A. Slack, D.T. Morelli, T.M. Tritt and A.C. Ehrlich, J. Appl. Phys. **79** (1996) 4002.

[3] C.B.H. Evers, W. Jeitschko, L. Boonk, D.J. Braun, T. Ebel, U.D. Scholz, J. Alloys Comp. **224** (1995) 184, and references therein.

[4] G.S. Nolas, G.A. Slack, T. Caillat, and G.P. Meisner, J. Appl. Phys. 79 (1996) 2622.

[5] H.J. Goldsmid, "Electronic Refrigeration", Pion Limited, London, 1986.

[6] See for example, N.W. Ashcroft and N.D. Mermin, "Solid State Physics", Holt, Rinehart, and Winston, Philadelphia, PA, 1976.

[7] G.A. Slack, in Solid State Physics, Vol. 34, edited by H. Ehrenreich, F. Seitz, and D. Turnbull, Academic Press, New York, NY, 1979.

[8] B.C. Sales, D.G. Mandrus, and R.K. Williams, Science **272** (1996) 1325.

[9] J.-P Fleurial, A. Borshchevsky, T. Caillat, D.T. Morelli, and G.P. Meisner, "High Figure of Merit in Ce-Filled Skutterudites", Proceedings of the Fifteenth International Conference on Thermoelectrics, edited by T. Caillat, IEEE Catalog No. 96TH8169, 1996, p. 91.

[10] T. Caillat, A. Borshchevsky, and J.-P. Fleurial, "Novel Transition Metal Compounds with Promising Thermoelectric Properties", Proceedings of the 12th International Conference on Thermoelectrics, edited by K. Matsuura, Institute of Electrical Engineers of Japan, Tokyo, 1994, p. 132.

[11] C.M. Bhandari, in "CRC Handbook of Thermoelectrics", edited by R.M. Rowe, CRC Press, Boca Raton, FL, 1995, and references therein.

[12] J.P. Dismukas, L. Ekstrom, E.F. Steigmeier, I. Kudman, and D.S. Beers, J. Appl. Phys. **35** (1964) 2899.

[13] G.A. Slack and M.A. Hussain, J. Appl. Phys. **70** (1991) 2694.

[14] D.T. Morelli and G.P. Meisner, J. Appl. Phys. **77** (1995) 3777.

[15] B. Chen, J. Xu, C. Uher, D.T. Morelli, G.P. Meisner, J.-P. Fleurial, T. Caillat, and A. Borshchevsky, Phys. Rev. **B** 55 (1997) 1467.

[16] L.D. Dudkin and N.Kh. Abrikosov, Sov. Phys. Solid State **1** (1959) 126.

[17] M.D. Hornbostel, E.J. Hyer, J. Thiel, and D.C. Johnson, J. Am. Chem. Soc. **119** (1997) 2665.

[18] J.L. Cohn, E.F. Skelton, S.A. Wolf, and J.Z. Liu, Phys. Rev. B **45** (1992) 13140.

[19] J.L. Cohn, E.F. Skelton, S.A. Wolf, J.Z. Liu, and R.N. Shelton, Phys. Rev. B **45** (1992) 13144.

[20] T.M. Tritt, G.S. Nolas, G.A. Slack, D.T. Morelli, A.C. Ehrlich, D.J. Gillespie, and J.L. Cohn, J. Appl. Phys. **79** (1996) 8412.

[21] D.J.Singh and W.E. Pickett, Phys. Rev. B **50** (1994) 11235.

[22] G.A. Slack, D.W. Oliver, and F.H. Horn, *Phys. Rev. B* **4** (1971) 1714.

[23] D.G. Cahill, S.K. Watson, and R.O. Pohl, *Phys. Rev. B* **46** (1992) 6131.

[24] D.T. Morelli,T. Caillat, J.-P. Fleurial, A. Borshchevsky, J. Vandersande, B. Chen, and C. Uher, Phys. Rev. B **51** (1995) 9622.

Effects of Doping Pd/Pt in $CoSb_3$ Crystals on Electrical and Thermoelectric Properties

H. Tashiro, [1]Y. Notohara, [2]T. Sakakibara, [3]H. Anno, and [3]K. Matsubara
Toyo Kohan Co.,Ltd. 1296 Higashitoyoi, Kudamatsu 744, Japan
Phone: +81(833)44-2541, FAX:+81(833)43-0295, E-mail: toyotec3@jsn.justnet.or.jp
[1]Kyushu Matsushita Electric Co.,Ltd. 4-1-62 Minoshima, Hakata-ku, Fukuoka 812, Japan
[2]Aisin Cosmos R&D Co.,Ltd. 5-50 Hachiken-cho, Kariya 448, Japan
[3]Science University of Tokyo in Yamaguchi, 1-1-1 Daigaku-dori, Onoda 756, Japan

Abstract

Double doping of palladium and platinum in Skutterudite $CoSb_3$ has been studied to improve thermoelectric properties. It was found that the solubility limit of Pd and Pt in $CoSb_3$ crystal amounted to about 10 at% and substitution of Pd and Pt for Co occurred. The carrier concentration increased to about 5×10^{20} cm^{-3} due to a higher degree of solutioning of Pd and Pt by double doping than that of Pd or Pt by single doping. Electrical conductivity of $\sigma = 1950$ S/cm at room temperature could be obtained for the double doping of 5 at% Pd and 5 at% Pt. Heavy doping by Pd and Pt was found to significantly reduce the lattice thermal conductivity, leading to the decrease in thermal conductivity from 0.1 (non-doped crystal) to 0.05 W/cmK. As a result , the figure of merit value Z was about 1.2×10^{-3} /K at temperatures between 500 and 800 K, and the maximum ZT = 0.9 was obtained at 750 K.

Introduction

Extensive interest has been focused on the skutterudite $CoSb_3$ as a new promising thermoelectric material because of its prominent transport properties, in particular, extremely high hole mobility over the past few years [1,2]. The value of materials for thermoelectric energy conversion or cooling applications is defined as the thermoelectric figure of merit Z, which is given by $Z=S^2\sigma/\kappa$, where S is the Seebeck coefficient, σ the electrical conductivity, κ the thermal conductivity. In spite of the desirable properties for the thermoelectric materials, the figure of merit Z for skutterudite compounds is limited due to their relatively high thermal conductivity, which is approximately 5 times as large as that of Bi_2Te_3-based materials. The reduction of the thermal conductivity is essential to improve the thermoelectric properties. Recently, several approaches have been attempted to reduce the thermal conductivity of skutterudites. For example , doping of some impurities [3-5], formation of solid solutions [6], synthesis of related compounds [7,8], and so on .

As reported previously, we have studied the effects of Pd-doping on the thermoelectric properties of $CoSb_3$ and found that the substitution of Pd for the Co sites successfully increases the thermoelectric figure of merit to a value of $Z = 0.6\times10^{-3}$ over a wide temperature range. However, increase in Z was suppressed by the low solubility of Pd [3].

In this paper ,we report a study on the effects of double doping of Pd and Pt on the thermoelectric properties of $CoSb_3$ crystals in order to increase the thermoelectric figure of merit. The double doping technique aims at an increase of the ratio σ/κ by both increasing the electrical conductivity and reducing the lattice thermal conductivity due to the electron-phonon scattering.

Experimental procedure

Powders of elements Co(99.998%), Sb(99.9999%), Pd(99.99%), and Pt(99.97%) were used as the starting materials. Mixtures of these powders were prepared in atomic percentage $Co_{1-X}M_XSb_3$ (M:Pd and Pt(Pd/Pt ratio =1), Pd, Pt, $0 \leqq x \leqq 0.2$). The mixtures were cold-pressed and sealed under vacuum in a carbon-coated quartz tube, and then annealed at 870 K for 2 days. The annealed samples were crushed to smaller particles less than 90 μ m in size, and hot-pressed under 15 MPa at 1020 K for 80 minutes.

The obtained samples were characterized by means of X-ray diffraction (XRD), and the quantitative analysis was performed by electron-probe microanalyzer (EPMA). The microstructure of samples was observed under an optical microscope. Measurements of the electrical conductivity and Seebeck coefficient were made in the temperature range from 300 to 800 K. Hall coefficient was measured by the van der Pauw technique, and the thermal conductivity was measured by the laser flash method.

Results and discussion

Figure 1 shows the dopant concentration measured by EPMA versus the weighed value of dopant. For the single doping of Pd or Pt, the maximum value of dopant concentration is 0.04 at most. On the other hand, the double doping permits higher doping level as compared to the single doping. The measured value increases with increasing the dopant concentration up to 0.07, and the value was saturated to about 0.1. More heavily doped samples can be obtained by double (Pt/Pd) doping. The saturation of dopant concentration may be attributed to flow out of liquid phases in the hot-pressing process, which are probably generated by melting of Sb-Pd or Sb-Pt compounds formed during annealing. XRD results showed that the lattice constant increases with increasing dopant concentration due to formation of a solid solution. From the results of XRD and EPMA, it was found that substitution of Pd and Pt for Co successfully occurred.

Figure 2 shows the Hall concentration as a function of dopant concentration. The carrier concentration increases monotonically with increase in dopant concentration. Higher

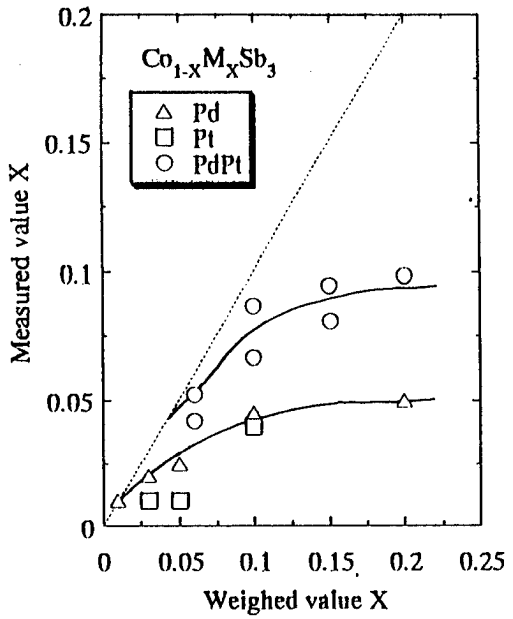


Fig.1 Dopant concentration measured by EPMA vs. weighed value.

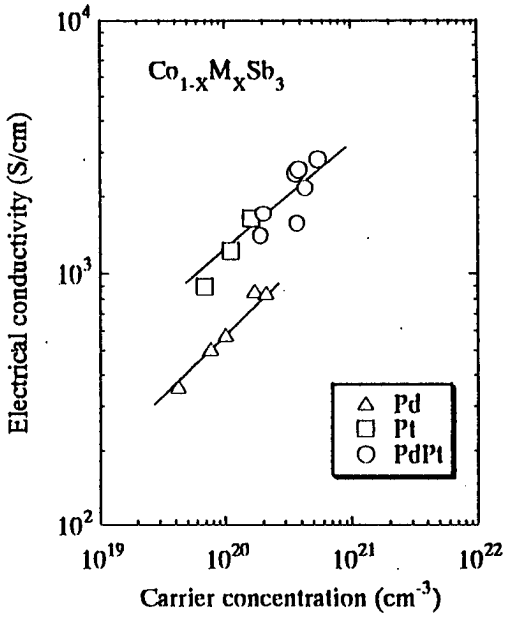


Fig.3 Electrical conductivity as a function of carrier concentration.

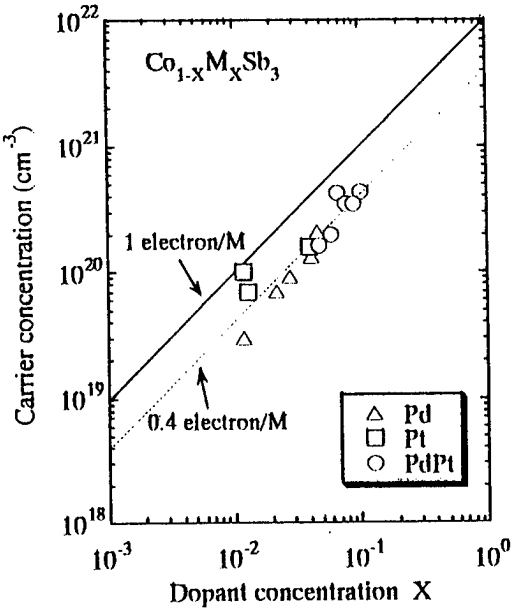


Fig.2 Carrier concentration as a function of dopant concentration.

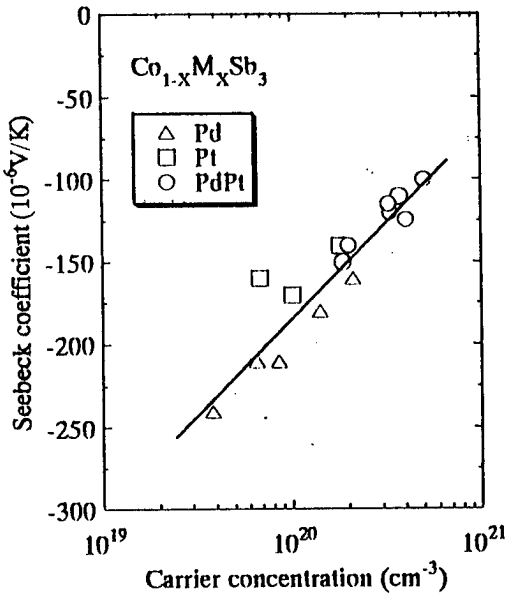


Fig.4 Seebeck coefficient as a function of carrier concentration.

carrier concentration can be obtained for the Pd/Pt-double doped samples as compared with the single doped samples. The solid line and dashed line indicate the calculated values for carrier activity of 100% and 40%, respectively. The experimental data goes along the dashed line (carrier activity:40%). In this system, the carrier activity is independent of the kind of dopant. The low carrier activity of about 40% may be due to the higher activation energy of carriers as compared with room temperature.

Figures 3 and 4 show the electrical conductivity and the Seebeck coefficient at room temperature as a function of carrier concentration, respectively. Electrical conductivity increases monotonically with increase in carrier concentration. Pd/Pt-doped $CoSb_3$ compounds have higher electrical

conductivity than Pt-or Pd-doped compounds(σ = 1950 S/cm at room temperature for the double doped $CoSb_3$ with 5 at% Pd and 5 at% Pt). For the single doping, Pt-doped samples have higher electrical conductivity than Pd-doped ones at a given carrier concentration. This can be explained by the fact that the carrier mobility of Pt-doped $CoSb_3$ is higher than that of Pd-doped one. On the contrary, the Seebeck coefficient decreases linearly with the carrier concentration, as observed usualy in thermoelectric semiconductors.

Power factor calculated from the results of the electrical conductivity and the Seebeck coefficient is shown in Fig.5. The value of power factor varies depending on the doping level of the sample, becoming higher for heavily doped samples. A maximum value of 4.5×10^{-5} W/cmK^2 was obtained for the double doped sample which has high electrical conductivity due to high carrier concentration. Power factor values may be increased by further heavy doping.

The ratio of the lattice thermal conductivity to the thermal conductivity of $CoSb_3$ was calculated and was found to be about 80 %. Thus, the reduction of the lattice thermal conductivity is essential to reduce the thermal conductivity. Figure 6 shows the lattice thermal conductivity as a function of carrier concentration. The lattice thermal conductivity decreases with increase in carrier concentration, reaching a value of about 2.5×10^{-2} W/cmK. The reduction of the lattice thermal conductivities ascribed mainly to lattice distortion due to the substitution of Pd and Pt for Co. The thermal conductivity of the Pd/Pt- double doped $CoSb_3$ compounds was found to be about half value of the non-doped samples.

Figure 7 shows the calculated dimensionless figure of merit value (ZT) as a function of temperature. ZT value

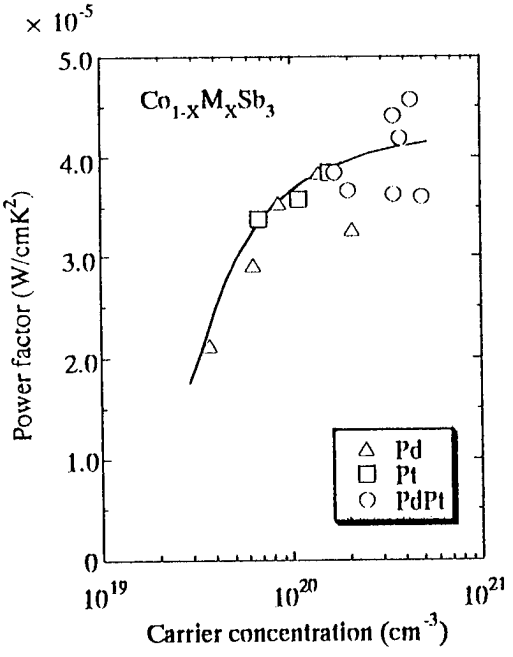


Fig.5 Power factor as a function of carrier concentration.

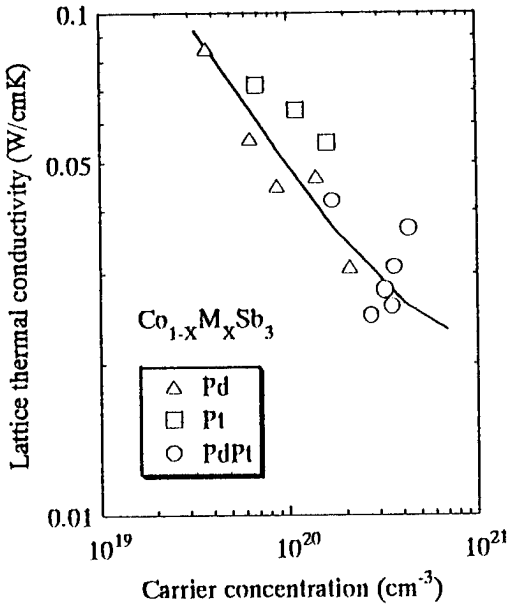


Fig.6 Lattice thermal conductivity as a function of carrier concentration.

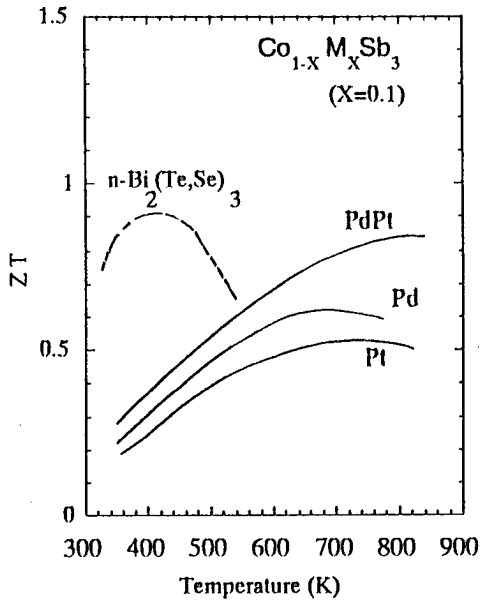


Fig.7 Dimensionless figure of merit ZT as a function of carrier concentration.

increases with temperature up to al out 700 K, and the ZT values of the double doped samples are higher than that of the single doped samples. A maximum ZT value of 0.9 was achieved around 800K for the double doped sample. This value is comparable with that of the Bi_2Te_3-based materiales. The double doped $CoSb_3$ has relatively high ZT value at high temperature range as compared to the Bi_2Te_3 compound.

Conclusion

Effects of Pd- and Pt-substitution for Co site in $CoSb_3$ on thermoelectric properties were investigated. Double doping of Pd/Pt was found to have a prominent effect on an increase of carrier concentration up to 5×10^{20} cm^{-3}. Electrical conductivity of about 1950 S/cm was obtained at room temperature for the double doped crystal, 5 at% Pd and 5 at% Pt. The thermal conductivity for the Pd/Pt-doped $CoSb_3$ was found to be about 0.05 W/cmK at room temperature. The figure of merit value $Z = 1.2 \times 10^{-3}$ /K was obtained in the temperature range of 500 - 800 K, and ZT value was 0.9 around 800 K.

Acknowledgement

This study was performed by financial supports of the Yamaguchi Prefectural Government and the Yamaguchi Industrial Technology Development Organization.

References

[1] D.T.Morelli, T.Caillat, J.-P.Fleurial, A.Borshchevsky, J.Vandesande, B.Chen, and C.Uher, "Low-temperature trasport properties of *p*-type $CoSb_3$", Phys. Rev. B, Vol.51, No.15, pp. 9622-9628(1995).

[2] T.Caillat, J.-P.Fleurial, and A.Borshchevsky, "Bridgman-solution crystal growth and characterization of the skutterudite compounds $CoSb_3$ and $RhSb_3$", J. Crys. Growth, 166, pp. 722-726(1996).

[3] K.Matsubara, T.Iyanaga, T.Tsubouchi, K.Kishimoto, and T.Koyanagi, "Thermoelectric Properties $(Pd,Co)Sb_3$ Compounds with the Skutterudite Structure", *Proc. XIII Int. Conf. on Thermoelectrics*, Kansas, USA, 1994, (AIP Press, New York), pp. 226-229(1995).

[4] T.Caillat, A.Borshchevsky, and J.-P.Fleurial, "Properties of single crystalline semiconducting $CoSb_3$", J. Appl. Phys., Vol.80, No.8, pp. 4442-4449(1996).

[5] T.Caillat, A.Borshchevsky, and J.-P.Fleurial, "Preparation and Thermoelectric Properties of p- and n-type $CoSb_3$", *Proc. XIII Int. Conf. on thermoelectrics*, Kansas, USA, 1994,(AIP Press, New York), pp. 41-44(1995).

[6] A.Borshchevsky, J.-P.Fleurial, E. Allevant, and T.Caillat, "$CoSb_3$-$IrSb_3$ solid solution: Preparation and Characterization", *Proc. XIII Int. Conf. on thermoelectrics*, Kansas, USA, 1994,(AIP Press, New York), pp. 3-6(1995).

[7] G.S.Nolas, V.G.Harris, T.M.Tritt, G.A.Slack, "Low-temperature transport properties of the mixed-valence semiconductor $Ru_{0.5}Pd_{0.5}Sb_3$", J. Appl. Phys., Vol.80, No.11, pp.6304-6308(1996).

[8] Y.Nagamoto, K.Tanaka, and T.Koyanagi, "Thermoelectric properties of the skutterudite-related phase $CoSn_{1.5}Te_{1.5}$", *Proc. XVI Int. Conf. on thermoelectrics*, (in this conference), Dresden, Germany,1997.

Thermoelectric Properties of the Skutterudite-Related Phase $CoSn_{1.5}Te_{1.5}$

Y. Nagamoto*, K. Tanaka and T. Koyanagi

Department of Electrical and Electronic Engineering, Yamaguchi University, 2557, Tokiwadai, Ube 755, Japan
Tel: +81-836-35-9453, Fax: +80-836-35-9452, *E-mail: nagamoto@aem.eee.yamaguchi-u.ac.jp

Abstract

A new skutterudite-related phase $CoSn_{1.5}Te_{1.5}$ was prepared. This new phase is one of a large family of skutterudites which have shown a good potential for thermoelectric applications. Polycrystalline samples were prepared by the spark plasma sintering method and were characterized by x-ray diffractometry. $CoSn_{1.5}Te_{1.5}$ has a cubic lattice, space group Im3, with a = 9.121 Å. The electrical conductivity, the Seebeck coefficient, and the thermal conductivity were measured over the temperature range 300–900 K. The temperature dependence of the electrical conductivity revealed that $CoSn_{1.5}Te_{1.5}$ was a semiconductor with a band gap of 0.7 eV. The electrical conductivity increased by doping with Ni. Large Seebeck coefficients up to –450 μV/K were obtained on the n-type undoped samples. The thermal conductivity of $CoSn_{1.5}Te_{1.5}$ was substantially lower than that of the binary isostructural compounds $CoSb_3$ and $IrSb_3$. The potential of this material for thermoelectric applications is discussed.

Introduction

Skutterudite materials have recently received considerable attention as attractive thermoelectric materials [1-3]. The binary skutterudite compounds possess reasonably large Seebeck coefficient and good electrical conductivity, resulting in large power factor values comparable to state-of-the-art thermoelectric materials. However, their thermoelectric figure of merit is limited by their relatively high thermal conductivity. If lowering the thermal conductivity of the binary compounds with a minimal reduction in the power factor can be achieved, high thermoelectric figure of merit values might be possible.

Several approaches have been recently attempted to reduce the lattice thermal conductivity of skutterudite materials. The first approach, used for many state-of-the-art thermoelectric materials, is to form solid solutions between isostructural compounds and to reduce the lattice thermal conductivity by increasing the point defect scattering [4, 5]. Another approach is the filling of the voids in skutterudite structures by rare-earth atoms to scatter the phonons by the "rattling" of these atoms [6-8].

Skutterudite-related phases can be formed by substitution of neighboring atoms for the anion or the cation in binary skutterudite compounds. The resulting phases are isoelectronic with the binary compounds. Many ternary skutterudite-related phases were reported in the literature [9]. However, few studies on the thermoelectric properties of the ternary skutterudite phases have been made [9-12]. Because of the additional atomic disorder introduced, one can expect some reduction in the lattice thermal conductivity for these materials. Thermal conductivity measurements of several ternary skutterudite-related phases showed that their thermal conductivity is substantially lower than that of the binary isostructural compounds [9-12].

A new skutterudite-related phase, $CoSn_{1.5}Te_{1.5}$, obtained by substitution of Sn and Te for Sb in the binary skutterudite compound $CoSb_3$ was found by Fleurial *et al.* [9]. However, no information is available in the literature about the thermoelectric properties of $CoSn_{1.5}Te_{1.5}$. We report here the results obtained on the preparation and thermoelectric properties of doped and undoped $CoSn_{1.5}Te_{1.5}$. The potential of this material for thermoelectric applications is discussed.

Experimental Procedure

Commercially available SnTe (99.9999%) and Co (99.99%) powders were used as starting materials. SnTe and Co powders were mixed in stoichiometric ratio in a plastic vial before being loaded in a steel die where they were compressed into a dense cylindrical pellet. The pellet was loaded on a graphite boat in an Ar atmosphere which was heated for 2 days at 873 K (lower than the melting point of SnTe). The product was then crushed and ground in an alumina mortar. The resultant powder was heated on a graphite boat for another 2 days at the same temperature. This last step was repeated once more. Following powder reaction, several samples of $CoSn_{1.5}Te_{1.5}$ were sintered by the spark plasma sintering method. The spark plasma sintering was performed at a pressure of 40 MPa and at a temperature of 853 K for 15 min. Undoped samples always showed n-type conduction. P-type samples were obtained by substituting Co for Ru (99.99%). N-type samples with high doping level were obtained by addition of Ni (99.9%). The dopants were introduced in the original mixed powders.

The crystal structure of the samples was investigated by the x-ray diffractometry (XRD) analysis. Silicon powder was used as a standard and was mixed with the powdered samples. The density of samples was measured by immersion technique using distilled water as the liquid. The Hall measurements were performed in a constant magnetic field of 0.5 T at room temperature. The electrical conductivity σ and the Seebeck coefficient S were measured between room temperature and about 900K. Measurements of the thermal conductivity κ were performed by a laser flash method in the temperature range from 300 to 800 K.

0-7803-4057-4/97 $10.00 ©1997 IEEE

Table I. Some properties at room temperature for n-type $CoSn_{1.5}Te_{1.5}$ and n-type $CoSb_3$ [3].

Property	Units	n-type $CoSb_3$	n-type $CoSn_{1.5}Te_{1.5}$
Lattice constant	Å	9.0345	9.121
X-ray density	g/cm^3	7.621	7.50
Electrical conductivity	$\Omega^{-1}cm^{-1}$	180	2.99
Hall mobility	cm^2/Vs	87.0	1.54
Hall carrier concentration	$10^{19}cm^{-3}$	1.287	1.21
Seebeck coefficient	μV/K	−373.0	−428
Lattice thermal conductivity	mW/cmK	100	39.9
Effective mass (m^*/m_0)	···	3.4	4.4
Band gap	eV	0.55	0.70

Results and Discussion

The x-ray diffraction pattern was indexed to a cubic unit cell corresponding to the skutterudite structure, space group *Im*3. The measured lattice constant at room temperature of the powdered sample was a_0 = 9.121±0.001 Å. This is slightly larger than that for the binary compound $CoSb_3$ (a_0 = 9.0345 Å [3]) from which $CoSn_{1.5}Te_{1.5}$ is derived. A similar fining was obtained for $CoGe_{1.5}Se_{1.5}$ (a_0 = 8.299 Å [13]), derived from the binary compound $CoAs_3$ (a_0 = 8.2043 Å [9]). The measured densities were found to be about 95% of the x-ray density of 7.50 g/cm^3. In addition, the x-ray diffractometry analysis of the sintered samples showed that the samples prepared in the stoichiometric ratio were predominantly $CoSn_{1.5}Te_{1.5}$ phase with a small amount of SnTe phase and that the samples prepared in Co-rich ratio were single phase.

Some room temperature properties of n-type $CoSn_{1.5}Te_{1.5}$ are summarized in Table I and are compared with the results of Caillat *et al.* obtained on an n-type single crystal $CoSb_3$ sample [3]. Hall coefficient measurements show that undoped samples have n-type conduction at room temperature. The room temperature Hall carrier concentration is 1.21×10^{19} cm^{-3} for undoped $CoSn_{1.5}Te_{1.5}$. $CoSn_{1.5}Te_{1.5}$ has Co-rich composition. Therefore, n-type conduction in undoped $CoSn_{1.5}Te_{1.5}$ is due to an anion deficiency [14]. The electrical conductivity of undoped $CoSn_{1.5}Te_{1.5}$ at room temperature is 2.99 $\Omega^{-1}cm^{-1}$ and the Hall mobility is 1.54 $cm^2V^{-1}s^{-1}$. The carrier mobility is significantly decreased in the ternary compound, as compared to binary compounds. The Seebeck coefficient at room temperature is relatively large with a value of −428 μVK^{-1}.

P-type $CoSn_{1.5}Te_{1.5}$ were obtained by substituting Co for Ru. The room temperature Hall carrier concentration is 2.33×10^{19} cm^{-3} for $Co_{0.95}Ru_{0.05}Sn_{1.5}Te_{1.5}$. The electrical conductivity of this sample at room temperature is 28.4 $\Omega^{-1}cm^{-1}$ and the Hall mobility is 7.62 $cm^2V^{-1}s^{-1}$. The Hall mobility for p-type $CoSb_3$ at the same doping level is about 1000 $cm^2V^{-1}s^{-1}$. The exceptionally high hole carrier mobility of $CoSb_3$ is drastically reduced by the substitution of Sn and Te for Sb. The Seebeck coefficient values are relatively small with a room temperature value of 39 μVK^{-1}.

The electrical conductivity values are shown as a function of inverse temperature for doped and undoped $CoSn_{1.5}Te_{1.5}$ in Figure 1. The electrical conductivity of the undoped $CoSn_{1.5}Te_{1.5}$ increases with temperature over the whole temperature range of measurements. A similar temperature-activated behavior of the electrical conductivity for $IrGe_{1.5}Se_{1.5}$ and $IrGe_{1.5}S_{1.5}$ was previously reported [15]. The exponential increase of the electrical conductivity at low temperatures represents the activation of the extrinsic electrons. Assuming that $\sigma = \sigma_0 \exp(-E_a/kT)$, we obtained E_a = 0.057 eV. The increase of the electrical conductivity above 700 K indicates the activation of the charge carriers across the intrinsic energy gap E_g. We estimated a band gap of 0.70 eV for $CoSn_{1.5}Te_{1.5}$ from the variation of the electrical conductivity in this temperature range. This is larger than a band gap of 0.55 eV for $CoSb_3$ [3] from which $CoSn_{1.5}Te_{1.5}$ is derived.

The electrical conductivity of $CoSn_{1.5}Te_{1.5}$ doped with Ni is

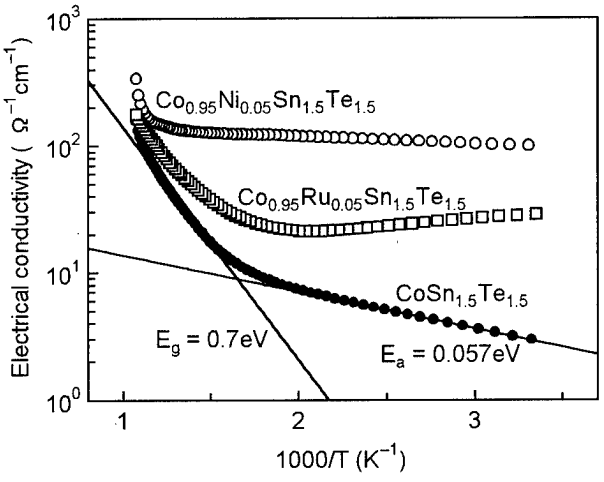


Fig. 1. Electrical conductivity values as a function of inverse temperature for doped and undoped $CoSn_{1.5}Te_{1.5}$.

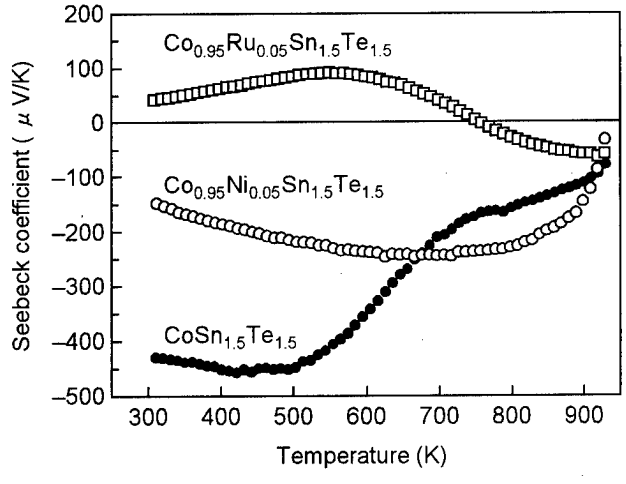


Fig. 2. Seebeck coefficient values as a function of temperature for doped and undoped $CoSn_{1.5}Te_{1.5}$.

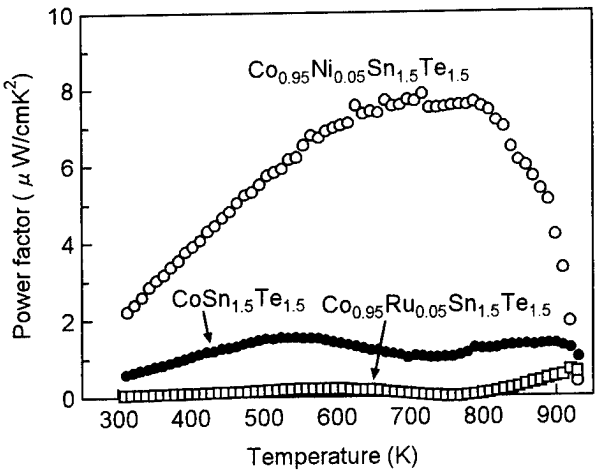


Fig. 3. Power factor values as a function of temperature for doped and undoped $CoSn_{1.5}Te_{1.5}$.

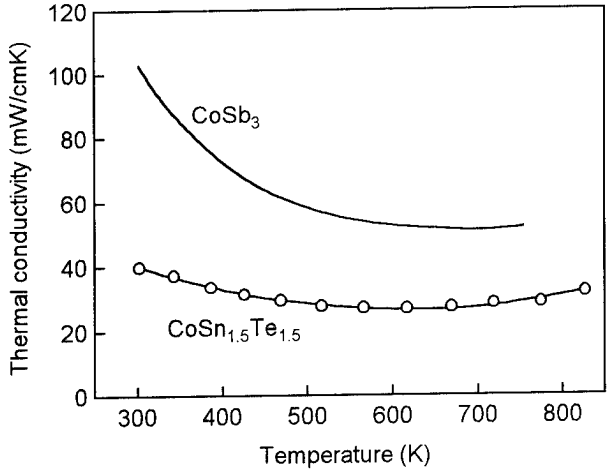


Fig. 4. Thermal conductivity values as a function of temperature for undoped $CoSn_{1.5}Te_{1.5}$. The solid line indicates the thermal conductivity values for n-type $CoSb_3$ [3].

increased, but it is still lower than that of state-of-the-art materials, about 1000 $\Omega^{-1}cm^{-1}$. The electrical conductivity of Ru-doped $CoSn_{1.5}Te_{1.5}$ is low. This is attributed to the relatively small carrier concentration and the low carrier mobility. The small carrier concentration is presumably due to the mixed-valency of Ru and self-compensation of Ru. The carrier mobility for p-type $Ru_{0.5}Pd_{0.5}Sb_3$ is relatively high [11]. The high mobility of binary skutterudite compounds is due to the predominantly covalent bonding in the skutterudite structure and valence band is essentially derived from pnicogen-pnicogen bonds in these materials [16]. Therefor, the substitution of Sn and Te for Sb causes more significant reduction of the carrier mobility than that of Ru and Pd for Rh.

The Seebeck coefficient values are shown as a function of temperature for the doped and undoped $CoSn_{1.5}Te_{1.5}$ in Figure 2. Large Seebeck coefficients up to –450 μV/K were obtained on the n-type undoped samples. The large n-type Seebeck coefficient is presumably attributed to a large electron mass. We calculated a room temperature effective mass of $4.4m_0$ for undoped $CoSn_{1.5}Te_{1.5}$ (m_0 is the free electron mass) using a single parabolic band model with acoustic phonon scattering. This value is comparable to the value of $3.4m_0$ obtained for n-type $CoSb_3$ [3]. The Seebeck coefficient of undoped $CoSn_{1.5}Te_{1.5}$ is negative over the whole temperature range of measurements. The Seebeck coefficient of the undoped sample increases slowly with increasing temperature in the extrinsic region and then decreases by increasing minority carriers. Above 750 K, the Seebeck coefficient decreases slowly. This behavior could be explained assuming the existence of an additional conduction band with a large effective mass. At high temperatures and at high doping level, the fraction of heavy electrons in the conduction electrons increases. The second conduction band electrons cause an increase in the magnitude of the n-type Seebeck coefficient, resulting in the slower decrease of the Seebeck coefficient of n-type $CoSn_{1.5}Te_{1.5}$. Above 750 K, the Seebeck coefficient values of p-type $CoSb_3$ decrease even faster and appear to become negative near 900 K [3]. This behavior can be also explained by the second conduction band model.

The Seebeck coefficient of $Co_{0.95}Ni_{0.05}Sn_{1.5}Te_{1.5}$ increases slowly with increasing temperature up to 750 K and tends to decrease at higher temperatures. This is due to an increase in the thermally excited minority carrier which causes a decrease in the magnitude of the Seebeck coefficient. The Seebeck coefficient of $Co_{0.95}Ru_{0.05}Sn_{1.5}Te_{1.5}$ is positive and relatively small at low temperatures corresponding to the extrinsic region. We estimated a room temperature effective mass of $0.16m_0$ for p-type $CoSn_{1.5}Te_{1.5}$. This value is comparable to the values $0.17m_0$, $0.153m_0$, and $0.28m_0$ obtained for p-type $IrSb_3$, $CoSb_3$, and $Ru_{0.5}Pd_{0.5}Sb_3$, respectively. The small p-type Seebeck coefficient is due to this small effective mass. When the conduction by minority carriers increases, the Seebeck coefficient decreases and becomes negative. This indicates the effect of the second conduction band.

The power factor values are shown as a function of temperature for the doped and undoped $CoSn_{1.5}Te_{1.5}$ in Figure 3. The power factor was improved by doping with Ni, but it was still low. A maximum power factor of about 8 $\mu Wcm^{-1}K^{-2}$ for Ni-doped $CoSn_{1.5}Te_{1.5}$ was achieved at 700K. The power factor of Ru-doped $CoSn_{1.5}Te_{1.5}$ was significantly decreased. This is attributed to the low carrier mobility and the small hole effective mass.

Figure 4 shows the thermal conductivity of the undoped sample as a function of temperature. The solid line represents the results of Caillat *et al.* for n-type $CoSb_3$ [3]. The room temperature thermal conductivity is about 40 $mWcm^{-1}K^{-1}$, about three times lower than for n-type $CoSb_3$. From the measurement value of the electrical conductivity and the Seebeck coefficient, we estimate using the Wiedemann-Franz law, that the electronic contribution to the thermal conductivity for undoped $CoSn_{1.5}Te_{1.5}$ can be ignored at room temperature. Thus the measured thermal conductivity of undoped

$CoSn_{1.5}Te_{1.5}$ is essentially the lattice thermal conductivity at low temperatures. The thermal conductivity of $CoSn_{1.5}Te_{1.5}$ decreases slowly up to about 600 K, and then increases slowly with increasing the electronic contribution. The room temperature lattice thermal conductivity value is relatively higher than that of the other ternary skutterudite compounds [9-12]. Recently it has been reported that the other ternary skutterudite compounds have an additional phonon scattering due to the mixed-valency of cation [11, 12]. This phonon scattering effect appeared to be not occurred for $CoSn_{1.5}Te_{1.5}$. The low thermal conductivity values of $CoSn_{1.5}Te_{1.5}$ are mainly caused by the differences of atomic mass and volume introduced by the substitution of Sn and Te for Sb.

The calculated dimensionless figure of merit *ZT* for Ni-doped $CoSn_{1.5}Te_{1.5}$ was reasonably low (ZT_{max} = 0.2 at 750 K) because of the low carrier mobility of the samples which results in low electrical conductivity values. Even though the thermoelectric figure of merit of this compound is improved by optimization of doping level, *ZT* values comparable to state-of-the-art thermoelectric materials will be unlikely to be achieved.

Conclusion

For the first time, the thermoelectric properties of a new skutterudite-related phase $CoSn_{1.5}Te_{1.5}$ were investigated. The temperature dependence of the electrical conductivity revealed that this compound was a semiconductor with a band gap of 0.7 eV. The Hall mobility in this compound was substantially low, as compared to binary compounds, leading the low electrical conductivity. The large Seebeck coefficient up to −450 μV/K was obtained on the undoped $CoSn_{1.5}Te_{1.5}$. This larger n-type Seebeck coefficient is due to a large electron mass. At high temperatures and at high doping level an additional conduction band with a large electron mass contributes to the Seebeck coefficient on $CoSn_{1.5}Te_{1.5}$. The thermal conductivity of this compound was substantially reduced from that of a binary compound $CoSb_3$. Because of the low carrier mobility, the dimensionless figure of merit was reasonably low, as compared to that of state-of-the-art thermoelectric materials. The results obtained showed that the thermoelectric potential of $CoSn_{1.5}Te_{1.5}$ was limited.

Acknowledgments

The authors would like to thank Prof. K. Matsubara and Dr. H. Anno of Science University of Tokyo in Yamaguchi and Mr. K. Kishimoto of Yamaguchi University for their available discussion. This work is supported in part by the Yamaguchi prefectural government.

References

[1] T. Caillat, A. Borshchevsky, J.-P. Fleurial, "Novel Transition Metal Compounds with Promising Thermoelectric Properties", Proc. 12th Int. Conf. on Thermoelectrics, Yokohama, Japan, IEEJ (1994), p.132.

[2] G. A. Slack, V. G. Tsoukala, "Some properties of semiconducting $IrSb_3$", J. Appl. Phys. **76**, 1665 (1994).

[3] T. Caillat, A. Borshchevsky, and J.-P. Fleurial, "Properties of single crystalline semiconducting $CoSb_3$", J. Appl. Phys. **80**, 4442 (1996).

[4] A. Borshchevsky, J.-P. Fleurial, E. Allevato, and T. Caillat, "$CoSb_3$-$IrSb_3$ solid solutions: preparation and characterization", Proc. 13th Int. Conf. on Thermoelectrics, Kansas City, MO, USA, (1995), p. 3.

[5] A. Borshchevsky, T. Caillat, and J.-P. Fleurial, "Solid Solution Formation: Improving the Thermoelectric Properties of Skutterudites", Proc. 15th Int. Conf. on Thermoelectrics, Pasadena, CA, USA, (1996), p. 112.

[6] D. T. Morelli and G. P. Meisner, "Low temperature properties of the filled skutterudite $CeFe_4Sb_{12}$", J. Appl. Phys. 77, 3777 (1995).

[7] G. S. Nolas, G. A. Slack, D. T. Morelli, T. M. Tritt, and A. C. Ehrlich, "The effect of rare-earth filling on the lattice thermal conductivity of skutterudites", J. Appl. Phys. **79**, 4002 (1996).

[8] B. C. Sales, D. Mandrus, and R. K. Williams, "Filled Skutterudite Antimonides: A New Class of Thermoelectric Materials", Science **272**, 1325 (1996).

[9] J.-P. Fleurial, T. Caillat, and A. Borshchevsky, "Thermoelectric Materials with the Skutterudite Structure: New Results", Proc. 14th Int. Conf. on Thermoelectrics, St. Petersburg, Russia, (1995), p.231.

[10] J.-P. Fleurial, T. Caillat and A. Borshchevsky, "Low Thermal Conductivity Skutterudite Materials for High Performance Thermoelectric Power Generation", Proc. 31st Intersoc. Energy Convers. Eng. Conf., Washington, DC, USA, (1996), p.914.

[11] T. Caillat, J. Kulleck, A. Borshchevsky, and J.-P. Fleurial, "Preparation and thermoelectric properties of the skutterudite-related phase $Ru_{0.5}Pd_{0.5}Sb_3$", J. Appl. Phys. **79**, 8419 (1996).

[12] G. S. Nolas, V. G. Harris, T. M. Tritt, and G. A. Slack, "Low-temperature transport properties of the mixed-valance semiconductor $Ru_{0.5}Pd_{0.5}Sb_3$", J. Appl. Phys. **80**, 6304 (1996).

[13] R. Korenstein, S. Soled, A. Wold, and G. Collin, "Preparation and characterization of the skutterudite-related phases $CoGe_{1.5}S_{1.5}$ and $CoGe_{1.5}Se_{1.5}$", Inorg. Chem. **16**, 2344 (1977).

[14] L. D. Dudkin, "The chemical bond in semiconducting cobalt triantimonide", Soviet Phys. - Tech. Phys., **2**, 216 (1958).

[15] A. Lyons, R. P. Gruska, C. Case, S. N. Subbarao, and A. Wold, "The preparation and characterization of some skutterudite related compounds", Mat. Res. Bul. **13**, 125 (1978).

[16] D. Jung, M.-H. Whangbo, and S. Alvarez, "Importance of the X_4 Ring Orbitals for the Semiconducting, Metallic, of Superconducting Properties of Skutterudites MX_3 and RM_4X_{12}", Inorg. Chem. **29**, 2252 (1990).

Effects of Defects and Impurities on Electronic Properties in $CoSb_3$

Koji AKAI, Hiroki KURISU, Toshiya SHIMURA and Mitsuru MATSUURA
Faculty of Engineering, Yamaguchi Univ., Japan
Tel.: +81 836 35 9111 ex8601, Fax.: +81 836 35 9956, E-mail: akai@po.cc.yamaguchi-u.ac.jp

Abstruct

The band structure and the density of states of doped and non-doped $CoSb_3$ were computed by using the super-cell. The computation has been done by the linear muffin-tin orbital method with non-overlapped-muffin-tin spheres. Based on the computational results, some doping effects were discussed.

Introduction

The skutterudite $CoSb_3$ and its mixed alloys have been recently investigated for its interesting thermoelectric properties.[1, 2, 3, 4, 5, 6, 7, 8] In $CoSb_3$, the hole mobility (μ_h) is extremely large, $\mu_h \sim 3000$ cm^2/Vs with the Hall carrier concentration about 10^{-18}cm^{-3}.[6] The similar transport property is observed in other skutterudites such as $IrSb_3$ and $RhSb_3$.[9]

By the band structure calculation using an extended general-potential linearized augumented-plane-wave method, Singh and Pickett[10] pointed out that $CoAs_3$ and $IrSb_3$ are zero-gap semiconductor, and $CoSb_3$ has a narrow gap of 50meV at the Γ point. Moreover, as the valence band has a linear dispersion, the density of states (DOS) is small and the pseudogap appears between the conduction band and the valence band. Mandrus et al.[11] reported that the results of the measurement for the transport properties are consistent with the theoretical prospects, especially the effective hole mass is rather small, m^*=0.01m_0.

As referred to the above, the electronic transport properties of pure or lightly doped skutterudities at low temperatures gradually get clear. Transport properties have been measured for non-doped and doped $CoSb_3$. But effects of defects and impurities are not clear with respect to such as the origin of the p-type of non-doped $CoSb_3$ and the nature of the pn-type of doped $CoSb_3$. In order to help understanding of these points, we pay attention to the impurity effects of the atoms from Pd to Sn in $CoSb_3$. These elements are between Rh and Sb in the periodic table, and the valency of doping-atoms is gradually varied from Pd to Sn. Experimental results for Pd[7] and Sn[8] shows the very good thermoelectric properties with n- and p-type characters, respectively. Our group made the experiment for Ag, Cd and In[13]. In-doped $CoSb_3$ shows the very good thermoelectric characteristics with n-type, being comparable to Pd-doped $CoSb_3$. We summarized the pn-character for the impurity from Pd to Sn in Table 1. The behavior is complex and the relation between pn-type and doping-atoms form microscopic viewpoints is not clear.

Table 1: pn-type in $CoSb_3$:X (X=Pd, Ag, Cd, In and Sn). [6,8,12,13]

X	[Rh(Co)]	Pd	Ag	Cd	In	Sn	[Sb]
type	-	n	p	n	n	p	-

In this paper we perform the preliminary study of the doping effects in the following cases; impurity atoms occupy void sites, existing in $CoSb_3$ structure, and Co and Sb atoms are exchanged for impurity atoms. The p- and n- types of carriers on impure semiconductors are determined from the position of impurity levels. We use the super-cell, including a defect or an impurity, and assume the periodic structure. Then the band structure in doped-$CoSb_3$ is computed by the linear muffin-tin orbitals (LMTO) method. From the calculated electronic structure near the Fermi energy, we discuss the pn-character.

Method of Computation

The skutterudite $CoSb_3$ is a Th^5 (Im3) bcc lattice with the lattice constant a=9.089Å.[14] The primitive cell is shown in Fig. 1, which consists of 16-atoms and a large void enclosed with those atoms. These Sb atoms are in the Wigner-Seitz(WS) cell of a bcc lattice and Co atoms are on the surface of the WS cell.

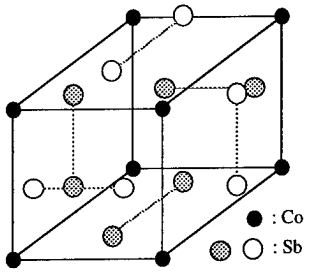


Figure 1: Primitive cell of $CoSb_3$. Small circles are Co atoms and large circles are Sb atoms.

The band structure of $CoSb_3$ is calculated by using the local-density-functonal approximation and the LMTO method with the most localized basis formalism.[15, 16] The Hedin-Lundqvist exchage-correlation function with Janak-Moruzzi-Williams parameters was used.[17]

0-7803-4057-4/97 $10.00 ©1997 IEEE

We compute the electronic band structure using the super-cell which is larger than the primitive cell. A super-cell used in this calculation is the conventional unit cell of $CoSb_3$ which consists of 8-Co atoms and 24-Sb atoms, totally 32-atoms, and 2-voids. We express the super-cell as $\square_2Co_8Sb_{24}$ in which $\square$ represents a void. The radii of MT spheres for Co and Sb atoms are given as $R_{Co} = 0.136a$ and $R_{Sb} = 0.143a$, respectively. The radii of MT spheres of impurities are given as the same radius as the atom at the doped site. When a impurity is put at the void site, the radius is taken as $R_{void} = 0.15a$.

The doping effects are investigated in three cases, i) a doping-atom occupies a void-site, ii) it occupies a Co-site, iii) it occupies an Sb-site. The DOS is calculated by using the tetrahedron method.[18] The integration in k-space were performed with a mesh of 816 points in the irreducible regions of the first Brillouin zone in the cases of (i) and (ii) and of 1000 points in the case (iii). Their regions are shown in Fig. 2 (a), (b), (c) for the cases of (i), (ii) and (iii), respectively.

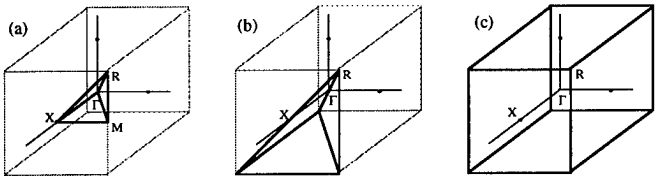


Figure 2: Irreducible regions of the first Brllouin zone, a) a doping-atom occupies a void site (the super-cell has rotational symmetry of the skutterudite structure), b) one of Co-atoms in the super-cell is exchanged for an impurity, c) one of Sb-atoms is exchaged. The cube is the first Brllouin zone of a simple cubic lattice.

Band structure on doped and non-doped $CoSb_3$

The band structure of $CoSb_3$ by the LMTO method is shown in Fig. 3. The general trends observed in the band-structure diagram is similar to that found by Singh-Pickett.[10] The characteristic feature of the band structure is the singlet valence band with a linear dispersion whose top reaches near the bottom of the conduction band at the Γ point. In our calculation, the slope of this band is -3.3 eVÅand the width of the narrow gap is 0.08eV.

The electronic density of states is shown in Fig. 4, in which the pseudogap due to the linear-dispersion band appears. This pseudogap lies below and above the Fermi energy, and the width is about 1eV. It is noted that in the general potential LAPW calculation[10], the pseudogap lies only below the Fermi energy and the width is about 0.5eV.

Impurities

Firstly, we investigate the effects of impurities which occupy one of the two void-sites, and the super-cell is given by $\square XCo_8Sb_{24}$, where X denotes a doping atom. Figures 5 show the DOS of $\square XCo_8Sb_{24}$ (X=Pd $\sim$ Sn). The origin of

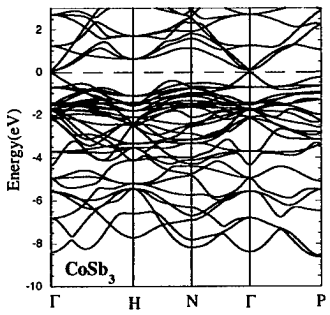


Figure 3: Band structure of $CoSb_3$. The origin of energy is the top of valence bands.

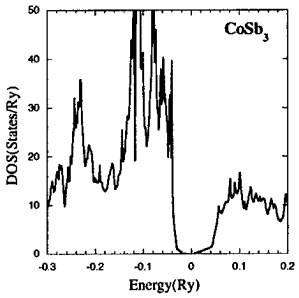


Figure 4: DOS of $CoSb_3$.

energy is the top of the linear band which is at the Γ point. Since its energy corresponds to the top of valence band in non-doped $CoSb_3$, a shift of the Fermi level is obtained. Thus we can determine whether the doping-atom acts as a donor or an acceptor. In Fig. 5(a), the sharp peak of the Pd-impurity states appears near the bottom of the conduction band, which is pointed by an arrow. The energy gap ΔE_{gap} between the top of valence bands and the bottom of the impurity band is smaller than 0.01eV. Thus Pd-impurities act as acceptors. There are mid-gap states of Ag impurities in Fig. 5(b). The states are partially occupied by electrons, and the Fermi energy is positive. It indicates that the excess electrons are supplied from Ag atoms and the Ag-doped $CoSb_3$ is a n-type semiconductor. In Fig. 5(c), the first peak of the DOS below Fermi energy denotes the impurity states of Cd which have s-like character. As the levels are very deep, Cd-impurities do not supply carriers. It is consistent that Cd-atom has a closed s-shell. When In-impurities or Sn-impurities occupy the void sites, the doping effects are clearly seen in Fig. 5(d) and (e). The Fermi level shifts to positive energy side due to the electron concentration from the doping atoms. This indicates In and Sn impurities at void site act as donors.

Figure 6 (a) and (b) show the DOS of $\square_2Co_7PdSb_{24}$ and $\square_2Co_8Sb_{23}Sn$, respectively. When Ag(Cd)-atom is doped and occupy Co-site, the DOS is qualitatively similar to Fig. 6(a), and when In-atom occupies Sb-site, it is similar to Fig. 6(b). From the shift of the Fermi level, electrons from

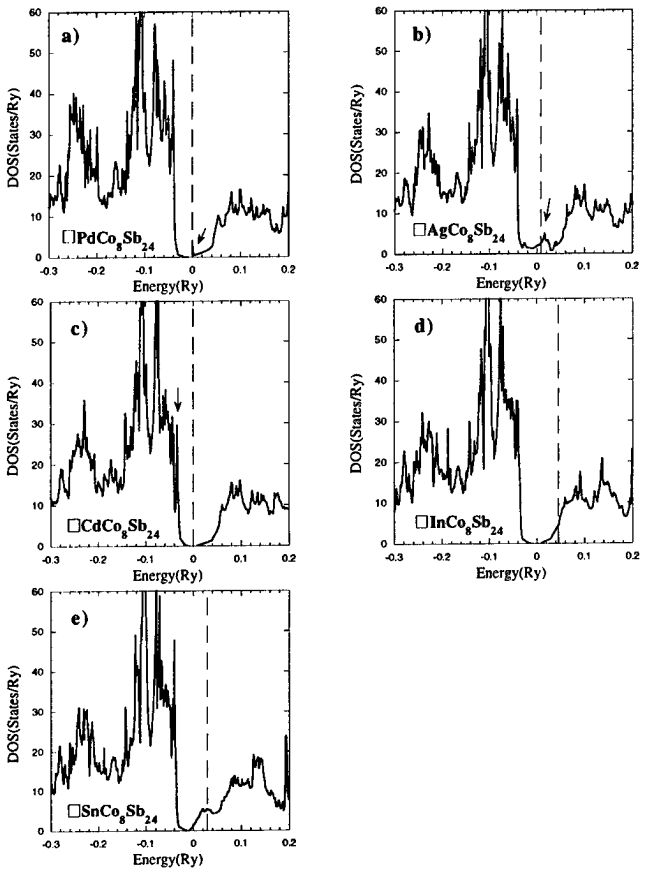


Figure 5: DOS of $\square XCo_8Sb_{24}$ (X=Pd~Sn). The origin of energy is the top of the linear band at Γ point. A straght broken line denotes the Fermi energy.

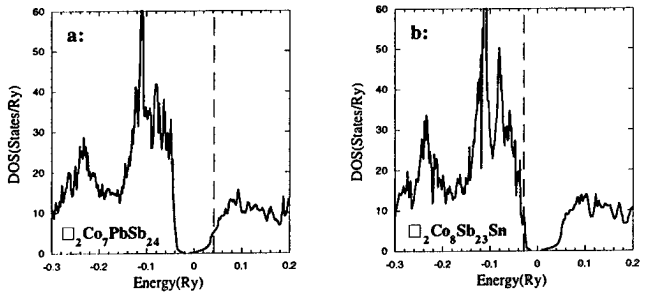


Figure 6: DOS of a: $\square XCo_7PdSb_{24}$ and b: $\square XCo_8Sb_{23}Sn$.

the impurity atoms are concentrated in $\square_2Co_7PdSb_{24}$ and holes are concentrated in $\square_2Co_8Sb_{23}Sn$. It indicate that Pd-impurities act as donors and Sn-impurities act as acceptors. These results are consistent with the filling of the outer shell of impurity atom.

Defects

The DOS of $CoSb_3$ with an empty sphere(ES) is shown in Fig. 7(a) and (b). The first is of the case that one of Co-atoms in the super-cell is exchanged for an empty sphere, the second is of the case Sb-atom is exchanged for an empty sphere. From the shift of the Fermi level, we can

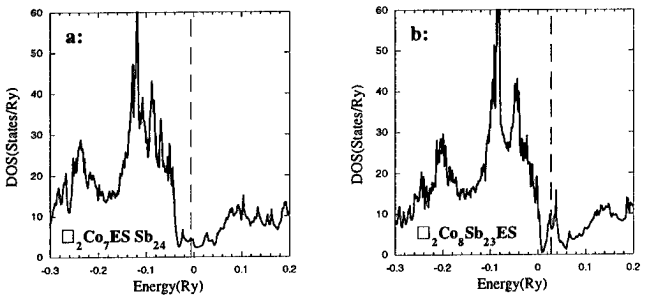


Figure 7: DOS of $CoSb_3$ with an empty spheres, a: one of Co-atoms in the super-cell is exchanged for an empty sphere, b: an Sb-atom is exchanged for empty sphere.

conclude that the empty sphere of the Co-site acts as an acceptor and the empty sphere of Sb-site acts as a donor. It is reasonable to the picture of bonds for $CoSb_3$.[19] As the DOS of skutterudite above the Fermi level is due mainly to ring antibonding π-type and σ-type molecular orbitals, 5p-electrons in Sb-atoms are exhausted for π- and σ- bonds of Sb-rings. 5s-electrons in Sb-atoms turn excess due to the hybridization with other atomic levels. Thus Sb-atoms supply electrons in $CoSb_3$ crystal. On the other hand, Co-atoms aquire electrons. In our calculation, d-orbitals of Co-atom is occupied with 8 electrons.

Conclusion

The electronic structure on doped and non-doped $CoSb_3$ were calculated with the super-cell model by using the LMTO method with non-overlapping-MT spheres and non-empty spheres. The calculated band structure of $CoSb_3$ is accord well with the results obtained earlier by other authors[10]. The results of our calculation to the pn-types of doped $CoSb_3$ are summarized in Table 2. From Tables 1 and 2, Pd-impurity atoms occupy Co-sites and Sn-impurity atoms occupy Sb-sites. On the other hand, for Ag, Cd and In the situation is not clear in the present calculation. About the origin of holes on non-doped $CoSb_3$, our results indicate that it may be occurred by defects at Co-sites. The above conclusion have preliminary aspects. For the quantitative discussion, we need further investigation with more exact methods such as the full-potential augmented-plane-wave method and the self-consistent impurity calculation based on the Green's function formal-

ism, and the total energy should be calculated to determine the favourable position for the impurity.

Table 2: pn-type of doped $CoSb_3$. The sign * denotes the case where there are few carriers, and in the cases with the sign -, the calculation has not been done.

X	Pd	Ag	Cd	In	Sn
$\square XCo_8Sb_{24}$	p	n	*	n	n
$\square_2Co_7XSb_{24}$	n	n	n	-	-
$\square_2Co_8Sb_{23}X$	-	-	-	p	p

Acknowledgement

We gratefully acknowledge Professor Setsuro Asano of the university of Tokyo for provideing LMTO program and useful discussions and comments. This work is partially supported by the Yamaguchi prefectural government.

References

[1] T. Caillat, A. Borshchevsky, and J.P. Fleureal, in *Proceedings of the XIth International Conference of Thermoelectrics*, pp. 98 (1992).

[2] T. Caillat, A. Borshchevsky, and J.P. Fleureal, in *Proceedings of the XIIth International Conference of Thermoelectrics*, pp. 132 (1993).

[3] J.P. Fleureal, T. Cailat, and A. Borshchevsky, in *Proceedings of the XIIIth International Conference of Thermoelectrics*, pp. 40 (1995).

[4] T. Caillat, A. Borshchevsky, and J.P. Fleureal, in *Proceedings of the XIIIth International Conference of Thermoelectrics*, pp. 31 (1995).

[5] K. Matsubara, T. Iyanaga, T.Tsubouchi, K. Kishimoto, and T. Koyanagi, in *Proceedings of the XIIIth International Conference of Thermoelectrics*, pp. 226 (1995).

[6] T. Caillat, A. Borshchevsky, and J.P. Fleurial, J. Appl. Phys., **80**, 4442 (1996).

[7] K. Matsubara, T. Sakakibara, Y. Notohara, H. Anno, H. Shimizu, and T. Koyanagi, in *Proceedings of the XVth International Conference of Thermoelectrics*, pp. 96 (1996).

[8] T. Koyanagi, T. Tsubouchi, M. Ohtani, K. Kishimoto, H. Anno, and K. Matsubara, in *Proceedings of the XVth International Conference of Thermoelectrics*, pp. 107 (1996).

[9] G.A. Slack and V.G. Tsoukala, J. Appl. Phys., **76**, 1665 (1994).

[10] D.J. Singh and W.E. Pickett, Phys. Rev. **B50**, 11235 (1994).

[11] D. Mandrus, A. Migliori, T.W. Darling, M.F. Hundley, E.J. Peterson, and J.D. Thompson, Phys. Rev. **B52**, 4926 (1995).

[12] B.N. Zobrina and L.D. Dudkin, Sov. Phys. Solid State **1**, 1668 (1960).

[13] The results for Ag, Cd and In were obtained by our group. The experimental details will be reported in other paper.

[14] T. Schmidt, G. Gliche, and H.D. Lutz, Acta Cryst., **C43**, 1678 (1987).

[15] O.K Andersen and O. Jepsen, Phys. Rev. Lett., **53**, 2571 (1984).

[16] O.K Andersen, O. Jepsen, and D. Grötzel, in *Highlight of Condensed Matter Theory*, edited by F. Bassai, F. Fumi, and M. Tosi (North-Holland, Amsterdam, 1985), pp59.

[17] J.F. Janak, V.N. Moruzzi, and A.R. Williams, Phys. Rev. **B12**, 1257 (1975).

[18] J. Rath and A.J. Freeman, Phys. Rev. **B11**, 2109 (1975).

[19] M. Llunell, P. Alemany, S. Alvarez, V.P. Zhukov, and A. Vernes, Phys. Rev. **B53**, 10605 (1996).

Preparation and Thermoelectric Properties of $CoSb_3$ Thin Films on GaAs(100) Substrate

H.Anno[1], T.Sakakibara[2], Y.Notohara[3], H.Tashiro[4], T.Koyanagi[5], H.Kaneko[1], and K.Matsubara[1]

[1] Science University of Tokyo in Yamaguchi, 1-1-1 Daigaku-dori, Onoda 756, Japan
Phone: +81(836)88-4541, Fax: +81(836)88-3844, E-mail: anno@ke.yama.sut.ac.jp
[2] Aisin Cosmos R&D Co., Ltd., 5-50 Hachiken-cho, Kariya 448, Japan
[3] Kyushu Matsushita Electric Co., Ltd., 4-1-62 Minoshima, Hakata-ku, Fukuoka 812, Japan
[4] Toyo Kohan Co., Ltd., 1296 Higashitoyoi, Kudamatsu 744, Japan
[5] Yamaguchi University, 2557 Tokiwadai, Ube 755, Japan

Abstract

The thin film growth of $CoSb_3$ on a semi-insulating GaAs(100) substrate was made by using magnetron rf-sputtering, and the electrical and thermoelectric properties of the films were studied with relation to annealing temperature and film thickness. Polycrystalline films with the skutterudite structure were successfully grown on the GaAs(100) substrate. The obtained films were found to be *p*-type, and their hole mobility, electrical conductivity, and Seebeck coefficient significantly changed depending on the annealing temperature and the thickness. A huge Seebeck coefficient of 600 μV/K, which is about three times as large as the value of a *p*-type single crystal, was obtained for a thin film annealed at 750 °C with thickness of 71 nm, and the power factor reached the value of 2×10^{-4} W/cmK^2. The variation in the thermoelectric properties with the annealing temperature and the thickness can be explained well in terms of a model which takes into account a carrier energy filtering effect by potential barriers at grain boundaries. According to the model, the Seebeck coefficient increases with increasing potential barrier height and also decreases with increasing carrier concentration.

1. Introduction

Much renewed interest is focused on the search for novel and efficient thermoelectric materials for cooling and energy conversion applications. For practical thermoelectric applications, materials must have a large thermoelectric figure of merit, defined as $Z=S^2\sigma/\kappa$, where S is the thermoelectric power (Seebeck coefficient), σ the electrical conductivity, and k the thermal conductivity. For over 30 years thermoelectric cooling and generation technology has been based virtually exclusively on bismuth telluride, silicon germanium, and their related compounds. Recently, $CoSb_3$ a member of the large family of skutterudite compounds has been identified as a new promising thermoelectric material because of its extremely high hole mobility, high thermoelectric power, and relatively low thermal conductivity due to complexity in the crystal structure [1, 2]. To maximize the thermoelectric figure of merit, a variety of approaches, doping of some impurities [1–4], formation of solid solutions [5], synthesis of related compounds [6, 7], and so on, have being made on this material. These conventional technique aims at the increase of the ratio σ/κ by reducing the lattice thermal conductivity κ_l. The improvements in Z by these approaches are however limited by the electronic contribution κ_e and by minimum limits of κ_l. A completely different approach to increasing Z is to attempt to increase the power factor $S^2\sigma$ through the quantum size effects, for example, changes of the scattering rates and/or the density of states [8–11]. In this point of view, Hicks and Dresselhous [8] considered the use of a superlattice structure, and found theoretically substantial improvement in Z through the change of the density of states on a Bi_2Te_3-based superlattice. According to their up-to-date investigation on a PbTe–based system, good agreement was found between the experimental result and their theoretical prediction, indicating that superlattice structure may indeed attain an enhanced Z [11]. In addition, the possibility of large enhancement in Z due to the manner of potential barriers as a carrier energy filter has been predicted for the transverse conduction through a superlattice structure [9, 10].

We have performed the thin film growth of skutterudite $CoSb_3$ on a semi-insulating GaAs(100) substrate and investigated the effects of annealing temperature and film thickness on the thermoelectric properties of obtained films. The thermoelectric properties are discussed in terms of a simple model taking into account a energy filtering effect due to potential barriers at grain boundaries.

2. Experiment

Thin film growth of $CoSb_3$ on a semi-insulating GaAs(100) substrate (the resistivity $\rho=10^7$ Ω cm) was made by magnetron rf-sputtering using a polycrystalline $CoSb_3$ target. Substrate temperature was kept at 300 °C during the deposition. Details about the sputtering conditions can be found elsewhere [12]. Some obtained films were annealed at 600 °C or 750 °C for 2 hours under flowing argon. The crystal structure of obtained films was checked by means of X-ray (Cu Kα) diffraction (XRD). The composition of the films was determined by electron probe microanalysis (EPMA), and was found to be closely stoichiometric. The observation of the film surface was made by using a scanning electron microscope (SEM) and an optical microscope. Measurements of the electrical and thermoelectric properties were carried out in the temperature range from 300 to 800 K. Hall measurements were performed between 80 and 300 K by using a van der Pauw technique.

3. Results and Discussion

3.1 Thin film growth and Annealing

From the XRD measurements, as-deposited films on

0-7803-4057-4/97 $10.00 ©1997 IEEE

GaAs(100) substrate were found to form polycrystalline skutterudite structure, including some other phases of $CoSb_2$, CoSb, and Sb. By annealing the as-deposited films at 600 °C in Ar atmosphere, the other phases nearly disappeared. The increase of the annealing temperature from 600 to 750 °C promoted full crystallization. Any diffraction peaks from the unexpected phases formed by the reaction between Co or Sb and GaAs were not detected by XRD. Surface morphology of the as-deposited films was smooth and dense, but that of the after-annealed films was rough.

The transport properties of the films were found to change largely by annealing. The changes in the values of the Hall mobility and the carrier concentration are listed in Table 1. The increase of the annealing temperature gives rise to a marked increase in the Hall mobility and also a decrease of about two orders magnitude in the carrier concentration as compared with that for an as-deposited film. The enhancement in the Hall mobility is attributed to the removal of lattice defects as well as the relaxation of lattice strain by annealing effect. But, the obtained value for the film annealed at 750 °C is about one order magnitude smaller than that for a single crystal yet [13] . In thin films, the surface and the grain boundary scattering should play an important role in the scattering mechanism along with the lattice defect scattering. In the carrier concentration, it is presumed that the drastic decrease arises from the decrease of the metallic phases in the films by annealing, according to the result of XRD. The electrical conductivity and the Seebeck coefficient of the films annealed at 600 °C as well as the as-deposited films showed irreversible changes during a heating and cooling process. This irreversible manner shows the presence of some residual lattice defects and the inhomogeneity of the films. However, for the films annealed at 750 °C, the irreversible manner was no longer observed, indicating that the higher temperature is required for the sufficient annealing effect.

Table 1 Changes in the transport properties by annealing (film thickness t=231 nm, RT data).

Annealing condition (°C)	Hall mobility (cm^2/Vs)	Carrier concentration (cm^{-3})
as-deposited	6.9	1.2×10^{19}
600	10	4.0×10^{18}
750	264	4.1×10^{17}

3.2 Thermoelectric Properties

Figure 1 shows the electrical conductivity versus inverse temperature for $CoSb_3$ films annealed at 750 °C with different thicknesses, as compared with the results for single crystals [13, 14] . The temperature dependence of the electrical conductivity varied markedly with film thickness. The variation with thickness is associated with the changes in both the scattering mechanism and the carrier concentration. In

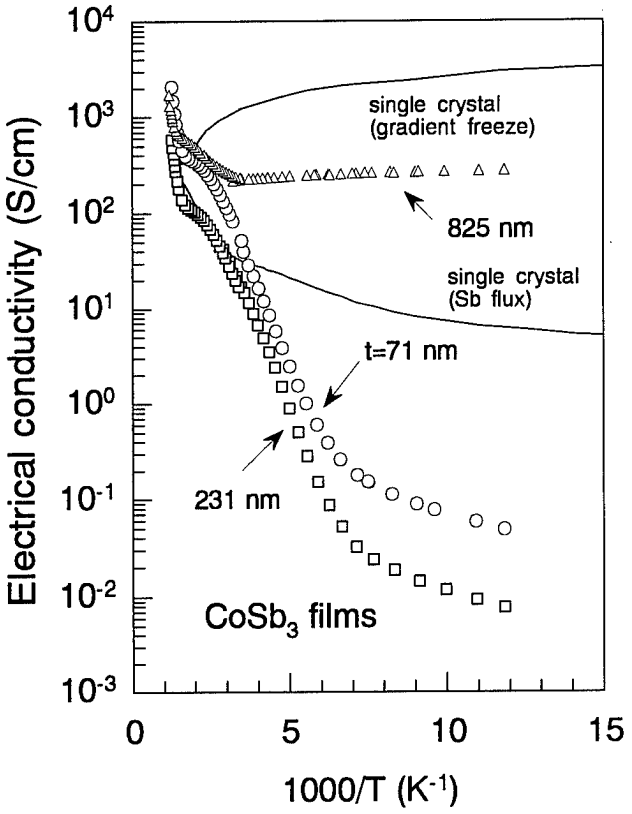


Fig. 1: Electrical conductivity versus inverse temperature for $CoSb_3$ films annealed at 750 °C with different thicknesses.

higher temperature, the saturation region was clearly observed between 300 and 500 K, and the intrinsic region above 500 K. The energy gap of approximately 0.9 eV was evaluated from the slopes of the linear potions above 500 K. The observed energy gap corresponds to the direct gap at the Γ point $E_{\Gamma-\Gamma}$, judging from the result of the energy band calculation made by Singh and Pickett [15]. Although the electrical conductivity values are much smaller than those of the single crystals at lower temperature, the situation is reversed at higher temperature. Namely, for the thin films, the electrical conductivity values become about one order magnitude larger than those for the single crystals at higher temperature.

Figure 2 shows the Seebeck coefficient as a function of temperature for $CoSb_3$ films annealed at 750 °C with different thicknesses. For the film with thickness of 825 nm, the Seebeck coefficient is comparable to that for a bulk sample [16]. However, the films with thicknesses of 71 and 231 nm were found to have huge Seebeck coefficients about 600 ~ 700 μV/K, which are about three times as large as that of the bulk sample. Rapid decrease in the Seebeck coefficient at higher temperature can be explained by the two band effect in the intrinsic region.

Figure 3 shows the power factor as a function of temperature for $CoSb_3$ films annealed at 750 °C with different thicknesses. Although the power factor values are smaller than that of the

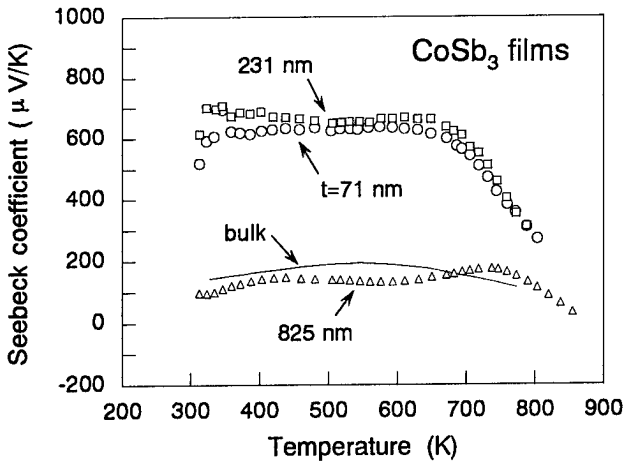


Fig. 2: Seebeck coefficient as a function of temperature for $CoSb_3$ films annealed at 750 °C with different thicknesses.

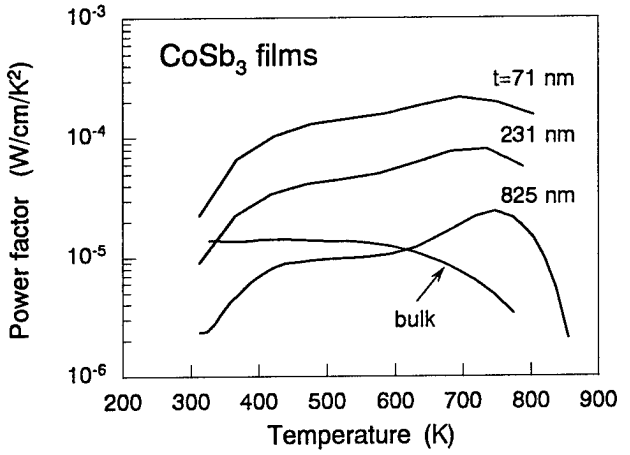


Fig. 3: Power factor as a function of temperature for $CoSb_3$ films annealed at 750 °C with different thicknesses.

bulk sample near room temperature due to the smaller electrical conductivity, the values become larger with increasing temperature up to the intrinsic region. The power factor tends to increase with decreasing thickness, and reached a maximum value of 2×10^{-4} W/cmK^2 around 700 K for the thickness of 71 nm. The improvement in the power factor for the thin films results mainly from the huge increase in the Seebeck coefficient and also the larger electrical conductivity at higher temperature as compared with the bulk sample.

The following three contributions can be regarded as the main causes of the observed large Seebeck coefficient: (1) effect of microstructure, (2) decomposition, and (3) interdiffusion between the film and GaAs substrate. The XRD results showed any clear decomposition or other phases (Ga- or As-related phases). Even though $CoSb_3$ can be expected to

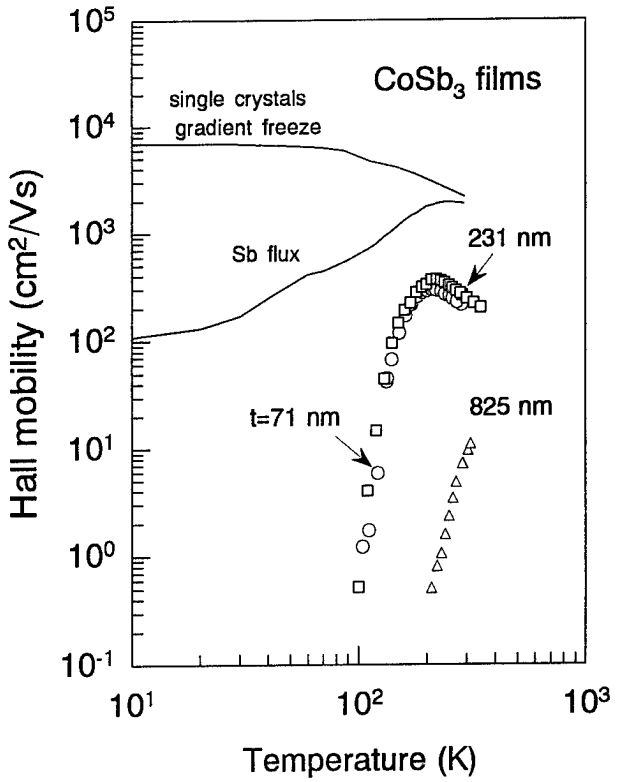


Fig. 4: Hall mobility as a function of temperature for $CoSb_3$ films annealed at 750 °C with different thicknesses.

partially decompose to a small amount of $CoSb_2$, CoSb, Sb, Co or other phases, this effect on the Seebeck coefficient may be small because of small amount and their small or comparable Seebeck coefficients [17]. In addition, the possibility of the substitution of Co or Sb for GaAs crystal lattice by interdiffusion may be probably low because of the lower annealing temperature than the melting point of GaAs (1238 °C). Thus, we discuss the effect of microstructure on the Seebeck coefficient. In the polycrystalline thin films, the scattering by grain boundaries and surface should be extremely important and may play a more prominent role in the thermoelectric properties as compared with bulk materials.

To have a clearer idea of the scattering mechanism, the Hall mobility as a function of temperature for $CoSb_3$ films annealed at 750 °C with different thicknesses is shown in Fig.4. The temperature dependence for the thin films is surprisingly different from those for the single crystals [13, 14]. For the films, the Hall mobility values increase rapidly with increasing temperature up to 200 K, then decrease as $T^{-3/2}$ behavior at higher temperature. For the grain boundary scattering, the carrier mobility μ is known to increase exponentially with temperature as the relation,

$$\mu = Le\left(\frac{1}{2\pi m^* k_B T}\right)^{1/2} exp\left(-\frac{E_b}{k_B T}\right), \quad (1)$$

Table 2 Carrier concentration and potential barrier height of $CoSb_3$ films annealed at 750 °C with different thicknesses.

Symbol	Thickness (nm)	Carrier concentration (cm^{-3})	Potential barrier height (eV)
○	71	1.1×10^{18}	0.16
□	231	5.5×10^{17}	0.15
△	825	1.4×10^{20}	0.19

where E_b is the potential barrier height at grain boundaries, L the grain size, m^* the effective mass of carrier, k_B Boltzmann's constant [18]. Thus, the relation between log ($\mu T^{1/2}$) and $1/T$ should be linear, and the potential barrier height E_b can be estimated from the slop. It was found that the plot of log ($\mu T^{1/2}$) vs $1/T$ was linear for the thin films, indicating that the grain boundary scattering is the predominant scattering mechanism. This result also suggests that the after-annealed films have fine-grained microstructures. On the other hand, at higher temperature T > 200 K, the acoustic phonon scattering is the predominant scattering mechanism. The carrier concentration and the potential barrier height are summarized in Table 2. The thin films were found to have extremely large potential barriers. The carrier concentration ranges from 10^{17} to 10^{20} cm^{-3} depending on the thickness.

As shown in Fig.5, based on the result of the Hall measurements, a model to explain the observed Seebeck coefficient can be drawn taking into account the carrier energy filtering effect due to the potential barriers at grain boundaries. Low-energy carriers are trapped between the potential barriers at grain boundaries, while high-energy carriers conduct normally, resulting in an increase of the Seebeck coefficient. On the contrary, the electrical conductivity decreases due to the grain boundary scattering, as shown in Fig. 1. Assuming the acoustic phonon scattering only (T > 200 K) as the charge carrier scattering, the Seebeck coefficient S can consequently be given by

$$S = \frac{k_B}{e}\left(\frac{7}{5}\frac{F_{5/2}(\eta)}{F_{3/2}(\eta)} - \eta\right), \qquad (2)$$

where $F_{5/2}(\eta)$ and $F_{3/2}(\eta)$ are the modified Fermi integrals, which are given by

$$F_n(\eta) = \int_\phi^\infty \frac{x^n}{exp\,(x-\eta)+1}\,dx, \qquad (3)$$

where $\phi = E_b/k_BT$ is the reduced barrier height of the potential barriers and $\eta = E_f/k_BT$ the reduced Fermi energy [19]. This model calculation takes into account the non-parabolic band dispersion in the vicinity of the top of the valence band. This treatment is based on the result of the band calculation, in which the linear dispersion at the valence band top is predicted for skutterudite $CoSb_3$ [15].

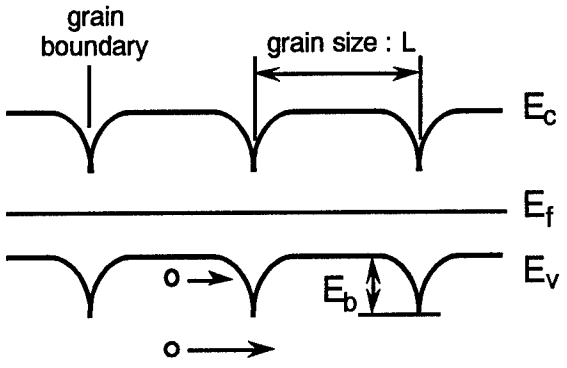


Fig. 5: Model of carrier energy filtering effect due to potential barriers at grain boundaries.

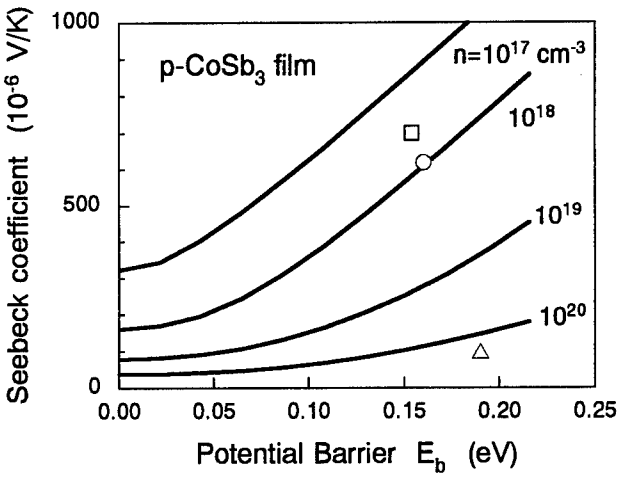


Fig. 6: Dependence of Seebeck coefficient on potential barrier height as a function of carrier concentration.

Figure 6 shows the dependence of the Seebeck coefficient on the potential barrier height as a function of the carrier concentration. The solid lines are results of the model calculation and the plots are experimental values denoted by the same symbols as Table 2. The calculated Seebeck coefficients without potential barriers agree well with those for bulk samples [16]. The interesting features of the calculation are the following: (1) the Seebeck coefficient increases with increasing potential barrier height due to the carrier energy filtering effect, and (2) the Seebeck coefficient at given potential barrier height decreases with increasing carrier concentration, similarly to an ordinary semiconductor manner. The model calculation reproduces satisfactorily well the observed values, indicating that the large increase in the Seebeck coefficient can be explained in terms of the proposed model. It turned out that the variation in the Seebeck coefficient with the thickness results from the changes in both the potential barrier height and the carrier concentration.

Conclusion

We have performed the thin film growth of skutterudite $CoSb_3$ on a semi-insulating GaAs(100) substrate and investigated the effects of annealing temperature and film thickness on the thermoelectric properties. Major results obtained in this study are as follows.

(1) Polycrystalline *p*-type $CoSb_3$ thin films with the skutterudite structure were successfully grown on a semi-insulating GaAs (100) substrate by using magnetron rf–sputtering.

(2) Annealing at 750 °C promotes full crystallization in the skutterudite structure, leading to fine-grained microstructures with considerably high potential barriers at grain boundaries.

(3) The electrical and thermoelectric properties (hole mobility, electrical conductivity, Seebeck coefficient) depend on the annealing temperature and the film thickness. A huge Seebeck coefficient of about 600 μV/K was obtained for the thin film annealed at 750 °C with thickness of 71 nm, and power factor reached a value of 2×10^{-4} W/cmK^2.

(4) The dependence of the Seebeck coefficient on the annealing temperature and the thickness can be explained in terms of a model which takes into account a carrier filtering effect due to potential barriers at grain boundaries. According to the model, the thickness dependence of the Seebeck coefficient for the after-annealed films is attributed to the changes in both the potential barrier height and the carrier concentration.

Acknowledgment

This work was performed by financial supports of the Yamaguchi Prefectural Government and the Yamaguchi Industrial Technology Development Organization.

References

[1] K.Matsubara, T.Iyanaga, T.Tsubouchi, K.Kishimoto, and T.Koyanagi, "Thermoelectric Properties of (Pd , Co)Sb_3 Compounds with Skutterudite Structure", *Proc. XIII Int. Conf. on Thermoelectrics*, Kansas, USA, 1994, (AIP Press, New York), pp.226-229 (1995).

[2] T.Caillat, A.Borshchevsky, and J.-P.Fleurial, "Preparation and Thermoelectric Properties of *p*- and *n*-type $CoSb_3$", *Proc. XIII Int. Conf. on Thermoelectrics*, Kansas, USA, 1994, (AIP Press, New York), pp.58-61 (1995).

[3] T.Caillat, A.Borshchevsky, and J.-P.Fleurial, " Properties of Single Crystalline Semiconducting $CoSb_3$", J.Appl.Phys., **80**, 4442 (1996).

[4] H.Tashiro, Y.Notohara, T.Sakakibara, H.Anno, and K.Matsubara, " Effects of doping Pd/Pt in $CoSb_3$ Crystals on Electrical and Thermoelectric Properties", *Proc. XVI Int. Conf. on Thermoelectrics,* (in this conference), Dresden, Germany, 1997.

[5] A.Borshchevsky, J.-P.Fleurial, E.Allevato, and T.Caillat, "$CoSb_3$ – $IrSb_3$ Solid Solutions: Preparation and Characterization", *Proc. XIII Int. Conf. on Thermoelectrics*, Kansas, USA, 1994, (AIP Press, New York), pp.3-6 (1995).

[6] T.Caillat, J.Kulleck, A.Borshchevsky, and J.-P.Fleurial, "Preparation and Thermoelectric Properties of the Skutterudite-Related Phase", J.Appl.Phys., **79**, 8419 (1996).

[7] Y.Nagamoto, K.Tanaka, and T.Koyanagi, "Thermoelectric Properties of the Skutterudite-Related Phase $CoSn_{1.5}Te_{1.5}$", *Proc. XVI Int. Conf. on Thermoelectrics*, (in this conference), Dresden, Germany, 1997.

[8] L.D.Hicks and M.S.Dresselhaus, "Effect of Quantum-Well Structures on the Thermoelectric Figure of Merit", Phys. Rev. B, **47**, 12727 (1993).

[9] L.W.Whitlow and T.Hirano, "Superlattice Application to Thermoelectricity", J.Appl.Phys., **78**, 5460 (1995).

[10] D.M.Rowe and G.Min, "Multiple Potential Barriers as a Possible Mechanism to Increase the Seebeck Coefficient and Electrical Power Factor", *Proc. XIII Int. Conf. on Thermoelectrics*, Kansas, USA, 1994, (AIP Press, New York), pp.339-342 (1995).

[11] L.D.Hicks, T.C.Harman, X.Sun, and M.S.Dresselhaus, "Experimental Study of the Effect of Quantum-Well Structures on the Thermoelectric Figure of Merit", Phys. Rev. B, **53**, R10493 (1996).

[12] H.Anno, K.Matsubara, Y.Notohara, T.Sakakibara, K.Kishimoto, and T.Koyanagi, "Thermoelectric Properties of RF-sputtered $CoSb_3$ Films", *Proc. XV Int. Conf. on Thermoelectrics*, Pasadena, USA, 1996, (IEEE Catalog # 96TH8169), pp.435-439 (1996).

[13] D.T.Morelli, T.Caillat, J.-P.Fleurial, A.Borshchevsky, J.Vandersande, B.Chen, and C.Uher, "Low-Temperature Transport Properties of *p*-type $CoSb_3$", Phys. Rev. B, **51**, 9622 (1995).

[14] D.Mandrus, A.Migliori, T.W.Darling, M.F.Hundley, E.J.Peterson, and J.D.Thompson, " Electronic Transport in Lightly Doped $CoSb_3$", Phys. Rev. B, **52**, 4926 (1995).

[15] D.J.Singh and W.-E.Pickett, "Skutterudite Antimonides: Quasilinear Bands and Unusual Transport", Phys. Rev. B, **50**, 11235 (1994).

[16] K.Matsubara, T.Sakakibara, Y.Notohara, H.Anno, H.Shimizu, and T.Koyanagi, " Electronic Transport Properties of the Skutterudite $CoSb_3$ and Mixed Alloys", *Proc. XV Int. Conf. on Thermoelectrics*, Pasadena, USA, 1996, (IEEE Catalog # 96TH8169), pp.96-99 (1996).

[17] T.Caillat, " Preparation and Thermoelectric Properties of $Ir_xCo_{1-x}Sb_2$ Alloys", J. Phys. Chem. Solids, **57**, 1351 (1996).

[18] J.Y.W.Seto, " The Electrical Properties of Polycrystalline Silicon Films", J.Appl.Phys. **46**, 5247 (1975).

[19] H.J.Goldsmid, "Electronic Refrigeration", (Pion Limited, London), Chap.2, (1986).

Electronic Transport Properties of *p*-type $CoSb_3$

H.Anno[1], H.Tashiro[2], Y.Notohara[3], T.Sakakibara[4], K.Hatada[1], K.Motoya[5], H.Shimizu[1], and K.Matsubara[1]

[1] Science University of Tokyo in Yamaguchi, 1-1-1 Daigaku-dori, Onoda 756, Japan
Phone: +81(836)88–4541, Fax: +81(836)88–3844, E-mail: anno@ke.yama.sut.ac.jp
[2] Toyo Kohan Co., Ltd., 1296 Higashitoyoi, Kudamatsu 744, Japan
[3] Kyushu Matsushita Electric Co., Ltd., 4-1-62 Minoshima, Hakata-ku, Fukuoka 812, Japan
[4] Aisin Cosmos R&D Co., Ltd., 5-50 Hachiken-cho, Kariya 448, Japan
[5] Science University of Yokyo, 2641 Yamazaki, Noda 278, Japan

Abstract

The electronic transport properties were investigated on polycrystalline *p*-type $CoSb_3$ with different grain sizes (about 3 and 3×10^2 μm) to clarify the important factors which affect the hole mobility. The magnetic susceptibility was also measured. Samples were found to be stoichiometric and homogeneous without any segregation of other phases. From the temperature dependence of the hole mobility, it was found that the predominant scattering mechanism depends significantly on grain size. The magnetic susceptibility was found to be diamagnetic independently of grain size, and to depend weakly on the temperature. The susceptibility can be explained by taking into account the three contributions due to ion cores, conduction electrons, and residual magnetic impurities. From the analysis of the susceptibility, the effects of residual magnetic impurities on the transport properties were found to be negligible. In addition, the band gap energy of $CoSb_3$ was determined to be about 70~80 meV. The grain size is one of the key factors determining the transport properties of polycrystalline *p*-type $CoSb_3$.

Introduction

$CoSb_3$ with the skutterudite structure has recently attracted much attention as a promising new thermoelectric material because of its extremely high hole mobility, high thermoelectric power, and relatively low thermal conductivity due to the complex crystal structure [1–8]. A variety of approaches have been considered to maximize the thermoelectric figure of merit of this material [6]. It is important to understand the electronic transport properties and the phonon scattering mechanism to achieve a further improvement in the thermoelectric performance of this material. Several researchers performed the *p*-type single crystal growth by a gradient freeze technique and the Sb flux method, and investigated the electronic transport properties in detail to reveal the nature of $CoSb_3$ [4, 5]. It can be considered that the important factors which bring about prominent effects on the transport properties are (1) stoichiometry, (2) residual impurities, and (3) microstructure. In a previous paper, we reported the effects of residual Ni impurity on the transport properties of polycrystalline $CoSb_3$ [7]. Recently, we also reported the effects of the segregation of other phases (Co, Sb, CoSb, and $CoSb_2$) on the hole mobility of polycrystalline *p*-type $CoSb_3$ [9]. However, there are few detailed studies on the effects of microstructure (such as grain size, grain boundary, and porosity) on the transport properties of polycrystalline *p*-type $CoSb_3$ [10].

To clarify the important factors which affect the hole mobility, we prepared polycrystalline *p*-type $CoSb_3$ with different grain sizes using extra pure source materials, and studied the relationship between the electronic transport and the structural properties. The effects of residual magnetic impurities on the transport properties are also discussed from the magnetic susceptibility.

Experiment

Polycrystalline *p*-type $CoSb_3$ samples were prepared by hot-pressing as follows. Extra pure powders of Co (99.998%: Ni-free) and Sb (99.9999%) were mixed in the Sb-rich molar ratio (Co : Sb = 1 : 3.2) to avoid the segregation of Co or other Co-Sb phases such as CoSb and $CoSb_2$. The mixed materials were sealed under vacuum in a carbon-coated quartz tube, and annealed at 873 K for 48 hours. Then, the resulting materials were hot-pressed under 60 MPa at 923 K for 1 hour (sample C01), and at 1023 K for 4 hours (sample C05). Excess Sb was melted and removed at the hot-pressing.

The crystal structure of samples was checked by x-ray diffraction. The composition and homogeneity of samples were checked by electron-probe microanalysis (EPMA). The microstructure of samples was observed under an optical microscope. The average grain size of samples was determined by a conventional method. The Hall measurements were carried out in the temperature range from 80 to 300 K using a van der Pauw technique. The Hall carrier concentration n was determined form the Hall coefficient R_H using $R_H=1/en$ relation. The Hall mobility μ was determined from the zero-field electrical conductivity σ and the Hall carrier concentration n using $\sigma=en\mu$. Measurements of the magnetic susceptibility were performed in the temperature range from 5 to 300 K using a Quantum Design superconducting quantum interference device (SQUID) magnetometer. Applied magnetic field was 2 T. The background susceptibility was independently measured and corrected for.

Results and Discussion

All samples were found to be single phase of the skutterudite structure from the x-ray diffraction measurements. The lattice constant of samples was about 9.036 Å, which agrees well with single crystal values [5]. The measured densities of samples were about 98% of the theoretical value of $CoSb_3$ (7.69 g/cm^3)

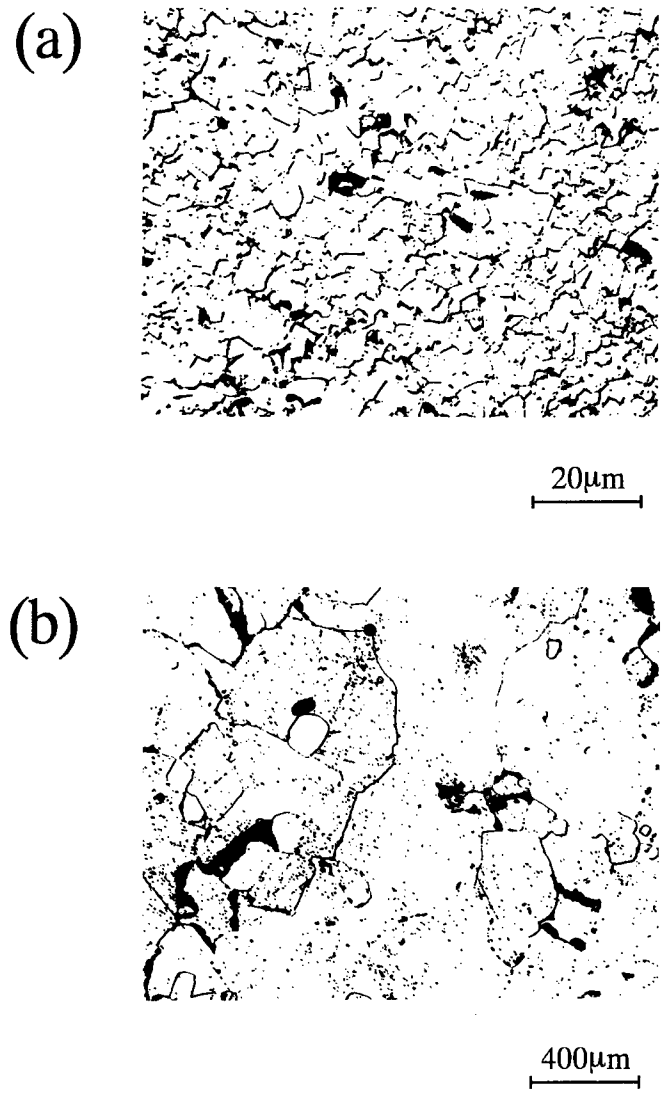


Fig. 1: Surface micrographs of polycrystalline $CoSb_3$ samples prepared by hot-pressing at (a) 923 K (sample C01) and (b) 1023 K (sample C05).

[4]. EPMA results showed that all samples were stoichiometric and homogeneous. The segregation of other phases (such as Sb, Co, CoSb, and $CoSb_2$) was not detected within the resolution of EPMA.

Figures 1 (a) and (b) show the surface micrographs of polycrystalline p-type $CoSb_3$ samples hot-pressed at 923 K (sample C01) and 1023 K (sample C05), respectively. The grain size of the samples depends on the sintering temperature. The average grain sizes of the samples C01 and C05 are about 3 and 3×10^2 μm, respectively.

Figure 2 shows the Hall mobility as a function of the temperature for polycrystalline p-type $CoSb_3$ samples with different grain sizes. The results are compared with those for two p-type single crystals: one was grown by the gradient freeze technique (sample GF) [4] and the other was grown by the Sb flux method (sample Sb-flux) [5]. In addition, results for polycrystal-

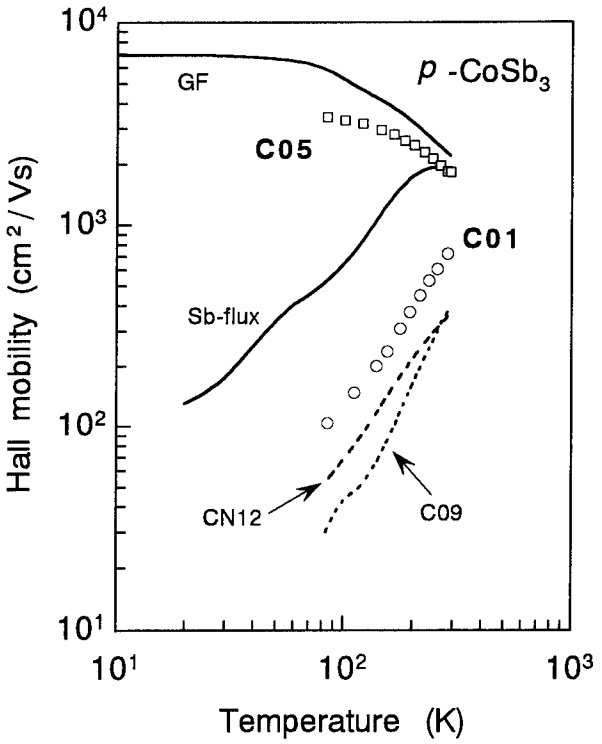


Fig. 2: Hall mobility as a function of the temperature for polycrystalline $CoSb_3$ samples with different grain sizes.

line p-type samples with residual Ni impurity of 230 ppm (sample CN12) [7] and a small amount of other phases (mainly $CoSb_2$ and CoSb) (sample C09) [9] are shown in Fig.2 as references. The average grain sizes of the samples CN12 and C09 are about 5 and 4 μm, respectively. In these polycrystalline samples with the impurities, the temperature dependence of the hole mobility can be explained in terms of the ionized impurity scattering model, in which the other phases (mainly $CoSb_2$ and CoSb) and the residual Ni impurity probably play dominant roles.

For the samples C01 and C05, the temperature dependence of the hole mobility depends significantly on the grain size. For large grain size (the sample C05), it can be considered that the predominant scattering mechanism is the combination of the neutral impurity scattering ($T < 100$ K) and the acoustic phonon scattering ($T > 100$ K). The carrier scattering mechanism for the sample C05 is in good agreement with that for the sample GF. On the other hand, for fine grain size (the sample C01) an indication of $T^{3/2}$ behavior shows that the ionized impurity scattering is the predominant scattering mechanism, similarly to the sample Sb-flux. For the samples C01 and C05, it should be noted that the Ni-free source powders were used and that there was no clear evidence of the segregation of other phases. Thus, some other types of impurities (except the residual Ni and other phases) probably act as the predominant scattering centers in the samples C01 and C05. Furthermore, from the relationship between the mean free path of phonon and grain size, it can be expected that the scattering by phonons is suppressed by grain size effects in the sample C01 with fine-

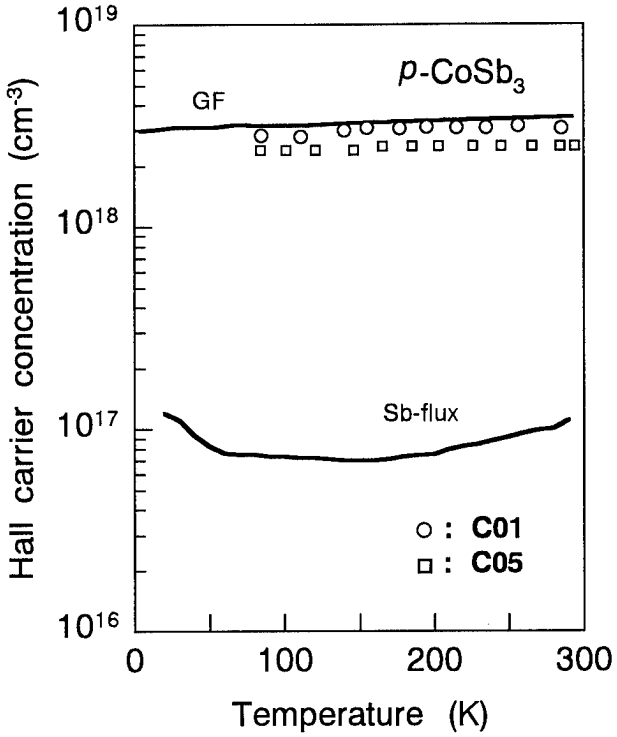


Fig. 3: Hall carrier concentration as a function of the temperature for polycrystalline $CoSb_3$ samples with different grain sizes.

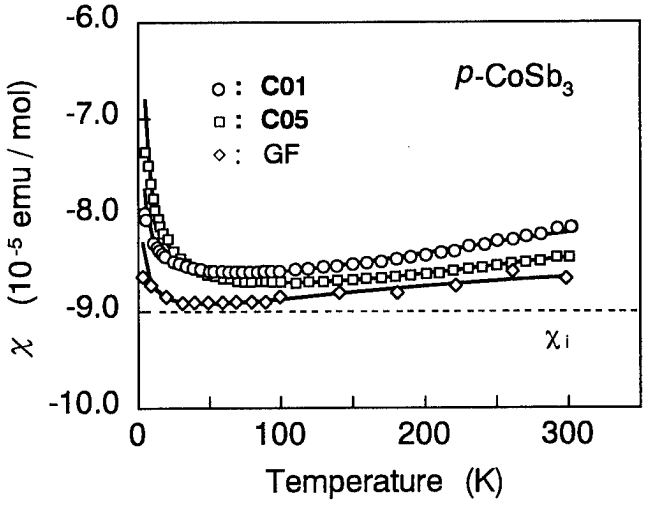


Fig. 4: Magnetic susceptibility χ as a function of the temperature for polycrystalline $CoSb_3$ samples with different grain sizes. Solid lines are results of fitting using Eq. (1) based on a proposed model. The dashed line indicates the estimated contribution of the ion cores χ_i.

grained structure.

The grain boundary scattering is also one of important factors for such fine-grained materials as the sample C01. In this case, the carrier mobility μ is known to increase exponentially with increasing temperature as the relation $\mu \propto T^{-1/2}\exp[-E_b/(k_B T)]$, where E_b is the energy barrier at grain boundaries and k_B the Boltzmann's constant [11]. Thus, the relation between $\log(\mu T^{1/2})$ and $1/T$ should be linear. However, it was found that the plot of $\log(\mu T^{1/2})$ vs $1/T$ is not linear for the sample C01, indicating that the grain boundary scattering is not the predominant scattering mechanism.

The values of the Hall carrier concentration are plotted as a function of the temperature for polycrystalline p-type $CoSb_3$ samples with different grain sizes in Fig.3. The values at room temperature for the polycrystalline samples are comparable to that for the sample GF, but approximately an order of magnitude larger than that for the sample Sb-flux. Interesting features seen in Fig.3 are the following: (1) although the temperature dependence of the hole mobility depends on the grain size, the temperature dependence of the Hall carrier concentration is almost independent of the grain size, and (2) for both the polycrystalline samples and the single crystals, the Hall carrier concentration depends slightly on the temperature.

Figure 4 shows the temperature dependence of the magnetic susceptibility χ for polycrystalline p-type $CoSb_3$ samples with different grain sizes. For the polycrystalline samples, the magnetic susceptibility is essentially diamagnetic independently of the grain size. However, the susceptibility depends weakly on the temperature. The results for the polycrystalline samples agree well with that for the sample GF [4]. These facts show that the crystal quality of the grains in the polycrystalline samples is as high as that of the single crystal. The magnetic susceptibility of ion cores is well known to be independent of the temperature. The ion core susceptibility of the samples was estimated to be approximately -9×10^{-5} emu/mol from the atomic susceptibility values of the constituents. Thus, the weak temperature dependence is due to some paramagnetic contributions.

The weak temperature dependence of the magnetic susceptibility can be divided into two different regions: (1) a relatively large decrease up to about 50 K, and (2) a slight increase from 50 to 300 K. The region (1) can be attributed to the paramagnetic contribution due to residual magnetic impurities. Since the paramagnetic susceptibility follows the Curie low, the paramagnetic contribution due to residual magnetic impurities decreases with increasing temperature. The region (2) can be explained by the semiconducting behavior of $CoSb_3$. As the temperature increases, the number of electrons in the conduction band increases, and consequently the paramagnetic contribution due to the conduction electrons increases. The appearance of the paramagnetic contribution due to the conduction electrons is reasonably consistent with the experimental result that the Hall carrier concentration increases gently with increasing temperature.

Therefore, the observed susceptibility χ can be explained by taking into account the three contributions, the diamagnetic susceptibility due to the ion cores χ_i (the negative constant value), the paramagnetic susceptibility due to the conduction electrons χ_e, and the paramagnetic susceptibility due to residual magnetic impurities χ_m. Solid lines in Fig.4 are the results of

fitting based on our model using the following relation,

$$\chi = \chi_i + \chi_e + \chi_m$$
$$= \chi_i + N_0 \exp[-E_g/(2k_B T)] + C/T \qquad (1)$$

where N_0 is the constant, E_g the band gap energy, and C the Curie constant. The contribution χ_e can be assumed to be simply proportional to the number of the conduction electrons [12]. Equation (1) can reproduce well the experiments, supporting our explanation of the temperature dependence of the susceptibility. The values of the band gap energy E_g were determined to be about 70 and 80 meV for the samples C01 and C05, respectively, from the fitting above 50 K. The obtained values are in reasonable agreement with the recent band-structure calculation of $CoSb_3$ made by Singh and Pickett, in which they predict a 50-meV narrow gap [13]. In addition, from the Curie constant, it was found that the quantity of residual magnetic impurities in the samples is so small that the effects of residual magnetic impurities on the transport properties can be negligible.

Conclusion

To clarify the important factors which affect the hole mobility, we have performed the detailed study on the electronic transport properties of polycrystalline *p*-type $CoSb_3$ with different grain sizes. We have also measured the magnetic susceptibility to obtain the data on the effects of residual magnetic impurities on the transport properties. Major results obtained in this study are as follows:

(1) The detailed impurity analyses strongly suggest that the effects of residual magnetic impurities and other phases on the transport properties can be negligible.

(2) The temperature dependence of the hole mobility shows that the predominant carrier scattering mechanism depends significantly on grain size. Thus, the grain size is one of the key factors determining the hole mobility of polycrystalline *p*-type $CoSb_3$.

(3) The magnetic susceptibility is diamagnetic independently of grain size. But the susceptibility depends weakly on the temperature. The susceptibility can be explained by the three contributions due to ion cores, conduction electrons, and residual magnetic impurities.

(4) The band gap energy of $CoSb_3$ can be determined to be about 70~80 meV from the analysis of the susceptibility.

Acknowledgments

The authors would like to thank Dr. J.W.Vandersande, Dr. T.Caillat, Dr. J.-P.Fleurial, and Dr. A.Borshchevsky of the Jet Propulsion Laboratory for their available discussion on the sample preparation. This work was supported by the Yamaguchi Prefectural Government and the Yamaguchi Industrial Technology Development Organization.

References

[1] T.Caillat, A.Borshchevsky, and J.-P.Fleurial, in *Proceedings of the 13th International Conference on Thermoelectrics*, AIP Conference Proceedings 316, edited by B.Mathiprakasam and P.Heenan, Kansas City, MO, USA, 1994 (AIP, New York, 1995), pp.58-61.

[2] K.Matsubara, T.Iyanaga, T.Tsubouchi, K.Kishimoto, and T.Koyanagi, in *Proceedings of the 13th International Conference on Thermoelectrics*, AIP Conference Proceedings 316, edited by B.Mathiprakasam and P.Heenan, Kansas City, MO, USA, 1994 (AIP Press, New York, 1995), pp. 226-229.

[3] J.W.Sharp, E.C.Jones, R.K.Williams, P.M.Martin, and B.C.Sales, J. Appl. Phys. **78**, 1013 (1995).

[4] D.T.Morelli, T.Caillat, J.-P.Fleurial, A.Borshchevsky, J.Vandersande, B.Chen, and C.Uher, Phys. Rev. B **51**, 9622 (1995).

[5] D.Mandrus, A.Migliori, T.W.Darling, M.F.Hundley, E.J.Peterson, and J.D.Thompson, Phys. Rev. B **52**, 4926 (1995).

[6] J.-P.Fleurial, T.Caillat, and A.Borshchevsky, in *Proceedings of the 14th International Conference on Thermoelectrics*, St.Petersburg, Russia, 1995, edited by M.V.Vedernikov, M.I.Fedorov, and A.E.Kaliazin, (A.F.Ioffe Physical-Technical Institute, St.Petersburg, Russia, 1995), pp. 231-235.

[7] K.Matsubara, T.Sakakibara, Y.Notohara, H.Anno, H.Shimizu, and T.Koyanagi, in *Proceedings of the 15th International Conference on Thermoelectrics*, IEEE Catalog Number 96TH8169, edited by T.Caillat, A.Borshchevsky, and J.-P.Fleurial, Pasadena City, CA, USA, 1996 (IEEE, Piscataway, 1996), pp. 96-99.

[8] H.Tashiro, Y.Notohara, T.Sakakibara, H.Anno, and K.Matsubara, in *Proceedings of the 16th International Conference on Thermoelectrics* (in this conference), Dresden, Germany, 1997.

[9] T.Sakakibara, Y.Notohara, H.Tashiro, H.Anno, and K.Matsubara, in *Extended Abstracts of the 57th Autumn Meeting of the Japan Society of Applied Physics*, JSAP Catalog Number AP961119-01, (JSAP, Tokyo, 1996), p.74.

[10] H.Nakagawa, H.Tanaka, A.Kasama, H.Anno, and K.Matsubara, in *Proceedings of the 16th International Conference on Thermoelectrics* (in this conference), Dresden, Germany, 1997.

[11] J.Y.W.Seto, J.Appl.Phys. **46**, 5247 (1975).

[12] Taking into account the Pauli paramagnetism and the Landau diamagnetism, the susceptibility χ_e due to conduction electrons is well known to be described by the relation, $\chi_e = \mu_B^2 n / E_F$, where μ_B is the Bohr magneton, n the number of electrons, and E_F the Fermi energy. In intrinsic region for semiconductors, the number of conduction electrons varies as $n = n_0 \exp[-E_g/(2k_B T)]$. Thus the combination of the relations χ_e and n produces $\chi_e = N_0 \exp[-E_g/(2k_B T)]$, where $N_0 = \mu_B^2 n_0 / E_F$.

[13] D.J.Singh and W.E.Pickett, Phys. Rev. B **50**, 11235 (1994).

Transport properties of the skutterudite $CoSb_3$

K. Fess, E. Arushanov, W. Käfer, Ch. Kloc, K. Friemelt, and E. Bucher
Universität Konstanz, P.O. Box X916, D-78457 Konstanz, Germany,
Tel.: +49/7531/88-3174, Fax: +49/7531/88-3895, e-mail:wolfgang.kaefer@uni-konstanz.de

Abstract
We prepared single crystals of $CoSb_3$ by chemical vapor transport and from Sb-rich melt. We performed measurements of the resistivity, the Hall-effect and thermoelectric power over a large temperature range.
The observed temperature dependence of the Hall-coefficient can be explained on the basis of an acceptor impurity band and an additional deep acceptor level. The values of the activation energies of the shallow and deep acceptors, their concentrations, as well as the concentrations of the compensating donors were calculated.
The contributions of different scattering mechanisms were determined on the basis of many available parameters from the literature and our own measurements. It is shown, that the scattering due to polar and nonpolar optical phonons is the dominant process at high temperatures. The value of the valence band deformation potential is estimated.

Introduction
Compounds with skutterudite structure are considered as very promising thermoelectric materials and found a lot of interest in the last few years. However the correct interpretation of the transport properties is still a matter of debate. Assuming that the knowledge of the fundamental physics of skutterudites is important for improving the technology, we took a closer look at the transport properties of $CoSb_3$.

Experimental Procedure
$CoSb_3$ exhibits a peritectical point at 873 °C. Therefore $CoSb_3$ single crystals were grown by chemical vapor transport in closed silica ampoules using iodine as transport agent (Fig. 1) and by a flux method in Sb-rich melts [1].

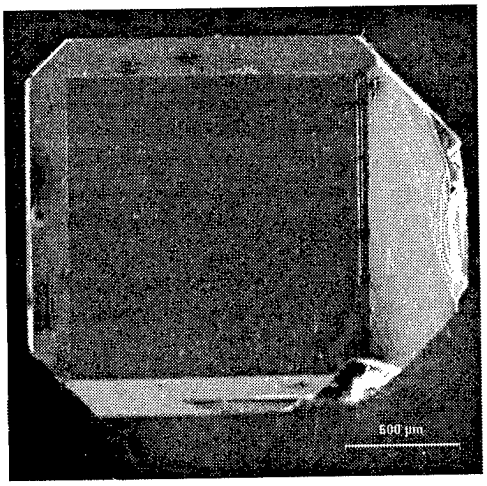


Fig. 1: CVT grown $CoSb_3$ single crystal.

The quality of the obtained crystals was checked by XRD analysis. Optical and EDX measurements carried out on polished samples did not show any inclusions of Sb (flux) or iodine (CVT).
The resistivity and the Hall-coefficient were determined in the temperature range from 4 K to 400 K in a dc magnetic field of 0.6 T.

Results and Discussion
The 1/T-dependence of the resistivity is nearly exponential in two temperature ranges (Fig. 2). The Hall-coefficient grows with decreasing temperature and shows a maximum at low temperatures (Fig. 3). The change in slope of the ρ(1/T) curves is observed near the temperatures corresponding to the maximum of the Hall-coefficient.

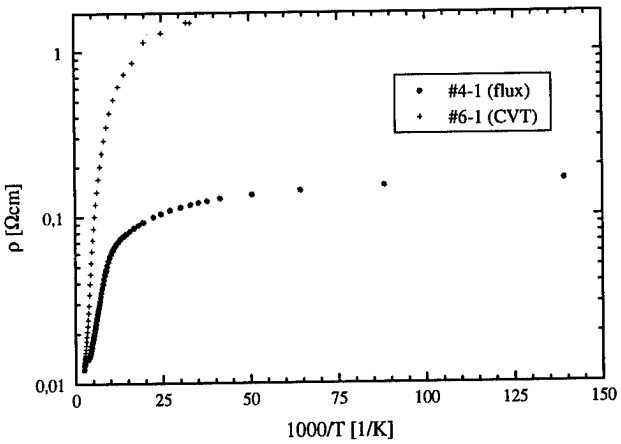


Fig. 2: Resistivity as function of reciprocal temperature.

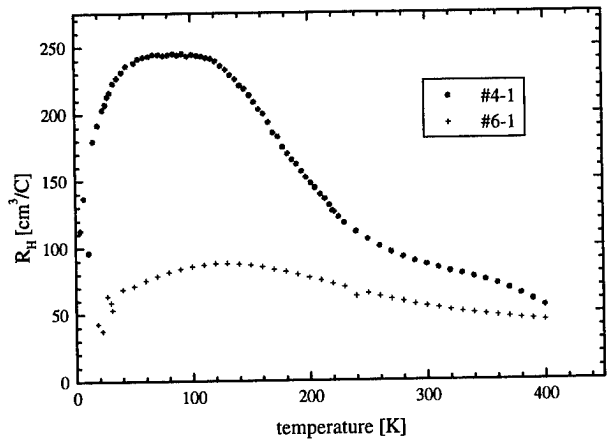


Fig. 3: Temperature dependence of the Hall-coefficient.

The value of the Hall-mobility (#4-1) increases with increasing temperature, reaches a maximum (up to 8000 $cm^2/(Vs)$) at about 200 K and decreases as T^{-n} (where n = 1.1) for higher temperatures (Fig. 4).

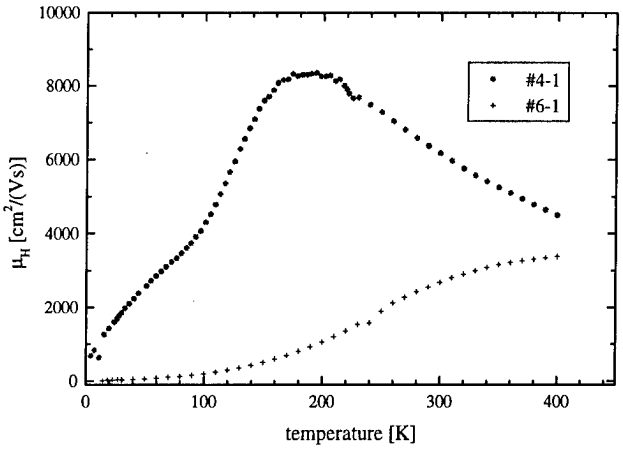


Fig. 4: Temperature dependency of the Hall-mobility.

The observed features of $R_H(T)$ as well as the character of the temperature dependencies of $\rho(T)$ and $\mu_H(T)$ could be explained assuming the existence of an acceptor impurity band formed by shallow impurity levels [2-7]. The value of the activation energy, estimated on the basis of the high temperature Hall-coefficient data is more than a magnitude higher than the value derived at low temperature. This suggests the existence of an additional deep acceptor level.
Assuming two acceptor and one additional donor level, the carrier density as a function of temperature can be given by the following expression [8]

$$p + N_d = \frac{N_{a1}}{1 + 2\frac{p}{N_v}\exp\frac{E_{a1}}{k_B T}} + \frac{N_{a2}}{1 + 2\frac{p}{N_v}\exp\frac{E_{a2}}{k_B T}}. \quad (1)$$

Where $N_{a1,2}$ is the concentration of the shallow and deep acceptor levels respectively and N_d is the concentration of compensating donors. $E_{a1,2}$ are the activation energies of the acceptors and N_v states the density of states in the valence band ($N_v = 1/4\ (8\pi m^* k_B T/h^2)^{3/2}$).
At high temperatures, where all the impurities are depleted, this leads to

$$p = \frac{1}{eR_{H,h}} = N_{a1} + N_{a2} - N_d. \quad (2)$$

At very low temperatures, in the carrier-freezing region, the conduction process only takes place in the impurity band and the Hall-coefficient is given by

$$\frac{1}{eR_{H,l}} = p_1 = N_{a1} - N_d. \quad (3)$$

Using Eq. (2) and Eq. (3) it is possible to estimate the value of the acceptor concentration N_{a2}.
In the case of high temperatures, assuming that $p >> N_d$, $2\frac{p}{N_v}\exp\frac{E_{a2}}{k_B T} >> 1$, Eq. (1) can be written as

$$p = \left(\frac{N_v}{2} N_{a2}\right)^{1/2} \exp\left(-\frac{E_{a2}}{2k_B T}\right). \quad (4)$$

Keeping in mind that N_v is proportional to $T^{3/2}$ the dependence of $\ln(p/T^{3/4})$ on 1/T should be a straight line. In fact this behavior could be observed, which confirms the assumptions made and permits us to determine the value of E_{a2}.
For low temperatures it is possible to neglect the deep acceptors and Eq. (1) simplifies to

$$p + N_d = \frac{N_{a1}}{1 + 2\frac{p}{N_v}\exp\frac{E_{a1}}{k_B T}}. \quad (5)$$

Assuming $p << N_d$ Eq. (5) could be reduced to

$$p = \frac{N_v}{2}\frac{N_{a1} - N_d}{N_d}\exp\left(-\frac{E_{a1}}{k_B T}\right). \quad (6)$$

Now the dependence of $\ln(p/T^{3/2})$ on 1/T is linear which allows us to estimate the value of E_{a1}.
Finally, if the value of m^*/m_0 is known, the application of Eq. (3) and Eq. (6) results in N_{a1} and N_d. The value of m^*/m_0 was estimated using the thermolectric power and Hall-mobility measurements and yields $m^* = 0.067\ m_0$ and $m^* = 0.036\ m_0$ for scattering by acoustical and polar optical lattice vibrations respectively.
The results are summarized in table 1.

Tab. 1: Parameters of $CoSb_3$ single crystals.

sample	N_{a1} [cm^{-3}]	N_{a2} [cm^{-3}]	N_d [cm^{-3}]	E_{a1} [meV]	E_{a2} [meV]
#4-1	$1.5\cdot10^{17}$	$1.37\cdot10^{17}$	$0.93\cdot10^{17}$	< 1	47
#6-1	$3.1\cdot10^{17}$	$1.24\cdot10^{17}$	$1.62\cdot10^{17}$	< 1	38

The value of E_{a2} is about 50 ± 10 meV. This energy is in an agreement with a recent band-structure calculation of $CoSb_3$ performed by Singh and Picket [9] in which they predict a 50 meV semiconducting gap.
For low temperatures a further analysis of the temperature dependence of the Hall-coefficient has been made on the basis of a two-band model. In accordance with the method presented in Ref. 6, the temperature dependence of p, the hole concentration in the valence band and p_1, the hole concentration in the impurity band, were calculated (Fig. 5).

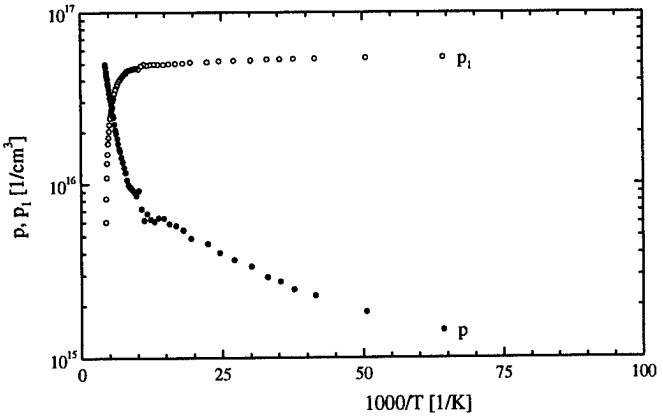


Fig. 5: Concentration of holes in the valence and impurity band respectively (#4-1).

The main scattering mechanisms in $CoSb_3$ are still unknown. In order to estimate the strength of different mechanisms the total mobility was calculated using Mathiessen´s rule

$$\mu^{-1} = \mu_{ac}^{-1} + \mu_{npo}^{-1} + \mu_{po}^{-1} + \mu_i^{-1}, \tag{7}$$

where μ_{ac}, μ_{npo}, μ_{po} and μ_i are the mobilities of the charge carriers due to scattering by acoustic lattice modes, nonpolar optical modes, polar optical modes and ionized impurities respectively.
For the acoustic mode scattering we used the expression [10]

$$\mu_{ac} = \frac{(8\pi)^{1/2} e\hbar^4 \rho_0 u^2}{3(k_B T)^{3/2} E_{ac}^2 (m^*)^{5/2}}, \tag{8}$$

where ρ_0 is the density, u is the longitudinal velocity of sound and E_{ac} stands for the valence band deformation potential. The velocity of sound can be estimated using [11]

$$u \cong \frac{k_B \Theta_D}{h}\left(\frac{V}{6\pi^2}\right)^{1/3}, \tag{9}$$

where V is the average atomic volume.
The combined effect of the acoustic and nonpolar optical modes is described by [12]

$$\mu_{anpo} = \mu_{ac} S(\Theta_D, x, T), \tag{10}$$

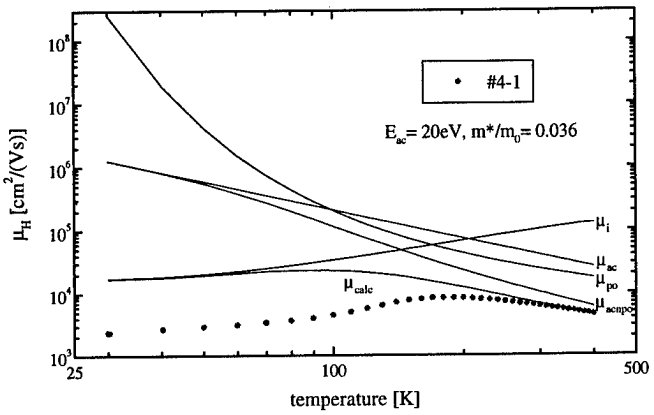
where x marks the squared ratio of the nonpolar optical and acoustic mode deformation potentials. The values for the function $S(\Theta_D, x, T)$ are tabulated in Ref. 11.
For the mobility due to scattering by polar optical phonons the following equation holds [13]

$$\mu_{po} = \frac{8\hbar^2 T^{1/2}(\exp z - 1)}{3(2\pi k_B)^{1/2} e\Theta_D (m^*)^{3/2}} G(z)\left(\frac{1}{\varepsilon_\infty} - \frac{1}{\varepsilon_0}\right)^{-1}, \tag{11}$$

where ε_∞ denotes the high frequency dielectric constant, z is the ratio Θ_D/T and G(z) is a tabulated function which could be approximated in the range of 100 K to 300 K by 0.56 + 26.93/T. The value of ε_0 was calculated using data on lattice vibrations in $CoSb_3$ and the Lyddane-Sachs-Teller relation [14].
The Hall-mobility due to ionized impurity scattering was calculated according to the Brooks-Herring formula [15]

$$\mu_i = \frac{2^{7/2}\varepsilon_0^2 (k_B T)^{3/2}}{\pi^{3/2} e^3 (m^*)^{1/2} N_i f(x)}, \tag{12}$$

where N_i is the concentration of the ionized impurities which is $N_i = 2N_d + p$ according to Eq. 2. The function f(x) is given by the relation $f(x) = \ln(1+x) - x/(1+x)$ with the abbreviation $x = 6\varepsilon_0 m^* (k_B T)^2 / (\pi e^2 \hbar^2 p)$.
For the simulation of the experimental data the values of m* obtained from thermopower measurements were taken into account. As free parameters the concentration of donors N_d and the deformation potential E_{ac} were used. The results are shown in Fig. 6 and Fig. 7.



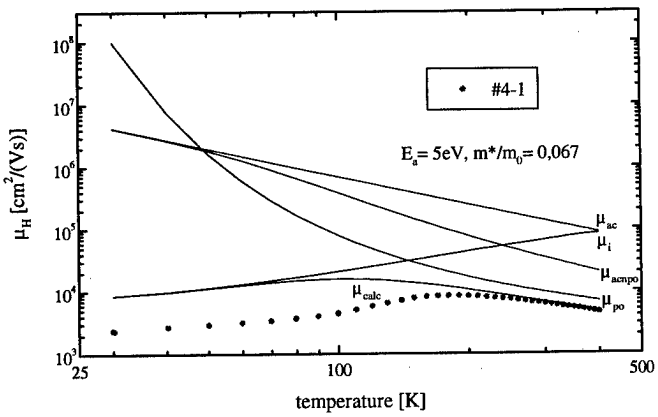


Fig. 6 and 7: Comparison of observed and calculated Hall-mobilities for different effective masses.

The values E_{ac} = 5 eV and E_{ac} = 20 eV for $m^*/m_0 = 0.036$ and $m^*/m_0 = 0.067$ respectively were estimated from the fitting procedure. N_d could be estimated to $N_d = 7.9 \cdot 10^{16}$ cm^{-3}, which

is in satisfactory agreement with the value determined from the Hall-coefficient data.
The scattering due to polar optical phonons and nonpolar optical phonons is most important at temperatures between 150 K and 400 K. The availability of a more exact value of m^*/m_0 is necessary to separate these two scattering mechanisms. Experiments to determine the effective mass using the Shubnikov-de Haas-effect are in operation. Furthermore the analysis of the scattering in the low temperature region is complicated due to the influence of the impurity band conduction.

Summary
$CoSb_3$ single crystals using two different techniques were grown. Low hole concentrations and a remarkable high Hall-mobility of up to 8000 $cm^2/(Vs)$ were observed.
The temperature dependence of the Hall-coefficient can be explained using the approximation of two acceptors and one donor. The value of the activation energy of the shallow and deep acceptors, their concentration as well as the concentration of the compensating donors were calculated.
The dominant scattering mechanisms were determined using analysis of the Hall-mobility data and the value of the valence band deformation potential was estimated.

Acknowledgments
The authors gratefully acknowledge financial support by the Deutsche Forschungsgemeinschaft DFG.

References
[1] Ch. Kloc, K. Fess, W. Käfer, K. Friemelt, H. Riazi-Nejad, M. Wendl, and E. Bucher, Proc. of the XVth Int. Conf. on Thermoelectrics, Pasadena, USA, 155 (1996)
[2] C.S. Hung and J.R. Gliessman, Phys. Rev. **79**, 726 (1950)
[3] E.M. Conwell, Phys. Rev. **98**, 1178 (1955)
[4] O.V. Emelyanenko, T.S. Lagunova, D.N. Nasledov, and G.N. Talalakin, Fiz. Tverd. Tela **7**, 1315 (1965)
[5] I.K. Andronik, E.K. Arushanov, O.V. Emelyanenko, and D.N. Nasledov, Fiz. Tekh. Poluprovodn. **2**, 1248 (1968)
[6] E. Arushanov, Ch. Kloc, and E. Bucher, Phys. Rev. B **50**, 2653 (1994)
[7] E. Arushanov, K. Fess, W. Kaefer, Ch. Kloc, and E. Bucher, Phys. Rev. **B**, accepted for publication
[8] J.S. Blakemore, Semiconductor Statistics (Pergamon Press), Oxford (1962)
[9] D.J. Singh, and W.E. Pickett, Phys. Rev. B **50**, 11235 (1994)
[10] J. Bardeen, and W. Shockley, Phys. Rev. **77**, 407 (1950)
[11] J.R. Drabble, and H.J. Goldsmid, Thermal conduction in semiconductors (Pergamon Press), Oxford, 191 (1961)
[12] J.D. Wiley, and M. Di Domenico Jr., Phys. Rev. B **2**, 427 (1970)
[13] H. Ehrenreich, J. Phys. Chem. Sol. **2**, 131 (1957)
[14] G. Kliche, and H.D. Lutz, Infrared Phys. **24**, 171 (1984)
[15] H. Brooks, Adv. Electron Phys. **7**, 85 (1955)

Grain Size Effects on Thermoelectric Properties of Hot-pressed $CoSb_3$

H. Nakagawa[1], H. Tanaka[1], A. Kasama[1], H. Anno[2] and K. Matsubara[2]
[1]Japan Ultra-high Temperature Materials Research Institute, 573-3 Okiube, Ube, Yamaguchi 755, Japan
Tel:+81/836/51-7160, Fax:+81/836/51-7165, e-mail:kasama@mb.infoweb.or.jp
[2]Science University of Tokyo in Yamaguchi, Faculty of Science and Engineering
1-1-1 Daigaku-Dori, Onoda, Yamaguchi 756, Japan

Abstract

To get high ZT values, grain size optimization of hot-pressed $CoSb_3$ is very important. Although single crystals of $CoSb_3$ have high electrical conductivities and moderate Seebeck coefficients, the ZT values are relatively low because of the high thermal conductivities. We tried to lower the thermal conductivity of hot-pressed $CoSb_3$ by reducing the grain size. Mechanical alloying of the raw material powders of Co and Sb was the very effective method to reduce the grain size of hot-pressed $CoSb_3$. This paper shows the relations between the thermoelectric properties (Hall mobility, Seebeck coefficient, electrical conductivity and thermal conductivity) and the grain size. The thermal conductivity of hot-pressed $CoSb_3$ decreased with reducing the grain size. The value of 4.19 $Wm^{-1}K^{-1}$, which is about 40% of the single crystals, was ultimately obtained at 293K for the hot-pressed material with an average grain size of 0.9 μ m. Although the larger grain size is preferable to attain a high ZT value at 293K, because of the greater decrease of the carrier mobility than the thermal conductivity with reducing the average grain size, the highest ZT value of 0.10 was obtained at 673K on the sample with an average grain size of 2.1 μ m.

1. Introduction

Skutterudite materials have been investigated as the promising candidates for advanced thermoelectric materials intensively for several years [1, 2]. To attain the high conversion efficiency of thermoelectric devices, thermoelectric materials used should have the high thermoelectric figure of merit (Z) which is a function of the Seebeck coefficient (S), electrical conductivity (σ) and thermal conductivity (κ), and is defined as

$$Z=S^2 \sigma / \kappa \qquad (1)$$

Although binary skutterudite antimonides such as $CoSb_3$ [3], $RhSb_3$ [4] and $IrSb_3$ [5] have the high electrical conductivities and the moderate Seebeck coefficients, Z values of the binary skutterudite antimonides are not high enough to get the high conversion efficiency because their thermal conductivities are relatively high. To obtain a high Z value, the electrical to thermal conductivity ratio should be enhanced.

The first approach to enhance the ratio is introducing point-defects into the skutterudite crystal structure [6]. The alloyings of these compounds have been investigated for the purpose, and some successful results have been obtained by A. Borshchevsky et al. [7].

The second approach is increasing the number of grain boundaries per unit length in the materials [6]. Although the thermal conductivity of $CoSb_3$ single crystals is as high as about 10 $Wm^{-1}K^{-1}$ at 293K [3], fine-grained sintered $CoSb_3$ materials are expected to have lower thermal conductivities due to boundary scattering. However, the electrical conductivity is also supposed to be reduced by the grain boundaries. The purpose of this work is to clarify the grain size effects on the thermal conductivity, electrical conductivity and Seebeck coefficient of $CoSb_3$, and optimize the grain size to maximize the Z value.

Grain size optimization is very important, in particular from the viewpoint of the advanced thermoelectric material processing. We must choose the best production method considering the production cost and the performance of candidate materials . Particularly in powder metallurgy, which is one of the promising mass production methods, we have to decide the processing conditions which have strong effects to change the grain size. We believe that this work will help to select a processing technique and fix the processing conditions for producing skutterudite thermoelectric materials in the near future.

Mechanical alloying of raw material powders with the subsequent hot-pressing is the very effective method to obtain fine-grained materials [8], which has been broadly used in powder metallurgy recently [9]. We applied the method to the preparation of $CoSb_3$ with an average grain size below 1 μ m. On the other hand, we annealed hot-pressed $CoSb_3$ to increase the grain size. And we obtained several $CoSb_3$ materials with the various average grain sizes of 0.9 to 40 μ m, and evaluated the thermoelectric properties.

2. Experimental procedure

2.1 Sample preparation

Figure 1 shows the schematic experimental procedure of $CoSb_3$ sample preparation. High purity granular Sb (99.999%) and Co powder (99.9985%) were used as raw materials. They were ground and mixed each other in the Sb/Co atomic ratio of 3.05 using a mortar and pestle made of WC and Co. The mixed Co and Sb powders were heated in argon at 923K for 50h to synthesize $CoSb_3$, and ground with the mortar and pestle. For the finer grinding of $CoSb_3$, the synthesized material was ground for 8h in argon using a planetary ball mill "pulverisette 5" of

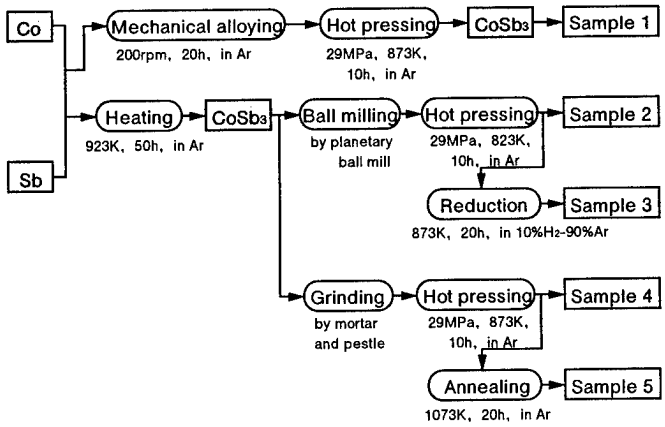


Figure 1. Schematic preparation procedure of $CoSb_3$ samples with various grain sizes.

FRITSCH, Germany. The grinding media and bowls of the mill were made of partially stabilized zirconia. The ground materials were hot-pressed at 823 or 873K for 10h at a pressure of 29MPa in argon. During the hot pressing, samples were enveloped by graphite foil. To get coarse-grained $CoSb_3$, the hot-pressed samples were annealed in argon at 1073K for 20h. The samples were cut into several pieces for the characterization and thermoelectric property measurement described in the following sections, after those surfaces were removed.

As described in the introduction, to prepare fine-grained $CoSb_3$ with an average grain size below 1 μ m, the raw materials were mechanically alloyed for 20h in argon using a planetary attrition mill and hot-pressed at 873K for 10h at a pressure of 29MPa in argon. The attrition mill was composed of steel ball media, a stainless steel central shaft with arms and a stainless steel container.

To reduce the oxygen concentration of the sample, the hot-pressed samples with an average grain size of 2.1 μ m were heated at 873K in argon containing 10% hydrogen for 20h.

2.2 Characterization

Cross sections of the prepared samples were polished, etched with conc. nitric acid, and observed by optical microscope and scanning electron microscope (SEM). The average crystal grain size of prepared samples was determined by the following method. Six micrographs were taken at random for the each sample and five lines were drawn at regular intervals in the each micrograph. The number of grains which an line crossed was counted and the length of the line was divided by the number of grains. By the same way, thirty values were obtained for the each sample and the average crystal grain size was determined by the arithmetic mean of the thirty values.

Crystal phases were analyzed by powder X-ray diffractmetry. Densities of the samples were calculated from the size and the mass of the rectangular samples. And, oxygen and metallic impurity contents were determined by the inert gas fusion method and electrothermal atomic absorption analysis, respectively.

2.3 Thermoelectric property measurement

The electrical conductivity and the Seebeck coefficient were measured simultaneously using ULVAC ZEM-1 at the temperature range of 210 to 680K in helium. In the measurement, the electrical conductivity was measured using the two probe method [10].

The thermal conductivity was calculated from thermal diffusivity, specific heat capacity and density. Thermal diffusivity was obtained by the laser flash measurements on ULVAC TC-7000 at 293 and 673K in vacuum. And specific heat capacity was measured using PERKIN ELMER DSC7 at the temperature range of 303 to 723K. The specific heat capacity at 293K was determined by extrapolation method.

The Hall coefficient (R_H) and the electrical conductivity (σ) were measured using the van der Pauw method [10]. The carrier density (n) was calculated from the Hall coefficient by

$$n=1/R_H e \qquad (2)$$

where e is the electronic charge of the hole. The Hall mobility (μ_H) was calculated from the Hall coefficient and the electrical conductivity by

$$\mu_H = R_H \sigma \qquad (3)$$

3. Results and discussion

3.1 Characterization

Table 1 shows the average grain size, impurity contents and density of the samples which were prepared by the methods described in Figure 1. The microstructures of the samples are shown in Figure 2. Although grain growth happened during the annealing at 1073K, grain size did not change during the reduction at 873K because the reduction temperature was not high enough for the grain growth. The microstructure of the sample 3 is same as of the sample 2 which is shown in Figure 2 (b).

Table 1. The average grain size, impurity contents and density of the samples which were prepared by the methods shown in Figure 1.

Sample	Average grain size (μm)	Impurity contents (ppm)			Density (g /cm^3)
		Oxygen	Fe	Ni	
1	0.9	2300	250	64	7.34
2	2.1	2500	<1	<1	6.82
3	2.1	1200	<1	<1	6.84
4	7.9	600	2	1	7.44
5	40	600	2	<1	7.20

The oxygen contents of the raw materials increased after the mechanical alloying or ball milling, because the surface areas of the milled powders were larger than the original powders. The reduction of the hot-pressed sample in 10%H_2-90%Ar was effective to decrease the oxygen content. The concentrations of metallic impurities, in particular Fe and Ni increased during the mechanical alloying of the raw materials, because the materials of the attrition mill wore and caused contamination of the sample. The measured densities of the prepared samples in this study are higher than 88% of the theoretical density (7.69 g/cm^3).

Powder X-ray diffractmetry (XRD) shows that the mechanically alloyed powder contains small percentages of a $CoSb_3$ and $CoSb_2$ phase besides a Co and Sb phase. And, XRD also shows that the all hot-pressed samples consist of a main $CoSb_3$ phase and a very slight Sb phase.

3.2 Thermoelectric properties

The thermoelectric properties of the hot-pressed samples which were measured at 293K are shown in Table 2. From the

Table 2. The thermoelectric properties of hot-pressed $CoSb_3$ materials which were measured at 293K.

Sample	S (μV/K)	κ (Wm^{-1}K^{-1})	σ (S/cm) by two probe method	σ (S/cm) by van der Pauw method	μ_H (cm^2/Vs)	n (10^{18}/cm^3)
1	140	4.19	74	87	70	7.71
2	185	5.43	97	93	271	2.13
3	182	5.61	93	67	216	1.92
4	150	9.23	328	320	794	2.52
5	156	9.36	571	590	1758	2.09

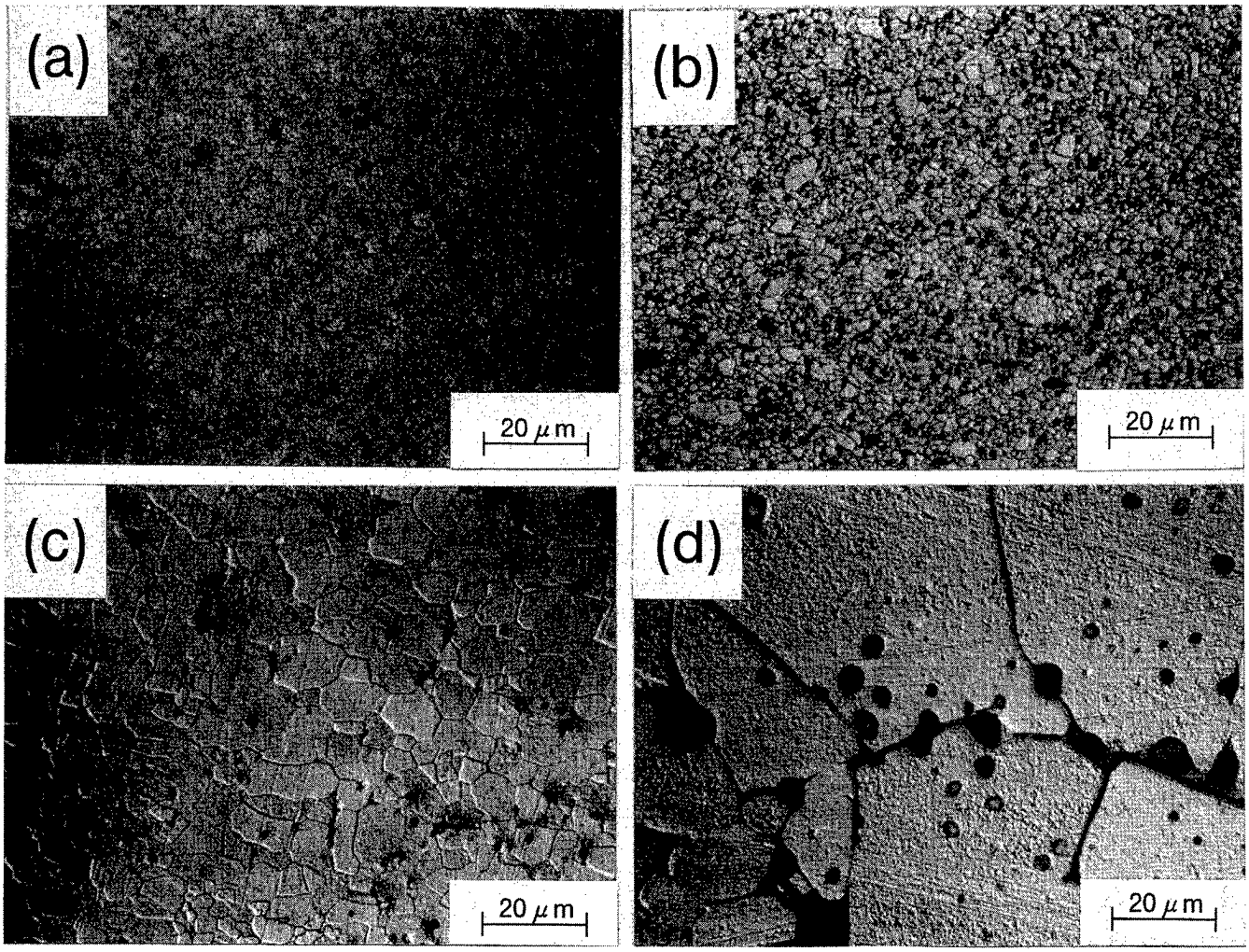


Figure 2. Optical micrographs of hot-pressed $CoSb_3$ (a) sample 1, (b) sample 2, (c) sample 4 and (d) sample 5, which were etched by conc.nitric acid. The microstructure of the sample 3 is same as of the sample 2.

comparison of the thermoelectric properties of the sample 2 with of the sample 3, oxygen content do not affect the properties in Table 2 considerably. The carrier densities of the samples are about 2 x 10^{18} cm^{-3} except 7.71 x 10^{18} cm^{-3} of the sample 1 which contains Fe of 250ppm and Ni of 64ppm. The relation between the Hall mobility at 293K and the average grain size is shown in Figure 3 based on the data of Table 1 and 2. As shown in Figure 3, the Hall mobility at 293K greatly decreases reducing the average grain size.

Figure 4 shows the relation between the average grain size and the thermal conductivity measured at 293 and 673K. The thermal conductivity considerably decreases reducing the average grain size, in particular below 8 μ m.

The electrical conductivities were measured by the two methods, namely, the two probe method and the van der Pauw method. Table 2 shows that the electrical conductivities measured by the two probe method nearly coincide with the values by the van der Pauw method. The values by the two probe method were used for the calculation of ZT. Figure 5 shows the electrical conductivity measured by the two probe method as a function of reciprocal temperature. The measured values in a cryo-furnace almost coinside with the values measured in an infrared image furnace, as shown as the data of the temperature range from 310 to 410K in Figure 5. The electrical conductivity depends greatly on the average grain size at lower temperature, as shown in Figure 5. Based on the data in Figure 5, the electrical conductivities at 293 and 673K as a function of the grain size are shown in Figure 6. The electrical conductivity at 293K decreases to 30% of the original value when the average grain size reduces from 7.9 to 2.1 μ m, because the Hall mobility greatly decreases reducing the average grain size as described above. However, the electrical conductivity of the sample 1 (an average grain size of 0.9 μ m) is almost same as of the sample 2 (an average grain size of 2.1 μ m) at 293K, because the increase of the carrier density compensates the decrease of the Hall mobility.

Figure 7 shows the Seebeck coefficient as a function of temperature. In the temperature range from 210 to 680K, all samples show the p-type conduction. Based on the data in Figure 7, the Seebeck coefficients at 293 and 673K as a function of the average grain size are shown in Figure 8. The Seebeck coefficient do not depend on the average grain size very much. The impurities of Fe and Ni may reduce the Seebeck coefficients of the sample 1 slightly.

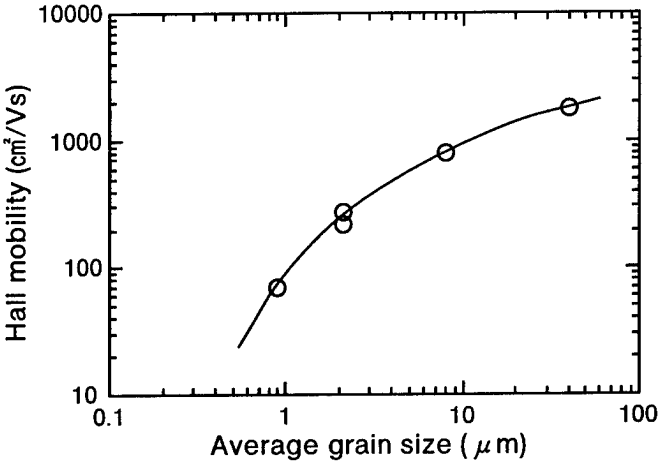


Figure 3. Hall mobility at 293K of hot-pressed $CoSb_3$ as a function of the average grain size.

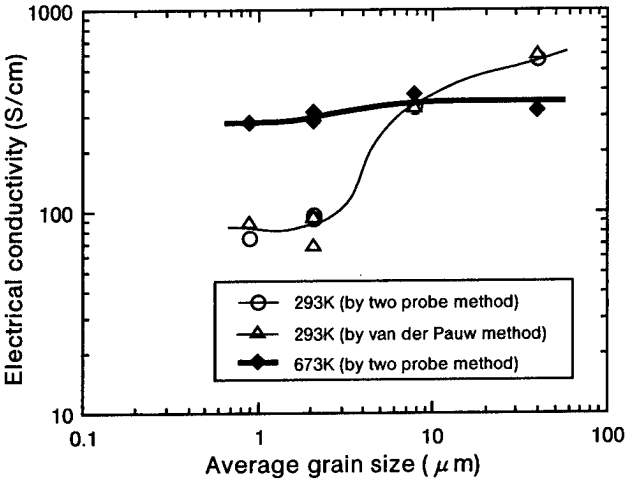


Figure 6. Electrical conductivities at 293 and 673K versus the average grain size of hot-pressed $CoSb_3$.

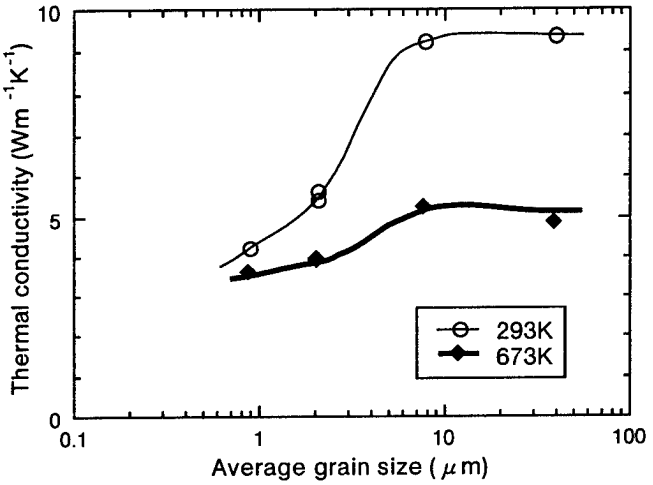


Figure 4. Thermal conductivities at 293 and 673K of hot-pressed $CoSb_3$ as a function of the average grain size.

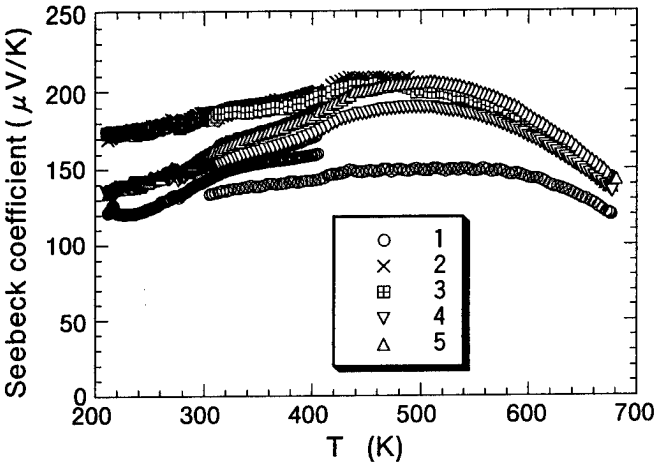


Figure 7. Temperature dependence of the Seebeck coefficient for the each hot-pressed $CoSb_3$ sample which has various average grain sizes. The each number in the figure shows the sample number in Table 1.

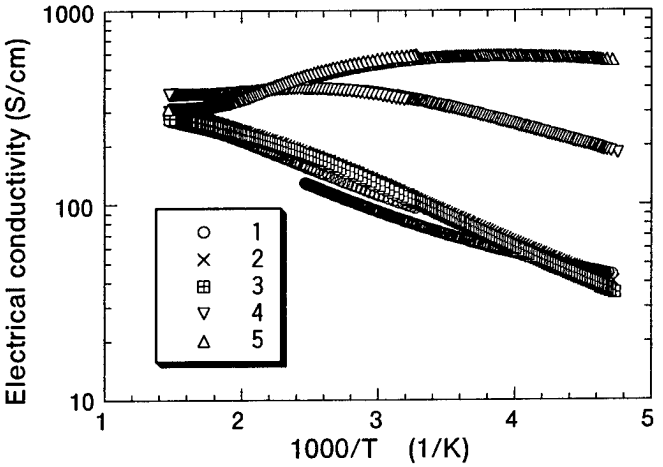


Figure 5. Reciprocal temperature dependence of the electrical conductivity for the each hot-pressed $CoSb_3$ sample which has various average grain sizes. The each number in the figure shows the sample number in Table 1.

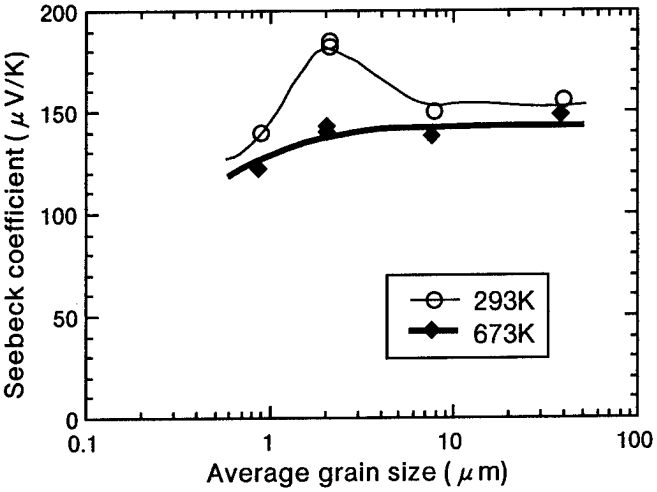


Figure 8. Seebeck coefficients at 293 and 673K of hot-pressed $CoSb_3$ as a function of the average grain size.

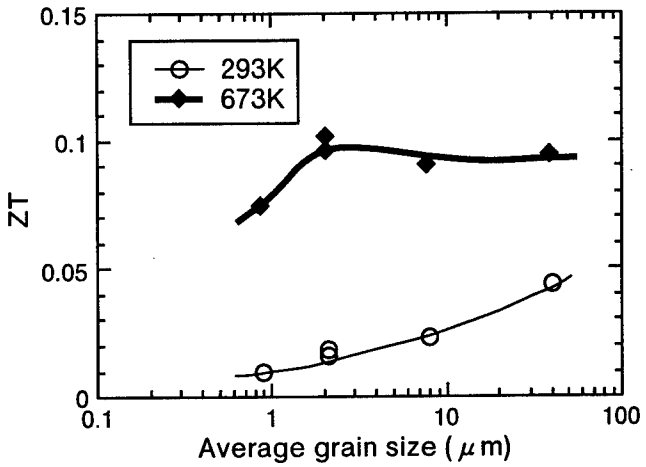


Figure 9. ZT versus the average grain size at 293 and 673K for hot-pressed $CoSb_3$.

ZT values were calculated from the data in Figure 4, 6 and 8. And the ZT values at 293 and 673K as a function of the average grain size are shown in Figure 9, which shows that larger grain size is preferable to attain a high ZT value, in particular at 293K. The highest ZT value of 0.044 at 293K was obtained on the sample 5 which has an average grain size of 40 μ m. The value is close to the single crystal's value of 0.05 [3].

Although ZT value do not depend very much on the average grain size at 673K, a maximum ZT value exists within the average grain size range of 1 to 10 μ m, which is similar to the calculated result of Si-Ge shown in the previous paper by G. A. Slack et al. [11]. The highest ZT value in this study of 0.10 at 673K was obtained on the sample 2 which has an average grain size of 2.1 μ m. The value is also comparable with the single crystal's value of 0.12 [3].

4. Conclusions

Several p-type $CoSb_3$ materials with various grain sizes of 0.9-40 μ m were prepared by changing the conditions of sample preparation. Mechanical alloying of raw materials was very effective to obtain fine-grained $CoSb_3$ materials. On the other hand, annealing of hot-pressed materials was a effective method to prepare coarse-grained $CoSb_3$ materials.

The thermal conductivity of hot-pressed $CoSb_3$ decreases considerably with reducing the grain size, particularly at 293K. The value of 4.19 $Wm^{-1}K^{-1}$, which is about 40% of $CoSb_3$ single crystals is ultimately obtained at 293K with an average grain size of 0.9 μ m. The Seebeck coefficient do not depend greatly on the average grain size. And ZT value decreases with reducing the average grain size at 293K because the grain size reduction has the greater effect on decreasing the carrier mobility than the thermal conductivity. Larger grain size is preferable to attain a high ZT value of hot-pressed $CoSb_3$ at 293K. The highest ZT value at 293K is 0.044 for the sample with an average grain size of 40 μ m.

At 673K, the grain size effects on the thermoelectric properties are weaker than at 293K and ZT value do not depend very much on the average grain size. The highest ZT value at 673K is 0.10 for the sample with an average grain size of 2.1 μ m.

Grain boundaries should be controlled to increase ZT of the skutterudite compound materials by the novel technique such as plasma processing [12].

Acknowledgement

This work was financially supported by Yamaguchi Prefectural Government and Yamaguchi Industrial Technology Development Organization. The authors would also thank Professor Toshikatsu Miki in Yamaguchi University for the helpful suggestions.

References

[1] K. Matsubara, T. Iyanaga, T. Tsubouchi, K. Kishimoto, and T. Koyanagi, "Thermoelectric properties of (Pd, Co)Sb_3 compounds with the skutterudite structure", Proc. XIII Int. Conf. on Thermoelectrics, Kansas City, USA, AIP Press No. 316, 226 (1994).

[2] T. Caillat, A. Borshchevsky and J.-P. Fleurial, "Novel transition metal compounds with promising thermoelectric properties", Proc. XII Int. Conf. on Thermoelectrics, Yokohama, Japan, IEEJ, 132 (1993).

[3] T. Caillat, A. Borshchevsky and J.-P. Fleurial, "Preparation and thermoelectric properties of p- and n-type $CoSb_3$", Proc. XIII Int. Conf. on Thermoelectrics, Kansas City, USA, AIP Press No. 316, 58 (1994).

[4] J.-P. Fleurial, T. Caillat and A. Borshchevsky, "Skutterudites: a new class of promising thermoelectric materials", Proc. XIII Int. Conf. on Thermoelectrics, Kansas City, USA, AIP Press No. 316, 44 (1994).

[5] G. A. Slack and V. G. Tsoukala, "Some properties of semiconducting $IrSb_3$", J. Appl. Phys. 76 (3), 1665 (1994).

[6] C. M. Bhandari, "Minimizing the thermal conductivity", CRC Handbook of Thermoelectrics, ed. by D. M. Rowe, CRC Press, Boca Raton, p.55 (1995).

[7] A. Borshchevsky, T. Caillat and J.-P. Fleurial, "Solid solution formation: improving the thermoelectric properties of skutterudites", Proc. XV Int. Conf. on Thermoelectrics, Pasadena, USA, IEEE, 112 (1996).

[8] H. Nakagawa, H. Tanaka, A. Kasama, K. Miyamura, H. Masumoto and K. Matsubara, "Thermoelectric properties of $CoSb_3$ prepared by copper mold quenching technique", Proc. XV Int. Conf. on Thermoelectrics, Pasadena, USA, IEEE, 117 (1996).

[9] B. A. Cook, J. L. Harringa and S. H. Han, "Preparation of thermoelectric materials by mechanical alloying", CRC Handbook of Thermoelectrics, ed. by D. M. Rowe, CRC Press, Boca Raton, p.125 (1995).

[10] L. Danielson, "Measurement of the thermoelectric properties of bulk and thin film materials: electric and magnetic measurements", Textbook of International Short Courses on Thermoelectrics, Pasadena, USA, pp.3-26 (1996).

[11] G. A. Slack and M. A. Hussain, "The maximum possible conversion efficiency of silicon-germanium thermoelectric generators", J. Appl. Phys. 70 (5), 2694 (1991).

[12] K. Kishimoto, T. Koyanagi and K. Matsubara, "Microstructure control of thermoelectric conversion materials by plasma processing", J. Mater. Sci. Soc. Japan, 33, 54 (1996).

Microstructures and Thermoelectric Properties of Spin-Cast $Co_{0.97}Cr_{0.03}Sb_3$ Ribbons

T. Morimura, H. Kitagawa, M. Hasaka, and S. Kondo
Department of Materials Science and Engineering, Faculty of Engineering, Nagasaki University,
1-14 Bunkyo-machi, Nagasaki 852, Japan

Abstract

The ribbons of $Co_{0.97}Cr_{0.03}Sb_3$ were fabricated by spin-casting on a rotating copper roll with the surface-velocity of 3-50m/s and were annealed for 10.8ks at 873K. The microstructures were investigated by means of X-ray diffraction measurements, scanning and transmission electron microscopic observations. The thermoelectromotive force and electrical conductivity were measured under a vacuum. As the surface-velocity increases, the amount of $CoSb_3$ in the as-cast ribbon decreases, because the peritectic reaction of $CoSb_2+L \rightarrow CoSb_3$ is suppressed due to rapid cooling. After annealing, the amount of $CoSb_3$ increases with increasing the surface-velocity, because the reaction of $CoSb_2+Sb \rightarrow CoSb_3$ proceeds more sufficiently during annealing. The morphology of crystal grains and lattice defects depend on the surface-velocity. As the surface-velocity increases, the thermo-electromotive force of the as-cast ribbon decreases, but the one of the annealed ribbon increases prior to decreasing. The maximum thermoelectromotive force and electrical conductivity, resulting in the maximum power factor, are attained at the surface velocity of 10m/s.

Introduction

A skutterudite among various intermetallic compounds is reported as a prospective candidate of thermoelectric semi-conductor [1]-[5]. The microstructures will be manipulated by heat treatments in order to improve the thermoelectric properties.

The objective of this paper is to elucidate the microstructures and thermoelectric properties of $Co_{0.97}Cr_{0.03}Sb_3$ ribbons by means of X-ray diffraction measurements, scanning and transmission electron microscopic observations, and the measurements of thermoelectromotive force and electrical conductivity. The ribbons were fabricated by spin-casting on a rotating copper roll and were annealed to control the two peritectic reactions of $CoSb+L \rightarrow CoSb_2$, $CoSb_2+L \rightarrow CoSb_3$.

Experimental

Pure materials of Co, Cr, and Sb were weighed at the composition of $Co_{0.97}Cr_{0.03}Sb_3$ and were melted in a high frequency induction furnace under an argon atmosphere. The melt was cast into a metal mold. The fragments of the cast were melted in a high frequency induction furnace, and were quenched on a rotating copper roll with the surface-velocity of 3-50m/s. The products were in the shape of ribbon, width of 5mm, thickness of 20μm. The ribbons were annealed for 10.8ks at 873K.

After powdering the ribbons, the crystal structures were investigated by an X-ray diffraction equipment, Rigaku RINT2200. The micropstructures were observed by a scanning electron microscope, Hitachi S-2250N. After thinning the ribbons by ion-milling, the bright field images were taken by a transmission electron microscope, JEOL JEM-2010.

Results and Discussion

Fig.1 shows the X-ray diffraction patterns of the as-cast ribbons. When the surface-velocity of a roll becomes large, the peaks of $CoSb_2$ and Sb are large, while the peaks of $CoSb_3$, skutterudite, are small. That is, the peritectic reaction of $CoSb_2+L \rightarrow CoSb_3$ is suppressed partially and the amount of $CoSb_3$ is small, because the cooling rate is large during casting. Conversely, when the surface-velocity becomes small, the amount of $CoSb_3$ increases through the sufficient progress of $CoSb_2+L \rightarrow CoSb_3$, as shown in the large peaks of $CoSb_3$.

Fig.2 shows the X-ray diffraction patterns of the annealed ribbons. When the surface-velocity becomes large, only the peaks of $CoSb_3$ can be observed, while the peaks of $CoSb_2$ and Sb disappear. The result suggests that the reaction of $CoSb_2+Sb \rightarrow CoSb_3$ proceeds more sufficiently during annealing if the surface-velocity is large.

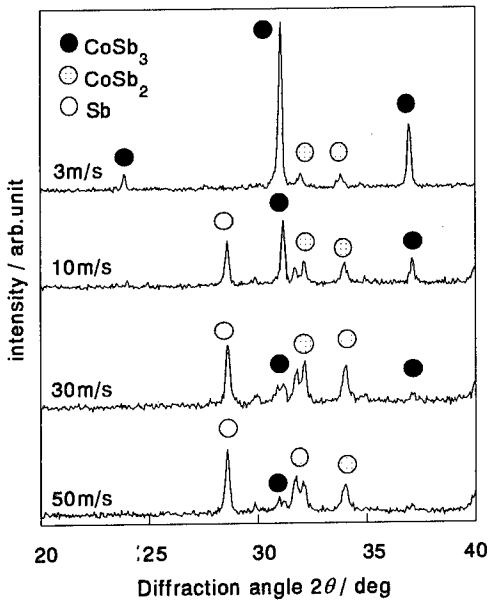
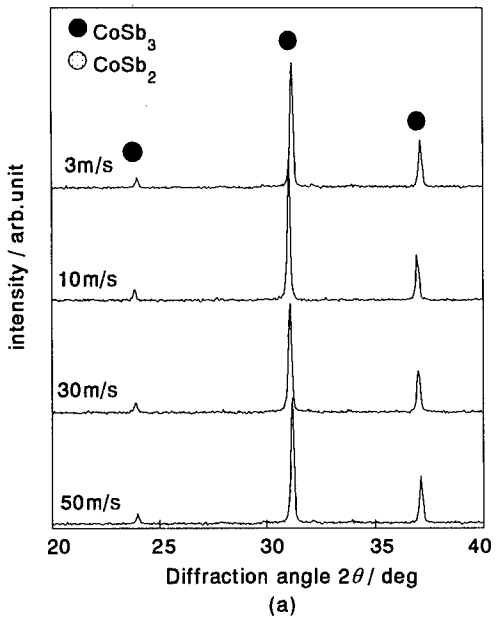


Fig.1 X-ray diffraction patterns of the $Co_{0.97}Cr_{0.03}Sb_3$ ribbons which were fabricated by spin-casting with the various surface-velocities of a roll.



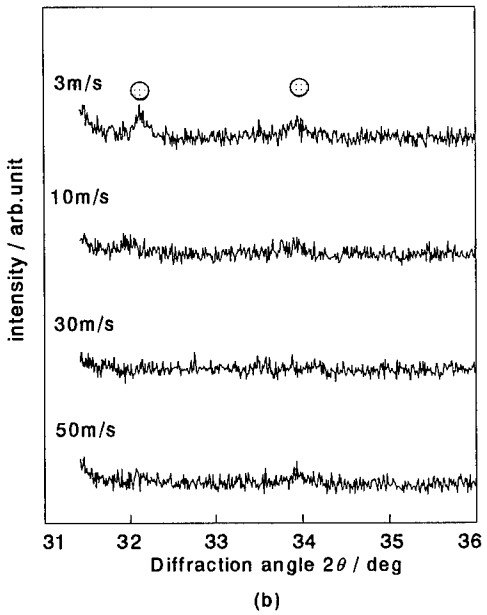


Fig.2 X-ray diffraction patterns (a) and their magnification (b) of the $Co_{0.97}Cr_{0.03}Sb_3$ ribbons which were annealed for 10.8ks at 873K.

Fig.3 shows the scanning electron microscopic images of the annealed ribbons. As the surface-velocity increases, the crystal grain size decreases to be smaller than 1μm, because crystal grains become uneasy to grow wide through the peritectic reaction of $CoSb+L \rightarrow CoSb_2$. Consequently, it is speculated in the case of large surface-velocity that there are a lot of interfaces between $CoSb_2$ and Sb, where the reaction of $CoSb_2+Sb \rightarrow CoSb_3$ proceeds. Namely, the amount of $CoSb_3$ increases during annealing with increasing the surface-velocity, as mentioned above.

Fig.4 shows the bright field images of the annealed ribbons with the surface velocity 3m/s (a) and 30m/s (b). The figure

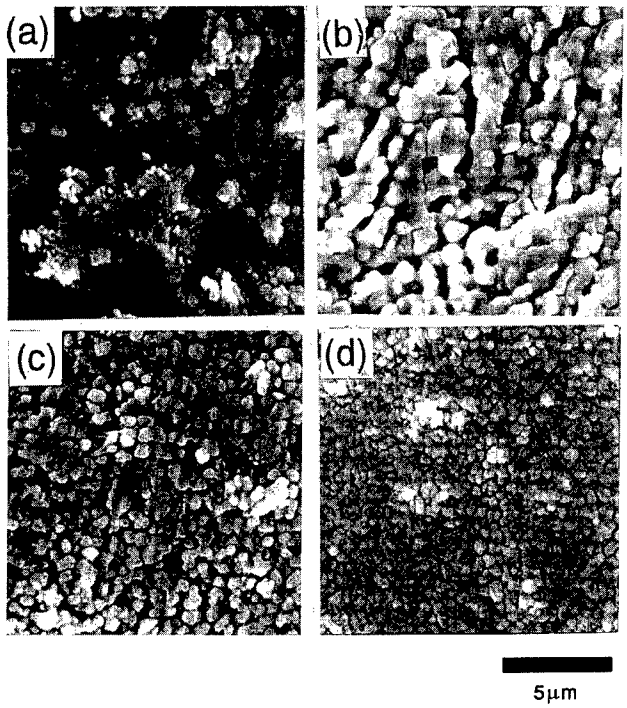


Fig.3 Scanning electron microscopic images of the annealed $Co_{0.97}Cr_{0.03}Sb_3$ ribbons. (a) 3m/s, (b) 10m/s, (c) 30m/s, (d) 50m/s.

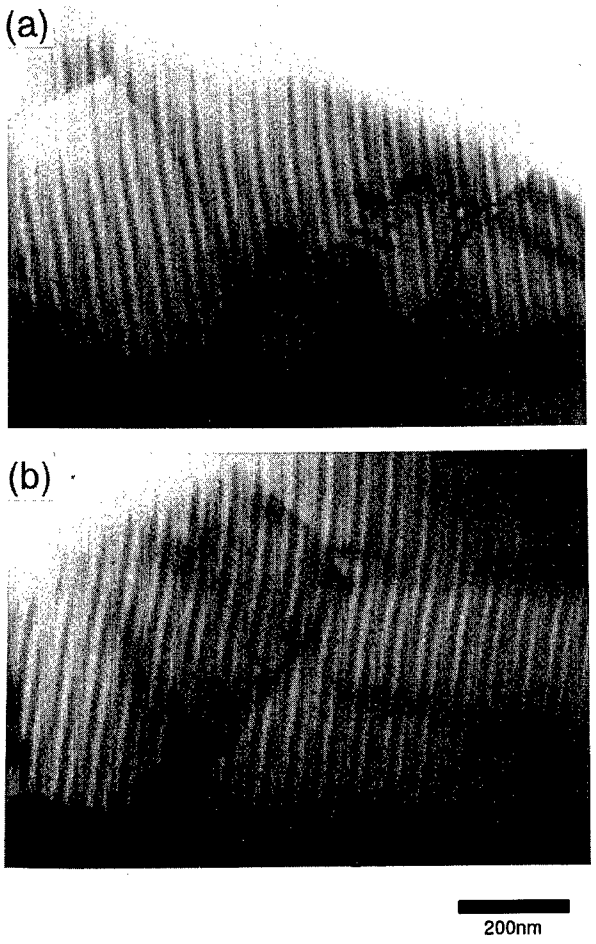


Fig.4 Bright field images of the annealed $Co_{0.97}Cr_{0.03}Sb_3$ ribbons. (a) 3m/s, (b) 30m/s.

shows the variation of lattice defects with changing the surface-velocity. Many dislocations can be seen along the boundaries of $CoSb_3$ grains in the figure (a), whereas they are invisible in the figure (b).

Fig.5 shows the changes of thermoelectromotive force with increasing temperature difference from the cooling edge of 300K of the annealed ribbons. The thermoelectromotive force increases with increasing temperature difference for 10, 20, 30m/s, while it remains almost zero below temperature difference 100K for 3m/s. Fig.6 shows the curve of thermoelectromotive force generated between the edges of 300K and 600K versus surface-velocity. The thermo-electromotive force of the as-cast ribbon decreases with increasing the surface-velocity, because the amount of $CoSb_3$ decreases. The thermoelectromotive force becomes larger after annealing. The thermoelectromotive force after annealing increases with increasing the surface-velocity from 3m/s to 10m/s. The behavior corresponds to increasing in the amount of $CoSb_3$. However, the thermoelectromotive force seems to decrease with increasing the surface-velocity above 10m/s, although the amount of $CoSb_3$ remains almost constant. The phenomenon may be attributed to change of lattice defects which are produced during rapid cooling and annealing.

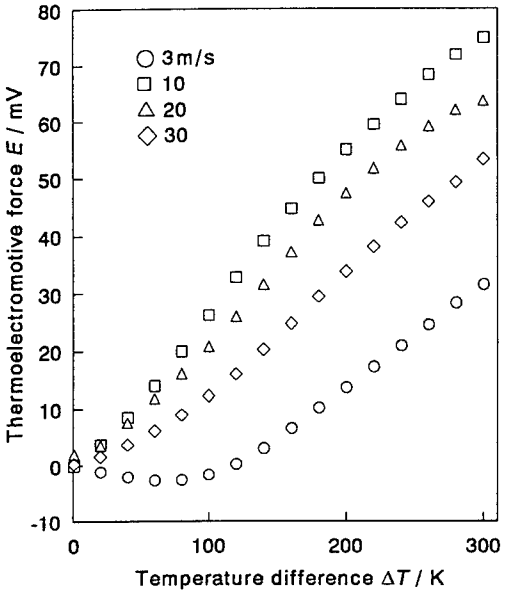


Fig.5 Changes of thermoelectromotive force with increasing temperature difference between both edges of the annealed $Co_{0.97}Cr_{0.03}Sb_3$ ribbons. The cooling edge was kept at 300K.

Fig.7 shows the changes of electrical conductivity with increasing temperature in the annealed ribbons. The electrical conductivity increases slowly below about 450K, and increases largely above the temperature. The electrical conductivity is large for 10m/s, especially below 450K. The electrical conductivity for 20m/s is almost the same as the one for 30m/s. These results suggest that the electrical conductivity may be varied by not only the amount of $CoSb_3$ but also by the morphology of lattice defects.

Fig.8 shows the changes of power factor with increasing temperature in the annealed ribbons. The power factor for 10m/s is large in the whole temperature range, because both the thermoelectomotive force and electrical conductivity are large.

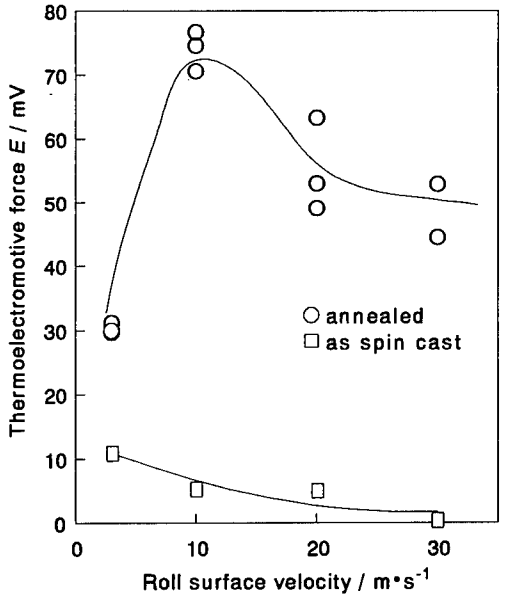


Fig.6 Thermoelectromotive force versus surface-velocity of a roll in the as-cast and the annealed $Co_{0.97}Cr_{0.03}Sb_3$ ribbons. The thermo-electromotive force was measured at the edges of 600K and 300K.

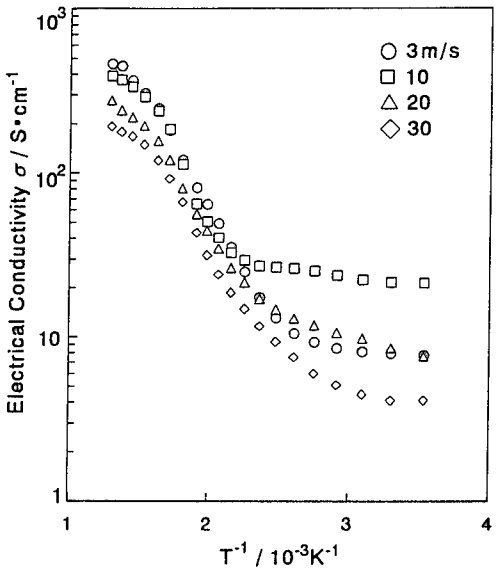


Fig.7 Changes of electrical conductivity with increasing temperature in the annealed $Co_{0.97}Cr_{0.03}Sb_3$ ribbons.

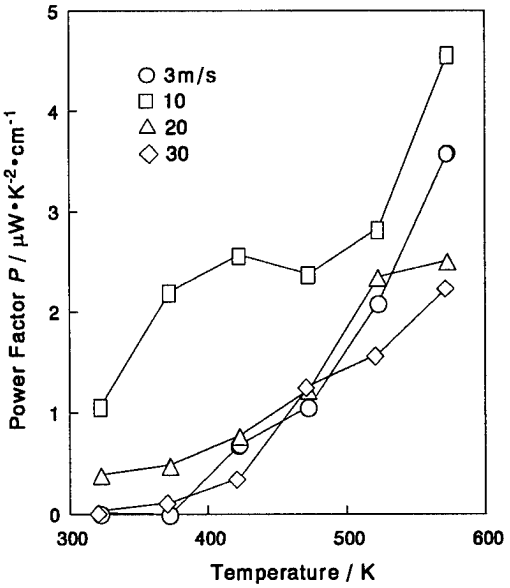


Fig.8 Changes of power factor with increasing temperature in the annealed $Co_{0.97}Cr_{0.03}Sb_3$ ribbons.

Conclusions

This paper showed the results of research on the microstructures and thermoelectric properties of $Co_{0.97}Cr_{0.03}Sb_3$ ribbons. The ribbons were fabricated by spin-casting on a rotating copper roll and then annealed for 10.8ks at 873K. The surface-velocity of roll was varied from 3 to 50m/s. The microstructures were investigated by means of X-ray diffraction measurements, scanning and transmission electron microscopic observations. The thermoelectromotive force and electrical conductivity were measured under a vacuum in the temperature range from 300K to 670K. The microstructures depend on the surface velocity which controls the process of the peritectic reactions of the Co-Sb system. After annealing, the large amount of $CoSb_3$ appeared together with small amount of $CoSb_2$ and Sb in the case of the surface-velocity below 10m/s, whereas $CoSb_2$ and Sb disappeared above 20m/s. The crystal grain size became small with increasing the surface velocity. The maximum thermoelectromotive force and electrical conductivity were attained for 10m/s, and the maximum power factor was observed for 10m/s. It is concluded that the thermoelectric properties of $CoSb_3$ are controlled by the lattice defects as well as the amount of $CoSb_3$.

References

[1] A. Borshchevsky, J.-P. Fleurial, E. Allevato, and T. Caillat, " $CoSb_3$-$IrSb_3$ Solid Solutions : Preparation and Characterization", Proc. of the 13th Int. Conf. on Thermoelectrics (ICT'94), Kansas City MU, USA, 1994, AIP Conf. Proc.(1995), 3-6.

[2] T. Caillat, A. Borshchevsky, and J.-P. Fleurial, "Preparation and Thermoelectric Properties of p- and n-type $CoSb_3$", Proc. of the 13th Int. Conf. on Thermoelectrics (ICT'94), Kansas City MU, USA, 1994, AIP Conf. Proc.(1995), 58-61.

[3] K. Matsubara, T. Sakakibara, Y. Notohara, H. Anno, H. Shimizu, and T. Koyanagi, "Electronic Transport Properties of the Skutterudite CoSb3 and Mixed Alloys", Proc. of the 15th Int. Conf. on Thermoelectrics (ICT'96), Pasadena CA, USA, 1996, IEEE Conf. Proc.(1996), 96-99.

[4] T. Caillat, J.-P. Fleurial, and A. Borshchevsky, "Skutterudite for Thermoelectric Applications", Proc. of the 15th Int. Conf. on Thermoelectrics (ICT'96), Pasadena CA, USA, 1996, IEEE Conf. Proc.(1996), 100-106.

[5] H. Nakagawa, H. Tanaka, A. Kasama, K. Miyamura, H. Matsumoto, and K. Matsubara, "Thermoelectric Properties of $CoSb_3$ Prepared by Copper Mold Quenching Technique", Proc. of the 15th Int. Conf. on Thermoelectrics (ICT'96), Pasadena CA, USA, 1996, IEEE Conf. Proc.(1996), 117-121.

Thermoelectric Properties of $Fe_{1-x}Ni_xSb_3$ Ribbons

M.Hasaka, H. Kitagawa, K. Matano T. Morimura, and S. Kondo
Department of Materials Science and Engineering, Faculty of Engineering,
Nagasaki University, 1-14 Bunkyo-machi, Nagasaki 852, Japan

Abstract

This paper deals with the microstructures and thermoelectric properties of $Fe_{1-x}Ni_xSb_3$ ribbons between x=0 and 1.0. The ribbons were fabricated by casting on a rotating copper roll with the surface velocity of 10m/s, and then annealed for 3.6ks at 873K. The microstructures were investigated by means of X-ray diffraction measurements and transmission electron microscopic observations. The $CoAs_3$ type of structure, namely skutterudite structure, appeared as well as the other structures of $FeSb_2$, $NiSb_2$ and Sb below x=0.45 and above 0.55. Only the skutterudite appeared and the other structures disappeared between x=0.45 and 0.55. The thermoelectromotive force and electrical resistivity were measured under a vacuum from 300K to 670K. The thermoelectromotive force was of p-type of semiconductor for x<0.5 and of n-type for x>0.5. The electrical resistivity recorded a maximum at x=0.5. The curve of electrical resistivity versus x was asymmetric at x=0.5. The electrical resistivity was larger for x<0.5 than for x>0.5 at the same deviation from x=0.5. The power factor, which was estimated from the thermoelectromotive force and electrical resistivity, reached to maximums at x=0.4 and x=0.6, and was small at x=0.5 at 300K.

Introduction

Semiconductors are requested for conversion from heat to electric power. Skutterudites, which have the $CoAs_3$ type of structure, have been reported to be attractive for this purpose [1]-[5]. The skutterudites were found in the ternary systems of $Fe_{0.5}Ni_{0.5}Sb_3$ etc. as well as the binary systems of $CoSb_3$ etc.

This paper lays emphasis on the microstructures and thermoelectric properties of $Fe_{1-x}Ni_xSb_3$ ribbons which were fabricated by spin-casting and annealing. X-ray diffraction measurements, transmission electron microscopic observations were performed together with the measurements of thermoelectromotive force and electrical resistivity.

Experimental

Ingots with the compositions of $Fe_{1-x}Ni_xSb_3$(x=0-1) were prepared by casting into a metal mold after high frequency induction melting under an argon atmosphere. The fragments of the cast were again melted in a high frequency induction furnace, and cast on a rotating copper roll with the surface velocity of 10m/s. The products were ribbons, width of 5mm, thickness of 20μm. The ribbons were annealed for 3.6ks at 873K.

After powdering the ribbons, the crystal structures were identified by X-ray diffraction measurements with Rigaku RINT2200. After thinning the ribbons by ion-milling, the electron diffraction patterns and high resolution images were taken by a transmission electron microscope, JEOL JEM-2010. The thermoelectromotive force and electrical resistivity were measured under a vacuum.

Results and Discussion

Fig.1 shows the X-ray diffraction patterns of the $Fe_{1-x}Ni_xSb_3$ ribbons. There exist several types of structure as follows :

x<0.45 $CoAs_3+FeSb_2+Sb$
$0.45 \leqq x \leqq 0.55$ $CoAs_3$
0.55<x $CoAs_3+NiSb_2+Sb$

The single structure of $CoAs_3$ type appears from x=0.45 to 0.55. This result suggests that the skutterudite is stable from Δn=-0.1 to 0.1 where Δn=2x-1 is difference of electron number between $Fe_{1-x}Ni_xSb_3$ and $CoSb_3$

Fig.2 shows the bright field TEM image of the ribbon of x=0.55. The ribbon is composed of many grains of about 100nm. Fig.3 and 4 show the high resolution TEM images in the grains of the ribbons of x=0.46 and x=0.55. Each image corresponds to atomic arrangement in the <001> projection and the <110> projection of the skutterudite.

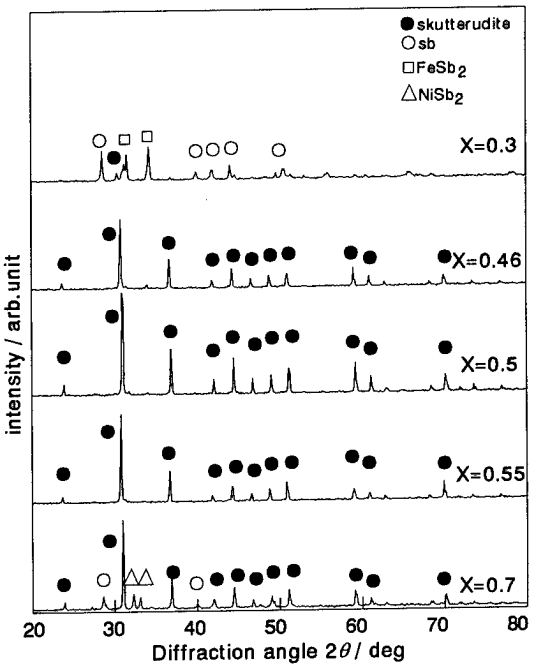


Fig.1 X-ray diffraction patterns of the $Fe_{1-x}Ni_xSb_3$ ribbons.

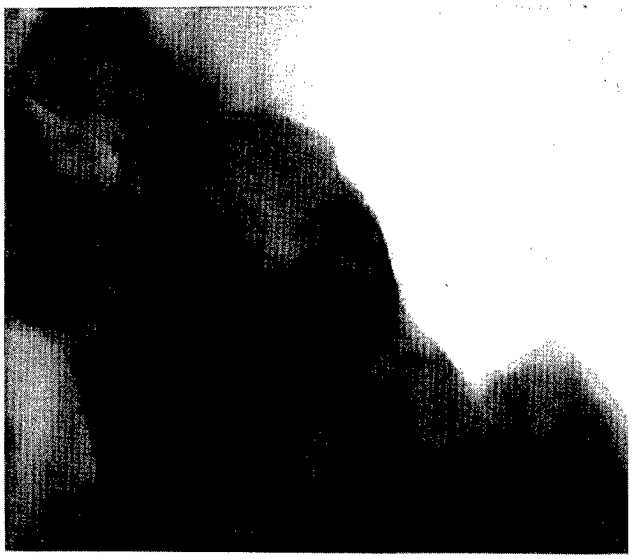


Fig.2 Bright field TEM image of the ribbon of x=0.55.

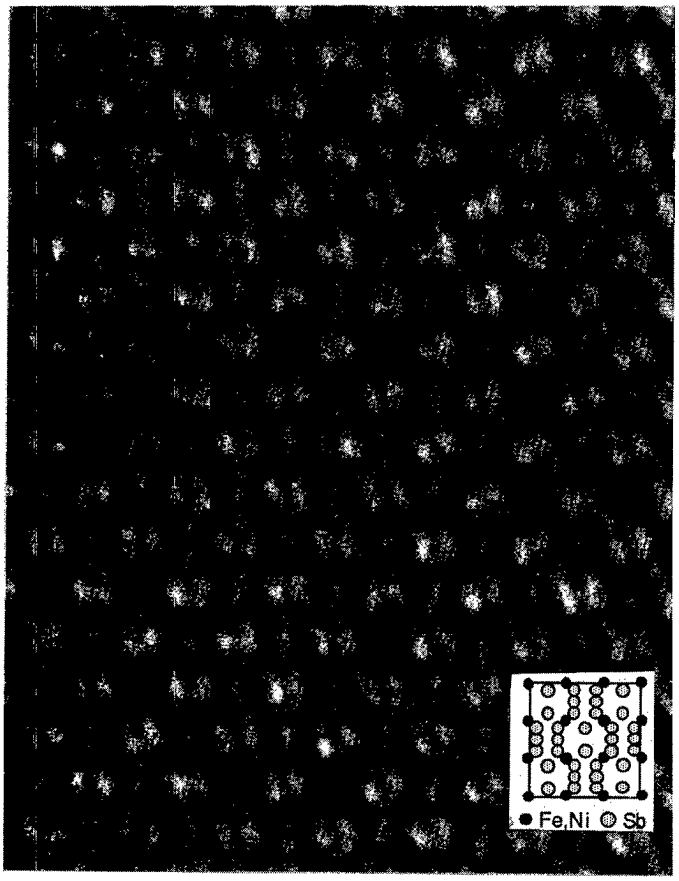


Fig.3 High resolution TEM image in the <001> projection of the ribbon of x=0.46.

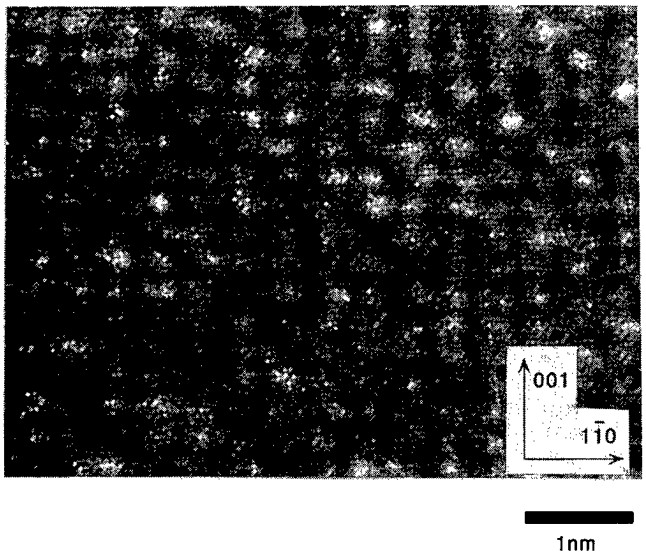


Fig.4 High resolution TEM image in the <110> projection of the ribbon of x=0.55.

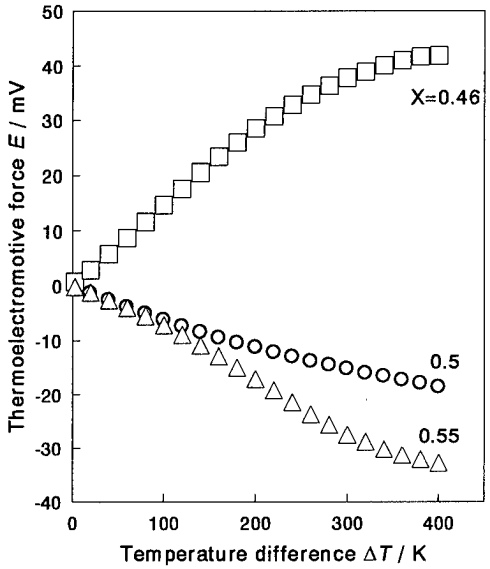


Fig.5 Changes of thermoelectromotive force with increasing temperature difference. The cooling edge is kept at 300K.

Fig.5 shows the changes of thermoelectromotive force with increasing temperature difference from the cooling edge of 300K in the ribbons of x=0.46, 0.5 and 0.55. The thermoelectromotive force increases positively for x=0.46 and negatively for x=0.55. The ribbon of x=0.46 is of p-type of semi-conductor and the ribbon of x=0.55 is of n-type. Fig.6 shows the curve of thermoelectromotive force versus x in the ribbons with the edges of 300K and 600K. The thermoelectromotive force is positive for x<0.5 and negative for x>0.5. It is zero at x=0.5. Consequently, the type of semi-conductor changes from p-type to n-type at x=0.5. The maximum thermoelectromotive forces are obtained at x=0.46, Δn=-0.08 for p-type and at x=0.53,Δn=0.06 for n-type.

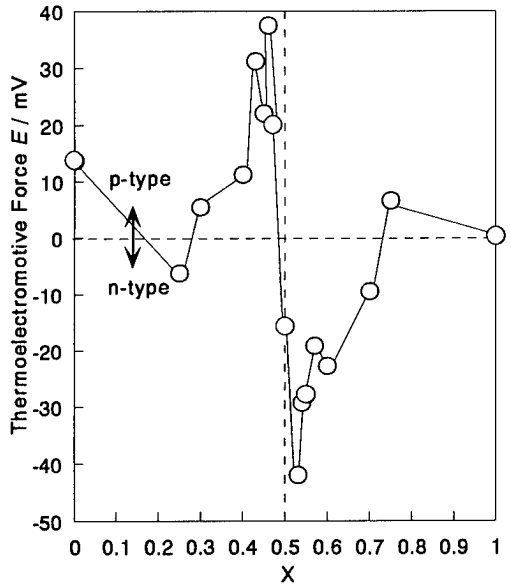


Fig.6 Thermoelectromotive force versus x. The heating edge is at 600K, the cooling edge being at 300K.

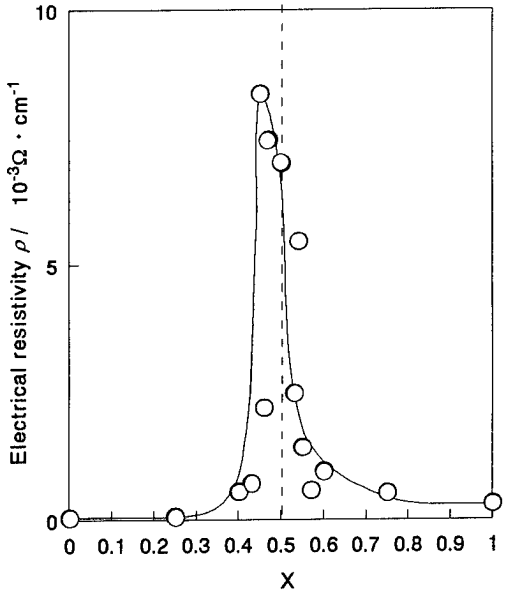


Fig.8 Electrical resistivity versus x at 300K.

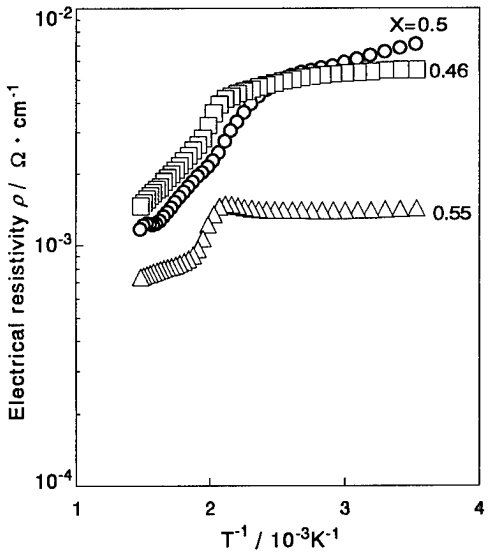


Fig.7 Changes of electrical resistivity with increasing temperature.

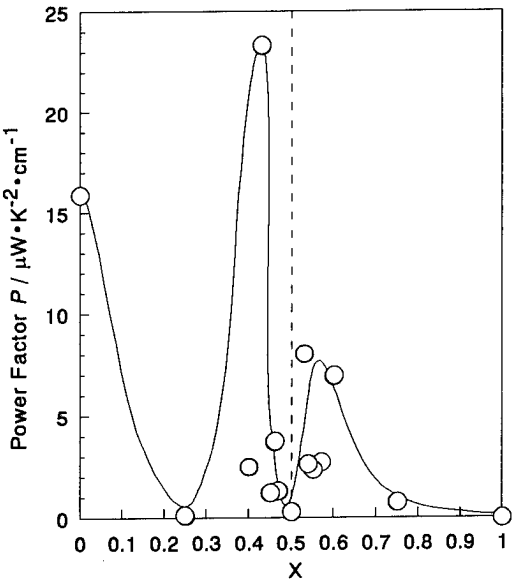


Fig.9 Power factor versus x at 300K.

Fig.7 shows the changes of electrical resistivity with increasing temperature in the ribbons of x=0.46, 0.5 and 0.55. The electrical resistivity is smaller for x=0.55 than for x=0.46, 0.5. It remains almost same, or becomes slightly smaller with increasing temperature, before it decreases abruptly above 450K. Fig.8 shows the curve of electrical resistivity versus x in the ribbons at 300K. The curve is not synmetric about x=0.5. The electrical resistivity is especially large in the range of x=0.46-0.53, Δn=-0.08-0.06

Fig.9 and 10 show the curve of power factor versus x in the ribbons at T=300K and 600K.The power factor is small at x=0.5 because of the small thermoelectromotive force. There are two maximums near x=0.4 and 0.6. That is, the power factor reaches to maximums in the mixed structure of semi-conductor and metals. It is possible to make the junction of semi-conductor with large power factor, if the ratio of Fe and Ni is selected properly.

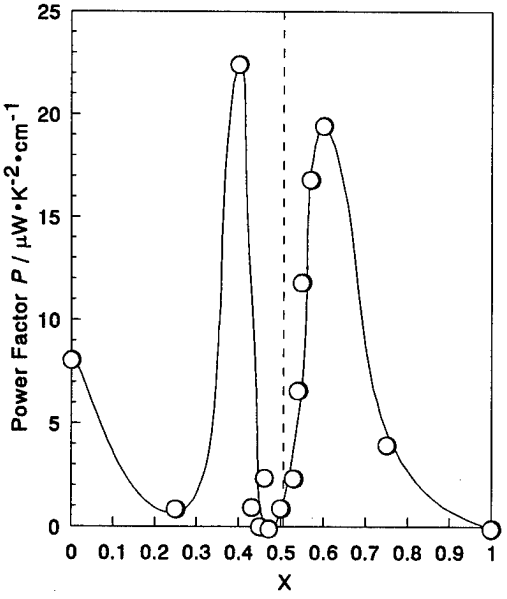


Fig.10 Power factor versus x at 600K.

Conclusions

The microstructures and thermoelectric properties of the annealed $Fe_{1-x}Ni_xSb_3$ (x=0-1.0) ribbons were investigated by means of X-ray diffraction measurements, transmission electron microscopic observations, and measurements of thermoelectromotive force and electrical resistivity. $CoAs_3$ type of structure was mixed with the other structures of $FeSb_2$, $NiSb_2$, Sb for x<0.45 and for x>0.55. Only the $CoAs_3$ type of structure appeared in the range of x=0.45-0.55. When x deviated slightly from x=0.5, the thermoelectromotive force reached to a maximum of p-type of semiconductor for x<0.5 and of n-type for x>0.5. The electrical resistivity was large near x=0.5 and decreased as x deviated largely from x=0.5. The maximum power factor was obtained near x=0.4 for p-type and x=0.6 for n-type.

References

[1] T. Caillat, A. Borshchevsky, and J.-P. Fleurial, "Preparation and Thermoelectric Properties of p- and n-type $IrSb_3$", Proc. of the 13th Int. Conf. on Thermoelectrics (ICT'94), Kansas City MU, USA, 1994, AIP Conf. Proc.(1995), 31-34.

[2] J.-P. Fleurial, "Modeling of the Thermoelectric Properties of p-type IrSb3", Proc. of the 13th Int. Conf. on Thermoelectrics (ICT'94), Kansas City MU, USA, 1994, AIP Conf. Proc.(1995), 86-91.

[3] K. Matsubara, T. Sakakibara, Y. Notohara, H. Anno, H. Shimizu, and T. Koyanagi, "Electronic Transport Properties of the Skutterudite CoSb3 and Mixed Alloys", Proc. of the 15th Int. Conf. on Thermoelectrics (ICT'96), Pasadena CA, USA, 1996, IEEE Conf. Proc.(1996), 96-99.

[4] T. Caillat, J.-P. Fleurial, and A. Borshchevsky, "Skutterudite for Thermoelectric Applications", Proc. of the 15th Int. Conf. on Thermoelectrics (ICT'96), Pasadena CA, USA, 1996, IEEE Conf. Proc.(1996), 100-106.

[5] A. Borshchevsky, T. Caillat, and J.-P. Fleurial, "Solid Solution : Improving the Thermoelectric Properties of Skutterudites", Proc. of the 15th Int. Conf. on Thermoelectrics (ICT'96), Pasadena CA, USA, 1996, IEEE Conf. Proc.(1996), 112-116.

Development of FGM thermoelectric materials in Japan -The state of the art-

Ichiro Shiota* and Isao A.Nishida**

*Dept.of Environmental Chemical Eng.,Kogakuin University,Hachioji,Tokyo 192,Japan
Tel.:+81-426-28-4568, Fax:+81-426-28-4596, E-mail:i-shiota@sin.cc.kogakuin.ac.jp

**National Research Institute for Metals, STA
Tel.:+81-298-59-2637, Fax:+81-298-59-2601, E-mail:albert@nrim.go.jp

Abstract

A higher figure-of-merit Z of a thermoelectric material shows a higher performance at a specific narrow temperature range. On the other hand, the specific temperature can be shifted to higher temperature by increasing the carrier concentration. Bismuth telluride(Bi_2Te_3), lead telluride(PbTe) and Si-Ge alloy(SiGe) are used for low, medium and high temperature range, respectively. Usually, a monolithic and uniform thermoelectric material is used, though a temperature gradient exists in the thermoelectric material. Therefore, each part has not proper carrier concentration for each temperature. Two times of higher performance than a traditional thermoelectric material can be expected, if the proper carrier concentration gradient is performed to fit with the temperature gradient. Performing stepwise change of carrier concentration is also a performing method for practical application. That is a fundamental concept of energy converting FGM. A national project by STA was started to develop the FGM in 1993.

It is essential to choose a proper material for each part to fit the temperature gradient. The proper material is a material with proper carrier concentration and a proper compound to match the temperature of each part along the temperature gradient.

FGM joining of these materials and fitting electrodes with FGM interface are also core technique, because thermal stress relaxation caused by the difference of thermal expansion coefficient is important at a high temperature.

Joining two Bi_2Te_3 with carrier concentrations n_e of 1.0 and 4.5×10^{25} was prepared by ordinal soldering technique or diffusion bonding. The specific temperature range of Seebeck coefficient α for the joined Bi_2Te_3 is extended from 50 to 100K, and the value of α at the valley between two materials with different n_e was higher than both materials. The sintered n-type PbTe FGM with 3 layers of n_e =3.51, 2.60 and 2.26×10^{25} was prepared by hot pressing. The effective maximum power P_{max} of the FGM at the temperature difference of $\triangle T$=310K is 150Wm/m^2 and is about 7% lager than that of the layer with n_e =3.51×10^{25} whose P_{max} is the greatest in all layers.

Introduction

A concept of the FGM(Functionally Graded Material) was proposed to establish the novel technique for thermal stress relaxation in 1987 in Japan. The fundamental concept of FGM was based on the gradual change of composition, structure or material to avoid the sharp interface where thermal stress concentrates. A 5-year national project to achieve the proposal was carried out by STA(Science and Technology Agency of Japanese Government). Heat resistive materials for a space plane and joining technique for high temperature application were successfully performed in the project, and the idea was widely spread out all over the world.

The idea of the FGM is pointed out to be applied not only to the field of the thermal stress relaxation but also to optical, electronic, energy conversion, or biological fields. These fields are very important for saving resources on the earth, effective utilization of unused energy or generating clean energy.

Another national project was started to create a high efficiency energy conversion material with FGM structure by STA in 1993, which is called as FGM-part II. Thermoelectric materials and thermionic materials were adopted as the energy conversion materials in the project. Main objectives of the project are developing of "designing the system", "controlling the structure", and "evaluation method". This project was revised in 1995, and the objectives were concentrated to thermoelectric materials and modules.

In these situation, the thermoelectric materials with FGM structure have attracted the attention of "The Japan Society of Applied Physics", "The Ceramic Society of Japan" and many other societies. Similar project, which is supported by Ministry of Education of Japanese Government, has been started since 1995.

Here, we describe the fundamental concept of high efficient thermoelectric materials with FGM structure. The state of the art is also presented in the field of thermoelectric materials with FGM structure in Japan.

Fundamental concept of FGM

As described above, temperature gradient exists in a thermoelectric material. Special carrier concentration of special material, usually intermetallic compound, show high efficiency at a special temperature. However, a monolithic thermoelectric material is usually used, and every part along the temperature gradient has not necessarily best properties. Then higher efficiency can be expected than traditional thermoelectric materials, if the best properties are given to each part to fit with the temperature gradient. Three kinds of approaches, carrier control, segmented joining and texture control, are adopted to form an FGM structure.

Carrier control

Performing higher Z over a wide temperature range is essential to obtain higher thermoelectric efficiency η. Fig.1 shows the temperature dependence of Z for 5 kinds of n-type PbTe with different carrier concentration, which was induced from a report of ZT-data by Goff and Lowney[1] as the parameter of carrier concentration. Every Z-curve has a

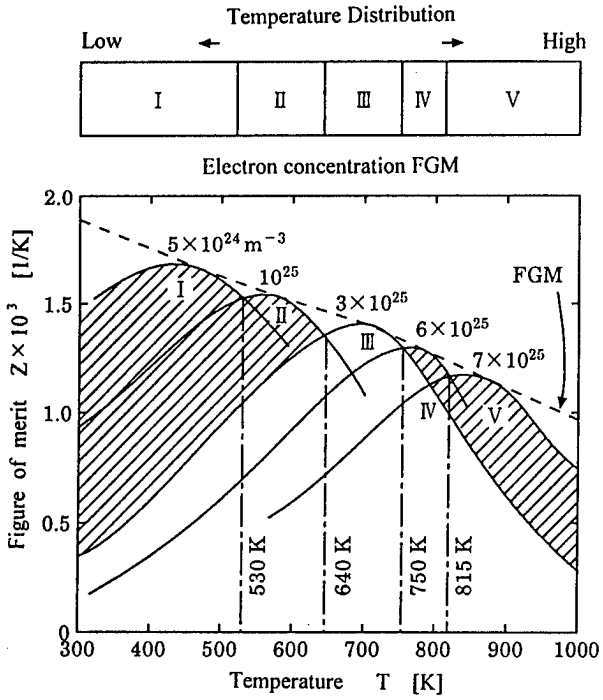


Figure 1 Temperature dependence of Z for n-type PbTe as parameters of carrier concentration.

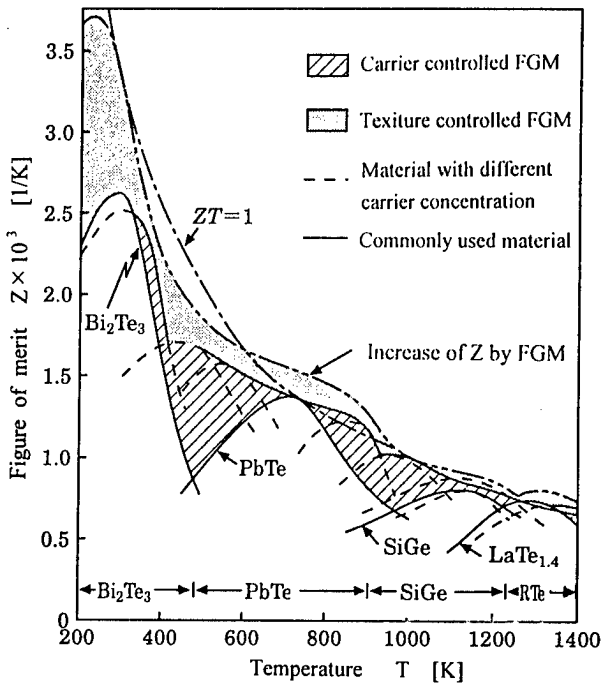


Figure 2 Temperature dependence of Z for monolithic thermoelectric materials, Bi_2Te_3, PbTe, SiGe and $LaTe_{1.4}$ FGMs, and improvement of Z by FGM forming.

maximum value, and the corresponding temperature shifts with the carrier concentration. If these materials are joined consequently to fit with the temperature gradient, higher performance than traditional thermoelectric materials can be expected.

When the FGM structure is applied to PbTe, the conversion efficiency can be improved remarkably[2]. Five kinds of PbTe in Fig.1 are joined in sequence at the intercept temperatures of 530, 640, 750 and 815K. This segmented PbTe has five kinds of different carrier concentration and shows five maximum values of Z at different temperatures. Comparing with the ordinal monolithic PbTe with a carrier concentration of $3 \times 10^{25}/m^3$, which show the highest efficiency in monolithic PbTe, the FGM exhibits a larger Z-value as shown in the hatched area. The broken line in Fig.1 shows an estimation on the assumption of continuous change of the carrier concentration for PbTe. This gradient PbTe has an ideal FGM structure and exhibits a higher Z than the segmented PbTe over a wide temperature range. It is estimated that the average Z of the ideal FGM should improve by 50% in comparison with a monolithic PbTe, and maximum thermoelectric efficiency η_{max} at T_h=950K should extend to 19%.

This concept can be applied not only to the carrier concentration gradient but also to joining different materials, such as Bi_2Te_3-PbTe-SiGe etc., corresponding to the temperature gradient. Fig.2 shows the Z values for monolithic materials and theoretically estimated values for FGM. The hatched area is the expected increase by FGM formation.

Segmented joining

Applicable maximum temperature to PbTe is about 950K.When higher temperature than 950K is preferable, refractory thermoelectric materials such as SiGe, Gd_2Se_3 and $LaTe_{1.4}$ are commonly used. If Si-Ge alloy(SiGe) and $LaTe_{1.4}$ have an ideal FGM structure of carrier concentration as same as PbTe in Fig.1, and these SiGe and $LaTe_{1.4}$ are joined to a PbTe-FGM, the maximum temperature rises up to 1400K. Then the Z curve shows a larger value than ZT=1 over the temperature ranges of 500 to 1400K as shown in Fig.2. The η_{max} of monolithic PbTe and SiGe are of 12 and 14%, respectively, while η_{max} of the segmented material of Bi_2Te_3/PbTe/SiGe/$LaTe_{1.4}$ would reach to 22.3% in the temperature ranges of 300 to 1400K[2]. Consequently, forming the FGM structure with different material is effective in improving the energy conversion efficiency.

Texture control

The thermoelectric performance of semiconductors is evaluated by Z related to three physical properties of Seebeck coefficient α, resistivity ρ and thermal conductivity κ. These properties are given as a function of the carrier concentration and each property can not be controlled independently. However, thermal conductivity in heavily doped semiconductor is mainly due to the electric contribution κ_{el} and lattice contribution κ_{ph}[3-5]. Then, thermal conductivity is given by

$$\kappa = \kappa_{el} + \kappa_{ph}. \qquad (1)$$

The thermal vibrations of the lattice are quantized and the quanta(phonons) migrate along the temperature gradient. Then a thermal current is caused as the result. The phonons are scattered and the thermal current is disturbed by collision among phonons, disorder in the lattice, and boundaries. The scattering is effectively caused when the wave length of the phonon is the same as the length between disorders. Then phonons with higher energy are effectively scattered by disorder in the lattice and phonons with lower energy are scattered by grain boundaries.

In many solid solution systems, the scattering due to disorder caused by alloying reduces κ_{ph} by almost one order of magnitude. Therefore, the Z of a solid solution or an alloy is higher than that of a single compound or an element because of the reduction effect of κ_{ph} due to the phonon scattering with a higher energy[6]. From this point of view, Si-Ge alloys are the most famous materials, as they consist of a solid solution of intermetallic compound and elemental semiconductors.

On the other hand, the grain boundaries scatter phonons with a lower energy remarkably. The reduction effect of κ_{ph} by the boundary scattering occurs in a polycrystal with fine grains and the sintered materials[2,4-6]. As an example, the relationship between the κ_{ph} and crystal grain size for p-type $Si_{70}Ge_{30}$ alloy[4,5] is shown in Fig.3. e and $1/(eR_H)$ are elemental electric charge and Hall concentration, respectively, and a line of No.1 is of a single crystal. It is shown in the figure that the κ_{ph} decreases with decreasing grain size L. Decreasing of the κ_{ph} with increasing $1/(eR_H)$ is also shown. This was caused by the disorder in the lattice induced by doped elements.

Theoretical approaches

Optimal designing based on potential gradient due to compositional change is essential to improve the properties. On the basis of this idea, FGM thermoelectric materials can be expected to have higher efficiency than monolithic materials[7,8]. However, this simple approach is on the basis

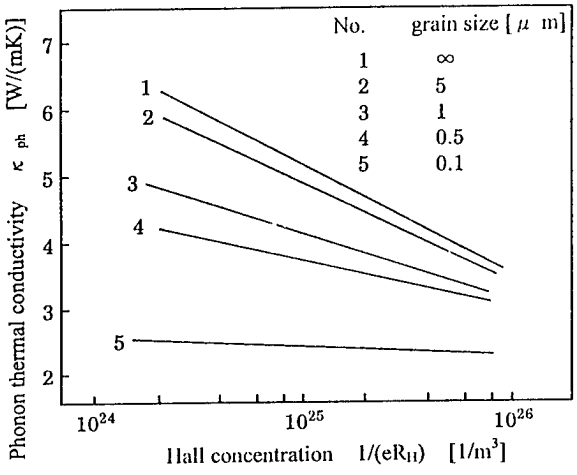


Figure 3 Relationship between the κ_{ph} and Hall concentration $1/(eR_H)$ for p-type $Si_{70}Ge_{30}$ alloys with various grain sizes.

Table 1 Maximum efficiencies of optimized FGM and monolithic materials (non-FGM).

Material	Bi_2Te_3	Pb	SiGe	Total
Temperature (K)	300-700	700-1000	1000-1300	300-1300
η_{max} for FGM (%)	12.25	5.20	4.51	20.56
η_{max} for non-FGM (%)	10.46	4.96	4.49	18.72

of interpolation between properties of combined imaginary materials. Therefore accuracy of the estimated value is not sufficient and the result is difficult to apply practically.

Designing of graded potential by using graded distribution of impurity in traditional semiconductor was proposed to estimate the macroscopic properties analytically by Teraki and Hirano[9] for promising thermoelectric material. By their analysis, η_{max} of Bi_2Te_3 and PbTe were higher than each monolithic material by forming the concentration controlled FGM as shown in Table 1. On the other hand, no remarkable improvement was recognized in SiGe. However, η_{max} of a segmented material of Bi_2Te_3, PbTe and SiGe, which is a stepwise FGM, has 10% higher than one of a monolithic material at the range of 300-1300K. Moreover, Teraki pointed that the thermoelectric properties of a segmented stepwise FGM has nearly equal to continuous FGM[10].

On the basis of the model proposed by Parrot and Stuckers[6], Rowe and Bhandari[11] analyzed the relationship between grain size L and κ_{ph} obtained by laser flash technique to improve the η_{max} of sintered PbTe by hot pressing. They concluded that κ_{ph} decreased as L became smaller, and the decrease of κ_{ph} was 5 and 10% less than one of the single crystal, when the L was 1.0 and 0.5 μ m respectively.

On the other hand, Yoshino[12] analyzed the temperature dependence of ZT for sintered SiGe and PbTe on the basis of heterogeneous grain boundary method. He reported that decreasing of κ_{ph} is very small even L is small as 1.0 μ m. He reported that ZT of PbTe can be increased by modifying grain boundaries when $L \leqq 0.1\ \mu$ m.

Yoneda et.al.[13] observed the temperature dependence of thermoelectric properties for sintered PbTe and uniaxially solidified PbTe with L=6-380 μ m which were fabricated by plasma activated pressing[14]. They found that κ_{ph} did not depend on crystal size at over 200K which agreed with the result by Yoshino.

Practical example

Bi_2Te_3 system compounds

The bismuth telluride system compounds and its solid solution have a higher Z in c-axis direction, then the uniaxial solidified materials generally utilized for applications of peltier heat and thermoelectric generator. Currently, the sintered Bi_2Te_3 system solid solutions with high Z and mechanical strength[15,16] are developed, and the productivity of minutiae shaped thermomodules has been grown. The sintered materials by hot pressing are anisotropic and have a higher Z in perpendicular to the hot pressing direction. Shiota[17] reported that κ_{ph} of the hot-pressed Bi_2Te_3 system and its solid solutions decrease with decreasing

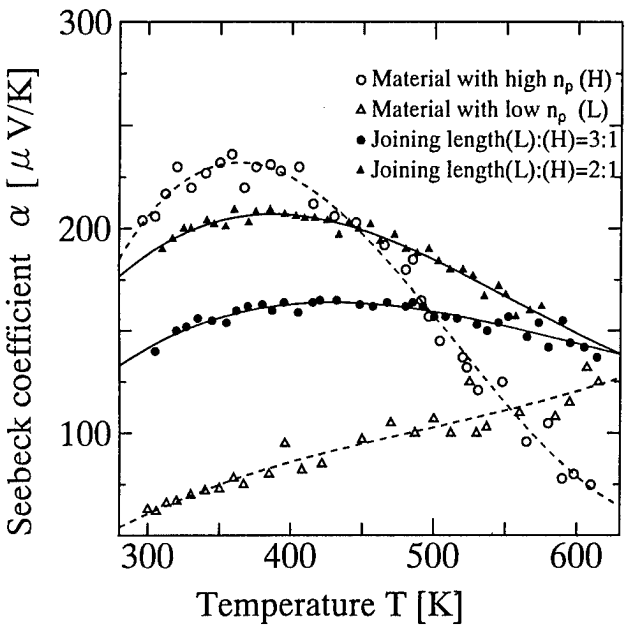


Figure 4 Temperature dependence of α for segmented Bi_2Te_3 with carrier concentration of 1.0 and $10\times10^{25}/m^3$.

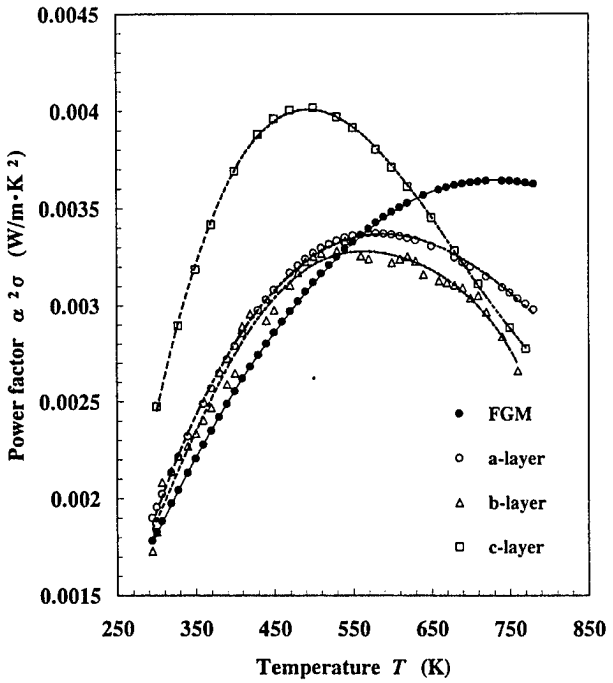


Figure 5 Temperature dependence of power factor $\alpha^2\sigma$ for the sintered n-type PbTe at 500K of the heat sink temperature T_c. FGM, a-, b- and c- correspond to the notes in Table 2.

L and reduce about 20% than uniaxial solidified materials, while sintered materials with $L\leqq1\mu m$ can not improve Z to decrease the carrier mobility. Fig.4 shows the temperature dependence of α for segmented $(Bi,Sb)_2Te_3$ with carrier concentrations of 1.0 and $10\times10^{25}/m^3$[18]. The joining to form the segmented material was performed by ordinal soldering, liquid state diffusion bonding and diffusion bonding techniques. The α-curve of the segmented material was broader than ones of homogeneous materials with different carrier concentration, and the value of α at the valley between two homogeneous materials was higher than both materials, resulting that the temperature range of high α-value was extended from 50 to 100K

PbTe system compounds

Imai et.al[19] fabricated three kinds of monolithic n-type PbTe with different electron concentration n_e and an FGM of 3-layer-segmented PbTe, which consists of three kinds of monolithic PbTe by hot pressing. Hot pressing was performed at 1100K for 750s in an Ar atmosphere. The size of the as-hot pressed FGM was 10mm in diameter and 6mm in thickness which consisted of three layers in 2mm thickness. The sample of 5mm×5mm×6mm for measurement was taken out from the central part of the hot pressed material. The thermoelectric properties of the monolithic materials and the FGM were observed.

Table 2 shows thermoelectric properties and transport parameters of the monolithic materials and FGM at room temperature. The n_e values of solidified materials are shown in the parentheses, and were 1.0, 0.6 and $0.3\times10^{25}/m^3$, which were planned to be the high temperature side, the middle temperature part and the low temperature side of an FGM,

Table 2 Thermoelectric properties of FGM composed of sintered n-type PbTe with 3 kinds of electron concentrations n_e at room temperature.

Layer	Seebeck Cof. α (μV/K)	Resistivity ρ (10^{-6} Ωm)	Hall Cof. R_H (m^3/C)	Electron n_e ($10^{25}/m^3$)	Mobility μ_e (m^2/Vs)	Power factor $\alpha^2\sigma$ (W/K²m)
High (a)	-67.1	2.540	1.78×10^{-7}	3.51 (1.00)	7.00×10^{-2} (11.0)	1.77×10^{-3}
Middle (b)	-72.3	2.831	2.30×10^{-7}	2.60 (0.60)	8.12×10^{-2} (11.0)	1.85×10^{-3}
Low (c)	-100.8	3.342	2.75×10^{-7}	2.26 (0.30)	8.22×10^{-2} (9.80)	3.04×10^{-3}
FGM	-85.0	3.94	--	--	--	1.11×10^{-3}

Values of n_e and μ_e for solidified materials which used as starting powders before FGM forming shown in parentheses.

respectively. They were pulverized and used as starting powders for monolithic sintered materials and an FGM. n_e of each layer has remarkably increased and electron mobility μ_e decreased during the hot pressing process as shown above the parentheses in Table 2. The increasing ratio of n_e in the low temperature layer is higher than that in the high temperature layer.

Fig.5 shows the temperature dependence of power factor(i.e. electrical figure-of-merit) α^2/ρ or $\alpha^2\sigma$ for the samples described above. The *a*-layer, *b*-layer and *c*-layer in Fig.5 correspond to the same notes in Table 2. The $\alpha^2\sigma$ of the FGM is lower than each monolithic layer below 500K because of high ρ. While the $\alpha^2\sigma$ of the FGM overcomes the others above 630K. Fig.6 also shows relationship between the effective maximum power P_{max} and temperature difference $\triangle T$ for the FGM and each layers at the heat sink temperature T_c of 500K. The P_{max} is 150mW/K^{2}m at $\triangle T$=310K and is about 7% lager than that of (*a*)-layer whose P_{max} is greatest in all layers. This value implies that the electric power reaches 25kW/m^2, if the operation temperatures of 500K for the cold side and 810K for the hot side are given to the FGM of 6mm thickness.

Yoneda et. al. [20] reported that thermoelectric properties of the solidified *n*-type PbTe with doped PbI_2 is stable below 700K in an Ar atmosphere. Then, joining two PbTe with n_e of 0.4 and 6×10^{25} was prepared by liquid state diffusion bonding technique. The insert material was 40wt%Pb-Sn solder with a thickness of 50 μm, and the joining was performed at 700K for 900s in an Ar atmosphere. Figs.7 and 8 show the temperature dependence of $\alpha^2\sigma$ for monolithic PbTe, and $\triangle T$ dependence of P_{max} for the joined PbTe, respectively[21]. The $\alpha^2\sigma$ of PbTe with higher n_e is larger than that of one with lower n_e above 500K, resulting that the P_{max} of the joined PbTe is higher than those of monolithic materials above $\triangle T$ =250K. As mentioned above, it is concluded that the highly efficient *n*-type PbTe FGM can be performed by the optimization of n_e graded structure.

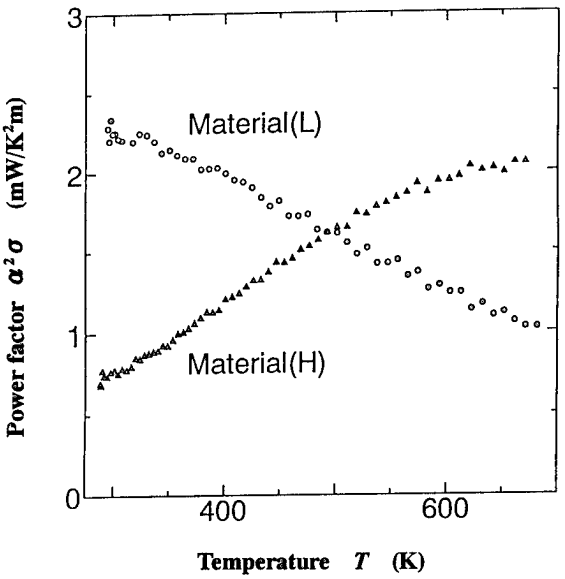


Figure 7 Temperature dependence of power factor $\alpha^2\sigma$ for the *n*-type PbTe joined by liquid state diffusion bonding.

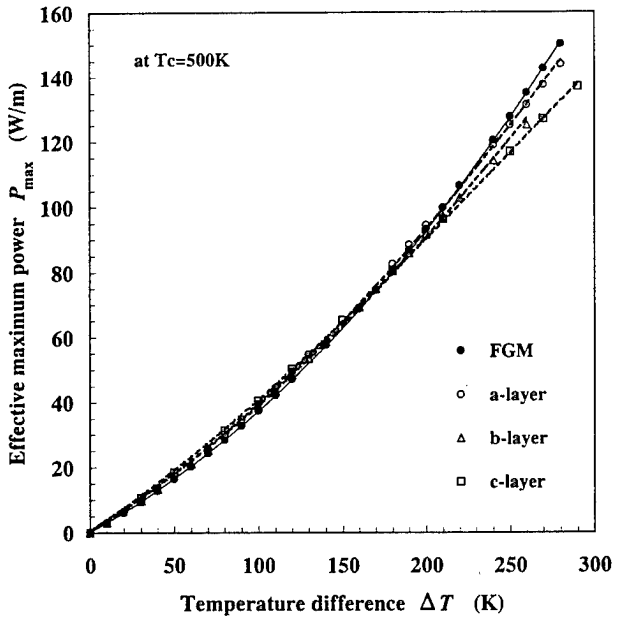


Figure 6 Relationship between effective maximum power P_{max} and temperature difference $\triangle T$ for sintered *n*-type PbTe.
FGM, *a*-, *b*-, *c*- correspond to the notes in Table 2 at 500K of the heat sink temperature.

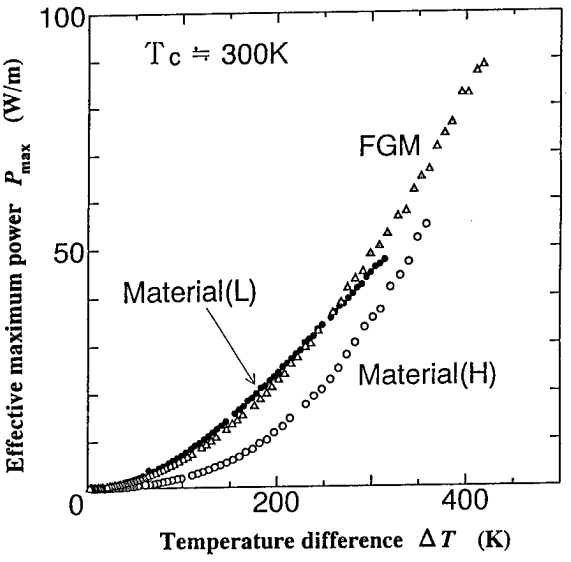


Figure 8 Relationship between effective maximum power P_{max} and temperature difference $\triangle T$ for the *n*-type PbTe by liquid state diffusion bonding.

Si-Ge alloy thin film

Hayashibara[22] reported thermoelectric properties of Si-Ge thin films with different gradient structure, which were formed by using a 2-target sputtering equipment. The slit driving speed and sputtering rate were simultaneously controlled during operation. He fabricated three FGM films with different B-concentration as shown in Fig.9. The thickness of each film was in 1 μm thickness. He reported that P_{max} was 0.87, 1.06, 0.98 μW, respectively, when $\triangle T$ =200K was applied between both ends of the film.

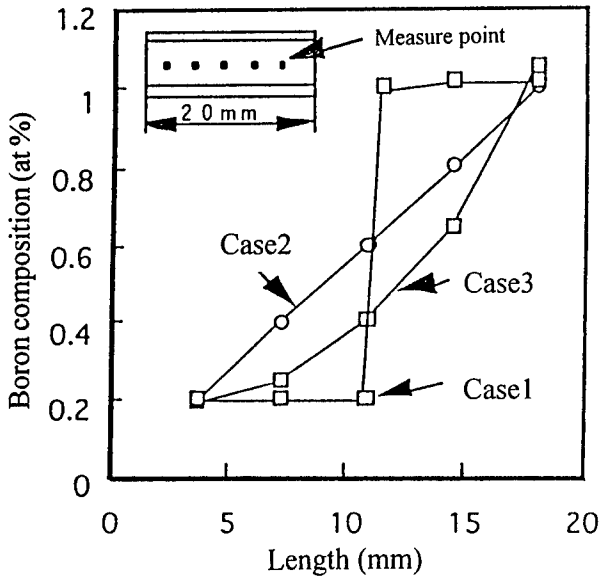


Figure 9 Compositional distribution of B in $Si_{80}Ge_{20}$ FGM film.

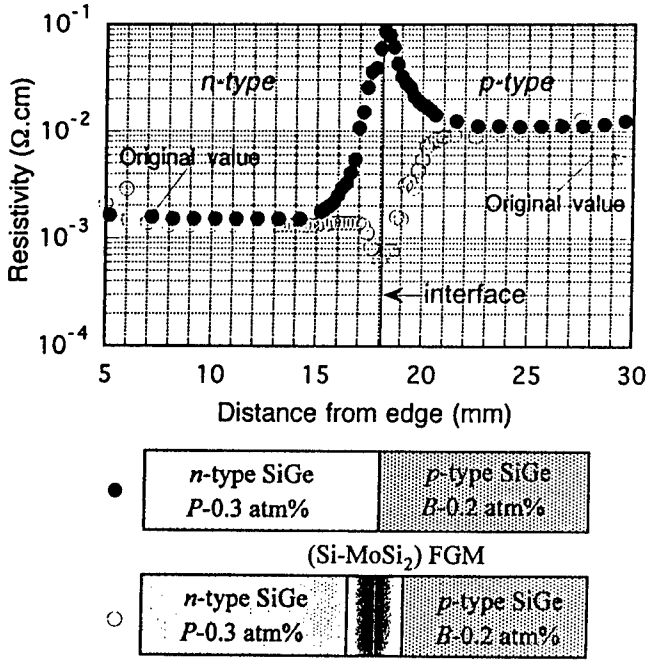


Figure 10 Resistivity around the directly joined interface of *n*-type and *p*-type Si-Ge, and the interface with Si-$MoSi_2$ FGM.

He concluded that P_{max} of continuous FGM, especially the linear gradient(case 2), is higher than the stepwise FGM.

Joining of electrode

Joining of an electrode and thermal stability at the high temperature side are also important objectives in the national project part II. This field is an application of the result obtained in part I, in which thermal stress relaxation and diffusion barrier were main objectives. In the project part II, joining of *n*-type and *p*-type Si-Ge was attempted[23]. Resistivity around the interface is one of important factor for thermoelectric properties. As shown in Fig.10, resistivity at the interface of direct joining is higher than both joined materials, while the resistivity is lower at the interface with Si-$MoSi_2$ of FGM structure. In the former case, compensation between electrons and holes was caused by interdiffusion between P- and B-dopants. In the latter case, the harmful interdiffusion is suppressed and the resistivity becomes lower than joined materials because of low resistivity of Si-$MoSi_2$. From these results, it is decided that an FGM of Si-$MoSi_2$ is not only a good conductor for an electrode, but also it is effective as a diffusion barrier.

Concluding remarks

As described above, it is shown theoretically and experimentally that thermoelectric materials with FGM structure showed a higher performance than monolithic materials. FGM joining is also useful technique for setting an electrode in order to relax the thermal stress and suppress the interdiffusion. However, it is difficult to improve the performance by controlling crystal size as long as we use an ordinal pulverization method.

On the other hand, exact measurement of thermal conductivity at a high temperature is another problem for accurate designing of an FGM. Therefore, we could not necessarily arrange the best material to fit the temperature gradient. If we can determine thermoelectric properties more exactly, we will be able to obtain much higher performance.

References

[1] J.F. Goff and J.R. Lowney, "The thermoelectric figure-of-merit", Proc. of 1st Int. Conf. on Thermoelectric Energy Conv., Arlington, (1976) 47.

[2] I.A. Nishida, "Highly efficient thermoelectric materials in FGM program", Proc. of Japan-Russia-Ukraine Int. Workshop on Energy Conv. Materials (ENECOM95), Sendai, Japan, (1995) 1.

[3] A.F. Ioffe, "Semiconductor thermoelements and thermoelectric cooling", Inforseach Ltd., London, (1956).

[4] D.M. Rowe and C.M. Bhandari, "Modern thermoelectrics", Holt, Rinehalt and Winston Ltd., London, (1983).

[5] K. Uemura and I.A. Nishida, "Thermoelectric semiconductors and its applications", Nikkan-Kogyo Shinbun Ltd., Tokyo, (1988).

[6] J.E. Parrot and A.D. Stuckers, "Thermal conductivity of solid", Pion Ltd., London, (1975).

[7] T. Hirano, L.W. Whitlow and M. Miyajima, "Numerical analysis of efficiency improvements in functionally gradient thermoelectric materials", Proc. of 5th FGM

Domestic Symposium, (1992) 197.
[8] L.W. Whitlow, T. Hirano and M. Miyajima, "Numerical analysis of efficiency improvements in functionally gradient thermoelectric materials", Proc. of 11th Int. Conf. Thermoelectrics, Arlington, (1992) 244.
[9] T. Teraki and T. Hirano, "An one-dimensional optimum design of functionally gradient thermoelectric materials", Proc. of 7th FGM Domestic Symposium, (1994) 133.
[10] T. Teraki, Report of FGM Project Meeting, Tohoku Univ., March, (1996), in Japanese.
[11] D.M. Rowe and C.M. Bhandari, "A review of lead telluride technology at UWIST", Proc. of 6th Int. Conf. on Thermoelectric Energy Conv., Arlington, (1986) 43.
[12] J. Yoshino, "Thermoelectric estimation of thermoelectric figure of merit in sintered materials and proposal of grain-size-graded structure", Proc. of 4th Int. Symposium on FGM, Tsukuba, Japan, (1996), in printing.
[13] S. Yoneda, E. Ohta, H.T. Kaibe, I. Shiota, K. Takahashi, Y. Shinohara, Y. Imai and I.A. Nishida, "Crystal grain size dependence of thermoelectric properties for sintered PbTe by spark plasma sintering technique", Proc. of 16th Int. Conf. Thermoelectrics, Dresden, (1997).
[14] T. Noguchi, "Powder processing of thermoelectric materials-focusing on GeSi with new sintering", ibid.
[15] H. Imaizumi, H.T. Kaibe and I.A. Nishida, "Thermoelectric properties of *n*-type $Bi_2(Te,Se)_3$ by hot-processing", Proc. of 7th Int. Conf. on Thermoelectric Energy Conv., Arlington, (1988) 141.
[16] H.T. Kaibe, "Thermoelectric properties of Bi_2Te_3 system semiconducting compounds", Doctoral thesis, Keio University, (1988).
[17] I. Shiota, Report of FGM Project Meeting, Tohoku Univ., March, (1996), in Japanese.
[18] I. Shiota, Report of FGM Project Meeting, Nat. Res. Inst. Metals., May, (1997), in Japanese.
[19] Y. Imai, Y. Shinohara, I.A. Nishida, M. Okamoto, Y. Isoda, T. Ohkoshi, T. Fujii, I. Shiota and H.T. Kaibe, "Joint of *n*-type PbTe with different carrier concentration and its thermoelectric properties", Proc. of 4th Int. Symposium on FGM, Tsukuba, Japan, (1996), in printing.
[20] S. Yoneda, H.T. Kaibe, T. Okumura, Y. Shinohara, Y.Imai, I.A. Nishida, T. Mochimaru, K. Takahashi, T. Noguchi and I. Shiota, "Improvement and thermal stability of thermoelectric properties for *n*-type PbTe", Proc. of 4th Int. Symposium on FGM, Tsukuba, Japan, (1996), in printing.
[21] Y. Shinohara, Y. Imai, Y. Isoda, I.A. Nishida and H.T. Kaibe and I. Shiota, "Thermoelectric properties of segmented Pb-Te systems with graded carrier concentration", Proc. of 16th Int. Conf., Thermoelectrics, Dresden, (1997).
[22] M. Hayashibara, Report of FGM Project Meeting, Nat. Res. Inst. Metals., May, (1997), in Japanese.
[23] Y. Miyamoto, ibid.

Preparation and Characterization of Segmented-Type Thermoelectric Branches of Bi_2Te_3/PbTe

Yasutoshi Noda(a), Yan-Sheng Kang(b) and Masayuki Niino(b)
(a)Department of Materials Science, Faculty of Engineering, Tohoku University, Sendai 980-77, Japan
Tel.:+81-22-217-7328, Fax.:+81-22-217-7328, E-mail:nodayasu@material.tohoku.ac.jp
(b) National Aerospace Laboratory, Kakuda Research Center, Kakuda City, Miyagi 981-15, Japan
Tel.:+81-224-68-3644, Fax.:+81-224-68-2483, E-mail:kang@kakuda-splab.go.jp

Abstract

Thermoelectric materials, metal/semiconductor joints and segmented-type thermocouple branches were prepared by plasma-activated sintering(PAS) using powdered source materials of Bi_2Te_3, PbTe and metals(Cu, Fe and Ni). The sintering was carried out in vacuum under a axial pressure of 45 MPa by pulse current heating followed by DC current heating, where temperature was differently controlled for sintering of Bi_2Te_3 and PbTe. The sintered materials were characterized by measuring the thermoelectric properties. The electron probe microanalyses indicated that no serious diffusion occurred at the joint interfaces of Fe/PbTe and Bi_2Te_3/PbTe where an abrupt change of the potential voltage was observed in their p-type joints. Therefore SnTe and Ni layers were inserted in the Fe/p-PbTe and Bi_2Te_3/PbTe joints, respectively, to keep low resistance. The thermoelectric branches were Ni/$Bi_2(Te,Se)_3$/Ni/PbTe/Ni for n-type and Ni/$(Bi,Sb)_2Te_3$/Ni/SnTe/PbTe/SnTe/Ni for p-type.

Introduction

The thermoelectric generator in a intermediate temperature range has been developed as the application in space exploration in 1960s, and now is expected as the one in effective utilization of untapped energy[1]. In the case of power generator application, it is desired to obtain a high value of figure of merit(Z) over as wide a temperature range as possible. Since no one material could provide the Z value necessary for high efficiency over the interest temperature range, the construction of the thermocouple branches has been directed to (1)solid solution-type[1] or carrier concentration functionally graded material(FGM)-type [2], (2)segmented(or stacked)-type[2][3], and (3)the combined type of (1) and (2). The segmented-type has firstly been proposed for the Bi_2Te_3/PbTe and Bi_2Te_3/$AgSbTe_2$ systems with the efficiency of 11 %[2], and then developed in space systems with light and compact power generator[4][5].

The present study concerns the fabrication of the metal-semiconductor and semiconductor-semiconductor joints by plasma-activated sintering(abbreviated as PAS) or spark plasma sintering(SPS)[6], where the powder particle surfaces are activated by plasma leading to an accelerated reaction or sintering. The potential profile measurements across the joint boundary will help the preparation of the thermocouple branches with long life and decreased energy loss.

Experimental

In construction of the thermoelectric branches, the p-type undoped PbTe for intermediate temperature range was prepared by Bridgman method and then ground into powder, while the n-type one by sintering a mixture of undoped PbTe and 4000 molppm PbI2 as the dopant. The powder materials of n-type ($0.85Bi_2Te_3$+$0.15Bi_2Se_3$) and p-type ($0.175Bi_2Te_3$+$0.83Sb_2Te_3$) (both abbreviated as Bi_2Te_3) for low temperature range were obtained from the commercial source prepared by mechanical alloying from the constituent elements.

Plasma-activated sintering of PbTe was performed at 1073 K in a carbon die of 11 mm ID in vacuum of about 10 Pa under 45 MPa load by pulse current heating, followed by DC current heating. The PAS condition was listed in Table 1, where it is noteworthy that heating temperature were differently controlled between Bi_2Te_3 and PbTe. The electrical properties were measured for the sintered materials.

The metal electrode - semiconductor joining, such as Fe/PbTe and Ni/ Bi_2Te_3 was made simultaneously by sintering under the same condition as the cases listed in Table 1. In case of metal - p-PbTe joining, thin SnTe layer was inserted between metal and PbTe layers in order to keep low joint resistance[7]. Because of the difference in heating temperature between PbTe and Bi_2Te_3, the joining of these two materials was made via the following two steps; first was to prepare metal/PbTe junction at ~1073 K, and then to joint metal/ Bi_2Te_3 at ~673 K, where a direct-type of PbTe/ Bi_2Te_3 and a sandwich-type of PbTe /Ni/ Bi_2Te_3 resulted.

The joint interfaces were inspected by optical microscope observation, electron probe microanalysis and measurements of potential voltage profile.

Results and discussion

Table 1. PAS condition for PbTe and Bi_2Te_3.

	Parameters	PbTe	Bi_2Te_3
I	Voltage	25 V	
	Current	400 A	
	Frequency	6 Hz	
	Time	90 s	
	Heating temperature	~1073 K	~673 K
II	Time	540 s	60 s
	Heating temperature	~1073 K	~673 K

Pulse current heating(I) followed by DC current heating(II).

Semiconducting properties of sintered materials

The density of sintered PbTe was more than 99 % that of calculated one. The SEM micrograph indicates a densified sintering structure and grain boundaries. Table 2 lists semiconducting properties of PbTe and Bi_2Te_3 prepared by PAS. The carrier concentration of p-PbTe exceeded those for melt-grown single crystals and Hall mobility were low lying. The carrier concentration of n-type PbTe was much lower than that of the melt-grown crystal, which suggests that the dopant was not fully resolved into PbTe crystal because of the short period of sintering. The data for Bi_2Te_3 correspond to those reported for the sintered materials.

Metal/semiconductor junction

The optical micrographs for the Fe/PbTe joints indicates that neither macroscopic defects nor cracks caused by stress were found at the joint boundary. Figure 1 shows the potential voltage profile across the interfaces of Fe/n-PbTe(a), Fe/p-PbTe(b) and Fe/SnTe/PbTe(c) junctions. The potential voltage profile for Fe/n-PbTe joint in Fig.1(a) indicates a gradual increase on leaving from the interface, while the one in Fig.1(b) for the Fe/p-PbTe joint shows an abrupt increase at the interface which causes additional resistance. The SnTe layer between metal and p-PbTe was effective to decrease the interface resistance as shown in Fig 1(c). Since the abrupt change in the potential voltage profile was limited in the Fe/p-PbTe joint, its origin might be sought in the reaction between Fe and PbTe. The reaction results in the formation of Fe donor atom in PbTe or metallic conductor of FeTe, which will produce a deformation of energy band or carrier compensation across the interface in the Fe/p-PbTe joint. The Fe/SnTe/p-PbTe joint is favorable without abrupt increase in the potential voltage profile, since the p-type conduction of SnTe is not significantly influenced by Fe doping. The above discussion is also suitable for the case of Ni/PbTe junctions.

The direct joining between Cu and Bi_2Te_3 was not favorable as is usual because of the diffusion of Cu into Bi_2Te_3. The reaction between Ni and Bi_2Te_3 was not serious and the voltage profile showed a favorable feature for both n- and p-type as shown in Fig.2.

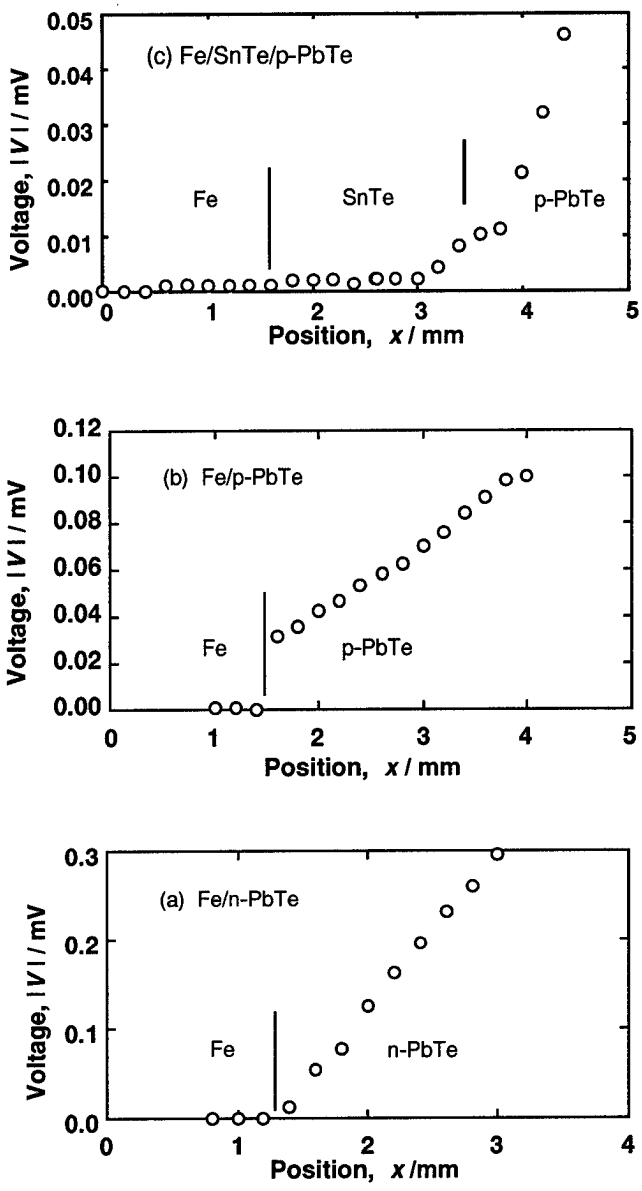
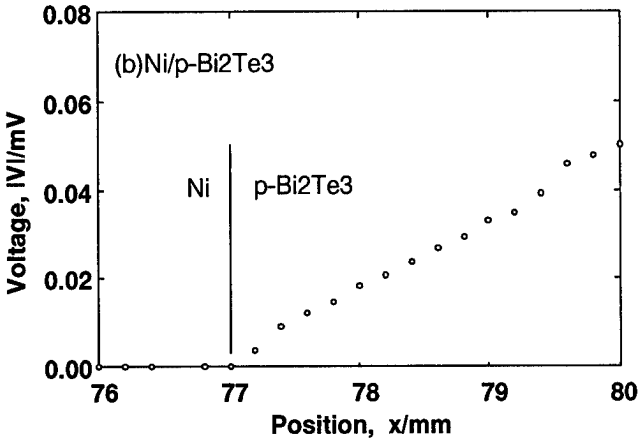


Fig. 1: Potential voltage profiles in the Fe/PbTe joints.

Table 2. Thermoelectric properties of PbTe and Bi_2Te_3 prepared by PAS(at 300 K).

	PbTe		Bi_2Te_3	
	n-type ($4000 mol ppm PbI_2$)	p-type (undoped)	n-type ($0.85Bi_2Te_3+0.15Bi_2Se_3$)	p-type ($0.18Bi_2Te_3+0.83Sb_2Te_3$)
Carrier concentration/(m^{-3})	$4.0x10^{23}$	$3.9x10^{24}$	$3.1\ x10^{25}$	$4.0\ x10^{25}$
Electrical conductivity ($W^{-1}m^{-1}$)	$5.2x10^{3}$	$2.6x10^{4}$	$1.1x10^{5}$	$8.7x10^{4}$
Hall mobility($m^2V^{-1}s^{-1}$)	$8.2x10^{-2}$	$4.3x10^{-2}$	$2.1x10^{-2}$	$1.4x10^{-2}$
Seebeck coefficient(VK^{-1})	-	-	$-1.3x10^{-4}$	$2.0x10^{-4}$
Thermal conductivity ($Wm^{-1}K^{-1}$)	-	-	1.72	1.32



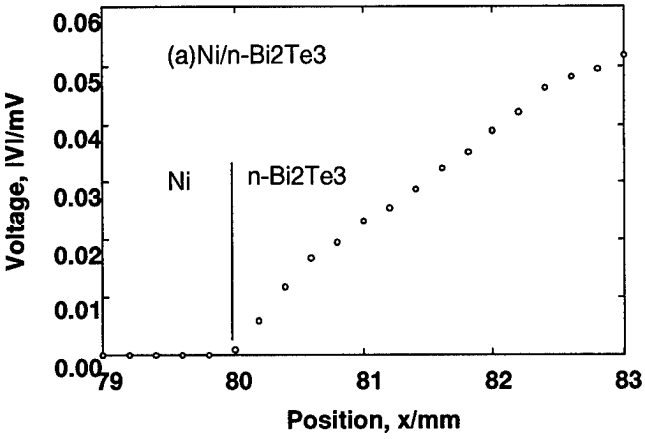


Fig. 2: Potential voltage profiles in Ni/ Bi 2Te3 joints.

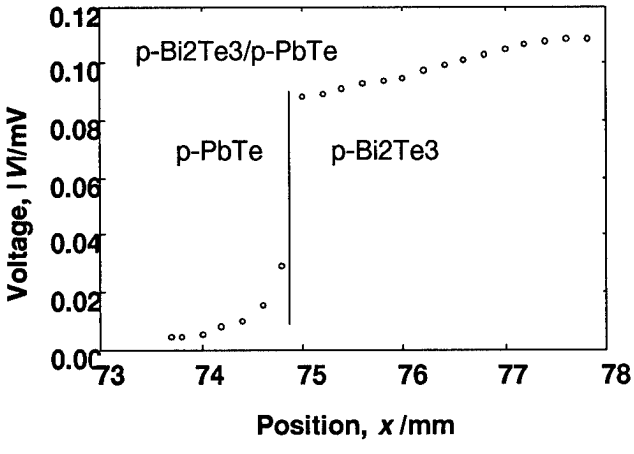


Fig. 3: Potential voltage profile in p-Bi 2Te3/p-PbTe joint.

PbTe/ Bi_2Te_3 segmented-type branches

Each layer in the branches was bound so tightly that the branches could be cut and shaped by high speed diamond saw. Figure 3 shows the potential voltage profile for the p-PbTe/p-Bi_2Te_3 joint, which indicates an abrupt change at the interface. The interface resistance may be due to the reaction between the two p-type phases, considering that the uncontrolled defects in the solid solution of $(PbTe)_{1-x}(Bi_2Te_3)_x$ (x«0.1) causes n-type conduction[8]. By inserting Ni layer as the barrier of reaction between the two layers, the segmented-type branches for n- and p-type were constructed as Ni/ Bi_2Te_3/Ni/ PbTe/Ni and Ni/ Bi_2Te_3/Ni/SnTe/ PbTe/SnTe/Ni, respectively. Fig. 4 and 5 show a segmented-type branch and its potential voltage profile, respectively. The voltage profile shows a smooth curve across the p-Bi_2Te_3/Ni/SnTe/p-PbTe joint, indicating minimized interface resistance. The Cu layer in Fig. 4 was connected to metal electrode in the double layer to keep good thermal conductivity.

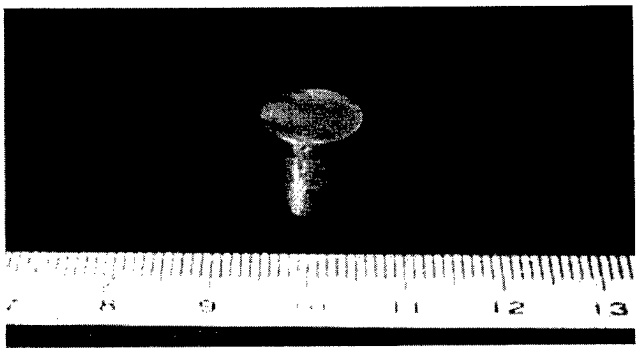


Fig. 4: A segmented type branch of Cu/Ni/p-Bi_2Te_3/Ni/SnTe/p-PbTe/SnTe/Ni for p-type.

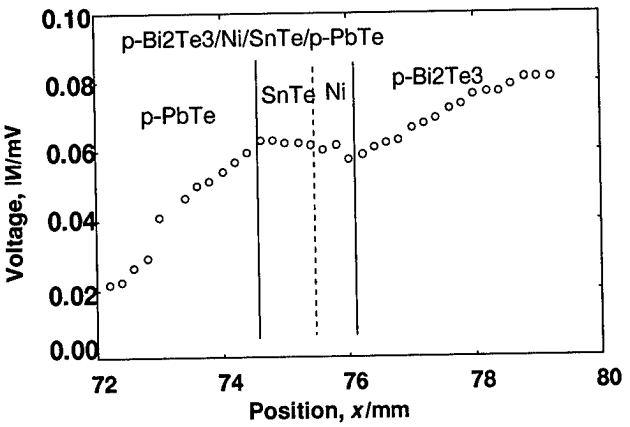


Fig. 5: Potential voltage profile in p-Bi2Te3/Ni /SnTe/p-PbTe joint.

The preparation and characterization of the branches designed for the optimum condition is currently being carried out[9].

Conclusion

Plasma-activated sintering was applied to preparation of thermoelectric materials, metal-semiconductor joining. On the basis of the results, the segmented-type thermoelectric branches of Bi_2Te_3/PbTe were prepared, where The thermoelectric properties of Bi_2Te_3 were comparable to the data for the existing sintered materials. The carrier concentration of p-PbTe by PAS was larger than that of the melt-grown crystal and the Hall mobility was low lying. The electric properties of n-type PbTe suggest that the doping was not completely performed by the sintering of a powder miture of undoped PbTe and PbI_2 as the dopant because of the short period of sintering. In stead, the control of carrier concentration could be made by PbI_2-doping on melt-growth of the PbTe crystals.

The sintering and joining were simultaneously performed by PAS to make metal/semiconductor and semiconductor /semiconductor joints. The microscopic observation at the joint interface revealed no cracks caused by the stress. The EPMA revealed no serious diffusion at the joint interface except in the Cu/ Bi_2Te_3 joints. The potential voltage measurements showed an abrupt change at the interface of Ni/p-PbTe and p-PbTe/p-Bi_2Te_3 joints. The results indicates that the reaction between the adjacent phases will influence more or less the interface resistance. From the inspection into low resistance metal/semiconductor joint, the segmented-type thermocouple branches resulted Ni/PbTe/Ni/Bi_2Te_3/Ni for n-type and Ni/SnTe/PbTe/SnTe/Ni/Bi_2Te_3/Ni for p-type, where the Ni layer between the two semiconductors stands the reaction barrier and the SnTe layer for the gradient joint between Fe(or Ni) and p-type PbTe. As well as low resistance, the blanche structure will be useful to keep long life by preventing deterioration due to diffusion and reaction between the layers. The joining strength are sufficient so that the blanches can be cut across the joint by a high-speed diamond blade.

References

[1]M.Niino, T.Ohshima and K.Matsubara: Proc. 16th Int. Conf. Thermoelectrics(ICT'97), submitted.

[2] F.D.Rosi, E.F.Hockings and N.E.Lindenblad: RCA Review, March(1961), 82.

[3]Y.Noda, M.Orihashi, H.Kaibe, Y.Imai, I.Shiota, and I.A.Nishida: Proc. 15th Int. Conf. Thermoelectrics(ICT'96), Pasadena(1996), p.146.

[4]J.B.Bass and N.B.Elsner:Proc. 4th ICTEC, Arlington(1982), p.26.

[5]P.Rouklove and V. Truscello: Proc. 10th IECEC, Delaware(1980), p.103.

[6] T.Hirai:Materials Science and Technology, A Comprehensive Treatment, ed. R.W.Cahn, P.Haasen and E.J.Kramer, Chapter 20 Functional Gradient Materials, VCH Verlag(Weinheim, 1996), p.293.

[7]Y.Suge: Thermoelectric Semiconductors, (Maki Shoten, 1966), p.434.

[8]T.A.Christakudi, G.Ch.Christakudis and L.D.Borissova: Phys. Stat. Sol.(b), 190(1995), 537.

[9]Y.S.Kang, S.Moriya, K.Kisara, M.Niino, Y.Noda, L.Chen and T.Sudo: Proc. 16th Int. Conf. Thermoelectrics(ICT'97), submitted.

Bismuth-Telluride / Iron-Disilicide Segmented Thermoelectric Elements: Patterning, Preparation and Properties

J. Schilz, L. Helmers

German Aerospace Research Establishment (DLR), Institute of Materials Research, Linder Höhe, D-51147 Köln, Germany

Y.S. Kang, Y. Noda, M. Niino

National Aerospace Laboratory (NAL), Kakuda Research Center, Koganezawa 1, Kimigaya, Kakuda-City, Miyagi 981-15, Japan

Abstract

We report on the development of a stacked thermogenerator element consisting of Bi-Te based materials for the low temperature and $FeSi_2$ for the high temperature stage. In order to determine the optimum segment length, a new numerical method was applied which maximizes the differential, i.e. local electrical power output. The resulting segment length for the Bi-Te stage is smaller than predicted by locally maximizing the figure of merit.

For the practical preparation of the anticipated structure, powdered semiconductors and metals were consolidated by means of a uniaxial hot-pressing method, i.e. so-called plasma activated sintering (PAS). It was also employed in directly forming the material junctions.

Due to the large differences in thermophysical and mechanical properties, Bi-Te and $FeSi_2$ cannot be directly joined in a single processing step. We employed Ni as a suitable common interface material with intermediate coefficient of thermal expansion. The joint to the low yield strength $FeSi_2$ requires however an additional layer, for which NiFe alloys were identified to be applicable. From the standpoint of electrical and thermal transport, all junctions exhibit reliable properties. Problems occur at the $FeSi_2$ / NiFe interface under high atmospheric temperatures due to the development of corrosion products and mechanical mismatch of the reaction layer.

Introduction

The so-called "FGM-concept" employs different material stages in a thermoelectric (TE) generator device in order to increase its overall efficiency by locally selecting temperature adapted materials [1]. In this sense, it is anticipated for example, to develop a segmented TE generator consisting of Bi-Te, PbTe, and Si-Ge (in the order of rising temperature) [2].

Besides an improvement of performance, the stacking of two or more materials can provide further advantages, such as simply extending the temperature range a specific material can be utilized in by covering it with a thermoelectric "heat shield". In this sense we have proposed the development of a stacked generator with a stage consisting of bismuth-telluride based alloys (Bi-Te) for the lower temperature range and a stage made from iron disilicide ($FeSi_2$) for the hot region. Such an element combines the high efficiency of the Bi-Te material with the high temperature stability and corrosion resistance of $FeSi_2$. Therefore it can be used in burner applications, where the temperature and atmosphere are usually adverse for the employment of Bi-Te alone [3,4].

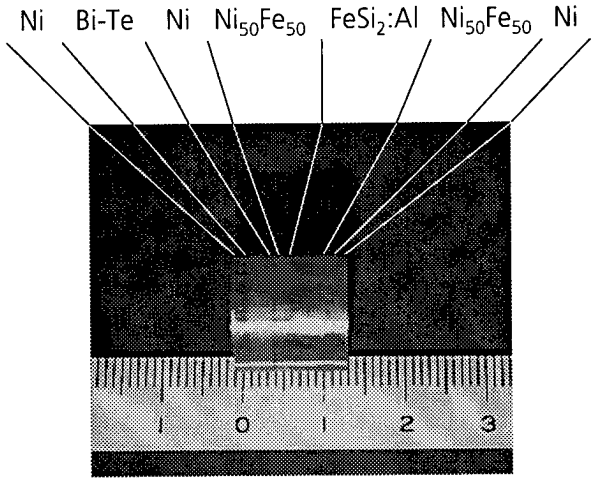


Fig. 1: Stacked Bi-Te/$FeSi_2$ element (15 mm diameter) with upper and lower Ni-contacts and common Ni interface produced by plasma activated sintering (PAS). The Ni50Fe50 interlayers relieve mechanical stresses to the $FeSi_2$.

Patterning a stacked thermoelectric element

There is no straightforward method to overlook the performance of a given combination of materials and it is even more difficult to find the particular design, i.e. segment length, of a given material combination to form a segmented TE generator which brings about maximum performance.

Different approaches to calculate the efficiency of an arbitrary thermoelectric leg have been published in the literature, either by employing a concept of (stepwise) average transport parameters to simplify the problem or by semi-analytical, iterative methods [5,6,7]. We have recently developed a more simple, but nevertheless exact, numerical access to the solution by using a finite-element (FEM) algorithm [8]. Thus, we are able to calculate the efficiency and the power output of an arbitrary thermoelectric generator — especially of a device with varying composition along the temperature axis.

The reverse question of finding that particular composition profile which maximizes the efficiency or power output has been previously treated by either probing discrete sets of compositions [9,10] or by parameterizing the transport parameter's

0-7803-4057-4/97 $10.00 ©1997 IEEE

temperature dependence and subsequently applying a standard mathematical maximization procedure [11]. Both procedures are cumbersome and it would be advantageous in having a *local* criterion, which prescribes the material to be chosen at a certain position along the element's leg.

It is often thought that maximizing the local (temperature dependent) figure-of-merit, $Z = S^2\sigma/\kappa$ (with Seebeck coefficient, S, electrical conductivity, σ, and thermal conductivity, κ) is a solution to the problem. This, however, is not right for a generator, where the current density is constant over the device leg. To be correct, the local Z adjustment requires additionally a local adjustment of the current density, which can only be achieved, when splitting the device into a (large) number of stages. The maximum performance of such a cascaded generator (and similarly a cascaded Peltier cooler) is then indeed determined by the (local) quantity Z.

Our new access in optimizing a graded device is based on the maximization of the electrical power output

$$P_{el} = A\left(i\int_{T_h}^{T_c} S(T)dT - i^2\int_0^L dx/\sigma(T)\right). \qquad (1)$$

This is the equation for a single element leg with cross section A and its spatial coordinate x, which is 0 at the hot side with temperature T_h and L at the cold side with T_c. The variable i stands for the electrical current density.

If one substitutes the temperature variable by x, one receives

$$P_{el} = A\int_0^L\left(iS\frac{dT}{dx} - \frac{i^2}{\sigma}\right)dx \quad \equiv \quad A\int_0^L \pi_{el}\,dx\,. \qquad (2)$$

This reveals that the output power can be written as an integral over the whole element. The integrand then indeed resembles a differential electrical power output, π_{el}. It contains local variables, i.e. transport parameters and temperature, but also the electric current density as a global environment variable. The temperature gradient can be substituted by $\nabla T = (iST - q)/\kappa$ (with $q = Q/A$ the density of heat flow) to get

$$\pi_{el} = \frac{i^2}{\sigma}\left(ZT - \frac{S\sigma}{\kappa}\frac{q}{i} - 1\right). \qquad (3)$$

The expression contains the figure-of-merit, but there is an additional correction term which contains the environment, i.e. q and i.

As this is a calculus for maximizing the element's electrical output power, it additionally requires a matching of the load to the internal element resistance.

We implemented this calculation procedure into our FEM program which determines device performance. First results on maximizing the power output of a $FeSi_2$/Bi-Te stacked generator revealed, that the interface temperature between the two materials has to be chosen considerably lower than predicted by the local Z argument. Input were the experimental data of p-$FeSi_2$:Al and (non-optimized) p-Bi-Te based material, which were prepared as described in the next paragraph. To achieve maximum power output for a hot side temperature of 600 °C and a cold side of 30 °C, the interface temperature should be 190 °C. This requires relative segment lengths of 0.08 for Bi-Te and 0.92 for $FeSi_2$. However, as can be seen from Fig. 1, below an interface temperature of 220 °C, the power output is almost constant, while the efficiency is still falling. Therefore 220 °C can be regarded to be the optimum value for a practical application.

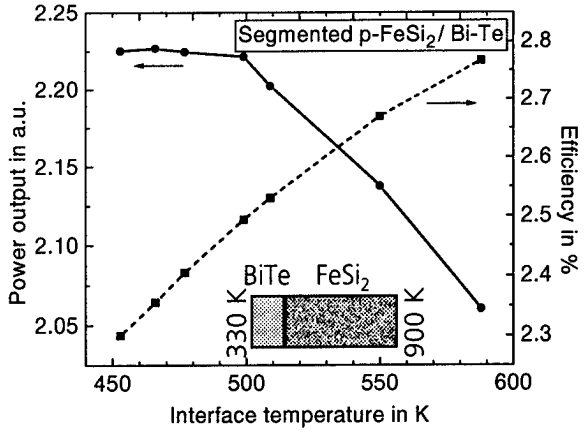


Fig. 2: Power output and efficiency of a segmented $FeSi_2$/BiTe element leg as a function of the interface position, i.e. temperature. It has to be noted that the materials are by no means optimized, which results in the low overall efficiency values. Here, the emphasis is on the performance of the calculus.

Preparation of segmented $FeSi_2$ / BiTe TE elements and properties of metal / semiconductor joints

For the practical development of a stacked TE element, the interfaces between the different segments must serve the conditions of having low thermal and electrical resistance as well as being mechanically stable. For a topologically flat surface a mechanical stable joint can only be formed if some kind of reaction, i.e. alloy formation or mutual diffusion between the two segment materials occurs. In this case a rigid joint develops, which mechanical stability is mainly determined by thermal expansion differences, which develop between the processing and operation (or room) temperature.

Plasma activated sintering

For all materials, i.e. TE semiconductors and metallic contact materials, prealloyed or elemental powders were used which were consolidated by means of so-called plasma activated sintering (PAS). PAS is essentially a uniaxial hot-pressing method in a vacuum chamber ($p < 10$ Pa) with an electrically, directly heated pressing die, which, in the present case, had an inner diameter of 15 mm. The die and punches were made of carbon and the applied axial pressure was 40 MPa. In contrast to normal hot pressing, where the die is heated by a controlled DC current, the mentioned plasma activation is achieved by periodically switching the heating current on and off. This alternate heating occurs at the beginning of the pressing proc-

ess for a chosen duration of 90 s. The duration of the pulse width was 80 ms with a duty cycle of 1. It is reported, that the periodical switching of the high current induces an ionization of the residual gases in the powder batch which, during subsequent recombination, can "activate" the powder particles through local heating or sputtering the surface. This activation should lead to a faster sintering and to compacts with higher electrical conductivity, due to the prior cleaning of the particle surfaces [12].

Compaction of homogeneous materials

The $(Bi,Sb)_2(Te,Se)_3$ powders (shortly referred as Bi-Te) in n- and p-type form were obtained from DTS, Halle, Germany. The nominal compositions were those used used for Peltier coolers, though their doping amounts were not optimized in the present case. The material originated from Bridgman grown crystals, ground in a planetary ball mill. The $FeSi_2$ powders were produced by inert gas atomization by H.C. Starck, Goslar, Germany. Doping was achieved by adding 2.5 at% Al for p-type and 5 at% Co for the n-type $FeSi_2$.

Fig. 3 shows a plot of reached end densities *vs.* temperature, as measured by a thermocouple in the carbon die. For Bi-Te materials, a temperature of 250 °C and a processing time of 3 minutes is sufficient to produce a compact with a relative density above 90%. The maximum die temperature, before melted regions due to local overheating occur, has experimentally been determined to be around 350 °C. This results in the indicated processing window for the Bi-Te based materials.

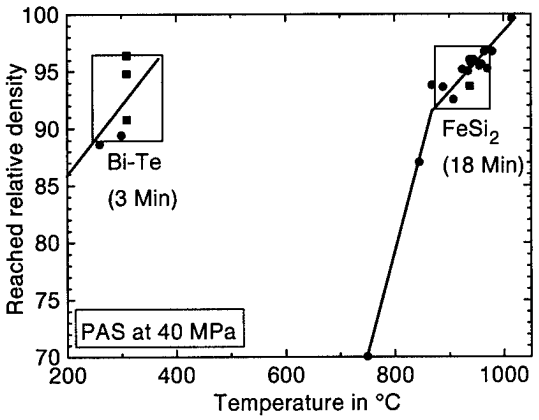


Fig. 3: Processing windows for PAS of Bi-Te and $FeSi_2$. As the windows are too distant on the temperature scale, several processing steps are necessary.

In the case of the $FeSi_2$, however, in order to reach a sufficient density, the temperature should be above 850 °C with a processing time of at least 13 minutes including heating. On the other hand the temperature should not exceed 960 °C, as this lead to frequent cracking of the ingot. After this comparably short compacting process, the $FeSi_2$ is still mainly in its metallic α-phase. A subsequent tempering is necessary to induce the transition into the semiconducting β-phase [13].

The processing windows for the two TE materials are therefore widely separated in temperature, which means that a stacked element cannot be formed in a single processing step. Therefore a method has to be developed, which joins Bi-Te to a preprocessed $FeSi_2$ compact.

First experiments on forming a direct joint by sintering Bi-Te powder to bulk $FeSi_2$ failed. Besides the fact that the thermal expansion coefficient (CTE) mismatch of Bi-Te and $FeSi_2$ is serious (CTE = $19 \cdot 10^{-6}\,K^{-1}$ for Bi-Te, and $10 \cdot 10^{-6}\,K^{-1}$ for $FeSi_2$), no junction was physically and chemically formed. Reason seems to be a thin oxide layer which develops on the $FeSi_2$ and could not be avoided.

Ni / $FeSi_2$ joints

From earlier experiments it is known, that Ni can be perfectly bond to Bi-Te under the given processing conditions for this TE material [14,15]. The resulting contacts have a low contact resistance and are mechanically and electrically stable. Thus it is advantageous to use Ni as a common interface for the two materials in question here. Joining Ni to $FeSi_2$, however, by processing a layered stack of Ni and $FeSi_2$ turned out to be not straightforward, since the large CTE of Ni ($14 \cdot 10^{-6}\,K^{-1}$) always caused a delamination crack near the Ni/$FeSi_2$ interface, which developed in the brittle and obviously low yield semiconductor. Microscopic investigations showed that under the given conditions a reaction layer of about 50 µm thickness develops at the interface. Measuring the voltage profile across this interface revealed that the layer is obviously metallic, since its contact resistance is very low.

The so-called FGM (functionally graded material) concept tries to release thermal stress by a continuous or stepwise change in composition of the two materials to be joined. Doing this, it is assumed that the material properties follow any mixing rule, i.e. the resulting material properties are between those of the two constituents. In the case of powder mixtures, this assumption is generally only valid, if there are neglecting amounts of reaction products between the components.

When forming a stepwise graded junction between Ni and $FeSi_2$, the appearing cracks become even severe. A thorough investigation by density measurements and x-ray diffraction indeed revealed, that a number of compounds were formed, which have unpredictable mechanical properties. As in the case of TE semiconductors usually many component systems occur which tend to form mutual reactions, one can conclude as a general rule that the simple FGM concept of material mixtures does mostly not lead to the expected results.

Thermal stress relieved Ni joint to $FeSi_2$

Instead, a different material system with the desired properties has to be employed to relieve the developing thermal stresses on cooling. In the present case we had success in forming junctions between $FeSi_2$ and nickel-iron based low CTE alloys. In particular, we present here results on joining Ni50Fe50, which has a thermal expansion coefficient between that of Ni and $FeSi_2$. The usually used low CTE alloy Ni36Fe64, commonly known as Invar, is not advantageous, since the CTE in the considered temperature range above 700 °C already reaches a value of $13 \cdot 10^{-6}\,K^{-1}$, which was found to be too large.

Ni50Fe50 can be processed together with $FeSi_2$. It develops a similar reaction layer as in the case of pure Ni (cf. Fig. 4). Striking is the point that at the metal side of the boundary always a large agglomeration of pores is seen, which shows up as a dark line in Fig. 4. This region indeed turned out to be the weakest element in the joint, since preliminary aging experiments in air at 600 °C revealed that corrosion, which started from the junction edges developed into the pore region causing the connection to break. This procedure may be enhanced by the fact that the reaction layer has probably different mechanical properties than the surrounding regions. The mechanisms of void formation and thermal stability has to be investigated further.

In a second processing step it is now possible to join a Ni layer to the Ni50Fe50, which then resembles the desired interface to the Bi-Te. As this joint can even be achieved at a temperature low enough to process Bi-Te, the aimed at segmented structure becomes feasible in only one additional processing step. It is possible to directly join a stack of Ni / Bi-Te / Ni to the Ni50Fe50 / $FeSi_2$ / Ni50Fe50 resulting in the structure shown in the photo of Fig. 1.

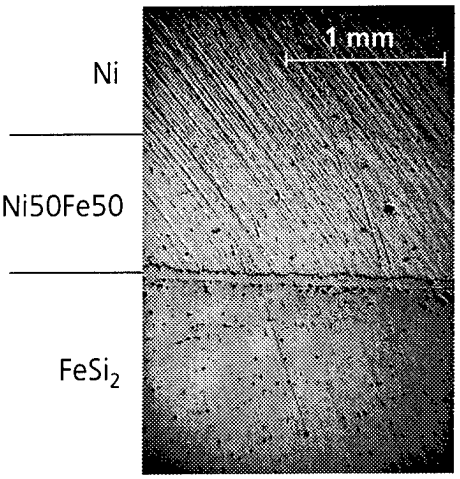


Fig. 4.: $FeSi_2$ / Ni joint with Ni50Fe50 interface to adapt the coefficients of thermal expansion (CTE). An about 50 µm thick reaction zone develops at the $FeSi_2$ boundary. The dark line in the Ni50Fe50 is an agglomeration of voids.

Conclusions and outlook

The application of our numerical model to a stacked Bi-Te / $FeSi_2$ structure revealed, that is not appropriate in terms of electrical power output to operate the Bi-Te stage at the highest possible temperature. With the data given here (for non-optimized material, but in comparison valid) the optimum operation temperature is around 220 °C, which is considerably low.

By means of a two stage uniaxial hot-pressing process it is possible to form a stacked Bi-Te / $FeSi_2$ structure, where Ni is employed as a common interface which simultaneously acts as a diffusion barrier for dopants between the stages. Ni can be directly joint to Bi-Te under the given processing conditions for this semiconductor. A direct joint to $FeSi_2$ is not possible as the developed mechanical stress is too severe. The yield strength of $FeSi_2$ turned out to be extremely low. Only when additionally inserting a Ni50Fe50 layer with intermediate CTE, a successful joint could be formed.

Preliminary experiments on joining plates of the low CTE material Kovar (Ni29Co17Fe54), showed some advantages. Firstly, the pore agglomeration always found when joining Ni containing powder to $FeSi_2$ did not develop, and secondly, the low CTE holds the semiconductor under pressure. Due to the low Ni content, however, we did not succeed in directly joining Ni under the low temperature conditions required to process Bi-Te. But the employment of bulk interlayers with a lower CTE should be anticipated when further improving the properties of the structure.

Acknowledgment: This work was made possible through a grant to J.S. by the Science and Technology Agency (STA), Japan, and a grant to L.H. by the Deutsche Forschungsgemeinschaft (DFG) within the Graduiertenkolleg "Schmelze, Erstarrung, Grenzflächen".

References

[1] A.F. Joffe, Pat. USSR No. 126158, Byulleten' izobretenii (Invention Review) **4** (1960) 22 (in Russian).

[2] Y. Miyamoto, M. Niino, M. Koizumi, Proc. of the 4th Int. Symposium on Functionally Graded Materials (FGM'96), Tsukuba, Japan, 1996.

[3] R. Kügele, W. Roth, W. Schulz, A. Steinhüser, Proc. of the 15th Int. Conf. on Thermoelectrics (ICT'96), Pasadena, California, USA (1996).

[4] W. Roth, J. Schilz, A. Steinhüser, Forschungsverbund Sonnenenergie, Jahrestagung 1996, Kassel, Germany (in German).

[5] B. Sherman, R.R. Heikes, R.W. Ure, Jr., J. Appl. Phys. **31** (1960) 1.

[6] B.W. Swanson, E.V. Somers, R.R. Heikes, Trans. ASME: J. Heat Transfer, Feb. (1961) 77.

[7] T. Hirano, L.W. Whitlow, M. Miyajima, Ceramic Trans., Functionally Gradient Materials, Ed. by J.B. Holt, M. Koizumi, T. Hirai, Z.A. Munir, The American Ceramic Soc. **34** (1993).

[8] L. Helmers, E. Müller, J. Schilz, W.A. Kaysser, to be published.

[9] L.I. Anatychuk, L.N. Vikhor, Proc. of the 4th Int. Symposium on Functionally Graded Materials (FGM'96), Tsukuba, Japan, 1996.

[10] L.I. Anatychuk, V.A. Semenyuk, Chernivsky, "Prut" (1992) 264.

[11] J. Teraki, T. Hirano, Proc. of the 4th Int. Symposium on Functionally Graded Materials (FGM'96), Tsukuba, Japan, 1996.

[12] N. Murazama, Ceramics **32** (1997) 445 (in Japanese).

[13] K. Schackenberg, J. Schilz, E. Müller, W.A. Kaysser, G. Langer, E. Lugscheider, Proc. of the XVI Int. Conf. on Thermoelectrics (ICT'97), Dresden, Germany, this volume.

[14] Y.S. Kang, Y. Noda, A. Moro, M. Niino, Proc. of the Fourth Int. Conf. on Composite Engineering (ICCE/4), July 6-12, 1997, Hawaii.

[15] Y. Noda, Y.S. Kang, M. Niino, Proc. of the XVI Int. Conf. on Thermoelectrics (ICT'97), Dresden, Germany, this volume.

Preparation and evaluation of PbTe-FGM by Joining Melt-grown Materials

Masaki Orihashi[(1)*], Yasutoshi Noda[(2)], Lidong Chen[(1)], Yansheng Kang[(3)], Akio Moro [(3)] and Toshio Hirai[(1)]

(1)Institute for Materials Research, Tohoku University, 2-1-1, Katahira, Aoba-ku, Sendai, Miyagi 980-77, Japan
Tel.: +81-22-215-2106, Fax: +81-22-215-2107, E-mail: orihashi@imr.tohoku.ac.jp

(2)Graduate School of Engineering, Tohoku University, Aramaki-Aza-Aoba, Aoba-ku, Sendai, Miyagi 980-77, Japan, Tel.: +81-22-217-7328, Fax: +81-22-217-7328

(3)National Aerospace Laboratory, Kakuda Research Center, Koganezawa 1, Kimigaya Kakuda, Miyagi 981-15, Japan, Tel.: +81-224-68-3644, Fax: +81-224-68-2483

Abstract

The 2-stage functionally graded materials (FGM) of carrier concentration controlled PbTe were prepared by plasma activated sintering (PAS) using the discs cut from melt-grown PbTe ingots. The component materials of PbTe ingots were prepared by the Bridgman method with 2000 or 4000 molppm PbI_2 as a n-type dopant. The thermoelectric characterization of the FGM was made in the temperature range from 300 to 700 K. The thermoelectric power (α) and the electrical conductivity (σ) for the FGM was almost intermediate between those for the components. In the measured temperature range, the power factor ($\alpha^2 \sigma$) value for the FGM was found to exceed that for the components. This results indicate the possibility to realize high efficiency of energy conversion with the well designed FGM structure.

Introduction

PbTe is one of the best materials used in construction of thermoelectric generators working at intermediate temperature region (450-840 K). The PbTe generators were developed as the special application in space exploration in 1960s and constitute the power supply unit using heat of gas combustion [1].

Since the maximum figure of merit (Z) shifts in wide temperature range depending upon carrier concentration, the functionally graded materials (FGM) of PbTe with controlled carrier concentration is expected to attain high efficiency of thermoelectric energy conversion.

Plasma-activated sintering (PAS) has been developed in the preparation of a variety of FGM [2], where the powder particle surface are activated by plasma leading to an accelerated reaction or sintering. The PAS has lately been applied to preparation of the thermoelectric materials such as SiGe and PbTe [3,4,5].

In the present study, we prepared the stepwise carrier concentration FGM of n-type PbTe by using PAS.

Experimental

Preparation of PbTe-FGM

The PbTe ingots as the source material were prepared by the Bridgman method after the direct melting of constituent elements of Pb and Te (nominal purity of 99.9999%). The weighed amount of the elements in the stoichiometric composition (Pb/Te=1) was vacuum sealed in a quartz ampule (10 mm ID and 120 mm length) with 2000 or 4000 molppm PbI_2 as the source of n-type dopant of iodine. The growth condition was as follows; the maximum heating temperature of 1223 K, the temperature gradient of about 1200 K/m at melting point, and growth rate of 4 mm/hr.

Table 1 shows thermoelectric properties of PbI_2 doped n-type PbTe at 300K [6].

The PAS was performed in a carbon die with 11 mm ID. The n-type 2-stage FGM was prepared by direct PAS of the two discs (~6.5 mm thickness × 10 mm diameter) cut from the 2000 and 4000 molppm PbI_2 doped ingots, where the powder from the 4000 molppm PbI_2 doped ingots was placed between the discs as the binder.

The PAS condition was; in a vacuum of about 10 Pa under the condition of load of 30 MPa, and pulse current of 600 A at 25 V with 6 Hz for 90 s, followed by the heating at 950 K for 540 s.

Measurement of thermoelectric properties

The Hall coefficient (R_H) and electrical conductivity (σ) were measured by van der Pauw configuration using the Pt-wire electrodes. The carrier concentration $|N_A-N_D|$ was estimated by using the equation $|N_A-N_D|=1/eR_H$ (e: electric charge). Hall mobility (μ_H) was obtained by using the equation $\mu_H = R_H \sigma$.

The thermoelectric properties of the FGM and its components were measured in 10^{-1} Pa in the temperature region from 300 to 700 K. The sample size was 5 × 5 × 13 mm^3. On the thermoelectric power measurement for FGM,

* Research Fellow of Japan Society for the Promotion of Science (JSPS Research Fellow)

Table 1 Thermoelectric properties of PbI_2 doped n-type PbTe at 300K[6].

No.	PbI_2 (molppm)	n (m^{-3})	σ ($\Omega^{-1}m^{-1}$)	μ_H ($m^2V^{-1}s^{-1}$)	α ($V \cdot K^{-1}$)
(1)	2000	4.2×10^{24}	4.6×10^{4}	1.1×10^{-1}	-2.4×10^{-4}
(2)	4000	4.9×10^{25}	3.5×10^{5}	5.4×10^{-2}	-1.1×10^{-4}

the components of high and low carrier concentration were arranged to high and low temperatures, respectively, and thermoelectromotive force (EMF) was measured at the temperature difference within about 10 K between the hot and cold ends. Fig. 1 shows schematic diagram of 2-stage carrier concentration FGM of PbTe. The temperature was monitored by using Pt-13%Rh thermocouples and the additional Pt electrodes were adopted for the EMF measurement. For the electrical conductivity measurement, the Pt wires of the thermocouples were served as the current lead and the additional electrodes as the potential lead.

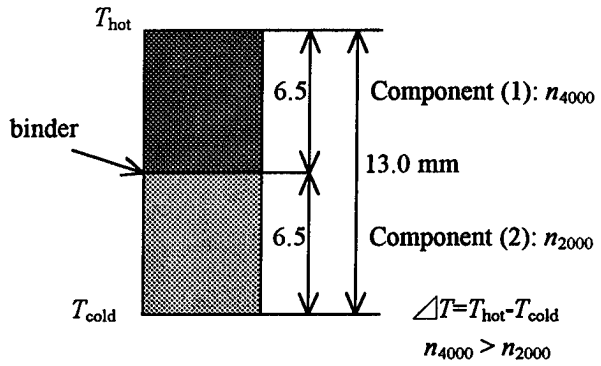


Fig. 1: Schematic diagram of 2-stage carrier concentration FGM of PbTe.

Results and Discussion

Figure 2 shows the temperature dependence of σ for the FGM and the components. The σ values of all the samples monotonously decreased with an increase of temperature, indicating that the samples are the typical degenerated semiconductors. The σ value for the FGM was almost intermediate between those for the components and get closer to that of component (2) with an increase of temeprature.

Figure 3 shows the temperature dependence of α for the FGM and the components. The α value for the component (1) linearly increased up to near 600 K with an increase of temperature and took a maximum of 3.2×10^{-4} $V \cdot K^{-1}$, while the maximum for (1) was 2.0×10^{-4} $V \cdot K^{-1}$ at about 700 K. The curve for the FGM was almost intermediate between

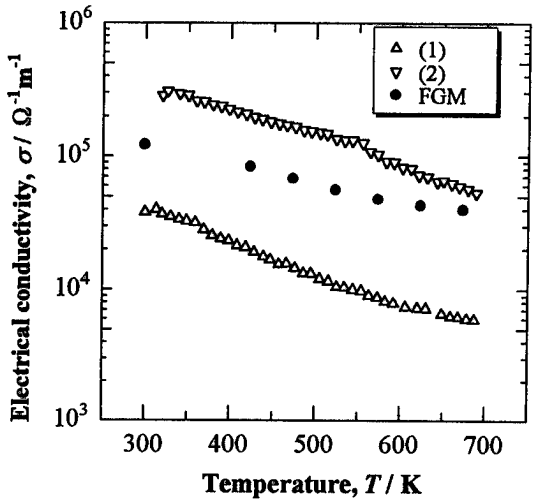


Fig. 2: Temperature dependence of electrical conductivity in 2-stage FGM and components of n-type PbTe.

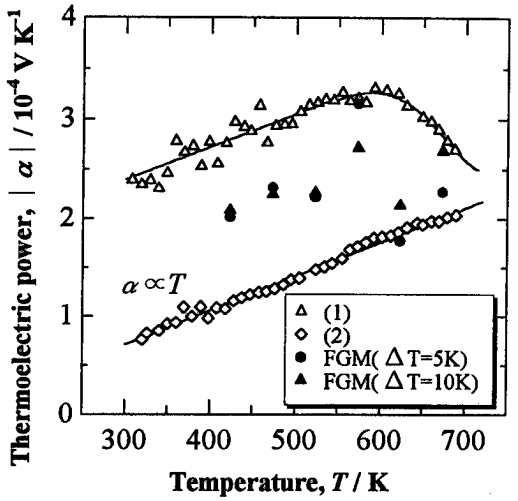


Fig. 3: Temperature dependence of thermoelectric power in 2-stage FGM and components of PbTe.

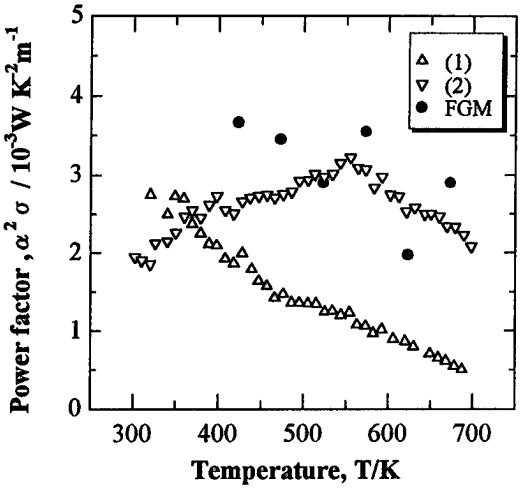


Fig. 4: Temperature dependence of power factor in 2-stage FGM and components of PbTe.

those for the components.

Figure 4 shows the temperature dependence of the electric figure of merit (or power factor, $\alpha^2\sigma$) for the FGM and the components. With an increase of temperature, the $\alpha^2\sigma$ value for the component (1) monotonously decreased with an increase of temperature, while that of (2) increased and took a maximum at about 560 K. At T>370 K, the $\alpha^2\sigma$ value for the component (1) was lower-lying than that for (2). In the measured temperature range, the $\alpha^2\sigma$ value for the FGM was found to exceed those for the components. This result indicates the part with lower carrier concentration of FGM-disc contributes to an increase of α value over a decrease of σ. This result indicates the possibility to realize high efficiency of energy conversion with the well-designed FGM structure.

The measurement of thermoelectric properties in the present study was performed under the small temperature span. It is necessary to measure the thermoelectric properties of well-designed samples under the large temperature span in order to visualize the effect of FGM.

Conclusion

In this study, 2-stage carrier concentration FGM of n-type PbTe was prepared by using PAS.

(1)The σ and α value for the FGM were almost intermediate between those for the components.

(2)In the measured temperature range, the $\alpha^2\sigma$ value for the FGM was found to exceed that for the components. This result indicates the part with lower carrier concentration of FGM-disc contributes to an increase of α value over a decrease of σ. This result indicates the possibility to realize high efficiency of energy conversion with the well-designed FGM structure.

(3)It is necessary to prepare a well-designed stepwise FGM and measure the thermoelectric properties the under the large temperature span in order to visualize the effect of FGM.

Acknowledgment

This work was supported by Research Fellowship of the Japan Society for the Promotion of Science for Young Scientist (JSPS Research Fellow).

References

[1] K. Uemura and I. A. Nishida: Thermoelectric Semiconductors and Their Applications, Nikkan Kogyo, Tokyo, (1988)

[2] T. Hirai: Materials Science and Technology, A Comprehensive Treatment, ed. R. W. Cahn, P. Hassen and E. J. Kramer, Chapter 20 Functional Gradient Materials, VCH Verlag. (Weinheim), (1996), 293.

[3] Takahashi, T. Masuda, T. Mochimaru and T. Noguchi: Proc. FGM symp. (FGM95), Tsukuba, (1995), 123.

[4] M. Miyajima, K. Fujii and T. Hirano: Proc X II Int. Conf. Thermoelectrics (X II-ICT), Yokohama, (1993), 272.

[5] Y. Noda, M. Orihashi, H. T. Kaibe, Y. Imai, I. Shiota and I. A. Nishida: Proc. Int. Conf. Thermoelectrics (ICT96), Pasadena, (1996), 146.

[6] Y. Noda, M. Orihashi and I. A. Nishida: Trans. IEE of Japan, **116-A** (1996), 242.

Improved materials for thermoelectric conversion (generation)

Z. Dashevsky[1], I. Drabkin[2], V. Korotaev[2], and D. Rabinovich[1]

[1] Department of Materials Engineering Ben-Gurion University of the Negev, P.O.B. 653, Beer-Sheva 84105, Israel

[2] Institute of Rare Metals, Moscow, 109017 Russia

Abstract

Thermoelectric conversion (TEC) presents several advantages compared to the other energy conversion technology: they are reliable, can operate untainted in hostile environments, and are also environmentally friendly. However their application has been limited up to now because of the relatively low conversion efficiency of traditional thermoelectric materials used in the devices. New more efficient materials are needed. The value of a material for thermoelectric power generation is defined by the thermoelectric figure of merit Z which is a function of the Seebeck coefficient S, electrical resistivity ρ, and thermal conductivity k and is defined as $Z = S^2/\rho k$. A choice of the optimal technique for the leg formations from synthesized thermoelectric materials, which are capable to provide the leg required forms and leg geometrical sizes, are determined by mechanical properties. Several methods for a thermoelectric efficiency increase that have been put forward over the past years. Among them we wish to focus our attention to produce segment thermoelectric leg with variation of the composition along legs. Calculated efficiency in this case is more than 10 % (Th = 500 ^{o}C, Tc = 50 ^{o}C). The first experimental results on 2-stage composite leg indicate the high efficiency in the thermoelectric energy conversion. Crystal-growth techniques with high crystalline perfection stimulates us to use this method for preparation the thermoelectric generator material.

Introduction

A major objective if this search addresses the crystal growth-concept towards the optimization of TEC. High carrier mobility μ ($Z \sim \mu$) is usually found in the structures with high crystalline perfection. The group IV and V tellurides are the most effective base materials for TEC. The thermoelectric properties are strongly dependent function of the carrier concentration. The formation of the gradient material is actually incidental to one of the main objectives of thermoelectric property optimization with goal the maximal achievement of Z in wide temperature range [1]. Doping in these compounds is achieving not only by impurity atoms, but also constituent elements themselves [2, 3].

The elimination of the negative influence of minority carriers in n- and p-type PbTe, that lead to decreasing Z values at high temperature, is suggested to achieve this by doping PbTe with III - Group impurities (for n-type - In and for p-type - Tl) [4]. Indium has a very favourable role as a dopant in PbTe. When PbTe is doped with indium, it forms an impurity level in the conduction band. When the concentration N_{In} is low, its electrons fill states in the conduction band made available by other impurities. At higher concentrations the Fermi level E_F becomes pinned at a position that is the energy level of the impurity E_i and it practically does not depend on N_{In}. When PbTe is doped with thallium, it forms an impurity level in the valence band and produces holes.

Moreover, for achieving optimal Z in the 50 - 500^{o}C temperature range, it is suggested to design 2-stage composite legs consisting of crystals for n-leg - $Bi_2Te_{2.4}Se_{0.6}$ (the temperature interval: 50 - 250 ^{o}C) and PbTe<In> (250 - 500 ^{o}C); for p-type - $Bi_{0.5}Sb_{1.5}Te_3$ (50 - 200 ^{o}C) and PbSnTe (200 - 500 ^{o}C).

Characterization of modern generator thermoelectric materials

Thermoelectric materials make up the "legs" of a thermoelement and are usually fabricated by powder technology methods [5]. Table 1 tabulates the most important materials for TEC applications, their effective temperature range of operation, the average value of the figure of merit in this range and the calculated efficiency value of a hypothetical thermoelement, the n- and p-legs of which have the same Z value at the same temperature interval. Chalcogenides of V group elements, such as bismuth, antimony (materials 1 and 2 in the above-table)

display the highest Z values in the low temperature 20 - 250 ^{o}C region of the requested temperature range. When crystallized in the tetradymit-type hexagonal lattice, both the *n*- and *p*-type materials are characterized by an appreciable anisotropy of an electrical and thermal conductivity. Thus, $Z = S^2/\rho k$ displays maximum in the direction perpendicular to the "*c*" axis of the crystal [3]. Material synthesis and the thermoelectric device leg formation are, therefore, designed and performed using techniques that provide maximum obtainable texture. The isostructural monotellurides of IV group elements (NaCl-type lattice) make up a subgroup of so called mid-temperature generator materials which are effective in the 500 - 600 ^{o}C temperature range of the hot junction. Finally, Co(Fe)Sb_3, $IrSb_3$ are most appropriate for the highest operating temperature. These materials are part of the large family of skutterudites, a class of compounds which have shown a good potential for thermoelectric application [6]. Figs. 1a and b show the temperature dependence of *Z*, typical for these materials. The maximum value *Z* for materials 1 and 2 is reached at 150 ^{o}C decreases sharply with, further temperature increase due to the negative influence of the intrinsic conduction (forbidden band for these materials is not more 0.2 eV). In general, the main disadvantage of the potential materials lies in the difficulty of getting high *Z* values in the 50 - 500 ^{o}C. It is also of relevance that in general, *p*-type materials in the 100 - 500 ^{o}C temperature range display serious drawbacks. Thus, GeTe has the highest in *Z* value, but only over a limited operating temperature range (Table 1). This is due to the polymorphic transition that takes place at 250 ^{o}C and causes a decrease of *Z* in the low temperature crystal modification. Legs from *p*-type PbTe is less expensive than GeTe, has a lower vapor pressure may be used over a wider operating temperature range and thus compensates to some extent its lower *Z* value. This material, however, displays an extremely brittle behavior, in particular at a hole concentration $p \geq 3 \cdot 10^{19}$ cm^{-3}. Presently, the segment (composite) *p*-leg by composition $Bi_{0.5}Sb_{1.5}Te_3$ (temperature interval: 50 - 300 ^{o}C) and GeTe (300 - 500 ^{o}C) was prepared by powder technology.

Table 1. Thermoelectric materials, prepared by powder technology [5, 6]

No	Base formula	Type	Melting point T, ^{o}C	Temperature range ΔT, ^{o}C	Average value $Z \times 10^3$, K^{-1}	Efficiency η, %
1	$Bi_2Se_{0.6}Te_{2.4}$	*n*	600	20 - 300	1.2	5
2	$Bi_{0.5}Sb_{1.5}Te_3$	*p*	620	20 - 300	1.2	5
3	GeTe	*p*	700	250 - 550	1.6	10
4	SnTe	*p*	780	300 - 600	0.7	4.3
5	PbTe	*n*	920	100 - 550	1.2	9.8
6	PbTe	*p*	920	100 - 550	1.4	11.3
7	Cu_2Se	*p*	1140	200 - 800	0.7	7.6
8	$CeFe_{3.5}Co_{0.5}Sb_{12}$	*p*	931	200 - 800	1.3	14
9	$CoSb_3$	*n*	931 (peritec. react.)	200 - 800	-	-

Development of thermoelectric material technology

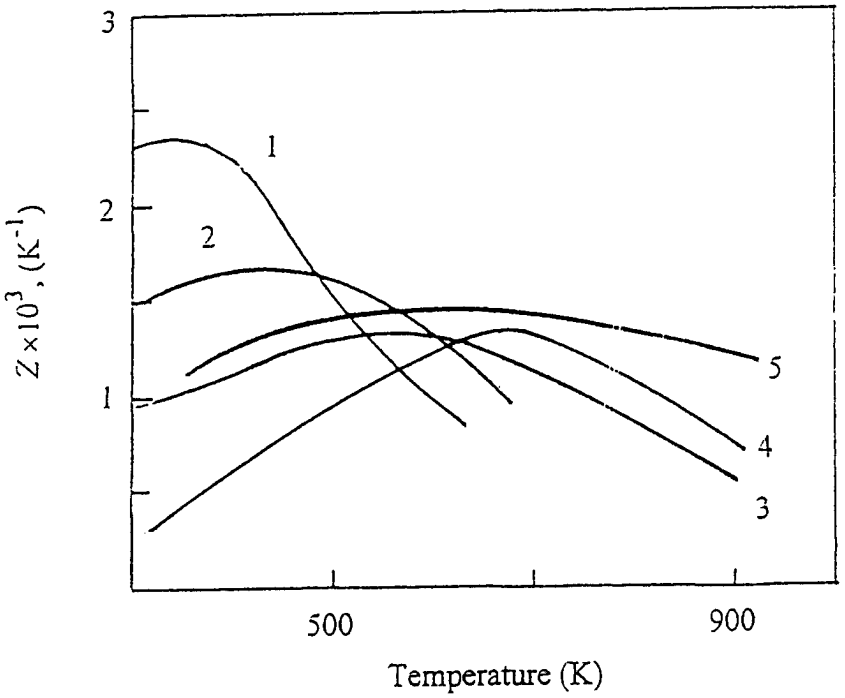


Fig 1.a: Figure of merit, Z as a function of temperature for n-type thermoelectric materials: 1- $Bi_2Te_{2.4}Se_{0.6}$, 2, 3, 4 - PbTe with increasing carrier density, 5 - PbTe<In>.

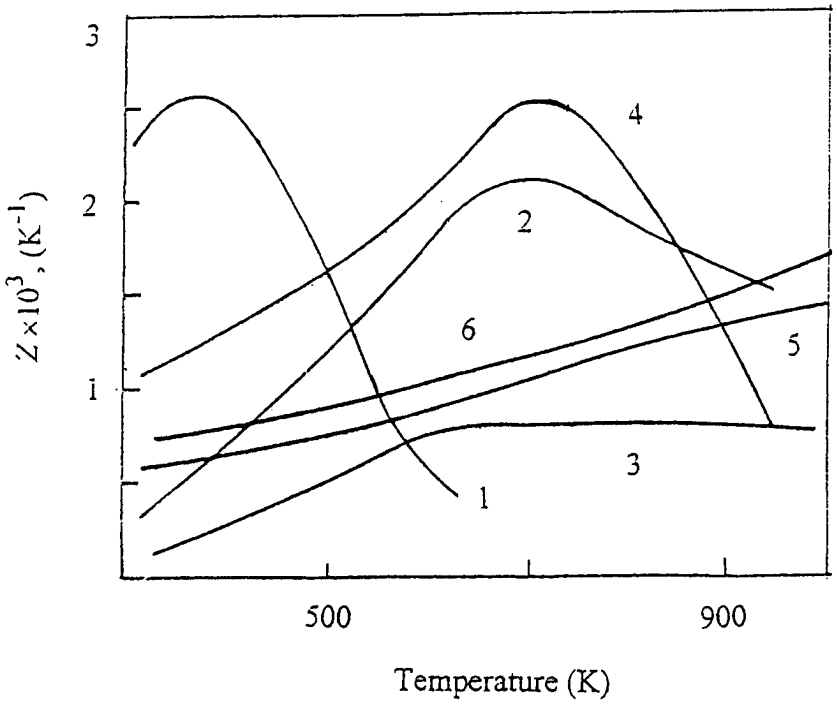


Fig 1.b: Figure of merit, Z as a function of temperature for p-type thermoelectric materials: 1- $Bi_{0.5}Sb_{1.5}Te_3$, 2 - PbTe, 3 - SnTe, 4 - GeTe, 5 - Cu_2Se, 6 -$CeFe_{3.5}Co_{0.5}Sb_{12}$.

The preparation of crystals and thermoelectric characterization

The crystals $Bi_2Te_{2.4}Se_{0.6}$ (doping impurity - Br, using $SbBr_3$ compound) and $Bi_{0.5}Sb_{1.5}Te_3$ (doping impurity - Pb) were grown by the Float Zone Process. These materials were developed to display appropriate anisotropy so as to yield maximal Z values. The crystals n-PbTe (doping impurity - I, using $PbBI_2$ compound) and p- PbSnTe (doping impurity - Na) were grown by the Czochralski technique. The parameters of process are next: crystal diameter, D = 25 - 30 mm, crystal growth v = 2 cm/hour, and rotation speed δ = 0.5 1/s. Distribution of Seebeck coefficient along crystals is not more than $\pm$ 10 μV/K.

The average Z for crystal legs PbTe of n- and p-type conductivity is higher (minimum on 25 %) than for the same composition legs, prepared by the powder technology.

Profile doping of preparing crystals

Doping in $A^{IV}B^{VI}$ (tellurides of VI group) is $A^{V}B^{VI}$ (chalcogenides of V group) these compounds is achieving not only by impurity atoms, but also constituent elements themselves. Thus, for case of PbTe carrier concentration is given by [2]

$$n\,(p) = -2[V_{Te}] + 2[V_{Pb}] + 0[I_{Te}] + 1[I_{Pb}], \qquad (1)$$

when total charge q is negative we have electron conductivity, when q is positive we have hole conductivity. Here $[V]$ and $[I]$ denote the vacancy and interstitial concentrations of lead and tellurium, respectively.

For case of compounds type Bi_2Te_3 and solid solutions on its base, carrier concentrations given by [3]

$$n(p) = -[M_{Te}] + [M_{Bi}]. \qquad (2)$$

Here $[M_{Te}]$ denote substitutional concentrations of Te atoms on Bi places and $[M_{Bi}]$ is contrary. The gradient thermal treatment and composition variation can be used to influence the concentration of native defects and thereby the thermoelectric properties.

Elimination the negative influence of minority carriers in n-PbTe at high temperature

We suggest to achieve this goal doping PbTe by III group impurities which as was discovered at the last time quasi-local (on the band spectrum background) or local (in the gap) levels. Among manifestations (very important for application in the thermoelectricity) of these impurities are: Fermi level pinning and carrier concentration stabilization, resonance scattering [4]. For n-leg preparation PbTe crystals were doped by indium PbTe<In>. Indium impurity in lead telluride definitely manifests donor properties, but in spite of a very high solubility of InTe in PbTe the electron concentration is practically constant. The additional doping of PbTe<In> with iodine I (one-charged donor) or sodium Na (one-charged acceptor) practically does not cause the change of electron concentration until the additional impurity concentration reaches the content of In. The same mechanism can explain the elimination the negative influence of minority carriers on the transport properties of PbTe crystals, doping In at high temperature. Therefore for this composition temperature dependence Z practically is constant (curve 5 on Fig. 1a) to T = 500 ^{o}C. Profile doping by indium (in n-type crystals from hot side) can be produced by the diffusion process.

The production of composite n-leg

For achievement optimal Z at temperature range: 50 - 500^{o}C we suggest composite n-leg consisting from two parts: crystals $Bi_2Te_{2.4}Se_{0.6}$ (50 - 250^{o}C) and PbTe<In> (250 - 500^{o}C). The first experimental results on composite leg indicate that high efficiency in the thermoelectric energy conversion (average $Z = 1.5\times 10^{-3}$ K^{-1}).

Conclusions

The crystal growth technique was developed for the preparation the generator thermoelectric materials. It was suggested the special doping by III group impurities for elimination the negative influence of intrinsic conductivity in PbTe at high temperature. We made considerable progress in the area of the development the composite thermoelectric leg for the temperature area 50 - 500 ^{o}C.

References

[1] M. Niino, The present situation of research on functionally grated materials in Japan", Proc. 4 Int. Symposium on FGM, Tsukuba, Japan, 25 (1996).

[2] L. Palmetshofer, Appl. Phys. A34, 139 (1984).

[3] B.M. Goltsman, V.A. Kudinov, I.A.Smirnov: *Semiconductor thermoelectric materials based on Bi_2Te_3*, (Nauka , Moscow 1970).

[4] V.I.Kaydanov, Defects and Diffusion Forum vol.103 - 105, 388, 1993.

[5] Z. Dashevsky, L.Dudkin, "Generator thermoelectric materials" J. of Thermoelectricity N1, 93 (1993).

[6] J. Fleurial, A. Borshchevsky, T.Caillat, Proc. 15 Int. Conf. on Thermoelectrics, Pasadena, USA, 91(1996).

Thermoelectric Properties of Segmented Pb-Te Systems with Graded Carrier Concentrations

Y.Shinohara[1)], Y.Imai[1)], Y.Isoda[1)], I.A.Nishida[1)], H.T.Kaibe[2)] and I.Shiota[3)]

1)National Research Institute for Metals, STA, 1-2-1, Sengen, Tsukuba-shi, Ibaraki 305, Japan

Tel: +81/298/59/2639, Fax: +81/298/59/2601, E-mail: shinohara@nrim.go.jp

2)Tokyo Metropolitan Univ., 1-1, Minamiohsawa, Hachioji, Tokyo 192-03, Japan

3)Kogakuin Univ., 2665-1, Nakanocho, Hachioji, Tokyo 192, Japan

Abstract

Thermoelectric properties have been investigated on the *n*-type PbTe material composed of 2 segments with different electron concentrations n_e. The 2-segment material was prepared by liquid state diffusion bonding of two kinds of solidified ingots. n_e of the ingots were 3×10^{24} and $6\times10^{25}/m^3$. The ingot of $3\times10^{24}/m^3$ had higher power factor below 500K, while the ingot of $6\times10^{25}/m^3$ had higher one above 500K. The ingot with higher n_e was for higher temperature use. When the temperature difference was given with the jointed interface of more than 450K, the 2-segment material was found to give higher maximum power than the original ingots. From these results, the segmentation with graded n_e is effective to improve the power generating performance of *n*-type PbTe.

Introduction

Lead telluride PbTe is typical *n*-type thermoelectric material used in the temperature range from 400K to 800K [1]. It has been already applied to power generating material at special locations, *i.e.* space, deep sea, desert, pole and so on[2]. Higher energy conversion efficiency is essential to its commoner applications. PbTe shows a maximum of figure of merit Z at a temperature T_{opt}. T_{opt} can be shifted with keeping ZT by changing electron concentration n_e; T_{opt} is higher by higher n_e[3]. When the segmented PbTe with graded n_e is developed, Z should be higher in a wider temperature range, resulting in higher energy conversion efficiency. In this paper, thermoelectric properties have been investigated on the *n*-type PbTe material composed of 2 segments with different n_e.

Experimental procedure

The mixtures of Pb and Te with dopant of PbI_2 were capsulated in evacuated quarts tubes under 1×10^{-3}Pa. The mixing ratio of Pb:Te was 1:1, and n_e was controlled by the amount of PbI_2. The mixtures were melted at 1300K by the rocking furnace with rocking cycle of 1 Hz to obtain homogeneous ingots, and solidified unidirectionally at the cooling rate of 30K/h. The slope of temperature given to the quarts tubes during cooling was 0.5K/mm. The two ingots with different n_e (Ingot(L): $n_e=3\times10^{24}/m^3$, Ingot(H): $n_e=6\times10^{25}/m^3$) were jointed by liquid state diffusion bonding technique in an Ar atmosphere. Pb-60wt%Sn was applied as soldering material and the Pb-60wt%Sn sheet was 50μm thick.

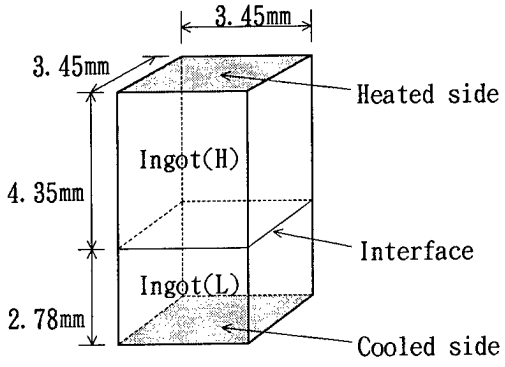


Fig.1 Schematic view of jointed PbTe material
Ingot(L): $n_e=3\times10^{24}/m^3$, Ingot(H): $n_e=6\times10^{25}/m^3$

Table 1 Thermoelectric properties of as-solidified ingots at room temperature prepared for jointing

	Electron Concentration n_e (/m^3)	Electrical Resistivity ρ (μΩm)	Seebeck Coefficient α (μV/K)	Thermal Conductivity κ (W/Km)	Figure of Merit Z (/K)
Ingot(L)	3×10^{24}	13.3	184	2.0	1.3×10^{-3}
Ingot(H)	6×10^{25}	1.63	30.4	5.6	1.0×10^{-4}

The jointing was under 2.0MPa at 700K for 15min. Pb-60wt%Sn was melted and reacted with PbTe at jointing to form a SnTe layer less than 10μm thick.

Electrical resistivity ρ and Hall coefficient R_H were measured by the DC method with high speed and high resolution, and thermal conductivity κ was by Harman method[4]. Seebeck coefficient α was obtained from a slope of (thermo-electromotive force, E_0)-(temperature difference, ΔT) curve. Resistance r_{int} under ΔT was also measured to evaluate maximum power P_{max}. P_{max} of thermoelectric material can be calculated from the following equation:

$$P_{max} = 1/4 \times E_0^2 / r_{int} \qquad (1)$$

A specimen of the jointed material for P_{max} evaluation is shown in Fig.1. Thermoelectric properties of PbTe are easy to change by thermal history of more than 700K[5]. In this study, the measurements were between 300K and 700K.

Results and Discussions

Thermoelectric properties of the as-solidified PbTe ingots at room temperature are shown in Table 1. Ingot(H) has 20 times higher n_e than Ingot(L). ρ and α of Ingot(H) are even lower than those of Ingot(L), and κ of Ingot(H) is higher than that of Ingot(L). As a result, the ingot with lower n_e results in higher Z at room temperature.

Temperature dependences of ρ and α of the as-solidified PbTe ingots are shown in Fig.2 and Fig.3, respectively. Ingot(H) has even lower ρ and α than Ingot(L) in the temperature range from 300K to 700K. The variation of ρ of Ingot(L) is gentler at more than 600K, and also α has a maximum at 620K. This tendency suggests that Ingot(L) is close to the intrinsic region at 700K.

Temperature dependence of power factor α^2/ρ of the as-solidified PbTe ingots is shown in Fig.4.

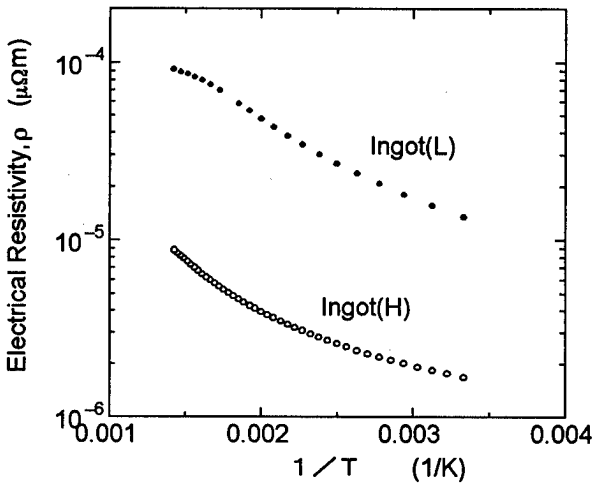


Fig.2 Temperature dependence of electrical resistivity of as-solidified ingots

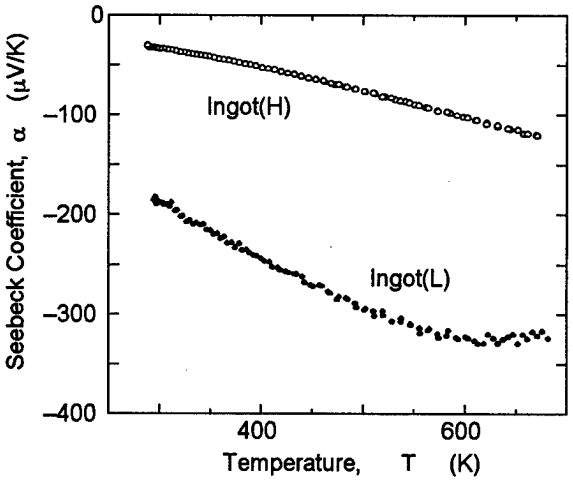


Fig.3 Temperature dependence of Seebeck coefficient of as-solidified ingots

α^2/ρ of Ingot(L) is decreased monotonously with increasing T, while that of Ingot(H) is increased and gives a maximum at 700K. The α^2/ρ curves of Ingot(L) and Ingot(H) have an intersection at 500K. Ingot(L) has higher power generating performance below 500K, and Ingot(H) has higher one above 500K. It is expected that the jointed material of Ingot(L) and Ingot(H) gives the best performance at the jointed interface temperature T_i of 500K.

Figure 5 shows maximum power P_{max} of the as-solidified ingots and the jointed material of two ingots as a function of T_h-T_c, ΔT_{hc}. T_h is heated side temperature and T_c is cooled side temperature. In the case of the jointed material, the heated side is in Ingot(H) and the cooled side is in Ingot(L), as shown in Fig.1. T_c was kept almost constant, 300K. Ingot(L) and Ingot(H) show the variations of P_{max} as expected from Fig.4. Both the ingots have the same slope of P_{max} curve at ΔT_{hc}=200K; this corresponds to the result that the α^2/ρ curves of Ingot(L) and Ingot(H) have an intersection at 500K.

The jointed material reveals higher P_{max} than Ingot(L) at $\Delta T_{hc} \geqq 250$K. It is demonstrated that the segmentation with graded n_e can improve power generating performance of n-type PbTe. The variation of T_i-T_c, ΔT_{ic}, as a function of ΔT_{hc} is shown in Fig.6. ΔT_{ic} is increased to 150K at ΔT_{hc}=250K; T_i=450K at T_h=550K. Figure 4 explains that the integrated area of α^2/ρ curve of Ingot(L) between 450K and 550K is almost same as that of Ingot(H). As a result, P_{max} of the jointed material agrees with that of Ingot(L) at ΔT_{hc}=250K.

A small specimen shown in Fig.1 generated 0.13W at ΔT_{hc}=400K with T_c=300K. Originally, n-type PbTe is used in the temperature range from 400K to 800K. PbTe with $n_e=1\times10^{25}/m^3$ has a maximum α^2/ρ of more than 3.2mW/K^{2}m at 400K, and also PbTe with $n_e=3\times10^{25}/m^3$ has a maximum of more than 2.5mW/K^{2}m at 600K. When these materials with $n_e=1\times10^{25}/m^3$ and $n_e=3\times10^{25}/m^3$ are jointed, approximately two times higher power generating performance than this study can be obtained at ΔT_{hc}=400K with T_c=400K.

From the above, it is concluded that the segmentation with graded n_e is effective to improve the power generating performance of n-type PbTe.

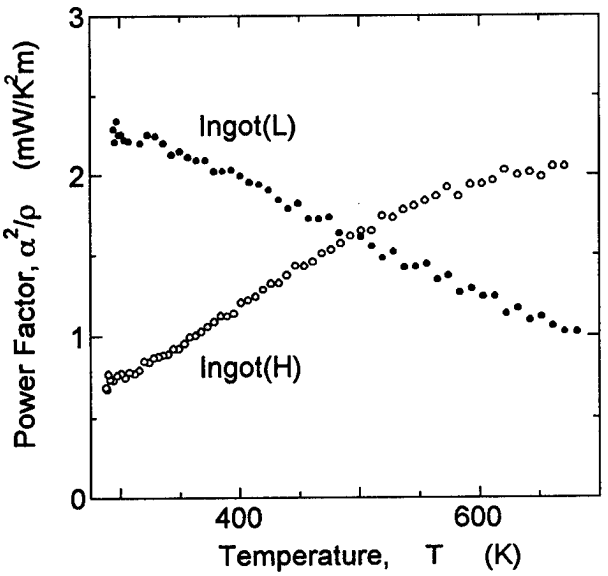


Fig.4 Temperature dependence of power factor of as-solidified ingots

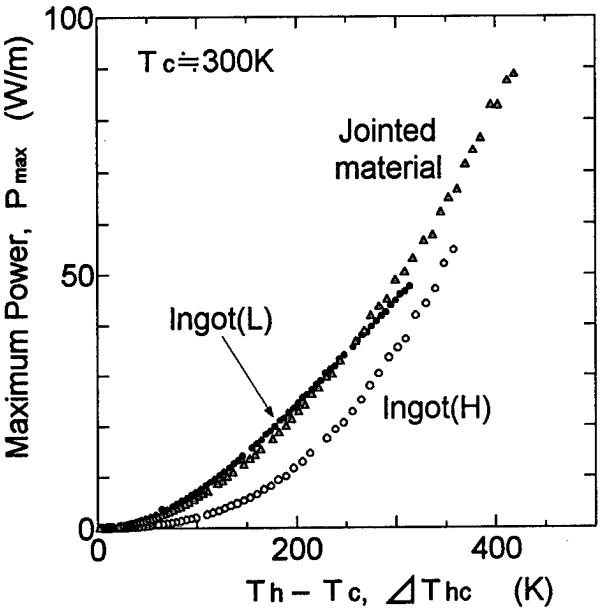


Fig.5 Maximum power of as-solidified ingots and jointed material as a function of T_h-T_c

References

[1] N.B.Elsner,J.Chen and G.H.Reynods, "Fabrication of selenide segented elements",Proc.3rd IETEC,(1980)105.

[2] D.M.Rowe ed., *CRC Handbook of THERMOELECTRICS*, CRC Press,Inc., New York, 459(1994).

[3] J.F.Goff and J.R.Lowney, "The thermoelectric figure-of-merit", Proc.1st ICTEC, (1976)47.

[4] T.C.Harman, "Measurement of thermoelectric materials and devices", Semiconductor Products, Sep.(1963)13.

[5] S.Yoneda,H.T.Kaibe,T.Okumura,Y.Shinohara,Y.Imai, I.A.Nishida,T.Mochimaru,K.Takahashi,T.Noguchi and I.Shiota, "Improvement and thermal stability of thermo-electric properties for *n*-type segmented PbTe", Proc. 4th Inter.Cof.on FGM(in printing).

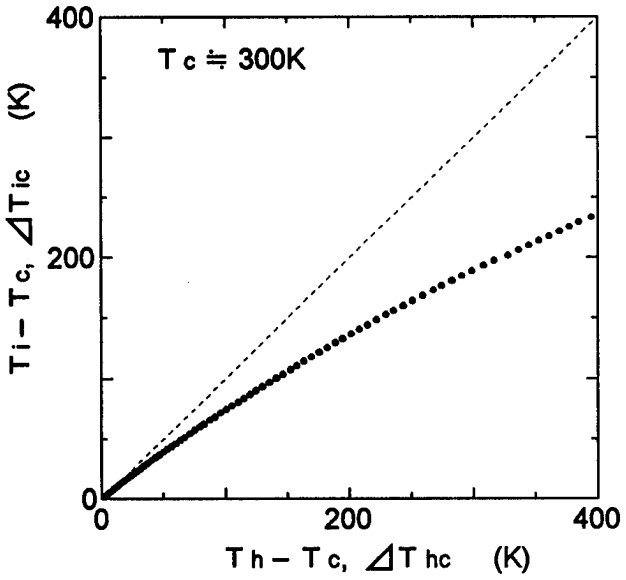


Fig.6 Variation of T_i-T_c as a function of T_h-T_c

Evaluation of monolithic and segmented thermoelectric materials by using a large-temperature-span apparatus

Y.S. Kang[1], S. Moriya[1], K. Kisara[1], M. Niino[1], Y. Noda[2], L. Chen[3] and T. Sudo[4]

[1] National Aerospace Laboratory (NAL), Kakuda Research Center, Koganezawa 1, Kimigaya, Kakuda-City, Miyagi 981-15, Japan

[2] Department of Materials Science, Faculty of Engineering, Tohoku University, Aoba-Aramaki, Aoba-ku, Sendai City, Miyagi 980-77, Japan

[3] Institute for Materials Research, Tohoku University, katahira 2-1-1, Aoba-ku, Sendai City, Miyagi 980-77, Japan

[4] National Space Development Agency of Japan (NASDA), Kakuda Propulsion Center, Koukuzo 1, Jinjiro, Kakuda-City, Miyagi 981-15, Japan

Abstract

In order to evaluate the thermoelectric properties and power output performance of a gradient TE material under a wide working temperature range, a large-temperature-span apparatus has been developed. However, an accurate evaluation is not so easy to put into practice on the gradient TE material because a lot of difficulties are associated with the heat flow controlling and the reducing of electrical resistance in measurement circuit.

Present work is a practice to characterize monolithic and segmented thermoelectric materials by the new developed apparatus and approach the method to evaluate a gradient TE material accurately and effectively. This work was carried out for evaluation of a stacked monolithic (SiGe, PbTe and Bi_2Te_3) TE leg and a segmented thermoelectric branch (PbTe/Bi_2Te_3), and we take the aim at to confirm their thermoelectromotive force, electrical resistance and temperature distribution both for the apparatus and for specimen stacks. We also made a trial of power output evaluation using an electronic load and explored some technical problems in the evaluation of TE materials under a large temperature span. The results of evaluation on power output by electronic load indicate much lower value than the calculation using the real electrical resistance in TE materials. We discuss some problems for the evaluation of stacked thermoelectric materials under a large temperature difference condition.

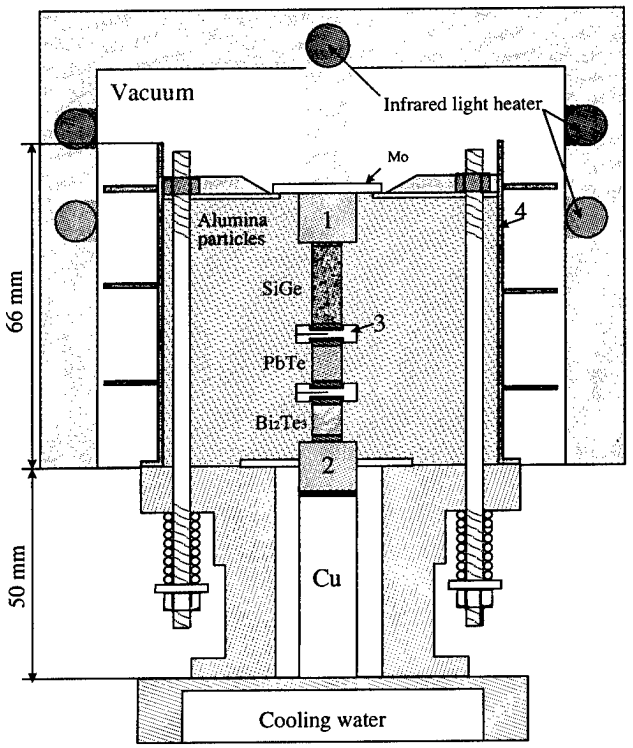
Introduction

Recent years, many efforts are devoted on development of high efficient thermoelectric materials[1-3]. Most of them are approached on the enhancement of TE figure of merit through functionally graded structures. An important point of the FGM concept may be summarized as, to maximize the figure of merit for monolithic thermoelectric materials and enhance the temperature covering range through a gradient structure. The gradient structure in a broad sense can be considered to include a segmented stack of different kind of thermoelectric materials and include the structure which composed of varied doped concentrations. In any case, the final evaluation of materials is an important work whatever the structure is.

On the evaluation of functionally graded thermoelectric materials, some theoretical method concerning computerized calculation are reported[4,5]. However, reports on the evaluation of FGM type of thermoelectric materials by a practical instrument are limited. The reasons may be in the practice of evaluation on the FGM type of TE materials need a specific apparatus which can provide a varied temperature condition, and some technical problems associated with the instrument. Beside of this, the research works on gradient thermoelectric materials are still under developing, only few high quality FGM type of thermoelectric materials those can be provide as a standard specimen.

Here we report the evaluation procedure and results of a stacked monolithic TE leg and a segmented thermoelectric branch by using a new developed large-temperature-span apparatus. The main object is to contribute both to the development of FGM processing and to the improvement of evaluation technique through the feedback of data.

Evaluation apparatus



Schematic of the TE evaluation apparatus

1. upper heat flow meter
2. lower heat flow meter
3. Copper electrode
4. Cylindrical heat shield

Fig. 1: Schematic of the large-temperature-span apparatus for the evaluation of TE materials those have various graded changed in composition and need a wide temperature condition.

Figure 1 shows schematic of the large-temperature-span apparatus used in this work. This apparatus is designed for evaluate a specimen in a dimension range of 10-20 mm in diameter and 5-30 mm in length by change corresponding probes (heat flow meters) [6]. The upper and lower heat flow meter, specimen are fastened on a base block with a disk shape holder through three alumina rods. The fastening force on the specimen is about 3 kgf/cm^2. The lower heat flow meter is electrical insulated to the base block copper rod by a ALN plate. The high temperature end of specimen is heated by three infrared light heater and the temperature is controlled by a thermocouple joined to a molybdenum disk plate on the upper heat flow meter. Cold end of the specimen is simply cooled by a copper rod which is stacked on the cooling water tank. The cylindrical shield serves as a wall to prevent the heat loss in radius direction, and alumina particles filled in the cylindrical shield is to expect preventing hear transfer by radiation.

Monolithic materials of n-type SiGe, Pbte and Bi_2Te_3 (5 X 5 X 30 mm) are stacked between two heat flow meters and joined by a copper plate each other. The copper is served as a connector of TE material and a terminal of measurement for thermoelectomotive force and electrical resistance. Temperature of each side of heat flow meter, specimen, and cylindrical shields are measured by thermocouples, respectively.

The segmented TE branch is composed by non-doped p-type PbTe and $Bi_2(Te,Se)_3$, the design in size is 10 mm in diameter and composition of PbTe/Bi_2Te_3 are not optimized [7]. The arrangement of segmented specimen is showing in figure 2.

All evaluations were in a vacuumed condition of about 0.003 Torr and measurements at every programmatic temperature were carried out after the specimen stacks become stable in temperature. The electrical resistance of specimen was measured by bring a source of 5 volts in voltage and 15 mA in current. During the measurement of electrical resistance, direction of current and time of source brought to the specimen were controlled to reduce the Peltier effect. Power output was measured by electronic load which can provide a minimum load resistance in 0.007 Ω.

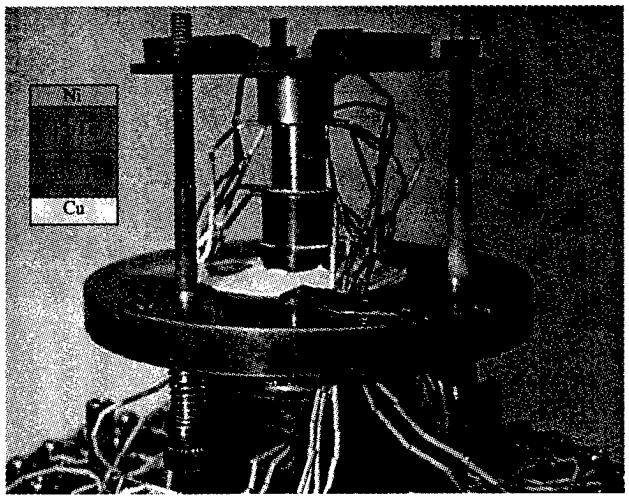


Fig. 2: An inner view of the arrangement of segmented PbTe/Bi_2Te_3. The stacks of specimen, heat flow meters and alumina rods will be wrapped by alumina particles.

Result and discussion

Figure 3 shows a measurement result of electrical resistance of the monolithic TE in the 3 stage stacked leg. The temperature axis shows the programmatic temperature of evaluation. Each monolithic TE has a real gradient temperature distribution. A temperature span of the 3 stage leg at programmatic 800℃ is showing in the schematic graph. VALLM is the total resistance and others indicate resistance of each stage, respectively.

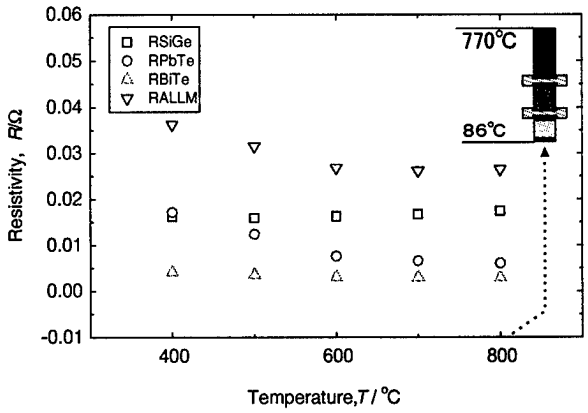


Fig. 3: Temperature dependence of the electrical resistance of 3 stage stacked monolithic TE leg. RALLM is the total resistance and others indicate resistance of each stage, respectively.

The total resistance decrease fast than single TE material, that can be considered the contact resistance between materials and copper electrode goes down with the temperature rising.

Figure 4 shows a temperature dependence of the Seebeck voltage of the 3 stage stacked monolithic TE leg. The temperature axis at here expresses a average vale of hot end and cold end for each stage. VALLM is the Seebeck voltage of 3 stage stacked leg that was measured through the top surface of SiGe and bottom surface of Bi_2Te_3. The Seebeck voltage of Bi_2Te_3 decrease with the temperature range rising, this give us a message that the temperature range for the Bi_2Te_3 seems too high.

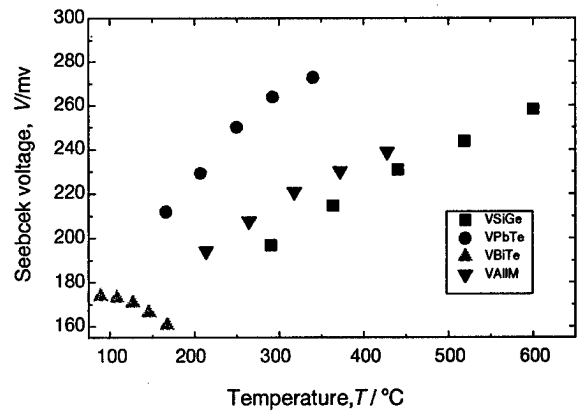


Fig. 4: Temperature dependence of the Seebeck voltage of the 3 stage stacked monolithic TE leg. The temperature here express a average vale of hot and cold end for each stage.

In the evaluation of power output for the 3 stage stacked leg, the current and voltage can be roughly measured by the electronic load directly in spite of the EL load can only express a rough value. Figure 5 shows the measure circuit composed of electronic load and TE. R_w is the resistance of lead wire which was much higher than the TE element.

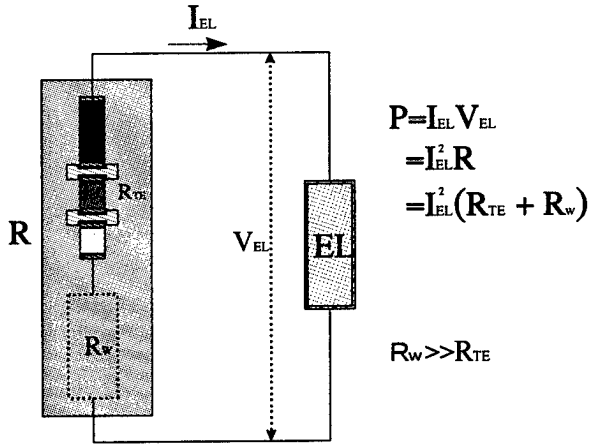


Fig. 5: Power output evaluation by using an electronic load.
R_{EL}: Resistance of electronic load;
R_w: Resistance of lead wire
R_{TE}: Resistance of TE
I_{EL}: Current in the electronic load
V_{EL}: Voltage in the electronic load

When the load was changed from the minimum value of the instrument to higher range, the current in the circuit continually reduced. The resistance of lead wire in our apparatus was about 0.134 Ω, it is about three times higher than the total inner resistance of the 3 stage leg. Therefor, the measured current can not find the maximum value. The result of the load resistance dependence of current is shown in figure 6. From the result, we can simply estimate the maximum of current, but in the sense of measurement technique, extremely reduce the electrical resistance of lead wire can not be ignore.

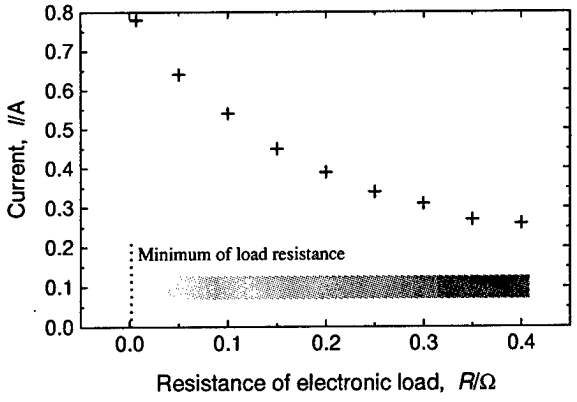


Fig. 6: Current variation in the 3 stage stacked monolithic TE leg.

Figure 7 shows a plot curve of power output of the 3 stage stacked monolithic TE leg. The value of power are calculated by current and voltage measured by electronic load. Considering the relation of load and inner electrical resistance, the peak of power output can express the real performance of the 3 stage stacked monolithic TE leg. In a theoretical calculation of maximum power output,

$$P_{max} = \frac{V_m^2}{4R_0}$$

where the V_m is Seebeck voltage, R_0 is internal resistance. In this work, the P_{max} calculated using above formula indicate near 10 times of the measured one.

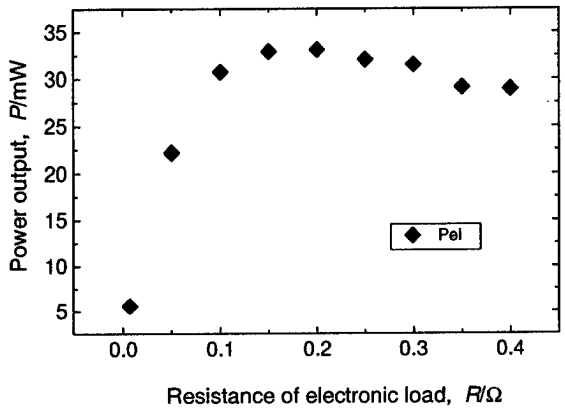


Fig. 7: Power output curve of the 3 stage stacked monolithic TE leg. The plots are calculated by current and voltage measured by electronic load.

Figure 8 shows the results of temperature drop and Seebeck voltage of the segmented branch. Temperature range in the branch and each part of TE indicate a reasonable distribution. However, when the temperature higher than 300℃, Seebeck voltage goes done fast, it is be considered that the PbTe was non-doped, the figure of merit is exist in a quite low temperature range, that may caused the performance down at a high temperature range.

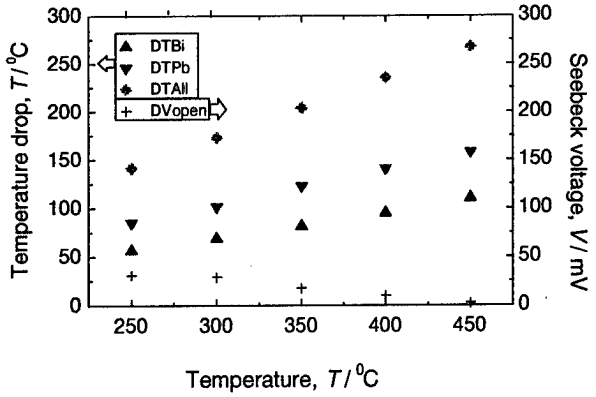


Fig. 8 Temperature drop and Seebeck voltage of the segmented branch. DTALL express the temperature drop between hot and cold ends.

The measured current and power output results has a similar tradition with the 3 stage stacked monolithic one, that means the internal electrical resistance is too small, and the evaluation of power output in a large area section specimen must be associated with a calculation.

Conclusions

Evaluation on monolithic (SiGe, Pbte and Bi_2Te_3) and segmented ($PbTe/Bi_2Te_3$) type thermoelectric materials are carried out by using a large-temperature-span apparatus. The evaluation of thermoelectromotive force, electrical resistance and temperature distribution are satisfied. Power output evaluation using an electronic load can be accurately carry out only in the case of lead wire has a electrical resistance which much lower than the TE materials.

The evaluation result of stacked and segmented type materials can provide a lot of experiences to evaluate FGM type TE, and the data is expected to improve the designing and processing of thermoelectric materials in FGM.

Acknowledgment: This work was partly supported by the Special Coordination Funds for Promoting Science and Technology from the Science and Technology Agency (STA), Japan. The authors grant to the financial support by STA.

References

[1] M. Niino and M. Koizumi, Proc. of the 3th Int. Symposium on Functionally Graded Materials (FGM'94), Lausanne, Switzerland, 1994.

[2] Y. Miyamoto, M. Niino, M. Koizumi, Proc. of the 4th Int. Symposium on Functionally Graded Materials (FGM'96), Tsukuba, Japan, 1996.

[3] T. Kajikawa, Proc. of the 4th Int. Symposium on Functionally Graded Materials (FGM'96), Tsukuba, Japan, 1996.

[4] J. Teraki and T. Jirano, Proc. of the Symposium on Functionally Graded Materials (FGM'95), Japan, p. 71, 1995. (in Japanese)

[5] L.I. Anatychuk, L.N. Vikhor, Proc. of the 4th Int. Symposium on Functionally Graded Materials (FGM'96), Tsukuba, Japan, 1996.

[6] T. Sudo, K. Kisara, L. Chen, M. Niino, T. Ohshima, R. kato, The 4th Asian Thermophysical Properties Conference, Tokyo, Japan, p.401, 1995.

[7] Y. Noda, Y.S. Kang, M. Niino, Proc. of the XVI Int. Conf. on Thermoelectrics (ICT'97), Dresden, Germany, this volume.

Catalytic Furnaces with Thermogenerators

Anatychuk L.I., Mikhailovsky V.Y.

Institute of Thermoelectricity, General Post-Office, Box 86, 274000, Chernivtsi, Ukraine
Tel:+380/3722/44422, Fax:+380/3722/41917, E-mail:Alex@ite.Chernovtsy.ua, WWW: http:\\www.ite.Chernovtsy.ua

Abstract

The results of investigations and development of catalytic heat sources with thermoelectric energy converters have been given. The efficiency of the catalytic oxidizers are about 5÷6%. Heat passed through thermobatteries is used for heating, electric energy is used where necessary. Structures and characteristics of such devices with heat power of 1,2,3kW have been given. Fields of practical applications have been analyzed.

The essence of the problem

Heat release during catalytic combustion of hydrocarbon fuels is widely used in various fields of heating engineering [1]. From the fuel oxidation efficiency point of view very promising are device where the combustion process is made on solid catalysts.

The essential advantage of the catalytic fuel oxidation is that the produced heat (about 80 %) is generated in the form of radiant energy [1] with wavelength of 2-16 mcm that is easily absorbed by the most of materials and can be directed only at objects that need heating. Fuel combustion on the catalyst is performed at relatively low temperatures (350-500°C) that allows to eliminate the formation of toxic nitrogen oxides and finely divided carbon that is inevitable at flame combustion of hydrocarbons.

Depending on purposes and consumer's qualities of catalytic heaters their structure and characteristics may vary widely. Among such types of devices we set aside burners which use separate fuel and air supple to the combustion zone. Such burners do not need special equipment for fuel-air mixture formation, operate independently, reliable and almost fire-proof. The positive is also lack of requirements to criticality of fuel-air mixture that means that changes in systems of air and fuel supply slightly effected on the combustion process.

The listed peculiarities enable to use effectively such heat sources both independently and as a part of thermoelectrogenerators of different power and purpose.

Institute of Thermoelectricity has conducted scientific work in this direction during several years. The use of the works results [2-4] made it possible to elaborate and develop a number of such devices on gaseous fuel. Schematic structure of such catalytic furnaces and generators with their characteristics are given in Fig.1-4, Table 1.

The presented devices used the elaborates catalysts based on oxides of variable valence metals such as iron, cobalt, chromium, nickel. For activity increase catalysts are promoted with small adding of palladium or platinum. For carrier a fiber silicium oxide with the following characteristics: fiber diameter is 5-7 mcm, d = 0.1 g/cm^3, moisture capacity of the carrier is 9.8 ml/g, coefficient of thermal conduction is 0.055 kKal/m.h.°C at 160°C and 0.12 at 460°C was used. Method of such type catalyst preparation was previously described in [5,6].

Conversion degree of gaseous hydrocarbons on the elaborated catalysts reaches 100%. It should be noted that almost all oxidation catalysts have definite rate range of fuel supply at which conversion degree is maximum at operating temperatures. For the developed catalysts fuel supply rate must be within 0.15-0.35 g/cm^2 under natural air supply Fig.1. Fig.1 shows that one can increase fuel consumption

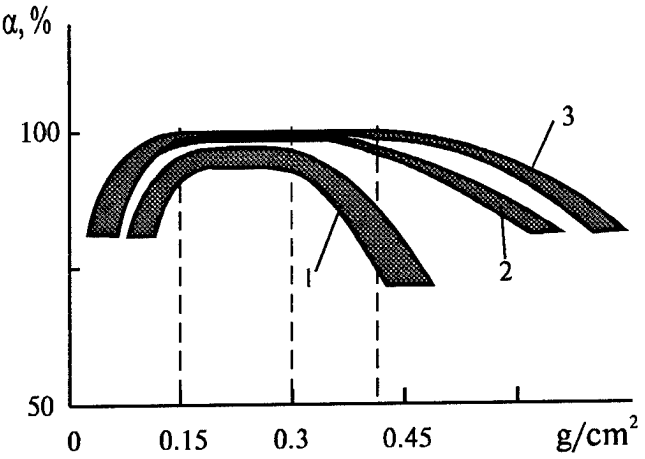


Fig. 1. Dependence of conversion degree (α) of catalysts on specific fuel consumption under the natural (1, 2) and forced (3) air supply.
1 is oxide catalysts; 2 is oxide promoted catalysts; 3 is oxide promoted catalysts under the forced air supply.

and so the catalyst thermal power by the use of forced air supply to the reaction zone. Mass transfer processes on the catalyst surface are intensified and as a result burning is enhanced.

The availability of the upper limit at fuel consumption increase depends on some factors. On the one side, even at sufficient temperature of the burner and air excess the fuel conversion degree may be limited by chemical activity of the catalyst that in its turn is determined by the carrier structure, nature and concentration of active components, availability of chemical interaction between them and so on [3]. On the other side, the way of fuel and air supply to the reaction zone has essential effects on α. In this case air access to the catalyst layer depth is controlled by the rate of fuel gas counter rate which increase decreased the depth of air access, and by temperature which increase gives the opposite effect. Mutual effect of these factors defines the location of the

0-7803-4057-4/97 $10.00 ©1997 IEEE

combustion zone where the reaction rate is maximum at the fuel-air optimal relation.

Structurally a catalytic furnace (Fig.2) consists of a catalyst (1) placed into a metal case (8). Just under the catalyst a porous distributor is placed through which a fuel gas is fed uniformly on the whole surface of the catalyst.

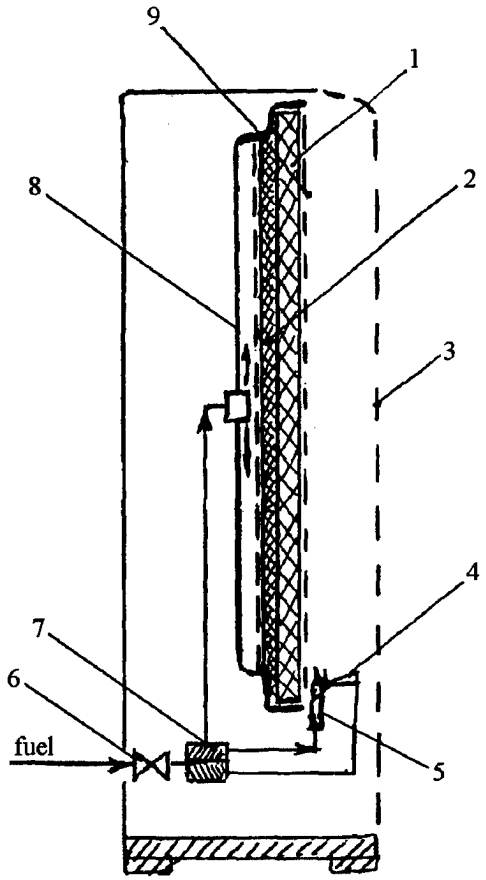


Fig. 2. Diagram of the catalytic furnace with flame start. 1 is a catalyst, 2 is distributor, 3 is perforated case, 4 is a thermocouple, 5 is starting fuse, 6 is input valve; 7 is magnetic valve; 8 is the burner case; 9 is reinforcing fabric.

In the lower part of the catalyst a flame a small power starting fuse (5) is placed. A thermocouple (4) is placed in the flame of the fuse, an electromagnetic valve (7) is connected to the thermocouple. Gas fuel is supplied to the catalyst through the valve (6). On the outer side the catalyst is protected by reinforcing fabric (9) from heat resistant metal.

With the aim of the catalytic power increase with the same catalyst area we have developed a structure with forced air supply to the reaction zone (Fig.3). The air is supplied on the catalyst by a low-power fan (4) placed in the lower part of the thermogenerator (3).A special thermobattery Altec-1010 developed by "Altec" company is used in the generator. Along with high efficiency the battery is characterized by the improved reliability and service life due to optimized thermoelectric material with high stability, by efficient anti-diffusion layer, commutation ensuring temperature compensation. The battery is enclosed into sealed filled with inert gas case made from special stainless steel. The generator is placed in such was that cold heat exchanger is in the air flow generated by the fan. Electric power of the fan is 1.8-2.0 W that is sufficient to burning process intensification on the catalyst areas of 500-800cm^2. Thermal capacity of the catalyst may be increased under definite conditions by 25-30%. The availability of fan makes it possible to improve convective heat exchange between radiating surface of the catalyst and environment. And the period of a unit of volume of a room is considerable reduced.

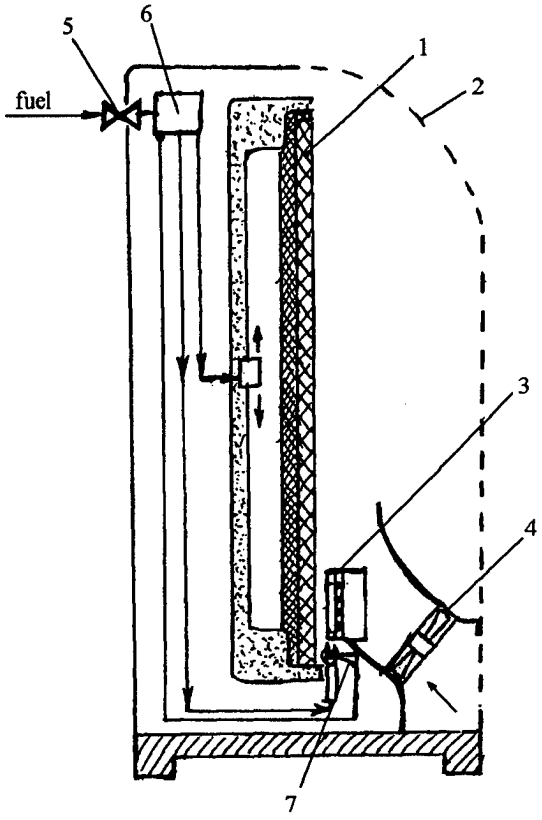


Fig.3. Diagram of the catalytic furnace with low-power thermoelectrogenerator. 1 is a catalyst; 2 is a case; 3 is a thermogenerator; 4 is electric fan; 5 is gas valve; 6 is magnetic valve; 7 is a thermocouple.

More universal is a catalytic furnace with large power thermoelectric generator. Heat passed through thermobatteries is used for heating, electric energy may be used for different consumers fed, for instance for illumination, domestic and special radio equipment, signal devices supply and so on.

Diagram of such thermogenerator with catalytic heat source is given in Fig. 4. In the present variant a double-side catalytic burner (1) was used, that permitted to reduce heat losses from nonoperating surface and by that manner to improve its thermal characteristics. Start of the catalytic furnace is performed by electric heaters (10).Operating time of the heaters is 3-5 min that is sufficient for the catalyst starting. Accumulator of proper power which is charged

during the thermogenerator operating time is used fro heaters supply.

The thermogenerator consists of cold (6) and hot (7) heat exchangers from aluminum between which standard batteries "Altec-1010" are placed. Two fans are placed in the center of cool heat exchangers outer plates. Cooling air is sucked through all side surfaces of heat exchangers and then the warm is rejected into the environment. Heat of the fuel combusted products is also used for rooms heating by means

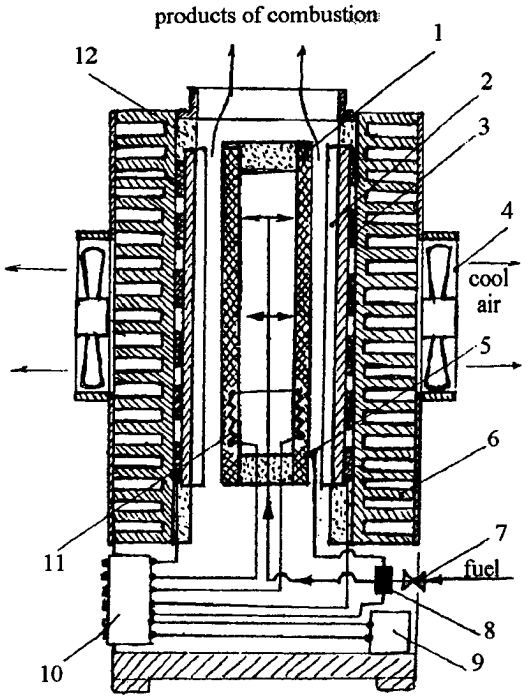


Fig.4. Diagram of the catalytic furnace with thermoelectro-generator. 1 is a catalytic burner; 2 is hot heat exchanger; 3 is thermoelectric batteries, 4 is a fan, 5 is a thermocouple, 6 is cold heat exchanger, 7 is gas valve; 8 is magnetic valve; 9 is accumulator; 10 is control unit for start and operation of the generator; 11 are electric starters; 12 is thermal insulation.

of air heat exchangers system placed on the chimney. In the case of the catalyst with 100% conversion degree use the chimney is unnecessary and the whole heat can be used for rooms and other objects heating.

Thus, catalytic furnaces with thermoelectric generators may be considered as one of the promising variants of the combined heat sources and electric energy. The expediency of such devices use is defined by their competitiveness in comparison with other sources as applied to particular fields of use. Autonomous catalytic furnaces with thermogenerators may be successfully used for heat and electric energy provision small houses, cottages ware-houses, hangars and so on. It counts in favor of their use that in most cases for a consumer is important not high efficiency but long service life, self-sufficiency, ecological purity.

Table 1. Characteristics of catalytic furnaces with thermogenerators (fuel is propane-butane)

Characteristics	Catalytic furnace		Catalytic furnace with TEG		
	НК-1	НК-2	НКТ-1	ТЭГ-2	ТЭГ-2
Thermal power, W	1000	3000	2000	950	2000
Electric power, W	-	-	2	30	60
Service life of the catalyst, h	11000	15000	11000	15000	15000
Temperature of the catalyst, °C	350-400	400-420	420-450	400-420	400-420
Fuel consumption , g/h	85	250	170	85	170
Weight without fuel, kg	4.0	5.0	5.5	10.5	12.7
Overall dimensions, mm, not more than					
length	335	385	385	310	310
width	140	145	180	220	240
height	335	370	370	370	390

References

1. Alkhazov T.G., Margolis L.Y. Deep catalytic oxidation of organic substances. M.: Khimia, 1985.
2. Mikhailovskyy V.Y., Konopelnyuk V.V. J.of Thermoelectricity, N 2, 1994, p. 76.
3. Mikhailovsky V.Y., Chervinsky K.A., Strutinskaya L.T. of Thermoelectricity, 1, 1996, p. 54.
4. Mikhailovsky V.Y., Strutinskaya L.T. J.of Thermoelectricity, N2, 1996, p. 58
5 Mikhailovsky V.Y., Chervinsky K.A., Lazaruk O.E. UKJ, 1994, v.61, N 1, p. 36.
6 Mikhailovsky V.Y., Chervinsky K.A., Fedunyak O.M. UKJ, 1994, v. 60, N 5-6, p 409.□

Low-temperature Thermoelectric Cooling under Optimal Legs Inhomogeneity in the Optimal Nonuniform Magnetic Field

L.I. Anatychuk, L.N. Vikhor

Institute of Thermoelectricity, General Post-Office, Box 86, 274000, Chernivtsi, Ukraine
Tel:+380/3722/44422, Fax:+380/3722/41917, E-mail:Alex@ite.Chernovtsy.ua, WWW: http:\\www.ite.Chernovtsy.ua

Abstract

The possibilities of optimal control theory use for coolers simulation under the conditions of combination optimal legs inhomogeneity with optimally magnetic field nonuniformity are investigated in present paper. The essential improvement of low-temperature cooling performances are demonstrated in this case.

The essence of the problem

At present one of the prospective approaches of thermoelectric cooling efficiency increase is the transition from a classic model of a thermoelectric battery, where legs are made of homogeneous materials to batteries, where legs are made of materials properties of which are coordinates functions. A vast number of investigations on the development and use of such inhomogeneous materials in cooling batteries are conducting in Ukraine in the Institute of Thermoelectricity. Based on mathematical methods of optimal control it was created a theory of computer simulation of the materials with predicted inhomogeneity [1-4]. The elaborated computer programs enable to determine inhomogeneity optimal functions of material properties and automatically use them for high quality cooling batteries designing. This have made possible to determine optimal functions of the magnetic field strength use of which is rather rational in the low temperature range for thermoelements efficiency increase. As is known at temperatures 80-160K the magnetic field leads to thermoelectric figure of merit increase by a factor of two-three of the alloy consisted from 88%*Bi* and 12%*Sb* and having electron type of conduction [5]. It is shown in [6] that the use for this material optimal functions of the magnetic field strength gives maximum temperature difference increase by a factor of 1.2 and coefficient of performance increase by a factor of 1.5 within one stage of the Peltier cooler in comparison with that of uniform field. The same method of low-temperature thermoelectric cooling efficiency increase was generalized in [7,8] for stage Peltier coolers that led to optimal functions determination of the magnetic field nonuniformity with taking into consideration of stages matching. These functions use allows additionally to increase maximum coefficient of performance of stage coolers in which $Bi_{98}Sb_{12}$ is used as *n*-type material. At temperature differences 60-70 degrees the gain in coefficient of performance reaches 75% in comparison with uniform version.

But in this problem solution two possibilities of low-temperature cooling energetic efficiency improvement were not used because of its severity. The first one is connected with figure of merit dependence of *n*-type material based on *Bi-Sb* not only on the magnetic field strength and temperature but also on percentage content of *Sb*. It follows from the experimental data given in Fig.1 that have been kindly submitted for study by Prof. Ivanov A.G. that maximum of this material figure of merit is shifted over the temperature scale in response to the magnetic field strength and Sb composition. So combination of optimal function of the field nonuniformity and optimal consumption of *n*-type material must produce additional increase of low-temperature cooling coefficient of performance.

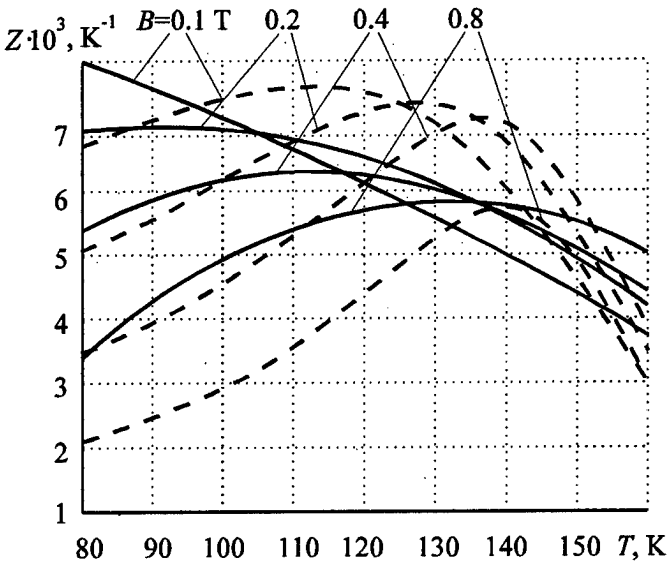


Figure 1: Figure of merit dependence of *n*-type material based on *Bi-Sb* on temperature for different compositions and strength of the magnetic field *B*.

The second possibility relates to improvement of *p*-type material properties. As is known one failed to get hole material with properties dependence on the magnetic field. So in [7,8] when designing low-temperature coolers material based on *Bi-Te*, homogeneous in composition, was used for *p*-legs of thermoelements. But [9] shows that the use of optimal functions of impurity concentration distribution in materials based on *Bi-Te* leads to coefficient of performance increase by a factor of 1.6-2.5 in comparison with the homogeneous material. That is why one may expect additional increase of cooling efficiency due to the use of optimally inhomogeneous materials of *p*-type in low-temperature batteries.

0-7803-4057-4/97 $10.00 ©1997 IEEE

In the present work we will try to use both possibilities and study new more efficient variant of problem of the optimal control by low-temperature cooling. It reduces to the agreed effect of two factors on the thermoelectric material: combination of optimal composition and optimal function of the magnetic field for *n*-leg of a thermoelement from *Bi-Sb* and optimal inhomogeneity of *p*-type material based on *Bi-Te*

Problem solution

A physical model for construction of the magnetic field optimal function computer design in combination with thermoelectric material inhomogeneity is presented in Fig.2.

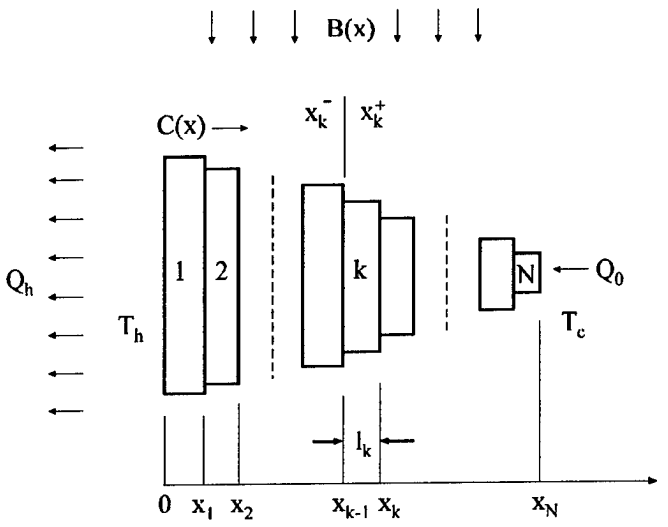


Figure 2: A diagram of *N*-stage thermoelectric cooler.

The controlled object is *N*-stage Peltier cooler. The magnetic field with intensity *B* which can be the *x* coordinate function is established in thermoelement legs perpendicular to the current direction. Material properties of *p*-legs: thermo-emf α, electric conduction σ, thermal conduction κ change with coordinate *x* because of their dependence on temperature and material inhomogeneity that characterized by charge carrier or doping impurity concentration. *N*-type material properties depend on temperature, composition and magnetic fields strength. Such assumption is justified because *p*-leg is made of material based on *Bi-Te* characteristics of which are weakly depend on the magnetic field, *n*-leg is made from the material based on *Bi-Sb* characteristics of which are strongly depend on the field.

The aim of control is the determination of *p*-material inhomogeneity optimal function, optimal composition and magnetic field strength function for *n*-type material, and optimal ratio of stage electric parameters that ensure the best coefficient of performance.

The initial data for the optimal control include cooling power Q_0, cooling temperature T_0, heat releasing surface temperature T_h.The model takes into account contact resistance r_0, interstage temperature differences δT and heat exchange with environment at the heat exchange coefficient α_T.

As limitations for control theoretical and experimental dependences α_p, σ_p, κ_p on temperature and value that characterizes the material inhomogeneity, and α_n, σ_n, κ_n on temperature, composition and magnetic field strength must be also specified.

Thus the problem covers adequately all required characteristics of the material, cooler and operating conditions.

Initial set systems describing thermal and electric processes in thermoelement legs and considering heat transfer due to thermal conduction, the Joule heat release, three-dimensional Peltier heat, is given by expressions:

$$\left.\begin{aligned} \frac{dT}{dx} &= -\frac{\alpha i_k}{\kappa}T - \frac{i_k}{\kappa}q, \\ \frac{dq}{dx} &= -\frac{\alpha^2 i_k}{\kappa}T + \frac{\alpha i_k}{\kappa}q + \frac{i_k}{\sigma}, \end{aligned}\right\}_{n,p} \quad k = 1,\ldots N \qquad (1)$$

Here $\alpha_n = \alpha_n\big(T,n,B(x)\big)$; $\sigma_n = \sigma_n\big(T,n,B(x)\big)$; $\kappa_n = \kappa_n\big(T,n,B(x)\big)$; where *n* is the value characterizing the material composition, *B(x)* is the magnetic field function, $\alpha_p = \alpha_p\big(C(x),T\big)$; $\sigma_p = \sigma_p\big(C(x),T\big)$; $\kappa_p = \kappa_p\big(C(x),T\big)$; here *C(x)* is the function of *p*-type material inhomogeneity. This may be current carrier concentration in a semiconductor, doping impurity concentration or other value characterizing inhomogeneity of a thermoelectric structure along the height of a thermoelement leg.

The boundary conditions of these expressions are written as the equality of temperatures between stages with account of interstages temperature losses and have the form:

$$\begin{aligned} &T_n(0^+) = T_p(0^+) = T_h, \qquad T_n(x_N^-) = T_p(x_N^-) = T_c \\ &T_n(x_k^+) = T_p(x_k^+), \qquad T_n(x_k^-) = T_p(x_k^-), \\ &T_n(x_k^+) = T_n(x_k^-) + \delta T, \end{aligned} \qquad (2)$$

with points x_k, k=1,...*N* location unfixed.

It is necessary to determine such conditions when the coefficient of performance reaches its maximum at the given cooling value.

Such problem was solved by means of a special computer program creation base on the use of mathematical theory of optimal control by Pontryagin [10]. In accordance to this theory the problem reduces to the study of functional *J* minimum which corresponds to maximum of the coefficient of performance and has the form

$$J = \sum_{k=1}^{N} (\ln q_1^k - \ln q_0^k). \qquad (3)$$

Here specific heat fluxes at junctions are determined by the expression

$$\begin{aligned} q_0^k &= \sum_{n,p}\left[q(x_k^-) + i_k r_0 + \frac{\alpha_T}{i_k}(T_h - T(x_k^-))\right], \\ q_1^k &= \sum_{n,p}(q(x_{k-1}^+) - i_k r_0). \end{aligned} \qquad (4)$$

They depend on the controlled parameters of current density $i_{n,p}$, n-type material composition n, inhomogeneity functions of the magnetic field $B(x)$ and p-type material $C(x)$. Starting approximations of these controls are fed into the computer program. The Pontryagin's method reduces to the determination of optimal expressions by means of J functional calculation for different values $i_{n,p}$, n and functions $B(x)$, $C(x)$ different from the given starting ones. Purposeful search for such controls is carried out on the following conditions:

1. Current density in stages must satisfy the equalities

$$-\frac{\partial J}{\partial i^k_{n,p}} + \int_{x^+_{k-1}}^{x^-_k} \frac{\partial H^k(\varphi, T, q, i^k_n, i^k_p)}{\partial i^k_{n,p}} dx = 0 \qquad (5)$$

where the Humilton function H^k has the form

$$H^k = \sum_{n,p} (\varphi_1 f^k_1 + \varphi_2 f^k_2) \qquad (6)$$

$\left(f^k_1, f^k_2\right)_{n,p}$ are the right parts of (1), $\varphi = \left(\varphi_1, \varphi_2\right)_{n,p}$ is pulses vector [10].

2. Optimal composition of n-type material must satisfy the equation

$$\int_{x^+_{k-1}}^{x^-_k} \frac{\partial H^k_n(\varphi, T, q, i^k_n, i^k_p, n)}{\partial n} dx = 0 \qquad (7)$$

3. Points coordinates of a joint x_k satisfy the equalities

$$H^k(x^-_k) = H^{k+1}(x^+_k), k = 1, \ldots N-1 \qquad (8)$$

4. Optimal functions of the magnetic field $B(x)$ strength and p-type material inhomogeneity $C(x)$ satisfy the conditions

$$H^k_n(\varphi(x), T(x), q(x), B(x), j, n) = \max_{B \in G_B} H^k_n(\varphi(x), T(x), q(x), B, j, n) \qquad (9)$$

$$H^k_p(j(x), T(x), q(x), C(x), j) = \max_{C \in G_C} H^k_p(j(x), T(x), q(x), C, j). \qquad (10)$$

Based on equations (1)-(10) the program for low-temperature Peltier coolers designing under optimal legs inhomogeneity at optimal magnetic field has been elaborated. The designing result of this program is determination of optimal agreed functions of the magnetic field and the material inhomogeneities in each stage and their use for calculation of magneto-thermoelectric Peltier coolers with the best characteristics.

Discussion of results

Calculations for low-temperature coolers optimized for temperature values in the range of 130-90K at T_h=160K were done by the computer designing methods. Experimental dependences of *Bi-Sb* n-type material properties on temperature, percentage composition of *Sb* and the magnetic field strength that result to material figure of merit dependences shown in Fig.1 have been used for calculations. Experimental dependences α, σ, κ on temperature for different starting electric conductivity σ^0_p (measured at 300K) proportional to charge carrier concentration and characterizes the material inhomogeneity have been used for p-type material based on *Bi-Te*. These dependences were taken from [11].

The results of the optimal control problem solution are given in Fig.3, 4. Each variant of cooler corresponds to its own variant of material optimal inhomogeneity combination with composition and nonuniformity of n-material magnetic field.

Fig.3 gives the examples of optimal functions of

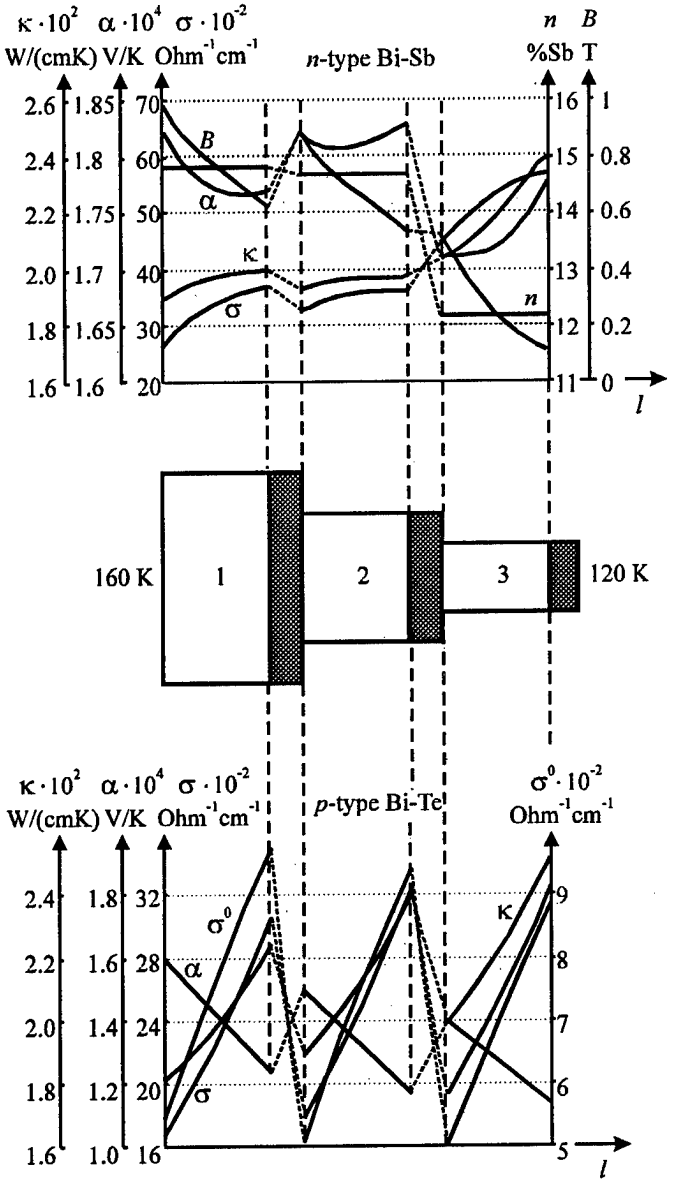


Figure 3: Optimal functions of material inhomogeneity σ^0_p, magnetic field B, composition n and the corresponding dependences of the material parameters for a 3-stage cooler.

inhomogeneities and the corresponding dependences of thermoelectric material characteristics received by the computer designing method for a three-stage cooler at the temperature difference 40K.

Fig.4 demonstrated the effect of such functions on the energy efficiency of cooling. Here two dependences are given for comparison. Dependence 1 was received previously in the work [8] and it shows the increase of the stage coolers coefficient of performance with the use of only an optimal function of the magnetic field strength nonuniformity in comparison with the best uniform variant. In that case *n*-material composition was the same for all stages with 12%*Sb* content, legs of *p*-type were of homogeneous material.

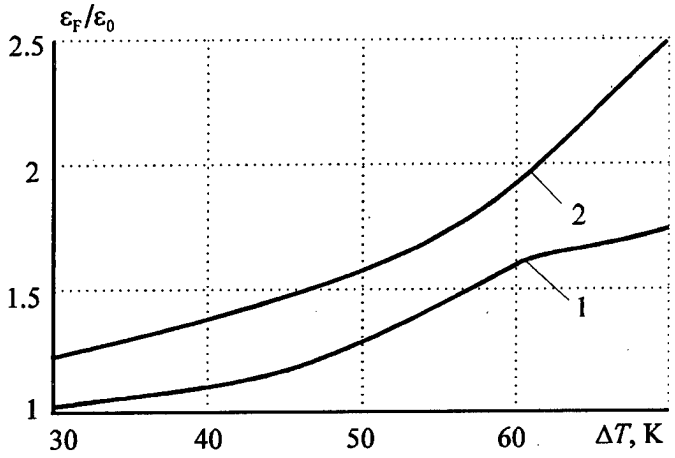


Figure 4: The coefficient of performance increase with the use of optimal functions ε_F in comparison with ε_0 for optimally homogeneous variant in coolers with different temperature difference. 1 - with consideration of optimal nonuniformity of the magnetic field; 2 - with consideration of optimal inhomogeneity of the material and the magnetic field nonuniformity.

Dependence 2 demonstrates the increase of the coefficient of performance caused by the agreed effect on the thermoelectric material of two functions, there are optimal inhomogeneity of *p*-type legs and optimal nonuniformity of the magnetic field in conjunction with optimal composition for *n*-type legs. As one can see the coefficient of performance with accounting for these effects can be increases by a factor of 2-2.5 in comparison with the variant of the optimally uniform magnetic field use and legs from optimally homogeneous materials for all stages. The comparison of 1 and 2 dependences shows that the coefficient of performance of low-temperature coolers due to simultaneous effect on the material of these two functions increases additionally by a factor of 1.5-2. It is very essential for low-temperature cooling.

References

[1] Anatychuk L.I., Semenjuk V.A. Optimal control by the Thermoelectric Material and Devices Properties. Chernivtsi, Prut, 1992, 264 p.

[2] Anatychuk L.I., Vikhor L.N., Kuznetsov A.V., Letiuchenko S.D. Functional-Gradient Materials for Thermoelectric Energy Converters, in Proceedings of the XIV International Conference on Thermoelectrics, St-Petersburg, Russia, June 27-30, 1995, p.7-9.

[3] Anatychuk L.I., Vikhor L.N. Computer design of thermoelectric functionally graded materials, in Proceedings of the Fourth International Symposium on FGM, Tsukuba, Japan, Oct. 21-24, 1996.

[4] Vikhor L.N. Optimal functions as a new step of the thermoelectricity development, J. of Thermoelectricity, N4, 1996, p.29-37.

[5] Ure Roland W.G. Theory of materials for thermoelectric and thermomagnetic devices, Proc.IEEE, 1963, v.51, N5, p.699-713.

[6] Anatychuk L.I., Vikhor L.N. Ivanov G.A. The Optimal Control Theory for Thermoelectric Cooler Design, in Proceedings of the Twelfth International Conference on Thermoelectrics, Japan, Nov., p.412-415.

[7] Anatychuk L.I., Vikhor L.N. Study on Cooler Design in Magnetic Field for Low Temperature Cascades, in Proceedings of the XIII International Conference on Thermoelectrics, Cansas, Aug.,1994.

[8] Anatychuk L.I., Vikhor L.N. Optimal functions of magnetic field for the Peltier coolers, in Proceedings of the XIV International Conference on Thermoelectrics, St-Petersburg, Russia, June 27-30, 1995, p.461-463.

[9] L.I.Anatychuk, O.J.Luste, L.N.Vikhor. Optimal Functions as an Effective Method for Thermoelectric Devices Design, in Proceedings of the 15 International Conference on Thermoelectrics, Pasadena,CA USA, March 26-29, 1996, p.223-226.

[10] Pontryagin L.S., Boltyansky V.G., Gamkrelidse R.V., Mischenko E.F. Mathematical Theory of Optimal Processes, Nauka, 1976, p.392.

[11] Vayner A.L. Thermoelectric Coolers, Moscow, 1983, p.176.

Thermoelectric tensor and figure of merit for a composite medium: some exact bounds

David J. Bergman
School of Physics and Astronomy, Raymond and Beverly Sackler Faculty of Exact Sciences
Tel Aviv University, Tel Aviv 69978 Israel

Abstract

Thermoelectric transport in a macroscopically heterogeneous or composite medium is considered for the most general case of n anisotropic components mixed together with an arbitrary microstructure (i.e., not necessarily disordered or isotropic or cubic, so that the macroscopic behavior can be anisotropic too). A figure-of-merit-tensor (FMT) is defined that generalizes the usual scalar figure of merit. Some general bounds are derived for the bulk effective electrical conductivity and heat conductivity tensors, and also for the FMT. In particular, it is proven that the figure of merit of any composite can never be greater than the largest figure of merit of any of its components.

Thermoelectricity is a particularly important example of a transport phenomenon involving coupled, curl free vector fields, and conserved (i.e., divergence free) fluxes. A succinct form for the equations that describe this phenomenon follows [1]:

$$J = \hat{Q}E, \tag{1}$$

$$E \equiv \begin{pmatrix} \mathbf{E}_1 \\ \mathbf{E}_2 \end{pmatrix} \equiv \begin{pmatrix} \nabla\psi_1 \\ \nabla\psi_2 \end{pmatrix} \equiv \begin{pmatrix} e\nabla\phi \\ k_B\nabla T \end{pmatrix}; \quad \nabla\times\mathbf{E}_1 = \nabla\times\mathbf{E}_2 = 0; \tag{2}$$

$$J \equiv \begin{pmatrix} \mathbf{J}_1 \\ \mathbf{J}_2 \end{pmatrix} \equiv \begin{pmatrix} -\mathbf{J}_E/e \\ -\mathbf{J}_S/k_B \end{pmatrix}; \quad \nabla\cdot\mathbf{J}_1 = \nabla\cdot\mathbf{J}_2 = 0; \tag{3}$$

$$\hat{Q} \equiv \begin{pmatrix} \hat{Q}_{11} & \hat{Q}_{12} \\ \hat{Q}_{12}^t & \hat{Q}_{22} \end{pmatrix} = \begin{pmatrix} \hat{\sigma}/e^2 & \hat{\sigma}\hat{\alpha}/ek_B \\ \hat{\alpha}\hat{\sigma}/ek_B & \hat{\gamma}/k_B^2T \end{pmatrix}. \tag{4}$$

Here $\mathbf{J}_E$ is the electric charge flux, $\mathbf{J}_S$ is the entropy flux, ϕ is the electric potential, T is the local temperature, $\hat{\sigma}$ is the electrical conductivity tensor at uniform T, $\hat{\gamma}$ is the heat conductivity tensor at uniform ϕ, $\hat{\alpha}$ is the tensor of thermoelectric coefficients or absolute thermopower, i.e., when the electric charge flux vanishes $\mathbf{J}_E = 0$, then the relation between electric field $-\nabla\phi$ and temperature gradient ∇T is

$$-\nabla\phi = \hat{\alpha}\nabla T, \tag{5}$$

e is the atomic unit of electric charge, and k_B is Boltzmann's constant. Note that these definitions imply that ψ has units of energy, while J has units of particle flux.

Restricting ourselves in this and in the following paragraph to isotropic media, where $\hat{\sigma}$, $\hat{\gamma}$, $\hat{\alpha}$ are all scalar tensors, the thermoelectric figures of merit ZT and Δ are defined by [2,1]

$$ZT \equiv \left(\frac{\gamma}{T\sigma\alpha^2} - 1\right)^{-1} = \frac{Q_{12}^2}{\det\hat{Q}} = \frac{\Delta}{1-\Delta}, \tag{6}$$

where

$$\Delta \equiv \frac{T\sigma\alpha^2}{\gamma} = \frac{Q_{12}^2}{Q_{11}Q_{22}} = \frac{ZT}{ZT+1}. \tag{7}$$

From the requirement, due to the second law of thermodynamics and to invariance under time reversal, that $\hat{Q}$ be a real, non-negative, symmetric matrix, the following equivalent inequalities must be satisfied

$$0 \le ZT < \infty; \quad 0 \le \Delta < 1. \tag{8}$$

For technological applications, large values of ZT or Δ are desirable, therefore it is of some interest to know whether it might be possible to increase these factors by macroscopically mixing together different thermoelectric materials, so as to form a heterogeneous or composite medium. For particular cases and models this was shown to be impossible. Those cases included isotropic n-component mixtures where all components satisfied $\Delta_i \ll 1, i = 1\ldots n$ [1]; isotropic two-component mixtures where Δ_1, Δ_2 could have any value between 0 and 1 [1]; some simple approximations, like Clausius-Mossotti and like Bruggeman's effective medium theory [1]; and a finite, three component, discrete network model, for which all possible configurations were checked [3].

Here we generalize those discussions as follows: For a general anisotropic thermoelectric medium a figure-of-merit-tensor (FMT) is defined. We then consider, alongside an actual composite thermoelectric, also a modified composite medium, with the same microstructure but with the thermoelectric coefficients artificially put to zero everywhere, and with a local electrical conductivity that is appropriate when the local entropy flux is made to vanish locally. In this way, we are able to derive some interesting bounds for the bulk effective conductivities of the actual composite, and also for the bulk effective FMT. In particular, we show that the bulk effective FMT is bounded from above by the largest eigenvalue of the

0-7803-4057-4/97 $10.00 ©1997 IEEE

component FMT's. The proof presented here is related to a mathematically similar problem that arises in connection with the electromechanical coupling tensor of a heterogeneous piezoelectric medium [4].

The FMT is denoted by $\hat{\Delta}$, and is defined so as to generalize the definition of the scalar figure of merit Δ in (7):

$$\hat{\Delta} \equiv \hat{Q}_{11}^{-1/2}\hat{Q}_{12}\hat{Q}_{22}^{-1}\hat{Q}_{12}^{t}\hat{Q}_{11}^{-1/2}. \tag{9}$$

With the help of this non-negative, symmetric matrix we can rewrite (1) by using $\mathbf{E}_1$, $\mathbf{J}_2$ instead of $\mathbf{E}_1$, $\mathbf{E}_2$, as independent fields:

$$\begin{pmatrix} \mathbf{J}_1 \\ \mathbf{E}_2 \end{pmatrix} = \begin{pmatrix} \hat{Q}_{11}^{1/2}(1-\hat{\Delta})\hat{Q}_{11}^{1/2} & \hat{Q}_{12}\hat{Q}_{22}^{-1} \\ -\hat{Q}_{22}^{-1}\hat{Q}_{12}^{t} & \hat{Q}_{22}^{-1} \end{pmatrix} \begin{pmatrix} \mathbf{E}_1 \\ \mathbf{J}_2 \end{pmatrix}. \tag{10}$$

The local rate of dissipation per unit volume is given by

$$\begin{aligned} W &= \mathbf{E}_1 \cdot \mathbf{J}_1 + \mathbf{E}_2 \cdot \mathbf{J}_2 \\ &= \mathbf{E}_1 \cdot \hat{Q}_{11} \cdot \mathbf{E}_1 \; + \; 2\mathbf{E}_1 \cdot \hat{Q}_{12} \cdot \mathbf{E}_2 \; + \; \mathbf{E}_2 \cdot \hat{Q}_{22} \cdot \mathbf{E}_2 \end{aligned} \tag{11}$$

$$= \mathbf{E}_1 \cdot \hat{Q}_{11}^{1/2}(1-\hat{\Delta})\hat{Q}_{11}^{1/2} \cdot \mathbf{E}_1 \; + \; \mathbf{J}_2 \cdot \hat{Q}_{22}^{-1} \cdot \mathbf{J}_2. \tag{12}$$

From the last expression it follows that the FMT is also bounded from above, thus it satisfies

$$0 \leq \hat{\Delta} < 1, \tag{13}$$

i.e., all its eigenvalues are between 0 and 1. The absence of of cross terms in (12), i.e., terms that involve both $\mathbf{E}_1$ and $\mathbf{J}_2$, is due to the fact that the off-diagonal blocks of the matrix in (10) are antisymmetric.

The total rate of dissipation of the entire system per unit volume $\langle W \rangle$ can likewise be written in two different forms

$$\langle W \rangle = \langle \mathbf{E}_1 \cdot \hat{Q}_{11} \cdot \mathbf{E}_1 \; + \; 2\mathbf{E}_1 \cdot \hat{Q}_{12} \cdot \mathbf{E}_2 \; + \; \mathbf{E}_2 \cdot \hat{Q}_{22} \cdot \mathbf{E}_2 \rangle \tag{14}$$

$$= \langle \mathbf{E}_1 \cdot \hat{Q}_{11}^{1/2}(1-\hat{\Delta})\hat{Q}_{11}^{1/2} \cdot \mathbf{E}_1 \; + \; \mathbf{J}_2 \cdot \hat{Q}_{22}^{-1} \cdot \mathbf{J}_2 \rangle, \tag{15}$$

where $\langle\ \rangle$ denotes a volume average. The first of these forms (14) is a functional of ψ_1, ψ_2 that attains its minimum value when ψ_1, ψ_2 assume their correct physical values at every point in the system [1]. That minimum value can also be written in two forms, using the appropriate blocks $\hat{Q}_{eij}$ [see (4)] of the matrix of bulk effective transport coefficients $\hat{Q}_e$

$$\begin{aligned} \langle W \rangle_{\min} &= \langle \mathbf{E}_1 \rangle \cdot \hat{Q}_{e11} \cdot \langle \mathbf{E}_1 \rangle \; + \; 2\langle \mathbf{E}_1 \rangle \cdot \hat{Q}_{e12} \cdot \langle \mathbf{E}_2 \rangle \\ &\quad + \langle \mathbf{E}_2 \rangle \cdot \hat{Q}_{e22} \cdot \langle \mathbf{E}_2 \rangle \end{aligned} \tag{16}$$

$$\begin{aligned} &= \langle \mathbf{E}_1 \rangle \cdot \hat{Q}_{e11}^{1/2}(1-\hat{\Delta}_e)\hat{Q}_{e11}^{1/2} \cdot \langle \mathbf{E}_1 \rangle \\ &\quad + \langle \mathbf{J}_2 \rangle \cdot \hat{Q}_{e22}^{-1} \cdot \langle \mathbf{J}_2 \rangle. \end{aligned} \tag{17}$$

The second expression was obtained by using the correct physical fields in the second form for $\langle W \rangle$ (15), even though those fields do not minimize that form, as will become clear from the subsequent discussion.

If we substitute $\mathbf{E}_1 = \nabla\psi_1$, $\mathbf{J}_2 = \nabla \times \mathbf{A}_2$ in (15), then we get a functional of ψ_1 and $\mathbf{A}_2$. It is not difficult to show that this functional is minimized when ψ_1, $\mathbf{A}_2$ are the solutions of the following equations

$$\begin{aligned} \nabla \cdot [\hat{Q}_{11}^{1/2}(1-\hat{\Delta})\hat{Q}_{11}^{1/2} \cdot \nabla\psi_1] = 0, \\ \langle \mathbf{E}_1 \rangle \equiv \langle \nabla\psi_1 \rangle = \text{given}, \end{aligned} \tag{18}$$

$$\begin{aligned} \nabla \times [\hat{Q}_{22}^{-1}(\nabla \times \mathbf{A}_2)] = 0, \\ \langle \mathbf{J}_2 \rangle \equiv \langle \nabla \times \mathbf{A}_2 \rangle = \text{given}. \end{aligned} \tag{19}$$

These solutions differ from the physical fields found in the actual composite medium: They are the fields that would be present in a medium with a local electric conductivity tensor equal to $\hat{Q}_{11}^{1/2}(1-\hat{\Delta})\hat{Q}_{11}^{1/2}$, a local heat conductivity tensor equal to $\hat{Q}_{22}$, and a thermopower tensor equal to 0. In this artificial medium, the potential gradient and the temperature gradient are completely decoupled. The minimum value thus achieved for $\langle W \rangle$ is equal to

$$\begin{aligned} &\langle \mathbf{E}_1 \rangle \cdot \hat{F}_e[\hat{Q}_{11}^{1/2}(1-\hat{\Delta})\hat{Q}_{11}^{1/2}] \cdot \langle \mathbf{E}_1 \rangle \\ &\quad + \langle \mathbf{J}_2 \rangle \cdot \frac{1}{\hat{F}_e[\hat{Q}_{22}]} \cdot \langle \mathbf{J}_2 \rangle, \end{aligned} \tag{20}$$

where $\hat{F}_e[\hat{\sigma}]$ is the bulk effective conductivity tensor of a simple conductivity problem, without any coupled fields, in a composite medium with local conductivity tensor $\hat{\sigma}$. We are assuming here that the composite medium has a microstructure that is macroscopically uniform, and that macroscopically uniform boundary conditions on ψ_1 and $\mathbf{A}_2$ are used in order to enforce the given average values $\langle \mathbf{E}_1 \rangle$ and $\langle \mathbf{J}_2 \rangle$.

In general, when $\hat{\sigma}(\mathbf{r})$ can be an arbitrary function of $\mathbf{r}$, $\hat{F}_e[\hat{\sigma}]$ must be considered as an order 1 homogeneous and monotonic functional of $\hat{\sigma}$, namely

$$\hat{F}_e[\lambda\hat{\sigma}] = \lambda\hat{F}_e[\hat{\sigma}] \quad \text{for any constant } \lambda, \tag{21}$$

$$\hat{F}_e[\hat{\sigma}_1] \geq \hat{F}_e[\hat{\sigma}_2] \quad \text{if } \hat{\sigma}_1 \geq \hat{\sigma}_2 \geq 0 \text{ everywhere}. \tag{22}$$

These properties follow from the variational properties of (14). However, in the case of a composite medium made of n constituents, characterized by uniform conductivity tensors $\hat{\sigma}_i$, $\hat{F}_e[\hat{\sigma}]$ can be considered as a function only of all the $\hat{\sigma}_i$, with the precise form of this function depending on the microstructure [5]. Note also that (18) corresponds to an electrical conductivity problem where the local entropy flux has been set to zero everywhere, while (19) corresponds to a heat conductivity problem where the local electric field has been set to zero everywhere. The results of (17) and (20) are different, even

though they were both calculated from the same expression (15), because different local fields $\mathbf{E}_1$, $\mathbf{J}_2$ were used to obtain them: The local fields used to obtain (17) are obtained from the solution of (1)–(3), and are thus the correct physical fields in the actual composite medium. By contrast, the local fields used to obtain (20) are obtained from the solution of (18) and (19), and are therefore fields of the above described artificial problem. Note, however, that both sets of local fields have the same volume average values $\langle \mathbf{E}_1 \rangle$ and $\langle \mathbf{J}_2 \rangle$.

We now consider the correct physical fields $\mathbf{E}_1$, $\mathbf{J}_2$ as trial fields for the functional of ψ_1, $\mathbf{A}_2$ that was obtained from (15). This means that (17) is an upper bound on (20) for any given values of $\langle \mathbf{E}_1 \rangle$ and $\langle \mathbf{J}_2 \rangle$. This leads to the following inequalities

$$\hat{Q}_{e22} \leq \hat{F}_e[\hat{Q}_{22}], \tag{23}$$

$$\hat{Q}_{e11}^{1/2}(1-\hat{\Delta}_e)\hat{Q}_{e11}^{1/2} \geq \hat{F}_e[\hat{Q}_{11}^{1/2}(1-\hat{\Delta})\hat{Q}_{11}^{1/2}]. \tag{24}$$

Note that the lhs of (24) is the bulk effective conductivity tensor of the actual physical composite when we impose boundary conditions such that $\langle \mathbf{J}_2 \rangle = 0$. By contrast, the rhs of (24) is the bulk effective conductivity tensor that we would get for our composite medium if we forced the local flux $\mathbf{J}_2(\mathbf{r})$ to vanish everywhere. If, instead of using $\mathbf{E}_1$, $\mathbf{J}_2$ as independent fields, we use $\mathbf{E}_2$, $\mathbf{J}_1$ as the independent fields, then we get similar inequalities where the indices 1, 2 are switched. For example, instead of (23) we now get

$$\hat{Q}_{e11} \leq \hat{F}_e[\hat{Q}_{11}]. \tag{25}$$

Two interesting consequences already follow directly from these inequalities:

1. From (25) and (23) we conclude that, if we turn off the (thermoelectric) coupling between the two fields when solving for the local fields ψ_1, ψ_2, (another way to think of this is that we force the local field $\mathbf{E}_2(\mathbf{r})$ to vanish everywhere when calculating ψ_1, and force $\mathbf{E}_1(\mathbf{r})$ to vanish everywhere when calculating ψ_2) then the bulk effective electrical and heat conductivity tensors which we get are, in fact, upper bounds on the correct values of the two tensors $\hat{\sigma}_e = e^2\hat{Q}_{e11}$ and $\hat{\gamma}_e = k_B^2 T\hat{Q}_{e22}$.

2. The meaning of (24) is that the bulk effective electrical conductivity tensor at *zero average entropy flux* $\langle \mathbf{J}_S \rangle = 0$, namely $e^2\hat{Q}_{e11}^{1/2}(1-\hat{\Delta}_e)\hat{Q}_{e11}^{1/2}$, is bounded from below by the bulk effective electrical conductivity tensor that we would get if we artificially made the local entropy flux vanish everywhere $\mathbf{J}_S(\mathbf{r}) \equiv 0$. Obviously, a similar statement holds for the bulk effective heat conductivity tensor at zero electric charge flux.

In order to obtain our third result, concerning an upper bound on the bulk effective FMT, we now use the above derived inequalities, together with (21) and (22), in order to produce the following chain of inequalities:

$$\begin{aligned}
&\hat{Q}_{e11}(1-\max_{i\alpha}\Delta_{i\alpha}) \leq \hat{F}_e[\hat{Q}_{11}](1-\max_{i\alpha}\Delta_{i\alpha}) \\
&= \hat{F}_e[\hat{Q}_{11}(1-\max_{i\alpha}\Delta_{i\alpha})] \leq \hat{F}_e[\hat{Q}_{11}^{1/2}(1-\hat{\Delta})\hat{Q}_{11}^{1/2}] \\
&\leq \hat{Q}_{e11}^{1/2}(1-\hat{\Delta}_e)\hat{Q}_{e11}^{1/2},
\end{aligned} \tag{26}$$

where $\Delta_{i\alpha}$, $i = 1 \ldots n$, $\alpha = 1,2,3$ are the eigenvalues of $\hat{\Delta}$ in the different components. From this it follows that

$$\hat{\Delta}_e \leq \max_{i\alpha}\Delta_{i\alpha}, \tag{27}$$

i.e., $\max_{i\alpha}\Delta_{i\alpha}$ is an upper bound on the eigenvalues of $\hat{\Delta}_e$.

In summary, we have shown that by mixing together macroscopically a number of different thermoelectric components, the figure of merit can never be enhanced to a value greater than the largest among the various component values. However, the figure of merit can definitely be degraded by making such a mixture, making it even smaller than the smallest among the various component values. In particular, by choosing an appropriate microstructure for a two component composite where the thermopower has opposite signs in the two components, it is possible to synthesize a composite medium that has zero thermopower, and hence also a zero figure of merit [1]

It is a pleasure to acknowledge a very useful conversation with and a critical reading of this manuscript by O. Levy. This research was supported, in part, by grants from the US-Israel Binational Science Foundation and the Israel Science Foundation.

---

[1] D. J. Bergman and O. Levy, J. Appl. Phys. **70**, 6821 (1991).

[2] T. C. Harman and J. M. Honig, *Thermoelectric and Thermomagnetic Effects and Applications*, (McGraw-Hill, New York, 1967).

[3] D. J. Bergman and O. Levy, MRS Symposium Proc. **234**, 39 (1991).

[4] M. Avellaneda and T. Olson, J. Intelligent Material Systems and Structures **4**, 82 (1993).

[5] D. J. Bergman and D. Stroud, Solid State Physics **45**, 147 (1992).

Thermoelectric properties of Bi and Bi_2Te_3 composites

Tito E. Huber* and Ricky Calcao

Polytechnic University, Brooklyn, New York 11201, USA
Tel.:(718)260-3294, Fax:(718)260-3139/3136, E-mail:thuber@photon.poly.edu

Abstract

It has been suggested that microengineering traditional thermoelectric materials into composites may lead to a significant improvement in their thermoelectric performance because of the reduction of phonon thermal conductivity from phonon scattering at the grain boundaries and interfaces. At the fundamental level the composite figure of merit ZT may be dramatically increased over that for bulk because of the increase of the electronic density of states that occur in low dimensionality systems. One approach for the fabrication of nanostructured materials is the utilization of nanochannel insulators as a matrix for the synthesis of dense composites using high pressure injection (HPI) of the semiconductor melt. We will discuss the synthesis and structural properties of oriented Bi_2Te_3 nanowire arrays in Anorore porous alumina as well as random networks of Bi_2Te_3 nanocrystals. The trigonal Bi_2Te_3 crystallites that form the wire are oriented with the basal plane of the hexagonal plane, i.e., the plane of highest conductivity, along the wire length. Bi wire arrays are similarly oriented. This structural effect is directly a result of the processing using the HPI technique. Another implication of our results is that wire arrays have a higher figure of merit than random networks.

Introduction

The area of thermoelectrics is one of opportunity for technical innovation. Thermoelectric cooler and generator performance has stagnated for the past thirty years or so. An important factor limiting this technology has been the availability of appropriate thermoelectric materials. The suitability of a material for thermoelectric cooling applications is defined by the thermoelectric figure of merit $Z = S^2 \sigma/\kappa$, where S is the Seebeck coefficient, σ is the conductivity, and κ is the thermal conductivity.[1] Efforts to increase Z in conventional, bulk materials have been hampered by the interrelation between the three parameters which results in an adverse effect on the other two parameters when improvement on one of them is attempted. Currently the materials with the highest figure of merit at room temperature are Bismuth Telluride and related ternary alloys such as $Bi_2 Te_{2.7}Se_{0.3}$ and $Bi_{0.5} Sb_{1.5}Te_3$ having a thermoelectric figure of merit ZT that peaks at around 0.96.[1] At low temperatures, in the range between 77 K and 200 K, $Bi_{1-x}Sb_x$ with $x \sim 0.1$ has a thermoelectric figure of merit that peaks at around 0.2. A closely related property, the thermomagnetic figure of merit Z_MT, which measures the cooling and heating efficiency of a given material when aided by an external magnetic field, is 0.5 for both pure Bi and some of its alloys with Sb at 0.75 T.[2] The Seebeck coefficient of these alloys, as well as the magnetoresistance, increase with the length-to-width ratio in the presence of a magnetic field[3] indicating that the thermoelectric figure of merit in the presence of a magnetic field is very dependent on the structure of the composite.

Bi is a semimetal since the three conduction band minima at the L-points lie 40 meV lower than the single valence-band maximum at the T-point. Bi electron effective mass is very small and therefore quantum confinement energies are very high. It is believed that quantum confinement leads to a semimetal to semiconductor (SMSC) transition for material thickness around 30 nm.[4] This is another strong motivation for studying Bi nanocomposites since semiconductors have a high figure of merit.

The mechanical properties of sintered elements are generally superior to those of samples cut from melt-grown ingots. Here we discuss a route to the synthesis of materials which may result in improved thermal and electric properties. Our approach is to tailor the structure of the thermoelectric material on a micrometer and nanometer scale so that the combination of the relevant parameters result in an improved Z with respect to the bulk phase. The benefits, in both function and performance, from the development of synthetic systems with hierarchical structure is well known.[5] The interest in low dimensional thermoelectric materials has been stimulated by suggestions that one- and two-dimensional systems would give a greatly enhanced figure of merit.[6,7,8] Realization of this potential, which is limited by processing technology and cost, is facilitated by recent advances in nanocomposite fabrication and in related analytical tools such a scanning electron and atomic force microscopies. Interesting materials in the context of thermoelectricity are superlattices, which are reviewed elsewhere.[9] Here we emphasize recent work on wire arrays. This is a type of composite that is made by injecting porous materials with a conductor phase. By utilizing microchannel and nanochannel insulators as hosts or template structures, we benefit from a increasing momentum[10] in the technology of microporous dielectrics,[11,12] The channels in the host can be filled with the conducting phase by high pressure injection of its melt,[13] This results in an interconnected conducting phase with highly reproducible properties since it essentially copies the channel structure of the matrix. In this way we have prepared composites where the active conducting phase occupies a large volume fraction, up to 76 percent. By controlling the microstructure of the composite

0-7803-4057-4/97 $10.00 ©1997 IEEE

we can microengineer some of the material parameters relevant to thermoelectricity.

The plan of the paper is as follows. First we describe the material preparation technique. Then we examine the material properties relevant to thermoelectricity of two types of composites: nanocomposites of Bi_2Te_3 and microwire arrays of Bi.

Composite synthesis

The composite preparation technique utilized in this work makes use of porous insulators with a regular pore structure as host or template. The host channels are filled with the conducting phase by high-pressure injection of the melt. This template strategy has been employed to chemically synthesize semiconductor and metal nanoparticles in microporous dielectrics and in cavities of zeolites. In those cases the conducting phase occupies a volume fraction typically less than a few percent. Many practical applications, such as those requiring electrical transport, require dense nanocomposites with high connectivity of the conducting phase.

We have prepared dense thermoelectric composites by high pressure injection (HPI) of the conducting phase into insulating templates. An externally applied hydrostatic pressure is needed to overcome surface tension effects. The magnitude of the pressure required depends on the surface tension of the melt and its wetting properties and is inversely proportional to the channel diameter. Details of this composite preparation method have been described elsewhere.[14]

The injection technique produces a dense nanocomposite and insures the desired interconnectivity of the conducting phase. It also present advantages over chemical and electrochemical preparation routes[13] with respect to the composition and chemical purity of the composite. The range of composites which can be prepared by injection is limited by the sintering of the template which is the consolidation of the pore structure with loss of surface area that takes place at an elevated temperature. The sintering temperature of porous Vycor glass and alumina are 850 C and 900 C, respectively.[15] Microchannel glass of the type utilized for our Bi experiment sinters at 450 C.

Bi_2Te_3 nanocomposites

Two types of Bi_2Te_3 composites are examined in this paper, namely wire arrays of oriented crystallites and semiconductor random networks in porous silica. We have prepared arrays of 200 nm diameter wires of oriented bismuth telluride crystallites. The nanowires have been prepared by injection of commercial anodic alumina

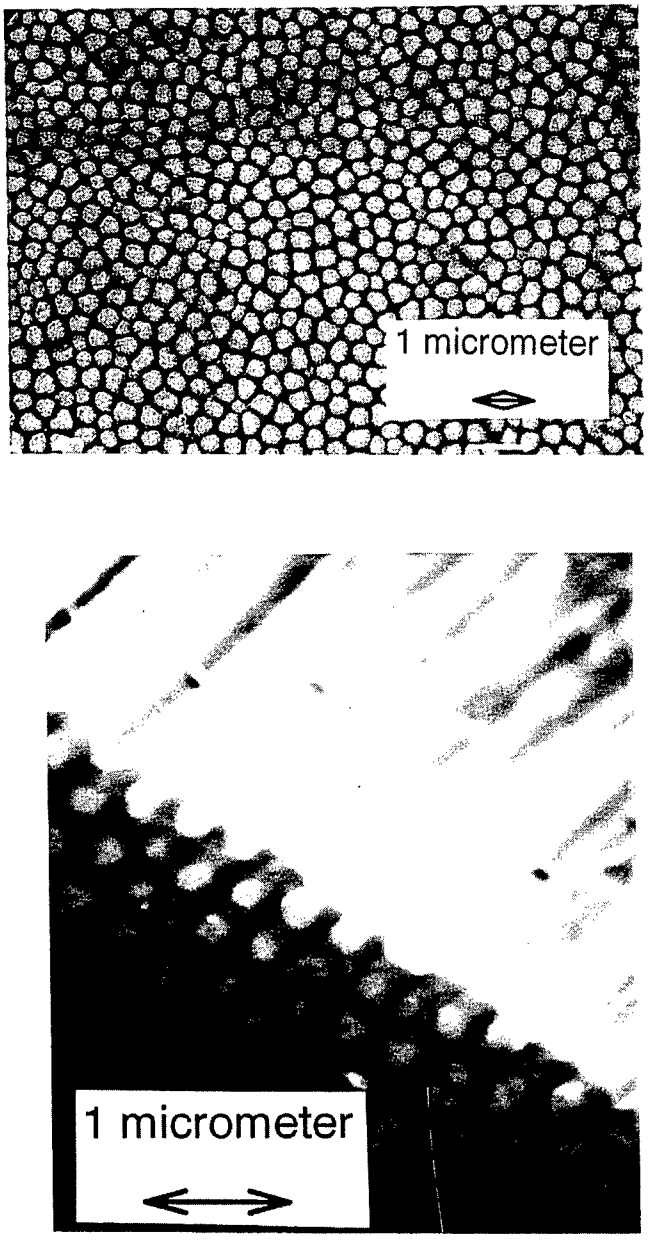


Fig. 1. Top and side views of an Bi_2Te_3 wire array composite prepared by pressure injection of the melt into an anodic alumina template. Dark corresponds to alumina.

templates[13] of about 50% porosity in the form of parallel, cylindrical channels. The anopore samples were injected with the Bi_2Te_3 melt at 700 C and 60,000 psi. Fig. 1 shows electron micrographs of the composite.

The nanowires grow with a preferred crystallographic orientation relative to their length. This is illustrated in Fig. 2 by the X-ray diffraction (XRD) spectra from bismuth telluride arrays. The spectrum is dominated by diffraction peaks from crystal planes parallel to the hexagonal c-axis. The trigonal bismuth telluride crystallites

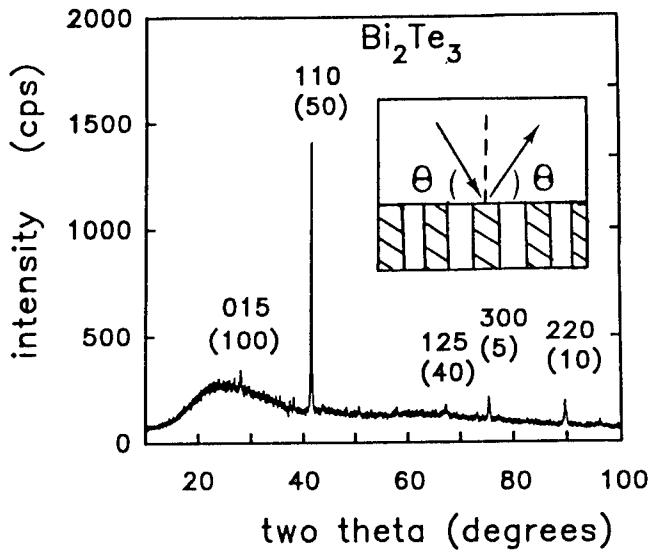


Fig. 2. X-Ray diffraction of an Bi_2Te_3 wire array composite. The inset shows the scattering geometry.

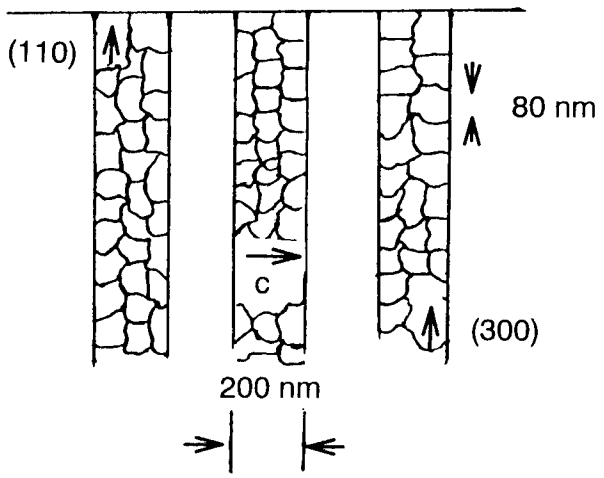


Fig. 3. Illustration of the crystalline structure of the Bi_2Te_3 wire array composite.

that form the wire are preferentially oriented with the basal plane of the hexagonal cell, i.e., the plane of highest conductivity, along the wire length (the c-axis perpendicular to the wire length). An estimate for the average semiconductor crystallite size D can be obtained from the widths of the XRD peaks through Scherrer's equation.[16] The value of D= 40 nm was determined from the width of the peak at $2\theta = 41.5°$ from the (110) plane, which is 0.24°. Figure 3 illustrates this condition. The preferential orientation of the crystallites in the nanowires is also exhibited by Te.[17] The orientation and size of the microcrystals forming the wires is determined during the nucleation process, where nuclei grow by adding single atoms to the growing cluster of atoms having the configuration of the solid. This may happen homogeneously somewhere in the volume of the melt or heterogeneously on the surface of the template. Since the surface area of the template is so large, the latter dominates. The existence of many nuclei may explain the small crystallite size. The reason that Bi_2Te_3 grows with the hexagonal c-axis perpendicular to the glass walls is that bismuth telluride tends to grow from the melt is such a way that the cleavage planes lie parallel to the growth direction.[18] This preferred crystallographic direction results from the significantly greater thermal conductivity and hence heat dissipation parallel to the c-plane.

We have also prepared and examined nanocomposites where the conducting phase is injected in porous Vycor glass. The Vycor glass used in this study has an average pore diameter of 5.6 nm as determined through nitrogen adsorption/desorption measurements. The interconnected porous network has a volume of roughly 32% of the total sample volume. The Bi_2Te_3 fills approximately 95% of the open volume. X-ray diffraction studies show that the Bi_2Te_3 retains its trigonal structure and the broadening of the X-ray peaks yields a characteristic indium crystallite size of roughly 30 nm, significantly larger than the pore size. This phenomenon has been recognized in other composites of metals in porous Vycor glass. [19] The Seebeck coefficient of the composite is decreased from the bulk. The Seebeck coefficient is strongly dependent on the concentration of donor and acceptor impurities. The impurities levels can change during processing and a similar phenomenon has been observed in powder metallurgy of bismuth telluride. Quantum effects are unlikely to play a role since our 5.6nm pore size is larger than the sizes for which quantum confinement effects would become significant for bismuth telluride.

Bi Composites

We measured the magneto-Seebeck coefficient of Bi wire arrays in the temperature range from 77 K to 300 K in magnetic fields of up to 1 Tesla. The material was prepared by the pressure injection method described in the previous sections using high purity 99.9999% Bi. The measurements were made in a cryostat that allowed the stabilization of

temperatures at any point between 77 K and 400 K. Each sample, typically 0.3mm x 0.3 mm in cross section and 3mm length, was soldered to copper end plates using Cerrolow low melting point solder through which electrical and thermal currents can be introduced. The electrical potentials and temperatures at the end plates were measured, allowing

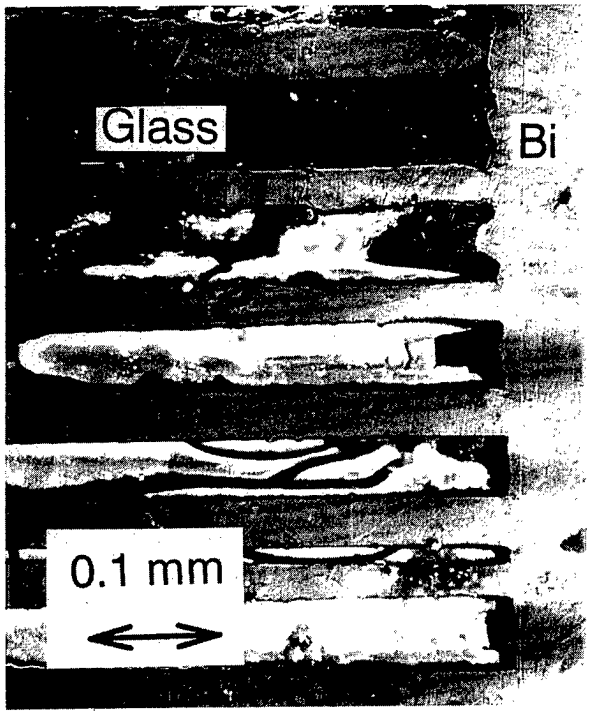


Fig. 4. Top view on the Bi microwire array.

the electrical and thermal conductivity, and the Seebeck coefficient, to be determined. It is important to realize that the overall length-to-width aspect ratio l/d is 10 for these samples. However, since the diameter of the wires in the composites is 0.05 mm, the wires aspect ratio is actually 60. For this sample we measured a Seebeck coefficient of -50μV. Gallo, Chandrasekhar, and Sutter measured the Seebeck coefficients for various orientations, and found then to be -50 μV and -70 μV for the current flow along and normal to the trigonal direction.[20] This confirms our expectation that the Bi microwires are oriented with the trigonal axis perpendicular to the wire length. This particular crystalline orientation of the wire crystallites is disadvantageous for thermoelectricity.

Conclusion

In this paper we have studied some thermoelectric effects of composite materials. The discussion has centered in off-the-shelf Bi_2Te_3. However, as we discussed in the introduction, it is well known that the figure of merit of this class of materials can be optimized by alloying with Sb_2Te_3 and Bi_2Se_3. Practical applications of composites would probably be based on these alloys. Our conclusions will likely apply to these compounds as well.

It is not difficult to show that the random network of B_2Te_3 has a low figure of merit. The large crystallite size of conductor in the pores means that the boundary scattering is small.[21] Since at room temperature the average phonon wavelength and mean free path are shorter than the pore diameter, the composite thermal conductivity is simply the sum of the contributions from the PVG matrix and the Bi_2Te_3 in the pores. Therefore, the composite thermal conductivity can be estimated from the expression $\kappa = (1-\phi)\,\kappa_{\text{Silica}} + \phi\,\kappa_{\text{Bismuth Telluride}}$. The result is shown in the table. The electrical conductivity of Bi_2Te_3 in PVG can be obtained from the empirical expression describing the conductivity of a porous system saturated with a conducting fluid,[22] $\sigma_c = \sigma_b\,\phi^m$, where σ_b is the conductivity of bulk Bi_2Te_3 and m is roughly 2. Accordingly, the electrical conductivity is depressed roughly one hundred-fold in the random

Table I. Thermoelectric properties of Bismuth Telluride composites

	bulk Bi_2Te_3 (1) (off-the shelf)	Bi_2Te_3- SiO_2 $\phi = 0.32$	Bi_2Te_3 in a wire array ($\phi = 0.5$)
S(μV/K)	230	164(2)	230
σ ($\Omega^{-1}.cm^{-1}$)	500	50	250
κ_L ($mW.cm^{-1}.K^{-1}$)	16	14	12.3
Z T (T = 300 K)	0.5	0.06	0.32

(1) Properties of the undoped material at 20 °C from Ref. 1.
(2) Measured.

composite. In order to estimate the properties ofwire arrays we have assumed that the matrix is glass, such as MCP's and the recently developed nanochannel glass. (In fact, we used Anopore in our experiments. Anopore is basically porous alumina and it has a higher thermal conductivity than glass). This allows comparison of the "geometrical" effects in the two composites. The table shows that random networks have a considerably lower figure of merit than the bulk material and wire arrays. The wire arrays suffer a 50% "geometrical" degradation in the figure of merit. This effect can be minimized using higher volume fraction matrices. For example, for MCP's, the decrease of the figure of merit is estimated to be only 25%.

It is known that sintered Bi_2Te_3 elements have superior mechanical properties to that of melt grown elements. However, the grains crystalline orientation is random. That means that the thermoelectric properties are an average over all orientations. As a result, the figure of merit is reduced. For n-type material the reduction amounts to about 20%. In contrast, in our method, the grains (crystallites) that form the wires are all properly alligned.

Quantum effects are not expected to be important for the large diameter wires studied here. The work presented here can be extended to very fine materials such as zeolites and nanochannel glasses for which the quantum effects are more relevant and may lead to an increase of the figure of merit.

This work is supported by the U.S. Army Research Office through Grant N0 DAAH04-95-1-0117 and U.S. National Science Foundation. The authors gratefully acknowledge the assistance of Carmen Huber, Ansil Dyal, and Daborah Chacko with sample preparation.

* Also at the Graduate School of Arts and Sciences, Howard University, Washington, DC .

References

1. H.J. Goldsmid in Electronic Refrigeration, 2nd edition (Pion Limited, London, 1986).
2. W.M. Yim and A. Amith, Solid-State Electronics 15 (1972) 1141.
3. M.E. Ertl, G.R. Pfister, and H.J. Goldsmid, Br.J. Appl. Phys. 14 (1963) 161.
4. C.A. Hoffman, J.R. Meyer, F.J. Bartoli, A. Di Venere, X.J. Yi, C.L. Hou, H.C. Wang, J.B. Ketterson, and C. K. Wong, Phys. Rev. B48, 11431 (1993).
5. Committee on Synthetic Hierarchical Structures, National Research Council, NMAB-464 (National Academic Press, Washington, D.C. 1994).
6. L.D. Hicks and M. Dresselhaus, Phys. Rev. B47 (1993) 12727.
7. L.D. Hicks, T.C. Harman, and M.S. Dresselhaus, Appl. Phys. Letters 63 (1993) 3230.
8. L.D. Hicks and M.S. Dresselhaus, Phys. Rev. B47 (1993) 16631.
9. T.L. Reineke and D.A. Broido, Phys. Rev. B51 (1995) 13797.
10. One indication of growing interest in the microporous templates is the large number of companies listed in the 1997 Physics Today Buyers's Guide under the classification of microchannel array plates.
11. R.J. Tonucci, B.L. Justus, A.J. Campillo, and C.E. Ford, Science 258 (1992) 783.
12. C.A. Huber, T.E. Huber, M. Sadoqi, J.A. Lubin, S. Manalis, and C.B. Prater, Science 263 (1994) 800.
13. Alternatively to pressure injection of the melt, electrochemical methods can be utilized to grow the conductive phase.
14. C.A. Huber and T.E. Huber, J. Appl. Phys. 64 (1988) 6588.
15. D. Chacko, C.Huber and T.E. Huber, to be published.
16. H.P. Plug and L.E. Alexander, X-Ray diffraction Procedures for Polycrystalline and Amorphous Materials, (J.W. Wiley and Sons, 2nd edition, New York, 1974).
17. C.A. Huber, M. Sadoqi, and T.E. Huber. Advanced Materials 7, (1995) 316.
18. F.D. Rosi, B. Abeles, and R.V. Jensen, J. Phys. Chem. Solids 10 (1959) 191.
19. W.H. Yang, T.E. Huber, J.A. Lubin, G.E. Walrafen, and C.A. Huber, Mat. Res. Symp. Proc. 286 (1993) 419.
20. G.F. Gallo, B.S. Chandrasehhar, and P.H. Sutter, J. Appl. Phys. 14 (1963) 161.
21. The thermal conductivity of porous glass is well known (M.P Zaitlin and A.C. Anderson, Phys. Rev. B12 (1975) 4475). At sufficiently low temperatures (T < 100 K) the voids in PVG scatter phonons. However, at room temperature this scattering is negligible and the thermal conductivity of porous glass is not different in magnitude and temperature dependence from that of silica glass, if the filling factor is taken into account.
22. M.J.Graf, T.E. Huber, and C.A. Huber, Phys. Rev. B45 (1992) 3133.

Thermoelectric Properties of Heterogeneous, Manyphase and Cosposite Materials

Yury Goryachev, Mykola Siman, Lyudmila Fiyalka, Ovsy Shvartsman

Institute for Material Problems of NAS of Ukraine, Krzhizhanovskogo Street 3, 252142, Kiev, Ukraine,
Tel.: (044) 444-23-71, Fax: (044) 444-20-78

Abstract

The model of formation of the thermoelectric properties of inhomogeneous matierials and the system classification of different structural classes and types of the materials are worked out. The analysis of the concentration dependences of thermoelectric properties is performed on the basis of the method. It is found that the thermoelectric properties of inhomogeneous materials are connected with their composition and internal structural characteristics (such as the coefficient of leakage, the leakage threshold, the contact potential difference and the coefficients of skeletonivity, matrixivity, chainivity).

The principal possibility of getting a higher thermoelectric figure of merit (TFM), Z, (in comparison with that of the initial material components) is shown. Such a possibility has been realized in the systems Bi_2Te_3 - C, $MnSi_{1,73}$ -CaF as well as in some composite materials, the most essential increase of the TFM being attained in cascade materials.

Introduction

The main aim of the work was to clear up the possibility of the TFM increase by means of formation of inhomogeneous (heterogeneous, manyphase and composite) structures. The method of the ivestigation is experimental-theoretic. The theoretic part consists of modelling and calculating kinetic properties (the electric and thermal conductivities) and potential ones (the thermoelectric power and elastic stress). The experimental part contains verifying the developed models on the systems of three kinds: metal - dielectric (MD), semiconductor - dielectric (SD), metal - semiconductor (MS).

The main regularities of formation of thermoelectric properties in complex objects like ceramics, composites and manyphase systems were investigated in many papers [1-3]. However, these works deal with the influence of some individual factors such as boundaries, the sample thickness, technological methods. As a rule, the authors did not aim at summarizing the data and their describing mathematically. Besides, the problem of getting high values of the TFM was not solved in these papers. Therefore the present study mainly deals with all these problems.

Theory

The analysis of the electric conductivity and thermoelectric power was perfomed on the basis of the developed physical model and electric scheme of inhomogeneous materials (Fig.1).

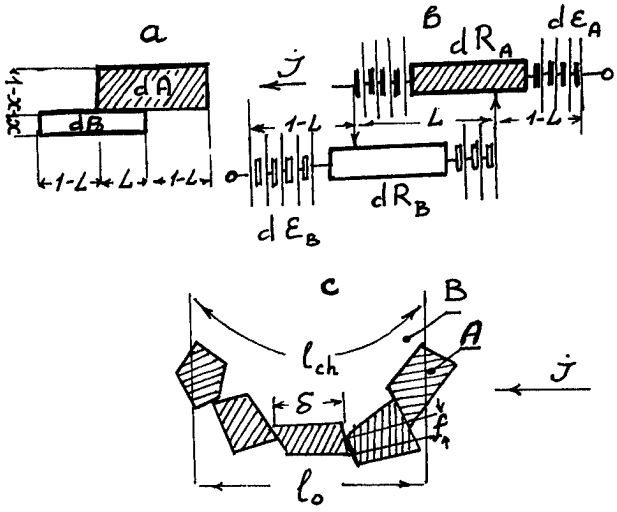


Fig.1: Physical model (a), electrical scheme (b) and fragment (c) of a disperse small volume of inhomogeneous material: A,B - low- and high-resistance material components, respectively; x - the volume fraction of the B -component; L - the fraction of a parallel electrotransfer; R_i and ε_i - the resistance and the thermoelectric power of the i-th component, respectively; δ - the average size of A - particles; f - the average size of the contact between A - particles; ℓ_0 - the leakage length along an electric field, ℓ_{ch} - the length of a chain of A - particles.

In the terms of the model the change of the material composition, $x = B/(A+B)$, leads to the following changes of the properties:

$$dR = dR_1 + dR_2 \qquad (1)$$

$$dR_1 = \mathrm{L}R^2\left(\frac{dR_A}{R_A^2} + \frac{dR_B}{R_B^2}\right) \qquad (2)$$

$$dR_2 = (1-\mathrm{L})(dR_A + dR_B) \qquad (3)$$

$$d\varepsilon = (1-\mathrm{L})(d\varepsilon_A + d\varepsilon_B) - \mathrm{L}d\varepsilon\frac{dR_A + dR_B}{dR} \qquad (4)$$

The analysis of these relations yields the two fundamental differential equations:

$$\begin{cases} \frac{d\rho}{dx} + \rho^2 L\left(\frac{1}{\rho_B} - \frac{1}{\rho_A}\right) + (1-L)\left(\frac{\rho_B}{x^2} - \frac{\rho_A}{(1-x)^2}\right) = 0 \quad (5) \\ \left(\frac{d\varepsilon}{dx}\right)\left(\frac{d\rho}{dx}\right) + L\frac{d\varepsilon}{dx}\left(\frac{\rho_A}{(1-x)^2} - \frac{\rho_B}{x^2}\right) + (1-L)\frac{d\rho}{dx}\left(\varepsilon_B - \varepsilon_A\right) = 0 \quad (6) \end{cases}$$

To solve the equations, the authors worked out the method of determing L as a function of numerous internal parameters. Among them the most essential are: the threshold, x_{th}, and coefficient, x_l , of the leakage; the coefficients of skeletonivity, x_{sk}, matrixivity, x_m, chainivity, x_{ch}, and the contact potential difference, φ_{ε}.

$x_l = l_0/l_{ch}$; $x_{sk} = f/\delta$; $x_{ch} = \left(l_{ch} - \delta\right)/l_0$ (the components of these expressions are shown in Fig.1(c)).

These parameters are used partly as fitting ones, partly as model factors.

To perform a generalized and comparative analysis, the whole set of inhomogeneous materials was divided into 4 structural classes (with 16 structural types) (Fig.2).

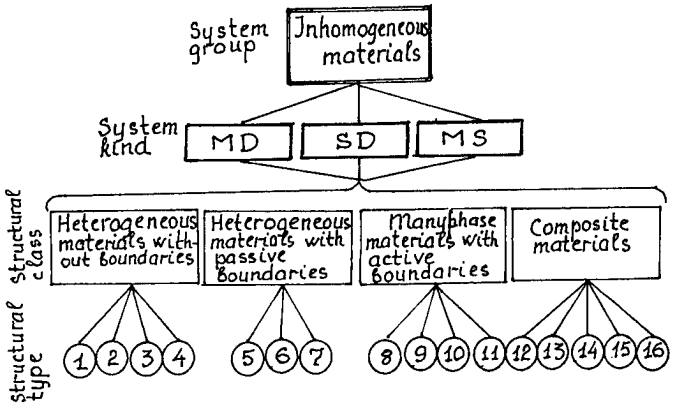


Fig.2. Classification of inhomogeneous materials:
1- Liquid materials (like emulsion), 2- Amorphous materials (like glass ceramics), 3 - Deeply doped materials, 4 - Partly amorphized materials, 5 - Materials with a small contact potential difference, 6 - Materials with the same carriers sign components, 7 - Thermodynamically equilibrium materials, 8 - Materials with porous boundaries, 9 - Materials with reactive boundaries, 10 - Materials with barrier boundaries, 11 - Materials with p - n and other junctions, 12 - Materials with governable shape of the particles, 13 - Materials with governable matrix - and skeletonivity, 14 - Fibre materials, 15 - Layer materials, 16 - Cascade materials.

Main results

The exact solution of the equations (5) and (6) can be only found in some simple cases. For example, in the simplest case (realized in the structures 14 and 15 in an electric field directed along the layers) the situation schemarically shown in Fig. 3 (a) takes place.

When an electric field is directed across the layers and in all the cases of the structural classes I and II the analogous schematic representation of the situation is given in Fig.3(b).

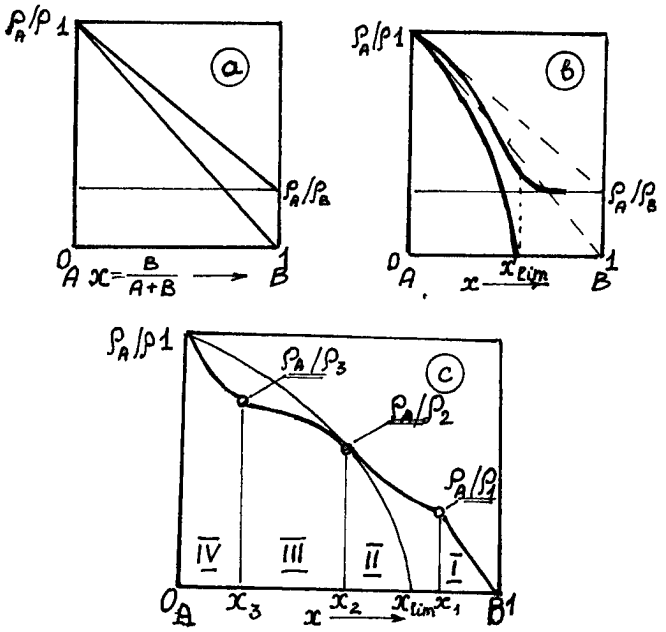


Fig.3. Concentration dependences of the inhomogeneous material conductivity with different values L: (a) - L=1; (b) - L=1 - x_{lim}; (c) L is changeable depending on x_i and ρ_A/ρ_i

Here x_{lim} - the limited content of the A-phase (in this case in the average there are no direct contacts between the particles of the B-phase). x_{lim} = 0,33 for sphera - shaped particles; x_{lim} = 0,50 for polyhedron-shaped particles and $x_{lim} > 0{,}7$ for needle - shaped particles (structural type 12).

In this cases:

$$\frac{\rho_A}{\rho} = 1 - \left(1 - \frac{\rho_A}{\rho_{\lim}}\right)x - \left(\frac{x}{x_{\lim}}\right)^2\left(1 - \frac{\rho_A}{\rho_B}\left(1 - \frac{\rho_A}{\rho_B}\right)x_{\lim}\right) \quad (7)$$

After similar considerating contact and by-passing phenomena in other structural classes and types the results given in the summarizing Table 1 were obtain.

It is seen that the dependence of an inhomogeneous material conductivity on structural characteristics is linear or quadratic. This is one of the main particularities of the developed model. In real conditions these dependences are probabilitive and can be described by means of exponential and hyperbolic functions. As for linear and quadratic approximations, they can only be used in a narrow range of changing the examined characteristics. They are quite suitable for the concentration regions I - IV (see Fig. 3(c)).

Table I

Connection of an ingomogeneous material conductivity with different factors of the structure

Structural class (and type)	Influencing factors	Dependence ρ_A/ρ on the factors
I (1,2)	x, x_{lim}	$\sim(a+bx+cx^2)$
II (5,6,7)		$\sim(d+l/x_{lim}+f/x_{lim}^2)$
III(8,9,10)	x_{ch}, x_l	$\sim x_{ch}$
IV(12,13,14,15)		$\sim x_{lim}$
I (3,4)	x	$\sim(1-x)$
III(8.9.10.11)	φ_c	$\sim(g/(h+\varphi_c+\varphi_c^2))$
IV(12,13,14,15)	x_m, x_{sk}	$\sim(1-x_m)$; $\sim x_{sk}$

When the ratio of the B-phase content to that of A-phase is widely changes, the change of the structural type occurs. As a rule, the material conductivity changes according to Fig. 3(c). Here Region I is the solid solution on the basis of the B-phase and corresponds to the structural types 2 and 3. Region II is a region with separated parts of the A-phase (in the form of particles, broken chains and islands); it corresponds to type 13 and partly overlaps the structural classes II and III. Region III is a region with direct or inderect (through surface thin layers) contacts of the small parts of the A-phase; it corresponds to the structural types 5,9,10. Region IV is a region of the maximum content of the A-phase with contacts through barrier layers, pores, inclusions and the like; it corresponds to the types 8,10,11.

The factor L changes broadly (from 0 to 1) in the investigated region of x-change. As a rule, it decreases with increasing a number of a structural type.

The application of the analysis to the thermoelectric power and the TFM is much more difficult because these values depend on more numerous factors. In the simplest case the following relations can be derived:

$$\frac{\varepsilon}{\varepsilon_A}=\left(1+\left(\frac{\varepsilon_B}{\varepsilon_A}\right)\left(\frac{\rho_A}{\rho_B}\right)\left(\frac{x}{1-x}\right)\right)^{2/3}; \qquad (8)$$

$$\frac{Z}{Z_A}=\left(\frac{\varepsilon}{\varepsilon_A}\right)^2\left(\frac{\rho_A}{\rho_B}\right)\left(\frac{\lambda_A}{\lambda}\right), \qquad (9)$$

$$\text{here } \frac{\rho_A}{\rho}=1-x; \quad \frac{\lambda}{\lambda_A}=\begin{cases}(1-x), & \text{for } x \ll x_p;\\ \left(1-x+\dfrac{\lambda_B}{\lambda_A}\right), & \text{for } x \gg x_p;\end{cases}$$

$x_p=\lambda_{pB}/\lambda_A$; λ_A, λ_{pB}- the thermal conductivity of the A-phase and the phonon component of the B-phase thermal conductivity.

The corresponding concentration dependences are given in Fig.4.

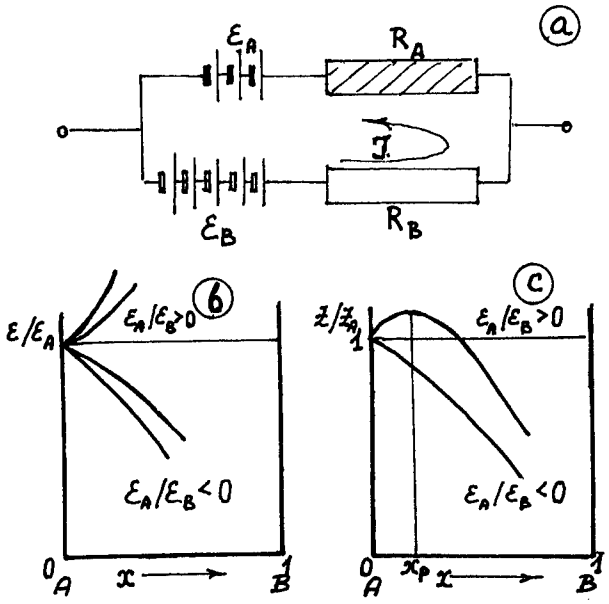


Fig. 4: Electrical scheme (a) and concentration dependences of the thermoelectric power (b) and the TFM (c) of inhomogeneous layer materials (for L=1)

On the basis of the performed experimental investigations some particularities of electrophysical and thermoelectric properties were determind in the main system kinds of inhomogeneous materials, MD, MS and SD. In the first kind there are wide regions of metallike conductivity with a sharp passage into a high-resistance state. In the second kind there is a wide region of metallic conductivity with a less sharp passage into a semiconductor state. In the third kind a semiconductor conductivity is observed with a smooth passage into a high-resistance state.

The inhomogeneous materials of the classes III andIV and the types 9,12 and 16 are the most perspective for receiving effective thermoelectric materials, the system types containing semiconducting phases being the most favourable.

The same sign of the majority carriers in the component phases is a nessesary condition to rise the TFM in an inhomogeneous material. A large value $(\mathcal{E}_B/\mathcal{E}_A)(\rho_A/\rho_B)$ and a small value of the thermal conductivity of the A-phase are also important conditions to increase the TFM. Cascade materials are the most perspective, especially materials with a smooth change of the cascade composition.

Some examples of effective inhomogeneous materials are given in Table 2.

The data demonstrate a real possiibility of rising the effectiveness of thermoelectric materials by means of formation them as inhomogeneous structures.

Table 2

Examples of effective composite thermoelectric materials

System	Class and type	Dominating factor (DF)	Optimum value of theDF	Mechanism and the indicator of effectiveness
Bi_2Te_3 - C	III -9	x x_p	0,03 0,01	Reduction of the oxide film $\Delta z / z_0 \simeq 0,1$
$MnSi_{1,73}$ - CaF	III - 9	x	0,05	Dissolution of the oxide film $\Delta z / z_0 \simeq 0,2$
Pr_6O_{11} - B_2O_3	III- 12	x x_{lim}	0,01 $\geqslant 0,7$	Dissociation of the oxide film $\Delta z / z_0 \simeq 0,3$
Bi_2Te_3 - CuSe - $MnSi_{1,73}$ -$CrSi_2$	IV- 16	l_i / l	$l_i = 0,25$	Optimization of Z_i ; Increase ΔT $\Delta\eta / \eta \simeq 2...5$

Here Z_0, ΔZ - the initial value and increase of the TFM, l_i - the height of the i-th cascade, η - the efficiency

Conclusions

The worked-out system classification of inhomogeneous thermoelectric materials and the generalized model for theoretic describing their properties permit to predict the possibility of increasing the material effectiveness by means of formation of manyphase and composite structures.

Inhomogeneous materials of the structural classes III and IV (types 9,11,13) are the most perspective, especially those containing semiconductor component or having a cascade structure with a smooth change of the cascade compositions.

The same sign of majority carries in the material components is a nessesary condition to increase the TFM.

References

[1] C.Himita, F.Provst, O.Gverdin and oth. "Electric properties of grain boundaries in ceramic components for thermoelectronics", Ann.Chin,16, #4 -6, (1991) 453.

[2] Ю.Горячев, В.Дехтерук, Е.Шварцман, Л.Фиялко. "Электронное строение и свойства композитов типа оксид-карбид". Сб. Теория и моделирование электронного строения и свойства тугоплавких соединений", ИПМ НАНУ (1997),44.

[3] Ю.Горячев,В.Черногоренко,Л.Фиялко. "Электронные параметры и термодинамика синтеза диоксид-оксидных керамик". Порошковая мет., Киев, 10,(1997) 183.

On the theory of thermopower in random two-component semiconductor systems

I.I.Fishchuk
Institute for Nuclear research, 47, pr.Nauki, Kiev , 252022, Ukraine
Fax:+380/44/2654463, E-mail: interdep@kinr.kiev.ua

Abstract

The previous theoretical results for the effective thermopower α_e in random two-component systems are extended and analyzed using the effective-medium theory. It is shown that in almost all cases of metallic and both degenerate and nondegenerate semiconductor components we can calculate independently the effective electrical conductivity σ_e and thermal conductivity χ_e, which determinate the value α_e in these systems.

Introduction

Theoretical studies of thermoelectric phenomena in inhomogeneous solids have been carried out in many papers. For example, the authors of [1] have used the effective-medium theory (EMT) and computer simulation for investigation of the thermopower in inhomogeneous systems. The exact formulae for thermopower in random two-component solids was obtained in [2]. In papers [3, 4] the general theory for thermoelectric properties was developed in a composite medium. The results of [3, 4] were analyzed in [5].
In this paper, we investigate the thermopower in random two-component systems by extending the results and methods of [2 *to* 5]. We find the conditions when these results are valid.

Theory

We consider a solid sample with random macroscopic inhomogeneities. The average size of separate inhomogeneities is much larger than the electron mean free path and much smaller than the sample size. In this case, local values of kinetic coefficients may be introduced. Then, for local densities of the electrical current $\mathbf{j}$ and thermal flow $\mathbf{q}$, we can write

$$\mathbf{j} = \sigma\mathbf{E} + \beta\mathbf{G}, \tag{1}$$

$$\mathbf{q} = T\beta\mathbf{E} + \gamma\mathbf{G}. \tag{2}$$

Here $\beta = \sigma\alpha$, $\gamma = \chi + T\sigma\alpha^2$. Values $\mathbf{E}$ and $\mathbf{G}$ are local intensities of the electrical and temperature fields, while σ, χ and α denote the local electrical conductivity, thermal conductivity and thermopower, respectively.
For effective densities of the electrical current $\mathbf{j}_e$ and thermal flow $\mathbf{q}_e$ in the sample we can write

$$\mathbf{j_e} = \sigma_e\mathbf{E}_o + \beta_e\mathbf{G}_o, \tag{3}$$

$$\mathbf{q_e} = T\beta_e\mathbf{E}_o + \gamma_e\mathbf{G}_o, \tag{4}$$

where $\beta_e = \sigma_e\alpha_e$, $\gamma_e = \chi_e + T\sigma_e\alpha_e^2$, $\mathbf{E}_o = \langle\mathbf{E}\rangle, \mathbf{G}_o = \langle\mathbf{G}\rangle$. Here σ_e, χ_e and α_e are the effective electrical conductivity, thermal conductivity and thermopower. Angular brackets denote the configuration averaging. Equations (1) to (4) may be rewritten in compact form

$$\mathbf{V} = \mathbf{Q}\mathbf{W}, \ \mathbf{V}_e = \mathbf{Q}_e\mathbf{W}_o, \tag{5}$$

where

$$\mathbf{V} = \begin{pmatrix} \mathbf{j}/e \\ \mathbf{q}/kT \end{pmatrix}, \ \mathbf{Q} = \begin{pmatrix} Q_{11} & Q_{12} \\ Q_{12} & Q_{22} \end{pmatrix}, \ \mathbf{W} = \begin{pmatrix} e\mathbf{E} \\ k\mathbf{G} \end{pmatrix}, \tag{6}$$

$$\mathbf{V}_e = \begin{pmatrix} \mathbf{j}_e/e \\ \mathbf{q}_e/kT \end{pmatrix}, \ \mathbf{Q}_e = \begin{pmatrix} Q^e_{11} & Q^e_{12} \\ Q^e_{12} & Q^e_{22} \end{pmatrix}, \ \mathbf{W}_o = \begin{pmatrix} e\mathbf{E}_o \\ k\mathbf{G}_o \end{pmatrix}, \tag{7}$$

$$Q_{11} = \frac{\sigma}{e^2}, \ Q_{12} = \frac{\beta}{ek}, \ Q_{22} = \frac{\gamma}{k^2T}, \tag{8}$$

$$Q^e_{11} = \frac{\sigma}{e^2}, \ Q^e_{12} = \frac{\beta_e}{ek}, \ Q^e_{22} = \frac{\gamma_e}{k^2T}. \tag{9}$$

For calculation of the effective tensor $\mathbf{Q}_e$ in three-dimensional sample we use the EMT equation (see, e.g.[3]) in the form

$$\langle(\mathbf{Q} + 2\mathbf{Q}_e)^{-1}(\mathbf{Q} - \mathbf{Q}_e)\rangle = 0. \tag{10}$$

From (10) we can calculate the values σ_e, χ_e and α_e. Inserting (8) and (9) into (10) we find the following system of equations

$$\langle\frac{(\chi + 2\chi_e)(\sigma - \sigma_e) - T\sigma_e\sigma(\alpha - \alpha_e)^2}{(\sigma + 2\sigma_e)(\chi + 2\chi_e) + 2T\sigma_e\sigma(\alpha - \alpha_e)^2}\rangle = 0, \tag{11}$$

$$\langle\frac{(\sigma + 2\sigma_e)(\chi - \chi_e) - 2T\sigma_e\sigma(\alpha - \alpha_e)^2}{(\sigma + 2\sigma_e)(\chi + 2\chi_e) + 2T\sigma_e\sigma(\alpha - \alpha_e)^2}\rangle = 0, \tag{12}$$

$$\langle \frac{\alpha(\sigma-\sigma_e)}{(\sigma+2\sigma_e)(\chi+2\chi_e)+2T\sigma_e\sigma(\alpha-\alpha_e)^2} \rangle = 0. \quad (13)$$

Calculations of the effective kinetic coefficients from (11) to (13) in general case are very difficult problem. We restrict ourselves to a simple case. Let us neglect the terms with $(\alpha-\alpha_e)^2$ in (11) to (13) and write

$$\langle \frac{\sigma-\sigma_e}{\sigma+2\sigma_e} \rangle = 0, \ \langle \frac{\chi-\chi_e}{\chi+2\chi_e} \rangle = 0, \quad (14)$$

$$\alpha_e = \frac{\langle \frac{\sigma\alpha}{(\sigma+2\sigma_e)(\chi+2\chi_e)} \rangle}{\langle \frac{\sigma}{(\sigma+2\sigma_e)(\chi+2\chi_e)} \rangle}, \quad (15)$$

where $\chi = \chi_E + \chi_L$, $\chi_E = TL\sigma$, χ_L is the uniform lattice part of thermal conductivity, L is the Lorentz number. Let us consider a random two component system with probabilities: p with values σ_1, χ_1, α_1 and $1-p$ with values σ_2, χ_2, α_2 in components. Here we take $\sigma_1 \gg \sigma_2$. From (14) and (15) after averaging, we obtain

$$\sigma_e = \sigma_1[A + \sqrt{A^2 + \frac{\sigma_2}{2\sigma_1}}], \quad (16)$$
$$A = \frac{1}{4}[(3p-1)(1-\frac{\sigma_2}{\sigma_1}) + \frac{\sigma_2}{\sigma_1}],$$

$$\alpha_e = \frac{p\alpha_1\sigma_1 B_2 + (1-p)\alpha_2\sigma_2 B_1}{p\sigma_1 B_2 + (1-p)\sigma_2 B_1}, \quad (17)$$
$$B_1 = (\sigma_1+2\sigma_e)(\chi_1+2\chi_e),$$
$$B_2 = (\sigma_2+2\sigma_e)(\chi_2+2\chi_e),$$

where $\chi_1 = \chi_{E1} + \chi_L$, $\chi_2 = \chi_{E2} + \chi_L$. To find χ_e we can substitute σ by χ in (16). Below we obtain the conditions when expressions (16) and (17) are valid. For that we perform the configuration averaging in (11) and write

$$p\frac{C_1(\sigma_1-\sigma_e) - T\sigma_e\sigma_1(\alpha_1-\alpha_e)^2}{B_1 + 2T\sigma_e\sigma_1(\alpha_1-\alpha_e)^2} +$$
$$(1-p)\frac{C_2(\sigma_2-\sigma_e) - T\sigma_e\sigma_2(\alpha_2-\alpha_e)^2}{B_2 + 2T\sigma_e\sigma_2(\alpha_2-\alpha_e)^2} = 0, \quad (18)$$
$$C_1 = \chi_1 + 2\chi_e, \ C_2 = \chi_2 + 2\chi_e.$$

Now we write down four inequalities concerning the numerators and denominators of (18)

$$T\sigma_e\sigma_1(\alpha_1-\alpha_e)^2 \ll |(\chi_1+2\chi_e)(\sigma_1-\sigma_e)|,$$
$$T\sigma_e\sigma_2(\alpha_2-\alpha_e)^2 \ll |(\chi_2+2\chi_e)(\sigma_2-\sigma_e)|,$$
$$2T\sigma_e\sigma_1(\alpha_1-\alpha_e)^2 \ll (\sigma_1+2\sigma_e)(\chi_1+2\chi_e), \quad (19)$$
$$2T\sigma_e\sigma_2(\alpha_2-\alpha_e)^2 \ll (\sigma_2+2\sigma_e)(\chi_2+2\chi_e).$$

Further we must examine these inequalities for the maximum degree of inhomogeneity, i.e. for the percolation threshold ($p = p_c = 1/3$). From (16) we have $\sigma_e \simeq \sqrt{\sigma_1\sigma_2/2}$. Let us investigate only three cases for inequalities (19):

1. In the case of high electron part of thermal conductivity when $\chi_{E1} \gg \chi_{E2} \gg \chi_L$ we have $\alpha_e \simeq (\alpha_1+\alpha_2)/2$. Then from (19) we obtain

$$\frac{(\alpha_2-\alpha_1)^2}{L} \ll K\sqrt{\frac{\sigma_1}{\sigma_2}}, \quad (20)$$

where K is a value of the order of unity for all inequalities in (19).

2. In the case of low electron part of thermal conductivity when $\chi_{E2} \ll \chi_{E1} \ll \chi_L$ we have $\chi_e \simeq \chi_L$, $\alpha_e \simeq \alpha_1$ and we obtain the inequality

$$\frac{(\alpha_2-\alpha_1)^2}{L} \ll K\frac{\chi_L}{\chi_{E2}}. \quad (21)$$

3. In the intermediate case when $\chi_{E2} \ll \chi_L \ll \chi_{L1}$ we obtain $\chi_e \simeq \sqrt{\chi_{E1}\chi_L/2}$, $\alpha_e \simeq \alpha_1$ and we have

$$\frac{(\alpha_2-\alpha_1)^2}{L} \ll K\sqrt{\frac{\sigma_1}{\sigma_2}\frac{\chi_L}{\chi_{E2}}}. \quad (22)$$

It is easy to see that far from p_c the inequalities (19) increase.

The same results can be obtained also for (12) and (13).

In paper [2] the exact expression for the effective thermopower in two-component systems was obtained in the form

$$\alpha_e = \alpha_1 + (\alpha_2-\alpha_1)\frac{(\frac{\chi_e}{\sigma_e} - \frac{\chi_1}{\sigma_1})}{(\frac{\chi_2}{\sigma_2} - \frac{\chi_1}{\sigma_1})}. \quad (23)$$

To use (23) we must calculate the values σ_e and χ_e. In general case it is not simple problem. In [3,4] the conclusions were made that $\sigma_e = \sigma_e(p, \sigma_2/\sigma_1, \chi_2/\chi_1, \alpha_2/\alpha_1)$ and $\chi_e = \chi_e(p, \chi_2/\chi_1, \sigma_2/\sigma_1, \alpha_2/\alpha_1)$. But if there are inequalities $Q_{12} \ll Q_{11}$ and $Q_{12} \ll Q_{22}$ in (6), i.e. $\alpha \ll k/e$ and $\alpha \ll eL/k$, we have $\sigma_e = \sigma_e(p, \sigma_2/\sigma_1)$ and $\chi_e = \chi_e(p, \chi_2/\chi_1)$. Consequently, in the EMT approximation we can use the equations (14). These inequalities occur only in the metallic and degenerate semiconductor components. In the nondegenerate semiconductor components usually the opposite inequalities hold. In this case, as it follows from conclusion of [3,4], the equations (14) are not valid. We found the new inequalities (20) to (22) when the equations (14) are valid. The inequalities (20) to (22) may occur even if $Q_{12} \gg Q_{11}$ and $Q_{12} \gg Q_{22}$, i.e. if $\alpha \gg k/e$ and $\alpha \gg eL/k$. Thus, the equations (14) may be used for calculation of the effective values σ_e and χ_e including the case of nondegenerate semiconductor components. The values α_2 and α_1 may be considerably large, but the difference $(\alpha_2-\alpha_1)$ must satisfy the inequalities (20) to (22).

In expression for α_e in the form (23) the condition $\sigma_1\chi_2 = \sigma_2\chi_1$ must be excluded. But the form (23) under this condition can be easy transformed to the following expression

$$\alpha_e = \alpha_1 + \frac{\sigma_2}{\sigma_1}(\alpha_2-\alpha_1)\frac{1}{\sigma_e}\frac{\partial\sigma_e}{\partial(\frac{\sigma_2}{\sigma_1})}. \quad (24)$$

Thus we have the complete theory for the thermopower

α_e. If for calculations of σ_e and χ_e is used the EMT approximation (16) we obtain that (23) and (24) coincide with (17) exactly for all p.
To calculate the critical behavior of α_e in the vicinity of the percolation threshold p_c it is necessary to use more accurate values of σ_e and χ_e in (23) and (24) [4].

Conclusions

The theory of thermopower α_e in random two-component systems is analyzed using the EMT. To calculate the value α_e using (15), (23) and (24) we have found the inequalities (20) to (22) when the independent calculations of values σ_e and χ_e by (14) are valid. The authors of [3, 4] conclude that such independent calculations of σ_e and χ_e are valid only if $\alpha \ll k/e$ and $\alpha \ll eL/k$, i.e. only in metallic and degenerate semiconductor components of system. Our inequalities (20) to (22) are valid even if $\alpha \gg k/e$ and $\alpha \gg eL/k$, i.e. in nondegenerate semiconductor components. Thus, the inequalities used in [3, 4] are very strong. These inequalities are not necessary to calculate the values σ_e and χ_e independently and without taking into account the thermoelectricity. For that kind of calculations the inequalities (20) to (22) are suffice. The obtained inequalities allow to use the equations (14) in almost all cases of random two-component solid systems especially outside of the percolation threshold vicinity.

References

[1] I.Webman, J.Jortner, M.H.Cohen, "Thermoelectric power in inhomogeneous materials", Phys.Rew.B **16** (1977) 2959.

[2] V.Halpern, "The thermopower of binary mixtures", J.Phys.C, **16** (1983) $L217$.

[3] D.J.Bergman, O.Levy, "Thermoelectric properties of a composite medium", J.Appl.Phys. **70** (1991) 6821.

[4] O.Levy, D.J.Bergman, "Scaling behaviour of the thermopower in a two-component composite near a percolation threshold", J.Phys.A **25** (1992) 1875.

[5] I.I.Fishchuk, "Theory of the Thermopower and Nernst Effect in Random Two-Component Solid Systems", Phys.Status Solidi (b) **190** (1995) 545.

Characterization of p-type PbEuTe/PbTe MQW Structures with High Thermoelectric Figures of Merit in the PbTe Quantum Wells

T. C. Harman, D. L. Spears, D. R. Calawa, S. H. Groves, and M. P. Walsh

Lincoln Laboratory
Massachusetts Institute of Technology
Lexington, MA 02173-9108, USA

Abstract

A large enhancement in the Seebeck coefficient, thermoelectric power factor and figure of merit ($Z_{2D}T$) is reported in very high carrier concentration p-type PbTe quantum wells grown by molecular beam epitaxy. The estimated $Z_{2D}T$ (using accepted bulk values for lattice thermal conductivity) is as high as 1.5 at 300 K. Power factor values up to 160 $\mu Wcm^{-1}K^{-2}$ were measured at 300 K, indicating a power factor in p-type quantum wells that is approximately five times the best bulk or homogeneous p-type value. Thinner barriers yielded lower thermoelectric power factors and figures of merit. The high power factor was achieved with a barrier thickness less than half that previously used to demonstrate enhanced thermoelectric power factors in n-type quantum wells. X-ray diffraction/reflection characterization results of the multiple-quantum-well (MQW) structures at both low and high Bragg angles yield precise values for the MQW periodicity.

Introduction

It has already been demonstrated that the $Pb_{1-x}Eu_xTe/PbTe$ quantum-well superlattice (QWSL) provides a useful vehicle for testing ideas on enhanced thermoelectric figures of merit Z in quantum confined systems.[1,2] Z is defined by the relation $Z = S^2\sigma/\kappa$ where S, σ, and κ are, respectively, the Seebeck coefficient, the electrical conductivity, and the thermal conductivity. In this earlier work it was demonstrated that an n-type multiple-quantum-well (MQW) structure based on the $Pb_{1-x}Eu_xTe/PbTe$ system yielded an enhanced value of the power factor $S^2\sigma$ arising from the quantum confinement of electrons in the PbTe quantum wells[1,2] using x = 0.073 for the barrier material and Bi as an n-type dopant which was introduced into the barrier regions. In the present work, we report even greater enhancement in the two-dimensional (2D) thermoelectric figure of merit $Z_{2D}T$ for p-type MQW samples of $Pb_{0.927}Eu_{0.073}Te/PbTe$. For the first time in any material, a value of $Z_{2D}T > 1.5$ at 300 K has been achieved within the quantum well.

A new acceptor dopant, i.e. BaF_2, has been found for PbTe and its alloys, that can be introduced continuously to grow homogeneous p-type layers or inserted as an acceptor δ-dopant in the middle of the $Pb_{0.927}Eu_{0.073}Te$ barriers, which are situated between the PbTe quantum wells, to increase the hole carrier concentration in the quantum wells to a very high density. $Pb_{0.927}Eu_{0.073}Te$ is desirable as a barrier material because it grows epitaxially on PbTe and provides high-quality interfaces between the barrier and the quantum-well regions of the MQW structure, and, because $Pb_{0.927}Eu_{0.073}Te$ has a bandgap[1] of 0.63 eV relative to that of PbTe (0.32 eV), it provides some confinement of the carriers to the quantum well. The $Pb_{0.927}Eu_{0.073}Te$ barrier material does not however have sufficient barrier height (bandgap and band offset) to confine the bound-state levels of the quantum well unless the barrier width is relatively large compared to the quantum-well width. Wide barriers are deleterious to realizing a high three-dimensional (3D) thermoelectric figure of merit $Z_{3D}T$ because of high parallel thermal conductance.[2,3]

BaF_2 inserted in the center of the $Pb_{0.927}Eu_{0.073}Te$ barrier did act as an acceptor δ-dopant and allowed the achievement of the highest estimated thermoelectric figure of merit of any material (quantum-wells part of the sample only) at 300 K as discussed below. We believe that the enhanced ZT is due to a combination of factors. One factor is believed to be the large enhancement in the Seebeck coefficient[1,2] in the quantum wells arising from the increased density of states per unit volume. A second factor is carrier mobility enhancement in the quantum wells when the dopant is placed only in the barrier regions. Impurity scattering contributes to a large degradation of the carrier mobility in uniformly doped bulk material at high acceptor impurity concentrations, but since the impurities are only placed in the middle of the barriers in this MQW structure, the carriers in the undoped PbTe quantum wells are not subjected to significant impurity scattering even though hole-hole,[4] hole-phonon, and hole-interface scattering does occur in the quantum wells. It was found that a hole carrier concentration level of 2×10^{20} cm^{-3} optimizes Z_{2D} at room temperature in the PbTe quantum wells for barriers 200 Å thick. For thinner barriers the maximum thermoelectric figure of merit Z_{2D} at room temperature decreases as the barrier thickness decreases due to tunneling through the barriers. A third factor in the enhancement of ZT in the quantum wells is believed associated with the Σ-valence-band pockets[5] of PbTe.

MBE Growth

A number of structures composed of p-type $Pb_{0.927}Eu_{0.073}Te/PbTe$ MQWs were grown by the previously described[2] (molecular beam epitaxial) techniques. In some initial

0-7803-4057-4/97 $10.00 ©1997 IEEE

experiments, thicker BaF_2 layers were grown to test a double-barrier concept where the first barrier (PbEuTe) provides high-quality interfaces to the quantum well and the second higher energy barrier (BaF_2) provides better carrier confinement, so that the overall barrier thickness can be minimized. Initial experiments involved placing a 2.0-nm-thick layer of BaF_2 in the center of the $Pb_{0.927}Eu_{0.073}Te$ barriers; however, we found that such layers produced high acceptor levels and degraded the crystal structure so severely that good thermoelectric properties were not realized. In subsequent experiments, δ-doping with BaF_2 was used in MQW structures as an acceptor impurity only. For p-type doping, chunks of BaF_2 were placed in one of the effusion cells and heated to the appropriate temperature. The computer-controlled BaF_2 shutter was opened to provide a flux of BaF_2 molecules which gave the desired hole carrier concentration. During BaF_2 deposition all the computer-controlled shutters were closed except the BaF_2 shutter. The substrate temperature was 573 K during growth of the MQW structure and the growth rate was typically 0.7 μm/hr. A schematic cross section of the $Pb_{0.927}Eu_{0.073}Te/PbTe$ MQW structure along with the $Pb_{0.958}Eu_{0.042}Te$ buffer layer and the BaF_2 substrate is shown in Fig. 1.

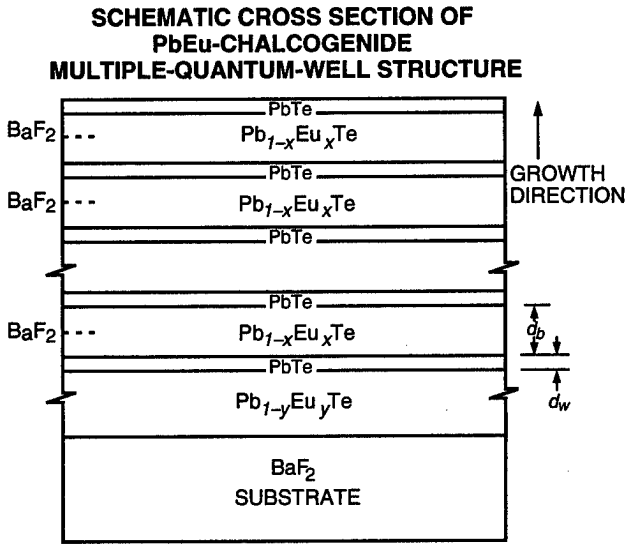


Figure 1. Schematic cross section of the PbEu-chalcogenide multiple-quantum-well (MQW) structure investigated

Superlattice Periodicity Measurements

1. High-Angle X-ray Diffraction

The structural properties of the samples were investigated by high resolution x-ray diffraction (XRD) for these measurements, a Philips horizontal MRD (materials research diffractometer) was used with Cu $K_{\alpha 1}$ radiation and a four-crystal (Ge 220) Bartels monochromator in the primary beam. The Bragg (444) $2\Theta/\omega$ XRD results for the MQW sample T-396, grown at a substrate temperature of 573 K, are shown in Fig. 2. Eight or more peaks

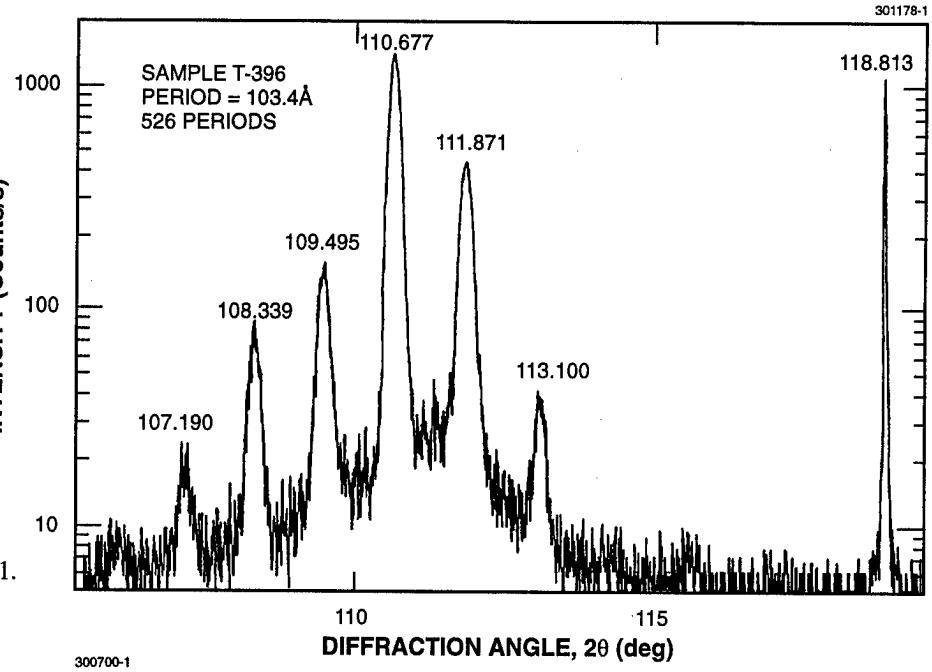


Figure 2. Reflected x-ray intensity vs double Bragg angle for (444) diffraction (Cu $K\alpha_1$ radiation) from $Pb_{0.89}Eu_{0.11}Te/PbTe$ MQW sample T-396 grown at 573 K. The structure of the sample consists of a BaF_2 substrate, a 106.2 Å/24.2 Å MQW on a 0.2 μm thick $Pb_{0.945}Eu_{0.055}Te$ buffer layer. The number of periods is 526

related to the superlattice are seen. The peak with the highest intensity is presumed to be closest to satisfying the Bragg condition for the fourth-order reflection for the average lattice constant, $\langle a_0 \rangle = (a_{0W} \cdot d_W + a_{0b} \cdot d_b)/(d_W + d_b)$. The peaks are caused by the superlattice periodicity, $P = d_W + d_b$, and are of order $m \approx 4 \cdot P / \langle a_0 \rangle$. From the Bragg condition,

$$m\lambda = 2P\sin\theta \qquad [1]$$

it is possible to determine P from adjacent peaks (where λ is the x-ray Cu $K_{\alpha 1}$ wavelength and θ is the Bragg angle):

$$P=(m_1-m_2)\lambda/[2(\sin\theta_1-\sin\theta_2)] \qquad [2]$$

where $m_1 - m_2 = 1$ for adjacent peaks and θ_1 and θ_2 are the respective Bragg angles. Upon applying Eq. (2) to the six largest satellite peaks around the (444) Bragg reflections (in Fig. 2) of the host lattice of the T-396 sample, we calculate P = 13.04 nm

for the superlattice period. The narrower line at a (444) double Bragg angle of 118.813 degrees is due to the BaF_2 substrate. For sample T-396, 526 periods were grown, giving 6.86 μm total MQW thickness. Also, from the fact that growth rates of PbTe and $Pb_{0.89}Eu_{0.11}Te$ were measured to be the same on homogeneous calibration films of the two materials, the proportional well and barrier growth times suggests d_b = 106.2 Å and d_w = 24.2 Å.

2. Low-Angle X-ray Reflection

The structural properties of the samples were also investigated by XRD in glancing incidence, just above the critical angle. For these measurements, a Philips vertical MRD instrument was used with Cu K_α radiation from a line-focus tube and parallel-plate collimator between the sample and detector. Figure 3

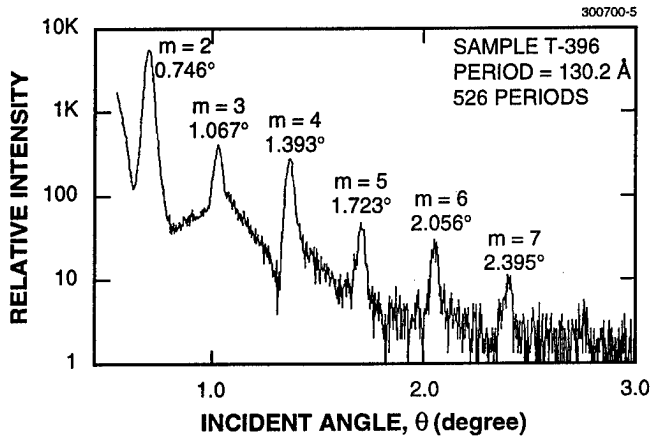


Figure 3. Low angle x-ray reflection of a $Pb_{0.89}Eu_{0.11}Te$/PbTe MQW superlattice sample T-396. The m numbers represent the order of the superlattice interference peak.

shows the reflected intensity vs θ for sample T-396 discussed in the previous section. Structure in the reflectivity curve is again causing the superlattice periodicity, but here the interference is of low order, as labeled in the figure. At low angles, it is necessary to include the effects of the small deviation of the refractive index from unity. For the superlattice, the modified[6] condition of Bragg's law is

$$d=P[1-(1-n_{SL})/\sin^2\theta_m], \qquad [3]$$

where $d = m\lambda/2\sin\theta_m$ and $n_{SL} = (d_b n_b$ and $d_w n_w)/P$ represents the refractive index of the superlattice; n_b and n_w are the refractive indices of PbEuTe and PbTe. Equation (3) shows that a plot of d vs $1/\sin^2\theta_m$ will yield a straight line and the x=0 intercept will be the value of the superlattice periodicity P. Figure 4 shows that, with the orders assigned in Fig. 3, we do obtain a straight line as expected. From the intercept of the best fit of the data (using Excel 7.0a) at the d-axis of Fig. 4, the superlattice period is calculated to be 130.2 Å for sample T-396, in excellent agreement with that of Sec. 1.

3. Periodicity from the Growth Parameters and Layer Thickness

Also, the superlattice period obtained from growth parameters

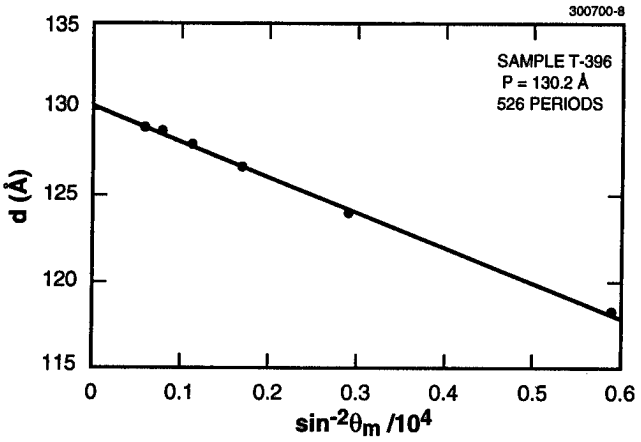


Figure 4. Plot of d (=m λ/2sin θ_m) vs $1/\sin^2\theta_m$ where m is the order of the interference peak.

was approximately 13.0 nm. For this method, we use the computer-controlled shutter counts to determine the total number of periods as mentioned above. The computer program count yields the ratio of the well thickness to the barrier thickness as mentioned above. Then the total thickness of the film is measured by scanning electron microscopy (SEM). The superlattice period is calculated from these data. However, we believe the x-ray diffraction data gives the most precise value for the period.

Alloy Compositional Measurements

The $Pb_{1-y}Eu_yTe$ buffer and $Pb_{1-x}Eu_xTe$ barrier layer compositions were determined by the following procedure. An approximately 6-μm-thick homogeneous calibration layer of a particular alloy composition was grown by MBE for a particular set of PbTe, Eu, and Te effusion cell temperatures and beam-equivalent vapor pressures. Then XRD spectra were recorded. Our (444) Bragg angle data for both $Pb_{1-x}Eu_xTe$ and BaF_2 were normalized to the accepted literature lattice constant value for the (444) Bragg angle of BaF_2 (6.200 Å lattice constant) in order to obtain the lattice constant of a specific composition of $Pb_{1-x}Eu_xTe$. Since we use the Cu $K_{\alpha 1}$ x-ray source, the lattice constant a_0 of the NaCl lattice structure $Pb_{1-x}Eu_xTe$ was determined from

$$a_0=5.3364/\sin\Theta_B \qquad [4]$$

where Θ_B is the (444) Bragg angle. The following equations[7] relating the mole fraction of EuTe to a_0 were used to calculate the mole fraction of EuTe in the $Pb_{1-x}Eu_xTe$ homogeneous layer:

$$y=A(\Delta a_0)^2+B(\Delta a_0), y<0.13 \quad [5]$$

where

$$(\Delta a_0)=a_{0PbEuTe}-a_{0PbTe}=a_{0PbEuTe}-6.462\text{Å} \quad [6]$$

and A = 37.3 $Å^{-2}$, B = 2.00 $Å^{-1}$. In Ref. 7, the lattice constant for PbTe is given as 6.460 Å but we measure 6.462 Å for our 6-μm-thick PbTe films on BaF_2 and used it in Eq. (6).

Results And Discussion

1. $Pb_{0.927}Eu_{0.073}Te$/PbTe MQW Structures with 20 nm Barriers

Hole charge carriers were provided to the p-type quantum wells by modulation doping of the $Pb_{0.927}Eu_{0.073}Te$ barriers as described in a previous section. Six $Pb_{0.927}Eu_{0.073}Te$/PbTe MQW structures were grown with undoped PbTe quantum wells and with BaF_2 δ-doping in the 20-nm barriers. Their characterization parameters are tabulated in Tables Ia , Ib, and Ic.

Table 1a

Some Parameters of the δ-Doped p-Type $Pb_{0.927}Eu_{0.073}Te$/PbTe Quantum-Well Superlattice Structures

Sample No.	Sample Thickness(μm)	Number of Periods	300 K Seebeck Coefficient (μV/K)	3D Carrier Concentration 300 K (cm^{-3})	3D Carrier Concentration 77 K (cm^{-3})	Carrier Mobility 300 K (cm^2/V-s)	Carrier Mobility 77 K (cm^2/V-s)
T-329	5.25	224	+241	$1.8x10^{19}$	$15x10^{19}$	77	345
T-331	5.25	224	+229	$1.3x10^{19}$	$1.3x10^{19}$	110	400
T-371	5.58	238	+206	$4.1x10^{19}$	$1.6x10^{19}$	39	190
T-368	4.59	205	+151	$6.2x10^{19}$	$2.4x10^{19}$	35	200
T-358	5.25	220	+242	$6.2x10^{18}$	$3.9x10^{18}$	120	720
T-332	4.76	204	+257	$4.1x10^{18}$	$2.3x10^{18}$	120	770

Table 1b

Some Parameters of the δ-Doped p-Type $Pb_{0.927}Eu_{0.073}$ Te/PbTe Quantum-Well Superlattice Structures

Sample No.	Thickness PbTe Well d_w(nm)	Thickness $Pb_{0.927}Eu_{0.073}Te$ Barrier d_b(nm)	Carrier Concentration 300 K (cm^{-3})	Carrier Concentration 77 K (cm^{-3})
T-329	1.91	19	$2.0x10^{20}$	$1.7x10^{20}$
T-331	1.91	19	$1.6x10^{20}$	$1.6x10^{20}$
T-371	2.07	20	$4.5x10^{20}$	$1.6x10^{20}$
T-368	1.97	19	$6.7x10^{20}$	$2.7x10^{20}$
T-358	1.90	19	$6.8x10^{19}$	$4.3x10^{19}$
T-332	1.88	19	$4.9x10^{19}$	$2.8x10^{19}$

Table 1c

Thermoelectric Properties at 300 K of p-Type $Pb_{0.927}Eu_{0.073}Te$/PbTe MQW Samples

Sample No	2D Power Factor P_{F2D} (μW/cm-K^2)	Electrical Conductivity σ_W (mho/cm)	Thermoelectric Figure of Merit* Wells Only $Z_{2D}T$
T-329	160	2700	1.5
T-331	150	2800	1.4
T-371	119	2800	1.1
T-368	88.5	3900	0.7
T-358	73	3900	0.9
T-332	63.5	960	0.8

* A literature value[14] of the lattice thermal conductivity of 20 mW/cm-K was assumed for the PbTe quantum wells

The hole carrier concentration increased as the BaF_2 effusion flux increased. All of these samples had high Seebeck coefficients, ranging from 151 to 257 μV/K. The 2D carrier concentrations are obtained by assuming that the carriers are confined to the PbTe quantum wells. At this point in time, modeling work[8] indicates that all of the carriers are confined to the PbTe quantum wells so the 2D assumption appears reasonable.

2. $Pb_{0.89}Eu_{0.11}Te/PbTe$ MQW Structures with 10 nm Barriers

Tables IIa, IIb, and IIc show a number of the characterization parameters for $Pb_{0.89}Eu_{0.11}Te/PbTe$ samples with approximately 10-nm-thick barriers. The hole carrier concentration increased as the BaF_2 effusion flux increased. Notice that the measured Seebeck coefficients for these QWSL samples are significantly smaller than the Seebeck coefficients of the $Pb_{0.927}Eu_{0.073}Te/PbTe$ QWSL samples measured with approximately 20-nm-thick barriers. We believe that the smaller S values are a result of tunneling between quantum wells, i.e. the holes are not totally confined to the wells. The 3D carrier concentrations and electrical conductivities were calculated by assuming the carriers are uniformly distributed throughout the samples whereas the 2D carrier concentrations and electrical conductivities were calculated by assuming the carriers are totally confined to the wells. Neither of these assumptions are believed correct but are made to tabulate the Hall coefficient and electrical conductivity data and indicate the range of possible carrier

Table IIa

Some Parameters of the δ-Doped p-Type $Pb_{0.89}Eu_{0.11}Te/PbTe$ Quantum Well Superlattice Structures Grown at 300°C

Sample No.	Sample Thickness (μm)	Number of Periods	300 K Seebeck Coefficient (μV/K)	Carrier Concentration 300 K (cm^{-3})	Carrier Concentration 77 K (cm^{-3})	Carrier Mobility 300 K (cm^2/V-s)	Carrier Mobility 77 K (cm^2/V-s)
T-383	6.23	408	+178	$1.6x10^{19}$	$1.3x10^{19}$	115	338
T-384	4.42	333	+134	$9.5x10^{19}$	$6.0x10^{19}$	45	100
T-385	4.10	331	+142	$3.2x10^{19}$	$2.9x10^{19}$	120	380
T-386	4.10	329	+126	$6.2x10^{19}$	$5.2x10^{19}$	80	290
T-396	7.06	526	+150	$4.4x10^{19}$	$5.3x10^{19}$	66	116

Table IIb

Some Parameters of the δ-Doped p-Type $Pb_{0.89}Eu_{0.11}$ Te/PbTe Quantum-Well Superlattice Structures

Sample No.	Thickness PbTe Well d_w (nm)	Thickness $Pb_{0.89}Eu_{0.11}Te$ Barrier d_b (nm)	2D Carrier Concentration 300 K (cm^{-3})	2D Carrier Concentration 77 K (cm^{-3})
T-383	2.27	12.5	$1.0x10^{20}$	$9.1x10^{19}$
T-384	2.21	11.1	$6.0x10^{20}$	$6.1x10^{20}$
T-385	1.92	10.5	$2.1x10^{20}$	$1.9x10^{20}$
T-386	1.92	10.6	$4.1x10^{20}$	$3.4x10^{20}$
T-396	2.42	10.6	$3.2x10^{20}$	$3.5x10^{20}$

Table IIc

Thermoelectric Properties of p-Type $Pb_{0.89}Eu_{0.11}Te/PbTe$ MQW Samples Measured at 300 K (δ-Doped with BaF_2)

Sample No.	2D Power Factor P_{F2D} (μW/cm-K^2)	Electrical Conductivity σ_w (mho/cm)	Thermoelectric Figure of Merit* Wells Only $Z_{2D}T$
T-383	60	1,900	0.6
T-384	74	4,150	0.6
T-385	80	3,900	0.6
T-386	85	5,400	0.6
T-396	70	1,880	0.6

*A literature value[14] of the lattice thermal conductivity of 20 mW/cm-K was assumed for the PbTe quantum wells and may be too high.

concentrations in the wells and barriers. The carrier mobility is the Hall mobility and is the same for either the 3D or 2D assumption, i.e. the geometry factor cancels out for the Hall mobility.

3. Bulk Materials

To evaluate the PbTe MQW data, we have compared these results with bulk PbTe. Properties of high quality bulk p-type PbTe samples[9,10] are listed in Table IIIa. These bulk materials were prepared from semiconductor-grade Pb and Te, grown by the Bridgman method, and were polycrystalline with large grain sizes. The low concentration samples were undoped whereas the higher concentration samples were doped with various impurities such as Ag, Au, and P. Seebeck coefficients at 300 K varied from +431 μV/K at low carrier concentrations to +95 μV/K at the highest concentration. At lower carrier concentrations the highest 300 K carrier mobility was 950 cm^2/V-s which decreases to 780 cm^2/V-s at a carrier concentration of 1.5 x 10^{19} cm^{-3}. Properties of a MBE-grown uniformly BaF_2-doped homogeneous PbTe film(T-376) are shown in Table IIIb. This sample has a power factor = 31.2 μW/cm-K^2 and a bulk $Z_{3D}T$ = 0.38 at 300 K, which are values slightly higher than those for any other p-type dopant in bulk PbTe. Also, we have included a MBE-grown δ-doped with BaF_2 homogeneous $Pb_{0.927}Eu_{0.073}Te$ film (T-393) in Table IIIc. Notice that the 300 K carrier mobility is a factor of eight larger for the PbTe sample even though the carrier concentrations are comparable.

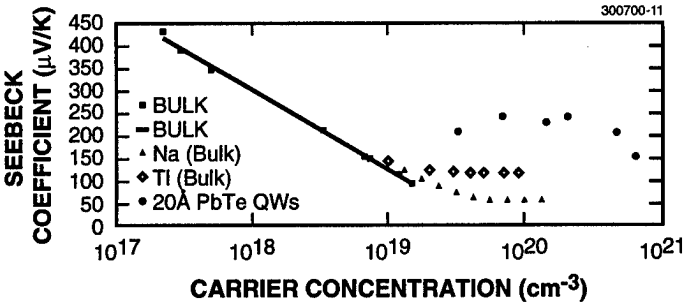


Figure 5. Seebeck coefficient vs hole carrier concentration for p-type $Pb_{0.927}Eu_{0.073}Te$/PbTe quantum-well superlattice structures and bulk PbTe.

Table III

Sample No.	300 K Seebeck Coefficient S(μV/K)	300 K Power Factor (μW/cm-K^2)	Carrier Concentration p (cm^{-3}) 300 K	77 K	Carrier Mobility μ(cm^2/V-s) 300 K	77 K
a. Bridgman-Grown						
3-69	+431	5.2	$2.2x10^{17}$	$2.1x10^{17}$	770	27000
5-70H1B	+388	5.4	$3.0x10^{17}$	$3.3x10^{17}$	740	23000
5-70H1A	+346	7.7	$4.9x10^{17}$	$5.4x10^{17}$	830	22000
2-71H1	+213	22.7	$3.3x10^{18}$	$4.6x10^{17}$	950	15000
1-72H1	+155	20.9	$6.7x10^{18}$	$9.7x10^{18}$	810	9000
12-71H1	+154	24.0	$7.4x10^{18}$	$1.1x10^{19}$	850	9100
1-72H6C	+117	21.4	$1.25x10^{19}$	$2.3x10^{19}$	780	4100
1-72H4B	+95	17.0	$1.5x10^{19}$	$2.8x10^{19}$	780	4800
b. MBE-Grown Epitaxial Homogeneous Layer of BaF_2-doped PbTe Samples						
T-376	+170	31.2	$1.7x10^{19}$	$2.2x10^{19}$	385	1700
c. MBE-Grown Epitaxial Homogeneous Layer of BaF_2-doped $Pb_{0.927}Eu_{0.073}Te$ Samples						
T-393	+206	8.7	$2.6x10^{19}$	$2.7x10^{19}$	48	185

Figure 5 shows a semilog plot of these S vs p data for bulk PbTe, which are fit by a straight line given by the simple expression

$$S\ (\mu V/K) = +477\text{-}175\ \log_{10}(p/10^{17}\ cm^3) \qquad [7]$$

Except for changes in signs, this is exactly the same expression that fit the best bulk n-type data[2] for n < 4 x 10^{19} cm^{-3}. This is to be expected because the L conduction band pocket is the mirror image of the L valence band pocket and the electron effective mass is equal to the hole effective mass for the same

carrier concentration. The effective mass of each L pocket increases with carrier concentration due to band nonparabolicity. Notice that above ~ 8 x 10^{18} cm^{-3}, the data become dependent on the impurity. The difference in Seebeck coefficient between the Tl-doped and Na-doped[11] bulk samples are attributed in the literature to resonance-impurity scattering[12,13] in the Tl-doped samples. From Eq. (7) and the slow mobility change with carrier concentration, we get a maximum power factor $S^2pe\mu_h$ = 24 $\mu W/cm\text{-}K^2$ at a concentration of 8 x 10^{18} cm^{-3}, but using literature values for Na-doped PbTe a maximum power factor of 28 $\mu W/cm\text{-}K^2$ is obtained at 1.0 x 10^{19} cm^{-3}. Using 20 mW/cm-K for the lattice thermal conductivity[14] of PbTe, we calculate a maximum figure of merit ZT_{max} = 0.35 for p-type bulk PbTe at 300 K.

These results for bulk PbTe are compared in Fig. 5 with S vs p data for the six BaF_2 δ-doped MQW structures with 20-nm barriers, and with data for one homogeneous epitaxial layer of p-type PbTe. The thick-barrier MQW-structure data show a nearly constant value of S (in the high 10^{19} cm^{-3} to 2 x 10^{20} cm^{-3} range) at high carrier concentrations similar to that of Na- and Tl-doped bulk material. Currently, we believe that this plateau is a consequence of the valence band structure of PbTe. Holes are predominantly in the L valence-band pockets for hole carrier concentrations below the mid-10^{19} cm^{-3}. Above 2x10^{20} cm^{-3}, holes are predominantly in Σ valence band-pockets. Constant energy surfaces of the PbTe valence-band extrema[5] are shown in Fig. 6. The maximum extremum is located at the L point (light hole band) of the Brillouin zone and there are eight half or four whole ellipsoids. This is important for thermoelectricity because ZT is directly proportional to the number of ellipsoids (valleys) through the density-of-states effective mass. The next highest valence-band extremum is located at the Σ point (heavy hole band) of the Brillouin zone and there are twelve whole ellipsoids, which is very favorable for high ZT. Thus, as the total hole carrier concentration increases the percentage of (heavy) Σ holes relative to (light) L holes increases with the result that a relatively high Seebeck coefficient persists to extraordinarily high carrier concentrations. The Tl-doped PbTe Seebeck coefficient of 120 μV/K at 2 x 10^{20} cm^{-3} can be calculated using a hole density-of-states effective mass of 1.2, which is reasonable in view of this valence band structure. For the early literature on the second valence band in PbTe see Refs. 15 and 16.

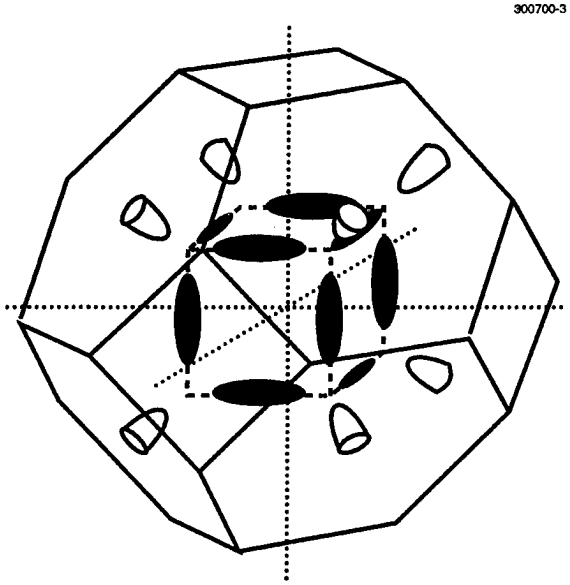


Figure 6. Constant energy surfaces of the PbTe valence band in the Brillouin zone.

Our measured Seebeck coefficients for the $Pb_{0.927}Eu_{0.073}Te$/PbTe MQW samples are approximately a factor of two larger than the Seebeck coefficients (assuming 2D conduction) of bulk Tl-doped PbTe, and at the very high carrier concentration of 2 x 10^{20} cm^{-3} we obtained a remarkably high Seebeck coefficient of +240 μV/K. We believe that the 2 x increase in S (4 x increase in power factor $S^2\sigma$ and ZT) is primarily from quantum-well enhancement due to the increased density of states per unit volume of the quantum wells. Furthermore, measurements indicate that the hole carrier mobility can be at least as high as 110 cm^2/V-sec, which is roughly 4 x higher than that of bulk Tl-doped PbTe at this carrier concentration. We hypothesize that this 4x mobility enhancement may be due in part to modulation doping. Since no impurities are placed in the quantum wells, mobility enhancement may occur due to the suppression of impurity scattering in the quantum wells. At the 2 x 10^{20} cm^{-3} impurity concentration level, ionized impurity scattering in bulk material probably contributes to some degradation of the carrier mobility. Since the impurities are placed in the barriers, the carriers in the undoped PbTe quantum wells are not subjected to impurity scattering. Thus, we believe a large carrier mobility enhancement occurs due to the δ-doping suppression of impurity scattering even though carrier-carrier, carrier-phonon and carrier-interface scattering may occur in the quantum wells.

In Tables Ic and IIc are listed the 2D power factor P_{f2D} = $S^2pe\mu_h$ and thermoelectric figure of merit $Z_{2D}T$ for the p-type PbTe MQW samples at 300 K, showing P_{f2D} values as high as 160 $\mu W/cm\text{-}K^2$. The power factor vs hole concentration for these samples and for the best bulk p-type PbTe (Table III) are displayed in Fig. 7.

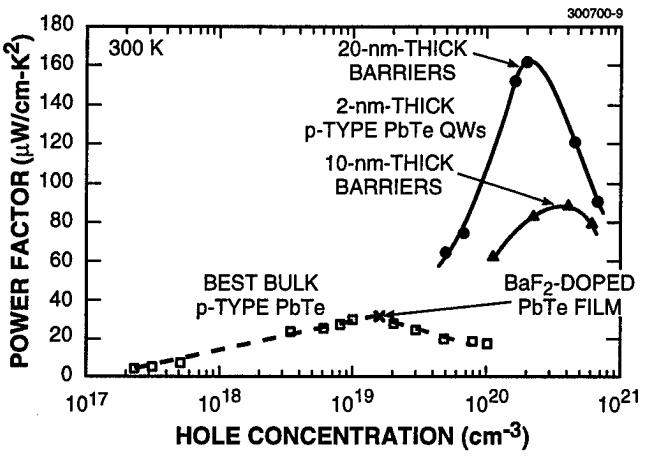


Figure 7. Thermoelectric power factor vs carrier concentration for the best p-type bulk PbTe samples, a single BaF_2 doped epitaxial PbTe layer, and p-type $Pb_{0.927}Eu_{0.073}Te/PbTe$ quantum wells.

Power factors ($S^2\sigma$ for bulk or single layer and $S^2\sigma_W$ for quantum well) from Tables II and III are presented in Fig. 7 as a function of the carrier concentration at 300 K. The bulk data show a very broad peak centered at a concentration $\approx 1.5 \times 10^{19}$ cm^{-3}, whereas the MQW data peak is much higher and narrower and centered at ~ 2×10^{20} cm^{-3}. The 2-nm-thick PbTe quantum wells with ~ 20-nm-thick barriers have higher 2D power factors than found for similar n-type quantum wells,[1,2] despite having a much lower carrier mobility. For the best sample (T-329) the power factor is 160 $\mu W/cm\text{-}K^2$, the highest reported to date for good thermoelectric materials.

Conclusions

Using the accepted bulk value of 20 mW/cm-K for the lattice thermal conductivity, we estimate $Z_{3D}T$ is as high as 0.24 and $Z_{2D}T = 1.5$ at 300 K. Since we expect phonon-interface scattering in the MQW structure is lowering the thermal conductivity, the actual ZT values may be considerably higher.

The 3D properties of these p-type quantum wells are intriguing with an electrical conductivity of 275 mho-cm^{-1} and a Seebeck coefficient S of +241 μV/K at 300 K. However, BaF_2 and $Pb_{0.927}Eu_{0.073}Te$ have negligible charge carriers and small $Z_{3D}T$. Thus, despite the fact that only the 9% PbTe part of the sample is thermoelectrically active, the overall estimated $Z_{3D}T$ is 0.24 at 300 K.

In summary the unusually high maximum thermoelectric power factor of 160 $\mu W/cm\text{-}K^2$ at 300 K in the quantum wells is believed to be the result of a combination of factors, such as the density of states per unit volume quantum well enhancement effect, the carrier mobility enhancement effect of modulation doping by δ-doping with an acceptor impurity in the barrier regions only of the MQW, and the enhancement effect of contributions to the density of states due to the presence of the high density-of-states effective mass hole pockets of the Σ valence band.

Acknowledgments

This work was sponsored by the Department of the Navy, the Army Research Office, and the Defense Advanced Research Projects Agency (DARPA) under AF Contract No. F19628-95-0002. The opinions, interpretations, conclusions and recommendations are those of the authors and are not necessarily endorsed by the United States Air Force.

References

[1]. L. D. Hicks, T. C. Harman, X. Sun, and M. S. Dresselhaus, Phys. Rev. B 52, R10493 (1996).

[2]. T. C. Harman, D. L. Spears, and M. J. Manfra, J. Electron. Mater. 25, 1121 (1996).

[3]. G. D. Mahan and H. D. Lyon, Jr., J. Appl. Phys. 76, 1899 (1994).

[4]. See R. D. S. Yadava, A. K. Gupta, and A. V. R. Warrier, J. Electron. Mater. 23, 1359 (1994) for a review of nine different hole scattering mechanisms in p-type HgCdTe.

[5]. H. Sitter, K. Lischka, and H. Heinrich, Phys. Rev. B 16, 680 (1977).

[6]. M. Sugawara, M. Kondo, S. Yamazaki, and K. Nakajima, J. Cryst. Growth 93, 318 (1988).

[7]. D. L. Partin, J. Electron. Mater. 13, 493 (1984).

[8]. T. Koga, S. B. Cronin, X. Sun, G. Dresselhaus, and M. S. Dresselhaus, personal communication.

[9]. A. J. Strauss, personal communication

[10]. A. J. Strauss, J. Electron. Mater. 2, 553 (1973).

[11]. B. F. Gruzinov, I. A. Drabkin, Yu. Ya. Eliseeva, E. Ya. Lev, and I. V. Nelson, Sov. Phys. Semicond. 13, 767 (1979).

[12]. V.I. Kaidanov, S. A. Nemov, and Yu I. Ravich, Sov. Phys. Semicond. 26, 113 (1992).

[13]. S. D. Darchuk, L. A. Korovina, and F. F. Sizov, Sov. Phys. Semicond. 26, 476 (1992).

[14]. See, for example, G. Nimtz and B. Schlicht, Narrow Gap Semiconductors, Springer Tracts in Modern Physics 98 (Berlin, Springer, 1983) and references therein.

[15]. R. S. Allgaier and B. B. Houston, Jr., J. Appl. Phys. 37, 302 (1966).

[16]. N. V. Kolomoets, M. N. Vinogradova, E. Ya. Lev, and L. M. Sysoeva, Sov. Phys. Solid State 8, 2337 (1967).

Thermoelectric Transport in Low Dimensional Superlattice Systems

T. L. Reinecke
Naval Research Laboratory
Washington DC 20375 USA

D. A. Broido
Dept. of Physics, Boston College
Chestnut Hill, MA 02167

Abstract:
We discuss the thermoelectric transport coefficients and the figure of merit of realistic quantum well and quantum wire superlattice systems. The electronic contribution to the transport is described in detail by including the effects of the heat current along the barriers, of carrier tunneling through the barriers, of well width dependence of the scattering rates, and of lifting of the valley degeneracy in realistic superlattice systems. The lattice thermal conductivity is described by including the effects of interface scattering.

Introduction:

In the past several years there has been considerable interest in quantum well and quantum wire superlattice systems in the search to find improved materials for applications in cooling and power generation [1]. The figure of merit [2], $ZT=\sigma S^2/\kappa$, where σ is the electrical conductivity, S the Seebeck coefficient and $\kappa = \kappa_e+\kappa_L$ is the total electron and lattice thermal conductivity, provides a measure of the quality of a material for such applications. These low dimensional superlattice systems are of interest because of the possibility of modifying their electrical properties through confinement and their lattice thermal properties through the introduction of additional scattering.

Interest in this area was stimulated by the proposal that these systems should exhibit a greatly enhanced figure of merit as a result of the effects of confinement on the electronic density of states [3-5]. These suggestions used arguments based on idealized two- and one-dimensional electronic systems. In subsequent work it has been shown that additional effects must be included in order to obtain a reliable understanding of electronic contribution to the thermoelectric transport in realistic systems. Among these effects are the heat current along the barrier layers, and carrier tunneling through the barriers [6-10]. Further, in recent work [11,12] we have pointed out that additional dependences of the figure of merit on the superlattice period come from the well width dependence of the carrier scattering rates and from the lifting of the valley degeneracy in multi-valley systems.

In addition to the electronic contribution to the thermoelectric transport, the phonon thermal conductivity plays an important role in determining the value of the figure of merit in these systems. It is expected that the interfaces and associated disorder will reduce the lattice thermal conductivity and thus will lead to increased figures of merit. Measurements of the phonon thermal conductivity of superlattices both parallel to the growth direction and also along the planes indicate that reductions of up to an order of magnitude occur over the corresponding quantity for pure bulk systems [13-15]. Calculations have been made which are consistent these findings [16-18].

Our interest in these systems has been to obtain a reliable, quantitative understanding of thermoelectric transport in realistic systems including all of the essential physical features. In the following we describe some work addressing this objective.

Electronic Transport:

In the following we consider quantum well superlattices with well and barrier widths, a and b, and period $d=a+b$. The direction of transport will be taken to be in the plane of the quantum well layers, which has been the direction of interest in most work to date. A Boltzmann equation approach is used for the steady state electron transport in the presence of a weak electric field $\mathbf{E}$ and a weak temperature gradient ∇T. The electric and heat currents in the superlattice are given by

$$\mathbf{J}_e = -e \sum_{nj} \int \frac{d\mathbf{k}}{4\pi^3} \mathbf{v}_{nj} \delta f_{nj} \qquad (1)$$

$$\mathbf{J}_Q = \sum_{nj} \int \frac{d\mathbf{k}}{4\pi^3} \mathbf{v}_{nj} (\varepsilon - \mu) \delta f_{nj} \qquad (2)$$

where δf_{nj} is the deviation from the equilibrium distribution function for the n^{th} carrier subband and j^{th} valley. δf_{nj} is given by

$$\delta f_{nj} = \left(-\frac{\partial f_{0nj}}{d\varepsilon} \right) \frac{\hbar \mathbf{k}_{||}}{m_{j||}} \cdot \left[-e\mathbf{E}\, \tau_{1nj}(k_{||}) - \frac{\nabla T}{T} \tau_{2nj}(k_{||}) \right] \qquad (3)$$

where the scattering functions, τ_{1nj} and τ_{2nj}, are determined from the solution of the Boltzmann equation for each well thickness. Here $\varepsilon = \varepsilon_{nj}(\mathbf{k})$ is the energy dispersion of the carrier in the nj^{th} subband, and $m_{j||}$ is the mass of the j^{th} valley for motion along the quantum well. The electric and heat currents are related to the transport coefficients by

$$\mathbf{J}_e = \sigma\mathbf{E} - \sigma S \nabla T$$
$$\mathbf{J}_Q = \sigma S T \mathbf{E} - \gamma_e \nabla T \qquad (4)$$

where $\gamma_e = \kappa_e + \sigma S^2 T$, and κ_e is the electronic contribution to the thermal conductivity.

First let us consider the effects of carrier confinement in realistic superlattices, including the thermal currents along the barriers and of carrier tunneling through the barriers. To do this, it will be adequate to neglect the well width and energy dependence of the scattering rates, which is done approximating τ_1 and τ_2 in eqn (3) by a single constant. In that case the transport coefficients are given by simple expressions in terms of the carrier density of states [3,19].

The density of states including the effects of carrier tunneling through the barriers with offset V_0 is described using a Kronig-Penny-like model. The carrier dispersion of the n^{th} subband is approximated by

$$\varepsilon_n(\mathbf{k}) = \varepsilon_n(k_z) + \frac{\hbar^2}{2}\left(\frac{k_x^2}{m_x} + \frac{k_y^2}{m_y}\right) \qquad (5)$$

Here, the superlattice axis is in the z-direction, m_x and m_y are the anisotropic effective masses in the plane of the layers, and $\varepsilon_n(k_z)$ is obtained by solution of the Kronig-Penney model. For relatively weak coupling between wells, $\varepsilon_n(k_z)$ is given by

$$\varepsilon_n(k_z) = \varepsilon_{n0} + \Delta_n \left(1 \mp \cos k_z d \right) \qquad (6)$$

where ε_{n0} is the energy at the bottom of the n^{th} subband, the overlap integrals, Δ_n , give the half-width of the subband, and the + (-) sign corresponds to negative (positive) band dispersion. Δ_n depend on potential height V_0, the barrier and well widths *a* and *b* and on the subband index n. For the range of parameters, *a*, *b*, and V_0, considered here, we find that this form gives a good fit to the relevant portion of the exact Kronig-Penney band structure. Then the density of states of the superlattice can be obtained analytically by summing over wavevectors at a given energy.

We give ZT for Bi_2Te_3 in order to illustrate the effects of the superlattice band structure of the electronic states. In the bulk, Bi_2Te_3 has the one of the highest *ZT* values known. Its transport properties are highly anisotropic. We take the x-direction to be in the quantum well plane and to be along the a_0 axis of the hexagonal unit cell. The superlattice direction z is taken to be along the c_0 axis of the unit cell, which gives [3] $m_x = 0.021$, $m_y = 0.32$ and $m_z = 0.081$ and a mobility $\mu_x = 1200$ $cm^2/Vsec$. These calculations were done at room temperature, T=300K, and in each case the carrier density is chosen to maximize *ZT*. The value of the phonon contribution to the thermal conductivity is taken to be [3] the bulk value $\kappa_{ph} = 0.015$ W/cmK for the well and barrier material. We have taken both the quantum well and barrier materials to be the same, and have put a potential barrier between them. In order to account in an approximate way for the six valleys of the conduction band of Bi_2Te_3, σ and κ_e have been multiplied by 6 for both bulk and superlattices [3]. This is expected to be an overestimate of these quantities in superlattices because the anisotropic masses partially lift the valley degeneracy.

The results for ZT_S for Bi_2Te_3 superlattices are shown in Figure 1. Here the barrier height, V_0, is taken to be 0.2 eV which is typical of off-sets in semiconductor superlattices. In Figure 1, ZT_S for thicker wells lies below the bulk value, and this effect is more pronounced for the larger barrier thicknesses. This behavior arises from the parasitic effects of the thermal current that flows through the barrier layers. For decreasing well widths, ZT_S increases and reaches a maximum, and then for still smaller well widths ZT_S decreases as a result of carrier tunneling through the barriers. The value of the well width at which the maximum occurs decreases for increasing barrier widths *b*. The maximum of ZT_S for superlattices is found to be enhanced over the bulk value and is nearly independent of the barrier width for this range *a* and *b*. This enhancement arises from the changes in the density of states upon electron confinement in relatively narrow wells.

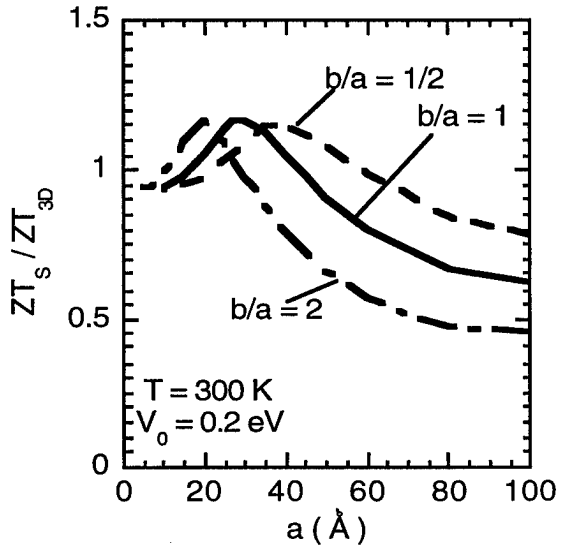


Fig. 1 The figure of merit ZT_S of Bi_2Te_3 superlattices scaled by ZT_{3D} for the corresponding bulk given as a function of the well width *a* for several ratios of the barrier width to well width, *b/a* = 1/2 (dashed line), 1 (solid line), and 2 (dashed - dotted line).

The dependence of ZT_S on the barrier height, V_0, is shown in Figure 2. For large periods *d*, ZT_S increases for decreasing V_0 and approaches the bulk value. In effect, the thermal conduction in the barriers becomes relatively less

important as the carriers spread out into the barriers. For superlattice periods near the maximum of ZT_S , its enhancement over the bulk value is larger for larger V_0, which arises from greater quantum confinement. This shows that the maximum in ZT_S arises from tunneling between the layers.

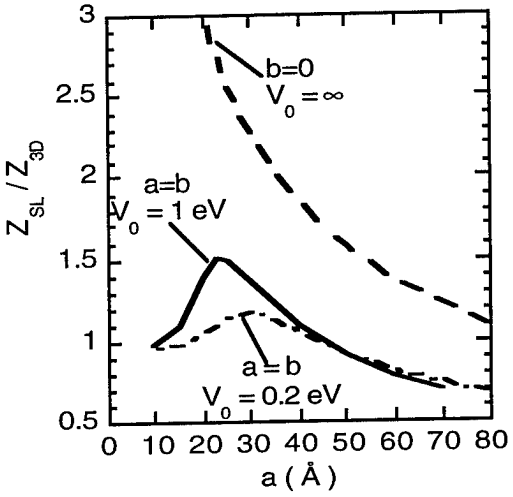


Fig. 2 The figure of merit ZT_S of Bi_2Te_3 superlattices (scaled by ZT_{3D}) as a function of the superlattice period d for potential barrier heights, V_0 = 0.2 eV (dashed dotted line),and 1 eV (solid line). Also shown is the ZT_S for $V_0=\infty$ and b=0 (dashed line).

We now consider the well width dependence of ZT_S that arises from the well width dependence of the carrier scattering rates. The constant relaxation time approximation (CRTA) used above neglects this dependence. It is well known that electron scattering rates in superlattices differ qualitatively from those in bulk materials [20,21]. Here we consider scattering due acoustic phonons, polar optical phonons, and impurities. In the following we will also consider the well width dependence of ZT that results from the lifting the valley degeneracy of multivalley systems due to confinement.

From the results above in the constant relaxation time approximation, we see that strong carrier confinement in the quantum well layers produces large ZT's. Thus, we will consider in the following the strong confinement limit in which the barrier height $V_0 \rightarrow \infty$. For this case, no tunneling occurs between the quantum wells. In order to solve the Boltzmann equation, we use an iterative approach that was developed to treat inelastic scattering mechanisms in bulk systems [22]. We have extended this approach to treat the multi-subband case of a quantum well superlattice. For transport in the plane of the well, the transport coefficients are given by

$$\sigma = \frac{e^2 k_B T}{\pi\hbar^2 d}\sum_{nj}\int_0^\infty dx\left(-\frac{\partial f_0(\zeta_{nj})}{\partial x}\right)\tau_{1nj}(x)x \qquad (7)$$

$$\sigma S = -\frac{e k_B}{\pi\hbar^2 d}\sum_{nj}\int_0^\infty dx\left(-\frac{\partial f_0(\zeta_{nj})}{\partial x}\right)\tau_{2nj}(x)x \qquad (8)$$

$$\gamma_e = \frac{k_B^2 T}{\pi\hbar^2 d}\sum_{nj}\int_0^\infty dx\left(-\frac{\partial f_0(\zeta_{nj})}{\partial x}\right)(x-\zeta_{nj})\tau_{2nj}(x)x \qquad (9)$$

Here the Fermi distribution $f_0=1/(\exp(x-\zeta_{nj})+1)$ involves the scaled chemical potential, $\zeta_{nj} = (\mu-\varepsilon_{nj})/k_BT$, where ε_{nj} is the energy at the bottom of the n^{th} subband deriving from the j^{th} valley. τ_{1nj} and τ_{2nj} are the scattering functions obtained by solving the full Boltzmann equation.

For illustration we evaluate the transport coefficients ZT for PbTe superlattices, which are of particular current interest experimentally. Bulk PbTe is a multi-valley semiconductor which has four parabolic anisotropic conduction band valleys along the [111] crystallographic directions. We consider explicitly here the lifting of the carrier valley degeneracy of multi-valley semiconductors due to confinement. The superlattice axis is along the [111] direction. We employ a two-band $\mathbf{k}\cdot\mathbf{p}$ model to obtain the band-edge masses for the j^{th} valley as

$$\varepsilon_j(\mathbf{k}) = \frac{\hbar^2}{2}\left(\frac{k_z^2}{m_{jz}} + \frac{k_{||}^2}{m_{j||}}\right) \qquad (10)$$

where m_{jz} and $m_{j||}$ are the masses along the superlattice axis and in the plane of the layers, respectively. Along the principal axes of the single longitudinal ellipsoidal valley aligned along [111] (z-direction) we find m_{lz}=0.35 and $m_{l||}$=0.034. The other three oblique valleys are equivalent, and the band-edge mass for these valleys projected along the [111] direction is m_{oz}=0.038. The corresponding density-of-states averaged in-plane mass is calculated to be $m_{o||}$=0.076. The parameters used in the calculations of the scattering rates are [23] the longitudinal optical phonon energy $\hbar\omega_0$ =14 meV, the static and high frequency dielectric constants, κ_0=33, κ_∞=414, the deformation potential constant, D=25eV, and ρv_l^2 = 486 meV/Å^3 where ρ is the density, and v_l is the average speed of the longitudinal acoustic phonons. The lattice contribution to the thermal conductivity in PbTe is taken to be κ_{ph}=2W/m-K.

Results of these calculations are show in Figure 3. Here the barriers have been taken to zero thickness and infinite potential height, which produces the highest ZT in the CRTA. Once again, the carrier density is chosen to maximize ZT. The solid line gives the results of the full calculation. With decreasing well thickness, ZT_{SL} first decreases and then increases for the narrowest wells. This behavior is caused by the lifting of the valley degeneracy due to the quantum

confinement, which occurs because of the large difference in effective masses for longitudinal and oblique valleys along the confinement direction. As the well thickness decreases further, the ZT of the system, now with only a single contributing valley, increases modestly. ZT_{SL} remains below the bulk value for wells down to 10Å. The dotted line is ZT_{SL} calculated in a multi-subband CRTA that uses the same relaxation time for each subband, which is chosen to match the bulk mobility [19], μ_{bulk} =1700cm^2/V-s. The same trend is evident in this case. Thus, for well widths of interest in practice the increase in ZT_{SL} brought about by the strong confinement is more than offset by a decrease in ZT_{SL} arising from the lifting of the valley degeneracy.

In order display the effects of the well width dependence of the scattering rates, we consider a model of a PbTe superlattice system in which all four valley are degenerate with the mass of the [111] valley. The dash-dotted line in Figure 3 gives results for ZT within the with this valley degeneracy. For small well thicknesses, ZT increases sharply, reaching a value almost 5 times the bulk value for the narrowest well considered, a=10Å. For comparison, the dashed line shows ZT obtained with the theoretical treatment given here. The increase in ZT is considerably smaller than that predicted by the CRTA. This difference arises from the decrease in the scattering functions, τ_{1nj} and τ_{2nj}, with decreasing well width.

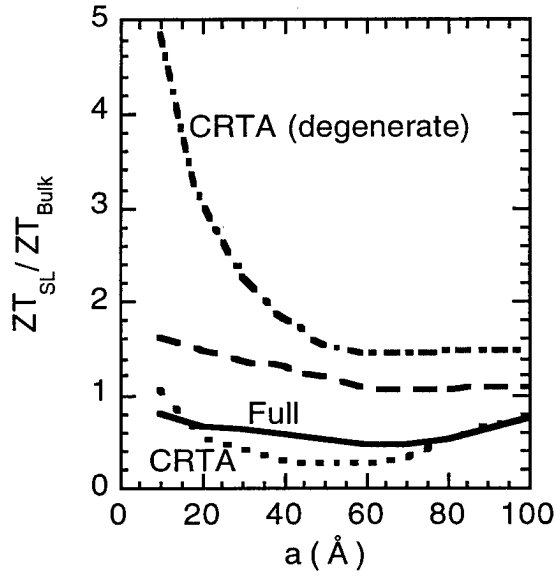


Fig. 3 ZT_{SL} /ZT_{Bulk} .vs. well thickness, a, for PbTe superlattices having zero barrier thickness with and without lifting of valley degeneracy. Solid line: full treatment in text including lifting of valley degeneracy; dotted line: CRTA with lifting of valley degeneracy; Dashed line: full treatment with enforced valley degeneracy; Dash-dotted line: CRTA with enforced valley degeneracy.

We have also studied the effects on the transport coefficients and on the figures of merit of a uniform distribution of ionized impurites equal in number to the carriers present, and we have included the screening due to the free carriers. The impurities are treated as Coulomb scattering centers. The screening is included in the Thomas-Fermi approximation, and both the impurities and the phonon interactions have been screened. In general the impurity scattering reduces ZT_S modestly at each well width, and the screening tends to increase it modestly. It is particularly noteworthy in PbTe that the impurity scattering has negligible effect on ZT_S because of the large background dielectric constant in this material. Thus control of the doping distribution in PbTe by, for example, modulation doping should not have an effect on ZT_S.

Lattice Thermal Transport:

In semiconductors the lattice contribution to the thermal conductivity typically dominates that of the electrons, and therefore the lattice thermal conductivity has a large influence on ZT_S of the system. In recent work [13-15] it has been found that the lattice thermal conductivity of semiconductor superlattices are decreased from the bulk values by up to a factor of 5 for transport along the quantum well planes and by up to a factor of 10 for transport along the growth direction.

Theoretical work has been done which associates the decreased thermal conductivity along the superlattice axis [16] and along the planes [17,18] to interface scattering. In particular, a Knudsen flow model for the phonon thermal transport along planes of a quantum well was introduced in Ref. [17], and it was extended to the case of transport in a quantum wire in Ref. [18]. Here we sketch these results using the case of a quantum wire for illustration.

The lattice thermal conductivity is treated using a linearized Boltzmann equation in the relaxation time approximation for the acoustic phonons. For a quantum wire with an axis in the z direction the Boltzmann equation becomes

$$v_x\frac{\partial N_1}{\partial x} + v_y\frac{\partial N_1}{\partial y} + \frac{N_1}{\tau} = v_z\frac{\partial N_0 \partial T}{\partial T\ \partial z} \qquad (11)$$

where v_i are the components of the velocity in the i directions, $N_0 = 1/(\exp(\hbar\omega(\mathbf{q})/k_BT)-1)$ is the equilibrium Bose distribution for the acoustic phonons, and N_1 is the deviation of the phonon thermal distribution from the equilibrium N_0 due to the thermal gradient along the wire. The phonon heat current then is

$$J_Q = \int \frac{d\vec{q}}{2\pi^3} v_z N_1 h\omega(\vec{q}) \qquad (12)$$

For most superlattice periods the well or wire width generally is smaller than the phonon mean free path. In the Knudsen

model, the Boltzmann equation is solved subject to the condition that the phonons are in equilibrium with the interfaces which are at a specified temperature. In addition, the scattering at the interfaces is specified as being either specular or diffuse [16-18], and in these calculations the relative amount of specular and diffuse scattering is varied.

Results for the phonon thermal conductivity of quantum wells and of cylindrical quantum wires are shown in Figure 4. Completely diffuse interface scattering was used in the figure. It is seen that the thermal conductivity decreases for smaller sizes, and for small sizes it can be an order of magnitude lower than the bulk value. We find that the resulting thermal conductivity depends on the choice of the form of phonon scattering time in the bulk. In Figure 4 we have used two forms for this relaxation time, one is a constant mean free path model, and the other is other is a frequency dependent relaxation time that has been used for the bulk [24].

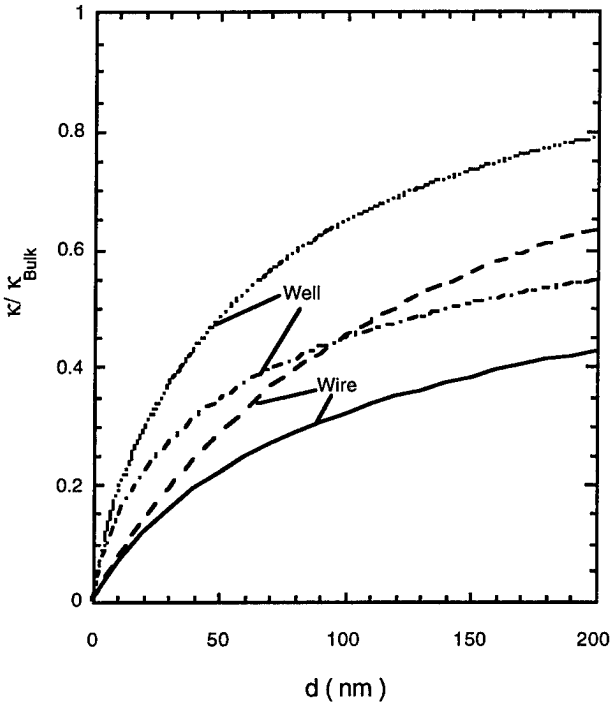


Fig. 4 Lattice thermal conductivity κ scaled by bulk value κ_{Bulk} for GaAs quantum wells and quantum wires as a function of well/wire thickness, d, for diffuse interface scattering. Dotted and dashed lines are for constant mean free path model of bulk phonon scattering, and dash-dotted and solid curves are frequency dependent relaxation time model.

Summary

Here we have discussed both the electronic and the thermal contributions to thermoelectric transport in superlattices. The issues involved in giving a quantitative understanding for the electrical contribution are coming to be relatively well understood, and progress is being made experimentally and theoretically in understanding the lattice contribution to the thermal conductivity.

Acknowledgments

This work was supported in part by the US Office of Naval Research.

References

[1] Gerald Mahan, Brian Sales and Jeff Sharp, Physics Today **50** (No. 3), 42 (1997)

[2] H. J. Goldsmid, in *Thermoelectric Refrigeration*, Plenum Press, NY (1964).

[3] L. D. Hicks and M. S. Dresselhaus, Phys. Rev. **B 47**, 12727 (1993).

[4] L. D. Hicks, T. C. Harman and M. S. Dresselhaus, Appl. Phys. Lett. **63**, 3230 (1993).

[5] L. D. Hicks and M. S. Dresselhaus, Phys. Rev. **B 47**, 16631 (1993).

[6] J. O. Sofo and G. D. Mahan, Appl .Phys. Lett. **65**, 2690 (1994).

[7] D. A. Broido and T. L. Reinecke, Phys. Rev. B **51**, 13797 (1995).

[8] D. A. Broido and T. L. Reinecke, Appl. Phys. Lett. **67**, 100 (1995).

[9] D. A. Broido and T. L. Reinecke, Appl. Phys. Lett. **67**, 1170 (1995).

[10] P. J. Lin-Chung and T. L. Reinecke, Phys. Rev. B **51**, 13224 (1995).

[11] D. A. Broido and T. L. Reinecke, Appl. Phys. Lett. **70**, 2834 (1997).

[12] D. A. Broido and T. L. Reinecke, Phys. Rev. B (submitted)

[13] T. Yao, Appl. Phys. Lett. 51, 1798 (1987).

[14] X. Y. Yu, G. Chen, A. Verman, and J. S. Smith, Appl. Phys. Lett. **67**, 3554 (1995).

[15] W. S. Capinski and H. J. Maris, Physica B **218@220**, 699 (1996).

[16] G. Chen, and C. Tien, Journal of Thermophysics and Heat Transfer **7**, 311 (1993).

[17] P. Hyldgaard and G. D. Mahan, Thermal Conductivity 23 (Technomic Publishing Co. Inc., Lancaster, Pennsylvania) pg. 172, (1996).

[18] S. G. Walkauskas, D. A. Broido, K. Kempa, and T. L. Reinecke, Appl. Phys. Lett. (submitted).

[19] N. D. Ashcroft and N. D. Mermin, *Solid State Physics*, (Saunders, Phildelphia, 1976), Chapt. 13.

[20] P. J. Price, Ann. Phys. (NY) **133**, 217 (1981).

[21] P. A. Knipp and T. L. Reinecke, Phys. Rev. B **48**, 5700 (1993).

[22] J. O. Sofo and G. D. Mahan, Phys. Rev. B **49**, 4565 (1994).

[23] Landholt and Bö rnstein, *Numerical Data and Functional Relationships in Science and Technology, New Series*, Vols. 17f (Springer-Verlag, Berlin, 1983) pp. 170-180.

[24] J. Callaway, Phys. Rev. **113**, 1046 (1959).

On the Use of Bismuth in Quantum Wells

A. Dauscher, B. Lenoir, O. Boffoué, X. Devaux, R. Martin-Lopez, H. Scherrer

Laboratoire de Physique des Matériaux, URA CNRS 155, Ecole des Mines, Parc de Saurupt, 54042 Nancy (France)
Tel.:+33/3/83584170, Fax:+33/3/83579794, E-mail:dauscher@mines.u-nancy.fr

Abstract

A rapid survey of some theoretical considerations concerning the use of multiple quantum well structures (MQWS) in thermoelectricity is given as well as why bismuth can be a perspective material for the development of a new class of thermoelectric systems. Problems arising from Bi film synthesis are discussed, in relation with the preparation of Bi-based MQWS. Some experimental results are reported on pulsed laser deposited Bi films prepared in our laboratory.

Introduction

Bismuth is a potentially interesting material to be used in multiple quantum well structures for thermoelectric applications. In the past and still nowadays, great emphasis was devoted to the study of bismuth in thin-film form due to its special properties (classical and quantum size effects, weak localization effects, elastoresistance effects, nonlinear optical properties). Particular care was taken to optimize the structure of the films for each specific application.

The aim of this paper is to have an in-depth look on the large amount of papers dealing with the preparation of thin bismuth films. The paper is divided in two parts. First, we will summarize why bismuth can be a choice material in quantum wells for the development of a new class of performant thermoelectric systems. Second, we will try to stand out of the literature the essential points concerning the problems linked to Bi film synthesis that can be useful for the preparation of Bi-based MQWS. Some experimental results obtained in our laboratory on the preparation and characterization of thin bismuth films synthesized by pulsed laser deposition (PLD), PLD being a new method to deposit Bi films, will be included in the paper.

Interest of Bismuth in MQWS

The dimensionless figure of merit ZT is a measure of the quality of a material to be used as a thermoelement and is given by $ZT = \alpha^2\sigma T/\kappa$, where α is the thermoelectric power, σ the electrical conductivity, κ the total thermal conductivity and T the absolute temperature. With conventional materials, the maximum limit of ZT has remained near 1. As it is highly desired to improve ZT, there has been recently many attempts in finding new bulk materials for the development of highly efficient thermoelectric systems for energy conversion applications [1]. In addition to the search of new thermoelectric materials, several papers were published analyzing the application of quantum wells [2-8]. By these two ways, it appears that the limit barrier $ZT \approx 1$ can be overcome.

The first quantitative theoretical investigations, performed by Hicks and co-workers [2], suggest that conventional semiconductor quantum wells would have an improved figure of merit. They show theoretically, and confirmed later experimentally [9], that ZT for a single quantum well increases as the well width decreases. The physical origin of the large increase of ZT proposed for such ideal quantum wells arises mainly from the large density of electron states per unit volume that occurs for small well widths in a two-dimensional geometry. These ideas used for a single quantum well were then extended to superlattices by Mahan, Lyon and Sofo [4,5] and Lin-Chung, Broido and Reinecke [6,7] who took into account the finite width of barriers and tunneling probability between quantum wells. Their conclusions were that the contribution of these two effects substantially decrease ZT for superlattices as compared to those of a single quantum well. Nevertheless, for a composite superlattice system, ZT could be increased above that of the maximum of the constituent bulk materials as a result of the two dimensional character of the electronic properties in one of the materials for small well widths. Moreover the non-zero barrier width has a significant effect in determining ZT of superlattice systems. The precise value of ZT for given well and barrier widths largely depends on the choice of materials in the superlattice.

Another interesting point underlined by Hicks et al. concerns the possibility of using two-band materials in quantum well superlattices [3]. In two-band bulk materials, the presence of both electrons and holes decreases α resulting in a lowering of ZT so that two-band materials such as semimetals are not performant thermoelectric materials. However, by preparing them in the form of two-dimensional quantum well superlattices, a significant increase in ZT over the bulk value may be achieved, allowing the possibility of using a new class of materials as thermoelectric refrigeration elements. Apart from the increase of the electronic density of states, the other factor responsible for the large increase in ZT over the bulk value is the separation of the two bands and the transformation of the materials into an effective one-band system.

Among two-band materials, semimetallic bismuth is certainly one of the most interesting due to its particular electronic properties. Electrons are located in three equivalent ellipsoids at the L-points of the Brillouin zone and the holes in a single ellipsoid at the T-point. The overlap energy of the

0-7803-4057-4/97 $10.00 ©1997 IEEE

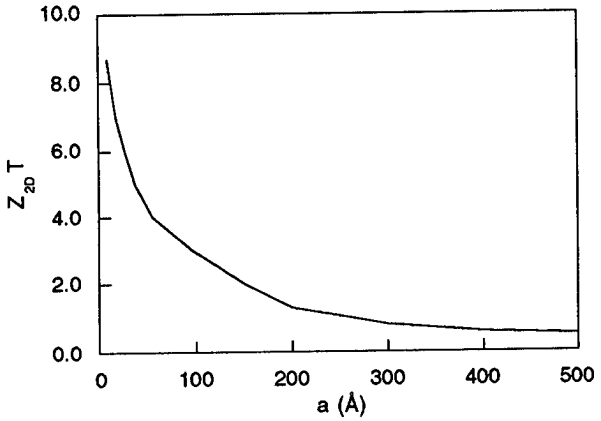


Figure 1: $Z_{2D}T$ vs layer thickness a for a quantum well of Bi at 300 K, after [3].

electron and hole bands in bulk Bi is 38 meV. Bulk dimensionless figure of merit in bismuth at 300 K is equal to 0.4 but as mentioned by Gallo et al. [10], ZT ≈ 2 would be achieved if the T-hole band is absent. Hicks and co-workers [3] calculated the figure of merit $Z_{2D}T$ at 300 K for a single Bi quantum well fabricated in the basal planes. Their results are reported in Fig. 1. The sharp increase of ZT for thicknesses lower than 30 nm is linked to the appearance of the semiconducting state.

This semimetal-semiconductor (SMSC) transition was postulated by Sandosmirskii [11] and Lutskii [12 and refs therein], and remains still nowadays a controversial issue despite many experimental and theoretical efforts. This feature gave rise to a lot of papers dealing with Bi thin film preparation, as will be seen later on in this paper.

Preparation of Pulsed Laser Deposited Bi Films

The bismuth films described in this study were deposited under vacuum (10^{-8}-10^{-7} mbar) from a pulsed, frequency-doubled Nd:YAG laser beam operating at 533 nm (repetition rate: 5 Hz, pulse duration: 10 ns, density of energy: 3 J/cm^2) onto glass substrates maintained at room temperature during deposition. The experimental set-up has been described in details elsewhere [13]. In order to study thickness effects on structure, morphology, roughness and transport properties, the deposition duration was varied between 30 and 180 min leading to film thicknesses between about 8.0 to 45.0 nm.

Overview of Thin Bismuth Film Synthesis

Synthesis of monolayers of thin bismuth films has been widely studied. Many works dealing on electronic diffraction and microscopy have been reported with the aim to determine the film characteristics as a function of film thickness, deposition rate, nature and temperature of the substrate. The investigations were performed to study either purely structure dependence of the films on the growth conditions and/or to correlate some electric (resistivity, Hall coefficient, magnetoresistance) and optic properties to the observed structure, morphology, roughness and surface defects of the films.

In the pioneer works, the bismuth films were generally grown by conventional thermal evaporation. If studies still deal with thermal evaporation nowadays, many other deposition methods have been developed this last decade, mainly with the aim to synthesize bismuth based multilayer or superlattice systems: molecular beam epitaxy (MBE) [14-18], sputtering [19-21], electron beam sputtering coupled with an electron cyclotron ion source [22], ionized [23] or low energy [24] cluster beam deposition and pulsed laser deposition [25]. The more commonly used substrates are glass, mica and oriented barium fluoride. Some studies were carried out on oriented silicon, sapphire, cadmium tellurium, silicon nitride and carbon coated substrates. Depending on the deposition method, numerous substrate temperatures (between room temperature and 240°C) and deposition rates (less than 0.01 nm/s to several nm/s) have been given as being the best to form smooth and continuous thin bismuth layers.

The main conclusions that can be pulled out from these studies are the following:

- the films directly deposited onto the substrate grow in an island growth mode out to a thickness of about 8.0 nm before coalescing into a continuous film, whatever the substrate.

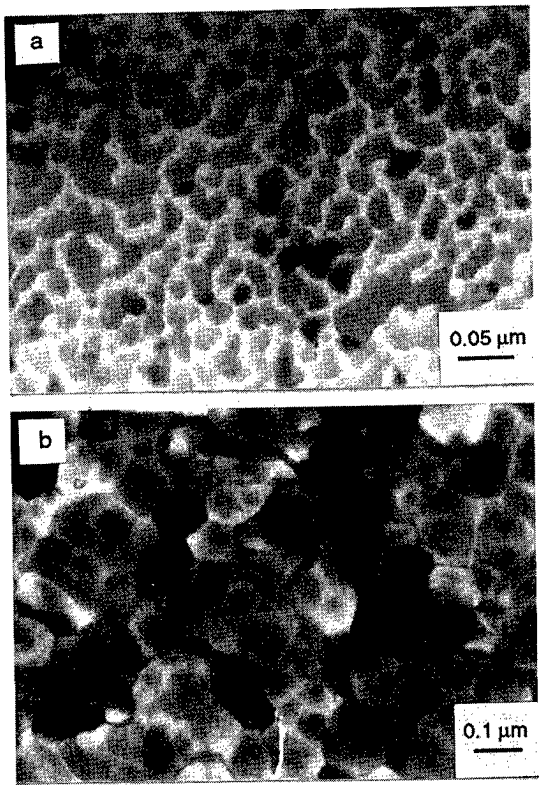


Figure 2: TEM images of a) 8 nm and b) 40 nm thick Bi films deposited by PLD.

The percolation threshold, determined by measuring "in situ" the changes of electrical resistivity as a function of film thickness is very sharp and occurs for thickness of about 9.0 nm [24,26]. These results were further confirmed by TEM [23], AFM [27], STM [28] and ellipsometry [29] measurements. This island formation complicates the study of the transport properties of very thin bismuth films. In figure 2 are reported TEM images of Bi films fabricated by PLD showing that the 8-nm-thick Bi film is discontinuous, the grains becoming however connected one to each other whereas the 40-nm-thick film is completely continuous with no voids at the grain junctions. These results agree with the previously mentionned studies performed on films synthesized by other deposition methods.

- the densest films are formed for substrate deposition temperature of around 70-80°C, as observed by SEM [30].

- surface roughness of about 3.0 nm are also achieved at these substrate temperatures according to TEM cross sectional [31], SEM [30] and AFM [27] studies. Films thicker than 10 nm generally exhibit smoother surfaces than thinner films due to the filling in of the channels between the growing grains.

Figure 3 shows AFM images (0.5 μm x 0.5 μm) of surface topographies of the same Bi films as in Figure 2. The root-mean-square roughness is equal to 2.8 and 4.2 nm for film thicknesses of 8 and 40 nm, respectively. The grain size increases as thickness becomes greater, as already observed by TEM. The grain shape also undergoes modifications, going from nearly spherical to faceted.

- bismuth films grown by thermal evaporation at substrate temperatures less than 100°C show in-plane polycrystalline structures. However, they present a texture with the trigonal axis of the Bi hexagonal structure normal to the film plane and a grain size of about 1 μm that are formed irrespective of the substrate nature. This texture is stable upon heat treatment at 200°C [32] while crystallites with random orientation are superimposed on the above mentioned ones when the substrate is heated above 150°C [33]. Higher resistivities than in bulk Bi are encountered in the films due to the problem of small grain sizes. In figure 4 are represented the $\theta/2\theta$ X-ray diffraction patterns of the same Bi films as in figure 2. At the beginning of film growth, only a low intense (012) peak is observed. The 40 nm thick film presents the (00*l*) peaks that are usually observed in Bi films, showing a preferential texture with the trigonal axis of Bi perpendicular to the film plane. A low intense (012) peak remains however present. This peak does no longer appear when the substrate is heated at 70°C during deposition. These results show that film structure changes as a function of film thickness. Growth goes through different steps: first growth develops in a random way and second with the densest planes parallel to the substrate plane. Such results have never been mentioned for Bi films in the literature.

- insulating Bi_2O_3 grows at the surface and internal boundaries when keeping the films under air at room temperature, leading in the reduction of the effective film thickness. Some result discrepancies observed by several authors may result from surface oxidation. Special care must therefore be taken in the handling of the films to avoid surface

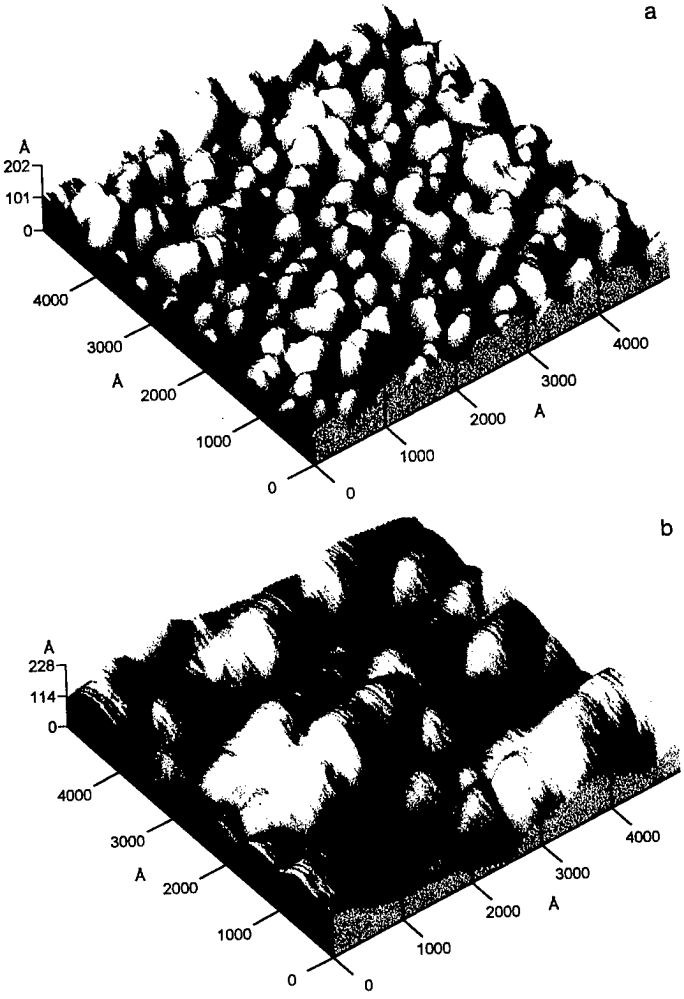


Figure 3: AFM surface images of a) 8 nm and b) 40 nm thick Bi films prepared by PLD.

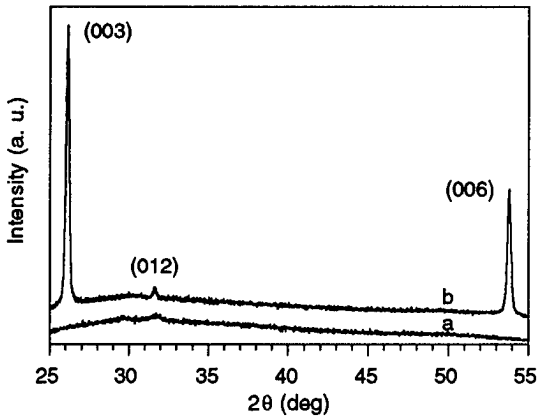


Figure 4: X-ray diffraction patterns of a) 8 nm and b) 40 nm thick Bi films prepared by PLD.

contamination even as during deposition where ultra-high vacuum is recommended.

- the history of substrate (cleaning, cleavage, presence of defects, preheating, temperature during deposition) is a very important factor that affects nucleation and growth of the Bi films [19,34].

For the use of bismuth in quantum wells, many efforts must be made to produce epitaxial thin films with the largest grain size, the smoothest surface and the sharpest interfaces between wells and barriers since grain boundaries and surface defects greatly affect the transport properties due to scattering effects. As bismuth layers have usually the (111) texture, one have to use a substrate commensurate with the (111) plane to synthesize epitaxial films. Mica and BaF_2(111) substrates, whose lattice mismatches with Bi in these planes is small (less than 4 %) are the two principal substrates reported in the literature. However, with mica twinning is possible because two different growth orientations are equally probable, leading to films with two crystal orientations containing twin boundaries. Jing et al. [34] reported a nice AFM study to image the growth of Bi surfaces on mica substrates. Their best growth conditions (substrate temperature 140°C, deposition rate 0.5 nm/s, annealing 1 hour at 160°C) lead to large (some μm) crystallites formation with monoatomic stepped topology and a surface roughness on the order of 1.0 nm.

MBE seems to be the choice method to realize epitaxial growth and superlattices on BaF_2(111) substrates. Actually, Partin et al. [14] obtained epitaxial Bi films at the elevated growth temperature of 240°C and observed for the first time Shubnikov-de Haas oscillations although the first 90 nm of their films were polycrystalline. Van Hulst et al. [18] reported on the fabrication of high quality Bi thin films and heterostuctures of typical roughness of 1.0 nm by epitaxially growing them between semiconducting Bi-rich $Bi_{1-x}Sb_x$ alloys, the first $Bi_{1-x}Sb_x$ layer being used as buffer. An optimal substrate temperature of 70°C was found to ensure smooth single crystalline growth, followed by in situ reflection high energy electron diffraction (RHEED) patterns, yet preventing significant interdiffusion of Bi and Sb. High carrier mobilities, but lower than in bulk materials, are achieved as well as clean termination of the film surfaces with little band bending. On the other hand, Yi et al. [17] successfully used CdTe($\bar{1}\bar{1}\bar{1}$) substrates and CdTe buffer layer to grow Bi/$Bi_{1-x}Sb_x$ superlattices. The lowest period was 14 nm. They observed by RHEED good crystal quality for substrate temperatures between 100 and 150°C. The same authors observed by cross-sectional TEM two kinds of coherent interfaces between Bi and CdTe layers in Bi/CdTe superlattices. Bi grows epitaxially on CdTe while CdTe grows in a columnar way on Bi [35]. Bi/Sb superlattices have also been fabricated [20-22]. Missana et al. [21] observed that in Bi/Sb layers, the morphology and the structure of the whole multi-layer system is determined by the first deposited layer.

All these results show that it is a tedious task to obtain simply high quality single layer bismuth films. It is nevertheless possible by the use of appropriate synthesis conditions to produce Bi-based multiple quantum well systems that can be optimized for thermoelectric applications. The choice of the barrier material is also of great importance as it has been discussed in part 1. PbTe-based alloys could be interesting barrier materials since PbTe has an electrical resistivity $\approx 10^3$ times higher than in Bi and has a low thermal conductivity. Bi and PbTe are structurally and chemically coherent: only small lattice mismatch (0.3 %) exists between the PbTe(111) cubic plane and Bi(111) trigonal plane, the lattice spacing of the constituents in adjacent planes being accommodated by biaxial strain rather by dislocations arrays, and both possess the same average number of valence electrons. Ketterson and co-workers [36,37] still reported the feasibility of compositionally modulated PbTe/Bi films deposited on mica at 100°C. Problem could arise from the easy diffusion of bismuth.

Conclusion

Although semimetallic bulk Bi has low thermoelectric properties, it could become interesting in thin film form due both to quantum size effects, particularly to the semimetal-semiconductor transition, and to the two dimensional nature of the density of states. MBE or any other ultra high vacuum deposition method seems to be particularly suitable to synthesize epitaxial films and Bi-based superlattices, combined with deposition on heated, at 70°C, oriented BaF_2 or CdTe substrates recovered by a buffer layer to smooth all the substrate defects. The choice of the barrier material remains a crucial problem. PbTe-based alloys or Bi-rich $Bi_{1-x}Sb_x$ alloys could be potential canditates.

References

[1] J.P. Fleurial, T. Caillat, A. Borshchevsky, "Skutterudites: an update", this conference.

[2] L.D. Hicks, M.S. Dresselhaus,"Effect of quantum-well structures on the thermoelectric figure of merit", Phys. Rev. B **47** (1993) 12727.

[3] L.D. Hicks, T.C. Harman, M.S. Dresselhaus, "Use of quantum-well superlattices to obtain a high figure of merit from nonconventional thermoelectric materials", Appl. Phys. Lett. **63** (1993) 3230.

[4] G.D. Mahan, H.B. Lyon, "Thermoelectric devices using semiconductor quantum wells", J. Appl. Phys. **76** (1994) 1899.

[5] J.O. Sofo, G.D. Mahan, "Thermoelectric figure of merit of superlattices", Appl. Phys. Lett. **65** (1994) 2690.

[6] P.J. Lin-Chung, T.L. Reinecke, "Thermoelectric figure of merit of composite superlattice systems", Phys. Rev. B **51** (1995) 13244.

[7] D.A. Broido, T.L. Reinecke, "Effect of superlattice structure on the thermoelectric figure of merit", Phys. Rev. B **51** (1995) 13797.

[8] L.W. Whitlow, T. Hirano, "Superlattice applications to thermoelectricity", J. Appl. Phys., **78** (1995) 5460.

[9] L.D. Hicks, T.C. Harman, X. Sun, M.S. Dresselhaus, "Experimental study of the effect of quantum-well structures on the thermoelectric figure of merit", Phys. Rev. B **53** (1996) R10493.

[10] C.F. Gallo, S.F. Chandrasekhar, P.H. Sutter, "Transport properties of bismuth single crystal", J. Appl. Phys. **34** (1963) 144.

[11] V.B. Sandomirskii, "Quantum size effect in a semimetal film", Sov. Phys. JETP **25** (1967) 101.

[12] V.N. Lutskii, "Quantum size effect - Present state and perspectives of experimental investigations", Phys. Stat. Sol. (a) **1** (1970) 199.

[13] A. Dauscher, A. Thomy, H. Scherrer, "Pulsed laser deposition of Bi_2Te_3 thin films", Thin Solid Films **280** (1996) 61.

[14] D.L. Partin, J. Heremans, D.T. Morelli, C.M. Thrush, C.H. Olk, T.A. Perry, "Growth and characterization of epitaxial bismuth films", Phys. Rev. B **38** (1988) 3818.

[15] S. Nahm, L. Salamanca-Riba, D.L. Partin, J. Heremans, "Transmission electron microscopy studies of bismuth films", J. Mater. Res. **5** (1990) 784.

[16] C.A. Hoffman, J.R. Meyer, F.J. Bartoli, A. DiVenere, X.J. Yi, C.L. Hou, H.C. Wang, J.B. Ketterson, G.K. Wong, "Semimetal-to-semiconductor transition in bismuth thin films", Phys Rev. B **48** (1993) 11431.

[17] X.J. Yi, H.C. Wang, A. DiVenere, C.L. Hou, J. Chen, J.B. Ketterson, G.K. Wong, "$Bi_{1-x}Sb_x$/Bi superlattice grown by molecular beam epitaxy", Appl. Phys. Lett. **64** (1994) 1283.

[18] J.A. Van Hulst, H.M. Jaeger, S. Radelaar, "Epitaxial growth of bismuth and bismuth-antimony heterostructures", Phys. Rev. B **52** (1995) 5953.

[19] A.V. Wagner, R.J. Foreman, L.J. Summers, T.W. Baebee, J.C. Farmer, "Multilayer thin film thermoelectrics produced by sputtering", Proc. of the XIV Inter. Conf. on Thermoelectrics, St Petersburg (Russia) (1995) 283.

[20] T. Missana, C.N. Afonso, "Microstructure and roughness improvment of polycrystalline Bi thin films upon pulsed-laser melting", Appl. Phys. A **62** (1996) 513.

[21] T. Missana, F. Catalina, C.N. Afonso, M.A. Ollacarizqueta, "Epitaxial effects on film growth and interdiffusion at Bi-Sb interfaces", Thin Solid Films **274** (1996) 76.

[22] J. Takahashi, T. Miyagawa, "Epitaxial growth of Bi/Sb superlattice", Jpn. J. Appl. Phys. **31** (1992) L1114.

[23] M. Nakada, N. Oshima, M. Okada, "Crystal orientation and surface roughness of Bi films prepared in ionized cluster beam apparatus", Jpn. J. Appl. Phys. **35** (1996) 714.

[24] G. Fuchs, C. Montandon, M. Treilleux, J. Dumas, B. Cabaud, P. Mélinon, A. Hoareau, "Low-energy Bi cluster beam deposition", J. Phys. D: Appl. Phys. **26** (1993) 1114.

[25] O. Boffoué, A. Dauscher, B. Lenoir, H. Scherrer, to be published

[26] N.T. Liang, Y. Shan, S.Y. Wang, "Electronic conductivity and percolation theory in aggregated films", Phys. Rev. Lett. **37** (1976) 526.

[27] T.M. Christensen, D.I. Dalton, "Effects of morphology on the electrical and optical properties of thin bismuth films", Surf. Inter. Anal. **18** (1992) 153.

[28] J.L. Cohn, C. Uher, "Electrical resistance and the time-dependent oxidation of semicontinuous bismuth films", J. Appl. Phys. **65** (1989) 2045.

[29] T.M. Christensen, "Bismuth film coalescence determined by ellipsometry", Thin Solid Films **292** (1997) 26-30.

[30] R. Atkinson, E. Curran, "Ellipsometric examination of the oxidation of vacuum-deposited bismuth films", Thin Solid Films **128** (1985) 333.

[31] Y. Namba, T. Mori, "Cross-sectional structure of Bi films and its phenomenological analysis", J. Appl. Phys. **46** (1975) 1159.

[32] A.A. Ramadan, A.M. El-Shabiny, N.Z. El-Sayed, "Size-dependent structural characteristics of thin bismuth films", Thin Solid Films **209** (1992) 32.

[33] J. Buxo, M. Saleh, G. Sarrabayrouse, G. Dorville, J. Berty, M. Brieu, "Structural study of bismuth films and its consequence on their electrical properties", Revue Phys. Appl. **15** (1980) 961.

[34] J. Jing, P.N. Henriksen, H.T. Chu, H. Wang, "Epitaxial growth of ultra thin films of bismuth: an atomic force microscopy study", Appl. Surf. Sci. **62** (1992) 105.

[35] J. Chen, A. DiVenere, X.J. Yi, C.L. Hou, H.C. Wang, G.K. Wong, J.B. Ketterson, "Interface structure between Bi and CdTe in molecular beam epitaxially grown Bi/CdTe and Bi/$Bi_{1-x}Sb_x$ superlattices", J. Electronic Mat. **23** (1994) 1255.

[36] S.C. Shin, J.E. Hilliard, J.B. Ketterson, "Preparation and X-ray diffraction studies of compositionally modulated PbTe/Bi films", Thin Solid Films **111** (1984) 323.

[37] A. DiVenere, S.C. Shin, B.Y. Jin, G.K. Wong, J.B. Ketterson, J.E. Hilliard, "Growth and structural characteristics of semiconductor-semimetal superlattices: CdTe-Bi, PbTe-Bi, SnTe-Sb", J. Crys. Growth **70** (1984) 452.

Thermoelectric Properties of Multilayeredp-type SiGe Thin Films

A.Yamamoto, H.Kato[1)], S.Kuwashiro[1)], M.Takimoto[2)], T.Ohta, K.Miki, K.Sakamoto, T.Matsui[1)], K.Kamisako[2)]

Electrotechnical Laboratory, AIST, MITI, Japan E-mail : a.yamamoto@etl.go.jp

[1)]Nagoya Univ. , [2)]Tokyo Univ. of Agriculture and Technology

Abstract

We fabricated thin films with SiGe/Si multilayered structure by using MBE and evaluated their low temperature transport properties in detail. Boron-doped $Si_{80}Ge_{20}$ wells separated with 500A Si barrier layers were formed on highly resistive Si (100) substrate. Measurements of resistivity and Seebeck coefficient clarify that the layered structure has an increasing power factor, α^2/ρ, with decreasing well width for temperatures below 300K.

Introduction

Since the strategy to use a superlattice / quantum well structure to enhance thermoelectric performance was first proposed by Hicks and Dresselhaus in 1993[1], several theoretical extensions were published[2]-[6] and efforts on proof-of-principle experiments have been made[7]-[8]. Enhancement of the thermoelectric power for a constant carrier concentration with two dimensional carrier gas in PbTe quantum well system was firstly observed by Harman[9], where the region of interest was focused only on the well. From the practical point of view, we need an evaluation of total film material including both well and barrier layer. According to the latest considerations including: the effect of the well width and energy dependence of carrier relaxation time and the effect of lifting the valley degeneracy, as well as the effect of heat conduction through the barrier materials[6]; it is concluded that the figure-of-merit value of parallel conduction over the total thin film material with quantum well structure does not exceed that of bulk materials.

However these predictions, based on the classical model, may not explain whole nature of the materials. There is room for different other possible effects to enhance the electrical performance of thin films. One is to realize high carrier mobility through the layered structure. Since thermoelectric materials often are optimized at high carrier concentration of the order of 10^{19} to 10^{20} cm^{-3}, carrier mobility is deteriorated by impurity scattering. By separating the ionized impurities from a carrier conducting channel with hetero-interface of semiconductors, a high mobility may be achieved in the layered structures. This increased mobility seems favorable for the thermoelectric properties.

Another possibility for enhancement of the electrical properties is to design energy band structures with artificial nano-structures. Alternating two semiconductors with different band gap in very narrow interval of angstroms. Furthermore, the band structure can be controllable by strain induced by lattice mismatch.

In this study we aim to prove the enhancement in the Seebeck coefficient in multilayered films due to confinements of the carriers. The background is basically based on the Hicks' model.

We selected Si/Si_xGe_{1-x} and Si/Ge superlattice and quantum well structures for the following reasons:
(1) The Si_xGe_{1-x} /Si system is well known as a strained superlattice. Since the band structure changes with existance of strain, by controlling this parameter, we have more freedom to optimize the performance. (2) Epitaxial growth of Si/Ge has well studied and the processing techniques are established.
(3) There is no need to control the exact stoichiometry for Si_xGe_{1-x} alloy. This makes the experiment much easier compared to materials such as PbTe and Bi_2Te_3.

Alternating epitaxial growth of $Si_{80}Ge_{20}$ and Si on Si-substrate produces well structure with band offset of 0.2eV in valence band[10]. This value is sufficient for carrier confinement when we focus on the low temperature properties.

In this paper we report initial data on the transport properties of thin films with $Si_{80}Ge_{20}$ /Si layered structure for low temperatures. We discuss the temperature dependences of resistivity and Seebeck coefficient and their comparisons with alloy thin films.

Experiment

Boron-doped $Si_{80}Ge_{20}$ and undoped Si layers were grown on a 2 inch (100) CZ silicon wafer with 1000 Ωcm. Initially the wafers are covered with a thin SiO_2 layer. After the loading into a

0-7803-4057-4/97 $10.00 ©1997 IEEE

Table 1. Thermoelectric properties at room temperatures

Sample	Resistivity	Hall mobility	Carrier density	Seebeck coefficient	Power Factor
	Ωcm	cm^2/Vs	cm^{-3}	μV/K	W/mK^2
40/500	1.11×10^{-2}	37.6	1.51×10^{19}	456	1.87×10^{-3}
60/500	7.50×10^{-3}	35.1	2.37×10^{19}	353	1.66×10^{-3}
100/500*	6.31×10^{-2}	4.53	2.19×10^{19}	263	1.10×10^{-4}
625/500	3.06×10^{-3}	20.0	1.00×10^{20}	214	1.50×10^{-3}
3000	1.27×10^{-3}	22.0	2.25×10^{20}	182	2.61×10^{-3}
Bulk	1.19×10^{-3}	29.9	1.89×10^{20}	130	1.50×10^{-3}

* this sample has a low mobility, that is, low quality.

modified ANELVA-620 MBE growth chamber with base pressure of $5x10^{-8}$ Pa, the protective SiO_2 layer was removed by exposure to weak Si beam at substrate temperature of 800 C.

A Si buffer layer of 200A was deposited and the flatness of the surface was checked by a RHEED pattern. Si and Ge were evaporated using a 10kW electron-gun and a Knudsen cell, respectively. Five $Si_{80}Ge_{20}$ /Si alternating layers were then deposited at 400C. A B_2O_3 source was used for born doping. We aimed to create heavily doped $Si_{80}Ge_{20}$ at a carrier concentration of $1x10^{20}$ cm^{-3} and this was achieved by evaporation from B_2O_3 Knudsen cell at 1200-1350C. Each $Si_{80}Ge_{20}$ layer was separated with 500A undoped Si layers and this width was fixed for each sample with different well width. For a comparison, we made $Si_{80}Ge_{20}$ alloy thin films which have the same total thickness (3000A) and almost the same level of the carrier concentration. We also cut a p-type $Si_{80}Ge_{20}$ polycrystalline bulk sample to the same dimensions.

We measured the electrical resistivity ρ, the mobility μ and the carrier concentration n of the films in a temperature range from 10K up to 300K. These data were determined by van der Pauw method and Hall measurement. We cut 5mm x 5mm samples for Hall measurement from middle of the 2 inch wafer and adjacent 5mm x 15mm samples were used for the Seebeck measurements. Seebeck coefficients α of the films were measured in the temperature range from 100K to 300K. The temperature difference, ΔT, over the length of 15mm sample was varied up to 4K and the Seebeck coefficient at the temperature was determined as the slope of the ΔV-ΔT plot. We used Chromel-Almel thermocouples for temperature measurement and Cu wire for the electromotiveforce detection. In order to remove uncertainty, we did not use silver pastes and just pressed the Cu wire to the film by a 300g weight.

Results

Table 1 shows the resistivity and the Seebeck coefficient of the samples at room temperature. All films showed a sheet electrical resistance lower than 500 Ω and the contact between a probe and the sample were fairly good. Since the resistance of Si substrate is $4x10^4$ Ω at room temperature, errors due to the substrate are less than 2% and we make no correction for the resistivities. The Seebeck coefficient of the substrate was +2mV/K at room temperature. We can treat the substrate and film as an equivalent circuit composed parallel connection of two voltage sources V_{film}, V_{subst} and internal resistances R_{film}, R_{subst}[11], we obtain measured voltage V as

$$V = \frac{R_{film}V_{subst.} + R_{subst.}V_{film}}{R_{film} + R_{subst.}} \qquad (1)$$

and in the case of $R_{film} << R_{subst.}$, measured V is much simpler as

$$V = V_{film} + \frac{R_{film}}{R_{subst.}}V_{subst.} \qquad (2)$$

As a result the correction does not exceed 6% at room temperature for the data listed in Table 1. As discussed later, we have to make correction to Seebeck coefficients for the temperature below 300K.

The carrier density decreases with decreasing well width, as we expected. This is understandable with changes in well/barrier width ratio. Since we made heavily doped $Si_{80}Ge_{20}$ of the order of 10^{20} cm^{-3} for the well layers and undoped Si layers for the barrier layers, it seems reasonable to suppose that the measured value corresponds to the mixed carrier concentration over both layers. The Seebeck coefficients of multilayered films are close to the ones of Si single crystal measured by Geballe and Hull[12], i.e., they reported 500μV/K at room temperature for Bridgemann sample with $1.5x10^{19}$ cm^{-3} boron.

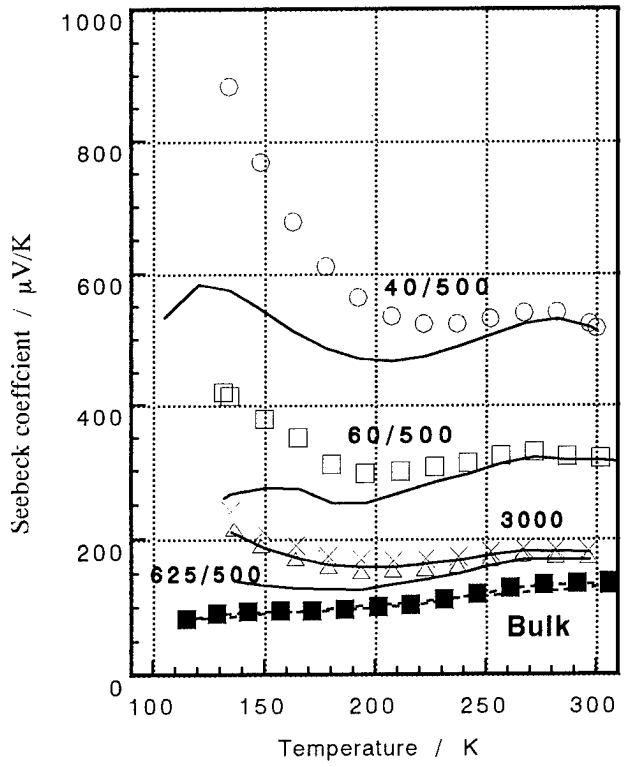


Figure 1. Temperature dependence of Seebeck coefficients Marks for as-measureddata and full lines for data with the correction.

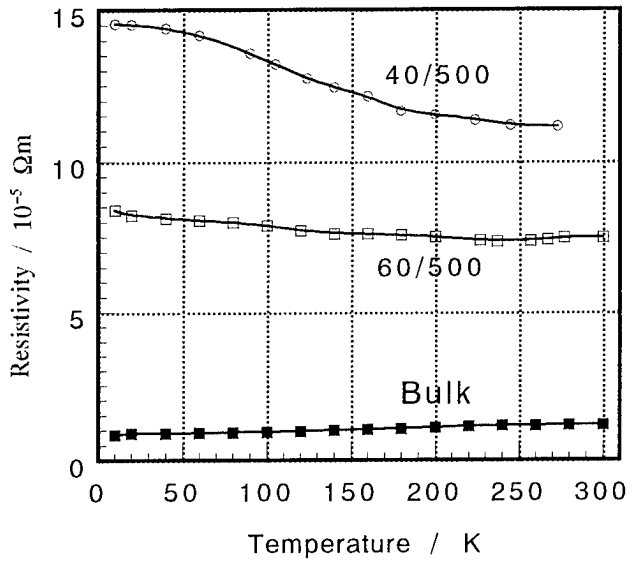


Figure 2. Temperature dependence of the resistivites

Mobility of the films is comparable to that of bulk materials, but we find that there are increasing mobilities with decreasing well width.

Figure 1. shows the temperature dependences of Seebeck coefficients. For lower temperatures, the resistivity of the Si substrate decreases rapidly and the Seebeck coefficient of the substrate increases simultaneously. According to the reference[12]-[14], V_{film}/R_{film} value in equation (2) becomes a hundred times larger than values for room temperature. Therefore the contribution to the film is no more negligible. In sample 40/500 and 60/500, the sharp rise in as-measured data for the temperature below 200K are suppressed with the correction. However, still the Seebeck coefficients slightly increase at 100 -150K.

Figure 2. shows temperature dependences of the resistivities. Sample 40/500 and 60/500 showed increasing resistivity with decreasing temperatures while the resistivity of bulk sample slightly decreases with decreasing temperature. For a heavily doped semiconductor of the order of $1x10^{18}$-10^{19} cm^{-3}, the resistivity does not show any increase for low temperatures in general. Therefore our results on the temperature dependence of the resistivity disagree with those of the bulk materials.

Discussion

The thermoelectric properties shown in table1 tell us :

(1) In multilayered films the power factors are comparable to that of the bulk sample. But the carrier concentration of the layered film,$1.5x10^{19}$ cm^{-3} , is much lower than that of bulk sample.

(2) The Hall mobilities of 40/500 and 60/500 samples are higher than that of bulk sample.

In general, the electrical properties such as power factor is uniquely determined when the material and its carrier concentration are fixed. Therefore there is a disagreement between our result and the general theory, since the same power factor is achieved with different carrier concentration.

We shall discuss it with simple single band model for thermoelectric properties[1]. In the model, when the mobility is increased, the optimizing fermi-level is reduced toward non-degenerate region. This means that the optimizing carrier concentration decreases with increasing mobility. For usual bulk materials, the mobility is strongly limited with the doping levels. It is reasonable to suppose that in this experiment we obtain the increased mobility by forming the multilayer structure and this makes it possible to optimize the electrical properties at one-order low carrier concentrations. This also means thorough change of balance of α-ρ for the optimized properties.

For temperature dependences of electrical properties, we have no interesting account for them. Unfortunately it was difficult to suppress completely the effects of the substrate for

this experiment and this makes it harder to understand the whole nature. We can observe peaks of Seebeck coefficient for low temperatures. It is appropriate to understand the exhibit of the multilayered films with simple electrical equivalent circuit. And the peaks in lower temperature may be accounted for the combination of both degenerated and non-degenerated alternating films.

Conclusions

In this paper we presented the thermoelectric properties of thin-film samples with $Si_{80}Ge_{20}$/Si layered structures. The electrical properties ρ, α and their balance are different from those of the bulk sample. We cannot confirm the enhancement in the Seebeck coefficient. We observed the larger mobility in 40/500 and 60/500 samples. These samples have almost the same performance as that of bulk sample but one-order lower carrier concentration. This seems due to increased mobilities which enabel to optimize at low carrier concentrations.

References

[1] L. D. Hicks and M. S. Dresselhaus, Phys. Rev. B 47, (1993) 12727.

[2] J. O. Sofo and G. D. Mahan, Appl. Phys. Lettt. 65, (1994) 2690.

[3] D. A. Broido and T. L. Reinecke, Phys. Rev. B 51 (1995) 13797.

[4] D. A. Broido and T. L. Reinecke, Appl. Phys. Lett. 67 (1995) 100.

[5] D. A. Broido and T. L. Reinecke, Appl. Phys. Lett. 67 (1995) 1170.

[6] D. A. Broido and T. L. Reinecke, Appl. Phys. Lett. 70 (1997) 2834.

[7] L. D. Hicks, T. C. Harman, X. Sun, and M. S. Dresselhaus, Phys. Rev. B 53 (1996) 10493.

[8] R. Venkatasubramanian, J. Crystal Growth, 170 (1997) 817.

[9] T. Harman, Proc. of ARPA Thermoelectric Materials Workshop, Arlington, VA, Nov. 1995.

[10] Erich Kasper edited, Silicon Germanium, INSPEC,IEE, London 1995.

[11] N.B.Elsner et al.,Proc. of XIII Int. Conference on Thermoelectrics, Kansas city (1994) 328.

[12] T. H. Geballe and G. W. Hull, Phys. Rev. 98 (1955) 940.

[13] F. J. Morin and J. P. Maita, Phys. Rev. 96 (1954) 28.

[14] C. Herring, Phys. Rev. 96 (1954) 1163.

Thermoelectrical properties of superlattices.

Melnichuk S.V., Kosyachenko S.V., Vozny M.V.
Institute of Thermoelectricity Box 86, General Post Office Chernivtsy , 274000, Ukraine,
Tel.:380/3722/44422, Fax: 380/3722/41917, E-mail:alex@ite.chernovtsy.ua

Abstract

Recent investigations show that thermoelectric properties of superlattices, where electronic density of states is two-dimensional, may be greatly improved. In our report the calculations of thermoelectric properties of Si/Ge superlattices are proposed. Superlattice band structure was calculated in the frame of tight-binding model (sp^3s^*). Obtained band structure allows us to calculate the electronic density of states. Fermi level was determined from neutrality equation. Kinetic coefficients were calculated within time relaxation approximation. The calculated figure of merit of superlattice is compared to that of Si-Ge alloy.

Introduction

The development of epitaxial techniques makes it possible to obtain different semiconductor superlattices (SL) with hopeful properties in different fields including thermoelectrics which causes tremendous interest towards the study of these objects. The theoretical calculations of the dependence of thermoelectric properties upon the layer thickness were done in [1-3]. It was shown, that thermoelectric efficiency may be increased. ZT may reach a value up to 14 at room temperatures in the ideal model when electrons move in wells' minibands and cannot penetrate through barriers. The experimental findings [4] show that ZT=2 at $T=300^0$ K for PbTe/PbEuTe superlattice.

Theoretical calculations of thermoelectric properties of Si/Ge superlattices are proposed in our work. With this purpose, the electronic energy spectrum is calculated for the structures with different number of layers. The thermoelectric properties and figure of merit of these SL are calculated as well.

Tight-binding model application to bulk Si and Ge

Band structure of crystals may be determined in the frame of the tight-binding model which is rather universal and simple in practical realization. This method uses sp^3 orthogonal basis set with nearest-neighbour interactions and makes it possible to obtain a quite accurate description of the valence bands but not the conduction bands. To eliminate this problem, Vogl et al. [5], have introduced one additional orbital to the minimum sp^3 orbital set. This new orbital has been termed as s^* and its purpose is to take into account the states which were not included in the minimum basis set. In the calculations above, the two-center approximation of the interatomic potential matrix elements has been used. sp^3s^* model has 13 parameters, their values for some elements, including Si and Ge, were given in [5].

The solution of a stationary Schrodinger equation in this model, may be reduced to secular matrix diagonalization. Matrix diagonalization was done numerically. Dispersive curves of bulk Si and Ge for some directions of Brillouin zone are shown in Fig.1a,b.

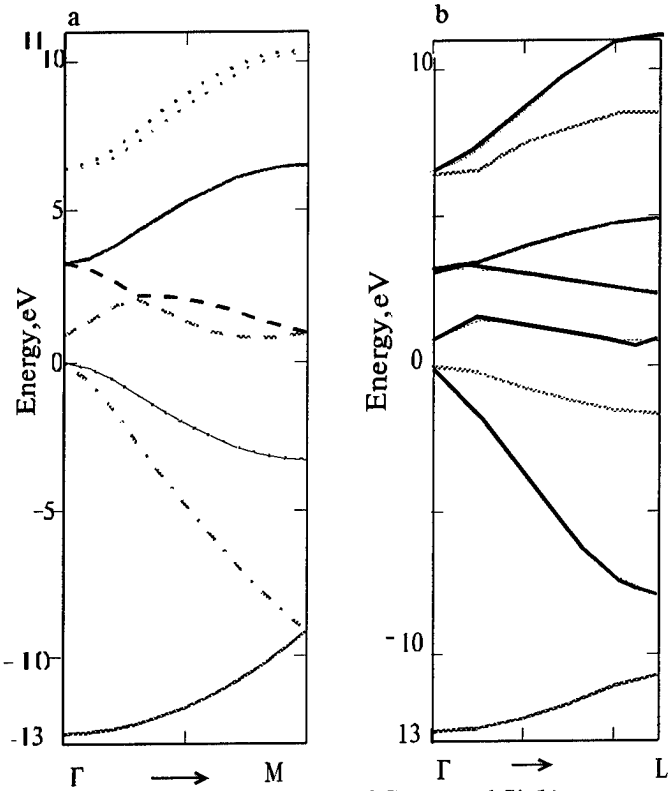


Fig.1 The energy band structure of Ge (a) and Si (b).

The results of these calculations are in good agreement with those obtained earlier for these materials through other methods.

Band structure of superlattices

Band structure of superlattices depends mainly upon growth direction and number of atomic layers in the superlattice period. Let us regard superlattice as a set of atomic layers, which are perpendicular to the [001] growth direction, repeating periodically in space. In this case each plane contains atoms of one type only, with two different atom positions. Different type planes alternate in space. These planes are simple two-dimensional square lattices. The distance between planes is a/4 (a is a lattice constant of diamond structure). The couple of such planes is called monolayer or simply layer. Band spectrum of superlattice with fixed layer number was calculated by numerical diagonalization of matrix in some point k of Brillouin zone [15]. Brillouin zone structure is determined by the number of Si and Ge layers in Si_n/Ge_m superlattice. For even (n+m)/2, superlattice structure is orthorhombic. If at least one of n or m is odd, then the structure is tetragonal. We will consider

the case when n and m are even.

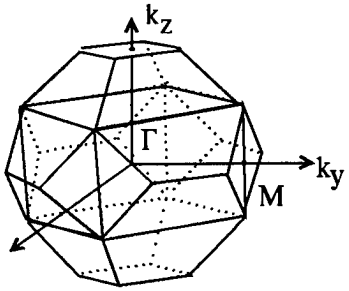


Fig.2 The Brillouin zone for superlattices with even (n+m)/2.

Band structure of Si_2/Ge_2 superlattice along Γ-M direction is shown, for example, in Fig.3

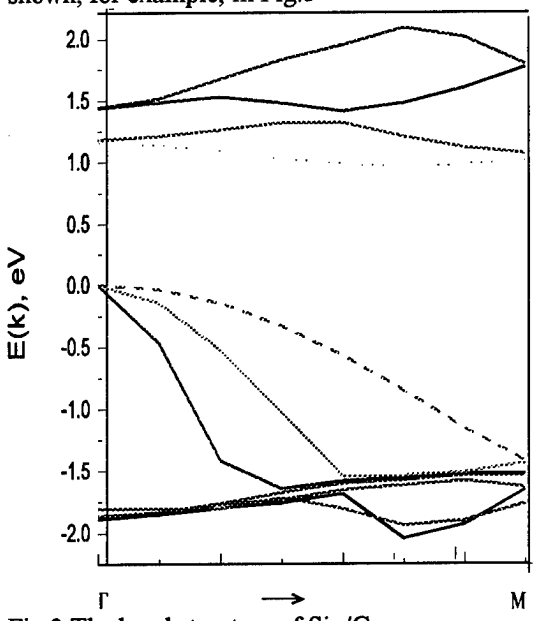


Fig.3 The band structure of Si_2/Ge_2 superlattice.

Heat conductivity

The determination of superlattice heatconductivity remains a complex problem. In [6] the authors estimate lattice contribution in heatconductivity κ by

$$\kappa_{ph} = 1 / 3 C_v v l \qquad (1)$$

where l is the phonon mean free path, v is the sound velocity, C_V is the heat capacity.

If the layer thickness is greater than 10A then the existence of superstructure does not effect the mean free path and the value of layer lattice heatconductivity is close to the bulk value. In [7] lattice heat conductivity is estimated as the mean value of heat conductivity components

$$\kappa = \frac{a\kappa_1 + b\kappa_2}{a + b} \qquad (2)$$

where a and b are layer thickness, κ_1 and κ_2 their heat conductivity.

The anysotropy of physical properties is a characteristic feature of SL structures, caused by layers growth direction. This fact is important for the study of heat and current flows. That is why the calculation of effective heat conductivity was done with inhomogeniousness of SL material being taken into account. Formula for this calculation is proposed in next section. However, such macroscopical evaluation of κ is rather rude for SL because it can not discribe the complex process of heat transfer through the boundaries of different layers in SL microscopically. In order to take into account the peculiarities of heat conductivity of microsystems one can use methods of computer modelling [8,9] and molecular dynamics method as well.

Thus we have used this method for heat transfer modeling in 1-dimensional chain with the aim to elaborate possible directions of solving of this complex problem.

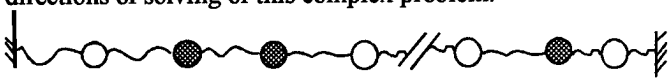


Fig.4. The model of one-dimensional chain.

Monoatomic chain, consisting of two atom species, which were disordered in some way as well as ordered combinations which model SL, were studied. It was supposed that the ends of chain are in contact with thermostat. Molecular dynamics method was used. According to this method all atoms were treated as rigid spheres. Interaction between the spheres is discribed by the Lenard-Jhons potential. The motion of such particles is discribed by the laws of classical mechanics. The atoms at the ends of chain interact in random moments of time with heat reservoirs. Only nearest neighboring interaction is taken into account. Zero and N+1 atoms have infinite masses, first and N-th atoms interact with thermostates (hot and cold ones). Numerical integration of equations of motion was done with the help of Verle algorithm in a rapid form [10]

We assume that initially the atoms are positioned along the chain with the equal distance between them. Every atom was characterised by the random value of velocity v_i, which correspond to the average temperature of hot and cold thermostats. Random parameters which were necessery for algorithm realization were generated with the help of random values generator.

The local temperature on the i-th particle was defined as a sum of kinetic and potential energy.

Heat flow stream through hot and cold ends of chain was determined as an energy of transition between the last atom of chain and thermostat divided by time interval of experiment.

At any specific moment the interaction energy was determined as difference of atom energy after the interaction with thermostat and before the interaction.

$$\delta E_{\alpha}^{s} = m_{\alpha}(v'_{\alpha})^2 / 2 - m_{\alpha}(v_{\alpha})^2 / 2 \qquad (3)$$

The cryterion of the equilibrium of the system is an equality of flows at the ends of chain. In our numerical expirement the difference of flows was at the level lower then 1%.

The heat conductivity κ was determined with the help of heat flow and gradient temperature. Obtained results are in a qualitative agreement with the results of other authors [11-12]. This fact may serve as an indication of correctness of the model and numerical calculations. Thus, this approach was applied to the modelling of the heat transfer processes in the SL. The results of calculation in this case are shown in Fig 5.

The dependence of heat conductivity upon the number of heavy atoms in the chain with a constant ratio of heavy and light atoms was investigated. The incresae of number of heavy atoms corresponds to the descrease of scattering centers per length unit. Therefore the heat conductivity increases.
This ideal model needs generalisation for two- and three-dimensional cases.

Electric conductivity and Zeebeck coefficient

The calculation of superlattice kinetic coefficients was done with account of SL structure peculiarities as a system of parallel layers of some materials [13]. To simplify the calculations we assumed both materials to be isotropic. The generalization for the anisotropic case is known [13,14] and does not change qualitatively the results.
There were regarded the cases when the currents are directed parallel and perpendicular to the SL layers.

1.Current is perpendicular to the SL layers.

$$\sigma_C = \left[\frac{\sigma_a \kappa_a}{a}\right](\sigma_a + q\sigma_b)W, \qquad (4)$$

$$\gamma_C = \left[\frac{\sigma_a \kappa_a}{a}\right](\gamma_a + q\gamma_b)W, \qquad (5)$$

$$\alpha_C = \frac{\sigma_a \alpha_a + q\sigma_b \alpha_b}{\sigma_a + q\sigma_b}. \qquad (6)$$

The parameters q,W, and h are

$$q = \frac{b\sigma_a \kappa_a}{a\sigma_b \kappa_b}, \qquad (7)$$

$$W \equiv (a+b)[(\gamma_a + q\gamma_b)(\sigma_a + q\sigma_b) - T(\sigma_a\alpha_a + q\sigma_b\alpha_b)^2]^{-1} \qquad (8)$$

$$h_\sigma = q\frac{\sigma_b}{\sigma_a}, h_\gamma = q\frac{\gamma_b}{\gamma_a}. \qquad (9)$$

$$\gamma = \kappa + T\sigma\alpha^2 \qquad (10)$$

where γ includes lattice and electron components of heat conductivity. The calculations of electric conductivity and Zeebeck coefficient were done in the relaxation time approximation with well known scattering mechanisms for the bulk materials being taken into account. Fermi level is calculated from the neutrality equation.
Density of states was calculated from the energy spectrum of SL which was found earlier

$$N(\varepsilon) = \sum \delta(\varepsilon - \varepsilon_n(k)) \quad , \qquad (11)$$

where n denotes bands. Summation over k was done with the help of uniform splitting of 1/8th part of Brillouine zone by 2000 points. N(ε) is shown in Fig.6.
The calculated density of states and Fermi level allow us to find α and σ, which are shown in Fig.7-8 (curve 1).

conductivity and Zeebeck coefficient have higher values for this current direction than in previous case.

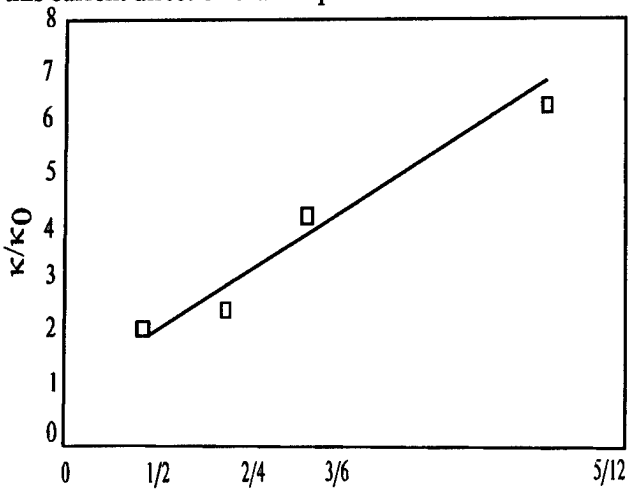


Fig.5 The dependence of heat conductivity upon the number of heavy atoms in the chain.

2.Current is parallel to the layers. In this case

$$\sigma_C = \frac{a\sigma_a + b\sigma_b}{a+b} \qquad (12)$$

$$\gamma_C = \frac{a\gamma_a + b\gamma_b}{a+b} \qquad (13)$$

$$\alpha_C = \frac{a\sigma_a\alpha_a + b\sigma_b\alpha_b}{a\sigma_a + b\sigma_b} \qquad (14)$$

The results of the calculations are represented in Fig.9-10 (curve 2). By comparing the figures we can see that the

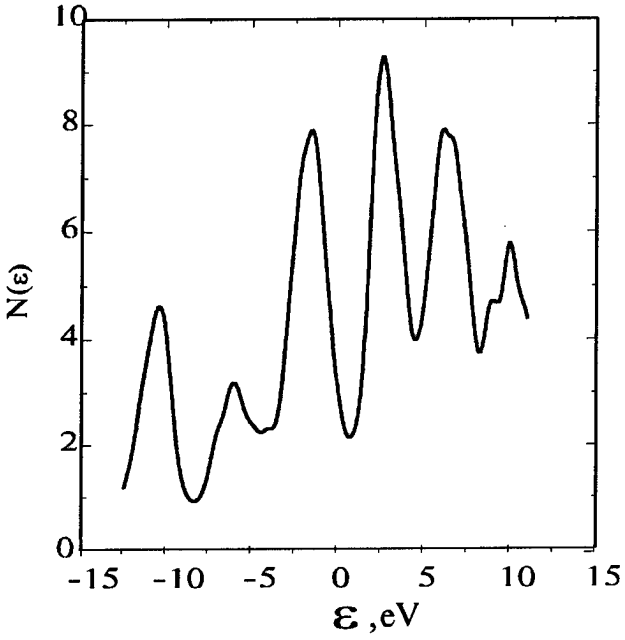


Fig.6 The density of states of Si_2/Ge_2 superlattice.

Figure of merit Z was calculated for different directions and layer thicknesses.

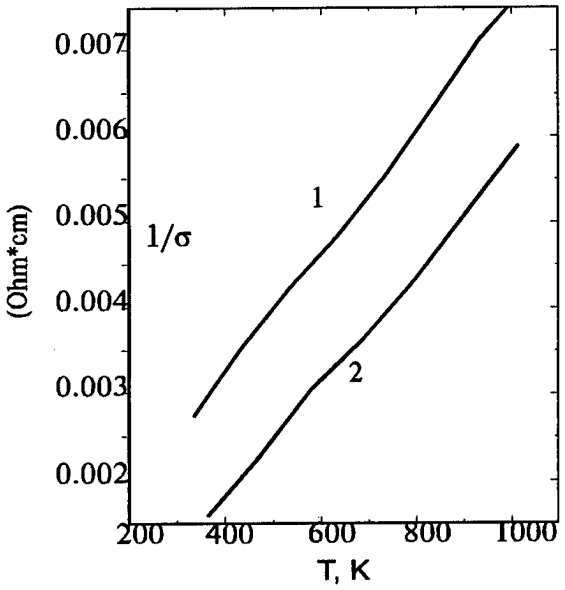


Fig.7 The dependence of 1/σ vs T.

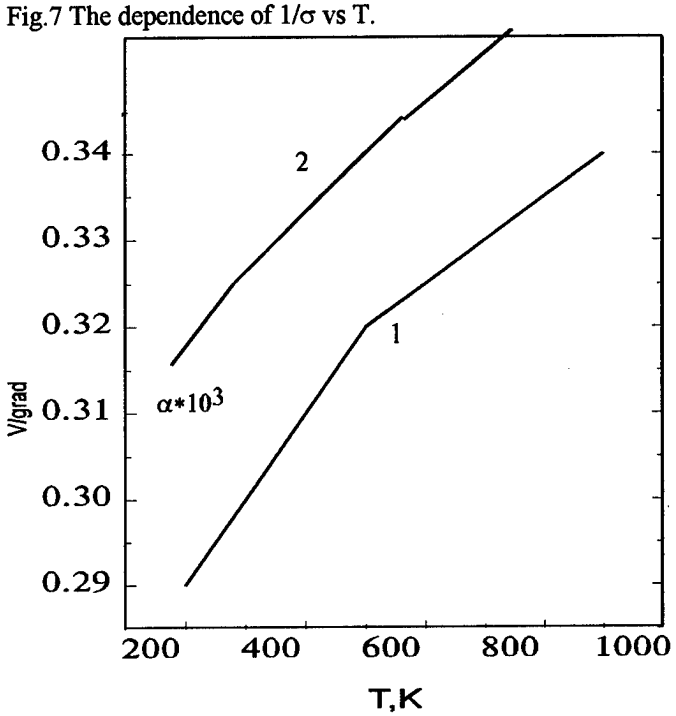


Fig.8 The dependence of Zeebeck coefficient vs T.

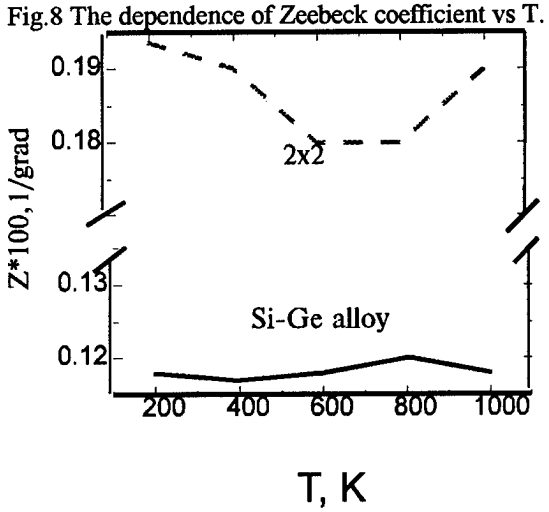


Fig.9 The dependence of figure of merit of Si-Ge alloy and Si_2/Ge_2 superlattice vs T.

Conclusion

After comparing calculated thermoelectric parameters of Si/Ge superlattices with the same parameters of bulk Si, Ge and Si-Ge alloys, we can make a conclusion about the higher (along-the-layer directions) values in the region of room (and higher) temperatures. However these estimations require the considaration of electron-phonon, spin-orbital and phonon-phonon interactions .

References

[1] L.D.Hicks, M.S.Dresselhaus. Phys.Rev.B 47 (1993) 12727.

[2] L.D.Hicks, T.C. Harman, M.S.Dresselhaus. Appl. Phys. Lett. 63 (1993) 3230.

[3] L.D.Hicks, M.S.Dresselhaus. Phys.Rev. B 47 (1993) 16631.

[4] L.D.Hicks, T.C.Harman, X.Sun, M.S.Dresselhaus. Phys.Rev.B53 (1996) R10493.

[5] P.Vogl, H.P.Hjalmarson, D.Dow. J.Phys.Chem. Solids 44 (1983) 365.

[6] P.J.Lin-Chung, T.L.Reinecke. Phys.Rev.B 51 (1995) 13244.

[7] A.Yamamoto, T.Ohta. Proceedings of the 15 Proc. of the XVth Int. Conf. on Thermoelectrics. (ICT'96), Pasadena CA, USA (1996) 464

[8] L.I.Anatychuk, S.V.Kosyachenko, S.V.Melnichuck. Proc. of the XVth Int. Conf. on Thermoelectrics. (ICT'96), Pasadena CA, USA (1996) 194.

[9] L.I.Anatychuk, S.V.Melnichuck, S.V.Kosyachenko. Proc. of the XIVth Int. Conf. on Thermoelectrics. St.Petersburg, Russia, (1995) 319.

[10] Guld H, Tobochnik J. Computernoye modelirovanie v physice, v.1,M.:Mir, 1990.-349p.

[11] D.N.Payton, M. Rich, W.M.Vissher. Phys.Rev., 160 (1967) 706.

[12] D.N.Payton, W.M.Vissher. Phys.Rev. 154 (1967) 802.

[13] G.S.Gudkin. E.K.Iordanishvily, V.A. Kudinov, E.E.Fiskind FTP 16 (1982) 1620.

[14] G.S.Gudkin, E.E.Fiskind FTP 18 (1984) 234.

[15] D.V.Korbutyak, S.G.Krylyuk, V.G.Litovchenko, S.V.Melnichuk,I.M.Yuriychuk.Phys.Low-Dim. Struct. 11/12 (1996) 97.

Effect of one dimensional quantum structures on the thermoelectric figure of merit

A. Casian, I. Sur, and A. Sandu
Technical University of Moldova, MD-2004, Kishinau

H. Scherrer and S. Scherrer
Laboratoire de Physique des Matériaux, Ecole des Mines, Parc de Saurupt, F-54042 Nancy, France

Abstract

Recently it was shown theoretically that the thermoelectric properties of certain materials can be enhanced very much by preparing them in the form of one-dimensional conductors or quantum wires. For this it was supposed, that the carriers mobility is the same both in quantum wire and in bulk material. Using the model of quasi-one-dimensional cylindrical quantum wire of finite radius with infinite potential confinement, we have calculated the mobility as a function of wire thickness. The carriers scattering both on optical and acoustical phonons is taken into account. It is found that the mobility decreases with wire thickness decreasing from values greater to values much smaller than bulk one. This result changes drastically the conclusion about significant increase in figure of merit of materials by preparing them in form of quantum wire structures.

Introduction

Recently, it was shown [1,2] that it may be possible to increase the figure of merit ZT of thermoelectric materials by preparing them in the form of quantum-well structures. This improvement of the thermoelectric properties of a material is achieved as a result of an effectively two-dimensional density of states for the free carriers. The preliminary experimental data were presented [3] for the confirmation of these predictions.

It was also investigated the figure of merit of materials prepared in the form of one-dimensional (1D) conductors or quantum wires [4]. It was shown theoretically that this approach could yield a more significant increase in ZT over both the bulk value and the calculated earlier two-dimensional quantum wells values. This increase is due to the change in the density of states in one dimension case.

At present the technological achievements make, in principle, possible to fabricate very narrow high quality quantum wires [5] in which only the lowest subband is carriers populated. In such systems the one-dimensional motion of carriers is realised with high degree of precision. One-dimensional conductors were also obtained by the encapsulation of metal filaments in carbon nanotubes [6,7]. Some of these tubes are 1.5 nm in diameter. These nanotubes could be encapsulated by semiconductor material too. So the prediction of significant increase in ZT [4] could be verified experimentally. However we would note that the most vulnerable approximation used in paper [4] is the supposition that the mobility of carriers is the same both in the one-dimensional conductors and in bulk material. If in the case of two-dimensional quantum -well structures [1,2] such assumption could be still admitted for the purpose of simplicity but in the case of one dimensional conductors the state of art is completely different.

The transport properties of quantum wires have been previously reported (see [8] and references therein). The calculation of carriers mobility in 1D conductor is, in general, a complicated problem, because the disorder, which always is present in real systems, leads at low temperatures to the localisation of one electron states and, as consequence, the method of Boltzmann kinetic equation is not applicable [9]. Although, as it was shown in [10], in reasonable high-quality low disorder quantum wires, the localisation length may be large sufficient for nanoelectronic or even microelectronic applications, but insufficient for thermoelectric utilisation.

On the other hand, for thermoelectric applications higher temperatures are available, and it is established, that when the phonon scattering becomes the main electron scattering mechanism the conductivity may be determined from the kinetic equation [11].

In this paper, our interest is focused on the study of the quantum-wire carrier mobility as a function of wire width when the 1D transport is realized. It is of special importance to analyse the carrier mobility in ultrafine semiconductor wires with a typical thickness of a few nanometers. In such thickness range, as was predicted in [4], it is expected to obtain a significant increase in ZT. Our treatment is based on the kinetic equation method. The quantum wire is modeled as a cylindrical thread of radius r_0 with infinite potential walls. The scattering of electrons both on optical and acoustical phonons is taken into account. It is found that the mobility decreases with the wire width decreasing and for widths larger than certain value, depending of material parameters, the mobility is higher than the bulk one. At the same time for smaller widths the mobility is less than in the bulk case and decreases more rapidly with the wire width decreasing.

0-7803-4057-4/97 $10.00 ©1997 IEEE

Wire model

In order to avoid cumbersome calculations we will consider that the bulk wire material has a simple band structure with spherical energy surfaces. We also assume that the crystal lattices and dielectric properties of both materials in the quantum well and an adjoining regions are the same so that the image potential contributions and the formation of localized phonons are ignored [12]. This means that electrons of quantum wire interact only with the bulk longitudinal phonons.

Let us take that the x direction is along the wire. We will use either rectangular coordinates x,y,z or cylindrical x,ρ,φ .The electron wave function $\Phi(\vec{r})$ is given by

$$\Phi(\vec{r}) = \Psi(x)\chi(\vec{\rho}), \quad \vec{r} = (x,\vec{\rho}) = (x,y,z), \tag{1}$$

where $\Psi(x)$ describes the free electron motion along the wire, $\Psi(x) = L^{-1/2}\exp(ik_x x)$, L is the wire length, k_x is the wave vector projection in the x direction. The function $\chi(\vec{\rho})$ describes the transversal motion of the electron. For the case when the electrons occupy only the lowest $(n=0)$ subband of quantum well we have

$$\chi(\vec{\rho}) = \begin{cases} \dfrac{1.92}{\sqrt{\pi}r_0} J_0\left(\dfrac{2.4\rho}{r_0}\right) & , \ \rho < r_0 \\ 0 & , \ \rho \geq r_0 \end{cases} \tag{2}$$

where J_0 is the Bessel function of zero index. The energy of electrons is

$$E(k_x) = \frac{\hbar^2 k_x^2}{2m} + E_0 \tag{3}$$

where E_0 is the energy of the lowest level in the well and m is the electron effective mass.

The kinetic equation for the nonequilibrium distribution function f_{k_x} takes the form of 1D Boltzmann equation with the collisional integral

$$I_C = \sum_{q_x}\Big[W_{k_x,k_x-q_x} f_{k_x-q_x}(1-f_{k_x}) - W_{k_x-q_x,k_x} f_{k_x}(1-f_{k_x-q_x})\Big] \tag{4}$$

where W_{k_x,k_x-q_x} is the scattering probability of an electron from the state with quasi-momentum $\hbar(k_x-q_x)$ to the state $\hbar k_x$, calculated in Born approximation ($\vec{q}$ is the phonon wave vector):

$$W_{k_x,k_x-q_x} = \frac{2\pi}{\hbar}\sum_{q_y,q_z}\left|I(q_y,q_z)\right|^2 A_q^2\Big\{ N(\omega_{\vec{q}})\,\delta\left[\hbar\omega_{\vec{q}} - E(k_x-q_x) + E(k_x)\right] + \left[N(\omega_{\vec{q}})+1\right]\delta\left[\hbar\omega_{\vec{q}} + E(k_x-q_x) - E(k_x)\right]\Big\} \tag{5}$$

Here the scattering form factor is given by

$$I(q_y,q_z) = \int d\vec{\rho}\,\chi^*(\rho)e^{-iq_y y - iq_z z}\chi(\rho) \tag{6}$$

and the matrix element A_q of electron-phonon interaction is the same as in the bulk case:

$$A_q^2 = (2\pi e^2\kappa\hbar\omega_q)/(V_q^2), \kappa = \varepsilon_\infty^{-1} - \varepsilon_0^{-1} \tag{7}$$

for the interaction with optical phonons and

$$A_q^2 = \hbar\theta q/(2V\eta s) \tag{8}$$

for the interaction with acoustical phonons, where θ is the deformation potential constant, s the sound velocity, $\omega_{\vec{q}}$ the phonon frequency, $N(\omega_{\vec{q}})$ the phonons distribution function, V the system volume, η the mass density, ε_0 and ε_∞ are the static and high frequency dielectric constants, respectively.

In order to carry out further analytical calculations we approximate the wave function (2) by a Gaussian [13]

$$\chi(\rho) = (\pi r_0^2)^{-1/2}\exp(-\rho^2/(2r_0^2)). \tag{9}$$

The integral (6) can be now calculated and we obtain

$$I(q_y,q_z) = \exp\left[-(q_y^2+q_z^2)r_0^2/4\right] \tag{10}$$

This expression describes (6) sufficiently well, especially for small values of qr_0. However, for large values of qr_0 (10) decreases to zero somewhat faster than the exact expression (6).

Mobility calculation

The kinetic equation for electron distribution function was linearised in weak field. In the case of scattering on optical phonons the linearised equation was resolved by the variational method using the simplest approximate function [14]. In the case of nondegenerate electron gas we obtain for 1D mobility μ_{1D}^{op}

$$\frac{\mu_{1D}^{op}}{\mu_{3D}^{op}} = 8K_1(\hbar\omega_0/(2k_0T))\times \left[3\int_0^\infty dx E_1\left(\frac{r_0^2 x}{2l^2}\right)\exp\left(\frac{r_0^2 x}{2l^2} - \frac{\hbar\omega_0}{2k_0Tx} - \frac{\hbar\omega_0 x}{8k_0T}\right)\right]^{-1} \tag{11}$$

where μ_{3D}^{op} is the mobility in the bulk $3D$ system, calculated with the same approximate function [14], K_1 is the modified Bessel function of the second kind [15], $E_1(x)$ is the exponential integral function [15], $l^2 = \hbar/m\omega_0$, ω_0 is the limit phonon frequency.

It is interesting to carry out the numerical calculations of (11) for a wire of a thermoelectric material. Note, that all thermoelectric materials have a many valley band structures and anisotropic effective masses. Therefore the calculation according to (11) can serve only for a qualitative estimate. Below we will discuss what modifications in the values of

μ_{1D} one can expect if a more accurate calculations will be made.

Numerical calculations were made for wires of material with parameters of bulk PbTe: $\varepsilon_\infty = 33$, $\varepsilon_0 = 400$, $\hbar\omega_0 = 13.6$ meV, $m = 0,038 m_0$ (m is the transport effective mass and m_0 is the free electron mass).

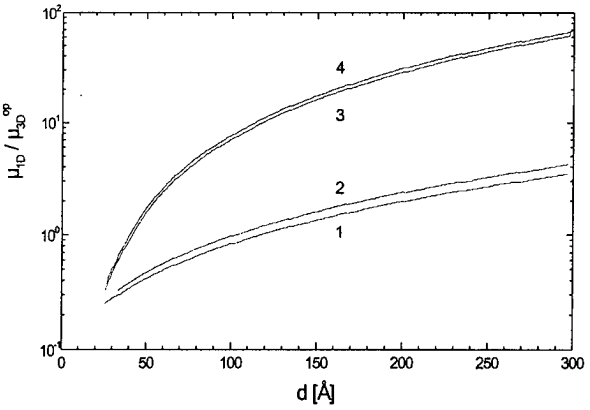


Figure 1 : Calculated mobilities μ_{1D}^{op} (curves 1 and 2) and μ_{1D}^{ac} (curves 3 and 4), expressed through μ_{3D}^{op}, as a function of wire diameter for PbTe parameters. Curves 1 and 3, T=200K; curves 2 and 4, T=300K.

Fig.1 shows the results and reveals clearly that $\mu_{1D}^{op}/\mu_{3D}^{op}$ decreases as the wire diameter $d = 2r_0$ decreases (curves 1 and 2). At $d < 110$Å μ_{1D}^{op} is less than mobility μ_{3D}^{op} in bulk material and drops sharply when d achieves values of 20Å. The explanation is as follows. In the *1D* case, the energy and momentum conservation laws impose restrictions only on the value of component q_x of phonon wave vector, but q_y and q_z remain arbitrary. For thin wires q_y, q_z less and of the order of $1/r_0$ are important, the phase-space region involved in scattering is large, the scattering probability is large too and, as consequence, the *1D* mobility is low. When the wire thickness increases the scattering phase-space decreases and μ_{1D} grows. At the thickness larger than approximately 300Å the electrons start to fill the second subband, the new scattering canal is opened and the mobility must drop to the bulk value.

In the case of electron scattering on acoustical phonons one can considered the scattering processes as elastic at room temperature. For the phonons the linear dispersion law may be still used $\omega_q = sq$, where s is the longitudinal sound velocity. For the mobility μ_{1D}^{ac} an analytical expression was obtained

$$\mu_{1D}^{ac} = \frac{\pi^{3/2} e\hbar^4 \eta s^2}{2^{3/2}\theta^2 m^{5/2}\left(k_0 T\right)^{1/2} E_0 \left[1 - pe^p E_1(p)\right]^{-1}}$$

$$p = \frac{ms^2 E_0}{4(k_0 T)^2} \qquad (12)$$

For PbTe $\eta = 7,6$ g/cm^3, $q = 18$ eV, $s = 3,6 \times 10^5$ cm/s [16]. As can be seen from (12), the mobility μ_{1D}^{ac} decreases when the energy E_0 increases and, consequently, the wire width decreases. Note that the value of E_0 can not be very small, so as only the lowest subband was occupied by electrons.

The comparison of μ_{1D}^{ac} with respective bulk value μ_{3D}^{ac} shows that as a result of increase of scattering phase-space μ_{1D}^{ac} is always lower than μ_{3D}^{ac}. But μ_{1D}^{ac} is much higher than μ_{3D}^{op} and μ_{1D}^{op} for $d > 40$Å (see curves 3 and 4 in Fig.1). So at room temperature for $d > 40$Å the main scattering mechanism in this approach is the electrons scattering on longitudinal optical phonons, while for smaller widths it need to take into account also the scattering on acoustical phonons. However resulting mobility drops sharply. In Fig. 1 one can see also, that in the examined temperature interval the temperature variation of 1D mobility is small as compared with bulk mobility for scattering both on acoustical and optical phonons.

The analysis of curves, presented in Fig. 1 show that the conclusion of potential significant increase in the figure of merit with decreasing well width in quantum wires is not so simple as it was demonstrated in [4]. At width of order of 10Å when $Z_{1D}T$ of up to 6 is predicted [4], the 1D mobility drops drastically. So the approximation of constant relaxation time, used in [4], can not be justified for 1D conductors. The expected values of $Z_{1D}T$ for the thinnest wires will be substantially lower than it was predicted in [4]. More accurate calculations taking into account the many valley band structure and anisotropic effective masses in PbTe does not change this conclusion. For example, if the wire is fabricated along the x direction which coincides with [100] all four valleys of the Brillouin zone in bulk PbTe give the same contribution to the conductivity. But the electron effective mass in this direction becomes $m_x = \left(2m_\perp + m_{||}\right)/3$, where $m_{||} = 0,24 m_0$ and $m_\perp = 0.024 m_0$ are the bulk longitudinal and transversal effective masses, respectively, and m_x is 2,8 times greater than transport effective mass. As a result, the 1D mobility will be lower as compared with calculated higher for scattering both on optical and acoustical phonons. A more realistic calculations of electrical conductivity, Seebeck coefficient and thermal conductivity of quantum wires are needed for the evaluation of thermoelectric opportunities of materials prepared in form of quantum wires.

Conclusions

We have calculated the carriers mobility in quasi-one-dimensional quantum wire on the basis of material with the parameters of bulk PbTe within the model of a cylindrical wire of finite radius r_0 with infinite potential walls. The wire are considered as thin so electrons populate only the lowest subband. In the nondegenerate case we found that for wire thickness greater than approximately 40Å the main scattering mechanism at room temperature is the electrons scattering on the optical longitudinal phonons. While for smaller thickness it need to take into account also the scattering on acoustical phonons. The electron mobility decreases rapidly with decreasing of quantum well width, especially at very thin wires. This effect changes considerably the predicted in [4] significant increase in the figure of merit of materials prepared in the form of quantum wires over both the bulk value and the two-dimensional structures values. In order to determinate the thermoelectric opportunities of materials prepared in form of quantum wires, a more detailed calculations of electrical conductivity of quantum wires , Seebeck coefficient and thermal conductivity are needed.

[1] L.D. Hicks and M.S. Dresselhaus, Phys. Rev. B 47 (1993) 12727.

[2] L.D. Hicks, T.C. Harman and M.S. Dresselhaus, Appl. Phys. Lett. 63 (1993) 3220.

[3] L.D. Hicks, T.C.Harman, X.Sun and M.S. Dresselhaus, Phys.rev. B 53 (1996) R 10494.

[4] L.D. Hicks and M.S. Dresselhaus, Phys. Rev. B 47 (1993) 16631.

[5] A.R. Goni *et al.*, Phys. Rev. Lett., 67 (1991) 3298.

[6] J. Meirav, M.A. Kastner, M. Heiblum, and S.J. Wind, Phys. Rev. B 40 (1981) 5871.

[7] J. Rodnev, S. Ruoff *et al.*, Science 259 (1993) 346.

[8] X.F. Wang and X.L. Lei, Phys. Rev. B 49 (1994) 478.

[9] V.L. Berezinsky. Journ. exp. and theor. phys. (Sov. Phys. JETP), 65 (1973) 1251.

[10] Dongzi Liu and S. Das Sarma, Phys. Rev. B 51 (1995) 1382.

[11] A.A. Gogolin, V.M. Mel'nicov and E.I. Rashba, Journ. exp. and theor. phys. (Sov. Phys. JETP), 69 (1975) 327.

[12] V.L. Gurevich and K.E. Shtengel, Phys. Rev. B 44 (1991) 8825.

[13] H.L. Cui and M.S. Horing, Phys. Rev. B 40 (1989) 2956.

[14] J. Ziman. Electrons and Phonons (Clarendon Press, Oxford, 1960), Chap. 10, p. 5.

[15] M. Abramovitz and J. Stegun, Handbook of Mathematical Functions, (National Bureau of Standarts, Applied Mathematics series 55, 1964).

[16] Yu.I. Ravich, B.A. Efimova and I.A. Smirnov, Methods of investigation of semiconductors applied to lead chalcogenides PbTe, PbSe, PbS (Nauca Press, Moscow 1968)

New Low Thermal Conductivity Materials for Thermoelectric Applications

T. Caillat* and J.-P. Fleurial
Jet Propulsion Laboratory/California Institute of Technology
4800, Oak Grove Drive, MS 277-207, Pasadena, CA 91109
*thierry.caillat@jpl.nasa.gov

Abstract

A low lattice thermal conductivity is one of the requirements to achieve high thermoelectric figures of merit. Several low thermal conductivity materials were identified and developed over the past few years at JPL, including filled skutterudites and Zn_4Sb_3-based materials. A study of the mechanisms responsible for the high phonon scattering rates in these compounds has demonstrated that materials with highly disordered or complex structures which can accommodate additional atoms in their lattice are likely to have low lattice thermal conductivity values. Several cluster compounds, including the Chevrel phases (Mo_6Se_8-type) and Re_6Te_{15}, are just such materials and are currently being investigated at JPL. The crystal structures of the Chevrel phases present cavities which can greatly vary in size and can contain a large variety of atoms ranging from large ones such as Pb to small ones such as Cu. These atoms are not localized in the structure and, depending on their size, can move between different sites and may produce significant phonon scattering. Although most of the Chevrel phases studied until now were reported to be metallic, it was found that semiconducting Chevrel phases can be engineered by controlling the number of electrons per [Mo_6] cluster. Initial results obtained on some cluster Chevrel phases and Re_6Te_{15} are presented and discussed. These materials possess very low thermal conductivity values (~ 10 mW/cmK at 300K) but optimization of their electronic properties will be required to achieve high thermoelectric figures of merit.

Introduction

Renewed interest in the search for thermoelectric materials with superior properties has been driven by several factors. The availability and identification of new compounds and concepts as well as economical and environmental concerns have substantially contributed to the revival of the thermoelectric field. Several new ideas have been recently reviewed [1]. One of the new approaches is to look at materials which can be referred to as "rattling" semiconductors. The idea was originally proposed by Slack [2] who suggested that, in crystals containing loosely bound atoms, phonons should be scattered more strongly than electrons (holes). He called such an ideal thermoelectric material a "phonon-glass, electron-crystal"-(PGEC). Efforts to identify new classes of thermoelectric materials initiated at the Jet Propulsion laboratory (JPL) in 1991 have resulted in the discovery of several materials with superior thermoelectric properties, including skutterudites and Zn_4Sb_3-based materials [3-5]. Studies on skutterudites initially focused on binary compounds but it became soon clear that thermoelectric figures of merit (ZT) greater than those obtained for state-of-the-art thermoelectric materials would not be achieved if the lattice thermal conductivity could not be significantly reduced. One of the features of the skutterudite compounds is the presence of voids in their crystal structure. These cavities can be filled by various atoms which are believed to produce an important phonon scattering, resulting in a significant reduction in lattice thermal conductivity and superior thermoelectric properties [5-8].

These findings support the concept initially proposed by Slack. Other crystalline materials containing loosely bound atoms have also been reported to posses thermal conductivity close to the calculated theoretical minimum [9]. We have conducted a search to identify new classes of materials with crystal structures that can host "rattling" atoms and to investigate their thermoelectric properties. We describe in this paper several cluster compounds which present such attributes: Chevrel phases and Re_6Te_{15}-based compounds recent experiments show that they possess very low thermal conductivity and a good potential for thermoelectric applications.

Chevrel phases

Structure and physical properties

Ternary chalcogenides of formula $M_xMo_6X_8$ (M= Cu, Ag, Ni, Fe, rare earth, etc.) and X = S, Se, or Te have been known since the 1970's. They have attracted considerable interest because of their superconducting properties with large critical magnetic fields [10]. They were first synthesized by Chevrel et al. in 1971 [11] and therefore are often referred to as Chevrel compounds. The ternary phases have structures closely related to those of binary molybdenum chalcogenides Mo_6X_8 (X= S, Se, Te).

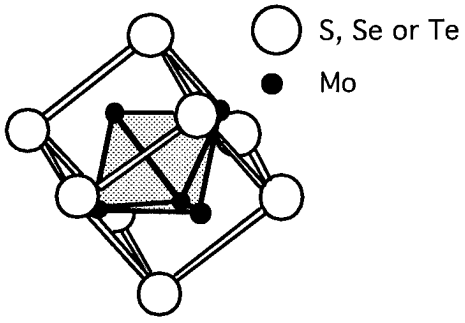


Figure 1: Illustration of the Mo_6X_8 (X = S, Se, Te) building block of the rhombohedral Chevrel phase structure.

The Mo_6X_8 unit is illustrated in Figure 1 and consists of an [Mo_6] octahedron "cluster" surrounded by eight chalcogens

arranged in a distorted cube. The rhombohedral Chevrel phase consists of a stacking of Mo_6X_8 units and contains channels where additional metal atoms can be inserted, forming MMo_6X_8 compounds where M can be a variety of atoms from small to large ones (M= Ag, Sn, Ca, Sr, Pb, Ba, Ni, Co, Fe, Cr, Mn, ... ; for a complete list see for example [12]). The cavities in the Chevrel structure are empty in the binary compounds such as Mo_6Te_8 and are filled by the M atoms in the ternary compounds $M_xMo_6X_8$. The largest of the voids in the Chevrel structure has nearly a cubic shape formed by 8 chalcogen atoms as illustrated in Figure 2a. Large atoms such as Pb or La can exclusively occupy these large voids with a filling factor limit corresponding to x~1. Smaller atoms such as Cu, Ni or Fe, for example can be inserted in 12 different smaller holes with irregular shapes in the chalcogen channels as illustrated in Figure 2b. For small atoms, the upper occupancy limit was experimentally found to be corresponding to x=4. It is also important to point out that the shapes and sizes of the interstices depend on the composition and degree of filling. The thermal behavior of $M_xMo_6X_8$ compounds has been studied by Yvon [10]. One of the results of these studies is that it appears that the M atoms are systematically not confined in a fixed position, are weakly bound and small atoms in particular are able to move between the 12 different lattice sites. The motion of these atoms within the lattice may be particularly effective in scattering. Data on thermal conductivity of $M_xMo_6X_8$ ternary compounds would therefore be of great interest.

As we mentioned above, these compounds have been mainly investigated for their superconducting properties. To the best of our knowledge, no data exists on the thermoelectric properties of Chevrel phases. Many of their physical properties appear to be linked to the number of electrons per Mo atom in the cluster. This quantity, often referred to as "cluster-valence-electron" (cluster-VEC) is calculated by adding the valence electrons of M atoms to the valence electrons of Mo atoms, by subtracting the number of electrons required to "fill" the octets of the chalcogen atoms and dividing the result by the number of Mo atoms [13]. Chevrel phases are formed for cluster VEC numbers between 3.3 and 4. [13]. In addition, band structure calculations results predicted an energy gap in the electronic structure for 4 valence electrons per Mo atom in the cluster [14]. The "magic" number of 4 is met in the compound $Cu_4Mo_6S_8$ although the semiconducting nature of this compound was not confirmed experimentally. Values of 4 are also attained in mixed-metal cluster compounds such as $Mo_2Re_4Se_8$ and $Mo_4Ru_2Se_8$ [15,16] and these compounds were found to be semiconductors, supporting the idea of an energy gap in the band structure of the Chevrel phases with a "magic" cluster VEC number of 4.

We have recently synthesized and investigated the thermoelectric properties of the compound $Mo_2Re_4Se_8$ [17], a pseudobinary compound with a VEC of 4. The results confirmed the expected semiconducting nature of this material. However, it was found that only very small amounts of an additional element M such as Sn can be introduced in the compound [15]. This might be explained by the fact that the cluster VEC is already at 4 and the bands below the gap are completely filled, preventing the insertion of additional M atoms. Other approaches must thus be considered to study the effect of void fillers on the thermal conductivity of

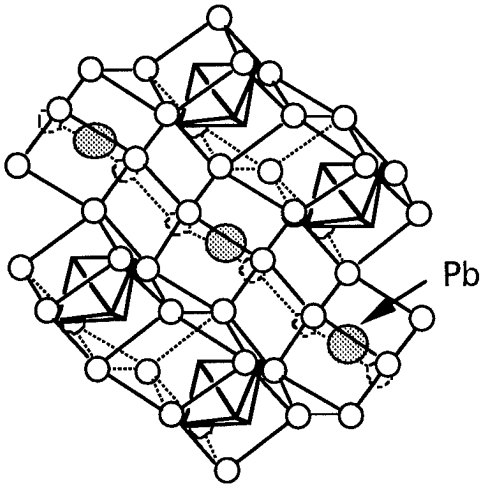


Figure 2a

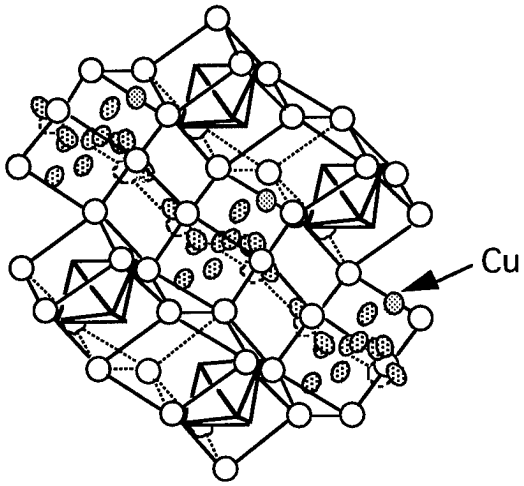


Figure 2b

Figure 2: Illustrations showing the positions of filling atoms in the cavities of the Chevrel crystal structure (after reference [10]). The figures represent a projection of the crystal structure on the hexagonal (1120) plane. The large atoms of Pb in $PbMo_6S_8$ occupy cube shaped chalcogen holes (2a) whereas small Cu atoms can be distributed over 12 different sites in the chalcogen network of $Cu_xMo_6S_8$ (x_{max}=4) (2b).

semiconducting Chevrel phases. In the $Cu_xMo_6S_8$ system, compositions with x=4 have been reported [18] and, assuming that the Cu has an oxidation state of +1, the ionic formula would be $Cu_4^{+}Mo_6^{2+}S_8^{2-}$. The "magic" cluster VEC number of 4 is met in this compound which should be semiconducting. Another possibility to explore is to prepare semiconducting Chevrel phases combining void fillers and a mixed cluster ($Mo_{6-x}M'_x$, where M' is a metal) to achieve the "magic" VEC number of 4. For example, an hypothetical compound $Cu_2Mo_3Re_3Se_8$ would have a cluster VEC of 4 and should be a semiconductor. Such a compound would be particularly attractive because phonons would presumably be scattered by both point defects and the void fillers. We are currently

investigating some of these approaches and synthesized several $(Fe,Co)_xMo_6Se_8$ filled compositions. Assuming an oxidation state of 2+ for Fe and Co these compositions have a VEC of 4 for x=2 and therefore should be semiconducting. The details of the sample preparation, characterization and transport properties measurements as well as their thermoelectric properties are presented and discussed in the following sections.

Experimental

Single phase, polycrystalline samples of $(Fe,Co)_xMo_6Se_8$ were prepared by mixing and reacting stoichiometric amounts of iron (99.99%), cobalt (99.999%), molybdenum (99.999%), and selenium (99.999%) powders. The powders were first mixed in a plastic vial using a mixer before being loaded into quartz ampoules which were evacuated and sealed. The ampoules were then heated at 1473K for 2 days. A total of three anneals at 1473K for 2 days each and with intermediate crushing and grinding was necessary to obtain single phase materials. The samples were analyzed by x-ray diffractometry (XRD) after each anneal. The powders were then hot-pressed in graphite dies into dense samples, 10 mm long and 6.35 mm in diameter. The hot-pressing was conducted at a pressure of about 20,000 psi and at temperatures between 1123 and 1273 K for about 2 hours under argon atmosphere. The density of the samples was calculated from the measured weight and dimensions and was found to be about 95% of the theoretical density.

X-ray diffractometry analysis (XRD) was performed at room temperature on a Siemens D-500 diffractometer using Cu-K_α radiation. Small additions of Si powders were made to the samples as an internal standard. Powder x-ray patterns were taken with scan steps of $2\Theta=0.05°$ and counting time of 3 s. Microprobe analysis (MPA) was performed on these samples to determine their atomic composition using a JEOL JXA-733 electron superprobe operating at $20x10^3$ Volts (V) of accelerating potential and $25x10^{-9}$ Amperes (A) of probe current. Pure elements were used as standards and x-ray intensity measurements of peak and background were conducted by wavelength dispersive spectrometry. The shear and longitudinal sound velocities were measured at room temperature on a sample about 8 mm long using a frequency of 5 Mhz.

Samples in the form of disks (typically a 1.0 mm thick, 6.35 mm diameter slice) were cut from the cylinders using a diamond saw (perpendicular to the pressing direction) for electrical and thermal transport property measurements. All samples were characterized at room temperature by Seebeck coefficient, Hall effect and electrical resistivity measurements. High temperature resistivity, Hall effect, Seebeck coefficient, thermal diffusivity, and heat capacity measurements were also conducted on selected samples between room temperature and about 1000K. The electrical resistivity (ρ) was measured using the van der Paw technique with a current of 100 mA using a special high temperature apparatus [19]. The Hall coefficient (R_H) was measured in the same apparatus with a constant magnetic field value of ~ 10,400 Gauss. The carrier density was calculated from the Hall coefficient, assuming a scattering factor of 1.0 in a single carrier scheme, by $p/n = 1/R_He$, where p and n are the densities of holes and electrons, respectively, and e is the electron charge. The Hall mobility (μ_H) was calculated from the Hall coefficient and the resistivity values by $\mu_H = R_H/\rho$. Errors were estimated to be ± 0.5% and ± 2% for the resistivity and Hall coefficient data, respectively. The Seebeck coefficient (α) of the samples was measured on the same samples used for electrical resistivity and Hall coefficient measurements using a high temperature light pulse technique [20]. The error of the Seebeck coefficient measurement was estimated to be less than ± 3%. The heat capacity and thermal diffusivity were measured using a flash diffusivity technique [21]. The thermal conductivity (λ) was calculated from the experimental density, heat capacity, and thermal diffusivity values. The overall error in the thermal conductivity measurements was estimated to be about ± 10%.

Results and discussion

The electrical resistivity and Seebeck coefficient values for Mo_6Se_8, $Mo_2Re_4Se_8$ and $(Fe,Co)_xMo_6Se_8$ Chevrel phases are shown in Figures 3 and 4, respectively.

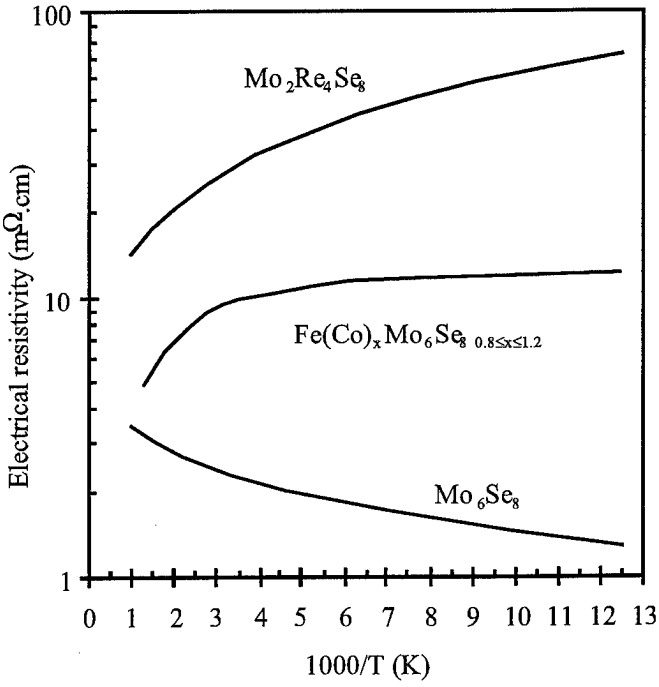


Figure 3: Electrical resistivity versus inverse temperature for Mo_6Se_8, $Mo_2Re_4Se_8$ and $(Fe,Co)_xMo_6Se_8$ Chevrel phases

The Seebeck coefficient and electrical resistivity for Mo_6Se_8 are typical of a metal. For $Mo_2Re_4Se_8$ (with a VEC of 4), the conductivity is n-type , the Seebeck coefficient values are relatively large (up to - 200 μV/K at 1100K) and the electrical resistivity decreases with increasing temperature. This clearly indicates a semiconducting behavior which is consistent with the VEC 'magic' number of 4. For $(Fe,Co)_xMo_6Se_8$ compositions, it was determined by MPA that the fraction, *x*, of Fe and Co in the samples was comprised between 0.8 and 1.2 presumably due to some material losses during the synthesis process. Therefore, the VEC for these compositions ranges between 3.6 and 3.7. For these samples, the Seebeck coefficient as well as the electrical resistivity are slightly increased compare to Mo_6Se_8 and the samples are semi-

metallic. Again, this seems to be consistent with the VEC rule for these materials. The carrier concentration for these filled compositions are about 2 x 10^{21} cm^{-3} and the carrier mobility is about 1 cm^2 V^{-1} s^{-1}.

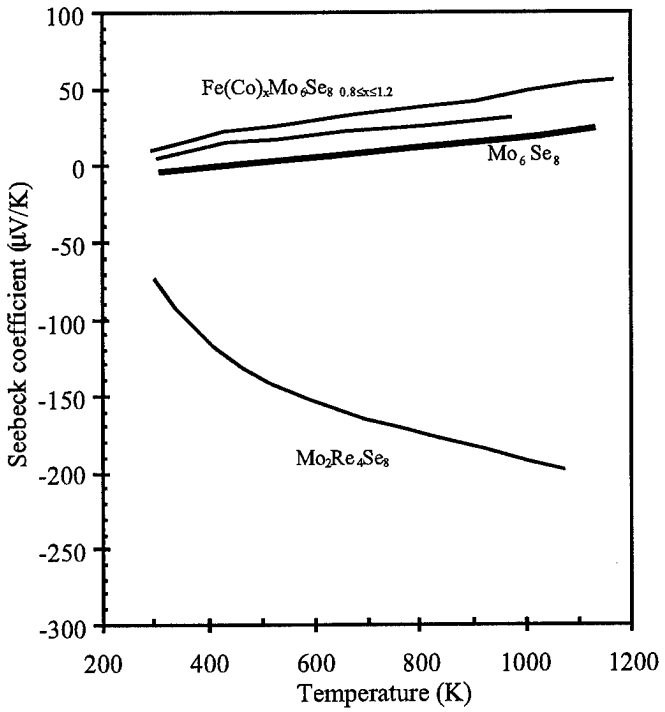


Figure 4: Seebeck coefficient versus temperature for Mo_6Se_8, $Mo_2Re_4Se_8$ and $(Fe,Co)_xMo_6Se_8$ Chevrel phases

The results of thermal conductivity measurements are shown in Figure 5. The room temperature thermal conductivity for Mo_6Se_8 is about 70 mW/cmK and the thermal conductivity decreases with increasing temperature to a minimum value of about 45 mW/cmK at 1100K. For $Mo_2Re_4Se_8$, the thermal conductivity is significantly decreased with a room temperature thermal conductivity of 40 mW/cmK. Considering the relatively large electrical resistivity values, the total thermal conductivity shown corresponds to approximately 98% of the lattice contribution. The thermal conductivity varies approximately as $T^{-1/2}$ which is indicative of a dominant phonon scattering by point defects introduced by the substitution of Re for Mo atoms. A remarkable decrease in thermal conductivity is obtained for $(Fe,Co)_xMo_6Se_8$ compositions. The room temperature thermal conductivity is about 13 mW/cmK for these compositions and the thermal conductivity rises with increasing temperature as for glass-like materials. The lattice thermal conductivity values, calculated using the Wiedemann-Franz law assuming the Lorenz number to be 2.44 x 10^{-8} V^2/K^2, are represented by the dashed lines in Figure 5 for Mo_6Se_8 and $(Fe,Co)_xMo_6Se_8$ compositions. For the filled compositions, the lattice thermal conductivity increases from a room temperature value of 10 mW/cmK to 13 mW/cmK at 1100K. As we pointed out above, these compositions are semi-metallic and one can expect a significant electrical carrier-phonon scattering which should lower the lattice thermal conductivity. However, it is known that this type of phonon scattering cannot lead to a glass-like behavior for the thermal conductivity and therefore the strong decrease in the thermal conductivity can predominantly be attributed to the "rattling" of the Co or Fe atoms in the voids of the Chevrel structure.

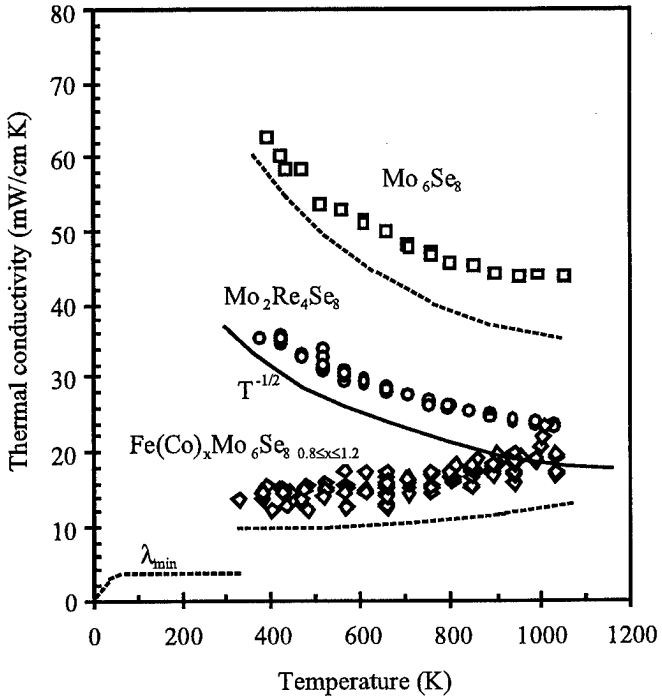


Figure 5: Thermal conductivity versus temperature for Mo_6Se_8, $Mo_2Re_4Se_8$ and $(Fe,Co)_xMo_6Se_8$ Chevrel phases. The dashed lines represent the lattice thermal conductivity for Mo_6Se_8 and $(Fe,Co)_xMo_6Se_8$ compositions. The calculated minimum lattice thermal conductivity is also reported (see text for details of calculations).

It was interesting to compare the experimental values obtained for $(Fe,Co)_xMo_6Se_8$ compositions to the calculated minimum thermal conductivity, a concept first proposed by Slack [22] and later developed by Cahill et al. based on a model due to Einstein [9]. The minimum thermal conductivity is expressed as a sum of three Debye integrals by [9]:

$$\lambda_{min} = \left(\frac{\pi}{6}\right)^{1/3} k_B\, n^{2/3} \sum_i v_i \left(\frac{T}{\theta_i}\right)^2 \int_0^{\theta_i/T} \frac{x^3 e^x}{(e^x-1)^2}\, dx$$

The sum is taken over the three sound modes (two transverse and one longitudinal) with speeds of sound v_i. k_B is the Boltzmann's constant, n the atomic density, T the temperature in K and $\theta_i = v_i\,(h/2\pi k_B)\,(6\pi^2 n)^{1/3}$. Using the measured transverse and longitudinal of 1.52 x 10^3 ms^{-1} and 2.63 x 10^3 ms^{-1}, respectively and an atomic density of 5.04 x 10^{28} m^{-3}, we calculated the minimum thermal conductivity values for $Fe_{1.2}Mo_6Se_8$. The results are reported in Figure 5. At room temperature, the calculated value is about 3 times the measured value, indicating that further reduction in thermal conductivity might be possible. The data reported for the filled compositions in Figure 5 correspond to materials which are about 50% filled and future studies on Chevrel phases will investigate the impact of various degree of filling on the thermal conductivity. In addition to the filling fraction, the

effect of introducing various large atoms well as a combination of small and large atoms in the voids should be studied. In selecting Chevrel phases for further investigations, one should obviously also pay attention to the VEC which should be close to 4 to achieve a semiconducting behavior. Preliminary data on the thermoelectric properties of Chevrel phases show that void fillers can be very effective in producing significant phonon scattering, resulting in relatively low lattice thermal conductivity values. The major questions which remain to be answered to fully assess the potential of thermoelectric applications are: 1) how low can the thermal conductivity be decreased ? and 2) can semiconducting Chevrel phases with good carrier mobility be obtained ?

Re_6Te_{15}

The structure of the cluster compound Re_6Te_{15} was studied in details by Klaiber et al. [23]. This compound, with 84 atoms per unit cell, belongs to the space group *Pbca* with a=13.003Å, b=12.935Å and c=14.212Å. The crystal structure presents some similarities with the Chevrel phases and the Re atoms are also arranged in octahedral [Re_6] clusters. The thermoelectric properties of this compound have been little studied but some Seebeck coefficient and electrical resistivity data can be found in the literature [23,24]. In general, the samples were characterized by high Seebeck coefficient values as well as high electrical resistivity values. To be best of our knowledge, there is no data on the thermal conductivity of this compound. The heavy atoms constituting the compound as well as the large number of atoms per unit cell could give low thermal conductivity. It was also found that up to 40% of the Te atoms can be replaced by Se atoms [23] and this offers further possibilities to achieve lower thermal conductivity than for the binary compound Re_6Te_{15} itself. For the reasons mentioned above as well as some others that will be discussed in the one of the following section, we have started the preparation and characterization of Re_6Te_{15}-based materials. Initial results of the synthesis and characterization of the thermoelectric properties of these materials is presented and discussed in the following sections.

Experimental

Single phase, polycrystalline samples of $Re_6Te_{15-x}Se_x$ were prepared by mixing and reacting stoichiometric amounts of rhenium (99.997%), tellurium (99.999%) and selenium (99.999%) powders. The powders were first mixed in a plastic vial using a mixer before being loaded into a quartz ampoule which was evacuated and sealed. The ampoules were then heated at 773K for 10 days with one intermediate crushing. The samples were analyzed by x-ray diffractometry (XRD) to check that they were single phase. The powders were then hot-pressed in graphite dies into dense samples, 10 mm long and 6.35 mm in diameter. The hot-pressing was conducted at a pressure of about 20,000 psi and at a temperatures of 773 K for about 2 hours under argon atmosphere. The density of the samples was calculated from the measured weight and dimensions and was found to be about 97% of the theoretical density.

The samples were characterized using the same microstructure and measurements techniques described in the experimental section for the Chevrel phases. All samples were found to be single phase by microprobe analysis. The transverse and longitudinal speed of sounds were measured to be 1.38 x 10^3 m s^{-1} and 2.35 x 10^3 m s^{-1}, respectively.

Results and discussion

The electrical resistivity and the Seebeck coefficient values are reported for Re_6Te_{15} and $Re_6Se_{2.25}Te_{12.75}$ in Figures 6 and 7, respectively. In general, the results are consistent with previous findings [23,24]: all samples showed p-type conductivity with large Seebeck coefficient values and large electrical resistivity values. The room temperature carrier mobility for Re_6Te_{15} was 4 cm^2 V^{-1} s^{-1} for a carrier concentration of 2 x 10^{18} cm^{-3}. The electrical resistivity are high, due to the low carrier mobility. For Re_6Te_{15}, both electrical resistivity and Seebeck coefficient decrease with increasing temperature, as expected for an intrinsic semiconductor. The electrical resistivity varies linearly with temperature at high temperatures. We calculated an activation energy of 0.8 eV, in good agreement with previous results [23]. A different behavior is observed for the $Re_6Se_{2.25}Te_{12.75}$ solid solution. Both Seebeck coefficient and electrical resistivity increase with increasing temperature and only at the highest temperatures of measurements, an onset of intrinsic behavior can be observed. However, the electrical resistivity are also relatively high which is due again to relatively poor carrier mobility of the order of 1-2 cm^2 V^{-1} s^{-1}.

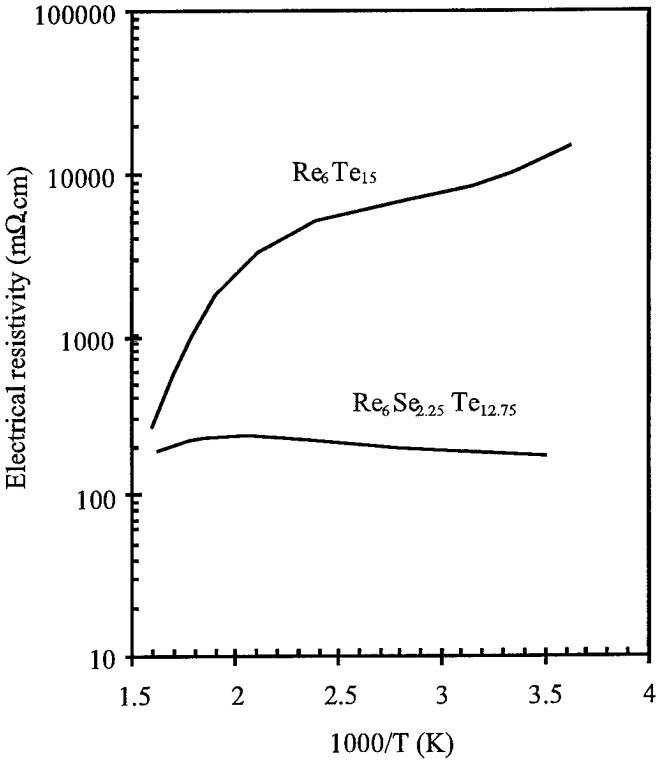


Figure 6: Electrical resistivity versus inverse temperature for Re_6Te_{15} and $Re_6Se_{2.25}Te_{12.75}$

The results of the thermal conductivity measurements for Re_6Te_{15} and $Re_6Se_{2.25}Te_{12.75}$ are shown in Figure 8 and compared to typical values obtained for p-type state-of-the-art thermoelectric materials. Considering the high electrical resistivity of the samples, the electronic component of the total thermal conductivity is negligible and the values shown

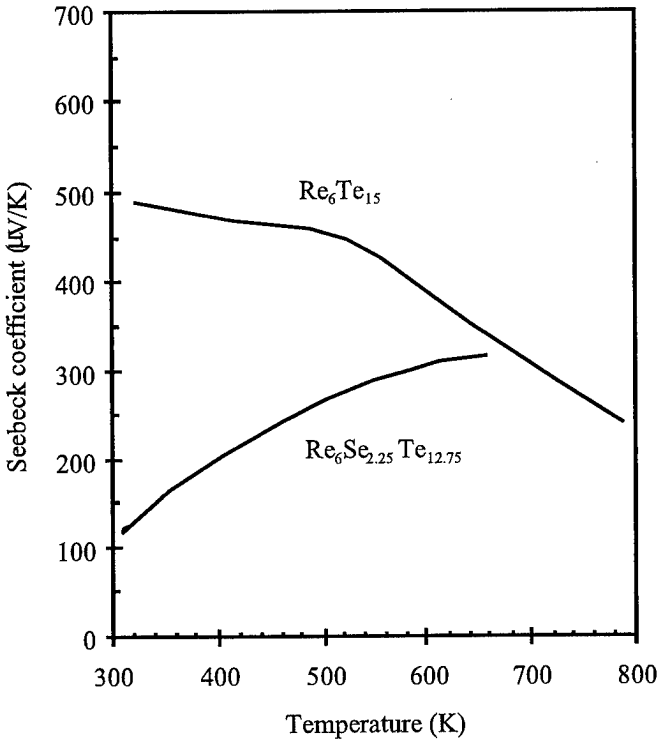


Figure 7: Seebeck coefficient versus temperature for Re_6Te_{15} and $Re_6Se_{2.25}Te_{12.75}$

in Figure 8 can be considered as being the contribution from the lattice only. At room temperature, the thermal conductivity for Re_6Te_{15} is about 14 mW/cmK and is comparable to p-type Bi_2Te_3-based alloys. The thermal conductivity of Re_6Te_{15} decreases with increasing temperature following reasonably well a 1/T dependence, as expected for phonon-phonon umklapp scattering. A minimum of 7 mW/cmK is reached at 800K, significantly lower than the values obtained for state-of-the-art thermoelectric materials. For the $Re_6Se_{2.25}Te_{12.75}$ solid solution, the thermal conductivity decreases with increasing temperature approximately as $T^{-1/2}$. This temperature dependence is typical of a phonon scattering by point defects. The values for the solid solution are lower than for the binary compound because of the mass and volume fluctuations introduced by the substitution of Se atoms for Te atoms. At room temperature the thermal conductivity is 10 mW/cmK, decreasing to a minimum of 6 mW/cmK at 600K.

Using the same formalism presented above, we have calculated the minimum thermal conductivity for Re_6Te_{15} which corresponds to the same material in the amorphous state. For the calculation, we used the measured speed of sounds and an atomic density of 3.52×10^{28} m^{-3}. The results are shown in Figure 8. At room temperature, the calculated minimum value is 2.3 mW/cmK and the minimum measured value is 10 mW/cmK for the $Re_6Se_{2.25}Te_{12.75}$ solid solution. This seems again to indicate that scattering of the phonons by point defects cannot yield thermal conductivity comparable to an amorphous material. As we mentioned earlier, the investigation of the thermoelectric properties of Re_6Te_{15} was primarily prompted by the possibility of achieving low thermal conductivity values because of the heavy masses of the elements forming the compounds as well as the large number of atoms per unit cell. The results show that indeed the thermal conductivity are low, significantly lower than for state-of-the-art thermoelectric materials between 300 and 800K. However, there also seems to be room for further reducing the lattice thermal conductivity. The second main reason which incited us to investigate the properties of Re_6Te_{15}-based materials is, as for the Chevrel phases, the presence of a number of voids in the structure. Figure 9 illustrates the location of the voids inside the crystal structure. The large spheres represent the atoms that can possibly be inserted in these voids. The radius of the voids is 2.754Å [23] and therefore each of the voids is large enough to accommodate a great number of different type atoms. Filled compositions can be represented by the formula $Re_6M_2Te_{15}$. Although the possibility of inserting additional atoms in the voids of the Re_6Te_{15} structure was suggested in the literature [23], this was not accomplished experimentally to the best of our knowledge.

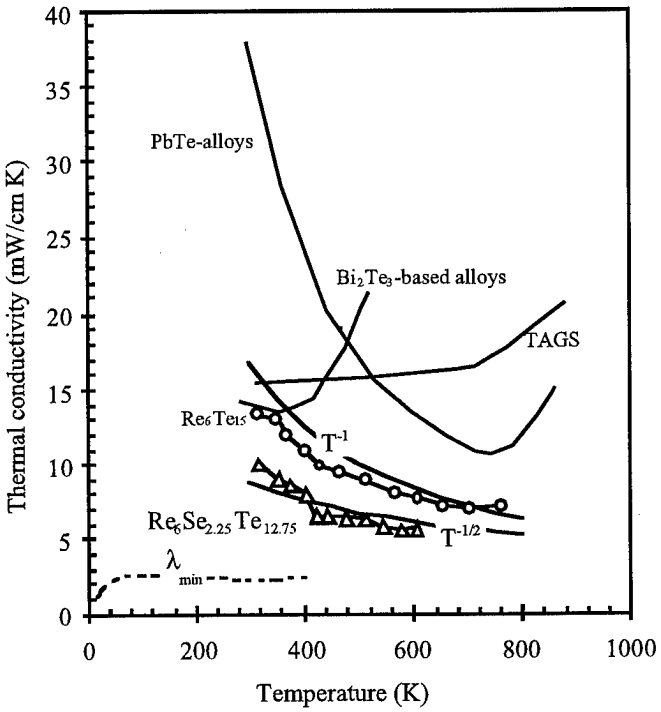


Figure 8: Thermal conductivity versus temperature for Re_6Te_{15} and $Re_6Se_{2.25}Te_{12.75}$. The calculated minimum lattice thermal conductivity is also reported (see text for details of calculations). The values for p-type state-of-the-art thermoelectric materials are also reported for comparison: Bi_2Te_3 and PbTe alloys and TAGS (Te-Ag-Ge-Sb alloys).

We have started the synthesis of filled Re_6Te_{15} samples with Ag, Cd and Fe. the filling elements were added to the pre-synthesized Re_6Te_{15} powders and the mixtures were annealed for 5 days at 773K. The powders were then hot-pressed under the same conditions as unfilled Re_6Te_{15} samples. MPA of the samples filled with Fe and Cd showed a significant amount of secondary phases and no phase corresponding to a filled composition could be detected. For Ag filled samples, the samples were essentially composed of

several filled compositions $Re_6Ag_xTe_{15}$ with $0.5 \leq x \leq 1.14$. This encouraging result suggests that it is indeed possible to fill the voids of the structure. The thermoelectric properties of the Ag filled sample are currently being investigated. Improvements are however needed to obtain homogeneous samples and also to ameliorate the synthesis technique and demonstrate the possibility of inserting other atoms in the voids. The study of the impact of the additional atoms on the thermal conductivity of these materials is of particular interest because it could result in very low thermal conductivity values, close to the theoretical minimum. Also, one can expect substantial modifications of the band structure of these materials and therefore different electrical properties.

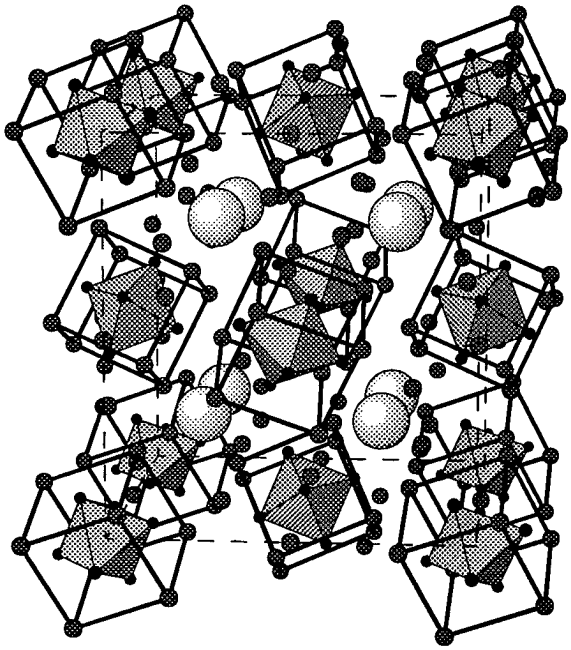


Figure 9: Illustration of the Re_6Te_{15} unit cell showing the $[Re_6]$ cluster surrounded by eight Te atoms. Large spheres representing atoms are inserted in the voids presented in the structure. Some Te atoms were omitted for clarity.

Conclusion

As part of an ongoing search for thermoelectric materials with superior thermoelectric properties, we have started to investigate the properties of two classes of cluster compounds: Chevrel phases and Re_6Te_{15}-based materials. A common property of these materials is the presence of voids in their crystal structure which can be filled with a variety of atoms. For the Chevrel phases, initial results showed that low thermal conductivity (~10 mW/cmK at 300K) can be achieved for filled compositions and even lower values might be possible by adjusting the nature of the filling element and its concentration. We have also shown that semiconducting Chevrel phases can be created by controlling the number of valence electrons. Semiconducting properties are observed for VEC of 4. Some of the compositions prepared showed good Seebeck coefficient values but also poor carrier mobility which will need to be improved to achieve good thermoelectric figures of merit. Re_6Te_{15}-based materials showed very low thermal conductivity in the 300-800K temperature range (6-13 mW/cmK), large Seebeck coefficient but also poor carrier mobility. The possibility of introducing Ag atoms in their voids of the structure was also demonstrated and such filled compositions should possess very low thermal conductivity, close to the theoretical minimum. The thermoelectric properties of Ag-filled compositions are currently being investigated as well as the synthesis of other filled compositions. In summary, we believe that these two new classes of materials offer a good potential for thermoelectric applications, including numerous possibilities for optimizing their properties. The concept of using loosely bound atoms in the crystal structure to obtain low thermal conductivity was demonstrated for the Chevrel phases.

Acknowledgments

The work described in this paper was carried out at the Jet Propulsion Laboratory/California Institute of Technology, under contract with the National Aeronautics and Space Administration. The authors would like to thank Dr. A. Borshchevsky, Dr. I. Mazin, Dr. D. J. Singh, Prof. Glen A. Slack, and Dr. G. J. Snyder for many helpful discussions. This work is supported by the U. S. Defense Advanced Research Projects Agency, Grant No. E407.

References

1. G. Mahan, B. Sales, and J. Sharp, *Phys. Today*, 50, 42 (1997).

2. Slack G. A., *Thermoelectric Handbook*, edited by M. Rowe (CRC, Boca Raton, FL, 1995), p. 407.

3. T. Caillat, J. -P. Fleurial, A. Borshchevsky, *J. Phys. Chem. Solids*, Vol. 58, 7, 1119 (1997).

4. T. Caillat, A. Borshchevsky, and J.-P. Fleurial, *Proceedings 7th International Conference on Thermoelectrics*, ed. K. Rao, University of Texas at Arlington, p. 98 (1993).

5. J. -P. Fleurial, A. Borshchevsky, T. Caillat, D. T. Morelli and G. P. Meisner, *Proceedings of the XV International Conference on Thermoelectrics,* Pasadena, CA, USA, IEEE Catalog Number 96TH8169, p. 91 (1996).

6. D. T. Morelli and G. P.Meisner, *J. Appl. Phys.* 77, 3777 (1995).

7. G. S. Nolas, G. A. Slack, D. T. Morelli, T. M. Tritt, and A. C. Ehrlich, *J. Appl. Phys.* 79, 4002 (1995).

8. B. C. Sales, D. Mandrus, R. K. Williams, *Science* 272, 1352 (1996).

9. D. G. Cahill, S. K. Watson, and R. O. Pohl, *Phys. Rev.* 46, 6131 (1992).

10. K. Yvon, *Current Topics in Materials Science* (E. Kaldis) Vol. 3, p. 53, North-Holland Amsterdam (1979).

11. R. Chevrel, M. Sergent and J. Pringent, *J. Solid State Chem.* 3, 515 (1971).

12. O. Fischer, Appl. Phys. 16, 1 (1978).

13. K. Yvon and E. Paoli, *Solid State Communication* 24, 41 (1977).

14. L. F. Matheiss and C. F. Fong, *Phys. Rev. B15*, 1760 (1977).

15. A. Perrin, M. Sergent and O. Fischer, *Mat. Res. Bul.* 13, 259 (1978).

16. A. Perrin, R. Chevrel, M. Sergent and O. Fischer, *J. Solid State Chem.* 33, 43 (1980).

17. T. Caillat and J. -P. Fleurial, *J. Phys. Chem. Solids*, in press (1997).

18. D. C Johnston., R. N. Shelton, and J. J. Bugaj, *Solid State Communication*, 21, 949 (1977).

19. J. A. McCormack and J. -P. Fleurial, *Modern Perspectives on Thermoelectrics and Related Materials*, MRS Symp. Proc. 234 (Materials Research Society, Pittsburgh, Pennsylvania), p. 135 (1991)

20. C. Wood, D. Zoltan and G. Stapfer, *Rev. Sci. Instrum.* 56, 5, 719 (1985).

21. J. W. Vandersande, C. Wood, A. Zoltan and D. Whittenberger, *Thermal Conductivity*, Plenum Press, New York, 445 (1988).

22. G. A. Slack, in *Solid State Physics*, edited by F. Seitz and D. Turnbull (Academic, New York, 1979), Vol. 34, p. 1.

23. F. Klaiber, W. Petter and F. Hulliger, *Journal of Solid State Chemistry* 46, 112 (1983).

24. T. Kh. Kurbanov, R. A. Dovlyatshina, I.A. Dzhavadova, and F. A. Akhmedov, *Zh. Neorg. Khim.* 22, 1137 (1977).

Potential of Quasicrystals and Quasicrystal Approximants for New and Improved Thermoelectric Materials.

Terry M. Tritt, [1,2], M. L. Wilson[1], A. L. Johnson[1], S. LeGault[3] and R. Stroud[4]
[1] Department of Physics and Astronomy, Clemson University, Clemson SC
[2] Materials Science and Engineering Department, Clemson University, Clemson SC
[3] McGill University, Department of Physics and Astronomy, Montreal Canada
[4] Naval Research Laboratory, Washington D.C.

Abstract:

The focus of our research revolves around a search for new thermoelectric materials with improved performance over present materials. We have performed preliminary experiments to assess the potential of quasicrystalline materials for thermoelectric applications. The investigation of known classes of quasicrystals and quasicrystal approximants is important for potential thermoelectric materials as well as a search for entirely new phases of these materials. The advantage of quasicrystals is that their electrical conductivity (and possibly their thermoelectric power) can be manipulated through variation of their composition, synthesis or annealing conditions without sacrificing their usually low thermal conductivity. Quasicrystalline materials exhibit characteristics which are suggestive of Slack's idea of a phonon-glass, electron-crystal material for thermoelectric applications. We will present some of our results of resistivity, thermopower, and thermal conductivity on measurements to show the potential of these materials. A more thorough investigation of this class of materials and a systematic search for new quasicrystaline and related compounds might very well yield new materials for thermoelectric devices.

Introduction:

Over the past 30 years, alloys based on the Bi_2Te_3 $\{(Bi_{1-x}Sb_x)_2$ $(Te_{1-x}Se_x)_3\}$ and $Si_{1-x}Ge_x$ have been extensively studied and optimized for their use as thermoelectric materials both for cooling (Bi_2Te_3) and power generation (SiGe) applications.[1,2,3]. Improvement over the past decade in Bi_2Te_3, in particular, has been relatively minor with the thermoelectric figure of merit ZT relatively constant at ZT=1. Due to this slow progress, recent research has focused on the investigation of new classes of materials as advanced thermoelectric systems.[4] Material classes currently under investigation include skutterudites,[5,6,7,8] quantum-well materials,[9,10] superlattice structures[11,12,] and low-dimensional systems.[13]

This recent activity has also been driven by advanced military and civilian applications that demand higher performance thermoelectric materials and systems operating at temperatures down to ~100 K. In particular, cryoelectronics and "cold computing" are emerging fields requiring reliable low-maintenance cooling and refrigeration technology. Sloan states that "speed gains of 30% - 200% are achievable in some CMOS computer processors" where "cooling is the fundamental limit to electronic system performance."[14] In addition, a limitation to cellular phone technology using superconducting narrow-band spectrum dividers is the lack of reliable refrigeration.

The potential of a material for thermoelectric applications is determined by the material's dimensionless figure of merit, $ZT = (\alpha^2\sigma/\lambda)T$, where α is the Seebeck coefficient, σ the electrical conductivity, λ the total thermal conductivity ($\lambda = \lambda_L + \lambda_E$; the lattice and electronic contributions respectively) and T the temperature. In most materials, α increases while σ decreases as the carrier concentration is lowered. This results in the ability to tune the power factor ($\alpha^2\sigma$) through control of the carrier concentration. In most materials the power factor is a maximum near a carrier concentration of $10^{19}/cm^3$, resulting in the feature that most thermoelectric materials are heavily doped semiconductors. High mobility carriers are most desirable, so as to have the highest possible electrical conductivity yet, still retain a low carrier concentration.

While $\alpha^2\sigma$ can be maximized through chemical doping, λ_{tot} is not so easily tuned. The electronic thermal conductivity, λ_E is tied to σ through the Wiedemann-Franz Law ($\lambda_E/\sigma = L_0T$, L_0 = Lorentz number ~2.3×10^{-8} $W\Omega/K^2$). Therefore, while doping may increase σ, and hence λ_E, doping is also known to lower λ_L, leading to unknown changes in λ_{tot}. State-of-the-art thermoelectric materials have a $ZT \approx 1$. This value has been a practical upper limit for more than 30 years, yet no theoretical or thermodynamic reason exists for why it can not be larger.

0-7803-4057-4/97 $10.00 ©1997 IEEE

In 1995, Glen Slack published a paper describing the chemical characteristics of materials which might be candidates for good thermoelectric materials.[15,16] The candidate material needs to be a narrow bandgap semiconductor with high mobility carriers. Typically this requires strong covalent bonding between elements with a small difference in electronegativity. This has lead to a thorough search of materials containing at least one element from the lower right section of the periodic table. Additionally, at lower thermal conductivity, the Seebeck coefficient and electrical conductivity (both in the numerator of ZT) are strong functions of the doping level and chemical composition, which must therefore be optimized for good thermoelectric performance.

The thermal properties of complex materials can often be modified by chemical doping. Understanding these various effects and selecting optimization strategies, however, can be an exceedingly difficult problem. In complex materials there are often many possible degrees of freedom.

Quasicrystals as thermoelectric materials:

Prior to 1983, single-crystals were defined as solids composed of a unit-cell repeated translationally throughout the crystal. This translational order required that the crystal contain either 2-, 3-, 4-, or 6-fold rotational symmetry so a unit cell can be repeated throughout space and have all space be filled. Quasicrystals break this rule in that they display a "forbidden" structural symmetry, typically 5-, 8-, 10- or 12-fold symmetry.[17,18,19] Rather than typical translational order evident in crystals, quasicrystals exhibit long-range positional order. Quasicrystals are argued to grow by means of local matching rules governing the orientation of new atoms, by which single-domain crystals can be formed. In these single-domain crystals, the position of all atoms in the lattice is uniquely determined, yet no repeating pattern exists. This positional order gives rise to observation of sharp x-ray diffraction lines similar to those of conventional single crystals.[20,21]

Icosahedral (5-fold symmetric) quasicrystals form the largest family of quasicrystalline materials with over 60 members known.[18] Of these systems 12 can be grown as stable, single-domain, macroscopic crystals of large enough size (~1 mm^3) to perform 'intrinsic' transport measurements. Most icosahedral quasicrystals are composed of icosahedral metal clusters known as Pauling triacontahedra (containing 44 atoms) or MacKay icosahedra (containing 54 atoms). These clusters are then arranged with additional linking atoms in a non-repeating pattern to form a quasicrystal. In some cases these clusters are arranged in a repeating pattern, resulting in a material known as a quasicrystalline approximant. Most of the understanding of electronic and phonon structure, and precision knowledge of atomic positions in quasicrystalline materials are actually determined from measurements on and calculations of stable approximant phases. One such approximant Al_5CuLi_3 is a bcc lattice of Pauling triacontahedra containing a total of 180 atoms per unit cell. This is actually a small approximant lattice, phases with lattice constants of up to 100 Å, containing over 50,000 atoms per unit cell, are known.[22]

For the best thermoelectric material, Slack suggested it should behave as a "phonon-glass, electron-crystal". It would have the thermal properties of a glass and the electronic properties of a crystal. Quasicrystals, which were discovered in 1984 by Shechtmann et. al.,[23] seem to possess properties usually associated with both crystalline and amorphous materials.[24,25] Single-domain quasicrystals exhibit the low thermal conductivity of amorphous materials in all the cases that have been studied and yet have electrical properties ranging from "dirty" metals to semiconductors. The advantage of quasicrystals is that one can vary the electrical conductivity (and possibly tune this thermoelectric power) by varying the composition or defect concentration without sacrificing the low lattice thermal conductivity. For these reasons, a systematic search through the different classes of existing and proposed quasicrystals is underway to develop new materials for thermoelectric applications; and possibly the phonon-glass, electron-crystal suggested by Slack.

Published data on the thermopower of quasicrystals is rather scarce with values ranging from -30 μV/K to +50 μV/K. While moderately large, these values are currently not large enough for thermoelectric application. However, we take interest in the fact that nearly this entire variability can be found in a single quasicrystalline system, AlCuFe. This may allow for both the n- and p-type legs in a thermoelectric device to be fabricated from the same system. For example, at 300 K iron-rich $Al_{62.5}Cu_{24.5}Fe_{13}$ has α = +45 μV/K, while iron-poor $Al_{62.5}Cu_{26.5}Fe_{11}$ has α = -30 μV/K.[26] This variance in stoichiometry is intrinsic to quasicrystals since they do not require a rigid chemical formula for stability. The elements in the crystal can typically be changed by a few atomic percent without changing the structure of the crystal. Lacking a unique empirical chemical ratio makes these crystals easy to dope, resulting in high tunability of the thermal and electrical properties. 62.5 24.5 13 26.5 11

In the search for new thermoelectric materials, we are investigating the resistance and thermopower of multi-domain stable icosahedral phase quasicrystals. Of the twelve stable icosahedral

quasicrystals, data will be presented for $Al_{62.5}Cu_{25}Fe_{12.5}$, $Al_{70}Pd_{20}Re_{10}$, $Ti_{45}Zr_{58}Ni_{17}$, and $Al_{70}Pd_{20}Mn_{10}$.

Experimental:

In determining the thermoelectric-figure-of-merit, several properties of the material must be quantified; thermal conductivity, electrical conductivity, and thermopower. Of these quantities, the thermal conductivity is one of the most difficult to control. Thermal conductivity is the sum of the lattice (phonon) and electronic contribution of the thermal conductivity. The electronic thermal conductivity is essentially the lower limit for the total thermal conductivity of an electrically conducting system. Consequently, it is always desirable to search for a system possessing a low lattice thermal conductivity in order for the total thermal conductivity to be as low as possible.

The thermoelectric figure of merit is inversely proportional to λ. Hence, low values of λ greatly enhance the potential of a material for thermoelectric application. While few studies of the thermal conductivity have been made on stable icosahedral quasicrystalline compounds, most materials examined have λ_{phonon} below about 2 W/m·K at temperatures below 150 K.

Thermal conductivity data for three multi-domain quasicrystalline materials; $Al_{62.5}Cu_{25}Fe_{12.5}$, $Al_{70}Pd_{20}Re_{10}$, and $Al_{70}Pd_{20}Mn_{10}$ are presented in Figure 1. AlPdRe and AlCuFe display nearly indistinguishable measurements of λ_{tot} yet, as will be discussed below, their electrical conductivities differed by more than a factor of 2, [Figure 2]. These thermal conductivity values resemble those of amorphous glasses which typically have λ_{tot}~1 W/m·K.[27]

Estimations of the electronic thermal conductivity using the Wiedemann-Franz law yields $\lambda_E \cong 0.03$ W/m·K, assuming L_0 is ~2.3×10^{-8} WΩ/K^2 at 150 K. This corroborates the idea that the majority of the total thermal conductivity in these samples is from lattice contributions.

The electrical properties of these materials are also related to their unique structure. Nearly all stable single-domain quasicrystals display semimetallic resistive behavior with ρ(300K) between 0.1 and 10 mΩ·cm. At low temperatures, the resistivity increases by a factor from 1 to 20 times the room temperature resistivity. These data imply that some quasicrystals have a band gap of less than 0.2 eV.[2] Previous studies have related this observed band gap to a pseudogap formed localization at the Fermi level. Thus, conduction at low temperatures is best described using models of weak localization and strong electron-electron scattering. Localization in these materials is enhanced by improved crystallinity of the sample. Consequently, as crystal quality is improved (evidenced by sharper x-ray or electron diffraction spots) the resistivity increases significantly.[28,29] This is contrary to typical observations for a metallic crystal. Consequently, the resistivities measured on high-quality single-domain samples provide a maximum limit to the resistivity in a tuned material.

Resistivity in quasicrystals is also reported to increases as the atomic number of the alloy increases. This is described in studies of single domain $Al_{70}Cu_{20}Fe_{10}$, $Al_{70}Cu_{20}Ru_{10}$ and $Al_{70}Cu_{20}Os_{10}$ quasicrystals.[30] Consequently, many avenues exist by which the conductivity of a quasicrystal can be tuned.

AlPdRe has a large room temperature resistivity (approximately 10 mΩcm) which increases rapidly as the temperature is lowered

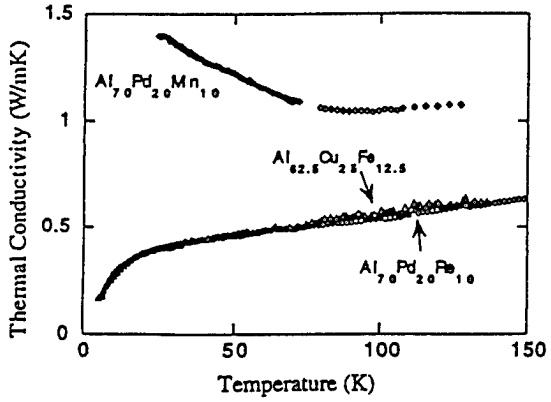


Figure 1: Thermal conductivity for AlPdRe, AlPdMn, and AlCuFe quasicrystals.

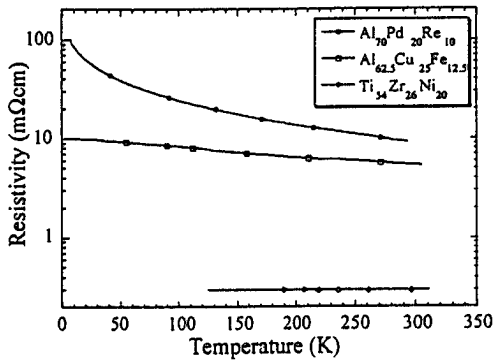


Figure 2: Resistivity vs. temperature for AlPdRe, AlCuFe, and TiZrNi quasicrystals.

AlPdRe has a large room temperature resistivity (approximately 10 mΩcm) which increases rapidly as the temperature is lowered [FIGURE 2]. AlCuFe, however, has a room temperature resistivity of about 5 mΩcm which only increases by a factor of two at 10 K. TiZrNi which displays the lowest resistivity, is virtually temperature independent for the range studied. This trend of lower overall resistivity correlating with a smaller temperature dependence of the resistivity is commonly found in quasicrystals, and some argue this is a universal property of these systems.[5] While the conductivity of the AlPdRe and AlCuFe samples appear to be too small for good thermoelectric materials, the TiZrNi sample does have a large enough conductivity to be of interest being ~3.4 $(m\Omega cm)^{-1}$.

For AlCuFe quasicrystals we find a thermopower of +12 μV/K which is in the range of the previously published data (Figure 3). AlPdRe on the other hand, is found to have a very large thermopower for a quasicrystal +55 μV/K and to be fairly constant near room temperature. This high thermopower over a broad temperature range is desirable for a widely useful low temperature thermoelectric cooling system. TiZrNi, while having the best conductive properties of the three systems studied has the lowest thermopower. AlPdMn also has a very large thermopower at room temperature, $\alpha = +61$ μV/K.

The variability and sensitivity of the thermopower to slight changes in the structure are also borne out through band structure calculations[31,32] and photoemission measurements.[33]

Summary:

At least a few of the challenges that are evident in relation to the potential of the quasicrystal class of materials for utilization in thermoelectric applications lie in achieving a higher thermoelectric power and a higher carrier mobility. One very important point should be made. Researchers are just beginning to thoroughly investigate the coupled thermal and electronic transport properties of these materials. Very little thermopower, thermal conductivity and carrier mobility data exist for any particular class of quasicrystals. Most of the research performed on these systems to date has been related to the structure, which is of course very reasonable given their complex nature.

Quasicrystals show potential as a new class of thermoelectric materials. The intrinsic chemical variability of these crystals allows for a high degree of tunability of their thermal and electrical properties. This should lead to a broad range within this class of materials. Known quasicrystals have thermal conductivities approaching that of an amorphous glass, yet their electrical conductivity is more akin to a small gap semimetal. These characteristics broadly meet Slack's "phonon-glass, electron-crystal" model. The sensitivity of the sign of the thermopower to elemental concentration raises hope that n- and p-type thermoelectrics could be found in the same material. Although the quasicrystals form a rather large class of compounds, for each quasicrystal, there also typically exists at least one conventionally ordered quasicrystalline approximant phase. These approximants will also be investigated for their potential as thermoelectric materials since they are known to have similar electrical and thermal properties to their related quasicrystals.[1]

Much more research must be done and an extensive data base must be established on the electrical and thermal properties of this large group of materials. Then, possibly, a much clearer indication of the potential of these materials can be established.

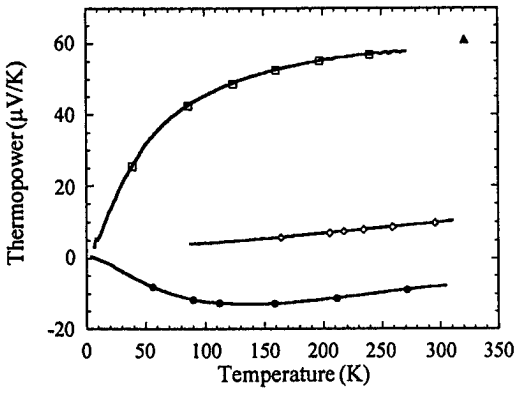


Figure 3: Thermoelectric power vs. temperature for AlPdRe (□), AlCuFe (◇), TiZrNi (▲), and AlPdMn (●).

References:

[1] H. J. Goldsmid, *Electronic Refrigeration*, (Pion Limited Publishing, London, (1986).

[2] *CRC Handbook of Thermoelectrics*, edited D. M. Rowe, CRC Press, Boca Raton (1995).

[3] C. W. Wood, Rep. Prog. Phys. **51**, 459-539 (1988).

[4] Terry M. Tritt, Science, **272**, 1276 (1996).

[5] B. C. Sales, D. Mandrus and R. K. Williams, Science, **272**, 1325 (1996).

[6] G. A. Slack and V. G. Toukala , Jour. Appl. Phys. **76**, 1635 (1994);
G. Nolas, *et al.*, Jour. Appl. Phys., **79**, 4002 (1996);
D. T. Morelli, *et al.*, Phys. Rev. B **51** 9622 (1995).

[7] T. M. Tritt, *et al.*, Jour. Appl. Phys., **79**, 8412 (1996).
[8] Baoxing Chen, *et al.*, Phys. Rev. B **55** 1476 (1997).
[9]L. D. Hicks and M. S. Dresselhaus, Phys. Rev. B. **47**, 12727 (1993).
[10] L. D. Hicks, *et al.*, Phys. Rev. B. **53**, R10493 (1996).
[11]R Venkatasubramanian, Proc. of the XIII International Conference on Thermoelectrics, AIP, p 40-44 (1995).
[12]R Venkatasubramanian,1997 Spring MRS Abstracts, 291 (1997).
[13]T. M. Tritt, *et al.*, submitted to 1997 MRS Symposium Q (San Francisco, CA).
[14]J. Sloan, Superconductor Industry, Fall 1996, p30 (1996).
[15]G. A. Slack, in CRC Handbook of Thermoelectrics, Rowe ed. 1995, ref. 2, p 407.
[16]G. A. Slack, in Solid State Physics, **34** 1 (1979), ed. by F. Seitz, D. Turnbull, and H. Ehrenreich, Academic Press, New York.
[17]S. J. Poon, Advances in Physics, **41**, 303-363 (1992).
[18]C. Janot, *Quasicrystals*, Clarendon Press, Oxford.
[19] A. I. Goldman and K. F. Kelton, Reviews of Modern Physics, **65**, 213 (1993).
[20] P. A. Bancel, Phys. Rev. lett. **63**, 2741 (1989).
[21] C. A. Guryan, *et al.*, Phys. Rev. Lett. **62**, 2409 (1989).
[22]T. L. Daulton and K. F. Kelton, Philos. Mag. B **66**, 37 (1992).
[23]D. Shechtman, *et al.*, Phys. Rev. Lett. **53**, 1951 (1984).
[24]S. Legault, *et al.*, Conference Proceedings "New horions in Quasicrystals: Research and Applications", August 19-23, 1996, Iowa State University, Ames, Iowa.
[25]A. Perrot, *et al.*, Proceedings of the 5th International Conference on Quasicrystals, World Scientific, 1995, p. 588.
[26]F.S. Pierce, *et al.*, Phys. Rev. Lett. **70**, 3919 (1993).
[27]M.A. Chernikov, A. Bianchi, and H.R. Ott, Phys. Rev. B **51**, 153 (1995).
[28]T. Klein, C. Berger, D. Mayou, and F. Cyrot-Lackmann, Phys. Rev. B **66**, 2907 (1991).
[29]R. Tamura, A. Waseda, K. Kimura, and H. Ino, Phys. Rev. B **50**, 9640 (1994).
[30]Y. Honda, K. Edagawa, S. Takeuchi, A.-P. Tsai and A. Inoue, Jpn. J. Appl. Phys. **34**, 2415 (1995).
[31]G. Kasner, H. Schwabe and H. Böttger, Phys. Rev. B **51**, 10454 (1995).
[32]S.E. Burkov, A.A. Varlamov and D.V Livanov, Phys. Rev. B **53**, 11504 (1996).
[33]U. Mizutani, Y. Yamada, T. Takeuchi, K. Hashimoto, E. Belin, A. Sadoc, T. Yamauchi and T. Matsuda, J. Phys: Conds. Matter **6**, 7335 (1994).

Complex Bismuth Chalcogenides as Thermoelectrics

Duck Young Chung[a], Tim Hogan[b], Jon Schindler[b], Lykourgos Iordanidis[a], Paul Brazis[b], Carl R. Kannewurf[b], Baoxing Chen[c], Ctirad Uher[c], Mercouri G. Kanatzidis[a],*

[a]*Department of Chemistry and Center for Fundamental Materials Research, Michigan State University, East Lansing, MI 48824.* [b]*Department of Electrical and Computer Engineering , Northwestern University, Evanston, IL 60208* [c]*Department of Physics, University of Michigan, Ann Arbor, MI 48109*

* corresponding author

Abstract

A solid state chemistry synthetic approach towards identifying new materials with potentially superior thermoelectric properties is presented. Materials with complex compositions and structures also have complex electronic structures which may give rise to high thermoelectric powers and at the same time possess low thermal conductivities. The structures and thermoelectric properties of several new promising compounds with K-Bi-S, K-Bi-Se, and Cs-Bi-Te.

Introduction

Interest in new thermoelectric (TE) materials with improved figures of merit is increasing rapidly [1,2]. The much increased sophistication of materials research coupled with many discoveries of new compounds, a wider variety of observed phenomena, and vastly improved capabilities for calculation of electronic structure and properties, provide a solid foundation for discovering new thermoelectrics once again. To improve device performance one needs to maximize the thermoelectric figure of merit, $ZT = (S^2\sigma/\kappa)T$; where S is the thermopower, σ the electrical conductivity, κ the thermal conductivity and T is the temperature. All three of these properties are determined by the details of the electronic structure and scattering of charge carriers (electrons or holes) and thus are not independently controllable parameters. κ also has a contribution from lattice vibrations, κ_l, the phonon thermal conductivity. Thus $\kappa = \kappa_e + \kappa_l$, where κ_e is the carrier thermal conductivity. Therefore one must increase σ and S while minimizing κ. Since the electrical conductivity and thermopower of optimally n or p doped Bi_2Te_3 is in the range of 500-800 S/cm and ± 220 μV/K [3] respectively, significant improvements in thermoelectric figure of merit could occur if materials of comparable conductivities but thermopowers of 300 to 350 μV/K can be found.

We are engaged in an exploratory synthesis program to identify new multinary phases with Bi and Sb which have narrow band-gaps and low thermal conductivity and may be suitable as thermoelectric materials. We believe that materials with more complex compositions and structures should have complex electronic structures which may give rise to high thermoelectric powers according to the Mott formula below, and at the same time possess low thermal conductivities. The thermopower S is given by the Mott equation:

$$S = \frac{\pi^2}{3} \cdot \frac{k^2T}{e} \cdot \frac{d\ln\sigma(E)}{dE}\Bigg|_{E=E_f}$$

where $\sigma(E)$ is the electrical conductivity determined as a function of band filling. The electronic conductivity $\sigma = \sigma(E)|_{E=E_f}$ where E_f is the Fermi energy. If the carrier scattering is independent of energy, then $\sigma(E)$ is just proportional to the density of states at E. In the general case, S is a measure of the difference in $\sigma(E)$ above and below the Fermi surface - specifically through the logarithmic derivative of it with respect to E, see the equation above. So by manipulating the energy dependence of $\sigma(E)$ one can control simultaneously σ and S. Since the thermopower of a material is a measure of the asymmetry in electronic structure and scattering rates near the Fermi level (E_f) [3], we aim to produce complexities in either or both in a small energy interval (a few kT) near E_f. While simple materials usually have simple band structures, cooperative electronic phenomena in a few materials lead to complex electronic structures and hopefully to high thermopowers. Because metallic compounds typically have small thermopowers and large thermal conductivities we focus our efforts in materials which are narrow gap semiconductors or semimetals (band-gap $0<E_g<0.5$ eV).

Despite the empirical guidelines one has, it is still challenging to choose the particular system for exploration. The fact that Bi_2Te_3 is the best material known to date suggests that it combines many of the necessary features for high TE response. If there is something special about bismuth in giving rise to simultaneously high electrical conductivity and thermoelectric power, it should be manifested in other compounds of Bi as well. Therefore we are exploring more complex chalcogenides of Bi hoping that some (or all) of the key properties would be superior to those of Bi_2Te_3. Because a structure with a large unit cell is expected for complex materials, which in turn would decrease the acoustic mode phonon velocities that are responsible for the transfer of heat in materials, we expect that structurally and compositionally more complex bismuth chalcogenides would, most likely, have a low lattice thermal conductivity. The relatively weak Bi-Te bonding and the large atomic masses contribute as well to the low phonon velocities. Therefore, exploratory synthesis in this region of the periodic table becomes a reasonable activity and, as the preliminary results show, quite promising. In this article we present our efforts to synthesize bulk materials with enhanced TE figures of merit.

0-7803-4057-4/97 $10.00 ©1997 IEEE

Results and Discussion

We are searching for more complex chalcogenide compounds using a low temperature synthesis method described elsewhere [4]. We have obtained many new phases of bismuth by reacting the metal with alkali metal chalcogenide salts in polychalcogenide melts [5]. Only a few promising materials will be elaborated upon here.

The sulfides $KBi_{6.33}S_{10}$ and $K_2Bi_8S_{13}$. [6] belong to the family of compounds $(A_2Q)_n(Bi_2Q_3)_m$ (A=alkali metal; Q=S, Se) with n=1 and m=6.33, 4, respectively. They have three-dimensional structures made up of Bi_2Te_3-type (NaCl-type) blocks and CdI_2-type fragments that connect to form tunnels filled with eight-coordinate K^+ cations. This may be beneficial to the electronic properties of the compounds which may bear similarities to those of Bi_2Te_3. The lower symmetry they possess may result in low thermal conductivity and could give rise to a superior thermoelectric material. The $[Bi_{6.33}S_{10}]^-$ framework is made of edge-sharing BiS_6 octahedra, as shown in Figure 1. The structure of $K_2Bi_8S_{13}$ is similar, but the Bi_2Te_3-type (NaCl-type) blocks and CdI_2-type fragments are arranged differently, Figure 2. The isostructural selenium analog of $K_2Bi_8S_{13}$ has also been prepared.

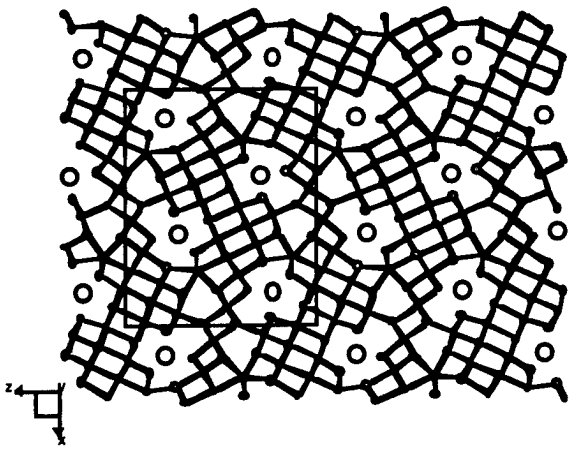


Figure 1. The structure of $KBi_{6.33}S_{10}$. Small white circles are sulfur atoms. Large circles are K atoms.

These ternary bismuth sulfides have promising electrical properties with maximum conductivity and thermopower of ~200 S/cm and ~-90μV/K, respectively. These are unoptimized values and we believe they can be greatly improved by further processing. Using the measured values of the electrical resistivity in conjunction with the Wiedemann-Franz law, we estimate the maximum possible value of the electronic thermal conductivity contribution to be below 1% of the total thermal conductivity. So almost all heat in these compounds is carried by lattice phonons. The sulfide $KBi_{6.33}S_{10}$ seems to have particularly low thermal conductivity. Taking as a bench mark the room temperature value of the total thermal conductivity of Bi_2Te_3 (κ_l = 1.6 W/m-K), we note that the total thermal conductivity of $KBi_{6.33}S_{10}$ is actually lower (Figure 3). Hence, at least from the perspective of thermal transport, these compounds satisfy one of the key requirements for a useful thermoelectric materials, they possess low lattice thermal conductivity. This is an important finding because $KBi_{6.33}S_{10}$, being a sulfide, is expected to possess higher thermal conductivity compared to the heavier tellurides. If controlled doping can enhance the electrical conductivity and at the same time preserve or even increase the thermopower, in the case of $KBi_{6.33}S_{10}$ we indeed might have a promising thermoelectric material. To achieve this, we need additional information regarding the transport properties including carrier concentrations and mobilities. Both $KBi_{6.33}S_{10}$ and $K_2Bi_8S_{13}$ melt with no decomposition at 710 °C and 713 °C respectively.

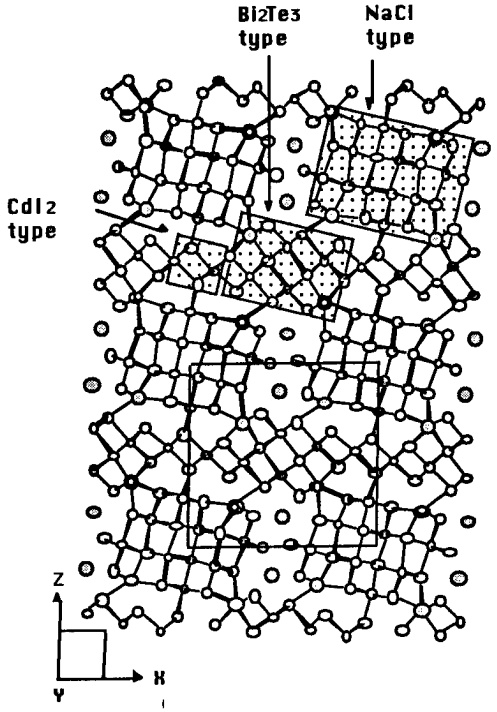


Figure 2. The structure of $K_2Bi_8S_{13}$ and β-$K_2Bi_8Se_{13}$.

We have also found two related selenides β-$K_2Bi_8Se_{13}$ and $K_{2.5}Bi_{8.5}Se_{14}$. These two compounds differ from one another by one half of an equivalent of "$KBiSe_2$". In $K_{2.5}Bi_{8.5}Se_{14}$ only NaCl- and Bi_2Te_3-type blocks exist. The addition of "$BiSe_2$" in the CdI_2-type blocks of β-$K_2Bi_8Se_{13}$ generates Bi_2Te_3-type blocks which are five-bismuth atoms wide. This small structural modification preserves the same connectivity of the NaCl-type fragments and the same size and shape of the K atom sites as in β-$K_2Bi_8Se_{13}$, see Figure 4.

The electrical properties of β-$K_2Bi_8Se_{13}$ and $K_{2.5}Bi_{8.5}Se_{14}$ were measured on single crystal samples and polycrystalline ingot samples [7]. The highest room temperature conductivity value obtained for single crystals of β -$K_2Bi_8Se_{13}$ was 240 S/cm with a weak negative temperature dependence consistent with a semi-metal or a narrow band-gap semiconducting material. There is a striking difference in conductivity when compared to α-$K_2Bi_8Se_{13}$ [8] which shows a room temperature value of 2 S/cm, and it is due to the substantial structural differences between the α- and β-

forms. Polycrystalline compactions of these materials show similar trends where at room temperature the α-$K_2Bi_8Se_{13}$ has a conductivity of 0.01 S/cm while β-$K_2Bi_8Se_{13}$ and $K_{2.5}Bi_{8.5}Se_{14}$ show ~ 30 and ~ 150 S/cm, respectively. This enormous difference is attributed to the fact that β-$K_2Bi_8Se_{13}$ and $K_{2.5}Bi_{8.5}Se_{14}$ have more dense three-dimensional structures than α-$K_2Bi_8Se_{13}$, which gives rise to greater orbital overlap in the Bi-Se network and consequently lower band gap.

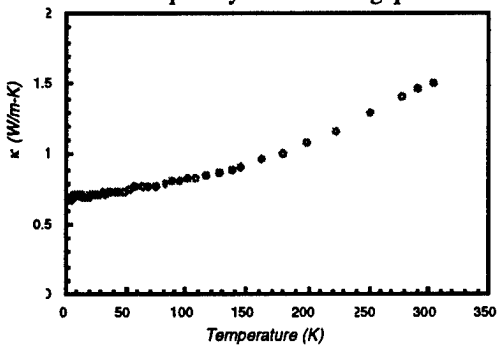


Figure 3. Variable temperature thermal conductivity data for a polycrystalline ingot of $KBi_{6.33}S_{10}$.

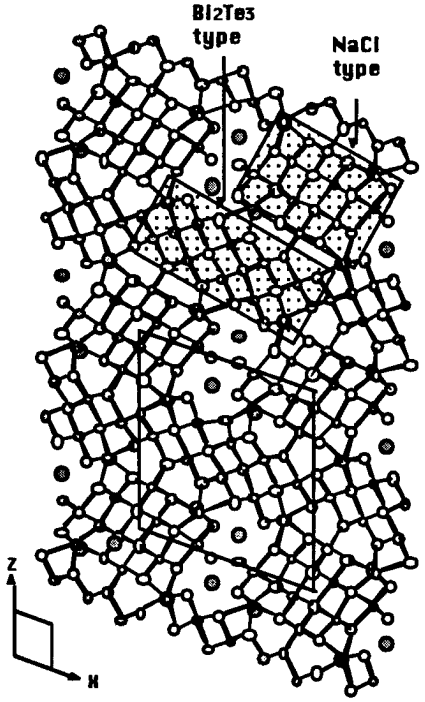


Figure 4. The structure of $K_{2.5}Bi_{8.5}Se_{14}$.

The thermopower data for β-$K_2Bi_8Se_{13}$ and $K_{2.5}Bi_{8.5}Se_{14}$ show large negative Seebeck coefficients (-200 and -100 μV/K at room temperature, respectively), which indicate the charge carriers are electrons (n-type), see Figure 5. It is remarkable that the thermopower behavior and magnitude of the β-$K_2Bi_8Se_{13}$ is similar to that of its α-analog [8] despite the large differences in conductivity. The thermopower values in these materials become less negative as the temperature is decreased from 300 K to 4 K, reminiscent of a metallic behavior, but the very large Seebeck coefficients suggest these materials are in fact semiconductors. The semiconducting character is also supported by the fact that optical gaps of 0.59 eV and 0.56 eV, respectively exist in β-$K_2Bi_8Se_{13}$ and $K_{2.5}Bi_{8.5}Se_{14}$ at room temperature.

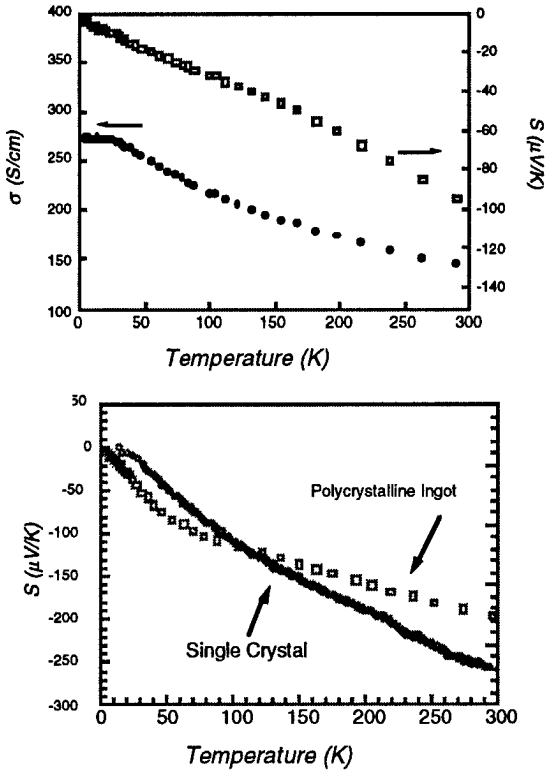


Figure 5. Top: Electrical conductivity and thermoelectric power data for a polycrystalline ingot of $K_{2.5}Bi_{8.5}Se_{14}$. Bottom: Thermoelectric power data for (a) a single crystal and (b) a polycrystalline ingot of β-$K_2Bi_8Se_{13}$.

The room temperature thermal conductivities of β-$K_2Bi_8Se_{13}$ and $K_{2.5}Bi_{8.5}Se_{14}$ are comparable (1.28 and 1.21 W/m-K, respectively) and lower than that of optimized alloys $Bi_2Te_{3-x}Se_x$. This demonstrates that it is possible to achieve lower thermal conductivity in ternary compounds with complex compositions and crystal structures compared to corresponding high symmetry binary compounds. Here again the maximum possible values of the κ_e contribution in both cases were estimated to be less than 10 % of κ_T, and so most of the heat in β-$K_2Bi_8Se_{13}$ and $K_{2.5}Bi_{8.5}Se_{14}$ is carried by lattice phonons. The thermal conductivity of β-$K_2Bi_8Se_{13}$ in the temperature range of 4-300 K is significantly lower than that of the isostructural compound $K_2Bi_8S_{13}$, which is consistent with the fact that the heavier Se atoms soften the lattice phonons thereby slowing down heat transport in the material.

Based on these results β-$K_2Bi_8Se_{13}$ and $K_{2.5}Bi_{8.5}Se_{14}$ seem to be quite promising as thermoelectrics. The figure of merit (ZT) as a function of temperature for "as prepared" β -$K_2Bi_8Se_{13}$ is shown in Figure 6. The room temperature ZT value is 0.22 (0.39 if the lower κ value of 0.83 W/m-K is considered). To improve the thermoelectric figure of merit of these ternary compounds we could pursue sulfur doping or solid solutions of $K_XBi_Y(SeS)_Z$

based on the fact that sulfide compounds can adopt the same structure types as corresponding selenide compounds.

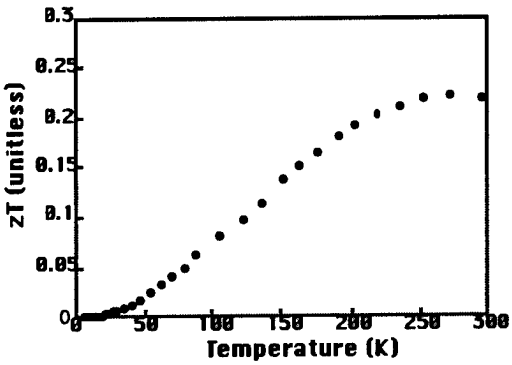


Figure 6. Temperature dependence of thermoelectric figure of merit (ZT) for a crystal of β-$K_2Bi_8Se_{13}$.

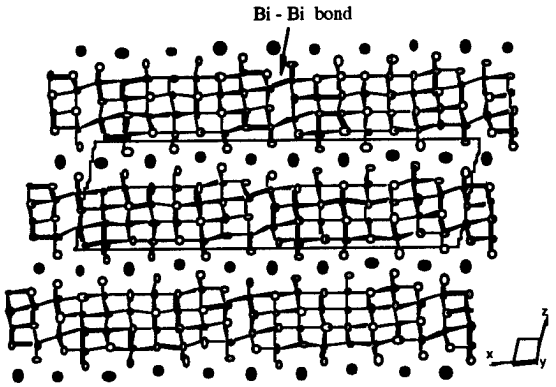


Figure 7. The structure of $CsBi_4Te_6$. Large black circles are Cs atoms, open circles are Te atoms [9].

Finally, the new phase $CsBi_4Te_6$ also seems very promising [12, 13]. The compound is a layered anisotropic material which grows in a needle type morphology. It is composed of anionic [Bi_4Te_6] layers alternating with layers of Cs ions, see Figure 7. The average oxidation state of Bi is less than three with some of the Bi atoms forming Bi-Bi bonds. The presence of such bonds is very unusual in bismuth chalcogenide chemistry and it is unclear what role they play, if any, in the thermoelectric properties of the material. The Bi coordination geometry is octahedral. Preliminary data show that crystals of $CsBi_4Te_6$ have room temperature electrical conductivities as high as 2440 S/cm which is much higher than that of optimized Bi_2Te_3 (~850 S/cm). The room temperature thermopower ranges from 90 to 120 μV/K, lower than the 220 μV/K typically found for optimized Bi_2Te_3.

The thermal conductivity of pressed pellets of $CsBi_4Te_6$ is in the range 0.9-1.8 W/m·K comparable to that of Bi_2Te_3. These values give rise to a relatively high room temperature ZT of 0.8 at a ZT_{max} of 0.95. To calculate the ZT we had to use thermal conductivity values obtained from a pressed pellet since we are unable to make such measurements on small single crystals. Therefore, the true ZT values may be off by 20-30%. Here we ask: does the Wiedeman-Franz law apply in such narrow gap semiconductors and if yes how much of the κ_e is accounted for by the measured value of the pressed pellet? To best address this question we need to obtain thermal conductivity data on large single crystals of $CsBi_4Te_6$. These ZT values are some of the highest ever reported (near room temperature) for a material other than Bi_2Te_3. Improvements in the sample preparation of $CsBi_4Te_6$ and appropriate doping should result in significant enhancements in TE properties.

Undoubtedly, exploratory synthetic investigations are needed to reveal promising new materials with superior thermoelectric properties. By creating complex multinary compounds with lower symmetry and larger cell asymmetric units, the thermal conductivity can be decreased substantially below that of optimized $Bi_2Te_{3-x}Se_x$ alloy.

Acknowledgments Financial support from the Office of Naval Research (contract # N00014-94-1-0935, MGK and CRK and N00014-96-1-0181 for C.U.) is gratefully acknowledged.

References

1. (a) *Naval Research Reviews*, 1996, vol. XLVIII, references therein. (b) Hicks, L. D.; Dresselhaus, M. S. Phys. Rev. B, 1996, 53, 1103.
2. (a) B. C. Sales, D. Mandrus, R. K. Williams, *Science*, **1996**, 272, 1325. (b) T. M. Tritt, *Science* 1996, 272, 1276.
3. *CRC Handbook of Thermoelectrics*; Rowe, D. M., Eds.; CRC Press, Inc.: Boca Raton, FL, 1995; references therein.
4. Sutorik, A. C.; Kanatzidis, M. G. *Prog. Inorg. Chem.* **1996**, 43, 151-265.
5. D. Y. Chung, T. Hogan, J. Schindler, L. Iordanidis, P. Brazis, C. R. Kannewurf, B. Chen, C. Uher, M. G. Kanatzidis. in "Thermoelectric Materials-New Directions and Approaches" *Mat. Res. Soc. Symp. Proc.* **1997**, 478, 333-344.
6. Kanatzidis, M. G.; McCarthy, T. J.; Tanzer, T. A.; Chen, L. -H.; Iordanidis, L.; Hogan, T.; Kannewurf, C. R.; Uher, C.; Chen, B. *Chem. Mater.*, **1996**, *8*, 1465-1474
7. Chung, D-.Y.; Choi, K.-S; Iordanidis, L; Schindler, J. L.; Brazis, P.; Kannewurf, C. R.; Chen, B.; Hu, S; Uher, C.; Kanatzidis, M. G. *Chem. Mater.* **1997**, in press..
8. McCarthy, T. J.; Ngeyi, S.-P.; Liao, J.-H.; DeGroot, D.; Hogan, T.; Kannewurf, C. R.; Kanatzidis, M. G., *Chem. Mater.*, **1993**, *5*, 331-340.
9. Chung, D-.Y.; Hogan, T.; Chen, X.; Schindler, J.; Brazis, P.; Kannewurf, C. R.; Chen, B.; Hu, S; Uher, C.; Kanatzidis, M. G. submitted.
10. Schindler, J.; Hogan, T.; Brazis, P.; Kannewurf, C. R.; Chung, D-.Y.; Kanatzidis, M. G. "Electrical Properties and Figures of Merit for New Chalcogenide-Based Thermoelectric Materials" "Thermoelectric Materials-New Directions and Approaches" *Mat. Res. Soc. Symp. Proc.* **1997**, 478, 327-332.

Thermoelectric Properties of β-Zn_4Sb_3 Doped with Sn

T. Koyanagi*, K. Hino, Y. Nagamoto, H. Yoshitake and K. Kishimoto
Department of Electrical and Electronic Engineering, Faculty of Engineering, Yamaguchi University
2557, Tokiwadai, Ube 755, JAPAN
*e-mail: koyanagi@aem.eee.yamaguchi-u.ac.jp

Abstract

We have tried to dope β-Zn_4Sb_3 with Sn for the purpose of the p-type doping and the enhancement of phonon scattering, which further improve the thermoelectric properties of β-Zn_4Sb_3. Polycrystalline samples doped with Sn were prepared by the spark plasma sintering method. Although no other phase was observed except for β-Zn_4Sb_3 in Sn-doped samples up to 3%, their lattice constants were not at all changed from that of bulk β-Zn_4Sb_3, indicating that Sn was not unfortunately substituted for Sb. These results suggest that microcrystals of Sn is dispersed in grain boundary regions of β-Zn_4Sb_3. The Seebeck coefficient was almost unchanged, and the electrical conductivity was slightly decreased by doping β-Zn_4Sb_3 with Sn, indicating that Sn dose not act as a dopant. On the other hand, the thermal conductivity was lowered from 8.66mW/cmK of the non-doped sample to 6.88mW/cmK of the 3% Sn-doped sample at room temperature. This lowering of the thermal conductivity was considered to be due to the point defect phonon scattering induced by inclusions of Sn.

Introduction

In the intermetallic compound Zn-Sb system, ZnSb, Zn_4Sb_3 and Zn_3Sb_2 compounds have been well identified. ZnSb has been known as a famous thermoelectric material since Seebeck reported it in 1820 to have a reasonably high figure of merit [1]. We investigated the growth and thermoelectric properties of ZnSb films [2] and sintered alloys [3] in order to obtain the single phase of ZnSb, of which growth is difficult due to the peritectic reaction [4]. Zn_4Sb_3 and Zn_3Sb_2 were reported to be stable and metastable, respectively [4]. For Zn_4Sb_3, three phases, α-, β- and γ-Zn_4Sb_3, are known [4]. β-Zn_4Sb_3, which is stable in the temperature range from -10 to 492℃ [5], was reported to have semiconducting properties [5,6] and abnormally low thermal conductivity (6.5mW/cmK) [7]. Recently, much attention to β-Zn_4Sb_3 has been attracted because of its p-type high thermoelectric performance since T. Caillat *et al.* reported its thermoelectric properties [8,9].

We have tried to dope β-Zn_4Sb_3 with Sn in order to improve further its thermoelectric performance. Since β-Zn_4Sb_3 is a p-type semiconductor, the substitution of Sb (V element) for Sn (IV element) leads to the generation of carriers (holes). Furthermore, the possibility exists that Sn might act as a inclusion which induces the point defect phonon scattering, leading to reduction of the thermal conductivity κ of β-Zn_4Sb_3. In this paper, we report some results on the preparation and thermoelectric properties of Sn-doped β-Zn_4Sb_3.

Experiment

Sn-doped β-Zn_4Sb_3 was sintered by the spark plasma sintering method. The crystal structure was checked by the x-ray diffraction measurement. The electrical conductivity σ and Seebeck coefficient S were measured in the temperature range from 300 to 800K. The Hall measurements were made at room temperature to examine the carrier concentration and the mobility. The thermal conductivity κ was calculated from the density, heat capacity and thermal diffusivity. The heat capacity and thermal diffusivity were measured by using the laser flush method in the temperature range from 300 to 700K

Zn (99.999% pure) and Sb (99.9999% pure) powders were mixed in the molar ratio Zn:Sb=4.03:3.00, which took account of deficiency of Zn due to evaporation during the following reaction and sintering processes. Sn powder (99.99% pure) was also mixed as a dopant with the mixture of Zn and Sb. The introduced dopant concentration was changed from 1% to 5% of an Sb amount. The mixture of these powders was molded into a pellet, and was reacted by the solid state interdiffusion at 220~400℃ for 48h in a Pyrex ampule filled with Ar gas. When the reaction temperature was lower than 300℃, only Zn, Sb and ZnSb phases were observed, and no β-Zn_4Sb_3 phase was grown. Although the β-Zn_4Sb_3 phase was grown at temperatures higher than 300℃, the ZnSb phase appeared again in addition to the β-Zn_4Sb_3 phase when the reaction temperature was increased beyond 400 ℃. From these results, we decided that the reaction temperature was 350℃. The resultant pellet was crushed and ground to powder diameter of several μm. The β-Zn_4Sb_3 was sintered using this obtained powder in an Ar atmosphere by the spark plasma sintering method. The sintering temperature, pressure and time were 400℃, 35MPa and 1 hour, respectively. The sintering temperature was limited to this temperature for obtaining the single phase. When the sintering temperature was higher than 400℃, the Zn_4Sb_3 phase was decomposed to ZnSb and Zn phases.

Results and Discussion

The density of the samples were typically as high as 98%, and tends to increase with an increase in the Sn concentration. This result suggests that Sn acts as a sintering aid for the sintered β-Zn_4Sb_3. An increase in the density by addition of Sn was also observed on the sintered ZnSb [3].

Figure 1 shows the x-ray diffraction patterns of 0~5% Sn-doped β-Zn_4Sb_3. In the patterns of the 0~3% Sn-doped samples only peaks of β-Zn_4Sb_3 phase are observed, whereas

0-7803-4057-4/97 $10.00 ©1997 IEEE

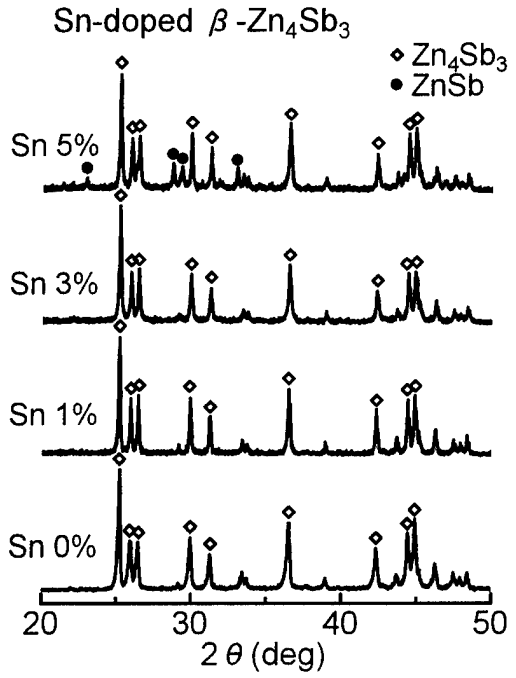


Fig.1 X-ray diffraction patterns of 0~5% Sn-doped β-Zn_4Sb_3.

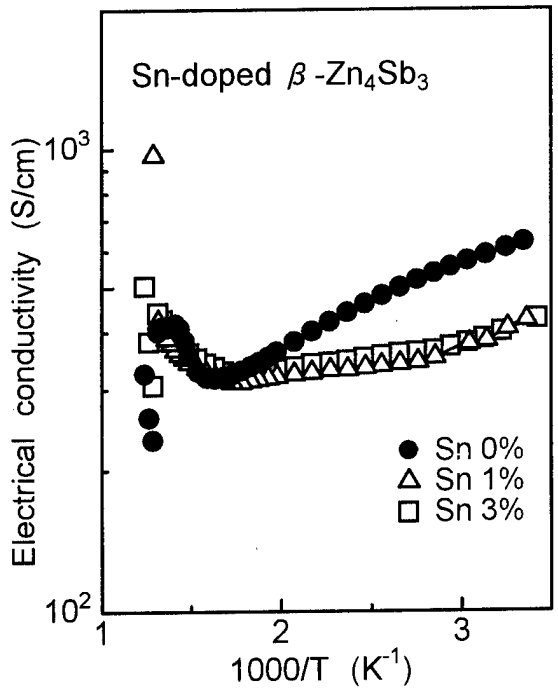


Fig.2 Temperature dependence of electrical conductivity σ for 0~3% Sn-doped β-Zn_4Sb_3.

for the 5% Sn-doped sample the ZnSb phase was grown in addition to the β-Zn_4Sb_3 phase. This growth of ZnSb phase is attributed to the deficiency of Zn due to the reaction between Zn and Sn at the reaction temperature of 350°C, judging from the Zn-Sn phase diagram [10]. Hereafter, for the 0~3% Sn-doped samples which have a β-Zn_4Sb_3 single phase their thermoelectrical properties were investigated.

From diffraction angles of these samples shown in Fig.1, the lattice constants *a* and *c* were calculated. Unfortunately, the values of *a* and *c* were hardly changed by changing the Sn concentration. These results suggest that microcrystals of Sn were dispersed in boundaries of β-Zn_4Sb_3 grains. An excess of Zn is considered to be evaporated due to its high vapor pressure.

Figures 2 and 3 show the temperature dependence of the electrical conductivity σ and the Seebeck coefficient *S*, respectively, for the 0~3% Sn-doped β-Zn_4Sb_3. The values of σ are scattered and the values of *S* suddenly drop at temperatures higher than ~750K, which is near the transformation temperature from β- to γ-Zn_4Sb_3. The results of σ and *S* measurements for our non-doped Zn_4Sb_3 sample are in agreement with the results of T. Caillat *et al.* [8]. For every samples, as the temperature is increased σ increases and *S* decreases in the temperature range above ~600K, indicating that β-Zn_4Sb_3 shows an intrinsic behavior. At temperatures lower than ~600K, the values of σ for Sn-doped samples are reduced from those for the non-doped one. In order to investigate this reduction of σ, measurements of the Hall coefficient were performed at room temperature. The carrier concentration of the 3% Sn-doped sample was $5 \times 10^{19} cm^{-3}$, and was approximately a quarter of that for the non-doped

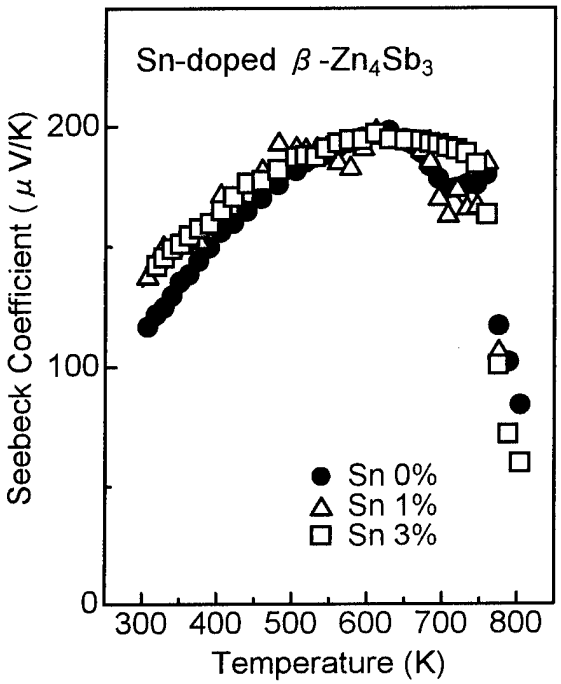


Fig.3 Temperature dependence of Seebeck coefficient *S* for 0~3% Sn-doped β-Zn_4Sb_3.

sample ($2 \times 10^{20} cm^{-3}$). From the fact that Sn was not substituted for Sb, it can be understood that Sn dose not act as a dopant contrary of our idea. Since carriers are compensated by Sn at grain boundaries, the carrier concentration is reduced. On the other hand, the Hall mobility for the 3% Sn-doped sample was increased to ~$44 cm^2/Vs$, as compared with the

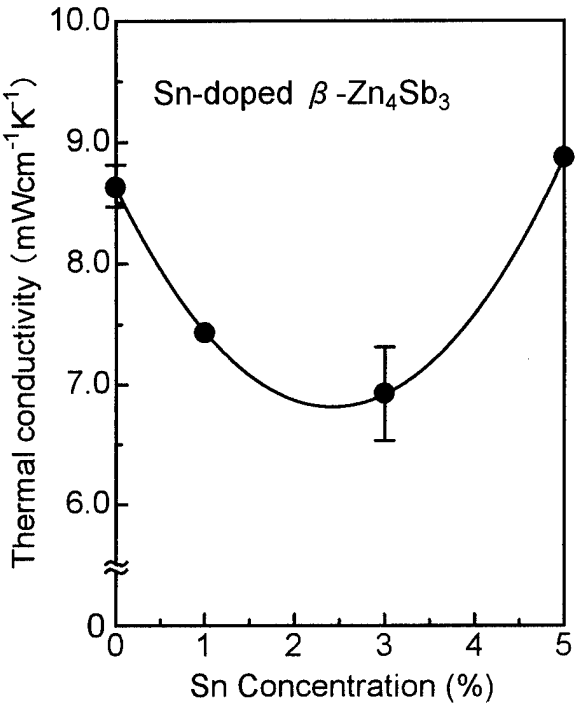


Fig.4 Thermal conductivity κ at room temperature as a function of Sn concentration.

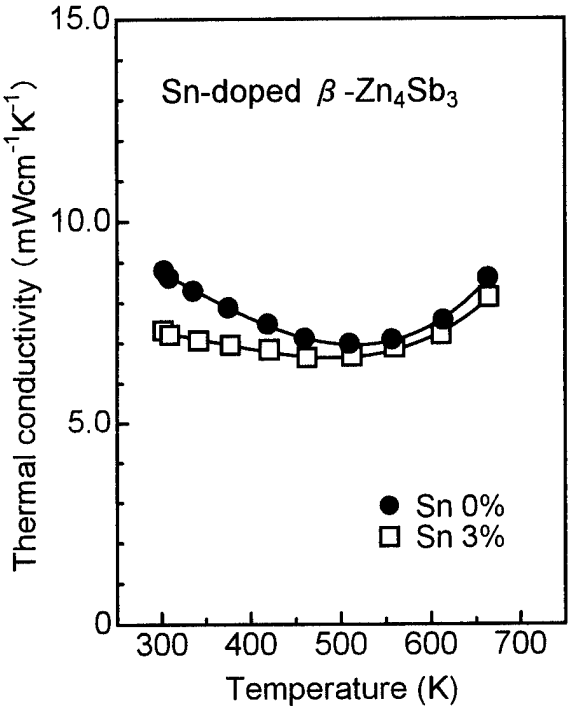


Fig.5 Temperature dependence of thermal conductivity κ for non- and 3% Sn-doped β-Zn_4Sb_3.

mobility of ~20cm^2/Vs for the non-doped sample. This reason is closely related to the improvement of the density of samples by doping β-Zn_4Sb_3 with Sn.

Although the Sn-doped samples have a similar temperature dependence of Seebeck coefficient to that of non-doped one, the values of Seebeck coefficient of the Sn-doped samples are slightly larger than those of non-doped one. Especially, for the 3% Sn-doped sample the values of S are larger than those of non-doped one at temperatures higher than ~650K. As a result, the power factor $S^2\sigma$ of the 3% Sn-doped sample was improved at temperatures higher than ~600K, and the maximum power factor of 14.4μW/cmK^2 was obtained at 733K.

Figure 4 shows the Sn concentration dependence of the thermal conductivity κ at room temperature for Sn-doped β-Zn_4Sb_3. The value of κ for our non-doped β-Zn_4Sb_3 sample was the almost same as for the sample of T. Caillat *et al.* [8]. As the Sn concentration is increased, the value of κ is reduced up to 3%, and then increased. The value of κ for the 3% Sn-doped sample is 6.88mW/cmK, which is about 20% lower than that for the non-doped samples (8.66mW/cmK). The decrease in κ caused by the Sn doping is attributed to the point defect phonon scattering by Sn at grain boundaries. The increase observed at 5% is related to the growth of ZnSb phase, of which value of κ is typically ~27mW/cmK [11]. From these results, it is found that the Sn addition is reasonably effective for the reduction of κ for β-Zn_4Sb_3.

Figure 5 shows the temperature dependence of the thermal conductivity κ for the non- and 3% Sn-doped β-Zn_4Sb_3. The thermal conductivity κ for the Sn-doped sample is lower in the whole temperature range than that for the non-doped sample. As the temperature is increased, κ is decreased up to ~500K because of the enhancement of the phonon-phonon scattering. At temperatures higher than ~550K, at which the samples almost had the intrinsic behavior, κ is increased with an increase in the temperature since the thermal conduction by electrons is dominant. A value of the minimum thermal conductivity κ for the non-doped sample is slightly high as compared with the result of T. Caillat *et al.* [3]. It seems probable that this increase in κ was related to the partial transformation to γ-Zn_4Sb_3 by repeated irradiation of the ruby laser with high power while the sample temperature was increased from room temperature.

Figure 6 shows the temperature dependence of the dimensionless thermoelectric figure of merit ZT of the 3% Sn-doped β-Zn_4Sb_3, as compared with that of the non-doped one. Since the reduction of the thermal conductivity κ canceled the reduction of the electrical conductivity σ for the Sn-doped sample, the thermoelectric figure of merit Z was not improved by doping β-Zn_4Sb_3 with Sn at temperatures lower than ~550K. However, the values of ZT for the Sn3%-doped sample are in excess of those for the non-doped sample at temperatures higher than ~550K owing to improvement of the Seebeck coefficient.

Conclusion

The thermoelectric properties of Sn-doped β-Zn_4Sb_3 have been investigated in order to improve further its good thermoelectric performance. Although the single phase of β-Zn_4Sb_3 was obtained up to 3% Sn concentration, the lattice constant of Sn-doped samples was hardly changed, indicating that Sn was

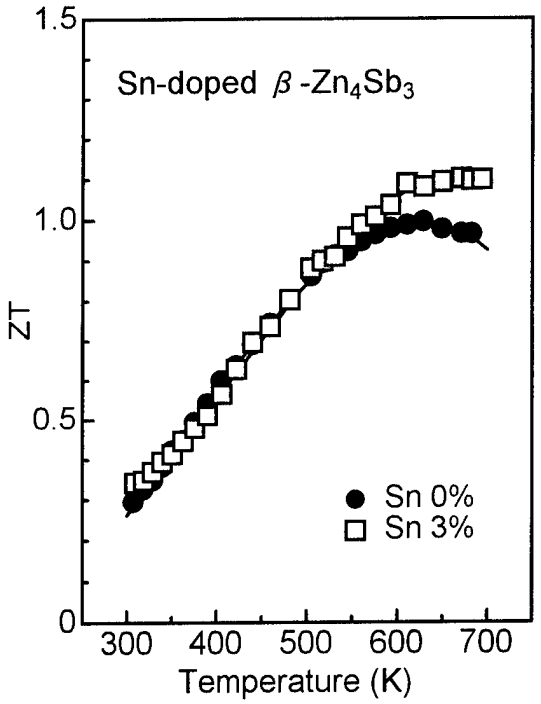


Fig. 6 Temperature dependence of dimensionless thermoelectric figure of merit for non- and 3% Sn-doped β-Zn_4Sb_3.

not substituted for Sb. From the results of x-ray diffraction measurements, it was suggested that microcrystals of Sn are dispersed in the region of grain boundaries. These microcrystals of Sn bring about the reduction of carrier concentration and thermal conductivity of β-Zn_4Sb_3. As a result, the thermoelectric figure of merit Z was hardly improved at temperatures lower than ~550K. However, above this temperature Z was improved because of an increase in the Seebeck coefficient. Based on the results, we expect that the addition of third element to β-Zn_4Sb_3 reduces the thermal conductivity without degrading the electrical properties.

Acknowledgement

We would like to thank Prof. K. Matsubara and Dr. H. Anno of Science University of Tokyo in Yamaguchi for helpful discussion. This work is supported in part by the Yamaguchi prefectural government.

References

[1] A.F. Joffe, *Semiconductor Thermoelements and Thermoelectric Cooling* (Infosearch, London, 1957).

[2] T. Koyanagi, K. Matsubara, K. Adachi and K. Kishimoto, "Thermoelectric Properties of ZnSb Films Prepared by Ionized-Cluster Beam Technique", Proc. 12th Int. Conf. on Thermoelectrics (IEE Jpn, Tokyo, 1994), pp.340-345.

[3] T. Koyanagi, K. Adachi, K. Kishimoto and K. Matsubara, "Thermoelectric Properties of ZnSb Ceramics Prepared by PIES Method", Trans. IEE Jpn **116-A** (3), 258-267 (1996) [*in Japanese*].

[4] M. Hansen and K. Anderko, *Constitution of Binary Alloys*, 2nd Ed. (McGraw-Hill Inc., New York, 1985), pp.1182-1185.

[5] M. Tapiero, S. Tarabichi, J.G. Gies, C. Noguet, J.P. Zielinger, M. Joucla, J.L. Loison, M. Robino and J. Herion, "Preparation and Characterization of Zn_4Sb_3", Solar Energy Mat. **12**, 257-274 (1985).

[6] Y.A. Ugai, E.M. Averbakh and V.V. Lavrov, "Some Electrical Properties of the Intermetallic Compound β-Zn_4Sb_3", Sov. Phys. Solid State **4** (11), 2393-2395 (1963).

[7] D.P. Spitzer, "Lattice Thermal Conductivity of Semiconductors: A Chemical Bond Approach", J. Phys. Chem. Solids **31**, 19-40 (1970).

[8] T. Caillat, J.-P. Fleurial and A. Borshchevsky, "A Low Thermal Conductivity Compound for Thermoelectric Applications: β-Zn_4Sb_3", Proc. 15th Int. Conf. Thermoelectrics (IEEE, Piscataway, NJ, 1996), pp.151-154.

[9] T. Caillat and J.-P. Fleurial, "Zn-Sb Alloys for Thermoelectric Power Generator", Proc. 31st Intersoc. Energy Convers. Eng. Conf. (IEEE, Piscataway, NJ, 1996), pp.905-909.

[10] M. Hansen and K. Anderko, *Constitution of Binary Alloys*, 2nd Ed. (McGraw-Hill Inc., New York, 1985), pp.1217-1219.

[11] R.R. Heikes and R.W. Ure, Jr. Eds., *Thermoelectricity: Science and Engineering* (Interscience Publishers, New York, 1961), Chap.17.

Huge Thermoelectromotive Force Generated by Porous Ceramics of Y_2O_3

K. Koumoto, W. S. Seo, S. Ozawa
Department of Applied Chemistry, Graduate School of Engineering,
Nagoya University, Furo-cho, Chikusa-ku, Nagoya 464-01, Japan

Abstract

Porous Y_2O_3 ceramic was found to show huge thermopower values up to -50 mV/K at 900-1,000 K in vacuum, but not in air. Such huge thermopowers may be generated by the electron gas emitted from the internal surfaces of the pores and are associated with some unknown effects. The non-dimensional thermoelectric figure of merit, ZT, of this porous ceramic was as large as ~0.95 at ~950 K, and hence it can be used as a new thermoelectric material.

Introduction

Tellurides and selenides of Bi, Sb, Pb, etc. and SiGe alloys have so far been developed as high-Z materials[1]. Recently investigations of new materials such as $CoSb_3$ solid solutions[2,3] and superlattice structured thin films[4-6] are actively carried out since they are expected to meet the criterion, ZT>1. We have recently discovered that huge thermopower values of about -50 mV/K can be generated by porous yttrium oxide (Y_2O_3) ceramic at high temperatures (900~1,000K) in vacuum (~1.3×10^{-3}Pa)[7] .

In general, metals show only small thermopowers of the order of a few tens of μV/K and semiconductors show some hundreds of μV/K. Insulators typically have very large thermopower values, but the thermopower of insulators is hard to measure. Sher has reported that a porous body of (Ca, Sr, Ba)O solid solution having low work function (~1.7 eV) also generates large thermopower of about -2 mV/K at 1,000K in vacuum (~1.3×10^{-5}Pa)[8]. In the present study, however, porous Y_2O_3 ceramic demonstrated one order of magnitude larger thermopower.

Experimental

Porous Y_2O_3 ceramic was fabricated by common ceramic processing techniques. The starting powder of Y_2O_3 (Kojundo Chemical Laboratory, 99.9% pure) was mixed with 20-25 wt% liquid paraffin. The mixture was packed in a rubber bag, isostatically pressed at 196 MPa, and fired at 1,723K for 1 h in air. The porosity was measured in pure water by an Archimedes method. Electrical conductivity and thermopower were simultaneously measured under vacuum (~1.3×10^{-3}Pa) or in air. Details of the method of measurement for ceramic specimens are described elsewhere[9].

Electrical conductivity was measured by the dc 4-probe method by using each Pt leg of the thermocouple as a current lead. Two more Pt leads wound around the specimen were used to measure the voltage drop. For thermoelectromotive force measurements, a temperature gradient in the specimen was generated by passing cool air in an alumina protection tube placed near one end of the specimen. The temperature difference between the two ends was controlled to be 2 to 15 K by varying the flow rate of air. Thermoelectromotive force measured as a function of the temperature difference gave a straight line and the Seebeck coefficient was calculated from its slope.

Thermal diffusivity and specific heat capacity were measured by the usual laser flash method. The disk specimen was set in an electric furnace, and heated up to a target temperature under vacuum. After the temperature became stabilized, the front surface of the specimen was irradiated with a ruby laser pulse. The temperature variation at the rear surface was monitored with a Pt-Pt13%Rh thermocouple and an InSb infrared detector. The thermal conductivity was calculated from thermal diffusivity, specific heat capacity, and

0-7803-4057-4/97 $10.00 ©1997 IEEE

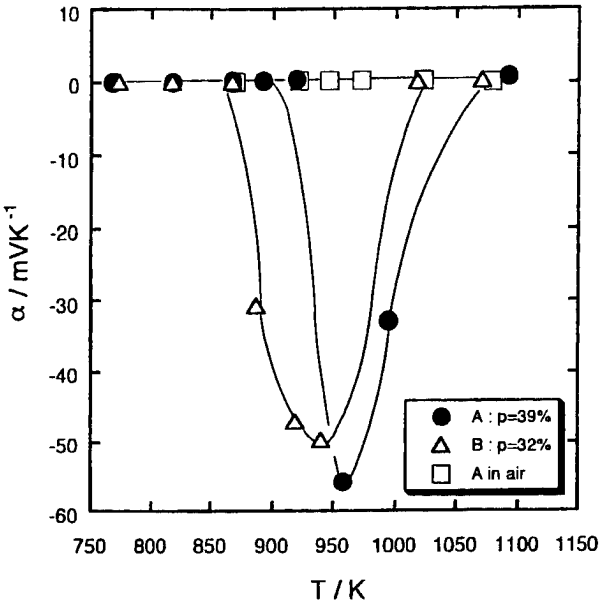


Fig. 1 Temperature dependencies of the thermopower, α, for two specimens, A and B, with different porosities, p. The values of α for specimen A measured in air are shown for comparison.

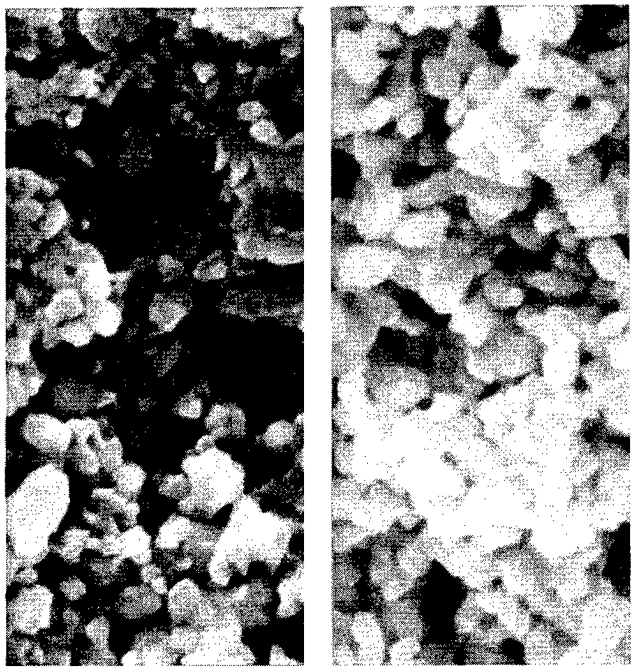


Fig. 2 SEM photographs of the fractured surfaces of the porous specimens; (A) porosity=39%, (B) porosity=32%.

density.

Results and Discussion

Figure 1 shows the temperature dependencies of the thermpower for two specimens with different porosities whose microstructures are shown in Fig. 2. It can be clearly seen that huge thermopower of the order of -50 mV/K is generated at 900-1,000 K in vacuum. The huge thermopower of porous Y_2O_3 ceramic is considered to be associated with the fact that Y_2O_3 possesses a rather low work function (~2.0 eV)[10]. Namely, when the temperature is raised in vacuum, thermionic emission takes place from the internal surfaces of the pores giving rise to an electron gas filling the pores. The huge thermopower must have been generated by applying the temperature difference to the electron gas. As shown in Fig. 1, only small thermopower was observed in air, which indicates that thermionic emission hardly took place because of the presence of air molecules. However, theoretical evaluation of the thermopower of free electrons using a simplified equation[11] cannot explain such a huge thermopower, so that some other unknown effects must be responsible, though they remain to be clarified in future studies.

Our measurement indicates the electrical conductivity, σ, (d.c. four probe technique) increases gradually with increasing temperature up to ~850 K under vacuum, and is approximately the same as that measured in air, as shoow in Fig. 3. Above ~850 K σ suddenly increases, deviating sharply from the value measured in air. This observation clearly indicates that thermionic emission takes place above ~850 K in vacuum but not in air. Both the electrical conductivity and the thermopower begin to decrease when the temperature is raised above ~1,000 K. The reason for this phenomenon is still unknown.

The thermal conductivity, κ, of specimen A with 39% porosity measured under vacuum by a laser flash method decreased

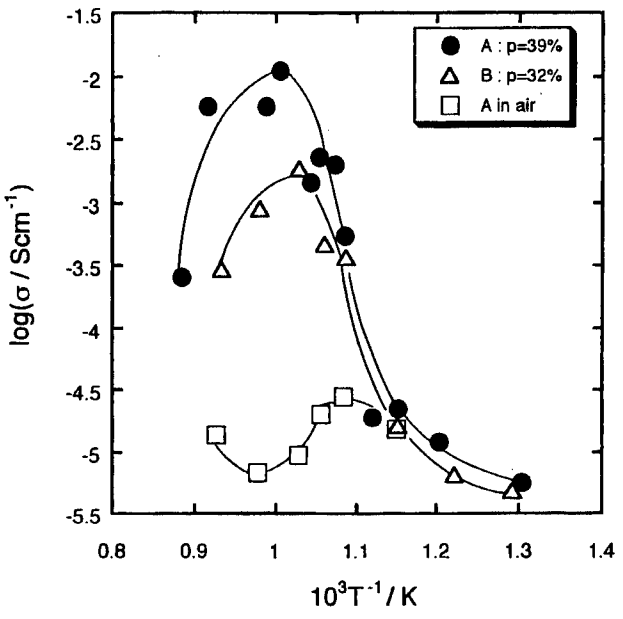


Fig. 3 Temperature dependencies of the electrical conductivity, σ, for two specimens, A and B, with different porosities, p. The values of σ for the specimen A measured in air are shown for comparison.

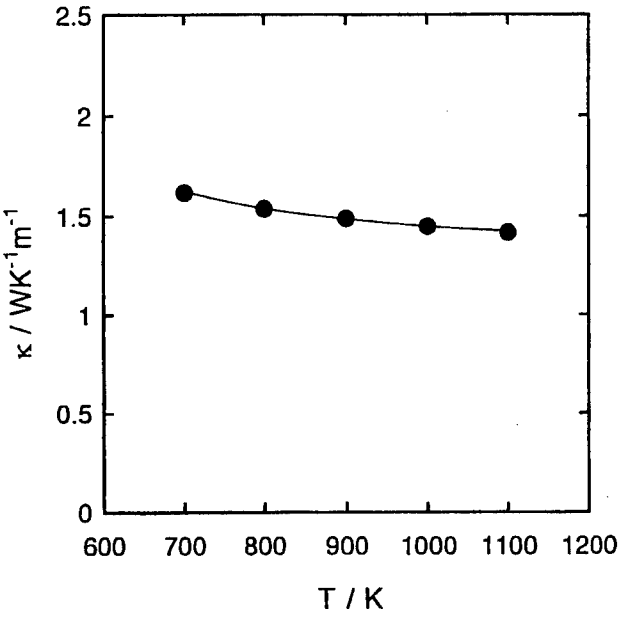


Fig. 4 Temperature dependence of thermal conductivity, κ, for specimen A with 39% porosity.

slightly with increasing temperature and was as low as 1.42~1.62 $WK^{-1}m^{-1}$ at 700 -1100 K as shown in Fig. 4. Sher has demonstrated that the thermal conductivity of a porous body of the (Ca,Sr,Ba)O solid solution was of the order of 10^{-3}~10^{-4} $WK^{-1}m^{-1}$, and that the radiation in the pores was the predominant mechanism for heat transport where κ increased with increasing temperature[8]. However, this was not the case for porous Y_2O_3 ceramics, and usual lattice thermal conduction in the Y_2O_3 matrix phase must have dominated the heat transport process in a porous body.

Combination of the measured σ, α, and κ enabled us to calculate the values of Z for porous Y_2O_3 ceramic. The obtained Z was as large as ~$1.0x10^{-3}$ K^{-1} at 950K (ZT~0.95), almost meeting the criterion, ZT>1. Although it should be possible to optimize for larger Z values in a wider temperature range, this new material is expected to become a promising candidate for the future thermoelectric energy conversion. The potential problem of integrating this material in working devices is that it only works at high temperatures in vacuum. However, this problem could be overcome if the devices can be suitably confined in a vacuum container, or if they are operated in space.

Acknowledgment

The authors thank Dr. K. Watari of the National Industrial Research Institute of Nagoya for his assistance in thermal conductivity measurements, Dr. E. M. Sher for helpful discussions providing them with valuable information, and Dr. C. B. Vining for critically reading the manuscript.

References

[1] K. Uemura, I. Nishida, Thermoelectric Semiconductors and their Applications, Nikkan Kogyo Shinbun, Tokyo(1988).

[2] T. Caillat, A. Borschevsky, and J.-P. Fleurial , J. Appl. Phys. 80(8), 4442(1996); ibid. 79(11), 8419(1996).

[3] B. C. Sales, D. Mandrus, and R. K.

Williams, Science 272, 1325(1996).
[4] L. D. Hicks T. C. Harman, X. Sun, and M. S. Dresselhaus, Phys. Rev. B53, R10493(1996).
[5] J. O. Sofo and G. D. Mahan, Appl. Phys. Lett. 65(21), 2690(1994).
[6] P. J. Lin-Chung and T. L. Reinecke, Phys. Rev. B51, 13244(1995).
[7] K. Koumoto, S. W. Seo and S. Ozawa, Appl. Phys. Lett. in press.
[8] E. M. Sher, Proc. 15th Int. Conf. Thermoelec., Edited by T. Caillat, IEEE, Piscataway, NJ, (1996)pp.168-171.
[9] H. Ohta, W. S. Seo, and K. Koumoto, J. Am. Ceram. Soc. 79(8), 2193(1996).
[10] Handbook of Chemistry - Fundamental Chemistry Edition, Edited by the Chemical Society of Japan, Tokyo(1993)pp.490.
[11] F. G. Baksht, G. A. Dyuzhev, A. M. Martsinovskiy, B. Ya. Moyzhes, G. Ye. Pikus, E. B. Sonin and V. G. Yur'yev, Thermionic Converters and Low-Temperature Plasma, US Department of Energy (1978) pp.16.

ENHANCED THERMOELECTRIC EFFICIENCY NEAR A CONDUCTIVITY THRESHOLD

Glen D. Guttman, Eshel Ben-Jacob and David J. Bergman
School of Physics and Astronomy
Raymond and Beverly Sackler Faculty of Exact Sciences
Tel-Aviv University
Ramat-Aviv 69978, Tel-Aviv, ISRAEL

We calculate the thermopower and efficiency of the thermoelectric effect in systems which have a conductivity threshold (as function of the electronic energy). For example, disordered metals near the mobility edge (i.e., at the metal–insulator transition). Near such a threshold the thermopower and thermoelectric efficiency (i.e, figure of merit) are enhanced. The figure of merit ZT can be made much larger than unity, however at the price of low power output. In the presence of minimal lattice heat conductivity we calculate $ZT \sim 6$ near the threshold. The enhancement effect is *universal* in the sense that it ensues from a competition between two physical mechanisms which sustain the the steady-state thermopower. Any system that exhibits an electrical conductivity threshold and low lattice thermal conductivity is a good candidate for observing such an enhancement.

I. INTRODUCTION

It is well known that the thermopower is sensitive to the energy dependence of the conductivity. This is demonstrated by the Mott formula for the thermopower of macroscopic metals which is (in the Sommerfeld approximation)

$$S = \frac{\pi^2}{3}\frac{k_B^2 T}{e}\left.\frac{d(\ln\sigma)}{dE}\right|_{E=\mu}. \qquad (1)$$

In Eq. (1) the temperature is denoted by T, k_B is the Boltzmann constant, μ is the chemical potential, e is the magnitude of the electronic charge unit and σ is the electric conductivity. However, the Sommerfeld approximation is only valid when the conductivity varies slowly on the scale of $k_B T$. Near a conductivity threshold (as function of energy) Eq. (1) breaks down, and one must calculate the transport coefficients more carefully. As we shall show, the thermoelectric properties change dramatically in the vicinity of such a threshold.

A wide variety of systems can be constructed in order to implement such a threshold. For example, one can exploit the Mott or Anderson metal-insulator transition. In general, any system in which one can control the conductance as function of energy and create a threshold beyond which the conductance is zero will suffice. In this sense the effects we will demonstrate are *universal*. The advances in fabrication of new materials is therefore very promising for the possibility to observe the effects we shall describe below.

We begin in Sec. II with a description of the expressions for the relevant thermoelectric properties. In Sec. III we explain the mechanisms which dictate the behavior of thermopower and the figure of merit. This leads to an understanding of the enhancement of both properties near a conductivity threshold, in the limit of zero lattice heat conduction. Finally, we discuss a realistic scenario which incorporates lattice conductance, and find that the figure of merit can reach values of $ZT \sim 6$. Such large values would provide significant benefits in many technological applications [1,2].

II. TRANSPORT COEFFICIENTS

Consider a typical transport measurement setup. Two electron reservoirs, with chemical-potentials μ_L, μ_R and temperatures T_L, T_R, are connected by a conductor. Within the linear response theory, thermoelectric transport between the two reservoirs can be formulated in a matrix form

$$\begin{pmatrix} I \\ Q \end{pmatrix} = \begin{pmatrix} \mathbf{L}_{11} & \mathbf{L}_{12} \\ \mathbf{L}_{21} & \mathbf{L}_{22} \end{pmatrix} \begin{pmatrix} \mu_L/e - \mu_R/e \\ T_L - T_R \end{pmatrix} \equiv \hat{\mathbf{L}}\mathbf{F} \qquad (2)$$

where $T_L - T_R = \Delta T$, $\hat{\mathbf{L}}$ is the transport coefficient matrix and $\mathbf{F}$ represents the thermodynamic generalized forces. The matrix elements are identified as follows: $\mathbf{L}_{11}$ is the electric conductance at zero temperature difference, $\mathbf{L}_{12}$ and $\mathbf{L}_{21}$ are the thermoelectric coefficients and $\mathbf{L}_{22}$ is the heat conductance at zero electric potential difference. In the continuum limit differences are transformed into gradients and conductances into conductivities. The transport coefficients can generally be written [3] as

$$\mathbf{L}_{11} = e^2 \int_{-\infty}^{\infty} \Sigma(E)\left(-\frac{\partial f}{\partial E}\right)dE, \qquad (3)$$

$$\mathbf{L}_{12} = \frac{1}{T}\mathbf{L}_{21} = \frac{e}{T}\int_{-\infty}^{\infty} \Sigma(E)\,(E-\mu)\left(-\frac{\partial f}{\partial E}\right)dE, \qquad (4)$$

$$\mathbf{L}_{22} = \frac{1}{T}\int_{-\infty}^{\infty} \Sigma(E)\,(E-\mu)^2\left(-\frac{\partial f}{\partial E}\right)dE, \qquad (5)$$

0-7803-4057-4/97 $10.00 ©1997 IEEE

where $\Sigma(E)$ includes all energy dependent properties of the conducting region. Physically, Σ determines the conductivity and contains information about the type of charge carrier (e.g., electrons or holes), the carrier scattering mechanisms, mobility, and density of states. The Fermi distribution function is denoted by $f(E)$.

The thermopower of a system is defined as the voltage bias V developed by the system in response to an applied temperature difference ΔT, under the constraint of an open circuit (i.e., $I = 0$). In order to evaluate the thermopower S we use the relation

$$S = -\mathbf{L}_{12}/\mathbf{L}_{11}. \tag{6}$$

It is useful to define the following additional quantity, which provides a measure for the efficiency of the thermoelectric effect [4]

$$\Delta \equiv \frac{\mathbf{L}_{12}\mathbf{L}_{21}}{\mathbf{L}_{11}\mathbf{L}_{22}}. \tag{7}$$

Note that Δ is related to the figure of merit of the system Z (the traditionally used quantity [1]) by $\Delta = ZT/(1 + ZT)$. Δ is a more natural quantity to define than Z, since $0 \leq \Delta \leq 1$ and since Δ is dimensionless, while Z ranges from zero to infinity and has the dimensions of inverse temperature. Δ is a measure of the rate of entropy production in the transport process. This can be seen by writing the entropy current $J_S \equiv Q/T$ as

$$J_S = SI + \frac{1}{T}\frac{D}{\mathbf{L}_{11}}\Delta T, \tag{8}$$

where S is the thermopower and $D \equiv |\hat{\mathbf{L}}| = \mathbf{L}_{11}\mathbf{L}_{22} - \mathbf{L}_{12}\mathbf{L}_{21}$. Indeed, when $I = 0$ and $\Delta = 1$, i.e., $D = 0$, then $Q = J_S = 0$. Therefore, the entropy production, which in the notation of Eq. (2) can be written as $\mathbf{F}\hat{\mathbf{L}}\mathbf{F}$, is zero and the thermoelectric effect is most efficient. When $\Delta < 1$, the second term on the right hand side of Eq. (8) leads to an entropy current, even in the absence of a net electric current: the net electric current vanishes because the current from the left is canceled by the current from the right. However, a charge moving from right to left changes the entropy by a different amount than a charge moving in the opposite direction. Thus, the temperature gradient results in generation of entropy, making the thermoelectric process less efficient.

III. THERMOPOWER AT A CONDUCTIVITY THRESHOLD

A. Specific Examples

Both the thermopower S and the efficiency Δ have a strong dependence on the functional form of the conductivity vs. energy relationship. We show specific examples of this behavior of S and Δ in the vicinity of a conductivity threshold. In practice, the state of the system is shifted with respect to the threshold by changing the chemical-potential.

The Anderson Metal-Insulator Transition: A conductivity threshold is realized by the mobility edge in disordered 3D metals. At a critical energy E_c a second order transition occurs, and the metal becomes an insulator. The behavior of the thermopower and its efficiency at the mobility edge have been studied before. On the insulating side ($\mu < E_c$), Cutler and Mott [5] noticed that the thermopower scales like $(\mu - E_c)/k_BT$, provided no hopping currents are present. Imry and Sivan [6] have shown that in the vicinity of this threshold the thermopower reaches a maximum in the conducting phase. It has also been shown [7] that the efficiency near the transition is enhanced (on the conducting side).

A Many-Channel Ballistic Wire: A quasi-1D ballistic conductor (e.g., a constricted 2D electron gas or a quantum point contact) consists of several channels corresponding to the transverse bound states. When a current is driven through the conductor, the conductance is characterized by a step-like curve as function of the chemical potential [8]. The thermopower has peaks at the step boundaries [9]. Substituting a step-like function for $\Sigma(E)$ in Eqs. (3) – (5), one can show [10] that the efficiency at the step boundary between different finite conductivities is much less (by an order of magnitude) than its value at the threshold. Below the threshold the efficiency reaches its maximum $\Delta \to 1$ (note that lattice heat conductance is neglected in these systems).

B. Interpretation

For simplicity let us consider the Landauer approach to transport. According to this picture transport can be viewed as a scattering process. The conductor is represented by a potential barrier which allows incident charge carriers to tunnel with a probability $t(E)$. Therefore, the transport coefficients are related to $t(E)$, and are described by Eqs. (3) – (5), substituting $\Sigma(E) = t(E)/\hbar$. This picture is particularly convenient when treating transport in mesoscopic systems, such as quantum wires, since quantum interference effects are naturally incorporated [10–12]. We also note that the following discussion does not account for lattice vibrations. Those degrees of freedom will be incorporated in the last section.

The anomalous behavior of the thermopower and its efficiency at a threshold of the conductivity is universal, and can be explained in the following way. Consider the model case of two particle and heat reservoirs connected by a *single* electronic state E_c, Fig. 1. We will refer to this as a *channel* and assume perfect (ballistic) transmis-

sion $t(E_c) = 1$. The initial state of the reservoirs is equal Fermi levels E_F and $T = 0$ for both reservoirs. Suppose the channel energy $E_c > E_F$ and the left hand reservoir temperature is raised to $T_L = \Delta T$. A net electron current, going to the right, develops due to thermally excited electrons in the left hand reservoir. In order to measure a thermopower we require an electrochemical bias to effectively raise the Fermi level in the right hand reservoir and impose the steady-state $I = 0$. The mechanism by which the electric current is set to zero is purely electrostatic. The single channel is blocked by the counteracting electric field of the bias. In the absence of currents in the steady-state no entropy is produced and therefore the efficiency is maximal. Indeed, when solving Eqs. (3) – (5) with $t(E) = \delta(E - E_c)$ one obtains $D = 0$ or $\Delta = 1$ (i.e., Z diverges). Examining Eq. (8) we observe that this mechanism is manifested in the thermodynamics by setting the term $D\Delta T/T\mathbf{L}_{11}$ to zero. This term is associated with entropy generation due to the transport process. The thermopower for this system behaves like $S \propto (E_c - E_F)$. This is because the bias ΔV must raise the Fermi-level in the right hand reservoir by the gap energy $E_c - E_F$ in order to make the current, driven by ΔT, vanish. (This follows from the definition of the thermopower, Sec. 2.)

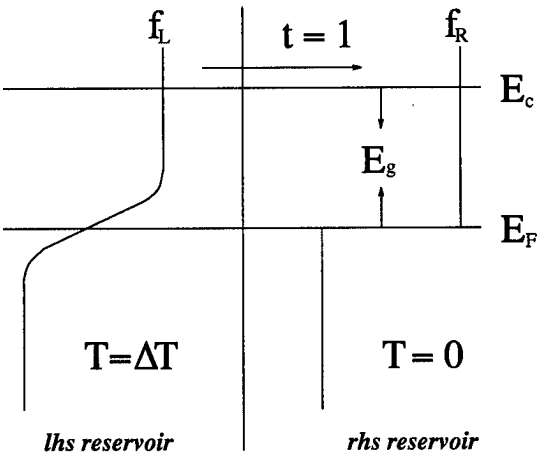


FIG. 1. **A schematic description of the transport between reservoirs through a single electronic state. The left hand (right hand) reservoirs are in equilibrium with Fermi functions f_L (f_R). The left hand reservoir is at temperature ΔT and the right hand at $T = 0$. The threshold energy is E_c, creating a gap of E_g above the Fermi level E_F.**

Now suppose we add one more ballistic channel of conductance. For instance, a channel below E_F in Fig. 1. Excluding the case of symmetric channels about the Fermi level, the currents in both channels will be different, owing to the different thermal occupancy of the levels. (Equivalently, we may consider channels with different transmissions). Applying an electro-chemical bias, the system will reach the steady-state $I = 0$. However, in contrast to the single channel, the net electric current is nullified by two mechanisms. One is the electrostatic field and the second is the cancellation of the currents in the two channels. This latter mechanism is not possible with one channel. The cancellation process is responsible for entropy production and is manifested by the term $D\Delta T/T\mathbf{L}_{11}$ in Eq. (8). Hence, for a system of more than one channel of conductance the efficiency is never maximal and $\Delta < 1$.

The distinction between these two mechanisms, which satisfy an open circuit steady-state, explains the behavior of the thermopower in more realistic systems. Consider the Landauer model illustrated in Fig. 2. The barrier (representing the conductor) is a generalization of the two channel model. Above a threshold E_c we have a continuum of channels with energy dependent transmission $t(E)$. As before, the initial state of the reservoirs is equal Fermi levels E_F and $T = 0$ for both reservoirs. The left hand reservoir temperature is raised to $T_L = \Delta T$.

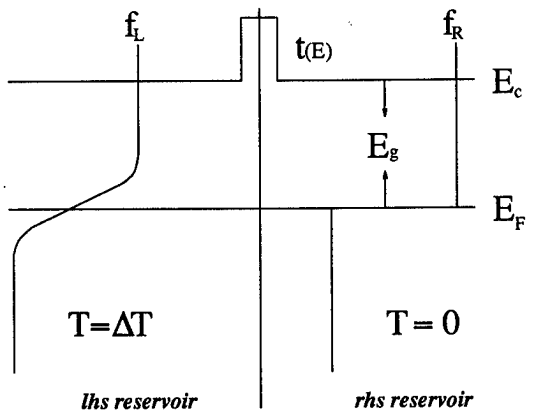


FIG. 2. **A schematic description of the transport across a barrier of transmission t. The left hand (right hand) reservoirs are in equilibrium with Fermi functions f_L (f_R). The left hand reservoir is at temperature ΔT and the right hand at $T = 0$. The barrier threshold energy is E_c. Here we illustrate a gap E_g above the Fermi level E_F.**

When the threshold energy E_c is lower than the chemical-potential of the reservoirs, electrons are free to conduct with transmission $t(E_F - E_c)$. Electrons from the left hand reservoir above E_F are compensated by a reverse current from beneath E_F in the right hand reservoir. Due to the energy dependence of the barrier transmission the total electron current (arising from ΔT) is non-zero. It is set to zero by a reverse bias ΔV. However, the main process nullifying the electric current is due to compensating currents. This is accompanied by

entropy production, and thus the efficiency is low. The thermopower is, hence, a result of the energy dependence of the transmission, leading to typical metallic behavior [Eq. (1)].

Suppose the channel energy is raised to the Fermi level. The reverse current from right to left is cut off. Therefore, in order to cancel the total current we need a larger counter-bias which will reverse the currents in higher energy levels until the steady-state is achieved. This enhances the thermopower and also, due to the smaller role of the current-cancellation mechanism, enhances the efficiency. If one raises E_c even more a gap is created in the conductivity, and only electrons with energy $E_g \equiv E_c - E_F$ above the Fermi level can conduct. Currents of electrons in energy levels above the threshold are strongly depleted since only thermally excited electrons contribute to the current (decreasing it exponentially in E_g/k_BT). The excess current from the left, due to ΔT, can only be compensated by a bias $\Delta V \cong E_g/e$, plus a correction to compensate for the small currents. Therefore, we expect $S \sim E_g$. The efficiency is greatly enhanced since the role of the electric field mechanism is dominant over the current-cancellation mechanism which produces entropy. As the gap is widened we reach the limit of a single channel conductance and $\Delta \rightarrow 1$. When both reservoirs have an initial temperature T one must account for the smearing of the Fermi level in the right hand reservoir. In particular, the limit $\Delta \rightarrow 1$ is reached for $E_g \gg k_BT$ and in this limit $S \sim E_g/k_BT$. This behavior can also be seen in Eqs. (3) – (5). In the limit $E_g = \mu - E_c \gg k_BT$ one can take $(-df/dE) \approx \exp[-(E-\mu)/k_BT]$. Expanding the transmission to first order around E_c one finds $S \approx (k_B/e)(const. + E_g/k_BT)$ and $\Delta \rightarrow 1$.

We note that when the system is below the conductivity threshold the electrical currents are exponentially reduced, and therefore the output power generated is also very small. In other words, the price we pay for maximal efficiency is minimal power. Also note that the effect discussed above is symmetric with respect to the threshold. If the conductivity vanishes above the threshold the enhancement effect is reversed accordingly.

IV. DISCUSSION

We have shown that in the absence of lattice heat conduction the efficiency of thermoelectric effects is greatly enhanced as the system moves through a conductivity threshold, albeit at the price of reduced output power. However, this limit is never satisfied. In the best thermoelectric materials the lattice heat conductivity is of the order of $\kappa_l \sim 10^{-2} W/cmK$. Although these values are small compared with the electronic heat conductance in metals ($\kappa_e \sim 1 W/cmK$), as we move towards the conductivity threshold the electronic contribution diminishes until $\kappa_l \sim \kappa_e$. In this case the efficiency is limited by κ_l. This is evident in the expression for ZT which then becomes

$$ZT = \frac{\Delta}{1 - \Delta + \kappa_l/\kappa_e^0}. \tag{9}$$

In Eq. (9) we used the relation for the heat conductance at zero electric current $\kappa^0 = \mathbf{L}_{22} - \mathbf{L}_{21}\mathbf{L}_{11}^{-1}\mathbf{L}_{12} = \mathbf{L}_{22}(1-\Delta)$, where $\mathbf{L}_{22} = \kappa_e^0 + \kappa_l$. Δ is the efficiency when excluding phonon conduction. In the limit $\Delta = 1$ we find that $ZT = \kappa_e^0/\kappa_l$. This value goes to zero as the system moves below the threshold where the conductance is zero. Therefore, in order to maximize ZT we must optimize the expression in Eq. (9) with respect to Δ and κ_e^0.

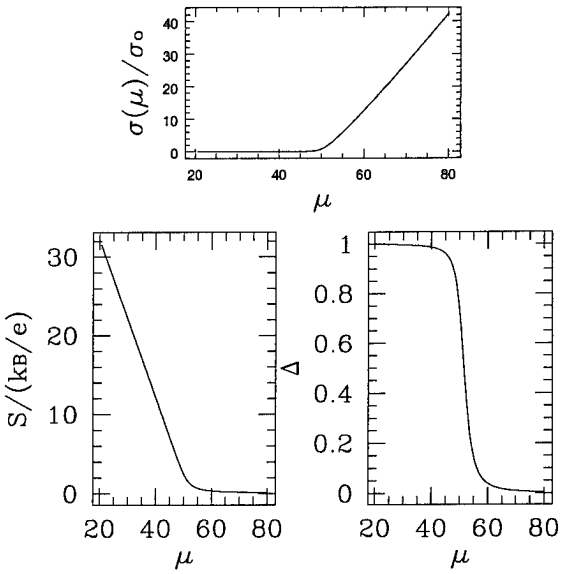


FIG. 3. **The conductivity, thermopower and efficiency (neglecting κ_l) as function of the chemical potential (in units of k_BT). We calculated Eqs. (3) – (5) when substituting a generic Σ function (see text).** $\sigma_0 \sim 46,000(\Omega cm)^{-1}$.

In order to demonstrate this we solved Eqs. (3) – (5) numerically with a generic function $\Sigma(E) = (E - E_c)^{0.5}/\hbar a_0$, where we chose a threshold energy $E_c = 50 k_BT$, and a_0 is the Bohr radius. In Fig. 3 we plot the results for the conductivity, the thermopower and the efficiency function Δ. We see that as expected the thermopower increases linearly as the gap opens up, and the efficiency quickly reaches maximum values. Above the threshold (i.e., in the metallic region) we obtain $\sigma \sim 10^5(\Omega cm)^{-1}$, $S \sim 10\mu V/K$, and $\kappa_e \sim 1 W/cmK$. These values agree with measured values for typical metals. Note that the value for κ_e is temperature dependent and was evaluated at room temperature. In Fig. 4 we plot the figure of merit including the effect of phonons $\kappa_l = 10^{-3} W/cmK$.

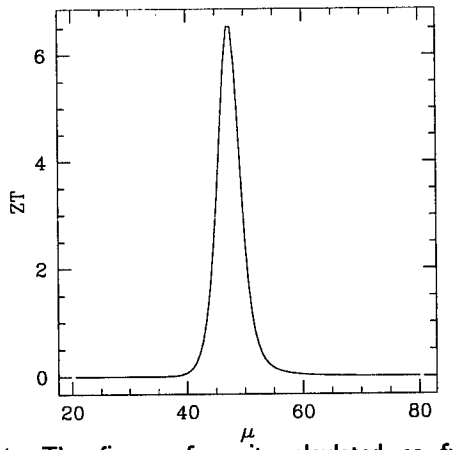


FIG. 4. **The figure of merit calculated as function of the chemical potential (in units of k_BT). We evaluated Eq. (9) which includes the effect of phonons. We chose $\kappa_l = 10^{-3}W/cmK$ and calculated κ_e^0 from Eq. (5) at room temperature.**

This is comparable with values of minimal heat conductivity of many non-metallic crystals [13]. Note that we are not limited to semiconductors. Any material that exhibits an electric conductivity threshold and these values of lattice conductivity is a good candidate for enhanced thermopower and ZT. In this realization we obtain a maximum value of $ZT \sim 6$. This occurs just below the threshold, which means we also achieve reasonable power output, since the electrical conductivity is still of the order of $10^4(\Omega cm)^{-1}$.

As yet, we have discussed the enhancement of the Seebeck effect. Obviously, the magnitude and efficiency of the Peltier effect will also be augmented. This is suggested by the Kelvin relation which relates the Peltier and Seebeck coefficients. The physical explanation is based on the discussion in Sec. III. In essence, the appearance of a gap acts like a "high-pass filter" which screens hot electrons from the externally driven electric current. Hence, the heat current that is generated by the electric current is larger than it would be in the absence of a gap. The enhanced efficiency is a direct result of the fact that the electric current is reduced by the gap.

Acknowledgments: Partial support for this work was provided by the Israel Science Foundation and the US-Israel Binational Science Foundation.

[1] H. J. Goldshmid, *Thermoelectric Refrigeration* (Plenum, New York, 1964).
[2] G. Mahan, B. Sales and J. Sharp, Physics Today (March 1997).
[3] N. W. Ashcroft and N. D. Mermin, *Solid State Physics*, (Asia, 1988).
[4] D. J. Bergman and O. Levy, J. Appl. Phys. **70**, 6821 (1991).
[5] M. Cutler and N. F. Mott, Phys. Rev. **181**, 1336 (1969).
[6] U. Sivan and Y. Imry, Phys. Rev. B **33**, 551 (1986).
[7] A. Kapitulnik, Appl. Phys. Lett. **60**, 180 (1992).
[8] B. J. van Wees, H. van Houten, C. W. J. Beenakker, J. G. Williamson, L. P. Kouwenhoven, D. van der Marel and C. T. Foxon, Phys. Rev. Lett. **60**, 848 (1988).
[9] P. Streda, J. Phys. Condens. Matter **1**, 1025 (1989).
[10] G. D. Guttman, E. Ben-Jacob and D. J. Bergman, Phys. Rev. B **51**, 17758 (1995).
[11] G. D. Guttman, E. Ben-Jacob and D. J. Bergman, Phys. Rev. B **52**, 5256 (1995).
[12] G. D. Guttman, E. Ben-Jacob and D. J. Bergman, Phys. Rev. B **53**, 15856 (1996).
[13] G. A. Slack, Solid State Phys. **34**, 1 (1979).

Thermopower and Thermal Transport in Metal-p-Type Semiconductor-Metal Structure

Yu. G. Gurevich, G. N. Logvinov,* O. I. Lyubimov,† O. Yu. Titov
Departamento de Fisica, CINVESTAV—I. P. N.,
Apdo. Postal 14–740, Mexico D. F. 07000, Mexico
*Teacher Training University, Avenue Krivonosa 2,
Ternopil 282009, Ukraine
†Physics Department, Kharkov State University,
Square Svoboda 4, Kharkov 310077, Ukraine

In this work we extend quantitatively the analysis of the thermoelectric phenomena in structure with charge carriers of the opposite signs.

In p-type semiconductor in the temperature field nonequilibrium holes have been shown to emerge, hence the necessity of taking recombination into account occur.

Boundary conditions for the electrons and holes on the p-type semiconductor-metal contact interface that take into account the surface recombination and the opportunity of current flow through the corresponding surfaces have been stated.

General expressions for thermo-emf and thermal flow in hole semiconductor are valid only at the existence of high recombination level. With a weak recombination the hole current which is not found in metals does not exist in p-type semiconductors either, and thermo-emf is constantly formed only by electrons.

Introduction.

We shall consider a one-dimensional problem: a monopolar p-type semiconductor ($-a \leq x \leq +a$) characterized by the chemical potential μ_s^0 with the forbidden band width ε_g and the work of exit χ_s is closed by a metal conductor with the work of exit χ_m and the chemical potential (counted off from the bottom of its conduction zone) μ_m (see Fig. 1).

At first we shall assume that the temperature at all circuit points is identical and is equal, for definiteness, to T^*. Then concentration of electrons on the semiconductor is determined by a well-known expression ($\mu_s^0 = \mu_n^0(T^*)$):

$$n_0(T^*) = \gamma_n(T^*) \exp\left[\frac{\mu_n^0(T^*)}{T^*}\right]$$

where $\gamma_n(T^*)$ is the density of states at the bottom of conduction zone.

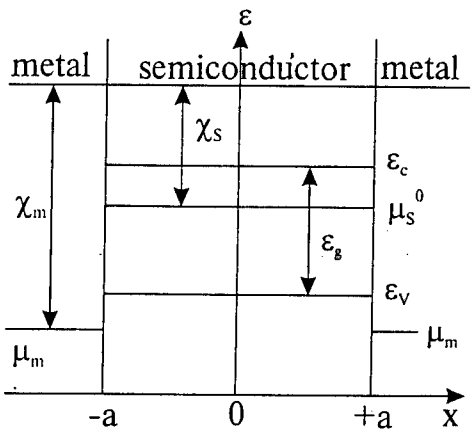
Chemical potential of holes $\mu_p^0(T^*)$ is related to $\mu_n^0(T^*)$ by a traditional (for equilibrium) relationship

$$\mu_p^0(T^*) = -\varepsilon_g - \mu_n^0(T^*), \qquad (1)$$

and their concentration is equal to

$$p_0(T^*) = \gamma_p(T^*) \exp\left[\frac{\mu_p^0(T^*)}{T^*}.\right]$$

Figure 1: Energy diagram of the structure under investigation before the establishment of equilibrium at $T = T^*$.



In the process of establishing equilibrium between semiconductor and metal in the vicinity of the surfaces $x = \pm a$ the space charge layers and contact potential differences will originate in the semiconductor.

Later we shall constantly deal with the approximation of quasi-neutrality which is valid at the satisfaction of the inequality

$$a^2 \gg {r_d}^2$$

where ${r_d}^2 = \frac{T^*}{4\pi e^2 p_0(T^*)}$ is Debye radius. In this case concentration change in the close to surface layers (of the order of r_d wide) is much less than the concentration itself, hence it can be ignored (Fig. 2). The absolute charge values in the close to surface layers can be rather significant resulting in the origination of sufficiently large built-in fields. In the quasi-neutrality approximation continuous distribution of built-in field potential is replaced by its abrupt change at the interface (Fig. 3 and 4) and Poisson equation becomes unnecessary. Contact potential difference φ_0 is easily found from the condition of electrochemical potential constancy in the closed circuit

$$\varphi_0 - \frac{\mu_n^0(T^*) - \mu_m}{e} + \frac{\Delta\varepsilon_c}{e} = 0 \qquad (2)$$

Figure 2: Distribution of electron concentration in semiconductor near the contact with metal.

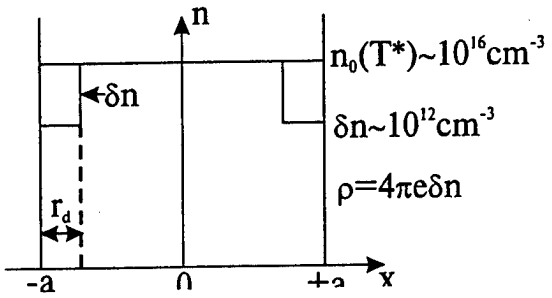


Figure 3: Similar to Fig. 1 after the establishment of equilibrium.

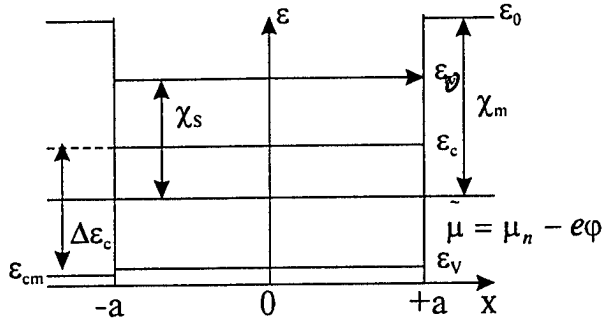
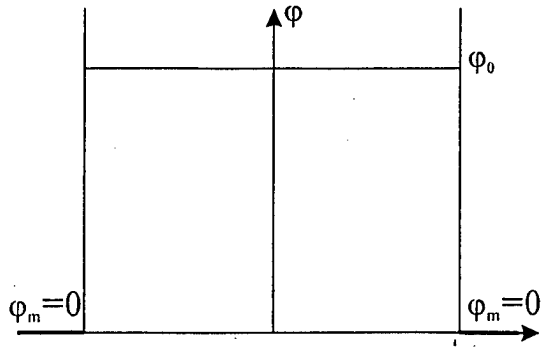


Figure 4: Distribution of built-in potential.



When writing the Eq. (2) it was taken into account that 1) chemical potential of metals is not changed with the establishment of equilibrium on the contact, 2) here and below $\varphi_m(-a) = 0$, 3) the energy reference points in metal and semiconductor are shifted relative each other by $\Delta\varepsilon_c$ (see Fig. 3). Then

$$\varphi_0 = \frac{1}{e}\left[\mu_n^0(T^*) - \mu_m - \Delta\varepsilon_c\right] \tag{3}$$

Bipolar Semiconductor in the Temperature Field.

Now we shall assume that temperature at point $x = -a$ is equal to T_1, and at point $x = +a$ it is equal to T_2. As long as chemical potential of metals is practically temperature independent, the changes in chemical potential and concentrations will concern only the semiconductor.

In the temperature field:

$$\begin{aligned}\mu_n^0(x) &= \mu_n^0(T^*) + \delta\mu_n^0(x)\\ \mu_p^0(x) &= \mu_p^0(T^*) + \delta\mu_p^0(x)\end{aligned} \tag{4}$$

As long as at this stage we do not take into account the possibility of carrier "overflow" from one semiconductor part to the other, here we deal with the "local" (at each point) equilibrium between electrons and holes, i.e.

$$\delta\mu_p^0(x) = -\delta\mu_n^0(x), \tag{5}$$

We must emphasize at once that at this stage there is no true equilibrium in the semiconductor. Really, chemical potential of electrons has become a coordinate function, while no electrical field has originated in the bulk of the sample, since there has been no electron and hole overflow inside the semiconductor and no space charge has originated.

At the same time the densities of surface charges on the planes $x = \pm a$ have changed, so that now inside the semiconductor we have:

$$\varphi_0(x) = \varphi_0 + \delta\varphi_0.$$

Metal potential at point $x = +a$ has also changed: $\varphi_m(+a) = \delta\varphi_m$. The values $\delta\varphi_0$ and $\delta\varphi_m$ are easily found from the condition of electrochemical potential continuity at points $x = \pm a$:

$$\delta\tilde{\varphi}_m(\pm a) = \delta\tilde{\varphi}_s(\pm a),$$

where $\tilde{\varphi}_m = \varphi_m - \frac{\mu_m}{e}$, $\tilde{\varphi}_s = \varphi - \frac{\mu_n}{e}$.

As a result, we have:

$$\delta\varphi_0 = \frac{1}{e}\delta\mu_n^0(-a) \qquad \delta\varphi_m = \frac{1}{e}\left[\delta\mu_n^0(-a) - \delta\mu_n^0(+a)\right] \tag{6}$$

Thus, at the given stage the first property of temperature field, namely generation of the "inhomogeneous" material has manifested itself.

At the third stage diffusion flows of electrons and holes originate (which tend to establish "equilibrium," i.e. to

make electrochemical potential constant in space). In so doing, naturally, a built-in thermoelectric field originates in the semiconductor. This situation is similar to the establishment of equilibrium in the inhomogeneously doped semiconductor. The only, though significant difference lies in the fact that in the inhomogeneously doped semiconductor we really have equilibrium, while in our case there is only the electrochemical potential equalization resulting in no true equilibrium due to the absence of temperature constancy.

Thus, diffusion of electrons and holes changes their chemical potentials as compared to Eq. (4), and

$$\begin{aligned} \mu_n^1(x) &= \mu_n^0(x) + \delta\mu_n^1(x) \\ \mu_p^1(x) &= \mu_p^0(x) + \delta\mu_p^1(x) \end{aligned} \tag{7}$$

and as long as we speak about the establishment of "equilibrium," there exists the relationship defined by Eq. (5). Then

$$\begin{aligned} n_1(x) = n_0(x) + \delta n_1 \qquad p_1(x) = p_0(x) + \delta p_1 \\ \varphi_1(x) = \varphi_0 + \delta\varphi_0 + \delta\varphi_1(x) \end{aligned}$$

Within the approximation of quasi-neutrality ($r_d \to 0$),

$$\delta n_1 = \delta p_1(x) = 0,$$

as long as all concentration changes will take place only in the space charge layers ($\propto r_d$), i.e. on the surface. Then

$$\delta\mu_n^1(x) = \delta\mu_p^1(x) = 0.$$

In this case the "equilibrium" condition (constancy of the electrochemical potential in space) is reduced to

$$\delta\mu_n^0 - e\delta\varphi_1(x) = C_0$$

from where

$$\delta\varphi_1(x) = -\frac{1}{e}\left[C_0 - \delta\mu_n^0(x)\right] \tag{8}$$

As long as chemical potential of metal is practically temperature independent, in the state of thermodynamic "equilibrium" the following conditions must be satisfied:

$$\delta\varphi_m^1(-a) = 0, \qquad \delta\varphi_m^1(+a) = -\delta\varphi_m(+a)$$

from where, using boundary conditions

$$\tilde{\varphi}_m(\pm a) = \tilde{\varphi}_n(\pm a)$$

we find that

$$C_0 = \delta\mu_n^0(-a).$$

Thus, the "equilibrium" concentration of electrons n_0 and holes p_0 which must appear in the expressions for space and surface recombination is determined by the Eq. (6).

The Basic Equations of Thermo-EMF Origination Theory and Their Solutions.

Now let us consider the second temperature field manifestation, namely, the force resulting in the quasi-particle movement. The usual expressions for the electron and hole currents in the presence of temperature gradient are as follows:

$$\begin{aligned} j_n &= \sigma_n\left[-\nabla\left(\varphi - \frac{\mu_n}{e}\right) - \alpha_n\nabla T\right] \\ j_p &= \sigma_p\left[-\nabla\left(\varphi + \frac{\mu_p}{e}\right) - \alpha_p\nabla T\right] \end{aligned} \tag{9}$$

The existence of the second components in the Eq. (9) leads to a new redistribution of concentrations attributable to thermal diffusion of carriers from the hot to the cold sample end:

$$\begin{aligned} n(x) &= n_0(x) + \delta n(x) \\ p(x) &= p_0(x) + \delta p(x) \end{aligned} \tag{10}$$

In this connection, there is also a change in space distributions of electron chemical potentials μ_n and hole chemical potentials μ_p.

$$\begin{aligned} \mu_n(x) &= \mu_n^0(x) + \delta\mu_n(x) \\ \mu_p(x) &= \mu_p^0(x) + \delta\mu_p(x) \end{aligned} \tag{11}$$

It is important to note that as long as both electrons and holes move from the hot to the cold sample end, their concentration near the heater will decrease, while near the refrigerator it will increase. It means that in a new stationary mode $\mu_p \neq -\varepsilon_g - \mu_n$ ($\delta\mu_p \neq -\delta\mu_n$), i.e. Fermi quasi-levels of the non-equilibrium (in the true sense of the word) electrons and holes appear.

According to the definition of Fermi levels, $\delta n(x)$, $\delta p(x)$ are obviously related to $\delta\mu_n(x)$, $\delta\mu_p(x)$:

$$\delta n(x) = \frac{n_0(T^*)}{T^*}\delta\mu_n(x) \qquad \delta p(x) = \frac{p_0(T^*)}{T^*}\delta\mu_p(x) \tag{12}$$

Space redistribution of electrons and holes will result in the change of coordinate dependence of potential $\varphi(x)$:

$$\varphi(x) = \varphi_0 + \delta\varphi_0 + \delta\varphi_1(x) + \delta\varphi(x) \tag{13}$$

and in the emergence of thermo-emf $\mathcal{E}$. It is obvious that the existence of non-equilibrium carriers will cause recombination processes. Then the expressions for the determination of δn, δp, $\delta\mu_n$, $\delta\mu_p$ and $\delta\varphi$ will take on the form:

$$\operatorname{div} j_n = 0, \qquad \operatorname{div} j_p = 0, \tag{14}$$

where the electron and hole recombination rates are, for simplisity, equal zero.

In the quasi-neutrality approximation $\delta n = \delta p$, $\delta\mu_p = \frac{n_0(T^*)}{p_0(T^*)}\delta\mu_n(x)$, and Poisson equation becomes unnecessary. The Eq. (14) can be rewritten as follows:

$$\begin{aligned} \frac{d^2\delta\varphi}{dx^2} - \frac{1}{e}\frac{d^2\delta\mu_n}{dx^2} = 0 \\ \frac{d^2\delta\varphi}{dx^2} + \frac{1}{e}\frac{n_0(T^*)}{p_0(T^*)}\frac{d^2\delta\mu_p}{dx^2} = 0 \end{aligned} \tag{15}$$

Note that thermoelectric coefficients α_n and α_p have fallen out of the Eq. (15).

The solution of the Eq. (15) is trivial:

$$\begin{aligned} \delta\mu_n &= C_1 x + C_2, \\ \delta\varphi &= C_3 x + C_4, \end{aligned} \tag{16}$$

To determine the constants C_i that are part of Eq. (16), one must lay down the boundary conditions on the planes $x = \pm a$, that take into account the surface recombination and the opportunity of current flow through the corresponding surfaces.

Boundary Conditions.

Let us consider the boundary of two conducting media in a one-dimensional model, when the electric current flows along the axis x. Then at the existence of electron and hole surface recombination we can write:

$$\begin{aligned} j_n(+0) - j_n(-0) &= eR_n^s \\ j_p(+0) - j_p(-0) &= -eR_p^s \end{aligned} \tag{17}$$

where R_n^s and R_p^s are the electron and hole surface recombination rates.

As long as $\operatorname{div} j_0 = 0$,

$$j_n(+0) + j_p(+0) = j_n(-0) + j_p(-0) = j_0,$$

we get a condition

$$R_n^s = R_p^s = R^s \tag{18}$$

In a quasi-neutrality approximation ($r_d \to 0$) recombination in the close to surface layers of the space charge of two contacting media is part of the surface recombination.

On the other hand, from Eq. (9), similar to Eq. (2), it is easy to get:

$$\begin{aligned} j_n(\pm 0) &= \sigma_n^s \{\tilde{\varphi}_n(-0) - \tilde{\varphi}_n(+0)\} \pm eR_{n\pm}^s \\ j_p(\pm 0) &= \sigma_p^s \{\tilde{\varphi}_p(-0) - \tilde{\varphi}_p(+0)\} \mp eR_{p\pm}^s \\ R_{p+}^s + R_{p-}^s &= R_p^s = R_{n+}^s + R_{n-}^s = R_n^s = R^s \end{aligned} \tag{19}$$

Here σ_n^s and σ_p^s are surface conductivities (conductivity of space charge layers).

Under the conditions considered one of the contacting media is bipolar semiconductor, while the other is metal, since in metals in virtue of high electron concentration δn can be assumed equal to zero, $\delta\mu_m = 0$ and no non-equilibrium carriers appear. It means that if semiconductor is on the left and metal is on the right, then (see Eq. (19)):

$$R_{n+}^s = R_{p+}^s = 0$$

and

$$R_{n-}^s = R_n^s = R_{p-}^s = R^s \tag{20}$$

In the simplest model of surface recombination

$$R^s = R_n^s = S_n \delta n|_{x=-0} = R_p^s = S_p \delta p|_{x=-0}, \tag{21}$$

and as long as in the quasi-neutrality approximation

$$\delta n|_{x=-0} = \delta p|_{x=-0},$$

we get:

$$S_n = S_p = S \tag{22}$$

Here S is the surface electron-hole recombination velocity.

Further, as long as holes do not pass to metal, the surface hole conductivity σ_p^s must be equal to zero (see the second Eq. (19) allowing for $j_p(+0) = 0$ and $R_{p+}^s = 0$.

$$\begin{aligned} j_n(\pm a) &= j_0 \mp eR_s^{\pm}, \qquad j_p(\pm a) = \pm eR_s^{\pm} \\ j_0 &= \pm\, \sigma_n^{s\pm} [\varphi_s(\pm a) - \varphi_m(\pm a)] \\ &\quad \mp \frac{\sigma_n^{s\pm}}{e} [\mu_n^s(\pm a) - \mu_m] \pm \frac{\sigma_n^{s\pm}}{e} \Delta\varepsilon_c \end{aligned} \tag{23}$$

Here index s refers to semiconductor, while m refers to metal,

$$R_s^{\pm} = S^{\pm} \delta n|_{x=\pm a}.$$

Besides, similar to the above,

$$\varphi_m(-a) = 0, \tag{24}$$

and

$$\varphi_m(+a) = V, \tag{25}$$

in so doing

$$V = j_0 R_v \tag{26}$$

Then thermal-emf of closed circuit $\mathcal{E}$ is equal to

$$\mathcal{E} = j_0 R, \tag{27}$$

where R is full resistance of closed circuit.

$$R = R_s + R_v + R_c,$$

$R_c = \frac{1}{\sigma_{n+}^S} + \frac{1}{\sigma_{n-}^S}$ is contact resistance. As regards the semiconductor resistance R_s, its value will be discussed later.

Further, as a simplification, it is assumed that

$$\sigma_n^{S+} = \sigma_n^{S-} = \sigma_n^S, \qquad S^+ = S^- = S$$

Note that in the boundary conditions defined by Eq. (23) there exist thermoelectric coefficients α_n and α_p (in the expressions for j_p^s and j_n^s).

Conclusions.

Substituting the Eq. (16) into the boundary conditions defined by Eqs. (23)-(27) it is easy to find the constants $C_{1,2,3,4}$, V, j_0 and $\mathcal{E}$.

We shall not bring here general answers in virtue of their awkwardness, but confine ourselves to the consideration of some specific and limiting cases.

If the resistance of connecting wires R_m is high as compared to R_s and R_c ($\sigma_m \to 0$, under no-load conditions), $j_0 = 0$, $V = \mathcal{E}$.

If, besides, the space or surface recombination is intensive enough

$$s \gg \frac{1}{\lambda^2 \tau a} \qquad \text{or} \qquad \tau^{-1} \gg \frac{1}{\lambda^2 \tau a^2}, \tag{28}$$

then

$$\delta n = \delta p = 0, \qquad \delta\mu_n = \delta\mu_p = 0, \qquad j_n = -j_p \neq 0,$$

and

$$\mathcal{E} = -\frac{\alpha_n\sigma_n + \alpha_p\sigma_p}{\sigma_n + \sigma_p} 2a\nabla T \tag{29}$$

i.e. we obtain the answer which coincides with the results of traditional theory. In so doing, naturally,

$$\nabla\left(\varphi - \frac{\mu_n^s}{e}\right) = \nabla\left(\varphi + \frac{\mu_p^s}{e}\right),$$

i.e. Fermi quasi-levels merge into a uniform Fermi level. In this case the semiconductor sample resistance R_s is determined by the standard expression $R_0 = \frac{2a}{\sigma_n + \sigma_p}$.

But if the circuit is open and recombination is inefficient

$$s, \frac{a}{\tau} \ll \frac{1}{\lambda^2 \tau a}, \tag{30}$$

then

$$\mathcal{E} = -2a\alpha_n \nabla T \tag{31}$$

i.e. it is only determined by electrons (even if it is a hole semiconductor). Here, naturally, $\delta n = \delta p \neq 0$, $\delta\mu_p \neq \delta\mu_n$ and $j_n = j_p = 0$. In this case the resistance R_s is equal to $R_s = \frac{2a}{\sigma_n}$.

If a short circuit is present ($\sigma_m \to \infty$, $V = 0$), then with a strong recombination the thermo-emf is still determined by the Eq. (29), and thermal flow is equal to

$$j_0 = -\frac{\alpha_n\sigma_n + \alpha_p\sigma_p}{\sigma_n + \sigma_p}\left(\frac{1}{a\sigma_n^s} + \frac{1}{\sigma_n + \sigma_p}\right)^{-1} \nabla T \tag{32}$$

In this case $j_n \neq 0$, $j_p \neq 0$.

But if no recombination is present, thermo-emf coincides with the Eq. (31) and thermal flow is equal to

$$j_0 = -\frac{\alpha_n \nabla T}{\frac{1}{\sigma_n} + \frac{1}{a\sigma_n^s}}, \tag{33}$$

in so doing, $j_p = 0$, $j_n = j_0$, i.e. all the dynamic processes are determined only by the electron gas.

In the monopolar case of n-type semiconductor irrespective of the recombination level the regular expression is present for thermo-emf:

$$\mathcal{E} = -\alpha_n 2a\nabla T \tag{34}$$

But if a hole semiconductor is used, then with a strong recombination we have

$$\mathcal{E} = -\alpha_p 2a\nabla T \tag{35}$$

i.e. thermo-emf is described by a general expression and with a weak recombination the Eq. (34) is present.

The above consideration has shown that the general expressions for thermo-emf and thermal flow in the bipolar and hole semiconductors are valid only at the existence of high recombination level. Note that within the traditional theory those expressions have been obtained ignoring recombination. With a weak recombination the hole current which is not found in metals does not exist in semiconductors either, and thermo-emf is constantly formed only by electrons.

The present work has been carried out with a partial support of CONACyT-México.

Crystal Structure and Thermoelectric Properties of the Mixed Layered Compounds of the $(GeTe)_n(Bi_2Te_3)_m$ Homologous Series

L.E.Shelimova[a], O.G.Karpinsky[a], M.A. Kretova[a], E.S.Avilov[a], J.-P.Fleurial[b]

a A.A.Baikov Institute of Metallurgy of Russian Academy of Sciences, Leninskii Pr-t 49, 117911 Moscow, Russia

b Jet Propulsion Laboratory/ California Institute of Technology, Pasadena, CA 91109, USA

Abstract

The initial members of the $(GeTe)_n(Bi_2Te_3)_m$ homologous series ($Ge_3Bi_2Te_6$, $GeBi_2Te_4$ and $GeBi_4Te_7$ compounds) have been investigated by X-ray diffraction study. High degree of lattice disorder is found in the melt-grown compounds. The dependences of the *a* and *c*/N parameters of the hexagonal lattices (N - number of layers per unit cell) on the cation-to-anion ratio have been analyzed for $nGeTe{\cdot}mBi_2Te_3$ compounds. These dependences were considered to be very close to linear. Based on these results, the lattice parameters were evaluated for another members of the homologous series for which experimental data are absent. A strong dependence of thermoelectric properties at 300 K on deviation from stoichiometry has been found for three above-mentioned compounds. All three compounds are characterized by extremely low lattice thermal conductivity what is probably related to high degree of disorder in cation sublattice as well as in anion one.

Introduction

An important class of the ternary layered compounds: $nA^{IV}B^{VI}{\cdot}mA_2^{V}B_3^{VI}$ (A^{IV} - Ge, Sn, Pb, A^{V} - Bi, Sb, B^{VI} - Se,Te) is known as tetradymite (Bi_2Te_2S)-like compounds with mixed layered structures. These compounds are formed in the $A^{IV}B^{VI}$ - $A_2^{V}B_3^{VI}$ quasi-binary systems and are interesting for thermoelectric applications.

The $nGeTe{\cdot}mBi_2Te_3$ compounds are the objects of the present work. Using electron diffraction and high-resolution electron microscopy, a homologous series of mixed-layer $(GeTe)_n(Bi_2Te_3)$ (n=1 to 9 and, may be to 18) [1] and $(Bi_2Te_3)_m(GeTe)$ (m=1 to, at least, 4) [2] compounds have recently been found in the GeTe-Bi_2Te_3 quasi-binary system.

A phase diagram of the GeTe-Bi_2Te_3 quasi-binary system has been constructed in [3]. According to [3], the $Ge_3Bi_2Te_6$ (A phase), $GeBi_2Te_4$ (B) and $GeBi_4Te_7$ (C) compounds are formed in the system by peritectic reactions.

The ternary compounds crystal structure has been investigated by electron diffraction of thin films [4-6]. The structures are represented by stacking of close-packed Te layers. The Ge and Bi atoms are distributed in octahedral interstices filling only a fraction of the cation positions. The atomic layers are arranged according ccp law. The number of the atomic layers per hexagonal unit cell is presented by the following equation: N = Z(2n + 5m), where Z is the number of molecules in the unit cell. The $Ge_3Bi_2Te_6$ unit cell contains three eleven-layer packets [4]. The $GeBi_2Te_4$ unit cell contains three seven-layer packets [5]. The $GeBi_4Te_7$ unit cell consists of twelve atomic layers [6]. The bonding between multi-layer packets is realized by weak van der Waals forces.

Experimental results and discussion

An isothermal section of the Ge-Bi-Te ternary system at 770 K has been constructed by metallography and X-ray diffraction study [7]. In addition to the known A, B, C homogeneity ranges, two new D and F phases have been found at this temperature. X-ray diffraction data for the ternary compounds are presented in Table 1. The F-phase has 39-layer structure. Its homogeneity range is probably displaced with respect to the $Ge_4Bi_2Te_7$ stoichiometric composition towards greater Bi/Ge ratio. This phase corresponds to the homologous series member with n=4, m=1.

Table 1
X-ray diffraction data for the ternary compounds in the GeTe-Bi_2Te_3 quasi-binary system

Composition	Space group	N	*a*, nm	*c*, nm
GeTe	$R3m$	6	0.4163	1.0657
$Ge_{3.7}Bi_{2.3}Te_7$ (F)		39	0.4265	7.328
$Ge_3Bi_2Te_6$ (A)	$R3m$	33	0.4268	6.264
$Ge_{1.5}Bi_{2.5}Te_5$ (D)	$P\bar{3}m1$	9	0.4305	1.7372
$GeBi_2Te_4$ (B)	$R\bar{3}m$	21	0.4322	4.127
$GeBi_4Te_7$ (C)	$P\bar{3}m1$	12	0.4348	2.392
Bi_2Te_3	$R\bar{3}m$	15	0.43835	3.0487

The intensity measurements for the $GeBi_2Te_4$ single crystal were completed by an automatic diffractometer "Syntex P1". The reliability index R=3.3% was reached for sixty reflections. The crystallographic data for B phase are presented in Table 2.

The interatomic distances are following: Me2-Te3 = 0.300, Me2-Te4 = 0.326, Me1-Te4 = 0.306, Te3-Te3 = 0.365 nm. The occupation factor is presented in atomic parts of the elements. It follows from occupation factors that the Ge and Bi atoms are statistically distributed in the octahedral interstices to form mixed-cation layers. In addition to disorder in the cation sublattice, the anti-structure defects were also discovered. The occupation

0-7803-4057-4/97 $10.00 ©1997 IEEE

factor data are very important as they give the direct information of the point defects which are responsible for conductivity type and carrier concentration.

Table 2
The atomic coordinates, occupation factors (μ), the equivalent positions (q) and isotropic temperature factors (B) for the $GeBi_2Te_4$ structure.

At.	x y z	μ	q	B
Me1	0 0 0	0.51Ge+0.49Bi	3a)	1.9
Me2	0 0 0.4273	0.65Bi+0.25Ge+ 0.10Te	6c)	1.5
Te3	0 0 0.1344	0.97Te+0.03Bi	6c)	1.3
Te4	0 0 0.2903	0.93Te+0.07Bi	6c)	1.1

The nine-layer lattice $Ge_2Bi_2Te_5$ (D) compound was not found earlier in [3] although there is information about the existence of the analogous compound in the GeTe-Sb_2Te_3 quasi-binary system [8]. In our work, a phase with the $Ge_2Sb_2Te_5$-type disorded structure was obtained for the $Ge_{1.5}Bi_{2.5}Te_5$ composition. The $Ge_{1.5}Bi_{2.5}Te_5$ single crystal structure was determined with the value R=4.8% for the 103 reflections. The crystallographic data for D phase are presented in Table 3. The interatomic distances are following: Me1-Te3 = 0.297, Me1-Te4 = 0.330, Me2-Te4 = 0.302, Me2-Te5 = 0.308, Te3-Te3 = 0.368 nm. It follows from the occupation factor data that mixed atomic layers exist in the $Ge_{1.5}Bi_{2.5}Te_5$ structure as well as in $GeBi_2Te_4$ one.

Table 3
The atomic coordinates, occupation factors (μ), the equivalent positions (q) and isotropic temperature factors (B) for D phase structure.

At.	x y z	μ	q	B
Me1	0 0 0.6716	0.63Bi+0.17Ge+ 0.20Te	2c)	3.7
Me2	2/3 1/3 0.8958	0.54Ge+0.46Bi	2d)	3.9
Te3	2/3 1/3 0.5779	0.96Te+0.04Ge	2d)	3.5
Te4	2/3 1/3 0.2035	0.94Te+0.06Bi	2d)	2.5
Te5	0 0 0	0.79Te+0.21Bi	1a)	3.1

An analysis of the $(GeTe)_n(Bi_2Te_3)_m$ homologous series structure demonstrates that the cation-to-anion ratio plays a fundamental role in the formation of the layered structures. The α-GeTe structure is formed when the cation-to-anion ratio (x) is equal to 1. The Bi_2Te_3 structure is formed when x is equal to 2/3. The layered ternary compounds have intermediate values of the cation-to-anion ratio. The lattice parameter dependences on the cation-to-anion ratio in the GeTe-Bi_2Te_3 system are presented in Fig. 1.

The *c*/N value is average distance between the two adjacent atomic layers. The use of *c*/N values lets to compare the *c* parameters of the compounds with the different number of layers per unit cell. The phase designations are accepted in the Fig.1 in accordance with [7]. The *a*(x) and *c*/N(x) dependences are very close to linear. These dependences may be represented by the following equations:

$$c(x) = (0.01514x^2 - 0.10214x + 0.26461)\ N,$$
$$a(x) = 0.179x^2 - 0.96x + 0.4942.$$

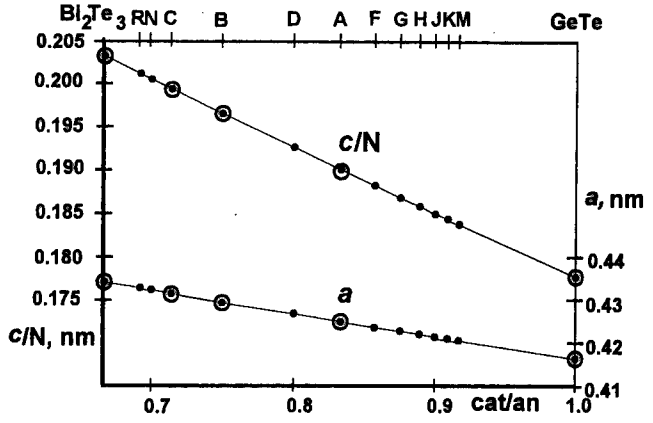


Fig.1 Dependences of the *a* parameter and the *c*/N average distance between the two adjacent atomic layers on the cation-to-anion ratio. Open circles are the experimental data, solid circles represent calculated values.

The existence of the almost linear *a*(x) and *c*(x) dependences for the complete range of x values (2/3 to 1.0) confirms the idea that all the ternary compounds structures are closely related. All the compounds are united by the same structural principle. The compounds are formed by the same structural units: the α-GeTe double-layer packet and the Bi_2Te_3 five-layer packet alternating orderly along the *c* direction. Based on the *c*/N(x) and *a*(x) dependences, the *a* and *c* values have been calculated [9] for high members of the $(GeTe)_n(Bi_2Te_3)_m$ homologous series for which experimental data were not reported.

Seebeck coefficient (α), electrical (σ) and thermal (κ) conductivity and Hall effect at 300 K have been measured for the initial members of the $(GeTe)_n(Bi_2Te_3)_m$ homologous series: $Ge_3Bi_2Te_6$, $GeBi_2Te_4$ and $GeBi_4Te_7$ compounds. The polycrystalline samples with different deviation from stoichiometry have been measured. The $Ge_3Bi_2Te_6$ compound has always p-type of conductivity. Thermoelectric properties of the $Ge_3Bi_2Te_6$ compound with different deviation from stoichiometry at 300 K are presented in Table 4. All the samples have rather low carrier mobility as well as the lattice thermal conductivity.

The density-of-states effective mass is calculated on the assumption that one type of carriers exists, the valence band is parabolic, and the basic mechanism of carrier

scattering is acoustic phonon scattering. The effective mass of holes in the $Ge_3Bi_2Te_6$ compound is about $m^*/m_0 \sim 1.2$ and does not practically depend on deviation from stoichiometry.

Table 4. Thermoelectric properties (300 K) of the $Ge_3Bi_2Te_6$ compound with different deviation from stoichiometry.*

Composition	$p \cdot 10^{-20}$, cm^{-3}	α, $\mu V/K$	σ, S/cm	μ	κ_{ph}
$Ge_{2.94}Bi_2Te_6$	3.3	48	1120	21	8.0
$Ge_3Bi_2Te_6$	1.9	62	600	20	8.0
$Ge_{3.06}Bi_2Te_6$	1.9	60	400	13	9.0
$Ge_3Bi_{2.04}Te_6$	1.6	65	510	20	7.0
$Ge_3Bi_2Te_{6.015}$	2.2	60	840	24	9.0
$Ge_3Bi_2Te_{6.05}$	3.5	45	1170	21	7.0

* In Table 4-6, μ ($cm^2/V \cdot s$) is Hall carrier mobility and κ_{ph} (mW/cm·K) is lattice thermal conductivity.

Thermoelectric properties at 300 K of the $GeBi_2Te_4$ compound with different deviation from stoichiometry are presented in Table 5. The samples with Bi or Ge excess have n-type of conductivity and high electron concentration. The samples with Te excess or Ge deficiency have p-type of conductivity. The effective mass of holes and electrons is equal to $0.6m_0$ and $0.8m_0$ in the $GeBi_2Te_4$ compound of p- and n-type of conductivity, correspondingly.

Based on above-mentioned X-ray diffraction data, any conclusions concerning to the nature of the predominant point defects in the $GeBi_2Te_4$ lattice have been made. The $Bi_{Ge}^{\bullet}$, $Ge_{Bi}^{'}$ substitution defects and the $Te_{Bi}^{\bullet}$, $Bi_{Te}^{'}$ anti-structure defects are probably the predominant point defects in the lattice. The electroneutrality condition may be represented by the following equation:
$n + [Bi_{Te}^{'}] + [Ge_{Bi}^{'}] \leftrightarrow p + [Bi_{Ge}^{\bullet}] + [Te_{Bi}^{\bullet}]$.
The $GeBi_2Te_4$ conductivity type is determined by the balance of the contribution of these point defects. The $GeBi_2Te_4$ lattice thermal conductivity is extremely low as well as the $Ge_3Bi_2Te_6$ one.

Table 5.
Thermoelectric properties (300 K) of $GeBi_2Te_4$ compound with different deviation from stoichiometry

Composition	$p(n) \cdot 10^{-19}$ cm^{-3}	α, $\mu V/K$	σ, S/cm	μ	κ_{ph}
$Ge_{0.96}Bi_2Te_4$	3.1	114	210	42	7.6
$Ge_{0.98}Bi_2Te_4$	9.0	76	320	22	8.0
$Ge_{1.02}Bi_2Te_4$	15.7	-51	378	15	8.0
$GeBi_{2.04}Te_4$	15.6	-75	250	10	9.0
$GeBi_2Te_{4.05}$	6.0	91	250	26	8.5

Seebeck coefficient decreases and electron concentration increases markedly in the $GeBi_4Te_7$ compound at Ge concentration growth (Table 6).

The effective mass of electrons in the $GeBi_4Te_7$ compound is about $m^*/m_0 \sim 0.9$ and weakly depends on deviation from stoichiometry.

The sharp increasing of electron concentration at Ge excess may be related to the incorporation into van der Waals gaps of excess Ge atoms acting as donors. The probability of the Ge excess atoms incorporation into van der Waals gaps is suggested to increase in the $nGeTe \cdot mBi_2Te_3$ compounds at the Bi_2Te_3 content growth as the percent of "empty" octahedrons in the lattices increases at the m/n ratio increasing.

Table 6
Thermoelectric properties (300 K) of $GeBi_4Te_7$ compound with different deviation from stoichiometry

Composition	$n \cdot 10^{-19}$ cm^{-3}	α, $\mu V/K$	σ, S/cm	μ	κ_{ph}
$Ge_{0.96}Bi_4Te_7$	2.4	-169	220	57	7.3
$GeBi_4Te_7$	4.0	-130	340	53	11.0
$Ge_{1.03}Bi_4Te_7$	9.5	-80	540	37	11.0
$Ge_{1.06}Bi_4Te_7$	20.0	-58	682	22	11.6
$GeBi_{4.10}Te_7$	35.0	-45	1100	20	16.0
$GeBi_4Te_{7.05}$	2.0	-180	130	41	9.4

Based on the carrier concentration change, it may be concluded that this particular mechanism of Ge incorporation into the lattice is not significant in the $Ge_3Bi_2Te_6$ compound but it is very probable in the $GeBi_2Te_4$ and $GeBi_4Te_7$ compound at Ge excess. It is worth to emphasize that the insertion of Ge excess atoms into van der Waals gaps between tetradymite-like five-layer packets in the Bi_2Te_3 compound was found earlier in [10] by X-ray diffraction study.

Conclusions

The cation-to-anion ratio (x) plays a fundamental role in the formation of the $nGeTe \cdot mBi_2Te_3$ layered structures. The *a* (x) and *c*/N(x) dependences are very close to linear what reflects the similarity of crystallographic constitution of the compounds. The substitution and anti-structure defects are probably the predominant point defects in the compounds lattices. The $Ge_3Bi_2Te_6$, $GeBi_2Te_4$ and $GeBi_4Te_7$ compounds have extremely low lattice thermal conductivity. The carrier mobility and μ/κ_{ph} ratio are not high, however, there is the possibility for optimization of the properties by the change of the composition and temperature.

Acknowledgements

This material is based upon work supported by the U.S. Civilian Research and Development Foundation under Award No RE1-262.

References

[1] S.Kuypers, G.van Tendeloo, J.van Landuyt and S.Amelinckx, " Electron Microscopic Study of the Homologous Series of Mixed Layer Compounds $R_2Te_3(GeTe)_n$ (R = Sb,Bi)", J. Solid State Chem., **76** (1988) 102.

[2] N.Frangis, S.Kuypers, C.Manolikas, J. van Landuyt and S.Amelinckx, "Continuous Series of One-dimensional Structures in the Compouds $Bi_{2+x}Se_3$, $Bi_{2+x}Te_3$, $Sb_{2+x}Te_3$, $(Bi_2Te_3)_nGeTe$ and $(Sb_2Te_3)_nGeTe$", Solid State Commun. **69** (1989) 817.

[3] N.Kh.Abrikosov and G.T.Danilova-Dobryakova, "Study of the Bi_2Te_3-GeTe Phase Diagram", Izv. AN SSSR, Neorg. Mater., **1** (1965) 57.

[4] I.I.Petrov and R.M.Imamov, "Crystal Structure of the $Ge_3Bi_2Te_6$ compound", Kristallographiya, **15** (1970) 168.

[5] Study of the $GeBi_2Te_4$ compound", Kristallographiya, **10** (1965) 109.

[6] K.A.Agaev, A.G.Talybov and S.A.Semiletov, "Electron Diffraction Study of the $GeBi_4Te_7$ compound", Kristallographiya, **13** (1968) 59.

[7] L.E.Shelimova, O.G.Karpinsky, M.A.Kretova and E.S.Avilov, "Phase Equilibria in the Ge-Bi-Te Ternary System at 570-770 K Temperature Range" J. Alloys and Compounds, **243** (1996) 194.

[8] N.Kh.Abrikosov and G.T.Danilova-Dobryakova, "Study of the Sb_2Te_3-GeTe Phase Diagram", Izv. AN SSSR, Neorg. Mater. **1** (1965) 204.

[9] O.G.Karpinsky, L.E.Shelimova, M.A.Kretova and J.-P.Fleurial, "X-ray Study of the nGeTe mBi_2Te_3 Mixed Layered Tetradymite-like Compounds", J. Alloys and Compounds, in press.

[10] M. Predota, L.Benes and J.Horak, "On the Incorporation of Germanium Atoms into the Bi_2Te_3 Crystal Lattice", Phys. Status Solidi (a) **100** (1987) 401.

Transport Properties of ZrNiSn-Based Intermetallics

Ctirad Uher, Siqing Hu, Jihui Yang
Department of Physics, University of Michigan, Ann Arbor, MI 48109, USA
Gregory P. Meisner and Donald T. Morelli
Physics and Physical Chemistry Department, GM Research and Development Center, Warren, MI 48090, USA

Abstract

Intermetallic compounds of the form MNiSn, where M is titanium, zirconium, or hafnium, are semiconductors with band gaps on the order of 0.2 electron volts. Due to their large conduction band masses, they show promise as thermoelectric materials with high figure of merit. In order to assess this potential, we have studied the thermoelectric properties of pure and doped ZrNiSn and $Zr_{0.5}Hf_{0.5}NiSn$ mixed crystals. Upon doping with Sb the resistivity can be reduced by a factor of 20-40 with a reduction in the Seebeck coefficient of only a factor of two. The resulting power factors of doped samples at room temperature are comparable to those of state of the art thermoelectric materials. The thermal conductivity of $Zr_{0.5}Hf_{0.5}NiSn$ is reduced strongly relative to ZrNiSn but must be reduced further to obtain a large figure of merit. The transport properties of these materials are very sensitive to annealing conditions.

Introduction

Over the past couple of years, several semiconducting systems with unique structural properties have attracted considerable attention and have become the focus of an intensive search for novel thermoelectric materials. This category of solids encompasses 2-dimensional quantum well structures for which record-high figures of merit are predicted [1] and bulk materials such as skutterudites [2]. The latter are characterized by the open "cage" structure which can be filled with appropriate foreign species that dramatically alter the phonon and carrier dynamics and such filled skutterudites then approach the desirable "phonon glass, electron crystal" characteristics [3].

Unique structural features are also manifested by a class of semiconducting intermetallics of composition MNiSn (M = Ti, Zr, Hf) that crystallize with the fcc MgAgAs structure and are often referred to as the half-Heusler intermetallics. This interesting structure consists of four interpenetrating fcc sublattices, one of which contains empty lattice sites. Such a vacancy sublattice reflects the missing atoms of Ni of the directly related Heusler intermetallics of the composition MNi_2Sn that are good metals and thus of no interest to thermoelectricity.

Earlier studies by Aliev et al. [4] established the semiconducting nature of transport with the experimental band gap of 0.1-0.2 eV, surprisingly large thermopower, low electrical resistivity but a modestly large thermal conductivity. Subsequent ab initio pseudopotential total-energy and band-structure calculations by Ögüt and Rabe [5] have shed light on the origin of the semiconducting gap and on the stability of the structure. With this as a background, the potential of RNiSn compounds as novel thermoelectric materials has been noted and some early data were reported by Cook et al. [6] and Hohl et al. [7] at recent conferences on thermoelectricity.

In our work we concentrate on the study of ZrNiSn and we explore the effect of substitutional disorder at various sublattices on the three important transport parameters that determine the thermoelectric figure of merit: electrical resistivity, thermal conductivity and thermopower. In addition, where relevant, we note the carrier density and mobility obtained from Hall measurements. We demonstrate that, by appropriate alloying, the thermal conductivity can be drastically depressed while by suitable doping one can control the electrical resistivity over at least two orders of its magnitude. Although our measurements are limited to temperatures not exceeding the ambient, it is clear that the half-Heusler intermetallics hold promise as thermoelectric materials for operation at the intermediate temperatures in the range 200-400C.

Materials and Experimental Technique

Samples for this investigation were prepared from high purity elements using arc-melting under an argon atmosphere. X-ray analysis of small sections of the as-prepared material revealed an essentially single phase structure with only a minute trace of a second phase. Upon annealing at 800 C, the second phase disappears completely. Samples with typical dimensions $2\times3\times8$ mm^3 were subjected to annealing treatment for either 2 days or 3 weeks. Measurements were made over the temperature range of 2-300K in a cryostat equipped with a radiation shield. Longitudinal steady-state technique was used to determine the thermal transport parameters. Hall effect data were generated over the same temperature range using a four-probe ac technique in a superconducting magnet cryostat capable of fields up to 5 Tesla.

Results and Discussion

Table 1 summarizes the relevant room-temperature transport parameters of the samples studied. It is immediately apparent that annealing has a strong influence on all transport properties. Structural improvement upon annealing of ZrNiSn is gleaned from the overall higher values of the thermal conductivity and especially from its magnitude at the dielectric peak, see Fig.1. We note that throughout the temperature range studied, the thermal conductivity of ZrNiSn and its alloys is essentially all due to lattice vibrations, the electronic term accounting for no more than 1-2% of the total heat flow. The time honored method of reducing the thermal conductivity by forming isostructural alloys is quite effective here too as demonstrated by a strong suppression of heat conduction in $Zr_{0.5}Hf_{0.5}NiSn$ samples, note the different scales in Fig.2 in comparison to Fig.1.

0-7803-4057-4/97 $10.00 ©1997 IEEE

Sample	ρ (mΩ-cm)	κ (mW/cm-K)	S (μV/K)	n (10^{20}cm^{-3})	μ_H(cm^2/V-s)
ZrNiSn	5.1	59.2	-167	1.84	6.7
ZrNiSn(*)	11.3	85.5	-171	0.90	6.1
ZrNiSn(**)	29.3	159.7	-226	0.80	2.7
$Zr_{0.5}Hf_{0.5}NiSn$	10.5	46.1	-136	1.00	6.0
$Zr_{0.5}Hf_{0.5}NiSn$(*)	16.1	42.7	-142	0.39	10.0
$Zr_{0.5}Hf_{0.5}NiSn$(**)	31.0	55.3	-223	0.30	6.8
$Zr_{0.5}Hf_{0.5}NiSb_{0.005}Sn_{0.995}$(**)	1.64	59.1	-194	1.32	28.8
$Zr_{0.5}Hf_{0.5}NiSb_{0.01}Sn_{0.99}$(**)	0.78	65.8	-147	2.12	37.9

Table 1: Room temperature values of the transport parameters. Samples without an asterisk were subjected to no annealing treatment. Samples marked with a single asterisk were annealed for 2 days, those with two asterisks were annealed for a 3-week period.

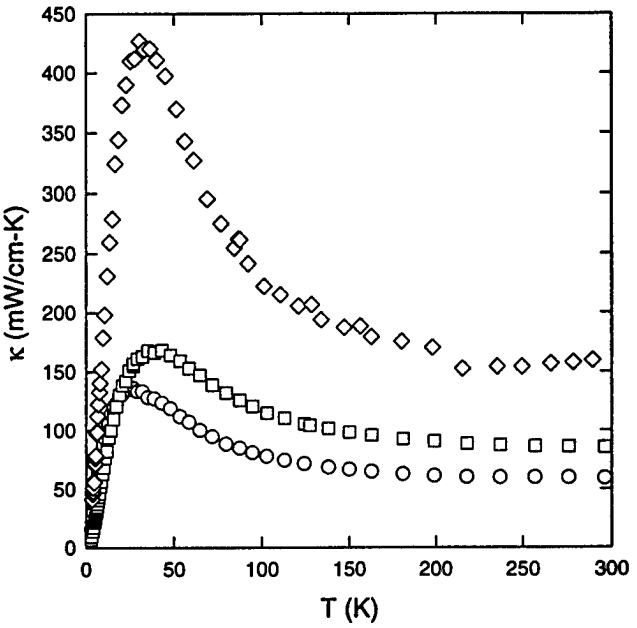


Figure 1: Thermal conductivity of ZrNiSn
- ○ as-prepared, no annealing
- □ 2 days at 800°C
- ◊ 3 weeks at 800°C

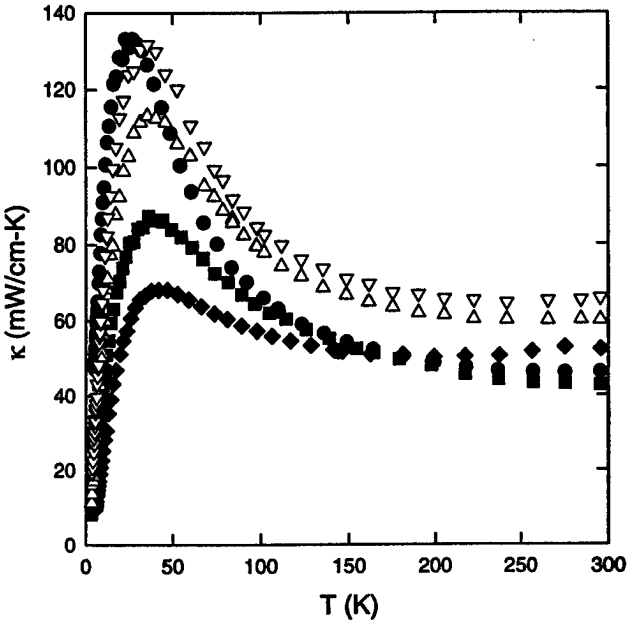


Figure 2: Thermal conductivity of $Zr_{0.5}Hf_{0.5}NiSn$
- ● as-prepared, no annealing
- ■ 2 days at 800°C
- ◆ 3 weeks at 800°C
- Δ $Zr_{0.5}Hf_{0.5}NiSb_{0.005}Sn_{0.995}$
- ∇ $Zr_{0.5}Hf_{0.5}NiSb_{0.01}Sn_{0.99}$

Furthermore, annealing appears to have an opposite effect on the alloys than on the pure compounds: with a prolonged annealing the thermal conductivity of the alloys decreases and, after three weeks at 800°C, the peak in the thermal conductivity is barely resolved. Movement of the Zr and Hf atoms during the heat treatment leads to a matrix that scatters phonons more effectively than that in the alloy subjected to no heat treatment. Further reduction of the thermal conductivity is desirable and it might possibly come from employing alloy scattering on the other two occupied sublattices.

Large thermopower of the half-Heusler intermetallics near and above the ambient temperature is perhaps the main reason why these compounds attracted attention as potentially useful thermoelectrics. With the room temperature values approaching -250 μV/K for well annealed specimens and even larger thermopower projected above 300K, see Figs. 3 and 4, one of the essential requirements for a good thermoelectric - large thermopower- is in these compounds readily satisfied. While the thermopower is sensitive to the annealing treatment, its magnitude is not compromised by forming isoelectronic alloys on the Zr sublattice. Perhaps the most intriguing feature of the thermopower is its temperature dependence. It is remarkable that the thermopower displays a typically metal-like behavior with a very weak temperature dependence and the magnitude on the order of or less than 1 μV/K up to at least 120K and then, above 150K, a sudden and rapid increase sets in and the thermopower quickly attains semiconductor-like values. The data on ZrNiSn and

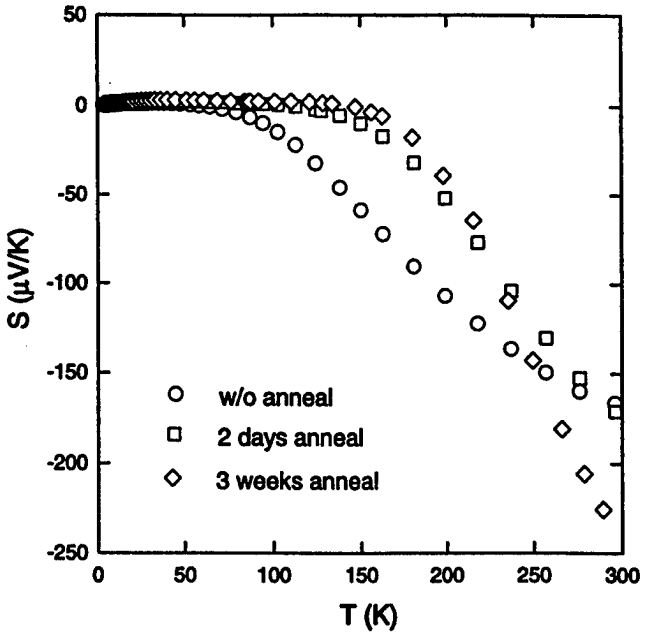


Figure 3: Thermopower of ZrNiSn

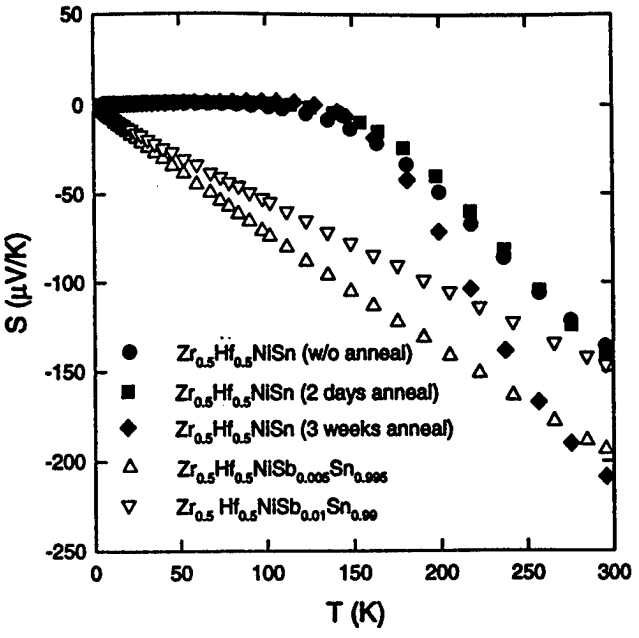


Figure 4: Thermopower of $Zr_{0.5}Hf_{0.5}NiSn$ alloys

on $Zr_{0.5}Hf_{0.5}NiSn$ clearly hint at some kind of metal (semimetal) - semiconductor transition in the vicinity of 150K. Upon doping with a rather minute amount of antimony on the tin sublattice, the thermopower acquires a substantially linear dependence, large magnitudes over the entire temperature range, and qualitatively different character.

The behavior of the electrical resistivity epitomizes the nature of the transport discussed above. Temperature dependence of the resistivity of ZrNiSn and its alloys attests to fundamentally different mechanisms of transport governing the low and high temperature domains and the changeover from the metal-like conduction to the region with a negative temperature coefficient of resistivity correlates well with the features noted in the behavior of the thermopower. Furthermore, while the resistivity of the as-prepared and two-days annealed samples of ZrNiSn and $Zr_{0.5}Hf_{0.5}NiSn$ are all comparable, the behavior of the well annealed ZrNiSn is very different from that of the well annealed $Zr_{0.5}Hf_{0.5}NiSn$. The latter never attains a metal-like character at low temperatures and its high resistivity reflects a strongly dissipative structural matrix noted in the context of a surprisingly low thermal conductivity measured on this sample in Fig.2.

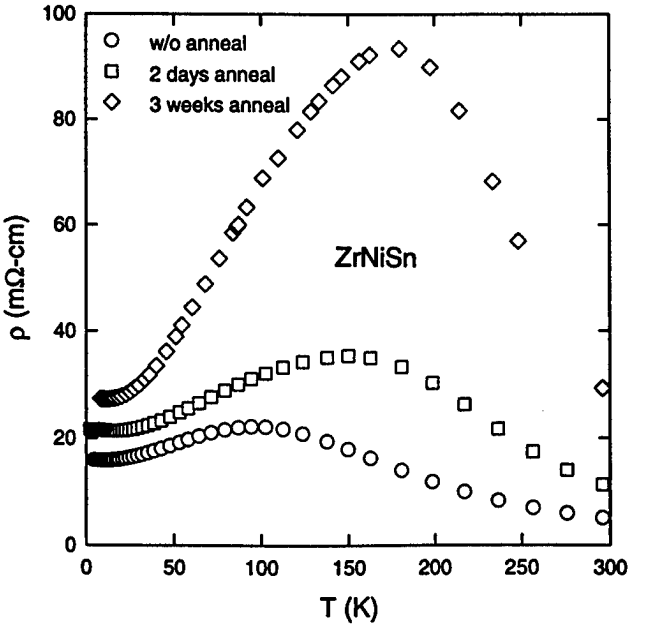


Figure 5: Electrical resistivity of ZrNiSn

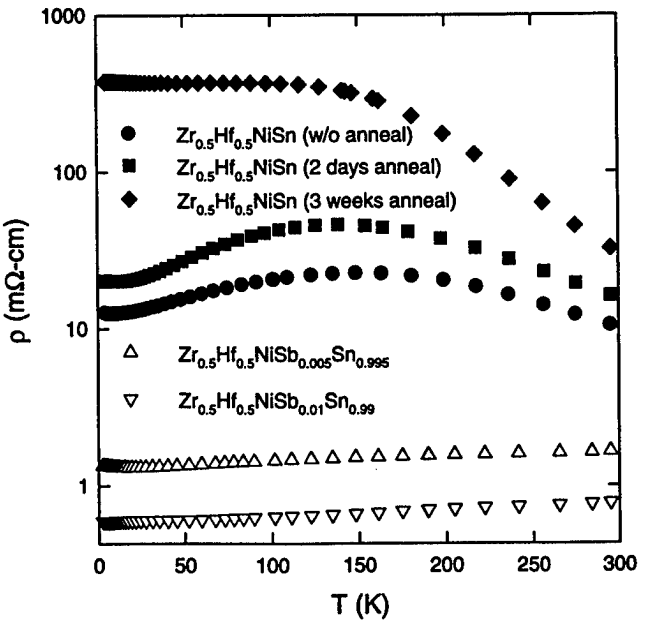


Figure 6: Electrical resistivity of $Zr_{0.5}Hf_{0.5}NiSn$ alloys

The most exciting feature from the perspective of thermoelectricity is a low resistivity displayed in Fig.4 for the weakly Sb-doped alloys. Being able to alter the resistivity over nearly two decades of its magnitude and, at the same time, preserving respectable values of the thermopower, is a very encouraging finding of this study. We note that the power factor, $P = S^2/\rho$, where ρ is the electrical resistivity and S the thermopower, at 300K reaches values of 23 and 28 $\mu W/cm\text{-}K^2$ for the $x = 0.005$ and 0.01 antimony doping concentrations, respectively. Such values are comparable to the best values obtained on the state-of -the-art thermoelectric materials.

From the thermopower and carrier density we estimate the corresponding effective masses for the two Sb-doped samples as $m^*=5.4$ ($x=0.005$) and $m^*=5.0$ ($x=0.01$). From the data in Table 1 it follows that the carrier density decreases upon annealing. For a well annealed sample of ZrNiSn in the temperature range down to 160K, the field dependence of the Hall resistivity is a linear function of the magnetic field with a rapidly diminishing slope, see Fig. 7. This implies that the Hall coefficient is field independent, a single carrier (electron) model appropriately describes the charge transport, and the carrier density rapidly rises as the temperature decreases. Below 150K, the Hall signal becomes very difficult to detect.

The nature of this metallic state, its dependence on annealing, and ultimately its influence on the nature of transport in this system deserves further detailed experimental and theoretical scrutiny.

The authors wish to acknowledge Charles Murphy for experimental assistance. The work was supported by the ONR Grant N00014–96–1–0181.

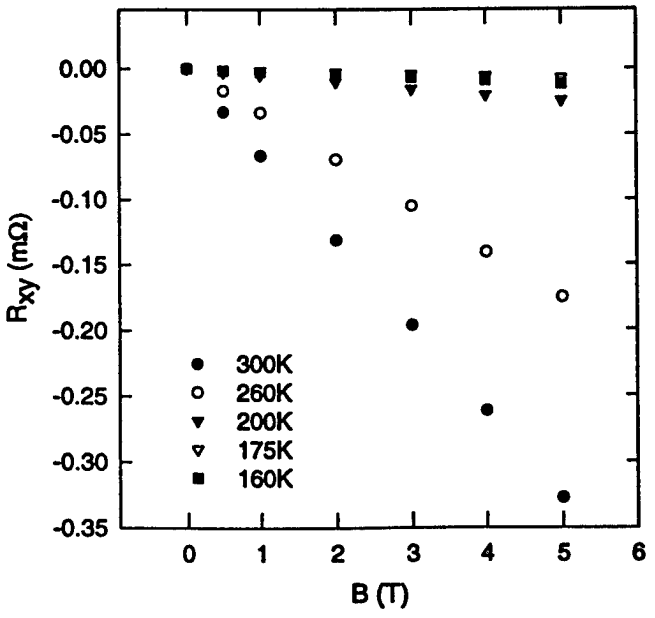


Figure 7: Field dependence of the Hall resistivity for a well annealed ZrNiSn.

References

[1] L.D. Hicks and M.S. Dresselhaus, "The effect of quantum well structures on the thermoelectric figure of merit", Phys. Rev. B47 (1993) 12727.

[2] J.-P. Fleurial, T. Caillat, and A. Borshchevsky, "Skutterudites: a new class of promising thermoelectric materials", Proc. of the XIII Intl. Conf. on Thermoelectrics, Kansas City, MO, USA, AIP Press NO. 316, (1995) 40.

[3] G.A. Slack, in *Thermoelectric Handbook* (CRC Press, Boca Raton, FL) (1995).

[4] F.G. Aliev, N.B. Brandt, V.V. Moshchalkov, V.V. Kozyrkov, R.V. Skolozdra, and A.I. Belogorokhov, "Gap at the fermi level in the intermetallic vacancy system RNiSn (R=Ti,Zr,Hf)", Z. Phys. B - Condensed Matter 75 (1989) 167.

[5] S. Ögüt and K.M. Rabe, "Band gap and stability in the ternary intermetallic compounds", Phys. Rev. B51 (1995) 10443.

[6] B.A. Cook, J.L. Harringa, Z.S. Tan, and W.A. Jesser, "TiNiSn: A gateway to the (1,1,1) intermetallic compounds", Proc. XV Intl. Conf. on Thermoelectrics, Pasadena, CA, March 26-29, 1996, IEEE Catlog Number 96TH8169, p. 122.

[7] H. Hohl, A.P. Ramirez, W. Kaefer, K. Fess, Ch. Thurner, Ch. Kloc, and E. Bucher, "A new class of materials with promising thermoelectric properties: MNiSn (M=Ti,Zr,Hf)", Abstracts of 1997 Spring Meeting of the Materials Research Society, San Francisco, CA, (1997) p. 291.

Thermoelectric properties of MNiSn (M=Ti, Zr, Hf) single crystals and related alloys

W. Käfer, K. Fess, Ch. Kloc, K. Friemelt, and E. Bucher
Universität Konstanz, P.O. Box X916, D-78457 Konstanz, Germany,
Tel.: +49/7531/88-3174, Fax: +49/7531/88-3895, e-mail:wolfgang.kaefer@uni-konstanz.de

Abstract
During the last few years a growing interest in new material classes for thermoelectric applications, such as intermetallic compounds, could be observed. Among others, the compounds MNiSn (where M=Ti, Zr, Hf) represent one of those systems and prompted us to study their properties thoroughly.
In contrast to the commonly used arc melting followed by long time heat treatment, we prepared our samples by melting the elements using a Sn flux technique [1].
The composition and structural quality was checked by different techniques, including x-ray diffraction and energy dispersive x-ray analysis EDX.
We determined the thermoelectric properties over a wide temperature range and were able to evaluate the figure of merit in the range between 90 and 360 K.
To reduce the thermal conductivity the possibility of alloying these ternaries was explored.

Introduction
MNiSn compounds crystallize in the MgAgAs structure and are characterized by the existence of a gap or pseudo-gap in the density of states at the Fermi level [2-4]. The magnitudes of the energy gaps [2] at RT are in sufficient agreement with the value 10 k_BT demanded for a high „figure of merit" [5-7].
Additionally the bonding in MNiSn seems to be covalent [8] and therefore the MNiSn compounds meet one of the criteria for the development of new thermoelectric materials recently discussed [7].

Experimental Procedure
Phase diagrams, melting points and the stoichiometric or nonstoichiometric character of the MNiSn compounds are still unknown. To obtain single crystals of these materials we used a Sn flux technique with stoichiometric amounts of Ti (Zr, Hf) and Ni and a five- to tenfold Sn surplus. Crystals were grown by flux technique in a two zone furnace or by Bridgman and Czochralski method.

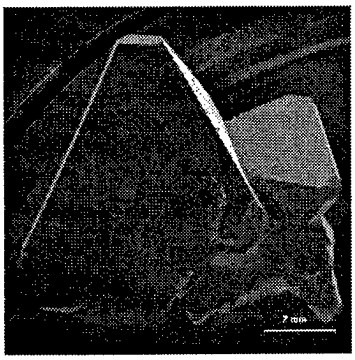


Fig. 1: ZrNiSn single crystal.

For all methods we used a maximum temperature of 1400 °C and varied cool down rates and growth velocity. Excess Sn could be removed by etching in HCl.
We obtained single crystals of TiNiSn and ZrNiSn up to dimensions between 8 and 10 mm, for HfNiSn in the range of 2 mm, respectively (Fig. 1). The composition and structural quality was checked by x-ray diffraction and EDX, where no secondary phases or indication of nonstoichiometrie were found. Moreover optical and EDX measurements carried out on polished samples did not show any inclusions of Sn.
The resistivity ρ and the Hall-coefficient were determined in the temperature range from 30 K to 400 K in a dc magnetic field of 0.6 T using a standard five-point technique.
Thermopower S and thermal conductivity λ were measured in the ranges from 90 to 400 K and 80 to 360 K, respectively. To obtain data for λ a steady state axial heat flow method was used.
To reduce the thermal conductivity of the pure ternaries, we made efforts to grow $Ti_{0.5}Zr_{0.5}NiSn$ and $Zr_{0.5}Hf_{0.5}NiSn$.

Results and Discussion
The temperature dependence of the resistivity for TiNiSn clearly shows two different behaviors depending on the sample. TiNiSn #2 and #4, which were grown in a two zone furnace with different cool down rates, exhibit a nearly temperature independent metallic slope. In contrast to this TiNiSn #5 , which was obtained by Bridgman method, shows an activated semiconductor like behavior (Fig. 2).

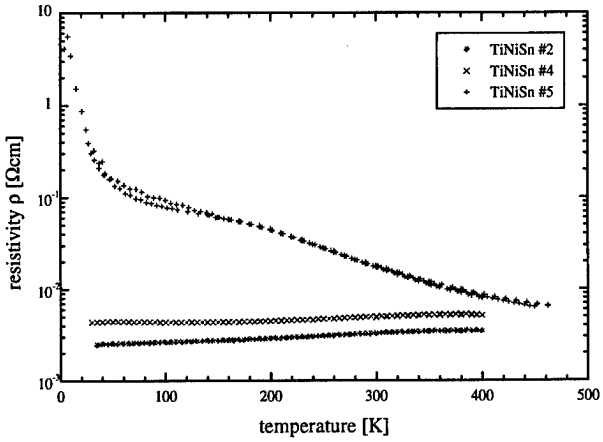


Fig. 2: Resistivity of TiNiSn as function of temperature .

The Hall-mobilities of all three samples reach a maximum of about 60 $cm^2/(Vs)$ between 100 and 200 K and decrease as T^{-r} (where r = 0.7) for higher temperatures.
TiNiSn shows n-type conductivity. The carrier concentrations for both #2 and #4 are temperature independent and in the

order of $3 \cdot 10^{19}$ cm^{-3} to $4 \cdot 10^{19}$ cm^{-3}. For TiNiSn #5 activation energies of 8 and 175 meV for low and high temperatures could be determined, according to $n \approx T^{3/2} \exp[-E_g/(k_B T)]$. The carrier concentration at room temperature is $1 \cdot 10^{19}$ cm^{-3}.
For ZrNiSn a similar situation was found. The Bridgman sample ZrNiSn #2 shows a semiconductor like temperature dependence, while for #1 and #13, which were obtained using the two zone furnace, the resistivity slightly increases with increasing temperature (Fig. 3).

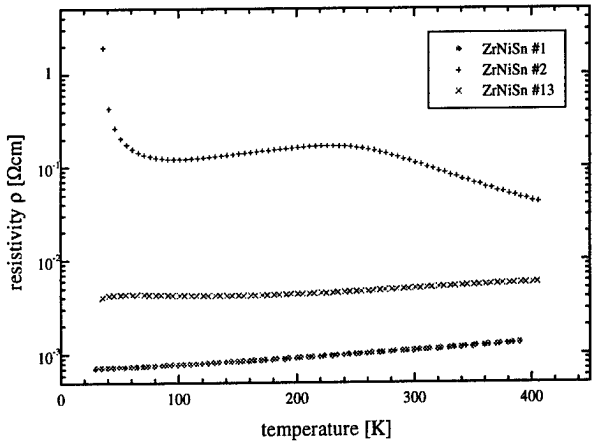


Fig. 3: Resistivity of ZrNiSn as function of temperature.

The maximum values of the Hall-mobility are between 125 and 300 cm^2/(Vs) for #1 and #2 respectively. In the high temperature range the Hall-mobility decreases with increasing temperature as T^r (where r = 1.4).
The concentration of the charge carriers for ZrNiSn #2 shows two activated regions with energies of 11 and 285 meV. The room temperature values for the carrier concentrations are $6 \cdot 10^{19}$ cm^{-3} for #1, $7 \cdot 10^{17}$ cm^{-3} for #2 and $8 \cdot 10^{18}$ cm^{-3} for #13. Therefore with carrier concentrations comparable to those in TiNiSn the higher mobilities in ZrNiSn lead to significant lower resistivities.
The two activation energies of 175 and 285 meV differ from previous reported values of 120 and 186 meV for TiNiSn and ZrNiSn found from analysis of temperature dependent conductivity measurements [2]. However these values are in reasonable agreement with the results found from optical measurements [2].

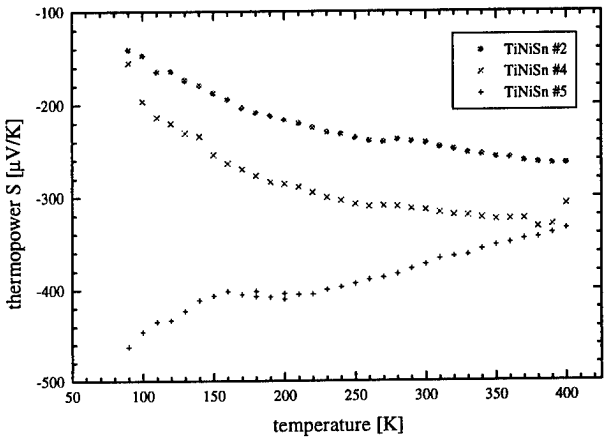


Fig. 4: Thermopower of TiNiSn.

The thermopowers of TiNiSn and ZrNiSn are represented in Fig. 4 and Fig. 5.

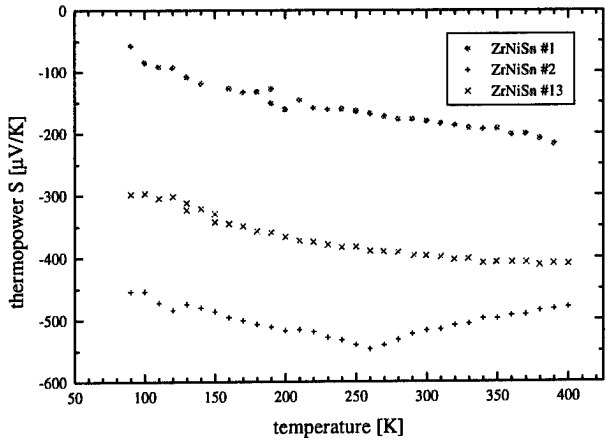


Fig. 5: Thermopower of ZrNiSn.

The Seebeck-coefficient is negative, confirming the carrier type found from Hall-data. The examined curves can be explained using either the model of a completely (TiNiSn #5, ZrNiSn #2) or weakly degenerate semiconductor. Comparing the observed thermopowers with calculations, using the scattering parameters found through Hall-measurements, the values of the effective masses can be estimated. This leads to the very high values of $m^* = 1.4\ m_0$ and $m^* = 1.5\ m_0$ for TiNiSn and ZrNiSn, respectively.
To summarize these results the power factors $S^2\sigma$ of TiNiSn and ZrNiSn are given in Fig. 6.

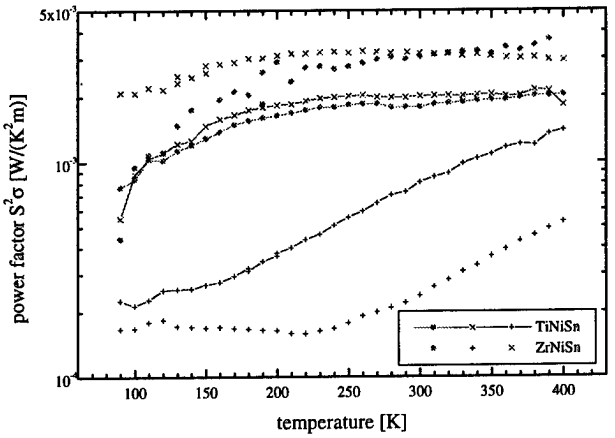


Fig. 6: Power factors of TiNiSn and ZrNiSn. The symbols used to mark different samples correspond with the previous notation.

A maximum power factor of $3.5 \cdot 10^{-3}$ W/(K^{2}m) is reached for ZrNiSn.
HfNiSn crystals were obtained using the flux technique in a two zone furnace. In this case the resistivity of HfNiSn shows a metallic temperature behavior.
The Hall-mobility reaches a maximum of about 80 cm^2/(Vs) and decreases as T^{-r} (where r = 0.7) for higher temperatures.
The charge carrier concentration is nearly temperature independent with a room temperature value of $5.9 \cdot 10^{19}$ cm^{-3}.
The thermopower shows the behavior of a weakly degenerate semiconductor. Taking into account a scattering factor of

r = -1/2 according to Hall-data, an effective carrier mass of $m^* = 0.9\ m_0$ can be estimated.
The results for HfNiSn are collected in Fig. 7.

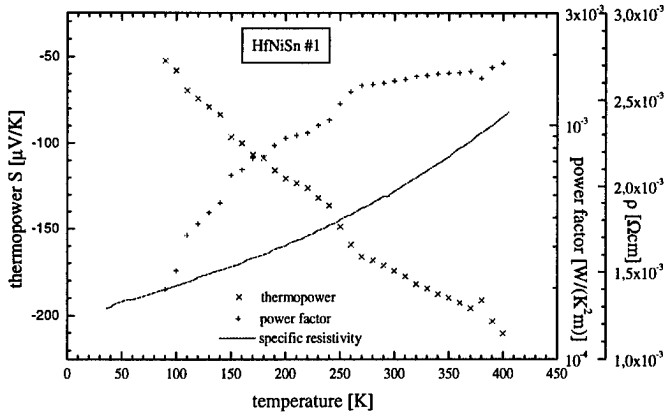


Fig.7: Resistivity, thermopower and power factor of HfNiSn.

For this particular sample of HfNiSn the maximum power factor reached is $1.8 \cdot 10^{-3}$ W/(K²m).
To complete the thermoelectric analysis of MNiSn the thermal conductivities of TiNiSn and ZrNiSn are depicted in Fig. 8.

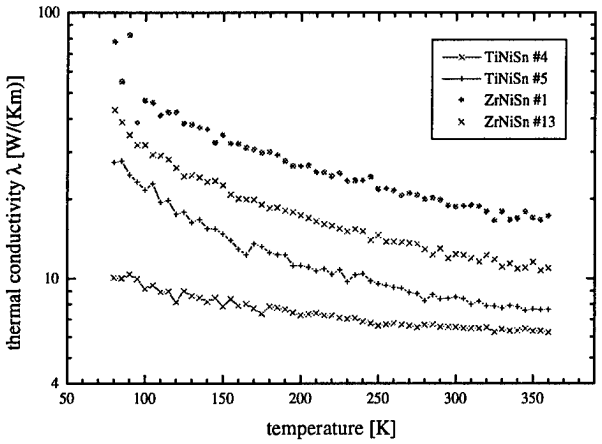


Fig. 8: Thermal conductivities of TiNiSn and ZrNiSn.

TiNiSn #2, ZrNiSn #2 and HfNiSn #1 were omitted, because the crystals did not reach the minimum dimensions of 5 mm requested for thermal conductivity measurements.
The temperature dependencies of λ as well as the comparison with the electrical conductivities show that the thermal conductivity in both TiNiSn and ZrNiSn is dominated by lattice contributions. ZrNiSn clearly exhibits higher values than TiNiSn, balancing the advantage gained in electrical conductivity and thermopower.
To conclude the „figure of merit" $Z = S^2\sigma/\lambda$ for both compounds is given in Fig. 9.
For all samples under investigation the „figure of merit" increases with increasing temperature and seems to saturate around 400 K. The highest Z is reached by TiNiSn #2 with $Z = 3.3 \cdot 10^{-4}$ 1/K.

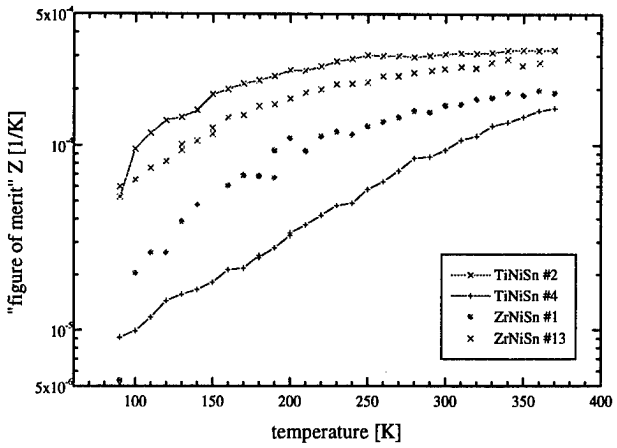


Fig. 9: „Figure of merit" of TiNiSn and ZrNiSn.

Keeping in mind the power factors obtained for the samples missing in this diagram, it is not likely to obtain higher values for one of them.
To reduce the thermal conductivity and thereby taking advantage of the high power factors, especially of ZrNiSn we made efforts to grow $Ti_{0.5}Zr_{0.5}NiSn$ and $Zr_{0.5}Hf_{0.5}NiSn$. In the first case we gained crystals with dimensions up to 6 mm, however the replacement of Zr by Hf was not successful. In both cases we used the flux technique in a two zone furnace to grow the alloys.
X-ray diffraction measurements carried out on $Ti_{0.5}Zr_{0.5}NiSn$ crystals which were ground before, indicated two different cubic phases with lattice parameters a = 5.954 Å and 6.022 Å. For TiNiSn and ZrNiSn we obtained values of 5.924 Å and 6.105 Å, respectively. Taking into account only the lattice parameters, this is a first hint that one phase lies close to TiNiSn, the other corresponds to $Ti_{0.5}Zr_{0.5}NiSn$. This suggestion could be verified using EDX measurements. Powder and single crystal x-ray diffraction carried out on particular crystals, showed that each specimen belonged either to one or the other phase. For the „TiNiSn" samples EDX yields approximately $Ti_{0.8}Zr_{0.2}NiSn$.
Temperature dependent resistivity measurements are shown in Fig. 10 together with TiNiSn #5.

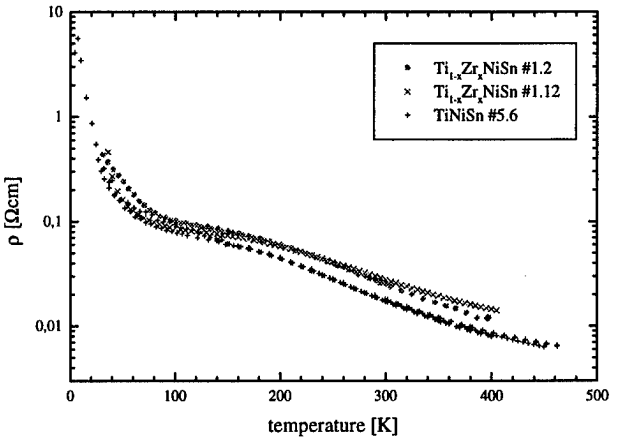


Fig. 10: Resistivity of $Ti_{1-x}Zr_xNiSn$ as function of temperature.

Both mixed samples show an activated behavior. From analysis of Hall-data the activation energies can be stated as 5 and 170 meV and 11 and 205 meV for $Ti_{0.8}Zr_{0.2}NiSn$ #1 and $Ti_{0.5}Zr_{0.5}NiSn$ #1, respectively.
Thermopower and power factor for this system are given in Fig. 11.

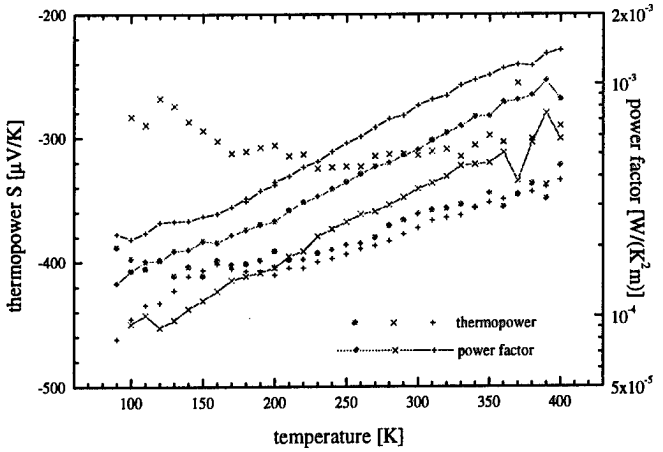


Fig. 11: Thermopower and power factor of $Ti_{1-x}Zr_xNiSn$ and TiNiSn #5. The symbols used to mark different samples correspond with the previous notation.

Nondegenerate and weakly degenerate behavior can be observed. The nearly perfect agreement of $Ti_{0.8}Zr_{0.2}NiSn$ #1 with TiNiSn #5 is remarkable and confirms the close relation of these samples.
The maximum power factor gained for the alloys is about three times smaller in comparison to the pure compounds.
To complete the picture the thermal conductivity and „figure of merit" are summarized in Fig. 12.

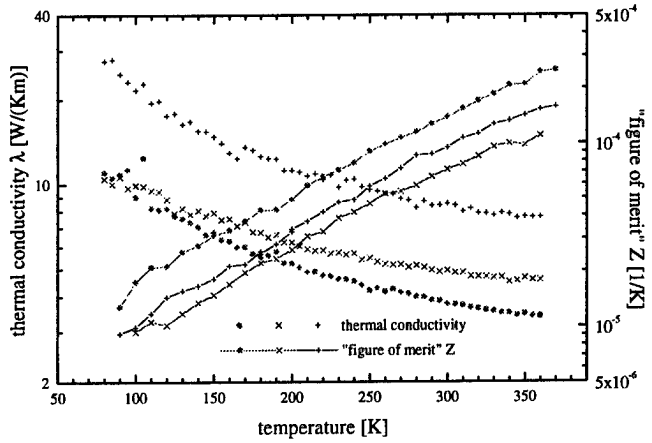


Fig. 12: Thermal conductivity and Z of $Ti_{1-x}Zr_xNiSn$.

It is evident, that the thermal conductivity is considerably reduced by alloying. The „figure of merit" increases with increasing temperature not reaching a maximum in the observed temperature range. The maximum value for Z is $2.5 \cdot 10^{-4}$ 1/K and not exceeding the values obtained for the pure compounds.

Conclusion

The thermoelectric properties of the system MNiSn (where M=Ti, Zr, Hf) were studied over a large temperature range. A new Sn-flux technique yielded single crystals of all three compounds belonging to this group.
With respect to the electronic parameters, ZrNiSn seems to be the most promising material. A maximum power factor of $3.5 \cdot 10^{-3}$ 1/K was obtained for this particular compound. However, the high thermal conductivity of ZrNiSn leads to a compensation of this advantage, so that the highest „figure of merit" $Z = 3.3 \cdot 10^{-4}$ 1/K was observed for TiNiSn.
A remarkable reduction of the thermal conductivity was obtained by alloying these compounds. Because only nondegenerate samples were found in the alloys, the maximum Z did not exceed $2.5 \cdot 10^{-4}$ 1/K. Improvement of the electrical parameters and better control of crystal growth remain as future tasks.
Just for further motivation and to show the direction of coming investigations, the high power factor of ZrNiSn can be mathematically combined with the reduced thermal conductivity of $Ti_{1-x}Zr_xNiSn$ resulting in $Z = 1.1 \cdot 10^{-3}$ 1/K!

Acknowledgments

The authors wish to thank M. Wendl and H. Riazi-Nejad for their technical support in crystal growth.

References

[1] Ch. Kloc, K. Fess, W. Kaefer, K. Friemelt, H. Riazi-Nejad, M. Wendl, and E. Bucher, Proc. Of the XVth Int. Conf. On Thermoel. , Pasadena, 155 (1996)
[2] F.G. Aliev, N.B. Brandt, V.V. Moshchalkov, V.V. Kozyrkov, R.V. Skolozdra, and A.I. Belogorokhov, Z. Phys. B **75**, 167 (1989)
[3] F.G. Aliev, V.V. Kozyrkov, V.V. Moshchalkov, R.V. Skolozdra, and K. Durczewski, Z. Phys. B **80**, 353 (1990)
[4] F.G. Aliev, Physica B **171**, 199 (1992)
[5] G.D. Mahan, J. Appl. Phys. **65**, 1578 (1989)
[6] J.O. Sofo and G.D. Mahan, Phys. Rev. B **49**, 4565 [1994]
[7] G.D. Mahan, B. Sales and J. Sharp, Physics Today **3**, 42 (1997)
[8] L.D. Dudkin, Z.M. Dashevskii, and R.V. Skolozdra, Inorg. Mat. **29**, 249 (1993)

Effect of Isoelectronic Substitution of Thermopower and Resistivity of $Hf_{1-X}Zr_XTe_5$

R. T. Littleton IV,[A] M. L. Wilson,[A] C. R. Feger,[B] M. J. Marone,[A]
J. Kolis,[B,C] and T. M. Tritt[A,C]
A. Department of Physics and Astronomy
B. Department of Chemistry
C. Materials Science and Engineering Department
Clemson University, Clemson, SC 29634 USA

F. Levy
Institut de Physique Appliquee, Laussanne, Switzerland

Abstract

The thermopower and resistance of single crystal pentatellurides in the series $Hf_{1-X}Zr_XTe_5$ (x = 0, .25, .50, and 1.0) have been measured as a function of temperature from 10 K to 300 K. The results show that $HfTe_5$ and $ZrTe_5$ contain broad resistance peaks at a temperature, T_P, of 76 K and 147 K respectively, which are in agreement with previous measurements. Both compounds possess relatively large p-type thermopower (~ +100 μV/K) which decreases rapidly through zero at a temperature T_0 before changing to an equally large n-type thermopower (~ -100 μV/K) at a temperature $T < T_0$. Through isoelectronic substitution of Zr for Hf ($Hf_{1-X}Zr_XTe_5$), systematic shifts are observed in both T_P and T_0 as the Zr concentration increases. These ternary compounds retain the large p- and n-type thermopowers.

Introduction

Prior research efforts on thermoelectric (TE) materials have focused on the Bi_2Te_3 and $Si_{1-X}Ge_X$ systems.[1-3] These materials have been investigated in great detail to enhance their properties in thermoelectric refrigeration and power generation application. These optimized systems prevail as the current state-of-the-art materials for applications at and above room temperature. There remains a necessity for progress on more efficient thermoelectric materials especially at temperatures T < 300K. This need for higher performance materials and extended temperature regimes for applicable thermoelectric devices has renewed interest in the field.[4] The need for lower temperature (100 - 200 K) thermoelectric materials is very important in fields such as cryoelectronics[5] and IR detection[6]. To develop devices for these applications, both p-type and n-type materials must be sought and optimized for this specific temperature range. The present study identifies the pentatelluride system as a potential class of materials for lower temperature thermoelectric applications. Not only do these binary and ternary systems contain both large p-type and n-type thermopowers, but they can easily be tuned over specific temperature regimes.

Experimental Technique

The preparation of pentatelluride single crystals is based on modifications of previously reported methods. Crystals were obtained by heating stoichiometric amounts of powered reagents in 10mm ID fused silica tubing. Approximately 5 mg/mL tube volume of iodine crystals were added as a transport agent. The sealed reaction vessels were placed in a single zone tube furnace with the charge located in the central, hot zone. The furnace was heated to 773 K and the temperature was held for 1-2 weeks. Powder x-ray diffraction of selected crushed crystals verified the formation of the pentatelluride structures. The quoted Zr fractions (x = .25 and x = .50) are only the nominal concentrations.

The thermopower and electrical resistance of the pentatelluride samples were measured using a four-point probe technique. A constant ΔT was established across the sample as the temperature was swept. Details of this experiment are discussed elsewhere.[8] Evaporated gold contact pads on the samples were necessary due to excess iodine from the growth procedure. Copper and gold probe leads were silver painted to the contact pads.

Results and Discussion

Resistance and thermopower measurements performed on single crystals of $Hf_{1-X}Zr_XTe_5$ where x = 0, .25, .50, and 1.0, are shown in Figures 1 and 2. The $HfTe_5$ and $ZrTe_5$ results were consistent with previous studies.[9-11] As Hf is replaced by Zr a steady temperature shift is observed in the measured resistivity. In each of the samples the resistivity decreases from high temperature before passing through a shallow minimum. As the temperature decreases, the resistance rises rapidly, passing through a maximum at T_p. At lower temperatures, $T < T_P$, the resistivity falls steadily, as shown in Figure 1.

In a similar manner, the thermopower of each sample reveals a systematic shift in temperature as the Zr concentration was increased, as shown in Figure 2. Each concentration exhibits the relatively large p-type thermopowers at room temperature. As the temperature decreases the thermopower for each sample increases until it

reaches a maximum. At lower temperatures the thermopower drops sharply, passes through zero (at T_0), and continues to decrease until reaching a maximum n-type thermopower. At even lower temperatures the thermopower begins to rise again going toward zero thermopower at T = 0 in a relatively linear fashion, characteristic of diffusion type thermopower. There was no evidence of any phonon drag effects at the much lower temperatures.

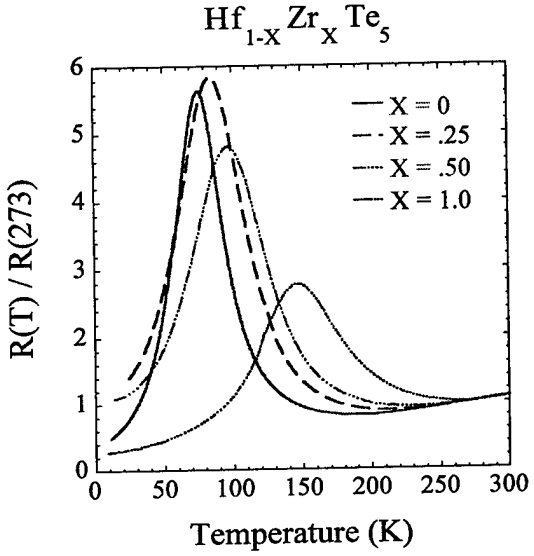


Figure 1. Normalized resistance of $Hf_{1-X}Zr_XTe_5$ as a function of temperature for x = 0, .25, .50, 1.0.

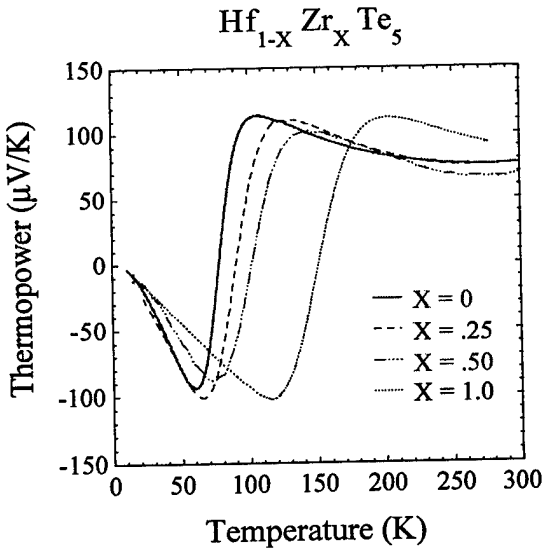


Figure 2. Thermopower of $Hf_{1-X}Zr_XTe_5$ as a function of temperature for x = 0, .25, .50, and 1.0.

The electrical transport properties of $HfTe_5$ and $ZrTe_5$ were examined previously.[10-17] The resistance transition or peak (T_p) was first thought to be evidence of charge density wave (CDW) phenomenon, but no supporting evidence was found. The origin of the transition in these pentatellurides, as discussed by Disalvo et. al., appears to be an electronic phase transition opposed to a structural phase transition. Therefore, the electronic properties of this system should be susceptible to doping which is evident with these results.

The agreement of the relative resistance peaks and zero thermopower of the substituted $Hf_{1-x}Zr_xTe_5$ series as a function of x is illustrated in Figure 3. The uncertainty in the concentrations of Hf or Zr does not allow for the prediction of an obvious dependency with regards to the zero thermopowers or resistance peaks. However, the correlation between the zero thermopower and the resistance peak at each concentration is quite impressive.

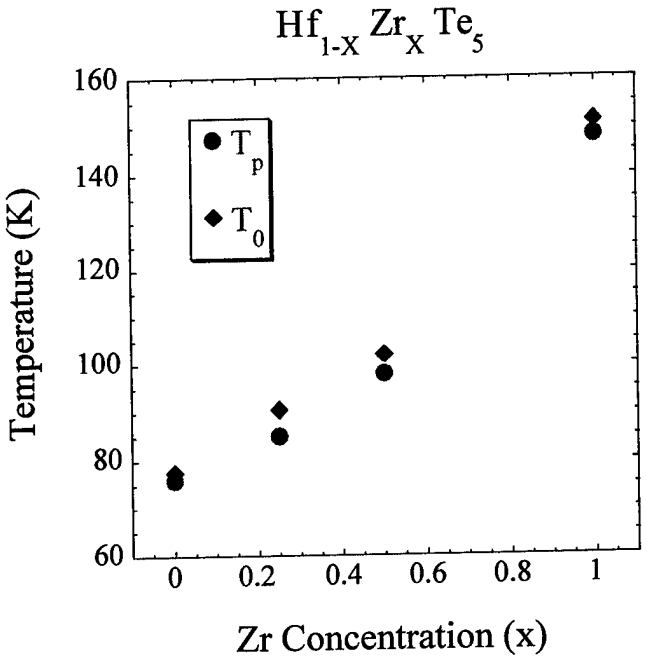


Figure 3. Temperatures of zero thermopower, T_0, and relative resistance peaks, T_P, for $Hf_{1-x}Zr_xTe_5$ where x = 0, .25, .50, and 1.0.

Summary

Resistance and thermopower of $Hf_{1-x}Zr_xTe_5$ have been measured as a function of temperature and Zr concentration. The temperature of the resistivity transition of these compounds can be systematically tuned, depending on the Zr concentration. Likewise, the temperature at which these systems exist with p- or n-type thermopower can also be manipulated by the Zr concentration over a large temperature regime. The existence of large p-type and n-type behavior over a relatively broad temperature range is necessary for any potential thermoelectric device application. More work is necessary to optimize the electronic properties of these pentatelluride materials. Work relating to the determination of the thermal conductivity of these materials is in progress.

Aknowledgement

This work is supported by an ARO/DARPA grant number AMXRO-AAA-37381-MS (1997).

References

1.) H.R.Goldsmid, Electronic refrigeration, Pion Limited Publishing, London, (1986)
2.) CRC Handbook of Thermoelectrics, edited by D.M. Rowe, CRC Press, Boca Raton (1995)
3.) C.W. Wood, Rep. Prog. Phys. **51**, 459-539 (1988)
4.) T.M. Tritt, Science, **272** 1276 (1996)
5.) J. Sloan, Superconductor Industry, Fall 1996, p 30 (1996)
6.) Laser Focus World, Detector handbook, March 97, **55** (1997)7.) S. Furuseth; L. Brattas; A. Kjekshus, Acta Chem. Scand., **27,** 2367 (1973)
8.) T.M. Tritt et. al., J. Appl. Phys., **79** 8412 (1996)
9.) T. M. Tritt, Materials Research Society Proceedings, Symposium on Thermoelectric Materials: New Directions and Approaches, Spring 97, edited by T.M. Tritt et. al., 349, (in press)
10.) T.E. Jones et. al., Solid St. Comm., **42**, 793 (1982)
11.) F.J. Disalvo, R.M. Fleming and J.V. Waszczak, Phys. Rev. B, **24**, 2935 (1981)
12.) M. Izumi, et. al., Solid State Comm., **42**, 773 (1982)
13.) W.W. Fuller et al., Journal de Physique, **C3**, 1709 (1983)
14.) D.W. Bullett, Solid State Comm., **42**, 691 (182)
15.) G.N. Kamm et. al., Phys. Rev. B., **35**, 1223 (1987)
16.) G.N. Kamm et. al., Phys. Rev. B., **31** 7617 (1985)
17.) E.P. Stillwell, A.C. Ehrlich, G.N. Kamm and D.J. Gillespie, Phys. Rev. B., **39**, 1626 (1989)

IR-Reflection Study of Sintered SiC/Al Thermoelectric Semiconductors

T.Miyakawa, Y.Okamoto*, T.Kawahara*, S.V.Ordin**, M.I.Fedorov**, Y.Miida
Department of Computer Science, Chiba Institute of Technology, Tsudanuma, Chiba, Japan
Phone:+81-474-78-0548, Fax: +81-474-78-0549, E-mail: miyakawa@cs.it-chiba.ac.jp
*Department of Materials Science & Engineering, National Defense Academy, Yokosuka, Japan
**Laboratory for Physics of Thermoelements, A.F.Ioffe Physico-Technical Institute, Sankt-Petersburg, Russia

Abstract.

IR-reflection spectra of sintered SiC/Al thermoelectric semiconductor samples are studied in its reststrahlen region and analysed using a 4-component effective medium model. The effects of Al impurities 1) reducing the pores 2) increase elctrical conductivity 3) acting as metallic inclusions, can be observed by the change of reflectance in and outside of the resonance, and that these effects can be separated by the proposed effective medium model. These results combined with the possibility of local probing offers a versatile means to characterize the quality of sintered samples especially of thermoelectric semiconductors.

1. Introduction.

Silicon carbide is a wide-band gap semiconductor stable even at high temperatures.Recently, active research effort is directed on the development of blue-emitting diodes as well as devices to be used at high temperature or under strong irradiation[1]. It is also known as a promissing material for thermoelectricsat high temperatures.

We have reported on the thermo-electric characteristics of sintered SiC samples which are expected to show the figure of merit Z approaching 1/T at 700°C[2]. The crucial point to achieve a high figure of merit Z is to reduce the high thermal conductivity of SiC by sintering while keeping the electrical conductivity as high as possible. To achieve this goal we have tried various dopants which have the temperature of vaporization higher than the sintering temperature.

SiC/Al is such a system in which Al impurities are expected to play three roles described in the following;

1) they are known to act as sintering additives which combine crystalline grains together,
2) increase the conductivity of the crystalline grains acting as the acceptors,
3) lower the resistivity of intergranular region.

Although the relative importance of these three effects also depends on the condition of sintering, especially sintering temperature, it is very interesting and important to have means to separate these effects.

In this paper we would like to show that the three effects of dopant can actually be observed in the IR-reflection[3,4,5] of sintered SiC and that the 4-component effective medium model can analyse the change in the spectral features almost quantitatively into these three effects.

The results can serve to characterize the quality of sintered samples and to improve the figure of merit of sintered thermoelectric semiconductors.

2. Samples and Measurements.

2.1. Samples.

Preparation of samples has already been described in our previous reports.[2]

2.2. Surface Treatment.

Mechanical grinding and polishing by diamond powder with water and by diamond paste were used basically for sample preparation for IR-measurements. After each stage of grinding on a glass polisher or on a soft plastic polisher a layer with thickness 10 or 1 times the size of the grain, respectively, of the powder or paste used were removed to avoid the effect of possible damage to the surface. At the final stage the diamond powder with grain size 7, 5, 3, 2, 1 and 0.5μm.were used

2.3. IR-measurements.

In Fig.1. we compare the IR-reflectance spectra of sintered SiC samples with that of powdered poly-crystal(6H) sample.From IR data alone it is difficult to discriminate 3C phase from 6H one.

0-7803-4057-4/97 $10.00 ©1997 IEEE

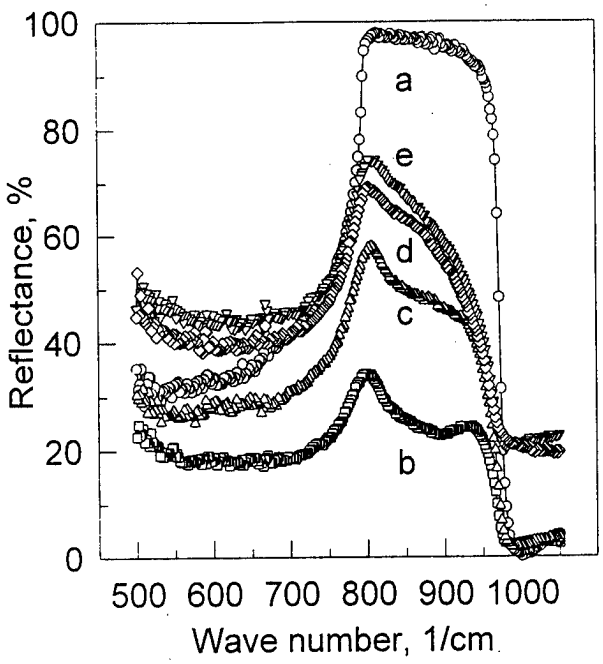


Fig.1. IR-reflectance spectra of SiC samples.
a) 6H poly-crystal powders, b) 0.5% Al,
c) 2% Al, d) 15% Al sintered at 1950°C,
e) 15% Al. T_s=2100°C for cases b),c),e).

We see that the reflectance decreases drastically at first but recovers as the Al concentration increases. The fact that no shift in phonon resosnance frequency is observed seems to imply that dominant part of crystal grains in our sintered samples remain 3C-type, and no appreciable change in the crystal structure is taking place. This is in agreement with our results of XRD observation on the samples which show only dominant 3C peaks.

Fig.2.a-c show results of IR-measurements for samples with Al impurities sintered at three different temperarures. Starting concentration of Al are indicated in the figures.

We note that while the magnitude of peak reflection varies widely, the shift in the resonance frequency is almost negligible. The peak reflectance is seen to increase as a function of Al concentration up to 5%. As this trend is in parallel with the change in sample density, we infer that sintered SiC have rather large number of pores which reduce the density of the sample, and part of added Al act as the sintering agent which reduce the pores and thus increase the density. This is also reflected in the increase of reflectance as a function of Al concentration.

The low value of reflectance outside the region of resonance seems to support the above inference. From this stand point the quality of sintered sample is best for the samples sinteredat 2100°C.

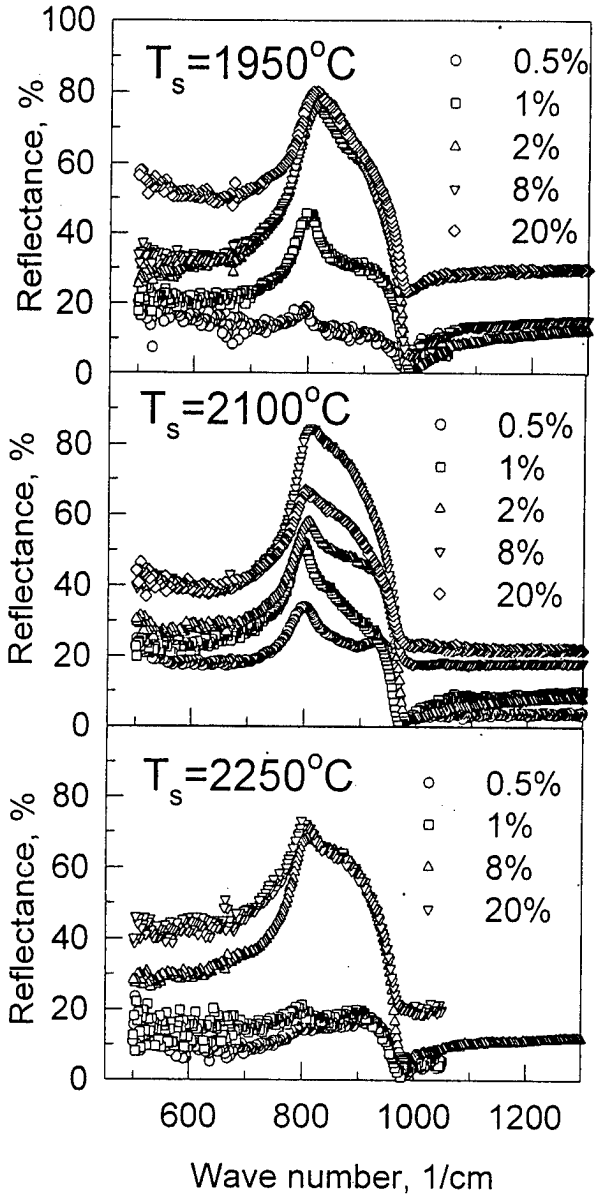


Fig.2. IR-reflectance spectra of SiC samples sintered at different temperatures T_s.
a) 1950°C, b) 2100°C, c) 2250°C.
Al concentrations y in the starting metrial are labeled in the figures.

The stability of reststrahlen maximum and sharp change of reflectance in the high-frequency region indicate the essential contribution of intergrain Al on the optical constants of samples containing more than 8% Al.

In the case of samples with 20% Al especially that sintered at 1950°C we see a strong increase in reflectance at lower wave number region. This effect reminds one of the similar effect found in Ni-MgO films[6] close to the percolation threshold.

3. EMA analysis.

3.1. 4-Component Effective Medium Model

To analyse these results we employed the following model.

We have pores with porosity f_1 besides the crystalline grains with a volume fraction f_3 and intergranular region with a volume fraction f_2, with f_4 denoting the fraction of metallic inclusions dispersed in the inter-granular region.

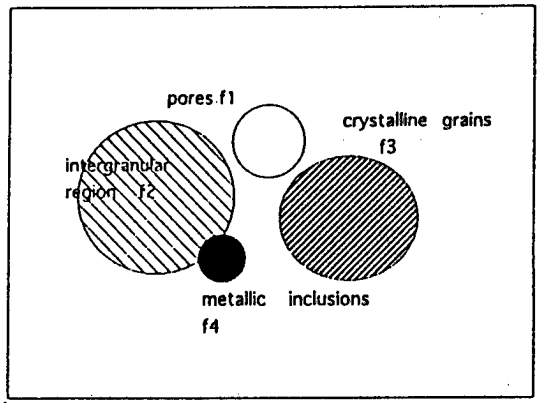


Fig.3. Effective medium model used in this analysis. Pores with a fraction f_1, intergranular region with f_2, crystalline grains with f_3, and metallic part with f_4.

3.2. Analysis in 4-component EM model

In this model the effective dielectric constant of the sintered samples can be found by solving the equation;

$$\Sigma^4_{i=1} f_i(\varepsilon_i-\varepsilon)/(\varepsilon_i+2\varepsilon)= 0 \qquad (1)$$

For pores we assume $\varepsilon_1 = 1$. For crystalline grains we use the two oscillator model of Spitzer etal.[3,4] neglecting the small contribution of the second oscillator;

$$\varepsilon_3(x) = 6.7 + 4\pi \times 0.263/(1-x^2-igx) \quad (2)$$

where, $x=\varpi/\varpi_0$, with $\varpi_0= 2.356\times10^{13}$Hz being the resonance frequency of the oscillator, $g = g/\varpi_0$, denotes the normalized damping factors of the oscillator.

As for the dielectric constant of the inter-granular material ε_2 we set $\varepsilon_2 = 2$. For a high Al concentration we assume that the metallic inclusion occupies a volume fraction f_4 with its ε_4 approximated by the Drude model.

$$\varepsilon_2(x) = 1 - r_2^2/(x^2+ig_2x) \qquad (3)$$

We used a value $r_2=100$ and $g_2 = 10g$.

We show in Fig.4. results of our 4-compnent effective medium analysis. Here, we simulate the effect of Al using three parameters described in the introduction. Namely, as the Al concentration y increases the volume fraction of pores f_1 decreases, fraction f_3 of crystalline grains will increase replacing intergranular part with fraction f_2, the damping coefficient g increases at the same time and finally, a component with metallic characteristics grows in the intergranular region.

Although we have arbitrarily selected parameters simulating these effects, one can see that the model reproduces almost quantitatively the main features of the observed IR-reflectance spectra.

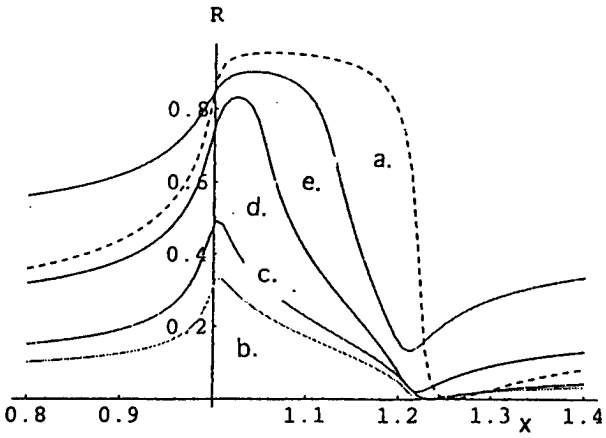


Fig.4. Effect of Al doping on the IR-reflectance spectrum analysed by the 4-component EMA model.

Values of f_1, f_2, f_3, f_4, ε_2 and g are as follows;

a) $f_1=0$, $f_2=0$, $f_3=1$, $f_4=0$, g=0.01 (single crystal),
b) $f_1=0.2$, $f_2=0.5$, $f_3=0.3$, $f_4=0$, $\varepsilon_2=2$, g=0.01,
c) $f_1=0.1$, $f_2=0.5$, $f_3=0.4$, $f_4=0$, $\varepsilon_2=2$, g=0.02,
d) $f_1=0.05$, $f_2=0.4$, $f_3=0.4$, $f_4=0.15$, $\varepsilon_2=2$, g=0.02,
e) $f_1=0.03$, $f_2=0.3$, $f_3=0.4$, $f_4=0.27$, $\varepsilon_2=2$, g=0.03.

4. Discussion.

As the sintered samples have intrinsic inhomogeneity the reflection spectrum measured on the external surface of it can differ strongly from that measured on an internal surface.

Also local resistance of the sample can differ when measured on the external surface from that measured on an internal surface. So we do not at this point try to fit the data with the available parameters but would like to point out the following; IR-reflectance in the region of reststrahlen provides a versatile means for analysing the effects of dopants and sintering quality in a sintered material, the fact that it can probe a region comparable to the focused area of the beam and that it is sensitive to local(not neccessarily microscopic) characteristics of the sample seems to show the promissing aspects of this method of analysis.

We are woking with samples with four kinds of impurities; Al, Cu, Ag and Si. Among these impurities Al is known to play the role of sintering additive, while Si is expected not to form inter-granular layers with "metallic" conductivity. So the comparison of IR-data on these samples will not only reveal the roles of these impurities on overall characteristics of the samples but also give information regarding their effects on the sintering quality.

Acknowledgements.

Two of the authors(S.V.O and M.I.F.) are grateful to Japan Society for the Promotion of Siences for the financial support which made this joint project possible. Three of the authors(Y.O., T.K. and T.M.) are grateful to Prof. J.Morimoto for valuable discussion and support.

References.

1) H.Morkoc, S.Strite,G.B.Gao, M.E.Lin:
Large-band-gap SiC, III-V nitrides, and II-VI ZnSe-based semiconductor device technologies
J.Appl.Phys. 76(3), pp1363-1398 (1994)

2) Y.Okamoto, A.Aruga, H.Tashiro, J.Morimoto, T.Miyakawa, S.Fujimoto:
Temperature dependence of thermoelectric properties of SiC/Al
Proceedings of XIV International Conference on Thermoelectrics St. Petersburg, pp269-273(1996)

3) W.G.Spitzer,D.A.Kleinman, C.J.Frosch:
Infrared Properties of Hexagonal Silicon Carbide
Phys.Rev. 113, pp127-132 (1959)

4) W.G.Spitzer, D.A.Kleinman, D.Walsh:
Infrared Properties of Cubic Silicon Carbide Films
Phys.Rev. 113, pp133-138 (1959)

5) M.F.MacMillan,R.P.Devaty, W.J.Choyke, D.Goldstein, J.Spanier :
Infrared Reflectance of Porous SiC Layers
Technical Digest of the International Conference on SiC and Related Materials
Technical Digest of ICSCRM-95-Kyoto
paper TuB-IV-5 pp248-249 (1995)

6) T.W.Noh,Y.Song,SI,Lee,J.R.Gaines:
Percolation effects in the optical properties of Ni-MgO composites
Phys.Rev.B33(6), pp3793-3802 (1986)

SYNTHESIS OF ZN_4SB_3 COMPOUND BY PIES METHOD

A.Yamamoto[1], Ichizuka[2], H.Takazawa[1], T.Ohta[1], T.Kajikawa[2]

[1]Electrotechnical Laboratory, AIST, MITI, Japan E-mail : a.yamamoto@etl.go.jp

[2]Shonan Institute of Technology, Kanagawa, Japan.

Abstract

An attempt was made to synthesize β-Zn_4Sb_3 semiconducting compound by PIES (Pulverized and Intermixed Elements Sintering) / hot-press method. We found that it is possible to synthesize β-Zn_4Sb_3 as a major phase without increased temperature when we start the ball milling process with Zn-rich composition. The power factor α^2/ρ at room temperature was 6.3×10^{-4} W/mK^2 and these initial data clarified that relatively high performance can be achieved with PIES/hot-press method.

Introduction

Zn-Sb compounds are well-known materials which have high Seebeck coefficients and complex crystal structures. The system have several stoichiometric compounds such as ZnSb, Zn_4Sb_3 and Zn_3Sb_2 at a room temperature. ZnSb, which has a stoichiometry of Zn:Sn is 1:1, was well studied by Telks et al. in 1950's[1]. Recently β-Zn_4Sb_3 have an increased interest since it was systematically studied by JPL, and Caillat reported a high figure-of-merit value of ZT=1.3 at 673K[2]. It is also reported by a group in Yamaguchi Univ. that the ZT value exceeds 1.3 with an atomic substitution of Sb for Sn[3].

According to the phase diagram, β-Zn_4Sb_3 phase is produced through peritectical reactions and this makes it difficult to obtain a homogeneous single phase sample. Several approaches including the quenching from the melt[2], long-term annealing after ball-milling[3], etc. In the latter case, long-time annealing is necessary to homogenize the distributions of elements and to achieve the exact stoichiometry.

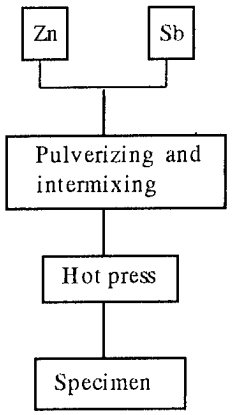
From the practical point of view, we have developed energy- and time-saving processing technique named PIES method[4]. This process is featured with a mechanical grinding of mixed powder-elements and subsequent low-temperature sintering. In the milling process, the starting powder is ground by mechanical energy input with ball-mill machine or an attritor. Under appropriate conditions, powder is mixed up to nano-meter size and forms a solid solution without increasing temperature. This makes it easier to densify the powder at low temperature sintering with good homogeneity. For synthesis of β-Zn_4Sb_3 phase, it is favorable not to exceed γ–β phase transition temperature at 492℃. From this point there is an enugh reason to apply the PIES method followed by low-temperature sintering to β-Zn_4Sb_3 synthesis.

In this paper we report the result of the synthesis of β-Zn_4Sb_3 with a centrifugal ball-mill and thier thermoelectric properties.

Experiment

Sample specimens of undoped β-Zn_4Sb_3 were prepared by PIES method which includes the pulverizing process of elemental zinc and antimony by high energy ball milling and the sintering process. We made 5 samples with different Zn/Sb ratio as shown in Table 1. The high energy ball milling process was accomplished in an atmosphere of argon. In this study hot pressing method were chosen as a sintering procedure. Hot pressing conditions were 673K and 773 K, 1500 kgf/cm^2 for five hours. Typical size of the specimens was 10 mmϕ x 5 mm thickness. The densities measured by the Archimedes' principle were about 80% of the ideal value for the samples sintered at 400℃ and 90 % for those sintered at 500℃. The preparation procedure and the conditions are shown in Figure 1.

Scanning Electron Microscopy-Electron Probe Micro Analyses



100 mesh, 99.999%

Ar atmospher, 20hours

Graphite Dies,
400℃/ 500℃, 1500kg/cm^2
5 hours

10mmϕ x 5mm

Figure 1. : Flow diagram of PIES method

0-7803-4057-4/97 $10.00 ©1997 IEEE

and X-ray diffractometry were performed for examining morphology and composition of the specimens. The Seebeck coefficients were calculated from measurements of the electromotive forces with temperature difference of 10K. The electrical resistivity was measured by van der Pauw method and the Hall measurements were performed. All measurements were performed from 300K to about 600K, except for the Hall measurement which was performed at 300K.

Results

1.Pulverizing process

Figure 2. shows the magnified view of powder after 20 hours pulverizing process with ball-mill. The size of the powder is about 1μm and we cannot find any macroscopic segrigations of Zn, Sb elements by EDX observation. Fig.3 shows the Zn/Sb ratio averaged in x100 view area. This graph indicates that the target compositions are achieved through the pulverizing process. However, we observed large variability of the Zn/Sb ratio when the area for the analysis is restricted within several μm.

Table 1. : Sample List

Sample	Mole ratio	Density(500℃)	Density(400℃)
	Zn:Sb	g/cm^3	g/cm^3
#1	1.4:1	4.877	4.455
#2	1.5:1	5.493	4.836
#3	1.6:1	5.492	4.714
#4	1.7:1	5.542	4.873
#5	1.8:1	5.539	5.183

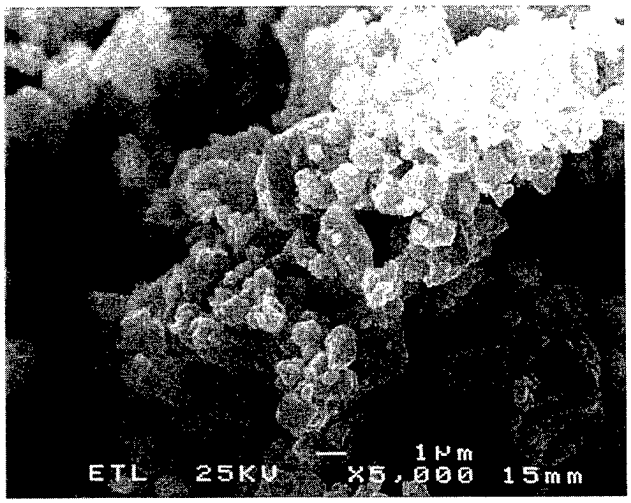


Figure 2. : A SEM image of the pulverized powder.

Figure 4. shows the XRD pattarn of the pulverized powder and dense sample sintered at 500℃. The XRD analysis indicate that the major phase is ZnSb when the starting Zn/Sb mole ratio is 1.4 while the Zn_4Sb_3 is dominant phase when the ratio Zn/Sb>1.4. There are weak peaks corresponding to Zn in the

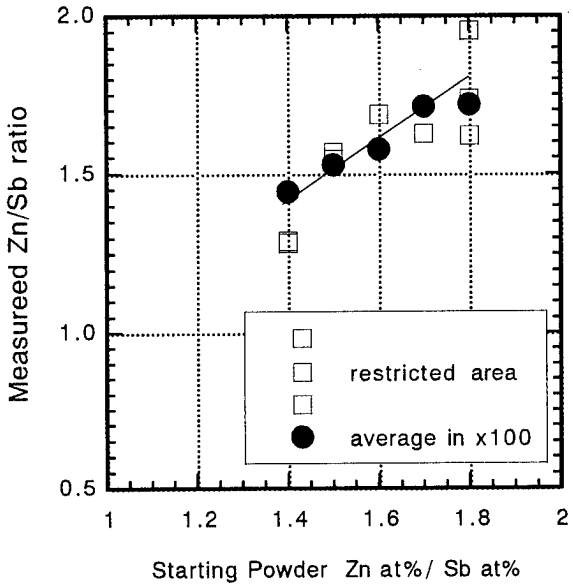


Figure 3. : The variability of the composition of the powders.

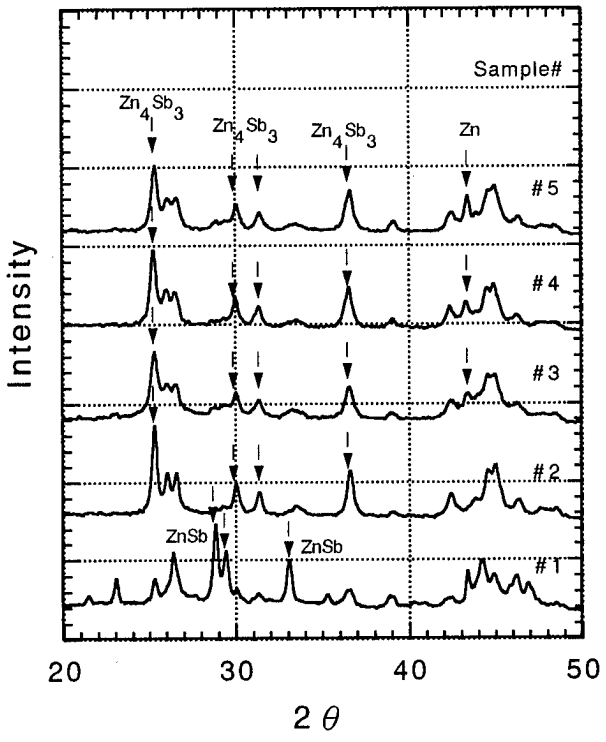


Figure 3. : XRD patterns of the pulverized powder.

sample with ratio Zn/Sb > 1.5 and the peak height is increasing with increasing the Zn/Sb ratio. This means the very fine excess Zn distribute in the sample. The XRD analysis also indicate that the β-Zn_4Sb_3 phase is synthesized only when the Zn/Sb mole ratio is higher than 1.5. These results disagree with the equilibrium phase diagram, in which the stoichiometoric Zn/Sb ratio is 1.33. There is no possibility of reducion of Zn in pulverizing process since the operating temperature dose not exceed 100℃. Therefore these results are supposed to stem from the non-equilibrium nature of the pulverizing process.

2.Hot-Pressed sample

Table 1 shows the densities of samples hot-pressed at 400C and 500℃, respectively. The relative densities to the ideal value (6.077g/cm^3)[5] are about 80% for the sintering temperature of 400℃ and 90% for 500℃. Clearly the longer sintering duration is favorable for the densification of the samples. But we also find that some samples sintered at 500℃ are very fragile, and this can be due to the γ–β phase transition at 492℃.

3.Thermoelectric Properties

Table 2. shows resistivities ρ and Seebeck coefficients α of the hot-pressed sample measured at room temperature. Except for sample #1,which is dominated with ZnSb phase, the resistivity is decreasing with increasing Zn/Sb ratio. This result is understandable as the influence of the excess Zn to the electrical conduction. Seebeck coefficients decrease with increasing the Zn/Sb ratio. The power factors α^2/ρ are around 6.3x 10^{-4} W/ mK^2 and these values are comparable to those prepared by melt-quenching process, which consists of Zn_4Sb_3 single phase.[5] The main reasons for the inferior electrical resistivities stem from both the lower densities of the sample and their low mobilities. The microscopic inhomogeneity of the composition is the main reason of the low mobility. The pulverized powders have a compositional distribution as shown in figure 3 and there are coexisting some other phases in it. In this experiment there are small improvement in the homogeneity through the diffusion of the elements in the hot-press process. Therefore the effort should be focused on the optimization of the pulverizing process so that the exact stoichiometry is achieved.

Figure 5 and 6 show the temperature dependence of the resistivities and the Seebeck coefficients. Both the resistivities and the Seebeck coefficients were measured in vacuum of 10^{-6} Torr. We have to note that the measured data were unstable with temperature changes. Plots shown in figure 5 and 6 are data measured after the several trials and they contain the annealing

Table 2. : Flow diagram of PIES method

Sample	Resistivity	Seebeck coef.	Power Factor
	Ω m	μ V ／K	W／mK^2
#1	1.04e-1	253	6.15e-7
#2	5.47e-5	175	5.60e-4
#3	7.86e-5	160	3.26e-4
#4	3.30e-5	125	4.73e-4
#5	2.47e-5	125	6.33e-4

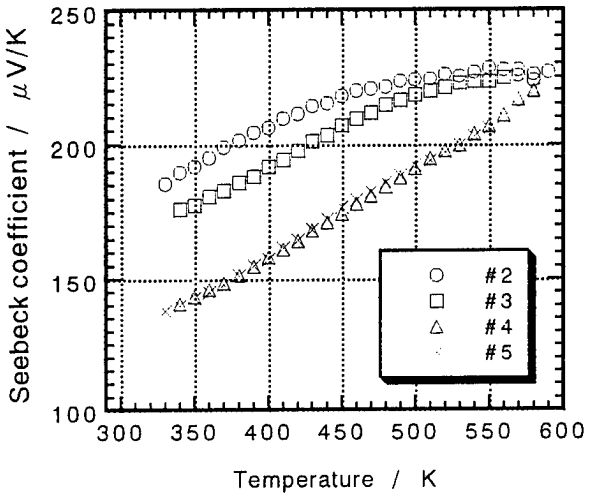


Figure 5. : Temperature dependences of the Seebeck coefficients.

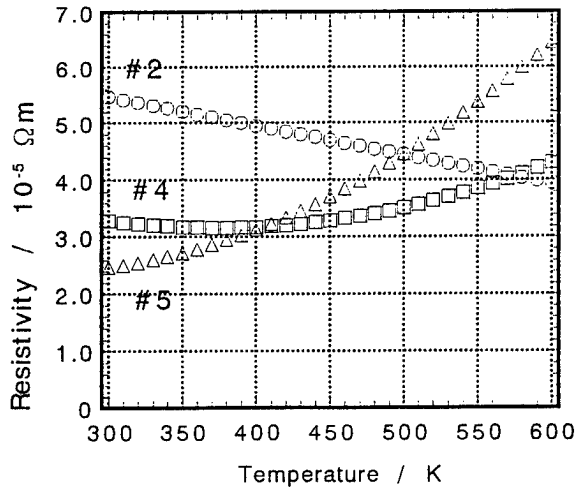


Figure 6. : Temperature dependences of the resistivity.

effects. The power factor values are calculated from figure 5 and 6. The highest power factor is 1.27×10^{-3} W/mK^2 and this is obtained for 600K for sample #2.

Conclusions

In this study we performed the synthesis of β-Zn_4Sb_3 by using PIES and hot-press method. It is clarified that we can obtain β-Zn_4Sb_3 phase by this method when we use Zn rich composition. But there exist minor phases and excess Zn in the hot-pressed samples. Relative densities of the samples are about 90%. Thermoelectric properties are comparable to the samples prepared by melt techniques. In conclusion, we need further optimization of the pulverizing and hot-pressing conditions for better homogeneity of the composition.

Acknowledgements

The authors would like to thank Akira Negishi for microscopic observation with SEM/EDX.

References

[1] M.Telkes : J. Appl. Phys., 25 (1954) 765.

[2] T. Caillat et al. : Proc. IECEC'96 Vol. 2 (1996) 905

[3] Hino, et al. : Proc. Spring Meeting of Japn. Appl. Phys. 1(1997) 80

[4] T. Ohta et al. : Proc. XIV Int. Conference on Thermoelectrics, St. Petersburg (1995) 24

[5] T. Caillat et al. : J. Phys. Chem. Solid, in press.

Low Temperature Thermoelectric Power of Amorphous Alloys Al-Y-Ni

K. PĘKAŁA

Institute of Physics, Warsaw University of Technology
Chodkiewicza 8, PL-02-524 Warsaw, Poland

Abstract

Low temperature thermoelectric power of amorphous alloys $Al_{90-x}Y_{10}Ni_x$ (x = 0, 2, 5 and 8) exhibits the characteristic "knee" which are related to the electron - phonon mass enhancement. The Debye temperature T_D and the electron - phonon mass enhancement parameter determined from the experimental data diminish with the rising Al content. This surprising observation suggests the reduction of the density of states at the Fermi level related to the attractive bonding force Al-Y which affects the nanocrystallization processes.

Introduction

In the nonmagnetic alloys the thermoelectric power (TEP) becomes often a linear function of temperature T above the Debye temperature T_D. At low temperature a slope of the TEP vs temperature curve increases giving rise to the characteristic so called "knee" observed e.g. in Fig. 1. In crystalline materials such a behavior is masked by the phonon drag effect. In the structurally disordered amorphous materials the the phonon mean free path is very short. Thus the phonon drag is negligible [1] and the "knee" can be observed.

The low temperature "knee" effect in TEP was first considered by Gallagher [2] who associated the experimental data with the the electron - phonon mass enhancement predicted theoretically by Opsal.[3]. Later on this effect was observed in various amorphous alloys [4-8].

The theoretical calculations of TEP performed by Kaiser [8] using the an experimental vibrational density of states and models of the electron - phonon coupling parameter $\alpha^2(E)$ for amorphous Cu-Zr and CuTi were in good agreement with the experimental results of Gallagher [2]. Then Kaiser and Stedman [9] showed that in amorphous alloys three effects related to the electron - phonon interaction play a role. This are 1) the energy renormalization, 2) velocity and relaxation time renormalization and 3) higher order scattering diagrams. All three effects have the same temperature dependence but the last two do not depend on the bare thermopower. In order to calculate the temperature variation of the function $\lambda(T)$ describing the thermoepower effects due to the electron - phonon interaction, Kaiser and Stedman [9] applied the Debye phonon spectrum F(E) and assumed that the Eliashberg function $\alpha^2F(E)$ varies as E^n with n = 1, 2 or 3. It was found that $\lambda(T)$ is a monotonically diminishing function of temperature when n = 1 whereas $\lambda(T)$ exhibits maximum for n = 2 or 3.

Generally, the simple metals with the atomic lattice easily transporting the electron - phonon interaction, are distinguished by the large interaction parameter $\lambda \geq 1$ and the relatively high transition temperature T_c. For such metals the Eliashberg function $\alpha^2F(E) \sim E$ and $\lambda(T)$ diminishes monotonically with rising temperature, as it was described by Bergmann [10].

On the other hand, in the amorphous transition metals $\lambda < 1$ due to the worse propagation of the electron - phonon interaction in their lattice. The exponent n in the Eliashberg function n = 2 or 3 [11,12]and then the $\lambda(T)$ exhibits the characteristic maximum.

The present work reports the results of the low temperature thermoelectric studies of amorphous alloys $Al_{90-x}Y_{10}Ni_x$ (x = 0, 2, 5 and 8) which were performed to elucidate an influence of the transition metals Ni on the electron - phonon interaction.

Experimental

The amorphous alloys were prepared by melt spinning method under an argon atmosphere. The alloy compositions were $Al_{90}Y_{10}$, $Al_{90-x}Y_{10}Ni_x$ (x = 2, 5, 8). Their amorphicity was checked by X - ray diffraction. TEP was mesured by differential method between 20 and 300 K [13]. Thermoelectric power of copper wires was subtracted.

Results

The values of TEP are negative ranging between 0 and -5 μV/K (Fig. 1). Above approximately 100 K TEP is a roughly linear function of temperature whereas in the low temperature range TEP exhibits a characteristic "knee" and an abrupt approach to about 0 μV/K at 0 K. TEP of the Ni containing alloys becomes more negative with increasing x.

The X(T) = S(T) / T variations plotted in Fig. 2 have the maxima around 50 K which suggest that the exponent in the Eliashberg function n is equal 2 or 3.

Data Analysis

Kaiser and Stedman [9] showed that

$$X(T) = S(T)/T = X_b\left[1+\lambda_0\lambda(T)\right]+\beta\lambda(T) \quad (1)$$

where the bare thermoelectric power S_b determined above the Debye temperature defines the bare thermopower parameter $X_b(T) = S_b / T$ and $\lambda(T)$ is written as

$$\lambda(T) = \frac{\int_0^\infty dE E^{-1}\alpha^2(E)F(E)G_s(E/kT)}{\int_0^\infty dE E^{-1}\alpha^2(E)F(E)} \quad (2)$$

with the universal function $G_s(y)$ proposed by Kaiser [3] as follows:

$$G_s(y) = \frac{3}{\pi^2}\int_0^\infty dz(-\partial f/\partial z)z\int_0^\infty dt\left[\frac{f(t)y^2}{(t-z)^2-y^2}\right] \quad (3)$$

where $f(t)$ is the Fermi function.

The second term in eq. 1 expresses the energy renormalization. The third term of eq. 1 is due to the velocity and relaxation time renormalization as well as the higher order scattering diagrams. A relative role of the third term becomes more important when a magnitude of the bare thermoelectric power is small [9]. For the Al-Y-Ni alloys the bare thermopower is small and the $\beta\lambda(T)$ term is negligible in the Al-Y-Ni alloys. However due to a presence of the magnetic Ni atoms the spin fluctuation effect should λ_{sf} be included. Then eq. 1 can be written as

$$X(T) = \frac{X_b\left[1+a\lambda_0\lambda(T)\right]}{\left(1+\lambda_{sf}\right)} \quad (4)$$

where $a = 1/(1+\lambda_{sf})$

It is assumed that λ_{sf} = const, which is true at temperature higher above the spin fluctuation temperature. Equation 2 is simplified in the extremal temperature ranges. At high temperature close to T_D when the X(T) approaches X_∞ and $\lambda(T) = 0$, eq. 2 becomes :

$$X_\infty = \frac{X_b}{1+\lambda_{sf}} \quad (5)$$

At very low temperature when $X = X_0$ and $\lambda(T) = 1$ the eq. 2 transforms to

$$X_0 = \frac{X_b}{1+\lambda_{sf}}\left[1+\frac{\lambda_0}{1+\lambda_{sf}}\right] \quad (6)$$

Thus the experimental data diplayed in Fig. 2 allow to determine some valuable parameters, like:

1) the Debye temperature T_D, above which the electron - phonon mass enhancement vanishes found from the X(T) slope,
2) the value of X_∞ from X(T) above T_D - according to eq. 4,
3) the X_0 value at low temperature,
4) the parameter $a\lambda_0 = \lambda_0/(1+\lambda_{sf}) = (X_0 - X_\infty)/X_\infty$

The fitting procedures applied to the experimental data resulted in the parameters listed in Tab. I.

Discussion

The parameters T_D, X_∞ and $a\lambda_0$ determined from the the experimental data and listed in Tab. I may be affected by the three factors: 1) ability of the atomic lattice to transfer the electron - electron interaction, 2) spin fluctuations due to the presence of the transition atoms of Ni and 3) electron structure of alloys.

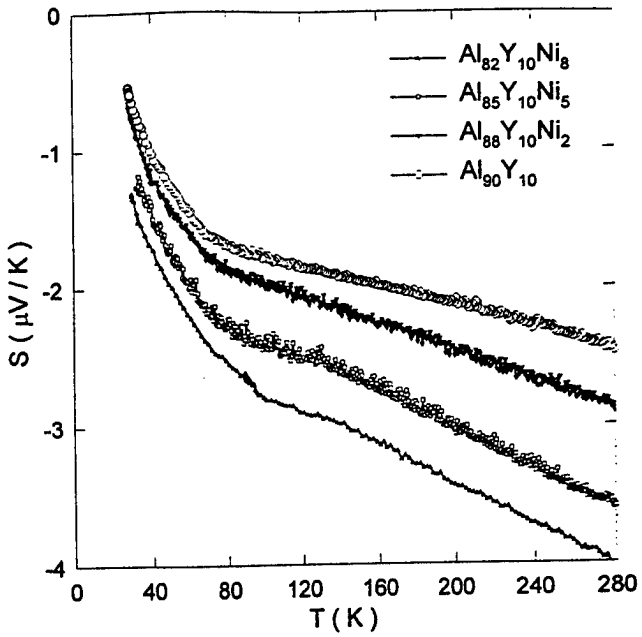


Fig. 1. Temperature dependence of thermoelectric power for $Al_{90-x}Y_{10}Ni_x$ alloys.

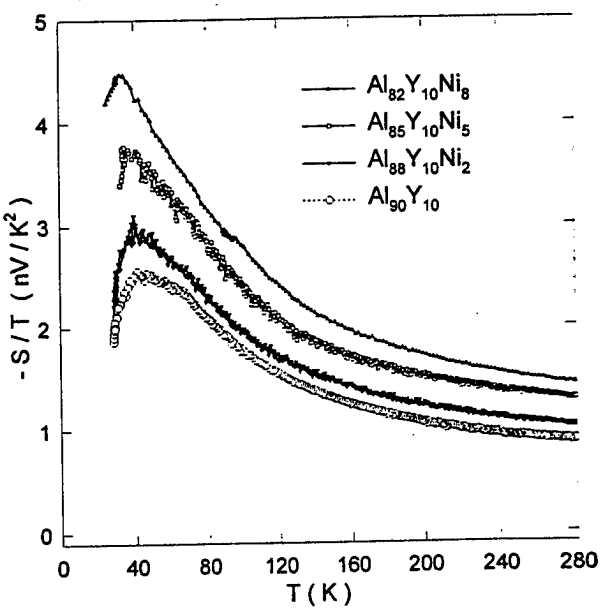


Fig. 2. Temperature variation of S(T) / T for $Al_{90-x}Y_{10}Ni_x$ alloys

In the amorphous alloys $Al_{90-X}Y_{10}Ni_X$ values T_D, X_∞ and $a\lambda_0$ diminish with the rising Al content. This appeals to consider separately an influence of the above mentioned factors.

1. One might expect that in the alloys studied containing 82 to 90 % of the simple metal as Al, values of T_D, X_∞ and $a\lambda_0$ parameters should increase, because the magnitude of the electron - phonon interaction should be stronger at higher Al content . Such a tendency contrasts with this one observed in Tab. I

Table 1. Parameters determined from TEP data analysis.

Alloy	T_D (K)	X_0 (nV/K^2)	X_∞ (nV/K^2)	$a\lambda_0 = \lambda_0 / (1 + \lambda_{sf})$
$Al_{90}Y_{10}$	220	12.5	- 9.0	0.39
$Al_{88}Y_{10}Ni_2$	240	15.0	-10.3	0.46
$Al_{85}Y_{10}Ni_5$	250	20.0	-12.7	0.57
$Al_{82}Y_{10}Ni_8$	270	25.0	-14.8	0.69

2. The magnetic Ni atoms present in the alloys studied should involve the spin fluctuation effects. Thus at the diminishing Ni content (equivalent to increasing Al %) the λ_{sf} should also decrease [6]. In turn, the $a\lambda_0$ parameter should rise up, just oppositely to the tendency seen in the last column of Tab. I.

3.The most plausible interpretation of the T_D, X_∞ and $a\lambda_0$ variations presented in Tab. I is related to the electron structure of the alloys. Values of λ_0 decreasing with the rising Al content may be due to the reduction of the density of states at the Fermi level N(0). Since there are no published data on the electron structure of the Al-Y-Ni alloys, the results of electron structure of the Al(ZrNi) alloys reported by Yamada et al [14] may be applied as the first approximation. This is justified since the Y atom has only one 4d electron less than Zr and the great similarity inthe electron structure of both the alloys may be assumed. The data of Yamada et al. prove that the density of states at the Fermi level is determined by 4d Zr electrons. The Y content is the same for each of the alloys studied. This should lead to the constant N(0) and λ_0 values. The observed λ_0 values diminishing at higher Al content reveal the simultaneous decrease of N(0). This may occur, if the 4d Y states are occupied by the 3p (and maybe also 3s) electrons of the Al atoms. Thus, the relation between λ_0 and Al content is caused by the occurence of the bonding force Al-Y. Such bonds were also reported by Matsubara et al. [15] and Audebert et al. [16] for amorphous Al-Y-Ni and Al-Fe-Nb respectively.

It is worth to notice that a very similar picture was proposed by Bhatnagar et al. [17]. They explained the decrease of λ_0 in the alloys Al(Zr/Ni) by the reduction of the density of states N(0) which was obviously caused by the diminishing Zr content.

The amorphous alloys Al-Y-Ni are known to transform to the nanocrystalline phase [18,19]. Thus, the model presented in point 3) is of relevance for the microstructural nanocrystallization processes in these alloys. Namely the attractive Al-Y forces may cause spatial atomic segragation in amorphous alloys. Then they may operate twofold: first creating the heterogeneous nucleation centers [18], which initiate the crystallization, and second by additionally inhibiting a growth of nanograins, since the diffusion of Al atoms is slowed down due to these forces.

Conclusion

The Debye temperature T_D and the electron - phonon mass enhancement parameter $a\lambda_0$ determined from the experimental thermoelectric data diminish with the rising Al content. Moreover the n exponent in the Eliashberg function is equal to 2 or 3. Such observations are in contradiction to the variations of these parameters expected for alloys containing the prevailing amount of simple metals. The most plausible reason of the reported dependences may be the reduction of the density of states at the Fermi level. This reduction may occur when the 4d Y states at the Fermi level are gradually filled by the the 3p and possibly 3s electrons of Al at rising Al content. The above picture corresponds to the attractive bonding force Al-Y reported also by other authors and correlates with the observed nanocrystallization of these alloys.

Samples were kindly supplied by Dr. J. Latuch. This work supported by grant PB/981/TO8/97/12 of KBN.

References

[1] J. Jäckle, J. Phys. F: Metal Phys. **10** (1980) L43
[2] B.L. Gallagher, J. Phys. F: Metal Phys. **11** (1981) L207
[3] J. L. Opsal, B. J. Thaler, J.Bass, Phys.Rev.Lett. **36** (1976) 1211
[4] B.L. Gallagher, A.B. Kaiser, D. Greig, J. Non-Crystalline Solids **61-62** (1984) 1231
[5] G. Fritsch, E. Luescher, A. Schutte, A. Eckert, J. Willer, W. Dyckhoff, J. Non-Crystalline Solids **61-62** (1984) 1225
[6] Z. Altounian, C.L. Foiles, W.B. Muir, J.O. Strom - Olsen, Phys. Rev. B **27** (1983) 1955
[7] D.G. Naugle, R. Delgado, H. Armbruster, C.L. Tsai, W.L. Johnson, A.R. Williams, J. Phys. F: Metal Phys. **15** (1985) 2189
[8] A.B. Kaiser, J. Phys. F: Metal Phys. **12** (1982) L223
[9] A.B. Kaiser, G.E. Stedman, Solid State Commun. **54** (1985) 91
[10] G. Bergman, Phys. Rev. B **3** (1971) 397
[11] S.J. Poon, Solid State Commun. **34** (1985) 659
[12] L.V. Meisel, P.J. Cote, Phys. Rev. B **23** (1981) 5834
[13] K. Pękała, P. Jaśkiewicz, J. Latuch, A. Kokoszkiewicz, J. Non-Crystalline Solids **211** (1997) 72
[14] Y. Yamada, Y. Itoh, U. Mizutani, N. Shibagaki, K. Tanaka, J. Phys. F **17** (1987) 2303
[15] E. Matsubara, Y. Waseda, A. Inoue, K. Ohtera, T. Masumoto, Z. Naturforsch. Teil A **44** (1989) 814
[16] F. Audebert, H. Sirkin, A. Garcia Escorial, Philos. Magazine B **76** (1997) 483
[17] A.K. Bhatnagar, R. Pan, D.G. Naugle, A.B. Kaiser, J. Phys.: Condens. Matter **2**, 6755 (1990)
[18] M. Calin, U. Köster, ISMANAM Conf. 1997 (preprint)
[19] X.Y. Jiang, Z.C. Zhong, A.L. Greer, Philos. Magazine B **76** (1997) 419

Transport Study of Hg - Based High Temperature Superconductors

M. Pękała[1], H. Bougrine[2,3], I. Sargankova[4], M. Ausloos[2]

[1] Chemistry Department, Warsaw University, Al. Żwirki i Wigury 101, PL-02-089 Warsaw, Poland
tel 48.22.220211, fax 48.22.230123, email pekala@chem.uw.edu.pl
[2] SUPRAS, Institut de Physique, B5, Universite de Liege, B-4000 Liege, Belgium
tel 32.4.3663752, fax 32.4.3662990, email ausloos@gw.unipc.ulg.ac.be
[3] SUPRAS, Institut d'Electricite Montefiore, B28, Universite de Liege, B-4000 Liege, Belgium
[4] Institute of Experimental Physics, Slovak Academy of Sciences, Watsonova 47, 04353 Kosice, Slovakia

Abstract

Polycrystalline superconductors $Hg_1Ba_2Ca_2Cu_3O_{8+\delta}$ were synthesized from oxides by the solid state reaction. Thermoelectric power, thermal conductivity and electrical resistivity of the Hg - based high temperature superconductors were measured in a broad temperature range between 20 and 300 K. The influence of magnetic fields up to 0.35 T was also studied. The superconducting transition starts at about 136 K and is completed in a relatively narrow temperature interval as revealed by thermoelectric power and resistivity measurements. The transition interval broadens in a magnetic field. The experimental data are used to determine and discuss the figure of merit for the Hg1223 superconductor. The figure of merit increases in an external small magnetic field.

Introduction

Peltier refrigerator junction consists of two thermoelectrically active materials, one n-type and the other p-type, mounted on the heat sink at one end and electrically connected at the other hand to form the cold junction. To characterize the Peltier refrigerator one uses the so-called "figure of merit" z: for a material $z = Q/(k\rho)$, where Q is the thermoelectric power (TEP) coefficient, k the thermal conductivity and ρ the electrical resistivity. The figure of merit of the refrigerator is approximately the average $\langle z \rangle$ of the components. Peltier coolers are traditionally used near room temperature in situations where compact, low power conditions are appropriate. For the low (50-200 K) temperature range, the best thermoelectric materials are layered monocrystalline Bi-Sb [1,2]. High T_c superconductors can be of p- or n-type [3].

Contrary to standard opinion thermoelectric effects appear in superconductors, in particular if they are granular ones [4-6]. The case of "transverse effects" (when a magnetic field H is perpendicular to the thermal current J and the electric field E) is of great interest [7]. If controlled, such effects would allow for the use of cryocoolers in magnetic fields near liquid nitrogen temperature. The Seebeck and Peltier effects of HTSC have been much studied by the Liege SUPRAS group, from a theoretical and experimental point of view [e.g.,8-12]. Here we report investigations of the basic transport coefficients and the electrothermal conductivity $P = Q/\rho$ for a new class of HTSC, i.e. a Hg-based HTSC [13].

Experimental

Samples with a composition $Hg_{1.4}Ba_2Ca_2Cu_3O_{8+\delta}$ were prepared by the solid state reaction starting with the stoichiometric mixtures of powdered of Hg-, Ba- Ca- and Cu-oxides, which were ground together under a dry nitrogen and pressed into pellets of a few mm diameter and heated in sealed quartz ampoules at 860 C for 5 hours. The transport measurements were made in a closed cycle refrigerator between 20 and 300 K. Electrical resistivity was measured using the precise four probe method reversing the electrical current direction in order to minimise noise and Peltier effects. Thermoelectric power and thermal conductivity coefficient were measured simultaneously by the differential and steady state methods, respectively. Temperature dependence of the electrothermal conductivity was determined from the electrical resistivity and thermoelectric power. A magnetic field up to 0.35 T was supplied by the electromagnet. More experimental details can be found in [10].

Electrical resistivity

The electrical resistivity is about 20 $\mu\Omega$m at 140 K and varies almost linearily with temperature in the normal state. Departure from linearity appears below 180 K. A transition to the superconducting state starts at about $T = 136$ K and is complete at the resistivity percolation temperature $T = 131$ K, where the electrical resistivity vanishes below the noise level. An application of the magnetic field does not affect the onset temperature of 136 K. However, the transition interval broadens monotonically and the superconducting state is chieved at last below $T = 121$ K.

Thermoelectric power

In analogy to the electrical resistivity also the thermoelectric power is found to be a linear function of temperature above 180 K (Fig. 1), where the slope of Q vs T is equal to -0.022 $\mu V/K^2$. The broad maximum of 6 $\mu V/K$ is located at 145 K, much above the transition temperature. The superconducting transition interval is about 10 K broad

without magnetic field. When a magnetic field of 0.1 T is applied the transition interval broadens and the thermoelectric power vanishes at a temperature 2 K lower, i.e. 129 K (Fig. 2).

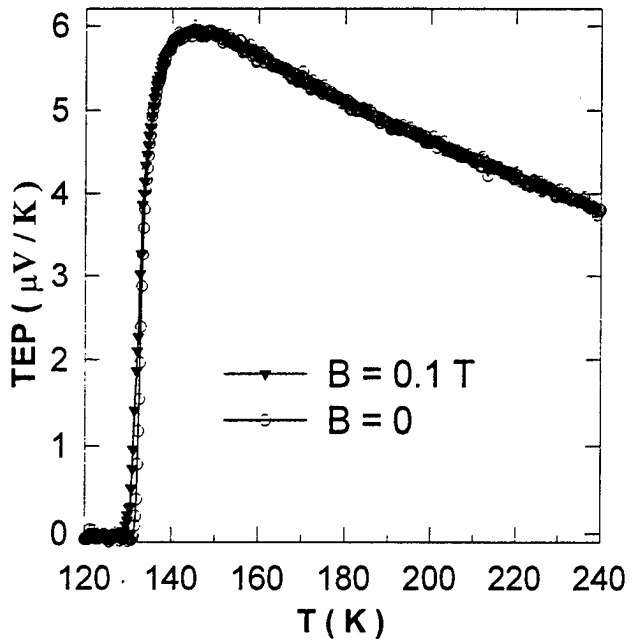


Fig. 1. Thermoelectric power of Hg1223 vs temperature.

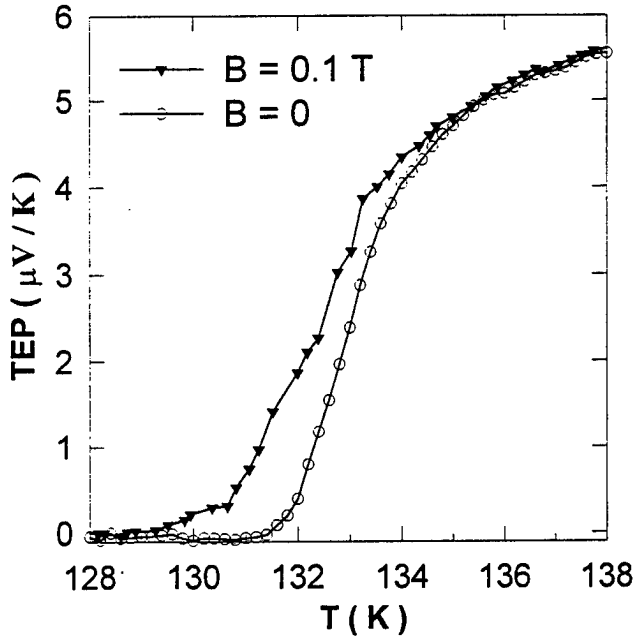


Fig. 2. Thermoelectric power of Hg1223 in the transition interval with and without magnetic field.

Electrothermal conductivity

The electrothermal conductivity describes the density of the normal state excitations driven by a thermal gradient. The temperature variation of the electrothermal conductivity P is typical of HTSC materials [10,14,15]. In the normal state it attains a value of 0.3 A/Km just above the t
transition temperature and is slowly decreasing with temperature with a slope of -0.34 A/K m. A huge and narrow maximum about 1.9 A/Km is seen in the transition interval (Fig. 3). A magnetic field of 0.1 T affects strongly P in the transition range. The maximum value becomes more than twice smaller and broader. Moreover the transition is completed at last at 129 K.

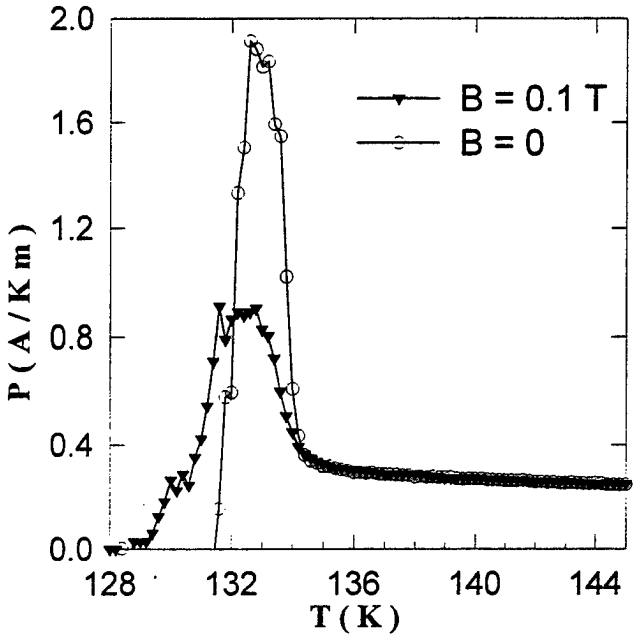


Fig. 3. Electrothermal conductivity vs temperature with and without a small external magnetic field.

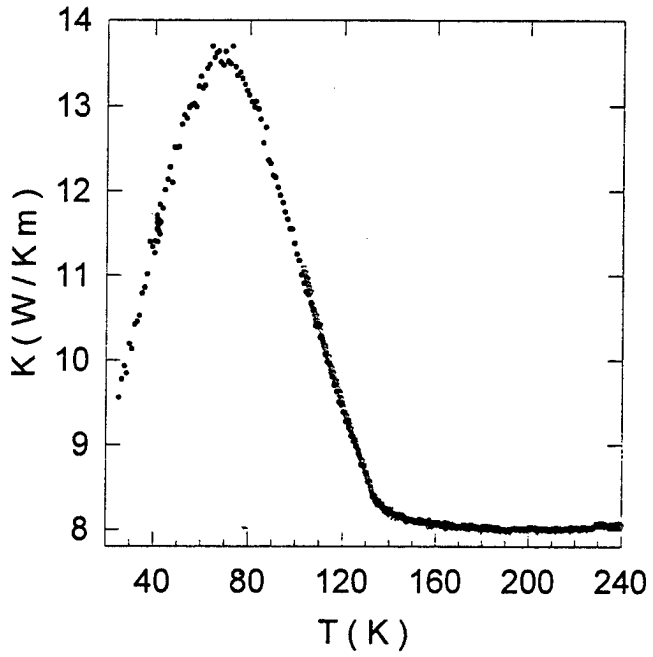


Fig. 4. Thermal conductivity of Hg1223.vs temperature.

Thermal conductivity

The thermal conductivity behavior in superconductors is very unique. In sharp contrast to the electrical transport parameters like the electrical resistivity and thermoelectric power vanishing in the superconducting state, the thermal conductivity reveals even a pronounced maximum in the superconducting phase (Fig. 4). This maximum equal to 13.8 W/Km is located approximately about T /2. There is a long lasting debate concerning the electron versus phonon origin of this maximum. In the normal state the thermal conductivity varies slowly around 8 W/Km. Application of a 0.35 T magnetic field does not alter the thermal conductivity both in the normal and superconducting states. The peak in the electrothermal conductivity has been shown to be highly dependent on the type of band structure in particular of the Van Hove singularities and of the order parameter symmetry of the compound [16-18].

Discussion

The electrical resistivity of the polycrystalline samples studied here is obviously higher than for the Hg1223 single crystals [19]. The relatively narrow transition interval confirms that the sample does not contain noticable amount of additional phases beyond Hg1223. The temperature derivative of the electrical resistivity (Fig. 5) for various magnetic fields shows that the superconducting transition critical region starts at 136 K independently of the applied magnetic field. A position of the dρ/dT peak shifts towards lower temperatures. Such a behavior shows that the samples are homogeneous and intergrain contacts are good.

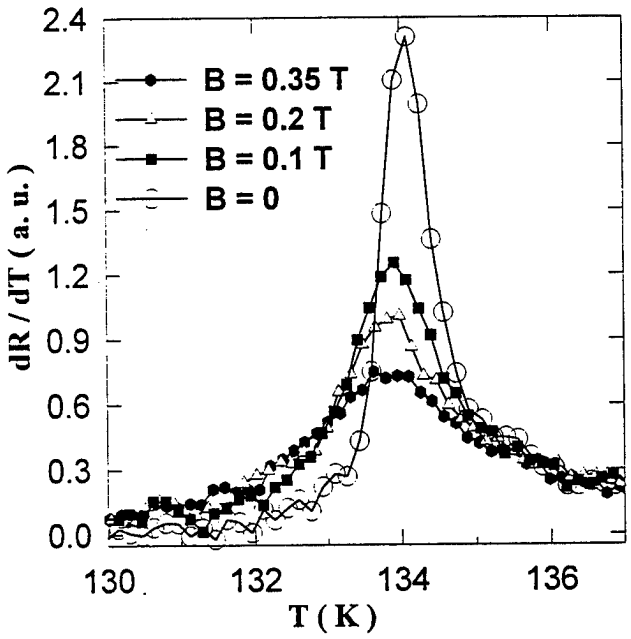


Fig. 5. Temperature derivative of electrical resistivity.

The broadening of the transition interval in the magnetic field is related to the existence of a so called mixed state. The electrical resistivity in the mixed state does not vanish due to the additional electron scattering on vortices. The transition interval width may also increase due to the degeneration of the intergrain contacts by the magnetic field.

In the mixed state the electrical resistivity vanishes at the so called resistivity percolation temperature varying with magnetic field strength as plotted in Fig. 6. Thus the Hg1223 superconductors seem to be strongly affected by a magnetic field since the application of the magnetic field of 0.35 T shifts the percolation temperature by 10 K.

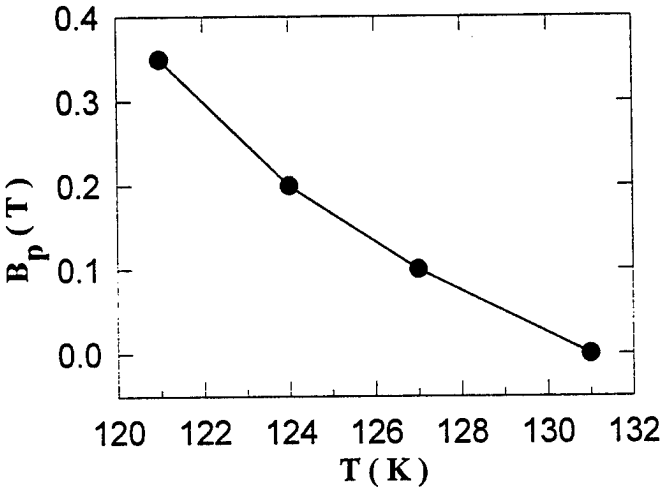


Fig. 6. Electrical resistivity percolation line

The thermoelectric power maximum is comparable or even lower than that reported by other authors [19-24]. The relatively low values of TEP in the normal state prove that the samples are well oxygenated. Moreover, the TEP values enable to determine the hole concentration to be 0.14, which is very close to the optimal one equal to 0.16. This corresponds to the overdoped system [25,26]. Assuming the diffusional mechanism for the normal state TEP one may write it as

$$Q(T) = Q_0 + \pi^2 k^2 T / e E_F \qquad (1)$$

and calculate the Fermi energy $E_F = 3 \pm 0.2$ eV. A value of E_F is rather large as compared with 1.5 ± 0.5 eV for the Bi2223 superconductors [27].

The behavior of the electrical resisitivity in a field, i.e. the broadening of the transition temperature range is usually interpreted through weak links and intrinsic effects. In the case of the thermoelectric power, the situation is more complex because one cannot superpose linearly various effects even in absence of field [28]; It is thought that the dissipation mechanisms contain scattering terms from electron and quasiparticle scattering with vortices and defects, but also an entropy term due to the inhomogeneous distribution of vortices in the sample. It has been thought that the behavior of the integrated excess TEP as a function of the field is likely a signature of the order parameter dominating symmetry [29,30] and therefore the broadening of the TEP transition is of very great interest.

The experimentally determined figure of merit z is about $2*10^{-7}$ K^{-1} in the normal state (Fig. 7) being drastically smaller as compared to the semiconductors working in Peltier refrigerators [31]. Values of z increase 3 times in the narrow transition interval. Additionally an application of magnetic field of 0.1 T causes that z rises by 50 % which is accompanied by a broadening of the transition interval by 2 K. This data shows that one may not expect to use Hg1223 superconductors as active Peltier elements. On the other hand, the Hg1223 material may play the role of the passive thermoelement working above the liquid nitrogen temperature as recently proposed [3,32-33].

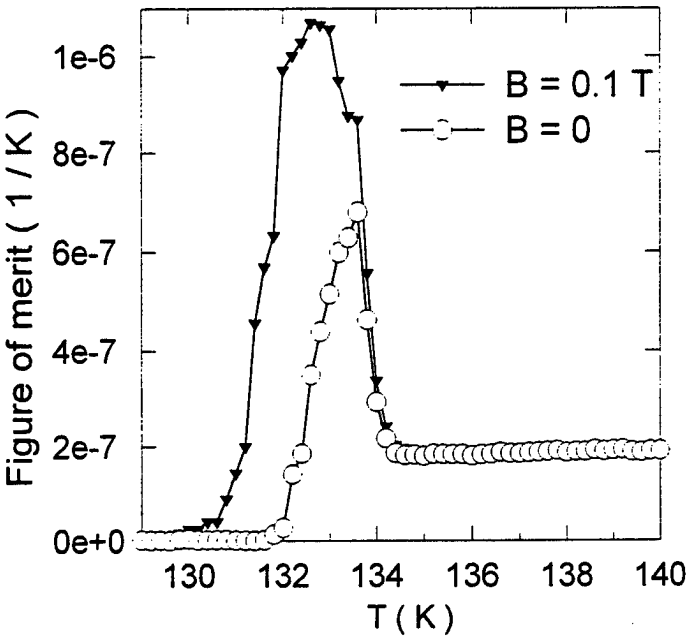


Fig. 7. Figure of merit for Hg1223 vs temperature in a presence or not of the magnetic field.

Conclusions

In view of the above it seems of interest to continue testing HTSC couples for Peltier cryocoolers, and in particular to optimize the material properties in order to improve the figure of merit. No need to say that many fundamental and technical questions are still unsolved.

Acknowledgment. Work was supported in parts by BW-1383-42/97 (MP), Project No. 2/1323/94 (IS) of Grant Agency of Slovak Academy of Sciences and ARC 94-99/174 of the Ministery of Higher Education through the University of Liege.

References

1. J. Navratil et al., Mater. Res. Bull. **31** (1996) 1559
2. N.A. Sidorenko et al., Supercond. Sci. Technol. **6** (1993) 63
3. H.J. Goldsmid et al. , J. Phys. D. **21** (1988) 344
4. V.L. Ginzburg, Sov. Phys. Usp. **34** (1991) 101
5. A.B. Kaiser and C. Uher, in "Studies of High Temperature Superconductors", vol.7 (Nova Sc. Publ., New York, 1990)
6. V.V. Gridin et al., Phys. Rev. B **47** (1993) 14 591
7. R.P. Huebener et al. , Phys. Rev. B **42** (1990) 4831
8. P. Clippe et al. , Phys. Rev. B **42** (1990) 8611
9. S. Sergeenkov and M. Ausloos, Phys. Rev. B **47** (1993) 14476
10. M. Pękała et al., Supercond. Sci. Technol. **8** (1995) 726
11. M. Pękała et al., Phys. Rev. B **52** (1995) 7647
12. M. Pękała et al., Supercond. Sci. Technol. **9** (1996) 644
13. H. Bougrine et al., Supercond. Sci. Technol. (1997 in press)
14. J. Mucha et al., Molecular Physics Rep. **15/16** (1996) 265
15. M. Houssa et al., Phys. Rev. B **54** (1996) R12713
16. M. Houssa and M. Ausloos, Physica C **265** (1996) 258
17. M. Houssa et al., Phys. Rev. B **54** (1996) 6126-6129
18. M. Houssa and M. Ausloos, J. Phys.: Condens. Mat. **9** (1997) 201
19. A. Carrington et al., Physica C **234** (1994) 1
20. C.K. Subramaniam et al., Phys. Rev. B **51** (1995) 1330
21. A.B. Kaiser et al., Synthetic Metals **71** (1995) 1583
22. F. Chen et al., (preprint 97:015)
23. F. Chen et al., (preprint 96:058)
24. G.C. McIntosh, A.B. Kaiser, Phys. Rev. B **54** (1996) 12569
25. J.L. Tallon et al., Phys. Rev. B **51** (1995) 12911
26. S.D. Obertelli et al., Phys. Rev. B **46** (1992) 14928
27. R. Cloots et al., Physica C **231** (1994) 259
28. K. Durczewski and M. Ausloos, Phys. Rev. B **53** (1996) 1762
29. M. Pękała and M. Ausloos, Physica C **235-240** (1994) 1385
30. M. Houssa et al., Czech. J. Phys. **46**, S2(1996) 1003
31. T.C. Harmon, J.M. Honig, Thermoelectric and Thermomagnetic Effects and Applications, (McGraw-Hill Co., N.Y. 1967) p.285
32. V.L. Kuznetsov et al., Sverhprovodimost (Russia) **4** (1991) 616
33. Z.M. Dashevskii et al., Supercond. Sci. Technol. **5** (1992) 690

Magneto - Thermoelectric Studies of High Temperature Superconductors

M. Pekala[1] and M. Ausloos[2]

[1] Chemistry Department, Warsaw University, Al. Zwirki i Wigury 101, PL-02-089 Warsaw, Poland
tel 48.22.220211, fax 48.22.230123, email pekala@chem.uw.edu.pl
[2] SUPRAS, Institut de Physique, B5, Universite de Liege, B-4000 Liege, Belgium
tel 32.4.3663752, fax 32.4.3662990, email ausloos@gw.unipc.ulg.ac.be

Abstract

The electrical resistivity and Seebeck effect probe the charge carrier currents caused by electric and temperature gradients. A magnetic field additionally superimposed on a superconducting sample allows to observe phenomena called excess electrical resistivity, excess thermoelectric power, Nernst effect and excess electrothermal conductivity. These parameters supply some consistent information on the kinetics of vortices and of quasi particle scattering in the mixed state. We stress apparently different behaviors for the various effects. We emphasize that more relevance should be put on sorting out the various dissipation mechanisms, like quasi particle scattering, vortex motion dissipation and superconductivity fluctuations. Several cases of Bi-based superconductors are reviewed with the aim of defining further investigation lines.

Introduction

Electric charge and heat transport processes proceed in various manner in the normal, superconducting and mixed states of high critical temperature superconductors (HTSC), since the carriers exhibit unique properties in these states. The so called mixed state where the quasiparticles (QP) and vortices (V) respond both to the electric and temperature gradients [1] is selected for discussion here below.

The electrical resistivity, thermoelectric power and electrothermal conductivity probe electric and heat currents and supply a characterization complementary to the data obtained from non-transport methods. When a magnetic field B is additionally superimposed on the superconducting sample with an orientation parallel or perpendicular to the electric or temperature gradient, effects called excess electrical resistivity, excess thermoelectric power, Nernst effect and excess electrothermal conductivity can be observed. The excess magneto-thermal conductivity is not discussed here.

The thermopower and Nernst effects may be thought as the thermal analogues of the electrical resistivity and the Hall effect with the heat current replacing the electrical current. Indeed, the Nernst effect is the off-diagonal element of the Seebeck coeficient tensor when the magnetic field is perpendicular to the plane of the thermal gradient and the induced, and measured, electric potential.These properties are markedly anisotropic due to the crystallographic layered structure of HTSC materials. The choice of the x, y, and z axes and of the measured tensor element will depend on the choice of the experimental probe positions. In fact, this will often practically depend on the geometry of the sample, and the available space for connecting such probes to the sample. However in single crystal materials or in their equivalent ones, like the textured materials, the intrinsic crystallographic anisotropy leads to an extra degree of freedom for the experimental investigation, i.e. specifically the orientation of the field can be parallel or perpendicular to the layers.

The correct choice of "currents" must be considered beside the proper choice of conjugate fluxes and forces [2] in a simple phenomenological description. The appropriate "scattering relaxation time(s)" and "density of carriers" have to be considered. It is known that a description of the anisotropy of such quantities is not trivial [3]. In such a spirit one can examine contributions to the traditional dissipation mechanisms from QP and V and propose new ones in HTSC. For example, the sign of the Nernst effect is properly determined by the energy dependence of the relaxation time in a kinetic theory [2]. This opens the possibility of finding whether any relaxation mechanism corresponds to carrier scattering by excitations having a linear spectrum, like trivially acoustic phonons or the vortex line thermal excitations. This can be related to the considerations of Coffey [4], who has further distinguished between Abrikosov and Josephson vortices, depending on the magnitude of the magnetic field. Let us also point out the relevant considerations of Samoilov et al. [5] for the TEP only of 2212 BSCCO single crystal systems. Moreover, the role of superconducting fluctuations below and above the Ginzburg - Landau temperature has already been considered by many authors but should be still rethought of in view of modern developments on QP and V dissipative mechanisms which should be better taken as a background to be extracted before looking for critical exponents.

This paper is aimed at presenting physically relevant features and parameters obtained from such magneto-transport measurements; we will concentrate our attention on Bi-based HTSC for which some anisotropy effects could be well marked. In the following the critical temperature T_c is that of the inflection point in the electrical resistivity or the thermoelectric power (TEP) accordingly, while the percolation temperature T_p is that at which the property vanishes. This occurs when a perfect phase coherence is established throughout the sample. Both T_c and T_p depend on B. In the framework of usual data analysis near phase transitions, we will compare the temperature shifts and transition widths with respect to their zero field value in the appropriate relative units.

0-7803-4057-4/97 $10.00 ©1997 IEEE

Experimental

Several polycrystalline samples, i.e. $Bi_{1.7}Pb_{0.3}Sr_2Ca_2Cu_3O_{10-x}$ (PA) [6], $Bi_{1.84}Pb_{0.34}Sr_{1.91}Ca_{2.03}Cu_{3.06}O_{10-y}$ (PB) [7], a lead-free $Bi_2Sr_2Ca_2Cu_3O_{10-v}$ textured (TA and TC - corresponding to the magnetic field oriented in the ab- plane and c- axis, respectively) [8,9] and a $Bi_2Sr_2Ca_1Cu_2O_{8-z}$ single crystal (SC) [10] were examined. They were structurally characterized by X - ray diffraction and electron microscopy. The transport measurements were made under helium atmosphere between 15 and 300 K. The electrical resistivity $\rho(T)$ and the thermoelectric power Q(T) were measured from the voltage and temperature drops along the sample. A magnetic field up to 4 T oriented perpendicular to the electric potential or temperature gradient was used to measure magnetoeffects in $\rho(T)$ and Q(T). In the case of the textured samples it was possible to orient the field transversally to the sample along the c-axis or along the ab-plane direction. The data are called TC and TA respectively in the following figures. The electrothermal conductivity $P = Q/\rho$ in a magnetic field B directly results from both Q(T, B) and ρ(T, B). The (transverse) Nernst coefficient N was calculated from the voltage appearing at right angle both to the temperature gradient and the magnetic field directions. The experimental details were described elsewhere [6-10].

Electrical resistivity in a magnetic field

The electrical resistivity and thermoelectric power measured in an external magnetic field unveil some additional structure as compared with the zero field case. The width of the transition is always finite even in zero field (Fig. 1). This indicates some weak link existence even in the case of the textured and single crystal samples. The external magnetic field enhances the intra- and inter-grain contributions in the resistivity through features appearing at the upper and at the lower end of the temperature intervals of interest. The relative transition intervals are the relative differences between T_c and T_p for each field. They are relatively broader in the polycrystalline HTSC than in the pressure textured and crystalline samples (Fig. 1). A relatively linear behavior is seen for all samples except for the PB sample for which a 3/4 power law can be well demonstrated on a log-log plot. Notice that this is different from Tinkham's law [11] which predicts a 2/3 power, likely valid for 3D systems only.

The different behaviors point to the different origins of the transition broadening. The most plausible explanation is that the main contribution below and close to T_c arises due to the intragranular transition. The contribution at lower temperature is more magnetic field sensitive and is related to intergranular phenomena for which the weak link distribution plays a major role. Let us recall that the usual geometry for measuring ρ(T, B) is not useful for distinguishing quasi particle scattering from vortex dissipation. However results obtained with an YBCO Corbino disk [12] suggest that the mixed state dissipation of high-T_c superconductors is very strongly influenced by the quasiparticle (QP) excitations. It would be interesting to reproduce the Corbino geometry disk experiment with Bi-based materials.

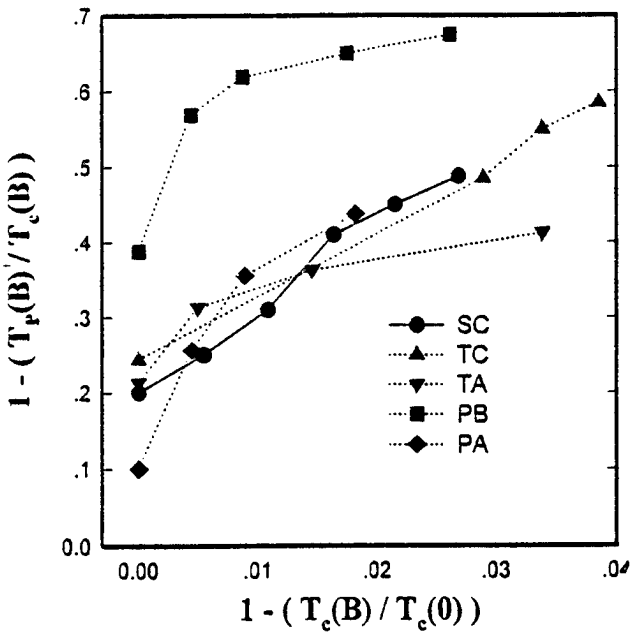


Fig. 1. Variation of the mixed state temperature interval as a function of the relative shift of the transition temperature at different fields and for different samples as defined in the text. Lines are guides to the eye only. Data are calculated from electrical resistivity measurements.

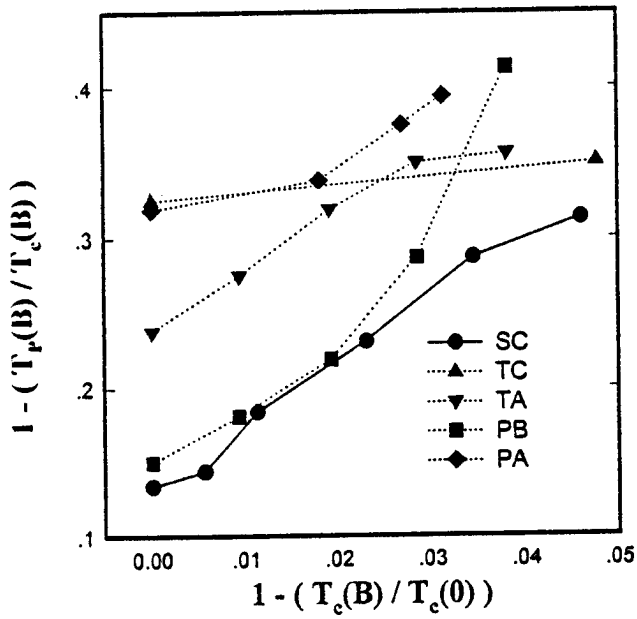


Fig. 2. Variation of the mixed state temperature interval as a function of the relative shift of the transition temperature at different fields and for different samples. Lines are guides to the eye only. Data extracted from thermoelectric measurements.

Thermoelectric power in a magnetic field

The normal state values of TEP data enable to determine the hole concentration, p, by fitting to the empirical formula [13]

$$T_c / T_{cmax} = 1 - 82.6 (p - 0.16)^2 \qquad (1)$$

The p values locate the HTSC samples studied here in the under-(below 0.16) and over-doped (over 0.16) ranges, as listed in Table I.

A very similar tendency as seen in the behavior of the resistivity is also observed for the thermoelectric power in the mixed state. The broadening of the transition width (Fig. 2) is wider in the TEP case than in the resistivity case and increases linearly even for the PB sample but not so much for TC, i.e. for B // c. This is usually related to the external magnetic field penetration into HTSC weak links [14] and the vortex motion dissipation in layers. However it would be of interest to investigate whether the quasiparticle dissipation is still as high as the vortex dissipation in HTSC as found for the electrical resistivity in the mixed state. Recent works by Clayhold et al.[15] seem to indicate that specific features might be explained at least at low field as due to the former (QP) effect also for this thermal transport property. Then the temperature and field range where an equal balance of dissipation contribution should occur is a question of great interest. It could be further investigated whether that temperature occurs above the equivalent phase coherence transition temperature T_p for TEP and whether the flux line lattice melting can be observed in such type of transport property. Let us recall the anomalous hysteresis seen in TEP in ref. 16, which was interpreted as due to weak links but might now be considered as a signature of the vortex lattice melting (first order) transition [17, 18].

Electrothermal conductivity in a magnetic field

The electrothermal conductivity is defined by $P = Q / \rho$. It probes the electrical current density of the normal excitations, driven by a thermal gradient [7,15,19]. P is a slowly varying function in the normal state of the type II HTSC. A 4/3 power law can also be seen on a log-log plot for the behavior of the temperature transition width of P as a function of the field for the PB case. The width gradually broadens when stronger magnetic fields penetrate in the HTSC samples. The finite value of P below the finite field phase coherence transition temperature T_p of the resistivity indicates that different mechanisms are responsible for the loss of superconductivity in various properties.

Nernst effect

The Nernst signal arises at a temperature about 5 to 10 K higher than the Ginzburg - Landau transition temperature indicated by the electrical resistivity and thermoelectric power inflection point [6-10,20,21]. Since the normal state Nernst effect has some small though finite value this shows that the superconductivity onset is much above T_c. The fact that the temperature at which N vanishes seems to increase from 90 to 95K when the field increases, points out to the

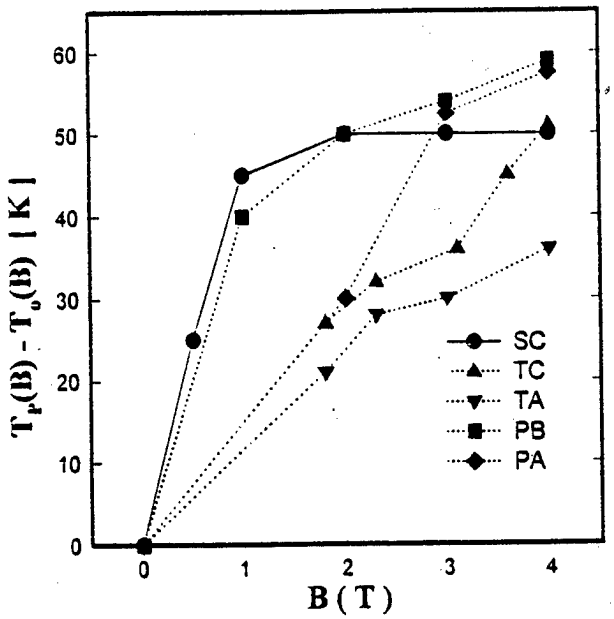


Fig. 3. Variation of the mixed state temperature interval as a function of the field strength for different samples as measured from Nernst data. Lines are guides to the eye only.

influence of superconductivity fluctuation contributions, and show that they exist quite above T_c in such anisotropic systems. The case is well seen in Fig. 8 of ref.7 for the PB sample. Similarly to the electrical resistivity and thermoelectric power data, the Nernst effect exhibits differences concerning the magnitude and behavior of the transition temperature interval in a field. This is demonstrated for various samples in Fig.3.

The range of finite Nernst signal approximately coincides with the temperature interval where the electrical resistivity is finite. In the mixed state the Nernst voltage is thought to be a direct evidence of vortex motion resulting from the Josephson - Lorentz relation, $\mathbf{E} = - (\mathbf{v} \times \mathbf{B})$, where v is the vortex velocity. In so doing it is often thought that the Nernst coefficient is related to the vortex transport entropy S_φ (Table I) by $N = S_\varphi / \Phi_0 B$ where Φ_0 is the flux quantum. An important assumption in this respect is that the electrical resistivity $\rho(T)$ in the mixed state is solely due to the vortex motion dissipation. Since the magnetic field is present in the vortex cores with a superconducting surrounding and the core states can be excited, this transport entropy might be overestimated in so doing. A correct theory should consider the contribution to heat flow performed by the excitations within vortices as well. In fact a difference with respect to standard arguments unexpectedly occurs in the decay of the entropy S_φ behavior just below T_c and reinforces our warning. The decay is found to be smoother than expected [7,8]. Nevertheless, assuming here that there is no contribution from quasi particle dissipation, the energy U(T) transported by vortices can be calculated. U(T) grows with magnetic field in the examined field range. Moreover, extrapolation of U(T) plots allowed us to determine the temperature dependence of the second critical field $B_{c2}(T)$ as displayed in Fig. 4.

TABLE I. Physical parameters deduced from magnetotransport data on various Bi-based superconducting samples as defined in the text: p = hole concentration; $S_{\varphi max}$ = maximum transport entropy; k_{GL} = Ginzburg - Landau parameter; ξ = coherence length at zero temperature and zero field; F_t = thermal force per unit length at (indicated temperature, in K); η = vortex viscous damping coefficient determined at (same temperature as F_t). When appropriate, it should be understood that the values are given for the 4T case.

sample	PA	PB	TA	TC	SC
p	0.19	0.12	0.11	0.11	0.14
$S_{\varphi max}$ (10^{-16} J/Km)	9.0	3.2	19.0	4.0	5.0
k_{GL}	85÷10	82÷18	25÷5	65÷10	95÷25
ξ (nm)	2 - 6	2 - 8	8 - 20	0.2 - 0.8	0.1 - 0.7
F_t (10^{-12} N/m)	2.5 (106)	5.0 (92)	2.0 (90)	2.0 (90)	2.0 (88)
η (10^{-9} Js/m^3)	1.6	1.4	4.1	2.3	1.2

Notice that from the behavior of N, and the above analysis, it can be argued that a finite B_{c2} value might exist above T_c, and likely up to the true onset temperature. The "fine structure sometimes observed below T_c in the Nernst signal and thought to be due to structural and chemical inhomogeneities [17] might also be reexamined in light of ideas on the vortex lattice melting transition [17].

We should note that contrary to TEP, the Nernst effect is independent of the charge carrier sign, and should be a positive / negative function (as it is most of the time) if the relaxation process is only a decreasing / increasing function of energy [2]. Therefore the mere sign of the Nernst effect is a key ingredient for understanding microscopic scattering processes and dissipation phenomena in HTSC.

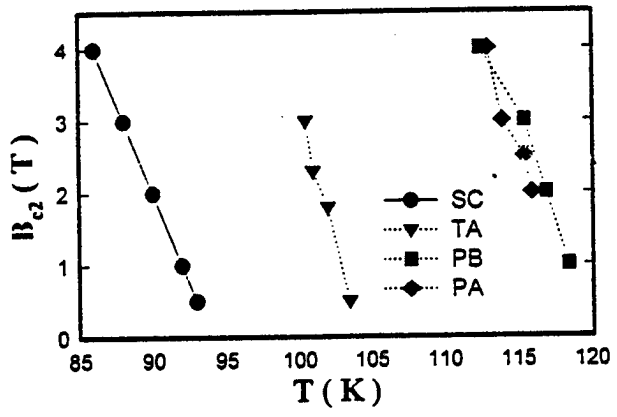


Fig. 4. Variation of the upper critical field B_{c2} as a function of temperature as deduced from vortex entropy data. Lines are guides to the eye only.

Transport entropy and upper critical field

The heat transported by normal excitations present in vortex cores embedded in the superconducting matrix is accounted for by the transport entropy calculated from the Nernst and resistivity data as

$$S_\varphi(T) = \Phi_0 N B/\rho \qquad (2)$$

S_φ sets on below the transition when a magnetic field starts to penetrate, then passes through a maximum and decays at lower temperature due to vortex pinning [1-4].
At various external magnetic fields the S_φ curves cross the temperature axis revealing thus the high temperature behavior of B_{c2} plotted in Fig. 4.

Ginzburg-Landau parameter and penetration depth

To determine the Ginzburg - Landau parameter k_{GL} we used

$$k_{GL} = [(\Phi_0 /9.28\,\pi)\,(dB_{c2}/dT)/(dU/dT)]^{1/2} \qquad (3)$$

This in turn allowed us to calculate the coherence length ξ using the penetration depth values λ taken from literature [1,5]. The k_{GL} and ξ values (Table I) determined from transport data reported for various Bi - based HTSC are in agreement with values inferred from magnetic measurements.

Thermal Hall angle and thermal force

In the case of a thermal current in the mixed state of HTSC it can be shown that the balance of forces leads to a much larger transverse voltage than the thermal one. One usually defines the thermal Hall angle like in the electrical case, i.e. by the ratio between the transverse and longitudinal voltages. The magnetic field dependent Seebeck and Nernst effects allow us to determine the thermal Hall angle

$$\alpha = \arctan (N B / Q) \qquad (4)$$

between the vortex velocity and the magnetic field [1,7,21]. In the range close to the transition temperature and due to the relatively weak thermal force $F_t = - S_\varphi \nabla T$, vortices move almost exactly along the direction of the magnetic field, as shown by the nearly zero a values for the case of the single crystal 2212 sample [10]. The thermal force (Table I) increases at lower temperatures and causes the vortex velocity vector to approach the thermal gradient direction when $\alpha = 90°$. The magneto transport data enable

us to estimate absolute values of the thermal force F_t experienced by the unit length of vortices. Such a force is of the order of 10^{-12} N/m just below T_c. In Tab. I we also list the value of the so called "vortex viscous damping coefficient" defined by [22] as

$$\eta = B_{c2}\,\Phi_o / \rho \qquad (5)$$

The η values for Bi - based HTSC are of the order of 10^{-9} Js/m^3. Due to a lacking data for Bi2223 materials we could compare them only with 5×10^{-5} Js/m^3 for the Y123 samples but at the temperature as low as 3 K [23].

Conclusions

The electrical and thermoelectrical transport studies of HTSC provide valuable experimental data for testing superconductivity models. The case of Bi based HTSC was summarized here for the finite magnetic field case. Similarities and differences in several data sets were briefly discussed. These properties and the derived parameters in fact allow to perform quick characterization of superconducting materials, necessary for optimization of the production, treatment and technological processes. Moreover, they serve to raise fundamental questions and automatically request new data to be collected and suggest better data analysis.

Acknowledgements. Support by a grants 3T09A 00811 and HTECH.EV.970414 is acknowledged. This work is also a part of an ARC (94-99/174) grant from the Ministry of Higher Education through the Research Council of the University of Liege. We thank Prof. H.W. Vanderschueren for allowing us to use the Measurement and Instrumentation Electronics Laboratory (MIEL) and all our coworkers in these studies.

References

1. R.P. Huebener, Supercond. Sci. Tech. **8** (1995) 189.
2. J.M. Ziman, Electrons and Phonons, Clarendon. Oxford. (1963)
3. M. Ausloos and K. Durczewski, J. Magn. Magn. Mater. **53** (1985) 243.
4. M.W. Coffey, Phys. Rev. B **48** (1993) 9767.
5. A.V. Samoilov, A.A. Yurgens, and N.V. Zavaritsky, Phys. Rev. B **46** (1992) 6643.
6. M. Pekala, H. Bougrine, and M. Ausloos, J. Phys.: Cond. Matter **7** (1995) 5607.
7. M. Pekala, A. Tampieri, G. Celotti, M. Houssa, and M. Ausloos, Supercond. Sci. Technol. **9** (1996) 644
8. M. Pekala, H. Bougrine, T. Lada, A. Morawski, and M. Ausloos, Supercond. Sci. Technol. **8** (1995) 729
9. M. Pekala, H. Bougrine, M. Ausloos, T. Łada, and A. Morawski, Molec. Phys. Rep. **7** (1994) 249.
10. M. Pekala, E. Maka, D. Hu, V. Brabers, and M. Ausloos, Phys. Rev. B **52** (1995) 7647.
11. M.H. Tinkham, Phys. Rev. Lett. **61** (1988) 1658.
12. V.V. Gridin, S. Sergeenkov, and M. Ausloos, Solid State Commun. **98** (1996) 623.
13. S.D. Obertelli, J.R. Cooper, and J.L. Tallon, Phys. Rev. B **46** (1992) 14 928.
14. R.P. Huebener, Magnetic Flux Structures in Superconductors, Springer Verlag, Berlin (1979)
15. J.A. Clayhold, Y.Y. Xue, C.W. Chu, J.N. Eckstein, and I. Bozovic, Phys. Rev. B **53** (1996) 8681.
16. S. Sergeenkov, M. Ausloos, H. Bougrine, R. Cloots, and V.V. Gridin, Phys. Rev. B **48** (1993) 16 880.
17. E. Brezin, D.R. Nelson, and A. Thiaville, Phys. Rev. B **31** (1985) 7124.
18. M. Ausloos, H. Bougrine, M. Houssa,and M. Pekala, submitted to Phys. Rev. B (1997)
19. M. Houssa, R. Cloots, S. Stassen, M. Pekala, and M. Ausloos, Czech. J. Phys. **46**, S2, (1996) 1003
20. S. Sergeenkov and M. Ausloos, Phys. Rev. B **47** (1993) 14476
21. S.A. Sergeenkov, V.V. Gridin, P. de Villiers, and M. Ausloos, Physica Scripta **49** (1994) 637
22. J. Bardeen and M.J. Stephen, Phys. Rev. **140** (1963) A1197
23. Y. Matsuda, N.P. Ong, Y.F. Yan, J.M. Harris, J.B. Peterson, Phys. Rev. B **49** (1994) 4380

MgAgAs structure type solid solutions as a new thermoelectric material

L.P.Romaka, Yu.V. Stadnyk, A.M.Goryn, Yu.K.Gorelenko, R.V. Skolozdra
Inorganic Chemistry Department, Lviv State University, Kirila and Methodia street 6,
Lviv 290005, Ukraine

Abstract

Solid solutions $TiNiSn_{1-x}Me'_x$ (Me'=Al, Sb, and Bi) and $ZrNi_{1-x}Me''_xSn$ (Me''=Cr, Mn, and Cu) with MgAgAs structure type were obtained on the basis of the TiNiSn and ZrNiSn semiconducting compounds. X-ray analysis was used to define the stability range of the solid solutions. The temperature dependence of the resistivity and thermopower showed a losses of semiconducting properties. The sign of thermopower remains negative for all solid solutions.

Introduction

The group of thermoelectric materials may be considerably expanded by the stannide compounds with the MgAgAs structure type. Their appropriate electrokinetic properties, high melting points, and a simple method of synthesis provide with ample opportunity to use these materials as a thermoelectrics but MeNiSn compounds (Me=Ti, Zr, Hf) can be so used in particular [1-4]. The stability of these phases is determined, in general, by the electron concentration (EC) factor that is equal to eight electrons per formula unit (8 el./f.u.) [1]. EC deviations in MeNiSn compounds that is caused by partial substitutions of the constituent elements may provide the appearance of the materials with different magnitudes of the resistivity (ρ) and thermopower (α). In this way we can also to reverse the type of conductivity [1,3,5]. The stability ranges of $TiNiSn_{1-x}Me'_x$ (Me'=Al, Sb, and Bi) and $ZrNi_{1-x}Me''_xSn$ (Me''=Cr, Mn, and Cu) solid solutions were investigated in this work and their electrokinetic properties were measured.

Experimental Procedure

Samples of nominal compositions were prepared by arc-melting of the pure metals (purity of the constituents is better than 99.9%) using a tungsten electrode under a high purity argon atmosphere. The ingots were homogenized by annealing at 1073 K for 720 h in evacuated quartz tubes. The phase composition of the samples was checked by X-ray analysis. The electrical resistivity and differential thermopower relative to copper were measured as described in [6].

Results and Discussion

TiNiSn and TiNiSb compounds (MgAgAs structure type, Space Group $F\bar{4}3m$) give rise to continuous solid solution because these compounds have the same crystal structure type and the difference of atomic radii of Sn and Sb is not significant. $TiNiSn_{1-x}Al_x$ and $TiNiSn_{1-x}Bi_x$ solid solutions are extended up to x=0.3 and x=0.1, respectively (Table 1). Insignificant replacement of Sn by Sb (x=0.05) in TiNiSn compound gives rise to losses in semiconducting properties and metallic type conductivity shows up but thermopower remains negative. $TiNiSn_{0.9}Bi_{0.1}$ alloy has the similar electrokinetic properties.

$TiNiSn_{1-x}Al_x$ solid solution has the gradual semiconductor-to-semimetal transition (Fig. 1).

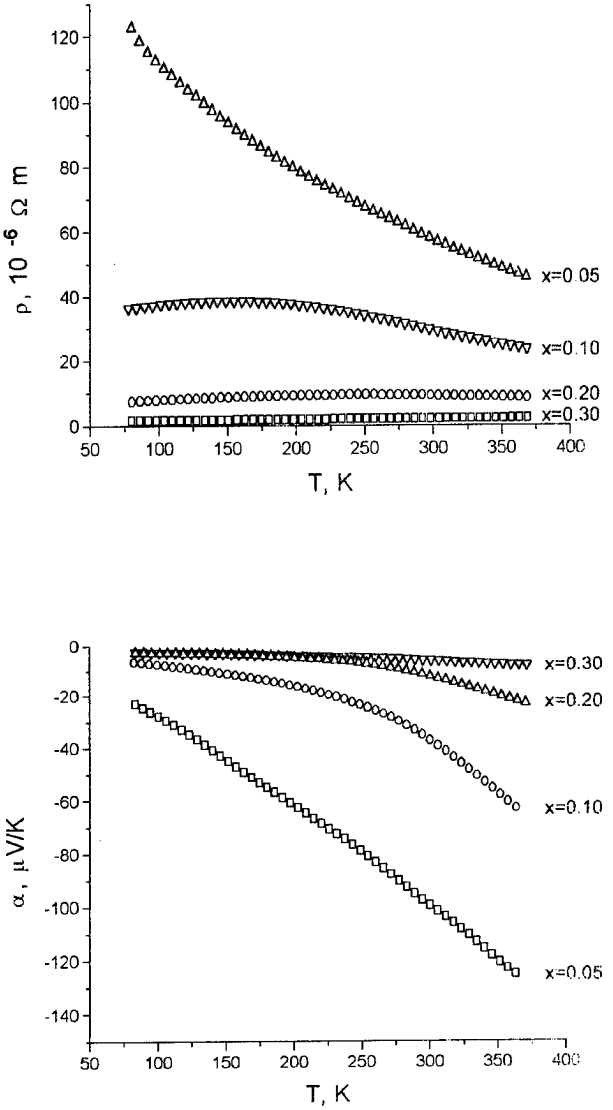


Fig. 1: Resistivity (ρ) and thermopower (α) as functions of temperature for $TiNiSn_{1-x}Al_x$ solid solution.

Al possesses the acceptor properties in the large majority of the well-known semiconductors. Since the doping of

Table 1
The characteristics of the MgAgAs structure type solid solution alloys at 293 K

Alloys composition	a, nm	ρ, μΩ·m	α, μV/K
$TiNiSn_{0.95}Al_{0.05}$	0.5922(2)	57.1	-100.0
$TiNiSn_{0.90}Al_{0.10}$	0.5918(2)	29.0	-35.8
$TiNiSn_{0.80}Al_{0.20}$	0.5916(2)	9.0	-11.0
$TiNiSn_{0.70}Al_{0.30}$	0.5913(2)	2.0	-6.0
$TiNiSn_{0.95}Sb_{0.05}$	0.5921(1)	2.2	-78.1
$TiNiSn_{0.90}Sb_{0.10}$	0.5921(1)	1.5	-32.0
$TiNiSn_{0.80}Sb_{0.20}$	0.5922(8)	3.3	-12.0
$TiNiSn_{0.70}Sb_{0.30}$	0.5923(1)	0.7	-20.5
$TiNiSn_{0.60}Sb_{0.40}$	0.5925(5)	0.7	-15.6
$TiNiSn_{0.50}Sb_{0.50}$	0.5928(2)	1.4	-15.6
$TiNiSn_{0.40}Sb_{0.60}$	0.5929(6)	1.0	-8.0
$TiNiSn_{0.30}Sb_{0.70}$	0.5908(3)	0.9	-8.7
$TiNiSn_{0.10}Sb_{0.90}$	0.5887(2)	2.0	-9.9
TiNiSb	0.5884(6)	2.4	-11.4
$TiNiSn_{0.90}Bi_{0.10}$	0.5924(1)	5.6	-52.0
$ZrNi_{0.95}Cr_{0.05}Sn$	0.6094(1)	25.0	-192.5
$ZrNi_{0.90}Cr_{0.10}Sn$	0.60952(9)	35.2	-66.3
$ZrNi_{0.80}Cr_{0.20}Sn$	0.60955(6)	8.3	-24.0
$ZrNi_{0.75}Cr_{0.25}Sn$	0.60968(6)	5.1	-14.8
$ZrNi_{0.70}Cr_{0.30}Sn$	0.6097(1)	3.3	-5.9
$ZrNi_{0.60}Cr_{0.40}Sn$	0.60981(7)	2.3	-4.5
$ZrNi_{0.95}Mn_{0.05}Sn$	0.6093(1)	84.5	-230.0
$ZrNi_{0.90}Mn_{0.10}Sn$	0.60944(8)	68.0	-137.6
$ZrNi_{0.80}Mn_{0.20}Sn$	0.60953(9)	26.0	-117.5
$ZrNi_{0.75}Mn_{0.25}Sn$	0.6096(1)	31.2	-45.8
$ZrNi_{0.70}Mn_{0.30}Sn$	0.60968(6)	-	-45.4
$ZrNi_{0.60}Mn_{0.40}Sn$	0.60966(7)	22.6	-31.6
$ZrNi_{0.50}Mn_{0.50}Sn$	0.60971(9)	15.3	-13.3
$ZrNi_{0.95}Cu_{0.05}Sn$	0.6102(3)	5.2	-78.5
$ZrNi_{0.90}Cu_{0.10}Sn$	0.6109(2)	3.7	-58.0

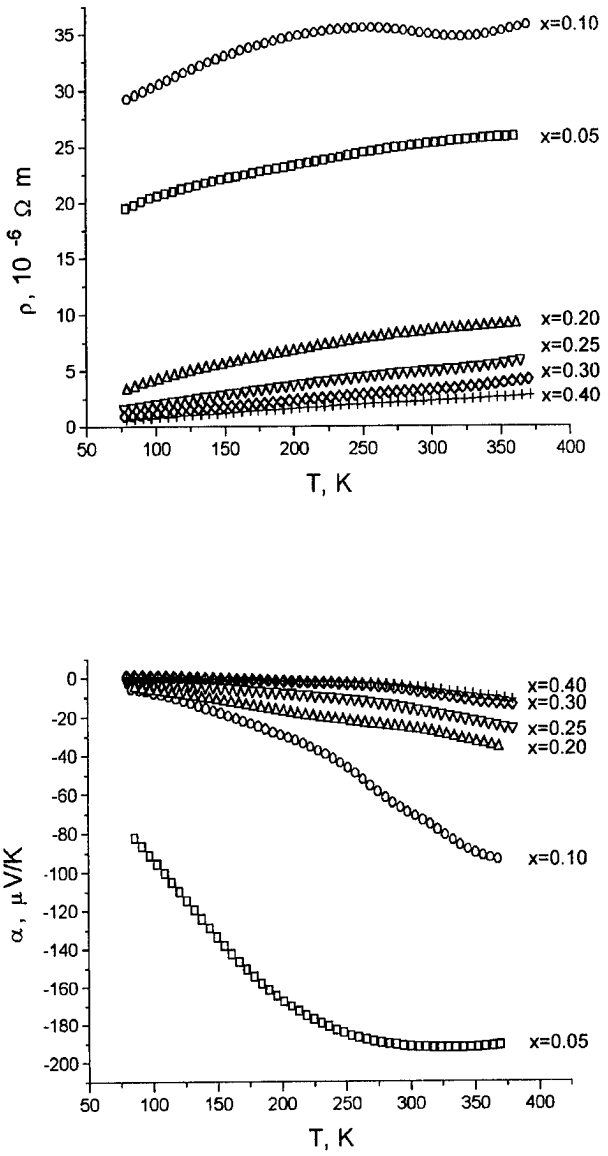
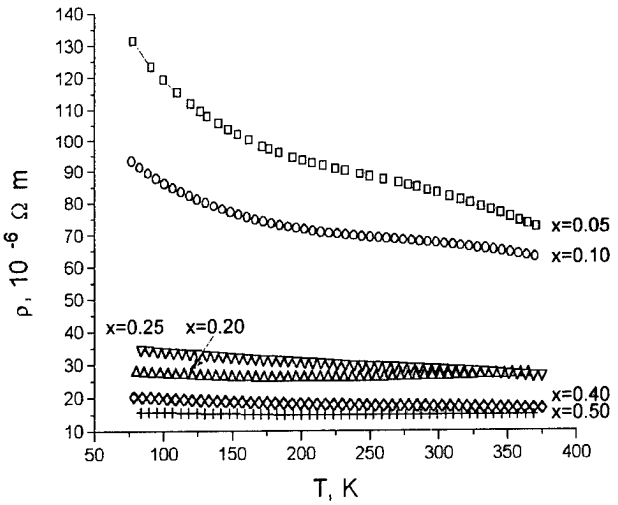
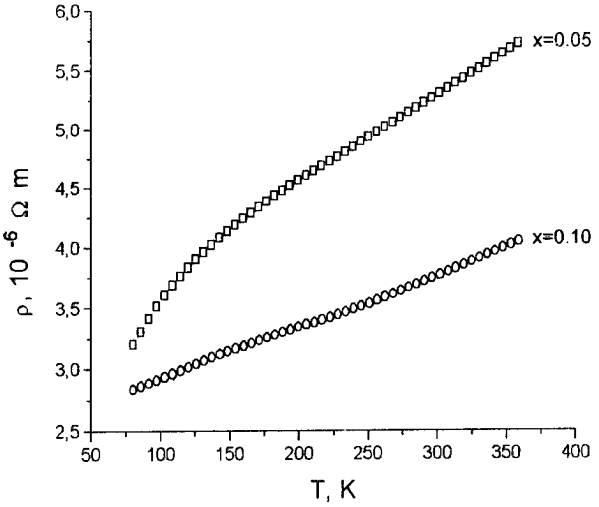


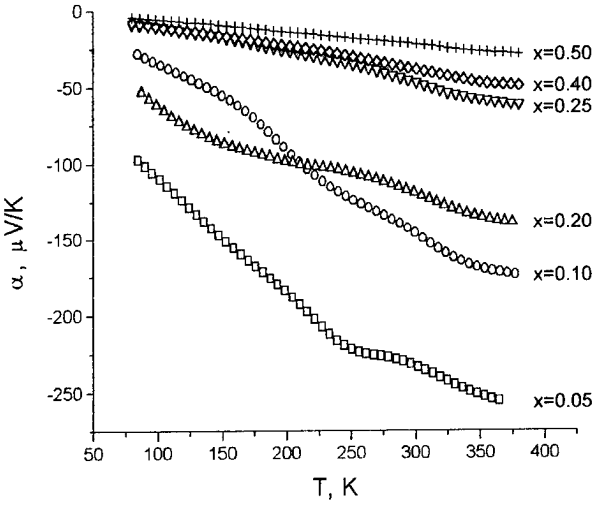
Fig. 2: Resistivity (ρ) and thermopower (α) as functions of temperature for $ZrNi_{1-x}Cr_xSn$ solid solution.

TiNiSn by Al results the increase of EC we have expected a p-type of conductivity as it took place when Ni by Co substitutions carried out in ZrNiSn and HfNiSn compounds [3,5]. But in this case the sign of the thermopower does not reverse (Fig.1). It may be supposed that Al atoms substitution is only partial for some Sn atoms in corresponding positions. It is also possible to suppose that Al atoms occupies the appropriate structure vacancies and thus Al impurity acquires the donor properties in this solid solution. An additional refined studies of the crystal structure are required for the verification of these assumptions.

Doping of ZrNiSn compound with Cr, Mn, and Cu gives rise to solid solutions. The gomogeneity range of these







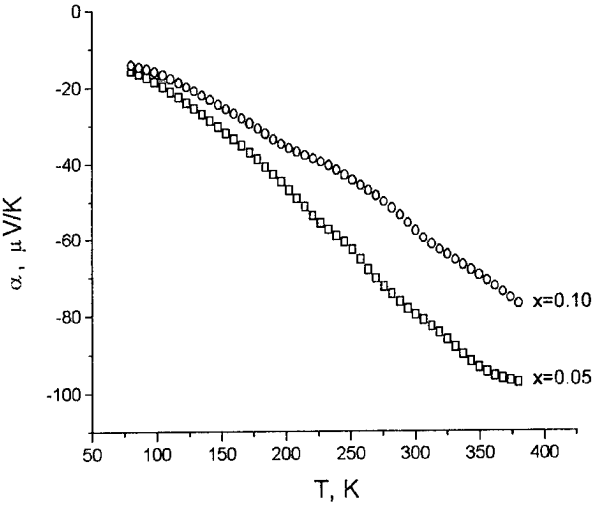


Fig. 3: Resistivity (ρ) and thermopower (α) as functions of temperature for $ZrNi_{1-x}Mn_xSn$ solid solution.

Fig. 4: Resistivity (ρ) and thermopower (α) as functions of temperature for $ZrNi_{1-x}Cu_xSn$ solid solution.

solid solutions depends on the kind of doping elements. $ZrNi_{1-x}Mn_xSn$ and $ZrNi_{1-x}Cr_xSn$ solid solutions range up to x=0.5 and x=0.4, respectively. $ZrNi_{1-x}Cu_xSn$ solid solution has a considerably smaller homogeneity range (up to x=0.1). A small variance of the lattice parameters (a) is observed (Table 1) because the difference of atomic radii of Ni and doping elements is insignificant. It is known that ZrNiSn compound is a narrow-gap n-type semiconductor characterized by EC=8 el./f.u. Doping of ZrNiSn compound with some elements that cause EC variance gives losses in semiconducting properties [3,7,8]. If ZrNiSn phase is doping with Cr, Mn, and Cu the number of the valent electrons in conduction band increases and thermopower remains negative. Different kinds of ρ(T) dependencies of alloys (Fig.1-4) with various doping metals may be explained by various location degree of valent electrons of these doping elements.

Conclusions

Homogeneity ranges of solid solutions based on TiNiSn and ZrNiSn compounds are depended on electronic structure and atomic radii of doping elements. The replacements of Sn atoms by Al, Sb, or Bi atoms in TiNiSn compound and the replacements of Ni atoms by Cr, Mn, or Cu atoms in ZrNiSn compound give losses in semiconducting properties. Doping of TiNiSn and ZrNiSn phases in this case do not reverse a type of conductivity.

References

[1] R.V. Skolozdra, "Stannides of rare earths and transition metals", Lviv, Ukraine, 1993.

[2] R.V. Skolozdra, Yu.V. Stadnyk, V.P. Sadov, "Synthesis and properties of Me'Me''Sn compounds", Proc. of the XIth Ukrainian Conf. on Inorganic Chemistry, Uzgorod, Ukraine, 1986.

[3] R.V. Skolozdra, Yu.V. Stadnyk, L.P. Romaka, F.G. Aliev, "Intermetallic compounds Me'Me''Sn the new semiconductor class with the narrow energy gap", J. of Thermoelectricity, 3(1994) 29.

[4] N.D. Marchuk, R.V. Skolozdra, Yu.V. Stadnyk, "Thermoelectric properties of new intermetallic compounds M'M''Sn, Proc. of the XIVth Int. Conf. on Thermoelectrics", St. Petersburg, Russia, 1995.

[5] A.O. Avetisian, O.M. Goriachev, S.V. Kalchenko, R.V. Skolozdra, Yu.V. Stadnyk, "Electrophysical properties of $HfNi_{1-x}Co_xSn$ compounds ($0<x<0.4$)", Ukrainian Phys. Journ. 36(1991) 773.

[6] R.V. Skolozdra, L.P. Komarovska, "Isotermic cross section at 670 K of Ce-Ni-Sn phase diagram", Izv. AN USSR, Metals, 2(1988) 214.

[7] L.P. Romaka, Yu.V. Stadnyk, A.M. Goryn, "The properties of $Zr_{1-x}Nb_xNiSn$ and $Zr_{1-x}Mo_xNiSn$ solid solutions", VIth Int. Conf. on Crystal Chemistry of Intermetallic Compounds, Lviv, Ukraine, 1995.

[8] Yu.V. Stadnyk, R.V. Skolozdra, Yu.K. Gorelenko, O.E. Terletska, "The influence of component substitution on the properties of ZrCoSn and ZrNiSn compounds", 35th IUPAC Congress, Abstracts II, Sections 4-6, Istanbul, Turkey, 1995.

Electronic transport in amorphous Ni-P alloys

Filip Skoropad, Bohdan Stadnyk

State University "Lviv Politechnic", 290646 Lviv, Ukraine,
Tel.: /0322/398-880, Fax: /0322/74-43-00, E-mail: skorp@polynet.lviv.ua

Abstract

We have measured the resistivity $\rho(T)$ and the thermoelectric power S(T) in the metallic glass system $Ni_{1-x}P_x$, with $0.10<x<0.25$.S(T) increases with increasing phosphorus concentration and changes sign, becoming positive above x=0.18. The S(T) is not linear over the entire measured temperature range for any of the samples. The samples with lowest x (x=0.142, 0.171) have negative S(T) with large positive curvatures which produce broad minima in S(T). This is also the ferromagnetic range of composition. Samples of intermediate-phosphorus content (x=0.176, 0.180) have small S(T) with both positive and negative curvatures in different temperature ranges. These compositions are near the transition from ferromagnetic to paramagnetic behaviour. Samples with large x (x=0.197, 0.200, 0.214, 0.220 and 0.245) have positive S(T) with negative curvatures. In this range of compositions S(T) fits a power law in T, $S(T) = CT^B$.

We find that as x increases, ρ increases, α [$\alpha=(1/\rho)d\rho/dT$] decreases and becomes negative, and S increases and becomes positive near x=0.18. These results agree with the Mooiji correlation and with a correlation of $S>0$ with high ρ and $S<0$ with low ρ, which is also seen in many nonmagnetic metallic glasses.Thus the$Ni_{1-x}P_x$ system spans the range of behaviour seen in many different metallic glasses. For $x<0.175$, $\rho(T)$ and S(T) are very similar to those seen in iron-based ferromagnetic glasses. The only clear difference between the transport properties of samples prepared by melt quenching and chemical deposition is in the temperature dependence of α. We compare our results with several theories for electron scattering.

Introduction

The larger the magnitude of ρ the more negative is the temperature coefficient of resistivity, $\alpha=(1/\rho)d\rho/dT$. In contrast, resistivities of normal crystalline metals are usually smaller and increase rapidly with increasing temperature. This dependence in metallic glasses of α on the magnitude of ρ is an example of a general trend diccovered by Mooij [1]. By looking at a variety of metallic systems Mooij found that α was lower in systems of higher ρ; in particular, most systems with $\rho<150\mu\Omega\bullet$cm have a positive α and those with $\rho>150\mu\Omega\bullet$cm have a negative α. A correlation is seen between the sign of the thermoelectric power and the sign of the temperature coefficient of resistivity (or the magnitude of ρ) in nonmagnetic metallic glasses. The glasses mentioned above all have $\rho>150\mu\Omega\bullet$cm, $\alpha<0$, and positive S. The correlation of positive S with high ρ and negative S with low ρ is very similar to the Mooij correlation exhibited by these same glasses.There has been little systematic investigation of the thermoelectric power, however. The purpose of this paper is to report a measurement of S(T) in a single metallic glass system , $Ni_{1-x}P_x$. By varying the composition in this alloy the resistivity can be varied from 100 to $170\mu\Omega\bullet$cm [2] (thus spanning the value $150\mu\Omega\bullet$cm, the resistivity which appears as the crossover point in the Mooij correlation). At the same time, α is positive at the lowest resistivities and decreases and becomes negative as the resistivity is increased. Therefore, we can observe S in a single system which spans the range of behavior of the resistivity in nonmagnetic metallic glasses.

Background

Several scattering mechanisms have been proposed to explain the negative values of α found at all temperatures in metallic glasses:- scattering from structural disorder, the Ziman theory;- Mott s-d scattering;- scattering from structural two-lewel systems ;- theories of incipient localization.

By assuming independent atomic vibrations, the resistivity as a function of temperature for such a glass is approximately [3]

$$r(T) = \frac{30p^3\hbar^3}{me^2k_F E_F W}\sin^2\left[h_2(E_F)\right]\left\{1+\left[S_0(2k_F)-1\right]e^{-2\left[W(T)-W(0)\right]}\right\}$$

Here k_F and E_F are the Fermi wave vector and energy, Ω is the atomic volume, $\eta_2(E_F)$ is the d-wave phase shift, $S_0(k)$ is the static structure factor at temperature T=0, and W(T) is th Debye -Waller exponent at temperature T.

Mott s-d scattering assumes that the electrons near the Fermi surface can be divided into two groups with very different mobilities[4]. The more mobile s or p carriers are strongly scattered into the less mobile d holes at the Fermi surface. The resistivity which is dominated by this scattering process is proportional to the number of such holes, i.e., to $N_d(E_F)$, the density of d states at the Fermi energy. In metals with partially full d bands $N_d(E)$ changes rapidly at E_F and ρ decreases with increasing temperature due to the thermal broadening of the electron distribution and the motion of the chemical potential. With the use of a simplified model where $\rho(E)\propto N_d(E)$ and the density of states does not change with temperature, the resistivity in this theory is [5]

0-7803-4057-4/97 $10.00 ©1997 IEEE

$$r(T) = r(0)\left\{1 - \frac{p^2}{6}(k_B T)^2\left[3\left(\frac{1}{N_d}\frac{dN_d}{dE}\right)^2 - \frac{1}{N_d}\frac{d^2N_d}{dE^2}\right]_{E_F}\right\}$$

If we assume for simplicity that the d band is nearly full and that $N_d(E) = C\sqrt{(E_0 - E)}$ (with $E_F<0$), then

$$\rho(T) = \rho(0)\left(1 - \frac{\pi^2}{6}(k_B T)^2 (E_0 - E_F)^{-2}\right).$$

Brouers and Brauwers [6] have considered the possibility that $N_d(E)$ does depend on temperature and found that there is a significant smearing out of $N_d(E)$ with increasing temperature. Aside from the effects of the thermal broadening of the electron distribution, this modification of $N_d(E)$ and the shift in E_F which is cused by it lead to a contribution to the resistivity which can either increase or decrease with temperature in a manner consistent with the Mooij correlation.

Each of these theories is able to predict a decreasing resistivity with increasing temperature. In order to distinguish between them another transport property must be measured. The thermoelectric power is a good choice because it is very sensitive to electron scattering mechanisms. In simple theories it is related to the resistivity by the Mott formula

$S(T) = \frac{\pi^2 k_B^2 T}{3|e|}\left(\frac{d\ln\rho}{dE}\right)_{E_F}$. We briefly describe the predictions for S for each of the scattering mechanisms discussed above. The thermoelectric power S(T) in the Ziman theory is [7] $S(T) = -\frac{\pi^2 k_B^2 T}{3|e|E_F}\left(3 - 2q - \frac{1}{2}r\right)$, where k_B is the Boltzmann constant, T is the absolute temperature, and

$$q = \frac{S(2k_F)|t(2k_F)|^2}{\int_0^{2k_F} dk\left[4(2k_F)^{-4}k^3 S(k)|t(k)|^2\right]}$$

. Here t(k) is the t matrix describing the muffin-tin potential. The quantity r in the expression for S(T) is the energy dependence of the t matrix:

$$r = \frac{\int_0^{2k_F} dk\left[4(2k_F)^{-4}k^3 S(k) k_F d|t(k)|^2 (d k_F)^{-1}\right]}{\int_0^{2k_F} dk\left[4(2k_F)^{-4}k^3 S(k)|t(k)|^2\right]}$$

. Note that S(T) is linear in temperature and can be either positive or negative depending on the magnitude of q. When $2k_F \approx k_p$ and $S(2k_F)$ is large then q is large and the thermoelecrtic power is positive. The condition $2k_F \approx k_p$ is also what is reguired to make the temperature coefficient of resistivity negative and the resistivity large.

The alloys $Ni_{1-x}P_x$ provide a single-alloy system in which the resistivity regime. At the same time, α is positive when ρ is low and decreases with increasing ρ. The thermoelectric power of one sample has been measured previously ($Ni_{0,76}P_{0,24}$) and a positive linear S(T) was found from 77,36K to room temperature [8].

Method

The resistivity of the samples were measured by the four-probe resistance method. The overall accuracy in the resistivity measurement is ±1%. The temperature dependence of the resistivity was measured from 4,2...300K. The accuracy in $\rho(T)/\rho(4,2K)$ is $\pm 2\bullet 10^{-5}$. The thermoelectric power was measured relative to pure Pb from 4,2...500K. The integral method was used; one end of the sample was kept at a constant temperature while the other end was raised in temperature. The derivative of the voltage measured with respect to temperature gives the relative thermoelectric power. The absolute thermoelectric power of the sample is obtained by subtracting the absolute thermoelectric power of the Pb standard from the measured relative thermoelectric power. Temperature was measured by copper-constantain thermocouples. The accuracy in S(T) is ±0,075μV/K.

Results

The temperature dependence of the resistivity $\rho(T)/\rho(4,2K)$ for each sample is shown in Fig. 1. With increasing phosphorus content the temperature coefficient of resistivity $\alpha=(1/\rho)d\rho/dT$ decreases and changes sign, becoming negative near x=0,23.

For each chemically deposited sample, $\alpha(T)$ decreases above T=80K, but for each melt quenched sample, $\alpha(T)$ increases above T=80K.

The thermoelectric power S(T) increases which increasing phosphorus concentration and changes sign, becoming positive above x=0,18. The temperature dependence of S is not linear over the entire measured temperature range for any of the samples. The samples with lowest x (x=0,143; 0,172) have negative S(T) with large positive curvatures which produce broad minima in S(T) . This is also the ferromagnetic range of composition. Samples of intermediate-phosphorus content (x=0,175; 0,181) have small S(T) with both positive and negative curvatures in different temperature ranges. These compositions are near the transition from ferromagnetic to paramagnetic behavior. Samples with large x (x=0.197, 0.200, 0.214, 0.220 and 0.245) have positive S(T) with negative curvatures. In this range of compositions S(T) fits a power law in T, $S(T) = C\cdot T^B$ with B=0,7.

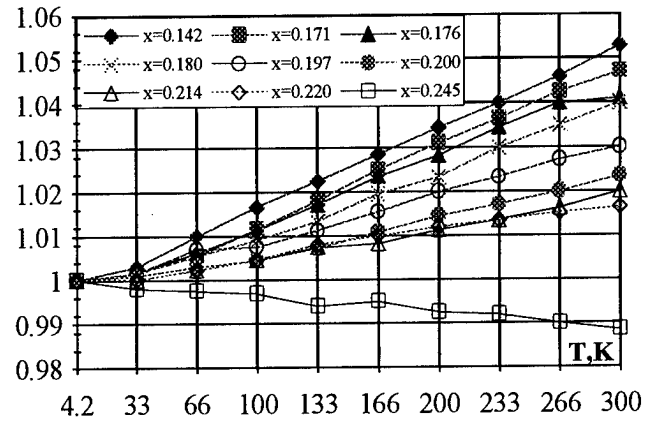


Fig 1: Resistivity vs temperature for each $Ni_{1-x}P_x$ sample normalized to the sample's resistivity at 4.2 K.

In conclusion, we have measured the temperature dependence of ρ and S in a single metallic glass system $Ni_{1-x}P_x$. We find that as x increases ρ increases, α decreases and becomes negative, and S increases and becomes positive. These results are in agreement with correlations between ρ and α and between ρ and S seen in many metallic glasses. At low-phosphorus concentrations, $x<0.18$, the transport properties are similar to those seen in iron-based metallic glasses, and as x increases above 0.18, the transport behavior becomes more similar to what is seen in nonmagnetic metallic glasses. The dependence on x of ρ, α, and the size of S are qualitatively consistent with the Ziman theory although it seems probable that other scattering mechanisms, such as s-d scattering, are important in the samples with low P concentration. There is a clear effect of the preparation technique on the transport properties only in the temperature dependence of α.

References

[1]. J.H. Mooij, Phys. Status Solidi A 17, 521 (1973).
[2]. P.J. Cote, Solid State Commun. 18, 1311 (1976).
[3]. R. Evans, D.A. Greenwood, and P. Lloyd, Phys. Lett. 35A, 57 (1971).
[4]. N.F. Mott, Philos. Mag. 26, 1249 (1972).
[5]. H. Jones, Hand Phys. 19, 267 (1956).
[6]. F. Brouers and M. Brauwers, J. Phys. (Paris) Lett. 36, L-17 (1975).
[7]. R.D. Barnard, Thermoelectricity in Metals and Alloys (Taylor and Francis, London, 1972).
[8]. P.J. Cote and L.V. Meisel, Phys. Rev. B 20, 3030 (1979).

Thermoelectric Properties of Transition-Metal Oxide $NaCo_2O_4$ System

H. Yakabe[1], K. Kikuchi[1], I. Terasaki[2], Y. Sasago[3] and K. Uchinokura[3]

1)*Frontier Technology Research Institute, Tokyo Gas Co., Ltd., Yokohama, 230, Japan*

2)*Department of Applied Physics, Waseda University, Shinjyuku-ku, Tokyo, 169, Japan*

3)*Department of Applied Physics, The University of Tokyo, Bunkyo-ku, Tokyo, 113, Japan*

Abstract

A transition-metal oxide $NaCo_2O_4$ system has been synthesized by a standard solid-state reaction method, and the thermoelectric properties have been measured. The resistivity ρ and the thermoelectric power α of the as-sintered $NaCo_2O_4$ is 2 mΩcm and 100 μV/K at room temperature, respectively. By hot-pressing, the electrical resistivity is reduced to about 60%, and by Ba- or Bi-substitution for Na, Cu- or Bi-substitution for Co, the thermoelectric power is enhanced up to 1.4 times. For all the samples, the figure-of-merit shows a flat temperature dependence over a wide range from 100 to 400°C, and in the hot-pressed $Na(Co_{0.95}Cu_{0.05})_2O_4$, the maximum value of 0.88×10^{-3} K^{-1} is achieved around 300°C, with ρ=2 mΩcm, α=147 μV/K, and the thermal conductivity κ=1.3 W/mK. In spite of a low carrier mobility material, $NaCo_2O_4$ system shows good thermoelectric performance. This indicates a possibility of applying low-mobility materials to thermoelectric devices, and thus $NaCo_2O_4$ system will be a prospective candidate for thermoelectric materials.

Introduction

Today, thermoelectric energy conversion is of great interest in terms of making best use of energy. However, the low conversion efficiency severely restricts the application of thermoelectric materials to the thermoelectric power generation. Although extensive studies have been made on searching thermoelectric materials with high figure-of-merit, only a few thermoelectric materials such as Bi_2Te_3, PbTe and SiGe systems have been applied to thermoelectric devices[1-3].

Most of the studies for thermoelectric materials have been concentrated on conventional semiconductors whose transport mechanism is well described by a conventional band theory, and most of the common thermoelectric materials belong to this category. Recently, a new approach to the research for thermoelectric materials, i.e. investigation of unconventional semiconductors or metals, has been tried[4-7, 9]. For example, strongly correlated systems which are not well described by the conventional band theory, such as heavy fermion compounds[4, 5] or 3d transition metal oxides[6, 7, 9], are expected to be candidate compounds. Heavy fermion compounds have 10^2-10^3 times larger effevtive mass than ordinary metals, and show enhanced thermoelectric power compared to the ordinary metals[8]. For 3d transition metal oxides, for example, high-temperature superconductors have been studied as thermoelectric materials[7, 9]. Among many superconducting cuprates, $La_{2-x}(Ba, Sr)_xCuO_4$ system is the most hopeful candidate with a figure-of-merit larger than 10^{-4} K^{-1}[9]. Thus investigation of strongly-correlated systems as thermoelectric materials is a promising way to discover new thermoelectric materials.

From the above viewpoint, $NaCo_2O_4$ is an interesting material. $NaCo_2O_4$ is a rather old material, which was first identified by Jansen and Hoppe[10]. As shown in Fig. 1, this material has a bronze-type layered structure[11]. CoO_2 sheets of edge-sharing CoO_6 octahedra are stacked along the c-axis, while Na ions occupancy 50% of the regular sites located between the CoO_2 sheets. The preliminary studies of $NaCo_2O_4$ were mainly concerned with the material syntheses and the structure analyses, and the transport properties recieved little scientific attention at that time. Recently, Tanaka, Nakamura, and Iida have found that polycrystalline $NaCo_2O_4$ is a good metal down to 4.2 K[12]. Motivated by their study, Terasaki, Sasago, and Uchinokura have studied the transport properties of single-crystal $NaCo_2O_4$ as a reference material for high-Tc superconductors, and discovered that the in-plane thermoelectric power is as large as 100 μV/K at 300 K[13]. Considering the low in-plane resistivity (200 $\mu\Omega$cm at 300 K), they pointed out that $NaCo_2O_4$ is a potential thermoelectric material[13].

In the present paper, we report the preparation and the thermoelectric properties of $NaCo_2O_4$ system which shows

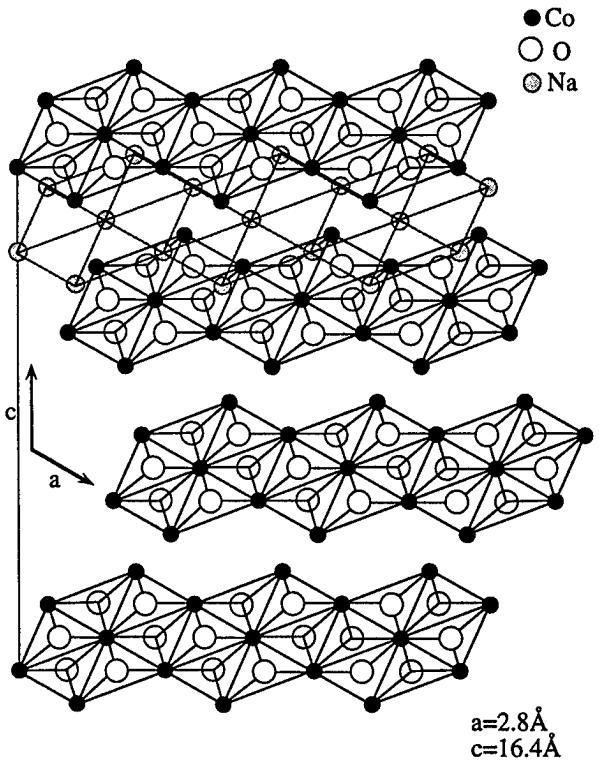


Fig. 1. Crystal structure of $NaCo_2O_4$. 50% of Na sites are randomly occupied. Only one Na layer is shown in the figure.

preferable thermoelectric performance. Substitution of some kinds of elements for Na or Co, improves the thermoelectric properties, and the results for the substitution are also reported.

Experimental

Polycrystalline $NaCo_2O_4$ were prepared by cold-pressing and hot-pressing methods. In both the preparation methods, fine Na_2CO_3 and Co_3O_4 powders were used as starting materials. The well-mixed powder was pressed into pellets and calcined at 860°C for 12 h. The calcined pellets were ground into powder, and the powder was pressed into a disk and sintered at 800°C for 12 h in air. For the hot-pressed sample, the sintered disk was further fired under a pressure of 255 kg/cm^2 at 800°C for 2 h. The effects of partial substitution were also studied. The substitution was done by 5 at.% each;Ba or Bi for Na, Mn or Cu for Co. These samples were prepared under the sample conditions as those for the non-substituted sample.

The crystal structures of the prepared samples were characterized by powder X-ray diffraction (XRD) using CuKα-radiation. In order to measure the transport properties, the samples were cut into rectangular shaped specimens of $1 \times 3 \times 20$ mm^3. The electrical resistivity was measured by the conventional four-probe method in a temperature range from room temperature to 400°C, and the thermoelectric power was estimated from the thermo-electromotive force between two pairs of chromel-alumel thermocouples under a temperature gradient of about 4K. The thermal conductivity was calculated from the thermal diffusivity and the specific heat measured by the laser flash method.

Results and discussion

The XRD patterns for the as-sintered and the hot-pressed $NaCo_2O_4$ are given in Fig. 2. For both the patterns, all the intensity peaks are assigned to $NaCo_2O_4$ structure without any impurity phases. Only the difference between these patterns is that the hot-pressed sample shows sharper peaks than the as-sintered sample, indicating that the hot-pressing process improves the crystallinity of the sample.

Figures 3(a) and 3(b) show the temperature dependence of the resistivity ρ and the thermoelectric power α, respectively, for the as-sintered and the hot-pressed $NaCo_2O_4$. Both the samples show a metallic temperature dependence of the resistivity, and the curvatures of the ρ-T curves are negative. The magnitude of ρ for the as-sintered sample is about 2 mΩcm at room temperature, and by means of hot-pressing, we have successfully reduce the resistivity down to about 1.1 mΩcm at room temperature. It has been reported that $NaCo_2O_4$ has an anisotropy in the resistivity, and for the single crystal, the magnitude of the in-plane resistivity ρ_{ab} is 200 μΩcm at room temperature, which is one order of magnitude smaller than that of the out-of-plane resistivity ρ_c[13]. In the present case, our samples are polycrystalline and the resistivity is a mixture of ρ_{ab} and ρ_c. Thus the magnitude of the resistivity for the present samples are reasonably higher than that of ρ_{ab} for the single crystal.

On the other hand, the magnitude of α for the present samples are about 100 μV/K at room temperature, and this value is almost the same as that of the single crystal. Moreover, the magnitude and the temperature dependence of α is identical between the as-sintered and the hot-pressed samples since the thermoelectric power is hardly affected by the crystallinity and the grain boundary. Using the data of Hall coefficient for the $NaCo_2O_4$ single crystal, which have been already reported [13], the carrier density n is estimated as ~10^{21} cm^{-3}, and thus $NaCo_2O_4$ is considered as a metal. However, as compared with other metals or metallic compounds whose α are about several μV/K, α of $NaCo_2O_4$ is one order of magnitude larger, suggesting that the transport properties of $NaCo_2O_4$ cannot be explained by the

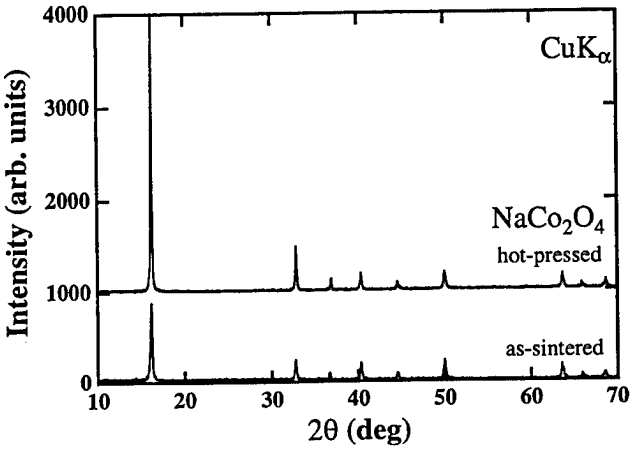
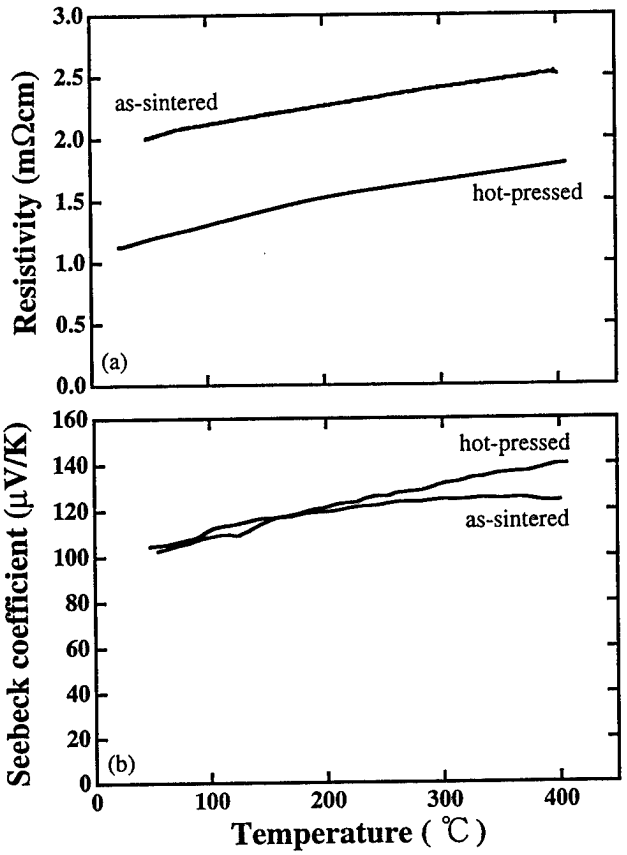


Fig. 2. XRD patterns for the as-sintered and the hot-pressed $NaCo_2O_4$. All the peaks are assigned to the structure of $NaCo_2O_4$.



Figs. 3. Temperature dependence of the resistivity (a) and the thermoelectric power (b) for the as-sintered and the hot-pressed $NaCo_2O_4$.

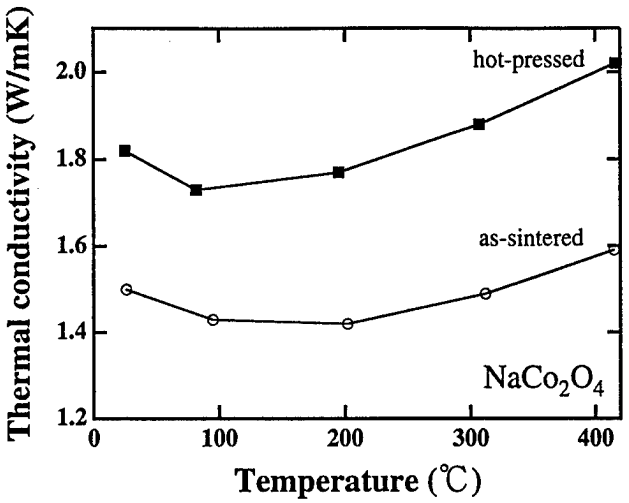


Fig. 4. Temperature dependence of the thermal conductiviy for the as-sintered and the hot-pressed $NaCo_2O_4$. The solid lines are guides for the eyes.

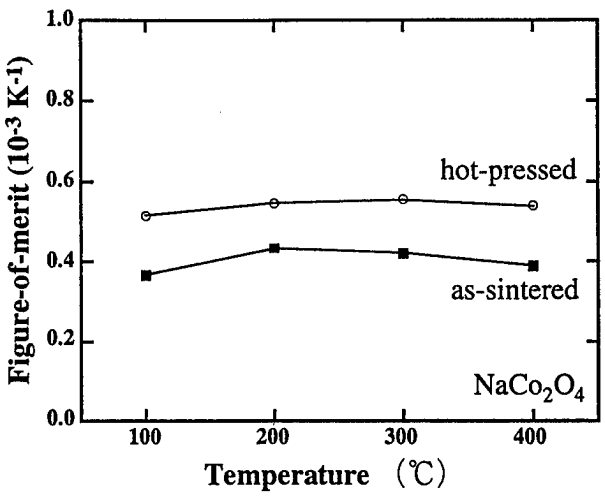


Fig. 5. Temperature dependence of the figure-of-merit for the as-sintered and the hot-pressed $NaCo_2O_4$. The solid lines are guides for the eyes.

conventional theory. Although the origin of the large α has not been explained clearly, a possibility that the large α would come from spin fluctuation as in the heavy fermion system or the valence-fluctuation system has been suggested[13].

Thermal conductivity measurements for $NaCo_2O_4$ show an intriguing result as the thermoelectric power measurements. Temperature dependences of thermal conductivity κ for the as-sintered and the hot-pressed $NaCo_2O_4$ are shown in Fig. 4. For the as-sintered sample, the magnitude of κ is ~ 1.5 W/mK at room temperature, and this value is as low as a typical value of the Bi_2Te_3 system. It has been generally accepted that compounds constituted of heavy elements, such as Bi or Te, exhibit low melting points and low thermal conductivity, whereas solid compounds with high melting points show high thermal conductivity. $NaCo_2O_4$ is constituted of light elements such as Na, Co, and oxygen, and thus it is expected that $NaCo_2O_4$ would show a high thermal conductivity. However, $NaCo_2O_4$ shows low κ as Bi_2Te_3 system, implying that the lattice thermal conductivity is extremely low. A possible reason to interpret the extremely low thermal conductivity of $NaCo_2O_4$ is that the randomly occupying Na ions work as scattering centers of phonon, and thus the phonon mean free path is reduced. The magnitude of κ for the hot-pressed sample is about 30% higher than that of the as-sintered sample, which is probably due to the increase in density. For both the samples, κ once decreases with increasing temperature, and above 200°C, increases monotonically with temperature.

The figure-of-merit $Z=\alpha^2/\rho\kappa$ for the as-sintered and the hot-pressed $NaCo_2O_4$ are estimated from the measured ρ, α, and κ, and displayed in Fig. 5. Both the samples show almost temperature-independent Z, coming from that ρ, α, and κ increase monotonically with temperature above 200°C. Reflecting the κ - T curve, Z attains the maximum value of 0.4×10^{-3} K^{-1} near 200°C for the sintered sample. Note that the magnitude of Z for the hot-pressed sample is about 30% larger than that of the as-sintered sample, because ρ is reduced by 40% while κ is increased by 30% with hot-pressing. For the hot-pressed sample, the maximum Z of 0.55×10^{-3} K^{-1} is achieved at 300°C. Although this value is not so high as those of other thermoelectric materials such as Bi_2Te_3 or PbTe system, it is higher than those of other oxides thermoelectric materials so far reported[6,15].

We turn next to the effects of the partial substitutionons on the thermoelectric properties for $NaCo_2O_4$. If we compare ρ, α, and κ of $NaCo_2O_4$ with those of other thermoelectric materials, $NaCo_2O_4$ shows comparably low ρ and κ whereas the magnitude of α for $NaCo_2O_4$ is about half. Therefore, a way to get larger Z is to increase α by modifying the composition. For this purpose, we tried to substitue some kinds of elements for Na or Co.

We obtained single-phase $(Na_{0.95}Ba_{0.05})Co_2O_4$ and $Na(Co_{0.95}Mn_{0.05})_2O_4$. However in the XRD patterns for $(Na_{0.95}Bi_{0.05})Co_2O_4$ and $Na(Co_{0.95}Cu_{0.05})_2O_4$, there were some peaks corresponding to raw maretials such as CuO or Bi_2O_3. Figures 6(a) and 6(b) display the temperature dependence of ρ and α, respectively, for the as-sintered $NaCo_2O_4$, $(Na_{0.95}Ba_{0.05})Co_2O_4$, $Na(Co_{0.95}Cu_{0.05})_2O_4$, $Na(Co_{0.95}Mn_{0.05})_2O_4$, and $(Na_{0.95}Bi_{0.05})Co_2O_4$. In all the samples, the substitution caused an increase in ρ, and especially for $(Na_{0.95}Ba_{0.05})Co_2O_4$, the increase in ρ was remarkable. One reason for the remarkable increase in ρ for $(Na_{0.95}Ba_{0.05})Co_2O_4$ may be a randomness induced by the Ba-substitution because the ionic radius of Ba is exceedingly larger than that of Na. α was also enhanced by the substitution, especially in $Na(Co_{0.95}Mn_{0.05})_2O_4$ and $(Na_{0.95}Bi_{0.05})Co_2O_4$. However, the increase in ρ canceled out the advantage of the increasing α, and thus the power factor α^2/ρ increased only for $Na(Co_{0.95}Cu_{0.05})_2O_4$ and $Na(Co_{0.95}Mn_{0.05})_2O_4$.

Next, we focus on the effects of the substitution on the thermal conductivity for $NaCo_2O_4$. It has been generally believed that scattering by lattice defects or phonons reduces the phonon mean free path, and thus substitution of heavy elements and introduction of impurities induce reduction of the lattice thermal conductivity. Accordingly, it is expected that substitution of some kinds of elements, especially heavy elements such as Ba, leads to a reduction of κ. However, amazingly, the substitutions, except for the Cu-substitution, brought about the increase in κ. In Fig. 7, κ is plotted as a function of temperature for the above mentioned samples. Despite the big difference of the atomic weight between

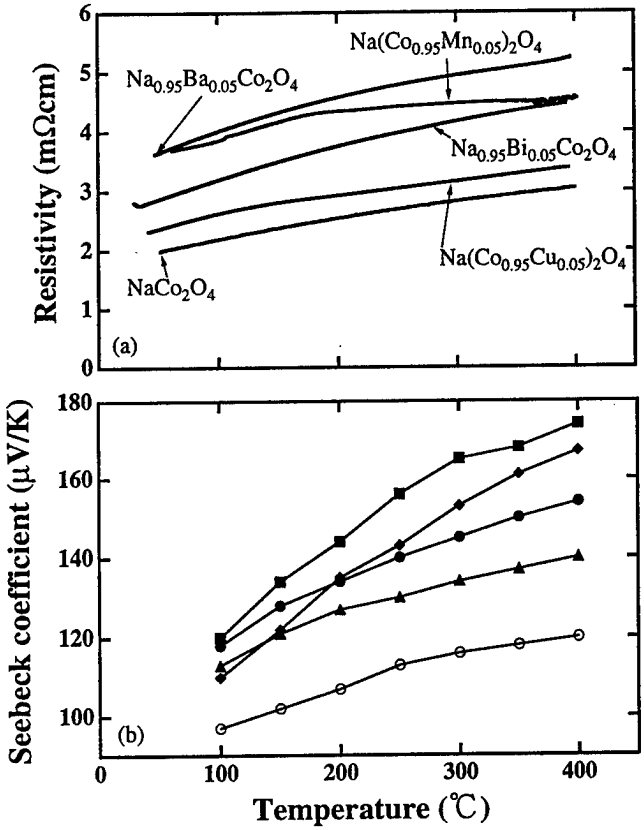


Fig. 6. Temperature dependence of the resistivity (a) and the thermoelectric power (b) for the as-sintered $NaCo_2O_4$ with different dopants. Open circles, solid triangles, solid circles, solid diamonds, and solid squares show the data for $NaCo_2O_4$, $(Na_{0.95}Ba_{0.05})Co_2O_4$, $Na(Co_{0.95}Cu_{0.05})_2O_4$, $(Na_{0.95}Bi_{0.05})Co_2O_4$, and $Na(Co_{0.95}Mn_{0.05})_2O_4$, respectively. The solid lines are guides for the eyes.

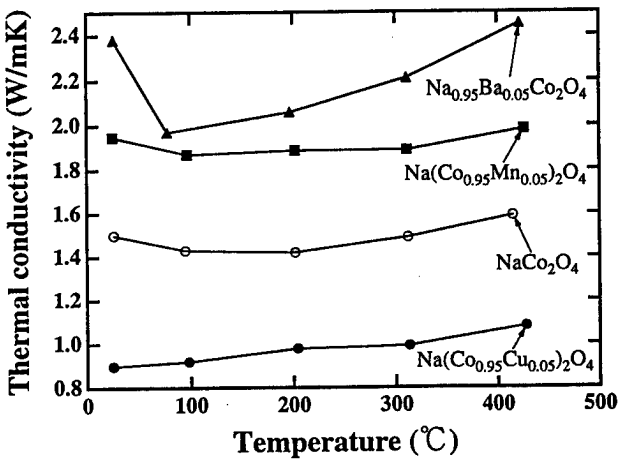


Fig. 7. Temperature dependence of the thermal conductivity for the as-sintered $NaCo_2O_4$ with different dopants. Open circles, solid circles, solid squares, and solid triangles show the data for $NaCo_2O_4$, $Na(Co_{0.95}Cu_{0.05})_2O_4$, $Na(Co_{0.95}Mn_{0.05})_2O_4$, and $(Na_{0.95}Ba_{0.05})Co_2O_4$, respectively. The solid lines are guides for the eyes.

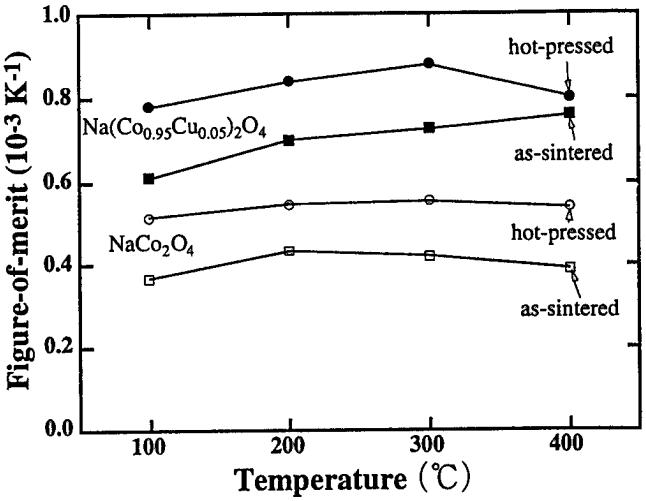


Fig. 8. Comparison of the figure-of-merit for $NaCo_2O_4$ and $Na(Co_{0.95}Cu_{0.05})_2O_4$. Open squares, open circles, solid squares, and solid circles correspond to the data for the as-sintered and the hot-pressed $NaCo_2O_4$, the as-sintered and the hot-pressed $Na(Co_{0.95}Cu_{0.05})_2O_4$, respectively. The solid lines are guides for the eyes.

Na and Ba, κ of $(Na_{0.95}Ba_{0.05})Co_2O_4$ is higer than that of $NaCo_2O_4$. Only $Na(Co_{0.95}Cu_{0.05})_2O_4$ exhibits the remarkable reduction of κ, and the value of ~1 W/mK is comparable to that of TAGS system. Although the reason for the increase of κ in the Ba-substitution is not clear, it would be related to the origin of the extremely low κ for the non-substituted $NaCo_2O_4$.

Finally, we show the comparison of Z for the as-sintered and the hot-pressed $NaCo_2O_4$, the as-sintered and the hot-pressed $Na(Co_{0.95}Cu_{0.05})_2O_4$ as a function of temperature in Fig. 8. In hot-pressed $Na(Co_{0.95}Cu_{0.05})_2O_4$, the highest Z of 0.88×10^{-3} K^{-1} is achieved around 300°C with ρ=2 mΩcm, α=147 μV/K, and κ=1.3 W/mK, and this value is larger than that of SiGe system. Here we comment on the mobility for $NaCo_2O_4$ system. Using the data of the transport measurement for $NaCo_2O_4$ single crystal, the mobility μ has been estimated to be about 13 cm^2/Vs at room temperature[13]. This value is almost the same as those of metals but one to two orders of magnitude smaller than those of semiconductors. Judging from the magnitude of ρ for the single crystal and the present samples, we may deduce that the present samples have one order smaller μ than the $NaCo_2O_4$ single crystal. According to the conventional semiconductor theory[16], materials with high-Z value will have a large carrier mobility, and thus low-mobility materials are regarded as having a poor thermoelectric capability for thermoelectric devices. However, $NaCo_2O_4$ system exhibits good thermoelectric performance despite the low μ. This indicates a possibility of low mobility materials to thermoelectric applications. The investigation of the thermoelectric $NaCo_2O_4$ system is just at the beginning, and we hope that Z will be improved by modifying the method of preparation, the preparing conditions, and the selection of dopants.

Conclusion

We have synthesized the transition-metal oxide $NaCo_2O_4$ system

by the cold-pressing and the hot-pressing methods, and measured the thermoelectric properties. The hot-pressed sample shows the lower resistivity and the larger thermal conductivity than the as-sintered sample. Ba-, Mn-, Cu-, and Bi-substitutions enhance the thermoelectric power, and thus the hot-pressed $Na(Co_{0.95}Cu_{0.05})_2O_4$ shows the maximum figure-of-merit of $0.88 \times 10^{-3} K^{-1}$ around 300 °C, with ρ=2 mΩcm, α=147 μV/K, and κ=1.3 W/mK. In spite of a low carrier mobility material, $NaCo_2O_4$ system shows good thermoelectric performance, implying that research on the low carrier mobility materials may be a promising way to discover new thermoelectric materials. It is expected that the thermoelectric properties of $NaCo_2O_4$ can be improved by modifying the method of preparation, the preparing conditions, and the selectin of dopants, and thus $NaCo_2O_4$ will be a prospective candidate for thermoelectric materials.

References

[1] W. C. Hall, in CRC Handbook of Thermoelectrics (ed. D. M. Rowe), 503-514(CRC Press, 1995).

[2] G. L. Benett, in CRC Handbook of Thermoelectrics (ed. D. M. Rowe), 515-538(CRC Press, 1995).

[3] K. Matsuura and D. M. Rowe, in CRC Handbook of Thermoelectrics (ed. D. M. Rowe), 573-594(CRC Press, 1995).

[4] C. B. Vining, XIIIth Int.Conf. on Thermoelectrics, ed. K. Matsuura, (Yokohama), 126-131(1994).

[5] B. Louie and R. Radebaugh, 1st National Thermogenic Cooler Conference, ed. S. Horn (Center for Night Vision and Electro-Optics, Fort Belvoir, Virginia, 17 September), 140(1992).

[6] M. Ohtaki et al., XIVth Int.Conf. on Thermoelectrics, ed. M. V. Vedernikov, (St.Petersburg), 245-248(1995).

[7] W. J. Macklin and P. T. Moseley, On the use of oxides for thermoelectric refrigeration, Mater. Sci. Eng. B7, 111-117(1990).

[8] C. S. Garde and J. Ray, Phys. Rev. B51, 2960-2965(1995).

[9] M. Cassart and J.-P. Issi, 8th International conference on Thermoelectric Energy conversion, Institue National Polytechnique de Lorraine, Nancy, 121(1989).

[10] M. Von Jansen and R. Hoppe, Z. Anorg. Allg. Chem. 408, 104-106(1974).

[11] C. Fouassier et al., J. Solid State Chem. 6, 532-537(1973).

[12] T. Tanaka, S. Nakamura, and S. Iida, Jpn. J. Appl. Phys. 33, L581-L582(1994).

[13] I. Terasaki, Y. Sasago, and K. Uchinokura, now submitting to Phys. Rev. B.

[14] C. Delmas, C. Fouassier, and P. Hagenmuller, J. Solid State Chem. 13, 165-171(1975).

[15] H. Ohta, W. S. Sep, and K. Koumoto, J. Am. Ceram. Soc. 79, 2193-2196(1996).

[16] H. J. Goldsmid, Application of Thermoelectricity, Methuen Monograph, London(1960).

Thermoelectric Properties of Hot-Pressed $YbAl_3$ Compound Over Temperature Range 150-800 K

D. M. Rowe, Gao Min and V.L. Kuznetsov
School of Engineering, University of Wales Cardiff, Cardiff, UK

Abstract

Small crystals of $YbAl_3$ compound have been obtained using the Bridgman or a direct synthesis method and subsequently disc-shaped compacts prepared using a hot-pressing technique. The Seebeck coefficient, electrical resistivity, thermal diffusivity and specific heat capacity were measured over a temperature range 200-800 K. Although the thermal conductivity of $YbAl_3$ is much higher than that of Bi_2Te_3 based alloys, $YbAl_3$ possesses an electrical power factor which is more than doubling those of Bi_2Te_3 based alloys. The thermoelectric figure of merit at room temperature is about $1.1x10^{-3}$ K^{-1}, which is only a third of Bi_2Te_3 based thermoelectric materials. However, $YbAl_3$ may be a useful material for electrical power generation using waste heat with its substantially large electrical power factor providing a large electrical power density.

Introduction

A thermoelectric energy converter is a unique and reliable heat engine in which the electron gas serves as the working fluid. However, its more wide-scale application has been limited by its relatively low energy conversion efficiency. Consequently, research effort has concentrated on improving its performance by increasing the figure of merit $ZT=\alpha^2\sigma T/\lambda$, of thermocouple materials, where α is the Seebeck coefficient, σ the electrical conductivity, and λ thermal conductivity, T the absolute temperature; $\alpha^2\sigma$ is referred to as the electrical power factor. Currently the best established thermoelectric materials possess a ZT value of about 1. In principle, very large $\alpha^2\sigma$ (>50 x 10^{-4} W/mK^2) may not be necessary to obtain ZT>1 if very low thermal conductivity can be achieved. However, recent studies show that a minimum lattice thermal conductivity exists which limits the lowest achievable thermal conductivity for a particular material [1]. Consequently, the search for the materials with large electrical power factor provide a more promising alternative. A literature survey of electrical power factor data indicates that the values for established thermoelectric materials are around 40-50 x 10^{-4} W/mK^2, with $Bi_{1-x}Sb_x$ an exception at low temperature (~200 x 10^{-4} W/mK^2 at 50 K). Recently it had been noted [2] that $YbAl_3$ exhibits a very large electrical power factor (~$100x10^{-4}$ W/mK^2 at 300 K), although its thermal conductivity is expected to be much higher than those of Bi_2Te_3 based alloys. In the present study, the thermoelectric properties of $YbAl_3$ is investigated experimentally in an attempt to assess its potential as a thermoelectric material and to identify possible avenues for further improvement of the thermoelectric figure of merit.

Experimental

Specimens with specific geometries are usually required in the assessment of thermoelectric properties and materials with relatively large dimension (over 1 x 1 x 1 mm^3) are usually required for the construction of thermoelements. Preparation of "large" specimens of pure $YbAl_3$ proved difficult due to the peritectic nature of the compounds formation. Although large dimension specimens can be prepared using arc-melting technique, materials prepared by this method are invariably a mixture of $YbAl_2$ and $YbAl_3$ with different proportion depending on the starting composition and preparation conditions.

In this study $YbAl_3$ prepared using two techniques. The Bridgman method was initially used in an attempt to grow crystalline $YbAl_3$ from the melt with a composition $Yb_{0.13}Al_{0.87}$. The ytterbium and aluminium mixture was placed into alumina (Al_2O_3) crucible and then sealed inside quartz ampoule under vacuum. Various growth conditions have been investigated. The best result obtained to date was a polycrystalline ingot of $YbAl_3$ which consisted of small crystals of about 0.5 x 0.5 x 1.0 mm^3 and surrounded by aluminium-rich matrix. Polycrystalline $YbAl_3$ compound was also prepared by direct synthesis in an alumina crucible at 1050 K from the elements taken in the proportion $Yb_{0.2}Al_{0.8}$. The initial exothermal reaction of aluminium with ytterbium resulted in a mixture of solid $YbAl_3$, $YbAl_2$ and Al-rich liquid. The continued synthesis encourages the further reaction towards $YbAl_2$ + Al = $YbAl_3$. As a result two phase ingot ($YbAl_3$ + Al) was obtained.

In order to obtain pure $YbAl_3$ compound, it is necessary to segregate $YbAl_3$ from aluminium and a number of techniques for achieving this have been reported [3]. The chemical nature of aluminium (i.e., it can be dissolved in alkali solution) makes it possible to remove easily the aluminium excess from the final ingot without the dissolution of $YbAl_3$. An X-ray analysis confirmed that the resulting powder-like crystals are pure $YbAl_3$ without second phase and possess a cubic Cu_3Au-type structure. The Seebeck coefficient of $YbAl_3$ prepared both by Bridgman and by direct synthesis methods was -75 μV/K.

Table 1 Hot-pressing conditions for specimen preparation (temperature T, pressure P, pressing period Δt) and the resultant density d. HP-16 and 26 were prepared using the steel die set and HP-17, 20 and 21 using the graphite die set.

	T (K)	P (MPa)	Δt (hrs.)	d (g/cm^3)
HP-16	823	6.9	6.5	5.00
HP-17	1000	0.5	1.5	4.37
HP-20	923	0.6	4.0	4.32
HP-21	823	0.7	1.0	3.98
HP-26	873	6.2	6.5	4.88

A hot pressing technique was then employed to prepare disk-shaped compacts of about 6 mm in diameter and 1.5 mm thick from polycrystalline powder of $YbAl_3$. Hot pressing was carried out in vacuum (about 10^{-2} torr) using a steel or

0-7803-4057-4/97 $10.00 ©1997 IEEE

graphite die. Typical hot pressing parameters for a number of specimens are listed in the table 1. After hot pressing, the specimens were placed in an alumina boat and annealed in a sealed quartz ampoule at 1000 K for 50 hours. A small quantity of aluminium was also placed inside the sealed ampoule to minimise the loss of aluminium from the specimen surface due to its high vapour pressure and reaction with quartz.

The Seebeck coefficient and electrical resistivity as a function of temperature over the range 150-800 K were measured "simultaneously" along disc plane using an α-ρ apparatus [4]. The thermal diffusivity as a function of temperature over the range 300-800 K was measured perpendicular to the disc plane using a laser flash technique [5]. $YbAl_3$ possess a cubic structure with isotropic transport properties, which enable its thermoelectric properties to be evaluated using data obtained along different specimen directions. The specific heat data was measured at National Physical Laboratory, UK. All properties were measured several times and the results presented in the following section are averaged values.

Results and discussions

The Seebeck coefficient, electrical resistivity and thermal diffusivity as a function of temperature for specimens HP-16, 20, 21 and 26 are shown in figure 1, 2 and 3, respectively. Both the electrical resistivity and thermal diffusivity increase with increasing temperature, while the Seebeck coefficient exhibit a maximum value of about -75 to -85 μV/K at a temperature around 250 K. $YbAl_3$ is reported to be a Kondo compound and its relatively large Seebeck coefficient can be explained based on the scattering of conduction electrons with magnetic moments [6,7]. However, the minimum electrical resistivity, which is a typical feature of Kondo system, was not observed in this study over the temperature range investigated.

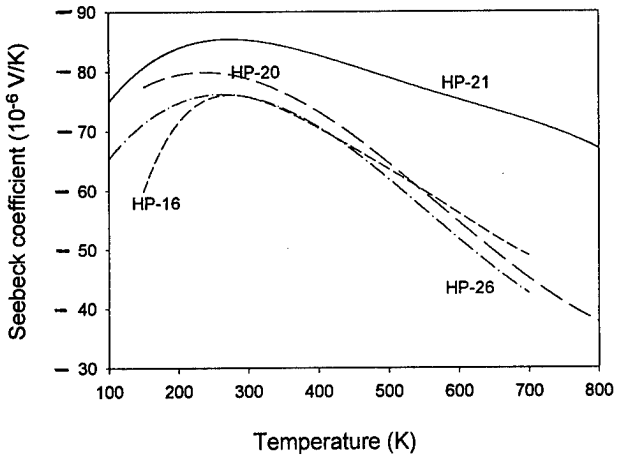


Figure 1. Seebeck coefficient as a function of temperature for different density.

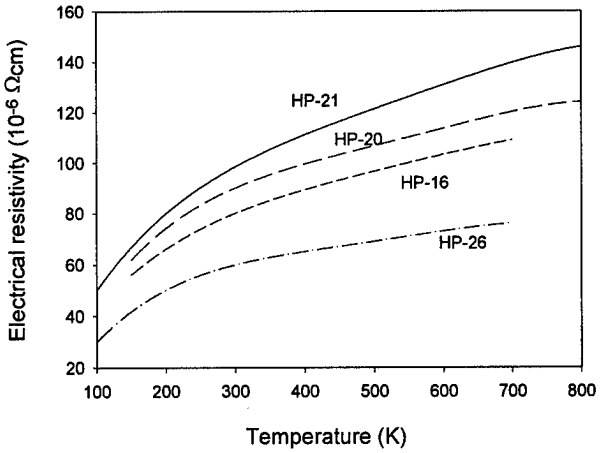


Figure 2. Electrical resistivity as a function of temperature for different density.

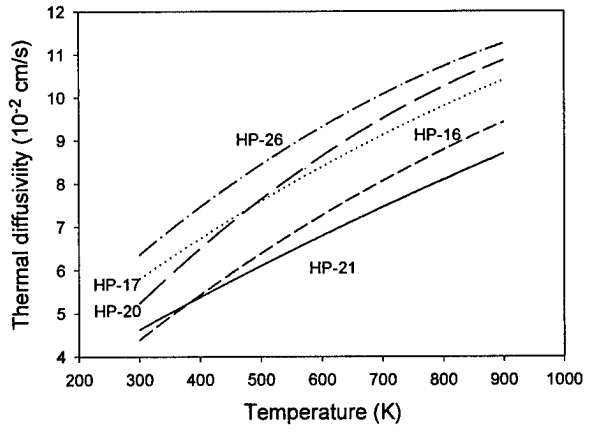


Figure 3. Thermal diffusivity as a function of temperature for different density.

As expected, the transport properties of $YbAl_3$ vary with specimen density. Both the Seebeck coefficient and electrical resistivity increase with a decrease in the density, while the thermal diffusivity decreases. The dependence of specimen HP-16 on the density appears less clear. This may be attributed to a crack in the specimen observed after thermoelectric properties assessment.

In figure 4 is shown the electrical power factor calculated using data from figures 1 and 2. The power factor of Bi_2Te_3 based alloys is also included as a dotted line for comparison. The electrical power factor of $YbAl_3$ is more than double that of Bi_2Te_3 based materials. To date, there is no other material which possesses such a large electrical power factor over this temperature range. However, $YbAl_3$ is an intermetallic compound which is expected to follow the Wiedemann-Franz-Lorenz law and possesses a relatively larger thermal conductivity than Bi_2Te_3 based alloys. In figure 5 is presented

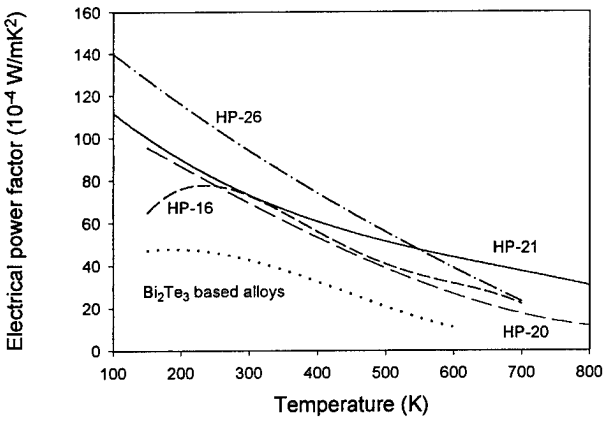


Figure 4. Electrical power factor as a function of temperature for different density.

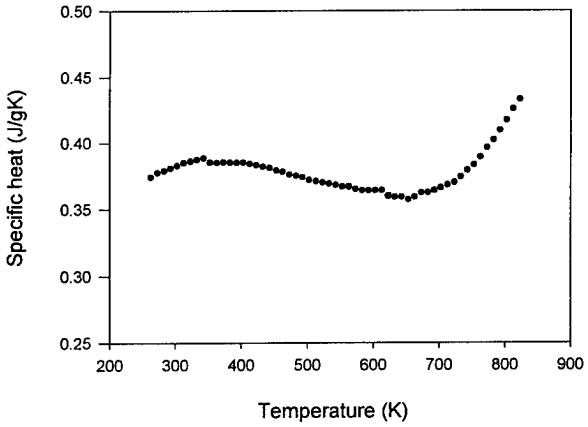


Figure 5. Specific heat capacity as a function of temperature for specimen HP-17.

the specific heat capacity as a function of temperature for specimen HP-17. It remains almost constant over the temperature range 250-750 K. Since the specific heat capacity is independent of the density, the thermal conductivity of specimens HP-16, 20, 21 and 26 can be calculated based on the data obtained from specimen HP-17 using $\lambda = c_p d\lambda'$ (where λ is the thermal conductivity, c_p the specific heat capacity and λ' the thermal diffusivity). The results are shown in figure 6. The increase in thermal conductivity with increasing temperature indicates that the electronic contribution is mainly responsible for the total thermal conductivity. This electronic contribution can be calculated using the Wiedemann-Franz-Lorenz law: $\lambda_e = L_o \sigma T$ (where, σ is the electrical conductivity, T the absolute temperature and Lorenz number L_O=2.45 x 10^{-8} V^2/K^2). The solid circles shown in figure 6 represents the electronic component of the thermal conductivity for specimen HP-26. Other specimens exhibit similar results but are omitted to simplify the graphs. It can be seen that the thermal conductivity values calculated using the Wiedemann-Franz-Lorenz law are larger than that obtained from thermal diffusivity measurement. This result indicates that the Lorenz number in $YbAl_3$ compound may be smaller than the classical value L_O. However, it should be noted that the thermal diffusivity apparatus has been calibrated against the standard reference materials (pure iron and stainless steel) using the reference data reported by Touloukian *et.al.* [8], which appears to be inconsistent with those reported in ref. [9]

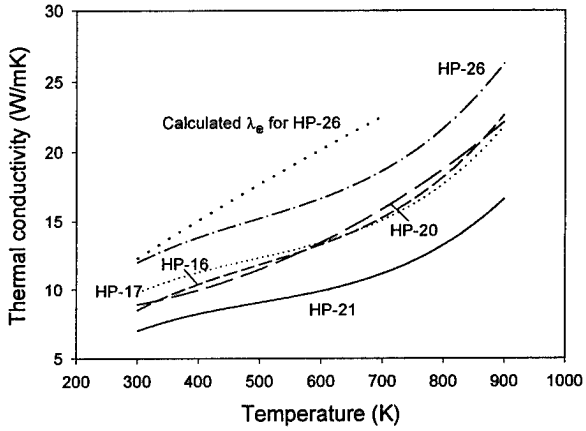


Figure 6. Thermal conductivity as a function of temperature for different density.

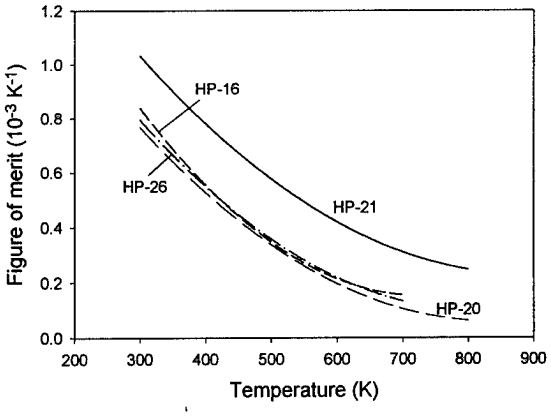


Figure 7. The figure-of-merit as a function of temperature for different density.

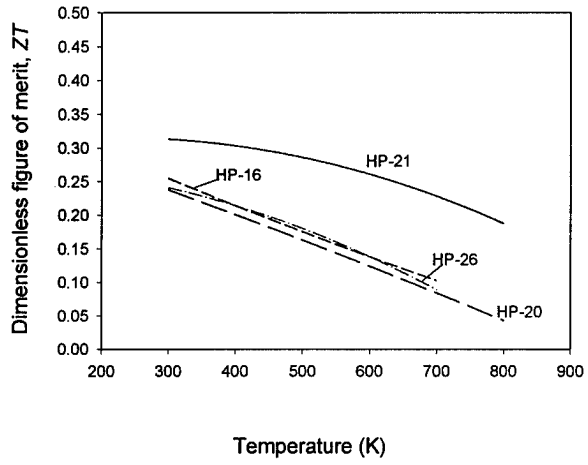


Figure 8. Dimensionless figure-of-merit as a function of temperature for different density.

In figure 7 and 8 are shown the figure-of-merit Z and its dimensionless value ZT, respectively, as a function of temperature for specimens HP-16, 20, 21, and 26. A value of $Z \sim 1.1 \times 10^{-3}\ K^{-1}$ (or $ZT \sim 0.3$) is obtained at room temperature for specimen HP-21 which, of the specimens investigated, possesses a relatively low thermal conductivity. Even so, this value is only a third of that obtained from Bi_2Te_3 based alloys due to very high thermal conductivity of $YbAl_3$ compound, its electrical power factor is more than doubled. $YbAl_3$ is not competitive with Bi_2Te_3 based alloys in terms of the conversion efficiency (or the coefficient of performance). Nevertheless, it exhibits a large power density than any other currently available thermoelectric materials. This is a distinctive advantage in electrical power generation using waste heat, where the power density rather than the conversion efficiency is overwhelming consideration. Furthermore, an improved understanding of its substantially large electrical power factor and possible deviation from the Weidemann-Franz-Lorenz law may provide insight into increasing the thermoelectric figure-of-merit in Kondo materials.

Acknowledgement

This work is supported by the New Energy and Industrial Technology Development Organisation (NEDO), the Energy Conversion Centre, Japan. Prof. R. J. D. Tilley, Dr. D. Pasero and Mr. R. Jones are thanked for preparation of arc-melting specimens and X-ray analysis.

References

[1] G. A. Slack, "New materials and performance limits for thermoelectric cooling" in *CRC Handbook of Thermoelectrics*, ed. D. M. Rowe, Boca Raton, (1995), chap.34

[2] G. D. Mahan and J. O. Sofo, "The best thermoelectrics" *Proc. Natl. Acad. Sci.* USA **93** (1996) 7436.

[3] P. C. Canfield and Z. Fisk, "Growth of single crystals from metallic fluxes", *Philosophical Magazine*, 65, 6 (1992) 1117.

[4] D. M. Rowe, Gao Min, S. G. K. Williams, V. L. Kuznestov and A. Aoune, *NEDO Technical Results Report: TR3* (1996-1997), University of Wales Cardiff, UK

[5] S. G. K. Williams, G. Min and D. M. Rowe, "Use of microcomputer for the analysis of thermal diffusivity data obtained by the laser flash technique", *Proc. of 10th Inter. Conf. on Thermoelectrics*, ed. D. M. Rowe, Babrow Press, Cardiff, UK, (1991) 74.

[6] E. Bauer, "Anomalous properties of Ce-Cu and Yb-Cu based compounds", *Adv. Phys.* 40 (1991) 471.

[7] A. C. Hewson, *The Kondo Problem to Heavy Fermions*, Cambridge University Press, Cambridge (1995)

[8] Y. S. Touloukian, *Thermal Properties of Mater (Volume 10): Thermal diffusivity*, IFL/Plenum, New York, (1973).

[9] J. G. Hust and A. B. Lankford, NBS Special Publication 260-90, (1984).

Development of Improved Modules for the Economic Recovery of Low Temperature Waste Heat

David Michael Rowe
NEDO Centre for Thermoelectric Engineering, Cardiff School of Engineering
PO Box 689, Newport Road, Cardiff CF2 3TF, Wales

Abstract

Waste heat recovery is an application of thermoelectrics where a high conversion efficiency is not of major importance. The economic competitiveness of this technology is determined by the capital investment (cost per watt) and reliability (module mean-time-between failures). This paper reports progress made in developing an improved module for use in the economic thermoelectric recovery of low temperature waste heat. It is predicted that these improved modules will generate at least three times the electrical power per unit area compared with Peltier modules currently available and reduce the break-even time (operating period required to produce electricity at a cost which matches that of the major electrical power generating utilities) from the present seven years to less than three years.

General Introduction

In general, applications of thermoelectric generators have been restricted to situations where combinations of their desirable properties such as reliability, silent operation and ability to operate in hostile environments outweigh their relatively high costs and low conversion efficiency [1]. By far the widest applications have been in Radioisotopic Thermoelectric Generators (RTGs) with the heat input being provided by a decaying radioactive isotope - an extremely expensive energy source. In order to maximise the conversion efficiency and hence reduce fuel costs, the generator's modules are designed to meet the requirements of the specific application, with effort concentrated on improving the thermocouple's figure-of-merit and operating the generator at as high a temperature as possible to increase the Carnot efficiency. The results are purposely built, expensive, high-tech modules which cannot be bought off the shelf. Examples are the multicouples used in the modular RTG (Figure 1) with its elaborate design features such as glass-coated thermoelements to prevent inter-element short-circuiting [2] and the SP-100 cell configuration (Figure 2) which uses compliance pads to minimise thermal expansion effects when operated at temperatures around 1000°C [3]. Fortunately, the module specification is far less stringent in thermoelectric waste heat recovery when the hot side temperature is less than 140°C. Commercially available Peltier module thermoelements, shown schematically in Figure 3, can readily be modified for generating application. In addition, when the cost of heat energy is low or is essentially free, as in the case of waste heat, the relatively low conversion efficiency of thermoelectric generation is not an important consideration. In some parasitic applications such as a power supply for a domestic central heating system it can be considered a distinct advantage [4]. Since 1994 a research project has been under way at the University of Cardiff to economically recover large quantities of low temperature waste heat using thermoelectric technology. In this paper is reported progress made in one aspect of this project which will result in the fabrication of modules based on commercial Peltier coolers which generate at least 3 times the electrical power per unit area compared to those currently available when operated over the same temperature range. It is predicted that these improved modules will reduce the economic break-even time (operating period required to produce electricity at a cost which matches that of the major electrical power generating utilities) from the present 7 years to less than three years.

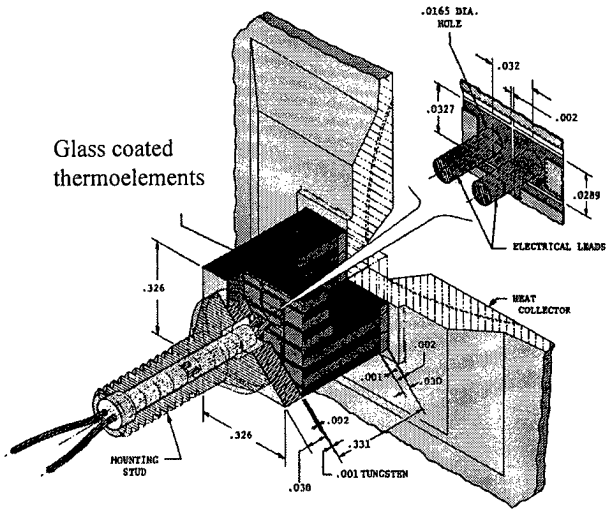


Fig 1: Modular RTG employing glass-coated thermoelements (courtesy General Electric)

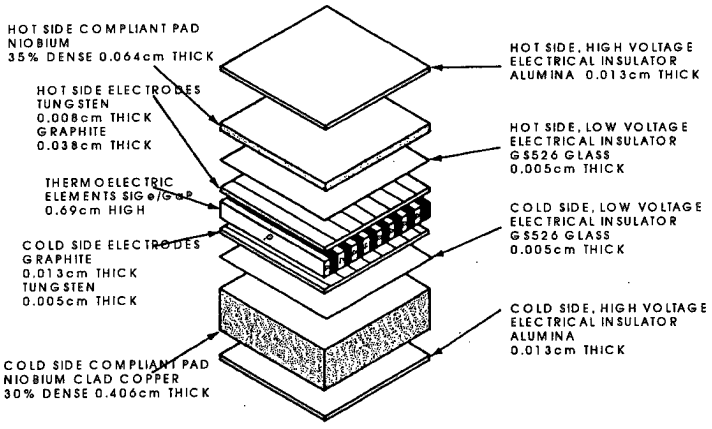


Fig 2: Thermoelectric cell configuration (SP-100) [ref 3]

Peltier module generating performance

As a first step an evaluation was undertaken of commercially available thermoelectric modules when operated in the generating mode. The modules tested, apart from one, were designed for operating in the cooling (Peltier) mode. A single

module test-generator was assembled and used to assess their performance. Maximum electrical power output was measured using a technique specifically developed to minimise module self-cooling and to overcome problems in measuring short-circuit current in these very low resistance devices. A selection of the results obtained for 127 thermoelement modules is displayed in Figure 4. Evidently the power output from different modules varies by more than a factor of 2. A very wide variation in the cost per watt is also evident as shown in Figure 5. Generating costs range from more than $100 a watt to less than $5 a watt when the module is operated with a temperature difference of 80K and an ambient temperature cold side.

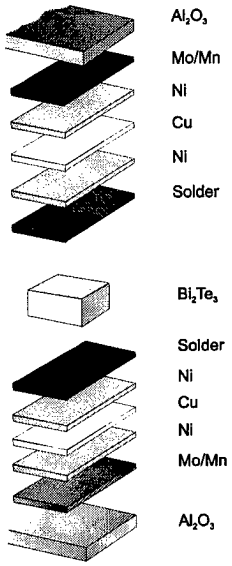


Fig 3: Construction of typical thermoelement

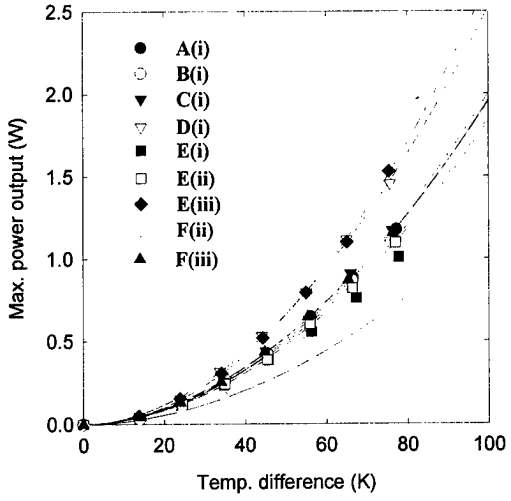


Fig 4: Maximum power output of commercial 127-thermocouples Peltier modules as a function of temperature difference (T_c at 300K)

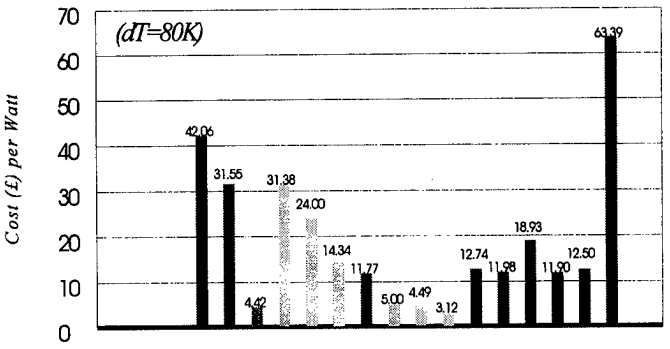


Fig 5: Comparison of cost (£) per WATT for thermoelectric modules when operating in generating mode (temperature difference 80K).

Theoretical model

In order to identify the parameters of a module which determine its performance in thermoelectric generation it is necessary to formulate a realistic theoretical model. The conventional design of a power generating thermoelectric module is usually based upon a set of formulae derived using a simple model in which the thermal and electrical contact resistances of the module are neglected [5] and expressions derived for the conversion efficiency which are independent of module geometry. In this situation the design of the thermoelectric generator is guided solely by matching the load resistance to achieve either of the two limiting cases; maximum conversion efficiency or maximum power output [6]. However, both power output and conversion efficiency of a thermoelectric module are dependent upon the thermoelement length for a given material figure-of-merit, contact properties and temperature regime of operation [7]. A schematic of a realistic single couple thermoelectric module is shown in Figure 6.

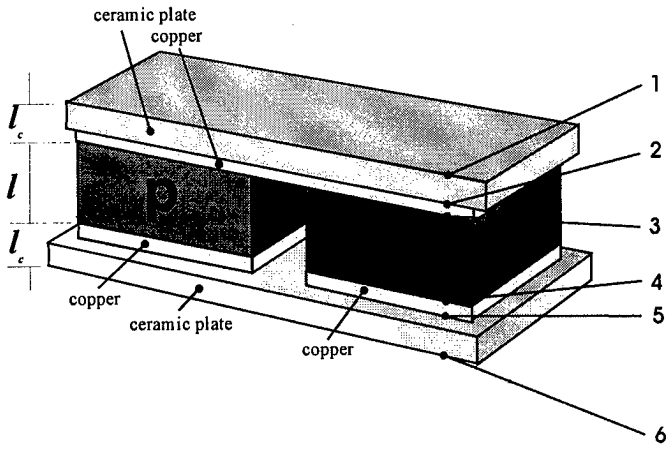


Fig 6: Simplified structure of Peltier module. Interfaces 1-6 contribute to the thermal contact resistance, Interfaces 3-4 contribute to the electrical contact resistance.

Based on this model the performance of a thermoelectric module operating as a generator can be described by the following set of equations:

$$V_m = \frac{\alpha N(T_h - T_c)}{1 + 2rl_c / l} \quad [1]$$

$$I_m = \frac{A\alpha(T_h - T_c)}{2\rho(n+l)(1 + 2rl_c / l)} \quad [2]$$

$$P = \frac{\alpha^2}{2\rho} \frac{AN}{(n+l)(1+2rl_c / l)^2}(T_h - T_c)^2 \quad [3]$$

$$\phi = \left(\frac{T_h - T_c}{T_h}\right)\left((1+2rl_c / l)^2\left[2 - \frac{1}{2}\left(\frac{T_h - T_c}{T_h}\right) + \left(\frac{4}{zT_h}\right)\left(\frac{l+n}{l+2rl_c}\right)\right]\right)^{-1} \quad [4]$$

$$P = F \cdot N\Delta T^2 \left(\frac{\alpha^2}{2\rho}\right)\left(\frac{A}{l}\right) \quad [5]$$

$$F = \frac{1}{\left(1+\frac{n}{l}\right)\left(1+\frac{2rl_c}{l}\right)^2} \text{ or } F = \frac{P}{N\Delta T^2\left(\frac{\alpha^2}{2\rho}\right)\left(\frac{A}{l}\right)}. \quad [6]$$

where α is the Seebeck coefficient of the thermoelement material, ρ its resistivity, N the number of thermocouples, A and l the cross-sectional area and length of the thermoelement respectively, l_c the thickness of contact layer, T_h and T_c are the temperatures of hot and cold side of module, $n=2\rho_c/\rho$, $r=\lambda/\lambda_c$, ρ_c is the electrical contact resistivity, λ the thermoelement thermal conductivity and λ_c the contact thermal conductivity.

Module fabrication quality factor

The wide variation in the performance of modules fabricated from essentially the same materials and operating over the same temperature regime reflects the differing standards in fabrication technology adopted by device manufacturers, viz. contact materials and the formation of electrical junctions and thermal contact layers. In equation 6, F is referred to as fabrication quality factor and is a measure of 'the quality of the module fabrication'. In Figure 7 the parameter F is plotted as a function of thermoelement length for different contact resistance. Each of the curves correspond to modules with identical contact properties (which reflect the fabrication process). Consequently this figure can be used to measure the quality of module fabrication. F values for a number of commercially available modules are plotted on the graph. It is apparent that the fabrication quality for a majority of manufacturers correspond to F values between 0.6 and 0.8 for the widely employed thermoelement lengths of around 1.5 mm. The module which does not fall on any of the curves was manufactured using a completely different (and inferior) contacting and fabrication process.

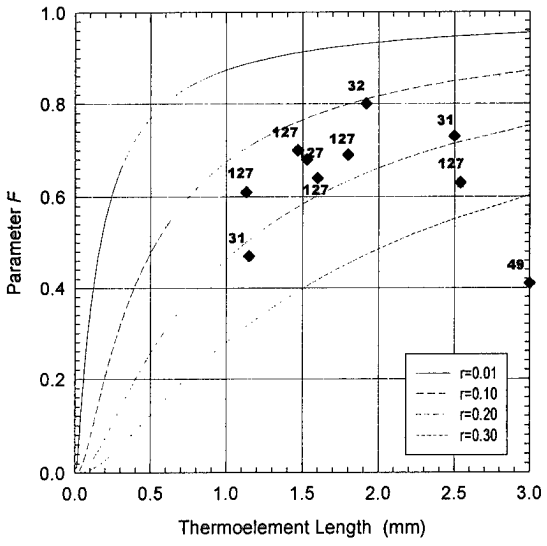


Fig 7: Procedure to assess quality of module fabrication quality

Contact improvement

Both the electrical power output and conversion efficiency of a module can be improved by reducing the thermal and electrical contact resistances. The electrical power output per unit area of the module are displayed as a function of the thermal and electrical contact parameters (n and r respectively) in Figure 8. Effort has concentrated on reducing the thermal contact resistance as the figure clearly illustrates that reducing the thermal contact resistance has a more significant effect on improving the power output than reducing the electrical contact resistance.

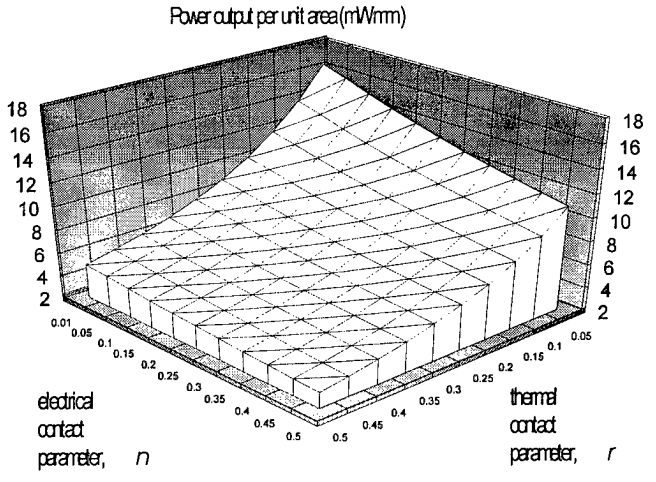


Fig 8: Improvement in power output per unit area of thermoelectric module based on parameters n and r.

Optimising thermoelement geometry

Traditional calculations of electrical power output and conversion efficiency of thermoelectric generating modules is

usually based upon an "ideal model" having long thermoelements to maximise efficiency and in which case the influence of electrical and thermal contacts can be neglected. However, in thermoelectric generation using waste heat short thermoelements are desirable and in this case both the power output and conversion efficiency would be over-estimated. In addition, an "ideal model" is unable to provide information on the relationship between thermoelement length and the electrical power output and conversion efficiency.

The "realistic model" outlined above revealed a length dependence of electrical power output which differs from that of conversion efficiency. The conversion efficiency increases with increasing thermoelement length while the electrical output increases with a decrease in thermoelement length, reaches a maximum and then decreases as indicated in Figure 9. The "realistic model" also facilitate the development of detailed design theory for the situation when fuel is not free and provides a practical procedure for optimising the module geometry guided by an economic factor (£/kWh).

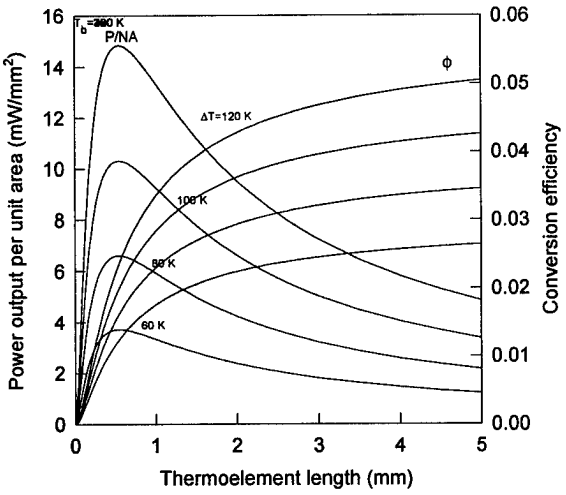


Fig 9: Power output per unit area and conversion efficiency as a function of thermoelement length

Generally in Peltier applications the volume to be cooled is large compared to the dimensions of the module, consequently the inter-thermoelement spacing is not of significant importance. In generation, however, a large power output per unit area is desirable and this can be almost doubled by halving the inter-element spacing.

Optimisation thermoelement materials

Materials currently employed in commercially available modules are optimised for Peltier applications around and below room temperature (apart from one manufacturer). Optimisation is achieved mainly by adjusting the carrier concentration and material composition. The effect on the electrical power factor and power output of shifting the optimised values from 300K to 350K is shown in Figures 10a and 10b respectively. Evidently an improvement of around 5% in power output can be achieved at $\Delta T \sim 100K$..

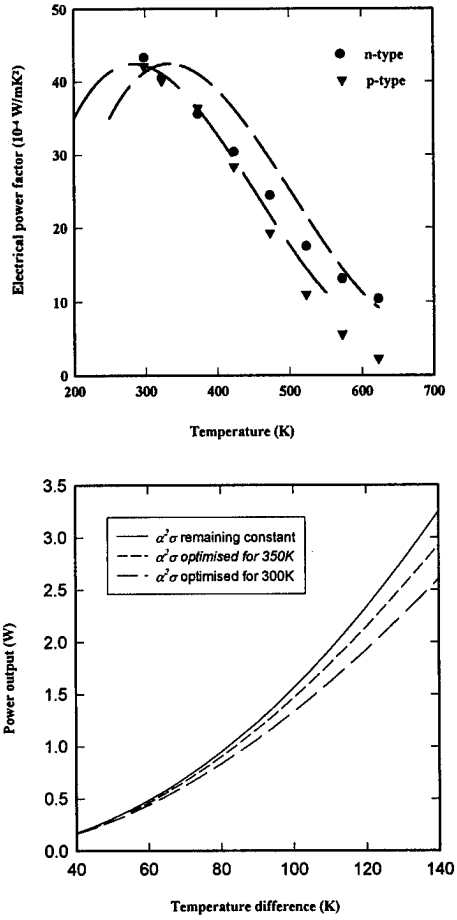


Fig 10(a)-(b): Electrical power factor and power output as a function of temperature difference

Search for new materials

In view of the daunting large numbers of possible material combinations, attempts have been made to identify general trends in the thermoelectric transport properties which provide guidelines to identify thermoelectric materials with a potentially good power factor. Trends were observed between the materials' electrical properties and the electronegativity differences of the elemental components, see figure 11. A modified "quantum structural diagram" (figure 12) which involves simple calculations using periodic table data enables potentially good binary compounds to be identified from their location in this diagram.

Material preparation

A quick and relatively simple method of producing materials has been developed using mechanical alloying followed by cold pressing and/or sintering. More than 500 materials have been prepared to date including over 250 binary compounds, 100 ternary compounds and 80 quaternary compounds.

Measured data on these materials serve to provide a material data base for the initial stage of thermoelectric properties mapping. High density samples of promising thermoelectric materials are prepared by vacuum hot pressing or Bridgeman's method. A phenomenological approach similar to the one used by Mendeleyev in constructing his periodic table was employed in attempting to identify promising trends. Computer graphics were used to superimpose measured thermoelectric transport data upon the periodic table. As an example the electrical power factor for ternary compounds based on SbTe is displayed in Figure 13.

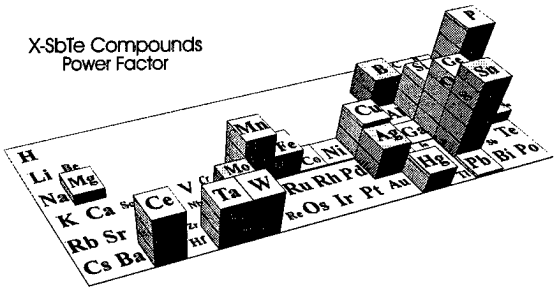


Fig 13: Electrical power factor of ternary compounds based on SbTe.

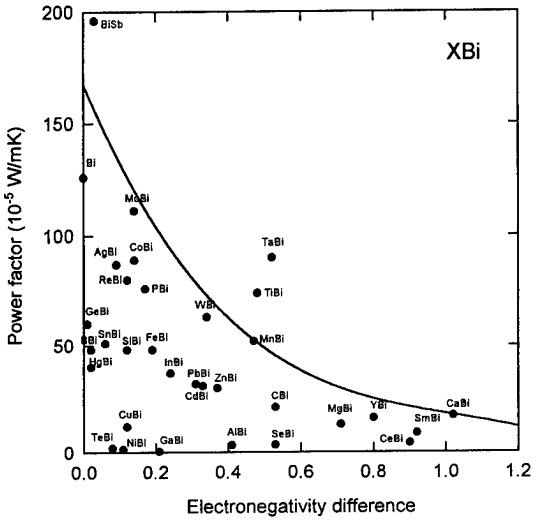


Fig 11: Electrical power factor as a function of electronegativity difference for binary compounds containing bismuth.

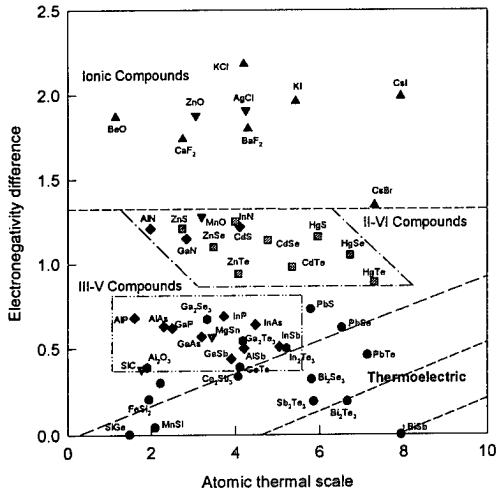


Fig 12: Thermoelectric properties "mapping" of binary compounds using a modified "quantum structural diagram".

Property screening

The search for a high figure-of-merit (electrical power factor) material involves a prohibitive amount of experimental work both in material preparation and subsequent transport properties evaluation. The optimum doping level of newly prepared materials is usually unknown. The thermoelectric property of non-optimum doped material is usually much small than those which are optimally doped. A technique has been developed [8] which eliminated the need to make measurements on a large number of specimens of a material with different doping levels. An α-$ln\sigma$ plot serves as a useful power factor indicator. The method is based on a relationship between the Seebeck coefficient and the electrical conductivity and enables the maximum electrical power factor to be readily estimated from Seebeck coefficient and electrical resistivity measurements on non-optimised specimens. The optimum electrical conductivity corresponding to the maximum electrical power factor can also be estimated. In Figure 14 is shown room temperature α-$ln\sigma$ plots obtained from published data for several thermoelectric materials. The intercept on the $ln\sigma$ axis exceeds 9 for good thermoelectric materials. The corresponding electrical power factors can be calculated using this Figure and the results are displayed as a function of electrical conductivity in Figure 15.

Reliability

Device reliability is a prerequisite for economic generation using waste heat as the operating lifetime of the generator is limited by the module's between failure time. Thermoelectric modules based on bismuth telluride technology are extremely reliable when operated in the cooling (Peltier) mode at and below room temperatures, with the life time, in general, considered to be more than 50 years. Although it has been reported that significant degradation occurs in modules when operated at 70°C for cooling laser diodes [9] very limited reliability information is available on modules operated in the generating mode. A programme of work was undertaken at Cardiff to determine the reliability of commercially available modules, identify failure mechanisms and where necessary take appropriate action.

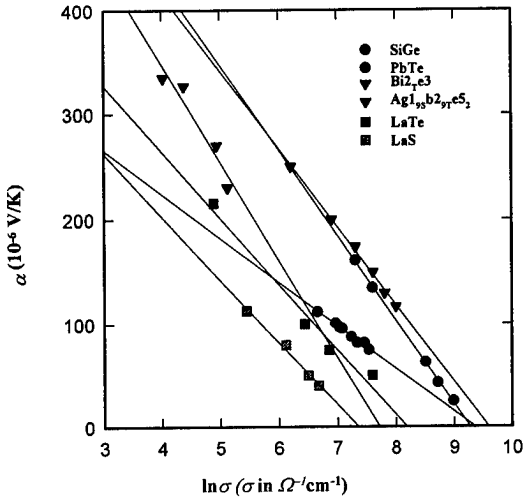


Fig 14: Room temperature plots of α–$ln\sigma$ for several thermoelectric materials

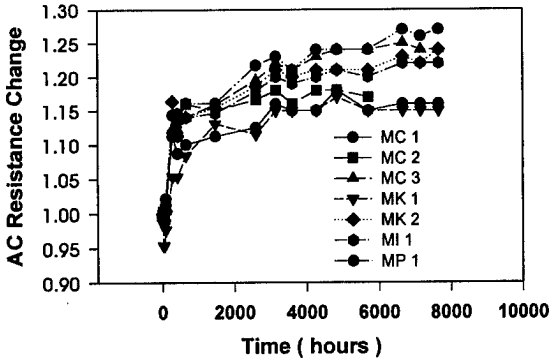


Fig 16: AC resistance change of Peltier cooling modules stored at 100 deg C as a function of time.

In Figure 17 is displayed that temperature dependencies of a typical module before and after continuous operation for 8500 hours under a temperature difference of 80°C and with a hot side temperature of 100°C. An average increase of about 3% was observed in the resistance of the module.

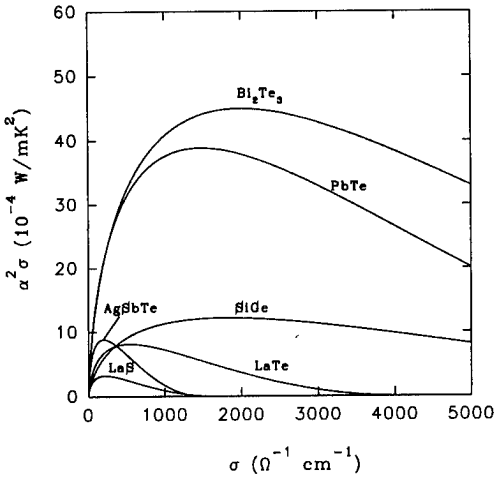


Fig 15: Electrical power factor as a function of electrical conductivity for several good thermoelectric materials

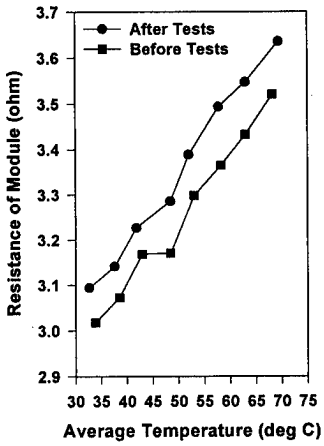


Fig 17: Temperature dependencies for typical Peltier cooling module before and after continuous operation for 8500 hrs at a temperature difference of 80 deg C and hot side 100 deg C.

Two reliability test procedures were employed, high temperature storage and continuous operation. Preliminary studies indicated that one of the dominant failure mechanisms of a module when operating at elevated temperatures was deterioration of the electrical properties and contacts. In high temperature storage tests AC resistance testing was adopted as an indicator of the module's integrity. Data obtained shows that significant performance degradation occurred in most tested modules as indicated in Figure 16. The electrical resistance of the modules increased by 5-14% during the first 300 hours and increased by up to 15-27% during the test period of 7600 hours at 100°C.

Estimation of median life

When a thermoelectric module operates in its cooling mode, the maximum temperature difference across it decreases with time due to an increase in the module's internal resistance. This increase in resistance is attributed to solid state diffusion and reactions between the semiconductor thermoelements and their solder pads. It is reasonable to assume that the degradation mechanism of modules operating in the generating mode is similar to that when operating in the cooling mode. The module life time can then be estimated using published cooling reliability data and Arrhenius's equation:

$$\frac{t_1}{t_2} = \exp\frac{E_a}{k}\left(\frac{1}{T_1} - \frac{1}{T_2}\right)$$

where t_1 and t_2 are the failure time of modules when operated at temperatures of T_1 and T_2, k is Bolzmann's constant and E_a is the processes activation energy taken as 0.55 eV for the continuous operation tests.

The medium life of the best modules investigated was calculated to be three years when operated in the cooling or generating mode at 100°C. This implies that the power output of half the tested modules will reduce by 10% after three years continuous operation at 100°C - a result in close agreement with our experimental results.

Economics

The cost per watt of a module provides a measure of its economic performance to some extent. However the ultimate cost of the electricity generated using a thermoelectric module is a function of the operating period and consequently related to its reliability. In general, the cost of electricity generated thermoelectrically using waste heat is given by:

$$\text{Economic factor} = \frac{\text{cost per watt}}{\text{mean time between failures}}$$

In Figure 18 is shown the cost of electricity as a function of operating period for several modules when operating at a temperature difference of 65K with a cold side at 300K. UK domestic electricity costs at about £0.08/kWh is also given as a comparison. The results indicate that high reliability modules are required for thermoelectric generation to be commercially competitive. For the best commercially available modules a minimum mean-time-between failures of around seven years is a minimum requirement which reduces to around three years for improved performance modules.

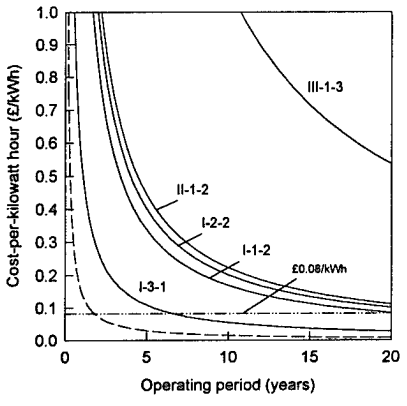


Fig 18: Cost per kilowatt hour as a function of operating period. Solid lines represent commercially available modules operated at ΔT=65K. Dashed lines indicate the predicted cost for a module with improved power-per-area operated at ΔT=100K.

The estimated costs in the figure exclude system construction costs but is unlikely to be double.

Conclusions

It has been demonstrated that Peltier modules can be used to generate electrical power using low temperature waste heat. When operated over a seven year period the cost of electricity produced by the best commercially available module matches that of the electrical utilities. The use of an improved module with thermoelement with optimised geometry and higher packing density would reduce the break even time to around three years. It is estimated that the break even time for a thermoelectric generating system would be around five years.

Acknowledgements

My co-workers Dr's Gao Min, S.G.K. Williams, V.Kuznetsov, A. Aoune and Professor L.Fu are acknowledged for their contributions to this paper. The work is supported by New Energy and Industrial Technology Development Organisation (NEDO), the Energy Conversion Centre, Japan.

References

[1] D.M. Rowe, "Thermoelectric power generation", Proc.IEE vol 125, No.11R, Nov. 1978, 1113

[2] D.Bunden and T.Albert, Space Nuclear Power Systems, Chapter 3, 1986, 15

[3] G.Stapfer and W.Carroll, "Thermoelectric power conversion for SP-100", Proc 8th International Conference on Thermoelectric Energy Conversion, July 10-13, Nancy, France, 143.

[4] D.M.Rowe, "Thermoelectric Recovery of Waste Heat - Case Studies", Proc 33 IECEC 1997, to be published.

[5] A.F.Ioffe, "Semiconductor thermoelements and thermoelectric cooling", Infosearch Ltd, London, 1957.

[6] R.R. Heikes and R.W.Ure, "Thermoelectricity, Science and Engineering", Interscience Publishers, New York 1961.

[7] Min Gao and D.M.Rowe, "Optimisation of thermoelectric module geometry for waste heat electrical power generation", Journal Power Sources 38, 1991, 253.

[8] D.M.Rowe and Gao Min, "α-$ln\sigma$ plot as a thermoelectric material performance indicator", Journal Mat. Science Letts., 14 (1995), 617.

[9] R.M.Redstall and R.Studd, "Reliability of Peltier Coolers in Fibre Optic Laser Packages", Proc 10th International Conference on Thermoelectrics, Cardiff, UK, 1991, 242.

Research Project on the Effective Use of Untapped Thermal Energy from Garbage Incineration etc.

M. Niino, T. Ohshima and K. Matsubara*

National Aerospace Laboratory (NAL), Kakuda Research Center, Koganezawa 1, Kimigaya, Kakuda-City, Miyagi 981-15, Japan

*Department of Electronics, Science University of Tokyo in Yamaguchi, Japan

Abstract

The objective of this project is to develop thermoelectric generation systems that convert untapped energy from such close-at-hand sources as garbage incineration heat, industrial exhaust, etc. into electricity. The project began in December 1995, supported by the Science and Technology Agency of the Japanese government. Four electric power generation systems have been under trial production and evaluation as to their reliability and advantages. Two of these (500W-class power generation systems) were linked to a conventional garbage incineration plant with a capacity of 80 tons/day. Another system was tested in conjunction with a gas co-generator. A fourth system, for solar thermal energy, was combined with a photovoltaic cell.

1. Introduction

Our modern day life-style has evolved within a mass-production, mass-consumption social structure supported by fossil fuels. As a result of this the global environment is facing such problems as warming due to greenhouse gases, acid rain and air pollution by such substances as dioxin. Also, the issue of the serious depletion of limited fossil fuel resources has been raised. Additionally, in Japan and elsewhere, disposing of the garbage produced by mass production/mass consumption has become a problem. In our attempts to deal with global environmental problems and, at the same time, avoid over-reliance on precious fossil fuel resources, there is a pressing need to develop new energy sources. In 1995 the Japanese government's Science and Technology Agency (STA) set up the "Research Project on the Effective Use of Untapped Thermal Energy from Garbage Incineration etc." (abbreviated title: UTP - Untapped Energy Project). In this project, some ten government, academic and commercial organizations are collaborating together to apply thermoelectric (TE) technologies used in space power generation systems to the development of power generation systems which make effective use of untapped thermal energy from the exhaust heat of garbage incineration plants and engines [1].

This paper describes the running project and outlines the present status of research. In particular, it will describe

1. the employment of two TE generating systems in a conventional, medium-size incineration plant,
2. the usage of exhaust heat of a gas-fired electricity generator to drive a TE system (co-generation of electricity),
3. the combination of a TE system with a photovoltaic generator to form a hybrid PV-TE system, and finally with
4. the popularization of thermoelectric power generation.

2. Development of garbage incineration driven power generation systems

In Japan, the majority of household and industrial waste is processed in garbage incineration facilities run by local government authorities. As of 1994 there were approximately 1850 of such facilities nationwide. Of these, some 130 facilities had steam generators attached summing up to an approximate electrical power capacity of 460 MW.

However, only 30% of the total volume of waste disposed in Japan contributes to the generation of electricity. The majority of waste is merely being discharged by the incineration plants into the atmosphere in the form of heat energy and gas. As the exploiting of such untapped energy sources will contribute to save fossil fuels, a positive attitude towards their development is looked for on the part of all parties involved.

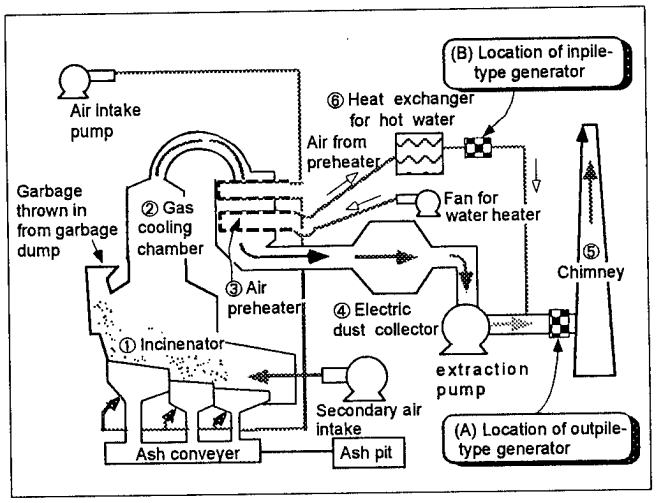


Fig. 1: Nishi-Tanaka garbage incineration plant in Sendai City with its two types of 500 W thermoelectric generating systems installed. (Capacity: 80t/16h. Type: Semi-uninterrupted stoker type. 2 automatic combustion control equipments. 2 water-spray gas cooling chambers. 2 electric dust collection equipments (< 0.05 g/Nm^3). 2 harmful gas disposal equipments (< HCl 150 ppm). Filtration of condensed water.)

Traditionally, steam turbine power generators are adopted by large-scale garbage incineration facilities. Its characteristics are such that it is appropriate for use in conjunction with large, continuously operated, facilities but not to smaller ones, with comparatively lower levels of processing capability, where the high cost of installation and repeated daily interruptions in operation would make it impracticable.

On the other hand, TE power generation can be used wherever there a heat source, irrespective of its size and operating conditions, and may therefore be adapted to these smaller type facilities. At their present stage of development, thermoelectric power generation only has an efficiency level of 4% as a power generation system but, as will be discussed later, an improved module is taken into account which will raise efficiency levels to 10~18%. In this case a thermoelectric power generation system will be a strong competitor to a steam engine.

The Nishi-Tanaka plant, owned by Sendai City, is an example for the majority of garbage incineration plants nationwide that are too small for the application of a steam power generator. The plant has a 80t/16h incineration capacity (2 x 40t/16h incinerators). A portion of the incineration heat it produces is used in heating the plant itself, in providing hot water and in melting snow that accumulates during the winter time but, beyond that, the heat is not utilized. With a view to putting that heat to good work, and with the cooperation of the Sendai City municipal office, two prototypes of TE generators (a so-called inpile- and an outpile-type generator) were installed at the plant and generation tests having been performing. Fig. 1 shows the way the incinerator system is laid out and where the power generators are located in the system.

The following steps are involved in the process of garbage disposal in the Nishi-Tanaka plant: combustible garbage is burned in an incinerator and the hot gases (950 °C) emitted by the high-temperature combustion, along with a small quantity of ashes, pass through the cooling chamber. From there they proceed through the air preheater, where they drop to a temperature of less than 300 °C as a result of thermal exchange. Fine, powder-like ashes are removed in an electric dust collector. Just before, the removal of harmful gases takes place. The gas, by now at a temperature of around 250 °C, passes through the flue and is discharged from the chimney.

The TE power generators were installed at the following two locations: the outpile-type thermoelectric generator on the flue immediately prior to where the flue joins the chimney (point A in Fig. 1) and the inpile-type generator towards the end of the duct leading out of the system's hot-water heater/heat exchanger (point B in Fig. 1)

2.1 Outpile-type Generator System [2]

This type of system has its generator located outside of the source of heat, i.e. the hot air duct, and uses heat pipes to direct the heat to the TE system, which is employs Bi-Te based modules HZ-14 from Hi-Z, USA. The heat pipes collect the heat with a fin structure and direct it to the TE modules by a gravity driven flow. Cooling is accomplished by means of a water cooling system using water from the incineration plant, which is a mixture of well water and tap water.

In the developmental stage, a 100 W type system was produced and its output checked using hot wind tunnel tests to simulate the generator's normal location on an incinerator plant's flue. Based on the results of these tests, a 500 W-class system was manufactured and installed at the Nishi-Tanaka facility, and long-term operation began.

The DC output of the generator is converted into 100 V alternating current, which is also used to feed the autonomous operation control equipment. Fig. 2 shows a photograph of the system before its installation and also a conceptual sketch of the way the generator works. Early on in the test operation of the generator, a DC output of 570 W was confirmed (exceeding its designed output) and, even after the passage of four months, a level of 400~500 W was being maintained with an integrated output reaching 400 kWh (approximately 5 kWh/day). Continued tests and long-term evaluation of the system's reliability are now undertaken.

Fig.3 shows a sample of data obtained over a period of approximately two days (45 hours) which were taken in the first month of operation. The DC output level of the TE modules reaches a maximum of around 500 W during the daytime, where the plant is in full operation. However, due to losses in the DC-AC converter, around 450 W are fed into the display equipment.

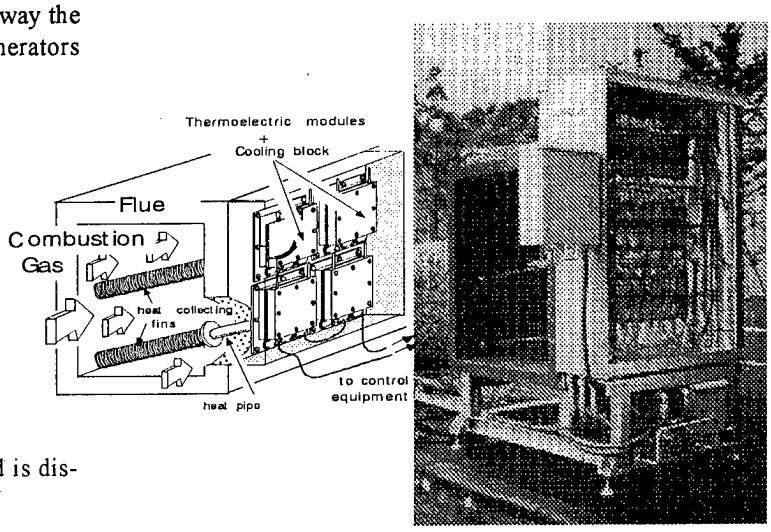


Fig. 2: Garbage incineration plant's outpile TE generator system.

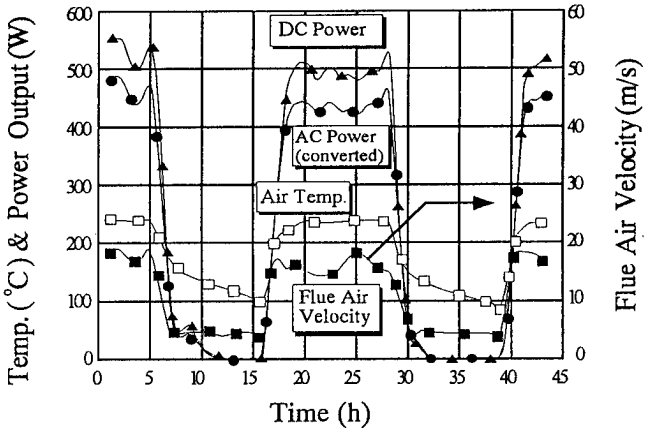


Fig. 3: Measurement data from the incineration plant's outpile TE generator system. The level changes reflect the plant's operation condition.

2.2 Inpile-type Generator System [3,4]

In the inpile generator system, thermal conversion takes place by having the main portion of the system located inside the heat source (hot air) itself. Fig. 4 shows a photograph of the generator together with a conceptual sketch. The heat-collection, thermoelectric conversion and cooling sections are located in the same unit and also here the cooler uses water from the garbage incineration facility. Problems with both, erosion of the heat collecting section and accumulation of dust, which usually have to be dealt with when locating the generator right in among burning gases have been avoided in the present case, as the generator was installed towards the end of the water heating system where the exhaust gas merely consists of clean hot air of about 250 °C. In this way problems with erosion and dust accumulation were removed.

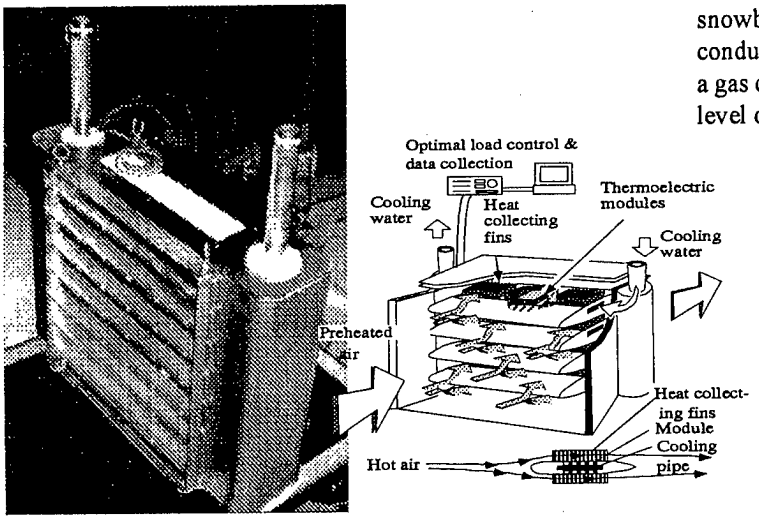


Fig. 4: Garbage incineration plant's inpile TE generator system.

The structure of the TE system consists of seven layers of twelve Bi-Te based TE modules laid side-by-side. The materials and modules have been manufactured by a Japanese company. Preliminary output tests conducted in a hot air wind tunnel before installation, confirmed the expected output of approximately 500 W. However, towards the end of the tests the generator sustained damage and four of its seven layers ceased functioning, thus the test was only valid for the remaining three layers. Output was around 200 W at the beginning of the tests but, after two months, it had gradually dropped to the 100 W level. The generator was dismantled and tests conducted to find the cause of the problem and a structural fault in the modules was found. Further tests are now being prepared for a new improved version of the modules.

2.3 Data collection and system evaluation

As both of the two above mentioned power generation systems require long-term testing, optimal electric load control and data collection were performed by a computer using a measurement and control system. Measurement control was automated and accomplished using a monitor with a computer graphics display and real time control.

3. Development of thermoelectric power generators for gas co-generation systems [5]

In Japan at present, there are about 3,000 stand alone gas-fired generators, mainly producing electricity for factories. The total volume of electricity produced is around 3,300 MW, with an increase at an annually rate of 10%. The efficiency of electricity generation by such a gas generator is approximately 30% and usually about 50% of the exhaust heat of such a co-generating system is recovered for heating purpose or as processing heat.

However, with the application of thermoelectric conversion techniques, the overall efficiency could be increased. If the effectiveness of thermoelectric power generation could be demonstrated with gas co-generation systems, it would be possible to apply them to co-generation systems as a whole, and the popularity of this form of power generation would snowball. In this present research project, experiments were conducted using a thermoelectric generator in conjunction with a gas co-generation system to establish its feasibility at a target level of 500 W electric power output.

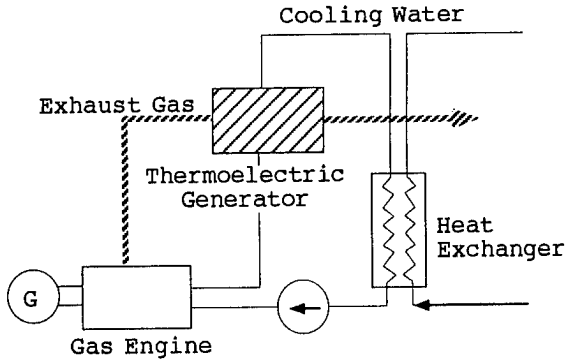


Fig. 5: Flow chart of a gas co-generation system with an additional TE converter attached.

3.1 Application of TE to a gas-fired electricity generator

Fig. 5 shows a system flow chart for a TE generator applied to a co-generation system. And as seen from Fig. 6, the TE generator consists of a heat exchanger and four layers of thermoelectric modules arranged in groups of 5 x 5 per layer. As in the case of the incinerator outpile system, Bi-Te type modules HZ-14 were used. The heat media of the heat exchanger were, on its hot side, exhaust from the gas co-generator's engine and, on its cool side, water. A plate fin type of heat exchanger was used, bearing in mind the thermal transfer efficiency ratio and size of the generator.

In TE power generation, the flow of heat through the thermoelectric modules determines the system's efficiency. In the case of a layered structure generator, it is necessary to apply pressure on the top of the plate fin heat exchanger so as to reduce thermal contact resistance between the heat exchanger and the thermoelectric module layer and, in designing a device to apply such pressure, it is necessary to ensure that the pressure is applied evenly to all of the thermoelectric modules. Based on preliminary tests to determine the level of pressure required and the method of applying it, an oil-filled bellows method

was adopted for the present thermoelectric generator because its pressure level may be regulated easily.

3.2 Performance Evaluation Tests

Performance evaluation tests were conducted using a hot air producing device and a cold water circulator. It was confirmed that the outputs for each of the modules for the preliminary test were approximately the same, and the tests were carried out under conditions of sufficient and uniform pressure application. Evaluation tests, using temperature of exhaust gas and its flow volume as parameters, were carried out to determine generator performance.

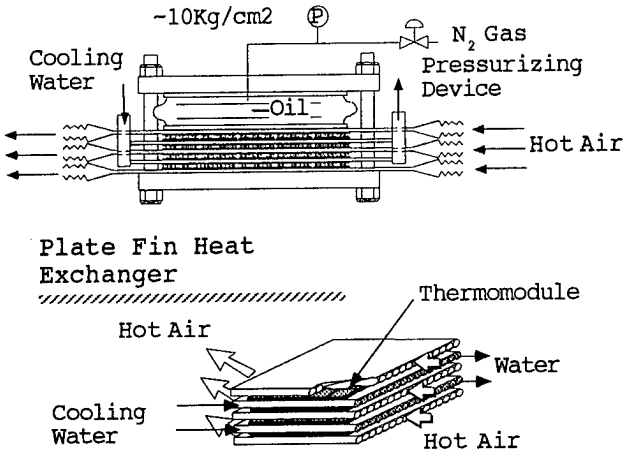


Fig. 6: Schematic of the TE assembly in the gas co-generation system.

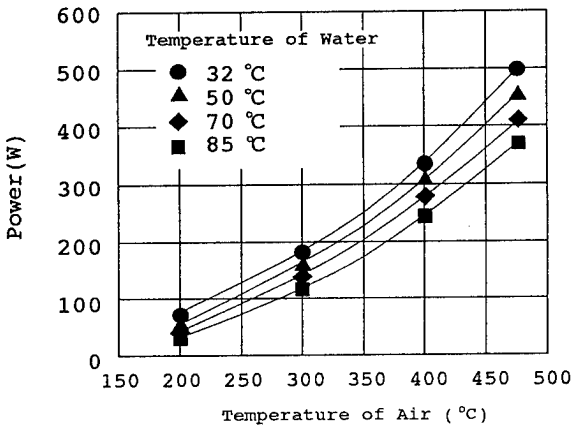


Fig. 7: Electrical output power *vs.* inlet air temperature at the gas co-generation system.

Fig. 7 shows the relationship between the temperature of the exhaust gas and generator power output when the flow volume of the exhaust gas is held at a fixed level. The power output for the thermoelectric generator is calculated as the highest output of the thermoelectric modules from the voltage values for the open ends and the internal resistance values of all the modules. It was confirmed that the volume of electricity generated increased in proportion to the square of the temperature difference of the thermal media and that, at the temperature at which it was designed to function, the goal of an output of 500 W was achieved.

4. Development of a hybrid photovoltaic/thermoelectric electrical power generation system [6]

4.1 Solar heat/light hybrid power generation

The previously described applications of TE indirectly still employ fossil fuel as heat source for the TE energy conversion. A source independent of limited fuel is solar radiation, though it has the disadvantage of a relatively low density and uncertainties in availability. The visible part of the solar spectrum is already successfully exploited by photovoltaic (PV) energy conversion systems, but as 50% of the radiated energy from the sun is transferred in the infrared (IR) region of the spectrum, there is still room for further improvement. Therefore the idea is at hand to divide the solar spectrum into the visible and the IR part which are separately lead to a PV and a TE system, respectively.

In order to investigate the performance of such a hybrid system, a concentrating solar receiver, with radiation separation through a wavelength selective filter has been set up.

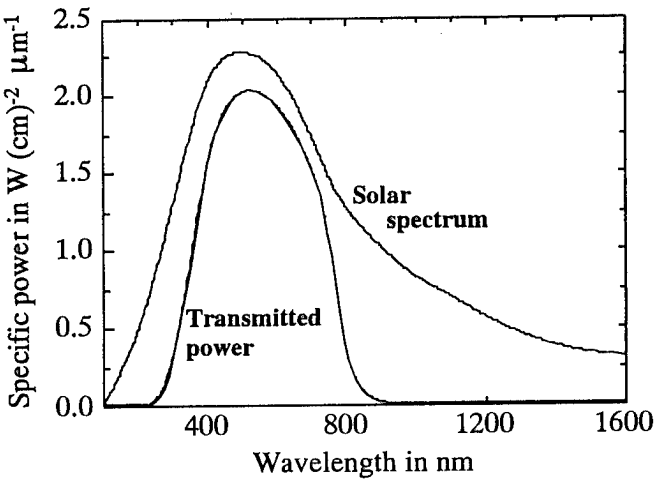


Fig. 8: Specific solar radiation power as a function of wavelength together with the transmission characteristics of the filter employed to separate the IR from the visible light.

4.2 The test heat/light hybrid solar power generation system

The solar receiver consists of a heliostat with a concentration factor of 3, and a heat linear concentrator made up of a selective wavelength reflector with a characteristic shown in Fig. 8. It serves as a heat/light separator, as it focuses the IR part of the solar spectrum with wavelengths above 800 nm onto a thermoelectric convertor which has TE modules in a row. For radiation below 800 nm the filter has a transmission characteristic of 90%. This radiation falls onto an array of amorphous silicon solar cells. Fig. 9 shows the overall concept of the system. The system was installed on the roof of the project research facility and tests were begun.

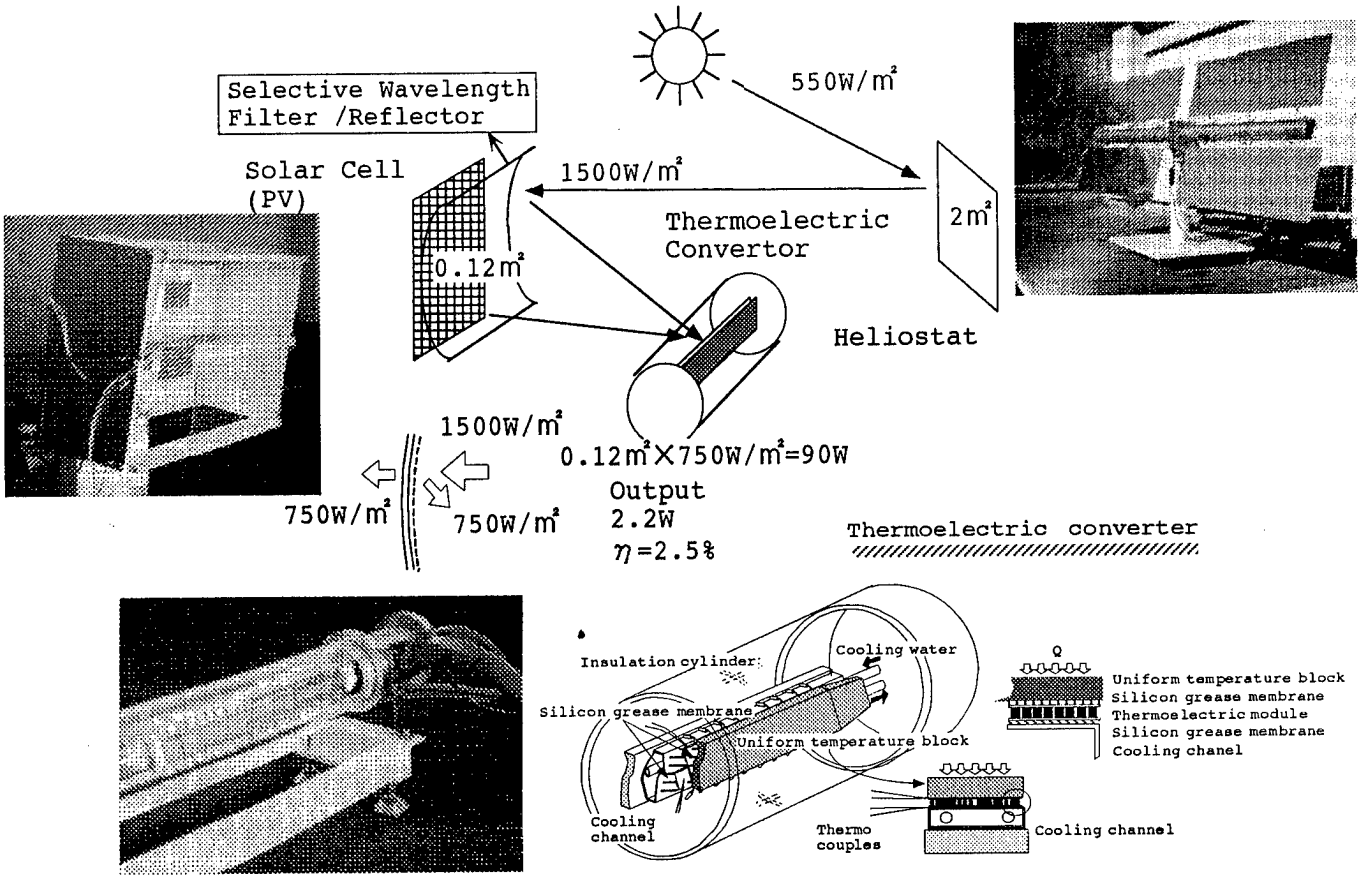


Fig. 9: Schematic and detailed views of the PV-TE hybrid system.

Two radiation power meters were attached into the reflected and transmitted radiation paths. Throughout the tests they indicated, that the radiation power was roughly divided into two equal parts. In order to determine the influence of the partly reflecting membrane on the output of the PV generator, we installed solar cells on both sides of the membrane. We could indeed verify that the outputs of both PV cells were equal, indicating that the influence of the employed filter is almost negligible.

As TE generating elements standard Peltier modules were used, which is the reason that the present tests are still seen to be preliminary. The concentrating solar receiver can generate hot side temperatures of the TE modules upto around 400 °C, but in the current case we were restricted to 150 °C. Cooling of the TE generator was achieved by tap water, which, in the current stage of experiment, did not gain a significant temperature rise during its flow.

Fig. 10 shows an example of the data obtained. The striking drop of temperatures in the chart is caused by an interruption of the solar radiation through a cloud. From the results shown in the chart, it may be seen that the TE conversion efficiency of the system was 2.5% when the hot side of the thermoelectric generator was 120 °C, with a temperature difference of 70 °C. If we did not have the restriction of the hot side temperature limit, the efficiency would be somewhat higher.

However, the present tests have fundamentally demonstrated that a hybrid PV-TE system, sharing the same incident radiation, without considerable mutual distortions is in fact realizable. Further setups of systems embodying amorphous solar cells and wavelength-selective filters have been scheduled with a view to developing a high output generator. By using BiTe-type and medium-temperature range PbTe-type materials in thermoelectric power generation, the aim is to achieve a thermal conversion efficiency level of 10% or more, thereby raising the compound thermal conversion efficiency of both, light and heat, to above 15%. If additionally the generated hot water is used, an overall system efficiency of 70% is expected.

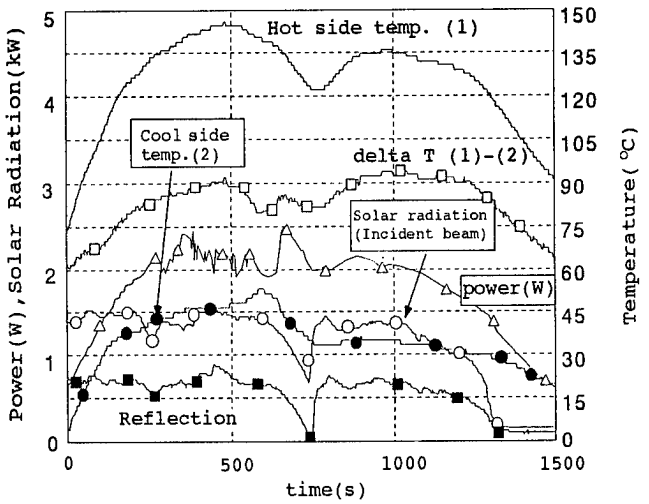


Fig. 10: Typical measurement data pattern of the PV-TE hybrid system.

5. Progressive increase in the efficiency of thermoelectric materials

The following points might be mentioned as challenges, or conditions that need to be met in order to achieve the popularization of thermoelectric generators powered by untapped exhaust heat such as garbage incineration heat: (1) thermoelectric power generation techniques must be demonstrated to have improved beyond their present 1 kW capacity to a level of 100 kW output and, (2) the durability and reliability of thermoelectric generating systems must be demonstrated and, finally, (3) it is vital that production costs become low enough to be commercially feasible. In order to achieve the first goal of increased output levels it is necessary, on the present materials development side, to improve the efficiency and thermal resistance of thermoelectric modules, and, in the area of thermoelectric generator design, it is vital to optimize system design so as to increase the temperature difference across the thermoelectric elements. One by-product of the increasing of combustion temperatures in incinerators in order to deal with the problem of dioxin emission is, that the temperature difference across the TE elements will grow, and so conditions will become progressively favourable for higher power output.

At present, the R & D work going into the development of more efficient thermoelectric materials can be roughly divided into two areas of effort. The first is research and development aimed at controlling the structure of existing materials and is being carried out with a policy emphasis on functionally graded (FGM) and quantum well structures. The second line of efforts involves the development of entirely new materials.

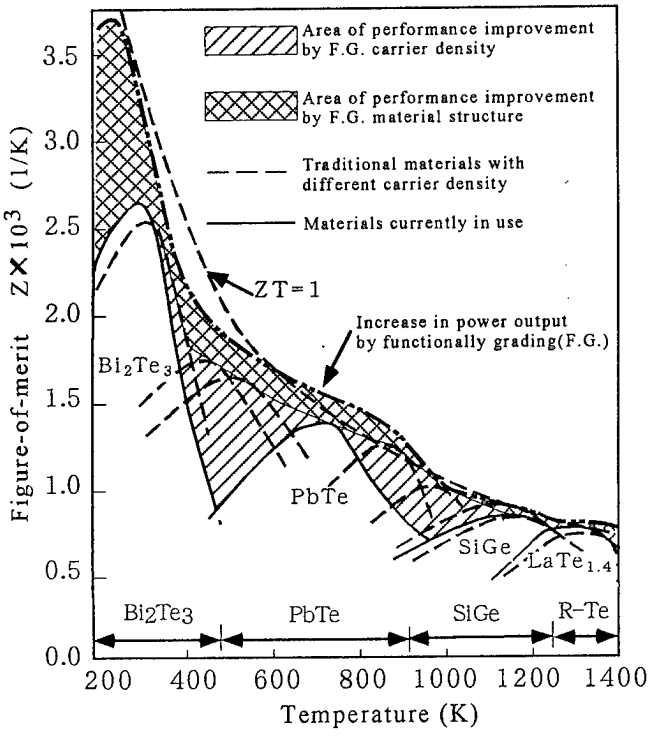


Fig. 11: Temperature dependent figure of merit for a series of TE semiconductor systems.

A typical example of the first of these two approaches is the advocating of an increase in performance levels by the joining together of functionally graded heterogeneous thermoelectric materials [7,8]. The particular approach seeks to increase generator efficiency by designing and joining together several types of thermoelectric materials in such a way that heat flows through each of these materials at optimum levels and by functionally grading the carrier density and structure of each of these materials, thereby improving their figures of merit over a wide thermal range. Fig. 11 shows a calculation based on the above approach. Specific details may be obtained from the reference materials but, the calculations shows that, by joining together and functionally graded various n and p elements of Bi_2Te_3-PbTe-SiGe-R*Te (R*: rare earth element), an average ZT level of 1 would be realized under a thermally gradient condition of a hot side temperature of 1100 °C with the cold side being at 30 °C. In this case the maximum conversion efficiency would be raised above a level of 23%.

On the other hand, since around 1990, extensive work has been done to seek out new kinds of thermoelectric materials. The thermoelectric elements developed thus far achieve a maximum score of $ZT = 1$, and for many years this was thought to have been the ceiling value on that scale. However, since a vast track record had been established for the element SiGe used in space probes, C. Vining was able to produce an accurate model of thermoelectric phenomena and it has been shown that, by changing microscopic parameters, the development of a material with a ZT of more 3 is possible [9,10]. As a result of this finding, much activity has been going on in the field of new materials development and promising new materials and families of materials are being discovered, and it is hoped that good results will come from the functionally grading of these new material families in the future. Also, in the area of module design and production, the need to raise the hot end temperature level of the thermoelectric elements used, makes it vital that these new materials be employed in developing highly durable modules (i.e. having high levels of heat resistance, thermal stress resistance and resistance to corrosion) with a structure that will reduce thermal stress.

6. Areas in which thermoelectric power generation methods may be applied and the popularization of thermoelectric power generation

The thermoelectric power generators that have been used thus far have been utilized in space exploration, military activities or in power generation in isolated areas and have had a maximum output level of around 1 kW, but it is now becoming technologically possible to manufacture large-capacity generators. Thermoelectric power generation can be accomplished no matter what the source of heat and, even with a low-level heat source, the process of taking in heat at one end of the system and generating electric power at the other can take

place. In addition to exhaust heat from incineration, other close-at-hand sources of untapped heat energy such as the hot wastes from steam-powered generators and factories, car exhaust heat and solar heat can be exploited. In Japan alone, the total annual power, when expressed in terms of cubic meters of crude petroleum, is 531,000,000 m^3, but only 67% of this quantity is effectively consumed, and the remaining amount, an equivalent of 173,000,000 m^3 of crude petroleum, is lost in the system — an amount which is equivalent to 2.4 times the total electrical power generated for the whole country. If methods of thermoelectric power generation could be applied to exploit this heat energy now being wasted, a valuable contribution could be made, both to the generation of electricity and to the saving of energy [11].

One of the hurdles that must be overcome in order to establish thermoelectric power generation technology as practical and commercially feasible is its cost. If the cost benefits are sufficiently large, the technology will naturally come into general use, and so the reduction of the manufacturing costs of these systems is closely tied in with their popularization. Fig. 12 shows a calculation originally done by the American Hi-Z Company [12] predicting quantities of thermoelectric generators manufactured when compared with the cost of power production. Additional data has been inserted into the chart to show the features of the process of the popularization of thermoelectric generation. The solid curve shows the specific investment costs as a function of the yearly manufactured power of thermoelectric modules. It is thought that the costs decrease as a result of mass production. If ten 100 kW-class generator systems using these thermoelectric modules were manufactured each year and installed at medium-sized incineration plants all over Japan, and if a production cost for these systems were assumed to be roughly 1.5 times that of the modules themselves, an annual demand for approximately 80,000 modules (estimated output of 13W/module) could be expected, thereby module production costs from the present \$10/W to half of that at around \$5/W. The electricity generated by incineration plants could be used to power their own facilities and, working with figures based on the savings and benefits obtained (calculated at an estimated rate of \$0.2/kWh), an estimate can be made of the number of years it would take to realize a full return for the expenses involved in manufacturing and installing the generation system. In the early stages of generator manufacture the \$1,500,000 cost would take eighteen years to pay back but, with the eventual drop of module costs to the \$5/W level, the period required to realize a return on the original expenses would be reduced to nine years [11]. Additionally, as was touched on in section 5, with the development of highly effective thermoelectric materials also proceeding parallel to this cost drop/popularization process, better thermoelectric modules will be produced.

In fact, our project team, while working on developing thermoelectric generation systems for garbage incinerators is also going on with research on basic techniques for thermoelectric module production (raising levels of heat and corrosion resistance, integration and shaping techniques), and is actively engaged in promoting the popularization of thermoelectric power generation technology.

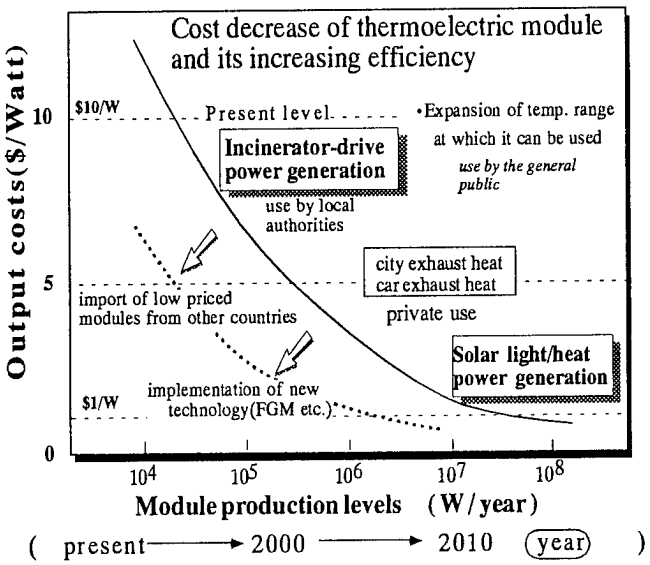


Fig. 12: Specific costs of TE modules as a function of their yearly manufactured power.

7. In Conclusion

The present problems of the global environment, energy and waste disposal demand a clear sense of direction in the development of energy sources. The effective exploitation of energy that was wasted or that simply dispersed without being utilized is an important concept in planning our communities as we approach the twenty-first century. Research into the effective exploitation of untapped thermal energy, such as that from garbage incineration, is extremely timely for Japan, a country with limited energy resources. In this report, the focus has been on incinerators, and the present stage in the development of thermoelectric power generation, the problems faced and the future prospects for a society in which the popularization of thermoelectric power generation has become a reality have been dealt with from the standpoint of those actually involved in the development of these systems. This development is still in progress and many technical problems remain but, at such a time as the present, when the means to increase the effectiveness of thermoelectric materials is within our grasp, it is important to establish basic techniques for producing generation systems that will make good use of achievements in the field thus far. Seeing that the Japanese government has expressed its policy decision to develop large-scale incinerators as a means of dealing with the restrictions placed on incinerator dioxin emission levels, it is unlikely that the impoverished local authorities who own the small and medium sized plants (that make up 90% of the total number of incinerators) will be able to afford to combine or otherwise adjust their facilities overnight in line with central government policy. It seems likely that these smaller facilities will have to work at improving the effectiveness of catalysts and filters, make effort for uninterrupted operation, raise the temperature of incinerator combustion and

effectiveness of catalysts and filters, make effort for uninterrupted operation, raise the temperature of incinerator combustion and seek any other ways for dealing with the problem of keeping dioxin emissions within the regulatory level while maintaining their present size. The movement in the direction of uninterrupted operation and high temperature combustion on the part of small and medium sized incineration facilities is not an unfavourable one in terms of the conditions for application of thermoelectric power generators.

It is highly hoped that thermoelectric power generation will prove to be the technology that will fill society's need for a constructive way of handling the vast amounts of exhaust heat involved. Steady reform of thermoelectric power generation technology is vital in order to further respond to this pressing need of society but, aided by the momentum from the thermoelectric module costs reductions that will result from the popularization of incinerator-driven generators, the exploitation of the ultimate reusable energy - that from the heat and light of the sun - will be within mankind's grasp and, in the coming twenty-first century, we will be able to benefit from this clean and unrestricted source of electricity.

It is the authors' desire that thermoelectric power generation technology will be of assistance in the construction of a "sustainable society" [13] wherein the use of fast-depleting fossils fuels is reduced and energy-awareness is highly valued.

8. Acknowledgement

The authors would like to thank all researchers of governmental, academic and comercial organizations who have collaborated together and who have been doing much effort in the present research project, and are also grateful for STA's Scinece and Technology Promotion Fund for its finantial support to this project.

References

[1] M. Niino et al., *„Research Project on the Effective Use of Renewable Thermal Energy such as Waste Incineration Heat"*, Collected Speeches of 9th Symposium on Thermal Engineering, 96-6, JSME, 33 (1996).

[2] I. Higashi et al., *„Thermoelectric Generator Systems"*, Technical Report of IEICE, EE97-19, 25 (1997).

[3] Y. Tada et al., *„An Experimental Study on Thermoelectric System by Hot Air in an Incinerator"*, Proceedings of the '97 Symposium on Environmental Engineering, JSME, 233 (1997).

[4] T. Kumagai et al., *„Evaluation of Thermoelectric System in Field Test"*, ibid., 235 (1997).

[5] M. Takeishi et al., *„Development of Thermoelectric Generator for Co-generation System"*, Proceedings of 34th Japan Heat Transfer Symposium, 325 (1997).

[6] K. Kisara et al., *„Development of Solar Power Generator System"*, Proc. of the '97 Symposium on Environmental Engineering, JSME, 368 (1997).

[7] I. Nishida, *„Highly Efficient Thermoelectric Materials in Functionally Graded Structures"*, Materials Science of Japan, 33, 42 (1996).

[8] I. Nishida, *„Evaluation of Thermoelectric Properties and High Performances in Improvement Program for Thermoelectric Materials"*, Materia Japan, 35, 943 (1996).

[9] Energy Technology Study Group of Electrotechnical Laboratory, *„Survey Towards Environment-Friendly Energy Technology"*, Circulars of the Electrotechnical Laboratory, 224, 80 (1993).

[10] C.B. Vining, *„The Thermoelectric Limit ZT=1: Fact or Artifact?"*, 11th ICT, Arlington, 223 (1993).

[11] Mitsubishi Research Institute, Research Report on the Popularization of Systems to Use Untapped Energy from Such Sources as Heat from Garbage Incineration - A Study Financed by the 1996 Science and Technology Promotion Fund, p 5-1, (1997).

[12] J.C. Bass et al., *„Thermoelectric Generator for Diesel Trucks"*, 10th ICT, Cardiff, 127 (1991).

[13] S. Ono, *„What does the Sustainable Society in the 21st Century Look Like?"*, Materia Japan, 36, JIM, 191 (1997).

Examples of Power From Waste Heat for Gas Fields

John C. Bass, Hi-Z Technology, Inc., San Diego, CA
Robert L. Farley, Power Sources, Inc., Farmington, NM

Abstract

This paper describes the design of three unique thermoelectric generators developed to supply electric power in natural gas fields. The unique feature of these generators is that they do not contain their own heat source but all convert the waste heat produced by equipment already used in the gas field as the thermal power source for the generators.

The first generator described uses the difference in temperature between the hot and cold legs of the glycol natural gas dehydrator cycle to produce power for cathodic protection of the well. The second system uses waste heat from the pilot light of the gas dehydrator boiler to produce power for electronic instruments. The third system used waste heat from the gas dehydrator boiler stack to provide power for instruments, communications, and other uses around the well site.

The description of these generators includes both photographs of the prototype units and performance curves from each of the generators. Each generator has unique features and advantages which are discussed in the paper.

Introduction

Oil and natural gas fields require electricity for several reasons. Among these are cathodic protection of the well casings and pipes, telemetry power, and lighting. If this power is not supplied by a connection to the grid, then it must be supplied from the field. The usual methods are to either provide small i.c. engine generator set, solar panels, or self-contained thermoelectric generator which is fueled with either propane or natural gas from the well.

For the low-power requirements motor generator sets are expensive to operate and maintain, so that either solar or self-contained thermoelectric generators have been the solutions of choice. Solar panels have their advantages and disadvantages for these applications. However, they are not the subject of this paper.

One of the disadvantages of the stand-alone thermoelectric generator is that it can represent an additional combustion source within the field, and therefore it represents a potential safety hazard. Also since it burns potential sale gas it represents a further energy depletion. In addition, a stand-alone thermoelectric generator can be expensive.

The alternative is to tap the sources of waste heat already available within the gas field. One widely used existing source is the natural gas dehydrator system in which a liquid descant such as triethylene glycol is employed to remove moisture from natural gas.

Gas extracted from a well is composed of a gaseous phase as well as distillate and water. Well-head gas and processing equipment is often situated at remote, relatively inaccessible locations and must be reliably continuously operable without attention by operating or maintenance personnel under variable and sometimes extreme climatic conditions. The well-head gas then must be transported, under pressure, great distances. Since well-head gas is usually at high pressure, the moisture, if not removed, tends to condense as the pressure is reduced upon entering the pipeline. This can lead to pipeline corrosion as well as the formation of water or ice within the distribution system subjecting the well producer to both expensive repair costs and loss of contracted sales gas.

A typical solution to the moisture problem is to pass the gas through a dehydrator to remove most of the water vapor an reduce the dew-point of the gas stream to a desired level for further handling or transportation of the gas. Gas dehydration is accomplished by passing the gas stream through an enclosure, including a pressure tower or vessel containing series of stacked liquid desiccant membranes, where gas is brought into intimate contact with a stream of triethylene glycol. Water from the gas and is absorbed in the triethylene glycol at 15 to 30°C. The absorbed water is subsequently removed from the triethylene glycol by circulating and heating the glycol/water solution to 175 to 200°C at atmospheric pressure.

A gas-fired boiler, such as the one shown in Figure 1, provides the source of heat to warm the glycol/water solution to separate and vaporize the water. The re-concentrated hot glycol is then cooled by means of well gas heat exchanger mechanisms and is returned to the contactor enclosure for absorption of moisture from further quantities of gas. The system is continuous in operation with the glycol circulation rate of 0.75 to 38 l/min depending on the capacity of the gas field.

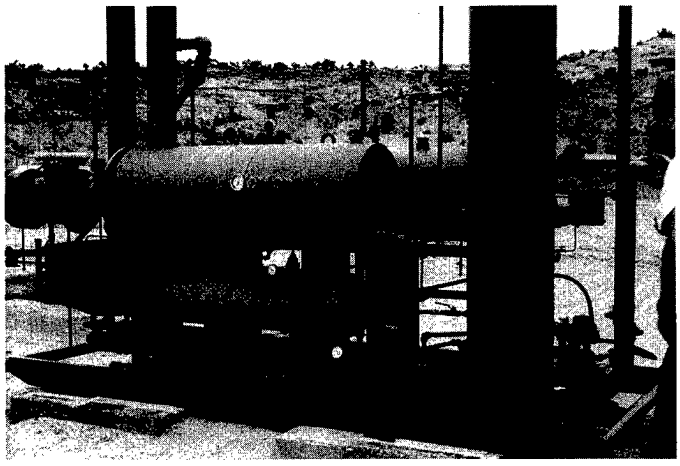


Figure 1: Gas-Fired Dehydrator Boiler In Field

0-7803-4057-4/97 $10.00 ©1997 IEEE

The dehydrator system represents a potential source of energy recovery for conversion into electricity. This paper describes three different applications of the thermoelectric conversion which are currently being built that use the waste heat in the gas dehydrator system as the energy source.

Glycol Generator

The first application described is a generator which uses the hot (dry) and cold (wet) glycol streams as a source of energy. The generator, shown in Figure 2, consists of a single high temperature heat exchanger of rectangular cross-section, eight HZ-14 thermoelectric modules, two cold side heat exchangers, and spring-loaded clamping system to hold the cold side heat exchangers and thermoelectric modules in good thermal contact against the central hot heat exchanger. The prototype generator shown in Figure 2 is made entirely from mild steel, however, aluminum is being considered in future production models.

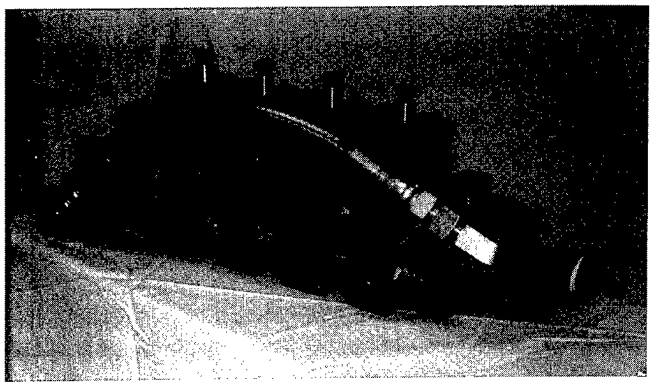


Figure 2: Glycol Generator

Hot triethylene glycol from the dehydrator boiler enters the hot heat exchanger through a straight section of pipe. It then flows by gravity through evenly spaced parallel rectangular passages in the center, giving up its heat to the thermoelectric modules. At the outlet end cooler glycol is collected and allowed to drain into the holding tank below the boiler.

Four HZ-14 modules, such as shown in Figure 3, are positioned on each side of the hot heat exchanger. Each is electrically insulated from the metallic heat exchanger by a 0.25 mm thick piece of aluminum oxide. Heat transfer grease is used on both sides of each insulator to minimize thermal contact resistance.

Cold glycol/water solution from the dehydrator column is pumped into one cold side heat exchanger by a double-acting circulation pump normally associated with the dehydrator system. The glycol flows through one cold heat exchanger and is then returned via flexible hose to flow through the second cold heat exchanger. From there, the glycol passes to a hot bubble tower located above the boiler where it is heated and the water is vaporized before the dry glycol returns to the boiler.

Figure 4 shows the installation of the glycol generator on a small dehydrator boiler. The generator is covered with a sheet metal jacket for weather protection during normal operation. With the installation of the glycol generator none of the dehydrator operating parameters are altered but are actually enhanced.

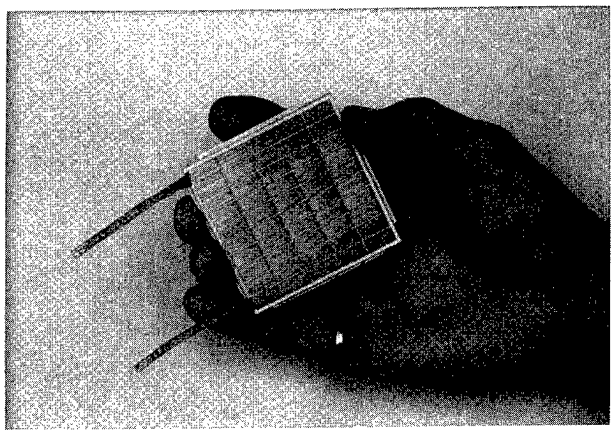


Figure 3: HZ-14 Module

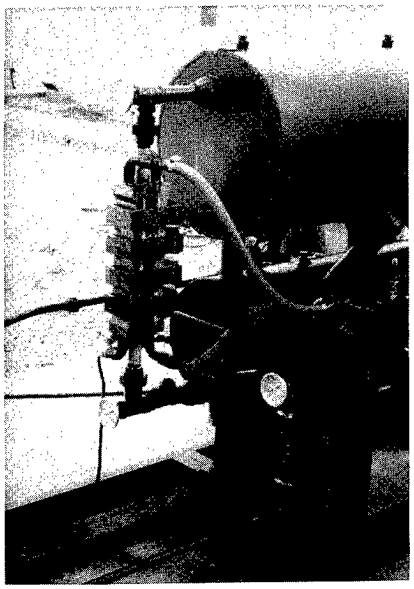


Figure 4: Glycol Generator Installed

While the eight HZ-14 modules are capable of producing in excess of 100 watts under their rated conditions, they only produce about 60 watts in this application because of the lower temperatures associated with the dehydrator glycol system. However, this low temperature system provides the potential for a long operating life with little degradation of the thermoelectric modules.

Figure 5 is a plot of output power from the glycol generator as a function of flow rate for three hot glycol temperatures and a cold glycol temperature of 15.5°C. One can see how quickly the output power falls for glycol flows of less than 4 liter per minute. One can also see the affect of temperature difference on power output.

The electric interface requirement for this generator depends on its use. If it is to be used solely for cathodic protection it would be connected to a DC/DC (buck) voltage converter and a constant current controller. If it is to be used to charge batteries or to provide power for transmission of wellhead data from a remote sit, it would probably be interfaced with a constant voltage DC/DC boost converter.

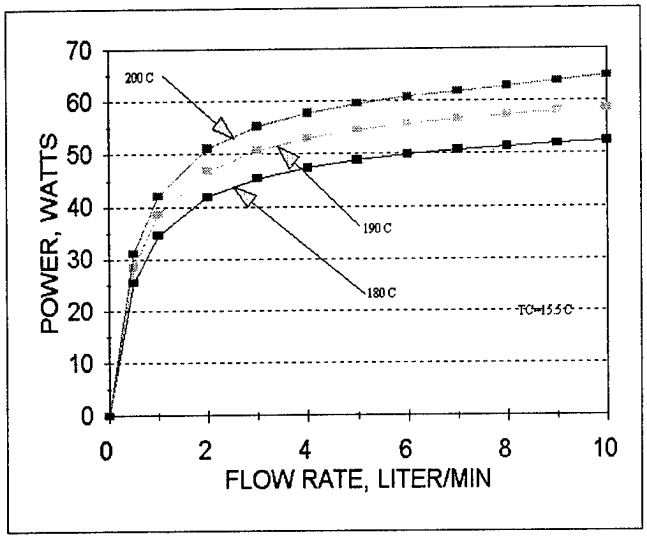


Figure 5: Glycol Generator Power Output vs Flow Rate for Various Hot Glycol Temperatures

The generator has no controls of its own. It depends totally on the existing controls of the dehydrator system. This should lead to low cost and reliable power solution without requiring additional combustion sources in the gas field.

This generator is currently being field tested on a gas well in Colorado where it is being used as the power source in a cathodic well protection system.

Pilot Generator

Another clear source of available energy is the pilot light for the dehydrator heating system boiler. Heating systems such as these consist of an elongated burner housing containing a main gas burner unit, which is operable intermittently on demand when heat is required, and a pilot gas burner unit which provides a continuous flame to ignite the main burner unit. The pilot burner has a thermal output of 29 kilowatts. This relatively high thermal output is dictated because of some of the special requirements of boiler operation.

Only a small fraction of the energy in the pilot has to be converted to provide a minimum 10 watts at 14.5 V necessary to maintain a typical remote telemetry system. One design challenge to overcome is how to get the thermal power out of the pilot when it is being fired by the pilot burner alone without being thermally overwhelmed when the much larger main burner is ignited. Another challenge is the restricted space available within the existing burner housing.

After some experimentation, it was found that the energy required to support a single HZ-14 module could be provided from the housing that encloses the pilot burner tip. The tip temperature remains essentially constant independent of main burner operation. Air flow to the pilot burner is sufficient to cool the cold side heat sink.

A machined copper hot side heat exchanger mounted perpendicular to and encompassing the pilot tip is used to conduct heat to the hot side of the thermoelectric module. The cold side of the module is mounted in the burner inlet airstream on an aluminum heatsink. The heatsink is machined to fit within the existing burner housing without excessively blocking air flow to the either the pilot or the main burner. The module power leads are connected to insulated conductions which penetrate the burner wall so that the burner flame arrestor system is not compromised. A drawing of the pilot generator is shown in Figures 6 and 7.

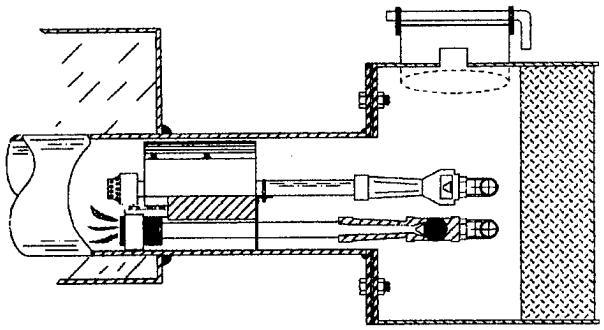


Figure 6: Drawing of Pilot Generator and Burner

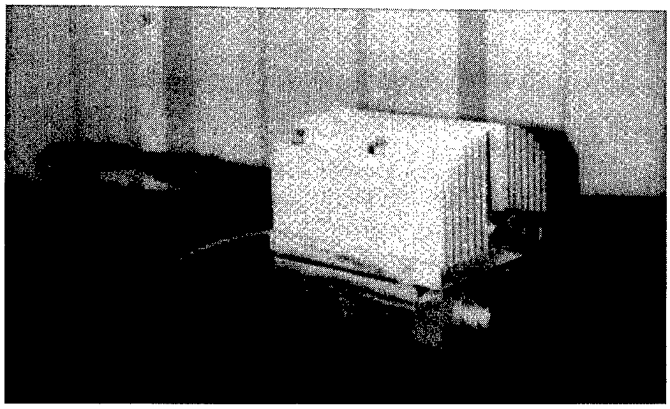


Figure 7: Components of Pilot Generator

The pilot generator will produce a maximum power of 14 watts and 1.65 volts at matched load. This system can be coupled with a DC/DC boost voltage converter and used to charge a battery and provide over 200 watt-hr per day of energy for various uses within the gas field, such as wireless data transmission from the wells. The burner housing described is typical of many types used in oil and gas fields. The pilot generator design can be adapted to most of these systems.

Stack Generator

The boiler emissions stack is also a considerable source of available energy to convert into electricity. The stack generator is shown in the drawing of Figure 8. This generator consists of two HZ-14 modules, a hot heat exchanger and a cold heat exchanger.

The generator obtains its energy from the hot combustion gasses leaving the dehydrator boiler. The energy at this point can be from 66 kilowatt to 293 kilowatt. The temperature of the stack gas can vary over a wide range

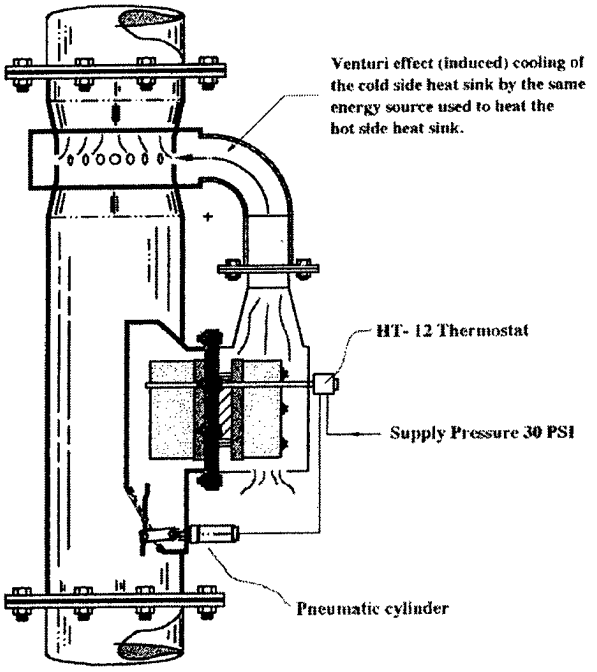


Figure 8: Drawing of Stack Generator

depending on boiler rating and whether only the pilot is burning or both the pilot and main burner are in operation. To handle this wide difference in gas temperature, a thermostat-actuated gas diverging valve is mounted upstream of the generator hot side compartment to divert combustion gas into and through the hot side compartment transferring heat through the hot side heat exchanger to the hot side of the thermoelectric modules when only the pilot burner is operating and around the hot side compartment when both burners are in operation.

A unique feature of this generator is that it uses induced air flow to cool the cold side heat sink. This is accomplished by connecting an air duct between the cold heat exchanger and a venturi section located within the stack above the generator as shown in Figure 8. The lower pressure in the stack at the throat of the venturi provides adequate suction of the air flow from the cold side heat sink compartment to cool the heat sink without consuming any energy. Eliminating the fan also eliminates possible gas ignition source.

The stack generator shown is capable of producing 28 watts of power at 3.3 volts. Again, this power can be used in several ways to provide electricity in the oil and gas field. It is obvious that a stack generator could be designed and built to provide much higher output power if there were a special need.

Conclusion

We have shown here three different examples of converting waste heat to electricity in the oil and gas field using thermoelectrics. These methods of producing useable electric energy do not add additional combustion sources within the field and therefore do not compromise field safety in any way.

We believe that such systems can be provided power at a lower cost than some of the stand-alone generators currently being used in the production fields. Both the acquisition cost and the maintenance cost can be lower than stand-alone systems as well as being hidden within the equipment assuring tamper-proof operation. The generators could be installed by original equipment manufacturing firms further reducing application and installation costs..

This technique of reusable energy can be readily extended to other operations where there are sources of thermal energy which are currently being wasted. The power obtained can be made available for an unlimited number of uses without any increase in energy usage. Another example of exploiting reusable energy in an unrelated field was the thermoelectric generator for the Diesel engine[1] which was presented at the 1994 ICT conference.

References

(1). Bass, J.C., N.B. Elsner, and F.A. Leavitt, "Performance of the 1 kW Thermoelectric Generator for Diesel Engines", Proceedings of the XIII ICT, 1994, Kansas City, MO, American Institute of Physics

Thermoelectric Power Generator Design and Selection from TE Cooling Module Specifications

Richard J. Buist and Paul G. Lau
TE Technology, Inc., 1590 Keane Drive, Traverse City, MI 49686 USA
Phone: (616) 929-3966, FAX: (616) 929-4163, E-mail: <cool@tetech.com>

Abstract

There are many applications where theromelectric (TE) coolers can be used effectively as power generators. In fact, where temperatures are less than 500K, TE cooling modules are the best choice for power generation, whether it be from a cost or performance standpoint. The literature available on this subject is scarce and very limited in scope. This paper describes the configuration, limitations and performance of TE coolers to be used as power generators. Also presented are performance curves generated using a new finite element thermoelectric model [1]. This enables the user to design the optimum TE module and select the nearest TE module (normally used for cooling) for this power generation application. A simple process is presented which provides detailed power generation specification (temperatures, watts in, current and voltage out) using the TE module's cooling specifications ΔTmax, Imax, Vmax, and Qmax).

Introduction

Generation of electrical power via thermoelectric devices has been a subject of interest for decades. Basically, thermoelectric power generation is a solid state means of converting heat flow directly into electrical power via the Seebeck effect. High temperature energy sources have historically been utilized because of the inherent higher efficiency at high temperature differences, ΔT's.

However, there are many low level energy sources plentiful in nature which are candidates for thermoelectric conversion. For example: ocean thermals, solar energy, steam and various forms of waste heat. TE modules normally designed for cooling are the best choice for these applications because they are manufactured from materials of highest efficiency at these nominal temperatures. As such, they represent the highest efficiency devices possible for use as thermoelectric power generators for low intensity energy sources.

This paper discusses some of the unique features of these versatile devices together with some limitations and precautions. Finally, design curves are presented enabling one to design or select the TE module to convert heat flow to DC power with the highest level of performance thermoelectrics can provide.

Theory of Operation

A thermoelectric cooler consists of several N & P pellets connected electrically in series and thermally in parallel sandwiched between two ceramic plates as illustrated in Figure 1. The bottom plate is bonded to a heat sink and, with the application of DC current of proper polarity, heat is pumped from the top plate to the bottom plate and into the heat sink, where it is dissipated to ambient. The resultant is that the top surface becomes cold. The top surface can also supply heat by simply reversing DC polarity.

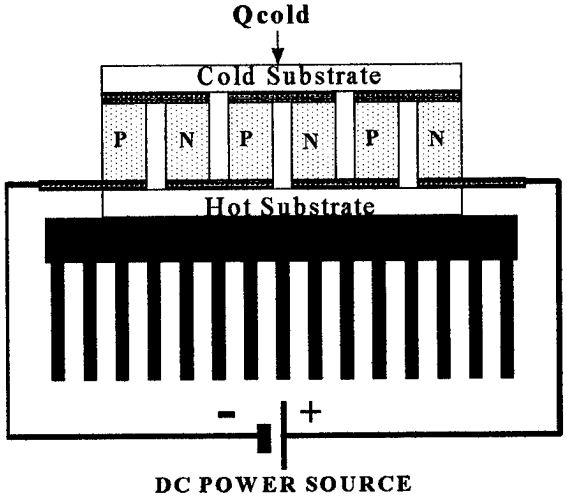


Figure 1. TE module in cooling mode.

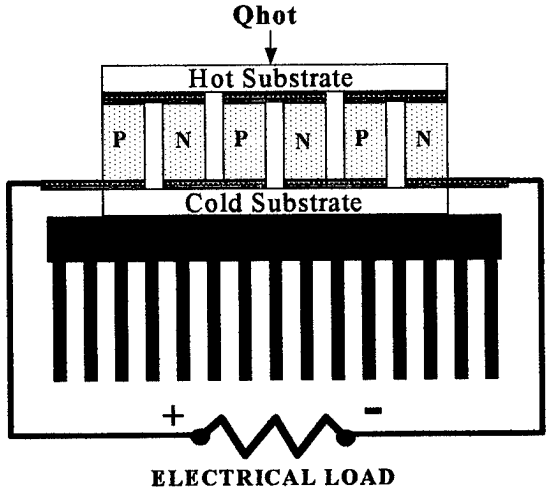


Figure 2. TE module in power generation mode.

The same unit can be made into a thermoelectric power generator by simply replacing the DC source with the load, or item to receive power, and apply heat to the top surface of the TE modules as illustrated in Figure 2. Note that the polarity of the power delivered is opposite the polarity for cooling. Electrical power is derived from the movement of electrical carriers brought on by heat flow through the TE pellets. Holes, or positive carriers, move to the heat sink side of the P-type pellet making that junction electrically positive. Similarly, electron flow in the N-type pellets results in a net negative charge at the heat sink side of the N-type pellet.

Coolers versus Generators

Technologically, most commercial TE power generators have little in common with TE coolers. Coolers have maximum COP or cooling "efficiency" at small ΔT's, whereas, generators have maximum efficiency at large ΔT's. The resulting high operating temperatures of TE generators demand different assembly technologies than for typical coolers, and different materials such as PbTe and Si/Ge alloys.

TE coolers are composed of alloys of Bi, Sb, Te, and Se optimized for operation in the temperature range of 180K to 500K. These materials have the highest thermoelectric efficiency in this range. Moreover, they have the highest efficiency regardless of whether the devices are used for cooling, heat pumping or for power generation. Consequently, devices normally designed for cooling are theoretically the most efficient TE generators to convert relatively low intensity energy sources with maximum temperatures of 550K.

Limitations and Precautions

There are some important practical considerations that should be made before attempting to use TE coolers in the power generation mode. Perhaps the most important consideration is the question of survivability of the module at the anticipated maximum temperature. Many standard TE cooling modules are fabricated with eutectic Bi/Sn solder which melts at approximately 138°C. However, there are some coolers being offered employing higher temperature solders designed for operation at temperatures of 200°C, even approaching 300°C.

In any case, consideration should be given to operational lifetime of a TE module exposed to high temperatures. Contaminants or even constituents of the solder can rapidly diffuse into the TE material at high temperatures and degrade performance and, in extreme cases, can cause catastrophic failure. This process can be controlled by the application of a diffusion barrier onto the TE material. However, some manufactures of TE coolers employ no barrier material at all between the solder and the TE material. Although application of a barrier material is generally standard on the "high temperature" TE cooling modules manufactured, they are mostly intended for only short-term survivability and may or may not provide adequate MTBF's (Mean Time Between Failures) at elevated temperatures. In summary, if one expects to operate a TE cooling module in the power generation mode, qualification testing should be done to assure long-term operation at the maximum expected operating temperature.

Performance Calculations

The finite element thermal model for a power generator developed by Lau[1] was used to calculate the maximum efficiency conditions of a TE module as a function of Tcold for selected constant values of Thot. This thermal model was especially effective for these calculations because, although the temperature gradient can be quite linear over a fairly large temperature difference, ΔT, the kinetic TE properties are not linear with temperature. Thus, these data are a marked improvement over those developed from equations using "temperature averaged" TE material parameters. The calculations produced from this model were the maximum efficiency, E; the voltage, V; and the current, I; of an arbitrarily chosen TE module at this maximum efficiency point. Of course, E is non-dimensional and, therefore, applies to all TE modules fabricated from the TE materials whose temperature dependent properties were used in the calculations. To normalize (and generalize) V and I, these values were divided by Vmax and Imax which are the voltage and current where maximum cooling ΔT would be achieved in a vacuum with the base plate held at a constant 300K. This condition is the usual performance specification by most, if not all, TE cooling module manufacturers of the world. It is for this reason why the power generation values V and I where normalized to V/Vmax and I/Imax. That is, not only does it generalize the results for all TE modules with a ΔTmax of approximately 67°C, it allows for easy identification of the TE module (or set of modules) needed to meet the desired power output from the generator. The final results of these calculations are illustrated in Figures 3, 4 and 5. Figure 3 is the maximum efficiency, E, obtainable from typical thermoelectric "cooling" modules with boundary temperatures Tcold and Thot. The corresponding optimum values of V/Vmax and I/Imax for each combination of Tcold and Thot are shown in Figures 4 and 5.

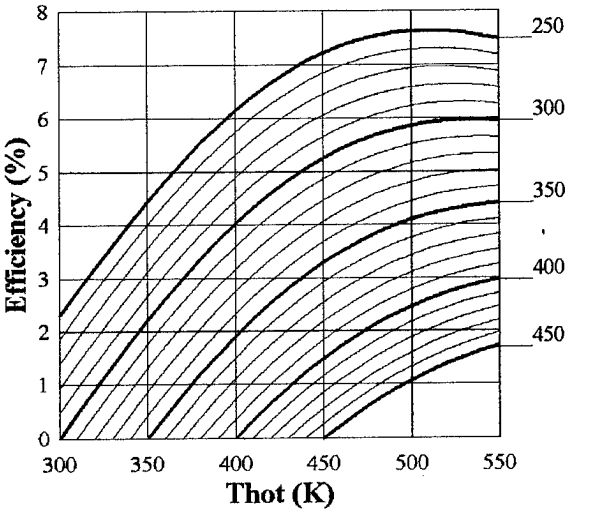


Figure 3. Maximum efficiency of a thermoelectric module as a function of junction temperatures.

These curves provide a simple graphical method to design or analyze TE power generators given only these boundary temperatures as shown in Figure 2. That is, the optimum variable set E, V/Vmax, and I/Imax is determinable by reading from the figures given only Thot and Tcold. TE module specifications, Imax and Vmax are subsequently determinable from these graphically determined ratio parameters using the user-desired power generator output current (I) and voltage (V).

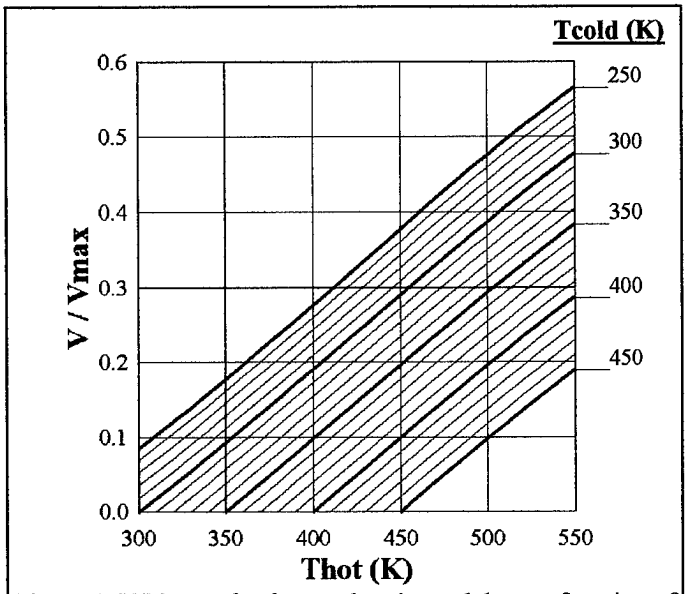


Figure 4. V/Vmax of a thermoelectric module as a function of junction temperatures.

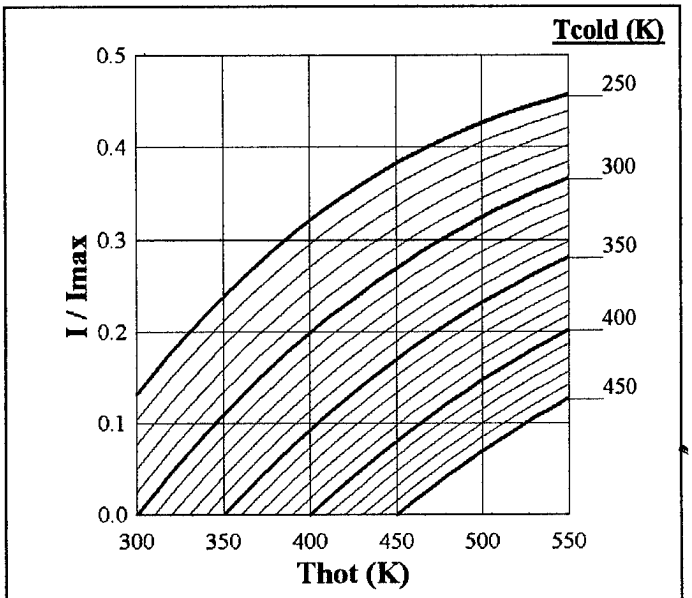


Figure 5. I/Imax of a thermoelectric module as a function of junction temperatures.

The amount of applied heat (Qhot) required at the hot side of the module is determinable from the formula for efficiency:

$$E = I * V / Qhot \qquad (1)$$

Electrical power is derived from energy flow, not just high temperature. Therefore, no TE generation system is complete without some means of heat sinking or dissipating the waste heat from the cold side (See Fig. 2). The overall performance of the heat sink is characterized by the heat sink resistance (HSR). This value is a measure of the temperature rise of the heat sink (Tcold) above ambient temperature (Ta) per watt of heat dissipated. This heat is essentially the applied heat (Qhot) at the hot side less the heat converted to electricity:

$$HSR = (Tcold - Ta) / (Qhot - IV) \qquad (2)$$

Examples

Two examples will be presented to provide an understanding of the use of the performance curves for two types of typical power generation applications.

Example 1: A thermoelectric power generator is to be used to supply power to a small sensing electronic system in a remote section of a processing plant using waste heat. The following conditions are given:

KNOWN	UNKNOWN
a) Thot = 440K	f) E
b) Tcold = 350K	g) Vmax
c) V = 1.5 volts	h) Imax
d) I = 0.6 amps	i) HSR
e) Ta = 300K	j) TE Module

STEP	FUNCTION	RESULT
1	Read E from Fig. 3	E = 3.0%
2	Read V/Vmax from Fig. 4	V/Vmax = 0.18
3	Read I/Imax from Fig. 5	I/Imax = 0.16
4	Calculate Vmax from c & 2	Vmax =8.33 volts
5	Calculate Imax from d & 3	Imax = 3.75 amps
6	Calculate Qhot = I*V / E	Qhot = 30.0 watts
7	Calculate HSR (Eq. 2)	HSR = 1.7°C/W

Two options exist to the designer at this point: 1) fabricate a custom module built to the optimum design or; 2) select a standard (HT) module, with the next largest Vmax and Imax. Note, however, that although that standard module will have ultimate capacity to deliver the needed I and V, this off-optimum design will have lower efficiency than the optimum module design depending on the degree of adjustment made. The TE module with approximately these specifications is a standard amongst most TE cooling module manufacturer's specifications as a 71 couple, 4.0 amp module.

Example 2: A solar collector is used to charge a 12 volt battery. It delivers a known flow of heat to a TE power generator with a known HSR. The following conditions and requirements are shown below. Note that in this example both Tcold and Thot are not given.

KNOWN	UNKNOWN
a) Qhot = 188 watts	f) Tcold
b) HSR = 0.14°C/W	g) Thot
c) Ta = 295K	h) Vmax
d) V = 15 volts	i) Imax
e) I = 0.5 amps	j) TE Module

STEP	FUNCTION	RESULT
1	Calculate E (Eq. 1)	E = 4.0%
2	Calculate Tcold (Eq. 2)	Tcold = 320K
3	Read Thot from Fig. 3	Thot = 430K
4	Read V/Vmax from Fig. 4	V/Vmax = 0.21
5	Read I/Imax from Fig. 5	I/Imax = 0.20
6	Calculate Vmax from d & 4	Vmax= 71.4 volts
7	Calculate Imax from e & 5	Imax= 2.5 amps

There are many standard TE modules to choose from with an Imax of 2.5 amps. However, none of them have a value of Vmax near the specified 71.4 volts. However, the set of 3 each 127 couple modules (Vmax=15.4V) plus 3 each 71 couple modules (Imax=8.6V), all wired electrically in series,. would have a Vmax of 72 V, but still with and Imax of 2.5 amps. Clearly, this set meets the requirement.

Conclusions

Thermoelectric coolers can be used as power generators using low intensity energy sources if consideration is made for effects of exposure to high temperatures. Moreover, they provide the highest conversion efficiency thermoelectrics can provide, at temperatures below 550K, since they are fabricated from the highest performance material available for that temperature range.

The data presented herein are based on standard TE materials which produce 68K ΔTmax at a 300K hot side temperature in a vacuum environment. TE modules with a higher ΔTmax would, of course, produce a proportionally higher power generation performance. Therefore, subject to the precautions and limitations described herein, the design curves presented in this paper enable the designer to define the ultimate capacity of thermoelectrics for use as a low-intensity power generator and to define in detail the actual device required.

References:

[1] P.G. Lau, R.J. Buist. "Calculation of Thermoelectric Power Generation Performance Using Finite Element Analysis", Proceedings of the XVI International Conference on Thermoelectrics, August 26-29, 1997 Dresden, Germany.

A Study of Commercial Thermoelectric Generation in a Processing Plant of Combustible Solid Waste

Akira Tsuyoshi (Kobe City College of Technology, Japan)
Shuzo Kagawa (KUBOTA Corporation, Japan)
Masanori Sakamoto (KUBOTA Corporation, Japan)
Kenji Matsuura (Osaka University, Japan)

Kobe City College of Technology,8-3 Gakuen-higashi-machi/Nishi-ku,Kobe city,651-21,JAPAN,
Tel.:+81/78-795-3234, Fax:+81/78-795-3314,E-mail:tsuyoshi@kobe-kosen.ac.jp

Abstract

This paper presents applicability of a commercially available thermoelectric generator for waste heat recovery in a processing plant of combustible solid waste. Heat transfer medium oil is utilized for heating of the commercially available thermoelectric generator employed in this study so that the generator could be operated in much lower pressure than using of water. Low pressure operation is not only reliable, it should have also safety and low maintenance cost. Each generator provides more than 500W and achieves relatively high efficiency with temperature of 220degC hot oil and around 30degC cold water. The result of the survey of a fitted position of a thermoelectric generator to a processing plant of combustible solid waste is summarized in this paper. Generator economics and goals of a thermoelectric generator to produce power in the similar rates of a steam turbine are also summarized to discuss applicability of a commercially available thermoelectric generator.

Conception of the Generating System

In this paper applicability of thermoelectric generator into a processing plant of combustible solid waste is discussed from the point of view where is the ideal position for the installation of a thermoelectric generator. Five positions which are investigated in the installation of thermoelectric generator are illustrated in Figure 1. Cooling methods, thermal conditions, adequate thermoelectric materials and issue of installation of thermoelectric generator, which are investigated respectively about the installation position, are summarized in Table1.

In any case amounts of heat flux applied for generation is restricted, and the fluctuation of heat source temperature and heat transfer condition should be large, so it is necessary to take effort to use waste heat totally in a processing plant . In case of total usage of separate heat sources, heat transfer from a heat source to heat transfer medium oil is the best way to intensive usage of waste heat. Thus, in this paper, a commercially available thermoelectric generator employing heat transfer

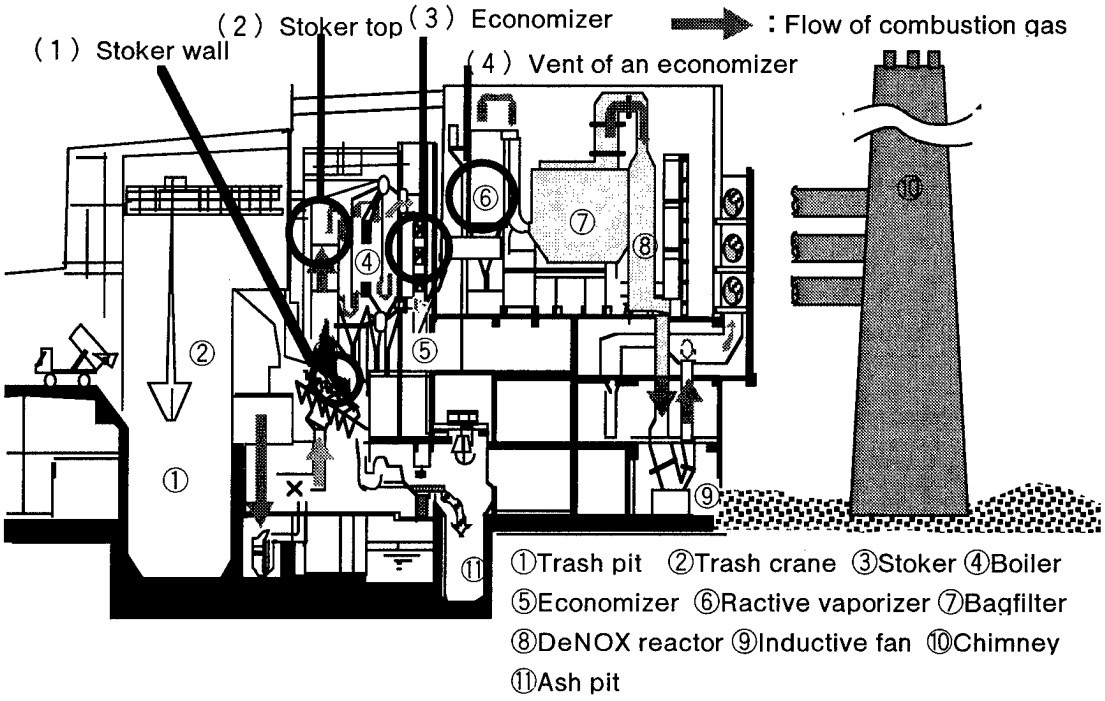


Figure1 Thermoelectric generator in processing plant of combustible solid waste

Table 1 Summary of installations of thermoelectric generators

Location	Heat transfer to OIL	Cooling	Junction Temp.[℃] (Hot side)	Junction Temp.[℃] (Cold side)	Usable material	Major point at issue
Stoker wall	No	Water or Indirect air cooling	300～700	100～200	FeSi2,PbTe,Bi-Te	Damage by mechanical shock at removing scale
↑	Yes	↑	250～400	80～160	FeSi2,PbTe,Bi-Te	↑
Stoker top	No	↑	250～400	80～160	PbTe,Bi-Te	Heat recovery in contaminatio
↑	Yes	↑	250～350	80～150	PbTe,Bi-Te	↑
Economizer	NO	↑	200～350	80～130	Bi-Te	Heat recovery efficiency of an economizer
↑	Yes	↑	200～300	80～120	Bi-Te	↑
Vent of a economizer	No	↑	200～300	80～130	Bi-Te	Less amount of usable heat
↑	Yes	↑	200～250	80～120	Bi-Te	↑
Condensor	No	Water cooling	50～75	20～30	Bi-Te	↑

medium oil is experimentally and theoretically investigated for waste heat recovery in the processing plant of combustible solid waste.

A test of a commercially available thermoelectric generator

The experimental apparatus for the test of a commercially available thermoelectric generator tested is illustrated in Figure 2 .The tested generator (ALTEC) employs 160 thermoelectric modules which are connected 40 in series and 4 in parallel as shown in Figure 3. Each module has 252 legs and indicates performance shown in Figure 4. Appearance of ALTEC is illustrated with its dimensions in Figure 5.

Experimental Results

The voltage and electrical output are measured with load current in various condition of a temperature of heat transfer medium oil. In this test a temperature of cooling water is controlled to be 25degC and a flow rate of cooling water and heat transfer medium oil is 6.0 liter/min and 10.8 liter/min respectively. These data are displayed in Figure 6 and Figure 7. In Figure 8 the gross power, required circulating power and the net power of the thermoelectric generator are displayed as a function of the flow rate of heat transfer medium oil. The required circulating power is calculated by using loss head measured in the test of ALTEC. To calculate the net power the total loss head is supposed to be twice of the loss head in

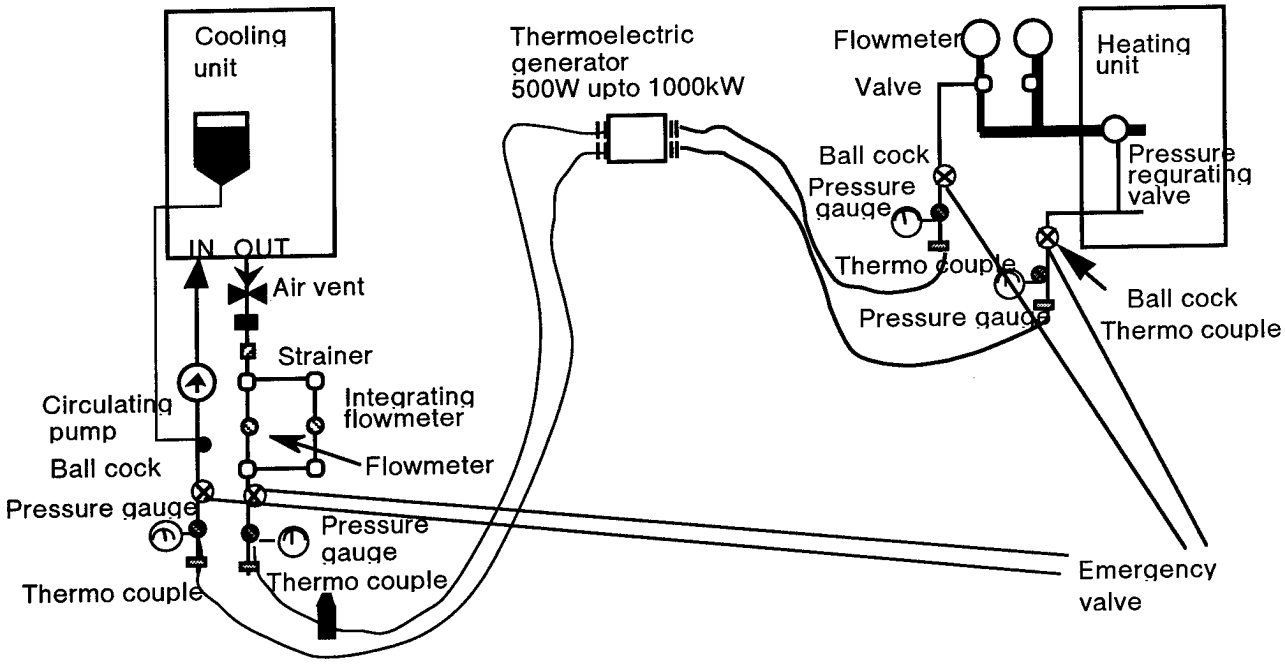


Figure 2 An experimental apparatus for the test of a commercially available thermoelectric generator

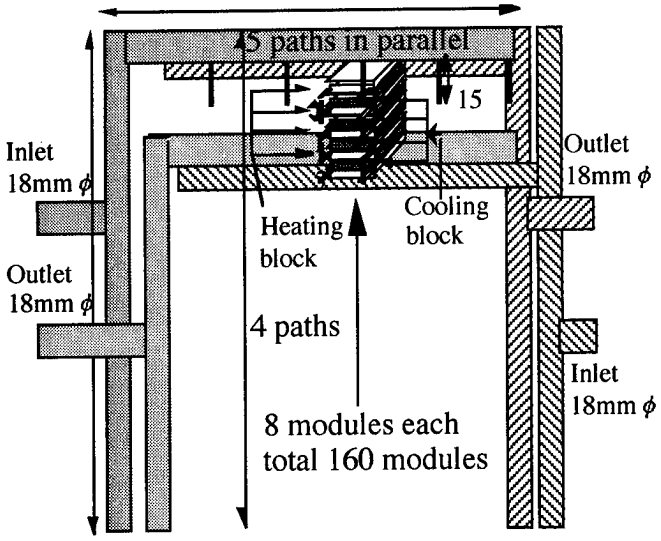


Figure 3 The configuration of the commercially available thermoelectric generator (ALTEC)

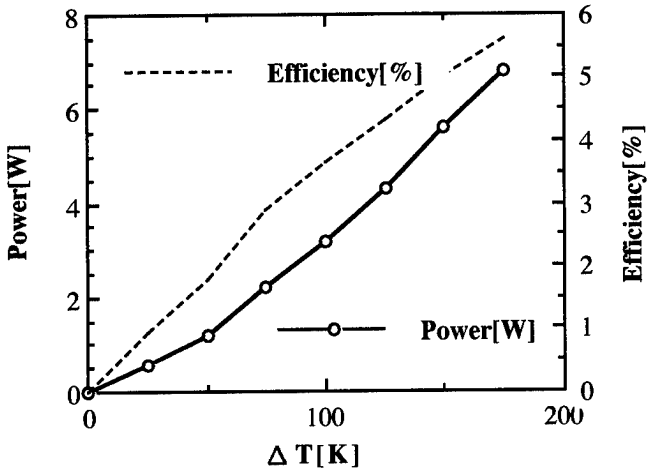


Figure 4 Performance of the thermoelectrical module employed in ALTEC [1]

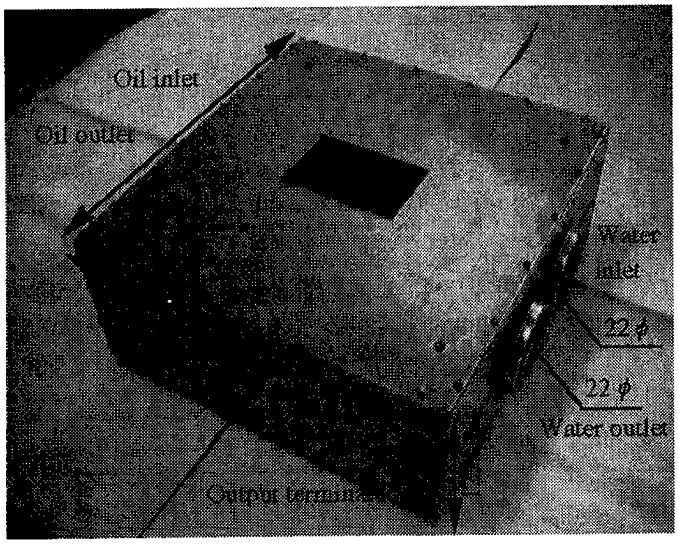


Figure 5 Appearance of a generator (ALTEC)

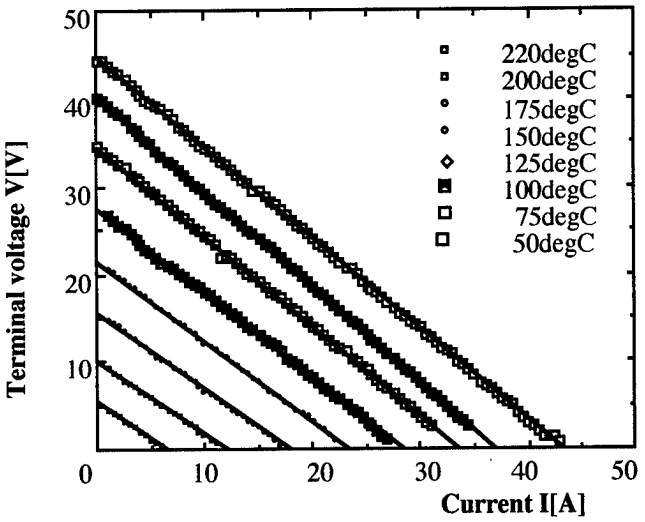


Figure 6 Voltage vs current in various temperatures

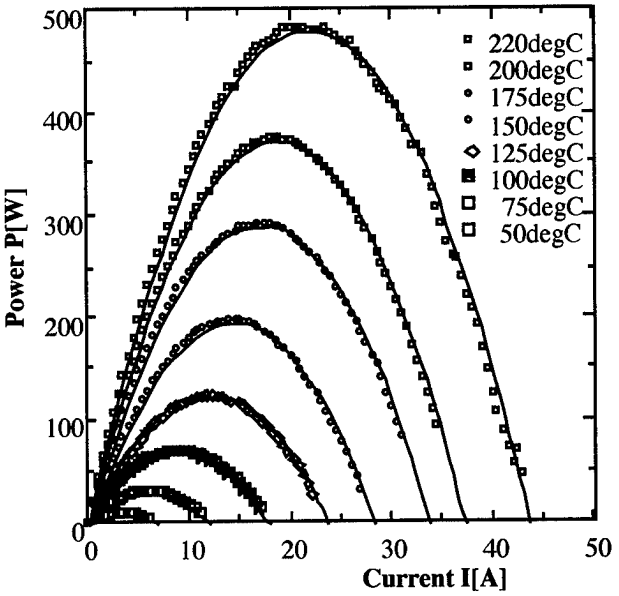


Figure 7 Elctrical outputs vs current in various temperatures

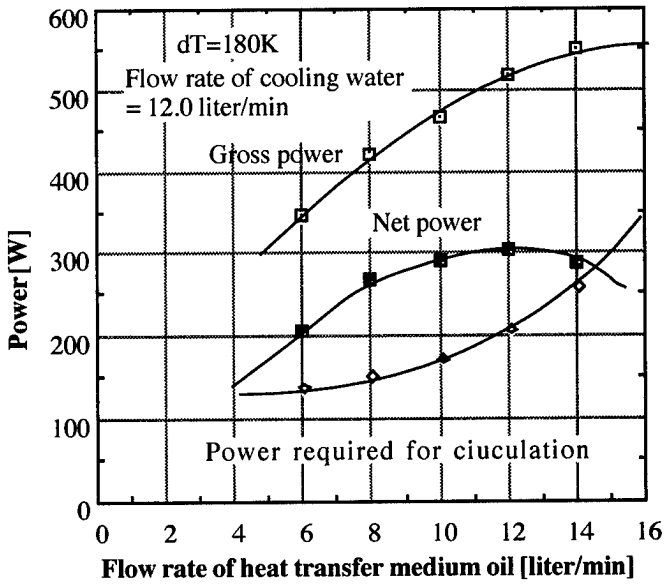


Figure 8 Gross power, net power and required pumping power as functions of flow rate of heat transfer medium oil

ALTEC. An increase of flow rates causes not only an increase of electrical output but an increase of the friction head in the generator. Thus excessive increase of flow rate causes a decrease of net power of generator, which is subtracted required pumping power from gross power of the generator as shown Figure 8.

Computer Analysis and Discussion

When an electricity is generated from waste heat in free of charge, the generator cost based on the net power rather than the efficiency is more influential parameter to minimize the generating cost. So an optimum operation of the thermoelectric generator for a processing plant of combustible solid waste was surveyed in referring of experimental data of ALTEC for variety of the thermal condition. For the desirable operation of the thermoelectric generator optimum flow rates of heat media shown in Figure 9 are determined, on the basis of ALTEC, as a function of a temperature difference of heat media.

In the next total economics of a thermoelectric generation by commercially available generators was investigated on the basis of a net power of ALTEC. When dT=180K and operated with optimum flow rates, a net power attains to 70% of a gross power. In this case for 10 years operation the thermoelectric generator obtains 30,660kWh, which is equivalent to about 2200 dollars. So allowing for a pipe work and installation of pumps[2], a cost of a thermoelectric generator for waste heat recovery should be reduced to around 1,000 dollars per kW at most.

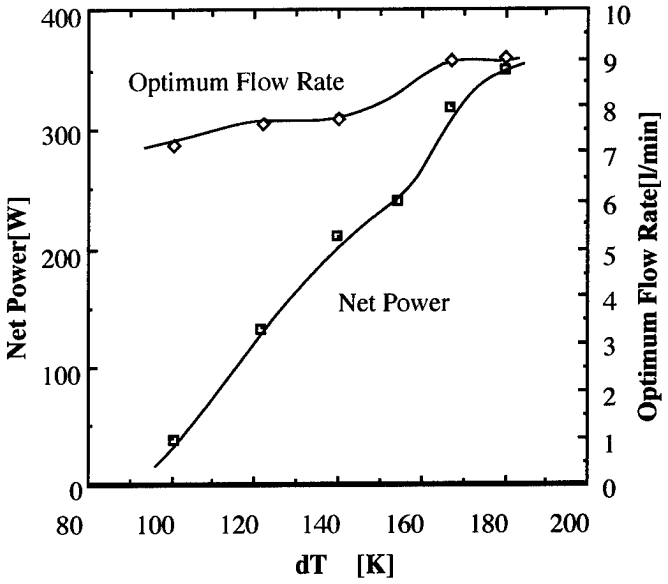


Figure 9 Net power and optimum flow rate as a function of temperature difference of heat media

Summary

The optimum operation and the economics of the commercially available thermoelectric generator are presented in this paper. For the commercial generation of electricity a configuration of a thermoelectric generator should be extremely simpler than ALTEC to reduce a production cost.

References

[1] Fujitaka Co.LTD.Japan,International Thermoelectric Academy. Ukline,Commercial reports of FSM-BT-4040(BiTe)

[2] A.Tsuyoshi,K.Matsuura,"Analysis of a Thermoelectric Generator Utilizing High Temperature Waste Heat and a Method of an Optimum Design",T.IEE Japan, Vol.116-A,No3(1996)

NUCLEAR THERMOELECTRIC POWER UNITS IN RUSSIA, USA AND EUROPEAN SPACE AGENCY RESEARCH PROGRAMS

A.A. PUSTOVALOV

Scientific and Industrial Enterprise "BIAPOS"
38-6, Leninskyi prospect, Moscow, Russia, 117334

ABSTRACT

The paper discusses the role and the significance of the radionuclide thermoelectric generators in space researches while using them as reliable long-life service autonomous sources of power and heat supply. There are considered approaches connected with the RTG design and the provision them with the radiation safety in the standard and emergency situations. There are given the main characteristics of basic RTG which were used in USA and Russia space programs. The prospects of the use of RTG in future USA, Russia and ESA space programs are shown.

INTRODUCTION

One of the main problems meeting the developers of any space program, and often restricting the circle and the depth of solving problems, is a problem of a reliable power supply of the SC support and scientific equipment. Solar panels, chemical current sources, fuel elements and, at last, radionuclide thermoelectric generators (RTG) should help, each in its field, to solve the standing problem. The RTG use as autonomous power supply sources of the SC on-board equipment became expedient and, in some cases sole, for solving space programs due to their unique technical and operational characteristics, namely:

full autonomy and high reliability during the service life; independence of the action of the solar radiation;
high specific power capacity (up to 100 kWh h/kg);
high life service (up to 20 years);possibility of the use of the spent heat of the equipment heating;
possibility of the work with the buffer accumulating systems;
high quality of the used power.

By present, using RTG there have been performed a number of space programs on researching the Moon, Mars and other planets of the Solar system [1]. Together with the incontestable advantages RTGs have the essential drawback lying in the potential danger of the radioactive pollution of the environment in case of the seal failing of the capsule with the radionuclide (radionuclide source of the heat - RSH). Especially keenly this problem appears while launching the SC with RTG aboard when the appearance of extremely hard emergency situations is possible with the rocket carrier (RC) during the launch and in the region of the SC ejection into the supporting orbit and the calculating trajectory. In these cases RTG can be effected by extremal influences caused by: the explosion of the RC and, as a consequence of it , the generation of the explosive wave and the formation of fragments of different masses with various rates of scattering; the fire and the burning of the rocket fuel components with the temperature in the epicenter up to 3800 C; the descent in the dense layers of the atmosphere by gentle or steep ballistic trajectories, accompanied by the aerodynamic heating, thermal shock, mechanical overloads; the blow on the Earth surface with the blow rates up to 80 m/sec; the fall on the ocean bottom and the effect of the hydrostatic pressure up to 1000 atm. etc.

The problem of the provision of the RTG radiation safety under the given conditions is solved due to the preservation of the integrity of the capsule with the radionuclide and the use of the radioactive matter in the form of the chemical composition with a high melting temperature, not soluble in water, alkaline solutions, acids and not diffused in air.

By this time, the sole radionuclide, meeting all above-mentioned requirements and having the acceptable radiation and physical characteristics, is plutonium-238. Plutonium-238 in RTGs is used as tablets of plutonium dioxide, caked at the temperature of 1200 C, which are placed in the sealed multishell capsule, additionally surrounded with the thermal protective body of the carbon-carbon materials. Such a construction is named as a radionuclide heat units - RHU. The development, design and creation of RHU should be done in full correspondence with the Principles referring the use of nuclear power sources in Space, approved by the United Nations General Assembly in resolution 47/68 of December 14, 1992 [2]. According to this document RTGs can be used in space only in cases if the physical form of the radioactive matter used in them and the system of the protective shells guarantee the absence of the ejection of the radioactive matter into the environment during the standard use and during the emergency effects connected with the unstandard situations which can appear during the SC launch and ejection into the supporting orbit and the calculating trajectory.

1. STATUS OF RTG DEVELOPMENT FOR SPACE IN USA

In USA the developments of RTG for space were performed by the SNAP program (Systems for nuclear auxiliary Power) [31].The first RTG (SNAP-3B) on plutonium-238 with the electric power of 2.7 W was launched into the near-Earth orbit in 1961 in the composition of the on-board equipment of the navigation satellite "Transit-4B". By present, in USA there have been done 25 launches of SC with RTGs aboard. In all there were launched in space 40 RTGs with the general number of plutonium of about 105 kg. RTGs were used in the composition of the navigation satellites ("Transit" series), communication satellites (LES series), meteorological satellites ("Nimbus" series), spacecraft for searching the Moon ("Apollo" series), Mars (Viking-1,

0-7803-4057-4/97 $10.00 ©1997 IEEE

and 2), Far space ("Pioneer-10, 11", "Voyager-1, 2", "Gallileo", "Uliss" [1].

The logical result of the completion of works on the SNAP program was the creation of fully unified RTG by the middle of 80th, the so called module isotopic thermal generator (MITG), afterwards named as [GPHS-RTG, 9], [4].

The typical peculiarity of the design of this RTG was, together with the achievement of optimum electrical characteristics, the possibility to vary the level of its electric power from tens of Watts up to hundreds of Watts due to the use of the standard radionuclide heat units (GPHS) and sections of thermal and electric panels while its manufacturing. Taking into the account the fact that in this case there was achieved a high level of the radiation safety.

GPHS-RTG was recommended as a main source of power supply for all following programs on Far space researches. Table 1 gives the main characteristics of GPHS-RTG.

GPHS-RTG was firstly mounted on the "Gallileo" SC which was launched in space in October, 1989. The purpose of the expedition was the research of Jupiter from the fly-by orbit and by the probe landed on its surface. The "Gallileo" SC reached Jupiter in August 1994 and from its board there was photographed the reverse side (invisible from the Earth) of the planet during its collision with the Shumeike-ra-Levi comet. At present, the researches on the "Gallileo" program are being continued. GPHS-RTG was used on the "Uliss" SC, launched in October 1990, as a main source of the power supply. The task of the "Uliss" SC was the research of the nearest vicinities of the Sun (corona, solar wing, magnetic field, solar radiation etc.).

Table 1. Main Characteristics of GPHS-RTG

Name of the parameter	Value
Electrical power, W - beginning of the resource - end of the resource (16 years)	 276 211
Output voltage, V	30
Fuel	Pu238O2
Fuel mass, kg	10.9
Heat power, W	4284
Number of single modules of GPHS, unit.	18
Thermoelectric materials	Si-Ge
Temperature of "hot seam", C	980
Efficiency, %	6.4
Sizes, m - diameter - height	 0.427 1.13
Weight, kg	56.2
Service life, years	16

In October 1997 USA are planning to launch the space expedition on the "KASSINI" project to research Saturn. The SC will include 3 GPHS-RTG and 157 tiny radionuclide heat units for the control of the temperature in compartments with scientific equipment.

2. STATUS OF RTG DEVELOPMENT FOR SPACE IN RUSSIA

In the USSR the practical use of RTG in space refers to 1965 when for supplying the onboard equipment of the Earth artificial satellites "Cosmos-84" and "Cosmos-90" there were used RTGs on polonium-210 with the conditional name "Orion-1" and "Orion-2". In 1969 and 1971 for heating the compartment with "Lunokhod-1" and "Lunokhod-2" equipment there were used radionuclide heat units on polonium-210 with the power of 800 W.

As is known not RTG were then used in space in the USSR but the nuclear power plants (NPP) with thermoelectric conversion (NPP "Buk") which were used in the satellites of the "Cosmos" series intended for the sea radiation probing and for the radar investigation of the ocean.

The output electrical power of NPP "Buk", 2.5-3 KW, was generated due to the thermoelectrically conversion of the heat released in the nuclear reactor by the heat power of 100 kW. More than 30 plants "Buk" were launched within the period from 1970-1988.

In 1987-1988 two NPP "Topaz" with the electrical power of 6 kW with the thermoemission conversion of the heat energy passed successful flight tests on "Cosmos-1818" and "Cosmos-1867" satellites. The nuclear power plants of the "Buk" and "Topaz" type were intended only for the use in the near-Earth space as their life time resource was limited to 1-2 years.

The problem of the space RTG development for the fulfillment of the Russian space programs became again actual with the beginning of the realization of the International project Mars-96 on the complex research of Mars (Fig.1) which as is known has been ended with the unsuccessful launch of the "Mars-96" SC. By this project small autonomous stations (SAS) and penetrators (PN) intended for the long work under Martian conditions should have been shot on the Mars surface from the orbite.

To provide the operation of the scientific equipment, processing and transmission of the obtained information the orbite included RTG in the SAS and PN composition with the electrical power of 200 and 400 mW, respectively, and radionuclide heat units with the heat power of 8.5 W intended for the station equipment heating (RHU "Angel").

The radionuclide heat units "Angel" were used both autonomously and in the RTG composition. The pilled plutonium-238 dioxide was the radionuclide fuel for them. The radiation safety was provided with the physical form of the used radionuclide, with the design of the heat unit and with the use while its manufacturing of anticorrosive, heat-resistant materials and coatings, including heatprotective materials on the basis of composition graphite materials.

Tables 2 and 3 give the main parameters of HU and RTG "Angel".

By the results of the ground tests the HU "Angel" was certificated by the Center of the certification of the rocket and space technics of the Russian Space Agency for the safety of its use in space [5].

Despite a small number of plutonium-238 (in comparison with the American projects) used in RTG "Angel" for the "Mars-96" project , and a milliwatt level of their output power, the completion of the developments of such RTG has a principle important significance for the Russian space programs on the Far Space researches.

Table 2. Main Characteristics of the RHU "Angel" for the "Mars-96" SC

Name of the parameter	Value
Heat power, W	85
Fuel	plutonium-238 dioxide
Mass of Pu-238,g	15
Sizes, mm diameter height	 40 60
Mass, kg	0.2
Design materials:	multishell
1st shell - anticorrosive	platinum-rhodium melts
2nd shell - power	tantalum-tungsten melts
3d shell - heatprotective	carbon-carbonic composition materials
Service life, years	10

Table 3. Main Characteristics of the RTG "Angel" for the "Mars-96" SC

Name of the parameter	Value
Electrical power, W	0.22
Voltage, V	15
Fuel	Pu-238 dioxide
Heat power, W	8.5
Thermoelectric battery	telluride`s vismuth
Temperature of "hot seams", C	160
Efficiency, %	2.6
Sizes, mm - diameter - height	 85 125
Mass, kg	0.5
Service life, years	10

First, it is caused by the fact that in Russia there has been fully completed the development of RTG on plutonium-238 of space purpose with the manufacture of flight samples satisfying both national and international requirements on the radiation safety.

Second, the radionuclide heat units, as potentially dangerous for the SC environment, were officially certificated by the state bodies for the safety of the use in space.

Third, the analysis of the existing approach in Russia and USA on the provision of the space RTG radiation safety and their certification for the safety of their use in the SC composition showed the proximity in this problem solution both in the certification of such products and in the scope of RTG tests during the standard usage and emergency situations.

Fourth, the RTG creation for the "Mars-96" project opens the prospects of the RTG use in other national and international space programs, which are planned to be fulfilled in future.

3. THE USE OF RTG IN THE EUROPEAN SPACE AGENCY SPACE PROGRAMS

By present there exists a number of projects developed by ESA which plan to use the radionuclide power sources. One of the most perspective is the "Rosette" project. This project SC is planned to be launched in January, 2003, for the rendezvous with the P/WIRTANEN comet in 2011 at the distance of 3 astronomical units from the Sun. "Rosette" will consist of 2 small landers (RoLand) which will be shot on the comet surface for performing a wide scope of scientific researches.

The consortium formed of the leading institutes of Europe includes the scientific organizations of Germany, Finland, Italy, Hungary, Great Britain and Austria.

"RoLand" is a small (45 kg) compact research station of the cubic form (the cube side length is 90 cm) will be landed on the comet surface for investigating the physical and chemical composition of the comet soil, its elementary composition etc.

"RoLand" includes the solar generator and RHU on plutonium-238 of the RHU "Angel" type. By the opinion of the project experts, the RHU use is the most desirable, sensible and reliable means for achieving the main goal of the "RoLand mission".

4. THE PERSPECTIVE OF THE RTG USE IN SPACE PROGRAMS OF THE XXI CENTURY

In the nearest years some space programs on a number of international projects with the use of RTG of American and Russian manufacture are planned to be developed and realized.

In 2001 it is planned to continue the complex researches of Mars in correspondence with the Russian-American project "Mars together". By this project the orbiter and the scientific complex are being developed by the American side, and the rover, shot on the Mars surface, and a part of scientific equipment - by the Russian experts.

The SC will be launched by the Russian rocket-carrier (RC "Molniya") from the Russian launching site "Plesetzk". For the rover operation there will be used the radionuclide heat units "Angel" and RTG with preliminary electric power of 3-5 W which will be developed and manufactured in Russia.

The future step of the Russian-American space cooperation in the Far space exploration which will use RTG is the "Solar probe" project for the direct investigations of the Sun coronas, solar wind and other important parameters of the near-Sun space.

Two SC of American and Russian manufacture are planned to be launched by one RC from the "Plesetzk" launching site. Aboard the American SC there will be used RTG of the GPHS-RTG type, on the Russian SC RTG will be used with the total electrical power of 40-50 W and the thermoelectrically generator with the output electrical power of the order of 500 W generated the electric power due to the thermoelectrically conversion of the solar radiation.

At last in 2003 it is planned to fulfill the Russian-American project on the research of the most removed planet from the Earth - Pluto and its satellite Harron ("Pluto Express" project) [6].There will be two RTGs on SC developed in USA:

- one of the American manufacture of the GPHS-RTG type with the electrical power of 90 W (of others, more effective radionuclide power sources providing the operation of the scientific equipment);
- the other RTG of the Russian manufacture of the RTG "Angel" type with the electrical power of 0.5-1.0 W is mounted on the probe (Drop Zond) separated from the SC while approaching the planet. The Drop Zond is used for more detailed research of the near planetary space.

It is proposed to use the "Molniya" RC as a rocket carrier as having the highest reliability and minimum cost. The "Molniya" will be launched from the Plesetzk launching site with the ejection of the SC into the orbit with the inclination of about 70 degrees to lay the flight route along the arctic sea-coast to decrease the consequences in case of hardly probable, but possible failures of RC and in case of the SC collapse with RTG.

It should be mentioned that the exploration of Far space and planets considerably removed from the Sun (such as Pluto) is possible only with the use of the radionuclide power sources as the solar panels with low levels of the solar radiation do not operate efficiently and the power capacity of chemical sources is not sufficient of the provision of the fulfillment of long-term space programs.

In this connection, taking into account a high cost of radionuclide power sources, the fulfillment of such projects becomes possible only with the participation of the international cooperation including the technically developed countries when each of the participating sides takes the obligations not only in the development of some aspects of scientific programs, but makes its contribution to the solution of problems connected with the financing of the project on the whole.

By present there are some projects developed by the European Space Agency (ESA) with the RTG use, such as the "Rosette" project and the also the project on the creation of the constantly acting moon stations. The realization of these projects is planned in the first decade of the next century.

The concept of the creation of power plants for the moon base is being developed also in Russia and Japan. In correspondence with this concept it is assumed to obtain the electrical power by a direct conversion of the solar energy in the module consisting of the thermoelectric and thermoemission units.

There is the information on works carried out in France on the RTG development for the ESA space program. But the absence of the concrete information on this question does not make it possible to draw conclusions about the achieved level of developments.

So, the development and the creation of RTG for space programs played a positive role and promoted the further profound research of space and planets of the Solar system.

At the same time, at present there is being developed a number of alternative radionuclide power sources such as AMTEC (Alkali metal thermal for electric conversion), thermophotoelectric power sources, installations with Stirling engine, having the efficiency 2-3 times higher than the efficiency reached in RTG [7, 8]. However, the practical use of such power plants in the nearest future remains rather problematic because of their insufficient high reliability and not long service life.

In conclusion it can be surely assumed that in the XXI century RTG will be used as before in large-scale projects on the space and Solar system planets exploration which will become possible only in case of close cooperation of technically developed countries.

ACKNOWLEDGMENT

I grateful NPP Biapos people who help me to make this paper. I acknowledge Space Research Institute Russian Academy of Sciences people for discussions the paper.

REFERENCES

1. J.A. Juri "The US Space Radioisotopes Power program", Nuclear power in Space Conference, Obninsk, USSR 15-18 May, 1990.
2. "Principles referring the use of the nuclear power sources in space". Adopted by the UN General Assembly, Resolution N 47/68 of 14.12.92.
3. U. Corlis, D. Harvi "Radioactive isotopes power sources", Translation from English, M., Mir, 1967.
4. A. Sock "Design and Analysis of RTGs for Solar and Martian Exploration Missions; Nuclear Power in Space" Conference Obninsk, 15-18 May, 1990.
5. Certificate on the safety of the HU "Angel" use, N FSSKT-13401-1.4-6943-01.95.
6. R.L. Staehle et al. "Pluto Mission Progress Report", 44th Congress of the International Astronautical Federation, Graz, Austria, 16-22 October, 1993.
7. A. Shock et al. "Design, Analysis and Optimization of a Radioisotope Thermophotovoltaic (RTPV) Generator and Its Applicability to an Illustrative Space mission" 45th Congress of the International Astronautical Federation, Jerusalem, 9-14 October, 1994.
8. R.K. Sievers and R.W. Wrigth "High Power Density Alkali metal Thermal to Electric Converter", "25th Intersoc. Energy Conversion Engineering Conference", v. 2, pp. 46-432.

Calculation of Thermoelectric Power Generation Performance Using Finite Element Analysis

Paul G. Lau and Richard J. Buist
TE Technology, Inc., 1590 Keane Drive, Traverse City, MI 49686
Tel: (616) 929-3966, FAX: (616) 929-4163, e-mail: cool@tetech.com

Abstract
Recent papers [1], [2] have covered the merits of using finite elements to calculate the thermoelectric device performance for steady-state conditions. Likewise, papers [3], [4] have covered the use of finite elements to model transient cooling conditions. It remains then to model power generation performance with finite elements and compare that model with various other modeling techniques.

Analysis was based on a single pellet for simplification. The pellet was modeled by treating the differential equations as closed form, finite equations across a small section of the pellet. The many sections, or finite elements, comprised the total pellet. Temperature dependent properties were incorporated into the model.

The finite element analysis predicted different results than the temperature-averaging techniques as was to be expected. Finite element analysis should be used when critical optimization is required since it is able to determine accurately the nature of the thermoelectric effects of materials whose properties are highly temperature dependent. Averaging schemes, by their very nature, lose modeling information and are less accurate.

Introduction
There are several ways to calculate the power generation performance of a thermoelectric couple, either by averaging schemes or by the use of finite elements. The advantage of the averaging schemes is that an immediate answer is obtained from simplified analytical equations. Finite elements require much iteration and, therefore, more time to obtain results. However, ever higher speed computers make this time difference increasingly negligible. The advantages of using finite elements over averaging techniques is accuracy and true optimizations. Prototype and experiment costs will surely be reduced when the model agrees precisely with experiment. Also, one can be certain that the higher performance will not be achieved by any other design.

The object of this study was to compare two models which used averaging techniques and a model which used finite element analysis. Graphs are presented to illustrate comparisons. For the purposes of this paper only one - dimensional analysis was investigated. Also, such effects as contact resistances were not included in the analysis since only a basic comparison of calculation methods was desired. Furthermore, the models did not include effects of passive heat losses from radiation and air conduction and convection. Such effects could readily be incorporated though to provide a model that would more closely match reality.

Computational Models
All three computational models are based on the following equations [5]:

$$Q_H = \alpha I T_H - \tfrac{1}{2} I^2 R + K \Delta T \quad (1)$$

$$P = I^2 R_L \quad (2)$$

$$I = V_{oc} / (R + R_L) \quad (3)$$

$$\Delta T = T_H - T_C \quad (4)$$

$$V_{oc} = \alpha \Delta T \quad (5)$$

$$R = \rho L / A \quad (6)$$

$$K = \kappa A / L \quad (7)$$

$$Q_H = P + Q_C \quad (8)$$

$$Z = \alpha^2 / \rho / \kappa \quad (9)$$

Q_H = heat input to the thermoelectric generator
Q_C = waste heat
Z = figure-of-merit
α = Seebeck coefficient
ρ = electrical resistivity
κ = thermal conductivity
I = current
T_H = hot side temperature
T_C = cold side temperature
P = output power
R_L = load resistance
V_{OC} = open circuit voltage
A = cross sectional area of pellet
L = length of pellet

Figure 1 shows a typical, schematic representation of a thermoelectric generator.

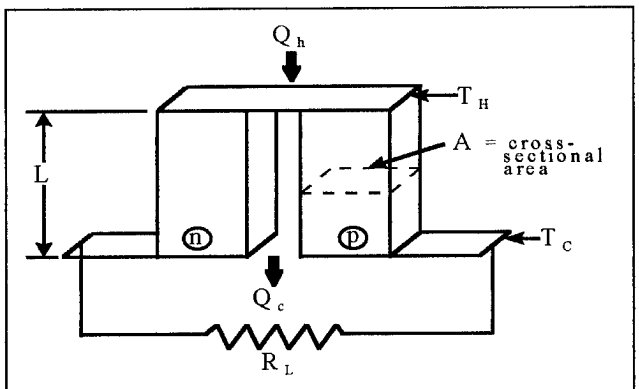


Figure 1. Thermoelectric Generator

The material properties of the thermoelectric material used for this analysis were obtained from an actual test result on a module as measured with TE Technology, Inc.'s TS-205. The temperature dependent properties were then extrapolated

at the extreme temperatures where test data was not available yet.

Model 1: $P(T_{HC})$
This model used material properties based on the average of T_H and T_C of the pellet.

Model 2: P_{avg}
This model used an integral average of the material properties. For example the average Seebeck coefficient was given by:

$$\overline{\alpha} = \frac{1}{T_H - T_C} \int_{T_C}^{T_H} \alpha(T)dT$$

Model 3: P_{fea}
This model splits the pellet into many small sub-sections, or elements. Eq. (1) was applied to each element whereby the heat leaving one element became the heat entering the subsequent element. The total power output was the sum of the power outputs of each element, as calculated from Eq. (8). The material properties were implicitly determined based on the temperature distribution calculated by a given heat flow. The heat flow, Q_H , into the pellet was parametrically altered by numerous iterations until the desired hot side temperature was obtained, assuming a given cold side temperature. Figure 2 shows a schematic of the P_{fea} model.

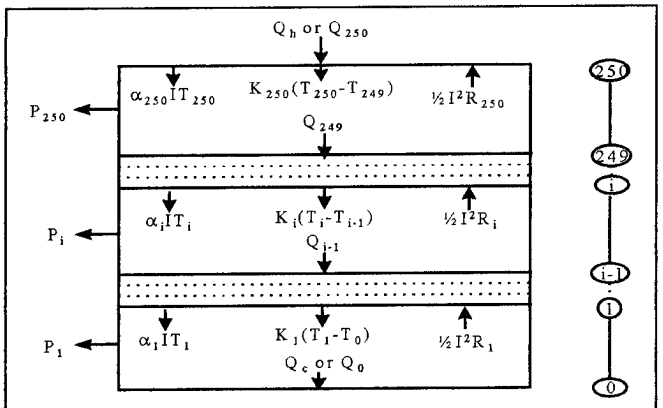


Figure 2. P_{fea} Model Schematic

Results
The determination of maximum efficiency was calculated by setting $R_L = (1+ZT_{HC})^{1/2} R$ [5] where Z was calculated at T_{HC} for $P(T_{HC})$; $T_{HC} = (T_H + T_C)/2$. For P_{avg}, R_L was calculated in the same manner except that the Z was calculated from the integral-averaged properties.

P_{fea} used a slightly different approach. The optimum R_L was not the true optimum when determined in the same manner as for $P(T_{HC})$ and P_{avg}. Rather the optimum was calculated from $(R_{L1} + R_{L2})/2$. R_{L1} was given by $(1+ZT_{avg})^{1/2} R$ where $T_{avg} = \left(\sum_{i=1}^{n} T_i\right)/n$. The Z was calculated at T_{avg}. R_{L2} was determined by $\left[\sum_{i=1}^{n}(1+Z_i(T_i+T_{i+1})/2)^{1/2}\right]\frac{R}{n}$.

However, there were only slight differences in the optimum R_L determined by any of the above means. The table below shows efficiency results from P_{fea} according to different methods used in calculating the optimum R_L.

The methods are identified in Table 1 as follows:
① $R_L = (1+ZT_{HC})^{1/2} R$
② $R_{L1} = (1+ZT_{avg})^{1/2} R$
③ $R_{L2} = \left[\sum_{i=1}^{n}(1+Z_i(T_i+T_{i+1})/2)^{1/2}\right]\frac{R}{n}$
④ $(R_{L1} + R_{L2})/2$

Table 1: Efficiency Based on Calculation of R_L

Method	efficiency, % T_H = 470K T_C = 300K	efficiency, % T_H = 600K T_C = 300K
①	5.608627	5.723894
②	5.608843	5.727157
③	5.608812	5.727169
④	5.608895	5.727174

At a ΔT = 170 K, the percent difference between method ① and ④ was only 0.005%. However, at a ΔT = 300 K, the percent difference between method ① and ④ was 5.73%. The averaging scheme represented by method ① is inadequate, especially at large ΔT's.

Figure 3 shows the maximum efficiency as determined by each model at different T_H's and at a constant T_C = 300K. For small temperature differences, the three models provided identical results. However, P_{fea} yielded a significantly lower efficiency at the higher temperature differences.

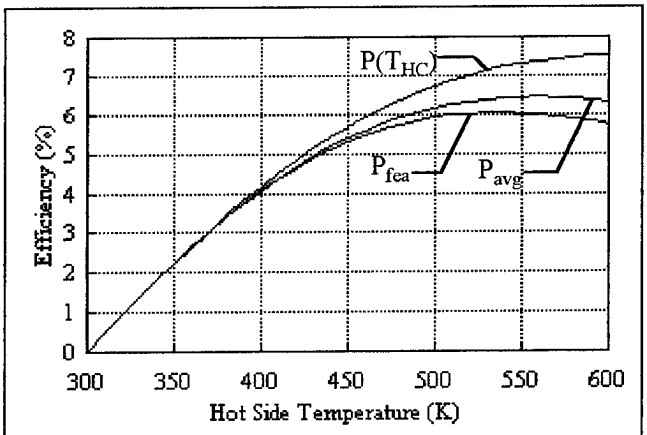


Figure 3. Maximum Efficiency (T_C = 300 K)

Figure 4 shows the maximum power as determined by each model at different T_H's and at a constant T_C = 300K. The maximum power was calculated by setting $R_L = R$. The models were based on 127 couples of 1.4 x 1.4 x 1.15mm pellet dimensions. Again at the smaller temperature differences, the $P(T_{HC})$ and P_{avg} provided sufficiently accurate answers when compared with P_{fea}. At the higher temperature differences, the variation was not quite as dramatic as for maximum efficiency. Nonetheless, the P_{fea} yielded a lower power output than calculated by $P(T_{HC})$ or P_{avg}.

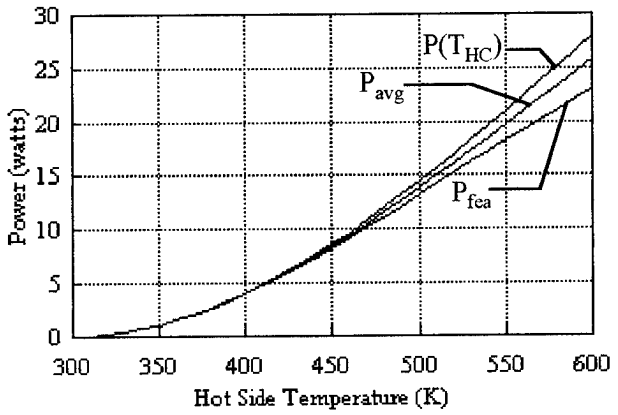


Figure 4. Maximum Power (T_C = 300 K)

Figures 5,6,7,8 and 9 show how current, load voltage, heat input and efficiency and output power compare according to the three models as a function of load resistance, keeping ΔT constant. Clearly, P_{avg} is a better model than $P(T_{HC})$. In Figure 5, P_{avg} and P_{fea} calculated essentially the same load voltage, indicating that P_{avg} is a superior model to $P(T_{HC})$. As shown in Figure 6, both $P(T_{HC})$ and P_{avg} over-predict the current. Figure 7 shows clearly that $P(T_{HC})$ was just too simplistic a model to provide sufficient accuracy.

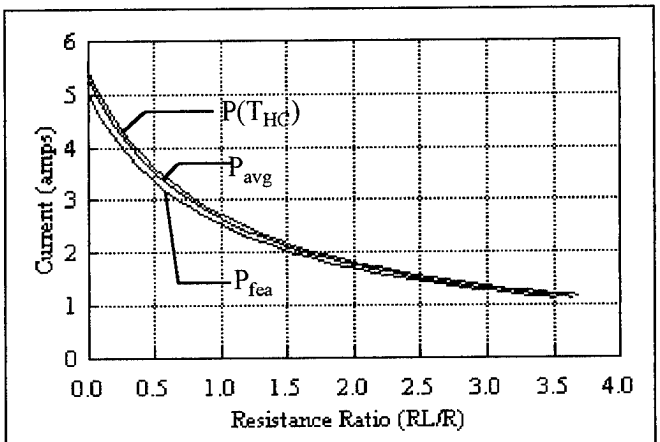


Figure 5. Effect of Load Resistance on Current
(T_H = 500 K, T_C = 300 K)

Figure 8 does show that the optimum resistance ratio for maximum efficiency was the same regardless of the model employed to determine it. However, the resistance ratios were not *exactly* the same. Table 2 shows how the ratios compared for the three models. While the optimum resistance ratios were essentially the same, the P_{fea} calculated significantly lower efficiencies than the other two models.

Table 2: Resistance Ratio for Optimum Efficiency

Model	R_L/R
$P(T_{HC})$	1.323393
P_{avg}	1.291606
P_{fea}	1.302489

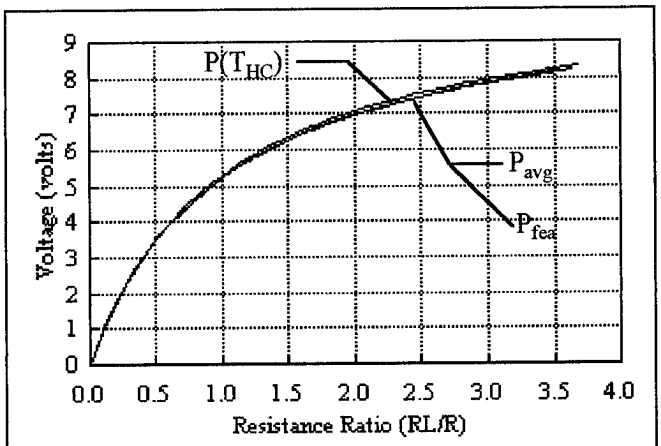


Figure 6. Effect of Load Resistance on Load Voltage
(T_H = 500 K, T_C = 300 K)

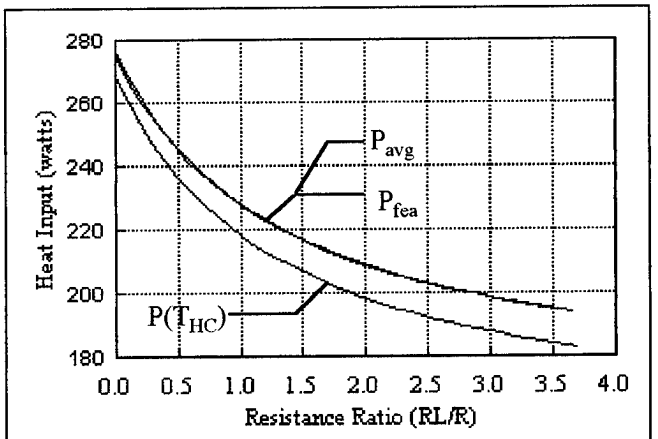


Figure 7. Effect of Load Resistance on Heat Input
(T_H = 500 K, T_C = 300 K)

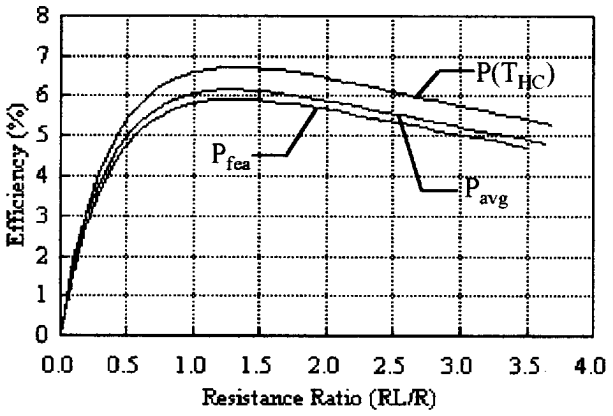


Figure 8. Effect of Load Resistance on Efficiency (T_H = 500 K, T_C = 300 K)

Figure 9 indicates that, regardless of the model, the resistance ratio for maximum power was unity, according to what the closed form, analytical equations predict. However, this may not be precisely true for all types of materials in all situations. As evidenced in Table 2, the closed form equations, do not necessarily predict the true optimum. Nonetheless, P_{fea} calculated a lower power level than the other two models.

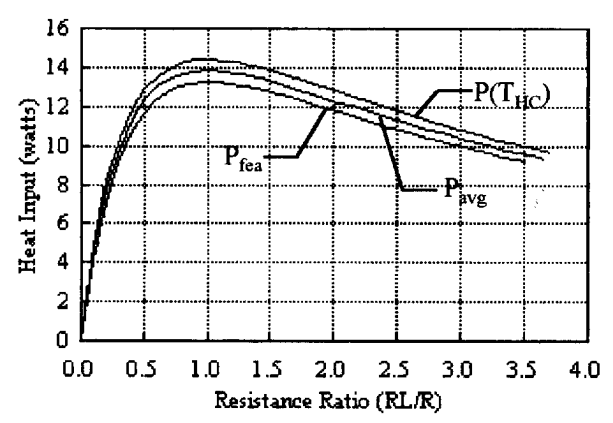


Figure 9. Effect of Load Resistance on Output Power (T_H = 500 K, T_C = 300 K)

Computation Time and Accuracy

The P_{fea}, using 250 elements in the model, required about 40 seconds to arrive at a solution when performed on a 90 MHz clock speed CPU. $P(T_{HC})$ and P_{avg} provided practically instantaneous results. When the temperature differences are large this additional computation time is probably justifiable. However, P_{fea} is itself only as accurate as the number of elements used in the model. The more elements that are used, the greater will be the internal accuracy, but also the greater will be the computation time. Table 3 shows comparisons of the P_{fea} model using 250 elements and 251 elements for the calculation of maximum efficiency at T_H = 600 K and T_C = 300 K, 127 couples, 1.4 x 1.4 x 1.5 mm pellet dimensions.

Table 3: P_{fea} Internal Accuracy Comparison

# of elements	Load Voltage V	Current A	Heat Input W	R_L/R
250	8.627417	2.652974	399.644	1.22133
251	8.626449	2.653348	399.651	1.22103
% change	0.011	0.014	0.0018	0.025

The use of 250 elements appears to have been sufficient for accurately calculating performance.

Conclusions

The P_{fea} has been shown to yield markedly different results when compared with $P(T_{HC})$ and P_{avg} results. The difference became more significant as the ΔT increased. There were also slight variations between the models for the determined optimum resistance ratio for maximum efficiency. While reasonable accuracy for determining the optimum resistance ratio for maximum efficiency could be achieved by using any of the three models, the variations could be much more exaggerated if the temperature dependent thermoelectric material properties were highly non-linear. Only the P_{fea} is sophisticated enough to correctly determine the true optimum. P_{fea} could be made even more sophisticated by including radiation, convection and conduction passive heat losses. These loss calculations could be easily included on an element-by-element basis whereas it would be quite difficult to correctly include in $P(T_{HC})$ or P_{avg}. Thus, the P_{fea} yields the best accuracy, it can easily model complex, real world situations and it calculates the true optimum.

References

[1] Buist, R. J., "Design and Engineering of Thermoelectric Cooling Devices," *Proceedings of the X Conference on Thermoelectrics*, Cardiff, Wales, September 10-12, 1991.

[2] Buist, R. J., "Calculation of Peltier Device Performance," *CRC Handbook of Thermoelectrics*, CRC Press, Inc., 1995.

[3] Lau, P. G. and R. J. Buist, "Temperature and Time Dependent Finite Difference Model of a Thermoelectric Pellet and Couple," *Proceedings of the XV Conference on Thermoelectrics*, Pasadena, California, March 25-28, 1996.

[4] Buist, R. J. and P. G. Lau, "Theoretical Analysis of Thermoelectric Cooling Performance Enhancement via Thermal and Electrical Pulsing," *Proceedings of the XV Conference on Thermoelectrics*, Pasadena, California, March 25-28, 1996.

[5] Cobble, M. H., "Calculations of Generator Performance," *CRC Handbook of Thermoelectrics*, CRC Press, Inc., 1995.

Effect of Electrons and Phonons Temperature Mismatch on Thermoelectric Properties of Semiconductors

Lev P. Bulat

Department of Electrical Engineering, St.Petersburg State Academy of Refrigeration,
Lomonosova St. 9, St.Petersburg, 191002, Russia,
Tel.: +7/812/164-7149, Fax: +7/812/31537-78, E-mail: bulat@ccref.spb.su

Abstract

A tendency of micro-miniaturisation of thermoelectric generators, coolers and sensors demands an increase of temperature gradients for preserving their power. It is impossible to consider that temperatures of electrons and phonons are equal in these conditions, so an electrons and phonons temperature mismatch begins to realise.

A system of non-linear equations for an energy balance of electrons and phonons and a continuity equation for current density is solved to study this mismatch. It is taken into account an electron-phonon energy interaction and a dependence of all kinetic coefficients on electrons and phonons temperatures.

It is shown that the three components of the mismatch are exist under large temperature gradients: the first component is proportional to a temperature gradient squared, the second component is proportional to a product of a temperature gradient and an electric field, and the third one - to an electric field squared. On the `volume of a sample the all components don't depend on coordinates and don't also depend on a type of heat boundary conditions for electrons and phonons.

The temperature mismatch is leading to a change of formulas for electric current density and heat flow density, for all kinetic coefficients and for the thermoelectric figure of merit. The figure of merit increase in consequence of the mismatch. This increase is starting to be shown up in thermoelectrics at temperatures gradients $\sim 10^5 K/cm$.

Introduction

A tendency of micro-miniaturisation of thermoelectric generators, coolers and sensors demands an increase of temperature gradients for preserving their power. On the other hand, experimental facilities already permit us to reach giant temperature gradients in solids (up to $10^{10} K/cm$) under laser beams, under electronic rays, at mechanical treatment, in welding, etc. [1]. There are a number of patents [2] in which are offered several thermoelectric generators with the temperature gradients $\sim 10^8 K/cm$.

It is impossible to consider that temperatures of electrons, phonons and others quasi-particles are the same under these conditions, so a temperature mismatch is beginning to realise.

The traditional theory of thermoelectricity assumes that a sample can be characterised with some common temperature. However, a semiconductor material really contains the whole complex of quasi-particles subsystems - electrons, holes, phonons etc., generally each is characterising with one's own temperature (if such temperature can be introduced). Yu. Gurevich at al [3, 4] were first who paid an attention to this fact.

We have to give an answer to the question: at what conditions it is necessary to take into account differences between the temperatures of different kinds of quasi-particles.

Let's take into consideration a homogeneous isotropic sample which consists from the only of two types of quasi-particles: from electrons and from phonons. Such material can be or an electronic semiconductor or a metal. If a different heat boundary conditions for electrons and phonons can be realized (such conditions can be fulfilled experimentally [5]) the first type of electrons and phonons temperatures mismatch can take place. Just that very case was thorough investigated by Yu. Gurevich at al [3, 4].

In the present paper, is investigating the other mechanism of electrons and phonons temperatures mismatch, this mechanism cause with the large temperature gradients. We can understand the reason of the temperature mismatch under large temperature gradients from the follow qualitative consideration. Heat conductivity coefficients of electrons and phonons depend on the temperatures in a different manner. Therefore the coordinate dependence of electrons and phonons temperatures must differ if an electron-phonon interaction does not take place. In the real case when the interaction takes place, it will somewhat reduce the temperature mismatch but it will remain other than zero is. This mismatch actually means peculiar warming (cooling) of electrons under large temperature gradients.

0-7803-4057-4/97 $10.00 ©1997 IEEE

Main Equations

Let's assume that a concentration of electrons in semiconductor is sufficiently large, so it is an energetic control in electronic system, the necessary criteria can be founded in [4]. In these assumptions the main equations of the problem are the energy balance equations for electrons and phonons

$$div\,\vec{q}_e = \vec{j}\,\vec{E} - P\cdot(T_e - T_p),$$
$$div\,\vec{q}_p = P\cdot(T_e - T_p), \qquad (1)$$

here $\vec{E}$ - electric field, $\vec{E} = -\nabla\,\Phi$ (Φ - electrochemical potential), $T_{e,p}$ - electrons and phonons temperatures, $P(T_e,T_p)\cdot(T_e - T_p)$ characterizes the electron-phonon energetic interaction [4].

We can write for the current density and for the heat flow densities of electrons and phonons the follows equations:

$$\vec{j} = \sigma\,(T_e)\,\vec{E} - \sigma\,(T_e)\,\alpha\,(T_e)\nabla T_e,$$
$$\vec{q}_e = -\kappa_e(T_e)\nabla T_e + \Pi(T_e)\,\vec{j} \qquad (2)$$
$$\vec{q}_p = -\kappa_p(T_p)\nabla T_p,$$

where $\sigma\,(T_e)$ - electrical conductivity, $\alpha(T_e)$ - thermoelectric power, $\kappa_e(T_e)$ - thermal conductivity of electrons and $\Pi(T_e) = T_e\alpha\,(T_e)$ - Peltier coefficient, $\kappa_p(T_p)$ - thermal conductivity of phonons.

The equations (1), (2) must be supplemented with the equation of current continuity

$$div\,\vec{j} = 0. \qquad (3)$$

Let's investigate the one-dimensional problem: a sample's length is $2a$.

The heat boundary conditions for the equations (1), (2) can be written in a form [3, 4]

$$q_{e,p}\Big|_{x=-a} = -\eta^{-a}_{e,p}(T_{e,p} - T_1)\Big|_{x=-a},$$
$$q_{e,p}\Big|_{x=a} = \eta^{a}_{e,p}(T_{e,p} - T_2)\Big|_{x=a}, \qquad (4)$$

where $\eta^{a}_{e,p}$ - phenomenological coefficients of heat changing, they connect with conditions in contact regions.

The system of non-linear differential equations (1)-(3) with boundary conditions (4) has not an analytical solution. Moreover, we can not find it's analytical solution in the case of one-temperature approximation $T_e = T_p$ and simplest boundary conditions (the first kind of heat boundary conditions: $\eta^{a}_{e,p} = \infty$). So we must use a perturbation theory to solve the problem. The small parameter is considered to be the follow

$$\gamma = \frac{T_2 - T_1}{T^*} << 1, \quad T^* = \frac{T_1 + T_2}{2}. \qquad (5)$$

The temperatures T_1, T_2 defined with the conditions (4).

We suggested a modification of the perturbation theory method to solve the system of equations (1)-(4) with temperature dependence of all kinetic coefficients. The use of this method gives us a possibility to reduce this non-linear system of differential equations to an unlimited chain of linear differential equations with constant coefficients. We founded a method of unhooking and integrating the chain of this differential equations. The results of solving these chain of equations (distributions of electrons and phonons temperatures and a distribution of electrical potential) was also corroborated with numerical experiment.

Main Results

The principal results of the investigation of the electrons and phonons temperatures mismatch can be illustrated on the properties of the mismatch value

$$\Theta = T_e - T_p. \qquad (6)$$

It turned out that the temperature mismatch (6) can be represented as a sum of three terms

$$\Theta = \Theta_q + \Theta_{q,j} + \Theta_j, \qquad (7)$$

where the term Θ_q connects only with a heat transport and exists in absence of an electric current (let's call the Θ_q as the heat mismatch), the term Θ_j connects only with an electric current and exists in absence of a heat transport (it is a well known Joule heating) and the term $\Theta_{q,j}$ take place in the case when both exist: a heat transport and an electrical current (let's call $\Theta_{q,j}$ as the interference mismatch).

The analysis of the structure of the temperature mismatch (7) leads to the follows general conclusions:

1. In the case when kinetic coefficients don't depend on electrons and phonons temperatures.

The temperature mismatch takes part (in isotropic media) only in the situation of different heat boundary conditions for electrons and phonons. This mismatch exists only in a locality of sample's boundary, as shown at the Figure 1.

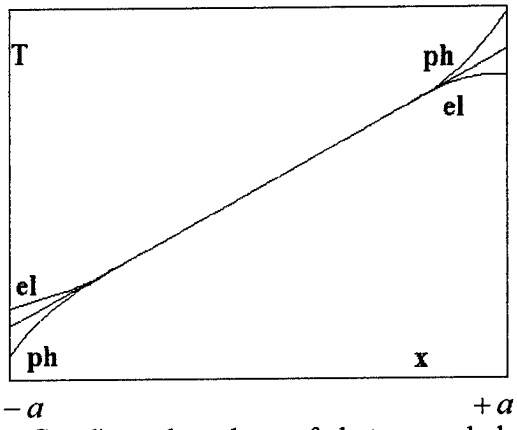


Figure 1: Coordinate dependence of electrons and phonon temperatures. Kinetic coefficients don't depend on temperatures, different heat boundary conditions for electrons and phonons take place.

2. In the case when kinetic coefficients depend on electrons and phonons temperatures.

The temperature mismatch exists in a whole volume of a sample at an arbitrary heat boundary conditions for electrons and phonons. Moreover, a temperature mismatch exists even in the case of equal heat boundary conditions for electrons and phonons. There is a characteristic length L^* with the follow property: in massive samples when $a >> L^*$ the heat mismatch Θ_q does not depend on coordinate, Θ_q does not depend on temperature dependence of energetic electron-phonon interaction, Θ_q is equal under arbitrary heat boundary conditions for electrons and phonons and it has the form:

$$\frac{\Theta_q}{T^*} = \frac{G^2}{k^2 T^2}\left(\frac{\kappa_e'}{\kappa_e} - \frac{\kappa_p'}{\kappa_p}\right) = \frac{\gamma^2 T^*}{4k^2 a^2}\left(\frac{\kappa_e'}{\kappa_e} - \frac{\kappa_p'}{\kappa_p}\right), \qquad (8)$$

and it has the order

$$\frac{\Theta_q}{T^*} \approx \frac{\gamma^2}{4k^2 a^2} = \frac{1}{L_T^2 k^2},$$

where k^{-1} is the characteristic cooling length of electrons and phonons [2, 5]:

$$k^2 = P(T^*)\left(\frac{1}{\kappa_e} + \frac{1}{\kappa_p}\right), \qquad (9)$$

(in the case of the first kind of heat boundary conditions $\eta^a_{e,p} = \infty$ we have $k^{-1} \approx L^*$), L_T - characteristic length of temperature changing [1, 5]

$$L_T = \frac{T}{|G|}, \qquad G = \frac{T_2 - T_1}{2a}, \qquad (10)$$

all the kinetic coefficients K in (8), (9) and in the follows formulas (11)-(13) have been calculated at the average temperature T^* (5); the stroke in (8) means

$$K' = \left.\frac{dK}{dT}\right| T = T^*.$$

A sign of the heat mismatch Θ_q (8) connects with a temperature dependence of electrons and phonons thermal conductivity and generally may be or «plus» or «minus». But in cases of real thermoelectric materials we have exclusively $\Theta_q > 0$. The heat mismatch of electrons and phonons temperatures is proportional to the heat flow density square. This mismatch is analogue to the Joule effect (the Joule mismatch is proportional to the current density square). So we can name the heat mismatch as the heat analogue of the Joule effect. The character of heat mismatch Θ_q are shown in Figure 2.

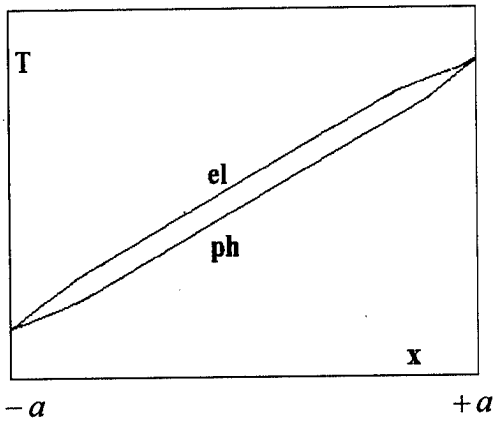


Figure 2: Coordinate dependence of electrons and phonon temperatures. Kinetic coefficients depend on temperatures, heat boundary conditions for electrons and phonons are equal.

Let's look at the value of the heat mismatch. At the room temperature ($T^* = 300K$) the heat mismatch reaches the value of $\Theta_q \approx 10K$ under temperature gradients $(4 \cdot 10^6 - 10^7)\, K/cm$ in metals and under temperature gradients $(3-8) \cdot 10^5 K/cm$ in semiconductors. The heat mismatch strongly increase with the increasing of the temperature gradient G, the heat mismatch also increase with the decreasing of the average temperature T^*.

A closing of a circuit leads to an appearance of the interference's mismatch $\Theta_{q,j}$ and Joule's Θ_j mismatch.

The last item in (7) (i.e. the Joule's heating) can be represented in the form:

$$\frac{\Theta_j}{T^*} = \frac{G^2 \nu^2 Z}{k^2 T^*}\frac{\kappa_e + \kappa_p}{\kappa_e}, \qquad (11)$$

where $Z = \dfrac{\sigma \alpha^2}{\kappa_e + \kappa_p}$ - thermoelectric figure of merit,

$\nu = \dfrac{R_{in}}{R_{in} + R_{out}}$, R_{in} - a resistance of a thermoelement, R_{out} - a resistance of a load.

It is obviously from (11) that always $\Theta_j > 0$.

If there is not non-thermoelectric types of electric power sources in a circuit the interference mismatch can be written in the form:

$$\frac{\Theta_{q,j}}{T^*} = \frac{G^2 \nu Z \tau_T}{k^2 T^* \alpha}\frac{\kappa_e + \kappa_p}{\kappa_e}, \qquad (12)$$

here τ_T - the Thomson coefficient.

We can see from (12) that $\Theta_{q,j} > 0$. But in a case of existence non-thermoelectric types of electric power sources, the sign of the interference mismatch $\Theta_{q,j}$ can be arbitrary.

A comparative values of different mechanisms of the mismatches can be represented as

$$\left|\frac{\Theta_j}{\Theta_q}\right| \approx \frac{\nu^2\alpha^2}{L}, \qquad \left|\frac{\Theta_j}{\Theta_{q,j}}\right| \approx \frac{\nu\alpha^2}{\tau_T}, \tag{13}$$

where $L = \frac{\kappa_e + \kappa_e}{\sigma T}$ - the Lorenz factor.

In pure semiconductors the ratio $\frac{\alpha^2}{L}$ can reach the value ~ 50, and in a closed circuit usually $\Theta_{q,j} > \Theta_q$. In typical thermoelectric materials under optimal for thermoelectric systems conditions $\nu \approx 0{,}5$ we have

$$\Theta_q \sim \Theta_{q,j} \sim \Theta_j .$$

So we must take into account all mechanisms of electrons and phonons temperatures mismatch in thermoelectrics.

Owing to approximation (5) we have $\Theta << T^*$. So in the zero assumption with the small parameter γ we can solve the traditional one-temperature equation of a heat conducting. Then a problem of calculating the electrons (phonons) kinetic coefficients comes to use the traditional formulas of the transport theory, but in these formulas we must change T on T_e (on T_p in formulas for phonons). Therefore, formulas for all kinetic coefficients can be written in the form:

$$K = K_0 + \gamma^2 K_1, \qquad \delta K = \frac{\gamma^2 K_1}{K_0} \tag{14}$$

where K_0 - a kinetic coefficient in the standard form.

It is found that

$$\delta(\sigma\alpha^2) > 0, \quad \delta\kappa_e < 0$$

at any type of electrons scattering mechanism and at any type of temperature dependence of phonons thermal conductivity, therefore in any case the change of the figure of merit is

$$\delta Z > 0 . \tag{15}$$

Consequently we have the increase of the figure of merit in any real thermoelectrics thanks to electrons and phonons temperatures mismatch. This increase starts to be shown up in thermoelectrics under temperatures gradients $\sim 10^5 K / cm$.

Conclusion

1. Under large temperature gradient the electrons and phonons temperature mismatch take place in whole volume of a sample.
2. The temperature mismatch can be represented as a sum of three terms: *the heat mismatch, the interference mismatch and the Joule heating.*
3. The temperature mismatch leads to a change of all kinetic coefficients and of the thermoelectric figure of merit.
4. We have an increase of the figure of merit in any real thermoelectrics. This increase starts to be shown up in thermoelectrics under temperatures gradients $\sim 10^5 K / cm$.

References

[1] L. I. Anatychuk, L. P. Bulat, Properties of thermoelectric materials under large temperature gradients (Revue), No.3 (1987) 5.

[2] R. Dahlberg, Deutsches Patentamt 2547262, 22.4.77; 3404137, 8.8.85; 3404138, 8.8.85.

[3] Yu. G. Gurevich, Thermoelectric and thermomagnetic effects in semiconductors, Ukrainian Phys. Journ., 24 (1979) 1601.

[4] F. G. Bass , V. S. Bochkov, Yu. G. Gurevich, Electrons and Phonons in limited semiconductors, Moscow, Nauka, 1984.

[5] A. I. Klimovskaya, O. V. Snitko, Absorption of hot electrons energy with semiconductor surface, Letters to JETP 7 (1968) 194.

[6] L. P. Bulat, V. A. Stefansky, Thermoelectric properties of high electron concentration materials under large temperature gradients, Proc. of the XIII-th Int. Conf. on Thermoelectrics, Kansas City, USA, 1994.

Thermoelectric Self-Powered Hydronic Heating Demonstration

Daniel T. Allen
Hi-Z Technology, Inc., San Diego, USA, tel. +1 619 695-6660, FAX +1 619 696-8870, e-mail d.allen@hi-z.com
Jerzy Wonsowski
Gas Research Centre, British Gas plc, Loughborough, Leicestershire, UK, tel. +44 (0)1509 282000, FAX +44 (0)1509 26464

Abstract

A residential-scale hydronic central heating unit was modified with the addition of a thermoelectric generating stage to demonstrate self-powered operation in a realistic environment. The unit was fabricated in the United States and tested in the US and in England. This paper describes the design, operation and testing history. The unit's performance was satisfactory, and the demonstration indicated the merit of further development of self-powered heating.

Background

A self-powered central heating unit is one that operates entirely on combustion fuel, independently from the electrical grid. Such a system would in theory be more reliable in providing heat through extreme weather conditions. It would also find application in remote habitations not served by the electrical grid. However, the main obstacle to integrating an electric generator into a heating unit is the selection of a convenient, cost-effective engine and generator. Thermoelectric generating modules are solid-state, compact, quiet, highly reliable and suited to self-powering central heating. A Hi-Z thermoelectric module is shown in Figure 1.

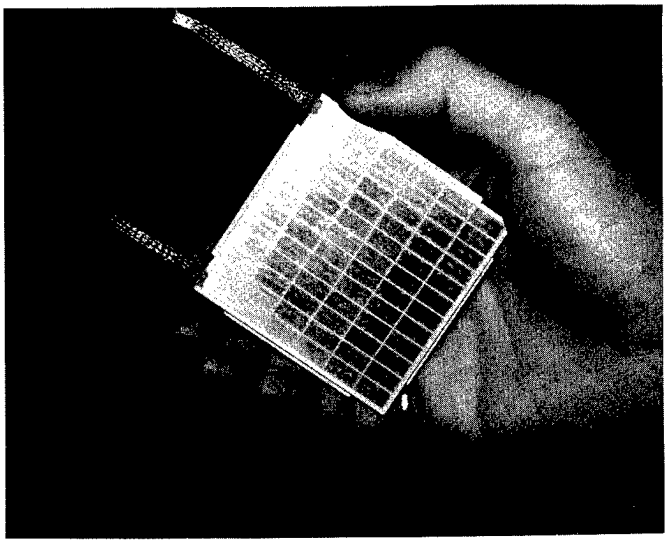


Figure 1 - Hi-Z 19 watt Thermoelectric Module

As power generators, thermoelectric modules have the disadvantage relative to other heat engines that their thermodynamic efficiency is low. However, regardless of stand-alone efficiency, if thermoelectrics is combined with a heating application, then the heat passing "inefficiently" through the thermoelectrics can still be fully utilized. In a system arranged schematically, such as is shown in Figure 2, the "cost" of the electricity generated by the thermoelectric stage is the cost of the

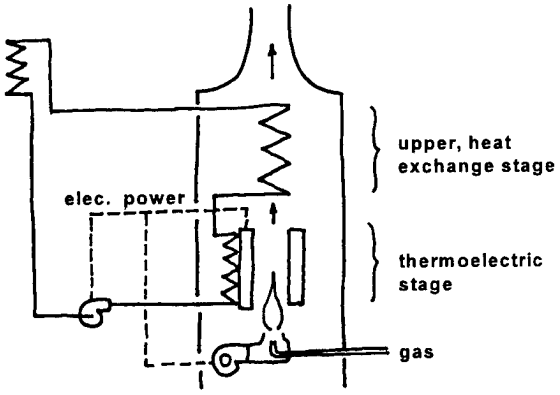


Figure 2 - Schematic Self-Powered Heat Unit

fuel for the equivalent heat energy. The electricity generation is essentially 100% efficient in this case. Consider the average US residential energy costs of $6.0/MBtu for natural gas and 8.4¢/kWh for electricity [1]. $6.0/MBtu is the equivalent of 2¢/kWh. That would be the cost for electricity generated in a thermoelectric self-powered heating system -- one-quarter of the cost of utility electricity. This is a real saving. Although not an enormous saving to the individual, in widespread use this is both an economic benefit to consumers and an energy conservation measure for the public benefit. It could be as well a new market for the fuel utility (at the expense of the electric utility).

Self-powered central space heating with forced air has been demonstrated previously utilizing thermoelectrics [2,3]. That unit incorporated lead-telluride-based thermoelectric alloys. Since the time of that demonstration, less costly bismuth-telluride alloy thermoelectric generating modules have become commercially available. The bismuth-telluride alloys operate at lower maximum hot side temperature (260°C *versus* 540°). Their integration with state-of-the-art central heating units is conceptually less complex.

Design and Objective

The objective of the project was not to build a prototype but to assemble and test a self-powered demonstration hydronic heater from existing components that would operate in a real environment. The assembly of the unit essentially followed the construction shown in the schematic of Figure 2.

The upper stage is a modified 15 kW compact, natural gas-fired heater which is used as a heat exchanger only. The burners were removed and discarded and most of that unit's gas controls and safety features were also removed but re-utilized as the final self-powered boiler controls.

The thermoelectric stage is a concentric assembly of a central steel heat receiver surrounded by an array of 18 bismuth-

telluride alloy thermoelectric modules such as shown in Figure 1. These are mounted on hexagonal flats on the heat receiver and surrounded by six water-cooled cold plates. This assembly is a modification of a generator designed originally used to extract electric power form the exhaust of a diesel truck engine. In that application it could generate up to 185 watts of power, rejecting heat to a water loop at near ambient temperatures (27°C). The exit end of the central cavity of this generator interfaces with a hole cut in the bottom of the upper stage.

The heat source used in the demonstration is a nominal 15 kW ceramic fiber burner 76 mm in diameter and 185 mm long inserted within the central cavity of the thermoelectric stage. Natural gas and air are mixed in a venturi. The air is supplied by a d.c. ultra-efficient, small high pressure blower rated at 7 watts. Fuel-to-air mixture is set by a variable resistor in series with the blower motor.

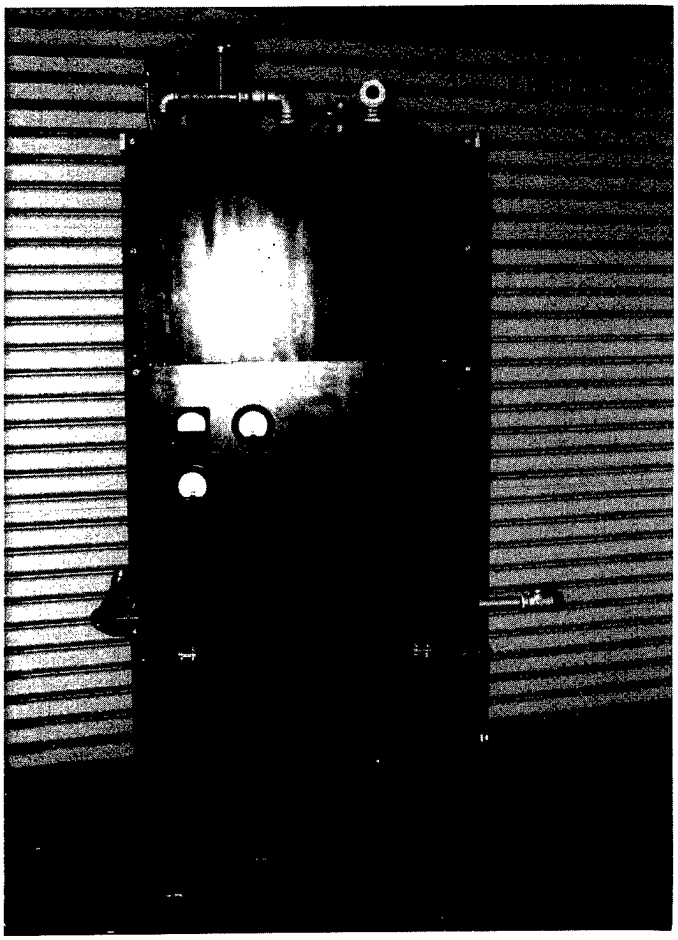


Figure 3 - Completed Heating Unit

The completed modified unit is shown in Figure 3, and in Figure 4 it is shown with exterior panels removed and test instrumentation in place. In Figure 4 the thermoelectric stage can be seen in the middle. Figure 5 is a schematic flow diagram.

Operation and Instrumentation

The boiler control system is based on the hardware furnished with the standard boiler. The control consists of a relay block actuated by the demand of an external thermostat,several safety interlocks in series, a damper actuator,

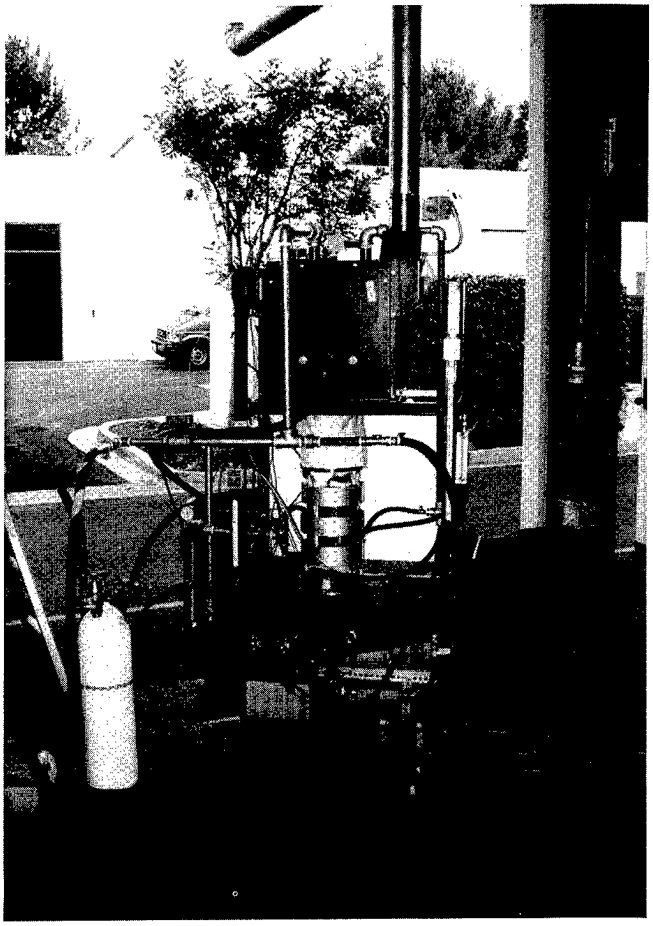


Figure 4 - Heater Unit on Test

an ignition unit for the burner pilot and a gas controller consisting of solenoid and servo control valves.

Of the interlocks on the standard boiler, the "roll-out" switch was eliminated. (This is a temperature switch on the air intake intended to shut off the gas in the event flue blockage causes the flame to move to the air intake. It could be eliminated on account of replacing naturally ventilated combustion with forced air.) An interlock consisting of pressure switch on the combustion air blower exit has been added to ensure that the main gas shuts off in any event that disables power to the air blower.

A delay timer has been interposed in the power relays for the water pump and combustion air blower. The timer allows the pump and fan to continue operation after the main gas is shut off. This delay was added for two purposes. On the water side it is necessary to continue cooling the thermoelectric generator because of its thermal inertia. On the gas side it is provided to clear unburned gas from the system.

The battery is fused and has an isolation switch. The switch is intended for use when the boiler is unused for any extended period in order to eliminate the small but continuous drain to the inverters. (In a commercial unit the inverter consumption would be eliminated or automatically switched.) A pair of diodes block reverse current flow from the battery through the thermoelectric generator. Two diodes in parallel are used to reduce the forward voltage drop. A loss of 0.4 volts was measured in testing.

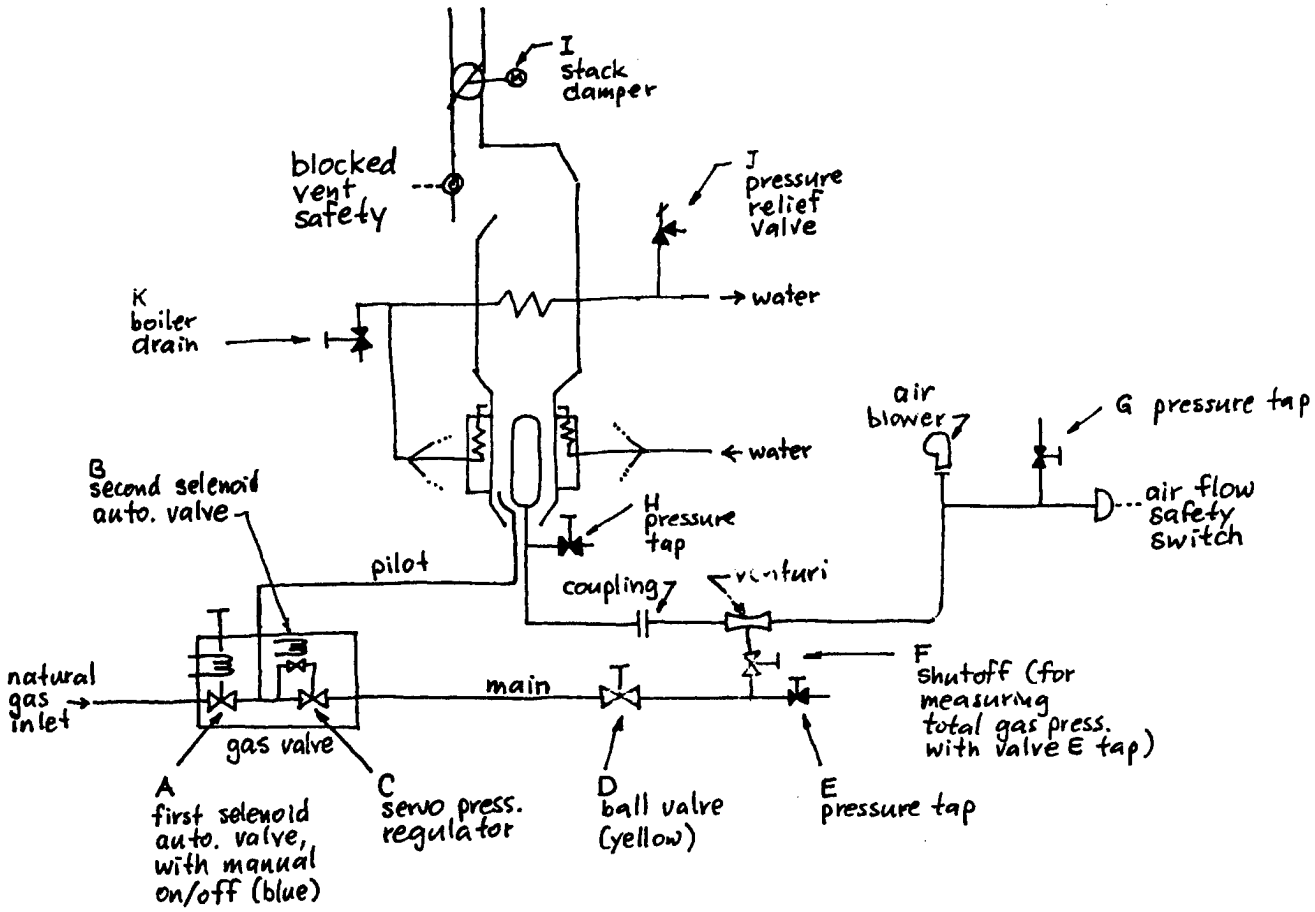


Figure 5 - Flow Diagram

In the resulting arrangement, the battery terminal voltage sets generator voltage and only the generator output current varies.

The combustion air blower operates on d.c. at battery voltage. An inverter changes power to 115 volt 60 Hz for the delay timer and the gas ignition and control. The control operates at 24 volts 60 Hz on the other side of a transformer. In a prototype unit the ignition and gas control would be designed to operate on d.c. in order to eliminate the need for this inverter and the associated power loss in converting to a.c.

For the demonstration a.c. water pumps were used requiring additional inversion (to 115 volt 60 Hz or 230 volt 50 Hz, depending on whether testing in the US or in England). Ideally d.c. system pumps would be employed because they are more efficient overall and since d.c. to a.c. inversion losses would not be present.

In place in a system, the unit operates automatically. The three gauges shown in Figure 3 monitor performance. A battery is included in the system to provide startup power, and one of the gauges reads battery current, plus and minus. Initially on a cold start current flows out of the battery, then as the thermoelectrics heat up there is significant excess power generated, and the battery is recharged in parallel with the system requirements. Thus as the water circuit comes to equilibrium, higher thermoelectric cold side temperatures reduce thermoelectric output and the battery gauge settles near zero. Finally, when the heating is shut off the system again draws from the battery to power a period of pump and blower run-on. The size of the battery needed depends on the cyclic demand of the heating system, and it can be significantly smaller than the automotive battery seen in Figure 4 used in the demonstration unit. The exact battery requirement was not determined in the work done thus far.

The other gauges are a volt meter, to check the system/battery voltage and monitor possible over- or under-charge of the battery, and an ammeter to verify thermoelectric output.

Performance and Test Results

The unit was tested 14 times in San Diego before being shipped to Loughborough. The objective of these tests was to check out intended operation, to set operating point parameters and to establish *bona fide* self-powering. The table following details the operating performance.

Input, Natural Gas	1.2 m^3/h
Thermal Power (@38.4 MJ/m^3)	12.9 kW
Thermal Output	11.0 kW
Of which transferred:	
in thermoelectric stage	43 %
in upper stage	57 %
Water Inlet Temperature	75°C
Water Outlet Temperature	80°C
Electrical Output, gross	109 W
System Voltage	13 volts
Power Utilized:	
Blower	4 W
Inverter Loss	1 W
Gas Control	24 W
Water Pump	80 W
Efficiency [(Thermal Power + Electric Power) / Input Power]	86 %

In England the pump was changed but all other unit components were the same. It was integrated into a computer controlled diagnostic system. Tests were run over a 1-1/2 month period to validate performance, and an overall heating efficiency of 85.6% was determined. Daily cyclic operation was imposed in "household simulation mode", for which representative performance is shown in Figure 6. In this testing, the unit fell short of zero net draw on the batteries for return water flow temperatures above 70°C.

Discussion and Conclusion

The demonstration unit met expectations in all respects except self-powering at the highest anticipated water return temperatures, which range to 80°C. Known losses in the gas control and inverters could be minimized, which would overcome some of that shortfall. Indeed more thermoelectric modules could have been added, but the objective of this demonstration was to use the diesel truck generator "as is". In fact, the demonstration points to the possibility of scale-up to a combined heat and power or cogeneration unit of modest net electrical output.

Operating experience emphasizes a need to optimize thermal mass in the thermoelectric stage, to reduce the need for battery-powered run on after the demand thermostat signals off. For the cold plates, fundamental thermodynamic principles indicate a maximization of module-to-cooling water heat transfer to assure the lowest possible cold side temperature and highest possible delta T across the generating elements.

The cylindrical configuration of the existing thermoelectric generator determined the use of a ceramic fiber burner, which worked very well but was somewhat fragile. Other burner configurations should be considered.

A next step would be integration of a purposefully designed thermoelectric stage into a state-of-the-art, high efficiency hydronic heating unit with design to address compactness, weight, and most importantly, low cost fabrication.

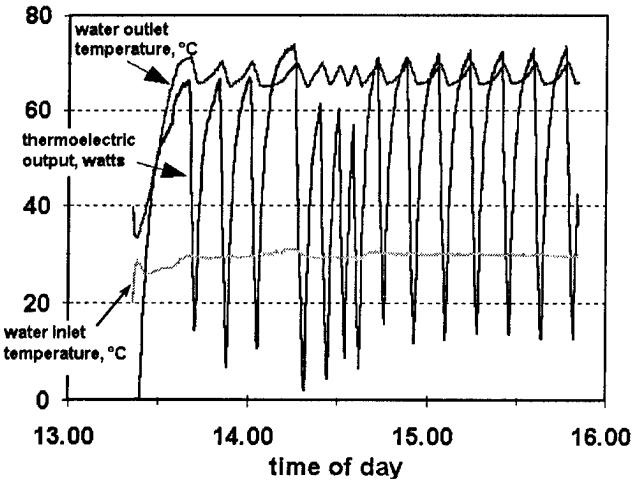


Figure 6 - Typical Cyclic Test Data

Acknowledgments

Design, construction, and testing of the self-powered gas-fired hydronic heater was fully funded by British Gas plc. The work reported was conducted by Hi-Z Technology, Inc., and the Gas Research Centre of British Gas plc in 1995 - 96. The thermoelectric generator originally designed for diesel engine exhaust heat recovery was built in 1990 - 91 by Hi-Z Technology, Inc. under a contract from the United States Department of Energy [4].

References

[1] DOE 1996. *Electric Power Annual 1995*, Table 22 & *Natural Gas Annual 1995*, Figure 13, Energy Information Administration, United States Department of Energy

[2] Babyak, R.J. 1993. Gas Furnace Unplugged. *Appliance Manufacturer*, May 1993, p. 76.

[3] Valenti, M. 1993. Keeping the Home Fires Burning. *Mechanical Engineering*, July 1993, p.66.

[4] Bass, J.C.; R.J. Campana and N.B. Elsner 1991. Thermoelectric Generator Development for Heavy Duty Truck Applications. *Proc. Annual Automotive Technology Development Contractors' Coordination Meeting*, SAE P-256.

Low Power Thermoelectric Generator - self-sufficient energy supply for micro systems

Matthias Stordeur, Ingo Stark

D.T.S. Gesellschaft zur Fertigung von Dünnschicht-Thermogenerator-Systemen mbH, D-06118 Halle (Germany),
Köthener Str. 34, Tel. & Fax: +49 345 52 44 292

Abstract

New micro and sensor systems are being rapidly developed for their application in all technology events in future. The energy consumtion of systems incorporated the latest technical advances decreases permanently to the range of only µW. For the applications in this low power range (a few 10 µW) D.T.S. has developed a new, self-sufficient power supply - the *Low Power Thermoelectric Generator*.
Whereas earlier with the help of MOS processing techniques manufactured thermoelectric generators reached only a nW-output, it was now possible to open up the µW-performance range on the basis of high effective thermoelectric compound semiconductor thin films, prepared by Physical Vapour Deposition on polyimid substrates.
The LPTG of D.T.S. is a small compact thermoelectric device, full hybrid compatible with micro electronic and micro matched systems.
Essential information about the LPTG-device-properties are given. E. g. at $\Delta T \cong 20$ K the first prototypes have a power output of 20 µW and a voltage of about 4.0 V under load. On the other hand the technological limit lies at about 60 µW.

Introduction

Thermoelectric Generators (TEG's), devices which convert thermal energy directly in electrical energy, exist in a broad power output spectra from the nW-range up to a few 100 kW /1/. The power output determines the different application fields, e. g. as power supply for micro systems or as nuclear power source in space. Even the used thermoelectric materials vary in connection with the working temperature range and of course the technical construction.
The TEG developed by D.T.S. is based on thin film thermoelectric materials and is therefore a Low Power Thermoelectric Generator (LPTG).
Whereas earlier with the help of MOS processing techniques manufactured thin film TEG's reached only a nW-output /2/ and have not existed as a device ready for use, it was now possible to open up the µW-performance range.

The Low Power Thermoelectric Generator Device

A first real LPTG-prototype is seen in Fig. 1. The working range is near room temperature not higher than 120 °C.
As active materials we have used the standard semiconducting compounds with the highest thermoelectric figure-of-merit in this temperature range /3-5/
p-leg: $(Bi_{0.25}Sb_{0.75})_2Te_3$; n-leg: $Bi_2(Se_{0.1}Te_{0.9})_3$
in each case with special dopands deposited by magnetron sputtering onto a polyimid-foil substrate (Kapton®, 75 µm).
Typical mean film values are for the electrical conductivity

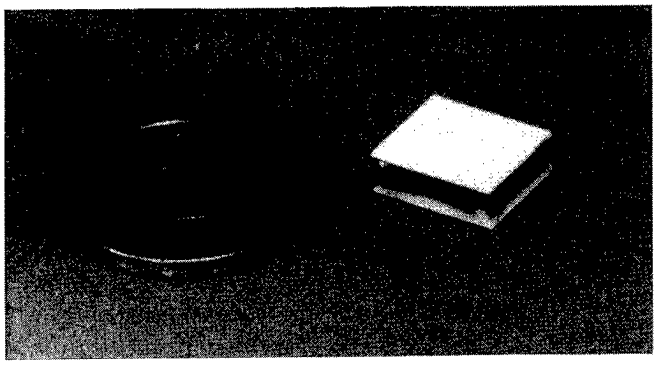


Fig. 1: µW-LPTG prototype in geometrical comparison with a german 1 Pfennig coin

$\sigma_p \cong 400\ \Omega^{-1}cm^{-1}$, $\sigma_n \cong 500\ \Omega^{-1}cm^{-1}$ and for thermopower $S_{n,p} \cong 370$ µV/K near room temperature. Therefore the data are very similar to the film properties prepared by flash evaporation onto glass substrates /6/ which led to laboratory function samples of thin film generator cells /7/. A selected set of film properties in the most technological relevant temperature intervall is shown in Figs. 2a and 2b.

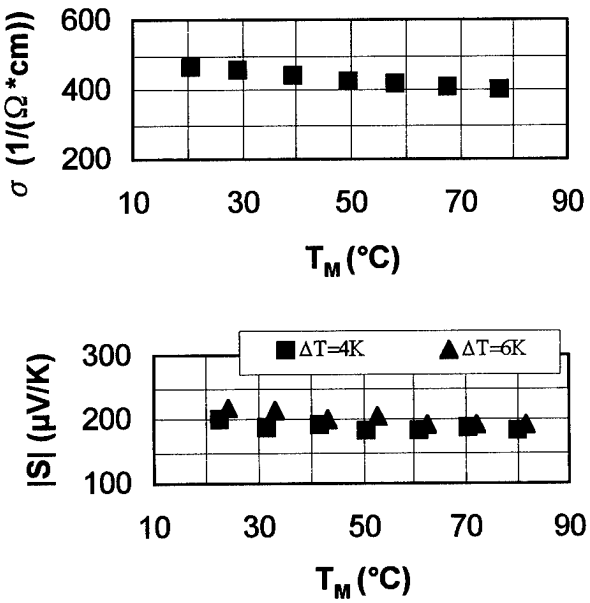


Fig. 2a: Electrical conductivity σ and thermopower S for p-semiconductor sputter films (d ≅ 1 µm, annealed) in dependence on mean temperature T_M

The LPTG was consequently manufactured with thin film technology methods and equipment by the batch processes

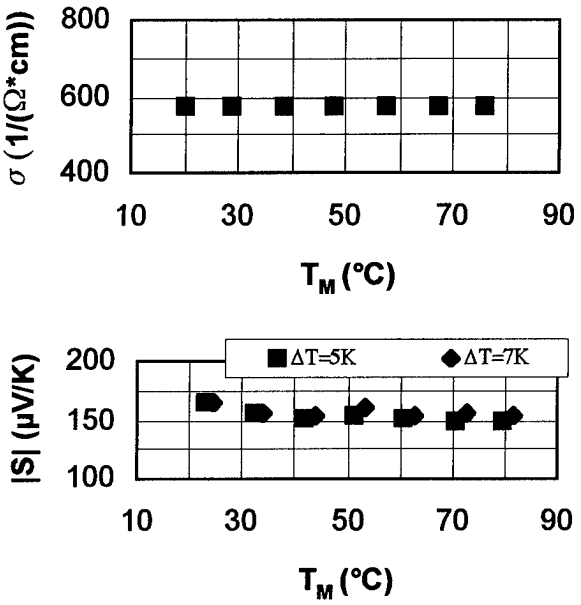


Fig. 2b: Electrical conductivity σ and thermopower | S | for n-semiconductor sputter films (d ≅ 1 µm, annealed) in dependence on mean temperature T_M

film generation, photolithography, pattern generation, wafer (foil) cutting and device assembly.
The demonstrated LPTG-prototype consists of 2250 thermocouples. The active films have a thickness of 2.5 µm, the internal electrical resistance amounts about 0.8 - 1.0 MΩ.

The same materials are also suited to realize high sensitive *plane* thermoelectric arrangements on foils /8/ used for active sensors like

* radiation sensors,
* heat flux sensors,
* temperature difference sensors with high output voltages up to about 100 mV/K.

The schematic structure of the LPTG is given in Fig. 3.
The LPTG consists of 70 so called segments. Each segment is a small foil with a chain of thermocouples.These segments are electrical connected in series and the segment package is at the top and the bottom covered with ceramic plates with a good thermal conductivity.

The real prototype values of Figs. 4 and 5 show, that the power output is available in adequate quantities (ΔT=20 K, P_0=20 µW) to supply e. g. a digital temperature sensor modul or a digital time display as application models to demonstrate the function principle of first LPTG-prototypes.
A second fact we can conclude from Fig. 4. At the present there is still a considerable discrepancy between the power output of the real devices and the technological limit at the same temperature differences. The plot for the technological limit was calculated taking into account all unavoidable losses caused by the real properties of the used materials and assembly techniques. That means, in the frame of permanent improvement of the LPTG performance there is a realistic way to increase especially the power output of LPTG.

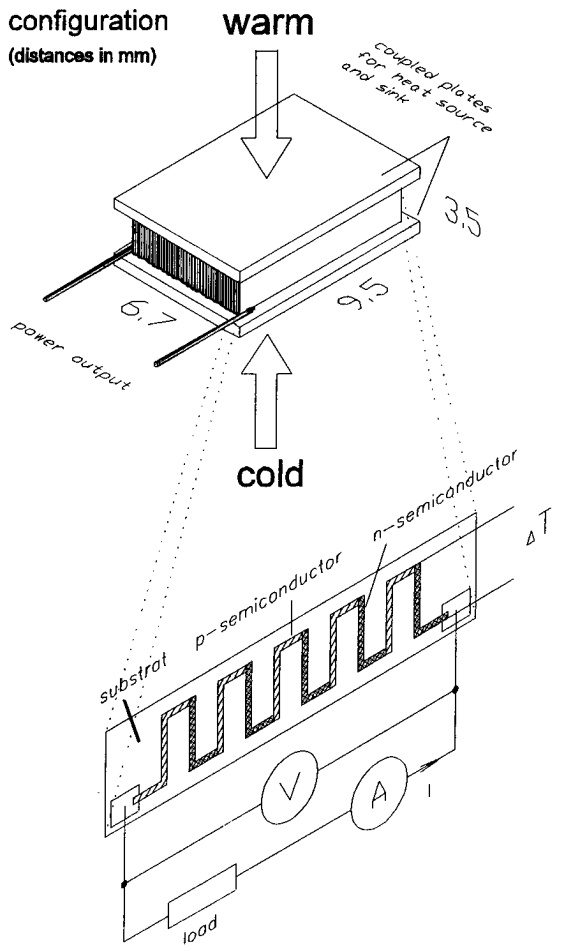


Fig. 3: LPTG-structure, schematically

LPTG-application aspects

Besides and in addition to the solar cells now the LPTG opens new possibilities to construct self-sufficient micro systems in the low power range by using the thermal energy.

Often it is necessary and at solar systems also usual to couple the LPTG with an electronic smart low power management. The management stores the electrical charge if the temperature difference is higher than necessary and supplies the micro system during the time, if the temperature difference is too small or even zero. In addition the LPTG output voltage has to be stabilized, because in many cases the temperature difference varies in the course of time. Furthermore features like over voltage protection and a switching of standby mode have to take into consideration.
For the LPTG there is a broad user spectra *as self-sufficient energy source* in the branches:

* *technique , technology* for e. g. temperature warning and registration systems,
  for charging system for small batteries or capacitances e. g. in hand held electronic devices
* *domestic appliances* e. g. for electronic heat cost allocators (simple models), for electronic temperature displays

* *automotive applications* for e. g. wireless controlling or sensor displays
* *consumer industry* e. g. for electronic wristwatches
* *medicine techniques* e. g. for temperature measurements

But in contrast to batteries for the adaption and optimization of the output energy the LPTG should be integrated in the

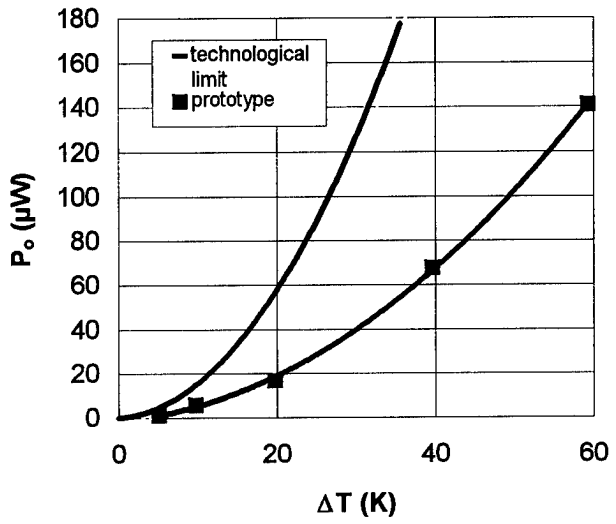


Fig. 4: Electrical power P_o in dependence on temperature difference ΔT

whole thermal and electrical design of the *complete* application, concerning also e. g. its geometrical sizes or the number of active thermocouples. Therefore for the conception of such systems it is always advantageously to consider both - application and LPTG - as an unit from the beginning. That saves money and time for the development.

In general the LPTG including its electronic smart low power management is able to supply self-sufficiently all sensor and micro systems, whose energy consumtion lie also in this low power range, a possible usage of thermal energy is provided.

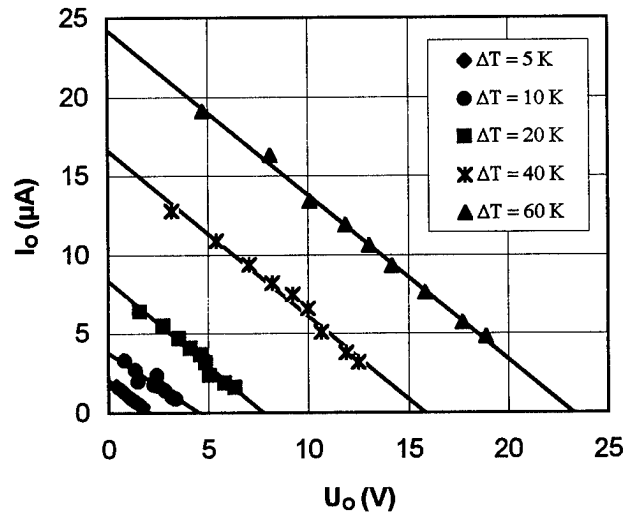


Fig. 5: Relationship between electrical voltage U_0 and current I_0 for different temperature differences ΔT

Conclusions

* Thin film thermoelectric generators are developed by D.T.S. as prototypes, manufactured with a technology which is full compatible with standard microelectronic technologies and suitable for process automatization.
* The low power thermoelectric generators have a power output of a few 10 µW and are able to supply self-sufficiently micro and sensor systems. For the realization of such systems a smart low power management is required.
* The increase of the output power is in the first line possible by an improvement of the present used technology, by decreasing the substrate thickness and by a raising of the film thickness, whereby for technological and economical reasons here seems to be a limit.
* Whereas in the present time it is not possible to supply such systems as micro mechanic pumps or turbines - their energy consumtion lies considerably higher than the LPTG can give - but in this field more and more applications will be generated in future.

References

/1/ J. H. Kiely, D. V. Morgan and D. M. Rowe: *The design and fabrication of a miniature thermoelectric generator using MOS processing techniques;* Meas. Sci. Technol. **8**, p. 182 (1994).

/2/ D. M. Rowe: *Miniature Semiconductor Thermoelectric Devices;* in: Handbook of Thermoelectrics (ed. D. M. Rowe), CRC Press, p.441 (1995).

/3/ M. Stordeur: *Valence Band Structure and the Thermoelectric Figure-of-Merit of $(Bi_{1-x}Sb_x)_2Te_3$ Crystals;* in: Handbook of Thermoelectrics (ed. D. M. Rowe), CRC Press, p. 239 (1995).

/4/ M. Stölzer, M. Stordeur and I. Stark: *Optimization of p-$(Bi_{0.25}Sb_{0.75})_2Te_3$ and n-$Bi_2(Te_{0.9}Se_{0.1})_3$ Films for Thermoelectric Thin Film Components;* in: Proceedings of 2nd Symposium on „Thermoelectrics - Materials, Processing Techniques and Applications", FAT, Dresden, p. 81 (1994).

/5/ M. Stölzer, M. Stordeur, and I. Stark: *Preparation of highly effective p-$Bi_{0.5}Sb_{1.5}Te_3$ and n-$Bi_2Te_{2.7}Se_{0.3}$ films;* in: Proceedings of XV ICT '96, Pasadena, p. 445 (1996).

/6/ Il-Ho Kim, Dong-Hi- Lee: *Preparation and properties of $(Bi,Sb)_2(Te,Se)_3$ Thin Film Thermoelectric Modules;* in: Proceedings of XII ICT '93, Yokohama, p. 328 (1993).

/7/ Il-Ho Kim, Dong-Hi- Lee: *Thin Film Thermoelectric Generator Cell of Bi-Sb-Te-Se System;* in: Proceedings of XV ICT '96, Pasadena, p. 425 (1996).

/ 8/ A. Mzerd, F. Tcheliebou, A. Sackada and A. Boyer: *Improvement of thermal sensor based on Bi_2Te_3, Sb_2Te_3 and $Bi_{0.1}Sb_{1.9}Te_3$;* Sensors and Actuators A 46-47, p. 387 (1995).

Thermoelectric and Heat-Transfer Properties in a New-Type Module Composed of Hamburger-Type Elements

Y. Tanji(1), Y.Nakagawa(2), S.Moriya(1), M.Niino(1), M.Yasuoka(2), R.Sato(3), Y.Tada(4).

(1) National Aerospace Laboratory, Kakuda, Japan, 981-15.
(2) Faculty of Engineering, Tohoku Institute of Technology, Sendai, Japan, 982.
(3) Faculty of Engineering, Tohoku Gakuin University, Tagajo, Japan, 985.
(4) Foundation for Promotion of Japanese Aerospace Technology, Sendai, Japan, 981-31.
Tel.: +81-224-68-3644; Fax: +81-224-68-2483, E-mail: tanji @ kakuda-slab-go.jp.

Abstract

We have proposed the use of hamburger-type thermoelectric elements for a new-type module assembled by screwing. In the present work, the new-type module is manufactured and tested. The thermoelectric materials used are quasi-single crystals of $(Bi,Sb)_2(Te,Se)_3$. The maximum electric power of the test module of 5.8 ×5.8 × 2.9 cm^3 in size at the temperature difference of 86 °C between end surfaces of thermoelectric material disks amounts to 1.14W with the current of 4.55A. The ratio of electrical contact resistance to the total resistance of thermoelectric material disks is unexpectedly large, caused by the unfit soldering between thermoelectric material disks and copper blocks composing the hamburger-type thermoelectric elements. The contact resistance between the metallic parts is reduced by spreading metallic paste composed of the two-phase structure of liquid InGa + solid Zn.

Introduction

Previously, the present authors have pointed out that conventional thermoelectric modules have a serious structural defect concerning thermal shear stress, and also have proposed the use of hamburger-type thermoelectric elements for a new-type module without the serious structural defect. The new-type module is assembled by screwing [1, 2, 3]. Generally, It is demanded simultaneously that both electrical and thermal contact resistances in the module are as small as possible, in addition to the prevention of thermal shear stress.
The purpose of the present work is to get technical data and know-hows necessary for designing and manufacturing the new-type module mentioned above.

Preparation of the new-type module

Thermoelectric element materials

Quasi-single crystal ingots of $(Bi,Sb)_2(Te,Se)_3$ of p and n types are prepared as the thermoelectric element materials, which are 10 cm in length and 1 cm in diameter. From the ingot, the 12 disks of p and n type materials are cut out, which are 0.3 cm in thickness and have a center hole of 0.32 cm in diameter. The manufacturing process of the quasi-single crystal ingots and test results of the thermoelectric properties were reported previously [3]. These properties are summarized in Table 1 .

Assembly of the new-type module

Fig. 1 shows the new-type module ; (a), (b), and (c) show a hamburger-type thermoelectric element, process of assembling, and top and side views of the module, respectively. The copper blocks and the thermoelectric

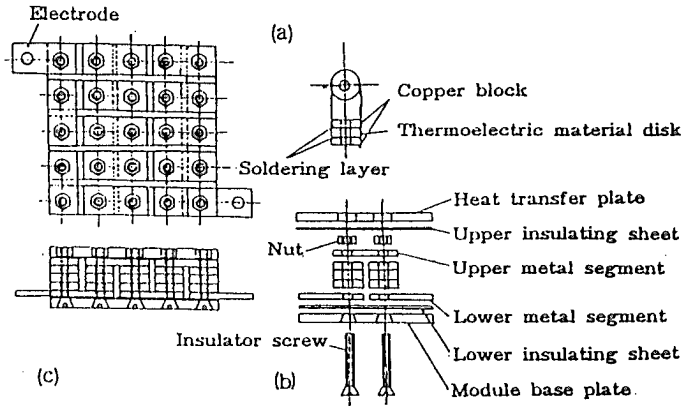


Fig. 1 The new-type module assembled by screwing using hamburger-type thermoelectric elements
(a) A hamburger-type thermoelectric elements
(b) Assembly of the module.
(c) Top and side views of the module.

material disk are soldered, the total length of the element being 0.9 cm. The module is assembled on a copper base-plate of 5.8×5.8 × 0.4 cm^3 having 25 holes of 0.4 cm in diameter, with two rubber insulating sheets of 5.8 ×5.8 ×0.01 cm^3, 24 hamburger-type thermoelectric elements, 24 metal segments of 1×2.2 × 0.2 cm^3 having two holes, two copper electrodes of 1×3.5×0.2 cm^3, a heat transfer plate of 5.8 ×5.8 ×

Table 1 Thermoelectric properties of quasi-single crystal disks of $(Bi,Te)_2(Te,Se)_3$ of p and n type used as thermoelectric elements

Physical properties / Specimens	$\rho \times 10^3$ Ω cm	$\alpha \times 10^6$ VK^{-1}	$\kappa \times 10^2$ $Wcm^{-1}K^{-1}$	$Z \times 10^3$ K^{-1}
$Bi_{0.5}Sb_{1.5}Te_{2.85}Se_{0.15}$ +0.15wt%Se (p-type)	1.37	233	1.29	3.14
$Bi_{1.8}Sb_{0.2}Te_{2.85}Se_{0.15}$ +0.09wt%$HgBr_2$ (n-type)	0.91	-241	2.00	3.19

0.4 cm^3 and 25 insulator screws of 0.3 cm in diameter. The new-type module has the π type structure, being connected electrically in series and thermally in parallel, similar to conventional modules. A concentration of shear stress due to thermal expansion, occurring near the contact planes between the metal segments and the thermoelectric elements, can be avoided by taking the screwing-structure. Ready-made insulator screws of strengthened synthetic resin are used for assembling the modules, which endure high temperatures up to 230 ℃. For reducing electrical contact resistances between the metal segments and hamburger-type thermoelectric elements, we have developed a metallic paste having the two-phase structure of liquid InGa + solid Zn. Although the eutectic point of InGa is 16.5 ℃, this paste is not completely molten up to about 200 ℃, being something like sherbet at room temperature.

Test results of the new-type module

Apparatus for test

Fig. 2 shows an apparatus for measuring heat transfer and thermoelectric properties of the test module, which is composed of two calorimeters, a heater block with a power supply, and an electronic load equipment. The test module is sandwiched between upper and lower calorimeters, each of which is composed of a nickel block and five thermocouples. The nickel block has five small holes for inserting CA-thermocouples in the side surfaces. The heat flow through the nickel block is estimated from the temperature distribution measured by these thermocouples and a digital thermometer with a changeover switch.

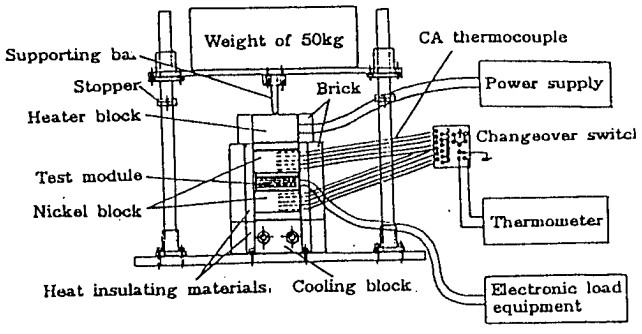


Fig. 2 Equipment for measuring heat transfer and thermoelectric properties of a thermoelectric module.

At the contact planes between the test module and the nickel blocks, silicon grease is spread to reduce the thermal contact resistance. Moreover, a constant weight of 50 kg is added on the heater block to keep the good thermal contact between the test module and the calorimeters. Surroundings of the calorimeters and the test module are enclosed with heat insulating materials and bricks. Thermoelectric properties are measured using an electronic load equipment FK-1000L of Takasago Co. Ltd. The electric power consumed by the load resistance R_L is measured as a function of R_L in the range of 0.007 to 2 Ω.

Heat flow through nickel blocks

Fig. 3 shows temperature distribution curves in the upper and lower nickel blocks when the heat source temperature is 150, 200 or 250 ℃ and the heat sink temperature is 17 ℃. The temperatures at the end surfaces of the nickel blocks are determined by linear extrapolation. In the case of a heat source temperature of 250 ℃, the upper and lower surface temperatures of the upper nickel block are 230 and 216 ℃, respectively, the difference being 14 ℃. The uniform heat flow through the nickel block is given by

$$Q = \kappa (S/L) \Delta T, \qquad (1)$$

where S is the cross sectional area, L the length, κ the thermal conductivity, and ΔT the temperature difference. In the case of the upper nickel block in the above example, $S = 42.3$ cm^2, $L = 2.45$ cm, $\Delta T =$ 14 ℃ and $\kappa = 0.73$ W $cm^{-1}K^{-1}$ at the average temperature of 223 ℃ [4], and thus the heat flow is calculated as $Q_H =$ 201 W. Similarly, the surface temperatures of the lower nickel block are 31 and 21 ℃ and $\Delta T = 10$ ℃. Since $\kappa = 0.90$ W $cm^{-1}K^{-1}$ at the average temperature of 26 ℃, the heat flow through the lower nickel block is $Q_L = 155$ W. The difference between Q_H and Q_L is mainly related to the Peltier and Joule heat in the thermoelectric elements, and also may be included heat leakage from the calorimeters and the test module.

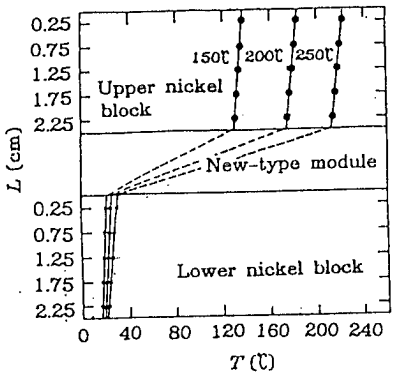


Fig. 3 Temperature distribution in the two nickel blocks at heat source temperature of 150, 200 or 250 ℃.

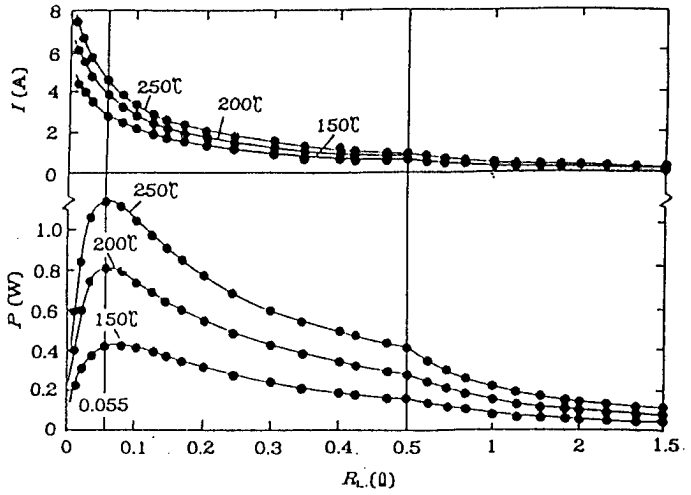


Fig. 4 The load resistance R_L dependences of electric power P and current I of the new-type e module at heat source temperature of 150, 200, or 250 ℃

Thermoelectric properties of the module

When a load resistance R_L is connected to electrodes of the module, the current I of the circuit is given by

$$I = \frac{E}{R_L + R_i} \qquad (2)$$

$$E = n\,\alpha\,\Delta\,\theta \quad \text{and} \quad R_i = r_E + r_M + r_C,$$

where E is the electromotive force and R_i is the internal resistance; n is the total number of thermoelectric elements, $\alpha = (|\alpha_p| + |\alpha_n|)/2$ is an average value of thermoelectric power of p and n type elements, and $\Delta\,\theta$ is temperature difference between the two ends of thermoelectric material disks; r_E, r_M and r_C are the resistance of thermoelectric material disks, the resistance of metallic parts, and the electrical contact resistance, respectively. The electric power P consumed by the load resistance R_L is given by

$$P = R_L I^2 = \frac{R_L E^2}{(R_L + R_2)} \qquad (3)$$

The P - R_L curve shows a maximum value when $R_L = R_i$. The maximum electric power P_{MAX} is given by

$$P_{MAX} = \frac{(n\,\alpha\,\Delta\,\theta)^2}{4R_i} \qquad (4)$$

Fig. 4 shows P- R_L and I- R_L curves of the module at heat-source temperatures of 150, 200 or 250 ℃. In the case of 250 ℃, P has a maximum values of 1.14 W at R_L = 0.055 Ω, where I = 4.55A. Thus we obtain R_i = 0.055 Ω.

Heat flow through the module

Temperature difference $\Delta\,\theta$ between the two ends of thermoelectric material disks can be estimated by Eq. (4) using P_{MAX} = 1.14W, R_i = 0.055 Ω, n = 24 and α =2.37 ×10^{-4} V ℃$^{-1}$, and so $\Delta\,\theta$ = 86 ℃. The total heat flow Q_E through the thermoelectric material disks can be estimated by Eq. (1) using κ =0.0165 Wcm^{-1} ℃$^{-1}$, S = 16.9 cm^2, L = 0.3 cm and $\Delta\,T$ = 86 ℃, as Q_E = 80 W. This value is fairly small in comparison with the heat flows through the nickel blocks (Q_H = 201 W ; Q_L = 155 W) .

Discussion

We have measured the heat flows Q_H and Q_L through the nickel blocks and compared them with the heat flow Q_E through the thermoelectric material disks calculated by using the value of $\Delta\,\theta$, which is estimated from the load resistance and the maximum electric power P_{MAX} of the test module. However, there are large differences among these values, which are related to the Peltier and Joule heat in the thermoelectric elements, and also to the heat leakage through the heat insulating materials and air convection.

The heat flow Q_S through the insulating screws can be easily calculated by Eq.(1) using κ =0.007 Wcm^{-1} ℃$^{-1}$, S =1.18 cm^2, L = 2.3 cm and $\Delta\,T$ = 184 ℃, as Q_S = 0.16W. This value is much smaller than Q_E.

To improve both the generating power and the energy conversion efficiency of the module, we have to reduce the thermal contact resistance between the module parts, and to get $\Delta\,\theta$ as large as possible at a given heat source temperature.

Next, let us consider the electrical contact resistance in the test module. We should note that the electrical contact resistance is important, especially in the case where very thin thermoelectric material disks are used.

The resistances of thermoelectric material disks and metallic parts in the present test module are estimated as $r_E = 1.2 \times 10^{-2}\ \Omega$, and $r_M = 1 \times 10^{-4}\ \Omega$, respectively. Since $R_i = 0.055\ \Omega$, the electrical contact resistance is estimated as $r_c = 4.3 \times 10^{-2}\ \Omega$, so r_c/r_E amounts to 3.6. This value is too large in comparison with that of the HZ-14 module of Hi-Z Technology Inc, which we also tested using the same equipment. We obtained r_c/r_E = 0.2 for the HZ-14 module on the same condition.

We have found a few of the hamburger-type thermoelectric elements in the test module show abnormally large values of electrical resistance, especially in the p type elements. This is considered to be caused by the unfit soldering between the thermoelectric material disks and the copper blocks. If the contact surfaces of the thermoelectric material disks would be plated by nickel in advance before the soldering in the present work, these resistances might be remarkably reduced. Other contact resistances between the metallic parts are also important in the new-type module assembled by screwing. We have confirmed that these contact resistances are sufficiently small by using the metallic paste of InGaZn mentioned above. Therefore, if the soldering of the elements is improved and the value of r_c/r_E of the new-type module is reduced down to 0.2, the maximum electric power may amount to more than 10 W at $\Delta\theta = 150$ ℃.

Conclusions

The maximum generating power of the test module at $\Delta\theta = 86$ ℃ amounts to 1.14W with the current of 4.55A. The ratio of electrical contact resistance to the total resistance of thermoelectric material disks amounts to 3.6, being unexpectedly large. This is caused by the unfit soldering between thermoelectric material disks and copper blocks composing the hamburger-type thermoelectric elements. If the contact surfaces of the thermoelectric material disks would be plated by nickel in advance before the soldering, we might be able to prevent the unfit soldering. The electrical contact resistances between the metallic parts are sufficiently small by spreading metallic paste composed of the two-phase structure of liquid InGa + solid Zn. If the soldering is improved, we can expect that the new-type module will generate more than 10 W at $\Delta\theta = 150$ ℃.

Acknowledgements

The present work is supported by the special coordination funds for promoting science and technology and other systems of the Science and Technology Agency of Japan. The present authors wish to express thanks to Mr. T. Ohshima of the National Aerospace Laboratory for his helpful advice for the measurement of heat transfer properties, and to Messrs. A. Yoshinari and H. Bansho of Tohoku Institute of Technology for the experiments on thermoelectric properties.

References

[1] Y Tanji et al.: Proceedings 12th ITC (1993, Yokohama) , 452-457.

[2] Y. Tanji et al. : Proceedings 13th ITC (1994, Kansas City), 332-338 .

[3] Y. Tanji et al. : Proceedings 14 the ICT (1995, Petersburg)140-144.

[4] Ed. Y.S.Toutoukian et al.: The TPPCD DATA Series, Thermoelectrical Properties of Matter. Vol. 1, Thermal Conductivity Metallic Elements and Alloys (IFI / PLENUM, New York,).1970).

GRID-INDEPENDENT POWER SUPPLY FOR REPEATERS IN MOBILE RADIO NETWORKS USING PHOTOVOLTAIC/THERMOELECTRIC HYBRID SYSTEMS

W. Roth, R. Kügele, A. Steinhüser, W. Schulz, G. Hille
Fraunhofer Institute for Solar Energy Systems ISE
Oltmannsstr. 5, D-79100 Freiburg, Germany
Tel. +49 (0) 761/4588-227, Fax. +49 (0) 761/4588-217
e-mail: roth@ise.fhg.de

Abstract

At Fraunhofer ISE, a photovoltaic/thermoelectric hybrid system has been developed as a power supply for repeaters (e.g. mobile telephone repeaters) and integrated into a newly constructed repeater station. A modified thermoelectric generator from the Canadian Global Thermoelectric company has been used as the auxiliary generator. A microprocessor-controlled energy management system (EMS) allows fully automatic operation with minimal use of fossil fuels and appropriate battery operation management.

As the auxiliary power supply can support the PV generator in supplying power to the load during periods with little sunlight, a very reliable power supply is achieved. Further, the dimensions of the PV generator and the battery capacity can be reduced without affecting the supply reliability. In Central Europe, for instance, the size of the PV generator can be reduced to a third of that needed for an exclusively PV system, if only 10 % of the annual demand is met by the auxiliary generator. This allows a compact construction of the photovoltaic hybrid system and helps the numerous requirements on isolated telecommunications facilities to be fulfilled.

Introduction

Repeaters are digital radio signal amplifiers, which increase the connection reliability of mobile telephones within radio cells and raise the accessibility level throughout the network. They receive the conversations, which have been converted to digital data, by radio, process them and transmit them on to a base station, also by radio. In rural areas and in mountainous regions, repeaters often have to be installed and operated at sites remote from the public electricity grid. The power supply for repeaters should be reliable and free of maintenance.

If a public electricity grid is not available to supply the repeaters, or if other reasons such as high connection costs, long waiting times or the need for local flexibility speak for a grid-independent supply, an autonomous electric power supply system must be constructed. To date, such stand-alone power supplies have mainly been based on fossil-fuelled motors coupled to generators. Apart from the consumption of limited fossil fuel reserves, the disadvantages of these systems include the creation of noise and exhaust gases, the constant need to obtain fuel and the high amount of maintenance, particularly for continuous operation. For these reasons, and due to the progress made in recent years on regenerative energy conversion, photovoltaic generators are being used increasingly often. Because of the seasonal fluctuations in solar radiation, an exclusively photovoltaic power supply leads to very large and thus expensive systems in the temperate zones. In order to avoid these disadvantages, the photovoltaic generator is usually combined with other power generators.

Within the research project on "Products with integrated photovoltaic power supply", supported by the German Federal Ministry for Education, Science, Research and Technology (BMBF), potential auxiliary generators were investigated at Fraunhofer ISE, and a photovoltaic hybrid system as a stand-alone power supply for repeaters in mobile telephone networks was designed and constructed (fig. 1).

Potential auxiliary generators for small photovoltaic hybrid systems

In general, diesel generators are used today in larger photovoltaic hybrid systems with an energy demand of around 10 kWh/day. For systems with a daily energy demand of a few hundred Wh up to a few kWh, small combustion motors, small fuel cells, thermoelectric generators (TEG), thermophotovoltaic generators (TPV) or appropriate thermodynamic converters such as small Stirling motors all come into question in principle. If adequate commercial availability is also required, at present the choice is narrowed essentially to small combustion motors (diesel, petrol) with a coupled generator, and thermoelectric generators. High reliability, almost silent operation and simple remote starts all speak for the application of thermoelectric generators in small PV hybrid systems.

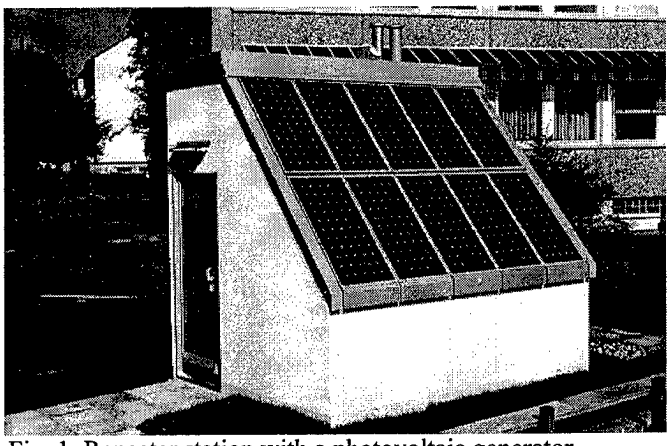


Fig. 1: Repeater station with a photovoltaic generator.

Configuration of the photovoltaic/thermoelectric hybrid system

Computer simulations made at Fraunhofer ISE have shown that in Central Europe, the size of the PV generator can be reduced to a third of that needed for an exclusively PV system, if only 10% of the annual demand is met by the auxiliary generator [1]. Further, the overall system reliability is higher for a hybrid system, as the redundancy means that if one energy supply breaks down, the load can be supplied temporarily by the other alone. The following diagram (fig. 2) illustrates the basic configuration of a repeater station.

The photovoltaic hybrid system consists of two solar generator arrays of different size, with a total power of 1100 W. The battery has a capacity of 480 Ah/12 V. The typical power drawn by a solar mobile telephone repeater is simulated by a permanent load of 50 W in the experimental system.

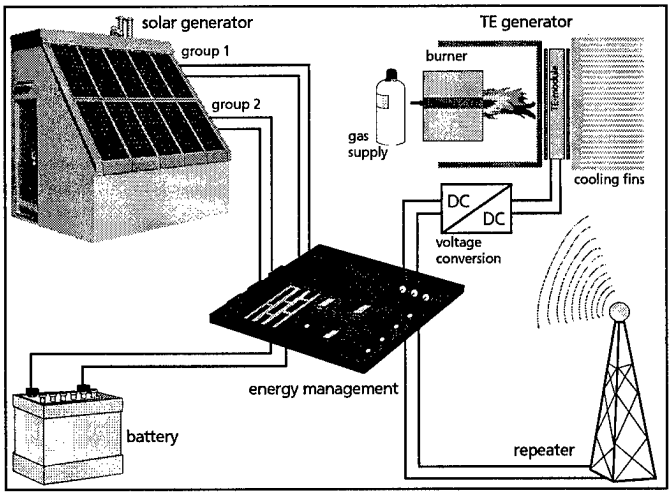


Fig. 2: Basic configuration of the energy supply for a repeater station.

A modified thermoelectric generator from the Canadian company, Global Thermoelectric, model 5120 (120 W), is used as the auxiliary generator (fig. 3).

A micro-controlled energy management system (EMS), newly developed at Fraunhofer ISE, ensures fully automatic operation with minimal consumption of fossil fuel and appropriate battery operation management.

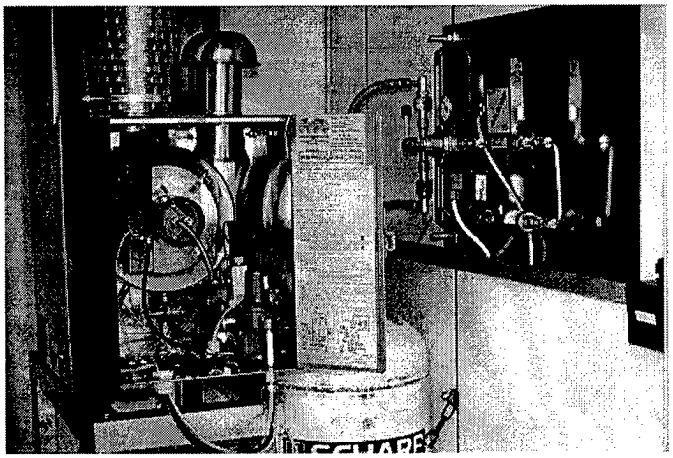


Fig. 3: Thermoelectric generator.

The energy management system with state-of-charge determination

The EMS is based on the electricity-saving micro-controller, H8/337 from Hitachi. It has a very low power consumption of less than 40 mW. The EMS is divided into a micro-controller and a power unit (fig. 4). This means that it can be adapted flexibly to different power requirements. In addition, it has a convenient operating system, with which the user can call up the system state onto the LC display with various menus. The system can also be simply configured and parametrised via the user interface. The EMS is thus open for many customer-specific settings. Further, care was taken to use standard components such as the I^2C bus and to develop the software in the high-level language C.

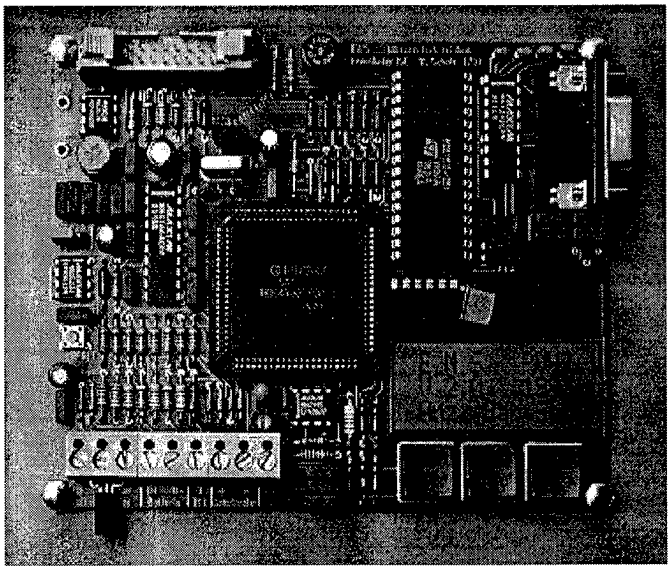


Fig. 4: Micro-controller unit of the EMS.

The central decision quantity for the energy management is the state of charge of the battery. It is determined with an adaptive state-of-charge method developed at Fraunhofer ISE. This is based on a current balance, which is recalibrated when the fully charged state of the battery is recognised. The recalibration is necessary, as errors in the current measurement and balance can occur over longer periods and allow the value of the state of charge to drift. During recalibration, the state of charge is reset to 100% and the loss current for the battery is recalculated. The fully charged state is recognised when first the battery voltage exceeds the equilibrium voltage for a long period, second the battery current is within the range of the loss current and third the change of the battery current with time is almost zero.

To control the battery, the EMS includes deep discharge protection and a guard against overcharging, which is independent of the state-of-charge determination. The solar generators can be controlled by the EMS in groups and sequentially. The decision to switch the load or the TEG on or off depends on the battery's state of charge.

Repeater station construction

The housing of the repeater station was completely reconstructed, to take account of the specific requirements on unmanned telecommunications facilities, remote from the grid. The repeater station is practically impregnable to burglars and vandals. Protection is achieved by use of a monolithic concrete building component and installation of burglar-proof doors. The solar modules are protected against theft by installation with a special substructure on a continuous concrete slab (fig. 5).

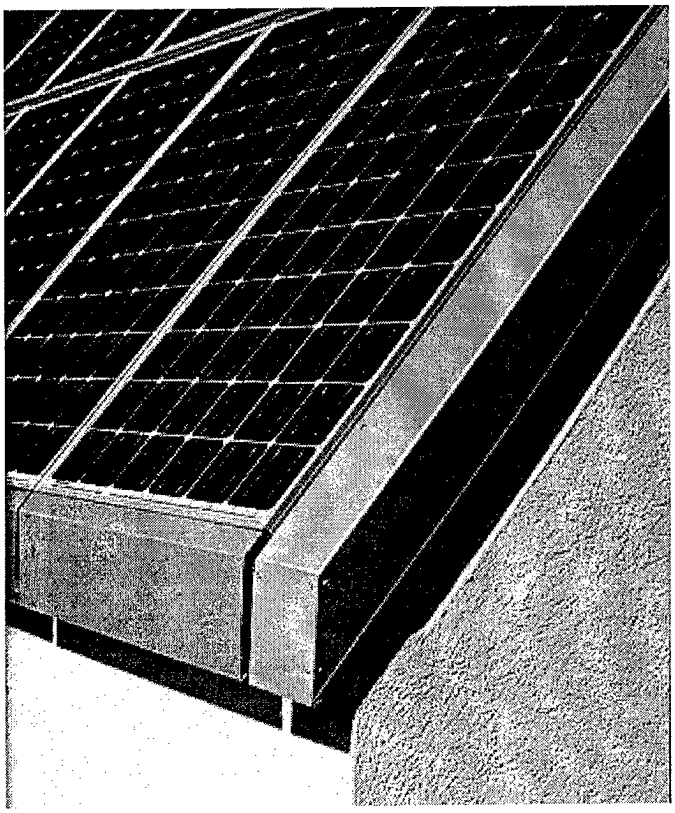


Fig. 5: Integration of the solar generator into the roof of the repeater station.

As the solar generator is tilted at 50°, dust, leaves and in particular snow can slide off the modules very easily. This ensures that the photovoltaic system will operate reliably in winter also, without serious losses due to shading.

Economic viability of the photovoltaic/thermoelectric hybrid system

The economics of the photovoltaic/thermoelectric hybrid system (770 W_{peak} solar generator; 5,8 kWh industrial battery; 120 W TEG; 50 W permanent output) has been analysed. The most important economic parameters are listed in table I:

In a first step, the sensitivity of the most cost relevant parameters are calculated based on the annuity method.

7.23 DM/kWh in the reference case is within the range of costs for autonomous power supplies. 23% of the annual costs are related to staff for operation and maintenance (O&M). Although TEG's are very reliable, most of the annual costs are spent on O&M. The largest cost reduction can be achieved by reducing the TEG as much as possible, here its annual cost share is 22%.

Battery investment as well as installation represent considerable factors in the investment costs. A reduction of 50% for one of them would reduce the levellised electricity costs by 9%.

The reduction of the lifetime of the stationary industrial batteries (reference: 8 years) will increase the levellised electricity costs appreciably. As the share of renewables is high in the total electricity production, two factors are of almost no significance for the total costs: the fuel price and the TEG efficiency.

	Costs investment maintenance fuel	**Depreciation time**	**Efficiency**
PV*	8.5 DM/W_p	20 a	14%
TEG	79.2 DM/W	20 a	3%
Gasoline generator	1.1 DM/W	10000 h	7%
Battery	460 DM/kWh	8 a	
EMS	1000 DM	15 a	
Charge controller	1 DM/W	15 a	
Maintenance	2% of the investment, at least 1 working day		
LPG	2.11 DM/kg in bottles 1 DM/kg refilling storage tank		
Gasoline	1.60 DM/l		

Tab. I: Economic parameters of the hybrid system and its alternatives. *(+15% support structure)

The crucial financial parameter is the real interest rate: doubling the rate from 4 to 8% means an increase in the levellised electricity costs of 22%.

In a second step the reference hybrid systems has been compared with all alternative power supplies. These are:

- an autonomous PV-battery system (0.77 kW_p; 4.8 kWh stationary industrial battery) for tropical climatic conditions
- an autonomous PV-battery system (2.3 kW_p; 12 kWh stationary industrial battery) for temperate zones
- one 120 W TEG generator
- one 120 W TEG with a 5.8 kWh battery
- one 2 kVA gasoline generator
- one 2 kVA gasoline generator with a 5.8 kWh battery
- one 2 kVA gasoline generator with a 5.8 kWh battery and 750 W_p PV
- one 3 kVA diesel generator

The following figure 6 shows the cost comparison based on the annuity method with a 4% real interest rate. The pure fossil-fuelled generator systems (gasoline, diesel) have not been included in the figure due to their enormous O&M costs, as the engines must be overhauled every 250 or 500 operation hours, respectively. These options are of relevance, if much more electricity is consumed.

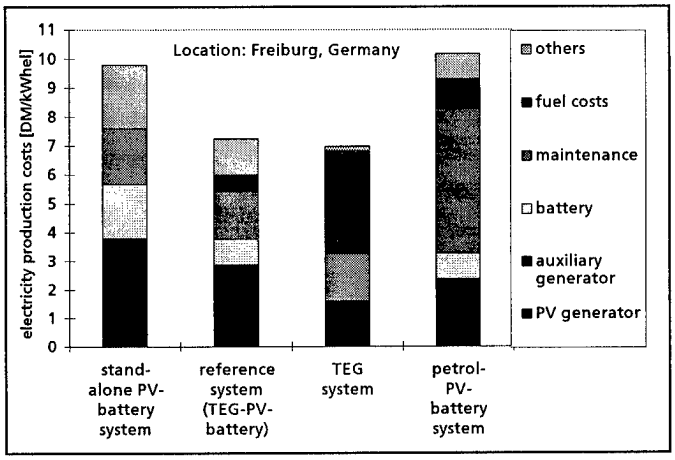


Fig. 6: Cost comparison of the reference case with its supply alternatives in temperate zones.

An autonomous PV-battery system is more expensive in temperate zones but the least cost option in tropical areas, as both the PV generator and the battery can be dimensioned smaller.

The reference TEG-PV-battery hybrid system and a pure TEG system are the cheapest alternatives. Low interest rates, cheap batteries, a further cost reduction of PV or LPG prices above 1 DM/kg makes the reference system the least cost alternative.

Moreover, the hybrid system with TEG and PV guarantees a lower loss-of-load probability and saves 2.4 t of CO_2 annually. This means that the annual CO_2 avoidance costs are 47 DM/t CO_2 which is cheap compared to other CO_2 reducing technologies for grid connected power supply.

In a third step the cost parameters of all system configurations listed above have been varied. The following conclusions can be drawn:

An autonomous PV-battery system is always the cheapest solution for this small load, if the site is located in tropical areas. Higher interest rates, typical for developing countries, improves the cost competitiveness of low investment alternatives. The operation in low income countries makes pure fossil-fuelled generator systems also attractive, if the regular maintenance checks can be guaranteed. The cost reduction of PV influences the ranking of all systems. If world market prices drop below 4 DM/W_p, autonomous PV-battery systems are cheaper than pure TEG systems. TEG are considered as very reliable, therefore they are the only fossil-fuelled alternative in this small power size.

Summary and outlook

The photovoltaic hybrid system presented is a very reliable and economically attractive power supply for grid-independent repeaters in mobile radio telephone networks.

Extensive investigations and measurements have shown that there is still considerable potential for optimisation, particularly concerning the gas burner and the connection of the thermoelectric modules to the heat source. For example, the total efficiency value and, in particular, the exhaust emission of the thermoelectric converter can be improved by using a large-area burner or a catalytic burner [2].

Due to the flexible configuration of the construction and the custom-programmable control, the system can also be used as the power supply for other facilities remote from the grid, such as environmental measurement stations, aviation safety equipment and traffic guiding systems.

The economics of the demonstration plant has been investigated in details.

A sensitivity analysis of all cost relevant parameters of the reference hybrid system shows that the TEG size needs to be reduced as much as possible.

In a second step the reference system has been compared with all relevant supply alternatives. The autonomous PV battery system is always the cheapest solution for this small load, if the site is located in tropical areas, but not in temperate zones. The fossil-fuelled generators (gasoline, diesel) are too expensive due to their enormous O&M costs.

It is proved that the hybrid system designed and operated by the Fraunhofer ISE is cost competitive with pure TEG generator systems. Moreover, the hybrid system guarantees higher reliability and avoids 2.4 t of CO_2 annually. Last but not least the use of PV means a positive and cheap public relation effort for any telecommunication operator.

Acknowledgement

The major part of this work was supported by the German Federal Ministry for Education, Science, Research and Technology (BMBF).

References

[1] R. Kügele, W. Roth, W. Schulz, A. Steinhüser, Thermoelectric Generators in Photovoltaic Hybrid Systems, Proceedings 15th International Conference on Thermoelectrics ICT '96, Pasadena, California, USA, March 26.-29.1996, Page 352-356

[2] W. Roth, J. Schilz, A. Steinhüser, Thermoelectric Generators as Auxiliary Electricity Generators, Research Association for Solar Energy, Proceedings Annual Conference '96, Kassel, Germany, September 04.-05.1996, Page 77-83

Thermal Generators for Waste Heat Utilization

Anatychuk L.I., Rozver Yu.Yu., Misawa K., Suzuki N.

Institute of Thermoelectricity, General Post-Office, Box 86, 274000, Chernivtsi, Ukraine
Tel:+380/3722/44422, Fax:+380/3722/41917, E-mail:Alex@ite.Chernovtsy.ua, WWW: http:\\www.ite.Chernovtsy.ua

Abstract

Technical and economical analysis of thermoelectric generators use for heat wastes from heat machines and industrial heat wastes utilization have been given. Generators' technical and economical data resulting from this analysis have been presented. Block concept of 100-200W generators development has been described. Development and test results of a 500W and 1kW generator blockshave been given.

The essence of the problem

The work of heat engines is accompanied by the release of a considerable amount of thermal energy. Diesel engines release as waste heat up to 55%, carburetor engines - up to 70%, gas-turbine plants - up to 65% of thermal energy spent on their operation. This is an enormous amount of waste heat, therefore its subsequent utilization for the electrical energy production is of great interest.

However, waste heat is a low-grade heat with temperature about 200-400°C. For such low temperatures the machine methods of thermal-into-electrical energy conversion are inefficient. Therefore, despite its comparatively low efficiency, thermoelectric method may become rational for this low-grade heat utilization. Really, the up-to-date thermoelectricity level allows to create thermogenerators with the efficiency about 5-6% at the hot temperature 250-300°C; 8-10% at the hot temperature 400÷500°C and 12-15% at the hot temperature about 600÷800°C.

Such generators can be used for the creation of additional low-temperature cascade in a heat engine. This device is schematically shown in Fig.1. It is seen from the figure that about 30% of the total fuel combustion thermal energy is converted to mechanical energy by the engine. The rest 70% is partially withdrawn for the engine cooling (about 20%) and about 50% is carried away by the spent gases. The utilization of thermal energy of spent gases by using thermogenerator with the efficiency of about 10% allows to obtain up to 5% of electrical energy in addition to the total

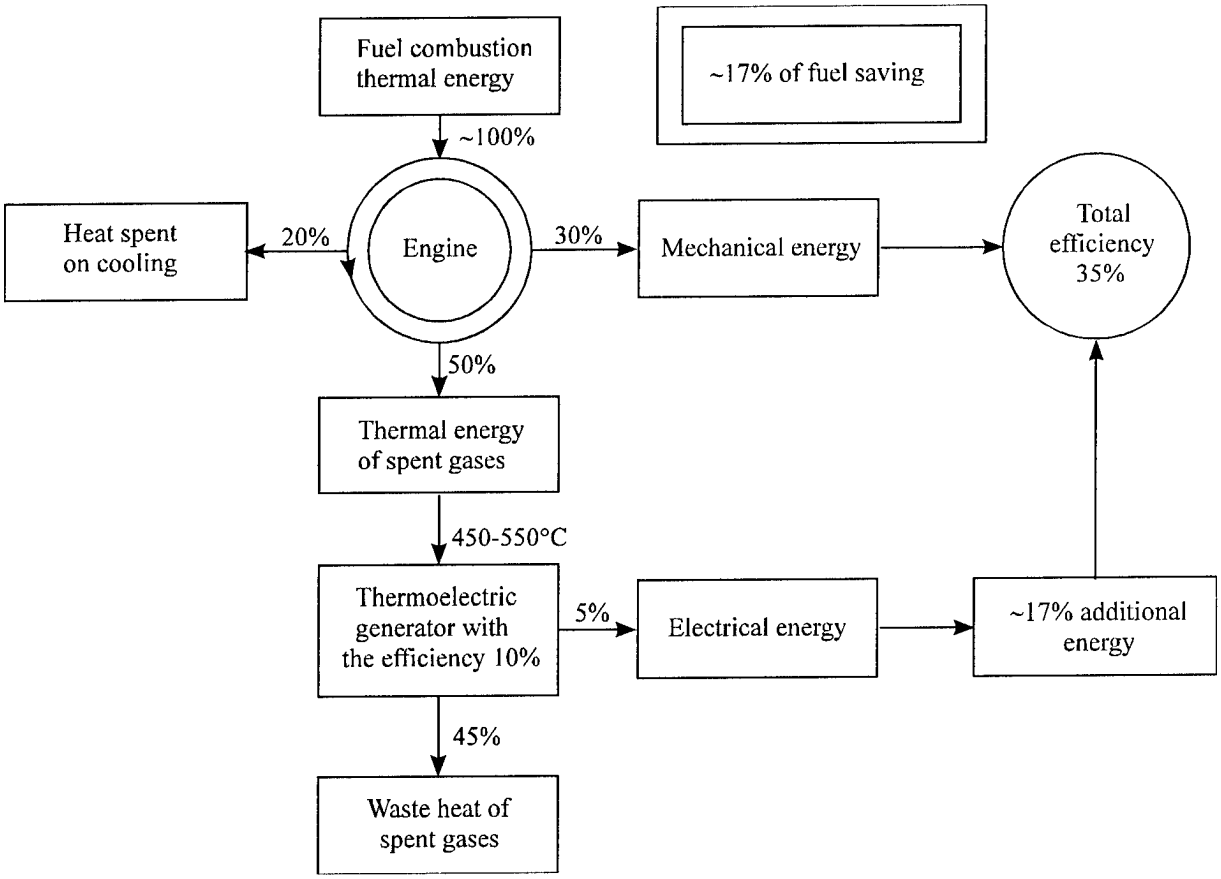


Fig.1. Diagram of low-temperature thermoelectric cascade of heat engines

energy of fuel combustion. This adds about 17% to the mechanical energy of the engine or provides up to 17% of fuel saving. These estimates are encouraging, however, one must take into account that technical-and-economic indexes of thermogenerators are no less important for their use.

The basic technical-and-economic indexes include the cost of mounting and service life of generators, or, in other words, their reliability. The analysis shows that economical expediency is present when the cost of thermogenerator mounting is 1-3 $/W with the service life 10-15 years. Under these conditions the mounting expenses may pay back in 3-5 years and bring profit in future. These conditions form an exceptionally complicated problem in thermoelectricity, namely, creation of thermogenerators that are superreliable and cheap at the same time. In the Institute of Thermoelectricity these investigations are being conducted in several directions: creation of *Bi-Te*-based thermoelectric material of increased efficiency using suitable optimization and material with programmed inhomogeneity; creation of superreliable thermoelectric modules; development of the reliability theory of thermoelectric devices which allows to develop the accelerated test methods and design thermoelectric modules and generators of increased reliability. The information on these investigations is given in Ref.[1, 2. 3].

Based on them, the Institute of Thermoelectricity, the "Altec" company (Ukraine) and the "Fudzitaka" company (Japan) are developing general-purpose thermoelectric generators for the utilization of low-grade heat. The generators use a block concept of power build-up. The primary block is a construction consisting of 8 modules with special liquid heat-exchangers [4]. Five blocks form a section which is a changeable component in the thermogenerator. Four blocks form a primary block thermogenerator with the electric power 500-800 W. Heat from the heat source is supplied to the generators by means of silicon liquids and corresponding heat exchangers at points of waste heat release. Heat withdrawal from the generators is provided by the running water. The parameters of a typical generator design with the power 500-800W are listed in Table 1. The data in the table correspond to parallel connection of primary blocks in the cold and hot liquid circuits and series connection of modules. However, depending on the requirements of consumers, there is a large range of other connections for convenient generator matching both in the liquid and electrical circuits.

These generators are used to form thermoelectric power plants of necessary power by their corresponding connection in the thermal and electrical circuits. The block design of these power plants seems preferable, since various consumers have different heat release values, as well as their specific requirements to the current and voltage values. This type of generator has been developed for the creation of thermoelectric power plant with the power 200 kW. However, these generators can be used practically in any area of human activity where there is waste heat. Investigations are carried out to reduce mass-dimensional characteristics, increase reliability parameters and reduce cost.

Table 1. Parameters of thermoelectric generator Altec-1017

		Mode 1	Mode 2	Mode 3
1	Hot input liquid temperature, °C	200	250	250
2	Hot output liquid temperature, °C	160	200	220
3	Hot liquid flow rate, ml/s	225	180	300
4	Hot input liquid pressure, M/Pa	0.34	0.22	0.61
5	Hot output liquid pressure, M/Pa	0.01	0.01	0.01
6	Cold input liquid temperature, °C	50	50	20
7	Cold output liquid temperature, °C	80	80	40
8	Cold liquid flow rate, ml/s	100	100	150
9	Cold input liquid pressure, M/Pa	0.12	0.12	0.12
10	Cold output liquid pressure, M/Pa	0.015	0.015	0.015
11	Electrical voltage, V	50	55	60.9
12	Electrical current, A	10	11	11.5
13	Electrical power, W	500	600	700
14	Efficiency, %	3.7	4.6	5.5
15	Number of permissible "on-off" cycles	10000	10000	10000
16	Service life, h	90000	90000	90000
17	Permissible short-time overheats in the hot part, °C	400	400	400
18	Permissible short-time overheats in the cold parts, °C	150	150	150
19	Dimensions, cm^3	11880	11880	11880
20	Weight, kg	14	14	14

References

[1] Anatychuk L.I., Vikhor L.N. Computer design of thermoelectric functionally graded materials, in Proc. of the IVth Int. Symposium on FGM, Tsukuba, Japan, Oct. 21-24, 1996.

[2] Anatychuk L.I., Razinkov V.V., Rozver Yu. Yu., Mikhailovsky V.Ya. Thermoelectric Generator Modules and Blocks. Report on ICT'97.

[3] Anatychuk L.I., Luste O.J. Relibility theory in thermoelectricity, in Proc. ICT'96, Pasadena, CA USA, p. 243-247

[4] Anatychuk L.I., Luste O.J. The effective thermoconductivity of the plate with the cylindrical opening calculation. J. of Thermoelectricity, N2, Oct., 1994.

Functionally Graded Materials and New Prospects for Thermoelectricity Use

Anatychuk L.I., Vikhor L.N.

Institute of Thermoelectricity, General Post-Office, Box 86, 274000, Chernivtsi, Ukraine
Tel.: +380/3722/44422, Fax:+380/3722/41917, E-mail:Alex@ite.Chernovtsy.ua, WWW: http:\\www.ite.Chernovtsy.ua

Abstract

Investigation results of state of the art and prospects of the theory, technology and practical use of thermoelectric FGM development have been presented. Computer technologies for the optimal predicted inhomogeneities determination have been considered. Data on the limiting possibilities of thermoelectric conversion efficiency improvement by means of FGM use as well as the data on the FGM technologies have been given. New possibilities of thermoelectric use have been considered.

Introduction

Achievements in thermoelectricity during the recent 30-40 years are first of all due to the progress in the creation of a thermoelectric material with high figure of merit values $z = \frac{\alpha^2 \sigma}{\kappa}$. The maximum figure of merit is achieved by way of material optimization. To reach the maximum of Z, one must find the optimal concentration from the extremum condition

$$\frac{dZ}{d(N_e, N_p)} = 0 \qquad (1)$$

Thus, the result of optimization is a number, namely the value of the optimal concentration of donor N_e or acceptor impurities N_p. Naturally, the theory cannot indicate the exact figure of doping impurity concentration. Therefore the optimal concentration is experimentally determined by way of creating materials with different impurity concentrations and determination of their Z.

This method served as the basis for highly efficient thermoelectric material technologies and guaranteed the progress of thermoelectricity on the whole.

However, by the present time these ways of improving the thermoelectric figure of merit have practically exhausted themselves. Despite the numerous efforts, the increase in the figure of merit is insignificant.

At present one of the most challenging trends of increasing the efficiency of thermoelectric materials is the transition from a classical thermopile model where legs are made of the homogeneous material, to the thermopiles where legs are made of materials whose properties are coordinate functions.

A large series of investigations on the use of the inhomogeneus materials in cooling batteries has been conducted in Ukraine. A theore of computer-aided design of materials with a programmable inhomogeneity has been developed. Fig. 1 shows an example of the optimal inhomogeneity functions for the materials based on *Bi-Te*.

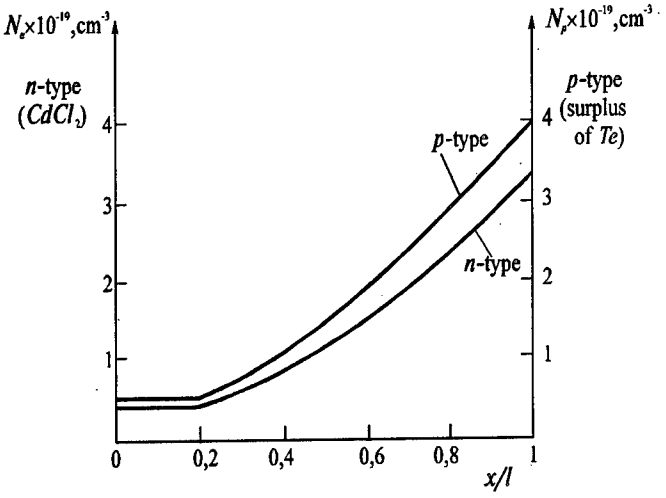


Fig.1. Optimal functions of thermoelectric material inhomogeneity: n-type $Bi_2Te_{2.7}Se_{0.3}$ + (0,09 ... 0,03)$CdCl_2$; p-type $Bi_{0.5}Sb_{1.5}Te_3$ + 4% Te

These investigations have been described in the monograph [1].

Technologies have been developed for obtaining these materials by pressing, extrusion, zone melting and Czochralski methods. These technologies are shown schematically in Fig. 2.

The process of the inhomogeneous material production from powder by pressing is shown in Fig.2A. The layers with

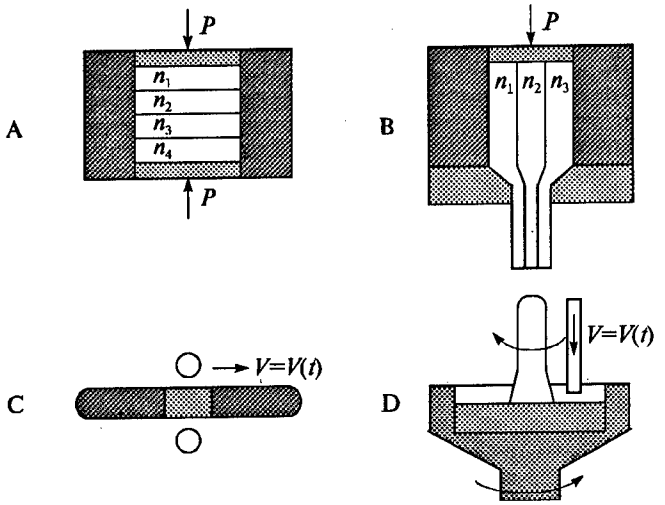


Fig.2. Technological schemes of thermoelectric material production with programmable inhomogeneity.
A - by pressing; B - by extrusion; C - by zone melting;
D - by Czochralski method.

different impurity concentrations are placed into pressing container. The step function of concentration is smoothed out by a high-temperature firing. Fig. 2B shows the technology of obtaining programmable inhomogeneity by extrusion method. Materials with the desired concentration are placed into extrusion container. After the extrusion the rods are also subjected to a high-temperature annealing. The inhomogeneous material production by zone melting method with changing the speed of melted zone motion is shown in Fig.2C, while Czochralski method of production is shown in Fig.2D. Inhomogeneity here is formed by changing the speed of the melt-replenishing rod used for material doping.

These materials have been used for the manufacturing of thermopiles whose properties are shown in Fig. 3.

It is seen from the figure that when materials with programmable inhomogeneity are used, the maximum temperature drop in cooling thermopiles increases from 70 to 90 degrees, i.e. by 25%, and the coefficient of performance can increase several times. To reach such parameters with the homogeneous materials, one must create a material with a thermoelectric figure of merit Z=4,5·10^{-3} K^{-1} which for the moment is impossible. This example shows that the use of thermoelectric materials with programmable inhomogeneity is a new efficient trend of improving the quality of thermoelectric devices.

Materials with programmable inhomogeneity can be also used to improve the efficiency of a generator. The generally accepted name for these materials in Japan is functionally graded materials. In conformity with the paper [2], FGM is defined as the envelope by the maximums of Z at various temperatures and, accordingly, at various concentrations. Equivalently, for wider temperature ranges FGM is formed as the envelope by the maximums of Z for various materials suitable for each temperature level.

In reality, to design FGM, use must be made of more accurate, hence more complicated methods. Let us consider them in more detail. The purpose of material design is to determine the distribution of impurity concentration along the leg where at the given temperature of hot and cold sides T_h and T_c the maximum efficiency or maximum power is reached. Thus, we have a basically new approach to the optimization of thermoelectric material. Really, if before optimization served the purpose of number, today it results in the optimal function of impurity concentration as coordinate function. To determine this optimal function is a complicated task.

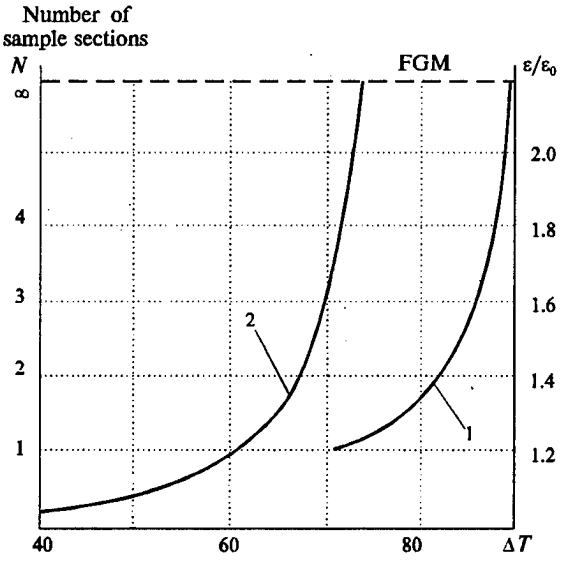


Fig.3. 1 - the increase in ΔT_{max} with approximation to the optimal function; 2 - the increase in the coefficient of performance ε for the optimal inhomogeneity; ε_0 is coefficient of performance of the homogeneous leg

Problem solution

Fig.4 gives a physical model for the construction of a computer-made FGM design. This model includes an inhomogeneous leg of n- and p-type of conduction, connected to electric and thermal circuits, external optimal electric load R_{opt} where electric power W is released. In the calculations one must take into account Joule heat release in the bulk of the leg, heat transfer by thermal conduction in the legs, release of Peltier bulk heat caused by material inhomogeneity and electric power release due to internal thermoelectromotive forces caused by different Seebeck coefficient values inside the leg. The model allows for the existence of contact resistances $r_0^{(n,p)}$, as well as losses of heat $\Delta T_k^{(n,p)}$ and electricity in commutation plates with the electric resistance R_k^0.

The source system of equations describing thermal and electric processes in the infinitesimal leg part dx is given by expressions

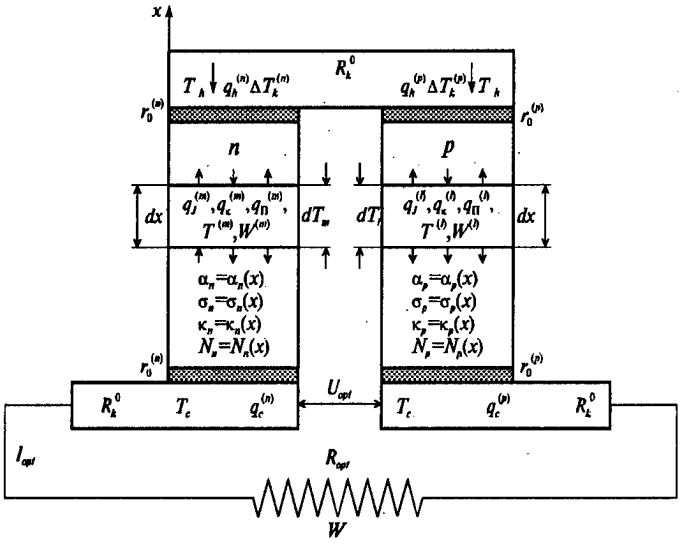


Fig.4. Physical model for construction of computer simulation of FGM.

$$\left.\begin{aligned} \frac{dT}{dx} &= -\frac{\alpha i}{\kappa}T - \frac{i}{\kappa}q \\ \frac{dq}{dx} &= \frac{\alpha^2 i}{\kappa}T + \frac{\alpha i}{\kappa}q + \frac{i}{\sigma} \end{aligned}\right\}_{n,p}, \qquad (2)$$

with the boundary conditions

$$\begin{aligned} T_n(0) &= T_p(0) = T_c, \\ T_n(l) &= T_p(l) = T_h, \end{aligned} \qquad (3)$$

where i is the density of generated current.

The equations are based on the differential Ohm's law for the circuit comprising thermoelectric sources and on the law of energy conservation. From the solution of the system of equations one can find temperature distribution in the legs $T_{n,p} = T_{n,p}(x)$; the distribution of thermal flow $q_{n,p} = q_{n,p}(x)$, as well as the thermal flow entering and leaving n- and p-type legs, the integral electric power on the external load and, accordingly, the generator efficiency. At the predetermined functions of the leg material inhomogeneity by varying the value of the external resistance R one can determine the maximum efficiency and the maximum circuit power, and here, as is well known, $R_{opt\,\eta max} \neq R_{opt\,W}$.

To solve this direct task that comes to finding efficiency and power, a program has been developed based on the combination of Euler method and the method of shooting for the system of differential equations (2).

However, our object in this investigation is to find the ways of solving the inverse task, namely, the search for the optimal function of p- and n- type leg material inhomogeneity at which the maximum efficiency of thermoelectric generator is reached. This task was solved by way of development of a special-purpose computer program based on the use of Pontryagin mathematical theory of optimal control [3]. The essence of the method lies in the fact that a zero approximation of the desired function is entered into the computer in the form of material parameters N_e and N_p that are coordinate independent or linearly changing. Pontryagin method comes to the search for the optimal function by calculating the efficiency for various functions that are different from the assigned initial ones.

Pontryagin method allows to make a purposeful search for function and thus considerably reduce the number of computer experiments. The essence of this method lies in the determination of the optimal functions $N_{n,p}(x)$, characterizing the inhomogeneity of thermoelectric materials of n- and p-type from the condition

$$\begin{aligned} &H_{n,p}(\psi(x), T(x), q(x), N(x), i) = \\ &= \max_{N_{n,p} \in G_N} H_{n,p}(\psi(x), T(x), q(x), N, i) \end{aligned} \qquad (4)$$

where Hamiltonian function H has the form

$$H_{n,p} = (\psi_1 f_1 + \psi_2 f_2)_{n,p} \qquad (5)$$

$(f_1, f_2)_{n,p}$ are right sides of equations (2), $\psi = (\psi_1, \psi_2)_{n,p}$ is pulse vector which is conjugate to the vector of phase variables $y = (T, q)_{n,p}$.

To use this method, the system of equations (2) must be complemented by the functions relate material parameters α, σ and κ to the impurity concentration $N_{n,p}$ and temperature. The more accurate the definition of these relations, the higher the accuracy of the method. Special investigations have been conducted based on our empirical data and the data from the world literature that allowed to approximate the functions of $\alpha_{n,p}$, $\sigma_{n,p}$ and $\kappa_{n,p}$ by the polynomials.

The system of equations (2)-(5) with the polynomials has served as the basis for the program of search for the optimal inhomogeneity functions of the materials of interest for us.

Discussion of results

Examples of the optimal inhomogeneity functions obtained by computer-aided design method are shown below. Fig. 5 shows an example of the optimal concentration functions for *Bi-Te* alloys, Fig. 6 - for *Pb-Te* alloys, Fig. 7 - for *Si-Ge* alloys. One of the dependencies can be obtained within 10-15 minutes of work of even not very high speed computer of the type IBM-486, which proves the efficiency of the developed program. Naturally, each specific case of FGM use requires individual function of material inhomogeneity, otherwise the use of FGM will be inefficient.

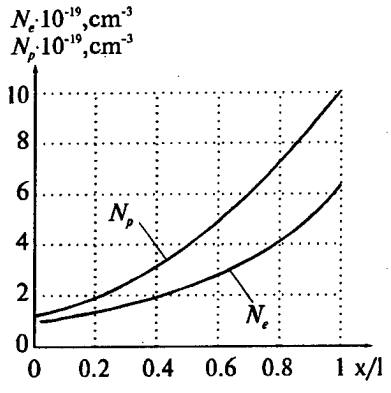


Fig.5. Optimal functions of N_e, N_p impurity concentration for n- and p-type alloys based on *Bi-Te*, accordingly

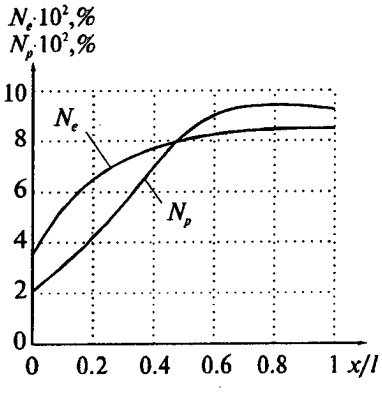


Fig.6. Optimal functions of N_e, N_p impurity percentage for n- and p-type alloys based on *Pb-Te*

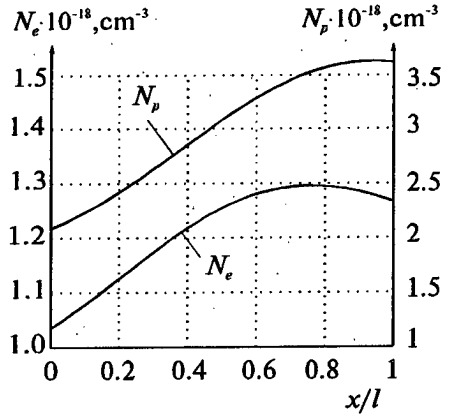


Fig.7. Optimal functions of N_e, N_p impurity concentration for n- and p-type alloys based on *Si-Ge*

The next important step of computer-aided design is the development of programs for the cascade thermoelectric generators. The program is complicated by the necessity to reach mutual match of the optimal inhomogeneities in each cascade at simultaneous finding of the best working temperature ranges for each of the cascades.

A program has been developed for the design of cascade thermoelectric generators with any number of cascades. Design according to this program results in the determination of the optimal matched inhomogeneities for each cascade, as well as in the determination of the optimal working temperature ranges for the materials of each cascade. It is quite obvious that no direct experimental methods seem to give these results. Fig.8 shows an example of a three-cascade thermopile design made of FGM.

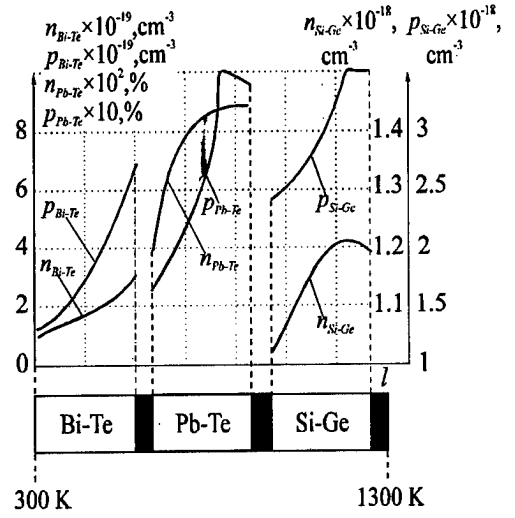


Fig.8. Optimal FGM for a three-stage generator.

In the cold cascade of the thermopile the alloys of *Bi-Te* have been used, in the medium-temperature cascade - the alloys of *Pb-Te*, in the high-temperature cascade - the alloys of *Ge-Si*.

The methods of computer simulation have been used to design 50 generators optimized for different hot temperature values in the range of 300÷1300 K. The results of these investigations are shown in Fig. 9. In the figure one can see the existence of rational temperature ranges for which it is advisable to use a one -, two- or three-cascade generator. The results of these investigations also determine the efficiency values of the generators that can be made of FGM. It is seen that at cold temperature of 300°C and the temperature drop of 1000 degrees one can expect the efficiency of 19%. It should be borne in mind that these efficiency values are realistic enough, since the program took into account thermal intercascade losses, as well as the losses in the thermopile contact resistances. The results obtained testify in favour of FGM use both for thermoelectric cooling and generation.

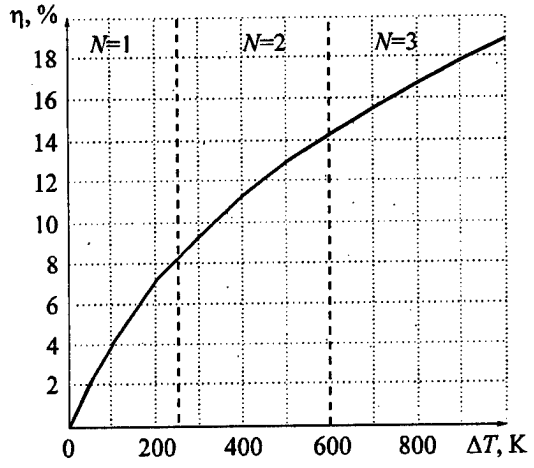


Fig.9. The efficiency of N-cascade generators with FGM material as function of temperature drop. T_c=300 K

Fig. 10 shows a tree of thermoelectricity development allowing for the prospects of using functionally graded materials.

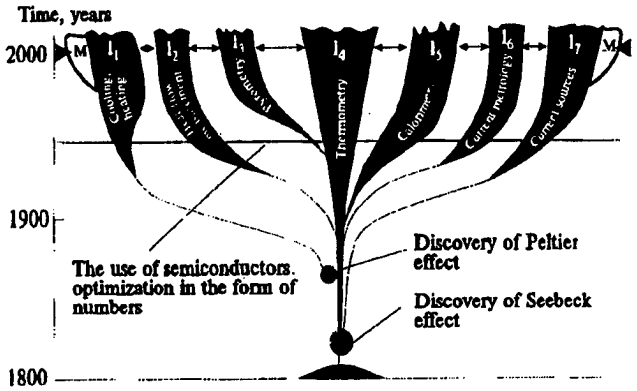


Fig.10. The tree of thermoelectricity evolution. The areas M indicate the prospects of FGM material use

One can expect that further progress in thermoelectricity will be closely associated with the use of the inhomogeneous thermoelectric structures.

References

[1] Anatychuk L.I., Semenyuk V.A. Optimal control of semiconductor material and device properties, Chernivtsy, 1992.

[2] Nishida I.A. Highly efficient thermoelectric materials in FGM program. In Proc. of Japan-Russia-Ukraine Int. Workshop on energy conversion materials, Japan 1995, p.1-6.

[3] Pontryagin L.S., Boltyanski V.G., Gamkrelidze R.V., Mishchenko E.F. Mathematical theory of optimal processes, Moscow, 1976.

Thermoelectric Generator Modules and Blocks

Anatychuk L.I., Razinkov V.V., Rozver Yu. Yu., Mikhailovsky V.Ya.

Institute of Thermoelectricity, General Post-Office, Box 86, 274000, Chernivtsi, Ukraine
Tel:+380/3722/44422, Fax:+380/3722/41917, E-mail:Alex@ite.Chernovtsy.ua, WWW: http:\\www.ite.Chernovtsy.ua

Abstract

Characteristics and elements of a new type structure of thermoelectric modules for electric power generation with output power of 10 W have been presented. It is proposed a parametric series of the indicated modules with rated output voltage of: 0.2; 0.4; 0.8; 1.6; 3.2 and 6.4 V.

Modules are designed for the use in thermoelectric generators of different purposes along with heat sources use that provide operation temperature level of the module warm side of 250-300 °C.

Optimization methods of known thermoelectric materials for the indicated modules conversion efficiency at a level of more than 6% have been examined.

The study results of commutations and anti-diffusion layers new types effect on the modules lifetime and resistance to climatic and temperature action have been given.

It is presented the reliability investigation results of the module as a whole.

It is presented examples of modules with heat exchangers arrangement into functional blocks that provide a user necessary overall dimensions and electric parameters for current and voltage.

Variants of specific applications of modules and blocks in thermoelectric generators with catalytic heat sources have been examined.

The essence of the problem

In recent years the interest for thermoelectric generation of electrical energy is ever growing. The hot temperature range 50-400°C is now most relevant for the generator operation. It is considered promising due to a large quantity of heat sources and high thermal power which can be used for electrical energy production in this temperature range. First of all, it is the utilization of all kinds of waste heat from power plants and industrial production. Among them there are internal combustion engines in all the variety of their use; gas turbines; waste heat of steel industry and non-ferrous metal industry, cement production, etc. The thermal power released by these devices is so high that its conversion into electrical energy, even with the modest efficiency values can be an appreciable contribution to power supply [1].

These factors stimulate investigations and development of thermoelectric modules for the creation of generators using the hot temperature level of 150-450°C. For the heat sources of lower temperature level use can be made of modified variants of thermoelectric cooling modules. Our purpose in this investigation and development is to create thermoelectric modules at the hot temperature level of 150-250°C. The analysis shows that these temperature levels have the largest application potential.

Crystalline substances based on *Bi-Te* doped so that the maximum efficiency corresponds to the assigned temperature range have been used as thermoelectric material. For further efficiency increase the materials with optimal inhomogeneity (FGM) have been developed as well. Our methods of designing these materials have been developed and described in Ref.[2, 3]. The technological methods of producing these materials have been described in [3]. In contrast to the traditional methods based on using pressed materials, we have used crystalline materials which help to achieve higher figure of merit values. Special emphasis has been placed on the problems of thermoelectric module reliability. For this purpose use was made of superreliable anti-diffusion layers based on *Co-Ni* and other materials. The thicknesses and structures of anti-diffusion layers were created so as to minimize the thermal stresses originating therein. On the whole, the module design features minimization of thermal influences on module reliability. To reduce the influence of the ambient atmosphere and heat loss, the modules were placed into thin-walled flexible hermetic containers made of stainless steels. The container volume was filled by the inert atmosphere. The module is schematically shown in Fig.1.

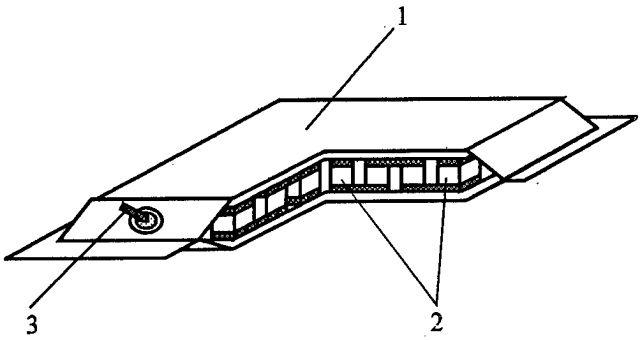


Fig.1. Scheme of generator module. 1 - metal container, 2 - thermoelectric module, 3 - hermetic leads.

It includes thermoelectric module, metal container, hermetic leads. The module design also features special measures for reliability increase, especially for the cases when the modules are used to produce thermogenerators having a large number of modules connected in series. This is the embodiment of a number of modules whose parameters are listed in Table 1.

The values of module parameters for the basic operating temperatures have been given in the table. The basic operating temperature on the hot side at continuous work is 250°C and lower. Short-time overheats of the hot side to 300-350°C are permissible. The basic operating temperature of the cold side at continuous work is 80°C and lower. Short-time overheats of the cold side to 120°C are permissible.

0-7803-4057-4/97 $10.00 ©1997 IEEE

Table 1. Parameters of "ALTEC" thermoelectric modules for thermogenerators.

The hot side temperature is 250°C, the cold side temperature is 30°C, the values of voltage, current and electrical power on the matched load under which the maximum efficiency value is reached.

Module type	Voltage, V	Current, A	Power, W	Efficiency, %	Module dimension, mm^3	Capsule dimension, mm^3	Reliability coefficient
Altec-1002	3	1.5	4.5	6.2	30×30×3	46×46×3.2	-
Altec-1010	5	1.5	6.5	6.2	40×40×3	56×56×3.2	-
Altec-1011	2.2	2.8	6.2	6	40×40×4.5	56×56×4.7	1
Altec-1012	1.1	5.6	6.2	6	40×40×4.5	56×56×4.7	20
Altec-1013	0.55	11.2	6.2	6	40×40×4.5	56×56×4.7	70
Altec-1014	0.27	23	6.2	6	40×40×4.5	56×56×4.7	120
Altec-1016	1.1	5.6	6.2	6	40×40×4.5	56×56×4.7	80
Altec-1017	0.55	11.2	6.2	6	40×40×4.5	56×56×4.7	350
Altec-1018	0.27	23	6.2	6	40×40×4.5	56×56×4.7	600

The modules permit multiple cyclic loads. A number of cycles when the module parameters are kept are listed in the table. One cycle corresponds to hot temperature increase from +30 to +250°C during 3-5 min and decrease from +250°C to +30°C during 3-5 min.

The modules to be used in high-power thermogenerators including a large number of modules connected in series have been designed so as to have the increased reliability. The increased reliability values are necessary to keep high reliability values of electric circuits with series connection of modules. Table 1 gives the values of reliability coefficient which is equal to the reliability ratio of this module with respect to ALTEC-1011 module. It is seen that the modules that develop reduced voltage for series connection are characterized by increased reliability values. This is an important factor of reaching high generator reliability.

Typical module characteristics are shown in Fig.2 and Fig.3. Fig.2 gives the characteristics of Altec-1010 module. Fig.3 - those of Altec-1011 module. Other modules have similar characteristics. The modules have been also developed that have the dimensions 60×60×4.5 mm, capsule dimensions 76×76×4.7 mm and electrical power 15 W.

As it has been mentioned above. the modules have been designed both for stand-alone use and as the basis for generator thermopiles. Of particular interest is the use of modules for the creation of " liquid-liquid" generators. They are most general-purpose and can be easily arranged with any heat source when there is a suitable heat exchanger.

To create these generators. the blocks have been developed that consist of hot and cold liquid heat exchangers with thermoelectric modules placed between them. The block is schematically shown in Fig.4. For this purpose special heat exchangers have been developed in the form of the plates having hermetic channels inside for passage of liquids. The dimensions and configuration of the channels provide the necessary extent of liquid turbulization with a view to reach

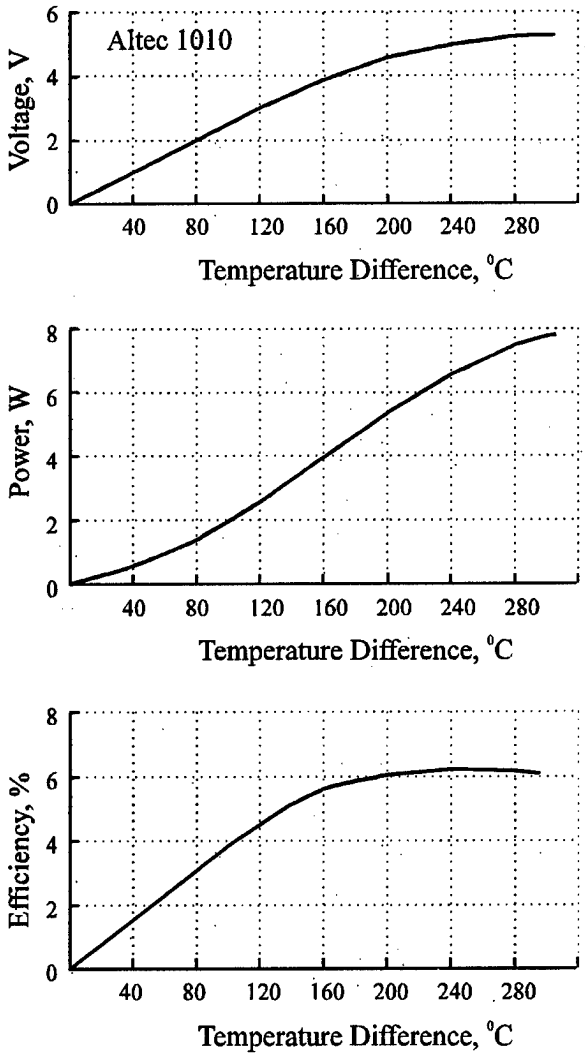


Fig.2. Characteristics of Altec-1010 module.

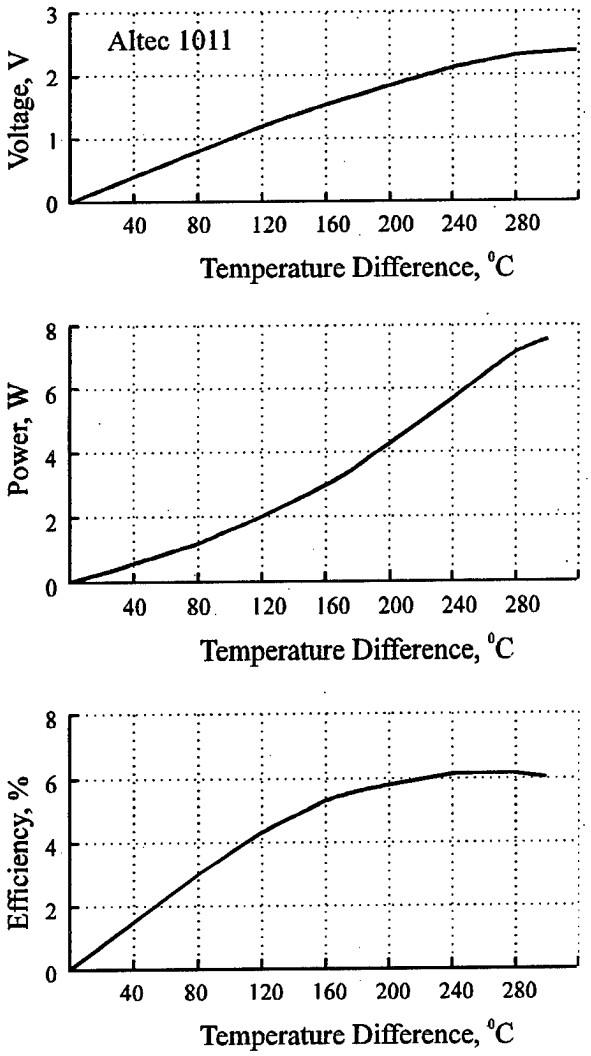


Fig.3. Characteristics of Altec-1011 module.

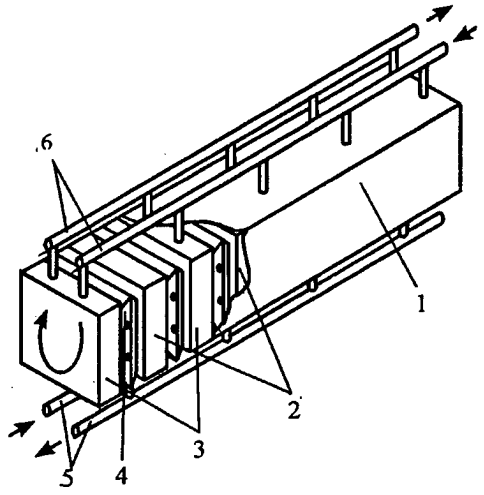


Fig.4. Scheme of block with generator modules. 1 - heat isolation, 2 - heat exchanger with "hot" carrier, 3 - heat exchanger with "cold" carrier, 4 - hermetic generator module, 5 - "hot" carrier channel, 6 - "cold" carrier channel.

the optimal values of heat transfer. At the same time it was intended to reach minimum energy loss for liquid pumping. as long as the use of this energy results in the reduction of thermogenerator efficiency. The heat exchangers are made of aluminum. copper or stainless steels depending on the liquid used. The block design features parallel. series or combined formation of liquid loops. The block parameters are listed in Table 2.

Table 2. Parameters of Altec-1041 block

1	Number of modules	8
2	Number of hot heat exchangers	4
3	Number of cold heat exchangers	5
4	Input hot liquid temperature	260 °C.
5	Output hot liquid temperature	230 °C.
6	Input cold liquid temperature	20 °C
7	Output cold liquid temperature	40 °C
8	Voltage	40 ± 2 V
9	Current	1.5± 0.1 A
10	Efficiency	6%

The above modules and blocks have been used to create the generators with catalytic heat sources [4] and the generators for waste heat utilization [1].

References

[1] L.I.Anatychuk. Yu.Yu.Rozver. K.Misawa. N.Suzuki. Thermogenerators for heat wastes utilization. Report on ICT'97.

[2] Anatychuk L.I.. Vikhor L.N. Computer design of thermoelectric functionally graded materials. in Proc. of the IVth Int. Symposium on FGM. Tsukuba. Japan. Oct. 21-24. 1996.

[3] Anatychuk L.I.. Vikhor L.N. Functionally graded materials and new prospects for thermoelectricity use. Report on ICT'97.

[4] Anatychuk L.I.. Mikhailovsky V.Y. Catalytic Furnaces with Thermogenerators. Report on ICT'97.

Thermoelectric Eddy Currents. Calculation and Control Methods

L.I. Anatychuk, O.J. Luste
Institute of Thermoelectricity, General Post-Office, Box 86, 274000, Chernivtsi, Ukraine
Tel: +380/3722/44422, Fax:+380/3722/41917, E-mail: anatychuk@ite.Chernovtsy.ua,
WWW: http:\\www.ite.Chernovtsy.ua

Abstract

Calculation methods of the thermoelectric eddy currents and electric potentials distributions in the non-isotermetral medium under arbitrary boundary conditions have been described. The problem of the thermoelectric eddy currents control have been formulated and solved for description of known energy converters and finding new ones. The examples of thermoelectric eddy currents control have been given.

Introduction

Eddy currents is the name for closed electric currents that originate in a conducting medium due to the external influences. Two kinds of eddy currents are known: eddy Foucault currents and thermoelectric eddy currents (TEC). Seebeck [1] was the first to observe TECs. But it was not earlier than in the 40-s of the 20-s century that the investigation of TECs began. The conditions for their origination were found out in the 60-s. At that time the methods of control of TECs were discovered alongside with their practical application [2-5].

TECs Calculation Methods

Scalar potential method. An equation for TECs calculation expresses the law of electrical charge conservation. It has a form

$$\frac{\partial}{\partial x_l}\left(\sigma_{lm}\frac{\partial U}{\partial x_m}\right)=\frac{\partial}{\partial x_l}\left(\sigma_{lm}\alpha_{ms}\frac{\partial T}{\partial x_s}\right), \qquad (1)$$

$$n_i\sigma_{ik}\frac{\partial U}{\partial x_k}\bigg|_\Gamma = n_i\sigma_{ik}\alpha_{ki}\frac{\partial T}{\partial x_l}\bigg|_\Gamma , \qquad (2)$$

where U is scalar potential of electric field, $\mathbf{n}_i$ is a normal vector to medium boundary Γ. The problem (1), (2) is a boundary problem for the inhomogeneous equation elliptical in the second-order partial derivatives with the inhomogeneous boundary conditions of second type. The existing analytical methods of solving these problems are efficient only in separate specific cases, which necessitates the use of numerical methods. Fast computer numerical methods of calculation of TECs have been worked out in the Institute of Thermoelectricity.

Vector potential method. Under steady-state conditions the vector field of TEC density has no internal sources, therefore one can introduce the vector potential **H:**

$$\mathbf{j}=\mathrm{rot}\,\mathbf{H},\ \mathrm{div}\,\mathbf{H}=0. \qquad (3)$$

The equations (3) agree with the Maxwell system of equations, and the vector potential **H** has a physical meaning of magnetic field intensity of TECs.

The vector potential **H** satisfies the Poisson equation

$$-\nabla^2\mathbf{H}=\mathrm{rot}\,\mathbf{j} \qquad (4)$$

with the boundary condition $\mathrm{rot}\,\mathbf{H}\big|_\Gamma = 0$.

The solution of boundary problem (4) for the two-dimensional medium with a homogeneous Seebeck coefficient has been obtained in the papers [3,5]. In this case $dT/dz = 0$, and the vector **H** has only one component $\mathbf{H}_z$. At the medium boundary $\mathbf{H}_z = 0$. The curves $H_z(x, y)$ = const are the lines of current. The function $H_z(x, y)$ magnitude is equal to the TEC integral value between the medium boundary and the point of the co-ordinates x, y.

TEC Spatial Configuration Control

Inverted thermoelectricity problems. In the general case inverted thermoelectricity problem (ITP) are formulated as follows (Fig. 1). Let us consider a simply connected spatial domain D of a medium which is characterized by tensors of the electric resistance $\hat{\rho}$, Seebeck coefficient $\hat{\alpha}$ which change with a radius-vector **r**. In the closed domain vector field of current density **j(r)** has been given.

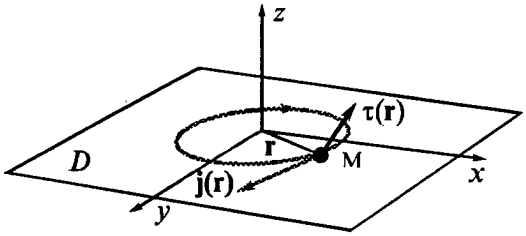


Fig. 1. A inverted thermoelectricity problem: r is radius-vector of point M in the co-ordinate system x,y,z. **j(r)** is vector function of the prearranged distribution of thermoelectric currents, **τ(r)** is desired vector function of temperature gradients in the medium domain D.

The inverted problem lies in the construction of such scalar field of temperatures T(**r**) (or vector field of temperature gradient **τ(r)**) which necessitates excitation of the prearranged current distribution **j(r)** in the domain D.

Under steady-state conditions

$$\mathrm{div}\,\mathbf{j}=0, \qquad (5)$$

and vectors **j** и **τ** are related by

$$\hat{\rho}\,\mathbf{j}=\mathbf{E}-\hat{\alpha}\tau \qquad (6)$$

where **E** is electric field intensity.

Having used the operator rot for both sides of the equation we get

$$\mathrm{rot}\,\hat{\alpha}\tau = -\mathbf{J}, \qquad (7)$$

here

$$\mathbf{J}=\mathrm{rot}\,\hat{\rho}\tau. \qquad (8)$$

Thus, the inverted thermoelectricity problem lies in the solution of a set of three differential equations in second-order partial derivatives with respect to the unknown temperature

$$\Omega_{ikl}\frac{\partial}{\partial x_k}\alpha_{lm}\frac{\partial}{\partial x_m}T(x_1,x_2,x_3)=-J_i, \quad (9)$$

where: Ω_{ikl} is the Levi-Chivita pseudotensor, *i, k, l, m* = 1, 2, 3; x_1, x_2, x_3 are radius vector **r** components in the Cartesian rectangular co-ordinate system.

The necessary conditions for the existence of the solution of the ITP conditions essentially depend on the Seebeck tensor structure and are formulated in different ways for various media (inhomogeneous, isotropic, gyrotropic, anisotropic, etc.).

Solutions of the inverted thermoelectricity problems

Control of eddy thermoelectric currents in the isotropic medium. The equation (7) for the isotropic medium has the form

$$\tau\times\mathbf{A}=\mathbf{J}, \quad (10)$$

where $\mathbf{A}=\nabla\alpha$, α is a scalar Seebeck coefficient.

The solution of the equation (10) can be written as

$$\tau=\varphi\mathbf{A}+|\mathrm{A}|^{-2}\mathbf{A}\times\mathbf{J}, \quad (11)$$

where $\varphi=\varphi(\mathbf{r})$ is a scalar function which must be found from the condition (10).

Let us indicate three possible solutions of the ITP for the isotropic medium. If the vector field $[\mathbf{A}\times\mathbf{J}]$ is potential, then the solution of the ITP is

$$T(\mathbf{r})=f(\alpha)+\int_0^r\frac{\mathbf{A}\times\mathbf{J}}{\mathbf{A}^2}d\mathbf{r}. \quad (12)$$

The second solutions corresponds to the case when vector fields $\mathbf{J}(\mathbf{r})$ and $\mathbf{A}(\mathbf{r})\times\mathbf{J}(\mathbf{r})$ are quasi-potential:

$$\mathbf{J}\,\mathrm{rot}\,\mathbf{J}=0, \quad (13.)$$

$$[\mathbf{A}\times\mathbf{J}]\,\mathrm{rot}[\mathbf{A}\times\mathbf{J}]=0.$$

The solution of the ITP has the form

$$T(q_1,q_2,q_3)=\frac{\int_0^{q_3}\frac{\partial}{\partial q_1}\lambda H_3\,dq_3}{|\mathrm{A}|H_1}+V(q_1), \quad (15)$$

$$\text{where } \lambda=\frac{|\mathbf{A}\times\mathbf{J}|}{\mathbf{A}^2}, \quad (16)$$

are the corresponding Lamais coefficients, $V(q_1)$ is arbitrary function.

If the vector field $\mathbf{A}\times\mathbf{J}$ is quasi-potential, and the vector field **J** is arbitrary solenoid one then the inverted thermoelectric problem solution has the form

$$T(r)=\xi(\alpha)\int_0^{\Phi\xi}\Phi(U)dU\int_0^r\mu\frac{\mathbf{A}\times\mathbf{J}}{\mathbf{A}^2}dr+f(\alpha). \quad (17)$$

Control of TECs in the gyrotropic medium

For the homogeneous gyrotropic medium

$$\partial\tau_1/\partial x_3=R_1(x_1,x_2,x_3),$$
$$\partial\tau_2/\partial x_3=R_2(x_1,x_2,x_3), \quad (18)$$
$$\partial\tau_1/\partial x_2+\partial\tau_2/\partial x_2=-R_3(x_1,x_2,x_3), \quad (19)$$

where $\mathbf{R}=|\mathbf{N}|^{-1}\mathbf{J}$, **N** is the constant Nernst vector. The solution of the ITP has the form:

$$\tau_1=\int R_1dx_3+\int\eta(x_1,x_2)dx_1+C_1x_2+C_2,$$
$$\tau_2=\int R_2dx_3+\int\eta(x_1,x_2)dx_2+C_3x_1+C_4, \quad (20)$$
$$\tau_3=\int R_1dx_3+F_1(x_2,x_3)=\int R_1dx_3+F_1(x_2,x_3),$$

where η is an arbitrary harmonic function of variables $x_1,x_2;F_1,F_2$ are arbitrary functions of their variables, C_i are arbitrary constants.

TEC Control in the Anisotropic Medium

For this medium so that the system (9) might be written in the form :

$$\frac{\partial^2T}{\partial x_2\partial x_3}=\frac{J_3}{\alpha_{22}-\alpha_{33}}=P_1(x_1,x_2,x_3),$$
$$\frac{\partial^2T}{\partial x_3\partial x_1}=\frac{J_3}{\alpha_{33}-\alpha_{11}}=P_2(x_1,x_2,x_3), \quad (21)$$
$$\frac{\partial^2T}{\partial x_1\partial x_2}=\frac{J_3}{\alpha_{11}-\alpha_{22}}=P_3(x_1,x_2,x_3),$$

where α_{ii} are the Seebeck tensor eigenvalues.

The solution is $\tau_1=\int_0^{x_2}P_3(x_1,\xi,x_3)d\xi-\int_0^{x_3}P_1(x_1,0,\xi)d\xi+f_1(x_1),$

$$\tau_2=\int_0^{x_3}P_1(x_1,x_2,\xi)d\xi-\int_0^{x_1}P_2(\xi,x_2,0)d\xi+f_2(x_2),$$
$$\tau_3=\int_0^{x_1}P_2(\xi,x_2,x_3)d\xi-\int_0^{x_2}P_3(0,\xi,x_3)d\xi+f_3(x_3), \quad (22)$$

where f_i are arbitrary functions.

Thermoelectric eddy currents of specified configurations

Circular TECs.

Determination of conditions for the excitation of circular TECs [3, 5] can serve as a simple example of the ITP solution.

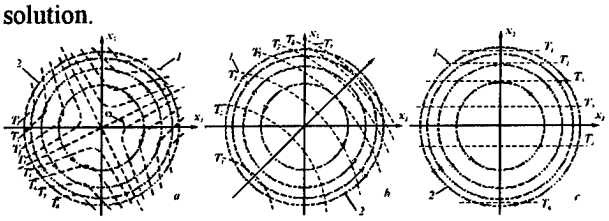


Fig. 2. Solutions of the inverted thermoelectricity problem for circular TECs 1 - lines of current, 2 - isotherm, a) homogeneous anisotropic medium, b) inhomogeneous medium, c) gyrotropic medium.

For the homogeneous anisotropic medium in the circular flat sample of radius R_0 (Fig. 2a) the following temperature distribution must be provided:

$$T(x_1,x_2)=T_0+\frac{\Delta T}{R_0^2}\left[x_1x_2\cos2\varphi+\frac{2\kappa_{22}x_2^2-2\kappa_{11}x_1^2+R_0^2(\kappa_{22}-\kappa_{11})}{2(\kappa_{22}+\kappa_{11})}\right], \quad (23)$$

where T_0 is the sample center temperature, ΔT - is maximum temperature difference, φ is the angle between the crystallographic axis and the line connecting the extreme points of equal temperature.

For the inhomogeneous isotropic medium with the Seebeck and electric conductivity coefficients that are co-ordinate dependent

$$\alpha(x_1)=B+D\frac{x_1}{G}, \qquad \sigma=\mathbf{A}\exp\left(\frac{x_1}{G}\right), \quad (24)$$

the sought temperature field is

$$T(x_1,x_2)=T_0-\frac{CG}{DA}x_2e^{\frac{x_1}{L}}\left[\frac{x_1}{G}+2\right], \quad (25)$$

where *A, B, C, D, G* are constants. The circular TECs can be also created in the homogeneous medium placed in magnetic field (Fig. 2c). The temperature distribution in this case has the form

$$T(x)=T_0-\frac{2C}{\sigma_s\alpha_\alpha}x^2, \quad (26)$$

where σ_s -is the component of the symmetrical part of electric conductivity tensor, α_α is the component of the antisymmetric part of Seebeck tensor, *C* is constant.

Helical TECs

We shall get the solutions of the ITP in the homogeneous anisotropic medium for the cases when the initial current distribution is characterized by the helical current lines. Let us consider one- and two-dimensional helical current lines. The current lines for the flat area will have the form of the Archimedean spirals (Fig. 3).

$$H(r,\varphi)=B(r-r_0)-C\varphi=const, \quad (27)$$

where *H* is the current function, , φ is the polar angle, *B, C* - are constants.

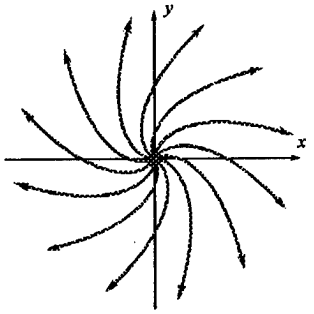


Fig. 3. Helical thermoelectric eddy currents of a two-dimensional area.

From the equation (22) we get:

$$\begin{aligned}T(r,\varphi)=&\left(\alpha_{11}-\alpha_{22}\right)^{-1}\{C(\rho_{11}-\rho_{22})\ln r-\\&-B\ln r(\rho_{22}\cos^2\varphi++\rho_{11}\sin^2\varphi)-\\&-Br[\rho_{22}\cos\varphi\ln(1+\sin\varphi)+\\&+\rho_{11}\sin\varphi\ln(1+\cos\varphi)]\}\end{aligned} \quad (28)$$

For a tree-dimensional case (Fig. 4) the current lines can be described by the vector field j(r) **j(r)** with the components

$$j_1=-Cx_2,\quad j_2=Cx_1,\quad j_3=D=\text{const}. \quad (29)$$

The ITP solution for this case has the form:

$$T(x_1,x_2,x_3)=\frac{2C}{\alpha_{11}-\alpha_{22}}x_1x_2+f_1(x_1)+f_2(x_2)+f_3(x_3)$$

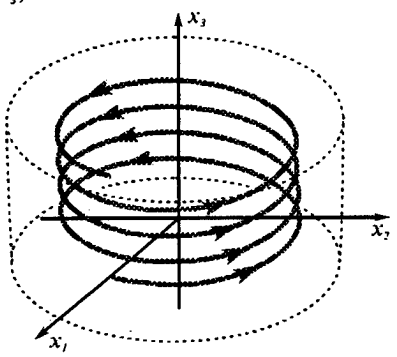


Fig. 4. Helical thermoelectric currents in a three-dimensional area.

TECs with changing configuration of current lines

Let us find the solutions of the ITP in the homogeneous anisotropic medium for which current distribution has been given by Lukosz function

$$H=\prod_{k=1}^{n}(y-\alpha_kx-b_k)h(x,y), \quad (30)$$

where *x* and *y* are the co-ordinates calculated along the tensor α axes, *h(x,y)* is arbitrary limited function.

The function (30) describes eddy currents whose form smoothly changes in going from one current line to the neighbor one. At the medium boundary the currents flow in the perimeter of the *n*-sided polygon the side equations of which have the form

$$y=\alpha_kx+b_k,\quad k=1,\ldots,n. \quad (31)$$

In proportion to the distance from the boundary, the current lines change their configuration from a polygon to a circle.

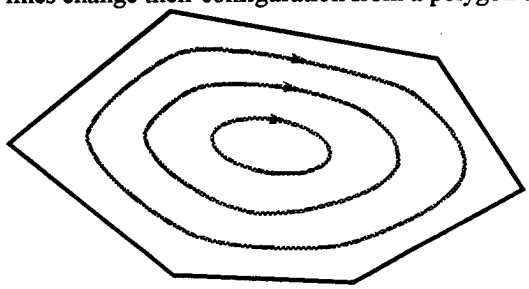


Fig. 5. Thermoelectric eddy currents with the variable configuration of the current lines.

The current distribution of this kind is schematically shown in Fig. 5.

To find the ITP solutions, one can write a system of differential equations in the first-order partial derivatives

$$\begin{aligned}-H_y=S_x,&\qquad H_x=D_y;\\S=U+T,&\qquad D=U-T.\end{aligned} \quad (32)$$

The integrated thermoelectricity problem solution is found by the integration (32) and has the form

$$T=-\frac{1}{2}\left\{\int_0^y H_x(x,\eta)d\eta+\int_0^x H_y(\xi,y)d\xi\right\}+ \quad (33)$$
$$+Y(y)-X(x),$$

To illustrate, let us consider as a boundary the equilateral triangle with the sides $y=\pm\sqrt{3}x$, $y=\sqrt{3}x/2$, and the current vector potential in the form $H=\left(2y-\sqrt{3}\right)\left(y^2-3x^2\right)$.

The resulting pattern of scalar fields *H, T, U* is shown in Fig. 6.

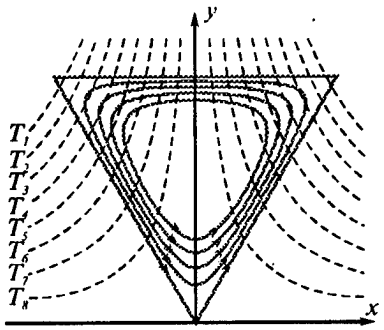


Fig. 6. Thermoelectric eddy currents in a regular triangle.

From the figure it is seen that the boundary current line coincides with the triangle perimeter, the current density being zero in its center. The solutions for regular pentagon and heptagon are given in Figs. 7 and 8.

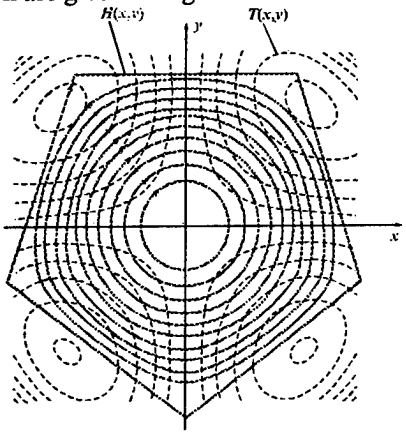


Fig. 7. Thermoelectric eddy currents in a regular pentagon: a) current lines, b) isotherms.

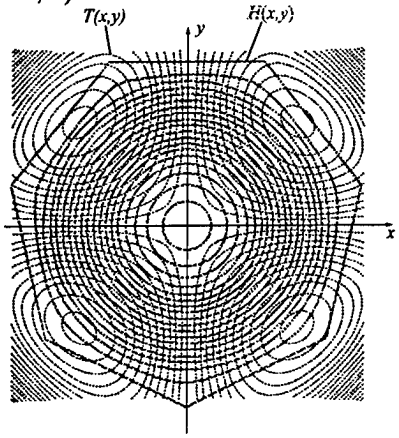


Fig.8. Thermoelectric eddy currents in a regular heptagon: a) current lines, b) isotherms.

Spatial-periodical configurations of thermoelectric eddy currents

Let us consider now current distributions that are periodically recurring in the space occupied by the medium. They can be described by the expression

$$H(x,y) = -\frac{1}{2}\sum_{-\infty}^{\infty}\sum_{-\infty}^{\infty} C_{mn} e^{i(mx+ny)}, \qquad (34)$$

The example of this current distribution is shown in Fig. 9.

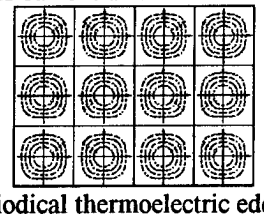


Fig. 9. Spatial-periodical thermoelectric eddy currents.

Based on the equation (33) the ITP can have the following solution:

$$T(x,y) = -\frac{1}{2}\sum_{-\infty}^{\infty}\sum_{-\infty}^{\infty} i\{mC_{mn}\int_0^y e^{i(mx+n_\eta)}d\eta + nC_{mn}\int_0^x e^{i(m\xi+ny)}d\xi\} + \text{The}$$

$$+ Y(y) - X(x).$$

above examples illustrate the possibility of inducing TECs of predetermined configuration. For the complex distributions of TECs the ITP can be solved by computer methods or electrical analogy method which allows to reduce the calculations of TECs to the determination of potentials and currents in the isothermal medium [13].

Thus, the developed theory is a powerful tool of TEC control and allows to create any possible two- and three-dimensional eddy current configurations. This theory is important for the development of generalized methods of thermoelectric energy conversion.

References

[1] Seebeck, T.J., Magnetic polarization of metals and minerals, Abhand. Deutsch. Akad. Wiss. Berlin, 265, p.1822 - 1823.

[2] Anatychuk, L.I., Thermoelectricity development prospects, *Acad. Sci. UkrSSR, Visnyk*, (9), p.30-44, 1975 (In Ukrainian).

[3] Anatychuk, L.I., Luste, O.J., Thermoelectric eddy currents and eddy thermoelements, *Fizika i tehnika poluprovodnikov*, 10, (5), p. 817-832, 1976 (In Russian).

[[4] Anatychuk, L.I., Luste, O.J., Thermoelectric eddy currents in CdSb, *Fizika tverdogo tela*, p. 2492-2494, 1966 (in Russian).

[5] Lukosz, W., Geschlossene elektrische Strome in thermoelektrische anisotropen Kristallen, *Z. Naturforsch.*, 19a, (13), s.1599-1610, 1964.

[4] Anatychuk, L.I., Bojko, V.N., Luste, O.J., Razinkov, V.V., Transverse thermopower in short-circited crystal, *Fizika i tehnika poluprovodnikov*, 9, (7), p. 1410-1413, 1975 (In Russian).

[5] Anatychuk, L.I., Dimitrashchuk, V.T., Luste, O.J., Transverse thermopower in short-circited anisotropic crystal, *Fizika i tehnika poluprovodnikov*, 3, (8), p. 1257-1259, 1969 (In Russian).

[6] Anatychuk, L.I., Dimitrashchuk, V.T., Luste, O.J., Transverse thermopower in semiconductor two-layers plate, *Fizika i tehnika poluprovodnikov*, 5, (5), p. 956-958, 1971 (In Russian).

[7] Anatychuk, L.I., Dimitrashchuk, V.T., Luste, O.J., Tsiganjuk, Yu.S., Thermoelectric eddy current in unsteady field, *Izvestija VUZov, Fizika,* (3), p.23 - 29, 1972 (In Russian).

[8]]Anatychuk, L.I., Iskra, V.D., Luste, O.J., Thermoelectric eddy currents in Ge. *Izvestiya vuzov, Fizika*, 2(69), p.127 - 128, 1969 (In Russian).

[9] Anatychuk, L.I., Luste, O.J., Investigations of closed thermoelectric currents in anisotropic media, *Ukrainskij fizicheskij zhurnal*, 12, (9), p. 1520-1529, 1967(In Russian).

[10] Anatychuk, L.I., Luste, O.J., Investigation of closed thermoelectric currents in zsone-heterogeneons media. *Ukrainskij fizicheskij zhurnal,* 14, (8), p. 1391-1395, 1969 (In Ukrainian).

[12] Anatychuk, L.I., Luste, O.J., Thermoelectric eddy currents and transverse thermopower in zone-heterogeneons plates, *Izvestija VUZov, Fizika,* (6), p. 134-136, 1969 (In Russian).

[13] Anatychuk, L.I., Luste, O.J., Method of resistivity measuring of semiconductor epitaxial films, USSR Authors Certificate SU372492, Publised 01.03.73.

Thermoelectric Semiconductor and Electrode-Fabrication and Evaluation of SiGe/Electrode

K. Hasezaki[1], H. Tsukuda[1], A. Yamada[1], S. Nakajima[2], Y. Kang[3] and M. Niino[3]
1) Nagasaki Research & Development Center, Mitsubishi Heavy Industries, Ltd.
2) Nagasaki Shipyard & Machinery Works, Mitsubishi Heavy Industries, Ltd.
3) Kakuda Research Center, National Aerospace Laboratory, Japan

Abstract
Joints between a Silicon-Germanium thermoelectric semiconductor and electrodes were prepared by hot-pressing. Tungsten or carbon electrodes were joined to either side of n-type Si0.8Ge0.2 (P 0.3 atomic %) respectively, with thin sheets of titanium foil inserted between them, and then pressed and joined at 1523K in vacuum. The size of the resulting electrode/SiGe semiconductor/electrode units measured 5mm × 5mm × 9mm.
Observations through SEM and EPMA showed the presence of many voids in the junction layers of the SiGe/tungsten electrodes, whereas the SiGe/carbon electrodes exhibited no voids in their junction layers. In the SiGe/carbon electrodes, the titanium atoms were enriched in the junction layer, and other atoms also remained undiffused. In the SiGe/tungsten electrodes, the tungsten and silicon atoms showed counter diffusion.
Resistance and Seebeck coefficient of the carbon/SiGe/carbon electrodes were measured in the temperature range from 600 to 1100K. Resistance ranged from 0.012 to 0.015Ω, and the Seebeck coefficient from 200×10^{-6} to 250×10^{-6} V/K.
To evaluate the upper limit of heating dependence, the carbon/SiGe/carbon electrodes were exposed in an argon atmosphere at 1273K and 1373K for 300 hours. After exposure testing, SEM observation showed the presence of many voids in the junction layer of the SiGe/carbon electrode, which had not previously shown any voids either at the stage of joining by hot-pressing or exposure at 1273K.

Introduction
The function of a thermoelectric semiconductor is to directly exchange thermal energy into electrical energy. Thermoelectric generators have no vibrating parts, are maintenance-free, and have a simple structure.
Because of these properties, a thermoelectric generator can be used for the electric power supply of a space probe. The efficiency of a thermoelectric generator is highly dependent on a figure of merit, ($Z=\alpha^2\sigma/\kappa$, where α is the Seebeck Coefficient (V/K), σ is electrical conductivity (S/m) and κ is thermal conductivity (W/mK). If Z can be improved, thermoelectric processes may be used in many important applications, such as power generators for space stations. Recently, a new concept known as gradually segmented thermoelectric materials is being investigated by many Japanese groups under the support of the Japan Science and Technology Agency[1]. One of the objectives of this project is to improve high-efficiency thermoelectric materials using the concept of Functionally Graded Materials (FGM).
Silicon Germanium (SiGe) has a high figure of merit at high temperatures[2]. The effect of high temperatures and heat treatment of isolated SiGe thermoelectric semiconductors has been reported to improve their thermoelectric properties[3]-[7]. In practice, however, a thermoelectric generator generally consists of many *p* type and *n* type semiconductors together with the jointed electrodes. It is therefore, necessary to combine low electrical resistivity and thermal stability, as well as improve the high-efficiency thermoelectric materials.
The long exposure time dependence of electrical properties can be important when assessing any overall improvement of thermoelectric generator performance. The paucity of reports on the long heating time dependence of joints between SiGe thermoelectric semiconductors and electrodes encouraged us to investigate.
In the present research, joints between SiGe thermoelectric semiconductors and electrodes were prepared by hot-pressing. The electrical properties of the resulting SiGe/electrodes were investigated under conditions of high operating temperature for a period of over 300h in an argon atmosphere. The morphology and elemental dispersion of the junction layers were observed.

Experimental Procedure
The material used in this investigation was *n* type SiGe thermoelectric semiconductor material that had been prepared by plasma activated sintering (PAS) and supplied by Vacuum Metallurgical Co., Ltd., Japan. The compositions of *n* type materials were Si0.8Ge0.2 + 0.3 atomic % phosphorus, which are typical for *n* type compounds. Specimens measuring 10mm × 10mm × 5mm were cut from sintered compact.
Figure 1 shows the schematic of the SiGe/electrode hot-pressing apparatus. The SiGe thermoelectric semiconductors were hot-pressed between tungsten or carbon electrodes respectively, and pure titanium foil was inserted between the SiGe thermoelectric semiconductor and each electrode. The thickness of the titanium foil was 2μm. The joint of each SiGe thermoelectric semiconductor and electrode was hot-pressed at 1523K under a vacuum, with a hot-press pressure of 19.6 MPa and keeping time of 5 min.
The junction areas of the joints of the SiGe/electrodes were observed using scanning electron microscopy (SEM) and EPMA element analysis.
The resistance and Seebeck coefficient were measured by a large-temperature-difference apparatus[3]. The joints of the SiGe/electrodes were then cut into quarters, approximately 5mm × 5mm × 9mm.
For long-term exposure testing, heat treatment of the joints of SiGe/carbon was performed from 1273K to 1373K using a

0-7803-4057-4/97 $10.00 ©1997 IEEE

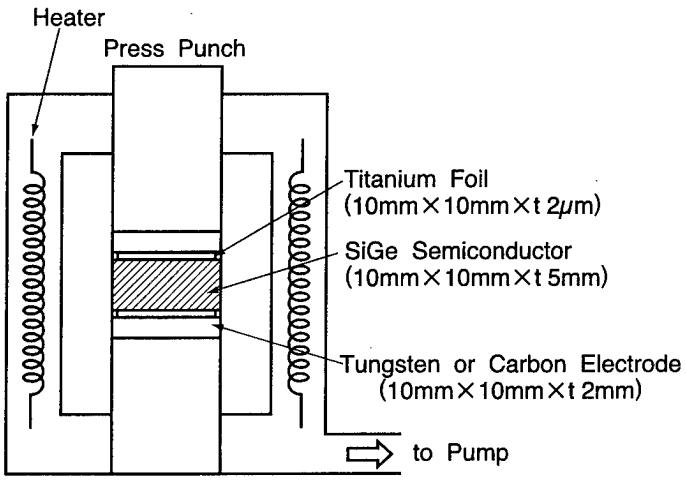


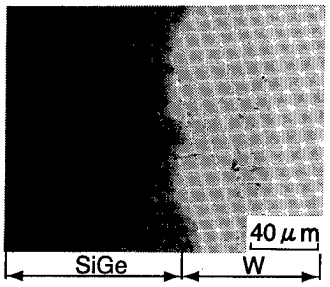
Fig.1 Schematic of Hot-Press Apparatus

vacuum furnace in an argon atmosphere. The joints of SiGe/carbon were fixed on silicon nitride plates, and around zirconium for the getter, and both heating and cooling rates were 100K/h.

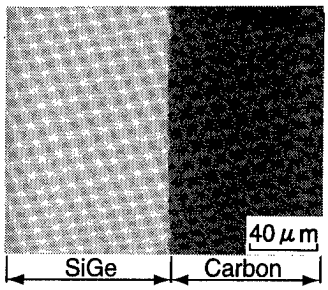
Results and Discussion

Figure 2 shows SEM microphotographs of the junction layers of SiGe/W and SiGe/C, and EPMA titanium elemental dispersion analysis. Microphotograph (a) shows the junction layer of an SiGe/W joint. A continuous void and an interactive layer were observed between the SiGe thermoelectric semiconductor and tungsten. This void occurred with increasing interface resistance, which would affect a thermoelectric generator. Microphotograph (b) shows the junction layer of an SiGe/C joint. No such continuous void and interactive layer was observed between the SiGe thermoelectric semiconductor and the carbon electrode. When the SiGe/W joint was cut to 5mm×5mm×9mm for the measurement of thermoelectric properties, it was found that it had fractured between the SiGe thermoelectric semiconductor and tungsten electrode. However, the SiGe/carbon joint was not fractured. Accordingly, the carbon electrode forms a better joint than the tungsten electrode, because of the absence of interface voids. Microphotograph (c) shows titanium elemental dispersion at the junction layer of an SiGe/C joint. The white brightness indicates the content of the titanium. Enriched titanium atoms were found between the SiGe thermoelectric semiconductor and the carbon electrode. From these results, it was decided to consuct the evaluation of thermoelectric properties only on the SiGe/C joint, using a large-temperature-difference apparatus.

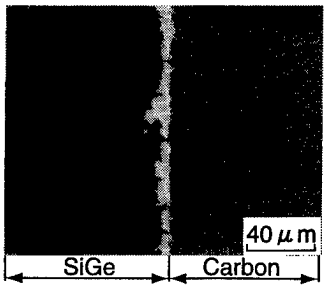
Figure 3 shows the Seebeck coefficient of the SiGe/C joint as a function of the average temperature between the top and bottom sides. In general, if external atoms diffuse in a thermoelectric semiconductor, the joint of the thermoelectric semiconductor/electrode affects the Seebeck Coefficient as a dopant. However, the Seebeck Coefficient of the joint of SiGe/C remained almost unchanged, because the titanium element condensed at the interface and the titanium atoms did



(a) SEM Microphotograph of the Junction Layer of SiGe/W



(b) SEM Microphotograph of Junction Layer of SiGe/C



(c) EPMA Titanium Elemental Dispersion Profile of SiGe/C

Fig.2 SEM Microphotographs and EPMA Titanium Elemental Dispersion

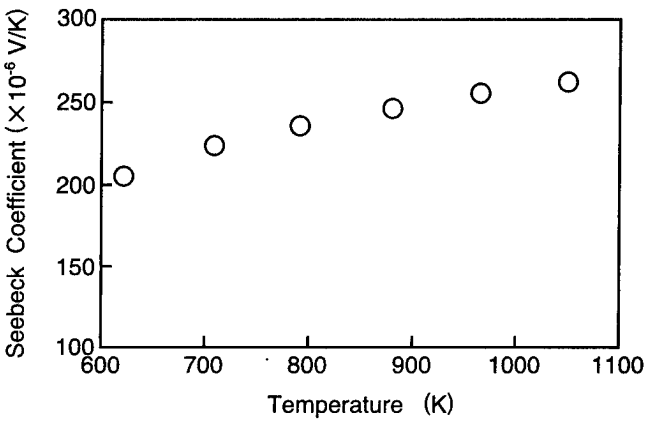


Fig.3 Seebeck Coefficient of the SiGe/C Joint as a Function of the Average Temperature

not diffuse in the SiGe thermoelectric semiconductor. The Seebeck Coefficient of the SiGe thermoelectric semiconductor is approximately 270 μV/K at 1000K[1], and approximately the same value was found for the SiGe/C joint.

Figure 4 shows the resistance of the SiGe/C joint as a function of average temperature between the top and bottom sides. The total resistance of an SiGe thermoelectric

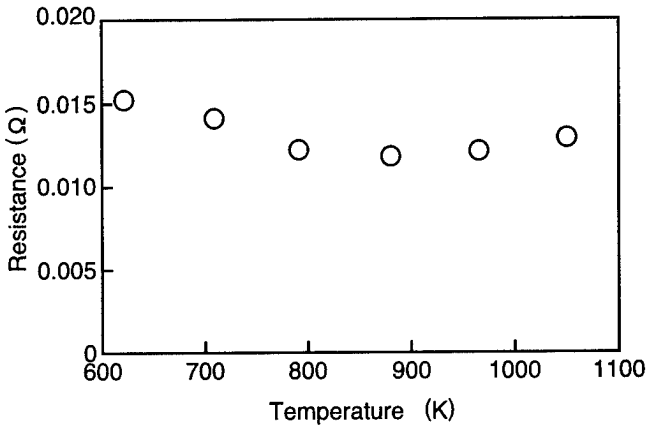


Fig.4 Resistance of the SiGe/C Joint as a Function of the Average Temperature

semiconductor and a carbon electrode of the same size is approximately 0.01Ω at 1000K[1]. The interface resistance of the SiGe/C joint is approximately 1/10 of total resistance.

Figure 5 shows SEM microphotographs of the junction layers of SiGe/C joints and EPMA titanium elemental dispersion analysis. Microphotograph (a) shows the junction layer of an SiGe/C joint after exposure at 1273K for 300h in an argon atmosphere. A number of pores were observed to occur between the SiGe thermoelectric semiconductor and the carbon electrode. Microphotograph (b) shows the junction layer of an SiGe/C joint after exposure at 1373K for 300h. A continuous void was observed between the SiGe thermoelectric semiconductor and the carbon electrode. Microphotograph (c) shows titanium elemental dispersion of the junction layer of joint SiGe/C after exposure at 1373K for 300h. The white brightness indicates the content of the titanium. The titanium atoms were diffused into the SiGe thermoelectric semiconductor.

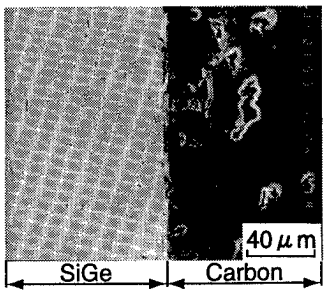
Figure 6 shows the Seebeck coefficient of the SiGe/C joint as a function of the average temperature between the top and bottom sides. The specimens exposed at 1273K for 100h and 300h showed a higher Seebeck Coefficient than prior to exposure. This is because of enhanced carrier mobility[4].

The specimens exposed at 1373K for 300h showed a lower Seebeck Coefficient than prior to exposure. This is because the titanium atoms were diffused into the SiGe thermoelectric semiconductor as seen in Figure 5-(c). The titanium atom acts as a dopant.

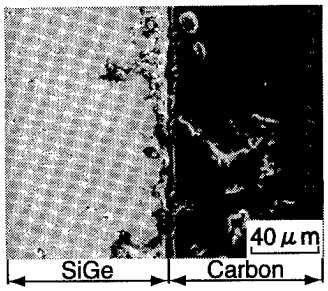
Figure 7 shows the resistivity of the SiGe/C joint, excluding the resistance of the carbon electrode, as a function of the average temperature between the top and bottom sides.

Specimens exposed at 1273K for 300h showed lower resistivity than prior to exposure. This is due to increased equilibrium carrier concentration or enhanced carrier mobility[4]. Specimens exposed at 1373K for 300h showed higher resistivity than prior to exposure. The reason for this is increased interface resistance due to the continuous voids as seen in Figure 5-(b).

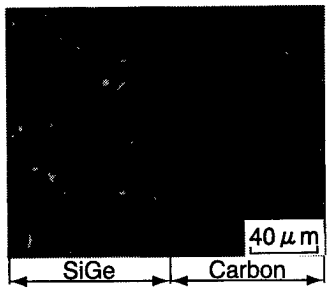
Figure 8 shows the power factor of the SiGe/C joint, excluding the resistance of the carbon electrode, as a function



(a) SEM Microphotograph of the Junction Layer of SiGe/C Expsoed for 300h at 1273K



(b) SEM Microphotograph of SiGe/C Exposed for 300h at 1373K



(c) EPMA Titanium Elemental Dispersion Profile of SiGe/C Exposed for 300h at 1373K

Fig.5 SEM Microphotographs and EPMA Elemental Analysis of Junction Layer in the SiGe/C Exposed in Argon

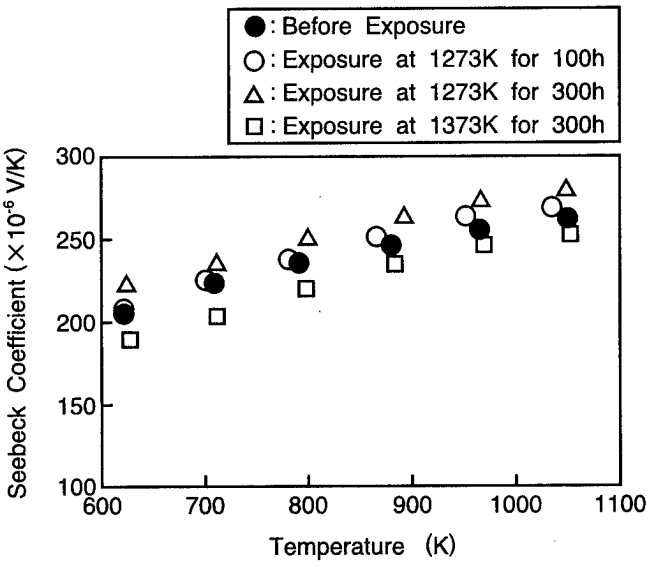


Fig.6 Seebeck coefficient of the SiGe/C Joint as a Function of the Average Temperature

of the average temperature between the top and bottom sides. The power factor of the SiGe/C joint is degraded at 1373K in an argon atmosphere.

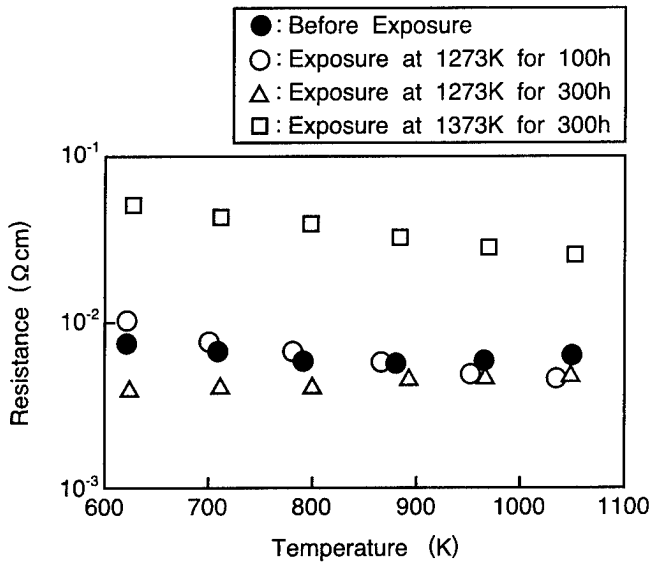


Fig.7 Resistance of the SiGe/C Joint as a Function of the Average Temperature, Excluding the Carbon Resistance

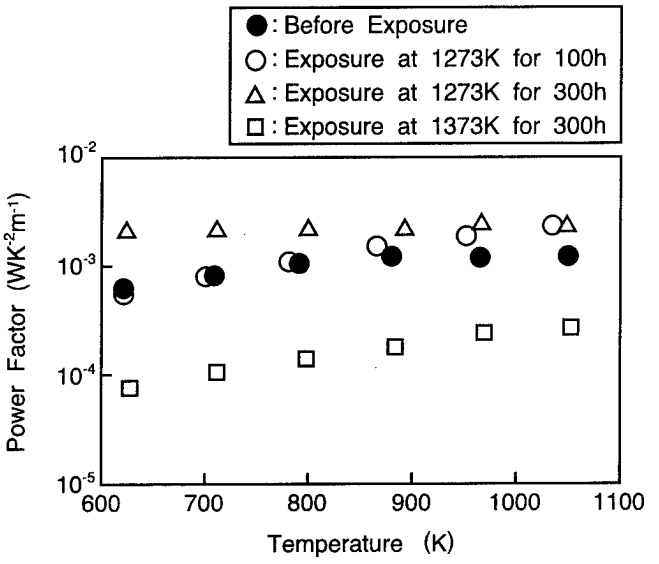


Fig.8 Power Factor of the SiGe/C Joint as a Function of the Average Temperature, Excluding the Carbon Resistance

Conclusions

This paper presented joints of Silicon-Germanium thermoelectric semiconductor and electrodes prepared by hot-pressing, as well as the investigation results of the electrical properties of SiGe/C joints under conditions of high operating temperature and a period of over 300h in argon. Conclusions are as follows:

1) The carbon electrode is better than the tungsten electrode for joints with SiGe thermoelectric semiconductors, as joints of SiGe/C did not exhibit a continuous void and interactive layer. On the other hand, the SiGe/W joints were observed to have continuous voids in conjunction with increasing interface resistance.
2) This SiGe/carbon electrode joining method is allowable for use up to 1273K. Because voids were formed in the junction layer of the SiGe/C joint during exposure at 1373K, the power factor decreased from 2.5×10^{-3} $WK^{-3}m^{-1}$ to 2.8×10^{-4} $WK^{-2}m^{-1}$.

Acknowledgement

This study was performed using special Coordination Funds of the Science and Technology Agency of the Japanese Government. We would like to thank Dr. Miyajima and Dr. Teraki of Daikin Industries, Ltd., MEC Laboratory for their valuable advice.

References

[1] A report on "Development of Energy Conversion Material through Formation of Gradient Structures" (Phase 1: Apr. 1993-Mar. 1996), supported by Special Funds for Promoting Science and Technology, STA, Japan, Feb., 1997.

[2] K. Uemura and I. Nishida: Thermoelectric semiconductor and its application, Nikkankougyo Shinbunsya, (1988).

[3] J. Fleurial and A. Borshchevsky, "Mechanisms of carrier concentration enhancement in multdoped SiGe". Proc. of the 9th Int. Conf. On Thermoelectrics (ICT'9), USA, (1990), 206.

[4] S. Loughin, J. Nakahara, B. Franklin, W. McGlinchey, J.P. Fleurial and J.W. Vandersande, "Thermal cycling of *n*-type silicon germanium thermoelectric material after annealing at 1225 degree C", Proc. of the 11th Int. Conf. On Thermoelectric (ICT'11), Arlington, (1992), 37.

[5] L.W. Fu, D.M. Rowe and G. Min, "Long term electrical power factor stability of high temperature annealed SiGe/GaP thermoelectric alloys", Proc. of the 11th Int. Conf. On Thermoelectrics (ICT'11), Arlington (1992), 83.

{6] D.M. Rowe, G. Min and Y.A. Chen, "Carrier enhancement mechanism in *n*-type SiGe-GaP alloys", Proc. of the 12th Int. Conf. On Thermoelectrics (ICT'12), Yokohama, (1993), 69

[7] J. Fleurial, J. Vandersands, N. Scoville, C. Bajgar and J. Rolfe, "Optimization of hot-pressed *n*-type SiGe/GaP SiGe/B thermoelectric materials", Proc. of the 12th Int. Conf. On Thermoelectics (ICT'12), Yokohama, (1993), 137.

[8] K. Kisara, L. Chen, T. Sudo, N. Sakuranaka, M. Nina, "A measurement system for thermoelectric properties of gradually-segmented composite elements over a large temperature span", 3rd Int. Symp. on FGM, Swiss (1994). 666.

Thermoelectric generator for underwater wellhead

Philippe Dubourdieu, Géry Tribou
DCN CHERBOURG, BP 10, 50115 Cherbourg Naval, France
Tél: 02.33.92.64.05, Fax: 02.33.93.47.40, E-mail: 106030,411@COMPUSERVE.com

Steve BYRNE
TOTAL OIL MARINE plc
Tel: 44 1224 858 154, Fax: 44 1224 858 305 E mail: Steve_BYRNE@total.com

Abstract

DCN CHERBOURG, the French submarine builder, has a great deal of experience in underwater equipment. The company also has experience in thermoelectric technology which is used in submarines for cooling systems. In light of this experience, DCN CHERBOURG was contacted two years ago by an oil company in order to develop a thermoelectric generator for an offshore subsea application
The requirements were:
- a thermogenerator able to be inserted as a spool in a submarine pipeline
- site: North Sea (sea water temperature = 4°C)
- fluid: mix of oil and gas, temperature between 90°C and 120°C, pressure 450 bar.
The design began with thermoelectric module tests (electrical, thermal and mechanical). The objective was to select the type of thermoelectric module and the assembly system. The ceramic technology from MELCOR was chosen.
DCN CHERBOURG then made and tested a prototype. The performance results were not as good as expected, however, the prototype proved that a thermoelectric generator for an offshore subsea application was feasible.
The next step was the assembling of two thermogenerators (THEGS) for an offshore application. The performance measurements obtained during on-shore testing were as expected: about 100W at 70V.

Introduction

One of the main cost elements of a subsea production control system is that of the umbilical required to power the equipment and to transmit data between the xmas tree subsea control module and the topside facility. All the technologies exist to suppress this cable, the THEG however, has yet to be field proven as a power source .
DCN, having experience on thermoelements used on cooling systems, proposed to TOTAL the development of an underwater generator. This development has been conducted under a THERMIE funded EC research programme.
This paper shows the process used to develop and to test the required generator.

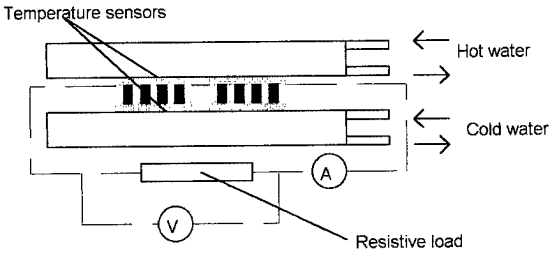
Requirements

The first requirement was the ability to deliver about 200W when the well is on stream.

The second requirement was the ability to work under water at depths up to 2000m and over.
The environemental conditions are:
- sea water temperature: 4°C
- effluent temperature over 100°C
- effluent pressure: 450 bar
- current around: 0 m/s

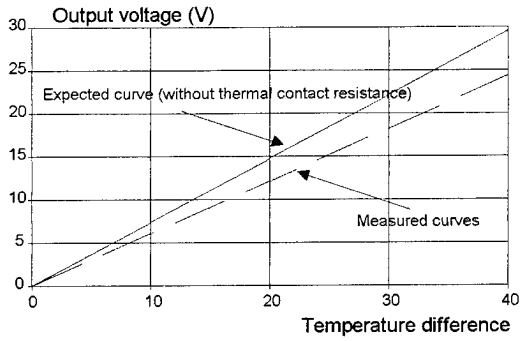
Development

The project started with a feasibility study. The purpose of this study was to verify the performance of different thermoelectric modules in several assembly concepts. The first part of the study determined the performance of the thermoelement: thermoelectric modules were placed between hot and cold plates and measurements of the voltage and power were taken.



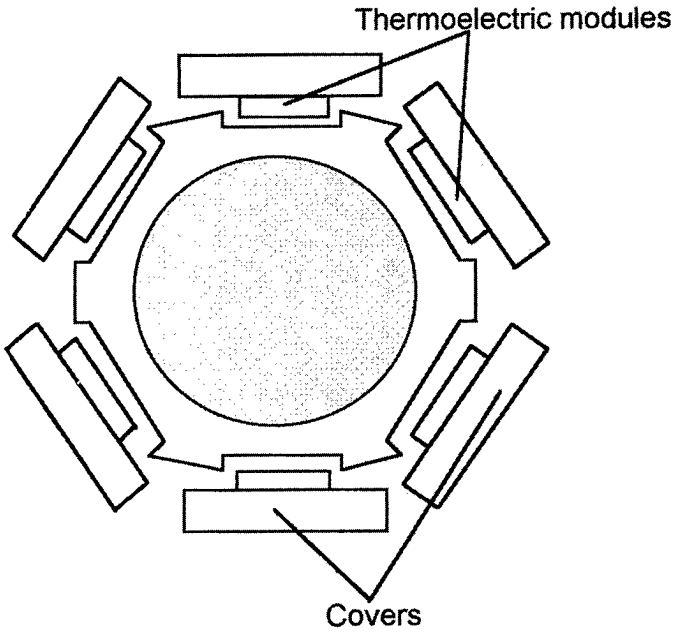
These tests were interesting because they allowed us to:
- choose the type of thermoelectric module,
- choose the interface material between modules, heater and cooler,
- check the performance of modules in comparison with theoretical values.

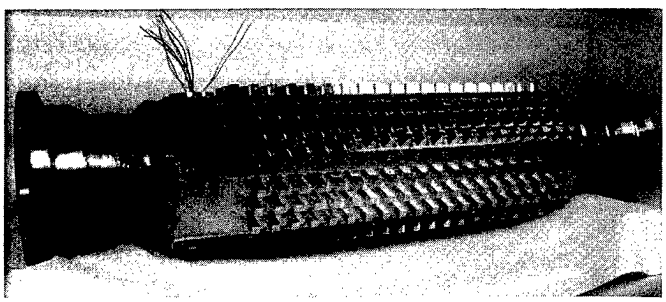
The main conclusions of the study are:
- The thermoelement choice: MELCOR thermoelectric modules Type CP 1.0-127-051-2, rated to 200°C
- The interface: even if the best interface material was chosen there would always be a voltage loss due to thermal resistance, as can be seen on the following figure:



The second stage of the project consisted of the manufacturing and testing of a Thermoelectric Generator (THEG) Prototype in order to validate the assembly concept and to determine the true performance of such a generator.

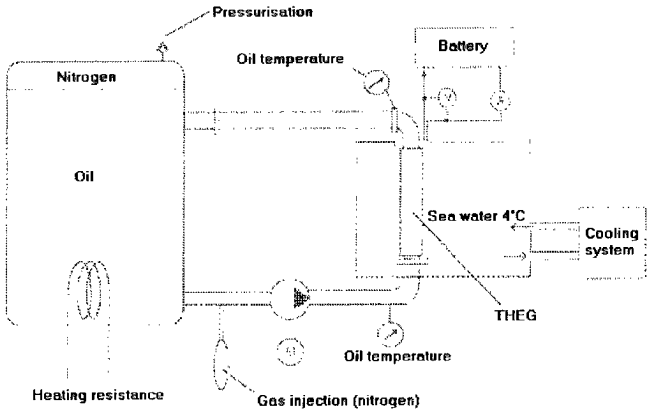
The prototype concept is:
- The body of the THEG is machined out of a piece of pipe. Six housings are machined so that the external shape looks like an hexagon. In each housing, two rows of 20 thermoelectric modules are placed. So, the THEG contains 12 rows of 20 modules. The modules in a row are connected in series and the 12 rows are connected in parallel.
- To protect thermoelectric modules from sea water, six covers in aluminium bronze are fixed onto the body (one per housing). These covers are used also as heat exchangers with sea water. they have a optimum thermal design.





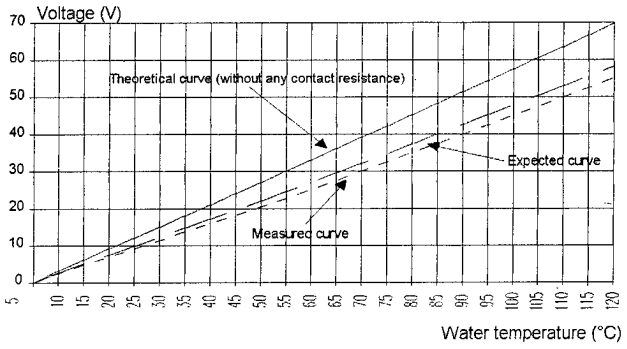
The THEG performance expected was deducted from thermal computation and from the test results made during the feasibility study.

Mechanical tests (internal and external pressure, vibrations) were made in order to check the resistance and the water tightness of the system. All the tests were successful.
To test the THEG performances, we had to define and assemble a specific test bench:

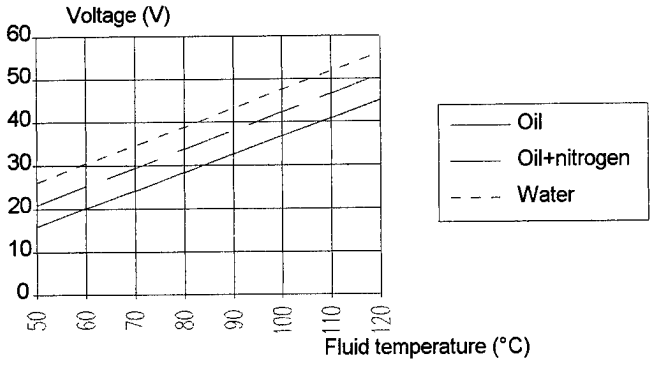


Tests for various conditions were performed:
- at several temperature
- at several flow rates
- using three different hot fluids: water, oil and oil+nitrogen

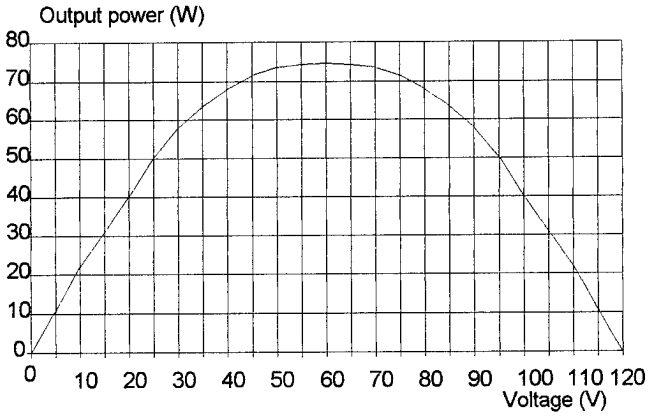
The first test was performed, with hot water. The output voltage (in open circuit) was measured and compared with that expected from computation. As can be seen on the following figure, the results are very close to the performance expected taking into account thermal contact resistance.



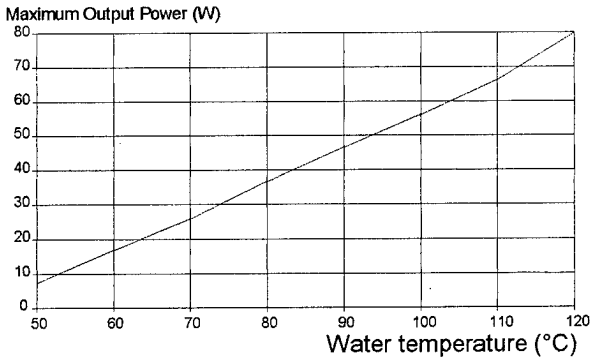
A large influence due to flow (comparison made between 500m3/day and 1000m3/day) was not seen, but we saw that the voltage depends on the fluid used. For a given temperature, we had a higher voltage with water than with oil, but the nitrogen in oil increases the voltage (this case should be representative of typical oil production).



With a resistive load, the output current was measured and hence the output power.
Maximum power is reached when the voltage reaches half open circuit voltage, as shown in figure following:

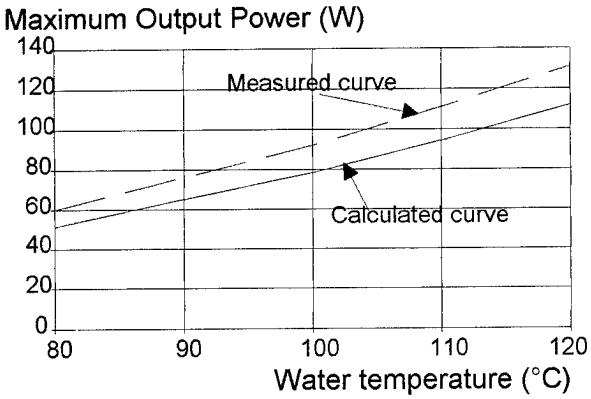


The maximum output power at various temperatures is also shown:



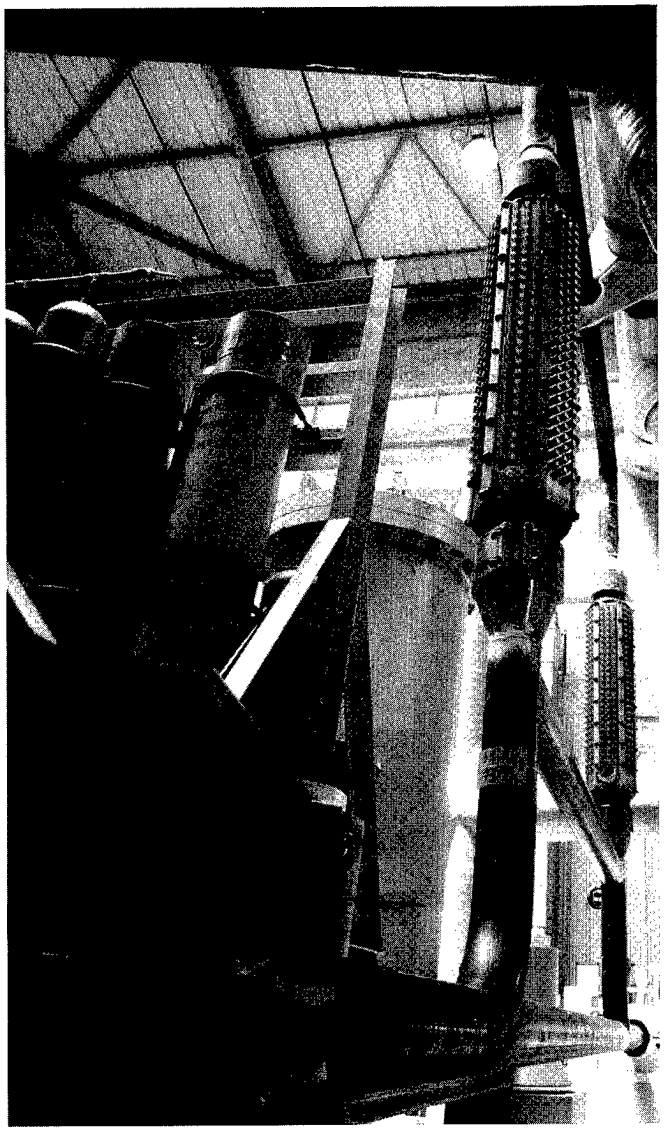
The battery was also charged by the THEG. The tests were successful and they proved that the system (battery+THEG) is efficient.
The advantage of such a system is the possibility to have large power amount of power available during a few minutes with a low average power provided by the THEG.

After initial prototype tests, DCN made two longer THEGS (length=prototype length X 1,4). The connections between thermoelectric modules were a little different (6 rows in parallel, 56 modules in series per row) in order to produce about 100W, 70V with 120°C oil. These two THEGs will be used on a subsea wellhead. For the THEG the characteristic curve mesured with water is shown below:



Present situation

The two THEGS have been on test, at the bottom of a wet dock in Cherbourg, for two months. The results are very good anf they prove the efficiency of the equipment. We are awaiting the moment when the THEGS will be used on a subsea oil production wellhead.



THEGS Before Dock Tests

Further developments

- The first is to adapt this equipment to other applications such as a gas field.
- The second is try to define and to use specific thermoelements deticated to electricity production.

THE USE OF THERMOELECTRIC CONVERTERS FOR THE PRODUCTION OF ELECTRICITY FROM BIOMASS

Markus Doloszeski, Alfred Schmidt
Institut für Verfahrens-, Brennstoff- und Umwelttechnik, Technische Universität Wien, Austria
Tel.: ++43-1-58801-5063; Fax.: ++43-1-5876397; mdolos@fbch.tuwien .ac.at

Abstract

The utilisation of renewable sources of energy to replace fossil fuels has been discussed in great detail in the last years. Their role in reducing carbon dioxide emissions and conserving natural resources has been widely realised. Among the renewable sources of energy bioenergy appears to have at the present the greatest potential. The use of biofuels for heating purposes in rural areas has been developed extensively in the past years especially in the Nordic countries and Austria. In these countries the contribution of biofuels to the total energy demand has reached 12 to 15%.

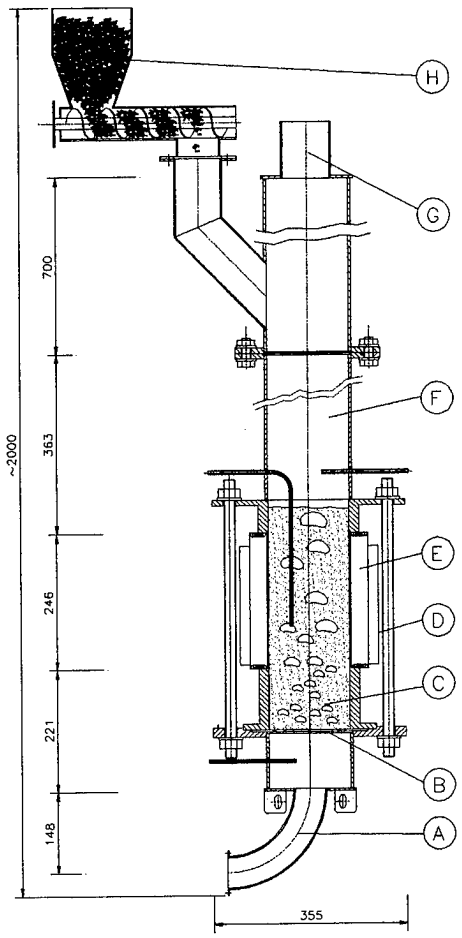
Efforts to produce electricity from biomass have been less successful although this would be for great interest for small scale decentralised power production in remote rural areas. Three technologies have been suggested: steam engines, gasification of biomass combined with gas motors and Stirling engines. All the technologies mentioned involve the use of elaborate mechanical equipment and, therefore, need for their operation and for their maintenance highly trained personnel.

During the past 25 years thermoelectric converters have been developed mainly for space applications. This technology is now also being applied to supply electricity in remote places such as light houses or on mountains but appear also possible in bioenergy applications. These installations are normally supplying hot water for space heating. Low conversion efficiencies to electricity are no problem as heat can also be utilised. First tests of the technology have been performed in a bench scale unit in the laboratory. It has a capacity of about 0.45 kW electricity and 6.8 kW of heat in form of hot water.

Experimental Setup

A Thermoelectric Generator (TG)[1] usually powered with Propane/Butane or Natural Gas has been installed in a special designed testrig for biomass combustion. BFBC combustion technology (Bubbling Fluidisised Bed Combustion) has been chosen to guarantee best heat transfer at moderate combustion temperatures at about 800°C. The TG has a cylindric cross section and is part of the combustion chamber. Combustion heat is transferred from the hot sand particles to the inner surface while the cold junction side is surrounded with a water jacket maintaining a large temperature gradient across the TG respectively the thermocouples. An additional shunt regulator circuit prevents the TG from an current more than 30 A and an open circuit voltage of more than 50 V.

The TG is based upon lead telluride technology. Similar TGs are used in a number of self powered devices in harsh and remote environment and military applications [1-3]. According to the company's specifications the electrical output at standard conditions is 550 W.



A...fluidisation-air inlet
B...windbox, distributor
C...BFBC bed
D...water jacket
E...TG
F...freeboard
G...exhaust
H...feeding assembly

Figure 1: Technical drawing of the testrig

Basic Equations

For the calculation of the thermoelectric properties S_{AB}, R_i and K a simple algorithm based on the following equations for thermoelectric power generation has been used [4, 5]:

Under steady state conditions, omitting the Thompson effects and following basic assumptions balancing the hot junction side equations (1) to (8) can be derived:

[1] 550 W Generator, Global Thermoelectric , Model 8550

- Any additional electrical resistance of the junction interfaces between the thermoelectric elements and the hot and cold plates and between adjacent thermoelectric materials are neglected.
- All heat from the source is assumed to pass into the thermoelectric elements, i.e. stray heat leakage is neglected.

$$Q_a = Q_p - \frac{1}{2}Q_j + Q_K \qquad (1)$$

$$Q_a = S_{AB} I T_i - \frac{I^2}{2} R_i + K\Delta T \qquad (2)$$

$$P = I \cdot U = \frac{(S_{AB}\Delta T)^2 R_l}{(R_i + R_l)^2} \qquad (3)$$

$$P_{\max} = \frac{(S_{AB}\Delta T)^2}{4R_l} \qquad (4)$$

with

$$R_i = R_A + R_B = \rho_A / D_A + \rho_B / D_B$$
$$K = K_A + K_B = k_A D_A + k_B D_B \qquad (5)$$
$$D_n = A_n / l_n$$

For a maximum power output from the TG, the load resistance R_l should be equal to the internal generator circuit resistance $R_i = R_1 + R_2$. Using definition (6) the maximum efficiency (7) is

$$\eta = P / Q_a \qquad (6)$$

$$\eta_{\max} = P_{\max} / Q_a = \frac{\Delta T}{2T_i - \Delta T/2 + 4/Z} \qquad (7)$$

with

$$Z = \frac{S_{AB}^{\ 2}}{(R_A + R_B)(K_A + K_B)} \qquad (8)$$

Z is called the "figure of merit". The quantity of Z is determined by the properties of the thermoelectric materials. For solids Z typically is of the order from $1 \cdot 10^{-3}$ to $3 \cdot 10^{-3}$ [C^{-1}].

Measurements and results

Measurements were carried out at different bed temperatures starting at about 330°C up to 800°C. The fluidisation air in a first step was preheated to warm up the bed particles and after gaining the ignition point, feeding of the biofuel (chips or pellets) was started. For determining the temperatures at the cold respectively at the hot junction side heat transfer coefficients for both, bed to hot shell and cold junction side to cooling water were calculated. The flow of the cooling water was adjusted to maintain a cold junction temperature of about 100 °C. At stable temperature gradients over the TG the load resistance was varied in the range from 0.05 to ~ 10.0 Ohm measuring current and voltage of the thermocouples.
The experimental determination of the resistivity R_i and the Seebeck Coefficient S_{AB} as a function of temperature difference was done using the basic equation for P (equation 3). The energy balance over the TG

$$Q_a = Q_c + P \qquad (9)$$

in combination with expressions (2) leads to values of K. Additional the momentary open circuit voltage was used calculating the internal resistance R_i.
The performance data of the TG are shown in figure 2. The maximum output at about 790 °C bed temperature is about 450 W at a hot junction temperature of 450°C with an optimal load resistance of 0,90 Ohm and an efficiency of 6,27% according to definition (6) (see figures 3 and 5).

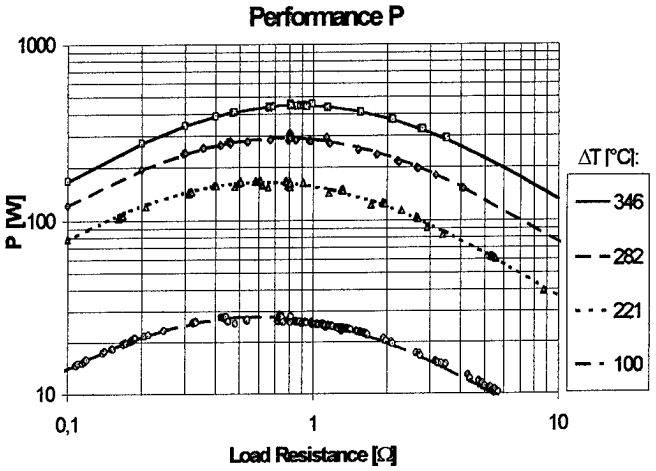


Figure 2: Performance at different temperature ΔT versus load resistance at a cold junction temperature of ~100 °C.

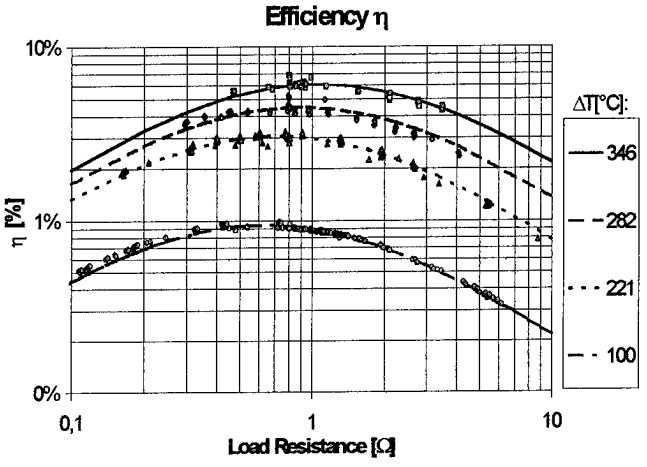


Figure 3: Efficiency according to definition (6) at different temperature gradients ΔT versus load resistance at a cold junction temperature of ~100 °C.

The allowed maximum temperature at this side of 580 °C could not be reached due to a bad heat transfer coefficient from bed particles to the hot shell (app. 230 W/m²K). The relative Seebeck Coefficients S_{AB} of the thermoelectric

material were found at 220 to 350 µV/°C with increasing thermoepower at high temperatures and are of same magnitude of highly doped PbTe materials.

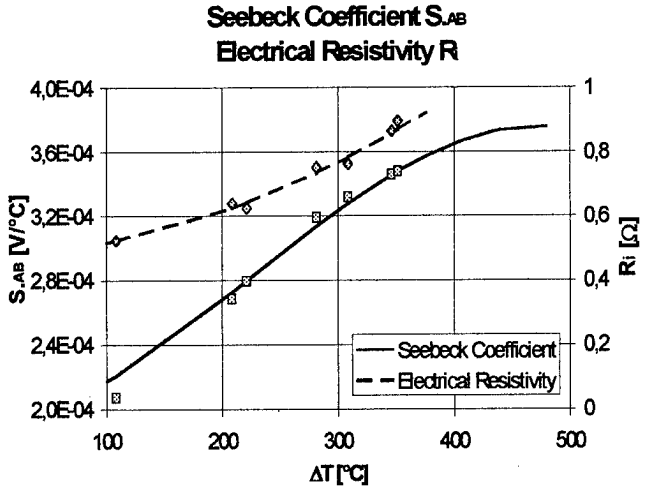


Figure 4: Seebeck Coefficient S_{AB} and internal generator circuit resistance versus temperature difference ΔT. Cold junction temperature at app. 100 °C.

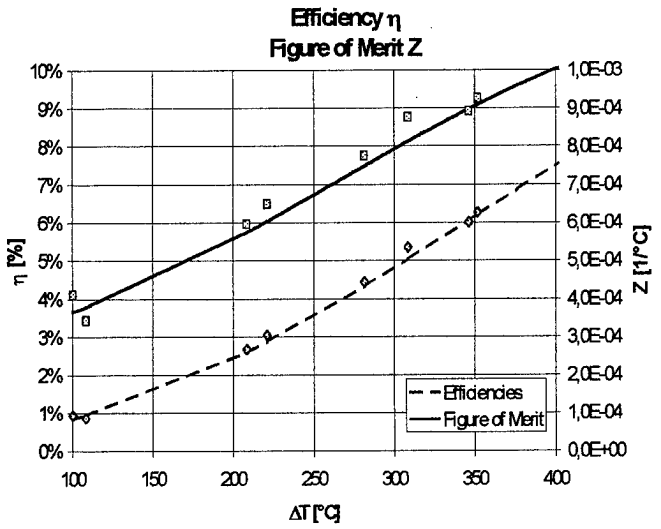


Figure 5: Efficiency and Figure of Merit versus temperature difference ΔT. Cold junction temperature at app. 100 °C.

Although the attained efficiency is in the range of comparable PbTe-TGs the overall efficiency of the test rig

$$\eta_0 = \frac{\text{electrical output}}{\text{fuel input}} \qquad (10)$$

is only about 1% due to great losses of heat in the freeboard and the exhaust.

The following table shows measured values for efficiencies and figure of merit compared to typical data from literature (Cold junction temperature 100 °C) [6, 7]. Parameters for Z are integrated values from T_i to T_a and represent average values for S, R and K neglecting again the Thomson heat (ref. [5]) .

	Temp. °C	Z [1/°C] measured	Literature
Hot	200	3,65E-04	1,18E-03
Junction	300	5,55E-04	1,21E-03
Temp.	400	7,91E-04	1,20E-03
	450	9,05E-04	1,22E-03

	Temp. °C	η [%] measured	Literature
Hot	200	0,84%	2,33%
Junction	300	2,42%	4,61%
Temp.	400	4,80%	6,61%
	450	6,15%	7,68%

Table 1: Comparison of measured data and literature data for a PbTe thermocouple.

Conclusions and Lookout

The current TG design is not optimised for biomass combustion. The high energy input provided through biomass requires a combustion air volume flow up to 50 m³/h. The relatively low cross section area of the TG leads to a high gas velocity of more than 2.5 m/s (usually maximum for BFCB combustion is about 1.0 m/s). Therefore a particle diameter of app. 800 µm has to be chosen to avoid elutriation of the bed material. Both, the high gas velocity and the large particle diameter result in a decrease of the heat transfer coefficient from the bed material to the hot shell (refer to figure 6).

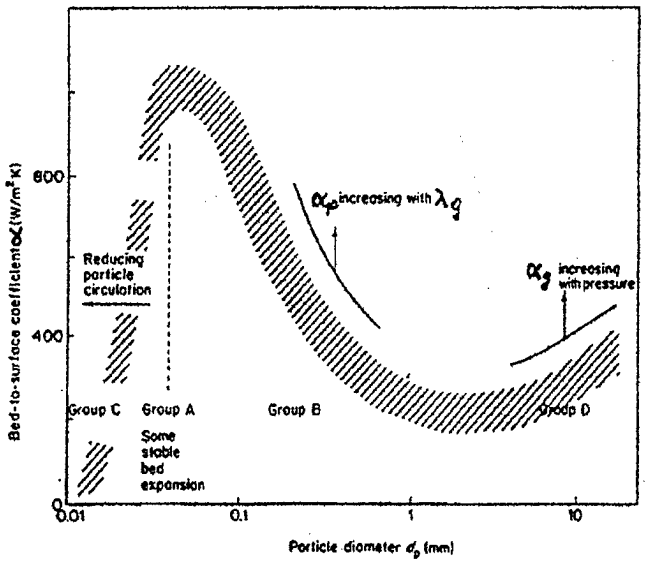


Figure 6: Bed-to-surface heat transfer [W/m²K] coefficient versus particle diameter [mm]

Furthermore the feeding point is about 400 mm above the BFBC surface. Devolatilisation of the biomass in the freeboard occurs and shifts the heat release from the bed to the freeboard. As a result less of the energy is transferred trough the TG and is lost by radiation in the freeboard. At high bed temperatures elutriation of the bed material and fuel (especially small wood chips) can be observed. Table 2 shows the energy

balance of the testrig in % of the fuel input. A special plant design with air preheating of the fluidisation air and assuming no radiation losses in the freeboard could gain an overall efficiency η_0 of app. 5% using the same PbTe materials.

energy	%
Electricity production	1
Cooling system heat production	14
Freeboard heat losses	51
Exhaust heat losses	34
Fuel input	100

Table 2: Energy balance.

References

[1] Valenti M., "Keeping the home fires burning", Mech. Eng. **115** (1993), p 66-96.

[2] Menchen W. R., "Development of a 0.1 kW thermoelectric power generator for military applications", Proceedings of the Intersociety Energy Conversion Engineering Conference 21st. Publ by ACS, Washington, DC, USA (1986), p1361-1366.

[3] Bass J. C., Elsner N. B., Leavitt F. A., "The preliminary design of a 500 watt thermoelectric generator", Proceedings of the Intersociety Energy Conversion Engineering Conference v 1 (1994), IEEE, Piscataway, NJ, USA,94CH3478-5, p 586-591.

[4] Cadoff Irving, Miller Edward, "The thermoelctric circuit",Thermoelectric materials and devices", New York 1960.

[5] Sherman B., Heikes R. R., Ure R. W. Jr., "Calculation of efficiency of thermoelectric devices", Journal of Aplied Physicys, **31**, No 1 (1960).

[6] Fritts, R. W., "Properties of lead telluride", thermoelectric materials and devices", New York 1960.

[7] Rowe D. M., Bhandari C. M., "Theoretical thermoelectric figure of merit of highly disordered lead telluride type materials", Energy Convers. Mgmt., **24**, No. 4 (1984), p 345.

[8] Hofbauer H., "Wirbelschichttechnik, Unterlagen zur Vorlesung", Institut für Verfahrens-, Brennstoff- und Umwelttechnik, Technische Universität Wien, Austria, (1996), p 65-76.

Nomenclature

Symbol		[*unit*]
Q_a...	heat transferred from the bed to the TG	*W*
Q_c...	heat transferred to cooling assembly	*W*
Q_j...	Joule heat	*W*
Q_K...	conduction heat flowing in the TG legs	*W*
Q_p...	Peltier heat	*W*
P...	performance	*W*
I...	current	*A*
U...	voltage	*V*
η, η_0...	efficiencies	-
R_l...	load resistance	*Ω*
R_i...	internal TG circuit resistance	*Ω*
$R_{(index)}$...	internal TG circuit resistance of material (index)	*Ω*
$\rho_{(index)}$...	specific resistivity of the material (index)	*Ωcm*
$K_{(index)}$...	total thermal conductance of the thermocouples	*W/°C*
$K_{(index)}$...	total thermal conductance of the material (index)	*W/°C*
$k_{(index)}$...	specific conductivity of the material (index)	*W/cm°C*
$A_{(index)}$...	area of the TG leg of material (index)	*cm²*
$D_{(index)}$...	form factor of material (index)	*cm*
$l_{(index)}$...	length of the TG leg of material (index)	*cm*
S_{AB}...	relative Seebeck Coefficient of the thermocouple V/°C	*V/°C*
Z...	figure of merit	*1/°C*
T_a...	hot junction side temperature	*°K*
T_i...	hot junction side temperature	*°K*
ΔT...	temperaturedifference over the TG	*°C, °K*

Index $_A$..Material A
Index $_B$..Material B

Comprehensive Research of the Institute of Thermoelectricity, Ukraine on the Theory, Material Science and Applications of Thermoelectricity

Anatychuk L.I.

Institute of Thermoelectricity, General Post-Office, Box 86, 274000, Chernivtsi, Ukraine
Tel:+380/3722/44422, Fax:+380/3722/41917, E-mail:Alex@ite.Chernovtsy.ua, WWW: http:\\www.ite.Chernovtsy.ua

Abstract

Results of works on the phenomenological and microscopic theory of thermoelectricity together with the theory of thermoelectric energy conversion have been presented. New thermoelectric effects, generalizations of the basic Thomson relations, generalizations of the electric current induction phenomena for the case of a thermoelectric medium, generalizations in thermoelements description as well as methods for new types of thermoelements discovery have been examined.

Examples of new types of thermoelements offering some advantages over the known ones have been given. Actual lines of the microscopic theory of thermoelectricity development and possibilities of new energy converters making based on the combined effect of electromagnetic and thermal fields have been studied.

In the field of thermoelectric material science the analysis results of thermoelectric materials figure of merit crisis, bounderline possibilities of thermoelectric figure of merit have been given, a new step of thermoelectric material science based on the use of materials with programmed inhomogeneity has been predicted. Results of combined study of such materials for the case of thermoelectric cooling and electric energy generation have been presented. Values of maximum possibilities for thermoelectric energy conversion efficiency improvement on the base of functionally graded materials have been given. Results of computer investigations and technology of materials with programmed inhomogeneity have been given. Other actual trends in further developments of thermoelectric material science have been considered.

In the field of practical use of thermoelectricity it was given the data on three basic directions - measuring equipment, thermoelectric cooling thermoelectric generators. Within the measuring equipment direction data on the achievements of the information-and-energetic theory as applied to thermoelectric detectors, devices and systems have been given. Data on the developed thermoelectric detectors with maximum values of sensitivity and devices on their basis have been given. Within the thermoelectric cooling direction the information about methods of computer design of cooling modules, developed series numbers of cooling modules of one to twelve stages for different temperatures levels; developed on their basis thermoelectric cooling and temperature stabilization devices, have been presented. Within thermo-electric generators direction results on reliability theory recent achievements as applied to thermoelectric energy converters, developments of a new number of modules for the operating temperature level up to 300°C with increased values of efficiency and reliability have been given. Information on generators based on such modules for restored energy sources, utilization of different heats, autonomous heat and electric sources have been given. Concept of cooling and generation modules optimal parameters, methods of their measurements, description of measuring equipment for modules parameters determination has been given.

Introduction

The Institute of Thermoelectricity is engaged in the complete set of interrelated scientific and applied research, design and process development, as well as manufacturing of thermoelectric products. It is our aspiration that theoretical research could continue in the engineering and technological developments and, further, in the manufacturing of thermoelectric products. The fundamental research includes phenomenological and microscopic theories of thermoelectric phenomena, as well as thermoelectric energy conversion. According to the requirement, the Institute is developing applied theoretical trends which basically include the theory of thermoelectric energy converters. The Institute is investigating the trends of thermoelectricity development and devising rational fields of thermoelectric device application. Computer methods of thermoelectric device design are being developed. Investigations in the field of thermoelectric material science are being carried out. The comprehensive character of the research carried out in the Institute is illustrated in the Fig.1.

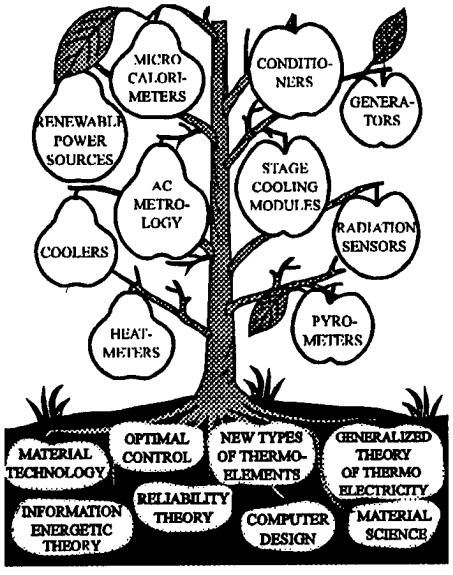


Fig.1. Pattern of research development in the Institute of Thermoelectricity of National Academy of Sciences and Ministry of Education of Ukraine.

Let us consider in more detail the state and prospects of each trend.

Phenomenological theory of thermoelectricity

To understand the potentialities of thermoelectricity, it is important to obtain full scope of possible thermoelectric effects. The necessary generalizations have been made within the linear and local thermodynamics for arbitrary homogeneous, inhomogeneous, anisotropic media affected by arbitrary physical fields and complete classification of thermoelectric, thermomagnetic and galvanothermomagnetic effects has been made (Fig. 2). In addition to the existing

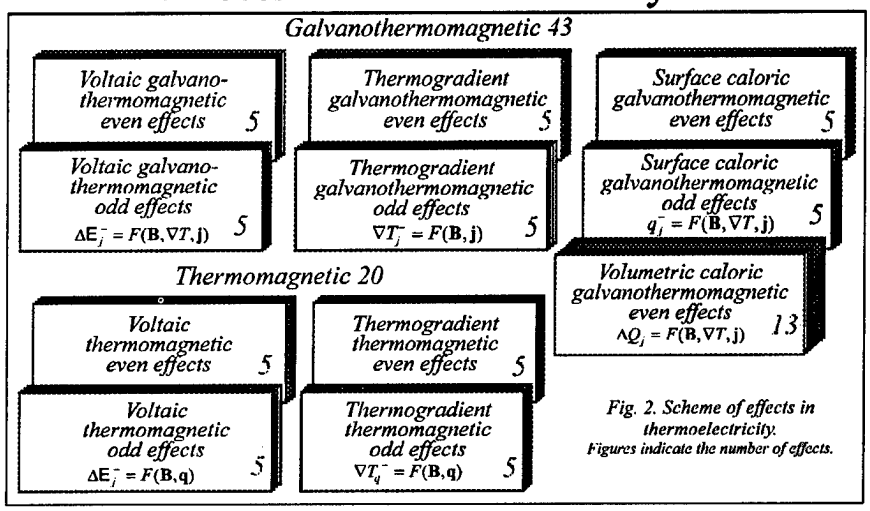


Fig. 2. Scheme of effects in thermoelectricity. Figures indicate the number of effects.

effects, the classification allows to discover a series of new effects, namely, thermogradient and caloric ones (Table 1).

Table 1. New predicted effects.

Medium			
Irregular	Quasi-Onsager	Gyrotropic	Isotropic
New thermogradient thermomagnetic effects			
$\Delta\tau_q^- C\perp$ $\Delta\tau_q P\perp G$ $\Delta\tau_q^+ C\perp$ $\Delta\tau_q^+ P\perp H$ $\Delta\tau_q^+ P\perp G$	$\Delta\tau_q^+ P\perp H$ $\Delta\tau_q^+ P\parallel G$ $\Delta\tau_j^+ C\perp$ $\Delta\tau_j^- P\parallel$ $\Delta\tau_j^- P\parallel G$	$\Delta\tau_j\parallel, \Delta\tau_j C\perp$ $\Delta\tau_j^- P\perp G, \Delta\tau_j^+ C\perp$ $\Delta\tau_j^+ P\perp H, \Delta\tau_j^+ P\perp G$ $\Delta\tau_j^- C\parallel, \Delta\tau_j^- C\perp$	—
New thermogradient galvanothermomagnetic effects			
$\Delta\tau_q C\perp$ $\Delta\tau_q^- P\perp G$ $\Delta\tau_q^+ C\perp$ $\Delta\tau_q^+ P\perp H$ $\Delta\tau_q^+ P\perp G$	$\Delta\tau_q^+ P\perp H$ $\Delta\tau_q^+ P\parallel G$ $\Delta\tau_j^+ C\perp$ $\Delta\tau_j^- P\parallel$ $\Delta\tau_j^- P\parallel G$	$\Delta\tau_j^-\parallel, \Delta\tau_j^- C\perp$ $\Delta\tau_j^- P\perp G, \Delta\tau_j^+ C\perp$ $\Delta\tau_j^+ P\perp H, \Delta\tau_j^+ P\perp G$ $\Delta\tau_j C\parallel, \Delta\tau_j C\perp$	—
New surface caloric effects			
$\Delta K_j P\parallel$ $\Delta K_j P\parallel G$ $\Delta K_j C\parallel$ $\Delta K_j C\perp$	$\Delta K_j^- C\parallel$, $\Delta K_j^+ P\parallel$	$\Delta K_j^- C\parallel, \Delta K_j^- P\parallel$ $\Delta K_j^- C\perp, \Delta K_j^- P\parallel G$ $\Delta K_j^- \perp, \Delta K_j P\perp H$ $\Delta K_j P\parallel G, \Delta K_j C\parallel$	—
New volumetric caloric effects			
$T\mathrm{Dev}(\hat{\alpha}^{s-}): \mathbf{Def}\,\mathbf{j}, -\mathbf{Tj}\,\mathrm{Div}, \hat{\alpha}^{s+}, -\mathbf{Tj}\frac{\partial}{\partial T}(\hat{\alpha}^{s-} - 2\hat{\alpha}^{s-})\tau$			—
Can occur in all the media		−TNrotj, − TjrotN	

The notations in conformity with Ref.[1] have been used in the table. More than two tens of new effects have been discovered. Their study can open the opportunities of new applications. It can also enrich the understanding of physics of thermoelectric phenomena.

Investigations have been carried out to discover the effects that are described by the nonlinear and nonlocal thermodynamics of irreversible processes. In addition to the well-known Benedics effect, this approach has allowed to discover a series of new effects which occur due to extreme influences on the thermoelectric medium. These data are generalized in Ref.[2]. An important result of this approach is the possibility of new situations occurring in the interaction of electron and phonon subsystems which contribute to favourable conditions for the increase of thermoelectric material figure of merit.

Modern thermoelectricity is known to be based on the Seebeck effect which is a particular case of thermoelectric effects in the inhomogeneous medium with a pronounced inhomogeneity. The model describing this effect is generally known and illustrated in Fig.3. However, there can exist another, more general approach to the formulation of the problems of thermal into electrical energy conversion based on the generalization of electromagnetic induction phenomena for the cases of nonisothermal media. This description is schematically shown in Fig.4. This approach allows to

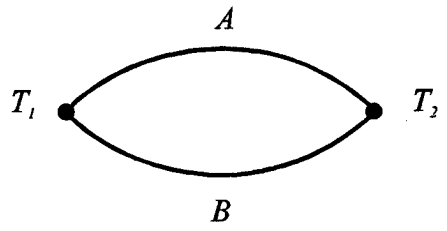


Fig.3. Diagram of Seebeck effect.

consider within the uniform treatment the process of energy conversion at the electromagnetic induction and the process of thermoelectric energy conversion. In the former case the Foucault currents originating in the conducting medium are used for the formation of current loop whose cut and current withdrawal to the external circuit results in the diagrams of electrotechnical devices (transformer, dynamo, etc.), which have formed electrical engineering. In the latter case the similar procedure leads to the generalized model of thermoelectric energy converter. Its consideration leads to a series of important consequences.

Firstly, the investigation of this model allows to answer the question: which media and which influences in the form of external physical fields result in thermoelectric conversion. The results of this investigation are illustrated in Table 2. The squares of the table classify the combinations of properties of

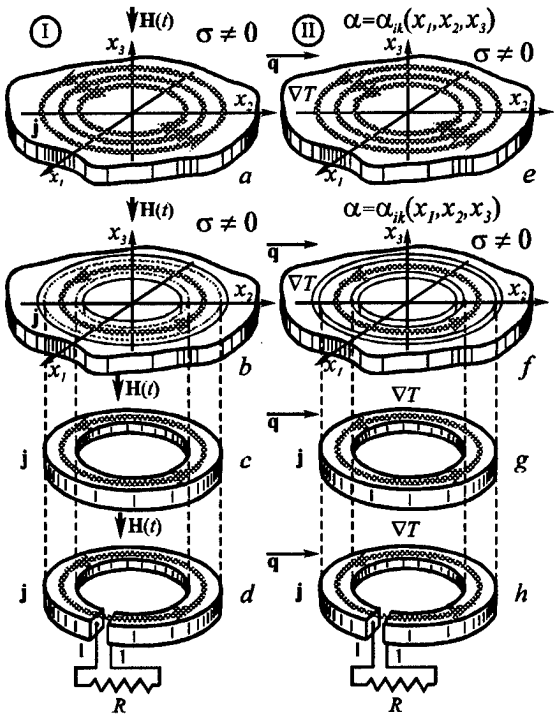


Fig.4. Diagrams leading to creation of energy converters based on the use of eddy current concept: I - diagram of creation of electromagnetic energy converter; II - diagram of creation of thermoelectric energy converter; a - eddy Foucault current induced in conducting medium; b - current loop formed by Foucault current lines; c - current loop in alternating magnetic field; d - current loop in alternating magnetic field with current tapping to external circuit; e - thermoelectric eddy currents induced in conducting thermoelectric medium, g - current loop from thermoelectric medium - generalized model of thermoelectric energy converter; h - current loop from thermoelectric medium with current tapping to external circuit; 1 - current tapping electrical contacts.

Table 2. Thermoelectric media and external influences leading to the thermal into electrical energy conversion.

External influences	Medium properties															
	σ	σ(x,y,z)	σ	σ(x,y,z)	σ_ik	σ	σ_ik	σ_ik(x,y,z)	σ_ik(x,y,z)	σ(x,y,z)	σ_ik	σ	σ(x,y,z)	σ_ik(x,y,z)	σ(x,y,z)	σ_ik(x,y,z)
	α	α	α(x,y,z)	α(x,y,z)	α	α_ik	α_ik	α	α_ik	α_ik	α(x,y,z)	α_ik(x,y,z)	α_ik(x,y,z)	α(x,y,z)	α_ik(x,y,z)	α_ik(x,y,z)
ΔT	0	0	+	*	0	+	*	0			+					
ΔT, H	+	*	+	*			+	+	+	+						
ΔT, P	+	+					+									
ΔT, E				*												
ΔT, H, P	+															
ΔT, H, E																
ΔT, H, P, E																
∇T	+															

Notations: 0 - conversion is impossible, + - conversion is under investigation, * - conversion is used, ΔT is temperature field, H is a magnetic field, P is force field, E is electric field, ∇T - is high temperature gradient, σ, α - are homogeneous and isotropic electrical conductivity and thermoemf, σ_{ik} , α_{ik} - are homogeneous and anisotropic electrical conductivity and thermoemf, $\sigma(x,y,z)$, $\alpha(x,y,z)$ are inhomogeneous and isotropic electrical conductivity and thermoemf, $\sigma_{ik}(x,y,z)$, $\alpha_{ik}(x,y,z)$ are inhomogeneous and anisotropic electrical conductivity and thermoemf.

thermoelectric media and fields which can induce thermoelectric currents, i.e. thermoelectric energy conversion. In one of the squares of this table there is a well-known thermocouple, in another there are well-known thermoelements using thermoemf anisotropy, for example Justi thermoelement, in the third square there are thermomagnetic energy converters based on the Nernst-Ettingsgausen effect. These squares illustrate the present state of thermoelectricity application. Still other fifteen squares have been filled with comparatively few investigations. The rest of the squares have not been studied at all and are blank spaces on the thermoelectricity map. It can be easily seen that the richest functional potentialities are in the squares that are still uninvestigated and embody, undoubtedly, the prospects of thermoelectricity. Let us illustrate this by several examples. At first the method was developed to find the way of discovering new thermoelement type from any square of the table (Fig.5). For this purpose the theory of solving the

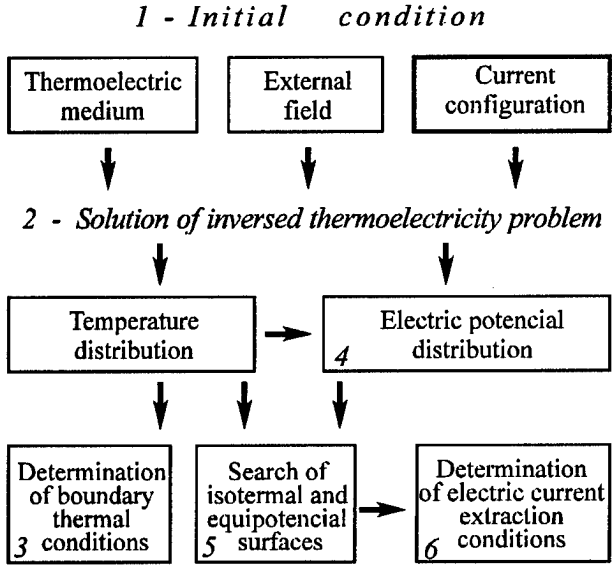


Fig. 5. Method of discovery of new thermoelement types.

inverted thermoelectricity problems has been developed [3]. It allows to find the temperature distribution at assigned current distributions in the medium and assigned medium properties. For example, to obtain circular currents, the current lines

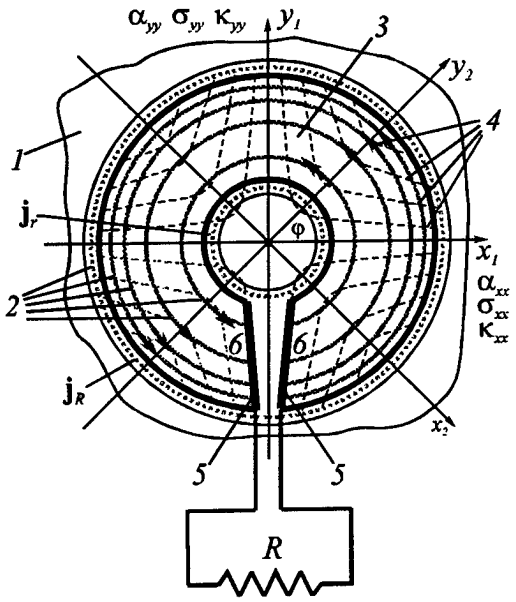


Fig. 6. Diagram for devising of thermoelectric converter with circular eddy currents. 1 - two-dimensional medium; 2 - circular eddy currents; 3 - current loop limited by current lines; 4 - equal temperature and equipotential lines; 5 - lines of current loop cut; 6 - electrical contacts.

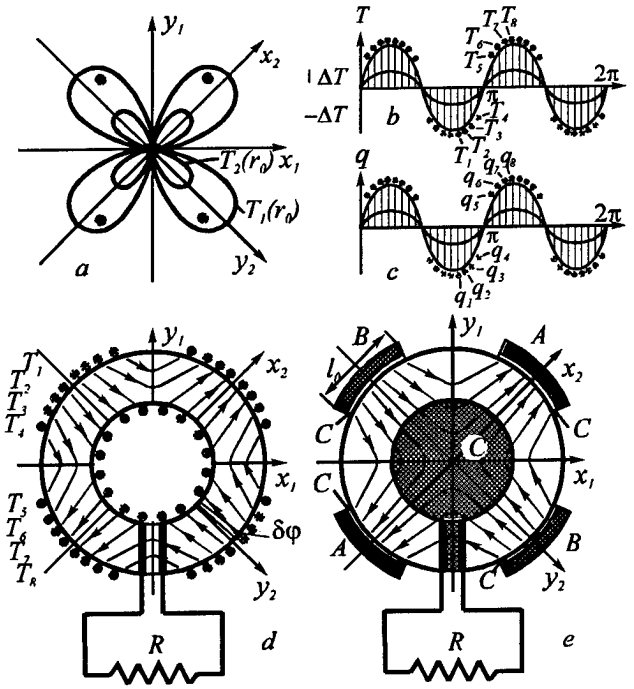


Fig. 7. Creation of thermal conductions in the anisotropic converter with circular currents. a, b - temperatures on the external and internal loop boundaries; c - thermal flows through the external and internal and loop boundaries; d - method of creating thermal conditions in the loop by using a set of heaters and coolers; e - method of creating thermal conductions in the loop by two heaters A and two coolers B; C - insulations with heat conductivity κ; l_0 - length of heaters and coolers.

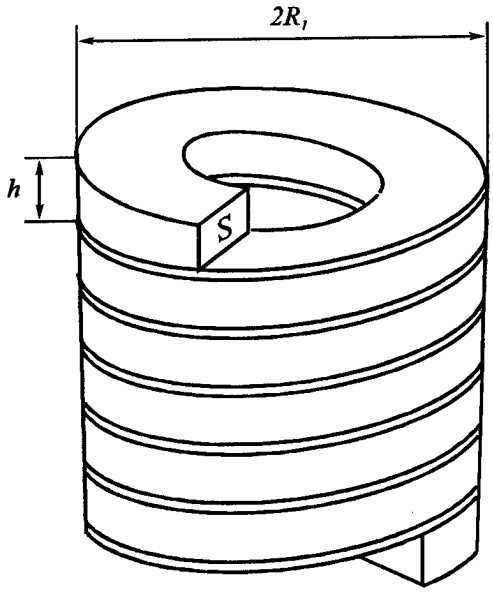


Fig. 8. Circular single-crystal-spiral for thermoelectro-generator.

must have the form of hyperbolae (Fig.6). Withdrawal of current originating in the medium to the external circuit is also shown in the figure. Fig.7 illustrates the variants of creating these temperature distributions by placing heat and cold sources on the inner and outer surface of the sample. A simplified variant is also shown which includes only two heat and cold sources. Actually, we have obtained a new thermoelement type with circular currents similar to Foucault currents. Similar to electrotechnical devices, this thermoelement can be made in the form of a single crystal spiral (Fig.8) which can serve as the basis for a new variant of helical generator with two heaters and coolers (Fig.9). This generator has no junctions, and the necessary currents and voltages develop by increasing the number of spiral coils and choosing the spiral coil cross section. This demonstrates full analogy between the thermoelectric and electrotechnical devices.

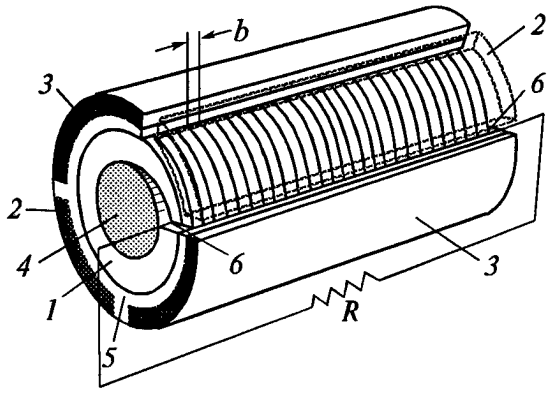


Fig. 9. Helical thermogenerator. 1 - spirals of single-crystal material; 2 - heaters; 3 - coolers; 4 - filling substance; 5 - insulation; 6 - electrical contacts.

The above example demonstrates the feasibility of method for devising new thermoelement types. This thermoelement type has not been discovered accidentally or by conjecture. It is a result of systematic approach with mathematical design of its configuration. This systematic approach opens up high potentialities of finding new thermoelement types. More than two tens of new thermoelement types have been developed in the Institute of Thermoelectricity thus far which have considerably expanded the potentialities of thermoelectricity.

Thus, for example, based on the rectangular helical structures (Fig.10) an exceptionally convenient and well-behaved helical rectangular thermoelement has been obtained which develops the voltage equivalent to tens of thousands of series connected thermocouples. This thermoelement successfully solves many problems of thermoelectricity use in measuring technique.

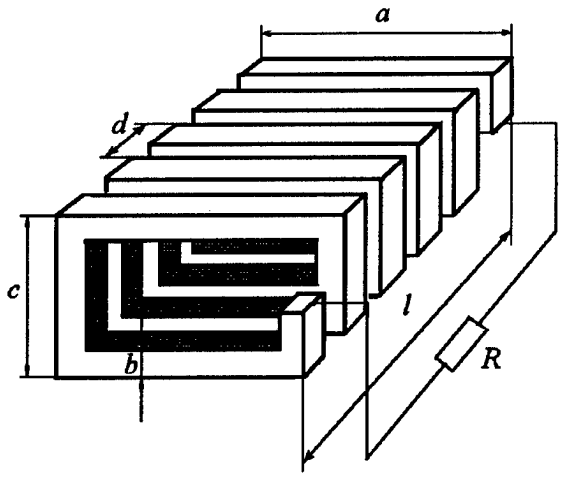


Fig.10. Rectangular single-crystal-spiral for thermogenerator.

The short-circuited thermoelements (Fig.11) created by this method can serve as another example. In this thermoelement combined actions of medium anisotropy and inhomogeneity have been considerably used. It can use the best materials with high values of thermoelectric figure of merit and natural or artificial electrical conduction anisotropy. These thermoelements are practically not inferior to traditional thermocouples in efficiency, but their reliability is considerably higher compared to them.

It is interesting to note that the method of Fig.5 usage leads to the thermocouple discovery once more. As mentioned, the thermocouple is inhomogeneous medium with sharp inhomogeneity (Fig.12). Maximal eddy current appears in this medium when the temperature gradient is directed along the medium interface. Using the method (Fig.5) one obtain the thermocouple model (Fig.12c). However such investigation did not lead to new type thermoelement discovery, but it confirmed this method efficiency new thermoelement types discovery.

On the whole, despite the fact that inhomogeneous medium in thermoelectricity has always been and still is the main object of research and application, it has not been inves-

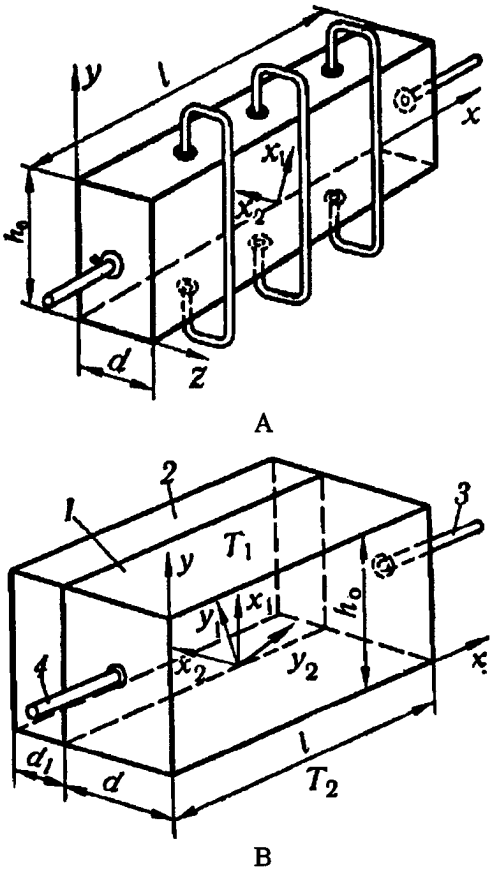


Fig. 11. Short-circuited thermoelectric converter of a single-crystal with anisotropic electrical conductivity. A - short-circuited current is formed by conductor short-circuit; B - short-circuited current is formed in two plates with anisotropic electrical conductivity.

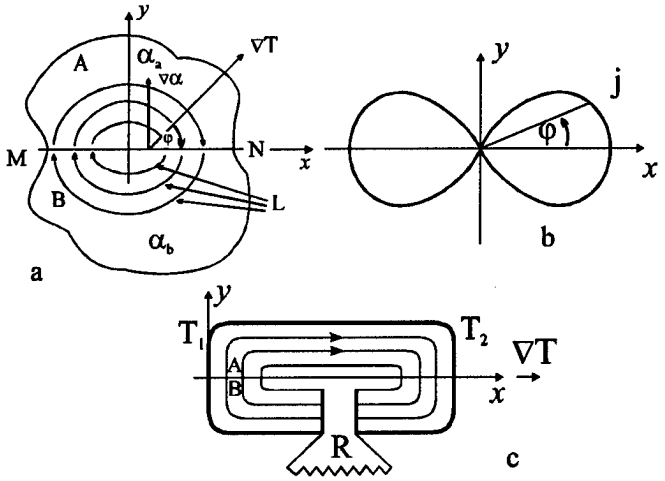


Fig. 12. Models of inhomogenious media for devising of thermocouple Seebeck energy converter; a - inhomogenious medium of two various inhomogenious media A and B with pronounced inhomogenity with respect to termoemf; L-eddy current lines. φ-the angle between the interface of two media MN and the direction of thermo-emf coefficient change; b-eddy current value as a function of temperature gradient orientation with respect to the direction of thermoelectric coefficient change; c - current loop between two current lines.

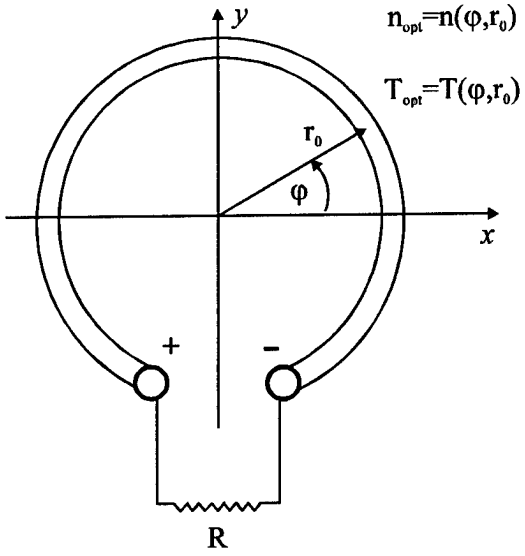


Fig. 13. Loop with optimal inhomogeneity and optimal temperature distribution.

tigated up to now as a loop with optimally changing homogeneity in optimal temperature fields with a view to reach maximum efficiency (Fig.13). Only recently the interest for this research has increased which has resulted in the formulation of problems on creation of function-graded materials. However, even during the formulation of this research specific problems of finding optimal inhomogeneity distribution in the thermocouple legs are solved. Mathematical methods of search for optimal functions by methods of optimal control theory have been developed. The basic results have been cited in the monograph [4] and are further developed in the Institute of Thermoelectricity [5].

The above-mentioned trends of phenomenological research include stationary processes. Non-steady thermoelectricity practically has not been developed up to now. Meanwhile, it is a completely new and promising trend of thermoelectricity where the processes of thermoelectric conversion are essentially different from those in stationary thermoelectricity. Under these conditions the restrictions imposed on the figure of merit of materials used in steady-state may change, which can create a favourable situation for the efficiency increase. The Institute of Thermoelectricity is carrying out a research in this direction [1]. In particular, the expression has been obtained for local efficiency at the moment of time t under the non-steady conditions

$$\eta(t)=\eta_{\text{Carnot}}\,T\left\{\frac{\alpha^*}{\Pi^*}\,\frac{i-\left(Z^*T\right)^{-2}}{i+1}+\frac{\frac{dU_0^*}{dt}}{\kappa^*}\right\}, \qquad (1)$$

where dU_0^* is the change in the internal energy of the elementary converter volume; α^*, Π^*, κ^*, Z^* are thermoemf, Peltier coefficient, thermal conductivity and material figure of merit in the elementary volume [1]. A table has been built that includes various medium and external field variants which contribute to thermoelectric conversion under the non-steady conditions. Pyroelectric and piezoelectric energy conversion can be found in this table as a particular case (Table 3). In the table α is thermoelectric medium, *p* piezoelectric medium, β pyroelectric medium.

Table 3. Mediums and influences leading to the thermal into electrical energy conversion in the transient state.

External influences	Medium properties					
	α	p	α, p	α, β	β, p	α, β, p
∇T	+	+	-	-	-	-
∇T, **B**	+	-	-	-	-	-
∇T, **E**	-	-	-	-	-	-
∇T, **p**	+	-	-	-	-	-
∇T, **B, E**	-	-	-	-	-	-
∇T, **B, p**	+	-	-	-	-	-
∇T, **E, p**	-	-	-	-	-	-
∇T, **B, E p**	-	-	-	-	-	-

The Institute of Thermoelectricity is engaged in applied research directed to creation of scientific fundamentals for functioning of thermoelectric instruments and devices. This includes information and energy theory of thermoelectric measuring systems.

When designing thermoelectric measuring devices the approaches are usually used which are valid for creating thermoelectric devices of energy purpose. However, the process of electric energy generation from the thermal energy and the process of getting information from the thermal channel are not identical. Accordingly, the descriptions of these processes are also different.

The information and energy theory has been developed in the Institute of Thermoelectricity with respect to the detectors and measuring devices in which thermoelectric energy conversion has been used. According to this theory, the efficiency has been replaced by the informative capacity parameter

$$\Omega=\frac{dI}{dt}, \qquad (2)$$

which determines the number of information units I that can be obtained per unit of time from the thermoelectric measuring device. Theoretical research has allowed to establish the elation between the informative capacity parameter, the design parameters of converters and the properties of thermoelectric materials used in converters [6]. It has been found out that to reach maximum informative capacity, the thermoelectric material must have not only high values of ZT, but also constant ratio $\frac{\alpha}{\kappa}$ in the operating temperature range.

For the realization of these conditions traditional methods of thermoelectric material optimization are not acceptable.

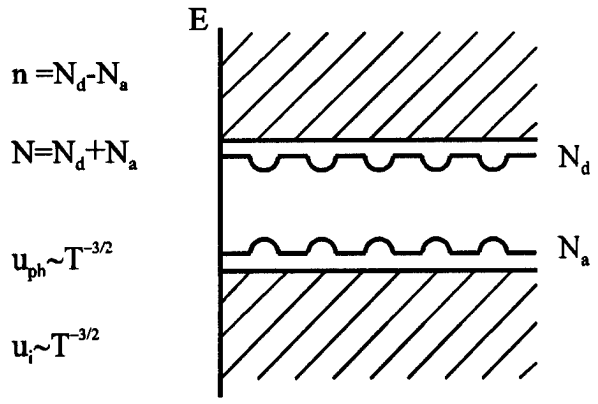


Fig. 14. Energy model of compensated semiconductor.

Therefore, the method of simultaneous optimization by the acceptor and donor impurities was used which realized the mechanism of partial electron and hole compensation (Fig.14). With proper choice of the difference between the acceptor N_a and donor N_d impurity concentrations the number of current carriers depends on the difference between their values, and scattering of current carriers depends on the sum of the acceptor and donor concentrations. Thus, two competing scattering mechanisms can be formed, namely, scattering of current carriers on the ionized impurity u_i and on the phonons u_{ph} and for reaching stability in the assigned temperature range. This method was used in the development of thermoelectric material technologies for thermoelectric detectors. Thus, various detectors have been produced - infra-red radiation detectors, microcalorimeters, heat flow meters and other measuring devices with high informative capacity values 50-250 bit/sec.

The development of reliability theory of thermoelectric devices and systems is an important trend of applied research. This trend of thermoelectricity is in a rather primitive state, therefore the data on the reliability of thermoelectric devices are not precise enough. In the Institute of Thermoelectricity the state of this problem has been analysed and the scope of research necessary for the improvement of situation has been determined. For this purpose a cycle of research to determine correct physical and mathematical reliability models has been carried out in the Institute, alongside with the analysis of the laws of thermoelectric device failure probability distribution, rational system of reliability parameters and characteristics, methods of reliability calculation, accelerated test methods for reliability determination. Detailed information on this matter can be found in Ref. [7]. The resultant data underlied the analysis of reasons for the insufficient reliability of thermoelectric devices and development of new designs and technologies for creation of highly reliable thermoelectric converters. The use of these achievements allowed, in particular, to create thermoelectric modules for the generators of Altec type with reliability values 10-1000 times higher than the traditional ones.

Numerous research cycles have been carried out in the Institute on the microscopic investigation of thermoelectric materials. Among them the investigations to specify the electron and phonon spectra of thermoelectric materials *Bi-Te*, *Cd-Sb*, *Zn-Sb*, *Pb-Te*, *Ge-Si* and others. The purpose of these investigations is to determine the microscopic characteristics for design and optimization of thermoelectric material properties. Particular emphasis has been placed on the anisotropic scattering processes and, on the whole, on the peculiarities of low-symmetry crystal properties. Two reasons prompted to study these problems in detail - the elevated figure of merit values that can be obtained in anisotropic materials and direct use of the anisotropy of crystal properties to create thermoelectric energy converters. The mechanisms of thermoemf anisotropy origination and the methods of its increasing have been discovered. Based on these data, the methods of anisotropic thermoelectric material optimization have been developed that underlied creation of proper technologies [1].

Marginal figure of merit potentialities of thermoelectric materials based on crystalline structures have been also studied from which it follows that maximum ZT values in homogeneous crystalline structures cannot, apparently, exceed 2-3. These results give grounds to concentrate the efforts on further investigation of the unusual thermoelectric materials, namely, composite structures, including powder materials, materials contributing to quantum well origination, etc. [8,9].

Practical works of the Institute of Thermoelectricity are concentrated in three basic directions - design and manufacturing of generators, coolers and measuring devices. Analysis shows that the low power range of 10^{-3} - 10^{3} W where thermoelectric generators have absolute advantages is most acceptable for generators today. To realize these potentialities, we have solved the technological problems of creating microminiature thermopiles that contain up to tens of thousands of legs in 1 cm^3 of the module. These modules are used to solve the problems of creating numerous sources of milliwatt range. The heat sources for these generators include isotopes (space and medical use), temperature differences in grounds, release of human heat, etc. These generators can work at low temperature differences (units and tens of degrees). The second problem included creation of reliable thermopiles for utilization of low-grade heat sources - waste heat from internal combustion engines, gas turbines, waste heat from industry, garbage combustion, etc. A series of modules of Altec type has been developed that allows to build module generator blocks of electrical power 10-1000W. These blocks can be used to create thermoelectric energy plants of various power depending on consumer demand (for example, 200kW for utilization of heat from garbage combustion [10].)

From the standpoint of creating efficient thermogenerators it is important to develop reliable devices that convert fuel energy into thermal energy. Highly efficient and reliable catalytic converters have been developed in the Institute of Thermoelectricity for this purpose. Their use in combination with thermoelectric modules allows to create reliable and easy to operate sources of heat and electrical energy. They are convenient not only as autonomous sources

but also as a means to formulate the problems of new general concepts of electricity and heat supply.

In the field of thermoelectric cooling the Institute has developed the efficient programs of cooling module design based on the optimal control theory. This is the way to reach the best cascade matching and optimization of cascade materials. In addition to existing modules, the modules with increased operating temperature range - up to 200°C, and recently up to 350-300°C, have been developed by the Institute. Single-cascade modules with increased cooling capacity, as well as two-cascade wide used modules have been created to replace single-cascade modules of numerous household and other technique. The Institute has developed the technologies of multi-cascade vacuum modules. These results are a good ground for development and manufacturing of numerous cooling and thermostatting devices for electronics, radio engineering, metrology, household technique, medicine. Besides, the theory of thermoelectric cooling based on function-graded materials has been developed, and the potentialities of using dynamic modes for thermoelectric cooling that add to the increase of coefficient of performance and ΔT_{max} by 20-30% have been studied. In the field of measuring engineering, as it was already mentioned above, the information and energy approach has served as the basis of instrument and device development. Computer programs have been created for the optimization of thermoelectric detectors and their materials. Numerous measuring devices have been created, namely, radiation detectors, microcalorimeters, alternating current transformers, pyrometers, etc. with parameters exceeding the existing analogues.

On the whole, analysis shows that the progress in the 21st century will be undoubtedly attributed to the development of information needs and, to a lesser extent, to the increase in power consumption. Therefore, the use of thermoelectricity must gradually tend to greater use of thermoelectric devices for obtaining information compared to thermoelectric devices for producing electrical energy and cold.

References

[1] L.I. Anatychuk. Physics of thermoelectricity. ITE, Chernivtsi, 1997.

[2] L.I. Anatychuk, L.P. Bulat. Thermoelectricity under high temperature gradient. To be published.

[3] L.I. Anatychuk, O.J. Luste. Thermoelectric eddy currents. Calculation and control methods. Report at ICT'97.

[4] L.I. Anatychuk, V.A. Semenyuk. Properties optimal control of thermoelectric materials and devices. Prut, Chernivtsy, 1992, 264 p.

[5] L.I. Anatychuk, L.N. Vikhor. Optimal control in stage thermoelectric generators design, in Proc. XIV ICT'95, St. Petersburg, 1995, p. 372-375.

[6] L.I. Anatychuk, O.J. Luste, E.L. Maslyanchuk. Informative - energetic description of thermoelectric converters, in Proc. XI ICT'92, Arlington, Texas, 1992, p. 160 - 163.

[7] L.I. Anatychuk, O.J. Luste. Reliability problems in thermoelectricity. Report at ICT'97.

[8] S.V. Melnichuk, S.V. Kosyachenko, M.V. Vozny. Thermoelectric properties of super lattices. Report at ICT'97.

[9] L.I. Anatychuk, S.V. Kosyachenko, S.V. Melnichuk. Texture influence on the forming of thermoelectric properties of pressed semiconductors, in Proc. XV ICT'96, Pasadena, CA, USA, 1996, p. 191 - 193.

[10] L.I Anatychuk, Yu.Yu. Rozver, K. Misawa, N. Suzuki. Thermogenerators for waste heat utilization. Report at ICT'97.

A Critical Evaluation of Today's Thermoelectric Modules

Todd M. Ritzer, Paul G. Lau, Andy D. Bogard
TE Technology, Inc., 1590 Keane Drive, Traverse City, MI 49686
Tel: (616) 929-3966, FAX: (616) 929-4163, e-mail: cool@tetech.com

Abstract

Today's thermoelectric module (TEM) users are experiencing a growing world marketplace filled with new or undiscovered sources for components. Selecting the right thermoelectric module supplier for a particular application is not as easy as it once was.

New applications in thermoelectrics are occurring faster now than ever before as more people learn the benefits of using the technology. As these applications become more diversified and the variety of the customer's needs expands, other criteria should be considered before selecting a TEM supplier based solely on price, performance and delivery.

This paper examines TEMs produced by manufacturers from all over the world. A module performance survey illustrates the range of products available today. Some of the TEM's were selected from this survey to undergo a variety of quality and reliability tests. These tests include electro-thermo cycling, high temperature ramp and soak, and thermal pulse. In addition, dimensional and visual inspections were performed and the results are included as a part of the over-all "vendor qualification" process described in this paper.

Introduction

A series of tests and measurements should be performed in order to thoroughly evaluate a TEM. Most of these tests are designed to examine the performance and reliability of the module. Failures, as a result of these tests, usually occur in the areas of pellet joining.

After a TEM has passed the performance requirements of a particular application, the next step is to determine whether or not the device will be reliable. To do this, the TEM is subjected to three standard tests incorporating various conditions designed to stress pellet diffusion barriers and the module's mechanical joining quality.

TEM Performance Test

The first area of interest when selecting a TEM is typically the performance of the device based on the particular requirements of the application. The test method most widely used to measure the performance characteristics of a TEM is referred to as the modified Harman technique.

This test, originally developed by T. Harman and J. Honig[1] in the early 1960's, was modified by R. Buist[2] to incorporate a "transient" method that enabled one to quickly and accurately measure the Seebeck coefficient, α; electrical resistivity, ρ; thermal conductivity, κ; and ZT.

The data presented in Figure 1 illustrates the ZT values for a standard 127 couple, 6 amp module. The Y-axis represents the ZT value measured in the thermocouple mode[2] at room temperature. Each letter designation on the X-axis represents a different TEM manufacturer. The second set of points for letters E, A, and F represents the values of modules commonly found in products produced by these vendors. The high levels of ZT by these vendors illustrates what they're capable of producing upon "special selection". This is especially interesting to note in the "A" vendors' case, having the capability of producing the best performing TEM in the lab and nearly the lowest in large volume production.

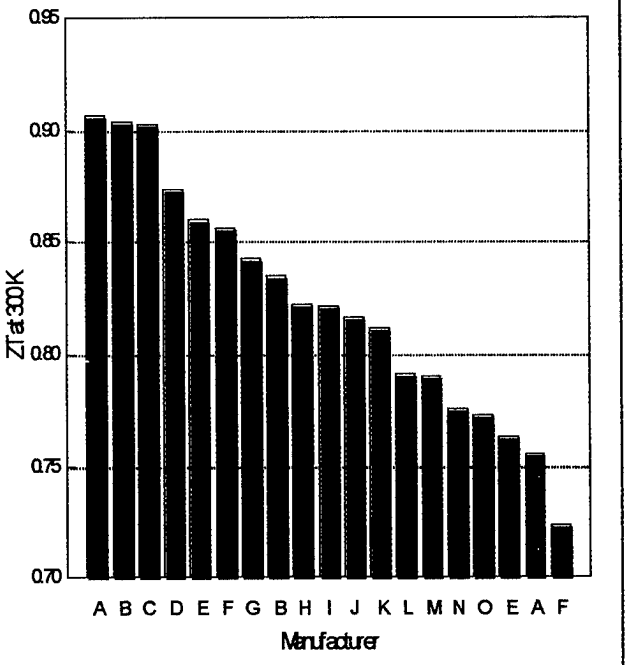


Figure 1 Thermoelectric Module Survey

Cycle Test

The next test, TEMs are commonly subject to undergo, is often referred to as the cycle test. Techniques of this type of test vary from manufacturer to manufacturer but the basic principle remains the same. The TEMs are usually temporarily assembled between two heat sinks. Power is then applied to the module for a short period of time, usually 5 to 10 minutes. An automatic timer switch then reverses (some only power off as in Bell 40/90 test) the power to the TEM for another short duration, thus completing a cycle.

The test method used for gathering this data applied approximately 12 VDC in the positive or "cooling direction" for 5 minutes. The power is then reversed to the negative direction for a 5 minute increment at approximately 5 VDC.

The temperatures that were produced during this particular test were approximately -15°C in the cooling mode and approximately 50°C when heating. A counter recorded the number of cycles completed throughout the test. The test apparatus incorporated the "bang-bang" or "full-power-on" process when power is applied to the module and was capable of testing up to 6 TEMs simultaneously. This particular method was more severe than the standard "Bell 90/40" test, therefore, reducing the time required to determine TEM reliability.

The data presented in Figure 2 illustrates the shift in AC resistance as a result of over three thousand temperature cycles. The test data shows rapid degradation in modules #4 and #5. This trend indicates likely catastrophic failure for these two modules. The continuing increase in AC resistance for the other three modules is further evidence this manufacturer has unreliable TEMs.

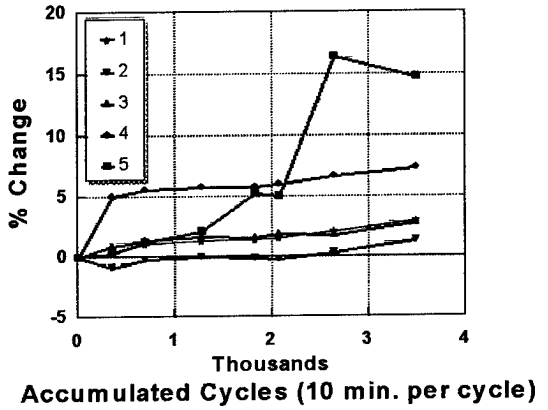


Figure 2 Percent Change in AC-Resistance Due to Temperature Cycling

Figure 3 is an example of a group of TEMs that have undergone the same test. These TEMs exhibit a slight shift in AC resistance initially, however, level-off at an acceptable value, <5% change.

High Temperature Ramp and Soak Test

This test, sometimes referred to as a bake test, is used to thermally stress a TEM. The TEM is subjected to elevated ambient temperatures near the maximum operating range for extended periods of time. The stresses incurred during this type of test affect both the effectiveness of the nickel diffusion barrier on the TE material and the mechanical integrity of the solder bonds at each junction.

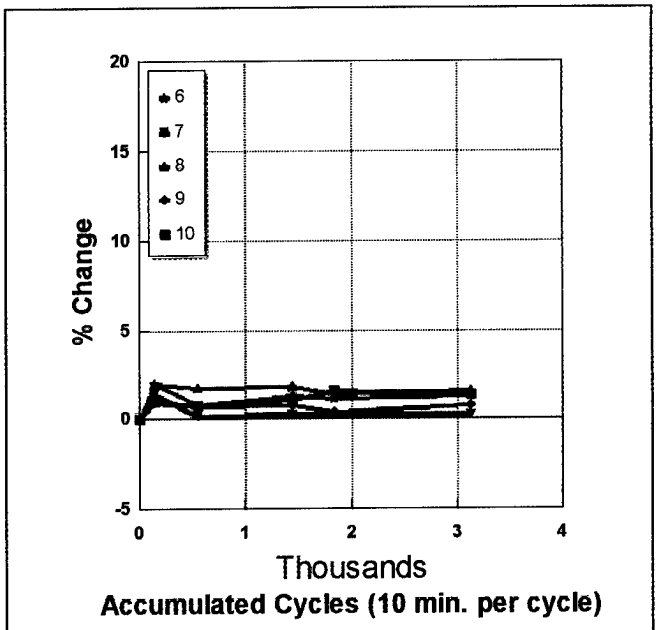


Figure 3 Percent Change in AC-Resistance Due to Temperature Cycling

The TEMs used for this test are standard high temperature devices that are rated for continual operation up to 200°C. Before exposure to the high temperature environment, the modules were tested to measure the AC resistance and ZT. Any increase in AC resistance and/or decrease in ZT observed in TEMs after this type of high temperature exposure would be an indication of an inferior TEM.

The TEMs were placed in a laboratory oven and heated to 160°C for a 24 hour period. The TEMs were then removed from the oven and allowed to cool to room temperature. The AC resistance and ZT values were measured again and TEMs were placed back into the oven for another heating interval at 160°C. After approximately 72 hours, the TEMs were removed from the oven, allowed to cool to room temperature, and the AC resistance and ZT measured again. A final sequence of baking at 160°C for 168 hours was completed and again, the values for AC resistance and ZT measured.

Figure 4 shows the effect on the AC resistance as a result of over 260 hours of exposure at 160°C. These 10 TEMs exhibit an alarming rise in AC resistance at a temperature 40°C lower than the specified operating range. Some TEMs changed over 40% and all of them continued to increase when the testing was stopped. It was clear from this dramatic increase that the TEMs would likely not survive an operating environment near 200°C. It was not certain whether the actual failure mechanism was due to a degradation in the diffusion barrier or a mechanical breakdown in the solder junctions. Further analysis is needed to make this determination.

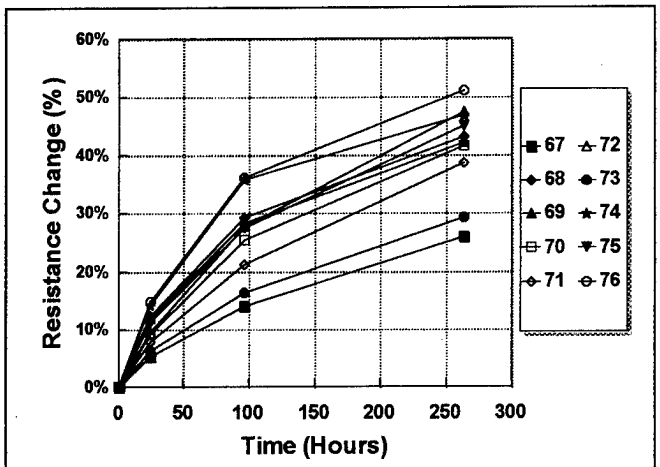


Figure 4 Effect of Exposure at 160°C on Resistance of TE Modules

Figure 5 illustrates the effect the high temperature exposure had on the ZT of the TEMs. It can be expected that a dramatic increase in AC resistance could result in a significant decrease in ZT. This phenomenon was observed in all 10 TEMs as a result of this test.

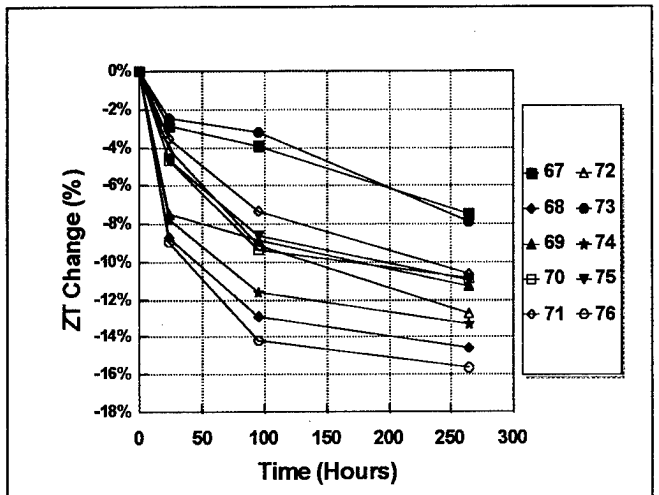


Figure 5 Effect of Exposure at 160°C on ZT of TE Modules

However, this degradation was not as extreme as in the case of the shift in AC resistance. In fact, the ZT failures made a significant shift initially, while beginning to level off after 100 hours. These observed changes could be as a result of diffusion of copper into the TE material. Since the magnitude of the AC resistance increase was so great and was continually rising, it can be surmised that the nature of the failure was more mechanical than chemical.

Thermal Pulse Test

There is another type of test that can be performed on TEMs to evaluate the integrity of solder junctions. This test applies a brief pulse of AC voltage to all the solder connections in a TEM. This instantaneous high voltage burst of energy will create substantial heat in solder connections that are inadequate. This heat energy, which is a function of contact resistance, can be observed by placing a piece of thermally activated paper, such as ordinary facsimile paper, against both surfaces of the TEM as the pulse is applied. Any extreme "hot-spots" in the TEM will expose the thermal paper somewhat like opening the shutter on a camera exposes film.

This test can be performed on any type of TEM and yield results in only a few seconds. Having the ability to quickly test a TEM for solder junction integrity has its advantages and disadvantages though. One shortcoming of this technique is that it is not very quantitative. It cannot always be determined whether or not the TEM is certain to fail during operation or not. It has been the author's experience, however, that these "hot-spots" are an indication of poor workmanship and/or inferior TEM components such as ceramic metalization, nickel plating on tabs or insufficient solder bonding.

The photograph in Figure 6 illustrates the results from a pulse test that was performed on two TEMs produced by different manufacturers. Both of the modules were similar in type and tested under the same conditions. The voltage was adjusted to 100 VAC and the pulse time to 1/10 of a second. It was determined through a few set-up runs that these parameters produced the best exposure for this particular type of TEM.

It can be observed that the thermal paper in the top of the photograph has a relatively uniform exposure of both sides of

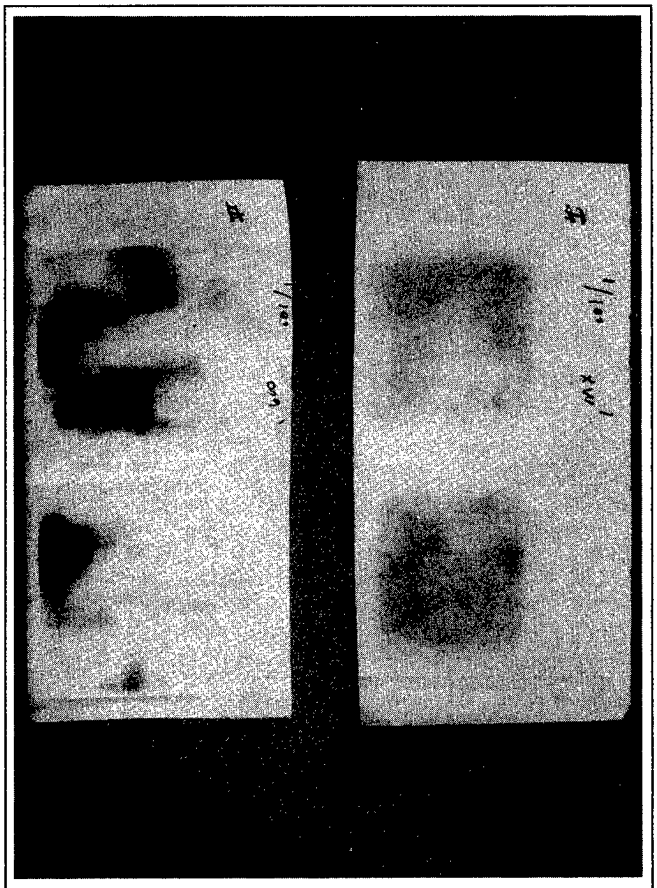


Figure 6 Exposed Thermal Paper due to Thermal Pulse Test

the TEM. From this type of even heat spreading throughout the module it can be surmised that this was a good module. However, the exposure pattern in the bottom sample shows evidence of extreme heating in several pellet junction areas on both sides of the TEM. This type of pattern is evidence of non-uniform contact resistance throughout the TEM.

Discussion

The data presented in the previous sections illustrated several cases where TEMs failed due to the rigors of vigorous testing. The actual cause for these failures is not always easily recognized from the results of the tests performed.

For example, the TEMs in Figure 4 exhibited extreme increases in AC resistance as a result of exposure to high temperatures. To determine the exact cause of the failure, further analysis is required.

The photo in Figure 7 was produced through use of a Scanning Electron Microscope (SEM). The TEM was sectioned through a row of TE pellet junctions to analyze the mechanical integrity of the solder joint and the effectiveness of the nickel diffusion barrier. It was determined from this analysis that there was no evidence present that would verify any copper had migrated into the TE material. This photo does, however, reveal a substantial crack along the entire solder connection between the flame sprayed nickel barrier and the TE material. This type of separation as result of poor nickel bonding verifies that these particular TEMs will not withstand the mechanical forces exerted by thermal stress and vibration.

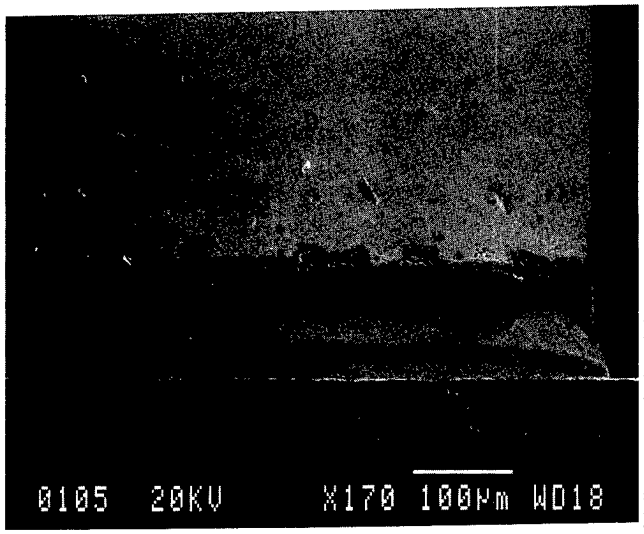


Figure 7 SEM Analysis of High Temperature TEM Solder Joint

Sometimes, mechanical failures in solder junctions are not caused by assembly process but by inferior raw materials such as ceramics and copper tabs. Figure 8 is a photograph illustrating an example of a standard alumina ceramic substrate (top) that was used in a TEM. The substrate had poor adhesion between the alumina and the metalization. The tab array patterns on the substrates in the bottom of the photo exhibits copper tabs that have insufficient nickel plating. When tabs of this nature are used in a TEM, the probability is quite high that the module will fail due to inadequate solder adhesion and/or copper diffusion.

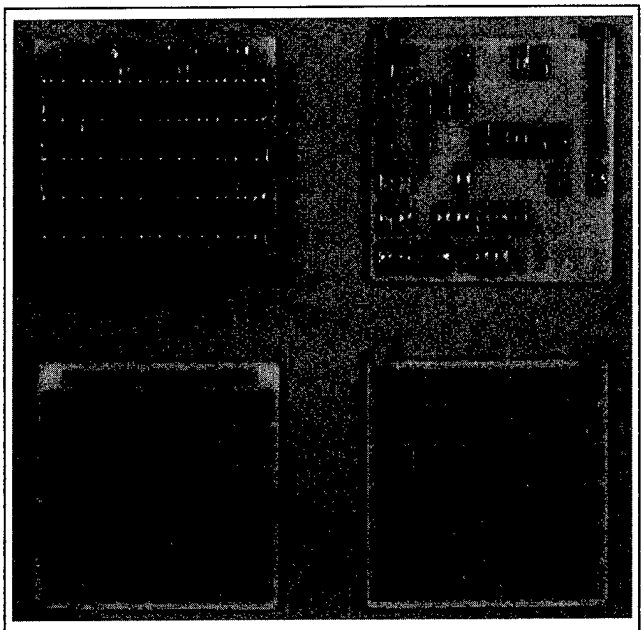


Figure 8 Sample of Inferior TEM Substrate Assemblies

Another condition that sometimes exists with the ceramic substrate is irregular surface finish or blemishes. A TEM should always be lapped or ground flat after assembly in order to achieve smooth, flat and parallel mounting surfaces. However, if the module has weak solder junctions, machining the ceramic surfaces can sometimes destroy the TEM. In one particular case, a TEM manufacture was unable to lap its modules due to weak solder connections. These modules had extremely wavy mounting surfaces. The measured "wave form" across the surface varied between 0.040mm to 0.072mm in height. Typically a TEM should have a surface finish that measures no more than 0.5µm and a flatness of ±0.025.

Excessive solder in a TEM can also be a problem for some manufactures. Electrical shorts between couples and excessive solder wicking can cause a TEM to perform lower than desired or may even become inoperable all together. Figure 9 is a photograph of a TEM magnified through a microscope, illustrating excessive solder wicking up the sides of the TE pellets. This type of condition can greatly reduce the overall performance of the module. Corrections in the assembly process should be made in order to minimize the amount of solder that is applied.

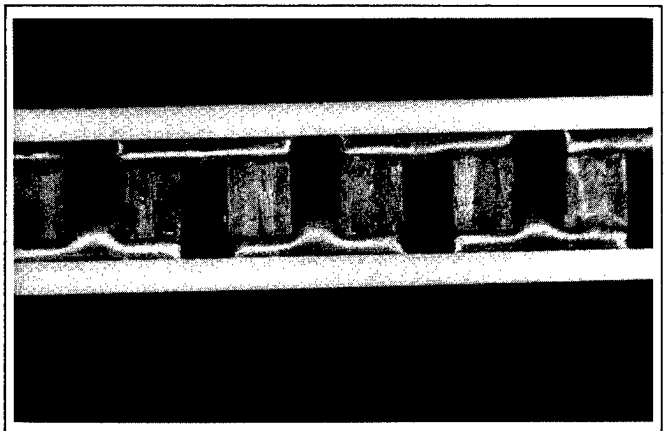


Figure 9 Excessive Solder Build Up in a TEM

Conclusion

The evaluation of TEMs is an on-going process at TE Technology, Inc. Verifying the performance and quality of the various suppliers from around the world is crucial to any manufacturer that needs to assure quality, performance and reliability.

It is apparent from this survey that not all TEMs produced today meet the specifications claimed. Differences in processes, raw materials and skill level all contribute to the variation in products that exist throughout the industry. Refining the techniques required to produce reliable TEMs is not as easy as it may appear. The delicate nature of the TE material, coupled with the difficulty in solder adhesion has made advancements in manufactureability a challenge for most, if not all, suppliers.

The future success of thermoelectrics is becoming increasingly more dependant on costs, performance and reliability. Experimentation in material science, material processing and assembly automation should be a priority for any supplier striving to improve its products. That is why we are continuing to explore new methods in TEM testing, manufacturing and design as part of our day to day operations.

References

[1] Harman, T. C. and Honig, J. M., "J. Appl. Phys.", 13, 440, 1962.

[2] Buist, R. J., "Methodology for Testing Thermoelectric Materials and Devices", *CRC Handbook of Thermoelectrics*, CRC Press, Inc., 1995

Influence of difference in dice properties on figure of merit of thermoelectric cooler

Igor Drabkin
Institute of Chemical Problems for Microelectronics, B. Tolmachevskij per. 5, Moscow 109017, Russia,
Tel, Fax: 7/812/1744365, E-mail: Igor@euphr.stud. pu.ru

Abstract

The influence of difference both in thermoelectric and dimension parameters of dice on the work of a thermoelectric cooler is investigated. It is shown that its work is described by the same equation as that for one die, with Seebeck coefficient, resistance and thermoconductance being replaced by average values. The analysis of the received equations is presented.It is shown that the distribution of dice properties may not diminish the figure of merit if thermoelectric materials in use are of high quality and the thermoconductivity of the ceramics is high. The rule to estimate the influence of dice distribution on the work of the thermoelectric cooler is proposed and it consists in small difference between the average dice resistance and the inverse value of dice conductivity. In practice the difference of the value of electroconductivity of dice ± 150 $1/\Omega$ cm is irrelevant for the work of the module. Besides, the influence of doping near the electrical contacts is analysed. It is shown that this can be used for the increase of figure of merit of the module.

Introduction

In a real thermoelectric battery there is a distribution of the electrical and geometrical properties of dice. It is supposed that this distribution of dice properties is not good for a battery because it diminishes the maximum temperature differential - ΔT_{max}. This conclusion is based on the analysis of work of one die. It is known that in this case the current for the regime of the maximum coefficient of performance depends on the electrical and geometrical parameters. Hence every die has its own current for that regime and the work of the battery becomes not very effective.

Mathematical analysis of the functioning of a battery with different dice has not been made. This article tries to fill in the above mentioned gap and to connect the properties of the battery with those of dice.

The analysis of the work of the battery with different dice

If the battery dice have different properties then it is possible to present the heat balance on the cold junction for every die:

$$|\alpha_i| T_{0i} I - \frac{1}{2} I^2 R_i - K_i \Delta T_i = Q_i \qquad (1)$$

where i - the number of a die i = 1...N, N - the total quantity of dice, α_i, R_i, K_i - the Seebeck coefficient, resistance and thermoconductance of i -die accordingly, Q_i - the heat load of i - die, T_{0i} - the temperature of cold end of i - die, ΔT_i - the temperature difference of i - die, I - current. Q_i can have both positive and negative sign, which corresponds to heat absorption or heat production by the die. Q_i has two parts: $Q_i = Q_{exi} + Q_{ini}$, where Q_{exi} - the heat load from external sources and Q_{ini} - the heat load from all the dice. Let the external heat load of the battery be zero, then every $Q_{exi} = 0$. If equations (1) for every die are summed up then it comes to the following:

$$\sum_{i=1}^{N} \alpha_i T_{0i} I - \frac{1}{2} I^2 \sum_{i=1}^{N} R_i - \sum_{i=1}^{N} K_i \Delta T_{0i} = \sum_{i=1}^{N} Q_{ini} \qquad (2)$$

All sources of internal heat are already taken into consideration in the left part of (2) therefore $\sum_{i=1}^{N} Q_{ini} = 0$. If the thermoconductivity of the heat junction is high then the heat loss along the junction can be neglected and all ΔT_i are equal $\Delta T_i = \Delta T$ for every i. It is also correct for $T_{0i} : T_{0i} = T_0$ for every i. This being accepted, equations (2) can be presented in the following form:

$$\bar{\alpha} T_0 I - \frac{1}{2} I^2 \bar{R} - \Delta T \bar{K} = 0 \qquad (3)$$

where $\bar{\alpha} = \frac{\sum_{i=1}^{N} |\alpha_i|}{N}$, $\bar{R} = \frac{\sum_{i=1}^{N} R_i}{N}$, $\bar{K} = \frac{\sum_{i=1}^{N} K_i}{N}$ are the average of the Seebeck coefficient, the resistance and the thermoconductance accordingly. Thus, the equation describing the work of the thermobattery is the same as that for a single die if the thermoconductivity of heat junction is infinitely high and the values of α, R and K are replaced by the average. According to it all the expressions concerning the battery work are the same as for a single die.

It is necessary to pay attention to the fact that the average electroconductance $\bar{\sigma}$ is not equal to $1/\bar{R}$. Let $\sigma_i = \bar{\sigma} + \Delta_i$ then with an accuracy of the second order on $\frac{\Delta_i}{\bar{\sigma}}$

$$\bar{R} = \frac{1}{\bar{\sigma}} \left(1 + \frac{\sum_{i=1}^{N} \frac{\Delta_i^2}{\bar{\sigma}^2}}{N} \right), \qquad (4)$$

i.e. always $\bar{R} \geq \frac{1}{\bar{\sigma}}$. Therefore there are two values of figure of merit : $Z_{\bar{R}} = \frac{(\bar{\alpha})^2}{\bar{R}\bar{K}}$ and $Z_{\bar{\sigma}} = \frac{(\bar{\alpha})^2 \bar{\sigma}}{\bar{K}}$, and always $Z_{\bar{\sigma}} \geq Z_{\bar{R}}$.

Now we consider how the difference of dice properties influence on the work of a thermobattery. First of all we

investigate the case when the geometric parameters of dice are equal but thermoelectric ones are different.
Let one half of the dice have the thermoelectric parameters α_1 , σ_{01} , κ_{01} and the other half - α_2 , σ_{02} , κ_{02}. The symbols σ_{0i} and κ_{0i} denote the electroconductivity and thermoconductivity of dice.
This case, though very simple, is very significant. In this case $\bar{\alpha} = \frac{\alpha_1 + \alpha_2}{2}$, $\bar{\sigma}_0 = \frac{\sigma_{01} + \sigma_{02}}{2}$, $\bar{\kappa}_0 = \frac{\kappa_{01} + \kappa_{02}}{2}$ and resistivity $\bar{\rho}_0 = \frac{\left(\frac{1}{\sigma_{01}} + \frac{1}{\sigma_{02}}\right)}{2}$. Then $\bar{K} = \bar{\kappa}_0 \frac{s}{l}$, $\bar{R} = \bar{\rho}_0 \frac{l}{s}$ and $\bar{\sigma} = \bar{\sigma}_0 \frac{s}{l}$, where l - the die length and s - the die crossection.

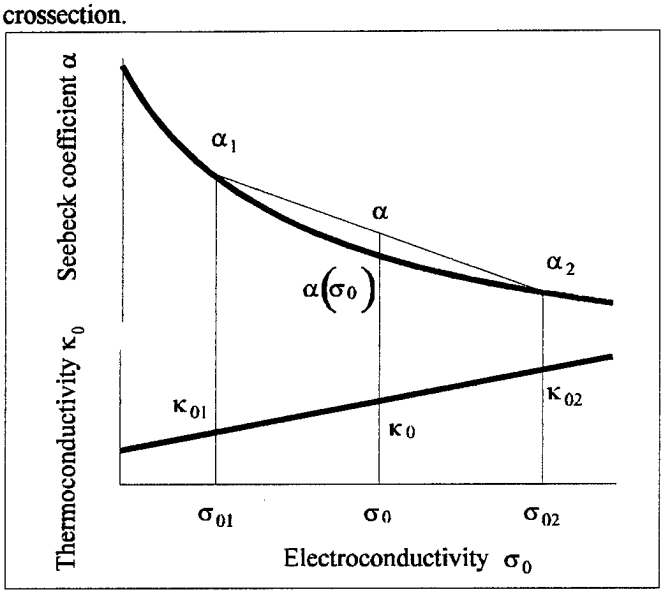


Fig 1: The dependence of average values of Seebeck coefficient α and the thermoconductivity κ_0 from the electroconductivity σ_0.

The dependence of $\kappa_0(\sigma_0)$ and $\alpha(\sigma_0)$ for thermoelectric materials is represented on fig. 1. As κ_0 has the linear dependence on σ_0 , $\bar{\kappa}_0 = \kappa_0(\bar{\sigma}_0)$. The dependence $\alpha(\sigma_0)$ has a convexity directed down, therefore $\bar{\alpha} > \alpha(\bar{\sigma}_0)$ and $Z_{\bar{\alpha}} = \frac{\bar{\alpha}^2 \bar{\sigma}_0}{\bar{\kappa}_0} > Z_{\bar{\sigma}_0} = \frac{\alpha^2(\bar{\sigma}_0)\bar{\sigma}_0}{\kappa_0(\bar{\sigma}_0)}$. Hence, an unexpected conclusion is obtained: the figure of merit $Z_{\bar{\alpha}}$ for the case with different dice properties is higher than the figure of merit of the thermoelectric material of electroconductivity of $\bar{\sigma}_0$. However the efficiency of the battery is defined by $Z_{\bar{R}}$.
The declining of the extrapolated value of α from the true one is proportional to $\frac{\Delta^2}{\bar{\sigma}_0^2}$. The influence of the growth of $\bar{\alpha}$ and $\bar{R}$ is defined by the members of the same order but with different signs. In a common case it can lead both to growing of $Z_{\bar{R}}$ and to diminishing of it, relatively of $Z\left(\sigma = \frac{1}{\bar{R}}\right)$.
The real dependence of $\alpha(\sigma_0)$ is likely to be of the kind that there is small diminishing of $Z_{\bar{R}}$.

Usually the accuracy of measurements of the value of σ is about 1%. Therefore it is natural to accept the error in difining the value of $\eta = \frac{\bar{R} - 1/\bar{\sigma}}{\bar{\sigma}}$ as 1 - 2 %. This value can be a measure of declination $Z_{\bar{R}}$ from $Z_{\bar{\sigma}}$.

For the case under consideration $\eta = \left(\frac{\Delta_0}{\bar{\sigma}_0}\right)^2$ where $\sigma_{01} = \bar{\sigma}_0 + \Delta_0$ and $\sigma_{02} = \bar{\sigma}_0 - \Delta_0$. As $\bar{\sigma}_0 \approx 1000\ \Omega^{-1}\text{cm}^{-1}$ the declination about 100 150 Ω^{-1} cm^{-1} from the average value of conductance dosn't lead to marked diminishing of Z of the battery. Now we'll investigate the case when the electrical parameters of the dice are equal but geometrical ones are different. In this case the values of α, σ, κ are equal for every die and the difference of dice length and crossection leads to the increase of R relative $1/\sigma$. Therefore geometrical difference always leads to diminishing the efficiency of the thermobattery. Expression (4) is valid irrespectively of the nature of the declination of R and σ from its average value.
Let us have two kinds of dice. One half has crossection $s_1 = (a_0 - \delta)^2$ where a_0 - average width of dice, and the other half - $s_2 = (a_0 + \delta)^2$. The thermoelectric parameters and lengths are regarded as equal for both halves. In this case $\eta = 2\left(\frac{\delta}{a_0}\right)^2$. Therefore for accepted value of η the declination of the width of the dice from the average value of a_0 can be 10 - 15 %. In the same way it can be shown that the tolerance of height is equal to 10 - 15 %.

The influence of dice doping near contacts on the work of the battery.
It is believed that contact resistance diminishes the figure of merit of a thermoelectric cooler. It is true if contact resistance takes place between a semiconductor and metal. But probably the contact resistance appears as a result of doping of semiconductor near a contact. Therefore a more realistic model of contact resistance of a die is represented on fig. 2, where near contacts there placed regions with length l and thermoelectric parameters σ_1, α_1, κ_1 (electroconductivity, Seebeck coefficient and thermoconductivity accordingly).

These parameters are different from those of basic material - σ_2, α_2, κ_2.The system of equations for such a layered die can be found anywhere [1-5] and is represented below:

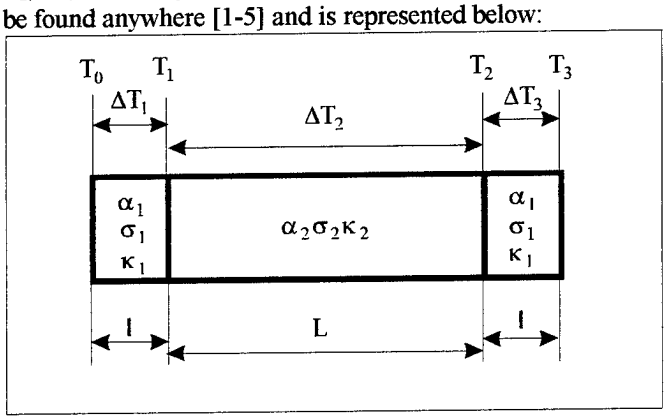


Fig.2. Distribution of doping regions in a die. L,l - length of the region, T_i - temperature,ΔT_i - temperature difference.

$$\alpha_1 I T_0 - \frac{1}{2} I^2 R_1 - k_1 \Delta T_1 = 0 \qquad (5.1)$$

$$\alpha_1 I T_1 + \frac{1}{2} I^2 R_1 - k_1 \Delta T_1 = \alpha_2 I T_1 - \frac{1}{2} I^2 R_2 - k_2 \Delta T_2 \qquad (5.2)$$

$$\alpha_2 I T_2 + \frac{1}{2} I^2 R_2 - k_2 \Delta T_2 = \alpha_1 I T_2 - \frac{1}{2} I^2 R_1 - k_1 \Delta T_3 \qquad (5.3)$$

$$R_1 = \frac{l}{\sigma_1 s}, R_2 = \frac{l}{\sigma_2 s}, k_1 = \kappa_1 \frac{s}{l}, k_2 = \kappa_2 \frac{s}{l} \qquad (5.4)$$

where s - crossection of a die, other designations correspond to those of fig.2.

ΔT_1, ΔT_2, ΔT_3 can be calculated from system (5). The total temperature difference of the die $\Delta T=\Delta T_1+\Delta T_2+\Delta T_3$ can be calculated also. Restricted by the terms of second order on I we can receive the followig expression for figure of merit of the die Z_{eff}:

$$Z_{eff} = Z_2 \frac{\left(1+2\frac{\alpha_1\kappa_2 l}{\alpha_2\kappa_1 L}\right)^2}{\left(1+2\frac{\sigma_2 l}{\sigma_1 L}\right)\left(1+2\frac{\kappa_2 l}{\kappa_1 L}\right)+Z_1T_0\frac{2\left(1-\frac{\alpha_2}{\alpha_1}\right)^2\sigma_2 l}{\sigma_1 L}} \qquad (6)$$

If l/L << 1 and the realistic thrmoelectric parameters for α_i, σ_i, κ_i i=1,2 are used then $Z_{eff} < Z_2$. The supposition about small current is natural because the control of module quality is fulfilled by Harman's method [6] or some modification of it. Antidiffusion layers are known to diminish the contact resistance. If an antidiffusion layer is placed on one end of a die then we receiwe the system which is represented on fig.3. Such a layered die can increase Z_{eff} relative to the figure of merit of the basic material - Z_2 [1-5].

The expression for Z_{eff} can be received by solution of equations (5.1) and (5.2):

$$Z_{eff} = Z_2 \frac{\left(1+\frac{\alpha_1\kappa_2 l}{\alpha_2\kappa_1 L}\right)^2}{1+2\frac{\sigma_2 l}{\sigma_1 L}+\frac{\sigma_2\kappa_2 l^2}{\sigma_1\kappa_1 L^2}-Z_1T_0\frac{2\sigma_2\left(\frac{\alpha_2}{\alpha_1}-1\right)}{\sigma_1 L}} \qquad (7)$$

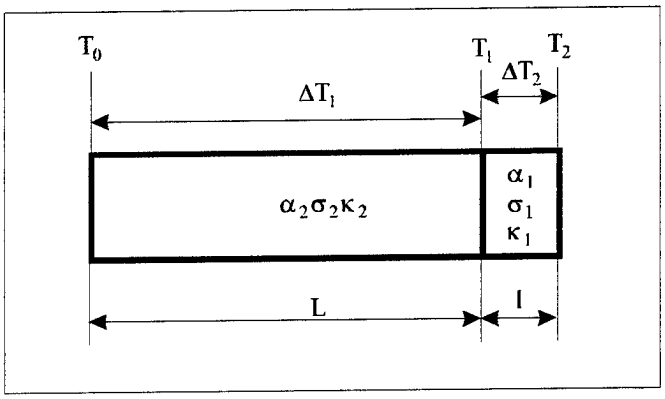


Fig.3: Distribution of doping regions in the die with antidiffusion layer on one end of the die

From (7) it is apparent that if $\alpha_1>\alpha_2$ and the doping layer is placed near the hot end of the die then $Z_{eff} > Z_2$.

Discussion

The above results are received for the case of infinitely big thermoconductivity of junctions, which is not true for a real thermobattery. If the thermoconductivity of junctions is finite then ΔT_i and T_{0i} are different and equation (3) becomes wrong. Different points of the junctions will have different temperature. Mathematical analysis of such a case is very complicated and the expected results don't justify the effort. But there is a method to minimize the unwanted sequence of finite thermoconductivity of junctions in a battery. For that it is necessary to minimize the length of the thermal flow from one die to another. The statistical distribution of the dice isn't a better case. The optimal distribution consists in the fact that a die of one sort has maximum number of neighbours of other sort. Such distribution takes place when dice with different properties of n - and p - type are used. In this case the communication lamels diminish the heat loss along the junction. The examined case of two kinds of dice is most unfavorable for declination from the average value. It is better to use a larger assembly of dice. This will diminish the declination of material properties from their average value.

As to doping near contacts it is difficult to determine the possibility of this method. But it is clear that some attention

must be paid to the solders which dope the die. These solders have been looked upon as not satisfactory ones so far.

References

[1] A.L.Vainer, ed, "Thermoelectric coolers", Moscow, Radio i Svjas, 1983.

[2] A.L. Vainer, N.V. Kolomoets, E.M. Lukishker, V.M. Rgevskiy, "To Theory of the Composite Thermoelemente", Fiz. Techn. Polupr., **11** (1977)546.

[3] C.A. Ball, W.A. Jesser, J.R.Muddux, "The Distributed Peltier Effect and its Influence on Cooling Devices", Proc. of the XIV Int. Conf. on Thermoelectrics (ICT'95), St. Petersburg, Russia, 1995.

[4] V.A.Semeniouk, T.E. Svechnikova, L.D. Ivanova,"Single Stage Thermoelectric Coolers with Temperature Difference of 80 K", ibid.

[5] R.J. Buist, "The Extrinsic Thomson Effect (ETE)", ibid.

[6] T.C.Harman, "Special Techniques for Measurement of Thermoelectric Properties" J.Appl. Phys.,**30** (1958)1351.

Thermal Properties of Commercial Thermoelectric Modules

Rafael Palacios, Miguel Angel Sanz-Bobi

Univerisidad Pontificia Comillas, Instituto de Investigación Tecnológica, Alberto Aguilera 23, 28015 Madrid, SPAIN
Tel: +34 1 541-9641, Fax: +34 1 542-3176, http://www.iit.upco.es
Rafael.Palacios@iit.upco.es, MiguelAngel.Sanz@iit.upco.es

Abstract

Thermoelectric semiconductors and the mass production of thermoelectric modules have experienced a big development in the last years, making thermoelectricity attractive for industrial and commercial applications. The design of industrial applications requires deep knowledge about how thermoelectric modules behave. Even in the case of an application designed to work at a certain operating point of the module, it is interesting to evaluate how would it behave at different working conditions. The thermal and electrical characteristics of the commercial thermoelectric modules, provided by the manufacturers, usually represent the optimal working condition or a few points in a narrow area around that point. But the characteristics can not be considered constant, the modules are specially sensitive to the temperature, which is very changeable in real applications and in fact depends on the heat transferred.

This paper shows the results of testing two commercial thermoelectric modules, one is the typical 12V, Tmax=80°C and the other, designed for high temperature, is a 50W, Tmax=200°C. All the results have been obtained experimentally using a test bench designed and built for this purpose. Special procedures were applied in order to be able to control the temperature in both sides of the thermoelectric module during the experiments. A description of the test bench (which is very easy to build for any laboratory) and the procedures for testing modules in a convenient way are also included. The results obtained correspond to a wide range of working conditions: a temperature from -15°C to 190°C, a range of heat power from 10W to 50W, and electric power from 0.1W to 80W.

Introduction

For the design and development of industrial applications, using commercial thermoelectric (TE) modules, it is necessary to know the thermal characteristics of the modules.

The behavior of the modules is mostly estimated using equations or graphs. Equations are based on theoretical aspects of thermoelectricity [4] and graphs are derived from the Universal Performance Graph [2][5]. The universal graph, already relabeled for a specific module, is sometimes provided by the manufacturer of the module. In most cases this is the only information used by engineers. However, these graphs are based on the temperatures at the faces of the module, which are difficult to estimate due to mounting uncertainties and because the temperatures depend on the amount of heat transferred by the module. It is also possible to find the application's working point out of boundary because the graphs provide data only for a few working conditions. Since the modules show quite an important dependency with the temperature, extrapolation is not suitable.

After testing some applications [1][3] we have found worse performance than that estimated using the graphs. The difference is due to a wrong estimation of the module's temperatures or simply because the performance of the modules is not as good as that shown in the graphs. We have also found disagreement in different graphs provided by the manufacturer for the same commercial TE module.

A comparative study of different modules based on the graphs is difficult because the manufacturers may not provide information at the same working points. For example, some graphs are valid for 27°C, 35°C or 50°C in the hot face of the module and other graphs are valid for 25°C, 35°C, 50°C or 65°C. In both cases the temperature range is fairly narrow taking into account that the operating temperature range of the module is -150°C to 80°C.

Information about special working conditions such as heat transfer with negative temperature gradient or electric generation is not available for most Peltier modules. These data are interesting to evaluate some applications out of the critical point used during the design.

A test bench has been designed and built in order to obtain the complete set of curves of commercial TE modules. This paper includes a description of the test bench and the procedures for testing modules in a convenient way. In addition, some experimental results obtained after testing two modules are also included. The first module, coded CP, is designed to be connected directly to a 12V source. It can work only at temperatures less than 80°C and its parameters are the following: Imax=8.5A, Qmax=68.8W, Vmax=15.4V, ΔTmax=65°C. The second module, coded HT, is designed for high temperature applications (up to 200°C) and has the following characteristics: Imax=6A, Qmax=51W, Vmax=14.4V, ΔTmax=63°C.

The notations used in this paper for the variables of the TE modules are the following:

- Qc is the thermal power absorbed in the cold side.
- Pe is the electric power supplied to the module.
- Qh is the thermal power given out of the hot side (Qh=Qc+Pe).
- I is the current applied to the module.
- V is the voltage applied to the module.
- Tc is the temperature at the cold face.
- Th is the temperature at the hot face.
- ΔT (also called DT in the graphs) is the gradient of temperature, that is Th-Tc.

0-7803-4057-4/97 $10.00 ©1997 IEEE

It is important to remark that the subscript 'c' means cold sink. The cold sink is the side in which the module absorbs heat, but not necessarily the side with the lowest temperature. Usually, the cold sink has a lower temperature than the hot sink and therefore ΔT is positive. But in some situations ΔT can be negative, for example to absorb more than 30W of heat in the cold side with just 1A, the temperature in the cold side must be higher than in the hot side. Another example is electric generation.

Description of the Test Bench

The test bench has been designed for commercial TE modules of standard dimensions 40x40mm, but smaller modules can also be tested. Using this bench it is also possible to compare the performance of different heat exchangers in real mounting conditions. The final mounting scheme usually involves several material, conductive gels and a clamping system; the thermal conductivity of the system can be estimated at real working conditions (working temperature and heat transfer).

The test bench has been designed with the following ideas in mind:

- Easy measurement of all thermal variables (heat transfer and temperatures).
- Simple control of the working conditions.
- Possibility to replace the TE module and the heat exchanger easily.
- Effortless testing, with short transients.

Figure 1 depicts the final design. Heat from the left isolated part is transferred to the right part through the TE module and then to the air or water (depending on the kind of heat exchanger).

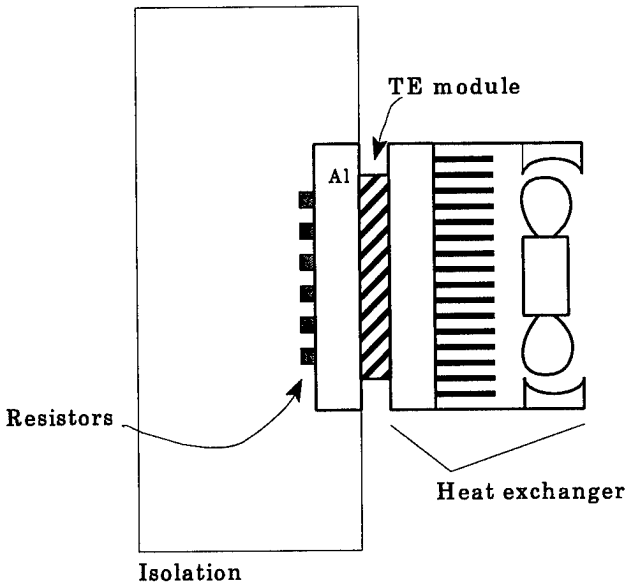


Figure 1: scheme of the test bench

On the left part, thermal power is generated by 6 resistors which are controlled using an external DC power supply. The DC source provides an accurate measure of the heat absorbed by the module, except for small losses through the polyurethane isolation. These losses have been estimated using a 3D finite element model. For the worst case (Tc=200°C and 15°C of ambient temperature) total heat through the isolation is 3.7W, and in most cases less than 1.5W. A correction can be applied rising in this amount the power generated by the resistors.

The resistors are mounted on a block of aluminum in order to have uniform temperatures in the face of the module and to make easier the module replacement. The whole system is put together using two screws (from the head exchanger to the Al block).

Temperatures at the faces of the TE module are measured using thermocouples. The thermocouples are inserted in small holes made in the aluminum block and in the heat exchanger. In the worst case, less than 1°C is the estimated difference between this measurement and the real temperature at the face of the module.

On the right part, the heat exchanger is mounted directly over the TE module, or using intermediate materials to imitate the mounting conditions of the application. It is possible to control the performance of the heat exchanger in order to change the working conditions of the test bench. The conditions are changed by adjusting the fan speed in finned heat exchangers or by adjusting the flow rate in liquid heat exchangers. These operations change the temperatures of the test bench; no additional systems to control the temperature of the cooling fluids are needed. The only limitation is to reach temperatures on the hot face below the temperature of the cooling fluid.

Procedure for Testing

There are three independent variables in the TE module: Th, ΔT, I and two dependent variables: Qc, V. The performance graphs are provided for fixed temperatures Th and then using ΔT and I you find Qc and V. Trying to obtain such graph directly from the test bench is somewhat complicated because it involves a control of the temperatures Th and Tc by changing Qc and the fan speed simultaneously. Temperature control is difficult, sometimes unstable and above all very slow.

In order to have easier testing we decided to fix Qc and I, then read the other variables. Qc and I are controlled using two DC power supplies, in few minutes the system is steady and then voltage and temperatures are read. Information for different temperatures is obtained by changing the performance of the heat exchanger. After a short transient, a different set of temperatures can be read.

Following this procedure, a big amount of reliable data can be obtained quickly. Other conditions, not directly measured, can be calculated by interpolation.

Experimental Results

Two commercial thermoelectric modules have been tested. A broad range of working conditions was studied (greater than that provided by the manufacturer). All tests were made for low electric currents (less than 5A) because the performance of the TE modules is better for lower current. For example, the CP module working at Th=25°C, ΔT=20°C absorbs 27W of heat at

the cold side and 30W of electric power when operated at I=4A (this means an efficiency of 0.9). On the other hand, when operated at I=8A, the heat Qc is only 46W and the electric power 116W (this means an efficiency of 0.4). Therefore for industrial applications it is more interesting to operate TE modules at lower power, using several modules if necessary.

The tests were achieved at I=1, 2, 3, 4, 5A and Qc=10, 20, 30, 40, 50W for both commercial modules (CP and HT). In this paper only a few graphs comparing experimental and theoretical results are shown, but all the measurements of the tests are available via Internet at `http://www.iit.upco.es/~palacios`.

As an example, figure 2 shows the measurements of the CP module when operated at I=3A.

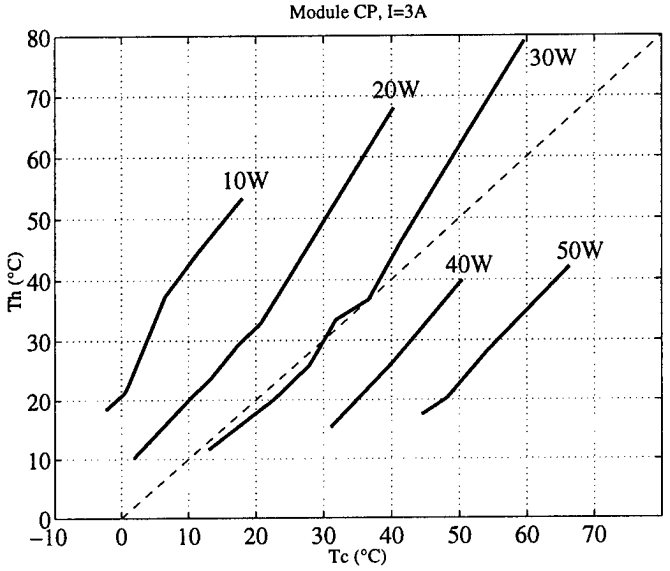


Figure 2: Experimental measurements

In this kind of representation it is easy to see that the CP module working at I=3A is not able to pump more than 40W unless ΔT is negative. More operating points for Qc=40W should have been measured to confirm this statement.

In the following graphs the thick line represents the experimental results, while the thin line represents the values calculated using the performance graphs provided by the manufacturer.

Figure 3 depicts a linear relationship between Qc and ΔT (DT in the graph) for a given Th and I, as illustrated on the universal performance graph. It is interesting to note that the experimental results also show the heat transferred by the module when ΔT is negative, this information is not shown in the manufacturer's graphs. It is also interesting to find that the heat power obtained experimentally is always lower than the power estimated using the performance graph. This difference is bigger for lower values of ΔT.

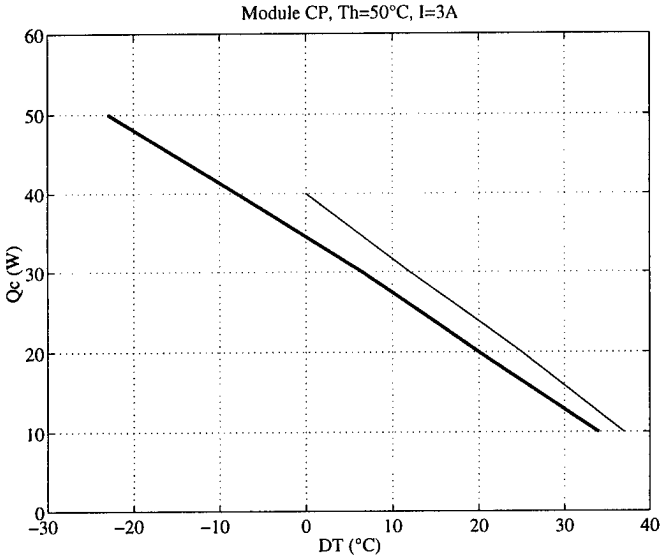


Figure 3: Linear relationship between Qc and ΔT

The proportionality between the voltage and the differential temperature has also been studied. Figure 4 shows the case of the CP module at Th=25°C and I=3A. The experimental values of the voltage are higher than those of the thin line. This means that the electric power needed to obtain a current of 3A is higher, and taking into account that the theoretical heat transfer is also higher (see figure 3), then the theoretical efficiency is unreachable.

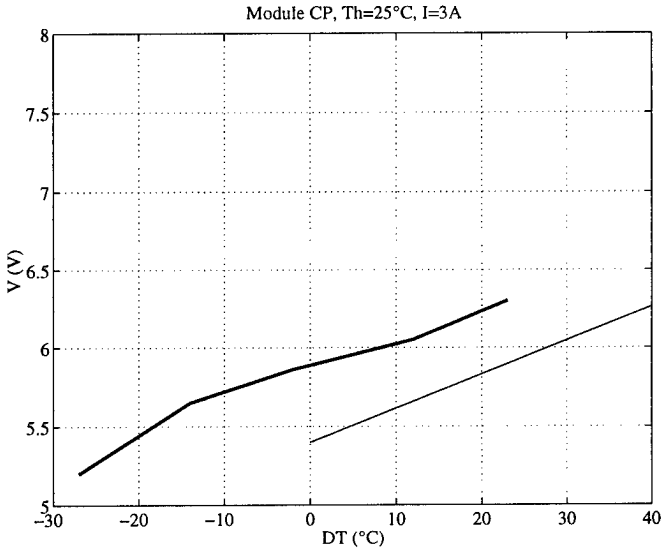


Figure 4: Linear relationship between voltage and ΔT

Finally, two more graphs represent the sensitivity of the TE modules to changes in the operating temperature. Figure 5 stands for the CP module, and figure 6 represents the behavior of the HT module. In the case of the CP module three lines have been drawn: the thick line means experimental, and the thin lines have been obtained using performance graph. The dashed line comes from a graph valid for Th=27°C, 35°C and 50°C, while the continuous line comes from a graph for Th=25°C, 35°C, 50°C and 75°C. Despite the fact that both graph were provided by the manufacturer of the TE module, they slightly disagree.

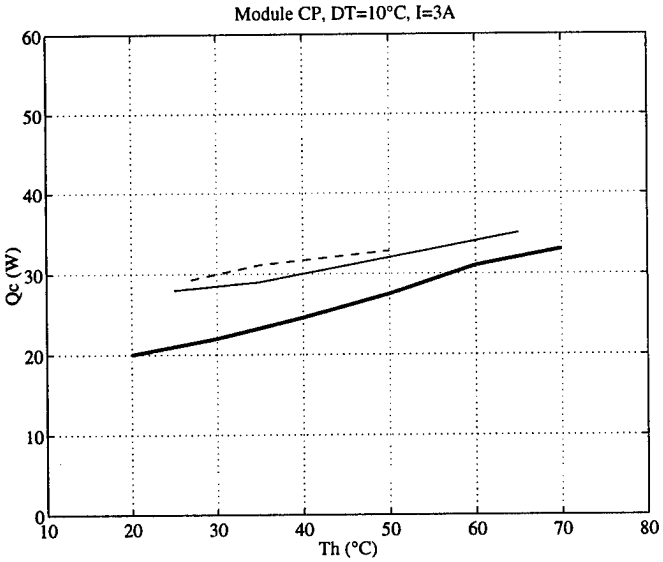


Figure 5: Module CP, sensitivity to the temperature

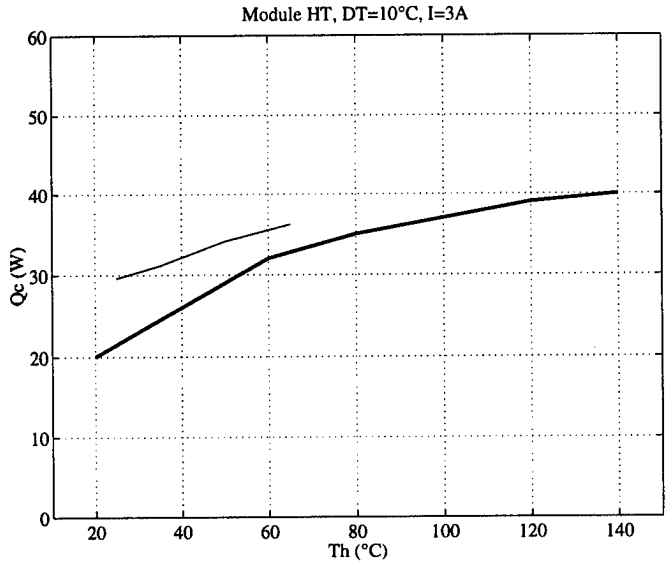


Figure 6: Module HT, sensitivity to the temperature

Figures 5 and 6 show that the heat transfer obtained experimentally is smaller than that estimated with performance graphs. The difference seems to be more significant for lower temperatures. In the case of the HT module a broad range of temperatures have been studied experimentally. In this graph it is clear that the linear extrapolation of the performance graph is not suitable.

Conclusions

This work is focused on obtaining the thermal properties of commercial thermoelectric modules at operating conditions not found in the performance graphs provided by the manufacturers. It is also interesting to be able to compare the characteristics of several modules operating at the same working conditions.

A test bench has been built to measure the thermal properties of commercial TE modules. In this paper the scheme of the test bench and a procedure for testing modules have been presented.

Finally, some experimental results have been included. Two commercial modules were examined in the test bench and the results have been compared with the performance graphs provided by the manufacturer.

- Linear relationships between some variables have been confirmed.
- It has been shown that data provided by the manufacturer for the same TE module can be inconsistent, questioning the validity of this information.
- Experimentally, we have obtained worse results of heat transfer and electric power than those predicted in the performance curves.
- A broad range of working conditions have been obtained.

In following papers we will show the results of the tests for electric generation which are now being performed in the test bench.

Acknowledgments

The authors would like to thank Luis Álvarez for his help building the test bench and performing most of the tests.

References

[1] Rafael Palacios, Miguel A. Sanz-Bobi, José Villar, Antonio Arenas. "Prototype of heat pump based on Peltier effect. Results of performance tests". ETS, European Thermoelectric Society Conference. Nancy, France, 1995.

[2] D.M. Rowe, et al. "CRC Handbook of Thermoelectrics". CRC Press 1995. ISBN 0-8496-0146-7

[3] Sanz-Bobi M.A., Palacios R.,Villar J.,Arenas A. "Prototype of heat pump based on Peltier effect for applications in ambient temperature condition". Proceedings of the XI International Conference on Thermoelectrics. Arlington, Texas, 1992.

[4] John G. Stockholm, Daniel W. Stockholm. "Thermoelectric Modeling of a Cooling Module with Heat Exchangers". Proceedings of the XI International Conference on Thermoelectrics. Arlington, Texas, 1992.

[5] K.I. Uemura. "Universal characteristics of Bi-Te thermoelectrics with application to cooling equipments". Proceedings of the X International Conference on Thermoelectrics. Cardiff, UK, 1991.

Problems of thermoelectric devices reliability

L.I. Anatychuk, O.J. Luste
Institute of Thermoelectricity, General Post-Office, Box 86, 274000, Chernivtsi, Ukraine
Tel: +380/3722/44422, Fax:+380/3722/41917, E-mail: anatychuk@ite.Chernovtsy.ua,
WWW: http:\\www.ite.Chernovtsy.ua

Abstract.
Problems of reliable operation of multi-element thermoelectric devices have been considered. Generalizations of reliability theory for thermoelectric devices include: physical and mathematical reliability models, rational system of reliability parameters and characteristics have been presented. The methods of parameters and characteristics calculation and the methods of accelerated reliability tests have been elaborated. The test results and comparative analysis of thermoelectric cooling modules reliability have been given. The ways of thermoelectric devices reliability increase have been considered.

Introduction.
Reliability problems belong to the most important problems in thermoelectricity. Thermoelectric instruments and devices have large potentialities for high reliability, long-term service life, capability of functioning under the extreme conditions without repair and maintenance. This provides conditions for thermoelectricity application in many prestigious fields of technique. Among them - autonomous supply sources, cooling devices, measuring instruments of space, terrestrial, naval and submarine purposes. For these and many other applications the determination, guarantee and prediction of reliability are the problems of paramount importance.
However, the works on reliability problems in the general scope of research and development make only a small part, which does not conform to the importance of these problems [1]. Only the simplest methods of reliability theory have been used in thermoelectricity up to now. The generally accepted system of reliability parameters and characteristics is practically absent. The parameters cited by the manufacturers of thermoelectric products are frequently of advertising nature and prevent the users from obtaining objective information on the products reliability.
Thermoelectric products have their own specific nature, and it is not always possible to use directly, without proper adaptation, the positive and rich experience of other engineering fields, for example, electronics, for solving the reliability problems in thermoelectricity.
Hence, the relevance of development of such methods of objective reliability estimation, guarantee and prediction which would consider the specific nature of thermoelectricity.
The results of solving these problems obtained in the Institute of Thermoelectricity have been presented in the report.

The existing solutions of reliability problems in thermoelectricity.
Probabilistic reliability models. Compared to such fields as electronics and measuring technique, in the thermoelectricity there have been used up to now only the simplest methods of the theory of reliability and processing of statistical material obtained while testing and use [2-9]. The so-called "human-like" version of failure statistics with the exponential law of sudden failure probability and normal law of parameter scattering of wear failures. This model can be presented by the equation

$$Q(t) = Q_{ac}(t) + F_{wear(}(t) - Q_{ac}(t)F_{wear(}(t) \qquad (1)$$

where Q(t) is failure probability during the time t, Q_{ac}(t) is sudden failure probability, F(t)$_{wear}$ is wear failure probability. In this model

$$Q_{ac}(t) = 1 - \exp(-t/MTBF) \qquad (2)$$

and sudden failures are described by the sole parameter of MTBF - mean time between failures.
The wear failure probability is described by a normal law

$$F_{wear}(t) = F_{wear}(t;p), \quad f(p) = \frac{\exp\left[-\frac{(p-p_0)^2}{2\sigma_p^2}\right]}{\sqrt{2\pi}\sigma_p}, \qquad (3)$$

where p is any of the operational parameters, $f(p)$ is the function of parameter p probability distribution, σ_p is this parameter dispersion. Of course, this description of complicated reliability processes is very simplified. In their prospects and catalogues the manufacturers of thermoelectric products never give the information on the mathematical reliability model which was used for the determination of parameters cited in these prospects and catalogues. One can only suppose that the exponential or normal model was most probably used.

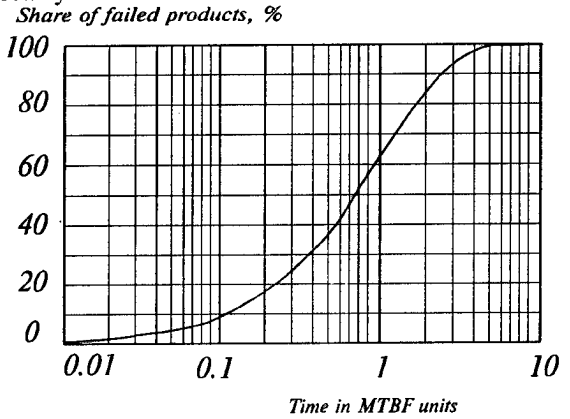


Fig. 1. The share of failed products as a function of time in the exponential model.

The exponential and normal models become more and more common and widely used, though the valid reasons for their use still do nor exist. A vicious circle appears when theoreticians think that traditional reliability models are well substantiated by the experimental data and long-term failure statistics of used products while manufacturers and users think that these models and all their consequences result from a trustworthy scientific theory, therefore they keep processing new statistical data based on the same unsubstantiated models. The readers of advertising prospects often do not even suspect that, for example, in the exponential model during the time MTBF 63% of products fail and are trusting

enough to identify the MTBF to the guaranteed period of product service (Fig. 1).

The existing methods of parameter calculation. Thermoelectric instruments and devices often contain thermopiles or multi-element thermoelectric modules. Knowing the reliability parameters of individual thermoelements (or their legs), it seems possible based on the probability theory to calculate the reliability parameters of the whole system.

The methods of these calculations have been described in literature. In Ref. [3] various variants of parallel-series connection of thermoelectric system components have been considered. Among them there are the cases when the components connected in parallel add to the system reliability. These components are redundant during the non-failure product operation. But when one of the components fails they can partially fulfill the functions of the failed component. Therefore, component failure does not result in the failure of the whole system, but only in the reduction of its operational parameters. If this reduction is less than the acceptable standard, the whole system does not fail. Similar circuits serve as the example of using unreliable elements for the construction of sufficiently reliable systems.

These calculations are based on a number of simplifications. The most significant assumption is that of the Boolean failure model. It means that the component under consideration can be only in two states - serviceable and switched off ones. The Markovian models of thermoelectric product failures have not been described yet. The second simplification is the use in the above circuits of the same type of elements with respect to their reliability and functions. Meanwhile it is known [11] that the use of at least two types of active and passive components for reservation can reduce the product cost while increasing its reliability. The active elements here fulfill the basic product functions, while the passive elements have only one function - to by-pass the open circuit on the failed element. Therefore, the passive elements can be manufactured in the form of rather cheap resistors.

The use of Arrhenius law [10]

$$\lambda(T) = \lambda_{T_0} \exp(-\frac{E_a}{kT}) \qquad (4)$$

is not substantiated enough for the processing of results of accelerated reliability tests at elevated temperatures. Taking the logarithm of dependence (4), where λ is failure intensity, T is temperature, E_a is activation energy, smoothes considerably the spread in experimental points. Small errors in the determination of activation energy result here in considerable mistakes.

The list of simplifications and shortcomings could be continued, but the above examples are enough to warn against the unwarranted trust to these methods.

Developed solutions of reliability problems of thermoelectricity.

The reliability theory developed in the Institute of Thermoelectricity contains:

- physical and mathematical reliability models,
- analysis of the laws of failure probability distribution,
- rational system of reliability parameters and characteristics.

There have been also developed:

- methods of calculation of reliability parameters and characteristics,
- determination of reliability prediction errors according to the test results depending on the number of tested products,
- methods of calculation of multi-element thermoelectric device reliability,
- methods of accelerated reliability tests.

There have been conducted

- tests and comparative reliability analysis of thermoelectric cooling modules produced by the leading manufactures of modules.

There have been determined

- promising ways of increasing the reliability of thermoelectric devices.

Let us consider the basic results of these efforts.

The analysis of failure distribution laws. The analysis of the laws of thermoelectric product failure probability distribution is based on the statistics of long-term tests of hundreds and thousands of samples carried out in the Institute. Sample lots of various manufacturers were tested with respect to mean time to failure, keeping quality, durability and other reliability parameters. The number of samples in each lot was determined based on the requirements of reliability theory so that to provide the accuracy not less than several % at confidence probability higher than 90-95%.

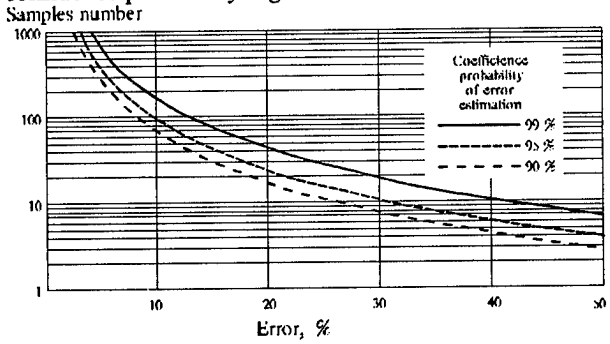


Fig. 2. Necessary samples number vs estimation error.

It has been established that for sudden failures the best approximations are given not by the exponential law (2), but the Weibull's law

$$R(t) = \alpha\lambda t^{\alpha-1} \exp(\lambda^{t^{\alpha}}); \alpha, \lambda > 0, \qquad (5)$$

Γ - law

$$R(t) = \frac{\lambda^{\alpha}}{\Gamma(\alpha)} t^{\alpha-1} \exp(\lambda t); \alpha, \lambda > 0 \qquad (6)$$

and their multi-parameter generalizations.

The check with the use of the χ^2 chi-square criterion shows that for wear processes the normal distribution law (3) is a sufficiently rough approximation. The real laws of distribution are asymmetrical, often having several maximums instead of one. Therefore, to describe the wear processes, instead of normally distributed random values we

have used random processes which to a high degree of accuracy can be considered stationary and ergodic.

Rational system of reliability characteristics

In the construction of the system of reliability characteristics we started from the fact that these characteristics must give the user a clear and unambiguous idea of changing product parameters in the use not only for large but also for small lots or even individual unique samples. With such approach one must refuse from the unsubstantiated and uncertain numerical parameters, such as MTBF of the exponential law (2). The reliability must be characterized not by the parameter-number, but by the characteristic-function of time. Thus, for example, for thermoelectric cooling modules this characteristics can be maximum temperature difference as function of time (Fig. 3).

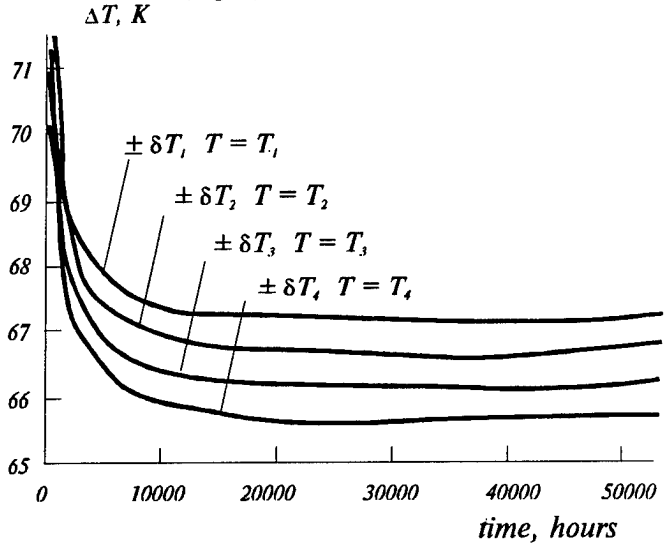


Fig. 3. Example of dependencies of maximum temperature difference of thermoelectric cooling modules on time.

It is also advisable to use as characteristics the functions of the type "failure quota - time", which give for each moment of time the percentage of failed goods on the level of confidence reliability assigned by the user.

Methods of calculation of multi-element thermoelectric systems.

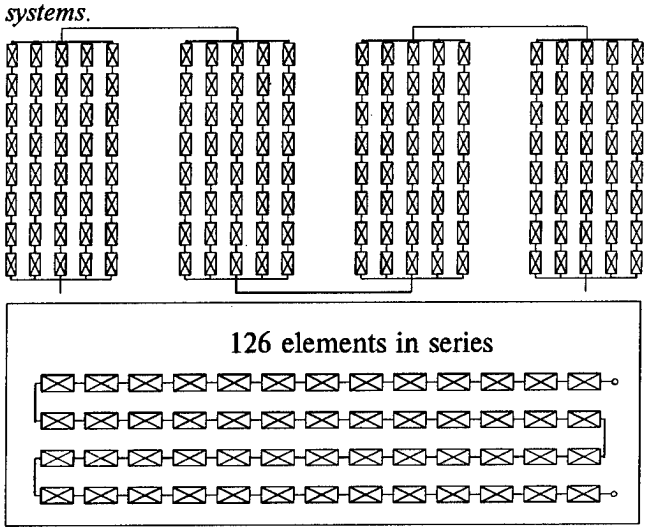


Fig. 4. TEG electrical connection. Diagram 1.

Fast computer methods of calculating multi-element thermoelectric devices have been developed in the Institute of Thermoelectricity. These methods allow to calculate the reliability of thermoelectric devices with the diagram of inner electrical connections of practically any complexity. An example of printing out the results of computer program work is given in Fig. 4. and 5. Fig. 4 illustrates the diagram of electric connections of thermoelectric generator. Fig. 5 is a dependence of TEG power on the operation time for seven variants of electrical diagram of TEG. Variant 1 corresponds to the scheme of Fig. 4, variants 2-6 differ in the methods of parallel-series connection of elements in block, blocks in section, sections in TEG.

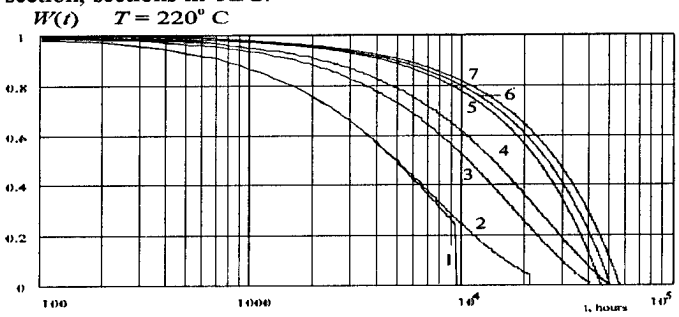


Fig. 5. Time dependence of thermoelectric generator output power.

The program allows to take into account any types of TEG element failures, simulating them as branching Markovian stochastic processes. Design and optimization of device electrical circuit is possible not only for any number of standard sizes of structural TEG elements, but also at any restrictions for economicity, dimensions and other parameters. In particular, from Fig. 5 it is seen that electric circuit optimization can give multiple reliability increase (variants 6-7).

Test results and comparative reliability analysis of thermoelectric cooling modules of leading manufacturers. Fig. 6 is a generalized representation of the results of testing thermoelectric cooling modules of a number of world leading companies producing these modules.

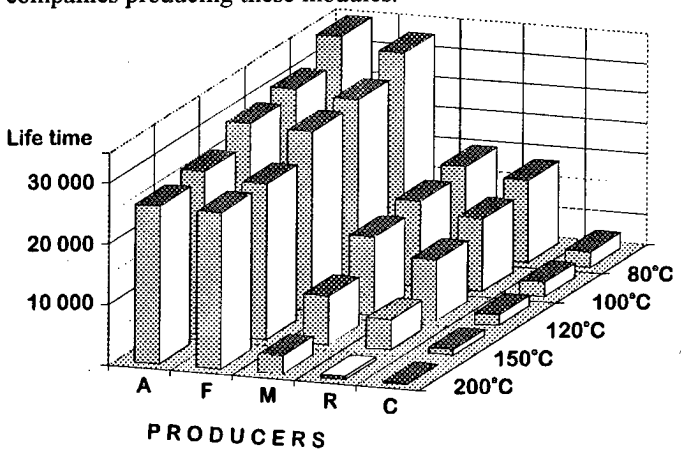


Fig. 6. Comparison of service life of thermoelectric cooling modules by various manufacturers.

The manufacturers are conventionally denoted by the letters A, F, M, R, C. The results allow objective estimate of the difference in module reliability. Thus, the modules of A company have successfully passed a set of tests during 25 000 hours and continue to work today under test conditions. The worst results have been obtained by the manufacturer C, whose all modules have worked not more than 2 500 hours at the temperature 120 °C. The manufacturers F, M, R give the intermediate values of service life.

Perspective ways of reliability increase.

The research of reliability problems carried out in the Institute of Thermoelectricity allows to assert that the indispensable condition of reliability increase is the availability of valid information on the failure statistics.

It allows to analyze and discover physical, technological and design factors of reliability reduction, to eliminate or minimize the influence of these factors.

Based on the statistical material accumulated in the Institute of Thermoelectricity, the following perspective directions can be indicated:

- reliability increase of thermoelectric device components, first of all, on the lowest structural levels- the reliability of legs, thermoelements, thermal and electrical contacts.
- introduction of reserving elements
- when necessary, radical change of design and principles of individual device parts and device on the whole.
- optimization of structure and technology of thermoelectric product to obtain the best reliability in combination with other technical parameters by optimal control methods.

References

[1] O. J. Luste, Reliability of Thermoelectric Devices, J. Of Thermoelectricity, (1), p. 5 - 13, 1996.

[2] P. Click, R. Marlow, Reliability and failure modes of thermoelectric heat pumps, Proc. 2nd Intl. Conf. On Thermoelectric Energy Conversion, Arlington, Texas 1978, pp. 115-120.

[3] D. A. Johnson, J. S. Kendrick, Improvements in reliability of thermoelectric coolers through the use of redundant elements, Proc. 7th Intern. Conf. On Thermoelectric Energy Conversion, Arlington, Texas 1988 Ed. K.R.Rao, Ph.D., pp. 95-100.

[4] Karr Charles H., Reliability of thermoelectric compile networks based upon couple catastrophic failures, IEEE Trans. Reliab. - 1970. - v. 19, N 3. - p. 116 - 119.

[5] Porter B. Click, Jr. R. Marlow, Reliability and failure modes of thermoelectric heat pumps. Receiving international conference of thermal energy conversion. - Arlington, 1978, IEEE.

[6] G. B. Bradskav, P. D. Postala, Modelling of radioisotopic thermoelectric generators reliability with long - duration service life. Intersoc. Energy Convers. Eng. Conf., Boston. - 1971. - p. 1003 - 1009.

[7] M. R. Seiler, T. S. Shilliddy, Reliability factors in thermoelectric generator design. Proc. of the IRE. - 1961. - v. 19, N 12. - p. 250 - 252.

[8] V. S. Truseello, G. Stapfer, Development of basic data for dogradating model of radioisotropic thermoelectric generators on the base of solenoids. Proc. 12 - th Inter. Energy Conf. - 1977. - v. 1. - p. 1271 - 1278.

[9] G. Stapfer, J. E. Cruver, ISOTEC thermoelectric generator for space power. Proc. 4 - th Intersoc. Energy Convers. Eng Conf., Washington. - 1989. - p. 515 - 521.

[10] Richard N. Alonso, Dwight A. Johnson, Roger Devilibiss, Predicting thermoelectric cooler reliability for the telecommunications industry, Proc. XI Intern. Conf. Thermoelectrics, Univ. Texas, Arlington, 1992, pp. 312-318.

[11] L I. Anatychuk, P. D. Mikityuk, Low voltage thermoelectric battery, USSR Author's Certificate SU1073824, 1984.

Heterostructure Integrated Thermionic Refrigeration

Ali Shakouri, and John E. Bowers
Department of Electrical and Computer Engineering
University of California, Santa Barbara, CA USA 93106

ABSTRACT

Thermionic emission in heterostructures is investigated for integrated cooling of high power electronic and optoelectronic devices. This evaporative cooling is achieved by selective emission of hot electrons over a barrier layer from the cathode to the anode. As the energy distribution of emitted electrons is almost exclusively on one side of Fermi energy, upon the current flow, strong carrier-carrier and carrier-lattice scatterings tend to restore the quasi equilibrium Fermi distribution in the cathode by absorbing energy from the lattice, and thus cooling the emitter junction. An analytic expression for the optimum barrier thickness is derived. It describes the interplay between Joule heating in the barrier and heat conduction from the hot to the cold junction. It is shown that by choosing a barrier material with high electron mobility and low thermal conductivity it is possible to cool electronic devices by 5 to 40 degrees in a wide range of temperatures.

INTRODUCTION

Thermoelectric (TE) coolers are important elements of many systems. TE coolers are used in most semiconductor laser modules because of the need to stabilize their characteristics (such as threshold, power output, and wavelength). TE coolers are essential in many infrared detectors applications because the sensitivity of the imaging array is much higher at low temperatures. TE coolers will become essential for many elements of modern optical telecommunications because the channel spacing of wavelength division multiplexed signals are quite close together (100 GHz or 0.5% of the optical frequency), and this wavelength will be used for many switching and routing elements. Consequently, we must stabilize not only the wavelength of the laser source, but also the wavelength of passive switching elements, tunable wavelength shifters and tunable receivers. In these cases the degree of cooling and the amount of the cooling power are not large, but the cost must be low. Since the conventional TE cooling devices based on BiTe or PbTe are not fabricated using integrated circuit technology [1], they can not be easily integrated with III-V or II-VI optoelectronic devices. This will increase the cost for packaging individual modules.

Recently, quantum wells, wires and superlattices have been extensively studied for thermoelectric cooling applications [2-5]. Modifying parameters such as electronic density of states and various relaxation time mechanisms, it is possible to alter electrical conductivity (σ) and Seebeck coefficient (S) of the material and thus increase the thermoelectric figure of merit $ZT = S^2\sigma T/\beta$, where β is the thermal conductivity. There have also been studies aiming to reduce the thermal conductivity by increasing phonon scattering at interfaces in superlattice structures. Heterostructures can modify electronic transport properties beyond *linear* regime where the concepts of electrical conductivity and Seebeck coefficient are usually defined [6]. Using the analogy with thermionic power generation by vacuum diodes, one can design new heterostructure devices (Fig.1) with high cooling power densities. More importantly, this will allow the use of conventional semiconductor materials for fabrication of cooling devices integrated with high power electronic and optoelectronic components. In the following, we will first review electrical power generation by vacuum diodes, and then look at the prospects of heterostructures for thermionic cooling. A simplified model which take into account main energy balance mechanisms is introduced [6]. It will be seen that a net cooling is achieved only for short devices (0.5-5 μm). In order to investigate accurately nonisothermal transport in these length scales, more elaborated Monte Carlo simulations are needed [7]. However, the simplified equations can give analytical expressions for the optimum device length and the maximum cooling temperature, which can be used for an initial evaluation of different material systems.

THERMIONIC POWER GENERATION

In the middle of fifties, when vacuum diodes and triodes were tested and analyzed, serious investigation of thermionic energy conversion began [8]. The idea is that a high work function cathode in contact with a heat source will emit electrons, a process which is called *thermionic emission*. These electrons are absorbed by a cold, low work function anode, and they can flow back to the cathode through an external load where they do useful work.

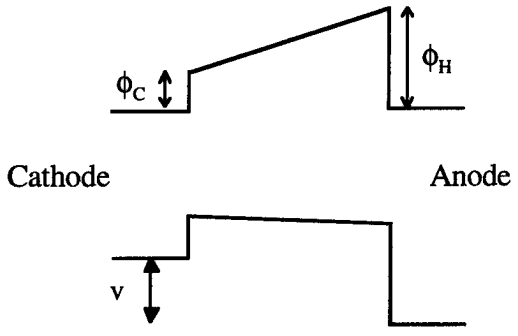


Fig.1 Conduction band diagram of a Heterostructure Integrated Thermionic (HIT) cooler at thermal equilibrium and under an applied bias.

0-7803-4057-4/97 $10.00 ©1997 IEEE

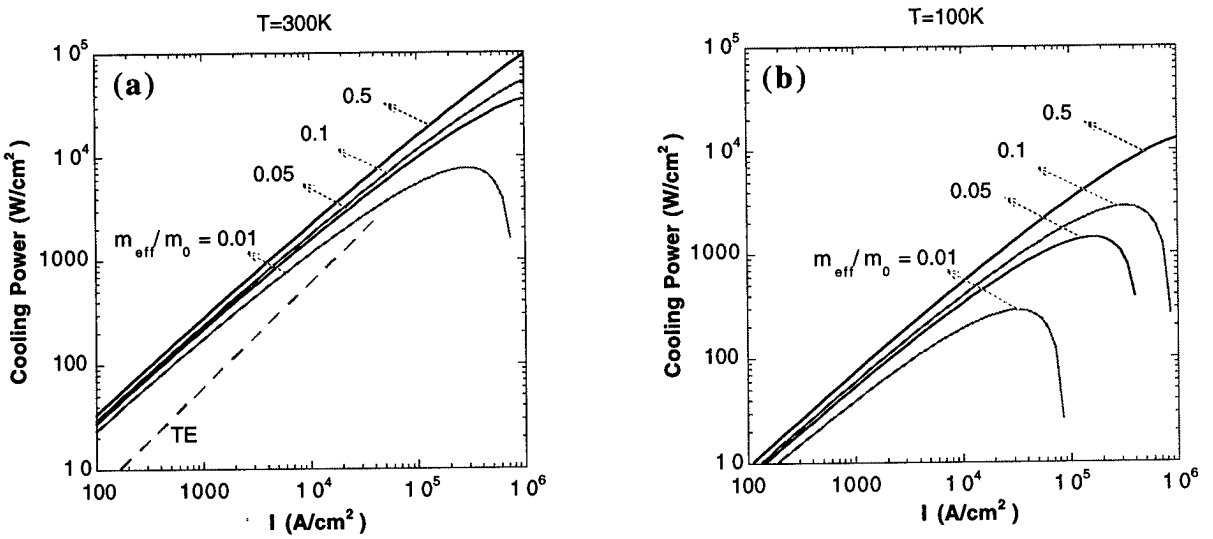


Fig.2 Thermionic cooling power as a function of current for different values of electron effective mass at (a) T=300K, (b) T=100K. The dashed curve corresponds to thermoelectric cooling power for a typical Bi_2Te_3 material.

Practical thermionic generators are limited by the work function of available metals or other materials which are used for cathodes. Another important limitation is the *space charge effect*. The presence of charged electrons in the space between cathode and anode will create an extra potential barrier, which reduces the thermionic current. Various means of reducing this space charge effect were proposed to improve the efficiency of thermionic generators, such as close-spacing of cathode and anode, or the use of a third positive electrode to counteract space charge. A major advance in the field occurred in 1957 when the introduction of positive ions (cesium vapor) in the inter-electrode space eliminated the need for close spacing and resulted in substantial improvement of performance.

The materials currently used for cathodes have work functions *> 0.7 eV*, this limits the generator applications to high temperatures *>500K*. Recently, Mahan have proposed these vacuum diodes for thermionic refrigeration [9]. Basically, the same vacuum diodes which are used for generators, under an applied bias will work as a cooler on the cathode side and heater on the anode side. Mahan predicted efficiencies over 80% of the Carnot value, but still these refrigerators only work at high temperatures (*>500K*).

HIT COOLING

The precise control of layer thickness and composition using various epitaxial growth techniques, allow the design of heterostructure devices with barrier heights in a wide range of 0 to 0.4 eV (Fig.1). Close and uniform spacing of cathode and anode is not a problem anymore and is achieved with atomic resolution. The problem of space charge can be controlled by modulation doping or bandgap engineering in the barrier region. One could use appropriate band offsets in conduction or valence band by choosing n or p type semiconductor material. The price for this flexibility is the large coefficient of barrier thermal conductivity (comparing to vacuum!). One could selectively remove this barrier material and recover the old vacuum thermionic generator but with extremely small and precise cathode-anode separation. In the following we will only consider thermionic cooling with semiconductor barriers. Because of the large backwards heat flux, these devices are not very efficient. We will see that it is still possible to pump heat at rates of 100s of W/cm^2 and maintain a steady state temperature gradients and cool the emitter junction by as much as 30-40 degrees. Cascading these devices in series and distributing the temperature gradient over longer distances might be used to increase the efficiency.

ENERGY BALANCE EQUATION

Assuming Richardson's expression for thermionic current, and Bethe criterion for voltage drop over the barrier, one can derive the following energy balance equation [6]:

$$Q_{TI} = \left(\phi_C(I,T_C) + \frac{2k_BT_C}{e}\right)I - \frac{k_B}{e}\left(T_C + \frac{\Delta T}{2}\right)\frac{d}{\lambda}I - \frac{\beta}{d}\cdot\Delta T$$

where ϕ_C is the cold side barrier height. It can be expressed as a function of the current as follows:

$$\phi_C(I,T_C) = \frac{k_BT_C}{e}\left[\ln\left(\frac{em^*k_B^2T_C^2}{2\pi^2\hbar^3}\right) - \ln(I)\right].$$

Here, T_C is the cold side temperature, m^* the minimum of electron effective mass in the emitter and barrier regions, λ and

β are respectively electron mean-free-path in the barrier and its thermal conductivity, and d is the barrier thickness.

Fig 2a and 2b display the thermionic cooling power (the first term in the energy balance equation) for two different temperatures 300K and 100K. The only material parameter is the electron effective mass which strongly affects the cooling performance by changing the density of "supply" electrons at the cathode or the density of available states in the barrier. For comparison a typical thermoelectric cooling term is also shown in the figure ($Q_{TE}=ST_CI$, S~200 μV/K for Bi_2Te_3 at room temperature). One should note that the expression for thermoelectric cooling is derived in linear transport regime and it is expected to hold for low and moderate current densities. The reduction of the cooling power at low temperatures is similar to thermoelectric case. This is a direct consequence of Fermi-Dirac distribution function, as the energy spread of electrons within the Fermi window is reduced.

Now if we look at the net thermionic cooling, we see that there is an optimum barrier thickness which balances Joule heating in the barrier and heat conduction form the hot to the cold junction. The maximum cooling temperature (ΔT) can thus be calculated:

$$\Delta T_{\max} = T_C\left(\sqrt{1+\frac{\lambda k_B}{2e\beta}\left(\frac{e\Phi_C(I,T_C)}{k_B T_C}+2\right)^2 I}-1\right)$$

$$d_{opt} = \sqrt{\frac{e\beta\Delta T\lambda}{k_B(T_C+\frac{\Delta T}{2})I}}$$

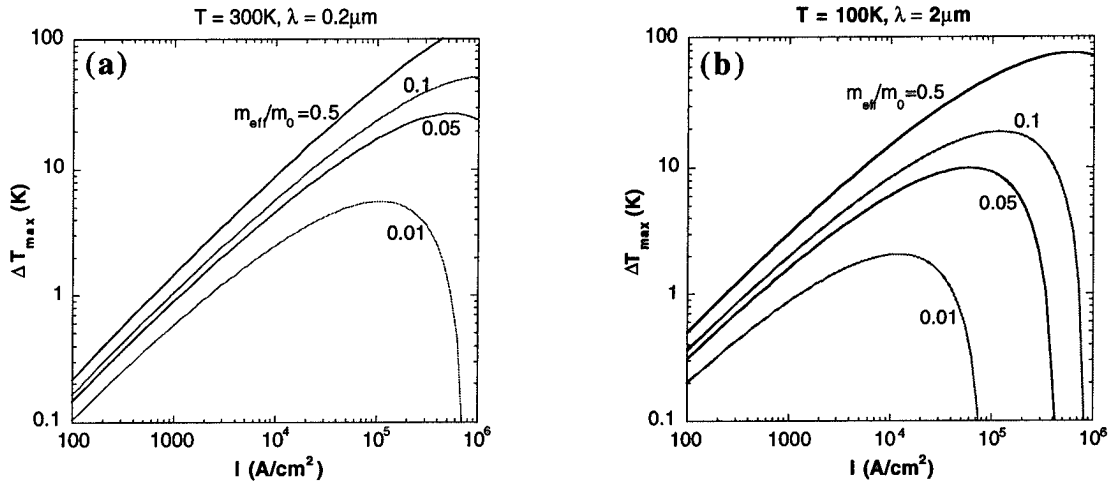


Fig.3 Maximum Cooling temperature as a function of current for different values of the electron effective mass.

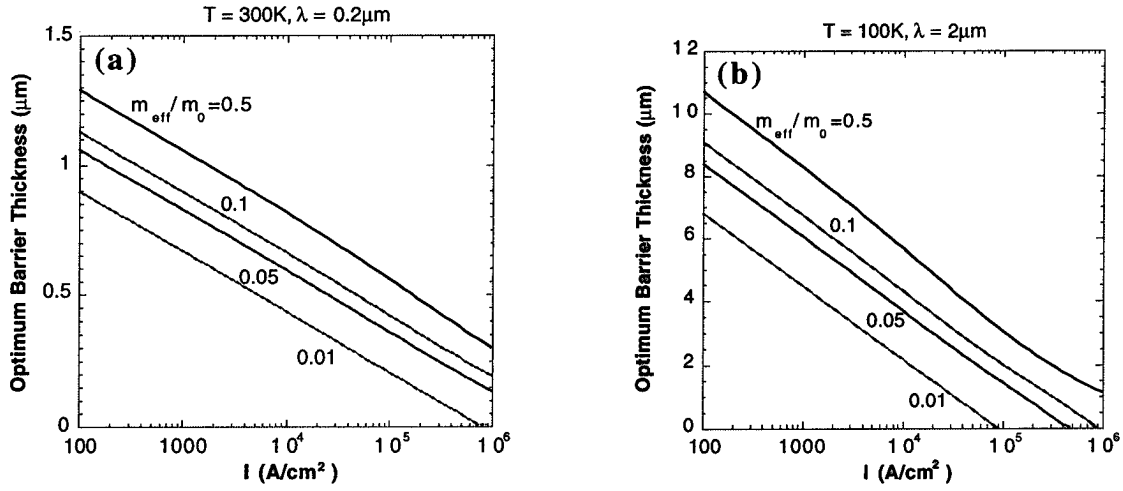


Fig.4 The optimum barrier thickness as a function of current for different values of the electron effective mass.

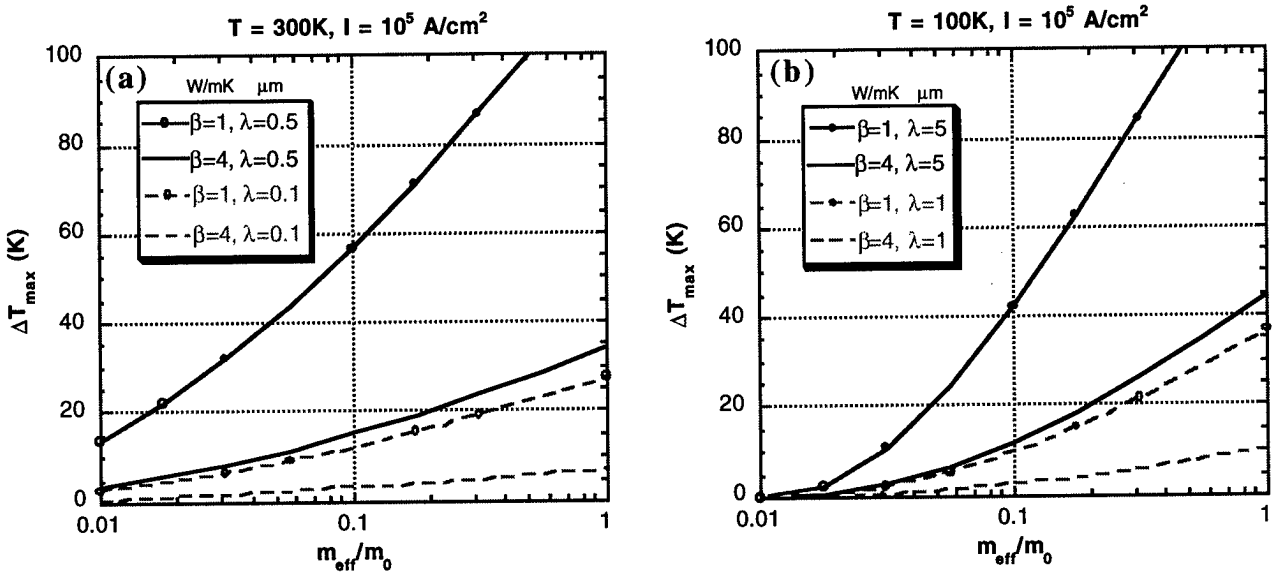


Fig.5 Effect of various material parameters on maximum cooling temperature.

ΔT_{max} at two different temperatures 300K and 100K is shown in Fig. 3a and 3b. The corresponding d_{opt} is displayed in Fig. 4a and 4b. The electron mean free path is taken to be 0.2 μm (2 μm) at 300K (100K), and a barrier thermal conductivity of 1 W/mk is assumed. One can see that cooling by 10-40 degrees (5-20 degrees) with a barrier thickness of ~0.4 microns (2 microns) is possible at 300K (100K). The required current densities are very high (10^4-10^5 A/cm^2), but this should not be a problem. The cooling area needed for an individual device is quite small and these level of currents are routinely achieved in various microelectronic devices (heterostructure bipolar transistors, lasers, etc.).

The thermionic cooling power density $((\phi_C+k_BT_C/e)I)$ is derived assuming Boltzmann distribution of carriers at the cathode junction. At high current densities the required cathode barrier height is small (on the order of k_BT), so this assumption is not valid anymore. In order to estimate more accurately the cooling power one should use the Fermi-Dirac distribution function, but we don't expect too much deviation from the above expression for ΔT_{max}. In fact, Boltzmann distribution over estimates the Joule heating term *more* than the thermionic cooling term. Electrons near the Fermi energy have a small contribution to the heat flux while their contribution to the current is identical to the high energy electrons (they both carry the same charge e!).

In order to study the importance of various material parameters, Fig. 5a (5b) shows the maximum cooling temperature as a function of the electron effective mass at 300K (100K). Different curves correspond to different electron mean free paths and barrier thermal conductivities. To improve the cooling performance, instead of maximizing Z $(=S^2\sigma/\beta)$ in a regular thermoelectric material, here one has to maximize $\lambda[\ln(m^*/m_0)]^2/\beta$.

An important characteristic of HIT coolers is the very small thickness of the barrier region on the order of microns. The large amount of heat conduction from the hot to the cold side is one of the main reasons for low efficiency. One possible remedy is to modify the device structure so that the electrons at the anode junction lose their energy by e.g. emitting photons rather than heating the lattice. Two possible schemes: intersubband [10] and interband light emitting devices are shown in Fig. 6. This concept of a heat pump without a hot side would seem to violate the second law of thermodynamics by reducing the total entropy. But, in fact, the amount of entropy reduction by cooling at the cathode junction, can be compensated by entropy generation at the anode side by emitting incoherent or partially coherent light.

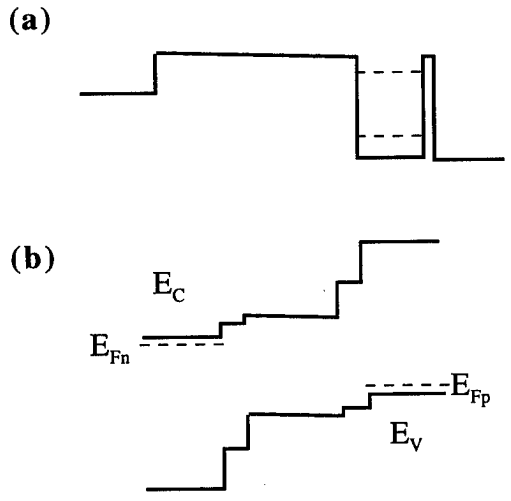


Fig.6 An intersubband (a) (interband (b)) light emitting thermionic cooler.

To realize light emitting devices with a net cooling power, further investigation of the required radiative efficiencies, and the optimum device design are needed.

In conclusion, single stage heterostructure integrated thermionic coolers are studied at different temperatures, using a simplified energy balance model. Analytic expressions for the optimum device thickness and the maximum cooling temperature are given, and important material parameters are identified.

Authors would like to acknowledge many stimulating discussions with Prof. Herb Kroemer.

This work was supported by DARPA and Office of Naval Research.

REFERENCES

[1] L. Rushing, A. Shakouri, P, Abraham, and J. E. Bowers, "Micro thermoelectric coolers for integrated applications", To be published in this proceedings (ITC97).

[2] L. D. Hicks, M. S. Dresselhaus, "Effect of quantum-well structures on the thermoelectric figure of merit", Physical Review B (Condensed Matter), vol.47, pp. 12727, 1993.

[3] T. C. Harman, D. L. Spears, M. J. Manfra, "High thermoelectric figures of merit in PbTe quantum wells", Journal of Electronic Materials, vol.25, pp. 1121-1127, 1996.

[4] J. O. Sofo, G. D. Mahan, "Thermoelectric figure of merit of superlattices", Appl. Phys. Lett., vol.65, pp. 2690-2692, 1994.

[5] D. A. Broido, and T. L. Reinecke, "Thermoelectric transport in quantum well superlattices", Applied Physics Letters, vol.70, pp. 2834-2836, 1997.

[6] A. Shakouri, and J. E. Bowers, "Heterostructure integrated thermionic coolers", to be published in Applied Physics Letters (1 September 1997).

[7] A. Shakouri, E. Y. Lee, D. L. Smith, V. Narayanamurti, and J. E. Bowers, "Thermoelectric effects in submicron heterostructure barriers", Submitted to Microscale Thermophysical Engineering (August 1997).

[8] Hatsopoulos, G.N.; Gyftopoulos, E.P., "Thermionic energy conversion I, II" (Cambridge, MIT Press 1973-79).

[9] G. D. Mahan, "Thermionic Refrigeration", Journal of Applied Physics, vol.76, p. 4362, 1994.

[10] J. Faist, F. Capasso, D.L. Sivco, C. Sirtori, A.L. Hutchinson, A.Y. Cho, "Quantum cascade laser", Science, vol.264, p. 553, 1994.

Thermoelectric Microcoolers for Thermal Management Applications

J.-P. Fleurial, A. Borshchevsky, M.A. Ryan, W. Phillips, E. Kolawa, T. Kacisch and R. Ewell
Jet Propulsion Laboratory/California Institute of Technology, Pasadena, California, USA

Abstract

Due to the combined increase in circuit integration and chip power dissipation, there is a rapidly growing demand for solving the thermal management issues of power microelectronics. We are pursuing a novel thermal management approach that actively cools only the key high power devices by using a novel thermoelectric microcooler located under each of these power devices. In this way the device can operate at temperatures at or even below the ambient temperature of the heat sink, resulting in increased reliability and efficiency. To successfully handle the high heat flux densities generated at the back of the power chips, a microcooler with thin legs and low thermal resistance at the interfaces must be built. We are currently developing a thermoelectric microcooler combining thick films of Bi_2Te_3-based alloys and very high thermal conductivity substrates, such as CVD diamond or AlN.

Electrochemical deposition is a very attractive process for depositing thick films of compound semiconductors on metallic surfaces. This paper presents recent results on the deposition of Bi_2Te_3 and related ternary solid solutions on a variety of metallic substrates. We also report on the development of Cu diffusion barriers for Bi_2Te_3 and stable metallizations and diffusion barriers for diamond and AlN substrates.

Introduction

The demand for increased processing speeds of integrated circuits, computers and other electronic systems requires higher power levels and a higher packaging density. The designing of microprocessors with faster clock rates call for faster logic, which necessitates more power, while an increase in the functional density of processors also results in a larger power requirement. In addition the growing digitalization and miniaturization of portable civilian and military electronic equipment necessitates ever increasing levels of integration between electronics, power sources and thermal control. Combined, these requirements result in very high power densities and thermal problems, which limits integration of devices and components.

At the chip level, the highest performance can be obtained if the junction temperature can be maintained at a tolerable level. Ideally, a reduced temperature and a closely controlled thermal environment is needed. Already, many high power electronic devices, such as power amplifiers and microprocessors, operate at high temperatures close to or at the edge of their reliability, which can severely impact performance and operating lifetime. Next generation power electronic chips, such as solid state power amplifiers, used for microwave applications, will have much higher power levels, with thermal power dissipation requirements increasing from 5 W to 30 W within a few years [1]. That increase will multiply the heat flux that has to be removed, from approximately 30 W/cm^2 to several hundreds W/cm^2. This higher heat flux density will result in a major thermal management problem that will have to be addressed using novel techniques. This is illustrated in Figure 1, which shows preliminary results from a thermal model of a next generation 20W GaN-based power amplifier with a 1.5x1.5 mm^2 footprint of which only 250x250 μm^2 is constituted by the electronic active layer. The very high heat flux densities in the immediate vicinity of the active layers (over 16000 W/cm^2) lead to an estimated 75-110°C temperature difference with respect to the back of the SiC substrate which still presents heat flux densities on the order of 100 W/cm^2.

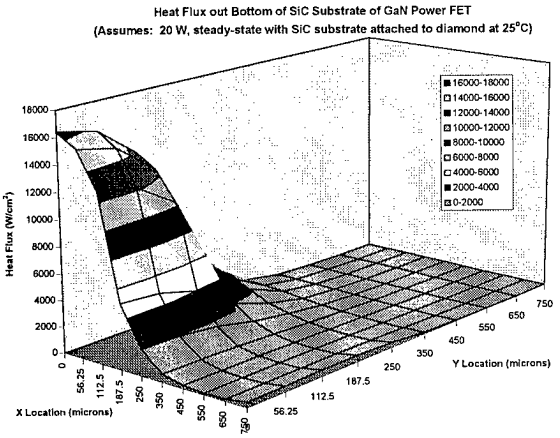


Figure 1: Heat flux profile for a 20W GaN FET using a 5 μm GaN buffer layer on top of a self-standing 100 μm SiC substrate, assuming steady state operation.

Conventional thermal management techniques are not well suited to the specific problem of cooling discrete or localized heat dissipating devices since they generally cool the whole board. Moreover these techniques have difficulty dealing with the large heat fluxes associated with the high density packaging of power devices. The specific problem of spot cooling of power devices can be very effectively solved by using a combination of diamond substrates and a thermoelectric microcooler. The highest power components would be mounted directly on a diamond substrate (ideally the top substrate of the cooler) allowing the cooler/diamond combination to maintain the temperature of the device from a few degrees to tens of degrees below that of the substrate on which the cooler is mounted (diamond or any other high thermal conductivity material such as AlN) and thermally

connected to the heat sink. The cold side diamond substrate will allow "thermal lensing" or spreading of the heat load as uniformly as possible onto a larger surface (for example such as a 10x10 mm^2 surface from the initial 1.5x1.5 mm^2 chip footprint). This will reduce the heat flux density to be cooled by the thermoelectric device from thousands of W/cm^2 to a more manageable 100-150 W/cm^2. The thermoelectric microcooler will then offset part of the temperature gradient across the chip substrate and allow the device to continuously operate at a low enough temperature to increase both reliability and clockspeed.

The main disadvantage of using thermoelectric coolers is the rejection of additional heat due to their low coefficients of performance (COP) at large temperature gradients. This additional heat has to be removed from the heat sink so an additional cooling technique is needed, such as a high thermal conductivity substrate, a heat pipe, microchannels or spray cooling [2-4]. The COP obviously varies over a large range depending on the temperature difference required, the thermal conductivity of the substrates and the thermal gradient. The cooling power density of state-of-the-art (SOA) bulk coolers is limited, which is why it is necessary to increase miniaturization in the cases of large heat fluxes.

Thick Film Microcoolers

The main benefit of going to thick film coolers is the dramatic increase in cooling power density which is inversely proportional to the length of the thermoelectric legs. Preliminary estimates have shown that heat flux densities up to several hundred W/cm^2 can now be removed with thick film coolers, with cooler leg lengths on the order of 10 to 50 μm.

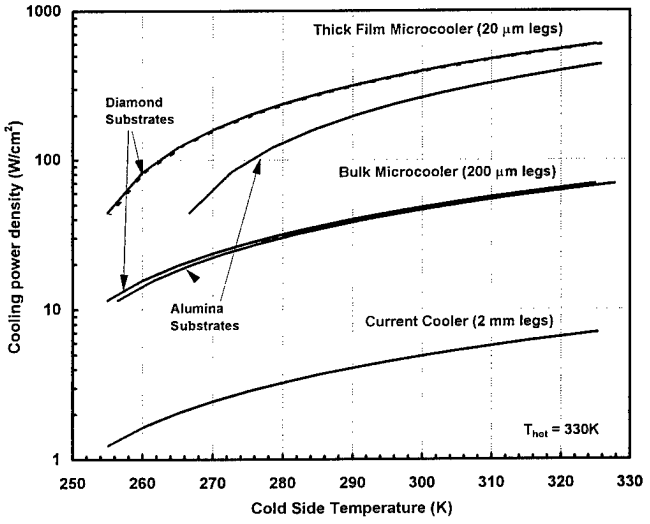


Fig. 2: Cooling power densities as a function of the temperature gradient across the thermoelectric device for three different kinds of coolers.

Figure 2 shows the cooling power density comparisons for a SOA commercial cooler with 2mm legs, for a bulk micro-cooler with 200μm legs, and for a thick film cooler with 20μm legs. These curves are for a hot side temperature of 330K and maximum cooling power operation. As can be seen from the figure, the cooling power density of the diamond substrates/thick film cooler combination is approximately two orders of magnitude greater than that for the SOA current cooler and one order of magnitude greater than that for the bulk micro-cooler. The reason to go to thick film coolers is thus very obvious.

Device considerations

However, considerable development work is still needed before thick film coolers are ready to be used. The limiting factors for microcoolers are the magnitudes of the electrical and thermal contact resistances. The contribution of these resistances become important parameters as the thermoelement length becomes smaller. They degrade the performance of the thermoelectric microcooler by decreasing the maximum COP, the maximum cooling capacity and the maximum temperature difference that can be achieved.

For resolving the thermal issues, the use of substrates such as AlN or diamond (thermal conductivity respectively one and two orders of magnitude higher than alumina, see Table 1) is necessary so that as small a ΔT as possible is dropped across the substrate. Assuming a uniform heat load on the cold side substrate, the performance of alumina based coolers was calculated and plotted in Figure 2. For the 20 μm cooler, the temperature gradient "lost" across alumina substrates ranges from 12 to 25°C, depending on the heat load. Moreover, if one considers a real case power chip with a much smaller footprint than the top cooler substrate, even larger additional temperature gradients will appear in the plane of the substrate (poor heat spreading). This will result in unacceptable operating temperatures for the power device being "cooled" (in some cases temperatures might even be higher with the alumina based cooler than without it).

For miniaturized thermoelectric devices comprised of thousands of thermoelements, electrical contact resistances can become a very large fraction of the total internal resistance. The degradation in performance for high electrical contact resistance values is illustrated in Figure 3. Low contact resistances (close to $1x10^{-6}$ $\Omega.cm^2$) can relatively easily be obtained using thin film processing technology developed for electronic semiconductors [5].

Table 1: Electrical resistivity (ρ in 10^{-8} Ω.cm), thermal conductivity (λ in W/mK) and thermal expansion coefficient (α in 10^{-6} K) at 300K of elements and compounds for thermoelectric microcoolers.

	Diamond	AlN	Al_2O_3	Ni	Pt	Cu	Bi_2Te_3
ρ				6.84	9.85	1.68	1000
λ	~1800	~180	20	91	72	400	1
α	1.5	4.4	7.1	13.3	9.1	16.4	12.9

In addition to the thermal and electrical contact resistances, other issues such as heat losses, mechanical strength and stress analysis must be considered. The low thermal expansion coefficient of diamond is of particular concern (see Table 1) to the ruggedness of thermoelectric microdevices,

and where appropriate from a thermal and cost aspect, AlN offer a better match to Cu and Bi_2Te_3.

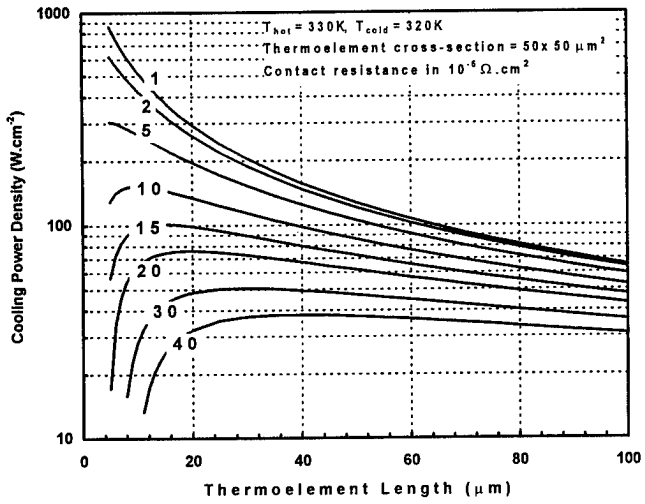


Figure. 3: Cooling power densities as a function of the thermoelement length and for increasing electrical contact resistances at the thermoelement/Cu electrode interface. Calculations performed for diamond-based microcoolers operating across a temperature gradient of 10°C.

Microcooler fabrication

Areas under development at JPL are the deposition and characterization of Bi_2Te_3-based thick films, bonding of metallized diamond or AlN substrates to the thermoelectric films, and the patterning, etching, bonding and testing of the cooler. Figure 4 shows the proposed schematic for the metallizations and bonding scheme for the diamond and the thick film thermoelectric material.

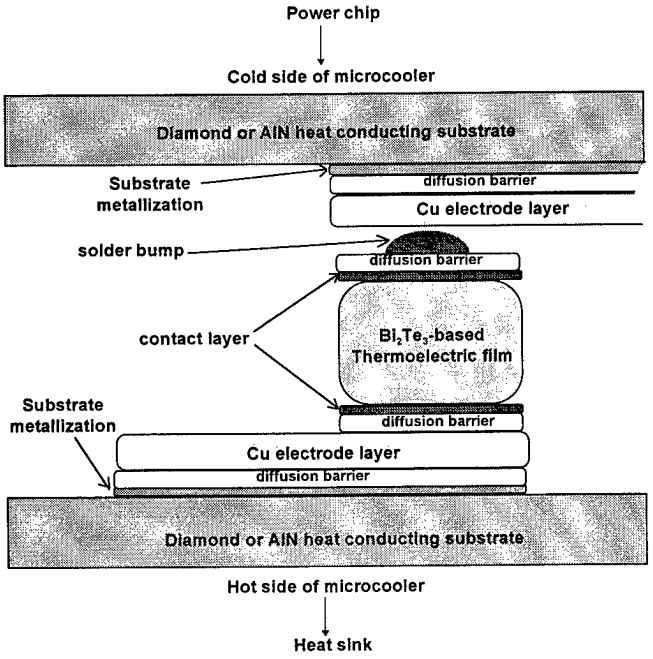


Figure 4: Schematic of a thick film thermoelectric cooling device with diamond or AlN substrates.

The scheme, similar to that for traditional bulk thermoelectric modules, involves many layers, including metallization to the high thermal conductivity substrate, diffusion barrier, Cu electrode, Cu diffusion barrier, contact layer and Bi_2Te_3 alloy film. Except for the Cu electrode and the thick thermoelectric film, all other metallic layers are of submicron thickness.

Thermoelectric Thick Films

A promising route for thick film preparation is electrochemical deposition (ECD) from aqueous solution. This is a fairly well known technique for the deposition of II-VI semiconductors such as CdSe, CdTe $CdSe_{0.5}Te_{0.5}$ and $CdSe_{0.65}Te_{0.35}$ [6,7]. In this technique the elements are deposited on an electrode using an aqueous solution of anions or anionic compounds. The advantage of this approach to the fabrication of films is that it is an inexpensive way to make films and, depending on the current density used in deposition, the deposition rate can be varied widely. Thick films can be difficult and time consuming to make using vacuum techniques such as sputtering or evaporation, but films several tens of microns thick can be made in a few hours using electrochemical deposition. In addition, slight variations in the deposition potential or solution concentration may possibly be used to induce off-stoichiometric films, thus providing p- or n-type doping through stoichiometric deviation. The preparation of thermoelectric material films by electrodeposition has been investigated very little [8,9] and the methods used in making the II-VI alloys must be adapted to the electrodeposition of thin films with p-type and n-type $Bi_{2-x}Sb_xTe_{3-y}Se_y$, compositions which are optimal for thermoelectric cooling applications. An additional advantage of this approach to the fabrication of thin film thermoelectric coolers is that some of the contact layers necessary to the fabrication of the cooling device, such as Cu for the electrical path or Ni or Pt for the Cu diffusion barrier can also be deposited by using a different aqueous solution.

Bismuth and tellurium metals dissolve in HNO_3 to make the oxide anions BiO^+ and $HTeO_2^+$. Bi_2Te_3 is insoluble in dilute HNO_3, so reduction of $HTeO_2^+$ to Te^{2-} at an electrode will result in the precipitation of Bi_2Te_3 on the electrode surface. The overall reaction for the process is:

$$13H^+ + 18e^- + 2BiO^+ + 3HTeO_2^+ \rightarrow Bi_2Te_3\downarrow + 8H_2O$$

Figure 5 shows the current-voltage behavior of an aqueous solution of $7x10^{-3}$ M BiO^+ and $1.0x10^{-2}$ M $HTeO_2^+$ in 1 M HNO_3. The reduction regions for each of these compounds overlie each other in the range -0.05 to -0.2 V versus a standard calomel electrode. BiO^+ is reduced to Bi^0 around -0.1 V. It is possible to co-deposit Bi_2Te_3 within this voltage range, probably more effectively in the range 0 to -0.1 V than within the region of the reduction wave for BiO^+. Preliminary studies have shown that variation in grain size and composition of the films can be introduced by changing the potential at which the deposition is carried out toward 0 V, as well as by changing the concentration of ions in solution.

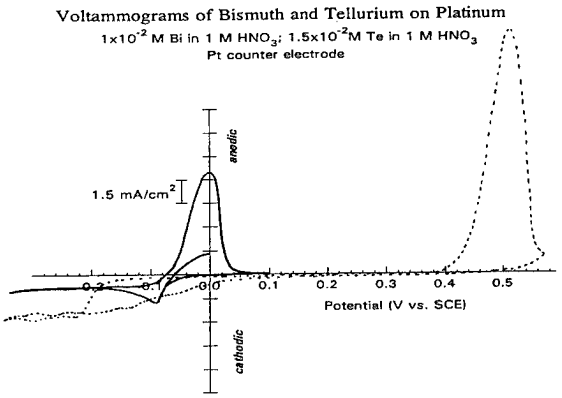


Figure 5: Current-Voltage graph for the electrochemical deposition of Bi and Te on a Pt substrate using a nitrate aqueous solution. (SCE is for standard calomel electrode)

Other parameters controlling the quality, composition and properties of the Bi_2Te_3 films grown by ECD are: temperature, Bi and Te molar concentrations in the HNO_3 solution, deposition time, substrate surface finish and geometry, active stirring of the bath, volume of the bath, distance between counter and deposition electrodes, and characteristics of the reference electrode. Such a large number of parameters means that many experiments (several thousand) must be run to determine the best experimental parameter values. We are currently developing a combination of statistical tools based on orthogonal arrays of control parameter values to optimize this deposition process and determine in a small number of experiments the best conditions for depositing high quality Bi_2Te_3-based films with good thermoelectric properties.

Initial deposition runs on Pt-coated substrates have shown that thick near-stoichiometric Bi_2Te_3 films could be grown from a $0.75x10^{-2}$ M/l [Bi] and $1.0x10^{-2}$ M/l [Te] concentrations. The thickness of the films measured with a profilometer ranged from 10 to 60 μm and the composition of the films was very close to the 40/60 at% ratio, as determined from electron microprobe analysis. In addition, back-scattering electron analysis indicated that films grown at low deposition voltages had very smooth top surfaces (less than 1 μm of roughness). The growth rates ranged from 10 to 20 μm/hour depending on the deposition voltage.

Measurements of the electrical transport properties has been conducted on some of the deposited films. Van der Pauw electrical resistivity and Hall effect were measured in the plane of the deposited films (after removal from the metallized substrates), and the Seebeck coefficient was measured in a cross-plane direction. Our results show heavily doped n-type behavior and are similar to those obtained previously by [9] except that we have achieved lower electron concentrations (~ $1x10^{20}$ cm^{-3}) and higher Hall mobility values (~ 26 cm^2/Vs). Seebeck coefficient values range from -50 μV/K to over -100 μV/K near room temperature. We are now working on optimizing the properties for n-type films as well as studying the possibility of achieving p-type conductivity. Recent experiments on ternary compositions demonstrated that $Bi_2Te_{3-x}Se_x$ ($0<x<0.1$) and $Bi_{2-y}Sb_yTe_3$ ($1.5<y<2$) films could also be obtained by ECD. Detailed experimental results will be published later [10].

Cu Diffusion Barrier

For the multilayer stack, Cu will be used for the electrical path (electrode) of the thermoelectric device, because Cu has low electrical resistivity and high thermal conductivity values (see Table 1), and can easily be deposited electrochemically. However a diffusion barrier must be found to prevent Cu from diffusing into Bi_2Te_3 and degrading the thermoelectric properties. Ni is the Cu diffusion barrier of choice in the thermoelectric industry, but unfortunately we have found that the Ni layer is dissolved in the nitrate solution used to grow Bi_2Te_3 by electrochemical deposition. After considering several options including a protective layer over the Ni barrier, the possibility of more suitable diffusion barriers was investigated.

Potential candidates included Cr, Pd and Pt as well as highly thermally stable amorphous nitride films previously developed for metallizations to diamond and AlN [5]. However, studies were required to demonstrate their effectiveness as diffusion barriers for Cu and to demonstrate that they do not contaminate the Bi_2Te_3 film.

A number of experiments were conducted on single crystalline Bi_2Te_3 bulk samples which were coated with Pt/Cu, Pd/Cu, Ni/Cu, Cr/Cu, TiSiN/Cu and TaSiN/Cu. The diffusion barrier thickness was typically 150 nm and the Cu overlayer was 250 nm. Several samples were prepared for each multilayer combination, and some of the samples were annealed for 1 hour at 150°C, 200°C, 250°C or 350°C in high vacuum. After completion of the anneals, as-coated and annealed samples for each materials combination were analyzed by Rutherford backscattering (RBS) microscopy.

Results showed that for temperatures in the 150-250°C range only Pt and the amorphous nitrides are suitable diffusion barriers (no Bi or Te detected on top of the Cu). For temperatures higher than 250°C the nitride films performed best. Both Ni and Cr samples showed some interdiffusion even at 150°C, and catastrophic results were obtained with Pd. Detailed results will be reported elsewhere [11]. Despite the apparent negative result of Ni as a Cu diffusion barrier, it must be noted that thermoelectric coolers are typically soldered at only 138°C (some at 189°C), and operated at 50-75°C maximum (hot side). Since Pt is well suited to the electrochemical deposition of Bi_2Te_3, we are now developing a Cu electrode/Pt barrier/Bi_2Te_3 combination by ECD.

Conclusion

The demand for increased speeds and higher power levels for electronic devices such as power amplifiers and microprocessors has resulted in thermal problems on the component and board level that need to be solved. The spot cooling of these power devices and microprocessors is needed to increase reliability, efficiency, and clockspeed. Thermoelectric microcoolers using high thermal conductivity substrates such as diamond or AlN are one of the most promising methods to address these thermal management issues. Very high cooling power densities (over 100 W/cm^2)

can be achieved with thick film coolers. We are currently developing such devices using a promising electrochemical technique to deposit Bi_2Te_3-based film on metallized and patterned diamond substrates.

Acknowledgments

The work described in this paper was performed at the Jet Propulsion Laboratory/California Institute of Technology under contract with the National Aeronautics and Space Administration. Part of this work was supported by the Ballistic Missile Defense Organization and managed by Wright Laboratory, WL/POO, MIPR # NFY14559600672.

References

1. P. Smith, Jet Propulsion Laboratory, private communication.
2. M.T. North, D.B. Sarraf, J.H. Rosenfeld, Y.F. Maidanik and S. Vershinin, *Proc. Space Technology and Applications International Forum*, AIP 387, 2, 561-566 (1997).
3. M.M. Sherman and G.O. Campbell, *Proc. Spacecraft Thermal Control Symposium*, Albuquerque, Nov. 1994
4. Isothermal Systems Research Inc., private communication.
5. E. Kolawa, J.S. Chen, J.S. Reid, P.J. Pokela, and M-A. Nicolet, *J. Appl. Phys.* 70, 1369 (1991).
6. K. Rajeshwar, *Adv. Mater.*, 4, 23 (1992) and references therein.
7. Y. Mirovsky, R. Tenne, G. Hodes and D. Cahen, *Thin Solid Films*, **91**, 49 (1982).
8. M. Takahashi, Y. Katou, K. Nagata and S. Furuta, *Thin Solid Films*, 240(1-2), 70 (1994).
9. P. Magri, C. Boulanger and J.M. Lecuire, *J. Mater. Chem.*, 6 (5) 773-779 (1996).
10. M.A. Ryan, A. Borshchevsky, W. Phillips, J.-P. Fleurial and T. Caillat, to be published in the Journal of the Electrochemical Society.
11. T. Kacisch, E. Kolawa, J.-P. Fleurial, T. Caillat and A. Borshchevsky, to be published.

Micro Thermoelectric Coolers for Integrated Applications

Lance Rushing, Ali Shakouri, Patrick Abraham and John E. Bowers
Department of Electrical and Computer Engineering
University of California, Santa Barbara, CA USA 93106

ABSTRACT

A different approach for manufacturing arrays of micro thermoelectric coolers using integrated circuit technology is presented. The idea is to fabricate a synthetic wafer containing the necessary thermoelectric elements by first bonding alternating p and n type wafers and then slicing them to obtain an array of thermocouples. This array is then metallized using standard photolithography and evaporation techniques to yield an array of coolers. To demonstrate this approach, six element Bi_2Te_3 cooler arrays were made and characterized. In this paper scaling laws, processing details, practical limitations, and preliminary experimental results are discussed.

INTRODUCTION

Increased demand in the optical communications industry has led to many advances in semiconductor laser sources. Now, these sources are efficient and operate at low threshold currents. As a result, heat dissipation is low (100's of mW) and temperature dependent parameters can be stabilized with little cooling (<20 °C). Still, the low heat dissipation in conjunction with very small surface area (100's of μm^2) results in a high heat flux density. Recent work in the miniaturization of thermoelectric coolers (TECs), has shown the advantages of smaller coolers in these applications.[1] Basically, element lengths in the submillimeter range produce greater cooling densities than conventional coolers and allow the overall size of the cooler to be greatly reduced.

As the cost of semiconductor laser sources decreases, it is important to maintain the cost of packaging as low as possible. This paper presents a novel approach to manufacturing micro TEC's with the desired goal to facilitate packaging with semiconductor laser sources and other opto-electronic devices and thus reduce the cost of packaging and production. In standard packaging procedures, a wafer is diced into single devices or groups of devices. These are then individually mounted into a package. The ultimate goal of our approach is to develop a synthetic "wafer" of TEC's that can be bonded to a wafer of lasers or other electronic devices or circuits. The synthetic "wafer" is made by bonding n and p type wafers, slicing them, and then metallizing the contacts. When this synthetic wafer is bonded to the wafer of lasers, the whole structure can be diced together and then mounted. This process allows the use of standard integrated circuit technology to enhance mass production of mountable devices.

SCALING LAWS

In order to understand submillimeter cooler operation, a set of design rules is needed. Also, the first set of rules should only depend on length. This will be done by considering the cooling density when operating in the maximum cooling regime. In this way, the scaling of device performance as element length decreases can be easily understood.

To start, the cooling capacity at the cold side of a single thermocouple (including contact resistance) is given by[2];

$$Q = \alpha T_C I - \frac{I^2}{2}\left(R_{mat} + 2R_{con}\right) - K\Delta T \qquad (1)$$

where α is the Seebeck coefficient (205 μV/K for Bi_2Te_3), R_{mat} is the material resistance (σ x area/length, σ_{ave}=1100 1/Ωcm), R_{con} is the contact resistance (r_c x area Ωcm^2)[3], and K is the thermal conductivity (κ x length/area, κ_{ave}=0.014 W/cmK). Next, cooling capacity in the maximum cooling regime is obtained from the condition dQ/dI=0. The cooling density is given by;

$$\frac{Q_{\max}}{a} = \frac{1}{L}\left[\frac{\alpha^2 T_c^2}{\left(\frac{2}{\sigma} + 4r_c\right)} - k\Delta T\right] \qquad (2)$$

at a current density of

$$\frac{I_{\max}}{a} = \frac{1}{L}\left[\frac{\alpha T_c}{\left(\frac{2}{\sigma} + 4r_c\right)}\right]. \qquad (3)$$

The results of Equations 2 and 3 are shown in Figure 1. This figure also shows similar expressions for the cooling and current densities in the maximum coeffecient of performance (COP) regime. Figure 1 shows that the maximum cooling increases as the element length decreases.

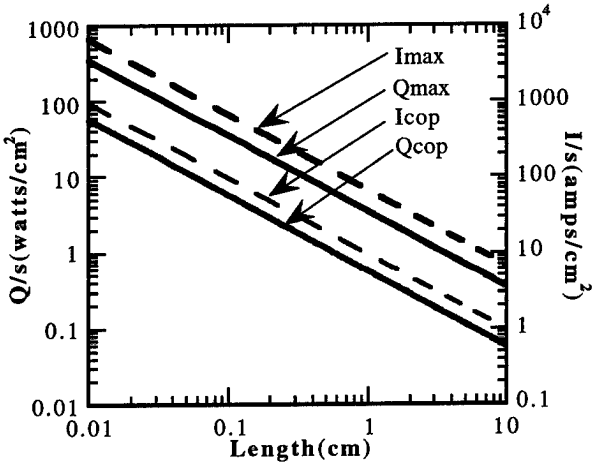


Fig 1. Cooling Density and Current Density vs Element Length in both the maximum cooling and maximum COP regimes. R_{con}=0, ΔT=17°C from a room temperature of 37°C

Also, an element length of 1mm produces a cooling density of 34.7 W/cm² and an element length of 100μm produces a cooling density of 347 W/cm². Of course, the maximum

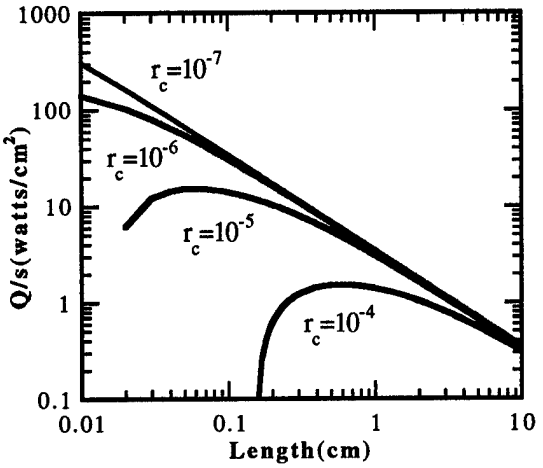


Fig 2. Cooling Density vs Element Length in the maximum cooling regime. Included is the effects of contact resistance: r_c (Ω/cm).

current density increases as well. An element of 1mm requires a current density of 654.7 A/cm^2, and an element length of 100μm requires a current density of 6547 A/cm^2.
Cooling densities in the range ≥100W/cm^2 are produced when the element length is smaller than 300μm.

The next step in the design rules is to determine the total cooling capacity and the total current for an array of thermocouples. These thermocouples are electrically in series and thermally in parallel, thus

$$Q_{total} = \frac{Q_{\max}}{a} A_{total}, \qquad (4)$$

$$I_{total} = \frac{I_{\max}}{a} \frac{A_{total}}{N}. \qquad (5)$$

The total current can be reduced by increasing the number of elements per area. Thus, a 1mmx1mmx100μm device with 65 elements would have cooling capacity of 3.47W with a total current of 1A at a temperature difference of 17°C.

The last step is to analyze the effect of contact resistance as the element length decreases. This is presented in Figure 2. This figure indicates that the effect of contact resistance is more pronounced at smaller element lengths. To make devices shorter than 1mm, a contact resistance of 10^{-6} or less is needed. But, a contact resistance of 10^{-6} greatly reduces cooling at lengths ≤ 300μm.

DEVICE PROCESSING

Figure 3 displays the processing steps necessary to fabricate a synthetic wafer of TECs. To demonstrate and develop this approach an array of 6 element bar coolers was made. The steps necessary for this are also presented in figure 3. An overview of the steps for the array and synthetic wafer will be presented and the remainder of this section discusses the specifics in the array fabrication.

To produce a synthetic wafer, alternating n and p type wafers are first bonded together (Fig.3a). Next, the resultant structure is cut into slices (Fig. 3b). These slices can be processed into an array of bar coolers. This is done by fabricating metal contacts and then mounting the array to a substrate(Fig. 3c). To further increase the number of cooling elements per unit area the slices in Figure 3b can be bonded together(Fig. 3d). This structure is once again sliced to yield a checker-board of alternating n and p type layers (Fig. 3e). Metal contacts are fabricated and the synthetic wafer of TECs is now bonded to the wafer with the opto-electronic devices(Fig. 3f). Finally, the bonded wafers are ready to be diced and mounted into a package. The remainder of this section presents the specific processing details for the array of bar coolers.

Before the wafers can be bonded, they must be prepared in order to insure periodicity in the stack which is necessary in the subsequent photolithography steps. To do this, they are lapped on a copper wheel using diamond grit to a desired thickness. Because Bi_2Te_3 is a soft material, care must

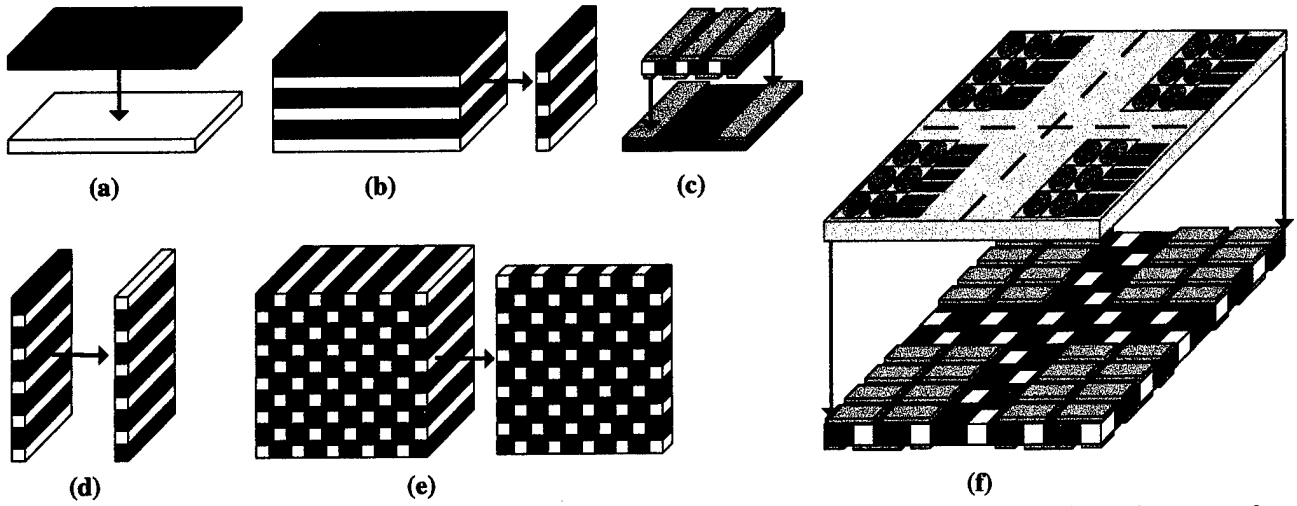


Fig3. Processing steps for a synthetic wafer of TECs. Also shown is the prototype array of bar coolers. a) p and n type wafers are bonded together. b) the resultant structure is cut into slices, c) a slice is patterned with metal contacts and mounted to a patterned substrate to make an array of bar coolers, d) to further process a synthetic wafer, the slices in b) are again bonded together. e) the resultant structure is again sliced to yield a synthetic wafer, f) the synthetic wafer is patterned with metal contacts and bonded to a wafer of opto-electronic devices(arrays of 6 PIN detectors). These can then be diced together, indicated by the dotted lines

be taken to reduce round off of the edges and scarring of the surfaces. Furthermore, polycrystalline Bi_2Te_3 has varying crystal grain structure which can produce an uneven surface with inappropriate lapping techniques. Finally, handling monocrystalline Bi_2Te_3 of thickness of 800μm or less requires special procedures as does polycrystalline Bi_2Te_3 of 400μm or less.

Next, the wafers are bonded together into a stack using a two part high temperature epoxy which will operate continuously up to 200°C. The procedure used produces an evenly thin epoxy layer between each wafer. This is done by first out-gassing the epoxy to remove any bubbles. Next, a thin layer of epoxy is spread on each wafer and then they are assembled into a stack. This stack is then placed into a vacuum press. The main features of this press are a dome shaped chuck and a silicone diaphragm. The press is exposed to house vacuum(≈150 Torr) which draws the diaphragm down on the dome shaped chuck which in turn applies an even pressure over the surface of the stack. Finally, the epoxy is cured with a temperature ramp that allows the whole press to remain at an uniform temperature . This technique produces an epoxy layer 1μm in thickness.

The bonded stack of wafers must now be sliced (shown in Figure 4). In this step, it is critical to use a procedure that will not destroy the stack and allows parallel slices to be made. To do this, a high concentration diamond grit wafering blade (thickness 325μm) is used on a slow speed spindle.

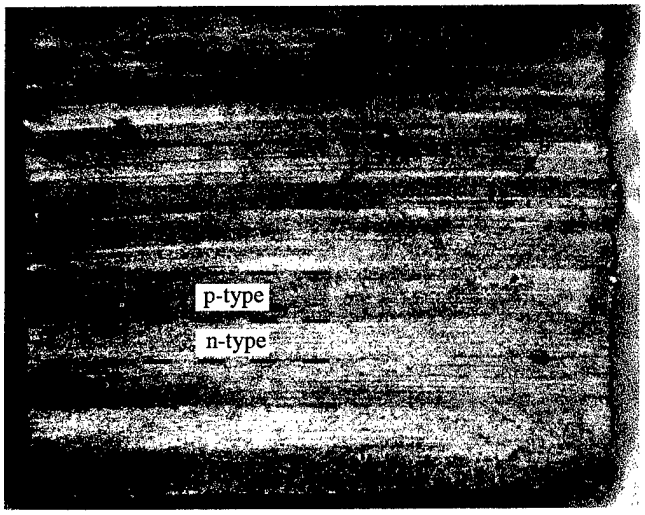


Fig 4. Top view of slice of bonded n and p wafers (refer to Fig3b).

At this point, each slice can be processed into a bar cooler. The next step is to fabricate metal contacts to allow current flow. To insure good adhesion of the metal to the Bi_2Te_3, the appropriate surfaces must be prepared. This is done by standard mechanical polishing techniques to remove any surface irregularities and damage. The metal contacts are fabricated using standard integrated circuit technology. First, the Bi_2Te_3 slice is cleaned and then a thin layer of polymer photoresist (Shipley AZ4210) is spun on. Next, a "chrome on quartz mask" with the appropriate metal contact pattern is placed into contact with the Bi_2Te_3 slice. These are exposed under a UV light source. After the photo resist is developed, the mask pattern has been reproduced on the slice. The sample is then O_2 plasma etched to remove any photo resist scum. Metal is deposited onto the slice using thermal evaporation. First, a 300Å of Ni is deposited as both a sticking layer and a diffusion barrier for a top Au layer. Next, a 1μm layer of Au is deposited as a thick metal layer to cover the epoxy and any surface irregularities still present. This also acts as a good layer for solder adhesion. After evaporation, the bar is placed in acetone for lift off. Because both sides of the bar cooler need metal contacts, this procedure is repeated on the second side of the bar cooler.

The remaining step in manufacturing a bar cooler is to mount the device to a thermally conductive substrate. BeO is used because of its high thermal conductivity (270 W/mK, 625μm thick). The BeO is metallized in the same method as described for the Bi_2Te_3 bar cooler. The only difference is that a Ti sticking layer is used on the BeO. The bar cooler is soldered into place on the BeO using In/Pb solder. To insure good thermal contact between the cooler and substrate, thermally conductive varnish is injected in-between the two. After soldering leads to the substrate, the cooler is now finished.

PRACTICAL LIMITATIONS

When operating in the maximum cooling regime there are no theoretical limits in the increase of cooling density with the decrease of element length. Of course there are practical limits in element size that can be manufactured and handled. The most destructive step in the process is handling the material after it has been lapped (before bonding). Because of this, wafer thickness (wafer thickness translates into one dimension of the element area, see Fig3b,c) of 800μm (single crystal Bi_2Te3) and 400μm (poly crystal Bi_2Te_3) are the practical limits when directly handling the material. Using special handling techniques Bi_2Te_3 (single or poly) can be easily lapped down to 100μm or less, thus lowering the limit on element areas. Minimum element length is less limited than area since the elements are already bonded with epoxy. This increases the mechanical integrity and allows easy handling. In this case element length are easily made to 100μm and care must be taken to make the length less.

EXPERIMENTAL RESULTS

The performance of the prototype 6 element bar cooler was evaluated by measuring the temperature at the cold side under an increasing DC current input. This was done at ambient pressure and temperature. The device was placed in good thermal contact with a heat sink using a thermally conductive paste. Thus, the hot side of the device remains at ambient temperature. The cold side temperature was measured using a thermister. In this prototype configuration, there is no cold side ceramic substrate and the thermister is placed directly on the thermocouples. The results of the temperature measurement are shown if Figure 7.

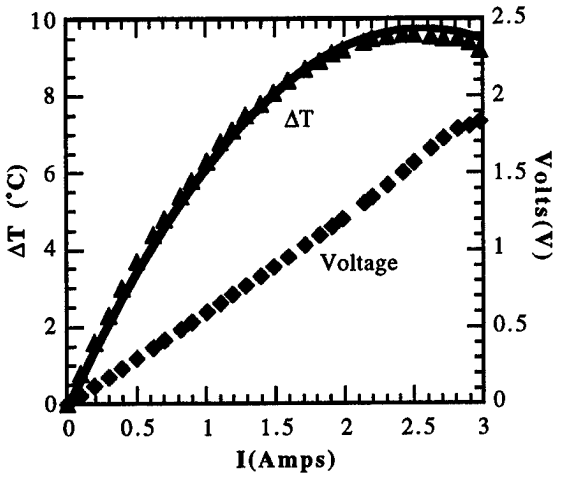


Fig7. Measurement results under DC input current. Vertical axis shows the temperature difference between the hot and cold sides and the voltage. The solid line shows the theoretical prediction.

In order to verify the results, a theoretical curve was calculated based on measured device and material parameters. The theoretical temperature difference is obtained by rearranging Equation 1 and is given by;

$$\Delta T = \frac{1}{K}\left[\alpha T_c I - I^2\left(\frac{1}{2}R_{mat} + R_{con}\right) - \frac{Q}{N}\right]. \quad (6)$$

To evaluate this, the Seebeck coefficient of the n and p type wafers was measured. This yielded average values of 203 μV/K and 230 μV/K respectively. Next, the resistance of the device was measured. This is obtained from the IV measurement (Figure 4). The voltage of the device is given by;

$$V = N\left[I\left(R_{mat} + 2R_{con} + R_{wire}\right) + \alpha\Delta T\right], \quad (10)$$

where R_{wire} is the resistance the current supply leads. The total resistance, given by the slope in Figure 4, is 0.63Ω. Subtracting the lead resistance, yields a device resistance of 0.15Ω. To use this value in Equation 6, it is multiplied by 1/2N(N=3), which yields 0.025Ω. Finally, the total thermal conductivity K, is obtained from the linear term of the measured temperature data, an average cold side temperature of 295 K, and the Seebeck coefficient(see Equation 6). These yield a K of 0.0166W/K. Substituting these values into Equation 1(with an estimation for ambient heat load) yields the following;

$$\Delta T = 1/.0166\left(-.002 + .128I - .025I^2\right) \quad (11)$$

Equation 11 is shown with the measured temperature difference in Figure 7. From this figure, the measured and calculated response show great similarity. The linear cooling term is due to the Peltier effect, and the quadratic roll off due to joule heating. Of course, the maximum temperature difference is much lower than desired. This is mostly due to the joule heating term, which is an order of magnitude more than expected. Preliminary measurements on conductivity and contact resistive reveal a material conductivity much lower than expected. Further investigation is necessary to determine the source of this high resistance. Using material with an expected conductivity(≈1000 1/Ωcm), should yield a device with a maximum temperature difference of 44°C. This fact is presented in Figure 8.

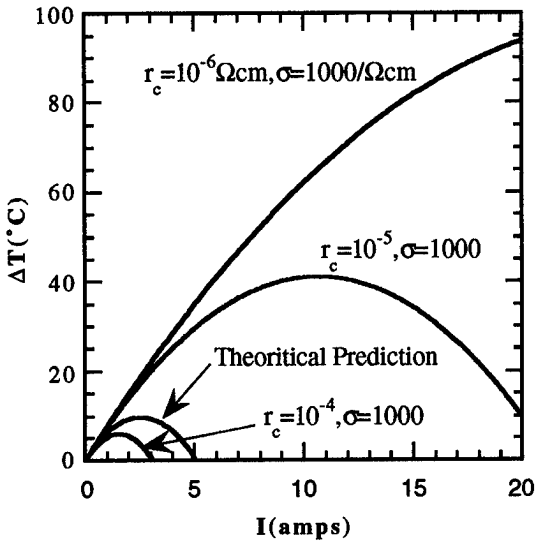


Fig8. Temperature difference vs input current for several different resistances. Also included is the theoritical prediction from Fig7.

CONCLUSIONS

This paper presented key developments in a manufacturing approach that can greatly enhance the ability to produce miniature TEC's and aid in packaging these to optoelectronic devices through the use of a synthetic wafer. These developments were validated by a prototype device which behaves as expected given the material limitations.

REFERENCES

1.Semenyuk V.A., Pilipenko T.V., Albright G.C., Ioffe L.A., and Rolls W.H."Miniature Thermoelectric Coolers for Semiconductor Lasers", *Proceedings of the Thirteenth International Conference on Thermoelectrics*, Kansas City, Mo, 1994, pp150-153.

2.Goldsmid H.J., *Electronic Refrigeration*, Pion Limited, London, 1986.

3.Sze S.M., *Physics of Semiconductor Devices*, John Wiley and Sons, New York, 1981.

Fast Thermoelectric Microcoolers

Vadim Galperin.

MGNPP «OSTERM» 15 Grazhdanskaia St.,190031
St. Petersburg, Russia
Tel. (812) 3-12-57-32, Fax : (812) 3-11-52- 39,
E mail : iib@ okb . cor. Neva.vu

Abstract

This paper is concerned with issues related to further examination of low-inertia thermoelectric microcoolers [1,2,3].Such devices are useful to deliver powerful short-term heating action an objects of low thermal capacity ,as for example ,in data recording or deletion using heating or cooling msec-pulses on thermochrome film.

Formulae suitable for engineering design have been obtained ,describing the opportunities of pulse cooling. It has been demonstrated that the mono-pulse /frequency mode change impose additional requirements on heat removal and contact heating resistance on the thermoelectric cooler hot side

Introduction

In spite of numerous publications on thermoelectric coolers these problems are urgented .Theoretically this fact is explained by cumbersome of numerical analytical procedures ,so that their practical application in engineering design and appraising of pulse cooling opportunities has been problematic .On practical view the interest to quick-operating microcoolers continually increase followed by intensive attempts of using their advantages sometimes it is impossible without them.Primarily, this is true in regard to film structure cooling, some medical and biological applications .The formulae suitable for engine design have been obtained by suggested method of the paper for temperature determination of the objects cooled with thermocouples during short time intervals; and on this base satisfactory analysis can be performed microcoolers operation in mono-pulse and frequency modes

Design model

Traditionally , time temperature dependence of cooling side of thermocouples have been determined from the solution of conductivity equation [1,2,4,5],one result in cumbersome procedures difficult to examine in all. Different approach to the solution of the problem is consider below.

Let heat transfer in thermocouple leg is with specific power $W = j^2\rho$ during the time (τ) ;cold source is on working surface with density of $q = j\Pi$,

where j-current density through thermocouple; ρ-specific resistance of thermoelectric material $\Pi = \alpha T_0$ -Peltiers coefficient; α -coefficient of the thermoelectric motive force T_0 -temperature of cold side

Then on the one hand ,temperature(T_0) of leg surface ,as and any point of it, must be increase on linear law at the sacrifice of internal heat source (without heat exchange with environment) :

$$T_0 = T_{st} + \frac{j^2\rho}{\lambda} a\tau \ , \qquad (1)$$

and on the other hand ,this temperature must be decrease in result by surface cooling on the law

$$T_0 = T_{st} - \frac{2q}{\sqrt{\pi}\lambda}\sqrt{a\tau} \ , \qquad (2)$$

where T_{st} -initial leg temperature; λ -and a- coefficients of heat conductivity and thermal conductivity of thermoelectrical material accordingly. It is follows that the total temperature difference is defined by expression :

$$\Delta T = \frac{2\alpha . jT_0}{\sqrt{\pi}\lambda}\sqrt{a\tau} - \frac{j^2\rho}{\lambda} a\tau \ , \qquad (3)$$

Offering ,that the Peltiers coefficient is not depend from temperature ,and using well-known expressions for $\Delta T_{max} = \frac{\alpha^2 T_0^{\,2}}{2\rho\lambda}$ and $j_0 = \frac{\alpha T_0}{2\rho h}$

where ΔT_{max} -maximum temperature difference on thermocouple in the steady -state mode ; j_0 -optimal current density in steady state mode; the expression for temperature difference depending on the time has been received in view :

$$\Delta T(\tau) = \Delta T_{max}\left[\frac{4}{\sqrt{\pi}}\frac{j}{j_0}\sqrt{\frac{\tau}{\tau_0}} - 2\left(\frac{j}{j_0}\right)^2\frac{\tau}{\tau_0}\right], \qquad (4)$$

Where $\tau_0 = \frac{h^2}{a}$ -thermocouple time constant;

From this expression it may be define the optimal current $j_0^{(p)}$ for maximum temperature difference $(\Delta T_{max}^{(p)}(\tau))$ during the time (τ) :

$$j_0^{(p)} = j_0\frac{1}{\sqrt{\pi}}\sqrt{\frac{\tau_0}{\tau}} \qquad (5)$$

and the value :

$$\Delta T_{max}^{(p)} = \frac{2}{\pi}\Delta T_{max} \qquad (6)$$

It is seen ,that for true theoretical approximation , ignoring the Joule heat in commutative plate and the capacity of cooled object ,temperature difference is not depend from current value and one is bounded by 0,637 ΔT_{max}

This assertion closely agrees with experimental data [2] and the expression (4) becomes precisely the same solution for with respect to the solution for small time values [5]. Establishing the correspondence between the received results and ideal model ones ,let us see how this related to actual conditions The Joile heat in commutative plate and load capacity must be taken into account.

Inserting additional leg surface density of heat transfer ($j^2 R_{k\delta}$)in expressions (1) and (2),liberated in commutative plate , and the value ($\approx C\frac{\Delta T}{\tau}$) ,characterizing heat content change of capacity (C),it is received ,that temperature increasing of cold object (ΔT_H) is determined by the expression:

$$\Delta T_h = \frac{j^2 \rho a \tau}{\lambda} + \frac{2 j^2 R_k S\sqrt{a\tau}}{\sqrt{\pi}\lambda} - \frac{2}{\sqrt{\pi}\lambda} C\frac{\Delta T}{\tau}\sqrt{a\tau} \ , \qquad (7)$$

and decreasing (ΔT_c) from one :

$$\Delta T_c = \frac{2(\alpha j T_0 - C\frac{\Delta T_s}{\tau})}{\sqrt{\pi}\lambda}\sqrt{a\tau} \ , \qquad (8)$$

and the total effect :

$$\Delta T = \Delta T_c - \Delta T_h \ , \qquad (9)$$

where

C-specific surface capacity of leg additional load ;

R_j -resistance of the commutative plate part , additional to the leg

S-leg cross section;

On the some simple rearrangements and it taken $\frac{2}{\sqrt{2\pi}} \approx 1$, general expression for temperature difference ,in time dependence at using of R_j and C has been obtained from expressions (7),(8),(9):

$$\Delta T(\tau) = \Delta T_{max}\frac{1}{f(c,\tau)}\left[\frac{4}{\sqrt{\pi}}\left(\frac{j}{j_0}\right)\sqrt{\frac{\tau}{\tau_0}}\right] -$$

$$- \Delta T_{max}\frac{1}{f(c,\tau)}\left[2\left(\frac{j}{j_0}\right)^2\frac{\tau}{\tau_0}f(R_j,\tau)\right], \qquad (10)$$

Where

$$f(c,\tau) = 1 + \frac{C}{\lambda}\sqrt{\frac{a}{\tau}} \qquad f(R_k,\tau) = 1 + \frac{R_j}{R}\sqrt{\frac{\tau_0}{\tau}} \ ,$$

where R- thermocouple leg resistance

Optimal current determined from the expression (10):

$$j_0^{(p)}(C,R_j) = j_0\frac{1}{\sqrt{\pi}}\sqrt{\frac{\tau_0}{\tau}}\frac{1}{f(R_j)} \ , \qquad (11)$$

except for time is depends on $f(R_j,\tau)$ and this current is unaffected by $f(c,\tau)$, there with maximum temperature difference is equal to:

$$\Delta T_{max}^{(p)}(R_j,C,\tau) = \frac{2}{\pi}\frac{\Delta T_{max}}{f(c,\tau)f(R_j,\tau)} \ , \qquad (12)$$

As it is seen from their structures functions $f(c,\tau)$ and $f(R_j,\tau)$ are dimensionless values , determined by the parameters of thermoelectric material and load , and time duration of cooling pulse also .With growth of R_j and C ,corresponding functions increase also, so that value $\Delta T_{max}^{(p)}(R_j,C,\tau)$ decrease. Similar dependence is observed at the decreasing of τ. Notice that application of this formulae is appropriate at leg length $h \geq 3\sqrt{a\tau}$ or it is the same situation at $\frac{j}{j_0} \geq 2$. For example ,at pulse duration of $\tau = 0{,}01s$ and $a = 4{,}9 * 10^{-7}\frac{m}{s^2}$, height (h), must be greater 0,2 mm, for any real thermocouple it is true . Examining the expression $f(c,\tau) * f(R_j,\tau)$ about minimum it may be obtained the optimal value of commutative plate thickness ,entering in the expressions for the capacity ($C_j = \delta_j S C_j$) and the resistance ($R_j = \frac{1}{3}\frac{\rho_j}{\delta_j}$). If cooled object is absent and only commutative plate capacity is considered ,that is $C = C_j$, so appear δ_j is in proportion to $\sqrt{s}$, it consist of 25 mc at s=1mm²

In this case the value of $\Delta T_{max}^{(p)}(R_j,C,\tau)$ is nothing more than (22-23)°C at $\tau = 0{,}01s$ Of course, it is upper apraised boundary ,if for no other reason than the estimation of contact resistance and heat transfer with environment ;somewhat it is the reason for increasing of second term in left part of the formula (10). Obtained expressions are in good agreememt with experimental data [3].

Frequency operating mode

As it is pointed above ,quick-operating microcoolers are useful for information systems,where data recording is carried out by phase transition in thin-film thermochrome

materials [7],for example, by laser ray and deletion using cooling pulse - it returns the film in initial state. If system has a chance to become thermodynamic-equilibrium during the spaces between deleting pulses, so it is mono-pulse mode ,fully described by proper approach.

However ,in view peceptible systems, using the devices of operating optical memory, it is necessary that the work is carried out in real time scale, that is, with frequency of change view . In this case cooling pulse duration is limited by 40 ms. The inefficient mode of deletion is observed at short pulse duration, that is, the spaces between pulses are reduced;consequently the system is not reduced to initial heat state. It may be two alternative cases therewith ;

- thermal contact of thermocouple heat side with heat removal is optimum one ,that is ,the junction temperature is constant at any allowable current through thermocouple. In this case every subsequent pulse initiate the cooling from more lower level, because the film is not reduced to starting state,that is , average temperature of cold side is decreased;on this reason the film ability is deteriorated for information memorizing.

-hermal contact of heat side with heat removal is not optimum.In this case the quantity of heat release (for 1 s) is not dissipated during total time of the spaces between pulses ,subsequently system superheating and loss of the ability to information recording take place.What this means is the transition from monopulse mode to frequency one requires either selection of thermal resistance contact value -"heat side - heat removal" (several for every frequency) or temperature selection of heat removal for providing the necessary heat flow through this contact,required to sustain the costant temperature of stability. On the practice , it is appear ,that starting from frequency (10-12) Hz for avoidance of superheating, it is necesary to decrease the amplitude of feed pulses; however it cause the lowering of cooling level..

In the same way , he optimal current amplitude exists for every cooling pulse recurrence frequency and every thermocouple construction,providing the maximum temperature difference without superheating:

$$j_0^{\,f} = j_0^{\,(p)}(C, R_j)\frac{1}{\sqrt{f}} \quad , \qquad (13)$$

In particular ,temperature difference ($\Delta T = 7^0 C$) can be obtained at current =5 A;frequency =25 Hz ,(τ_p =35ms) constant conditions of heat removal during transition from mono-pulse mode to frequency one by optimization of cooling pulse amplitude .

Conclusions

Simple analitical useful expressions have been received for engine design of thermoelectrical coolers, operating in pulse feed mode. Cooler potential on temperature lowering during short time spaces may be appraised on the knowledge of its parameters. And conversely, if necessary temperature differences are given at fixed time , optimal construction and required feed currents will be determined . It is shown ,that certain features of frequency mode must be taken into account at development of microcoolers with heat removal.

References

[1] M.A. Kaganov, M.R. Privin, " Thermoelectric heat pumps",L.,: Energiya (1970)

[2] E.K. Iordanishvili, V.P. Babin,"Non-steady process in thermoelectric and thermomagnetic energy-transformation systems," M.:Nauka,1983

[3} V.L. Galperin, "Non-steady processes in pulsed-mode thermoelectric devices," Proc. of the 14 International Conference on Thermoelectrics (ICT'95),St-Petersburg,Russia (1995) 446

[4] L.S. Stilbans, N.A.Fedorovich,"Thermoelectric coolers oerated in the non-steady mode " 2h.Tekn.Fiz 3 1958) 489

[5] A.D. Reich, T.Arai, J.R. Madigan,"Transient effects in Peltier coolers," J.Appl.Phys. 32 (1961) 2493

[6] G.N.Dulnev,E.M.Semayshkin"Heat transfer in radio-electron devices", L(1969)

[7] G.N. Galperin ,I.A. Khakhaev, F.A.Chudnovskii, E.B. Shadrin,"Optical memory device on the base of vanadium dioxide film and fast thermocooler,"SPIE proceedings 3000 (1996)

Fabrication of a miniature thermoelectric module with elements composed of sintered Bi-Te compounds

M. Kishi, Y. Yoshida, H. Okano, H. Nemoto, Y. Funanami, M. Yamamoto,and H. Kanazawa

Seiko Instruments Inc., 563, Takatsukashinden, Matsudo-shi, Chiba 271, Japan
Tel : +81/47/392/7819, Fax ; +81/47/392/2025, E-mail ; matsuo. kishi@sii.co.jp

Abstract

A new manufacturing process of a π-shaped miniature thermoelectric module composed of sintered Bi-Te compounds has been developed. The manufacturing process is suitable for mass production as it is comprised of simple technologies such as conventional photolithography technology, micro-bonding technology using the solder bump method and precise cutting technology using a dicing machine. A miniature module with the dimensions of 3 mm X 3 mm X 1.3 mm in which 102 elements (51 junctions) with the dimensions of 120 μm X 120 μm in cross section parallel to the substrates and a height of 600 μm were included was fabricated while developing the process. The maximum temperature difference ΔT_{max}, and the heat absorption Q_{max} of the module were 61.3 °C and 0.36W, respectively. This indicates that the performance of the module as a cooling device was equivalent to that of conventional modules. The specification for high voltage and low current input, a significant purpose in addition to the miniaturization of the module, was achieved because the maximum voltage V_{max} and current I_{max} were 6.7 V and 110 mA, respectively.

Introduction

Millimeter sized thermoelectric modules are widely utilized as cooling devices for micro-electronic devices such as laser diodes, infrared detectors and CCDs (charge couple devices). However, there is a constant push to improve the performance of power input because a large difference exists between the input voltage of the electronics devices and that of the thermoelectric modules. In other words, the former is several times greater than the later.

The input voltage to a module does not only depend on the properties of the materials composed of the elements, but also on the size and the number of the elements. It is obvious that the input voltage can be increased by making the elements more slender and by increasing the number of the elements in the module. However, several problems arise when trying to miniaturize the elements. it is especially difficult to prepare elements with leg dimensions of below several hundred micrometer (estimated to be below 300 μm) because single crystals of Bi-Te compounds, which have the highest performance of all thermoelectric materials, are too fragile to create such slender elements. Recently, sintered Bi-Te compounds using hot pressing techniques have been prepared in order to increase the strength without degradation of the thermoelectric properties of starting compounds.[1)]

In the present work, a manufacturing process for miniature modules, which include elements with leg dimensions of below a few hundred micrometers in cross section parallel to the substrates, was developed. The process is principally based on photolithography, micro-soldering exemplified by solder bump technology and dicing technologies, and can be expected to be superior in productivity and costs in mass production to the conventional manufacturing process which could be adopted only for preparation of "large size modules". Furthermore, a module including 102 elements with leg dimensions of 120 μm × 120 μm × 600 μm in 3 mm × 3 mm substrates was fabricated using the process, and the properties of the module were measured.

Experimental Procedure

Thermoelectric materials used were hot pressed Bi-Te-Sb compounds ($z=3\times10^{-3}$ K^{-1}) with a thickness of 600 μm as p-type material and Bi-Te ($z=2.3\times10^{-3}$ K^{-1}) as n-type. The process developed mainly consists of the five stages shown in Fig.1.

0-7803-4057-4/97 $10.00 ©1997 IEEE

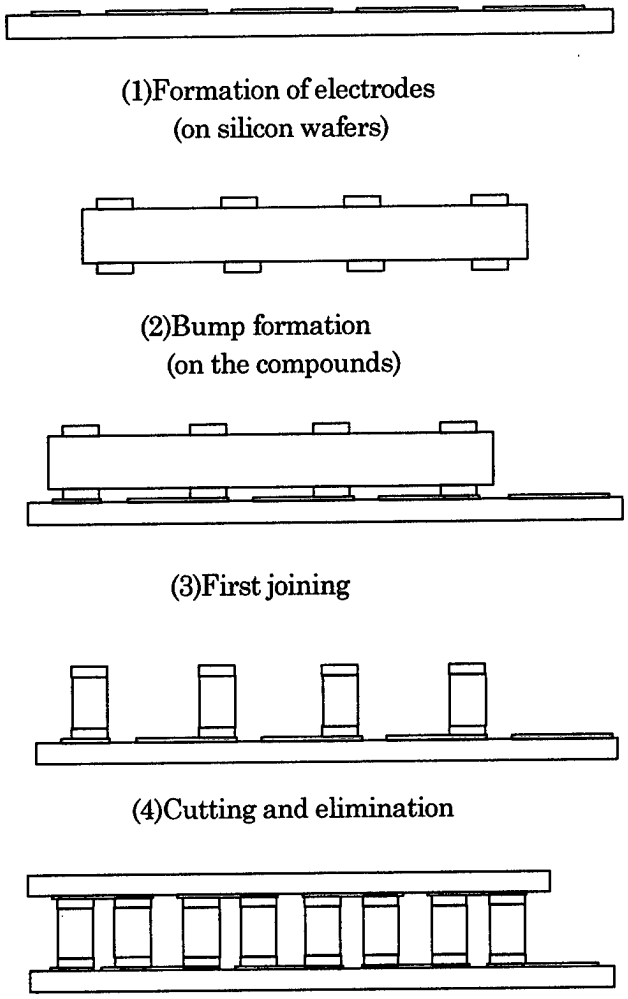


Fig.1 Schematics of the manufacturing process

Thin film consisting of three layers of Cr-Ni-Au with a total thickness of 1 μm was formed by sputtering method on thermally oxidized silicon wafers with thickness of 300 μm to form the electrodes for pn-junctions. Afterward, the electrodes were patterned using conventional photolithography technology.

A resist layer containing circular openings with a diameter of 120 μm for the formation of bumps was created on both sides of the thermoelectric materials. Nickel bumps with a height of 40 μm were electroplated on both sides of the sintered thermoelectric materials prior to the formation of solder bumps. The electroplating method was used to form solder layers with a composition of Sn : Pb = 6 : 4. The solder layers were re-flowed to prepare solder bumps by heating them with rosin flux after removing the resist layer.

The thermoelectric materials were bonded to the electrodes for pn-junctions on the substrates with solder bumps by heating.

Cut and elimination of unnecessary portions of the thermoelectric material was carried out with a dicing saw with a 200 μm thick blade to prepare the elements, which are bonded to the substrates. Here, a gap between the thermoelectric material and the substrate, which was formed by the nickel bumps, was utilized for preventing the electrodes from being cut. This process produced two types of substrates, one with p-type elements and the other with n-type elements.

The module was completed by positioning the two types of substrates and bonding the elements on one substrate to the electrodes on the other substrate with solder.

Results and discussion

Plural modules could have been fabricated at the same time as silicon wafers and Bi-Te plates were used throughout the process. Thus, the process could be a candidate for mass production.

A micrograph of the miniature module is shown in Fig.2. The size of the module was 3 mm wide × 3 mm long × 1.3 mm high. The dimensions of the element composed of sintered Bi-Te compounds were 120 μm × 120 μm in cross section parallel to the substrates and 600 μm in height. The module consisted of 112 legs, with 102 utilized for pn-junctions and the remaining 10 not functioning as thermoelectric elements because of the design of the module and the manufacturing process.

Some attempts to prepare miniature thermoelectric modules using the thin film method or using silicon surface technologies were carried out. [2,3] However, there is no report related to π-shaped miniature modules composed of bulk Bi-Te compounds.

Although the module fabricated in the present works was miniaturized as shown in Fig.2, it had an equivalent performance to that of conventional cooling modules as described below.

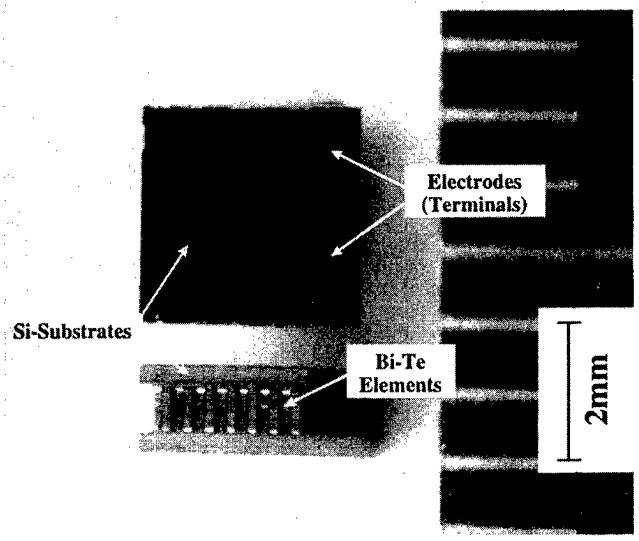


Fig.2 Photograph of the miniature module

The cooling properties of the module were measured using CA thermocouples with a diameter of 25 μm. The substrate to which the heat generated in the module should be released was kept at a constant temperature of 300 K, while the measurement was carried out in a vacuum chamber evacuated up to 10^{-1} Pa to prevent the occurrence of condensation from the surroundings. The dependence of the temperature difference between the substrates on the input current is indicated in Fig.3.

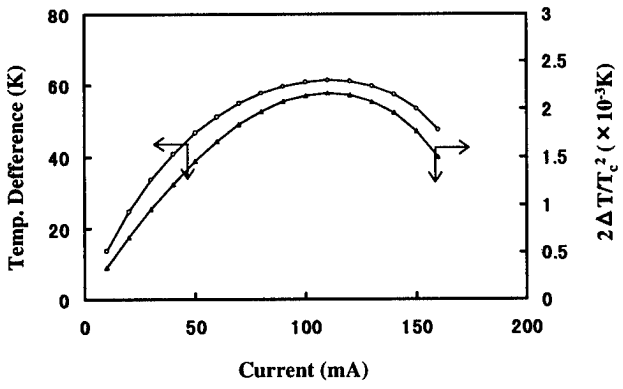


Fig.3 Temperature difference between the substrates and 2 Δ T/T_c^2 values as a function of the current through the module.

The temperature difference ΔT increases with a rise in the input current and the maximum temperature difference ΔT_{max} of 61.3 °C appeared at an input current of 110 mA. Afterward, the temperature difference ΔT decreased above the current at which the maximum temperature difference was given because the joule heat by electric current was superior to the heat transfer by Peltier effect.

The relationship between figure-of-merit z, the maximum temperature difference ΔT_{max} and the temperature of cold side ΔT_c is given by

$$Z = \frac{2\Delta T_{max}}{\Delta T_c^{\,2}} \qquad (1)$$

The value of z calculated from the equation (1) is 2.15×10^{-3} K^{-1}. This value is significantly smaller than those of the materials whose mean value is 2.65×10^{-3} K^{-1}. The decrease in ΔT_{max} and z is not only brought about by the heat resistance related with the substrates, but also by heat flow through the 10 dummy legs which were inevitably formed due to the design of the module. The later especially effects the performance of the module. The ratio of heat flow through the dummy legs should amount to 10/112 of the total heat flow through the legs. If the legs between the substrates create the temperature difference between the substrates, the following equations should be developed because the temperature difference should be inversely proportional to the thermal conductance.

$$\Delta T'_{max} = \Delta T_{max}\frac{112}{112-10}$$
$$= 67.3K$$

$$T'_c = T_c - (\Delta T'_{max} - \Delta T_{max})$$
$$= 226.7K$$

where $\Delta T'_{max}$ and $\Delta T'_c$ are estimated values of the maximum temperature difference and of the cooling side temperature without the dummy legs, respectively. These values give the figure-of-merit, z, of 2.49×10^{-3} K^{-1}. Accordingly, eliminating the dummy legs is expected to improve the performance of the module to a level equivalent to commercially supplied

modules.[4]

Figure 4 shows the dependence on the input power of the heat absorption and the coefficient of performance (COP) at the temperature difference of 0, 15, 30 and 45 °C. It was found that the module produces a maximum heat absorption Q_{max} of 0.36 W at the input current of 110 mA. This result indicates that the module has an enough ability of heat absorption to utilize it as a cooling module for electric devices such as laser diodes.

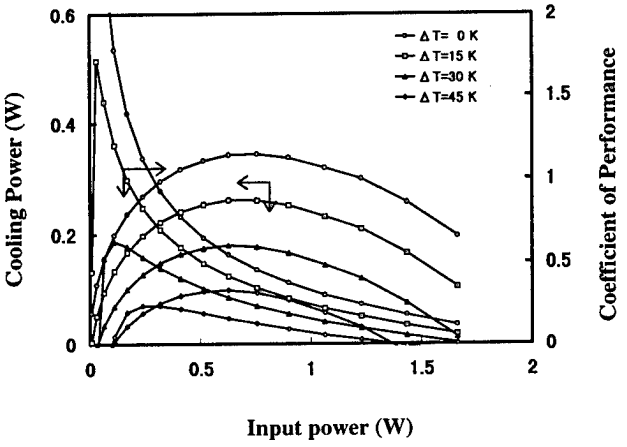


Fig.4 Dependence of the cooling power and COP on input power

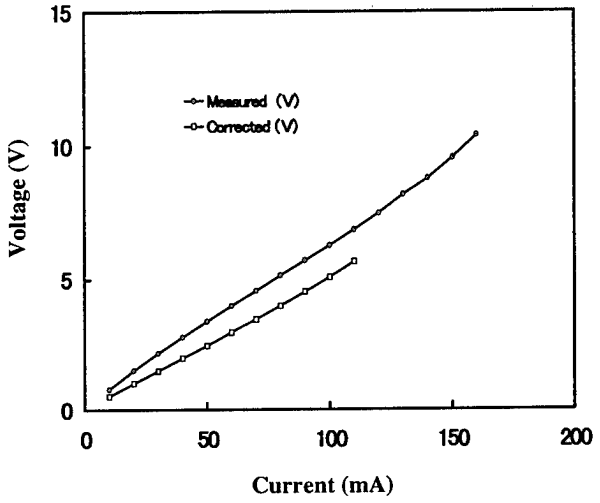


Fig.5 Relationship between input current and voltage.

The input voltage increases nearly in proportion to the increase of the input current as shown in Fig.5. The maximum voltage, which is significant for the use of the module as a electric device, is 6.7 V at the maximum current. The voltages was corrected neglecting the term of Seebeck effect, the value of α times ΔT and the internal electric resistance of the module is about 50 Ω which is calculated from the corrected voltages. The values of the voltage and current imply that the module can be powered by the same electric power source that supplies voltage to ordinary electric devices, which usually range from 1.5 V to 12 V.

Conclusions

The manufacturing process and technology to prepare millimeter sized miniature module in which the elements with leg dimensions of 120 μm × 120 μm and a heights of 600 μm are included has been established. It is certain that the process is suitable for mass production. The module which was fabricated using the process had suitable performances as a cooling device for applying to electric devices.

Acknowledgments

The authors would like to thank T. Ishii, S. Fujita, N. Echigo, S. Natori, S. Yamamoto and R. Ataka of Seiko Instruments Inc. for their useful advice.

References

1. H. T. Kaibe, M. Sakata and I. A. Nishida, "Thermoelectric cooling properties of the π-shaped thermocouples consisting of the sintered Bi_2Te_3 and Sb_2Te_3 based compounds", Proc. 12th ICT(1993) 165.
2. I. H. Kim and D. H. Lee, "Preparation and properties of $(Bi,Sb)_2(Te,Se)_3$ thin film thermoelectric modules", Proc. 12th ICT (1993) 328.
3. J. H. Kiely, D. V. Morgan and D. M. Rowe, "The design and fabrication of a miniature thermoelectric generator using MOS processing techniques", Meas. Sci. Technol. 5 (1994) 182.
4. H. P. Ha, Y. W. Cho, J. Y. Byun and J. D. Shim, "Simple and quick characterization of thermoelectric modules", Proc. 12th ICT (1993) 404.

Peltier Current Lead Experiments with a Thermoelectric Semiconductor near 77 K

S. YAMAGUCHI, H. NAKAMURA, K. IKEDA
National Institute for Fusion Science (NIFS), Oroshi 322-6, Toki 509-52, Japan

T. SAKURAI, I. YOSHIDA, S. TANUMA
Iwaki Meisei Univ.,Chuodai-Iino 5-5-1, Iwaki 970, Japan.

S. TOBISE, K. KOUMOTO
Nagoya Univ., Furo-cho, Chikusa-ku, Nagoya 464-01, Japan.

Abstract − **Peltier current lead was proposed to reduce heat leak from the current lead. The temperature of the hot side of semiconductors was kept to be a room temperature and the liquid nitrogen was used to cool the system in the experiment. The experiment confirmed the principle of the Peltier current lead, and the reduction of the heat leak is calculated to be 30 % for the liquid helium system and 40 % for the liquid nitrogen system. We also proposed a new current lead system which is composed of semiconductors and high temperature superconducting material (HTS). This idea bases on the functionally gradient material (FGM), and the HTS is connected to the semiconductor directly. The temperature of the hot side of semiconductor is kept to be the liquid nitrogen temperature, the temperature of HTS can be expected to be lower than 77 K. Therefore, we can expect high current capacity of the HTS and/or high stability of the HTS. We use BiSb as a N-type semiconductor and BiTe as a P-type semiconductor in the experiment, and the temperature of the cold side of the semiconductor is 73 K in this experiment.**

I. INTRODUCTION

Peltier current lead was proposed, and the P-type and N-type semiconductors made of BiTe were kept at the hot side of room temperature side in the demonstration experiment. The temperature difference between the high and low temperature sides of the semiconductors was around 100 K, which confirmed the principle of the Peltier current lead [1]. A superconducting magnet system includes a room temperature power supply and a low temperature magnet, which creates a temperature difference in the electric circuit. This can be dealt with by using an thermoelectric element take the Peltier current lead. Analyzing and numerical calculations gave theoretical results that confirmed the original experimental findings [2]. While liquid nitrogen was used as a coolant in the experiment, resulting in a 40 % reduction in the heat leak from the current lead, the estimated reduction in a liquid helium superconducting system would be about 30 %. If the system did not use a coolant, the Peltier current lead would be even more effective.

Electric power consumption increases when the semiconductors are inserted, but the efficiency of the electric power is improved ten times because the heat leak is reduced and the efficiency of refrigerator is low. Since A cooling system is not cheap, the Peltier current lead can reduce not only the running costs but also the instrument costs of the system. It has an active element, i.e. its thermoelectric effect. Moreover, since the thermal conductivity of BiTe is only 0.3 to 0.5 % that of copper around room temperature, so even if the current of the current lead is zero, the heat leak is reduced. This is a passive effect.

A high temperature superconductor (HTS) has recently been used in so-called HTS current leads [3]. It is a passive element, i.e. the thermal conductivity of HTS material is currently about 0.1 % that of the copper below 77 K, reducing the occurrence of the heat leak from 77 K to the temperature of liquid helium. The conductivity of HTS is of the same order as that of the semiconductor in this temperature range. While BiTe is a good semiconductor material near room temperature, i.e. a BiTe semiconductor offers low thermal conductivity, high electrical conductivity and high thermoelectric power, other semiconductors and/or multistage elements are needed because the low temperature side of the semiconductor reaches around 200 K in the maximum temperature difference operation. BiSb is a good N-type semiconductor material in low temperatures and it is connected with HTS [4]. BiSb also has a magnetic field effect, so its performance improves [4] when a magnetic field is applied.

A number of HTS materials has been developed and studied and Bi-2223 is one of the best HTS material for the current lead. All materials of the semiconductor and HTS are, therefore, based on Bi alloy designed for temperature from room temperature to 77 K. Yamaguchi et al [5] proposed a new current lead concept based on functionally gradient material (FGM).

Manuscript received October 21, 1997.

Low temperature experiments were needed to realize this concept. We conducted and analyzed these low temperature experiments, where the hot temperature side of the semiconductors was set at the temperature of liquid nitrogen.

II. Experimental Set Up

Figure 1 shows the experimental device. We used liquid nitrogen to keep the temperature constant, on the hot temperature side of the semiconductors which were connected to the immersed copper plate electrodes by low temperature solder. The semiconductors were set in a vacuum vessel with a vacuum of 2.0×10^{-6} torr for thermal insulation. The N-type semiconductor, made of BiSb, was 12 mm diameter and 10 mm length, the P-type semiconductor, a made of BiTe, and has a cross section of 13×13 mm and the length of 10 mm. The transport coefficients of these semiconductors and the copper near 77 K are listed in Table 1, α the thermoelectric power, κ the thermal conductivity and η the electrical resistivity. The thermal conductivity of copper is increases with a decrease in temperature and reaches about 1200 W/m/K near 20 K. The thermal conductivity of the semiconductors decreases with the decreasing temperature but no more than 30 %. The electrical resistivity of copper decreases with a decrease in temperature and reaches saturation of 0.0002 to 0.0001 μΩm below 20 K, while the resistivity of the semiconductors increases with a decrease in temperature without reaching saturation. Since the low temperature sides of the two semiconductors are connected by a flexible copper cable, its temperature is lower than that of the liquid nitrogen. The performances and the cold temperatures of BiTe and BiSb are different from each other, but this difference is not so big because the thermal conductivity of the copper cable is high.

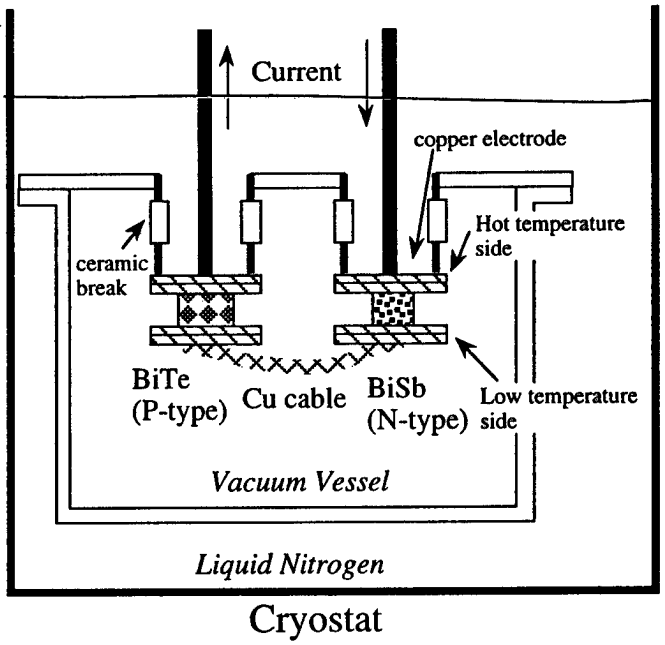


Fig.1. Experimental device. Semiconductors are set in a vacuum vessel for thermal insulation. The temperature of the hot side of the semiconductors is kept at the temperature of the liquid nitrogen.

Temperatures were measured by Type C thermocouples, directly connected to the electrodes by the low temperature solder, and voltages were measured by the thermocouples cable. Electrical current is controlled by the power supply with an accuracy of 3 digits.

III. Experimental Result and Calculation

Figure 2 shows the voltages of the semiconductors at different currents. The voltages were fairly proportional to the currents. The semiconductor resistance accounted for the main part of their inclines. Others, small factors were the electrode contact resistance measured at 3 to 6 μΩ, the copper electrode resistivity is quite small (see Table 1) and the thermoelectric voltages can be estimated from Table 1. These estimations indicate that the main part of the inclines come from the resistance of the semiconductors. The estimated semiconductors resistances was 132 μΩ for BiTe and 83 μΩ for BiSb.

Figure 3 shows the measured temperatures of the semiconductors at different currents. Measured in the center of the copper plate electrodes, the lowest temperature of BiTe was occurred at a current of 30 to 40 A, while the lowest temperature of BiSb did not materialize over the current range of our experiment. The temperature difference between the hot and the cold side was greater with BiSb than with BiTe, which makes BiSb a better material for the temperature range of our experi-

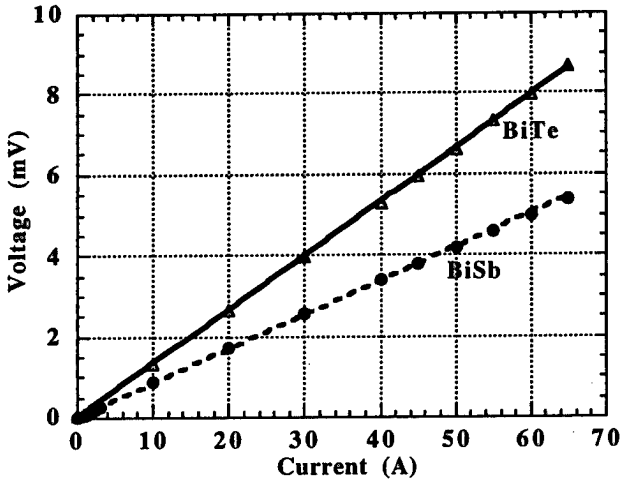


Fig.2. Currents and voltages of the semiconductors.

Table.1
Transport coefficients of BiTe, BiSb and copper near 77 K.

Material	κ (W/m/K)	η (μΩ m)	α (μV/K)
BiTe	1.78	2.20	75
BiSb	3.80	1.10	-160
Cu	600	0.002	0.1

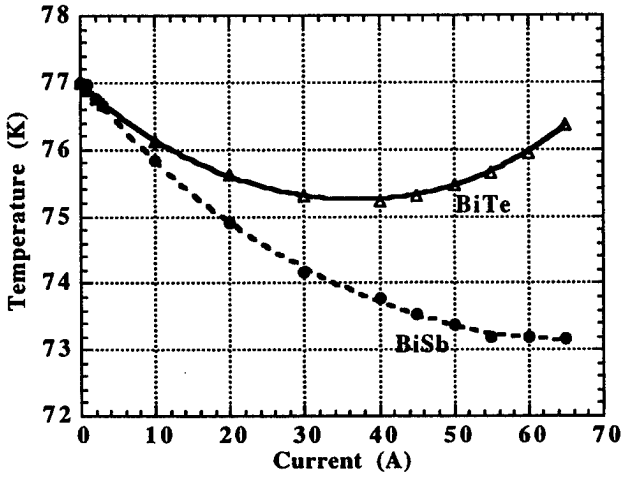


Fig.3. Current versus the low temperatures of semiconductors in the experiment.

ment.

Theoretically, the optimum current I_{opt}, i.e. the maximum temperature difference between two sides of a semiconductor, is

$$I_{opt} = \alpha \frac{T_c}{r_e} = \frac{K_e}{\alpha}\left\{\left(1+2Z\left(T_h+\frac{q_c}{K_e}\right)\right)^{0.5}-1\right\} \quad (1)$$

given by

where T_c is the temperature of the cold side i.e., T_h is the temperature of the hot side, almost 77 K in our experiment; and q_c is the heat flux to the cold side. The other parameters are defined by

$$K_e = \kappa \frac{S}{l} \quad (2)$$

$$r_e = \eta \frac{l}{S} \quad (3)$$

$$Z = \frac{\alpha^2}{\kappa \eta} \quad (4)$$

where K_e is the thermal conductance, r_e is the electrical resistance, Z is the figure of merit, S is the cross section area of the semiconductor, and l is its length.

The optimum current was calculated to use Table 1, and was about 43 A for the BiTe and 140 A for the BiSb. The temperature of the cold side of semiconductor is a function of current and given by

$$T_c = \frac{1}{\alpha I + K_e}\left(\frac{1}{2} r_e I^2 + K_e T_h + q_c\right) \quad (5)$$

where I is the current of the semiconductor.

In order to calculate the temperature of the cold side, we

$$T_h = 77\,K \quad (6)$$

$$q_c = R_{int} I^2 \quad (7)$$

assumed the followings;

where R_{int} is the total resistance of the cold side of the semiconductors.

We measured the voltage of the copper cable in the experiment, and the result is Fig. 4. R_{int} could be estimated as 38.8 μΩ. Having determined the other parameters of Eq. (5) based on the coefficients of Table 1, we could finally calculate the temperature of the cold side of the semiconductors at different currents. See Fig. 5. The lowest temperature of BiTe was obtained at a current of 30 A, while the lowest temperature of BiSb had not been obtained at the upper end of the current range of our calculation. While the graphs of the measured temperatures in Fig. 3 are very much like the graphs of the calculated temperature in Fig. 5, however, the absolute temperature values are different.

One reason for this difference is the copper cable connection between two semiconductors . Its thermal conductivity is high, so the BiSb would pump out the heat flux from the BiTe side through the copper cable. Because of this, the assumption of Eq. (7) is not suitable or the values of the R_{int} is not the same

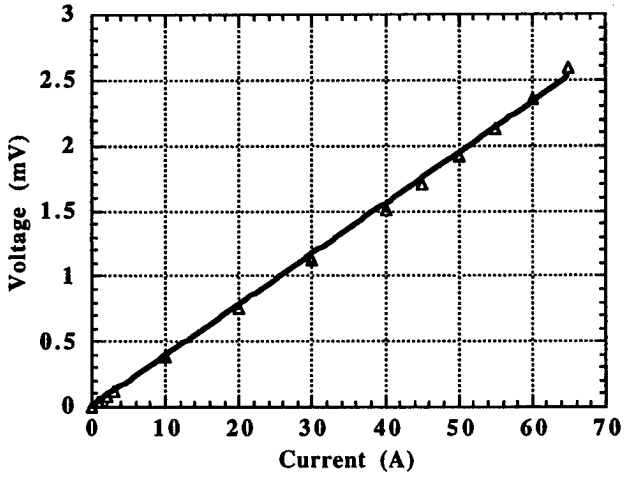


Fig.4. Currents and voltage of the copper cable.

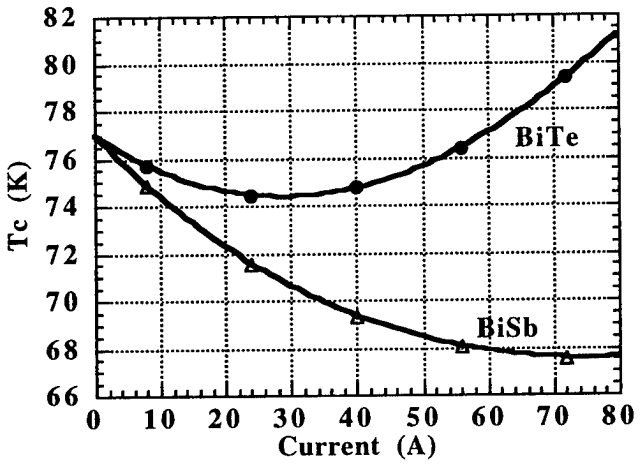


Fig.5. Currents and calculated temperature on the cold side of the semiconductors.

for the two semiconductors. The transport coefficients (thermoelectric power, electrical resistivity and thermal conductivity in this study) are temperature-dependent, so we should analyze a nonlinear equation.

IV. Discussion and Conclusion

Both the P-type BiTe and N-type BiSb semiconductors work below the temperature of liquid nitrogen, but their performances are different. In an actual current lead, the semiconductors are individually connected to the HTS component, and thus thermally insulated. This will simulate our experiment and the next experiments by inserting the HTS component into the cold side of the two semiconductors. With the thermal conductivity of HTS material only absent 0.1 % that of copper below 77 K, it will be easy to thermally insulated the two semiconductors even if we use only a short HTS component. We will also improve the shape of the semiconductors to take into account that the optimum currents of BiTe and BiSb are so different from each other, and that this reduces the overall performance of the Peltier current lead.

The BiTe and BiSb materials were not optimized. BiTe is would have been most efficient around room temperature, and the BiSb sample was hand made with less than optimal for the doping material and density. Having used these multi-crystal materials, we should also consider using single-crystal material.

On the other hand, multi-crystal materials have been described with higher performance atomic ratios than Bi and Sb (88 % and 12 %). These materials have a magnetic field effect, and the magnetic field effect should improve overall performance.

With the high temperature on the hot side of the HTS material being brought down from 77 K by the semiconductors, its current capacity is increased and/or its stability improved. Using the parameters from the references, the temperature drop was calculated to have been 7 to 12 K for BiTe and BiSb at optimal currents. The drop in temperature is more effective to use HTS.

Acknowledge

The authors would like to thank Prof. K. Kuroda, Nagoya University for his constructive criticism, and Prof. A. Iiyoshi, director general of the National Institute for Fusion Science, for his support through this study.

References

[1] S. Yamaguchi, K. Takita and O. Motojima, "A proposal for Peltier current lead", *Proc. Int. Conf. Cryog. Eng. 11 and Int. Conf. Cryog. Mat.* Part-2, pp. 1159-1162, 1997.

[2] H. Okumura and S. Yamaguchi, "A Simulation for Peltier Current Lead", Applied Superconductivity Conf. (ASC96), LMB-10, Aug. 1996, accepted for publication in *IEEE Trans. in Applied Super.*

[3] M. V. Vedernikov and V. L. Kuznetsov, "Cooling thermoelements with superconducting leg", *CRC Handbook of Thermoelectrics*, pp. 609-616, CRC Press Inc., 1995.

[4] K. Ueda, "Techological aspects and recent advances in HTS current lead", *J. Cryog. Eng. Japan*, vol. 30, pp. 552-559, 1995.

[5] S. Yamaguchi, H. Nakamura, K. Ikeda, K. Kuroda and K. Takita, "Proposal for peltier current lead and FGM for current lead of superconducting magnet system", *J. Adv. Science*, vol. 8, pp. 143-146, 1996.

[6] W. M. Yim and A. Amith,"Bi-Sb alloys for magneto-thermoelectric and thermomagnetic cooling", *Solid-State Elect.* vol. 15, pp. 1141-1165, 1972.

New Physical Point of View on the Peltier effect

O. Yu. Titov, G. Gonzalez de la Cruz,
G. N. Logvinov,* Yu. G. Gurevich
Departamento de Fisica, CINVESTAV—I. P. N.,
Apdo. Postal 14-740, Mexico D. F. 07000, Mexico
*Ternopil Pedagogical State University,
2 Krivonosa Str., Ternopil, Ukraine

We bring to your notice a novel physical point of view on the Peltier effect which is appropriate for any type of contact. Peltier heating or cooling are the work of build-in contact electric and valence forces on moving charges and the generation (or recombination) in space charge region.

Introduction

The Peltier effect is usually expressed as (see Fig. 1):

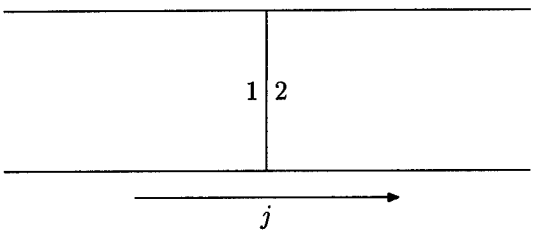


Figure 1: Junction for Peltier effect.

$$Q = (\Pi_1 - \Pi_2)j, \tag{1}$$

where Q is the heat at junction (when $Q > 0$ we have heating, when $Q < 0$—cooling), j—the electric current, $\Pi_{1,2}$—the Peltier coefficients of the first and second materials.

For non-degenerate electrons (n) and holes (p)

$$\Pi_{n,p} = \mp\frac{1}{e}\left[(q_{n,p} + 5/2)T - \mu_{n,p}\right]. \tag{2}$$

Here T is the temperature, $\mu_{n,p}$—the chemical potentials of the electrons and holes which are measured from the botton of the conduction band and the top of the valence band respectively ($-\mu_n - \mu_p = \varepsilon_g$—the band gap), e—hole charge.

Dependence of the momentum relaxation times $\tau_{n,p}$ from energy $\varepsilon_{n,p}$ are given by:

$$\tau_{n,p}(\varepsilon) = \tau_{n,p}^{(0)}\left(\frac{\varepsilon_{n,p}}{T}\right)^{q_{n,p}}. \tag{3}$$

For degenerate gases of charge carriers

$$\Pi_{n,p} = \mp\frac{1}{e}\frac{\pi^2}{3}(q_{n,p} + 3/2)\frac{T^2}{\mu_{n,p}} \tag{4}$$

For a physical interpretation, Eqs. (2) and (4) are usually rewritten as:

$$\Pi_{n,p} = \mp\frac{1}{e}\left[\langle\varepsilon\rangle_{n,p} - \mu_{n,p}\right] \tag{5}$$

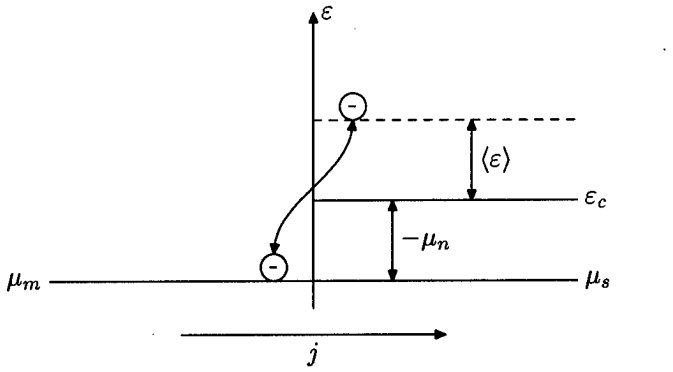


Figure 2: Heating of metal-n-type semiconductor contact.

where

$$\langle\varepsilon\rangle_{n,p} = \frac{\int_0^\infty \tau_{n,p}(\varepsilon)\varepsilon^{5/2}\frac{\partial f_0^{n,p}}{\partial\varepsilon}\,d\varepsilon}{\int_0^\infty \tau_{n,p}(\varepsilon)\varepsilon^{3/2}\frac{\partial f_0^{n,p}}{\partial\varepsilon}\,d\varepsilon}$$

are the average kinetic energies in the flow. They are measured (as $\mu_{n,p}$) from the bottom of the conduction band and the top of the valence band, $f_0^{n,p}$ are distribution functions. One usually interprets $-\mu_{n,p}$ as the potential energies of the electrons and holes,

$$\langle\varepsilon\rangle = \begin{cases}(q+5/2)T & |\mu| \gg T, \quad \mu < 0,\\ \mu + \frac{\pi^2}{3}(q+3/2)\frac{T^2}{\mu} & \mu \gg T, \quad \mu > 0.\end{cases} \tag{6}$$

For a demonstration of the physics meaning of the Peltier effect consider usually a metal-n-type semiconductor contact (Fig. 2). The surplus the electron energy in a semiconductor (as compared with metal) is $\Delta\varepsilon = \langle\varepsilon\rangle - \mu_n = (q+5/2)T - \mu_n$ and $\Pi_1 - \Pi_2 = -\frac{\Delta\varepsilon}{e}$.

Unfortunately this consideration involves difficulties:

1. What does the potential energy for degenerate gas of charge carriers mean?
2. About what energy must we speak when we have a p-n or a metal-p-type semiconductor junction?
3. Where in this scheme do the work of electrostatic force contribute?
4. Taking into account that in equilibrium $\langle\varepsilon\rangle - \mu$ may be different in different parts of the junction (Fig. 3), the scheme which was stated above is not understandable!

0-7803-4057-4/97 $10.00 ©1997 IEEE

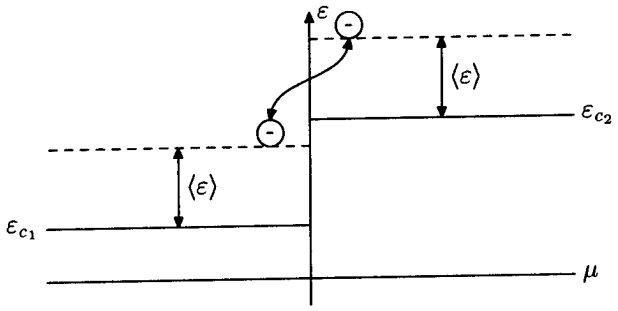


Figure 3: Contact in equilibrium ($j = 0$)

Peltier effect from the new physics point of view.

Actually, in p-p or n-n junctions it is necessary to calculate the change of the kinetic energy which is measured from a common Fermi level.

In a p-n junction it is necessary to talk about electron-hole generation or recombination from levels of the kinetic energies for electrons and holes again measured from a common Fermi level.

But it is possible to present another physical picture of Peltier effect.

Let us consider an n-n non-degenerate contact (Fig. 4). In

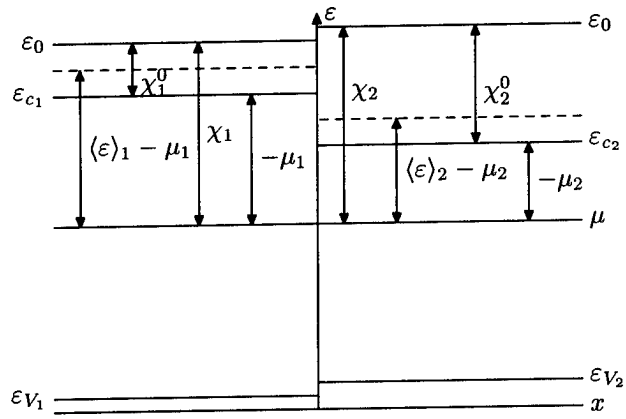


Figure 4: Nondegenerate contact. ε_0—vacuum level, χ and χ^0 are workfunctions and electron affinity.

this case (see Eq. (5))

$$\Pi_1 - \Pi_2 = \frac{\mu_1 - \mu_2}{e} \tag{7}$$

$$= \frac{1}{e}\left(\chi_1 - \chi_1^0 - \chi_2 + \chi_2^0\right) \tag{8}$$

$$= \varphi_c - \frac{\Delta\varepsilon_c}{e}, \tag{9}$$

where $\varphi_c = (\chi_1 - \chi_2)/e$ is the contact voltage difference and $\Delta\varepsilon_c = \chi_1^0 - \chi_2^0$ is the work of a valence force. It means that Peltier cooling or heating are connected with the work of a built-in electric field E_{int} ($\mathbf{jE}_{\text{int}}$) and valence forces F_v ($\mathbf{j}\Delta\varepsilon_c$).

For a p-p non-degenerate junction this picture is preserved.

If we have an n^+-n or a p^+-p junction (see Fig. 2), the Peltier effect is unaffected by the properties of the contact, but is depended only on the parameters of the non-degenerate semiconductor:

$$\Pi_1 - \Pi_2 = -\frac{\mu_n}{e} \tag{10}$$

and, of cource, it is improper to talk about the "changing" of some physical value on contact.

But, if we have a contact of two degenerate n- or p-type semiconductors (or two metals) the value of Peltier effect will be depend on properties of the contact again (see Fig. 5 and Eq. (6)) and it is possible to talk about work

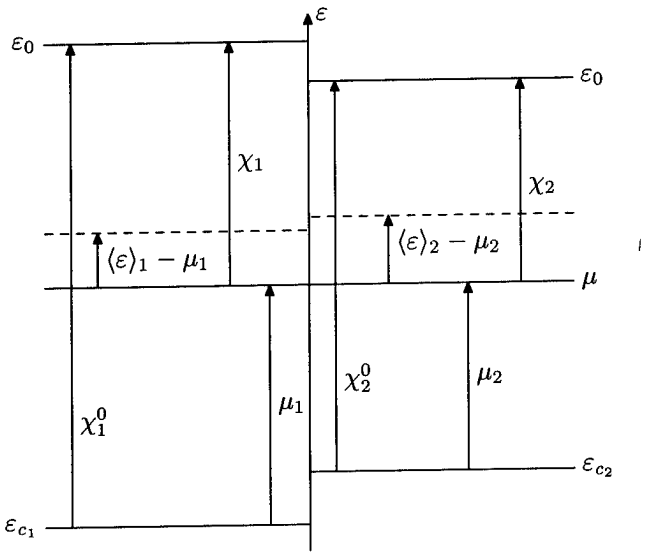


Figure 5: Contact of two metals.

of a built-in electric field and a valence force. At the same time it is necessary to keep in mind that for a degenerate electron gas

$$\mathbf{jE} \propto \frac{\pi^2}{4}\frac{T^2(E) - T_0^2}{\mu}$$

(in the case of a non-degenerate gas $\mathbf{jE} \propto \frac{3}{2}[T(E) - T_0]$) and $\Pi_1 - \Pi_2 = \frac{\pi^2}{3}(q + 3/2)\frac{T^2}{\mu_1\mu_2}(\mu_1 - \mu_2)/e$ (compare with Eq. (7)).

It is interesting to note that in equilibrium ($j = 0$) $\langle\varepsilon\rangle_1$ measured from a common Fermi level may be greatter or less then $\langle\varepsilon\rangle_2$.

Now let us examine a p-n junction (Fig. 6). The difference between the Peltier coefficients in this situation for non-degenerate media is

$$\Pi_1 - \Pi_2 = -\frac{\mu_n + \mu_p}{e}. \tag{11}$$

This difference corresponds to the energy liberated (or absorbed) under the recombination (or generation). But this pattern is correct only if the surface recombination is strong enough. Otherwise, when the surface recombination velocity $s \ll \frac{n}{p}\frac{T\tau_p}{m_p}\frac{1}{a}$, where m_p is the effective hole

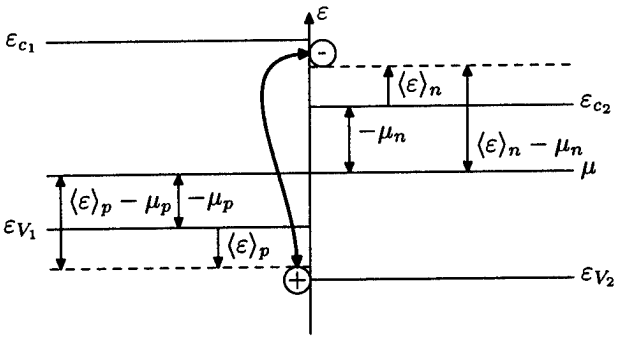


Figure 6: p-n junction.

mass and a is the length of p-type part of contact, the heating is reduced into cooling (see Fig. 7). This picture was

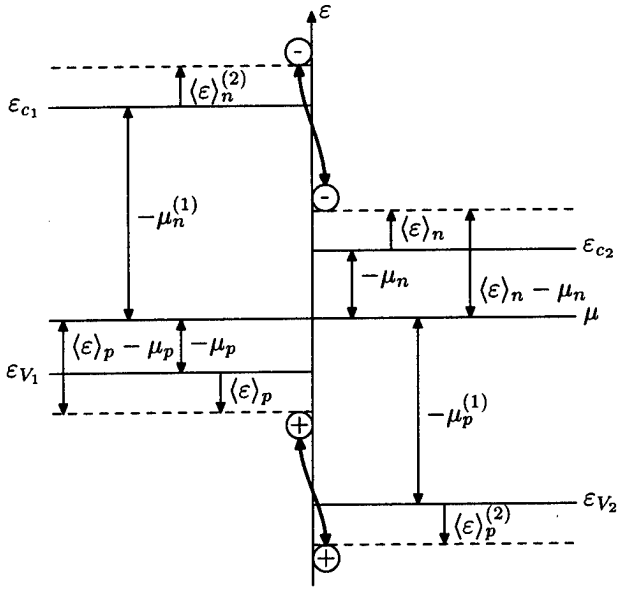


Figure 7: p-n junction without recombination.

described in more detail by Gurevich, et. a.l. in Ref. [1]. In conclusion, note that it is possibly the case (and for non-degenerate, and for degenerate contact) that a heterojunction exists, but the Peltier effect is absent (see Fig. 8).

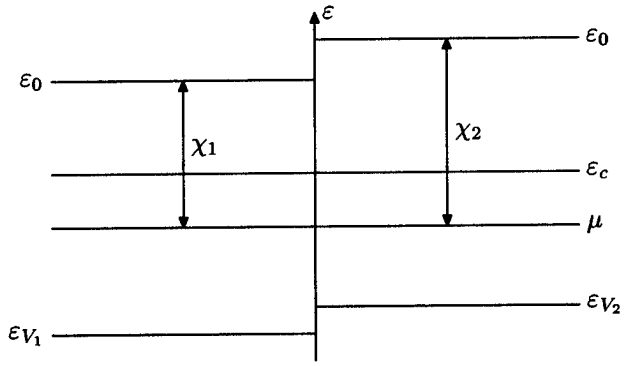


Figure 8: Heterocontact under condition $e\varphi_k = \Delta\varepsilon_c$.

This work is partially supported by CONACyT-México.

[1] Yu. G. Gurevich, O. Yu. Titov, G. N. Logvinov, O. I. Lyubimov, *Thermopower and thermal transport in metal-p-type semiconductor-metal structure,* Proceedings of the XVI ICT'97, Dresden (in press).

A New Concept of Porous Thermoelectric Module Using a Reciprocating Flow for Cooling/Heating System (Numerical Analysis for Heating System)

*Shigeru Tada, Ryozo Echigo and Hideo Yoshida

Dept. of Mech. Eng. & Sci., Tokyo Institute of Technology,
2–12–1 Ohokayama, Meguro–ku, Tokyo 152, Japan,
Phone ; +81–3–5734–2179, E–Mail ; stada@mech.titech.ac.jp

Abstract

The paper presents the conceptual design of a novel thermoelectric cooler and/or heater utilizing the heat transfer effect due to forced convection. A porous thermoelectric converter combined with a reciprocating flow system in which the flow direction of air passing through the element is reversed after regular intervals is proposed. This flow system in effect makes the thermal conductivity insignificant and contributes toward the achievement of a high efficient cooler and/or heater. A one-dimensional numerical analysis is performed to examine the detailed characteristics of the porous thermoelectric heater by systematically varying the relevant thermo-fluid parameters. In the calculation, for a fixed ambient temperature of 27 [degree C], dependences of the flow velocity, material porosity, and input power on the system performance are clarified. Moreover, a series of computation is carried out in order to obtain the system's COP.

Nomenclature

A	: surface area of an equivalent particle	[1/m]
c_p	: specific heat of gas	[kJ/kgK]
c_s	: specific heat of solid	[kJ/kgK]
d_p	: diameter of solid particle	[m]
h	: heat transfer coefficient	[W/m^{2}K]
h_e	: heat transfer coefficient at the end surface	[W/m^{2}K]
j	: electric current density	[A/m^2]
P	: input power ($=j \times V_{Bat}$)	[W]
Q	: heat	[W/m^2]
q_h	: absorbing heat	[W/m^2]
r_e	: internal specific electric resistance	[Ωm]
T	: temperature	[K]
T_0	: inlet air temperature (= 300)	[K]
T_{ex}	: outlet air temperature	[K]
$\overline{T}_{max}$	: average temperature in porous medium	[K]
$\triangle T$	: temperature difference ($= T^+ - T^-$)	[K]
$\triangle T_0$	: temperature difference ($= \overline{T}_{max} - T_0$)	[K]
t	: time	[s]
u	: apparent flow velocity	[m/s]
V_{Bat}	: battery voltage	[V]
x	: axial coordinate	[cm]
x_e	: thickness of thermoelectric module	[cm]
x_p	: thickness of porous material	[cm]
Z	: figure-of-merit ($= \alpha^2\sigma/\lambda_s$)	[1/K]

Greek Symbols

α	: Seebeck coefficient	[V/K]
δ	: control volume thickness	[cm]
ϵ	: porosity	
λ	: thermal conductivity of gas	[W/mK]
ρ	: density	[kg/m^3]
σ	: electric conductivity ($= 1/r_e$)	[S/m]
τ	: half cycle	[s]
ϕ	: coefficient of performance (COP)	

Superscripts and Subscripts

$+$	: hot junction
$-$	: cold junction
J	: Joule heat
P	: Peltier heat
s	: solid

Introduction

On the thermoelectric (TE) conversion system, the theoretical studies have been executed to give the technical bases and to show the most important parameter, figure of merit Z. Thereafter the extensive studies have been directed toward the development of materials in order to separate the heat and electric conduction processes rather than the successive effort so as to improve the efficiency of the TE device in the light of energy conversion system.

The temperature differences are produced and maintained by heat conduction for the conventional solid state TE modules. However, it is important to notice that in the porous TE modules the convective heat transfer is dominant rather than the conduction, which may results in a separation of the conduction processes for the heat and electric current [1]. The porous TE module with the reciprocating flow system in which air is introduced alternately from both ends of the device with regular intervals is one of the most prominent schemes for the TE cooling/heating system. For instance in the porous TE cooler[2], ambient air entering from the one end of the device cools the hot junction at the inlet surface and releases the waste heat at the another end until the flow direction changes. The air flowing in this way effectively decreases the temperature of the cooling region of the device. That is, this flow system in effect makes the thermal conductivity of the TE module insignificant.

In this paper, on the basis of the heat transfer mechanism of the porous TE module, the theoretical investigation of design and construction development of porous TE heating devise combined with a reciprocating flow system is performed. Numerical calculations are conducted to study the effects of the relevant parameters, i.e., flow velocity, porosity of the porous materials, and input power, on the thermoelectrical conversion installed in the reciprocating flow system.

Mathematical Formulation

Figure 1 shows a schematic view of the porous TE reciprocating flow system and physical model assuming one-dimensional flow and heat transfer. A pair of porous TE modules of thickness x_e and porosity ϵ are located in an insulated channel with a spacing x_p. Further, a plain porous material of thickness x_p with the same porosity ϵ as porous TE modules is inserted in the center space of the device. In this system, the convective heat exchange between air and porous medium is primarily important because it leads to a favourable working performance as well as adverse heat losses to the up- and downstream sides. Here, we assume the porous medium are homogeneous and all the porous medium , i.e., the porous TE modules and the plain porous medium at the center, have the same thermal properties. The insu-

0-7803-4057-4/97 $10.00 ©1997 IEEE

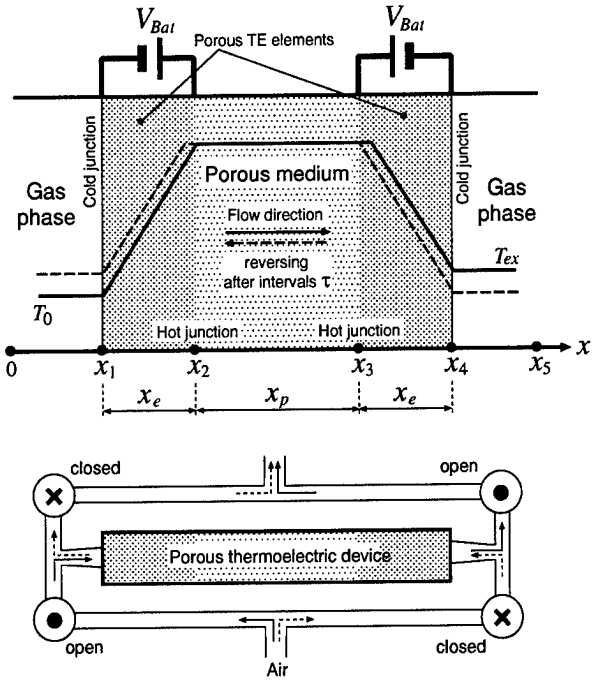


Figure 1: Schematics of the system

lated channel is non-porous elsewhere. For each TE module, D.C. power is supplied in order to sustain a constant electric potential between the hot and cold junctions. The flow direction is reversed at the regular intervals τ, which represents the half cycle of the operation. The other assumptions taken are that:

- the flow velocity is constant during each half cycle.
- the physical properties are constant.

The governing equations for heat transfer in the system are derived from the conservation laws of energy. With the preceding assumptions the energy equation for both gas and solid phases, taking into account the thermoelectric terms, can be formulated as follows:

- Gas phase in free space

$$\rho c_p \frac{\partial T}{\partial t} + \rho c_p u \frac{\partial T}{\partial x} = \lambda \frac{\partial^2 T}{\partial x^2} \tag{1}$$

- Gas phase in porous medium of porosity ϵ

$$\epsilon \rho c_p \frac{\partial T}{\partial t} + \rho c_p u \frac{\partial T}{\partial x} = \epsilon \lambda \frac{\partial^2 T}{\partial x^2} - Ah(T - T_s) \tag{2}$$

- Thermoelectric porous medium of porosity ϵ

$$(1-\epsilon)\rho_s c_s \frac{\partial T_s}{\partial t} = (1-\epsilon)\lambda_s \frac{\partial^2 T_s}{\partial x^2} + Ah(T - T_s) + Q_J \tag{3}$$

- Plain porous medium of porosity ϵ

$$(1-\epsilon)\rho_s c_s \frac{\partial T_s}{\partial t} = (1-\epsilon)\lambda_s \frac{\partial^2 T_s}{\partial x^2} + Ah(T - T_s) \tag{4}$$

The terms in eq. (1) represent the energy balance between the conduction and convective heat of the air. The terms in eq. (2) represent an energy balance between the enthalpy change of the air and the convective heat into or out of the solid. The terms in eq. (3) represent the conducted heat and the Joule heat in the solid. The terms in eq. (4) represent an energy balance between the enthalpy change of the air and the conducted heat into or out of the solid.

The surface area of an equivalent particle per unit volume A can be written in the form:

$$A = \frac{6(1-\epsilon)}{d_p} . \tag{5}$$

The heat transfer coefficient h is given by:

$$h = 2\frac{\lambda}{d_p} . \tag{6}$$

where the constant "2" is the Nusselt number around a sphere in thermo-fluid mechanics.

For the cold and hot junctions, located at x=x_1, x_4 and x=x_2, x_3 respectively, boundary conditions are given by introducing the Peltier heat terms into the energy equations at each junction. Equations (3), (4) are integrated over the control volume δ at $x = x_1, \cdots, x_4$:

- For the cold junction at x=x_1

$$(1-\epsilon)\rho_s c_s \frac{\partial T_s}{\partial t} = \frac{1-\epsilon}{\delta}\lambda_s \frac{\partial T_s}{\partial x}\bigg|_{x+\delta} + \frac{Q_P^-}{\delta} + Q_J + Ah_e(T - T_s) \tag{7}$$

- For the cold junction at x=x_4

$$(1-\epsilon)\rho_s c_s \frac{\partial T_s}{\partial t} = \frac{1-\epsilon}{\delta}\lambda_s \frac{\partial T_s}{\partial x}\bigg|_{x-\delta} + \frac{Q_P^-}{\delta} + Q_J + Ah_e(T - T_s) \tag{8}$$

where h_e represents the sum of the heat transfer coefficient of the porous end surface and h which is the heat transfer coefficient between porous medium and gas phase, given by eq.(6). From the detailed investigation performed previously[2], the heat transfer coefficient h is much higher than those at the end surfaces. Therefore, we assume that the end surfaces have no influence on the energy balance of the porous TE module. Namely, h_e is approximated as:

$$h_e \simeq h . \tag{9}$$

- For the hot junction at x=x_2, x_3

$$(1-\epsilon)\rho_s c_s \frac{\partial T_s}{\partial t} = \frac{1-\epsilon}{2\delta}\lambda_s \frac{\partial T_s}{\partial x}\bigg|_{x+\delta} - \frac{1-\epsilon}{2\delta}\lambda_s \frac{\partial T_s}{\partial x}\bigg|_{x-\delta} - \frac{Q_P^+}{2\delta} + Q_J + Ah(T - T_s) \tag{10}$$

The Joule heat and the Peltier heat are evaluated in terms of the electric current density j and the battery voltage V_{Bat} imposed on the open circuit of the module. They are:

- Joule heat

$$Q_J = j^2 \frac{r_e}{1-\epsilon} = \frac{(1-\epsilon)(V_{Bat} - \alpha \triangle T_s)^2}{r_e {x_e}^2} \tag{11}$$

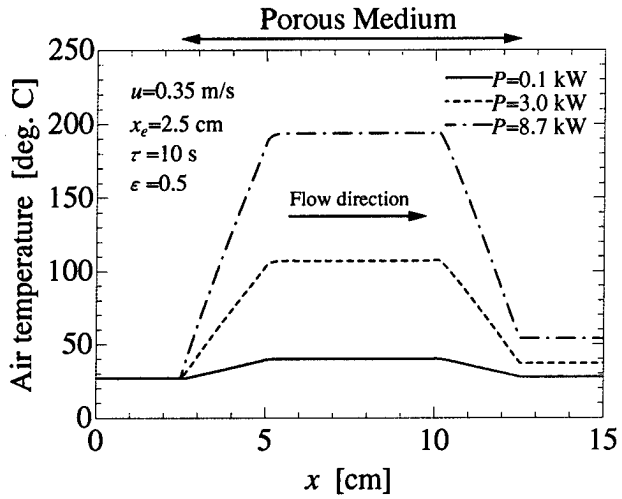


Figure 2: Temperature distribution in the device for various power input

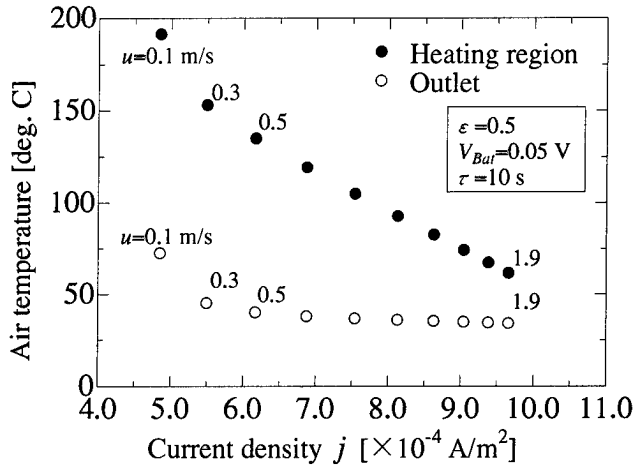


Figure 4: Temperatures as a function of current density for various flow velocity u

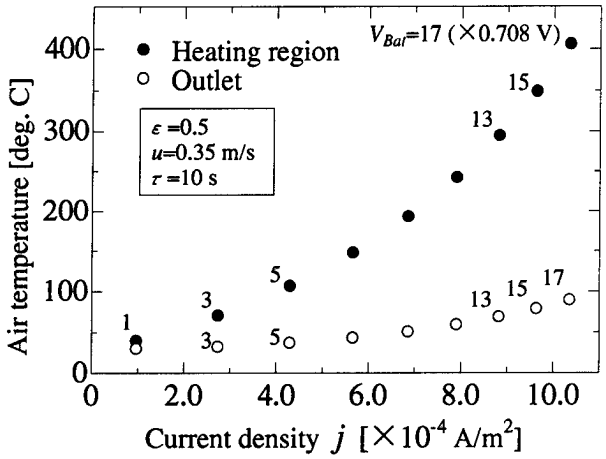


Figure 3: Temperatures as a function of current density at different battery voltage V_{Bat}

• Peltier heat

$$Q_P^{\pm} = j\,\alpha\,T_s^{\pm} = \frac{(1-\epsilon)(V_{Bat}-\alpha\,\Delta T_s)\,\alpha\,T_s^{\pm}}{r_e\,x_e} \qquad (12)$$

Results and Discussion

Here, the figure-of-merit of the porous TE modules is assumed to be $ZT_0 = 1$, which is the most likely performance for future TE materials. Other relevant physical properties are assumed to be the same as for Bi_2Te_3-based TE materials.

The flow velocity u (or the TE module thickness x_e) and porosity of materials ϵ are expected to be the most important parameters which directly affect the device performance so that a series of computations to systematically study their influence was carried out. The thickness of the porous TE module x_e and of the porous material x_p were taken to be 2.5 cm and 5 cm, respectively. The half cycle of the operation is fixed to τ=10 s. During calculations, a relative convergence criterion of 10^{-6} was specified for the iterations and an overall energy balance of approximately 1% (maximum 4%) was achieved for most of the cases.

Figure 2 shows the typical air temperature distribution developed within the device. Figure shows the temperature profiles at the end of a half cycle τ just before the flow direction is reversed. It can be seen that inside both porous TE modules, temperature distributions with steep gradients are sustained and that the portion with the highest temperature in the device is established along the entire length of the center porous medium (x=5~10cm). Air of initially ambient temperature T_0=27 °C coming from the outside with velocity 0.35 m/s is cooled when it reaches the cold junction (x_1=2.5cm). Thereafter, the temperature rapidly increases as the air travels through the porous TE module, until it reaches the upstream hot junction (x_2=5cm). The air passes through the center porous medium with constant temperature until it reaches the downstream hot junction (x_3=10cm). Here, the air is further heated by the Peltier heat generation before it is cooled with distance x_e from $x = x_3$, and finally leaves the porous body with a temperature T_{ex} at x_4=12.5cm. The heat conducting from the heating region back to the cold part is markedly reduced. Furthermore, cold junctions located at both ends of the system are always heated by the inlet air of room temperature or the exhaust air which leaves the system. Therefore, the hot junction whose temperature is related to that of cold junction through the Seebeck effect is able to sustain a higher temperature than that of the conventional TE module without any additive heat source for the cold side.

Figure 3 shows the dependence of the air temperatures at the heating region and outlet on the current density at different battery voltage V_{Bat}. The "temperature at the heating region" is the time average of the mean air temperature within the center porous material. The "outlet temperature" is also the time averaged temperature of the exhaust air. The porosity of the material ϵ, air velocity u, and half cycle τ were kept constant; they were ϵ=0.5, u=0.35 m/s and τ=10 s , respectively. Temperatures of the air at the heating region and outlet increase parabolically with the increase in the input power P ($=j \times V_{Bat}$). The temperature difference between the heating region and outlet also increases with increasing V_{Bat}. For lower input powers, temperatures of the heating region and outlet take almost the same value, however for V_{Bat}=17 (× 0.708 V), temperature difference between them becomes ~ 310 °C.

Figure 4 shows the dependence of the temperatures at the heating region and outlet on the flow velocity u. Temperatures of the air both at the heating region and outlet of

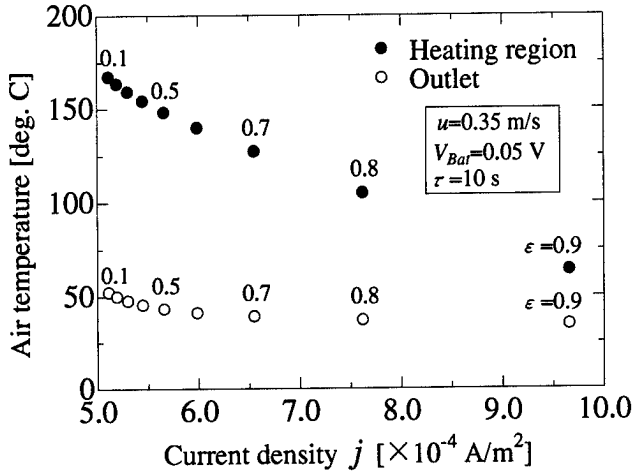


Figure 5: Temperatures as a function of current density at different material porosity ϵ

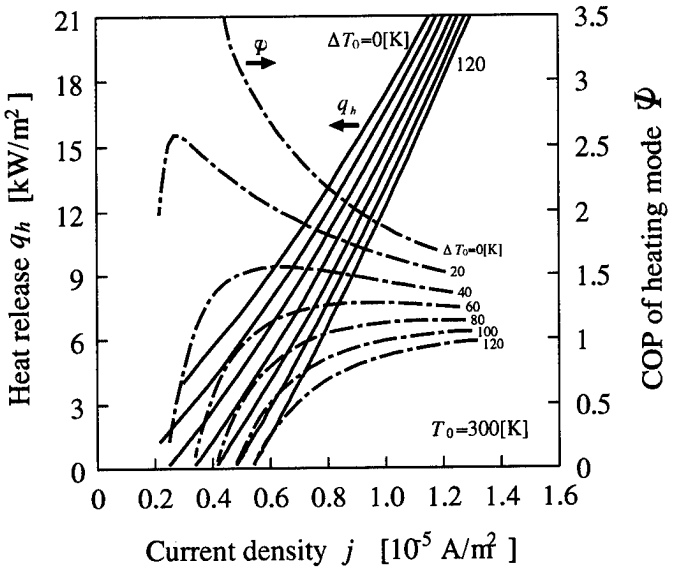


Figure 6: ΔT_0 and COP (u=0.35 m/s, ϵ=0.5, τ=10 s)

the device decrease with increasing air velocity. Contrasting with the temperature at the heating region, that gradually decreases with the increase in the flow velocity, the outlet air temperature rapidly decrease over the range where the air velocity is smaller than $\simeq$ 0.5 m/s. For higher velocity greater than u=0.5 m/s, outlet temperature asymptotically closes to the room temperature with increasing flow velocity. In addition, the current density also increases when the air velocity increases. The reason is as follows. In the calculation, the electric potential between the hot junction and cold electrode was kept constant during the operation. Therefore, even if the amount of heat transferred by convection to the outside becomes greater, the system can compensate for such a heat loss by the "ideal" power source which would be able to infinitely supply the electric energy to the system.

Figure 5 shows the dependence of the temperature of the heating region and outlet on the material porosity ϵ. A larger value of ϵ means that the mesh of the porous medium is denser. For ϵ=0.1, the temperature of air rises from 27 °C to 167 °C at the heating region. The outlet temperature for ϵ=0.1 is 52 °C. The temperature of the heating region gradually decreases with increasing porosity of the porous medium while the outlet air temperature hardly decrease. As the calculation were carried out under the condition of a constant mass flow rate, the flow velocity inside the porous media increases with the increase in material porosity ϵ; leading to a stronger heat convection by the air flow.

Figure 6 shows both the dependence of the rate of heat release q_h on the electrical current density j and COP of heating mode for several temperature differences $\Delta T_0 (= \overline{T}_{max} - T_0)$. The COP for the overall heating cycle ψ in the present device is defined as:

$$\psi = \frac{\text{heat release}}{\text{required input}} = \frac{q_h}{P} , \qquad (13)$$

where the "heat release" is the heat transfer from the heating region to the ambient air and the "required input" is the electric power necessary to generate such a heat release. In the calculations, heat sinks are located on both end surfaces of the center porous medium. The rate of the heat absorption is varied for each calculation in order to evaluate the system performance.

The device performance parameters to be calculated are specified at a constant inlet air temperature T_0=300 K, contrary to that conventionally specified at a constant cold junction temperature, since the cold junction temperature T_s plays a minor role in evaluating the COP of the device.

The heating performance gradually decreases with respect to the increase in the temperature difference ΔT_0. Furthermore, the result shows a higher performance than that of conventional TE modules. This is because in conventional TE modules which consist of heat sink, TE module and cold sink, significant thermal resistances existing between the heat sink and the hot junction, and between the cold junction and the cold sink, can not be avoided. In other words, in the proposed device, the heat is mainly transferred by the effect of convection, unlike in conventional TE modules. Therefore, thermal resistances present among constituent items have fairly small influence on the device performance.

Concluding Remark

A porous thermoelectric module employing a reciprocating flow for heating system is proposed. A set of basic equations which governs the heat transfer within the system is solved numerically. The dependence of temperatures of the heating part and outlet air on the imposed power, flow velocity of the air, and the porosity of the material is clarified. Moreover, a set of COP curves for overall heating cycle is obtained through the additional parameterised calculations.

Although discussion herein is just limited on showing a highly potential of the corresponding system as a heater and/or cooler, results presented in the paper indicate that a properly designed porous TE heater is expected to be a novel TE heating device having markedly higher performance than the conventional TE device.

References

[1] R. Echigo, et al., "An Extended Analysis on Thermodynamic Cycle of Advanced Heating/Cooling Method by Porous Thermoelectric Conversion Device", 12th ICT, Yokohama, JAPAN, VI-5(1993).

[2] S. Tada, et al., "A New Concept of Porous Thermoelectric Module Using a Reciprocating Flow for Cooling/Heating System", 15th ICT, Pasadena, U.S.A, 264(1996).

Quality Testing of Two-Stage Thermoelectric Cascades

Solomon M. Gorodetskiy
Cryotherm, 6 Aerodromnaya Street, Saint Petersburg, 197348, Russia
Phone: 812-394-1310, FAX: 812-394-1267, E-mail: <cryotherm@infopro.spb.su>

and

Richard J. Buist and Paul G. Lau
TE Technology, Inc., 1590 Keane Drive, Traverse City, MI 49686 USA
Phone: (616) 929-3966, FAX: (616) 929-4163, E-mail: <cool@tetech.com>

Abstract

The usual practice of quality testing manufactured two-stage thermoelectric modules (TSTM's) is to measure their maximum temperature differential in a high-vacuum system using a temperature-controlled, constant base plate. This is very difficult, time-consuming, expensive and requires sophisticated, complex equipment. As such, it is not practical to assure quality of TSTM's on a 100% basis. Therefore, it is desirable to create a new test method for these TE coolers which shortens test time and minimizes experimental error.

This paper describes the development of a new testing method for TSTM's which takes advantage of the transient method developed by Buist [1] and/or the modified Harman [2] method developed by Gorodetskiy [3]. This method basically consists of electrically isolating the bottom and top stages and testing the characteristics of the bottom and top stages individually by auxiliary wires, if needed.

The accuracy and validity of this test method was developed by pre-characterizing each stage (prior to TSTM assembly) as individual TE modules via methods [1] and [3]. After TSTM assembly, the proposed new test method was applied and compared with component test results. Although the implied "modular" approach to TSTM fabrication was applied to validate results, this new test method applies to all TSTM's if auxiliary wires are either not needed or attachable.

Introduction

If a TM has two stages connected in series and if top stage current terminals are accessible, or, at least, two auxiliary wires can be attached thereto, it is possible to test the top and the bottom stages in separate measurements. To measure the top stage parameters the computer-aided test system has to be connected to these inter-stage test points (or auxiliary wires). When the computer-aided system is connected to a TSTM input terminals and the inter-stage test points are short-circuited, the bottom stage parameters can be measured.

It has been previously shown by Lau [4] that although the time constant of a TE module is doubled by being "heat sunk" (compared to a suspended module), the measured figure of merit, Z, of a typical TE module via the Transient Method [1] agreed within 0.8%. Therefore, for practical purposes, it was inferred through these tests that the correction factors due to the dormant, passive stage would be quite small in most cases. This observation was the key to accurately testing the individual stages of a TSTM using either method [1] or [3]. That is, it would be only necessary to isolate the test current to either stage, top or bottom. These two separate tests could then be used to ascertain the overall quality of the TSTM.

Correction Factor Analysis

The resistance of the auxiliary wires must be considered in the measurement of the figure of merit, Z, and resistance, R, of the top and bottom stages. In order to have negligible corrections for resistance of the wires, their length/area must be small enough to have negligible resistance compared with the resistance of each stage. Therefore, if auxiliary wires are needed, they should be only long enough for connecting with Kelvin clips.

In both test procedures, test current does not flow through one of the stages. The additional heat exchange of this dormant stage with environment has to be taken into account, when the corrections to measurement results are made. The corrections to Harman expression can be made as in [3], where the calculations were performed by thermoelectric module (TM) energy balance analysis in steady state conditions. When a test current flows through the stage under test, the Joule heating, thermal conductance of air, heat flow through wires, and heat exchange with environment by radiation and convection were taken into account using an energy balance analysis. For this purpose, a simultaneous solution of the following two heat exchanger heat balance equations must be obtained:

$$-Sm*I*Tc + I^2*R/2 + (K+Ka)*\Delta T + Hv*(Ta-Tc) = 0 \qquad (1)$$

$$Sm*I*Th + I^2*R/2 - (K+Ka)*\Delta T - Hn*(Th-Ta) = 0 \qquad (2)$$

Equations (1) and (2) are related to cold and hot heat exchangers, respectively. The symbols used in the equations are defined as follows:

Sm is the Seebeck coefficient of the stage under test defined by: $Sm = N*(|Sn|+|Sp|)$ where |Sn| and |Sp| are the absolute values of n-type and p-type element Seebeck coefficients, respectively. N denotes the number of thermocouples in the stage under test. R and K are stage resistance and thermal conductance, respectively. Ka designates the thermal conductance of air, sandwiched between stage ceramics. I is the test current. $\Delta T = Th - Tc$. Tc, Th and Ta are the temperatures of cold and hot heat exchangers and of the

environment, respectively. Hv and Hn are effective heat conductances of heat exchange processes between a corresponding exchanger and environment.

Effective heat exchange coefficients due to convective and radiative processes between the heat exchange coefficient due to heat contact between the plate and lead wires is also included in Hn as the sum, or effective overall coefficient of all of these effects. It is considered, that lead wires have heat exchange with environment due to convective and radiative processes and current wires Joule heating could be neglected. If the current were reversed, one would have to interchange the position of Hv and Hn in (1) and (2). When the top stage of the TSTM is under test, its Hv will be the same as for a usual thermoelectric module. However, Hn includes an additional heat exchange owing to the passive bottom stage. When the bottom stage of the TSTM is under test, Hn will be the same as for a usual thermoelectric module and Hv will include an additional heat exchange owing to the passive top stage.

Hv and Hn can be estimated by methods described by Dulnev [5], if all heat exchanger dimensions and distances between its outer surface and thermostat inner walls are known. Let us denote temperature difference Th - Ta by ΔTh, Ui = I*R + Us and Us = Sm*ΔT; and point out, that the difference Ta - Tc is equal to ΔT - ΔTh. Subtracting (1) from (2) one can obtain:

$$Z = \frac{Us}{Ta(Ui-Us)} * \frac{Ta}{Ta+\Delta Th-\Delta T/2} * \left(1+\frac{(Hv(\Delta T-\Delta Th)+Hn\Delta Th)}{(2*(K+Ka)\Delta T)}\right) \quad (3)$$

Where denoted by Z a TM figure of merit in air is equal to:

$$Z = Sm^2/(R*(K+Ka)) \quad (4)$$

The equation (3) differs from the Harman expression by two correction factors that, by first approximation, may be taken as 1. The first of them is a ratio of environment temperature Ta to stage under test mean temperature, that is equal to Ta+ΔTh-ΔT/2. The second one takes properly into account the influence of heat exchange between the stage under test and environment on stage figure of merit. A following equation can be obtained from the sum of (1) and (2):

$$\Delta Th = (Hv*\Delta T + I*Ui) / (Hv+Hn) \quad (5)$$

A stage resistance, R, that was measured at mean TM temperature, is to be related to a temperature of 295K by temperature coefficient of TM resistance that is equal to 0.45 percent/K :

$$R = ((Ui-Us)/I)*(1+0.0045*(295-Ta-\Delta Th+\Delta T/2)) \quad (6)$$

By the first approximation, the values ΔT and ΔTh in (6) may be taken as zero.

By successive approximation, the Seebeck coefficient Sm can be calculated from expression (4) if the heat conductivity of TM elements and air, and dimensions of all TM parts are known.:

$$Sm = (Z*R*(K+Ka))^{1/2} \quad (7)$$

Thus, the temperature difference ΔT can be calculated from:

$$\Delta T = Us/Sm \quad (8)$$

By successive approximation, the ΔTh, Z and R values can be calculated from expressions (5), (4) and (6), respectively. The iterative scheme converges to unique solution rapidly for a TSTM stage.

All numerical calculations were performed for a TM suspended on wires by Kelvin clips and located in a space of the passive thermostat. The resistance of the auxiliary wires was taken equal to zero. Calculations were performed on a TSTM fabricated from a TM, model TB-83-1.0-1.3 as the bottom stage and a TM, model TB-31-1.0-1.3 as the top stage. These results indicated that the as-measured, non-corrected Z was reduced by approximately 0.7 percent and 2.3 percent for the bottom stage and top stage, respectively

It was also determined that the vacuum value of the TM figure of merit can be obtained, if the corrected value of Z is multiplied by a factor (1+Ka/K).

Experimental

A set of thermoelectric modules were designed and manufactured by Cryotherm, St. Petersburg, Russia especially for experimentally verifying the TSTM test procedures described in this paper. The module designated for the top stage was a 31 couple module with TE pellets 1.0 x 1.0mm in cross-section and 1.3mm tall (model TB-31-1.0-1.3). The only difference between this TE module and "regular" TE modules was that both substrate surfaces were metallized and pre-tinned with low temperature solder for joining to the bottom stage.

The TE module designated for the bottom stage was a 83 couple module with TE pellets identical to the top stage. This module was designated: model TB-83-1.0-1.3. This "bottom stage" was also metallized on both substrate surfaces, but also had some other unique features. One of its cold side conducting tabs, which would normally connect the cold sides of the adjoining TE pellets, was replaced with two separate conducting tabs which faced outward. This modification, therefore, created an open circuit.

Of course, these "output tabs" could be easily electrically shorted to complete the normal TE module electrical network and, thus, provide the means for testing it as a "normal" TE module. Indeed, this was done in order to test it, and the top stage separately as "normal" TE modules for their thermoelectric parameters. This "Before" test data is given in Tables 1 and 2 for two sets of bottom and top stages, serial numbers #1 and #2 for each pair of stages.

The TSTM fabrication process was to solder the smaller TE module onto the cold side of the larger TE module, thereby forming the structure of a TSTM. The final step in this procedure was to connect wire "jumpers" from the un-shorted output tabs of the bottom stage to the electrical input tabs of the smaller, top stage. The resultant was the formation of two each 2-stage thermoelectric modules, TSTM#1 and TSTM#2, on which subsequent testing was performed in normal, room-temperature, still air.

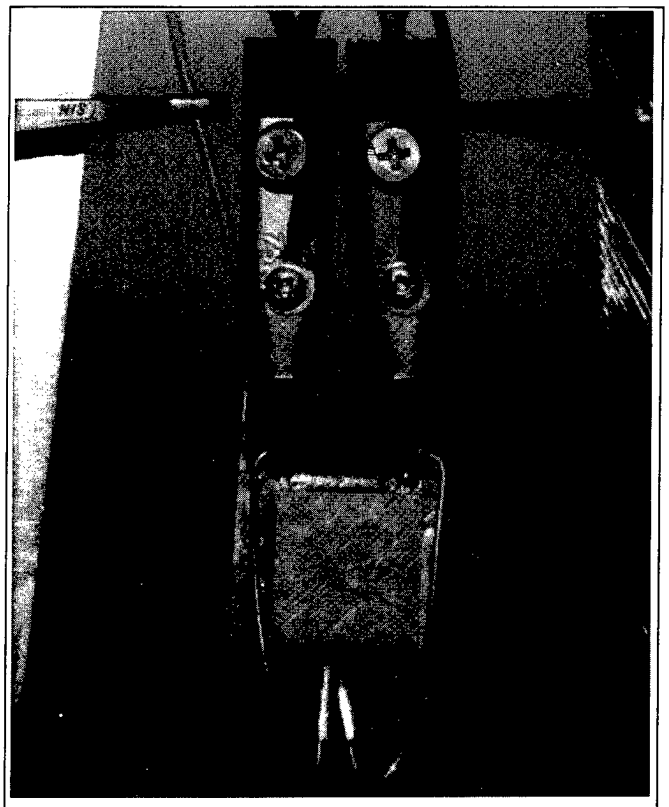


Figure 1. Configuration for testing the top stage in air.

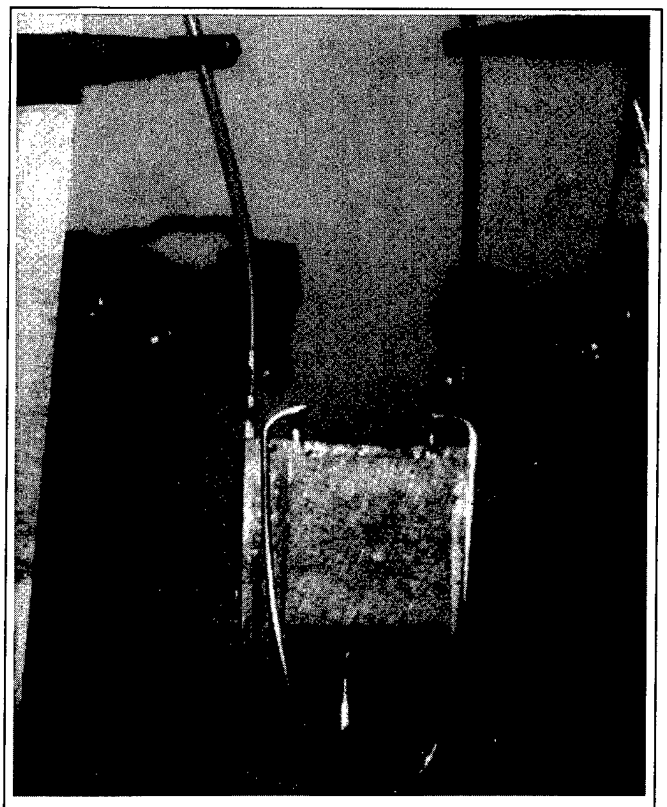


Figure 2. Configuration for testing the bottom stage in air.

Testing the Top Stage of the TSTM's

To test the top stage of the 2-stage cascades, it was very important to suspend the TSTM such as that shown in Figure 1, where extra clips are fastened to the insulated input leads of the TSTM. Significant errors were observed when the TSTM was attached to a heat sink. This was because the passive stage already acted as a heat sink and an additional heat sink significantly thermally loaded the stage under test and reduced the measured Z. Finally, "Kelvin" clip test probes were clipped to each of the "jumpers" to the top stage as illustrated in Figure 1, leaving the electrical input leads of the bottom stage totally isolated. For some manufactured TSTM's it may have been necessary to attach auxiliary test probes at these points as described above. However, for this case it was quite easy to simply clip to the jumper wires at their point of connection to the top stage. All that was needed was to test the top stage just as if it were a separate, independent TE module. During the test, the test current passed only through the top stage. The dormant bottom stage acted as a heat sink, as mentioned before. Certainly, the bottom stage slightly heated during one test current polarity and slightly cooled during the other test current polarity. However, as described in the introduction and analysis given above, this was only a minor perturbation from the fully isolated tests on this same stage performed before cascade assembly. The data from this test of the assembled TSTM's #1 and #2 are given in Tables 1 and 2, designated "After".

Testing the Bottom Stage of the TSTM's

This test configuration required that the top stage be electrically shorted to eliminate any test current from entering the top stage. This was accomplished by clipping an extra clip lead to the two jumper wires, shorting them together as shown in the lower portion of Figure 2. Whenever auxiliary wires are needed, this same condition can be accomplished by simply shorting these wires together. After this top stage shorting was secured, test Kelvin clips were applied to the bottom stage input wires as shown in the upper portion of Figure 2. Testing was subsequently performed on the bottom stages of both TSTM's. The test data gathered is given in Tables 1 and 2, designated "After". It is clear that good agreement exists between the "Before" and "After" data sets, proving the effectiveness and dependability of this procedure to quickly and accurately ascertain TSTM quality.

Table 1.
Tested Resistance and uncorrected Z of TSTM#1 stages

	Top Stage		Bottom Stage	
	Resistance (Ohm)	Z*1000 (/K)	Resistance (Ohm)	Z*1000 (/K)
Before	0.775	2.394	2.227	2.574
After	0.808	2.415	2.294	2.553
Diff.	4.25%	0.88%	3.01%	-0.82%

Table 2.
Tested Resistance and uncorrected Z of TSTM#2 stages

	Top Stage		Bottom Stage	
	Resistance (Ohm)	Z*1000 (/K)	Resistance (Ohm)	Z*1000 (/K)
Before	0.794	2.440	2.288	2.602
After	0.806	2.465	2.339	2.550
Diff.	1.51%	1.02%	2.23%	-2.00%

Conclusions

The testing required to assure the quality of a 2-stage cascade by conventional cooling performance test methods can be a long and laborious problem. Therefore, it is not practical to test the TE cooling modules at a very high acceptance quality level (AQL). However, a method has been presented in this paper which reduces test time to such a degree that 100% testing of 2-stage thermoelectric cascades is now economically practical and effective.

Obviously, the key to this test method is to have a computer-aided test system that is capable of quickly and accurately obtaining data such as that described in [1] or [3]. It is then only necessary to suspend the 2-stage cascade (in open air) and configure the test probes equivalent to that shown in Figures 1 and 2. The actual test procedure is then as simple and quick as testing individual single-stage TE modules, taking only a minute or two for the bipolar testing of each stage. The data gathered can not only be used to ascertain and validate the quality of the cascade, it also provides the TE material property data which can be used in an effective TE modeling program [6] to determine the cooling performance of the cascade at literally any thermal and electrical condition.

Acknowledgments

The authors would like to acknowledge the contributions of Todd M. Ritzer and Julie A. Witkop of TE Technology, Inc., USA for assembling and instrumenting the two-stage cascades fabricated from individual single-stage TE modules provided by Cryotherm, St. Petersburg, Russia. The authors would also like to acknowledge the support and contributions to the hardware and the assistance provided in the preparation of the manuscript by V.E. Baukin and S.V. Zarubo of Cryotherm, St. Petersburg, Russia.

References:

[1] R.J. Buist, "A New Method for Testing Thermoelectric Materials and Devices", Proceedings of the XI International Conference on Thermoelectrics, October 7-9, 1992 Arlington, TX, USA.

[2] T.C. Harman and J.M. Honig, J. Appl. Phys., 13, 440, 1962.

[3] V.P. Babin, S.M. Gorodetskiy. "Thermoelectric Modules Quality Testing by a Manufacturer.", Proceedings of the XIV International Conference on Thermoelectrics, June 27-30, 1995 St. Petersburg, Russia, pp. 338-340.

[4] P.G. Lau and R.J. Buist, "Temperature and Time Dependent Finite-Element Model of a Thermoelectric Couple", Proceedings of the XV International Conference on Thermoelectrics, Pasadena, California, March 25-28, 1996

[5] B.N. Dulnev, E.M. Semyashkin, "Heat exchange in radioelectronic devices", Energiya, Leningrad, 1968 (in Russian).

[6] R.J. Buist, "Calculation of Peltier Device Performance", CRC Handbook of Thermoelectrics, CRC Press, Inc., 1995.

Precise Methods and Equipment for Thermoelectric Cooling Modules Parameters Measurement

Anatychuk L.I., Varich N.,I., Shchedrin A.A.

Institute of Thermoelectricity, General Post-Office, Box 86, 274000, Chernivtsi, Ukraine
Tel:+380/3722/44422, Fax:+380/3722/41917, E-mail:Alex@ite.Chernovtsy.ua, WWW: http:\\www.ite.Chernovtsy.ua

Abstract

The investigation results of thermal compensation systems for thermoelectric cooling modules parameters determination have been given. Thermoelectric thermal meters were used as heat balance sensors, 2-stage thermoelectric batteries were used as compensating heat and cold sources. Methods and devices made it possible to determine parameters of thermoelectric cooling modules with increased accuracy.

The essence of the problem

The necessity for more accurate determination of thermoelectric cooling modules parameters becomes more actual in connection with their use growth. By now rather rational set of parameters has been established which uniquely determines a thermoelectric cooling module properties as an object of use.

Such parameters are following:

- maximum temperature difference at zero cooling power - ΔT_{max};
- maximum cooling power at ΔT equals to zero - Q_{max};
- electric resistance of a module at ΔT equals to zero - R;
- electric current value when ΔT max is reached - I_{max};
- voltage value at which ΔT_{max} is reached - V_{max}; where ΔT is temperature difference at outside surfaces of a module ceramic plates (or between outside surfaces of commutating plates if modules do not have any ceramics).

Such parameters uniquely determine module's quality but they are not enough for design of the module's rational use depending on its specific operating conditions. For this purpose modules characteristics in the form of dependences on current in the temperature range of $I=I_{max}$ and $I=0$ are additionally presented. By now a unified approach to description of modules functional characteristics has been not formed. But more often they have the form given if Fig.1. It should be noted that regardless of the form of the given characteristics their use for calculations is very inconvenient because of insufficient accuracy of the information obtained from such calculations.

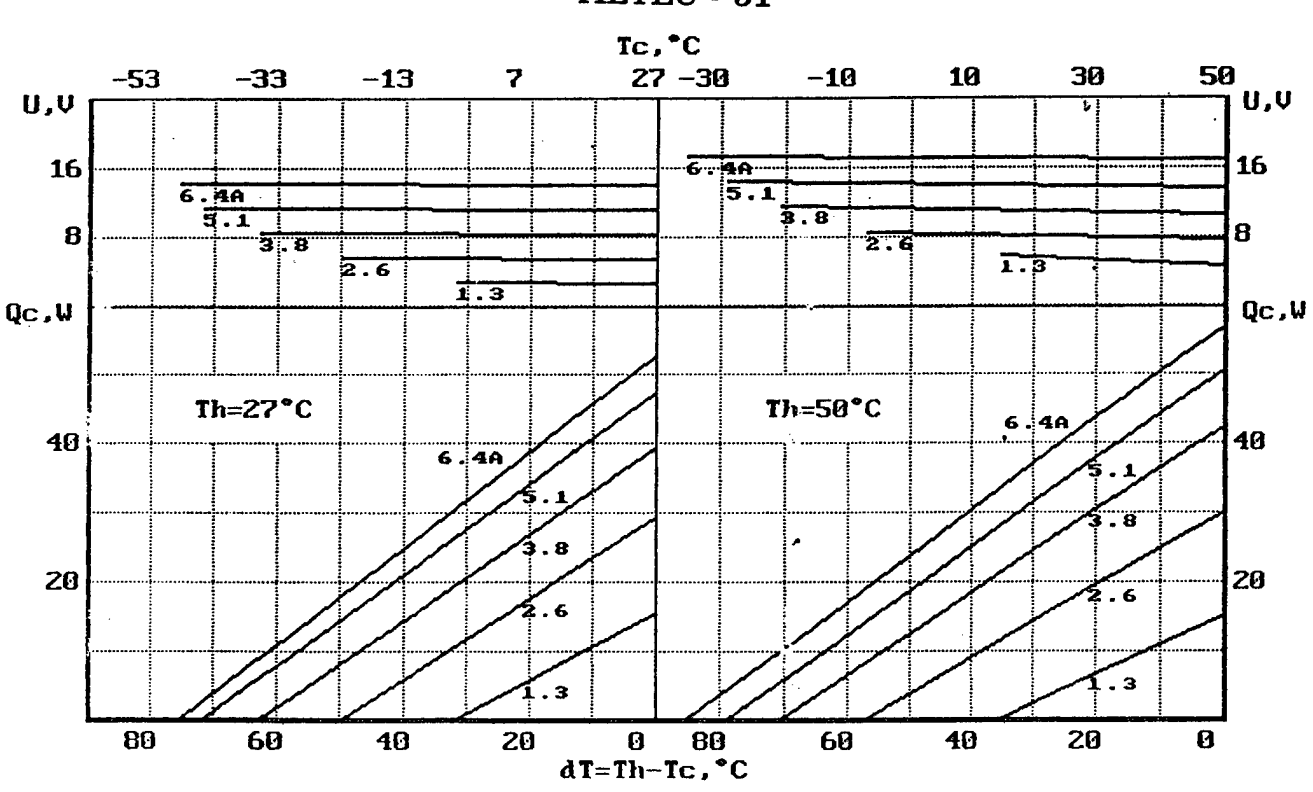


Fig.1. Typical module perfomances.

That is why we recommend to accompany modules with a computer diskette which contain the necessary set of information, and with a program for modules design in any intermediate operating conditions.

Modules parameters and their functional dependences determination itself meets at least two basic difficulties. The first implies that the given above parameters were formulated for idealized thermal models which it is difficult to reproduce in real condition and thus the discrepancy between measurement conditions and model's requirements becomes the cause of considerable errors

.Let us examine in detail the general. Fig. 2a gives the diagram of a module measurement at ΔT_{max} conditions. Here we come up against at least three causes of errors.

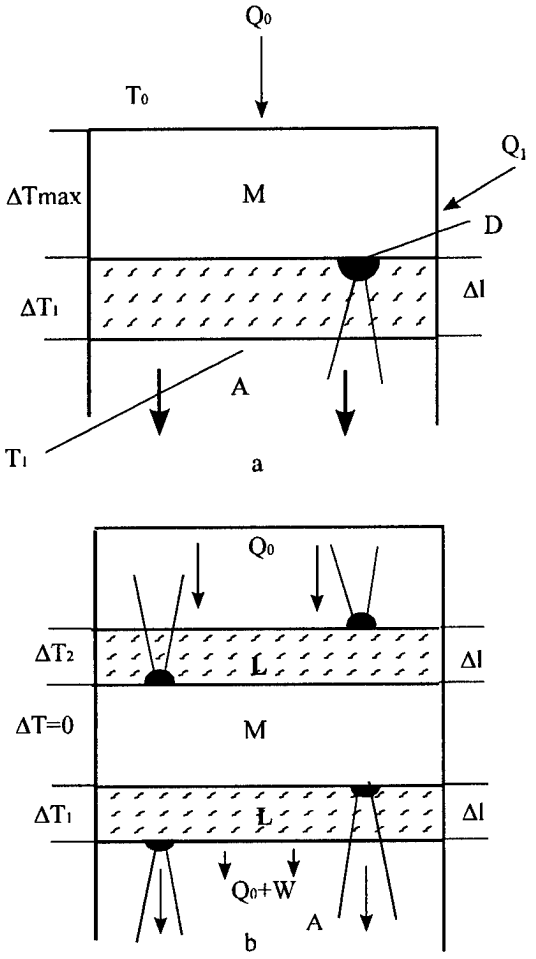


Fig.2.

The first is the departure from adiabaticity.

In real measurement conditions heat exchange with environment leads to a considerable error at ΔT_{max} measurement. Really, cooling power is rather small in the regime close to ΔT_{max} so even small heat inflows lead to considerable ΔT_{max} changes. Measurement in vacuum or in an inert medium with small coefficient of thermal conduction though decrease such errors but made difficulties in measurements and some ambiguity which depend on radiant heat exchange conditions and configuration of different objects placed close to the module. Errors as a whole at ΔT_{max} measurements can reach 5% and more as module's power decreases that makes difficult correlation of modules quality.

The second error is connected with heat removal conditions from the module's hot side.

Hot side temperature determination meets with serious difficulties. As Fig 2a shows heat removal from the hot surface of ceramics is effected through a contacting layer with thickness Δl. This layer may be air if a module is placed just on the heat removing object A, liquid (water, glycerol, oils) or as heat removing pastes. Thermal flow from the module to a heat removing object A causes temperature difference ΔT_1 in a layer L. As a result temperature measurement on the surface of worm ceramic plate is difficult. If temperature T_1 is measured near the surface of heat removing plate that error ΔT_1 is appeared which ultimately result in real value of ΔT_{max} decrease for ΔT_1 value. If temperature detector D is placed just on the surface of warm ceramic plate then it makes distortions in the heat removes pattern on the region to which it is adjoin, so it also result if uncontrolled errors in temperature measurements. Analysis of errors value arising by this cause shows that absolute error in ΔTmax measurement may reach 3-6°C.

Third cause if mistakes is connected with uncontrolled heat inflows Q_1 to the side surfaces of the module which also lead to adiabaticity disturbance and, as a result to an error in ΔT_{max} determination which also result in reduction of real values of ΔT_{max}. Its effect is smaller and is usually 0.2-0.5 degrees.

Thus error in ΔT_{max} measurement in the worse case can result in the error of 10-15%, in the best case - 3-5%. Since the modules quality is defined first of all by ΔT_{max} value, uncontrolled errors in ΔT_{max} determination may become the cause of errors in modules quality determination.

Rather great errors also arise at maximum cooling capacity measurements. In this case measurement regime is such that temperature difference between ceramic plates surfaces must be equal to zero. Such conditions are favorable for errors minimization which results due to uncontrolled heat exchange of the module with environment. So we may neglect the environment influence at such measurement regime.

But increases the errors connected with temperature of ceramic plated surface determination. As a result the condition ΔT=0 is satisfied with an error that leads to the error in Q_0 determination. It should be noted that errors resulted from uncontrolled temperature differences ΔT_1 will be larger than in the ΔT_{max} regime due to heat flow growth through a contact region L. As a whole, error in the departure from the condition ΔT=0 may be easily reach 5-8 degrees, that is also insufficient for modules parameters determination.

The second problem is great period of time that is necessary to use for their characteristics determination. Relations for modules parameters calculation were obtained on the assumption that stationary thermal conditions were formed in the module. For such conditions errors which are

permitted in measurements (usually 0.2-0.5%) are reached under a period of time of about 3-10min depending on the modules geometric size. To determine ΔT_{max} and ΔQ_{max} it is necessary to conduct several measurements and that additionally increases measurement time. So the studied above method of direct measurements id noneffective for modules parameters control on their serial production.

Apart from direct or absolute methods given in Fig. 2, there occurred a great number of works that analysis a possibility of the Harman method use for modules parameter determination. The essence of the method is reduced to electric resistance of the module measurement at passing constant and alternating currents through it. In conditions of numerous idealizing prerequisites it is assumed that some parameter Z generally called as thermoelectric figure of merit can be determined from the expression $ZT=R_a/R_i$ -1

It should be noted that this parameter in fact has physical uniqueness only as applied to thermoelectric materials properties. Its use for determination of Q_0 and ΔT_{max} of a module can be made at the availability of information about a whole number of modules properties: contact resistance value, electric and thermal resistances of commutating plates or their efficient thermal resistance, thermoelectric characteristics of legs material and so on. So it is rather difficult using such method to get reliable information about basic characteristics of a module, ΔT_{max} and Q_0. In literature there is a number of works devoted to the attempts to improve this situation and thus to elaborate methods for ΔT_{max},, Q_{max} , I_{max},, V_{max} measurements based on the Harman's method [2,5]. The essence of those proposals reduced to the use of different sometimes very witty measurement conditions and errors consideration by means of different corrections introduction. But against all the odds the Harman method is indirect method of module parameters determination and so has rather limited possibilities in their measurement accuracy accomplishment. To the advantages of the Harman's methods may be referred the possibility of receiving the results considerably faster than by the absolute methods.

Institute of Thermoelectricity has conducted the studies of this problem that resulted to the elaboration of procedure for modules parameters measurement, which combined both methods (Fig.3).

In thermoelectric modules production of N number each of them is subject to testing by the Harman method for determination of module's figure of merit Z_m. A module is chosen for the rational lot and is subject to precise certification by the absolute method. By that a correspondence between ΔT_{max}, ,Q_{max} and Z_m is established by determination the corresponding coefficients K_1 and K_2. By this manner measurement results of one module of the lot may be used for accurate determination of ΔT_{max} and Q_{max} of the whole lot. Naturally, this procedure is valid at rational choice of modules number in a lot and for the case when Z_m measured values of different modules do not drastically differ from each other.

For modules parameters measurement in large-scale production we have designed a unit realizing the stationary

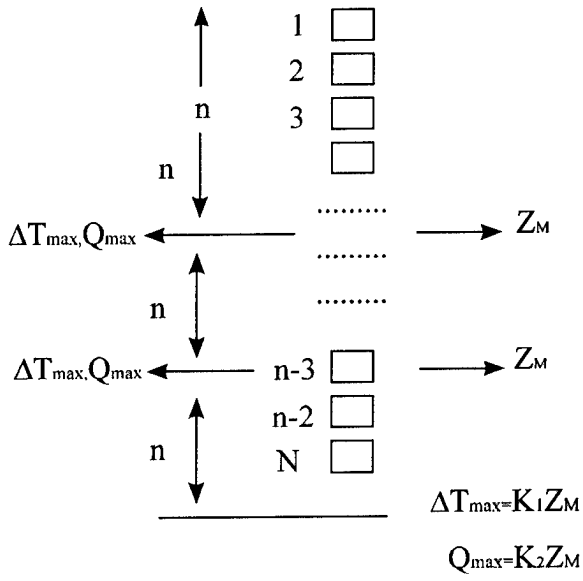
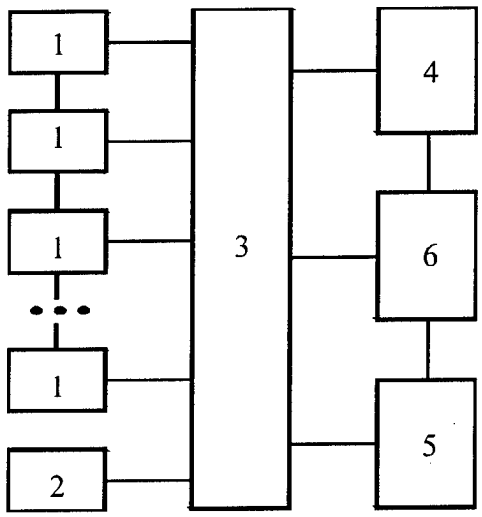


Fig.3.

Harman method implying that at small currents (less than 0.02 of the operated one) the module's resistance is measured at alternating R_i and constant R_a currents. Module's figure of merit $ZT = R_a/R_i$ - 1 and resistance R_i on alternating current define the module's quality. Measurement accuracy of module's figure of merit andresistance at alternating current is not worse than 1%. Fig 4 presents the units diagrams.



1 - TE module
2 - Thermometer
3 - Commutator
4 - AC source
5 - DC source
6 - PC

Fig 4.

Similar to [2] and [4] ΔT_{max} ,I_{max} ,V_{max} and Q_{max} are determined as reference ones. In terms of [4] ΔT_{max} and Q_{max} are determined by P(Thot) method; I_{max} and V_{max} - by P(Tavg). In calculation of Q_{max} a correction for ceramics thermal resistance was made. All this permits to get design parameters of a module with accuracy not worse than 5%.

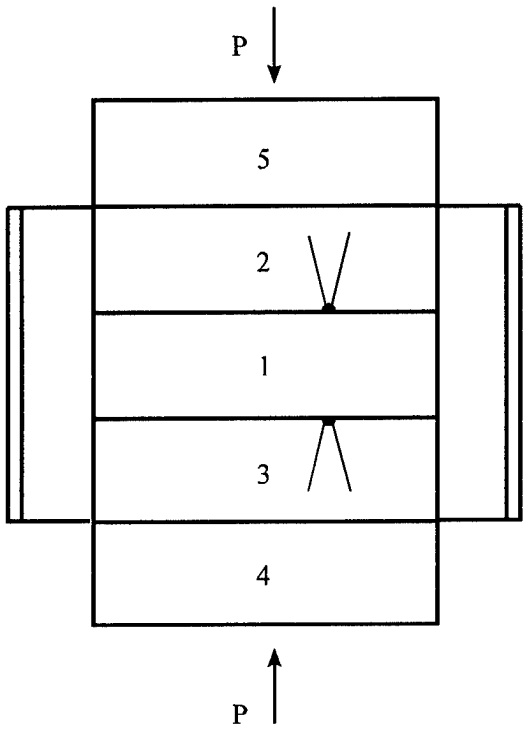


Fig.5.

Computer governing the unit's operation provides statistic treatment of results and printing of the protocol.

Now consider how to improve accuracy of modules parameters measurement at their measurement by the absolute method. Fig.5 shows a thermoelectric module 1place between two heat meters 2 and 3. Heatmeter 3 is also in thermal contact with thermostat 4 and heatmeter 2 with stage thermoelectric cooler 5. Heatmeter with the module is enclosed by a radiating screen which contacts both with the cooler 5 and thermostat 4. The heatmeter peculiarity is the possibility of measurements not only thermal flows but precise temperature measurements on its surface. For this purpose institute of Thermoelectricity has designed special heatmeters based on high sensitive anisotropic thermoelectric converters with resolution 10^{-4} W and dynamic range 10^{7}. At ΔT_{max} measurement in the cooler 5 is produce such temperature at which a thermal flow through the heatmeter 2 equals to zero. In this case the condition of adiabaticity has been fulfilled, and error connected with the outside thermal flows are minimized with the accuracy which the heatmeter allows to resolve. Temperature meter of the heatmeter 2 registers cooling degree at ΔT_{max} conditions. As this takes place a temperature gradient similar to the temperature gradient in the module has been formed and decreases the effect of side heat exchanges of the module with environment.

Error of ΔT_1 in temperature determination of the module's hot side is determined in the following way. First heatmeters 2 and 3 placed in thermal contact. Thermal transferring liquid (glycerol for example) is put between them. Creating by the cooler 5 thermal flows it is easy to determine ΔT_1 between heatmeters at thermal flows which amount equals to flows at module's measurement. Here it is important that pressure P compressing heatmeters and pressure, compressing modules under measurements be equal. The same method of experimental determination of error may be used for Q_{max} determination.

Total error in ΔT_{max} measurement with the use of such method can be reduced to 0.5% and more, and in measurements of Q_{max} up to 0.8-1% and more.

References

[1] Harman T.C., Cahn J.H., Logan M.J. J. Appl. Phys., 1959, v.30, p.1351.

[2] Buist R.J. In Proc. XI ICT'92, Texas, Arlington, 1992, p.196.

[3] Nagy M.J., Buist R.J. In. Proc. XIII ICT"94, Kansas City, USA, 1994, p.147.

[4] Buist R.J. In Proc. X ICT'91, Cardiff, UK, 1991, p.84.

[5] Anatychuk L.I. Thermoelements and thermoelectric devices, Kiev, Naukova dumka, 1976.

Rapid method of defining the quality of multistage thermoelectric cooler based on measurements of voltage from every stage

Igor Drabkin, Oleg Jouranlev
Institute of Chemical Problems for Microelectronics, B. Tolmachevskij per. 5, Moscow 109017, Russia,
Tel, Fax: 7/812/1744365, E-mail: Igor@euphr.stud. pu.ru

Abstract
A method for defining the quality of multistage thermoelectric coolers is proposed .This method is based on measurements of voltage from every stage of the cooler with the current on and at the first moment after switching it off. Heat transfer with ambient environment is taken into consideration. This method also takes into account the thermal load for the lower stage received from the upper one. The causes which can lead to the wrong results are also investigated.

Introduction
Harman's ideas [1] lie at the base of a rapid control of thermoelectric modules. In his papers it was shown that the figure of merit Z was connected with the measured values for small currents by the equation:

$$Z\bar{T} = \frac{u_\alpha}{u_R} \qquad (1)$$

where $u_R = IR$ - the Ohm voltage on a die and u_α - the Seebeck voltage on it, $\bar{T}$ - the average temperature of a die.
All methods of express -control of the thermoelectric module use expression [1] or some modification of it [2]. It is a pity but to apply [1] to the multistage module is not correct because the temperature difference on different stages is not the same. The quality control of multistage modules is fulfilled by the measurement of maximum temperature differential ΔT_{max}. This method is demanding too much effort and slow. In this article the express - methods of the control of multistage modules are given. It is assumed the modules have the series connection of the stages.

Results
First of all we investigate the behavior of n - stage module when the external heat flows are neglected. The designation used below is clear from fig. 1. Let n be the total number of stages, ΔT_i - the temperature difference of i - stage, N_i - the quantity of dice of i - stage, T_0 - the temperature of cold junction, T_i - temperature of i - junction which numeration corresponds to fig. 1.
We investigate the case when the thermoelectric parameters of material are independent from temperature and they are the same both for n- and p-types. Further, let the thermoelectric parameters of the material and the dice length and width be the same for every stage. The equations of the heat balance on junctions have the following form:

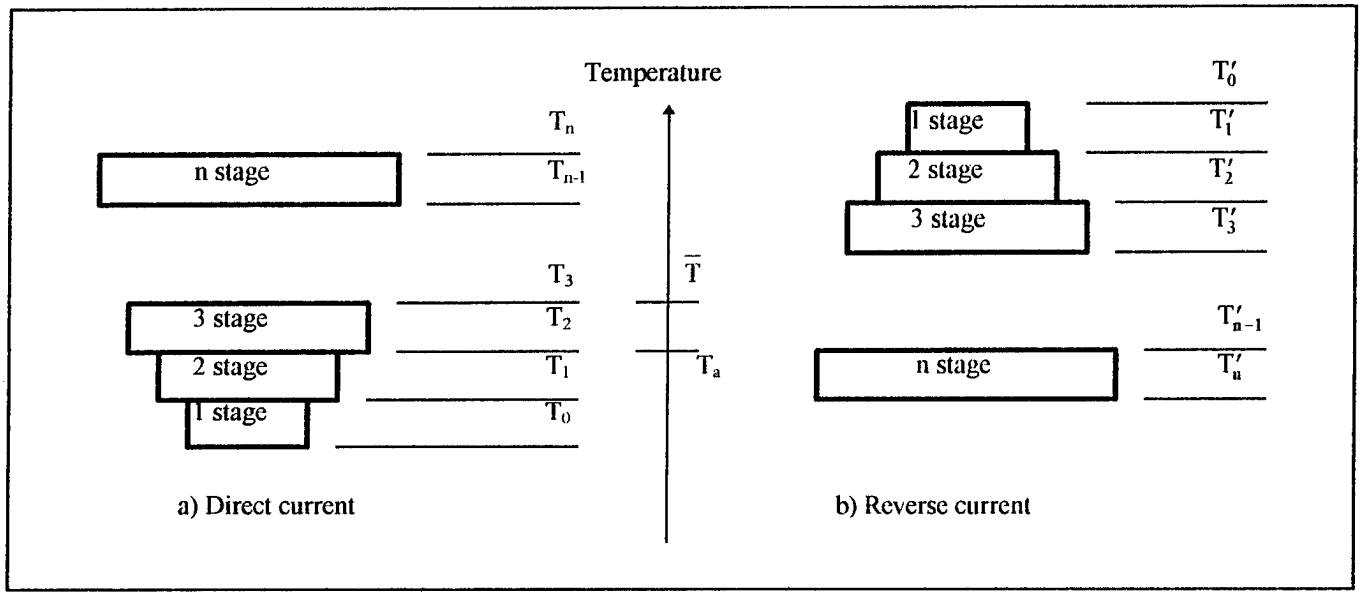


Fig. 1: The distribution of temperatures on the stages.

$$N_1\left(\alpha T_0 I-\frac{1}{2}I^2 r-k\Delta T_1\right)=0 \qquad (2.1)$$

$$N_1\left(\alpha T_1 I+\frac{1}{2}I^2 r-k\Delta T_1\right)=N_2\left(\alpha T_1 I-\frac{1}{2}I^2 r-k\Delta T_2\right) \qquad (2.2)$$

$$N_3\left(\alpha T_2 I-\frac{1}{2}I^2 r-k\Delta T_3\right)=N_2\left(\alpha T_2 I+\frac{1}{2}I^2 r-k\Delta T_2\right) \qquad (2.3)$$

. . . . . .

$$0=N_n\left(\alpha T_n I+\frac{1}{2}I^2 r-k\Delta T_n\right) \qquad (2.4)$$

where r - resistance of a die, k - thermoconductance of a die, α - Seebeck coefficient of a die, I - current.

It is possible to give the analogous system of equations for the reverse current. The stage difference of temperature corresponds to the designations given on fig. 1b and value $\Delta T_i' = T_{i-1}' - T_i'$.

If the equations of this system are added to the corresponding equations of system (2) then the following result is received:

$$Z\bar{T}=\left(\frac{U_{R1}-U_{R2}+U_{R3}+\ldots+(-1)^n U_{Rn}}{\bar{U}_{\alpha 1}-\bar{U}_{\alpha 2}+\bar{U}_{\alpha 3}+\ldots+(-1)^n \bar{U}_{\alpha n}}\right) \qquad (3)$$

where $Z = \alpha^2/rk$, $\bar{U}_{\alpha i}=\frac{U_{\alpha i}+U_{\alpha i}'}{2}$ for i = 1, 2,...,n (here and further the sign ′ is placed after values measured for reverse current), U_{Ri} - the Ohm voltage of i - stage, $U_{\alpha i}$ - Seebeck voltage of it i = 1, 2 ,...,n. The value $\bar{T}$ is defined by the following equations:

$$\bar{T}\approx\frac{1}{2}\left(\frac{T_0+T_1}{2}+\frac{T_1'+T_0'}{2}\right)\approx\frac{1}{2}\left(\frac{T_1+T_2}{2}+\frac{T_2'+T_1'}{2}\right)\approx$$

$$\approx\frac{1}{2}\left(\frac{T_{n-1}+T_n}{2}+\frac{T_n'+T_{n-1}'}{2}\right) \qquad (4)$$

Expression (3) for multistage modules is analogous to expression (1) for one-stage modules. Let us consider this expression in a more detailed way.

The value of $Z\bar{T}$ in a one - stage module is connected directly with ΔT_{max} . But such connection is absent in multistage modules. $Z\bar{T}$ corresponds in (3) to one die and shows the possible ΔT_{max} for this die. In other words the measured value of ΔT_{max} is a quality index of the module assembly. The temperature $\frac{T_{i-1}+T_i}{2}$ is the average temperature of i - stage for direct current and $\frac{T_i'+T_{i-1}'}{2}$ is the same for reverse current.The former one is higher than the ambient temperature and the latter is smaller. The average of two directions of the current must give the value which is close to the ambient temperature. In practice, when (1) is used, the value $\bar{T}$ is changed by the ambient temperature T_a. The supposition that the average temperature of different stages received in this way is almost the same does not seem artificial due to small temperature difference on the module. It is clear that the module current must be small in this case.

Different signs before terms of (3) are connected with the fact that the upper stage is a heat load for the lower one. The diminishing of this heat load can bring to the seeming growth of $Z\bar{T}$ because equations (2) have a rigid connection between the stages, which creates basic difficulties for using expression (3).

Every mistake in assembling a one-stage module must diminish $Z\bar{T}$, i.e. the maximum of the latter is received when the quality of the module is high. Different signs of the terms in (3) made it untrue for a multistage module. For example, the denominator in (3) can become zero if the resistance of one of the upper stages increases. This leads to increasing of $Z\bar{T}$. The same can be received if some part (or all) of the dice of a stage has the wrong type of conductivity. Therefore the direct use of (3) is very complicated and it is necessary to rely on the results of (3) very carefully.

It is better to analyse every stage of a module. For this purpose it is necessary to analyse only two equations of system (2): the equation of the heat balance on a free junction - (2.1) and the one on an intermediate junction - (2.2) or (2.3) type. If in these equations the external heat flow on the junctions is taken into consideration then they have the following form:

$$N_1\left(\alpha T_0 I-\frac{1}{2}I^2 r-k\Delta T_1\right)=Q_0 \qquad (5)$$

$$N_{i-1}\left(\alpha T_i I-\frac{1}{2}I^2 r-k\Delta T_{i+1}\right)=N_i\left(\alpha T_i I+\frac{1}{2}I^2 r-k\Delta T_i\right)+Q_i \qquad (6)$$

where Q_o and Q_i are the heat flow on 0- and i- junction .

Let

$$Q_0 = hN_1\left(T_a - T_0\right) \qquad (7)$$

$$Q_i = h\left(N_{i-1}-N_i\right)\left(T_a - T_i\right) \qquad (8)$$

where h - heat exchange coefficient, T_a - ambient temperature.For the case when h<<k it is possible to receive (with very rough approximation $\Delta T_i \approx \frac{\Delta T}{n}$, where ΔT is the temperature difference on the module):

$$Z_r\bar{T}=\frac{\frac{1}{2}\left(U_{\alpha 1}+U_{\alpha 1}'\right)}{U_{R1}} \qquad (9)$$

where $Z_r = Z\frac{k}{\left(k+\frac{hn}{2}\right)}$ and $\bar{T}=\frac{T_0+T_0'}{2}$. This expression is analogous to (1) for a one - stage module. In practice the correction to Z_r is a value defined by an experiment and therefore the introduced rough approximation isn't very essential.

In the similar way it can be received from (6):

$$Z_{1r}\,\bar{T} = \frac{\frac{1}{2}\left(U_{\alpha(i+1)} + U'_{\alpha(i+1)}\right) - \frac{1}{2}\left(U_{\alpha i} + U'_{\alpha i}\right)}{U_{R(i+1)} - U'_{Ri}} \qquad (10)$$

where $\bar{T} = \frac{T_i + T'_i}{2}$ and $Z_{1r} = Z\frac{k}{\left(k + \frac{h|n-2i|}{2}\right)}$.

Therefore it is possible to analyse the work of a multistage module on the base of expressions (9) and (10). Such analysis is conducted for every stage, from top to bottom of a module.

Discussion

The measurement of voltage of every stage can be fulfilled by special probe leads . Thin wires can be soldered to the stage leads or sharp thin wires can be pressed to it.

The analysis of the first stage is little different from that of a one-stage module and can be realized in the way usual for such modules . The analysis of the following stages is fulfilled after the measurement of the preceeding ones.

The quantity of equations in system (2) is by one more than that of the stages in a module. It is possible to analyse the work of the last stage on the base of both equation (9) and (10). It can be very useful for two - stages modules. If the heat excange coefficients are close in their value for both stages then it is possible to receive the following expression for a two - stage module:

$$Z_{eff} = \frac{\left(U_{\alpha 1} + \frac{U_{\alpha 2}}{m}\right)(1+m)}{U_{R1} + U_{R2}} \qquad (11)$$

where $m = \frac{N_2}{N_1}$.

This method is applied to modules with series connection of stages but it can also be applied to modules with direct connection of stages. In this case such modules must have special strips which are removed at mesurement time.

References

[1] T.C. Harman, "Special Techniques for Measurement of Thermoelectric Properties", J. of Appl. Phys.**30** (1958) 1351.

[2] V.P.Babin, S.M. Gorodetskiy, "Thermoelectric Modules Quality Testing by a Manufacturer", Proc. of the XIV Int. Conf. on Thermoelectrics (ICT'95), St.Petersburg, Russia,1995.

Generalized Formulas to Express Maximum Temperature Difference for Two-Stage Thermoelectric Cooling Modules

Dow-Bin Hyun[1], N. V. Kolomoets[1], Tae-Sung Oh[2], Jong-Seung Hwang[1] and Jae-Dong Shim[1]

1. Division of Metals, Korea Institute of Science and Technology(KIST), P.O. Box 131, Cheong-Ryang, Seoul 130-650, Korea, Tel.: +82/2/958-5464, FAX: +82/2/958-5379, E-mail: dbhyun@kistmail.kist.re.kr
2. Dept. of Metallurgy and Materials Science, Hong Ik Univ., Mapo-ku, Seoul 121-791, Korea, Tel.: +82/2/320-1655, FAX: +82/2/337-8460, E-mail: ohts@wow.hongik.ac.kr

Abstract

Application of the two-stage modules has been widely considered to obtain a large temperature difference, required for devices such as a freezer, by thermoelectric cooling. Due to the complexity of the formulas for maximum parameters, however, design of the application devices in practical use has been limited. Generalized formulas have been derived to express the maximum temperature difference and maximum current at ΔT_{max} -mode for two-stage thermoelectric modules connected electrically in series or in parallel: $\Delta T_{max} = T_h \frac{a}{c} \frac{M'-1}{M'+1}$, $I_{max} = 2T_h \frac{a}{b} \frac{e_1}{R_1} \frac{1}{M'+1}$, and $M' = (1+2T_h \frac{ac}{b} \frac{Z_1}{K_2/K_1})^{1/2}$. Corresponding to these expressions, $\Delta T_{max} = T_h - \frac{M'-1}{Z_1} = T_h \frac{M'-1}{M'+1}$, $I_{max} = \frac{K_1}{e_1}(M'-1) = 2T_h \frac{e_1}{R_1} \frac{1}{M'+1}$, and $M' = (1+2 \cdot Z_1 \cdot T_h)^{1/2}$ for one-stage modules.

Part 1. Series Mode

Generally, a temperature difference (ΔT) in a two-stage module is the summation of the temperature difference in the upper cascade ($\Delta T_1 = T_m - T_c$) and that in the lower cascade ($\Delta T_2 = T_h - T_m$): $\Delta T = \Delta T_1 + \Delta T_2$. When a two-stage module connected electrically in series is operated in the maximum-temperature-difference (ΔT_{max}) mode, the applied current can not meet the ΔT_{max} condition for both the upper and the lower cascade simultaneously, and ΔT_{max} is not the simple summation of $\Delta T_{1,max}$ and $\Delta T_{2,max}$. When a two-stage cascade module is operated in the ΔT_{max}-mode, i.e. the heat load to the upper cascade is zero, the heat balance for the upper cascade is given by

$$e_1 \cdot I \cdot T_c - 0.5 \cdot I^2 \cdot R_1 - K_1 \cdot \Delta T_1 = 0 \quad (1)$$

where e_1, R_1 and K_1 are the Seebeck coefficient, the electrical resistance and the thermal conductance of the thermocouples in the upper cascade, respectively. From Eq. (1), one can derive the temperature difference in the upper cascade as

$$\Delta T_1 = \frac{e_1 \cdot I \cdot T_c - 0.5 \cdot I^2 \cdot R_1}{K_1} = \frac{e_1 \cdot I \cdot T_h - e_1 \cdot I \cdot \Delta T - 0.5 \cdot I^2 \cdot R_1}{K_1} \quad (2)$$

Due to the heat load dissipated from the upper cascade, the heat balance for the lower cascade is given by

$$e_1 \cdot I \cdot T_m + 0.5 \cdot I^2 \cdot R_1 - K_1 \cdot \Delta T_1 = n \cdot (e_2 \cdot I \cdot T_m - 0.5 \cdot I^2 \cdot R_2 - K_2 \cdot \Delta T_2) \quad (3)$$

where n is the ratio of the numer of thermocouples in the lower cascade to the upper cascade. From Eq. (3), the inter- cascade temperature, T_m, can be derived and expressed simply as follows:

$$T_m = \frac{0.5 \cdot I^2 \cdot R_1 \cdot X_R + K_1 \cdot X_{K,T}}{e_1 \cdot I \cdot X_e + K_1 \cdot X_K} \quad (4)$$

where

$$X_e = n\frac{e_2}{e_1} - 1$$

$$X_R = n\frac{R_2}{R_1} + 1$$

$$X_K = n\frac{K_2}{K_1} + 1$$

$$X_{K,T} = n\frac{K_2}{K_1} T_h + T_c \quad (5)$$

And, the temperature difference in the lower cascade can be derived as:

$$\Delta T_2 = \frac{(ne_2 - e_1) \cdot I \cdot T_m - 0.5I^2 \cdot (nR_2 + R_1) + K_1 \cdot \Delta T_1}{n \cdot K_2} = \frac{e_1 \cdot X_e \cdot I \cdot (T_h + \Delta T_1 - \Delta T) - 0.5I^2 \cdot R_1 \cdot X_R + K_1 \cdot \Delta T_1}{n \cdot K_2} \quad (6)$$

The temperature difference in a two-stage module is the summation of Eqs. (2) and (6), and can be expressed as

$$\Delta T = \frac{e_1 \cdot I \cdot [T_h \cdot (e_2/e_1 + K_2/K_1) + (e_2/e_1 - 1/n) \cdot \Delta T_1] - 0.5 \cdot I^2 \cdot R_1 \cdot (R_2/R_1 + K_2/K_1 + 2/n)}{e_1 \cdot I \cdot (e_2/e_1 + K_2/K_1) + K_2}$$

$$= \frac{e_1 \cdot I \cdot [T_h \cdot (X_e + X_K) + X_e \cdot \Delta T_1] - 0.5 \cdot I^2 \cdot R_1 \cdot (X_R + X_K)}{e_1 \cdot I \cdot (X_e + X_K) + n \cdot K_2} \quad (7)$$

Since ΔT is the additive function of ΔT_1 and ΔT_2, the maximum of ΔT appears at $\Delta T_1 = \Delta T_2 = \Delta T/2$. In this condition, the maximum temperature difference of a two-stage module can be derived from Eq. (7) as follows:

$$\Delta T_{max} = \frac{e_1 \cdot I \cdot T_h (X_e + X_K) - 0.5 I^2 \cdot R_1 (X_R + X_K)}{e_1 \cdot I \cdot (0.5 X_e + X_K) + n \cdot K_2} \quad (8)$$

By letting

$$a = X_e + X_K$$
$$b = X_R + X_K$$
$$c = 0.5 X_e + X_K \quad (9)$$

Eq. (8) can be rewritten in a generalized fomula as

$$\Delta T_{max} = \frac{a \cdot e_1 \cdot I \cdot T_h - 0.5 \cdot b \cdot I^2 \cdot R_1}{c \cdot e_1 \cdot I + n \cdot K_2} \quad (10)$$

From Eq. (10), the maximum current in the ΔT_{max}-mode can be obtained by $d(\Delta T_{max})/dI = 0$ as

$$I_{max} = \frac{n \cdot K_2}{c \cdot e_1} (M'' - 1)$$

$$= \frac{e_1}{R_1} \frac{1}{Z_1} \frac{n \cdot K_2/K_1}{c} (M'' - 1) \quad (11)$$

or

$$I_{max} = \frac{e_1}{R_1} \frac{a}{b} \frac{2 \cdot T_h}{M'' + 1} \quad (12)$$

where

$$M'' = \left[1 + 2 \cdot Z_1 \cdot T_h \frac{1}{n \cdot K_2/K_1} \frac{a \cdot c}{b} \right]^{1/2} \quad (13)$$

In the case of an one-stage module, it is general to express the maximum current, $I_{I,max}$, as follows:

$$I_{I,max} = \frac{e}{R} \frac{1}{Z} (M_I - 1) \quad (14)$$

or

$$I_{I,max} = \frac{e}{R} \frac{2 \cdot T_h}{M_I + 1} \quad (15)$$

where

$$M_I = (1 + 2 \cdot Z \cdot T_h)^{1/2} \quad (16)$$

From Eqs. (12), (13), (15) and (16), one can generalize the M value and maximum current in the ΔT_{max}-mode as Eqs. (12) and (14) with $a = b = c = 1$ for an one-stage module.

Furthermore, by inserting Eq. (11) into Eq. (10) and simplifying the equation using the relation of Eq. (13), ΔT_{max} for a two-stage module, connected electrically in series, can be reformulated into a generalized formula as:

$$\Delta T_{max} = T_h \frac{a}{c} \frac{M' - 1}{M' + 1} \quad (17)$$

as well known, ΔT_{max} for an one-cascade module is expressed as:

$$\Delta T_{I,max} = T_h \frac{M_I - 1}{M_I + 1} \quad (18)$$

With comparison of Eq. (17) and Eq. (18), the differences in ΔT_{max} between a two-stage and an one-stage module can be described using the parameters, a, b and c which are determined by thermoelectric properties of the thermocouples in the lower and upper cascade, dimension of the thermoelements, and the ratio of n.

Using the thermoelectric properties written in Table 1, ΔT_{max} for a two-stage module was calculated from Eq. (17) with varying the ratio of the number of thermocouples in the lower cascade to the upper cascade, and plotted in Fig. 1. ΔT_{max} increases rapidly with n up to 3 - 4, and then increases more moderately with further increase of n. From this result, one can notice that the number of thermocouples in the lower cascade should be at least 3 or 4 times larger than that in the upper cascade to get a large temperature difference using a two-stage module.

As the conventional one-stage module, ΔT_{max} of a two-stage module can be also expressed using the effective figure-of-merit:

$$\Delta T_{max} = 0.5 \cdot Z_{eff} \cdot T_c^2 = T_h - \frac{\sqrt{1 + 2 \cdot Z_{eff} \cdot T_h} - 1}{Z_{eff}} \quad (19)$$

where Z_{eff} is the effective figure-of-merit. The calculated Z_{eff} at T_h = 300K is also plotted in Fig. 1.

Table 1. Thermoelectric properties of thermocouples in the upper and lower cascades.

upper cascade		lower cascade	
e_1 [x10^{-3}V/K]	0.36	e_2	0.41
R_1 [x10^{-3}Ohm]	2.7	R_2	3.4
K_1 [W/K]	2.10	K_2	1.87
Z_1 [x10^{-3}K^{-1}]	2.3	Z_2	2.5

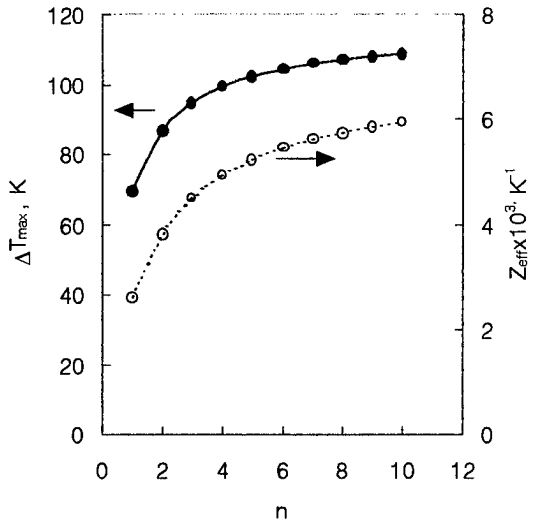


Fig. 1 Calculated values of ΔT_{max} and Z_{eff} with the ratio of the number of thermocouples in the lower cascade to the upper cascade. (T_h = 300K)

Although Z_{eff} is a hypothetical value, ΔT_{max} of a two-stage module can be considered to be that of an one-stage module having figure-of-merit of Z_{eff}, and the high Z_{eff} value in Fig. 1 confirms the possibility of utilizing the two-stage modules in many application fields.

Part 2. Parallel Mode

When a two-stage module, connected electrically in parallel, is operated in the ΔT_{max}-mode, the heat balance in the upper cascade is given by

$$e_1 \cdot I_1 \cdot T_c - 0.5 \cdot I_1^2 \cdot R_1 - K_1 \cdot \Delta T_1 = 0 \qquad (20)$$

and the heat balance in the lower cascade is given by

$$e_1 \cdot I_1 \cdot T_m + 0.5 \cdot I_1^2 \cdot R_1 - K_1 \cdot \Delta T_1 = n \cdot (e_2 \cdot I_2 \cdot T_m - 0.5 \cdot I_2^2 \cdot R_2 - K_2 \cdot \Delta T_2) \qquad (21)$$

where

$$I_1 = I \cdot (1 - 1/X_R) \text{ and } I_2 = I/X_R \qquad (22)$$

Following the steps given in Eqs. (2) - (7), one can derive ΔT_{max} in a two-stage module, connected electrically in parallel, as follows:

$$\Delta T_{max} = \frac{e_1 \cdot I \cdot T_h \cdot [(1+X_e)/X_R - (1-X_K)(1-1/X_R)] - 0.5 \cdot I^2 \cdot R_1 \cdot [(1-1/X_R) + X_K(1-1/X_R)^2]}{e_1 \cdot I \cdot [0.5(1+X_e)/X_R - (0.5-X_K)(1-1/X_R)] + n \cdot K_2} \qquad (23)$$

Although Eq. (23) seems to be a little more complicated than for the series mode, it also can be expressed in the generalized fomula of Eq. (10) with the parameters of

$$a = (1+X_e)/X_R - (1-X_K)(1-1/X_R)$$
$$b = (1-1/X_R) + X_K(1-1/X_R)^2$$
$$c = 0.5(1+X_e)/X_R - (0.5-X_K)(1-1/X_R) \qquad (24)$$

Furthermore, using M' value, defined as Eq. (13), the maximum current and the maximum temperature difference can be expressed simply as Eqs. (12) and (17) for different ratio of number of thermocouples in the lower and upper cascade, n.

Part 3. Combined "Series and Parallel" Mode

Besides two-stage modules, connected electrically in series or in parallel, various kinds of two-stage modules, connected electrically both in series and parallel, can be designed. Simplest example of such a module is shown in Fig. 2, where the current flows along each branches in the parallel part, I_2, is

$$I = \frac{(n+1)}{2} I_2 \qquad (25)$$

In the middle part of the two-stage module, the current is redistributed by I_1, across the thermocouple of the upper cascade, and I'_2, across the $(n-1)/2$ thermocouples of the lower cascade, as follows:

$$I = I_1 + \frac{(n-1)}{2} I'_2 \qquad (26)$$

As the voltage on the thermocouples in the upper and lower cascade is the same in the intermediate electrodes, the following relation can be obtained:

$$I_1 \cdot R_1 + e_1 \cdot \Delta T_1 = I'_2 \cdot R_2 + e_2 \cdot \Delta T_2 \qquad (27)$$

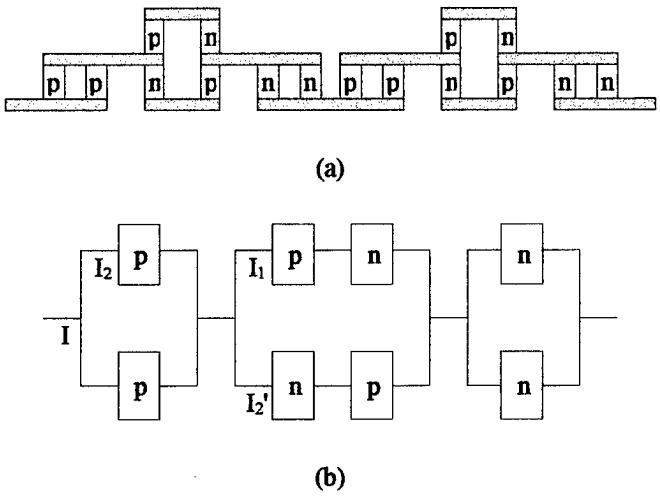


Fig. 2 (a) Example of a two-stage module connected electrically in series and parallel, and (b) the electrical block diagram.

Since the difference in the counter-emf., $(e_2 \cdot \Delta T_2 - e_1 \cdot \Delta T_1)$, is relatively small compared to the total voltage on the thermocouples, it can be neglected. Inserting $I_1 \cdot R_1 = I'_2 \cdot R_2$ into Eq. (26), one can derive I_1 and I'_2 in terms of n as:

$$I_1 = \frac{2(X_R - 1)}{n^2 - n + 2(X_R - 1)} \tag{28}$$

and

$$I'_2 = \frac{2n}{n^2 - n + 2(X_R - 1)} \tag{29}$$

When a two-stage module shown in Fig. 2 is operated in the ΔT_{max}-mode, the heat balance in the upper cascade is given by

$$e_1 \cdot I_1 \cdot T_c - 0.5 \cdot I_1^2 \cdot R_1 - K_1 \cdot \Delta T_1 = 0 \tag{30}$$

and the heat balance in the lower cascade is given by

$$\begin{aligned}(e_1 \cdot I_1 \cdot T_m + 0.5 \cdot I_1^2 \cdot R_1 - K_1 \cdot \Delta T_1) \\ = 0.5\frac{(n-1)}{2}(e_2 \cdot I'_2 \cdot T_m - 0.5 \cdot I'^2_2 \cdot R_2 - K_2 \cdot \Delta T_2) \\ + 0.5\frac{(n+1)}{2}(e_2 \cdot I_2 \cdot T_m - 0.5 \cdot I_2^2 \cdot R_2 - K_2 \cdot \Delta T_2)\end{aligned} \tag{31}$$

Following the steps given in Eqs. (2) - (7), one can derive ΔT_{max} in the generalized fomula as Eq. (10) with the parameters of

$$\begin{aligned}a &= \frac{2(X_R-1)}{2(X_R-1)+n(n-1)} \cdot \left\{X_K - 1 + \frac{[(X_R-1)+n(n-1)](X_e+1)}{n(X_R-1)}\right\} \\ b &= \left[\frac{2(X_R-1)}{2(X_R-1)+n(n-1)}\right]^2 \cdot \left\{X_K - 1 + \frac{n^2(n^2+n+4)+2(X_R-1)[X_R-1+n(n-1)]}{n^2(n+1)}\right\} \\ c &= \frac{2(X_R-1)}{2(X_R-1)+n(n-1)} \cdot \left\{X_K + 0.5\left[\frac{(X_R-1)+n(n-1)(1+X_e)}{n(X_R-1)} - 1\right]\right\}\end{aligned} \tag{32}$$

As a conclusion, the generalized formulas for the M value, maximum temperature difference, maximum current, and the parameters a, b and c for the different cases of the two-stage modules are summarized in Table 2.

Table 2. Summary of the generalized formulas for the two-stage modules in the mode of ΔT_{max}.

Generalized expression		
$\Delta T_{max} = \frac{a}{c} 2T_h \frac{M'-1}{M'+1}$	$I_{max} = \frac{e_1}{R_1}\frac{a}{b}\frac{2T_h}{(M'+1)}$	$M' = \left(1 + 2T_h \frac{Z_1}{n \cdot K_2/K_1}\frac{a \cdot c}{b}\right)^{1/2}$
one-stage module		
$a=1;\ b=1;\ c=1;\ K_2=K_1$		
two-stage module with "series mode"		
$a = X_e + X_K$ $b = X_R + X_K$ $c = 0.5X_e + X_K$		
two-stage module with "parallel mode"		
$a = (1+X_e)/X_R - (1-X_K)(1-1/X_R)$ $b = (1-1/X_R) + X_K(1-1/X_R)^2$ $c = 0.5(1+X_e)/X_R - (0.5-X_K)(1-1/X_R)$		
two-stage module with "series and parallel mode"		
$a = \frac{2(X_R-1)}{2(X_R-1)+n(n-1)}\left\{X_K - 1 + \frac{[(X_R-1)+n(n-1)](X_e+1)}{n(X_R-1)}\right\}$ $b = \left[\frac{2(X_R-1)}{2(X_R-1)+n(n-1)}\right]^2\left\{X_K - 1 + \frac{n^2(n^2+n+4)+2(X_R-1)[X_R-1+n(n-1)]}{n^2(n+1)}\right\}$ $c = \frac{2(X_R-1)}{2(X_R-1)+n(n-1)}\left\{X_K + 0.5\left[\frac{(X_R-1)+n(n-1)(1+X_e)}{n(X_R-1)} - 1\right]\right\}$		

Novel High Performance Thermoelectric Microcoolers with Diamond Substrates

Vladimir Semeniouk [1], J.-P. Fleurial [2]
(1) Odessa State Academy of Refrigeration, Thermion Company, E-mail: semeniou@thermion.tenet.odessa.ua
(2) Jet Propulsion Laboratory/California Institute of Technology, Pasadena,CA 91109.

Abstract

The concepts discussed in previous papers [1-3] have been implemented in novel miniature thermoelectric coolers (TECs) with diamond substrates. Micromodules with TE legs 0.2mm long and 0.4×0.4mm^2 in cross-section were developed. A maximum temperature difference of 67K was obtained, a value comparable to the ones obtained for commercial TECs with TE leg length of 1mm and higher. Heat flux densities of 70W/cm^2 at cold junctions were achieved. Taking into consideration the hot side thermal resistance, the minimum TE leg length was calculated. It was found that using high thermal conductivity substrates allows miniaturization of the TE legs near its lower theoretical limit defined by electrical contact resistance only. Cold side heat flux densities in excess of 100W/cm^2 can be attained in such coolers. This makes them ideal to solve thermal problem of high density localized heat sources such as power amplifiers, microprocessors and other power electronic devices which are already operating at the edge of their reliability.

Introduction

Many electronic components need active cooling for safe operation. The thermal issues are particularly severe for high power devices such as power amplifiers, microprocessors, semiconductor lasers and other electronic and electro-optic devices which act as high density localized heat sources. To maintain control of their operating temperature, TECs with exceptionally high cooling capacity must be developed. It is well known that heat flux densities q_0 and q_1 at the TEC cold and hot junctions increase in inverse proportion to TE leg length l. With l=0.1mm, for instance, q_0 values can exceed 100W/cm^2. Thus, developing extremely short-legged TEC is required to meet the cooling requirement of high density heat sources. However, hot side heat rejection issues must also be resolved because q_1 values can reach 250-350 W/cm^2. For alumina substrates, which are commonly used, the resulting hot side temperature gradient can be more than 30K. So the use of substrates from high thermal conducting materials, such as diamond, is the most promising trend for extremely short-legged TECs development.

Theoretical maximum of cooling capacity

Heat flux densities at the TEC cold and hot sides are bound by the following system of equations (1), where α, ρ, κ are the Seebeck coefficient, electrical resistivity and thermal conductivity of TE materials, i is the input current density, T_c and T_1 are the temperatures of cold and hot junctions respectively, T_e is the temperature of environment, r_c is the contact electrical resistance referred to junction area unit, R_t is the TEC hot side thermal resistance defined as the ratio of the temperature drop to the hot side heat flux density.

$$\begin{aligned} q_0 &= \alpha T_c i - \frac{1}{2} i^2 (\rho l + 2r_c) - \frac{\kappa}{l}(T_1 - T_c) \\ q_1 &= \alpha T_1 i + \frac{1}{2} i^2 (\rho l + 2r_c) - \frac{\kappa}{l}(T_1 - T_c) \\ T_1 &= T_e + R_t q_1 \end{aligned} \qquad (1)$$

(1) gives the $q_0(i,l)$ dependence in indirect fashion. For any fixed l value the set of equations (1) determines the maximum of $q_0(i)$ as a function of current density. The calculated maxima for different R_t values are given in Fig.1. One can see that for a fixed contact resistance optimal l values corresponding to absolute maximum of cooling capacity can be determined. Such l values are the minimum acceptable TE leg lengths since smaller values result in simultaneous q_0 and COP reductions. This dramatic degradation in TEC performance is mostly due to catastrophic superheating of the TEC hot side.

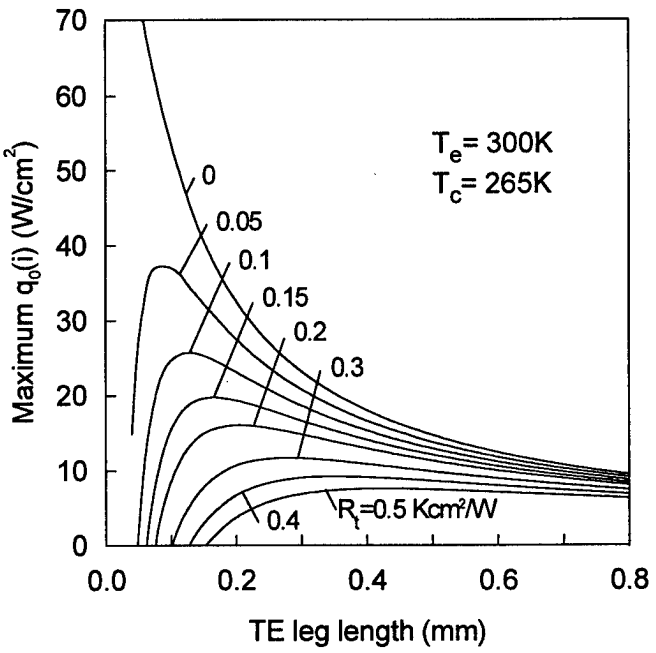


Figure 1: Maximum (by current density) cold side heat flux density versus TE leg length for different R_t values.

Fig.2 shows the variations of l_{min} and q_{0max} with increasing R_t values and highlights the importance of using high heat conducting substrates. For alumina substrates (thermal

conductivity of 0.2W/cmK) R_t values are usually of the order of 0.1-0.2Kcm^2/W, minimum TE leg lengths range from 0.1 to 0.7mm, depending strongly on the operating temperature difference $\Delta T=T_e-T_c$. This gives q_{0max} values considerably below 50W/cm^2 for $\Delta T>20$K.

Because of the much higher thermal conductivity of diamond substrates (12 to 18W/cmK), the thermal resistance practically vanishes. This enables reducing l_{min} to its theoretical limit defined by electrical contact resistance only (estimated here as $1.5\cdot10^{-6}$ Ωcm^2). Lower l_{min} values means that q_{0max} values can be increased to over 150W/cm^2.

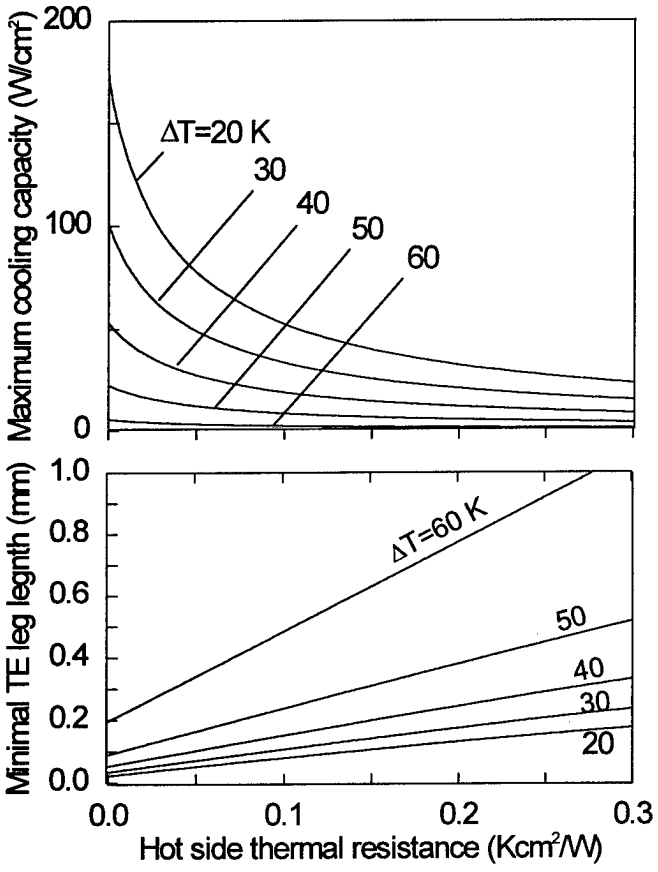


Figure 2: Minimal TE leg length and maximum cold side heat flux density versus hot side thermal resistance.

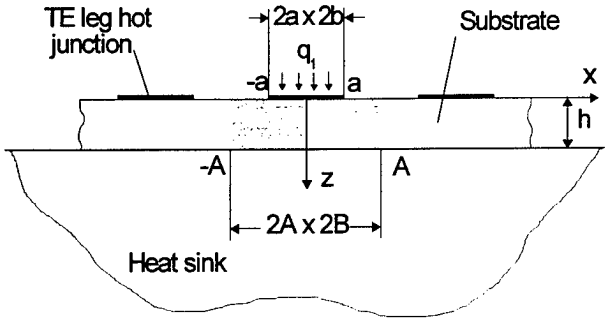


Figure 3: Scheme of TEC hot side substrate.

In real devices however, the hot side TEC thermal resistance also depends on the heat sink thermal resistance, R_{hs} for a total value of $R_t=R_{ts}+R_{hs}$. To estimate the TEC characteristics, separate modeling of the substrate and heat sink thermal resistances must be conducted.

Substrate thermal resistance

Let us consider a substrate section related to a TEC junction (Fig. 3) with dimensions $2A\times2B$ and thickness h. Heat is generated in a junction area $2a\times2b$ with uniform density q_1 and flows three-dimensionally into the highly conductive sink having zero temperature. Other top and side surfaces of this section are adiabatically insulated. The substrate thermal resistance is defined as the ratio of the mean integral temperature at the junction area to the heat flux density q_1. A solution of Laplace's equation for the temperature $T(x,y,z)$ within the substrate element leads to the following equation for R_{ts}:

$$R_{ts}=\frac{h}{\kappa_s}\Phi\left(\frac{a}{A},\frac{b}{B},\frac{h}{A},\frac{A}{B}\right) \qquad (2)$$

where

$$\Phi=\beta\left(1+2S_1+2S_2+4S_3\right) \qquad (3)$$

Φ is a form factor characterizing the influence of TE leg spacing, and S_1, S_2 and S_3 are expressed as:

$$S_1=\sum_{n=1}^{\infty}\left(\frac{\sin(\lambda a)}{\lambda a}\right)^2\frac{\tanh(\lambda h)}{\lambda h}$$

$$S_2=\sum_{m=1}^{\infty}\left(\frac{\sin(\mu b)}{\mu b}\right)^2\frac{\tanh(\mu h)}{\mu h} \qquad (4)$$

$$S_3=\sum_{n=1}^{\infty}\left(\frac{\sin(\lambda a)}{\lambda a}\right)^2\sum_{m=1}^{\infty}\left(\frac{\sin(\mu b)}{\mu b}\right)^2\frac{\tanh(\alpha h)}{\alpha h}$$

$$\lambda=\frac{n\pi}{A},\qquad \mu=\frac{m\pi}{B},\qquad \alpha^2=\lambda^2+\mu^2$$

where $\beta=ab/AB$ is the TE leg packing density and κ_s is the substrate thermal conductivity.

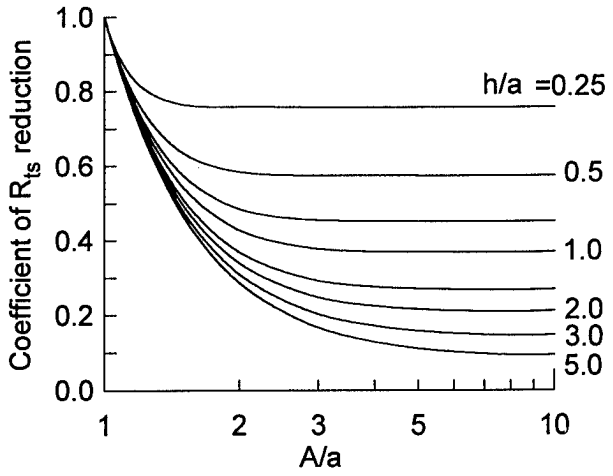


Figure 4: Reduction of substrate thermal resistance with TE legs spacing.

Fig.4 shows the dependence of the form factor Φ on TE legs spacing. In a boundary case when the packing density is unity (a=A, b=B), one has Φ=1 and $R_{ts}=h/\kappa_s$, which corresponds to the one-dimensional heat flow. Increasing leg spacing considerably reduces substrate thermal resistance, the effect being particularly significant for high values of h/a ratio. It is also clear that increasing legs spacing to $A/a > 3$ does not result in any significant additional gains.

Thermal resistance of a heat sink

Let us consider the physical model of a heat sink in a form of semi-infinite section with a rectangular heat source at its surface. Heat flow from the substrate with dimensions of $2A_s \times 2B_s$ enters uniformly into heat sink, heat flux density being of $q_s=q_1\beta$. The supporting surface is adiabatically insulated and the heat sink temperature at infinity is zero. The thermal resistance of such heat sink, defined as the ratio of the integral mean temperature at the substrate bottom area to heat flux density q_1, can be expressed as:

$$R_{hs}=\frac{\beta}{\pi\kappa_{hs}}\left\{A_s\ln\frac{R+B_s}{R-B_s}+B_s\ln\frac{R+A_s}{R-A_s}-\frac{2}{3}\frac{R^3-A_s^3-B_s^3}{A_sB_s}\right\} \quad (5)$$

where $R=\sqrt{A_s^2+B_s^2}$ and κ_{hs} is the heat sink thermal conductivity. If A_s=B_s, (5) can be reduced to the formula:

$$R_{hs}=0.947\beta A_s/\kappa_{hs}. \quad (6)$$

Results show that the heat sink thermal resistance is proportional to the substrate linear dimensions. So for fixed q_1 and β values, hot side substrate superheating increases linearly with increasing module edge dimension. For example, using a substrate with dimensions A_s=B_s=10 mm and β=0.25, the calculated thermal resistance of a copper heat sink is 0.06 Kcm²/W. This resistance approaches the value obtained for 0.5mm thick alumina substrates but is much larger than the one achieved for diamond substrates. A heat flux of 250W/cm² can result in a 15K temperature gradient at the substrate-heat sink interface. This additional superheating by no means can be eliminated in such a model. It must be noted that the temperature decrease in the direction of the heat sink depth is rather slow. Even at a depth equal to the substrate edge dimension, the calculated overheating is close to half the maximum temperature rise which occurs at the center of the sink surface. Thus, heat sink thin plate geometry combined with intensive heat removal from its bottom surface are highly desirable for cooling short-legged TECs. Another alternative is a heat sink with a two-phase heat pipe embedded under the substrate bottom and directly in the zone of maximum superheating. To estimate R_{hs} for this model equations (2)-(4) can be used with A_s and B_s as a and b respectively.

Experimental details

Self-standing diamond films were produced by CVD technique and used as substrates for short-legged TECs. Similar TE modules with alumina substrates were also fabricated to provide a baseline. Some details of these TECs arrangement are given in Table 1.

Table 1. Characteristics of experimental samples

Parameter	TECs with diamond substrates	TECs with alumina substrates
Number of TE legs	120	120
TE leg length (mm):	0.2	0.2
TE leg cross-section (mm):	0.4×0.4	0.4×0.4
TE leg spacing (mm)	0.4	0.4
Top substrate thickness (mm):	0.56	0.5
Top substrate are (mm):	10.4×14.1	9.6×8
Bottom substrate thickness (mm):	0.56	0.5
Bottom substrate area (mm):	10.4×14.1	9.6×9.6
metallized and patterned area Substrate dimensions (mm)	9.2×7.6	9.2×7.6
Substrate thermal resistance per unit area (Kcm²/W)	1.5×10^{-3}	0.1

The modules were tested in vacuum, operating with no load operation (ΔT_{max}) as well as with heat load at the cold side (Q_{max}). The hot side of the modules was maintained at 303K using ultra thermostat with heat-transfer liquid. The temperature-sensitive micro resistor mounted at the heat sink close to the bottom substrate edge was used for hot side temperature control.

The dynamic thermal behavior of the TECs after switching the DC source on was also studied. Using thermocouples from copper and constantan wires 0.03mm in diameter, the cold side temperature was recorded as a function of time.

Results and discussion

Fig. 5 plots the variations in temperature gradient at the TECs hot and cold junctions as a function of the input electrical current and under zero thermal load conditions.

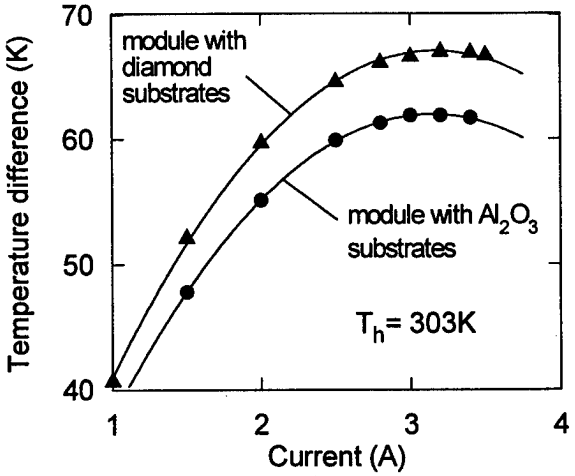


Figure 5: Dependence of TEC temperature difference with input electrical current.

In spite of extremely short TE legs, a maximum temperature difference of 67K was obtained for the cooler with diamond substrates, a result comparable to the performance of commercial coolers with TE leg length of 1mm and higher. Because of the hot side substrate superheating, a lower ΔT_{max} of 62K only was measured for the alumina-based module.

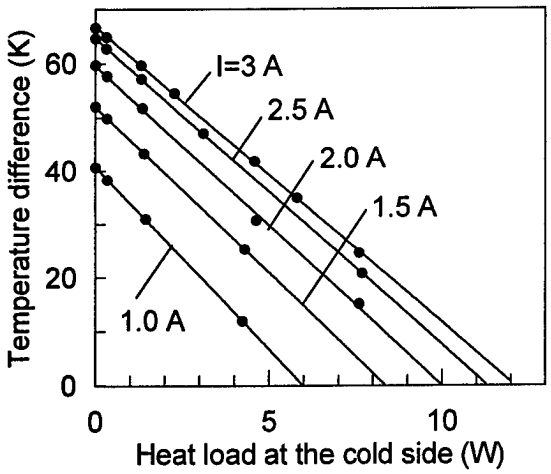


Figure 6: Heat load characteristics of TE microcooler with diamond substrate (measured).

It should be noted that the preliminary configuration of the diamond-based microcoolers was far from optimal because their substrate area substantially (more than twice) exceeded the patterned area (see Table 1), resulting in increased heat losses at the cold side. Thus, the potential for further performance improvement exists and can be realized in future. Fig. 6 plots the variations of ΔT with different heat loads at the cold side for the diamond-based microcoolers. One can see that the device can maintain a ΔT of 25K even with a heat load of up to 8W. This makes it possible to use such devices for cooling solid state power amplifiers in spacecraft applications [2]. When ΔT is completely suppressed the module has a cooling capacity of more than 12W which corresponds to a heat flux density of 65W/cm^2 at the cold junctions.

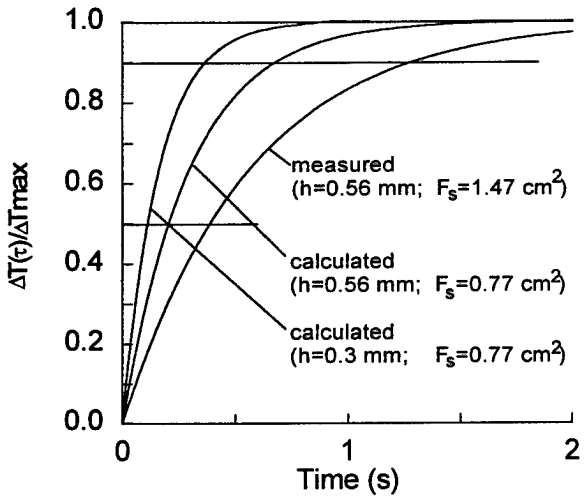


Figure 7: Dynamic characteristics of experimental sample.

The recorded dynamic characteristic of the experimental module with diamond substrates is displayed in Fig.7. The calculated characteristics for optimal top substrate dimensions are also presented here. The results are treated in the form of $\Delta T/\Delta T_{max}$ time dependence and show that the device required about 2s to achieve its ΔT_{max}. Much better results should be achieved when superfluous parts of the top substrate are removed and its thickness is diminished. Corresponding data are shown in Table 2. For TEC with substrate thickness of 0.3mm the time to achieve $0.9\Delta T_{max}$ is expected to be reduced to only 0.36s only.

Table 2. Time to achieve specified ΔT (s)

Top ceramic dimensions (mm)	Specified temperature difference (K)		
	$0.37\Delta T_{max}$	$0.5\,\Delta T_{max}$	$0.9\,\Delta T_{max}$
h=0.56, F_s=10.4×14.1	0.25	0.4	1.3
h=0.56, F_s=9.6×8	0.13	0.20	0.67
h=0.3, F_s=9.6×8	0.07	0.11	0.36

Conclusion

Use of diamond substrates in short-legged TE microcoolers resulted in near complete elimination of the undesirable superheating at the TEC hot side. A maximum temperature difference of 67K was demonstrated in TECs with TE legs 0.2mm long, a value approaching ΔT_{max} for commercial samples with TE leg length of 1mm and higher. Cold side heat flux densities over 60W/cm^2 can be reached by such coolers under maximum cooling power conditions. This makes them ideal to solve thermal issues related to high density localized heat sources, such as power electronic devices. Moreover, 50% shorter cool down time have been obtained in diamond-based coolers compared to alumina- or berilla-based coolers, because of shorter TE legs and lower substrate specific heat.

References

[1] Vladimir A. Semeniouk, Tatyana V. Pilipenko, Grant C. Albright, Leonid A. Ioffe, William H. Rolls, "Miniature Thermoelectric Coolers for Semiconductor Laser", Proc. of the XIIIth Int. Conf. on Thermoelectrics (ICT'94), Kansas City MO, USA, 1994, AIP Conf. Proc. 316 (1995) 150.

[2] Jan W. Vandersande, Richard Ewell, Jean-Pierre Fleurial and Hylan B. Lyon, "Thermoelectric Devices and Diamond Films for Temperature Control of High Density Electronic Circuits", Proc. of the XIIIth Int. Conf. on Thermoelectrics (ICT'94), Kansas City MO, USA, 1994, AIP Conf. Proc. 316 (1995) 174.

[3] Jan W. Vandersande and Jean-Pierre Fleurial, "Thermal Management of Power Electronics Using Thermoelectric Coolers", Proc. of the XVth Int. Conf. on Thermoelectrics (ICT'96), Pasadena, CA, USA, 1996, IEEE (1996) 252.

The Effectiveness of Water Vapor Sealing Agents When Used in Application with Thermoelectric Cooling Modules

Michael J. Nagy
TE Technology, Inc., 1590 Keane Drive, Traverse City, MI 49686
Tel: (616) 929-3966, FAX: (616) 929-4163, e-mail: cool@tetech.com

Abstract

The inherent reliability of thermoelectric modules (TEMs) can be destroyed when water vapor is allowed to condense within the device. This causes corrosion in the TEM and eventually leads to catastrophic failure. TEM manufacturers and users combat this problem by applying sealing agents to the perimeter of the devices. However, not all sealing agents are equally effective or even beneficial to long-term, reliable operation of the TEM.

This paper presents an analysis on the various sealing agents used through out the industry. Sealed TEMs were cooled in a high humidity environment and monitored for the visual evidence of water and it's associated weight gain.

A marked difference in the effectiveness of the various sealing agents was noted. Some sealing agents, such as the ubiquitous silicone rubber, yielded unacceptable sealing capability. That is, water vapor was shown to easily penetrate the silicone based "sealant" leaving trapped liquid water inside. In sharp contrast, the epoxy sealant was found to be essentially impervious to vapor penetration.

Introduction

Thermoelectric modules (TEMs) are used in medical, military and aerospace applications where reliability is of utmost importance. They can be made to operate for hundreds of thousands of hours when utilized properly. However, their inherent reliability can be destroyed when water vapor is allowed to condense within the device.

Condensation leads to corrosion within the TEM. Water mixes with residual acidic solder flux (used during the module's assembly) and creates an active electrolyte which can be highly corrosive. Solder junctions eventually degrade until the TEM is rendered useless and the cooling system has undergone catastrophic failure. These failures occur most rapidly when TEMs are operated continuously in a high humidity environment.

Engineers have combated this problem by applying sealing agents to the outer perimeter of the TEM between the substrates. Several classes of sealing agents are used throughout the industry. These include acrylics, epoxies, urethanes, and silicone rubbers.

Each sealant has different water vapor permeability characteristics. Consequently, their effectiveness also varies. Some sealing agents are permeable to water vapor, allowing moisture to enter a sealed TEM, yet they prohibit the condensed water from escaping. The use of such a sealing agent can actually be more detrimental than not sealing the device because the water can neither dry or drain out of the module. Conversely, other sealing agents are practically impervious to water vapor and can make otherwise unreliable products highly reliable.

This paper rates the effectiveness of four sealing agents by employing two different test methods. The visual test used specially made TEMs with transparent substrates (see Figure 1). The TEMs were sealed with the various sealing agents and cooled below dew point in a high-humidity environment. Visual inspection and comparison of moisture within the TEMs was facilitated through the transparent substrates. The crux of this method was that it allowed periodic inspection for internal condensation without physically destroying the TEM (separating one substrate from another).

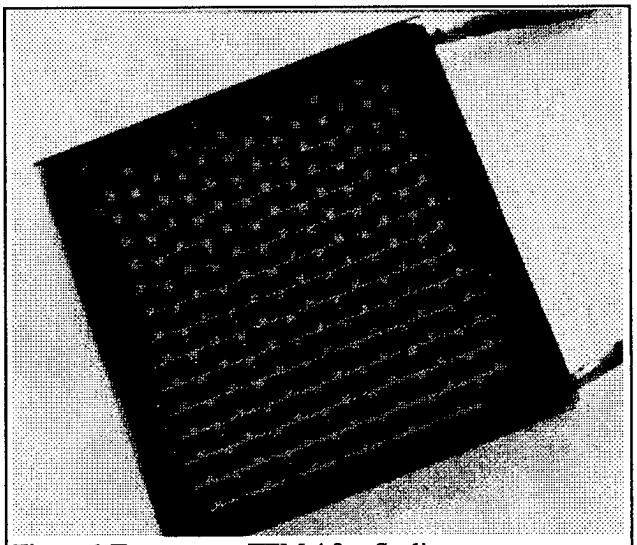


Figure 1 Transparent TEM After Sealing

The second test monitored moisture penetration by tracking the weight gain of a TEM. Standard TEMs were sealed with the various sealing agents. Next, they were cooled below dew point in a high-humidity environment. The TEMs were then periodically removed and weighed on a high resolution laboratory scale. The effectiveness of each sealing agent was determined by measuring the weight gained by each of the TEMs. This weight gain is directly correlated to the amount of water condensed within each TEM.

Selection of Sealants

The four classes of sealants chosen for this study were acrylics, epoxies, polyurethanes, and silicone rubbers. All classes are currently being used in the thermoelectric industry. One specific sealant was chosen to represent each class. The Dow Corning 738 silicone rubber and TE

0-7803-4057-4/97 $10.00 ©1997 IEEE

Technology 1034-01 epoxy were chosen because they are known to be used on existing products. 3M 606NF acrylic and Sikaflex 221 were recommended by a sealant distributor because they offered good adhesion characteristics, were relatively common, and were easy to work with. No vapor permeability data was available for any specific sealant in any of the classes.

Experimental Apparatus

The experimental apparatus consisted of a thermoelectrically cooled cold plate contained within a high humidity environment. The cold plate was a 19 mm thick aluminum base plate, approximately 150 x 200 mm in length and width, which provided an isothermal platform to cool the TEMs. Aluminum pedestals (40 mm square, 14 mm thick) were evenly spaced and bonded to the cold plate. All areas of the cold plate not covered by the pedestals were covered with insulation. Band clamps were then placed on the cold plate, strapping the TEMs against the pedestals. Figure 2 details this apparatus. The thermoelectric cold plate was driven by a power supply / temperature controller which maintained the temperature of the pedestals at 4 ± 1°C.

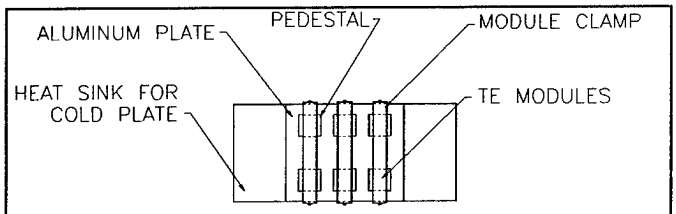


Figure 2 Thermoelectrically Cooled Cold Plate

The environmental chamber consisted of an enclosure with dimensions of 0.75 x 0.75 x 1.25 mm. A small humidifier was placed inside the chamber to elevate the relative humidity above 90%. The temperature within the chamber was 28 ± 2°C throughout the experiment. The entire experimental apparatus is depicted in Figure 3.

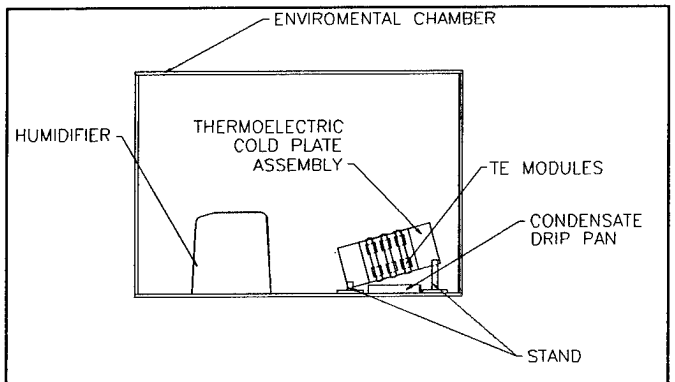


Figure 3 Complete Experimental Apparatus

Visual Test Method

The visual test for moisture penetration utilized four specially fabricated TEMs with transparent substrates. These substrates, made from highly polished, single-crystal aluminum oxide, allowed visual means for inspection of condensation within the TEM. An industry standard 40 x 40 mm, 127 couple device was chosen for these tests. Pellet geometry was 1.4 x 1.4 mm square by 1.6 mm tall. Separation between the substrates was 2.2 mm (the thickness of two conducting tabs plus the pellet height).

Each of the four TEMs were sealed with one of the commonly used sealing compounds (acrylic, epoxy, polyurethane, or silicone rubber). The sealant extended into the TEM approximately 3.0 mm between the pellets. The TEMs were clamped onto the cold plate and placed in the environmental chamber. Moisture within the TEMs condensed and dried the air trapped within the TEM. Thus, an absolute humidity differential was established across the potting compound which "pumped" water into the module via osmosis. The TEMs were then removed and inspected on a daily basis.

Weight Gain Test Method

The weight gain test method monitored the weight of a TEM as it was exposed to a humid environment.

This test for moisture penetration utilized four TEMs with standard pressed and sintered ceramic substrates. A 40 x 40 mm, 127 couple TEM was chosen for this test as in the previous test. Pellet geometry of the TEMs was 1.4 x 1.4 mm square by 1.5 mm tall. Separation between the substrates was 2.3 mm. Lead wires were not attached to the TEM.

Each of the four TEMs were sealed and subjected to the same high humidity environment as in the visual test. The TEMs were periodically removed, dried, and weighed on a laboratory scale with a resolution of 0.0001 grams. Weight gain was directly attributed to the penetration and collection of moisture within the TEM.

Results and Discussion

The results of the visual test method are compiled in Table 1. The TEMs sealed silicone rubber and acrylic sealants both showed condensation within 24 hours of exposure to the test environment. The TEM sealed with the polyurethane sealant underwent 72 hours of exposure before showing condensation within the TEM.

Table 1

Sealant Type	Exposure Time Before Condensation Detected
3M 606NF Acrylic	24 Hours
TET 1034-01 Epoxy	Data Not Meaningful
SIKAFLEX 221 Polyurethane	72 Hours
DOW 738 Silicone Rubber	24 Hours

Condensation also appeared inside the epoxy sealed TEM within 24 hours of exposure. This TEM, in fact, absorbed more water than any other in the initial 24 hours of testing. The data was judged not meaningful, however. Inspection of the TEMs before testing revealed that the epoxy would not properly bond to the highly polished substrates. Slight shrinkage of the epoxy upon curing, combined with this insufficient bond, yielded an air gap between the substrate and the sealing agent. Thus, the TEM was not adequately sealed and condensation fully expected.

The results of the weight gain test method are shown in Figure 4. Clearly, the epoxy sealant had the lowest weight

gain (zero, within the error of measurement). TEMs used in this test were made with pressed and sintered ceramic substrates. These substrates had a rougher surface texture and facilitated a proper bond with the epoxy sealant. Therefore, the epoxy was capable of sealing the TEM (unlike the visual test). The remainder of the weight gain results seemed to correlate with the visual test results. Silicone rubber and acrylic sealants gained the most weight; and the polyurethane sealant was considerably better but far from perfect.

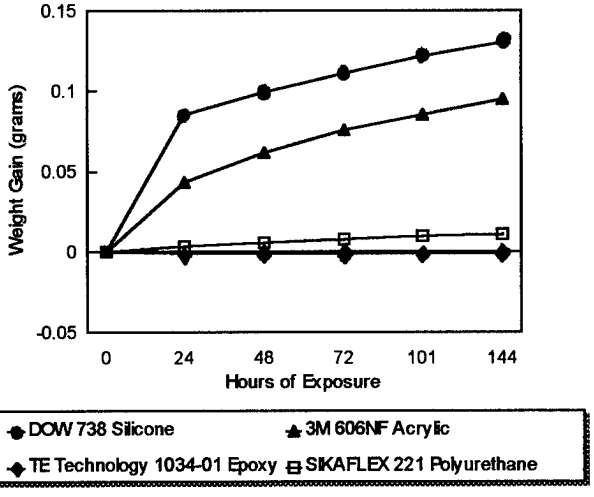


Figure 4 Weight Gain of Thermoelectric Modules

The results obtained in these tests are relative in nature. They do not yield TEM failure rates relative to the amount of internal condensation. One can only make the inference that failure rates will increase with increasing condensation levels.

Published data regarding the vapor transmission rates of the sealant classes is shown in Table 2[1] (data was unavailable for the specific sealants). This data supports the effectiveness as ranked by the testing. The published data also indicates that, while polyurethanes can have lower transmission rates than silicones, they can also have higher transmission rates. Epoxies, as a rule, have lower transmission rates than polyurethanes and silicones.

Table 2

PUBLISHED PERMEABILITY DATA	
Type	Vapor Transmission Rate $g \bullet mm/m^2 \bullet day$
Acrylic	Not Listed
Epoxy	0.7 - 0.94
Polyurethane	0.94 - 3.43
Silicone Rubber	1.73 - 3.11

Conclusion

Epoxy based materials should be used when sealing TEMs against water vapor. Acrylic, silicone rubber, and polyurethane based sealants proved inferior to epoxy in direct comparison testing. Published vapor transmission data for the various classes of sealants also indicates that epoxies are the most effective choice for TEM sealing.

Silicone rubber, the most commonly used sealant, proved to be the least effective of all the types tested. This sealant was very permeable to water vapor yet blocked condensed water from leaving the TEM. Using such a sealant would actually be detrimental and not beneficial for many applications.

References

[1] Permeability And Other Film Properties Of Plastics And Elastomers, Plastics Design Library, 1996

A Method of Diode Parallel to Improve the Reliability of the Thermoelectric Coolers

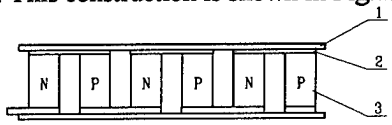
Zhang Jianzhong, Zhang Hua, Wang TieminChen Song , Ji Zhaonan
Tianjin Institute of Power Sources. Tianjin, P.O.BOX 296, 300381 P.R.CHINA
Tel: (86-022)23382851-6278, Fax:(86-022)23383783

Abstract

Thermoelectric Coolers (TECs) are a kind of very reliable solid-state devices which do not make any noise, harmful fluids or gases. TECs have been widely used in fields of industry, agriculture, science research and national defense. In pace with the increasing use, TECs' research on reliability is putting on the order of day. This paper introduces the method for reliability design, which is in parallel with diode. Thermoelectric cooling module is consist of some couples of thermoelements, connected in series by copper tabs. If a solder joint breaks, the thermoelectric cooling module fails. So redundancy can be used. The thermoelements is divided into some groups, and every group is parallel with a diode. If a thermoelement fails, the parallel diode conducts, so the thermoelectric cooling module continues operating. Thus the reliability is improved greatly. As a result of abundant calculation and series experiments, the failure rate of thermoelectric cooling module decrease by 40%, the electric current reduce by 4%, the cooling power cut down by 4%. The negative function is not obvious. The design method will satisfy high reliable demand of some circles.

Introduction

Thermoelectric cooling modules (TEMs) are Peltier effect based heat pumps, which are solid state devices without mechanical rotating parts. TEMs have long life times, operate noiselessly and release off no harmful substances. They can operate independently on the direction and the place of arrangement. For these advantages, TEMs are widely applied on industry, medical science, agriculture and communication. TEMs consist of several couples of thermoelement, electrically connected in series by copper tabs, thermally coupled with heat sinks on hot side and cold side by alumina ceramic. This construction is shown in Fig.1.



1 - ceramic
2 - copper tab
3 - thermoelement

Fig 1: The construction of TEM.

Now, TEMs are broadly used, especially in missile guidance, radar systems, communication etc. The reliability of the TEMs are required highly. So it is very important to improve the reliability of TEMs.

There are several methods for reliability design of TEMs, such as derating, redundant design, thermal design and waterproof techniques. When other methods are exhausted, and the reliability can not be satisfied yet, the redundant design, which is a method adding the number of parallel unit to arrange one or more substitute passage on a system, could be used.

Principle of reliability design

1 The Model of Reliability of TEM

Typically, thermoelectric cooling modules consist of several couples of thermoelement, connected in series by copper tabs. Every themoelement in TEMs includes two solder joints. When a solder joint breaks, the TEM fails. So the model of reliability of TEM is shown as Fig.2.

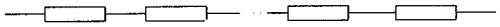


Fig 2: The reliability model of TEM.

The failure rate of TEMs can be regarded as the sum of failure rate of all solder joints. If λ is regarded as the mean failure rate of each solder joints, then we find out:

$$\lambda = 4n\lambda_i \qquad (1)$$

λ — the failure rate of TEM

n — the couple numbers of thermoelement

2 The principle of redundancy

Redundancy is an added device or method to complete a given function. Even if a part of system is out of order, the system can also work normally. Redundancy can increase the reliability of system greatly. Redundancy include system redundancy and element redundancy. The reliability of the latter is higher than the former. The latter can be used to increase the reliability of TEM.

Parallel redundancy is used widely. The main using range is to provide inconvertible protection against failure for a continuous running system. Because all thermoelement are in series, diode is in parallel with thermoelement to achieve parallel redundancy, as shown in Fig 3:

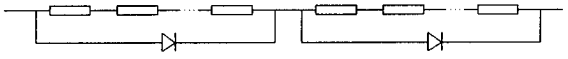


Fig 3: Parallel redundancty.

Thermoelements are divided into some groups, each of which

is in parallel with a diode. When TEM works normally, the voltage of every group thermoelements is lower than the conduction voltage of diode, so the diodes don't conduct. When a solder joint of any group fails, the voltage of diode exceeds the conduction voltage , the diode which is parallel to this group conducts, so other groups of thermoelement can also work normally. TEM can be on operation.

Mathematics model

1 General Mathematics Model of Redundancy

(1) serial system

$$\lambda = \lambda_1 + \cdots + \lambda_n \qquad (2)$$

n — the number of serial units

λ — the failure rate

(2) Parallel system with two units

$$\lambda = 1/MTBF \qquad (3)$$

$$MTBF = \frac{1}{\lambda_1} + \frac{1}{\lambda_2} - \frac{1}{\lambda_1 + \lambda_2} \qquad (4)$$

MTBF — the Mean Time Between Failure

(3) series/parallel mixed system

In mixed system, a independent parallel system, when regarded as a unit to combine with other unit, so supposed as a parallel system. For example, numbers of parallel system which include two units is in series connection:

$$\lambda = n \times \left(\frac{1}{\lambda_1} + \frac{1}{\lambda_2} - \frac{1}{\lambda_1 + \lambda_2} \right) \qquad (5)$$

2 Reliability of TEM:

The mean failure rate(λ_i) of each solder joint for TEMs which reported from Marlow Industries Inc. is 3×10^{-8}/h [2].

Such as TEC1-12703, n=127, when rated voltage is 12V, then

$\lambda = 4n\lambda_i = 1.524 \times 10^{-5}$/h (6)

If we increase two diodes on the TEM, then the structure is :

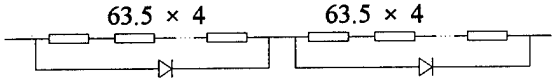


Fig 4: The structure with two diodes parallel.

From the table, appendix 2 'failure rate of diode' [3] , we have λ_0, the failure rate of diode, is 2×10^{-8}/h.

We can see from Fig.4 that the reliability model is series by two parallel branchs, and the failure rate of each parallel branch is:

$$\lambda_1 = 1/MTBF \qquad (7)$$

$$MTBF = \frac{1}{254\lambda_i} + \frac{1}{\lambda_0} - \frac{1}{254\lambda_i + \lambda_0} \qquad (8)$$

$$= 50000343.54h$$

$$\lambda_1 = 2.0 \times 10^{-8} / h \qquad (9)$$

So for the whole system, we have

$$\lambda = 2\lambda_1 = 4.0 \times 10^{-8} / h \qquad (10)$$

and so on, when the TEM is in parallel with four diodes, then

$$\lambda = 8.0 \times 10^{-8} / h \qquad (11)$$

when eight diodes is parallel

$$\lambda = 1.6 \times 10^{-7} / h \qquad (12)$$

The above calculation shown that eight diodes parallel redundancy decrease the failure rate by 10^{-2} times , and the reliability increase by a big margin.

The redundancy structure and its effect

1 Choose of the Reliability Structure

As a result of the calculation above, the number of the diode parallel takes effect on the reliability in equal degree. But it is different for the thermoelectric performance. If two diodes were in parallel, only half of the thermoelements of TEM would work when a solder joint failed. So the cooling power and the temperature difference is obvious decreased. The more diodes were in parallel, the less effect to performance from solder joint failing would be. But it's not absolute, when a TEM works normally, excessive parallel diode will affect the performance. So in TEM with 127 couples we use eight diodes, the thermoelements are divided into eight group, every two line is in parallel with a diode. Show as Fig.5. This structure reduces the diode's effect to the lowest.

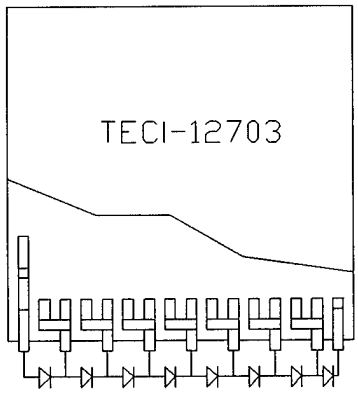


Fig 5: TEM with eight diodes.

2 Estimation of the Effect

From the above mentioned structure, diode parallel take effect on the performance. On the same working voltage, because diode have a little leakage of current, the working current of TEM is less than that of before.

$$\frac{\Delta T_m - \Delta T}{\Delta T_m} = \frac{(I - I_m)^2}{I_m^2} \qquad (13)$$

When current deviate 20% from normal value, the temperature difference deviate 4%.

$$Q_{cm} = K\Delta T_m\left(1 - \frac{\Delta T}{\Delta T_m}\right)$$
$$Q_c = K\Delta T_m\left(2i - i^2 - \frac{\Delta T}{\Delta T_m}\right) \qquad (14)$$

where $i = I/\ I_m$, when current deviate 20%, Qc deviate 4%.

From the calculation, parallel diode do not affect the performance obviously. Supposed a solder joint fails, one diode would conduct and replace a group of no working thermoelements, so it would not affect every working thermoelement, the TEM continues working. But, for 1/8 thermoelements are loss, the cooling power decrease 1/8, the temperature difference on the broken thermoelement is lower, others are not taken any effect. Because the substrate conduct heat, there is uniform in the surface of the temperature. But if two and more solder joints failed, the cooling power would decrease more than 1/4, then TEM could not work normally, the temperature difference would not satisfy the user's demand.

Experiment

We can demonstrate from experiment for the discussion above. We take one TEC1-12703, firstly we test the thermoelectric performance, then we divide the thermoelements into eight groups, every of which is in parallel with a diode, the structure is shown in Fig.6. Then we measure the thermoelectric performance once more.

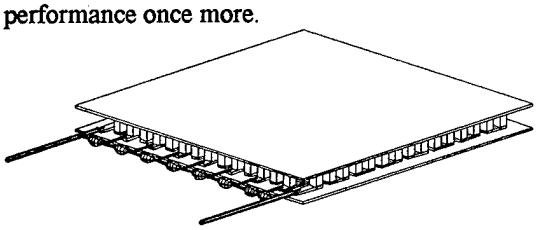


Fig 6: The TEM for experiment.

The result of experiment is shown in table 1.

	Voltage V	Current A	Qcmax W	Th ℃	Tc ℃
before soldering	5.0	1.21	18.9	30.0	-6.0
after soldering	5.0.	1.02	18.3	30.0	-5.4

Table 1: the performance parameter of TEM before and after soldering diode

From the table 1 we found that soldering of diodes take little effect on the thermoelectric performance.

Then, we break a center solder joint of TEM, measure the temperature difference and the cooling power. The result is shown in table 2.

	Voltage V	Current A	Qcm W	Th ℃	Tc ℃
before breaking	5.0	1.02	18.3	30.0	-5.4
after breaking	5.0	0.99	13.2	30.0	center 1.1 side 0.5

Table 2: the performance parameter of TEM before and after breaking the solder joint

From the table 2 we found the measure result consistent with the preceding calculation.

Conclusion

Discussion and experiment on the above has proved that the method of diode parallel increase the reliability of TEM. Soldering of diode takes little effect on the performance. In normal working the diode don't conduct. When a solder joint fails, the diode conduct, the TEM continue working. So the reliability is increased, high reliability demand in some application is satisfied. However, because the replace passageway is diode, it replaces a part of thermoelement, some cooling power and temperature difference would been lost. When more than two solder joints in different branch break, the TEM could not satisfy the user's demand yet. So other redundancy design could been required. Such as redundancy inside the TEM, change the arrange of thermoelements, use thermoelemants as replace passageway, so as to reduce the effect to lowest.

References

[1] Lu Zhongkun , The Theory and the Pagmatic Technology of Reliability Disign, Tianjiin Science and Technology press, Chinese, 1987.

[2] P.Click & R.Marlow, "Reliability and failure modes of thermoelectric heat pumps", Proc. 2nd International Conference on Thermoelectric Energy Conversion, Arlington, Texas, 1978.

[3] Mei Qizhi & Liao Jongsheng et., Reliability Engineering Basis of System, The science Press, Chinese, 1992.

THERMOELECTRIC COOLERS WITH VORTEX APPARATUS

G.A.Smolyar

Institute of Thermoelectricity, General Post-Office, Box 86, 274000, Chernivtsi, Ukraine
Tel:+380/3722/44422, Fax:+380/3722/41917, E-mail:Alex@ite.Chernovtsy.ua, WWW: http:\\www.ite.Chernovtsy.ua

Abstract

Results of thermodynamic characteristics of the combined cooling system consisting of a thermoelectric cooler and a jet cooler in the form of a vortex tube have been given. General relations for their description based on the exergetic method of thermodynamic system calculations have been obtained. Results supporting such devices efficiency have been presented. Experimental results of such system variations study have been given. Possibilities of their use in flying vehicles for electronic equipment cooling have been considered.

The essence of the problem

Solid state thermoelectric coolers (TEC) characterized by unique operating properties find wider application in developing of cooling devices and heat protective devices of various purposes starting from 50th.

In particular, it is known the achievements of specialized companies of thermoelectric instrument building in design of a number of thermoelectric modules for IR-detectors cooling; heat protection of semiconductor elements of units for information processing and laser radiators OKG; electric energy generation by thermogenerators (TEG) with different sources of thermal energy [1, 2, 3].

It should be noted that an elaborator of complex modern machinery could not always manage to solve optimization problems in designing of cooling devices based on TEC not solving at the same time problems of maximum allowable temperature (T_h) of its radiator (heat remover) ensuring. Energy consumption of TEC can be realized both as in quasi-stationary regime (a cooler of a standard IR-radiator, a module within TEC) and in intensive regimes with given cycling (thermal protection of OKG radiator).

The conducted analysis of technical solutions on the choice of a generator variant that enable to state TEC's heat remover temperature in the given operation regimes revealed the prospectiveness of vortex apparatus (VA) application that realized the Rank effect (1931).

Vortex apparatus (or usually called as vortex tube) consists of nozzle unit (a body with axial openings in the front wall and tangently located channel (channels) for compressed gas input and giving it an initial rotation); a chamber of energy interaction of axial and marginal gas flows; a unit for control of "cold" and "hot" gas flows relation that traditionally made in a cone form and padding with respect to the chamber end, and further a constrictor.

The compressed gas is carried to the nozzle unit, the cooled flow is removed through an axial opening, the hot one from the constrictor over its margin. In accordance to the hypothesis of eddy interaction [4] the eddy effect nature is explained by the energy redistribution between axially rotated gas flows characterized by a quasi-solid body rotation law (axial zone, "forced" eddy) and quasi-potential flow (marginal zone, "free" eddy).

Various problems predetermined the development and investigation of vortex apparatus special structures VA: dividing counterflow (DVA); cooled (CVA); self-vacuuming (SVA) ones. The indicated types of VA are used both as independently and as a part of staged, step circuit of connection. The listed basic variants of apparatus are characterized by simplicity, reliability of structure (no moving and rotating parts), normal operation in the wide range of media parameters change by pressure, temperature, moisture content. They are essentially differed by structures, thermodynamic characteristics and mode of heat delivery to a consumer (Fig.1, 2).

Thus, under the operation of CVA the relation of "cold" (G_c) and "hot" (G_h) flows (valuable for consumers) characterizes the apparatus work at the regimes of maximum temperature efficiency $\mu = G_c / (G_c + G_h) = 0.2 - 0.3$ and maximum energy efficiency $\mu = 0.7 - 0.9$. For instance, CVA with the nozzle sectional diameter of 20 mm (180 mm long) at the flow expansion degree $\pi = P_{in}/P_c = 3$ (where P_{in}, P_c is pressure of input and "cold" gas flows, respectively) at the regimes μ=0.2 and 0.8 provides the flux cooling for 39 and 18 K, respectively; $G_c = 0.01$ and 0.04 kg/sec.

The relative temperature of the CVA with the 24 mm in diameter "cold" flow ($\Theta_c = T_c / T_{in}$, where T_c and T_{in} are temperatures of "cold" and output gas flows for $\mu = 0.2 \ldots 0.8$ and $\pi = 1.05 \ldots 9.0$, is described by the dependence

$$\Theta^{24}_{\pi,\mu} = 1.02777704 - 0.06452358 \cdot \pi + 0.0033602791 \cdot \pi^2 + \\ + \mu \cdot \left(-0.02886561 + 0.047720934 \cdot \pi - 0.00210673 \cdot \pi^2\right)$$

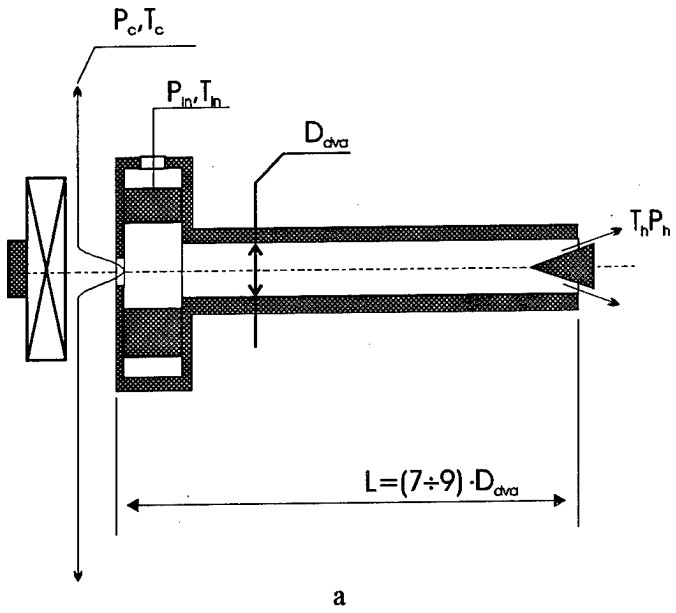
The inclusion of the scale factor at the CVA dimension reduction to d=8mm is recommended to make according to the dependence

$$\Theta_{\pi,\mu,d} = \Theta^{24}_{\pi,\mu} \cdot \left(1 + \left\{0.36 + \left(\pi - 4.2\right) \cdot 0.06\right\} \cdot \left(0.024 - d\right)\right),$$

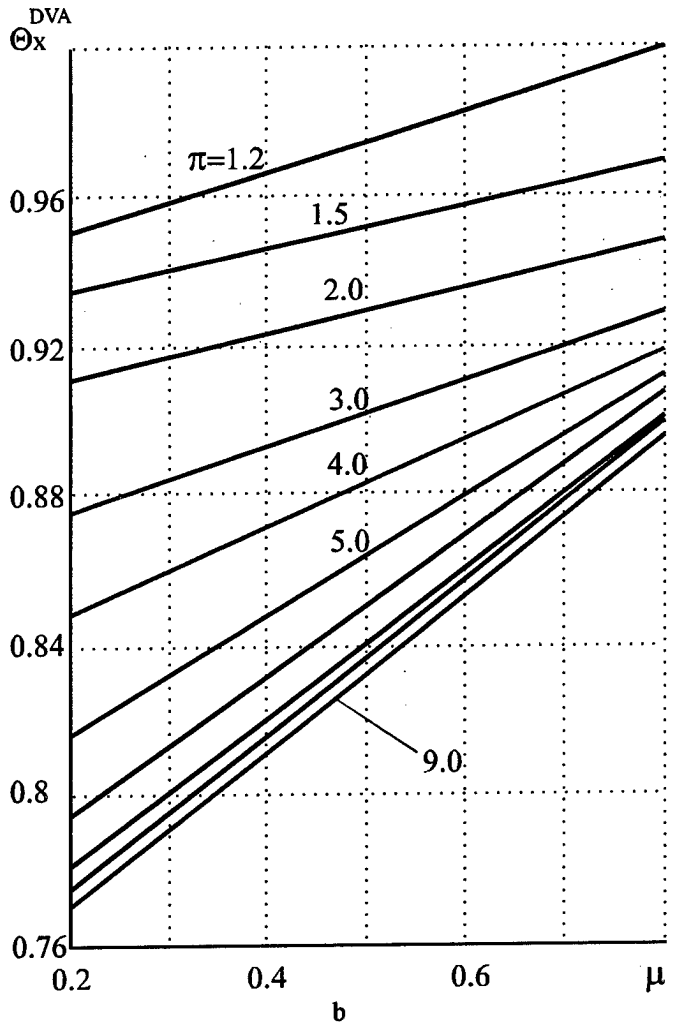
here d [m].

Cooled VA are made with flowing liquid heat exchangers placed on the forming chamber of energy interaction; cooled liquid input is performed near the nozzle unit, its disposal is at the constrictor. The effected in such structure additional intensive cooling allows to increase the apparatus figure of merit by a factor of 3-4.

Described VA structures allows to cool TEC radiator-heat exchanger from a distance to the temperature T_c that is

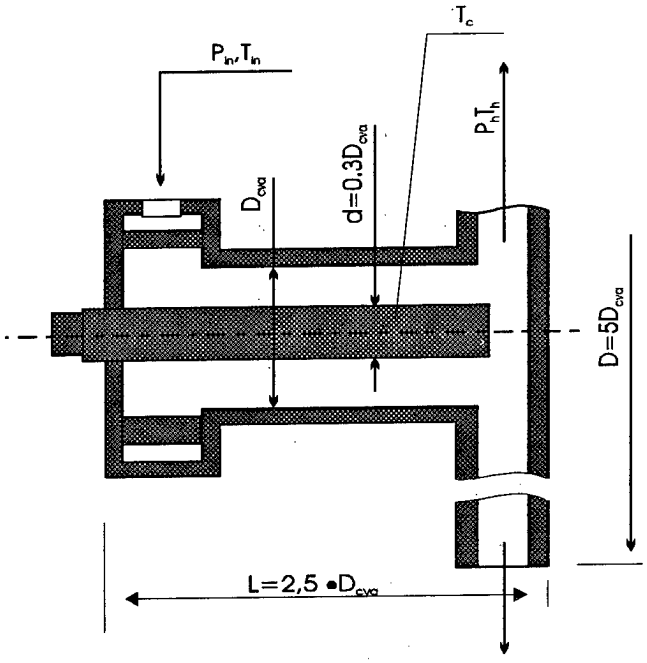


a

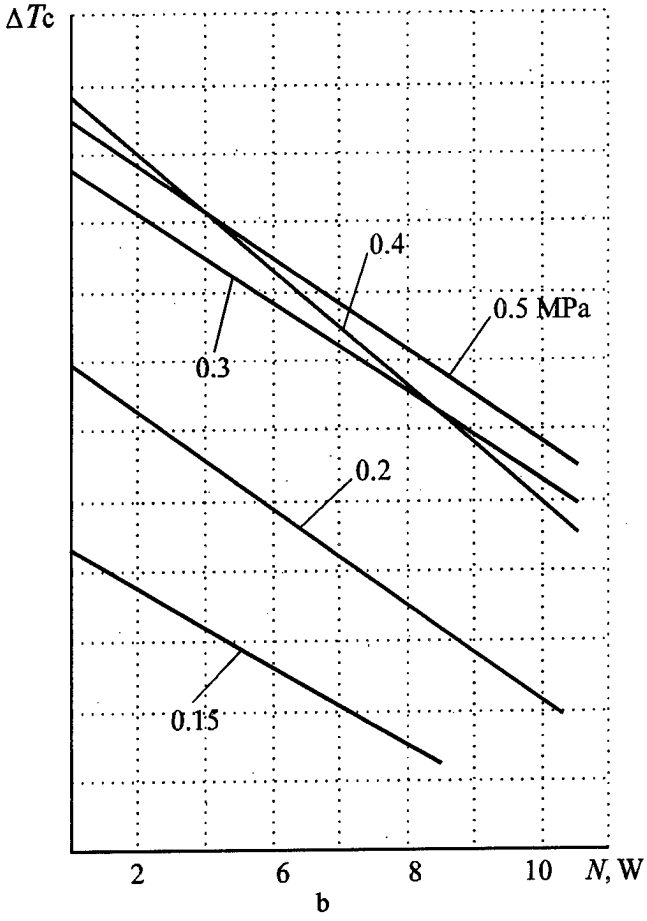


b

Fig.1. TEC with deviding vortex apparatus. Basic arrangement (a). Dependence of relative temperature of DVA cold flow on relative portion of the cold flow (b).



a



b

Fig.2. TEC with self-vacuumized vortex apparatus. Basic arrangement (a).Cylinder cooling effect dependence on additional heat load value supplied to the cylinder P_{in} =0.75÷0.5 MPa, T_{in} = 293K, $\Delta T_c = T_{in} - T_c$ (b).

very promising for a number of problems. S_0, according to [1] two -, three- and four-stage modules (Mj2063, Mj3021T and Mj4012, respectively) can be used when designing a combined cooler (TEC+VA) for the level T_c = 210K at the heat load on TEC Q_0 = 0.08 W (T_{oc} = 33K) depending on T_h=300 - 333 K. Cost of the indicated modules at a lot of 10-90 pieces is $140-490, respectively. Here the essential dimensions and electric power consumption increase with stage increase at T_{max} regimes should be taken into account. It was stated by the design investigations over the given dependences $\Theta_{\pi,\mu,d}$ that DVA with 10 mm in diameter at T_{in}=333K and π = 2.0 will make it possible to state T_h at the level of 300K. Cooling performance of DVA is 6.5 W and two stage TEC consumption at $\Delta T_{max} \approx$ 90K is 5.5W. Thus the stated problem solution is possible with the use of a two-stage TEC cooled by a 10 mm DVA; when thermostatting a TEC base at the level of 333K it is necessary to use a four-stage module (P_{TEC} = 7.5 W, cost - $490). For a number of devices characterized by a radical possibility of a radiator cylindrical heat sink placement in VA the promising may be the use of SVA. The distinctive feature of SVA from the previously described types is the insertion an open unwinded diffuser instead of an usual restrictor [5]. This provides the possibility of more full conversion of the kinetic energy of the entered into the "hot" zone of VA flow into the pressure energy. A sharp pressure decrease along the apparatus axis is occurred at the simultaneous improvement of the heat exchange conditions between axial and marginal vortexes, the cooling effect of axial elements in comparison with DVA is increased. The relative temperature of the axial cylinder dependence on its relative diameter for different values of the supplied additional electric energy is given in Fig.2. The calculated values of the "cylinder surface- gas" heat exchange coefficient are varied from 400 to 700 W/mK that is impossible in principle in low-pressure pneumatic systems. When inserting an axially symmetric cylinder of 10mm in diameter into SVT of 30 mm in diameter the effect of its cooling ΔT_{ef} for 68K at P_{in} = 0.2 MPa is observed. So to solve the previously given problem of IR-detector cooling a single stage TEC cooled by SVT will be sufficient.

The use of the indicated coolers containing TEC and VA is the most promising for mobile units (VA feed is the head of running air flow, built-in systems of pneumatic control, conditioning) and with the availability of pneumatic mains of waste gas.

The temperature efficiency coefficient ($\eta_T = \Delta T_x / \Delta T_s$) and adiabatic efficiency $\eta = \mu \cdot \Delta T_x / \Delta T_s$, where ΔT_x, ΔT_s are effect of the flow cooling (T_{in} - $T_c(c) = \Delta T_c$) and the cooling effect at isoentropic gas expansion with parameters (P_{in}, T_{in}) to the cooled flow pressure (of the cylinder) are used for performance evaluation of VA operation and for their comparison with other types of energy converters. According to data of [4] the level of η_T = 0.7; η = 0.32 has been reached; for SVT η_T reaches 0.83.

Thermodynamic perfection of the combined device containing TEC and VA must be evaluated on the base of the exergetical method because only exergetical efficiency (η_e) considers temperature levels of gas flows, ambient; fairly evaluates the converters perfection degree of different energy type [5]. The exergetic efficiency of the combined cooler is determined from the equality [6]:

$$\eta_e^{co} = \frac{E_{out} + E_{out}^{VA}}{E_{in}^{VA} + P_{TEC}} = \frac{P_{TEC} \cdot \eta_e^{TEC} + E_{in} \cdot \eta_e^{VA}}{E_{in} + P_{TEC}}, \qquad (1)$$

where $E_{out} = Q_0^{TEC} \cdot (T_{oc} - T_c) / T_c$ is the useful exergy of TEC.

$E_{out}=M_{in}^{VA} \cdot e_i$ - useful exergy of VA; M_{in}^{VA} is mass of a gas introduced in VA,

$$\eta_e^{TEC} = [Q_o^{TEC} \cdot (T_{oc} - T_c) / T_c] / P_{TEC}$$

is the exergic efficiency of TEC.

$$\eta_e^{VA} = \frac{\mu \cdot e_c + (1-\mu) \cdot e_h}{e_c}$$

is the exergic efficiency of VA;

$$e_i = C_P(T_i - T_{OC}) - T_{OC}\left(C_P \ln\frac{T_i}{T_{OC}} - R\ln\frac{P_i}{P_{OC}}\right),$$

where e_i is the specific exergy value of "cold" (e_c), "hot" (e_h) and introduces gas flows (e_s), C_p is gas heat capacity at constant pressure, R is an universal gas constant.

To determine the extremum of the value η_e^{co} it is necessary to have constraint equations between cooled gas flow temperature and TEC heat sink temperature; VA cooling performance and power value supplied to TEC (P_{TEC}).

The following inequalities must be fulfilled:

$$T_c^{VA} < K_T T_h, \qquad (2)$$

$$\frac{M_{in}^{VA} \mu C_p \Big|_{T_L^{VA}}^{T_{0C}} (T_{0C} - T_C)}{P_{TEC} + Q_{0C}} > 1, \qquad (3)$$

where K_T is the coefficient characterizing thermal resistance of heat bridge "VA-TEC".

Having the equations (1)-(3) and using VA, TEC structures calculation methods optimized over the required parameters (dimensions, temperature, cooling performance) determine the optimized construction (OC).

Value T_h connected by the equation (2) with T_c is the controlling factor when determine (η_e).

Varied parameters: to TEC - properties of TEC semiconductor materials, number of stages, limitations to thermobattery feed and dimension conditions; to VA - flow π expansion degree (min ... max); overall dimensions.

Under the failure of requirements (2), (3) by independent VA one should evaluate the use prospectiveness of two or more VA stage or step connections [7].

The evaluation of OC perfection as an integral part of a mobile unit (where fuel is combusted for set in motion), the necessity of η_e use is determined by the possibility of fuel consumption in the same analytical system for transportation

consideration, VA functioning: $\left(\eta_e^{OC}\right)^{mob} = E_f / E_{cons}$,. where E_f is exergetic cooling performance of OC, $E_{cons.} = M_{\Sigma}^{F} l_F$ is the fuel exergy consumed for transportation and functioning of OC, l_T is specific exergy of fuel combustion; $M\Sigma^T = M_1 + M_2 + M_3 + M_4$ is mass of additional take-off fuel storage consumed for compensation of aerodynamic drag of VA air vent (M_1); electric energy amount generation consumed by TEC (M_2); transportation of the positioning mass (M_3); transportation of variable mass (with supply system).

Results of comparison of the required conditions of IR-detector operation control (T_c = 210K, Q_0 = 0.08 W) made on the base of OC and/or cylinder restriction system (nitrogen, nitrogen-hydrocarbonic mixture as cryoagent; mass of cylinder systems is 15 and 9 kg respectively) confirm the essential advantage of OC:

by (η_e) by a factor of 12 - 7;

by cost by a factor of 10- 12.

Practical unlimited service life without maintenance-reconstruction works are provided in this case.

The given examples of thermoelectric coolers combination with vortex apparatus is the most easy in realization. Analysis of heat technological problems reveals the large reserves of VA and cooling systems on their basis use for thermoelectric energy converters operating conditions optimization, improvement of their competitiveness.

References

[1] Prospects of "Marlow Industries", 1991.

[2] Thermoelements and thermoelectric devices. Reference book, L.I.Anatychuk. Kiev; Naukova dumka, 1979, 768 p.

[3] Compact nuclear electric power sources. Lazorenko Y.V., Pustovalov A.A., Shapovalov V.P. M. Energoatomizdat, 1992, 208 p.

[4] Vortex apparatus. Suslov A.D., Ivanov S.V., Murashkin A.V., Chizhikov Y.V. M.: Mashinostroyenie, 1985, 256 p.

[5] Exergetic method of thermodynamic analysis. Brodyanskii V.M. M.: Energiya, 1973.

[6] G.A.Smolyar. On power system design on the basis of thermoelectric energy converters. J. of Thermoelectricity, 1996, N2, p.75-100.

[7] Merkulov A.P., Biryuk V.V., Smolyar G.A. Stage vortex independent cooling systems for vehicle elements. Izvestiya VUZov, ser. Aviazion.tekhnika, 1980, N3, p.69-73.1

Thermoelectric cooling devices based on bismuth telluride alloys: data of the patent documentation of the USSR and Russia

B.Sh.Malkovitch

Engineering & Production Firm "Cryotherm", 197348 St.Petersburg, Russia
Tel.: +7/812/394-1318, 394-5414, Fax: +7/812/394-1267, E-mail: cryotherm@infopro.spb.su

Abstract

The overview of the patent documents of the USSR and Russia over the period from October 1957 up to June 1997 in the field of the cooling thermoelectric devices based on bismuth telluride alloys is presented.

Introduction

Bismuth telluride alloys are the best materials for making of the cooling thermoelectric batteries nowadays. These materials were first prepared and investigated in the 50's after Professor A.F.Ioffe has shown the possibility of the practical use of the thermoelectric cooling based on the theory he has developed [1].
The thermoelectric cooling has found widespread application in various areas of engineering, medicine, everyday life [2,3]. Many aspects of the practical use and manufacture of the thermoelectric cooling units are embodied in the patent documentation.
We have analysed more than 600 published documents of the Patent File of the USSR (from 1993 - of Russia) in which the inventions in the scope of use of the thermoelectric cooling based on bismuth telluride alloys are described.
The first document concerned the elaboration of the most effective n-type thermoelectric material, based on bismuth telluride, was the author's certificate (a.c.) of the USSR N107420 issued to the collaborators of the Institute of Semiconductors of the Academy of Sciences of the USSR S.S.Sinani, G.V.Kokosh, G.N.Gordyakova, A.N.Shadrina and published in October 1957 (application pryority 6.07.1956). The authors of this invention elaborated the alloy Bi_2Te_3 - Bi_2Se_3 with a dopant such as halogenides, or copper, or silver.
Among documents found in the Patent File of the USSR the patent N1836755 (published 1993; the authors-owners of the patent V.G.Kopaev and I.K.Batrack) is the youngest in the field of the thermoelectric cooling. The patented knowledge proposed by the authors of this document relates to the technique of fabricating of the thermoelements. Further, from the N2000000, the patents of Russia follow. The patent N2005461 (published 15.01.1994) is the first patent of Russia within the range for consideration. The authors of this patent (V.N.Fedorov, V.V.Fedorov, and V.I.Jarich) elaborated the device for the thermal effect on the biological active points of the skin. The owners of this patent are the TOO "Cosmocrator" and Russian Research Institute of Cosmic Instrument- making.
According to the subject of invention the patent documents of the Patent File of the USSR and Russia relevant to the thermoelectric cooling devices based on bismuth telluride alloys may be classified under three groups: (1) technique of fabricating and design of the cooling thermoelectric batteries, (2) measuring of the characteristics of the cooling thermoelectric batteries, (3) devices utilized the cooling thermoelectric batteries.

Technique of fabricating of the cooling thermoelectric batteries

The author's certificates of this group are concerned with the following aspects of the cooling thermoelement fabricating technique: (1) preparing of the materials for the legs of the thermoelement, (2) the form of the thermoelement leg, (3) preparing of the planar thermal coupler (bridging and insulating elements), (4) thermoelectric battery design, including the design of the individual thermoelements and of the single stage and of the multistage thermobatteries, (5) assembly process of the thermobattery including the elaboration of the solders, fusing agents as well soldering conditions , the mechanization of assembly process including assembly jigs. In the Patent File of the USSR and Russia we found 75 patent documents which may be assigned to this group.
The technique of the thermoelectric battery (TEB) fabricating has been intensively elaborated in the 50-60's (30 a.c.). At this time there was elaborated the thermoelectric material for the negative leg of the thermoelement (a.c. N107420 noted above), there were suggested the solder and the nickel solderer for the thermoelement leg soldering (a.c. NN123030, 123315, 194528, 271273), there were found the methods of fabricating and design of the planar thermal coupler (a.c. NN199948, 240064, 267645), the methods to connect the legs of the thermoelement (a.c. NN123216, 131736, 199946, 274173), the method of optimization of the carrier concentration (a.c. N190448), there was proposed the form of the thermoelement legs to impart the flexibility to the TEB (a.c. NN104467, 114216), there was elaborated the design of the multistage cooler (a.c. N225285), it was designed a jig for thermoelectric modules (a.c. N199223), etc.
Only three organizations were indicated as applicants (see List of applicants: 1,2,7). It is important to note that up until December 1964 in the bibliographical part of the

0-7803-4057-4/97 $10.00 ©1997 IEEE

specification of the author's certificate the heading "Applicant" was not specified at all.
In the 70's developments within the range of technique of TEBs continued (22 a.c.). The attention of the elaborators predominantly focused (1) on increase in the mechanical strength by fabricating the legs by extrusion (a.c. NN320236, 534812), (2) on decrease a stress in TEBs by placing of the lead wafer between the bridging element and the leg of the thermoelement (a.c. N472402), (3) on decrease of the contact resistance either by deposition the Bi-Sb sublayer onto the thermoelement ends (a.c. N323823) or by plating with nickel (a.c. N361748), (4) on improvement of planar thermal couplers (a.c. N395674), (5) on protection of the TEB by its encapsulation by the polyethylene film (a.c. N313252), etc. In this time the developments of the jig design of the thermoelectric module fabricating (a.c. N546047), of the design of the multistage TEBs (a.c. NN342025, 444294, 514171, 556685, 693096), of the methods of the TEBs fabricating (a.c. NN669432, 690576) have been continued.
In this period besides organizations mentioned above another ones take an active part in patenting their inventions concerned the technique of cooling TEBs making (see List of applicants: 3,12,14). For instance, the TEB bridging element in the corrugated tape form with the flat apexs (a.c. N422059) and the method of making the diffusion-protective barrier (a.c. N361748) were elaborated in the organization indicated in the List of applicants: 3.
The two-stage TEB, in which the base stage thermoelements were placed on five sides of the cube and on the sixth side was placed the cold stage, was designed in the organization indicated in List of applicants:14. Spurious heat gains are absent here because the heat conductor is located internally (a.c. N444294). In TEB designed in organization indicated in List of applicants:12 the thermoelements pressed by their side surfaces to each other through the electroinsulation spacers were succesively displaced along the length (a.c. N514171).
In the 70's seven organizations were indicated as the applicants. Six of them are specified in the List of applicants: 1,2,3,12,14,17. It will be noted that in 70's the information about the development of the unified TEBs (so called "thermoelectric modules") in the USSR has been appeared. The characteristics of these TEBs are presented in the monography [3].
In the 80's the number of patent documents within the range of consideration rather decreased (19 a.c.). Nevertheless the development of the technique intensively continued in the direction of miniaturization (a.c. NN813540, 831878, 885558 etc.) and mechanization of the assembly process (a.c.NN918996, 927458, 1038985,1119931, 1454746, etc.).
In this period as the applicants there were indicated also seven organizations so as in the 70's. Three of them are certificated in the List of applicants: 1,12,13. Another ones are not included in the List because they are the applicants less than four inventions.
In the 90's the total number of the patent documents concerned the technique of TEB production sharply decreased. We were successful in finding only four patents within the range of consideration: patent of the USSR N1836755 (mentioned above) and patents of Russia NN2033583, 2075138, 2076286. The peculiarity of these patent documents is that the authors are the applicants and the owners of the invention at the same time.

Measuring of the characteristics of the cooling TEBs and their components

The thermoelectric efficiency is the most important property of the TEB. In the Patent File of the USSR and Russia we have found 25 relevant patent documents.
In the 50-60's the attention of the elaborators was concentrated on the estimation of the thermoelectric efficiency of the material or of the operating TEB by measuring of the resistance (a.c. NN171461, 230458, 243679), or by measuring of the thermal conductivity of the material (a.c.N186538), or by continuous recording of the temperature dependence of the material parameters (a.c.N196143).
A considerable body of patent documents in the field cited falls at 70's (13 a.c.). In this period there were elaborated the methods of measuring thermoEMF of the material (a.c.NN392386, 512145, 529400, 529401, 554576) and the thermoelectric efficiency of TEBs, particularly under the conditions of mass production of TEBs (a.c.NN319019, 527603, 694775). The design of the heat exchangers of the measuring devices have been devised also.
Relative to miniaturization of the TEBs and increase of the number of the thermoelements in the TEBs a necessity arised in express methods of determination of proper alternation of the legs during packing the thermoelements in jig under conditions of large-scale production of the TEBs. Thus, in a.c.N616599 the tracer was offered to identify the conductivity type - an aqueous solution of nitric acid copper.
The most active elaborator in the field of measuring was the organization specified in List of applicants:1 (5a.c.).
In the 80's the patent documents in the field cited (6 a.c.) predominantly concern the methods of TEB efficiency determination (5 a.c.). One document is referred to identification of the conductivity type by means of epoxy compound (a.c. N716009).
As regards the 90's, we found only two patent documents: a.c. N1597971 "The device for the thermal measurements of TEBs and thermoelement legs" (an applicant is not indicated) and a.c. N1787271 "The device for measuring the semiconductor material characteristics" (the applicant is specified in the List of applicants:4).

Devices utilized the cooling thermoelectric batteries.

During the period under review, from October 1957 to June 1997, in the Patent File of the USSR and Russia we found 529 patent documents in which the devices utilized the cooling TEBs are described. Among them 75 documents (14%) account for the 50-60's, 133(25%) - for the 70's, 229(43%) - for the 80's, and 92(18%) - for the 90's.

The following fields of the potential application of TEBs are indicated in patent documents: (1) thermostats (devices with constant temperature volume), (2) air-conditioning, (3) cooling of the electronic components of communications-electronics equipment and the radiation detectors, (4) food-stuffs cooling, (5) air dehumidification, (6) measuring of the humidity, (7) measuring of the liquids and gas flows, (8) ice making, (9) cooling of the medicaments and tissues, etc.

The distribution of the patent documents over the fields of application is following: the various use coolers including microminiature coolers - 136(25%), the air conditioners 64(12%), the thermostats - 59(11%), the medical and biological devices - 48(9%), dew-point hygrometers - 41(8%), ice-makers - 39(7.5%), temperature controllers - 37(7%), air dehumidifiers - 32(6%), other devices - 72.

There are 91 organizations indicated as the applicants of the inventions in the field cited. Among them 6 organizations are indicated as the applicants of more than 10 inventions, 6 - more than 4 inventions, 12 are indicated as applicants of 3 inventions, 17 - of 2 inventions, and 48 - as applicants of the only invention.

The organization indicated as applicant of the largest number of published inventions (57 a.c.) is the State Specialized Designer's Office of Thermal Instrument-making (formerly: The Specialized Designers' Office of Semiconductor Devices). The subject of inventions: thermostats (17 a.c.), coolers including ones for an automobile industry (9 a.c.), temperature controllers of TEB including the TEB operating under heating and cooling condition (8 a.c.), devices for the measurements of the thermo-physical properties (7 a.c.), air dehumidifiers (4 a.c.), ice-makers (3 a.c.), devices for biological and physical measurements (3 a.c.), the flow rate regulator (1 a.c.), the mean for a body transference (1 a.c.), etc. This organization is indicated also as the applicant of 13 published inventions concerning the technique of TEB fabricating and measuring of the TEB properties.

Odessa Technological Institute of a Refrigeration Industry is indicated as applicant of 23 published inventions. The subject of inventions: ice-makers (7 a.c.), portable automobile coolers (3 a.c.), domestic food-stuff refrigerators (2 a.c.), cascade refrigeration systems for medical use and for instrument-making (2 a.c.), cooler for the electronic components of communications-electronics equipment, thermostat, air-conditioner, gas dehumidifier, liquid stream cooler, device for the heat exchange intensification, power supply stabilizer, flow rate regulator and the device for testing of the stability of bottled off wine, cognac and similar drinks - one invention each. This institute is also indicated as applicant of four published inventions concerning the technique of TEB fabricating.

The Research and Experimental Institute of Electrical Equipment and Motor Devices is indicated as applicant of 23 published inventions. The subject of inventions: coolers for the motor transport (15 a.c.), air conditioners (4 a.c.), ice-makers (3 a.c.), electrostatic generator operating under high dust loading conditions (1 a.c.). This institute is also indicated as applicant of three published inventions concerning the technique of TEB fabricating.

Dagestan Polytechnical Institute is indicated as applicant of 18 published inventions. The subject of inventions: coolers (3 a.c.) and thermostat (1 a.c.) for the electronic components of communications-electronics equipment, cooling devices for medical uses (3 a.c.), the device for heat exchange intensification of TEB (3 a.c.), the dew-point hygrometers (2 a.c.), the air conditioner, the temperature controller, the device to make visible the ultrasound field, time-defining element of the infra-low frequency generator, the device to take the finger-prints, method of supervising heat supply - one invention each. This institute is also indicated as applicant of the published invention of the 90's, concerning the measuring of the semiconductor material properties.

The Engineering Thermal-Physics Institute of the Academy of Science of the Ukrainian SSR is indicated as the applicant of 17 published inventions. The subject of inventions: cooling devices (7 a.c.) including the optimization of cooling conditions, coolers of electron photomultipliers, cascade refrigeration systems, etc.; thermostats (7 a.c.) including thermostats for the objects with nonstationary heat generation, for testing of the communications-electronics equipment; conditioner for vehicles (1 a.c.) , device for medical use (1 a.c.).

Dnepropetrovsk Civil-Engineering Institute is indicated as applicant of 12 published inventions. The subject of inventions: driver's cab air-conditioning unit (11 a.c.), including cabins of the farm lorries, of the electric locomotives, of the coal-loading trucks; device for the controlled hypothermia treatment and correction of the human being functional state (1 a.c.).

Following is the List of 17 organizations indicated each as the applicant of four published inventions and even more.

1. The State Specialized Designers' Office of Thermal Instrument-making (70 a.c.).
2. Odessa Technological Institute of a Refrigeration Industry (27 a.c.).
3. The Research and Experimental Institute of Electrical Equipment and Motor Devices (26 a.c.).
4. Dagestan Polytechnical Institute (19 a.c.).
5. The Engineering Thermal-Physics Institute of the Academy of Science of the Ukrainian SSR (17 a.c.).
6. Dnepropetrovsk Civil-Engineering Institute (12 a.c.).
7. All-Union Research Institute of Power Sources (9 a.c.).
8. Specialized Designers' Office of the A.F.Ioffe Physico-Technical Institute (7 a.c.).
9. OKTB "Ukrtorgtekhnika" (6 a.c.).
10. Kiev Scientific and Production Association "Analytpribor" (5 a.c.).
11. Specialized Designers' Office "Tellur" with the Pilot Production of Physics Institute of the Academy of Science of the Azerbaijanian SSR (5 a.c.).
12. A.I.Gertsen Leningrad State Pedagogical Institute (5 a.c.).
13. Chernovtsi State University (5 a.c.).
14. All-Union Research Institute of a Refrigeration Industry (4 a.c.).

15. A.F.Ioffe Physico-Technical Institute (4 a.c.).
16. G.V.Plekhanov Moscow National Economy Institute (4 a.c.).
17. Riga wagon-building works (4 a.c.).

In Engineering & Production Firm "Cryotherm" the database "Thermoelectric cooling with the use of semiconductors based on bismuth telluride alloys" is produced. In every patent document of this database together with the traditional International Patent Classification codes the numbers of the later patent documents are indicated in which the involved one is referred to.

References

[1] A.F.Ioffe. Semiconductor thermoelements. Nauka, M.-L., 1956.
[2] E.A.Koienko. Thermoelectric cooling devices. Nauka, M.-L., 1967.
[3] L.I.Anatychuk. Thermoelements and thermoelectric arrangements. Naukova dumka, Kiev, 1979.

Modeling and Minimization of Intercascade Thermal Resistance in Multi-Stage Thermoelectric Cooler

Vladimir A. Semeniouk, Dmitri B. Bezverkhov

Odessa State Academy of Refrigeration, Thermion Company,
Phone/Fax: (0482) 638324, E-mail: semeniou@thermion.tenet.odessa.ua

Abstract

The problem of achieving highest temperature difference ΔT in cascade thermoelectric cooler (TEC) is solved with consideration of intercascade thermal resistance. The model of three-dimensional heat spread in substrates is considered. Existence of substrate optimum thickness corresponding to highest ΔT is established. It is shown that correct choice of substrate configuration permits to receive considerable increase in TEC efficiency. In particular, it concerns short-legged TECs having extremely high heat flux densities.

Introduction

Cascade thermoelectric coolers (TECs) are finding wide application in cooling electronic and electro-optic components. As a rule, these devices need rather low operating temperatures in combination with acceptably small power consumption. So in most applications cascade TECs operate near physical limit of their possibilities. In this connection, the reduction of irreversible losses in these devices is the problem of great importance.

Electrical contact resistance and heat gains from environment are regarded traditionally as the main undesirable factors which greatly affect TEC efficiency. As to intercascade thermal resistance, it is being usually neglected or rough approximations are used for want of something better. Meanwhile, the losses at intercascade thermal resistance can predominate over other kinds of losses. In particular, it concerns short-legged TECs having extremely high heat flux density.

This paper presents solution of a problem of cascade TEC maximum efficiency with consideration of thermal resistance at cascade boundaries. Model of three-dimensional heat spread in substrate is considered. Substrate dimensions which provide minimal thermal resistance are find at this basis.

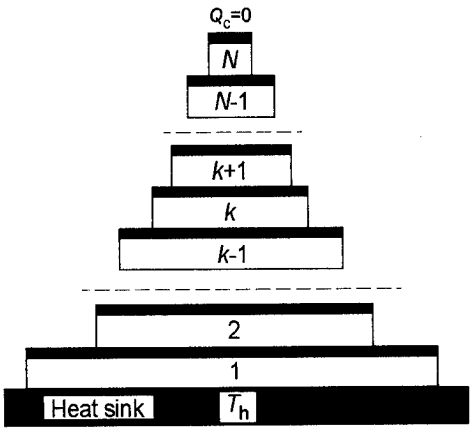


Figure 1: Scheme of N-cascade TEC.

Interconnection of temperatures and heat fluxes

Let us consider a model of N-cascade TEC in no-load operation. The TEC (Fig.1) is adjusted to a heat sink having fixed temperature T_h. Outer surfaces of the cooler are insulated adiabatically. Heat conducting substrates in a form of rectangular plates are mounted between cascades. All cascades have series connection. The typical situation when TE legs of all cascades have identical dimensions and the same packing density is under consideration. Together with condition of successive connection this gives the same electrical current density in all TE legs. Besides, the sidelong heat conductance in cascades is supposed to be absent because their discrete structure, so the temperature distribution in TE leg is one-dimensional.

Under the assumptions made, the distribution of the temperatures and heat fluxes at cascades boundaries is defined by the system:

$$
\begin{aligned}
q_0^{(k)} &= \alpha i T_0^{(k)} - \frac{1}{2} i^2 \rho l - \frac{\kappa}{l}\left(T_1^{(k)} - T_0^{(k)}\right), \quad k = 1,\ldots,N \\
q_1^{(k)} &= \alpha i T_1^{(k)} + \frac{1}{2} i^2 \rho l - \frac{\kappa}{l}\left(T_1^{(k)} - T_0^{(k)}\right), \quad k = 2,\ldots,N \\
F_k q_1^{(k)} &= F_{k-1} q_0^{(k-1)}, \qquad k = 2,\ldots,N \\
T_1^{(k)} &= T_0^{(k-1)} + R_{tk} F_k q_1^{(k)}, \qquad k = 2,\ldots,N \\
q_0^{(N)} &= 0, \qquad T_1^{(1)} = T_h
\end{aligned}
\tag{1}
$$

where α, κ, ρ are the Seebeck coefficient, thermal conductivity and electrical resistivity of TE material, l is TE leg length, i is electric current density, $q_0^{(k)}$, $q_1^{(k)}$ and $T_0^{(k)}$, $T_1^{(k)}$ are mean integral heat flux densities and mean integral temperatures at the cold and hot sides of kth cascade, F_k is the total junction area of kth cascade, R_{tk} is thermal resistance of kth substrate.

System (1) includes $4N$-1 equations linear as regards to unknown temperatures $T_0^{(k)}$, k=1,...,N, $T_1^{(k)}$, k=2,...,N, and heat flux densities $q_0^{(k)}$, k=1,...,N-1, $q_1^{(k)}$, k=2,...,N. For each set of initial parameters F_k, R_{tk}, α, κ, ρ, l and i, the system has unique solution and the cold side temperature takes certain value $T_0^{(N)}=T_c$. The change of the current density i, the rest parameters being the same, gives new T_c value. The problem is to find such i value which provides minimum T_c.

To solve this problem one must learn how to define thermal resistance of the substrate. The peculiarity and complexity of the problem in question is in the fact that one has three-dimensional temperature distribution in substrate which depends on substrate configuration as well as on distribution of temperatures and heat fluxes at its surfaces.

0-7803-4057-4/97 $10.00 ©1997 IEEE

Model of intercascade substrate

Model of kth substrate mounted between kth and (k-1)th cascades is shown at Fig.2. Z axes is directed in heat sink, the origin of coordinates for each substrate being adjusted to its top side.

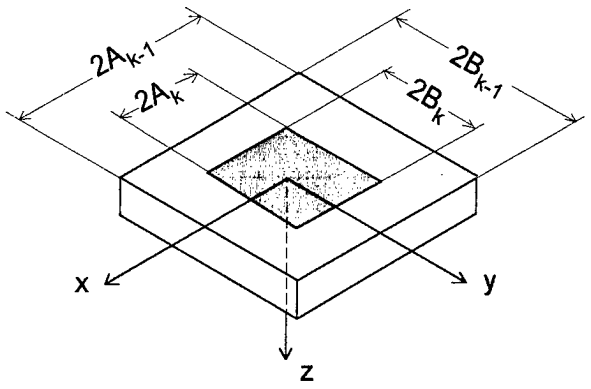


Figure 2: Scheme of intercascade substrate.

External heat flux $Q_k=q_1^{(k)}F_k$ from kth cascade enters into substrate through rectangular area $F_{sk}=2A_k x 2B_k$ at the center of its top surface and removes through the all surface of its bottom. The rest substrate surface is insulated adiabatically. This gives boundary conditions as following:

$$\frac{\partial T^{(k)}\left(|A_{k-1}|,y,z\right)}{\partial x}=0,\quad \frac{\partial T^{(k)}\left(x,|B_{k-1}|,z\right)}{\partial y}=0, \tag{2}$$

$$\frac{\partial T^{(k)}(x,y,0)}{\partial z}=\begin{cases}-\dfrac{q_{ek}(x,y)}{\kappa_s}, & |x|\le A_k,\ |y|\le B_k\\ 0, & A_k<|x|<A_{k-1},\ B_k<|y|<B_{k-1}\end{cases} \tag{3}$$

$$\frac{\partial T^{(k)}\left(x,y,h^{(k)}\right)}{\partial z}=-\frac{q_{ek-1}(x,y)}{\kappa_s} \tag{4}$$

$$k=2,\ldots,N-1$$

where q_{ek} and q_{ek-1} are external heat flux densities from kth and (k-1)th cascades:

$$q_{ek}=\beta\left[\alpha i T^{(k)}(x,y,0)+\frac{1}{2}i^2\rho l-\right.$$
$$\left.-\frac{\kappa}{l}\left(T^{(k)}(x,y,0)-T^{(k+1)}(x,y,h_{k+1})\right)\right] \tag{5}$$
$$q_{ek-1}=\beta\left[\alpha i T^{(k)}(x,y,h_k)-\frac{1}{2}i^2\rho l-\right.$$
$$\left.-\frac{\kappa}{l}\left(T^{(k-1)}(x,y,0)-T^{(k)}(x,y,h_k)\right)\right]$$

h is substrate thickness, k_s is substrate thermal conductivity, $\beta=F_k/F_{sk}$ is TE leg packing density.

Thus, the temperature distribution within substrate and at its surfaces is defined by Laplase's equation with linear boundary conditions (2)-(4). Solution of this problem makes it possible to find thermal resistance of intercascade substrate which is defined as follows:

$$R_{tk}=\frac{T_1^{(k)}-T_0^{(k-1)}}{Q_k} \tag{6}$$

where

$$T_1^{(k)}=\frac{1}{F_{sk}}\int_{F_{sk}}T^{(k)}(x,y,0)dxdy$$
$$T_0^{(k-1)}=\frac{1}{F_{sk-1}}\int_{F_{sk-1}}T^{(k)}(x,y,h_k)dxdy \tag{7}$$

As to TEC cold side substrate its temperature is regarded as to be uniform $T_0^{(N)}=T_c$ due to adiabatic insulation.

Solution for 2-stage cooler

For 2-stage cooler which includes only one intercascade substrate the k index at T, h and R_t can be removed. The boundary conditions (3),(4) reduce to the form:

$$\frac{\partial T(x,y,0)}{\partial z}=\begin{cases}-\dfrac{q_{e2}}{\kappa_s}, & |x|\le A_2,\quad |y|\le B_2\\ 0, & A_2<|x|<A_1,\ B_2<|y|<B_1\end{cases} \tag{8}$$
$$\frac{\partial T(x,y,h)}{\partial z}+g_1T(x,y,h)=g_2$$

where

$$g_1=\frac{\beta}{\kappa_s}\left(\alpha i+\frac{\kappa}{l}\right),\quad g_2=\frac{\beta}{\kappa_s}\left(\frac{1}{2}i^2\rho l+\frac{\kappa}{l}T_h\right) \tag{9}$$

It have to be noticed that in no-load operation heat flux $q_{e2}(x,y)$ is formed mainly at the expense of Joule heat which is spread uniformly in TE legs of upper cascade. Thus, the coordinate dependence of variable $q_{e2}(x,y)$ can be neglected, this being replaced by the equality $q_{e2}=\beta q_1^{(2)}$=const.

Solution of Laplase's equation for the temperature $T(x,y,z)$ within substrate with specified boundary conditions (8),(9) as well as the formula for substrate thermal resistance are given in Appendix.

Calculation results and discussion

Solution obtained was used for calculation of temperature distribution at substrate outer surfaces as well as for evaluation of its thermal resistance. All calculations are made using following data: T_h=303K, $\alpha=205\cdot10^{-6}$V/K, $\rho=10^{-3}\Omega\cdot$cm, κ=0.015W/cm/K, , TE leg cross-section is 0.6x0.6mm^2, β=0.36, κ_s=0.25W/cm/K (alumina substrate). Calculation results are represented at Fig. 3-6.

Fig.3 shows temperature distribution at substrate external surfaces along x axis for different h values. The ΔT_{max} operation is under consideration.

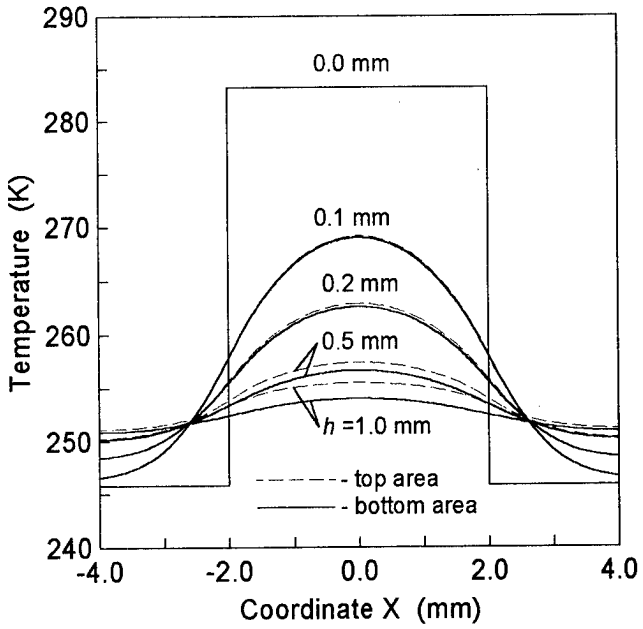


Figure 3: Temperature distribution along x axes for different substrate thickness. F_{s1}=8x8 mm^2, F_{s2}=4x4 mm^2, l=1 mm.

It is seen that for small h values (up to h=1mm) temperature drop along z axis is negligibly small. Much greater temperature non-uniformity is observed in substrate plane. Even for h value of 0.5mm which is typical for miniature cascade TECs temperature difference between substrate center and its periphery reaches 7K. Some more superheat (about 15K) arises at h=0.2mm. When $h\rightarrow 0$ sidelong heat spread vanishes and cascade cooler degenerates in a system of two insulated from each other one-stage batteries (the central cooler and peripheral one). The increase in h value leads to opposite result. Heat spread improves greatly but thermal resistance of substrate central part is rising. Thus the optimal substrate thickness h_{opt} must exist which provides minimal R_t and maximum ΔT values.

This thesis is confirmed by calculations represented at Fig.4. The difference of mean integral temperatures at the substrate outer surfaces ΔT_s as well as ΔT_{max} values are shown at this Figure as a function of substrate thickness.

For the cooler under consideration the h_{opt} value is about 1mm. It is seen that deviation to the greater h values has insignificant influence at TEC performance. On the contrary, deviation to lower h values results in great reduction in ΔT_{max} because of significant increase in substrate thermal resistance. The h value of 0.3mm is such a limit which being crossed the catastrophic reduction of ΔT_{max} is observed.

It is seen also from Fig.4 that the influence of substrate thermal resistance becomes especially significant for short-legged TECs. For l=0.5mm the minimal superheat at substrate surfaces is of 6K and this leads to reduction in ΔT_{max} about 4K as compared to idealized TEC with κ_s=∞. Further l reduction can result in ΔT_{max} loss up to 10K.

It is of great interest to compare the losses connected with substrate thermal resistance R_t and electrical contact resistance R_c. Fig.5 shows the dependence of ΔT_{max} on l value. Two variants are considered, each assumes only one kind of losses. Actual R_c and κ_s values are taken into account.

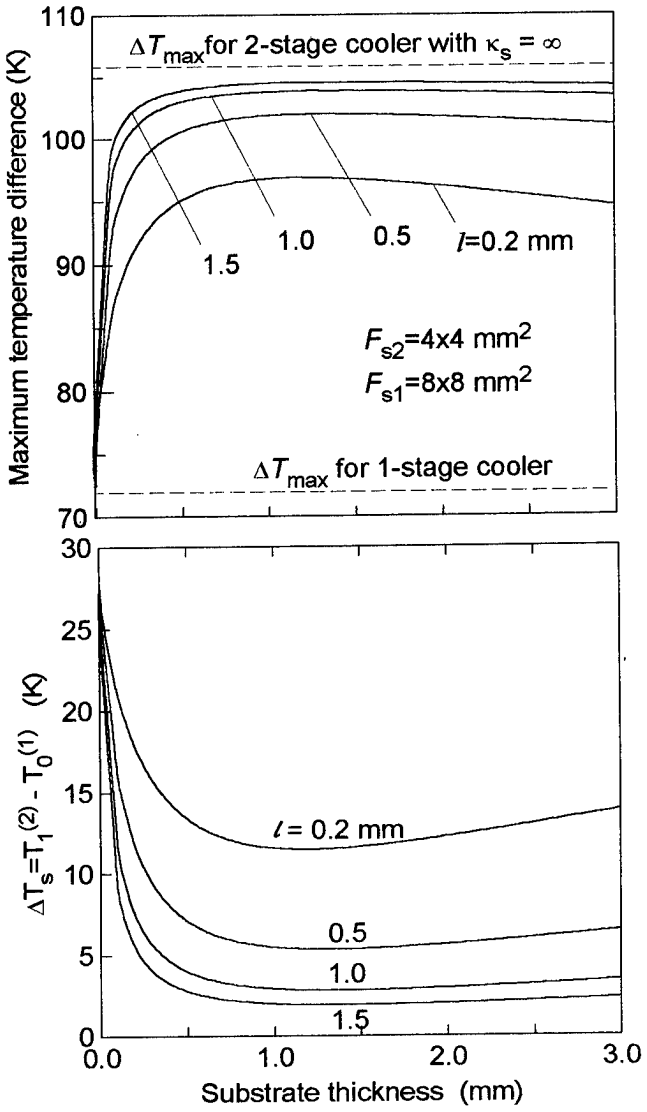


Figure 4: Dependence of mean integral temperatures difference at the substrate surfaces on substrate thickness.

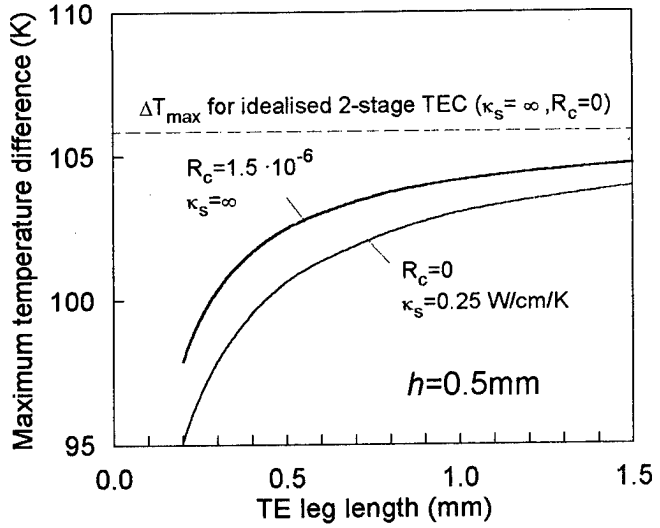


Figure 5: Comparison of influence of intercascade thermal resistance and electrical contact resistance on TEC efficiency. F_{s1}=8x8 mm^2, F_{s2}=4x4 mm^2.

It is seen that for h=0.5mm the losses at alumina substrate predominate over ones connected with electrical contact resistance.

It is worth to be noted that above-mentioned results and conclusions relate to rather small TEC with F_{s1}=64mm^2 and F_{s2}=16mm^2. For larger coolers the h_{opt} value increases and the losses are rising greatly (Fig.6).

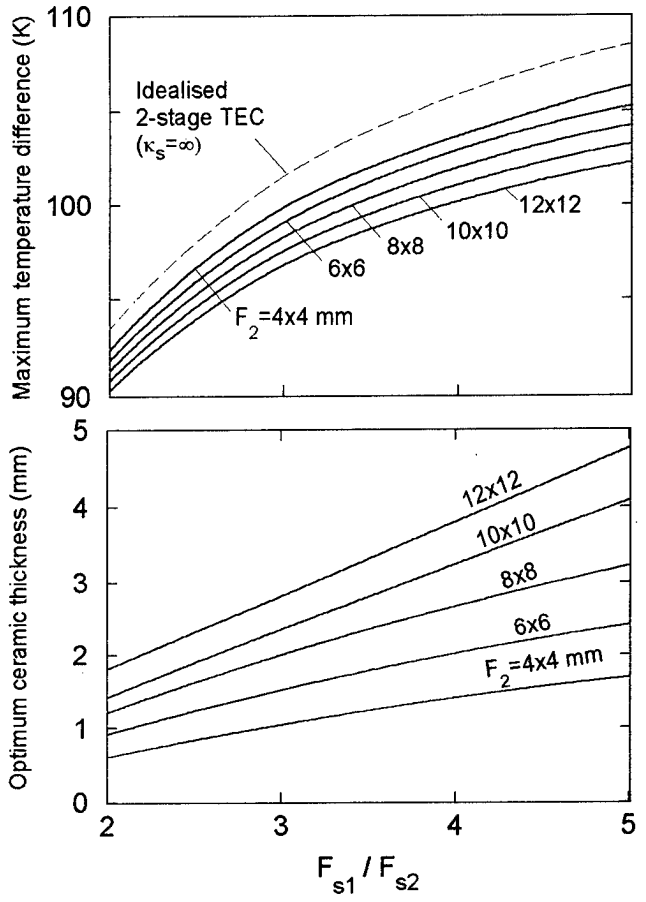


Figure 6: Dependence of maximum temperature difference and optimum ceramic thickness on TEC dimensions. l=1mm.

For TE coolers with top cascade dimensions of 10x10mm^2 the optimal substrate thickness is in the region of 2 to 4mm and losses in ΔT_{max} can rise up to 6K.

As to the TECs with three and more cascades the solution of the problem is much more complicated. But some estimations shows that irreversible losses due to substrate thermal resistance are essentially higher in these devices as compared to 2-stage ones.

It must be noted in conclusion that h_{opt} value is independent of substrate heat conductivity, but its thermal resistance reduces with κ_s value in reverse proportion. Thus high thermal conductivity substrates such as beryllia or aluminum nitride ceramic are desirable for the TECs with increased dimensions.

Conclusion

Existence of substrate optimum thickness corresponding to highest temperature difference ΔT_{max} in cascade cooler is established. It is shown that even significant increase of substrate thickness as compared to optimum one has small affect on ΔT_{max} value, and vice versa, shift to smaller thickness is extremely undesirable as resulting in considerable losses.

For miniature TECs with bottom cascade surface of 8x8mm^2 the optimal thickness of alumina substrate is about 1 mm. This have to be enlarged up to 3 mm in cascade TECs with F_1=20x20mm^2 when the F_1/F_2 ratio is 4 and more.

For alumina ceramic the losses in ΔT_{max} due to intercascade thermal resistance are essentially higher than the losses connected with electrical contact resistance.

Correct choice of substrate material and configuration can result in considerable improvement in cascade TEC efficiency.

Appendix

Solution of Laplase's equation for temperature distribution within intercascade substrate for 2-stage TEC has the form:

$$T(x,y,z) = \frac{g_2}{g_1} + \frac{4q_{e2}}{\kappa_s}\sum_{m=0}^{\infty}\sum_{n=0}^{\infty}(-1)^{m+n}\sigma_{\lambda\mu}\sin(\lambda A_2)\times$$

$$\times\frac{\cos(\lambda(x+A_1))}{\lambda}\frac{\sin(\mu B_2)\cos(\mu(y+B_1))}{\mu}G(\alpha,h,z)$$

where

$$G(\alpha,h,z) = \frac{g_1\sinh(\alpha(h-z)) + \alpha\cosh(\alpha(h-z))}{g_1\cosh(\alpha h) + \alpha\sinh(\alpha h)}$$

$$\sigma_{\lambda\mu} = \begin{cases} 1/F_{s1} & m = n = 0 \\ 2/F_{s1} & mn = 0 \\ 4/F_{s1} & mn > 0 \end{cases}$$

$$\lambda = \frac{n\pi}{A_1},\quad \mu = \frac{m\pi}{B_1},\quad \alpha^2 = \lambda^2 + \mu^2$$

Substrate thermal resistance is as follows:

$$R_t = \frac{h}{\kappa_s F_{s1}}\Phi$$

where

$$\Phi = 1 + 2S_1 + 2S2 + 4S_3$$

$$S_1 = \sum_{n=1}^{\infty}\left(\frac{\sin(\lambda A_2)}{\lambda A_2}\right)^2\frac{R(\lambda h)}{\lambda h}$$

$$S_2 = \sum_{m=1}^{\infty}\left(\frac{\sin(\mu B_2)}{\mu B_2}\right)^2\frac{R(\mu h)}{\mu h}$$

$$S_3 = \sum_{n=1}^{\infty}\left(\frac{\sin(\lambda A_2)}{\lambda A_2}\right)^2\sum_{m=1}^{\infty}\left(\frac{\sin(\mu B_2)}{\mu B_2}\right)^2\frac{R(\alpha h)}{\alpha h}$$

$$R(\nu h) = \frac{g_1\sinh(\nu h) + \nu\cosh(\nu h)}{g_1\cosh(\nu h) + \nu\sinh(\nu h)}$$

Thermoelectric Cascade for Cryosurgical Destroyer

Tomasz Wartanowicz [1], Aleksander Czarnecki [2]
[1]Institute of Heat Engineering, University of Technology
Nowowiejska 25, 00-665 Warsaw, Poland
[2]Foundation of Applied Physics
Nowickiego 7/22, 02-105 Warsaw, P.O.Box 40, Poland

Abstract

The paper is a continuation of our investigations on a thermoelectric cooling system for medical applications in the cryosurgical destroyers. It concerns experimental analysis of a three-stage thermoelectric cascade based on the Melcor modules. The experimental works have been conducted for two working conditions: first - maximum temperature difference ΔT_{max} and the second - maximum cooling capacity Q_{0max}. The best obtained results are as follows:

- maximum temperature difference ΔT=115.5K for supplying current I=3.1A,
- maximum cooling capacity Q_0=8.05W for supplying current I=2,8A.

Moreover the results have been applied to verify the method of numerical optimization of thermoelectric multistage systems elaborated in the frame of our previous research works [1,2]. That verification is in good compliance with the experimental results.

The experiments have confirmed that the temperature of the cold side of the cascade can reach the level of 200K (-73^{0}C) while the cooling capacity at the same time equals Q_0=1W.

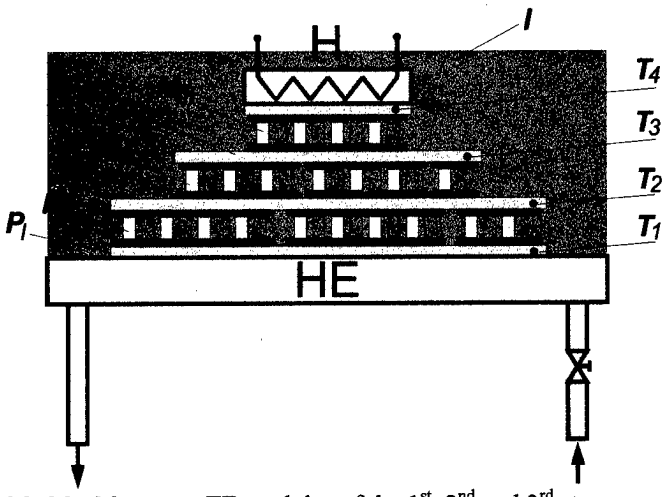
Introduction

For many years we have been working on low-temperature „cold sources" for cryosurgical destroyers [1,2] in the aspect of achieving the lowest possible temperatures for required cooling capacity. It should be underlined that one of the most important constructional constraint is the weight as well as dimensions of the cascade.

The experimental model

A three-stage experimental model have been constructed according to the elaborated by the authors optimization method of multistage thermoelectric systems [3]. In the cascade the Melcor modules have been tested with the same geometry and the same maximum current, in the considered case 3,9A.

Modules and stages have been connected between themselves in series with the double circuit electrical connection what eliminates „heat bridges". The scheme of the tested cascade is shown in fig.1. The cascade is placed in a vacuum chamber and additionally it is prevented against radiation losses. On the cold side of the cascade an electrical heater simulates the heat flux to the cascade i.e. cooling capacity. The hot side is in thermal contact with a liquid heat exchanger which allows to keep the constant temperature on that side.



M_I, M_{II}, M_{III}	- TE modules of the 1st, 2nd and 3rd stages,
T_2, T_3, T_4	- thermocouples of the cold sides of the 1st, 2nd and 3rd stages respectively,
T_1	- thermocouple of the hot side,
I	- vacuum chamber and insulation,
HE	- liquid heat exchanger,
H	- electrical heater,
P_I, P_{II}, P_{III}	- inter-stage spacer blocks,

Fig.1. Tested cascade

Results

The investigations have been carried out for two regimes of working conditions:

- maximum temperature difference - fig.2 and
- maximum cooling capacity - fig.3.

Fig.2. illustrates the dependence of temperature difference ΔT between cold and hot side of the cascade as a function of supplying current for given cooling capacity and for temperature on the hot side T_h=300K. Four values of the cooling capacity have been chosen for tests: 0,1,2,5 W. The temperature difference tends to increase along with the current and achieves its maximum value in the current range from 2.6 to 3.1 A. Further current increase causes decreasing tendency in ΔT. The maximum value of ΔT=115,5K was obtained for I=3.1 A and obviously for Q_0=0 W.

Fig.3 presents the cooling capacity as a function dependent on supplying current for a given temperature difference. During increase the supplying current the cooling capacity getting higher till its maximum value in the range between 2,75 - 3,0A than significantly decreases. Maximum

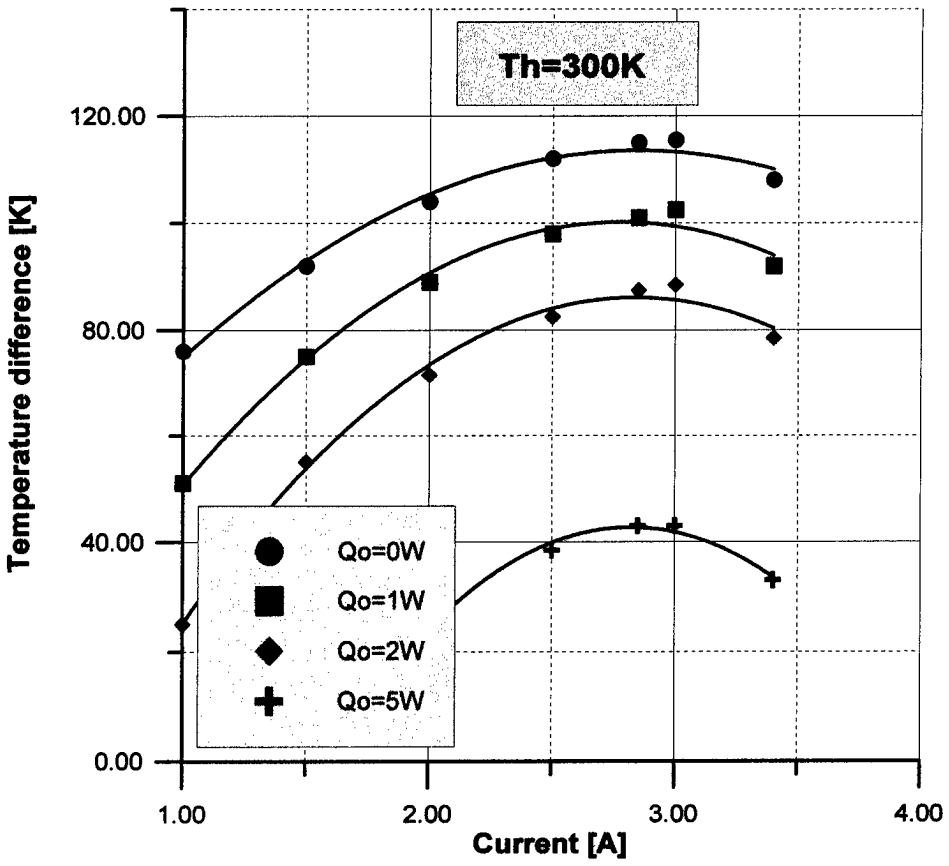


Fig.2. Temperature difference vs. supplying current

Tab.1

		Qo=0W	Qo=1W	Qo=2W	Qo=5W
Experimental results	ΔT_{max}[K]	115.50	102.50	88.50	43.00
	I [A]	3.10	3.00	2.90	2.85
Numerical results	ΔT_{max}[K]	119.50	113.49	107.09	92.04
	I [A]	2.95	2.96	2.94	2.54

Tab.2

		ΔT=0K	ΔT=60K	ΔT=80K	ΔT=90K
Experimental results	Qo_{max}[W]	8.05	3.95	2.50	1.90
	I [A]	2.80	3.00	3.10	3.00
Numerical results	Qo_{max}[W]	9.01	4.33	3.14	1.97
	I [A]	3.10	2.73	2.39	2.73

cooling capacity Q_{0max}=8.05W is reached for I=2.8A (for ΔT=0K).

The mentioned optimization method of a multistage thermoelectric system covers two cases of the target function: maximum temperature difference or maximum cooling capacity which depends on supplying parameters of the cascade and its geometry. The comparison of numerical results of the optimization process and results from the experiments is presented in tab.1 and tab.2. These tabs correspond to fig.1 and fig.2 respectively. It could be noticed that the results obtained on the base of theoretical considerations shows quite good correctness with the experimental measurements.

Next figure i.e. fig.4 is given as an example of temperature distribution on particular stages of the cascade for Q_0=0W. It could be underlined that temperature differences are getting smaller on the succeeding stages and minimum temperatures on particular stages are obtained for the same supplying current what prove correct of working conditions and that stages are well-matched.

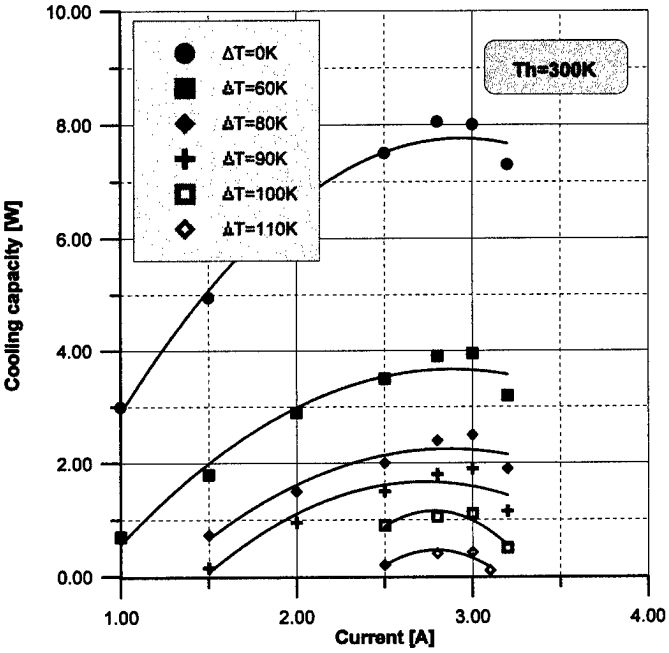


Fig.3. Cooling capacity vs. supplying current

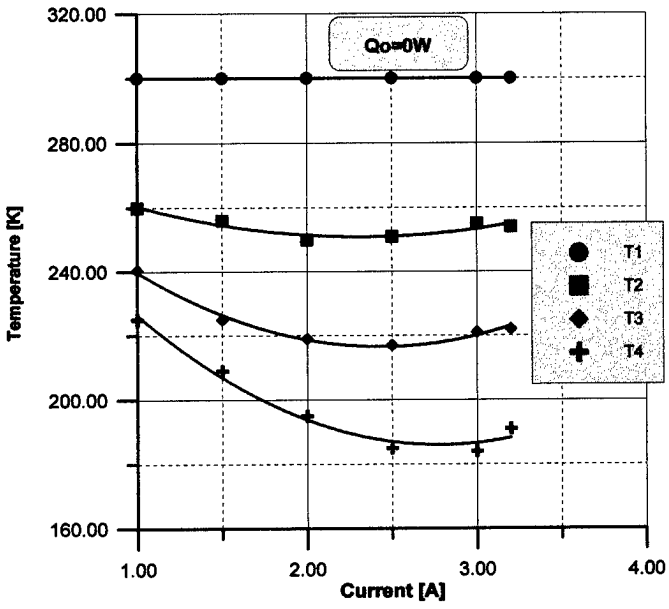


Fig.4. Temperature distribution on the stages vs. supplying current

Summary

1. The experiments have shown that the cold side temperature of the tested three stage cascade can reach 200K (-73^{0}C) for cooling capacity Q_0=1W what is one of the essential conditions for application it as a cooling unit in cryosurgical destroyers while for Q_0=0W the cold side temperature decreases down to 183K (-90^{0}C).
2. The temperature distribution on the particular stages of the cascade proves correct selection of geometrical parameters.
3. The numerical computations show good compliance with the experimental results.
4. Actually next research works will be undertaken concerning a new version of the cascade for significant improvement of parameters in the clinical aspect.

References

[1] T.Wartanowicz, A.Czarnecki, „Cryosurgical Thermoelectric Destroyer", Proc. Of the Xth Int. Conf. On Thermoelectrics (ICT'91), Cardiff, UK, 1991.

[2] T.Wartanowicz, A.Czarnecki, D.Prokop, „Hybrid Thermoelectric Cooling System for Cryosurgical Destroyer", Proc. Of the XIVth Int. Conf. On Thermoelectrics (ICT'95), St.Petersburg, Russia, 1995.

[3] T.Wartanowicz, A.Czarnecki, „Analysis of Thermoelectric Energy Conversion in a Multistage Cooling System", Proc. Of the XIth Int. Conf. On Thermoelectrics (ICT'92), Arlington, USA, 1992.

Reliability investigation of semiconductor coolers

Liu Zhenmao, Wang Xilian, Liu Xiaowei, Quan Wuyun, Sun Shufang, Ye Shuichi, Lui Jingwei
Harbin Institute of Technology, Harbin, China
Tel: 86/0451/6413441, FAX: 86/0451/6221048, E-mail: zmliu@hitnet.hit.edu.cn
Chen Lunqiang
Pengxian Refrigeration and Air Conditioning Equipment Company

Abstract

The life tests on the thermoelectric shock of semiconductor coolers show that the life of semiconductor coolers follows the Weibull distribution. After the early failed devices are removed, the failure rule of the devices can be described as an exponential distribution. The main failure mode is the crack between electric couple material and welding pad. The failure mechanism is the orientated incline and easy splitting of the thermoelectric materials and the stress of substrate deformation due to the temperature difference between the two sides of the cooler. The reliability of the devices can be increased by using multilayer metalization in electric couple welding.

Introduction

Semiconductor coolers have been produced for four decades. With the progress of science and technology, the application of semiconductor coolers has been gradually increasing[1] because of their following advantages: small size, light weight, no mechanical vibration, no wear and no noise, no effect of gravity and no pollution; furthermore, adjustable cooling speed and easily temperature and heat transfer control by not only cooling but also heating. Since the first International Thermoelectricity Conference took place in 1976, 15 sessions have held, and new research fields (such as thermoelectric materials, thermoelectricity theories, test methods and equipment, thermoelectric devices and systems, etc.) have been created. Attention to the thermoelectric device development and the need for semiconductor coolers increase rapidly.

The semiconductor cooler is a kind of solid-state devices, and its reliability should be extremely high theoretically. However in practical use, after short working time, the internal resistance of some coolers increases, and the cooling value and efficiency decrease. The catastrophic failure occurs due to open circuit. This has been proved in thermoelectric shock test[2]. So far except for the property of thermal couple metalization[3] and stability[4], the research on the life characteristics and failure distribution of semiconductor has not been reported. The semiconductor cooler is different from ordinary semiconductor devices, and, it has its instinct features, such as functional material, device structure, manufacture process, working conditions and property parameters, etc. Therefore the research on the failure modes and principles of semiconductor coolers should be carry out, and the quantitative and qualitative description of the life characteristics and their distribution will be the reference to increase the reliability of semiconductor coolers and their efficient use.

Life Test

In order to reflect the real working life of the coolers, the tests were executed in accord with the true working state and conditions of the coolers. While working, DC passed through the cooler with the temperature differential between the two sides of the cooler. In some use, the hot side and the cool side often change alternatively. The widely used working condition is that the current is about 1/2~2/3 of the maximum current I_{max}, and the temperature difference ΔT between the hot side and the cool side is proximately (1/3~1/2) ΔT_{max}. The best testing method to simulate the above working state and condition is to apply the constant current on the coolers which changes in its polarity periodically. The test mentioned above is called thermoelectric shock test. Fig.1 and Fig.2 show the shock current curve applied to the coolers and the temperature changes on the hot and the cool sides in the test respectively. I_p and $-I_p$ are the positive and negative current applied on the coolers respectively. T is the cycle time of the shock. Because the time constant when the coolers reach the maximum temperature difference is about one minute, T is determined as three minutes. T_L and T_H are the temperatures on the cool side and the hot side of the cooler respectively. By the above method, the wire welding, the couple metalization, the couple welding, the thermal matching and the adaptability of the couple material are examined efficiently.

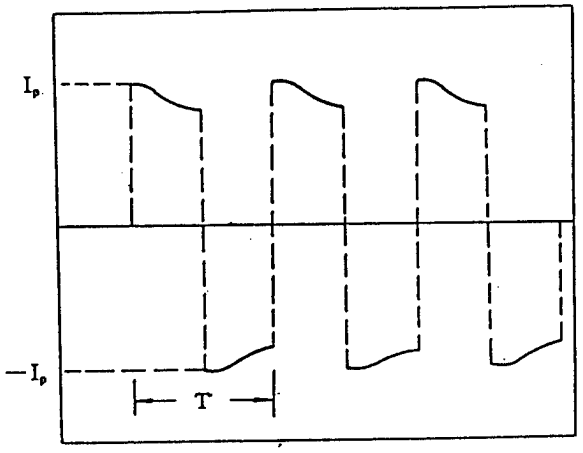


Fig.1 The shock current curve applied to the cooler

* The project is financially supported by the China National Natural Science Fund

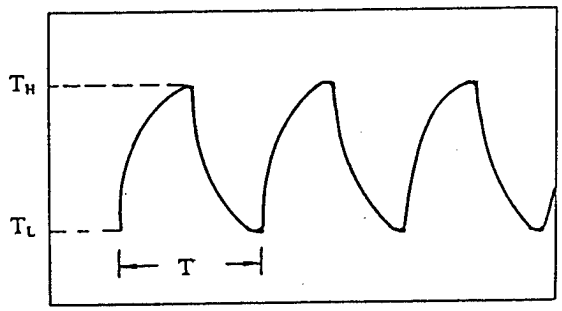


Fig.2 The alternative temperature change on the two sides of the cooler

Test results and analyses

The failure distributions of the coolers, after the thermoelectric shock repeated 5000 times, are shown as Tab.2. From the data in Tab.2, the reliability features of the two types of coolers are calculated by the Weibull graphic evaluation. Fig.3 and Fig.4 show the regression curve of the type TEC1-09702 and TEC1-03104 coolers on the Weibull probability papers (in the figures, the true shock time $t=t' \times 10^2$). Then from the lines, the reliability characteristics are given in Tab.3.Under the thermoelectric shock, the failure rule, or life distribution, follows the Weibull distribution, and is extremely close to the exponential distribution used in semiconductor devices reliability analyses. Thus the reliability of semiconductor coolers can be described or predicted by the exponential distribution.

Tab.1 Test parameters and cooler dimension

type	cooler dimension (mm^3)	couple size (mm^3)	cycle time (min.)	$I_p(=\|-I_p\|)$ (A)	T_H (℃)	T_L (℃)	Δ T (℃)	sample number (n)
TEC1-03104	20 × 20 × 4.0	1.37 × 1.37 × 2.2	3	1.6	45	19	26	20
TEC1-09702	26 × 26 × 3.5	0.8 × 0.8 × 1.5	3	0.7	48	24	24	16

The coolers used in the test are type TEC1-03104 and TEC1-09702. At normal temperature and pressure, the coolers were not mounted with heat sink. The test parameters and the structures of the coolers are shown in Tab.1.

Before the test, the samples were applied by shock tests 100 times, and the early failure coolers were removed. In the test, the maximum temperature differential ΔT_{max} was measured before test and when the shock cycle reached 80, 160, 320, 640, 1280, 2560, 5000 times. The failure criterion is defined as the comparison between the measured ΔT_{max} and the original ΔT_{max0} measured before the test. When the relative change $(\Delta T_{max}-\Delta T_{max0})/\Delta T_{max0} \geq 10\%$, The cooler is regarded as failure, which is called degradation failure. If the cooler circuit is open, the catastrophic failure happens.

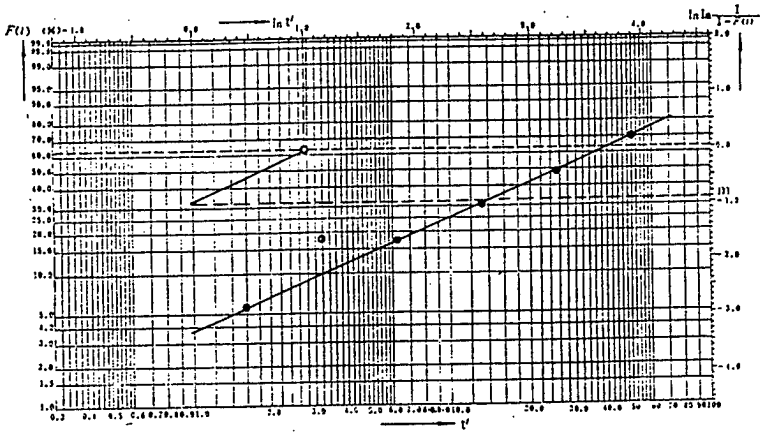


Fig.3 The regression curve of the life distribution of the type TEC1-09702 coolers on the Weibull probability paper

Tab.2 The failure distribution and accumulated failure probability of the coolers

	TEC1-09702			TEC1-03104		
shock time (t')	failure number (Δ i)	accumulated failure number (i)	accumulated failure probability (%)	failure number (Δ i)	accumulated failure number (i)	accumulated failure probability (%)
80	0	0	0	1	1	5
160	1	1	6	1	2	10
320	2	3	18	3	4	20
640	0	3	18	3	7	35
1280	2	5	29	2	9	45
2560	3	8	47	2	11	55
5000	4	12	70	4	15	75

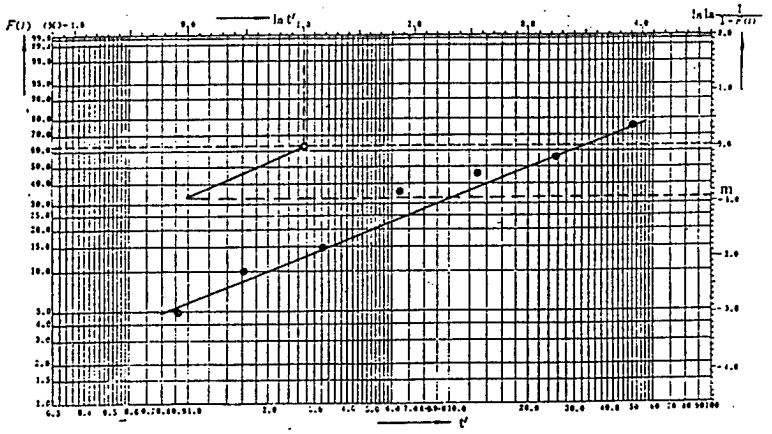


Fig.4 The regression curve of the life distribution of the type TEC1-03104 coolers on the Weibull probability paper

Tab.3 The reliability characteristics and the distribution function of the coolers

parameter / type	shape parameter m	scale parameter (time) t_0	eigenlife (time) η	average life (time) μ	standard deviation (time) σ	distribution function
TEC1-09702	0.9	1.6×10^3	4.0×10^3	4.2×10^3	4.7×10^3	$F(t)=1-e^{-\frac{t^{0.9}}{1.6\times10^3}}$
TEC1-03104	0.9	1.1×10^3	3.0×10^3	4.7×10^3	4.7×10^3	$F(t)=1-e^{-\frac{t^{0.9}}{1.6\times10^3}}$

Among the failure coolers, about 10% are degradation failure due to the internal resistance increase and the cooling efficient decrease, and 90% are catastrophic failure from the open circuit. In the catastrophic failure coolers, the separation of wire welding takes up about 5%, and thermoelectric material splitting causes nearly another 5%. The majority of the catastrophic failure is due to the welding pad separation of thermoelectric couples, which is mainly caused by the exfoliating of the metalization layer on the welding end of thermoelectric couples. It is noticeable that more than 80% of these kinds of the failure thermoelectric couples are located in the periphery of the cooler. That means that in thermoelectric tests, the failure is easy to occur on the edge of the cooler. The reason is understandable. After the current passes the cooler, the temperatures on the two sides are different, which create about 20~30 ℃ differential which produces 3~6 μ m move from the center to the edge of the ceramic plates on the cooler's two sides. The thermal stress exerts on the ends of the couples in opposite directions, and penetrate into the welding plane and the inside of the couple. In addition, in the test, the stress changes its direction at every three minute. After the stress repeats certain times, with the continuous deformation of the welding layer and material of the cooler, the tired splitting occurs at the weak place, then extends continuously and leads to the separate of the welding or the splitting of the couple. Since the adhesion of the metalization layer and thermoelectric material is weaker, this becomes the place where failure is easy to happen. The maximum stress is located on the edge of the device and thermal material has its easy splitting defects. For this reason, the thermal stress makes the couples on the edge of the cooler easy to increase the internal resistance or open the circuit, which cause the degradation or catastrophic failure of the cooler.

Conclusion

By using the dynamic thermal shock test which the hot and the cool side change alternatively, the semiconductor cooler reliability found in the test follows the Weibull distribution. This method is much more strict than the static test which keeps the cool side and the hot side unchanging. And it has an acceleration affect, but the acceleration ratio needs to be investigated. From the experiment, it is found that the test method is an effective way to proceed reliability screening of the coolers. The key to increase to cooler reliability is to improve the adhesive strength of the couple's metalization and reduce the deformation stress in the structure of the cooler.

Reference

[1] TAKI NOBU, KAJI KAWA, "Thermoelectric energy conversion systems", Realize INC., 1995.

[2] Zhang Guowei, et al, "Electric shock testing reaserch on the nickel-tin metallizing contact thermomodule", Journal of Harbin Institute of Technology, 5(1993)32-36.

[3] Isao Nishida, "Thermoelectric materials and itsjoining technique", Transactions of National Research Institute for Metals, Vol.31, No.1, (1989)1-7.

[4] Liu Zhenmao, "The adhesive strength research of thermoelectric couple-metallized Layers", Proceedings of the 12th International Conference on Thermoelectrics, Japan, (1993)569-572.

[5] R.M.Redstall, "Reliability of peltier coolers in fibre-optic laser packages", 10th International Conference on Thermoelectrics, Programme & Abstracts, (1991)VI.5.

Thermal Conductivity of Thin Films - Experimental Methods and Theoretical Interpretation

Friedemann Völklein, Thomas Stärz
FH Wiesbaden, Faculty of Physical Technology, Am Brückweg 26, D - 65428 Rüsselsheim, Germany
Tel.: +49/6142/898531, Fax: +49/6142/898528, E-mail: voelklein@physik.fh-wiesbaden.de

Abstract
The determination of the thermal conductivity of thin films is of great interest both for understanding the structure and conduction mechanism and for numerous technical applications of these films. The thermal conductivity λ is a crucial term of the thermoelectric figure of merit $z = \alpha^2\sigma/\lambda$ and consequently an important parameter for the design of thermoelectric thin film devices. Usually the film properties differ considerably from the bulk. Recently research activities are focused on thermoelectric thin film materials, since high z values can be expected in lowdimensional structures. Standard methods for the investigation of the Seebeck coefficient α and the electrical conductivity σ are well established. However, measurements of the thermal conductivity of thin films are sofisticated and associated with various problems. New methods for the measurement of the thermal conductivity of thin films are reviewed. The problems of stationary and transient measuring techniques are discussed. The results are interpreted with models of surface scattering and grain boundary scattering of charge carriers and phonons.

Features and problems of stationary and transient measuring techniques

Measurements of the thermal conductivity of thin films with thicknesses $d < 1$ µm are associated with some crucial experimental problems. Therefore only few experimental investigations have been performed in the temperature range 80 - 400 K /1-5/.

i) One crucial problem arises from the anisotropy of the film structure. For example, bulk thermoelectric materials like $(Bi_{1-x}Sb_x)Te_3$ solid solutions show strong anisotropy of the thermal conductivity. Thin films of this material have a polycrystalline columnar film structure, where the crystallographic c-axis of the grains is perpenticular to the substrate. In such films the thermal conductivity in the direction perpenticular to the film surface $\lambda_\perp$ differs from the thermal conductivity in any direction parallel to the film surface $\lambda_\parallel$. Therefore, measuring techniques for thin films should take into consideration these effects of anisotropy and should enable the separate determination of $\lambda_\perp$ and $\lambda_\parallel$.

ii) The principle of stationary measurements of $\lambda_\parallel$ is shown in Fig.1. By using a heat sink and a heat source (heating power Q) a heat flux is generated through the film. By temperature sensors (e. g. thermocouples or bolometers) the temperatur gradient $[T(x_1) - T(x_2)]/l$ in the film can be detected. Usually the film thickness d is determined during the deposition process by a quartz microbalance. With the measured quantities Q and $[T(x_1) - T(x_2)]/l$ and with the known film cross section $A = d \cdot b$ (where b is the film and substrate width), λ can be calculated according to equ. (1)

$$Q = \lambda \, d \, b \, [T(x_1) - T(x_2)]/l \qquad (1)$$

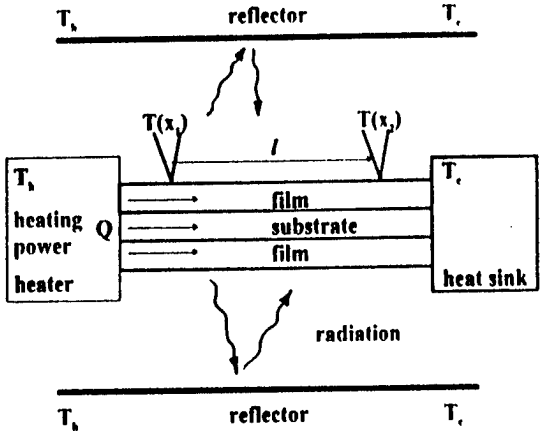


Fig. 1: Principle of steady state measurements of $\lambda_\parallel$

The most important problem for such stationary measurements of $\lambda_\parallel$ consists in the the influence of the substrate. For sufficient measuring accuracy, the product of thermal conductivity λ and film thickness d should be equal to or higher than the corresponding product $\lambda_S \cdot d_S$ of the substrat.

$$\lambda \cdot d \geq \lambda_S \cdot d_S \qquad (2)$$

In order to increase the measuring accuracy, sometimes both sides of the substrate are deposited with identical films (Fig. 1). Measurements were carried out preferably on metal films of high thermal conductivity like Ag, Au, Cu, /1, 3, 5, 6-7/. In order to achieve a small heat flux through the substrate, thin mica, glass or polymer substrates with a typical value $\lambda_S \cdot d_S \cong 10^{-6}$ W/K are used. For semiconducting films with λ in the order of magnitude 1 W/mK we learn from equ. (2), that only films with $d \geq 1$µm can be investigated with sufficient measuring accuracy. However, for many applications and for theoretical works we are interested in measurements with film thickness $d < 1$ µm.

Boiko et al /6/ have developed a sofisticated method for the preparation of self-supporting films on heat sinks. The measurement is based on the analysis of the temperature distribution in the film by using electron diffraction. Measurements were performed on Ag films in the temperature range 300-900 K.

iii) A further crucial problem is the emission of a considerable portion of the heat flux by thermal radiation. Therefore, stationary measuring methods should include a simultaneous evaluation of the emissivity ε of the film or the elimination of "radiation losses". A decrease of thermal radiation can be achieved by the application of radiation shields with appropriate temperature profiles or reflecting mirrors (Fig. 1).

Other problems arise from the heat losses of the heater or by the temperature sensors (e. g. thermocouples), since the heat flux through the film is very small and the heat losses

through the electrical connections of temperature sensors and heaters can be in the same order of magnitude.
Finally, a portion of the heat flux through the films can be delivered by thermal conduction and convection of the surrounding gas. These heat losses are eleminated by the application of an evacuated measuring setup with vacuum pressures $p < 10^{-5}$ mbar.

Transient methods apply an ac elctrical heating power $Q \propto \exp(i\omega t)$, which generates a thermal wave propagation through the film. The application of the well known Angström method for thin films /8/ is an example of such a transient measuring technique (Fig. 2).

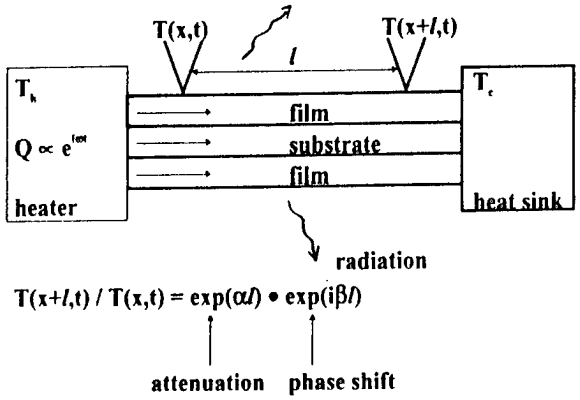


Fig. 2: Principle of the transient Angström method

Here, no precautions for the elimination of radiation losses are necessary. The ratio of the temperatures T(x+l, t) and T(x, t) at two positions with a distance l yields the attenuation factor $\exp(\alpha l)$ and the phase shift $\exp(i\beta l)$ of the thermal wave. Using these two quantities, the thermal diffusivity

$$a = \lambda / (\rho \cdot c) = \omega / \left(2\alpha\beta - \alpha^2 + \beta^2\right) \qquad (3)$$

can be calculated. ρ is the density and c the specific heat capacity of the film. The emissivity of the film can also be determined. With respect to the measuring accuracy, in addition to equ. (2) an analogous equation should be fulfilled for the specific heat capacitances of film and substate, respectively:

$$\rho \cdot c \cdot d \geq \rho_S \cdot c_S \cdot d_S \qquad (4)$$

However, the disadvantage of most of the transient methods is the fact that only the thermal diffusivity can be determined. Usually the thermal conductivity is deduced with the help of the bulk values of density and specific heat capacity. This procedure is very questionable, since the values of ρ and c in thin films may differ considerably from the bulk /9, 10/.

Transient 3ω method

The transient 3ω-method which yields the thermal conductivity (not the diffusivity a) was developed by Cahill and Pohl /11/. Fig. 3 shows a sample with the metal line that serves simultaneously as heater and thermometer. It is in intimate thermal contact with the sample. The narrow metal line and the rectangular pads are produced on the sample either by photolithography (with line widths of 5 µm or 35 µm) or by evaporation through masks (with line width of 90 µm). In order to avoid reflections, the sample thickness must be at least five times the width of the line and the surface of the sample must be large enough to accommodate the length of the metal line and the electrical connections for the four point probe technique.

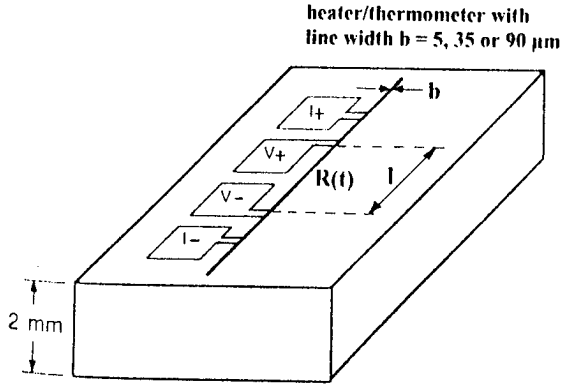


Fig. 3: Evaporated metal pattern on the face of a sample for 3ω measurements

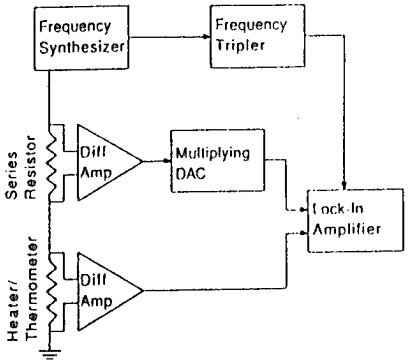


Fig. 4: Diagram of the equipment used for the 3ω method

Fig. 4 shows a schematic diagram of the equipment. A frequency synthesizer supplies the driving current, which is a very pure sine wave. The sinusoidal current of angular frequency ω heats the sample at 2ω. The heating produces a temperature oscillation with frequency 2ω. The metal line also serves as a thermometer; the resistance of the line is a function of the temperature. The resistance oscillation at 2ω multiplied by the exitation current at ω produces a voltage oscillation at 3ω. The amplitude of this 3ω voltage is measured by the lock-in amplifier (hence, the name: 3ω method). In addition to the voltage at 3ω, a very large voltage at ω is present across the heater-thermometer; the ω voltage is typically 1000 times larger than the 3ω voltage. To reduce this large voltage at frequency ω, a resistor is placed in series with the heater-thermometer resistance. By adjusting the gain of the multiplying digital-to-analog converter, the ω voltage from the series resistor can be made equal to the ω voltage from the heater-thermometer. The differential input of the lock-in amplifier can then reduce the ω content of the input voltage to an acceptable level. A frequency tripler provides a reference signal at 3ω. By measuring the third-harmonic signal at

two frequencies, f_1 and f_2, we obtain the thermal conductivity

$$\lambda = \frac{V^3 \ln(f_1/f_2)}{4\pi l R^2 [V_3(f_1) - V_3(f_2)]} \frac{dR}{dT} \quad (5)$$

R is the average resistance of the metal line, V is the voltage across the line at frequency ω, and $V_3(f_1)$, $V_3(f_2)$ are the voltages at the third harmonic for frequencies f_1 and f_2, respectively. dR/dT is the slope of the calibration of the metal line (resistance as a function of temperature) at the temperature of the measurement.

By increasing the frequency ω, the technique can be adapted to measuring the thermal conductivity of films on substrates. If the heater-thermometer is evaporated onto a dialectric film of thickness d, situated on some substrate (Fig. 5), the thermal wave will be confined to the film if the penetration depth $(a/2\omega)^{1/2} < d$.

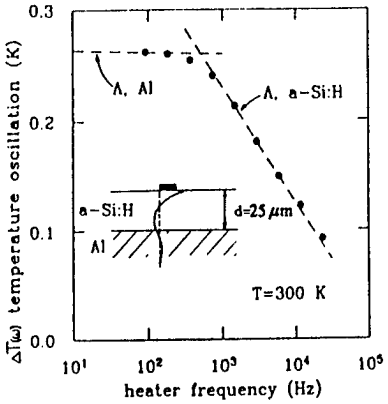


Fig. 5: Amplitude of temperature oscillation of the heater-thermometer for a 25-μm-thick film of a-Si on Al substrat

If, however, $(a/2\omega)^{1/2} >> d$, the film can be neglected, and the thermal wave can be considered as diffusing entirely in the substrate. The temperature amplitude ΔT as a function of the frequency of the temperature oscillation 2ω is shown in Fig. 5 for an amorphous silicon film (a-Si) adhering to an aluminium substrate. For small frequencies, the small slope of the straight line obtained when ΔT is plotted versus the natural logarithm of this frequency is the result of the large thermal conductivity of the aluminium (obviously, the frequency range is inadequate to measure λ in this case). As the frequency increases beyond ~ 10^3 Hz, ΔT decreases rapidly, and approaches a staight line in Fig. 5, from which the thermal conductivity of the a-Si can be determined.

For films < 10 μm thick the frequencies ω needed to satisfy $(a/2\omega)^{1/2} < d$ quickly become cumbersome because of the required lock-in technique, and thus the 3ω method becomes less suitable for very thin films. In addition, the technique yields no information regarding the anisotropic behaviour of the thermal conductivity.

Steady state and transient measuring technique using microsensors prepared by micromachining

Völklein et al /12, 13/ have developed a new steady state and transient technique by using silicon chips with extremly thin membranes. Fig. 6 shows such a microsensor prepared by micomachining.

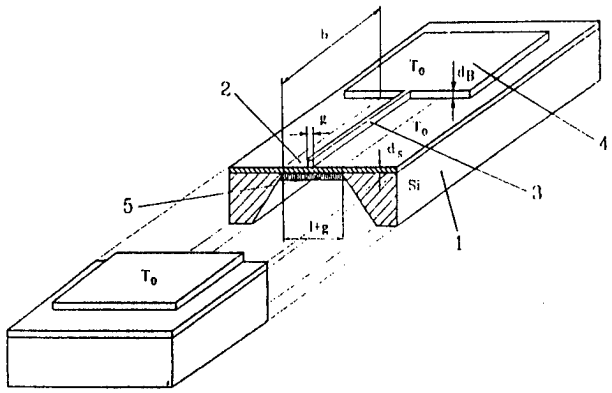


Fig. 6: Schematic of a sensor chip for thermal conductivity measurements

The membrane (2) consists of a set of SiC/Si_3N_4 layers (total thickness d_S = 100 nm) with poor thermal conductivity. This SiC/Si_3N_4 sandwich system is deposited on both sides of a silicon wafer (1) by Plasma Enhanced Chemical Vapor Deposition (PECVD). The back sandwich system is patterned by photolithographic and plasma-etching techniques. Then, anisotropic etching of the silicon wafer with KOH solution forms a self-supporting membrane (2; width $l+g$ and length b, where $b >> l+g$) on the front side. A thin stripe of aluminium (3; called bolometer hereafter) with a narrow width g ($g << l$) and thickness d_B = 200 nm is deposited by vacuum evaporation and is patterned by photolithography on the membrane. The bolometer is connected with bonding pads (4) on the bulk silicon frame. The film (5) to be investigated is deposited onto the bolometer-free side of the membrane by any deposition technique. For thermal conductivity measurements as a function of temperature T_0, the sensor with a silicon frame temperature T_0 is placed in a "black environment" of the same temperature T_0 and in a vacuum chamber with a pressure of less than 10^{-5} mbar. The bolometer is heated electrically (heating power N). This leads to an increase of the average bolometer temperature $\Delta T = T - T_0$, whereas the silicon frame acts as a heat sink with unchanged temperature T_0. The temperature rise is determined from the resistance change of the bolometer:

$$\Delta T = \frac{R(T) - R(T_0)}{R(T_0) \cdot \beta} = \frac{\Delta R}{R(T_0) \cdot \beta} \quad (6)$$

where $R(T_0)$ and $R(T)$ are the resistances of the unheated and heated bolometer, respectively, and β is the temperature coefficient of resistivity. Experimentally, the resistance $R(T_0)$, the heating power N and the resistance change ΔR are determined by a four-point probe method. The membrane thermal conductivity λ_S can be calculated from the measured thermal conductance G = N/ΔT of the sensor by

$$\lambda_S \cdot d_S = \frac{G \cdot l}{4 \cdot b} = \frac{N \cdot R(T_0) \cdot b \cdot l}{\Delta R \cdot 4 \cdot b} \quad (7)$$

For a sensor chip with a deposited thin film (thermal conductivity λ, thickness d) on the bolometer-free side of

the membrane, we must replace the product $\lambda_S \cdot d_S$ by the sum $(\lambda_S \cdot d_S + \lambda \cdot d)$. For the unknown thermal conductivity of the film, we obtain

$$\lambda \cdot d = \frac{N \cdot R(T_0) \cdot \beta \cdot l}{\Delta R \cdot 4 \cdot b} - \lambda_s \cdot d_s \qquad (8)$$

where N is the heating power and ΔR is the resistance change for a sensor chip with the deposited thin film.

Time response analysis of the sensor chip

If we apply a constant heating power to the bolometer at time t = 0 (Fig. 7), its time response is

$$\frac{\Delta R(t)}{R(T_0) \cdot \beta} = \Delta T(t) = \frac{N}{G}\left[1 - \exp\left(-\frac{t}{\tau_s}\right)\right] \qquad (9)$$

where τ_S is the thermal time constant of the sensor, which is measured according to Fig. 7.

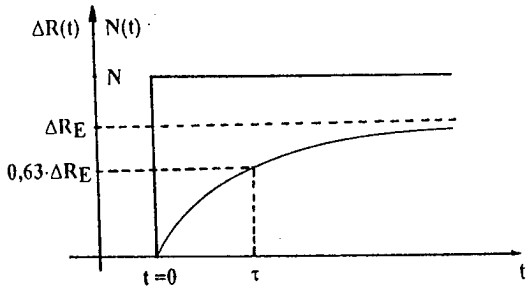


Fig. 7: Heating power N(t) and resistance change ΔR(t) as a function of time t. ΔR_E is the stady state resistance change (for $t \Rightarrow \infty$) and the thermal time constant τ is determined at $(1 - e^{-1}) \cdot \Delta R_E = 0{,}63 \cdot \Delta R_E$.

Owing to the optimization of the membrane dimensions, τ_S can be described by a simple expression:

$$\tau_s = (\rho_s \cdot c_s \cdot d_s) \cdot \left(\frac{l}{3} + g\right) \cdot b / G \qquad 10)$$

Here, ρ_S and c_S are the mass density and the specific heat capacity of the membrane, respectively. Using the experimentally determined time constant τ_S, equ. (10) yields the membrane specific heat capacitance $\rho_S \cdot c_S$, and the thermal diffusivity $a_S = \lambda_S / \rho_S \cdot c_S$ can be calculated, since λ_S is known from the steady state measurement. The typical thermal time constant τ_S of our sensor is about 1 ms at T_0 = 295 K. After deposition of any film onto our sensor chip, the specific heat capacitance $\rho \cdot c$ of this film is deduced from

$$\tau = (\rho_s \cdot c_s \cdot d_s + \rho \cdot c \cdot d) \cdot \left(\frac{l}{3} + g\right) \cdot b / G \qquad (11)$$

where τ and G are the time constant and the thermal conductance of the deposited sensor chip, respectively.

Figure 8 shows the application of the sensor for in situ thermal conductivity measurements. The sensor chip is placed in a water-cooled sensor head with constant temperature T_0 and is electrically connected with a Wheatstone bridge. Before film deposition, the resistance of the unheated bolometer $R(T_0)$ is measured and the Wheatstone bridge is balanced (signal voltage $U(d) = 0$) by using a very small voltage U_B. This small voltage is required to prevent a temperature rise of the bolometer.

Then, using a higher U_B, a temperature increase of about 10 K is caused by the heating power $N = U_B^2/(n+1)^2 \cdot R(T_0)$ with $n = R_A / R_B$ (see Fig. 8). The temperature rise leads to a resistance change ΔR and to the signal voltage U_0.

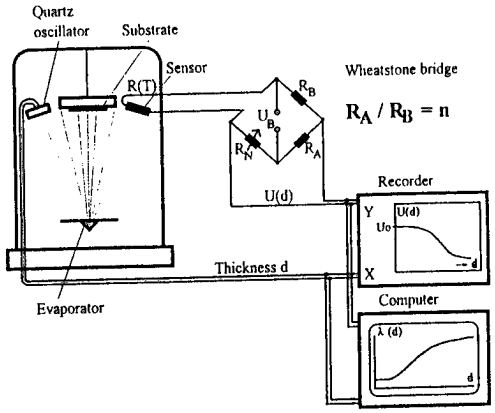


Fig. 8: Principle of in situ measurement

During the deposition of a thin film, the thermal conductance of the membrane increases according to

$$G = [\lambda_S \cdot d_S + \lambda(d) \cdot d] \cdot b / l \qquad (12),$$

where the thermal conductivity of the growing film $\lambda(d)$ is usually a function of thickness, and where d increases with increasing deposition time. Therefore, the temperature rise of the bolometer and its resistance change ΔR are reduced during the film deposition. Hence, the signal voltage decreases according to

$$U(d) = \frac{n}{(n+1)^4} \cdot \beta \cdot \frac{U_B^3}{R(T_0)} \cdot \frac{1}{[\lambda_s \cdot d_s + \lambda(d) \cdot d]} \qquad (13)$$

We simultaneously record this voltage $U(d)$ and the signal of a quartz oscillator monitor, which is proportional to the thickness d of the growing film. These two signals are evaluated during the deposition, by a PC. Thus the thermal conductivity is calculated according to

$$\lambda(d) = \frac{n}{(n+1)^4} \cdot \beta \cdot \frac{l}{4 \cdot b} \cdot \frac{U_B^3}{R(T_0)} \cdot \frac{1}{d} \cdot \left(\frac{1}{U(d)} - \frac{1}{U_0}\right) \qquad (14)$$

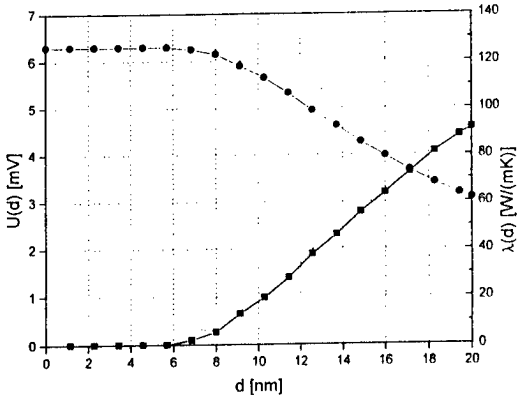


Fig. 9: In situ measured signal voltage $U(d)$ (●) and thermal conductivity $\lambda(d)$ (■) of growing silver film.

Fig. 9 shows an example of an in situ measurement. It represents the signal voltage $U(d)$ and the thermal conductivity $\lambda(d)$ of a silver film during a deposition

process of up to 20 nm film thickness. Fig. 9 demonstrates the very high sensitivity of the sensor. Above the average film thickness of 8 nm, thermal conduction of the film is observed. The start of thermal conduction corresponds to the coalescence state of the silver film islands.

Fig. 10 shows the thermal conductivity of antimony films with thicknesses ranging from 27 nm to 230 nm.

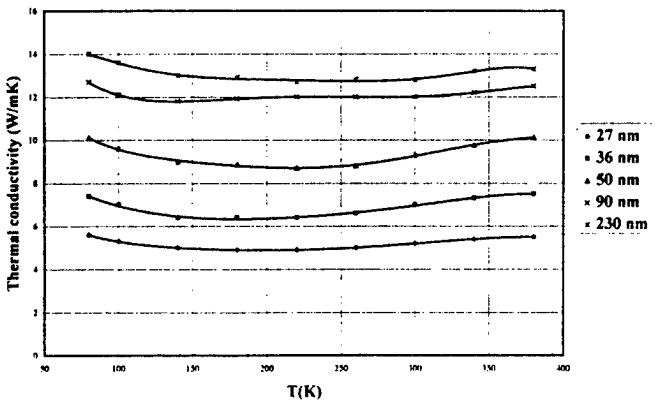


Fig. 10: Thermal conductivity of Antimony films as a function of temperature

Fig. 11 represents thermal conductivity measurements on bismuth films in the temperature range 80 - 400 K.

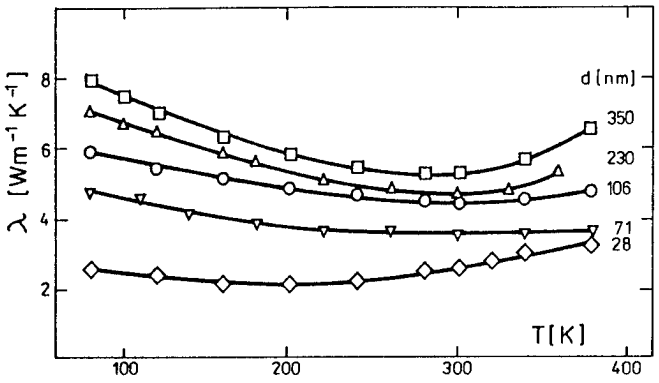


Fig. 11: Thermal conductivity of Bismuth films as a function of temperature

Investigations of extremely thin films

Measurements of $\lambda_{\parallel}$ on extremely thin films require the preparation of a self-supporting film. This can be performed by a removal of the substrate using bulk or surface micromachining (e. g. by a sacrificial layer technology or by selective plasma dry etching) /14-16/. Fig. 12 shows the cross sectional view of an experimental setup. The technique can be applied only for electrically conducting films with a temperature coefficient of resistivity β of about 10^{-3} K^{-1}. Then, the film can be heated by a current I and its resistance serves as a temperature sensor Fig. 12 shows a film with length l, thickness d and width b, which rests on a heat sink with temperature T_0 in a black ambient of temperature T_0. The temperature profile T(x) in the film and the mean temperature T_M, respectively, can be calculated with regard to the boundary conditions. T_M is given by

$$T_M - T_0 = \frac{R(T_M) - R(T_0)}{R(T_0)\cdot\beta} = \frac{I^2 R(T_0)}{(\pi^2 \lambda db / l) + 8\varepsilon\gamma T_0^3 lb} \qquad (15)$$

where ε is the emissivity of the film and γ is the Stefan-Boltzmann constant. Equ. (15) demonstrates that the mean temperature is a function of the two unknown parameters λ and ε. However, if we perform two measurements on identical films, which are produced at the same deposition process, but with different lengths l_1 and l_2, respectively, we are able to determine as well as the thermal conductivity and emissivity.

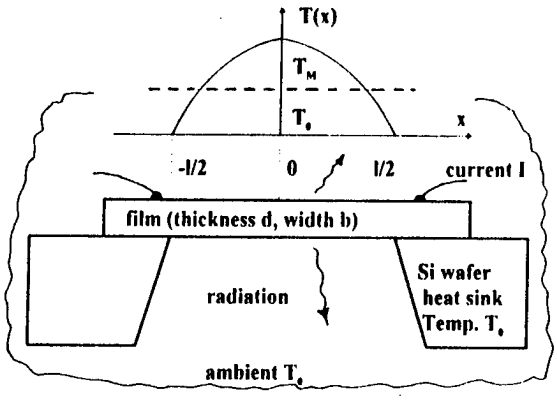


Fig. 12: Experimental setup for self-supporting thin films

For transient measurements the heating current I(t) is switched on at t = 0 in form of a step function. From the experimentally observed temperature increase $[T_M(t) - T_0] \propto [1 - \exp(-t/\tau)]$ we deduce the time constant τ, which is related to the specific heat capacitance $\rho\cdot c$ by

$$\tau = \frac{\rho c d l b}{(\pi^2 \lambda db / l) + 8\varepsilon\gamma T_0^3 lb} \qquad (16)$$

Obviously, the combination of the steady state and transient measurement yields the thermal diffusivity a.

Measurements of $\lambda_{\perp}$

Fig. 13 demonstrates the problems associated with the measurement of $\lambda_{\perp}$ and a method, which overcomes these problems. Interfaces between substrate and film or between film and heater/thermometer may have a thermal resistance equal to the thermal resistance of the investigated film /17-18/. However , the investigation of two identical films with different film thicknesses d_1 and d_2 enables the elimination of these interface effects.

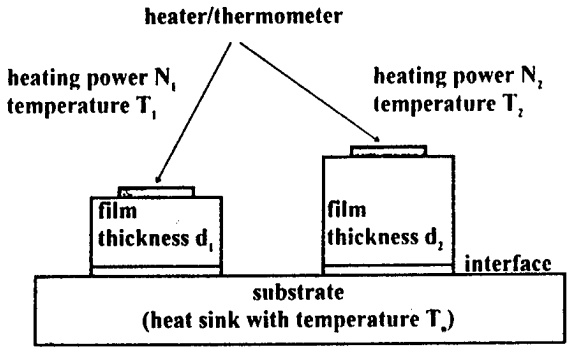


Fig. 13: Principle of $\lambda_{\perp}$ measurement

Such identical films can be prepared during one and the same deposition process by the application of a shutter. Two thin film heaters/thermometers are heated by the heating power per unit square N_1 and N_2, respectively. Its temperature increase T_1 and T_2, respectively are detected, where T_0 is the temperature of the substrate, which acts as a heat sink. The thermal conductivity is calculated according to

$$\lambda = N_1 \cdot N_2 \cdot (d_1 - d_2) / [N_2 \cdot (T_1 - T_0) - N_1 \cdot (T_2 - T_0)] \quad (17)$$

Theoretical interpretation

The presented theoretical interpretation is focused on thin polycrystalline films. The electrical resistivity of these films can be described by the well established Fuchs-Sondheimer /19-20/ and Mayadas-Shatzkes /21/ models. We have extended these models to the interpretation of the thermal conductivity. With a model of surface and grain boundary scattering of charge carriers *and* phonons we can analyze the charge carrier component and the lattice component of the thermal conductivity. The theoretical results are compared with experimental results of Bismuth and Antimony films /22-26/.

Description of the model (Fig. 14)

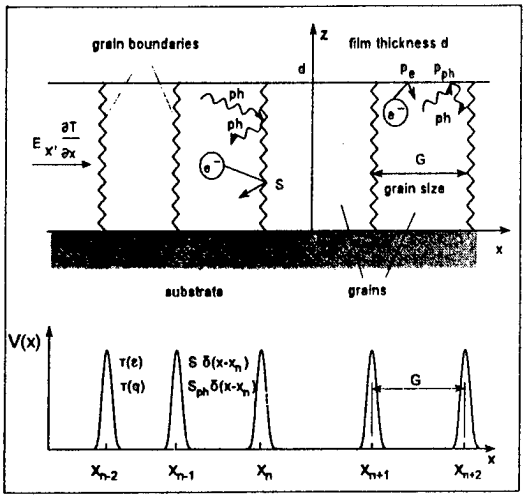


Fig. 14: MS model of surface and grain boundary scattering

Charge carrier and phonon scattering occurs within the grains and at the film surfaces and grain boundaries. At the film surface partial diffuse reflection (scattering perameter $0 \le p_e, p_{ph} \le 1$ as fraction of the specularly reflected carriers) is assumed. The grain boundaries are oriented perpenticular to the direction of the external fields (E_x, $\partial T/\partial x$) and descriebed by δ-shaped scattering potentials of strength S at the positions x_n, which are distributed according to a Gaussian with the mean grain boundary distance G. For the crystallites the properties of the bulk material and its band structure are assumed. The scattering processes within the grains (background scattering) can be described by relaxation times $\tau(\varepsilon)$ and $\tau(q)$, where ε is the charge carrier energy and q is the phonon (lattice) mode. There is no preferential orientation of the films in the x-y-plane. Therefore, the x- and y-axes of the coordinate space are arranged arbitrarily. The external fields shall be oriented parallel to the x-axis.

Thermal conductivity in polycrystalline metal films

Presumtions of the MS model and of our calculations are:

i) complete degeneration of the electron gas:

$-\partial f_0/\partial \varepsilon = \delta(\varepsilon - F)$,

where $f_0 = [\exp(\varepsilon - F)/kT + 1]^{-1}$ and F is the Fermi level

ii) sherical Fermi surface (isotropy)

In the framework of this model, the electrical conductivity $\sigma(d, G)$ as a function of film thickness d and grain size G is given by

$$\sigma(d,G) = \sigma_{bulk} \cdot g(d,G) \quad (18)$$

where σ_{bulk} is the bulk electrical conductivity and the function g(d, G) include the grain boundary and surface scattering of the electrons. A useful approximation of this function is

$$g(d,G) = \left(1 + \frac{3(1-p_e)l}{8d} + \gamma(S)\frac{l}{G}\right)^{-1} \quad (19)$$

where l is the mean free path of the carriers (in the bulk material), $\gamma(S) = 6\pi^2 m S^2/h^2 F$, m is the effective mass and h is Plancks constant. Calculations of the thermal conductivity demonstrate that it can also be described by the bulk value λ_{bulk} and the same function g(d,G):

$$\lambda(d,G) = \lambda_{bulk} \cdot g(d,G) \quad (20)$$

Therefore, the quotient of thin film thermal and electrical conductivities is equal to the quotient of the bulk:

$$\lambda(d,G)/\sigma(d,G) = \lambda_{bulk} / \sigma_{bulk} = L_0 \cdot T \quad (21)$$

This theoretical result demonstrates, that the Wiedemann-Franz law is valid even for very thin polycrystalline metal films with the Lorenz-Number L_0 of the bulk material.

An experimental verification of the theory is represented in Fig. 15 and Tab. 1.

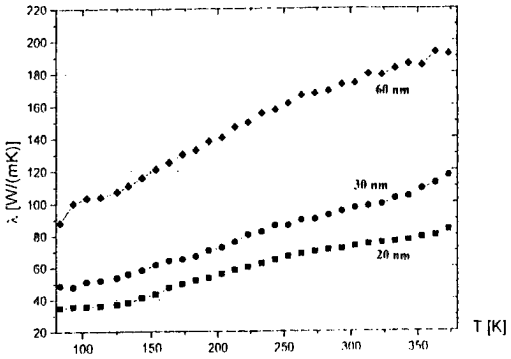


Fig. 15: Thermal conductivity of Aluminium films

Tab. 1: Thermal and electrical conductivity and Lorenz-Number L_0 of Aluminium films at room temperature

d (nm)	λ (W/mK)	σ (10^7/Ωm)	L_0 (V^2/K^2)
20	72,5	1,00	$2{,}42 \times 10^{-8}$
24	83,5	1,15	$2{,}42 \times 10^{-8}$
30	94,8	1,30	$2{,}43 \times 10^{-8}$

Thermal conductivity in bipolar films with anisotropic transport coefficients

As an example of the thermal conductivity in bipolar semimetal films with anisotropic transport coefficients we

discuss the properties of Bismuth and Antimony. Their transport coefficients can satisfactorily be interpreted only by means of a two-band model. At temperatures of 80 to 400 K Bismuth with its small band overlap is within the transient range between degeneration and non-degeneration. For Antimony, the bulk material has been analyzed in the framework of a partially degenerate two-band many-valley-model. In this model the Fermi level is pinned between the two band edges. Therefore, the presumption $(-\partial f_0/\partial\varepsilon) = \delta(\varepsilon-F)$ of the MS model is not justified. The band structure of Bismuth and Antimony crystallites can be described by elliptical Fermi surfaces (many-valley-model). The grains are generally columnar and oriented perpendicular to the substrate with their c-axis.In the framework of this model we calculate the

i) electrical conductivity:

$$\sigma = en\mu_n g_{0n}(d,G) + ep\mu_p g_{0p}(d,G) = \sigma_n + \sigma_n \qquad (22)$$

ii) Seebeck coefficient:

$$\alpha = (\sigma_n\alpha_n + \sigma_p\alpha_p)/\sigma \qquad (23)$$

$$\alpha_i = (\mp)\frac{k}{e}\left[\frac{2\Im_1(\zeta_i)}{\Im_0(\zeta_i)}\frac{g_{1i}(d,G)}{g_{0i}(d,G)} - \zeta_i\right] \qquad (24)$$

iii) thermal conductivity (charge carrier contribution)

$$\lambda_e = L_n\sigma_n T + L_p\sigma_p T + (\alpha_p-\alpha_n)^2\sigma_n\sigma_p T/\sigma = \lambda_n+\lambda_p+\lambda_{bi} \qquad (25)$$

$$L_i = \left(\frac{k}{e}\right)^2 \frac{3\Im_2(\zeta_i)\Im_0(\zeta_i)g_{2i}(d,G)g_{0i}(d,G) - [2\Im_1(\zeta_i)g_{1i}(d,G)]^2}{[\Im_0(\zeta_i)g_{0i}(d,G)]^2} \qquad (26)$$

Here, μ_n and μ_p are the carrier mobilities in the bulk material, n and p are the electron and hole concentration, respectively, $F_i = F-E_c$ for electrons and $F_i = E_v - F$ for holes, $\zeta_i = F_i/kT$, E_c and E_v are the edges of the conduction and valence band, respectively. i= n denotes the electrons, i=p denotes the holes. L_i are the Lorenz-Numbers for the two bands. $\Im_r(\zeta_i)$ are the well known Fermi integrals with r = 0, 1, 2.

The functions $g_{ri}(d,G)$ are not equal for electrons and holes, respectively, and they take into consideration the anisotropy of the Fermi surfaces. These functions can be approximated by

$$g_{ri}(d,G) \approx \frac{\int_0^\infty \left(-\frac{\partial f_{0i}}{\partial\varepsilon_i}\right)\varepsilon_i^{r+3/2}\tau_i(\varepsilon_i)\left(1+\frac{3}{2}\gamma_i(S_i)+\frac{3(1-p_i)}{8K_i(\varepsilon_i)}\right)^{-1}d\varepsilon_i}{\int_0^\infty \left(-\frac{\partial f_{0i}}{\partial\varepsilon_i}\right)\varepsilon_i^{r+3/2}\tau_i(\varepsilon_i)d\varepsilon_i} \qquad (27)$$

where $\gamma_i(S_i) = \frac{\sqrt{2m_i}S_i^2\tau_i(\varepsilon_i)}{\hbar^2 G\sqrt{\varepsilon_i}}$, $K_i(\varepsilon_i) = \frac{d\sqrt{m_{3i}}}{\tau_i(\varepsilon_i)\sqrt{2\varepsilon_i}}$ and $2(m_i)^{-1} = (m_{1i})^{-1} + (m_{2i})^{-1}$. $(m_{1i})^{-1}$, $(m_{2i})^{-1}$ are the axes of the effective mass tensor in the x-y-plane, $(m_{3i})^{-1}$ is the axis perpenticularly to this plane. We analyze the charge carrier thermal conductivity λ_e with the help of equs.(22) to (27), assuming charge carrier scattering by acoustic phonons. The quantitative analysis requires the partial conductivities σ_n, σ_p and the partial Seebeck coefficients α_n, α_p. However, measured quantities are the total electrical conductivity σ, the Seebeck coefficient α and the total thermal conductivity λ. With these quntities σ_n, σ_p, α_n and α_p cannot be determined. However, the theoretical analysis of the functions $g_{ri}(d,G)$ shows, that the quotients $g_{1i}(d,G)/g_{0i}(d,G)$ and $g_{2i}(d,G)/g_{0i}(d,G)$ can be approximated by unity for film thickness larger than 30 nm. Therefore, we can use the bulk values for α_n, α_p and L_n, L_p. With α_{ibulk} and the measuring results of α and σ, the partial conductivities σ_n, σ_p are determined. Then, using equ. (25) the charge carrier thermal conductivity λ_e is deduced by the calculation of the Wiedemann-Franz contributions λ_n, λ_p and the bipolar term λ_{bi}. With the total thermal conductivity λ, the lattice thermal conductivity λ_{ph} (phonon contribution) is determined by $\lambda_{ph} = \lambda - \lambda_e$. Applying this procedure, the thermal conductivities of Bismuth and Antimony were studied for film thicknesses ranging from 30 to 400 nm in the temperature region 80-400 K. Fig. 16 demonstrates the results for Antimony films. Results for $Bi_{1-x}Sb_x$ films are published in /24/.

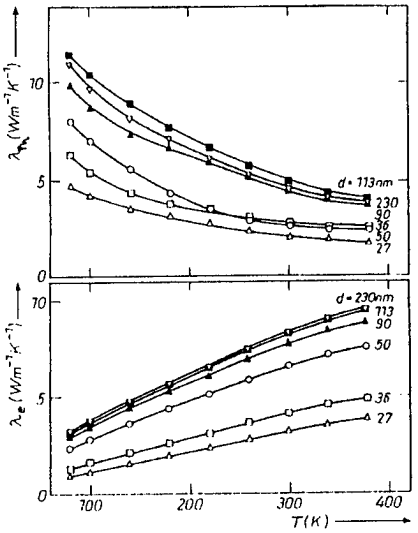


Fig. 16: Lattice and charge carrier component of the thermal conductivity of Antimony films as a function of temperature

From these investigations the lattice thermal conductivity of Bismuth films and Antimony films is deduced as a function of thickness and represented in Figs. 17 and 18.

Theory of the lattice thermal conductivity in thin polycrystalline films

The experimental results shown in Figs. 17 and 18, can be interpreted by means of phonon scattering on surfaces and grain boundaries. Using the model of Fig. 14, the Boltzmann equation for the calculation of the phonon occupation number N(q, r, t) is

$$v_z\frac{\partial n(q)}{\partial z} + v_x\frac{\partial N_0}{\partial T}\frac{\partial T}{\partial x} = \frac{n(q)}{\tau(q)} - \int P(q,q')[n(q)-n(q')]dq' \qquad (28)$$

where $n(q) = N(q,r,t) - N_0(q)$. q is the lattice mode vector, $N_0(q) = \{\exp[\hbar\omega(q)/kT]-1\}^{-1}$ is the equilibrium occupation number. The background scattering processes within the crystallites are described by the isotropic relaxation time $\tau(q) = \tau(\omega)$. v_x and v_z are the x- and z-components of the velocity vector. The term $v_z \partial n(q)/\partial z$ takes the scattering effect of the surfaces into account; the integral describes the grain boundary scattering, where $P(q,q')$ is the transition probability for a phonon in state q to be scattered to q' by the grain boundaries. $P(q, q')$ is calculated using perturbation theory.

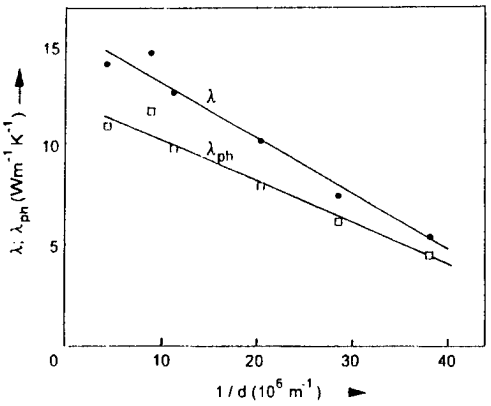


Fig. 17: Lattice thermal conductivity of Antimony films as a function of film thickness at T=80K (lines: theory)

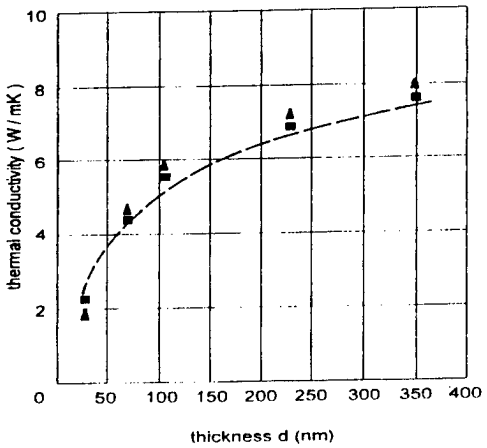


Fig. 18: Lattice thermal conductivity of Bismuth films as a function of film thickness at T=80K (dashed line: theory)

We obtain the lattice thermal conductivity:
$\lambda_{ph} = \lambda_{ph,bulk} \cdot g_{ph}(d,G)$, where the first factor is the lattice thermal conductivity of the bulk material and the function $g_{ph}(d,G)$ describes the dependence of λ_{ph} on thickness and grain size:

$$g_{ph}(d,G) \approx \frac{\int_0^{\Theta/T} \frac{x^4 e^x}{(e^x-1)^2}\tau(x)\left[1+\frac{3}{2}\gamma+\frac{3(1-p_{ph})}{8K}\right]^{-1} dx}{\int_0^{\Theta/T} \frac{x^4 e^x}{(e^x-1)^2}\tau(x)dx} \qquad (29)$$

with $\gamma = \frac{2S_{ph}^2 \tau(x)}{\hbar^2 vG}$, $x = \frac{\hbar\omega}{kT}$ and $K = \frac{d}{\tau(x)v}$.

Here, v is the velocity of sound, Θ is the Debye temperature and p_{ph} is the parameter of surface scattering. Phonon-phonon umklapp scattering with $\tau(\omega) = \tau_0 / kT\omega^2$ is the essential scattering mechanism in bulk Bismuth and Antimony in the temperature range 80-400 K. The results of our theoretical calculations are compared with experimental results for $\lambda_{ph}(d, G)$ of Bismuth and Antimony films in Figs. 17 and 18. A more extended interpretation is given in /23/.

References

/1/ V. M. Abrosimov, B. N. Egorov, Fiz. Tverd. Tela. 11 (1969) 530
/2/ J. Z. Okun, B. S. Frajman, A. F. Cudnowskij; Fiz. Tekh. Poluprov. 5 (1971) 242
/3/ P. Nath, K. L. Chopra, Thin Solid Films 18 (1973) 29
/4/ J. A. Boikov, B. M. Golcman, S. F. Sinenko, Prib. i Tekh. Eksp. 2 (1975) 230
/5/ F. Kelemen, Thin Solid Films 36 (1976) 199
/6/ B. T. Boiko, A. T. Pugachev, V. M. Bratsychin; Thin Solid Films 17 (1973) 157
/7/ R. L. Filler, P. Lindenfeld, G. Deutscher, Rev. Sci. Instr. 46 (1975) 439
/8/ B. Sundquist, G. Bäckström, Rev. Sci. Instr. 47 (1976) 177
/9/ M. S. Blois, L. M. Rieser, J. Appl. Phys. 25 (1954) 338
/10/ H. Ebel, F. Hengstberger, Z. Naturf. 25a (1970) 1984
/11/ D. G. Cahill, R. O. Pohl, Phys. Rev. B 35 (1987) 4067
/12/ F. Völklein, Thin Solid Films 188 (1990) 27
/13/ T. Stärz, U. Schmidt, F. Völklein, Sensors and Materials 7 (1995) 395
/14/ P.G. Borden, J. Electrochem. Soc.: Solid-state Sci. and Techn. 127 (1980) 2454
/15/ F. Völklein, E. Kessler, Phys stat sol (a) 81 (1984) 585
/16/ Y. C. Tai, C. H. Mastrangelo and R. S. Muller, Appl. Phys. **63** (1988) 1142.
/17/ V. E. Holt, J. Appl. Phys. 37 (1966) 798
/18/ D. G. Cahill, H. E. Fischer; T. Klitsner, E. T. Swartz, R. O. Pohl, J. Vac. Sci. Techn. A7 (1989) 1259
/19/ K. Fuchs, Proc. Cambridge Phil. Soc. 34 (1938) 100
/20/ E. H. Sondheimer, Phys. Rev. 80 (1950) 401
/21/ A. F. Mayadas, M. Shatzkes, Phys. Rev. B 1 (1970) 1382
/22/ F. Völklein, E. Kessler, Phys stat sol (b) 134 (1986) 351
/23/ F. Völklein, E. Kessler, Thin Solid Films 142 (1986) 169
/24/ F. Völklein, E. Kessler, Phys stat sol (b) 143 (1987) 121
/25/ F. Völklein, E. Kessler, Phys stat sol (b) 158 (1990) 521
/26/ F. Völklein, T. Franke, Proc. 23rd Int. Therm. Cond. Conf., Nashville, Tennessee (USA), 1995

Thermal and Electrical Imaging of Surface Properties with High Lateral Resolution

E. Oesterschulze and R. Kassing

Institute of Technical Physics, University of Kassel, Heinrich-Plett-Strasse 40, D-34109 Kassel, Germany
Phone: 49 561/804-4519; FAX: 49 561/804-4136, EMail: oester@physik.uni-kassel.de

Abstract

The demand to increase the bandwidth of very large scale integrated curcuits for future applications in computer and communication electronics has led to device structure dimensions in the sub-micrometer range. The ability of the device materials to withstand stress due to the growing electrical and thermal loading will be of particular importance. The design optimization as well as the material analysis thus demand analytical tools with high lateral resolution, high bandwidth capability, and high sensitivity. In this paper we demonstrate that scanning probe microscopy (SPM) employing integrated probes is a promising candidate for not only imaging topography but simultaneously electrical and thermal device properties. For voltage contrast imaging a coplanar waveguide cantilever was designed and fabricated to be used in high frequency scanning electrical force microscopy (HFSEFM). Additionaly it is demonstrated that an in a tip of a cantilever probe integrated Schottky diode is useful for thermal surface imaging with highest temperature resolution in scanning thermal microscopy (SThM). The batch fabrication processes of both probes will be briefly introduced. Fabricated probes are characterized and first results obtained with these novel probes are presented.

Introduction

In digital computer and analog communication electronics future applications of data processing demand signal frequencies in the microwave range. Due to the physical limits of signal transfer speed this requires the device structures to be shrunken to sub-micrometer dimensions. Nowadays typical structure dimensions of very large scale integrated digital circuits are about 0.1–0.25 μm and signal frequencies reach the GHz range whereas in case of monolithic microwave integrated circuits (MMIC) in analog communication electronics frequencies already exceed some ten to hundred GHz. This development implies that the microscopic properties of substrate and layer materials are of crucial importance to withstand the increasing stress. Electrical failure due to break through on a rather microscopic scale and also - more pronounced - thermal destruction due to the increase of the dissipation energy inherent to shrinking dimensions are the future problems of microelectronics.

In present times a variety of different analytical tools are available for electrical (e.g. voltage contrast imaging via optical sampling or electron beam testing, optical and electron beam induced current (OBIC, EBIC) measurements) and thermal (e.g. infrared microscopy, fluorescence microscopy, photothermal and photoacoustic spectroscopy etc.) failure analysis in semiconductor industries. However, most of them suffer from their limited spatial and/or frequency resolution. This gets apparent defining 10 μV voltage resolution with a bandwidth of better than 1 THz in case of electrical anaylsis and 10 μK resolution in case of thermal analysis with both 1 nm spatial resolution as key parameters for future analytical tools.

Scanning probe microscopy (SPM) was introduced to be the most promising tool to fulfill these requirements. The most versatile one scanning force microscopy (SFM) was introduced by Binnig et al. for high resolution topography imaging of electrical non-conducting surfaces employing cantilever probes with an integrated sharp tip at is very end [1]. With respect to electrical and thermal characterization two distinct SPM techniques based on SFM are already available and were proven to be useful: high frequency scanning electrical force microscopy (HFSEFM) and scanning thermal microscopy (SThM) [2, 3, 4, 5, 6]. Both methods have been successfully applied for testing of electronic devices using different techniques as well as different proximal probes [2, 7, 8, 9, 10].

But in almost any case probes were single manufactured although the base component - the cantilever probe with an integrated tip of high aspect ratio made of silicon or silicon nitride - is commercially available. With very few exceptions, no attention was focused on the integration of electrical or thermal sensors on a silicon cantilever by means of microsystem technology. The advantages of micromachining – high reproducibility of technology processes and batch fabrication capability – have almost exclusively been used for the manufacturing of bare silicon cantilevers.

In this paper we describe the development and batch fabrication of novel monolithic silicon probes with integrated sensors for HFSEFM and SThM. The fabrication of these probes is based on almost identical technology processes to simplify the combination of both concepts in future. The probes have been electrically and thermally characterized to determine the voltage and temperature sensitivity.

In HFSEFM an electrical conducting cantilever and tip is used to investigate the voltage distribution of the device under test (DUT). In the non-contact mode the cantilever deflection is used to measure locally the Coulomb force between the biased tip and the operating device. For measuring the voltage contrast with high detection bandwidth of some ten to hundred GHz the cantilver has to be provided with an integrated microwave structure to obtain a well defined and sufficiently high tip voltage. Kubalek et al. employed commercially available SFM cantilevers which were completely metal coated for HF-

0-7803-4057-4/97 $10.00 ©1997 IEEE

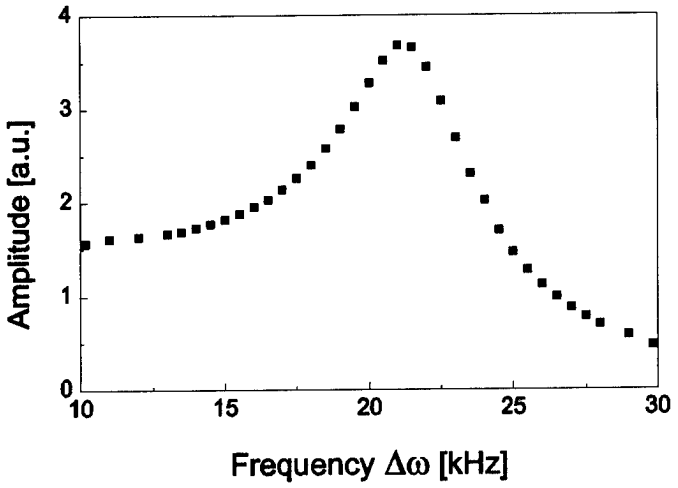


Figure 1: HFSEFM beat response to signal mixing at 1GHz as a function of the difference frequency $\Delta\omega$.

SEFM [2, 11, 12]. In this case the waveguide impedance of the probe is not well defined and thus precludes the prediction of the voltage at the tip. Nevertheless, a measurement bandwidth of up to 104 GHz and a spatial resolution below 100 nm have been demonstrated. The probe design was altered, integrating a coplanar wave guide structure in the metal layer by focused ion beam erosion [13]. Here we describe the batch fabrication of HFSEFM probes with reproducible mechanical and electrical properties. The design of the waveguide structure was improved to adjust its wave impedance for power matching over the entire coplanar line.

In case of SThM a silicon cantilever probe was batch fabricated integrating a temperature sensitive Schottky diode in the very tip. Earlier sensor concepts employing thermocouple probes suffer from the low sensitivity of less than 40–50 μV/K [5, 14] in comparison to the sensitivity of typically 1–3 mV/K for almost any semiconductor diode. Davies et al. demonstrated that Schottky photodiodes on silicon tips can be fabricated by micromachining [15]. In this case the diode was formed by an aluminium/silicon Schottky contact on a pyramidal tip which was placed on a plane silicon substrate without having a cantilever structured. Danzebrink et al. fabricated a Schottky diode cantilever by evaporating aluminium on a commercial silicon cantilever [16]. The Schottky diode was formed by the entire cantilever structure and thus was not restricted to the silicon tip. Akamine et al. integrated a planar p/n junction in the very end of a silicon cantilever without having any kind of tip [17]. We present a technological process for the micromachined fabrication of complete Schottky diode cantilevers. The diodes have been integrated on the tips of the silicon cantilevers and consist of a miniaturized titanium/silicon contact.

High frequency scanning electrical force microscopy

Working principle of HFSEFM

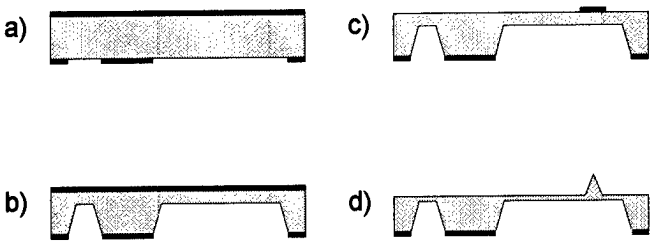


Figure 2: Microfabrication of a monolithic force cantilever based on (100) oriented silicon wafer. Steps of cantilever fabrication: a) lithography and etching process for the definition of the probe shape, b) KOH etching of a 10-30 μm thin membrane, c) definition of a circular oxide pad necessary for tip fabrication, d) underetching the oxide pad allows to get a very sharp tip on top of the silicon membrane.

In HFSEFM electrical conducting probes are utilized to measure the potential distribution of integrated circuits in the non-contact mode. Conventional probes consist of completely metallized cantilevers where the tip is biased with an external voltage $U_P(t)$. Assuming a time dependant signal $U_S(t)$ on the operating device, the cantilever deflects mechanically due to the local Coulomb force $F(U_{SP})$ between tip and sample which is proportional to the square of the voltage difference [13]:

$$F(U_{SP}) \sim (U_P(t) - U_S(t))^2 \qquad (1)$$

Detection of the cantilever deflection is performed with a conventional laser beam deflection technique. Scanning the probe above the device surface in constant height allows to image the potential distribution. A detailed description of the experimental set-up is given elsewhere [18].

The limited bandwidth of the mechanical response characteristic of the HFSEFM cantilever precludes the investigation of potential distributions in the high frequency range, e.g. the microwave range. Taking advantage of the non linear electrical force dependence in accordance with Eq. 1 allows to circumvent this restriction introducing a heterodyne technique. The tip and the device under test (DUT) are biased with sine wave signals of frequency ω_P and ω_S respectively. The difference frequency $\Delta\omega = \omega_P - \omega_S$ is adjusted to be below the mechanical resonance frequency of the cantilever. Thus the high frequency signal of the DUT is down converted to the difference frequency $\Delta\omega$ which can easily be detected measuring the cantilever deflection. Figure 1 shows the mechanical response of a metal coated cantilever applying sinusoidal signals of 1 GHz and 1 GHz-Δf sweeping the difference frequency Δf. A strong broading of the resonance peak occurs due to the electrostatic damping of the cantilever oszillation amplitude which reduces the quality factor of the cantilever dramatically as expected from theory [19].
A quantitative determination of the sample potential amplitude $U_S(\omega_S)$ of the DUT requires the knowledge of the tip voltage $U_P(\omega_P)$ as is apparent from Eq. 1. To achieve a sufficient signal to noise ratio in particular for high fre-

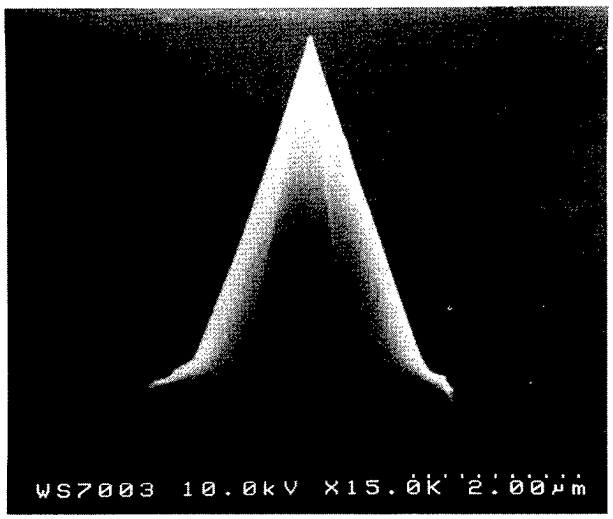


Figure 3: SEM image of an anisotropic etched silicon tip.

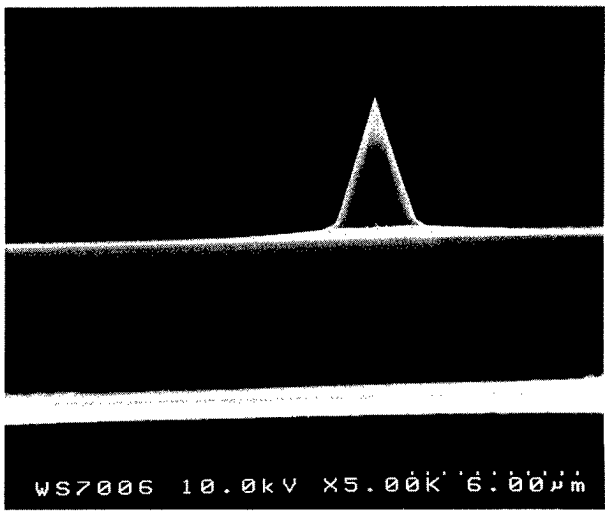


Figure 4: SEM image of the side view of the membrane including the tip.

quencies demands the integration of a wave guide structure on the cantilever with an impedance matched to that of the external syntheziser. In the following the batch fabrication process of novel coplanar wave guide cantilevers for HFSEFM is described in detail.

Fabrication of coplanar waveguide probes for HFSEFM

Probes were fabricated in a batch process from boron doped (100) oriented silicon wafers. The technological processes necessary for the fabrication of the base element of both HFSEFM and SThM probes - the cantilever with the integrated tip - are sketched in Fig 2. After thermal oxidation of a silicon wafer the bottom oxide layer is structured via optical lithography and subsequently etching with BHF in step a) to open windows for the definition of the holder and cantilever membrane. In stpe b) the

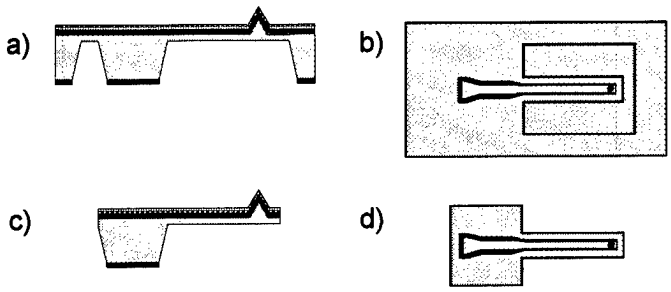


Figure 5: Microfabrication process of combined HFSEFM/SFM probes: a) metal coating of the oxidized silicon membrane of Fig. 2 d) with a thin aluminium layer, b) top view of the coplanar wave guide structure etched in the metal layer on top of the silicon membrane, c) probes are released by reactive ion etching (RIE), d) top view of the complete HFSEFM/SFM cantilever.

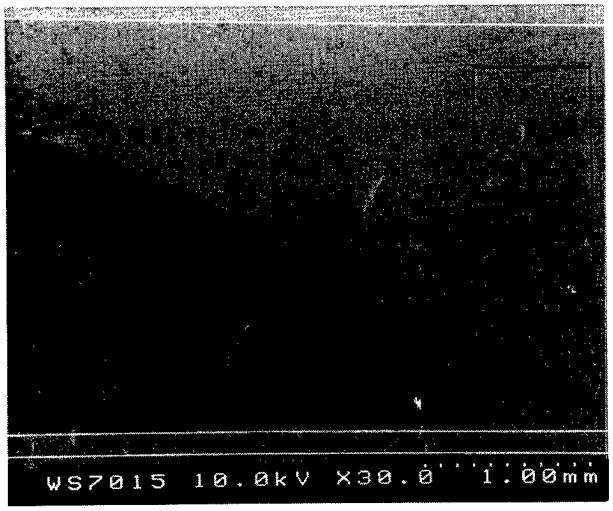


Figure 6: SEM image of the top view of the coplanar wave guide structure.

exposed silicon is etched in an aquaeous solution of potassium hydroxide (40 wt%, 60 °C) until a 30 μm membrane as well as the holder is left. On the unprocessed wafer side an oxide pad is defined utilizing a second lithography and BHF etching step. Anisotropic underetching of this pad originates in a sharp silicon tip with high aspect ratio (step d)). The height of the tip depends on the etching time as well as on the size of the oxide pad. Before proceeding with the integration of the specific sensor the wafer is thermally oxidized for a second time. The oxide layer is used as mask material for the definition of the cantilever as well as for electrically insulating it. Figure 3 shows a SEM image of a typical anisotropically etched silicon tip whereas Fig. 4 gives a side view of the ca. 6 μm thick membrane including the tip.

For the integration of the coplanar wave guide necessary for biasing the tip in HFSEFM the specific processes depicted in Fig. 5 are necessary. In step a) the cantilever is completely metallized with a 0.5 μm thick layer of alu-

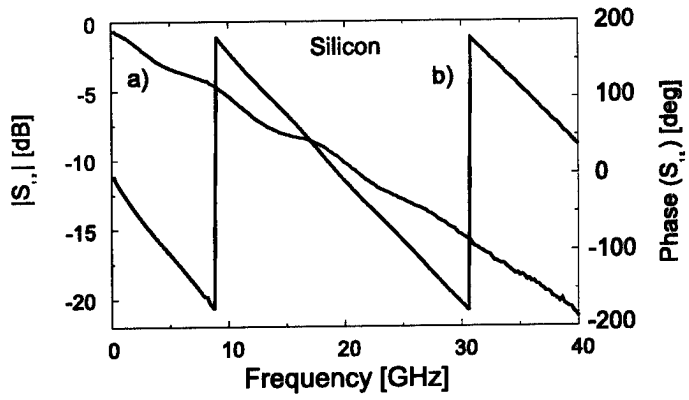


Figure 7: Power coupling coefficient S_{12} (port 1: bond pad, port 2: cantilever) as a function of the frequency (200 MHz - 40.2 GHz) for a HFSEFM probe with an integrated coplanar waveguide: a) amplitude (S_{12}) and b) phase (S_{12}).

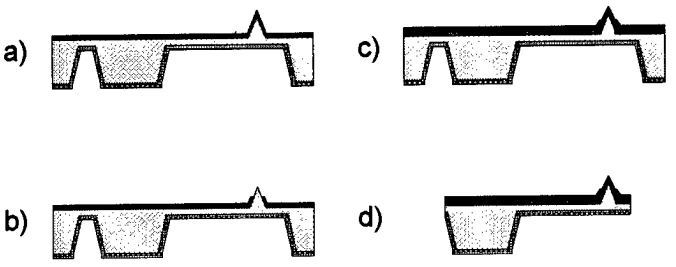


Figure 8: Microfabrication process of SThM/SFM probes: a) fabrication of an ohmic contact on back of the silicon membrane (see Fig. 2 d)) depositing a thin aluminium layer, b) the bare silicon tip is obtained removing the oxide layer at the tip apex, c) fabrication of a miniaturized Schottky contact at the silicon tip by deposition of a thin titanium layer and subsequent thermal annealing, d) Schottky diode probes are released by reactive ion etching (RIE).

minium to minimize conduction losses. The coplanar wave guide structure is transferred in a photo resist layer via optical lithography where the center electrode is carefully aligned to overlap with the sharp silicon tip. Subsequently the exposed aluminium is removed with a standard aluminium etchant to obtain the signal electrode insulated from the ground electrode. In the last step another lithograpyh process is used to define the cantilever geometry. Cantilevers are released etching first the aluminium layer wet chemically and furthermore the silicon oxide and silicon layer via reactive ion etching. The remaining cantilever is 700 μm long, 200 μm wide and about 3–8 μm thick.

Figure 6 shows a SEM image of the HFSEFM cantilever before releasing. From left to right the contact pad, the wave guide on the substrate as well as on the cantilever can be seen. The center electrode is separated by a slot from the ground electrode to either sides. The dimension of the contact pad was chosen large enough to facilitate wire bonding as well as to accomodate on-wafer microwave prober. The pad was tapered to match its wave impedance to that of the coplanar line. At the interface between holder and cantilever a second tapering of the coplanar line is necessary owing to their different substrate thickness. Due to the open end termination of the line a maximum voltage amplitude is obtained at the tip.

Characterization of HFSEFM probes

First of all the microstructured HFSEFM cantilevers were mechanically characterized. The resonance frequency of the cantilever was determined to be 15.5 kHz (quality factor 126) which is in good agreement with the theoretical value of 15.9 kHz if the above cantilever geometry is assumed.

For the electrical characterization of the probes the wave guide properties of the coplanar line were investigated. To diminish the influence of parasitic inductances or capacitances and additionally improve the measurement accuracy the coplanar line was directly connected to the contact pad with a network analyzer (HP8510) via a standard RF-probe (Cascade wph GSG). For our application it is important to determine the tip voltage $U_P(t)$ if the coplanar probe is biased with an external microwave signal. The transmission coefficient given by the scattering coefficient S_{12} was determined in a linear frequency sweep from 200 MHz up to 40.2 GHz by connecting a second RF-probe with the very end of the coplanar wave guide on the cantilever. In case of a lossless coplanar line a linear phase dependence as well as a constant amplitude is expected. Figure 7 shows the amplitude and phase of S_{12}. It is apparent that the phase varies linearly with frequency which is in correspondence to the ideal line. Additionally the amplitude decreases only slightly, which is expected for a low-loss coplanar wave guide. To reduce losses furthermore the substrate material has to be insulating which was demonstrated to work in case of semi-insulating GaAs HFSEFM probes elsewhere [20, 21].

Preliminary Results

For the sake of simplicity in first experiments the voltage distribution of metall lines on an insulating substrate were investigated. The sample imaged with the HFSEFM system was a 800 nm wide and 200 nm thick gold line on top of a silicon dioxide substrate. Both topography and voltage contrast images of this sample are shown in Fig. 9, with an applied sinusoidal signal of 8dBm at 1 GHz at the device and a sinusoidal signal of 8 dBm at 1 GHZ+20 kHz at the tip. Measurements were performed in the lift mode (Nanoscope III, Digital Instruments) keeping a constant distance of about 50 nm between tip and sample. The maximum voltage signal in this image is about 3 V. Taking a lock-in amplifier sensitivity of 200 mV and a photodiode sensitivity of approximately 33 mV/nm into account this results in a deflection amplitude of the cantilever of 1.5 nm, which is much larger than the thermal noise of the vibrating cantilever. This first result underlines the suitability of the concept and the resolution capabilities of HFSEFM.

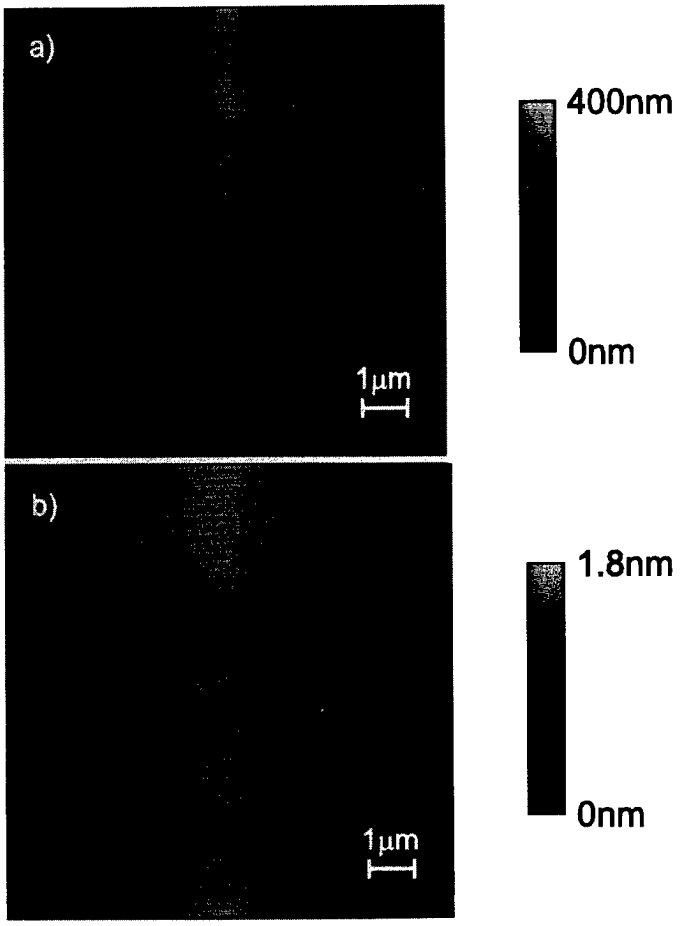


Figure 9: Topography (top), and voltage contrast (bottom), of a single gold line.

Scanning thermal microscopy

Working principle of SThM

With the SThM the surface temperature is mapped instead of the voltage. In this case it is more advantageous to perform imaging in the contact mode rather than in the non-contact mode to improve the lateral resolution and the measurement accuracy. Scanning the thermal probe over the device the heat transfer mechanism is dominated by the heat conduction between the sample and the tip [22].

Furthermore, if the temperature sensitive area is miniaturized and is placed at the very tip of the thermal probe, heat losses are diminshed and the detected temperature corresponds in a good approximation to the actual local device temperature. We suggest near-field temperature mapping by a Schottky diode probe. To fulfill the requirement of local temperature detection, the Schottky contact was embedded in the probe tip and the contact size was decreased. From the temperature dependence of the DC I-V curve of the diode two measurement modes can be established for the probe operation in the SThM. When the diode is forward biased with a constant current, the voltage shift of the diode is measured. In case the diode is reversed biased with constant voltage, measurement of the reverse bias current has to be performed.

Fabrication of Schottky diode probes for SThM

For the SThM probe the basic technological steps are shown in Fig. 8. A more detailed description of the fabrication process is given elsewhere [23]. In the first step an ohmic contact is produced on the backside of the cantilever. For this purpose the oxide is removed on the same side and a thin aluminium layer is deposited. The wafer is then sintered at 580 °C for 20 min to produce the ohmic contact between the silicon and the aluminium (step a)). In the next step the Schottky diode is constructed on the silicon tip. To restrict the diode to the very tip photoresist is spun on leaving the tip apex uncovered [15]. The latter is opened by wet chemical etching in buffered HF to

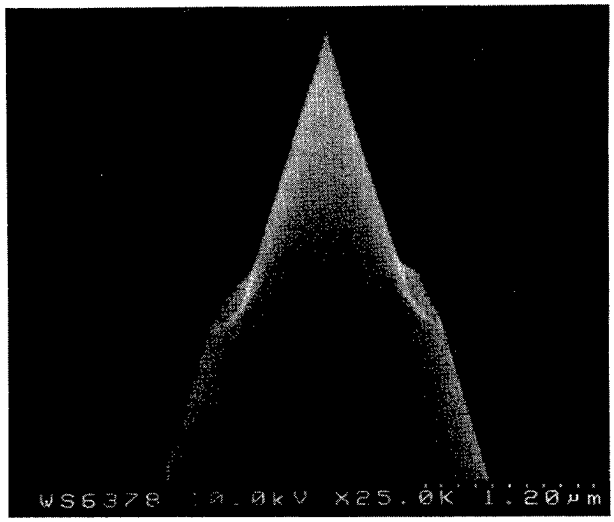


Figure 10: SEM image of a silicon tip with opened oxide layer at the tip apex.

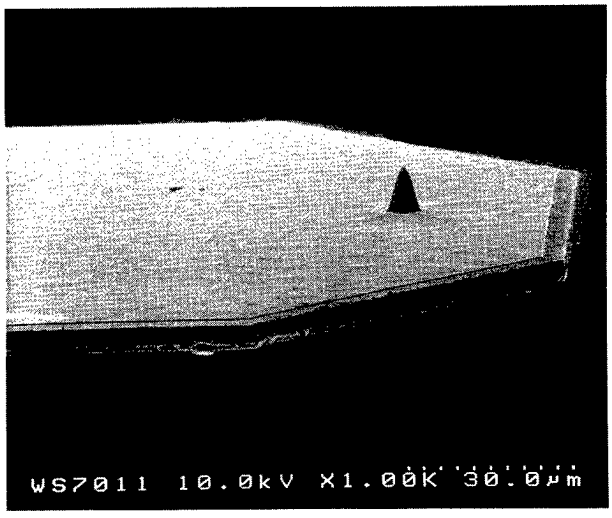


Figure 11: SEM image of the micro-structured Schottky diode cantilever.

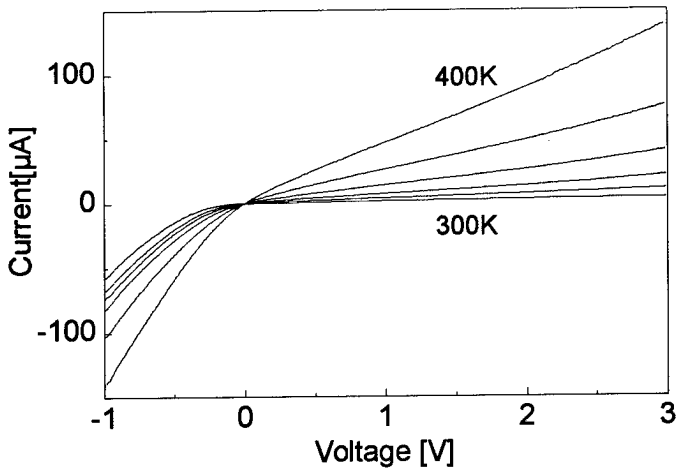


Figure 12: I-V curve of the Schottky diode cantilever for six different temperatures starting with 300 K and increasing by 20 K steps.

obtain bare silicon at the tip apex (step b)). Subsequently a titanium layer is deposited on the entire structure, originating a Schottky diode at the very end of the tip (step c)). In the last lithographic step the cantilever is defined. The exposed titanium is removed by wet chemical etching in buffered HF (step d)). As was already mentioned in case of the HFSEFM probe the exposed SiO_2 layer as well as the silicon was etched through by reactive ion etching to free cantilevers. The dimension of the STHM cantilever are identical with those of the HFSEFM probe.

Figure 10 shows a SEM image of an opened tip. The opening in the oxide is approximately 1 μm and the tip radius is less than 50 nm. In Fig. 11 an SEM image of the micro-structered Schottky diode cantilever is depicted where the cantilever thickness is approximately 5 μm.

Characterization of SThM probes

The mechanical, electrical, and thermal properties of SThM probes have been characterized. Due to the same probe geometry the mechanical cantilever properties resemble that of HFSEFM probes already discussed above. The resonance frequency was determined to be typically in the range of 14-18 kHz with a quality factor of about 120-140. For the electrical characterization of the Schottky diode integrated in the tip I-V measurements were performed at varying temperature. Figure 12 shows the latter for discrete temperatures between 300 K and 400 K. As expected from theory the curves shift to smaller voltages in the forward bias range when temperature is increased. The shift was found to be approximately 3 mV/K which corresponds to the theoretical value [24]. The high sensitivity enables the probes to be used in SThM. In the reverse bias range the reverse current is nearly independent of the applied voltage for room temperature but rises strongly when the probe is heated. For the probes investigated quality factors of 1.7–2.5 were determined. The barrier height varried between 0.7 eV and 0.8 eV, which is slightly higher than stated in literature [24, 25]. This might be due to the influence of the surface pretreatment before titanium deposition.

Summary

For the electrical and thermal characterization of surfaces with scanning probe microscopy techniques novel proximal probes based on the scanning force microscopy (SFM) cantilever concept were introduced. A coplanar wave guide structure was integrated on an insulating cantilever to bias the tip. These probes were used to investigate the voltage contrast distribution of electronic devices utilizing a heterodyne technique. First results of the investigation of metal lines on an insulating substrate were discussed. Furthermore a miniaturized diode probe integrated in a cantilever tip was presented. The temperature sensitivity of up to 3 mV/K underlines already the suitability of the probe for SThM when compared to conventional thermocouple probes with a sensitivity of less than 40-50 μV/K. Although not discussed in this paper there are a variety of other microscopy techniques where the diode concept is of value; e.g. as miniaturized photo detector in scanning near-field microscopy (SNOM), as non-linear electrical mixer in HFSEFM, etc. The fabrication process of both probes relies on batch processes to obtain cantilever with reproducible properties. The combination of both concepts was taken into account adapting the technological processes in a way which makes the fabrication of a single probe for both HFSEFM and SThM feasible.

Acknowledgement

We like to thank A. Majumdar, (University of California, Berkeley, Department of Mechanical Engineering) for his support on HFSEFM. Furthermore we are thankful to G. Kompa and F. van Raay for the electrical characterization of the coplanar wave guide probes.

References

[1] G. Binnig, C. F. Quate, and C. Gerber, "Atomic Force Microscope," *Phys. Rev. Lett.* **56**, pp. 930–933, 1986.

[2] C. Böhm, F. Saurenbach, P. Taschner, C. Rohts, and E. Kubalek, "Voltage contrast in integrated circuits with 100 nm spatial resolution by scanning force microscopy," *J. Phys. D* **26**, pp. 1801–1805, 1993.

[3] A. Majumdar, J. P. Carrejo, J. Lai, and M. Chandrachood, "Thermal imaging of electronic materials and devices using the atomic force microscope," *SPIE Vol.* **1855**, pp. 209–217, 1993.

[4] R. Kassing and E. Oesterschulze, "Sensors for scanning probe microscopy." Nato workshop, Portugal, Lissabon, to be published in *NATO ASI Series*, Kluwer Academic Publishers, 1996.

[5] E. Oesterschulze, M. Stopka, L. Ackermann, W. Scholz, and S. Werner, "Thermal imaging of thin

films by scanning thermal microscopy," *J. Vac. Sci. Technol. B* **14**(2), pp. 832–837, 1996.

[6] M. Maywald, R. J. Pylkki, and L. J. Balk, "Imaging of local thermal and electrical conductivity with scanning force microscopy," *Scanning Microsc.* **8**, pp. 181–188, 1994.

[7] A. S. Hou, F. Ho, and D. M. Bloom, "Picosecond Electrical Sampling Using A Scanning Force Microscope," *Electronic Letters* **28**(25), p. 2302, 1992.

[8] R. A. Said, G. E. Bridges, and D. J. Thomson, "Scanned electrostatic force microscope for noninvasive high frequency potential measurement," *Appl. Phys. Lett.* **64**(11), pp. 1442–1444, 1994.

[9] B. A. Nechay, F. Ho, A. S. Hou, and D. M. Bloom, "Applications of an Atomic Force Microscope Voltage Probe with Ultrafast Time Resolution," *J. Vac. Sci. Technol. B* **13**(3), p. 1369, 1995.

[10] A. S. Hou, B. A. Nechay, and D. M. Bloom, "Scanning Probe Microscopy for Testing Ultrafast Electronic Devices," *Optical and Quantum Electronics* **28**(7), pp. 820–841, 1996.

[11] C. Böhm, J. Sprengepiel, M. Otterbeck, and E. Kubalek, "Voltage contrast in submicron integrated circuits by scanning force microscopy," *J. Vac. Sci. Technol. B* **14**(2), pp. 842–844, 1996.

[12] A. Leyk, C. Böhm, D. van der Weide, and E. Kubalek, "104 GHz Signals Measured by a High Frequency Scanning Force Microscope Testsystem," *Electron. Lett.* **31**(13), pp. 1046–1047, 1995.

[13] C. Böhm, M. Otterbeck, S. Lipp, L. Frey, R. Reuter, A. Leyk, W. Mertin, F. J. Tegude, and E. Kubalek, "Design and Characterization of Integrated Probes for Millimeter Wave Applications in Scanning Probe Microscopy." *IEEE MTT-S*, pp. 1529-1532, 1996.

[14] E. Oesterschulze and M. Stopka, "Photothermal Imaging by Scanning Thermal Microscopy ," *J. Vac. Sci. Technol. A* **14**(3), pp. 1172–1177, 1996.

[15] R. C. Davis, C. C. Williams, and P. Neuzil, "Micromachined submicrometer photodiode for scanning probe microscopy," *Appl. Phys. Lett.* **66**, pp. 2309–2311, 1995.

[16] H. U. Danzebrink, O. Ohlsson, and G. Wilkening, "Fabrication and characterization of optoelectronic near-field probes based on an SFM cantilever design," *Ultramicroscopy* **61**, pp. 131–138, 1995.

[17] S. Akamine, H. Kuwano, and H. Yamada, "Scanning near-field optical microscope using an atomic force microscope cantilever with integrated photodiode," *Appl. Phys. Lett.* **68**(5), pp. 579–581, 1994.

[18] S. Münster, T. Chang[a], E. Oesterschulze, A. Majumdar[a], and R. Kassing, "Micromachined Probes for High Frequency Scanning Electrical Force Microscopy and Scanning Joule Expansion Microscopy," presented at Scanning Tunneling Microscopy 97 (STM97), Hamburg, Germany, 1997.

[19] D. Sarid, *Scanning-Force-Microscopy*, Oxford University Press, New York, 1991.

[20] M. Stopka, S. Münster, T. Leinhos, C. Mihalcea, W. Scholz, A. Leyk, W. Mertin, and E. Oesterschulze, "Micromachined Probes for High Frequency Scanning Force Microscopy and Scanning Thermal Microscopy," vol. 3009 of *Proceedings of SPIE*, pp. 92–100, 1997.

[21] S. Heisig, H.-U. Danzebrink, A. Leyk, W. Mertin, S. Münster, and E. Oesterschulze, "Monolithic Gallium Arsenide Cantilever for Scanning Near-field Microscopy," to be published in Ultramicroscopy, presented at Near-fiel Optical Microscopy NFO-4, Jerusalem, Israel, 1997.

[22] M. Stopka, *Rasterwärmemikroskopie mit thermoelektrischen Mikrosonden.* PhD thesis, Universität Gesamthochschule Kassel, 1996.

[23] T. Leinhos, M. Stopka, and E. Oesterschulze, "Micromachined Fabrication of Silicon Cantilevers with in the Tip Integrated Schottky Diodes," presented at Scanning Tunneling Microscopy 97 (STM97), Hamburg, Germany, 1997.

[24] E. H. Rhoderick and R. H. Williams, *Metal-Semiconductor contacts*, vol. 19 of *Monographs in electrical and electronic engineering*, Clarendon Press, Oxford, second ed., 1988.

[25] W. D. Bosscher, R. L. V. Meirhaeghe, P. L. Hanselaer, L. Caenepeel, W. H. Laflère, and F. Cardon, "The influence of silicide formation on the barrier height of Ti/Si MIS Schottky barriers," *Semicond. Sci. Technol.* **1**, pp. 376–382, 1986.

Thermal Conductivity Measurement and Microscopy of Thin Film Structures

T.Borca-Tasciuc,[1] G.Chen,[1] D. Wang,[2] and K. L. Wang[2]

[1]Mechanical and Aerospace Engineering Department
[2]Electrical Engineering Department USA
University of California, Los Angeles, CA 90095

Abstract

This work discusses two techniques for thermophysical property characterization: scanning laser thermoelectric microscope (SLTM) and scanning thermal microscope (SThM). The SLTM can be used to measure thermal diffusivity of thin films as well as bulk materials. In SLTM, a modulated laser beam is focused through a transparent substrate onto the film-substrate interface. The generated thermal wave is detected using a fast responding thermocouple formed between the sample surface and the tip of a sharp probe. By scanning the laser beam around the thermocouple, the amplitude and phase distributions of the thermal wave are obtained with micrometer resolution. Thermal diffusivity of the film is determined by fitting the obtained phase signal with a three dimensional heat conduction model. The SThM technique is based on measuring the temperature variations of a laser heated nanoscale temperature sensor when the sensor is scanned over the sample surface. The temperature sensor is a thermistor film deposited onto the tip of an atomic force microscope cantilever. Although the SThM shows a high spatial resolution, the thermal image is strongly coupled to topographical variations.

Introduction

Thermophysical properties are the most difficult parameters to characterize in the evaluation of thermoelectric materials. The recent interest in low-dimensional thermoelectric structures [1] makes these characterizations even more challenging. A complete physical understanding of transport mechanisms in low-dimensional structures calls for measurements at both macroscopic and microscopic scales.

At the macroscopic scale, thermophysical property characterization is more difficult for thin films than for bulk materials [2-5]. Heat conduction in thin films is often anisotropic and thermophysical properties are different in the in-plane and cross-plane direction. One major difficulty is determining the in-plane thermophysical properties of thin films because in this case most heat is conducted through the substrate rather then through the film. Two possible ways to overcome this problem are substrate removal or obtaining the two dimensional temperature distribution generated around a microscale heat source. The substrate removal [6-7] is usually done by selective chemical etching but is limited only to film-on-substrate systems for which there are selective etchants. In the other approach a microscale heat source is created into the film [8-10] and from the spread of the heat source, it may be possible to obtain anisotropic thermophysical properties of the thin film and/or the bulk material.

Macroscopic thermophysical properties characterization often provides the effective thermophysical properties of a whole structure such as the thermal conductivity of superlattices. From these measurements models can be developed to assist the understanding of transport processes [11-12]. More physical understanding of the transport mechanisms at the nanometer scale could be realized if local thermophysical property can be measured. One possible technique that can enable this measurement is the scanning thermal microscope (SThM) [13-17]. In this technique a temperature probe is scanned in contact or at a constant distance over the sample surface and the temperature of the sensor is recorded. The spatial resolution of the temperature measurement is related to the dimensions of the temperature sensor and also to the probe-sample thermal interaction. Because the heat transfer parameters between the probe and the sample surface are unknown, the SThM is useful mainly for qualitative measurements and contrast imaging.

This work discusses two techniques that can be used for thermophysical property characterization. At the macroscopic scale, a scanning laser thermoelectric microscope (SLTM) is used for determining the anisotropic thermophysical properties of thin films for film-on-substrate systems without the removal of the substrate. At the microscopic scale, an SThM based on atomic force microscopy (AFM) is employed for local thermophysical property characterization.

The SLTM employs modulated laser radiation to generate a thermal wave in the sample, and scans the focused laser beam over the area of interest. The laser wavelength is tuned to a range where the substrate is transparent such that the laser beam penetrates the substrate and acts as a micrometer scale heat source in the film. The detection is done using a fast thermoelectric effect created by direct contact between the metallically covered surface of the sample and the sharp tip of an electrochemically etched wire. Thermophysical properties of the film or the substrate material can be determined from the amplitude and/or the phase of the thermoelectric voltage signal.

The presented SThM is based on the AFM setup. A temperature sensor is deposited onto the cantilever tip. The feedback laser used for monitoring the cantilever deflection also acts as a heat source due to its partial absorption onto the cantilever. When the tip is scanned in contact to the sample surface, the temperature of the sensor varies as a function of the local thermal properties of the sample and tip-surface interaction. Simultaneous topographical and thermal images are obtained. This setup allows imaging for both electrically conductive and insulating samples. Experimental results are presented for the cross-section of a 700Å/700Å AlGaAs superlattice structure. Although the SThM shows a high spatial resolution, the thermal image is strongly influenced by topographical variations.

0-7803-4057-4/97 $10.00 ©1997 IEEE

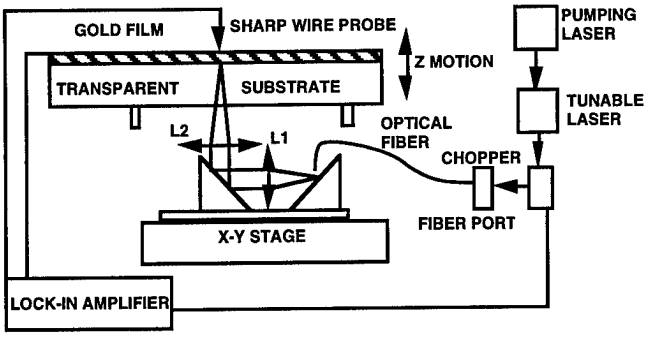


Fig.1. Scanning Laser Thermoelectric Microscope.

Scanning Laser Thermoelectric Microscope(SLTM)

The method is designed to measure thermophysical properties of films on a substrate or bulk materials. A focused laser beam is scanned through the transparent substrate over the film-substrate interface in order to produce thermal waves that are detected using a fine thermocouple formed between the sample and the probe. Thermophysical properties can be determined from the amplitude and phase profiles of the data.

Our current experimental setup is shown in Fig.1. An argon laser is used to pump a tunable Ti-Sapphire laser that may output laser radiation with a wavelength between 700-900 nm. The modulated radiation is coupled into a single mode optical fiber. The optical system used to focused the laser radiation is assembled onto a base plate, which is placed onto a x-y scanner (in our case, it is fitted into the scanner of an AFM). A specially designed holder is used to maintain the sample at an adjustable distance above the scanning laser such that the laser beam diameter at the film-substrate interface can be varied. The top surface is a conducting element that absorbs the laser radiation and also forms one leg of the thermocouple. The other leg of the thermocouple is formed by a fine wire contacting the surface. The thermocouple junction formed between the film and the wire has virtually no mass and is thus expected to be fast responding.

An experiment is conducted with a 150nm gold film evaporated on the top surface of a glass slide. The probe used to detect the thermal wave is a sharp K-type thermocouple wire obtained through electrochemical etching in a solution of sulfuric acid. The tip is brought into contact with the gold

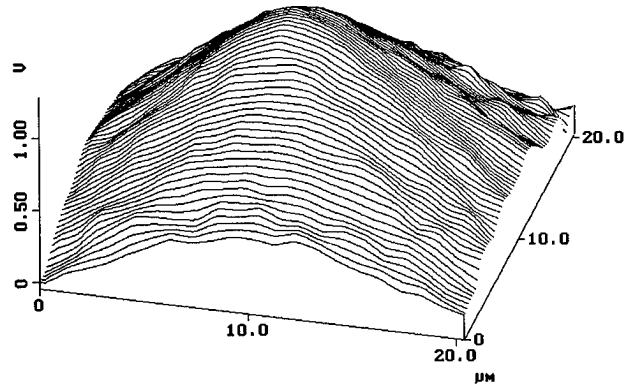


Fig.2 Distribution of phase of the thermal signal.

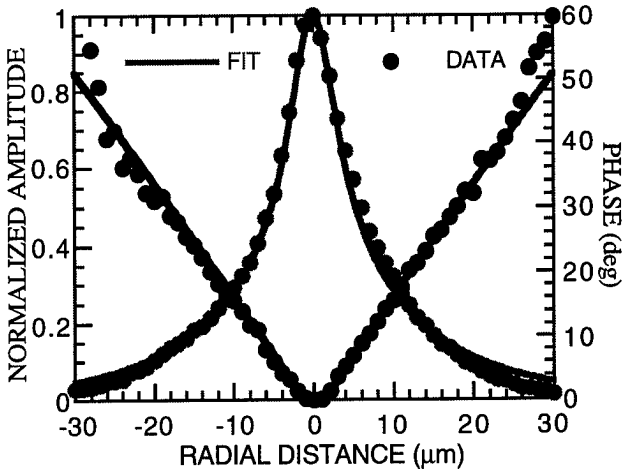


Fig.3 Fitting of phase and amplitude of the experimental signal of a gold-on-glass sample with a film diffusivity of $0.96 cm^2 s^{-1}$, modulation frequency at 3200Hz.

film. The ac components of the amplitude and the phase of the thermoelectric voltage developed at the tip-surface junction are picked-up by a lock-in amplifier.

Figure 2 shows the distribution of the phase of the experimental thermal signal. Based on a 3-dimensional heat conduction model, a fitting scheme is employed to determine the thermal diffusivity of the thin film [8]. Figure 3 shows the phase and the amplitude fits of the experimental signals for the gold film with a thermal diffusivity value of $0.96\ cm^2\ s^{-1}$.

Scanning Thermal Microscope (SThM)

The purpose of the method is to image thermophysical properties variations at the nanometer scale. The experimental setup is a Digital Instruments Multimode Scanning Probe Microscope. The microscope is design to image simultaneously the topography and the temperature variations on the sample surface. The temperature measurement is performed by a thin film thermistor deposited onto the cantilever tip.

The experimental setup is shown in Fig. 4. Topography imaging is done by a classic AFM setup. A laser beam is employed to probe the cantilever deflection that occurs when the tip is scanned over the sample surface. However, some of the incident laser radiation is absorbed onto the cantilever, generating a steady heat source. As a result of the laser absorption the overall temperature of the cantilever system increases. If the cantilever system is brought into the proximity of the sample surface, the tip temperature will change due to the heat exchange with the surface. The new tip temperature is dependent on the local thermal conductivity and tip-surface thermal conductance. If the tip-sample thermal conductance is constant during scanning it is possible to image the relative contrast in the local thermophysical properties since variations in the tip temperature are proportional to thermal conductivity variations. The temperature dependent resistance variations of the thermistor are monitored by a Whetstone bridge setup.

Figure 5(a) shows the topography and Fig. 5(b) the thermal signal at the same location obtained for a 700Å/700Å

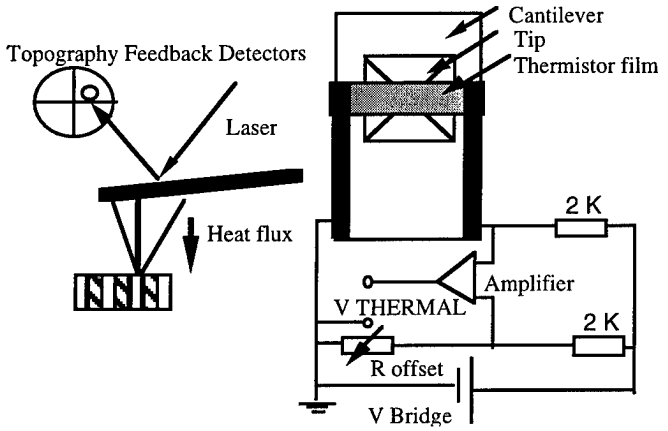


Fig. 4 Scanning Thermal Microscope.

GaAs/AlAs periodic structure deposited onto a GaAs substrate. The imaging is obtained by scanning over the cross-section of a freshly cleaved sample. Immediately after the cleavage, being exposed to air, the AlAs and GaAs layers oxidize at different rate. This behavior enables the layer identification since the AlAs layers have now higher topography and are shown in bright colors in the topography image [Fig. 5(a)]. The contrast is reversed in the thermal image [Fig. 5(b)], higher temperatures being shown in dark colors. The spatial resolution of the temperature sensor seems to be very close to the spatial resolution of a regular AFM probe since both images shown common features having almost the same dimensions.

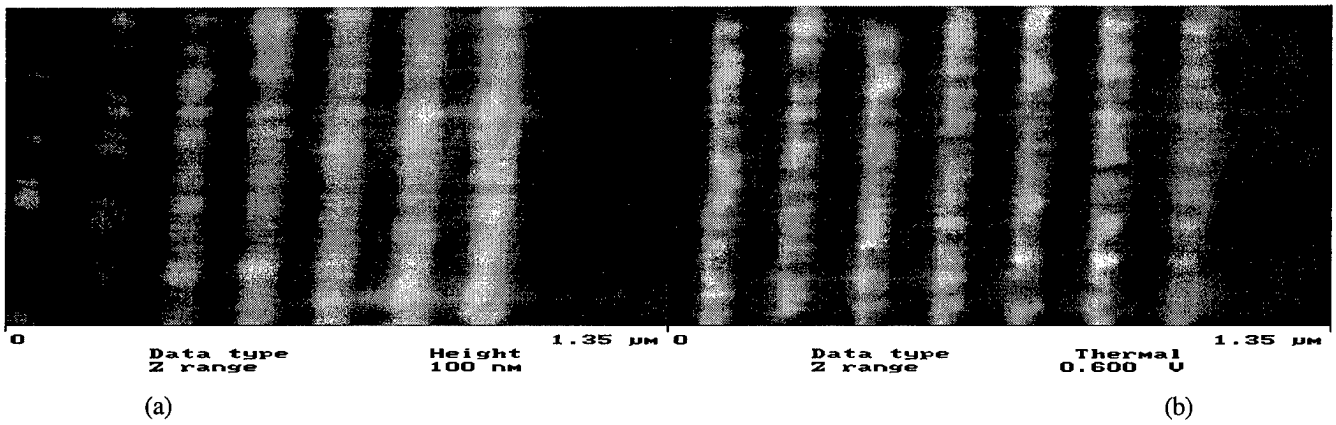
In order to see more clearly the correlation between the sample topography and the temperature signal, Fig. 6 shows a plot of the temperature and height signals along the same scan line. The temperature is constant when the probe is scanned over the GaAs substrate but decreases when approaches the lattice side. Over the GaAs layers the temperature is smaller than over the GaAs substrate. The largest temperatures are recorded over the AlAs layers. The temperature variations are not consistent with the variations in the thermophysical properties of superlattices [11] since the highest temperatures are expected to occur over the GaAs layers, which have the lowest thermal conductivity on this sample. A more complex tip-sample thermal interaction has to be assumed in order to explain these results.

One possible explanation is based on the influence that the sample topography may have on the heat transfer between probe and surface. In a simple model it can be considered that the tip and sample surface thermally interact through direct heat conduction and air conduction. Both heat transfer mechanisms may have a large effect in determining the tip temperature. The direct heat conduction contact region is very small since the tip radius is usually around 10-50 nm. However a nm scale liquid layer usually found over samples surface can increase this effective area [16]. Local contact area variations depend on various factors including the probe geometry, sample topography, hardness variations, temperature, adhesion forces between the liquid layer and tip and sample surfaces. These variations can strongly affect the sensor temperature and can explain the temperature spikes when the tip is scanned over a hill or a surface impurity. In addition to direct heat conduction through the contact, the tip temperature is also influenced by the thermal interaction between the cantilever and the sample through air or radiation. During scanning the contact area and also the air gap and the air-conduction affected areas are not constant. When the probe approaches a topographical feature the lateral heat conduction can occur. The magnitude of the heat flux exchanged through the air is strongly dependent on the air gap between the two surfaces. This mechanism can explain the temperature drops that occur when the probe is scanning through a "valley" .

In order to obtain thermophysical property characterization at nanometer scale the influence of the above discussed factors in establishing the tip temperature must be minimized. One possible way to reduce the air conduction influence is to conduct the experiment in vacuum. Furthermore, using modulation techniques may reduce the influence of the above parameters on the phase signal.

Conclusions

Two scanning techniques, the SLTM and SThM, are employed for thermophysical property characterization at macroscopic and microscopic scales. A SLTM is developed for thin film thermophysical properties characterization at



(a) (b)

Fig.5 Imaging of (a) topography and (b) thermal signal for a 700Å/700Å GaAs/AlAs lattice structure.

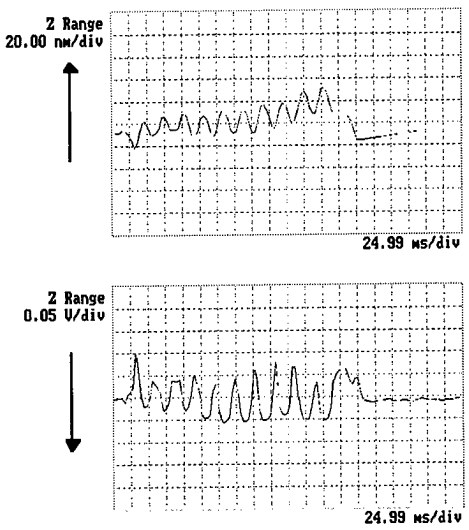


Fig.6 Height (up) and temperature signal (down) obtained along a single scan line over a AlGaAs superlattice.

micrometer scale without the removal of the substrate. Thermophysical properties of the film can be obtained from the amplitude or the phase images. Experimental results are presented for a 150nm gold film deposited onto a glass substrate. In a different setup, a SThM based on a thermistor deposited at the tip of an AFM cantilever is used for local thermal conductivity imaging. Experimental results lead to the conclusion that when the sensor dimensions and the surface topography approach the same dimensional scale, the heat transfer between the sensor and the sample becomes more complex and the sensor temperature is strongly influenced by the local topography of the sample. However, by employing a modulated technique and conducting the experiment under vacuum it may be possible to image the local thermal diffusivity of the sample.

Acknowledgments

This work is supported by an NSF young investigator award to G. C., NSF grant CTS 96-22274, and a DOD/ONR MURI grant on thermoelectricity.

References

[1] L. D. Hiks and M. S. Dresselhaus, "Effect of quantum-well structures on the thermoelectric figure of merit," Phys. Rev. B. **47**(1993) 12727.

[2] C. L.Tien and G. Chen, "Challenges in microscale radiative and conductive heat transfer," J. Heat Transf. **116**(1994) 799.

[3] D.G. Cahill, H.E. Fischer, T. Klitsner, E. T. Swartz, and R. O. Pohl, "Thermal conductivity of thin films: measurement and understanding," J. Vac. Sci. & Tech. A. **7**(1989) 1259.

[4] I. Hatta, "Thermal diffusivity measurement of thin films and multilayered composites," Int. J. of Thermophys. **11**(1990) 293.

[5] K. E. Goodson and M. I. Flik, "Solid layer thermal-conductivity measurement techniques," Appl. Mech. Rev. **47**(1994) 101.

[6] X. Y. Yu, G. Chen, A. Verma, and J. S. Smith, "Temperature dependence of thermophysical properties of GaAs/AlAs periodic structure," Appl. Phys. Lett. **67**(1995) 3554.

[7] X. Y. Zhang, S. Z. Li, M. Chen, and K. L. Wang, "Giant reduction in lateral thermal conductivity of thin nitride/ silicon/oxide membrane measured with a suspended microstructure," ASME DSC-**59**, (1996) 93.

[8] T. Borca-Tasciuc and G. Chen, "Scanning laser thermoelectric microscope for thin film thermophysical property measurement," submitted for presentation at 1997 IMECE Dallas USA.

[9] J. Hartmann, P. Voigt, and M. Reichling, "Measuring local thermal conductivity in polycrystalline diamond with a high resolution photothermal microscope," J. Appl. Phys. **81** (1997) 2966.

[10] L. Pottier, "Micrometer scale visualization of thermal waves by photoreflectance microscopy," Appl. Phys. Let. **64**(1994) 1618.

[11] G. Chen, "Size and interface effects on thermal conductivity of superlattices and periodic thin film structures," J. Heat Trans. **119**(1997) 220.

[12] G. Chen, "Heat transport in the perpendicular direction of superlattices and periodic thin film structures," ASME DSC **59**(1996) 13.

[13] M. Nonnenmacher and H.K. Wickramasinghe, "Scanning probe microscopy of thermal conductivity and subsurface properties," Appl. Phys. Lett. **61**(1992) 168.

[14] A. Majumdar, J. Lai, M. Chandrachood, O. Nakabeppu, Y. Wu, and Z. Shi, "Thermal imaging by atomic force microscopy using thermocouple cantilever probes," Rev. Sci. Instrum. **66**(1995) 3584.

[15] E. Oesterschulze, M. Stopka, 1. Ackermann, W. Scholz, and S. Werner, "Thermal imaging of thin films by scanning thermal microscope," J. Vac. Sci. & Technol. B. **14**(1996) 832.

[16] A. Majumdar, K. Luo, Z. Shi and J. Varesi, "Scanning thermal microscopy at nanometer scales: A new frontier in experimental heat transfer," Experim. Heat Transf. **9**(1996) 83.

[17] R. J. Pylkki, P. J. Moyer, and P. E. West, "Scanning near field optical microscopy and scanning thermal microscopy," Jpn. J. Appl. Phys. **33**(1994) 3785.

Damped Thermoelectric Waves

C. B. Vining
ZT Service, Inc., 2203 Johns Circle, Auburn, AL 36830 USA, vining@zts.com

Abstract

Dynamic measurement techniques such as ac resistivity and the Cahill 3-ω [1] thermal conductivity method induce periodic currents in materials. In thermoelectric materials the coupling between electrical and thermal effects means the normal mode excitations are generally attenuated waves of mixed electrical/thermal character. Since ZT is one measure of the coupling between the electrical and thermal effects it is perhaps not surprising that ZT is also a measure of the mixing. This paper examines solutions to the coupled thermoelectric diffusion problem and discusses some implications for measurements.

Introduction

Diffusion of heat and charge in solids is ordinarily well described by the approximate diffusion equations

$$\begin{aligned}\dot{\eta} &= d_e \nabla^2 \eta \\ \dot{T} &= d_q \nabla^2 T\end{aligned} \tag{1}$$

where η is the electrical potential (or more precisely, the electrochemical potential), T is the temperature, and d_e and d_q are the electrical and thermal diffusivities. These diffusion equations derive from conservation of energy and charge considerations, with only a few simplifying assumptions.

In thermoelectric materials heat and electricity are coupled, an effect neglected above. This paper seeks to identify when the above expressions are adequate and when a more complete treatment is required.

First, the coupled diffusion equations are derived and the characteristic eigenvalue problem is solved to identify the normal modes. The resulting eigenvalues represent diffusivity values for coupled temperature-potential diffusion and the eigenvectors indicate the degree to which temperature and potential diffusion are mixed in the normal modes. Next the behavior of the normal mode diffusion constants is examined as a function of coupling. And as an example, the coupled boundary-value problem corresponding to the 'flash' method of determining the thermal diffusivity is considered.

Thermoelectric Diffusion Equations

The first task is to write the problem in terms of measurable properties. Start with conservation of charge and energy

$$\begin{aligned}\dot{\rho} + \nabla \cdot \bar{i} &= 0 \\ \dot{U} + \nabla \cdot \bar{U} &= 0\end{aligned} \tag{2}$$

and definitions of the entropy flux ($\bar{S}$) and time rate of change of the entropy density ($\dot{S}$)

$$\begin{aligned}T\bar{S} &= \bar{U} - \eta \bar{i} \\ T\dot{S} &= \dot{U} - \eta \dot{\rho}\end{aligned} \tag{3}.$$

Combining (2) and (3) and defining an entropy source term, s,

$$\begin{aligned}s &\equiv \frac{1}{T}\left(\bar{S} \cdot \left(-\nabla T\right) + \bar{i} \cdot \bar{E}\right) \\ \dot{S} + \nabla \cdot \bar{S} &= s\end{aligned} \tag{4}$$

allows connection to the ordinary transport coefficients, assuming the currents are linearly proportional to the gradients of the potentials, by

$$\begin{aligned}\bar{i} &= \sigma\left(\bar{E} - \alpha \bar{\nabla} T\right) \\ \bar{S} &= \alpha \bar{i} - \left(\frac{\lambda}{T}\right)\bar{\nabla} T\end{aligned} \tag{5}.$$

Using a more compact matrix notation.

$$\begin{pmatrix} \bar{i} \\ \bar{S} \end{pmatrix} = L \begin{pmatrix} \bar{E} \\ -\bar{\nabla} T \end{pmatrix} \tag{6}$$

with the transport matrix L given by

$$L = \begin{pmatrix} \sigma & \sigma\alpha \\ \sigma\alpha & \lambda \gamma_L / T \end{pmatrix} \tag{7}.$$

Here i is the electric current density, E is the electric field, ∇T is the temperature gradient, σ is the electrical conductivity, α is the Seebeck coefficient and λ is the thermal conductivity (measured under the condition $\bar{i}$=0). γ_L is a convenient measure of the relative strength of the thermoelectric effects

$$\begin{aligned}\gamma_L &\equiv 1 + \frac{{L_{12}}^2}{L_{11}L_{22} - {L_{12}}^2} \\ &= 1 + \frac{\sigma \alpha^2 T}{\lambda} \\ &\equiv 1 + ZT\end{aligned} \tag{8}$$

where ZT is the dimensionless thermoelectric figure of merit.

Within the same linear response regime, the time variations as can be written

$$\begin{aligned}\dot{\rho} &= C_{11}\dot{\eta} + C_{12}\dot{T} \\ \dot{S} &= C_{21}\dot{\eta} + C_{22}\dot{T}\end{aligned} \tag{9}$$

which is conveniently summarized in matrix form as

$$\begin{pmatrix} \dot{\rho} \\ \dot{S} \end{pmatrix} = C \begin{pmatrix} \dot{\eta} \\ \dot{T} \end{pmatrix} \tag{10}.$$

with the capacity matrix, C, given by various thermodynamic derivatives.

The symmetry of C is a consequence of the second law of thermodynamics and the off-diagonal elements (C_{12} and C_{21}) are exactly equal. C_{22}-C_{12}^2/C_{11} is essentially the heat capacity. C_{11} is related to the carrier concentration although in general it is a slightly more complex quantity. C_{21} represents the change

in entropy (or heat) when the charge is changed isothermally and C_{12} represents the change in charge with temperature, keeping the electrochemical potential constant. In principle each coefficient can be both calculated and measured, although the cross coefficients rarely are.

A 'γ' can be defined for the C matrix as well

$$\gamma_C = 1 + \frac{C_{12}^{\ 2}}{C_{11}C_{22} - C_{12}^{\ 2}},$$

which again is a convenient measure of the relative magnitude of the cross effects.

Combining conservation of energy and charge with linear response considerations yields the coupled diffusion equations

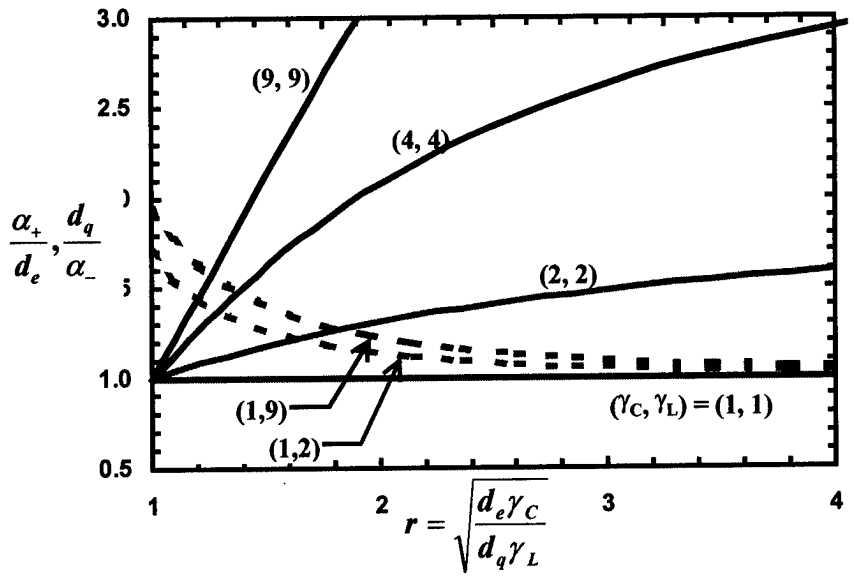


Figure 1: Actual diffusivity values α_+ and α_- as functions of the diffusion constants d_e and d_q neglecting coupling and the magnitude of thermoelectric coupling (γ_C, γ_L).

$$\left[C\frac{\partial}{\partial t} - \nabla L \nabla\right]\begin{bmatrix}\eta \\ T\end{bmatrix} = \begin{bmatrix}0 \\ s\end{bmatrix} \qquad (11).$$

For the remainder of this paper the entropy source term will be neglected and the C and L matrices will be treated as constants, independent of chemical potential and temperature. The non-linearities so neglected, however, can in principle lead to a variety of interesting behavior.

The coupled diffusion problem may be solved using the usual methods. Solutions which oscillate in space and decay with time like

$$\begin{bmatrix}\eta \\ T\end{bmatrix} = \begin{bmatrix}\eta_o \\ T_o\end{bmatrix} e^{-\alpha k^2 t + jkx} \qquad (12)$$

or which oscillate in time and decay exponentially in space like

$$\begin{bmatrix}\eta \\ T\end{bmatrix} = \begin{bmatrix}\eta_o \\ T_o\end{bmatrix} e^{j\omega t + (j-1)\sqrt{\frac{\omega}{2\alpha}}x} \qquad (13)$$

are possible. The first case is often useful for initial value problems, where for example the potential and temperature distribution are known at some initial time and one wishes to know the future time evolution of these functions. This case will be examined below. The second case occurs in methods where the potential (or temperature) is forced to oscillate at a fixed frequency, such as in an ac resistivity measurement (or an Ångstrom [2] or Cahill 3-ω [1] thermal conductivity measurement).

Solution of the characteristic equation yields the eigenvalues

$$\alpha_\pm = \frac{1}{2}\sqrt{d_e d_q \gamma_C \gamma_L}\left(b \pm \sqrt{b^2 - 4/\gamma_C\gamma_L}\right)$$

$$b = r + 1/r - 2\sqrt{\left(1 - \frac{1}{\gamma_C}\right)\left(1 - \frac{1}{\gamma_L}\right)} \qquad (14)$$

$$r = \sqrt{\frac{d_e\gamma_C}{d_q\gamma_L}}$$

where

$$d_e = \frac{L_{11}}{C_{11}}$$

$$d_q = \frac{L_{22} - L_{12}^{\ 2}/L_{11}}{C_{22} - C_{12}^{\ 2}/C_{11}} \qquad (15)$$

are the usual electrical and thermal diffusivity values for the respective uncoupled diffusion problems.

Thus the eigenvalues depend on the two uncoupled diffusivity values and on the coupling between electrical and thermal effects represented by the two γ values.

The two eigenvectors are given by

$$\frac{\eta_{o\pm}}{T_{o\pm}} = -\frac{(\alpha_\pm C_{12} - L_{12})}{(\alpha_\pm C_{11} - L_{11})} \qquad (16),$$

which again illustrates that in the absence of thermoelectric coupling (C_{12}=L_{12}=0), the solutions uncouple to one purely electrical diffusion solution and another purely temperature diffusion solution.

Behavior of the eigenvalues

The two eigenvalues α_+ and α_- represent two diffusion constants which appear in two independent solutions of the form given by Eqs. 12 or 13. In a great many materials the electrical diffusivity (d_e) is greater than the thermal diffusivity (d_q), sometimes very much greater, so it is natural to identify the larger eigenvalue α_+ as an 'electric-like' diffusion coefficient and the smaller eigenvalue, α_-, as a 'heat-like' diffusion coefficient. It is important to note, however, that so long as thermoelectric coupling is not zero each solution involves time and spatial variations of both the electrochemical potential and the temperature. Further, when $d_e < d_q$ (which is true for some poor mobility materials) the identification of 'electric-like' or 'heat-like' can become ambiguous and the roles of α_+ and α_- can reverse.

The constants d_e and d_q represent the diffusivity values expected in the absence of thermoelectric effects, but α_+ and α_- are the diffusivity values which one observes in dynamic laboratory measurements. Fig. 1 illustrates how the observed diffusivity values (α_+ and α_-) depend on d_e and d_q and on the degree of coupling.

Fig. 1 shows the thermoelectric coupling can significantly modify the actual diffusivity values compared to the values expected in the absence of coupling. The situation is particularly severe when both types of coupling are large (i.e. when γ_C and γ_L>>1). For most materials, however, thermoelectric coupling is small (γ_C and γ_L only slightly greater than 1) and the actual diffusivity values are little modified from the uncoupled values d_e and d_q.

For d_e>>d_q the first order corrections to the diffusivity is given by

$$\alpha_+ \cong d_e\gamma_C + d_q\left(\gamma_L - \frac{1}{\gamma_C}\right) - 2\sqrt{d_e d_q(\gamma_C - 1)(\gamma_L - 1)} \quad (17).$$

$$\alpha_- = d_e d_q/\alpha_+$$

Eq. 17 illustrates that the corrections depend on the departure from no coupling (i.e. γ_C-1 and γ_L-1), a delicate balance between the two types of thermoelectric coupling (γ_C vs. γ_L), and on the relative magnitudes of the two uncoupled diffusivity values (d_e and d_q).

Thermal Flash Diffusivity

The flash technique (Fig. 2) developed by Parker et al [3] for determining thermal diffusivity is relatively simple, fast and insensitive to heat loss.

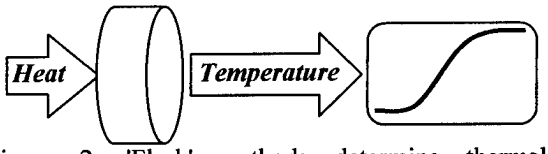


Figure 2: 'Flash' methods determine thermal diffusivity on thin, disk-shaped samples from the temperature vs. time response of the front face.

The boundary conditions for the flash method are that no heat or charge enters or leaves the sample, except during a brief period (short compared with any characteristic internal diffusion time) when heat is deposited on the rear face of the sample. The mathematical problem including the effects of thermoelectric coupling is solved using techniques essentially identical to a heat flow problem discussed by Carslaw and Jaeger [4], except that here two independent solutions are required to conserve charge. The time dependence of the electrochemical potential and temperature of back face of the sample are given by

$$\eta = T_\infty\left\{A_+B_+f\left(\alpha_+t/L^2\right) + A_-B_-f\left(\alpha_-t/L^2\right)\right\}$$
$$T = T_\infty\left\{A_+f\left(\alpha_+t/L^2\right) + A_-f\left(\alpha_-t/L^2\right)\right\} \quad (18)$$

with

$$A_\pm = \mp\frac{\left(\frac{C_{12}}{C_{11}} + B_\mp\right)}{(B_+ - B_-)}$$

$$B_\pm = -\frac{(\alpha_\pm C_{12} - L_{12})}{(\alpha_\pm C_{11} - L_{11})} \quad (19)$$

$$f(x) = 1 + 2\sum_{n=1}^{\infty}(-1)^n e^{\left(-n^2\pi^2x\right)}$$

and

$$T_\infty = \frac{Q_o/T_o}{C_{22} - C_{12}^{\ 2}/C_{11}} \quad (20)$$

Q_o is the total heat deposited in the sample at temperature T_o. These solutions ensure that no electrical charge enters or leaves the surfaces at any time, even during the heat flash itself.

The time dependence of the temperature of the back face is given by the sum of two terms: 1) an 'electric-like' term with amplitude A_+ propagating with a characteristic diffusion time governed by $\alpha_+$and 2) a 'heat-like' term with amplitude A_- propagating with a characteristic diffusion time governed by α_-. Fig. 3 illustrates how the amplitude of more slowly propagating 'heat-like' portion of the temperature response varies with relative magnitude of the two uncoupled diffusivity values (d_e and d_q) and the degree thermoelectric coupling (represented by γ_C and γ_L).

Again, thermoelectric coupling significantly modifies the results compared to the values expected in the absence of coupling. When both types of coupling are large (i.e. when γ_C and γ_L>>1) the 'heat-like' contribution can actually become a small faction of total temperature response. For most materials, however, thermoelectric coupling is small (γ_C and γ_L only slightly greater than 1) and the 'heat-like' component dominates the temperature response, as expected

When corrections are large

From the above discussion it appears that no special precautions are required when interpreting diffusivity measurements when both types of thermoelectric coupling are small (i.e., when γ_C and γ_L are only slightly greater than 1) When only one type of coupling is strong (i.e. γ_C>>1 or γ_L >>1, but not both) the actual diffusivity values will be given by the uncoupled values (d_e or d_q) except when these are similar in magnitude. In other cases, the full roots given by Eq. 14 are required.

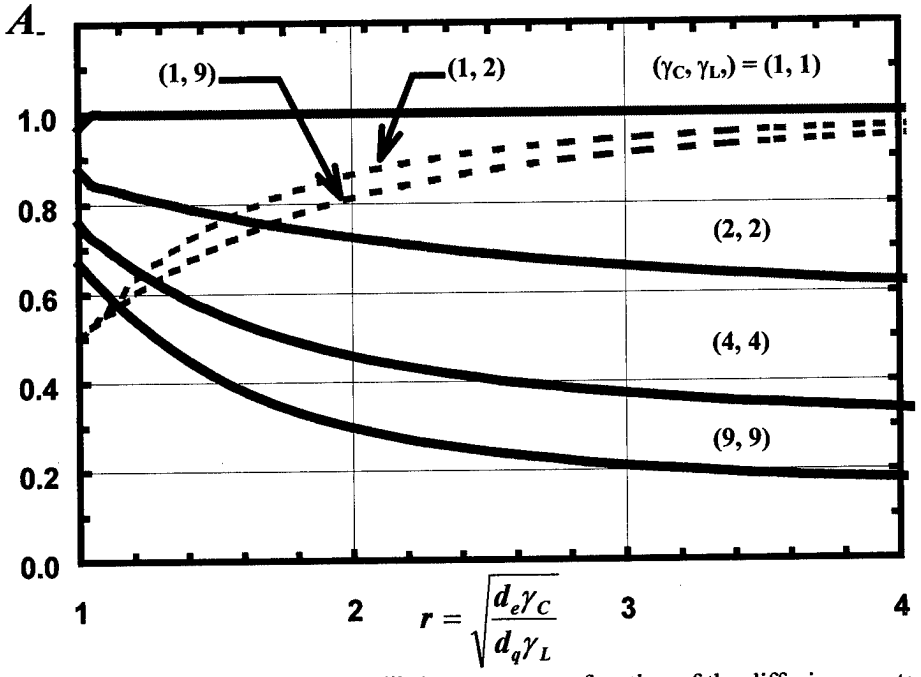


Figure 3: Amplitude of the 'heat-like' response as a function of the diffusion constants neglecting coupling (d_e and d_q) and the magnitude of the coupling (γ_C and γ_L).

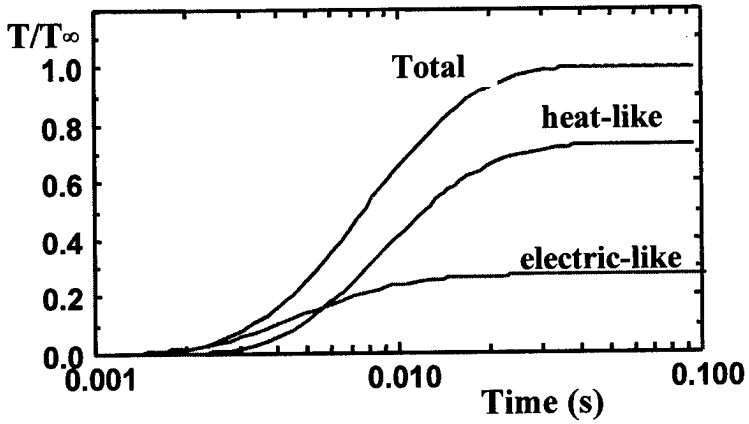


Figure 4: Temperature vs. time response for a flash diffusivity measurement on a hypothetical metal 1 mm thick with γ_C~2 and γ_L~2.

Fig. 4 illustrates one kind of error which can occur in extreme cases. Here, diagonal coefficients corresponding approximately to Pd have been combined with hypothetical off-diagonal coefficients to give γ_C~2 and γ_L~2 and the results of a flash diffusivity experiment on this hypothetical metal was calculated. While the total time dependence of the back face looks qualitatively similar to the uncoupled case (which has the shape of either of the individual contributions labeled 'heat-like' and 'electric-like'), it is acually much more complex depending on three new materials parameter (d_e,, γ_C, and γ_L) in addition to the uncoupled thermal diffusivity (d_q).

This example is not intended to represent realistic properties, but it illustrates some difficulties which may be encountered. Ordinarily, a key advantage of diffusivity measurements is that only a single number (such as $t_{0.5}$, the time required for the backface temperature to reach 1/2 of its' final value) is required. Times can be determined with great precision and accuracy, so a simple measurement of times can yield important experimental information.

In the case of thermoelectric coupling, four materials parameters (two diffusivities and two coupling parameters) determine the time dependence of the temperature of the backface temperature and more careful analysis is required to extract the material properties. Indeed, when other corrections such as heat loss and finite duration of the flash are considered (as has been done for the uncoupled problem [3]), extraction of reliable values for materials properites becomes problematic.

Conclusion

Characterization of electrical and thermal properties of materials using dynamic methods (i.e. using time dependent external perturbations) is more complex in materials with strong thermelectric effects because the response generally exhibits both 'electric-like' and 'heat-like' components, each with characteristic diffussion constants modified compared to the uncoupled diffusion constants. In most materials thermoelectric coupling will be negligible but it would be of interest to confirm the effects described in this paper by analysis of high-precision diffusivity experiments on, for example, metallic thermocouple .materials where the coupling effects may be within experimental resolution.

References

1. Cahill, D. G. (1990). Rev. Sci. Instrum. **61**: 802.
2. Sidles, P. H. and G. C. Danielson (1960). Thermal Diffusivity Measurements at High Temperatures. Thermoelectricity. P. G. Egli. New York, John Wiley & Sons, Inc.: 270-287.
3. Parker, W. J., R. J. Jenkins, et al. (1961). J. Appl. Phys. **32**: 1679.
4. Carslaw, H. S. and J. C. Jaeger (1959). Conduction of Heat in Solids. New York, Oxford University Press: 101.

A 256 pixel linear thermopile array using materials with high thermoelectric efficiency

E. Kessler, U. Dillner, V. Baier, J. Müller

Institute of Physical High Technology e.V. (IPHT), Dept. Microsystems, P.O.Box 100239, D-07702 Jena, Germany
Phone: +49-3641-657712, Fax: +49-3641-657700, E-mail: kessler@b3.ipht-jena.de, dillner@b3.ipht-jena.de

Abstract

First results are presented concerning a recently developed thermopile array with 256 linearly arranged pixels within a total width of 23 mm. Thermal simulation studies were performed by means of 3-D finite element calculations to optimize the specific detectivity D^* of the pixels and to find the conditions for the cross-talk between adjacent pixels as low as possible.

Resulting from this, two designs with different element lengths of 1.2 and 0.4 mm, respectively, but equal pixel pitch of 175 mm and pixel width of 89 mm each, have been investigated. Each pixel consists of a thermopile of ten thermocouples built up in a multilayer technology. These thermopiles are arranged on free-standing, stress-compensated SiON membranes formed by anisotropic wet-etching of the 4" silicon wafer from the backside. The thermoelectric material combinations typically used are BiSb/Sb and BiSb/BiSbTe, respectively, deposited by vacuum evaporation and patterned microlithographically. The absorbing layer is silver black.

To reduce the cross-talk the whole array is built up in a staggered arrangement of two subarrays of 128 pixels shifted by half a pitch against each other and separated by a narrow bar of bulk silicon. Furthermore, the membrane region between the pixels is removed by RIE thus creating a slit. For the one design with an element length of 1.2 mm and an absorbing area of 0.6 x 0.089 mm^2 (110) Si wafers are used to reduce the width of this bar, not to exceed the whole length of the sensitive area of 2 mm. This type shows a D^* of 5...9×10^7 cmHz$^{1/2}$/W per pixel and a cross-talk of about 50 % in normal pressure air, which is reduced to about 35 % in normal pressure Xe with an increase of D^* to 2...3×10^8 cmHz$^{1/2}$/W. These considerable cross-talk values are due to the thermal coupling between the pixels by the surrounding gas. Therefore, best results can be achieved by housing the array under vacuum conditions with a D^* of 0.7...1.7×10^9 cmHz$^{1/2}$/W and a negligible cross-talk.

Since the cross-talk is correlated with the pixel dimensions, a second design has been investigated with a reduced element length of 0.4 mm and an absorbing area of 0.2 x 0.089 mm^2. In this case the cross-talk is reduced to 16 % in air and about 8 % in Xe, respectively, but also the output signal voltages are reduced by a factor of about 2.

Introduction

At present there is a renaissance of thermopile infrared radiation sensors. The new interest in these sensors stems from the potential of microsystem technologies, which has led to far-reaching improvements of their parameters as well as to low-cost batch fabrication. Thermopile sensors belong to the class of thermal infrared sensors. All detectors of this class have in common that the incident radiation causes a temperature difference between the absorbing medium and a heat sink. This working principle implies that thermal sensors respond unselectively to a wide spectral range and do not require cooling. In thermopile sensors the temperature increase due to the absorbed radiation is converted into an electrical signal by means of the Seebeck effect. As microsensors these devices are of small size and their manufacture is based principally on the concepts of microsystem technologies, e.g., silicon chips, micromachining, selective etching techniques, thin-film deposition methods, packaging and interconnection technologies as well as monolithic or hybrid integration.

Thermopile linear arrays are one-dimensional arrangements of a number of pixels comprised by thermopiles. The arrangements of several elements of a size $l \times w$ with length l and width w are characterized by pixel number n, pixel size A (the assembly of thermocouples to a thermopile as a sensitive area) and pixel pitch p (the distance from a center of a sensitive area to the center of the neighboring pixel). In addition to the single element performance data, i.e. detectivity D^* and time constant τ, the performance of the array is characterized by the cross-talk c to adjacent pixels. Essentially, one-dimensional arrangements are useful as detectors in two important applications: spectrometers (spectral photometers) and line scanning pyrometers.

The first micromachined thermopile-based linear infrared sensing arrays were reported by Choi and Wise [1]. After some refinement they showed the following parameters [2]: n=2×16 in an arrangement of two staggered subarrays, $l \times w$=(0.8×0.4) mm^2, p=0.6 mm, $D^* \approx 7.7 \times 10^7$ cmHz$^{1/2}$/W and $\tau \approx 10$ ms. Each element of these arrays consists of a thin membrane spanning a silicon rim. The rim acts as heat sink and results in a negligible cross-talk. Alternatively to membranes cantilevers were used as infrared sensing array elements [3]. Here the parameters were n=8, $l \times w$=(3×0.44) mm^2, p=0.5 mm, $D^* \approx 5 \times 10^7$ cmHz$^{1/2}$/W and $\tau \approx 180$ ms. A cross-talk of $c \approx 15$ % was observed due to heat conduction through the air. Contrary to [1-3] where the thermopiles were fabricated using doped polysilicon, the use of $Bi_{0.87}Sb_{0.13}$ for the n-type thermopile layer and of Sb for the p-type layer was reported in [4]. These materials show a high efficiency of the thermoelectric conversion characterized by the thermoelectric figure of merit $Z = S^2 \sigma \lambda^{-1}$ (S: Seebeck coefficient, σ: electrical conductivity, λ: thermal conductivity), e.g., Z is about 0.5×10^{-3} K^{-1} for thin films of $Bi_{0.87}Sb_{0.13}$ [5]. Due to the low thermal conductivity of these films (about 3 WK^{-1}m^{-1}) this Z value is nearly one order of magnitude higher than the corresponding one of polysilicon. As in [1,2] an element of the array described in [4] consisted of a thin membrane supported and thermally isolated from its

0-7803-4057-4/97 $10.00 ©1997 IEEE

neighbors by a silicon rim. The parameters of this linear array were n=2×8 (staggered), $l \times w$=(2×0.6) mm², p=1.5 mm, $D^* \approx 3 \times 10^8$ cmHz$^{1/2}$/W, $\tau \approx 20$ ms and $c \approx 0$.

Sensor array design

A schematic top view of a typical layout of a thermopile array is shown in Fig. 1. A free-standing stress-compensated membrane made by anisotropic etching of a Si wafer covered with a silicon oxinitride (SiON) layer serves as a substrate for the thermopiles patterned microlithographically by wet chemical etching. We employ thin films of 0.4 µm thickness using n-type $Bi_{0.87}Sb_{0.13}$ against p-type Sb as thermocouple materials with a Seebeck coefficient S=135 µV/K per couple. Each thermopile is covered by an absorption layer corresponding to the pixel size A. Note that, contrary to [1,2,4] where every single array element is completely surrounded by a Si rim acting as heat sink and serving also to separate the pixels thermally, this is not the case for the layout of Fig. 1 where the heat sink is only provided under the cold junctions of the thermopiles. Instead of a bulk heat sink, there is a pixel separating region between two pixels, which is essentially formed by a slit in the membrane to reduce thermal cross-talk.

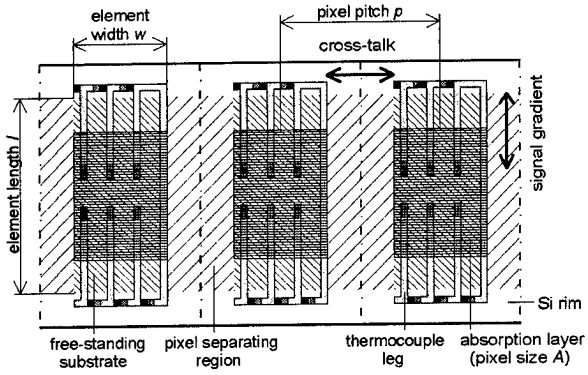


Figure 1. Top view of a linear thermopile array chip (schematically), thermocouple legs arranged using a multi-layer technology.

The n-type and the p-type legs of the thermopiles are arranged one on the top of the other using a multi-layer technology [6]. This arrangement, which has the advantage of doubling the package density of the thermocouple legs, is illustrated in Fig. 2.

Aimed to provide a device for resolving an infrared spectrum of about 22.5 mm width and 2 mm height with 256 pixels, a high resolution sensor array was designed as a staggered array with n=2×128, p=0.175 mm, p_{eff}=0.0875 mm, A=(0.6×0.089)mm² and $l \times w$=(1.2×0.089) mm². The thermopiles consist of 10 thermocouples having a width of 8 µm each.

The distance between the membranes of the two subarrays is to be 0.2 mm only. To realize such a structure using bulk micromachining by anisotropic etching it is favorable to choose a (110) cut wafer, since here the etch-stopping (111) planes are perpendicular to the surface and, hence, vertical walls can be etched [7]. Using a (100) instead of a (110) wafer gives, on the

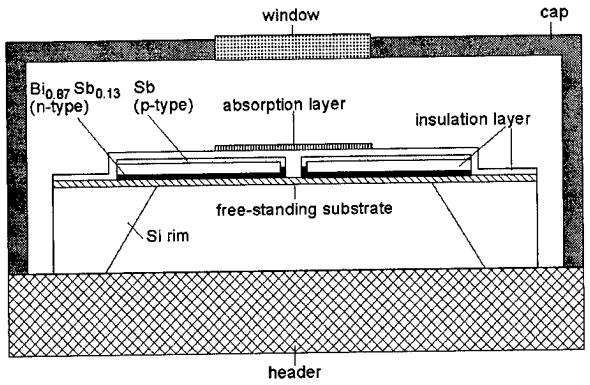


Figure 2. Cross-sectional view of a linear thermopile array (schematically), thermocouple legs arranged using a multi-layer technology.

other hand, merely inclined walls or V-grooves. This is a drawback when high aspect ratio structures are required. In Fig. 3 one can see that only a (110) cut wafer is suitable to realize an appropriate structure to separate the two subarrays with a small distance of 0.2 mm. If such a small distance is not necessary a (100) cut wafer can be used. Therefore, a second variant for the 2×128 pixel array is based on that wafer type. The second variant differs from the first one in element length, which is divided by three in the second variant compared to the first one (cf. Fig. 3). Here the distance between the two subarrays can be larger.

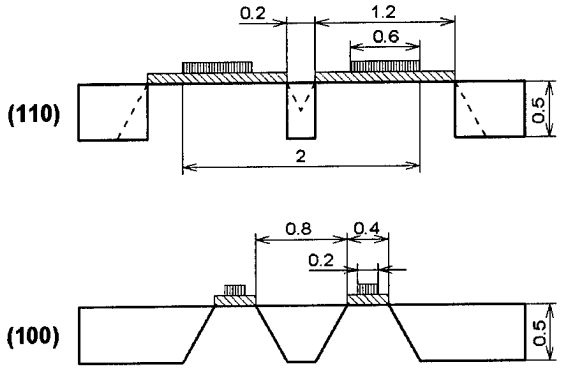


Figure 3. Cross-sectional view of the chips of two variants for the 2×128 pixel staggered linear thermopile array based either on a (110) wafer or on a (100) wafer. The dashed line denotes the result to be expected when employing a (100) instead of a (110) wafer in the first variant.

Thermal analysis

From Fig. 1, we see that the temperature gradient leading to the pixel signal voltage (the signal gradient) and the cross-talk between pixels have different directions. Hence, both dimensions of the membrane region should be included in the thermal analysis. Since the heat transfer by a surrounding gas has also to be considered, the problem of calculating the signal gradient and cross-talk of array layouts described in the previous section

requires a full 3-D treatment. This was performed by a 3-D finite element analysis (FEA) using the FEA code ANSYS to simulate the stationary and transient temperature distribution in a modeling region depicted schematically in Fig. 4.

The modeling region comprises a quarter (due to symmetry) of three elements of the sensor array as well as the gas-filled or evacuated space above and below the selected elements. The silicon rim, the header and the cap are not included in the FEA modeling region, since they are regarded as heat sinks at sensor temperature T_S or temperature of the surroundings T_U. The pixel (or absorber) area of the middle element is loaded by a heat flux equivalent to the incident infrared radiation while the neighboring pixels are not loaded but receive the thermal cross-talk from the middle element.

The FEA modeling region is subdivided in five regions of different material properties. MAT2 referring to the pixel area, MAT1 and MAT4 belong to the free-standing substrate while MAT5 comprises the pixel separating region and MAT3 the gas filling. The thin-film thermal conductivity and heat capacity data for the various components of the membrane including the thermopiles and photoresist insulation layers published in [8] were used in the calculations.

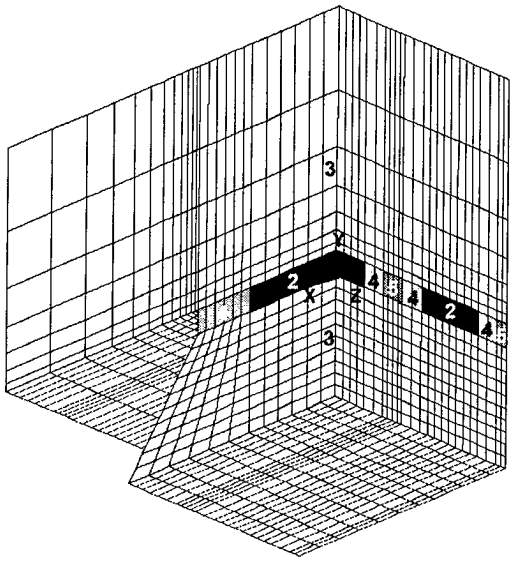


Figure 9. 3-D FE model of the membrane and its surroundings (not to scale). The numbers 1 to 5 denote regions of different materials (MAT1 to MAT5).

Results of the thermal simulation calculations

The pixel's signal voltage and the thermal cross-talk between adjacent pixels, both extracted from the stationary FEA, the thermal time constant of a pixel calculated from the transient FEA as well as the electrical resistance of an array element and its detectivity are given in Tables 1 to 4 for different array design variants and thermocouple material combinations.

It can be seen, that a vacuum encapsulation of the array chip would be the best way to obtain a maximum signal voltage and detectivity with vanishing thermal cross-talk. On the other hand, the corresponding thermal time constants are relatively large. A nitrogen-filled array gives considerably lower signal voltages, detectivities and, even worse, a large cross-talk due to the thermal conductivity of the gas. Using xenon instead of nitrogen results in considerable improvements of signal voltages and detectivities. However, this is not connected with a equivalent improvement in the cross-talk values. They are only acceptable for the design variant with the short element length (cf. Tables 3 and 4). A xenon-filled array with 0.4 mm element length requires the best thermoelectric materials possible (in particular, $Bi_{0.5}Sb_{1.5}Te_3$, for the p-type leg, cf. Table 4) for a reasonable detectivity.

	N_2 (normal pressure)	Xe (normal pressure)	vacuum
signal voltage (mV) at 100 W/m² irradiance	0.2	0.7	2.5
detectivity (10^8 cmHz$^{1/2}$/W)	0.5	2	7
time constant (ms)	11	30	90
resistance (kΩ)	17	17	17
cross-talk (%)	47	37	0

Table 1. Calculated array performance data referring to the 2×128 pixel array with 1.2 mm element length for the case of $Bi_{0.87}Sb_{0.13}$ /Sb as thermocouple materials.

	N_2 (normal pressure)	Xe (normal pressure)	vacuum
signal voltage (mV) at 100 W/m² irradiance	0.5	2	10
detectivity (10^8 cmHz$^{1/2}$/W)	0.9	3	17
time constant (ms)	8	30	200
resistance (kΩ)	50	50	50
cross-talk (%)	47	37	0

Table 2. Calculated array performance data referring to the 2×128 pixel array with 1.2 mm element length for the case of $Bi_{0.87}Sb_{0.13}$ /$Bi_{0.5}Sb_{1.5}Te_3$ as thermocouple materials.

	N_2 (normal pressure)	Xe (normal pressure)	vacuum
signal voltage (mV) at 100 W/m² irradiance	0.09	0.2	0.3
detectivity (10^8 cmHz$^{1/2}$/W)	0.7	1.5	2.3
time constant (ms)	4	8	13
resistance (kΩ)	6	6	6
cross-talk (%)	16	8	0

Table 3. Calculated array performance data referring to the 2×128 pixel array with 0.4 mm element length for the case of $Bi_{0.87}Sb_{0.13}$ /Sb as thermocouple materials.

	N_2 (normal pressure)	Xe (normal pressure)	vacuum
signal voltage (mV) at 100 W/m² irradiance	0.25	0.7	1.7
detectivity (10^8 cmHz$^{1/2}$/W)	1.3	3.5	7
time constant (ms)	5	15	30
resistance (kΩ)	17	17	17
cross-talk (%)	16	8	0

Table 4. Calculated array performance data referring to the 2×128 pixel array with 0.4 mm element length for the case of $Bi_{0.87}Sb_{0.13}$ / $Bi_{0.5}Sb_{1.5}Te_3$ as thermocouple materials.

Experimental results

Microfabricated samples of the 2×128 pixel array with 1.2 mm element length employing of $Bi_{0.87}Sb_{0.13}$ /Sb as thermocouple materials have been tested in an air environment at normal pressure. The measured electrical resistance was 14 kΩ, for the thermal time constant a value of 13 ms was found while the thermal cross-talk was measured to be about 45 %. These experimental values are in good agreement with the simulation results (cf. Table 1).

However, the measured signal voltage of 0.9 mV at an irradiance of 100 W/m² and the resulting detectivity of 1.9×10^8 cmHz$^{1/2}$/W are much higher than the predicted values given in Table 1. This can be explained as follows. In the experiments the complete array chip was irradiated using a black body source to determine the signal voltage while in the simulation only one pixel area was loaded referring to the most stringent arrangement for a spectroscopic application. Therefore, we have done additional simulations where the thermal load of 100 W/m² is applied to all pixels. This modification in the thermal model results in a signal voltage of 0.6 mV and even 1 mV, respectively, if the radiation reflected at the header of the chip was also included in the model. Thus the experiments and the simulation results agree with each other also in the case of signal voltage and detectivity. Hence it can be concluded that the employed 3-D FEA model is adequate to describe the temperature field within the sensor array membrane and in its surroundings.

Conclusion

Applying a 3-D finite element analysis to model the stationary and transient temperature distribution within the sensor array membrane and its surroundings we calculated the signal voltage, detectivity, pixel-to-pixel thermal cross-talk and time constant for two designs of a 2×128 pixel staggered linear thermopile infrared radiation sensor array in dependence on different types of the filling gas. As tested for arrays with elements of a length of 1.2 mm on (110) wafers in an air environment, the calculated signal voltages, time constants and thermal cross-talk data are in a reasonable agreement with the measured data. Due to the small pixel pitch a high performance of the array (i.e. high detectivity and negligible cross-talk) can only be achieved by its vacuum encapsulation. Thus a D^* of 0.7×10^9 cmHz$^{1/2}$/W can be expected for the thermoelectric material combination $Bi_{0.87}Sb_{0.13}$ /Sb while a D^* of 1.7×10^9 cmHz$^{1/2}$/W is possible for the thermoelectric material combination $Bi_{0.87}Sb_{0.13}$ / $Bi_{0.5}Sb_{1.5}Te_3$.

Acknowledgment

This work has been supported by the Federal Ministry of Education, Science, Research and Technology (BMBF), collaborative project THERMAP, Grant No. 16 SV 283/9.

References

[1] I.H. Choi, K.D. Wise, A silicon-thermopile-based infrared sensing array for use in automated manufacturing, *IEEE Trans. on Electron Devices, ED-33* (1986) 72-79.

[2] W.G. Baer, K. Najafi, K.D. Wise, R.S. Toth, A 32-element micromachined thermal imager with on-chip multiplexing, *Sensors and Actuators, A48* (1995) 47-54.

[3] P.M. Sarro, H. Yashiro, A.W. v. Herwaarden, S. Middelhoek, An integrated thermal infrared sensing array, *Sensors and Actuators, 14* (1988) 191-201.

[4] W. Schnelle, U. Dillner, S. Poser, A linear thermopile infrared sensing array, *VDI-Berichte, 982,* (1992) 261-264.

[5] F. Völklein, E. Kessler, Thermal conductivity and thermoelectric figure of merit of $Bi_{1-x}Sb_x$ films with $0<x\leq0.3$, *Physica Status Solidi, B143* (1987) 121-130.

[6] F. Völklein, A. Wiegand, High sensitivity and detectivity radiation thermopiles made by multi-layer technology, *Sensors and Actuators, A24* (1990) 1-4.

[7] W. Lang, Silicon microstructuring technology. *Materials Science and Engineering, R17* (1996) 1-55.

[8] U. Dillner, Thermal modeling of multilayer membranes for sensor applications, *Sensors and Actuators, A41-A42* (1994) 260-267.

Thermoelectric Detection of Photothermal Signals in Semiconductors

G. N. Logvinov, M. N. Kasyanchuk
Ternopil Pedagogical State University; 2, Krivonosa str., P.O. 282009, Ternopil, Ukraine,
Tel: (380)352334006, Fax: (380)35220176, E-mail: logvinov@ecolab.ternopil.ua

Yu.G. Gurevich, G. Gonzalez de la Cruz
Departamento de Fisica, Centro de Investigacion y de Estudios Avanzados del Instituto Politecnico Nacional, Apartado Postal 14-740, 07000, Mexico, Distrito Federal, Mexico,
Tel: (525)7477000, Fax: (525)7477096, E-mail: gurevich@fis.cinvestav.mx

Abstract

Thermal waves are theoretically investigated in electron and phonon subsystems of nondegenerate semiconductors. Periodic thermo-e.m.f., which appears in the sample under propagation of thermal waves is calculated. Amplitude and phase frequency dependencies of thermo-e.m.f. is received.

Introduction

The basis of all photothermal methods of a solid states research is formed by detecting the thermal waves appearing in a sample as a result of absorption of modulated laser radiation energy , which is converted into periodic thermal flux on a surface and in volume (thermal waves) [1]. The thermal response measured by either methods and the analysis following it, allows to get an extensive information about heat sources generating thermal waves; characteristic of a medium in which they are propagated; light absorption factor; characteristic times of physical processes etc.

At once we have to mark, that the process of thermal waves propagation has specific singularities in semiconductors, which are linked in the elementary case with the presence of two nonequilibrum, nonstationary temperature distributions - electron's $T_e(\mathbf{r},t)$, and phonon's $T_p(\mathbf{r},t)$, where $\mathbf{r}$ is a position vector, t-time [2]. This distinction is exhibited on distances l_ε from surfaces contacting to a heater and a refrigerator in bulk semiconductors [$2a \gg l_\varepsilon$, when 2a - sample's length, l_ε - the cooling length (effective length of energy electron-phonon interaction)]; the stratification of this temperatures takes place in the whole volume of a sample in submicron films ($2a \le l_\varepsilon$). In typical semiconductors the length l_ε is the value of order 10^{-4}-10^{-2} cm. The heterogeneity of temperature distribution $T_e(\mathbf{r},t)$ leads to the appearance of non-stationary thermo-e.m.f. with the necessary, that entails in addition to being available another one method of thermal waves detecting. Theoretical calculation of this thermo-e.m.f. and its singularities analysis is the purpose of the present work.

Thermal electron and phonon waves

With the purposes of simplicity we will consider, that the nondegenerate isotropic, monopolar semiconductor has the form of a parallelepiped, on one of which surfaces (x = - a) the laser radiation, modulated with frequency ω, falls. The surface x = a is hold under the constant temperature T_0. Lateral sides are adiabatically isolated. We assume, that the semiconductor opaque and whole energy of an incident radiation is absorbed on a surface. All kinetic factors are assumed not depending on temperature.

The temperatures of electrons and phonons can be selfcoordinate defined from the following set of equations of energy balance, taking into account the electron - phonon energy interaction [3]:

$$\begin{cases} \dfrac{\partial^2 T_e(x,t)}{\partial x^2} - k_e^2 [T_e(x,t) - T_p(x,t)] = \dfrac{1}{\alpha_e}\dfrac{\partial T_e(x,t)}{\partial t} \\ \dfrac{\partial^2 T_p(x,t)}{\partial x^2} + k_p^2 [T_e(x,t) - T_p(x,t)] = \dfrac{1}{\alpha_p}\dfrac{\partial T_p(x,t)}{\partial t}. \end{cases} \quad (1)$$

Here $k_{e,p}^2 = \dfrac{P}{\chi_{e,p}}$; $P = n\omega_\varepsilon$ [2] is a coefficient, which determines the intensity of electron-phonon energy interaction; $\alpha_{e,p} = \dfrac{\chi_{e,p}}{\rho_{e,p} c_{e,p}}$ are the thermal diffusivity for electron and phonon systems; $\chi_{e,p}$, $\rho_{e,p}$, $c_{e,p}$ are electron and phonon thermal conductivity, density and specific heat respectively; n is electron's concentration; ω_ε is electron - phonon energy relaxation frequency.

The boundary conditions are represented by the following system of relations [3]:

$$\begin{cases} Q_{e,p}(x,t)\big|_{x=-a} = Q_{e,p}^0 + \Delta Q_{e,p} e^{i\omega t} \\ T_{e,p}(x,t)\big|_{x=a} = T_0 \end{cases} \quad (2)$$

here $Q_{e,p}^0$ are the static electron's and phonon's heat fluxes appearing as a result of high-frequency carrying radiation energy absorption; $\Delta Q_{e,p}$ are dynamic electron's and phonon's fluxes, generated by a modulating component of an incident radiation. The magnitudes ΔQ_e and ΔQ_p can be different each time that are depended on thermophysical characteristics of a surface.

Being limited by the condition $\chi_p \gg \chi_e$, that is typical characteristic for nondegenerated semiconductors, it is possible to receive:

$$T_e(x,t) = T_e^s + e^{i\omega t}\frac{\Delta Q_p}{\chi_p}\left(F_1\frac{\mathrm{sh}\sigma_1(a-x)}{\mathrm{ch}2\sigma_1 a} + F_2\frac{\mathrm{sh}\sigma_2(a-x)}{\mathrm{ch}2\sigma_2 a}\right); \quad (3)$$

$$T_p(x,t) = T_p^s + e^{i\omega t}\frac{\Delta Q_p}{\chi_p} G \frac{\mathrm{sh}\sigma_2(a-x)}{\mathrm{ch}2\sigma_2 a}, \qquad (4)$$

where

$$T^s_{e,p} = T_0 + \frac{Q_e + Q_p}{\chi_p}(a-x) \pm \frac{k^2_{e,p}}{k_e^3}\left(\frac{Q_e}{\chi_e} - \frac{Q_p}{\chi_p}\right)\frac{\mathrm{sh}k_e(a-x)}{\mathrm{ch}2k_e a}$$

are the static parts of temperature distributions;

$$F_1 = \frac{1}{\sigma_1}\left(K - \frac{k_e^2}{\sigma_1^2 - \sigma_2^2}\right);\ F_2 = \frac{k_e^2}{\sigma_2\left(\sigma_1^2 - \sigma_2^2\right)};\ G = \frac{1}{\sigma_2};$$

$$K = \frac{\Delta Q_e}{\chi_e}\frac{\chi_p}{\Delta Q_p};\ \sigma_1^2 = k_e^2\left(1 + \frac{i\omega}{\omega_\varepsilon}\right);\ \sigma_2^2 = \frac{2i\omega}{a^2\omega_a};$$

$\omega_a = \frac{2\alpha_p}{a^2}$, $\omega_\varepsilon = k_e^2\alpha_e$ are characteristic frequencies; ω_a determines the frequency of relaxation of a temperature fluctuations in phonon's subsystem.

It is essential to mark, that four thermal waves are propagated in electron subsystem and only two waves are propagated throw phonon subsystem. The reason is that, when $\chi_p >> \chi_e$, the value of phonon's thermal flux practically does not vary under inflow of heat from electron's subsystem. On the contrary, the electron gas takes a noticeable periodic thermal perturbation from the phonon's subsystem. By other words, the electron gas is warming by the surface and bulk sources of heat, and phonon's gas only by surface sources of heat. As a result, dynamic part of electron temperature depends on electron's and phonon's subsystems parameters, and the dynamic part of phonon's temperature is defined only by phonon's gas characteristic.

The corresponding waves lengths and damping length look like the following:

$$\lambda_1 = \frac{2\pi}{\mathrm{Im}\,\sigma_1} = 2\sqrt{2}\pi l_\varepsilon\left(\sqrt{1+\left(\frac{\omega}{\omega_\varepsilon}\right)^2} - 1\right)^{-1/2};$$

$$\lambda_2 = \frac{2\pi}{\mathrm{Im}\,\sigma_2} = 2\pi a\left(\frac{\omega}{\omega_a}\right)^{-1/2}; \qquad (5)$$

$$L_1 = \frac{1}{\mathrm{Re}\sigma_1} = \sqrt{2}l_\varepsilon\left(\sqrt{1+\left(\frac{\omega}{\omega_\varepsilon}\right)^2} + 1\right)^{-1/2};$$

$$L_2 = \frac{1}{\mathrm{Re}\sigma_2} = a\left(\frac{\omega}{\omega_a}\right)^{-1/2}.$$

The characteristic frequencies ω_ε and ω_a essentially differ in bulk semiconductors ($\omega_\varepsilon >> \omega_a$) and are commensurable among themselves in submicron films ($\omega_\varepsilon \sim \omega_a$). So the evaluations show, that $\omega_a = 8{,}6\cdot10^3$ sec^{-1}, when a = 10^{-2} cm in p-Ge for T=300 K, $\omega_a = 8{,}6\cdot10^9$ sec^{-1}, when a = 10^{-5} cm. Cooling length $l_\varepsilon = 2\cdot10^{-4}$ cm, $\omega_\varepsilon = 1{,}1\cdot10^9$ sec^{-1}.

The theoretically calculated frequency dependence of electron's and phonon's amplitudes of thermal waves on the surface x = -a in a sample p-Ge (a = 10^{-3} cm) are shown on figure 1.

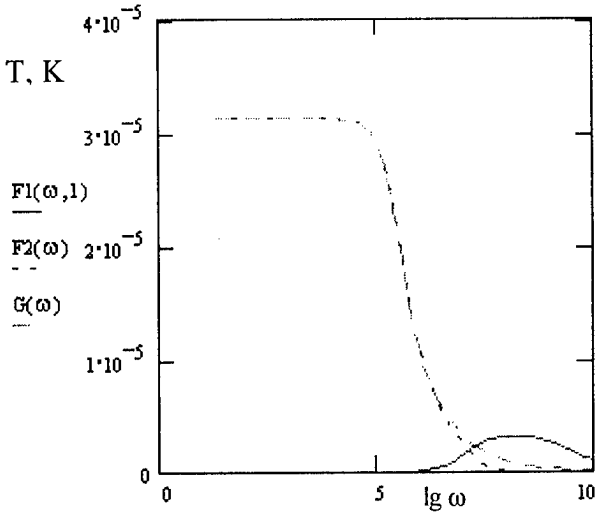


Figure 1.

It was selected for a determinacy, that K=1; $\Delta Q = \Delta Q_e + \Delta Q_p = 10^{-2}$ Wt/cm^2. From the shown graphs it is visible, that the amplitude F_1 is negligible small for frequencies $\omega \le 10^7$ sec^{-1} and, on the contrary, it is dominating in some interval of frequencies near the frequency 10^8-10^9 sec^{-1}.

Periodic thermoelectric response

A required thermo-e.m.f. in a quasistationary approximation

$$E(t) = -\int_{-a}^{a} \alpha \frac{dT_e(x,t)}{dx}dx, \qquad (6)$$

where α - factor of a differential thermo-e.m.f.

We can come to the following expression, by taking expression (3) and after conducting some formal transformations:

$$E(t) = E_0 + e^{i\omega t}\alpha\frac{\Delta Q_p}{\chi_p}\sqrt{E_1^2 + E_2^2 + 2E_1E_2\cos(\mathrm{Arg}E_1 - \mathrm{Arg}E_2)}\cdot e^{i\phi}, \qquad (7)$$

where

$$E_0 = \alpha\left(2a\frac{Q_e + Q_p}{\chi_p} - \frac{1}{k_e}\left(\frac{Q_p}{\chi_p} - \frac{Q_e}{\chi_e}\right)\mathrm{th}(2k_e a)\right) \qquad (8)$$

is the static part of thermo-e.m.f.;

$$E_1 = 1_\varepsilon \frac{\sqrt{\left(K - \left(1+W^2\right)^{-1}\right)^2 + W^2\left(1+W^2\right)^{-2}}}{\sqrt{1+\left(\frac{\omega}{\omega_\varepsilon}\right)^2}} \times$$

$$\times \frac{\sqrt{ch\frac{4a}{L_1} - \cos\frac{8\pi a}{\lambda_1}}}{\sqrt{ch\frac{4a}{L_1} + \cos\frac{8\pi a}{\lambda_1}}}; \qquad (9)$$

$$E_2 = \frac{a}{\sqrt{2}}\sqrt{\frac{\omega_a}{\omega}}\frac{1}{\sqrt{1+W^2}}\frac{\sqrt{ch\frac{4a}{L_2} - \cos\frac{8\pi a}{\lambda_2}}}{\sqrt{ch\frac{4a}{L_2} + \cos\frac{8\pi a}{\lambda_2}}}; \qquad (10)$$

$$Arg(E_1) = -arctg\frac{2\pi L_1}{\lambda_1} - arctg\frac{W}{K\left(1+W^2\right)-1} +$$

$$+ arctg\frac{tg4\pi a\lambda_1^{-1}}{th2aL_1^{-1}} - arctg\left(tg4\pi a\lambda_1^{-1}\cdot th2aL_1^{-1}\right); \qquad (11)$$

$$Arg(E_2) = -\frac{\pi}{4} + arctg\frac{tg4\pi a\lambda_2^{-1}}{th2aL_2^{-1}} -$$

$$- arctg\left(tg4\pi a\lambda_2^{-1}\cdot th2aL_2^{-1}\right) + arctgW; \qquad (12)$$

$$W = \frac{\omega}{\omega_\varepsilon}\left(\frac{\alpha_e}{\alpha_p} - 1\right); \qquad (13)$$

$$\phi = arctg\left(\frac{E_1 \sin ArgE_1 + E_2 \sin ArgE_2}{E_1 \cos ArgE_1 + E_2 \cos ArgE_2}\right) \qquad (14)$$

is the phase of dynamic part of thermo-e.m.f.

The graphs of an frequency dependence of thermo-e.m.f. amplitude and their phases for p-Ge (α=1 mV/K [4]) are shown on figure 2, 3.

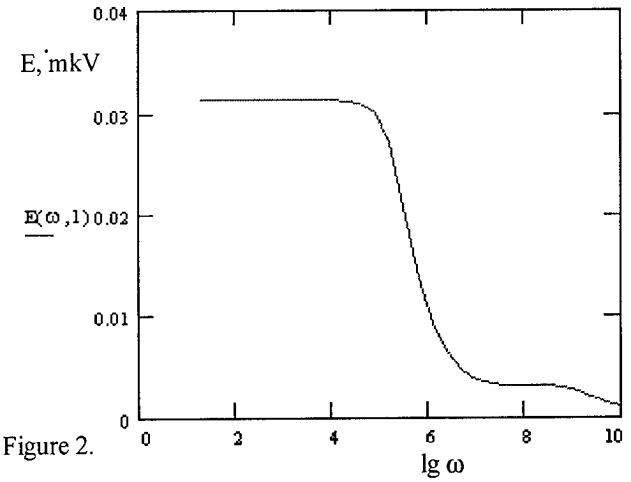


Figure 2.

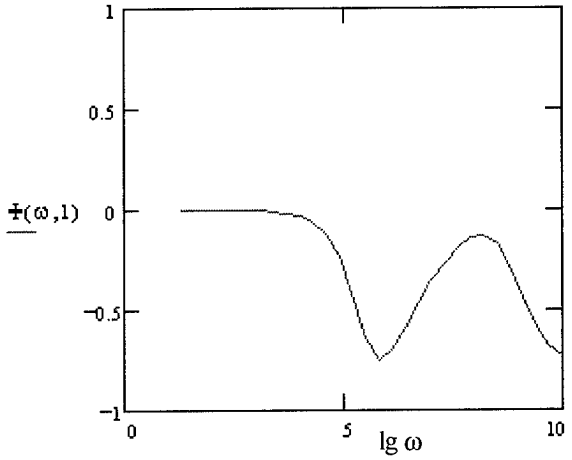


Figure 3.

The characteristic of a special future frequency dependence of a phase is the presence of extremums. In experiment, measurements of frequencies of these extremums together with extremes of a phase, and also the magnitude of thermo-e.m.f. allows to receive an extensive information about various parameters of a semiconductor in particular about parameters α_e and α_p.

Acknowledgments

This work is partially support by Consejo Nacional de Ciencia y Tecnologia (CONACYT), Mexico.

References

[1] "Progress in Photothermal and Photoacoustic Science and Technology" edited by A. Mandelis (Prentice Hall, N. Y.), 1994.

[2] F. G. Bass, V. S. Bochkov, Yu. G. Gurevich. Electrons and Phonons in Limited Semiconductors. — M.: Nauka. 1984.-287 (in Russian).

[3] G. Gonzalez de la Cruz and Yu. G. Gurevich. J. Appl. Phys. 80(3), 1996, p. 1726.

[4] T. N. Geballe, G. W. Hull. Phys. Rev., 94, 1134 (1954).

EDDY THERMOELECTRIC CURRENTS. MEASURING DEVICES ON THEIR BASIS

L.I. Anatychuk, O.J. Luste
Institute of Thermoelectricity, General Post-Office, Box 86, 274000, Chernivtsi, Ukraine
Tel: +380/3722/44422, Fax:+380/3722/41917, E-mail: anatychuk@ite.Chernovtsy.ua,
WWW: http:\\www.ite.Chernovtsy.ua

Abstract
It has been shown that eddy thermoelectric currents could be used for conducting inhomogeneous and anisotropic media parameters determination. Eddy currents flowing in a media bulk lead to surface electric potential distributions which are used for undestroyed test methods.
Methods and devices for eddy currents excitation and measurement have been described.

Introduction
Eddy thermoelectric currents (ETC) appear in inhomogeneous and anisotropic media under nonisothermal conditions [1-3]. Similar to the Foucault currents in electrical engineering, ETC are usually an undesirable phenomenon in thermoelectric devices.
They result in additional heat losses due to the Joule heat, decrease thermoelectric devices voltage and efficiency. The present work examine the possibilities of ETC use for material parameters measurement. Measuring devices based on ETC usage, namely heat flow detectors and radiation sensors are described.

Measurement of layer structure parameters
ETC and related transverse EMF were studied in Refs. [1-4,6]. ETC (Fig.2,3) and transverse EMF (Fig.4) appear in two-layer plates (Fig.1) if temperature gradient is directed along layers interface.

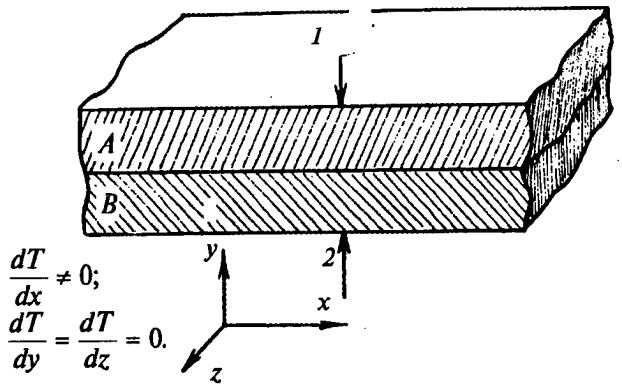


Fig. 1. A zone - inhomogeneous plate. *A* and *B* are materials with electrical conductivity σ_A and σ_B and coefficients of Seebeck α_A and α_B, 1, 2 are measuring probes.

Calculation of the transverse thermo-emf in a two-layer plate with p-n junction has been made. The following expression has been got

$$V_\perp = \frac{\Delta T}{2b}(\alpha_n - \alpha_p)\left\{y - \frac{8b}{\pi^2 Z_0}\left(\frac{L_{pn}}{L_{np}}\frac{1}{\operatorname{sh}\frac{\pi d}{2b}} + \frac{1}{\operatorname{sh}\frac{\pi a}{2b}}\right)\sin\frac{\pi y}{2b}\right\}, \quad (1)$$

where $Z_0 = \frac{P_p}{P_n}\frac{L_{pn}}{2b}1.312\pi + \frac{L_{pn}}{L_{np}}\operatorname{cth}\frac{\pi a}{2b}$,

$\Delta T/2b$ is the temperature gradient, α_n, α_p are a film and a substrate Seebeck coefficient, L_{pn} and L_{np} are diffusion lengths for holes and electrons, P_p is equilibrium concentration of holes in the *p*-region, P_n is equilibrium concentration of holes in the *n*-region.

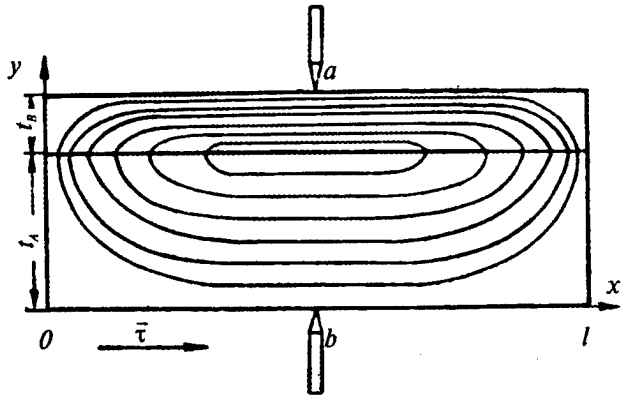


Fig. 2. Eddy currents in a zone inhomogeneous plate.

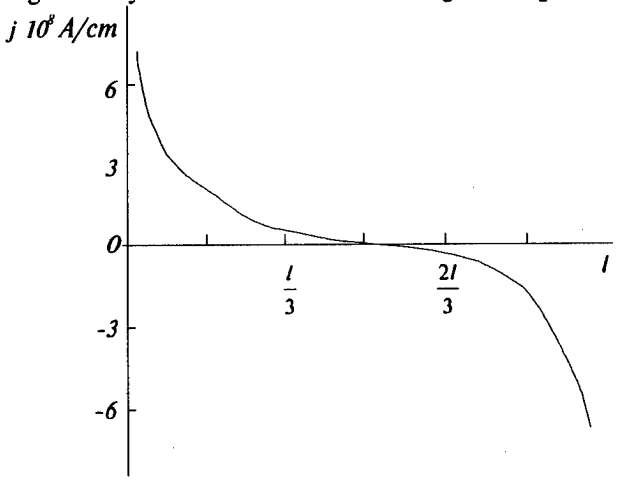


Fig. 3. Density of thermoelectric current crossing the interface of two zones at α_A = 700 μV/K, α_B = 700 μV/K, $\sigma_A = \sigma_B$ = 1.42 10 Ohm^{-1} cm^{-1}, dT/dx = 4 K/cm, t_B/t_A = 5, $l/(t_A + t_B)$ = 1.5

Analysis of expression (1) shows that at $b >> a + d$ the second term in the braces is small for a wide range of P_p/P_n, L_{pn}/L_{np}, relations so $V_\perp$ for the majority of crystals is determined within accuracy exceeding the experiment accuracy only by the difference of a film and substrate, Seebeck coefficient, crystal length and temperature gradient:

$$V_{\perp} = \frac{\alpha_n - \alpha_p}{2b} \Delta T y . \qquad (2)$$

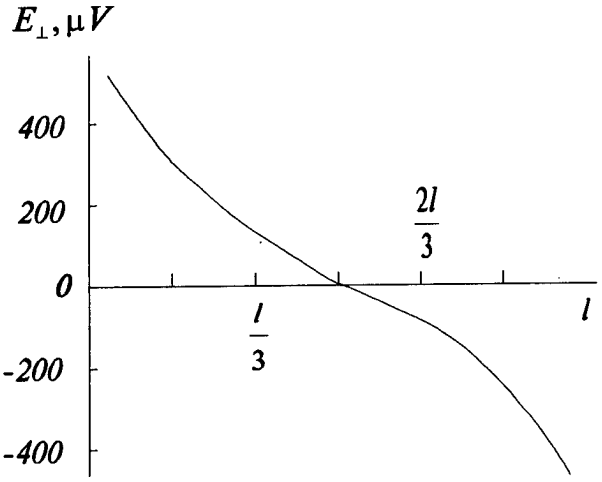


Fig. 4. Distribution of transverse thermo-emf in a zone inhomogeneous plate. Parameters are the same as in Fig. 3.

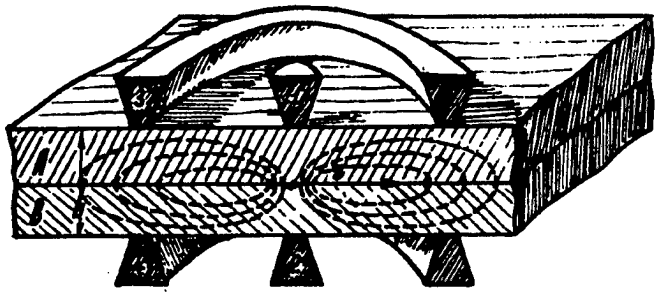


Fig. 5. Thermal contacts location on the sample.

By the temperature field choice it is possible to change the value and spatial distribution of ETC in a small volume. Under such conditions measuring of $V_{\perp}$ in different regions of a crystal it is possible to determine about the epitaxial layers homogeneity degree.

Fig.5 shows a device for axially symmetrical temperature distribution excitation in an epitaxial film.

Fig.6 shows the temperature distribution profile in a sample,

Fig.7 shows distribution of ETC located in a heater region (a), distribution of transverse thermo-emf (b) and temperature in an epitaxial film.

Measurements of $V_{\perp}$ for epitaxial films homogeneity determination is best to use when samples contain a low-ohmic substrates. In such cases standard probe measurement methods do not provide necessary accuracy.

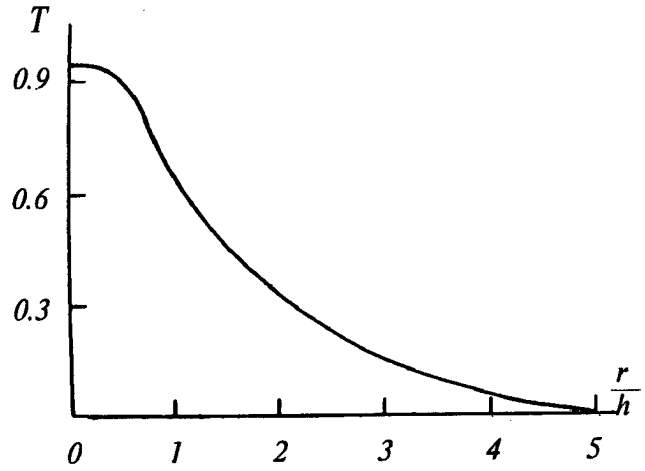


Fig. 6. Temperature distribution along the interface of contacting media at axially symmetrical temperature distribution.

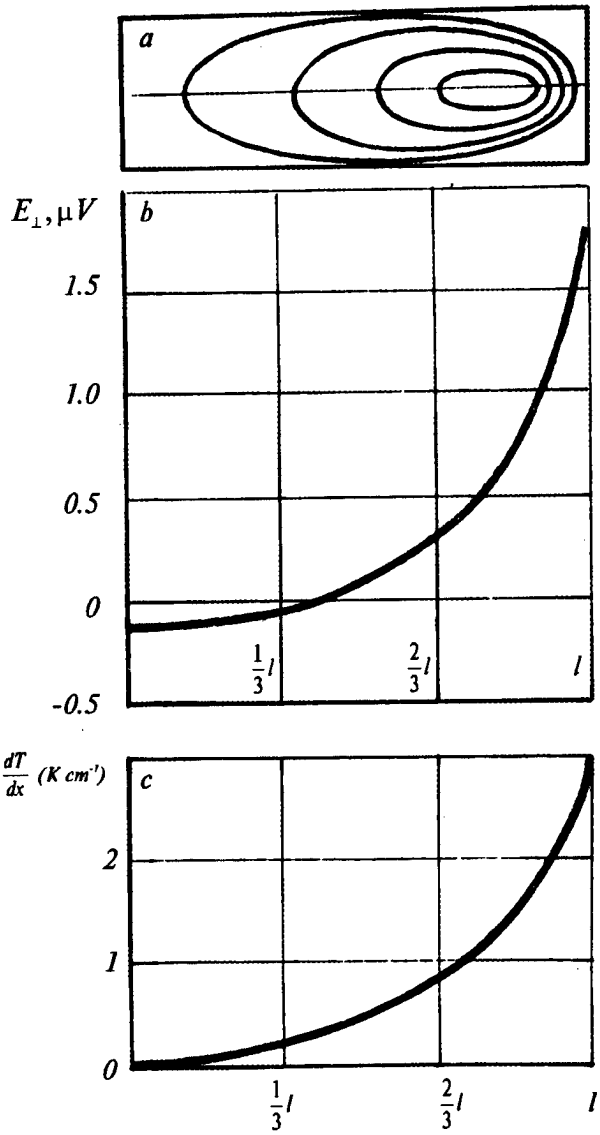


Fig. 7. Distribution of eddy current (a) and transverse thermo-emf (b) at axially symmetrical temperature distribution (c).

Eddy thermoelectric detectors of IR radiation

It is well known that a thermocouple radiation detector's responsibility can be increased by a couple thermal resistance decrease that results at the same time in sensitivity decrease. With the use of thermoelements generating transverse thermo-emf sensitivity does not depend on a thermoelement geometric size along the thermal flow that in principle removes restrictions in possibility to develop fast radiation detectors without sensitivity losses. This peculiarity is used in design of radiation detectors with eddy thermoelements [1] generating transverse thermo-emf.

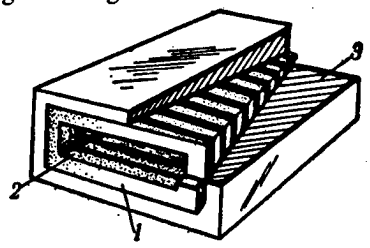


Fig. 8. Eddy thermoelement us radiation detector : 1 - single crystal spiral of pyramidal form; 2 - hollow; 3 - thermostat.

A detector diagram with an eddy thermoelement is given in Fig. 8. Expressions for sensitivity and time constant of the detector have the form

$$S_U^a = \frac{\varepsilon_0(\alpha_\parallel - \alpha_\perp)}{2\kappa b}, \quad \tau = \frac{4}{\pi^2}\frac{h_0^2}{a_0},$$

where α_0 is a material temperature conduction along a thermal flow direction, κ is a material thermal conduction, a, b - spiral turn sizes, h_0 thickness.

Table. Parametres of radiation detectors

Time constant τ, s	Detectivity D^*, cm $Hz^{1/2}W^{-1}$	Resistance r, Ohm	Spiral thickness h_0, μm
CdSb - 400 K			
2.2	$7\ 10^7$	17.5	2850
$2.2\ 10^{-2}$	$2.2\ 10^7$	175	285
$2.2\ 10^{-4}$	$0.7\ 10^7$	1750	28.5
$8.9\ 10^{-6}$	$3.2\ 10^6$	8750	5.70
$2.2\ 10^{-6}$	$2.2\ 10^6$	17500	2.85
Bi-Sb - 300 K			
2.2	$4\ 10^8$	0.005	6240.00
$2.2\ 10^{-2}$	$1.2\ 10^8$	0.053	624.00
$2.2\ 10^{-4}$	$4\ 10^7$	0.53	62.40
$8.9\ 10^{-6}$	$1.8\ 10^7$	2.65	12.50
$2.2\ 10^{-6}$	$1.2\ 10^7$	5.3	6.25

Table presents parameters of detectors with eddy thermoelements form materials with anisotropic Seebeck coefficient. Table shows that these detectors at high frequencies are competitive with the best samples of bolometers retaining all advantages of thermoelectric detectors.

The use of spiral eddy thermoelements for IR radiation registration enable to increase non-selectivity especially in far region of IR spectrum and decrease additional losses appearing at a thermal junction between a receiving site and a detector.

Microcalorimetric eddy detectors

A spiral shape and transverse mode of operation are very convenient for the thermoelements [5] usage in microcalorimeters (Fig. 9).

A studied object is placed into the spiral hollow. Outer surfaces of the spiral are thermostatted. Heat release or heat absorption are registered by the appeared thermoelectric voltages at the ends of the spiral (2, 3, 4). The use of two spirals made it possible to use a differential diagram.

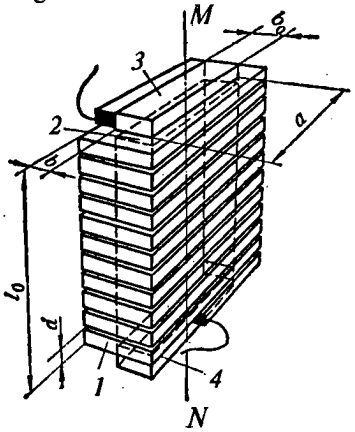


Fig.9. Eddy thermoelectric sensor for a microcalorimeter: 1 - single crystal spiral; 2 - reaction chamber hollow; 3, 4 - thermal insulation of the low and top space of the chamber [4].

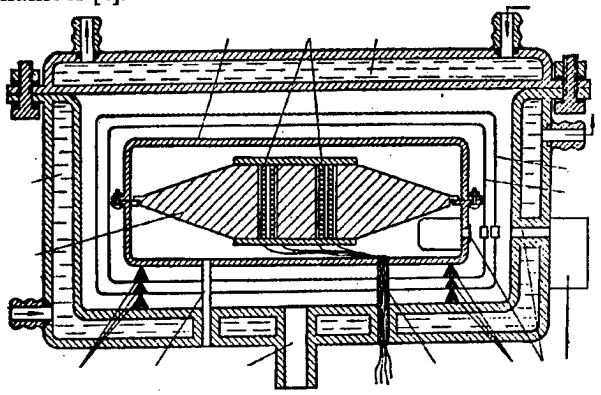


Fig.10. A diagram of a microcalorimeter with eddy thermosensors [5]: 1 - liquid thermostatted vacuum bulb; 2 - thick-wall unit for outer thermal disturbances equalizing; 3 - single crystal spirals; 4 - unit cover; 5, 6 - radiation shields; 7 - photo amplifier; 8 - windows; 9, 13 - fluoroplastic thrust bearings; 10 - electric contacts; 11 - pine connection for evacuation; 12 - tube for pressure equalizing between calorimeter and environment; 14 - thermal unit [5].

Fig. 10 presents a variant of a microcalorimeter with spiral eddy sensors. It has an outer jacket, radiation shields and copper thermostatting units. Outer jacket temperature is maintained within ± 0.01 K. A unit with eddy thermoelements is protected form the outer influences by a thick-wall copper unit and two alumina shields. To decrease outer thermal disturbance the units are symmetrical with respect to the reaction chambers. The device structure provides a vacuum protection from outer thermal effects. Eddy sensors are inserted into differential circuit and connected with a galvanometer of

a photo amplifier which is built-in into the microcalorimeter thermostatted unit for error decrease. Heat release compensation may be performed by the use of double spirals, one part of which is used for thermal flow registration, the other for cooling or heating by the transverse Peltier effect when electric current passed through the spiral. Minimum detected power is 10^{-6} W, a sensor time constant is 1.5 s, reaction chambers volume is 10 cm^3, temperature range of measurements is 50-150 C, internal resistance of sensors is 10 Ohm. Single crystal spirals are made of bismuth. Microcalorimeter is used for registration of fast thermal processes. Measurements can be done in any non - aggressive gaseous medium under the pressure from 5 Atm to 10^{-3} mm Hg .

References

[1] Anatychuk, L.I., Luste, O.J., Thermoelectric eddy currents and eddy thermoelements, *Fizika i tehnika poluprovodnikov*, 10, (5), p. 817-832, 1976 (In Russian).

[2] Anatychuk, L.I., Luste, O.J., Investigation of closed thermoelectric currents in zone-heterogeneous media, *Ukrainskij fizicheskij zhurnal,* 14, (8), p. 1391-1395, 1969 (In Ukrainian).

[3] Anatychuk, L.I., Luste, O.J., Thermoelectric eddy currents and transverse thermopower in zone-heterogeneons plates, *Izvestija VUZov, Fizika,* (6), p. 134-136, 1969 (In Russian).

[4] Anatychuk, L.I., Luste, O.J., Method of resistivity measuring of semiconductor epitaxial films, USSR Authors Certificate SU372492, Publised 01.03.73.

[5] Anatychuk, L.I., Luste, O.J., Microcalorimetry, L'vov, 1986 (In Russian).

[6] Hirose, A., Mathematical theory of multi-dimensional thermoelectricity with some experimental proofs, *J. Inst. Electr. Eng. Jap.*, 74, (9), p. 1056-1062, 1954.

Film manometric thermocouple transducer

Roman Bychkovskii

State University "Lviv Politechnic", 290646 Lviv, Ukraine,
Tel.:380/0322/398619, Fax: 380/0322/744300,
E-mail: oresti@polynet.lviv.ua

Abstract

An analog of the PMT-2 tube manometer thermocouple transducer fabricated using thin-film technology is described. The transducer may have a wider range of application because the source and the heat detector are separated and the output signal is higher due to larger number of thermocouples. The transducers fabricated on mica substrates operate at pressures ranging from 760 to 10^{-5}, 10^{-1} to 10^{-3} and 50 to 1 torr, those on polyimyde substrates operate in the range of 10^{3} - 10^{2} torr. The transducers have passed mechanical and climatic, a 500-h time-to-failure, and ozone tests.

Introduction

Existing pressure transducers operate in wide pressure ranges. Their sensitivity, however, is often non-linear and too low. Although one can correct for these defects of primary converters by using electronic devices and computers, improvement of thermoelectric pressure transducers is also possible [1-3]. The aim of this work was to develop a device similar to the PMT-2 thermocouple manometer transducer and to improve its structure and parameters using thin-film technology.

Background

The sensitive element of the unified film transducer on mica or polyimyde substrate contains a current-heated resistor and a package of thermocouples instead of wires of the PMT-2 transducer. Given the thin-film technique of transducer production, separation of the heat source and detector, and a package of several thermocouples (Fig.1), its parameters may be varied over a wide range. The parameters were optimized by varying separation between the sensitive element and the vacuum case walls (the walls may be either polished or black), the substrate thickness, the distance between the resistor and the thermocouple package, and the number of thermocouples in the package. The upper measurable pressure is reached when the gas thermal conductivity become independent from pressure, i.e., the mean free path of gas molecules is shorter then the distance between heat-exchanging surface. The upper measurable pressure can be increased by decreasing the distance between the surfaces (the highest measured pressure is 0.1 torr when the separation is ~1 cm and 1 torr with ~1 mm). The lower limit of the measured pressure is reached when heat transfer through gas becomes negligible

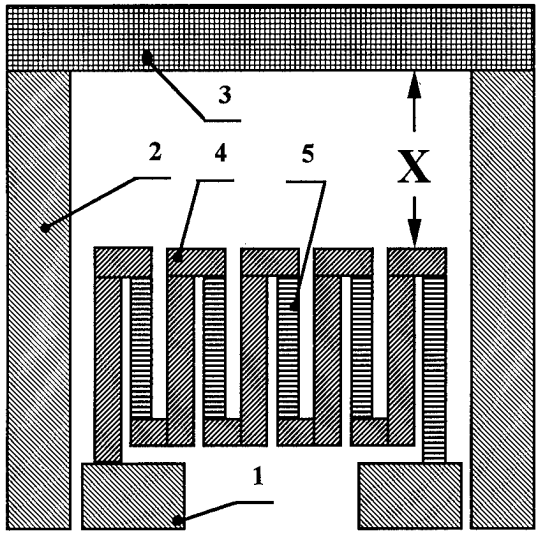


Fig 1: Diagram of the film manometer thermocouple transducer: 1) thermocouple package contact pads; 2) resistor paths; 3) resistor; 4) *p*- branch; 5) *n*- branch of the thermocouple package.

as compared to the radiative heat exchange. The lowest measurable pressure can be decreased by increasing the distance between the surfaces exchanging heat (the limit is 10^{-5} torr when the distance is 1 cm and 10^{-3} torr when the gap is 1 mm wide). The heat transfer through thermal conductivity is minimal at the lowest measurable pressure (the radiative heat transfer is practically constant over the entire range), and the temperature of the resistor and thermocouple hot junctions, and the total thermal emf are the highest. The total thermal emf can be made equal to 10 mV in order to match the device to common electronic potentiometers [4]. In order to find the output thermal voltage as a function of pressure at various distances between the heater and hot junctions of the thermocouples (X in Fig. 1) and the separation between the sensitive element and the chamber walls, the heat exchange has been calculated on a computer. The model is based on the stationary equation of heat conductivity with radiation taken into account. The following parameters were assumed in the model: the power released in the resistor was 0.5 W, the number of thermocouples n=15, the thermal emf α_{te}=100 μV/K, the substrate thermal conductivity k_s=0.03 W/cm·K, the substrate thickness t_s=15μm.

The calculations presented in Fig. 2 show that with the increasing distance between the heater and hot

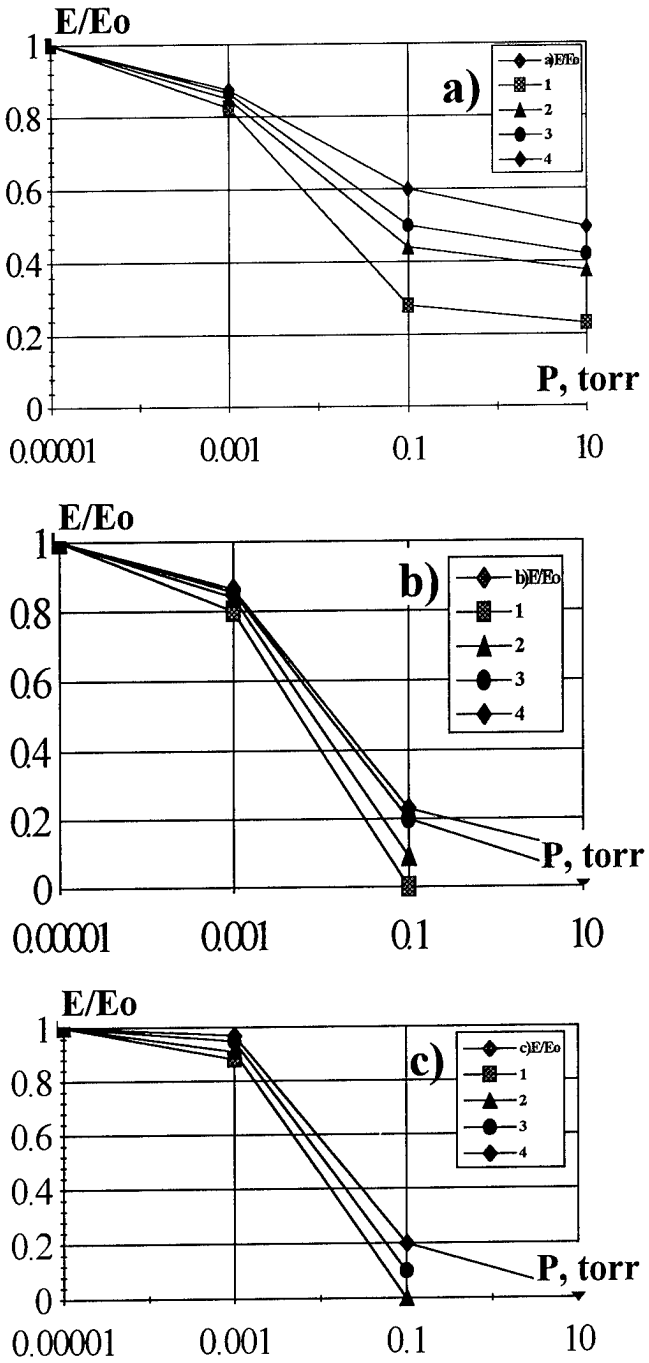


Fig 2: Computed characteristics of film thermocouple transducers at various distances between the transducer and the case walls a) 1cm; b) 0.1 cm; c)0.0015cm; and between he resistor and hot junctions of thermocouples1)-0; 2)-0.2; 3)-0.5; 4)-1 cm.

junctions of thermocouples, the upper measurable pressure rises and the measurable pressure range widens, but the output thermal emf drops; it is more sensitive to the distance between the heater and thermocouples than between the heat-exchanging surfaces.

The signal drop is compensated for by increasing the number of thermocouples. With the thin film technology, it does not make the fabrication process more labor-consuming because a new mask resolves all problems. Mica (muscovite) plates and polyimyde film were used as substrates. Mica has sufficient strength, low thermal conductivity, and perfectly structured smooth surface. Polyimyde film is thin and highly resistant against chemical agents. Both materials have fairly high adhesion to the selected film materials provided that the deposition and pumping regimes are optimized and films of optimal thickness are deposited. The upper layers were deposited under a temperature below that of the lower layers.

The contact pads and current paths were produced from copper on a chrome underlayer, the resistor was fabricated from bismuth [5], the thermocouple package from bismuth and antimony [6,7], and the protecting layer from germanium oxide. The circuit shape was defined by deposition through a mask made by photolithography from beryllium bronze foil 50μm thick.

The substrate holes are made by a calibrated drill with a jig. The masks are set in mask and substrate holders on pins. The transducer elements coincide to within ±10μm. The film geometry and electric parameters were checked in process using a "witness".

The film resistor ~1μm thick has a width of 0.6 mm and 0.4 mm. The film thermocouple elements ~1μm thick have a width of 0.6 mm, are spaced at 0.4 mm their branches overlap in junction over 0.4 mm. The protecting layer has a thickness of 1 mm, the contact pads are not protected. The distance between the heater and the junctions is 0.1 mm to several millimeters, depending on the desired range. The number of thermocouples was up to fifteen, the distans between the sensitive element and the case walls is 2-3 mm.

The film structures were annealed in order to stabilize the microstructure [5-7]. A current of 100 mA was passed through the transducer for 24 h.

The sensitive element is set in a separate case with a lid connected to a gas-filled or vacuum volume via a sealed connection, as in PMT-2. The current (connected to the resistor) and potential (to the thermopackage) leads are passed through cover seals and a case connector and welded to the sensitive element contact pads on the assembly holder. The transducer is set vertically with the resistor in the top position in order to decrease the convection at the upper measurable pressure.

A B018P reference manometer, and PMT-2 and LM-2 tubes were used to calibrate the transducer. The rated heating current through the resistor (several or tens of milliamperes) was adjusted so that the dial limit correspond to 10 torr (10 mV) or 760 torr (1 mV). The possibilities of measuring pressure using one transducer in both manometer (>3 atm) and vacuummeter ($<10^{-5}$ torr) modes, and of transducer fabrication for required measuring range have been checked (Fig. 3).

The transducers made on mica substrate 20 ± 2μm thick for the ranges of 760-10^{-5} torr, 10^{-1}-10^{-3} torr and 50-1 torr and on polyimyde film 20μm thick for the range of 10^{3}-10^{2} torr have been tested for 500 h. The transducers retained their parameters after being subjected to 25 Hz vibrations with an amplitude of up to 0.1 mm, and after exposure to temperatures of +60 and -40°C and an ambient with a relative humidity of 80% at 35°C. The transducers operated

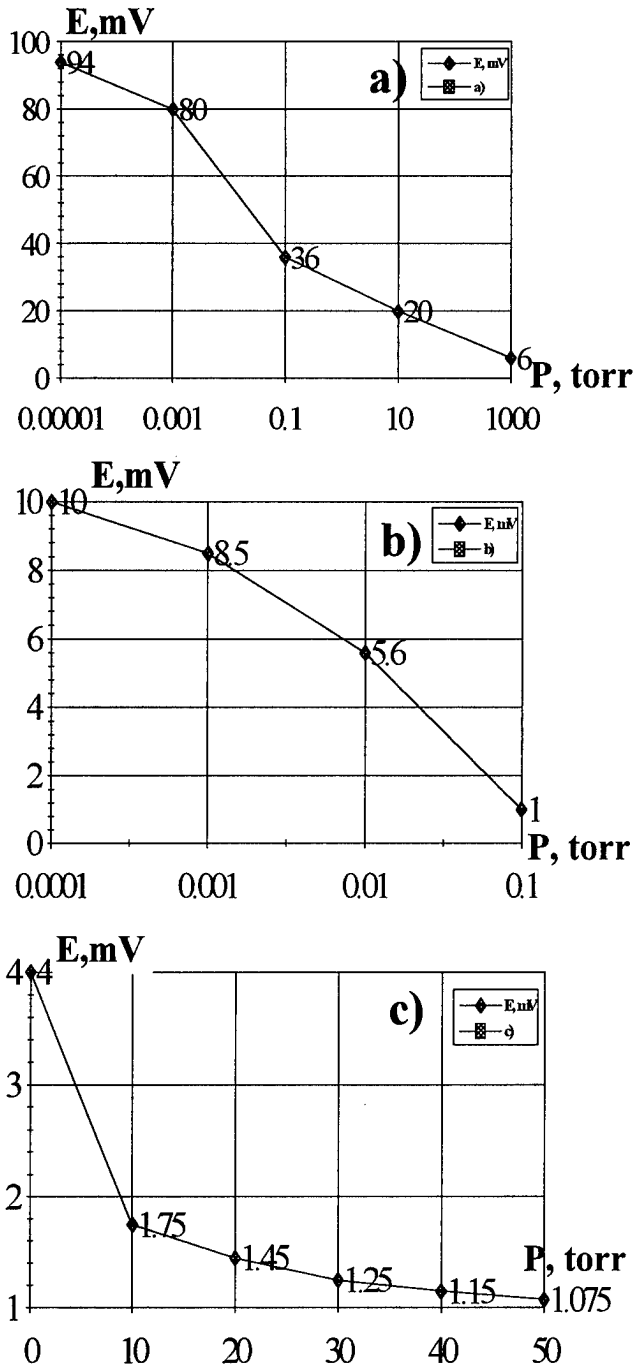


Fig 3; Measured characteristics of the film thermocouple ransducers for the ranges: a) 760-10^{-5}, b) 10^{-1} - 10^{-3} and c) 50 - 1 torr.

for a long time in a device for ozone analysis, which may characterize them as fairly reliable.

References

[1] V. N. Vigdorovich, V. G. Gontar', V.A. Kuznetsov, and F.V. Markov, Collection of Pre-prints NITs TL RAN, NITs TL RAN, Shatura (1991), p. 245-286.

[2] R.V. Bychkovskii, V. N. Vigdorovich, and I.M. Domin'uk, Film Thermometric Transducer. Film Thermocouples (technical instructions) [in Russian], L'vov Polytechnical Institute, L'vov (1989).

[3] V. N. Vigdorovich, F.V. Markov, and G.A. Ukhlinov, Electronnaya Promyshlennost', No. 2 (140), 10 (1985).

[4] R.V. Bychkovskii, V. N. Vigdorovich, E.A. Kolesnik, et al., Instrument for Temperature Contact Measurements. Handbook [in Russian], Editor R.V. Bychkovskii, Vishcha shkola, L'vov (1978).

[5] R.V. Bychkovskii, E.A. Kolesnik, G.A. Ukhlinov, and B.A. Shvarts, Selected Works on Problems of Microelectronics [in Russian], MIET, Moscow (1976), No. 28, p. 53-55.

[6] V. N. Vigdorovich, G.A. Ukhlinov, B.A. Shvarts, and E.N. Andronova, Izvestiya AN SSSR. Nonorganic Materials, 21, No. 6, 905 (1985).

[7] N.F. Bondarchuk, V. N. Vigdorovich, G.A. Ukhlinov, Izvestiya AN SSSR. Nonorganic Materials, 24, No. 11, 1805 (1988).

[8] K.D. Mgaloblishvili and T.G. Rukhadze, Metrology and Precision Measurements [in Russian], 3, 3 (1977).

[9] K.D. Mgaloblishvili and T.G. Rukhadze, Metrology and Measuring Techniques [in Russian], 8, 1 (1975).

THE THERMOCOUPLE TEMPERATURE INSTABILITY

B.M.Goltsman
A.F.Ioffe Physical-Technical Institute, Russian Academy Science, St.Petersburg, Russia,
Yu.I.Ravich
Technical University, St.Petersburg, Russia

Abstract
It has demonstrated, that the thermocouple with strong dependence of the thermoelectric parameters can be in the regime of the temperature instability. The criterion of the instability origin has calculated in the case, when the Joule heat flow to the external junctions is absorbed by the Peltier effect and the temperature deviations of thermoelectric parameters can strongly break the heat balance. In this case only the Seebeck coefficient temperature dependence and the thermocouple figure of merit value determine the instability criterion. The thermocouple in the insatiable regime can be used as a memory cell, a temperature amplifier and a temperature element very sensitive to the voltage.

Theory
This report presents an analysis of temperature instability of the thermocouple (TC) with strong temperature dependence of the thermoelectric parameters. Let us consider TC with the some thermostabilized junctions and the other external junctions, which temperature depends on the external heat flow, the electric current in TC and thermoelectric parameters. TC supply voltage supposed to be constant. Let dT is a deviation of the external junctions temperature, owing to a fluctuation or a small thermal signal, and dQ is a corresponding heat, emanated or absorbed in these junctions due to the change of the current I and the change of the thermoelectric parameters. The instability can be realized if dT and dQ have the same sign (or $dQ/dT>0$) [1]. Really, in this case the temperature growth causes the heat growth, that in turn causes the further temperature growth and so on.

Let us calculate the expression for dQ/dT. For simplicity we neglect the heat exchange of TC with surroundings. The initial equations are; the thermal balance at the external junctions

$$Q = \frac{1}{2} J^2 R - \alpha J T - K \Delta T ; \qquad (1)$$

and the Ohm law for TC

$$U = JR - \alpha \Delta T ; \qquad (2)$$

Here R, α and K are the TC electric resistance, Seebeck coefficient and thermal conductivity of thermocouple respectively, $\Delta T = T\text{-}T_0$, T and T_0 are the temperatures of the external and thermostabilized junctions.

It is interesting to consider the instability in the case, when the Joule heat flow to the external junctions is completely absorbed by the Peltier effect. In this case the temperature deviations of thermoelectric parameters can strongly break the heat balance at the external junctions and cause the considerable variation of junctions temperature. The compensation of Joule and Peltier heats take place when $\Delta T=0$ and the electric current is $2I_m$. Here $I_m=\alpha T/R$ - the current, corresponding to the maximal temperature drop in TC. In this case from (1) and (2) we get:

$$\frac{dQ}{dT} = -\frac{\alpha^2 T}{R}\left(1 + \frac{1}{zT} + \frac{d\ln\alpha}{d\ln T}\right); \qquad (3)$$

It follows from (3) that temperature instability ($dQ/dT>0$) exists ,when the logarithmic derivative $d\ln\alpha/d\ln T$ has the negative sign and its absolute value is more than $1+1/zT$. Then. the TC state with $\Delta T = 0$ is instable and TC have to pass to one of stable states: $\Delta T>0$ and $\Delta T<0$. Such TC can act as a memory cell.

If $I = 2I_m$ and $d\ln\alpha/d\ln T \approx -(1 + 1/zT)$ the derivative dQ/dT has a small value and the temperature of external junctions is very sensitive to the thermal signal. Such TC can act as a temperature amplifier. In these conditions TC has another interesting properties. So, the calculation shows that in the case, when $J=2J_m$ and $d\ln\alpha/d\ln T\approx-(1+1/zT)$ the derivatives dT/dU and dT/dT_0 aspire to infinity.

For example the derivative dT/dU is expressed as:

$$\frac{dT}{dU} = \frac{1}{\alpha\left(1 + \frac{1}{zT} + \frac{d\ln\alpha}{d\ln T}\right)}; \qquad (4)$$

Therefore the temperature of the external junctions is also very sensitive to the supply voltage and the thermostabilized junctions temperature deviations.

Practical realization of TC instability effects requires a special elaboration of thermoelectrics, having sufficiently high value of zT and high negative value of $d\ln\alpha/d\ln T$. Such properties can have for instance the Bi_2Te_3 - based materials in the region of a intrinsic conductivity beginning. In accordance with [2] at 400K for p-Bi_2Te_3 values of $1+1/zT$ and $d\ln\alpha/d\ln T$ can be 4,3 and -4 respectively. The thermoelectrics with phase transition such as Cu_2Se [3] also can be useful.

References
[1] Goltsman B.M., Ravich Yu.I. IFJ. 51 (1986) 770 (in Russian)
[2] Kutasov V.A., Moizes B.J., Smirnov I.A. FTT. 7 (1965) 1065 (in Russian)
[3] Ogerelec Z., Celustka B. J.Phys. Chem. Solids, 27 (1966) 615.

0-7803-4057-4/97 $10.00 ©1997 IEEE

Unsteady-State Thermoelectric Response For a Thermal Pulse in Semiconductors

G.N. Logvinov, Yu.V. Drogobitskiy
Institute of Thermoelectricity, Post Box 86, Chernivtsi, Ukraine, Tel: (380) 3722 41917; E-mail Alex@ite.chernovtsy.ua
Yu.G. Gurevich, A.F. Carbalo Canchez, O.Yu. Titov
Departamento de Fisica Centro de Investigasion y de Estudios Avanzados del I.P.N., Apaetado Postal 14-740, 07000 Mexico, Distrito Federal, Mexico Tel: (525) 7477000, Fax: (525) 7477096, E-mail: gurevich@fis.cinverstav.mx

Abstract

Thermoelectric signal appeared in the result of the propagating the rectangular thermal flux through the geometrically bounded sample has been theoretically investigated. The possibility of obtaining of the thermal diffusivity by thermo-e.m.f. maximum registration is shown.

Last years, the experimental method based on transient thermoelectric effect (TTE) became widespread for the determine different electrophysical and relaxation parameters of semiconductors [1]. With it's aid it was succeeded to understand the electron's and hole's kinetic properties in Si_4GaAs, quasitwodimensional materials γ-Mo_4O_{11}, narrow gap semiconductors $Bi_{2-x}Sn_xTe_3$. On it's base, most probable band model of the solid solutions $Sb_{2-x}In_xTe_3$ and $Sb_2Te_{3-x}Se_x$ has been proposed. An idea of this method is simple and consists of measuring thermoelectric voltage appeared as a result of short-term thermal disturbance, caused by absorbtion of the energy impulse of the incident electromagnetic radiation, as a rule - laser radiation. Detected thermoelectric signal carries on the information about medium thermal parameters, relaxation characteristics, lite absorbtion factor etc.

One of the many important theoretical problems concerning TTE is calculation of the non-stationary and inhomoheneous thermal fields in bounded samples and corresponding thermoelectric responses. Just this is the problem this work devoted to.

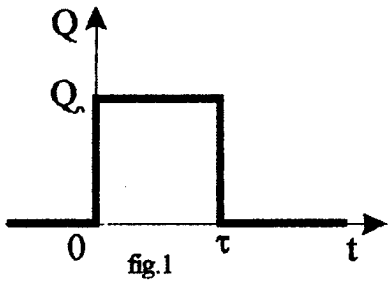


fig.1

Let the pulse of the thermal flux with the value Q_0 and duration τ falls on the surface x = 0 of homogeneous and isotropic sample parallelepiped-shaped (fig.1). Right surface x = 1 is hold under the constant temperature T_0. The lateral sides are adiabaticaly isolated (fig.2). To simplify we will consider all thermal flux is absorbed on the sample surface, electron and phonon temperature are equal and kinetic coefficients are not depend on temperature.

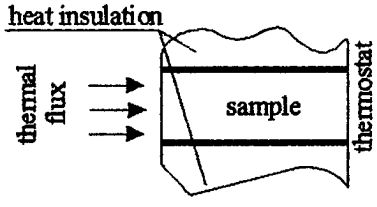


fig.2

To determine temperature T(x,t) let's use well-known heat conduction equation

$$\frac{\partial^2 T(x,t)}{\partial x^2} = \frac{1}{\beta}\frac{\partial T(x,t)}{\partial t}, \qquad (1)$$

Here $\beta = \frac{\kappa}{\rho c}$ is the thermal diffusivity, k is the thermal conductivity, ρ is the density and c is the specific heat capacity. It is convenient to model the considerable problem by two heat processes:

1. When $0 < t \le \tau$, the boundary and initial conditions for the equation are:

$$\begin{cases} -\kappa \left.\frac{dT}{dx}\right|_{x=0} = Q_0 \\ T(x,t)\big|_{x=1} = T_0 \\ T(x,t)\big|_{t=0} = T_0 \end{cases} \qquad (2)$$

2. When $t > \tau$, corresponding boundary and initial conditions are the following:

$$\begin{cases} \left.\frac{\partial T}{\partial x}\right|_{x=0} = 0 \\ T(x,t)\big|_{x=1} = T_0 \\ T(x,t)\big|_{t=\tau} = T_1(x,\tau) \end{cases} \qquad (3)$$

At a moment $t = \tau$ thermal flux ends. The initial temperature in this process is the same as the final temperature $T_1(x,t=\tau)$ in the previous process.

The solution of the equation (1) may be presented by the next expression:

$$T(x,t) = A + Bx + X(x)U(t), \qquad (4)$$

where A, B are unknown constants; X(x), U(t) are unknown functions. Finally, inserting (4) into (1) and using (2), (3) the following expression for the temperature could be obtained:

$$T(x,t) = \frac{Q_0}{\kappa} l \cdot \left\{ \left(1 - \frac{x}{l}\right) - \right.$$

$$\left. - \frac{2}{\pi^2} \cdot \sum_{n=0}^{\infty} \frac{1}{\left(n+\frac{1}{2}\right)^2} \cdot \cos\left(\pi\left(n+\frac{1}{2}\right)\frac{x}{l}\right) \cdot \exp\left(-\pi^2\left(n+\frac{1}{2}\right)^2 \frac{t}{\tau_1}\right) \right\} -$$

$$- \eta(t-\tau)\frac{Q_0}{\kappa} l \cdot \left\{ \left(1 - \frac{x}{l}\right) - \right. \qquad (5)$$

$$\left. - \frac{2}{\pi^2} \cdot \sum_{n=0}^{\infty} \frac{1}{\left(n+\frac{1}{2}\right)^2} \cdot \cos\left(\pi\left(n+\frac{1}{2}\right)\frac{x}{l}\right) \cdot \exp\left(-\pi^2\left(n+\frac{1}{2}\right)^2 \frac{t-\tau}{\tau_1}\right) \right\}$$

where $\eta(t-\tau)$ is the Heaviside function [3], $\eta(y) = \begin{cases} 1, & y > 0, \\ 0, & y \le 0; \end{cases}$ $\tau_1 = \frac{l^2}{\beta}$ is the characteristic parameter that has a meaning of the thermal conductivity process relaxation time.

Estimations show, the series in (5) convergent slowly when $t \ll \tau_1$ and are equal to their first terms with the good precision when $t \ge 0{,}1\tau_1$.

In a general case, two-dimensional dependence T(x,t) is shown on fig.3.

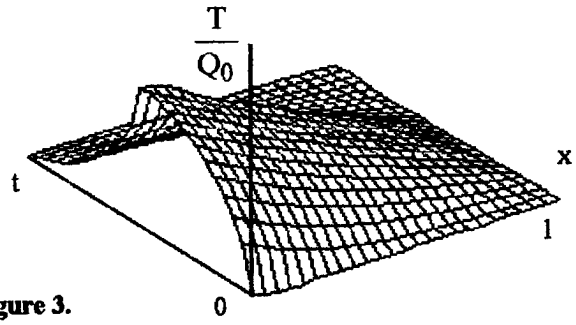


figure 3.

As a example Si ($a = 0{,}4$ mV/K) was taken [1], under $T_0 =$ 300 K, $\tau = 1*10^{-8}$ sec, $l = 1$ cm.

It is easy to see that in general case the function T(x,t) is non-linear on both arguments. As for the argument t the function is non-monotonous on it. Evidently these singularities have to be reflected on the character of the thermoelectric voltage appeared in the sample.

Let us illustrate the dynamic of the temperature response in the sample. There are two cases that are interest to observe: $\tau_1 > \tau$ and $\tau_1 < \tau$. In the first case when $t < \tau$ the graphs of temperatures $\left(\frac{K}{Q_0} \cdot 10^{-3}\right)$ are shown on the figure 4 ($t_1=0{,}1\tau_1$, $t_2=0{,}5\tau_1$, $t_3=0{,}7\tau_1$), and when $t>\tau$ on fig.5 ($t_1=1{,}1\tau$, $t_2=1{,}3\tau$, $t_3=2\tau$). In the second case the graphs are shown on the fig.6,7.

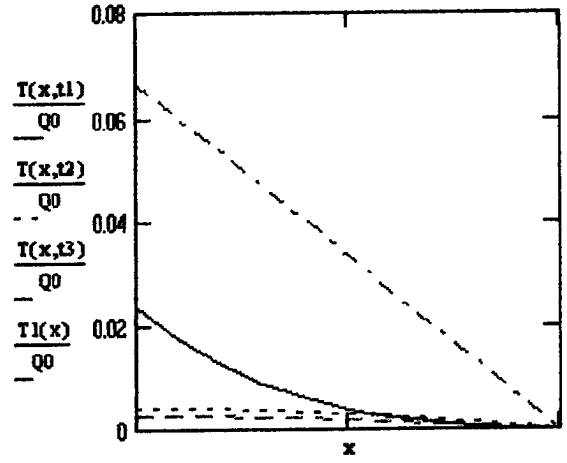


figure 4.

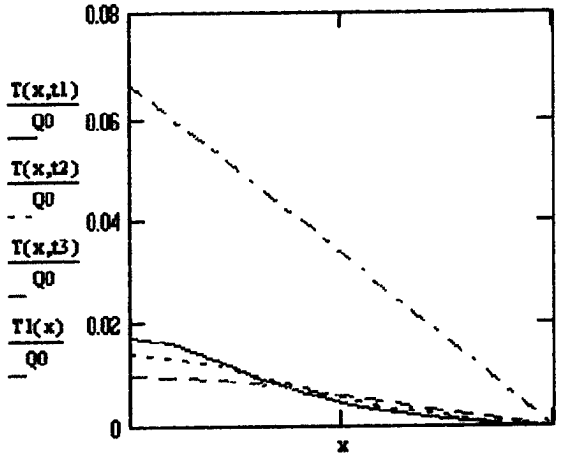


figure 5.

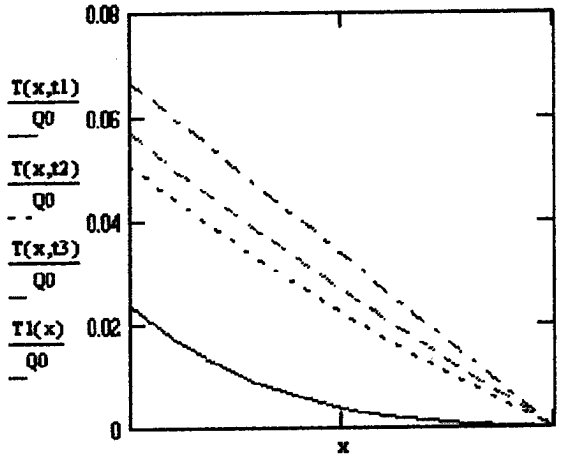


figure 6.

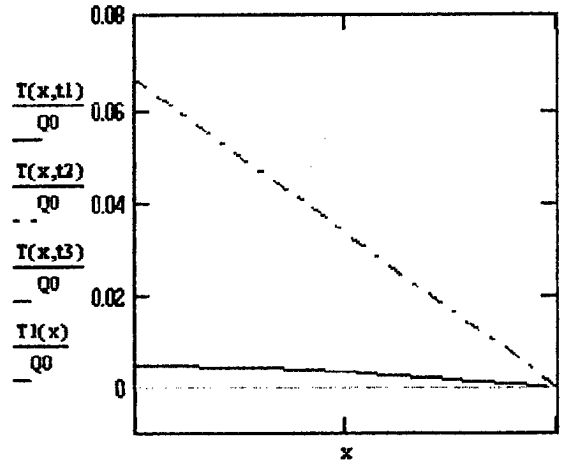


figure 7.

Limiting ourself by quasistationary approximation with the condition of open circuit (no load regime), generating thermoelectric voltage could be determine as:

$$E(t) = -\int_0^1 \alpha \cdot \frac{dT(x,t)}{dx}\,dx, \qquad (6)$$

where α is the thermoelectric voltage coefficient.
With the initial conditions of the problem, using (5), it is easy to receive:

$$E(t) = \alpha \frac{Q_0}{\kappa} 1 \cdot \left\{ -1 + \frac{2}{\pi^2} \cdot \sum_{k=0}^{\infty} \frac{1}{\left(k+\frac{1}{2}\right)^2} \cdot e^{-\pi^2\left(k+\frac{1}{2}\right)^2 \frac{t}{\tau_1}} \right\} + \qquad (7)$$

$$+ \eta(t-\tau)\alpha \frac{Q_0}{\kappa} 1 \cdot \left\{ 1 - \frac{2}{\pi^2} \cdot \sum_{k=0}^{\infty} \frac{1}{\left(k+\frac{1}{2}\right)^2} \cdot e^{-\pi^2\left(k+\frac{1}{2}\right)^2 \frac{t-\tau}{\tau_1}} \right\}$$

The thermoelectric voltagies accounted for the unit of the heat flux $\varepsilon(t) = \frac{E(t)}{Q_0}\left(\frac{mkV}{Q_0}\cdot 10^{-3}\right)$ for different correlations between t and τ_1 is shown on figures 8,9,10.

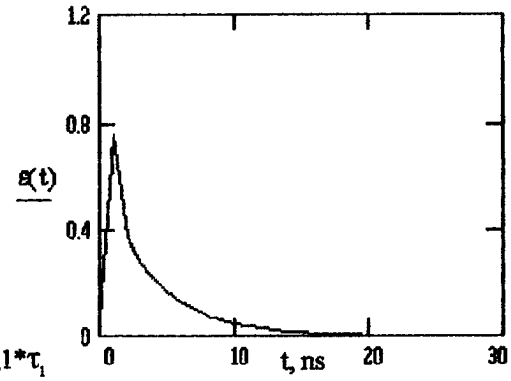


figure 8. $\tau = 0{,}1^*\tau_1$

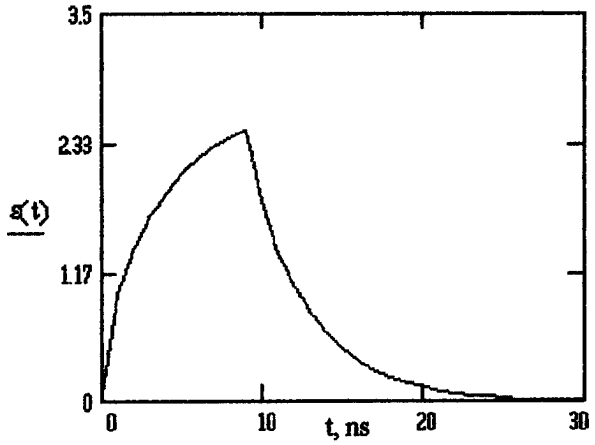


figure 9. $\tau = \tau_1$

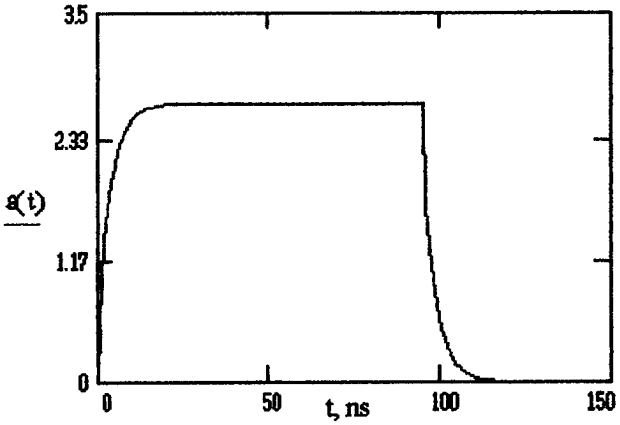


figure 10. $\tau = 10^*\tau_1$

Characteristic pecularity of those graphs is the presence of thermoelectric voltage maximum, that appears each time when t = τ. When τ is large ($\tau >> \tau_1$) maximum degenerates into horizontal plateau, that is entirely coordinates with the qualitative physical view. When $t \to \infty$ the problem is reducing to the determination of thermoelectric voltage when the incident radiation is continuous.
The registration of that thermoelectric voltage maximum allows to obtain the information about different substance parameters. The situation is the most simple in those cases when the series could be approximated by the first terms. Really, in that case (7) reduces to:

$$E(t) = \alpha \frac{Q_0}{\kappa} 1 \cdot \left\{ -1 + \frac{8}{\pi^2} \cdot e^{-\frac{\pi^2}{4}\frac{t}{\tau_1}} \right\} +$$

$$+ \eta(t-\tau)\alpha \frac{Q_0}{\kappa} 1 \cdot \left\{ 1 - \frac{8}{\pi^2} \cdot e^{-\frac{\pi^2}{4}\frac{t-\tau}{\tau_1}} \right\} \qquad (8)$$

and,

$$\text{Max } E_1(t) = \alpha \frac{Q_0}{\kappa} l \cdot \left(-1 + \frac{8}{\pi^2} \cdot e^{-\frac{\pi^2}{4} \cdot \frac{\tau}{\tau_l}} \right) \qquad (9)$$

From the expression (9) follows that when we know, for instance, the values Q_0, l, τ and max $E_1(t)$ we can trivially obtaine the parameter τ_l (and that means that we can obtaine thermal conductivity factor β too). Or, knowing the other set of the values and max $E_1(t)$ obtained in experiment we can obtaine the sample width, the intensity of the incident radiation, etc.

References

[1] Minoru Sasaki, Hiroshi Negishi, and Masasi Inoue. J.Appl. Phys., Vol. 59, 1986, p. 796-802.

[2] V. A. Kulbachinskii, Z. M. Dashevsky, M. Sasaki, H. Negishi, W. X. Gao, P. Lostak, J. 'Horak and A. de Visser, Phys. Rev. B., V. 52, p. 10915-10922, (1995).

[3] Granino A.Korn, Theresa M.Korn. Mathematical Handbook for Scientists and Engineers, New York - Toronto - London, 1961.

AKNOWLEDGMENTS

This work is partially support by Consejo Nacional de Ciencia y Tecnologia (CONACYT), Mexico.

Features of thermoelectromotive force in Au/p-Ge junctions

S.Ašmontas, J.Gradauskas, A.Sužiedėlis, G.Valušis

Semiconductor Physics Institute, A.Goštauto 11, 2600 Vilnius, Lithuania
Tel.: 3702/627124, Fax: 3702/627123, E-mail: asmontas@uj.pfi.lt

Abstract

We demonstrate the experimental fact that in Au/p-Ge junctions which are annealed at temperatures close to that of eutectic, the voltage-power characteristic of thermoelectromotive force in microwave electric fields deviates from the linear law. Even more, at certain range of lattice temperatures it becomes non-monotonical and, in definite range of electric fields, the inversion of its sign is observed. We attribute this phenomenon to the hole cooling effect in microwave electric fields. Experiments at various lattice temperatures and in transverse magnetic fields confirmed the validity of the model suggested. The essence of the hole cooling effect in germanium is described, possible features for the application are considered.

Introduction

Usually, the usage of the l-h junctions for microwave power measurements is determined by the fact that the thermoelectromotive force of hot carriers (TEMF) arising on the junction is directly proportional to incident power of the electromagnetic radiation [1 and literature cited herein]. As a typical example of such kind of application is silicon junctions of n- and p- type [2], where the TEMF is linearly proportional to the incident power. Nevertheless, such a rule can not be approximated as a general law for the l-h junctions produced on the base of the different materials. Under a certain conditions, however, the detected signal can depend nonmonotonically on the applied microwave power. This circumstance restricts the talk about possible application for microwave detection, however, it reveals new area for the basic physics. In particular, the case of $n\text{-}n^+$-junctions in highly compensated n-InSb<Cr> can serve as an illuminating example of this matter [3]. Experiments shows [4] that here at first, voltage-power characteristics follows the linear law, reaches a maximum, decreases rapidly and, finally, a negative region of the TEMF appears. This effect of a negative detected signal was attributed to the electron cooling effect [3]. Since the TEMF reflects the behaviour of the mean carrier energy, it means that the latter can be lower than the equilibrium one. For the observation of the carrier cooling effect the strong scattering of the momentum of low energy electrons by complexes of ionised impurities, the dominance of optical phonon emission, and negligible electron-electron interaction are necessary. The essence of the phenomenon can be described in the following way. An electric field accelerates electrons in a passive region of the k-space. When the electrons reach the energy of an optical phonon, the emission of the optical phonon occurs, the electrons lose all its energy and get in the state with energy close to zero, i.e. in the bottom of random valleys. Due to additional scattering of electrons by the complexes of ionised impurities, electrons remain localised in the neighbourhood of the conduction band bottom, where their mobility is low. For that reason the mean energy of electron gas becomes smaller than the equilibrium value.

In a given communication we report on the experimental findings in Au/p-Ge junctions. We determined the conditions suitable for detection of microwave power and the circumstances enabling the TEMF exhibit nonmonotonical dependence on the incident microwave power.

Samples and technique

Samples under test were prepared from germanium of p-type with specific resistance of 30 Ω·cm. Small area Au/p-Ge junctions were made by electrochemical deposition of gold with subsequent annealing in the H_2 atmosphere for 10 minutes at 350 °C. The carriers were heated by a microwave electric field with frequency of 10 GHz. In order to avoid crystal lattice heating, the duration of the pulses was up to a few microseconds, while the repetition rate was 40 Hz.

Experimental results and discussion

Recent investigation of microwave signal detection using small area l-h junctions made on the bases of p-Ge with annealed Au contacts at different annealing temperatures revealed the non-traditional behavior of detected voltage depending on the value of microwave power [5]. We bear in mind the fact that the shape of the TEMF power dependence is strongly defined by the annealing temperature of the junction. If junctions are

0-7803-4057-4/97 $10.00 ©1997 IEEE

not annealed or the annealing temperature are far below /above than that of eutectics, voltage-power characteristics follows the linear law. Consequently, such a junctions are suitable for the detection of microwave power [6], and the reason of choice is determined whether the sensitivity fulfils the desirable requirements or not. However, when the junction is annealed at temperature close to the eutectic one ($T_{Au\text{-}Ge}$=356 °C), the TEMF at low lattice temperature began to depend on the incident power nonmonotonically. Namely, these peculiarities and related effects are focus of our attention in this paper.

Figure 1 depicts the dependencies of the detected signal on the applied microwave power at different lattice temperatures. It is seen that the TEMF has the region where its sign is negative. If the change of mobility in electric fields is negligible, then the behaviour of the TEMF signal directly reflects the change of the mean electron energy. Following the scenario developed in [3,4], we attributed the existence of the negative region of the TEMF to the hole cooling effect. Hence, we suppose that the holes after optical phonon emission are localised at the tops of the valence band, randomly modulated by the inhomogeneities occurring during eutectic process in the junction. Therefore, it is reasonable to suppose that elimination of one of these reasons (random potential or optical phonon emission) should lead to the destruction of the effect.

One of the ways to change the carrier concentration, and, correspondingly, the screening of the random barriers, is the variation of the lattice temperature. The hole mobility in our case increases more than one order of magnitude getting down from the room temperature to the liquid nitrogen one. Concentration effects become pronounced in the vicinity of 100 K, therefore, this temperature can serve as a guide for the expectable effects. Indeed, in our samples we observed non-traditional behaviour of the TEMF below 110 K . In higher temperatures the random inhomogeneities can be screened by carriers causing the disappearance of the cooling effect .That is why the negative region of the TEMF on incident microwave power vanishes with the increase of the lattice temperature (Figure 1) and at 170K the dependence becomes monotonical. Although the temperature dependence confirms our model, the question concerning existence of random inhomogeneities remains to be clarified.

As a background for the ideology from this point of view we used works [7,8] where the main features of the highly compensated or disordered semiconductors were determined. Since the current depends on the applied electric field by a law

$$I \sim \exp\left[-\left(\mathcal{E}_a - \alpha E^{1/2}\right)/kT\right], \qquad (1)$$

where $\mathcal{E}_a$ indicates the activation energy of Ohmic conductivity , α is parameter of the inhomogeneity, E denotes the electric field strength, k is the Boltzmann constant, T stands for the lattice temperature, we have measured the current-voltage (I-V) characteristics at different lattice temperatures. Figure 2 shows the I-V characteristics measured at room (light dots) and at liquid nitrogen (dark dots) temperatures. We have found

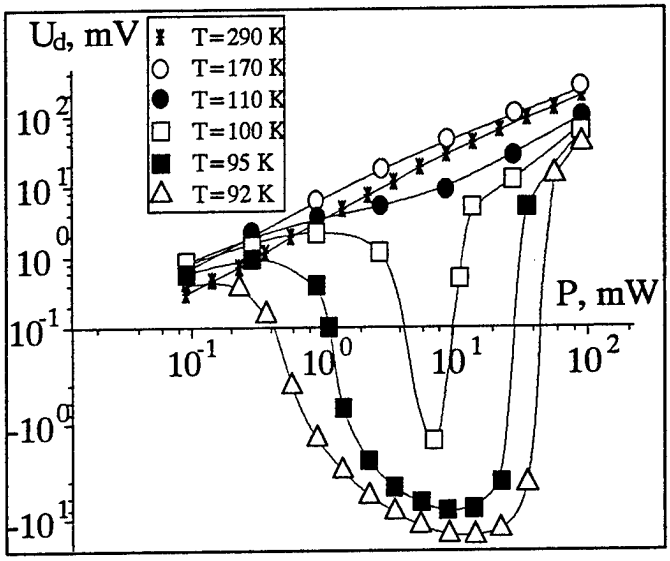


Fig. 1: The dependence of detected voltage on the applied microwave power at different lattice temperatures

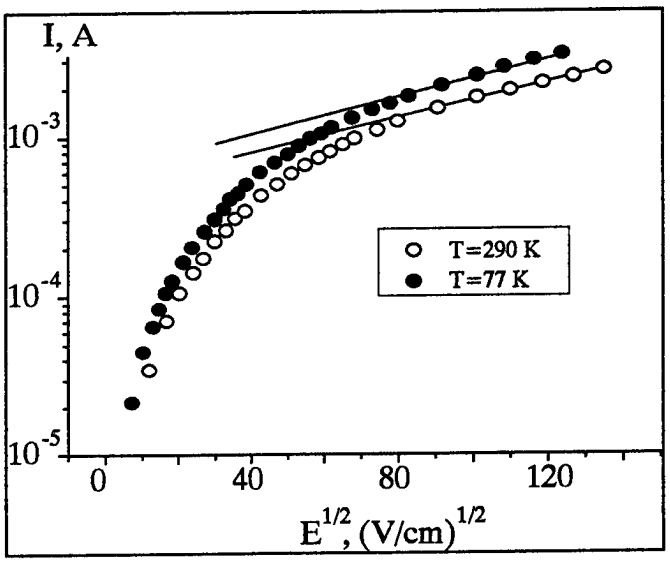


Fig. 2: The I-V characteristic of the Au-p-Ge junction at room and liquid nitrogen temperatures

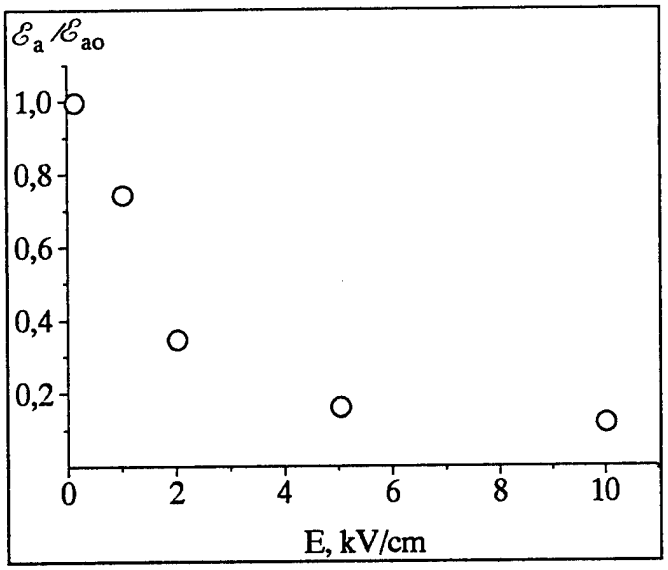


Fig. 3: The dependence of activation energy of Ohmic conductivity on electric field strength

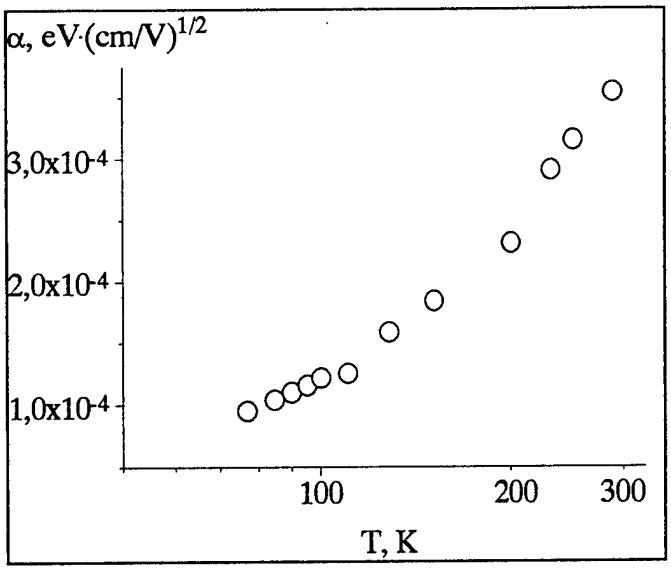


Fig. 4: The temperature dependence of inhomogeneity parameter α

that the electrical conductivity has an activation character, and these characteristics are very similar to that of disordered material [8] or highly compensated semiconductors [9,10]. These findings suggested the idea that the inhomogeneities can play an important role in studied junctions and be responsible for the new effects of the TEMF in microwave electric fields. From the I-V experimental data at various lattice temperature we evaluated the dependence of activation energy of electrical conductivity

$$\mathcal{E}_E = \mathcal{E}_a - \alpha E^{1/2} \qquad (2)$$

on the strength of electric field (Figure 3 shows the relative activation energy dependence on electric field strength, and $\mathcal{E}_{ao}$ denotes the activation energy at weak electric field). It is clearly seen that the activation energy decreases with increase of the electric field as predicts the percolation theory [7].

The temperature dependence of carrier concentration revealed two values of activation energy. At lattice temperature higher than T=120 K $\mathcal{E}_a$=30 meV, whereas, at lattice temperature close to liquid nitrogen one $\mathcal{E}_a$=15 meV. Evaluation of the parameter of the inhomogeneity α at different lattice temperature from eq. (1) have shown its strong temperature dependence (Figure 4). The parameter α is related with energetical and spatial quantity of inhomogeneity [7]

$$\alpha = (0.25eaV_0),^{1/2} \qquad (3)$$

where e is electron charge, *a* denotes the length of inhomogeneity, and V_0 is the fluctuation magnitude of random potential. Taking into consideration the fluctuation magnitude equal to the activation energy values, mentioned above, we have, that at low temperatures holes feel inhomogeneities which length are *a*=30 nm, while at higher temperatures *a*=150 nm. We suppose that the small barriers are screened , but the biggest ones being important to the carrier transport, however, are not sufficient for the existence of the hole cooling effect. Probably, due to the low density of big barriers.

As concerns another approach, i.e. the elimination of optical phonon scattering, we have measured the TEMF dependence on incident microwave power in transverse magnetic fields (Figure 5). It is evident that the negative region of the TEMF with the increase of the induction of the magnetic field decreases and when it reaches 0.5 T. the TEMF negative region is replaced by the kink . It indicates that the magnetic field prevents the holes to reach the energy of optical phonon, i.e. the trajectories of holes are bent due to the influence of the Lorenz force. Therefore, the energy gain from the electric field decreases. The suppression of optical phonon emission decreases the number of holes which can reach the top of the random potential after optical phonon. emission. Consequently , one of the main mechanisms of the localisation is excluded, and the hole cooling disappears. This finding strengthened our consideration concerning origin of the nonmonotonical behaviour of the TEMF in microwave electric fields.

As for application, the cooling effect seems also illuminating: Since it is related to the decrease in mean

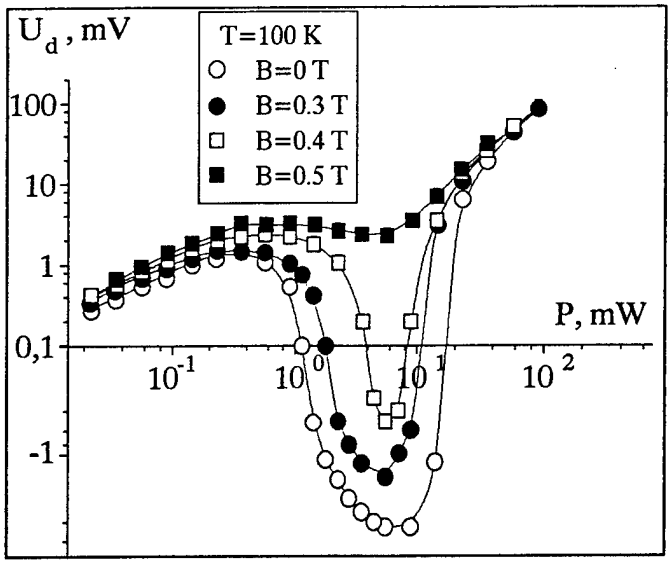


Fig. 5: . The dependence of detected voltage on the applied MW power at different strength of transverse magnetic field

carrier energy, the decrease of the noise temperature here, as in the case of highly compensated InSb [11,12], also should be expected.

Conclusions

We have examined the features of the Au-p-Ge junctions annealed at the temperature close to that of eutectic of Au-Ge. Firstly, the thermoelectromotive force caused by microwave electric fields of 10 GHz frequency depends nonmonotonically on the applied microwave power. This effect was explained by the hole cooling in heating electric fields. Secondly, it was established that the increase of lattice temperature and transverse magnetic field destroys the hole cooling effect in germanium. Thirdly, the parameter of inhomogeinety and its temperature dependence is determined. Finally, we hope that the experimental data presented here can be usual for practical purposes.

We are deeply indebted to Dr. S. Bumelienė for valuable discussions.

References

[1] S. Ašmontas, A. Sužiedėlis, "Thermoelectromotive force of hot carriers in metal p-Ge and -GaAs contacts", Proc. of the XIV Intern. Conf. on Thermoelectrics, (ICT'95), St.Petersburg, Russia, 1995, A.F.Ioffe - Physical Institute, (1995) 334.

[2] S.Ašmontas, "Electrogradient phenomena in semiconductors, Mokslas", Vilnius, 1984, P. 183.(in Russian)

[3] S.Ašmontas, L.Subačius, J.Požela, "Heating and cooling of electron gas in electric fields in compensated indium antimonide", Zh.Ekspr. Theor. Fiz. Lett., **33**, (1981), 580.

[4] S.Ašmontas, J.Požela, L.Subačius, G.Valušis, "Electron gas heating and cooling effects by microwave electric fields in compensated InSb" 'Solid St. Electronics, **31**, (1988), 701.

[5] S. Ašmontas, A. Sužiedėlis, G. Valušis, "Carrierr cooling effect in nonuniform germanium", Lithuanian Journ. of Phys., **35**, (1995), 412.

[6] S. Ašmontas, A. Sužiedėlis, "A study of small area contacts of different metals to the p-type germanium", Physics and Technics of Semiconductors, **30**, (1996), 1163.

[7] B.I.Schklovskii, "Percolation conductivity in strong electric fields", Soviet Physics - Fiz. Techn.Poluprovodn., **13**, (1979), 93.

[8] A.Y.Vul, S.V.Kidalov, "Influence of nonhomogeneous doping impurities distribution for the photoelectric characteristic of resistivity structures based on solid solution $GaAs_{1-x}Sb_x$", Soviet Physics - Fiz. Techn.Poluprovodn., **21**, (1987), .804.

[9] S.Ašmontas, A.Skučienė, "Electrical properties of compensated n-InP", Lithuanian Journ. of Phys, **32**, Suppl, (1992), 205.

[10] S.Ašmontas, S.Dedulevičius, Ž.Kancleris, L.Subačius, G.Valušis, "Investigation of hot electron relaxation in electric fields in compensated InSb<Cr>", Lithuanian Journ. of Phys, **32**, (1992), 425.

[11] S.Ašmontas, G.Valušis, J.Liberis , L.Subačius, "Noise temperature in compensated n-InSb<Cr>, Soviet Physics - Fiz. Techn.Poluprovodn., **24**, (1990), .2214.

[12] S.Ašmontas, J.Liberis , L.Subačius, G.Valušis, "Electron gas cooling studied by measurements of noise temperature", Semicond. Sci. Technol., **7**, (1992), B331.

Nature of thermoelectric anisotropy in semiconductors at the lower temperatures

E.V.Osipov, A.Aulas
Semiconductor Physics Institute, A.Gostauto 11, 2600 Vilnius, Lithuania, unicorn@uj.pfi.lt .

Abstract
It is found, that on the base of the anisotropic scattering theory for monovalley semiconductor and experimental dates of electrical conductivity and Seebeck coefficients measured at lower temperatures on pure single crystals of ZnSb become possible to evaluate relaxation times and effective masses of charge carries.
It is obtained analytical expressions for TE anisotropy and components of Seebeck coefficients tensor for such semiconductors at lower temperatures, in which phonon drag effect predominate. Method are illustrated on example of p-type ZnSb single crystals various purity.

Introduction
The most detailed theoretical investigation of TE anisotropy on the base of the anisotropy scattering theory was developed by Professor A.G.Samoilovich more 30 years ago. In this report we made the attempt to continue development of this theory to explain of arising TE anisotropy in semiconductors at lower temperatures, when phonon drag effect predominate. Exactly such type of semiconductor is single crystals of ZnSb. This theory is espacial utility in ZnSb as it removes the extremely large TE anisotropy in the region of nitrogen temperatures. Namely in this region of temperatures purest single crystals of ZnSb are successfully used for manufacture of Samoilovich's TE element. This is unconventional TE element which does not have traditional junctions between two dissimilar materials and consist of homogeneous materials [1 , 2].

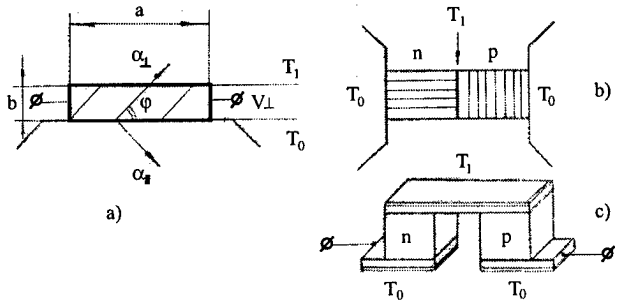


Fig 1. Samoilovich`s TE element (a) in contrast to ordinary TE elements (b,c).

The simplest Samoilovich's TE element is shown in Fig.1. This is a rectangular slice cut from a single crystal. That one has different components of Seebeck coefficient, which distinguish at least in two mutually perpendicular directions : $\alpha_\parallel$ - along the principal TE axis component and $\alpha_\perp$ - transverse to principal TE axis component. The principal TE axis of the crystals lies in the plane of the slice and makes an angle e.g. $\varphi=45^0$ with the side and the end faces of the slice. The upper and lower side faces of the slice have different temperatures T_1 and T_0 so the temperature gradient (∇T) is parallel to the end faces of the slice. The length of the slice a greatly exceeds its height **b**. Under this conditions, between the end faces of the slice, take place a transverse to ∇T TE motive force, denoted as $V_\perp$ is defined by equation below:

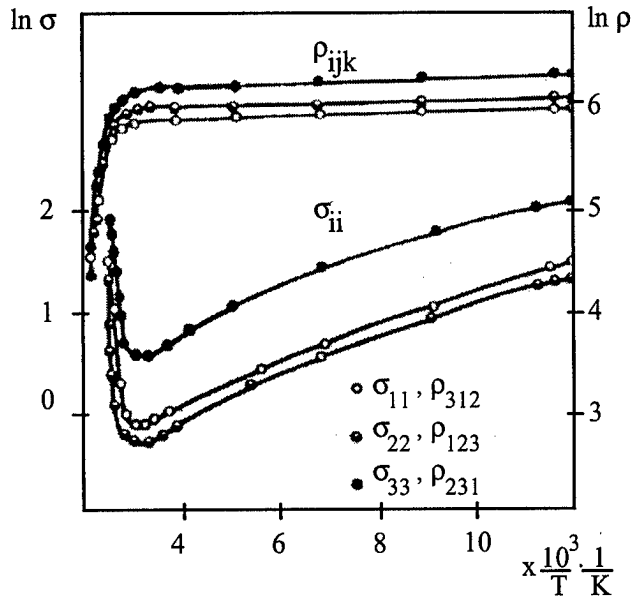


Fig. 2. Components of electric conductivity and Hall tensor for pure single crystals of ZnSb.

$$V_\perp = \frac{1}{2}\cdot\Delta\alpha\cdot\Delta T\cdot\frac{a}{b}, \qquad (1)$$

where in $\Delta\alpha=(\alpha_\parallel-\alpha_\perp)$ is TE anisotropy, $\Delta T=(T_1-T_0)$.
In contrast to the isotropic case depends on the geometry factor **a / b** . Currently ratio **a / b** reaches about one thousand . If other conditions being the same we obtain a considerable increase over the TE motive force of a conventional TE elements. Besides, ordinary TE elements can not perform such a feet as direct measurement of temperature gradient and heat flux with tiny little own thermal resistance for heat flow.

Experiment
We analyzed electric , thermoelectric, galvanomagnetic and thermomagnetic characteristics of single crystals ZnSb various purity. In Fig.2 are shown electrical conductivity and Hall coefficient as function of reverse temperature. At region of temperatures higher 350 K extrinsic conductivity is replaced intrinsic one. Energy gap is estimated from these curves consist of 0.56-0.59 eV and carrier density of ~10^{16} hole /cm^3 at T < 200 K and scattering of charge carriers take place mainly on acoustic phonon (mobility u ~ $T^{-3/2}$).

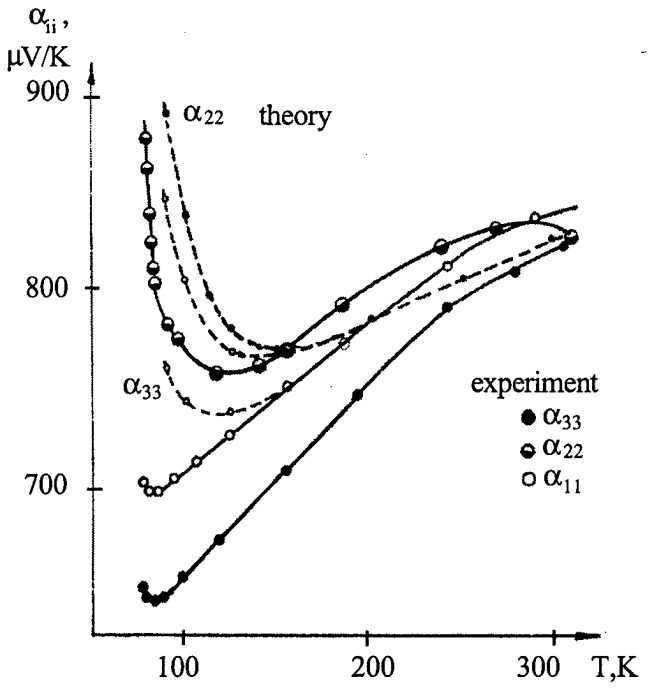


Fig.3. Components of Seebeck coefficient tensor as function of temperature for pure single crystals of ZnSb

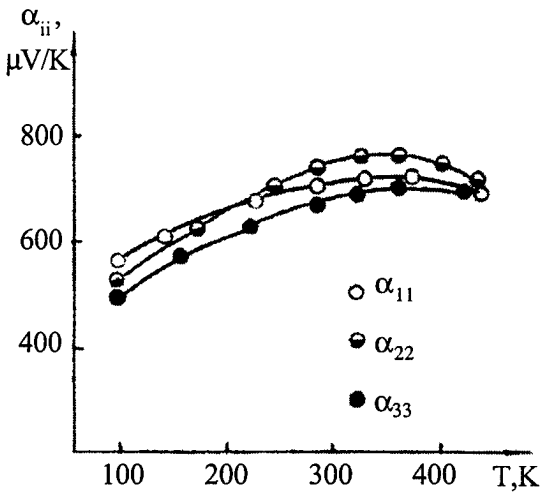


Fig.4. Components of Seebeck coefficient tensor as function of temperature for single crystals of ZnSb ($p \sim 6 \cdot 10^{16} cm^{-3}$).

In Fig.3 are shown α_{11}[100], α_{22}[010] and α_{33}[001] as function of temperature for single crystals ZnSb with $p \sim 10^{16}$ cm^{-3}. At T< 150 K arise essential TE anisotropy $\Delta\alpha=(\alpha_{22}-\alpha_{33})=136\mu V/K$ at 90 K and $\Delta\alpha=236\mu V/K$ at 80 K.

Investigation of transverse thermomagnetic effect showed negative value of Nernst - Ettingshausen coefficients in all region of temperatures. These experimental dates confirm that in condition when phonon drag effect predominate, presence of charge carries with anisotropic effective masses reduced to considerable TE anisotropy.

However another behavior of components tensor of Seebeck coefficients are observed on single crystals of ZnSb with carrier density of $\sim 6 \cdot 10^{16}$ holes / cm^3 (Fig. 4). Just as electric anisotropy stays invariable, small difference in density of charge carriers essential changes TE anisotropy which became practically isotropic. So TE anisotropy has been found sensitive to purity of TE anisotropic crystals.

Theory

First of all we suppose the next model : semiconductor is monovalley, degeneration is absent, tensor of effective masses is diagonal and relaxation time is scalar . In this case Seebeck coefficient in condition acoustic phonon scattering is commonly expressed [3] by equation below :

$$\alpha_e = \frac{k}{e}\left[2 - \ln\frac{nh^3}{2(2\pi m_d kT)^{3/2}}\right], \qquad (2)$$

where for hole $m_d = (m_1 \cdot m_2 \cdot m_3)^{1/3}$ - average for zones effective masses density of state ; m_1, m_2, m_3 - components of diagonal tensor of effective masses of the charge carriers in principal axis.

To receive into account phonon drag effect we change common equation in isotropic case for not in equilibrium addition n'_{ph} to distribution function, which are caused by phonon drag in case of scattering on acoustic phonon in the next form :

$$n'_{ph} = \frac{\upsilon_0^2}{T} \cdot \tau_{ph} \frac{\partial n^0}{\partial \varepsilon} \sum_i m_i \upsilon_i \nabla_i T, \qquad (3)$$

where n^0 - equilibrium distribution function of charge carriers

τ_{ph} - phonon relaxation time,

υ_0 - velocity of longitudinal sound wave.

The components of diagonal tensor of Seebeck coefficients caused by phonon drag effect in the case of scattering on acoustic phonon will have the next form :

$$\alpha_{ii}^{ph} = \frac{m_i \upsilon_0^2}{eT} \frac{\langle \tau_{ph} \rangle}{\langle \tau_{ac} \rangle}, \qquad (4)$$

and accordingly the components of total Seebeck coefficients tensor are :

$$\alpha_{ii} = \alpha_e + \alpha_{ii}^{ph}. \qquad (5)$$

At scattering on acoustic phonon relaxation time for holes scattering on acoustic phonons have the next expression [3] :

$$\tau_{ac} = \frac{a}{T\sqrt{\varepsilon}}, \qquad (6)$$

where **a** - constant of interaction charge carriers with phonons. In our case not so lower temperature (liquid nitrogen) and not so much density of charge carriers ($\approx 10^{16}$cm^{-3}) τ_{ph} is approximately phonon-phonon relaxation time. Moreover, if anisotropy of effective masses is not so much, it is appropriately select longitudinal acoustic phonon, which is more large in this case the transverse acoustic phonon [2].

If this assumption is substantively, τ_{ph} can be expressed so :

$$\tau_{ph} = \frac{b}{\varepsilon T^3}. \qquad (7)$$

Substitution of equations (6) and (7) into (5) yields :

$$\alpha_{ii} = \frac{k}{e}\left[2 - \ln\frac{nh^3}{2(2\pi m_d kT)^{3/2}} + \frac{\sqrt{\pi}\upsilon_0^2 b m_i}{2k^{3/2}aT^{7/2}}\right]. \qquad (8)$$

From this expression it is possible to obtain TE anisotropy :

$$\Delta\alpha = \alpha_{ii} - \alpha_{jj} = \frac{k}{e}\cdot\frac{\sqrt{\pi}\upsilon_0^2 b(m_i - m_j)}{2k^{3/2}aT^{7/2}}. \qquad (9)$$

From this equation we conclude that TE anisotropy is directly proportional to the anisotropy of effective masses . Consequently, to find the TE anisotropy it is need to find m_1, m_2 ,m_3.
If degeneration is absent electric conductivity have the next form [3] :

$$\sigma_{ii} = \frac{e^2 p}{m_i}\cdot\langle\tau\rangle, \qquad (10)$$

where

$$\langle\tau\rangle = \frac{4}{3\sqrt{\pi}(kT)^{5/2}}\int e^{-\varepsilon/kT}\varepsilon^{3/2}\tau\cdot d\varepsilon. \qquad (11)$$

So corresponding to equation (6) diagonal tensor electric conductivity is :

$$\sigma_{ii} = \frac{4e^2 na}{3\sqrt{\pi}km_i T^{3/2}}. \qquad (12)$$

From (12) for primary acoustic phonon scattering , e.g. at 200 K < T < 300 K the ratio of components of the tensor electric conductivity at T = const are :

$$\sigma_{11}:\sigma_{22}:\sigma_{33} = \frac{1}{m_1}:\frac{1}{m_2}:\frac{1}{m_3}. \qquad (13)$$

At the other hand, at the same temperature Seebeck coefficients are isotropic and determined by equation (2). Having experimental dates of α_e for given T and **p** it is possible to find $m_d = (m_1\cdot m_2\cdot m_3)^{1/3}$. After that using experimental dates of σ_{ii} we can find m_1, m_2 and m_3. For example, for ZnSb with $p \approx 10^{16}$cm^{-3} at 250 K (Fig. 2) we have: $\sigma_{11}:\sigma_{22}:\sigma_{33} = 1.1:0.93:2.1$ (ohm^{-1}cm^{-1}).
Using (13) yields $m_2/m_1 = 1.18$; $m_2/m_3 = 2.26$; $m_1/m_3 = 1.90$.
At the same temperature 250 K $\alpha \approx \alpha_e \approx 800\mu V/K$ so we can find $m_d = 0.86m_0$ and finally

$$m_1 = m_0 ; \quad m_2 = 1.2\ m_0 ; m_3 = 0.53\ m_0 \qquad (14)$$

It must be noted, that if measurements of kinetic coefficients are produced on doping crystals of ZnSb it is possible take place mixed scattering and ratio $\sigma_{11}:\sigma_{22}:\sigma_{33}$ will depend from temperature thus relation (13) will not be correct. So accuracy of determination of effective masses will be considerably smaller [4]. Substitution of experimental date of σ_{22} (250 K) = 0.93 ohm^{-1}cm^{-1} in (12) give the possibility to evaluate τ_{ac}. Besides from (12) we can have **a** = $2.5\cdot 10^{-17} erg^{1/2}\cdot K\cdot s$.
Now we can use equation (9) to evaluate phonon-phonon relaxation time τ_{ph}. Substitution in (9) the obtained values $\mathbf{m_i}$, **a** and $\mathbf{v_0} = 5\cdot 10^5$ cm/s and experimental date $\Delta\alpha = 136\mu V/K$ at 90 K it is possible to find **b** = $3\cdot 10^{-18} erg\cdot K^3\cdot s$.
Finally we have the next resultant expression for tensor components of Seebeck coefficients :

$$\alpha_{ii} = \frac{k}{e}\cdot\left(1.02 + \frac{3}{2}\ln T + 1.63\cdot 10^7\frac{m_i}{m_0 T^{7/2}}\right). \qquad (15)$$

Results

Using (15) we can obtain theoretical curves of various components of Seebeck coefficients tensor, which are shown on Fig.3. As a result we have good coincidence theoretical and experimental dates in the range of acoustic phonon scattering and quality description in the range of temperatures between 80 K< T < 150 K in which phonon drag effect predominate. In this conditions pure semiconductor must have one constant-energy ellipsoid. Obtained results of investigation

monovalley semiconductors did not lose generality as far as in specific conditions multivalley semiconductors are converted in monovalley one (e.g. it is possible in the presence of deformation). TE motive force is integral of all valleys phenomenon, but TE anisotropy is degree of asymmetry in disposition of valleys. For example in n-Ge in ordinary conditions TE anisotropy equal to zero because of disposition of valleys is symmetric. So the simplest model of crystal with TE anisotropy is monovalley.

Conclusions

Analytical expression for TE anisotropy obtained on the base of anisotropic scattering theory is permitted to compare theoretical and experimental results for pure single crystals of ZnSb at low temperatures. The most convincing evidence as to the validity of the proposed model is the ability of the theory to predict the dependence of the TE anisotropy correctly. It is allowed to explain nature of TE anisotropy at low temperatures : semiconductor must have one constant-energy ellipsoid , one mechanism of scattering and region of temperatures in which phonon drag effect predominate. All of them can take place only in TE anisotropic single crystals with homogeneous and perfect structure. Besides TE anisotropy has been found ultrasensitive to discover nongomogeneity and purity of anisotropic crystals. The measurement technology of TE anisotropy have self-dependent sense as the way to indicate the homogeneity and quality of the TE anisotropic crystals. Moreover TE anisotropy have unique property to stay independent of extremely action of electric and magnetic fields, laser radiation and radioactivity. But it is not always valid for individual components of Seebeck coefficient.

Acnowledgments

The authors wish to express gratitude for attention to their problems of ICT'97 Conference Chaiman Professor Armin Heinrich. Also the authors are grateful to Professor P.I.Baranski (Ukrainian Institute of Semiconductor in Kiev) for useful discussions.

References

1. A.G.Samoilovich , E.V.Osipov , I.M.Pilat and K.D.Soliychuk, "Anisotropic thermoelement", Patent of Germany, # 2000088, 1971.
2. E.V.Osipov , "Solid State Cryogenics", edited by Ukrainian Academy of Science, Kiev, 1977, 234p.
3. P.I.Baranski, I.S.Buda, I.V.Dahovski and V.V.Kolomoec , "Electric and Galvanomagnetic phenomenon in anisotropic semiconductors" , edited by Ukrainian Academy of Science, Kiev , 1977 , 270p.
4. P.I.Shaver and J.Blair, Phys. Rev., "Thermal and electronic transport propierties of p-type Zn Sb" **141**, (1966), 649 .

Determination of Structural Changes and Temperature Distribution within Crystals

V.P.Shafranyuk

Institute of Thermoelectricity, General Post-Office, Box 86, 274000, Chernivtsi, Ukraine
Tel:+380/3722/44422, Fax:+380/3722/41917, E-mail:Alex@ite.Chernovtsy.ua, WWW: http:\\www.ite.Chernovtsy.ua

Abstract

Results of the X-ray method of contactless determination of structural changes within crystals with simultaneous temperature distribution determination in it have been presented. The method of temperature distribution determination uses the X-ray topography based on the use of phenomena of diffraction patterns change with the change of inter-atom distance in crystals under the temperature effect. Methods of double-crystals spectrometry and topographic methods of Berch-Barrett and Lang the structural changes in crystals are determined at cyclic temperature effects which enable consecutively observe aging and degradation processes of materials under the cycling loads effect. Experimental methods, investigation results, errors analysis have been given.

Introduction

Investigation of X-rays dynamic scattering in real crystals with constant gradient of deformation presents a particular interest because with the help of this simplest kind of distortions one can determine the mechanisms of diffraction contrast forming and find a single-valued relation between diffraction image and parameters of crystal deformation [1-5]. Even under mechanical bending the stimulated distortions in a crystal not always correspond to real ones. As is shown in [4] in the case of mechanical bending the diffraction planes may be not only turned but bent that is the reason of discrepancy between experimental and theoretical results. In the given case three-dimension elastic deformation is to be discussed.

The real distribution of the deformation fields in a distorted crystal can be obtained by an X-ray interferometer. It is known that X-ray interferometry has no equal by measurement accuracy of relative deformations and atomic planes turns. It makes possible to observe fields of elastic shifts just on diffraction moiré patterns and to get reliable quantitative information about deformation and stress distributions in a crystal [6-9]. A study of structure moiré bands change on the temperature gradient value and point of application in units of an interferometer has been made in [6]. But in the given case the real distribution of shift and deformation fields in a crystal do not determined because of structural moiré bands presence in the interferometer.

The study of thermoelastic fields of shift and deformation appearing at the perfect interferometer temperature gradient effect on the analyzer has been conducted by the X-ray diffraction moiré method.

Experimental procedure

A perfect X-ray three-crystal LLL-interferometer made from dislocationless single crystal $S1$ was used for the given problem solution. Each unit of the interferometer was 420mm thick, 25 mm wide and 15 mm high. Spaces between the units were equal and were 4.525mm (Fig.1). The investigations were conducted with the use of reflection $(\bar{2}20)$ in CuK_α-radiation. Temperature gradient was generated in the crystal-analyzer by a thermoelement placed at 0.5 mm from the top part of the unit. The gradient vector was oriented in $[11\bar{2}]$ direction along the reflecting planes $(\bar{1}10)$. Temperature was measured in several points of the crystal-analyzer by thermocouples for the gradient dT/dy values determination. The gradient value was varied within 0.29 to 2.4 K/cm. Interferometer's units S and M were thermostatted by metal thermal screen.

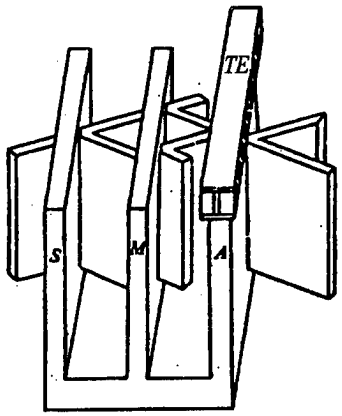
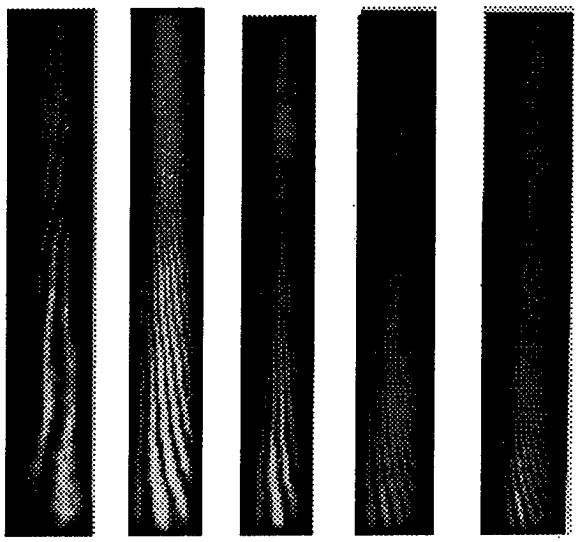


Fig. 1. Scheme of experiment. S, M, A - interferometer components, TE - thermoheter.

Investigation results and discussion

Fig.2 gives a number of experimental interferograms got at different temperature gradient values in a crystal-analyzer of the perfect interferometer. With on temperature gradient the moire bands are absent that is indicative of a high interferometer perfection. Moire patterns were got by scanning along diffraction vector. Interferograms present a family of moire bands with different period. With the temperature gradient increase the moire bands periods are decreased in the top part of interferograms. Moire bands interpretation is convenient to made by U_x shift in values of interplanes distances d_0.

0-7803-4057-4/97 $10.00 ©1997 IEEE



A B C D E

Fig.2. Experimental Moire patterns got in CuK_α-radiation. A- dT/dy=0.29K/cm, B- 0.57 K/cm, C - 0.79 K/cm, D - 1.07K/cm, E - 1.87 K/cm.

Under the crystal deformation by a uniform temperature gradient the shift vector in the general case has the form:

$$U = r\{r\nabla_r\{\alpha T\}\} - 0.5\{(rr)\nabla_r(\alpha T)\}, \qquad (1)$$

where α is the coefficient of linear expansion, T is temperature. In the given case the temperature gradient is directed perpendicular to the diffraction vector then the component of the shift field along OX axis (in the direction of the diffraction vector) in the Decart coordinate system will be

$$U_X = xy\frac{d(\alpha T)}{dy} = \frac{xy}{R}, \qquad (2)$$

where `R is the radius of the reflecting planes bending, $\alpha\frac{dT}{dy} = R^{-1}$. A component of the shift field is the quadratic function of coordinates. Considering that the moire band is the locus of similar relative shifts in the direction of the diffraction vector (shift value equals to interplane distance of the perfect lattice d_0) at the distance equals to the moire bands period then $U=d_0n + \Delta U_X$, where n is integral number.

Change of interplane distance Δd under the temperature gradient effect takes the form

$$\Delta d(y) = d_0\left(\alpha\frac{dT}{dy}y\right) = d_0\frac{y}{R}. \qquad (3)$$

Thus, under temperature gradient in the crystal-analyzer the moire bands periods will be y-coordinate dependent and equal to

$$\Lambda(y) = \frac{d_0 d(y)}{\Delta d(y)} = d_0\left[1 + \frac{1}{\alpha\cdot y\cdot \text{grad}\, T}\right]. \qquad (4)$$

Atomic planes slope in the deformed crystal-analyzer in respect to undeformed lattice equals to

$$\theta \cong \text{arctg}\left(n\cdot\alpha_0\cdot d\cdot \text{grad}\, T\right) \qquad (5)$$

and depends on X (this dependence is fed into n). Ideally the moire bands under the uniform temperature gradient according to (4) must have the form of hyperbolic curves.

The similar conclusions may be obtained if to represent atomic planes of the deformed analyzer in the form of radial line with some step θ proportional to ΔT and coefficient of the crystal thermal expansion α. Then in parametric view the moire bands location can be represented as

$$X = Y\cdot \text{tg}\left[(x/\alpha - n)\varphi\right], \qquad (6)$$

where n is integral number and φ is the moire bands slope to etalon grid. In the given case a crystal lattice of the first and second crystals is taken as the etalon grid. But the experimentally obtained moire patterns are differed from theoretically predicted. Measuring the distance between moire bands in Fig.2 and using the relation

$$d = \Lambda\left[1 + \left(\frac{\Lambda}{d_0}\right)^2 + 2\frac{\Lambda}{d_0}\cos\varphi\right]^{-1/2} \qquad (7)$$

we have determined the relative deformations of atomic planes in the analyzer. Fig.3 gives the dependence of atomic planes ($\Delta d/d$) relative deformations value on temperature gradient along the atomic planes.

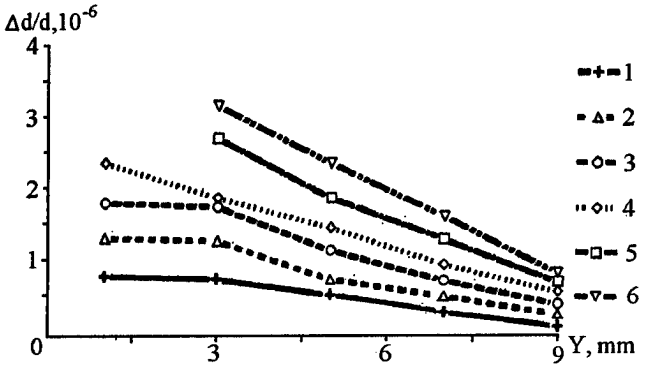


Fig.3. the dependence of atomic planes ($\Delta d/d$) relative deformations value on temperature gradient along the atomic planes. 1 - dT/dy=0.29K/cm, 2- 0.57 K/cm, 3 - 0.79 K/cm, 4 - 1.07 K/cm, 5 - 1.46 K/cm, 6 - 1.87 K/cm.

Using the experimental values $\Delta d/d$ one can calculate the planar temperature distribution in the interferometer analyzer by the relation

$$\Delta T = \frac{d_0}{\alpha}\frac{\Delta\Lambda}{\Lambda_n\Lambda_{n-1}}, \qquad (8)$$

where Λ_n and Λ_{n-1} are moire bands periods in different points of the interferogram. The relation (8) shows that contactless

accuracy of ΔT is defined by α measurement. It follows from Fig.3 and moire patterns (Fig.2) that in the case of the uniform temperature gradient in the real crystal appears a complicated bending of the atomic planes. Thus, under the negligible gradients for example, (dT/dy = 0.29 K/cm) when the atomic planes deformation values are comparable with deformations appearing in the regions of nonuniform impurity distribution or cluster formations a local bending of the reflecting planes is observed (Fig.2a). When temperature gradient value reaches $dT/dy \geq 2.9$ K/cm, distances between moire bands are comparable with photoemulsion resolution Λ= 10 mcm. In this case relative deformation reaches the values $\Delta d/d = 2 \cdot 10^{-5}$. Further increase of the temperature gradient value in the crystal-analyzer practically excludes the possibility of the X-ray diffraction moire method use for deformation determination because of small resolution of the photo materials used. One can extend the application limits of the interferometer using it as a three-crystal spectrometer. Measuring integral reflection intensity from planes (hkl) and ($\overline{h}\overline{k}l$) and taking into account the deviation from the Fidel's law one can determine the bending radius R of the atomic planes and consequently, the deformation in a crystal by the procedure described in [10].

It should be noted that a thermocooler operation stability during the moire patterns receiving (5-6 hours) is rather large and is about 0.05 °C.

Studies of crystals Bi_2Te_3 homogeneity have been also conducted in the present work with the help of X-ray interferometer. The studied samples were made as plane-parallel plates. If the studied sample density is not homogeneous over the whole volume then on the interferograms moire bands are forming, period and slope of which is closely connected with density distribution as other phase inclusions. So using phase moire topography the study of structural perfection of Bi_2Te_3 crystals got by directed crystallization and Czochralski methods have been conducted.

Phase moire patterns offers the possibility to determine a transverse bending in crystals which origin is likely connected with bands of growth. It was determined that crystals got by the Czochralski method have more perfect structure that crystals got by other methods.

X-ray interferometry allows to stimulate any interferentic moire pattern (lattice) with the period less that 0.1 mcm using photomaterials with high resolution (X-ray photoresist). Such use of X-ray interferometry offers possibilities to new technologies on diffraction lattice formation for integral-optical devices with the use of X-ray photolithography.

References

[1] Penning P., Polder A. Anomalous transmission of X-rays in elastically deformed crystals. Philips. Res.Repts., 1961. v.16, N 2, p.419-440.

[2] Collela E. Anomalous transmission of X-ray in slightly deformed crystals. Phys. Rev. 1972. v.B6, N12, p.4857-4860.

[3] Kato N., Patel I. X-ray diffraction topographs in silicon crystals with superposed oxid films. J.Appl.Phys., 1973, v.44, p.965-970.

[4] Kushnir V.I., Suvorov E.V., Mukhin K.Y. To the problem of Laue diffraction of X-rays by uniformly bent crystal. FTT, 1980, v,7, p.2135-2143.

[5] Hart M. Pendellosung Fringes in elastically deformed silicon. Z.Phys., 1966. v.189, p.269-291.

[6] Navasardian M.F., Nazarian Y.P., Arutyunian V.V. Temperature gradient effect on the interference bands pattern in X-ray interferometer. Crystallography. 1979. v.24, vyp.2. p.368-370.

[7] Raranskii N.D., Shafranyuk V.P., Fodruk I.M. Moire patterns of the growth bands in *Si* dislocationless single crystal. UFJ, 1985, v.30, N1, p.133-135.

[8] Raranskii N.D., Shafranyuk V.P. Defects of interface boundaries and stress relaxation epitaxial systems *Si-Si*, *GaP-Si*. UFJ. 1985, v.1 p.127-132.

[9] Raranskii N.D., Shafranyuk V.P., Fodchuk I.M. X-ray interferometric image of deformation fields around dislocation pile-ups. Metallofizika, 1985. v.7, p.63-71.

[10] Datzenko L.I., Kislovskii E.N., Prokopenko I.V. X-ray dynamic scattering by *Si* crystals elastically bent by homogeneous oxidation.UFJ, 1977. v.22, p.513-515.

About the Possibilities of Transverse Termoelectromotion Force in the case of Optical Media

Ashcheulov [2] A.A., Gutsul[1] I.V., Rarenko[1] A.I

[1] Chernivtsi State University, Kotsubinskogo 2, 274012, Chernivtsi, Ukraine, Tel.:+380/372/598461
[2] Institute of Thermoelectricity, General Post-Office, Box 86, 274000, Chernivtsi, Ukraine
Tel.: +380/3722/44422, Fax:+380/3722/41917, E-mail:Alex@ite.Chernovtsy.ua, WWW: http:\\www.ite.Chernovtsy.ua

Abstract

The possibility of conversion and registration of high intensive radiant flows by transverse thermo-emf arose in anisotropic media with different degree of optical transparency has been studied. The basic expressions for the studied opticothermoelements as well as thermogenerators and receiving devices based on the use of the "transparent wall" method have been obtained.

The possibilities of practical use have been analyzed and the demands to materials properties have been determined. The investigation results for the first time have allowed to propose the method of high density radiant energy registration. The device performances as volt-watts sensitivity, limit sensitivity, time constant, registration power limit value, optical transmissivity have been received from heat balance equation. Some constructions of optical and infrared wavelength radiant energy measuring devices have been produced.

Introduction

The advantage of science and technology has been brought into existence several sources which energy in some cases was highly conjectural converted and registrated by the existed methods. To solve this problem the present work proposes to use media with different degree of optical transparency. This result in its turn to the possibility of a new method of radiant flows registration called as the "transparent wall" method based on the partial absorption of the passing radiation by transparent media with simultaneous conversion of the absorbed portion of energy by the known thermal pyrocalorimetric effects. The conducted analysis shows that for the radiant fluxes of UV, visible and IR-region of spectrum the realization of this method particularly promising for the case of the transverse thermo-emf phenomena application [1] arising in anisotropic media. This provides the basis for the production of anisotropic opticothermoelements (AOT) [2,3]. Below is given the AOT theory and their parameters and potentialities are examined.

Problem solution

Let us consider AOT consists of a plate with the given dimensions a, b, c from a material that is anisotropic be the coefficients of thermo-emf $\hat{\alpha}$ and thermal conductivity $\hat{\kappa}$. Tensors $\hat{\alpha}$ and $\hat{\kappa}$ at the system of co-ordinates (X,Y,Z) rotated to the angle φ in XOY plane in respect to the crystallographic (X',Y',Z') one have the form

$$\hat{\alpha} = \begin{vmatrix} \alpha_{\parallel}\sin^2\varphi + \alpha_{\perp}\cos^2\varphi & (\alpha_{\parallel} - \alpha_{\perp})\sin\varphi\cos\varphi & 0 \\ (\alpha_{\parallel} - \alpha_{\perp})\sin\varphi\cos\varphi & \alpha_{\parallel}\cdot\sin^2\varphi + \alpha_{\perp}\cos^2\varphi & 0 \\ 0 & 0 & \alpha_{\perp} \end{vmatrix},$$

$$\hat{\kappa} = \begin{vmatrix} \kappa_{\parallel}\sin^2\varphi + \kappa_{\perp}\cos^2\varphi & (\kappa_{\parallel} - \kappa_{\perp})\sin\varphi\cos\varphi & 0 \\ (\kappa_{\parallel} - \kappa_{\perp})\sin\varphi\cos\varphi & \kappa_{\parallel}\sin^2\varphi + \kappa_{\perp}\cos^2\varphi & 0 \\ 0 & 0 & \kappa_{\perp} \end{vmatrix}. \quad (1)$$

A radiant flux with density q_0 is incident on the upper surface of this thermoelement, it lower face is in the thermal contact with a thermostat at a temperature $T=T_0$. Lateral faces of the plate are adiabatically insulated edge effects therewith are ignored ($a=c>>b$) [4]. Uniform monochromatic flux with density q_0 and wavelength λ_0 passing through such late initiates a temperature gradient and transverse thermo-emf unambiguously connected with it.

Temperature distribution in the plate is determined from the fundamental law of thermal conduction at the availability of inner heat source

$$\frac{\partial T}{\partial t} = -\frac{1}{dC}\sum_{i=1}^{3}\frac{\partial q_i}{\partial x_i} + \frac{q_V}{dC}, \quad (2)$$

where d is density, C is AOT material thermal capacity, q_v is a quantity of heat released by the inner sources in a unit volume in a unit time.

In case of stationary temperature distribution $\frac{\partial T}{\partial t} = 0$, for approximations $\kappa_{12} < \kappa_{22}$ the equation (2) has the form

$$\kappa_{22}\frac{d^2T}{dy^2} + q_V = 0. \quad (3)$$

Using the known Burger-Lambert law , obtain

$$q_V = q_0(1-r)\gamma e^{-\gamma(b-y)}, \quad (4)$$

where r, γ are coefficients of reflection and absorption of AOT material.

Substituting (4) into (3) and solving (3) at the edge conditions

$$T\big|_{y=0} = T_0, \qquad \left.\frac{dT}{dy}\right|_{y=b} = 0$$

get the temperature difference within the AOT volume

$$T(y) = T_0 + \frac{q_0(1-r)}{\kappa_{22}}\left[y + \frac{e^{-\gamma b}}{\gamma}\left(1-e^{\gamma y}\right)\right]. \quad (5)$$

Thermoelectric field strength $\vec{E}_T$ is determined by the relation

$$\vec{E}_T = \hat{\alpha}\nabla T. \quad (6)$$

Substitution (5) into (6) gives

$$E_x^T = \alpha_{12}\frac{\partial T}{\partial y} = q_0(1-r)\frac{\alpha_{12}}{\kappa_{22}}\left[1-e^{-\gamma(b-y)}\right]. \quad (7)$$

According to [5] the transverse thermo-emf is determined by the following relation

$$\varepsilon = \frac{1}{bc}\int_0^b dy\int_0^c dz\int_0^a E_x^T dx. \quad (8)$$

Then substituting (7) into (8), get the expression for AOT

$$\varepsilon = q_0(1-r)a\frac{\alpha_{12}}{\kappa_{22}}\left[1-\frac{1}{\gamma b}\left(1-e^{-\gamma b}\right)\right]. \quad (9)$$

the efficiency of such devices [6] is determined by the following relation [7]

$$\eta = \eta_C\frac{1}{1+\Lambda}, \quad (10)$$

where η_C is the Carnot cycle efficiency, $\Lambda = \frac{BT_0}{A}$, $A = I^2R_{in}$ - the work performed by AOT in a time unit, B is the rate of the entropy change within AOT volume which has the following form

$$B = \frac{Q_0}{T_0} - \frac{Q_1}{T_1} = \kappa_{22}S\left[\frac{1}{T_0}\frac{dT}{dy}\bigg|_{y=0} - \frac{1}{T_1}\frac{dT}{dy}\bigg|_{y=b}\right], \quad (11)$$

where Q_0, Q_1 is the heat amount on the lower and upper sides of AOT, $S = a \times c$ is the area of these sides, T_1 is the temperature of the upper side.

For the studied AOT with account of (5) we get for (11)

$$B = q_0(1-r)acT_0^{-1}\left(1-e^{-\gamma b}\right) \quad (12)$$

Current I flowing through AOT

$$I = \frac{\varepsilon}{R_i + R_{in}} = \frac{q_0a(1-r)\alpha_{12}}{(R_i+R_{in})\kappa_{22}}\left[1-\frac{1}{\gamma b}\left(1-e^{-\gamma b}\right)\right], \quad (13)$$

where $R_i = \rho\frac{a}{bc}$ is the inner resistance of AOT, ρ is the specific resistance of the material, R_{in} is the load resistance. In the case R_i=R_{in} the expression for work A with regard for (13) takes the following form

$$A = \frac{q_0^2(1-r)^2abc\alpha_{12}^2}{4\rho\kappa_{22}^2}\left[1-\frac{1}{\gamma b}\left(1-e^{-\gamma b}\right)\right]^2. \quad (14)$$

Then dimensionless parameter Λ involving into the expression for the efficiency, η

$$\Lambda = \frac{4\rho\kappa_{22}^2\left(1-e^{-\gamma b}\right)}{q_0(1-r)^2b\alpha_{12}^2\left[1-\frac{1}{\gamma b}\left(1-e^{-\gamma b}\right)\right]^2}. \quad (15)$$

The substituting (15) into (10) with account for (5), get

$$\eta = \frac{q_0(1-r)b\kappa_{22}^{-1}\left[1+\frac{1}{\gamma b}\left(e^{-\gamma b}-1\right)\right]}{T_0 + q_0(1-r)b\kappa_{22}^{-1}\left[1+\frac{1}{\gamma b}\left(e^{-\gamma b}-1\right)\right]}\times$$
$$\times\left[1+\frac{4\rho\kappa_{22}^2\left(1-e^{-\gamma b}\right)}{q_0(1-r)^2b\alpha_{12}^2\left[1-\frac{1}{\gamma b}\left(1-e^{-\gamma b}\right)\right]^2}\right]^{-1}. \quad (16)$$

Analysis of (9) and (16) shows that maximum value of transverse thermo-emf ε and efficiency η is determined by anisotropy both as of a coefficient of thermo-emf $\hat{\alpha}$ and coefficient of thermal conduction $\hat{\kappa}$ and is observed at some optimal value of angle φ_{opt} determined from the conditions $\frac{\partial\varepsilon}{\partial\varphi} = 0$, $\frac{\partial^2\varepsilon}{\partial\varphi^2} < 0$ [1].

It follows from (9) and (16) with account of (1) that for AOT operating conditions called by the regime of optical passing (γ_i is the coefficient of optical absorption of a thermostat material with the height b_1), the expression for thermo-emf ε, efficiency η and figure of merit of AOT material z_A are shown up as

$$\varepsilon_1 = \frac{q_0(1-r)a\alpha_{12}\gamma b}{2\kappa_{22}}, \quad (17)$$

$$\eta_1 = \frac{q_0(1-r)b\kappa_{22}^{-1}\gamma b}{2T_0 + q_0(1-r)b\kappa_{22}^{-1}\gamma b}\times$$
$$\times\left[1+\frac{8\rho\kappa_{22}^2(2-\gamma b)}{q_0(1-r)^2b\alpha_{12}^2\gamma b}\right]^{-1}, \quad (18)$$

$$Z_{A1} = \frac{\alpha_{12}^2(1-r)^2\gamma b}{\rho\kappa_{22}}. \quad (19)$$

For the regime of the volume absorption $\gamma_1 b_1 << \gamma b \cong 1$

$$\varepsilon_2 = \frac{q_0(1-r)a\alpha_{12}e^{-1}}{\kappa_{22}}, \quad (20)$$

$$\eta_2 = \frac{q_0(1-r)b\kappa_{22}^{-1}e^{-1}}{T_0 + q_0(1-r)b\kappa_{22}^{-1}e^{-1}}\times$$
$$\times\left[1+\frac{4\rho\kappa_{22}^2\left(1-e^{-1}\right)}{q_0(1-r)^2b\alpha_{12}^2e^{-2}}\right]^{-1}, \quad (21)$$

$$Z_{A2} = \frac{\alpha_{12}^2(1-r)}{\rho\kappa_{22}}\left(1-e^{-1}\right). \quad (22)$$

In case of the regime of surface absorption $\gamma b >> 1$

$$\varepsilon_3 = \frac{q_0(1-r)a\alpha_{12}}{\kappa_{22}}, \quad (23)$$

$$\eta_3 = \frac{q_0(1-r)b\kappa_{22}^{-1}}{T_0 + q_0(1-r)b\kappa_{22}^{-1}} \times \left[1+\frac{4\rho\kappa_{22}^2}{q_0(1-r)^2 b\alpha_{12}^2}\right]^{-1}, \quad (24)$$

$$Z_{A3} = \frac{\alpha_{12}^2(1-r)}{\rho\kappa_{22}}. \quad (25)$$

It follows from (17)-(25) that the good use of the studied thermoelements as energy converters is promising for AOT operating in the regime of the surface absorption. Use of such anisotropic thermoelectric materials as superconductive ceramics ($Ybe_2Cu_3O_3$, T_r = 300K) crystals of chrome silicide and manganese (T_r = 100K) single crystals *Be* and *Re* (T_r=1400-200K) [8-9] makes possible to develop high temperature thermogenerators with high value of efficiency.

Discussion of results

Thermoelements operating at the regime of optical penetration pioneered to realize the "transparent wall" method and to develop means for registration and continuous control of radiant flows if different intensity. As it was shown in [10,11] the basic parameters of those AOT such as volt/watt sensitivity S_o, equivalent noise power *ENP* , limiting value of the controlled power q_r, optical transparency F and time constant τ are represented by the following relations

$$S_0 = \frac{\gamma(1-r)^2\alpha_{12}b}{\kappa_{22}c}, \quad (26)$$

$$ENP = \left(k_0 T\rho\frac{ac}{b}\right)^{1/2}\left[(1-r)^2\frac{\alpha_{12}}{\kappa_{22}}\gamma b\right]^{-1}, \quad (27)$$

$$q_r = 2\Delta T\kappa_{22}\left[(1-r)^2\gamma b^2\right]^{-1}, \quad (28)$$

$$F = (1-r)^2\gamma b, \quad (29)$$

$$\tau = 0.04b^2a_0^{-1}, \quad (30)$$

where k_o is Boltzman constant, ΔT is the admissible temperature of AOT material overheating, a_0 is AOT material thermal diffusivity.

Table 1 gives characteristics of really existing optically transparent anisotropic single crystals [12-14], which are the most suitable for development of feed-through power detectors. Table 2 gives parameters of some detectors on their basis. These table data correspond temperature T=300K.

Changing the geometry of AOT refracting surfaces and a thermostat, their cross-section forms it is possible to develop different structures of detectors that allow along with radiant flows registration to perform the required power spectral redistribution at the simultaneous their use as windows of various radiators.

Table 1. Characteristics of optically transparent anisotropic single crystals

Material	Optical transmission electric region λ, mcm	Coefficient of optical absorbity γ, cm^{-1}	Coefficient of transverse thermo-emf $\Delta\alpha$, mcV $\cdot K^1$	Coefficient of thermal conductivity κ, $W\cdot cm^{-1}\cdot K^1$	Coefficient of conductivity σ, $Ohm^{-1}\cdot cm^{-1}$
CdSb	2.6-40.0	0.2	200	$1.5\cdot10^{-2}$	0.3
ZnSb	2.4-27.0	0.5	150	$1.1\cdot10^{-2}$	1.5
$CdAs_2$	1.25-16.0	0.5	350	$2\cdot10^{-2}$	0.03
$ZnAs_2$	1.36-21.0	1.0	220	$6\cdot10^{-2}$	0.01
CdS	0.5-18.0	0.5	150	$2\cdot10^{-1}$	0.6
Te	3.6-30.0	0.2	160	$3\cdot10^{-2}$	4.0

Table 2. Parameters of detectors

Type of detector	Material of a thermoelement	Material of a thermostat	Volt/Watt sensitivity S, $V \cdot W^{-1}$	Maximum density of energy q_0, $W \cdot cm^{-2}$	Working sides area $a \times c$, cm^2
АПП-1	CdSb	CdTe	$2 \cdot 10^{-5}$	$5 \cdot 10^{3}$	0.3 ×0.3
АПП-2	CdSb	CdTe	$2 \cdot 10^{-6}$	$4.5 \cdot 10^{2}$	1.0×1.0
АПП-3	$CdAs_2$	CdTe	$1 \cdot 10^{-7}$	$3.6 \cdot 10^{3}$	4.0×4.0
АПП-4	$ZnAs_2$	CdTe	$1 \cdot 10^{-7}$	$1 \cdot 10^{4}$	0.8×0.8
АПП-5	CdS	CdTe	$1 \cdot 10^{-7}$	$2 \cdot 10^{4}$	0.5×0.5

References

[1] Tomson W. On thermoelectric currents in linear conduction of crystalline substance. - Math.Phys.Pap., 1882, N 1, p.266-273.

[2] Ashcheulov A.A., Kondratenko V.M., Pilyavskii Y.B., Rarenko I.M. EMF of an anisotropic material in the passing power condition. - UFJ, 1984, v.29, N 9, p. 1427-1429.

[3] Ashcheulov A.A. Anisotropic radiation thermoelement for passing power measurement. - OMP, 1989, N 12, p. 48-49.

[4] Snarskii A.A., Slipchenko B.N. Thermal conduction anisotropy effect on the transverse thermo-emf. - FTP, 1974, v.8, 10, p.2010-2012.

[5] Snarskii A.A. EMF of thermoelements using anisotropy of thermo-emf. 1. Anisotropic thermoelements of rectangular shape. - FTP, 1977, v.11, 10, p.2053-2055.

[6] Ashcheulov A.A. Gutsul I.V., Rarenko A.I. Anisotropic thermoelement of internal reflection. UFJ, 1993, v.38, N 6, p.923-928.

[7] Slipchenko B.N. On the problem AT efficiency. UFJ, 1976, v,21, N 1, p.126-131.

[8] Burkov A.T., Heinrich A., Vedernikov M.V. Anisotropic thermoelectric materials properties and applications. - XIII Int.Conf. of Thermoel. USA, N.Y., 1995, p.76-80.

[9] Ordin S.V. Thermoelectric waves in anisotropic crystal of Higher Manganese Silicide (HMS) - XIII Int.Conf. of Thermoel. USA, N.Y., 1995, p.212-214.

[10] Ashcheulov A.A., Gutsul I.V., Rarenko A.I. Anisotropic radiation thermoelement operating in the internal reflection regime. - OJ, 1993, N4, p.78-79.

[11] Ashcheulov A.A. On the possibility of parametric control of anosotropic thermoelements using the effect of thermal conduction anisotropy. - J.of Thermoelectricity, 1995, N4, p.59-64

[12] Marenkin S.F., Raukhmyan A.M., Pishchikov D.I., Lazarev V.B. Electric and optical properties of zink and cadmium diarcenides. - Neorganic materialy, 1992, v.28, N.9, p.1813-1828.

[13] Ashcheulov A.A., Rarenko I.M., Voronka N.K. Optimized materials based on Cadmium Antimonide and their application. J. of Thermoelectricity, 1995, N3, p.73-88.

[14] Anatychuk L.I. Thermoelements and thermoelectric devices. Kiev, Naukova dumka, 1979.

Devices for Temperature Measurement and Laser Profile Analysis Using $YBa_2Cu_3O_{7-\delta}$ Atomic Layer Thermopiles

W. Brozio, F. Wolf, C. Ferstl, O. Kus, F. Lankes, T. Honke, J. Betz*, and K.F. Renk
Institut für Angewandte Physik, Universität Regensburg, D-93040 Regensburg, Germany

Abstract

We report on the application of the atomic layer thermopile for the determination of both the temperature profile near a heated surface and the radiation profile of laser radiation. As thermopile we used a $YBa_2Cu_3O_{7-\delta}$ (YBCO) film grown epitaxially on a substrate with the crystal c–axis tilted away from the substrate normal. Irradiating the film (at room temperature) leads to a temperature gradient in the film, resulting in a voltage signal parallel to the film surface. The origin of the signal is due to the transverse Seebeck effect, which is a consequence of the anisotropy of YBCO. We made use of this effect for developing several devices. For fast non-contact temperature measurement we prepared a small sensor (response time less than 30ns). For profile analysis of laser radiation we developed two complete systems. One is suitable for cw lasers, in particular for CO_2 lasers. The cross-section of the laser beam is scanned by a rotating aperture facility. For the analysis of pulsed laser radiation we built an array of atomic layer thermopiles, which is moved stepwise across the laser beam. This system is suitable for the determination of radiation profiles of pulsed lasers from the UV to the FIR. Finally, we are developing the detector head of a third system. It consists of 100 small atomic layer thermopile pixels for fast online profile analysis of cw lasers.

Introduction

The transverse Seebeck effect was described theoretically already in 1941 [1]. Recently, the effect was observed for $YBa_2Cu_3O_{7-\delta}$ thin films [2], which were characterized as atomic layer thermopiles [3]; besides the transverse Seebeck effect, various other effects have been discussed as possible origins of voltage signals of YBCO films [4, 5, 6, 7, 8]. Now, the transverse Seebeck effect has also been observed for $TlBa_2Ca_2Cu_3O_9$ [9], $PrBa_2Cu_3O_{7-\delta}$ [10], $Bi_2Sr_2Ca_2Cu_3O_9$ [11], and Bi single crystals [12].
The atomic layer thermopile combines several detector properties, such as a wide spectral range, a large dynamical range of more than 11 orders of magnitude [2], a high damage threshold ($1\,MW/cm^2$) for laser radiation. For very thin $YBa_2Cu_3O_{7-\delta}$ films the electrical bandwidth extends from *dc* up to ~ 1 GHz, i.e. the response time is ~1ns [13]. These properties are not attainable at once with a conventional detector, such as a thermopile or a pyroelectric detector [14].

The transverse Seebeck effect

For our devices we used thin YBCO films. The films were grown epitaxially on $SrTiO_3$ or $LaAlO_3$ substrate crystals by pulsed laser deposition. The substrate of a film was cut in a special way so that the crystal c–axis (fig.1) of the film material had a tilt angle (α) with respect to the surface normal (z-direction). Perpendicular to the c–axis is the (ab)–plane of the YBCO material, which is characterized by CuO_2 atomic layers and intermediate layers (containing BaO atomic layers and CuO chains).

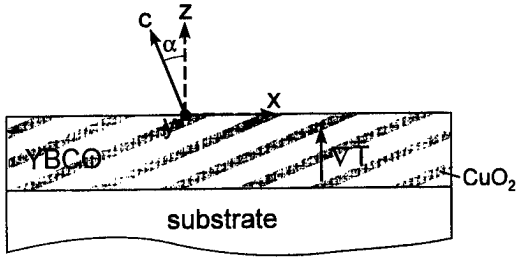


Fig. 1: YBCO film with the c–axis tilted by an angle α with respect to the macroscopic surface normal

Applying a temperature gradient, $\vec{\nabla}T$, leads to a thermoelectric voltage signal, according to the equation [3, 15]

$$\vec{E} = \hat{S}\,\vec{\nabla}T \tag{1}$$

where $\vec{E}$ is the electric field in the film and $\hat{S}$ the Seebeck coefficient, which is a 2nd rank tensor. Equation (1) follows from the first Onsager equation

$$\vec{j} = \hat{\sigma}(\vec{E} - \hat{S}\,\vec{\nabla}T) = 0 \tag{2}$$

in the currentless state ($\hat{\sigma}$, conductivity). For a YBCO film with the c–axis tilted with respect to the direction of the temperature gradient, the Seebeck tensor has the form

$$\hat{S} = \begin{pmatrix} S_{xx} & 0 & S_{xz} \\ 0 & S_{yy} & 0 \\ S_{zx} & 0 & S_{zz} \end{pmatrix} \tag{3}$$

where y is the tilt axis and x, lying perpendicular to z and y, is directed along the film surface. Inhomogeneous heating of the film either by laser radiation or by a thermal source leads to a temperature gradient $\vec{\nabla}T = \Delta T/d$ (d, film thickness) perpendicular to the film surface, where ΔT is the temperature difference between film surface and backside (at the film/substrate interface). The temperature gradient causes a thermoelectric field

$$E_x = S_{xz}\,\Delta T/d \tag{4}$$

which is oriented parallel to the film surface. The thermoelectric voltage resulting from the electric field is then given by

$$U_x = S_{xz}\,\Delta T\,l/d \qquad (5)$$

where l is the length of the heated area. The off diagonal element is given by

$$S_{xz} = (S_{ab} - S_c)\,\sin\alpha\cos\alpha \qquad (6)$$

where S_{ab} and S_c are the Seebeck coefficients perpendicular and parallel to the c–axis, respectively. For tilt angles $\alpha \lesssim 20°$, equation (5) can be written as

$$U = \Delta S\,\Delta T\,\alpha\,l/d\,. \qquad (7)$$

For $YBa_2Cu_3O_{7-\delta}$, with $\delta \approx 0$, $S_{ab} \approx -2\mu$V/K and $S_c \approx 25\mu$V/K [16], so that $\Delta S \approx -30\mu$V/K. Laser radiation has a small penetration depth in the film ($\sim$ 100nm). Accordingly, the temperature gradient $\Delta T/d$ and the ratio l/d can be very large (e.g. $l/d \sim 10^5$). For a 100nm thick film with $\alpha = 20°$ and a heated area of a length l = 1cm, equation (7) gives a senstitvity $U/\Delta T \approx 1$ V/K. Thus, even a small temperature difference leads to a significant output voltage. The response time of the detector depends on the film thickness, which determines the heat diffusion from the film to the substrate [13]. For very thin films ($d <$ 40nm) the heat escapes very fast leading to a response time of $<$ 1ns. YBCO and other cuprate films have low penetration depths (of the order of 100nm) for radiation from the UV to the far-infrared (FIR) frequency range. The atomic layer thermopile is therefore applicable for detection of radiation from the UV to the FIR range, and even for detection of millimeter wave radiation.

Temperature sensor

We have built a small and fast temperature sensor for non contact temperature measurements. For this purpose we used a commercially available $YBa_2Cu_3O_{7-\delta}$ atomic layer thermopile on a $SrTiO_3$ substrate [17]. Electrical contacts with a distance of 200μm were made by sputtering gold onto the film surface. With a diamond wire saw we cut off a small piece ($\sim 300 \times 300\mu m^2$) and fixed it on the tip of a glass rod (fig.2). The gold contacts of the sensor were connected with 90μm thick copper wires with silver paste. The atomic layer thermopile can be applied for a temperature measurement, because heat conduction through the substrate acts as a heat sink, which leads to a temperature gradient in the film. To demonstrate the capability for a local temperature measurement, we heated a 0.1mm thick sheet steel from one side with pulses of a laser (duration 5ms; energy 4J; beam diameter 0.8mm) and measured the local distribution of the temperature at the other side of the sheet. The detector, scanned over the hot spot, indicated a signal (fig.3) of a half width slightly larger than the heated spot — corresponding to the heat diffusion in the sheet steel. In the experiment we used a low noise *dc* amplifier at an amplification factor of 2000. At a distance of 1mm between metal and sensor, the maximum voltage was $\sim$ 400mV. In another experiment, using a cw laser for heating, we calibrated the sensor in the range of 300°C to 400°C, using a Ni/NiCr thermocouple as reference. In this experiment we reached an accuracy of 2°C for the temperature measurement.

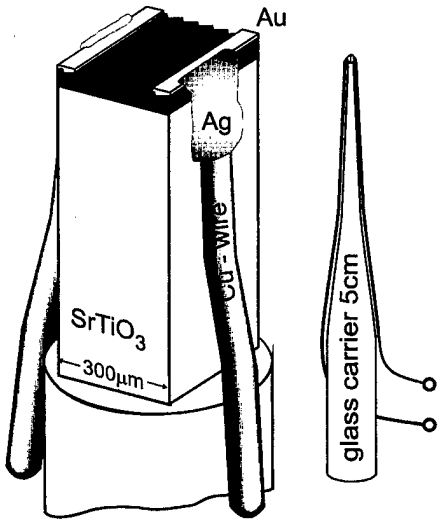


Fig. 2: Atomic-layer thermopile temperature sensor

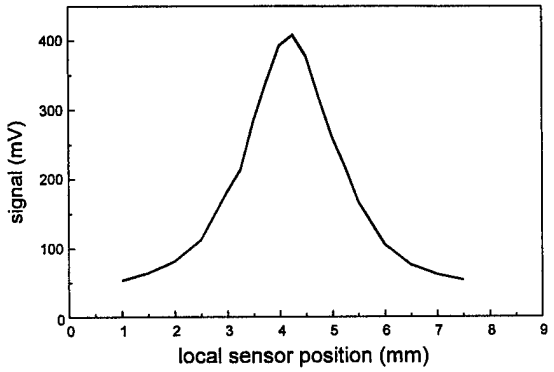


Fig. 3: Temperature distribution across a heated spot on a sheet steel

Analysis of a cw laser profile

We have developed an atomic layer thermopile (area 15×15 mm^2) for cw laser beam analysis. The detector is placed behind a rotating metal disk. The disk has 15 small apertures of the same size (diameter 800μm) with equal distance from each other but increasing distance from the center of the disk (fig. 4). This kind of mechanical scanner was used for the first time by the television pioneer Paul Nipkow in 1884. During one rotation, i. e. within 200ms, the cross-section of the laser beam is completely scanned. Each aperture produces a one-dimensional profile. The 15 profiles are digitized, patched together and displayed on a computer screen. The resolution was $\sim$ 660 pixels/cm^2 and the maximum area was 15×12 mm^2. As an example, fig. 5 shows the intensity profile of the farfield of a diode

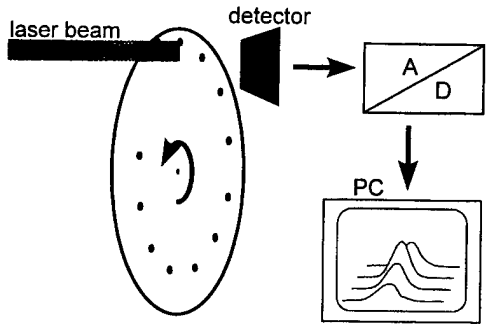


Fig. 4: Atomic-layer thermopile Nipkow system

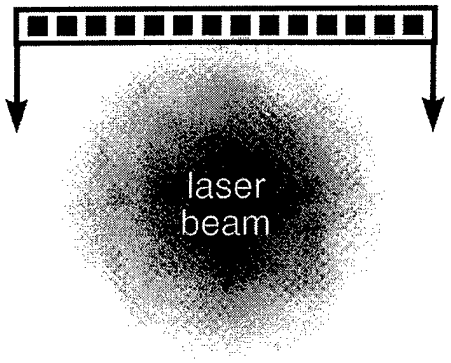


Fig. 6: Pixel array of atomic layer thermopiles and scanning direction (arrows) with respect to a laser beam

laser at a wavelength of 807nm. It shows the typical hare ear shape.

The Nipkow system, with a resolution of 8 bit, is suitable for laser powers from 100mW/cm^2 up to $\sim$ 1kW/cm^2 (maximum power on the detector $\sim$ 30W). The Nipkow system is applicable for the analysis of radiation of lasers from the UV to the FIR. Because the reflectivity increases for YBCO with increasing wavelength, the YBCO film has been covered, for the FIR detection, with an absorbing film. This leads to a rise of the response time to $\sim 1\mu$s because of the increased heat resistance, which is, however, no disadvantage of the system.

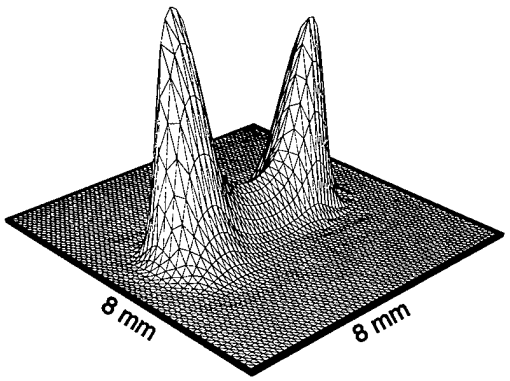


Fig. 5: Profile of the radiation of a diode laser (farfield)

Analysis of pulsed laser radiation

For the analysis of pulsed-laser radiation we manufactured an array of a 16-pixel YBCO atomic layer thermopile with gold contacts. By a simple mechanical arrangement, the array is moved stepwise across a laser beam (fig.6). The array is placed in a dual-in-line (DIL) housing with the gold contacts of the pixels bonded to the housing base. The DIL housing is plugged to the scanning facility, which is integrated with an electronic processing unit. The DIL housing with the array can easily be removed from the complete system. In this way the system can be adapted to different requirements. We have prepared an array with a pixel width of 800μm and another with a pixel width of 300μm. The dimension in the scan direction was variied by slit apertures from 0.1 to 1mm, which were fixed above the array. The scan length was 45mm. The system was designed for pulse lengths $\leq$ 100ns. The power was integrated for 100ns. Fig.7 gives an example for the intensity distribution of the radiation of a pulsed FIR laser with a wavelength of 250μm. The distribution is almost gaussian with a half width of about 2mm.

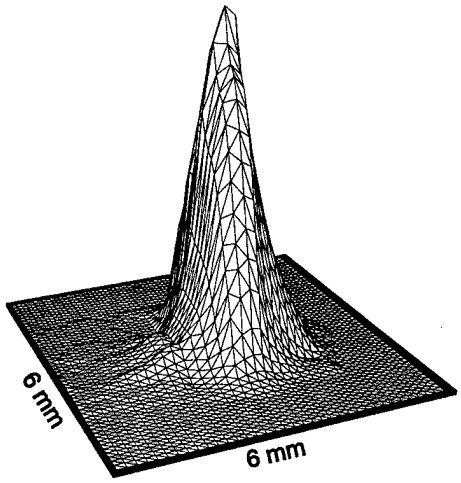


Fig. 7: Profile of pulsed FIR laser radiation (250μm)

Conclusion

We have developed a sensor suitable for temperature measurements and, furthermore, two systems for laser beam profiling, one for cw lasers and the other for pulsed lasers, using $YBa_2Cu_3O_{7-\delta}$ atomic layer thermopiles. The systems should be suitable to control lasers in material processing and medicine.

The detector sizes of the devices can be structured to reach

higher spatial resolution. At present, we are developing a detector head with a 10×10 pixel matrix of atomic layer thermopiles. The size of one pixel is 0.5×0.7 mm^2. The signals of the atomic layer thermopiles can be stored in amplifier-multiplexer array chips and forwarded to a digital signal processor. With such a system, one can achieve a fast online profile analysis of cw laser radiation.

Acknowledgment

The work was supported by the Bayerische Forschungsstiftung through the Bayerischer Forschungsverbund Hochtemperatur-Supraleiter (FORSUPRA). For helpful discussions we would like to thank Dr. H.L. Althaus (Siemens, Regensburg).

References

[*] ForTech HTS GmbH

[1] M. Kohler, "Abhängigkeit der thermoelektrischen Erscheinungen in Metalleinkristallen von der kristallographischen Orientierung", Annalen der Physik, 5.Folge, Band 40, S.196-206 (1941).

[2] H. Lengfellner, S. Zeuner, W. Prettl, and K.F. Renk, "Thermoelectric Effect in Normal-State $YBa_2Cu_3O_{7-\delta}$ Films.", Europhys. Lett., vol.25, no.5, pp.375-378 (1994).

[3] H. Lengfellner, G. Kremb, A. Schnellbögl, J. Betz, K.F. Renk, and W. Prettl, "Giant voltages upon surface heating in normal $YBa_2Cu_3O_{7-\delta}$ films suggesting an atomic layer thermopile", Appl. Phys. Lett., vol.60, no.4, pp.501-503 (1992).

[4] J.F. Scott, "Interpretation of photovoltaic pulses in normal $YBa_2Cu_3O_7$", Appl. Phys. Lett., vol.56, no.19, pp.1914-1915 (1990).

[5] D. Mihailovic and A.J. Heeger, "Pyroelectric and piezoelectric effects in single crystals of $YBa_2Cu_3O_{7-\delta}$", Solid State Comm., vol.75, no.4, pp.319-323 (1990).

[6] C.L. Chang, A. Kleinhammes, W.G. Moulton, and L.R. Testardi, "Symmetry-forbidden laser-induced voltages in $YBa_2Cu_3O_7$", Phys. Rev. B, vol.41, no.16, pp.11564-11567 (1990).

[7] K.L. Tate, R.D. Johnson, C.L. Chang, E.F. Hilinski, and S.C. Foster, "Transient laser-induced voltages in room-temperature films of $YBa_2Cu_3O_{7-x}$", J. Appl. Phys., vol.67, no.9, pp.4375-4376 (1990).

[8] H.S. Kwok and J.P. Zheng, "Anomalous photovoltaic response in $YBa_2Cu_3O_7$", Phys. Rev. B, vol.46, no.6, pp.3692-3695 (1992).

[9] W. Brozio, Diplomarbeit, Universität Regensburg (1996), unpublished.

[10] F. Lankes, unpublished.

[11] S.T. Li, A. Ritzer, E. Arenholz, D. Bäuerle, W.M. Huber, H. Lengfellner, and W. Prettl, "Step-like growth of $Bi_2Sr_2CaCu_2O_8$ films on off-axis oriented (001) $SrTiO_3$", Appl. Phys. A, vol.63, no.5, pp.427-429 (1996).

[12] J. Betz, B. Lenoir, and D. Perrin, "Transversal thermoelectric voltage in single crystalline bismuth material for detection of electromagnetic radiation", Proceedings of the 2nd European Workshop on Thermoelectrics (ETS), pp.87-90, Nancy (1995).

[13] S. Zeuner, W. Prettl, and H. Lengfellner, "Fast thermoelectric response of normal state $YBa_2Cu_3O_{7-\delta}$ films", Appl. Phys. Lett., vol.66, no.14, pp.1833-1835 (1995).

[14] M. Kauf, S. Schuberth, J. Hutfless, J. Betz, S. Zeuner, and H. Lengfellner, "Atomlagen-Thermosäule. Ein neuartiger Detektor für die Laserstrahldiagnose", Laser Magazin, Nr.5, S.12-17 (1994).

[15] K.F. Renk, J. Betz, S. Zeuner, H. Lengfellner, and W. Prettl, "Thermopile effect due to laser radiation heating in thin films of high-T_c materials", Physica C, vol.235-240, pp.37-40 (1994).

[16] I. Terasaki, Y. Sato, S. Miyamoto, S. Tajima, and S. Tanaka, "Normal-state transport properties of slightly overdoped $YBa_2Cu_3O_y$ crystals prepared by a crystal-pulling technique", Phys. Rev. B, vol.52, no.22, pp.16246-16254 (1995).

[17] ForTech HTS GmbH, Weiherweg 3, 93051 Regensburg (Germany).

INTERNATIONAL ADVISORY COMMITTEE

J.-P. Fleurial	*Pasadena, USA*
H. J. Goldsmid	*Kingston Beach, Australia*
T. Kajikawa	*Kanagawa, Japan*
K. Matsubara	*Ube, Japan*
M. Rowe	*Cardiff, UK*
H. Scherrer	*Nancy, France*
G. A. Slack	*Troy, USA*
T. M. Tritt	*Clemson, USA*
M. Vedernikov	*St. Petersburg, Russia*
H. Warlimont	*Dresden, Germany*

ORGANIZING COMMITTEE

A. Heinrich, Conference Chairman	*IFW Dresden*
J. Schumann, Technical Program Chairman	*IFW Dresden*
A. Hellwig, Exhibition Chairman	*IFW Dresden*
U. Brüstel, Secretary	*IFW Dresden*
G. Minar, Accomodation	*IFW Dresden*
C. B. Vining	*Auburn, USA*
H. Böttner	*Fh IPM Freiburg*
E. Müller	*DLR Köln*
J. Schilz	*DLR Köln*
M. Stölzer	*Universität Halle*
F. Völklein	*FHS Wiesbaden*

ICT'97 EXHIBITORS

Cosmos Italia s.r.l.	*Borgoticino, Italy*
Cryotherm	*St. Petersburg, Russia*
Crystal Ltd.	*Moscow, Russia*
D.T.S. GmbH	*Halle, Germany*
Fraunhofer Institute for Solar Energy Systems	*Freiburg, Germany*
HL Planar GmbH	*Dortmund, Germany*
Institute of Physical High Technology	*Jena, Germany*
Institute of Thermoelectricity	*Chernivtsi, Ukraine*
L.O.T.-Oriel GmbH	*Darmstadt, Germany*
Marlow Industries Inc.	*Dallas, Texas, USA*
Melcor Corporation	*Trenton, New Jersey, USA*
Noranda Advanced Materials	*St.-Laurent, Quebec, Canada*
Oxford Instruments SRD	*Wiesbaden, Germany*

ICT'97 SPONSORSHIP

The Organizing Committee thanks for their contribution to the conference:

SPONSORS OF THE ICT'97

Deutsche Forschungsgemeinschaft

Sächsisches Staatsministerium für Wissenschaft und Kunst

European Commission, Directorate General XII

United States Air Force European Office of Aerospace Research and Development

SUPPORTING ORGANIZATIONS

Bundesministerium für Bildung, Wissenschaft, Forschung und Technologie

Institute of Electrical and Electronics Engineers, Inc – the Components, Packaging, and Manufacturing Technology Society

International Thermoelectric Society

European Thermoelectric Society

Author Index

A

Abraham, Patrick 646
Akai, K. 334
Alekseeva, G. T. 105
Allen, Daniel T. 571
Anatychuk, L. I. .. 394, 397,586,
... 588, 592, 595, 611,632, 672
Anno, H. 326, 338, 343, 351
Anukhin, A. I. 159
Aoyagi, Eiji 215
Arai, Hiromichi 224, 240
Arushanov, E. 347
Ausloos, M. 507, 511
Avilov, E. S. 481

B

Bass, John C. 547
Bechstein, V. 93
Behr, G. 267, 287
Ben-Jacob, E. 471
Bergman, David J. 401, 471
Bezverkhov, D. B. 701
Boffoué, O. 429
Bogard, Andy 619
Boikov, Yu. A. 89
Borisenko, V. E. 267
Borshchevsky, A. 1, 641
Bougrine, H. 507
Boulouz, A. 167
Bowers, John E. 636, 646
Boyer, A. 163, 167
Brazis, P. 459
Brehme, S. 267
Brochin, F. 199
Broido, D. A. 424
Bublik, V. T. 118
Bucher, E. 347, 489
Buist, Richard J. . 551, 563, 668
Bulat, Lev P. 567
Byrne, Steve 603

C

Caillat, T. 1, 446
Calawa, D. R. 416
Calcao, R. 404
Casian, A. 442
Chen, B. 459
Chen, G. 12
Chen, L. 215, 251, 379, 390
Cho, S. 188
Choi, J. S. 127, 228, 263
Chung, D.-Y. 459
Claeson, T. 89
Cohn, J. L. 321
Cronin, S. B. 12
Czarnecki, A. 705

D

Danilov, V. A. 89
Das, V. Damodara
..... 101, 147, 259
Dashevsky, Z. 255, 382
Dauscher, A. 184, 199, 429
Demouge, A. 192
Devaux, X. 184, 199, 429
DiVenere, A. 188
Doettinger, Chr. A. 138
Doettinger, S. G. 138
Doloszeski, Markus 607
Drabkin, I. A. 382, 624, 676
Dresselhaus, M. S. 12
Dubourdieu, Philippe 603
Duvankov, N. I. 122

E

Echigo, Ryozo 664
Edelman, F. 232
Eguchi, Koichi 224, 240
Erts, D. 89
Ewell, R. 641

F

Farley, Robert.L. 547
Fedorov, M. I. 291, 496
Feger, C. R. 493
Fejchouk, P. 244
Fess, K. 347, 489
Filonov, A. B. 267
Fishchuk, I. I. 413
Fiyalka, L. 409
Fleurial, J.-P. .....
..... 1, 446, 481, 641, 683
Foucaran, A. 163, 167
Friemelt, K. 347, 489
Frolov, A. M. 118
Funanami, Y. 653

G

Galperin, Vadim 650
Ganesan, P. Gopal 147
Gasenkova, I. 151
Giani, A. 163, 167
Goldsmid, H. J. 171, 196
Gonzalez de la Cruz, G. 661
Gorelenko, Yu. K. 516
Gorodetskiy, Solomon M. ... 668
Goryachev, Yu. 409
Goryn, A. M. 516
Goto, Takashi 215, 251
Grabov, V. M. 176
Granatkina, Yu. V. 111
Griessmann, H. 267, 287
Groves, S. H. 416
Gurevich, Yu. G. 476, 661
Guttman, G. D. 471

H

Harman, T. C. 416
Hasaka, M. 356, 360
Hasezaki, K. 599
Hatada, K. 343
Hatta, E. 97
Heinrich, A.
..... 267, 287, 299, 303
Helmers, L. 375
Henrion, W. 267
Herwaarden, Sander van 47
Hille, G. 582
Hino, K. 463
Hirai, Toshio
..... 215, 251, 379, 251, 275
Hoffman, C. A. 188
Hogan, T. 459
Horak, J. 68
Hu, Siqing 485
Hua, Zhang 690
Huber, T.E. 404
Huebener, R. P. 138
Hwang, Jong-Seung 679
Hyun, D.-B.
..... 76, 127, 228. 263, 679

I

Ichizuka, T. 500
Ikeda, K. 142, 155, 657
Ilaschouk, M. 244
Imai, Y. 247, 386
Iordanidis, L. 459
Isobe, R. 203
Isoda, Yukihiro 279, 386
Ivanov, Yu. V. 192, 291
Ivanova, L. D. 111
Iwata, Y. 97

J

Jang, Kyung-Wook 76
Jianzhong, Zhang 690
Jingwei, Lui 708
Johnson, A. L. 454
Jouranlev, O. 676
Ju, M. 114

K

Kacisch, T. 641
Kagawa, Shuzo 85, 555
Kaibe, H. T. 247, 279, 386
Kajikawa, T. 28, 275, 500
Kamisako, K. 434
Kanatzidis, M. G. 459
Kanazawa, H. 653
Kaneko, H. 338
Kang, Y. S.
..... 371, 375, 379, 390, 599
Kannewurf, C. 459
Karamazov, S. 68
Karataev, V.V. 118
Karpinsky, O. G. 481
Kasama, A. 351
Kato, H. 434
Kato, Kazuhiko 236
Kawahara, T. 496
Kawashima, Seiji 63
Kaysser, W. A. 307
Kemmler-Sack, S. 138
Ketterson, J. B. 188
Khazan, M. A. 291
Kikuchi, K. 523
Kikuchi, S. 97
Kim, H. C. 127, 228, 263
Kim, H. J. 127, 228, 263
Kim, J. 114
Kisara, K. 390
Kishi, M. 653
Kishimoto, K. 463
Kita, Takuji 311
Kitagawa, H. 356, 360
Klingesberger, K.-J. 138
Kloc, Ch. 347, 489
Koga, T. 12
Kohno, Mizuki 311
Kolawa, E. 641
Kolis, J. 493
Kolomoets, N. V. 679
Komem, Y. 232
Kondo, S. 356, 360
Konstantinov, P. P.
..... 56, 105, 109
Korotaev, V. 382
Kosyachenko, S. V. 438
Koumoto, K. 467, 657
Koyanagi, T.
..... 203, 330, 338, 463
Kretova, M. A. 481
Kueffel, V. 219
Kurisu, H. 334
Kurt, R. 303
Kutasov, V. A. 56, 105
Kuwashiro, S. 434
Kuznetsov, V. L. 528
Käfer, W. 347, 489
Kügele, R. 582

L

Lange, H. 267
Langer, G. 307
Lau, Paul 551, 563, 619, 668
LeGault, S. 454
Lee, C. 81, 114
Lee, D. M. 81
Lee, Dong-Hi 76, 315
Lee, H. W. 228
Lee, Y. H. 203
Lenoir, B. 184, 192, 199, 429
Levy, F. 493
Li, Jianhui 215
Little IV, R. T. 493
Logvinov, G. N. 476, 661
Lostak, P. 68
Lugscheider, E. 307
Luk'yanova, L. N. 56, 105
Lundström, T. 219
Lunqiang, Chen 708
Luste, O. J. 595, 632
Lyon, Hylan B. 321
Lyubimov, O. I. 476

M

Mahan, G. D. 21
Maksimova, N. M. 109
Malkovitch, B. Sh. 697
Marone, M. J. 493
Martin-Lopez, R.
..... 184, 199, 429
Matano, K. 360
Matsubara, K.
..... 326, 338, 343, 351, 539
Matsui, T. 434
Matsuura, Kenji 555
Matsuura, M. 334
Meisner, Gregory P. 485
Melnichuk, S. V. 438
Meusel, J. 93
Meyer, J. R. 188
Miida, Y. 496
Mikhailovsky, V. Ya. ... 394, 592
Miki, K. 434
Min, Byoung-Gue 76, 315
Min, Gao 528
Misawa, K. 586
Mishima, Yoshinao 295
Miura, Seiji 295
Miyakawa, Toru 236, 496
Morelli, Donald T. 485
Morimoto, Jun 236
Morimura, T. 356, 360
Moriya, S. 390, 578
Moro, A. 379
Motoya, K. 343
Mukasa, K. 97
Muller, E. 307

N

Nagai, Hiroshi 311
Nagamoto, Y. 330, 463
Nagao, J. 97
Nagy, Michael J. 687
Nakagawa, H. 351
Nakagawa, Y. 578
Nakajima, S. 599
Nakamoto, I. 203
Nakamura, Hiroaki
..... 142, 155, 657
Navratil, J. 68
Nemoto, H. 653

Nemov, S. A. 72
Niino, M. 371, 375,
..... 390, 539, 578, 599
Nishida, I. A.
..... 247, 279, 364, 386
Nissel, T. 138
Noda, Y. 375
Noda, Y. 379
Noda, Yasutoshi
..... 279, 371, 390
Nogi, Kiyoshi 311
Noguchi, Teruo 207
Nolas, George S. 321
Notohara, Y. 326, 338, 343
Oh, T. S. 127, 228, 263, 679
Ohmori, Mamoru 275
Ohshima, T. 539
Ohta, E. 247
Ohta, T. 85, 434, 500
Ohta, Yoriko 295
Ohtaki, Michitaka 224, 240
Okamoto, Y. 236, 496
Okano, H. 653
Ordin, S. V. 496
Orihashi, M. 379
Osvenski, V. B. 118
Ozawa, S. 467

P

Pascal-Delannoy, F. ... 163, 167
Palacios, Rafael 628
Park, K. 81, 114
Pekal, M. 507
Pekala, K. 504
Pekala, M. 511
Phillips, W. 641
Pitschke, W. 299, 303
Popov, V. V. 291
Pustovalov, A. A. 559

R

Rabinovich, D. 382
Rath, S. 138
Ravich, Yu. I. 192
Raz, T. 232
Razinkov, V. V. 592
Reinecke, Thomas L. 424
Riffel, M. 283
Ritzer, Todd M. 619
Romaka, L. P. 516
Roth, W. 582
Rowe, D. M. 528, 532
Rozver, Yu. Yu. 586, 592
Rushing, Lance 646
Ryan, M. A. 641

S

Sackda, A. 163
Sagalova, T. B. 118
Sakakibara, T. 326, 338, 343
Sakamoto, K 434
Sakamoto, Masanori 85, 555
Sakurai, M. 180
Sakurai, T. 657
Sandu, A. 442
Sanz-Bobi, Miguel Angel 628
Sargankova, I. 507
Sasago, Y. 523
Satake, Hideki 85
Sato, R. 578
Satoh, N. 180
Schackenberg, K. 307
Scherbak, L. 244
Scherrer, H.
..... 184, 192, 199, 429, 442
Scherrer, S. 199, 442
Schilz, J. 283, 307, 375
Schindler, J. 459
Schmechel, R. 219
Schmidt, Alfred 607
Schulz, W. 582
Schumann, J. 299, 303
Sekine, Rika 63
Selme, M. O. 192
Selvaraj, S. 101
Semeniouk, V. A. 683, 701
Seo, J.H. 81, 114
Seo, W. S. 467
Shakouri, Ali 636, 646
Shchedrin, A. A. 672
Shelimova, L. E. 481
Shida, Keisuke 275
Shim, Jae-Dong 679
Shimizu, H. 343
Shimura, T. 334
Shinohara, Y. 247, 386
Shiota, I. 247, 364, 386
Shufang, Sun 708
Shuichi, Ye 708
Shvartsman, O. 409
Sidorov, Yu. A. 111
Siman, M. 409
Skipidarov, S. Ya. 122
Skolozdra, R. V. 516
Skoropad, F. 520
Slack, G. A. 321
Smolyar, G. A. 693
Sokolov, O. B. 122
Song, Chen 690
Spears, D. L. 416
Stadnyk, B. 520
Stadnyk, Yu. V. 516
Stark, I. 575
Steinhüser, A 582
Stockholm, John 37
Stolzer, M. 93
Stordeur, M. 575
Straehle, J. W. 138
Stroud, R. 454
Stärz, T. 711
Stölzer, M. 232
Sudo, T. 390
Sugihara, Sunao 63, 275
Sun, X. 12
Sur, I. 442
Suzuki, Hiroaki 63
Suzuki, N. 586
Svechnikova, T. E. 72, 109

T

Tada, Shigeru 664
Tada, Y. 578
Takahashi, K. 247
Takazawa, H. 500
Takimoto, M. 434
Tanaka, H. 351
Tanaka, K. 330
Tanji, Y. 578
Tanuma, S. 180, 657
Tashiro, H. 326, 338, 343
Terasaki, I. 523
Tiemin, Wang 690
Titov, O. Yu. 476, 661
Tobise, S. 657
Tokunaga, Tsutomu 224
Tribou, Gery 603
Tritt, T. M. 321, 454, 493
Tsubota, Toshiki 240
Tsukuda, H. 599
Tsuyoshi, Akira 555
Tu, Rong 251
Tuomi, Donald 131

U

Uchinokura, K. 523
Ufimtsev, V. B. 118
Uher, C. 459, 485
Uryupin, O. N. 176

V

Vackova, S. 244
Varich, N. I. 672
Vedernikov, M. V. 56
Vikhor, L. N. 397
Vining, C. B. 232
Volckmann, E. H. 171, 196
Vozny, V. M. 438
Vykhor, L. N. 588
Völklein, F. 711

W

Walsh, M. P. 416
Wang, K. L. 12
Wartanowicz, T. 705
Werheit, H. 219
Wetzig, K. 303
Wilson, M. L. 454, 493
Wong, G. K. 188
Wonsowski, Jerzy 571
Wuyun, Quan 708

X

Xiaowei, Liu 708
Xilian, Wang 708

Y

Yakabe, H. 523
Yamada, A. 599
Yamaguchi, S. 142, 155, 657
Yamamoto, A. 85, 434, 500
Yamamoto, M. 653
Yang, Jihui 485
Yasuoka, M. 578
Yomura, M. 203
Yoneda, S. 247
Yonekura, Isaku 63
Yoshida, Hideo 664
Yoshida, I. 180, 657
Yoshida, Y. 653
Yoshitake, H. 463

Z

Zaitsev, E. V. 122
Zaitsev, V. K. 291
Zandona, M. 184
Zaumseil, P. 232
Zdansky, K. 244
Zeindl, H. 232
Zhaonan, Ji 690
Zhenmao, Liu 708
Zhitinskaya, M. K. 72

PROCEEDINGS
1997 International Conference on Thermoelectrics

You are invited to attend the International Conference on Thermoelectrics in Nagoya, Japan, May 24-28, 1998, supported by the Aichi Prefectural Government, the City of Nagoya, and Nagoya University. Please send inquiries to:

Secretariat, ICT98
c/o Inter Group Corp.
3F Sakae East Bldg, 4-2-7, Sakae, Naka-ku
Nagoya, 460, Japan
TEL: +81-52-263-6334 FAX: +81-52-263-6298
Email: ignagoya@po.iijnet.or.jp

Visit our Website: http://www.its.org/ict98

JOIN ITS

For information on membership in the International Thermoelectric Society, please visit our Website at:

http://www.ict.org

or contact:

Dr. Jean Pierre Fleurial, ITS Secretary
Jet Propulsion Laboratory/California Inst. of Technology
4800 Oak Grove Drive
Pasadena, CA 91109-8099 USA
Phone: +1-818-354-4144, FAX: +1-818-393-6951

JOIN IEEE

For information on membership in the Components, Packaging, & Manufacturing Technology Society of the IEEE, a free back issue of a CPMT *Transactions*, or participation in one of the Technical Committees or local Chapters within the Society, please visit our Website at:

http://www.cpmt.org

or contact:

Marsha Tickman, CPMT Executive Director
IEEE
PO Box 1331
Piscataway, NJ 08855 USA
m.tickman@ieee.org

Or, in the U.S.A., call IEEE at:
+1-800-678-IEEE